

DOCTOR OF  
PHILOSOPHY

GEOLOGICAL GEOPHYSICAL AND SEISMOLOGICAL INVESTIGATIONS FOR  
EARTHQUAKE HAZARD ESTIMATION IN WESTERN CRETE

*A THESIS SUBMITTED FOR THE DEGREE OF DOCTOR OF PHILOSOPHY*

*by*

*Margarita Moisidi*

INSTITUTE FOR THE ENVIRONMENT, BRUNEL UNIVERSITY

July 2009

## ***Abstract***

---

The purpose of the thesis is the determination of potentially seismic active sources and of the dynamic response evaluation of surface and subsurface structure at sites where the geometric and dynamic properties of the ground can strongly amplify seismic motions. A combination of methods involving the study of geology, geophysics and seismology disciplines permitting cross-comparison of techniques in a robust approach is applied to address these issues. The study area is focused in Kastelli-Kissamou and Paleohora half graben basins in northwestern and southwestern Crete that is located in one of the most seismically active parts of the Africa-Eurasia collision zone. Ground truthed geological field survey, 2D Electrical Resistivity Tomography (ERT), Horizontal to Vertical Spectra Ratio (HVSr) technique using microtremors and microseismicity study are conducted. Microseismicity study involves two different earthquake dataset acquired from a regional permanent network installed on Crete and local temporal network installed on Paleohora. 2D Electrical resistivity tomography (ERT) reveals seven faults in the territory of Kastelli-Kissamou and three faults large scale faults in the territory of Paleohora basin. HVSr technique using microtremors is applied only in the populated area of Kastelli and Paleohora basins and reveals five fault zones in Kastelli and four major fault zones in Paleohora crosscutting the densely populated areas. The effects of the surface and subsurface structure are well patterned in the horizontal to vertical spectra ratios. One amplified clear frequency, two high amplified clear frequencies, broad and flat or low amplitude HVSr peaks attributes the effects of surface and subsurface structure on seismic ground motion. The effects of soft rocks, stiff soils, thick and thin alluvial deposits, fault zones, lateral heterogeneities and discontinuities on seismic ground motion are determined. The higher ground amplification level is observed in Paleohora ( $A=5.7$ ) compared to Kastelli ( $A=3.4$ ). Three case studies of building vulnerability evaluation in Paleohora half-graben basin using HVSr technique and microtremors are presented. Temporal seismological network is installed in the territory of Paleohora to study the seismotectonic setting of southwestern Crete. Microseismicity using data from the permanent seismological regional network of Crete is used to compare the seismicity of the study areas.

## Contents

---

<b>CHAPTER 1: INTRODUCTION</b>	1
1.1 RATIONALE AND AIMS OF THE THESIS	1
1.2 ORGANIZATION OF THE THESIS	3
1.3 THE STUDY REGION: THE SEISMOTECTONIC SETTING OF THE REGION UNDER STUDY AND THE MAIN TOPOGRAPHIC FEATURES OF THE SOUTH AEGEAN REGION	3
1.4 SEISMICITY OF CRETE IN RELATION TO THE PURPOSE OF THE STUDY	4
1.5 GEOLOGY OF THE INVESTIGATED SITES IN PALEOHORA AND KASTELLI KISSAMOUI IN WESTERN CRETE	5
1.5.1 GEOLOGY OF THE INVESTIGATED SITES IN KASTELLI KISSAMOU IN NORTHWESTERN CRETE	6
1.5.2 GEOLOGY OF THE INVESTIGATED SITES IN PALEOHORA IN SOUTHWESTERN CRETE	8
1.6 A BRIEF OUTLINE OF METHODOLOGY APPLIED IN THIS RESEARCH	10
1.7 POTENTIAL CONTRIBUTION TO FUTURE RESEARCH	11
<b>CHAPTER 2: LITERATURE REVIEW THEORETICAL BACKGROUND OF THE COMBINED APPROACH</b>	12
2.1 THE LITERATURE REVIEW OF TECTONIC AND GEOLOGICAL SETTING OF CRETE	12
2.1.1 TECTONIC SETTING OF THE HELLENIC SUBDUCTION ZONE	12
2.1.2 THE UPLIFT OF CRETE	14
2.1.3 TECTONIC EVOLUTION OF THE NORTHWESTERN AND SOUTHWESTERN BASINS ON CRETE	15
2.1.4 TECTONIC AND GEOLOGICAL SETTING OF TOPOLIA AND LISSOS BASINS IN NORTHWESTERN AND SOUTHWESTERN CRETE BASINS: A MODEL PROPOSED BY SEIDEL (2007)	16
2.1.4.1 TOPOLIA BASIN	17
2.1.4.2 LISSOS BASIN	18
2.1.5 GEOLOGY OF NORTH AND SOUTH CRETE	19
2.1.5.1 GEOLOGY OF NORTHWESTERN CRETE	20
2.1.5.2 GEOLOGY OF SOUTHWESTERN CRETE	22
2.2: LITERATURE REVIEW OF SEISMICITY STUDY OF THE STUDIED AREAS IN NORTHWESTERN AND SOUTHWESTERN CRETE	23
2.2.1 SEISMOLOGICAL NETWORK ON CRETE AND SURROUNDING AREA	23
2.2.2 EARTHQUAKE DATABASE OF GREECE AND SURROUNDING AREA	23
2.2.3 SEISMICITY AND MICROSEISMICITY STUDY OF THE HELLENIC SUBDUCTION ZONE	24
2.3 LITERATURE REVIEW OF EARTHQUAKE GROUND MOTION: SITE EFFECTS AND SEISMIC GROUND RESPONSE	29
2.3.1 INFLUENCE FACTOR OF SEISMIC MOTION	29
2.3.1.1 THE FAULT RUPTURE EFFECT (SOURCE EFFECT) ON SEISMIC GROUND MOTION	31
2.3.1.2 THE INFLUENCE OF TRAVEL PATH ON SEISMIC GROUND MOTION	31
2.3.1.3 THE INFLUENCE OF SITE EFFECTS ON SEISMIC GROUND MOTION	35
2.3.1.3.1 SOFT SEDIMENTS EFFECTS ON SEISMIC GROUND MOTION	35
2.3.1.3.2 TOPOGRAPHY EFFECTS ON SEISMIC GROUND MOTION RESPONSE	36
2.3.2 SPECTRA CHARACTERISTICS OF SEISMIC GROUND MOTION RESPONSE	37
2.3.3 AMPLIFICATION OF GROUND SEISMIC RESPONSE	38
2.3.4 SOIL AND BUILDING STRUCTURE INTERACTION	40

2.3.5	MICROTREMOR RECORDINGS FOR SEISMIC GROUND RESPONSE EVALUATION	41
2.3.5.1	ORIGIN AND NATURE OF NOISE WAVEFIELD	43
2.3.5.1.1	ORIGIN OF NOISE WAVEFIELD	43
2.3.5.1.2	NATURE OF MICROTREMORS	43
2.3.6	HVSR TECHNIQUE FOR SITE EFFECT ESTIMATION	45
2.3.7	MICROZONATION STUDY USING HORIZONTAL TO VERTICAL SPECTRA RATIO (HVSR) TECHNIQUE	47
2.3.8	MICROTREMOR MEASUREMENTS AND BUILDING DAMAGES	47
2.3.9	HVSR TECHNIQUE IN GEOPHYSICAL AND GEOTECHNICAL PROSPECTING	48
2.4	ELECTRICAL RESISTIVITY TOMOGRAPHY (ERT) TO IMAGE SUBSURFACE STRUCTURE	51
2.4.1	ELECTRODE RESISTIVITY CONFIGURATION ARRAYS	51
2.4.2	ADVANTANTAGES AND DISANTANTAGES OF WENNER-SCHLUMBERGER AND DIPOLE-DIPOLE ARRAYS	55
2.4.3	ELECTRICAL RESISTIVITY TOMOGRAPHY (ERT)	55
2.4.4	THE 2-D INVERSION OF GROUND SURFACE AND SUBSURFACE RESISTIVITY DATA USING ACCURATE INVERSION TECHNIQUE PROCEDURE	56
<b>CHAPTER 3: METHODOLOGY</b>		57
3.1	HORIZONTAL TO VERTICAL SPECTRA RATIO (HVSR) FOR SITE EFFECTS STUDY	57
3.1.1	THEORETICAL BACKGROUND OF HVSR TECHNIQUE PROPOSED BY NOGOSHI-IGARASHI (1971)	57
3.1.2	EXPLANATIONS ON HVSR TECHNIQUE, NAKAMURA (1989, 1996, 2000)	58
3.1.2.1	K-VALUES TO DETERMINE BUILDING STRUCTURAL DAMAGE (NAKAMURA 1996)	62
3.1.2.2	VULNERABILITY INDEXES, K-VALUES FOR SURFACE GROUND	63
3.1.2.3	BASEMENT DEPTH RELATED WITH NAKAMURA TECHNIQUE	66
3.1.3	DATA ACQUISITION AND PROCESSING	66
3.1.3.1	DATA ACQUISITION RECOMMENDATIONS	66
3.1.3.2	DATA PROCESSING PROCEDURE	68
3.1.3.3	RELIABILITY OF THE RESULT	68
3.1.3.4	J-SESAME SOFTWARE FOR SITE EFFECTS STUDIES	69
3.2	ELECTRICAL RESISTIVITY TOMOGRAPHY INSTRUMENTATION	73
3.2.1	FIELD RESISTIVITY SURVEY PROBLEMS	75
3.2.2	ELECTRICAL RESISTIVITY TOMOGRAPHY INVESTIGATION	75
3.2.3	RES2DINV FOR ELECTRICAL RESISTIVITY TOMOGRAPHY INVESTIGATION	76
3.2.4	ELECTRICAL RESISTIVITY TOMOGRAPHY USING RES2DINV IN KASTELLI KISSAMOU AND PALEOHORA REGIMES	78
3.3	METHODOLOGY OF THE SEISMOLOGICAL APPROACH TO LOCATE EPICENTER AND TO DELINEATE ACTIVE STRUCTURES	79
3.3.1	METHODOLOGY OF THE SEISMOLOGICAL APPROACH TO LOCATE EPICENTER AND TO DELINEATE ACTIVE STRUCTURES IN NORTHWESTERN AND SOUTHWESTERN CRETE	81
3.4	SUMMARY	82
<b>CHAPTER 4: RESULTS</b>		83
4.1	GEOLOGICAL FIELD SURVEY IN KASTELLI AND PALEOHORA IN NORTHWESTERN CRETE	83
4.1.1	GEOLOGICAL FIELD SURVEY IN POPULATED AREA OF KASTELLI KISSAMOU (NORTHWESTERN CRETE)	83

4.1.2 UPLIFT EVIDENCE IN KASTELLI KISSAMOU AREA	89
4.1.3 GEOLOGICAL FIELD SURVEY OF PALEOHORA IN SOUTHWESTERN CRETE	93
4.2 RESULTS: ELECTRICAL RESISTIVITY TOMOGRAPHY (ERT) IN KASTELLI KISSAMOU AND PALEOHORA REGIMES	106
4.2.1 ELECTRICAL RESISTIVITY SURVEY IN KASTELLI KISSAMOU REGIME	106
4.2.2 EAST OF KASTELLI	107
4.2.2.1 EAST OF KASTELLI (PROFILE 1)	107
4.2.2.2 EAST OF KASTELLI (PROFILE 2)	108
4.2.2.3 EAST OF KASTELLI (PROFILE 3)	110
4.2.3 ELECTRICAL RESISTIVITY TOMOGRAPHY WESTERN OF KASTELLI	112
4.2.3.1 WEST KASTELLI (PROFILE 5)	112
4.2.3.2 WEST KASTELLI (PROFILE 6)	113
4.2.3.3 WEST KASTELLI (PROFILE 7)	115
4.2.3.4 WEST KASTELLI (PROFILE 8)	116
4.2.4 ELECTRICAL RESISTIVITY TOMOGRAPHY IN KERA FAULT LOCATED IN THE SOUTHERN PART OF KASTELLI (PROFILE 4)	118
4.2.5 ELECTRICAL RESISTIVITY SURVEY (ERT) IN PALEOHORA IN SOUTHWESTERN CRETE	121
4.2.6 FAULT IN THE NORTH EASTERN PART OF PALEOHORA	122
4.2.6.1 SHALLOW ELECTRICAL RESISTIVITY PROFILE	122
4.2.6.2 DEEP ELECTRICAL RESISTIVITY PROFILE	123
4.2.7 ELECTRICAL RESISTIVITY PROFILE IN THE URBAN AREA OF PALEOHORA AND GRAMMENO PENINSULA	124
4.2.7.1 ERT IN PALEOHORA PENINSULA IN THE URBAN AREA (PAHIA AMMOS)	124
4.2.7.2 SHALLOW ELECTRICAL RESISTIVITY PROFILE	125
4.2.7.3 DEEP ELECTRICAL RESISTIVITY PROFILE	126
4.2.7.4 ERT IN GRAMMENO PENINSULA	127
4.2.8 ELECTRICAL RESISTIVITY TOMOGRAPHY IN THE NORTHEASTERN, NORTHWESTERN AND SOUTHERN PART OF PALEOHORA	131
4.2.8.1 WATER SURFICIAL DEPOSITS NORTHEASTERN OF PALEOHORA	132
4.2.8.2 WASTE SURFICIAL DEPOSITS NORTHWESTERN OF PALEOHORA (WESTERN OF PANORAMA)	133
4.2.8.3 WATER SURFICIAL DEPOSITS IN THE ARCHAEOLOGICAL SITE FORTEZA (SOUTHERN OF PALEOHORA)	134
4.3 RESULTS: SEISMIC GROUND MOTION EVALUATION AND MICROZONATION STUDY USING HVSR TECHNIQUE AND MICROTREMORS	136
4.3.1 SITE EFFECTS AND MICROZONATION STUDY USING MICROTREMORS AND HVSR TECHNIQUE URBAN AREA OF KASTELLI HALF-GRABEN BASIN	136
4.3.2 SITE EFFECTS EVALUATION USING HVSR TECHNIQUE AND MICROTREMORS IN ROKA VILLAGE	143
4.3.3 SEISMIC GROUND MOTION EVALUATION AND MICROZONATION STUDY USING HVSR TECHNIQUE AND MICROTREMORS IN PALEOHORA HALF-GRABEN	144
4.3.4 SINGLE POINT EARTHQUAKE AND MICROTREMORS RECORDINGS	148
4.3.4.1 EARTHQUAKE AND MICROTREMOR RECORDED IN THE CENTRE OF PALEOHORA BASIN	149
4.3.4.2 EARTHQUAKE AND MICROTREMOR RECORDED ALONG THE BASIN EDGE	152
4.3.5 BUILDING VULNERABILITY ESTIMATION USING HVSR TECHNIQUE: A CASE STUDY OF SEISMIC GROUND-BUILDING INTERACTION	157

4.3.5.1 BUILDING VULNERABILITY ESTIMATION USING HVSR TECHNIQUE IN A MASONRY CONSTRUCTED HOUSE LOCATED SOUTHEASTERN OF PALEOHORA CLOSE TO THE EDGE OF THE BASIN	158
4.3.5.2 BUILDING VULNERABILITY ESTIMATION USING HVSR FOR A THREE-FLOOR CONCRETE HOUSE LOCATED NORTHEASTERN OF PALEOHORA IN THE CENTRE OF THE BASIN	160
4.3.5.3 BUILDING VULNERABILITY ESTIMATION USING HVSR IN THE ELEMENTARY AND HIGH SCHOOL LOCATED IN THE CENTRE OF THE BASIN (b2)	163
4.4. MICROSEISMICITY USING A NEW PERMANENT SEISMOLOGICAL NETWORK INSTALLED IN THE WHOLE TERRITORY OF CRETE AND A TEMPORAL LOCAL SEISMOLOGICAL NETWORK OF PALEOHORA	172
4.4.1 MICROSEISMICITY OF NORTH AND SOUTH WESTERN CRETE USING A NEW TELEMETRIC SEISMOLOGICAL NETWORK INSTALLED IN THE WHOLE TERRITORY OF CRETE	172
4.4.2 MICROSEISMICITY OF SOUTHWESTERN CRETE USING TEMPORAL LOCAL SEISMOLOGICAL NETWORK INSTALLED IN PALEOHORA	174
<b>CHAPTER 5: DISCUSSION</b>	176
5.1 INTRODUCTION TO DISCUSSION	176
5.2 DIRECT INTERRELATION OF THE COMBINED MULTI-PROXY METHODOLOGY AND JUSTIFICATION OF THE COMBINED METHODOLOGIES IN FAULT IDENTIFICATION IN KASTELLI-KISSAMOU AND PALEOHORA BASINS	178
5.2.1 THE SYNTHESIS OF THE COMBINED MULTI-PROXY APPROACH OF GEOLOGY, HVSR USING MICROTREMORS, ERT AND MICROSEISMICITY STUDIES IN FAULT DETERMINATION IN KASTELLI-KISSAMOU AND PALEOHORA BASINS	179
5.3 SITE EFFECTS ASSESSMENT AND SEISMIC GROUND RESPONSE ZONING USING MICROTREMORS IN PALEOHORA AND KASTELLI-KISSAMOU BASINS	191
5.4 COMPARISON OF SEISMIC GROUND ZONING BASED ON HVSR TECHNIQUE USING MICROTREMORS AND GREEK EIROCODE (EC8) IN KASTELLI AND PALEOHORA	199
5.5 TECTONIC DIFFERENCES IN SEISMIC GROUND RESPONSE BETWEEN THE TWO STUDY AREAS BASED ON THE MULTI-PROXY APPROACH	200
5.6 SUMMARY OF DISCUSSION	204
<b>CHAPTER 6: CONCLUSIONS</b>	205
6.1: MAIN CONCLUSIONS POINTS OF THE RESEARCH STUDY	205
6.2 CONTRIBUTION TO FUTURE RESEARCH	205
<b>REFERENCES</b>	208
<b>APPENDICES</b>	228
APPENDIX I: HVSR, HNS/V and HEW/V RATIOS USING MICROTREMOR RECORDINGS IN KASTELLI-KISSAMOU ROKA AND PALEOHORA BASINS	228
APPENDIX II: LIST OF TABLES	275
APPENDIX III: MICROTREMOR RECORDINGS (TIME SERIES) IN KASTELLI-KISSAMOU AND PALEOHORA BASINS	313
APPENDIX IV: EARTHQUAKE SAMPLES RECORDED FROM THE REGIONAL AND PERMANENT SEISMOLOGICAL NETWORK OF CRETE	389

APPENDIX V: EARTHQUAKE SAMPLES RECORDED FROM THE TEMPORAL SEISMOLOGICAL NETWORK OF THREE SHORT PERIOD SEISMOMETERS INSTALLED IN THE TERRITORY OF PALEOHORA	464
APPENDIX VI: SAMPLES OF SITES OF MICROTREMOR RECORDINGS USING LENNARTZ 3D/5sec SEISMOMETER	818

## List of Figures

---

**Figure 1.1:** Landsat satellite image of the location of the research areas in western part of Crete in the southern Aegean region. Faults of Crete derived from geological and satellite image maps are presented with yellow lines. The location of the investigated regions in Kastelli-Kissamou and Paleohora basins located in northwestern and southwestern Crete is shown with red rectangles.

2

**Figure 1.2:** Main topographic features of the southern Aegean region (Papazachos & Papazachou, 1997). The Hellenic arc consists of an external sedimentary arc, which connects the Dinaric Alps with the Turkish Taurides and of an internal volcanic arc, which is parallel to the sedimentary arc. The southern Aegean trough is located in between the sedimentary and volcanic arc.

4

**Figure 1.3:** Epicenters of earthquakes with magnitude  $M > 5.0$ . Greece is separated into seismogenic zones. High seismicity distribution is observed along the Hellenic arc. The red circles present the two major events in southwestern Crete (AD 365,  $M = 8.3$ ) and in the easternmost part of the Hellenic trench (AD 1303,  $M = 8.0$ ). The green circles present the earthquakes with magnitude  $5.0 \leq M < 6.0$ . The blue circles present earthquakes with magnitude  $6.0 \leq M < 7.0$  and the yellow circles presents earthquakes events with magnitude  $7.0 \leq M < 8.0$ , (Morrato et al., 2007).

5

**Figure 1.4:** Geological map of Kissamou basin in northwestern Crete (Karageorgiou, 1968). The red circles represent the sites where ERT measurements were conducted. The blue triangle represents the site where the permanent seismological station installed. **Figure 1.5:** Geological map of Paleohora territory in southwestern Crete (Tsalahouri & Fontou, 1972). The sites where ERT performed are presented on the map with coloured red circles. The permanent seismological station installed in southwestern Crete is presented with the blue triangle. The two temporal seismological stations are presented with the yellow triangles

7

**Figure 1.5:** Geological map of Paleohora territory in southwestern Crete (Tsalahouri & Fontou, 1972). The sites where ERT performed are presented on the map with coloured red circles. The permanent seismological station installed in southwestern Crete is presented with the blue triangle. The two temporal seismological stations are presented with the yellow triangles.

9

**Figure 2.1:** Cross-section of the Hellenic subduction zone and the southern Aegean region (southern margin of the Aegean microplate) for early to middle Miocene times. The supra-detachment basins Topolia and Lissos in the northern and southwestern Crete are presented. The Kastelli Kissamou and Paleohora half graben basins are presented (modified after Seidel et al., 2007).

16

**Figure 2.2:** (a) Schematic figure of the structure of the Topolia basin in the middle Miocene, and the depositional features of the alluvial fans. The fault-scarp of a major normal fault separates the hangingwall block (basin floor) from the footwall block (mountain range) from which the clastic sediments were derived (catchment area) (extracted from Seidel et al., 2007).

17



**Figure 2.3:** (a) Schematic Figure of the middle Miocene half-graben, the catchment (footwall uplands) and the depositional features of the coastal alluvial fans in the surroundings of Lissos basin (extracted from Seidel et al., 2007).

18

**Figure 2.4:** (Upper) Generalized geological map of western Crete (modified after Seidel et al., 2007, Trypali Unit included in the Plattenkalk Unit). Neogene Topolia and Lissos basins, the underlying tectono-stratigraphic units, and the detachment fault is presented. The Topolia basin is located in the surroundings of the villages of Roka, Topolia and Kakopetros (modified after Seidel et al., 2007) (Lower right): Geological map of Crete where paleobathymetry sections performed on northwestern and southwestern part. The H-H' line represents the WNW-ESE fault. The segment H' is located in the eastern part of Crete and therefore not presented in the Figure. The cross-section of site 7 corresponds to Paleohora half-graben basin, site 3 corresponds to Koundoura territory, site 4 corresponds to Grammeno peninsula, site 16 Chairetiana (south of Kastelli) and 18 corresponds to Kera village (extracted from van Hinsbergen, 2006). Lower left Figure: Cross-section of Crete (van Hinsbergen, 2006). The cross section of Paleohora and Kastelli Kissamou are presented. Paleohora half-graben basin and the investigated area Kastelli are characterized of Pindos zone, Lower to Middle Miocene and Upper Miocene to Pliocene, Pindos and Middle to Upper Miocene (extracted from van Hinsbergen, 2006).

19

**Figure 2.5:** Seven sedimentary units on Kera fault (unit 0: limestones, unit 1: marls, unit 2 and unit 3 are recognized during the logging of the trenches, unit 4: conglomerates, unit 5: material composed of limestones, marls and conglomerates, unit 6: fine conglomerate clasts and unit 7: thin dark colour soil covering (Mouslopoulou et al., 2001). Right upper: Map showing the study area in Kera Fault (5 Km) is located in the second segment with an NE-SW orientation Kastelli; The three active segments on Spatha peninsula in a N-S fault system. The uplift (+) and subsidence (-) motion of Gramvousa is presented. Red circles present earthquake recordings provided by NOA (extracted from Mouslopoulou et al., 2001).

21

**Figure 2.6:** Time variation of known strong earthquakes ( $M \geq 6.0$ ) in Greece since 550 BC up to AD 1990 (Papazachos & Papazachou, 1997). The vertical scale of this graph corresponds to the number of earthquakes. During the first time interval spans from the sixth century BC until the middle of the sixteenth century (550 BC - AD 1550) information exists for a total number of about 150 strong earthquakes. For the second time interval from the middle of the sixteenth century up to the middle of the nineteenth century (1550-1845), the total number of recorded earthquakes of this interval is about 170. The third time interval covers the period 1845-present and is divided into three phases (AD 1845-1928, 1928-1964, 1964-2000).

24

**Figure 2.7:** a) Spatial distribution of the earthquake foci in the central part of the arc where dipping of the Wadati-Benioff zone starts (point B Figure 2.7a) in the convex side of the arc under the Hellenic trench, b) Cross-section of the earthquake foci along the line ABCD. In the convex (outer) arc beneath or very close to the Hellenic trench, strong intermediate depth earthquakes with relatively large focal depths ( $h > 100$  km) occur, denoted by solid triangles. Point B is located in southwestern Crete, which is near the study area of this thesis (modified after Papazachos et al., 2000b). The relative location of Kastelli and Paleohora in the northwestern and southwestern Crete in respect to the spatial distribution is presented.

26

**Figure 2.8:** Site effects on seismic ground motion response. Source effects, travel path effects from fault to ground surface and local site effects are presented (modified after Murono, 1999).

30

**Figure 2.9:** The theoretical and actual way path of a seismic way travels from source to the seismological station. Seismic wave amplitude decrease is observed through the theoretical path compared to seismic wave amplitude through the actual path. Velocity models should account the actual ray path for accurate earthquake solutions (Stein & Wysession, 2003).

34

**Figure 2.10:** Schematic representation of the dependance of ground fundamental frequency and depth of sediments ( $H_{12}$ ,  $H_2$ ) of two sedimentary basins. The ground fundamental frequency increases with decreasing depth of the sediments (modified after Dorwick, 2003).

40

**Figure 2.11:** (Upper): HVSR technique in the archaeological site Aptera (western Crete) in seismic ground response evaluation. Figures 2.11a and 2.11b present the Doric Temple and the Dipartite Temple, respectively where HVSR using microtremor recordings conducted. Figures 2.11c and 2.11d present the HVSR ground seismic response of Doric Temple and the Dipartite Temple, respectively. The vertical scale of the graphs corresponds to the ground amplification while the horizontal component corresponds to the ground frequency. (Lower): Electrical resistivity tomography using Schlumberger array to verify the validity of HVSR technique is performed in the Doric Temple. Two large scale voids are revealed corresponding to ancient reservoirs. The data presented here are from the author's own preliminary work, undertaken in preparation for the current PhD thesis.

50

**Figure 2.12:** The equipotential and the current lines for the case of two point source configuration (modified after Reynolds, 1997).

52

**Figure 2.13:** Generalized electrode configuration (modified after Reynolds, 1997).

53

**Figure 3.1:** Fourier spectrum of horizontal (dashed lines) and vertical components (solid lines) at Hakodate ENG (Nogoshi-Igarashi, 1971, extracted from Nakamura, 2000).

57

**Figure 3.2:** A typical sedimentary basin.  $H_r$ ,  $V_r$  are the horizontal and vertical motion on the exposed rock ground near the basin,  $H_b$ ,  $V_b$  are the spectra of the horizontal and vertical motion in the basement under the basin,  $H_f$ ,  $V_f$  are the spectra of the horizontal and vertical motion on the surface ground of the sedimentary basin (Nakamura, 1996; Nakamura, 2000).

60

**Figure 3.3:** Surface ground deformation (extracted from Nakamura, 2000).

63

**Figure 3.4:** Relationship between vulnerability indexes and earthquake damage after the Kobe earthquake (extracted Nakamura et al., 2000b).

65

**Figure 3.5:** Ground vulnerability distribution in Kobe city based on HVSR technique using microtremors (extracted from Nakamura et al., 2000b). 65

**Figure 3.6:** The general layout of the J-SESAME graphical user interface. The selected time series windows are shown in green (J-Sesame guidelines manual). 70

**Figure 3.7:** The selected time window for the HVSR calculation (green time windows). The selected time window for H/V (left lower) and spectra (right lower) is denoted with red zone. For each selected window the H/V ratio (left lower) and the vertical and horizontal spectra (right lower) are calculated. 71

**Figure 3.8:** a) Average H/V spectral ratio and standard deviation using JS software, b) The spectra ratio of the horizontal NS components to vertical ( $H_{ns}/V$ ) to characterize the seismic motion in the NS direction, c) the spectra ratio of the horizontal EW components to vertical ( $H_{ew}/V$ ) to characterize the seismic motion in the EW direction. The HVSR,  $H_{ns}/V$  and  $H_{ew}/V$  spectra ratio are presented with the black curve. The blue and red line curve represents the standard deviation of the HVSR,  $H_{ns}/V$  and  $H_{ew}/V$  spectra ratio. In the upper right (green panel) of the average HVSR (a),  $H_{ns}/V$ ,  $H_{ew}/V$  are presented the extracted HVSR when a 20 sec window is adopted. 72

**Figure 3.9:** a) The main characteristics of the resistivity meter, b) Central switching unit and c) Distributed switching unit (modified by Tsourlos, 1995). 74

**Figure 3.10:** An example of the observed and calculated apparent resistivity pseudosections for ERT data acquired eastern of Kastelli-Kissamou (ERT\_P5) territory located in northwestern Crete. The red zone represents the high resistive zone corresponding to fault. This is an example of the type of result given in Chapter 4. 77

**Figure 4.1.1:** a) Overall view of the urban area of Kastelli-Kissamou half-graben basin, b) View of the coastal site in the northwestern part of the basin where the active fault determined. Photos a and b are derived from google earth software. 84

**Figure 4.1.2** Fault system coastal of northwestern Crete. The green line represents the identified large scale fault trending NNW-SSE and the red lines the series of actives fault cutting the beachrock and trending almost N-S. Yellow lines indicate the already identified faults using geological (Karageorgiou, 1968) and satellite image data. 84

**Figure 4.1.3:** a) The observed apparent offset west of the northwestern part of Kastelli could be the result of erosion exposing the fault plane. The fault causing the uplift of the wave-cut slab that contains the fault shown in the figure might lies hidden just offshore. The very visible fault may be linked to this structure as a subsidiary fault (green line), b,c,d,e) The NNE-SSW faulting eastern of northwestern Kastelli, f) Segment of an opened 30 cm (blue arrow) almost WNW-ESE striking fault. The one meter scale is used as a scale (red arrow). The coast of northwestern Kastelli is characterized of well-lithified limestone. 86

**Figure 4.1.4:** a,c,d,e,f,j,k) Numerous active fault cutting the beachrock and striking almost N-S are identified in the northwestern part of Kastell-Kissamou half-graben basin. The identified N-S faults extended for several meters inland, a) Eastern of the northwestern Kastelli the site is characterized of well lithified limestone without evidences of debris layer, b) Western of northwestern part of Kastelli a debris layer is overlying the well-lithified limestone site. The dashed yellow line on this photo distinguishes the overlying debris layer of the limestone bedrock, e, f, j,k and l) N-S fault filled with recent alluvial fan deposits. The recent lateral trends of faulting justify the fault activity of the faulting coastal of northwestern Kastelli. One meter scale, 10 cm meter and a regular hand bag are used as a scale (red arrow). The green arrows show the N-S faulting.

88

**Figure 4.1.5:** a,b,f) The maximum footwall uplift at beach end of northwestern part of Kastelli is measured of up to 6.8m. c) Evidences of uplifted dead trottoir almost 60 cm. d) The hanging wall of the fault also moved up to 60 cm.

90

**Figure 4.1.6:** a,b) Eroded bedrock level without debris on top and c,d) eroded bedrock level with debris on top of it. The trottoir is the algal encrustation on the vertical cliff face next to the sea.

91

**Figure 4.1.7:** a,b,c) Dead Trottoir at present sea level.

92

**Figure 4.1.8:** The uplifted dead trottoir undercut by small notch at present sea level.

92

**Figure 4.1.9:** Main Fault system of the Geological observations in Paleohora and Grammeno peninsulas in southwestern Crete. The red lines represent the identified faults in Paleohora and Grammeno peninsulas during the fieldwork. Yellow lines indicate the already identified faults using geological and satellite image data.

94

**Figure 4.1.10:** Overall view of Paleohora and the site of en-echelon fault northeastern of the basin where the pottery was found. a) Segment of normal fault striking E-W identified northeastern of Paleohora. On top of the limestone are gravels containing pottery shards (red circle) that have been downfaulted against the limestone in a normal fault (green dashed line). b) Segment of a fault striking E-W identified northeastern of Paleohora. The hammer is used as a scale. The yellow line represents the E-W strike of the fault zone.

95

**Figure 4.1.11:** a,b) In the northern side of Paleohora where the pottery (Upper right) is en-echelon fault is identified. The characteristics of the fault are: strike E-W  $66^{\circ}$ S, slicks (trend  $063^{\circ}$ S, plunge  $062^{\circ}$ S). The fault scarp presents relatively degraded and the fault plane characteristic is  $012/70^{\circ}$ E, c) The downfaulted pottery shards against the limestone in a normal fault, d,e) Samples of the pottery.

97

**Figure 4.1.12:** a, b, d) Fault network indicating oblique slip northwestern of Paleohora. Visible patches of fault planes indicating oblique slip, d) a second en-echelon range front fault with very well developed slicks, c) infilled earlier fractures with the same orientation. The coin on figure (c) and the hammer on figure (d) are used as a scale.

99

**Figure 4.1.13:** a) Cave where the notch is located, b,c) An uplifted notch (3.5-4.5 m) that is an abrasion notch, and therefore not an indicator of an older relative sea-level position, d,e) basal conglomerates in the cave. The hammer, the coin (d) and the 10 cm meter (d) are used as a scale.

101

**Figure 4.1.14:** a) Trottoir located below the bench of the uplifted abrasion notch. b, c) The photo of trottoir and the associated beachrock at the base of the trottoir is an uplift indicator which must have occurred quickly because the trottoir is well-preserved.

102

**Figure 4.1.15:** a) View of a flat topped headland where Fortezza castle is located north of Paleohora. The flat topped headland is characterized of beachrock platforms, b) Beachrock platforms on the flat topped Fortezza headland, c and d) fault evidences of an  $120^{\circ}$  fault that cuts the beachrock and three to four fault system are existent.

104

**Figure 4.1.16:** In the central part of Paleohora evidence of uplift is identified. The late Quaternary post-glacial deposits that overly (Jurassic) marly limestone.

105

**Figure 4.2.1:** Landat (TM8) image of the area under investigation in Kastelli-Kissamou region. The sites where electrical resistivity profiles conducted are denoted with P1 to P8. The orientation of the 2D electrical resistivity tomographies is denoted with the green lines represents the orientation of the electrical resistivity tomography profiles. The length of the ERT profiles is: 185 m for P8, 235 m for P5, 280 m for P7 and 310 m for P1, P2, P3, P4 and P6. The yellow lines represent the already identified faults extracted from geological and satellite images.

107

**Figure 4.2.2:** ERT profile east of Kastelli (P1) on the map in Figure 4.2.1. The thick dashed line shows the unconformity between the bedrock and sedimentary formations saturated with seawater. The electrode spacing of 10 m is presented in the lower left corner of the ERT model. The RMS error is presented in the right upper corner and the resistivity scaling (measured in  $\text{ohm} \cdot \text{m}$ ) is presented in the left lower corner of the ERT model.

108

**Figure 4.2.3:** ERT profile east of Kastelli (P2) on the map in Figure 4.2.1. An almost NNW-SSE normal fault zone using ERT method is depicted with the dashed line to a depth of 50 m. The electrode spacing of 10 m is presented in the lower left corner of the ERT model. The RMS error is presented in the right upper corner and the resistivity scaling (measured in  $\text{ohm} \cdot \text{m}$ ) is presented in the left lower corner of the ERT model.

109

**Figure 4.2.4:** ERT profile in the eastern part of Kastelli (P3). The identified almost N-S normal fault at a depth of 40 m using ERT method is presented with the dashed line. The electrode spacing of 10 m is presented in the lower left corner of the ERT model. The RMS error is presented in the right upper corner and the resistivity scaling (measured in  $\text{ohm} \cdot \text{m}$ ) is presented in the left lower corner of the ERT model.

110

**Figure 4.2.5:** Landsat (TM8) image presenting an overall view of the inverted 2D the electrical resistivity tomographies (P1, P2 and P3 on Figure 4.2.1) in the northeastern part of Kastelli. The green lines represent the orientation of the ERT profile. The yellow lines represent the already identified faults extracted from geological and satellite images.

111

**Figure 4.2.6:** ERT profile in the Western Part of Kastelli (P5) on the map in figure 4.2.1. An almost NNW-SSE normal faulting zone using ERT method is depicted with the dashed line. The electrode spacing of 5 m is presented in the lower left corner of the ERT model. The RMS error is presented in the right upper corner and the resistivity scaling (measured in  $\text{ohm} \cdot \text{m}$ ) is presented in the left lower corner of the ERT model. 112

**Figure 4.2.7:** Landsat (TM8) image presenting the ERT profile P5 in the northwestern part of Kastelli. The green lines represent the orientation of the electrical resistivity tomography. The yellow lines represent the already identified faults extracted from geological and satellite images. 113

**Figure 4.2.8:** ERT profile in the western part of Kastelli (P6) on the map in Figure 4.2.1. An almost NNW-SSE fault using ERT method is depicted with the dashed line. The electrode spacing of 10 m is presented in the lower left corner of the ERT model. The RMS error is presented in the right upper corner and the resistivity scaling (measured in  $\text{ohm} \cdot \text{m}$ ) is presented in the left lower corner of the ERT model. 114

**Figure 4.2.9:** Landsat (TM8) image presenting the ERT profile P6 in the northwestern part of Kastelli. The green lines represent the orientation of electrical resistivity tomography. The yellow lines represent the already identified faults extracted from geological and satellite images. 114

**Figure 4.2.10:** ERT profile western of Kastelli (P7) on the map in Figure 4.2.1. An almost normal N-S faulting zone using ERT method is depicted with the dashed line. The electrode spacing of 10 m is presented in the lower left corner of the ERT model. The RMS error is presented in the right upper corner and the resistivity scaling (measured in  $\text{ohm} \cdot \text{m}$ ) is presented in the left lower corner of the ERT model. 115

**Figure 4.2.11:** Landsat (TM8) image presenting the ERT profile P7 in the northwestern part of Kastelli. The green lines represent the orientation of the electrical resistivity tomography. The yellow lines represent the already identified faults extracted from geological and satellite image data. 116

**Figure 4.2.12:** ERT profile in the west Kastelli (P8). An almost normal N-S faulting zone using ERT survey is depicted with the dashed line. The electrode spacing of 10 m is presented in the lower left corner of the ERT model. The RMS error is presented in the right upper corner and the resistivity scaling (measured in  $\text{ohm} \cdot \text{m}$ ) is presented in the left lower corner of the ERT model. 117

**Figure 4.2.13:** Landsat (TM8) image presenting the ERT profile P8 in northwestern Kastelli. The green lines represent the orientation of the ERT. The yellow lines represent the already identified faults extracted from geological and satellite images. 117

**Figure 4.2.14:** a) ERT line configuration along a segment of Kera fault. The yellow line is the cable connected with electrodes to model subsurface structure, b) close view of the determined faulting, c) very clear faulting along Kera Fault using ERT survey. An almost normal N-S faulting zone using ERT method is depicted with the dashed line. The RMS error is presented in the right upper corner. 118

**Figure 4.2.15:** Landsat (TM8) image presenting the ERT profile P4 in Kera located in the southeastern part of Kastelli. The green lines represent the orientation of the ERT line. The yellow lines represent the already identified faults extracted from geological and satellite image data.

119

**Figure 4.2.16:** Identified faults using ERT and their possible extension of existing faults derived from geological and satellite image data. All ERT profiles conducted in Kastelli region are dominantly occupying a sector between NNE and NNW. The green line represent the orientation of the ERT profiles. The red lines represent the possible extension of the identified faults based on ERT survey. The yellow lines represent the known faults based on geological and satellite images.

120

**Figure 4.2.17:** Landsat (TM8) image of the area under investigation in Paleohora located in southwestern Crete. The ERT profiles are denoted with P1 to P6. The green lines represent the orientation of the ERT profiles. The yellow lines represent the already identified faults extracted from geological and satellite images.

121

**Figure 4.2.18:** Shallow Electrical Resistivity Tomography profile. Red colours define the resistive structure. The estimated ENE-WSW reverse faulting zone using ERT method is depicted with the thick dashed line. The questionmarks represents that the fault extend to an unknown depth. The electrode spacing of 5m is presented in the lower left corner of the ERT model. The RMS error is presented in the right upper corner and the resistivity scaling (measured in  $\text{ohm}\cdot\text{m}$ ) is presented in the left lower corner of the ERT model.

122

**Figure 4.2.19:** Deep ERT profile P1 in northeastern of Paleohora. Red colours define the resistive structure. The estimated ENE-WSW reverse faulting zone using ERT method is depicted with the dashed line. The electrode spacing of 15 m is presented in the lower left corner of the ERT model. The RMS error is presented in the right upper corner and the resistivity scaling (measured in  $\text{ohm}\cdot\text{m}$ ) is presented in the left lower corner of the ERT model.

123

**Figure 4.2.20:** Landsat (TM8) image presenting the inverted 2D ERT profile (P1) of the northeastern Paleohora near pottery findings. The green lines represent the orientation of the ERT profiles. The yellow lines represent the already identified faults extracted from geological and satellite images.

124

**Figure 4.2.21:** Shallow ERT profile at Paleohora peninsula. Red colours define the resistive structure. The tectonic zone is depicted with the dashed line. An almost E-W faulting zone using ERT method is depicted with the thick dashed line. The thin short-dashed black line represents the unconformity. The electrode spacing of 5 m is presented in the lower left corner of the ERT model. The RMS error is presented in the right upper corner and the resistivity scaling measured in ( $\text{ohm}\cdot\text{m}$ ) is presented in the left lower corner of the ERT model.

125

**Figure 4.2.22:** The deep electrical tomography profile at Paleohora peninsula (Pahia Ammos). Red colours define the resistive structure. The tectonic zone is depicted with the dashed line. An almost E-W faulting zone using ERT method is depicted with the dashed line. The thin short-dashed black line represents the unconformity. The electrode spacing of 15 m is presented in the lower left corner of the ERT model. The RMS error

is presented in the right upper corner and the resistivity scaling (measured in ohm\*m) is presented in the left lower corner of the ERT model.

126

**Figure 4.2.23:** Landsat (TM8) image presenting the deep ERT profiles along Pahia Ammos site of Paleohora. The green lines represent the orientation of the ERT profiles. The deep ERT profile reveals large scale fault. The yellow lines represent the already identified faults extracted from geological and satellite image maps.

127

**Figure 4.2.24:** Electrical resistivity tomography profile in Grammeno peninsula. The red colours represent the high resistivity structure (bedrock) and the blue colours correspond to the low resistivity structure (seawater intrusion). A large scale almost E-W fault dipping to North and two possible 'faults' dipping to South are observed and depicted with dashed black lines. The two speculated 'faults' on the right-hand of the profile might instead be buried rock platforms. The evidence for a fault in these places is not strong. The questionmarks indicate the unknown fault depth.

128

**Figure 4.2.25:** Landsat (TM8) image presenting the proposed tectonic model based on ERT survey in Grammeno peninsula. A large scale E-W fault dipping to North and two possible faults dipping to South are observed and depicted with dashed black lines. The green line represents the site of the ERT profile. The yellow lines represent the already identified faults extracted from geological and satellite image maps.

129

**Figure 4.2.26:** The configuration of the two large scale identified faults striking almost E-W in Paleohora and Grammeno peninsulas. The similarities in the subsurface model suggest that Grammeno peninsula is the miniature of Paleohora. The aforementioned configuration suggests that the coastline of Paleohora is characterized of of a large scale fault or of a system of faults. The dashed yellow line represents the fault or the system of faults in the coastline of the investigated area.

131

**Figure 4.2.27:** ERT profile P4 in northeastern of Paleohora. Water surficial deposits are identified. The red colour corresponds to the resistive structure (bedrock) and the green colour to conductive structure (water contaminant). The RMS error is presented in the right upper corner and the resistivity scaling (measured in ohm\*m) is presented in the left lower corner of the ERT model.

132

**Figure 4.2.28:** ERT profile west of Panorama of the northeastern part of Paleohora reveals a thick layer of waste disposal at a depth of 30 m. The red colour corresponds to the resistive structure (bedrock) and the blue colour to conductive structure (waste disposal). The electrode spacing of 15 m is presented in the lower left corner of the ERT model. The RMS error is presented in the right upper corner and the resistivity scaling (measured in ohm\*m) is presented in the left lower corner of the ERT model.

133

**Figure 4.2.29:** (Upper): ERT in the archaeological site Fortezza located on beach-gravels hydrogeneous surficial deposits. (Lower): Water surficial deposits in the archaeological site south of Paleohora peninsula extracted from ERT model. The red colour corresponds to the resistive structure (bedrock) and the green colour to conductive structure (water contaminant). The electrode spacing of 15 m is presented in the lower left corner of the ERT model. The RMS error is presented in the right upper corner and the resistivity scaling (measured in ohm\*m) is presented in the left lower corner of the ERT model.

134



**Figure 4.2.30:** Landsat (TM8) image presenting an overall view of the derived surface and subsurface structure northeastern, northwestern and southern of Paleohora. The green line represents the orientation of the ERT profile. The yellow lines represent the already identified faults extracted from geological and satellite images.

135

**Figure 4.3.1:** a) HVSR using microtremors conducted northwestern of Kastelli characterized of a well- lithified limestone site, b, c, d, e) Average HVSR (sites MK5-MK8) on a multi-fractured well-lithified limestone site without the effect of alluvial/sedimentary deposits. The one clear amplified HVSR peak in the medium frequency corresponds to the spectra characteristics of the fractured system of a single site microtremor recording. At each HVSR curve the blue line represents the HVSR curve and the black lines the standard deviation. The one clear amplified HVSR peak in the medium frequency correlates to the spectra characteristics of the fractured system.

140

**Figure 4.3.2:** The main seismic ground fundamental frequency map of Kastelli-Kissamou half-graben basin. The yellow circles represent sites of ground fundamental frequency in the medium frequency range corresponding to the effect of a fault zone on ground seismic motion. The red circles represent sites of two amplified frequencies. The fundamental frequency in the low frequency range corresponds to the effect of thick alluvial deposits and the second amplified in the medium frequency range to the effect of a fault zone. The blue circles represent sites of flat or low amplitude fundamental frequency. The green circles represent sites of ground fundamental frequency in the low frequencies due to the thick alluvial deposits, b, c) Cross-sections delineating fault zones AB, CD,EF, GH, KL based on HVSR technique using microtremors.

142

**Figure 4.3.3:** Seismic ground amplification map of Kastelli Kissamou half-graben basin using HVSR technique. The red circles represent sites of ground amplification ranging from 3.02-3.34. The orange circles represent sites of ground amplification ranging from 2.03-2.90 and the yellow area the ground amplification ranging from 1.10-1.99.

143

**Figure 4.3.4:** a) Ground fundamental frequency map in Paleohora basin and fault delineation based on HVSR technique using microtremors. Red circles correspond to sites characterized of one clear HVSR peak in the medium frequency range. The brown circles correspond to low frequency HVSR peaks. The pink circles correspond to broad HVSR curves. The dark blue, pale blue, green and yellow correspond to the effect of subsurface structure (attributed to fault zone) and to the effect of the thickness variation of the alluvial deposits on seismic ground motion. Four main fault zones (blue, red, orange-green (Fortezza) and yellow clusters) are delineated using HVSR technique and microtremors, b) Microtremor profile recordings (A1A2) performed along Pahia Ammos where ERT profile conducted. In the southern part of Pahia Ammos the clear amplified low frequency corresponds to the thick sand layer overlying the bedrock. The two amplified frequencies correspond to the surface and subsurface structure. The first amplified in the low corresponds to the effect of the sandy layer while the second amplified in the high frequencies to the effect of the lateral heterogeneities of the subsurface. The first amplified in the high frequencies corresponds to the effect of the lateral heterogeneities of the subsurface while the second amplified to the low frequencies to the effect of the sandy layer.

144

**Figure 4.3.5:** Ground seismic amplification map in Paleohora basin. The red zones (A) represent sites with the higher amplification (5.68, 5.75). The orange zone (B)

represents sites of ground amplification ranging from 3.0-4.66. The yellow area zone (C) represents sites of ground amplification 1.88-3.36.

147

**Figure 4.3.6:** Sites of HVSR comparison between simultaneously recorded microtremor and earthquake data using Cityshark II.

148

**Figure 4.3.7:** (Upper) Microtremor and earthquake time series. (Lower): The green time window is the earthquake recording.

149

**Figure 4.3.8:** (Upper): HVSR curves using microtremors and earthquake data recorded at the same site in the centre of the basin. The horizontal axis presents the HVSR ground fundamental frequency and the vertical axis presents the HVSR ground amplification. The HVSR fundamental frequency using microtremors and earthquake data is in the low frequency (0.75 Hz). For microtremors and the recorded earthquake the second HVSR amplified frequency is observed in the high frequencies (7.11 Hz). Similarities in the HVSR, Hns/V and Hew/V spectra curves and in fundamental frequencies for the average HVSR (blue curve), Hns/V (red curve) and Hew/V (green curve) spectra ratios are observed. (Lower): Comparison between HVSR (blue curve), Hns/V (pink curve) and Hew/V (grey curve) using microtremors and HVSR (black curve), Hns/V (green curve) and Hew/V (red curve) using earthquake recording. The HVSR ground amplification is underestimated using microtremors (blue curve) compared to HVSR ground amplification using earthquake recording (black line) in the centre of the basin.

151

**Figure 4.3.9:** (Upper) Microtremor and earthquake time series. (Lower) The green time window is the magnification of the earthquake recording.

152

**Figure 4.3.10:** (Upper): HVSR curves using microtremors and earthquake data recorded at the same site in the basin edge and the comparison of microtremor and earthquake data. The horizontal axis presents the HVSR ground fundamental frequency and the vertical axis presents the HVSR ground amplification. Similarities in the HVSR (blue curve), Hns/V (red curve) and Hew/V (green curve) spectra curves and in fundamental frequencies using microtremors and earthquake recording are observed. (Lower): Comparison between HVSR (blue curve), Hns/V (red curve) and Hew/V (black curve) using microtremors and HVSR (green curve), Hns/V (grey curve) and Hew/V (pink curve) using earthquake recording. The HVSR ground amplification using microtremors is overestimated compared to recorded earthquake recorded along the basin edges.

154

**Figure 4.3.11:** Building Vulnerability estimation using HVSR and microtremors in three case studies located in the centre of the basin (b2,b3) and near to the basin edge (b1).

157

**Figure 4.3.12:** (Upper): Building vulnerability estimation using HVSR and microtremors for the masonry constructed house, located in the southeastern part of Paleohora close to the edge of the basin (b1). Similarities in the HVSR (blue curve), Hns/V (red curve) and Hew/V (green curve) spectra curves in fundamental frequencies and amplification of ground structure response and ground floor foundation are observed. (Lower): Comparison between HVSR ground response and HVSR ground floor foundation. Similarity in the fundamental frequency ( $F_0=2.3-2.4$  Hz) and in the amplification is observed ( $A=2.3-2.5$ ).

159

**Figure 4.3.13:** Building Vulnerability estimation using HVSR and microtremors for three-story concrete constructed house, located northeastern of Paleohora in the centre of the basin (b3). Similarities in the HVSR (blue curve),  $H_{ns}/V$  (red curve) and  $H_{ew}/V$  (green curve) spectra curves in fundamental frequencies and amplification of ground freefield underground foundation and third floor are observed. (Lower): Comparison between HVSR ground response and HVSR ground floor foundation. Similarities in the fundamental frequencies of ground freefield 100 m (green line) ground freefield of the construction (black line), of the underground foundation (blue line) and of the third floor (red line) are observed.

162

**Figure 4.3.14:** Building vulnerability estimation using HVSR and microtremors for the elementary and high school located northeastern of Paleohora in the centre of the basin (b2). The fundamental frequency of the first and fundamental frequency second floor of the masonry building is observed in the similar frequency range of the second floor amplified frequency of the ground freefield. The second amplified frequency of the first and second floor in the low frequency coincidence with the fundamental frequency of the ground freefield. The fundamental frequency of the ground floor foundation in the concrete building construction coincidence with ground freefield fundamental frequency located 50 m west of the concrete building while the second amplified frequency in the medium frequency range coincidence with the second amplified frequency located 5m northeast of the concrete building construction. High amplification ( $A=5$ ) is observed in the first floor in the medium frequency band that coincidence with the HVSR fundamental frequency of ground response (ground freefield) located 50 m west of the reinforced concrete building.

169

**Figure 4.3.15:** Microseismicity of Crete during the period of 01/07/07 to 31/08/2007. The red cycles represent the earthquake epicenter using the local network of Crete. The list of seismological stations is presented in the Appendix II (Tables 4.5 and 4.7).

173

**Figure 4.3.16:** Microseismicity of Crete recorded from the temporal seismological network of Paleohora. The red cycles represent the earthquake epicenter using the local network of Crete. The list of seismological stations is presented in the Appendix II (Tables 4.6 and 4.8).

175

**Figure 5.1:** a) One HVSR clear peak in the medium frequency ( $F_0=3.93\text{Hz}$ ,  $A=2.66$ ) on an opened with recent infilling alluvial fan N-S fault segment located on a well-lithified limestone structure. The yellow dashed line represents the N-S fault, b) One HVSR clear peak in the medium frequency ( $F_0=2.98\text{Hz}$ ,  $A=1.66$ ) along a subsidiary fault coastal of northwestern Kastelli characterized of a well-lithified limestone structure. The green dashed line represents the subsidiary fault. In both sites microtremors are collected using Cityshark II connected with Lennartz 3D/5sec seismometer oriented to north.

181

**Figure 5.2:** A synthesis of the combined multi-proxy approach of geological ground truthed field survey, electrical resistivity tomography, HVSR using microtremors and microseismicity recorded from the permanent seismological network of Crete for fault delineation in Kastelli-Kissamou basin. All recorded data are described and interpreted in Chapter 4. Geological investigation and HVSR using microtremors revealed five fault zones. ERT revealed four fault zones and microseismicity recorded from the permanent network verified the moderate seismic activity of northwestern Crete recorded for the time period of two months.

184

**Figure 5.3:** View of the tectonic model along Pahia ammos (western part of Paleohora profile A1A2) based on the combined methodologies HVSR using microtremors (upper figure) and ERT (lower figure): HVSR curves pattern the surface and subsurface variations along Pahia Ammos. The numbering (A-D) in the lower right part of the HVSR curves depicts the site where HVSR was conducted in Pahia Ammos. In the southern part of Pahia Ammos the clear amplified low frequency corresponds to the thick sand layer overlying the bedrock. The two amplified frequencies correspond to the surface and subsurface structure. The first amplified low frequency corresponds to the effect of the sandy layer while the second amplified in the high frequencies to the effect of the lateral heterogeneities of the subsurface due to the fault zone. The first amplified in the high frequencies corresponds to the effect of the lateral heterogeneities of the subsurface while the second amplified in the low frequencies to the effect of the sandy layer, (lower figure): the ERT profile showing the resistivity variations in depth along Pahia Ammos.

187

**Figure 5.4:** A synthesis of the combined multi-proxy approach of geological ground truthed field survey, electrical resistivity tomography, HVSR using microtremors and microseismicity recorded from the permanent seismological network of Crete and temporal local seismological network of Paleohora for fault delineation in Paleohora basin. All recorded data are described and interpreted in Chapter 4. Geological investigation revealed numerous fault zones, HVSR using microtremors revealed four fault zones. ERT revealed two fault zones in the populated Paleohora half-graben and one fault in Grammeno peninsula. Microseismicity recorded from the temporal network revealed a large scale fault or a system of fault striking almost E-W and trending for approximately 46 km from east of Grammeno-Pahia Ammos-Lissos basin (western of Paleohora) in agreement with the tectonic model proposed from ERT. Microseismicity from the permanent network verifies the high activity of southwestern Crete compared to northwestern Crete is due to the heterogeneous structure characterized of large scale faults.

190

**Figure A:** HVSR using microtremors to determine the ground seismic spatial variation response in the populated of Kastelli Kissamou (MK1-MK38) basin and Roka village (MKR1-MKR4). The horizontal scale of the HVSR curves represents the fundamental frequency range (0.2-20Hz) while the vertical scale represents the ground seismic amplification. The black lines in all graphs correspond to the standard deviation of each  $H/V$ ,  $H_{ns}/V$ ,  $H_{ew}/V$  curve. The grey zone presented in all graphs corresponds to the standard deviation of fundamental frequency. The blue line of the curves represents the average  $H/V$  ratios (HVSR average ratios) of microtremor component recordings.

228

**Figure B:** HVSR technique using microtremors recorded in urban Paleohora half-basin to determine ground seismic spatial variation response. The horizontal scale of the HVSR curves represents the fundamental frequency range (0.2-20Hz) while the vertical scale represents the ground amplification. The blue curves represents the average  $H/V$  ratios (HVSR average ratios) of microtremor component recording recorded in a single station site. The red curve of each graph represents the north-south horizontal to vertical spectra ratio ( $H_{ns}/V$ ) of microtremor component recorded in a single station site. The green curve of each graph represents the east-west horizontal to vertical spectra ratio ( $H_{ew}/V$ ) of microtremor component recordings. The black curves in all graphs correspond to the standard deviation of each  $H/V$ ,  $H_{ns}/V$ ,  $H_{ew}/V$  curve. The grey zone presented in all graphs corresponds to the standard deviation of fundamental frequency.

274

## **List of Tables**

---

<b>TABLE 4.1:</b> <i>ERT survey in Kera and Kastelli-Kissamou region</i>	275
<b>TABLE 4.2:</b> <i>ERT survey in Paleohora region</i>	275
<b>TABLE 4.3:</b> <i>Microtremor recordings in Kastelli-Kissamou basin</i>	276
<b>TABLE 4.4:</b> <i>Microtremor recordings in Paleohora basin</i>	278
<b>TABLE 4.5:</b> <i>Permanent Seismological Network of Crete</i>	282
<b>TABLE 4.6:</b> <i>Temporal seismological network of Paleohora</i>	282
<b>TABLE 4.7:</b> <i>Samples of earthquake epicenters recorded from the permanent seismological network of Crete</i>	283
<b>TABLE 4.8:</b> <i>Samples of earthquake epicenters recorded from the temporal seismological network of Paleohora</i>	293

## **List of abbreviations**

---

<b>HVSR</b> : <i>Horizontal to Vertical Spectra Ratio</i>	i
<b>ERT</b> : <i>Electrical Resistivity Tomography</i>	i
<b>RMS</b> : <i>Root Mean Square</i>	25
<b>ERH</b> : <i>Error in Epicenter</i>	25
<b>FEM</b> : <i>Finite Element Method</i>	55
<b>JS</b> : <i>J-SESAME Software</i>	66

## ***Acknowledgments***

---

**I own appreciation to:**

**Dr Stephen Kershaw for the paramount efforts and support dedicated to a thorough and complementary thesis**

**Dr Derek Rust for the significant contribution in the determination of fault zones in the study areas**

**Dr Philip Collins for the precise amendments that improved the thesis**

**Dr Filippos Vallianatos for introducing me to this field of science**

**This work is supported by the Greek State Scholarship Foundation  
My thankfulness to the Greek State Scholarship Foundation**

**Instrumentation is provided by the Laboratory of Geophysics and Seismology of  
Crete of the Technological Educational Institute of Crete**

---

***To my brother Konstantinos  
and to my parents, Dimosthenis and Maria***



## **CHAPTER 1: INTRODUCTION**

---

### **1.1 RATIONALE AND PURPOSE OF THE THESIS**

The study of earthquake hazards is a critical issue in the preparedness, mitigation and management of earthquake disasters, especially in populated regions located in highly seismic environments. A comprehensive seismic hazard assessment of a site is mainly focused on the estimation of the dynamic response of surface and subsurface structures subjected to the seismic ground motion and on the determination of spatial and temporal earthquake occurrence (Reiter, 1990; Morrato et al., 2007).

In urban areas, the key issues in the estimation of seismic hazards (Morrato et al., 2007; Pitilakis et al., 2007) that should be considered for earthquake loss mitigation (McGuire, 1993) are the:

- 1) determination of potentially seismic active sources; and
  - 2) dynamic response evaluation of surface and subsurface structure at sites where the geometric and dynamic properties of the ground can strongly amplify seismic motions.
- This thesis addresses these two issues, by evaluating seismic ground motion in a populated active tectonic area using a combination of methods involving the study of geology, seismology and geophysical disciplines permitting cross-comparison of techniques in a robust approach.

The purpose of the thesis is to develop an understanding of the nature of ground response subjected to earthquakes using a multiproxy approach, in order to advance the science of ground seismic motion evaluation in seismically active populated regions.

The study area is focused in western Crete, in the forearc of the Hellenic subduction zone of the southern Aegean region of Greece in one of the most seismically active parts of the Africa-Eurasia collision zone. Two sites are chosen for detailed study: Paleohora half-graben basin, close to the Hellenic trench in southwestern Crete and Kastelli-Kissamou half-graben basin, located in northwestern Crete, located further from the trench, in order to compare the seismic ground responses of the two areas. The location of the studied areas of Kastelli-Kissamou and Paleohora basins located in northwestern and southwestern Crete, respectively are presented in Figure 1.1. A clear indicator of the intense seismic activity that can occur in this area is shown by uplift of up to 10 m of southwestern Crete, which occurred synchronously with the AD 365 earthquake. The precise cause of that uplift is not determined, but it is related to either the subduction of Mediterranean ocean crust beneath Crete (Pirazzoli et al., 1982; Meulenkaamp et al., 1994) or to a fault dipping at about 30° within the overriding Eurasia plate (Shaw et al., 2008).

Both Paleohora and Kastelli areas have high human population densities in this highly seismic environment. Thus, the combination of a highly seismic environment, the proximity of active faults, the geometry of the subsurface structure and the dynamic properties of the uppermost sedimentary deposits (that can strongly amplify earthquake ground motion) characterize the investigated areas as an ideal natural laboratory to address the effect of surface geological and subsurface structure on seismic ground motion.

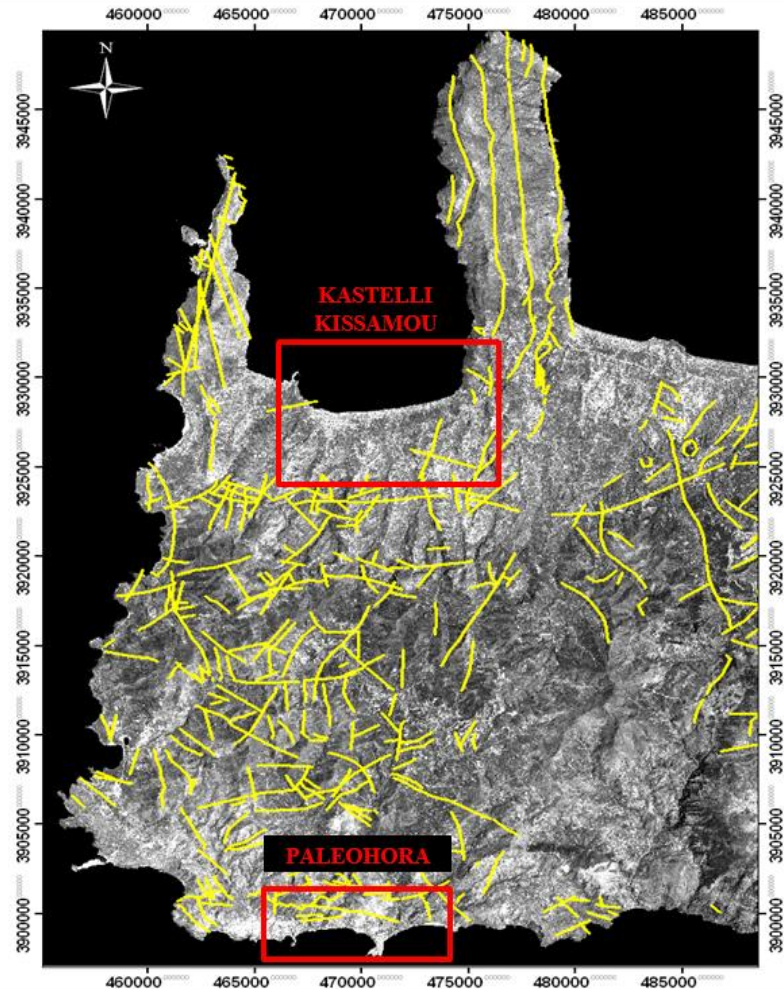


**Figure 1.1:** Landsat satellite image of the location of the research areas in western part of Crete in the southern Aegean region. Faults of Crete derived from geological and satellite image maps are presented with yellow lines. The location of the investigated regions in Kastelli-Kissamou and Paleohora basins located in northwestern and southwestern Crete is shown with red rectangles.

The methodologies of this thesis use a combination of four approaches including geological, geophysical, seismological and geotechnical engineering disciplines. These four areas are investigated to collect specific information needed to address the aims:

- Geological investigation is conducted to define the location, configuration and potential of seismically active faults or rupture zones. This information forms a background to the remaining three techniques, in to attempt to provide ground-truthing. Geological ground thruthing evidences verify the research outcomes of the applied experimental techniques.
- Geophysical 2D Electrical Resistivity Tomography (ERT) technique is implemented to experimentally identify the location of seismic sources and to directly cross-compare with the geological field observations.
- Seismology is performed to reveal active ruptures zones (faults) which are possibly not observable at the Earth's surface (Reiter, 1990).

- Geotechnical engineering technique is used to determine fault zones that may be active, to estimate the effect of local soil conditions (site effects) due to surface and subsurface structure on seismic ground motion and to finally present a microzonation study. The microzonation study involves the presentation of ground seismic fundamental frequencies and amplification maps based on the Horizontal to Vertical Spectra Ratio (HVSR) or Nakamura technique using microtremors.

Therefore the four methodologies provide a robust system of cross-comparisons of different types of datasets in relation to the aim of this research.

## **1.2 ORGANIZATION OF THE THESIS**

The remaining parts of this Chapter provide a brief description of the seismotectonic background to the study area. Chapter 2 is a review of published work relevant to this subject area. Chapter 3 describes the methods used in the research. Chapter 4 presents the results and Chapter 5 discusses the research outcomes. The thesis ends with conclusions in Chapter 6 involving a short note of future research studies that can be conducted based on the research outcomes. The reference list follows in the end of the thesis. A CD is provided in the end of the thesis presenting the Tables and samples of the data acquired in the frame of this thesis.

## **1.3 THE STUDY REGION: THE SEISMOTECTONIC SETTING AND THE MAIN TOPOGRAPHIC FEATURES OF THE SOUTH AEGEAN REGION**

The study regions are presented in Figure 1.1. Crete is located in the plate boundary between Africa-Eurasia plates. The Africa plate motion relative to Eurasia plate and the presence of Anatolian, Aegean and Apulian microplates affect the active tectonics of the southern Aegean region and the surrounding area of Greece (Papazachos et al., 1998). The westward drift and counter-clock wise rotation of Anatolia plate due to the northward drive of Arabia results in the southward movement of Aegean plate towards Africa. In the Aegean Sea the collision of Africa-Eurasia plates forms an inclined seismic zone, the Wadati-Benioff zone (Hellenic subduction zone), (Papazachos & Comninakis, 1970, Papazachos & Comninakis 1971; Papazachos et al., 2000b), that follows the convex side of the sedimentary arc including Western Peloponnese, west of Kythira, south coast of Crete and east of Rhodes (Fig.1.2).

The Hellenic subduction zone is characterised by high seismic activity, while high uplift rates are evident in southwestern Crete (Papazachos & Comninakis, 1970; Papazachos & Comninakis 1971; Papazachos et al., 2000b). The plate convergence creates a parallel extension (Papazachos & Papazachou, 1997; Jost et al., 2002; Duermeijer et al., 2000) that results in thrust faults bounded by north-south trending normal faults (Armijo et al., 1992). Transtensional trenches (named Ptolemy, Pliny, and Strabo) within the continental Aegean plate in the southeastern Crete that parallels the Hellenic arc and formed due to the oblique angle of subduction towards central and eastern Crete picturizes a general overview of the main tectonics of Crete.

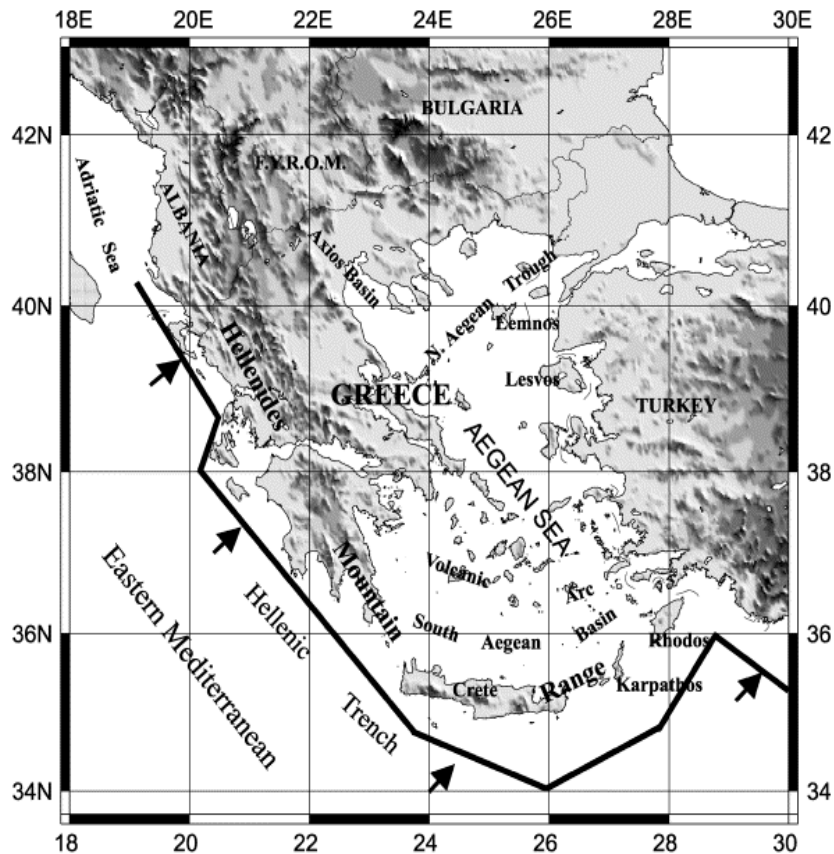


**Figure 1.2:** Main topographic features of the southern Aegean region (Papazachos & Papazachou, 1997). The Hellenic arc consists of an external sedimentary arc, which connects the Dinaric Alps with the Turkish Taurides and of an internal volcanic arc, which is parallel to the sedimentary arc. The southern Aegean trough is located in between the sedimentary and volcanic arc.

#### 1.4 SEISMICITY OF CRETE IN RELATION TO THE PURPOSE OF THE STUDY

Historical data (Papazachos & Papazachou, 1997; Papazachos & Papazachou, 2003) source report that the strongest earthquake event in Crete was in AD 365 in southwestern Crete ( $M_s = 8.3$ , Lat: 35.20, Long: 23.20,) and in AD 1303 in the easternmost part of the Hellenic trench (east of Rhodes island) ( $M_s = 8.0$ , Lat: 36.10, Long: 29.00). Higher seismic activity is observed in southwestern Crete compared to northwestern Crete. During the period from 426 BC to AD 1995 four strong events occurred in southwestern Crete and one in northwestern Crete. Recent deterministic seismic hazard analysis for shallow earthquakes in Greece confirms that the most seismically hazardous zones are the western Crete and the central Aegean sea (Morrato et al., 2007). Figure 1.3 presents earthquake data of magnitude  $M > 5.0$  historically and instrumentally recorded for the period 426 BC to AD 2003, and the seismogenic zones of Greece subdivided by Moratto et al. (2007). In Figure 1.3 (Morrato et al., 2007) red circles, present the strongest earthquakes events occurred in AD 365 in southwestern Crete and in AD 1303 in the easternmost part of the Hellenic trench (east of Rhodes island).

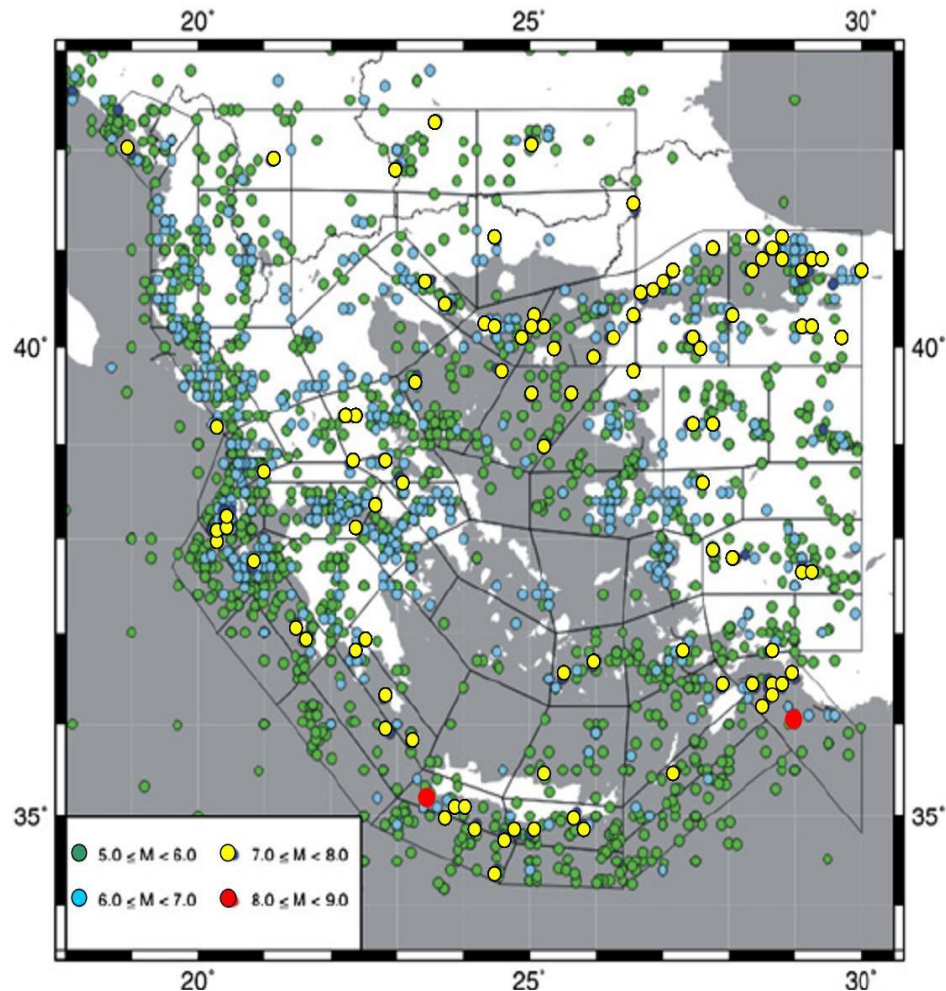


**Figure 1.3:** Epicenters of earthquakes with magnitude  $M > 5.0$ . Greece is separated into seismogenic zones. High seismicity distribution is observed along the Hellenic arc. The red circles present the two major events in southwestern Crete (AD 365,  $M = 8.3$ ) and in the easternmost part of the Hellenic trench (AD 1303,  $M = 8.0$ ). The green circles present the earthquakes with magnitude  $5.0 \leq M < 6.0$ . The blue circles present earthquakes with magnitude  $6.0 \leq M < 7.0$  and the yellow circles presents earthquakes events with magnitude  $7.0 \leq M < 8.0$ , (Morrato et al., 2007).

### 1.5 GEOLOGY OF THE INVESTIGATED SITES IN PALEOHORA AND KASTELLI IN WESTERN CRETE

The crustal extension in the forearc region driven by the: a) rollback of the subducting African slab (Thomson et al., 1998; Thomson et al., 1999), and b) westward motion of the Anatolian plate resulted in north-south and east-west extension in Crete. The extensional basins in northwestern and southwestern Crete filled with breccio-conglomerates, are complex multi-fractured neotectonic small scale half-graben basins bounded by N-S fault zone. Moreover, bounded by a W-E trending normal fault, basins of northwestern and southwestern Crete can be characterized as alluvial fan, submarine

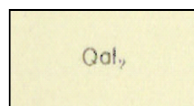
steep-faced and basin-plain environments (Seidel et al., 2007). The characteristic of the basins in the two localities is the subparallel fault blocks mountains separated by broad alluvium-filled half-graben (van Hinsbergen, 2006; Seidel et al., 2007). Geological maps used in the frame of the study in Kastelli-Kissamou and Paleohora basins are derived from Karageorgiou (1968) and Tsalahouri & Fontou (1972), respectively.

### **1.5.1 GEOLOGY OF THE INVESTIGATED SITES IN KASTELLI KISSAMOU IN NORTHWESTERN CRETE**

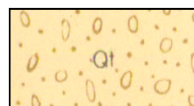
In Figure 1.5 is presented the geological map (Karageorgiou, 1968). The surface geological setting of the investigated sites in Kastelli Kissamou region is characterized by a diversity of rock types, shown in Figure 1.4, including the following:

- i) carbonate rocks (marble and thin-bedded limestones that are dolomitic, white grayish, compact crystalline with blue-brownish to very dark brown thin layers)
- ii) mica schists and graphitic chloritic phyllites,
- iii) marls,
- iv) Cretaceous limestones (white to brown, locally compact lithographic thin bedded commonly fine grained or even microcrystalline in banks strongly karstified).
- v) older Fluvial-Terraces (Pleistocene: loose deposits of red brownish clays containing a great percentage of sand granules and pebbles and sometimes boulders deriving from limestones, hornstones and rarely from flysch sandstone). Some beds of the older fluvial terraces are alternating shales and argillaceous sandstones.
- vi) alluvial deposits (Holocene: Loose loams, clays, sands and gravel with thickness not exceeding 3 m).

ERT profiles were performed on marbles, schists, marls, alluvial deposits, Cretaceous limestones and alternating beds of shales and argillaceous sandstones. The sites where the ERT profiles conducted to model the subsurface structure are presented on the map in Figure 1.4 with red circles. The permanent seismological station is installed on older fluvial terraces. The site where the permanent seismological station installed to determine the effect of the subsurface structure in seismic hazards of the area are presented on the map in Figure 1.4 (blue triangle). Microtremor measurements are conducted in the whole territory of the populated area of Kastelli characterized of alluvial deposits (Holocene: loose loams, clays sands and gravels), older fluvial terraces (Pleistocene; loose clay deposits containing sand granules, pebbles and boulders derived from limestones or flysch sandstone) and limestones (Cretaceous).



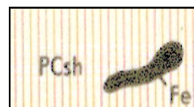
**Alluvial deposits (Holocene)** : Loose loams, clays, sands and gravel with thickness not exceeding the 3m



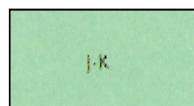
**Older Fluvial-Terraces (Pleistocene)**: Loose deposits of red brownish clays containing a great percentage of sand granules and pebbles and sometimes boulders deriving from limestones, hornstones and rarely from flysch sandstone



**Limestones (marble) (Metamorphic)**: Dolomitic, white grayish, compact crystalline with blue brownish to very dark brown thin bedded limestones



**Crystalline Schists (Metamorphic)**: Shining mica schists or graphitic chonitic phyllites. Iron ore occurrences.



**Limestones (Cretaceous)**: White to brown, compact locally lithographic thin bedded commonly fine grained or even microcrystalline in banks strongly kastrified

**Figure 1.4:** Geological map of Kissamou basin in northwestern Crete (Karageorgiou, 1968). The red circles represent the sites where ERT measurements were conducted. The blue triangle represents the site where the permanent seismological station installed.

### **1.5.2 GEOLOGY OF THE INVESTIGATED SITES IN PALEOHORA IN SOUTHWESTERN CRETE**

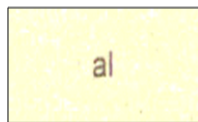
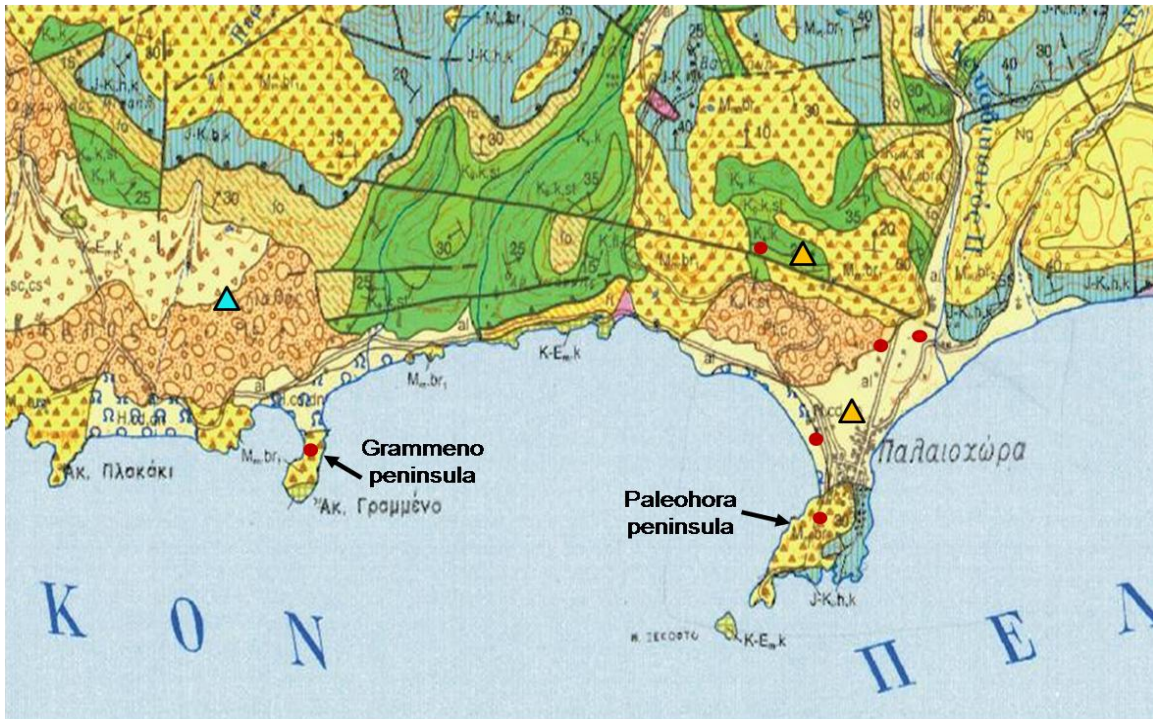
In Figure 1.5 is presented the geological map (Tsalahouri & Fontou, 1972).

The surface geological setting of the investigated sites in Paleohora area is characterized by a diversity of rock types, shown in Figure 1.5, including the following:

- i) alluvial deposits,
- ii) conglomerates alternating with sandstone clays and loams,
- iii) transition beds composed of platy limestones alternating with sandstone and shales,
- iv) Lissos beds composed of cobbles and rubbles of pre-neogene series consolidated with calcitic and marly cement, fluvio-terrestrial deposits.

Red circles on the map (Fig.1.5) represent the sites where ERT survey conducted. ERT profiles applied on alluvial deposits, transition beds composed of platy limestones alternating with sandstone and shales, Lissos beds composed of cobbles and rubbles of pre-Neogene series consolidated with calcitic and marly cement. The sites where the permanent and temporal seismological station installed to determine the effect of the subsurface structure in seismic hazards of the area are presented with blue and yellow triangle, respectively. The temporal seismological stations (yellow triangles) were installed on limestones and on alluvial deposits. The permanent station (blue triangle) is installed on fluvio-terrestrial deposits (composed of carbonate and phyllite cobbles of various size and lithologic composition locally of conglomerates with sandstone, clays and loams. Microtremor measurement are conducted in the whole territory of the populated area of Paleohora characterized of alluvial deposits (Holocene: clayey-sandy), fluvio-terrestrial deposits (Pleistocene; rubbles, conglomerates alternating with sandstone, clays and loams (thickness: 100 m).





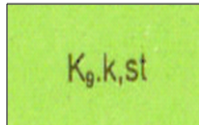
**Alluvial deposits (Holocene):** Clayey-sandy material in small internal basins and unconsolidated material of clay sand, cobbles and rubbles on the torrents beds and outlets



**Fluvio-terrestrial deposits (Pleistocene):** Carbonate and phyllitic rubbles of various size and lithologic composition, locally conglomerates alternating with sandstones, clays and loams. Thickness: up to 100m approximately



**Lissos Beds (Serravallian):** Cobbles and rubbles of preneogene series consolidated with calcitic and marly cement. Thickness: maximum 150m approximately



**Transition beds (Maastrichtian):** Composed of platy limestones alternating with sandstone and shales

**Figure 1.5:** Geological map of Paleohora territory in southwestern Crete (Tsalahouri & Fontou, 1972). The sites where ERT performed are presented on the map with coloured red circles. The permanent seismological station installed in southwestern Crete is presented with the blue triangle. The two temporal seismological stations are presented with the yellow triangles.

## 1.6 A BRIEF OUTLINE OF METHODOLOGY APPLIED IN THIS RESEARCH

The multi-proxy approach of this study is conducted to evaluate the effect of the geological structure and complex subsurface structure in seismic ground motion of Paleohora and Kastelli half-graben. Geological field evidence is used to study the tectonic environment and to reveal active tectonic structures not previously presented; thus geological field observations enrich the database of the studied areas. Moreover, the recognition of active fault zones in close proximity to the studied urban areas is important in site effect studies and in earthquake damage distribution. ERT survey based on ground resistivity variations with depth, profiled across known faults, is used to identify buried faults that are not visible on the ground.

Destructive earthquake consequences (for example in the events at Northridge, 1994, Turkey, 1999, Loma Prita, 1989, Kobe 1995, California, 1983; Mexico City, 1985) confirm the importance of the effects of local site condition in the earthquake damage distribution. Considering the importance of site effects in earthquake distribution and taking account that the effect of surface and subsurface structure of Paleohora and Kasteli half-graben basins is unknown, dense microtremor measurements were performed to evaluate soil characterization according to the Greek seismic ground vulnerability code (EC8). Moreover, the effect of the strong lateral heterogeneities on seismic ground motion is studied. A microzonation study based on local site conditions due to geological structure and complex subsurface structure is presented.

HVSR using microtremor measurements is implemented to evaluate the effect of the geological structure and subsurface structure on ground seismic motion. Spatial distribution of similar HVSR curves delineates fault zones that may be active. Dense microtremor measurements performed at sites where the characteristics of the seismogenic or active faults neighbouring populated areas suggest possible co-seismic deformations at the surface and at sites where the geometric and dynamic properties of the soil can strongly amplify seismic motions. A microzonation study that is an assessment of seismic potential hazard, based on site effects of both the geologic structure and subsurface soil conditions is proposed.

Instrumental seismology using earthquake data from a new telemetric local seismological network installed on Crete is implemented to reveal and delineate active faults. A seismological database has been acquired from a seismological network of permanent and temporary field stations installed across the whole territory of Crete. The aforementioned instrumentation provides the seismicity data for the determination of the seismotectonic setting in western Crete. Earthquake data were acquired from the local network of Crete (that comprises one permanent short-period station in Kastelli and in Paleohora) to compare the seismicity rate of northwestern and southwestern Crete. In the analyzed time period higher seismicity is observed in southwestern compared to northwestern Crete. In addition to this permanent network, a three - temporary seismological network was installed for a period of 45 days in Paleohora area to record the local microseismicity. The purpose of the local temporal seismological network is to record the spatio-temporal microseismicity after the 27<sup>th</sup> April 2007 earthquake in southwestern Crete and to model the strong heterogeneities of the most active seismic part of Crete. The seismological database of this temporary network provides detailed knowledge of the spatial distribution of microearthquakes in the convex (outer) part of the Hellenic arc. Moreover seismological data extracted from the

temporal network installed in Paleohora enriches the earthquake database of the substructure underneath southwestern Crete. Electrical resistivity tomography performed in both Kastelli and Paleohora is used to model the substructure. HVSR technique is used to model the substructure and the surface and subsurface seismic response of Kastelli-Kissamou and Paleohora basins. Geophysical methods used in this proposal to model soil structure and substructure are more flexible in their application as can be performed in various structural topographies and topologies. All the geophysical, earthquake geotechnical and seismological results are compared with the field data of a geological survey. Thus the multidisciplinary approach allows cross-comparison of techniques, resulting in a robust study of the subject matter of this thesis.

### **1.7 POTENTIAL CONTRIBUTION TO FUTURE RESEARCH**

The outcome of this thesis has the potential to significantly contribute to a future detailed seismic hazard scenario and to the seismic risk assessment of the investigated sites of Paleohora and Kastelli regions. The combined approach involving the study of geology, seismology and geophysics disciplines is a robust methodology used in the frame of this thesis and provides the basis for a seismic hazard assessment. A future milestone is the contribution to a future improvement of the deterministic model proposed by Morrato et al., (2007) considering the local site effects and soil classification given in the Greek Eurocode (EC8). The Nakamura (1989, 1996, 1997, 2000, 2000a) technique can be applied to estimate structural building vulnerability indices, to identify vulnerable weak points and to evaluate the damage risk or collapse of various points of the structure. Earthquake building vulnerability response estimation techniques in relationship with the known ground seismic response contributes to the estimation of a ground-building seismic interaction that increases seismic motion intensities and the earthquake damage distribution in the nearby structures. Microearthquake data suggests an ideal case for relocation techniques to precisely delineate activated structures (Becker et al., 2006) near subduction zones. The microearthquake clustering recorded from the temporary network installed southwestern of Crete provides the basis to improve the (1D) velocity model proposed by Papazachos & Nolet (1997). The potential contribution of the thesis to further research milestones is detailed presented in Chapter 6.

## **CHAPTER 2: THEORETICAL BACKGROUND OF THE COMBINED APPROACH - A LITERATURE REVIEW-**

---

### **2.1 LITERATURE REVIEW OF TECTONIC AND GEOLOGICAL SETTING OF CRETE**

In order to provide background to the aims of this study, relevant geological and geophysical literature is reviewed in this Chapter, prior to description of methodology in Chapter 3. The review is divided into several sections below, appropriate to different parts of the literature; the purpose of this Chapter is to inform the reader of the range of available information relevant to this research. The literature review is focused on the studied area in the northwestern and southwestern Crete; the rest of Crete is out of the frame of this thesis and therefore not analyzed in details.

#### **2.1.1 TECTONIC SETTING OF THE HELLENIC SUBDUCTION ZONE**

The study area is presented in Figure 1.1. The Africa plate motion relative to Eurasian plate and the presence of Anatolian, Aegean and Apulian microplates affect the active tectonics of the southern Aegean region and the surrounding area of Greece (Papazachos et al. 1998). The westward drift and counter-clock wise rotation of Anatolia plate due to the northward drive of Arabia results to the southward movement of Aegean towards Africa. Migration of the active margin is confirmed by of neotectonic reconstructions studies (ten Veen & Meijer, 1998; ten Veen & Kleinspehn, 2003). Global positioning system surveys demonstrate that the rate of southwestward movement of Aegean towards Eurasia increases in the southern part (McKenzie, 1970; McKenzie, 1972a; McKenzie, 1972b; McKenzie, 1978; Le Pichon et al., 1995; McClusky et al., 2000). At present times McClusky et al. (2000) proposed that the Aegean plate is moving towards the southwest of the Eurasia with an approximately velocity of 3.0-4.5 cm/a, while the Africa exhibits a northward drift of less than 1 cm/a. The seismic crustal deformation along the convex side of the Hellenic arc is 1.3 cm/yr (Kastens, 1991). This rollback of the subducting African slab leads to the extension in the overriding Aegean plate (Le Pichon & Angelier, 1979; Angelier et al., 1982; ten Veen & Meijer, 1998; Armijo et al., 1992).

The main characteristic of the Mediterranean region is the plate boundary between Eurasia and African plates. The collision of Africa-Eurasia plates forms an inclined seismic zone, the Wadati-Benioff zone or the Hellenic subduction zone, revealed by Papazachos & Comninakis (1970, 1971) based on tomographic studies. The Wadati-Benioff zone follows the convex side of sedimentary arc including western Peloponnese, west of Kythira, south coast of Crete east of Rhodos and dips at low angle  $30^{\circ}$  to the Aegean Sea is characterised by high seismic activity (Papazachos & Comninakis, 1970; Papazachos & Comninakis, 1971; Papazachos, 1990, Papazachos et al., 2000b). In the Aegean region, the front part of the African oceanic lithosphere is subducting under the continental Aegean sea lithosphere as part of the collision process of Africa–Eurasia plates. Earthquake focal mechanisms studies reveal that this convergence creates a parallel extension in the Hellenic subduction zone (Jost et al., 2002; Benetatos et al., 2004). The subduction of the front part of the African oceanic lithosphere under the continental Aegean sea lithosphere as part of the collision process of Africa–Eurasia plates are extensively studied (McKenzie, 1972a; McKenzie, 1972b; McKenzie, 1978; Taymaz et al., 1990, Taymaz et al., 1991; Jackson, 1994; Le

Pichon et al., 1979; Le Pichon et al., 1995; Papazachos & Kiratzi, 1996; Papazachos, et al.; 1998; Papazachos, et al., 2000b; Papadimitriou & Sykes, 2001; Laigle et al., 2004; Karagianni & Papazachos, 2007; Meier et al., 2007; Endrun et al., 2004; Endrun et al., 2008).

In the region of western Crete continent-continent collision is observed in the Hellenic Subduction zone (ten Veen & Kleinspehn, 2003; Meier et al., 2004b). In western Crete the subduction occurs almost normal to the continental margin of the Aegean plate, while subduction becomes oblique towards the east (Le Pichon et al., 1995). The oblique subduction towards central and eastern Crete and the roll back of the downgoing slab (Kahle et al., 1998, Kahle et al., 2000; ten Veen & Kleinspehn, 2003; Bohnhoff et al., 2005; Becker et al., 2006; Meier et al., 2004a) likely formed transtensional (Ionian, Pliny, Strabo, Ptolemy) WSW-ENE trending trenches within the continental Aegean plate in the southeastern Crete that parallel the Hellenic arc. Intense seismicity is observed south of Crete where the plate interface reaches depths of 20 km. North of Crete seismicity is low where the plate interface reaches depths of 40 km (Meier et al., 2007). Higher seismicity rate is observed in the forearc of the Hellenic subduction zone compared to the southern Aegean sea.

Intense shallow earthquake clustering within the forearc delineates NE-SW striking segments of increasing depth from west (100 km) to east (160 km) defining a curved shaped Wadati-Benioff zone (Engdahl et al., 1998; Hatzfeld & Martin, 1992; Knapmeyer & Harjes, 2000; Papazachos et al., 2000b), enhanced by the rollback (ten Veen & Kleinspehn, 2003). The higher seismicity rate (hypocenter of 100 and 150 km) observed in the western part of Hellenic subduction zone compared to eastern part shows that dips westwards from western to the eastern part of Crete (Hatzfeld & Martin, 1992).

Similar observation of the increased angle of the oceanic dip from west to east is reported by Knapmeyer & Hayes (1999). Beneath western Crete the slab dips at  $15^{\circ}$  while beneath eastern Crete at  $19^{\circ}$  (Meier et al., 2004a). Le Pichon et al. (1995) proposed that this subduction becomes more oblique from west towards east. Body and surface wave studies in the Libyan sea south of Crete conducted by Marone et al. (2004) reveal that the segmentation of the subducting slab can be due to the lateral heterogeneity of the Africa plate that enters the Hellenic subduction zone to the south of western Crete (Meier et al., 2004a). The low seismic velocities in the mantle lithosphere to the south of western Crete indicates this continental-continental collision to the south of western Crete (Marone et al., 2004; Meier et al., 2004a), while in the southeastern Crete oceanic crust is subducted south of eastern Crete (ten Veen & Meijer et al., 1998; ten Veen & Postma, 1999b; ten Veen & Kleinspehn, 2003; Marone et al., 2004). Papazachos & Kiratzi (1996) suggested that the major AD 365 earthquake event near the southwestern Crete probably ruptured the plate interface between Africa and Aegean on a lateral extent of 300 km from south of central Crete to  $22^{\circ}$ .

East-west segmentation of the subducting slab in the Hellenic subduction zone and of the overriding Aegean is revealed from tomography results (Papazachos & Nolet, 1997) and from intermediate depth seismicity (Papazachos et al., 2000b). Indicators for this east-west segmentation and lateral heterogeneities of the Aegean are :1) the dip and depth changes of the Wadati Benioff zone (Papazachos et al., 2000b; Becker et al., 2006; Meier et al., 2004a) and of the structure of the Hellenic trench system along the

forearc (LePichon et al., 1995); 2) remarkable uplift in the southern border of the Aegean plate; 3) the lateral heterogeneity within the Aegean plate (receiver function, surface wave and seismicity studies); 4) changes in the position of the southern border of the Aegean lithosphere (seismic studies (Lallemant et al., 1994; Bohnhoff et al., 2001). High uplift rates evident in southwestern Crete are discussed in the following paragraph.

Focal mechanisms studies (Papazachos et al., 1991; Papazachos et al., 1998) also reveal that the convex (outer) Hellenic arc is associated with low angle thrust faults attributed to the collision of Eurasia-Adriatic and to the northward motion of Africa and the subduction along the Hellenic trench. Hatzfeld et al. (1993) using focal mechanisms studies suggested reverse faulting along the Hellenic arc and normal faulting in the southern Aegean region, in the outer arc of the subduction zone. Normal faulting is revealed offshore to the southeast of Crete in the region of Pliny and Strabo trenches (Huchon et al., 1982; Le Pichon et al., 1982; Huguen et al., 2001; Becker et al., 2006).

### **2.1.2 THE UPLIFT OF CRETE**

The uplift of Crete is considered recent and rapid. The geological structure of Crete is characterized by a rather complex pattern of uplifted massifs (Angelier et al., 1982) and subsident basins filled with unconformable Neogene and Quaternary sediments. Neogene marine deposits of Middle Miocene to early Late Pliocene age that have been uplifted up to several hundreds of meters above the present sea-level indicate a rapid uplift (Meulenkamp et al., 1988; Meulenkamp et al., 1994). The rapid uplift is also confirmed by the morphology of the stepped shorelines showing that they developed during a period of almost stable relative sea level and that the changes from one shoreline to another occurred by rapid uplift (Pirazzoli et al., 1996). Angelier et al. (1982) correlated the uplift with underplating of subducted sediments. Numerical modelling proposed by Gerya & Stöckhert (2006) suggest that the material included hydrated material extracted from the subduction are spread out beneath the forearc and progressively growth of part of the lower Aegean lithosphere, leading to sudden uplift of Crete.

Pirazzoli et al. (1982) studied notches that were raised since approximately 5 kyr ago and subdivided Crete into two blocks, the eastern which tilted slightly to the NE during one seismic episode the western block underwent uplift without significant tilting. This uplift was associated with NNW tilting along a ENE-WSW trending axis and probably resulted from friction with the subducting African plate or even the African promontory during southwestward motion of Crete. Pirazzoli et al. (1982) concluded that the uplift in southwestern Crete is related to the AD 365 event. Shaw et al. (2008) proposed that the uplift in western Crete is associated with a fault dipping at about  $30^{\circ}$  within the overriding plate. Meulenkamp et al. (1994) associated the uplift of Crete as the result of friction of the external part of the overriding plate with the subducting African plate. The combination of the late Pliocene uplift and the simultaneous left-lateral strike slip activity suggests that the friction of Crete with the Africa plate was contemporaneous with southwestward motion. The higher rate of tectonic uplift on Crete is observed in western part (Meulenkamp et al., 1994). According to Pirazzoli (2005) the vertical displacements of a sequence of ten rapid small relative sea-level rises without noticeable tilting (10–25 cm each time) between about 4000 and 1500 years BP,

followed a sudden emergence reaching 2.7 m in Antikythira and 9 m in southwestern Crete and a general northwest tilting. The stepped shorelines and the erosional ripple notches are the evidences of the sequence of sea-level changes between about 4000 and 1500 years. Stiros (1996) correlated the uplift with the earthquake in the Hellenic subduction arc of magnitude  $M > 8$ . Pirazzoli (2005) proposed that the isostatic sea level rise modeling should include the rigidity of the second plunging lithosphere slab (Pirazzoli, 2005). Meier et al. (2007) proposed that the uplift of Crete is driven by return flow in the upper portion of the subduction and by material extrusion into the deeper crust. Recently, Shaw et al. (2008) suggested that the assumption that the uplift of southwestern Crete and its surrounding sea floor occurred slowly within few decades of AD 365 and the tsunami that destroyed Alexandria are two events directly connected. Further studies are needed to verify the finding proposed by Shaw et al. (2008) since these two events might be independent, occurred synchronously.

### **2.1.3 TECTONIC EVOLUTION OF NORTHWESTERN AND SOUTHWESTERN BASIN ON CRETE**

In the Aegean region the convergence of African–Eurasian plates formed a Mesozoic-Cenozoic nappe stack and resulted to a complex tectonic region characterized of strong lateral variations (van Hinsbergen et al., 2005). The southward rollback of Africa towards the Aegean and of the associated crustal extension led to a development of a series of sedimentary basins in Crete (Meulenkamp et al., 1979; Fortuin & Peters, 1984; Meulenkamp et al., 1994; ten Veen & Postma, 1999a). In the Hellenic segment of the Alpine orogen, a series of nappes was progressively stacked from north to south (Jolivet et al., 2003; Le Pichon et al., 1982; Meulenkamp et al., 1988).

The series of these nappes are separated by each other by a low angle normal detachment fault (Seidel & Theye, 1993; Jolivet et al., 1994; Fassoulas et al., 1994; Kiliyas et al., 1994), known as the Cretan detachment fault (Ring et al., 2001a; Ring et al., 2001b; Reischmann, 2002). The southward rollback of the African plate since the Late Eocene extended the Mesozoic-Cenozoic nappe stack and formed extensional detachments and exhumed metamorphic core complexes (Jolivet et al., 1994, Jolivet et al., 2003; Ring & Layer, 2003; Ring et al., 2001a, Ring et al., 2001b; van Hinsbergen et al., 2005).

Armijo et al. (1992) proposed that simultaneously to the extension of the Aegean plate (Le Pichon & Angelier, 1979; Angelier et al., 1982; ten Veen & Meijer, 1998) the Hellenic subduction zone is characterized of thrust faults bounded by north-south trending normal faults. The crustal extension formed a low angle normal detachment fault (Cretan detachment fault) cutting through the nappe pile down to a depth more than 30 km. The hangingwall to the Cretan detachment fault underwent minor stretching and the W–E trending half-grabens filled by coarse-grained clastic sediments were formed. Basins in the southwestern Crete represent the footwall of the Cretan detachment fault (Rahl et al., 2004). The sequence of the tectonic process is integrated by: a) the thinning and disintegration of the low-angle detachment fault and b) the exposure of the HP-LT (High Pressure-Low Temperature) metamorphic units of the footwall.

#### 2.1.4 TECTONIC AND GEOLOGICAL SETTING OF TOPOLIA AND LISSOS BASINS IN NORTHWESTERN AND SOUTHWESTERN CRETE BASINS: A MODEL PROPOSED BY SEIDEL (2007)

The purpose of presenting the tectonic model of Topolia and Lissos Basins is the close proximity of these basins to Kastelli-Kissamou and Paleohora basins. Topolia is located 7 km south of Kastelli and Lissos basin is located 7 km from Paleohora. Moreover, microseismicity recorded from local network in southwestern Crete delineates an earthquake clustering extending at about 46 km reaching Lissos basin. For this reason it would be beneficial to gain a better insight of the geometry and sedimentary evolution of both basins. The following paragraph is modified after Seidel et al. (2007).

Seidel et al. (2007) presented the geometry and sedimentary evolution of the supra-detachment Topolia and Lissos basins located in northern and southern Crete. They are the result of this crustal extension and developed between c.20 and 15Ma (Burdigalian-Langhian/Serravallian) (Seidel et al., 2007). Both basins are fault bounded, situated in the hangingwall of the detachment fault and are characterized by subparallel fault block mountains separated by broad alluvium-filled half-graben (Seidel et al., 2007). Both basins Topolia and Lissos can be characterized as half-graben geometry basins bounded by a W-E trending normal fault characterized as alluvial fan, submarine steep-faced and basin-plain environments (Seidel et al., 2007) with typical features of slope-type fan delta (Postma,1990; Prior & Bornhold, 1990). In Figure 2.1 is presented a schematic cross-section of the Hellenic subduction zone and the southern Aegean region in the early to middle Miocene times.

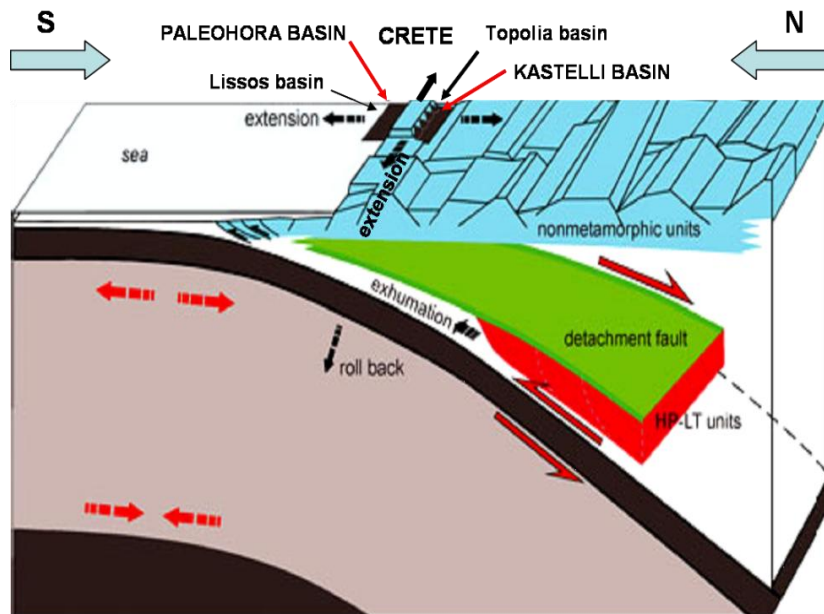


**Figure 2.1:** Cross-section of the Hellenic subduction zone and the southern Aegean region (southern margin of the Aegean microplate) for early to middle Miocene times. The supra-detachment basins Topolia and Lissos in the northern and southwestern Crete are presented. The Kastelli Kissamou and Paleohora half graben basins are presented (modified after Seidel et al., 2007).



#### 2.1.4.1 TOPOLIA BASIN

Topolia Basin is a large scale ( $15 \text{ km}^2 \times 8 \text{ km} \times 500 \text{ m}$ ) basin of a thick alluvial fan deposits covering an area of  $15 \text{ km}^2$  and of width of 8 km. The thickness of the alluvial fan is approximately more than 500 m (Seidel et al., 2007). The geological characteristic that forms the alluvial fan deposits of Topolia is presented in Figure 2.2 by Seidel et al. (2007). Debris flow of very poorly sorted matrix-supported, pebble, cobble and boulder gravel (Seidel et al., 2007) are observed. The coarsest deposits are located in the southern part of the basin, while closer to the catchment, the sediments are mostly debris-flows (Seidel et al., 2007). Limestones, dolomites, and recrystallized limestones are derived from the Tripolitza nappe whiler fossils might correspond to Tripolitza unit (Seidel et al., 2007). Moreover, other types of cobbles, including radiolarites, calcarenites, and micritic limestone are consistent with derivation from the Pindos unit. The oldest sediments of the Tefelion Group belong to the Fotokadhon or Roka Formation (Rahl et al., 2004).

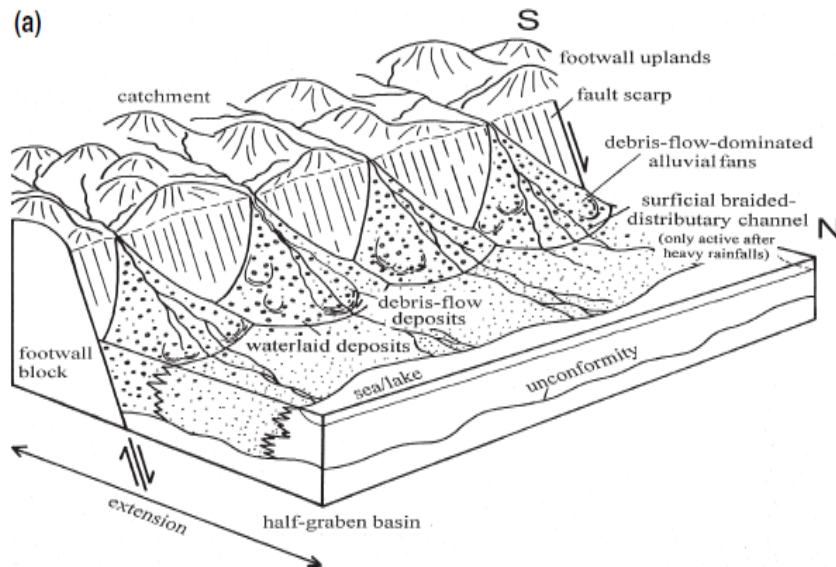


**Figure 2.2:** (a) Schematic figure of the structure of the Topolia basin in the middle Miocene, and the depositional features of the alluvial fans. The fault-scarp of a major normal fault separates the hangingwall block (basin floor) from the footwall block (mountain range) from which the clastic sediments were derived (catchment area) (extracted from Seidel et al., 2007).

#### 2.1.4.2 LISSOS BASIN

The middle Miocene half-graben Lissos basin, located 7 km east of Paleohora, is characterized of sub-aerial, marine debris flow and turbidite deposits as presented in the fault scarp of Figure 2.3 (Seidel et al., 2007). The thickness of the coastal alluvial fan is more than 250 m. Rockfall and debris flow deposits are deposited southern near to the steep-faced slope. Seidel et al. (2007) suggested that western of Lissos the basin fills is Cretaceous dolomites and limestones with rudists that possibly belong to Tripolitza unit or represent huge olistholites.

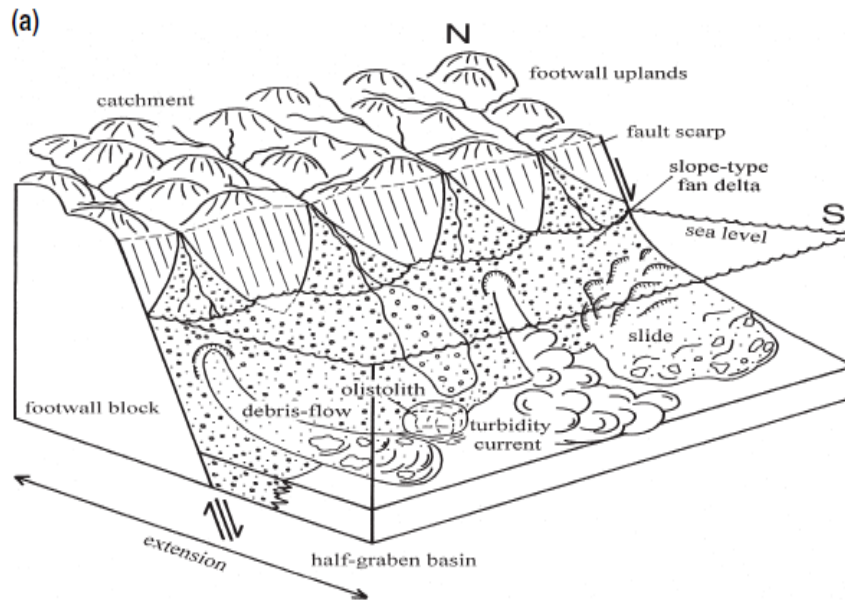


**Figure 2.3:** (a) Schematic Figure of the middle Miocene half-graben, the catchment (footwall uplands) and the depositional features of the coastal alluvial fans in the surroundings of Lissos basin (extracted from Seidel et al., 2007).

## 2.1.5 GEOLOGY OF NORTH AND SOUTH CRETE

In the following paragraphs is presented a brief literature review of the geological setting of the investigated sites. Geological maps of Kastelli and Paleohora basins that contribute to the significance of the research outcomes are presented in Chapter 1, paragraph 1.5.1 and 1.5.2.

Normal faults that bound the lower and upper tectonic unit in northwestern and southwestern Crete are partly covered by the Neogene sediments. Neogene sediments (deposited between c.9 and 5 Ma) overlay breccio-conglomerates older than 9 Myr (pre-Neogene) (or lower Miocene to middle Miocene) (Keupp & Bellas, 2000). In Figure 2.4 (Seidel et al., 2007) is presented the exhumation of Neogene in north and south western Crete. Kastelli Kissamou basin, including Roka and Kera village (northwestern Crete) and Paleohora territory (southwestern Crete) are also presented in Figure 2.4.

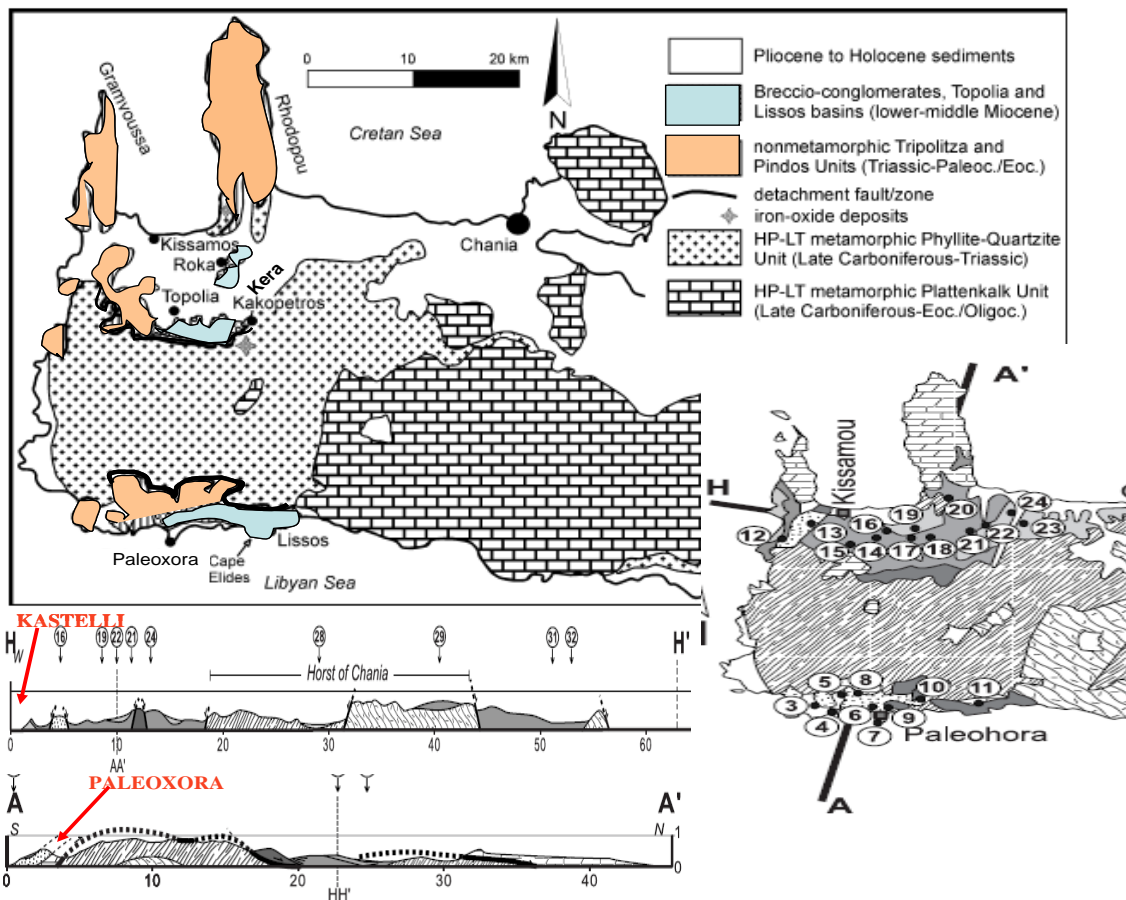


**Figure 2.4:** (Upper) Generalized geological map of western Crete (modified after Seidel et al., 2007, Trypali Unit included in the Plattenkalk Unit). Neogene Topolia and Lissos basins, the underlying tectono-stratigraphic units, and the detachment fault is presented. The Topolia basin is located in the surroundings of the villages of Roka, Topolia and Kakopetros (modified after Seidel et al., 2007) (Lower right): Geological map of Crete where paleobathymetry sections performed on northwestern and southwestern part. The H-H' line represents the WNW-ESE fault. The segment H' is located in the eastern part of Crete and therefore not presented in the Figure. The

*cross-section of site 7 corresponds to Paleohora half-graben basin, site 3 corresponds to Koundoura territory, site 4 corresponds to Grammeno peninsula, site 16 Chairetiana (south of Kastelli) and 18 corresponds to Kera village (extracted from van Hinsbergen, 2006). Lower left Figure: Cross-section of Crete (van Hinsbergen, 2006). The cross section of Paleohora and Kastelli Kissamou are presented. Paleohora half-graben basin and the investigated area Kastelli are characterized of Pindos zone, Lower to Middle Miocene and Upper Miocene to Pliocene, Pindos and Middle to Upper Miocene (extracted from van Hinsbergen, 2006).*

van Hinsbergen (2006) performed paleobathymetry investigations at 75 sites distributed throughout the whole territory of Crete. In Figure 2.4 (upper left) are presented the sites that are directly associated with the aims of the thesis where paleobathymetry sections performed in northwestern (sections: 13-21) and in southern western (sections: 3-11) Crete to determine the depth of the sediments (van Hinsbergen, 2006). Neogene exhumations in the northern and southern part of western Crete is divided by a WNW-ESE striking antiform fold (Meulenkamp et al., 1988; Kiliyas et al., 1994; ten Veen & Postma, 1999a) that is crosscut by a complex mosaic of normal faults that formed basins throughout the late Neogene, presented on Figure 2.4 (upper left). Faults in the western part of Crete have a NW-SE predominant direction (Angelier et al., 1982).

#### **2.1.5.1 GEOLOGY OF NORTHWESTERN CRETE**

The horsts of northwestern Crete are bounded by N-S striking normal faults implying late Tortonian to early Messinian E-W extension (Rahl et al., 2004). Angelier et al. (1982) performed field measurements of outcropping faults and studied the geometry of the slickenside lineations and proposed an E-W distribution of fault strikes in the western Crete. The upper Tortonian southern marginal calcarenites of the Kissamou basin reveal tapering features indicating syn-sedimentary tilting (van Hinsbergen, 2006). This tilting possibly occurred synchronously with subsidence of the basin due to the E-W extension, active with approximately N-S compression (van Hinsbergen, 2006). The extent of the iron-oxides in Rabdouxa region northwestern Crete related with the large scale extensional low angle shear zone indicates fluid flow circulation at a regional scale and at shallow crustal level depths (Seidel et al., 2005)

Paleobathymetry sections in northwestern Crete (van Hinsbergen, 2006) reveal deep depositional sedimentation. Chairetiana (section:16 on Figure 2.4) presents 463 m depositional depth, Kera (section:18 on Figure 2.4:upper left) (Upper Tortonian to late Messinian) presents 624 m depositional depth, Kaloudiana (section:19 on Figure 2.4:upper left) (Late Pliocene) presents 1039 m depositional depth and Nokhia (section: 20 on Figure 2.4:upper left) (Upper Tortonian to late Messinian) presents 636 m depositional depth. Northwestern Crete was subdivided by Meulenkamp et al., (1979) into the Kissamou and Voukolies basins, separated by the Roka /Kera ridge (Rahl et al., 2004). Kera fault is a NE-SW oriented bend in an N-S fault system along the Spatha peninsula with a left lateral strike-slip component (strike:  $0.36^{\circ}$ NE, dip:  $70^{\circ}$ NW, rake:  $20^{\circ}$ SW, after Mouslopoulou et al., 2001). Kera fault extending along a segment of 5 Km is presented in Figure 2.5 (upper left) (Mouslopoulou et al., 2001). On Kera fault, Mouslopoulou et al., (2001) identified seven sedimentary units. The identified units are presented in Figure 2.5.

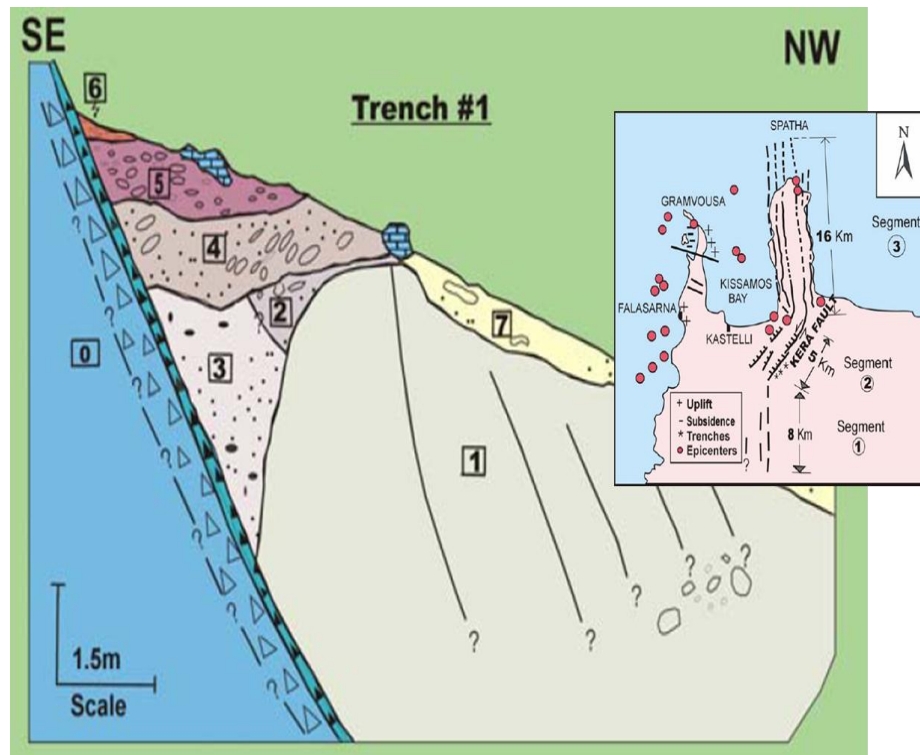


**Figure 2.5:** Seven sedimentary units on Kera fault (unit 0: limestones, unit 1: marls, unit 2 and unit 3 are recognized during the logging of the trenches, unit 4: conglomerates, unit 5: material composed of limestones, marls and conglomerates, unit 6: fine conglomerate clasts and unit 7: thin dark colour soil covering (Mouslopoulou et al., 2001). Right upper: Map showing the study area in Kera Fault (5 Km) is located in the second segment with an NE-SW orientation Kastelli; The three active segments on Spatha peninsula in a N-S fault system. The uplift (+) and subsidence (-) motion of Gramvousa is presented. Red circles present earthquake recordings provided by NOA (extracted from Mouslopoulou et al., 2001).

Mouslopoulou et al., (2001) used the surface fault's length and estimated the paleoearthquake minimum magnitude of Kera fault. The N-S fault system consisting of three segments can infer an earthquake magnitude of ( $M=6.7\pm0.05$ ). The major outcome of the survey conducted by Mouslopoulou et al., (2001) is that Kera fault can cause an earthquake of magnitude  $M=5.9\pm0.2$ . Segments 1<sup>st</sup> and 2<sup>nd</sup> (13 km fault length, on Figure 2.5) the magnitude is calculated  $M=6.3\pm0.1$  and along the 2<sup>nd</sup> and 3<sup>rd</sup> (21 km fault length) the minimum magnitude is calculated  $M=6.6\pm0.2$ . Three earthquakes in 1980, 1987 and 1988 with magnitudes ranging from 4.5-5.2 are associated with Kera fault and three small offshore events in 1999 are probably associated with Kera N-S fault system along Spatha peninsula confirming that the study area can generate earthquakes of significant magnitude. Mouslopoulou et al., (2001), concluded that the 30 Km N-S fault system along Spatha peninsula can generate earthquake of magnitude ranging from 6.0 to 6.7. The average slip rate of the last three Holocene events is 0.63 mm/year, taking account that the initial Kera scarp height is 6.3

m (Mouslopoulou et al., 2001). Moreover, paleoseismological analysis based on the deposition of the colluvial wedge sediments, by Mouslopoulou et al., (2001) on two trenches along the Kera fault provide evidences of five tectonic deformational events. The first two correspond to an Upper Cretaceous-upper Miocene deformation period while the two breccias of the fault surface indicate a series of tectonic deformational episodes. The remaining three identified tectonic events are interpreted as individual paleoearthquake possibly in Quaternary/Holocene as indicated by the unconsolidated colluvial wedges of the fault scarp. The last tectonic event may be associated with historical earthquake events. Andreou et al. (2001), incorporating paleoseismological data (Mouslopoulou et al., 2001) associated the parameters of the Kera fault zone with the subduction of the Benioff zone.

### **2.1.5.2 GEOLOGY OF SOUTHWESTERN CRETE**

In the southwestern Crete large isolated blocks of Upper sequence (Tripolitza unit or Prina Group conglomerates (Profile A-A' in Figure 2.4) overlay the Lower Sequence of the Neogene. The Prina Group contains the oldest Neogene rocks (Topolia breccias: Meulenkamp, et al., 1979) that unconformably overlie dominantly the Tripolitza unit (Rahl et al., 2004).

Deep marine sections and paleobathymetry sections in southwestern Crete are presented by van Hinsbergen (2006). The depositional depth of the sediments in Koundoura territory (3), Grammenos (4), Paleohora (6) and Paleohora campsite (9) extracted by paleobathymetry sections is 36 m, 935 m, 775 m and 136 m, respectively (van Hinsbergen, 2006). In the gorge of Anidri (10), few metres of Topolia breccias that grade into shallow marine sands and marls (assigned to the Tefelion Group overlay limestone formation. van Hinsbergen (2006) comparing the continuous profile of short, deep marine sections Grammenos (section: 4) Paleohora (section: 6), Sellino (section: 7) and Voutas (section: 8) into the shallow marine sediments near Anidri (section:10) on Figure 2.4 (upper right), suggests that the subsidence continued in the late Serravallian or early Tortonian to reach deep marine conditions. In southwest near Paleohora formations of Prina group exist (Fortuin & Peters, 1984). In Koundoura (west of Paleohora) a swarm of wave-cut terraces are exposed in the northern part and formed as a result of sea-level fluctuations (eustasy) and/or to elastic deformation related to the earthquake circle (Rahl et al., 2004). The beach-rock of Paleohora is composed of cemented conglomerate and sand and contains cobbles derived from the adjacent Cretan nappes (Phyllite-Quartzite and Tripolitza) (Rahl et al., 2004).

## **2.2: LITERATURE REVIEW OF SEISMICITY STUDY OF THE STUDIED AREAS IN NORTHWESTERN AND SOUTHWESTERN CRETE**

### **2.2.1 SEISMOLOGICAL NETWORK ON CRETE AND SURROUNDING AREA**

In 1965 a Wood-Anderson seismograph (2 horizontal components) was installed in the village Vamos in the northwestern Crete east of Chania and during July 1973 a new station was installed in Neapolis (Eastern Crete) (Papazachos & Papazachou, 1997). In 1994 a new digital station, part of the Mediterranean Network (MEDNET), was installed by INGV (Rome) in Anogia (north-central Crete) operating from 1995 until 1999. Since 1998 up to now the Geodynamic Institute of the National Observatory of Athens and the Seismological Laboratory of the University of Athens and the seismological centres of the Geophysical Laboratory of the University of Thessaloniki have installed several permanent and temporary seismometers in the whole territory of Crete. Temporary seismometers in the northern and southern part of Crete have also been installed by (Hatzfeld et al., 1989; Scordilis et al., 1995 and Meier et al., 2004a). Several temporary short period networks have been installed on the islands of Crete and Gavdos to study the distribution of microseismic activity of the region.

### **2.2.2 EARTHQUAKE DATABASE OF GREECE AND SURROUNDING AREA**

Up to the middle of the nineteenth century earthquake events are derived from historical, paleoseismological and archaeoseismological studies (macroseismic effects destructions of buildings, ground changes, tsunamis) after strong shocks (Papazachos & Papazachou, 2003). In the 20<sup>th</sup> century seismicity studies were mainly based on data from earthquake catalogues comprises macroseismic effects and epicentres of earthquakes of the Aegean region. Earthquake data catalogues for the Cretan region and the surrounding Aegean region are provided by the seismological centers of Geodynamic Institute of the Observatory and the Geophysical Laboratory of the University of Thessaloniki. Papazachos & Papazachou (1997) presented the distribution of epicenters of known strong  $M \geq 6.0$  shallow ( $h=0-60$  km), intermediate depth and deep (61-300 km) earthquakes, which have occurred in the broader Mediterranean area during 1901-2002.

During the last four decades earthquake catalogues included the basic focal earthquakes parameters of the area of Greece (Galanopoulos; 1960; 1961; 1963; Karnik, 1969; 1971; Makropoulos, 1978; Makropoulos & Burton, 1984; Papazachos & Comninakis, 1982; Comninakis & Papazachos, 1972; Comninakis & Papazachos, 1978; 1986; 1989; Makropoulos et al., 1989; Papazachos & Papazachou, 1997; Papazachos et al., 2000a). Papazachos & Papazachou (1997), presented the time variation of the number of earthquakes derived from historical data, destructive earthquakes in the area of Greece since 550BC up to AD 1990 (Fig. 2.6). The total number of studied strong earthquakes during this period is 270 ( $M \geq 6.0$ ).

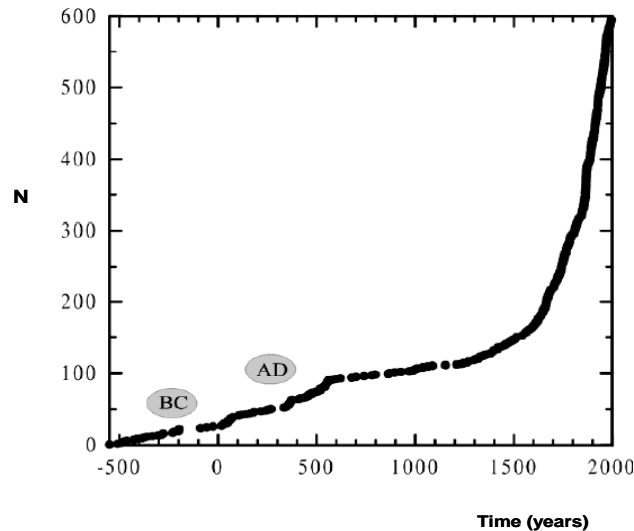


**Figure 2.6:** Time variation of known strong earthquakes ( $M \geq 6.0$ ) in Greece since 550 BC up to AD 1990 (Papazachos & Papazachou, 1997). The vertical scale of this graph corresponds to the number of earthquakes. During the first time interval spans from the sixth century BC until the middle of the sixteenth century (550 BC - AD 1550) information exists for a total number of about 150 strong earthquakes. For the second time interval from the middle of the sixteenth century up to the middle of the nineteenth century (1550-1845), the total number of recorded earthquakes of this interval is about 170. The third time interval covers the period 1845-present and is divided into three phases (AD 1845-1928, 1928-1964, 1964-2000).

### 2.2.3 SEISMICITY AND MICROSEISMICITY STUDY OF THE HELLENIC SUBDUCTION ZONE

Microseismicity study in the frame of this thesis is an attempt to image seismogenic zones beneath the forearc using earthquake data acquired from a local network. The contribution of data in the forearc is highlighted by Meier et al. (2007). Spatial-temporal earthquake recordings are used to: 1) compare the seismic activity of northwestern and southwestern Crete and 2) delineate active fault zones that contribute in site effects study and in the seismic hazards of the studied areas in northwestern and southwestern Crete. Microseismicity study is divided into two sections:

- i) the usage of a new seismic network of permanent seismic stations installed in the whole territory of Crete to determine faults and to verify the existence of those already known. The microseismicity study in the frame of this thesis is focused in the estimation of reliable P and S time arrivals and accurate earthquake hypocenter localization.
- ii) the usage of a new local seismological network of three short period seismological stations installed in southwestern Crete to detect seismic activity that may be related to faults within seismogenic regions.

In the following is presented a brief review of the seismicity studies conducted in the region of the Hellenic subduction zone. In recent years, due to the recognition of crucial issues derived from earthquakes many seismicity research studies have been performed. The extent catalog of historic catalogues of Crete and the Hellenic



subduction zone spanning the last 2500 years (Papazachos & Papazachou, 1997), global catalogues, microseismicity studies of the forearc of Crete (Hatzfeld et al., 1993; Delibasis et al., 1999; Meier et al., 2004a; Becker et al., 2006) comprise the available earthquake data for the spatial and temporal seismicity study of Crete and Hellenic subduction zone.

Makris (1973, 1976, 1978) and Makris & Veis (1977) conducted deep seismic sounding in the Aegean area and proposed for the Aegean and southern Aegean (forearc of the Hellenic subduction zone) an average crustal thickness between 30-44 km and 20-25 km, respectively. Similar results for the crustal thinning are presented by Delibasis et al. (1988), Bohnhoff et al. (2001). Papazachos (1994), Papazachos et al. (1995) using travel time arrivals of regional and local earthquakes concluded to similar results for crustal thickness. The velocity structure of the whole Aegean region is evaluated from tomography studies (Papazachos & Nolet, 1997; Karagianni et al., 2002, Karagianni et al., 2005). The evaluated velocity structure of the whole Aegean region is used in earthquake hypocenter studies.

Hypo71 software has been used in seismicity studies to accurately identify the Wadati-Benioff zone of the Hellenic arc (Papazachos, 1990; Papazachos et al., 2000b) and the seismicity and microseismicity of Crete (Meier et al., 2004a; Becker et al., 2006). For the determination of the location of regional earthquakes velocity model was proposed by Papazachos et al. (2000b). The aforementioned velocity model is based on a model using tomographic results for the Aegean area proposed by Papazachos & Nolet (1997). Papazachos et al. (2000b) used a velocity ratio  $V_p/V_s$  equal to 1.78 to define the geometry of the Wadati-Benioff zone.

Accurate hypocenter location of intermediate depth earthquakes using the difference in arrival time at the seismological station reveals the Wadati-Benioff zone (Papazachos et al., 2000b) based on tomography studies proposed by Papazachos & Nolet (1997). Papazachos & Nolet (1997) based on tomography results calculated P and S wave velocity distribution in the Aegean area using a non-linear inversion of travel times to model the regional 3D structure of the crust and uppermost mantle (up to 160 km).

According to Papazachos et al. (2000b): 1) the mean Epicenter Error (ERH) equal to  $mERH=2.5\pm 2.5$  km, 2) the average depth error (ERZ) equal to:  $mERZ=2.7\pm 2.4$  km and 3) the RMS (**R**oot **M**ean **S**quare) errors of the travel times obtained from the location process smaller than 1.2 s, do not necessarily correspond to the 'true' error estimates. These values are only a valid indicator that the focal coordinates of the earthquakes, located by the local network data are of high accuracy and can be used for the purposes of study. In Figure 2.7a is presented the spatial distribution of the earthquake foci in the central part of the arc where dipping of the Wadati-Benioff zone starts (point B Figure 2.7a) in the convex side of the arc under the Hellenic trench. In Figure 2.7b is presented the cross-section of the earthquake foci along the line ABCD. In the convex (outer) arc beneath or very close to the Hellenic trench, strong intermediate depth earthquakes with relatively large focal depths ( $h > 100$  km) occur, denoted by solid triangles in Figure 2.7b (located in distances 350-400 km in the cross-section). Point B is located in southwestern Crete, which is near the study area of this thesis. In Figure 2.7a is presented the comparison of the seismicity in the southwestern and northwestern part of Crete. The southwestern part of Crete is

characterized of shallow and strong earthquakes while the northwestern part of intermediate and strong magnitude earthquakes.

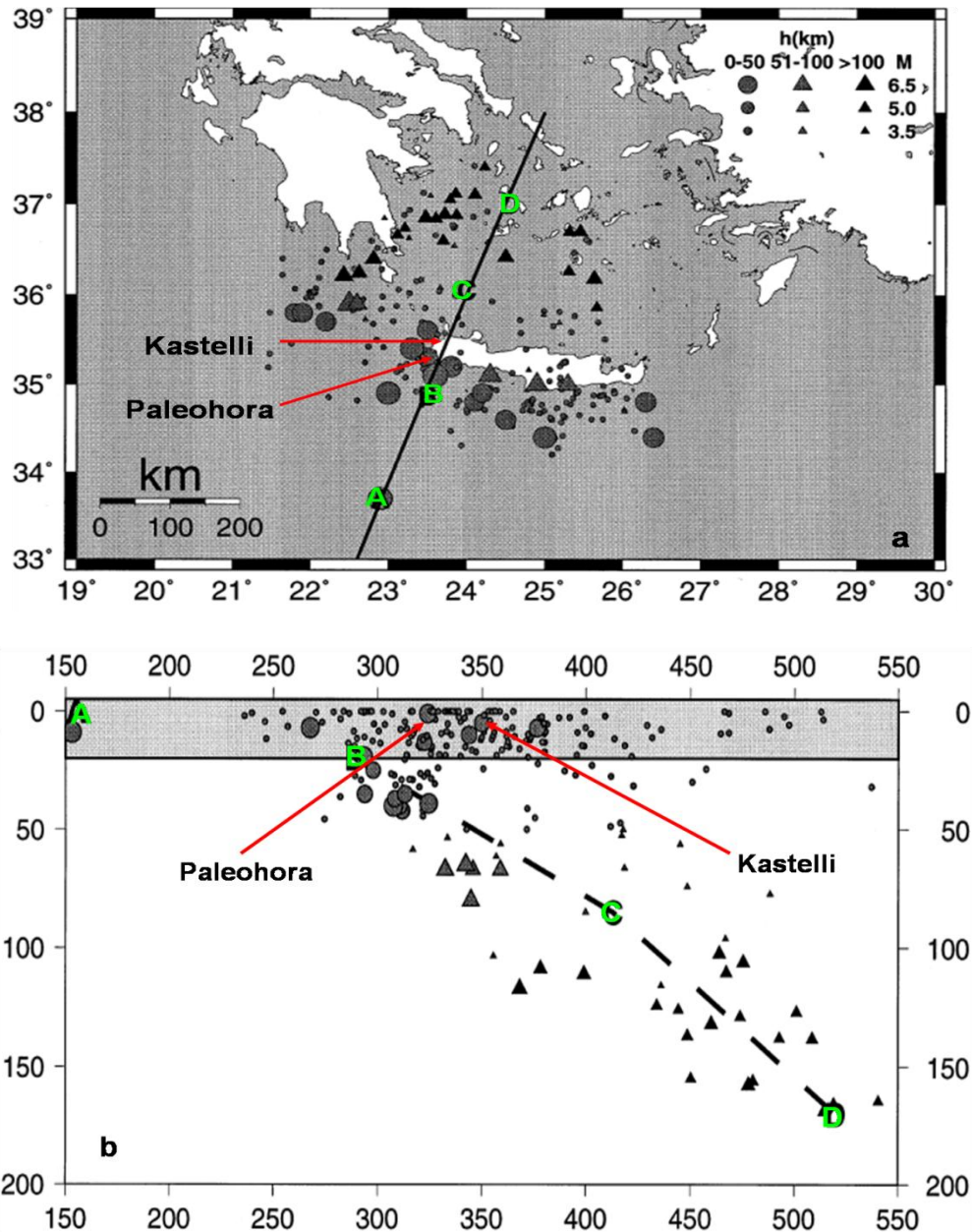


**Figure 2.7:** **a)** Spatial distribution of the earthquake foci in the central part of the arc where dipping of the Wadati-Benioff zone starts (point B Figure 2.7a) in the convex side of the arc under the Hellenic trench, **b)** Cross-section of the earthquake foci along the line ABCD. In the convex (outer) arc beneath or very close to the Hellenic trench, strong intermediate depth earthquakes with relatively large focal depths ( $h > 100$  km) occur, denoted by solid triangles. Point B is located in southwestern Crete, which is near the study area of this thesis (modified after Papazachos et al., 2000b). The relative location of Kastelli and Paleohora in the northwestern and southwestern Crete in respect to the spatial distribution is presented.

North of Crete strong and intermediate depth (70-300 km) earthquakes are observed. High shallow seismicity ( $h < 20$  km) is observed in the southwestern convex (outer) side of the arc (Ionian Sea) due to the fast southwestward motion of the Aegean plate. Strong intermediate earthquakes ( $h > 100$  km) in the fore-arc area of the southwestern part of the Hellenic arc are reported. This earthquake clustering indicates a thinning of oceanic crust in this part of the Hellenic trench due to roll-back of the descending lithospheric slab (Papazachos et al., 2000b). Karagianni & Papazachos (2007) evaluating the S-wave velocity structure of the Aegean confirmed the presence of a thin crust typically less than 28–30 km in the whole Aegean sea, which in some parts of the southern and central Aegean sea becomes significantly thinner (20-22 km).

In southcentral and southeastern Crete medium magnitude and shallow depth earthquake are reported. Similar results for southcentral and southeastern Crete are reported by Becker et al., (2006) and Meier et al., (2007). In the Ionian trench low seismicity is observed (Meier et al., 2004a). Seismicity in the northeastern part of Crete is much strongest than the northwestern part of Crete. In the eastern part of the Hellenic arc where deep earthquakes occur ( $100 < h < 180$  km) the combination of a free sinking of an oceanic lithosphere slab and the lack of strong coupling is the reason for no earthquakes with magnitude up to 7.0 (Papazachos et al., 2000b) occur. In the following is presented a brief review of microseismicity studies on Crete. Microseismicity studies are proposed to image seismogenic zones within seismically very active region (Deshcherevsky & Zhuravlev, 2004). Despite the recording time span to only few months is efficient to model to geometry of seismic faults and plate contacts even when was operated for only few weeks or months (Meier et al., 2004). An amphibian seismological network operated for 8 days in southeast Crete to study microseismicity (Kovachev et al., 1991a; Kovachev et al., 1991b; Kovachev et al., 1992). Becker et al. (2006) used an amphibian network installed in southcentral and southeastern Crete for microseismicity study.

Several microseismicity studies based on earthquake data from temporary dense seismic networks have been performed in the Cretan region (Hatzfeld et al., 1993; de Chabaliér et al., 2007; Delibasis et al., 1999; Igarashi et al., 2003; Becker et al., 2006; Meier et al., 2004; Meier et al., 2007; Bohnhoff et al., 2006). Intense interplate seismicity is observed to south of Crete at depth of 20km compared to north of Crete (Meier et al., 2007). Microseismically active zone south of western (southeastern Crete reaches to a depth of 100 km (Meier et al., 2004) that may associated with the fault plane of the 8.3 magnitude AD 365 earthquake. The length of the activated segment of a fault in southeastern Crete estimated from paleoseismological studies is approximated at 200 Km (Pirazzoli et al., 1982; Stiros, 2001). Hatzfeld et al. (1993) studied microseismicity of the forearc and Delibasis et al. (1999), and Meier et al. (2004b) observed seismic activity in the southcentral and southeastern offshore Crete. Meier et al., (2004a) reported an offset between the southern border of the Aegean lithosphere and the southern border of active interplate seismicity. Meier et al. (2007) proposed a new model for the Hellenic subduction zone based also on seismological studies.

Hatzfeld et al. (1993) estimated a  $V_p/V_s$  velocity ratio equal to 1.79 and de Chabaliér et al. (2007) a velocity  $V_p/V_s$  ratio equal to 1.80 for the Aegean area. Becker et al. (2006) used an amphibian network that covers the trench system in the central and eastern Crete to study microseismicity. Becker et al. (2006) used Hypo71 and a

velocities model ( $V_p/V_s=1.78$ ) based on refraction seismic studies (Bohnhoff et al., 2001) and receiver function and surface dispersion studies (Endrun et al., 2004) to study the effect of the slab and of the thick sedimentary layer in the southern part of the amphibian network. The proposed 3D velocity model did not perform better than the 1D velocity model due to the insufficient knowledge of the velocity structure in the off-shore region.

Meier et al. (2004a) observed intense microseismicity in the southcentral Crete. Spatio-temporal clustering of microseismicity in the central forearc of the Hellenic subduction zone in the area of southeastern Crete is investigated by Becker et al. (2006). The hypocenter estimator is lower in southwestern offshore Crete due to the fact that these events are far outside the networks. A southward microseismicity dipping zone pattern to a depth of 40 km is formed in the southcentral Crete. The southern and northern interplate seismicity in the region of Strabo reaches depths of 20 km and 40 km, respectively. The swarm like earthquake cluster observed by Becker et al. (2006) in southcentral and southeastern Crete from an amphibian network was not attributed to a main earthquake and a power of law distribution of the inter-event times was observed. Becker et al. (2006) performed relocation techniques based on P–S travel time difference derived from waveform cross-correlations to accurately relocate the initial hypocenter. This study of Becker et al. (2006) suggests the possible correlation of the observed microseismicity in southcentral and southeastern Crete with fluids transported along the plate interface escaping towards the surface through zones of crustal weakness. Becker et al. (2006) concluded that the shallow plate contact in the southwestern Crete was recently coupled with strong seismic activity (magnitudes up to 6) and can generate larger earthquakes.

Seismological studies and focal mechanism studies (Papazachos & Delibasis, 1969; McKenzie, 1970; McKenzie, 1972a; McKenzie, 1972b; McKenzie, 1978; Taymaz et al., 1990; Taymaz et al., 1991; Papazachos et al., 1991; Papazachos et al., 2000b) reveal that the outer arc is characterized of thrust faulting due to the convergence and relative motion between the Aegean and eastern Mediterranean plates. Parallel to the Hellenic arc shallow strike slip faulting with thrust components are evident while normal and thrust faulting bound north of Crete (Kiritzi & Papazachos, 1995; Papazachos & Kiritzi, 1996).

## **2.3 LITERATURE REVIEW OF EARTHQUAKE GROUND MOTION: SITE EFFECTS AND SEISMIC GROUND RESPONSE**

The following sections provide a comprehensive overview of the relationships between seismic ground response and surface structures in general and local situations. The purpose is to demonstrate the complexity that exists in local settings, so that the results of ground movement may be very different even within a relatively small area of a landscape upon which buildings are constructed. In the frame of this thesis the effect of surface geology on seismic ground motion and the importance of the effect of subsurface structure (faults and lateral subsurface heterogeneities) located in a close proximity to urban installation on seismic ground motion are discussed and briefly presented.

### **2.3.1 INFLUENCE FACTOR OF SEISMIC MOTION**

Seismic ground response evaluation due to geological and subsurface structure (site effects) is a necessity in microzonation studies and of paramount importance in seismic hazards estimation (Reiter, 1990; Field, 2000; McGuire, 2001; Steimen, 2004; Morrato et al., 2007). Active (seismic wave methods, downholes, drillings) and passive methods (surface wave methods such as SSR, HVSR) are used in seismic site characterization studies. Surface ground recordings for seismic site characterization in microzonation studies is a flexible and low cost tool to determine seismic ground response mostly in urban areas. The dynamic characteristics of the seismic motion recorded at a specific site in the surface include the source effects characteristics, the dynamic travel path characteristics and the dynamic characteristic of the surface layer at the investigated site. The geological and tectonic factors that influence the seismic ground motion response are: a) the fault rupture characteristics (source effects), b) the travel path effects and c) the local site effects, presented in Figure 2.8.

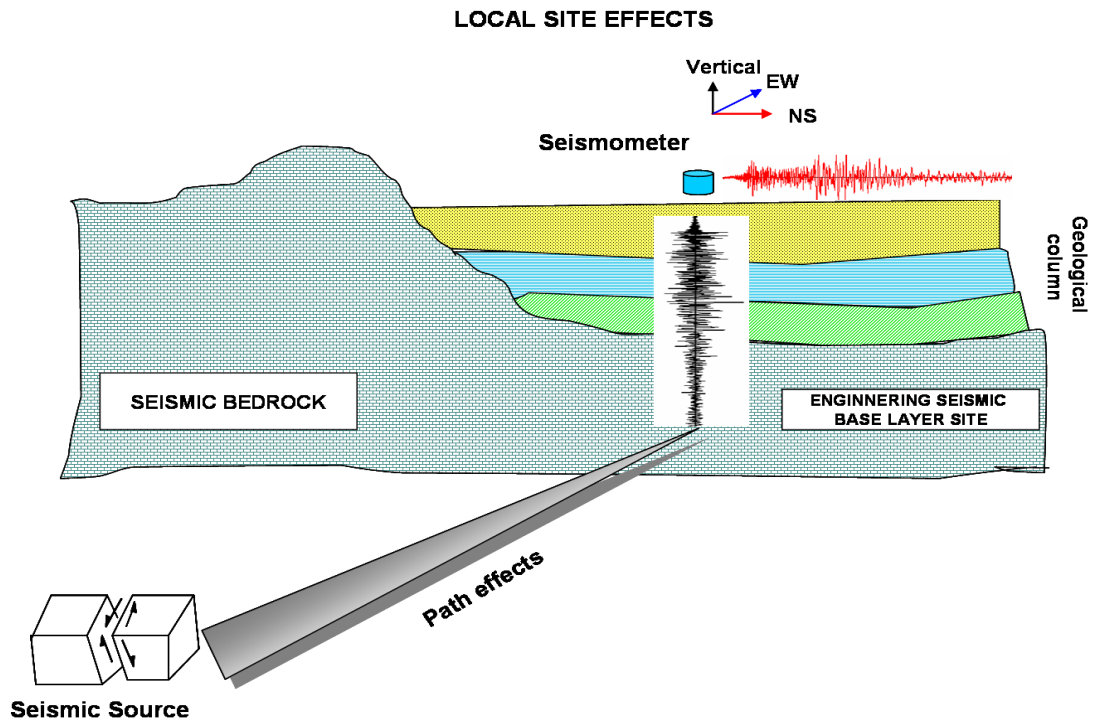


**Figure 2.8:** Site effects on seismic ground motion response. Source effects, travel path effects from fault to ground surface and local site effects are presented (modified after Murono, 1999).

The fault rupture characteristics (source effects), the travel path effects and the local site effects are directly interrelated as a convolution function  $r(t)$  recorded at one single seismological station. The convolution function describing the factors that influences the seismic motion (Andrews, 1986; Bard, 1999) is given by the equation (2.3.1)

$$r(t) = e(t) * p(t) * s(t) \quad (2.3.1)$$

where  $e(t)$  is the source function,  $p(t)$  is the function of the travel path and  $s(t)$  is the site effects function. The frequency content of ground motion assesses the resonance response of geological structures. The ground motion frequency characteristics are well defined by the Fourier response spectrum. The Fourier spectrum of a record at a single station is given by the equation (2.3.2):

$$R(f) = E(f) \cdot P(f) \cdot S(f) \quad (2.3.2)$$

where  $R(f), E(f), P(f), S(f)$  are the Fourier transforms of the functions  $r(t), e(t), p(t), s(t)$ , respectively.

### **2.3.1.1 THE FAULT RUPTURE EFFECT (SOURCE EFFECT) ON SEISMIC GROUND MOTION**

In the frame of this thesis the fault rupture zones (source effects) underlain sedimentary/alluvial basin considerably affect seismic ground motion. The determination of fault zones in northwestern and southwestern Crete are presented in Chapter 4 and discussed in Chapter 5. In the following are briefly discussed the fault rupture effects on seismic motion. The fault rupture characteristics that affected the ground motion behaviour are the stress drop, the total fault displacement, the length of the fault break, the nature of the rupture process, the proximity of the fault plane to the ground surface and the fault shape. Fault mechanisms and directivity are the most important factor that affects ground seismic response. Near field strong motion recordings after Loma Pieta earthquake (1989), Northridge (1994), Hyogoken Nanbu earthquake (1995) confirm the significance of near source effects in seismic design structures located about 10 km from the rupture zone. The faulting type also affects the earthquake damage distribution. Reverse thrust type earthquakes induce higher horizontal accelerations at site located above the faulting zone (Campbell, 1985; Sen, 2007). Seismic ground acceleration and velocity increase when the dip of the fault decreases. In such cases the strain relief is higher and causes large seismic wave amplitude. The distribution of seismic intensities of the AD 1953 earthquake in Ker County of California along the fault edge-ends is due to the seismic wave propagation fault rupture in the direction of the rupture. The high seismic intensities (high frequency seismic wave) distribution is observed along the direction of the fault rupture (Yamamoto, 2002). Directivity describes the seismic wave release associated with the rupture direction and velocity. The single direction and the bi-lateral rupture affect the duration of ground shaking and the earthquake damage distribution (Loma Pieta earthquake, 1989; Hyogoken Nanbu earthquake, 1995). Consequently, the site effects due to or near to a rupture fault zone amplify the earthquake motion causing excessive damages.

### **2.3.1.2 THE INFLUENCE OF TRAVEL PATH ON SEISMIC GROUND MOTION**

Earthquake events involve release of strain energy accumulated in the focal area and of the propagation of a part of energy released in the surrounding rock (Nakamura, 1989). The effect of seismic travel path on earthquake seismic motion is related to the seismic wave amplitude attenuation propagating from the seismotectonic source to the recording station. The important outcome discussed in the frame of this thesis related with travel path effects is: 1) the determination of the effect of the direction of fault zones on seismic motion in populated area, 2) the effect of lateral heterogeneities in the velocity model of the Aegea proposed by Papazachos et al. (2000b).

It is well stated that the seismic wave amplitude decreases as the distance source from the seismotectonic source to the recording increases (Stein & Wysession, 2003). The travel path effect on seismic motion is summarized on the following:

1. The total energy over a wavelength of a volume is proportional to the square of the amplitude and frequency (Stein & Wysession, 2003). Important outcome in site effects studies is that waves of the same amplitude the higher frequency waves transmit more energy.

$$Et = \frac{1}{2} A^2 \omega^2 p = \frac{A^2 2\pi^2 \rho}{T^2} \quad (2.3.3)$$

2. The seismic wave amplitude decreases with distance from source (Papazachos, 1996) is given by the equation.

$$\frac{A_1}{A_2} = \frac{r_2}{r_1} \quad (2.3.4)$$

To provide a better understanding of the physical mechanisms describing the amplitude decrease as the seismic wave propagates through geological materials the strain potential energy from source (fault) to the recorded site is presenting. Considering the simple case of a spring that extends in the x direction the potential energy to extend the spring at dx is determined according to equation (2.3.5). The strain energy accumulated in a volume (dV) is the sum of the stress and strain components (equation 2.3.6).

$$E = \frac{1}{2} kx^2 \quad (2.3.5)$$

$$E = \frac{1}{2} \int \sigma_{xy} e_{xy} dV \quad (2.3.6)$$

where  $\sigma_{xy}$  and  $e_{xy}$  describe the strain and stress of the volume.

The harmonic wave wave equation is given (Stein & Wysession, 2003) by the equation (2.3.7)

$$u(x, t) = A \exp[i(\omega t - kx)] \quad (2.3.7)$$

Considering the symmetricity of a strain tensor it is extracted that the nonzero strain components is given by the equation 2.3.8

$$e_{xy} = e_{yx} = \frac{1}{2} \frac{\partial u_y}{\partial x} = -\frac{1}{2} ika \exp[i(\omega t - kx)] \quad (2.3.8)$$

The shear stress and strain are described by the rigidity  $\mu$

$$\sigma_{ij} = 2\mu \varepsilon_{ij} \quad (2.3.9)$$

The nonzero stress components (Stein & Wysession, 2003) considering equation (2.3.9) and the symmetricity of the stress tensor are given by the equation (2.3.10).

$$\sigma_{xy} = \sigma_{yx} = -ik\mu A \exp[i(\omega t - kx)] \quad (2.3.10)$$

The strain energy per unit area of wave front averaged over a wavelength in the propagation direction considering the Lamé constants  $\mu$ ,  $\lambda$  ( $\mu = \beta^2 \rho$ ,  $\beta = \lambda/T$ ) is given by the equation (2.3.11)



$$E = \frac{1}{2\lambda} \int_0^\lambda k^2 A^2 \mu \sin(\omega t - kx) dx = \frac{1}{4} A^2 \mu k^2 = \frac{1}{4} A^2 \omega^2 \rho \quad (2.3.11)$$

The total energy averaged over a wavelength is the sum of the kinetic and the strain energy and is given by the equation (2.3.12)

$$Et = \frac{1}{2} A^2 \omega^2 \rho = \frac{A^2 2\pi^2 \rho}{T^2} \quad (2.3.12)$$

The average energy flux in the propagation direction is found by multiplying by the S velocity (Stein & Wysession, 2003). The total energy and flux are proportional to the square of the amplitude and frequency resulting that for waves of the same amplitude the higher frequency waves transmit more energy (Stein & Wysession, 2003).

Considering  $A_1$  and  $A_2$  the amplitude of seismic waves through spherical cells located in a distance  $r_1$  and  $r_2$  from the rupture source and  $E_1$  and  $E_2$  the total energy averaged over a wavelength per unit area, the principle of energy conservation suggest that equal total energy is propagated through each cell (Papazachos, 1996). The principle of energy conservation is given by the equation (2.3.13) and (2.3.14).

$$4\pi r_1^2 E_1 = 4\pi r_2^2 E_2 \quad (2.3.13)$$

or

$$4\pi r_1^2 \left( \frac{2\pi \rho A_1^2}{T^2} \right) = 4\pi r_2^2 \left( \frac{2\pi \rho A_2^2}{T^2} \right) \quad (2.3.14)$$

It is derived from equation (2.3.14) that the amplitude of seismic waves is decrease with increase the distance from the source. The amplitude decrease with distance from source (Papazachos, 1996) is given by the equation (2.3.15).

$$\frac{A_1}{A_2} = \frac{r_2}{r_1} \quad (2.3.15)$$

According to Reiter (1990) the major processes of seismic wave attenuation is geometric spreading and absorption. Geometric spreading, multipathing, scattering and intrinsic attenuation are four of the processes of amplitude reduction described by Stein & Wysession (2003). Geometric spreading describes the inversely proportional amplitude decrease to the distance from the source.

Multipathing described the phenomenon of amplitude variations as seismic wave focused or defocused along lateral variations of the substructure. The seismic waves refract towards low velocity anomalies and away from high-velocity anomalies. In subduction zones where strong velocities heterogeneities are existent the effect of multipathing are significant; small velocity heterogeneities located near an earthquake are capable of inducing large amplitude variations at distance. In Figure 2.9 is presented an example illustrating the predicted and actual travel path along which the

seismic wave propagates. In focal mechanisms studies the actual ray path that the seismic wave propagates characterized of lateral heterogeneities (high-velocity region) should be consider in seismicity studies (Stein & Wysession, 2003).

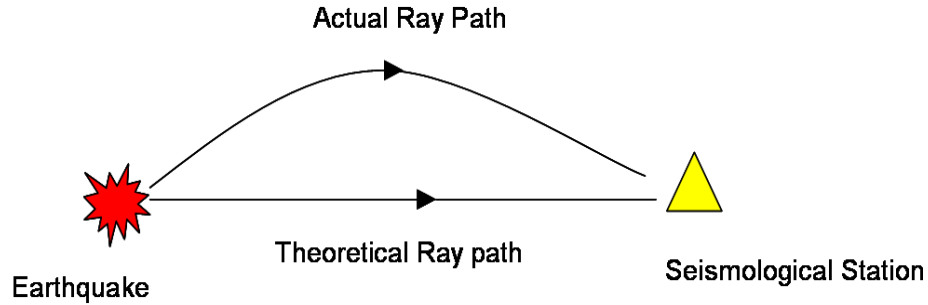


**Figure 2.9:** The theoretical and actual way path of a seismic way travels from source to the seismological station. Seismic wave amplitude decrease is observed through the theoretical path compared to seismic wave amplitude through the actual path. Velocity models should account the actual ray path for accurate earthquake solutions (Stein & Wysession, 2003).

Seismic wave scattering is also due to the effects of inhomogeneities (heterogeneities) along the seismic wave travel path. There is a slight discrimination between scattering and multipathing and is based on the ratio of the heterogeneity size to the wavelength and the distance the seismic waves travels through the heterogeneous region. Absorption (or damping) Intrinsic physical loss mechanisms such as sliding friction across cracks, internal friction and grain boundary effects as seismic wave propagates through rock, background temperature where hotter rocks results in higher absorption and scattering (Reiter, 1990) can cause seismic wave damping. The seismic wave amplitude  $A$  in distance  $r$  from the source is related with the distance from the source and with the coefficient  $q$ , describing the rate of attenuation with distance is given by the equation (2.3.16) (Reiter, 1990).

$$A = \frac{A_0}{r} \exp(-qr) \quad (2.3.16)$$

where  $A_0$  is the maximum amplitude. The coefficient  $q$  is related with frequency and seismic wave velocity ( $V$ ) and is given by the equation 2.3.17.

$$q = \frac{\pi f}{QV} \quad (2.3.17)$$

where  $Q$  is a quality factor. The amplitude decrease with distance considering equations (2.3.16) and (2.3.17) is presented in equation (2.3.18)

$$A = \frac{A_0}{r} \exp\left(-\frac{\pi r}{QTc}\right) \quad (2.3.18)$$

As the seismic wave propagates from the rupture zone, the high frequency components of the motion are attenuated more quickly than the lower frequency motions due to the damping by the transmitting rock that dissipates a fraction of the wave energy per travel

cycle (the high frequency waves have shorter wave lengths and attenuate more quick with distance from the rupture than the longer period motions). Consequently, the dynamic characteristics/properties and the topographic complexity of the surface geological structure may increase or decrease the amplitude of seismic motion. The absorption or damping is substantially higher on soft soil than on rocks.

The travel path effect on earthquake damage distribution depends on the azimuth of the site with respect to the direction of the rupture. In the near surface higher displacements are observed in the case the propagation of the rupture towards a site allows most of the seismic energy to arrive from the rupture to the surface. In the earthquake building engineering field, fault mechanisms and travel path effects should be incorporated into the design of mid to long period structures and in base isolation systems that are sensitive to large velocities and displacement.

### **2.3.1.3 THE INFLUENCE OF SITE EFFECTS ON SEISMIC GROUND MOTION**

Site effect is the most important factor in the earthquake damage distribution and refers to the effect of the geological surface and subsurface structure characteristics on seismic ground motion. Destructive earthquake consequences (Northridge, 1994; Turkey, 1999; Loma Prieta, 1989; Kobe 1995; California, 1983; Mexico City, 1985) confirm that the local site effects are the major important factor in the earthquake damage distribution compared to the effects induced of the proximity of earthquake sources and of the travel path effects. Local site effects moderate the effect of seismic ground motion on structural damage. The influence of local site effects on the earthquake damage distribution has been studied extensively and well documented (Borcherdt, 1970; Borcherdt & Glassmoyer, 1992; Aki, 1965; Mucciarelli & Monacheri, 1998; Mucciarelli & Monacheri, 1999; Nakamura, 1989; Nakamura et al., 2000a; Nakamura et al., 200b). Nakamura (1989), comparing earthquake events of different magnitudes recorded at the same site observed that the: 1) seismic waveform is similar for all the data set recorded at the same observational point even when the radiation or travel path characteristics are different, 2) the seismic waveforms of an earthquake recorded at different seismological stations substantially differ. The effect of the surface geological and subsurface structure as well as topographical characteristics on seismic motion is a key element in the earthquake damage distribution. In the following are briefly described the effects of soft sediments and topography on seismic motion.

#### **2.3.1.3.1 SOFT SEDIMENTS EFFECTS ON SEISMIC GROUND MOTION**

Earthquake damage distribution is generally larger on soft sediments rather than on bedrock outcrops. Examples of earthquake damaged cities located on soft sediments effects on seismic motion are the San Francisco, Lima, Tokyo, Osaka, Kobe 1995; Lisbon, and Mexico City Mexico City, 1985. In the time domain the soft soil effects influence the peak amplitudes, the waveform and the duration of seismic motion. At long periods the duration of seismic motion is increased mostly on soft sediments (Theodoulidis & Bard, 1995). The duration of seismic motion in the low frequency band (2-3Hz) is longer on alluvial deposits rather than on rock sites (Theodoulidis et.al, 1995). The non-linear behaviour of soft soil is characterized by a decrease of shear modulus and increase of material damping as shear strain increases. The decrease of the shear modulus decreases the shear velocity and the consequence is the shifting of

fundamental frequency towards lower values. The increase of the material damping decreases the spectral amplification and peak acceleration especially in the high frequency range (Bard, 1999).

#### **2.3.1.3.2 TOPOGRAPHY EFFECTS ON SEISMIC GROUND MOTION RESPONSE**

Earthquake damage is focused at sites where strong lateral discontinuities and heterogeneities are existent (Lambesc, France, 1909; Irpinia, Italy 1980; Liège, Belgium, 1983). Faults, voids, caves, basin edge effects, abnormal contacts, debris zones, etc are considered as lateral discontinuities. The amplitude and frequency of seismic motion is considerably affected by local surface topographical effects (Celebi, 2000; Giampicollo et al., 2001, Moisiidi et al., 2004; Gueguen et al., 2007, Cornou & Bard, 2003). The duration increase of seismic motion is correlated with the diffraction of seismic waves along the lateral heterogeneities (Frankel & Vidale 1992). Lateral heterogeneities within sediments induce significant differential seismic motion over spatial distances (Bard, 1999).

Theoretical and numerical models report high amplification of seismic motion at ridge crests or convex topographies and in controversy de-amplification over concave topographies (valleys, base of hills) (Bard, 1999). Instrumental studies verify the effects of surface topography and geology on amplitude and frequency content of seismic motion. Large ground amplification and abrupt amplitude seismic motion variations are observed along the slopes (Lebrun et al., 2001). The focusing or defocusing of seismic waves are reflected along the topographic surface. The effect of focusing and defocusing of seismic rays in the case of a wedge-shaped medium is well documented by Sanchez-Sesma (1990).

The diffraction of body and surface wave along a topographic feature forms interference patterns between direct and diffracted waves inducing abrupt amplitude variations of seismic motion and an increased ground amplification (Bard, 1999; Bonnefoy-Claudet et al., 2008a). Diffraction of body and surface wave is based on Huygen's principle stating that each point of a wavefront can be considered as a focal point of a secondary wave. The focal point permits the wave movement outwardly of that point. Huygen's principle describes the incidence of an elastic wave to discontinuities or wedge shaped structures. These structures behave as a secondary focal elastic wave points. Diffraction of direct and diffracted waves possesses interference of direct and diffracted waves. The result of that seismic wave interference is the inhomogeneous energy distribution at large distances and consequently the amplification or de-amplification of seismic motion. In the case of a simple topography the amplitude of the diffracted wave is smaller than the amplitude of the direct body waves.

The sediments response in the very near field due to the possible effects of complex incident wavefield, and of sub or super-sonic rupture velocities for near-surface faults may induce amplification effects (Chavez-Garcia et al., 1995; Bard, 1999). The lateral discontinuities and heterogeneities generate local surface waves in the softer medium that enhance seismic ground motion and earthquake damage distribution (Bard, 1999). The locally generated waves can be the cause of long period duration of seismic motion during an earthquake. Frankel & Vidale (1992) reported that these waves are the cause of long period duration of seismic motion in San Clara valley

during Loma Prieta earthquake. Kinoshita (1992), Phillips (1993) and Hisada (1993), report that these locally surficial generated waves along the edge valley have larger amplitudes than the S waves. Among to other authors, Frankel & Vidale (1992), Frankel et al. (2001), Field et al. (1995) observed long period surface generated waves along valleys. Bonnefoy-Claudet et al. (2008a) observed long period surface generated waves along Coachella valley and Santiago de Chile valley.

### 2.3.2 SPECTRA CHARACTERISTICS OF SEISMIC GROUND RESPONSE

Ground response is related with the depth of the sediments and with the shear wave velocity. The vibrational period  $T$  of a simple sedimentary layer overlying a stiff substratum (1D) structure of depth  $H$  is related with the depth of the sediments and with the shear wave velocity of the sediments. Kanai (1961) proposed the numerical estimation of ground period presented in equation (2.3.19).

$$T_n = \frac{4H}{(2n-1)u_s} \quad (2.3.19)$$

where  $U_s$  is the shear seismic wave velocity of the layer. The fundamental period ( $T_0$ ) is extracted from 2.3.20 substituting  $n = 1$ .

$$T_0 = \frac{4H}{u_s} \quad (2.3.20)$$

In the case of a multi layer (more than one soil layer) soil column the average shear seismic wave velocity is given by the equation (2.3.21).

$$u_s = \frac{\sum_{i=1}^n u_{si} H_i}{H} \quad (2.3.21)$$

The resonance frequency response is related to the thickness and to the S-wave velocity of the surface layers. In the case of 1D layered structures the fundamental frequency is given by the equation (2.3.22) and the harmonics are extracted from equation (2.3.23).

$$f_0 = \frac{\beta_1}{4H} \quad (2.3.22)$$

$$f_n = (2n+1) f_0 \quad (2.3.23)$$

The second amplified frequency is given from equation 2.3.23 for  $n=2$ , the third for  $n=3$ . The fundamental frequency ranges in the low frequencies for thick deposits or for extremely soft material and in high frequency band for very thin layers. In the case of 1D layer one clear fundamental frequency ranges in the low frequencies for thick deposits or for extremely soft material and in high frequency band for very shallow layers is observed (Nakamura, 1989; Nakamura, 1996; Nakamura, 2000). In Figure 2.10 is presented a schematic representation of the dependance of ground fundamental frequency and depth of sediments ( $H12$ ,  $H2$ ) of two sedimentary basins.

In the case of a complex (2-D or 3-D) structure the surface waves are reverberating into the lateral heterogeneities of the complex structure. The mechanical and geometrical characteristics of the geological structure construct the resonance frequency. The resonance patterns of 1D, 2D and 3D structures in the frequency domain present single peak for a simple 1-D structure and multiple peaks for complex substructure 2-D or 3-D structure (Bard & Bouchon, 1985; Bard, 1999; Bonnefoy-Claudet, 2008a). Bard (1999) proposed that the width of the sedimentary basin and the depth of the sediment control the ground frequency pattern. The 2D effects of a thick basin ( $h/w=0.7$ ) cause higher seismic ground resonance phenomena compared to the 2D effects of a shallow basin ( $h/w=0.06$ ) (Bard, 1999).

### 2.3.3 AMPLIFICATION OF GROUND SEISMIC RESPONSE

The term site amplification refers to the increase in the amplitude of seismic waves as they propagate through the surface geological structure. The amplitude of that peaks are related to the impedance contrast between the surface layer and the underlying bedrock, to the lateral heterogeneities, to the material damping of sediments and to the characteristics of the incident wavefield. In the case of 1-D structures the amplification level neglecting the energy loss due to material damping is simply defined by the principle of energy conservation. In the case that the impedance changes gradually through the soil layers from the sedimentary layer  $(pV)_1$  to bedrock  $(pV)_2$  and considering that the seismic energy flux  $E(t)$  along a tube of seismic rays is given by the equation (2.3.24) the amplification is estimated (equation 2.3.26) using the principle of energy conservation (equation 2.3.25).

$$E(t) = \frac{1}{2}(pV) \cdot \dot{x}^2(t) \quad (2.3.24)$$

$$E(t)_1 = E(t)_2 \quad (2.3.25)$$

$$A = \left[ \frac{x_2(t)_{\max}}{x_1(t)_{\max}} \right] = \sqrt{\frac{(pV)_1}{(pV)_2}} \quad (2.3.26)$$

In the case that the impedance changes sharply through the soil layers the amplitude usually increases as the seismic wave transverses the boundary between the soil layers with different impedances. The amplification of the fundamental frequency is a function of the impedance contrast between the surface and subsurface structure and the material damping of sediments (equation 2.3.27) (Bard, 1999).

$$A_0 = \frac{1}{\left( \frac{1}{C} + 0.5\pi\zeta_1 \right)} \quad (2.3.27)$$

Where  $C = (\rho_2 V_2)/(\rho_1 V_1)$  represents the impedance contrast,  $\rho_1, \rho_2$  is the density of sedimentary and bedrock, respectively and  $\zeta_1$  is the material damping. In the case of very small material damping ( $\zeta_1 = 0$ ) the maximum amplification is equal to impedance contrast between the surface (sedimentary) and subsurface (bedrock) structure.

Impedance is a dynamic property that can substantially affect the seismic motion and is used to characterize the material's resistance in seismic motion. The impedance contrast between the surface and surface structure substantially affect the seismic wave amplitude. The resistance to seismic motion is increased in an increasing impedance environment (rock site). The impedance of a soil layer ( $\rho V$ ) is defined as a function of mass material density ( $\rho$ ), shear wave velocity ( $V$ ) and of the incidence angle. The angle of incidence is the angle between the vertical and the direction of seismic wave propagation. Near the surface layer the cosine of the incidence angle is equal to unity (Reiter, 1990) and the impedance is defined of the soil mass density and wave propagation soil velocity (impedance = density\*propagation velocity). Amplitude seismic wave increase at soft soil sites is due to the low impedance of soil layers near the surface structure. The cause of the high amplification level of sediments is the trapping of seismic waves due to the high impedance contrast between the sediments and the underlying bedrock (Ojeda & Escallon, 2000).

In 2D or 3D complex structures the lateral heterogeneities strongly influences the amplification level especially in the case of small material damping. The lateral thickness variations generate local surface waves trapped within the soft layers and induce an increased amplification. The width of an embanked 2-D or 3-D valley structure modifies the frequency resonance pattern (Cueguen et al., 2007).

In Figure 2.10 are presented the factors that influence seismic motion according to Dorwick (2003). The most important factors that influence the ground seismic response are: 1) the horizontal extent of soft deposits ( $L_1, L_2$ ), the less the extent the higher the effect of the lateral variations on seismic motion, 2) the depth of the sedimentary deposits, 3) the effects of valleys (1, 2, 3) and 4) the lateral variations and heterogeneities of the surface (F,G) and subsurface structure that induces important variations in the spectral response of the site. These lateral heterogeneities induce seismic wave reflection, refraction and scattering that affect the ground seismic response. These factors enhanced earthquake damage distribution after the Mexico City (1985). Consequently, based on the previous studies the seismic response of the surface and subsurface structure is of paramount importance in earthquake damage distribution in near and far field.

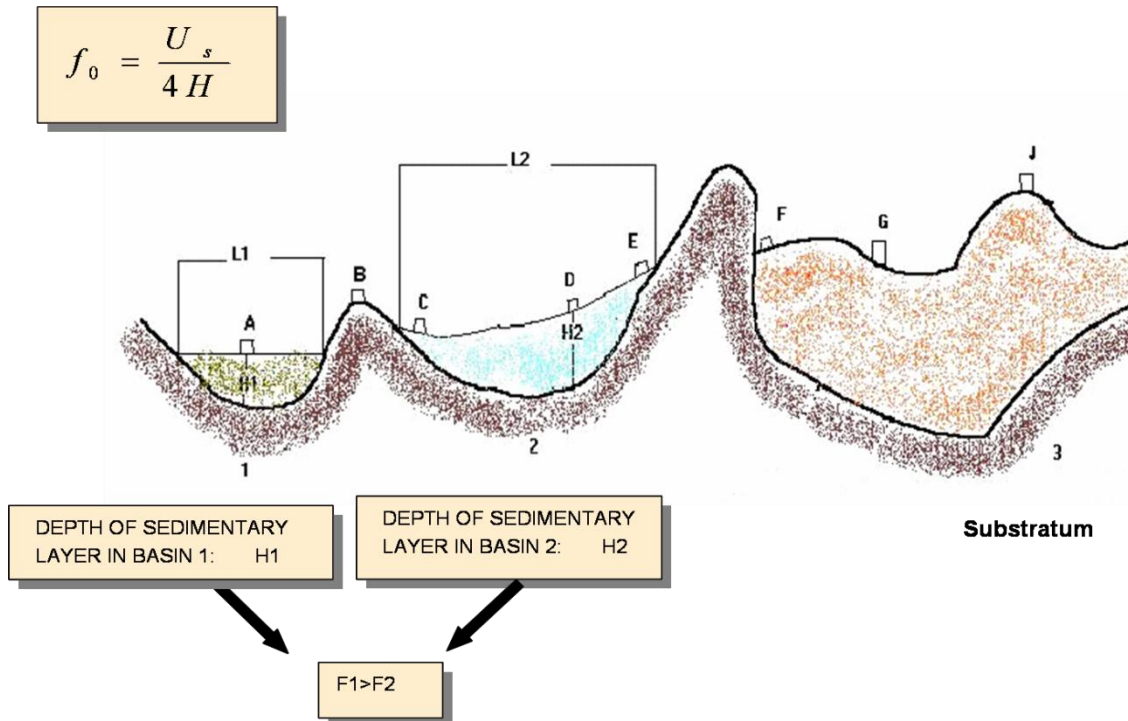


**Figure 2.10:** Schematic representation of the dependence of ground fundamental frequency and depth of sediments ( $H_1$ ,  $H_2$ ) of two sedimentary basins. The ground fundamental frequency increases with decreasing depth of the sediments (modified after Dorwick, 2003).

### 2.3.4 SOIL AND BUILDING STRUCTURE INTERACTION

Large magnitude seismic events verify the effect of soil-structure interaction in earthquake damage distribution. The coincidence of the fundamental period of soil and structure interaction is the most important factor in earthquake building damage distribution. The natural frequency of vibration of a multi-degree of freedom system (MDF) is given by the equation (2.3.30) (Chopra, 2001).

$$T_n = \frac{2\pi}{\omega_n} \quad (2.3.29)$$

and

$$f_n = \frac{1}{T_n} \quad (2.3.30)$$

To preclude the effects of ground and building (or the so called soil-site effects) resonance that may lead to building failure the coincidence of the ground and building fundamental frequency should be avoided. The earthquake building damage distribution depends on both the response of local site effects and on the soil-structure interaction.



The comprehensive evaluation of site effects on seismic motion is an important factor in building vulnerability estimation. HVSR technique using microtremors is a flexible, reliable and low cost estimation technique of ground and building resonance response. HVSR technique and microtremor can be used for preliminary estimation of building vulnerability without the need of structural details (number of width of frames, openings, and mass of floors, number of columns). A brief literature review of the applicability of HVSR and microtremors to characterized building vulnerability studies is presented in the following.

### **2.3.5 MICROTREMOR RECORDINGS FOR SEISMIC GROUND RESPONSE EVALUATION**

The use of microtremors to model near surface structure is of major practical importance in geotechnical engineering especially for microzonation studies of densely populated areas where the use of other techniques are either invasive or very expensive or not applicable to perform due to civilization. In urban planning studies high density microtremor recordings are necessary to perform for a complement microzonation study and to identify hazardous seismic zones where possible additional geophysical explorations should be performed.

Site effects studies are used to estimate dynamic response of various types of geological structures and the tectonic environment of the area under study, to estimate the ground amplification effects and to evaluate local site effects due to surface and subsurface structure. The importance of these effects in the present research is highlighted.

Microtremors are the small vibrations of the ground caused by natural or anthropogenic noise. The amplitude of this vibrations is  $10^{-6}$  - $10^{-3}$  cm. According to Okada (1999) the wavefield of the ground motion vibrations (microtremors) consist of surface waves and of body waves. This wavefield contains information of the complex subsurface sources, of the wave travel way and of the subsurface structure. In the earthquake event in Guerrero-Michoacan (Mexico, 1985) spectral microtremor characteristics are well correlated with strong motion data. Microtremor measurements is a preferable geotechnical method for site effects estimation for the following reasons:

1. Easiness of applicability mostly in urban areas.
2. Instrumental Simplicity and flexibility
3. Non-invasion technique. No environmental impacts.

#### **Techniques used in microtremor analysis**

Three main innovative techniques have been introduced in microtremor analysis and to estimate the effect of surface and subsurface structure on seismic ground motion response: a) Kanai, b) Kagami and c) HVSR techniques.

1. **Kanai Technique (Absolute spectra).** Kanai's technique based on the assumptions: 1) microtremors are composed of vertically incident S waves and 2) the incident spectrum is white. The assumptions proposed by Kanai were questioned. The first one based on previous studies for the composition of the nature of the noise wavefield. The second one based on studies where predominant periods of microtremors exhibit clear time - variations of amplitudes and on studies about the influence of human activity in the amplitude variations (Gauil et al., 1995; Milana et al., 1996) (the existence of clear peaks on the noise

spectra recorded on soil and on rocks). Bard (1999) proposed that: 1) microtremors are also composed of surface waves, 2) the natural noise spectrum is not flat, and 3) the anthropic noise may contain band limited components and also the noise level may exhibit time variations. The advantage of Kanai's technique provides reliable estimates for the fundamental frequency of soft soils while the amplification is not well defined.

2. **Kagami Technique (Standard Spectra Ratio):** Kagami technique (Kagami, et al. 1982) is based on the selection of the S part of the seismogram. A hard rock site is needed as a reference site. The ratio of the smoothed amplitude Fourier spectra is the transfer function between the soft soil site and the reference station used for microtremors analysis. The disadvantages of that method are:
  - Usually rock sites are covered with sedimentary/alluvial layer and therefore it not always an easy task to identify a rock site.
  - The distance between the rock site and the sedimentary site should be less than 300 m to exclude source and travel path effects.
3. **HVSR or Nakamura Technique:** In the frame of this thesis HVSR or Nakamura technique (1989, 1996, 2000) is conducted to model surface and subsurface structure and to determine the site effects on seismic ground motion. Nakamura technique is used as a major method in the research of this study. The spectra ratio of horizontal to vertical components of microtremors using one recording station was introduced by Nogoshi & Igarashi (1971). To estimate fundamental frequency Nogoshi & Igarashi (1971) based on the assumption that microtremors are composed of surface seismic waves. Nakamura (1989) proposed that HVSR technique for incident S seismic waves provides reliable estimate of fundamental frequency and amplification. In comparison to Kanai (1961) and Kagami techniques, Nakamura technique estimates the effects of local condition (geological and subsurface structure) on seismic motion. Moreover, Kanai and Kagami technique provide an approximate estimation of seismic ground amplification, while Nakamura technique provides a more reliable estimate of the ground soil amplification. Since the pioneering work of Kanai (1961) the interpretation of site effects using Fourier spectra of horizontal and vertical noise component is extensively studied. Specifically, the peak frequency of microtremor spectra is related to the fundamental resonance frequency of the investigated site. Despite the controversies arises relatively to the assumptions of the nature of noise wavefield, many studies verify the validity of the spectra characteristics of microtremors in the interpretation of site geological deposits. An important application of HVSR is in the earthquake structural engineering field. The HVSR technique using microtremor is a valid estimator of natural building frequency. The natural frequency estimation of structural building vibration is a very important factor in seismic codes of building construction. The spectral ratio of horizontal to vertical components evaluates the fundamental frequencies, amplification factors, vulnerable points and modal shapes. The seismic building response is estimated using microtremor measurements in the buiding construction (ground foundation and in each n-floor) and in ground surface.

## **2.3.5.1 ORIGIN AND NATURE OF NOISE WAVEFIELD**

### **2.3.5.1.1 ORIGIN OF NOISE WAVEFIELD**

The small ambient ground vibrations caused by natural or cultural sources are characterized as noise. The amplitude of these small vibrations is usually between  $10^{-5}$ - $10^{-3}$ cm. The origin of the noise is natural induced by natural sources, such as tides, water waves striking the coast, effects of wind on trees or buildings and cultural induced by industrial machinery, cars, trains, traffic, human footsteps.

A classification of ambient noise sources is presented according to the frequency content, proposed by Asten (1978), Asten & Henstridge (1984) and reviewed by Bonnefoy-Claudet et al. (2006b). Based on this difference between natural and cultural noise, the terms microseisms and microtremor respectively are proposed as a further discrimination of noise. The discrimination of long period noise ( $T > 1$ sec) and short period noise ( $T < 1$ sec) was based on the natural origin microseisms and on cultural origin noise (microtremors) (Horike, 1985). Microseism amplitude is strongly correlated with meteorological activities (Tindle & Murphy, 1999; Bromirski & Duennebieer, 2002). Long period microseisms in the Los Angeles basin are related with the ocean disturbances and short period microtremors are clearly associated with cultural noise (Yamanaka et al., 1993). At long period ( $T > 2$ sec) noise is generated by oceanic and large scale meteorological conditions, in the intermediate periods between  $1 < T < 2$ sec the origin of noise is due to wind effects and to local meteorological condition and at the short periods ( $T < 1$ sec) the origin of noise is mostly cultural (Bonnefoy-Claudet et al., 2006b). The spectral discrimination boundary between microseisms and microtremor is specified around 1 Hz. Nakamura (1996) studied long and short period microtremors in different geological sites. The results of their observations are briefly presented in the following:

1. Microtremors in the long periods or in the low frequencies (0.3-0.5Hz) are due to the oceanic wave (sea waves) and to large scale meteorological conditions.
2. The origin of microtremors in the frequencies between 0.5 and 1 Hz is due to the tidal waves and to the influence of wind.
3. Microtremors in frequencies higher than 1 Hz is related to cultural noise.

High frequency microtremor measurements exhibit clear daily and weekly variations are linked with cultural activities (Bonnefoy-Claudet et al., 2004) and low frequency microseisms are related with natural phenomena most often with oceanic activity for long period noise (Bonnefoy-Claudet et al., 2004). The minimum and the maximum Fourier spectra amplitude of cultural noise is observed during midnight and midday, respectively (Yamanaka et al., 1993; Okada, 2003).

### **2.3.5.1.2 NATURE OF MICROTREMORS**

The nature of wavefield of microtremors is extensively studied. Gutenberg in 1911 studied the nature and origin of microseisms and presented the first major review of seismic noise. Kanai (1961) considered that microtremors consist mostly of vertically incident S-waves, similar with the seismic signals. Nogoshi & Igarashi (1971), Horike (1985), Milana et al. (1996) and Chouet et al. (1998), proposed that the wavefield of microtremors is composed of surface waves. Horike (1985) investigated the noise wavefield of Osaka basin in Japan with f-k analysis and observed that for frequencies

between 0.5 to 0.9 Hz and 0.9 to 3.0 Hz microtremor noise wavefield consist of higher mode of fundamental Rayleigh wave.

Chouet et al. (1998) performed array measurements observed significant proportion of surface waves (77% Rayleigh and 23% Love waves) in the noise wavefield. Arai & Tokimatsu (1998, 2000) and Ohmachi & Umezono (1998) analyzed HVSR ratio and synthetic noise and proposed a qualitative estimate of a relative proportion of Rayleigh and Love waves in the noise wavefield. Applying the SPAC method to detect Rayleigh and Love waves from array measurements, the energy power fraction of Love waves at 1 sec increases from about 50% and at longer period (>3 sec) reaches the 90% (Okada, 2003). In the frequency range 3-8Hz, 60% to 85% of noise microtremor energy corresponds to Love waves, applying Spac technique (Yamamoto, 2000). Arai & Tokimatsu (1998, 2000) used f-k analysis and Spac method and proposed a relative proportion of 60% Love and 40% Rayleigh waves in the microtremor wavefield. The predominance of Love waves in the noise wavefield is verified using spatial auto-correlation method (Arai & Tokimatsu, 1998; Yamamoto, 2000). The three component array measurements and more specific the Spac method are the key element in determining the relative proportion of Love and Rayleigh waves in the noise wavefield and are only mentioned to gain a better insight of the nature of the noise wavefield. The few quantitative results have been obtained through array measurements. Spac method and autocorrelation method is out of the frame of this thesis and will not be extensively studied.

Few studies about the proportion of Love and Rayleigh waves of H/V ratio are published. The interrelation between the HVSR technique and the ellipticity of Rayleigh wave is estimated (Nogoshi & Igarashi, 1971; Konno & Ohmachi, 1998; Chouet et al., 1998). Milana et al. (1996) noticed surface wave in the frequency band 2-10 Hz. Bonnefoy-Claudet et al. (2008b) concluded that the noise wavefield is sensitive to the spatial noise source distribution (source-receiver distance and source depth). Consequently, it is documented that the nature of microseisms wavefield is composed of fundamental Rayleigh waves. In controversy it is not yet well defined the nature of microtremors as some authors claim that the microtremor wavefield is composed either of P waves, of predominant surface waves and or of a mixture body and surface waves. The proportion between surface and body waves (Rayleigh and Love waves, fundamental and higher modes) of the microtremor wavefield is not proved through well accepted method that can directly lead to these ratios (J-Sesame manual, 2004).

Nogoshi-Igarashi (1971) interpreted the spectra H/V ratio using microtremors with the ellipticity of Rayleigh effects. Among to Nogoshi-Igarashi many authors (Lachet & Bard, 1994; Field & Jacobs, 1995; Ansary et al., 1995; Bard, 1999) suggested that the fundamental peak of H/V is explained with the fundamental mode of Rayleigh wave. Konno & Ohmachi (1998) suggested a proportion of 60% Love and 40% Rayleigh waves. Arai & Tokimatsu (2000) proposed theoretical explanation of HVSR technique including also Love waves. Theoretical explanations of HVSR technique using only the S waves are given by Nakamura (2000). Parolai et al. (2002) proposed a model based on summation of different body wave phases. Yamanaka et al. (1994) observed similarities between the HVSR curves and the theoretical ellipticity curves of the fundamental Rayleigh mode waves on a sedimentary site.

Bonnefoy-Claudet et al. (2004) using HVSR curves concluded that for high and low impedance contrast substructure the noise wavefield is composed of surface waves and of both surface and body waves, respectively. The cultural activity, geological, geotechnical and topographical characteristics (Bard, 1999) of the site and the source properties (Ohmachi & Umezono, 1998) influence the proportion of surface and body waves.

The existence of higher modes at the trough frequency (corresponding to the vertical polarization of the fundamental mode of the Rayleigh waves) explains why in most cases a peak/trough structure is not observed in HVSR curves (Bonnefoy-Claudet, et al., 2004). The second observed HVSR peak corresponds to the first higher harmonic of Rayleigh waves (Bodin et al., 2001). The second HVSR peak is associated with the peaks observed at higher frequencies of the ellipticity curves of higher modes of Rayleigh waves (Asten & Dhu, 2002; Asten, 2004). In controversy, the higher peaks are explained due to the body wave resonance (Bonnefoy-Claudet et al., 2004). Site effects dominates also an important role in the excitation of higher modes of Rayleigh waves in the noise wavefield (Zhang & Chan, 2003; Cornou & Bard, 2003; Roten et al., 2006). Main conclusion is that the noise wavefield is composed of body and surface waves. The proportion of body/surface, Rayleigh/Love, fundamental/higher modes is affected by the site effects and source properties. Independently of the noise wavefield HVSR technique is a valid estimator of resonance frequency Site effects studies proves that despite the impedance contrasts environment, the seismic wave focusing due to the surface topography, the existence of water contaminant, cavities and voids and the strong lateral variations and heterogeneities of the surface topography are factors that strongly affect site amplification (Giampiccollo et al., 2001; Moisiidi et al., 2004).

### **2.3.6 HVSR TECHNIQUE FOR SITE EFFECT ESTIMATION**

Theoretical investigations (Lachet & Bard, 1994; Lermo & Chavez Garcia, 1994b) and experimental data (Lermo & Chavez-Garcia, 1993; Lermo & Chavez-Garcia, 1994a; Duval et al., 1994; Field et al., 1995; Fäh, 1997; Lebrun et al., 2001) suggests that the observed HVSR peak on soft sites is strongly correlated with the ground fundamental resonance frequency. Teves-Costa (1996) indicated that singled peaked curves are associated with soft and flat curves with rock sites. On the contrary, few studies exhibit a more complex pattern presenting two or more peaks due to the topographic effects (Lebrun et al., 2001) due to thin alluvial topmost layer (Gueguen et al., 2000) or due to the high impedance contrast of the substructure (Giampiccollo et al., 2001, Moisiidi et al., 2004).

Earthquake damage due to strong lateral heterogeneities using HVSR method is extensively reported (Mucciarelli et al., 2001; Gueguen et al., 2007; Bonnefoy-Claudet et al., 2008a). The lowest frequency defines the resonance frequency of the whole soil layer above the bedrock, while the higher frequency attributes the response of the soft superficial layer. Teves-Costa et al. (1996) examined the seismic behaviour of two sedimentary basins (Alcantara and Praca do Comercio) with different geotechnical characteristics and verified using the HVSR method that the amplitude and frequency depends on the geotechnical characteristics and mostly on the impedance contrast between the surface and subsurface structure. In particular, the high impedance contrast between the geological layers induces high amplification level and the

fundamental frequency is correlated with the thickness of alluvial deposits (Teves-Costa et al., 1996).

Surface waves are generated and clearly identified along to basin edge of large size valleys (Bonney-Claudet et al., 2008b). Kawase (1996) report the effect of direct S wave and diffracted wave in the edge of the basins. Few detailed investigations on the edge effects have been reported. According to Bard (1999), in the case of small dimension valleys the fundamental frequency is in the high frequency band and the travel wave duration is smaller. In controversy, diffracted waves are clearly identified in small scale valleys. Some authors questioned the validity of HVSR technique in the case of 2D or more complex structures.

In controversy the strong 2D effects due to the shape of the valley on the resonance frequency deduced from ambient seismic noise is well established (Steimen, 2004; Roten et al., 2006). The trapping of earthquake surface waves in sedimentary basins can amplify the magnitude and lengthen the duration of seismic shaking at the surface (Louie, 2001). Theoretical studies reveal that the basin geometry, particularly in narrow sedimentary basin ( $w/H$  small) may have major effect on resonance frequency (Gueguen et al., 2007). The fundamental frequencies extracted from HVSR are considered as the fundamental frequencies at which the local site effects amplify the seismic motion regardless of the 1D, 2D or 3D geometry of the site (Gueguen et.al, 2007).

The HVSR technique reveals the main characteristics and features of a small basin in southern Spain (internal zone, Beltic Cordillra) and provides sufficient estimator of the resonance response of soft sediments (peats), while it does not guarantee a perfect determination of coarse sediments (Delgado et al., 2002). Amplification effects of soft soil on seismic motion are extensively studied (Finn, 1991; Chavez-Garcia et al., 1995). The use of HVSR technique verified that the surficial recent (alluvial) deposits in valleys amplify the seismic motion up to 50 in the frequency band 0.3-0.7Hz; while no amplification is observed at sites where andeside is located as andeside has the characteristics of a rock site. Larger amplification has been observed due to the wave scattering in the substructure.

A short predominant period ( $T_0=4H/V_s$ ) indicates a rather stiff rock while a larger period indicates softer and thicker deposits. This period lengthening with increasing softness is often associated with an amplitude increase. Large fundamental period or low fundamental frequency using microtremors recordings indicates softer and thicker deposits. Shorter period corresponds to rather stiff soil or rock site. Experimental evidences in the long period range ( $T>1\text{sec}$ ) verify that these peak frequencies are related to the fundamental resonance frequency of the investigated sites (Yamanaka et al., 1993). A proposed explanation is that the very soft soils lead to high impedance contrast at depth, or when this impedance contrast does not exist to the existence of natural origin of microseisms at long periods and their relative spectra smoothness (Bard, 1999). Spectral ratios using microtremors and strong motion data at periods longer than 5 sec are in agreement (Yamanaka et al., 1993). At shorter periods spectra microtremor are representative of the geological site characteristics (Gitterman et al., 1996; Mucciarelli & Monacheri, 1998). In controversy, some authors consider that at shorter period the validity of microtremors is questionable (Yamanaka et al., 1993; Milana et al., 1996; Toshinawa et al., 1996). Sharp spectral peaks are associated with

high impedance contrast between the surface and the subsurface structure; particularly when the impedance contrast exceeds a value of 3 to 4 (Bard, 1999). If the impedance contrast between the surface and the subsurface structure is high, the surface and body waves are trapped and a sharp spectral peak is observed at the fundamental frequency (Bard, 1999). At sites where the impedance contrast of the surface and subsurface layers is low, the trapping is not efficient to create sharp peaks (Bard, 1999).

### **2.3.7 MICROZONATION STUDY USING HORIZONTAL TO VERTICAL SPECTRA RATIO (HVSr) TECHNIQUE**

A microzonation study is an assessment of seismic potential hazard consulting the seismic regime and the local geological, topographical and geotechnical conditions. A detailed and complementary microzonation study necessitates an inter-scientific synergy of data collection and analysis concerning the disciplines: the seismicity, the local geology and tectonics, the surface and subsurface geotechnical characteristics and the seismic response of the soil. Estimation of local response of a site (site effects) is a key element-component of local seismic hazards (Bour, 1998). The major factor in the earthquake damage distribution is the effects of the surficial geological characteristics. The most important part of a microzonation study that influences the accuracy of the results is the valid determination of the topmost soil properties or the site effects on seismic motion. The most popular techniques developed for this purpose is the site to reference spectra ratio and the HVSr technique. The validity of HVSr technique for microzonation studies is well established (Field et al, 1995; Teves-Costa, 1996; Mucciarelli & Monacheri, 1998; Gallipoli et al., 2003; Gallipoli et al., 2004; Cara et al, 2003; Cardarelli et al, 2008; Bonnefoy-Claudet et al, 2008; Picozzi et al., 2009).

### **2.3.8 MICROTREMOR MEASUREMENTS AND BUILDING DAMAGES**

Nakamura et al. (2000a) used the spectral characteristics of the horizontal to vertical components of microtremors to identify vulnerable points of the Roman colliseum. Measurements performed at each floor and vulnerability indices value are estimated from ground and structure strains (Nakamura, 1996; Nakamura et al., 2000a) and vulnerable points are finally estimated for the Roman colliseum. Nakamura et al. (2000a) described the determination of the fundamental frequencies of cultural structure vibration applying the innovative HVSr technique.

The importance of building eigen-modes and soil frequency resonance is extensively investigated (Mucciarelli & Monacheri, 1998; Mucciarelli et al., 2001; Mucciarelli & Gallipoli, 2001). Microtremor measurements are used to assess the dynamic structural characteristics. Microtremor measurements have been used worldwide to investigate the dynamic structural characteristics and to identify the damage mechanisms and to evaluate the damage risk or collapse of various points of the structure (Nakamura, 2000b). Vulnerability indices ( $K_g = A^2 / F_0$ -values) proposed by Nakamura (1989, 1996, 1997) and derived from the ground and structure strains are specified to estimate possible weak points that may collapse during an earthquake. Moreover, Nakamura (1997) consider that the damage in soils and structures is basically controlled by the shear strain in soils. This consideration is based on the derivation of the above formula on the following two assumptions: i) the amplification of

the fundamental frequency represents the S-wave amplification and ii) the peak acceleration and displacements may be simply related with the fundamental frequency.

The building vibration radiates a diffracted wavefield into soil, trapped into the soil foundation and produces a frequency and amplitude seismic motion variation producing the site-city seismic interaction (Mucciarelli et al., 2001; Gallipoli et al., 2004). The modifications of seismic ground motion are caused by the effects of soil-structure interaction of massive/tall buildings and strong impedance contrast between surface and subsurface. The consequences of these “site-city interaction” are the increase of motion intensities and the increased damage distribution in the nearby structures. The spectral ratio of horizontal to vertical components evaluates the fundamental frequencies, amplification factors, vulnerable points and modal shapes. The possible coincidence of fundamental frequencies of building and the building ground foundation that induces resonance phenomena capable of compromising building’s stability during earthquakes is the main outcome estimated with the spectra ratio of horizontal and vertical components.

Kawase (1996) performed a microzonation study after the Kobe earthquake using microtremor recordings and noticed that the high structural damages were focused in a specific zone. Microtremor soil spectra exhibit a clear peak in the period 0.2-0.5s that coincides with the fundamental vibrational period of wooden houses. Morimoto (1996) observed in the vicinity of Mukogawa River in Kobe interrelations between noise spectra characteristics and damage distribution.

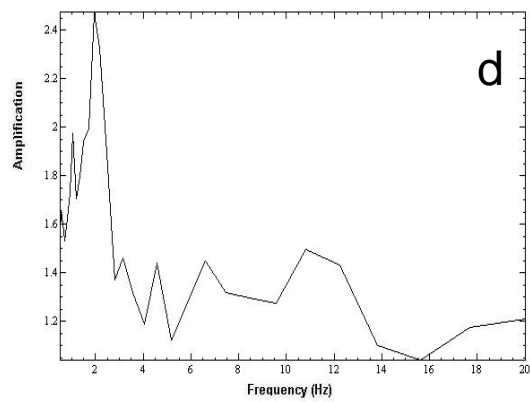
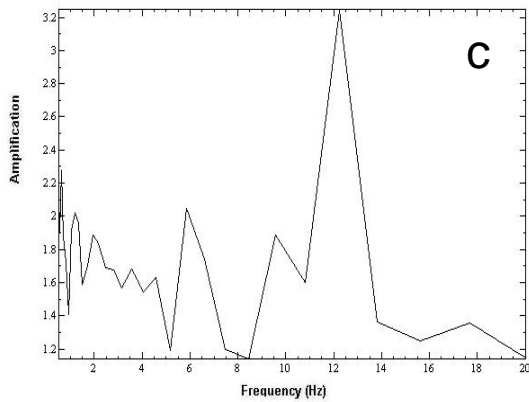
### **2.3.9 HVSR TECHNIQUE IN GEOPHYSICAL AND GEOTECHNICAL PROSPECTING**

Recent studies focus their interests in the application of HVSR technique in geophysical prospecting studies. The resonance frequency pattern variation with depth of a sedimentary basin is one application of HVSR technique (Chavez-Garcia et al., 1995; Dravinski, et al., 1996; Al-Yuncha & Luzon, 2000; Duval et al., 1994; Ansary et al., 1995; Teves-Costa, 1996; Ojeda & Escallon, 2000; Gosar et al., 2001; Louie, 2001). HVSR technique has been used as a geophysical exploration tool (Toshinawa et al., 1996; Toshinawa, 2000; Delgado et al., 2000; Ins-Von Seht & Wohlkenberg, 1999; Parolai et al., 2002). An important component of site response estimates of ground shaking is the evaluation of shallow shear velocity structure (Louie, 2001). The estimation of shear wave resonance of sediments is an important factor in earthquake risk assessment (Konno & Ohmachi, 1998; Asten & Dhu, 2002; Asten, 2004; Gallipoli et al., 2004). Moreover, the average shear wave velocity of the soil column is estimated from the HVSR soil frequency and from the knowledge of soil layer depth provided by geophysical methods such as the electrical resistivity tomography.

The HVSR technique is used to estimate the geometry of the main seismic reflectors such as the interface between basin alluvial deposits and the underlying bedrock. Considering constant S-wave velocity, Yamanaka et al. (1994), Giampicollo et al. (2001), Moisiidi et al. (2004) used the HVSR to identify lateral heterogeneities and irregularities that induce amplification effect on seismic motion. Ibs-von Seth & Wohlenberg (1999) considered the velocity variations with depth. Moisiidi et al. (2004) combined HVSR technique with high resolution electrical resistivity tomography (ERT) to identify large scale voids that correspond to ancient large scale reservoirs (Fig. 2.11). Strong spatial variability of ground seismic motion is observed at Doric Temple and



Dipartite Temple. The distant between two sites is 13 m. HVSR spectra characteristics in the Doric Temple indicate a strong lateral heterogeneities and irregularities. Electrical resistivity tomography using Schlumberger array is applied along the Doric Temple to verify the validity of HVSR technique. Two large scale voids are revealed using ERT and Schlumberger array in aggrement with HVSR results using microtremors.



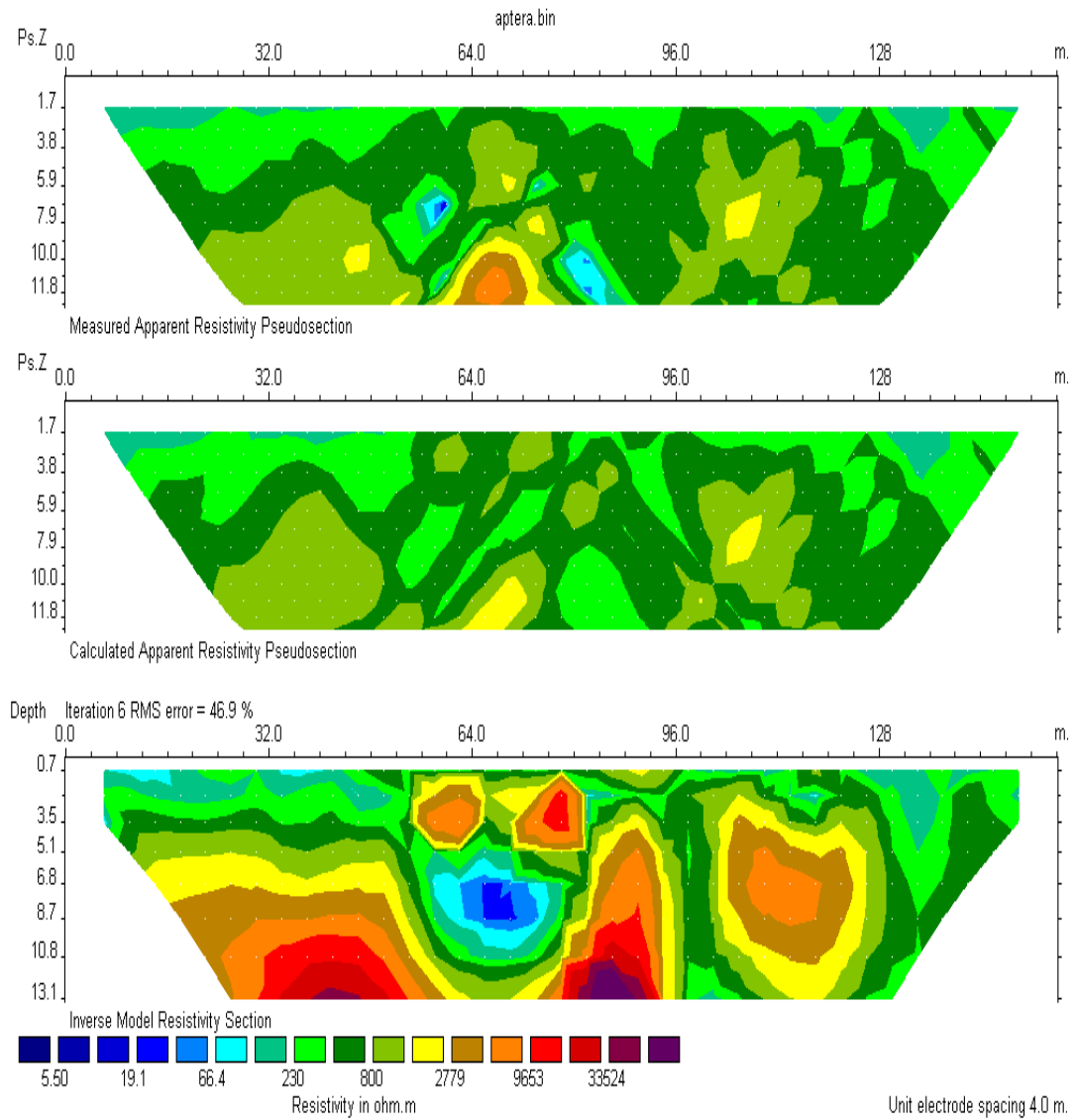


**Figure 2.11:** (Upper): HVSR technique in the archaeological site Apera (western Crete) in seismic ground response evaluation. Figures 2.11a and 2.11b present the Doric Temple and the Dipartite Temple, respectively where HVSR using microtremor recordings conducted. Figures 2.11c and 2.11d present the HVSR ground seismic response of Doric Temple and the Dipartite Temple, respectively. The vertical scale of the graphs corresponds to the ground amplification while the horizontal component corresponds to the ground frequency. (Lower): Electrical resistivity tomography using Schlumberger array to verify the validity of HVSR technique is performed in the Doric Temple. Two large scale voids are revealed corresponding to ancient reservoirs. The data presented here are from the author's own preliminary work, undertaken in preparation for the current PhD thesis.

## **2.4 ELECTRICAL RESISTIVITY TOMOGRAPHY (ERT) TO IMAGE SUBSURFACE STRUCTURE**

Geophysical exploration studies in determining the subsurface structure characteristics not directly observable at the surface are of paramount importance in earthquake hazards estimation. Electrical Resistivity methods are introduced to model the subsurface geological structure determining the subsurface resistivity distribution of geological units. High-resolution electrical resistivity methods are widely used in geotechnical and tectonic, hydrogeological studies in groundwater pollution evaluation, geothermal and archaeological studies and in borehole logging. Mainly, they are used to allocate faults, voids subsurface heterogeneities, groundwater contaminants, and the extent of ground water pollution.

The method of electrical resistivity tomography is based on Ohm's law. Estimating the geoelectrical properties of the surface and subsurface the geological and tectonic characteristics is determined. The basic concept of ERT profile is the existence of high apparent resistivity anomalies and low apparent resistivity anomalies over conductive geological structures. The most widely geo-electrical method dedicated to image subsurface structure is the two-dimensional (2D) electrical resistivity surveying. The two-dimensional (2D) resistivity surveying has also been used for environmental, geological and engineering studies (Meads et al., 2003; van Schoor, 2002; Demanet et al., 2001; Lapenna et al., 2003; Reynolds, 2004; Reynolds, 2006). The 2D geo-electrical profiling provides an accurate, practical and a moderate low cost modelling of the subsurface structure.

In the frame of this thesis 2D ERT survey using Schlumberger, Wenner and dipole-dipole array is conducted at several sites in the broader area of Paleohora basin in southwestern Crete and in Kastelli-Kissamou territory in northwestern Crete. The purpose of the ERT survey is to verify ground truthing field observations and to reveal different geological and tectonic structures not directly observable at the Earth's surface. The recorded ERT data are collected to provide apparent resistivities inverted to a 2D geoelectrical resistivity model.

### **2.4.1 ELECTRODE RESISTIVITY CONFIGURATION ARRAYS**

To determine the subsurface electrical resistivity measurements are conducted by inducing electrical current in the surface and measuring the derived potential difference. The acquisition system is composed of a voltmeter to measure the voltage (V) and an amperometer to measure current flowing (I) through geological layers. The amperometer measures the induced electric current (I) with the use of current electrodes well embedded in the surface layers and the voltmeter the voltage between the electrodes. The calculated resistivity value is the apparent resistivity that corresponds to the resistivity of a homogeneous ground structure. The true ground structure resistivity is given by the inversion of the measured apparent resistivity values.

In Figure 2.12 is presented a schematic figure of the embanked electrodes in the surface, the measured voltage between the two electric current and the equipotential and electric current lines through subsurface produced by two point source configuration in a homogeneous geological layer of resistivity ( $\rho$ ). Figure 2.12 is modified after Reynolds (1997). In the ERT prospecting a sequence of electrodes

configurations are used to model the subsurface structure. The simplified case of two electrodes is presented in the following Figure 2.13 (modified by Reynolds, 1997).

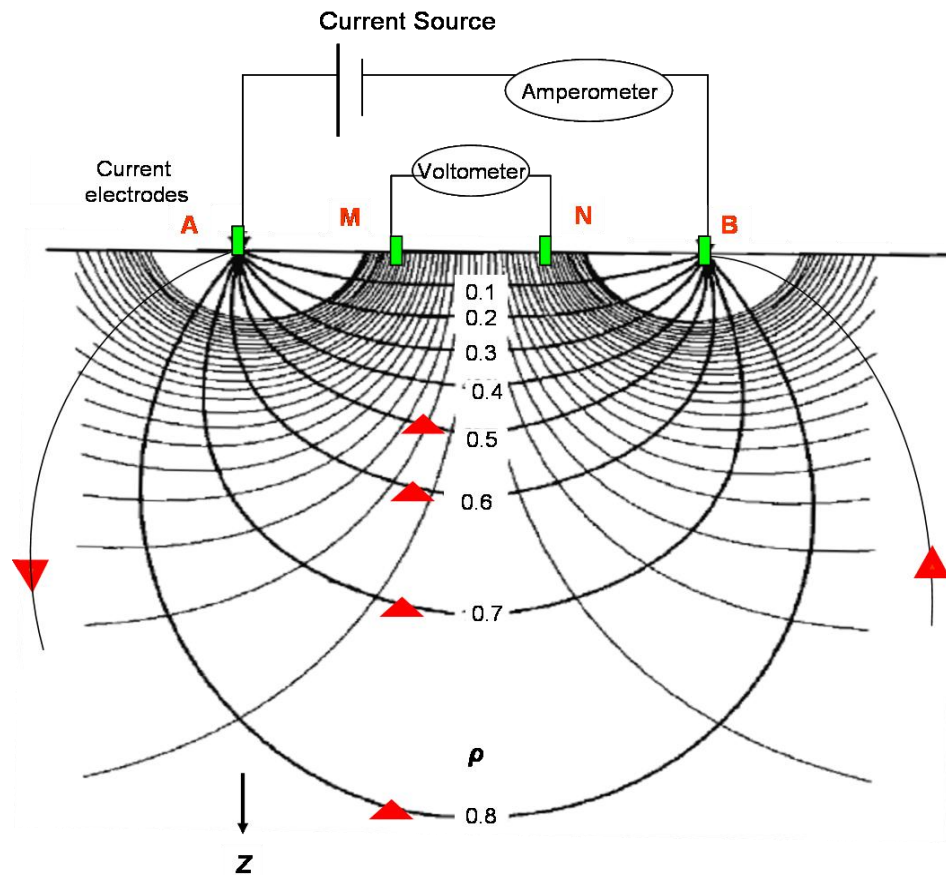


**Figure 2.12:** The equipotential and the current lines for the case of two point source configuration (modified after Reynolds, 1997).

The proportion of current that penetrates into subsurface at a depth  $z$  using two point electrodes A, B at a distance  $d$  is given by the equation (2.4.1) (Telford, 1990; Tsourlos, 1995; Reynolds, 1997). From the equation (2.4.1) it is extracted that the penetration depth ( $z$ ) increases with the current electrode distance ( $d$ ). A proportion of 50% of the current ( $I_z=0.5$ ) penetrates from an interface at depth  $z$ , half the current electrode separation ( $d$ ).

$$I_z = \left[ \frac{2}{\pi} \tan^{-1} \left( \frac{2z}{d} \right) \right] \quad (2.4.1)$$

The current penetration depth depends not only on the current separation but on the position of the potential electrodes and on the earth's inhomogeneity (Roy & Apparao, 1970; Tsourlos, 1995; Reynolds, 1997).

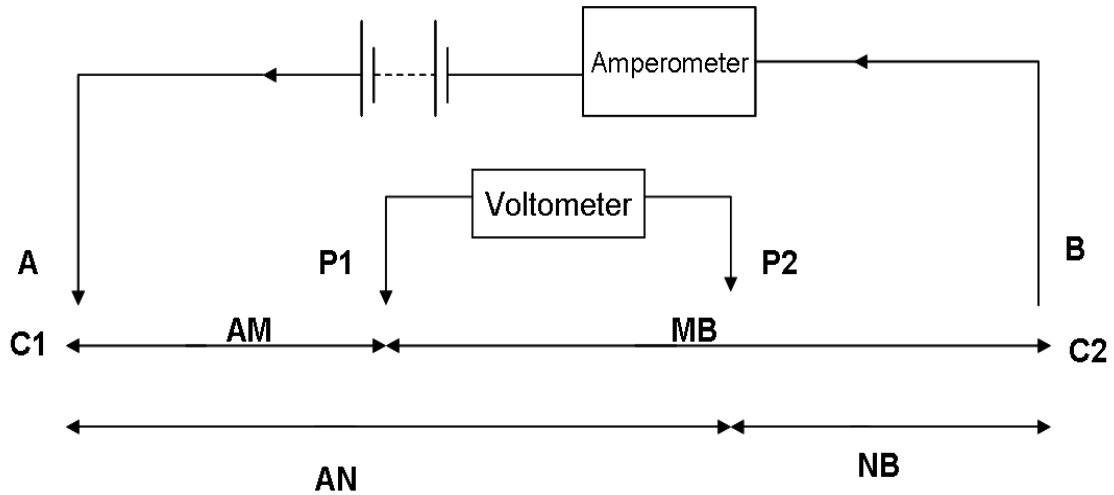


**Figure 2.13:** Generalized electrode configuration (modified after Reynolds, 1997).

The potential measured at a point P at a distance  $r_A$  and  $r_B$  from electrodes A and B is given by the equation 2.4.2.

$$V_p = \frac{Ip}{2\pi} \left( \frac{1}{r_A} - \frac{1}{r_B} \right) \quad (2.4.2)$$

The potential  $V_M$  and  $V_N$  at the electrode M and N are respectively given by the equations 2.4.3 and 2.4.4:

$$V_M = \frac{pI}{2\pi} \left[ \frac{1}{AM} - \frac{1}{MB} \right] \quad (2.4.3)$$

and

$$V_N = \frac{pI}{2\pi} \left[ \frac{1}{AN} - \frac{1}{NB} \right] \quad (2.4.4)$$

The potential difference measured at the voltage electrodes M and N is given by the equation (2.4.5):

$$\delta V_{MN} = V_M - V_N = \frac{pI}{2\pi} \left\{ \left[ \frac{1}{AM} - \frac{1}{MB} \right] - \left[ \frac{1}{AN} - \frac{1}{NB} \right] \right\} \quad (2.4.5)$$

The resistivity  $p$  is extracted solving the equation (2.4.6)

$$\rho = \frac{2\pi\delta_{MN}}{I} \left\{ \left[ \frac{1}{AM} - \frac{1}{MB} \right] - \left[ \frac{1}{AN} - \frac{1}{NB} \right] \right\}^{-1} \quad (2.4.6)$$

In inhomogeneous structure the apparent resistivity ( $\rho_a$ ) is the measured resistivity of the electrical resistivity surveys. The apparent resistivity is the product of the resistance ( $\delta V/I$ ) and of the geometric factor ( $K$ ) of the electrode array configuration used. The factor that describes the electrode configuration that is used is known as geometric factor given by the equation 2.4.7. The apparent resistivity is given by the equation 2.4.8.

$$K = 2\pi \left[ \frac{1}{AM} - \frac{1}{MB} - \frac{1}{AN} + \frac{1}{NB} \right]^{-1} \quad (2.4.7)$$

$$\rho_a = KR \quad (2.4.8)$$

The apparent resistivity value depends on the electrode configuration array. Several resistivity arrays (deployments of current and voltage electrodes) can be used to model subsurface structure. The use of the most appropriate configuration is based on the purpose of the study. In the frame of this thesis the Wenner, Schlumberger and the dipole-dipole arrays are used to verify the subsurface structure and to locate active faults. Equations 2.4.9, 2.4.10, 2.4.11 present the apparent resistivity of Wenner, Schlumberger, dipole-dipole arrays. Wenner array was proposed by Frank Wenner in 1912. The potential electrodes M, N in the Wenner array configuration are equally spaced between the current electrodes A, B. The apparent resistivity is equal to:

$$\rho_a = 2\pi\alpha R \quad (2.4.9)$$

Schlumberger array was proposed by Conrad Schlumberger in 1920. The voltage and current electrode are symmetrically placed around the centre of the array. The apparent resistivity is equal to:

$$\rho_a = \frac{\pi\alpha^2}{2b} R \quad (2.4.10)$$

In dipole-dipole array the potential and current electrodes are closely spaced while potential electrode configuration is separated from current electrode configuration. The distance between current dipoles ( $a$ ) is equal with the distance between the potential dipoles ( $a$ ). The distance between the current and potential electrode is proportional to distance between current or potential dipoles, equal to ( $na$ ). The apparent resistivity is equal to equation.

$$\rho_a = \pi n(n+1)(n+2)aR \quad (2.4.11)$$

#### **2.4.2 ADVANTAGES AND DISADVANTAGES OF WENNER-SCHLUMBERGER, AND DIPOLE-DIPOLE ARRAYS**

The Wenner, Schlumberger and the dipole-dipole that have specific advantages and disadvantages and sensitivities depth penetration, to signal strength, to sensitivity to lateral variations/inhomogeneities (Habberjam & Watkins, 1967; Barker, 1981; Loke, 2000) and to dipping interfaces (Broadbent & Habberjam, 1971; Loke, 2000). Wenner is characterized by easiness of applicability in the fieldwork, the strong signal strength (vertical resolution) and of less demand of instrumental sensitivity. The disadvantages of Wenner for 2D surveys is the poor horizontal coverage as electrode spacing increase and the need of large cables for estimating resistivity model at large depths. Moreover, Wenner has high sensitivity in lateral heterogeneities. Schlumberger needs shorter potential cables and long current electrodes. Schlumberger requires a sensitive equipment. Dipole–dipole has a better horizontal coverage than Wenner. Dipole-dipole uses shorter cables for deep soundings. The disadvantage of dipole-dipole is the small strength signal (Loke, 2000). Dipole-dipole array is the most preferable among Wenner and Schlumberger since it provides good lateral and vertical resolution, easiness of applicability (requires the minimum electrodes motions) and adequate investigation depth (Tsourlos, 1995; Loke, 2000; Papadopoulos et al., 2006; Caputo et al., 2007). Dipole-dipole array is more effective in karst hazards evaluation compared to Wenner and Schlumberger arrays (Wanfang-Zhou et al., 2002).

#### **2.4.3 ELECTRICAL RESISTIVITY TOMOGRAPHY (ERT)**

In electrical resistivity arrays the vertical and lateral resistivity variations are acquired (Griffiths & Baker, 1993; Loke, 1999; Tsourlos, 1995; Acworth, 1999). The forward resistivity modeling methods are used to calculate the apparent resistivity pseudosection. Forward resistivity modeling is a procedure to estimate the potential subsurface distribution solving the mathematical equations of the electrical current flow through inhomogeneous subsurface structure for the applied resistivity distribution and current configuration array. The forward resistivity calculations were executed by applying an iterative algorithm based on a **F**inite **E**lement **M**ethod (**FEM**). The basic assumption of the FEM method is that the field is subdivided into sub-regions where the unknown potential is approximated by suitable interpolation function attributed to specific points of sub-regions that are called nodes. These functions contain the potential value at the respective nodes of each sub-region. The minimization of the residuals results in an algebraic system of linear equations. The solution of this system leads to the determination of the potential values at the nodes. The advantages of the FEM method compared are: 1) the applicability in heterogeneities and irregular boundaries and 2) time consuming and therefore used in the frame of this study. The other differential methods for resistivity modeling (2.5D and 3D) are out of the frame of the thesis, not used in the experimental part and therefore not presented.

The pseudosection method was firstly proposed by Hallof (1967) for a dipole-dipole array. The apparent resistivity obtained from ERT measurements are plotted on a pseudosection to provide an approximate picture of the true subsurface resistivity (Loke, 1999). It is assumed that every measured resistivity value is arbitrary placed at the intersection of two 45-degree lines through the centers of the dipoles. The pseudosection of the Wenner-Schlumberger and dipole-dipole is constructed by

projecting each apparent resistivity measurement to the midpoint of the (MN) electrodes at a depth equal to the inter-electrode spacing of the measurement, (Loke, 1999; Tsourlos, 1995). The pseudosection resistivity recorded data set are inverted to image the subsurface structure.

#### **2.4.4 THE 2-D INVERSION OF GROUND SURFACE AND SUBSURFACE RESISTIVITY DATA USING ACCURATE INVERSION TECHNIQUE PROCEDURE**

The true subsurface resistivity is estimated by inversion of the measured apparent resistivity. The inversion principle is based both on: 1) subdividing the studied 2D geological structure into a number of cells and 2) determining the resistivity within the cells that produce a subsurface model fitting reliably to the recorded data (Nguyen et.al, 2005). Extended reviews of the type of inversions have been presented by many authors (Press et al., 1988, Tsourlos, 1995).

For the purpose of this thesis the geoelectrical data collected have been processed by means of the RES2DINV (Loke, 1997) modelling software in order to perform 2D geoelectrical data inversion. The inversion routines are based on the smoothness-constrained least squares method (deGroot-Hedlin & Constable 1990; Constable et al. 1987; Sasaki 1989, 1992; Loke & Barker 1995; Loke & Barker, 1996a; Loke & Barker 1996b; Tsourlos 1995) and the forward resistivity calculations were executed by applying an iterative algorithm based on a FEM. The detailed mathematical considerations are out of the scope of the thesis and therefore not presented.

---

## **2.5 SUMMARY**

The above literature review demonstrates the range of information available about the various aspects of the study area and processes. The following Chapter 3 describes the methods applied in this research project.

---



## CHAPTER 3: METHODOLOGY

### 3.1 HORIZONTAL TO VERTICAL SPECTRA RATIO (HVSR) FOR SITE EFFECTS STUDY

#### 3.1.1 THEORETICAL BACKGROUND OF HVSR TECHNIQUE PROPOSED BY NOGOSHI-IGARASHI (1971)

Nogoshi & Igarashi (1971) proposed the applicability of horizontal to vertical spectra ratio (HVSR) using only one single-station in site effect studies and specifically in determining rock or soft sites. The Nogoshi–Igarashi interpretation is based on the assumption that the noise wavefield is mostly composed of surface waves. According to Nogoshi & Igarashi’s interpretation the spectra H/V ratio using microtremors is correlated with the ellipticity of Rayleigh effects and can be used to estimate the fundamental frequency of soft soils. To provide evidences of their assumption, they compared the spectra characteristics of the horizontal and vertical components of microtremor recordings at specific sites at Hakodate city in Japan. Fourier spectrum of the horizontal and vertical components at the site Hakodate ENG in a linear scale are presented in Figure 3.1.

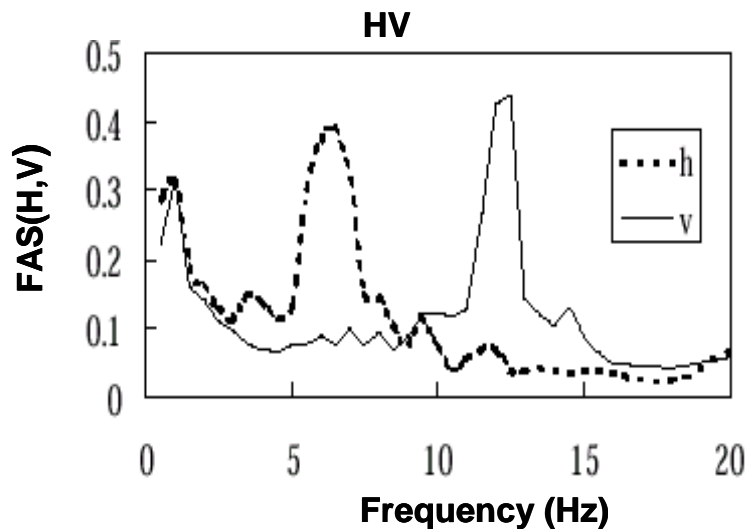


**Figure 3.1:** Fourier spectrum of horizontal (dashed lines) and vertical components (solid lines) at Hakodate ENG (Nogoshi-Igarashi, 1971, extracted from Nakamura, 2000).

The comparison study presented above results to Nogoshi-Igarashi (1971) interpretation of HVSR spectra ratio with surface waves in site effects studies. The Nogoshi-Igarashi assumptions and arguments (1971) presented by Bard (1999) are:

1. The microtremors wavefield is mostly composed of Rayleigh waves.
2. The H/V ratio is related to the ellipticity of Rayleigh waves.
3. The ellipticity of Rayleigh waves is frequency dependent and exhibits a sharp peak around the fundamental frequency at sites of high impedance contrast between the surface and subsurface structure.

4. The impedance contrast threshold above which the horizontal to vertical spectra ratio HVSR peaks coincidence with the ellipticity curves of Ryleigh ranges between 2.5 and 3.

Many authors (Lachet & Bard, 1994; Field & Jacobs, 1995; Ansary et al., 1995; Bard, 1998) have suggested that the fundamental peak of H/V is explained with the fundamental mode of the Rayleigh wave. Bard (1999) suggested that the theoretical explanation is provided by the ellipticity ratio of Rayleigh waves is preferred but not fully satisfactory. These theoretical definitions are based only by observing the similarity of the H/V ratio of microtremors and the fundamental mode Rayleigh waves (Nakamura, 2000a). Konno & Ohmachi (1998) compared the ellipticity curves for Rayleigh waves in soils with different and complex velocity profiles and the transfer function for S-waves and the microtremor H/V ratio and observed similarities. According to Bard (1999) the Nogoshi & Igarashi interpretation is not valid in the case of significant proportion of body waves in the noise wavefield.

Konno & Ohmachi (1998) estimated an impedance contrast threshold value around 2.5. Ansary et al. (1995) proposed an impedance contrast threshold between 3.3 and 5.5 for simple one layered structure and above 2.5 for complex structures. The H/V peak frequency and the fundamental S-wave resonance frequency coincidence using impedance contrast threshold around 3 (Bard, 1999). Trifunac & Todorovska (2000) suggested that the HVSR technique is more valid for high impedance contrast of surface and subsurface structures, while Al-Yuncha & Luzon (2000) used HVSR technique for low impedance contrast of surface and subsurface structures.

### **3.1.2 EXPLANATIONS ON HVSR TECHNIQUE, NAKAMURA (1989, 1996, 2000)**

Nakamura (1989) based on the effect of seismic ground response in earthquake distribution, presented the applicability of the horizontal to vertical spectra ratio technique using microtremor in estimating the dynamic ground response characteristics. Nakamura (1989) based on the observed similarity of earthquake waveforms recorded in same seismological station concluded that site effect is the most important factor in earthquake hazards assessment. Nakamura (1989) to test the applicability of microtremor in geotechnical engineering field examined the Fourier spectra of 24-hour microtremor measurements recorded at two underground stations, Kamonomiya and Tabata in Japan. The velocity amplitude and the spectra characteristics of microtremor at Kamonomiya and Tabata underground station are varying over time. The observed fluctuation in the amplitude of microtremor is considered due to the effect of the artificial noise wavefield induced by train in the vicinity of the investigated sites. The effect of the train was observed in the vertical component of the recordings implying that Rayleigh waves effects are included in the vertical spectrum in the surface. The amplitude of the incident seismic motion waves on surface layers estimated from boring survey and PS velocity logging was used in the comparison. Nakamura (1989) concluded that the observed differences in the transfer functions calculated from the horizontal components recorded at the surface and from boring investigation data are due to the effect of the surface Rayleigh waves. Nakamura (1989), proposed a new transfer function method for the estimation of ground seismic response of surface layer considering the Rayleigh wave effect as noise that should be eliminated from the transfer function. The basic concept of this interpretation is based on the following

observations: 1) Horizontal and vertical microtremors present similar characteristics. The horizontal component of microtremor is amplified through multi-reflections of the S-wave and the vertical tremor is amplified through multi-reflection of the P-wave, 2) the vertical component of ambient noise keeps the characteristics of source to sediments surface ground and the Rayleigh wave effects in the vertical spectrum are existent only in the surface layer, 3) the amplification ratio of horizontal and vertical ratio at a rock site is close to unity (no amplification on bedrock). Nakamura (1989) presented the new transfer function for estimating ground spectra characteristics. The transfer function ( $S_T$ ) of the surface layer is given by the equation (3.2.1):

$$S_T = \frac{S_{HS}}{S_{HB}} \quad (3.2.1)$$

where  $SH_S$  and  $SH_B$  are the horizontal spectra of microtremor recorded on the surface and the horizontal spectrum of the basement, respectively.

The assumptions proposed by Nakamura (1989) are presented in the following:

1. The Rayleigh wave effect is included only in the vertical spectrum at the surface ( $S_{VS}$ ) but not in the vertical spectrum ( $S_{VB}$ ) in the basement.
2. For a wide frequency range (0.2-20Hz), the spectra ratio of the horizontal and vertical components in the stiff substratum is close to unity (equation 3.2.2). This ratio is free of Rayleigh effects.

$$\frac{H_B}{V_B} = 1 \quad (3.2.2)$$

3. Assuming that the vertical component of microtremor is not amplified propagating through the soft soil layer, the Rayleigh wave effect on the vertical component ( $E_S$ ) is given by the equation (3.2.3).

$$E_S = \frac{S_{VS}}{S_{VB}} \quad (3.2.3)$$

4. If there is no Rayleigh effect (hard rock),  $E_S$  equals to unity.

Assuming that the effect of Rayleigh is equal for vertical and horizontal component, the ratio  $S_T/E_S$  is considered as a reliable transfer function of the geological column after eliminating the Rayleigh wave effects and is simply derived from the equation (3.2.4).

$$S_{TT} = \frac{S_T}{E_S} = \frac{\frac{S_{HS}}{S_{HB}}}{\frac{S_{VS}}{S_{VB}}} = \frac{\frac{S_{HS}}{S_{HB}}}{\frac{S_{VS}}{S_{VB}}} = \frac{R_S}{R_B} \quad (3.2.4)$$

$R_S$  and  $R_B$  are the horizontal to vertical spectra ratio of microtremors in the surface and subsurface structure. Considering assumption 2 that for a wide frequency range, the

spectra ratio of the horizontal and vertical components in the stiff subsurface structure is close to unity ( $R_B=1$ ), equation (3.2.4) is modified to (3.2.5):

$$S_{TT} = R_s = \frac{S_{HS}}{S_{VS}} \quad (3.2.5)$$

It is therefore possible to estimate the dynamic characteristics of the surface layers using microtremors recorded on the surface.

Summarizing, Nakamura (1989) compared bore-hole data, strong motion and microtremor including train induced tremors data at the two underground stations in Japan to verify the validity of the new proposed transfer function of microtremor after eliminating Rayleigh effects in estimating ground dynamic characteristics. The observed stability in the fundamental frequency, amplification and in the shape of the spectra characteristics provides evidences of the verification of the method. Nakamura (1989) explained the peak of the H/V ratio with multiply refracted vertical incident SH waves and eliminated the Rayleigh wave effects from the H/V ratio, considered it as noise. Moreover, with the use of the new transfer function for estimating the dynamic ground characteristics after eliminating the Rayleigh effects proposed by Nakamura (1989), there is no restriction in the recording time of microtremors during midday or midnight.

Nakamura (1996) presented a more detailed study of horizontal to vertical spectra ratio (HVSR) in determining seismic ground characteristics and considered both the influence of body and surface wave on the microtremor wavefield. Nakamura (1996) renamed HVSR technique to QTS (Quasi Transfer Function) and introduced the applicability of microtremor spectra ratio in estimating structural seismic response characteristics. Nakamura (1996) proposed that building vulnerability can be estimated using microtremor recordings on buildings and ground surface. Building vulnerability indices ( $K_g$ ) were also presented. Nakamura (2000) presented the revised explanation provided. A typical geological structure of a sedimentary basin is used to define the ground motions spectra is presented in Figure 3.2 (Nakamura, 1996; Nakamura, 2000). The revised explanation (Nakamura, 2000) considers that the microtremor wavefield in this sedimentary basin is composed of body and surface waves.

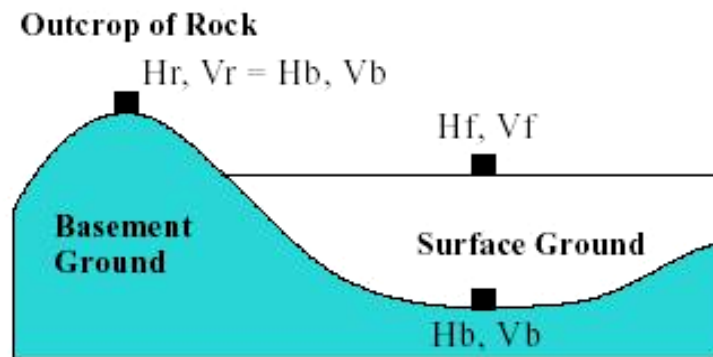


**Figure 3.2:** A typical sedimentary basin.  $H_r, V_r$  are the horizontal and vertical motion on the exposed rock ground near the basin,  $H_b, V_b$  are the spectra of the horizontal and vertical motion in the basement under the basin,  $H_f, V_f$  are the spectra of the horizontal and vertical motion on the surface ground of the sedimentary basin (Nakamura, 1996; Nakamura, 2000).

Under this assumption the horizontal (H<sub>f</sub>) and vertical (V<sub>f</sub>) spectra of the horizontal and vertical motion on the surface ground of the sedimentary basin are given by the equations (3.2.6) and (3.2.8) (Nakamura, 1996, 2000):

$$H_f = A_h \cdot H_b + H_s \quad (3.2.6)$$

$$T_h = \frac{H_f}{H_b} \quad (3.2.7)$$

$$V_f = A_v \cdot V_b + V_s \quad (3.2.8)$$

$$T_v = \frac{V_f}{V_b} \quad (3.2.9)$$

where,

- H<sub>r</sub> and V<sub>r</sub> are the horizontal and vertical spectra motion on the basement ground.
- H<sub>b</sub> and V<sub>b</sub> are the spectra of the horizontal and vertical motion in the basement beneath the sedimentary layer.
- H<sub>s</sub> and V<sub>s</sub> are the spectra of the horizontal and vertical motions of surface waves.
- A<sub>h</sub> and A<sub>v</sub> are the amplification of horizontal and vertical motions of vertically incident body wave, respectively.
- T<sub>h</sub> and T<sub>v</sub> is the amplification of horizontal and vertical motion of the surface sedimentary layer.

The horizontal (H<sub>f</sub>) and vertical (V<sub>f</sub>) spectra recorded on the surface ground of the sedimentary basin provides the transfer function of the seismic response of the sedimentary basin given by equation (3.2.10):

$$QTS = \frac{H_f}{V_f} = \frac{A_h \cdot H_b + H_s}{A_v \cdot V_b + V_s} = \frac{H_b}{V_b} \cdot \frac{\left[ A_h + \frac{H_s}{H_b} \right]}{\left[ A_v + \frac{V_s}{V_b} \right]} \quad (3.2.10)$$

The basic assumptions of QTS are:

1. The H<sub>b</sub>/V<sub>b</sub> spectra ratio of a rock site is close to unity.
2. No influence of Rayleigh effects suggests that QTS=A<sub>h</sub>/A<sub>v</sub>.
3. In the case that there is no Rayleigh wave effect the vertical spectra on the surface ground of the sedimentary basin is almost equal (V<sub>f</sub> ≅ V<sub>b</sub>) to the vertical spectra motion in the basement under the basin.
4. In the case that the vertical spectra on the surface ground of the sedimentary basin is larger than the vertical spectra motion in the basement under the basin (V<sub>f</sub>>V<sub>b</sub>), the effect of Rayleigh wave is existent. Under this specification horizontal amplification can be written as:

$$T_h^* = \frac{T_h}{T_v} = \frac{\frac{H_f}{V_f}}{\frac{H_b}{V_b}} = \frac{QTS}{\frac{H_b}{V_b}} \quad (3.2.11)$$

$$T_h^* = \frac{T_h}{T_v} = \frac{\frac{H_f}{V_f}}{\frac{H_b}{V_b}} = \frac{QTS}{\frac{H_b}{V_b}} = \frac{\left[ A_h + \frac{H_s}{H_b} \right]}{\left[ A_h + \frac{V_s}{V_b} \right]} \quad (3.2.12)$$

Considering that  $H_b/V_b$  is almost equal to unity equation (3.2.12) is modified to:

$$T_h^* \cong QTS \cong \left( 1 + \frac{A_v}{\beta} \right) \quad (3.2.13)$$

Where  $\beta=V_s/V_b$  and is related with the effect of Rayleigh wave.

- No Rayleigh effects (the vertical spectra on the surface ground of the sedimentary basin is almost equal to the vertical spectra motion in the basement under the basin) suggests that  $\beta=0$  and  $QTS=A_h/A_v$ .
- Rayleigh wave dominance suggests that  $QTS=H_s/V_s$ .
- The vertical component is not amplified at the fundamental frequency  $F_0$ .

Nakamura (1996) concluded that :1) QTS presents stability in the fundamental frequency  $F_0$  and 2) is a valid estimator of ground fundamental frequency due to multi-reflection of SH-wave in the surface layers regardless the degree the Rayleigh wave effects. The comparison of  $H_f$ ,  $V_f$ ,  $H_f/H_b$  using the SSR technique and  $H/V$  proposed by Nakamura (1996, 2000) suggests that the amplitude of QTS is smaller than the amplitude of the theoretical transfer function. Nakamura (2000) proposed that QTS explanation (or HVSR technique) can be valid interpreted by the multi-reflection of SH-wave in the surface layers.

### 3.1.2.1 K-Values to determine building structural damage (Nakamura 1996)

Nakamura (1996) presented the applicability of K-value of column of rigid frame viaduct. Nakamura (1996) considering that concrete columns are designed to collapse by bending moment, proposed that vulnerability index  $K_{sg}$  for a column of rigid frame can be derived from marginal column due to the bending moment at the upper and lower points of the column. Specifically,  $K_{sg}$  multiplied with maximum acceleration of basement layer specifies the marginal strain of the upper and lower columns ends. In the case of a two story rigid frame viaduct is defined from the equation (3.2.14):

$$K_{sg} = \frac{\left(\frac{7500}{\pi^2}\right)\left(\frac{A_{sg}}{F^2}\right) \times (bh_i)}{(h_1^3 + h_2^3)} \quad (3.2.14)$$

Where  $A_{sg}$  is a combined amplification factor of surface ground and of the viaduct,  $F$  is the fundamental frequency of the viaduct,  $b$  is the width of the column in vibrating direction and  $h_i$  is the column height of  $i$ -th story. The value of  $7500/\pi^2$  is a coefficient to adjust the calculated results in unit  $10^{-6}$  strain, when seismic acceleration is measured in Gal ( $\text{cm}/\text{sec}^2$ ). In Hyogo-Ken-Nanbu earthquake higher values of  $K_{sg}$  are presented for the higher column of the two-story rigid frame viaduct in accordance with the actual viaduct damage during the earthquake. The  $K_{sg}$  values calculated before the earthquake event using microtremor recordings on surface ground and rigid frame viaduct along Shinkansen correlates very well with the observed structural damage after Hyogo-Ken-Nanbu earthquake event.

### 3.1.2.2 VULNERABILITY INDEXES, K-VALUES FOR SURFACE GROUND

Vulnerability index  $K_g$  values estimation to determine earthquake damage of surface ground and structures are also presented in Nakamura (1996, 2000a). In Figure 3.3 the shear strain deformation of surface ground is presented.

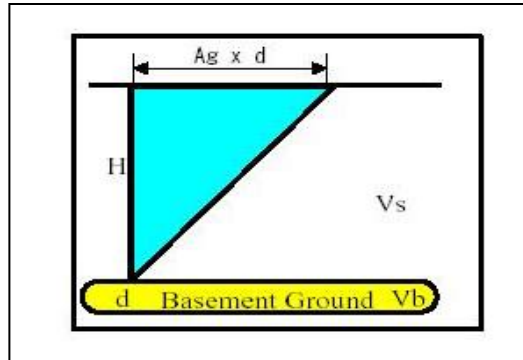


**Figure 3.3:** Surface ground deformation (extracted from Nakamura, 2000).

The shear strain deformation of surface ground is given by the equation:

$$\gamma = A_g \cdot \frac{d}{h} \quad (3.2.18)$$

$A_g$  is the amplification factor of surface layer,  $h$  is the thickness of surface layer and  $d$  represents the seismic displacement. Considering the S wave velocities of the basement and surface layer the fundamental frequency  $F$  of the surface layer is given by the equation:

$$F_g = \frac{V_b}{4 * A_g * h} \quad (3.2.19)$$

The shear strain ( $\gamma$ ) is given by the equation (3.2.20):

$$\gamma = \frac{A_g \alpha_b}{(2\pi f_g)^2} 4A_g \frac{F_g}{C_b} = \frac{A_g^2}{f_g} \frac{\alpha_b}{\pi^2 C_b} = c \cdot K_g \cdot \alpha \quad (3.2.20)$$

where ( $\alpha_b$ ) is the basement acceleration, ( $c$ ) is an almost constant value for various sites and ( $v_b$ ) is the shear wave in bedrock.

$$\alpha_b = (2\pi f_g)^2 d \quad \text{and} \quad c = \frac{1}{\pi^2 v_b}$$

$K_g$  vulnerability index is given by the equation (3.2.21):

$$K_g = \frac{A_g^2}{f_g} \quad (3.2.21)$$

According to Nakamura (2000a),  $K_g$  value can be considered as the vulnerability index of the site and it is useful to determine sites where major damages might be observed in the case of a strong earthquake.  $K_g$  values for various types of structures might be found in Nakamura (1996, 1997). The vulnerability index  $K_g$  in areas that suffered major damages during the Loma Prieta earthquake ranges between 20~100. High  $K_g$  values indicate liquefaction phenomena. In Loma Prieta 1989 earthquake sites where  $K_g$  values were higher than 20 ( $K_g > 20$ ) liquefied while sites with small  $K_g$  values suffered low damages during the 1989 earthquake event. At sites where there is no structural damage vulnerability index  $K_g$  ranges from 0.5~5. Vulnerability index using microtremors to evaluate the ground failure/liquefaction potential hazards after the Chi-Chi Taiwan is higher in areas where liquefaction occurred (Huang & Tseng, 2002). Nakamura (2000) concluded that the H/V peak ratio using microtremors or earthquake data can be explained with SH waves. With the re-examination of H/V spectra ratio Nakamura (2000a) verified his first proposed explanation in 1989. Detailed reviews can be found by Mucciarelli & Gallipoli (2001). Nakamura (1996, 1997) observed very good compatibility between the Vulnerability index  $K_g$  and the earthquake building damage. According to Nakamura this compatibility is based on two reasons. Firstly, the vulnerability index is a scaling factor providing direct estimates of ground shear strain given by the equation:

$$\gamma = c \cdot K_g \cdot a_{\max} \quad (a)$$

Secondly, Nakamura consider that the damage in soils and structures is basically controlled by the shear strain in soils. Under these assumptions equation (a) is based on the following two assumptions:

- the amplification of the fundamental frequency represents the S-wave amplification
- the peak acceleration ( $a$ ) and displacements ( $d$ ) can be related with the fundamental frequency

$$a_{\max} = 2 * \pi F_g * d_{\max} \quad (3.2.22)$$



Gueguen et al. (2000) observed in the high frequencies ( $F=10\text{Hz}$ ) considerable compatibility between the HVSZ amplification and building damage after the Pujili earthquake (Equador, 1996). Duval et al. (1994) observed in the low frequency range ( $F<0.8\text{Hz}$ ) considerable compatibility between building damages after the Garacas Earthquake and the H/V ratios. In Figures 3.4 and 3.5 are presented the vulnerability index  $K_g$  and earthquake damage after the Kobe earthquake (Nakamura et al., 2000b).

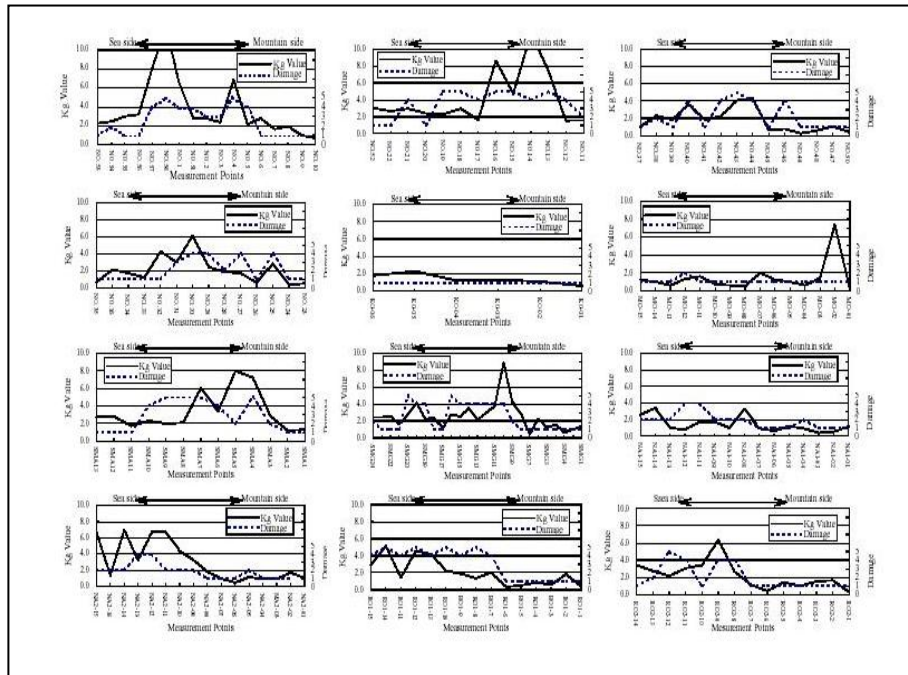


**Figure 3.4:** Relationship between vulnerability indexes and earthquake damage after the Kobe earthquake (extracted Nakamura et al., 2000b).

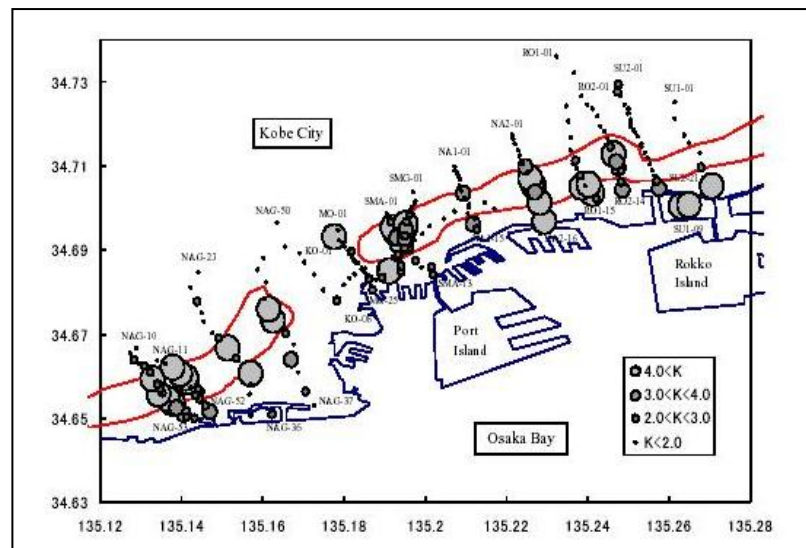


**Figure 3.5:** Ground vulnerability distribution in Kobe city based on HVSZ technique using microtremors (extracted from Nakamura et al., 2000b).

These examples provide evidences of the valid applicability of HVSR technique to estimate  $K_g$  value as a vulnerability index of a site to determine sites where major damages might be observed in the case of a strong earthquake.

### 3.1.2.3 BASEMENT DEPTH RELATED WITH NAKAMURA TECHNIQUE

The ground resonance response on the amplitude of the incident seismic wave is major near the fundamental frequency of the soil deposit (Nakamura, 2000). The fundamental frequency of vertically propagating waves in a linear (1D) elastic soil layer is a function of the depth ( $h$ ) and of the average shear wave velocity ( $V_s$ ) of the soil deposit. The soil fundamental frequency is extracted from the equation:

$$F_o = \frac{C_s}{4h} \quad (3.2.23)$$

The amplification factor is a function of the soil thickness and stiffness, of the impedance contrast between surface and subsurface layers and of the strain dependent properties of the soil. Considering similar densities of surface and subsurface structure the amplification is equal to :

$$A_o = \frac{C_b}{C_s} \quad (3.2.24)$$

Substituting in equation (3.2.23) the equation (3.2.24) the depth of deposit is equal to:

$$h = \frac{C_b}{4A_o \cdot F_o} \quad (3.2.25)$$

## 3.1.3 DATA ACQUISITION AND PROCESSING

### 3.1.3.1 DATA ACQUISITION RECOMMENDATIONS

Duval et al. (1994), Nakamura (1996), Mucciarelli (1998) and Mucciarelli et al. (2003) and **J-Sesame (JS)** project guidelines (2005) presented recommendations concerning data acquisition and processing.

1. Accelerometers produce very unstable results and not sensitive enough at frequencies lower than 1Hz (JS manual WP12, D23.22) and should be avoided as their resolution power is too low to resolve noise on a broad frequency band in the three components (Mucciarelli, 1998). Velocimeters coupled with a high gain acquisition system are preferable. At periods longer the 1s velocimeter of 5 or 10sec are preferable (Mucciarelli, 1998; Bard, 1999). The Lennartz 5 sec sensors are the best performing in terms of the frequency range, sensitivity and stability (JS manual WP12). The Lennartz (LE- 3D/5s) seemed the overall best sensor if response down to 0.1 Hz or below if required. To ensure stability of the sensor broadband seismometers with natural period higher than 20 sec are recommended (Jsesame manual WP12, D23.22). Therefore, spurious noise recordings and not desired signal such as electronic noise induced by wiring between electronic parts not coupled with the ground (Mucciarelli, 1998;

Mucciarelli et al., 2005). The cable length that connects the sensor and the station is suggested not to exceed the length of 100 meters based on JS guidelines.

**2.** Microtremor measurements should not be performed in rainy or windy days (Mucciarelli, 1998, Mucciarelli et al., 2005) or after heavy rain (JS manual WP12, D23.22). Cara et al. (2003) analyzed two weeks of continuous microtremor recordings at the Colfiorito Basin, Umbria in Italy to study variations in noise HVSR from meteorological condition, and observed very strong variations in the low-frequency range (<1Hz) in the case the wind speed exceeds 18 km/hr. The wind effect on microtremor measurements near coastline is related to stronger sea swells during windy weather (Gaul et al., 1995). Mucciarelli (1998), investigating the effects of gusts of compressed air on sensors, wires and digitizers - to simulate wind acting directly on instruments deployed in the field - observed a strong enhancement of HVSR below 1Hz. Wind disturbs only low frequencies (Mucciarelli et al., 2005; JS manual WP12, D23.22). Mucciarelli et al. (2005) studied the effect of wind variation on HVSR at a permanent three-component seismological station in a controlled wind speed condition experiment equipped with a laser particle velocimeter. The effect of increasing wind speed on various sensor/digitizer configurations were analyzed by numerical modelling conducting. Numerical experiment performed by Mucciarelli & Gallipoli (2004) and experimental study performed by Mucciarelli et al. (2005) and Chatelain et al. (2008) suggest that the wind increases the amplitude of horizontal and vertical components of microtremor recordings but does not influences the fundamental HVSR frequency. In the case of quick microzonation studies the sensors protection against wind is suggested (Mucciarelli et al., 2005).

**3.** Asphalt or concrete generate in the frequency band 7-8Hz small perturbations in the HVSR pattern while for a broad frequency range 0.2-20Hz no artificial peaks are observed (JS manual WP12, D23.22). Reinforced concrete inserts small attenuation in the amplification content while it does not affect the fundamental frequency content. Ground floor or basements are points for reliable microtremor measurements, as they are well coupled with the ground and protect the instrumentation from the weather (Mucciarelli et al., 2005). 'Soft and non-cohesive' materials such as foam-rubber should be avoided (Jsesame manual WP12, D23.22).

**4.** It is recommended to avoid measurements in a noisy environment. The additional external noise created by a seismic sledgehammer experiment (Mucciarelli et al., 2003) increases the amplification factor and does not affect the frequency pattern. Monochromatic sources (construction and industrial machines, pumps) and short duration disturbances should be disregarded using either an anti-trigger window selection (JS WP12, D23.22) or manually using the J-sesame program. The movement of buildings and trees induce low frequency perturbations in the ground mostly in the case of strong wind. The synergy between building structural type, the wind strength, soil type increases these movements (JS WP12, D23.22).

**5.** Daytime or night time microtremor measurements provide reliable site effect estimate (Mucciarelli, 1998).

6. Sesame project recommends that the recording duration should fulfill the condition  $f_0 > 10/lw$  to ensure that at the fundamental frequency there are at least 10 significant cycles in each window. The total number of significant cycles is recommended to be larger than 200. According to Mucciarelli (1998) and Mucciarelli & Gallipoli (2001) ten time series of 1 sec is enough to guarantee 'valid' signal windows for site effect estimation.

7. For microzonation studies the measurement spacing in the case of lateral variation environment a grid of 250 m and in a simple (1D) structure a large spacing of a grid of 500 m are sufficient (JS WP12, D23.22).

### **3.1.3.2 DATA PROCESSING PROCEDURE**

Mucciarelli & Gallipoli (2001) proposed the data processing procedure. The selected time windows of each time series are corrected for the base line and for anomalous trends, tapered with a cosine function to the first and last 5% of the signal, and band pass filtered from 0.5 to 20 Hz with cut off frequencies at 0.3 and 22 Hz, selected in order to preserve energy and avoid spurious maxima due to unrealistic low vertical spectra (Castro et al., 1997). The arithmetic average of all horizontal-to-vertical ratios represents the HVSR site amplification function (Mucciarelli & Gallipoli, 2001). In the frame of this thesis J-Sesame software is applied following the guidelines proposed by Mucciarelli (1998). The J-Sesame software is a Java application for site effects studies and is mainly a tool for: 1) organizing the input data, 2) executing window selection and processing and 3) displaying the processing results (JS WP12, D23.22).

### **3.1.3.3 RELIABILITY OF THE RESULT**

In the frame of this thesis the following steps of JS software are used:

#### **1. The optimum window length and number of noise time windows.**

According to Bard (1999) the window length depends on the bandwidth of interest. When the interest is focused around 1 Hz a window length of 20 sec is sufficient for reliable site effect estimates. The stability of the results through a standard deviation estimates is an estimator of an acceptable and valid of time windows number (Bard, 1999). The recommendation provided by Sesame Software proposes that a large number of time windows and cycles is required. More specifically, in the case that the automatic window selection is used the total number of significant cycles to be larger than 200 (scientific interest at 1 Hz and at 0.5 Hz peak requires at least 20 windows of 10sec each and 10 time windows of 40 sec each, respectively). Five recordings of one minute are sufficient for reliable site effect estimation (Albarelo, 2001). According to Mucciarelli (1998) ten time window recordings of 1 minute are sufficient for reliable results. In the frame of this thesis guidelines proposed by Mucciarelli (1998) and JS software are followed. Moreover, in the frame of this thesis a 50 sec time window length is selected. The number of 50 sec time windows ranging from 5-25.

## **2. Merging the Horizontals components to calculate the ‘H’ horizontal component.**

The computation of the geometrical mean or the root mean square average provides reliable merging estimations (Bard, 1999). Merging the horizontal (NS and EW) components with a quadratic mean or geometric mean is recommended by the JS software. In the frame of this thesis geometric mean is adopted. Haghshenas et al. (2008) used geometry average (as arithmetic average was inconsistent of with the actual residual distribution) to calculate the HVSR ratio using earthquakes and microtremors because of the lognormal distribution of residuals on spectra ratios. Geometric averaging spectra are preferred (Bard, 1999). Field & Jacob (1995) and Bard (1999) concluded to similar results.

## **3. Smoothing Spectra**

Smoothing is of paramount importance to avoid spurious peaks (linked with sharp troughs) on the vertical component spectrum that alters the spectra shape and the fundamental peak estimate. Konno-Ohmachi (1998) proposed a new logarithmic window function and the H/V ratios (NS/UP and EW/UP) are calculated separately for the three individual records and then averaged arithmetically. To detect the low and high frequencies a complement smoothing solution is to adapt the width of the smoothing window to the frequency of interest (Bard, 1999).

## **4. Averaging Spectra**

Mucciarelli (1998), Bard (1999) proposed to compute first the H/V ratio and then average the ratios obtained from various windows. The procedure proposed by Mucciarelli (1998) is also adopted in the frame of this thesis.

## **5. Standard Deviation Values**

A large standard deviation value is an indicator that ambient vibrations are strongly non-stationary that may significantly affect the H/V peak frequency. It is recommended the standard deviation value to be lower than a factor of 2 for fundamental frequency higher than 0.5 Hz and lower than a factor of 3 for fundamental frequency lower than 0.5 Hz over a frequency range at least equal to  $[0.5f_0, 2f_0]$  (JS software).

### **3.1.3.4 J-SESAME SOFTWARE FOR SITE EFFECTS STUDIES**

The general layout of the J-SESAME graphical user interface for site characterization studies is based on four main modules: 1) browsing, 2) window selection module, 3) processing module and 4) display module (Figures 3.6, 3.7, 3.8). The processing is based on the J-Sesame guidelines provided by (<http://SESAME-fp5.obs.ujf-grenoble.gr>) In the following sections J-SESAME software will be referred as (JS). The steps for ground seismic response estimation are briefly described:

1. Manual window selection of the stationary signal window was adopted. The option of automatic (STA/LTA) is also available using JSexame software. In the following figure a time series of 800sec versus the amplitude of the recording is presented. The green windows indicate the manually selected windows for the HVSR ground response evaluation. The first (black) time series corresponds to

the vertical component and the two remaining (red, blue) correspond to the (NS) and (EW) horizontal components.

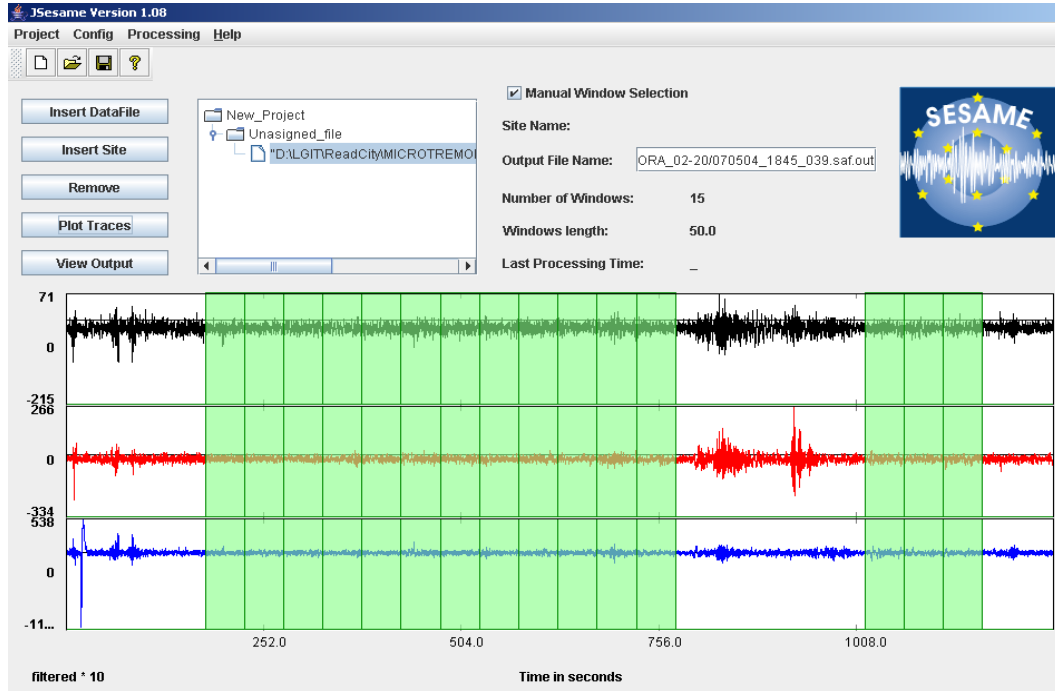


**Figure 3.6:** The general layout of the J-SESAME graphical user interface. The selected time series windows are shown in green (J-Sesame guidelines manual).

2. The selected time windows of each time series are corrected for the base line and for anomalous trends (DC-offset removal: r-mean is selected), tapered with a cosine function to the first and last 5% of the signal (tapering: cos), and band pass filtered from 0.2 to 20 Hz (frequency spacing selection: 0.2-20Hz) and smoothing, and merging of horizontal components. Several smoothing options are available. In the frame of this thesis Konno-Ohmachi smoothing is recommended as it accounts for the different number of points at low frequencies. Geometric mean for merging two horizontal components is adopted:

$$H_{(Ni)} = \sqrt{[EW_{(Ni)} \cdot NS_{(Ni)}]}$$

3. The spectra of each component vertical and horizontal (NS and EW) for each selected window ( $N_i$ ). In Figure 3.7 (upper) is presented the selected windows and the derived calculated spectra of the three components (lower right) for the selected window. In Figure 3.7 (lower left) is presented the calculated the HVSR (or H/V) for each time window ( $N_i$ ):

$$HVSR_{(Ni)} = \frac{H_{(Ni)}}{V_{(Ni)}}$$

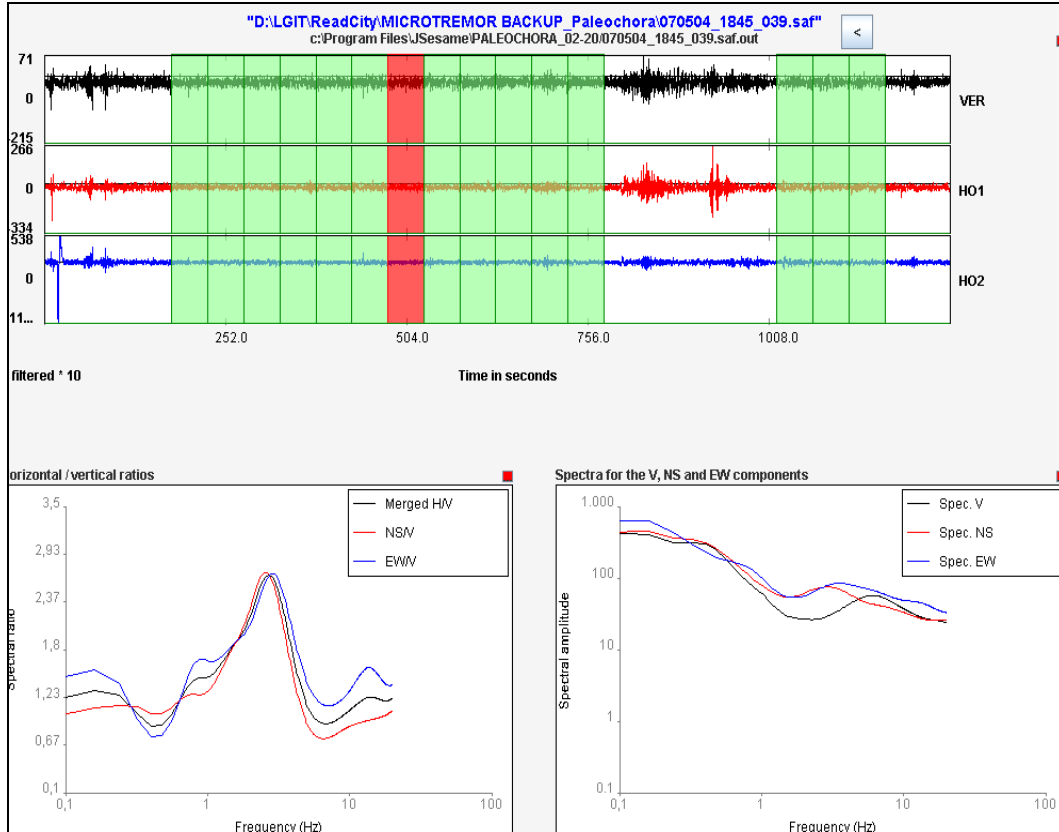


**Figure 3.7:** The selected time window for the HVSR calculation (green time windows). The selected time window for H/V (left lower) and spectra (right lower) is denoted with red zone. For each selected window the H/V ratio (left lower) and the vertical and horizontal spectra (right lower) are calculated.

4. The average HVSR spectra ratio calculation of the selected N time series window is calculated :

$$HVSR = 10 \frac{\sum \log_{10} \left( \frac{H_i}{V_i} \right)}{N}$$

5. The HVSR, Hns/V and Hew/V ratios are calculated and the HVSR, Hns/V and Hew/V fundamental frequency, amplification and the standard deviation representation are extracted. The average HVSR spectra ratio (Fig 3.7 and 3.8a) is presented with the black line curve. The X-axis shows the frequency range of investigation (0.2-20Hz) and the y-axis corresponds to the HVSR amplification. The fundamental frequency is presented in the graph with the grey vertical line while the shadow grey zones (Fig 3.8) represents the standard deviation of the fundamental frequency. The red and blue curves represent the standard deviation of the average HVSR curve (Fig.3.8a). The HVSR (Fig.3.8a), Hns/V(Fig.3.8b) and Hew/V (Fig.3.8c) spectra ratio are presented with the black curve. The blue and red line curve represents the standard deviation of the

HVSR, Hns/V and Hew/V spectra ratio. The pink zone (Fig. 3.8, green panels) presents the frequency range where the spectra ratio results are considered low statistical significant due to time window length selection ( $f_0=10/w$ ).

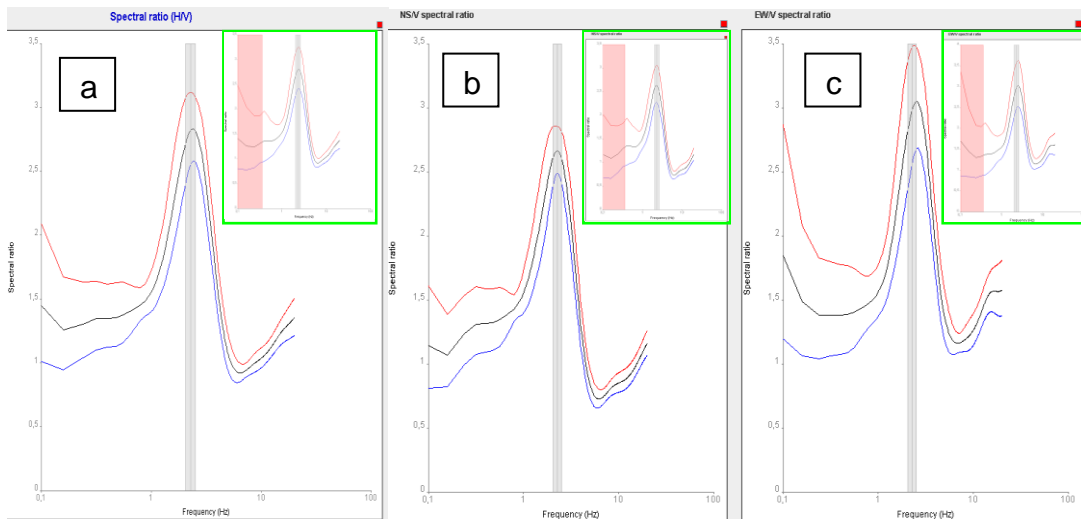


**Figure 3.8:** a) Average H/V spectral ratio and standard deviation using JS software, b) The spectra ratio of the horizontal NS components to vertical (Hns/V) to characterize the seismic motion in the NS direction, c) the spectra ratio of the horizontal EW components to vertical (Hew/V) to characterize the seismic motion in the EW direction. The HVSR, Hns/V and Hew/V spectra ratio are presented with the black curve. The blue and red line curve represents the standard deviation of the HVSR, Hns/V and Hew/V spectra ratio. In the upper right (green panel) of the average HVSR (a), Hns/V, Hew/V are presented the extracted HVSR when a 20 sec window is adopted.



### **3.2 ELECTRICAL RESISTIVITY TOMOGRAPHY INSTRUMENTATION**

The instrumentation used to model the subsurface structure is known as resistivity meter (RM). This consists of the power source and the measuring system that measures the resistance (Tsourlos, 1995). DC or AC power source can be used. The AC power source is preferable to the DC since the DC power source induces polarization effect and spontaneous potential. AC power source eliminates electric polarization effect and nullifies the spontaneous potential. However, AC power source induces capacitance effects and electromagnetic coupling (EM) between current and potential electrodes. Low frequencies are used in the AC source to minimize electromagnetic induction effects and to achieve deep investigation depth. The measuring system consists of an ammeter and of a voltmeter to measure subsurface resistivity. The automatic resistivity meter is connected to a switching unit. The switching units are controlled by a laptop computer that can switch any of the two current or potential cables.

Electrode selection, triggering the measuring meters, current intensity, measurement sampling and the measuring storage are controlled automatically by the computer. Using computer control a variety of electrode configurations and separations can be selected and a resistance measurement can be acquired (Reynolds, 1997). A central or distributed switching unit can be used (Figure 3.9, Tsourlos, 1995). In the case of the central switching unit the channels of the multi-core cable are equal to the probes used for the array. The distributed switching unit consists of controlled switching circuits mounted at every probe (Tsourlos, 1995). The automatic resistivity measuring systems are time-consuming but easy to apply and flexible in the choice of the array and costly endeavor. The only disadvantage is the increased equipment cost. A variety of automatic multiplexing systems can be used (OYO, AGI, Campus, ABEM, IRIS). In the frame of this study the IRIS Syscal Switch 48 electrodes automatic multiplexing system is applied to determine subsurface structure and the existence of large or small scale faults.

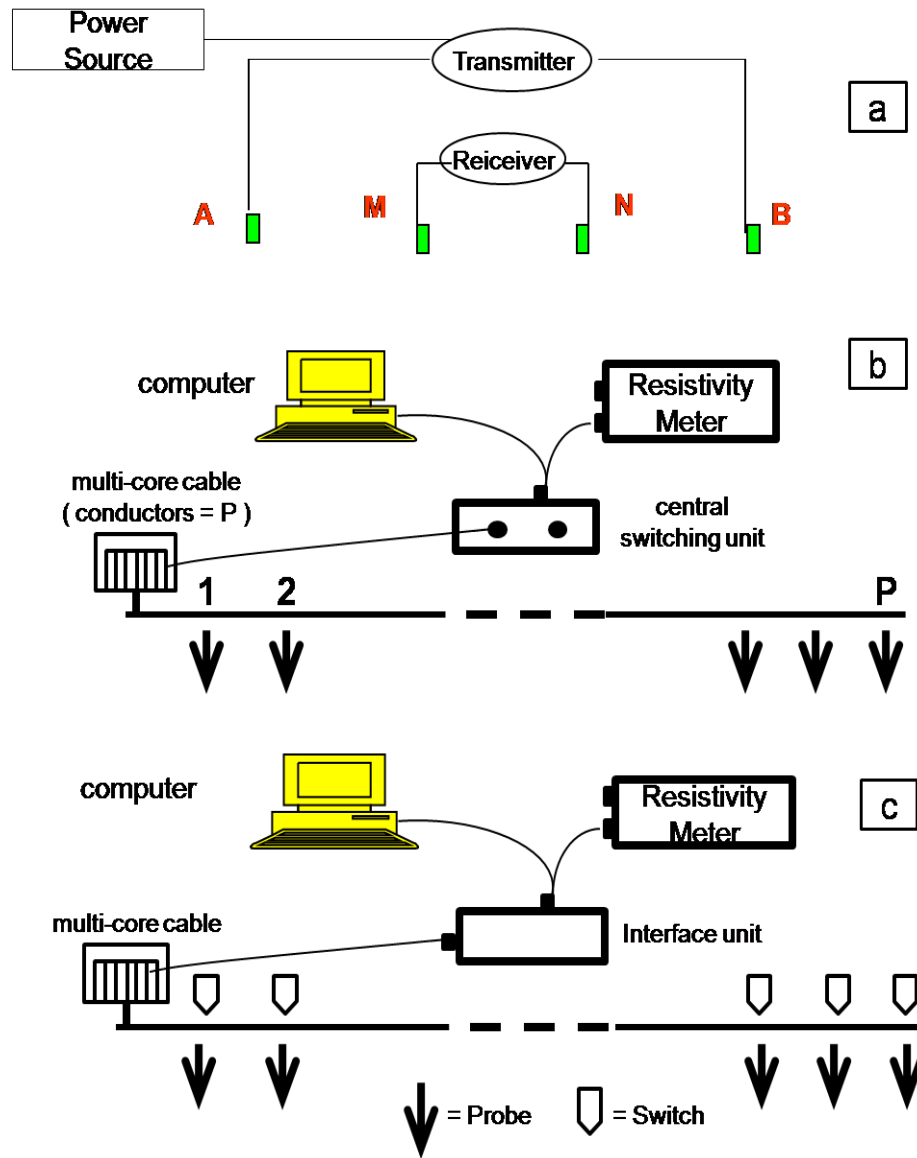


**Figure 3.9:** a) The main characteristics of the resistivity meter, b) Central switching unit and c) Distributed switching unit (modified by Tsourlos, 1995).

### 3.2.1. FIELD RESISTIVITY SURVEY PROBLEMS

Electromagnetic coupling, probe positioning and the induced effects of topography are factors that may cause problems in field surveys. Several studies report the field resistivity survey problems. *The following field resistivity problems are reported by Tsourlos (1995).*

- 1. Electromagnetic coupling (E.C):** Electromagnetic coupling occurs when charging the transmitted current. The electromagnetic coupling is reduced using arrays that have separate receiving and transmitting cables. To reduce electromagnetic coupling phenomena it is preferable to use dipole-dipole rather than Wenner and Schlumberger arrays. However, cable length, sampling frequency and earth conductivity increase coupling (Tsourlos, 1995).
- 2. Probe Positioning (P.P):** Effective probe positioning results in an accurate estimation of the geometrical factor and finally in valid apparent resistivity estimation. Automatic positioning instruments can highlight errors in probe positioning. In the frame of this thesis the electrodes are carefully placed.
- 3. The Effect of Topography (T.E):** Geological surface and subsurface irregularities and topography effects near the electrodes induce noise due to the focusing or defocusing of the current distribution in the resistivity surveying (Telford, 1991). The effect of topography should be considered and corrected in the surveys. Dipole-Dipole array is suggested for correcting 2-D and 3-D topography effects (Tsourlos, 1995).

### 3.2.2 ELECTRICAL RESISTIVITY TOMOGRAPHY INVESTIGATION

In the frame of this study the true subsurface resistivity model is estimated by inversion of the measured apparent resistivity using the RES2DINV software. RES2dinv is an automatically software program that delineates a two dimensional (2-D) resistivity model of the subsurface structure using data extracted from electrical resistivity tomography method (Griffiths & Barker, 1993). A forward modelling subroutine and a non-linear least squares optimization is used to calculate the apparent resistivity values and to perform the inversion routine (deGroot-Hedlin & Constable, 1990; Loke & Barker, 1996a) to adequately image the subsurface. The principle consists in subdividing the studied 2D surface into a number of blocks and in determining the resistivity within the cells that provides a model response fitting well with the measured data. The distribution and the size of the blocks that the inversion program RES2dinv uses are generated by the program using the distribution of the electrode spacing data. The grid can be dense (half of the electrode spacing) on request. The depth of the bottom row of blocks is set to be approximately equal to the equivalent depth of investigation of the data points with the largest electrode spacing. Uniform or non-uniform electrode spacing depending on the inhomogeneity/heterogeneity of the structure of can be inserted into the RES2dinv software for modeling the subsurface structure. In this study Wenner, Schlumberger and dipole-dipole arrays are used for subsurface determination and uniform electrode spacing is used in all array configurations.

### **3.2.3 RES2DIV FOR ELECTRICAL RESISTIVITY TOMOGRAPHY INVESTIGATION**

The RES2div program is used to determine the resistivity of the rectangular blocks that constitute the 2D model of the subsurface and to manage the well fitting between the calculated and the measured values from the field survey. The RES2div automatically subdivides the subsurface into a number of blocks and performs a least-square inversion routine to specify the appropriate resistivity for each block. The location of the electrode inserted into the soil layer and the extracted apparent resistivity values are stored into the field work into a text file that can be opened and read by the Res2div.

Prosys Software is used to 'read' raw resistivity data (.bin format) collected in the field. The data are filtered, ignored when noise signal or modified through recomputing procedure of the Rho value. Topography is inserted in case studies when necessary. The Rh graph is used to check the data resolution. Finally, the data are exported and saved in dat. format used in RES2DINV software for ground subsurface modelling.

#### **1. RES2DInv Data file operations**

Read data file menu displays the list of files in the current directory with extension -.dat - and is used to read and import data file format. The program provides a detailed description of the data format for Wenner, Schlumberger and dipole-dipole arrays. The example data file format acquired in the eastern part of Kastelli territory (ERT\_P5) located in Northwestern Crete (Kast2.dat) and the observed and calculated apparent resistivity pseudosection for a dipole-dipole array is presented in Figure 3.10. For dipole-dipole, Wenner, Schlumberger arrays "a" spacing is defined as the distance between the P1 and P2 potential electrodes and "n" factor that is an integer value is the ratio of the C1-P1 distance to the P1-P2 distance.

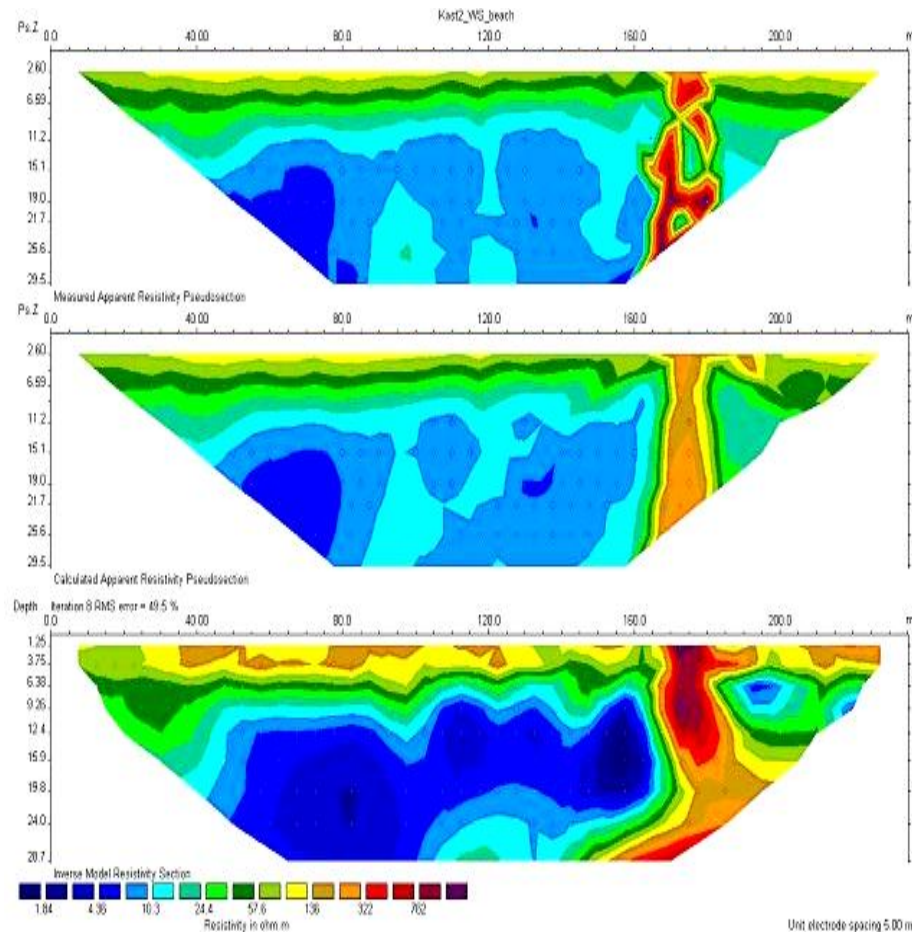


**Figure 3.10:** An example of the observed and calculated apparent resistivity pseudosections for ERT data acquired eastern of Kastelli-Kissamou (ERT\_P5) territory located in northwestern Crete. The red zone represents the high resistive zone corresponding to fault. This is an example of the type of result given in Chapter 4.

## 2. Editing the data

In the frame of this study the Editing file operation is used for:

1. Removing the bad data points - Exterminate bad data points (based on error analysis).
2. Selecting a section of the data set - Splice large data sets
3. Changing the location of the first electrode (when necessary).

## 3. Change Settings operation

Change Settings operation is used for selecting the (FEM) to calculate the apparent resistivity values.

## 4. Inversion Options

The inversion of the data set file is performed using the inversion toolbar. The inversion starts with the least-squares inversion routine. The robust model constrain inversion

method is used to delineate sharp geological interfaces of different resistivity values or faulted blocks and their surrounding.

### **5. Topographical modelling**

Topography option calculates topography effects due to significant topographical relief along the survey line. In such cases the geographical coordinates of a number of points along the survey are inserted into the data file format with topography data. The software automatically selects the FEM method and incorporates the topography into the modelling. The topographic modeling is automatically carried out when inverting the data set. The RES2dinv software uses four different methods to incorporate the topography into the inverted model. Topographic corrections are accounted for in the case of Kera fault and on Kastelli area (P3, P7, P6, and P8) where significant changes in the elevation are observed.

### **6. Displaying the inversion result option**

Displaying the inversion result option is basically used to read the data file after the inversion subroutine and to display the measured and calculated apparent resistivity pseudosections and the final model section. Moreover, it is used to modify the contour interval used for drawing the pseudo and model sections, the vertical scale of the sections and to insert the topography in the model section. It is also used to change the parameters that control the way the apparent resistivity pseudo-sections and the model sections are displayed.

### **7. Editing data option**

Editing data option is used to display the distribution of the datum points according to the percentage difference between the observed and calculated apparent resistivity values.

### **3.2.4 ELECTRICAL RESISTIVITY TOMOGRAPHY USING RES2DINV IN KASTELLI KISSAMOU AND PALEOHORA REGIMES**

The geoelectrical data were collected using an IRIS-Syscal Jr. Switch 48 instrument with accuracy of 0.1 mV. The system features 48 electrodes, enabling fully automated measurements of the shallow subsurface apparent resistivity using dipole–dipole, Wenner and Schlumberger configurations. Two current (C1, C2) and two potential (P1, P2) electrodes, are connected to a take-out on the multicore cable and the cable is connected to a switching box which is manually controlled, or to a switching module which is computer controlled (Paragraph 3.2). Typical cables have between 20 and 25 take-outs with 2m, 5m or 10m separation between each take-out. A resistivity traverse is carried out with the electrodes separated by single electrode spacing. A convention exists in that measurements taken with adjacent electrodes connected are referred to as N = 1 (5) measurements, N = 2 (4) to N = 4 (2). The numbers in parenthesis show the number of readings in each traverse. As the electrodes are all connected to the switching module, it is not required that the measurements be collected as a traverse.

The recorded ERT data, using 5m and 15m electrode spacing are collected to provide apparent resistivities inverted to a 2D geoelectrical resistivity model. For imaging depths of about 30 m it is convenient to use electrode spacing of 5 m to 10 m,

depending on the subsurface resistivity. The spacing of 5 m and 15 m enables the possible detection of bodies and/or structures down to 90 m depth. The above arrangement provides the required information for the near-surface geological/tectonic features. The dense configuration of 5 m electrode spacing is used to acquire high-resolution data and reduce uncertainty due to topographic effects and consequently to accurately image the complex subsurface geological structure. The 15 m electrode spacing is selected as the best choice to resolve the geometry of the subsurface structure.

The geoelectrical data collected have been processed by means of the RES2DINV (Loke, 1997) modelling software in order to perform 2D geoelectrical data inversion. The inversion routines are based on the smoothness-constrained least squares method (deGroot-Hedlin & Constable 1990; Constable et al. 1987; Sasaki 1989, 1992; Loke & Barker 1995, 1996a,b; Tsourlos 1995) and the forward resistivity calculations were executed by applying an iterative algorithm based on FEM. The quality of the fit is expressed in terms of the RMS error. In this work, the mean RMS errors for all the conducted profiles ranged from 133.7% to 2.8%. RMS error greater than 40% could be reasonably explained by the highly inhomogeneity of the area under investigation (high resistivity contrast between the sea water intrusion and the calcitic bedrock). All measurements are collected, filtered and corrected for baseline and for anomalous trends and simultaneously inverted for the final tomographic image.

### 3.3 METHODOLOGY OF THE SEISMOLOGICAL APPROACH TO LOCATE EPICENTER AND TO DELINEATE ACTIVE STRUCTURES

The basic concept for locating the epicenter of earthquakes is based on the determination of the difference of the S and P travel time arrivals. Accurate epicenter location is determined by the travel times of at least three seismological stations. The S-P arrival travel time is a function of  $V_p/V_s$  and origin time ( $t_0$ ) and is given by the equation 3.2.26.

$$t_s - t_p = \left(\frac{V_p}{V_s} - 1\right)(t_p - t_0) \quad (3.2.26)$$

The origin time of an earthquake event can be determined by plotting the Wadati-Benioff diagram of the S and P arrival time difference versus the arrival time of P waves at different station. The origin time corresponds to the intercept ( $t_0$ ) of the straight line with the arrival time axis. The slope of the line of the Wadati-Benioff diagram is equal to  $V_p/V_s - 1$ . The  $V_p/V_s$  ratio can be easily determined using an earthquake event recorded on two different stations by the equation (3.2.28) based on equations (3.2.26) and (3.2.27).

$$t_{s2} - t_{s1} = \left(\frac{V_p}{V_s} - 1\right)(t_{p2} - t_{p1}) \quad (3.2.27)$$

and

$$\frac{V_p}{V_s} = \frac{t_{s2} - t_{s1}}{t_{p2} - t_{p1}} + 1 \quad (3.2.28)$$

where  $V_p$ ,  $V_s$  are the P and S wave velocities,  $t_{s2}$ ,  $t_{s1}$  are the S wave arrival times in stations 2 and 1 respectively and  $t_{p2}$ ,  $t_{p1}$  are the P wave arrival times at stations 2 and 1 respectively.

HYP071 is a computer program for determining hypocenter, magnitude, and first motion pattern of local earthquakes (Lee & Lahr, 1972). For earthquake localization both P and S arrival times have been used. Both P and S arrival times are used for epicenter determination. In the frame of this thesis the importance of P and S for accurate epicenter determination is highlighted and denoted in Hypo 71 with low weight. The weight value used in Hypo71 for P and S arrival times is zero. Weighting of P and S time arrivals is an important factor for accurate epicenter determination. Earthquake events where the P and S time arrivals are not clearly identified are not included in the epicenter delineation. The velocity model ( $V_p/V_s=1.78$ ) for the Aegean, proposed by Papazachos & Nolet (1997) is inserted in Hypo 71 and adopted for earthquake epicenter localization.

HYP071 provides an assessment of the quality of the epicenter solution (Lee & Lahr, 1972). The theoretical travel time model used for epicenter determination that is an symmetric earth model - without considering the lateral heterogeneities - for each station do not corresponds to the real travel time due to the complicated geometry of ray paths in the Earth. The difference between the observed and calculated travel time is called residuals and are used as indicators for a reliable earthquake epicenter but not always a guarantee for accurate hypocenter solution. Root mean square of time residuals in sec (RMS) is defined as the sum of the squared residuals for  $n$  observations (equation 3.2.29)

$$RMS = \sqrt{\frac{\sum_i^n R_i^2}{n}} \quad (3.2.29)$$

where  $R_i$  is the time residual for the  $i$  station.

ERH is the standard error of the epicenter in Km defined by the equation (3.2.30):

$$ERH = \sqrt{(SDX^2 + SDY^2)} \quad (3.2.30)$$

where SDX and SDY are the standard error in latitude and longitude of the epicenter. Hypo 71 guidelines manual suggest ideal values for residuals lower than 1.0 for accurate epicentral determination. Earthquake events in regions where the velocity inhomogeneity is low the residual value is close to zero (Sleep & Fujita, 1997). In subduction zones that are characterized of high lateral velocity heterogeneities although accurately earthquake localization have a relative high root-mean square (RMS) residual; while at the end of the slab the residuals are expected to be close to zero (Sleep & Fujita, 1997). The lateral velocity variation in the Wadati–Benioff zone caused by the descending high-velocity slab can introduce location errors (McLaren, 1985). Near subduction zones systematic epicenter mislocation is observed due to an incorrect average P velocity model or due to an incorrect P to S velocity ratio (McLaren, 1985).



### **3.3.1 METHODOLOGY OF THE SEISMOLOGICAL APPROACH TO LOCATE EPICENTER AND TO DELINEATE ACTIVE STRUCTURES IN NORTHWESTERN AND SOUTHWESTERN CRETE.**

In the frame of this thesis the purpose of instrumental seismicity study is to locate earthquake epicenter, to reveal and delineate active fault zones in northwestern and southwestern Crete. Seismological data are extracted from a new seismic network of permanent and temporal seismological station configuration installed on Crete.

For the purpose of this thesis microseismicity study is divided in two sections. The first section involves earthquake data acquired from a telemetric seismological network comprised of 8 seismological stations (seven short period) and one broad band station) equipped with high resolution 24-bits Reftek-130 digitizers, and three component Gurup CMG -40T and Sercel L-4-3D, 1Hz sensors. Earthquake data from this database collected for two months from July to August 2007 to record the spatiotemporal microseismicity of northwestern and southwestern Crete.

In addition, to the regional seismological network of Crete, the second section of microseismicity study involves a temporal seismological station comprised of three short-period installed in Paleohora to image seismogenic zones beneath the forearc. The small network aperture and the proximity of the local network aperture contribute to a detailed clustering delineation in the outer arc of southwestern Crete with higher resolution and lower detection threshold. Earthquake data from the local network are acquired from one permanent and two temporal short period stations, equipped with high resolution 24-bits Reftek-130 digitizers, and three component Gurup CMG-40T, 1Hz sensors. The seismological stations form an almost triangular network. The local network operated for 45 days to record the local microseismic activity of southwestern Crete.

For the purpose of this thesis earthquake epicenters of seismological data extracted from permanent and temporal seismological stations have been analyzed using Hypo71 software (Lee & Lahr 1972). The 1D velocity model proposed by Papazachos et al. (2000b) based on tomography studies by Papazachos & Nolet (1997) for the Aegean is used for epicenter delineation. This velocity model is a linear representation of subsurface structure (1D) where lateral heterogeneities of the subducting zone are not inserted. The high velocity inhomogeneity induced by small or large local lateral heterogeneities of the area in the proximity of the subducting zone (small or large local variations of the lateral velocity variation in the Wadati–Benioff zone caused by the descending high-velocity slab) is not considered in the proposed (1D) velocity model. The velocity model used in the frame of this thesis and proposed by Papazachos et al. (2000b) is presented in Table 3.1. The arrival S-P travel time is based on a calculated  $V_p/V_s$  ratio equal to 0.78 ( $V_p/V_s=1.78$ ).

<b>VELOCITY MODEL PROPOSED BY PAPAACHOS et al. (2000b)</b>	
<b>P wave velocity</b>	<b>Depth (km)</b>
6.00	0.0
6.60	19.0
7.90	31.00
7.95	50.00
8.00	100.00
8.05	120.00

**Table 3.1:** Velocity model used in Hypo71 for epicenter delineation in northwestern and southwestern Crete. The velocity model proposed by Papazachos et al. (2000b) is based on tomography studies proposed by Papazachos & Nolet (1997).

Epicenter delineation is acquired using P and S time arrivals. The results are presented in Chapter 4 and discussed in Chapter 5. In southwestern Crete the  $V_p/V_s$  velocity ratio is determined by Wadati plots between two suggestive earthquake events recorded by the three temporal seismological stations. The importance of this microseismicity study provides earthquake data

In this thesis it is highlighted the importance of an accurate: 1) P and S time arrivals in earthquake delineation and 2) a velocity model that characterizes the heterogeneities of the subsurface structure. The lack of reliable 3D structural model considering also the strong lateral heterogeneities of Crete, especially of the western part of Crete is also considered in the epicentre localization.

---

### 3.4 SUMMARY

An introductory description of the purpose of the study, of the geological setting, the seismotectonic setting of the study area and the applied methodologies for the purpose of this thesis is presented in Chapter 1. The literature review of the theoretical background of the combined methodologies applied and the validity of each method based on previous studies are presented in Chapter 2. The methodology of each technique and method is described in Chapter 3. In the following Chapter 4 are presented the results of the proposed combined methodologies in the study areas.

---

### **4.1 GEOLOGICAL FIELD SURVEY IN KASTELLI AND PALEOHORA IN NORTHWESTERN CRETE**

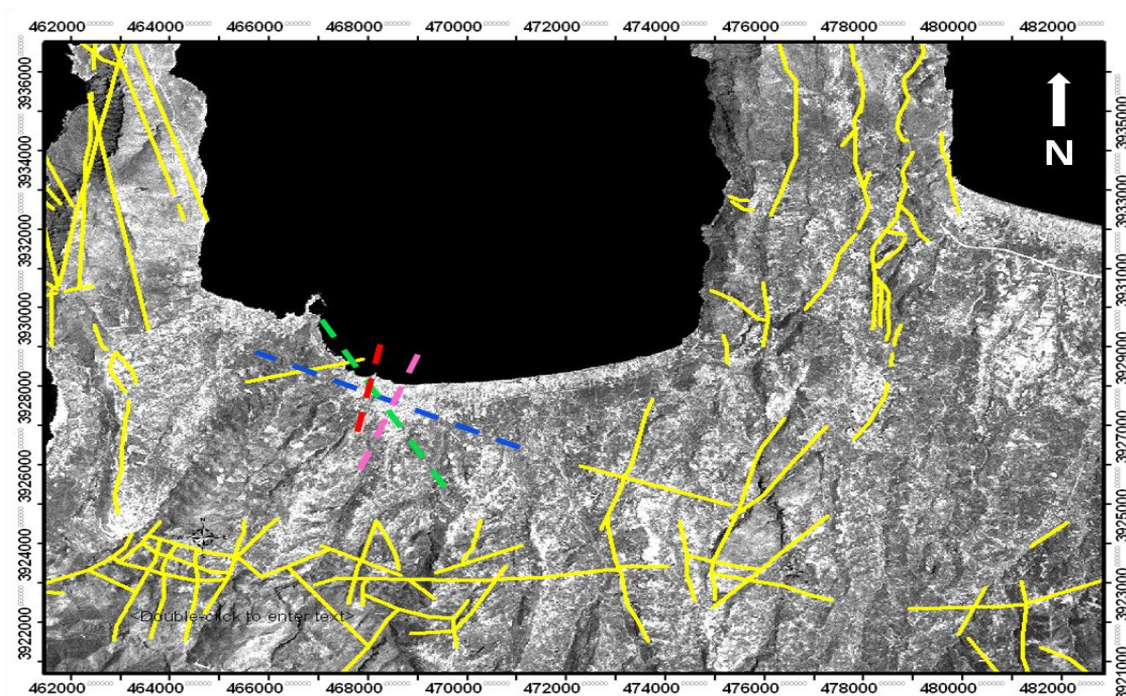
Geological survey was conducted in the frame of this thesis to characterize the tectonics of the two investigated areas. Several faults are determined along Kastelli-Kissamou and Paleohora. Sections 4.1.1 and 4.1.2 present the research outcomes of the ground truthed geological survey in both investigated basins.

#### **4.1.1 GEOLOGICAL FIELD SURVEY IN KASTELLI-KISSAMOU (NORTHWESTERN CRETE)**

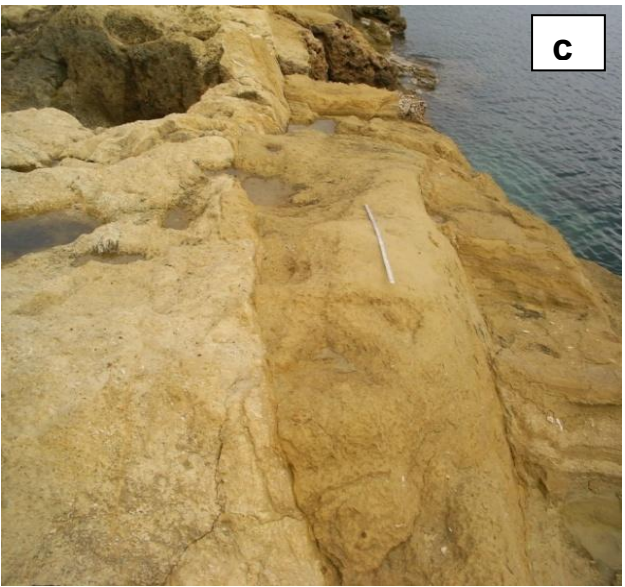
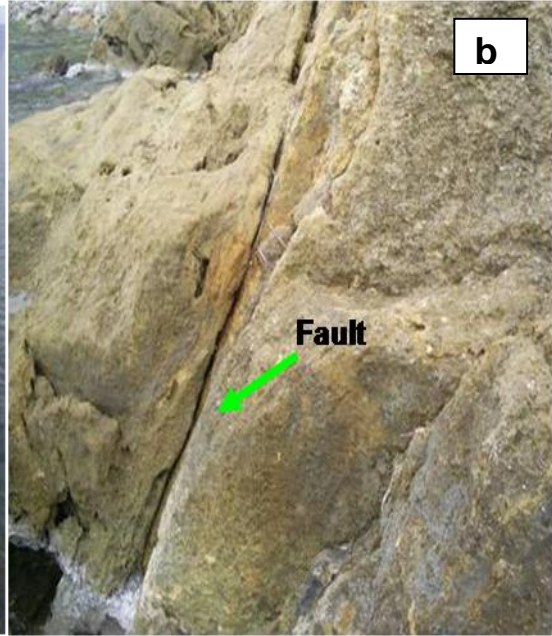
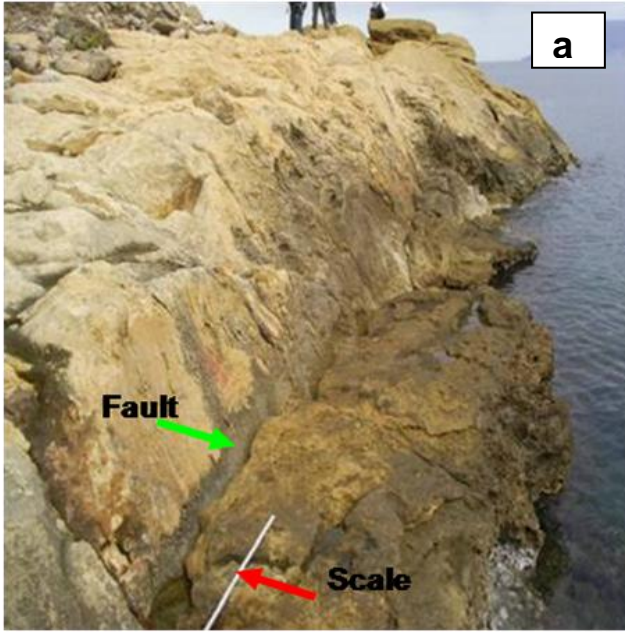
Geological survey in this study reveals coastal uplift of up to 6.8 m, probably in association with the AD 365 earthquake and numerous active faults. Figure 4.1.1a present the urban area of Kastelli-Kissamou half-graben basin. Clear active fault evidences are observed coastal in northwestern of Kastelli (Fig.4.1.1b). Southwest of Kastelli no outcrops are observed. Figure 4.1.2 shows satellite image of the main active faults identified in this study (green, blue, red and pink dashed lines). Active faults dominantly are occupying a sector between NNE and NNW crosscutting the populated area. Figures 4.1.3 and 4.1.4 show the identified fault features. Northwestern of Kastelli a subsidiary fault striking NNW-SSE (green dashed line on figure 4.1.2) and a series of 12-15 active fault cutting the beachrock and striking almost N-S (red dashed lines) are identified. The visible NNW-SSE fault that might be resulting as an erosion process is subsidiary to a larger structure just offshore; evident by the very small amount of displacement on the visible fault and the fault itself appears to be a minor structure. The identified faults extend for several meters inland from the coastline. These faults are located on a well-lithified limestone site. Eastern of northwestern part of the coastline the site is characterized of well lithified limestone without evidences of debris layer, while western of northwestern Kastelli a debris layer is evident. Figures 4.1.2, 4.1.3 and 4.1.4 present the geological evidences of this study. Evidences of the coastal uplift of up to 6.8 m are presented in Figure 4.1.5.

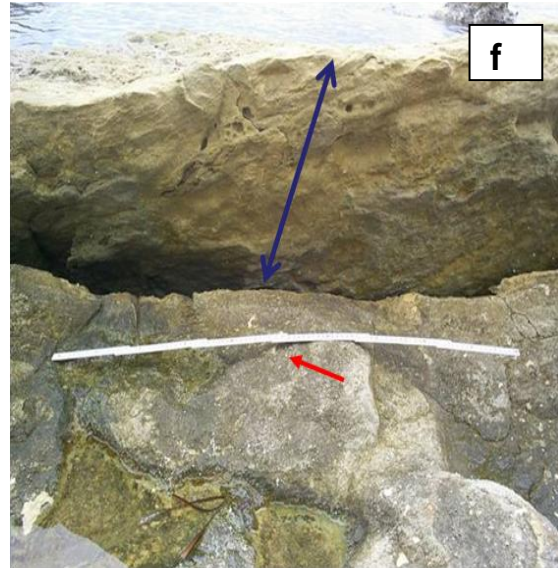
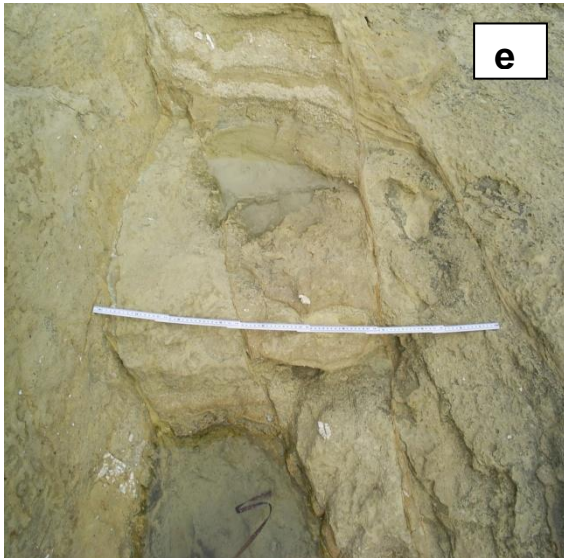


**Figure 4.1.1:** a) Overall view of the urban area of Kastelli-Kissamou half-graben basin, b) View of the coastal site in the northwestern part of the basin where the active fault determined. Photos a and b are derived from google earth software.

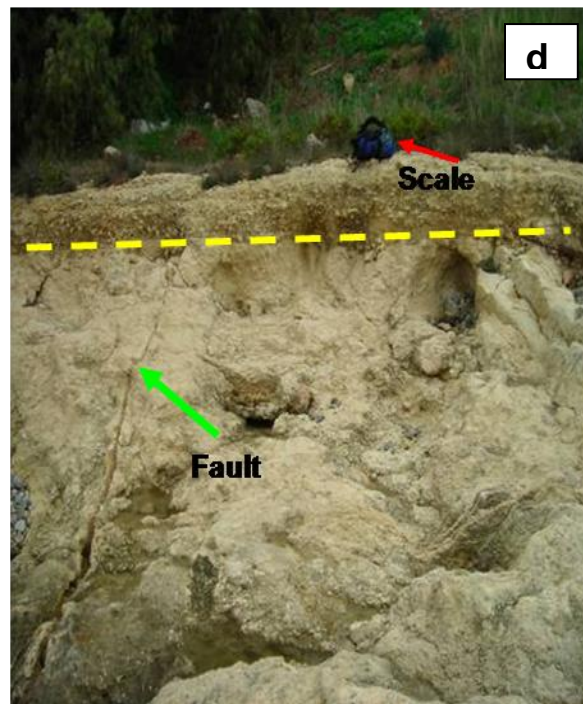
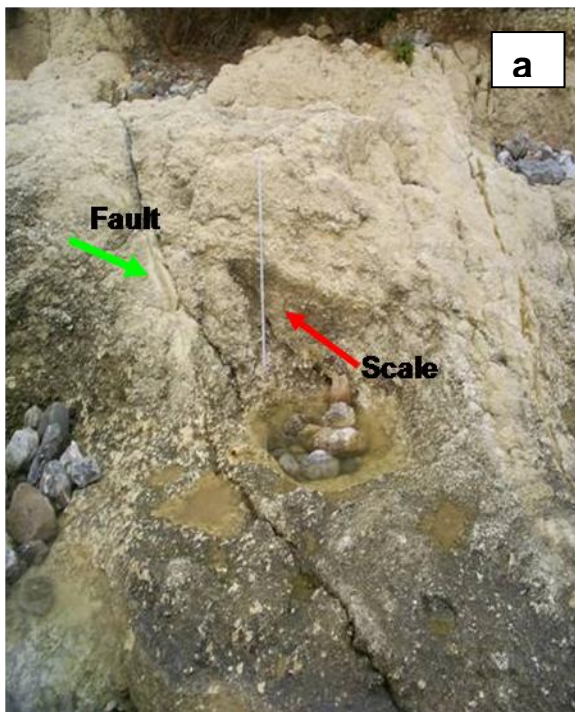


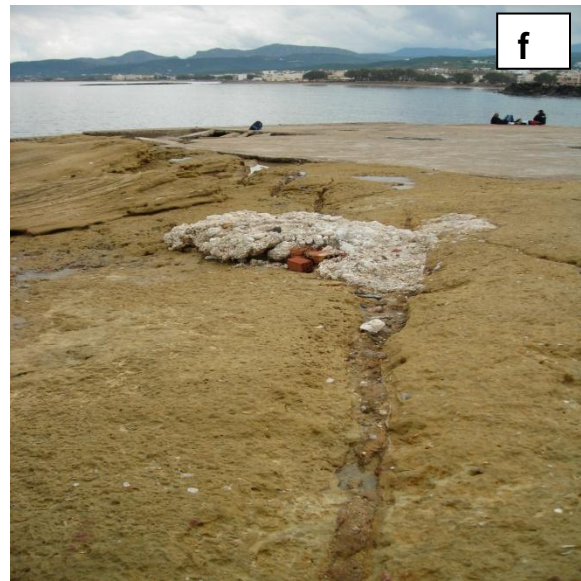
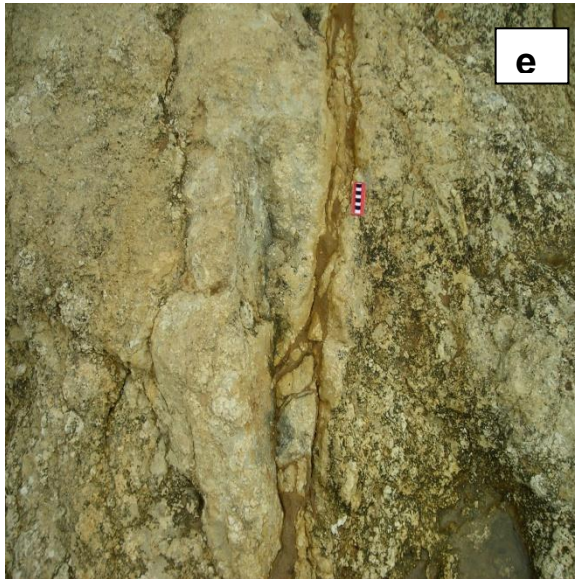
**Figure 4.1.2** Fault system coastal of northwestern Crete. The green line represents the identified large scale fault trending NNW-SSE and the red lines the series of actives fault cutting the beachrock and trending almost N-S. Yellow lines indicate the already identified faults using geological (Karageorgiou, 1968) and satellite image data.





**Figure 4.1.3:** a) The observed apparent offset west of the northwestern part of Kastelli could be the result of erosion exposing the fault plane. The fault causing the uplift of the wave-cut slab that contains the fault shown in the figure might lie hidden just offshore. The very visible fault may be linked to this structure as a subsidiary fault (green line), b,c,d,e) The NNE-SSW faulting eastern of northwestern Kastelli, f) Segment of an opened 30 cm (blue arrow) almost WNW-ESE striking fault. The one meter scale is used as a scale (red arrow). The coast of northwestern Kastelli is characterized of well-lithified limestone.





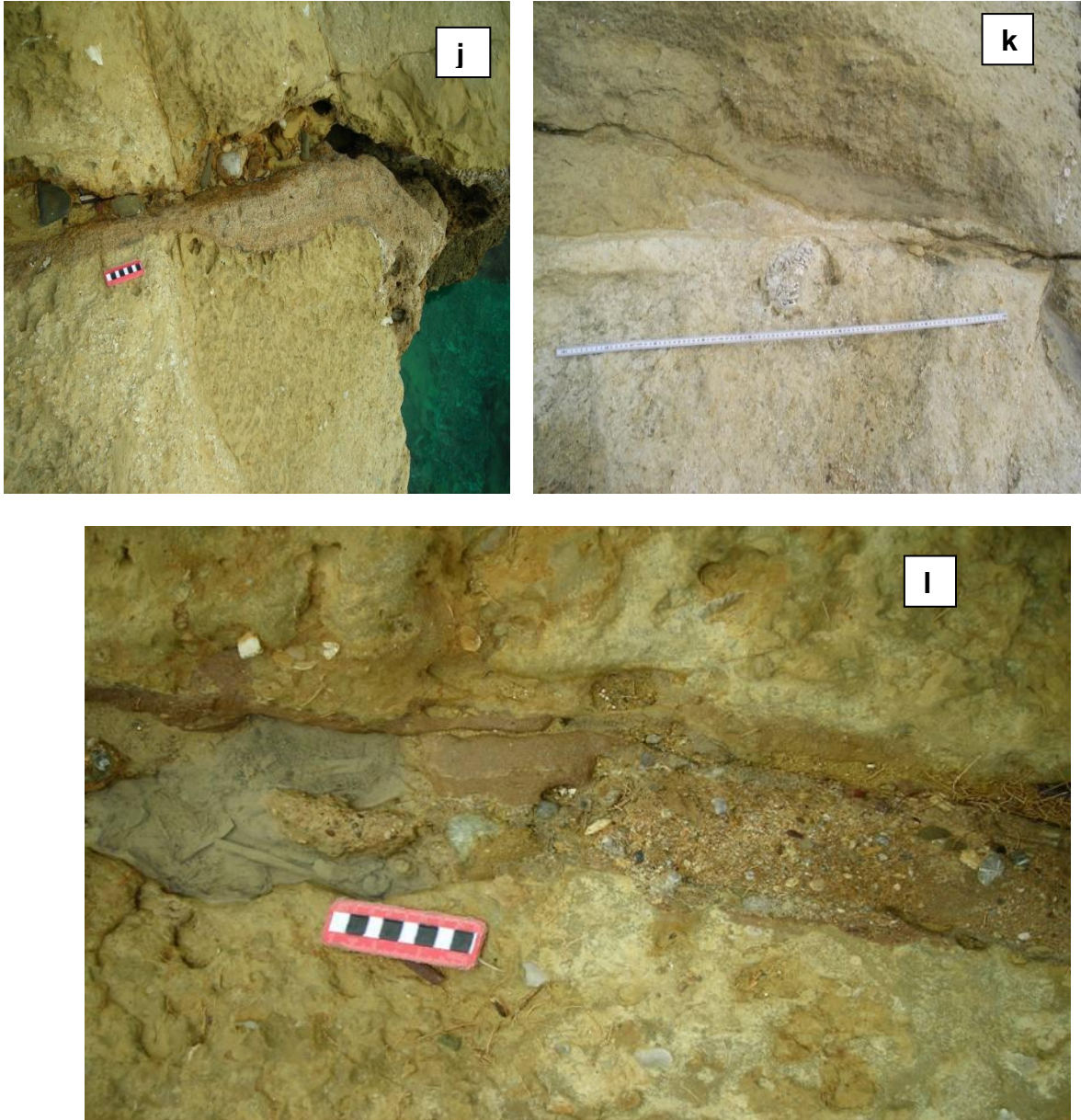


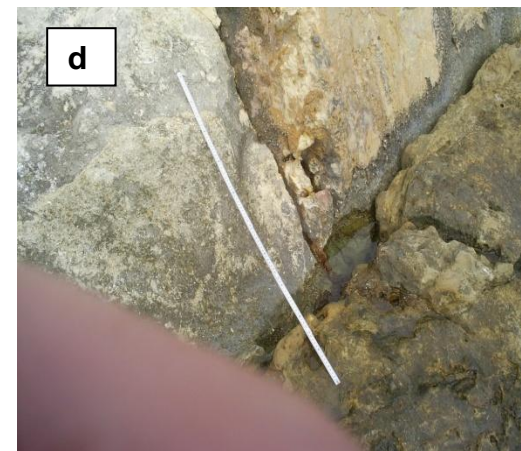
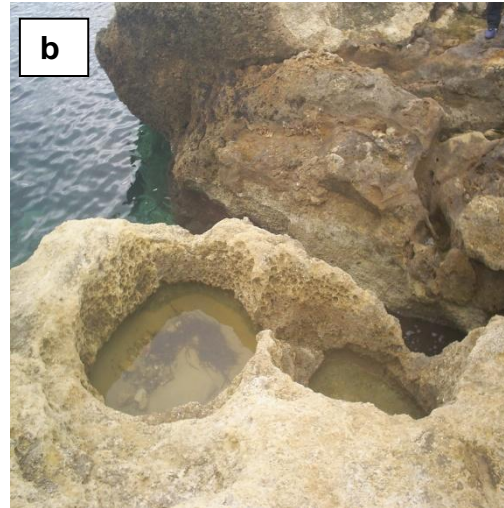
**Figure 4.1.4:** a,c,d,e,f,j,k) Numerous active fault cutting the beachrock and striking almost N-S are identified in the northwestern part of Kastell-Kissamou half-graben basin. The identified N-S faults extended for several meters inland, a) Eastern of the northwestern Kastelli the site is characterized of well lithified limestone without evidences of debris layer, b) Western of northwestern part of Kastelli a debris layer is overlying the well-lithified limestone site. The dashed yellow line on this photo distinguishes the overlying debris layer of the limestone bedrock, e, f, j,k and l) N-S fault filled with recent alluvial fan deposits. The recent lateral trends of faulting justify the fault activity of the faulting coastal of northwestern Kastelli. One meter scale, 10 cm meter and a regular hand bag are used as a scale (red arrow). The green arrows show the N-S faulting.



#### 4.1.2 UPLIFT EVIDENCE IN KASTELLI KISSAMOU AREA

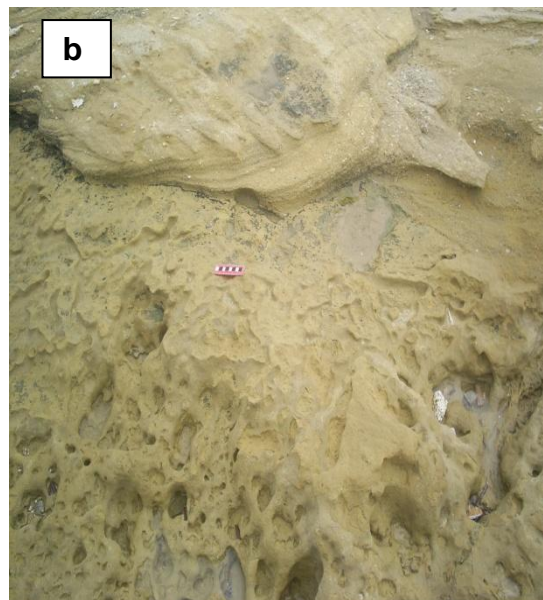
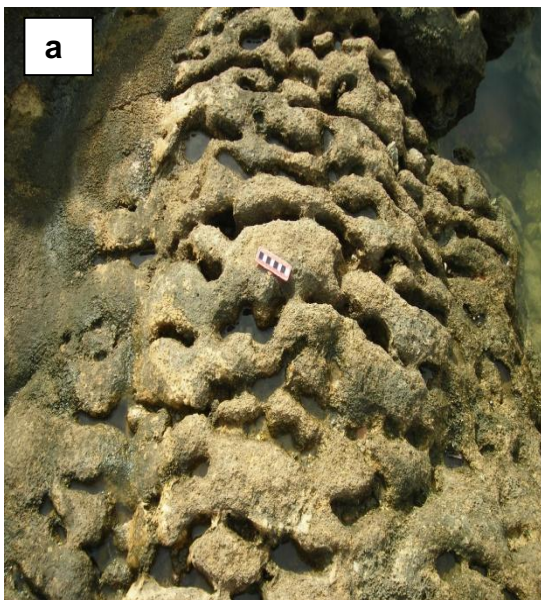
The outcome of previous studies that the sea level has not fallen eustatically in the last few thousand years, as a result of the recent tectonic uplift is also evident in the frame of the geological survey in the frame of this thesis. Geological field observations reveal the high rate of the emergence.

In Kastelli-Kissamou Bay within the beachrock fault plane  $020/63^{\circ}\text{E}$  with vertical slicks is identified. The measured max footwall uplift at beach end of northwestern part of Kastelli is 6.8 m possibly associated with the AD 365 earthquake is presented in Figures 4.1.5a, 4.1.5b and 4.1.5f. Evidences of uplifted dead trottoir almost 60 cm confirm the uplift (Fig.4.1.5c). The hanging wall of the fault within beach rock also moved up to 60 cm (Fig.4.1.5d). The uplifted dead trottoir almost 60 cm are undercut by small notch at present sea level. Evidence of erroded bedrock level and dead trottoir are presented in Figure 4.1.6. The dead trottoir is also presented in Figure 4.1.7. The uplifted dead trottoir is undercut by small notch at present sea level is presented in figure 4.1.8.





**Figure 4.1.5:** a,b,f) The maximum footwall uplift at beach end of northwestern part of Kastelli is measured of up to 6.8m. c) Evidences of uplifted dead trottoir almost 60 cm. d) The hanging wall of the fault also moved up to 60 cm.



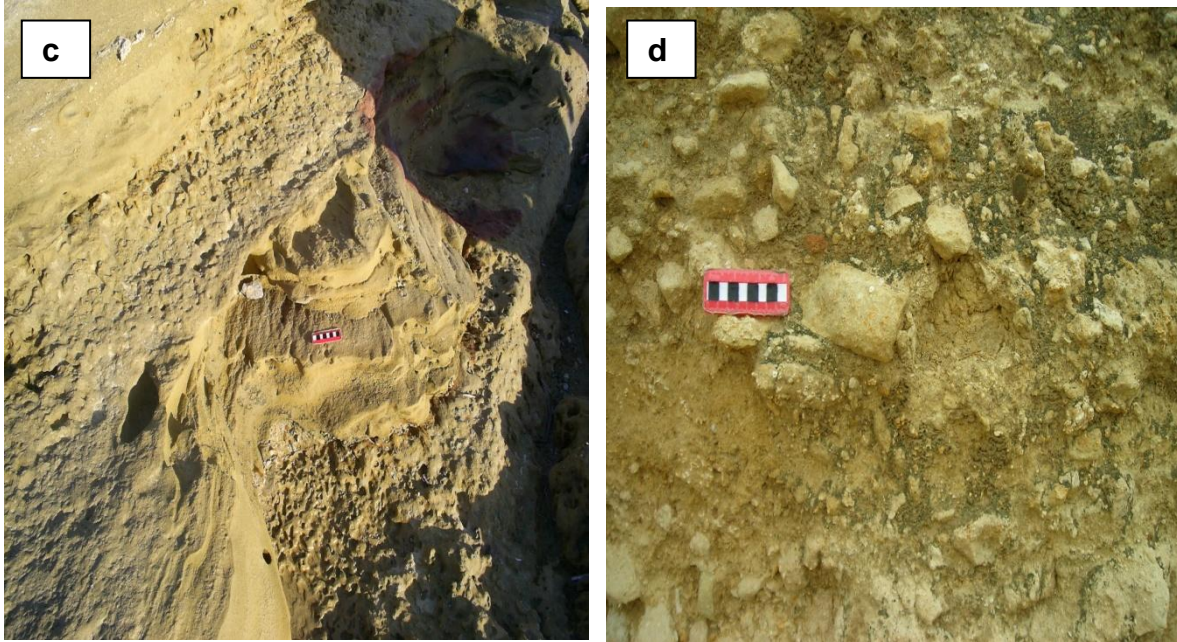


**Figure 4.1.6:** a,b) Eroded bedrock level without debris on top and c,d) eroded bedrock level with debris on top of it. The trottoir is the algal encrustation on the vertical cliff face next to the sea.

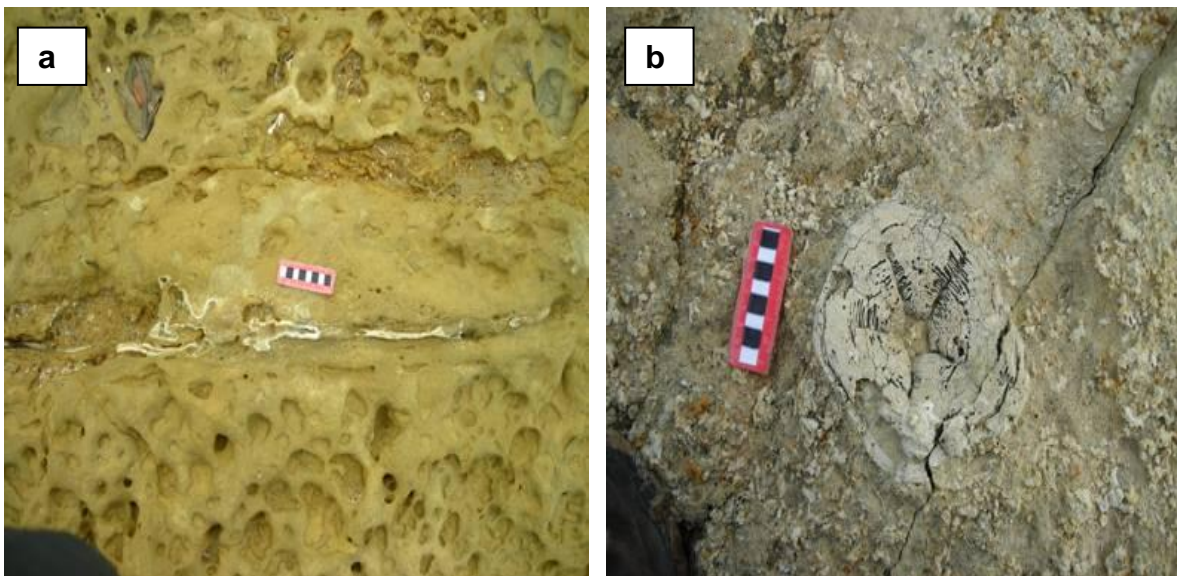




**Figure 4.1.7:** a,b,c) Dead Trottoir at present sea level.



**Figure 4.1.8:** The uplifted dead trottoir undercut by small notch at present sea level.

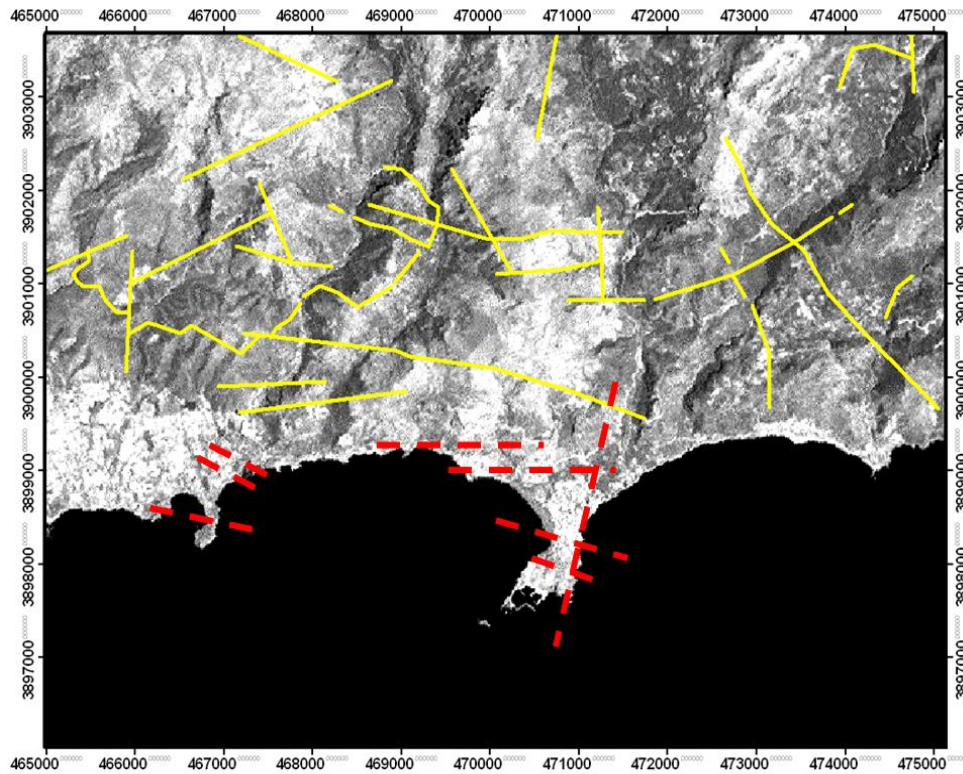
### 4.1.3 GEOLOGICAL FIELD SURVEY OF PALEOHORA IN SOUTHWESTERN CRETE

The geological survey field survey conducted in this thesis suggests that the town of Paleohora is the most remarkable peninsula that originates from breaking of the coastline by NNE-SSW-striking left-oblique extensional faults, traced for several kilometres inland. The faults segment the E-W coastline which is itself bounded by a continuous E-W normal fault which is one of a series of E-W faults that occur at intervals up to several kilometres inland. Offshore the faults created headlands and peninsulas. Fault activity segments the coast into blocks exhibiting long-term patterns of relative uplift and subsidence. A right-stepping series of short (few hundred meters) en-echelon faults at an almost 50 degrees strike oblique to the coast evident the coastline segmentation and disrupted coastal terraces, notches, pottery bearing sediments.

Figure 4.1.9 shows the identified faults in Paleohora and Grammeno peninsulas. During the fieldwork in the northeastern side of Paleohora where pottery was found is one segment of en-echelon fault (4.1.10a). In Figure 4.1.10 is presented the northeastern side of Paleohora where the pottery was found. According to archaeological dating the pottery is highly prone to belong in the Roman era (first Century B.C to first century A.C). Particles of the pottery might belong to the Classic Era (4<sup>th</sup> century AD to the beginning of the 5<sup>th</sup> century AD). A very small piece of pottery is assumed to be dating to the prehistory; however further dating should be performed for that piece of pottery to verify the prehistory dating. The verified dating in the Roman Era is an indicator of the recent activity of the fault. Samples of the pottery are presented in Figures 4.1.11d and 4.1.11e. The bedrock lithology is limestone, on top of which are gravels containing pottery shards that have been downfaulted against the limestone in a normal fault (Fig. 4.1.11c). The characteristics of the fault are: strike E-W 66°S, slickenlines on the fault plane (trend 063°S, plunge 062°S) shows oblique slip. The fault scarp is relatively degraded and characteristic of the fault plane is 012/70°E. The site is characterized of marine terrace with boulder basal conglomerate (in an altitude 4.2 m calibrated to the sea level) and possibly equivalent to marine conglomerate on the west side of the fault (Fig. 4.1.11c). The altitude where marine terrace with boulder basal conglomerate is 4.2 m estimated with GPS calibrated to the sea level. Moreover, a fault segment in the direction of the normal fault of Figure 4.1.11a is observed in Figures 4.1.10b and 4.1.11b. ERT conducted near pottery findings to verify that fault zone striking almost E-W (Fig. 4.1.10). To Koundoura road west of Paleohora, patches of fault planes are visible, with indication of slickenlines pitching 24°N, directly on strike with gorge 015°/90° and therefore indicate oblique slip (Figs. 4.1.12a, b and Fig. 4.1.12d). Infilled earlier fractures with the same orientation are observed (Fig. 4.1.12c). A second en-echelon range front fault with very well developed slicks (strike: 110°, dip: 78° South, Pitch: 50° West).

A 3.5 m notch (or 4-4.5 m), in the cave located to east and in the adjacent headland (near the main beach) is observed (Fig. 4.1.13). The 3.5 m notch (or 4-4.5 m), in the cave is associated with the 9 m uplift. The notch presents different cuts at various points ranging from 3.5 m to 4.5 m. The altitude of the main beach is 5.0 m. The better estimate of the offset is 3.5m. An E-W fault (90°) is well defined. On the ridge west of the fault boulder outcrop is observed. In the coast of the beach degraded notch are obvious. Well-preserved trottoir located below the bench of the uplifted abrasion notch

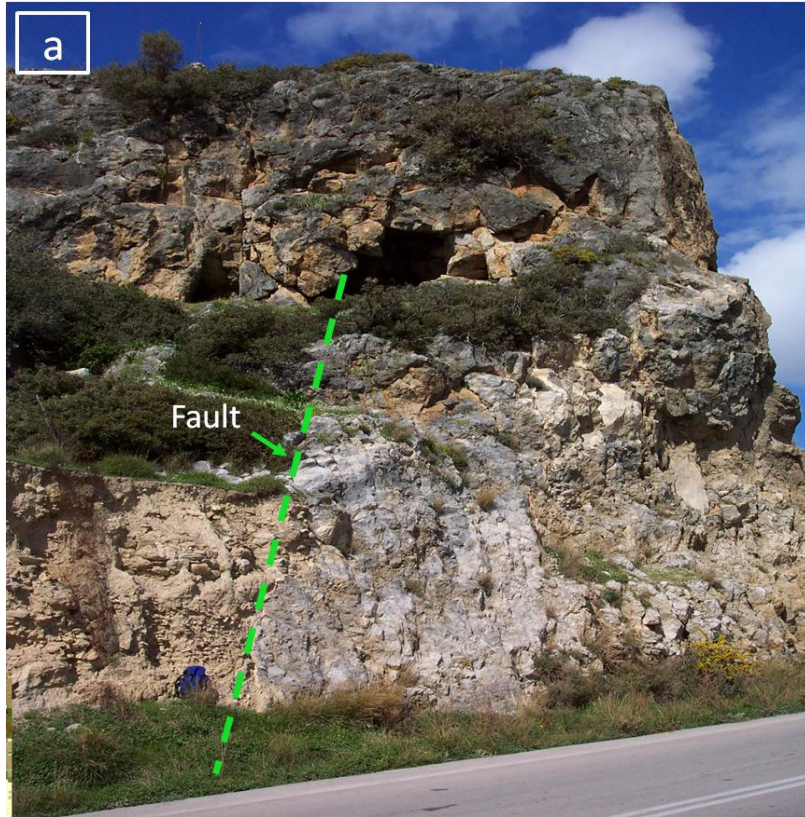
is observed (Fig. 4.1.14). The altitude of the marine terraces is measured almost 80 m above the sea level. In the southern part a flat topped headland where an old castle (Fortezza) is located is characterized of beachrock platforms (Fig. 4.1.15). An  $120^{\circ}$  fault that cuts the beachrock while 3 to 4 fault system are existent. In the central part of Paleohora evidences of uplift are identified. The late Quaternary post-glacial deposits overly (Jurassic) marly limestone (Fig.4.1.16).



**Figure 4.1.9:** Main Fault system of the Geological observations in Paleohora and Grammeno peninsulas in southwestern Crete. The red lines represent the identified faults in Paleohora and Grammeno peninsulas during the fieldwork. Yellow lines indicate the already identified faults using geological and satellite image data.



**Figure 4.1.10:** Overall view of Paleohora and the site of en-echelon fault northeastern of the basin where the pottery was found. a) Segment of normal fault striking E-W identified northeastern of Paleohora. On top of the limestone are gravels containing pottery shards (red circle) that have been downfaulted against the limestone in a normal fault (green dashed line). b) Segment of a fault striking E-W identified northeastern of Paleohora. The hammer is used as a scale. The yellow line represents the E-W strike of the fault zone.





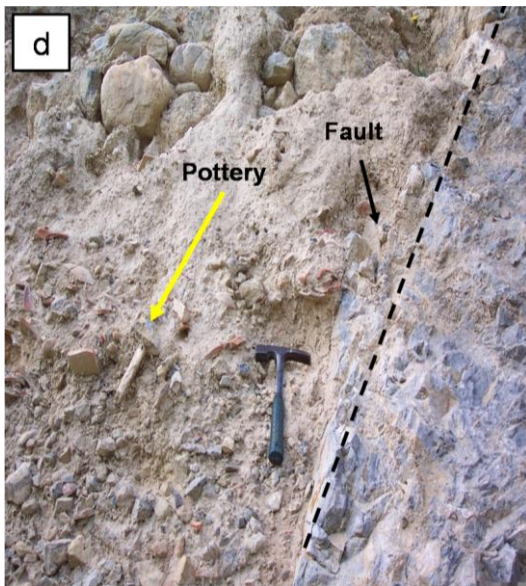
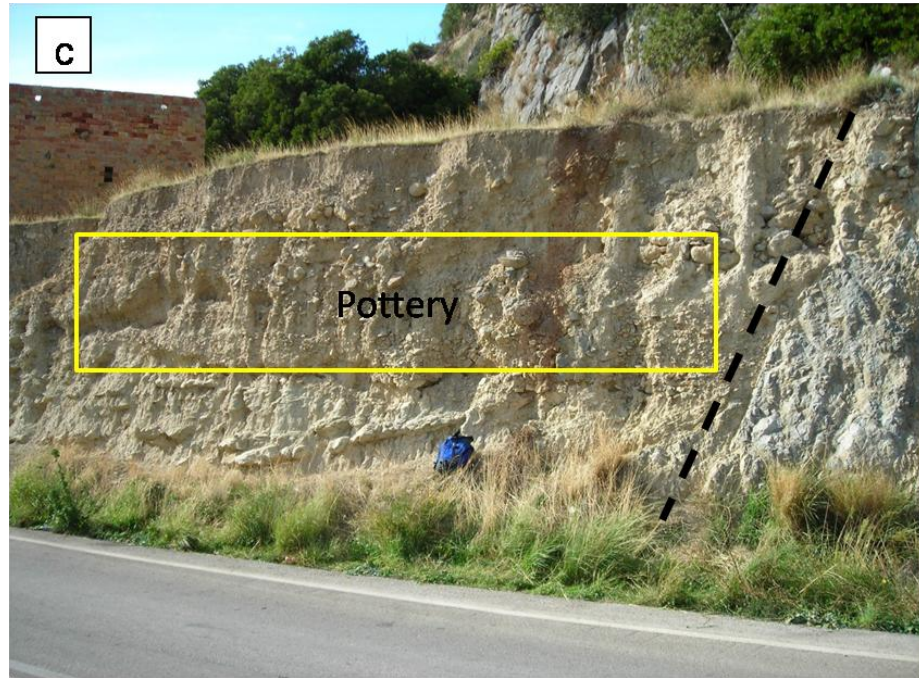


**Figure 4.1.11:** a,b) In the northern side of Paleohora where the pottery (Upper right) is en- echelon fault is identified. The characteristics of the fault are: strike E-W  $66^{\circ}\text{S}$ , slicks (trend  $063^{\circ}\text{S}$ , plunge  $062^{\circ}\text{S}$ ). The fault scarp presents relatively degraded and the fault plane characteristic is  $012/70^{\circ}\text{E}$ , c) The downfaulted pottery shards against the limestone in a normal fault, d,e) Samples of the pottery.

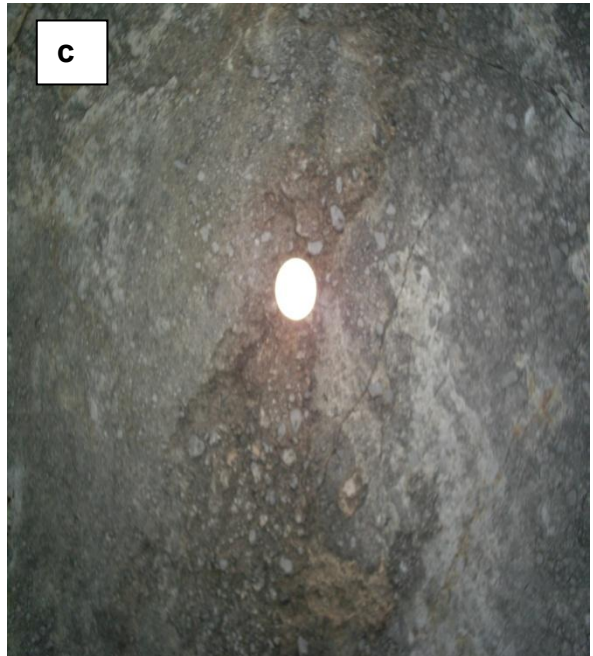
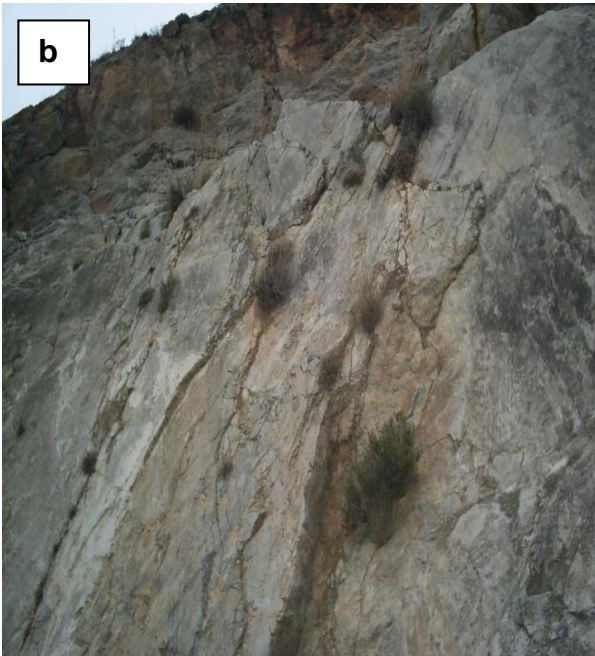




**Figure 4.1.12:** a, b, d) Fault network indicating oblique slip northwestern of Paleohora. Visible patches of fault planes indicating oblique slip, d) a second en-echelon range front fault with very well developed slicks, c) infilled earlier fractures with the same orientation. The coin on figure (c) and the hammer on figure (d) are used as a scale.





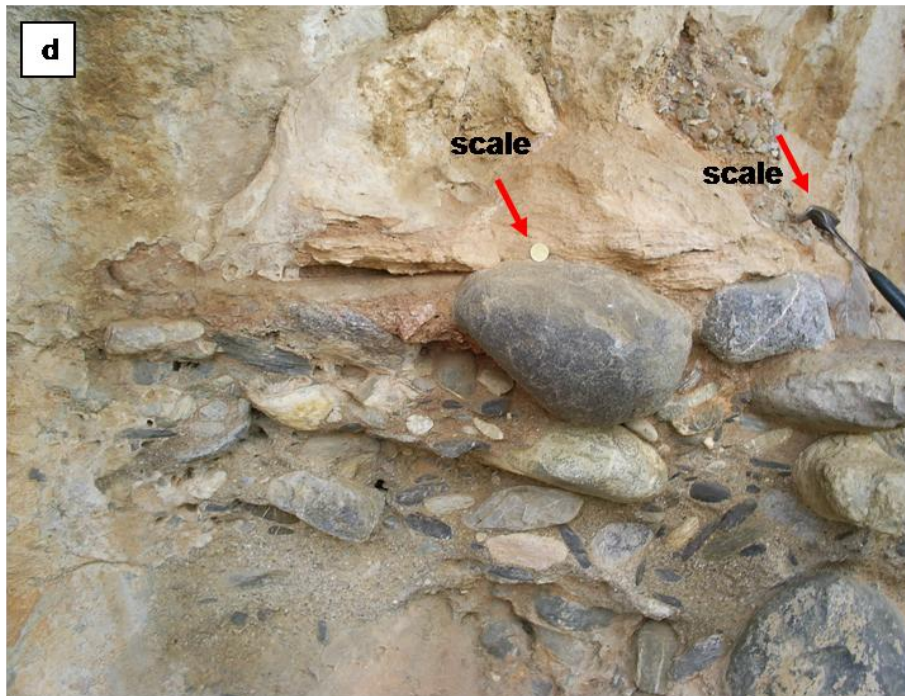


**Figure 4.1.13:** a) Cave where the notch is located, b,c) An uplifted notch (3.5-4.5 m) that is an abrasion notch, and therefore not an indicator of an older relative sea-level position, d,e) basal conglomerates in the cave. The hammer, the coin (d) and the 10 cm meter (d) are used as a scale.

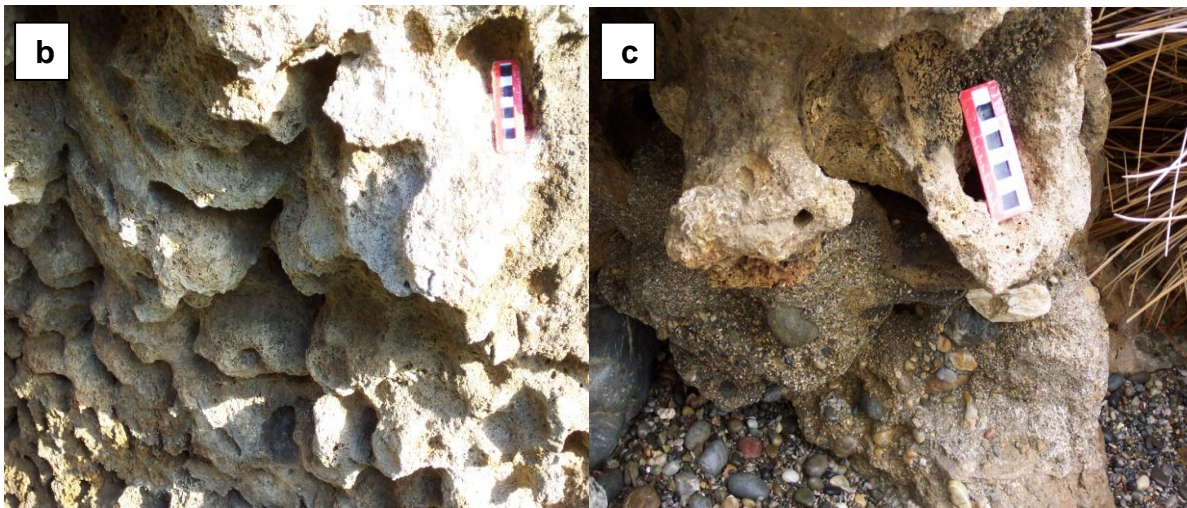


**Figure 4.1.14:** a) Trottoir located below the bench of the uplifted abrasion notch. b, c) The photo of trottoir and the associated beachrock at the base of the trottoir is an uplift indicator which must have occurred quickly because the trottoir is well-preserved.





**Figure 4.1.15:** a) View of a flat topped headland where Fortezza castle is located north of Paleohora. The flat topped headland is characterized of beachrock platforms, b) Beachrock platforms on the flat topped Fortezza headland, c and d) fault evidences of an  $120^{\circ}$  fault that cuts the beachrock and three to four fault system are existent.





**Figure 4.1.16:** In the central part of Paleohora evidence of uplift is identified. The late Quaternary post-glacial deposits that overly (Jurassic) marly limestone.

## **4.2 RESULTS: ELECTRICAL RESISTIVITY TOMOGRAPHY (ERT) IN KASTELLI - KISSAMOU AND PALEOHORA REGIMES**

### **4.2.1 ELECTRICAL RESISTIVITY SURVEY IN KASTELLI KISSAMOU REGIME**

Two periods of fieldwork were organized in Kastelli territory to determine the subsurface structure at specific sites, 10<sup>th</sup> September 2006, and 1<sup>st</sup>, 10<sup>th</sup>, 11<sup>th</sup> and in 13<sup>th</sup> June, 2007. Electrical resistivity tomography survey applied on marbles, schists, marls, alluvial deposits, Cretaceous limestones and alternating beds of shales and argillaceous sandstones. In Figure 4.2.1 are presented the sites where ERT conducted and the orientation of the 2D ERT profiles (green lines). Wenner-Schlumberger and Dipole-dipole configurations are conducted at each site to improve the lateral and in depth accuracy of the measurements. The length of the ERT profiles is varying from 185 m to 310 m at the investigated sites. In Appendix Table 4.1 presents the sites of ERT investigation.

Eight ERT profiles were conducted at several sites in Kastelli-Kissamou region, to model the surface subsurface structure and to reveal fault zones that might be active. Three of the ERT profiles (P1, P2 and P3) are conducted east of Kastelli (near Spatha peninsula) and one profile southeast of Kastelli along a segment of Kera fault (P4). Four ERT profiles (P5 to P8) are conducted west of Kastelli to reveal fault zones crosscutting the dense populated area. ERT profiles P2 to P8 reveal that the investigated area is characterized of a fault system dominantly occupying a sector between NNE and NNW. The extracted 2D ERT profiles are presented in Figures 4.2.2, 4.2.3, 4.2.4, 4.2.6, 4.2.8, 4.2.10, 4.2.12, 4.10.14.

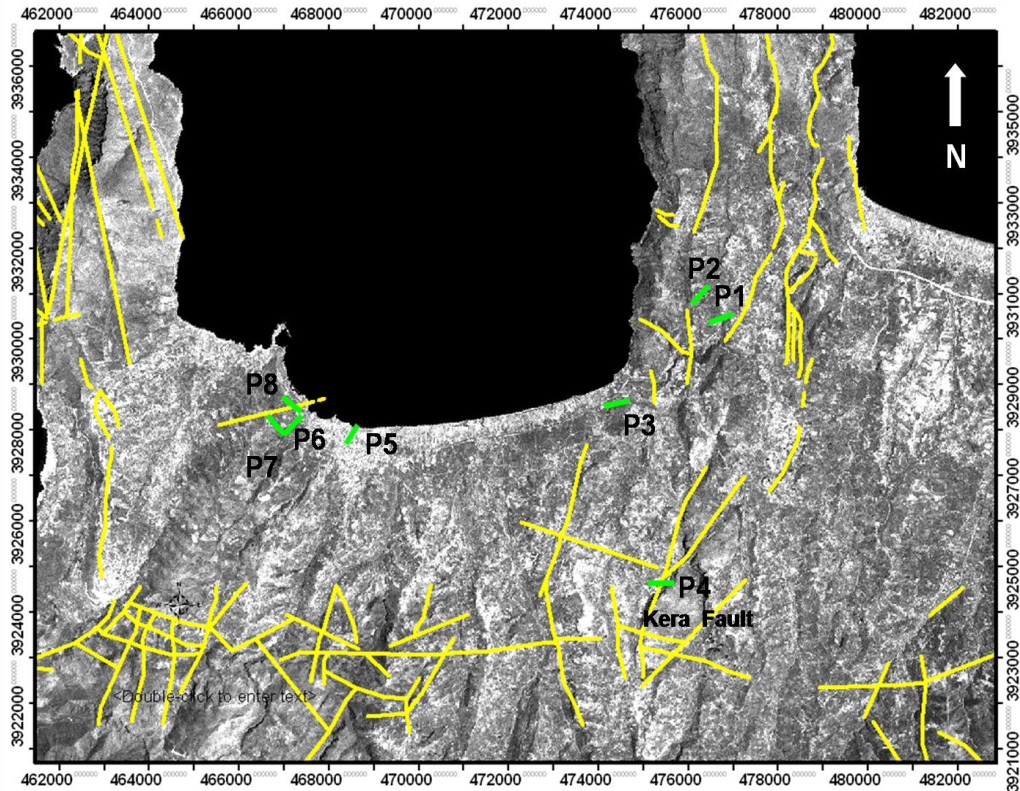


**Figure 4.2.1:** Landat (TM8) image of the area under investigation in Kastelli-Kissamou region. The sites where electrical resistivity profiles conducted are denoted with P1 to P8. The orientation of the 2D electrical resistivity tomographies is denoted with the green lines represents the orientation of the electrical resistivity tomography profiles. The length of the ERT profiles is: 185 m for P8, 235 m for P5, 280 m for P7 and 310 m for P1, P2, P3, P4 and P6. The yellow lines represent the already identified faults extracted from geological and satellite images.

## 4.2.2 EAST OF KASTELLI

East of Kastelli three ERT profiles (P1, P2, and P3) on Figure 4.2.1 were conducted at specific sites of that regime to model the surface and subsurface structure.

### 4.2.2.1 EAST OF KASTELLI (PROFILE 1)

The shallow ERT profile P1 east of Kastelli is presented in Figure 4.2.2 and reveals the interface between the bedrock and the saturated sedimentary formations. ERT along profile P1 defines the unconformity between the saturated sedimentary layer and the bedrock or the observed planar resistivity discontinuity that might contribute to low angle fault. The low resistivity zone (blue colour, 7-20  $\Omega\text{m}$ ) correlates with the conductive material (small scale water contaminants). The high resistivity colour (red colour) defines the resistive tectonic structure. The dashed black line represents the unconformity between the bedrock and the saturated sedimentary formations. The electrodes are grounded by electrode spacing 10 m and the total length of the ERT profile is 310 m (32 electrodes with spacing between them equal to 10 m were used).

The root mean square (rms) was 13.3%. Possible reasons for the derived low angle planar discontinuity feature (dashed black line on Fig.4.2.3) are: a) thrust faults, or b) buried rock platforms of a former shoreline positions that may have been displaced. Given that the region is a tensional setting the likelihood of a thrust fault is less than a rock platform.

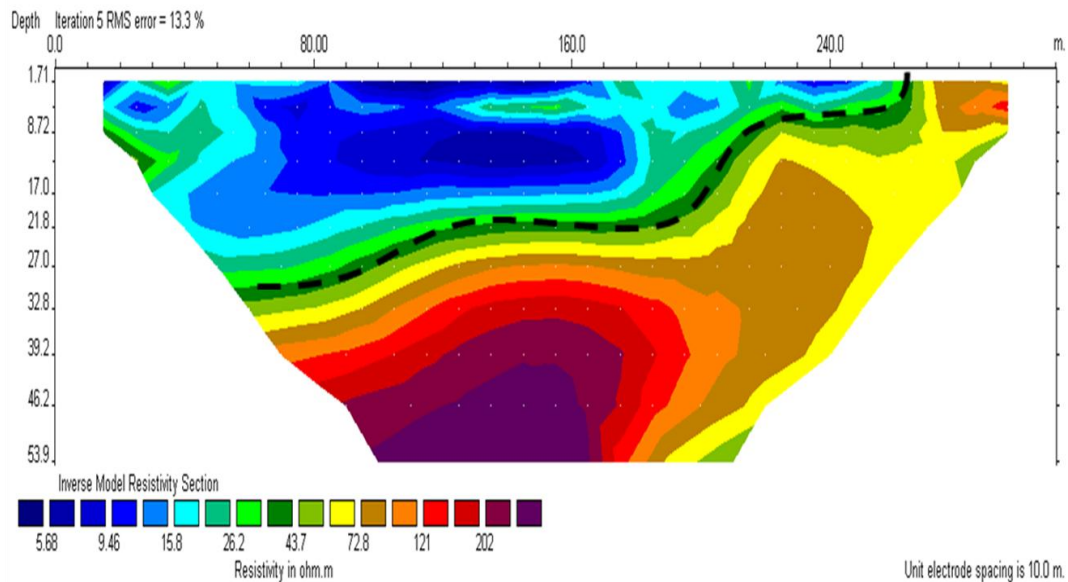


**Figure 4.2.2:** ERT profile east of Kastelli (P1) on the map in Figure 4.2.1. The thick dashed line shows the unconformity between the bedrock and sedimentary formations saturated with seawater. The electrode spacing of 10 m is presented in the lower left corner of the ERT model. The RMS error is presented in the right upper corner and the resistivity scaling (measured in ohm\*m) is presented in the left lower corner of the ERT model.

#### 4.2.2.2 EAST OF KASTELLI (PROFILE 2)

The 2D inverted resistivity profile of the shallow ERT line verifies the presence of a fracture zone of width 80m (figure 4.2.3), approximately dipping to north and trending to almost NNW-SSE direction. The low resistivity zone (blue colour) correlates with the conductive structure. The high resistivity colour (red colour) defines the resistive tectonic structure. The dashed black line represents the fault zone. The electrodes ERT line are grounded by electrode spacing 10 m and the total length of the ERT profile is 310 m. The root mean square (rms) was 14.1%.

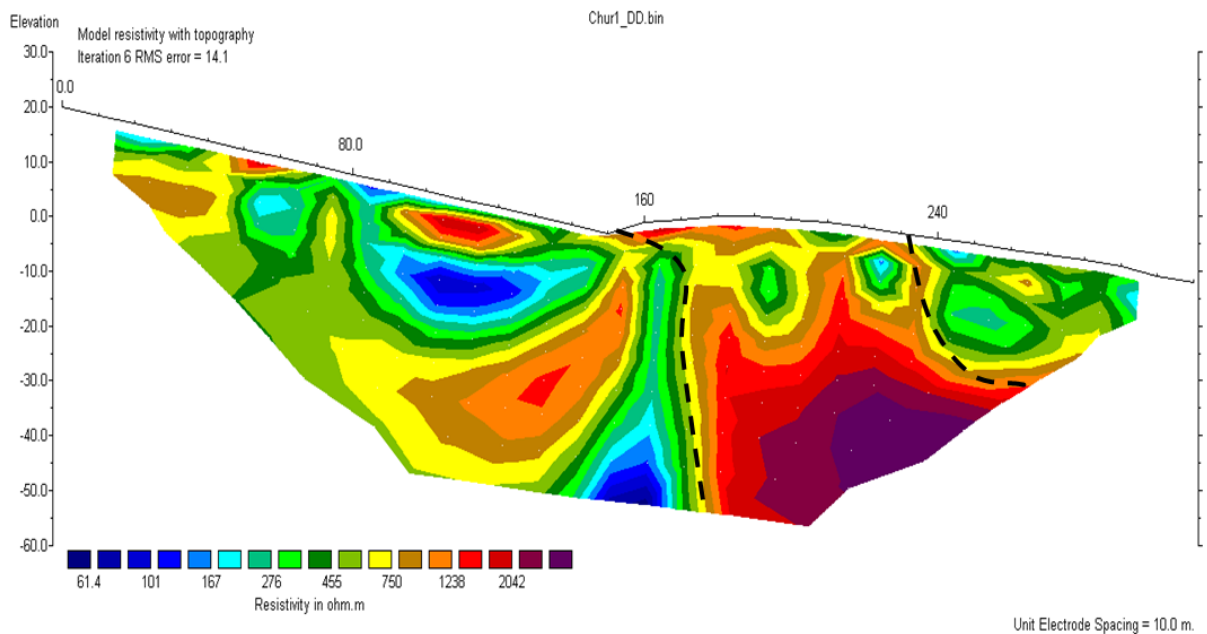


**Figure 4.2.3:** ERT profile east of Kastelli (P2) on the map in Figure 4.2.1. An almost NNW-SSE normal fault zone using ERT method is depicted with the dashed line to a depth of 50 m. The electrode spacing of 10 m is presented in the lower left corner of the ERT model. The RMS error is presented in the right upper corner and the resistivity scaling (measured in ohm\*m) is presented in the left lower corner of the ERT model.

#### 4.2.2.3 EAST OF KASTELLI (PROFILE 3)

The 2D inverted resistivity profile of the shallow ERT line (P3) is presented in figure 4.2.4 and reveals an almost N-S striking fault zone. The dashed black line represents the fault structure at a depth of 40 m. The electrodes ERT line are grounded by electrode spacing 10m and the total length of the ERT profile is 310 m. The low resistivity zone (blue colours) correlates with the conductive structure. The root mean square (rms) was 9.4%.

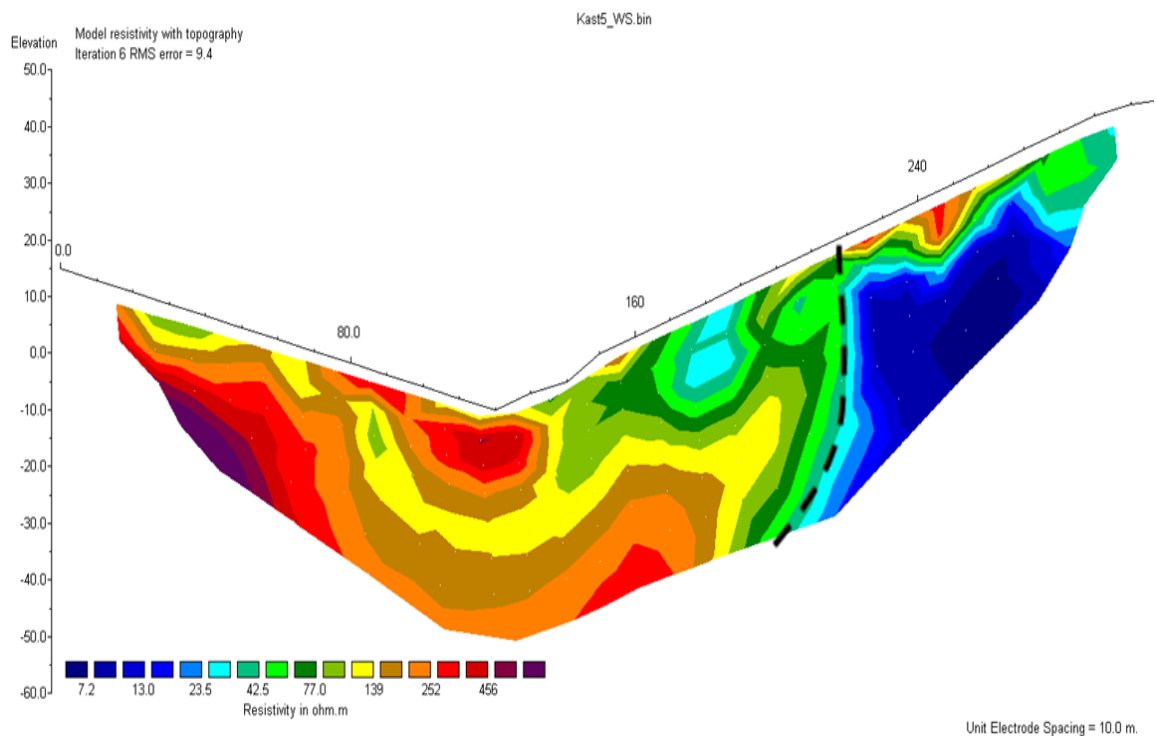


**Figure 4.2.4:** ERT profile in the eastern part of Kastelli (P3). The identified almost N-S normal fault at a depth of 40 m using ERT method is presented with the dashed line. The electrode spacing of 10 m is presented in the lower left corner of the ERT model. The RMS error is presented in the right upper corner and the resistivity scaling (measured in ohm\*m) is presented in the left lower corner of the ERT model.

The overall view of the inverted 2D electrical resistivity tomographies (P1, P2 and P3 on Figure 4.2.1) and the identified subsurface structure in the northeastern part of Kastelli is presented in Figure 4.2.5.

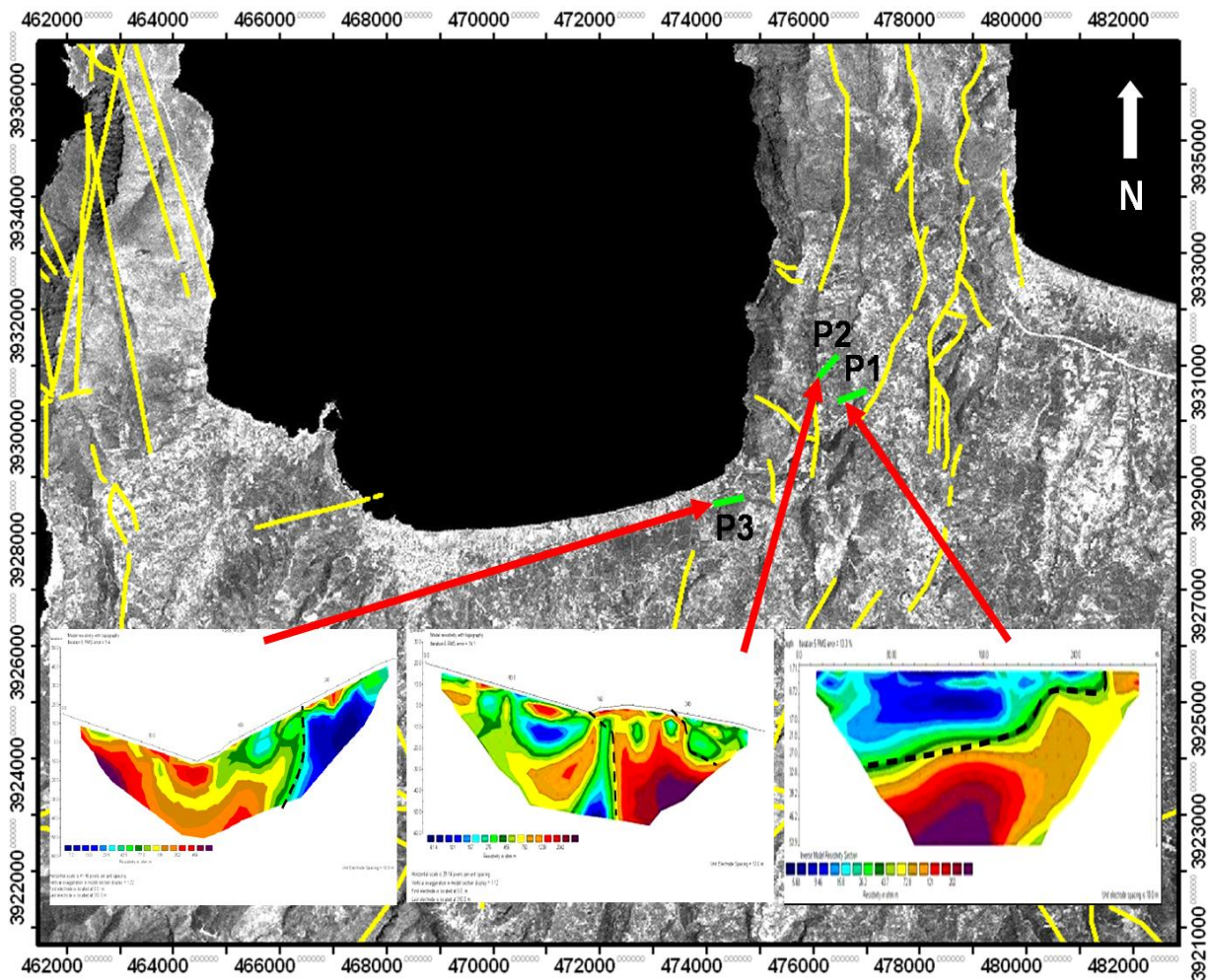


**Figure 4.2.5:** Landsat (TM8) image presenting an overall view of the inverted 2D the electrical resistivity tomographies (P1, P2 and P3 on Figure 4.2.1) in the northeastern part of Kastelli. The green lines represent the orientation of the ERT profile. The yellow lines represent the already identified faults extracted from geological and satellite images.

### 4.2.3 ELECTRICAL RESISTIVITY TOMOGRAPHY WESTERN OF KASTELLI

In west Kastelli four ERT profiles (P5, P6, P7 and P8 , Figure 4.2.1) were used to match known faults at the surface with ERT profiles. Electrical resistivity tomography in western Kastelli reveals an NNW-SSE and N-S faulting network.

#### 4.2.3.1 WEST KASTELLI (PROFILE 5)

The 2D inverted resistivity profile of the shallow ERT line reveals the presence of an almost NNW-SSE trending fault zone at a depth of 28 m. The 48 electrodes of the ERT line are grounded by electrode spacing 5 m and the total length of the ERT profile is 235 m. The low resistivity zone (blue colour) correlates with the conductive structure. The dashed black line represents the fault structure. The root mean square (rms) was 9.5%. In Kastelli profile P5 reveal a very clear faulting and also a decrease in resistivity at depth that it is likely related to an increase in water content of the sediments patterned in the ERT model.

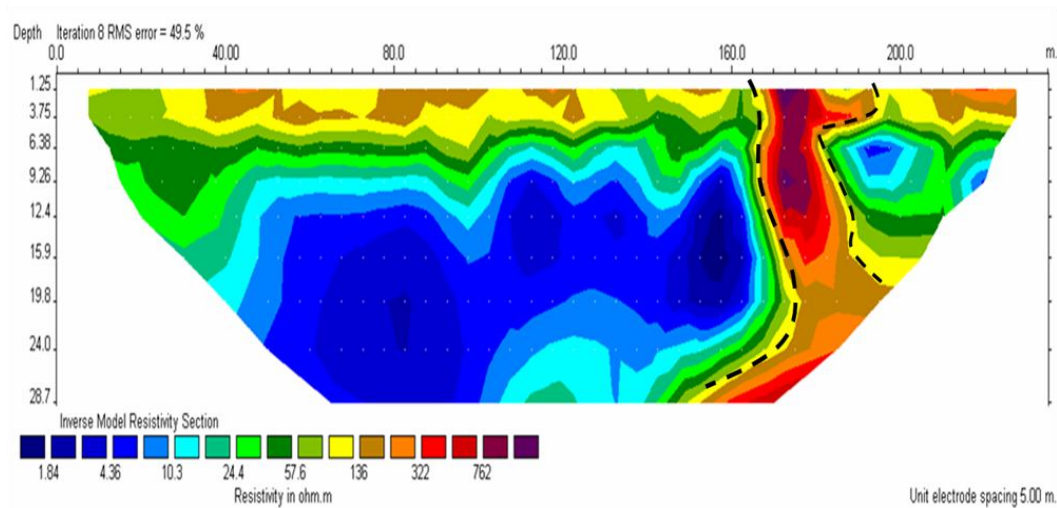


**Figure 4.2.6:** ERT profile in the Western Part of Kastelli (P5) on the map in figure 4.2.1. An almost NNW-SSE normal faulting zone using ERT method is depicted with the dashed line. The electrode spacing of 5 m is presented in the lower left corner of the ERT model. The RMS error is presented in the right upper corner and the resistivity scaling (measured in ohm\*m) is presented in the left lower corner of the ERT model.



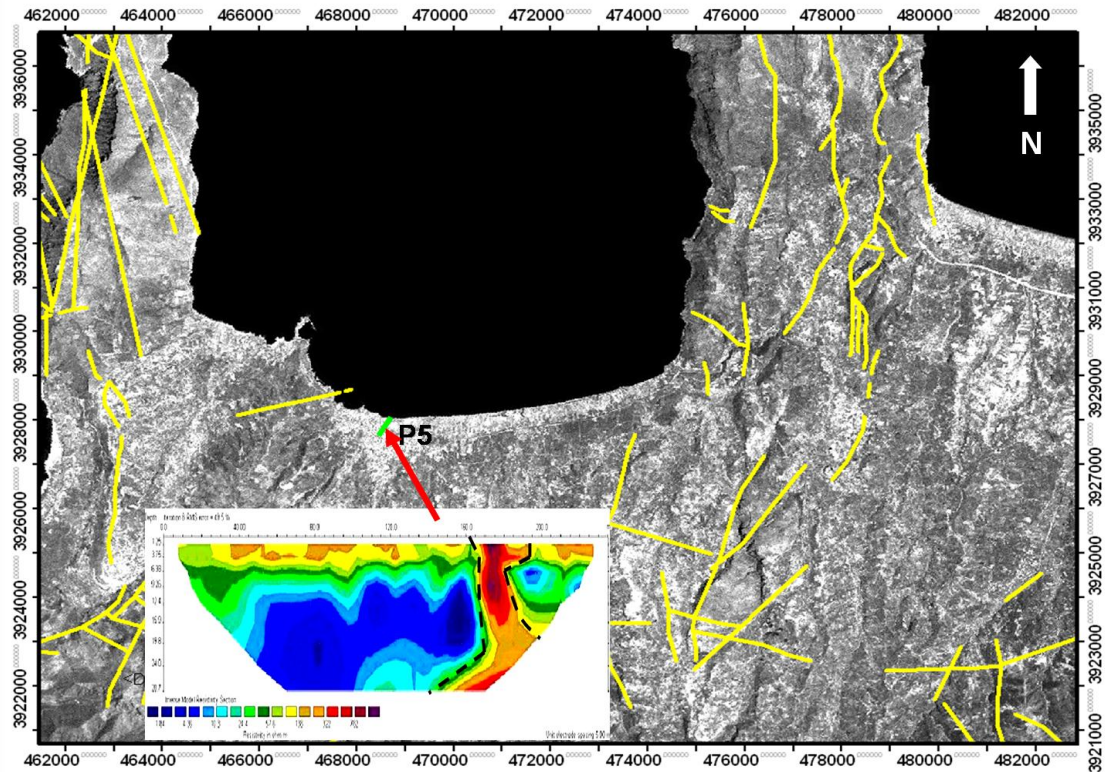


**Figure 4.2.7:** Landsat (TM8) image presenting the ERT profile P5 in the northwestern part of Kastelli. The green lines represent the orientation of the electrical resistivity tomography. The yellow lines represent the already identified faults extracted from geological and satellite images.

#### 4.2.3.2 WEST KASTELLI (PROFILE 6)

The 2D inverted resistivity profile of the shallow ERT line verifies the presence of an NNW-SSE trending fault zone. The dashed black line represents the fault structure at a depth of 30 m. The electrodes ERT line are grounded by electrode spacing 5m and the total length of the ERT profile is 210 m. The low resistivity zone (blue-green colour) correlates with the conductive structure while the red colour is associated with the resistive structure. The root mean square (rms) was 6.9%.

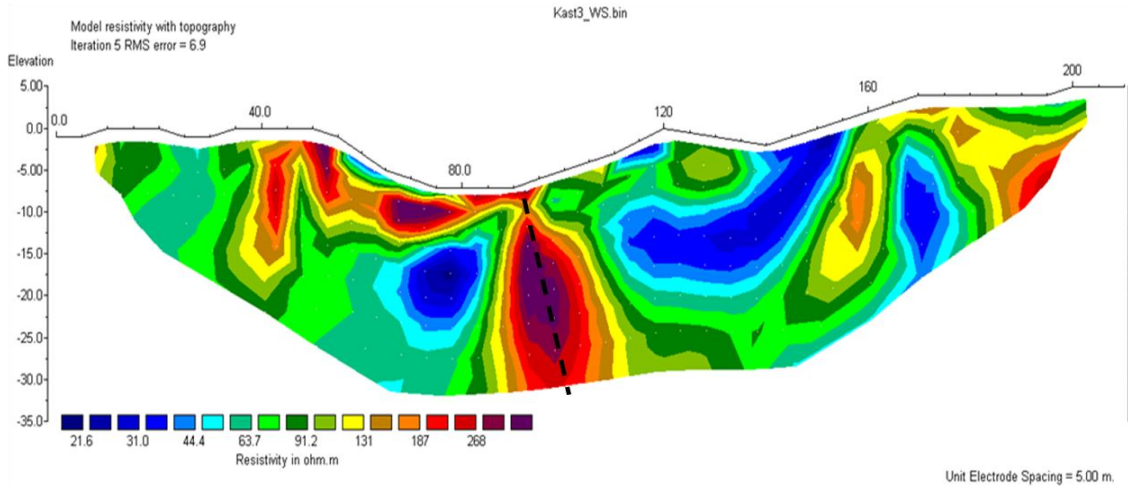


**Figure 4.2.8:** ERT profile in the western part of Kastelli (P6) on the map in Figure 4.2.1. An almost NNW-SSE fault using ERT method is depicted with the dashed line. The electrode spacing of 10 m is presented in the lower left corner of the ERT model. The RMS error is presented in the right upper corner and the resistivity scaling (measured in ohm\*m) is presented in the left lower corner of the ERT model.

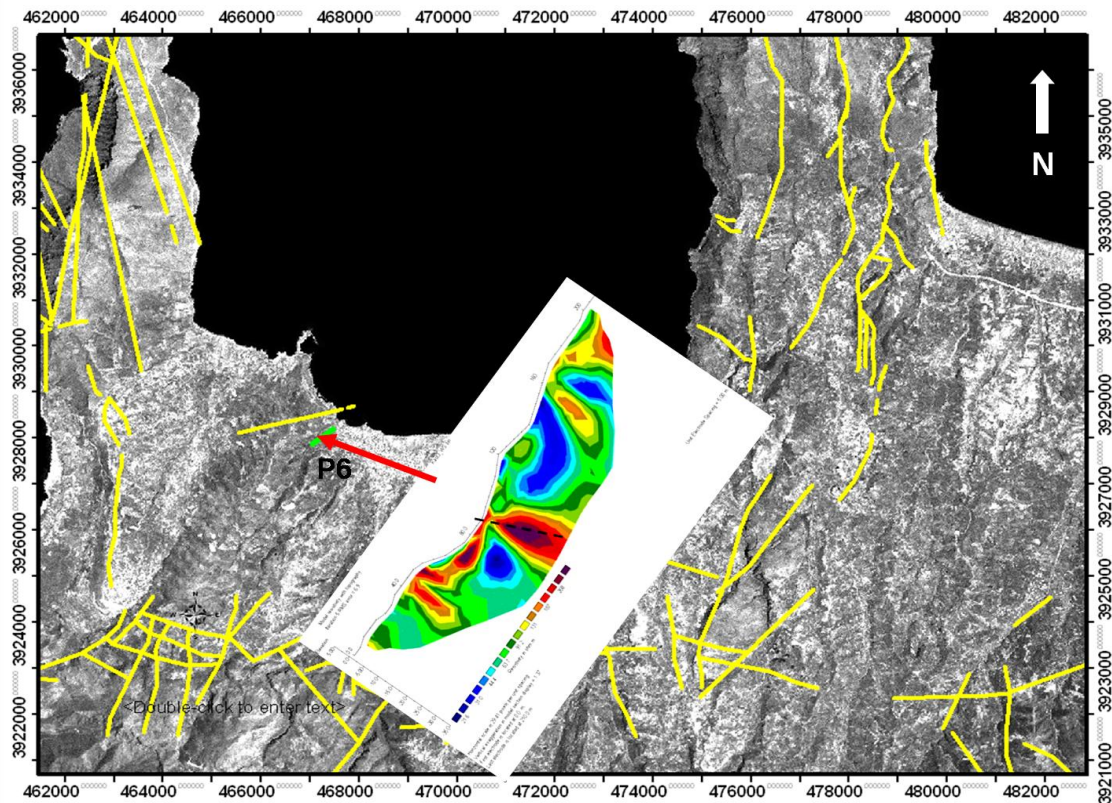


**Figure 4.2.9:** Landsat (TM8) image presenting the ERT profile P6 in the northwestern part of Kastelli. The green lines represent the orientation of electrical resistivity tomography. The yellow lines represent the already identified faults extracted from geological and satellite images.

#### 4.2.3.3 WEST KASTELLI (PROFILE 7)

The 2D inverted resistivity profile of the shallow ERT line verifies the presence of an N-S trending fault zone at a depth of 60 m. The dashed black line represents the fault structure. The electrodes ERT line are grounded by electrode spacing 10m and the total length of the ERT profile is 280 m. The low resistivity zone (blue-green colour) correlates with the conductive structure while the red color is associated with the resistive structure. The root mean square (rms) was 6.9%. The site where profile P7 conducted is presented in Figure 4.2.11.

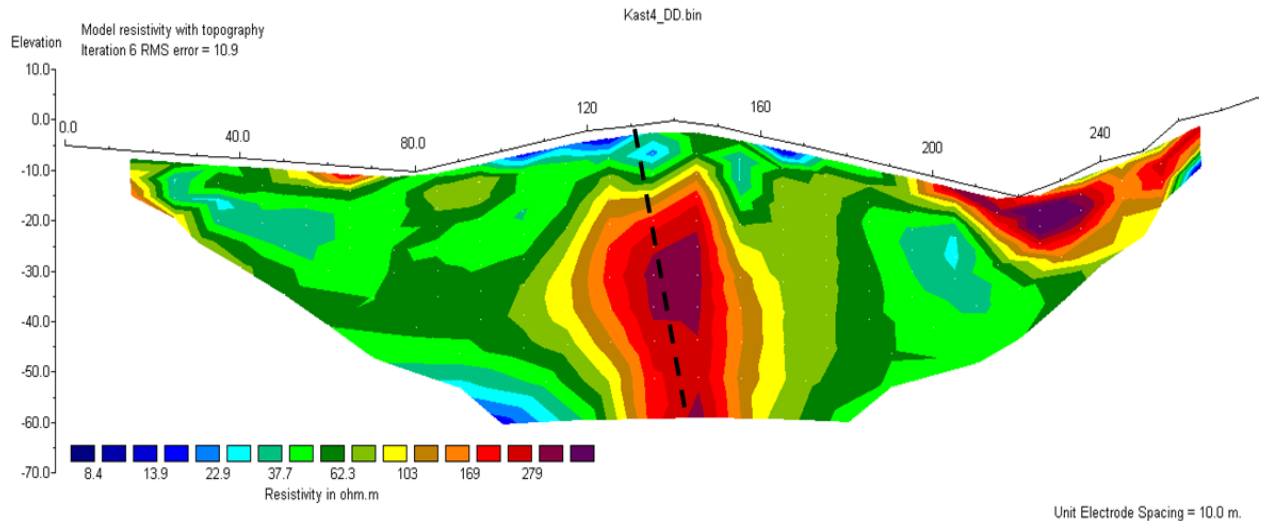


**Figure 4.2.10:** ERT profile western of Kastelli (P7) on the map in Figure 4.2.1. An almost normal N-S faulting zone using ERT method is depicted with the dashed line. The electrode spacing of 10 m is presented in the lower left corner of the ERT model. The RMS error is presented in the right upper corner and the resistivity scaling (measured in ohm\*m) is presented in the left lower corner of the ERT model.

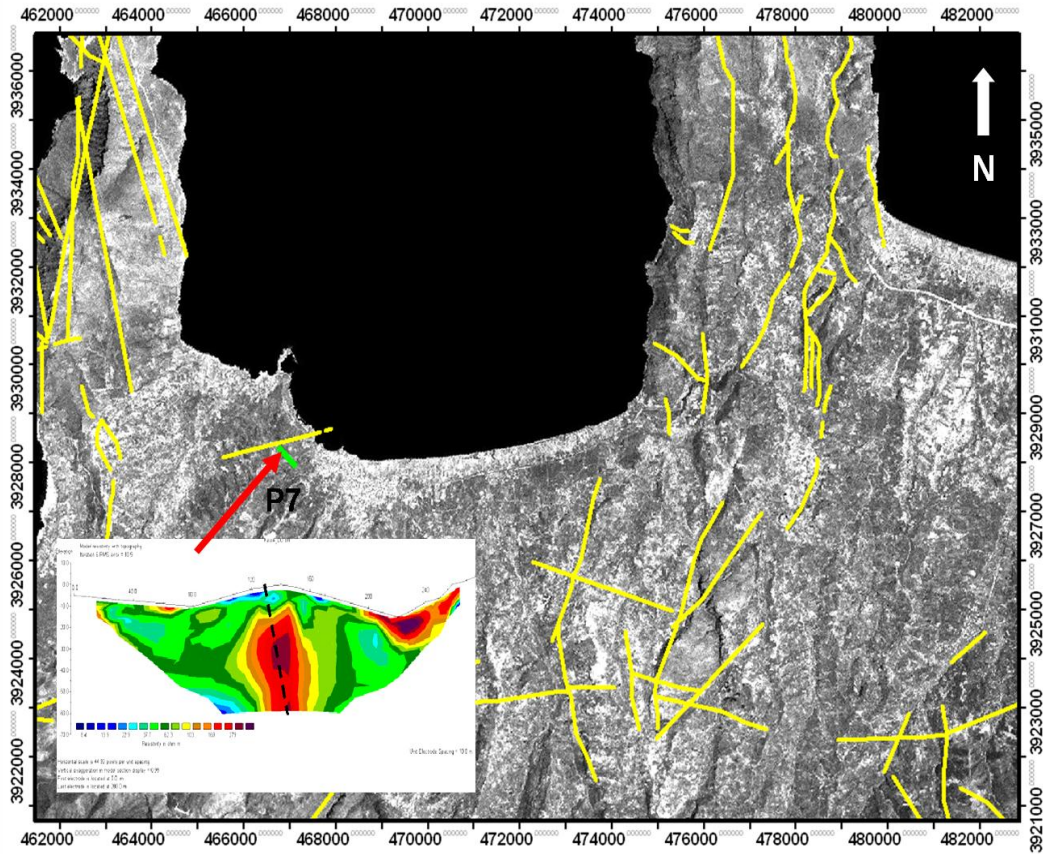


**Figure 4.2.11:** Landsat (TM8) image presenting the ERT profile P7 in the northwestern part of Kastelli. The green lines represent the orientation of the electrical resistivity tomography. The yellow lines represent the already identified faults extracted from geological and satellite image data.

#### 4.2.3.4 WEST KASTELLI (PROFILE 8)

The 2D inverted resistivity profile of the shallow ERT line verifies the presence of an N-S trending fault zone at a depth of 30 m. The electrodes ERT line are grounded by electrode spacing 5m and the total length of the ERT profile is 185m. The low resistivity zone (blue-green colour) correlates with the conductive structure while the red colour is associated with the resistive structure. The fault structure is represented with the dashed black line. The root mean square (rms) is 20.7%. The site where profile P7 conducted is presented in figure 4.2.1.13. In Kastelli profile P8 reveal a very clear faulting and also a decrease in resistivity at depth that it is likely related to an increase in water content of the sediments patterned in the 2D electrical resistivity tomography.

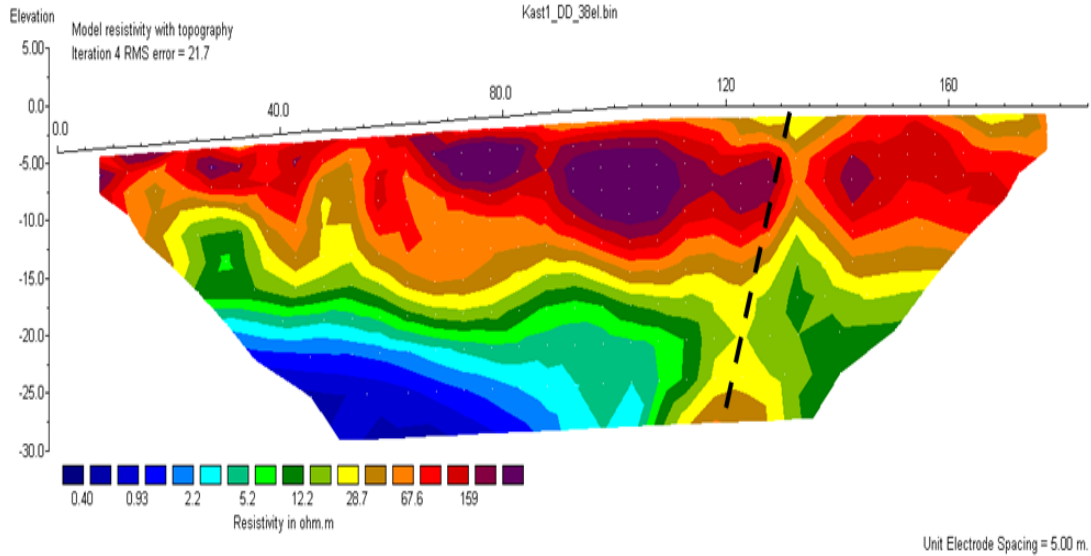


**Figure 4.2.12:** ERT profile in the west Kastelli (P8). An almost normal N-S faulting zone using ERT survey is depicted with the dashed line. The electrode spacing of 10 m is presented in the lower left corner of the ERT model. The RMS error is presented in the right upper corner and the resistivity scaling (measured in ohm\*m) is presented in the left lower corner of the ERT model.

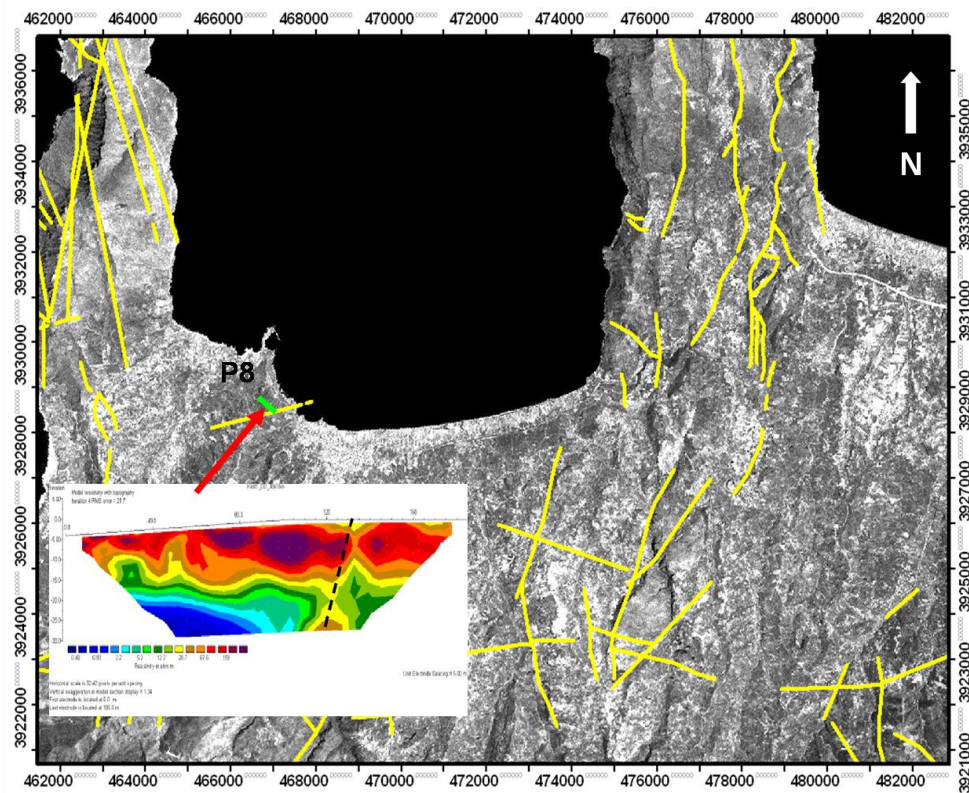


**Figure 4.2.13:** Landsat (TM8) image presenting the ERT profile P8 in northwestern Kastelli. The green lines represent the orientation of the ERT. The yellow lines represent the already identified faults extracted from geological and satellite images.

#### 4.2.4 ELECTRICAL RESISTIVITY TOMOGRAPHY IN KERA FAULT LOCATED IN THE SOUTHERN PART OF KASTELLI (PROFILE 4)

ERT profile P4 along Kera located south-east of Kastelli reveals a large scale N-S fault zone. The RMS of the proposed model is 2.8.

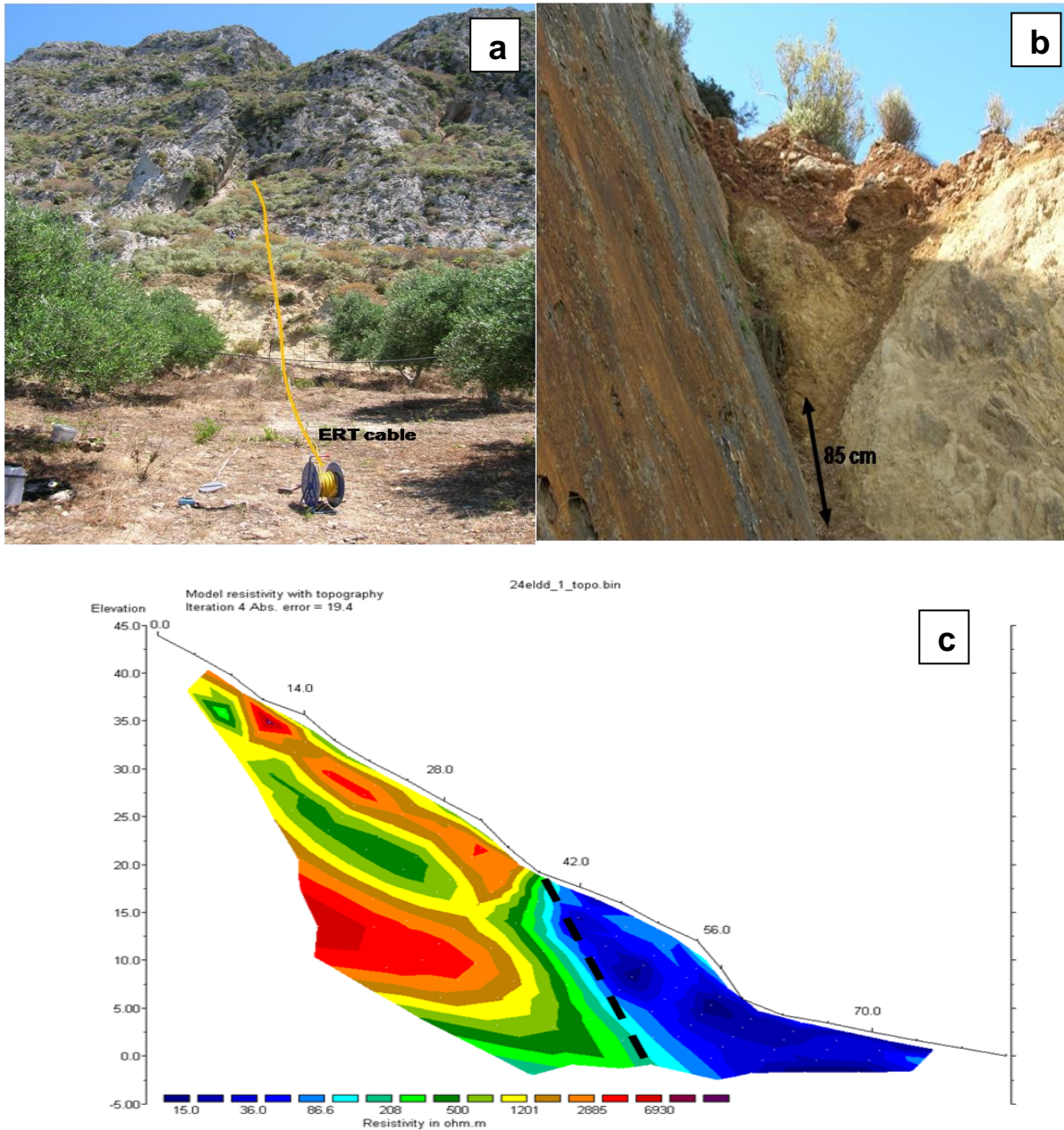


**Figure 4.2.14:** a) ERT line configuration along a segment of Kera fault. The yellow line is the cable connected with electrodes to model subsurface structure, b) close view of the determined faulting, c) very clear faulting along Kera Fault using ERT survey. An almost normal N-S faulting zone using ERT method is depicted with the dashed line. The RMS error is presented in the right upper corner.

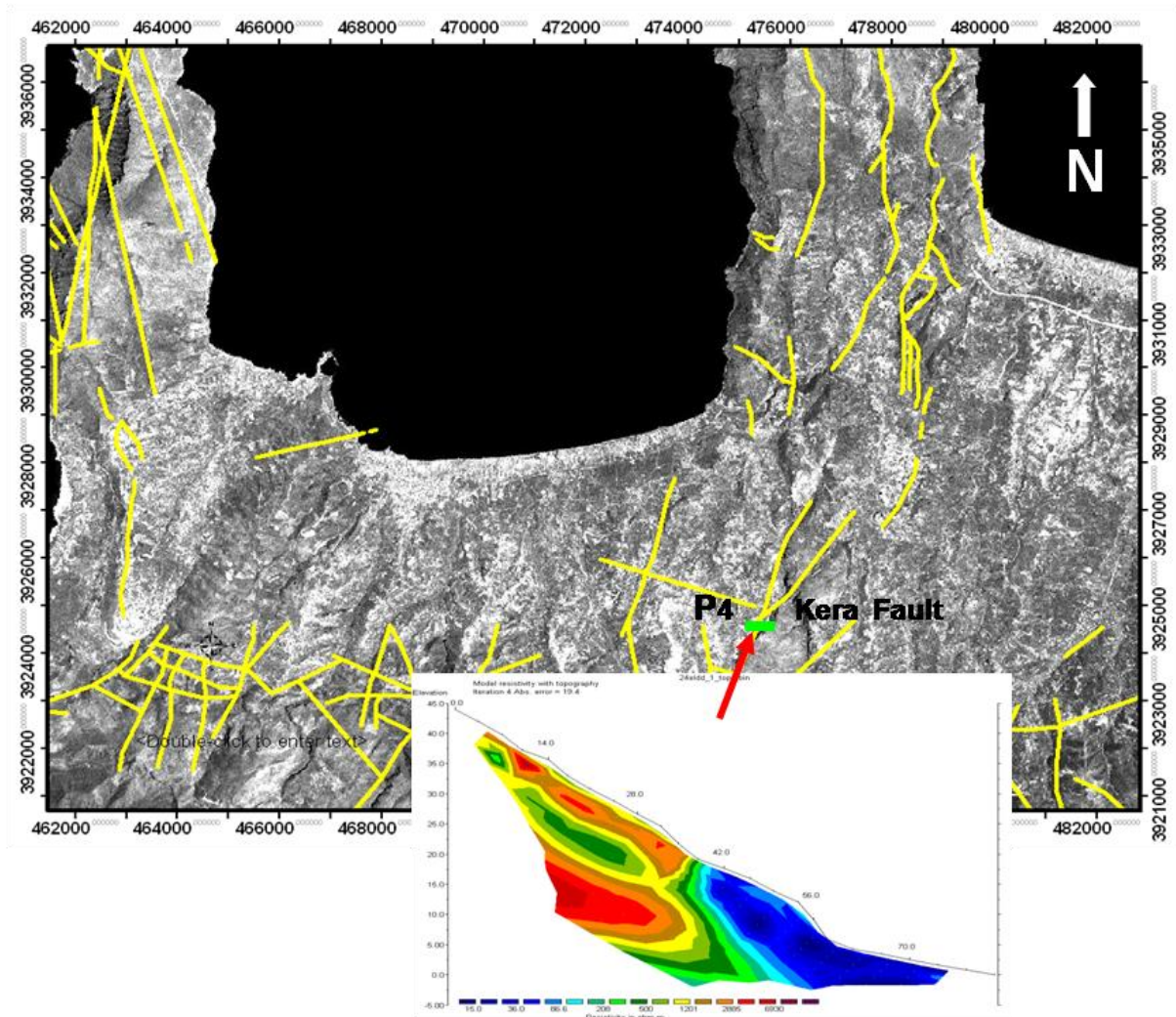


**Figure 4.2.15:** Landsat (TM8) image presenting the ERT profile P4 in Kera located in the southeastern part of Kastelli. The green lines represent the orientation of the ERT line. The yellow lines represent the already identified faults extracted from geological and satellite image data.

The identified faults based on ERT are the possible extension of existing faults derived from ground thruthed geological investigations and geological and satellite image maps are presented in Figure 4.2.16. ERT along profile P1 defines a clear unconformity between the saturated sedimentary layer and the bedrock. The unconformity (planar resistivity discontinuity) might be part of the segment of low angle fault. ERT profile P1 that does not present a clear fault feature might be a part of the segment of the low angle fault (cross-sections F-G, Figure 4.2.16) denoted by FK7 on figure 4.2.16 or to the low angle fault (cross-section K-L, on Figure 4.2.16). The likelihood of a thrust fault is less than a rock platform in this tensional region. Further geophysical techniques are required to justify the proposed fault delineation (cross-sections F-G and K-L on figure 4.2.16).

ERT profile 2 is the possible extension of a fault presented on figure 4.2.16 (point K on Fig. 4.2.1.16) and contributes to the delineation of a fault segment striking almost NNW-SSE (cross-section K-L on fig 4.2.1.16) denoted by FK6 on figure 4.2.16. ERT profile 3 is the possible extension of a fault (point D on Fig. 4.2.16) and contributes to the delineation of the fault segment (cross-section D-E on fig 4.2.16) striking almost NNE-SSW and denoted by FK5 on Figure 4.2.16. ERT profiles P5 and P6 are the extension of fault southeast of Kastelli (point A on Fig. 4.2.16) and contribute to the delineation of the fault segment (section A-B-C on Fig 4.2.16) striking almost NNW-SSE denoted by FK3 on figure 4.2.16. ERT profiles P7 and P8 are the extension of a fault (point M on Fig.4.2.16) denoted by FK2 and FK1 respectively. These faults contribute to the delineation of a fault segment (cross-section M-N on Fig 4.2.16) striking NNE-SSW. ERT along Kera village located almost 6 km southeast of Kastelli (P4) reveals a clear N-S fault zone. ERT profiles conducted in Kastelli region are dominantly occupying a sector between NNE and NNW.

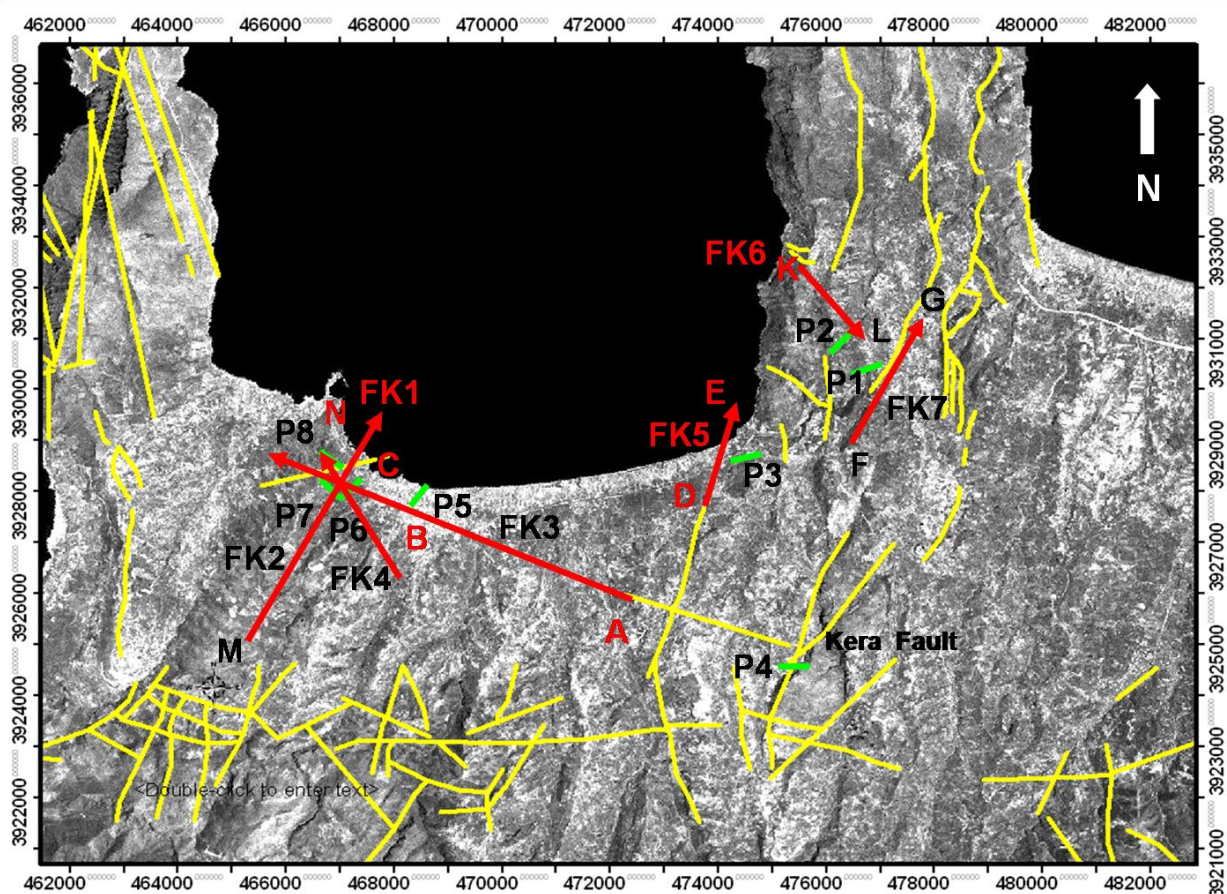


**Figure 4.2.16:** Identified faults using ERT and their possible extension of existing faults derived from geological and satellite image data. All ERT profiles conducted in Kastelli region are dominantly occupying a sector between NNE and NNW. The green line represent the orientation of the ERT profiles. The red lines represent the possible extension of the identified faults based on ERT survey. The yellow lines represent the known faults based on geological and satellite images.



#### 4.2.5 ELECTRICAL RESISTIVITY SURVEY IN PALEOHORA IN SOUTHWESTERN CRETE

Three periods of fieldwork were organized in Paleohora territory to determine the subsurface structure at specific sites, 13<sup>th</sup> September 2006, 30<sup>th</sup> November 2006 and June, 2007. Six ERT profiles were conducted at several sites in the Paleohora basin to model the subsurface structure and to reveal fault zones that might be active. ERT profiles applied on alluvial deposits, transition beds composed of platy limestones alternating with sandstone and shales, on Lissos beds composed of cobbles and rubbles of pre-Neogene series consolidated with calcitic and marly cement (maximum depth 150 m). In Figure 4.2.17 are presented the sites and the orientation of the ERT survey. In Table 4.2 (Appendix I) is presented the location of the sites of ERT investigation.

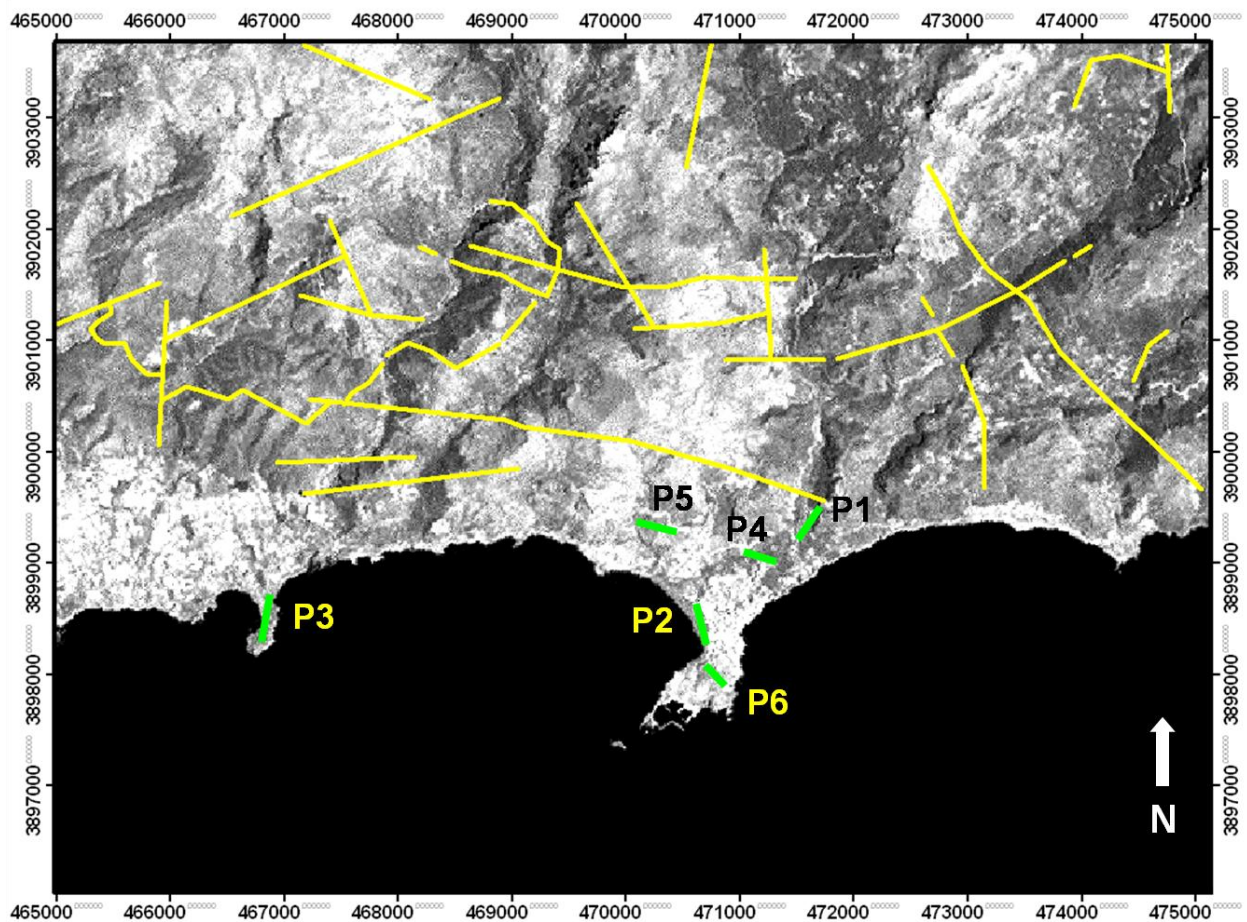


**Figure 4.2.17:** Landat (TM8) image of the area under investigation in Paleohora located in southwestern Crete. The ERT profiles are denoted with P1 to P6. The green lines represent the orientation of the ERT profiles. The yellow lines represent the already identified faults extracted from geological and satellite images.

#### 4.2.6 FAULT IN THE NORTHEASTERN PART OF PALEOHORA

During the first period of field work a geoelectrical resistivity tomography, based on the geological field survey was implemented at the site where the pottery bearing sediments is located to verify the presence of the en-echelon faults at that site. ERT profiles are conducted in the northern part of Paleohora regime to locate the north-dipping extensional fault. Based on geological field survey the fault creates a coast-parallel graben structure. Shallow and deep ERT profiles at site P1 (Fig. 4.2.18 and 4.2.20) verify the presence of a fracture zone, a reverse fault dipping to north and trending to almost ENE-WSW direction. The shallow and deep 2D electrical resistivity profiles are shown in Figures 4.2.18 and 4.2.20. The shallow and deep ERT profiles (Figs 4.2.18 and 4.2.20) at site profile P1 reveal reverse fault near the site where the pottery findings identified from geological survey (Fig. 4.1.10 ).

##### 4.2.6.1 SHALLOW ELECTRICAL RESISTIVITY PROFILE

The ERT profile of electrodes spacing 5m along a 235 m long ERT line, verify the presence of a reverse fault of width approximately 30 m, dipping to North and trending to almost ENE-WSW direction. The shallow ERT profile is shown in Figure 4.2.18. The orientation of the profile is presented in Figure 4.2.20.

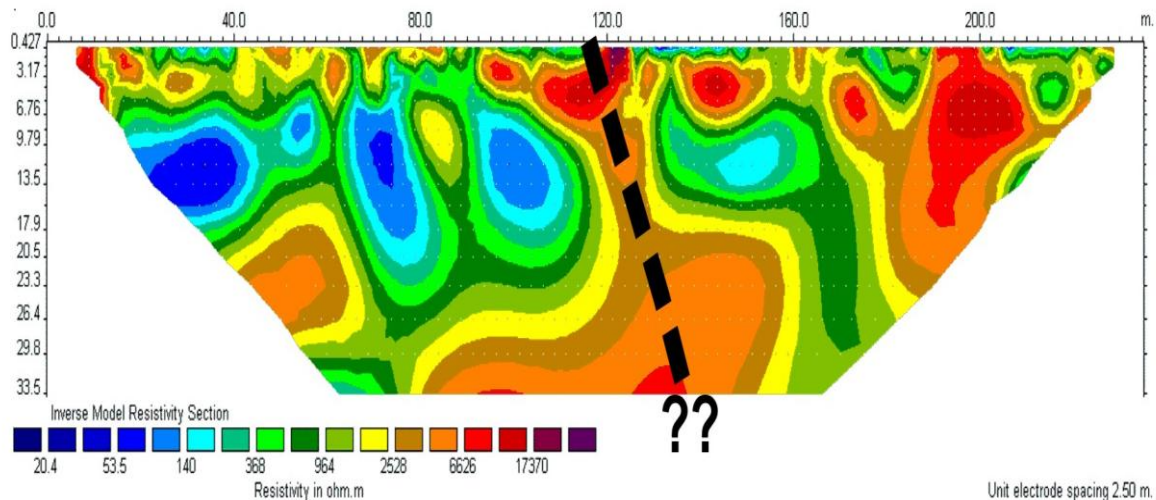


**Figure 4.2.18:** Shallow Electrical Resistivity Tomography profile. Red colours define the resistive structure. The estimated ENE-WSW reverse faulting zone using ERT method is depicted with the thick dashed line. The questionmarks represents that the fault extend to an unknown depth. The electrode spacing of 5m is presented in the lower left corner of the ERT model. The RMS error is presented in the right upper corner and the resistivity scaling (measured in ohm\*m) is presented in the left lower corner of the ERT model.

#### 4.2.6.2 DEEP ELECTRICAL RESISTIVITY PROFILE

To determine the depth of the substructure fracture zone a deep ERT resistivity line (345m) with electrode spacing 15 m is conducted. The 2D inverted resistivity profile (Figure 4.2.19) of the deep ERT line verifies the presence of a fracture zone, a reverse fault, of width 30 m, dipping to north and trending to almost ENE-WSW direction. The low resistivity zone (7-90  $\Omega\text{m}$ ) correlates with a clay layer while the high resistivity zone consists primarily of terrace gravel. The final rms was 133.6%. The orientation of the profile is presented in figure 4.2.20.

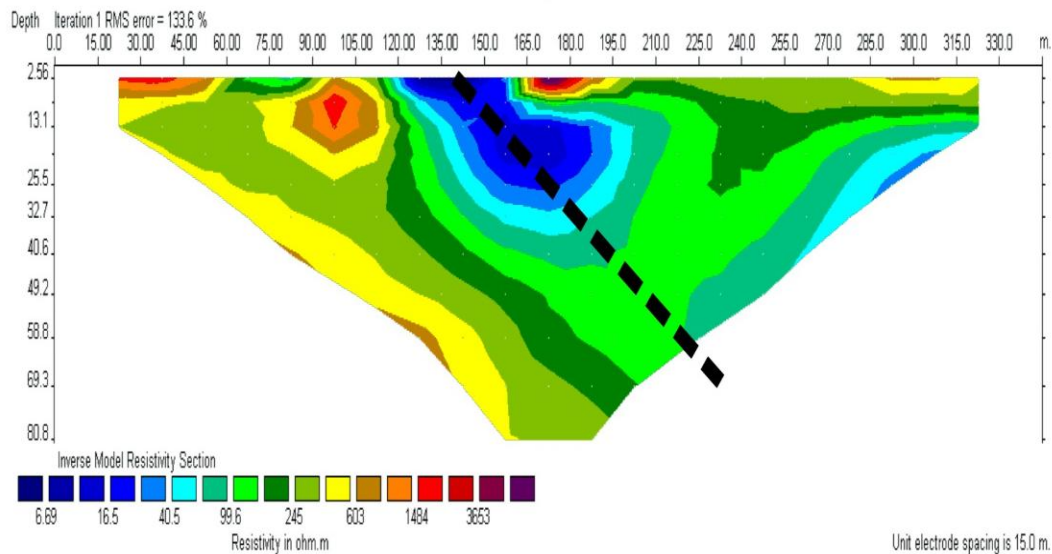


**Figure 4.2.19:** Deep ERT profile P1 in northeastern of Paleohora. Red colours define the resistive structure. The estimated ENE-WSW reverse faulting zone using ERT method is depicted with the dashed line. The electrode spacing of 15 m is presented in the lower left corner of the ERT model. The RMS error is presented in the right upper corner and the resistivity scaling (measured in ohm\*m) is presented in the left lower corner of the ERT model.

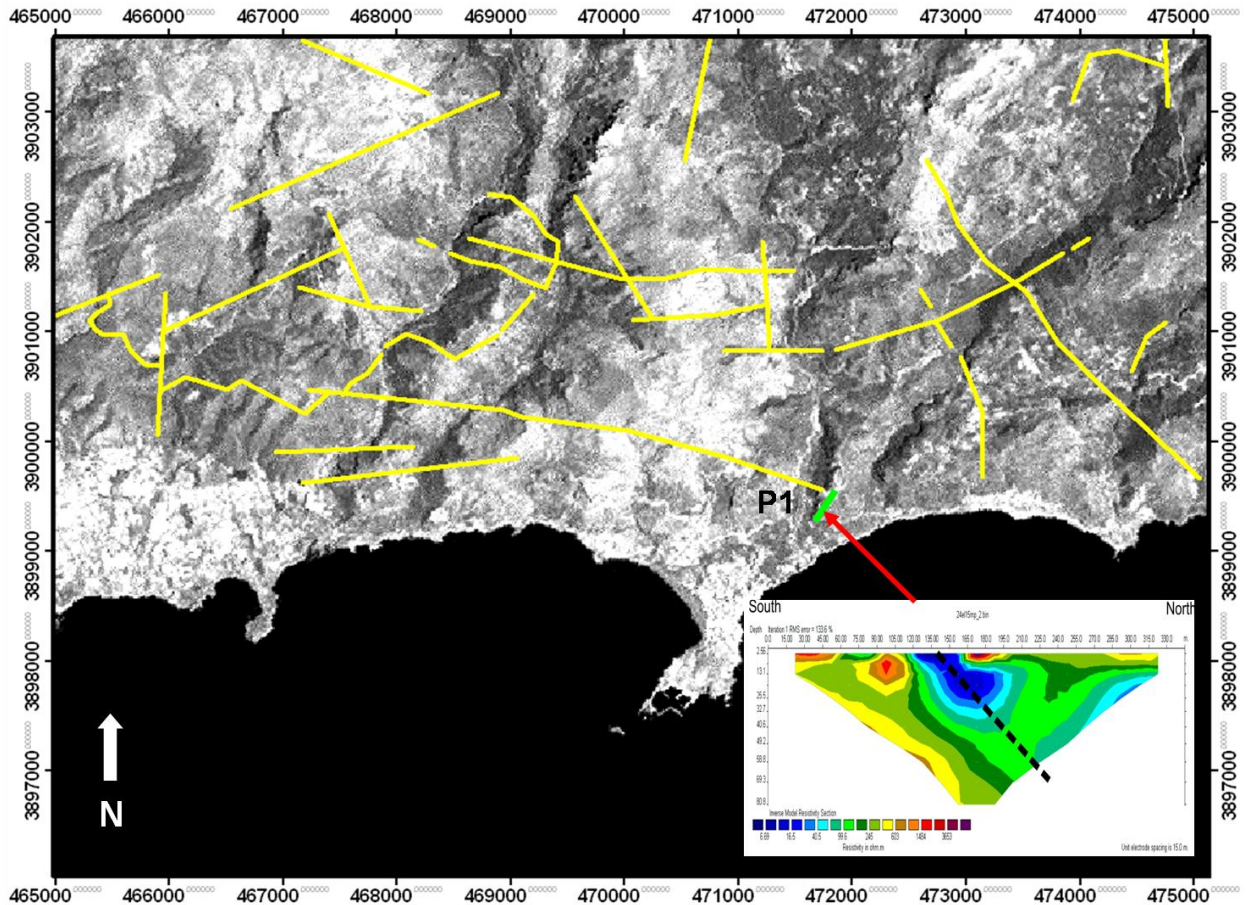


**Figure 4.2.20:** Landsat (TM8) image presenting the inverted 2D ERT profile (P1) of the northeastern Paleohora near pottery findings. The green lines represent the orientation of the ERT profiles. The yellow lines represent the already identified faults extracted from geological and satellite images.

## 4.2.7 ELECTRICAL RESISTIVITY PROFILE IN THE URBAN AREA OF PALEOHORA AND IN GRAMMENO PENINSULA

### 4.2.7.1 ERT IN PALEOHORA PENINSULA IN THE URBAN AREA (PAHIA AMMOS)

Electrical Resistivity tomography performed in shallow and deep profiles along the coastline of Pahia Ammos site, is consistent with the presence of a large scale fault, dipping to south and trending almost E-W. The fracture zone revealed by the ERT is verified by the geological fieldwork. ERT profile in Pahia Ammos beach is characterized by a thick cemented sandy layer. In the southern part of Pahia Ammos The high electrical resistivity value (711 to 3500  $\Omega\text{m}^*\text{m}$ ), extracted either from shallow and deep ERT profiles is presented with red colour and corresponds to the electrical physical properties of the limestone/calclitic bedrock. The blue colour corresponds to seawater intrusion (0.34-4.4  $\Omega\text{m}^*\text{m}$ ) while the green colour contributes to fresh groundwater (15.6-55.8  $\Omega\text{m}^*\text{m}$ ) that discharged into the seawater. Personal communications with

locals verifies the existence of the aforementioned discharge of the groundwater into the sea.

The investigated site in Pahia Ammo in Paleohora urban area where the ERT profile carried out is presented in figure 4.2.23. The shallow and deep 2D inverted electrical resistivity profiles are presented in figures 4.2.21 and 4.2.22. An overall schematic section of the investigated site and the corresponding shallow 2D resistivity model is presented in figure 4.2.23.

#### 4.2.7.2 SHALLOW ELECTRICAL RESISTIVITY PROFILE

The 2D inverted resistivity profile of the shallow ERT line reveals the presence of a left-oblique normal fault of width of almost 80 m in the near surface, dipping to south and trending almost E-W. The electrode spacing is 5 m along a 235 m line. The final rms was 44.5%.

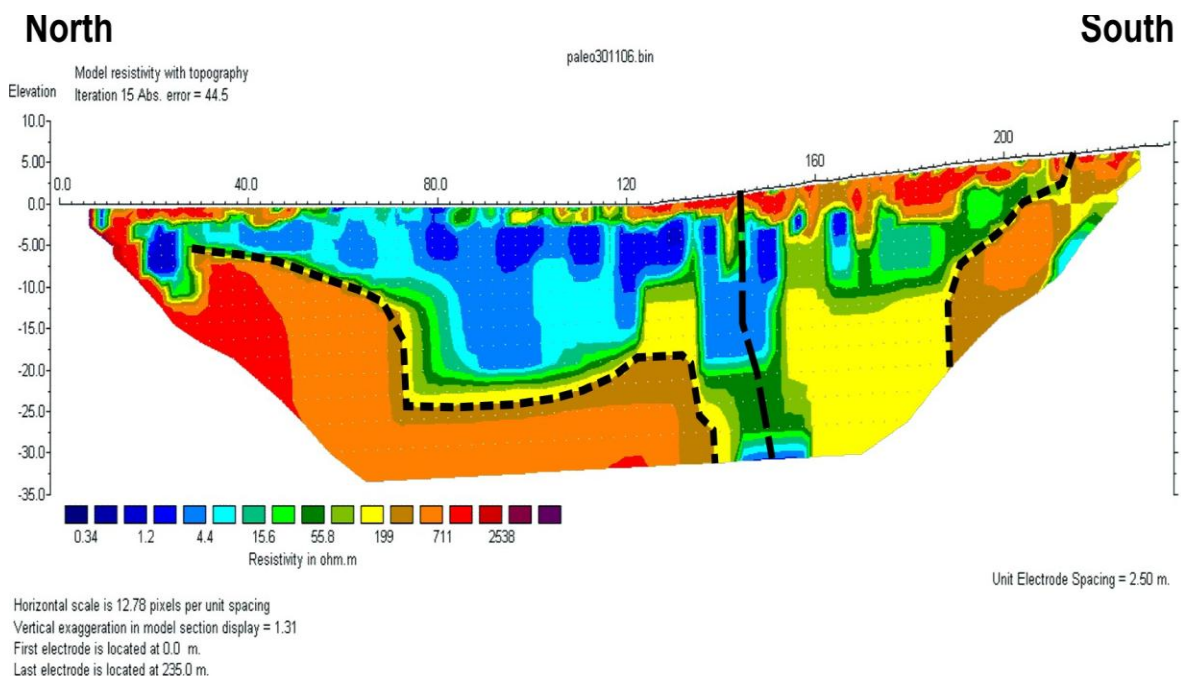


**Figure 4.2.21:** Shallow ERT profile at Paleohora peninsula. Red colours define the resistive structure. The tectonic zone is depicted with the dashed line. An almost E-W faulting zone using ERT method is depicted with the thick dashed line. The thin short-dashed black line represents the unconformity. The electrode spacing of 5 m is presented in the lower left corner of the ERT model. The RMS error is presented in the right upper corner and the resistivity scaling measured in(ohm\*m) is presented in the left lower corner of the ERT model.

### 4.2.7.3 DEEP ELECTRICAL RESISTIVITY PROFILE

The 2D inversion resistivity profile of the deep ERT line verifies the presence of a large scale fault of width 80 m in the near surface, dipping to south and striking almost E-W at a depth of at least 50 m. The fracture zone might be saturated with saltwater. The electrode spacing of deep ERT resistivity line (345 m) is 15 m. The final rms was 58.9%.

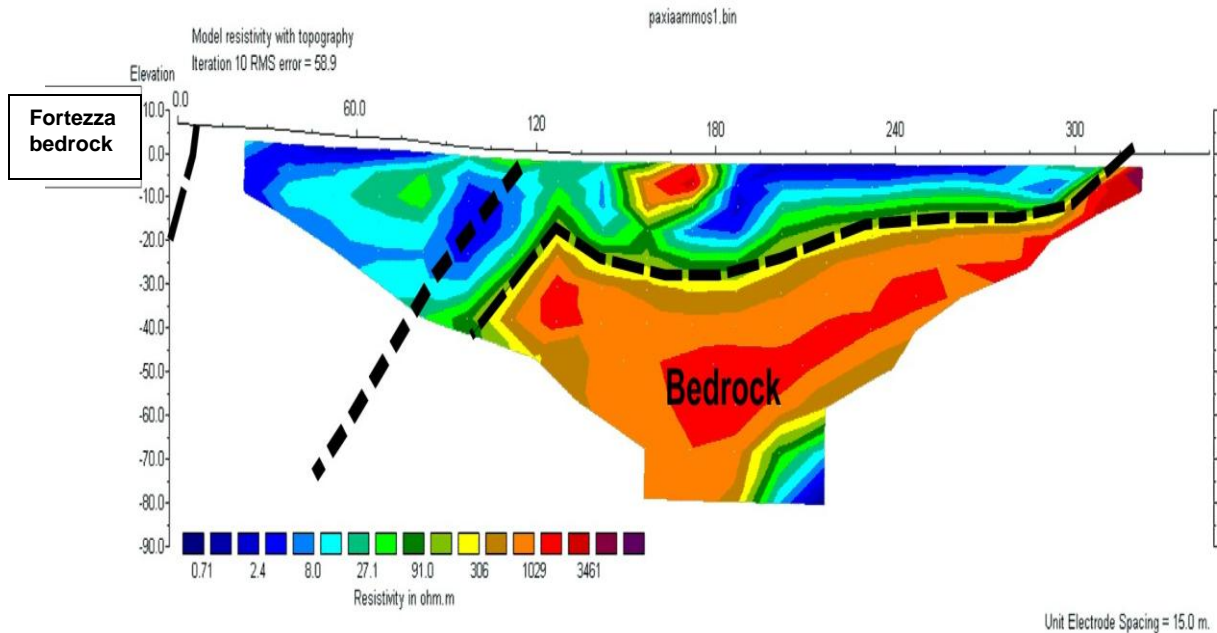


**Figure 4.2.22:** The deep electrical tomography profile at Paleohora peninsula (Pahia Ammos). Red colours define the resistive structure. The tectonic zone is depicted with the dashed line. An almost E-W faulting zone using ERT method is depicted with the dashed line. The thin short-dashed black line represents the unconformity. The electrode spacing of 15 m is presented in the lower left corner of the ERT model. The RMS error is presented in the right upper corner and the resistivity scaling (measured in  $\text{ohm}\cdot\text{m}$ ) is presented in the left lower corner of the ERT model.

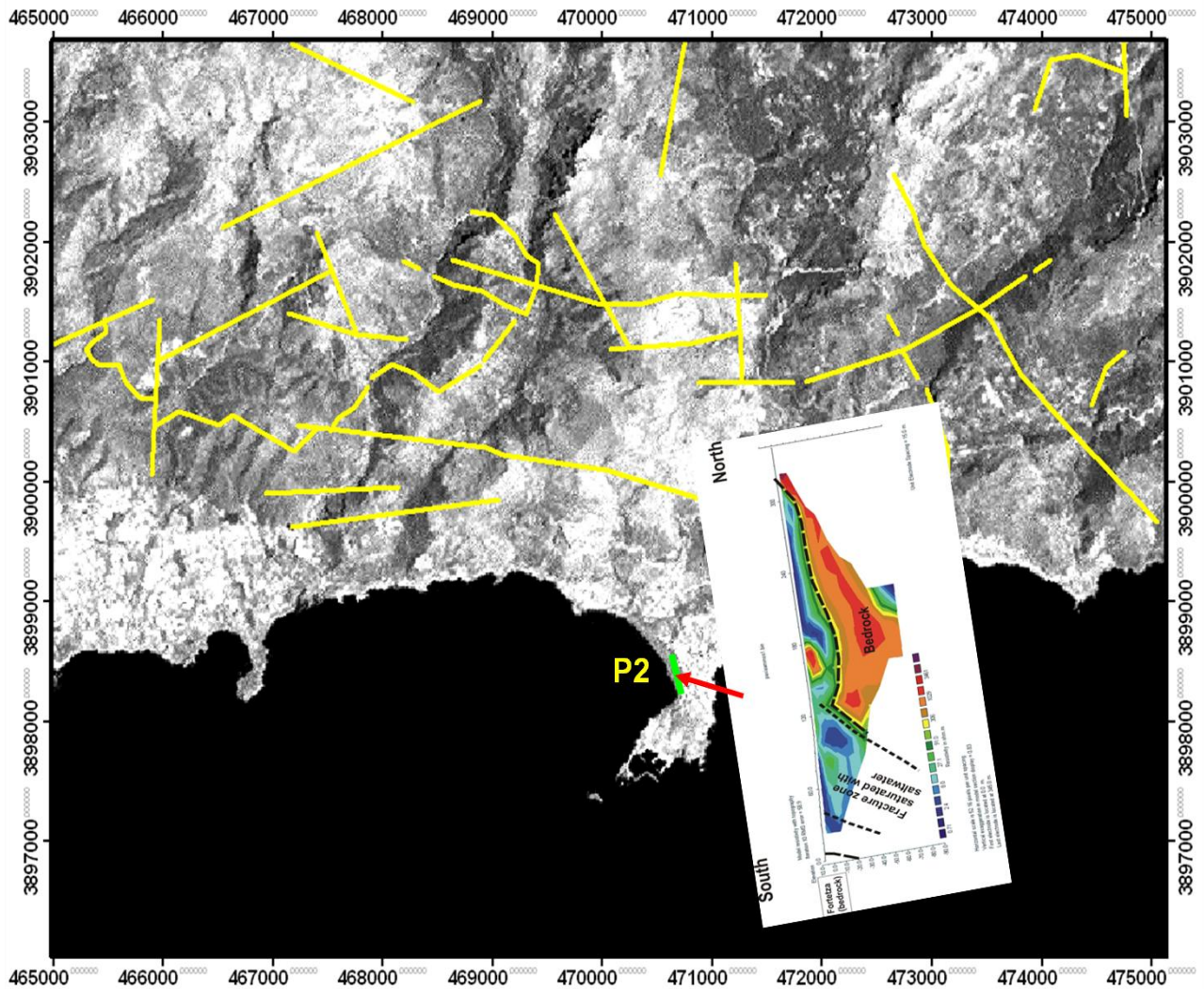


**Figure 4.2.23:** Landsat (TM8) image presenting the deep ERT profiles along Pahia Ammos site of Paleohora. The green lines represent the orientation of the ERT profiles. The deep ERT profile reveals large scale fault. The yellow lines represent the already identified faults extracted from geological and satellite image maps.

#### 4.2.7.4 ERT IN GRAMMENO PENINSULA

To estimate the subsurface structure of Grammeno peninsula two different field campaigns performed on 30/11/2006 and 30/03/2007. The distance between the two study areas of Pahia Ammos and Grammeno peninsulas is 3.67 km. The ERT profile in Grammeno peninsula is extracted from the joint interpretation of the resulted tomographic images acquired during the two field campaigns. Mathematical modifications and data regularization have been performed. The final tomographic model is derived applying several inverse methods, using all the available regularization parameters and removing the high noise data. The resulted ERT model extracted from simultaneous interpretation of the geoelectrical resistivity tomography profile at Grammeno peninsula is presented in figure 4.2.24. ERT profile in Grammeno peninsula

suggests a large scale E-W striking fault and dipping to north at a depth of at least 80 m. The red colours represent the high resistivity structure (bedrock) and the blue colours correspond to the low resistivity structure (seawater intrusion). At the southern part of Grammeno site the main observation is the dominance of a series of beach rock outcrops (-125 m) and the penetration of seawater into the fractured bedrock. Both the surficial beach rock outcrops and the penetration of the seawater under the surface observed at that southern part of the investigated site are also well presented in the ERT profile. The resulting filtered tomographic image shows that the bedrock is continued along the lower part of the resistivity model as is depicted from the thick dashed line (-112 m to 0 m). The observed discontinuity of the bedrock could be safely assumed as a fracture zone based on both geology survey and ERT survey. A large scale fault dipping to north and two possible small scale faults dipping to south are observed and depicted with dashed black lines. Grammeno peninsula where electrical resistivity tomography method applied is presented in the satellite image in Figure 4.2.17. An overall schematic section of the investigated site and the corresponding 2D resistivity model is presented in Figure 4.2.25. In Figure 4.2.26 is presented the configuration of the two identified faults in Paleohora and Grammeno peninsulas.

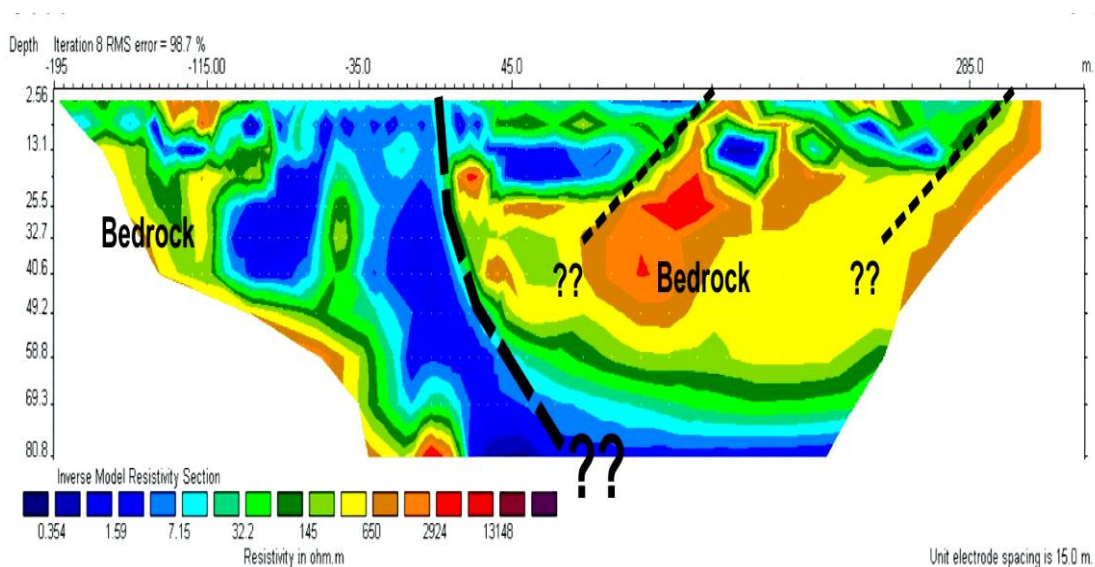


**Figure 4.2.24:** Electrical resistivity tomography profile in Grammeno peninsula. The red colours represent the high resistivity structure (bedrock) and the blue colours correspond to the low resistivity structure (seawater intrusion). A large scale almost E-W fault dipping to North and two possible ‘faults’ dipping to South are observed and depicted with dashed black lines. The two speculated ‘faults’ on the right-hand of the profile might instead be buried rock platforms. The evidence for a fault in these places is not strong. The questionmarks indicate the unknown fault depth.



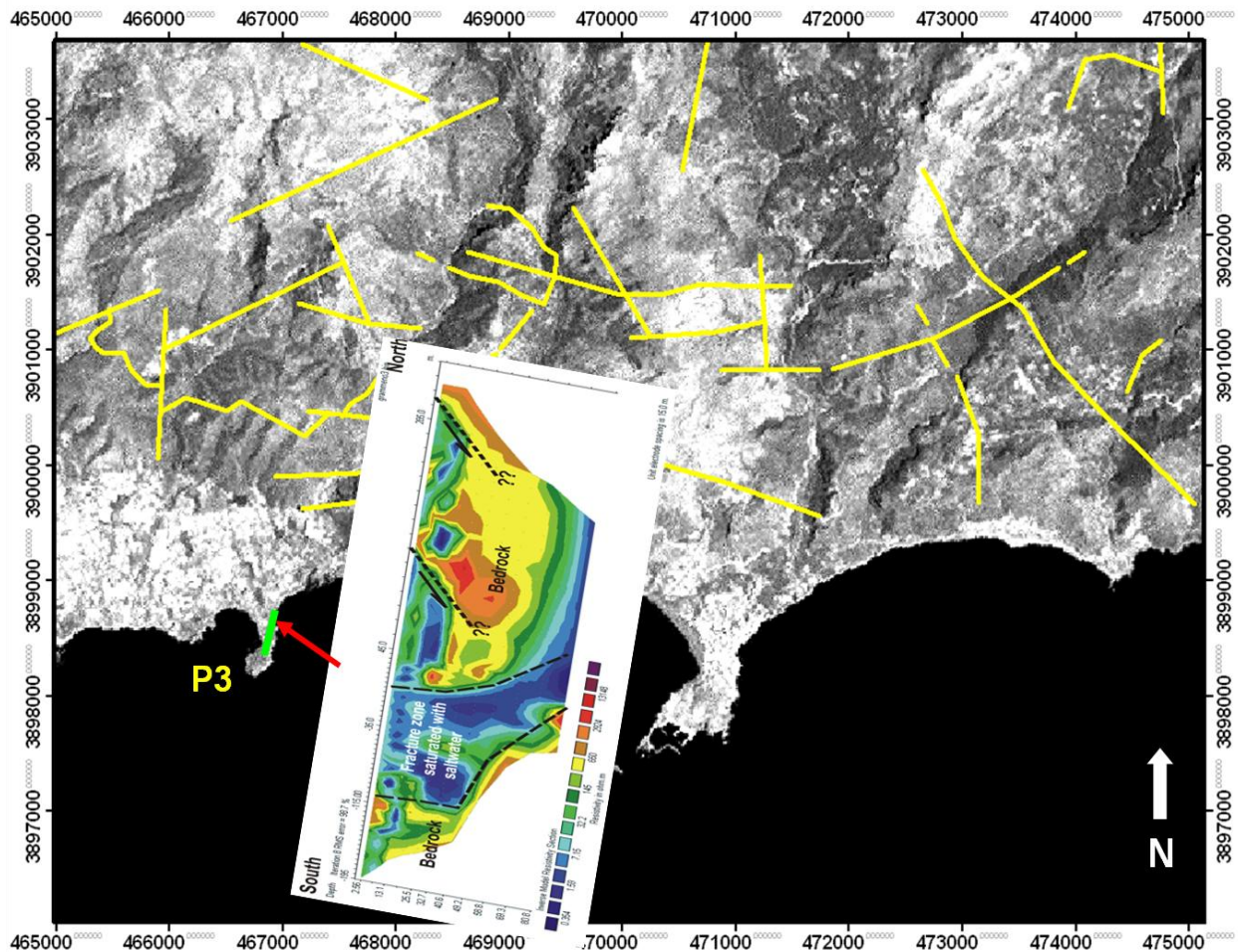


**Figure 4.2.25:** Landsat (TM8) image presenting the proposed tectonic model based on ERT survey in Grammeno peninsula. A large scale E-W fault dipping to North and two possible faults dipping to South are observed and depicted with dashed black lines. The green line represents the site of the ERT profile. The yellow lines represent the already identified faults extracted from geological and satellite image maps.

ERT profiles were performed in Pahia Ammos coastline (P2, Fig. 4.2.23) and Grammeno peninsula (P3 Fig. 4.2.25) to identify the subsurface tectonic structures which govern Paleohora and Grammeno peninsulas. The configuration of the two large scale identified faults in Paleohora and Grammeno peninsulas is presented in Figure 4.2.26. The aforementioned configuration of the two large scale identified faults suggests a new tectonic model coastal of southwestern Crete. According to the new proposed ERT model of the subsurface structure it is revealed: 1) along the coastline of Pahia Ammos site (profile 2), the presence of large scale fault, dipping south and trending to an almost E-W direction at a depth of at least 50 m and 2) along Grammeno peninsula a large scale almost E-W fault dipping to north at a depth of at least 80 m. The new proposed substructure model for the investigated area in Pahia Ammos, Grammeno and surrounding area suggest that the coastline of Paleohora and

Grammeno are associated with a system of fault zones or to a large scale fault (Figure 4.2.26). New Indicators of similarities in tectonics of both Paleohora and Grammeno peninsulas are revealed. ERT profiles in Grammeno and Pahia Ammos reveal similarities in the tectonic setting of the two areas suggesting that Grammeno is a miniature of Paleohora. In the northern and southern part of Grammeno the high resistivity zones (red colours) are defined at a depth of 10 m (that may correspond to Lissos beds -Late Serravallian- or Palaeozoic rocks that also outcrop in the area. In the southern part of the profiles in Grammeno and Pahia Ammos the low resistive zone (blue colours) is consistent with the Quaternary alluvial fan deposits. The resistivity discontinuity in the subsurface forms the fault scarp shown with the black dashed line in both areas. Outcrop of Lissos beds (Late Serravallian) in the southern part of the areas based on ground thruthed geological observations and on the geological map, coinciding with the high resistive zone, suggest that the high resistive zone can be attributed to the Lissos beds. It is possible that these faults are extensional considering that the exposures of Paleozoic rocks in the southern part indicate that the hanging wall of the rocks is down thrown and that is opposite to the reverse movement of the Quaternary sediments along the fault scarp. Moreover, the low resistivity value along the fault might suggest high permeability.

The new proposed tectonic model based on ERT consisting of either a large scale fault or of a system of faults striking almost E-W, crosscutting Pahia Ammos and Grammeno is presented in Figure 4.2.26. The dashed yellow line represents the fault or the system of faults in the coastline of southwestern Crete.

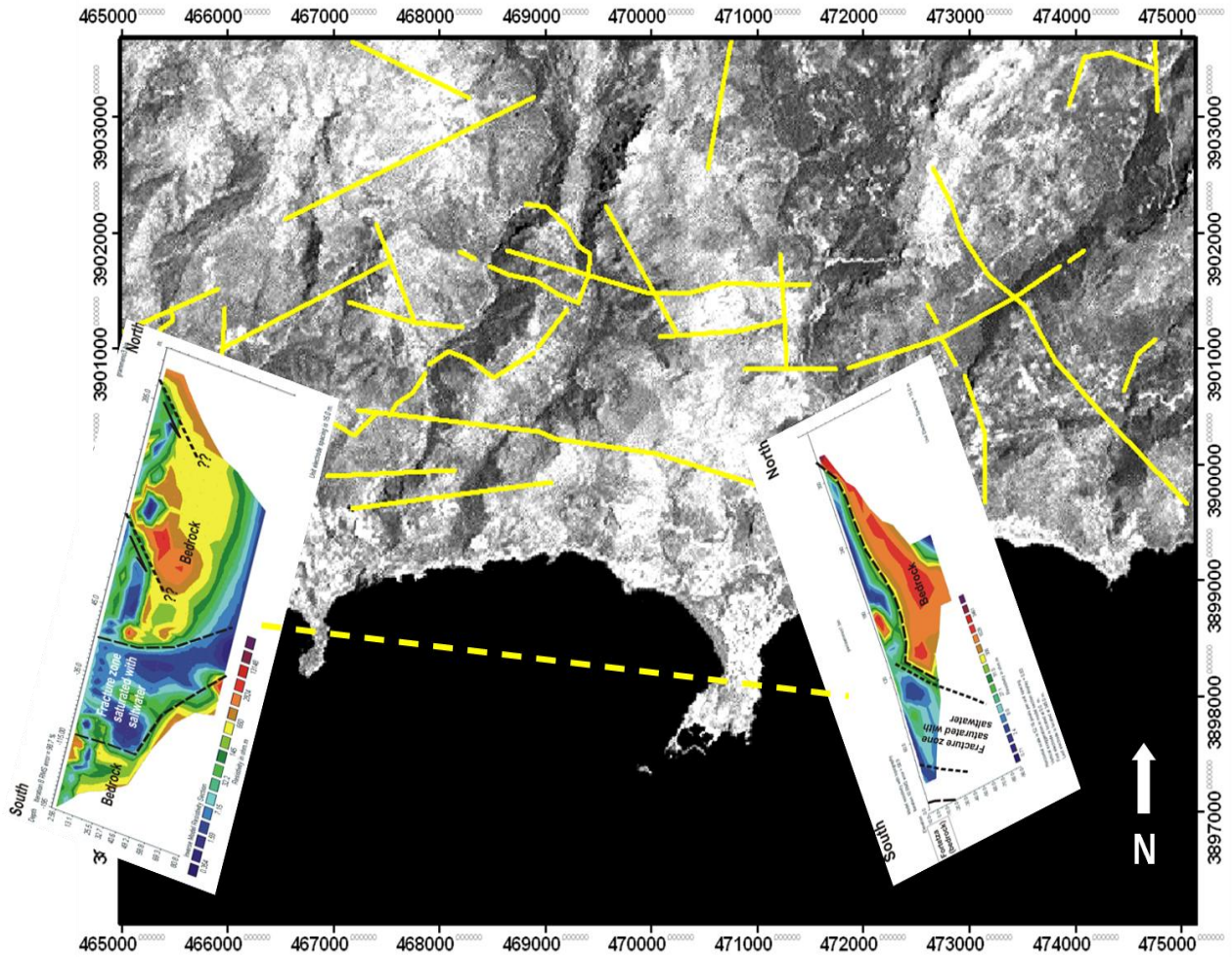


**Figure 4.2.26:** The configuration of the two large scale identified faults striking almost E-W in Paleohora and Grammeno peninsulas. The similarities in the subsurface model suggest that Grammeno peninsula is the miniature of Paleohora. The aforementioned configuration suggests that the coastline of Paleohora is characterized of of a large scale fault or of a system of faults. The dashed yellow line represents the fault or the system of faults in the coastline of the investigated area.

#### 4.2.8 ELECTRICAL RESISTIVITY TOMOGRAPHY IN THE NORTHEASTERN NORTHWESTERN AND SOUTHERN PART OF PALEOHORA

Electrical resistivity profiles were conducted in the northeastern, southwestern and southern areas of Paleohora. ERT profile P4 in the northeastern part of Paleohora reveals surficial water deposits to a depth of 20 m (Figure 4.2.27). The ERT profile 4 conducted northeast of Paleohora, to verify the existence of the fault trending almost N-S, revealed water surficial deposits and not a fault feature. The reason for the lack of ERT along P4 to verify the N-S fault is that the profile did not extend far enough to crosscut the fault. At that site the presence of private land prevented extension of the profile. In Panorama (northwestern of Paleohora) ERT profile P5 was conducted over a

waste disposal site. This kind of “landfill” can amplify seismic motion and the purpose of ERT measurements was to define the geometrical characteristics of the site. Waste disposal site is identified from a shallow ERT performed in western of Panorama (Figure 4.2.28). The very low resistivity zone (blue zone) corresponds to topmost surficial debris layer covered by thin soil layer. A shallow ERT profile P6 in the archaeological site (Fortezza castle) located south of Paleohora peninsula and characterized of beachrock platforms was conducted. The ERT profile P6 revealed a planar discontinuity between the beach-gravels hydrogeneous surficial deposits and the bedrock (Figure 4.2.29). An overall schematic section of the investigated sites and the corresponding ERT model is presented in Figure 4.2.30.

#### 4.2.8.1 WATER SURFICIAL DEPOSITS IN THE NORTHEASTERN SITE OF PALEOHORA

The extracted shallow ERT profile P4 conducted in northeastern of Paleohora is presented in figure 4.2.27. The electrode spacing is 15 m along a 240 m line. The rms was 52.7%. The ERT profile P4 conducted northeast of Paleohora, revealed water surficial deposits at a depth of 25 m. Water deposits are estimated to a depth of 25 m.

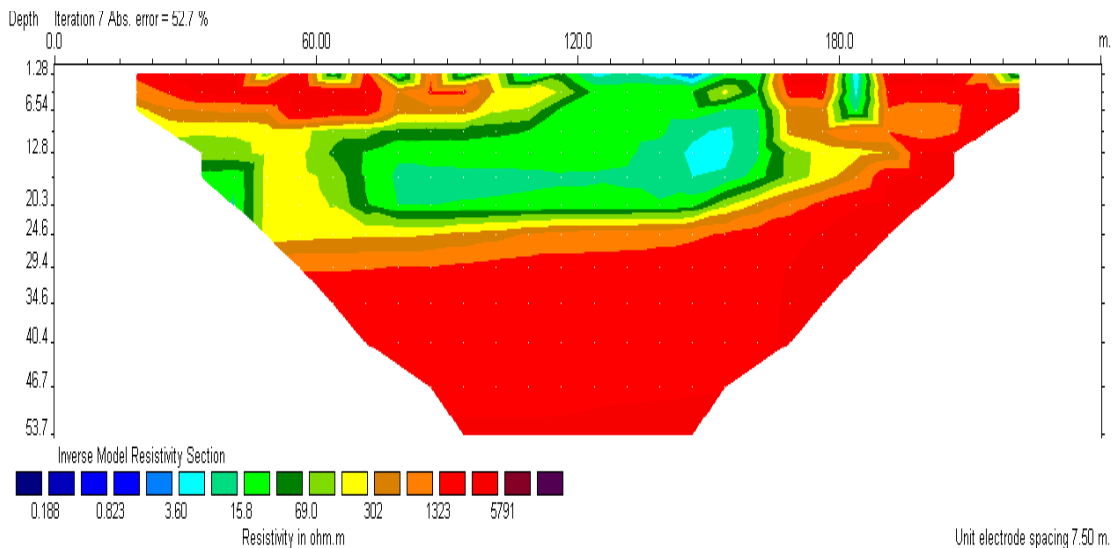


**Figure 4.2.27:** ERT profile P4 in northeastern of Paleohora. Water surficial deposits are identified. The red colour corresponds to the resistive structure (bedrock) and the green colour to conductive structure (water contaminant). The RMS error is presented in the right upper corner and the resistivity scaling (measured in ohm\*m) is presented in the left lower corner of the ERT model.

#### 4.2.8.2 WASTE SURFICIAL DEPOSITS IN THE NORTHWESTERN SITE OF PALEOHORA WESTERN PART OF PANORAMA

The extracted shallow ERT profile P5 in Panorama site located northwestern of Paleohora is presented in Figure 4.2.28. The electrode spacing at each site is 15 m along a 225 m ERT line. The rms is 11.8%. The ERT profile P5 conducted northeast of Paleohora, revealed a thick layer of waste disposal to a depth of 30 m.

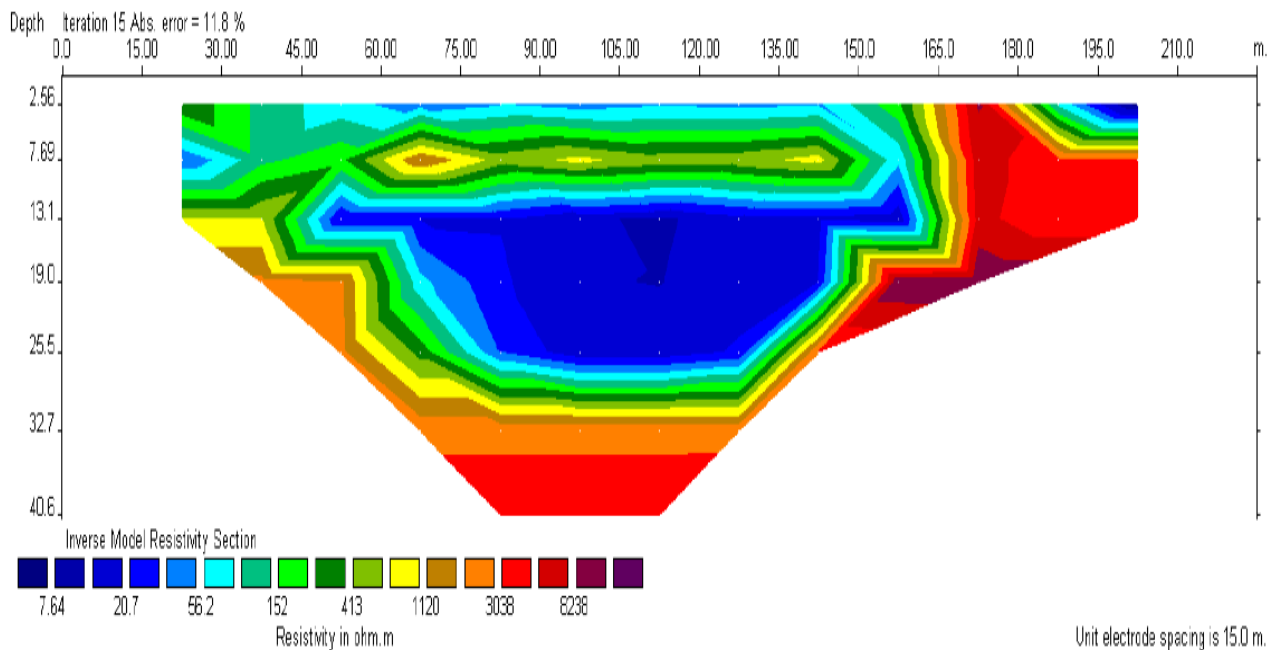


**Figure 4.2.28:** ERT profile west of Panorama of the northeastern part of Paleohora reveals a thick layer of waste disposal at a depth of 30 m. The red colour corresponds to the resistive structure (bedrock) and the blue colour to conductive structure (waste disposal). The electrode spacing of 15 m is presented in the lower left corner of the ERT model. The RMS error is presented in the right upper corner and the resistivity scaling (measured in ohm\*m) is presented in the left lower corner of the ERT model.

### 4.2.8.3 WATER SURFICIAL DEPOSITS IN THE ARCHAEOLOGICAL SITE IN THE WESTERN PART OF PANORAMA

The extracted ERT profile (P6) in the archaeological site Fortezza south of Paleohora is presented in Figure 4.2.29. The electrode array conducted on a water surficial contaminants site is presented in figure 4.2.29. The electrode spacing of ERT resistivity 210 m line is 15 m. The rms is 96.8%. The ERT profile P6 revealed hydrogeneous surficial deposits at a depth of 20 m.

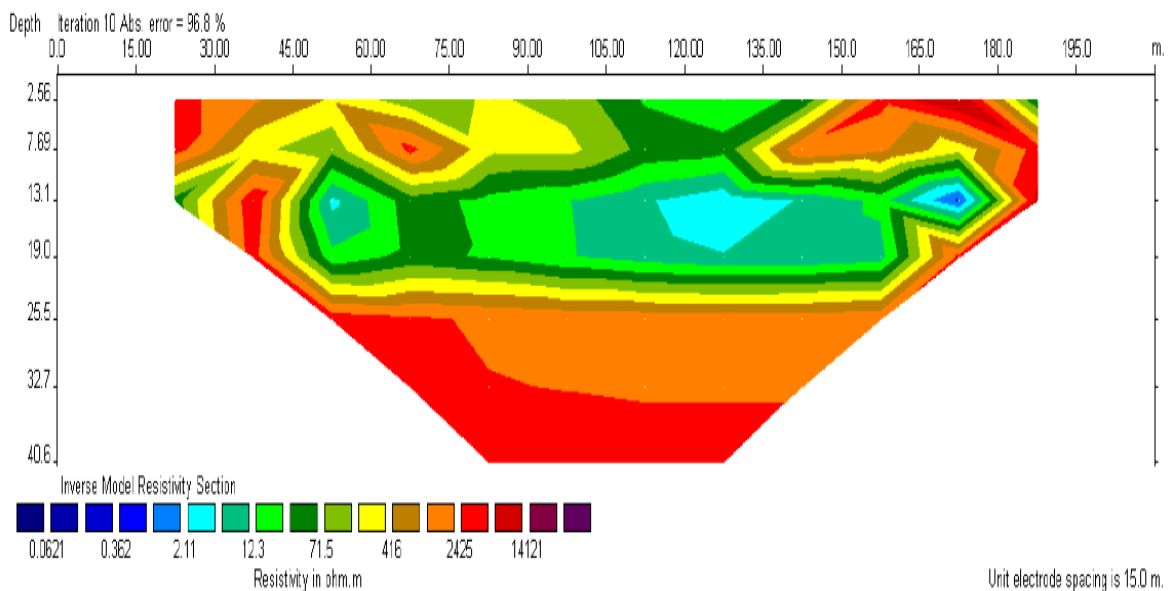


**Figure 4.2.29:** (Upper): ERT in the archaeological site Fortezza located on beach-gravels hydrogeneous surficial deposits. (Lower): Water surficial deposits in the archaeological site south of Paleohora peninsula extracted from ERT model. The red colour corresponds to the resistive structure (bedrock) and the green colour to conductive structure (water contaminant). The electrode spacing of 15 m is presented in the lower left corner of the ERT model. The RMS error is presented in the right upper corner and the resistivity scaling (measured in ohm\*m) is presented in the left lower corner of the ERT model.

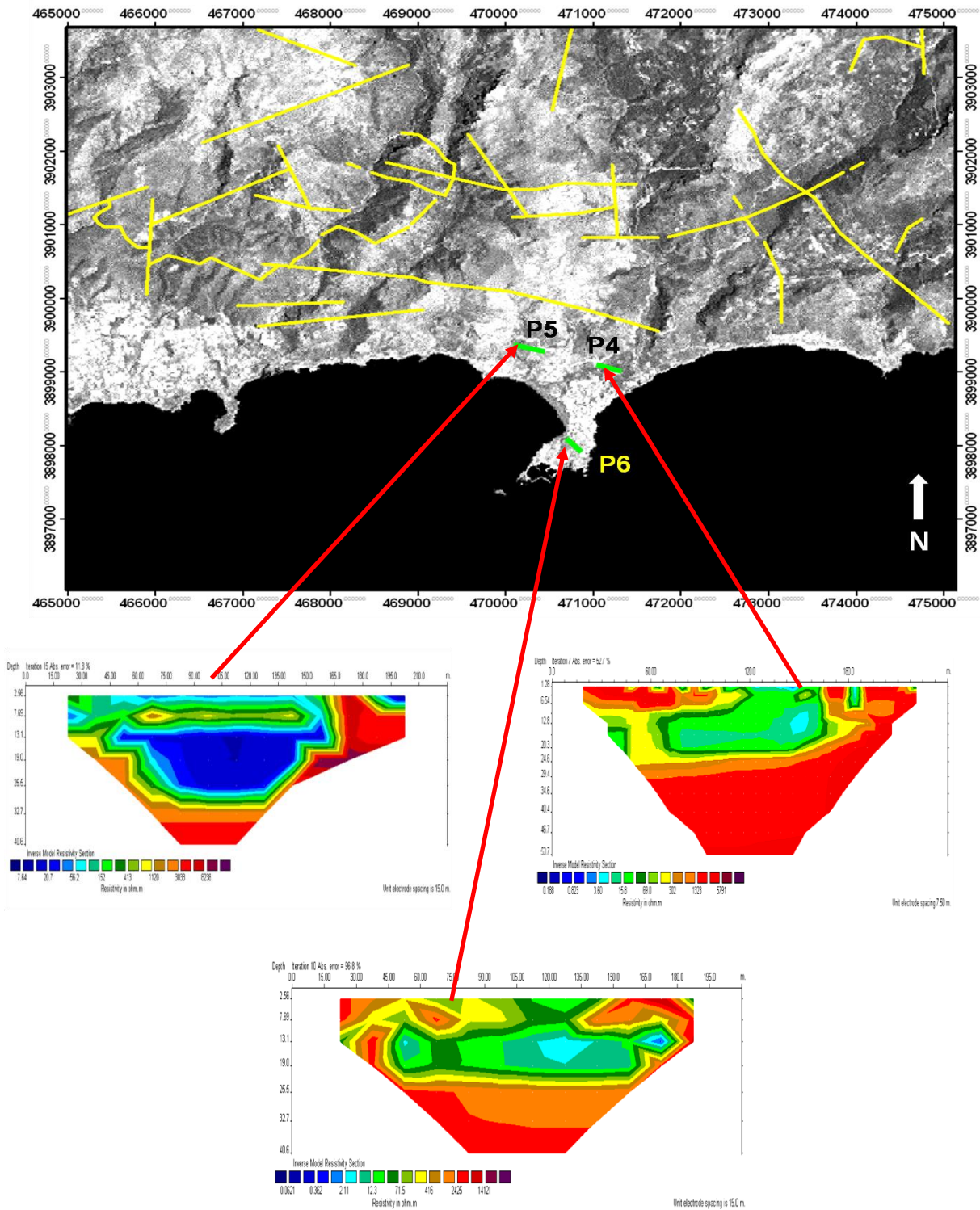


**Figure 4.2.30:** Landsat (TM8) image presenting an overall view of the derived surface and subsurface structure northeastern, northwestern and southern of Paleohora. The green line represents the orientation of the ERT profile. The yellow lines represent the already identified faults extracted from geological and satellite images.

### **4.3 RESULTS: SEISMIC GROUND MOTION EVALUATION AND MICROZONATION STUDY USING HVSR TECHNIQUE AND MICROTREMORS**

Site effects substantially modify seismic motion in the time domain and spectra characteristics and consequently its potential to cause earthquake damage. The HVSR technique proposed by Nakamura (1989, 1996, 2000a) using microtremors is conducted to determine the nature of the subsurface structure that can strongly amplify earthquake seismic ground motion and to classify ground seismic response into seismic zones. The proximity of the populated basin to large scale active faults, the strong lateral heterogeneities and irregularities of the topographical characteristics and the presence of deep basin sediments infilling are parameters to enhance seismic ground motion and the earthquake damage distribution. The microzonation study models seismic soil response and provides the crucial step in seismic regulation, in land use planning, in earthquake hazard reduction programs and in determining future seismic risk scenarios of Paleohora and Kastelli areas.

Site effects and microzonation study using microtremor recordings in the populated area of Kastelli Kissamou, in Roka village located along the segment of Kera fault in the northwestern Crete and in Paleohora basin located in southwestern Crete is presented. The Greek Vulnerability Code (EC8) characterizes soil into five categories. The main discrimination of the soil categories according to (EC8) are: Category (A) describes rock or semi-rock formations covering large distance and depth without strong weathering. Categories (B) and (C) describe highly weathered rock. Category (D) characterizes soils of soft marls of thickness more than 10 m. Category X describes: a) Loose grain size sand-silt soils that can be easily liquefied, b) Soils near fault zones, c) Steep slopes with loose material surficial layer, d) Loose granules or soft sand-silty soils (non-cohesive) and e) Recent rubbles or cobbles, f) soils of category B or C are those located in a high steep slope environment.

#### **4.3.1 SITE EFFECTS AND MICROZONATION STUDY USING MICROTREMORS AND HVSR TECHNIQUE IN THE URBAN AREA OF KASTELLI HALF-GRABEN BASIN**

Microtremors data recorded with 100-250 meters spacing in the whole territory of the dense populated and large scale (7x1km) alluvial fan Kastelli basin in the northwestern Crete. An approximate estimation of the permanent inhabitants of the urban area of Kastelli-Kissamou is 3.909. The surface geology (Karageorgiou, 1968) of the urban area of Kastelli-Kissamou is characterized of: a) Cretaceous limestones (white to brown, locally compact lithographic thin bedded commonly fine grained or even microcrystalline in banks strongly karstified), b) older Fluvial-Terraces Some beds of the older fluvial terraces are alternating shales and argillaceous sandstones and c) alluvial deposits (Loose loams, clays, sands and gravel with thickness not exceeding 3 m).

Thirty-eight microtremor measurements of 10, 15 and 20 minutes duration with sampling frequency at 125 Hz are acquired. Microzonation study using microtremor recordings distinguish the town of Kastelli into five seismic zones (KA-KF) based on the ground seismic response. The HVSR data are presented in Appendix I. Zone KA categorizes sites of a fundamental frequency in the medium frequency band that is characterized of a well-lithified (limestone) site without the effect of the alluvial fan deposits. Microtremor recordings conducted northwestern of Kastelli along the ground

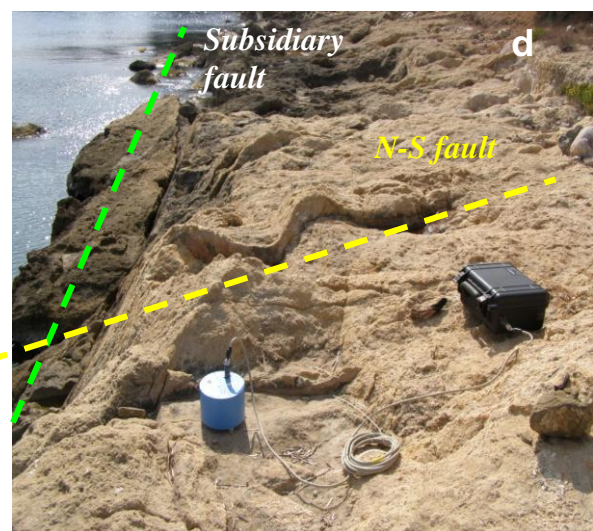
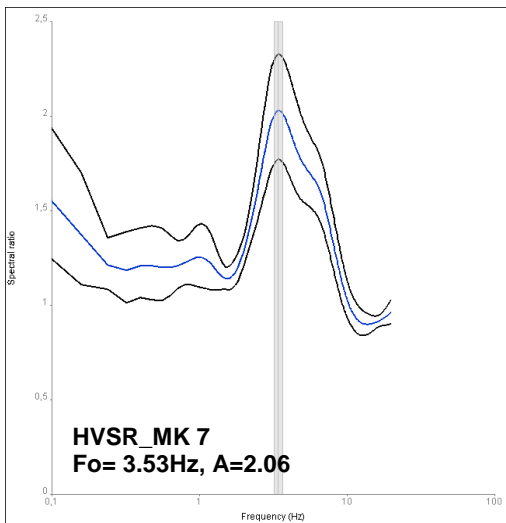
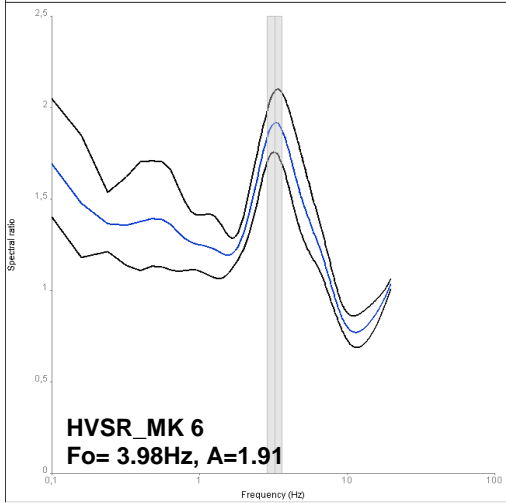
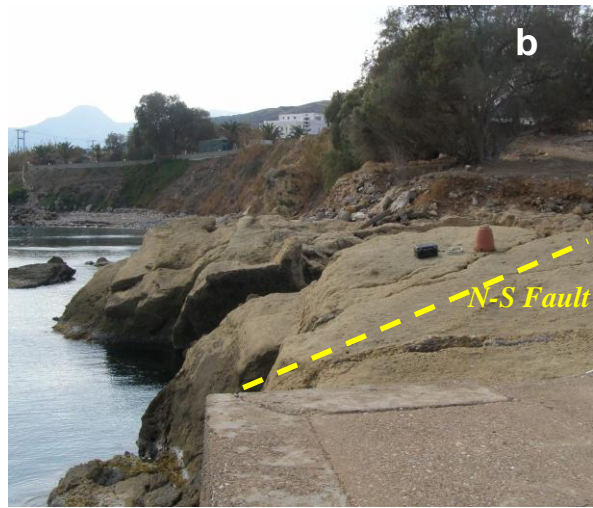
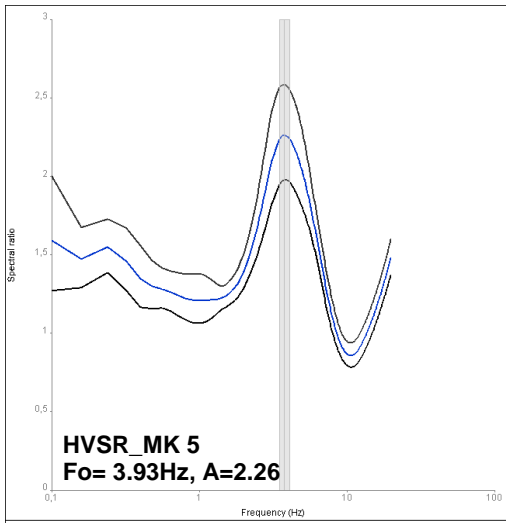


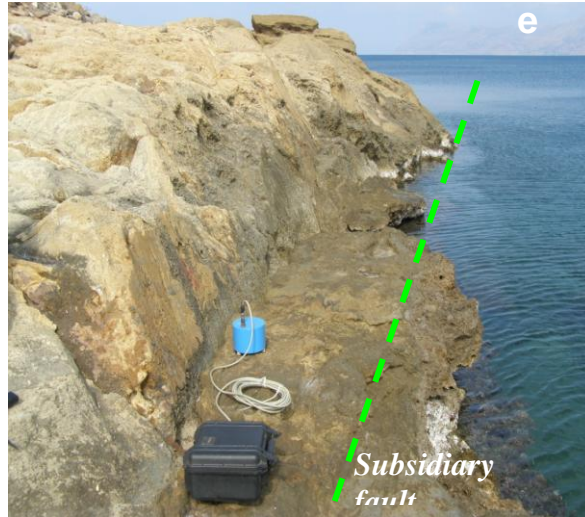
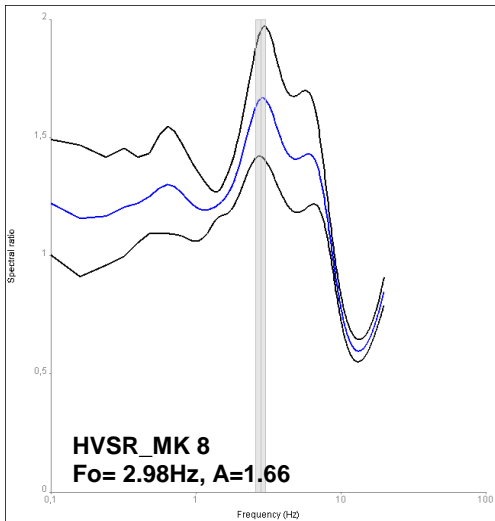
thruted complex faulting system (Figs. 4.1.3 and 4.1.4) on a well-lithified limestone site. The sites where microtremor measurements performed coastal northwestern of Kastelli are denoted as MK5-MK8 on Figure 4.3.2. HVSR using microtremor coastal northwestern of Kastelli characterized of multi-fracture well-lithified limestone site without the effect of alluvial fun deposits, presents an amplified frequency in the range (2.98-3.93 Hz) with ground amplification factor 1.66 to 2.26. Fault delineation based on microtremor spectra characteristics using HVSR technique at the multifracture well-lithified limestone is verified with geological observations (Figs. 4.1.3 and 4.1.4). At that site there is no impedance contrast between the surficial and subsurface structure, since there is no alluvial fun deposits layer effect on ground motion.

Zones KB, KC and KD are characterized of two amplified frequencies indicating highly complex environment. These sites are characterized of the effect of lateral heterogeneities and irregularities associated to a fault structure and of the effects of the thickness of overlying deposits on seismic ground motion. These sites are MK2, MK3, MK4, MK11, MK12, MK13, MK14, MK15, MK16, MK24, MK25, MK31, MK32, MK33 and MK37. The spectra characteristics of sites (MK11, MK33) corresponding to zone KB present the fundamental frequency in the medium and the second amplified in the low frequency band. Zone KB characterize sites of both lateral heterogeneities and irregularities due to the possible presence of a fault and of the effects of the thick overlying alluvial deposits on seismic ground motion. The first amplified in the medium frequency attributes to the effects of lateral heterogeneities associated to a fault structure (2D/3D effects). The second amplified frequency in the low frequency band attributes to the overlying thick sedimentary/alluvial layer. This zone corresponds to rupture zones/faults not directly observable at the surface covered with thick sedimentary layer. The spectra characteristics of sites corresponding to Zone KC (MK3 and MK4) present the fundamental frequency in the high frequency band and the second amplified in the low frequency band. The second amplified frequency in the low frequency corresponds to thick alluvial deposits or very soft deposits (older fluvial terraces). The fundamental (higher) frequency in the high frequency range is associated with the very shallow structure and it indicates strong lateral heterogeneities and irregularities. Considering the geology setting and the depth of the geological column derived from ERT, it is proposed that these strong lateral heterogeneities and irregularities are associated with the existence of a fault zone or with large scale discontinuities. Zone KD present the fundamental frequency in the low frequency band and the second amplified in the high frequency band. The site presenting the fundamental in the low and the second amplified in the high frequency band is MK12. The fundamental frequency in the low frequency corresponds to thick alluvial deposits or to the very soft deposits. The fundamental frequency in the high frequency range is associated with the very shallow structure that might indicates strong lateral heterogeneities and irregularities of the near subsurface. The main characteristic of zone KC and KD is the variation in the thickness of the alluvial deposits. The depth of alluvial deposits in Zone KC is shallower compared to Zone KD or Zone KC is characterized of softer deposits compared to zone KD. Moreover, the difference of zone KC compared to zone KD, in relation to the effect of the lateral heterogeneities in the HVSR spectra characteristics, is its closer proximity to the lateral discontinuity that infer the two amplified frequency in the HVSR curve. Zone KE characterizes site (MK9)

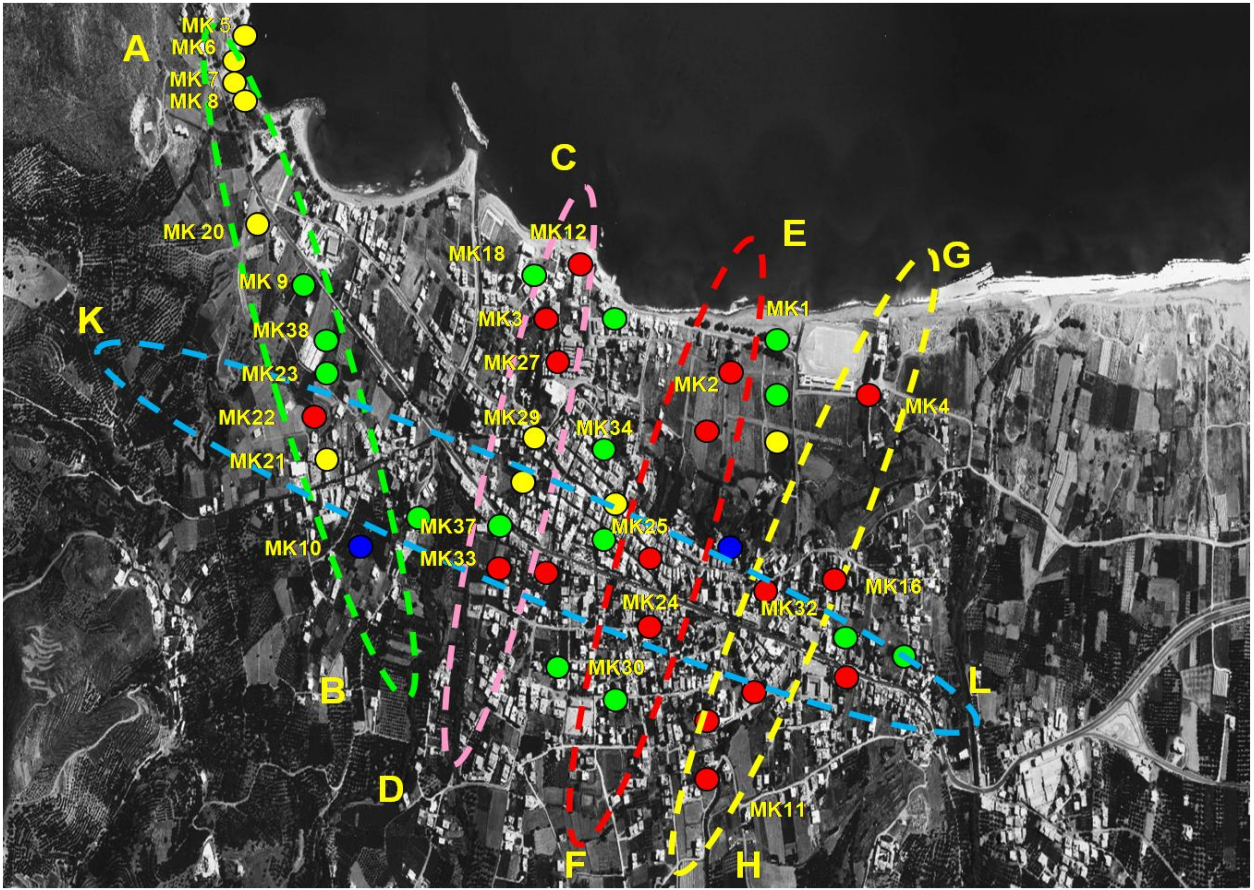
where the fundamental frequency is in the high frequency band (7.11 Hz) with amplification 3.16. The fundamental frequency in the low frequency range corresponds to thin alluvial deposits. Zone KF is used to describe sites (MK1, MK17, MK23, MK34, MK36, and MK38) of one clear fundamental frequency at low frequencies. This zone characterizes sites of thick or very soft deposits (older fluvial terraces). Zone KG characterizes sites of one fundamental in the low and a second amplified in the medium frequency band (MK2, MK14, MK6, MK24, MK25, MK31, MK32, MK35 and MK37). The frequency in the medium frequencies correlates with the lateral heterogeneities of the subsurface and the low frequency to the thick deposits. Zone KH characterizes sites (MK10, MK19, MK26) of flat or low HVSR amplitude curves. These sites are characterized of low impedance contrast between surface and subsurface contrast. Zone KH that presents low amplification is an indicator of rock or of stiff sediments overlay bedrock at a non rock site. Zones KA, KB and KC, KD and KG correspond to category X of the (EC8). Zone KE corresponds to category X of the (EC8) considering the close proximity of that site to fault zone. Zone KF corresponds to category D of the (EC8). Zone KH correspond to category A of the (EC8). Ground seismic response data applying HVSR technique and microtremors in Kastelli-Kissamou is presented in Appendix. Microtremors of similar spectra characteristics in the northwestern, northern and southeastern are identified and delineate fault zones crosscutting the dense populated area. The HVSR curves for Kastelli-Kissamou and Roka village are presented in the Appendix I. The fundamental frequency map of Kastelli-Kissamou based on HVSR curves and the identified fault zones are presented on Figure 4.3.2. The HVSR ground amplification is presented on Figure 4.3.3. HVSR curves, fundamental frequencies ground amplification and ground vulnerability index are presented in Appendix I and Appendix II (Table 4.3). A significant outcome of this study is that the extracted HVSR curves using microtremors (Appendix I) can be used to delineate fault zones. For Kastelli the variation of the ground spectra characteristics delineates five fault zones.



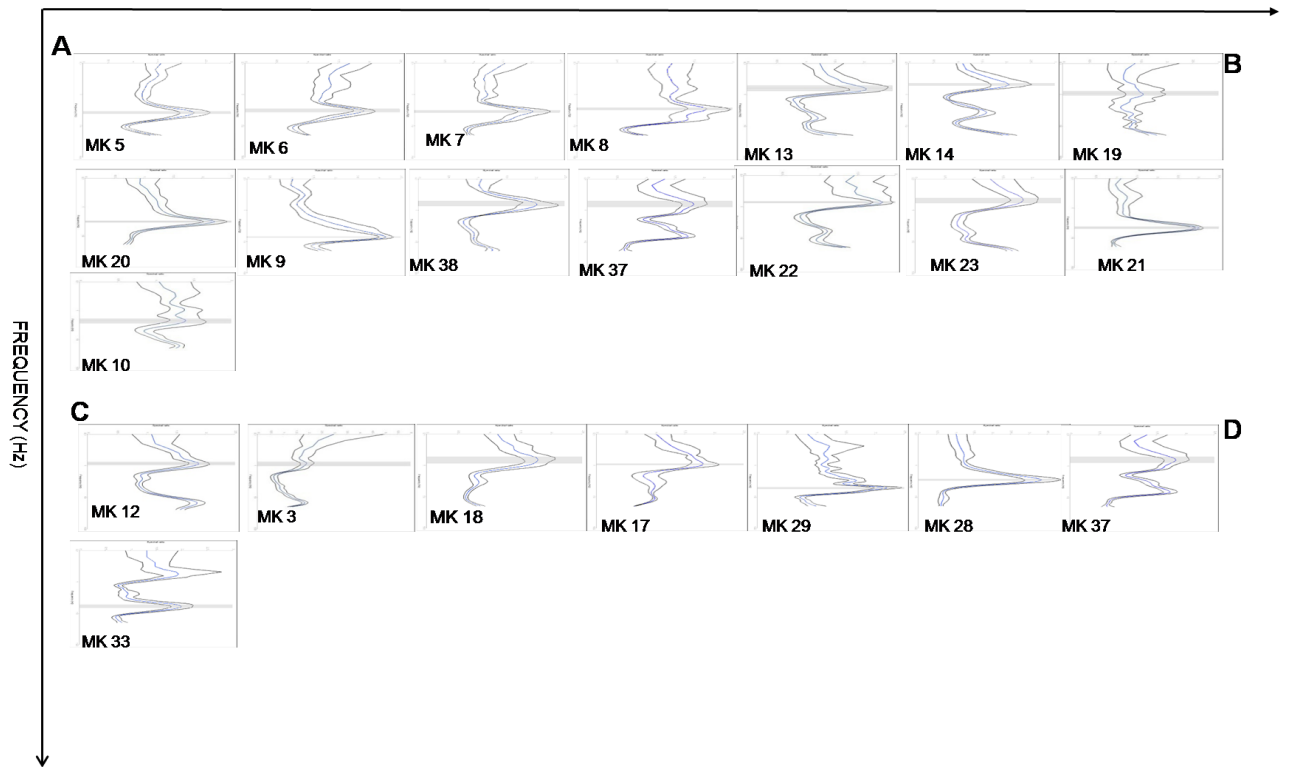




**Figure 4.3.1:** a) HVSr using microtremors conducted northwestern of Kastelli characterized of a well- lithified limestone site, b, c, d, e) Average HVSr (sites MK5- MK8) on a multi-fractured well-lithified limestone site without the effect of alluvial/sedimentary deposits. The one clear amplified HVSr peak in the medium frequency corresponds to the spectra characteristics of the fractured system of a single site microtremor recording. At each HVSr curve the blue line represents the HVSr curve and the black lines the standard deviation. The one clear amplified HVSr peak in the medium frequency correlates to the spectra characteristics of the fractured system.



HVSR SPECTRA RATIO (AMPLIFICATION)



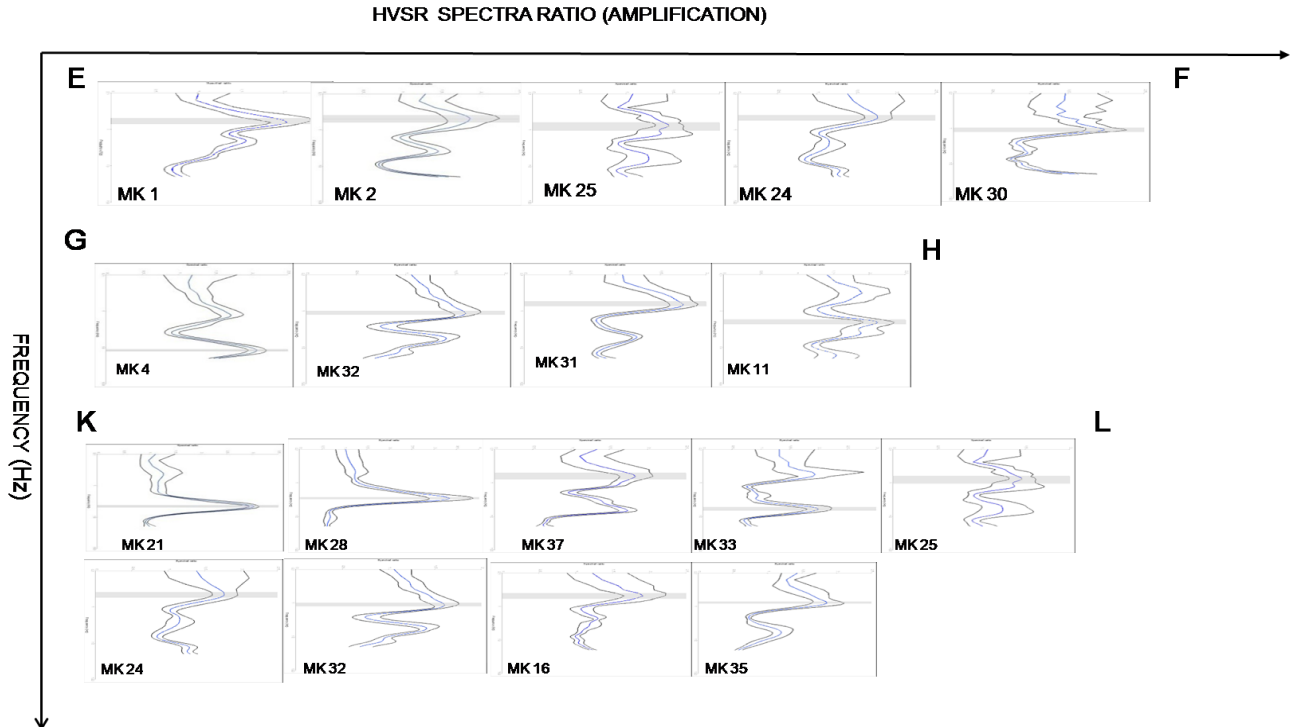


**Figure 4.3.2:** The main seismic ground fundamental frequency map of Kastelli-Kissamou half-graben basin. The yellow circles represent sites of ground fundamental frequency in the medium frequency range corresponding to the effect of a fault zone on ground seismic motion. The red circles represent sites of two amplified frequencies. The fundamental frequency in the low frequency range corresponds to the effect of thick alluvial deposits and the second amplified in the medium frequency range to the effect of a fault zone. The blue circles represent sites of flat or low amplitude fundamental frequency. The green circles represent sites of ground fundamental frequency in the low frequencies due to the thick alluvial deposits, b, c) Cross-sections delineating fault zones AB, CD,EF, GH, KL based on HVSr technique using microtremors.

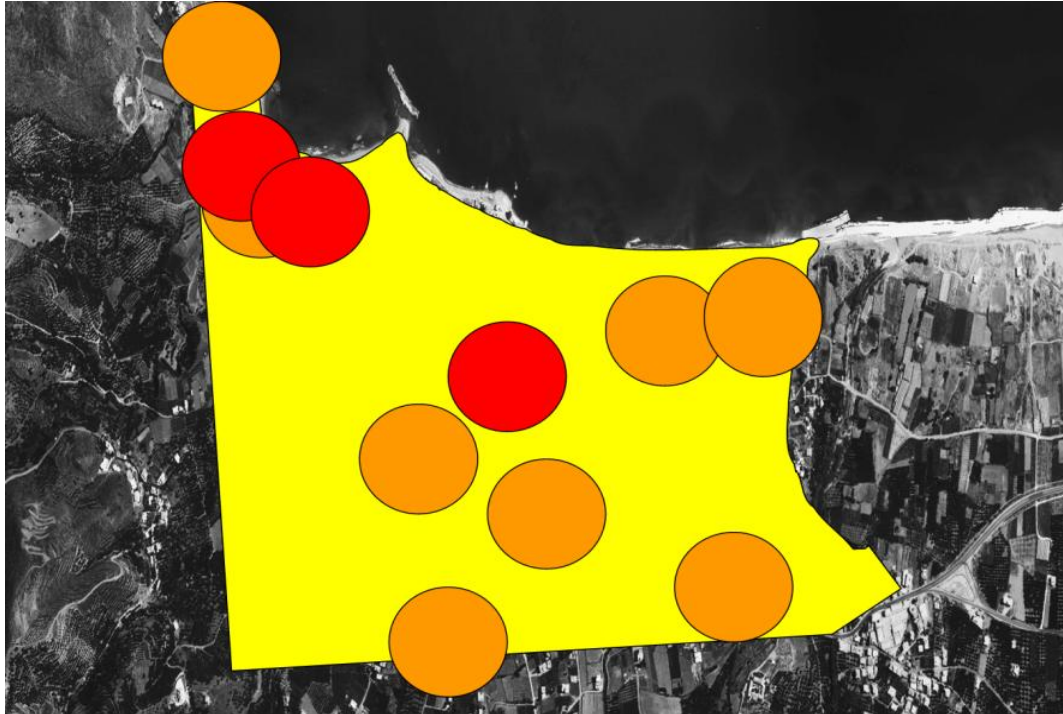


**Figure 4.3.3:** Seismic ground amplification map of Kastelli Kissamou half-graben basin using HVSR technique. The red circles represent sites of ground amplification ranging from 3.02-3.34. The orange circles represent sites of ground amplification ranging from 2.03-2.90 and the yellow area the ground amplification ranging from 1.10-1.99.

#### 4.3.2 SITE EFFECTS EVALUATION USING HVSR TECHNIQUE AND MICROTREMORS IN ROKA VILLAGE

In Roka village at sites MKR1, MKR2 the fundamental frequency is observed in the medium frequency band, while the amplification is rather low. The fundamental frequency in the medium frequency range is associated with the fractured marly limestone substructure. Stability of spectra microtremors characteristics is observed at sites MKR1, MKR2 in Roka village and at sites MK1-MK4 in the northwestern part in the coast of Kastelli. Roka village corresponds to seismic zone KA. From borehole logging data it is confirmed that Roka village is located on marly limestone formations. The observed high frequency (8Hz) at site MKR3 is due to the very shallow rubbles/cobbles, while the second amplified frequency in the medium frequency band corresponds to fractured marly limestone geological column. It is proposed that the dip sloping environment and the effect of shallow Neogene sediments northeastern of Roka are patterned in microtremor HVSR spectra ratio at site MKR4. The very close proximity of Roka village to Kera fault categorize Roka village in seismic ground category X of the Greek vulnerability code (EC8). Moreover, site MKR3 located on very shallow rubbles/cobbles corresponds to category X of EC8. The HVSR (H/V average,  $H_{ns}/V$  and  $H_{ew}/V$  curves for Roka village located near Kera are presented in Appendix I.

### 4.3.3 SEISMIC GROUND MOTION EVALUATION AND MICROZONATION STUDY USING HVSR TECHNIQUE AND MICROTREMORS IN PALEOHORA HALF-GRABEN

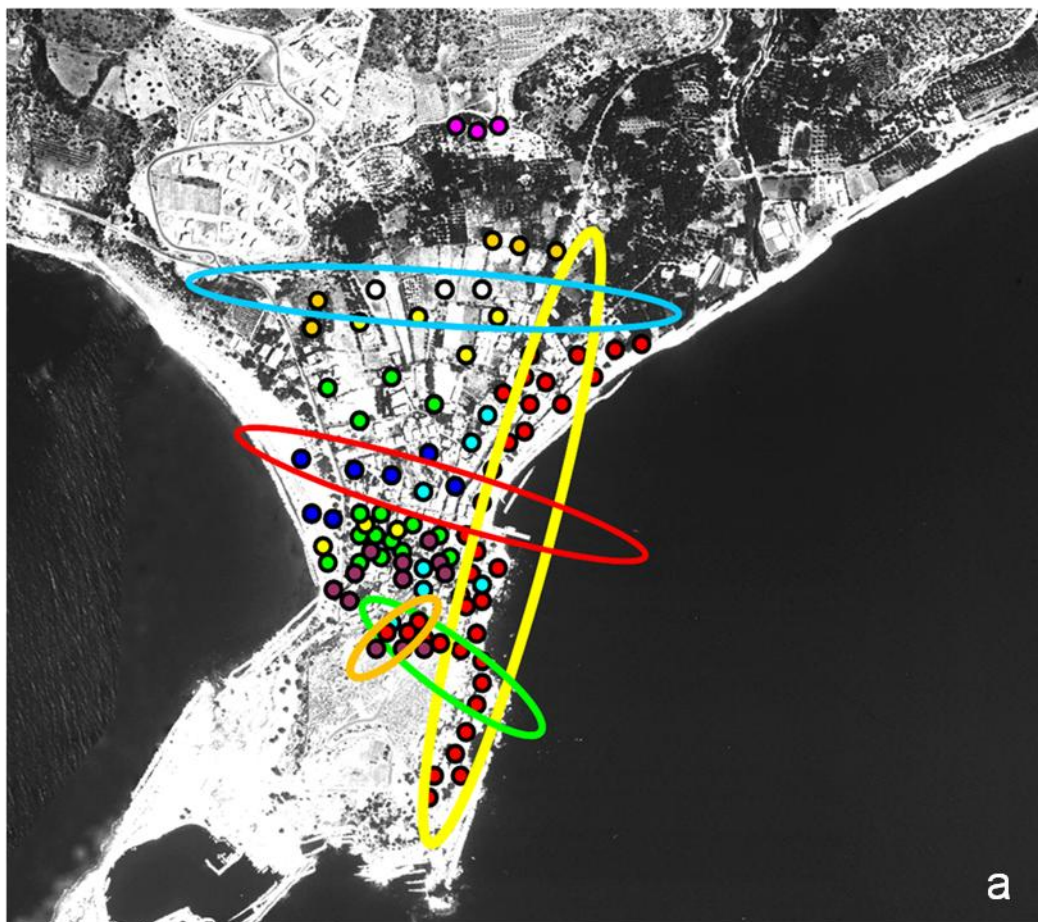
Dense spatial grid of ninety-six microtremor recordings performed with 5-8m spacing in the whole territory of the dense populated small scale (4 km x 1 km) half-graben Paleohora basin. The approximate estimation of the permanent inhabitants of Paleohora basin is 2.219. At various sites the spacing of microtremor recordings is 2 m. 120 microtremor measurements of 10, 15 and 20 minutes sampled at 125 Hz are acquired. Microzonation study in Paleohora using HVSR technique classifies ground seismic response study into seven main zones of seismic resonance. In Appendix I and Appendix II (Table 4.4) are presented the extracted average HVSR,  $H_{vs}/V$  and  $H_{ew}/V$  results leading to main conclusion for site characterization. The one clear fundamental frequency in the low frequency range characterizes thick or soft material deposits. The clear fundamental frequency in the high frequency attributes the ground response of the thin material deposits and compared to the near site effects can be an indicator of faults zones. Two or more peaks is an indicator of a highly complex environment. Soft rocks (conglomerates), soft (clay-sand) and stiff (gravels and sand) soils, possible transition zones, high substructure impedance contrast, strong lateral heterogeneities and irregularities of the subsurface and are identified. Ground seismic zones PA to PC are characterized of two amplified peaks. Ground seismic zone PA characterizes sites of two clear amplified peaks with the fundamental peak identified in the medium frequency band and the second amplified in the low frequency. Zone PB characterizes sites of two clear amplified peaks with the fundamental peak identified in the low frequency band and the second amplified in the medium frequency band. Zone PC is characterized of two clear amplified peaks with the fundamental peak identified in the low frequency band and the second amplified frequency in the high frequency band. Zone PD characterizes sites of highly amplified fundamental frequency in the medium frequency band. Zone PE characterizes sites of one clear peak at the low frequencies.

In Paleohora basin zone PD is characterized by one clear peak in the medium frequency band. This zone delineates lateral heterogeneities of large scale faults. A dense grid of microtremor recordings in the coastline eastern of Paleohora reveals stability of HVSR pattern. One clear fundamental frequency is observed in the medium frequency band ( $F_0=2.5$  Hz,  $A=2-3.5$ ). Microtremor recordings reveal the existence of an almost NNE-SSW fault (yellow cluster on Figure 4.3.4) extending at least 700 m from north to south in the eastern coastline of Paleohora. In the archaeological site Fortezza located in the southern part of Paleohora, a cluster of microtremor recordings presents fundamental frequency at the medium frequency band and is classified in zone PD. The stability of the fundamental frequency (2.3-3.0Hz) parallel to a fault zone is capable to delineate fault zone and is also an indicator of a fault zone (Pahia Ammos eastern part of Paleohora). Zone PF characterizes sites of broad HVSR peak possibly due to the effect of the complexity of the wavefield of the underlain 2D or 3D effects (heterogeneities, slope discontinuities). Zone PG is characterized of flat or low ground amplification.

Seismic ground zoning in Paleohora using HVSR technique and microtremor recordings delineates a very complex fault zone system (Fig. 4.3.4a) that significantly contributes in the seismic hazards of the studied area. Four main fault zones are



identified along the populated area are identified. Dense microtremor measurements performed perpendicular and parallel of the area of Pahia Ammos located western of Paleohora village, clearly define an E-W fault zone of complex ground resonance pattern. The HVSR seismic ground response due to the discontinuity of the fault in the N-S cross-section is patterned in the HVSR. A shift in the fundamental frequency in the northeastern (Pelekanos) and northwestern (Pahia Ammos) part is observed. In the archaeological site Fortezza, located in the southern part of Paleohora, a cluster of microtremor recordings presents fundamental frequency at the medium frequency band (3.0-5.0 Hz) with amplification factor is around 2.5 to 3. Stability of the spectra HVSR ratios along an almost NNE-SSW zone is presenting. The observed stability correlates with an almost NE-SW fault zone. HVSR spectra ratios in the central part of Paleohora basin delineate two faults trending almost E-W (Fig. 4.3.4a). Ground-truthed geological investigations and ERT conducted in this thesis cross-correlate the research outcomes of HVSR technique. An example of HVSR using microtremors in determining fault zones is presenting in Figure 4.3.4b. HVSR curves, fundamental frequencies ground amplification and ground vulnerability index are presented in Appendix I and Appendix II (Table 4.4). The ground seismic amplification map is presented on Figure 4.3.5.



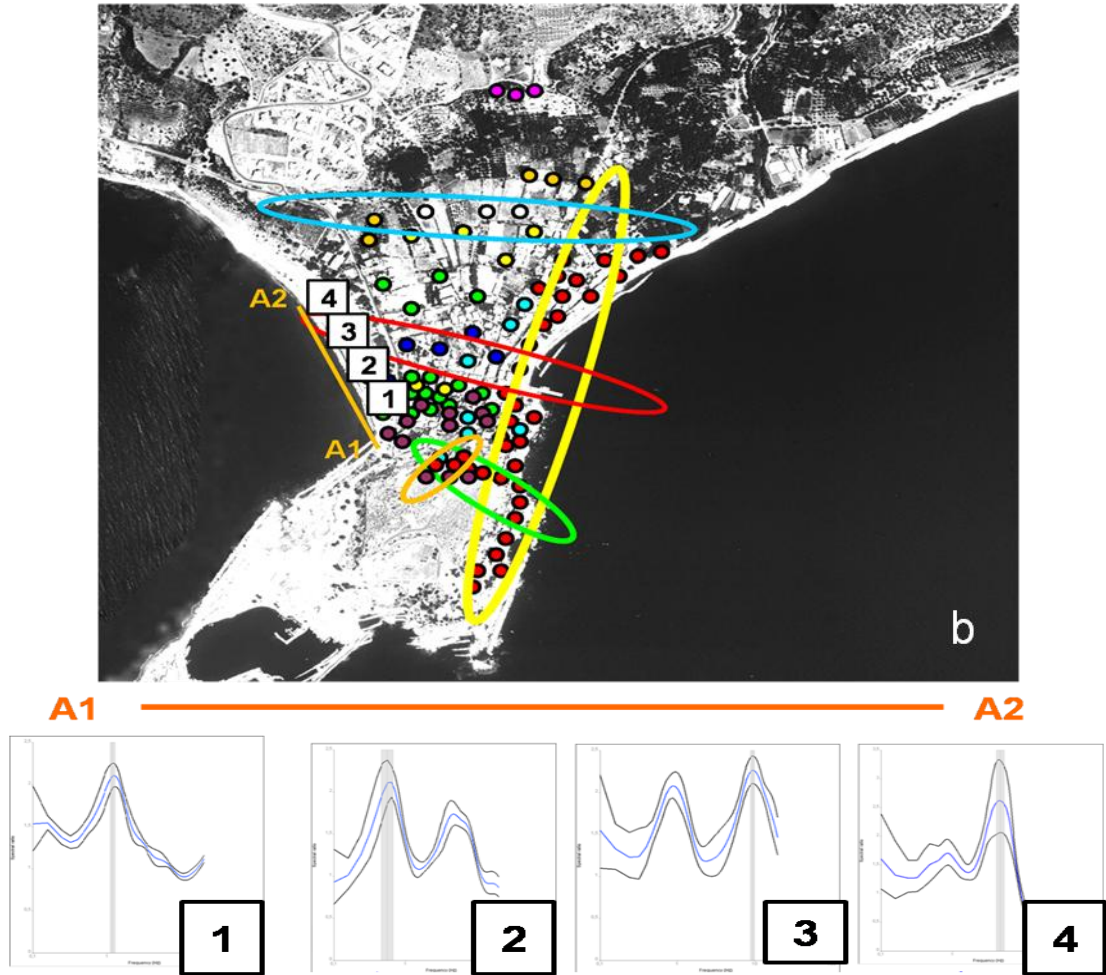


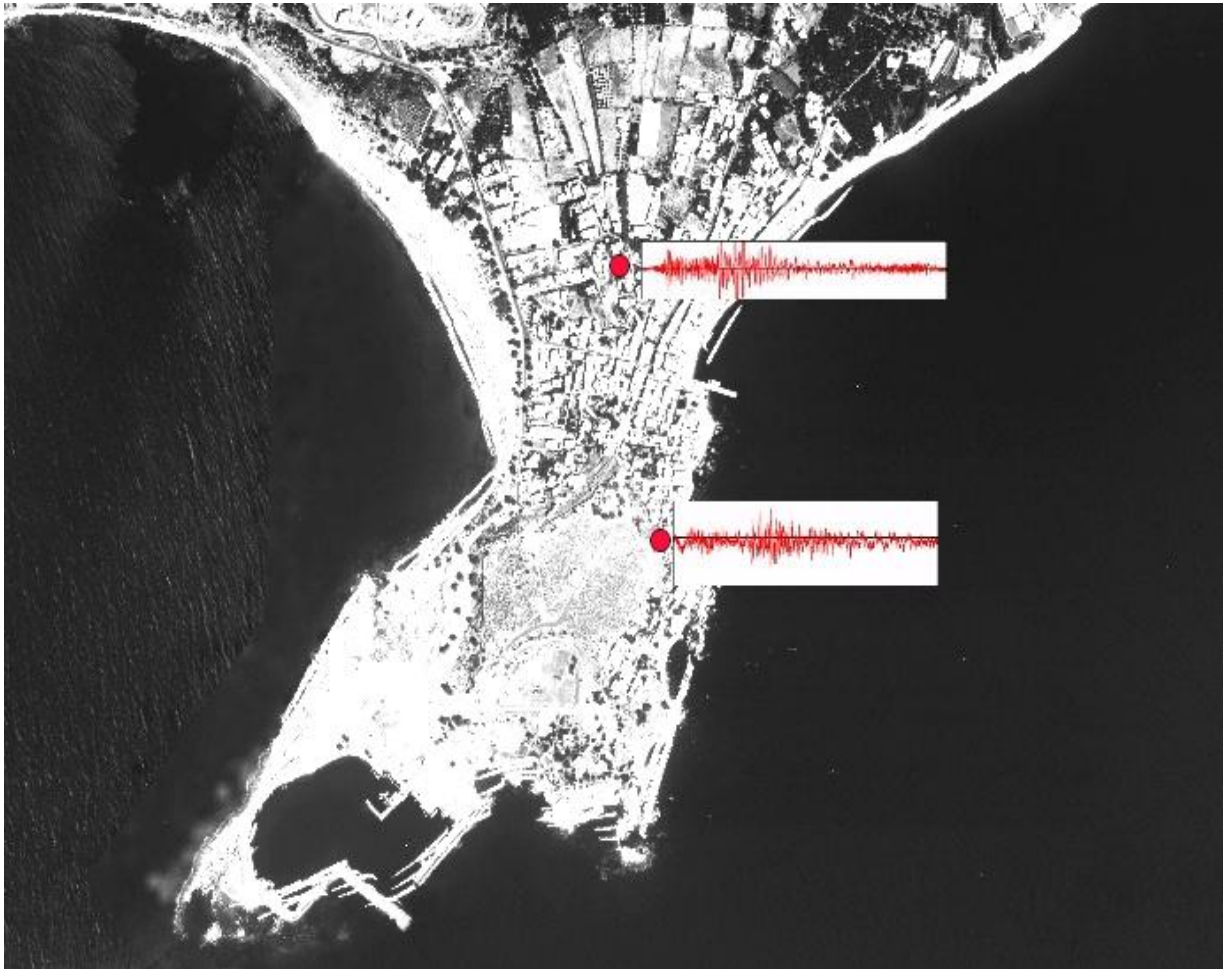
**Figure 4.3.4:** a) Ground fundamental frequency map in Paleohora basin and fault delineation based on HVSR technique using microtremors. Red circles correspond to sites characterized of one clear HVSR peak in the medium frequency range. The brown circles correspond to low frequency HVSR peaks. The pink circles correspond to broad HVSR curves. The dark blue, pale blue, green and yellow correspond to the effect of subsurface structure (attributed to fault zone) and to the effect of the thickness variation of the alluvial deposits on seismic ground motion. Four main fault zones (blue, red, orange-green (Fortezza) and yellow clusters) are delineated using HVSR technique and microtremors, b) Microtremor profile recordings (A1A2) performed along Pahia Ammos where ERT profile conducted. In the southern part of Pahia Ammos the clear amplified low frequency corresponds to the thick sand layer overlying the bedrock. The two amplified frequencies correspond to the surface and subsurface structure. The first amplified in the low corresponds to the effect of the sandy layer while the second amplified in the high frequencies to the effect of the lateral heterogeneities of the subsurface. The first amplified in the high frequencies corresponds to the effect of the lateral heterogeneities of the subsurface while the second amplified to the low frequencies to the effect of the sandy layer.



**Figure 4.3.5:** Ground seismic amplification map in Paleohora basin. The red zones (A) represent sites with the higher amplification (5.68, 5.75). The orange zone (B) represents sites of ground amplification ranging from 3.0-4.66. The yellow area zone (C) represents sites of ground amplification 1.88-3.36.

#### 4.3.4 SINGLE POINT EARTHQUAKE AND MICROTREMORS RECORDINGS

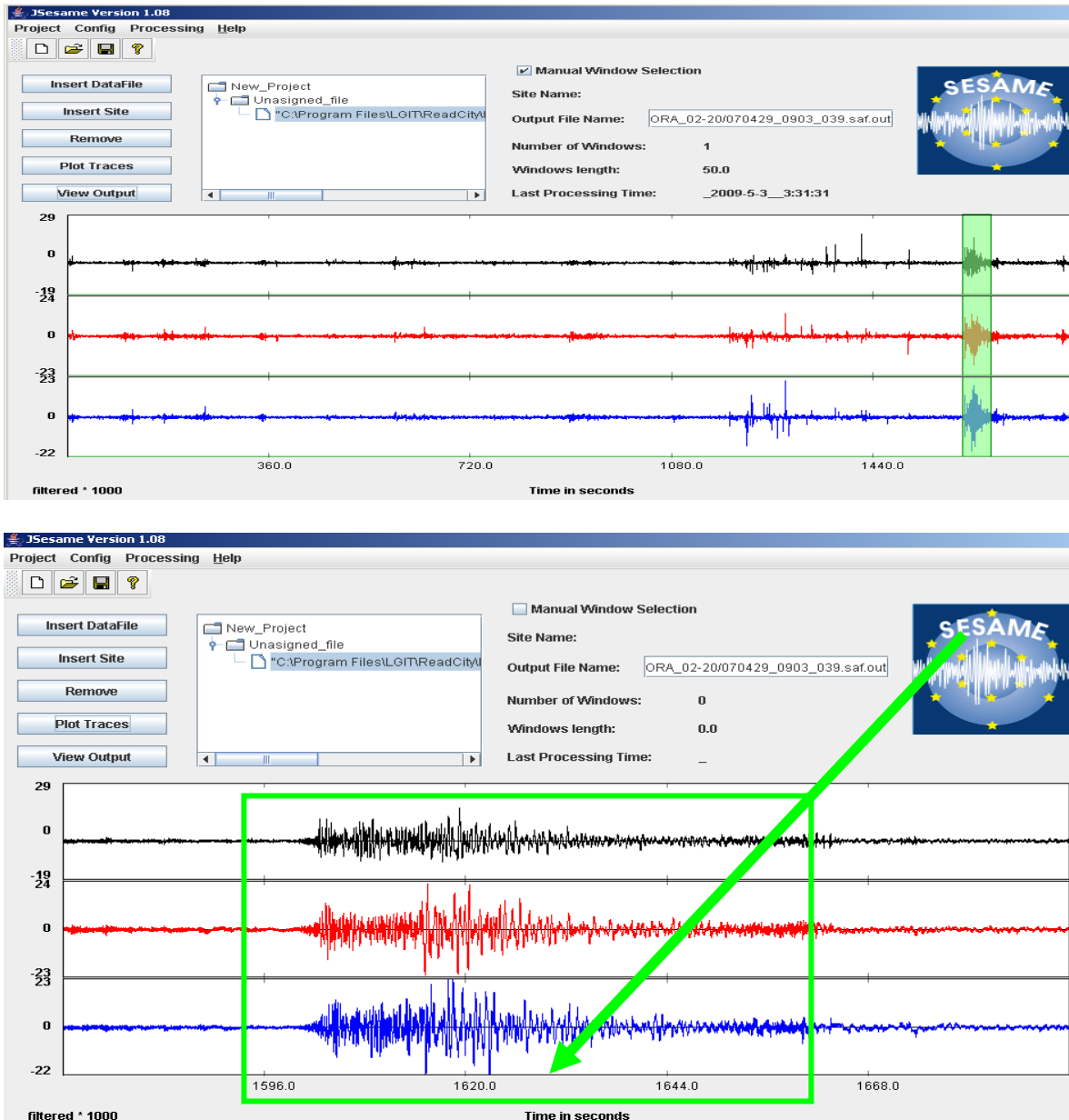
Microtremor and earthquake HVSR spectra are compared in the centre of the basin and along the basin edge to: 1) verify the applicability of HVSR using microtremors to determine the surface and subsurface structure structure and 2) to preliminary study the the basin effect in the two localities on seismic ground motion. Simultaneously microtremor and earthquake data recorded on 29<sup>th</sup> of April 2007 at 09:03 in the centre of the basin and on 4<sup>th</sup> of May 2007 at 18:45 in the basin edge (Figure 4.3.6). In both cases similarities are observed between the microtremors and earthquake spectra.



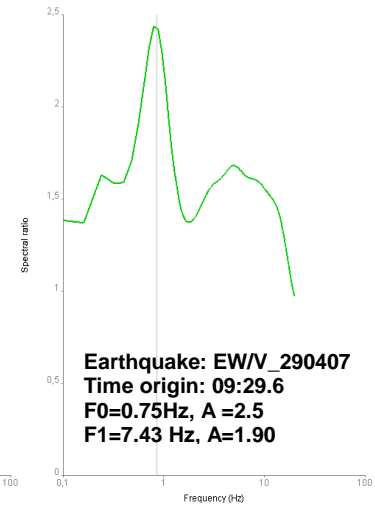
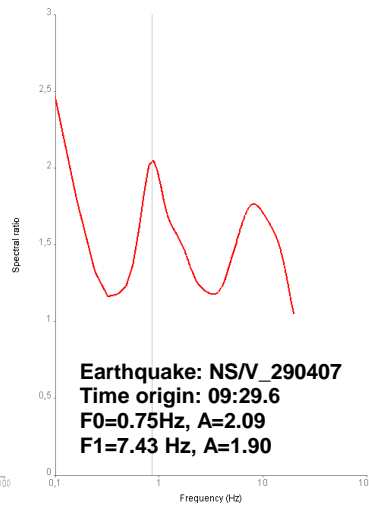
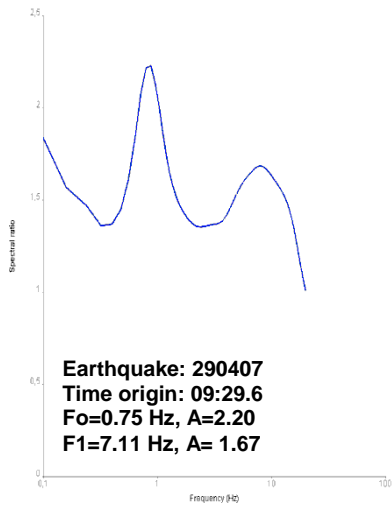
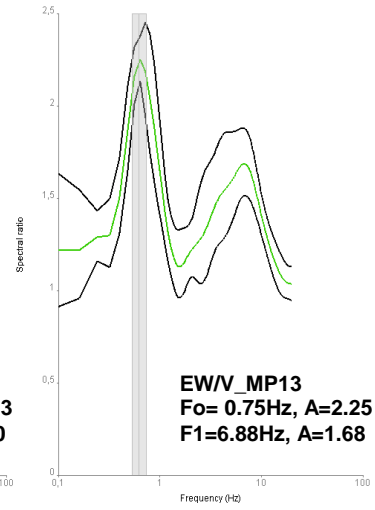
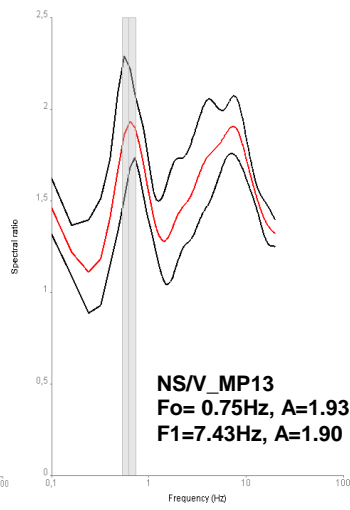
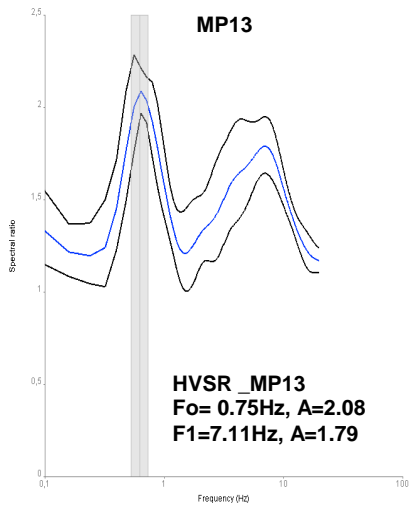
**Figure 4.3.6:** Sites of HVSR comparison between simultaneously recorded microtremor and earthquake data using Cityshark II.

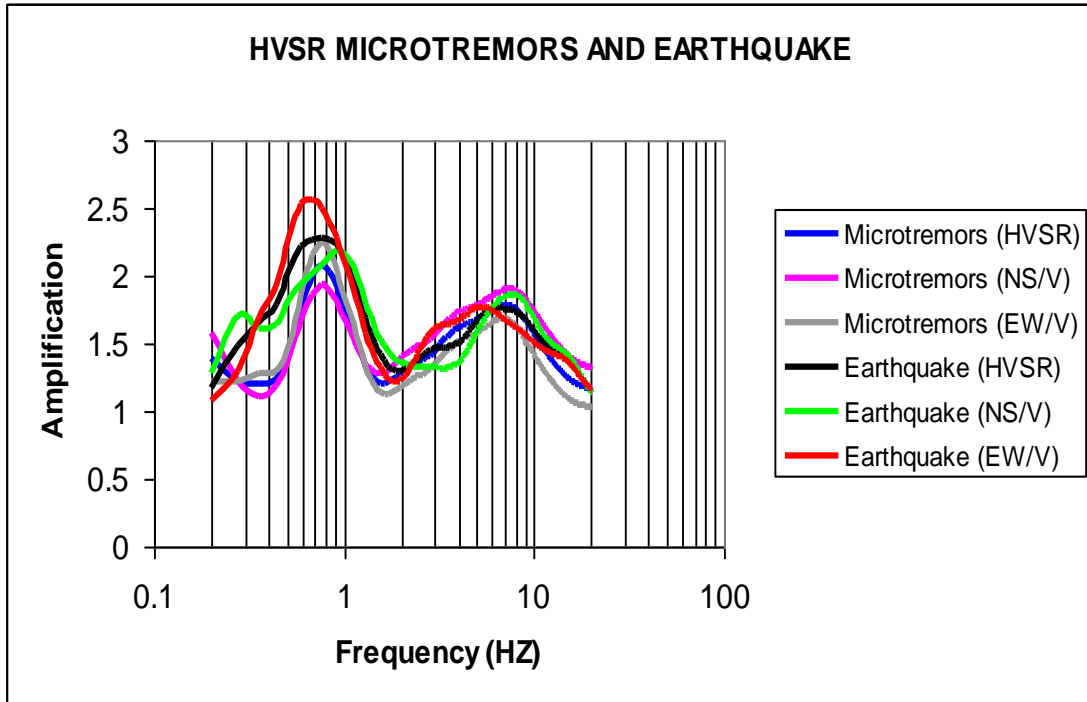
#### 4.3.4.1 CASE STUDY: EARTHQUAKE RECORDED IN THE CENTRE OF THE BASIN

In the following is presented the time series recorded on 29<sup>th</sup> of April 2007 at 09:03 in the centre of the basin. In the center of the basin the HVSR ground fundamental frequency using microtremors is observed in the same frequency range compared to the HVSR ground frequency using earthquake data. Two amplified frequencies are observed using microtremors and earthquake recording. The fundamental frequency in both cases is observed at  $F_0=0.75$  Hz, while the second amplified frequency is observed at 7.11 Hz. The HVSR ground amplification using microtremors is underestimated compared to HVSR ground amplification using earthquake recording.



**Figure 4.3.7:** (Upper) Microtremor and earthquake time series. (Lower): The green time window is the earthquake recording.

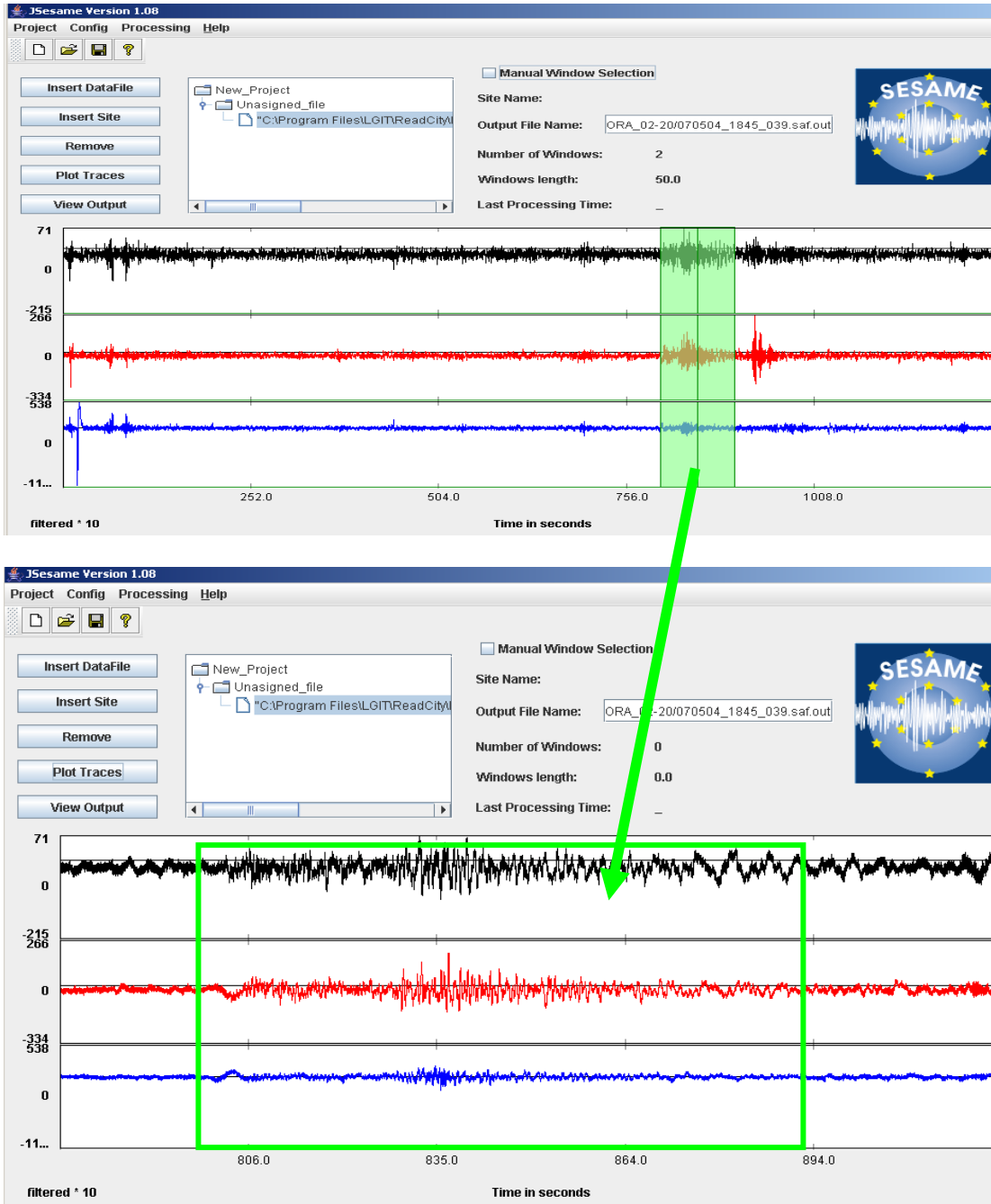




**Figure 4.3.8:** (Upper): HVSR curves using microtremors and earthquake data recorded at the same site in the centre of the basin. The horizontal axis presents the HVSR ground fundamental frequency and the vertical axis presents the HVSR ground amplification. The HVSR fundamental frequency using microtremors and earthquake data is in the low frequency (0.75 Hz). For microtremors and the recorded earthquake the second HVSR amplified frequency is observed in the high frequencies (7.11 Hz). Similarities in the HVSR, Hns/V and Hew/V spectra curves and in fundamental frequencies for the average HVSR (blue curve), Hns/V (red curve) and Hew/V (green curve) spectra ratios are observed. (Lower): Comparison between HVSR (blue curve), Hns/V (pink curve) and Hew/V (grey curve) using microtremors and HVSR (black curve), Hns/V (green curve) and Hew/V (red curve) using earthquake recording. The HVSR ground amplification is underestimated using microtremors (blue curve) compared to HVSR ground amplification using earthquake recording (black line) in the centre of the basin.

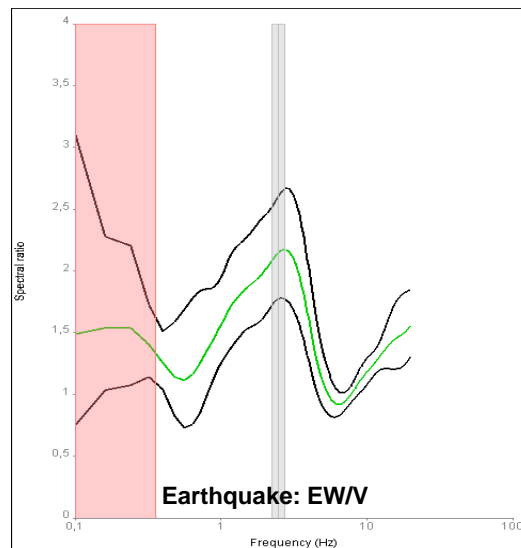
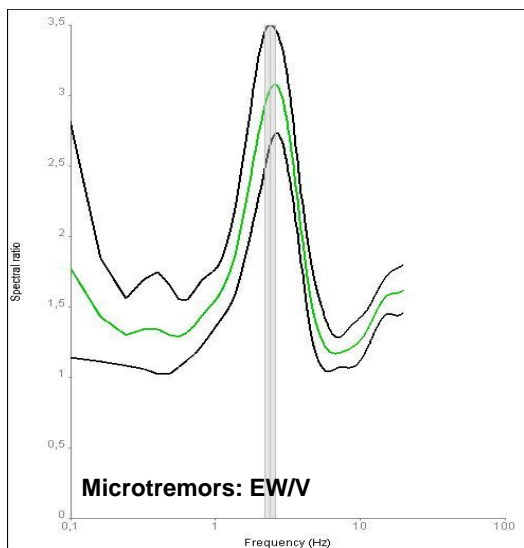
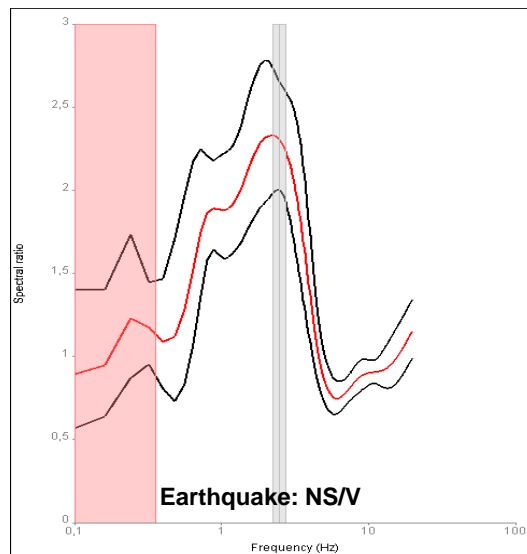
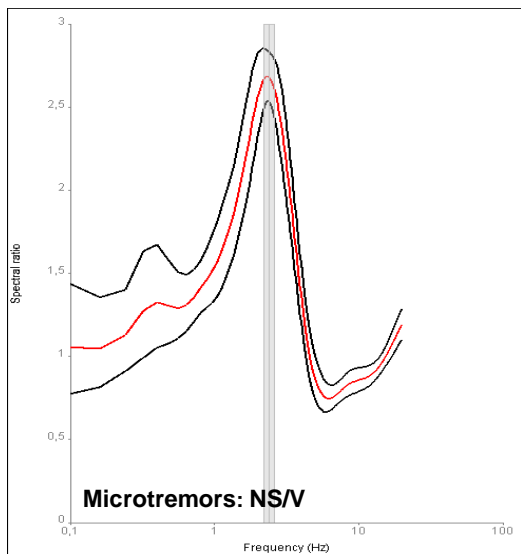
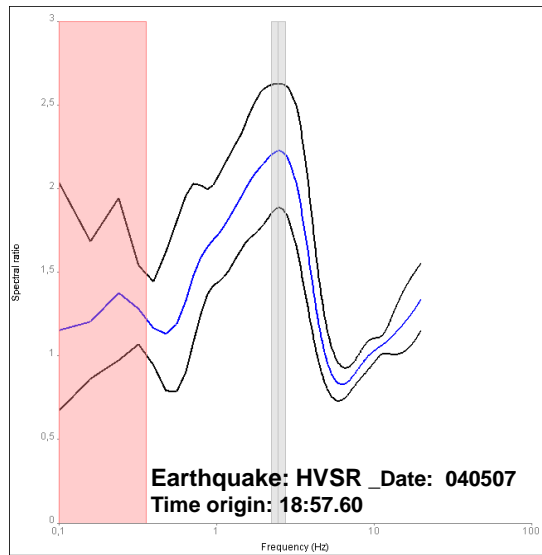
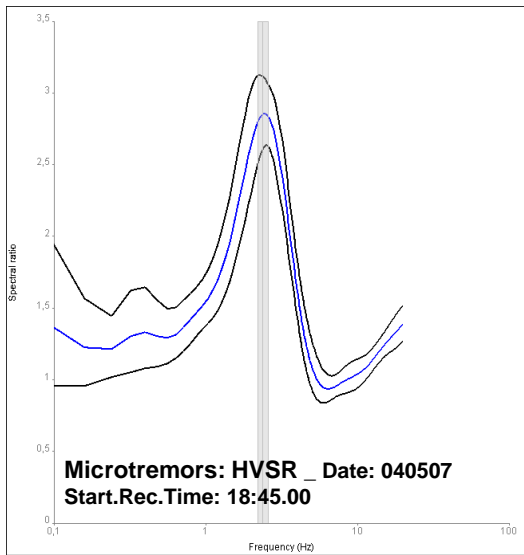
#### 4.3.4.2 CASE STUDY: EARTHQUAKE RECORDED ALONG THE BASIN EDGE

In Figure 4.3.9 is presenting the time series of microtremors and earthquake data recorded on 29/04/07 at 18:45 in the edge of the basin. Along the basin edge similar HVSR ground fundamental frequency using microtremors and earthquake recording is observed. The HVSR ground amplification using microtremors is overestimated compared to HVSR ground amplification using the earthquake recording.



**Figure 4.3.9:** (Upper) Microtremor and earthquake time series. (Lower) The green time window is the magnification of the earthquake recording.





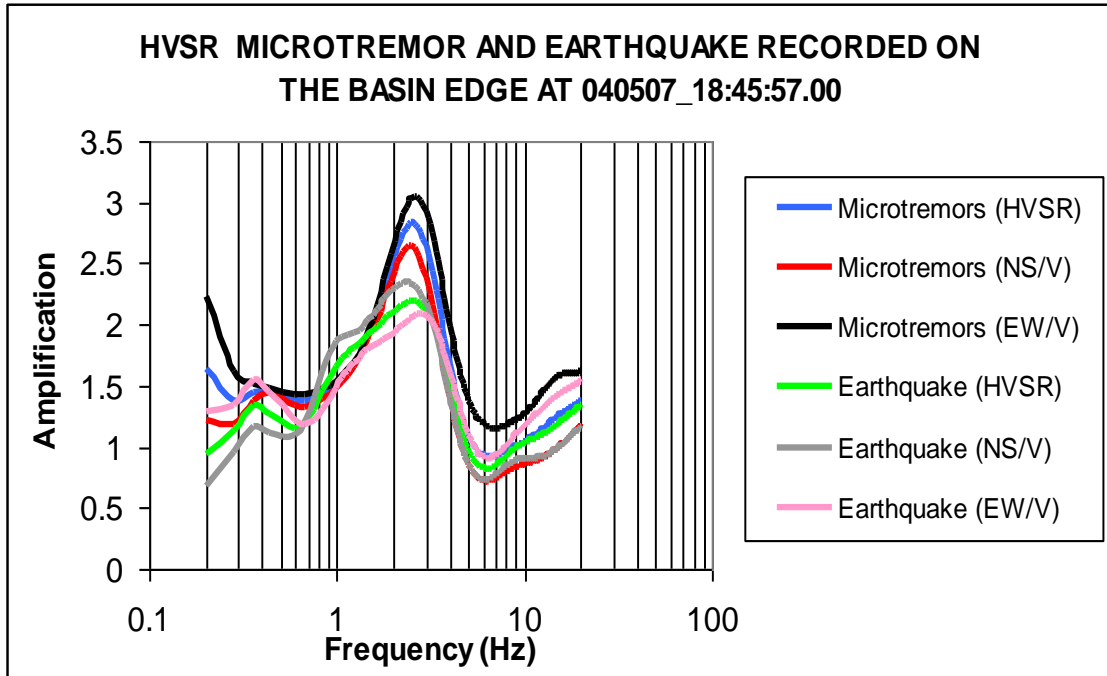


**Figure 4.3.10:** (Upper): HVSr curves using microtremors and earthquake data recorded at the same site in the basin edge and the comparison of microtremor and earthquake data. The horizontal axis presents the HVSr ground fundamental frequency and the vertical axis presents the HVSr ground amplification. Similarities in the HVSr (blue curve), Hns/V (red curve) and Hew/V (green curve) spectra curves and in fundamental frequencies using microtremors and earthquake recording are observed. (Lower): Comparison between HVSr (blue curve), Hns/V (red curve) and Hew/V (black curve) using microtremors and HVSr (green curve), Hns/V (grey curve) and Hew/V (pink curve) using earthquake recording. The HVSr ground amplification using microtremors is overestimated compared to recorded earthquake recorded along the basin edges.

In Paleohora basin a comparison of the HVSr spectra characteristics of the S-wave earthquake wavefield and microtremors recorded simultaneously on: a) the edge of Paleohora basin in the southern part (Fig 4.3.8) and b) in the center of the basin is presented (Fig. 4.3.10). The comparison of HVSr spectra using microtremors and earthquake data purposes to present the applicability of HVSr technique of microtremors in evaluating the seismic ground response fundamental frequency without the occurrence of an earthquake. Similarities in the fundamental frequency between the HVSr using microtremors and earthquake data in the centre and in the basin edges are observed. In the centre of the basin slightly lower (underestimated) HVSr amplification using microtremors is observed compared to earthquake data. The HVSr ground amplification using microtremors is higher (overestimated) compared to recorded earthquake at the same site along the basin edges.

The shallow sedimentary layer and the surficial generated wave along the edge of the basin induce amplification of ground seismic motion. It is observed that along the edge of the valley the locally shallow layer generate larger amplitudes than the

earthquake S direct wave. The HVSR ratio of microtremor along the edge of the valley verifies that these locally surficial generated waves (due to the strong diffractions on the edges of the basins) have larger amplification than the HVSR ratio of the S earthquake wavefield (Fig. 4.3.8). The HVSR fundamental frequency is the same while the seismic ground response amplification is higher when using microtremors.

The outcome of comparison of single-point microtremor and earthquake HVSR ratios recorded at the same site in Paleohora (Fig. 4.3.8) along the edge of basin is in agreement with Bard (1999) and Bonnefoy-Claudet et al. (2008b) observations. These authors reported that along the edge of a valley the locally surficial generated wave have larger amplitudes than the S direct wave of the substratum. According to Bard (1999), the amplitude of the locally generated waves (depending on the impedance contrast and damping) is higher than the amplitude of the incident wave especially near the lateral discontinuity and their short wavelength induces large differential motions and enhanced earthquake damage distribution. Frankel & Vidale (1992) reported the consequences of these waves on seismic ground motion and mentioned that these waves are the cause of long period duration of seismic motion in San Clara valley during Loma Prieta earthquake.

The HVSR fundamental frequency using microtremors and earthquake data is similar but the amplification level using microtremors is slightly underestimated in the low frequency range compared to the HVSR amplification using earthquakes in the centre of the basin. Raptakis et al. (2005) compared the HVSR curves using microtremors and earthquake data (HVSR, HVSR\_NS, HVSR\_EW) recorded in Mygdonia basin and found also similarities in the HVSR fundamental frequency. Similar results in the HVSR fundamental frequency (ranging between 0.4-0.6Hz) were observed using either microtremors or earthquakes, while at some sites the amplification using microtremors is underestimated or overestimated. Bonnefoy-Claudet et al. (2008a) observed similarities in the ground fundamental frequency using microtremors and earthquake recorded in Santiago de Chile valley. In contrast, at one site there is no similarity in the HVSR curves in the case of broad band amplification using earthquake data and microtremors either in frequency or in amplification; there is no clear explanation yet for the lower HVSR amplification level using microtremors (Bonnefoy-Claudet et al. (2008a). Possible explanation for the lower HVSR amplification level using microtremors might be related to influence of the polarization of Rayleigh (Konno & Ohmachi, 1998; Bonnefoy-Claudet et al., 2006a) or the effect of Love waves in HVSR curve (Arai & Tokimatsu, 2000; Bonnefoy-Claudet et al., 2008a). Zare et al. (1999) compared HVSR using microtremors and earthquake data recorded in Iran. No correlation of HVSR curves using microtremors and earthquakes at all sites was observed possibly related to the low velocity contrast of the site. Haghshenas et al. (2008) compared the HVSR amplitude peak using microtremors and earthquake, SSR and RF techniques and found similar fundamental frequencies even though the HVSR curves do not fulfill the strict reliability criteria by JS (J-Sesame guidelines). Volant et al. (2002) calculated the spectra ratio (site/reference) of an earthquake with epicenter 150km from the recorded site and the spectra ratio of microtremors on fractured rock soil (limestone) and found good correlation. Mucciarelli et al., (2003) compared microtremors and earthquake data recorded at the same site and observed similarities in the fundamental frequency but the amplification is underestimated. Haghshenas et al. (2008) comparing

HVSR using microtremors and earthquake data concluded that the fundamental frequency is similar but the amplification is underestimated. The amplification level using microtremors is higher than the amplification level using earthquakes along basin edges. Ergin et al. (2004) compared HVSR using microtremors and SSR using earthquake data and found good correlation in the fundamental frequency. At low frequency the ground amplification using microtremors is lower than the ground amplification using earthquakes. The underestimation in the amplification using microtremors suggests that the energy of microtremors at the low frequencies is not sufficient to induce oscillation modes at that site. D'Amico et al. (2002) compared the HVSR amplification and macroseismicity data at various sites in Italy and found good correlation. Rodriguez (2003) proposed that HVSR provides a relatively better estimate of soil response than the S-wave and coda.

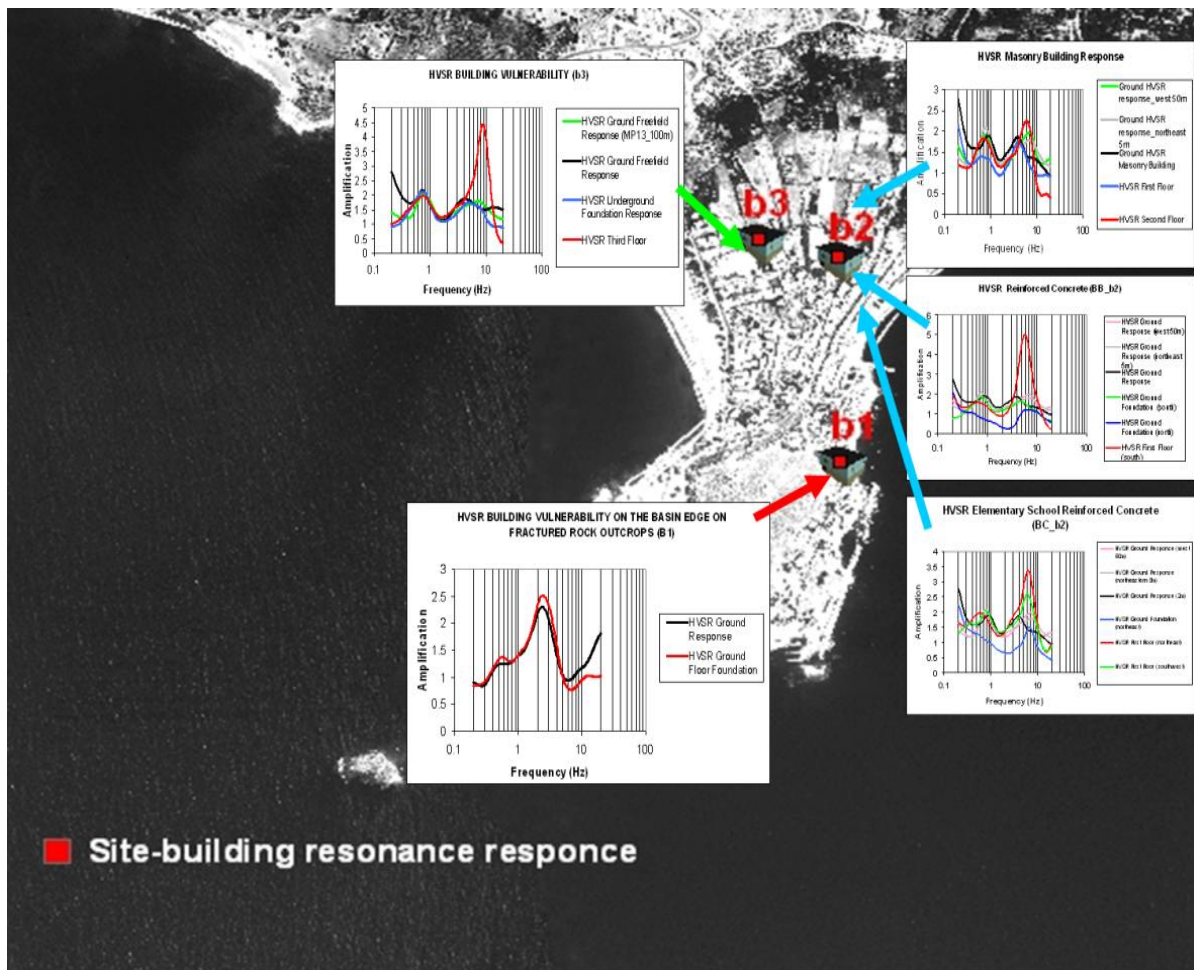
In the frame of this thesis the comparison between HVSR using microtremors and earthquake data suggests similar results to Mucciarelli et al. (2003), to Bonnefoy-Claudet et al. (2008a) and Haghshenas et al. (2008) for the two investigated sites at Santiago de Chile valley. Arai & Tokimatsu (1998), Yamamoto (2000), Okada (2003) Köhler et al. (2004), Bonnefoy-Claudet et al. (2006a,b) showed that the effect of relative proportion of Love waves in the seismic noise wavefield patterned on H/V curves may vary from site to site.

In the frame of this thesis it is proposed comparing HVSR earthquake and microtremors that HVSR technique can be used to infer site amplification in environments where 2D/3D (lateral variations of subsurface structure) effects are existent. The amplification is underestimated but the fundamental frequency remains the same. The underestimations might be related to the composition of complex noise wavefield diffracted along the basin edge or due to the large scale fault. The major outcome is the importance of the shallow layer on seismic ground motion.

Moreover, the comparison of HVSR spectra using microtremors and earthquake data verifies that the spectra characteristics of microtremors can be used to the seismic ground response fundamental frequency without the occurrence of earthquake. It is highlighted that a wealth of data of microtremors and earthquakes recorded at the same site are necessary to perform a comprehensive statistical significant result. The statistical analysis of microtremors and earthquake data is out of the frame of this thesis. The two earthquake data recorded in the centre and along the basin edge are only presented to examine the validity of HVSR in identifying ground the fundamental frequency resonance response using microtremors without the occurrence of earthquake. Moreover, Dravinski et al. (1996), Coulet & Mora (1998) compared the HVSR using microtremors and S waves of earthquake recordings.

### 4.3.5 BUILDING VULNERABILITY ESTIMATION USING HVSR TECHNIQUE: A CASE STUDY OF SEISMIC GROUND-BUILDING INTERACTION

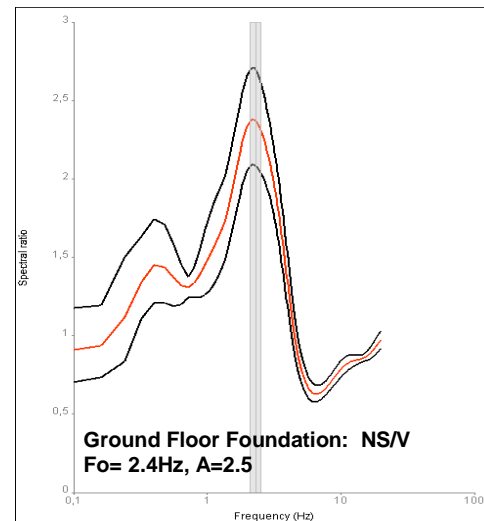
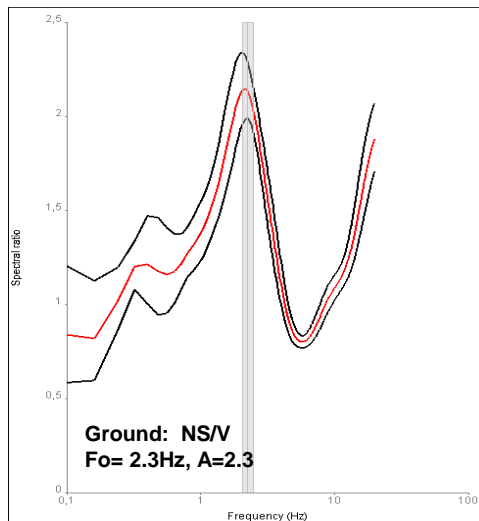
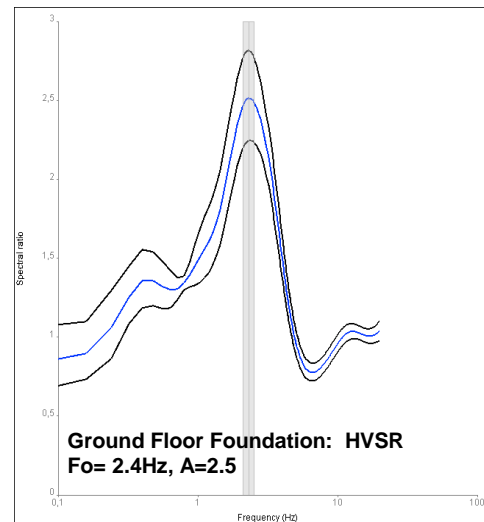
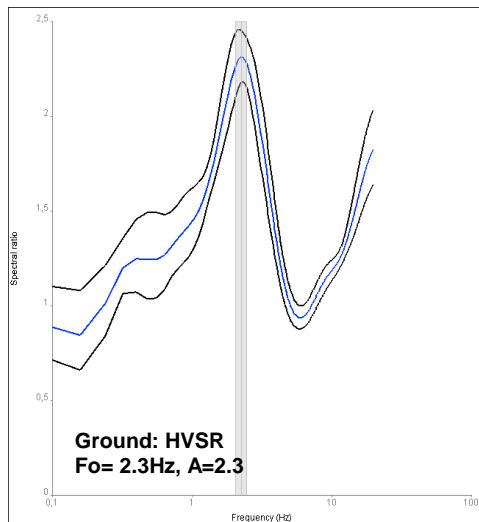
HVSR technique and microtremors is used to estimate the building vulnerability response of three selected building constructions located in the centre and on the edge of the basin. A comprehensive ground-building vulnerability interaction study involves microtremor recordings in all directions at each floor of the building. In the frame of this thesis microtremors performed at floor level where permission was given, therefore the ground-building seismic response study purposes only to preliminary evaluation. Building vulnerability evaluation of three case studies using HVSR technique and microtremors are presented for: a) a small sized one-storey masonry house located on the rock fractured outcrop in the edge of the basin (b1), b) a reinforced concrete three-floor building near Pahia Ammos (b3) and c) the High School in the middle of the basin in Paleohora (b2). Ground and building resonance phenomena are observed and highlight the importance of site effects in civil engineering constructions.

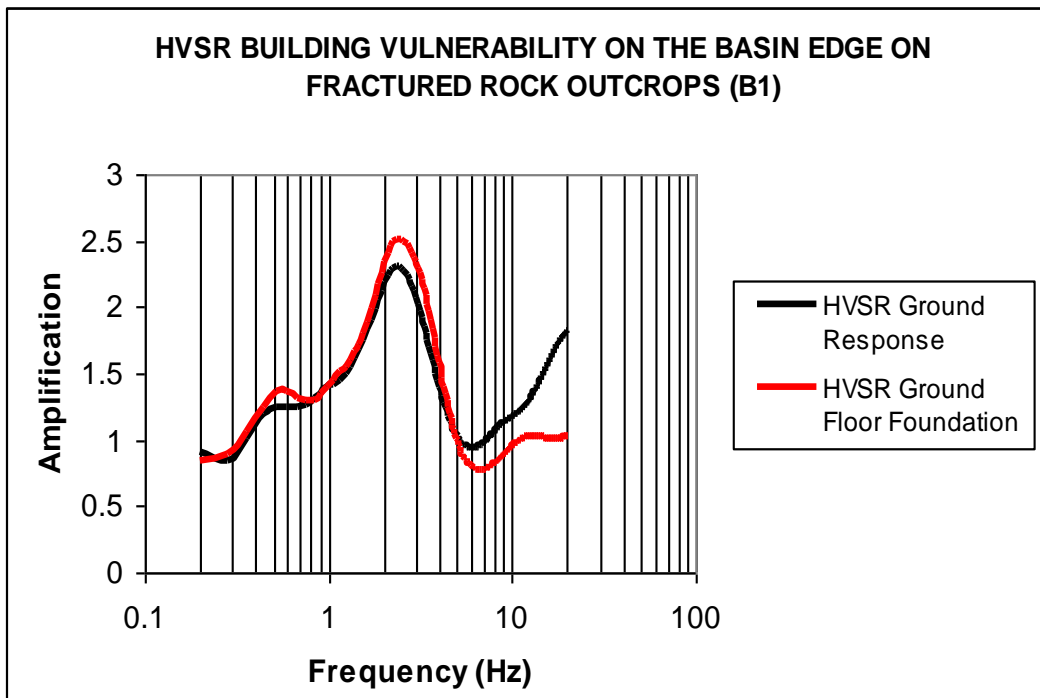
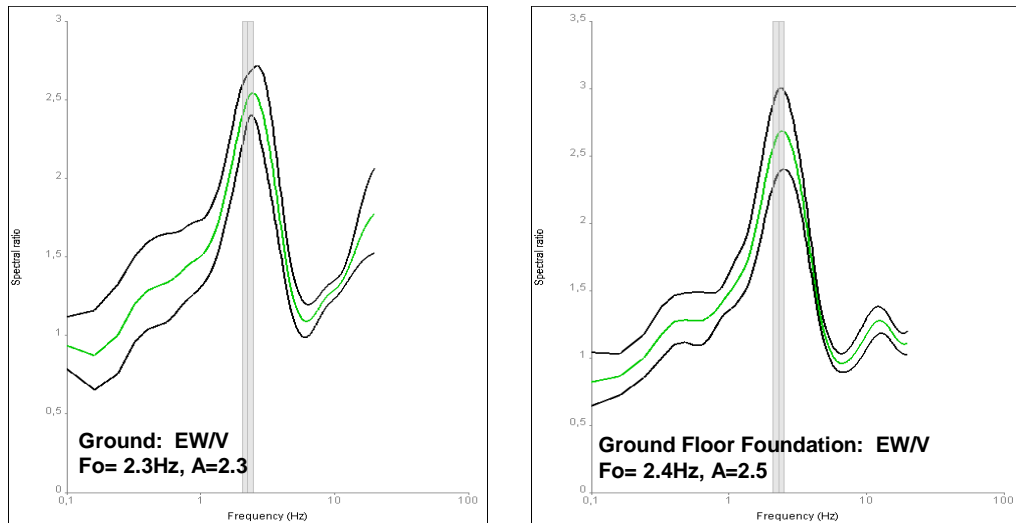


**Figure 4.3.11:** Building Vulnerability estimation using HVSR and microtremors in three case studies located in the centre of the basin (b2,b3) and near to the basin edge (b1).

#### 4.3.5.1 BUILDING VULNERABILITY ESTIMATION USING HVSR FOR A MASONRY CONSTRUCTED HOUSE, LOCATED IN THE SOUTHEASTERN PART OF PALEOHORA CLOSE TO THE EDGE OF THE BASIN (b1)

HVSR fundamental frequency using microtremors for a masonry constructed house, located in the southeastern part of Paleohora close to the edge of the basin (b1) coincidence with the ground HVSR fundamental frequency. The ground fundamental frequency is observed at 2.3 Hz with amplification 2.3. The ground floor foundation of the masonry frequency is observed at 2.4 Hz. The amplification of the floor foundation is 2.5. Coincidence between the ground freefield and ground floor foundation in the frequency and amplification is observed.

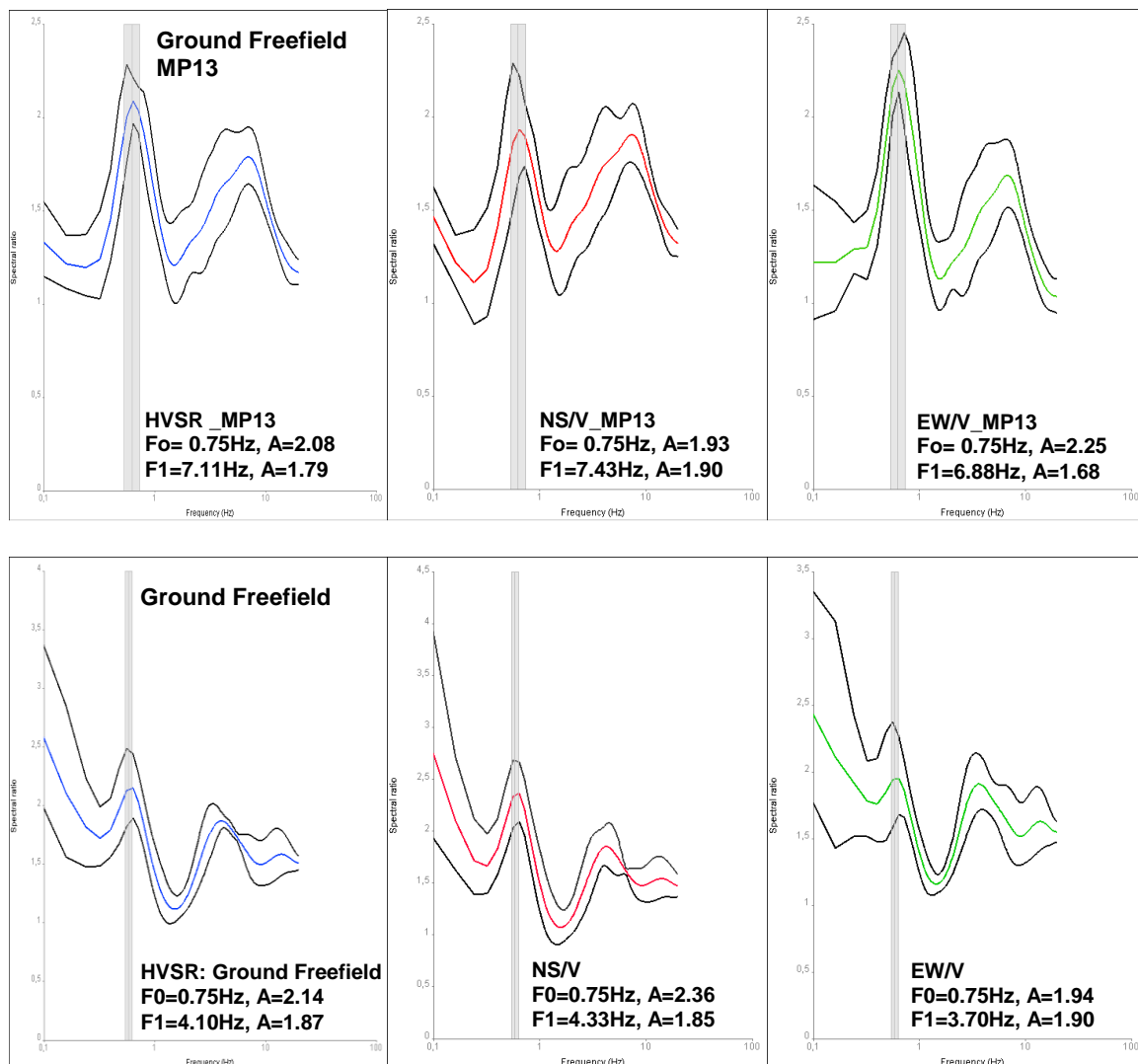




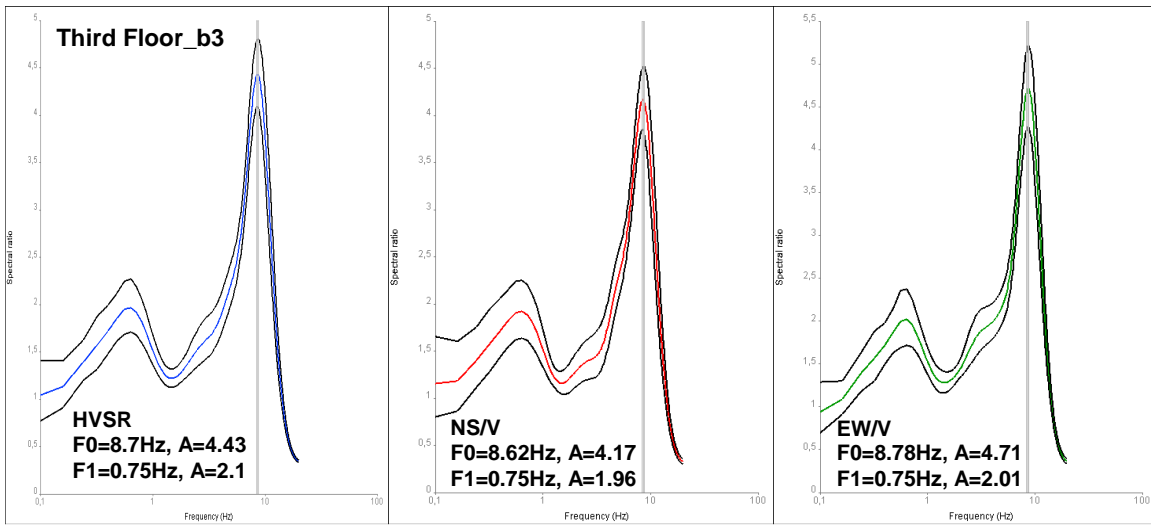
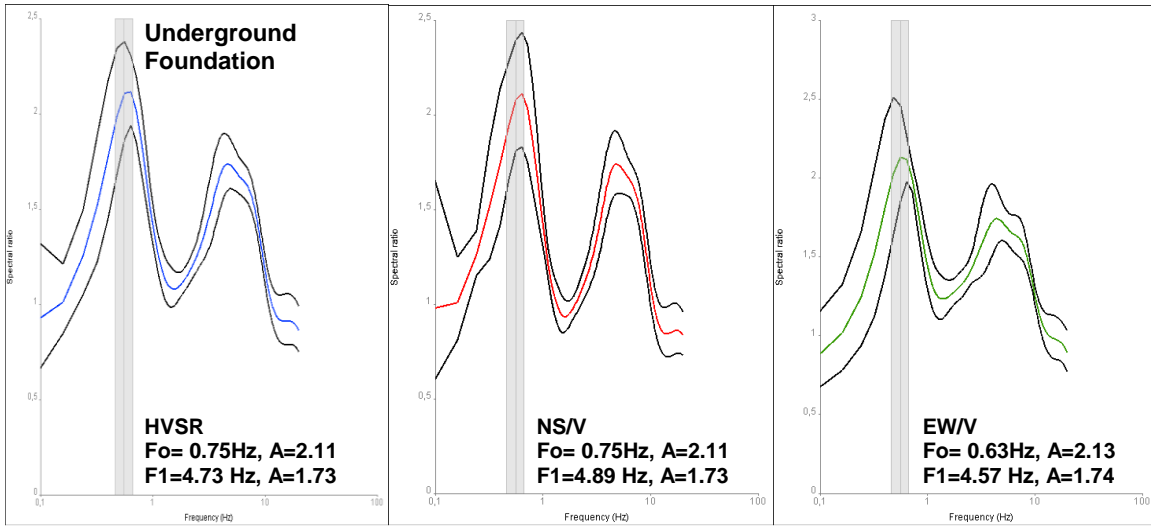
**Figure 4.3.12:** (Upper): Building vulnerability estimation using HVSr and microtremors for the masonry constructed house, located in the southeastern part of Paleohora close to the edge of the basin (b1). Similarities in the HVSr (blue curve), Hns/V (red curve) and Hew/V (green curve) spectra curves in fundamental frequencies and amplification of ground structure response and ground floor foundation are observed. (Lower): Comparison between HVSr ground response and HVSr ground floor foundation. Similarity in the fundamental frequency ( $F_0=2.3-2.4$  Hz) and in the amplification is observed ( $A=2.3-2.5$ ).

### 4.3.5.2 BUILDING VULNERABILITY ESTIMATION USING HVSR FOR A THREE-FLOOR CONCRETE HOUSE, LOCATED NORTHEASTERN OF THE CENTRE OF THE BASIN

HVSR fundamental frequency using microtremors for the concrete constructed house, located northeastern of Paleohora in the centre of the basin (b3) coincidence with the ground HVSR fundamental frequency. Microtremor recordings conducted on the ground freefield (MP13) in the underground foundation and in the third floor present similar fundamental frequency. Fundamental frequency of the third floor at  $F_0 = 8.7$  Hz is in the same frequency range with the second amplified frequency of the ground freefield (MP13 located 100 m far from the building construction) that is observed at 7.11 Hz. The first amplified frequency of : a) the ground freefield (located 100 m and 2 m), b) the first amplified frequency of the building ground foundation and c) the second amplified frequency of the underground foundation is observed at 0.75 Hz. Similarities in the fundamental frequencies of ground freefield, of the underground foundation and of the third floor are observed.







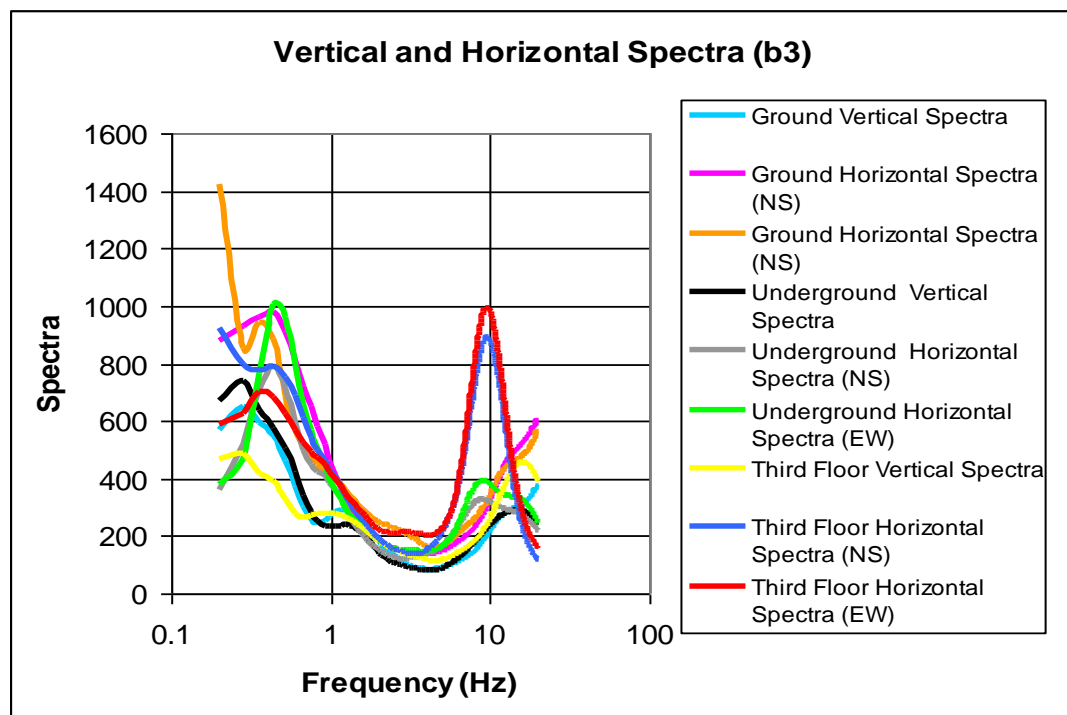
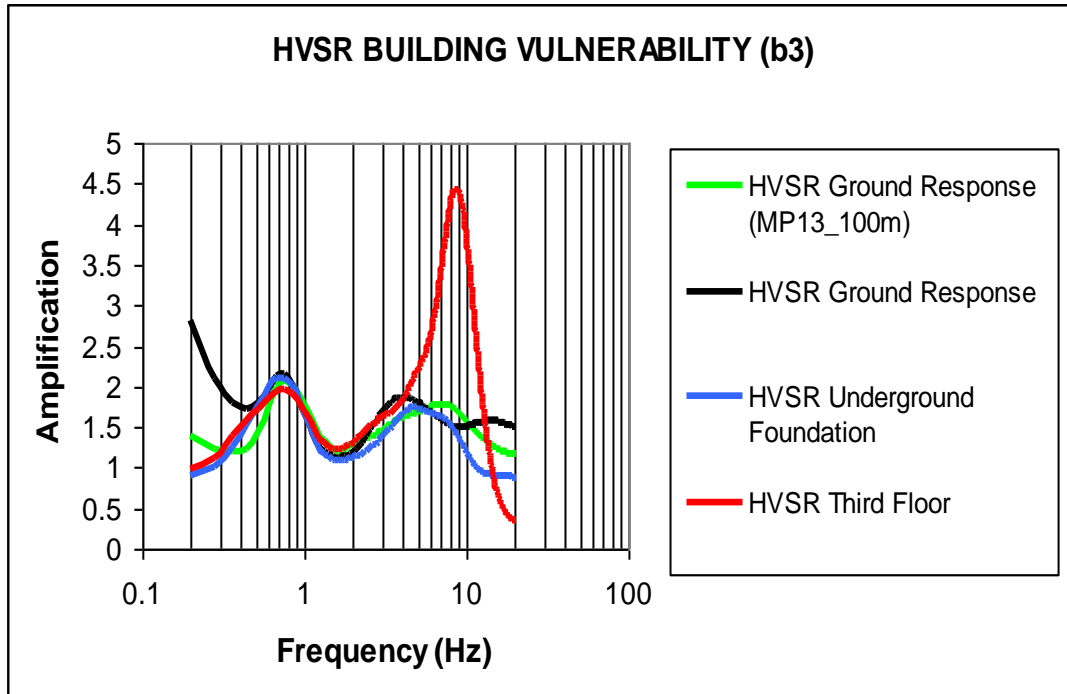
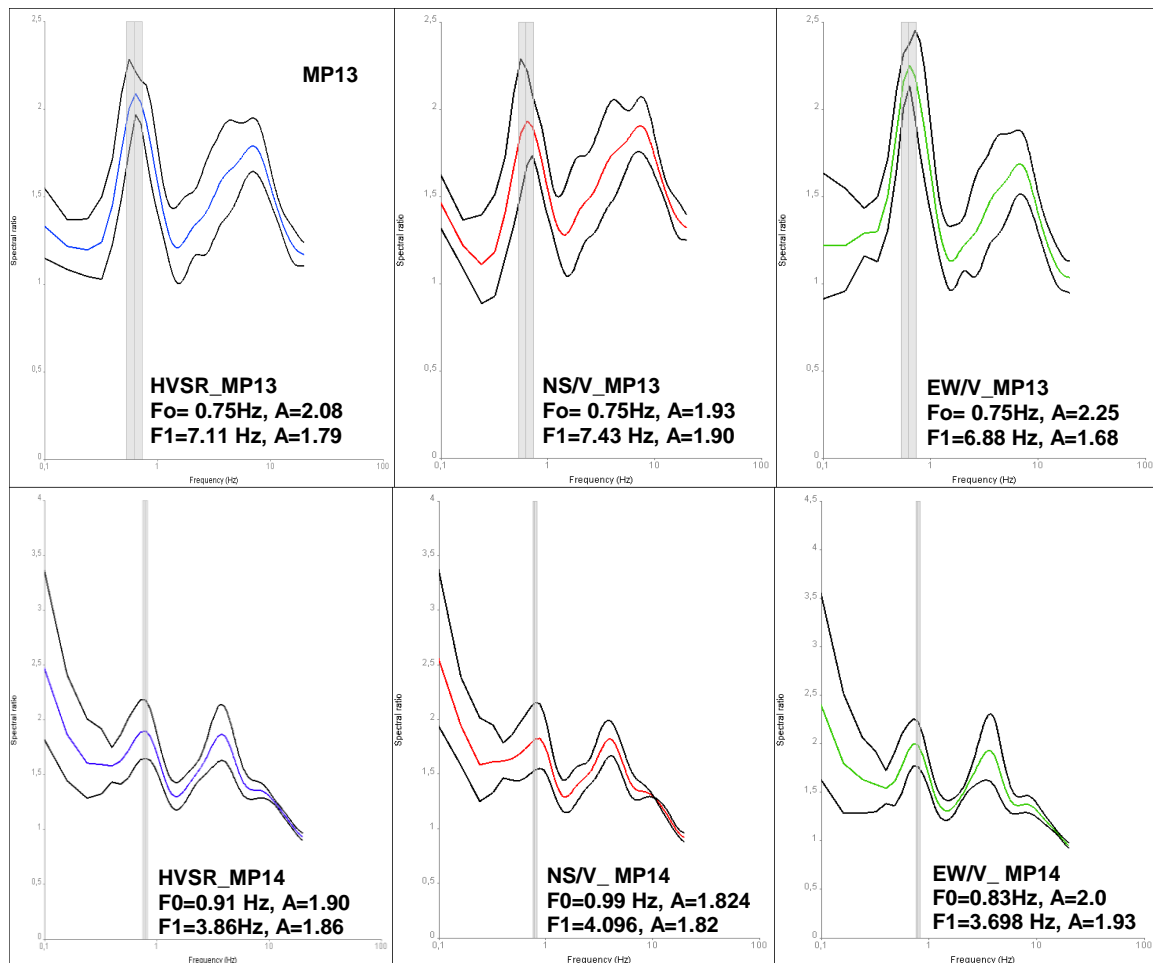


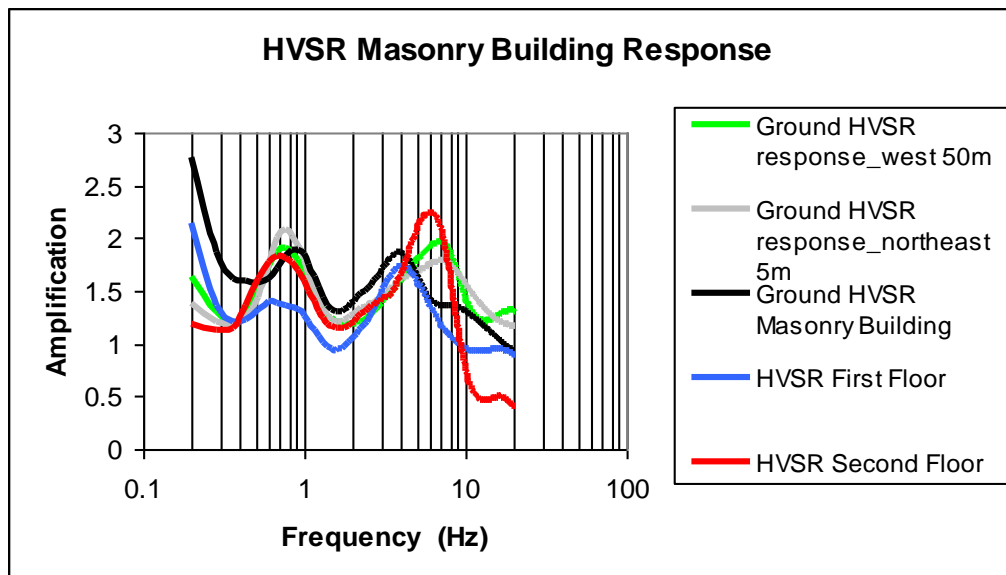
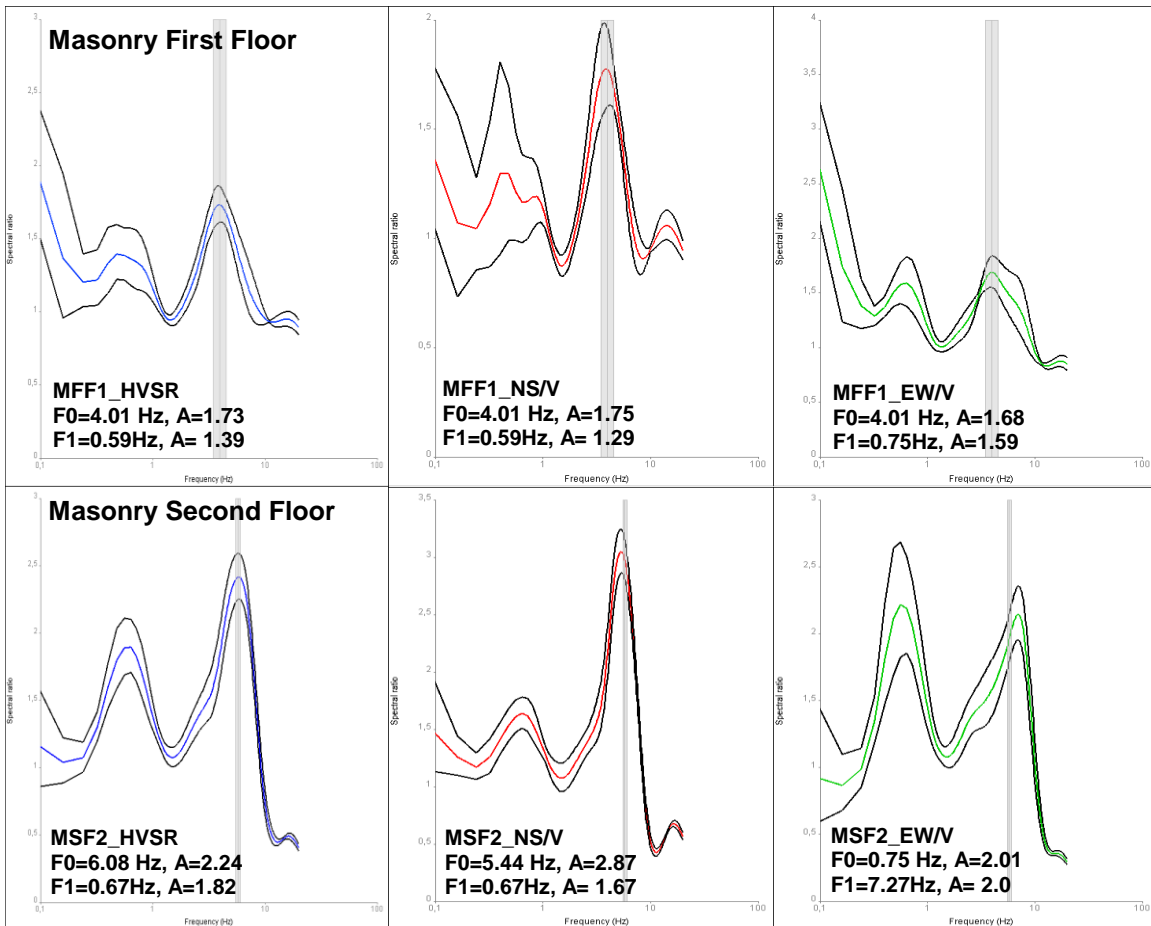
**Figure 4.3.13:** Building Vulnerability estimation using HVSR and microtremors for three-story concrete constructed house, located northeastern of Paleohora in the centre of the basin (b3). Similarities in the HVSR (blue curve), Hns/V (red curve) and Hew/V (green curve) spectra curves in fundamental frequencies and amplification of ground freefield underground foundation and third floor are observed. (Lower): Comparison between

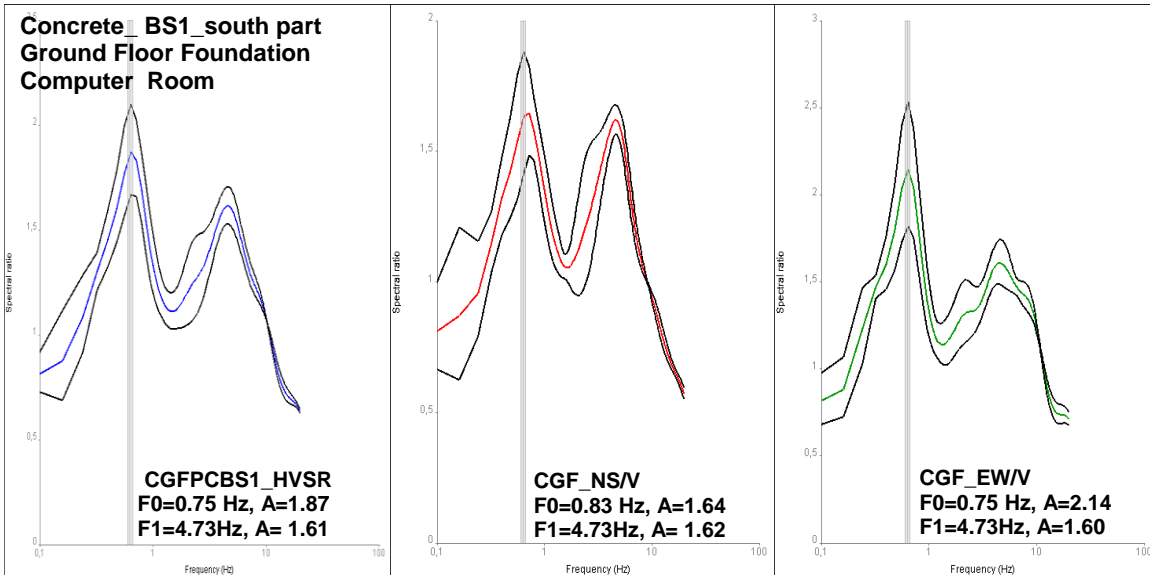
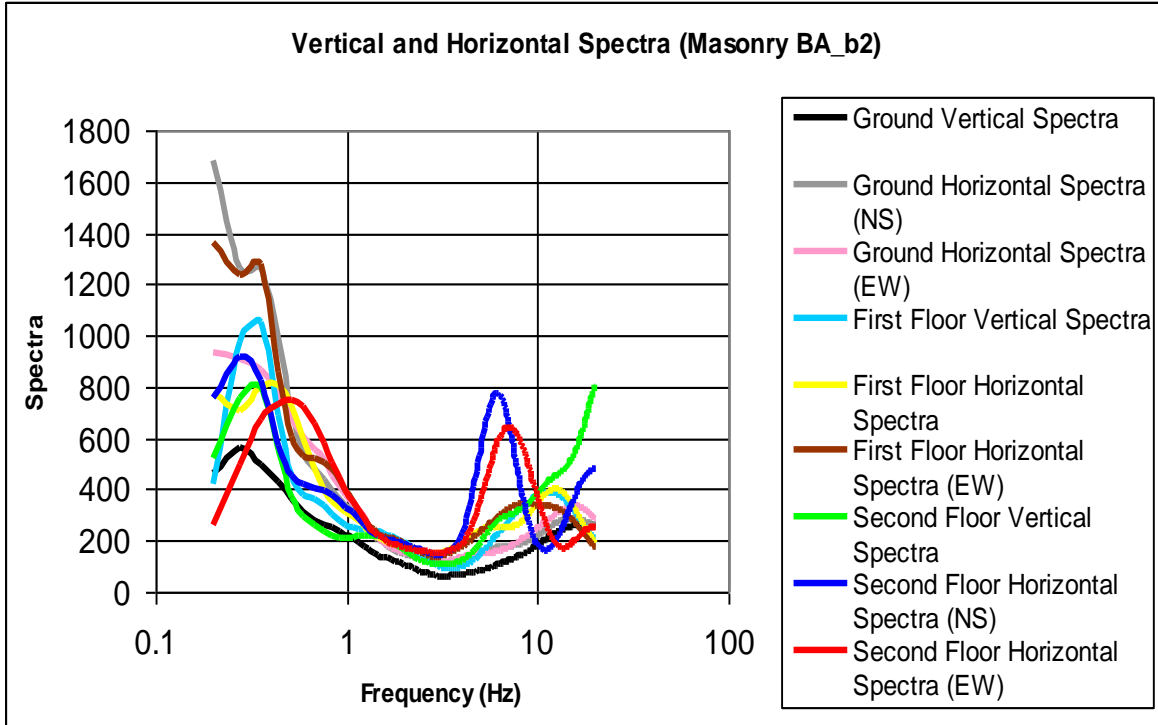
*HVSR ground response and HVSR ground floor foundation. Similarities in the fundamental frequencies of ground freefield 100 m (green line) ground freefield of the construction (black line), of the underground foundation (blue line) and of the third floor (red line) are observed.*

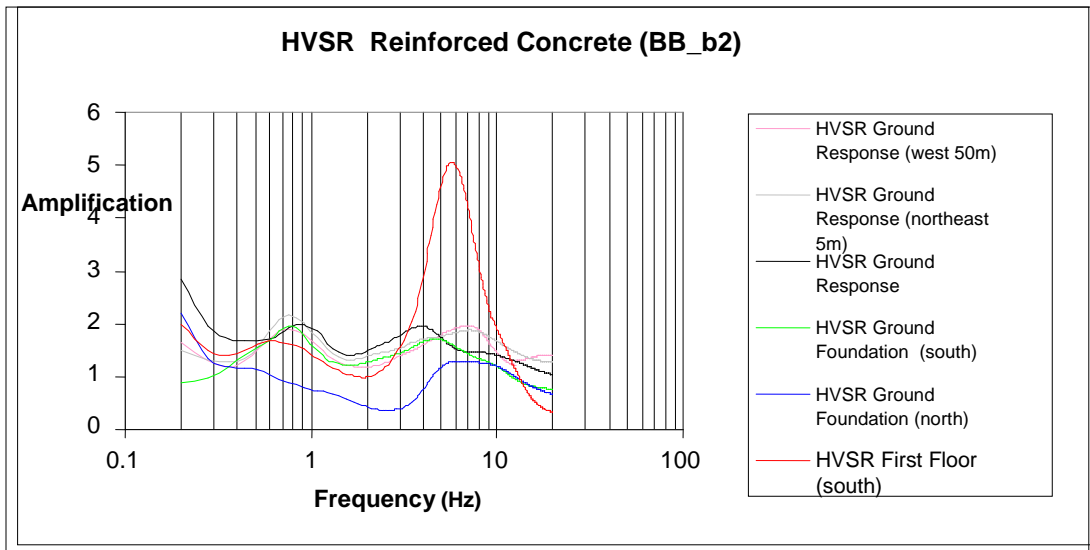
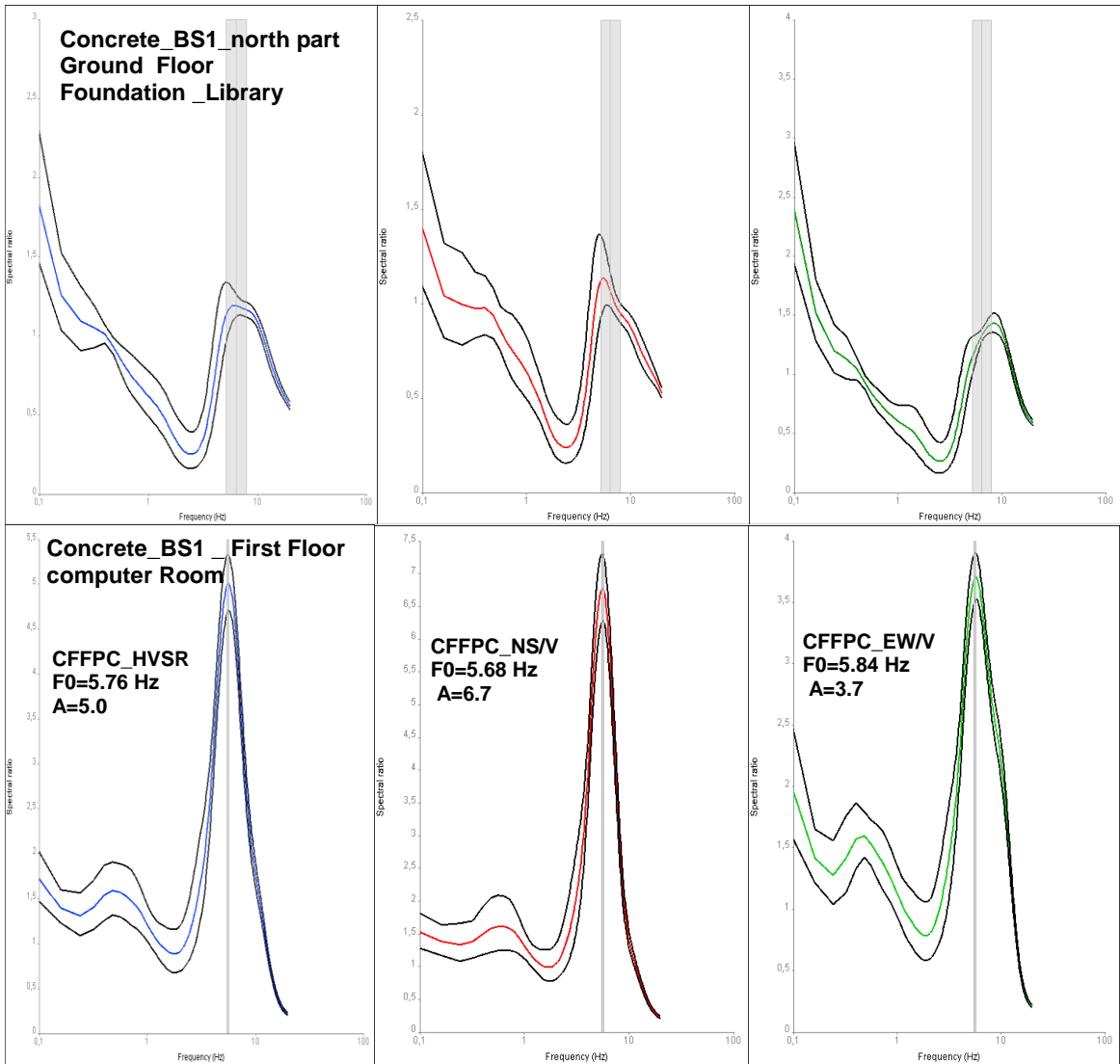
#### 4.3.5.3 BUILDING VULNERABILITY ESTIMATION USING HVSR FOR THE ELEMENTARY AND HIGH SCHOOL LOCATED IN THE CENTRE OF THE BASIN (b2)

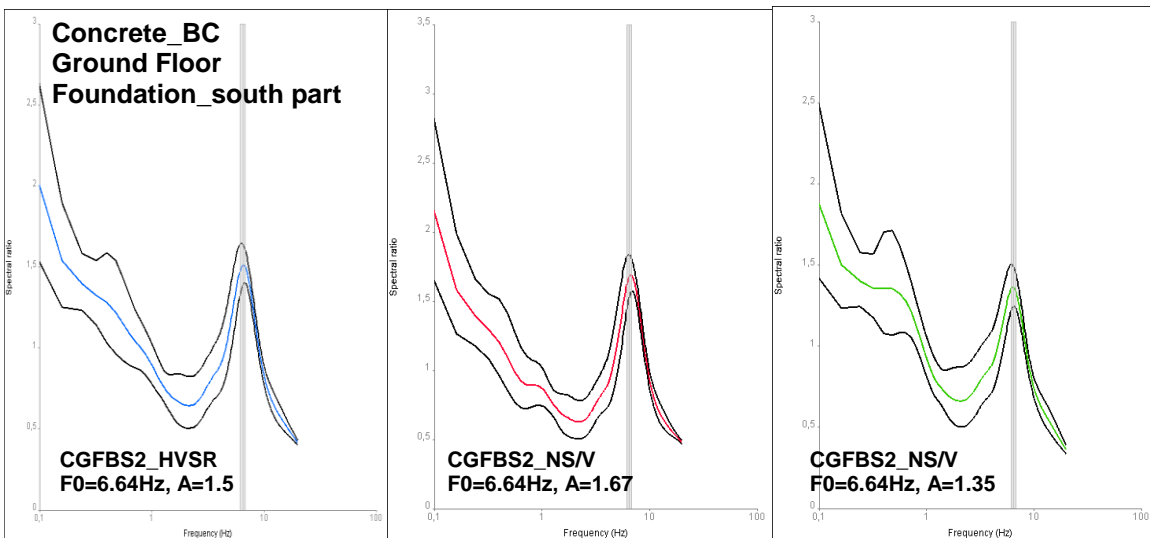
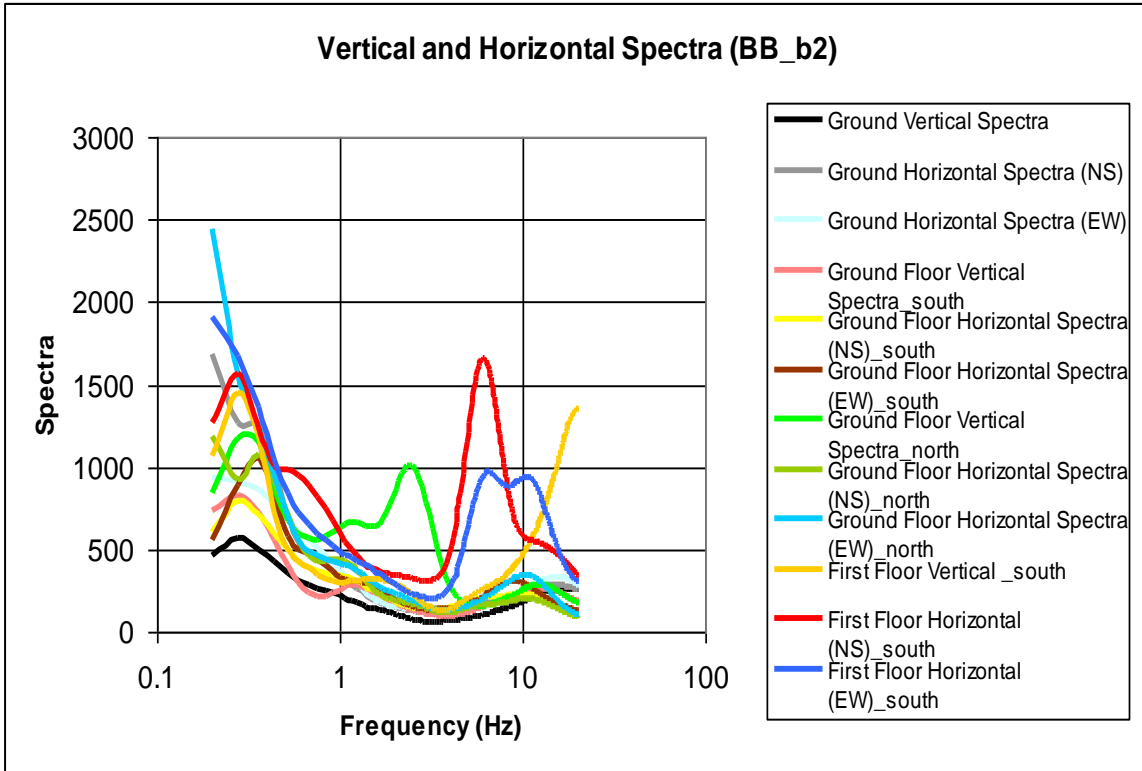
The HVSR soil-structure resonance respond of case study (b2) is presented in the following. HVSR ground seismic respond and the vertical and horizontal spectra at 5 m 10 m, 50 m far from the Elementary and High school are presented in the following Figures.

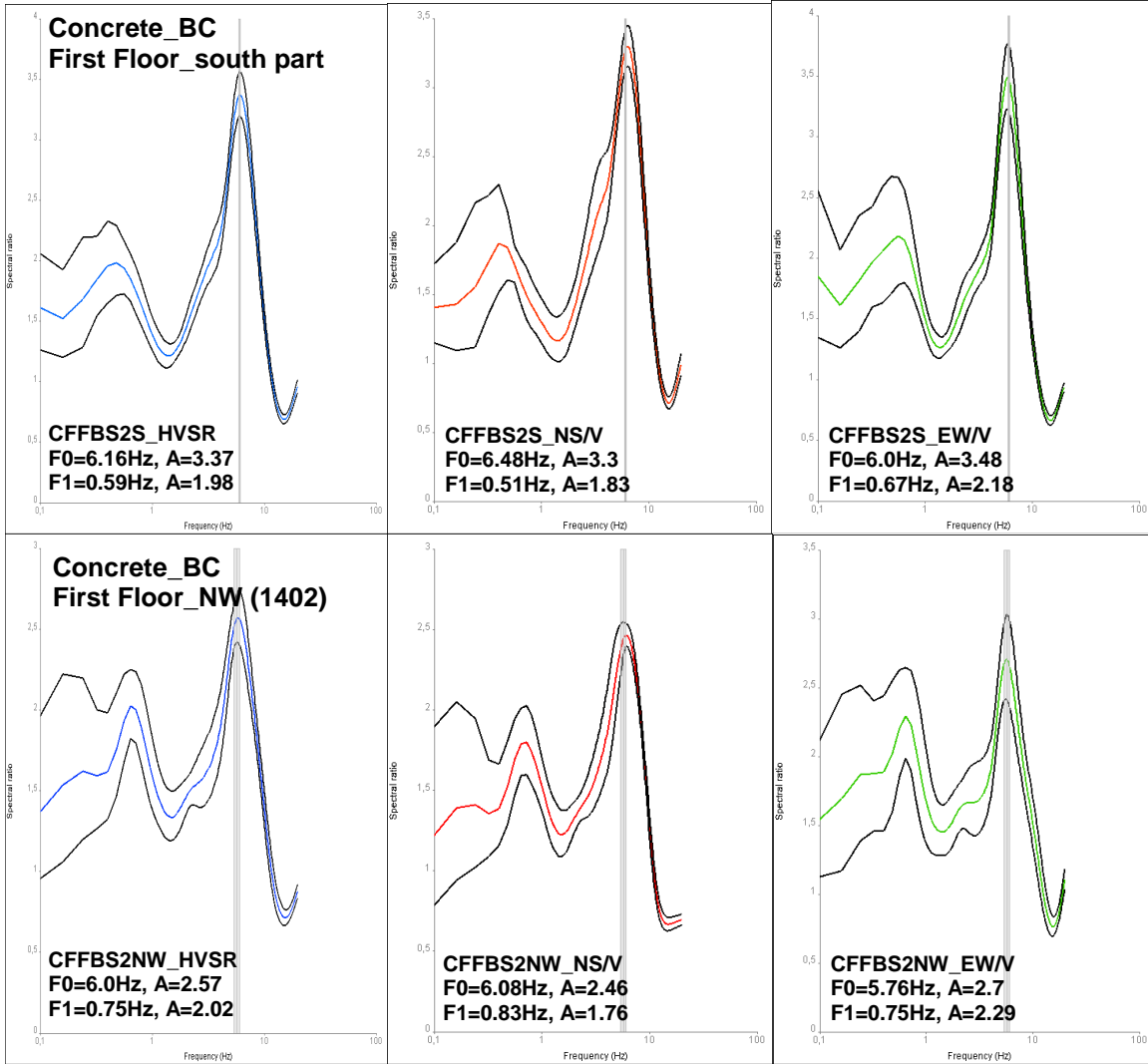














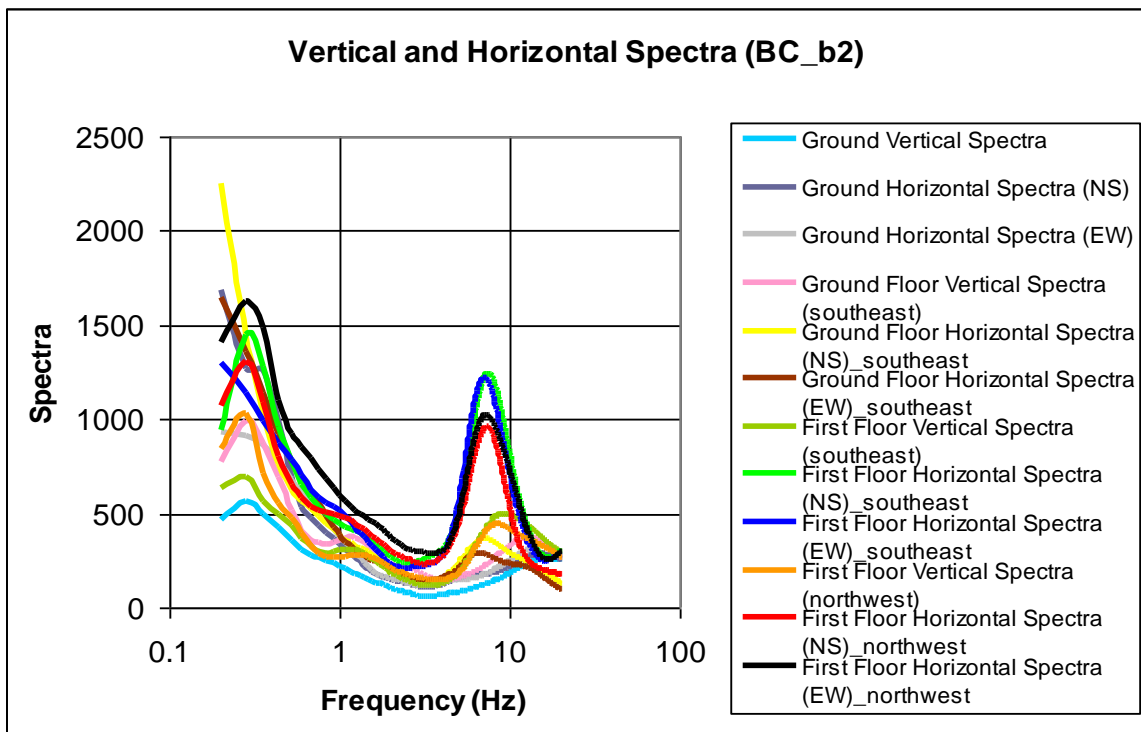
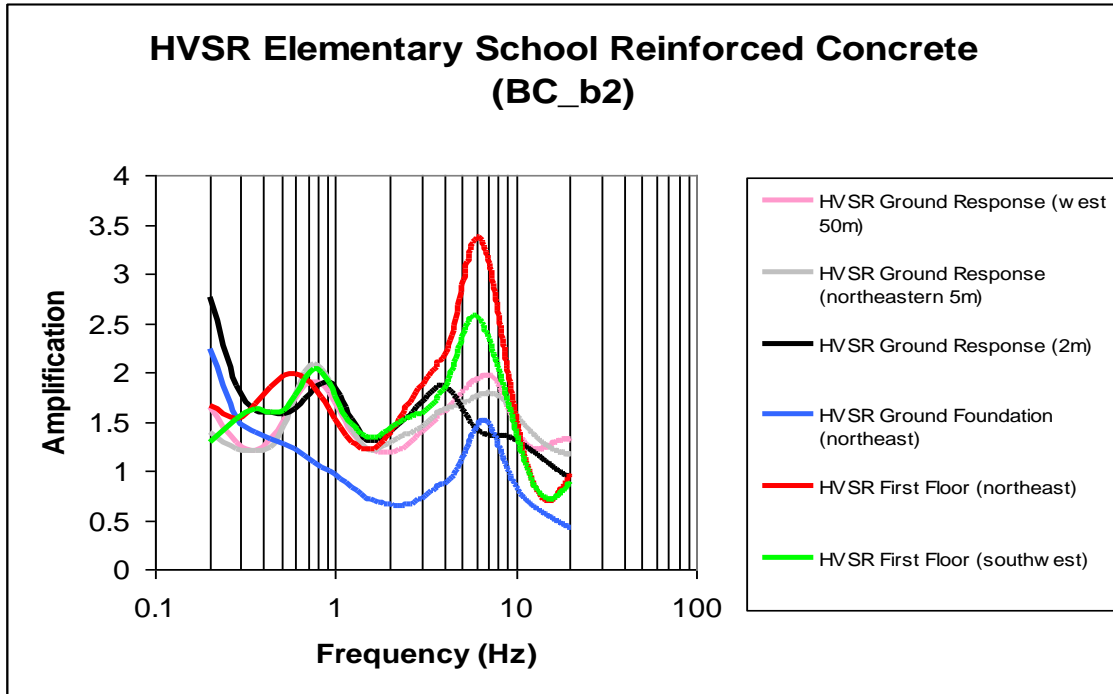


**Figure 4.3.14:** Building vulnerability estimation using HVSr and microtremors for the elementary and high school located northeastern of Paleohora in the centre of the basin (b2). The fundamental frequency of the first and fundamental frequency second floor of the masonry building is observed in the similar frequency range of the second floor amplified frequency of the ground freefield. The second amplified frequency of the first

*and second floor in the low frequency coincidence with the fundamental frequency of the ground freefield. The fundamental frequency of the ground floor foundation in the concrete building construction coincidence with ground freefield fundamental frequency located 50 m west of the concrete building while the second amplified frequency in the medium frequency range coincidence with the second amplified frequency located 5m northeast of the concrete building construction. High amplification ( $A=5$ ) is observed in the first floor in the medium frequency band that coincidence with the HVSR fundamental frequency of ground response (ground freefield) located 50 m west of the reinforced concrete building.*

Three case studies of ground-building resonance response study using HVSR and microtremors are presented. In all cases the building constructions are vibrating in the same fundamental frequency in both E-W and N-S direction. The fundamental frequency of the first and second floors is observed in the same frequency range of the HVSR fundamental or second amplified frequency of the ground freefield. Frequency ground-building coincidence is a preliminary indicator of building vulnerability. In all in-situ building microtremor recordings the N-S microtremor component corresponds to the longitudinal and E-W microtremor component corresponds to transverse direction of the building. The vertical and horizontal spectra components of the ground foundation, of the first and second floor are in coincidence. The spectra of the vertical and horizontal components are also presented. The possible coincidence of fundamental frequencies of building and the building soil foundation that induces resonance phenomena capable of compromising building's stability during earthquakes is the main outcome estimated with the spectra ratio of horizontal and vertical components. The arisen ground and building resonance phenomena at the vulnerable recorded points are capable for building failure in the case of strong seismic activity. In the following is presented the research outcomes of other's researcher's work for ground-building frequency resonance response identified from HVSR using microtremors.

The importance of building eigen-modes and soil frequency resonance is extensively investigated. The seismic building damage is mainly controlled by the effects of soil-structure interaction of massive/tall buildings and strong impedance contrast between surface and subsurface. This impedance contrast is the result of seismic wave trapping in soft surface layer (Bard & Wirgin, 1995). The consequences of these "site-city interaction" are the increase of motion intensities and the increased damage distribution in the nearby structures. Major damages in Santiago de Chile basin, after the Valparaiso earthquake 1985, were observed in small-sized abode houses, while many high rise structures (10-20 stories) behaved well with minor damages or non-structural features (Wyllie, 1986). In controversy, to other HVSR building vulnerability studies, in the area of the major damage in Santiago basin, the HVSR ground fundamental frequency is around 4-5Hz while the damaged small sized building natural frequency is higher than 5Hz. Gosar (2007) applied HVSR technique using microtremor measurements in six buildings (the N-S microtremor component corresponds to the longitudinal and E-W microtremor component corresponds to transverse direction of the building) located on terraces and on younger Quaternary gravels in Bovec basin that were damaged during 1998-2004 earthquakes and found

coincidence of ground and building fundamental frequency. At several buildings the ground HVSR fundamental frequency coincided with the HVSR longitudinal (N-S) and HVSR transverse (E-W) building fundamental frequency of each floors. The soil-structure resonance is the probable reason for very high damage after the 1998 and 2004 earthquakes. In heavily damaged buildings the ground fundamental frequency coincided with the buildings fundamental frequency. Gosar (2007) applied HVSR technique using microtremor measurements in six buildings located on terraces and on younger Quaternary gravels in Bovec basin. Four of six houses were moderate to heavily damaged after earthquakes and soil-structure resonance response was determined using HVSR technique. In the two slightly damaged houses soil-structure resonance phenomena are not observed using HVSR technique and microtremors. An example of a very highly damaged house after the 1998 earthquake in Bovec and HVSR soil-structure resonance (Gosar, 2007) is presented in the following. Ground fundamental frequency in Bovec-Mala (House 1) is observed at  $f_0=8\text{Hz}$  while the fundamental frequency in the N-S (longitudinal) and E-W (transverse) direction are observed at 8.7Hz and 7.6Hz respectively.

Gosar et al. (2009) used HVSR technique using microtremor recordings in the region of Ilirska Bistrica (south Slovenia). The HVSR fundamental frequency range lower than 10Hz are attributed to the extent of Pliocene clays and sand overlain by alluvium, while the HVSR fundamental frequency to the flysch rocks (Gosar et al., 2009). Gosar et al. (2009) observed soil-structure resonance effects using microtremors in buildings located in in the region of Ilirska Bistrica (south Slovenia). In that case study the main longitudinal and transverse HVSR frequencies (ranging between 3.8-8.8Hz) of microtremor recordings inside buildings at various stories coincided with the fundamental frequency range of Pliocene and Quaternary sediments (2-10Hz), (Gosar et al., 2009). Volant et al. (2002) used HVSR and microtremors in a reinforced concrete frame with masonry in-fills building composed of three different and independent blocks located on fracture rock site (limestone) (SE France) to study: 1) the seismic dynamic building behavior, 2) to identify the mode shape at the high roof and 3) to study the behaviour of the joints between independent blocks.

Microtremor performed on the high roof (15sec) and at different levels of the building and on the ground to study possible resonance phenomena and good coincidence between the HVSR fundamental frequency of the high roof and the HVSR of the ground foundation of the building (4 and 6.5Hz) in the NS direction. Moreover, the mode shapes (modal nodes) of the main column vibrate in the same frequencies (4 and 6.5Hz). Volant et al. (2002) concluded that there is strong interaction between the building and the cell and an influence of masonry in-fills under the low roof level. Volant (2002) concluded that the massive concrete cell and external walls with masonry in-fills strongly contribute to the dynamic response of the building. Volant (2002) used numerical simulations to improve the seismic behaviour of building observed with microtremor recordings. Gosar et al. (2001) found good correlation between the higher amplification ( $A=6$ ) and building damage at sites in the Upper Soca valley that occurred after the 12 April earthquake in the Krn mountains (Slovenia). The results of these studies show that HVSR technique can be used to determine soil-structure resonance phenomena and to predict possible structural damage in the case of an earthquake.

The validity of microtremor measurements in estimating building damage is extensively tested (Nakamura, 1989, 199; Gueguen et al., 2000; Gallipoli et al., 2004). The natural period of vibration of high level storey building (4-6 storey buildings) that were heavily damaged after the 1999 Dinar earthquake coincidence with the period of seismic wave vibration due to basin structure Yalcinkaya & Alptekin (2005).

#### **4.4.MICROSEISMICITY USING A NEW PERMANENT SEISMOLOGICAL NETWORK INSTALLED IN THE WHOLE TERRITORY OF CRETE AND A TEMPORAL LOCAL SEISMOLOGICAL NETWORK OF PALEOHORA**

##### **4.4.1 MICROSEISMICITY OF NORTHWESTERN AND SOUTHWESTERN CRETE USING A NEW PERMANENT SEISMOLOGICAL NETWORK INSTALLED IN THE WHOLE TERRITORY OF CRETE**

The purpose of seismicity study is the accurate determination of spatial and temporal earthquake occurrence. The precise delineation of the active fracture zones is one of most important tasks in practical seismology. The contribution of seismogenic faults is of paramount importance in earthquake hazards estimation of Crete (Papazachos et al., 2000b). Seismicity study is focused to the delineation of active seismogenic zones in northwestern and southwestern Crete using seismological data extracted from a new seismic network of seven permanent seismological stations (Appendix II, Table 4.5) and Appendix III) installed in the whole territory of Crete comprised of short-period and one long-period seismological stations.. Microseismicity study is mainly focused in Paleohora regime located in southwestern Crete in one of the most active region of Crete and of Europe (Papazachos et al., 2000a). The innovation of this seismicity study is the delineation of new seismic active faults in northwestern and southwestern Crete. In addition, a temporal seismological station comprised of three short-period stations is installed in Paleohora to record the local seismic activity. The lack of reliable 3D structural model, and the difficulties arisen in the seismometer calibration for accurate amplitude determination is considered for magnitude and depth determination of Crete. Moreover, the lack of an accurate 3D velocity model considering also the strong lateral heterogeneities of Crete, especially of the western part of Crete is also considered in the epicentre localization.

Two earthquake datasets are studied:

1. Microseismicity of northwestern and southwestern Crete from the permanent network installed on Crete.
2. Microseismicity of southwestern Crete using the short-period temporary network comprised of three stations.

Epicentre distribution using data from local network is derived from at least three stations installed on Crete using both six phases (three P and three S phases). The importance of accurate P and S wave picking using full P and S weighting, in the determination of the earthquake distribution is highlighted. RMS and ERH values for the earthquake epicenter distribution using the local permanent seismological network present varying values. To reduce the ERH, several re-examination of P and S values

with varying weight from (0-4) are performed. In many cases the reduction of ERH value inserts mislocation in the earthquake epicentral location.

The outcome of this re-examination is:

- i. The importance of both P and S phase using full P and S weighting from at least three stations in determining earthquake epicenter location.
- ii. High ERH value is not always an indicator of the epicenter mislocation, as also proposed by Papazachos et al. (2000b).

Spatio-temporal microseismicity on Crete for the examined time period delineates a large scale N-S fault crosscutting western Crete, near Falasarna. Moreover, microseismicity delineates an earthquake clustering in northcentral Crete that might correspond to a fault zone. Further microseismicity studies or geophysical techniques are necessary to verify the existence of that speculated fault zone. Microseismicity study in northwestern and southwestern Crete enriches the earthquakes database.

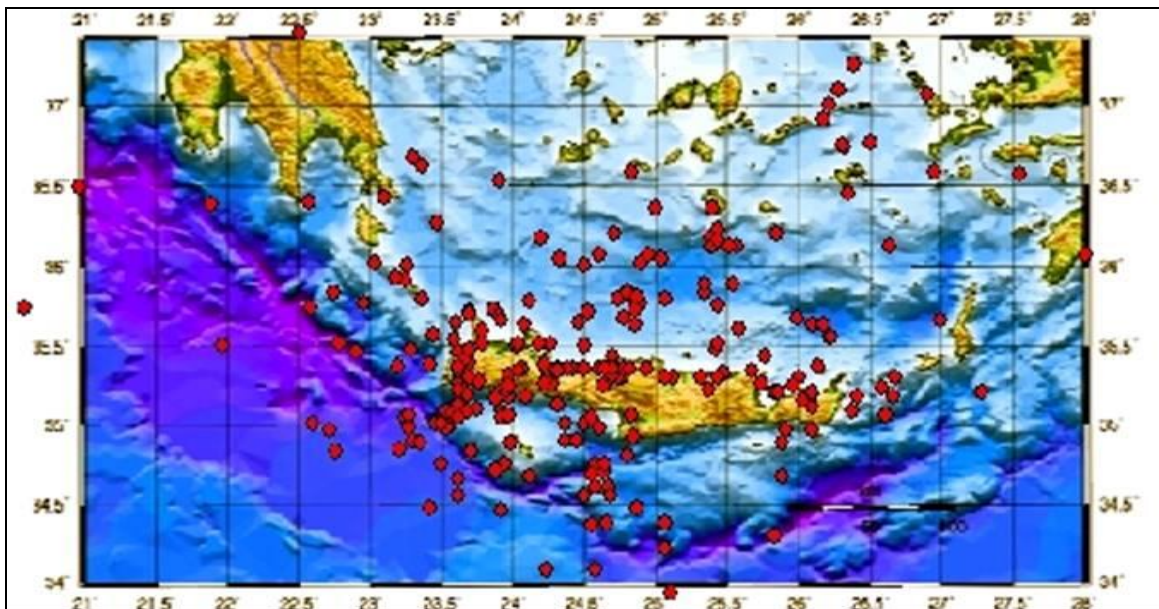


**Figure 4.3.15:** Microseismicity of Crete during the period of 01/07/07 to 31/08/2007. The red cycles represent the earthquake epicenter using the local network of Crete. The list of seismological stations is presented in the Appendix II (Tables 4.5 and 4.7). Samples of microearthquake recordings are presented in the Appendix IV.

#### 4.4.2 MICROSEISMICITY OF SOUTHWESTERN CRETE USING TEMPORAL LOCAL SEISMOLOGICAL NETWORK OF PALEOHORA

To investigate the local spatio-temporal clustering microseismicity and to detect active seismic zones, of Paleohora located in the southwestern Crete, a local network of three temporal short period seismological stations is installed. The purpose of the small network is to detect zones of seismic activity within seismogenic structures in the outer-arc, after the 27 April of 2007 earthquake of magnitude  $M_L=4.0$  (UTC time: 18:19:07.04, 35.24N, 21.19E) in southwestern Crete. The small aperture of the network close to the outer-arc and the proximity of the network to the investigated seismic zones of Paleohora enhance the mapping of the cluster activity with higher accuracy and with a lower detection threshold. The temporal seismological network comprised of three short period seismological stations operated for 45 days and records nearly constant interval repeating earthquake events with similar waveform and almost identical amplitude and duration. The recorded earthquake events are processed manually by picking both P and S arrival time using Hypo 71 location software (Lee & Lahr, 1972). Earthquake datasets based on the RMS and ERZ values are categorized into three datasets:

- i) RMS <1 and ERH < 1km
- ii) RMS <1 and ERH > 1km
- iii) RMS and ERH not calculated/detected.

After 27<sup>th</sup> April 2007 earthquake in the southwestern Crete two distinguished microearthquake clusters are extracted from the epicenter location of microearthquakes recorded from a three short-period local seismological station network in Paleohora operating for 45 days (Figure 4.3.16). One distinct cluster comprises sparse earthquake located in the subduction zone. The second cluster that comprises the majority of microearthquakes, trenches from Gramenno to Lissos basin and extending at about 40 km west from Paleohora to 6 km east of Paleohora near Lissos basin. The  $V_p/V_s$  value using travel time P and S arrivals for the recorded dataset using Wadati-Benioff plots is calculated equal to 1.99 and the Poisson ratio is calculated to  $\sigma=0.333$  (the reader is referred to Chapter 3, Sections 3.3 and subsection 3.3.1 for the description of the methodology). Microearthquake clustering delineates a fault zone or a system of faults zones in the coastline of Paleohora in southwestern Crete.

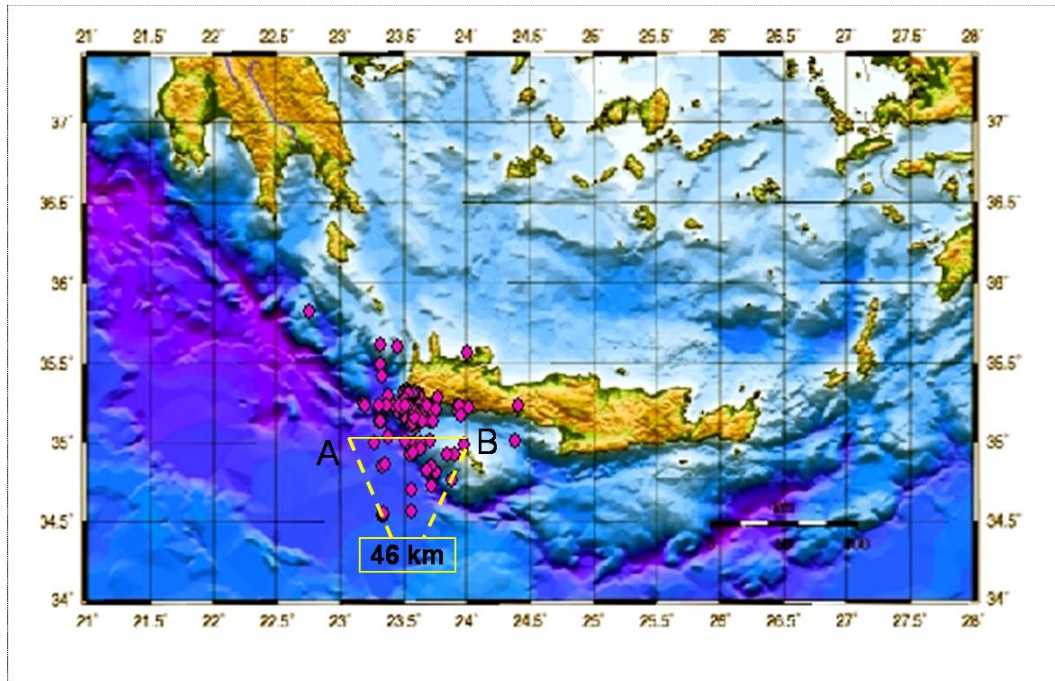


**Figure 4.3.16:** *Microseismicity of Crete recorded from the temporal seismological network of Paleohora. The red cycles represent the earthquake epicenter using the local network of Crete. The list of seismological stations is presented in the Appendix II (Tables 4.6 and 4.8). Samples of microearthquake recordings are presented in the Appendix V.*

## **CHAPTER 5: DISCUSSION**

---

### **5.1 INTRODUCTION TO DISCUSSION**

The overall purpose of this thesis is to evaluate the effect of local site conditions (due to surficial geological features and complex subsurface structure) on seismic ground motion in the densely populated Kastelli-Kissamou and Paleohora basins of western Crete. As described in the introduction to this thesis (Chapter 1) western Crete was selected for study because of its close proximity to the Hellenic subduction zone which dips northwards beneath Crete. These two sub-areas were chosen for detailed analysis because Paleohora in the south is closer to the subducting slab than Kastelli in the north. Thus, an important aspect of this work is to assess the differences between the two areas in relation to the seismic ground response.

The previous chapters demonstrate a robust combined methodological approach involving the study of geology, geophysics, instrumental seismology and earthquake engineering geophysics disciplines. The data produced are used to locate possible seismic faults (that may be active) and to evaluate ground seismic response due to site effects of the investigated areas. Moreover, three examples of building vulnerability estimation provide evidence of the applicability of microtremors to study the site-structure interaction and make preliminary estimation about the likely damage caused during an earthquake event.

The parameters that enhance the importance of seismic hazards assessment in Paleohora and Kastelli basins are:

- 1) the highly populated environment located in a highly seismic environment near the subduction zone; (discussed in Chapter 2, Section 2.2)
- 2) the proximity of active faults; (presented in Chapter 4, Sections 4.2, 4.3 and 4.4) and discussed in the following Section 5.2
- 3) the dynamic properties of the uppermost sedimentary deposits and the geometry of the basins' structure that can strongly amplify earthquake ground motion (presented in Chapter 4, Section 4.3) and discussed in Section 5.3.

Thus the investigated areas can be characterized as an ideal natural laboratory to address the effect of subsurface structure in seismic ground motion.

The combined methodologies of ground truthed geological survey, electrical resistivity tomography (ERT), Horizontal-Vertical Spectral Ratio (HVSr) using microtremor measurement, and the seismicity methods applied, described in detail in Chapter 3, have created a wealth of data presented in Chapter 4.

The reader is reminded here the uses of the four methods:

1. The purpose of the geological survey is to reveal the complex tectonic structure and fault localization of the investigated sites based on surface ground-truthed observations. Moreover, the geological ground truthed observations are used as indicators to verify the results extracted from the applied geotechnical techniques.
2. The purpose of ERT is threefold: 1) to reveal faults not previously recognized that may be active during earthquakes and significantly contribute in the seismic hazard of the studied areas; 2) to try to identify faults that may be active during earthquakes; and 3) to model the surface and subsurface variations in depth-



used also as a correlation of the research outcomes produced from site effects study.

3. The purpose of the HVSR method is: 1) to delineate faults that may be active during earthquakes; 2) (as for ERT) to reveal faults not previously recognised that may be active during earthquakes but may significantly contribute to the seismic hazard of the studied areas; and 3) to assess the effects of local ground response on seismic ground motion. Microzonation study is focused in Kastelli and Paleohora urban areas.
4. The purpose of microseismicity study using earthquake data (recorded from the regional seismological station on Crete and the local seismological station in Paleohora territory) is to: a) determine earthquake clustering that may correspond to active zones and b) estimate local  $V_p/V_s$  value using travel time P and S arrivals. The high value of  $V_p/V_s$  is an indicator of strong heterogeneities of the subsurface of southwestern Crete near the subduction zone.

The basic concept of combining the above proxies is to compare and verify the research outcomes of each proxy and to eliminate any arisen uncertainties of the results. It is emphasized that the study of the multi-proxy approach for surface and subsurface determination that posses an important role in site effects and future earthquake hazard methods is mainly focused in the populated area of the studied basins. All the applied proxies are interrelated in discussion of the data. ERT profiles were also conducted in proximity of Spatha peninsula in northwestern Crete (Kastelli-Kissamou area) and Grammeno peninsula in southwestern Crete (Paleohora area), respectively. The purpose of applying ERT in those former peninsulas is to determine an overall view of the tectonic environment of the investigated half-graben basins. A major outcome is that faults recognized using geophysical (ERT) and earthquake engineering geophysics (HVSR) methods are ground-truthed by geological field survey and data extracted from geological and satellite image maps. Thus, there is great confidence in the techniques for locating faults that may be active in seismic response studies.

The following critical questions need to be addressed in order to relate the aims and data together:

1. How successful is the combined approach of field geological investigation and geophysical methods for the identification of faults that may be active during earthquakes? This research question is addressed in section 5.2.
2. Do the HVSR using microtremors techniques satisfactorily characterize the local seismic ground motions which may cause damage in earthquakes? What is the extent of the efficiency of these methods to provide evidence appropriate or useful for the Greek Euro code (EC8)? This research question is addressed in sections 5.3 and 5.4
3. What are the tectonic differences in seismic ground response between the two study areas? This research question is addressed in section 5.5.

The following sections of this discussion Chapter: a) address these three principal questions b) provides verification of the validity of the research outcomes through comparisons with other case studies and c) address the main points of the research,

leading to conclusions, in Chapter 6, about the overall effectiveness of this work in assessing seismic ground response.

## **5.2 Direct interrelation of the combined multi-proxy methodology, and justification of the combined methodologies in fault determination in Kastelli-Kissamou and Paleohora half-graben basins**

In the following is presenting a summary to remind the reader the research outcomes of the multi-proxy approach in fault determination.

Compatibility of the research outcomes of fault identification in the dense populated areas of Paleohora and Kastelli extracted from geological field survey ERT, HVSR using microtremors and microseismicity is observed. Specifically, geological ground-truthed investigations in Kastelli-Kissamou and Paleohora half-graben basin verify the validity of the research outcome of the electrical resistivity tomography, the HVSR using microtremors and the microseismicity surveys in fault determination.

ERT profiles were conducted at several sites in the populated regime of Kastelli-Kissamou and Paleohora half-graben basins, described and interpreted in Chapter 4 (section 4.2) to reveal fault zones that might be active. Specifically, eight ERT profiles at eight selected sites were conducted at several sites in Kastelli-Kissamou while nine shallow and deep ERT profiles were conducted at six selected sites Paleohora half-graben basin located in southwestern Crete. The reader is referred to Chapter 4 (section 4.2) for the description and interpretation of the data.

Microtremor measurements were conducted across only densely populated sites in Kastelli and Paleohora half-graben basins. In the case of Kastelli and Paleohora the HVSR ground frequency that attributes the rupture velocities due to faulting is observed in the medium frequency band and in the high frequency band. The sites that attribute to faults or rupture zones in Kastelli and Paleohora half-graben basins are characterized by: i) one clear HVSR fundamental frequency in the medium frequency zone and ii) two amplified frequencies with the first (fundamental) or the second amplified either in the medium or in the high frequency range. The reader is referred to Chapter 4 (paragraphs 4.3.1, 4.3.2 and 4.3.3) for the description of HVSR seismic ground response classification.

Similarities in the fundamental frequency and the shape of the spectra ratio of microtremor recordings at several sites in this area were observed. The observed similarities in HVSR fundamental frequency and HVSR spectra ratio shape using microtremor recordings delineate fault zones crosscutting the dense populated area.

In Kastelli-Kissamou and Paleohora half-graben basins seismic ground zoning based on HVSR technique using microtremor recordings delineates a fairly to very complex fault zone system crosscutting the dense populated area (Figs. 4.3.2 and 4.3.4). Five and four fault zones are respectively identified using HVSR technique in the two case study half-graben basins. The reader is referred to Chapter 4 for the description and interpretation of the data. The complexity of the data are described and interpreted in Chapter 4. The fault zone delineation based on HVSR technique in Kastelli is verified from the geological ground-truthed field and electrical tomography surveys and from data from satellite image maps. Geological, ERT, microtremor and microseismicity data given in Chapter 4 are discussed below in relation to identification of fault zones. In sections 5.2.1 and 5.2.2 are briefly presented the synthesis of the data

highlighting the main results of fault determination in the two case studies. Comparison of the research outcomes with other case studies is also presented for each approach.

### **5.2.1 The synthesis of the combined multi-proxy approach of geology, HVSR using microtremors, electrical resistivity tomography and microseismicity studies in determining active faults in Kastelli-Kissamou and Paleohora half-graben basins**

The importance of combining the four proxies for fault determination is the verification of validity of the of the research outcomes of the multi-proxy approach. The research outcomes for fault determination of each approach are cross-correlated to verify all the produced results. All geotechnical methods (HVSR, ERT, seismology) are used to reveal suspected fault not directly observable at the earth's surface while the geological survey justifies the fault activity not directly determined by HVSR and ERT methods. The multi-proxy approach is mainly focused in the populated area of the studied half-graben basins since fault determination and site effects (local site conditions; surface and subsurface estimation) possess an important role.

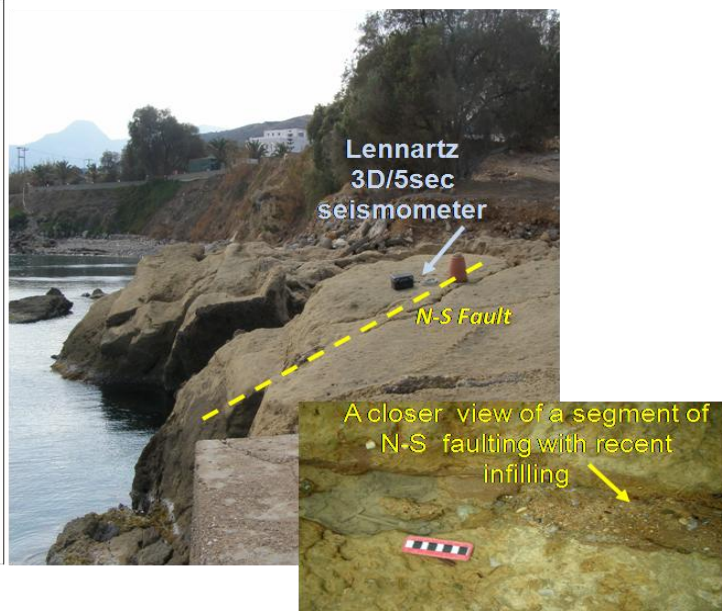
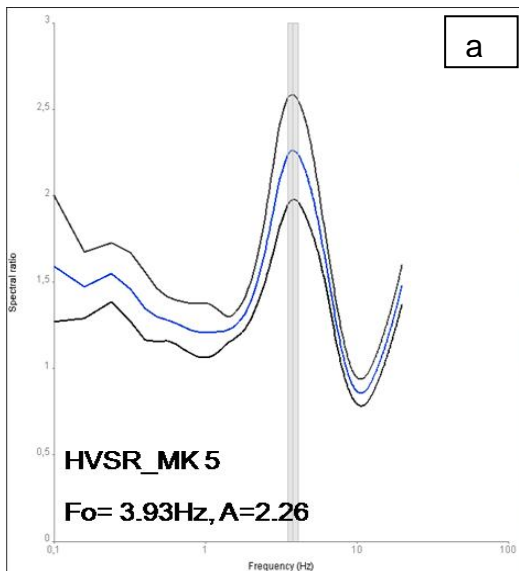
#### **a) The synthesis of the combined multi-proxy approach of geology, HVSR using microtremors, electrical resistivity tomography and microseismicity studies in determining active faults in Kastelli-Kissamou half-graben basin.**

Geological ground field survey in the densely populated area of the northwestern coastal locations of Kastelli Kissamou basin reveals a multi-fractured well-lithified limestone site. Specifically, a series of 12-15 N-S striking faults cutting the beachrock and subsidiary faults striking almost NNW-SSE, (resulting as an erosion process), located on a well-lithified limestone site are identified. The recent lateral trends fault (Chapter 4, Fig. 4.1.4) justifies the activity of the faulting coastal of northwestern Kastelli.

HVSR using microtremors conducted on the above fractured well-lithified limestone site coastal of northwestern Kastelli. The research outcome of microzonation study conducted in the fracture well-lithified limestone site without the effect of alluvial fan deposits is that the one HVSR amplified frequency in the medium frequency ( $F_0=2.98-3.98\text{Hz}$ ) correlate with the opening of the fault. The low HVSR ground amplification level ( $A=1.66-2.26$ ) in Kastelli and Roka correlates with the well-lithified limestone structure. The higher HVSR amplification ( $A=2.5$ ) is observed along the opened with recent sedimentary (alluvial fan) infilling N-S fault, whose recent lateral trends (based on geological survey, (Chapter 4, Fig. 4.1.4) which justified fault activity. The higher HVSR ground amplification ( $A=2.26$ ) is associated to the recent alluvial fan fault infilling. The sites where lower amplification ( $A=1.66$ ) is observed are characterized of 'closed' faulting (MK8, Fig. 4.3.1, Appendix II, Table 4.3) without the effect of alluvial fan infilling. It is highlighted that the overall area coastal of northwestern Kastelli is characterized of a well-lithified limestone site without the effect of the alluvial fan deposits. In the following figures is presented the fractured well-lithified limestone site coastal of northwestern Kastelli and an example of HVSR conducted on an opened with recent infilling alluvial fan N-S fault segment (Fig. 5.3a) and along a subsidiary fault (Fig. 5.3b). The reader is needed to refer to Chapter 4 Section 4.3, (Figs. 4.3.1 (MK5-MK7 and MK8) and Section 4.1.3 (Fig. 4.1.4).

Moreover, HVSR and microtremors (sites MKR1, MKR2) was conducted in Roka village (approximately 20 km southeast of Kastelli and 300 m from Kera fault) located on a fractured well-lithified limestone site. The HVSR spectra ratio presents one clear peak in the medium frequencies 2.0Hz and 3.5Hz. The low HVSR ground amplification level (1.51-1.8) in Roka correlates with the fracture well-lithified limestone structure. The fractures of that site are closed.

It is emphasized that in Kastelli Kissamou there is no other site effect study presented for comparison of the aforementioned results. The only literature review for the applicability of HVSR using microtremors on a fracture well-lithified structure is proposed by Volant et al. (2002). Similar to the result proposed in Kastelli Kissamou basin (NW Crete) for the validity of HVSR ground fundamental frequencies in the medium frequencies in the case of a fracture well-lithified site is proposed by Volant (2002) for seismic evaluation of nuclear facility (SE France). Volant et al. (2002) applied HVSR using microtremors on a fractured rock (Cretaceous limestone) site a few kilometers from a main active fault (southeastern Durance Fault) that is also composed of two sub parallel faults. HVSR present fluctuations but the shape of the HVSR curves is similar in the lower frequencies. HVSR fundamental frequency is observed at 1.5-2.0Hz on fractured rock (Cretaceous limestone) site few kilometers far from the main fault. Volant's et al (2002) work therefore shows how this method is successfully applicable in other areas, and provides confidence in the interpretations in this study.



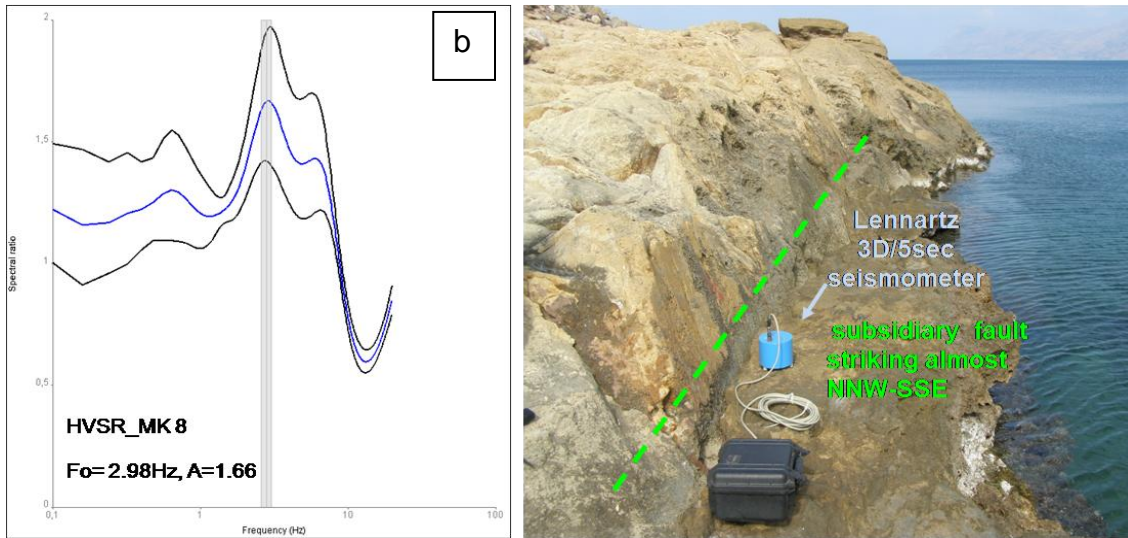


**Figure 5.1:** a) One HVSR clear peak in the medium frequency ( $F_0=3.93\text{Hz}$ ,  $A=2.66$ ) on an opened with recent infilling alluvial fan N-S fault segment located on a well-lithified limestone structure. The yellow dashed line represents the N-S fault, b) One HVSR clear peak in the medium frequency ( $F_0=2.98\text{Hz}$ ,  $A=1.66$ ) along a subsidiary fault coastal of northwestern Kastelli characterized of a well-lithified limestone structure. The green dashed line represents the subsidiary fault. In both sites microtremors are collected using Cityshark II connected with Lennartz 3D/5sec seismometer oriented to north.

Microtremor measurements were conducted across only densely populated sites in Kastelli half-graben basin. Similarities in the HVSR fundamental frequency and the shape of the spectra ratio using microtremor recordings at several sites were observed. The observed similarities delineate fault zones crosscutting the dense populated area of Kastelli-Kissamou half-graben basin.

In Kastelli it is proposed that an HVSR curve of two amplified frequencies with the fundamental frequency (the higher amplified frequency) either in the medium or in the high frequencies is also an indicator of subsurface lateral heterogeneities induced by the effect of fault zone. In Kastelli-Kissamou half-graben basin the second amplified frequency, either in the medium (1.51-2.0Hz and 3.5-4.5Hz) or high frequencies (7-12Hz) respectively indicate the effect of lateral heterogeneities induced by fault zones. The fundamental frequency in the high frequency range ( $F_0=7-12\text{Hz}$ ) is associated with the very shallow structure. The high frequencies correspond to the lateral heterogeneities induced by the fault structure and the second amplified to the rest geological column. The second amplified frequency can range from low to high frequencies according to the thickness of the rest geological column (the reader is reminded to refer to the theoretical background of HVSR technique in Chapter 3. Moreover, comparison of this research outcome with other case studies is given in Section 5.3). The reader is referred to Sections 4.3.1 for interpretation of the produced HVSR data in fault delineation.

Similar results compared to the one observed in this thesis are obtained from Lombardo & Rigano (2007). Lombardo & Rigano (2007) used HVSR technique and

microtremors across the Tremestieri fault and an eruptive fracture and found amplification in two frequencies (1.5-2.0Hz) and (4.0-8.0Hz). Significant ground amplification is observed at sites located close to the fault at the frequency range 4.0-8.0Hz. Yellampalli et al. (2005) applied a technique integrating the oscillation and proposed that the natural oscillation frequency of a short and open fault is 7Hz while the natural oscillation frequency of a short fault is 2.3Hz.

The comparison of the research outcomes with the research study of Lombardo & Rigano (2007) using HVSR technique and microtremors along fault zones confirms the validity of the two HVSR amplified frequencies in fault determination. Moreover, the study presented by Yellampalli et al. (2005) applied a technique integrating the oscillation and justifies that the natural oscillation frequency of fault is modified from the characteristics of the opening of the fault. The research outcome of Yellampalli et al. (2005) is confirmed from the study in northwestern of Kastelli where the fundamental frequency along a fault zone with opening (of approximately 10 cm) of recent alluvial fan fault infilling is 3.93Hz while HVSR using microtremors along the subsidiary fault and along N-S faulting (without openings) presents fundamental frequency in lower frequencies ( $F_0=2.98\text{Hz}$ ). HVSR using microtremors southcentral of Kastelli half graben basin in an area crosscutted by a clear open N-S fault (2 m fault) presents the fundamental frequency in the high frequencies ( $F_0=7-12\text{Hz}$ ). This finding is in accordance with Yellampalli et al. (2005) using a technique integrating the oscillation proposed that the natural oscillation frequency of an opened fault is 7Hz. Moreover, Lombardo & Rigano (2007) found significant ground amplification at the frequency range 4.0-8.0Hz at sites located close to the Tremestieri fault. At sites located near the eastern master fault, between Weil and Lorrach, clear HVSR peak were observed in the medium frequency range between 3.5-8Hz (Roten et al., 2008).

For the Kastelli study it is proposed that: 1) the fault characteristics (openings, alluvial fan infillings) are patterned in HVSR technique using microtremors, 2) the shift of ground fundamental frequency from medium or higher frequencies of microtremors with distance perpendicular to a fault zone is capable to pattern the variation of lateral heterogeneities induced by fault zones. Moreover, the importance of HVSR using microtremors in the northwestern part of Kastelli located on a fractured well-lithified limestone site is threefold: a) the low amplification HVSR curves (i.e  $A=1.8-2.26$ ) is a valid estimator of site effects characterization, b) HVSR using microtremors is a valid technique to determine faulting and c) HVSR using microtremors is a valid technique to determine fault zones on a well-lithified structure located at coastal sites. The cross-correlation of the extracted HVSR results (Fig. 5.2b) with the geological results (Fig. 5.2a) for fault zones determination justifies the proposed result. This study suggests to broaden the criteria of J-Sesame guidelines. According to J-Sesame guidelines (2005), it is suggested to avoid recording along coastal areas because frequencies around 0.5 Hz are emitted between the interaction of sea waves and coasts that may influence HVSR spectra.

In conclusion the HVSR ground frequency that attributes the rupture velocities due to faulting is observed in the medium frequency band and in the high frequency band and delineates five fault zones; the reader is referred to Chapter 4 paragraph 4.3.1. The validity of research outcome of fault delineation using HVSR technique is

shown by ground-truthed geological field survey, ERT survey and from geological data extracted from satellite image maps.

Four of eight electrical resistivity tomography profiles were conducted in the populated area of Kastelli and reveal four striking NNW-SSE (P5 presented in Figure 4.2.6 and P6 presented in Figure 4.2.8), and almost NNE-SSW (P7 presented in Figure 4.2.10, and P8 presented in Figure 4.2.12) fault. In Kastelli profiles P5 and P8 reveal a very clear faulting and also a decrease in resistivity at depth that is likely related to an increase in water content of the sediments as interpreted in Chapter 4. Similar observations of a decrease of resistivity in depth that delineates fault zones is observed from Fazzito et al. (2009). Nguyen et al. (2005) proposed that the transition zone from low resistive to high resistive zone indicates fault zone in the lower Rhine system (Germany). In Kastelli profiles P2-P4 and P6, P7 reveal a clear Quaternary fault. Quaternary active faults have been also revealed using 2D ERT survey by; Störz et al., 2000 ; Suzuki et al., 2000; Demanet et al., 2001; Caputo et al., 2003 ; Caputo et al., 2007; Wise et al., 2003; Nguyen et al., 2007).

The aforementioned faults identified from ERT survey are the possible extension of existing faults derived from: 1) new ground truthed geological survey conducted in the frame of this thesis and 2) geological map (Karageorgiou, 1968) and satellite image map are presented in Chapter 4 in Figure 4.2.16. The possible extension of ERT profiles P5-P8 for Kastelli half-graben basins are extensively presented and interpreted in Chapter 4. The reader is referred to Chapter 4, Section 4.2.

In the following is presented a simple graph of the interrelation of the multi-proxy approach adopted for fault determination in the populated Kastelli-Kissamou half-graben basin. The research outcomes of multi-proxy are cross-correlated. All the aforementioned research outcomes of the multi-proxy approach adopted for fault determination in Kastelli-Kissamou half-graben basin are presented in Figure 5.2.

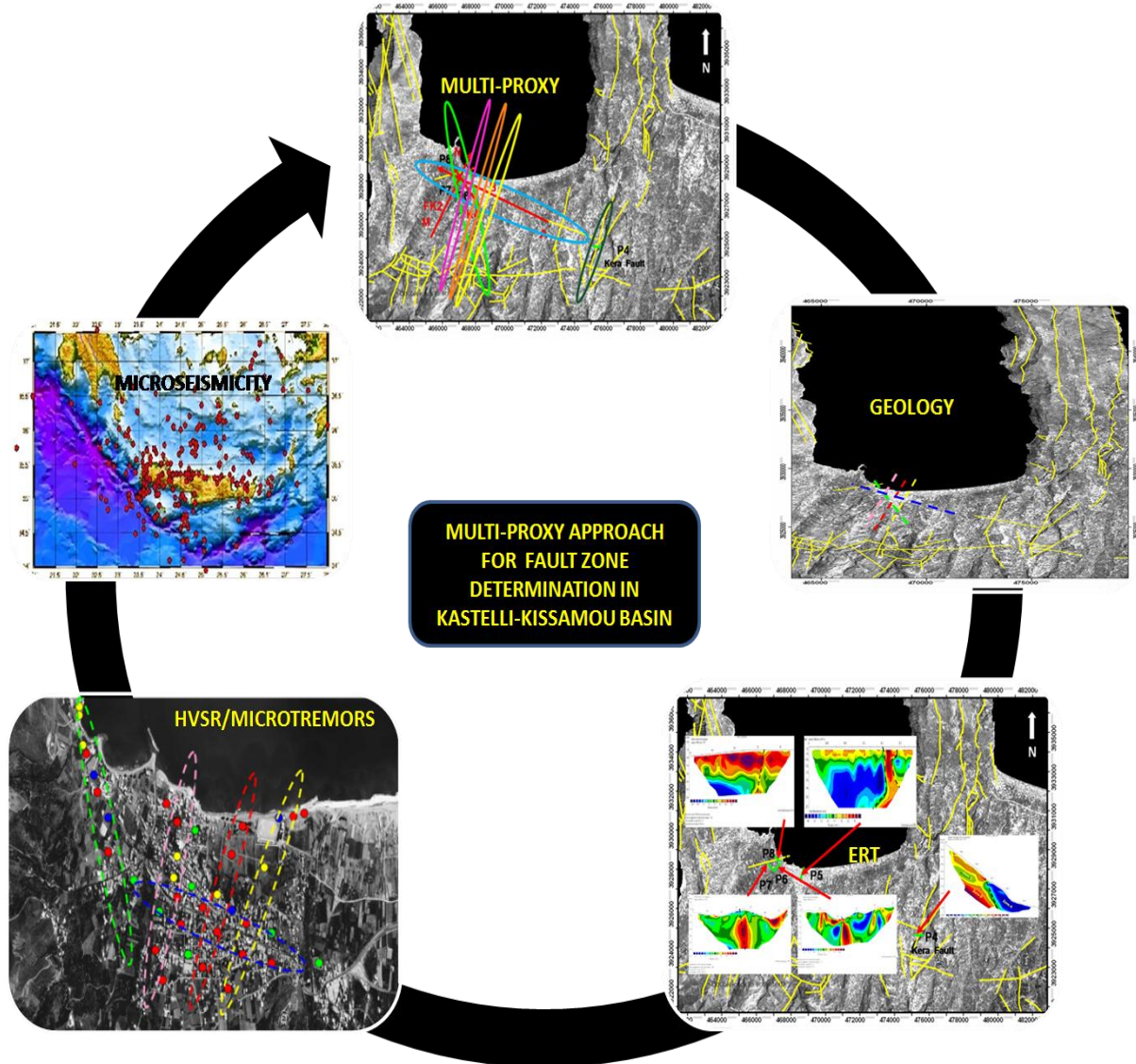


**Figure 5.2:** A synthesis of the combined multi-proxy approach of geological ground truthed field survey, electrical resistivity tomography, HVSR using microtremors and microseismicity recorded from the permanent seismological network of Crete for fault delineation in Kastelli-Kissamou basin. All recorded data are described and interpreted in Chapter 4. Geological investigation and HVSR using microtremors revealed five fault zones. ERT revealed four fault zones and microseismicity recorded from the permanent network verified the moderate seismic activity of northwestern Crete recorded for the time period of two months.

**b) New combined multi-proxy approach of geology, HVSR using microtremors, electrical resistivity tomography and microseismicity studies in determining active faults in Paleohora half-graben basin.**

Geological ground field survey in the densely populated area of Paleohora regime reveals a complex tectonic setting characterized mainly by NNE-SSW-striking left-



oblique extensional faults, traced for several kilometres inland (Figure 5.2). The faults segment the E-W coastline which is itself bounded by a continuous E-W normal fault crosscutting Paleohora and Grammeno peninsulas. This E-W fault zone which is one of a series of E-W faults that occur at intervals up to several kilometres inland. A second major outcome is that Pahia Ammos (located eastern of Paleohora half-graben basin) and Grammeno produce similar geo-tectonic subsurface characteristics that possess the assumption that Grammeno peninsula is a miniature of Paleohora. The two peninsulas are assumed to be associated with a system of fault zones or to a large scale fault. The reader is referred to Chapter 4 and paragraph 4.2.5 for a detailed description of the geological survey. Northeastern of Paleohora basin a recent pottery bearing, located on a segment of an echelon fault and dating in the Roman Era is an indicator of the recent fault activity.

In Paleohora territory six shallow and deep electrical resistivity tomography (ERT) profiles (P1, P2, and P3) conducted at three selected sites and revealed clear faulting. ERT conducted northeastern of Paleohora (P1) at the site where the pottery bearing was found and in agreement with the geological survey ERT verified a clear faulting. The extracted ERT profiles in Pahia Ammos (P2) and Grammeno (P3) reveal similar geo-tectonic subsurface setting of the two peninsulas that in agreement with the geological survey possess the assumption that Grammeno peninsula is a miniature of Paleohora. The proposed substructure model for the investigated area in Pahia Ammos, Grammeno and surrounding area (Fig 4.2.26) suggest that the area that covers the coastline of Paleohora and Grammeno can be associated with a fault zone or to a large scale fault striking E-W from Grammeno to Paleohora. The reader is referred to Chapter 4 for the description and interpretation of the identified tectonic structure.

The resistivity discontinuity in the subsurface forms the fault scarp dipping to north in both peninsulas. In the northern part of the peninsulas a high resistivity is defined at a depth of 10 m and likely it correspond to Lissos beds (Late Serravallian) or Palaeozoic rocks that also outcrop in the area. In the southern part of the two profiles a low resistive zone is identified that is consistent with the Quaternary alluvial fan deposits. These faults are interpreted as extensional considering that the exposures of Paleozoic rocks in the southern part indicate that the hanging wall of the rocks is down thrown and that is opposite to the reverse movement of the Quaternary sediments along the fault scarp. Moreover, the low resistivity value along the fault might suggest high permeability.

Similar considerations suggested for the tectonic setting of Grammeno and Pahia Ammos (Fig.4.2.26) have been proposed by Fazzito et al. (2009) for faults Precordillera in western Argentina using 2D electrical resistivity tomography (ERT). In this case study the identified resistivity discontinuity is consistent with a west-dipping high angle fault where the high resistivity zone is related to exposures of Paleozoic rocks and the low resistivity zone with Quaternary alluvial fans. The investigated fault of that area is considered as extensional fault based on: 1) exposures of Paleozoic rocks in the west part indicates that the hanging western block is down thrown and 2) to opposite to the reverse movement of the Quaternary sediments along the fault scarp. Fazzito et al. (2009) suggested the low resistivity value along to another fault indicate high permeability in that area. The shallow profile in Pahia Ammos suggest fresh groundwater intrusion ( $15.6-55.8\Omega\text{hm}^*\text{m}$ ) below 25 m that discharged into the seawater

(0.34-4.4  $\Omega\text{m}\cdot\text{m}$ ). Personal communication with locals verifies the existence of the aforementioned discharge of the groundwater into the sea. It is speculated that the fault acts a barrier to water circulation. Fazzitto et al. (2009) observed significant presence of fresh groundwater indicating the near fault might act as a barrier to water circulation. Fresh groundwater resistivity of about 25 $\Omega\text{m}$  floating over the sea water (2 $\Omega\text{m}$ ) using 2D electrical resistivity tomography (ERT) in Salento (Italy) is also reported by Margiotta & Negri (2008). ERT profiles in Pahlia Ammos and Grammeno insert high RMS values due to the high large contrasts resistivity environment. Large RMS values have been reported by Martinez et al. (2009) and suggested that large RMS values are acceptable in large contrasts resistivity environments.

HVSR using microtremor recordings in the populated Paleohora half-graben basin delineates four fault zones that significantly contribute in the seismic hazards of the studied area. Similar to Kastelli basin microzonation study based on HVSR using microtremor recordings in Paleohora basin verifies that the HVSR ground frequency that attributes the rupture velocities due to fault is observed at: i) one clear HVSR fundamental frequency in the medium frequencies (1.50- 4.5Hz) and ii) two amplified frequencies with the fundamental either in the medium or in the high frequencies (7-12Hz), correlates with fault zones. The high frequencies correspond to the lateral heterogeneities induced by the fault structure and the second amplified to the rest geological column. The second amplified frequency can range from low to high frequencies according to the thickness of the rest geological column (comparison of this research outcome with other case studies is given in section 5.3). The reader is referred to Chapter 4 (Section 4.3) for the description of HVSR seismic ground response classification. Comparison of the research outcomes in Paleohora basin with Yellampalli et al. (2005) and Lombardo & Rigano (2007) verify the validity of HVSR using microtremors in fault determination (see section 5.2.1a, case study Kastelli). More comparison of the one clear amplified in the low and high frequencies and the two HVSR amplified frequencies observed in Paleohora case study with other case studies is presented in section 5.3. Four fault zones are identified using HVSR technique in Paleohora half-graben basin. The fault zone delineation based on HVSR technique in Paleohora is verified from the geological ground-truthed field and electrical tomography surveys and from data from satellite image maps.

HVSR technique revealed an E-W striking fault in Pahlia Ammos in agreement with geological and ERT survey. Moreover, HVSR in the archaeological site Fortezza revealed clear faulting in agreement with the geological survey that suggests the presence of a 120° fault that crosscuts the beachrock, while 3 to 4 system faults are existent. In contrast, ERT did not revealed any clear faulting because the profile was inadvertently placed parallel to the fault. However, ERT revealed planar discontinuity between the beach-gravels hydrogeneous surficial deposits and the bedrock, in agreement with ground-truthed surficial geological environment (Fig.4.2.27) composed of beachrock platforms. Geological survey in Fortezza verifies the existence of a fault and the validity of HVSR technique for fault determination. Fault delineation extracted from HVSR using microtremors is verified from geological ground truthed and ERT survey survey. The reader is referred to Chapter 4 for the description and interpretation of the data.

An example in Figure 5.3 of the combined approach of HVSR using microtremor recordings and ERT profile along Pahia Ammos verifies the effectiveness of the research outcomes in surface and subsurface modeling. Figure 5.4 presents the cross-correlation of HVSR and ERT survey in identifying fault zones. The aforementioned results of an almost E-W fault are verified from ground truthed survey along Paxia Ammos (Section 5.2b).

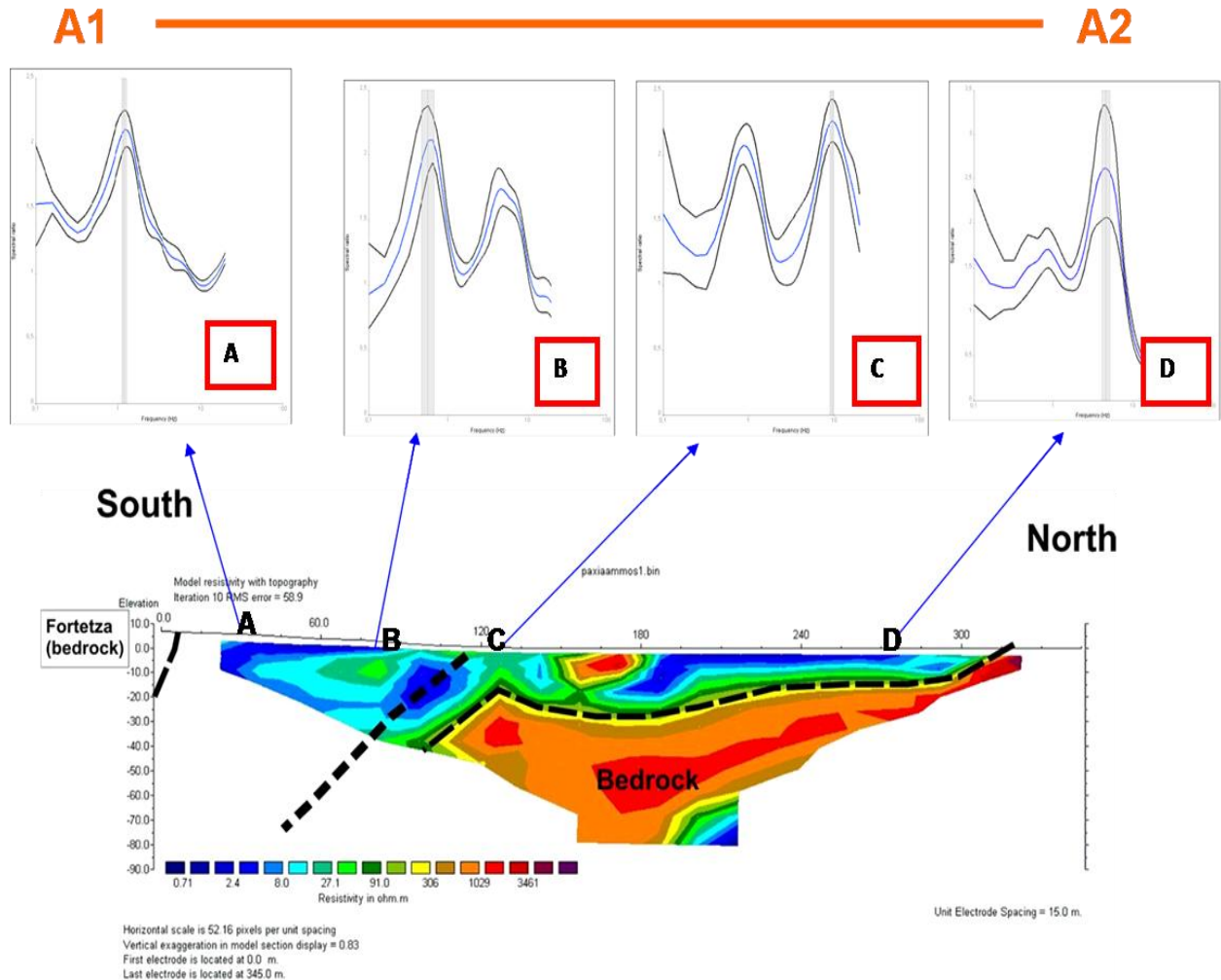


**Figure 5.3:** View of the tectonic model along Pahia Ammos (western part of Paleohora profile A1A2) based on the combined methodologies HVSR using microtremors (upper figure) and ERT (lower figure): HVSR curves pattern the surface and subsurface variations along Pahia Ammos. The numbering (A-D) in the lower right part of the HVSR curves depicts the site where HVSR was conducted in Pahia Ammos. In the southern part of Pahia Ammos the clear amplified low frequency corresponds to the thick sand layer overlying the bedrock. The two amplified frequencies correspond to the surface and subsurface structure. The first amplified low frequency corresponds to the effect of the sandy layer while the second amplified in the high frequencies to the effect of the lateral heterogeneities of the subsurface due to the fault zone. The first amplified in the high frequencies corresponds to the effect of the lateral heterogeneities of the

*subsurface while the second amplified in the low frequencies to the effect of the sandy layer, (lower figure): the ERT profile showing the resistivity variations in depth along Pahia Ammos.*

Microseismicity of southwestern Crete recorded from the local temporal network comprised of three seismological stations installed in Paleohora after 27th April 2007 earthquake in the southwestern Crete delineates a fault zone or a system of faults zones striking almost E-W in the coastline of Paleohora of southwestern Crete. The reader is referred to Chapter 4 for a detailed description of the network. That microearthquake clustering is trending from Grammeno to Lissos basin and extending at about 46 km west from Paleohora to 6km east of Paleohora near Lissos basin (Section 4.4). The aforementioned microearthquake delineation defining a large scale fault trending from Grammeno to Lissos basin in the southwestern Crete is previously unreported therefore no correlation is presented from literature review. This microearthquake epicenter delineation is well correlated with the proposed tectonic model from ERT method in Pahia Ammos suggesting also the activity of the large scale E-W fault or a system of E-W faults

Microseismicity study suggests that the southwestern Crete is characterized by strong lateral heterogeneities in the subsurface. This suggestion is based on the following two observations: a) the observed high root-mean square (RMS) residual and standard errors in the epicenter (ERH) is an indicator of the strong lateral heterogeneities of the subsurface structure of southwestern Crete. The up-to-date velocity models inserted in Hypo 71 for earthquake epicenter solutions uses the 1D velocity model ( $V_p/V_s=1.78$ ) proposed by Papazachos & Nolet (1997) that does not take into account the heterogeneities and irregularities of the active subsurface region.

Model calculations by McLaren (1985) of earthquake regional network location near subduction zones suggests that the complexity of the lateral velocity variations (due to the exaggerated low velocity wedges above the subducting slab and of a region of higher velocity within the slab) introduce large location errors or produce accurate locations which have larger residuals. McLaren (1985) inserted a complex velocity structure including features that may occur near Wadati-Benioff zone (exaggerated low velocity wedges above the subducting slab and of a region of higher velocity within the slab). The study conducted by McLaren suggests that RMS residuals are seldom a good indicator of location quality even in the case of well-recorded events; shallow events may have either large or small RMS residuals and deep events with severe mislocations may have small residual'. The factor that causes large mislocations or large rms residuals is the travel-time rays in the dipping slab. Moreover, Papazachos (2000) suggested that the high ERH value of the output solution file of HYPO71 software is not always an indicator of epicentral mislocation.

Furthermore, it is proposed that the reason that the ERH and RMS errors could not be calculated or detected might be associated with the seismic velocity structure on each side of the fault, due to the lateral heterogeneities of that structure. A similar result is observed in the case of San Andreas Fault in California (Reiter, 1990) proposed that the reason that ERH and RMS errors could not be calculated or detected might be associated with the seismic velocity structure on each side of the fault, due to the lateral heterogeneities of that structure.

b) The calculated high value of  $V_p/V_s$  ratio ( $V_p/V_s=1.99$ ) and Poisson ratio ( $\sigma=0.333$ ) from the time delay P to S phases of the microseismicity in southwestern Crete suggests the existence of strong heterogeneities and conductive structures (that attribute fault zones) near the subduction zone. Moreover, the calculated high value Poisson ratio from the proposed velocity model for southwestern Crete that is equal to  $\sigma=0.333$  may be attributed to: 1) the fractured upper oceanic crust, 2) thin cracks (aspect ratio $<0.005$ ), and 3) to shallow unconsolidated sand (that might have the same behavior of a fault zone).

The important research outcome of the microseismicity study in relation to fault determination conducted is that the origin of microseismicity clustering in the vicinity of the coastline of Paleohora observed from the local network of Paleohora can be related to the activity of the large scale E-W fault verified also from ground-truthed geological and ERT survey. This consideration is mainly based on the identification of a large scale fault or to a system of faults striking E-W coastal from west of Grammeno to Lissos basin extracted from microseismicity study. The reader is referred to Chapter 4 for the calculated interrelation of high  $V_p/V_s$  ratio and poisson ratio with the origin of the microseismicity study and for the comparison of the research outcomes with other case studies. All the aforementioned research outcomes of the multi-proxy approach adopted for fault determination in Paleohora half-graben basin are presented in Figure 5.4

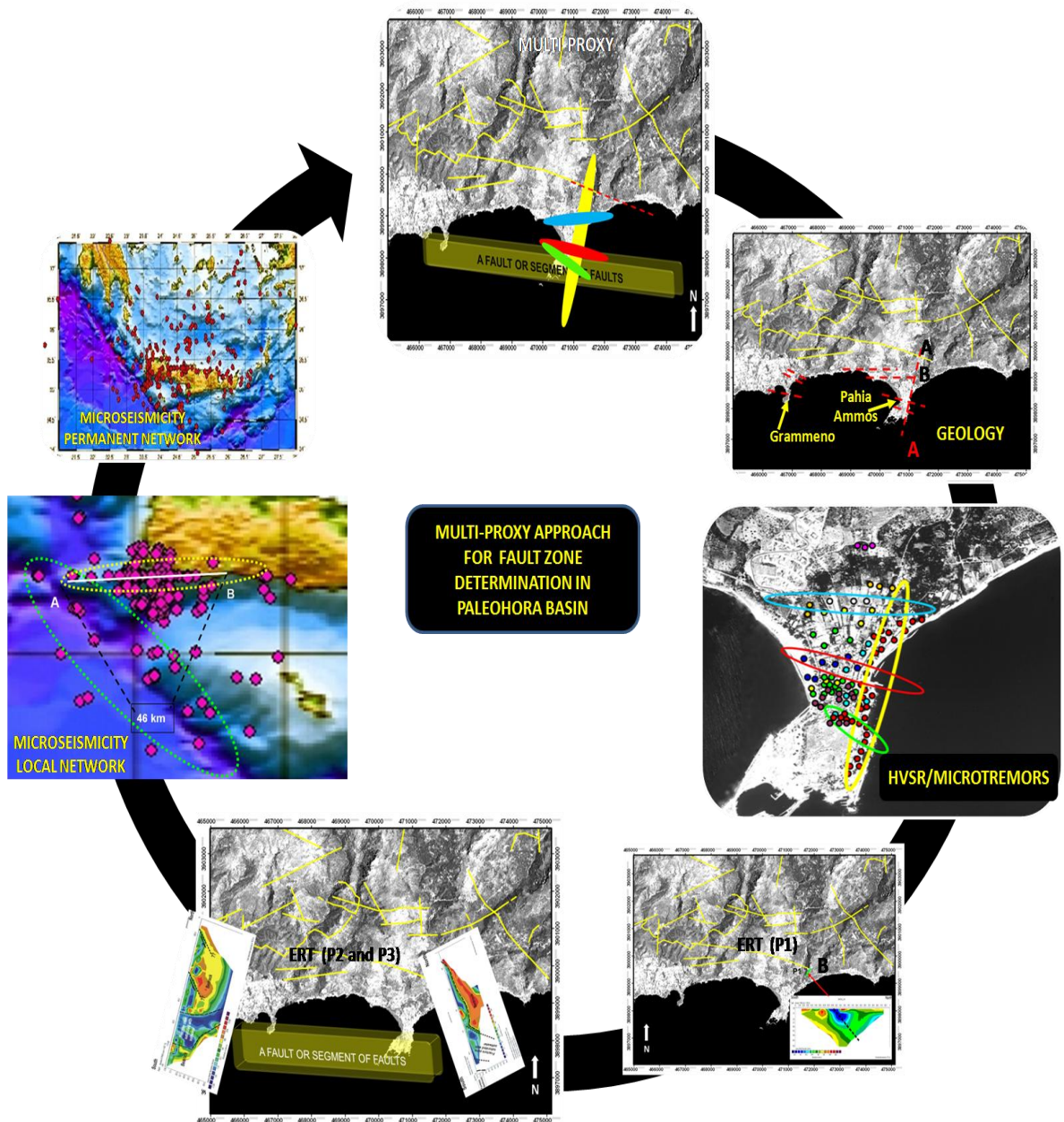


**Figure 5.4:** A synthesis of the combined multi-proxy approach of geological ground truthed field survey, electrical resistivity tomography, HVSR using microtremors and microseismicity recorded from the permanent seismological network of Crete and temporal local seismological network of Paleohora for fault delineation in Paleohora basin. All recorded data are described and interpreted in Chapter 4. Geological investigation revealed numerous fault zones, HVSR using microtremors revealed four fault zones. ERT revealed two fault zones in the populated Paleohora half-graben and one fault in Grammeno peninsula. Microseismicity recorded from the temporal network revealed a large scale fault or a system of fault striking almost E-W and trending for

*approximately 46 km from east of Grammeno-Pahia Ammos-Lissos basin (western of Paleohora) in agreement with the tectonic model proposed from ERT. Microseismicity from the permanent network verifies the high activity of southwestern Crete compared to northwestern Crete is due to the heterogeneous structure characterized of large scale faults.*

### **5.3 SITE EFFECTS ASSESMENT AND SEISMIC GROUND RESPONSE ZONING USING HVSR TECHNIQUE AND MICROTREMORS IN KASTELLI-KISSAMOU AND PALEOHORA BASINS.**

In this section is addressed the second research question of the effectiveness of HVSR using microtremors techniques in site effect characterization on ground seismic motion which may cause damage in earthquakes. The extent of the efficiency of these methods to provide evidence appropriate or useful for the Greek vulnerability code (EC8) is discussed in section 5.4.

The purpose of the microzonation studies in Kastelli and Paleohora basins based on HVSR and microtremors is to characterize the surface and subsurface structure on ground seismic motion (site effects) that posses an important role in earthquake hazards. HVSR technique using microtremor measurements recorded in Kastelli-Kissamou and Paleohora basins reveals ground seismic spatial variability. The reader is needed to infer to Chapter 4 for details in site effect characterization based on HVSR in both case studies. In both investigated basins: i) one amplified clear frequency, ii) two high amplified clear frequencies, iv) broad and iiv) flat or low amplitude HVSR peaks are observed and model the surface and subsurface structure. The majority of microtremor recordings present one and two amplified frequencies.

The ground seismic spatial variability derived from HVSR technique in Kastelli-Kissamou and Paleohora indicates a fairly to very complex subsurface structure, respectively characterized by lateral heterogeneities and irregularities and by variation of the thickness of alluvial deposits. The effects of soft rocks (conglomerates), soft (clay, sand) and stiff (sandy-clay) soils, possible transition zones due to slopes, substructure impedance contrast environment, heterogeneities and irregularities of the subsurface are attributed in the HVSR curves. In the case studies of Kastelli and Paleohora basins the HVSR using microtremors reveals: 1) one amplified clear frequency, 2) two high amplified clear frequencies, 3) broad and 4) flat or low amplitude HVSR peaks, that are all associated with the surface and subsurface ground response.

The validity of the effectiveness of HVSR using microtremors in Kastelli-Kissamou and Paleohora case studies in determining surface and subsurface structure is verified based on: a) the cross-correlation of the research outcomes of each proxy and a) through comparisons of the research outcomes in Kastelli and Paleohora with other case studies. In the following is presented a comparison of the identified HVSR ground fundamental frequencies in Paleohora and Kastelli-Kissamou basins with other case studies for the: 1) one amplified clear frequency, 2) two high amplified clear frequencies, 3) broad and 4) flat or low amplitude HVSR peaks. The importance of determining the HVSR frequencies is that they are associated with the surface and subsurface ground response evaluation. The effectiveness of the derived HVSR peaks in evaluation of surface and subsurface structure is verified from the research outcomes of the ground – thruthed geological and ERT surveys. The extracted HVSR seismic ground

characterization is also well correlated with the geological surficial formations presented from geological maps and satellite image data in Kastelli and Paleohora basin. All the results are cross-correlated thus there is a great confidence of the research outcomes. Moreover, a comparison with previous studies verifies the validity of the research outcomes presented in the frame of this thesis. In the following section is presented the comparison of the research outcomes of the identified HVSR frequencies and its interpretation with the local site conditions in Kastelli and Paleohora basins with the research outcomes of relevant case studied.

### **1) One clear HVSR fundamental frequency.**

In Kastelli and Paleohora basins the one clear HVSR fundamental frequency in the low or high frequency band are related with the thickness of the alluvial/sedimentary layer. In both basins the one clear HVSR fundamental frequency in the medium frequencies is related to the lateral discontinuities and attributes the effect of fault zone. The level of HVSR ground amplification is correlated with the impedance contrast of the surface and subsurface structure. Specifically, in the above case studies the one clear HVSR fundamental frequency in the low frequencies (0.5-1.4Hz) is related with thick deposits or extremely soft material and the fundamental frequency in the high frequencies (6.0-15.0Hz) is related with shallow deposits (the reader is referred to Sections 4.3 and 4.4 for data interpretation). It is worth noting an example in the northwestern part of Kastelli characterized by fractured well-lithified limestone without the effects of surficial alluvial deposits, where the amplification is rather low 1.8-2.26. The reader is referred to Section 5.2a to remind the HVSR result in this site. Moreover, the reader is referred to Section 5.2b (Fig. 5.3) presenting the combined HVSR and ERT survey in modeling surface and subsurface structure. The low frequency (HVSR\_A) at  $F_0 = 1.2\text{Hz}$  with amplification of 2.0 corresponds to a site of sediments thickness of 50 m (site A, Fig. 5.3). The high frequency (HVSR\_D) at  $F_0 = 7.0\text{Hz}$  with amplification of 2.7 corresponds to a site of sediments thickness of 10 m (site D, Fig. 5.3).

Similar results to Kastelli and Paleohora basins for the correlation of the one HVSR fundamental frequency in the low and high frequencies with the thickness variation is proposed by several authors (Yamanaka et al., 1993; Teves-Costa & Matias, 1996; Gitterman et al., 1996; Mucciarelli et al., 2001; Giampicollo et al., 2001).

Köhler et al (2004) concluded that HVSR fundamental frequency correlates very well with the sediment thickness variation in the southern Rhine Graben close to Basle. Tuladhar (2004) performed microzonation study in Hanoi (Vietnam) using HVSR method and microtremors and observed good correlation between: 1) HVSR and geology, 2) fundamental frequency and variation of thickness of soft sediment. In the eastern part where the thickness decreases the fundamental period ranges between (0.6-0.8 sec) while in western part where the thickness increases the fundamental period ranges between (0.6-1.1 sec). Gosar et al., (2009) related the observed HVSR ground frequency, ranging from 0.9 Hz to 10 Hz, with the thickness of soft sediments in Ljubjana (Central Slovenia). In Ljubjana the low amplitude HVSR peaks were related with the low impedance contrast between the surface deposits (gravels) and the underlying bedrock. The high HVSR amplitude peaks were related with the high impedance contrast soft sediments with the bedrock. Gosar (2007) related the high fundamental frequency HVSR (18-22Hz) with the very shallow geological formations



(very shallow till or sand gravel layer overlying flysch bedrock or shallow conglomerates) in Bovec basin (NW Slovenia). The observed HVSR lower frequencies (3-6Hz) in Bovec basin (NW Slovenia) were related to flysch and deep sea clastic rocks outcrop. HVSR fundamental frequency (6-14Hz) are related to the generally thin Quaternary deposits. Specifically, HVSR fundamental frequency (8-10Hz) are related to shallow 15-25m thick layer of younger sand and gravel overlying lacustrine chalk. Raptakis et al. (1998) correlated the low HVSR fundamental frequency ( $f_0=0.7\text{Hz}$ ) with the thick and soft site ( $h>200\text{ m}$ ) characterized of lateral heterogeneities (2D) in Thessaloniki (Volvi). Gueguen et al. (2007) in Grenoble, France, related the HVSR low fundamental frequency ( $f_0=0.3\text{Hz}$ ) with the very thick and stiff site (3D site) of a typical alpine valleys. The amplification at this site is large and broad. In Colfiorito (Apennines, Central Italy) that is a small scale valley the HVSR fundamental frequency of that a deep site ( $h>100\text{ m}$ ) is rather low ( $f_0=1\text{Hz}$ ). In Basel, Switzerland (Fäh, 1997), the HVSR fundamental frequency ranges between 0.5-2Hz for rather thick sites ( $h>200\text{ m}$ ). Ergin (2004) found HVSR fundamental frequency ( $f_0=0.8-3\text{Hz}$ ) at a site on the shores of Kucuk Cekmece lake, in Turkey, that is considered to reflect the effects of a thick deposit. Clear HVSR peaks related with one dimensional alluvial/sedimentary layered geological structure are also observed by Chavez-Charcia et al. (1995), Fäh (1997), Bour (1998), Duval et al. (1994), Köhler et al. (2004) and Bonnefoy-Claudet et al. (2008b). According to Teves-Costa & Matias (1996) high frequency is observed at shallow topmost sedimentary layer, while fundamental frequency in the low frequency band is observed at thick sedimentary sites in two investigated basin in Lisbon.

Several results gave similar results to the Kastelli and Paleohora basins where the HVSR ground level amplification is correlated with the impedance contrast of the surface and subsurface structure. The example in the northwestern part of Kastelli characterized by a fractured well-lithified limestone without the effects of surficial alluvial deposits, where the amplification is rather low 1.8-2.26 is mentioned. This research outcome shows that in a well-lithified structure where the impedance contrast between surface and subsurface structure is low the ground seismic amplification is low.

The higher HVSR ground amplification in Kastelli and Paleohora is observed at 3.58 and 6.8 at sites characterized by a high impedance contrast environment. Bonnefoy-Claudet et al. (2008a) observed the fundamental frequency above 5.01Hz for thick deposits in Santiago de Chile basin, which are similar to the results from Kastelli. The observed low shear wave velocity at sites characterized of soft sediments unconsolidated (alluvial deposits or stiff pumice deposits) overlying the bedrock and the high shear wave velocity of the bedrock in Santiago de Chile basin indicates strong velocity contrast between the unconsolidated and consolidated sediments. The clear HVSR peaks in Kastelli and Paleohora are probably correlated with the sharp contrast velocity between the surface and subsurface geological structure. A clear peak indicates that the site presents high velocity contrast and is highly prone to amplify seismic motion (Konno-Ohmachi, 1998; Bard, 1998; Bonnefoy-Claudet et al., 2008a). Gueguen et al. (2000) applied the HVSR technique in Pujili, Equador, and verified that the surficial alluvial deposits in valleys amplify the seismic motion up to 50 in the frequency band 0.3-0.7Hz. Generally, very soft soils leading to high impedance contrast at depth and insert high amplification (Yamanaka et al., 2005). At sites where the

impedance contrast of the surface and subsurface layers is low, the amplification value at rock site is close to unity (Nakamura, 1989, 1996).

In conclusion, for Kastelli and Paleohora basins the one clear HVSR fundamental frequency in the low frequencies is related to thick alluvial/sedimentary deposits. The high frequencies are related with to the shallow deposits that may be induced by the effect of thin deposits or by lateral heterogeneities. The one clear HVSR frequency in the medium frequencies is related to the lateral discontinuities indicating fault /fracture zone. Section 5.2a describes the case study of northwestern part of Kastelli. Section 5.2b discusses the example of the combined methodology of HVSR and ERT in Pahia Ammos of Paleohora discussed. In that example the one clear amplified low frequency (HVSR\_A, Fig 5.2b) corresponds to the thick sand layer overlying the bedrock.

In Kastelli and Paleohora the one clear amplified low and high frequency correlates to the thick and shallow sedimentary layer overlying the bedrock. This is in agreement with other studies cited in the text above, showing correlation between one clear HVSR curve and thick shallow features (in this case sediments) overlying bedrock.

## **2) Two HVSR amplified fundamental frequencies**

Two amplified frequencies are observed in Kastelli and Paleohora basins. The two peaks identified in this research indicate both the lateral heterogeneities/irregularities and the effects of variations in the thickness of alluvial layer. In Kastelli-Kissamou basin zones KB, KC and KD are characterized by two amplified frequencies and correspond to sites characterized of lateral heterogeneities/irregularities and of the effects of variation in the thickness of the surficial layer. In Paleohora basin zones PA, PB, PC, PD, PE, PF, PG and PH indicate the effect of subsurface lateral heterogeneities and the effect of thickness variation of the surficial deposits.

In Kastelli and Paleohora basins the HVSR curve presenting two amplified frequencies is an indicator of a fault zone. The amplified frequency in the medium or high frequency correlates with the fault zone while the amplified frequency in the low frequency range correlates with the thick or very soft sedimentary/alluvial deposits. Moreover, the higher amplified frequency (fundamental frequency) correlates with the topmost layer (that may be associated to the effect of a fault zone located near the surface) while the second amplified to the rest geological column. See Chapter 4 for the detailed description and interpretation of the HVSR data, and Section 5.2b for the example of the combined methodology of HVSR and ERT in Pahia Ammos of Paleohora for the interrelation of the ground fundamental frequency and the determination of: a) variation in the thickness of the surficial geological structure and b) the surface and subsurface structure. The clear amplified low frequency corresponds to the thick sand layer overlying the bedrock, while the two amplified frequencies correspond to the surface and subsurface structure. The first amplified low frequency corresponds to the effect of the sandy layer while the second amplified in the high frequencies to the effect of the lateral heterogeneities of the subsurface due to the fault zone. The first amplified in the high frequencies corresponds to the effect of the lateral heterogeneities of the subsurface while the second amplified to the low frequencies to the effect of the sandy layer.

Similar to Kastelli and Paleohora basins, Gueguen et al. (2000) in Pujili (Equador) and Gueguen et al. (2000) in Quito (Equador) proposed that the higher

amplified frequency (fundamental frequency) correlates with the topmost layer while the second amplified to the rest geological column. Köhler et al. (2004) correlated the observed clear second amplified frequency around 7-10Hz to the shallow Quaternary deposits of low velocity layers overlying the Tertiary sediments, in Southern Rhine Rift valley, close to Basle in Switzerland. Köhler et al., (2004) performed microtremor measurements along observed clear HVSR peaks in the low frequency band (0.5-0.9Hz) and high frequency band (7-10Hz) related with the sediments thickness variations. Roten et al., (2008) using numerical simulations found one clear fundamental frequency at the low frequency band (0.6Hz) correlated a the deep embanked valley with high impedance contrast in Rhône valley in Switzerland. According to J-SESAME recommendation in a Y-shaped basin of 800 m depth composed of Quaternary deposits that overly bedrock of Jurassic marls to marly limestone, in Grenoble (SE France), the HVSR amplified frequency presents two amplified peaks in the low and high frequency band. In such a case, the amplified frequency in the high frequency range corresponds to the very shallow Quaternary deposits that overly bedrock. Cornou et al. (2003) in Grenoble basin observed one fundamental frequency at 0.3Hz and a second amplified frequency at 2.5-4.4Hz. The second amplified (2.5-4.4Hz) is correlated with topmost layer of the basin. Lebrun et al. (2001) correlated the second amplified frequency at 3Hz with the resonance response of the surficial topmost layer in a depth range 20-40 m of the Grenoble basin. Oros (2009) used HVSR technique in Timisoara (western part of Romania) observed two fundamental frequencies ranging from  $F_0=0.6$  Hz. According to Oros (2009) the low frequency corresponds to Quaternary layer while the high frequency might be correlated with the subsurface structure few meters under the surface. Among to others, Toshinawa et al. (1996) in Santiado (Chile) and Delgado et al., (2002) in Padul- Nigüelas basin (South Spain) proposed that the higher amplified frequency corresponds to the ground response of the soft superficial layer while the second amplified frequency defines the resonance frequency of the whole soil layer above the bedrock.

The above case studies confirm the results from Kastelli and Paleohora thereby verifying that HVSR higher amplified frequency (fundamental frequency) correlates with the topmost layer (that may be associated with the effect of a fault zone located near the surface) while the second correlates to the rest geological column. Summarizing, in Kastelli and Paleohora basins the HVSR curve presenting two amplified frequencies is an indicator of fault zones. The amplified frequency in the medium or high frequency correlates with the fault zone while the amplified frequency in the low frequency range correlates with the thick sedimentary deposits. Moreover, the higher amplified frequency (fundamental frequency) correlates with the topmost layer (that may be associated to the effect of a fault zone located near the surface) while the second amplified to the rest geological column.

### **3) Flat or low amplitude fundamental frequency peaks**

In Kastelli and Paleohora basins the low HVSR ground amplification is related to low impedance contrast of surface and subsurface structure. In Kastelli and Paleohora basins flat HVSR or low amplitude peaks (low amplification) are observed in areas lacking solid bedrock near the surface. The extracted HVSR curves at such sites are an indicator of stiff sediments overlying bedrock.

In Kastelli Kissamou and Paleohora basins, flat or low HVSR amplification describes rock or semi-cemented/semi-consolidated outcrop and/or a stiff sediment overlay the bedrock. In Paleohora flat or low amplification HVSR characterizes stiff (sandy-clay) soils or soft rocks (conglomerates). In northwestern part of Kastelli and Roka village characterized by a fractured well-lithified limestone structure the HVSR ground amplification is rather low. See Chapter 4 for the characterization of flat or low amplitude fundamental frequencies in Kastelli and Paleohora.

Flat HVSR peaks with amplification close to unity are also observed by (Nakamura, 1996; Duval et al., 1994; Bour, 1998). Lachet & Bard (1994), Bard (1998), Konno & Ohmachi (1998), and Bonnefoy-Claudet et al. (2008a) concluded that the observed a rather small amplification on rock site is an indicator of stiff sediments that overlie bedrock and at these sites a rather small ground amplification in a case of an earthquake is expected. According to Bonnefoy-Claudet et al. (2008a) the observed flat or low amplification HVSR peaks at sites characterized of stiff sediments overlying bedrock are likely due to the weak velocity contrast between stiff sediments and bedrock. Experimental and numerical studies verify the relation of low amplification and weak velocity contrast (Konno & Ohmachi, 1998; Bonnefoy-Claudet et al., 2008b).

Northwest of Kastelli and in Roka village, located 20 km southern of Kastelli, the HVSR fundamental frequency is observed at 1.66-3.98Hz and the amplification ranges between 1.8-2.26. Those sites are located on fractured rock of well lithified limestone without the effect of sedimentary/alluvial deposits. In the southwestern part of Kastelli several microtremor recordings performed presenting ground fundamental frequency at 2.5Hz while the amplification ranging between 1.8-2.26. A similar result was observed by Volant et al. (2002), at a site characterized of fractured rock soil (limestone) and concluded that the HVSR fundamental frequency is observed at 1.5-2.0Hz and the amplification is lower than 2 .

Moreover, very good correlation was observed in the shape of HVSR curves using microtremors and earthquake data recorded in Paleohora with amplification lower than 2 (the reader is referred to Chapter 4, section 4.4). Several microtremor measurements performed in the southern part of Pahia Ammos depicting amplification factor of 1.8-2.5 at fundamental frequency of 2.5Hz.

Bonnefoy-Claudet et al. (2008a) in the case of Santiago de Chile basin mentioned that HVSR curves of amplification lower than 2 might possible indicate the soil resonance frequency and suggested that more detail study will verify the threshold of a clear HVSR peak higher than 2. According to Bonnefoy-Claudet et al. (2008a) further experiments should be conducted to evaluate quantitative information at sites characterized of low amplitude H/V peaks. According to JSESAME guidelines (Bard & SESAME-Team, 2005, <http://sesame-fp5.obs.ujf-grenoble.fr>) in the case of low amplitude peaks lower than 2 it is suggested not to extract site effect interpretations using HVSR curves. Bard (1998) suggested that an unclear HVSR peak followed by a clear trough is a reliable estimate of fundamental frequency. Haghshenas et al. (2008) suggested that the observed flat HVSR curves extracted comparing H/V ratios using microtremors and earthquake data are reliable indicator of absence of large effects, using data from 104 sites located in Europe, Caribbean and Tehran. In conclusion, the work of this thesis shows that the HVSR peaks of low amplitude spread among clear HVSR peaks can be used in estimating site resonance frequency.

#### 4) Broad HVSR fundamental frequencies

Broad HVSR fundamental frequencies in Kastelli Kissamou and Paleohora basins are observed and related to the effect of the complexity of the wavefield of the underlain 2D or 3D subsurface structural (transition zones-slopes, discontinuities) variations. Similar results are observed by Bonnefoy-Claudet et al. (2008a). Three or more amplified peaks are observed along the edge basin. For the purpose of this thesis the HVSR (or the H/V spectra ratio) of both horizontal components, the HVSR of the N-S component and the HVSR of the E-W component were calculated. In several sites the average HVSR of both components and the HVSR of the two horizontal components ( $H_{ns}/V$ ,  $H_{ew}/V$ ) have similar fundamental frequency ( $f_{0ew}$ ,  $f_{0ns}$ ) and amplification ( $A_{0ew}$ ,  $A_{0ns}$ ). The correlation between the coefficients of determination ( $R^2$ ) of fundamental frequencies ( $R^2 f_{0ew}$ ,  $f_{0ns}$ ), amplification ( $R^2 A_{0ew}$ ,  $A_{0ns}$ ) and ground vulnerability index ( $R^2 k_{gew}$ ,  $k_{gns}$ ) for the case of Paleohora is very low that might indicate strong subsurface heterogeneities. In Kastelli-Kissamou the correlation between the fundamental frequencies and amplification is higher than Paleohora basins. The observed similarity between fundamental frequency ( $f_{0ew}$ ,  $f_{0ns}$ ) and dissimilarity of amplification ( $A_{0ew}$ ,  $A_{0ns}$ ) of the two horizontal components might be an indicator of strong heterogeneities of the subsurface (2D/3D) structure. In Kastelli and Paleohora the one amplified frequency in one of the two horizontal components is an indicator of 2D/3D effects.

Similar to Kastelli and Paleohora basins, Panou et al. (2005) correlated the observed differences in the HVSR amplitude of the horizontal components to vertical ( $Ns/V$  and  $Ew/V$ ) component with the possible effects of 2D/3D effects. The correlation of the  $F_o$ ,  $A_o$  and  $K_g$  (vulnerability index) between the two horizontal components were not good enough to exclude the 2D/3D effects; but neither could they confirm the 2D/3D effects in Thessaloniki (northern Greece). Bonnefoy-Claudet et al. (2006b) compared the spectra of horizontal components to vertical ( $X/V$  and  $Y/V$ ) and observed one clear H/V peak at 4Hz only in one of the spectra ratio  $Y/V$  of the horizontal component. The observed H/V fundamental frequency at 4Hz is possible related to the strong contribution of Love waves compared to Rayleigh waves.

The strong 2D effects due to the shape of the valley on the resonance frequency deduced from ambient seismic noise are recently well established (Steimen, 2004; Roten et al., 2008). Bonnefoy-Claudet et al. (2008a) considering the steep slope basement concluded that the broad HVSR peaks along topographic slopes and deep depression are due to the complexity of the seismic wavefield. The broad HVSR peaks in Santiago de Chile basin (are indicators of dipping underground interface between softer and harder geological formations. This underground structure is characterized of significant lateral variations that could lead to 2D or 3D effects. Similar observations to Bonnefoy-Claudet et al. (2008a) of site effects along topographic slopes are experimentally observed by Rovelli (2001) in Colfiorito basin and by Yalcinkaya & Alptekin (2005) in Dinar basin. Mucciarelli (2008) mentioned the importance of 2D effects in the seismic ground amplification and in the earthquake damage distribution in Umbria-Marche.

In the Paleohora case study broad low amplitude HVSR curve due to the edge-basin effect is observed. In Paleohora basin the maximum amplification due to the edge-basin effect was observed at 2.0Hz. Similar to Paleohora basin, Guillier et al. (2006) found broad peaks or plateau-like HVSR curves of low amplitude (lower than

2.0) at sites of strong lateral sediments thickness variation (along valley edge) suggested that broad peaks and low amplitude H/V curves indicate strong underground lateral thickness variation. Woolery & Street (2002) observed broad and relatively low amplitude H/V peaks (lower than 2.0) at sites characterized of sharp shear velocity contrast in non-horizontal near surface soil layer. Irregularities of the basement lead to focusing or defocusing of seismic ground noise wavefield at the surface (Woolery & Street, 2002; Cornou et al., 2003). Bonnefoy–Claudet (2008) proposed that ground amplification phenomena can be inserted due to presence of lateral seismic wave propagation but further clearer evidences of such effects should analyzed in more details.

Moreover, in Paleohora basin soil fundamental frequency shift to the higher frequency band up to 1Hz is observed close to the edge of the basin where the sediment thickness decreases. Specifically, systematic amplified frequencies  $f_0=3\text{Hz}$  with amplification around 2.5 to 3 are observed around the edge of the basin. The observed shift of the fundamental frequency up to 1Hz around the edge of the basin and lower amplification around the edge of the basin is also observed by Delgado et al. (2000) and Gueguen et al. (2007). Gueguen et al. (2007) observed soil fundamental frequency increase up to 1Hz on the edge of the basin in Grenoble valley and correlated with thickness decrease around the basin's edge. Delgado et al. (2000) mentioned highly rapid increase of fundamental frequency around the edge of the Segura river valley (SE Spain), compared to the fundamental frequency the center.

In this study to determine the effects of basin margins on seismic ground motion two earthquake data sets and microtremors were recorded at the same site: a) in the centre of the basin and b) along the basin margins. Similarities in the fundamental frequency between the HVSR using microtremors and earthquake data in all cases are observed. In the centre of the basin slightly lower (underestimated) HVSR amplification using microtremors is observed compared to HVSR amplification using earthquake data. The HVSR ground amplification using microtremors is higher (overestimated) compared to recorded earthquake at the same site along the basin edges.

This observation for Paleohora suggests the higher seismic ground amplification along the basin margins due to the basin effects. The HVSR ratio of microtremor along the edge of the valley verifies that these locally surficial generated waves (due to the strong diffractions on the edges of the basins) have larger amplification than the HVSR ratio of the S earthquake wavefield (Section 4.3.4). It is observed that along the edge of the valley the locally shallow layer generate larger amplitudes than the earthquake S direct wave. The HVSR fundamental frequency is the same while the seismic ground response amplification is higher when using microtremors.

Among to other, Haghshenas et al. (2008) comparing HVSR using microtremors and earthquake data concluded that the fundamental frequency is similar but the amplification is underestimated. The amplification level using microtremors is higher than the amplification level using earthquakes along basin edges (Haghshenas et al. 2008). Ergin et al. (2004) compared HVSR using microtremors and SSR using earthquake data and found good correlation in the fundamental frequency. At low frequency the ground amplification using microtremors is lower than the ground amplification using earthquakes. The underestimation in the amplification using

microtremors suggests that the energy of microtremors at the low frequencies is not sufficient to induce oscillation modes at that site.

The outcome of comparison of single-point microtremor and earthquake HVSR ratios recorded at the same site in Paleohora (Fig. 4.3.4) along the edge of basin is in agreement with Bard (1999, Bonnefoy-Claudet et al., 2008b). These authors reported that along the edge of a valley the locally surficial generated wave have larger amplitudes than the S direct wave of the substratum. According to Bard (1999), the amplitude of the locally generated waves (depending on the impedance contrast and damping) is higher than the amplitude of the incident wave especially near the lateral discontinuity and their short wavelength induces large differential motions and enhanced earthquake damage distribution. Frankel & Vidale (1992) reported the consequences of these waves on seismic ground motion and mentioned that these waves are the cause of long period duration of seismic motion in San Clara valley during Loma Prieta earthquake. Mucciarelli (2008) in several towns in Umbria Marche mentioned: 1) the importance of 2D effects of sedimentary basins in seismic ground motion 2) strong morphological effects (using experimental and numerical modeling, 3) the importance of soil-building resonance effect in damage enhancement. Mucciarelli (2001) mentioned the importance of 2D effects in the seismic ground amplification and in the earthquake damage distribution in Umbria-Marche.

In the case of Paleohora in addition to the basin margin effects on ground seismic motion, the effect of the strong lateral heterogeneities induced by the rupture fault zone should also be considered as a factor that influences the resonance frequency pattern. The two above combined effects on seismic ground motion in Paleohora are discussed in Section 5.5

In conclusion, in Kastelli and Paleohora basins broad HVSR fundamental frequencies are observed and related to the effect of the complexity of the wavefield of the underlain 2D or 3D subsurface structural (transition zones-slopes, discontinuities/heterogeneities) variations, in agreement to the above research outcomes of other case studies.

#### **5.4 COMPARISON OF SEISMIC GROUND ZONING BASED ON HVSR TECHNIQUE USING MICROTREMORS AND GREEK EUROCODE (EC8) IN KASTELLI AND PALEOHORA.**

Considering the importance of site effects in earthquake distribution and taking account that the effect of surface and subsurface structure of Paleohora and Kasteli half-graben basins is unknown, dense microtremor measurements were performed to evaluate soil characterization according to EC8 (see Chapter 4, Section 4.3) for the EC8.

The microzonation study based on HVSR technique specifies sites of different expected ground seismic response during an earthquake event. Four sets of seismic ground responses are expected:

- 1) Sites where no significant ground seismic amplification is expected. These sites are characterized by stiff sediments;
- 2) Sites where significant ground seismic amplification is expected. These sites are characterized by soft sediments;
- 3) Sites where significant ground seismic amplification is expected due to both the effects of soft sediments and strong lateral heterogeneities and irregularities.

- 4) Sites where significant ground seismic amplification could be due to the basin-edge effects and the proximity of underground structure.

The reader is referred to Section 4.3 for the detail description of the seismic ground response classification based on HVSR technique using microtremors in Kastelli and Paleohora.

Microzonation study using HVSR technique and microtremor recordings distinguish the populated Kastelli basin into six zones based on the ground seismic response. Seismic ground zones KA, KB and KC, KD correspond to category X of the (EC8). Zone KE corresponds to category B of the (EC8). Zone KF corresponds to category D of the (EC8). Zone KG correspond to category A of the (EC8). The very close proximity of Roka village to the Kera fault categorizes Roka village in seismic ground category X of the Greek Eurocode Regulations (EC8). Moreover, site MKR3 located on very shallow rubbles/cobbles corresponds to category X of EC8.

Microzonation study using HVSR technique and microtremor recordings distinguish Paleohora basin into eleven zones based on the ground seismic response. Seismic ground zones PA, PB, PC, PD, PE, PF, PH, PJ and PK correspond to category X of the (EC8). PG corresponds to category B of the (EC8). PL zone corresponds to category A of the (EC8). The efficiency of geological, electrical resistivity HVSR using microtremors and seismological techniques in sites located across fault zones is verified from the aforementioned sections. Moreover the effectiveness of HVSR in characterizing the surface geological formations that correspond to EC8 is also presented. See Chapter 4 for the EC8 eurocode characterization.

## **5.5 TECTONIC DIFFERENCES IN SEISMIC GROUND RESPONSE BETWEEN THE TWO STUDY AREAS BASED ON THE MULTI-PROXY APPROACH**

The major tectonic difference between the two investigated half-graben basins located in southwestern and northwestern Crete is the closer proximity of Paleohora than Kastelli to the Hellenic subduction zone (Chapter 2, section 2.1.1). This proximity to subduction zone is most likely to be the major reason for the higher activity in Paleohora than Kastelli.

In this study the geological ground-truthed investigation conducted revealed a higher tectonic uplift of Paleohora compared to Kastelli-Kissamou, since measured uplift coastal of Paleohora is of up to 9 m, while measured uplift coastal of Kastelli-Kissamou is of up to 6.8 m. The measured tectonic uplift in Paleohora and Kastelli might be associated with the AD 365 earthquake. The cause of the uplift is not studied in this thesis; see Chapter 2, Section 2.1.2 for the possible reasons of the high amount of observed uplift proposed by several authors. Several authors report an uplift of 9 to 10 m in southwestern Crete (Meulenkamp et al., 1994; Lambeck, 1995; Pirazzoli et al., 1982). Pirazzoli et al. (1982), proposed an uplift of 6-7 m near Falasarna in northwestern Crete associated with AD 365.

The high seismic tectonic environment of northwestern and southwestern Crete is also verified from microseismicity study. Earthquake data were recorded from a permanent seismological network consisting of six stations installed in the whole territory of Crete and from three temporal seismological stations installed in southern Crete; see Chapter 4, Sections 4.4.1 and 4.4.2 for details for the seismological networks. Analysis of earthquake data recorded from the permanent seismological



network Crete reveals that the interplate seismicity is more intense to the south compared to the north part of western Crete (Fig. 4.4.1). Moreover, it is evident that the north part of western Crete is more seismically more active than the rest part of Crete. Seismicity studies confirm that the southwestern part of Crete is seismically more active than the rest Crete.

Microseismicity recorded from the temporary seismological network installed in the territory of Paleohora reveals a highly seismically active tectonic environment coastal of southwestern Crete. The time delay of P to S phases of the swarm-earthquake clustering recorded from the three short-period temporary seismological network was calculated. The calculated high  $V_p/V_s$  ratio ( $V_p/V_s=1.99$ ) and Poisson ratio ( $\sigma=0.333$ ) observed in southwestern Crete suggests the existence of strong heterogeneities and suggests the existence of strong heterogeneities and conductive structures (that attribute fault zones) near the subduction zone. This conductive structure might correlate with the fault zone striking almost E-W identified coastal of Paleohora from geological ground-truthed and HVSR and ERT surveys.

The comparison of the calculated high  $V_p/V_s$  ratio ( $V_p/V_s=1.99$ ) of this study with the calculated  $V_p/V_s$  ratio of other studies conducted in the Aegean area explains the strong heterogeneities of bedrock in southwestern Crete. Specifically, Hatzfeld et al. (1993) estimated a  $V_p/V_s$  velocity ratio equal to 1.79 and de Chabali er et al. (2007) a velocity  $V_p/V_s$  ratio equal to 1.80 for the Aegean area. Becker (2007) used an amphibian network that covers the trench system in the central and eastern Crete to study microseismicity and a velocity model with  $V_p/V_s=1.78$ .

In conclusion, this comparison of the calculated  $V_p/V_s$  velocity ratio of this study with  $V_p/V_s$  velocity ratio of other previously mentioned studies, confirms that southwestern Crete is seismically more active to the rest Crete.

HVSR using microtremors and ERT in the populated Kastellii-Kissamou patterns five and four fault zones, respectively crosscutting the area discussed in section 5.2.1a. HVSR using microtremors and ERT in the populated Paleohora basin patterns four and one fault zones, respectively discussed in section 5.2.1b.

Broader HVSR fundamental frequencies peaks in Paleohora basin compared to Kastelli are observed and are related to the effect of the complexity of the wavefield of the underlain 2D or 3D subsurface structural (transition zones-slopes, discontinuities) variations. Moreover, in Paleohora the one amplified frequency in the one of the two horizontal components is due to the complexity of the wavefield suggesting strong 2D/3D effects. Specifically, in Paleohora at sites (MP25 and MP27, Chapter 4) the HVSR of the EW horizontal component (EW/V) presents one clear amplified frequency at 0.9 Hz with a relatively high amplification of 2.5. At that site the HVSR of the NS horizontal component (NS/V) presents no clear low amplified frequencies. HVSR of the EW horizontal component (EW/V) at site MP3 presents a clear amplified frequency at 0.9Hz with amplification 2.3Hz, while the HVSR of the NS component presents on clear amplified frequency at frequency 8.0Hz. In controversy, in Kastelli-Kissamou basin the fundamental frequencies of the two HVSR are observed in the same frequency. Similar results to Paleohora are observed by Bonnefoy-Claudet et al. (2008a). Bonnefoy-Claudet et al. (2006b) compared the HVSR spectra ratio of the horizontal to vertical components of the horizontal components (X/V (EW) and Y/V (NS/V) and observed one clear H/V peak at 4Hz only in one of the spectra ratio Y/V of the horizontal component.

The observed H/V fundamental frequency at 4Hz is possible related to the strong complexity of the wavefield and particularly the contribution of Love waves compared to Rayleigh waves. Panou et al. (2005) correlated the observed differences in the HVSR amplitude of the horizontal (NS/V and EW/V) components to the possible effects of 2D/3D effects.

The multiple amplified HVSR peaks along the edge of Paleohora basin suggest the effect of basin margins on ground seismic motion. The steep dipping (or sloping) environment of the edge basins is well-patterned in HVSR curves and infer high ground seismic amplification ( $A=3-3.5$ ). Similar to this study Köhler et al. (2004) concluded that the multiple peaks are due to the complicated inclined dipping structure. Moreover, the correlation of the  $F_0$ ,  $A_0$  and  $K_g$  (vulnerability index) between the two horizontal components in Kastelli and Paleohora suggest 2D/3D effects due to strong lateral heterogeneities in Paleohora. Panou et al. (2005) used correlation  $F_0$ ,  $A_0$  and  $K_g$  (vulnerability index) between the two horizontal components to confirm 2D/3D effects in Thessaloniki (northern Greece).

Higher HVSR ground seismic amplification level is observed in Paleohora basin compared to Kastelli basin. In Kastelli Kissamou ground seismic amplification ranges from 1.5 to 3.58 while in Paleohora ranges from 1.5-6.2. The higher amplification ground soil seismic response ( $A=6.2$ ) using HVSR technique and microtremor data is observed northeastern near the centre ( $A=6.2$ ) and near the basin edge ( $A=5.8$ ) in the southern part of the sedimentary half-graben Paleohora basin at frequency 2.5Hz.

In the northeastern part of Paleohora ground soil amplification effects are enhanced due to the effect of both the fault striking almost E-W and NNE-SSW (identified using HVSR technique) of the diffraction of seismic waves on the edges of the valley (northwest basin margin) and of the sediments thickness deposits. The observed higher amplification in the center of the valley is in accordance with Cornou et al. (2003) observations. Cornou et al. (2003) observed the higher amplification level in the centre of the valley and showed the role of strong diffractions on the edges of the basins in the total seismic ground motion in the centre of the valley. Moreover, the sediments response in the very near field, in the centre of the valley, considering also the effects of complex incident wavefield, and of sub or super-sonic rupture velocities for near-surface faults induces amplification effects. Bard (1999) mentioned the amplification effects due to sediment effects in the very near field due to the effects of complex incident wavefield, and of sub or super-sonic rupture velocities for near-surface faults. Raptakis et al. (2005) observed the maximum amplification using HVSR technique in both horizontal components near to the centre of Mygdonia basin.

In the southern part of Paleohora basin the high ground HVSR amplification is observed due to : 1) the basin margin effects, 2) the lateral heterogeneities induced by the large scale E-W (identified using multi-proxy approach) and NNE-SSW faults (identified using HVSR technique) or 3) to the high impedance contrast between the surface and subsurface structure. At this site, the impedance contrast is due to: a) the sediment thickness decrease along the basin edges that induce higher impedance contrast and higher amplification b) personal communications on 28<sup>th</sup> April 2007 with local people confirm the existence and the recent refilling of concrete over sea water intrusion at that site, that verifies the high impedance contrast between concrete refilling and sea water in the southern part of the basin.

In conclusion, the higher amplification level in Paleohora compared to Kastelli is due to: a) the smaller scaling of the basin and b) steeper dipping margins of the edge of the basin and c) the complex fault network. In Paleohora basin the seismic waves travel shorter distances to the basin margin and the seismic energy is diffracted along the basin margins and higher seismic wave energy is focused near the center of the basin. In the case of a larger scale basin the seismic waves travel further to reach the basin margins and seismic wave energy is scattered along the basin margins. The amplitude of the locally generated waves near the edge of the basin (depending on the impedance contrast and damping) is higher than the amplitude of the incident waves and especially near the lateral discontinuity induces large differential motions that enhance earthquake damage distribution. A similar explanation is given by Bard (1999). Frankel et al. (2001) and Joyner (2000) mentioned the amplification effects due to edge basin effects. Moreover, multipathing and scattering effects (Chapter 2, Paragraph, 2.3) due to large heterogeneities, where the seismic waves are focused or defocused by substructure lateral variations, are capable of inducing velocity variations at distance (Chapter 2).

The large scale faults crosscutting Paleohora inferred higher impedance contrast between the surface and subsurface structure. The high amplification level is an indicator of high impedance contrast of the surface and subsurface structure. Moreover sharper and high amplitude HVSR peaks are observed in Paleohora compared to Kastelli. Zhao (1996, 1999) suggested sharp peak and amplification in high impedance contrast between the surface and the subsurface structure environments. Bonnefoy-Claudet et al. (2008b) mentioned the high amplification effects at sites located near basin–edge effects and next to underground structures. The seismic energy is also amplified when the seismic wave travels through the sedimentary layer. Ground HVSR amplification effects due to sedimentary layers are well presented by several research studies. Gueguen et al. (2000) applied the HVSR technique and verified that the surficial alluvial deposits in valleys amplify the seismic motion up to 50 in the frequency band 0.3-0.7Hz. Generally, very soft soils leading to high impedance contrast at depth and insert high amplification. Amplification effects on seismic motion in soft soil are extensively studied and presented in Chapter 2. At sites where the impedance contrast of the surface and subsurface layers is low, the ground HVSR amplification value at rock site is close to unity (Nakamura, 1989, 1996). The final difference between the two case basins is that the calculated ground vulnerability indices  $K_g$  values for Paleohora are more than 10 times higher than Kastelli (Tables 4.3 and 4.4, Appendix II). High  $K_g$  values are related to liquefaction phenomena. Based on  $K_g$  values it is proposed that liquefaction is highly prone to occur in Paleohora compared to Kastelli. This study suggests that the  $K_g$  value extracted from HVSR can be used as a preliminary indicator of liquefaction phenomena.

## 5.6 SUMMARY OF DISCUSSION

1. The conduction of ERT method applied in ground-truthed faults in Kastelli and Paleohora verifies the validity of ERT method in identifying fault zones. Moreover, ERT method is a reliable method at identifying fault zones, when conducted at sites to an almost perpendicular orientation to the fault. Therefore the ERT method is very good at identifying faults as long as the ERT profiles are correctly aligned in relation to the fault. Thus, in the case of uncertain results, the obvious approach is to repeat the ERT profiles in an orientation almost perpendicular zone to the fault.
2. This thesis proposes that although the ERT and microtremor methods are able to allow identification of the location of a fault, the activity of a fault can not be directly estimated using ERT and microtremors. Currently discrimination between active and inactive faults can be available by the field observation of the fault plane surface; however, fault activity can be monitored using displacement gauges placed across faults (outside the scope of this study), although this cannot be done so easily in the case of buried faults. In seismic hazards studies the importance is the delineation of faults, since active and inactive faults behave as a wave-guides in an impinging seismic wave front (Cornier & Spudich, 1984). Moreover, it is possible that a previously inactive fault may become active during an earthquake.
3. Geological and seismological approach confirms the higher activity of southwestern Crete than northwestern Crete.
4. Geological, HVSR, ERT, and seismological research outcomes are cross-correlated.
5. The high  $V_p/V_s$  ratio value extracted from the P and S travel time arrival of microseismicity study of the local network in Paleohora reveal a strong conductive tectonic structure characterized of strong heterogeneities that can contribute to the future seismic studies of the convex part of the Hellenic arc. The observed high root-mean square (RMS) residual and standard errors in the epicenter (ERH) are attributed to the lack of a representative (3D) velocity model accounting the strong lateral heterogeneities especially of the southwestern part of Crete. The representative (3D) velocity model accounting the strong lateral heterogeneities especially of the western part of Crete is a necessity for earthquake localization studies.
6. HVSR technique using microtremors is a valid estimator in determining the surface and subsurface structure. HVSR with amplification lower than 2.0 is a valid estimator of ground response.
7. It is proposed that the fracture conditions affect the HVSR ground response spectra characteristics.

## **CHAPTER 6: CONCLUSION**

---

### **6.1 MAIN CONCLUSIONS POINTS OF THE RESEARCH STUDY**

Several major outcomes are derived from this research, stated in the following:

The robust combined multi-proxy approach involving the study of geology, geophysics, instrumental seismology and earthquake engineering geophysics disciplines reveals seismic faults (that may be active) (Figs. 5.1 and 5.2) and evaluate the ground seismic response due to surface and subsurface structure (site effects) of the investigated areas. 2D electrical resistivity tomography (ERT) delineates fault zones when applied perpendicular to faults. ERT reveals a highly tectonic environment of Paleohora compared to Kastelli Kissamou half-graben basin. HVSR technique using microtremors is a powerful tool in estimating surface and subsurface variations that are capable to infer ground seismic motion enhancement during an earthquake event. HVSR may reveal a more complex environment of Paleohora compared to Kastelli half-graben basin. Microzonation study based on HVSR technique and microtremors presents the ground seismic response fundamental frequency, amplification. It is proposed that clear HVSR peaks of low amplitude ( $<2$ ) can be used to infer reliable estimates of ground seismic response.

Microseismicity of Crete using earthquake data from the regional network of Crete confirm that the southwestern part of the Crete is more active than northwestern Crete and of the other parts of Crete. A large scale fault N-S near Falasarna is revealed. Microseismicity clustering using data from the temporal network in Paleohora is conducted to reveal fault zones of the region and to estimate the  $V_p/V_s$  ratio of the recorded events. The large scale fault in Pahia Ammos identified from ERT, microtremors and cross-correlated with microseismicity clustering delineation extending almost 46 km from western of Grammeno to Lissos basin eastern of Paleohora. The high  $V_p/V_s$  value can be attributed to a strong conductive tectonic structure. It is proposed that this value is an indicator of strong heterogeneities of the subsurface structure of southwestern Crete near the subduction zone. For Paleohora considering the building vulnerability of three buildings located in the basin margins and in the centre of the basin are estimated. Coincidence between the building and ground fundamental frequencies is observed for all cases.

The experimental multiproxy research outcomes are verified from ground thruthing geological field survey and crosscorrelated. Therefore there is a great confidence of the research outcomes of the study and is proposed that can be the basis of a future research study.

### **6.2 CONTRIBUTION TO FUTURE RESEARCH**

The outcome of this thesis can significantly contribute to a future detailed seismic hazard scenario and to the seismic risk assessment of the investigated sites of Paleohora basin and Kastelli territory. The combined approach involving the study of geology, seismology and geophysics disciplines is a robust methodology used in the frame this thesis and provides the basis for a seismic hazard assessment.

One of the major contributions of this thesis in future research studies is the improvement of the deterministic model proposed by Moratto et al. (2007). The estimated local site effects, the soil classification given in the Greek vulnerability code

(EC8) and the strong heterogeneities of southwestern Crete indicated by the high velocity contrast identified from microearthquakes recorded from the local network in Paleohora can contribute to the deterministic earthquake hazards model in northwestern and southwestern Crete. Moreover, other passive techniques using microtremors (SSR, Vs30) can be applied to compare the proposed amplification level considering that the HVSR amplification is underestimated, as long as the soil remains in an linear elastic domain (Haghshenas et al., 2008).

Microearthquake data clustering suggests an ideal case for relocation techniques to precisely delineate activated structures. Moreover, prediction of the next major event can be extracted from microseismicity studies by mapping the b-value variations on the rupture surface (Schorlemmer & Wiemer, 2005). The advantage of microseismicity studies, using a small network aperture, that focus and concentrate only on a specific area is the higher mapping resolution of seismic events (Becker, 2007).

Further microseismicity study can be conducted to verify the proposed velocity model for southwestern Crete. The observed high velocity ratio value observed in the southwestern Crete can be used to improve the 1D velocity model proposed by Papazachos & Nolet 1997) for the whole Aegean. Further seismicity study can be conducted in the southwestern Crete to verify the origin of microseismicity patterns. The possible relation of microseismicity clustering to fluids transported along the plate interface escaping towards the surface in zones of crustal weakness, triggering swarm like cluster activity along its way can be estimated using further seismicity studies. Becker et al. (2006) suggested the possible relationship of microearthquake clustering near Ptolemy trench with fluid circulation in the fore-arc of the Hellenic subduction zone and concluded that microseismicity patterns may be related to fluids transported along the plate interface escaping towards the surface in zones of crustal weakness, triggering swarm like cluster activity along its way.

This microearthquake clustering might be attributed to the pore pressure increase due to the subduction of portion of water contained as pore fluids within the sediments or in the form of hydrated rock within the upper part of the ocean crust. Further seismicity study is required to verify the assumptions. Future fluid mechanics studies are needed to study the origin of the microseismicity clustering. Moreover, future detailed studies of the seafloor (using amphibian network, OBS, ROVs or towed cameras) in the region of southwestern Crete could reveal the surficial existence of such fluid\_circulation.

Rock mass classification systems studies used by civil engineering (Waltham, 2002) have potential to be applied to verify the relation of fracture conditions and rating of Paleohora and Kastelli that can be used for a detailed seismic hazards assessment. Future mathematical experimental modeling equations can prove that the length and the width of the fault affect the HVSR fundamental frequency. It is proposed that the fracture conditions affect the HVSR ground response spectra characteristics. It is also speculated that the width and the length of a fault may affect the HVSR fundamental frequency of microtremors recorded on a fault site. It is also proposed that the fault activity might be evaluated using microtremors. Further geological field investigations are required to record the possible rough tight or gouge faults of Paleohora and Kastelli. Future studies based HVSR technique using microtremors and verified by rock mass classification and can be used to verify fault activity.

Detailed microtremor measurements on building structures in Kastelli and Paleohora can be performed to evaluate the damage risk or collapse of various points of the structure before an earthquake. Numerical studies can be performed inside buildings to repair parts of vulnerable points of building. Volant et al. (2002) performed numerical study and based on the microtremors findings proposed solutions to repair vulnerable points. Earthquake building vulnerability response estimation techniques in relationship with the known ground soil response will contribute to the estimation of a ground-building seismic interaction that increases seismic motion intensities and the earthquake damage distribution in the nearby structures. Further geophysical techniques is suggested to be applied to confirm the proposed identified faults using HVSR technique.

## REFERENCES

---

- Acworth, R., 1999, Investigation of dryland salinity using the electrical image method, *Australian Journal of Soil Research*, vol. 37, pp.623-636
- Aki, K., 1965, A note on the use of microseisms in determining the shallow structures of the earth's crust, *Geophysics*, vol. 30, pp.665–666
- Albarello, D., 2001, Detection of Spurious Maxima in the site Amplification Characteristics estimated by the HVSR Technique, *Bulletin of the Seismological Society of America*, vol.91, pp.1562-1536
- Al-Yuncha, Z., Luzon, F., 2000, On the horizontal-to-vertical spectral ratio in sedimentary basins, *Bulletin of the Seismological Society of America*, vol.90 pp.1101–1106
- Andreou, C., Mouslopoulou, V., Fountoulis, I., Atakan, K., 2001, Implications of paleoseismology in seismic hazard analysis in NW Crete and Kythira Strait (Greece), *Bulletin of the Geological Society of Greece, Proceedings of the 9<sup>th</sup> International congress*, vol. XXIV/4, pp.1465-1472
- Andrews, D.J., 1986, Objective determination of source parameters and similarity of earthquakes of different size, *Earthquake source mechanisms, S. Das.J.Boatwright, AGU, Washington, D.C*, pp. 259-268
- Angelier, J., Lyberis, N., Le Pichon, X., Barrier, E., Huchon, P., 1982, The tectonic development of the Hellenic arc and the sea of Crete: A synthesis, *Tectonophysics*, vol.86, pp. 159-163
- Ansary, M.A., Yamazaki, F., Fuse, M., Katayama, T., 1995, Use of microtremors for the estimation of ground vibration characteristics, *Third International Conference on Recent Advances in Geotechnical Earthquake Engineering and Soil Dynamics. St. Louis, Missouri*
- Arai, H., Tokimatsu, K., 1998, Evaluation of local site effects based on microtremor H/V spectra, *Proceeding of the Second International Symposium on the Effects of Surface Geology on Seismic Motion, Yokohama, Japan*, pp. 673–680
- Arai, H., Tokimatsu, K., 2000, Effects of Rayleigh and love waves on microtremor H/V spectra, *Proceedings of the 12th World Conference on Earthquake Engineering, Auckland, New Zealand*
- Armijo, R., Lyon-Caen, H., Papanastassiou, D., 1992, East-west extension and Holocene normal fault scarps in the Hellenic arc, *Geology*, vol. 20, pp.491-494
- Asten, M.W., 1978, Geological control of the three-component spectra of Rayleigh wave microseisms, *Bulletin of the Seismological Society of America*, vol.68, pp.1623–1636
- Asten, M.W., Henstridge, J.D., 1984, Arrays estimators and the use of microseisms for reconnaissance of sedimentary basins, *Geophysics*, vol.49, pp.1828–1837
- Asten, M.W., Dhu, T., 2002, Enhanced interpretation of microtremor spectral ratios using multimode Rayleigh-wave particle-motion computations, *Proceedings of Total Risk Management in the Privatised Era, Australian Earthquake Engineering Society Conference, Adelaide, Australia*
- Asten, M.W., 2004, Comment on “Microtremor observations of deep sediment resonance in metropolitan Memphis, Tennessee” by Paul Bodin, Kevin Smith, Steve Horton and Howard Hwang, *Engineering Geology*, vol.72, pp.334–343



- Bard, P.Y., Bouchon, M., 1985, The two-dimensional resonance of sediment-filled valleys, *Bulletin Seismological Society of America*, vol.75, pp. 519–541
- Bard, P.Y., 1998, Microtremor measurements: a tool for site effect estimation?, In *Proceedings of the Second International Symposium on the Effects of Surface Geology on Seismic Motion*, vol. 3, pp. 1251–1279
- Bard, P.-Y., 1999, Seismotectonic and microzonation techniques in earthquake engineering: Intergrated training in earthquake risk reduction practices, *Proceedings of the Advanced study course*, European Commision Research Directorate General, Kefallinia, Greece
- Bard, P.-Y., SESAME-Team, 2005, Guidelines for the implementation of the H/V spectral ratio technique on ambient vibrations—measurements, processing and interpretations, *SESAME European research project* EVG1-CT-2000–00026, deliverable D23.12 (<http://sesamefp5.obs.ujf-grenoble.fr>)
- Barker, R.D., 1981, Offset system of electrical resistivity sounding and its use with a multicore cable, *Geophysical prospecting*, vol.29, pp. 128-143
- Becker, D., Meier, T., Rische, M., Bohnhoff, M., Harjes, H.P., 2006, Spatio-temporal microseismicity clustering in the Cretan region, *Tectonophysics*, vol. 423, pp. 3-16
- Becker, D., 2007, Spatio-temporal microseismicity clustering in the Cretan region, *Phd thesis*, Hamburg
- Benetatos, C., Kiratzi, A., Papazachos, C., Karakaisis, G., 2004, Focal mechanisms of shallow and intermediate depth earthquakes along the Hellenic arc, *Geodynamics*, vol.37, pp. 253-296
- Bodin, P., Smith, K., Horton, S., Hwang. H., 2001, Microtremor observations of a deep sediment resonance in metropolitan Memphis, Tennessee, *Engineering Geology*, vol.62, pp. 159-168
- Bohnhoff, M., Makris, J., Stavrakakis, G., Papanikolaou, D., 2001, Crustal investigation of the Hellenic subduction zone using wide aperture seismic data, *Tectonophysics*, vol. 343, pp. 239–262
- Bohnhoff, M., Meier, T., Harjes, H.P., 2005, Stress regime at the Hellenic Arc from focal mechanisms, *Seismology*, vol.9, pp. 341–366
- Bohnhoff, M., Rische, M., Thomas Meier, Dirk Becker, George Stavrakakis, Hans-Peter Harjes, 2006, Microseismic activity in the Hellenic Volcanic Arc, Greece, with emphasis on the seismotectonic setting of the Santorini-Amorgos zone, *Tectonophysics*, vol.423, pp. 17-33
- Bonnefoy-Claudet, S., Cornou, C., Bard, P.-Y. and Cotton, F., 2004. Nature of noise wavefield, SESAME report, D13.08 (<http://sesame-fp5.obs.ujf-grenoble.fr>)
- Bonnefoy-Claudet, S., Cornou, C., Bard, P.-Y., Cotton, F., Moczo, P., Kristek, J., Fäh, D., 2006a. H/V ratio: a tool for site effects evaluation. Results from 1-D noise simulations, *Geophysical Journal International.*, vol.167, pp. 827–837
- Bonnefoy-Claudet, S., Cotton, F., Bard, P.-Y., 2006b, The nature of noise wavefield and its applications for site effects studies, A literature review, *Earth.Sciences. Revolution*, vol. 79, pp. 205–227
- Bonnefoy-Claudet.S., Baize.S., Bonilla.LF., Berge-Thierry.C., Pasten.C., Campos.J., Volan.P., Verdugo.R., 2008a, Site effect evaluation in the basin of Santiago de Chile using ambient noise measurements, *Geophysical Journal International*, doi: 10.1111/j.1365-246X.2008.04020.x

- Bonnefoy-Claudet, S., Köhler, A., Cornou, C., Wathelet, M., Bard, P.-Y., 2008b, Effects of Love waves on microtremor H/V ratio, *Bulletin Seismological Society of America*, vol. 98, pp. 288-300
- Borcherdt, R.D., 1970, Effects of local geology on ground motion: San Francisco Bay, *Bulletin Seismological Society of America*, vol.60, pp. 29-61
- Borcherdt, R.D., Galssmoyer, 1992, On the characteristics of local geology and their influence on ground motions generated by the Loma Prieta earthquake in the San Francisco Bay region, California, *Bulletin Seismological Society of America*, vol.82, pp. 603-641
- Bour, M., Fouissac, D., Dominique, P., Martin, C., 1998, On the use of microtremor recordings in seismic microzonation, *Soil Dynamics and Earthquake Engineering*, vol.17, pp.465-474
- Broadbent, M., Habberjam, G.M., 1971, A solution to the dipping interface problem using the square array resistivity technique, *Geophysical prospecting*, vol.19, pp. 321-338
- Bromirski, P.D., Duennebier, F.K., 2002, The near-coastal microseism spectrum: spatial and temporal wave climate relationships, *Journal of Geophysical Research*, vol.107, pp. 510–520
- Campbell, K., 1985, Strong motion attenuation relationships: a ten-year perspective, *Earthquake Spectra*, vol.1, pp.759-804
- Caputo, R., Pitsitelli, S., Oliveto, A., Rizzo, E., Lapenna, V., 2003, The use of electrical resistivity tomographies in active tectonics: examples from the Tyrnavos Basin, Greece, *Journal of Geodynamics*, vol.36, pp.19-35.
- Caputo, R., Salviulo, L., Pitsitelli, S., Loperte, A., 2007, Late Quaternary activity along the Scorciabuoi Fault (Southern Italy) as inferred from electrical resistivity tomographies, *Annals of Geophysics*, vol.50, pp.213-224
- Cara, F., Di Giulio, G., Rovelli, A., 2003, A study on seismic noise variations at Colfiorito, central Italy: implications for the use of H/ V spectral ratios, *Geophysical Research Letters*, vol. 30, No 18, art number 1972
- Castro, R.R., Mucciarelli, M., Pacor, F., Petrangaro, C., 1997, S-wave site-response estimates using HVSR, *Bulletin Seismological Society of America*, vol.87, pp.256-260
- Celebi, M., 2000, Revelation from a single strong motion record retrieved during the 27 June 1998 Adana (Turkey) earthquake, *Soil Dynamics and Earthquake Engineering*, vol.20, pp.283-288
- Chatelain, J.-L., Guillier, B., Cara, F., Duval, A.-M., Atakan, K., Bard, P.-Y., 2008, Evaluation of the influence of experimental conditions on H/V results from ambient noise recordings, *Bulletin Earthquake Engineering*, vol. 6, pp.33–74
- Chavez-Garcia, F.J., Guenca, G., Sanchez-Sesma, F.J., 1995, Site effects in Mexico City urban zone, A complementary Study, *Soil Dynamics and Earthquake Engineering*, vol.15, pp.141-146
- Chopra, A.K., 2001, Dynamics of structures: Theory and Applications to Earthquake Engineering (Second Edition), *Pearson, Pentice Hall Editions*
- Chouet, B., De luca, G., Milana, G., Dawson, P., Martini, M., Scarpa, R., 1998, Shallow velocity structure of Stromboli Volcano, Italy, derived small aperture array

- measurements of strombolian tremor, *Bulletin Seismological Society of America*, vol.88, pp. 653-666
- Comninakis, P.E., Papazachos, B.C., 1972, Seismicity of the Mediterranean ridge. *Geological Society of America*, vol.83, pp.1093–1102
- Comninakis, P.E., Papazachos, B. C., 1978, A catalogue of earthquakes in the Mediterranean and surrounding area for the period 1901-1975, *Publication of the Geophysical Laboratory, University of Thessaloniki*, vol.5, 96pp
- Comninakis, P.E., and Papazachos, B.C., 1986, A catalogue of earthquakes in the Aegean and surrounding area for the period 1901-1985, *Publication of the Geophysical Laboratory, University of of Thessaloniki*, vol.1, 167pp
- Comninakis, P. E. and Papazachos, B.C., 1989, Aftershock and foreshock sequences in Greece and surrounding area during the period 1911-1985, *Laboratory of Geophysics, University of Thessaloniki*, vol.5, 156pp
- Constable, S., Parker, R., Constable, C., 1987, Occam's inversion: A practical algorithm for generating smooth models from electromagnetic sounding data, *Geophysics*, Vol. 52 pp.289-300
- Cornier, V., and Spudich, P., 1984, Amplification of ground motion and waveform complexity in fault zones: examples from the San Andreas and Calaveras fault zones: *Geophysical Journal of the Royal Astronomical Society*, vol. 79, pp. 135-152
- Cornou, C., Bard, P.-Y., 2003, Site-to-bedrock over 1D transfer function ratio: An indicator of the proportion of edge-generated surface waves? *Geophysical Research Letters*, vol. 30, pp.1453-1457
- Cornou, C., Bard, P.-Y., Dietrich, M., 2003, Contribution of dense array analysis to identification and quantification of basin-edge induced waves, part II: Application to the Grenoble basin (French Alps), *Bulletin of the Seismological Society of America*, vol. 93, pp. 2624–2648
- Cornou, C., Kristek, J., Ohrnberger, M., Di Giulio, G., Schissele, E., Guillier, B., Bonnefoy-Claudet, S., Wathelet, M., Fäh, D., Bard, P.-Y., Moczo, P., 2004, Simulation of seismic ambient vibrations-II H/V and array techniques for real sites, *Proceedings of the 13th World Conference on Earthquake Engineering*, Vancouver, Canada
- Coulet, F., Mora, P.,1998, Simulation based comparison of four site-response estimation techniques, *Bulletin of the Seismological Society of America*, vol.88, pp. 30–42
- D' Amico, V., Albarello, D., Mucciarelli, M., 2002, Validation through HVSR measurements of a method for the quick detection of site amplification effects from intensity data: an application to a seismic area in Northern Italy, *Soil Dynamics and Earthquake Engineering*, vol.22, pp. 475-483
- de Chabaliier, J.B., Lyon-Caen, H., Zollo, A., Deschamps, A., Bernard, P., Hatzfeld, D., 2007, A detailed analysis of microearthquakes in western Crete from digital three-component seismograms, *Geophysical Journal International*, vol.110, pp.347–360
- de Groot-Hedlin, C., Constable, S., 1990, Occam's inversion to generate smooth, two-dimensional models from magnetotelluric data, *Geophysics*, vol. 55, pp. 1613–1624

- Delgado, J., Lopez Casado, C., Giner, J., Estevez, A., Cuenca, A., Molina, S., 2000, Microtremor as a geophysical exploration tool: Application and limitations, *Pure and applied Geophysics*, vol.157, pp. 1445–1462
- Delgado, J., Alfaro, P., Galindo-Zaldivar, J., Jabaloy, S., Lopez Garrido, A.C., Sanz De Galdeano, C., 2002, Structure of the Padul- Nigüelas basin (South Spain) from H/V ratios of ambient noise: application of the method to study peat and coarse sediments, *Pure and Applied Geophysics*, vol.159, pp. 2733–2749
- Delibasis, N., Makris, J., and J. Drakopoulos, 1988, Seismic investigations in the crust and upper mantle in Western Greece, *Anall Geol. Pays Hell*, vol. 33, pp. 69-83
- Delibasis, N., Ziazias, M., Voulgaris, N., Papapdopoulos, T., Stavrakakis, G., Papanastassiou, D., Drakatos, G., 1999, Microseismic activity and seismotectonics of the Heraklion area (central Crete Island, Greece), *Tectonophysics*, vol.308, pp. 237–248
- Demanet, D., Pirard, E., Renardy, F., Jongmans, D., 2001, Application and processing of geophysical images for mapping faults, *Computers & Geosciences*, vol. 27, pp.1031–1037
- Deshcherevsky, A.V., Zhuravlev, V.I. 2004, Temporal regime of microearthquakes in the Garm research area, *Physics of the Solid Earth*, vol. 40, pp. 66–82
- Di Giulio, G., Cornou, C., Ohrnberger, M., Wathelet, M. & Rovelli, A., 2006, Deriving wavefield characteristics and shear-velocity profiles from two-dimensional small-aperture arrays analysis of ambient vibrations in a small-size alluvial basin, Colfiorito, Italy, *Bulletin of Seismological Society of America*, vol.96, pp.1915–1933
- Dorwick, D., 2003, Earthquake risk reduction, *Willey Publications*
- Dravinski, M., Ding, G., Wen, K. L., 1996, Analysis of spectral ratios for estimating ground motion in deep basins, *Bulletin of the Seismological Society of America*, vol.86, pp.646–654
- Duermeijer, C.E., Nyst, M., Meijer, P.T., Langereis, C.G., Spakman, W., 2000, Neogene evolution of the Aegean arc: paleomagnetic and geodetic evidence for a rapid and young rotation phase, *Earth Planetary Science Letter*, vol.176, pp. 509–525
- Duval, A.M., Meneroud, J.-P., Vidal, S. & Singer, A., 1994, Relation between curves obtained from microtremor and site effects observed after Caracas 1967 earthquake, in *Proceedings of the 11th European Conference on Earthquake Engineering*, Paris, France, 6–11 September
- Endrun, B., Meier, T., Bohnhoff, M., Harjes, H.P., 2004, Lithospheric structure in the area of Crete constrained by receiver functions and dispersion analysis of Rayleigh phase velocities, *Geophysical Journal International*, vol. 158, pp 592-608
- Endrun, B., Meier, T., Lebedev, S., Bohnhoff, M., Stavrakakis, G., Harjes, H.P., 2008, S velocity structure and radial anisotropy in the Aegean region from surface wave dispersion measurements, *Geophysical Journal International*, vol. 174, pp. 593-616, [doi:10.1111/j.1365-246X.2008.03802.x](https://doi.org/10.1111/j.1365-246X.2008.03802.x).
- Engdahl, E.R., van der Hilst, R., Buland, R., 1998, Global teleseismic earthquake relocation with improved travel times and procedures for depth determination, *Bulletin of the Seismological Society of America*, vol.88, pp. 722– 743
- Fäh, D., 1997, Microzonation of the city of Basel, *Journal of Seismology*, vol.1, pp.87-102

- Fazzito, S.Y., Rapalini, A. E., Cortés, J. M., Terrizzano, C.M, 2009, (accepted manuscript), Characterization of Quaternary Faults by Electric Resistivity Tomography in the Andean Precordillera of Western Argentina, *Journal of South American Earth Sciences*, doi: [10.1016/j.jsames.2009.06.001](https://doi.org/10.1016/j.jsames.2009.06.001).
- Fassoulas, C., Kiliadis, A. and Mountrakis, D., 1994, Postnappe stacking extension and exhumation of high-pressure/low temperature rocks in the island of Crete, Greece, *Tectonics*, vol.13, pp. 127–138
- Field, E.H., Clement, A.C., Jacob, S.M., Aharonian, V., Hough, S.E., Friberg, P.A., Babaian, T.O., Karapetian, S.S., Hovanessian, S.M., Abramian, H.A., 1995, Earthquake site-response study in Giumri (formerly Leninakan), Armenia, using ambient noise observations, *Bulletin of the Seismological Society of America*, vol. 85 pp.349–353
- Field, E.H., Jacob, K.H., 1995, A Comparison and Test of Various Site Response Estimation Techniques, Including Three That Are Not Reference Site Dependent, *Bulletin of the Seismological Society of America*, vol. 85, No.4, pp. 1127-1143
- Field, E.H., 2000, Earthquake site Response study in Giumri (formerly Leninakan), Armenia, using ambient noise observations, *International Journal of Rock Mechanics and Mining Sciences*, vol.33, p.122-124
- Fortuin, A.R., Peters, J.M., 1984, The Prina complex in eastern Crete and its relationship to possible strike-slip tectonics, *Journal Structural Geology*, vol.6, pp. 459-476
- Frankel, A., Vidale, J., 1992, A three-dimensional simulation of seismic waves in the Santa Clara Valley, California, from a Loma Prieta aftershock, *Bulletin Seismological Society of America*, vol. 82, pp. 2045–2074
- Frankel, A., Carver, D., Cranswick, E., Bice, T., Sell, R., Hanson, S., 2001, Observations of basin ground motion from a dense seismic array in San Jose, California, *Bulletin of the Seismological Society of America*, vol.91, pp.1–12
- Galanopoulos, A.G., 1960, Tsunamis observed on the coast of Greece from antiquity to present time, *Annali di Geofisica*, vol.13, pp.369-386
- Galanopoulos, A.G., 1961, A catalogue of shocks with  $Io \geq VI$  for the years prior to 1800 Athens, 19 pp.
- Galanopoulos, A.G., 1963, On mapping of seismic activity in Greece. *Annali di Geofisica*, vol.16, pp. 37-100
- Gallipoli, M.R., Mucciarelli, M., Albarello, D., Lapenna, V., Schiatarella, M., Calvano, G., 2003, Hints about site amplification effects comparing macroseismic hazards estimate with microtremor measurements: The Agri valley (Italy) example, *Journal of Earthquake Engineering*, vol. 7, pp. 51-72
- Gallipoli, M.R., Mucciarelli, M., Gallicchio, M., Tropeano, M., Lizza, C., 2004, Horizontal to Vertical Spectral Ratio (HVSr) measurements in the area damaged by the 2002 Molise Italy, earthquake, *Earthquake Spectra*, vol.20, pp. 581-593
- Cardarelli, E.M., Cercato, M., de Nardis, R., Di Filippo, G., Milana, G., 2008, Geophysical investigations for seismic zonation in municipal areas with complex geology: The case study of Celano, Italy, *Soil Dynamics and Earthquake Engineering*, vol.28, pp. 950-963

- Gaull, B.A., Kagami, H., Eeri, M., Taniguchi, H., 1995, The microzonation of Perth, western Australia, using microtremor spectral ratio, *Earthquake Spectr.*, vol.11, pp.173–191
- Gerya, T.V., Stöckhert, B., 2006, 2-D numerical modeling of tectonic and metamorphic histories at active continental margins, *International Journal of Earth Sciences*, vol. 95, pp.250–274
- Giampiccolo, E., Gresta, S., Mucciarelli, M., De Guidi, G., Gallipoli, M.R., 2001, Information on subsoil geological structure in the city of Catania (Eastern Sicily) from microtremor measurements, *Annali di Geofisica*, vol.44, pp.1-11
- Gitterman, Y., Zaslavsky, Y., Shapira, A., Shtivelman, V., 1996, Empirical site response evaluations: case studies in Israel, *Soil Dynamics and Earthquake Engineering*, vol.15, pp. 447-463
- Griffiths, D., Barker, R., 1993, Two-dimensional resistivity imaging and modelling in areas of complex geology, *Journal of Applied Geophysics*, vol.29, pp. 211-226
- Gueguen, P., Chatelain, J.L., Guillier, B., Yepes, H., 2000, An indication of the soil topmost layer response in Quito (Ecuador) using noise H/V spectral ratio, *Soil Dynamics and Earthquake Engineering*, vol.19, pp.127-133
- Gueguen, P., Cornou, C., Garambois, S., Banton, J., 2007, On the limitation of the H/V spectral ratio using seismic noise as an exploration tool: application to the Grenoble valley (France), a small apex ratio basin, *Pure and applied Geophysics*, vol.164, pp.115–134
- Gosar, A., Stopar, R., Car, M., Mucciarelli, M., 2001, The earthquake on 12 April 1998 in the Krn mountains (Slovenia): ground–motion amplification study using microtremors and modeling based on geophysical data, *Journal of Applied Geophysics*, vol.47, pp.153-167
- Gosar, A., 2007, Microtremor HVSR study for assessing site effects in the Bovec basin (NW Slovenia) related to 1998 Mw 5.6 and 2004 Mw 5.2 earthquakes, *Engineering Geology*, vol.91, pp.178-193
- Gosar, A., Rosek, J., Motnikar, B., Zupancic, P., 2009, Microtremor study of site effects and soil-structure resonance in the city of Ljubljana (central Slovenia), *Bulletin of Earthquake Engineering*, doi: 10.1007/s10518-009-9113-x
- Guillier, B., Cornou, C., Kristek, J., Moczo, P., Bonnefoy-Claudet, S., Bard, P.-Y., Fäh, D., 2006, Simulation of seismic ambient vibrations: does the H/V provide quantitative information in 2D-3D structures? *Proceedings of the Third International Symposium on the Effects of Surface Geology on Seismic Motion*, Grenoble, France, August 29–September 1, Paper No 185.
- Ibs-Von Seht, M., Wohlenberg, J., 1999, Microtremor measurements used to map thickness of soft sediments, *Bulletin Seismological Society of America*, vol.89, pp.250– 259
- Igarashi, T., Matsuzawa, A., Hasegawa,., 2003, Repeating earthquakes in interplate aseismic slip in the northeastern Japan subduction zone, *Journal Geophysics Research*, vol.108, No.B5, pp.1-8, doi:10.1029/2002JB001920
- Habberjam, G.M., Watkins, G.E., 1967, The reduction of lateral effects in resistivity probing. *Geophysical Prospecting*, vol.15, pp.221-235
- Haghshenas, E., Bard, P.Y., Theodulidis, N., SESAME WP04 Team, 2008, Empirical evaluation of microtremor H/V spectral ratio, *Bull Earthquake Eng*, vol 6, pp.75–108

- Hallof, P.G., 1967, An Appraisal of the variable frequency IP method after twelve of Application, *Phoenix Geophysics*, Ltd, Markham, Ontario
- Hatzfeld, D., Pedotti, G., Hatzidimitriou, P., Panagiotopoulos, P., Scodilis, M., Drakopoulos, J., Makropoulos, K., Delibasis, N., Latoussakis, J., Baskoutas, J., Frogneux, M., 1989, The Hellenic subduction beneath Peloponnesse: first results of a microseismicity study, *Earth Planetary Scientific Letter*, vol.93, pp.289-293
- Hatzfeld, D., Martin, C., 1992, The Aegean intermediate seismicity defined by ISC data, *Earth Planet Scientific Letter*, vol.113, pp.267–275
- Hatzfeld, D., Besnard, M., Makropoulos, K., Voulgaris, N., Kouskouna, V., Hatzidimitriou, P., Panagiotopoulos, P., Karakaisis, G., Deschamps, A., Lyon-Caen, H., 1993, Subcrustal microearthquake seismicity and fault plane solutions beneath the Hellenic arc, *Journal of Geophysical Research*, vol.98, pp.9861–9870
- Horike, M., 1985, Inversion of phase velocity of long period microtremors to the S-wave velocity structure down to the basement in urbanized areas, *Journal of Physics Earth*, vol.33, pp.59-96
- Hypo71 (manual revised), 1975: A computer program for determining hypocenter magnitude and first motion pattern of local earthquakes, Department of Interior, *Geological survey*, National center for earthquake research
- Huchon, P., Lyberis, N., Angelier, J., LePichon, X., Renard, V., 1982, Tectonics of the Hellenic trench: a synthesis of Sea-Beam and submersible observations, *Tectonophysics*, vol.86, pp.69-112
- Huguen, C., Mascle, J., Chaumillon, E., Woodside, J.M., Benkhelil, J., Kopf, A., Volkonskaia, 2001, Deformation styles of the eastern Mediterranean Ridge and surroundings from combined swath mapping and seismic reflection profiling, *Tectonophysics*, vol. 343, pp.21-47
- Jackson, J., 1994, Active tectonics of the Aegean region, *Annual Revision Earth planet Sciences*, vol.22, pp. 239-271
- Jolivet, L., Daniel, J.M., Truffert, C., 1994, Exhumation of deep crustal metamorphic rocks and crustal extension in arc and back-arc regions, *Lithos*, vol. 33, pp. 3– 30
- Jolivet, L., Facenna, C., Goffé B., Burov, E., Agard, P., 2003, Subduction tectonics and exhumation of high-pressure metamorphic rocks in the Mediterranean Orogen, *Am. Journal of Science*, vol. 303, pp.353-409
- Jost, M., Knabenbauer, O., Cheng, J., Harjes, H.P., 2002, Fault plane solutions of microearthquakes and small events in the Hellenic Arc, *Tectonophysics*, vol. 356, pp. 87-114
- Joyner, W.B., 2000, Strong motion from surface waves in deep sedimentary basins, *Bulletin Seismological Society of America*, vol.90, pp. 95–S112.
- Kagami, H., Duke, C.M., Liang, G.C., Ohta, Y., 1982, Observation of 1-5 second microtremors and their application to earthquake engineering, Part II. Evaluation of site effect upon seismic wave amplification due to extremely deep soil deposits, *Bulletin of the Seismological Society of America*, vol.72, pp.987-998
- Kahle, H-G., Straub, C., Reilinger, R., McClusky, S., King, R., Hurst, K., Veis, G., Kastens, K., Cross, P., 1998, The strain rate field in the eastern Mediterranean region, estimated by repeated GPS measurements, *Tectonophysics*, vol.294, pp.237-252.

- Kahle, H-G., Cocard, M., Peter, Y., Geiger, A., Reilinger, R., Barka, A., Veis, G., 2000, GPS derived strain rate field within the boundary of the Eurasia, African and Araboian plates, *Journal of Geophysics Research*, vol.105, pp.23353-23370
- Köhler, A., Ohrnberger, M., Scherbaum, F., Stange, S., Kind, F., 2004, Ambient vibration measurements in the southern Rhine Graben close to Basle, *Annals of Geophysics*, vol. 47, n.6, pp. 1771-1781
- Kanai, K., Tanaka, T., 1961, On microtremors VIII, *Bulletin of the Earthquake Research Institute*, vol.39, pp.97-114
- Karageorgiou, K., 1968, Geological map of Kastelli
- Karagianni, E.E., Panagiotopoulos, D.G., Panza, G.F., Suhadolc, P., Papazachos, C.B., Papazachos, B.C., Kiratzi, D., Hatzfeld, D., Makropoulos, K., Priestley, K., Yuan, A., 2002, Rayleigh wave group velocity tomography in the Aegean area. *Tectonophysics*, vol.358, pp.187-209
- Karagianni, E.E., Papazachos, C.B., Panagiotopoulos, D.G., Suhadolc, P., Yuan, A., Panza, G.F., 2005. Shear velocity structure in the Aegean area obtained by inversion of Rayleigh waves, *Geophys. Journal International*, vol.160, pp. 127-143
- Karagianni, E.E., Papazachos, C.B., 2007, Shear velocity structure in the Aegean region obtained by joint inversion of Rayleigh and Love waves, *Geological Society of London*, Special Publications, vol. 291, pp. 159-181
- Karnik, V., 1969, Seismicity of the European Area, Part I. *D. Reidel Publ. Comp., Dordrecht, Netherlands*, 364 pp.
- Karnik, V., 1971, Seismicity of the European Area, Part II, 1801-1900. *D. Reidel Publ. Comp., Dordrecht, Netherlands*, 218 pp.
- Kawase, H., 1996, The cause of the damage belt in Kobe: "the basin-edge effect", constructive interference of the direct S-wave with the basin induced diffracted Rayleigh waves, *Seismological Research Letter*, vol.67, pp.25-34
- Kastens, K.A., 1991, Rate of outward growth of the Mediterranean Ridge accretionary complex, *Tectonophysics*, vol.199, pp.25-50
- Keupp, H. and Bellas, S.M., 2000, Neogene development of the sedimentary basins of NW Crete island, Chania Prefecture, South Aegean Arc System (Greece), *Berliner Geowiss. Abh*, vol. 34, pp.3-117
- Kilias, A., Fassoulas, C., Mountrakis, D., 1994, Tertiary extension of continent crust and uplift of Philoritis metamorphic core complex in the central part of the Hellenic arc (Crete, Greece), *Geol.Rundsch*, vol.83, pp.417-430
- Kiratzi, A.A., Papazachos, C.B., 1995. Active seismic deformation in the southern Aegean Benioff zone, *Journal Geodynamics*, vol.19, pp. 65-78
- Knapmeyer, M., Harjes, H.-P., 2000, Imaging crustal discontinuities and the downgoing slab beneath western Crete, *Geophysical Journal International*, vol.143, pp. 1-21
- Konno, K., Ohmachi, T., 1998, Ground-motion characteristics estimated from spectral ratio between horizontal and vertical components of microtremor, *Bulletin Seismological Society American*, vol.88, pp.228-241
- Kovachev, S.A., Kuzin, I.P., Soloviev., S.L., 1991a, Spatial Distribution of microearthquakes in the Frontal Part of the Hellenic Arc according to Observations of Bottom Seismographs, *Geotektonika*, vol.25, pp.155-160



- Kovachev, S.A., Kuzin, I.P., Shoda, O.Yu., Soloviev, S.L., 1991b, Attenuation of S-waves in the lithosphere of the Sea of Crete according to OBS observations, *Physics of the Earth and Planetary Interiors*, vol.69, pp.101-111
- Kovachev, S.A., Kuzin, I.P., Soloviev, S.L., 1992, Microseismicity of the frontal Hellenic arc according to OBS observations, *Tectonophysics*, vol.201, pp.317-327
- Lachet, C., Bard PY, 1994, Numerical and theoretical investigations on the possibilities and limitations of Nakamura's technique, *Journal of Physics of the Earth*, vol. 42, pp. 377-397
- Laigle, M., Sachpazi, M., Hirn, A., 2004, Variation of seismic coupling with slap detachment and upper plate structure along the western Hellenic subduction zone, *Tectonophysics*, vol.391, pp.85-95
- Lallemant, S., Truffert, C., Jolivet, L., Henry, P., Chamo-Rooke, N., de Voogd, B., 1994, Spatial transition from compression to extension in the Western Mediterranean Ridge accretionary complex, *Tectonophysics*, vol.234, pp.33-52
- Lapenna, V., Pietro, P., Perrone, A., Piscitelli, S., Sdao, F., Rizzo, E., 2003, High resolution geoelectrical tomographies in the study of Giarrossa landslide (southern Italy), *Bulletin Engineering Geology*, vol. 62, pp. 259-268
- Lebrun, B., Hatzfeld, D., Bard, P.-Y., 2001, Site effect study in urban area: experimental results in Grenoble (France), *Pure and Applied Geophysics*, vol.158, pp.2543–2557
- Lee, W.H.K., Lahr, J.C., 1972, Hypo71: A computer program for determining hypocenter, magnitude and first motion pattern of local earthquakes, *Open file report, US Geological survey, Menlo Park, California, 100pp.*
- Le Pichon, X., Angelier, J., 1979, The hellenic arc and trench system: A key to the neotectonic evolution of the eastern mediterranean area, *Tectonophysics*, vol. 60, pp.1-42
- Le Pichon, X., Angelier, J., Sibuet, J-C., 1982, Plate boundaries and extensional tectonics, *Tectonophysics*, vol.81, pp.239-256
- Le Pichon, X., Chamot-Rooke, N., Lallemant, S., 1995, Geodetic determination of the kinematics of central Greece with respect to Europe, *Journal Geophysical Research*, vol.100, pp. 12675-12690
- Lermo, J., Chavez-Garcia, F., 1993, Site effect evaluation using spectral ratios with only one station, *Bulletin Seismological Society America*, vol.83, pp.1574–1594
- Lermo, J., Chavez-Garcia, F.J., 1994a, Site effect evaluation at Mexico City: dominant period and relative amplification from strong motion and microtremor records, *Soil Dynamics and Earthquake Engineering*, vol.15, pp.141-146
- Lermo, J., Chavez-Garcia, F., 1994b, Are microtremors useful in site response evaluation? , *Bulletin Seismological Society of America*, vol. 84, pp.1350–1364
- Loke, M.H., Barker, R.D., 1995, Least-squares deconvolution of apparent resistivity pseudosections, *Geophysics*, vol. 60, pp.1682–1690
- Loke, M.H., Barker, R.D., 1996a, Rapid least-squares inversion of apparent resistivity pseudosections by a quasi-Newton method, *Geophysical Prospecting*, vol.44, pp.131–152
- Loke, M.H., Barker R.D., 1996b, Practical techniques for 3D resistivity surveys and data inversion, *Geophysical Prospecting*, vol. 44, pp.499-523
- Loke, M.H., 1997, Rapid 2D resistivity inversion using the least-squares method, *RES2DINV Program manual*, Penang, Malaysia

- Loke, M.H., 1999, Electrical imaging surveys for environmental and engineering studies - *A practical guide to 2D and 3D surveys*, <http://www.abem.se>
- Loke, M.H., 2000, Topographic modelling in electrical imaging inversion, *Proceedings*, 62<sup>nd</sup> Conference and Technical Exhibition
- Louie, J.N., 2001, Faster, Better: Shear-Wave Velocity to 100 Meters Depth from Refraction Microtremor Arrays, *Bulletin of the Seismological Society of America*, vol.91, pp.347-364
- Lombardo, G., Rigano, R., 2007, Local seismic response in Catania (Italy): A test area in the northern part of the town, *Engineering Geology*, vol.94, pp.38-49
- Makris, J., 1973, Some geophysical aspects of the evolution of the Hellenides, *Bulletin Geological Society of Greece*, vol. 10, pp. 206-213
- Makris, J., 1976, A dynamic model of the Hellenic Arc deduced from Geophysical data, *Tectonophysics*, vol.36, pp.339-346
- Makris, J., Veis, R., 1977, Crustal structure of the central Aegean Sea and the islands of Evia and Crete, Greece, obtained by refraction seismic experiments, *Journal of Geophysical Research*, vol.42, pp.329-341
- Makris, J., 1978, The crust and upper mantle of the Aegean region from deep seismic soundings, *Tectonophysics*, vol.46, pp.269-284
- Makropoulos, K.C., 1978, The statistics of large earthquake magnitude and an evaluation of Greek seismicity, *PhD Thesis*, University of Edinburgh, Edinburgh, UK
- Makropoulos, K.C, Burton, P.W., 1984, Greek tectonics and seismicity, *Tectonophysics*, vol. 106, pp. 275-304
- Makropoulos, K.C., Drakopoulos, J.K., Latoussakis, J.B., 1989, A revised earthquake catalogue for Greece since 1900. *Geophysical Journal International*, vol.98, pp. 391-394
- Margiotta, S., Negri, S., 2008, Stratigraphic and geophysical integrated methodologies for the interpretation of sulphur water formational environment in Salento (Italy), *International Journal of Coal Geology*, vol. 75, pp. 27-39
- Marone, F., Lee, S., Giardini, D., 2004, Three Dimensional upper mantle S velocity model for the Eurasia-Africa plate boundary region, *Journal Geophysical International*, vol.158, pp. 109-130
- Martinez, J., Benavente, J., Garcia-Arostegui, J.L., Hidalgo, M.C., Rey, J., 2009, Contribution of electrical resistivity tomography to the study of detrital aquifers affected by seawater intrusion-extrusion effects: The river Velez delta (Southern Spain), *Engineering Geology*, doi: [10.1016/j.enggeo.2009.07.004](https://doi.org/10.1016/j.enggeo.2009.07.004).
- McLaren, J.P., Frohlich, C., 1985, Model calculations of regional network locations for earthquakes in subduction zones, *Bulletin of the Seismological Society of America*, vol. 75, pp. 397-413
- McClusky, S., S. Balassanian., A. Barka, C. Demir, S. Ergintav, I. Georgiev, O. urkan, M. Hamburger, K. Hurst, H. Kahle, K. Kastens, G. Kekilidze, R. King, V. Kotzev, O. Lenk, S. Mahmoud, A. Mishin, M. Nadariya, A. Ozounis, D. Paradissis, Y. Peter, M. Prelipin, R. Reilinger, I. Sanli, H. Seeger, A. Tealeb, M.N. Toksöz, and G. Veis, 2000, Global Positioning System constraints on plate kinematics and dynamics in the eastern Mediterranean and Caucasus, *Journal Geophysical Research*, vol.105, pp. 5695-5719

- McGuire, R.K., 1993, Computations of seismic hazard, *Annali di Geofisica*, vol. 36, pp.181-200
- McGuire, R.K., 2001, Deterministic vs Probabilistic Earthquake Hazards and Risks, *Soil Dynamics Earthquake Engineering*, vol. 21, pp. 377- 384
- McKenzie, D.P., 1970, The plate tectonics of the mediteranean region, *Nature*, vol. 226, pp. 239-243
- McKenzie, D.P., 1972a, Active tectonics of the Mediterranean region, *Geophysical Journal of the Royal Astronomics Society*, vol.30, pp.109-185
- McKenzie, D.P., 1972b, Active tectonics of the Alpine-Himalayan belt: the Aegean Sea and surrounding regions, *Geophysical Journal of the Royal Astronomics Society*, vol.55, pp. 217-254
- McKenzie, D.P., 1978, Active tectonics of the Alpine-Himalayan belt: the Aegean Sea and surrounding regions, *Geophys. J. R. Astron. Soc*, 55, 217–254.
- Meads, N.L., Bentley, L.R., Mendoza, C.A., 2003, Application of electrical resistivity imaging to the development of a geologic model for a proposed Edmonton landfill site, *Canadian Geotechnical Journal*, vol. 40, pp. 551–558
- Meier, T., Rische, M., Endrun, B., Vafidis, A., Harjes, H.P, 2004a, Seismicity of the Hellenic subduction zone in the area of western and central Crete observed by temporary local seismic networks, *Tectonophysics*, vol. 383, pp.149-169
- Meier, T. Dietrich, K., Stöckhert, B., Harjes, H.-P., 2004b, One dimensional models for shear wave velocity for the Eastern Mediterranean obtained from the inversion of Rayleigh wave phase velocities and tectonic implications, *Geophysical Journal International*, vol. 156 pp. 45–58
- Meier, T., Becker, D., Endrun, M., Rische, M., Bohnhoff, M., Stöckhert, B., Harjes, H-P., 2007, A model for the Hellenic subduction zone in the area of Crete based on seismological investigations, *Geological Society of London*, Special Publications, vol. 291, pp. 183-199
- Meulenkamp, J.E., Dermitzakis, M., Georgiadou-Dikeoulia, E., Jonkers, H.A., Böger, H., 1979, *Field Guide to the Neogene of Crete*, Publications of the Department of Geology and Paleontology, University of Athens, A32
- Meulenkamp, J.E., Wortel, M.J.R., van Wamel, W.A., Spakman, W., Hoogerduyn Strating, E., 1988, On the Hellenic subduction zone and the geodynamic evolution of Crete since the late Middle Miocene. *Tectonophysics*, vol. 146, pp. 203-215
- Meulenkamp, J.E., van der Zwaan, G.J., van Wamel, W.A., 1994, On Late Miocene to recent vertical motions in the Cretan segment of the Hellenic arc, *Tectonophysics* vol.234, pp. 53-72
- Milana, G., Barba, S., Del Pezzo, E., Zambonelli, E., 1996, Site response from ambient noise measurements: new perspectives from an array study in central Italy, *Bulletin of the Seismological Society of America*, vol.86, pp. 320–328
- Moisidi, M., Vallianatos, F., Soupios, P., Makris, J.P., Nikolintaga, M.I., 2004, Estimation of seismic response of historical and monumental sites using microtremors: a case sudy in ancient Aptera, Chania, Crete (Greece), *Bulletin of the Geological Society of Greece*, Proceedings of the 10<sup>th</sup> Int. Congress, Thessaloniki, vol. XXXVI, pp.1441-1450

- Morrato, L., Orlecka-Sikora, B., Costa, G., Suhadolc, P., Papaioannou, Ch., Papazachos, C.B., 2007, A deterministic hazard analysis for shallow earthquakes in Greece, *Tectonophysics*, vol. 442, pp.66-82
- Mouslopoulou, V., Andreou, C., Atakan, K., Fountoulis, I., 2001, Paleoseismological investigations along the Kera fault zone, Western Crete: Implications for seismic Hazards Assesment, *Bulletin of the Geological Society of Greece*, Proceedings of the 9<sup>th</sup> International congress, vol. XXIV/4, pp. 1531-1537
- Mucciarelli, M., 1998, Reliability and applicability range of the Nakamura's technique using microtremors – An experimental approach, *Journal of Earthquake Engineering*, vol.2, pp.625-638
- Mucciarelli, M., Monacheri, G., 1998, A Quick survey of local amplifications and their correlation with damage observed during the Umbro-Marchesan earthquake of September 26, 1997, *Journal of Earthquake Engineering*, vol.2, 2, pp.1-13
- Mucciarelli, M., Monacheri, G. 1999, The Bovec (Slovenia) earthquake April, 1998: Preliminary quantitative association among damage , ground motion amplification and building frequencies, *Journal of Earthquake Engineering*, vol 3, Issue 3, pp.317-327
- Mucciarelli, M., and Gallipoli, M. R., 2001, A critical review of 10 years of microtremor HVSR Technique, *Bolletino di Geofisica Teorica e Applicata*, vol.42, pp. 255–266
- Mucciarelli, M., Contri, P., Monacheri, G., Calvano, G., Gallipoli, M.R, 2001, An empirical method to assess the seismic vulnerability of existing buildings using the HVSR technique, *Paleography*, vol.158, pp. 2635-2647
- Mucciarelli, M., Gallipoli, M.R., Arcieri, M., 2003, Stability of Horizontal-to-Vertical Spectral Ratio by triggered noise and earthquake recordings, *Bulletin Seismological Society of America*, vol. 93, pp. 1407-1412
- Mucciarelli, M., Gallipoli, M.R, 2004, The HVSR technique from microtremor to strong motion: empirical and statistical considerations; *13th World Conference on Earthquake Engineering Vancouver*, Paper No. 45
- Mucciarelli, M., Gallipoli, M., Di Giacomo, D., Di Nota, F., Nino, E., 2005, The influence of wind on measurements of seismic noise, *Geophysical Journal International*, vol.161, pp. 303 -308
- Mucciarelli, M., 2008, Codes, models and reality: reductionism vs holism in a review in the Umbria-Marche region, *Annals of Geophysics*, vol.51, pp. 491-498
- Murono, Y., Nishimura, A., 1999, Characteristics of Local Site Effects on Seismic Motion Non-linearity of Soil and Geological Irregularity, *Quarterly Report of RTRI*, vol.40, pp.139-145
- Nakamura, Y., 1989, A method for Dynamic Characteristics Estimation of Subsurface using Microtremor on the Ground surface, *Quarterly Report of RTRI* , Railway Technical Research Institute , vol.30, pp. 25–30
- Nakamura, Y., 1996, Real Time Information systems for seismic Hazards Mitigation UREDAS, HERAS, PIC, *Quarterly Report of RTRI*, vol.37, No3
- Nakamura, Y., 1997, Seismic vulnerability Indices for ground and structures Using microtremor, *World Congress on Railway Research in Florence*, Italy
- Nakamura, Y., 2000, Clear identification of fundamental idea of Nakamura's method for dynamic characteristics estimation of subsurface using microtremor on the ground

- surface and its applications, *Proceedings of the 12th World Conference on Earthquake Engineering*, Auckland, New Zealand
- Nakamura, Y., Gurler, E.D., Saita, J., Rovelli, A., Donati, S., 2000a, Vulnerability investigation of Roman Colliseum using microtremor, *World Conference on Earthquake Engineering*, N. Zealand
- Nakamura, Y., Sato, T., Nishinaga, M., 2000b, Local site effect of Kobe based on microtremor measurement, *Proceedings of the sixth international Conference on Seismic Zonation (6ISCZ)*, EERI, Palm, Springs, California
- Nguyen, F., van Rompaey, G., Teerlynck, H., Van Camp, M., Jongmans, D., Camelbeeck, T., 2004, Use of microtremor measurement for assessing site effects in Northern Belgium-interpretation of the observed intensity during the Ms=5.0 June 11, 1938 Earthquake, *Journal of Seismology*, vol.8, pp.41–56
- Nguyen, F., Garambois, S., Jongmans, D., Pirard, E., Loke, M.H., 2005, Image processing of 2D resistivity data for imaging faults, *Journal of Applied Geophysics* vol. 57, pp. 260-277
- Nguyen, F., Garambois, S., Chardon, D., Hermitte, D., Bellier, O., Jongmans, D., 2007, Subsurface electrical imaging of anisotropic formations affected by a slow active reverse fault, Provence, France, *Journal of Applied Geophysics*, vol. 62, pp. 338–353.
- Nogoshi, M. & Igarashi, T., 1971, On the amplitude characteristics of microtremor, Part 2 (In Japanese with English abstract), *Journal of Seismological Society of Japan*, vol. 24, pp. 26-40
- Ohmachi, T., Umezono, T., 1998, Rate of Rayleigh waves in microtremors, *Proceeding of the Second International Symposium on the Effects of Surface Geology on Seismic Motion*, Yokohama, Japan, pp. 587–592
- Ojeda, A., Escallon, J., 2000, Comparison between different techniques for evaluation of predominant periods using strong ground motion records and microtremors in Pereira Colombia, *Soil Dynamics and Earthquake Engineering*, vol.20, pp.137-143
- Okada, H., 1999, A new Passive Geophysical Survey Method (BEM) using microtremors, *Lecture in the One day Seminar held in 1997 at the Hokkaido University by the Society of Exploration Geophysicists of Japan*
- Okada, H., 2003, The microtremor survey method, *Geophysical Monograph Series*, Society of Exploration Geophysicists, Number 12
- Oros, E., Site effects investigation in the city of Timisoara using spectra ratio methods., 2009, *Romanian Reports in Physics*, vol.61, pp. 347-358
- Panou, A.A., Theodulidis, N.P., Hatzidimitriou, P.M., Stylianidis, K., Papazachos, C.B., 2005, Ambient noise horizontal-to-vertical spectral ratio in site effects estimation and correlation with seismic damage distribution in urban environment: the case of the city of Thessaloniki (Northern Greece), *Soil Dynamics and Earthquake Engineering* vol.25, pp. 261–274
- Papadimitriou, E.E., Sykes, L. R., 2001, Evolution of the stress field in the northern Aegean Sea (Greece), *Geophysical Journal International*, vol. 146, pp. 1-20
- Papadopoulos, N. G., Tsourlos, P. G., Tsokas, N., Sarris, A., 2006, Two-dimensional and three-dimensional resistivity imaging in archaeological site investigation, *Archaeological prospecting*, vol. 13, pp. 163-181

- Papazachos, B.C., Delibasis, N.D., 1969, Tectonics stress field and seismic faulting in the area of Greece, *Tectonophysics*, vol. 7, pp. 231-255
- Papazachos, B.C., Comninakis, P.E., 1970, Geophysical features of the Greek Island arc and Eastern Mediterranean Ridge, *Com.Rend.des Seasens de la Conf.Reunie a Madrid*, vol.16, pp. 74-75
- Papazachos, B.C., Comninakis, P.E., 1971, Geophysical and tectonic features of the Aegean arc, *Journal of Geophysical Research*, vol.76, pp. 8517-8533
- Papazachos, B. C., Comninakis, P.E., 1982, A catalogue of historical earthquakes in Greece and surrounding area, 479BC- AD1900, *Publication Geophysical Laboratory, University of Thessaloniki*, vol.6, 24 pp.
- Papazachos, B.C., 1990, Seismicity of the Aegean and the surrounding area, *Tectonophysics*, vol.178, pp. 287-308
- Papazachos, C.B., 1994, Structure of the crust and upper mantle in SE Europe by inversion of seismic and gravimetric data, *PhD Thesis*, University of Thessaloniki (in Greek), 208pp.
- Papazachos, B.C., Kiratzi, A., Papadimitriou, E., 1991, Regional focal mechanisms for earthquakes in the Aegean area, *Pure Applied Geophysics*, vol.136, pp. 405-420
- Papazachos, C.B., Hatzidimitriou, P.M., Panagiotopoulos, D.G., Tsokas, G.N., 1995. Tomography of the crust and upper mantle in southeast Europe, *Journal of Geophysical Research*, vol.100, pp.12405–12422
- Papazachos, B.C., Kiratzi, A.A., 1996, A detailed study of the active crustal deformation in the Aegean and surrounding area, *Tectonophysics*, vol. 253, pp.129-153
- Papazachos, B.C., 1996, Introduction to Applied Geophysics, *Ziti Editions* (in Greek), Thessaloniki
- Papazachos, C.B., Nolet, G., 1997, P and S deep velocity structure of the Hellenic area obtained by robust nonlinear inversion of travel times, *Journal of Geophysical Research*, vol. 102, pp. 8349–8367
- Papazachos, B.C., Papazachou, K., 1997, The earthquakes of Greece, Ziti edition, Thessaloniki
- Papazachos, B.C., Papadimitriou, E.E., Kiratzi, A.A., Papazachos, C.B., Louvari, E.K., 1998. Fault plane solutions in the Aegean Sea and the surrounding area and their tectonic implication, *Bolletino di Geofisica Teorica e Applicata*, vol.39, pp.199–218
- Papazachos, B.C., Comninakis, P.E., Karakaisis, B.G., Karakostas, V.G., Papaioannou, C.A., Papazachos, C.B., Scordilis, E.M., 2000a, A catalogue of earthquakes in Greece and Surrounding Area for the Period 550BC-AD1999, *Publication Geophysical Laboratory, University of Thessaloniki*
- Papazachos, B.C., Karakostas, V.G., Papazachos, C.B., Scordilis, E.M., 2000b, The geometry of the Wadatti-Benioff zone and lithospheric kinematics in the Hellenic arc, *Tectonophysics*, vol. 319, pp. 275-300
- Papazachos, B.C., Papazachou, C.C., 2003, Earthquakes of Greece, *Ziti Editions* (in Greek), Thessaloniki, 286 pp.
- Parolai, S., Bormann, P., Milkreit, C., 2002, New relationships between Vs, thickness of sediments, and resonance frequency calculated by the H/V ratio seismic noise for the Cologne area (Germany), *Bulletin Seismological Society of America*, vol. 92, pp. 2521–2527

- Picozzi, M., Strollo, A., Parolai, S., Durukal, E., Ozel, O., Karabulut, S., Zschau, J., Erdik, M., 2009, Site characterization by seismic noise in Istanbul, Turkey, *Soil Dynamics and Earthquake Engineering*, vol. 29, pp.469-482
- Pirazzoli, P.A., Thommeret, J., Thommeret, Y., Laborel, J., Montag-Gioni, L.F., 1982, Crustal block movements from Holocene shorelines: Crete and antikythira (Greece), *Tectonophysics*, vol. 86, pp. 27-43
- Pirazzoli, P.A., Laborel, J., Stiros, S.C., 1996, Earthquake clustering in the Eastern Mediterranean during historical times, *Journal of Geophysical Research*, vol.101, pp. 6083-6097
- Pirazzoli, P.A., 2005, A review of possible eustatic, isostatic and tectonic contributions in eight-late Holocene relative sea-levels histories from the Mediterranean, *Quaternary Science Reviews*, vol. 24, pp.1989-2001
- Pitilakis, K., Cultreras, G., Margaris, B., Ameri, G., Anastasiadis, A., Franceschina, G., Koutrakis, S., 2007, Seismic hazard assessment :Probabilistic and deterministic approach for rock site conditions, *4<sup>th</sup> International Conference on Earthquake Geotechnical Engineering* , Number 1701
- Postma, G., 1990, Depositional architecture and facies of river and fan deltas: a synthesis. In coarse and grained deltas, *Special Publications International Association Sedimentology*, vol.10, pp.13-27
- Press, W.H., Flannery, B.P., Teukolsky, S.A., Vetterling, W.T., 1988, Numerical Recipes in Cambridge University Press, Cambridge, UK
- Prior, D.B., Bornhold, B.D., 1990, The underwater development of Holocene fan deltas, In coarse and grained deltas, *Spec. Publ. Int. Assoc. Sediment*, vol.10, pp.75-90
- Rahl, J.M., Fassoulas, C., Brandon, T., 2004, Exhumation of high pressure metamorphic rock within an active convergent margin, Crete, Greece, *32<sup>th</sup> International Geological Congress, Field guide book B32*, Firenze, Italy, n2, pp. 3-36, B32
- Raptakis, D., Theodoulidis, N., Pitilakis, K., 1998, Data analysis of the EUROSEISTEST strong motion array in Volvi (Greece): Standard and horizontal to vertical spectra ratio techniques, *Earthquake Spectra*, vol. 14, pp.203-240.
- Raptakis, D.G., Manakou, M.V., Chávez-García, F.J., Makrac, K.A., Pitilakis, K.D., 2005, A 3D configuration of Mygdonian basin and preliminary estimate of its site response, *Soil Dynamics and Earthquake Engineering*, vol.25, pp.871-887
- Reiter, L., 1990, Earthquake Hazards Analysis, Issues and insights, Columbia University press, New York
- Reynolds, J.M., 1997, An introduction to applied and environmental Geophysics, John Wiley and Sons Ltd, Chichester.
- Reynolds, J.M., 2004, Geophysics in engineering investigations, *Quarterly Journal of engineering geology and hydrology*, vol.34, pp. 369-370
- Reynolds, J.M., 2006, The role of geophysics in glacial hazard assessment, *First Break* vol.24, pp.61-66
- Ring, U., Brachert, T., Fassoulas, C., 2001a, Middle Miocene graben development in Crete and its possible relation to large-scale detachment faults in the southern Aegean, *Terra Nova*, vol.13, pp. 297-304

- Ring, U., Layer, P.W., Reischmann, T., 2001b, Miocene high-pressure metamorphism in the Cyclades and Crete, Aegean Sea, Greece: evidence for large-magnitude displacement on the Cretan detachment, *Geology*, vol.29, pp. 395–398
- Ring, U., Layer, P.W., 2003, High-pressure metamorphism in the Aegean, eastern Mediterranean: underplating and exhumation from the Late Cretaceous until the Miocene to Recent above the retreating Hellenic subduction zone, *Tectonics*, vol. 22, pp.1022, doi:10.1029/2001TC001350
- Rodriguez, H.S., Midorikawa, S., 2002, Applicability of the H/V spectral ratio of microtremors in assessing site effects on seismic motion, *Earthquake Engineering Structural Dynamics*, vol.31, pp.261–279
- Roten, D., Fäh, D., Cornou, C., Giardini, D., 2006, Two-dimensional resonances in Alpine valleys identified from ambient vibration wavefields, *Geophysical Journal International*, vol.165, pp. 889–905
- Roten, D., Fäh, D., Olsen, K.B., Giardini, D., 2008, A comparison of observed and simulated site response in Rhône valley, *Geophysical Journal International*, vol.173, pp.958-978
- Rovelli, A., Scognamiglio, L., Marra, F., Caserta, A., 2001, Edge-diffracted 1-sec surface waves observed in a small-size intramountain basin (Colfiorito, Central Italy), *Bulletin Seismological Society of America*, vol.91, pp.1851–1866
- Roy, A., Apparao., 1970, Depth of investigation in direct current methods, *Geophysics*, vol.36, pp.943-959
- Sanchez-Sesma, F.J., 1990, Elementary solutions for the response of a wedge-shaped medium to incident SH and SV waves, *Bulletin Seismological Society of America*, vol.80, pp. 737-742
- Sasaki, Y., 1989, 2-D joint inversion of magnetotelluric and dipole-dipole resistivity data, *Geophysics*, vol.54, pp. 254-262
- Sasaki, Y., 1992, Resolution of resistivity tomography inferred from numerical simulation, *Geophysical Prospecting*, vol.40, pp. 453-464
- Seidel, E., Theye, T., 1993, High-pressure/ low-temperature metamorphism in the external Hellenides (Crete, Peloponnese), *Bulletin of Geological Society of Greece*, vol. 28, pp. 49–55
- Seidel, M., Pack, A., Sharp, Z.D., 2005, The Kakopetros and Ravdoucha iron- oxide deposits, western Crete, Greece: fluid transport and mineralization within a detachment zone, *Economic Geology*, vol.100, pp. 165–174
- Seidel, M. Seidel., Stöckhert, B., 2007, Tectono-sedimentary evolution of Lower to Middle Miocene half-graben basins related to an extensional detachment fault (western Crete, Greece), *Blackwell Publishing, Terra Nova*, 19, pp. 39 - 47
- Sen, S., 2007, A fault zone cause of large amplification and damage in Avclar (west of Istanbul) during 1999 Izmit earthquake, *Natural Hazards*, vol.43 pp. 351–363
- Schorlemmer, D., Wiemer, S., 2005, Microseismicity data forecast rupture area, *Nature*, vol. 434, pp.1086, doi:101038/4341086a
- Scordilis, E., Voidomatis, F., Delibasis, N., Stavrakakis, G., Papanastasiou, D., Karakaisis, G., Panagiotopoulos, D., Papadimitriou, E., Tsapanos, T., Karagianni, E., Mpaka, A., Drakopoylos, I., Papazachos, B., 1995, Microseismicity of the Heracleion (Crete island) region, *Publication Geophysical Laboratory, University of Thessaloniki* vol.16, 15pp.



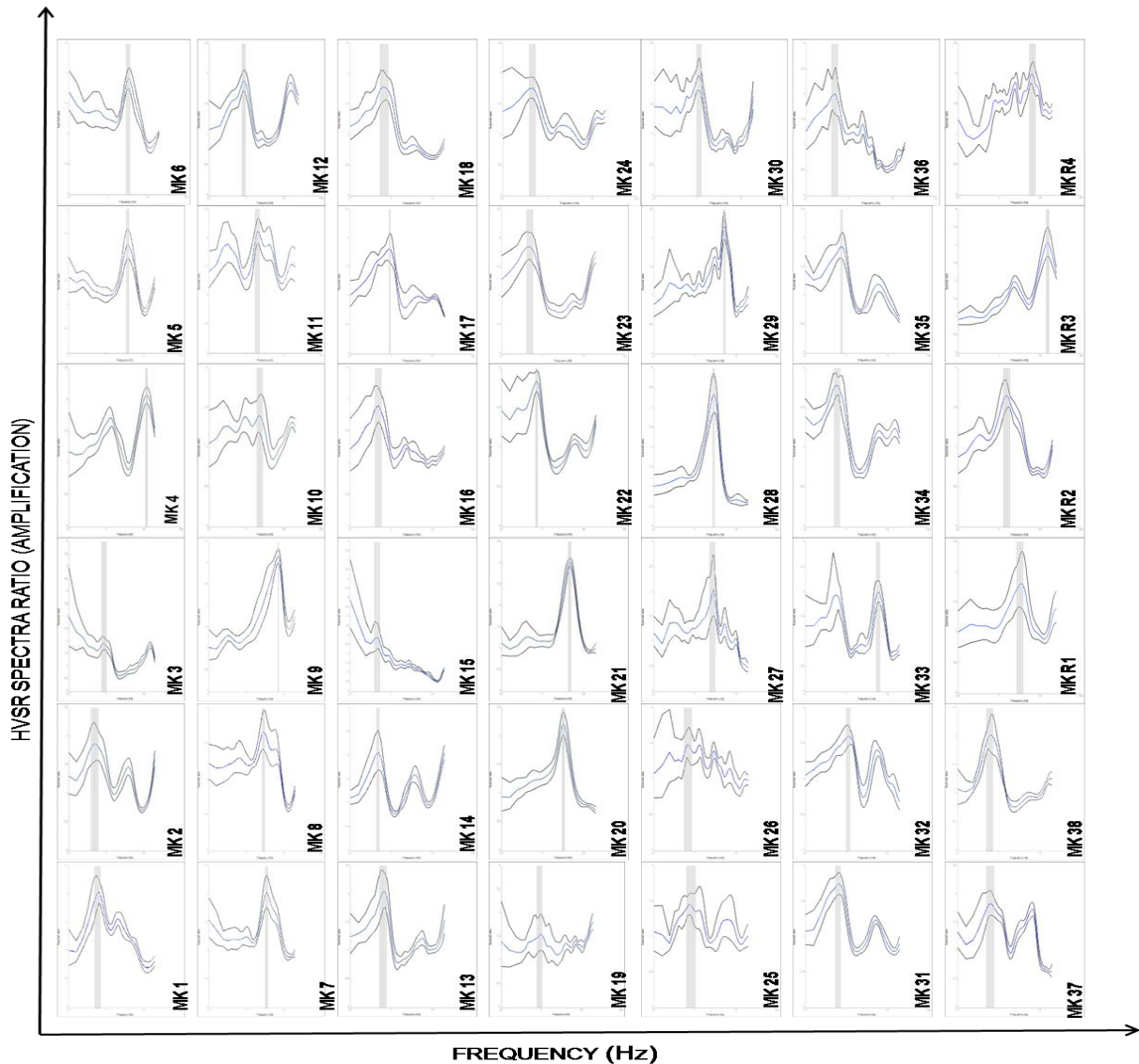
- Shaw, B., Ambraseys, N.N., England, P.C., Floyd, M.A., Gorman, G.J., Higham, T.F.G., Jackson, J.A., Nocquet, J.-M., Pain, C.C., Piggott, M.D., 2008, Eastern Mediterranean tectonics and tsunami inferred from the AD 365 earthquake, *Nature Geoscience*, doi:10.1038/ngeo151
- Sleep, N.H., Fugita, K., Principles of Geophysics, 1997, *Blackwell Publications*
- Spakman, W., Wortel, M.J.R., Vlaar, N.J., 1988, The Hellenic subduction zone: a tomographic image and its geodynamic implications. *Geophysical Research Letters* vol. 15, pp. 60-63
- Stein, S., Wysession, M., 2003, An introduction to seismology earthquakes and earth structures, *Blackwell publishing*
- Steimen, S., 2004, Uncertainties in Earthquake Scenarios, Phd thesis, Swiss Federal institute of technology Zurich, *Dissertation*, ETH No. 15740
- Stiros, S., 1996, Late Holocene relative sea-level changes in SW Crete: evidence of an unusual earthquake cycle, *Annali di Geofisica*, vol. 39, pp. 677–687
- Stiros, S.C., Papageorgiou, S., 2001, Seismicity of Western Crete and the destruction of the town of Kisamos at AD 365: Archaeological evidence, *Journal of Seismology*, vol 5, pp. 381–397
- Störz, H., W, Storz, W., Jacobs, F., 2000, Electrical resistivity tomography to investigate geological structures of the earth's upper crust, *Geophysical Prospecting*, vol. 48, pp. 455-471
- Taymaz, T., Jackson, J., Westaway, R., 1990, Earthquake mechanisms in the Hellenic trench near Crete, *Geophysical Journal International*, vol.102, pp. 695-731
- Taymaz, T., Jackson, J., McKenzie, D., 1991, Active tectonics of the north and central Aegean Sea, *Geophysical Journal International*, vol. 106, pp. 433-490
- ten Veen, J.H., Meijer, P.T., 1998, Late Miocene to Recent tectonic evolution of Crete (Greece): geological observations and model analysis, *Tectonophysics*, vol.298, pp. 191-208
- ten Veen, J.H., Postma, G., 1999a, Neogene tectonics and basin fill patterns in the Hellenic outerarc. *Basin Research* , vol.11, pp. 223-241.
- ten Veen, J.H., and Postma, G., 1999b, Roll-back controlled vertical movements of outer-arc basins of the Hellenic subduction zone (Crete, Greece), *Basin Research* vol. 11, pp. 243-266
- ten Veen. J., Kleinspehn. K, 2003, Incipient continental collision and plate-boundary curvature: Late Pliocene–Holocene transtensional Hellenic forearc, Crete, Greece *Journal of the Geological Society of London*, vol. 160, 2003, pp. 161-181
- Teves-Costa, P., Matias, L. and Bard, P.Y., 1996, Seismic Behaviour estimation of thin alluvium layers using microtremors recordings, *Soil Dynamics and Earthquake Engineering*, vol.15, pp. 201-209
- Theodoulidis, N., Bard, P.Y., 1995, Horizontal to vertical spectral ratio and geological conditions : an analysis of strong motion data from Greece and Taiwan (SMART-1), *Soil Dynamics and Earthquakes Engineering*, vol. 14, pp. 177-197
- Theodoulidis, N., Cultrera, G., De Rubeis, V., Cara, F., Panou, A., Pagani, M., Teves-Costa, P., 2008, Correlation between damage and ambient noise H/V spectral ratio: the SESAMEproject results, *Bulletin of Earthquake Engineering*, vol.6, pp. 109-140

- Thomson, S.N., Stöckhert, B., Brix, M.A., 1998, Miocene high pressure metamorphic rocks of Crete, Greece: Implications for the speed of tectonics, *Geology*, vol.26, pp.259-262
- Thomson, S.N., Stöckhert, B., Brix, M.R., 1999, Miocene high-pressure metamorphic rocks of Crete, Greece: rapid exhumation by buoyant escape, In: Ring, U., Lister, G., Willet, S., Brandon, M. (Eds.), *Exhumation Processes: Normal Faulting, Ductile Flow and Erosion*, *Special Publications of the Geological Society of London*, vol.154, pp. 87-107
- Toshinawa, T., Matsuoka, M. & Yamazaki, Y., 1996, Ground-motion characteristics in Santiago, Chile, obtained by microtremor observations, in *Proceedings of the 11th World Conference on Earthquake Engineering*, Acapulco, Mexico, 23–28 June, paper 1764
- Tindle, C.T., Murphy, M.J., 1999, Microseisms and ocean wave measurements, *Journal of Oceanic Engineering*, vol. 24, pp. 112–115
- Trifunac, M.D., Todorovska, M.I., 2000, Long period microtremors, microseisms and earthquake damage, Northridge, CA, 17 January 1994, *Soil Dynamics and Earthquake Engineering*, vol.19, pp.253-267
- Tsalahouri & Fontou, 1972, Geological map of Palleohora
- Tsourlos P., 1995, Modeling interpretation and inversion of multi-electrode resistivity survey data: D.Phil. Thesis, University of York
- Tuladhar, R., Cuong, N.N., Yamazaki, F., 2004, Seismic microzonation of Hanoi, Vietnam using microtremor observations, *13<sup>th</sup> World Conference on earthquake engineering*, Vancouver, Canada, Paper No, 2539
- Uebayashi, H., 2003, Extrapolation of irregular subsurface structures using the horizontal-to-vertical ratio of long-period microtremors, *Bulletin Seismological Society of America*, vol.93, pp. 570–582
- Uetake, T., Kudo, K., 1998, The excitation of later arrivals in Ashigara valley during earthquakes occurring in east part of Yamanashi prefecture, in *Proceedings of the Second International Symposium on the Effects of Surface Geology on Seismic Motion*, pp. 427–434, Balkema: Rotterdam, Yokohama, Japan
- van Hinsbergen, D.J.J., Hafkenscheid, E., Spakman, W., Meulen Kamp, J.E., Wortel, M.J.R., 2005, Nappe stacking resulting from subduction of oceanic and continental lithosphere below Greece, *Geology*, vol. 33, pp.325-328
- van Hinsbergen, D.J.J. and Meulen Kamp, J.E., 2006, Neogene supradetachment basin development on Crete (Greece) during exhumation of the South Aegean core complex, *Basin Research*, vol.18, pp.103–124
- van Schoor, M., 2002. Detection of sinkholes using 2D electrical resistivity imaging, *Journal of Applied Geophysics*, vol. 50, pp.393– 399
- Volant, Ph., Orbovica, N., Dunandb, F, 2002, Seismic evaluation of existing nuclear facility using ambient vibration test to characterize dynamic behavior of the structure and microtremor measurements to characterize the soil: a case study, *Soil Dynamics and Earthquake Engineering* vol. 22, pp.1159–1167
- Wanfang-Zhou, W., Beck, B.F., Adams, A.L, 2002, Effective electrode array in mapping karst hazards in electrical resistivity tomography, *Environmental Geology*, vol. 42, pp. 922-928

- Waltham, T., 2002, Foundations of Engineering Geology, Second edition, *Spon Press*, 104pp.
- Wen, Z. P., Hu, Y. X., Chau, K. T., 2002, Site effect on vulnerability of high-rise shear wall buildings under near and far field earthquakes, *Soil Dynamics and Earthquake Engineering*, vol. 22, pp.1175-1182
- Wise, D.J., Cassidy, J., Locke, C. A., 2003. Geophysical imaging of the Quaternary Wairoa North Fault, New Zealand: a case study, *Journal of Applied Geophysics*, vol. 53, pp. 1-16
- Westcott, W.A., Ethridge, F.G., 1980, Fan-delta sedimentology and tectonic setting – Yallahsfan delta, southeast Jamaica, *Bulletin American Association Petroleum*, vol.64, pp.374-399
- Woolery, E.W., Street, R., 2002, 3D near-surface soil response from H/V ambient-noise ratios, *Soil Dynamic Earthquake Engineering*, vol.22, pp. 865–876
- Yalcinkaya, E., Alptekin, O., 2005, Contributions of basin-edge-induced surface waves to site effect in the Dinar basin, Southwestern Turkey, *Pure applied Geophysics*, vol. 162, pp. 931–950
- Yellampalli, S., Srivastava, A., Pulendra, V., 2005, A combined oscillation power supply current and I<sub>DDQ</sub> Testing methodology for fault detection in floating gate input CMOS operational amplifier, *IEEE*, doi:0-7803-9197-7/05, pp. 503-506
- Yamamoto, H., 2000, Estimation of shallow S-wave velocity structures from phase velocities of Love waves and Rayleigh waves in microtremors, *Proceedings of the 12<sup>th</sup> World*, Auckland, New Zealand
- Yamamoto, H., 2002, Source characteristics and propagation effects of the Puebla, Mexico earthquake of 15 June 1999, *Bulletin of the Seismological Society of America*, vol.92, pp. 2126-2138
- Yamanaka, H., Dravinski, M., Kagami, H., 1993, Continuous measurements of microtremors on sediments and basement in Los Angeles, California, *Bulletin of the Seismological Society of America*, vol. 83, pp. 1595–1609
- Yamanaka, H., Takemura, M., Ishida, H., Niwa, M., 1994, Characteristics of long-period microtremors and their applicability in exploration of deep sedimentary layers, *Bulletin of the Seismological Society of America*, vol. 84, pp. 1831–1841
- Yamanaka, H., Motoki, K., Fukumoto, S., Takahashi, T., Yamada, N., Asano, K., 2005. Estimation of local site effects in Ojiya city using aftershock records of the 2004 Mid Biigata Prefecture earthquake and microtremors, *Earth Planets and Space*, vol. 57, pp. 539–544
- Zare, M., Bard, P.Y., Ghafory-Ashtiany, M., 1999, Site characterizations for the Iranian strong motion network, *Soil Dynamics and Earthquake Engineering*, vol.18, pp.101-123
- Zhang, S., Chan, L., 2003, Possible effects of misidentified mode number on Rayleigh wave inversion, *Journal of Applied Geophysics*, vol.53, pp.17–29

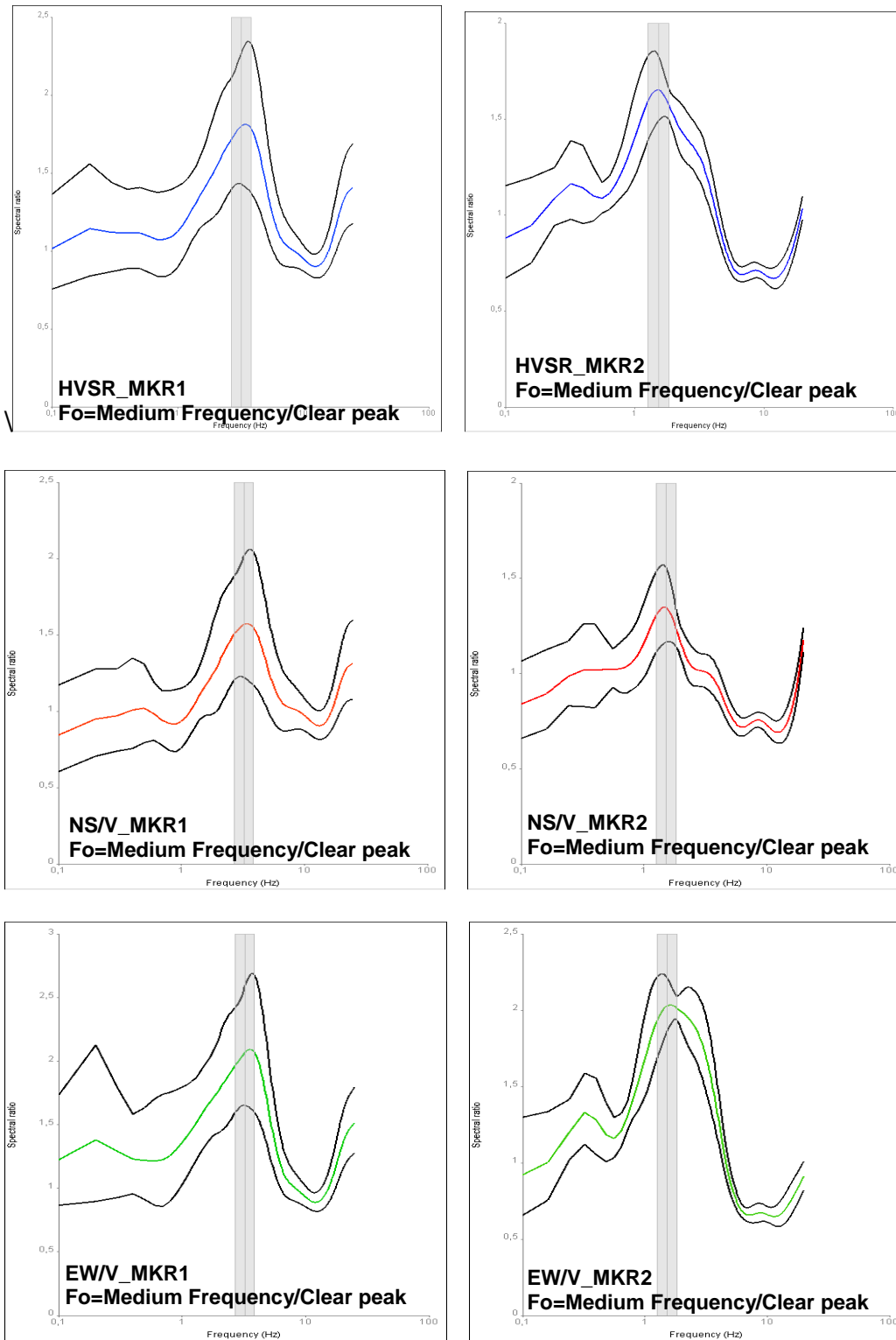
## APPENDIX I: HVSR CURVES IN KASTELLI AND PALEOHORA BASINS

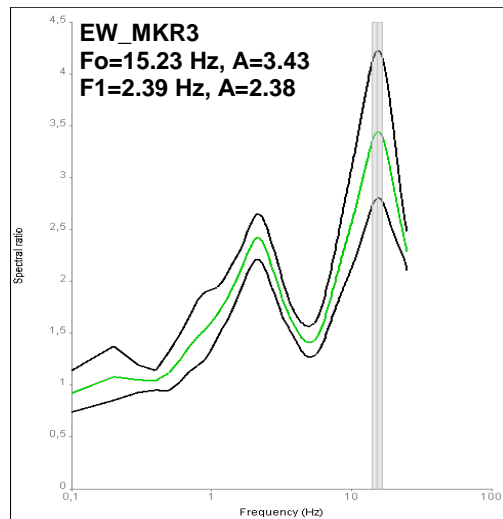
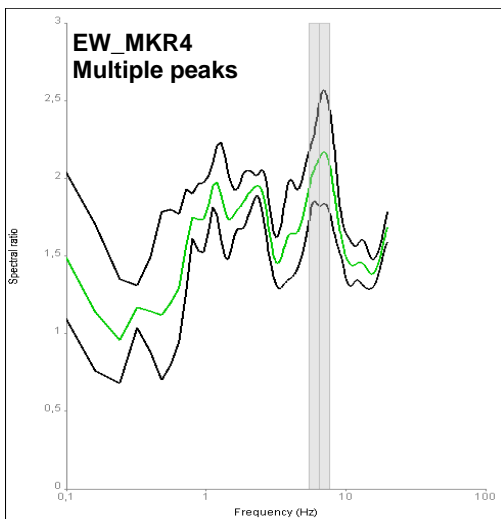
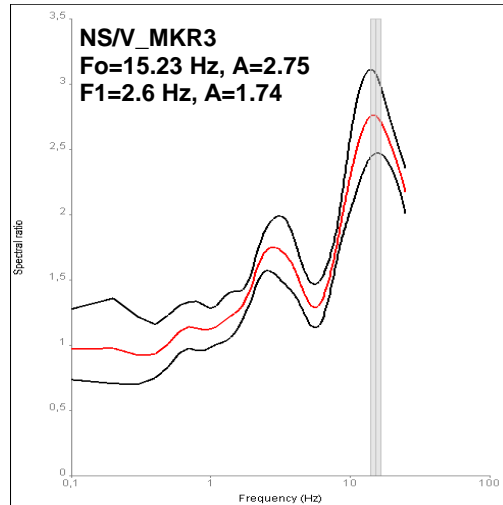
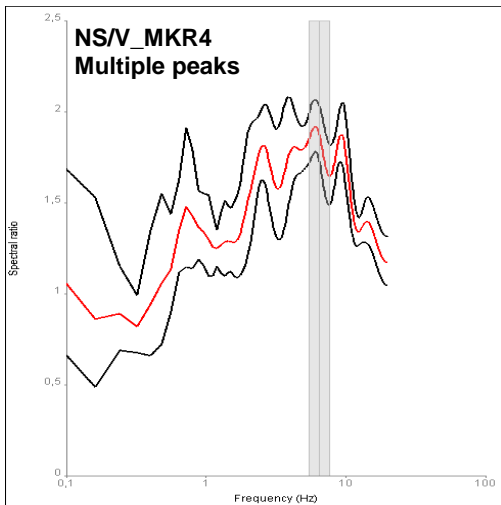
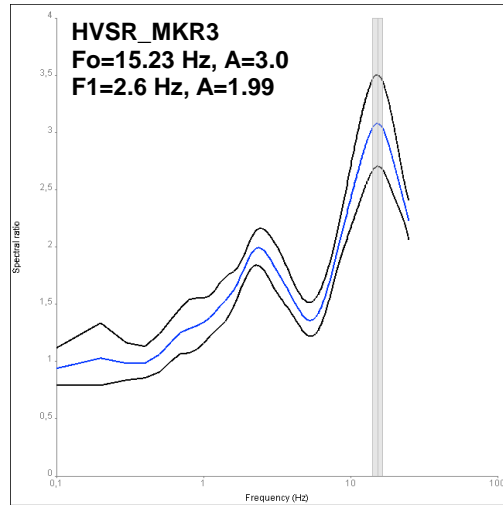
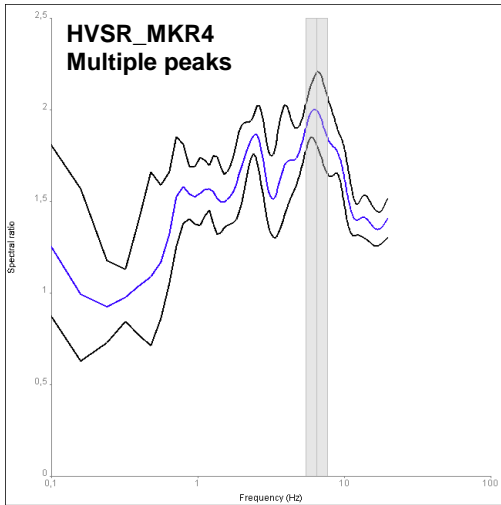
### A1: HVSR, $H_{NS}/V$ and $H_{EW}/V$ RATIOS USING MICROTREMOR RECORDINGS IN ROKA AND KASTELLI-KISSAMOU BASIN

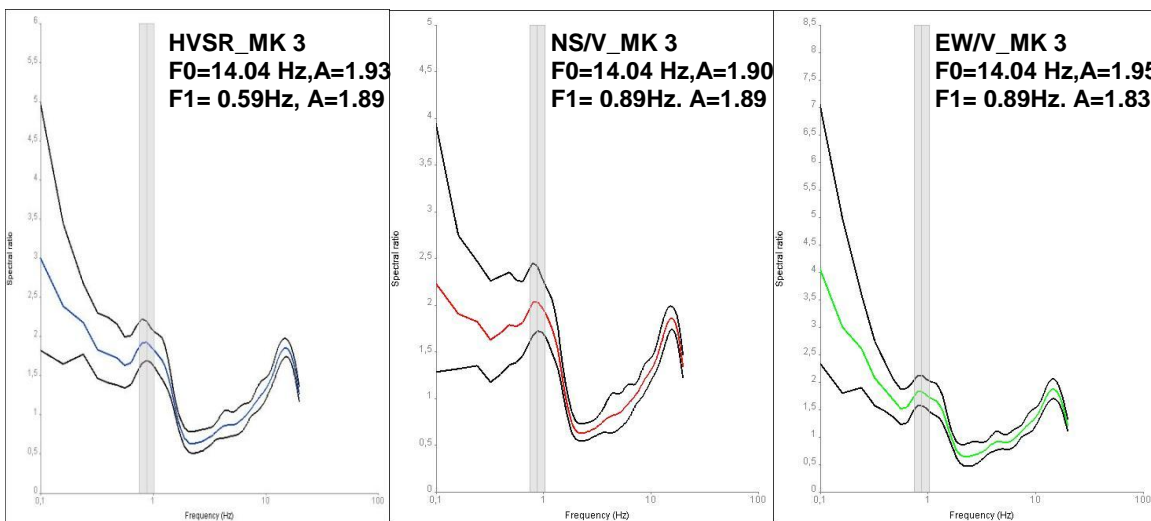
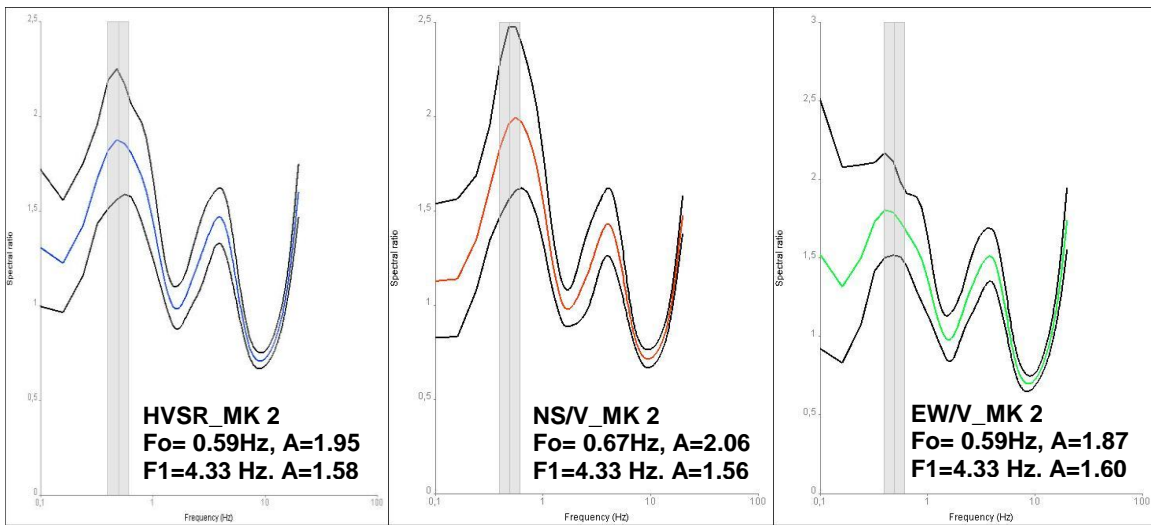
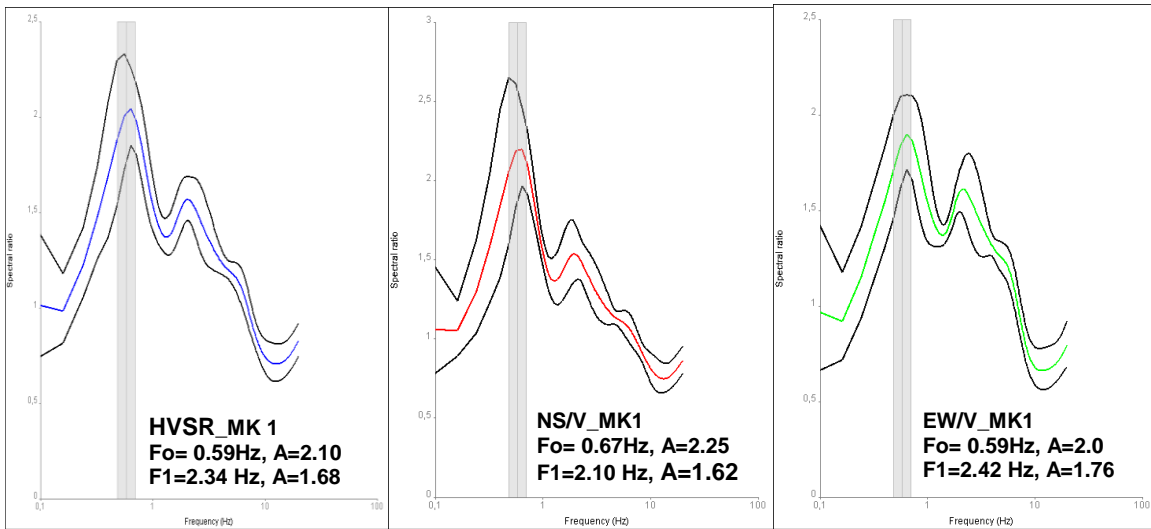


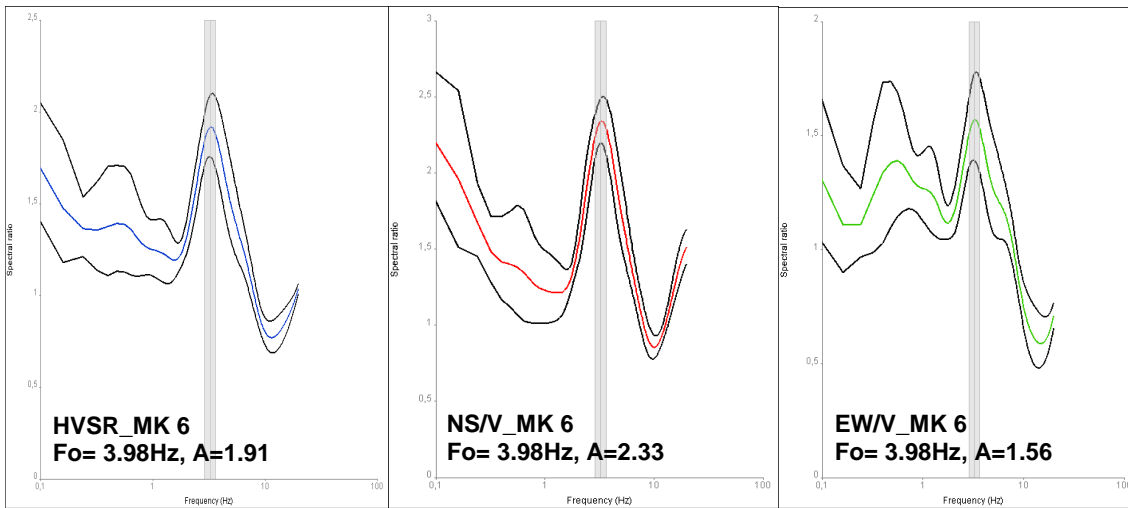
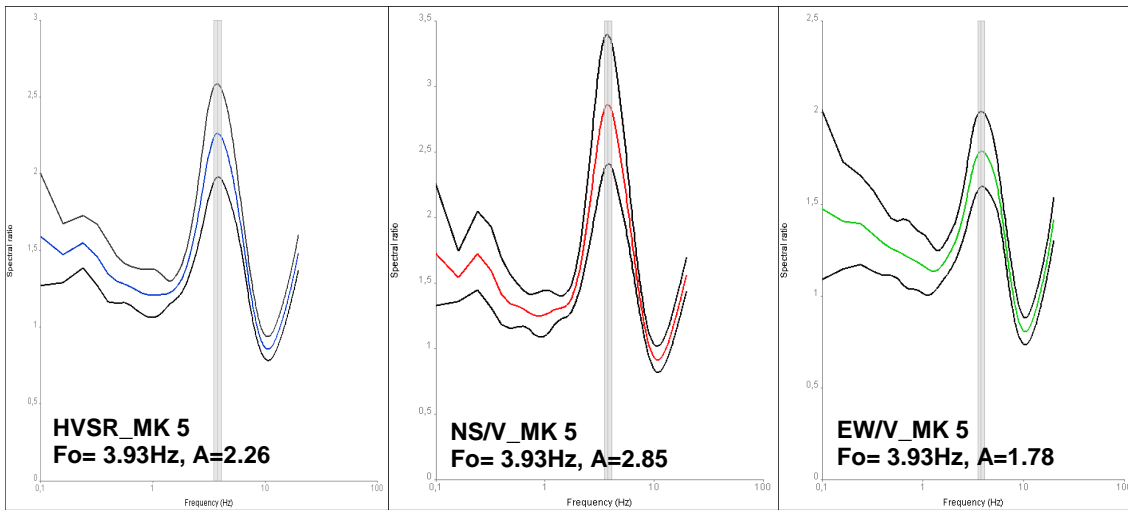
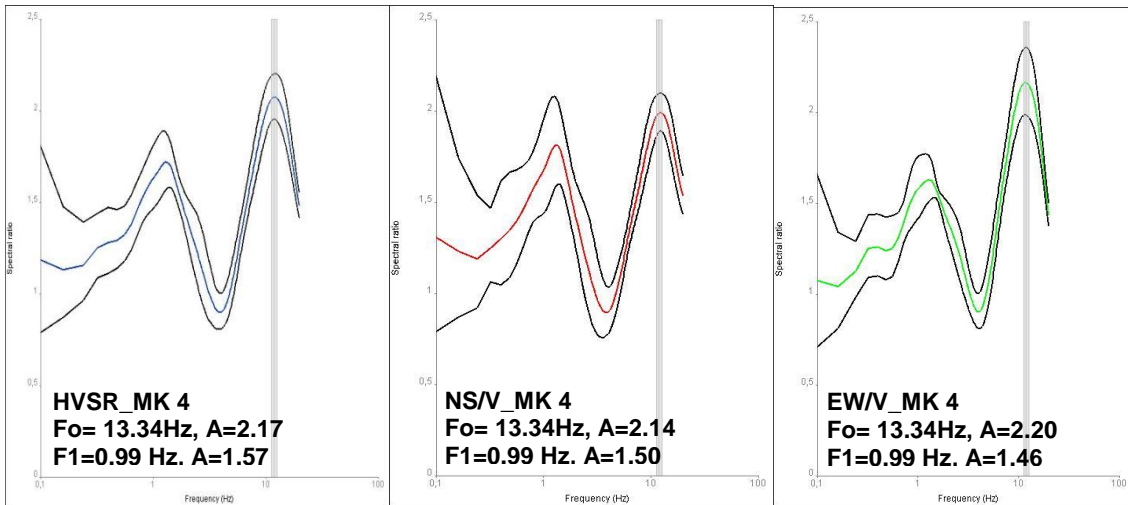
**Figure A:** HVSR using microtremors to determine the ground seismic spatial variation response in the populated of Kastelli Kissamou (MK1-MK38) basin and Roka village (MKR1-MKR4). The horizontal scale of the HVSR curves represents the fundamental frequency range (0.2-20Hz) while the vertical scale represents the ground seismic amplification. The black lines in all graphs correspond to the standard deviation of each  $H/V$ ,  $H_{ns}/V$ ,  $H_{ew}/V$  curve. The grey zone presented in all graphs corresponds to the standard deviation of fundamental frequency. The blue line of the curves represents the average  $H/V$  ratios (HVSR average ratios) of microtremor component recordings.

The ground seismic spatial variation based on HVSr technique in the populated area in Kastelli ( MK1-MK38) and Roka village (MKR1-MKR4) is presented in Figure B.

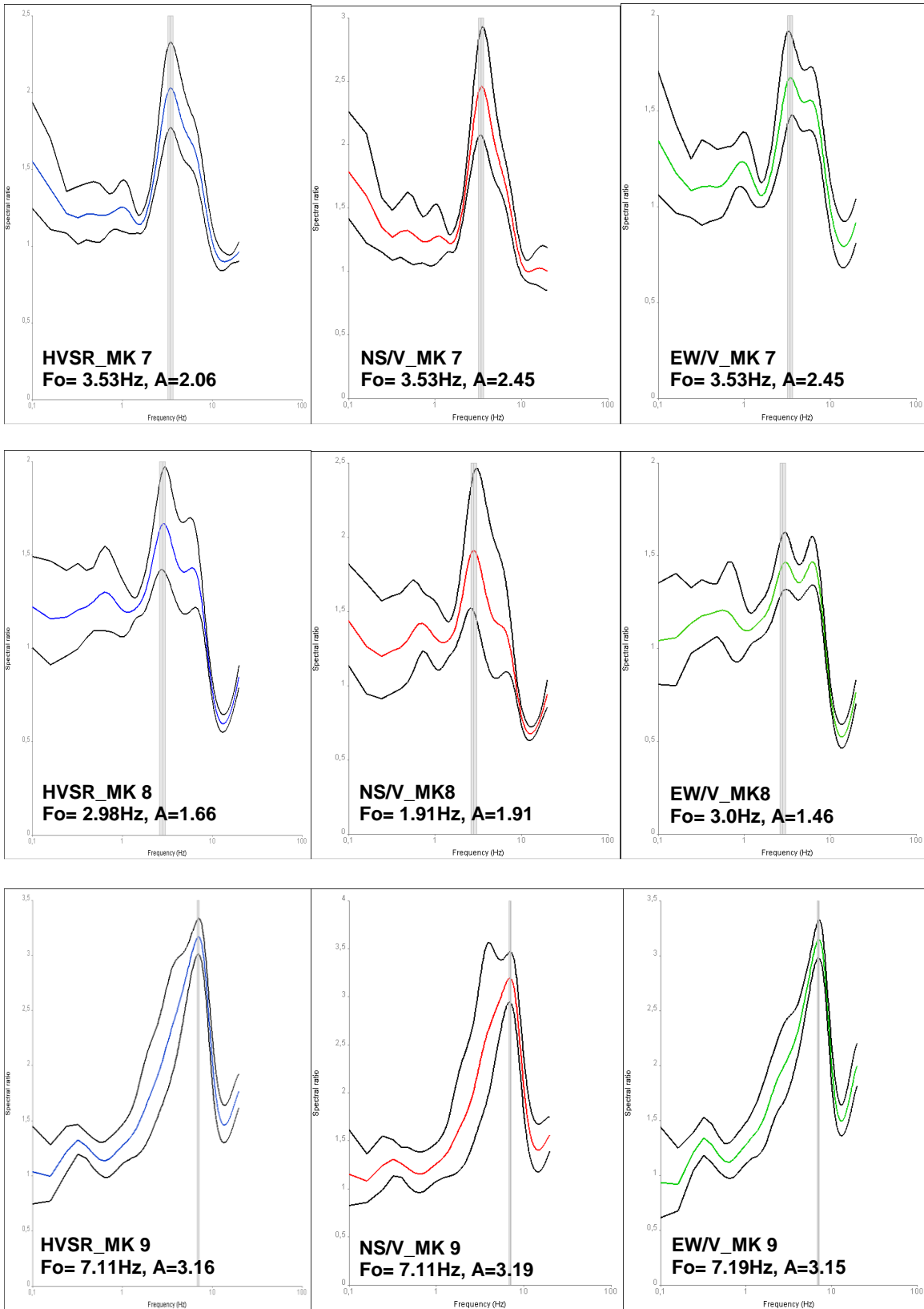


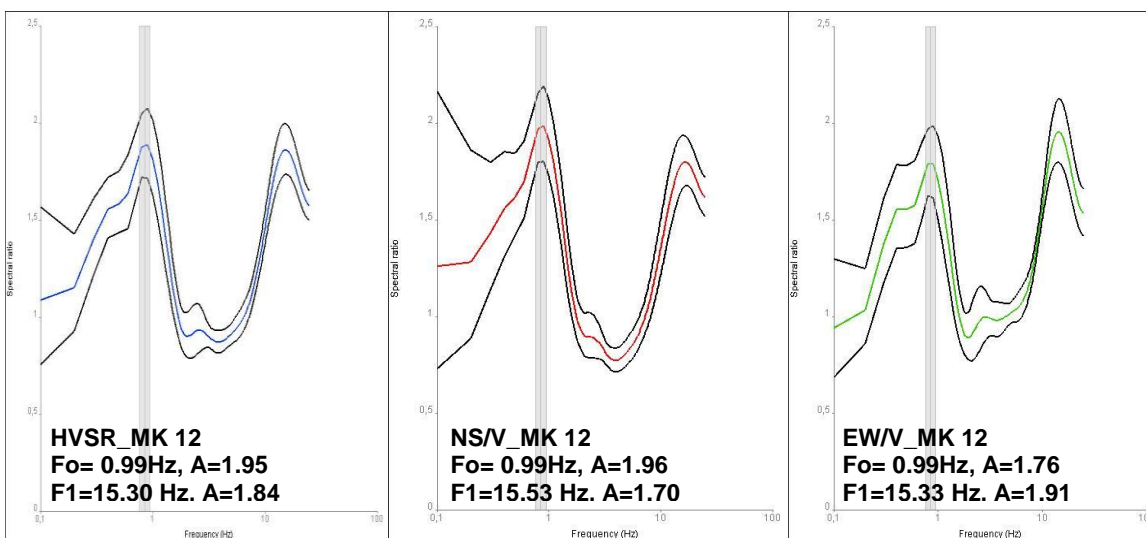
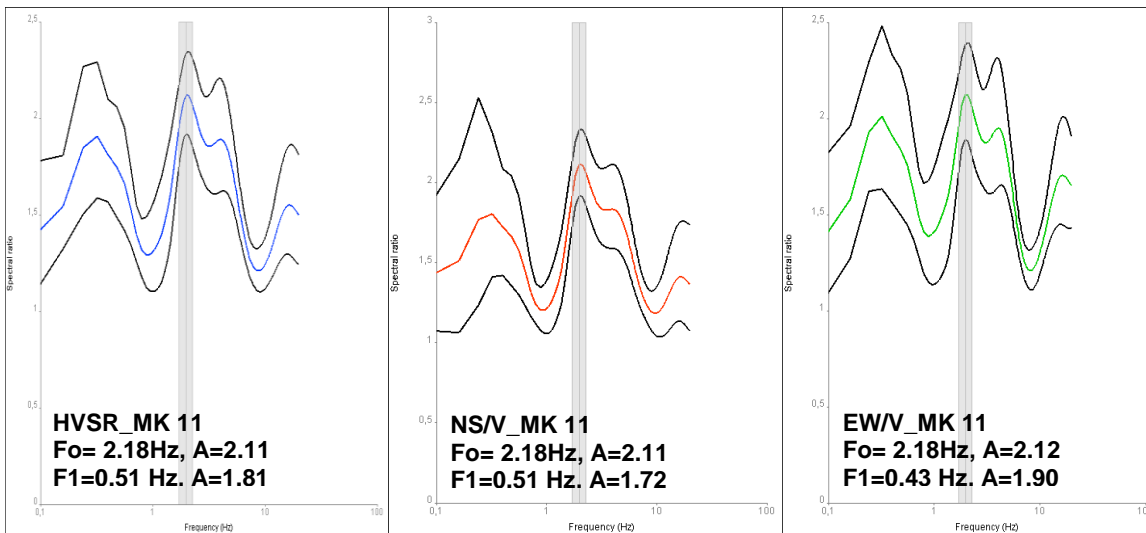
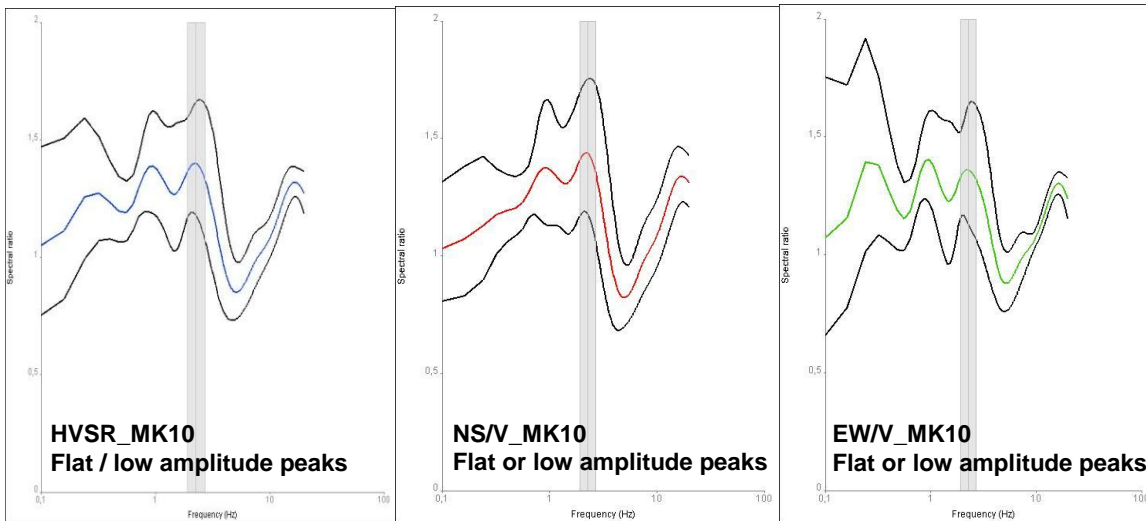


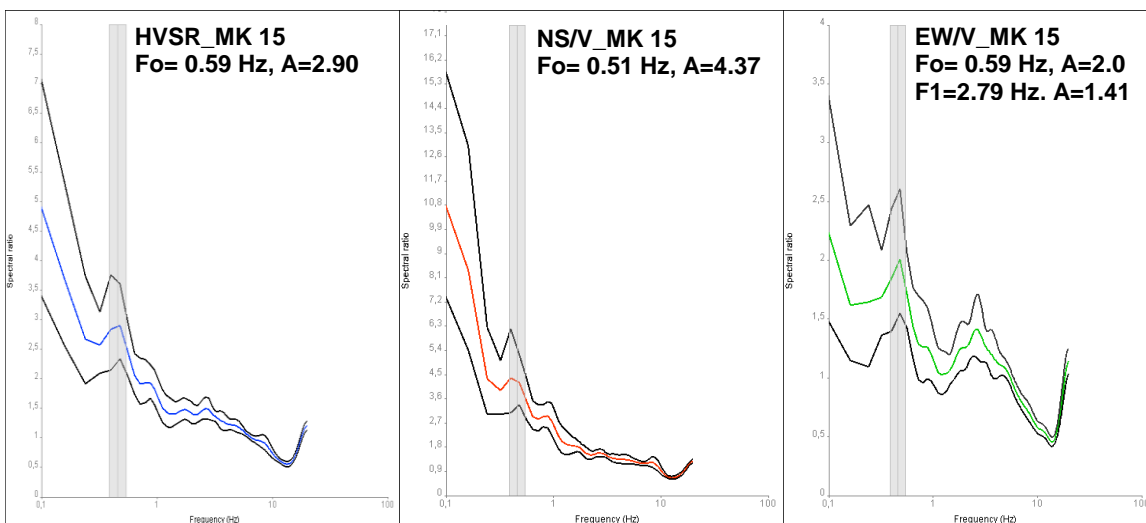
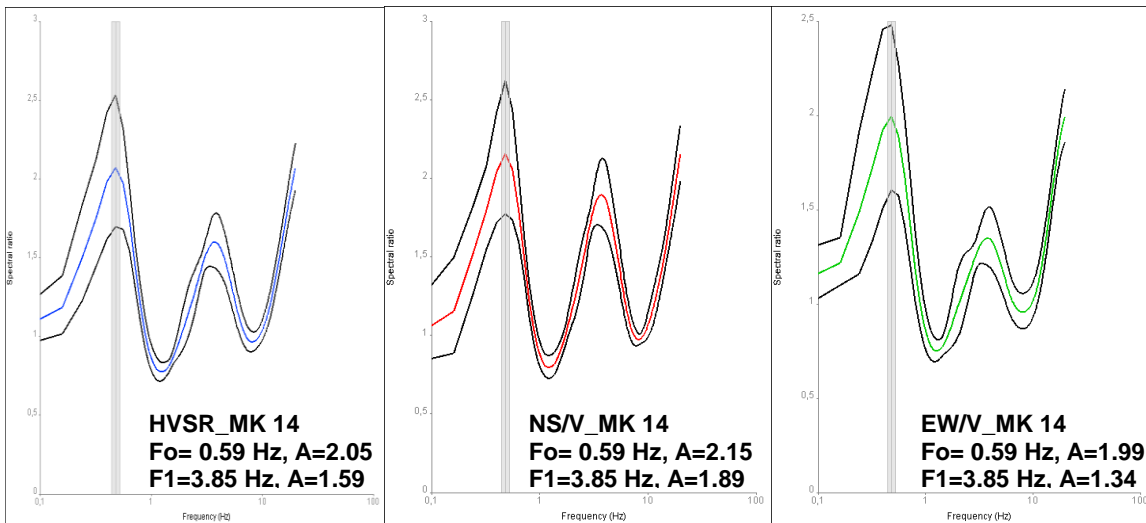
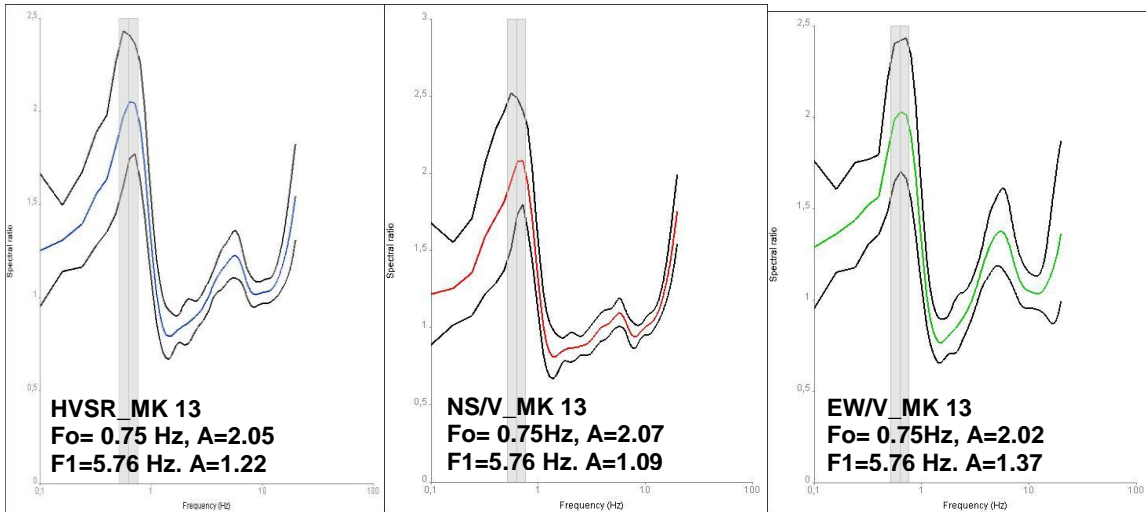


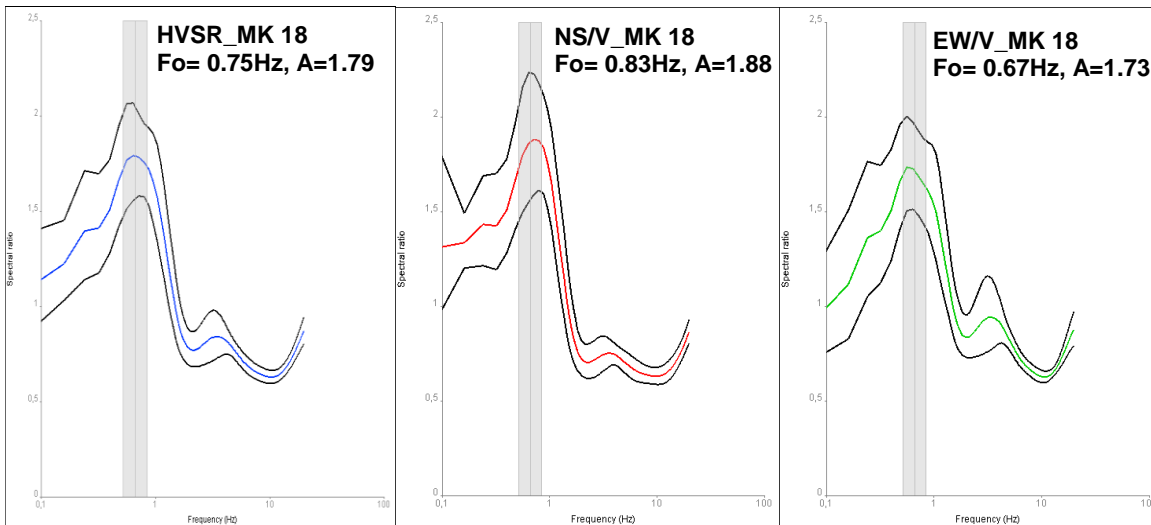
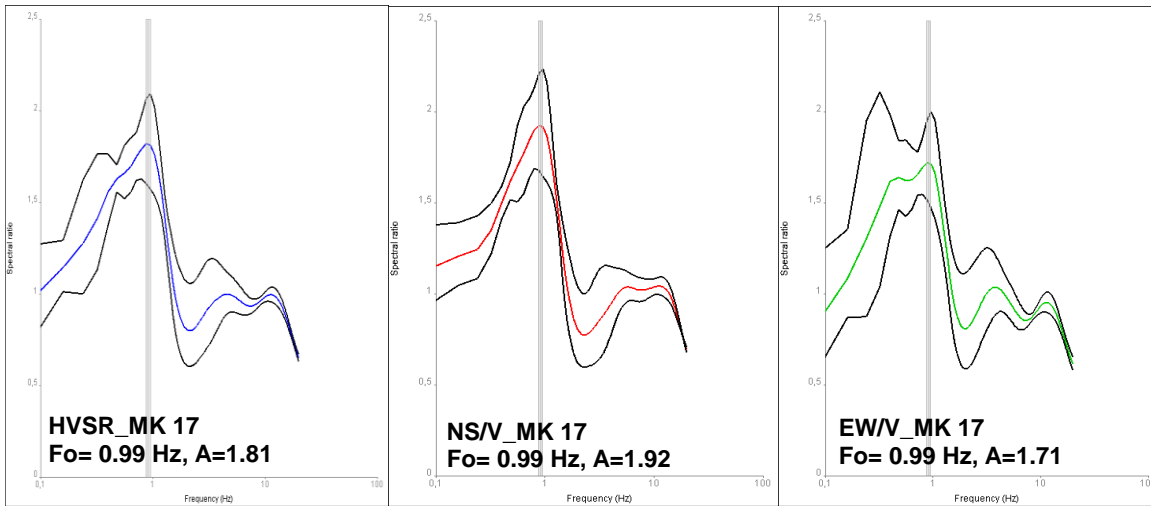
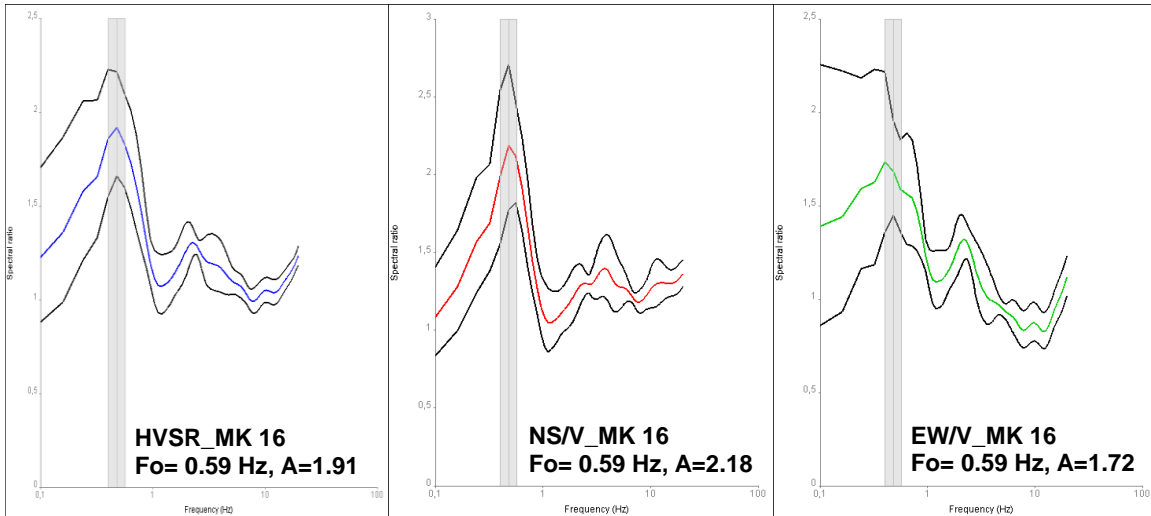


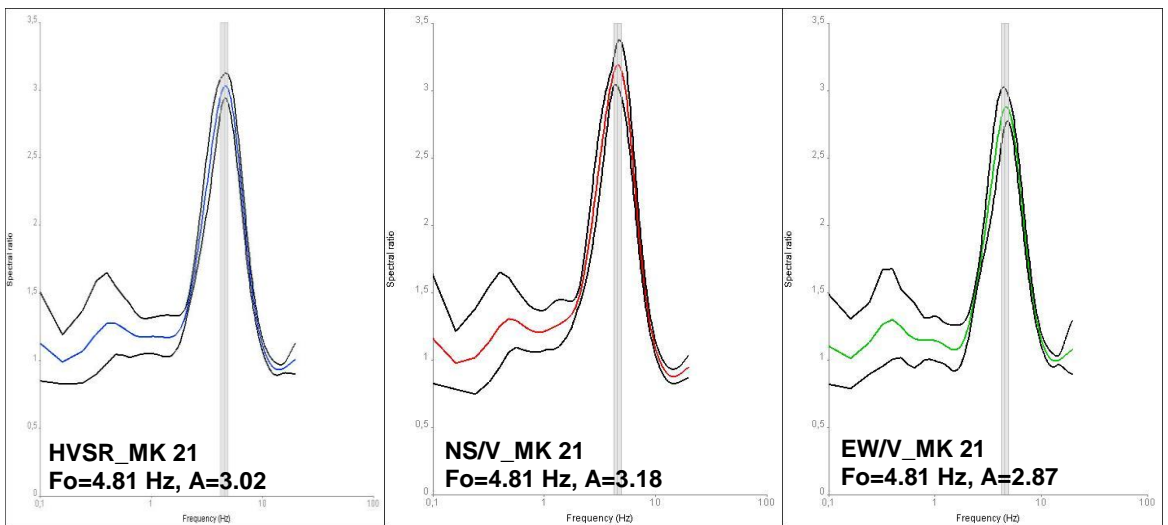
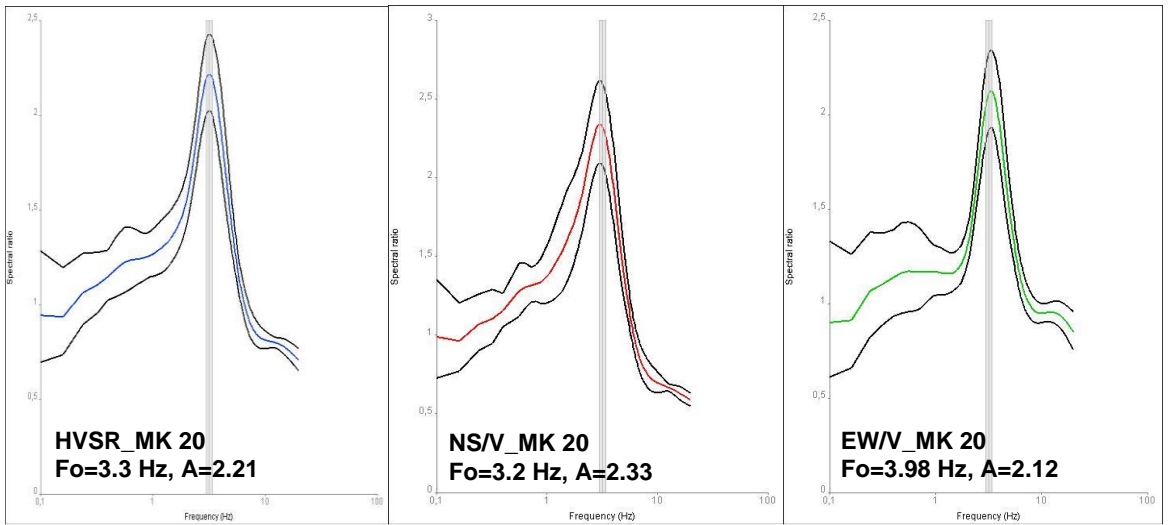
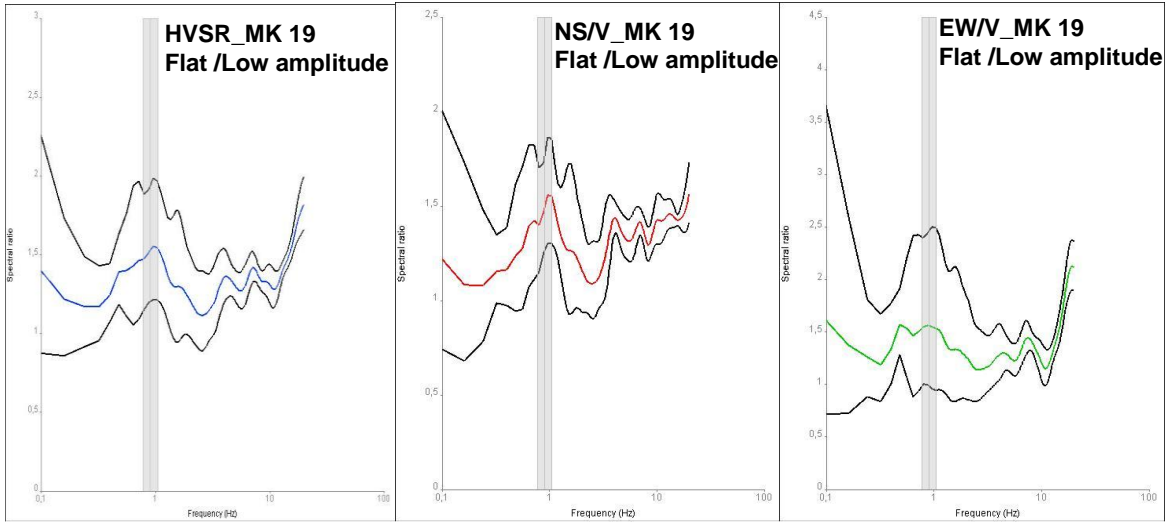


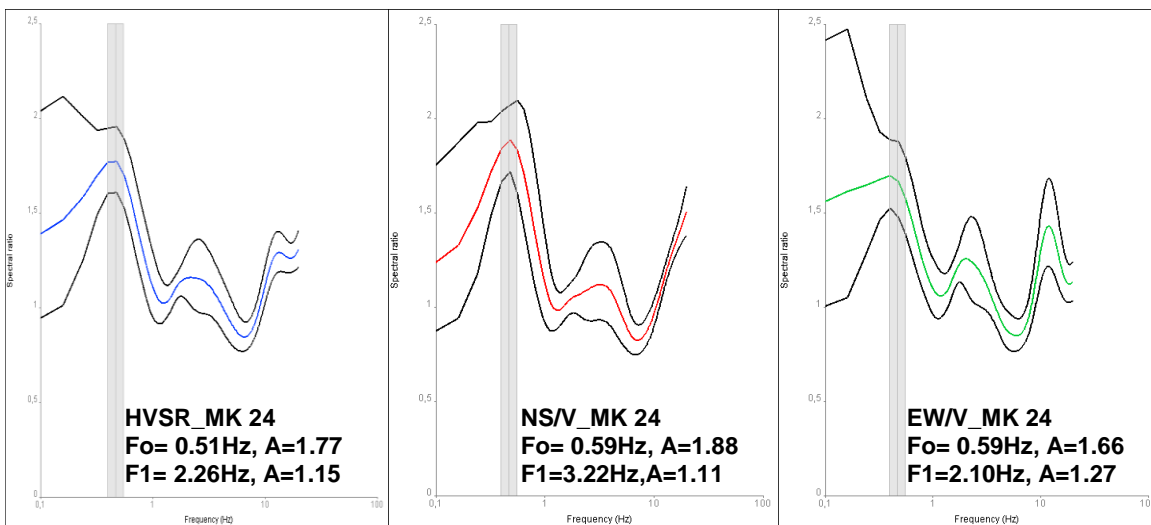
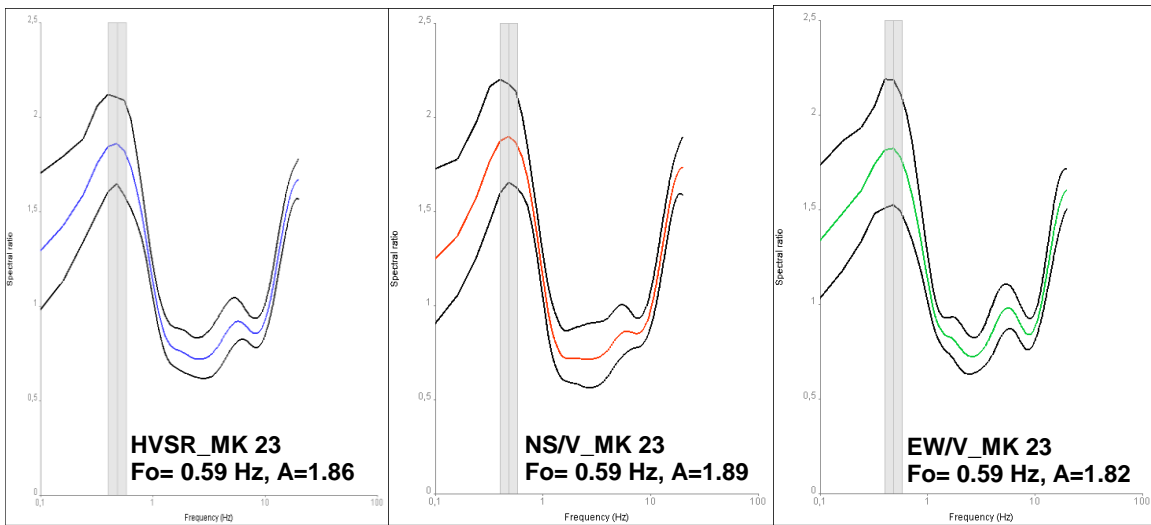
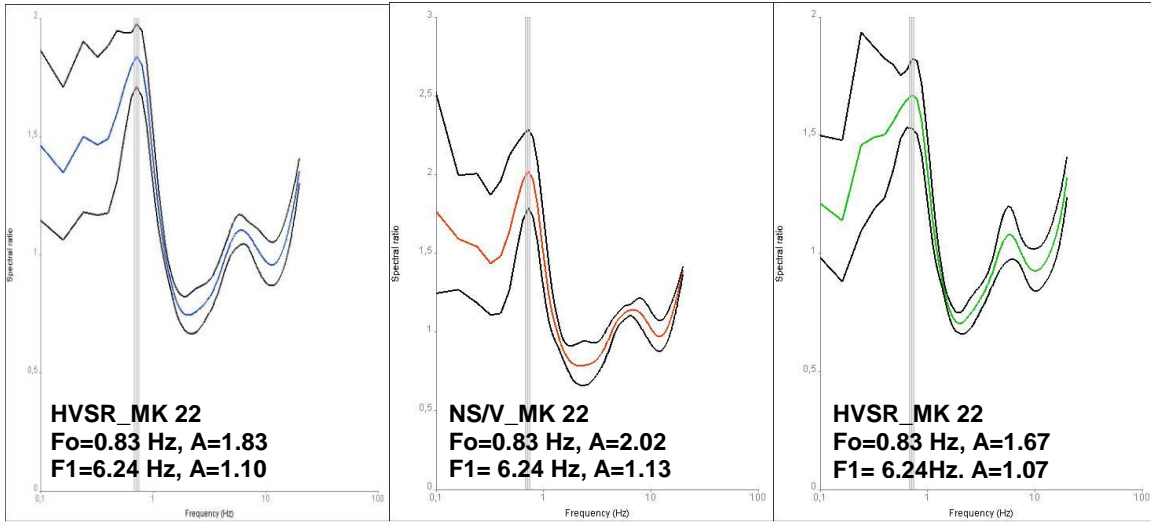


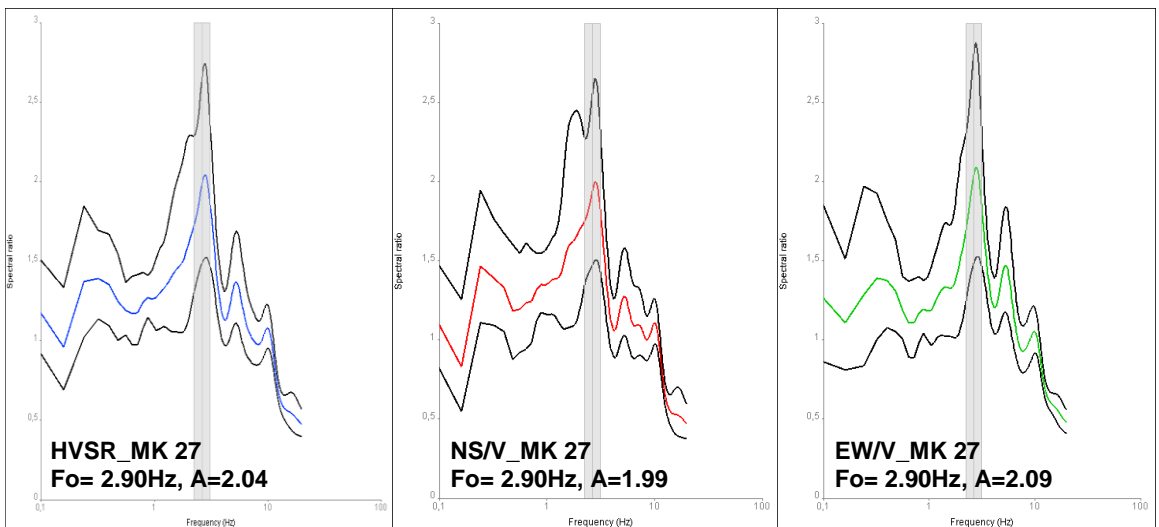
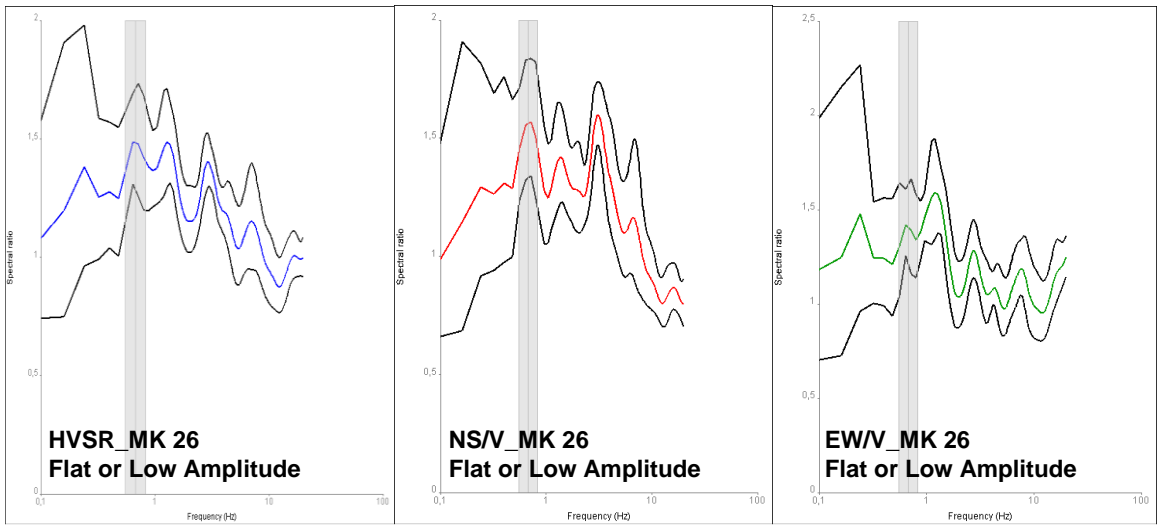
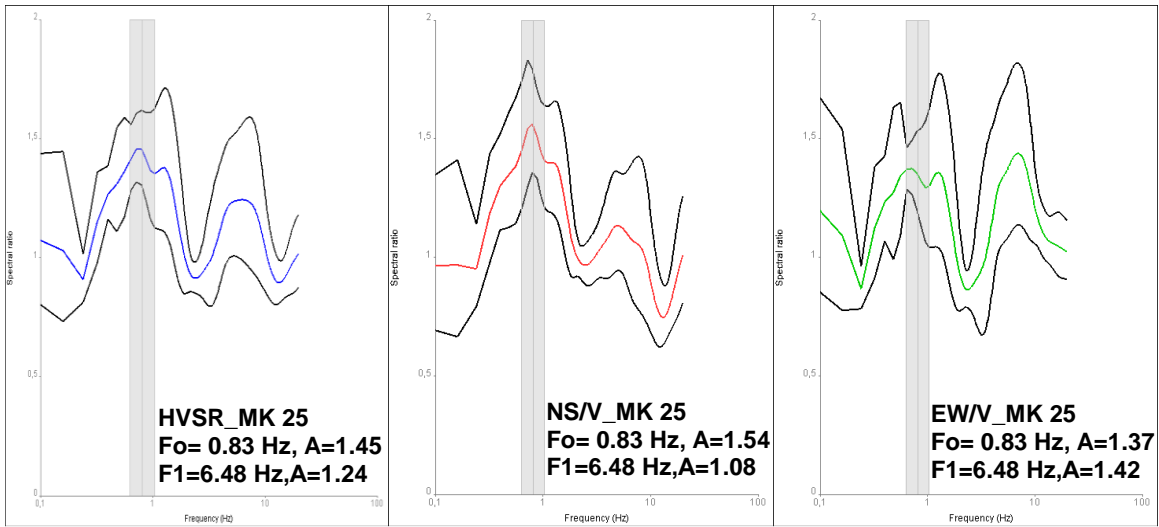


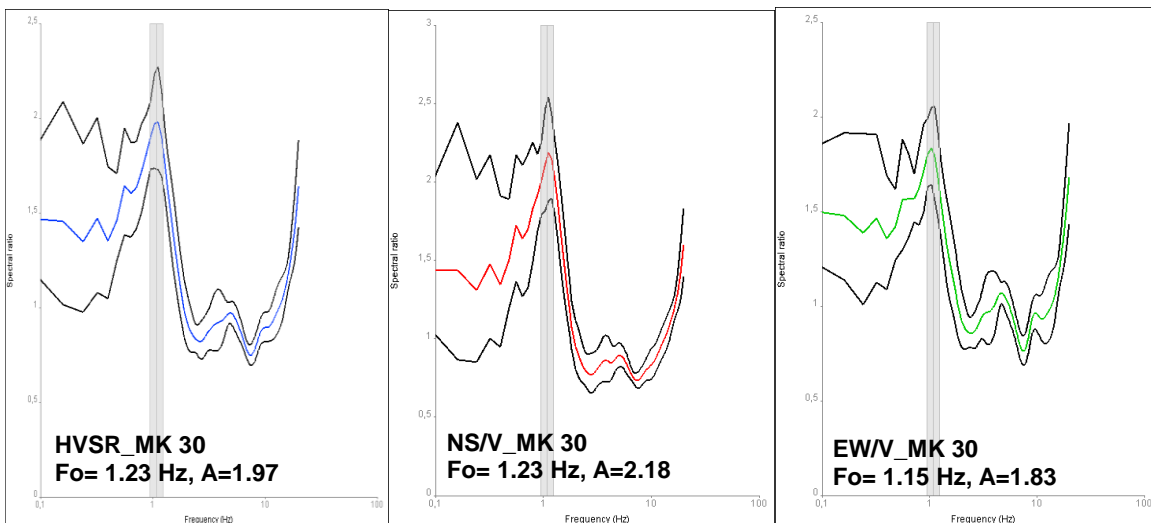
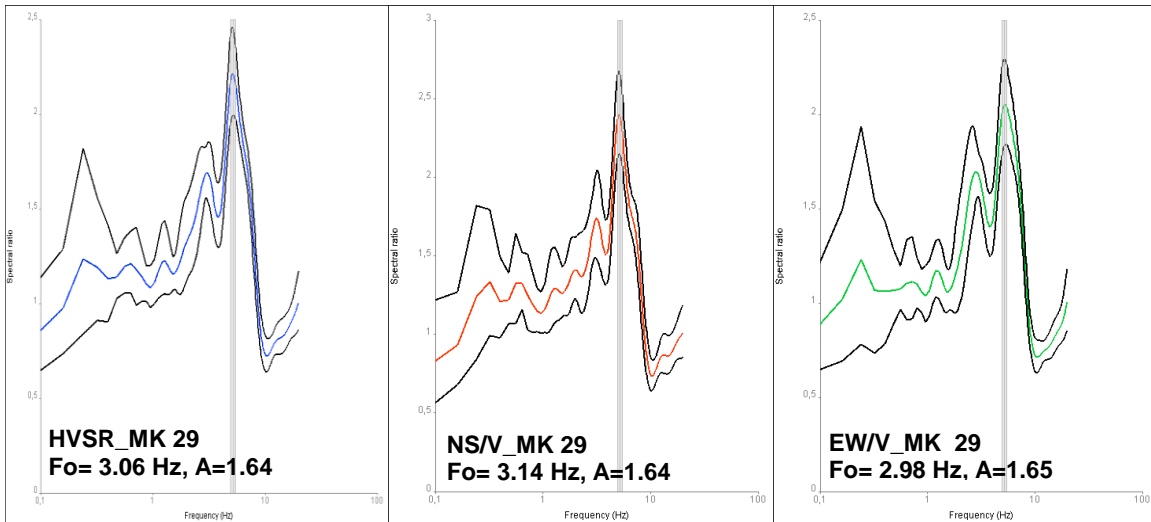
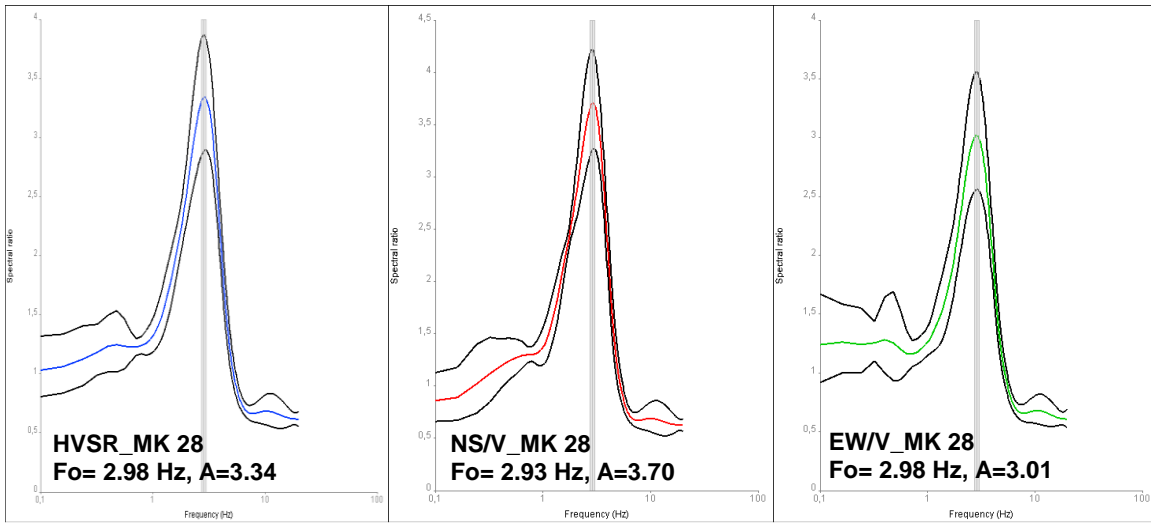




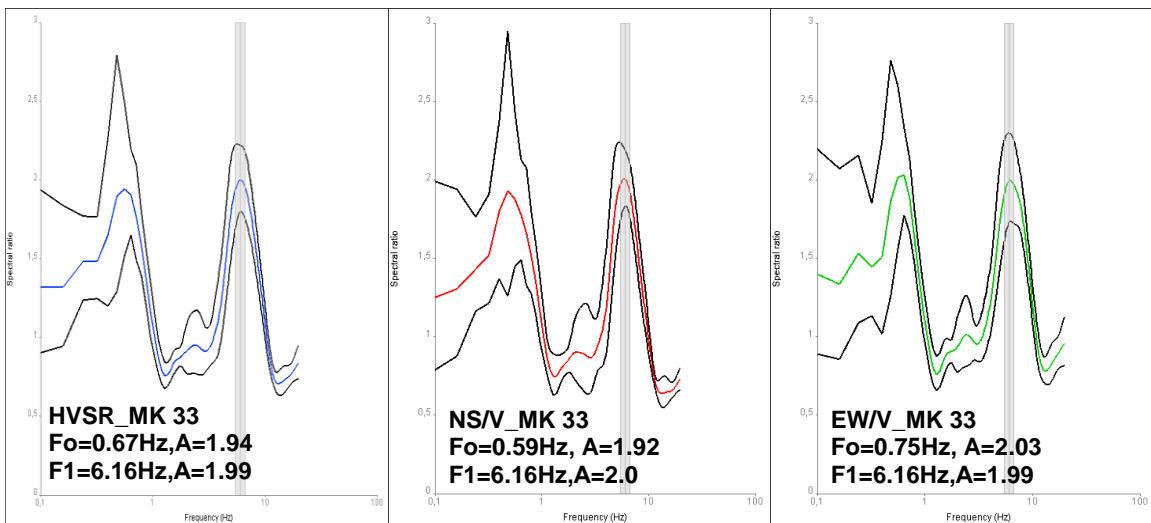
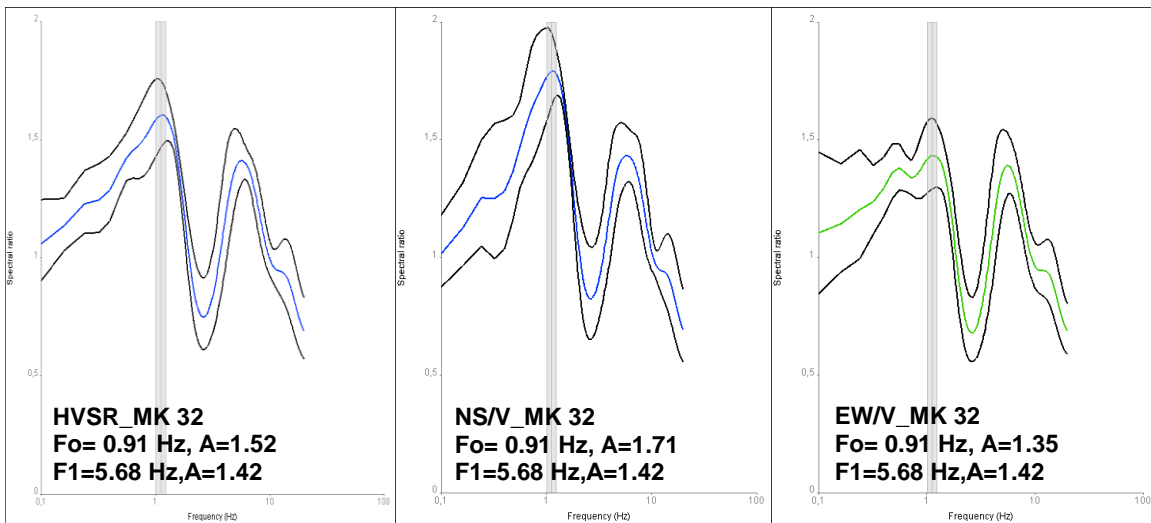
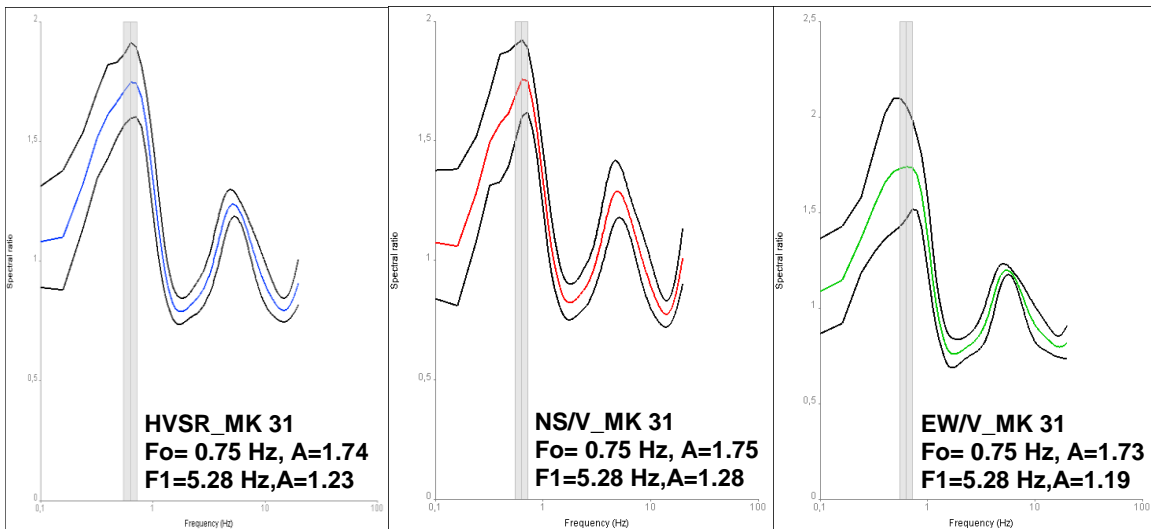


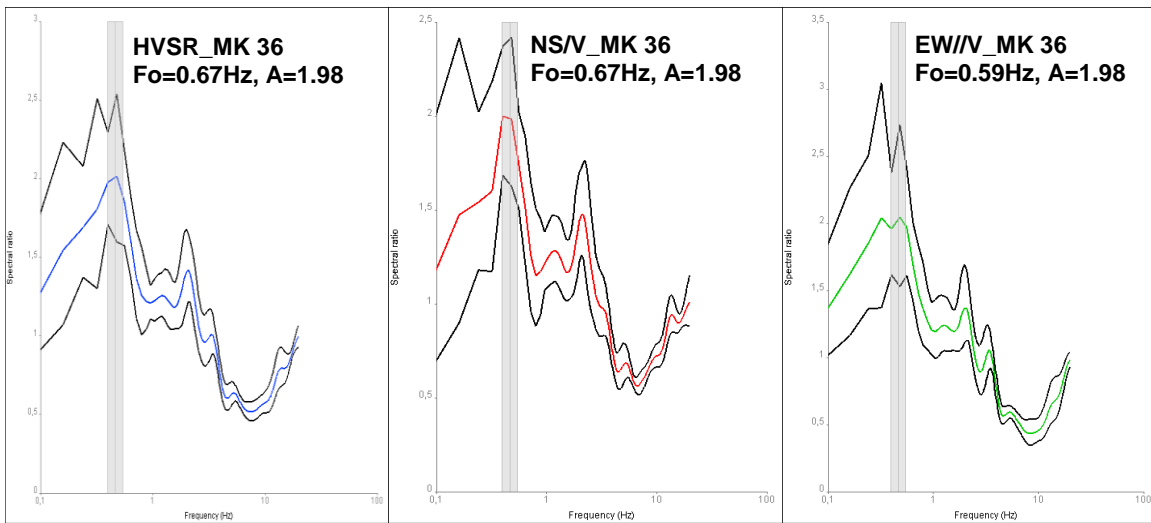
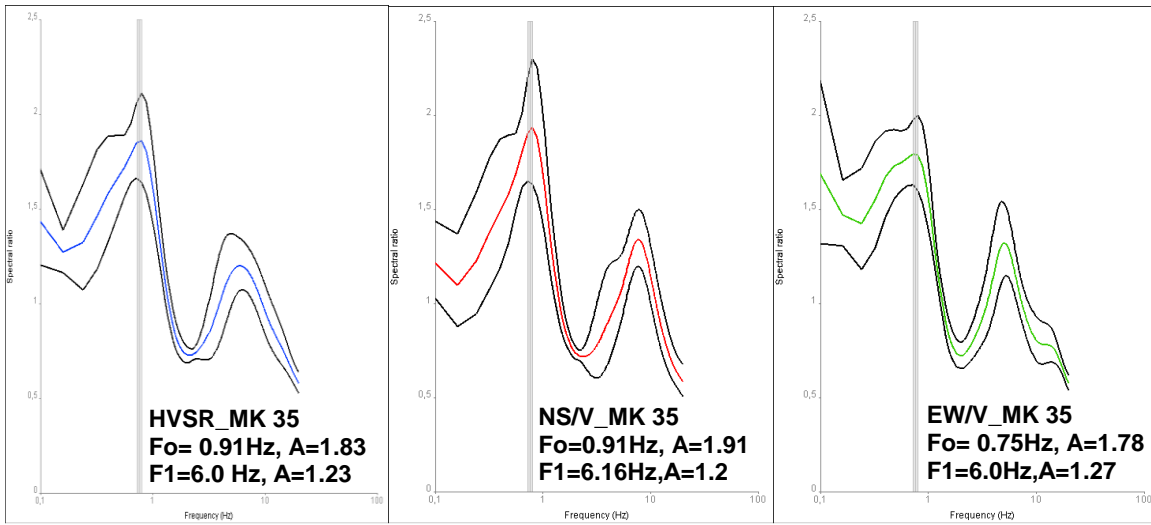
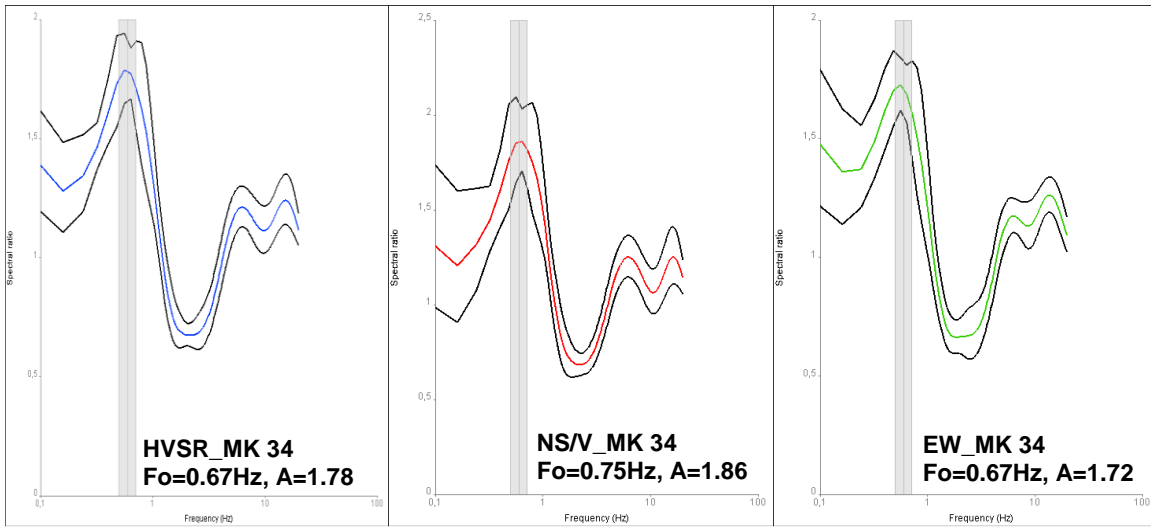


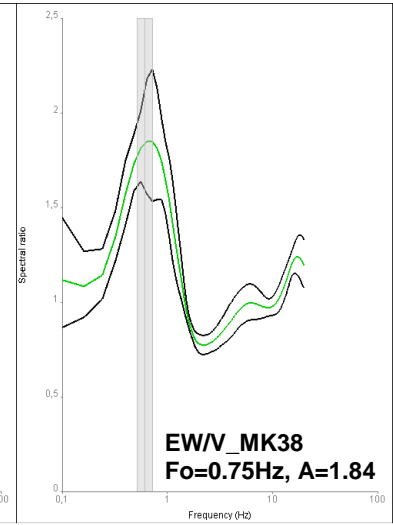
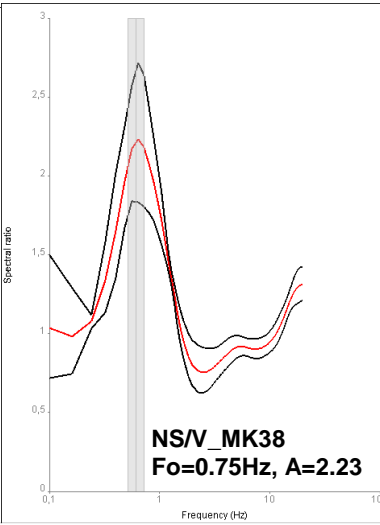
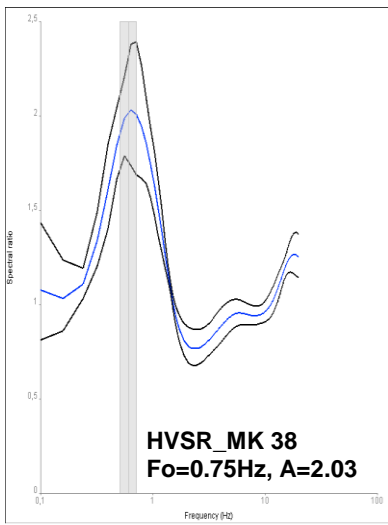
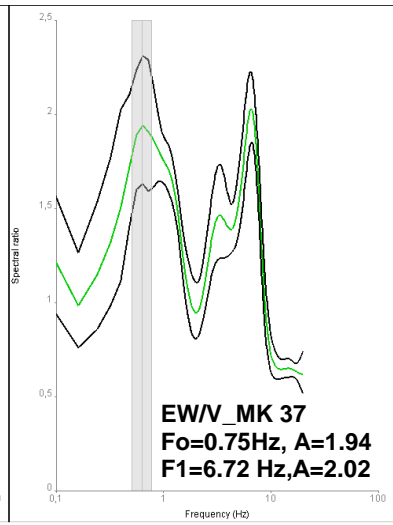
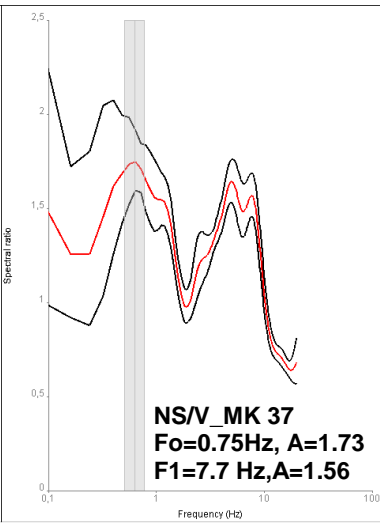
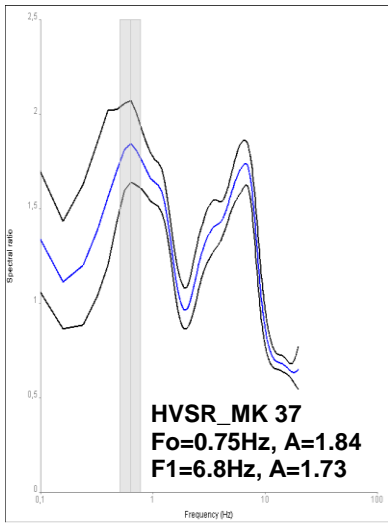




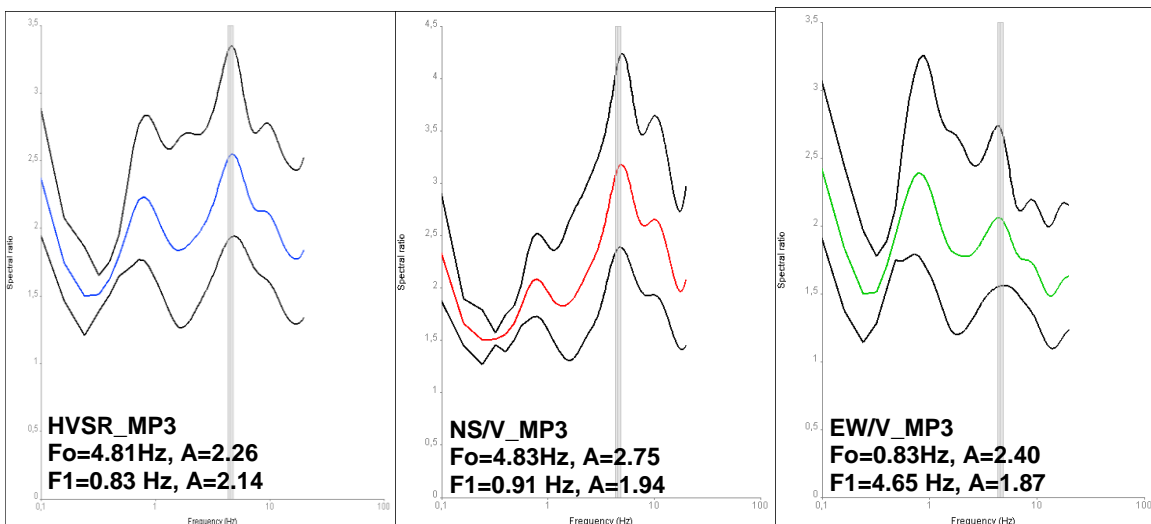
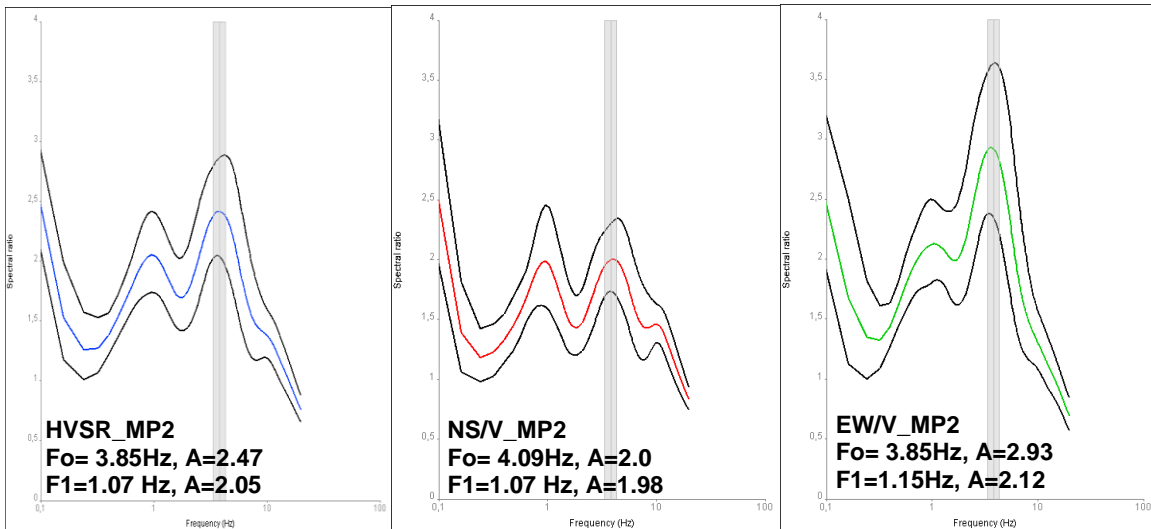
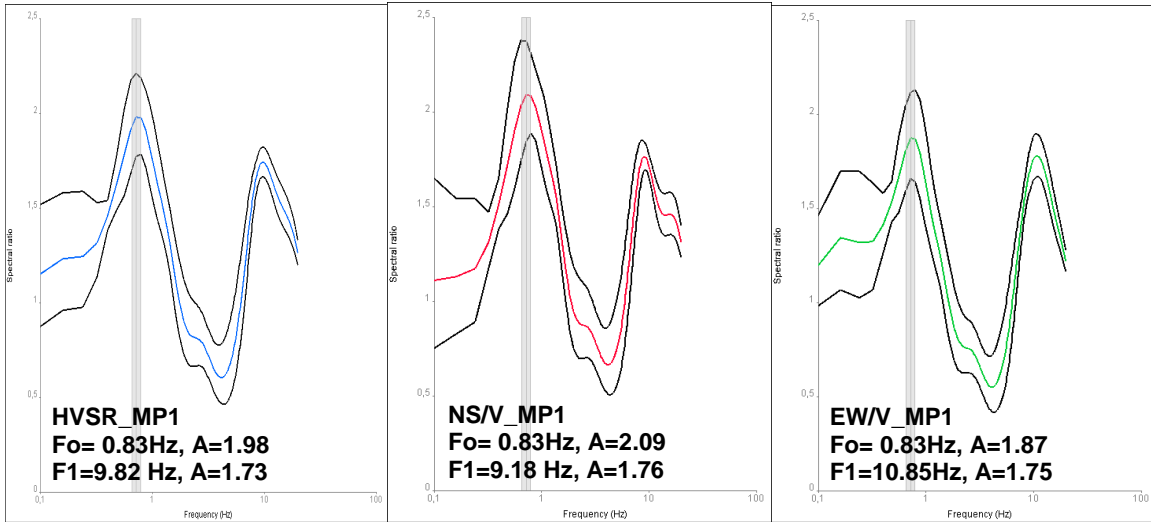


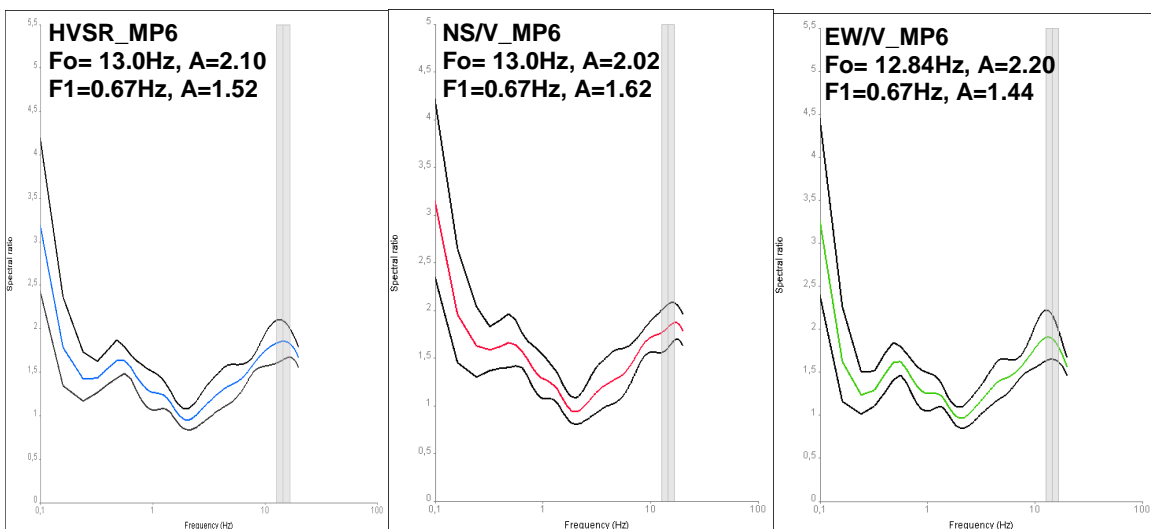
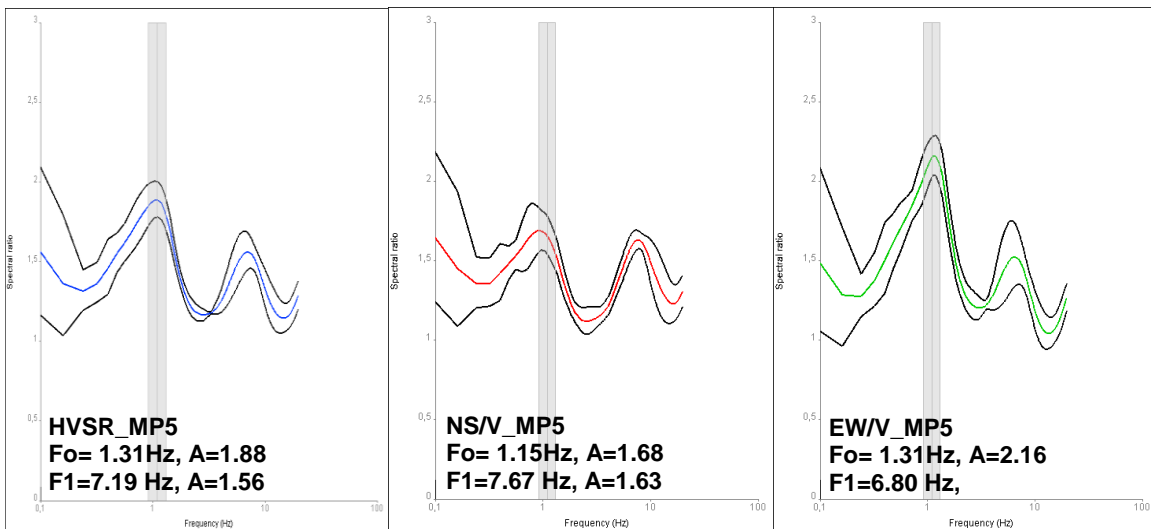
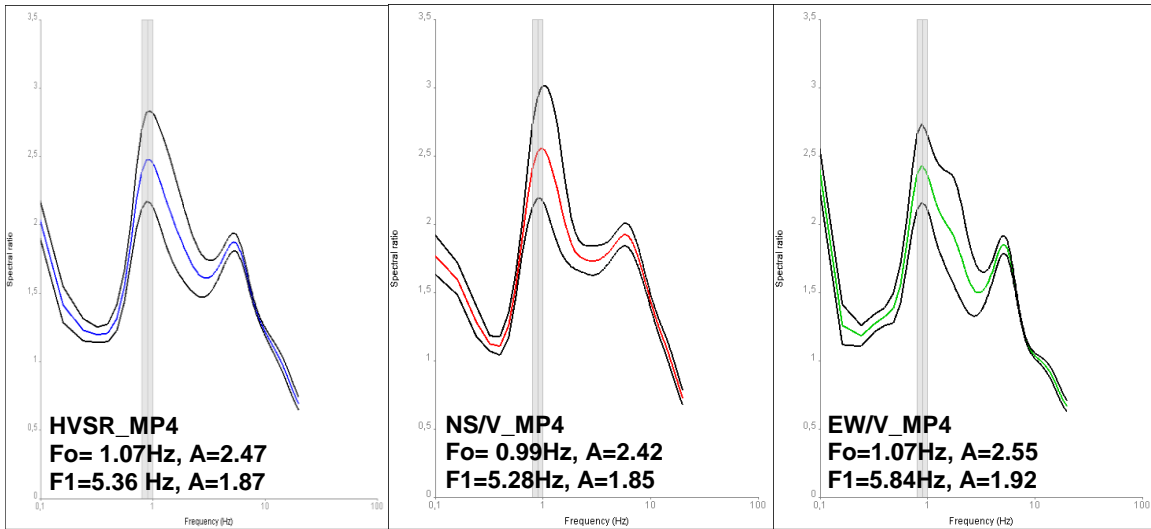


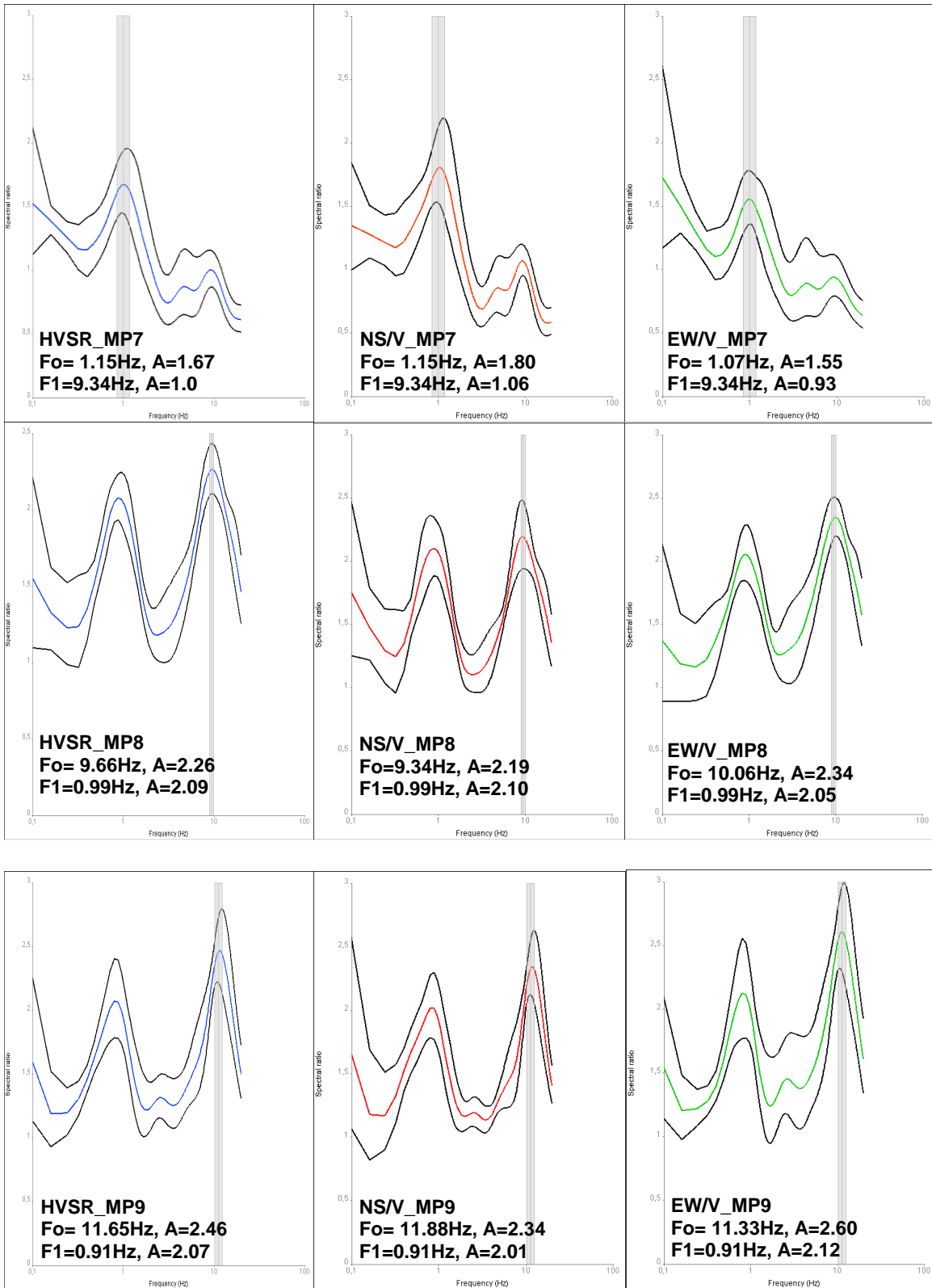


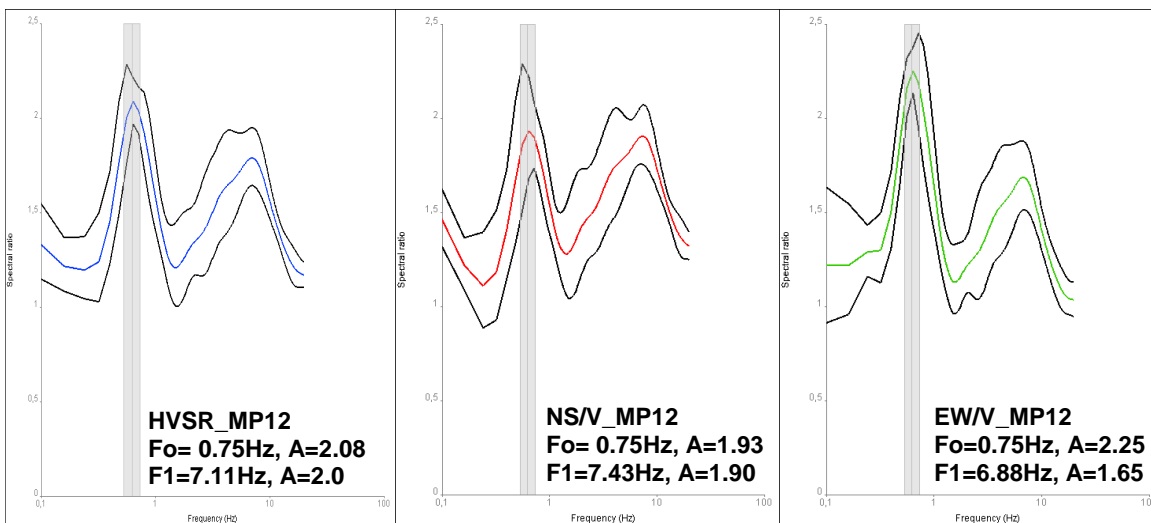
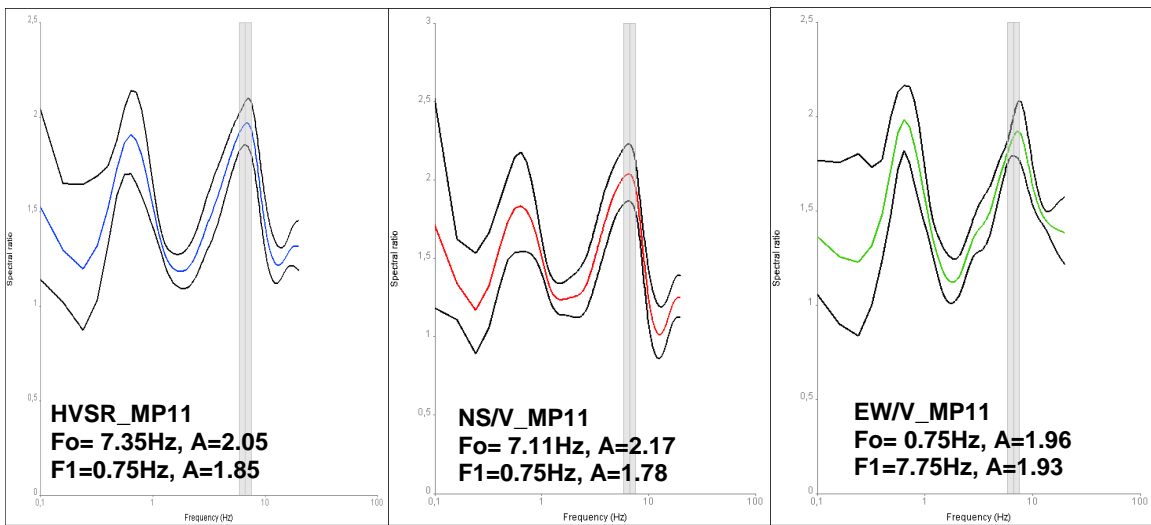
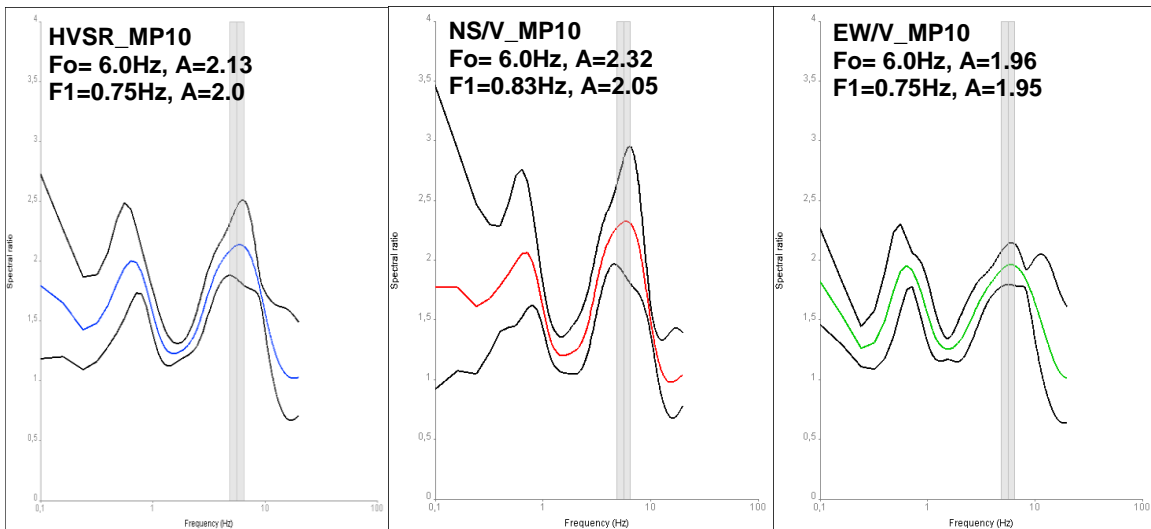


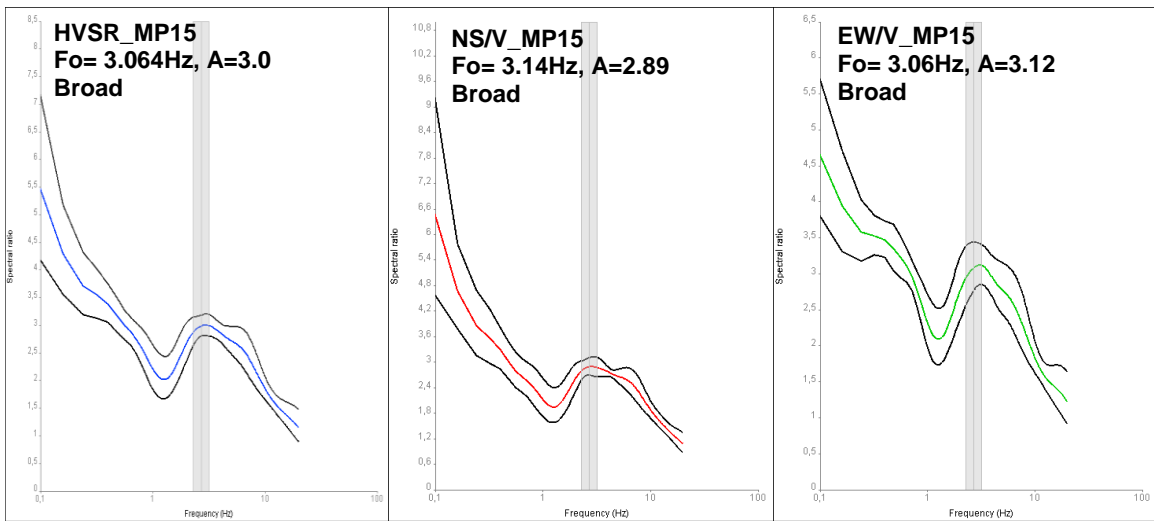
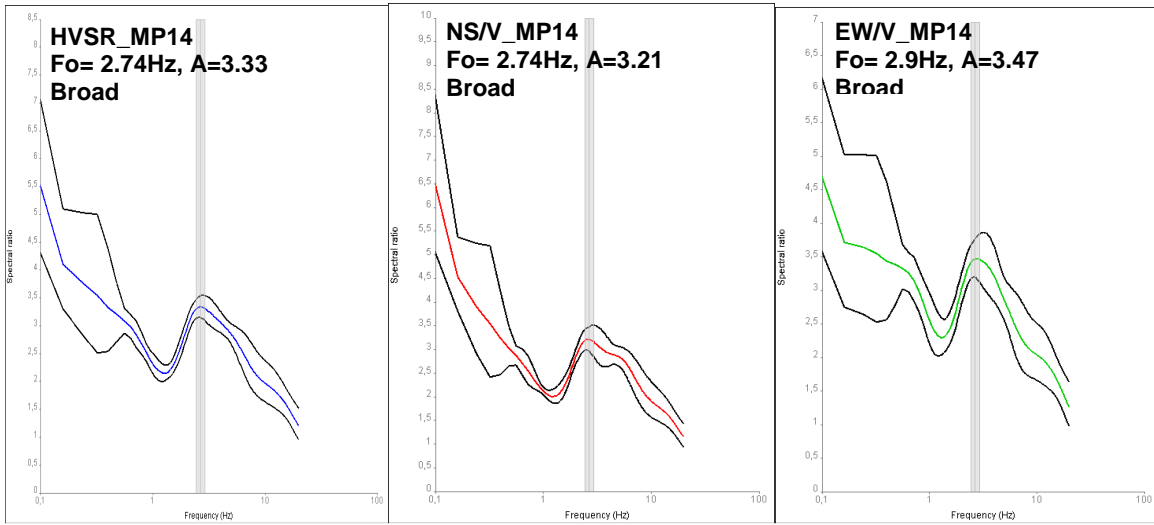
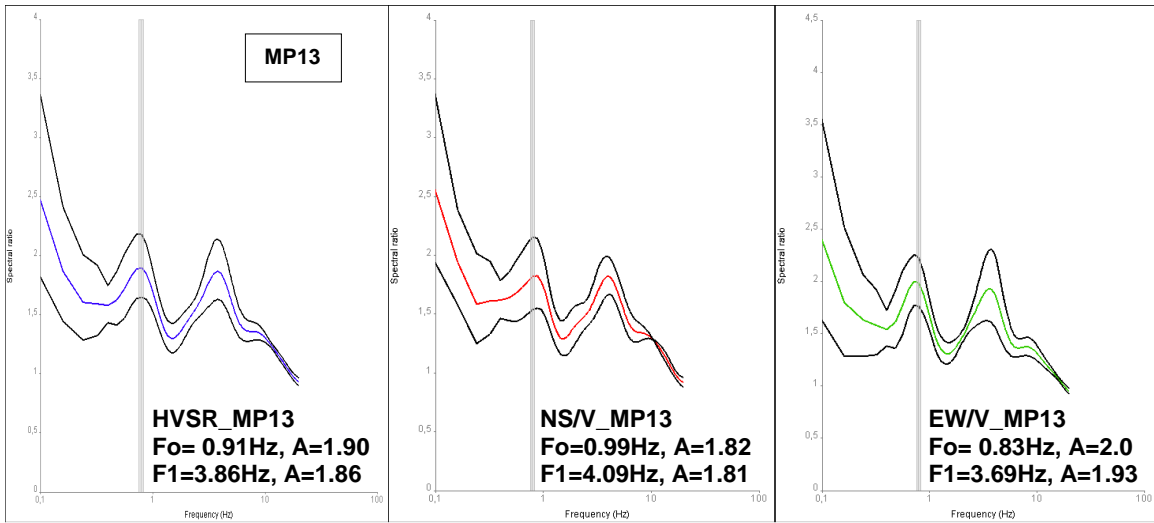
## A2: HVSR, $H_{NS}/V$ and $H_{EW}/V$ USING MICROTREMOR RECORDINGS IN PALEOHORA BASIN



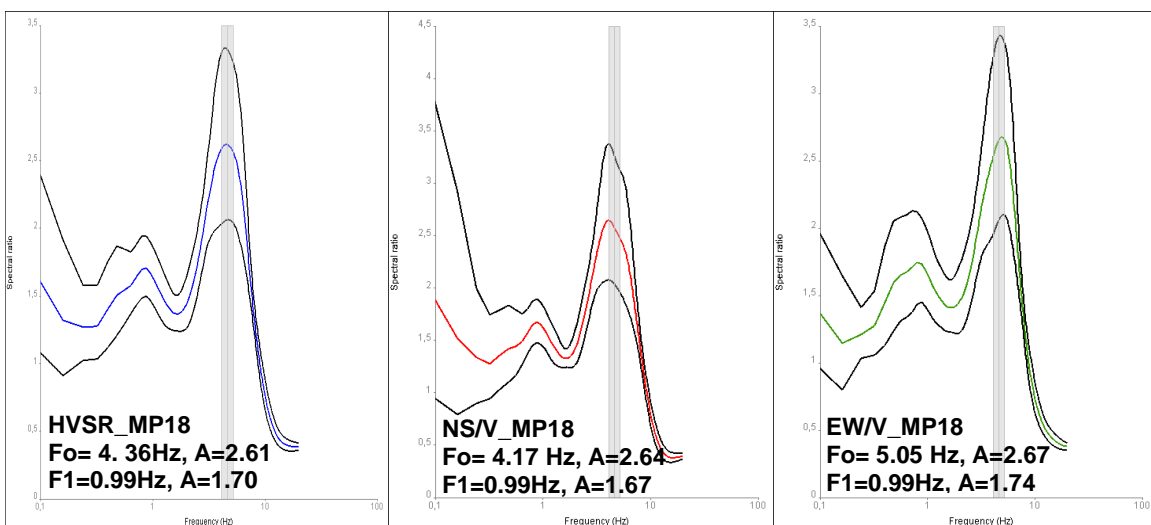
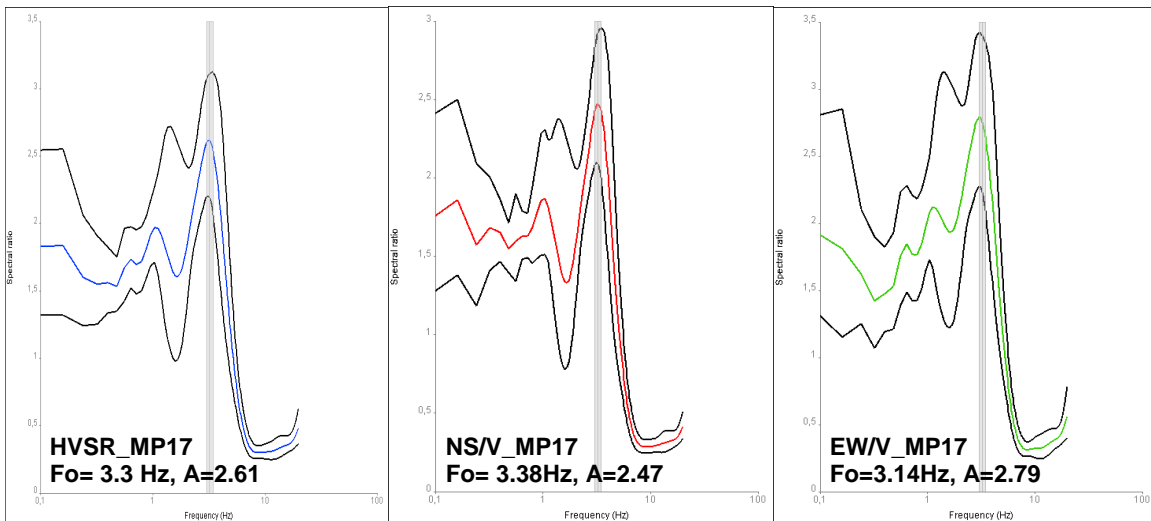
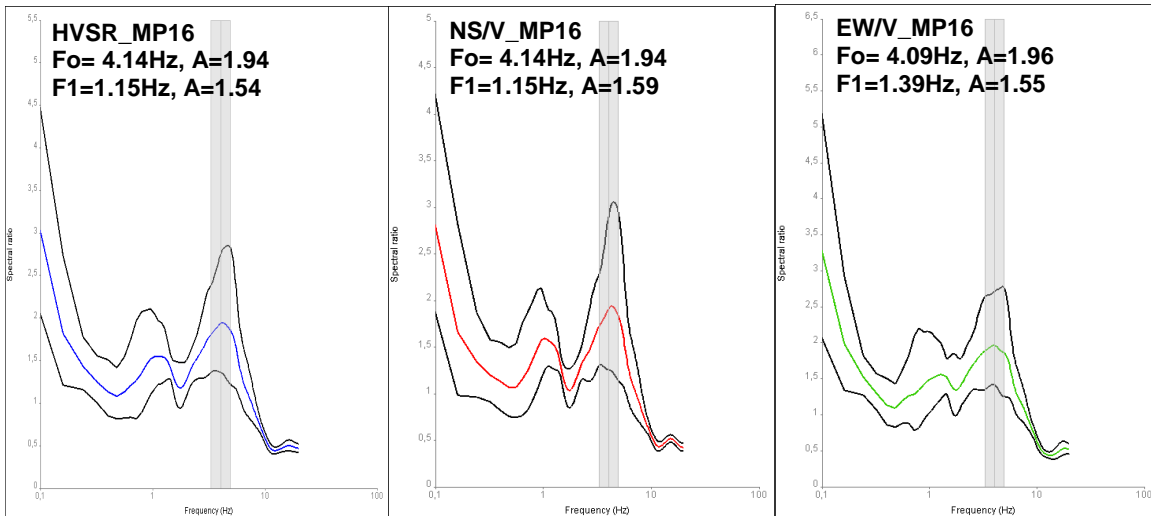


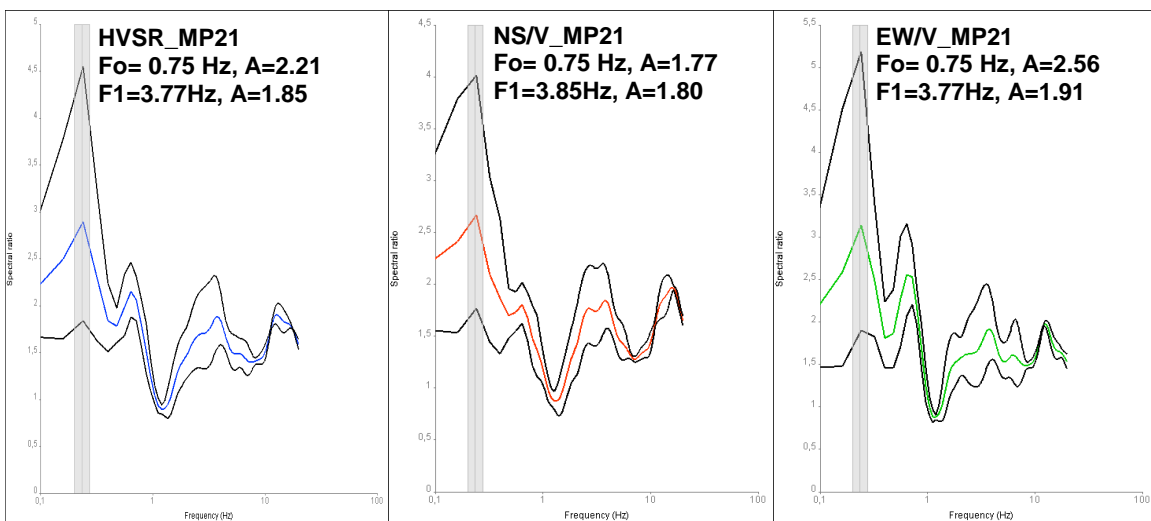
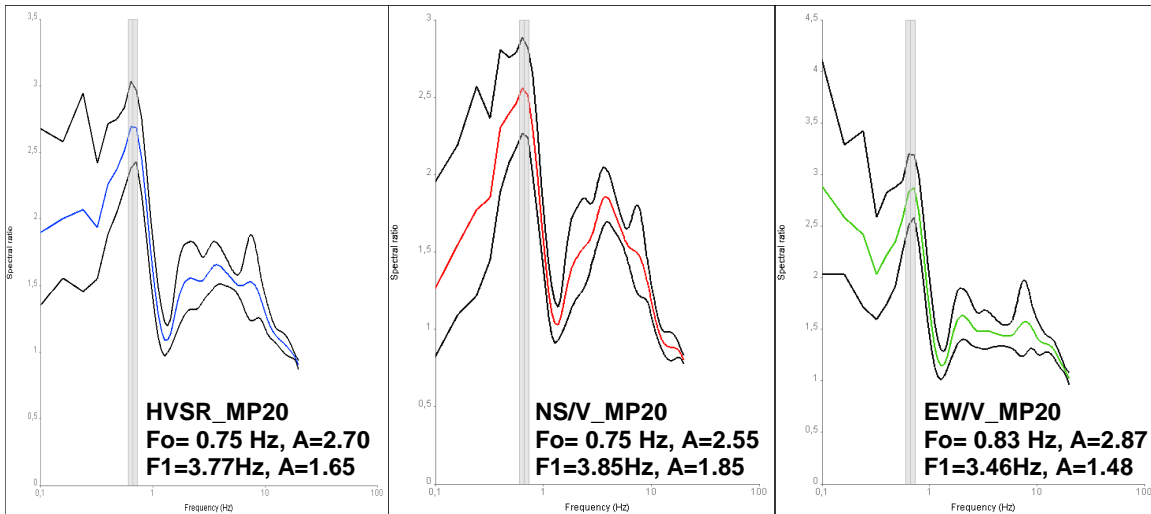
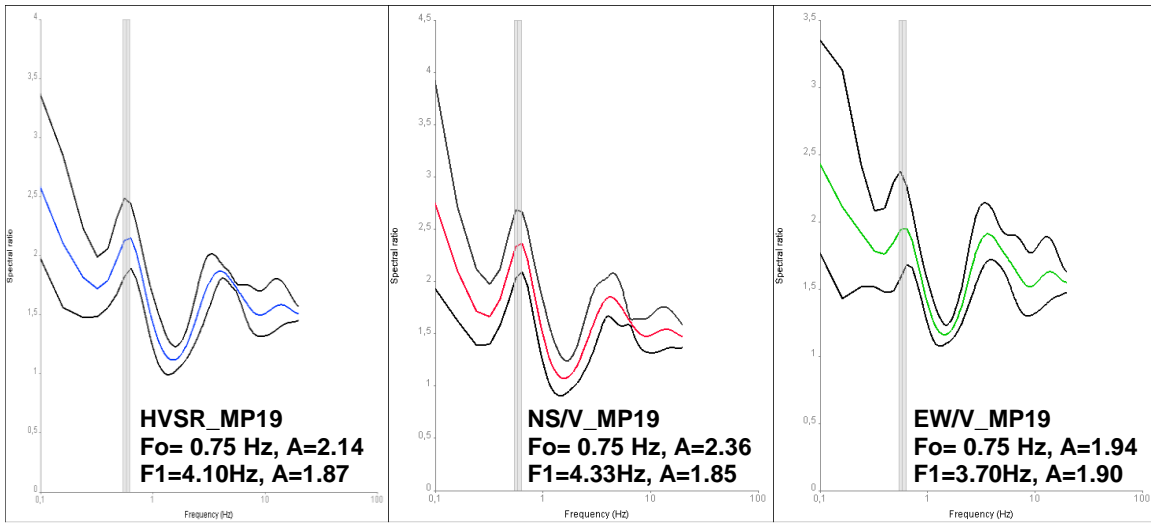


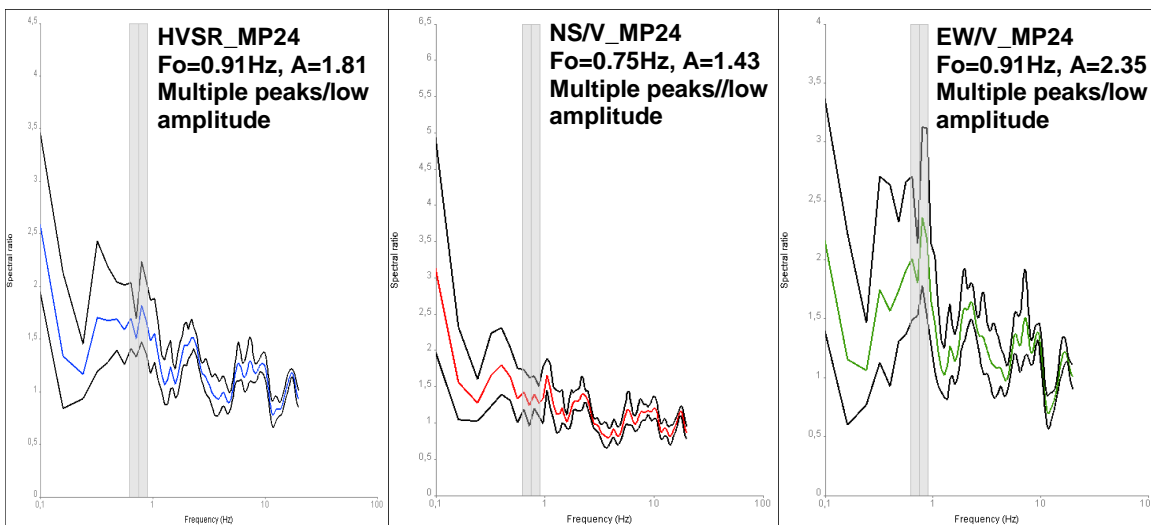
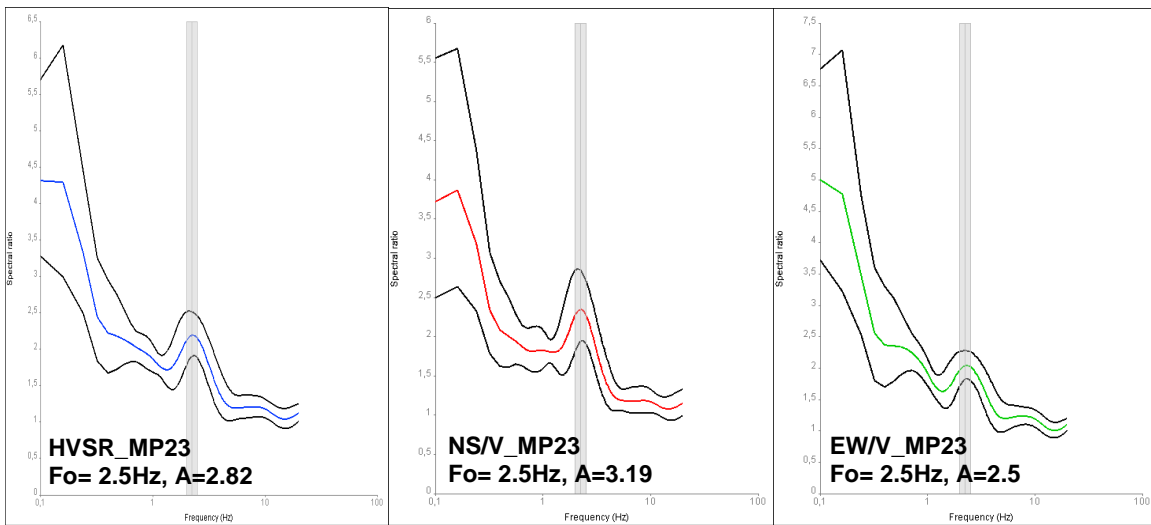
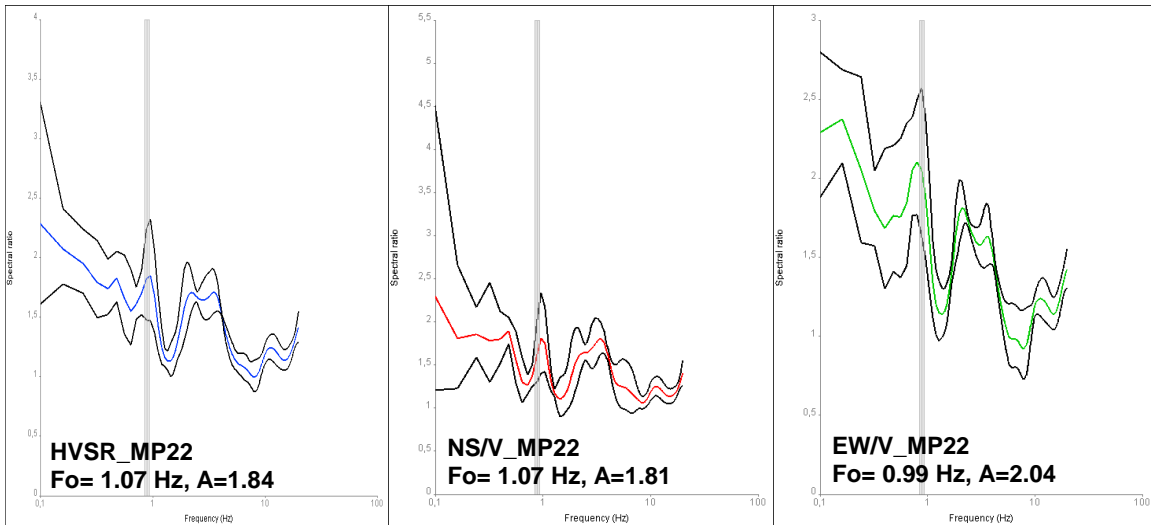


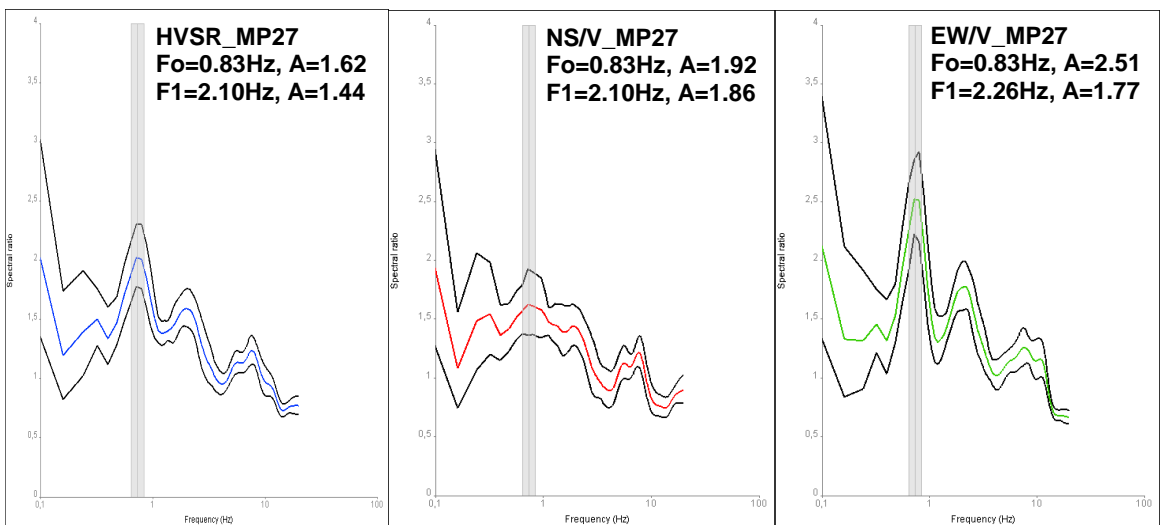
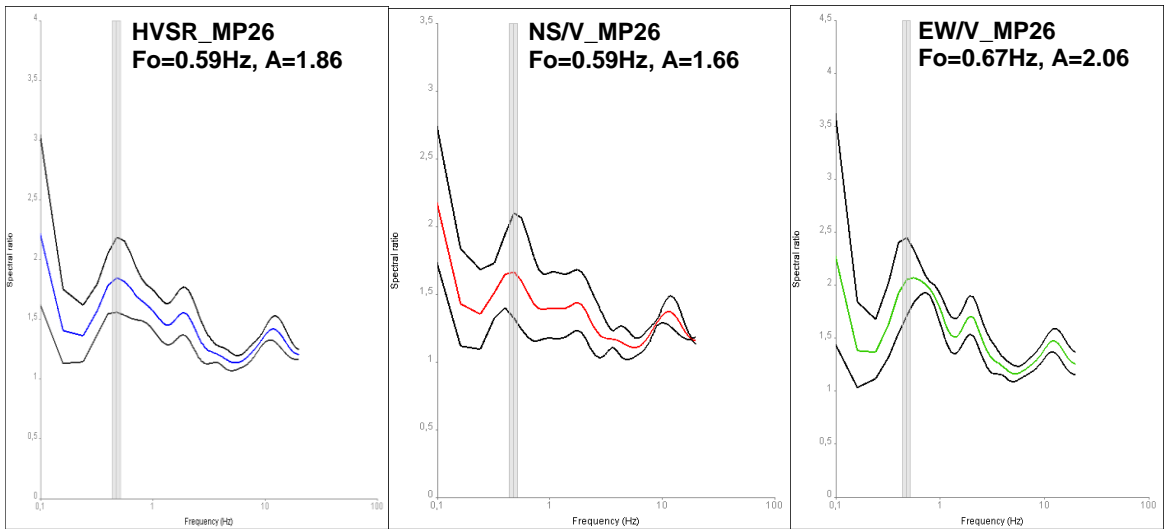
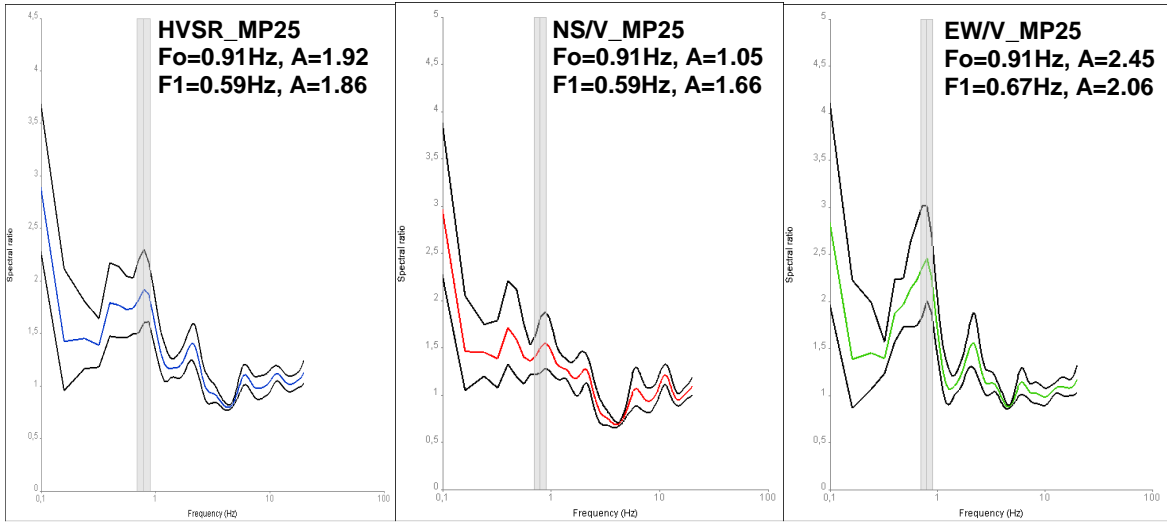


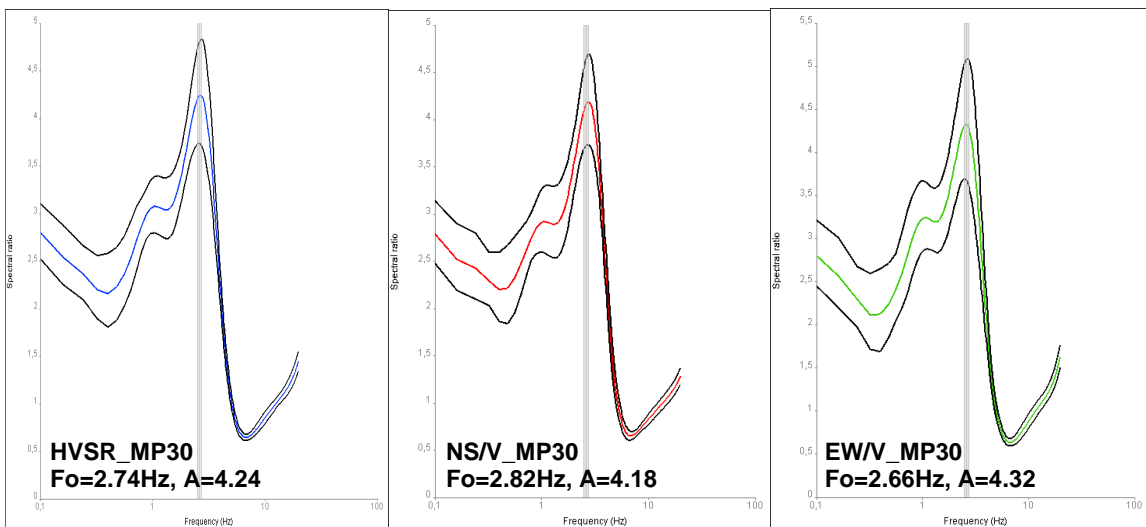
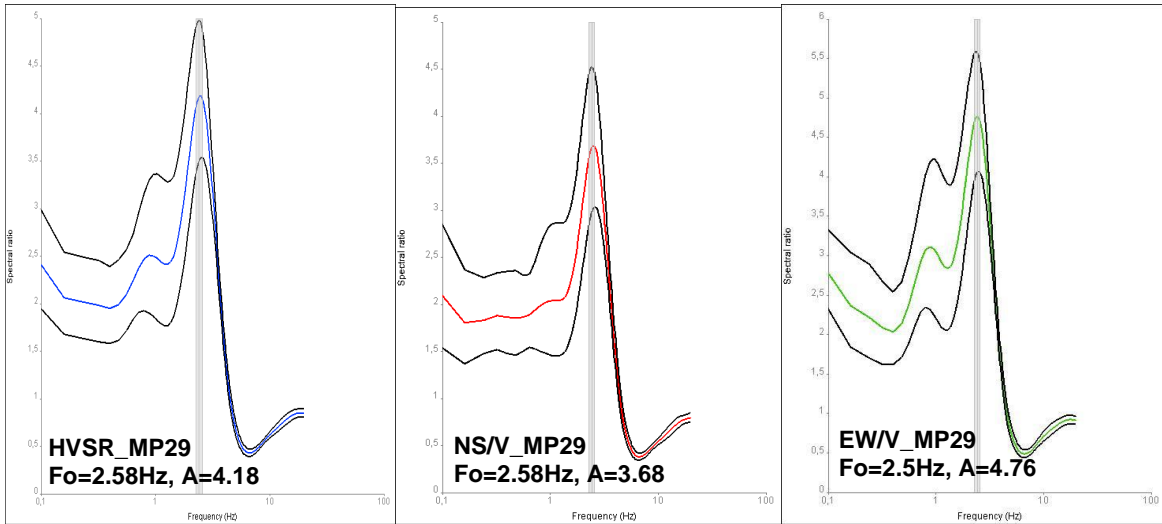
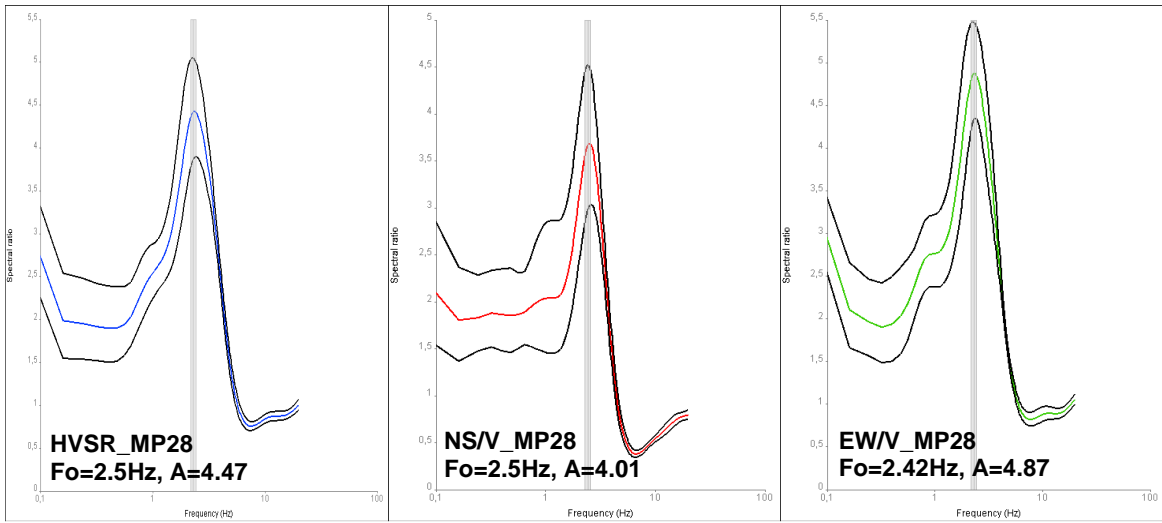


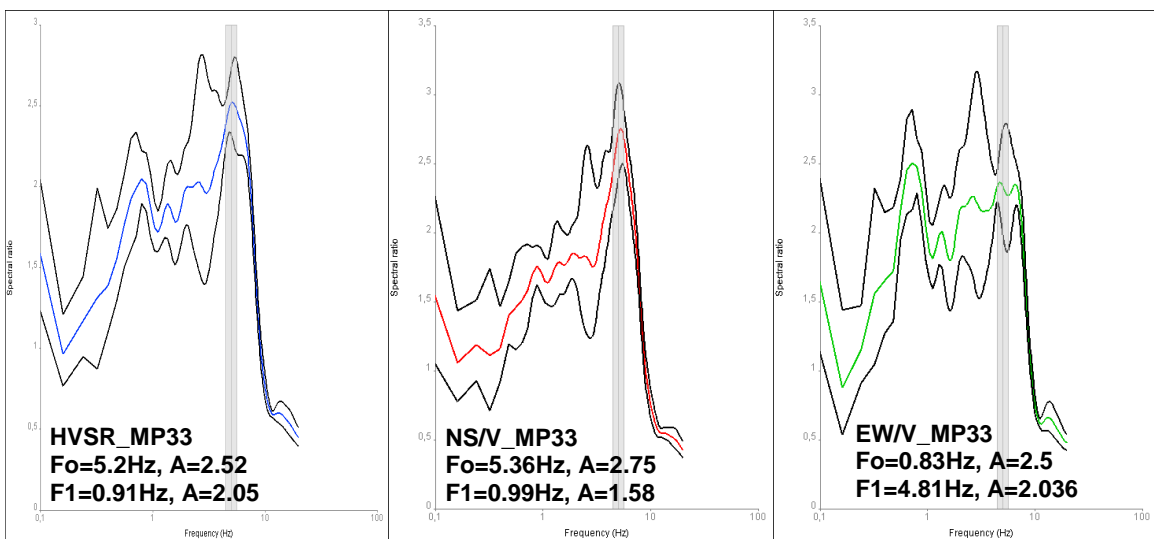
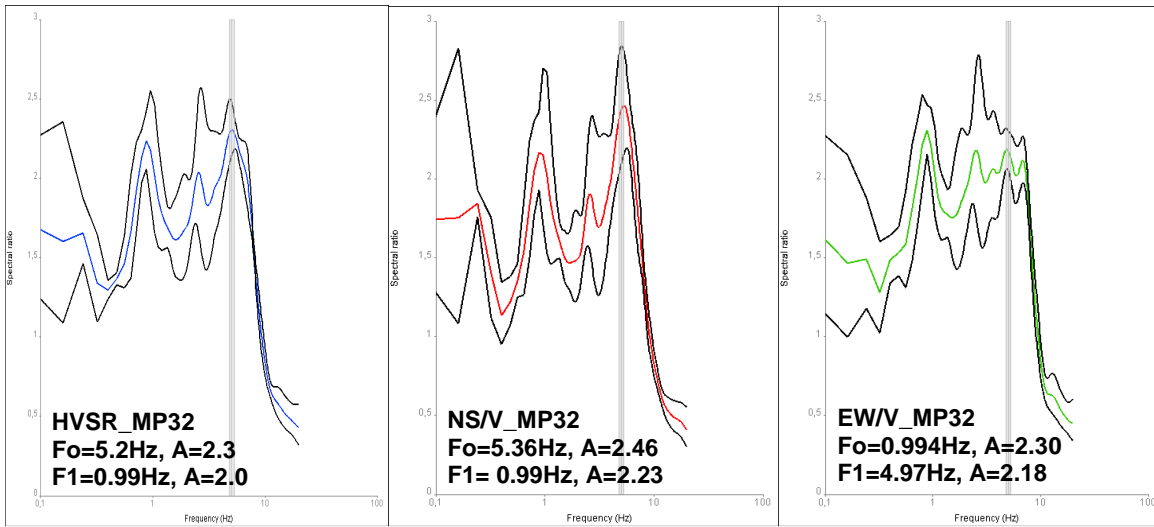
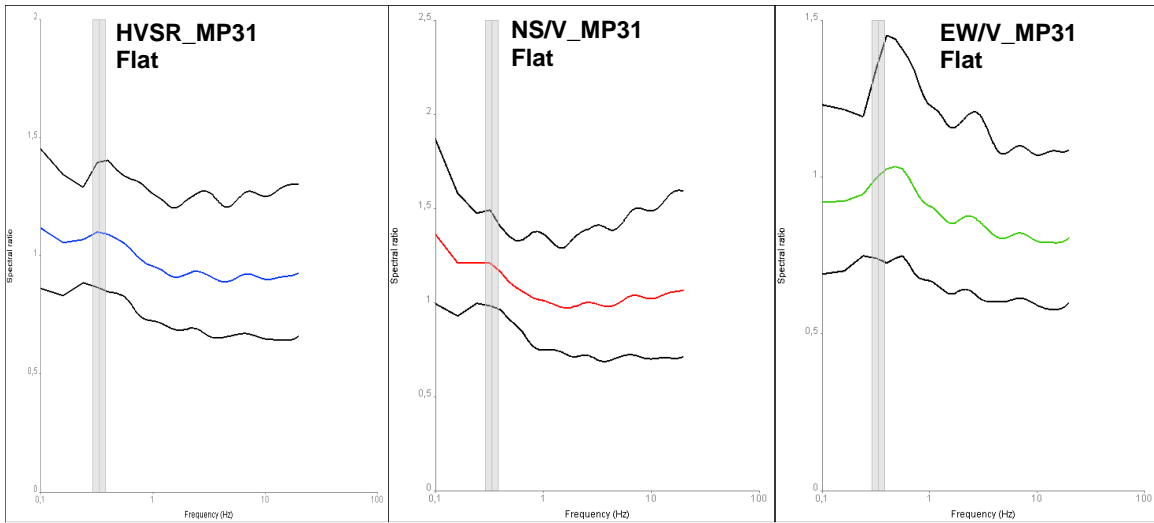


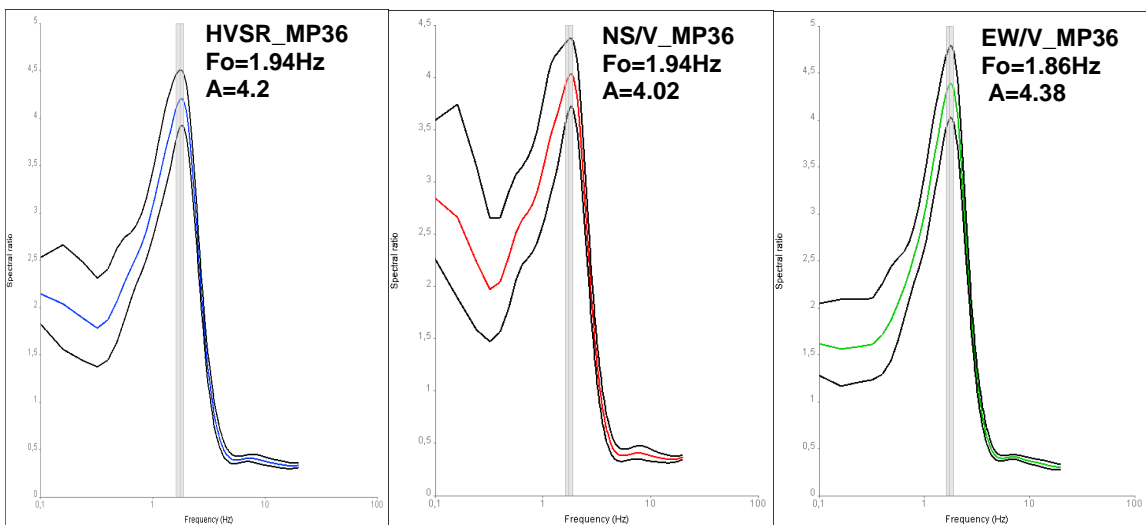
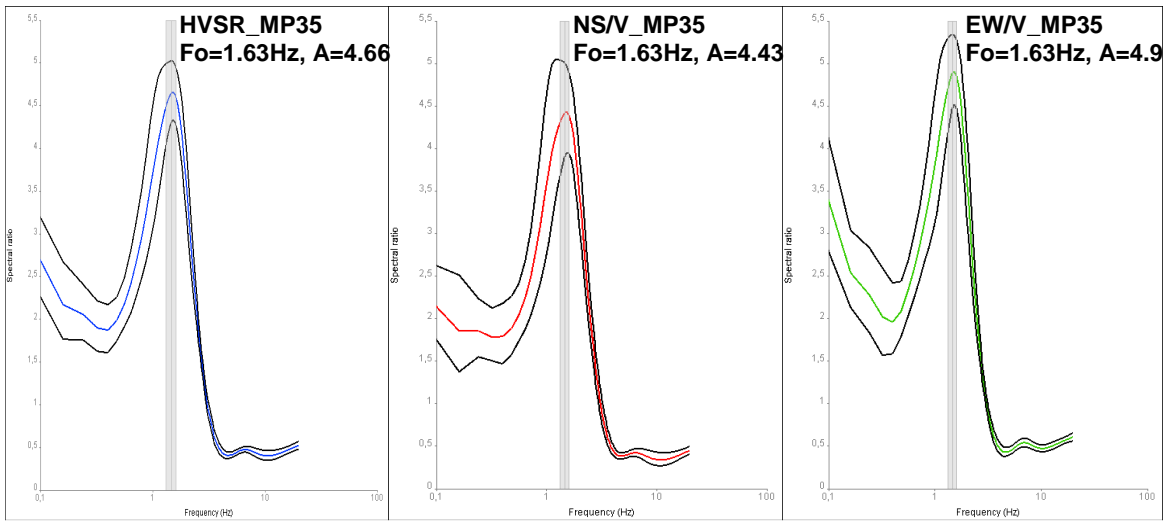
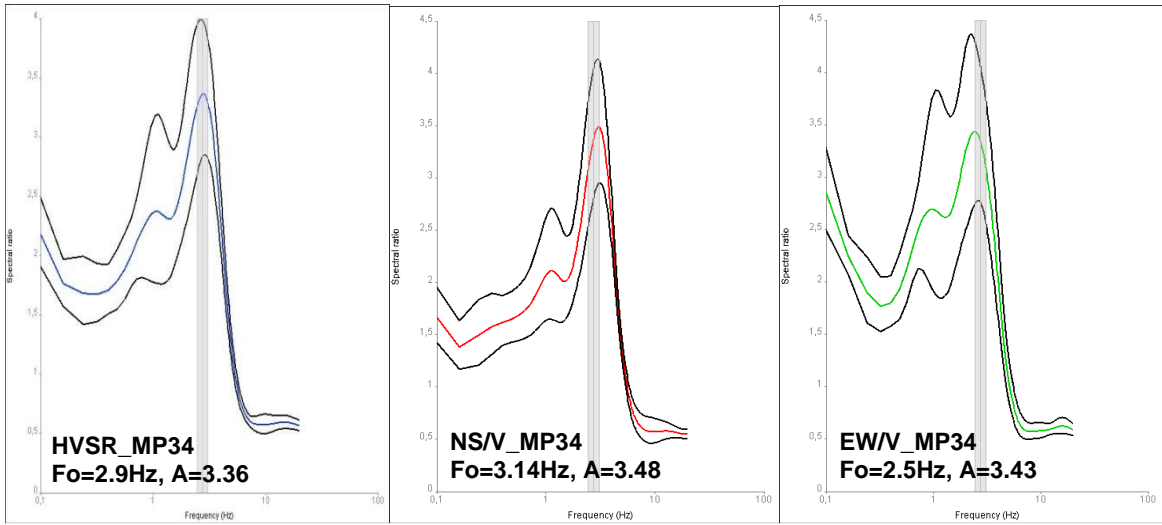


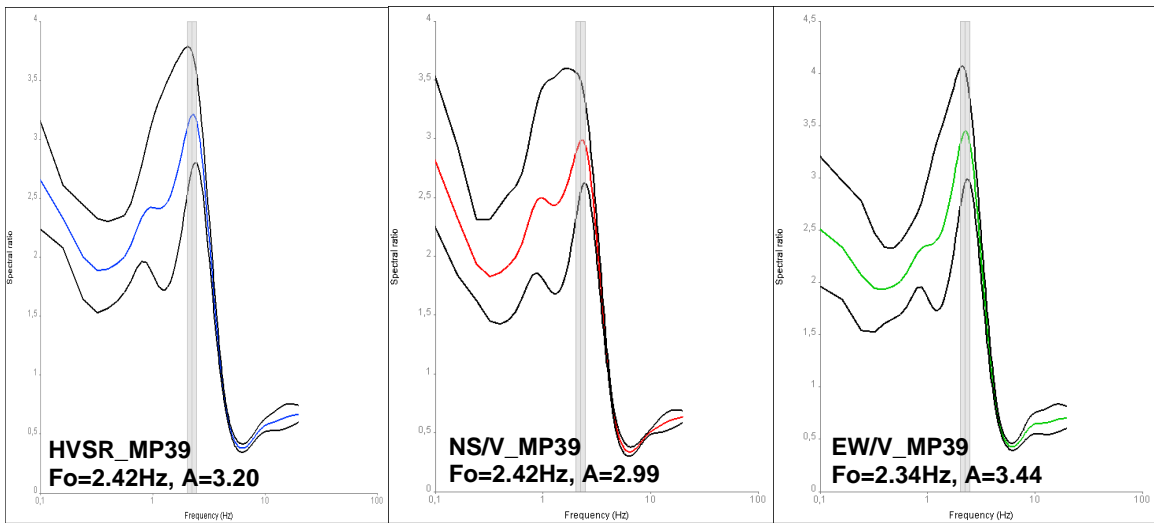
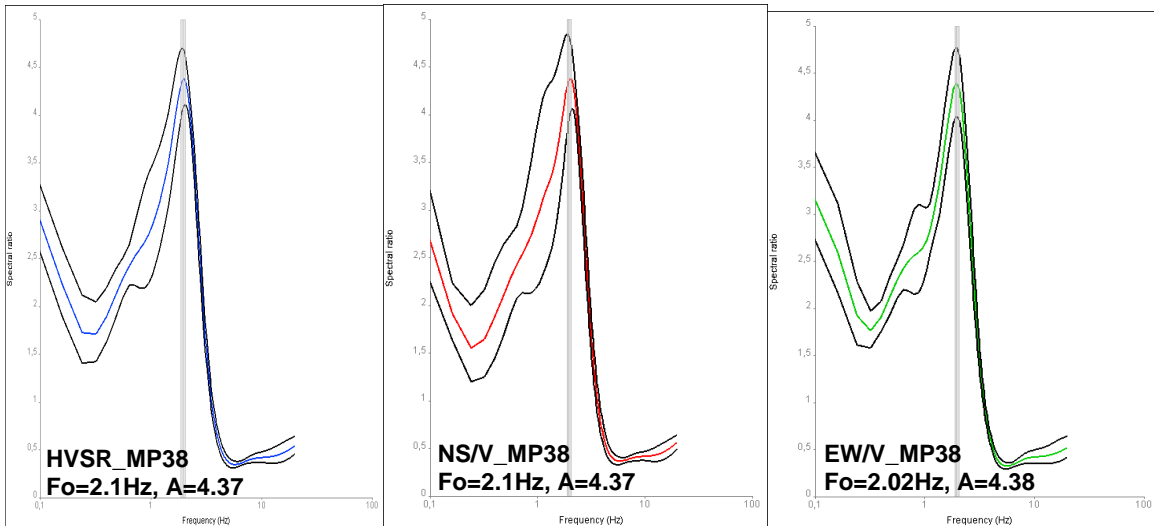
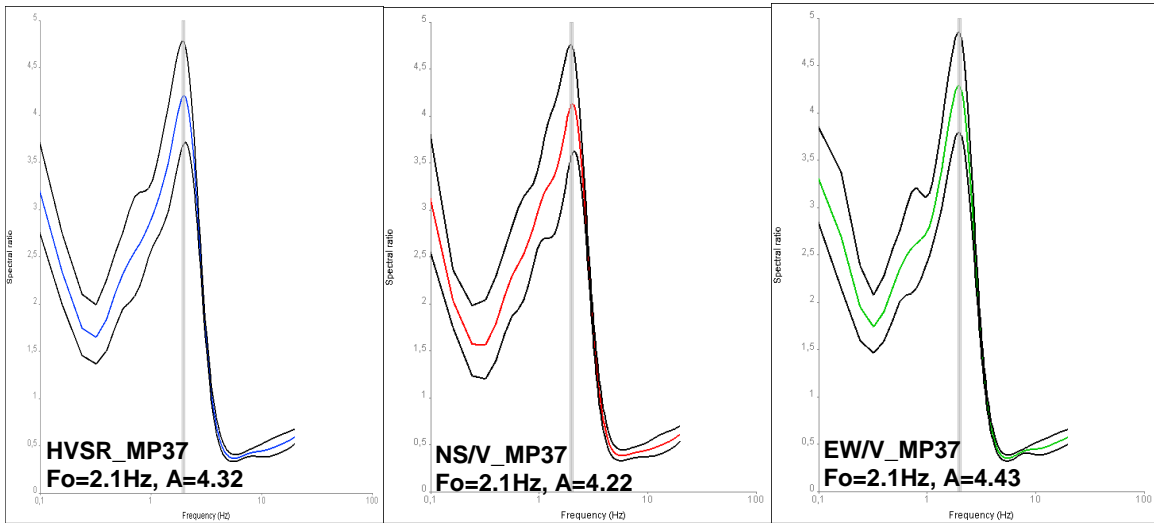




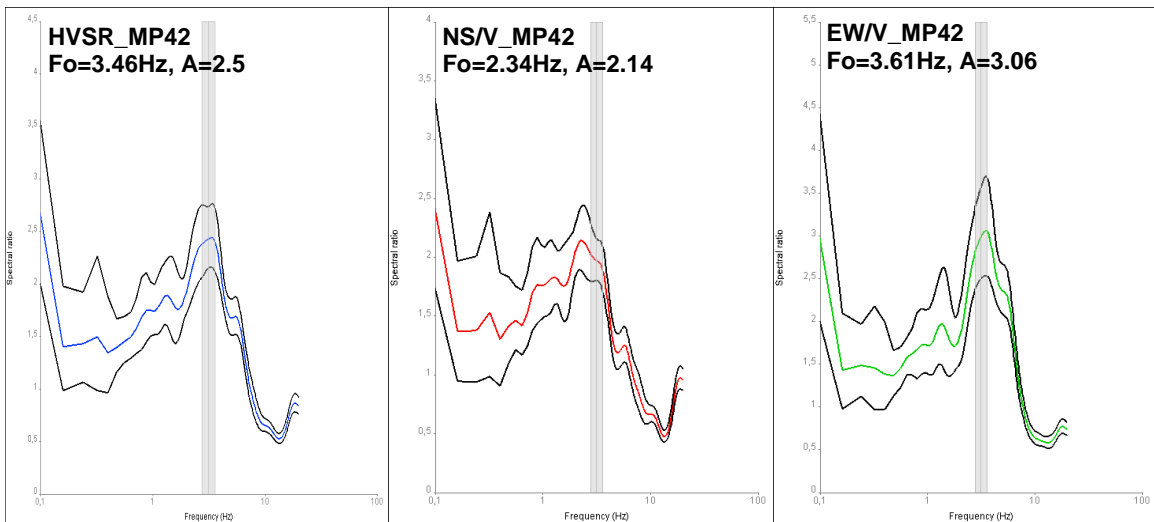
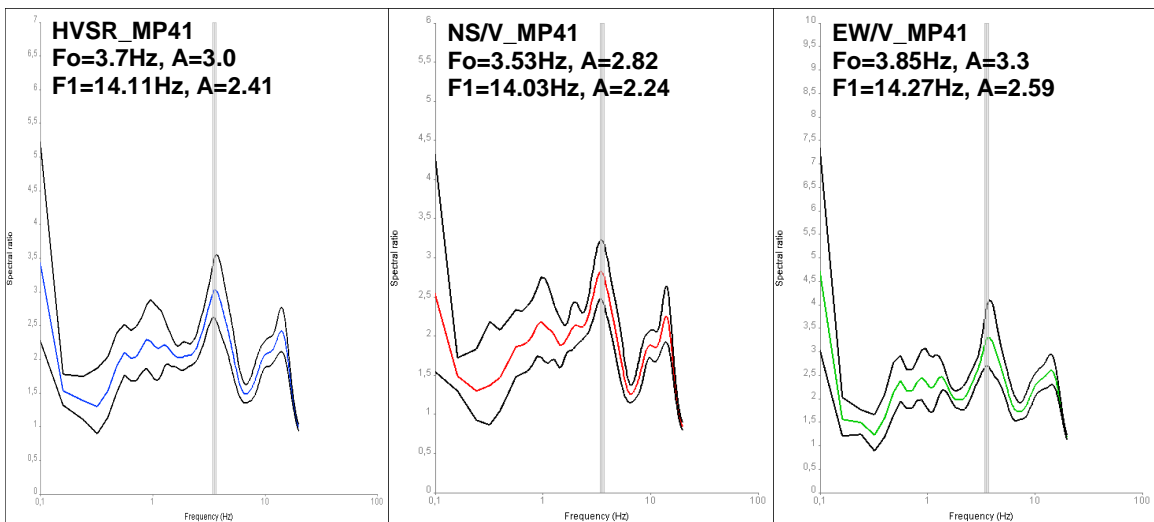
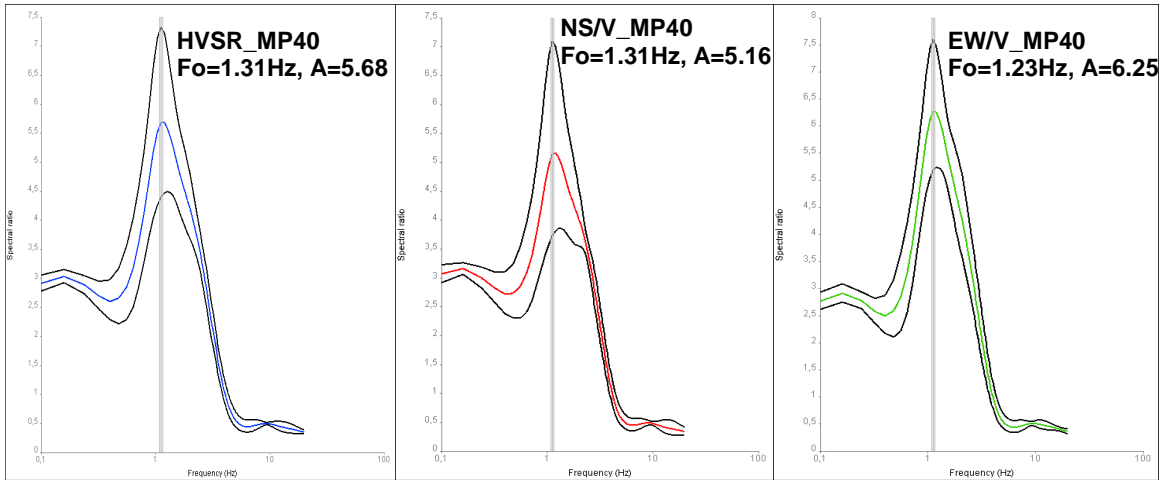


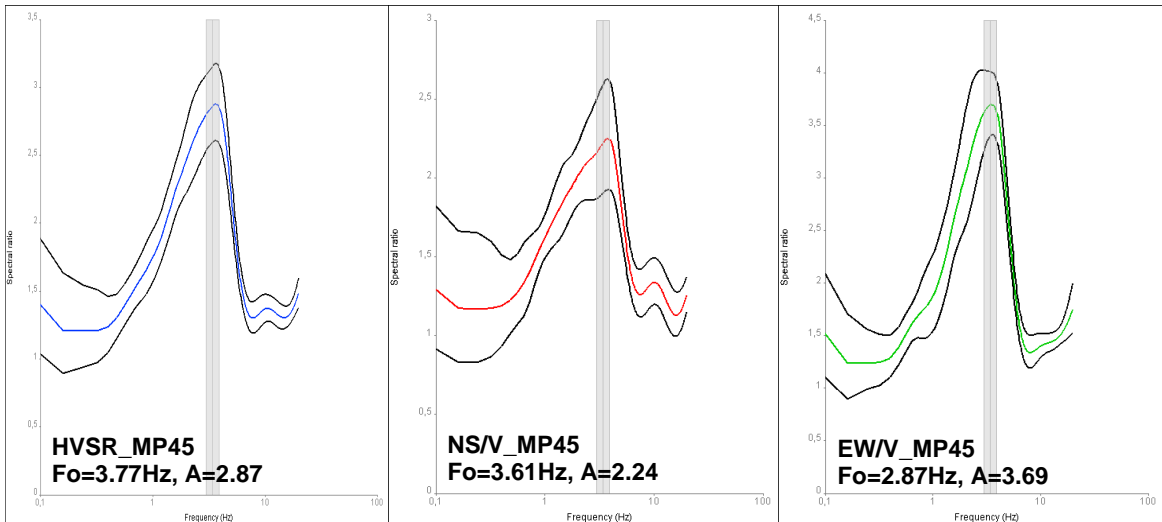
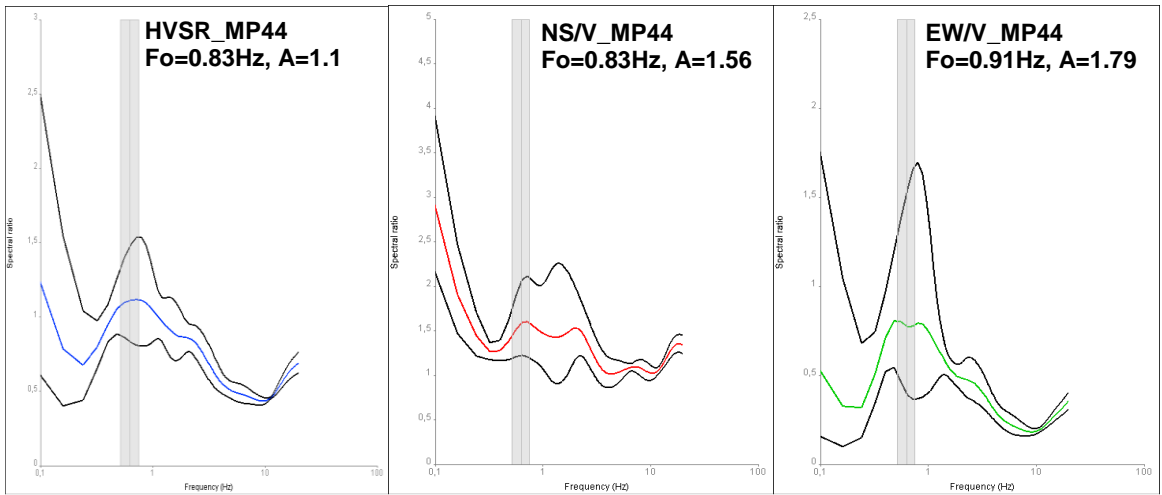
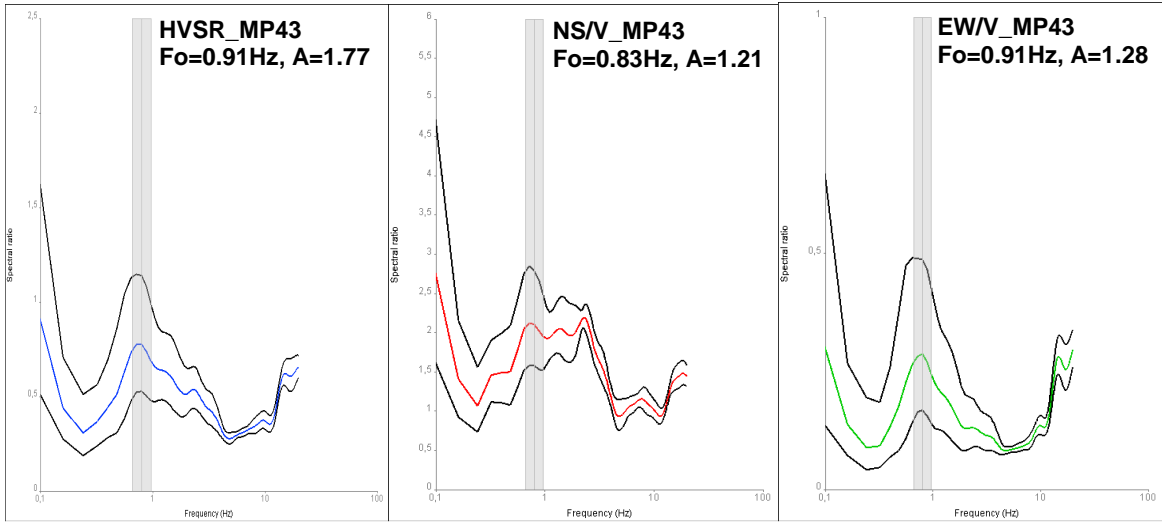


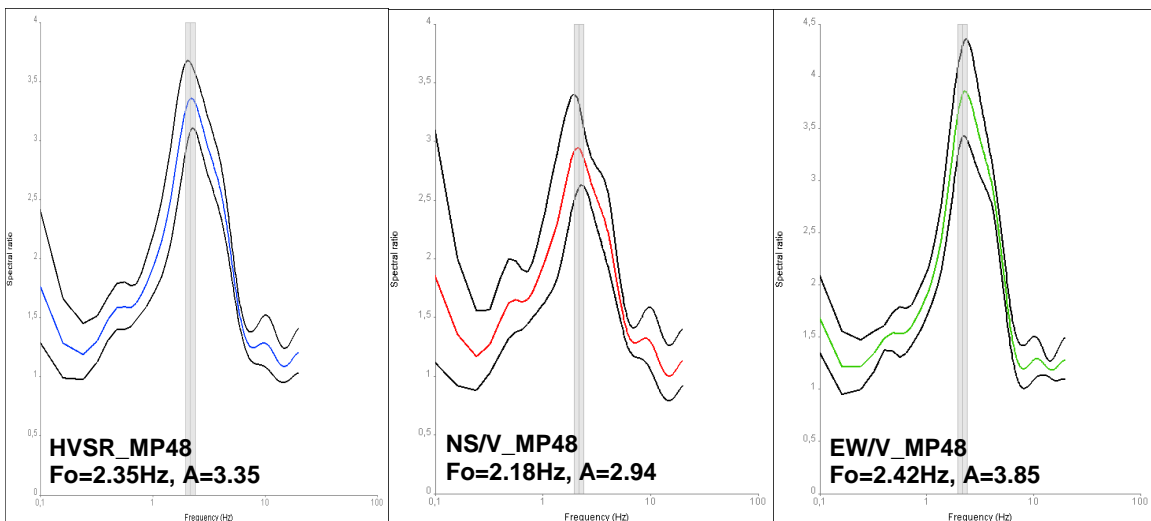
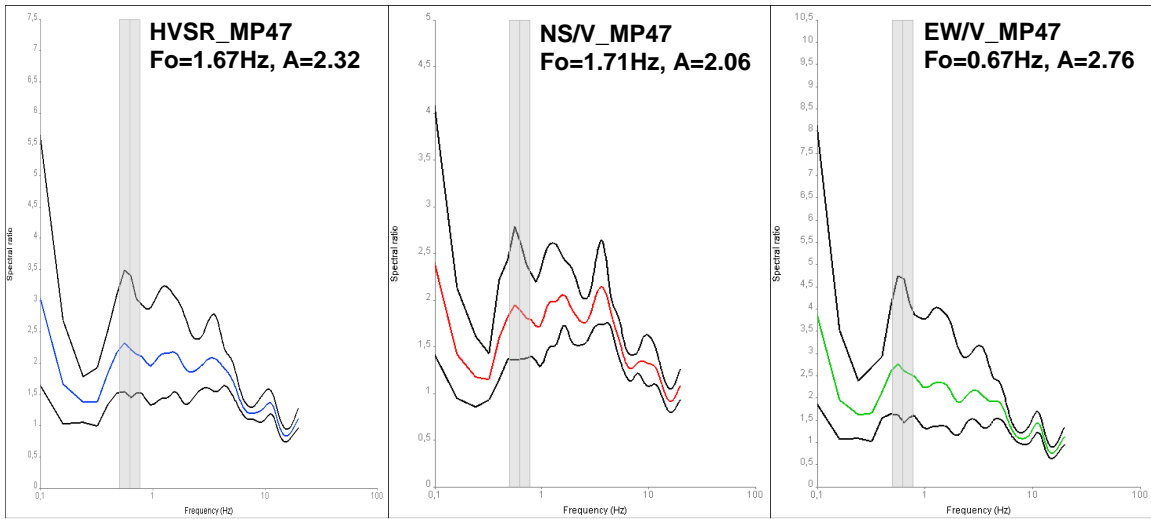
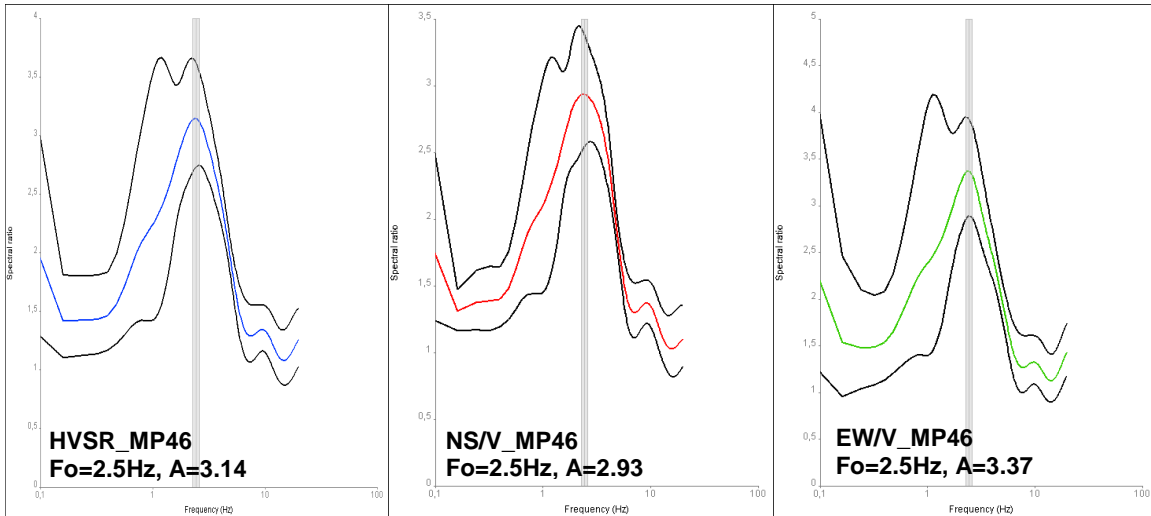


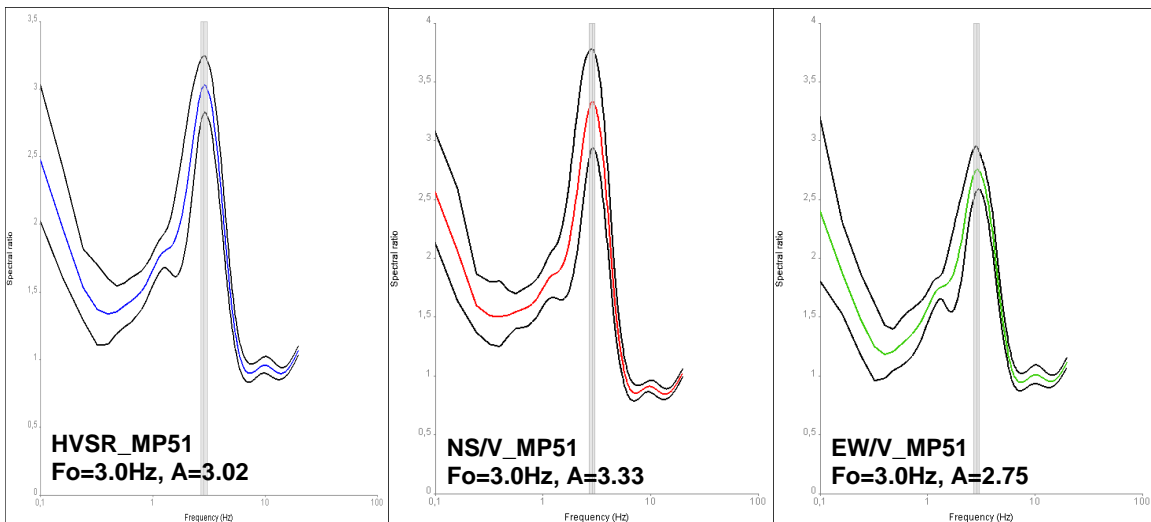
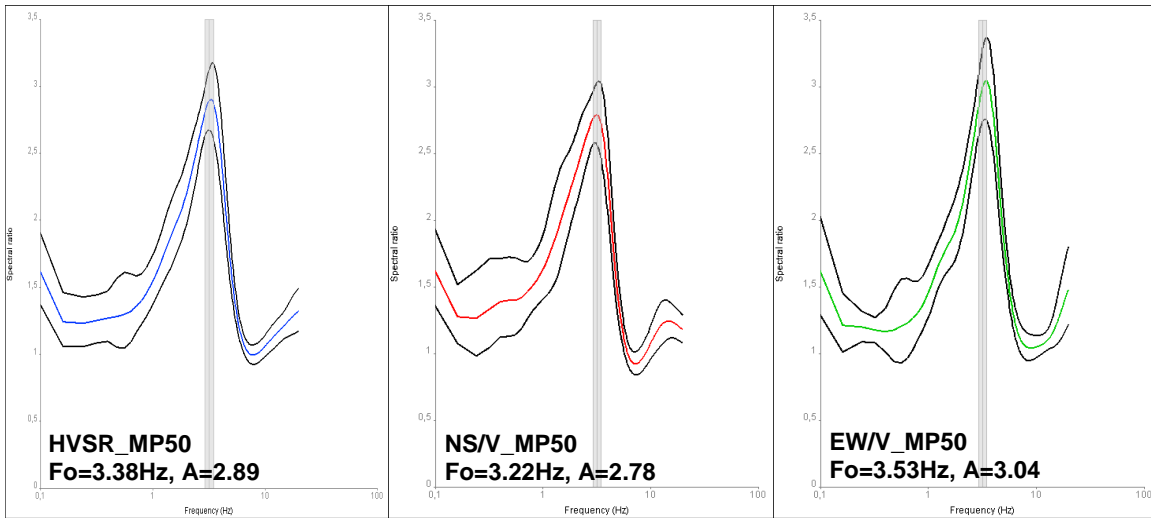
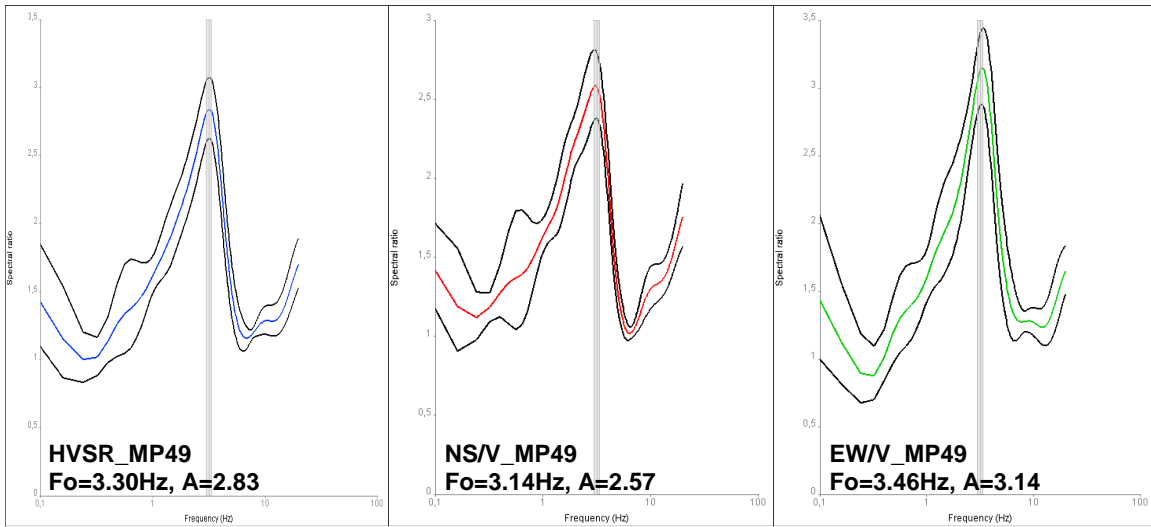


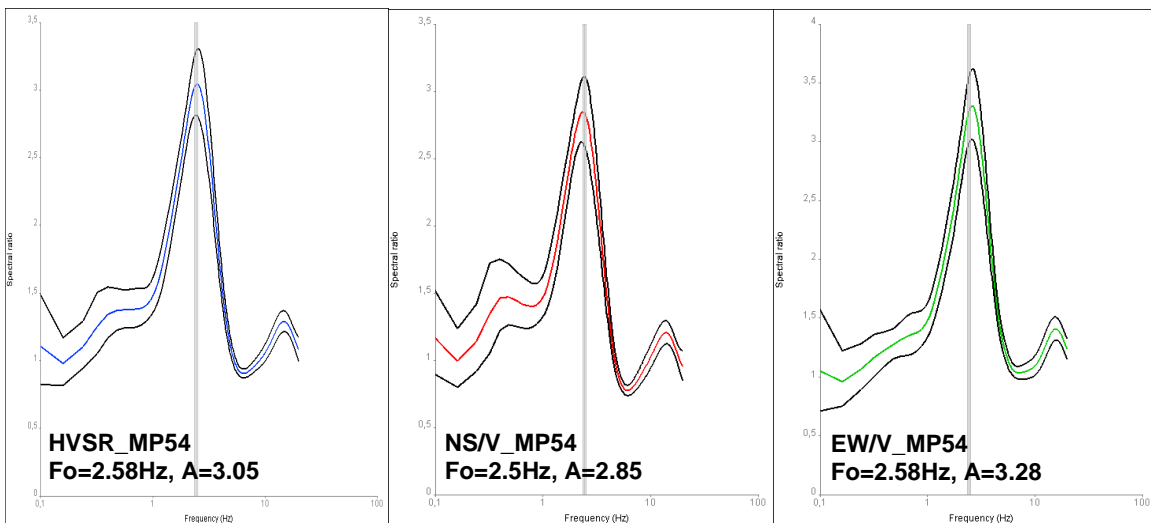
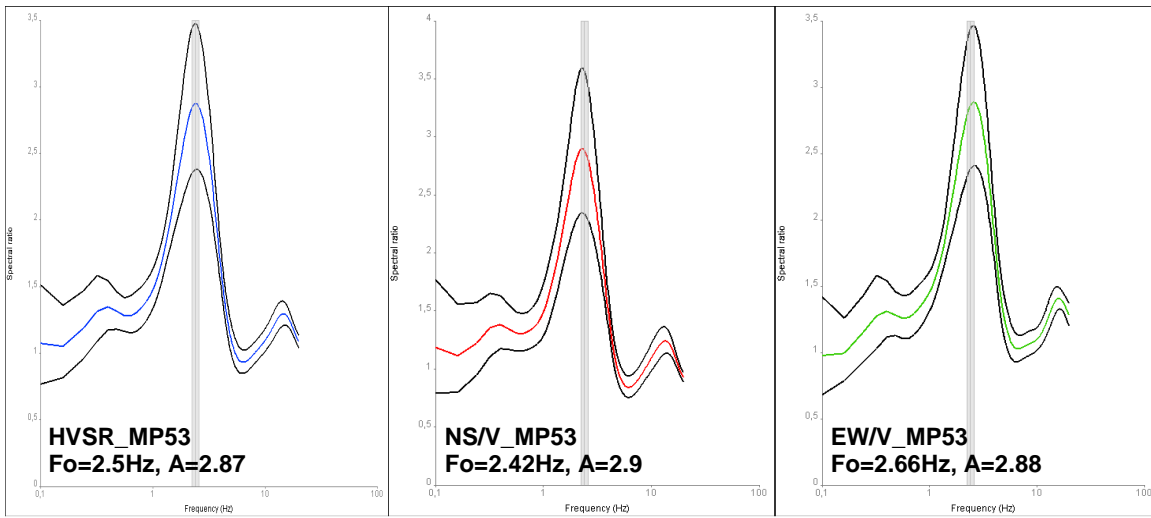
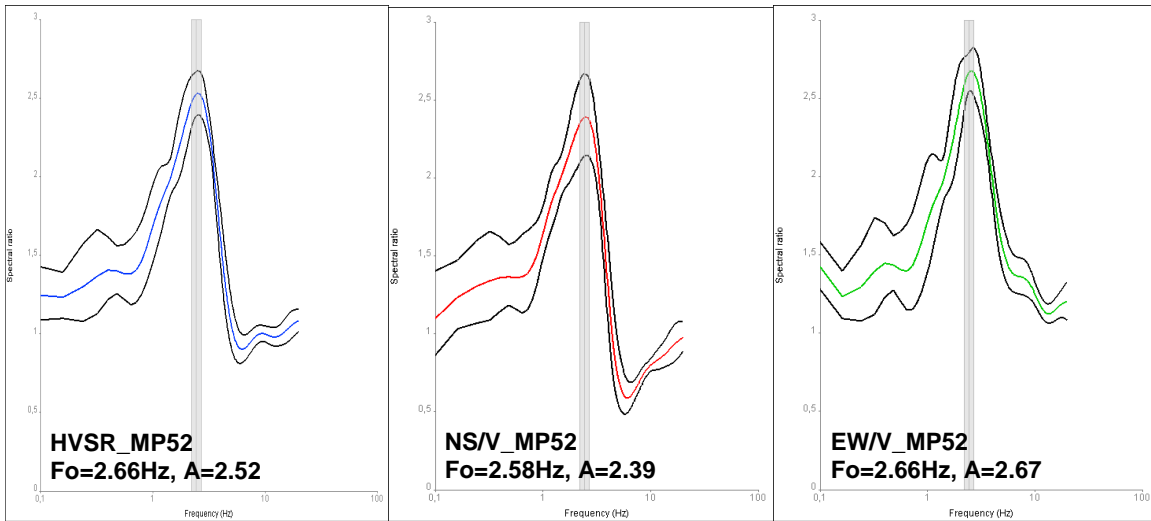


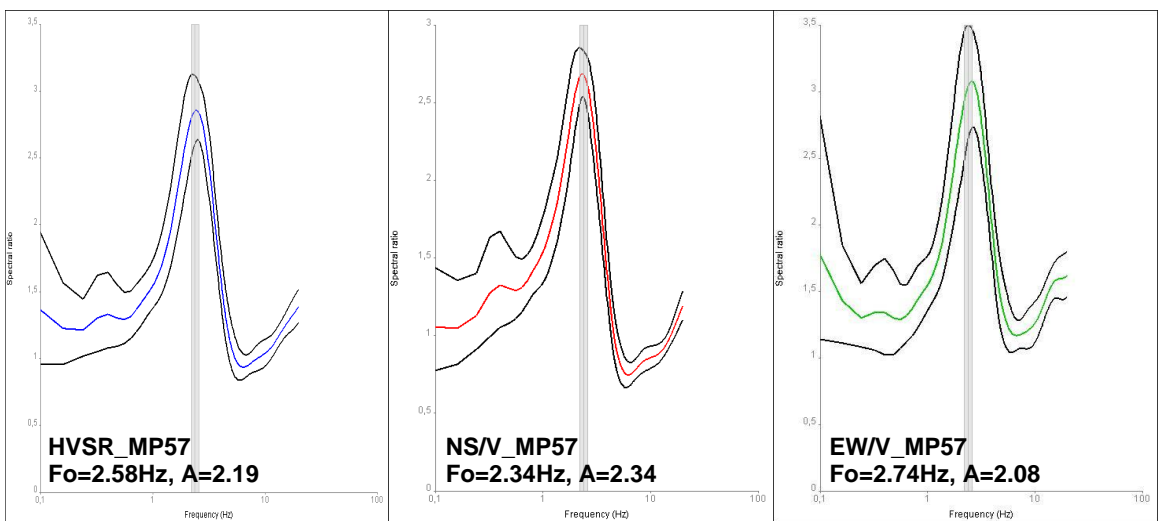
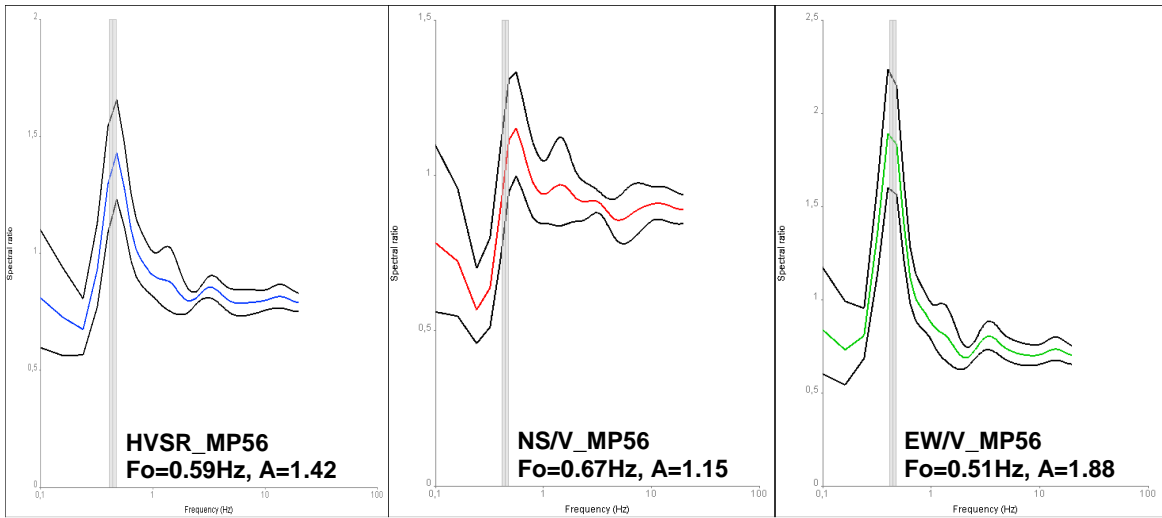
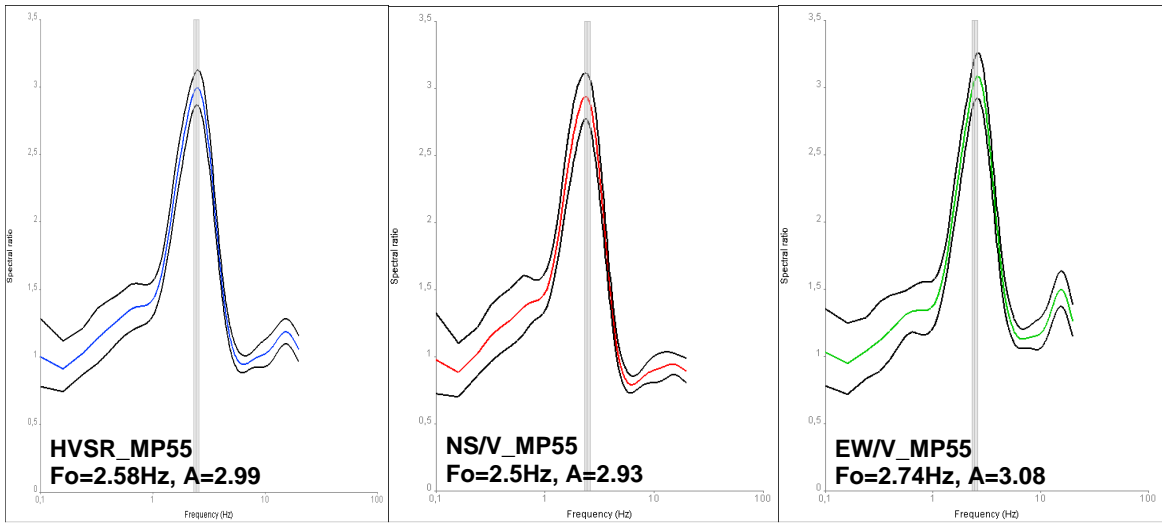


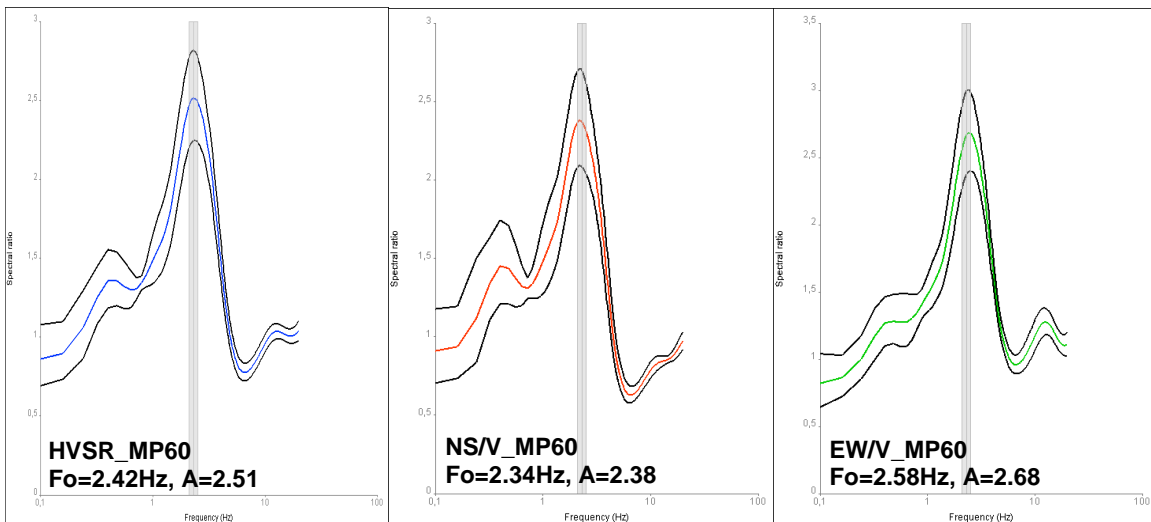
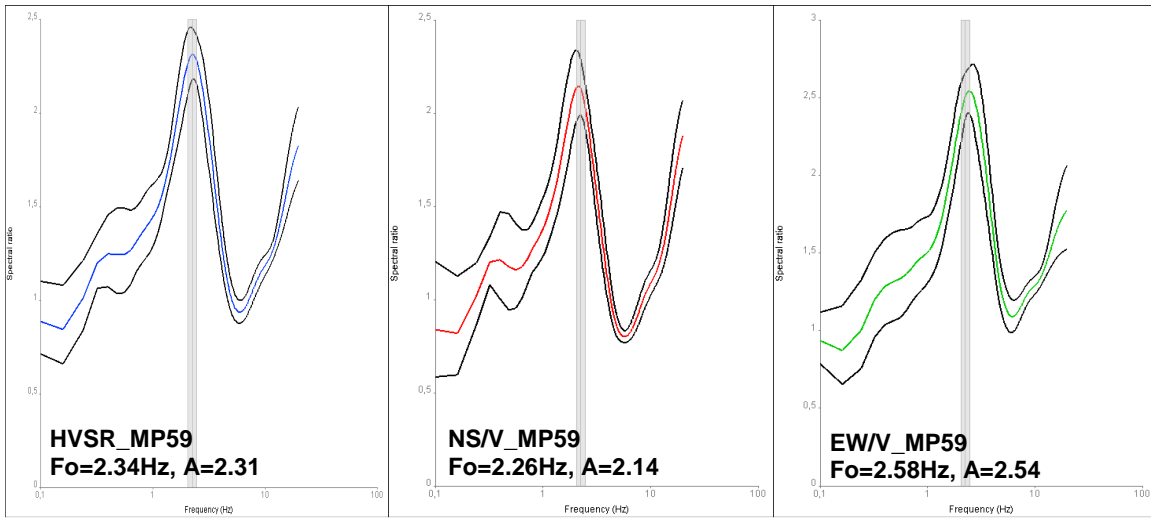
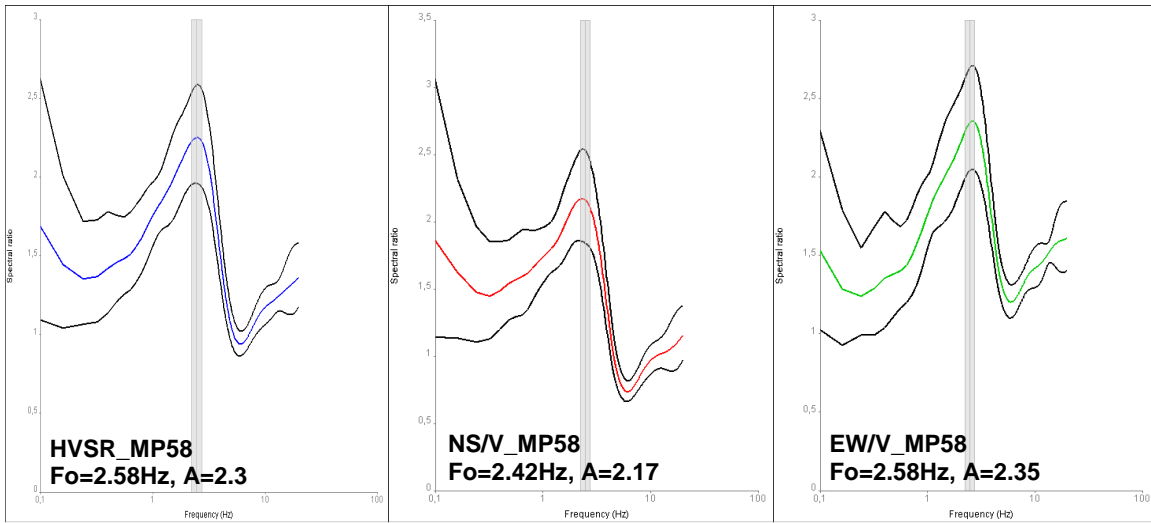


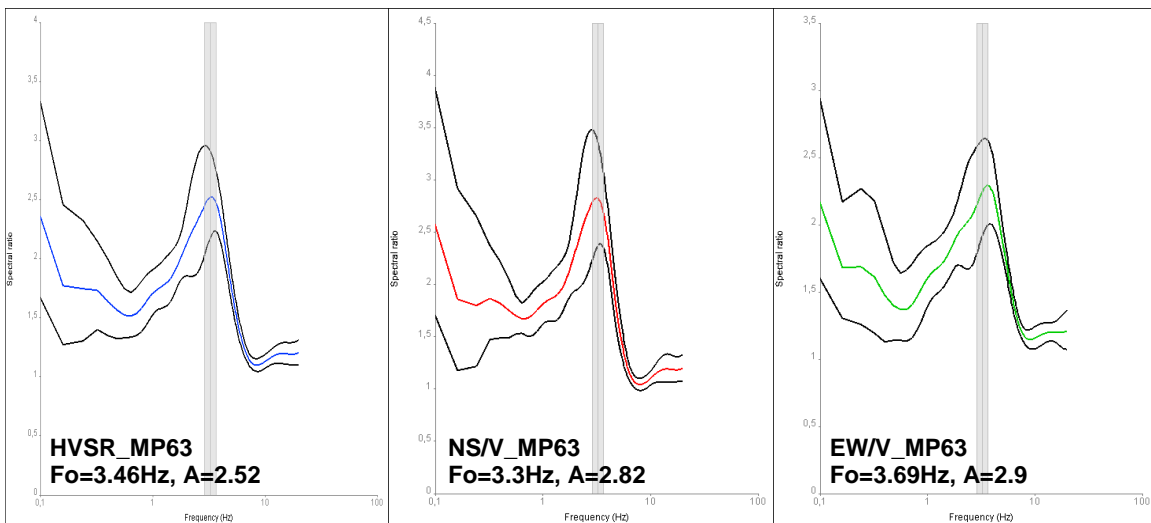
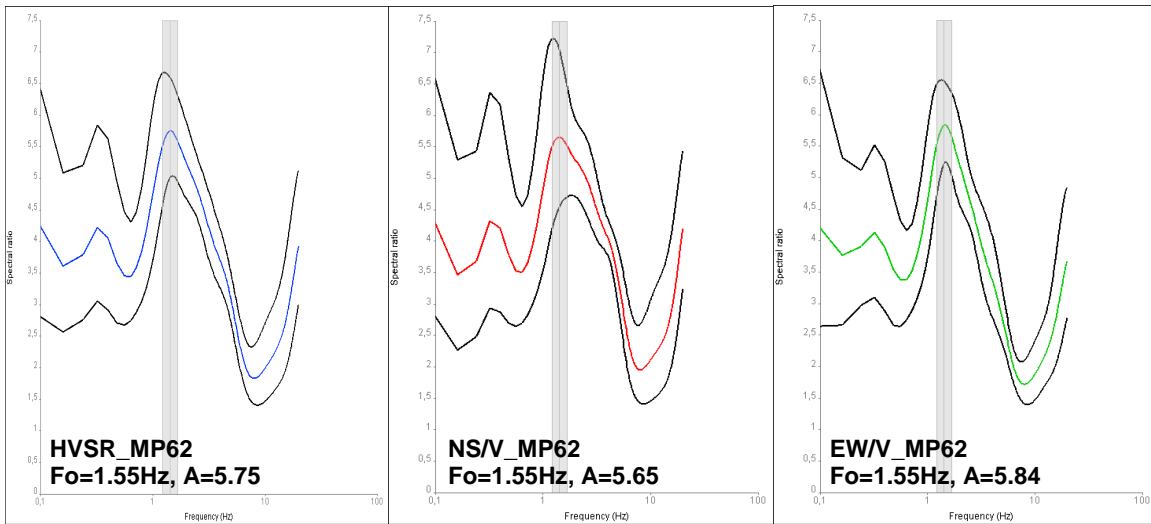
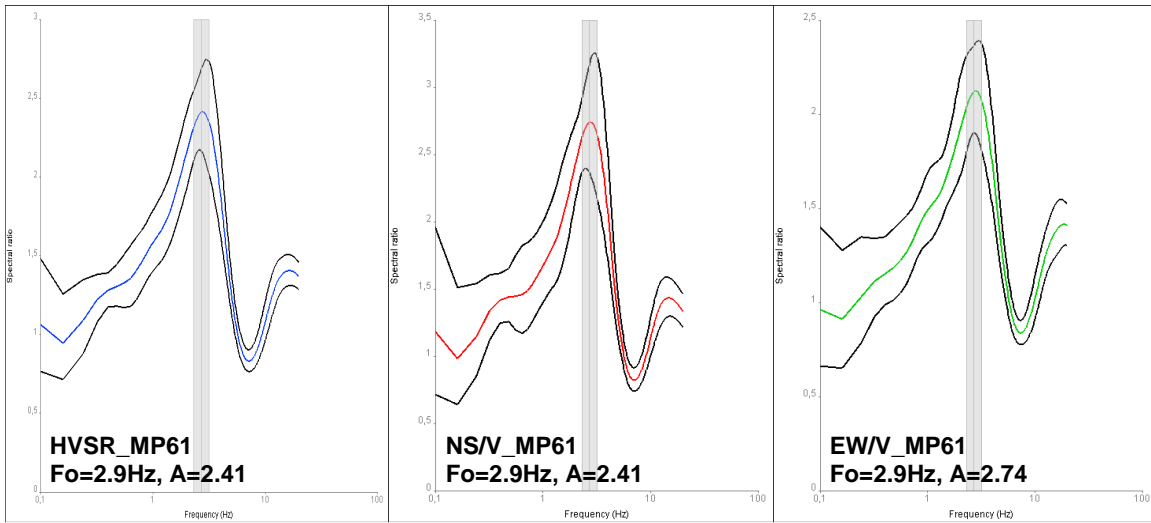




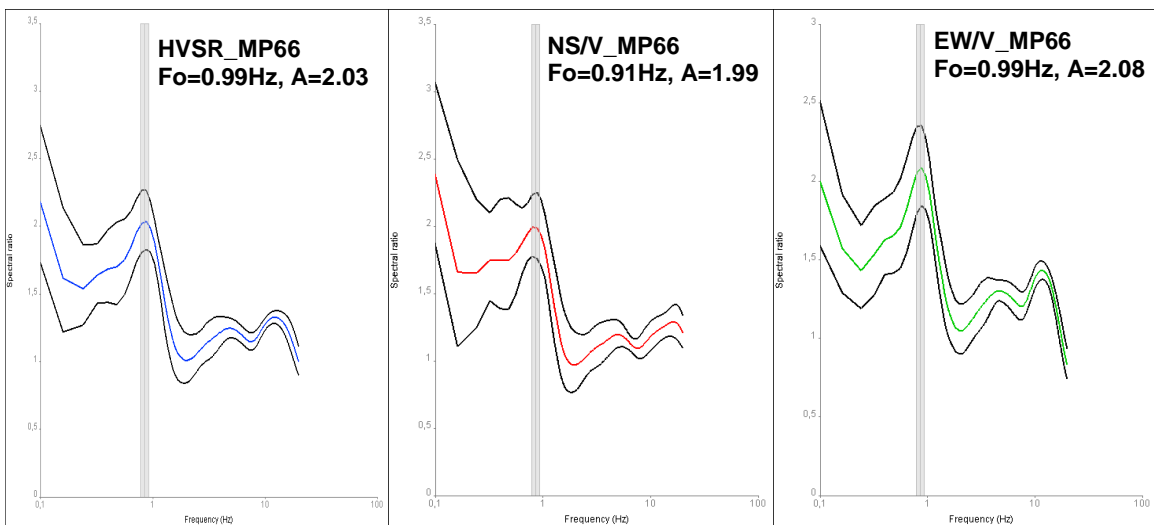
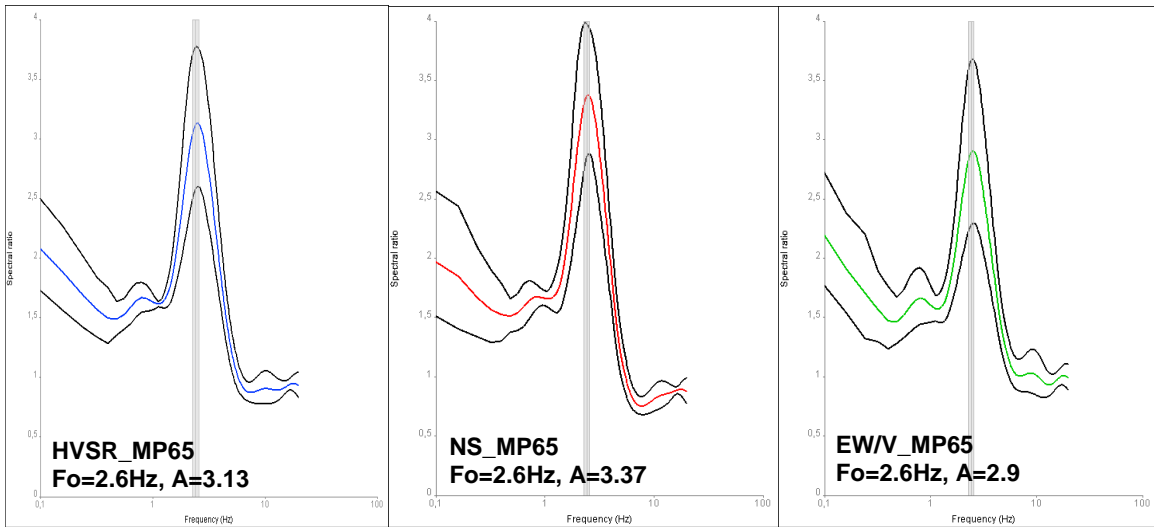
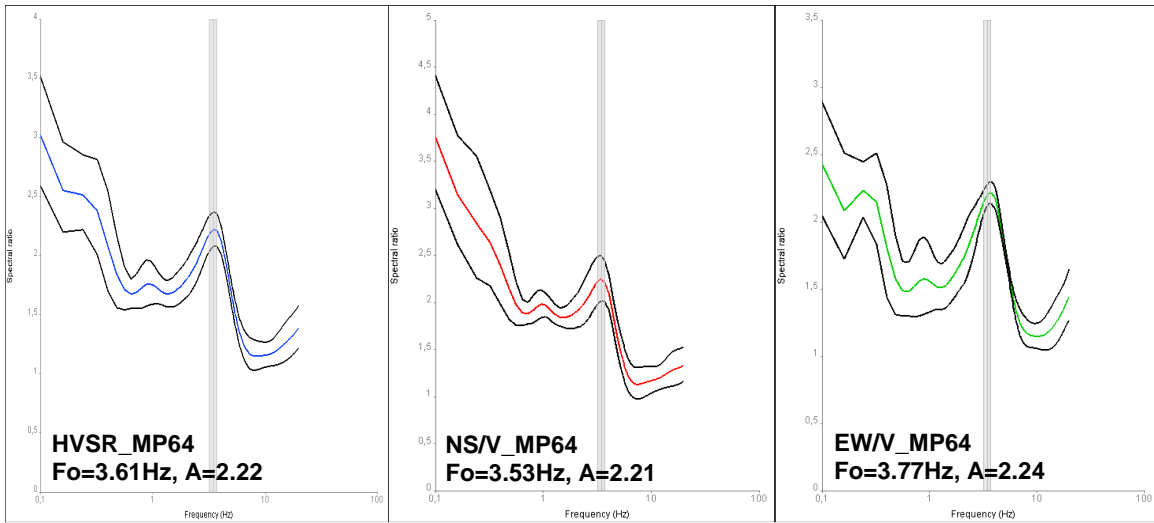


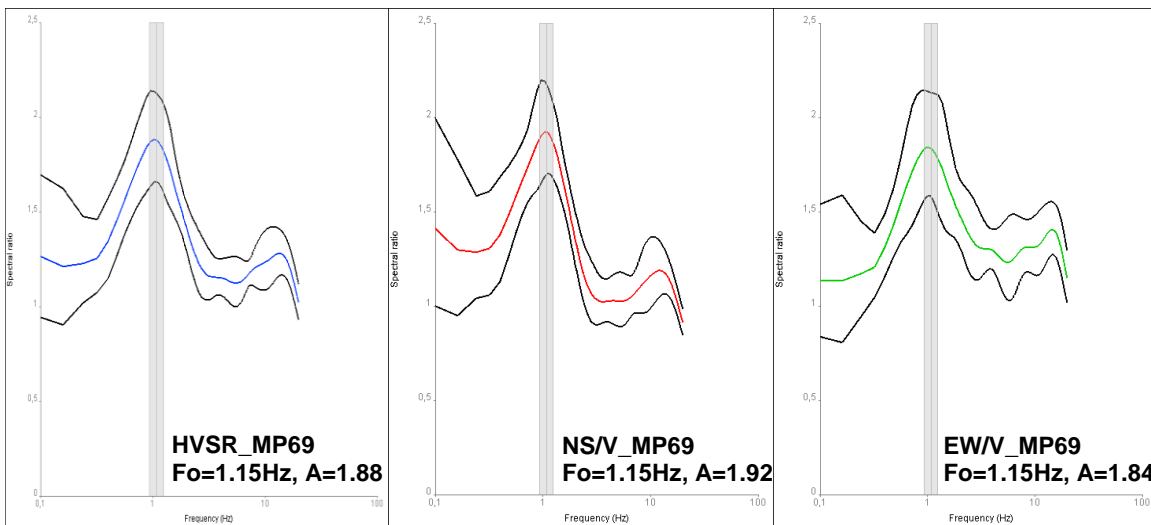
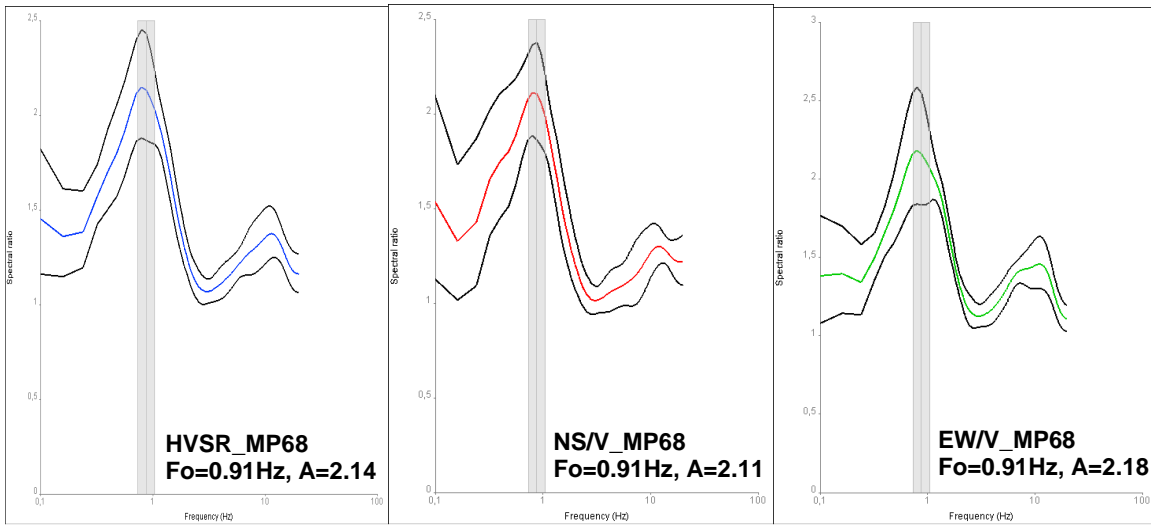
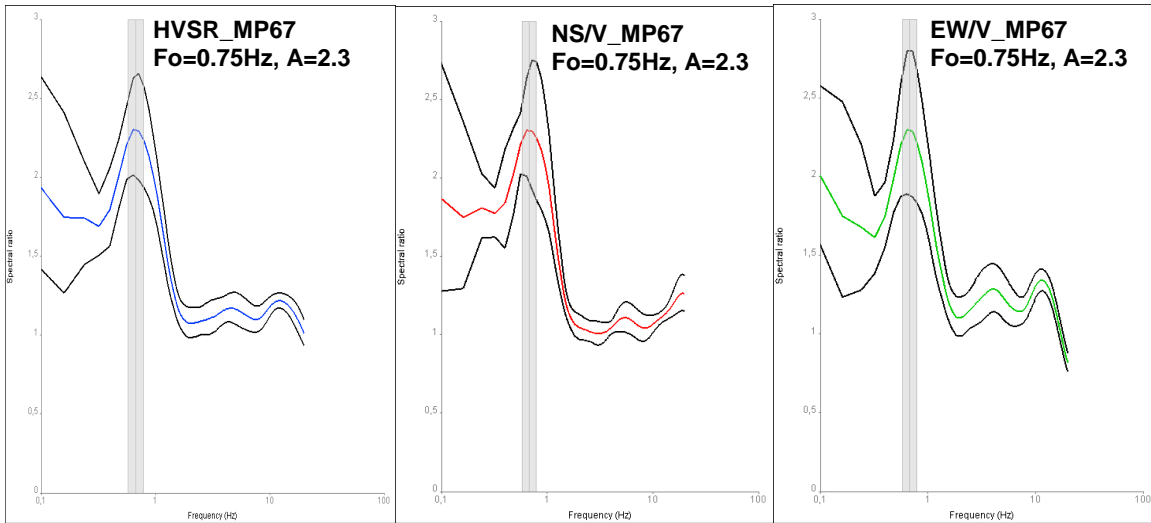


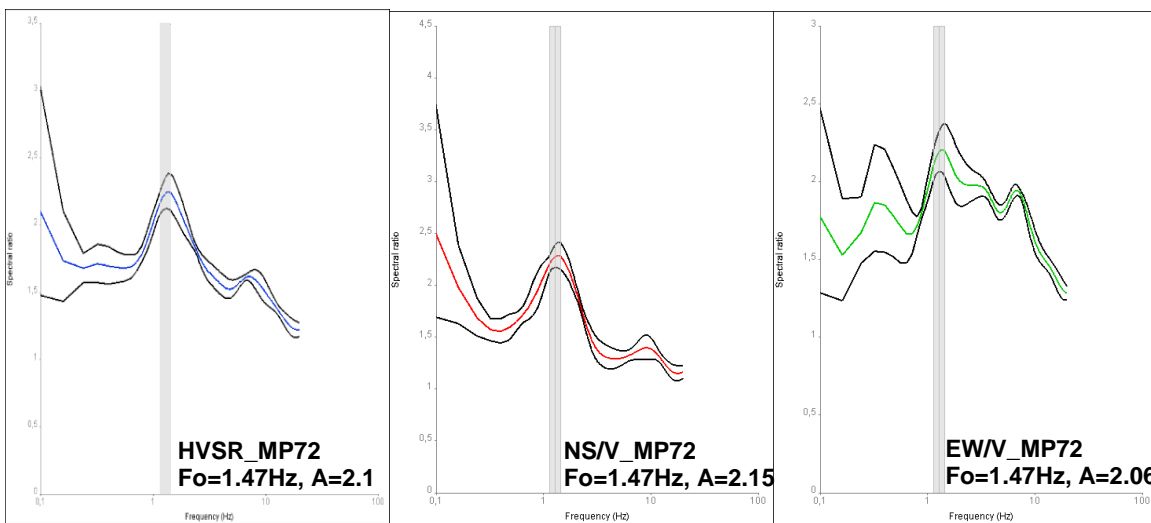
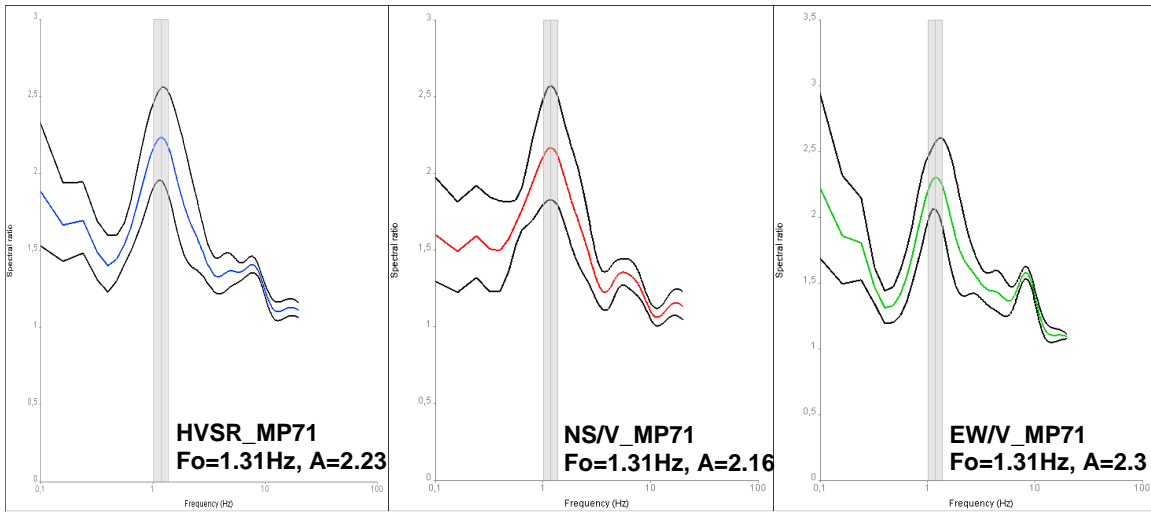
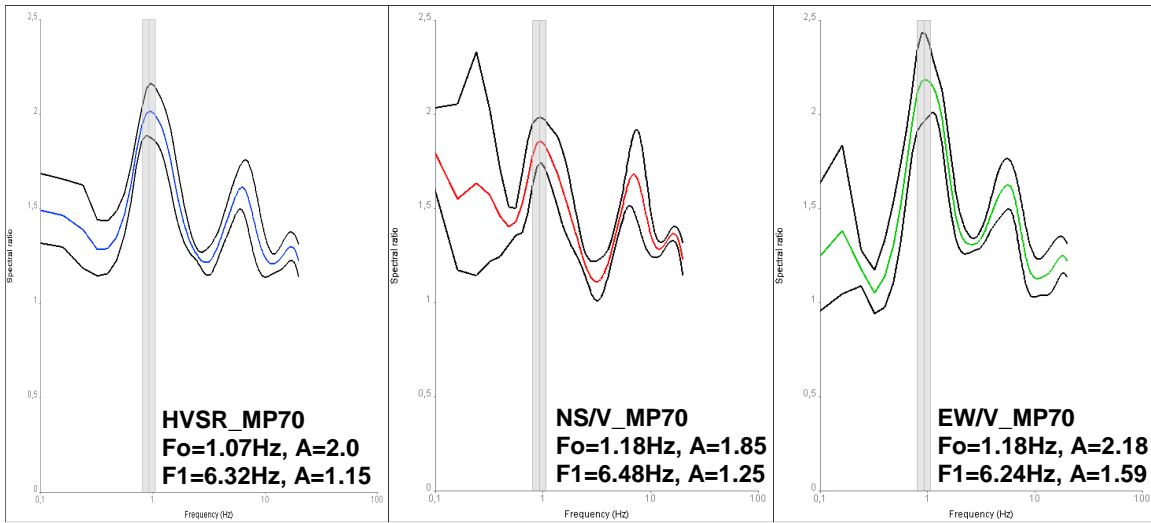


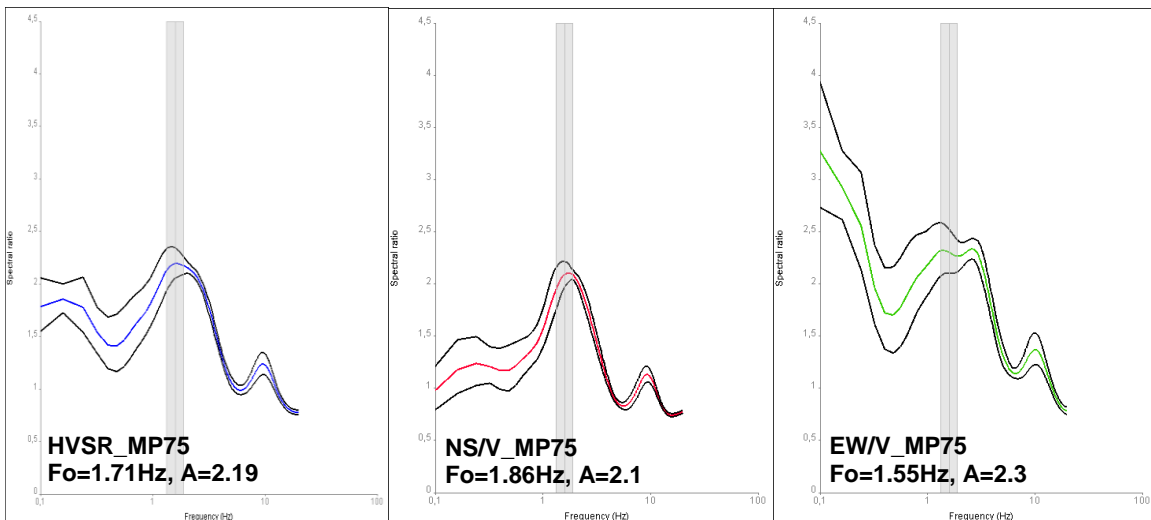
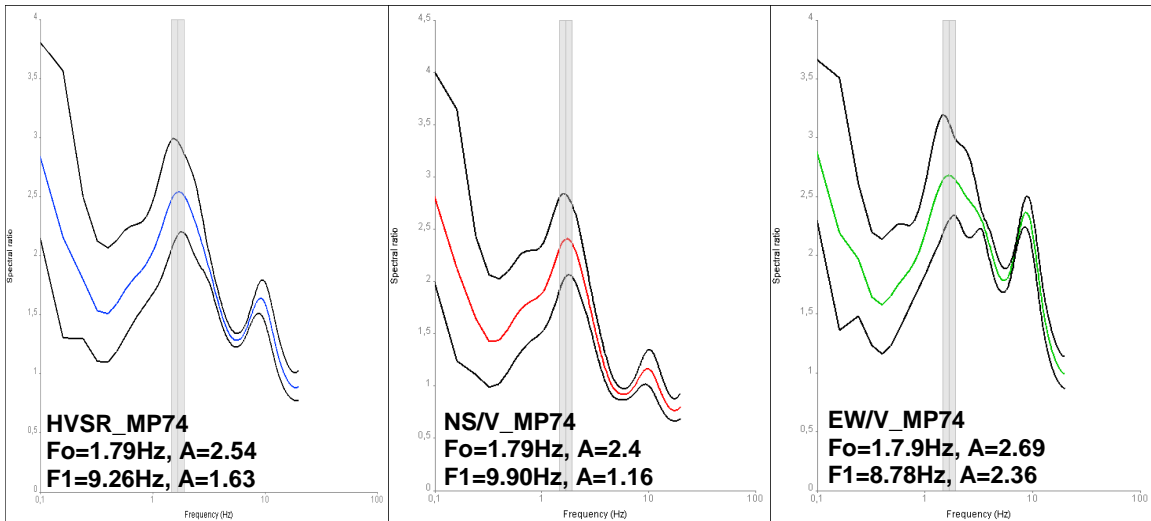
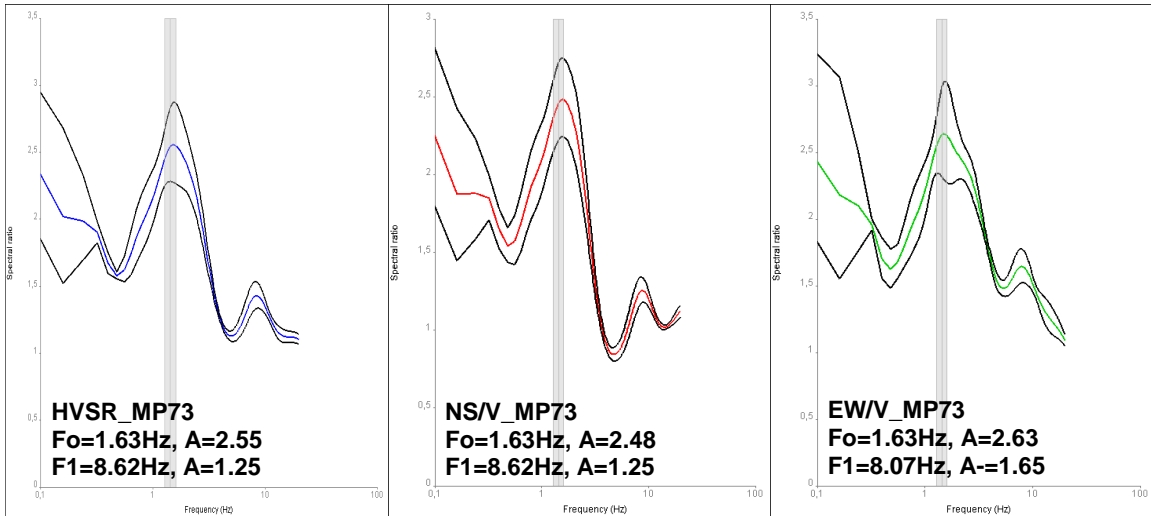


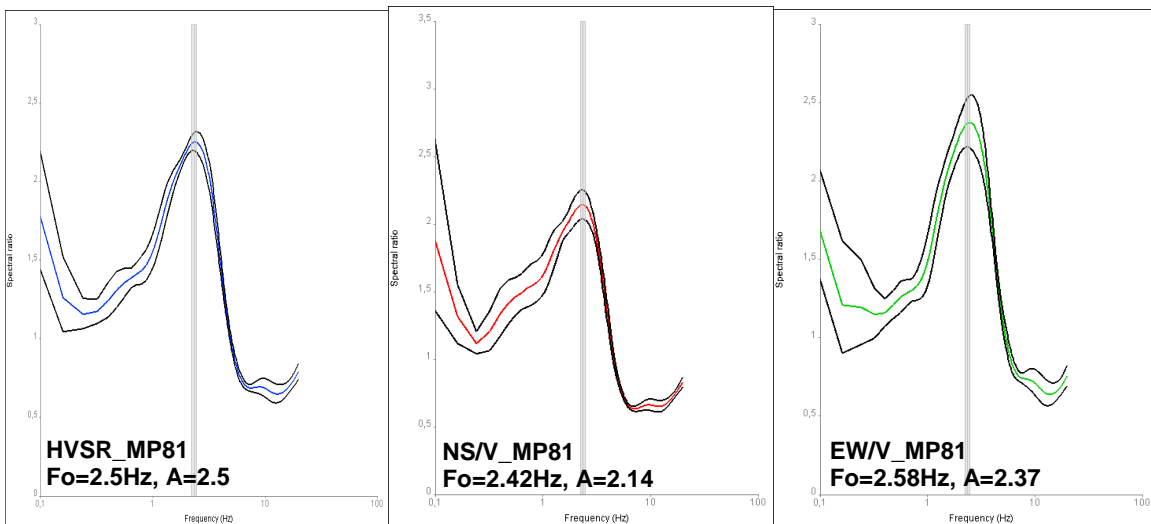
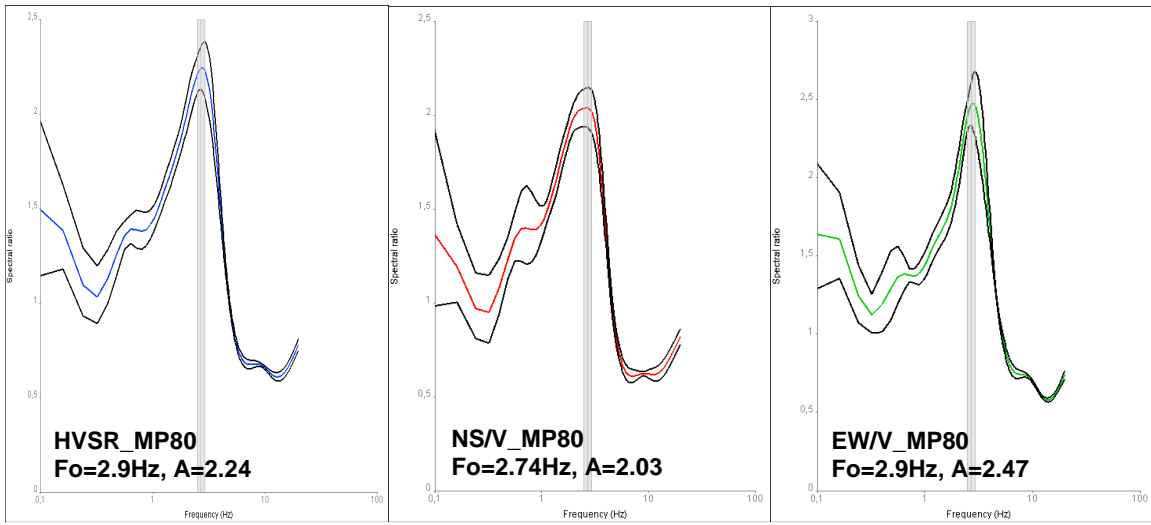
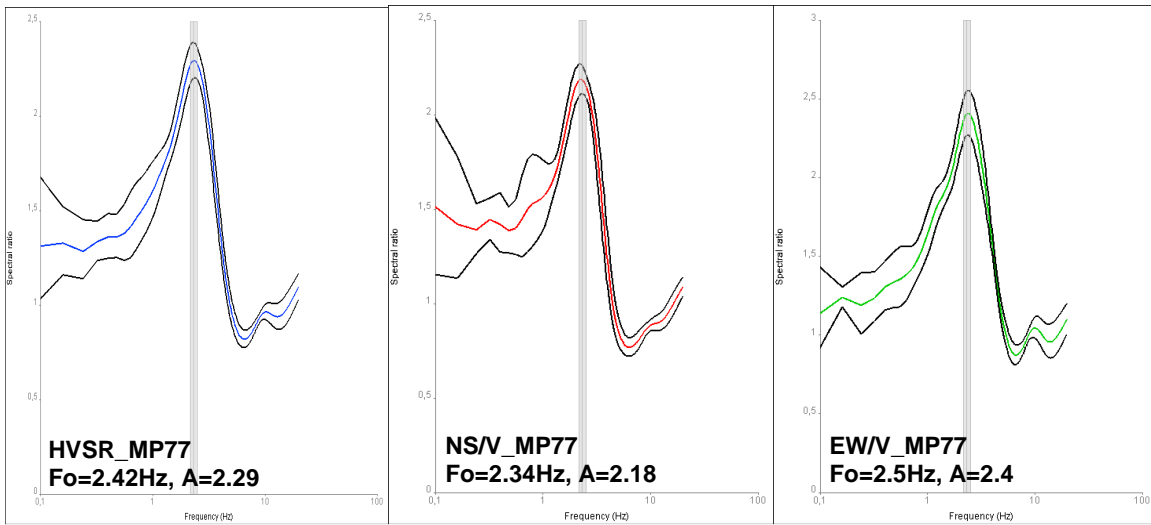


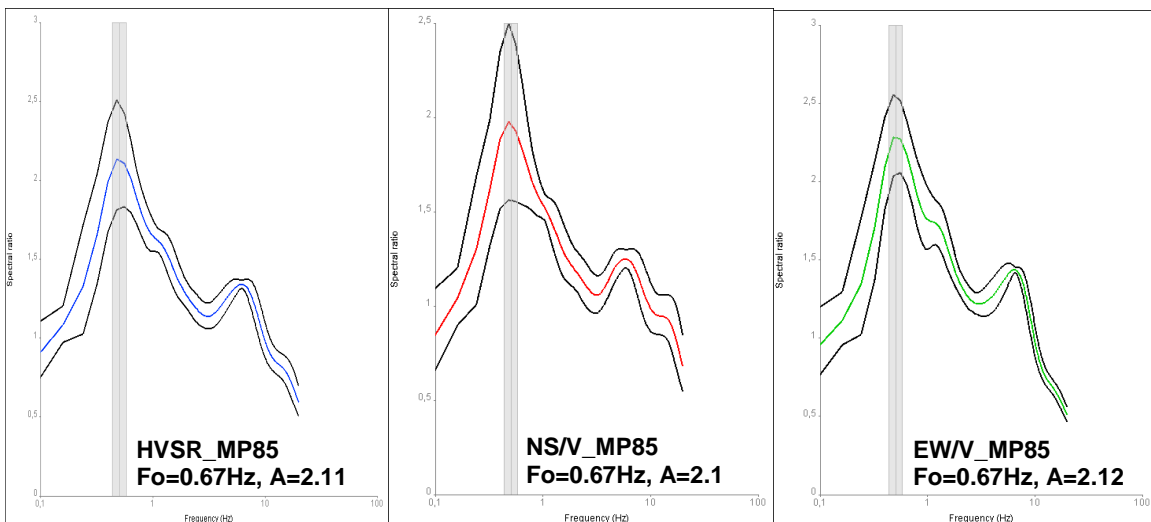
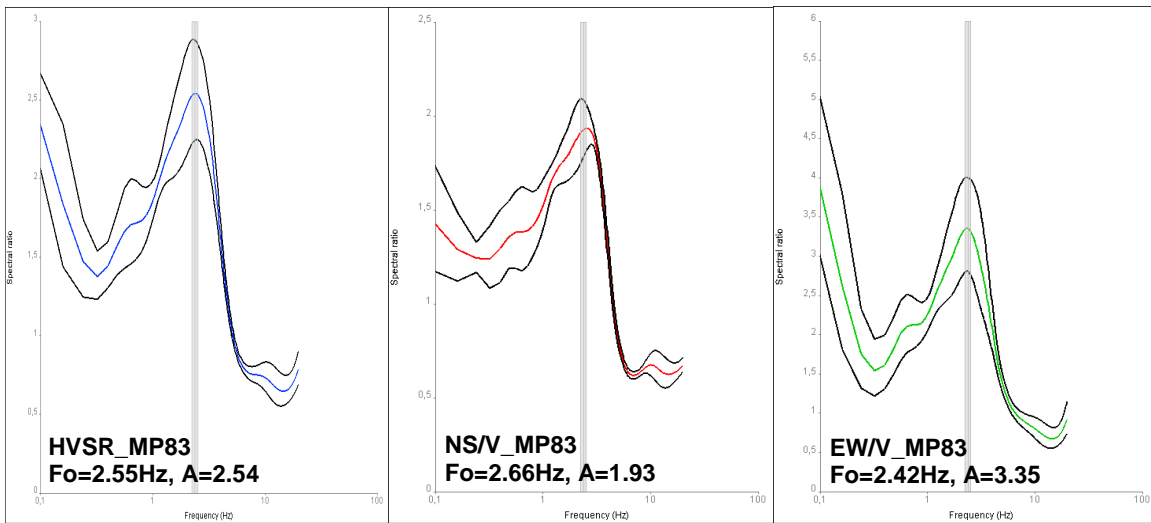
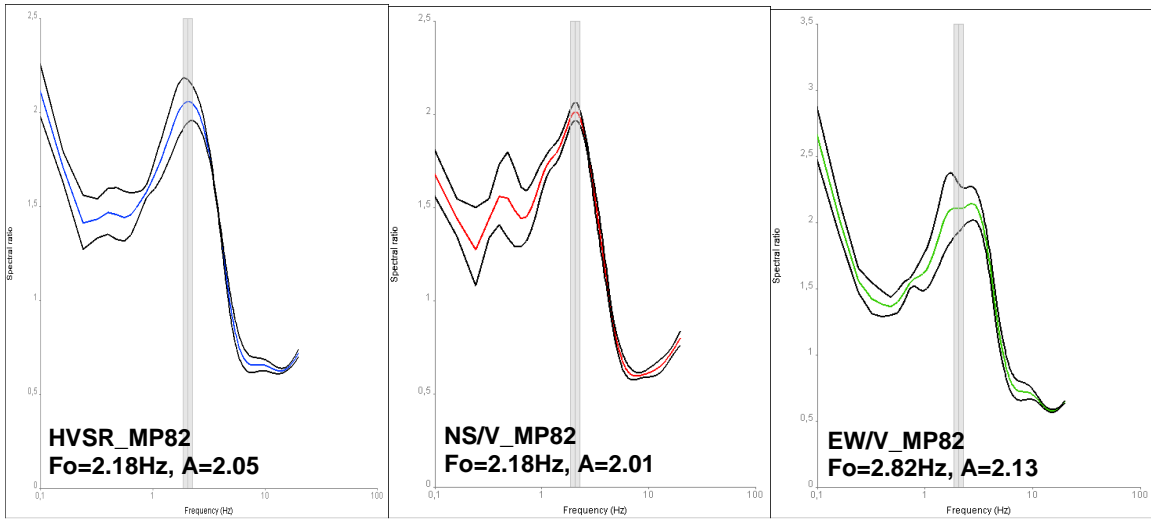


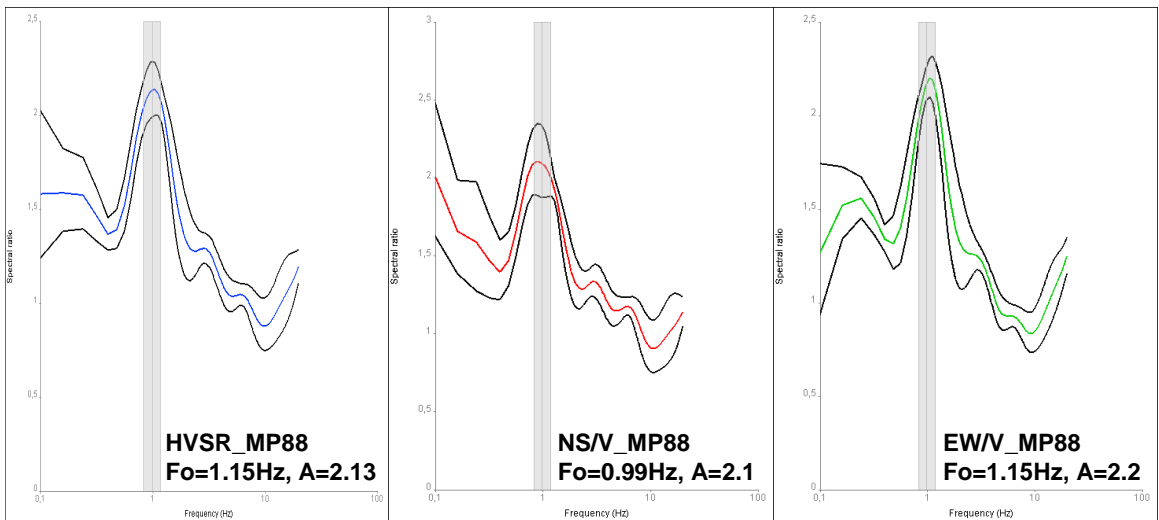
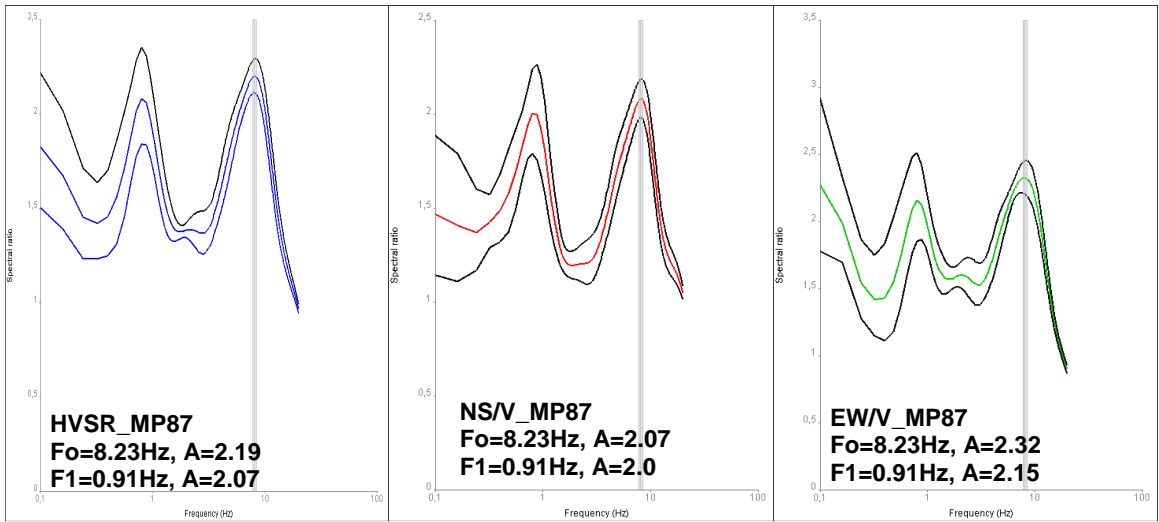
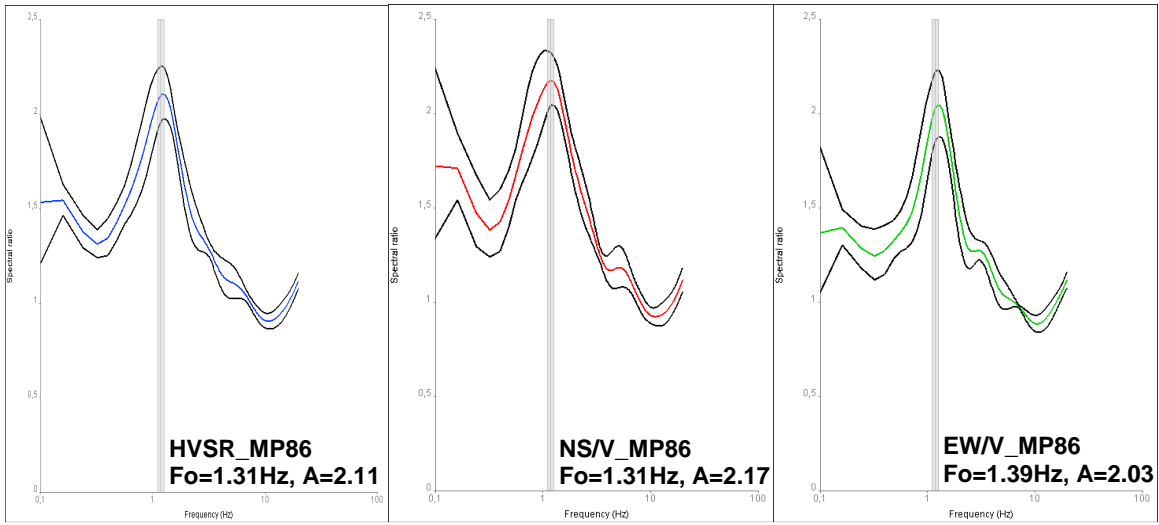


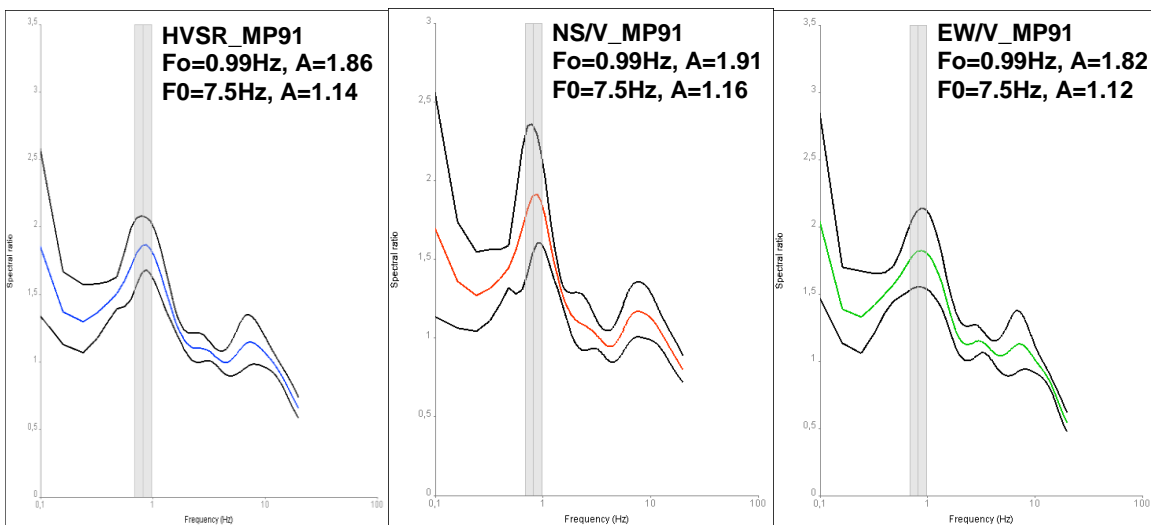
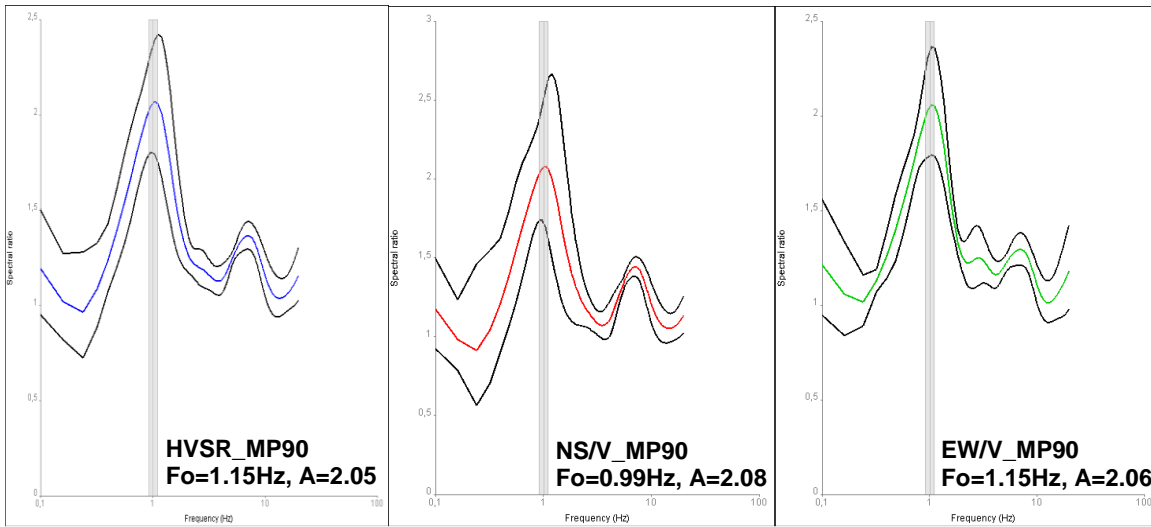
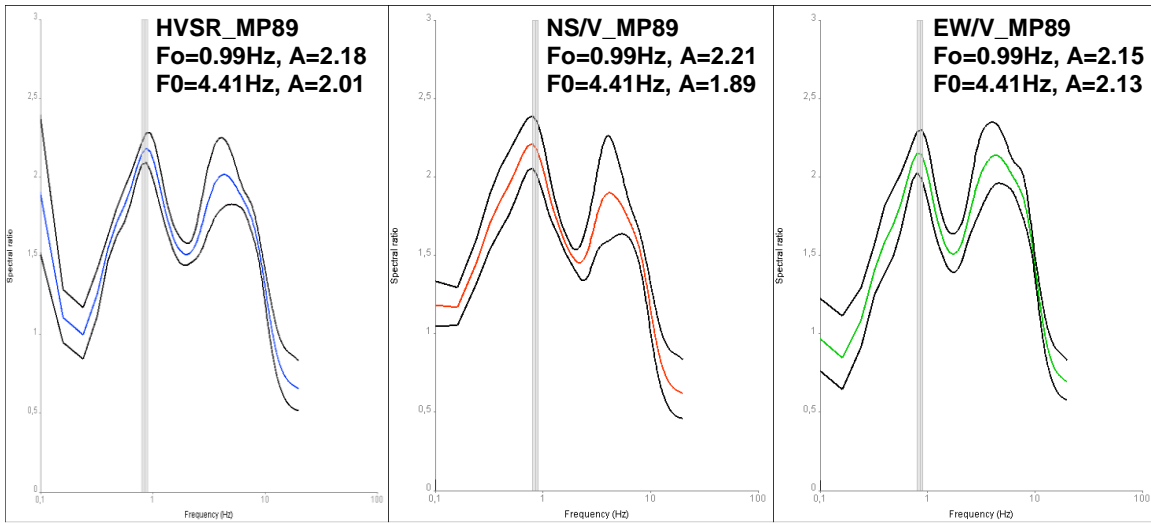




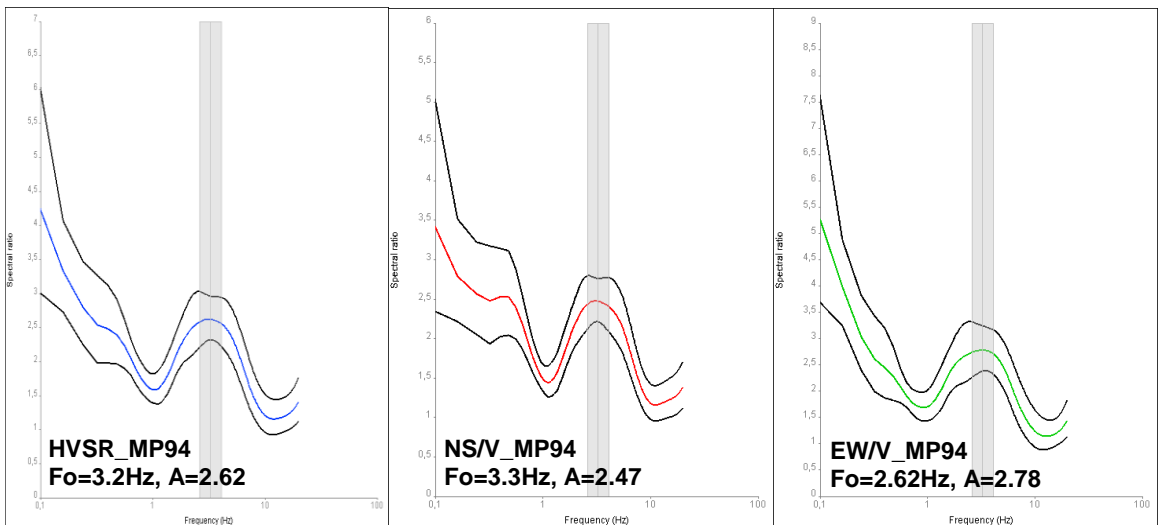
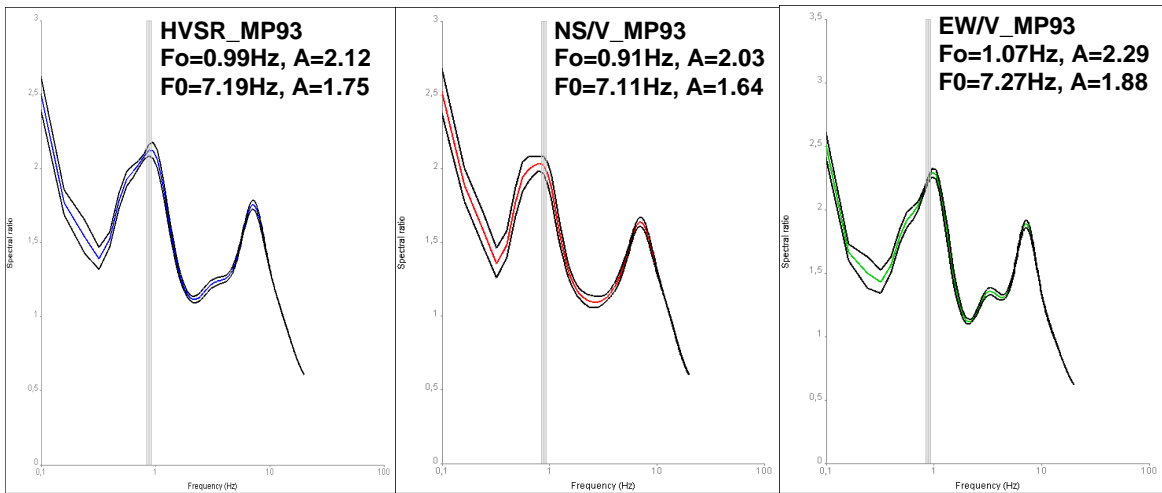
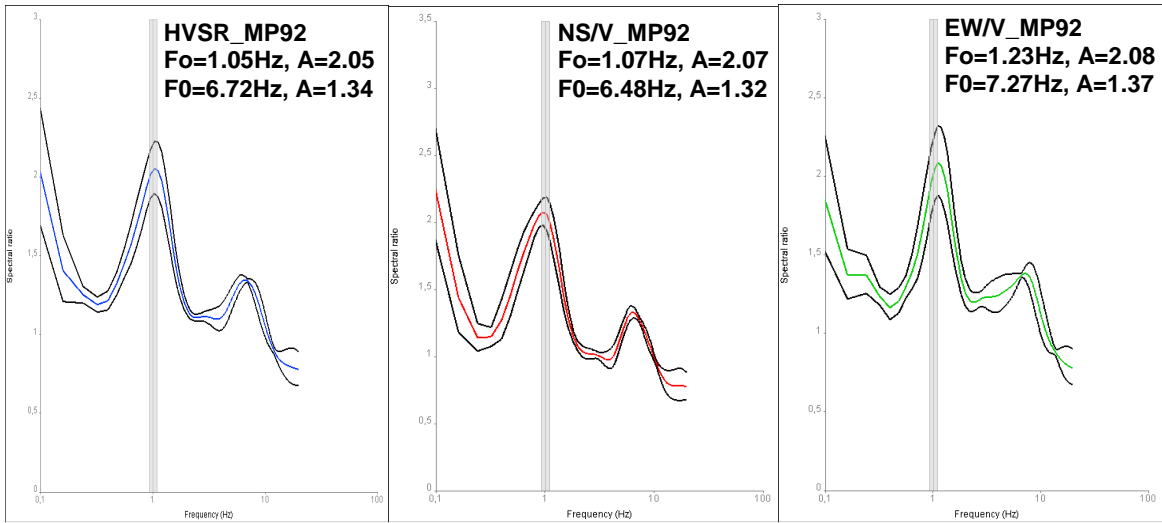












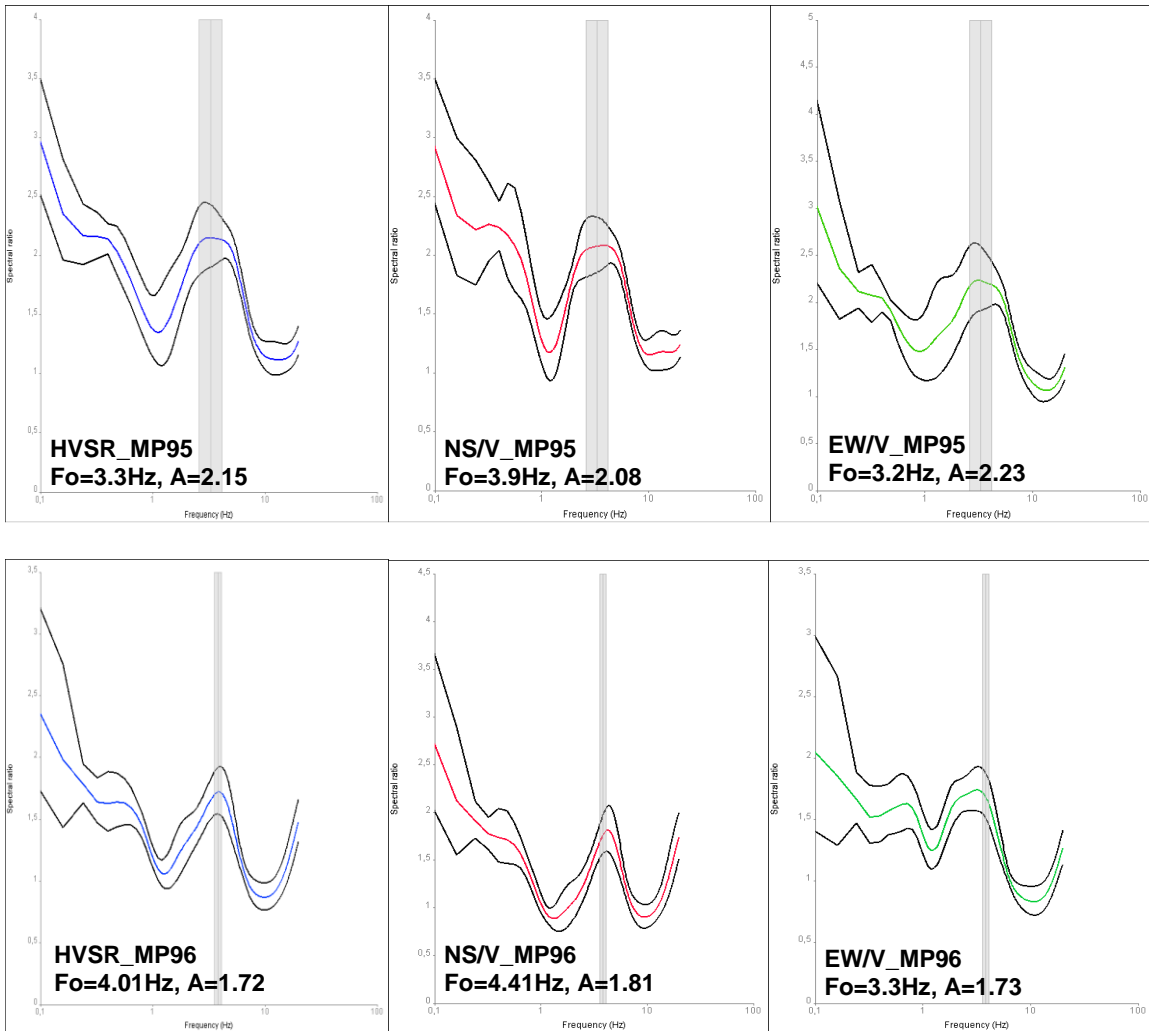


**Figure B:** HVSr technique using microtremors recorded in urban Paleohora half-basin to determine ground seismic spatial variation response. The horizontal scale of the HVSr curves represents the fundamental frequency range (0.2-20Hz) while the vertical scale represents the ground amplification. The blue curves represents the average H/V ratios (HVSr average ratios) of microtremor component recording recorded in a single station site. The red curve of each graph represents the north-south horizontal to vertical spectra ratio ( $H_{ns}/V$ ) of microtremor component recorded in a single station site. The green curve of each graph represents the east-west horizontal to vertical spectra ratio ( $H_{ew}/V$ ) of microtremor component recordings. The black curves in all graphs correspond to the standard deviation of each H/V,  $H_{ns}/V$ ,  $H_{ew}/V$  curve. The grey zone presented in all graphs corresponds to the standard deviation of fundamental frequency.

**APPENDIX II: LIST OF TABLES**

**TABLE 4.1: ERT survey in Kera and Kastelli-Kissamou region**

P1	35 31.179	23 44.925	32 electrodes 10 m spacing wenner-schlumberger + dipole
	35 31.160	23 44.854	
P2	35 31.047	23 44.271	32 electrodes 10 m spacing wenner-schlumberger + dipole
	35 31.058	23 44.476	
P3	35 30.343	23 43.334	32 electrodes 10 m spacing wenner-schlumberger + dipole
	35 30.260	23 43.160	
P4	35 27.918	23 43.723	24 electrodes 5 m spacing wenner-schlumberger + dipole
	35 27.793	23 43.715	
P5	35 29.866	23 39.367	48 electrodes 5 m spacing wenner-schlumberger + dipole
	35 29.830	23 39.365	
P6	35 29.877	23 38.518	43 electrodes 5 m spacing wenner-schlumberger + dipole
	35 29.969	23 38.589	
P7	35 29.900	23 38.448	29 electrodes 10 m spacing wenner-schlumberger + dipole
	35 29.922	23 38.618	
P8	35 30.061	23 38.698	33 electrodes 5 m spacing wenner-schlumberger + dipole
	35 30.104	23 38.595	

**TABLE 4.2: ERT survey in Paleohora region**

P1	35° 14.382	23° 40.559	16 electrodes, 224 meters, wenner-schlumberger + dipole
	35° 14.328	23° 40.692	
P2	35° 13.890	23° 40.770	electrode spacing 15m, 345 meters array , wenner- schlumberger + dipole
P3	35° 13.890	23° 38.245	electrode spacing 15m, 345 meters array , wenner- schlumberger + dipole
P4	35° 14.235	23° 41.146	17 electrodes , 240 meters, wenner-schlumberger + dipole
	35° 14.218	23° 41.296	
P5	35° 14.464	23° 41.357	24 electrodes, 345 meters, wenner- schlumberger + dipole
	35° 14.291	23° 41.314	
P6	35° 13.703	23° 40.840	15 electrodes, 210 meters, wenner-schlumberger + dipole
	35° 13.601	23° 40.890	

**TABLE 4.3: Microtremor recordings in Kastelli-Kissamou basin**

Microtremor Code	LAT	LONG	F0 (HVSr)	F0 (H/Vns)	Fo (H/Vew)	Amplification	Vulnerability Kg
<b>MK1</b>	35° 29.865	23° 39.551	0.59	0.67	0.59	2.10	7.47
<b>MK2</b>	35° 29.800	23° 39.453	0.59	0.67	0.59	1.95	6.44
			4.33	4.33	4.33	1.58	0.57
<b>MK3</b>	35° 29.870	23° 39.196	14.04	14.04	14.04	1.93	0.26
			0.59	0.89	0.89	1.89	6.05
<b>MK4</b>	35° 29.909	23° 39.919	13.34	13.34	13.34	2.17	0.35
			0.99	0.99	0.99	1.57	2.48
<b>MK5</b>	35° 30.173	23° 38.637	3.93	3.93	3.93	2.26	1.29
<b>MK6</b>	35° 30.158	23° 38.638	3.98	3.98	3.98	1.98	0.98
<b>MK7</b>	35° 30.152	23° 38.637	3.53	3.53	3.53	2.06	1.20
<b>MK8</b>	35° 30.147	23° 38.637	2.98	1.91	3.0	1.66	0.92
<b>MK9</b>	35° 29.833	23° 38.820	7.11	7.19	7.19	3.16	1.40
<b>MK10</b>	35° 29.440	23° 38.988	Flat/low amplitude				
<b>MK11</b>	35° 29.479	23° 39.421	2.18	2.18	2.18	2.11	2.04
			0.51	0.51	0.43	1.81	6.42
<b>MK12</b>	35° 29.502	23° 39.277	0.99	0.99	0.99	1.95	3.84
			15.30	15.53	15.33	1.95	0.24
<b>MK13</b>	35° 30.152	23° 38.637	0.75	0.75	0.75	2.05	5.60
			5.76	5.76	5.76	1.22	0.25
<b>MK14</b>	35° 30.505	23° 38.700	0.59	0.59	0.59	2.05	7.12
			3.85	3.85	3.85	1.59	0.25
<b>MK15</b>	35° 29.532	23° 39.919	0.59	0.59	0.59	2.90	14.25
					2.79	1.41	0.71
<b>MK16</b>	35° 29.605	23° 39.740	0.59	0.59	0.59	1.91	6.18
			2.34	2.42	2.34	1.90	1.54
<b>MK17</b>	35° 29.835	23° 39.213	0.99	0.99	0.99	1.81	3.3
<b>MK18</b>	35° 29.930	23° 39.163	0.75	0.75	0.75	1.79	4.27
<b>MK19</b>	35° 30.058	23° 38.595	Flat/low amplitude				
<b>MK20</b>	35° 29.896	23° 38.688	3.3	3.2	3.98	2.21	1.48

<b>MK21</b>	35° 29.630	23° 38.863	4.73	4.73	4.81	3.02	1.92
<b>MK22</b>	35° 29.609	23° 38.354	0.83	0.83	0.83	1.83	4.03
			6.24	6.24	6.24	1.10	0.19
<b>MK23</b>	35° 29.699	23° 38.805	0.59	0.59	0.59	1.86	5.86
<b>MK24</b>	35° 29.638	23° 39.287	0.51	0.59	0.59	1.77	6.14
			2.26	3.22	2.10	1.15	0.58
<b>MK25</b>	35° 29.660	23° 39.287	0.83	0.83	0.83	1.45	2.53
			6.48	6.48	6.48	1.24	0.23
<b>MK26</b>	35° 29.688	23° 39.386	Flat/low amplitude				
<b>MK27</b>	35° 29.696	23° 39.296	2.90	2.90	2.90	2.04	1.43
<b>MK28</b>	35° 29.755	23° 39.161	2.98	2.93	2.98	3.34	3.74
<b>MK29</b>	35° 29.819	23° 39.193	3.06	3.14	2.98	1.64	0.87
<b>MK30</b>	35° 29.551	23° 39.271	1.23	1.23	1.15	1.97	3.15
<b>MK31</b>	35° 29.496	23° 39.357	0.75	0.75	0.75	1.74	4.03
			5.28	5.28	5.28	1.23	0.28
<b>MK32</b>	35° 29.514	23° 39.521	0.91	0.91	0.91	1.52	2.53
			5.68	5.68	5.68	1.42	0.35
<b>MK33</b>	35° 29.612	23° 39.192	0.67	0.59	0.75	1.94	5.6
			6.16	6.16	6.16	1.99	0.64
<b>MK34</b>	35° 29.725	23° 39.226	0.67	0.75	0.67	1.78	4.72
<b>MK35</b>	35° 29.502	23° 39.780	0.91	0.91	0.75	1.83	3.68
			6.0	6.16	6.0	1.23	0.25
<b>MK36</b>	35° 30.089	23° 39.075	0.67	0.67	0.67	1.98	5.85
<b>MK37</b>	35° 29.055	23° 39.045	0.75	0.75	0.75	1.84	4.5
			6.8	7.7	6.72	1.73	0.4
<b>MK38</b>	35° 29.744	23° 38.754	0.75	0.75	0.75	2.03	5.49

**TABLE 4.4: Microtremor recordings in Paleohora basin**

Microtremor Site Code	LAT	LONG	F0 (HVSR)	F0 (H/Vns)	F0 (H/Vew)	A0 (H/V)	A0(H/Vns)	A0 (H/Vew)	Vulnerability index Kg
<b>MP1</b>	35 13.812	23 40.860	0.836	0.836	0.836	1.98	2.09	1.87	4.68
			9.82	9.18	10.85	1.73	1.76	1.75	0.3
<b>MP2</b>	35 13.858	23 40.850	3.85	4.09	3.85	2.47	2	2.93	1.95
			1.07	1.07	1.15	2.05	1.98	2.12	3.92
<b>MP3</b>	35 13.820	23 40.853	4.81	4.83	0.83	2.26	2.75	2.4	1.06
			0.83	0.91	4.65	2.14	1.94	1.87	5.5
<b>MP4</b>	35 13.858	23 40.890	1.07	1.07	0.99	2.47	2.55	2.42	5.7
			5.36	5.84	5.28	1.87	1.92	1.85	0.65
<b>MP5</b>	35 13.794	23 40.957	1.31	1.15	1.31	1.88	1.68	2.16	2.6
			7.19	7.67	6.8	1.56	1.63	1.52	0.32
<b>MP6</b>	35 13.808	23 40.868	13	13	12.84	2.1	2.02	2.2	0.33
			0.67	0.67	0.67	1.52	1.62	1.44	3.44
<b>MP7</b>	35 13.808	23 40.866	1.15	1.15	1.07	1.67	1.8	1.55	2.42
			9.34	9.34	9.34	1	1.06	0.93	0.1
<b>MP8</b>	35 13.785	23 40.784	9.66	9.34	10.06	2.26	2.19	2.34	0.52
			0.99	0.99	0.99	2.09	2.1	2.05	4.41
<b>MP9</b>	35 13.782	23 40.789	11.65	11.88	11.33	2.46	2.34	2.6	0.51
			0.91	0.91	0.91	2.07	2.01	2.12	4.7
<b>MP10</b>	35 13.877	23 40.782	6	6	6	2.13	2.32	1.96	0.75
			0.75	0.83	0.75	2	2.05	1.95	5.33
<b>MP11</b>	35 13.871	23 40.783	7.35	7.11	0.75	2.05	2.17	1.96	0.57
			0.75	0.75	7.75	1.85	1.78	1.93	4.5
<b>MP12</b>	35 13.918	23 40.897	0.75	0.75	0.75	2.08	1.93	2.25	5.76
			7.11	7.43	6.88	1.79	1.9	1.68	0.45
<b>MP13</b>	35 13.959	23 40.948	0.91	0.99	0.83	1.9	1.82	2	3.96
			3.86	4.09	3.69	1.86	1.81	1.93	0.89
<b>MP14</b>	35 13 .977	23 40.959	2.74	2.74	2.9	3.33	3.21	3.47	4.04

			Boad						
<b>MP15</b>	35 13 .990	23 40.940	3.06 Broad	3.14	3.06	3.0	2.89	3.12	2.94
<b>MP16</b>	35 13.897	23 40.979	4.25	4.14	4.09	1.94	1.94	1.96	0.8
			1.15	1.15	1.39	1.54	1.59	1.55	2.72
<b>MP17</b>	35 13.918	23 41.051	3.3	3.38	3.14	2.61	2.47	2.79	2.06
<b>MP18</b>	35 13.925	23 40.986	4.36	4.17	5.05	2.61	2.64	2.67	1.56
			0.99	0.99	0.91	1.7	1.67	1.74	2.91
<b>MP19</b>	35 13.980	23 40.830	0.75	0.75	0.75	2.14	2.36	1.94	6.8
			4.1	4.33	3.7	1.87	1.85	1.9	0.85
<b>MP20</b>	35 13.944	23 40.804	0.75	0.75	0.83	2.7	2.55	2.87	9.72
			3.77	3.85	3.46	1.65	1.85	1.48	0.72
<b>MP21</b>	35 13.984	23 41.119	0.75	0.75	0.75	2.21	1.77	2.56	6.5
			3.77	3.85	3.77	1.85	1.8	1.91	0.9
<b>MP22</b>	35 13.987	23 40.980	1.07	1.07	0.99	1.84	1.81	2.04	3.16
<b>MP23</b>	35 13.966	23 40.975	2.5	2.5	2.5	2.82	3.19	2.5	3.1
<b>MP23</b>	35 13.966	23 40.975	2.5	2.5	2.5	2.82	3.19	2.5	3.1
<b>MP24</b>	35 14.045	23 41.021	0.91	0.75	0.91	1.81	1.43	2.35	3.6
<b>MP25</b>	35 14.056	23 41.005	0.91	0.91	0.91	1.92	1.5	2.45	4.05
<b>MP26</b>			0.59	0.59	0.67	1.86	1.66	2.06	5.86
<b>MP27</b>	35 14.015	23 41.010	0.83	0.83	0.83	2.02	1.62	2.51	4.91
			2.1	2.02	2.26	1.59	1.44	1.77	1.43
<b>MP28</b>	35 13.991	23 41.064	2.5	2.5	2.42	4.42	4.01	4.87	7.8
<b>MP29</b>	35 13. 992	23 41.065	2.58	2.58	2.5	4.18	3.68	4.76	6.77
<b>MP30</b>	35 13.997	23 41.065	2.74	2.82	2.66	4.24	4.18	4.32	6.56
<b>MP31</b>	35 14.108	23 40.778	flat						
<b>MP32</b>	35 14.071	23 41.180	5.2	5.36	0.99	2.3	2.46	2.3	1.01
			0.99	0.99	4.97	2	2.23	2.18	4.04
<b>MP33</b>	35 14.078	23 41.190	5.2	5.36	0.83	2.52	2.75	2.5	1.22
			0.91	0.99	4.81	2.05	1.58	2.36	4.61

<b>MP34</b>	35 13.951	23 41.040	2.9	3.14	2.5	3.36	3.48	3.43	3.8
<b>MP35</b>	35 14.430	23 41.257	1.63	1.63	1.63	4.66	4.43	4.9	13.32
<b>MP36</b>	35 14.020	23 41.191	1.94	1.94	1.86	4.2	4.02	4.38	9.09
<b>MP37</b>	35 14.012	23 41.162	2.1	2.1	2.1	4.32	4.22	4.43	8.8
<b>MP38</b>	35 14.057	23 40.979	2.1	2.1	2.02	4.37	4.37	4.38	9.09
<b>MP39</b>	35 13.984	23 41.119	2.42	2.42	2.34	3.2	2.99	3.44	4.23
<b>MP40</b>	35 13.945	23 41.091	1.31	1.31	1.23	5.68	5.16	6.25	24.62
<b>MP41</b>	35 13.754	23 40.992	3.7	3.53	3.85	3	2.82	3.3	2.4
			14.11	14.03	14.27	2.41	2.24	2.59	0.41
<b>MP42</b>	35 13.766	23 40.962	3.46	2.34	3.61	2.5	2.14	3.06	1.8
<b>MP43</b>	35 18.768	23 40.940	0.91	0.83	0.91	1.77	2.1	1.28	3.44
<b>MP44</b>	35 13.760	23 40.940	0.83	0.83	0.91	1.11	1.56	1.79	1.48
<b>MP45</b>	35 13.724	23 40.948	3.77	3.85	3.61	2.87	2.24	3.69	2.18
<b>MP46</b>	35 13.708	23 40.932	2.5	2.5	2.5	3.14	2.93	3.37	3.9
<b>MP47</b>	35 13.708	23 40.939	1.67	1.71	0.67	2.32	2.06	2.76	3.22
<b>MP48</b>	35 13.708	23 40.932	2.35	2.18	2.42	3.35	2.94	3.85	4.77
<b>MP49</b>	35 13.732	23 40.963	3.3	3.14	3.46	2.83	2.57	3.14	2.42
<b>MP50</b>	35 13.732	23 40.972	3.38	3.22	3.53	2.89	2.78	3.04	2.47
<b>MP51</b>	35 13.701	23 40.952	3	3	3	3.02	3.33	2.75	3.04
<b>MP52</b>	35 13.690	23 40.965	2.66	2.58	2.66	2.52	2.39	2.67	2.38
<b>MP53</b>	35 13.690	23 40.966	2.5	2.42	2.66	2.87	2.9	2.88	3.29
<b>MP54</b>	35 13.691	23 40.967	2.58	2.5	2.58	3.05	2.85	3.28	3.54
<b>MP55</b>	35 13.690	23 40.965	2.58	2.5	2.74	2.99	2.93	3.08	3.46
<b>MP57</b>	35 13.690	23 40.965	2.58	2.34	2.74	2.19	2.34	2.08	1.85
<b>MP58</b>	35 13.690	23 40.965	2.58	2.42	2.74	2.3	2.17	2.35	2.05
<b>MP59</b>	35 13.686	23 40.944	2.34	2.26	2.58	2.31	2.14	2.54	2.28
<b>MP60</b>	35 13.690	23 40.965	2.42	2.34	2.58	2.51	2.38	2.68	2.6
<b>MP61</b>	35.13.623	23 40.947	2.9	2.9	2.9	2.41	2.41	2.74	2
<b>MP62</b>	35 13.584	23 40.948	1.55	1.55	1.55	5.75	5.65	5.84	21.33
<b>MP63</b>	35 13.581	23 40.941	3.46	3.3	3.69	2.52	2.82	2.9	1.83



<b>MP64</b>	35 13.551	23 40.906	3.61	3.53	3.77	2.22	2.24	2.21	1.36
<b>MP65</b>	35 13.602	23 40.902	2.6	2.6	2.6	3.13	3.37	2.9	3.76
<b>MP66</b>	35 13.840	23 40.790	0.99	0.91	0.99	2.03	1.99	2.08	4.16
<b>MP67</b>	35 13.821	23 40.813	0.75	0.75	0.75	2.3	2.3	2.3	7.05
<b>MP68</b>	35 13.814	23 40.826	0.91	0.91	0.91	2.14	2.11	2.18	5.03
<b>MP69</b>	35 13.693	23 40.952	1.15	1.15	1.15	1.88	1.92	1.84	3.07
<b>MP70</b>	35 13.818	23 40.930	1.07	1.07	1.07	2	1.85	2.18	3.73
			6.32	6.48	6.24	1.5	1.25	1.59	0.35
<b>MP71</b>	35 13.790	23 40.924	1.31	1.31	1.31	2.23	2.16	2.3	3.79
<b>MP72</b>	35 13.757	23 40.897	1.47	1.47	1.47	2.1	2.15	2.06	3
<b>MP73</b>	35 13.757	23 40.904	1.63	1.63	1.63	2.55	2.48	2.63	3.98
			8.62	8.62	8.07	1.25	1.25	1.65	0.18
<b>MP74</b>	35 13.758	23 40.905	1.79	1.79	1.79	2.54	2.4	2.69	3.6
			9.26	9.9	8.78	1.63	1.16	2.36	0.28
<b>MP75</b>	35 13.730	23 40.895	1.71	1.86	1.55	2.19	2.1	2.3	2.8
<b>MP76</b>	35 13.717	23 40.899	flat						
<b>MP77</b>	35 13.717	23 40.887	2.42	2.34	2.5	2.29	2.18	2.4	2.16
<b>MP78</b>	35 13.714	23 40.886	flat						
<b>MP79</b>	35 13.730	23 40.894	2.66	2.34	2.9	2.17	2.05	2.32	1.77
<b>MP80</b>	35 13.730	23 40.895	2.9	2.74	2.9	2.24	2.03	2.47	1.73
<b>MP81</b>	35 13.725	23 40.880	2.5	2.42	2.58	2.25	2.14	2.37	2.02
<b>MP82</b>	35 13.704	23 40.889	2.18	2.18	2.82	2.05	2.01	2.13	1.92
<b>MP83</b>	35 13.702	23 40.889	2.55	2.66	2.42	2.54	1.93	3.35	2.29
<b>MP84</b>	35 13.703	23 40.890	flat						
<b>MP85</b>	35 13.825	23 40.919	0.67	0.67	0.67	2.11	2.1	2.12	6.64
<b>MP86</b>	35 13.713	23 40.779	1.31	1.31	1.39	2.1	2.17	2.03	3.36
<b>MP87</b>	35 13.897	23 40.938	8.23	8.23	8.23	2.19	2.07	2.32	0.58
			0.91	0.91	0.91	2.07	2	2.15	4.7
<b>MP88</b>	35 13.726	23 40.778	1.15	0.99	1.15	2.13	2.1	2.2	3.94
<b>MP89</b>	35 13.762	23 40.782	0.99	0.99	0.99	2.18	2.21	2.15	4.8

			4.41	4.41	4.41	2.01	1.89	2.13	0.91
<b>MP90</b>	35 13.740	23 40.773	1.15	1.15	1.15	2.05	2.08	2.06	3.65
<b>MP91</b>	35 13.763	23 40.804	0.99	0.99	0.99	1.86	1.91	1.82	3.49
			7.5	7.75	7.5	1.14	1.16	1.12	0.17
<b>MP92</b>	35 13.773	23 40.796	1.05	1.07	1.23	2.05	2.07	2.08	4
			6.72	6.48	7.27	1.34	1.32	1.37	0.26
<b>MP93</b>	35 13.729	23 40.802	0.99	0.91	1.07	2.12	2.03	2.29	4.5
			7.19	7.11	7.27	1.75	1.64	1.88	0.42
<b>MP94</b>	35 14.267	23 40.993	3.3 Broad	3.2	3.3	2.62	2.47	2.78	2
<b>MP95</b>	35 14.267	23 40.993	3.3	3.9	3.2	2.15	2.08	2.23	1.4
<b>MP96</b>	35 14.259	23 40.987	4.01	4.41	3.3	1.72	1.81	1.73	0.73

**TABLE 4.5:** *Permanent Seismological network of Crete*

PERMANENT SEISMOLOGICAL NETWORK OF CRETE		LATITUDE	LONGITUDE
<b>CHANIA</b>	<b>CHN</b>	35 31.16	24 02.54
<b>KALOYDIANA</b>	<b>KLD</b>	35 29.21	23 41.42
<b>KOYNTOYRA</b>	<b>KNDR</b>	35 14.09	23 37.49
<b>RETHIMNO</b>	<b>RTH</b>	35 21.89	24 30.09
<b>HERAKLION</b>	<b>HRK</b>	35 18.22	25 04.24
<b>IERAPETRA</b>	<b>IER</b>	35 00.86	25 43.99
<b>SITIA</b>	<b>SIT</b>	35 12.53	26 06.33

**TABLE 4.6:** *Temporal seismological network of Paleohora*

TEMPORAL SEISMOLOGICAL NETWORK OF PALEOHORA		LATITUDE	LONGITUDE
<b>KOUNTOURA</b>	<b>KNDR</b>	35 14.09	23 37.49
<b>PANORAMA</b>	<b>KNS</b>	35 14.26	23 40.77
<b>CENTRE OF THE BASIN</b>	<b>KNM</b>	35 13.88	23 40.95

**TABLE 4.7:** Samples of earthquake epicenters recorded from the permanent seismological network of Crete

DATE	ORIGIN TIME	LONGITUDE	LATITUDE	DEPTH	RMS	STATIONS
70701	01:07;26	24.36	34.91	10	8*****	sit,hrk,chn
70701	03:22;28	24.83	35.07	10	0.7	sit,hrk,chn
70701	04:24;21	24.5	35.36	10	4	sit, hrk, chn, kld
70702	00:07;50	25.34	35.84	10	2	hrk, chn
70702	01:20;40.51	23.24	35.06	14.59	0.1	kld, chn, hrk
70702	05:10;39.10	26.03	35.16	<1km	4.89	sit, hrk, rth, chn
70702	06:18;08.92	26.61	35.07	10	3.6	sit, hrk, rth, chn
70702	21:18:00.04	26.03	35.16		4	kld,rth, hrk,sit
70703	00:43;02	22.59	35.74	<1Km	1.6	kld, chn, rth
70703	01:54;16	23.3	34.91	2.54	0.5	kld, chn, hrk, rth, sit
70703	18:23;47	24.26	35.52	10	4.7	kld, chn, hrk, rth, sit
70703	19:54;;42	23.27	35.07	23.37	0.98	kndr, kld, chn
70703	21:34;54	23.62	35.23	10	2.8	kndr, kld, chn
70703	23:36;55	23.62	35.13	23.41	0.6	kld, kndr
70704	00:17;01	23.62	35.27	4.36	0.12	kndr, kld
70704	16:23;18	23.27	34.99	31.39	0.17	kndr, kld
70704	23:57;22	23.76	35.28	24.17	1.34	kndr, kld, hrk, rth, chn, sit
70704	23:58;42	23.78	35.52	17.43	6.12	kndr, kld, hrk, rth, chn, sit
70705	08:01;28	23.92	35.1	36.76	0.5	kndr, kld
70705	17:01;17	23.74	35.11	<1km	0.94	sit, hrk
70706	07:01;19.32	23.67	35.39	7.89	0.11	kld,kndr
70706	19:02;51	22.5	37.46	10	1.25	sit, kndr
70707	16:53;40	26.1	35.12	10	0,21(****)	kld, chn, rth, sit, hrk
70707	17:15;26	26.5	36.77	10	0.01	sit, hrk
70707	22:04;16	26.58	35.24	<1km	1.64	sit,kld,chn, hrk,rth,
70708	03:28;41	26.1	35.21	10	(****)	sit, hrk, kndr
70708	07:32;25	24.87	33.72	10	(****)	

70708	12:48;00	23.62	34.67	10	0.66	kld, kndr, chn , hrk
70708	14:20;22	24.04	35.52	10	0,2*****	chn, sit, kld
70709	13:46;27	24.94	35.36	10	(****)	chn, kld, hrk, kndr,rth
70710	01:58;38	23.91	35.21	24.5	0.07	knldr, kld
70710	03:05;58	23.1	36.43	10	1.4	knldr, kld, hrk, chn , rth
70710	03:57;22	23.97	35.18	10	1.08	knldr, kld, hrk, chn, rth
70711	02:12:35.36	26.38	35.1	10	1.37	hrk, rth, chn, kld
70711	01:56:10.89	26.68	35.3	10	0.5	hrk, chn, kld, rth
70711	11:16:01.20	24.09	35.18	28.07	0.11	chn, kld
70713	14:21:55.59	25.91	34.97	1.68	1.46	knldr, kld, hrk, chn, rth
70714	00:19:19.49	23.88	35.17	9.36	0.63	chn, kld, rth, hrk
70716	01:25:37.04	23.41	34.49	50.55	****	kld, hrk, chn
70716	01:32:16.14	25.42	35.48	10	****	kld, hrk, chn
70716	14:38:56.34	24.5	35.36	10	4.6	rth,kld, chn, hrk
70716	19:36:39.88	25.12	35.3	19.99	1.1	hrk,sit,rth, chn
70717	03:38:18.37	23.97	35.32	<1km	0.6	hrk, rth,kld
70717	08:51:58.38	25.32	35.3	19.51	***	sit,chn,rth,hrk
70718	00:15:05.04	24.37	35.02	25.32	1.62	kld, hrk,rth,chn,
70718	18:43:54.92	23.69	35.48	10	2.69	sit,hrk,rth
70718	01:40:53.54	24.31	35.14	20.9	0.42	sit, hrk,chn,kld,rth,
70718	01:31:44.39	25.85	36.2	10	2.45	sit, hrk, rth,chn, kld
70718	15:25:26.10	25.04	36.04	<1km	1.02	sit, hrk,chn,kld,rth,
70718	18:43:00.27	23.69	35.48	10	2.65	kld, chn
70719	23:29:30.09	22.95	35.77	<1km	1.54	kld, chn rth
70720	00;23;03	25.99	35.68	48.67	0.4	sit, hrk
70720	01:18;49	24.74	35.79	21.91	0.46	sit, hrk
70720	04:33;15	25.89	34.68	49.7	0.05	sit, hrk
70720	10:14;58	25.54	35.89	51.41	3.2	chn, kld, rth, sit, hrk
70721	00:13;40	24.46	35.65	39.83	0.11	hrk, chn, sit, rth, kld
70721	01:01;10	24.42	35.36	10	3.32	hrk, chn, rth, kld

70721	01:21;19	24.04	35.52	10	0.2	kld, chn
70721	02:37;07	24.04	35.52	10	0.2	kld, hrk, chn
70721	05:40;17	24.89	36.02	19.4	1.98	rth, kld
70721	07:48;54	24.38	35.36	10	3.7	rth, kld, chn, hrk
70721	09:14;48	22.6	35.01	10	3.2	kld, chn
70721	15:02;54	23.2	34.85	18.03	1.14	kld, rth, chn, hrk
70721	17:02;50	24.76	35.3	<1km	2.56	chn, hrk
70721	17:53;38	24.18	35.52	1.57	1.52	chn, kld
70721	20:32;08	23.69	35.72	<1Km	9.51	kld, rth, chn
70721	23:44;00	24.5	35.02	1.77	5.52	sit, rth
70722	04:34;07	23.6	35.65	10	1.41	rth,kld, chn,hrk
70722	04:44;26	23.03	36.02	10		kld, chn, rthn, hrk
70722	06:43;30	24.73	35.3		5.51	hrk, chn, rth, kld
70722	07:18;07	23.91	36.54	18.63	1.02	hrk, chn, rth, kld
70722	08:26;41	25.07	35.3	10	****	rth, kld, hrk
70722	14:02;27	23.69	35.48	10	4.91	chn, kld
70722	14:50;43	23.69	35.7	11.85	0.75	chn, kld
70722	16:25;08	23.96	35.22	49.66	1.22	kld, rth
70722	23:10;20	26.18	36.92	10	1	rth, kld
70722	23:25;28	20.96	36.5	10	****	rth, chn, kld
70723	01:12;44	25.83	34.32	10	****	rth, chn, hrk
70723	05:49;30	24.23	34.1		****	rth, chn, hrk
70723	22:48;42	26.01	35.3	17.84	1.3	rth, chn, hrk
70724	03:33;30	23.87	35.73	2.41	1.2	kld, chn, hrk
70724	03:58;33	23.25	35.91	2.97	0.5	rth, chn, kld
70724	06:15;23	25	36.36	47.98	1.86	kld, chn, hrk
70724	13:45;57	24.84	34.93	10	1.12	kld, chn, hrk
70725	02:19;46	24.2	36.18	47.88	0.83	chn, hrk
70725	09:57;18	23.69	35.48	10	0,2*	kld, chn
70725	14:36;10	23.44	35.57	<1km	0.62	kld, hrk,chn

70726	22:03;18	23.62	35.23	10	1.92	kld, kndr
70726	23:48;34	25.43	35.52	10	9.11****	kld, kndr,chn
70726	00:02;44	23.92	34.47	19.67	1.06	kld, kndr,chn, hrk
70726	02:06;02	23.62	34.56	10	1.1	kld, kndr,chn
70726	04:19;28	23.65	35.23	10	****	kndr, chn
70726	05:53;55	22.74	35.83	15.94	1.1	kndr,hrk,chn
70726	06:04;30	23.26	36.01	25.71	0.85	kld, kndr
70726	09:05;13	23.88	40.43	25.57	0.7	kld, hrk,kndr
70726	11:26;36	23.28	35.48	10	1.8	kld, kndr,chn, hrk
70726	18:56;04	24.66	35.26	<1km	4.14	kndr, rth
70726	22:02;52	26.21	35.55	26.53	0.09	sit, hrk,chn
70726	23:16;15	27.55	36.57	18.68	4.05	hrk, chn, sit,kndr
70727	01:47;51	26.1	35.21	16.07	5.38	hrk, chn, sit,kndr,kld,rth
70727	02:03;18	27.29	35.21	10	3	hrk, chn, sit,kndr,kld
70727	04:18;55	24.61	35.36	18.18	1.7	rth, chn,hrk
70727	09:56;38	22.9	35.47	4.92	0.66	rth, kld
70727	09:59;44	23.69	35.48	10	****	rth, kld
70727	15:05;34	25.39	36.36	29.45	*****	hrk, sit chn
70727	22:02;02	24.5	35.36	18.79	*****	rth, sit, hrk
70727	22:15;17	23.69	35.48	10	2	kld, chn
70727	22:25;26	26.41	35.19	10	0.6	sit, hrk
70727	23:50;29	23.9	35.69	<1km	0.08	kld, chn
70728	19:08;28	26.1	35.21	10	1.8	sit,hrk,rth
70729	05:06;76	25.35	35.89	60.63	4.93	hrk, sit, chn
70729	08:25;39.19	21.89	36.39	10	1.74	kld, chn, rth
70729	15;35;02	24.12	34.68	19.14	1.59	chn, kld,rth,kndr,hrk
70729	01:08;41.19	25.74	35.26	<1km	1.94	sit,kld,hrk
70729	01:19;70	23.69	35.48	10	4	kld, chn
70730	10:51;55	23.3	36.68	10	5.5	sit, hrk
70730	22:25;23.46	25.43	36.23	23.48	****	hrk,sit, chn, kld

70730	23:12;41	23.68	3,.05	25.81	0.7	kndr, kld
70730	09:17;32	23.97	35.25	2.25	0	kndr, kld
70730	17:11;36.73	24.5	36.01	10	1.77	rth, chn,hrk,sit
70731	02:27;36	24.55	34.38	19.24	0.7	rth, kndr, chn
70731	11:03;28	25.06	34.4	39.27	0.41	sit,hrk
70731	17:11;46	24.32	35.36	10	4.48	sit, hrk, chn, rth
70731	21:29;02	24.5	35.36	18.52	5****	rth, sit, chn,hrk
70731	23:04;29	24.6	36.07	19.17	4.34	rth, sit, chn, hrk
70801	00:10;41.78	23.78	35.6	<1km	0.6	chn, sit
70801	00:09;37.72	23.18	35.92	<1m	1,74***	hrk,sit, chn,rth
70801	17:47;52.30	26.96	36.58	19.53	2.84	chn, rth, sit, hrk
70801	18:55;21.33	25.06	34.23	2.81	0.13	hrk, sit
70801	12:14;40.97	26.1	35.21	10	2.2	sit, hrk
70802	16:44;42.72	23.69	35.4	10	4.56	kld, chn
70802	08:43;32.48	25.07	35.3	10	2.75	rth,hrk
70802	07:51;06.61	23.36	35.79	10	*****	rth, chn, hrk
70802	03:44;43.81	26.28	37.1	10	8.61	sit, hrk, chn
70804	13:25;58	27	35.66	2.13	3.3	chn, rth
70804	21:50;18	23.69	35.48	10	2.1	kld, chn, hrk, sit
70804	22:38;29	26.1	35.21	10	****	sit, hrk
70804	23:15;27	26.66	35.18	<1km	0.02	sit, hrk
70805	00:51;26	23.69	35.48	10	4.28	kld, chn
70805	02:56;34	25.07	35.8	6.72	0.94	hrk, sit, chn, rth,kld
70805	09:47;07	24.83	36.59	35.65	2.2	hrk, chn, kld
70806	01:48;50.72	24.58	34.62	19.83	0.71	sit, hrk
70806	05:27;54.78	24.11	35.78	<1km	6.62	sit, Hrk
70806	00:39;40.00	24.85	35.75	49.23	3.9	chn, sit,hrk
70806	15:18;30	23.42	35.38	21.82	0.11	kld,plc,chn
70806	22:59;59	22.57	36.4	10	4.34	sit,hrk
70807	01:11;28	23.92	35.05	0.3	0.05	kld,plc

70807	4:24;23	24.52	35.71	0.2	0.49	sit, HRk
70807	11:28;21	23.57	35.03	8	0.18	sit, plc
70807	11:26;00	23.68	35.09	15.86	0.21	sit, plc
70807	14:40;10	23.46	35.03	2.18	0.29	plc, kld, chn
70807	16:55;	23.19	35.37	10	6.69	sit, hrk
70807	17:25;17	24.22	35.38	<1km	0.62	sit, kld
70807	22:24;28	23.69	35.48	10	****	kld, plc, chn, hrk
70807	23:53;06	23.68	35.2	10	0.4	kld, plc
70808	02:23;18	24.55	35.05	8.16	0.46	plc, kld, chn
70808	17:17;08	24.45	34.91	<1km	1.69	sit, hrk,chn, kld
70808	01:11:00.0	23.92	35.05	<1km	0.05	kld, Kndr (plc)
70809	14:52;43	23.98	34.9	18.82	2.17	chn, kld, hrk
70810	03:44:09.20	24.5	35.5	30.89	1,8****	rth, chn ,kld
70810	10:45;19	24.27	35.33	18.42	0.12	rth, chn,sit, hrk,kld
70810	01:42;45	24.5	34.57	10	5.17	hrk, sit, chn, kld
70810	10:21;36	24.69	35.32	<1km	****	chn, rth, sit
70810	12:41;06	24.7	35.44	<1km	****	chn, kld, sit, rth
70810	14:30;39	24.27	35.27	<1km	0.31	chn,kld,hrk
70811	00:59;14	24.02	35.5	<1km	0.54	kld,chn,rth
70811	01:03;11	24.04	35.52	10	8.2	kld, chn,rth
70811	01:48;49	24.63	35.25	1.48	2.1	kld,sit
70811	08:10;21	23.61	35.46	<1km	4.2	rth,chn,kld
70811	09:52;21	24.5	35.36	17.57	1.27	chn, rth, sit
70811	14:30;03	23.58	35.02	10	****	rth, chn
70811	14:33;08	24.31	35.35	25.05	0.26	rth,kld, chn
70811	17:17;23	24.24	35.29	<1	0.27	sit, chn, kld
70812	02:36;31	26.35	36.45	<1	<1	sit,hrk,chn,rth
70812	21:56;45	24.08	35.63	<1	<1	sit, chn
70812	23:49;18	24.63	34.71	5.53	0.66	kld, chn,rth,sit, hrk
70812	11:22;40	24.08	35.63	24.44	0.16	hrk,chn,rth



70813	0321 11.72	24.95	36.07	45.73	1.73	hrk, chn, rth, kld
70813	0324 18.66	25.77	35.44	10	2.47	hrk, chn, rth, kld
70813	0334 39.59	24.67	34.62	0.89	3.17	sit,hrk, chn,rth, kld
70813	0342 45.35	24.5	35.36	10	4	chn, rth, kld
70813	0344 45.35	23.41	33.38	8	*****	chn, rth, kld
70813	0918 21.09	24.89	35.77	15.84	1.32	hrk, rth, chn, kld, sit
70813	11:14:12.26	24.78	35.67	12.63	0.24	rth, sit, hrk,chn
70813	14:26:49.60	24.58	34.77	<1km	0.55	sit, hrk,rth
70813	14:31:56.46	24.85	35.64	18.44	1.1	hrk,sit, rth, kld
70813	18:33:50.00	24.68	34.57	19.33	3	hrk,sit, rth, kld,chn
70813	20:31:46;44	35.37	35.63	18.98	0.53	kld, chn, rth
70814	00:37:57.53	24.8	35.85	1.4	0.53	rth, kld, chn, sit, hrk
70814	00:38;07	24.8	35.84	1.74	<1	kld,hrk,sit,rth
70814	01:39:40.91	24.5	35.36	10	<1	sit,rth,kld,chn, hrk
70814	02:04;15.29	25.68	35.35	51.57	****	kld, chn, sit,hrk
70814	11:25;27.13	25.88	34.89	1.49	1.58	hrk,sit, rth, kld
70814	12:32;31.7	24.8	34.82	10	3	rth,kld, chn, hrk
70814	12:42;13.23	24.55	34.7	10	1.53	chn, sit,rth, kld,hrk
70814	17:20;24	26.1	35.2	10	****	sit,hrk,chn
70814	20:02;14.43	24.86	35.73	<1km	2.45	rth, chn, kld
70815	01:01:11.29	23.65	35.41	4.46	0.34	kld, chn, rth
70815	06:30:07.44	22.82	37.85	10	5.36	chn, rth
70815	08:58:20.13	26.1	35.21	10	****	sit, hrk, chn
70817	05:04:16.38	26.1	35.21	10	****	chn, rth, sit, kld, hrk
70817	05:43:49.13	24.78	35.36	16.94	1.2	rth,hrk, chn
70817	06:20:24.22	25.47	35.33	<1km	0.2	rth, sit, hrk
70817	16:35:31.31	26.1	35.21	10	6.21	sit,hrk
70817	22:14:13.00	24.7	35.36	18	2.56	chn, rth, sit, kld, hrk
70817	23:00:26.16	23.71	34.84	10	0.85	kld,rth, chn
70817	23:24:02.10	26.32	36.74	19.7	3.2	rth, sit, hrk

70818	00:05.28	24.5	35.36	10	3.4	kld,rth, chn
70818	00:05.33	24.87	35.81	10	0.76	sit,hrk,chn
70818	00:56.29	24.64	34.76	<1km	1.89	sit, hrk, chn
70818	01:25.00	24.81	35.36	26.06	2.41	rth, kld, chn,sit, hrk
70818	19:52:13.43	24.71	36.2	39.34	****	rth,hrk, chn
70818	20:13:53.62	24.65	35.36	10	2.17	rth, kld, chn, hrk
70818	22:44:19.76	23.69	35.48	10	2.72	kld, chn
70818	23:39:43.80	25.83	35.21	10	1.72	sit, hrk
70819	07:21:41.07	26.1	35.21	10	*****	sit,hrk,chn,rth
70819	14:03:13.29	25.57	36.12	29.49	3.11	rth,kld,chn, sit, hrk
70819	01:56:01.01	26.1	35.21	10	*****	sit, hrk, rth
70819	18:47:52.72	25.37	35.23	<1km	2.14	hrk,sit
70820	08:39:02.7	23.54	34.99	6.11	0.48	rth, kld, chn,
70820	16:32:39.06	26.39	37.26	19.52	*****	rth, sit, hrk
70820	17:50:45.24	24.06	35.36	10	****	rth, hrk chn
70820	22:52:51.09	23.97	35.07	27.54	2.97	rth, kld, kndr, chn,sit, hrk
70820	23:13:45.08	23.45	35.01	15.82	0.74	chn, rth, kld, kndr
70820	23:57.00	28.01	36.07	10	***	kld, rth, sit,hrk
70821	08:59:27.61	23.5	35.02	14.14	0.06	kndr, kld
70821	09:20:0.60	23.54	35.09	16.16	1.03	kndr, kld,chn, rth,hrk
70821	10:19:09.44	24.22	35.26	1,67km	0.93	kndr, kld,chn, rth,hrk
70821	12:30:20.85	23.57	35.08	16.26	1.02	rth, kndr, kld,chn
70821	14:13:39.30	26.64	36.13	10	1.7	sit, hrk, kndr, chn
70822	05:30:06.10	23.95	34.76	34.76	0.62	kndr, kld, chn
70822	08:30:46.34	20.57	35.74	<1km	****	hrk, rth, chn, kld, sit
70822	18:34:06.28	23.69	35.48	10	****	kld, kndr, hrk, chn, rth
70823	01:32.00	23.49	34.77	10	0.9	chn, rth, kld, kndr
70823	03:54:46.00	23.69	35.48	10	3.76	kndr, kld, chn
70823	11:57:17.15	24.04	35.34	<1km	2.15	kndr, kld
70823	17:11:35.39	23.35	34.89	10	1.53	chn, hrk, rth, kndr

70823	19:14:23.44	26.31	36.76	18.69	4.91	sit,hrk
70823	19:34:35.36	23.62	35.05	27	0.7	kndr, kld, chn, rth
70823	21:25:44.36	22.76	34.84	10	0.79	kndr, kld,chn
70823	22:11:38.83	24.58	34.11	10	1.85	hrk,sit,kndr,rth
70823	22:19:37.22	24.87	34.49	22.18	1.14	hrk, sit
70824	08:22:29.70	26.1	35.21	10	****	kndr, kld,rth
70824	14:03:14.15	23.59	35.54	25.14	0.06	kndr, kld
70824	15:08:17.45	23.47	36.27	5.37	0.76	kndr, kld,chn, hrk, rth
70824	22:42:53.51	23.62	35.23	10	3	kndr,kld,chn
70824	22:54:06.82	25.07	35.3	10	6.69	chn, hrk, rth, kndr, sit
70824	23:02:04.00	25.43	35.3	18.47	****	chn, hrk, rth, kndr, sit
70825	01:21:02.77	25.38	36.12	10	0.75	chn, hrk, rth, kndr, sit
70825	18:11:45.34	26.1	35.64	10	7.93	sit, hrk, chn
70826	02:17:25.62	26.1	35.21	20.26	0.47	sit, hrk
70826	05:05:45.33	26.23	35.56	3.19	0.45	sit, hrk
70826	06:42:06.71	26.13	35.37	18.09	0.14	sit, hrk
70826	12:06:13.48	26.1	34.97	13.3	0.19	sit, hrk
70826	12:07:40.07	25.07	35.3	10	6.82	sit, hrk, chn
70826	13:21:21.33	25.96	35.25	1.82	0.86	sit, hrk, chn, kndr, kld
70826	13:51:58.04	25.51	36.13	5.12	0.88	sit, hrk, chn, kld
70826	14:02:34.86	25.07	35.3	10	7.1	sit, hrk, chn
70826	15:45:08.42	23.69	35.48	10	2.38	chn, kld
70827	01:30:37.56	25.38	36.18	6.78	0.81	hrk, sit, chn, kld,rth
70827	10:31:47.62	25.4	36.13	2.6	1.41	hrk,sit, rth, kld, kndr
70827	22:37:01.71	24.6	34.99	<1km	0.53	rth, kndr, hrk
70828	03:12:44.92	25.44	36.17	3.37	0.63	chn, rth,kld, kndr, sit, hrk
70828	04:36:25.17	22.86	37.98	10	1,80****	rth, kld,chn, hrk
70828	09:06:38.26	22.29	37.75	10	0,7****	rth, kld chn, kndr, hrk
70829	00:48:36.62	26.1	35.21	10	****	rth, kld, chn, kndr, sit, hrk
70829	02:08:05.54	23.88	34.72	10	0.88	kndr, kld

<b>70829</b>	06:12:55.96	22.78	35.52	17.28	0.36	rth, kld, kndr, chn
<b>70829</b>	07:301:04.46	26.18	35.64	2.62	1.1	sit, kndr, hrk, kld, rth
<b>70829</b>	13:08:31.29	25.86	35.21	10	****	sit, hrk, chn, rth
<b>70830</b>	01:03:47.81	24.66	34.4	<1km	1.45	rth, kld, ferm, chn, kndr, hrk
<b>70830</b>	01:19:18.18	23.62	35.35	3.82	1.08	rth, kld, ferm, chn, kndr, hrk
<b>70830</b>	01:47:22.93	23.62	35.37	16.67	1.26	rth, kld, chn, kndr, hrk
<b>70830</b>	07:58:58.13	25.43	35.75	24	0.2	chn, sit, hrk
<b>70830</b>	09:49:58.36	22.72	34.98	<1km	0.99	rth, kld, ferm, chn, kndr, hrk
<b>70830</b>	20:23:12.96	21.96	35.5	10	****	kndr, hrk, chn, kld, rth
<b>70830</b>	22:26:02.04	23.69	35.31	23.85	1.23	kndr, kld, chn
<b>70831</b>	02:07:59.01	23.36	36.63	10	0.91	kndr, kld, chn, kast, rth, ferm
<b>70831</b>	12:34:00.0	23.92	35.66	18.02	0.1	kndr, chn, rth, kld
<b>70831</b>	20:53:08.09	26.21	37.01	10	1.87	kndr, kld, chn, kast, rth, ferm, hrk
<b>70831</b>	21:49:04.36	26.9	37.07	10	1,53*****	kndr, kld, chn, kast, rth, ferm, hrk

**TABLE 4.8:** Samples of earthquake epicenters recorded from the temporal seismological network of Paleohora

DATE	ORIGIN	LATITUDE	LONGITUDE	DEPTH	MAG	NO	GAP	DMIN	RMS ERH ERZ	QM
70331	1450 30.79	34 55.71	23 34.28	10	0.82	6	351	34.3	2.25134.4455.2	D1
70331	1831 13.26	34 55.06	23 34.35	10	0.92	6	352	35.5	2.28154.3540.9	D1
70331	2129 7.52	34 57.61	23 34.42	10	0.42	6	350	30.8	2.21123.2374.2	D1
70331	2212 27.72	34 56.68	23 34.46	10	0.7	6	351	32.5	2.18135.4434.3	D1
70331	2213 27.91	34 55.43	23 34.37	10	0.71	6	351	34.8	2.30143.7493.9	D1
70331	2251 47.39	34 55.41	23 34.42	10	0.92	6	351	34.9	2.31172.4593.3	D1
70331	23 4 27.86	34 56.36	23 34.28	10	0.71	6	351	33.1	2.20128.2418.8	D1
70331	23 9 4.23	34 55.05	23 34.52	10	0.71	6	352	35.5	2.29152.3534.0	D1
70401	048 25.40	34 56.03	23 34.41	10	0.78	6	351	33.7	2.17142.7474.9	D1
70401	048 25.15	34 55.59	23 34.27	10	0.78	6	351	34.6	2.26140.8479.9	D1
70401	052 12.60	34 55.94	23 34.47	10	0.65	6	351	33.9	2.09156.1521.9	D1
70401	056 17.65	34 56.33	23 34.45	10	0.82	6	351	33.2	2.19142.3465.4	D1
70401	121 31.64	34 55.05	23 34.50	10	0.96	6	352	35.5	2.13185.8651.8	D1

<b>70401</b>	150 21.92	34 56.05	23 34.44	10	0.82	6	351	33.7	2.22147.3489.3	D1
<b>70401</b>	154 51.93	35 4.56	23 38.53	0.35	0.65	6	343	17.6	2.21173.9****	D1
<b>70401</b>	2 4 19.98	35 24.94	23 19.62	5.93	0.83	6	356	33.7	2.07*****	D1
<b>70401</b>	2 6 4.51	34 55.52	23 33.16	10	0.44	6	352	35	2.36415.8****	D1
<b>70401</b>	2 9 55.31	34 55.77	23 34.10	10	0.62	6	351	34.3	2.14207.6700.9	D1
<b>70401</b>	3 0 46.48	34 56.04	23 34.47	10	1.57	6	351	33.7	2.17152.5506.9	D1
<b>70401</b>	836 36.51	35 13.12	23 33.89	0.41	0.73	6	349	5.7	0.15 14.3 68.7	D1
<b>70401</b>	1851 25.89	34 56.09	23 34.43	10	0.71	6	351	33.6	2.14102.0338.1	D1
<b>70401</b>	22 0 32.58	35 14.19	23 31.07	3.85	0.63	6	357	9.7	0.30 18.9 5.9	D1
<b>70401</b>	2234 13.70	35 14.19	23 31.79	3.23	0.67	6	357	8.6	0.26 18.8 6.2	D1
<b>70401</b>	23 5 53.12	35 14.19	23 31.06	0.72	0.68	6	357	9.8	0.17 6.6 10.9	D1
<b>70401</b>	2325 24.35	35 14.19	23 31.68	3.91	1.08	6	357	8.8	0.27 18.6 5.2	D1
<b>70402</b>	018 25.10	35 14.19	23 30.96	4.05	0.59	6	357	9.9	0.28 17.7 5.4	D1
<b>70402</b>	018 25.13	35 14.19	23 30.99	2.51	0.59	6	357	9.9	0.11 9.5 5.0	D1
<b>70402</b>	018 25.02	35 14.19	23 30.72	3.17	1.25	6	357	10.3	0.13 10.4 4.5	D1

<b>70402</b>	023 33.33	35 14.19	23 31.01	2.64	0.73	6	357	9.8	0.22 17.2 7.8	D1
<b>70402</b>	040 9.50	35 14.19	23 30.85	4.62	0.63	6	357	10.1	0.30 16.7 4.6	D1
<b>70402</b>	111 6.69	35 14.19	23 30.77	4.45	0.36	6	357	10.2	0.33 22.4 6.4	D1
<b>70402</b>	210 46.88	35 12.17	23 28.69	0.1	0.76	6	355	13.8	0.41 12.8496.8	D1
<b>70402</b>	156 56.68	35 14.19	23 31.37	0.41	0.92	6	357	9.3	0.20 15.6 42.6	D1
<b>70402</b>	244 37.55	35 15.64	23 29.10	0.15	0.37	6	356	13	0.21 15.4316.0	D1
<b>70402</b>	3 4 23.31	35 14.19	23 32.24	0.2	0.74	6	357	8	0.21 16.9 81.5	D1
<b>70402</b>	343 10.99	35 14.19	23 29.26	1.29	0.75	6	358	12.5	0.07 2.4 2.7	C1
<b>70402</b>	354 13.82	35 9.63	23 32.37	1.18	0.82	8	344	11.3	0.68 69.9505.2	D1
<b>70402</b>	430 19.59	35 14.61	23 31.27	0.13	0.63	6	357	9.5	0.23 21.2232.8	D1
<b>70402</b>	627 34.75	35 17.00	23 30.96	0.2	0.64	6	350	11.3	0.28 24.0641.6	D1
<b>70402</b>	816 58.63	35 14.19	23 30.73	4.54	0.64	6	357	10.3	0.32 22.0 6.0	D1
<b>70402</b>	816 59.13	35 14.19	23 31.58	0.21	0.63	6	357	9	0.22 14.6 76.1	D1
<b>70402</b>	842 14.80	35 14.19	23 30.71	4.74	0.64	6	357	10.3	0.35 33.7 9.0	D1
<b>70402</b>	9 7 34.51	35 14.82	23 29.48	0.13	0.64	6	357	12.2	0.12 2.4 36.0	D1

<b>70402</b>	9 7 34.06	35 14.19	23 37.59	18.68	0.6	6	229	0.2	0.31 59.6 3.5	D1
<b>70402</b>	1221 42.44	35 14.19	23 30.48	4.85	0.64	6	357	10.6	0.32 21.8 5.9	D1
<b>70402</b>	1838 24.73	35 5.84	23 36.30	2.33	0.75	6	341	15.4	0.61 9.8 63.8	D1
<b>70402</b>	2313 44.06	35 14.19	23 31.81	0.38	0.63	6	357	8.6	0.20 17.2 46.5	D1
<b>70402</b>	2328 23.48	35 14.19	23 30.91	2.89	0.36	6	357	10	0.22 17.9 7.5	D1
<b>70403</b>	053 44.45	35 4.36	23 34.13	4.34	0.66	6	345	18.7	0.61 12.2 50.5	D1
<b>70403</b>	8 8 41.70	35 14.19	23 32.66	2.6	0.62	6	357	7.3	0.32 28.4 9.8	D1
<b>70403</b>	1159 17.65	35 14.19	23 30.60	4.73	0.36	6	357	10.5	0.34 27.6 7.6	D1
<b>70403</b>	1430 31.60	35 14.19	23 30.91	3.07	0.93	6	357	10	0.20 11.8 4.7	D1
<b>70403</b>	1518 43.28	35 14.19	23 29.98	5.1	0.75	6	358	11.4	0.19 6.3 1.8	D1
<b>70403</b>	1539 58.59	35 19.06	23 35.10	6.94	0.36	4	359	12.4	0.05	C1
<b>70403</b>	1623 45.55	35 14.00	23 28.78	2.65	0.94	6	358	13.2	0.28 14.7 9.0	D1
<b>70403</b>	1649 47.78	35 14.19	23 30.85	4.53	0.62	6	357	10.1	0.34 28.8 7.9	D1
<b>70402</b>	2226 24.24	35 14.19	23 30.93	1.02	0.63	6	357	10	0.19 17.5 20.4	D1
<b>70403</b>	1652 34.13	35 14.19	23 30.80	4.63	0.84	6	357	10.2	0.32 23.0 6.3	D1



<b>70403</b>	1819 50.14	35 14.19	23 29.61	1.43	0.75	6	358	12	0.07 5.8 5.7	D1
<b>70403</b>	1838 13.80	35 14.19	23 28.32	2.69	0.65	6	358	13.9	0.19 36.2 22.7	D1
<b>70403</b>	19 4 45.15	35 14.19	23 30.13	0.16	0.64	6	358	11.2	0.33 22.8185.7	D1
<b>70403</b>	1949 14.48	35 14.19	23 31.32	0.32	0.63	6	357	9.4	0.20 12.8 45.2	D1
<b>70403</b>	2132 51.49	35 0.96	23 34.25	16.78	1.87	6	348	24.8	0.19 52.7 76.0	D1
<b>70403</b>	2247 40.77	35 14.19	23 31.23	0.53	1.17	6	357	9.5	0.20 16.5 35.7	D1
<b>70403</b>	2256 10.54	35 14.19	23 29.89	3.98	0.64	6	358	11.5	0.17 6.0 2.2	D1
<b>70403</b>	2328 31.65	35 14.19	23 30.26	4.4	0.75	6	358	11	0.17 6.3 2.0	D1
<b>70403</b>	2332 45.06	35 14.19	23 29.22	7.05	0.75	6	358	12.5	0.09 16.7 3.7	D1
<b>70404</b>	058 19.78	35 14.19	23 30.79	1.8	0.63	6	357	10.2	0.24 29.3 19.8	D1
<b>70404</b>	1 5 41.05	35 14.19	23 30.86	3.72	0.74	6	357	10.1	0.26 23.0 7.6	D1
<b>70404</b>	0 5 0.51	35 14.19	23 34.98	10.72	0.91	6	356	3.8	0.06 8.9 0.8	D1
<b>70404</b>	113 23.98	35 14.19	23 31.20	3.42	0.84	6	357	9.5	0.27 18.8 6.5	D1
<b>70404</b>	149 42.39	35 14.19	23 31.52	3.98	0.63	6	357	9.1	0.37 33.1 9.3	D1
<b>70404</b>	225 45.86	35 14.19	19 33.41	0.22	1.9	6	360	370.3	18.92*****301.3	D1

<b>70404</b>	4 4 50.67	35 14.19	23 31.14	1.54	0.74	6	357	9.6	0.22 12.0 9.1	D1
<b>70404</b>	416 50.03	35 14.19	23 30.79	4.62	0.95	6	357	10.2	0.44 46.0 12.4	D1
<b>70404</b>	5 2 33.72	35 14.19	23 25.54	2.31	0.87	6	358	18.1	0.98 19.0 18.4	D1
<b>70404</b>	528 51.65	35 16.22	23 30.30	2.21	0.93	6	353	11.6	0.23 14.8 27.1	D1
<b>70404</b>	549 1.11	35 14.19	23 29.81	4.44	0.75	6	358	11.7	0.20 18.0 5.8	D1
<b>70404</b>	632 48.28	35 14.19	23 32.04	0.45	0.83	6	357	8.3	0.23 19.8 43.8	D1
<b>70404</b>	8 5 2.74	35 14.19	23 30.67	4.73	0.64	6	357	10.3	0.32 24.0 6.5	D1
<b>70404</b>	946 34.60	35 14.36	26 48.20	10	1.69	6	3602	84.11	3.42*****	D1
<b>70404</b>	14 4 8.22	35 14.19	23 35.44	11.86	0.9	6	355	3.1	0.10 13.0 1.2	D1
<b>70404</b>	1447 21.79	35 11.81	23 36.60	9.13	0.61	6	318	4.4	0.11 4.7 2.2	D1
<b>70404</b>	19 2 0.73	35 14.19	23 35.26	10.02	0.24	6	355	3.4	0.01 1.6 0.2	C1
<b>70404</b>	2042 32.49	35 11.78	23 37.39	10.15	0.9	6	308	4.3	0.14 6.6 2.8	D1
<b>70404</b>	2237 2.39	35 10.36	23 36.09	8.14	0.34	6	329	7.2	0.08 2.8 2.4	D1
<b>70405</b>	022 53.09	35 13.38	23 35.11	9.69	0.82	6	346	3.8	0.03 3.8 0.7	D1
<b>70405</b>	025 46.79	35 14.19	23 35.50	10.76	0.9	6	355	3	0.08 10.4 1.0	D1

<b>70405</b>	053 7.07	35 25.91	23 26.96	26.95	0.9	6	352	27.1	0.07 25.8 22.4	D1
<b>70405</b>	331 11.20	35 18.33	23 34.72	7.36	0.63	6	338	8.9	0.09 13.0 13.8	D1
<b>70405</b>	512 35.61	35 17.85	23 34.63	6.71	0.83	6	337	8.2	0.20 25.8 26.7	D1
<b>70405</b>	746 47.50	35 14.19	23 16.08	18.38	1.16	6	359	32.5	0.71283.9 61.2	D1
<b>70405</b>	746 54.58	35 14.19	23 37.59	10	1.13	4	229	0.2	1.63	D1
<b>70405</b>	950 39.40	35 16.26	23 34.94	9.51	0.91	6	337	5.6	0.04 5.2 2.2	D1
<b>70405</b>	1024 59.54	35 14.19	23 35.42	9.33	1.17	6	355	3.2	0.05 6.3 0.6	D1
<b>70405</b>	1040 51.34	35 14.19	23 33.16	19	0.73	6	357	6.6	0.03 7.5 0.6	D1
<b>70405</b>	1040 51.34	35 14.19	23 33.16	19	0.73	6	357	6.6	0.03 7.5 0.6	D1
<b>70405</b>	1122 29.81	35 14.19	23 35.33	9.66	1.05	6	355	3.3	0.02 2.7 0.3	D1
<b>70405</b>	1133 28.66	35 10.18	23 37.59	7.07	0.68	6	322	7.2	0.23 17.0 17.5	D1
<b>70405</b>	14 0 50.58	35 15.95	23 35.34	9.05	0.98	6	334	4.7	0.05 6.3 2.4	D1
<b>70405</b>	1447 22.15	35 14.19	23 35.55	10.1	0.65	6	355	2.9	0.05 5.9 0.6	D1
<b>70405</b>	1725 0.18	35 14.19	23 33.14	17.85	0.7	6	357	6.6	0.21 33.8 2.5	D1
<b>70405</b>	1947 48.51	35 14.19	23 35.70	9.65	0.72	6	355	2.7	0.02 2.2 0.2	C1

<b>70405</b>	23 3 51.43	35 14.19	23 37.59	10	1.33	6	229	0.2	6.56 43.8 4.4	D1
<b>70406</b>	026 57.56	35 14.19	23 34.11	12.46	0.73	6	356	5.1	0.22 32.1 2.9	D1
<b>70406</b>	151 1.66	35 14.19	25 35.28	10	1.2	6	360	173.5	18.06*****292.4	D1
<b>70406</b>	428 4.11	35 19.40	23 32.19	6.15	0.51	6	345	12.7	0.33 28.1 44.5	D1
<b>70406</b>	513 58.21	35 14.19	23 37.59	16.92	0.47	6	229	0.2	0.45 73.4 4.7	D1
<b>70406</b>	524 41.08	35 14.19	23 33.20	21.92	0.73	6	357	6.5	0.10 25.2 1.7	D1
<b>70406</b>	558 7.15	35 23.75	23 48.31	8.06	0.66	6	349	20.9	0.42 15.0 33.6	D1
<b>70406</b>	1324 46.66	35 14.19	23 35.09	10.22	0.81	6	355	3.6	0.03 3.9 0.4	D1
<b>70406</b>	1338 55.31	35 14.19	23 35.22	10.77	0.9	6	355	3.4	0.02 3.1 0.3	D1
<b>70406</b>	1340 10.43	35 14.19	23 35.65	13.06	0.72	6	355	2.8	0.12 16.5 1.4	D1
<b>70406</b>	1614 37.01	35 16.24	23 35.11	8.23	0.62	6	335	5.4	0.02 3.0 1.4	D1
<b>70406</b>	1834 16.10	35 14.19	23 35.00	9.25	0.72	6	356	3.8	0.03 3.6 0.4	D1
<b>70406</b>	1916 44.93	35 19.55	23 32.17	1.39	0.75	6	346	12.9	0.13 19.9143.7	D1
<b>70406</b>	20 7 19.11	35 14.19	23 35.20	8.98	0.72	6	355	3.5	0.02 2.0 0.2	C1
<b>70406</b>	21 6 59.26	35 14.19	23 35.16	10.72	0.61	6	355	3.5	0.03 4.8 0.5	D1

70408	030 57.69	35 5.74	23 31.28	2.34	0.57	6	347	18.1	0.74 58.2385.5	D1
70408	042 23.20	34 43.71	23 43.23	10	1.08	6	355	55.9	5.27544.4*****	D1
70408	250 38.10	35 10.33	23 35.58	7.61	0.91	6	331	7.5	0.07 7.8 7.2	D1
70408	255 36.08	35 10.86	23 36.12	8.44	0.49	6	326	6.3	0.04 5.3 3.8	D1
70408	257 1.96	35 14.19	22 43.69	33.01	1.18	6	360	81.6	0.35388.0 29.8	D1
70408	313 24.17	35 14.19	23 35.74	9.36	0.76	6	355	2.7	0.08 8.9 0.9	D1
70408	3 1 42.31	35 13.98	24 26.44	18.6	1.88	6	359	69	0.39*****	D1
70408	415 10.05	35 .04.24	23 42.4	<sup>4</sup> 17.23	1.2	2	6 34	5 18.	0 0.14 15.5 16.2	D1
70408	425 51.51	35 .04.85	24 23.1	<sup>5</sup> 19.63	2	2	6 35	9 66	2 0.13 76.9357.2	D1
70408	435 27.14	34 59.60	23 58.55	6.55	1.59	6	355	37.6	0.12 9.4 37.7	D1
70408	257 1.96	35 14.19	22 43.69	33.01	1.18	6	360	81.6	0.35388.0 29.8	D1
70408	5 0 8.02	35 9.19	23 35.49	7.55	0.92	6	335	9.6	0.12 15.1 18.1	D1
70408	854 34.88	34 51.54	23 19.86	18.68	0.97	6	355	49.6	0.14 55.0123.7	D1
70408	9 1 6.21	35 14.90	23 39.14	13.47	1.22	6	237	2.8	0.00 0.2 0.0	C1
70408	925 17.06	35 11.58	23 35.61	9.15	0.82	6	329	5.4	0.02 2.5 1.3	D1

<b>70408</b>	943 34.78	35 16.42	23 35.56	8.75	0.59	6	331	5.2	0.04 5.5 2.7	D1
<b>70408</b>	1057 35.42	35 14.19	23 36.02	12.7	0.61	6	354	2.2	0.10 14.3 1.2	D1
<b>70409</b>	211 43.22	35 43.01	23 34.94	10	0.68	6	355	53.6	2.94645.6*****	D1
<b>70409</b>	4 9 58.82	35 14.36	24 19.56	18.7	1.66	6	359	58.6	0.33211.0 9.3	D1
<b>70409</b>	415 42.38	35 14.19	23 35.76	10.65	0.52	6	355	2.6	0.07 8.7 0.8	D1
<b>70409</b>	439 44.45	35 13.98	23 41.05	17.11	0.88	6	259	0.2	0.16*****	D1
<b>70409</b>	446 10.24	35 15.14	23 35.17	8.85	0.34	6	342	4	0.00 0.4 0.1	C1
<b>70409</b>	5 4 43.08	35 10.73	23 35.97	6.47	0.62	6	328	6.6	0.16 5.4 5.2	D1
<b>70409</b>	510 0.52	35 11.93	23 35.79	9.08	0.49	6	328	4.8	0.05 5.8 2.6	D1
<b>70409</b>	510 0.52	35 11.93	23 35.79	9.08	0.49	6	328	4.8	0.05 5.8 2.6	D1
<b>70409</b>	854 40.37	35 15.12	23 35.43	8.46	0.61	6	340	3.7	0.02 1.9 0.5	C1
<b>70409</b>	2238 24.04	35 10.21	23 35.58	8.07	0.72	6	332	7.7	0.05 5.4 4.8	D1
<b>70409</b>	23 2 6.53	35 9.90	23 35.32	7.36	0.73	6	334	8.4	0.05 6.8 7.2	D1
<b>70410</b>	217 38.39	35 10.21	23 35.55	5.7	0.83	6	332	7.8	0.04 4.6 5.8	D1
<b>70410</b>	239 6.22	35 14.36	23 38.16	15.82	0.71	6	209	1.1	0.28 43.5 3.2	D1

<b>70410</b>	244 32.70	35 11.23	23 35.69	8.11	0.48	6	329	5.9	0.04 2.7 1.8	D1
<b>70410</b>	446 59.72	35 10.62	23 35.81	8.41	0.91	6	329	6.9	0.06 7.8 6.0	D1
<b>70410</b>	516 30.86	35 11.47	23 35.82	8.27	1.31	6	327	5.5	0.04 5.5 3.3	D1
<b>70410</b>	619 18.85	35 10.32	23 35.67	8.03	0.78	6	331	7.5	0.05 4.0 3.5	D1
<b>70410</b>	626 18.52	35 10.29	23 35.52	8.3	0.44	6	332	7.6	0.04 5.1 4.3	D1
<b>70410</b>	1530 49.08	35 14.19	23 35.03	7.33	0.64	6	355	3.7	0.03 3.7 0.4	D1
<b>70410</b>	1729 15.47	35 10.41	23 39.00	12.63	0.65	6	317	7.1	0.09 13.4 7.2	D1
<b>70410</b>	1817 54.53	35 14.19	23 35.73	8.58	0.65	6	355	2.7	0.15 15.9 1.7	D1
<b>70410</b>	1951 53.95	35 14.19	23 35.87	12.87	0.55	6	355	2.5	0.12 17.9 1.5	D1
<b>70410</b>	2345 4.60	35 10.88	23 36.54	8.2	0.61	6	323	6.1	0.10 10.0 7.3	D1
<b>70411</b>	047 15.75	35 11.26	23 35.73	7.8	0.82	6	329	5.9	0.06 7.7 5.3	D1
<b>70411</b>	130 45.37	35 14.19	23 36.31	10	0.33	6	353	1.8	0.05 6.2 0.6	D1
<b>70411</b>	137 57.39	35 14.19	23 35.36	10	0.33	6	355	3.2	0.06 7.2 0.7	D1
<b>70411</b>	225 27.13	35 15.05	23 35.82	8.56	0.33	6	336	3.1	0.04 4.8 1.1	D1
<b>70411</b>	312 56.61	35 10.76	23 35.73	7.38	0.62	6	329	6.7	0.06 6.7 5.6	D1

<b>70411</b>	341 24.84	35 3.07	24 16.23	8.01	1.77	6	358	57.2	0.26 79.0203.1	D1
<b>70411</b>	655 52.10	35 14.19	23 35.92	10	0.33	6	355	2.4	0.09 11.3 1.1	D1
<b>70411</b>	817 29.19	35 15.81	23 35.42	8.3	0.44	6	334	4.5	0.04 5.1 2.0	D1
<b>70411</b>	841 12.34	35 10.66	23 35.94	7.01	0.48	6	328	6.8	0.03 2.7 2.5	D1
<b>70411</b>	1156 20.27	35 14.19	23 36.16	10	0.4	4	359	2	0.06	C1
<b>70411</b>	1255 25.51	35 10.96	23 35.43	7.79	0.44	6	331	6.6	0.05 5.3 4.0	D1
<b>70411</b>	1629 56.00	35 11.49	23 35.90	7.29	0.49	6	327	5.4	0.01 0.6 0.4	C1
<b>70411</b>	1758 2.50	34 52.05	23 21.56	18.21	1.49	6	355	47.4	0.09 38.0 85.3	D1
<b>70411</b>	2234 2.33	35 7.64	23 35.82	1.86	0.36	6	338	12.2	0.12 16.6106.6	D1
<b>70412</b>	255 8.42	34 45.77	23 53.17	34.87	1.7	6	355	55.2	0.09*****	D1
<b>70412</b>	321 15.47	35 14.19	23 18.72	29.66	1.21	6	359	28.5	0.33*****	D1
<b>70412</b>	1753 16.55	35 40.13	23 18.46	19.79	1.98	6	356	56.1	0.07 32.1264.8	D1
<b>70412</b>	2033 13.46	35 13.98	23 41.05	10	2.16	6	259	0.2	9.86 23.8 2.5	D1
<b>70412</b>	2046 20.67	34 56.53	23 54.16	32.47	1.5	6	354	37.8	0.07*****	D1
<b>70412</b>	2225 47.04	35 8.18	23 35.80	1.05	0.74	6	337	11.2	0.07 7.5 78.4	D1



<b>70413</b>	119 5.90	35 14.19	23 35.88	8.02	0.48	6	355	2.4	0.05 4.9 0.5	D1
<b>70413</b>	620 5.98	35 13.48	23 35.96	8.9	0.61	6	340	2.6	0.01 0.9 0.1	C1
<b>70413</b>	835 8.74	35 14.19	23 35.32	8.78	0.48	6	355	3.3	0.08 8.2 0.9	D1
<b>70413</b>	1035 38.51	35 14.19	23 34.36	8.88	0.62	6	356	4.8	0.11 14.3 1.6	D1
<b>70413</b>	1112 25.77	35 17.36	23 35.95	5.98	0.62	6	329	6.5	0.09 9.8 9.9	D1
<b>70413</b>	1924 49.46	35 19.42	23 32.32	13.8	0.93	6	345	12.6	0.09 19.0 13.4	D1
<b>70413</b>	2230 53.08	35 19.12	23 35.44	5.73	0.92	6	337	9.8	0.11 15.2 24.5	D1
<b>70414</b>	043 40.66	35 15.93	23 36.65	7.08	0.61	6	317	3.6	0.16 14.6 7.1	D1
<b>70414</b>	056 55.65	35 10.58	23 36.63	8.11	0.49	6	324	6.6	0.07 8.0 6.4	D1
<b>70414</b>	124 11.07	35 14.19	23 55.86	10	0.56	6	358	22.6	2.46403.2144.2	D1
<b>70414</b>	130 35.49	33 17.42	23 22.57	10	1.26	6	359	216.9	18.69*****	D1
<b>70415</b>	23 0 37.68	35 14.19	23 36.35	10.9	0.9	6	353	1.7	0.12 14.9 1.4	D1
<b>70415</b>	015 49.20	35 13.98	23 41.05	10	0.8	6	259	0.2	0.41 37.6 4.2	D1
<b>70415</b>	015 48.60	35 11.50	23 36.04	8.15	0.91	6	325	5.3	0.06 3.7 2.2	D1
<b>70415</b>	246 4.75	35 13.98	22 22.06	19.78	2.43	6	360	114.4	12.04*****	D1

<b>70415</b>	3 5 27.29	35 16.70	23 46.01	10	1.82	3	346	9.1	0.01	C1
<b>70415</b>	6 7 2.44	36 11.89	23 55.68	22.54	2.17	6	357	108.9	0.07773.0*****	D1
<b>70415</b>	720 42.64	35 8.71	23 43.52	3.02	0.74	6	340	10.3	0.36 3.3 10.7	D1
<b>70415</b>	8 9 20.65	35 7.16	23 33.76	2.59	0.94	6	343	14	0.17 27.9138.2	D1
<b>70415</b>	835 43.41	35 14.19	23 31.52	10	0.92	6	357	9.1	0.58 97.2 12.6	D1
<b>70415</b>	835 42.94	35 14.19	23 34.47	15.43	0.91	6	356	4.6	0.38 58.7 4.9	D1
<b>70415</b>	916 52.47	35 10.35	23 35.74	7.62	1.25	6	331	7.4	0.06 5.7 5.1	D1
<b>70416</b>	1149 15.89	35 14.19	23 36.14	11.88	0.63	6	354	2.1	0.11 15.4 1.3	D1
<b>70415</b>	12 1 10.28	35 36.72	23 19.47	20.37	1.93	6	355	50	0.10 41.4126.5	D1
<b>70415</b>	1259 28.58	35 14.19	22 42.65	10	2.32	3	360	83.2	0.43	D1
<b>70415</b>	1924 41.98	35 14.19	23 31.73	10	1.11	6	357	8.7	0.55 92.3 11.8	D1
<b>70415</b>	2115 26.36	35 11.31	23 35.34	9.23	0.62	6	332	6.1	0.02 2.1 1.2	C1
<b>70415</b>	2137 21.98	35 11.72	23 43.97	0.72	0.34	6	340	6.1	0.20 4.2 24.4	D1
<b>70415</b>	2232 38.50	35 8.32	23 42.99	2.36	0.35	6	339	10.7	0.44 5.1 22.6	D1
<b>70415</b>	23 0 37.50	35 9.76	23 35.91	7.79	0.92	6	332	8.4	0.03 2.8 2.9	D1

<b>70415</b>	7 6 54.91	35 33.53	24 2.11	12.33	1.49	5	355	48.1	0.13 83.3248.0	D1
<b>70416</b>	2 3 11.91	35 14.19	23 35.51	8.82	0.33	6	355	3	0.05 6.0 0.6	D1
<b>70416</b>	745 39.28	35 14.36	24 56.49	10	0.87	6	360	114.6	*****	D1
<b>70416</b>	744 46.74	35 18.33	23 37.59	4.58	0.53	6	326	7.8	0.30 21.0 35.8	D1
<b>70416</b>	8 0 31.02	34 54.51	23 32.85	17.85	1.34	6	352	36.9	0.13 5.9 11.9	D1
<b>70416</b>	1149 16.26	35 18.33	23 34.93	5.78	0.35	6	337	8.7	0.22 26.6 36.0	D1
<b>70416</b>	13 8 38.61	36 34.46	23 25.34	10	1.97	6	358	149.7	2.27*****	D1
<b>70416</b>	1848 20.81	35 10.48	23 35.70	8.49	0.62	6	330	7.2	0.00 0.5 0.4	C1
<b>70416</b>	1848 20.72	35 10.13	23 35.69	8.42	0.62	6	331	7.8	0.06 5.7 5.0	D1
<b>70416</b>	1913 17.88	35 9.69	23 35.24	5.33	0.63	6	335	8.8	0.00 0.3 0.5	C1
<b>70416</b>	2126 6.48	35 16.35	23 30.65	4.11	0.64	6	352	11.2	0.51 14.3 14.7	D1
<b>70417</b>	938 20.33	34 59.82	23 38.20	16.84	0.97	6	349	26.3	0.13 12.3 19.2	D1
<b>70417</b>	22 2 47.45	35 3.62	24 18.48	2.34	2	6	358	60.1	0.19108.9921.8	D1
<b>70418</b>	0 1 15.54	35 11.69	23 34.19	12.65	0.91	6	340	6.7	0.31 46.3 16.9	D1
<b>70418</b>	012 23.36	35 14.19	23 36.04	12.14	0.9	8	354	2.2	0.05 4.9 0.4	D1

<b>70418</b>	028 8.30	35 11.57	23 36.71	9.09	0.61	6	318	4.8	0.04 4.3 2.2	D1
<b>70418</b>	041 32.20	35 14.19	23 35.18	8.47	0.9	6	355	3.5	0.18 22.2 2.4	D1
<b>70418</b>	1250 22.01	35 14.19	23 33.88	10	0.73	6	356	5.5	0.46 63.3 6.7	D1
<b>70418</b>	1544 40.64	35 14.19	22 18.28	4.31	2.63	6	360	120.2	0.10156.6 0.8	D1
<b>70418</b>	2153 48.78	35 32.61	23 22.45	10	1.6	6	354	41.1	0.76269.5912.9	D1
<b>70418</b>	2323 27.43	35 13.98	23 41.05	10	2.36	6	259	0.2	7.02 4.8 0.5	D1
<b>70419</b>	0 1 15.54	35 11.40	23 34.18	12.45	0.91	6	339	7.1	0.00 0.2 0.1	C1
<b>70419</b>	129 25.11	35 8.65	23 31.88	15.54	0.64	6	345	13.2	0.00 0.5 0.3	C1
<b>70419</b>	149 35.76	35 11.50	23 36.43	8.53	0.61	6	321	5	0.01 0.8 0.5	C1
<b>70419</b>	443 14.64	35 7.43	23 34.01	16.72	0.75	6	342	13.4	0.01 3.1 2.3	D1
<b>70419</b>	555 55.51	35 11.81	23 37.45	8.96	0.33	6	307	4.2	0.13 8.7 4.2	D1
<b>70419</b>	1137 40.55	35 9.92	23 34.70	3.61	0.63	6	336	8.8	0.03 4.1 8.7	D1
<b>70419</b>	1137 40.42	35 13.27	23 35.62	10	0.61	6	340	3.2	0.14 17.0 3.1	D1
<b>70419</b>	1231 29.81	35 10.75	23 34.97	7.88	0.62	6	334	7.3	0.07 8.2 6.5	D1
<b>70419</b>	1749 48.52	35 11.16	23 36.01	7.5	0.62	6	326	5.9	0.09 8.8 6.4	D1

<b>70419</b>	1754 41.07	35 10.32	23 35.75	5.15	0.34	6	331	7.4	0.00 0.2 0.2	C1
<b>70419</b>	1934 15.36	35 12.34	23 36.34	8.8	0.9	6	320	3.7	0.10 7.3 2.8	D1
<b>70419</b>	2020 1.41	35 11.28	23 36.64	9.09	0.61	6	320	5.4	0.03 1.4 0.8	C1
<b>70419</b>	21 0 21.78	35 12.44	23 36.59	9.18	0.48	6	316	3.3	0.09 5.6 1.9	D1
<b>70419</b>	2049 35.10	35 11.26	23 36.49	8.55	0.49	6	322	5.4	0.08 6.7 4.2	D1
<b>70419</b>	2140 42.47	35 11.28	23 36.18	7.42	0.61	6	325	5.6	0.18 15.5 11.0	D1
<b>70420</b>	013 41.30	35 12.08	23 36.84	9.44	0.48	6	313	3.9	0.03 3.4 1.4	D1
<b>70420</b>	1 0 1.92	35 11.67	23 35.66	8.16	0.61	6	329	5.3	0.16 12.7 7.1	D1
<b>70420</b>	120 54.09	35 14.19	23 37.59	3.9	0.47	6	229	0.2	1.76102.3 19.2	D1
<b>70420</b>	142 51.66	35 14.19	23 37.59	10	1.79	6	229	0.2	6.49 15.0 1.5	D1
<b>70420</b>	2 4 12.00	35 13.98	23 41.05	10	1.46	6	259	0.2	14.30 29.8 3.2	D1
<b>70420</b>	212 45.88	35 12.07	23 36.33	8.94	0.48	6	321	4.1	0.11 5.6 2.4	D1
<b>70420</b>	255 10.03	35 12.09	23 37.40	10	0.61	6	304	3.7	0.13 7.4 2.8	D1
<b>70420</b>	334 52.86	35 10.38	23 35.37	8.25	0.73	6	333	7.6	0.08 4.9 4.1	D1
<b>70420</b>	4 9 57.66	35 10.24	23 35.83	7.03	0.49	6	330	7.5	0.10 7.2 7.3	D1

<b>70420</b>	622 40.41	34 49.49	23 40.93	0.01	0.75	6	353	45.1	19.15907.2*****	D1
<b>70420</b>	849 58.26	35 10.96	23 36.09	7.85	0.73	6	326	6.2	0.07 4.7 3.5	D1
<b>70420</b>	1031 9.56	35 11.53	23 35.97	6.59	0.61	6	326	5.3	0.07 6.0 4.3	D1
<b>70423</b>	1046 29.66	35 36.26	23 27.11	19.44	1.61	6	354	43.9	0.13 32.8102.9	D1
<b>70420</b>	1222 26.79	35 11.02	23 36.33	8.39	0.61	6	324	5.9	0.09 7.4 5.1	D1
<b>70420</b>	14 9 10.58	35 10.96	23 36.03	6.86	0.73	6	327	6.2	0.00 0.3 0.3	C1
<b>70420</b>	1532 32.10	35 10.33	23 37.16	10.14	0.62	6	323	7	0.12 12	D1
<b>70420</b>	1651 11.41	35 7.96	23 38.62	1.99	0.35	6	333	11.5	0.34 5.4 30.4	D1
<b>70421</b>	546 33.93	35 13.98	23 41.05	10	0.59	6	259	0.2	6.19 43.2 4.6	D1
<b>70421</b>	139 28.04	35 9.27	23 35.61	6.95	0.63	6	334	9.4	0.13 11.7 15.0	D1
<b>70423</b>	855 0.79	35 12.41	23 45.85	2.63	0.62	6	350	7.9	0.49 27.7 33.2	D1
<b>70423</b>	228 27.59	35 14.19	22 25.88	25.56	2.59	6	360	108.6	0.37568.1 7.8	D1
<b>70423</b>	10 2 38.18	35 55.63	23 50.56	10	2.06	6	356	77.9	0.85318.1*****	D1
<b>70423</b>	1046 29.66	35 36.26	23 27.11	19.44	1.61	6	354	43.9	0.13 32.8102.9	D1
<b>70405</b>	816 6.12	35 14.19	23 35.65	7.63	0.61	6	355	2.8	0.07 7.7 0.9	D1

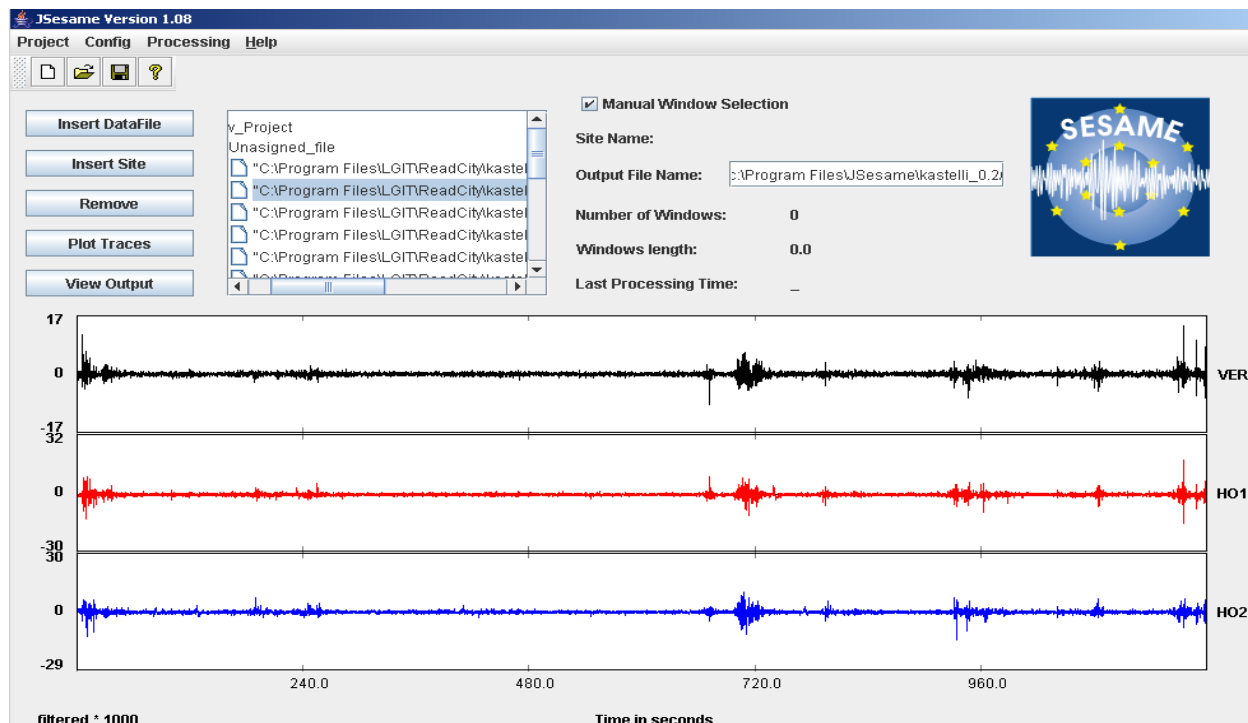
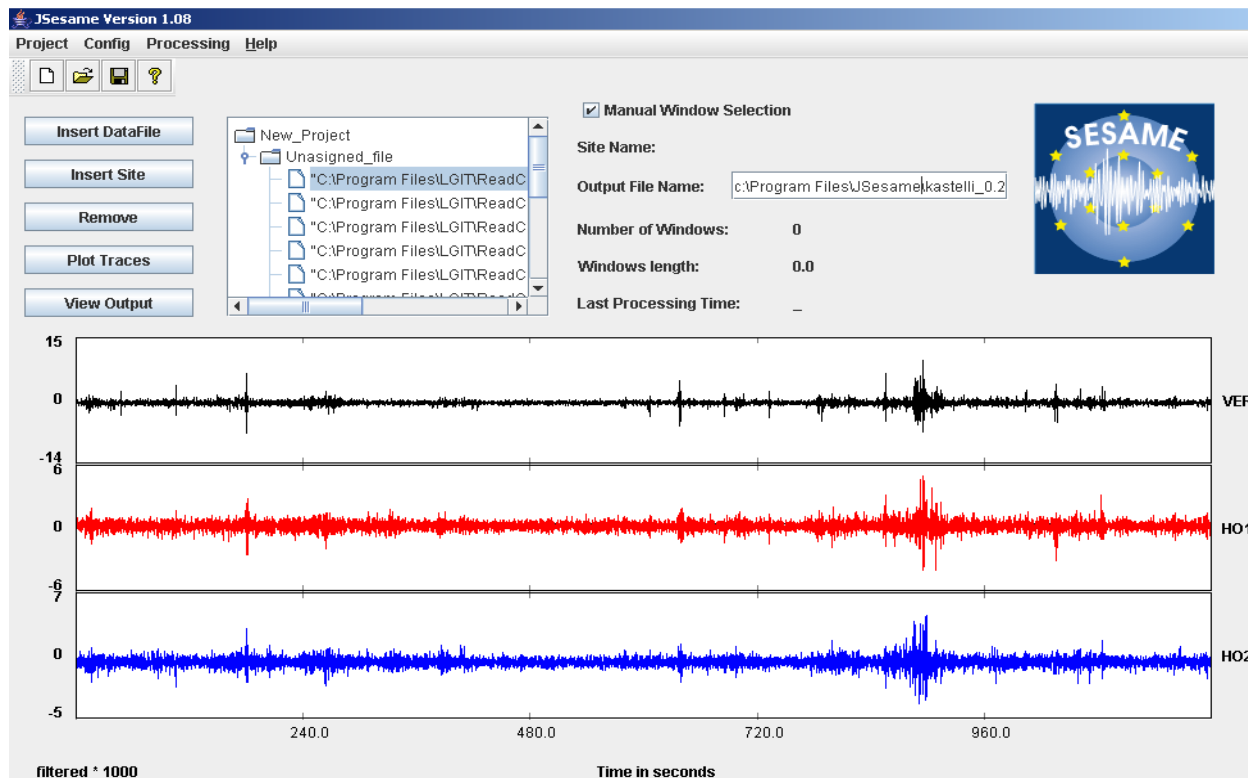
<b>70424</b>	1316 40.49	35 3.63	23 28.01	0.57	1.54	6	351	24.1	0.23 46.8****	D1
<b>70424</b>	2133 30.74	35 0.97	24 5.08	0.98	1.04	6	356	43.7	0.16 29.1719.8	D1
<b>70424</b>	2249 30.38	35 13.98	23 41.05	10	1.87	6	259	0.2	5.67 8.4 0.9	D1
<b>70424</b>	23 3 55.49	35 7.52	23 47.07	10	0.65	6	347	15	0.37 20.7 24.7	D1
<b>70424</b>	2314 28.68	35 9.43	23 36.08	8.34	0.62	6	332	8.9	0.10 4.3 4.5	D1
<b>70425</b>	340 2.54	35 13.98	23 41.05	10	2.48	6	259	0.2	14.35 14.1 1.5	D1
<b>70425</b>	836 43.90	35 14.19	23 22.93	27.25	0.68	6	359	22.1	0.27*****	D1
<b>70425</b>	1044 52.55	35 9.34	23 37.19	8.02	0.85	6	329	8.8	0.11 6.7 7.3	D1
<b>70425</b>	1442 44.23	34 43.39	24 11.46	19.18	1.14	6	357	73	0.09 10.2134.9	D1
<b>70425</b>	2213 23.64	35 0.85	23 30.63	17.35	1.73	6	350	26.6	0.11 24.5 34.7	D1
<b>70425</b>	2324 36.20	34 55.74	24 2.78	10	1.61	6	360	47.2	0.15101.1336.4	D1
<b>70418</b>	028 8.20	35 11.56	23 36.54	9.44	0.61	6	320	4.9	0.09 9.2 4.7	D1
<b>70501</b>	1 2 23.58	35 13.98	23 41.05	10	1.46	6	259	0.2	9.17 41.7 4.4	D1
<b>70501</b>	220 7.43	35 6.81	23 33.65	5.35	0.85	6	343	14.7	0.23 32.3 81.4	D1
<b>70501</b>	620 0.33	35 11.61	23 37.51	10.18	0.72	6	308	4.6	0.14 6.7 3.0	D1

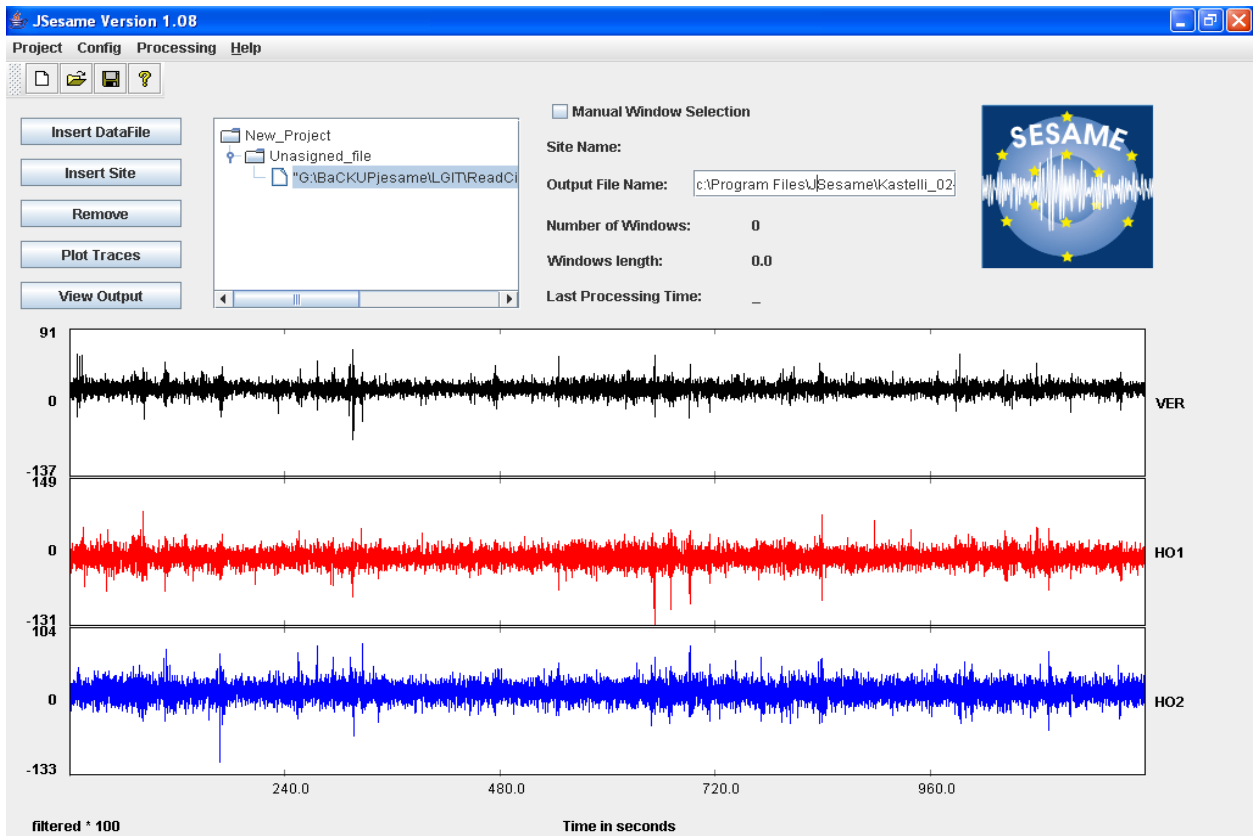
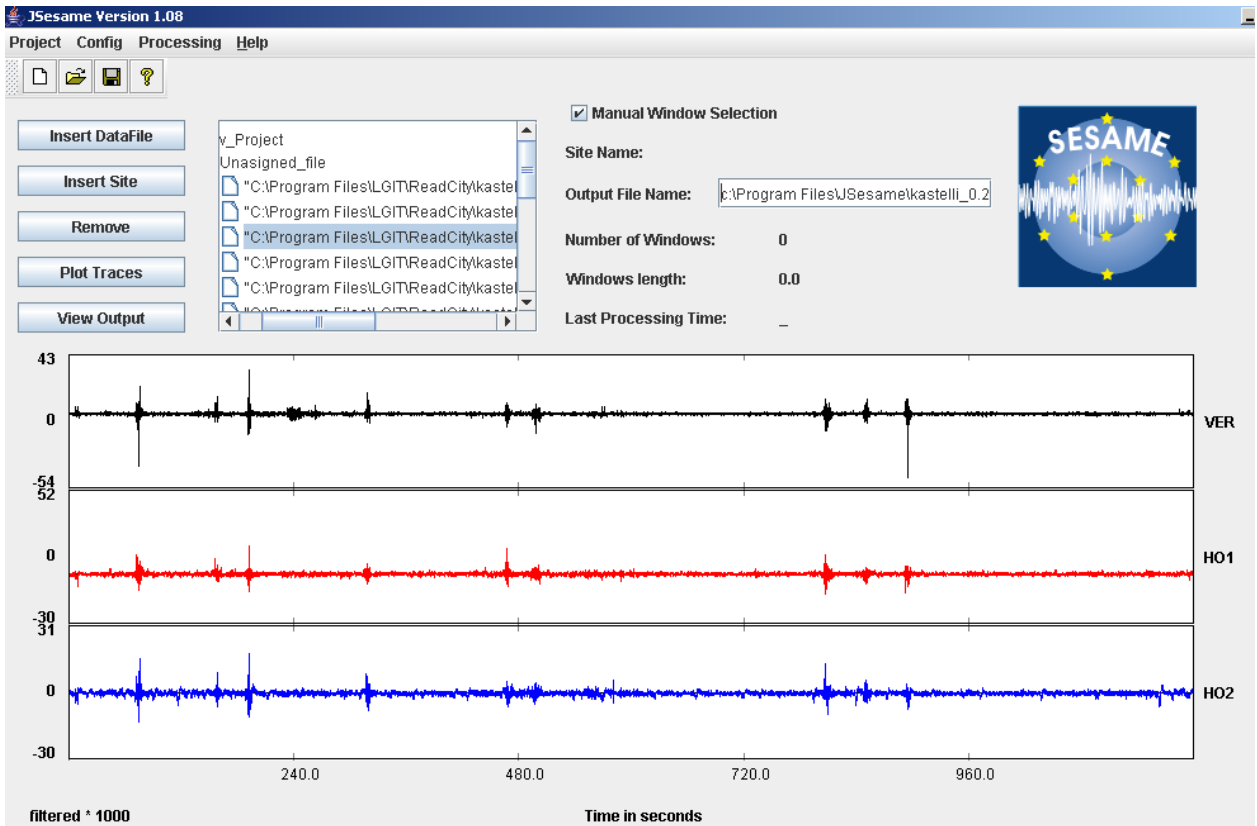
<b>70503</b>	142 54.79	35 13.98	23 41.05	10	0.89	6	259	0.2	8.54 23.0 2.4	D1
<b>70503</b>	13 2 45.97	35 14.19	23 31.67	12.23	0.74	5	357	8.8	0.15 66.0 4.6	D1
<b>70504</b>	1030 37.16	35 11.41	23 37.49	10.23	0.82	6	311	5	0.14 5.5 2.7	D1
<b>70504</b>	1531 28.99	37 23.92	24 15.62	10	1.65	6	359	245.4	0.88*****	D1

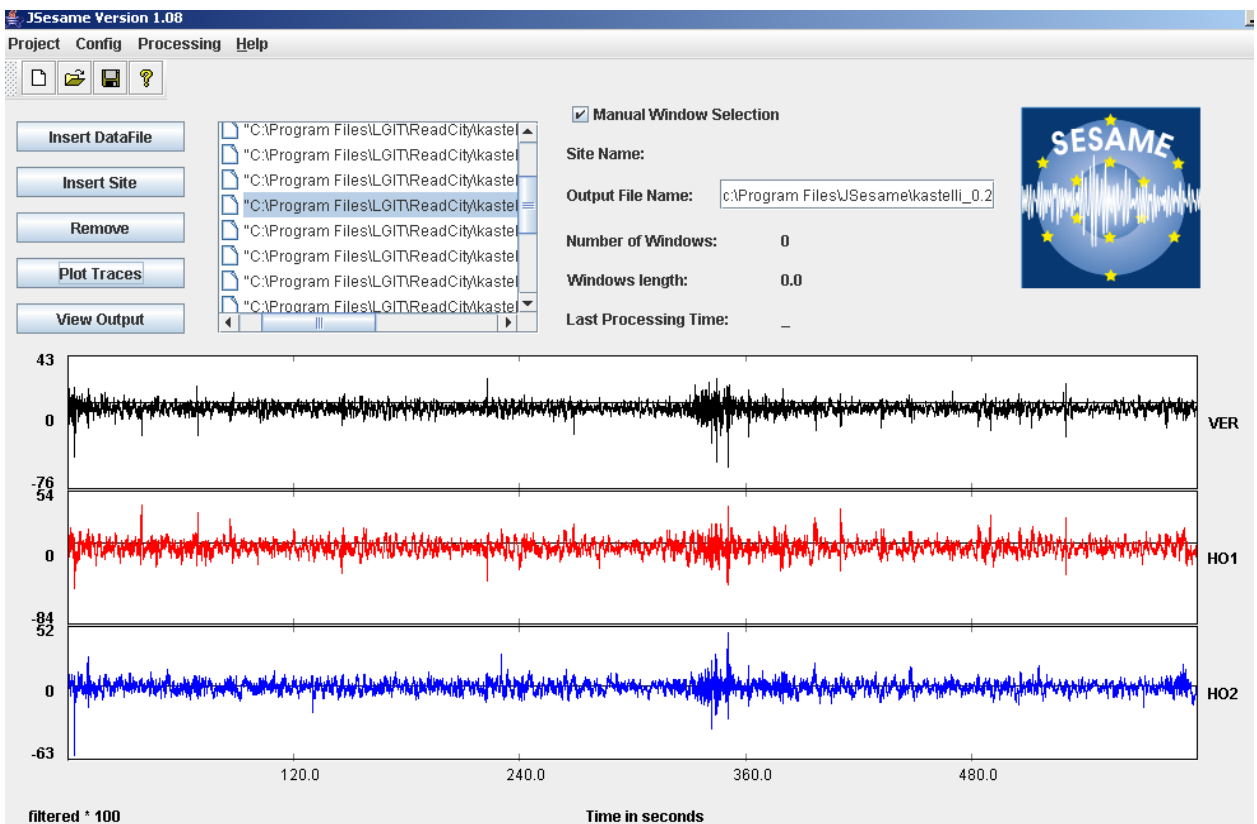
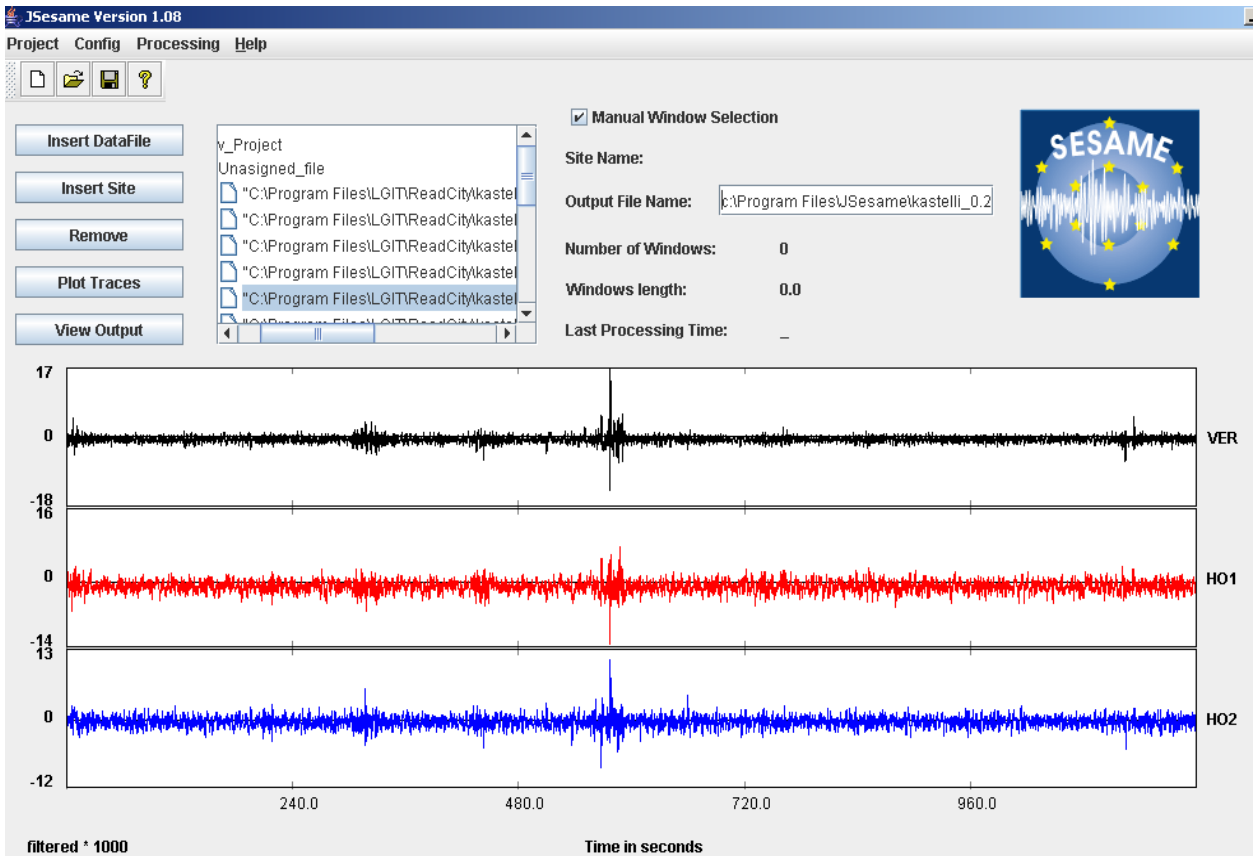


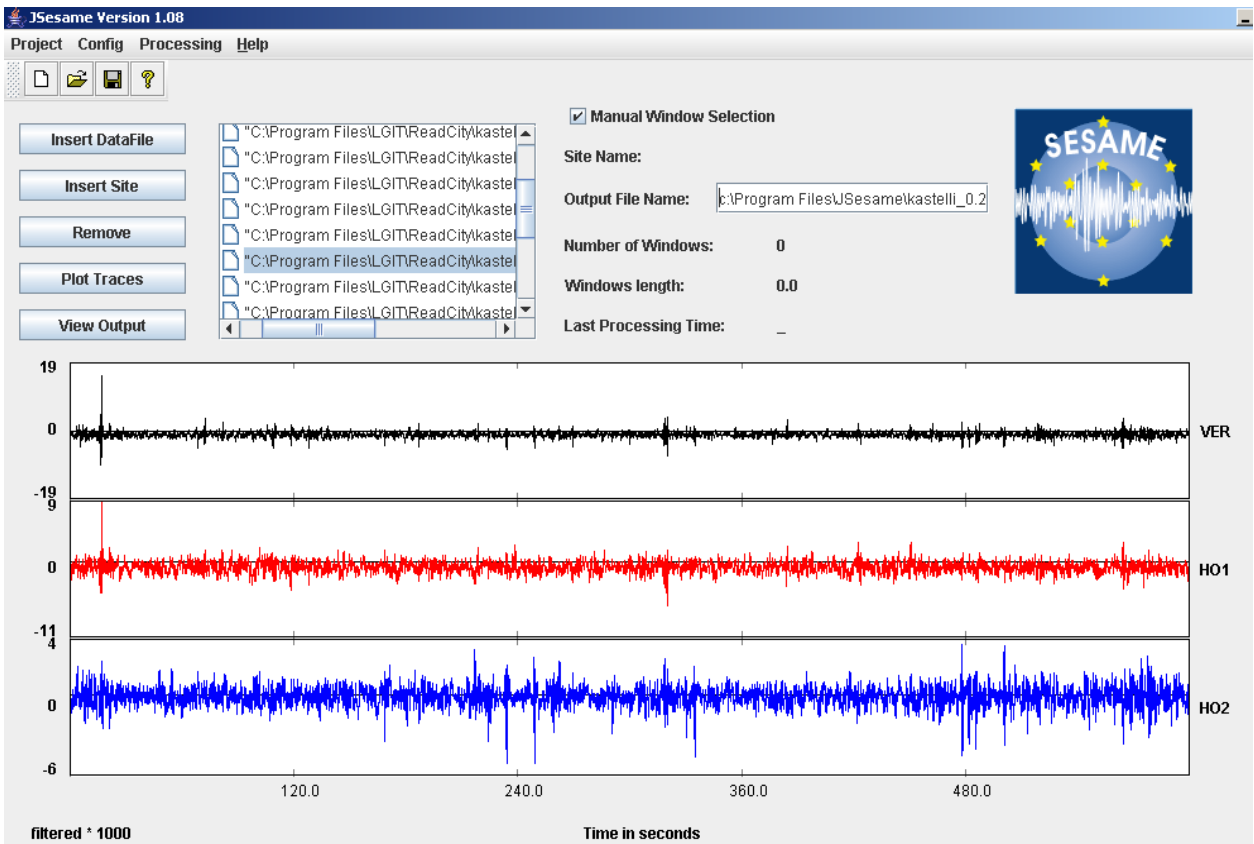
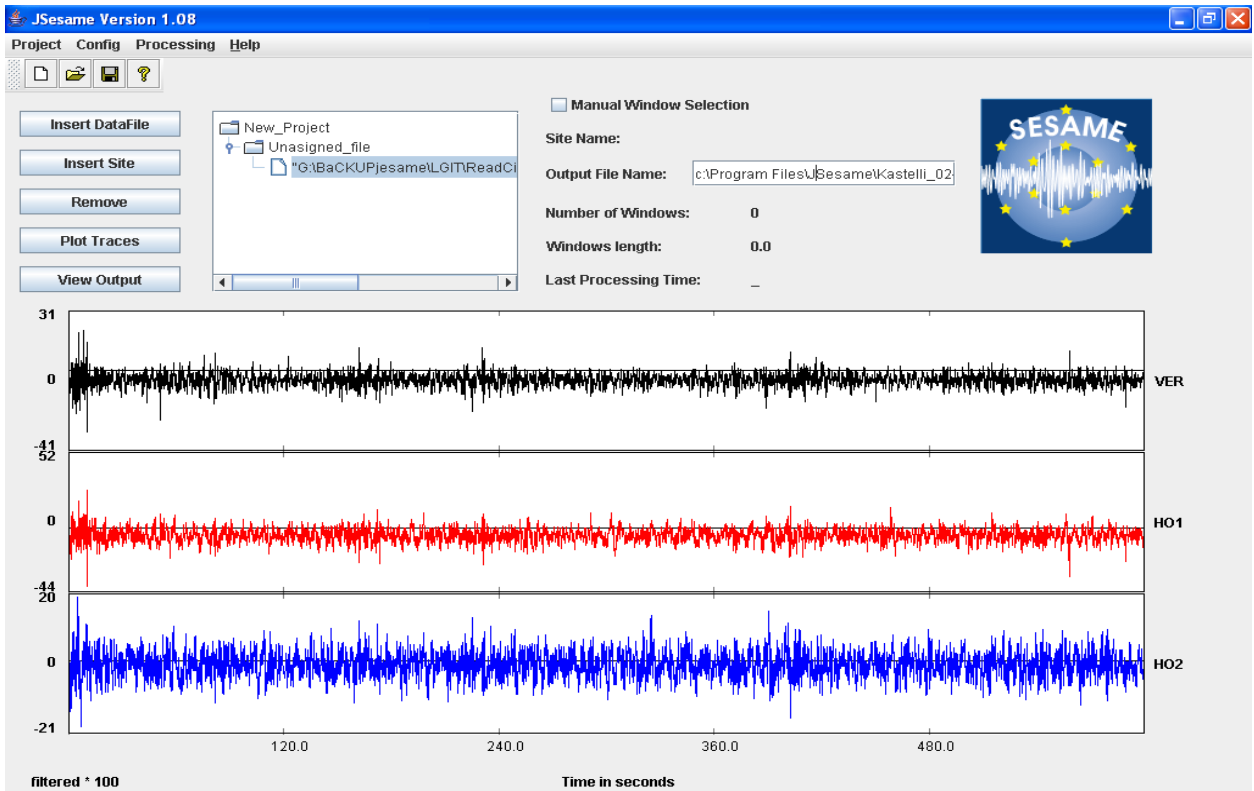
# APPENDIX III: MICROTREMOR RECORDINGS IN KASTELLI-KISSAMOU AND PALEOHORA BASINS

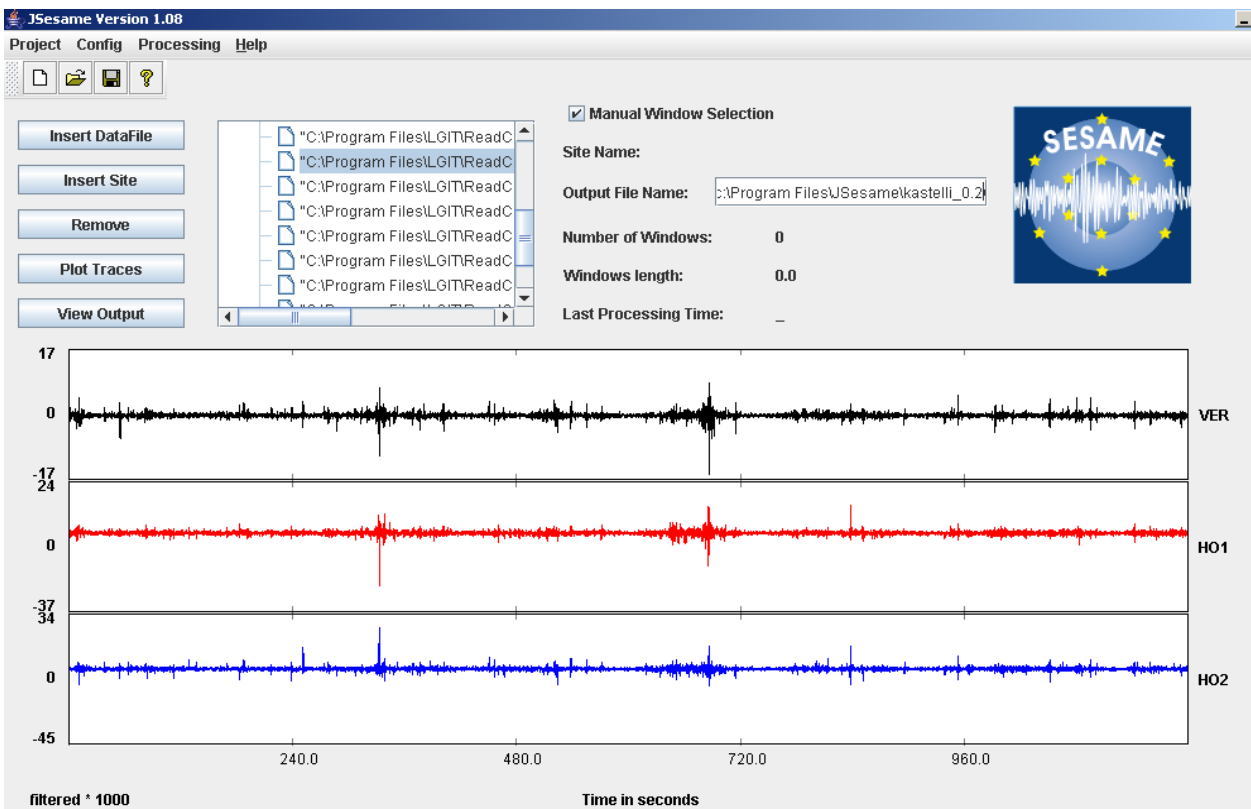
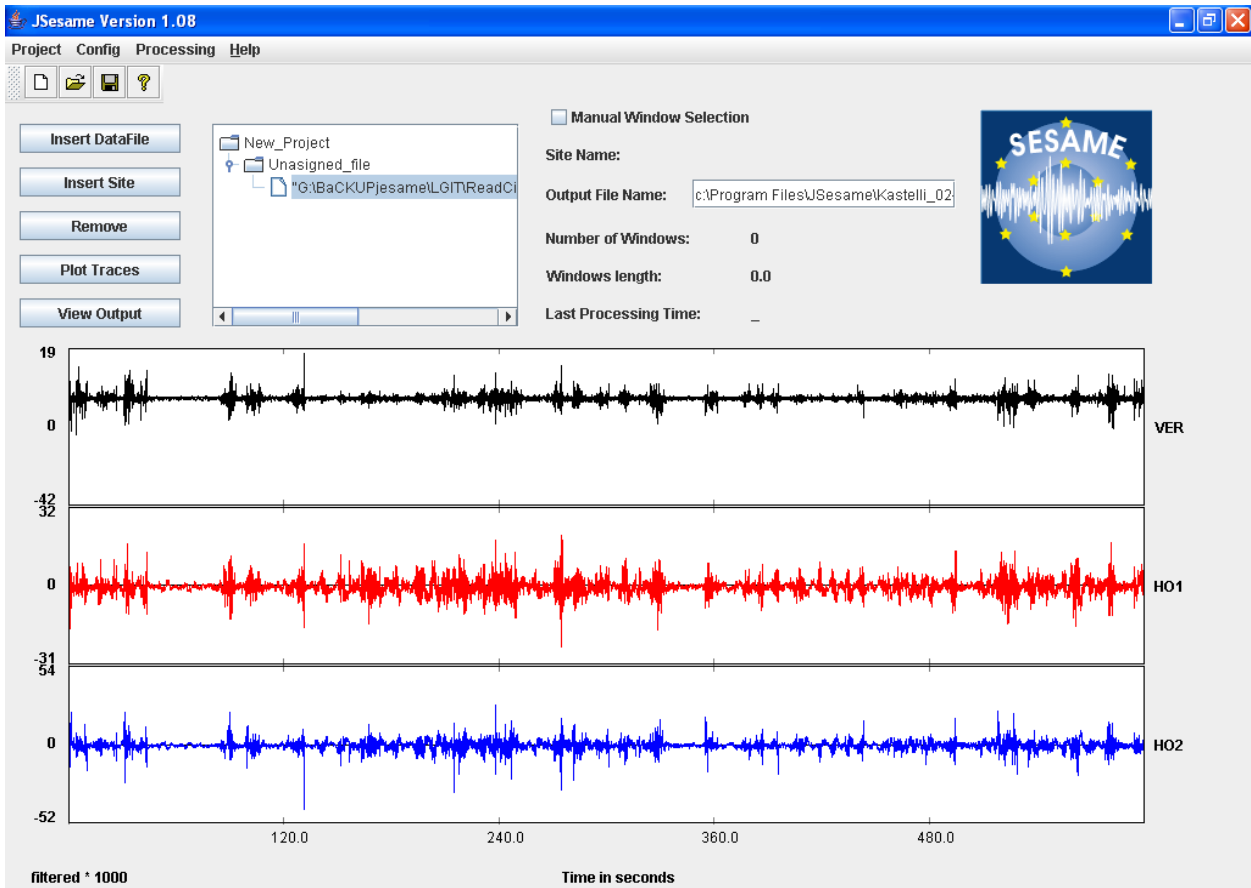
## A1: MICROTREMOR RECORDINGS IN KASTELLI-KISSAMOU BASIN

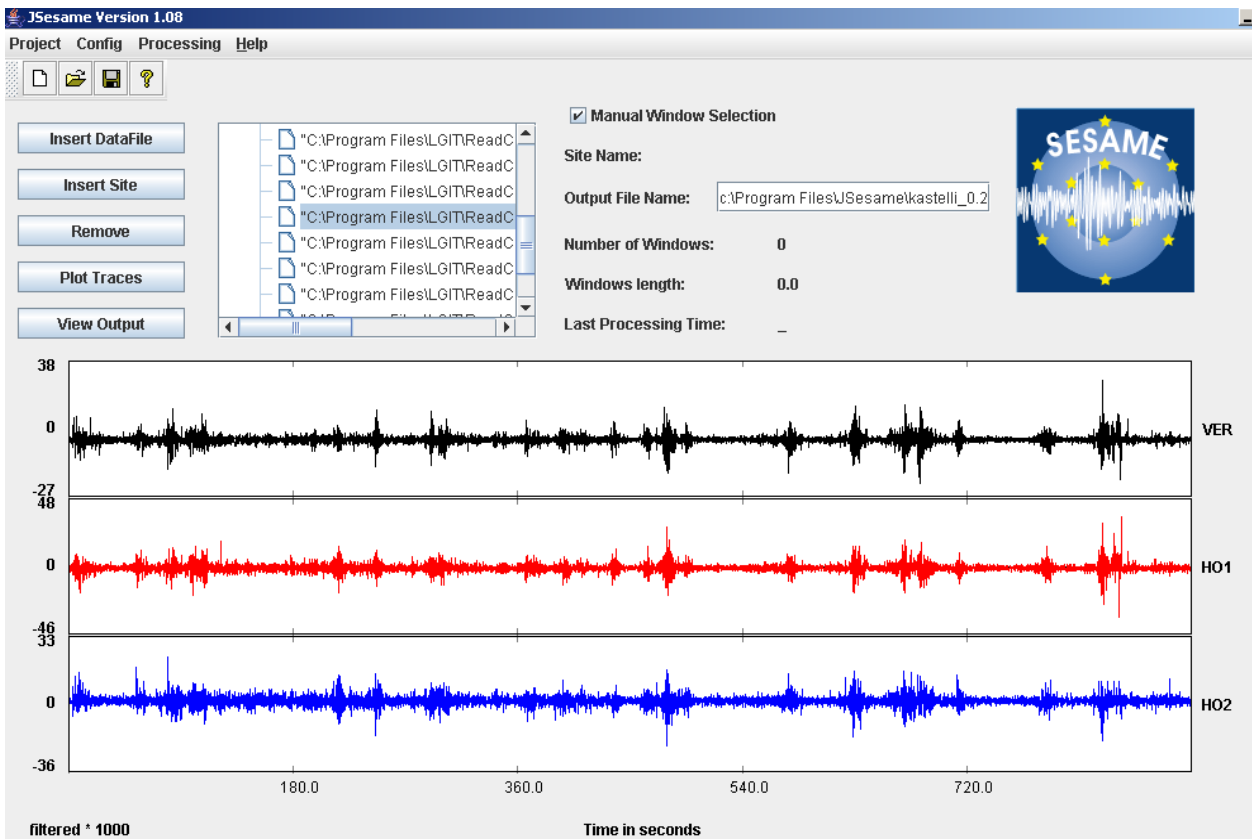
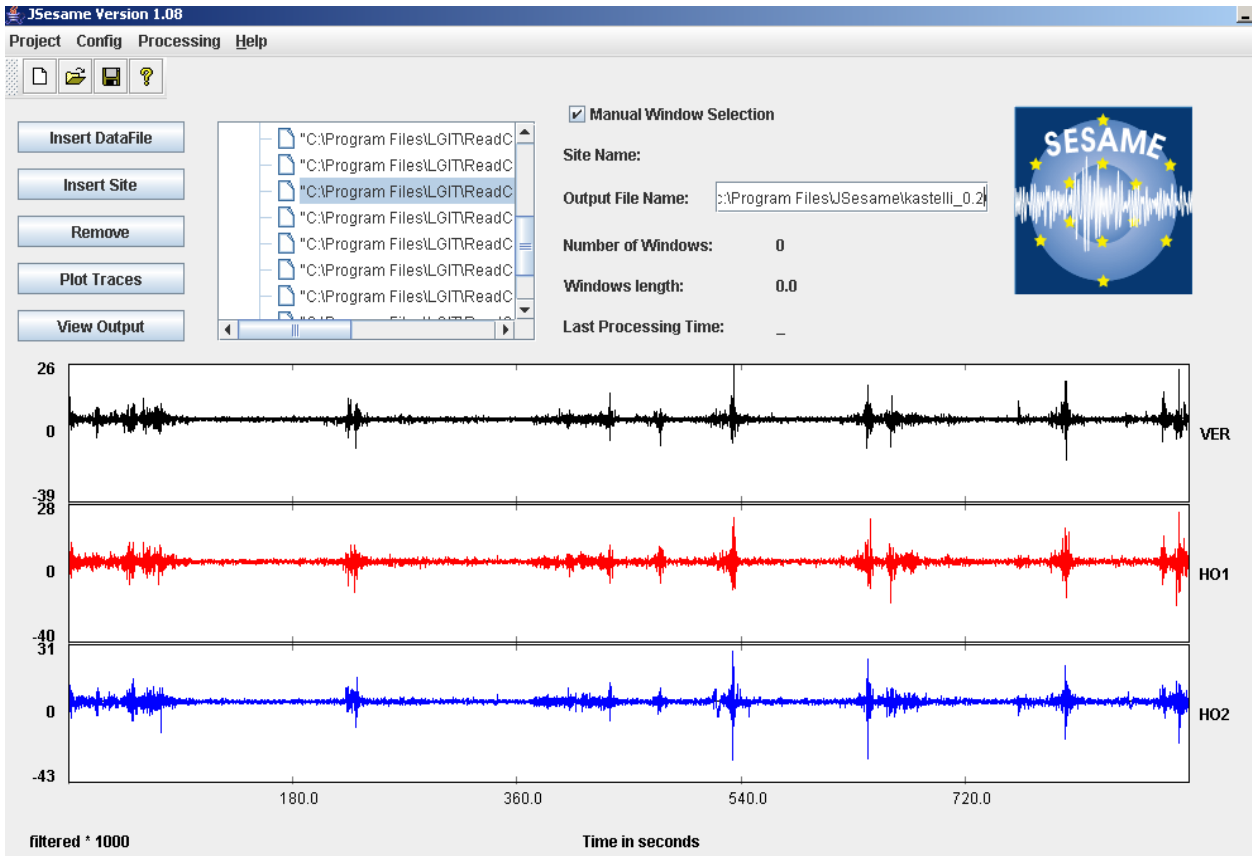


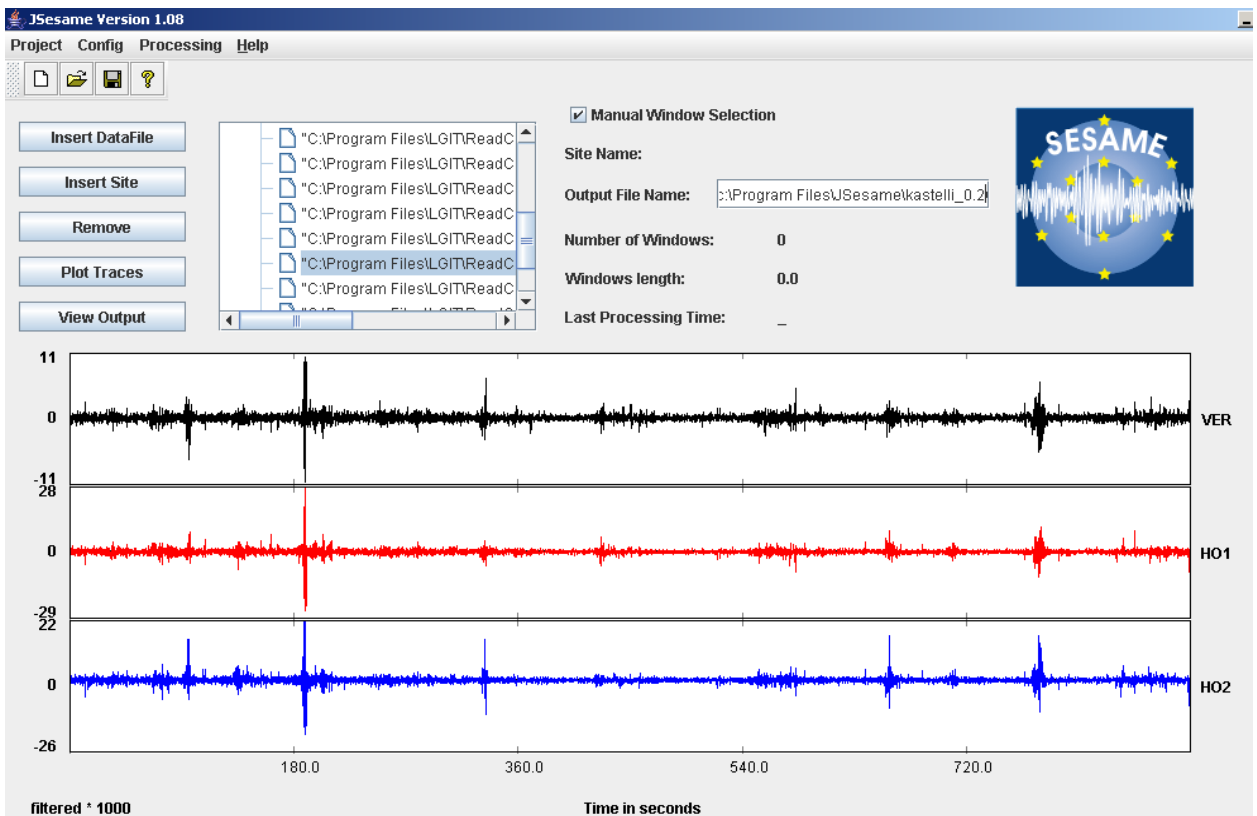
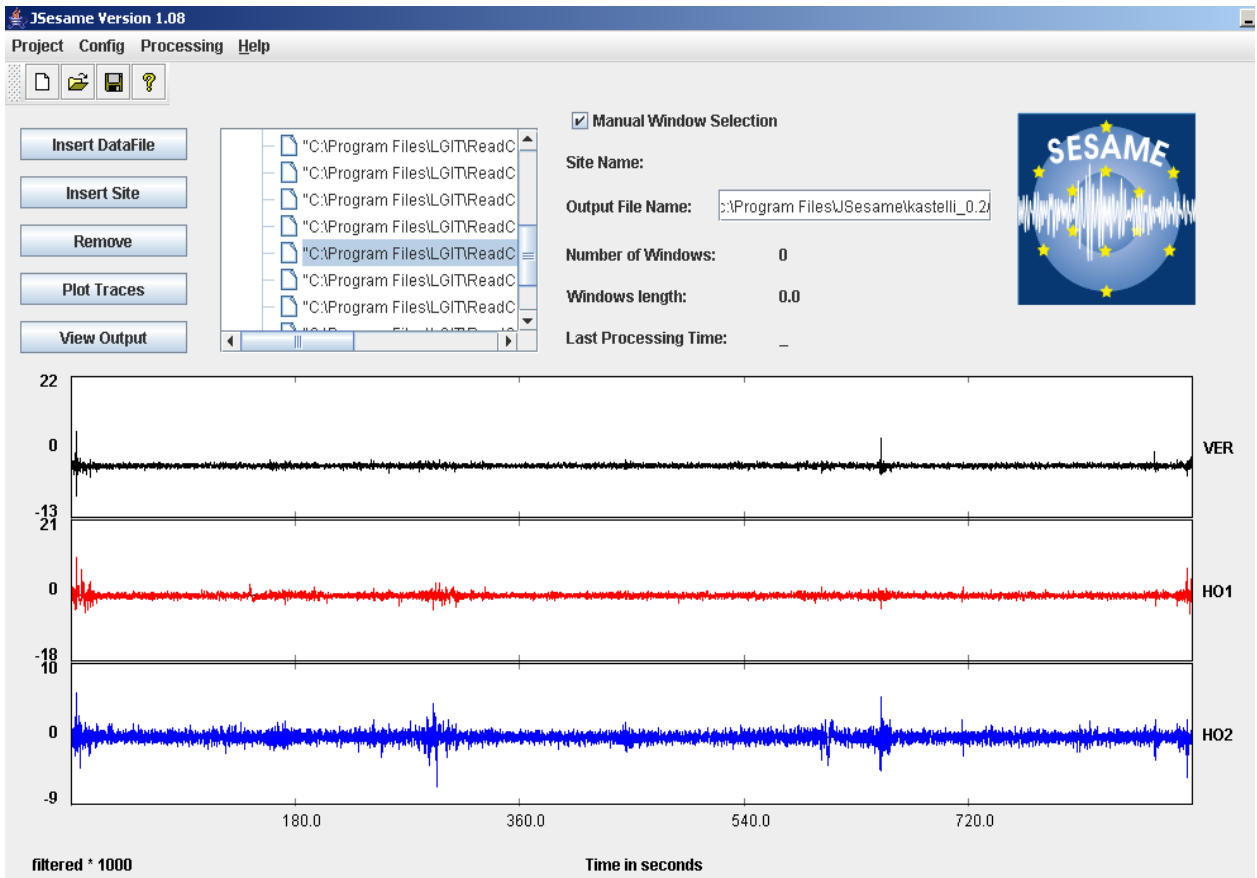


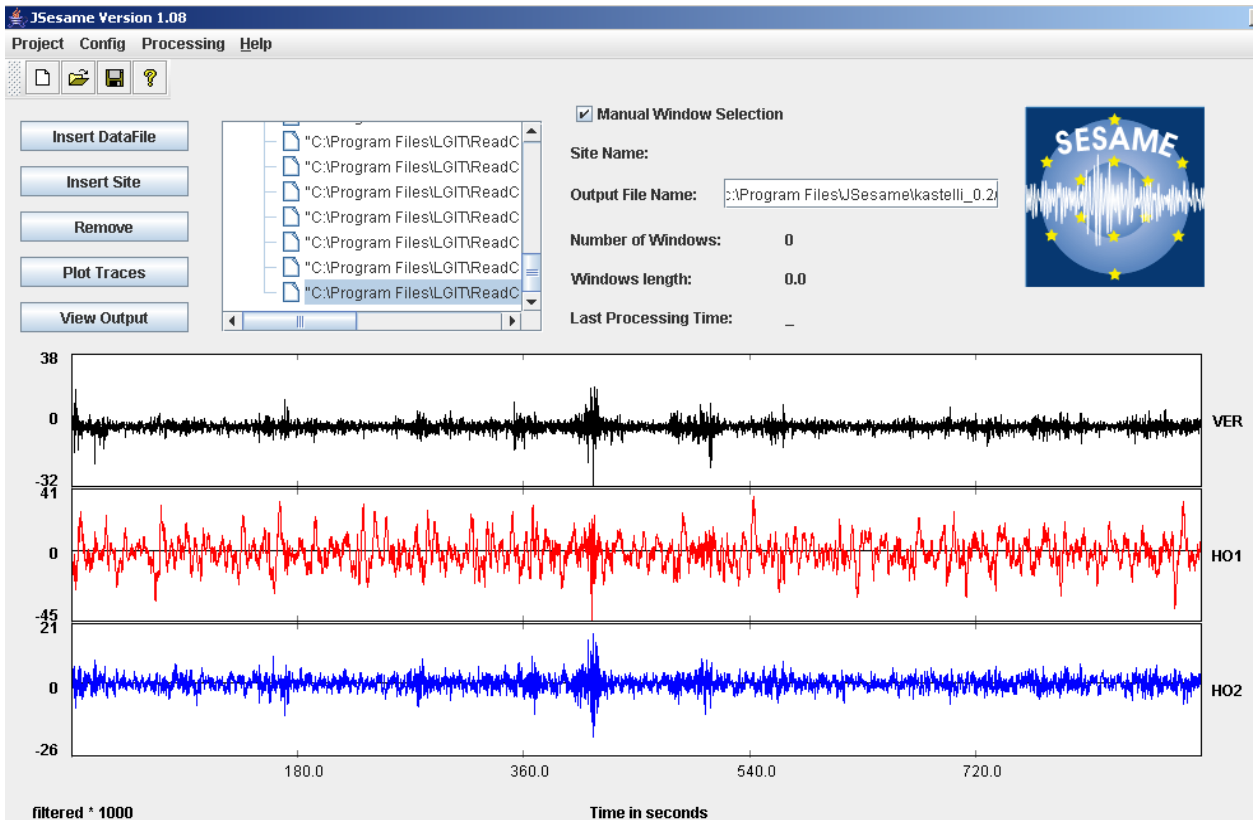
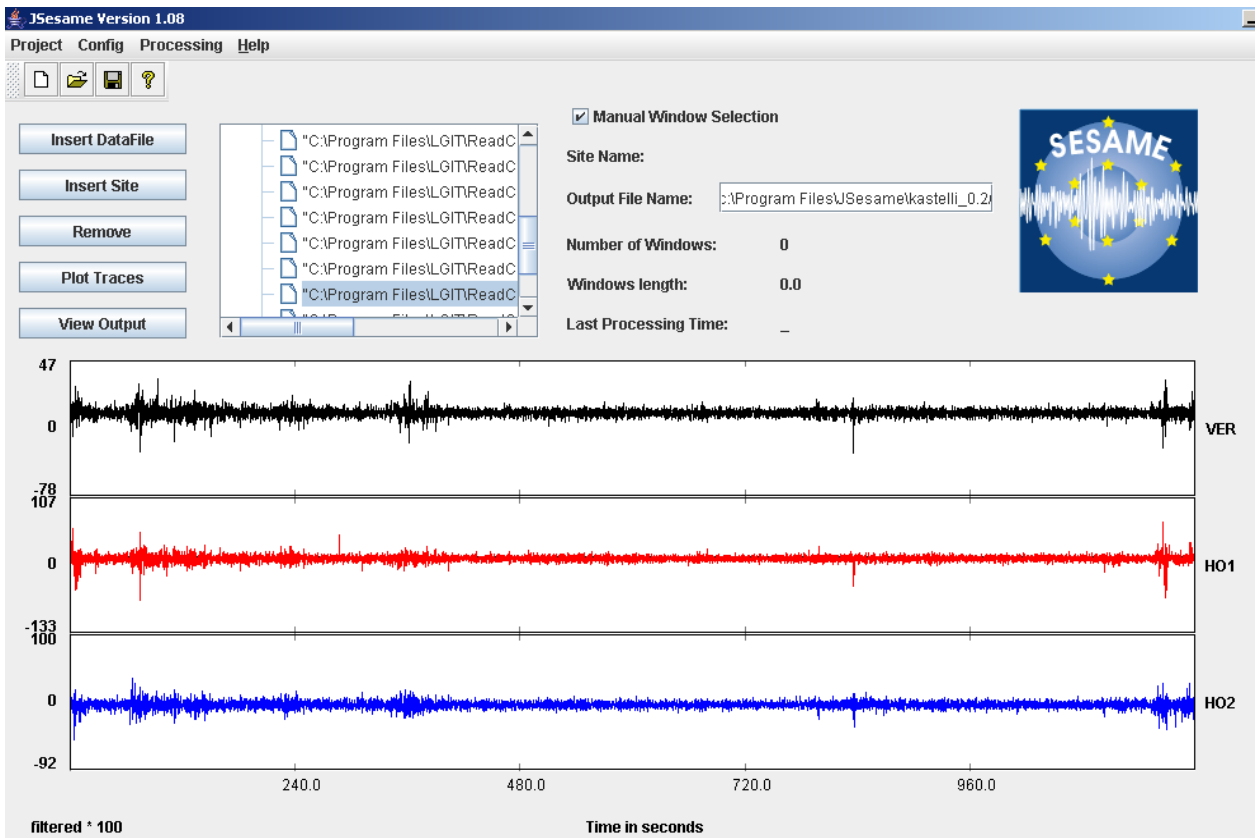




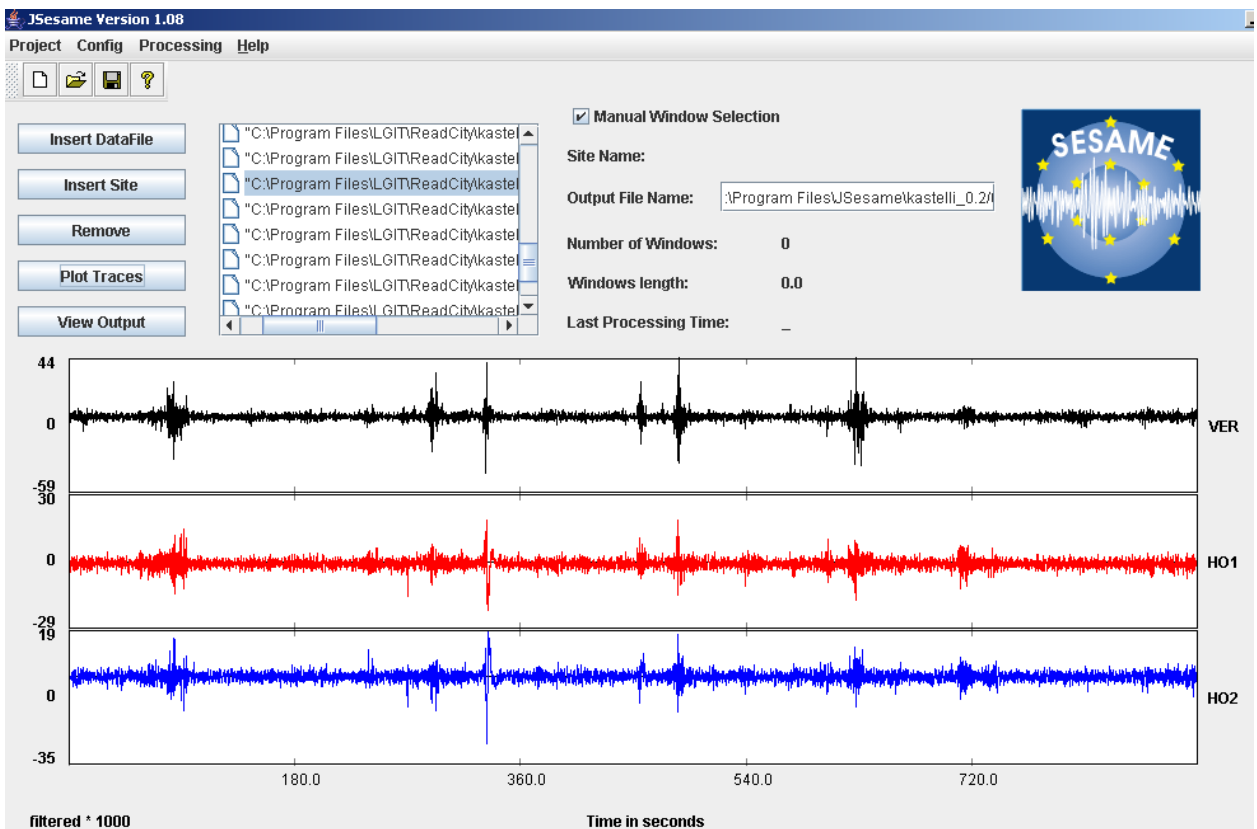
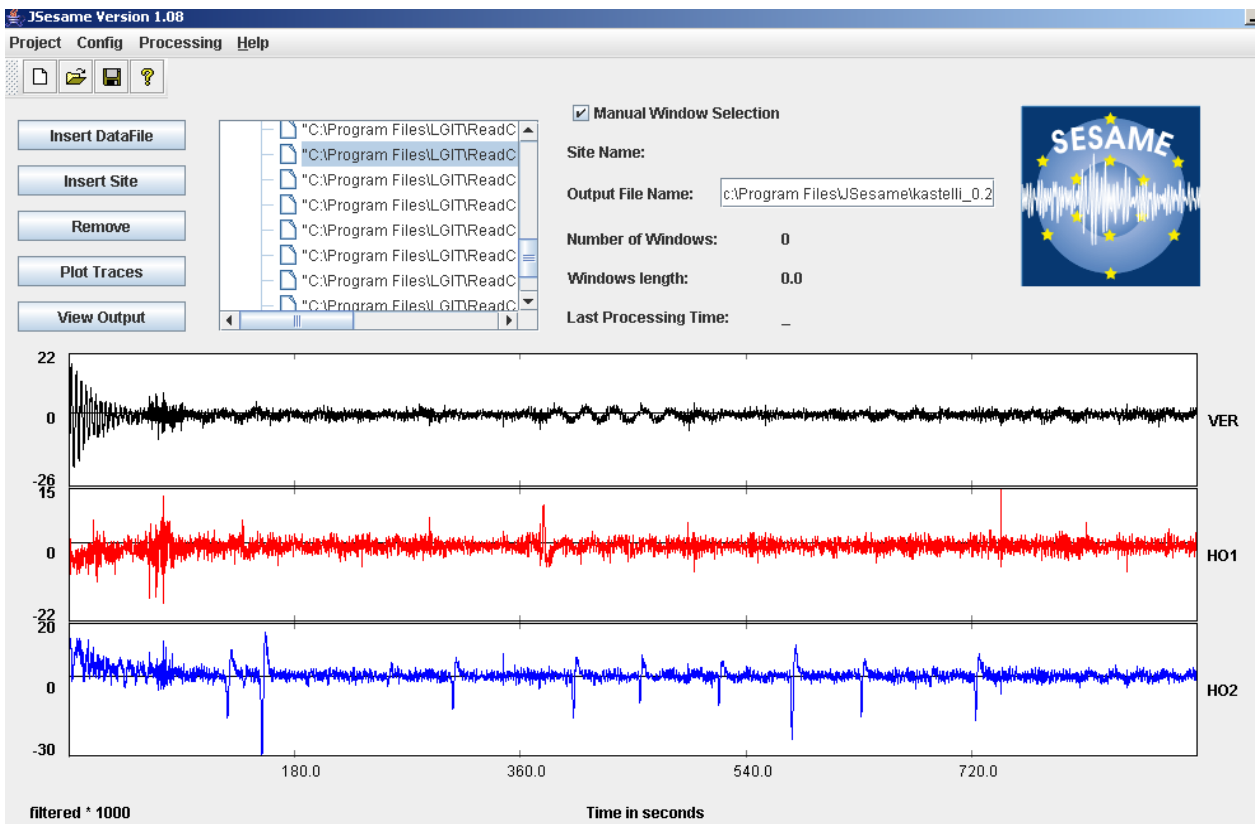


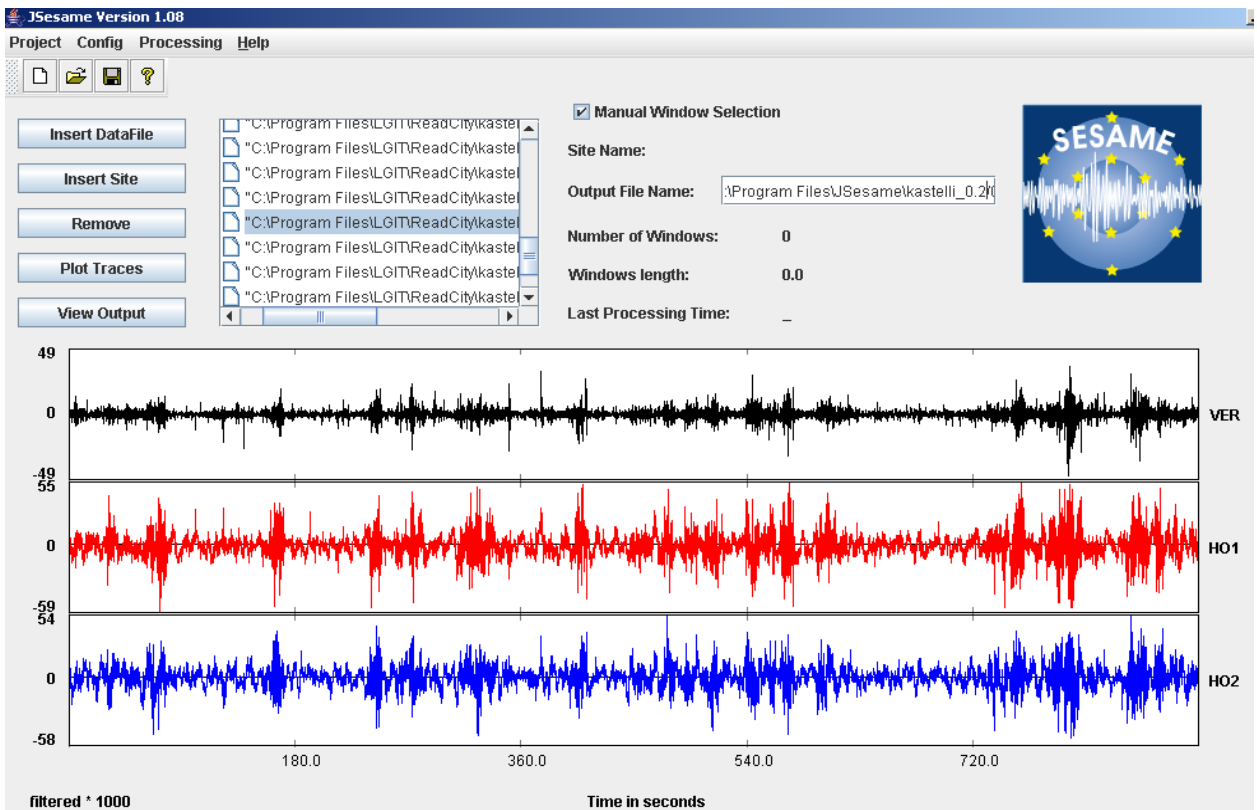
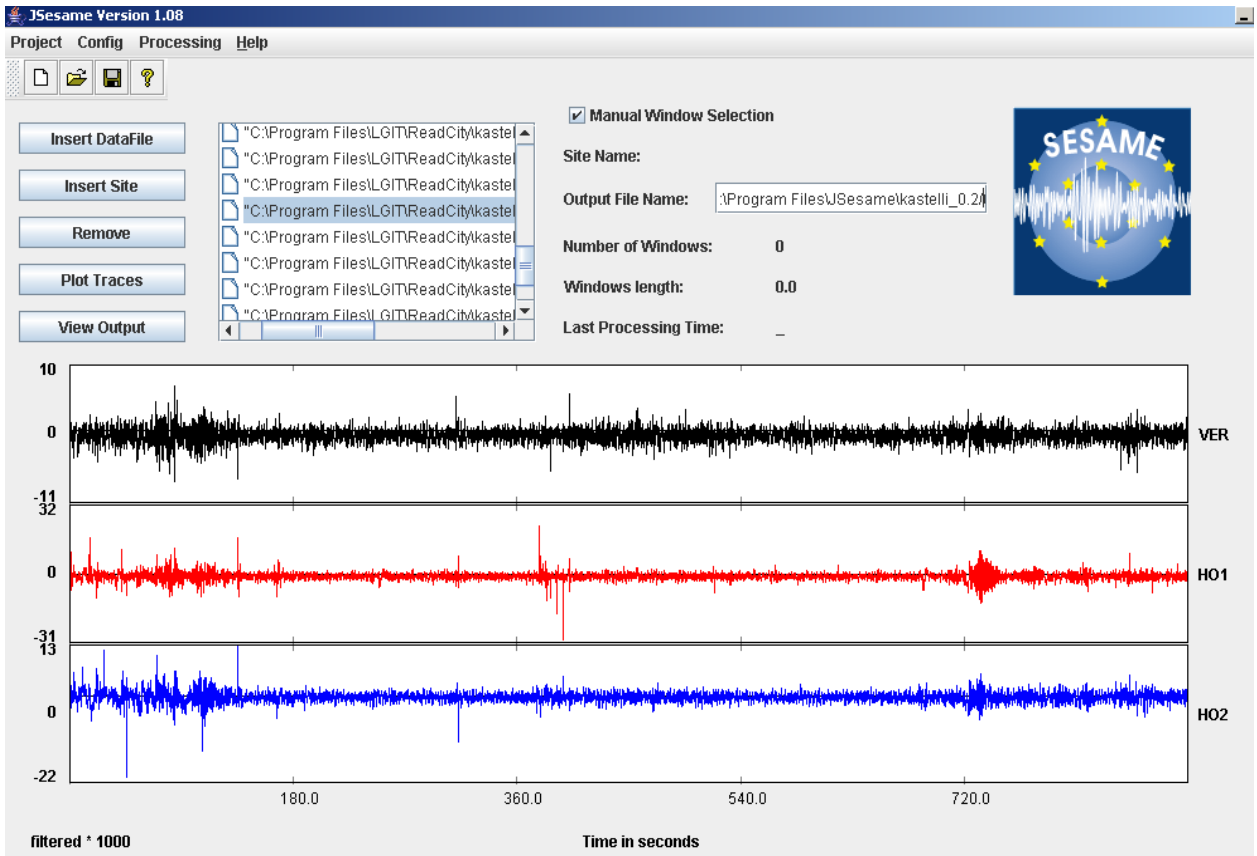


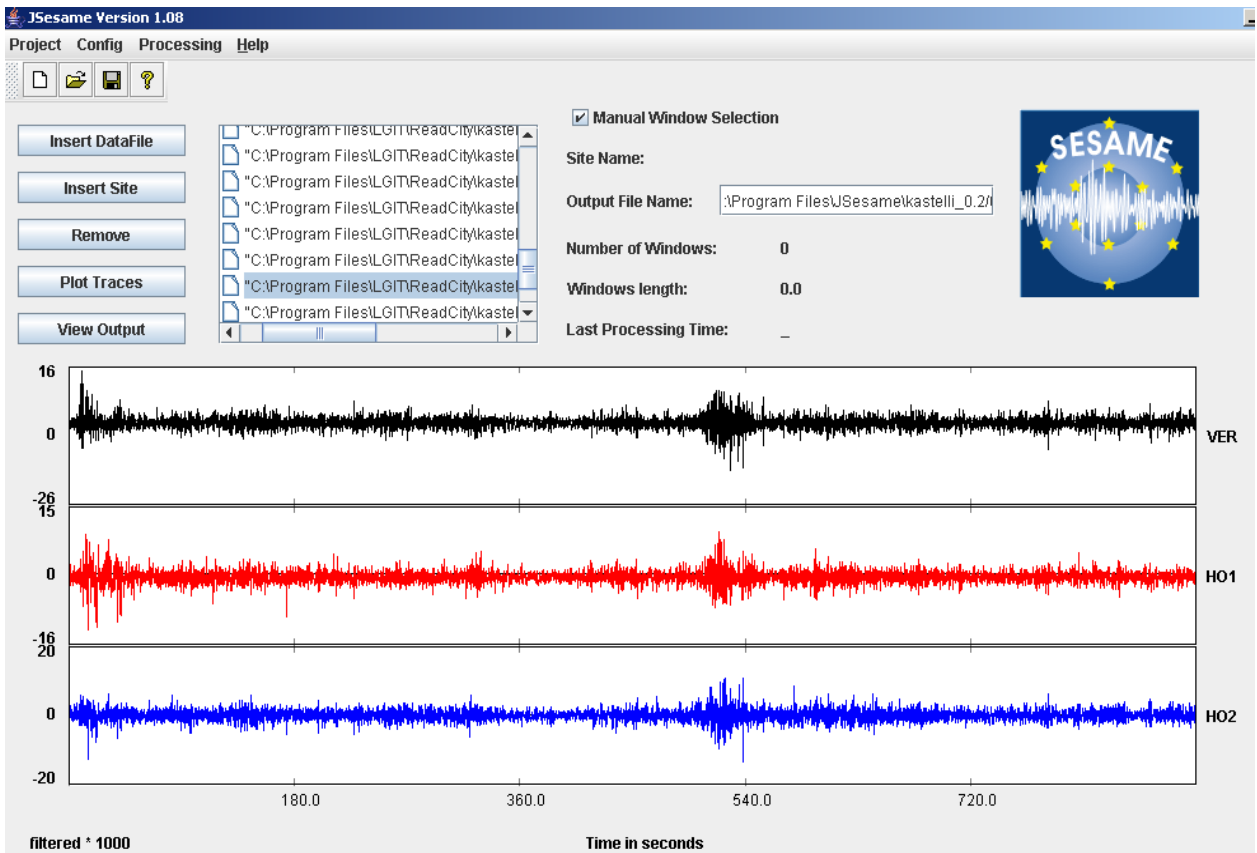
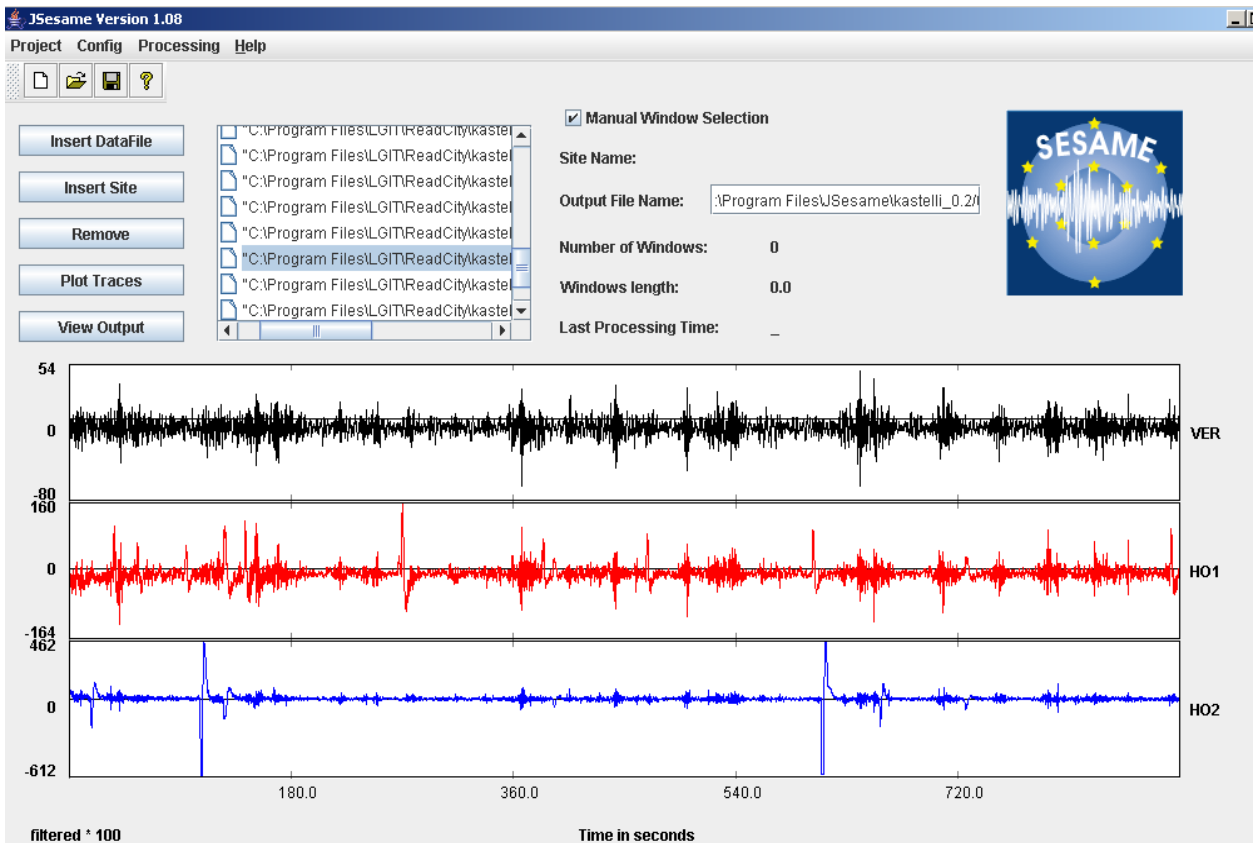


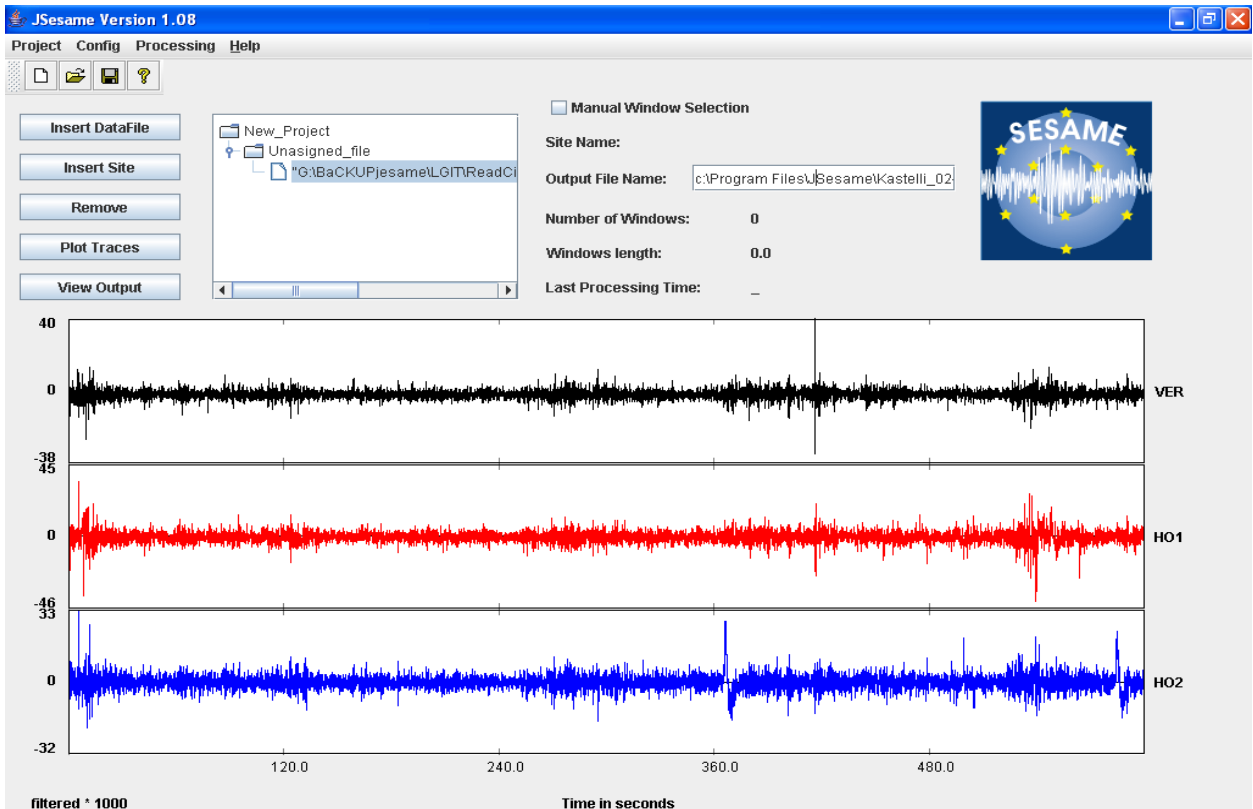
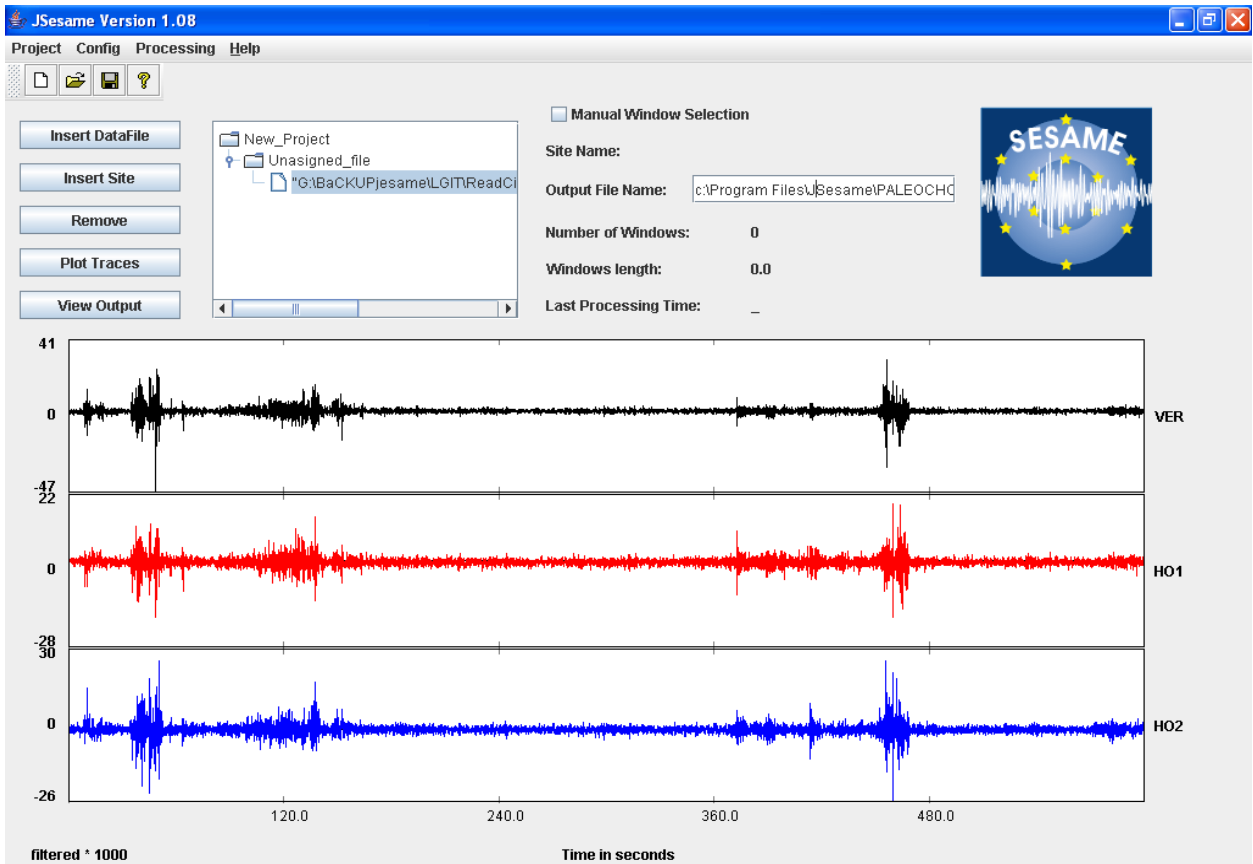


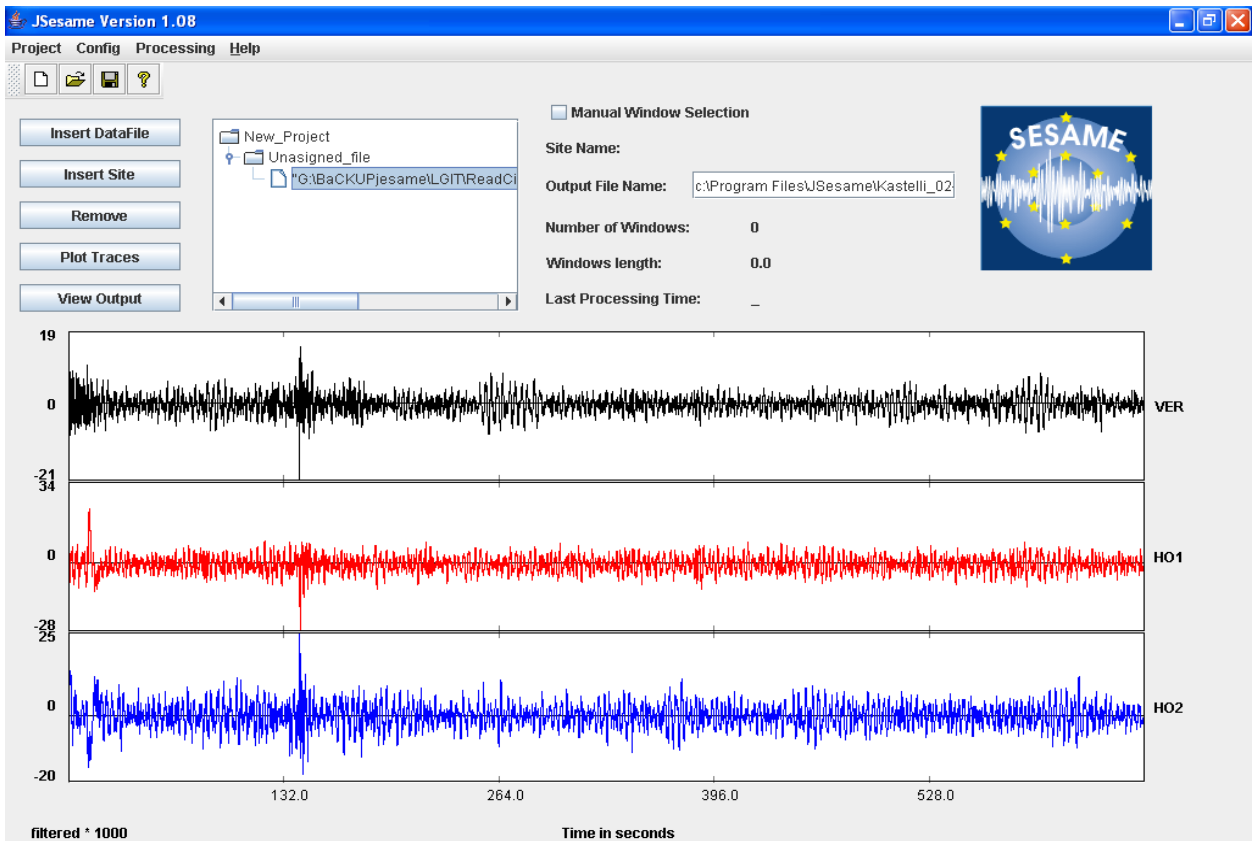
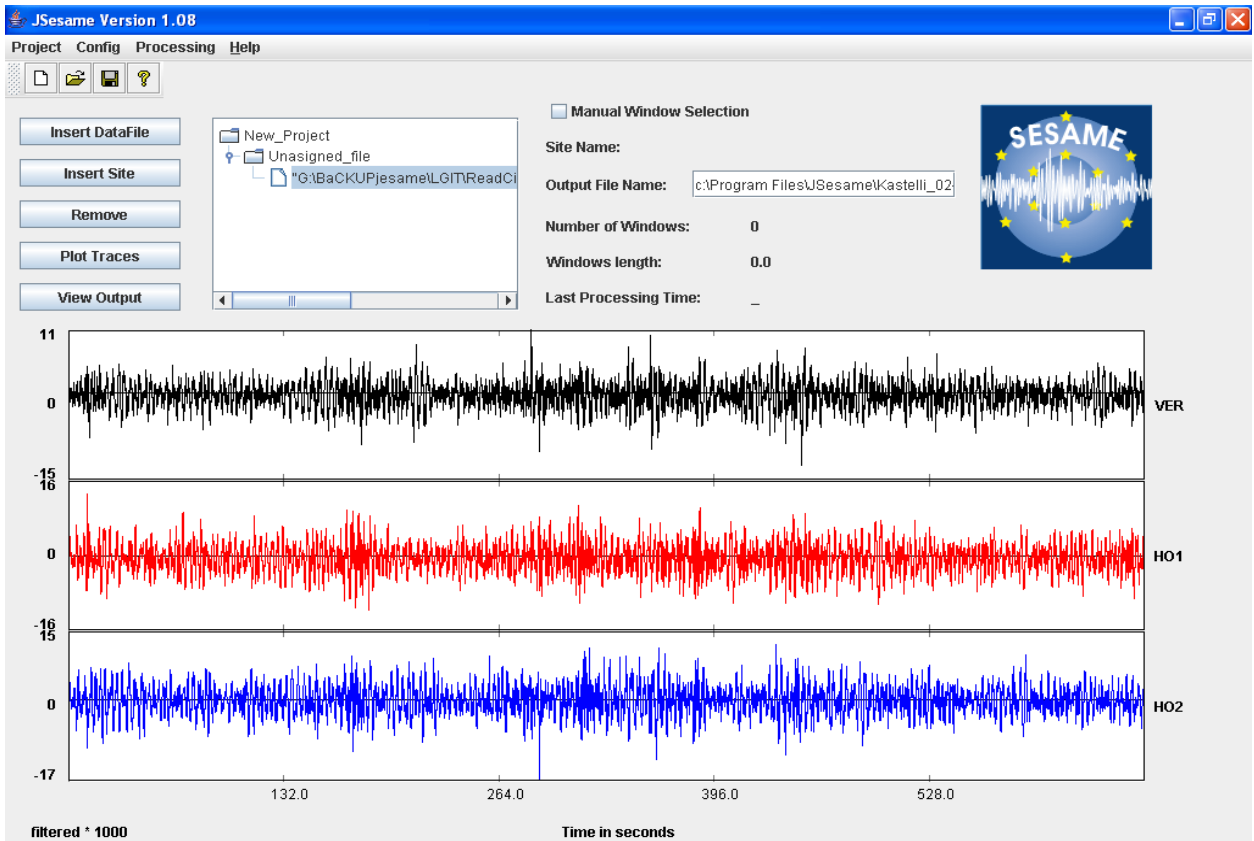


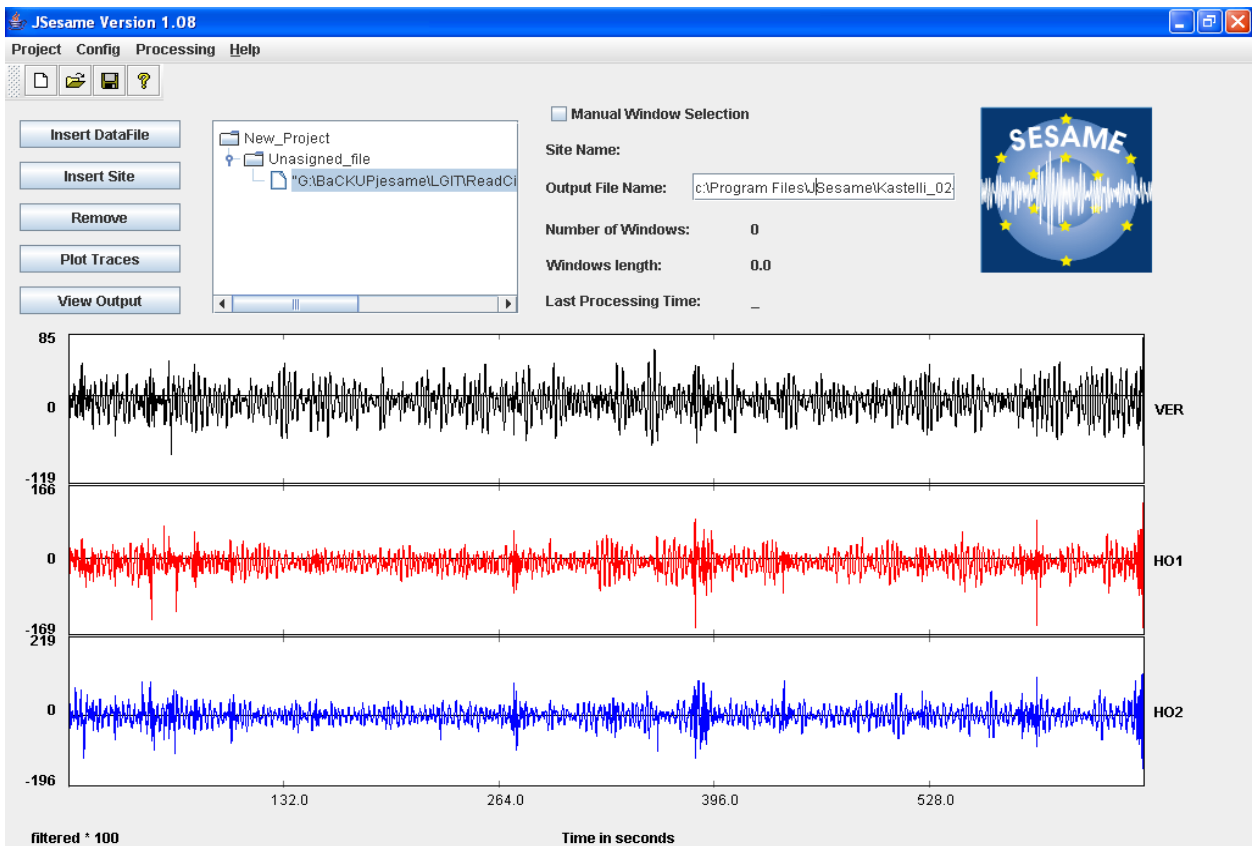
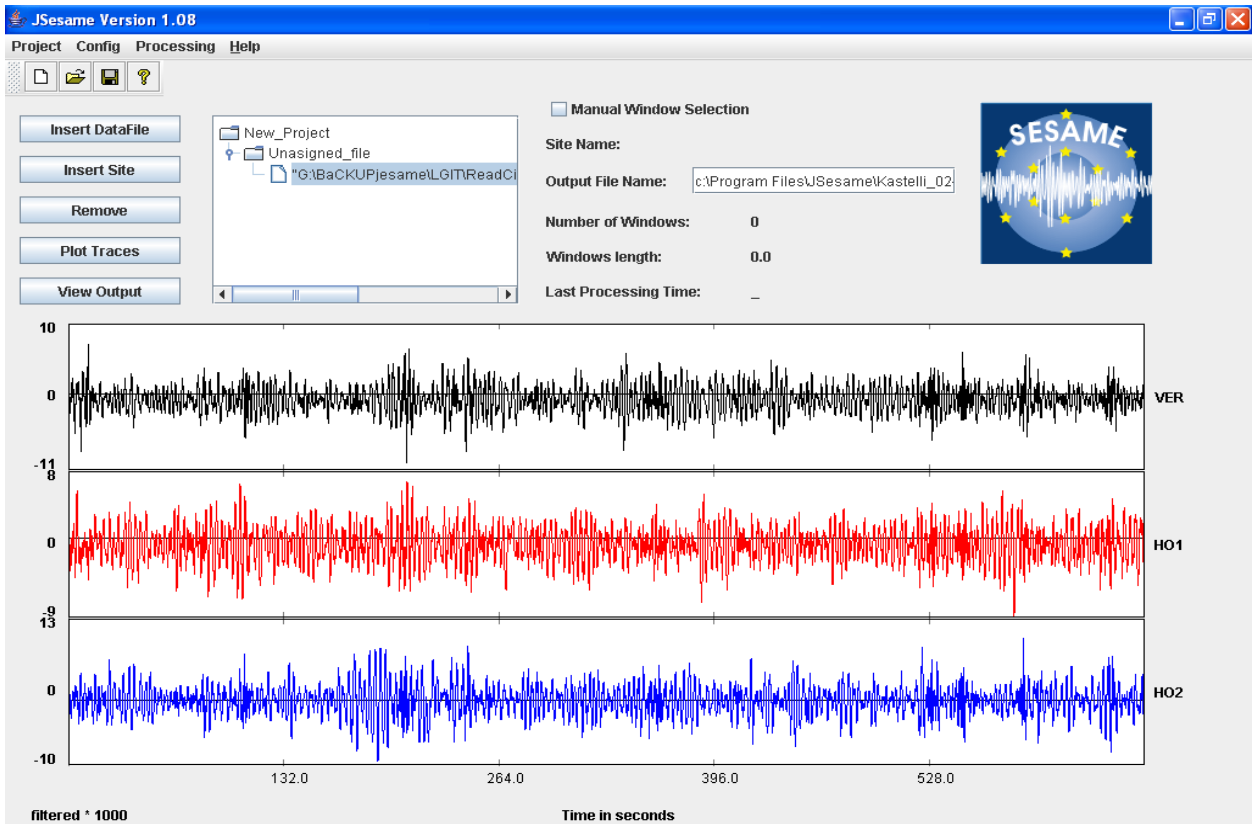


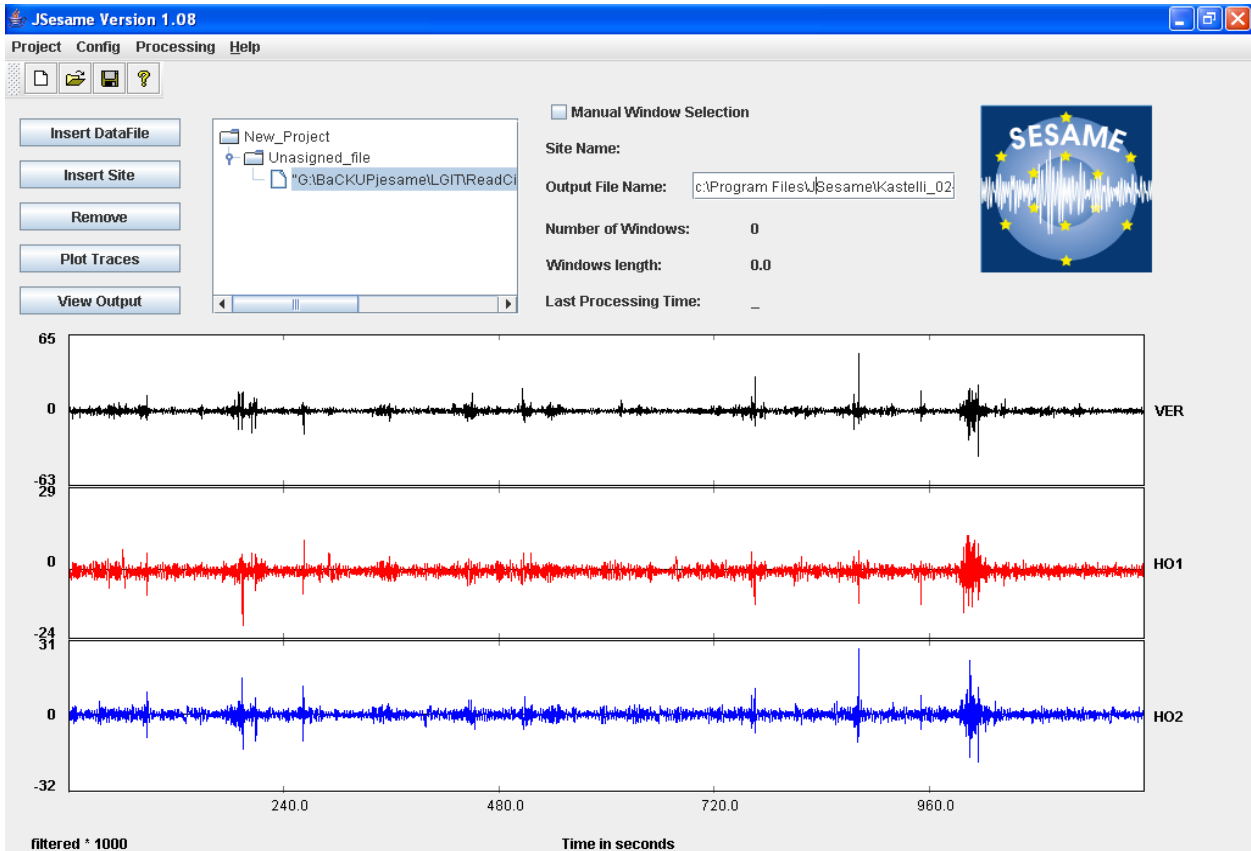
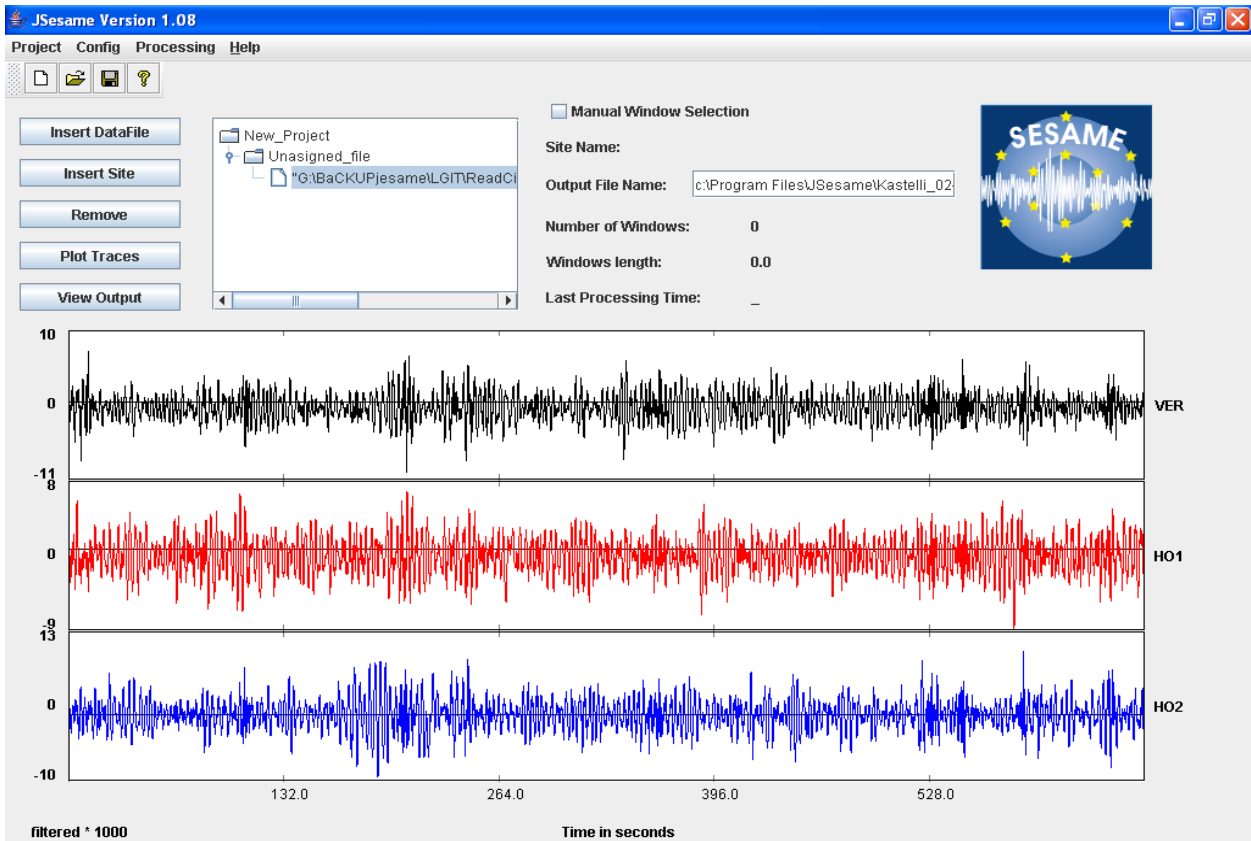


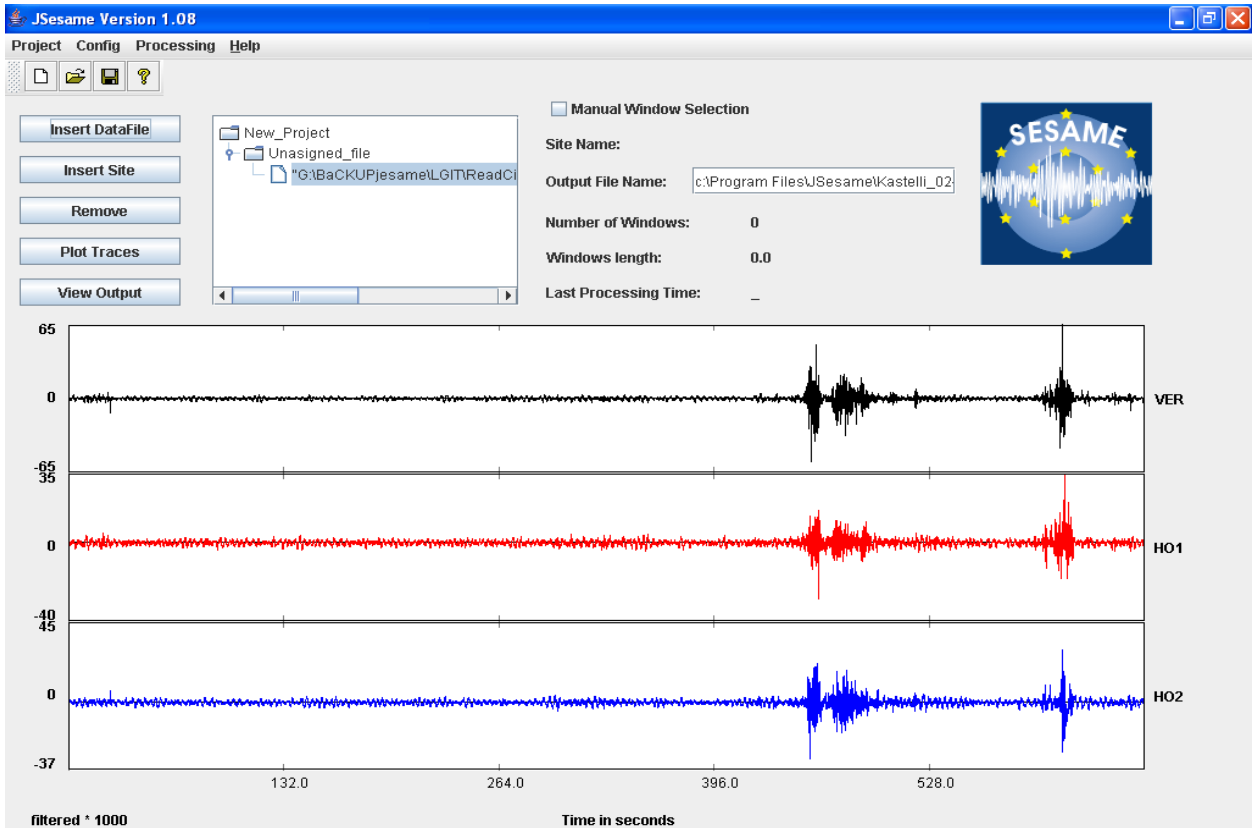
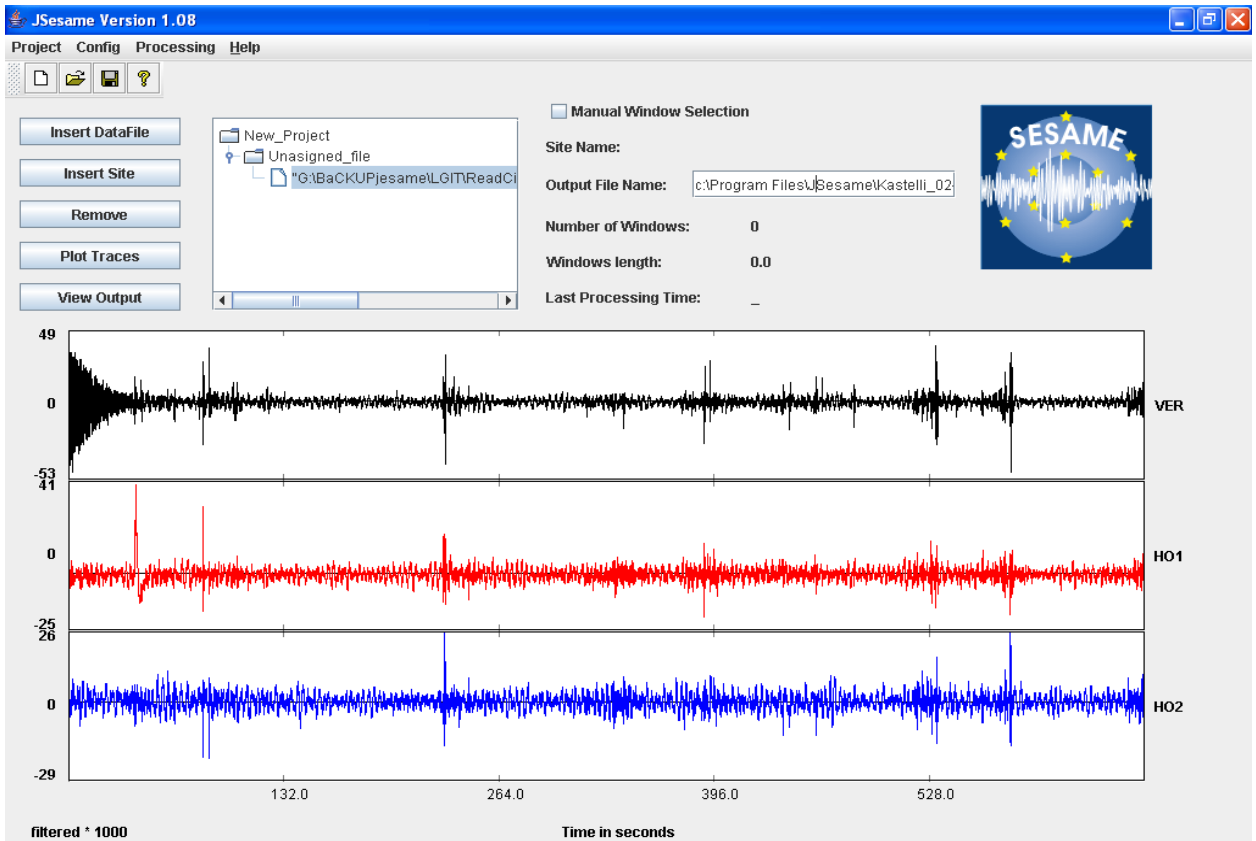




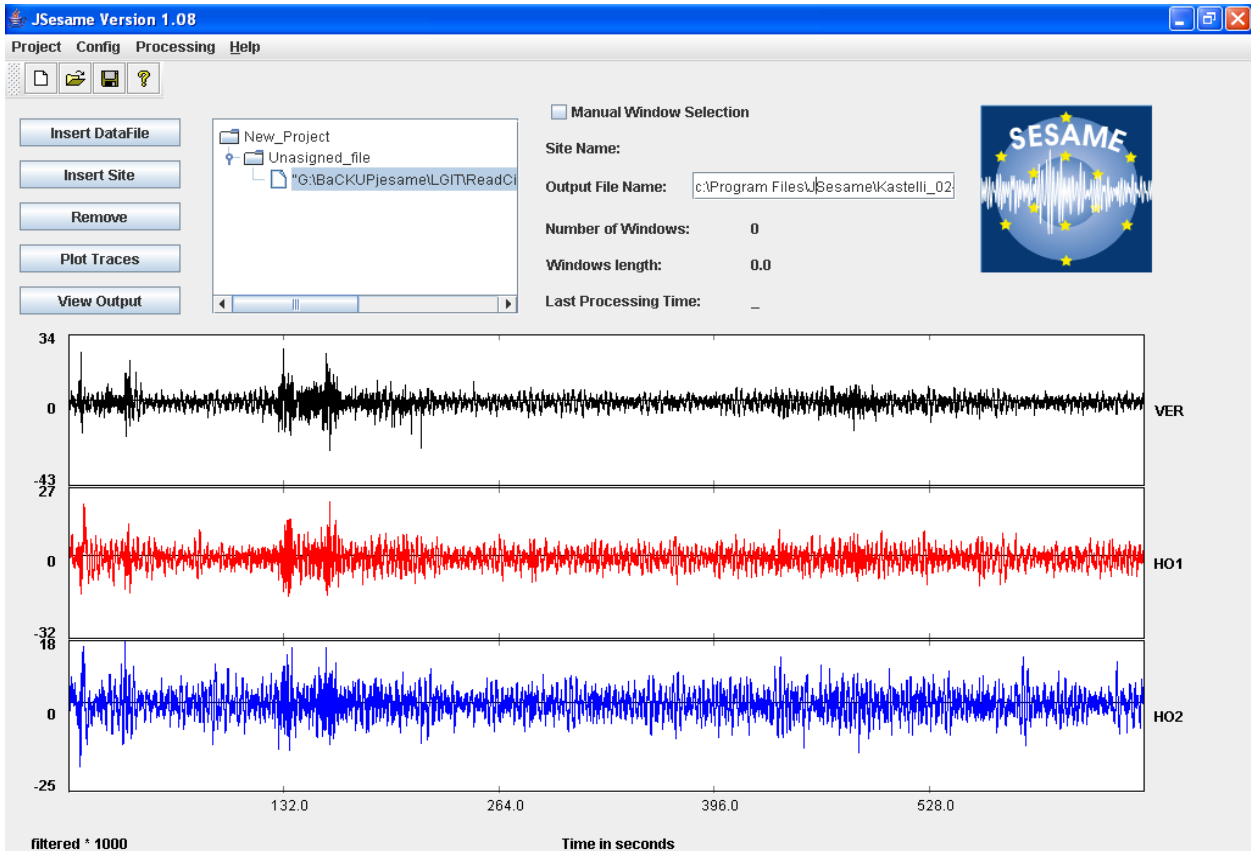
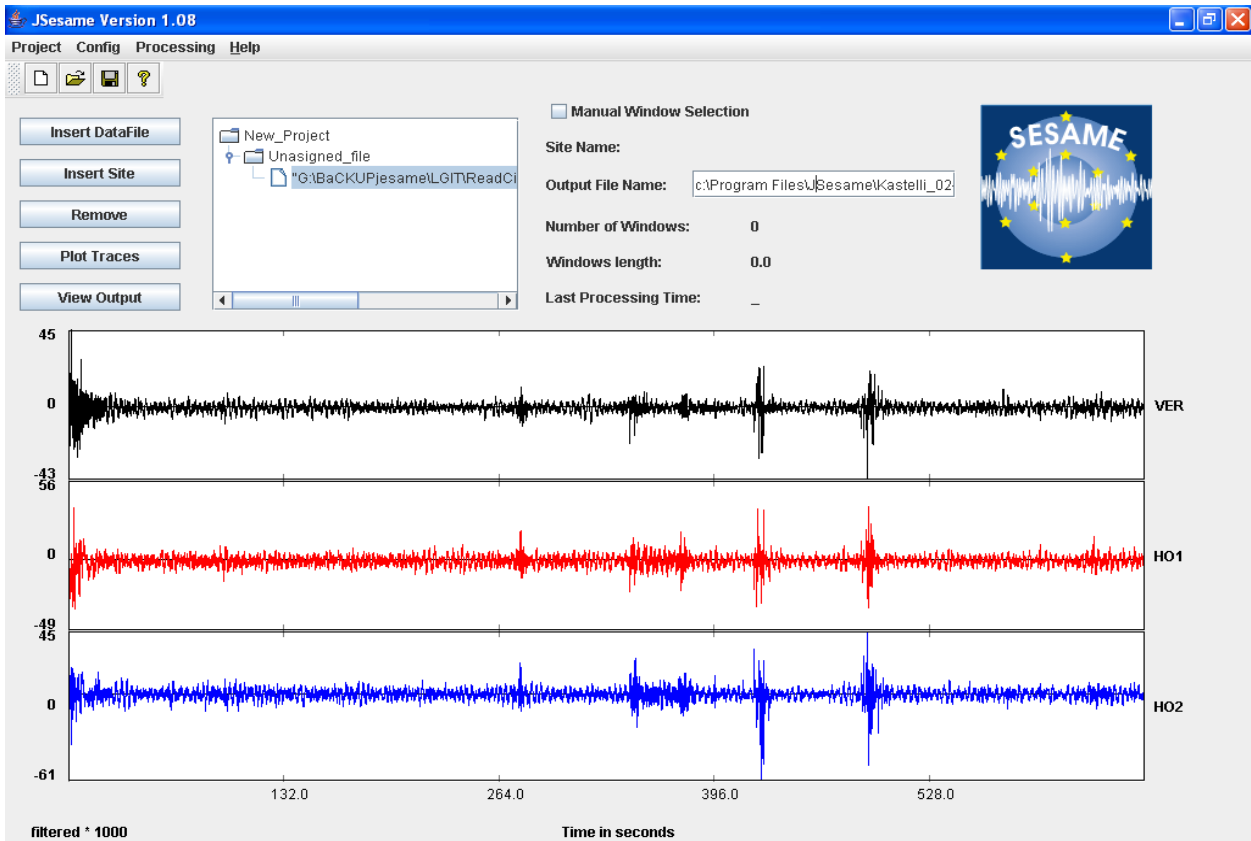


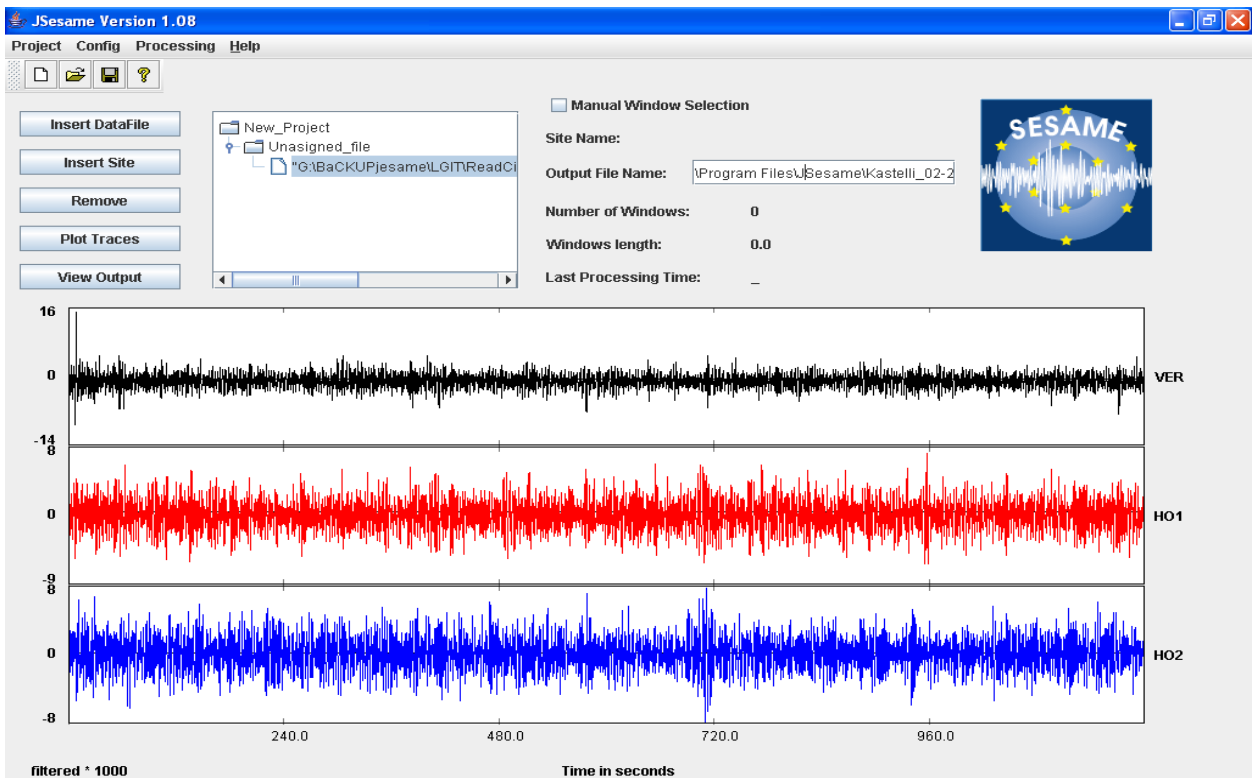
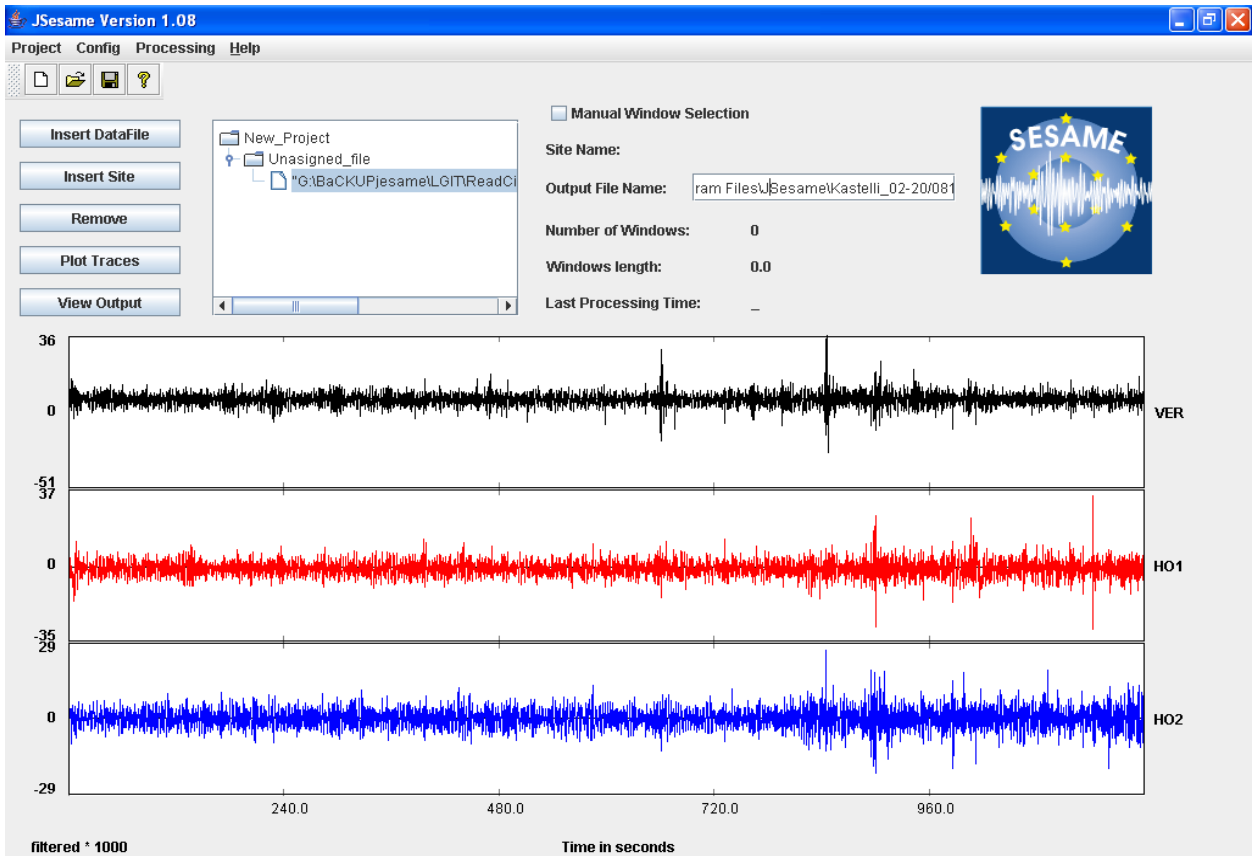


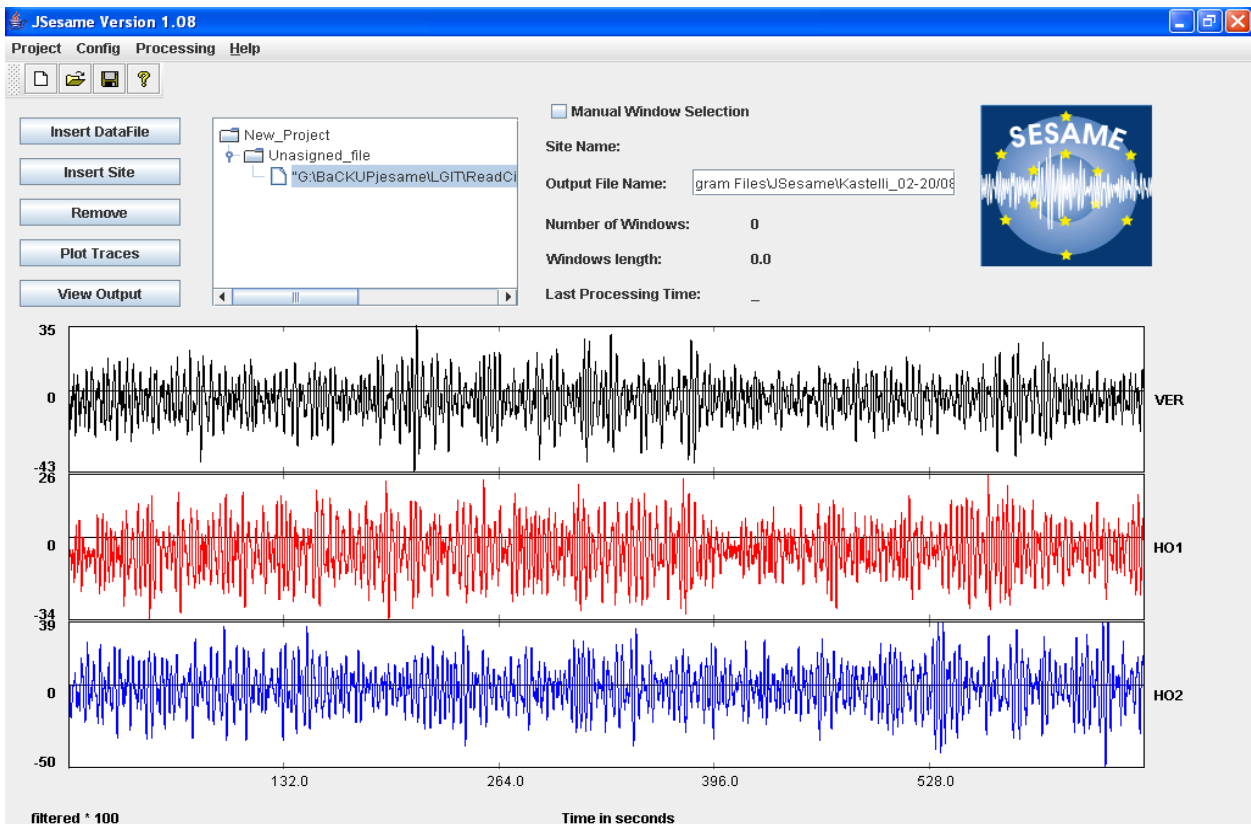
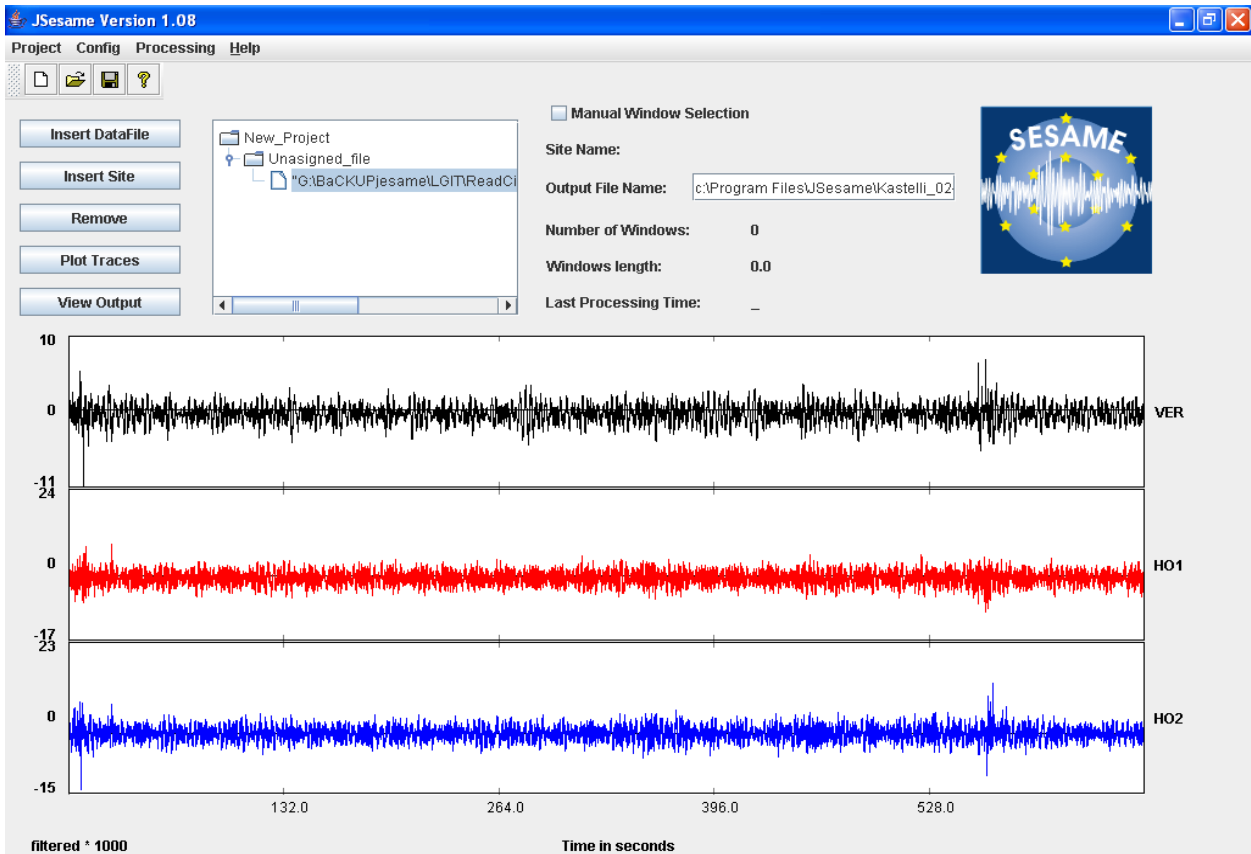


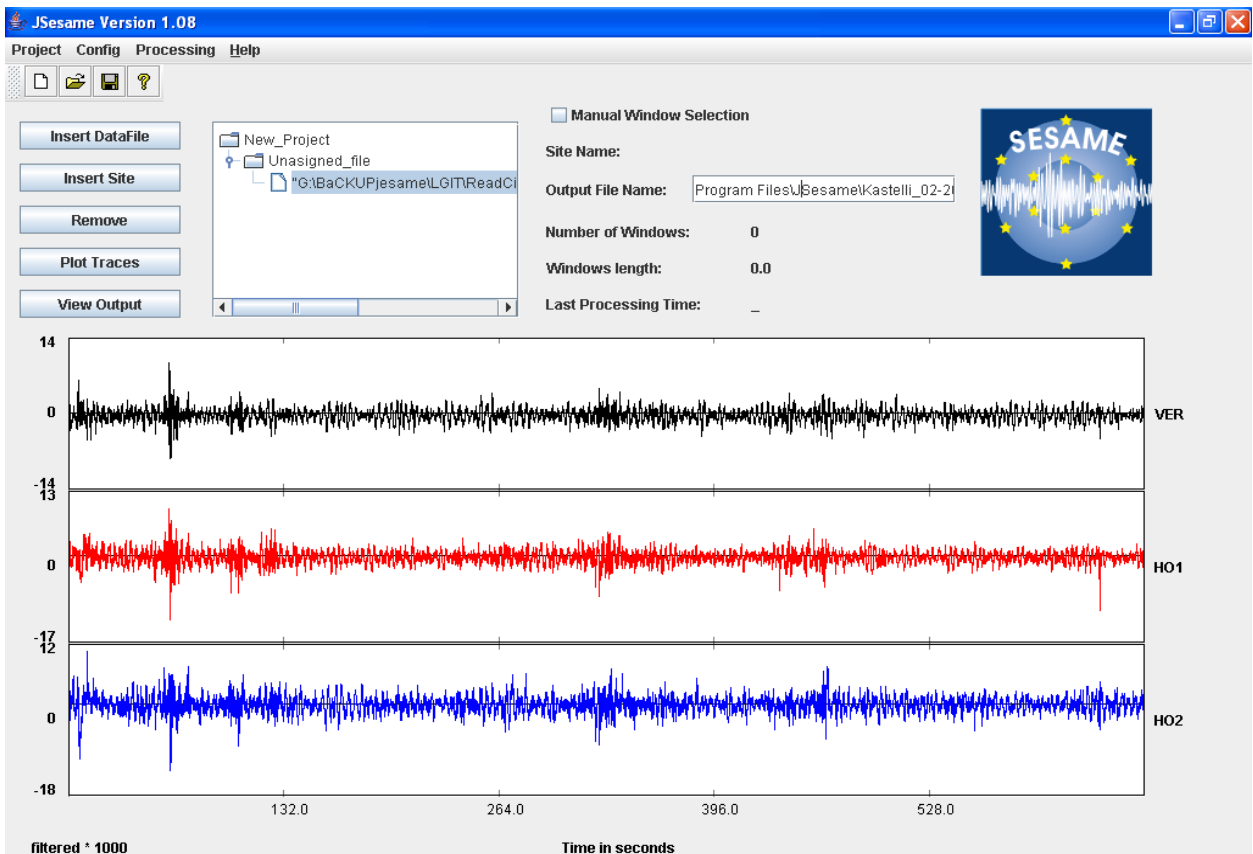
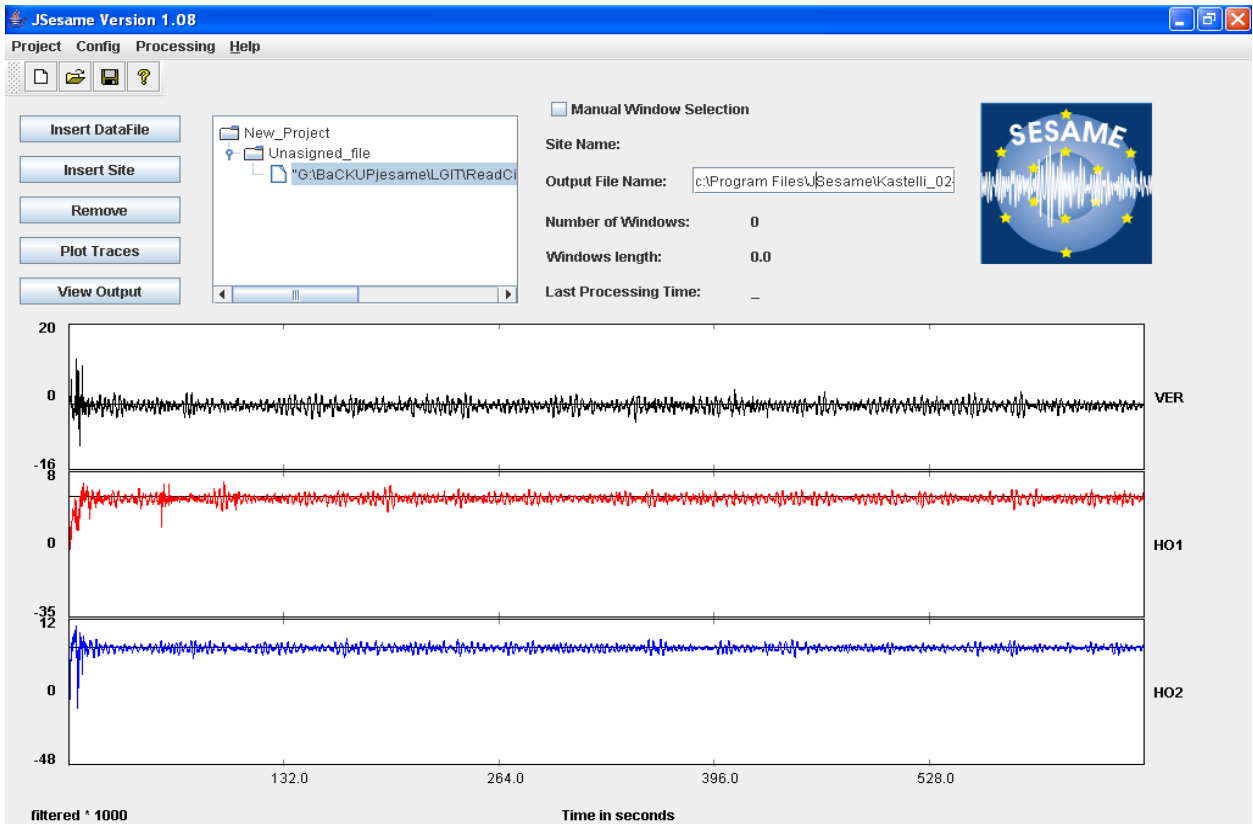


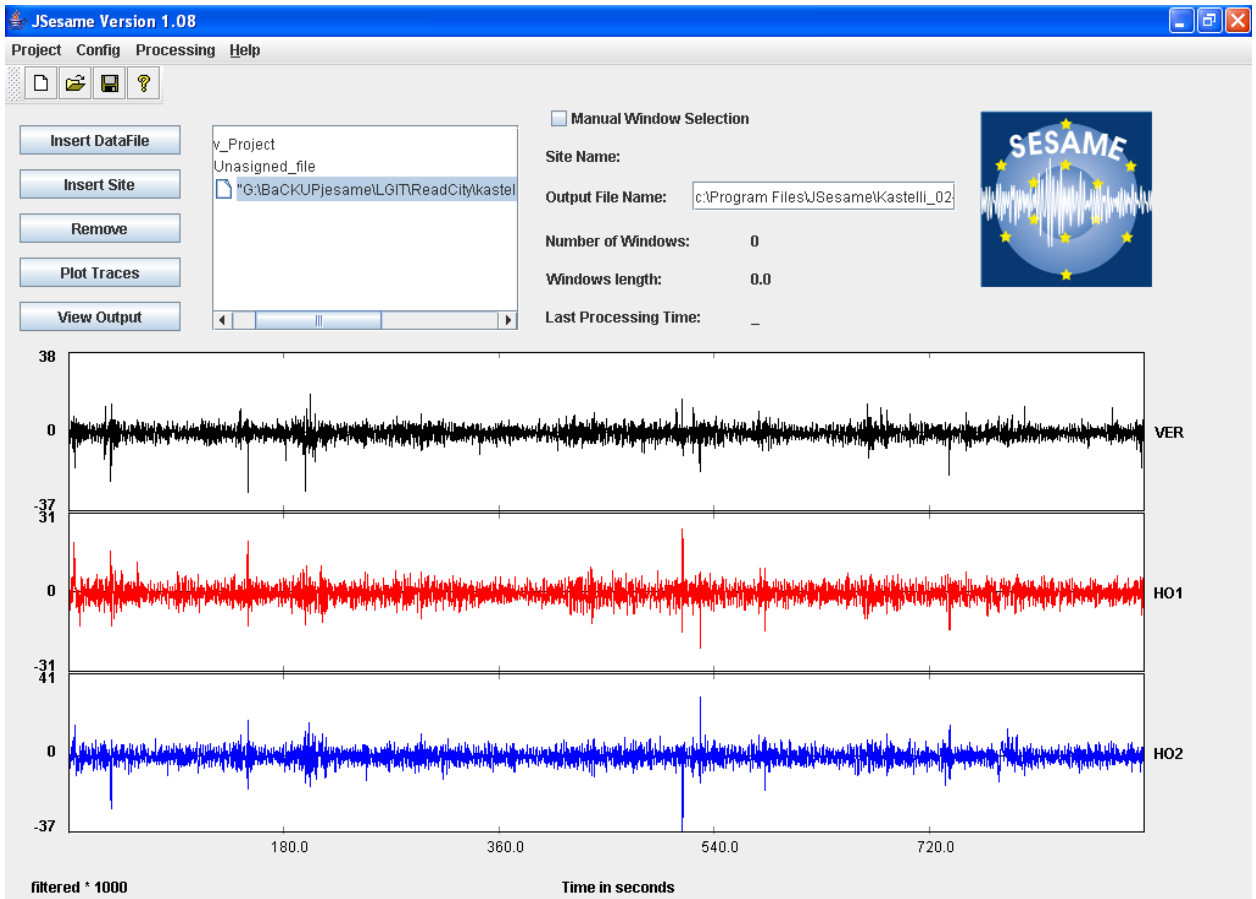


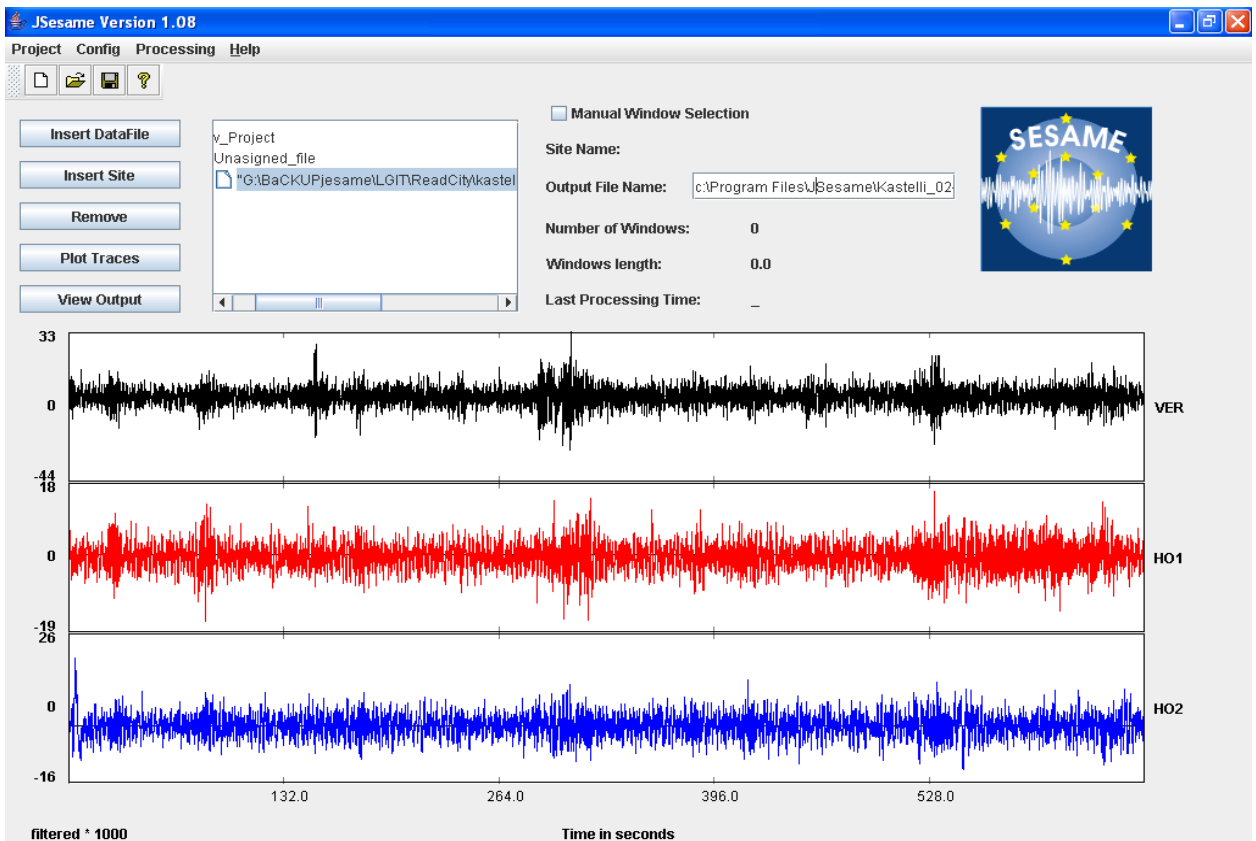
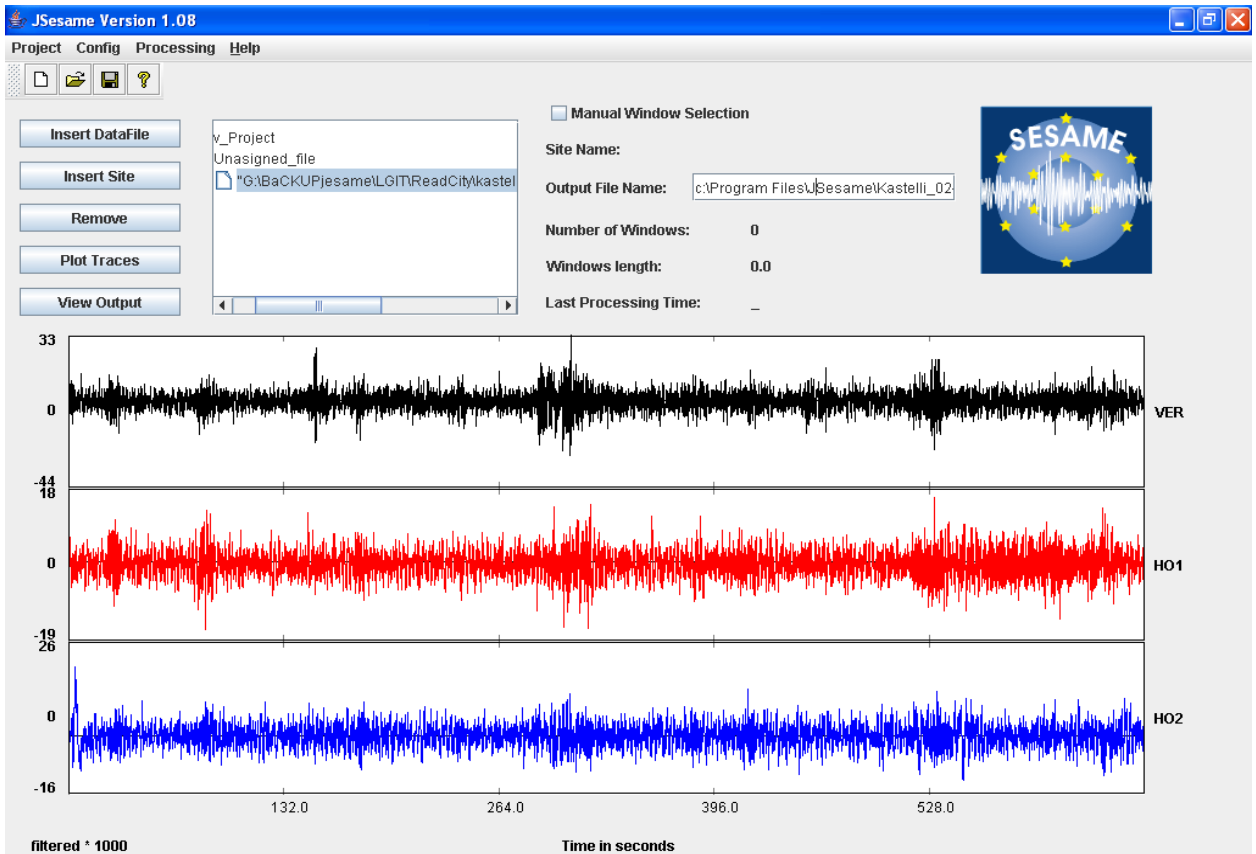


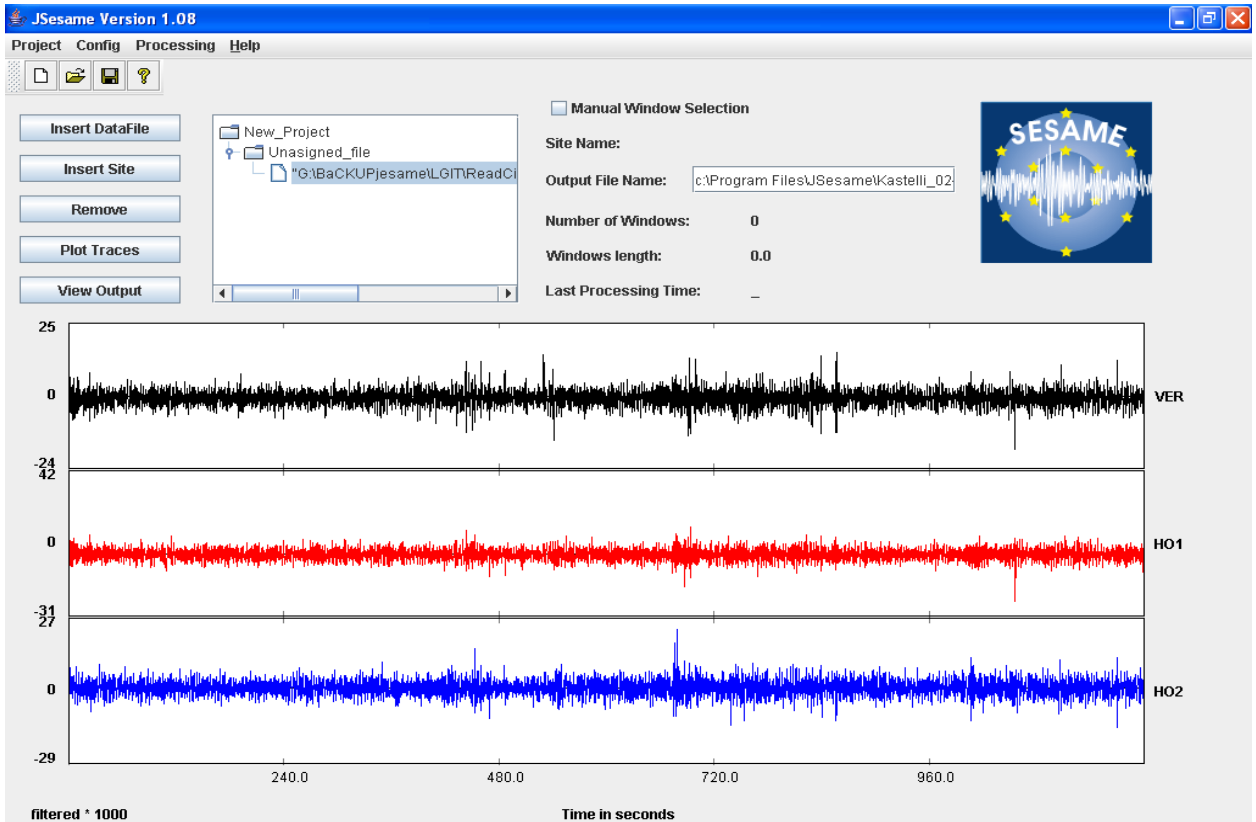
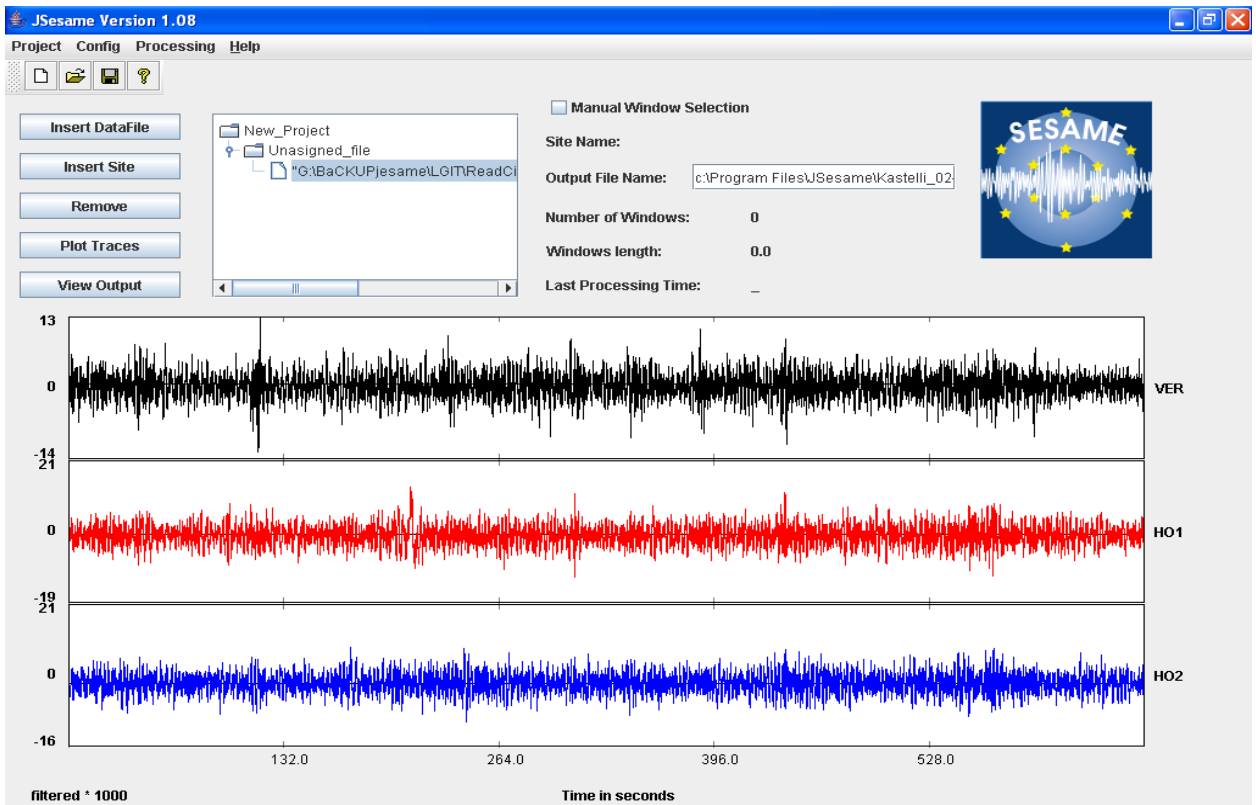


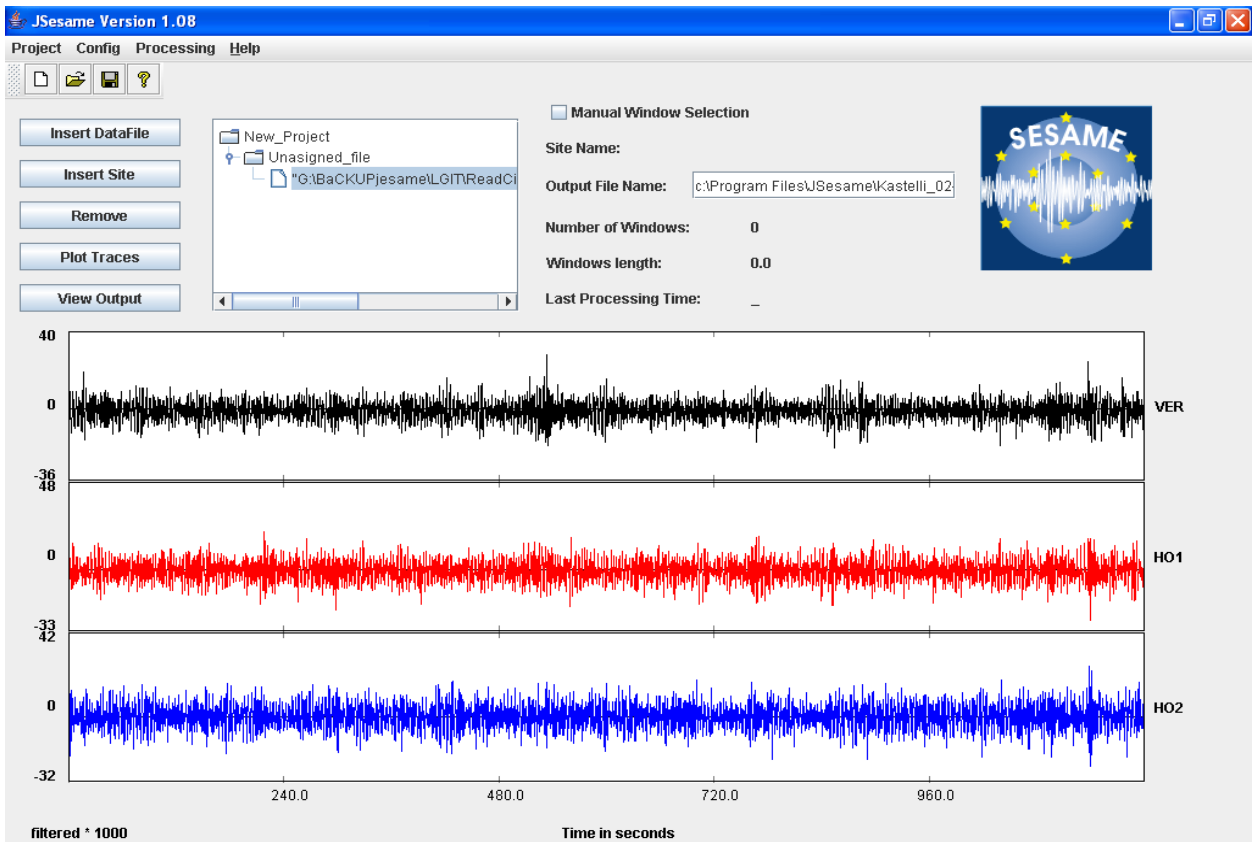
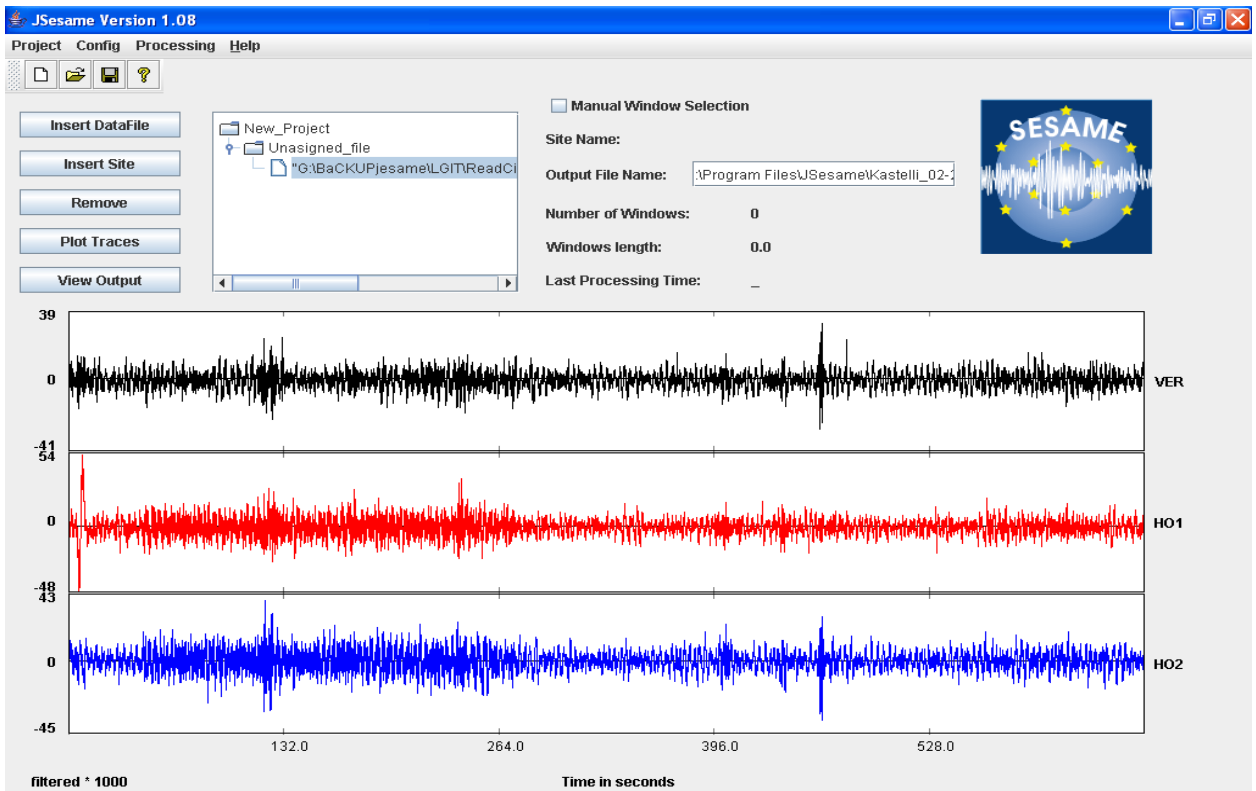






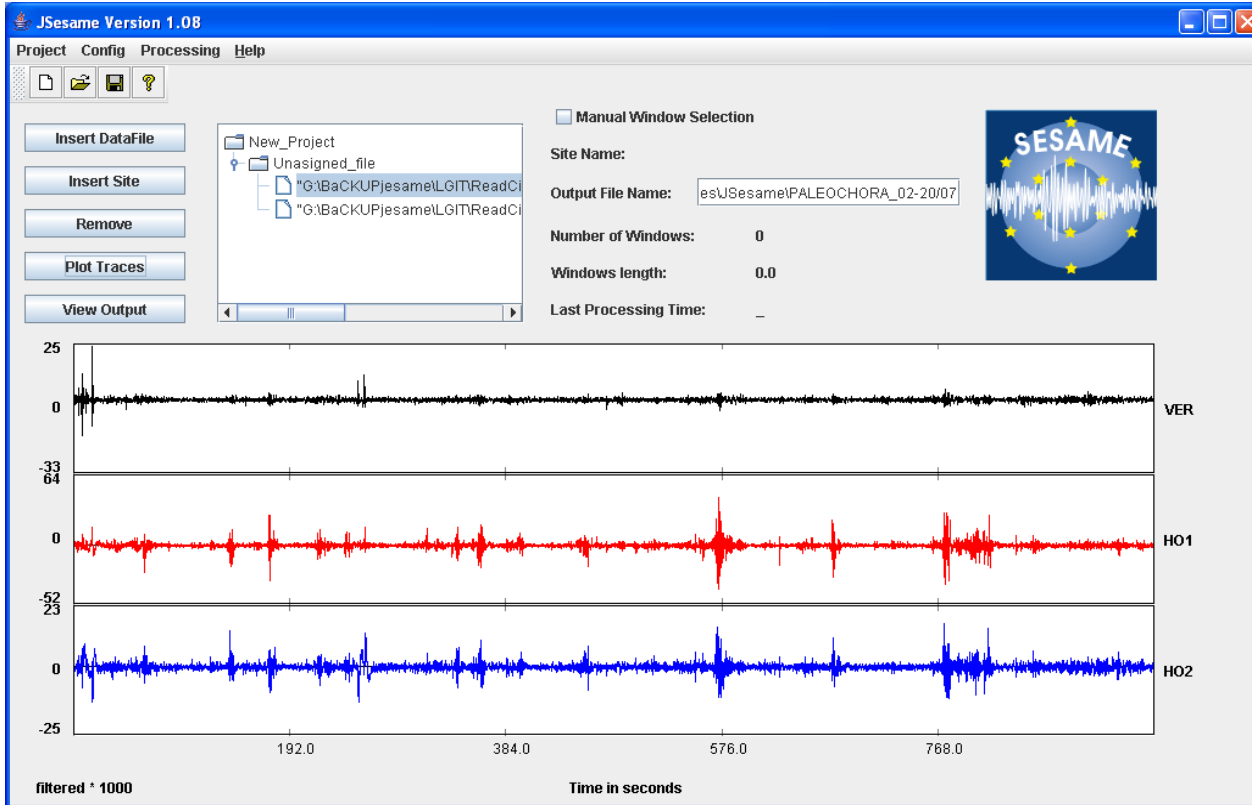
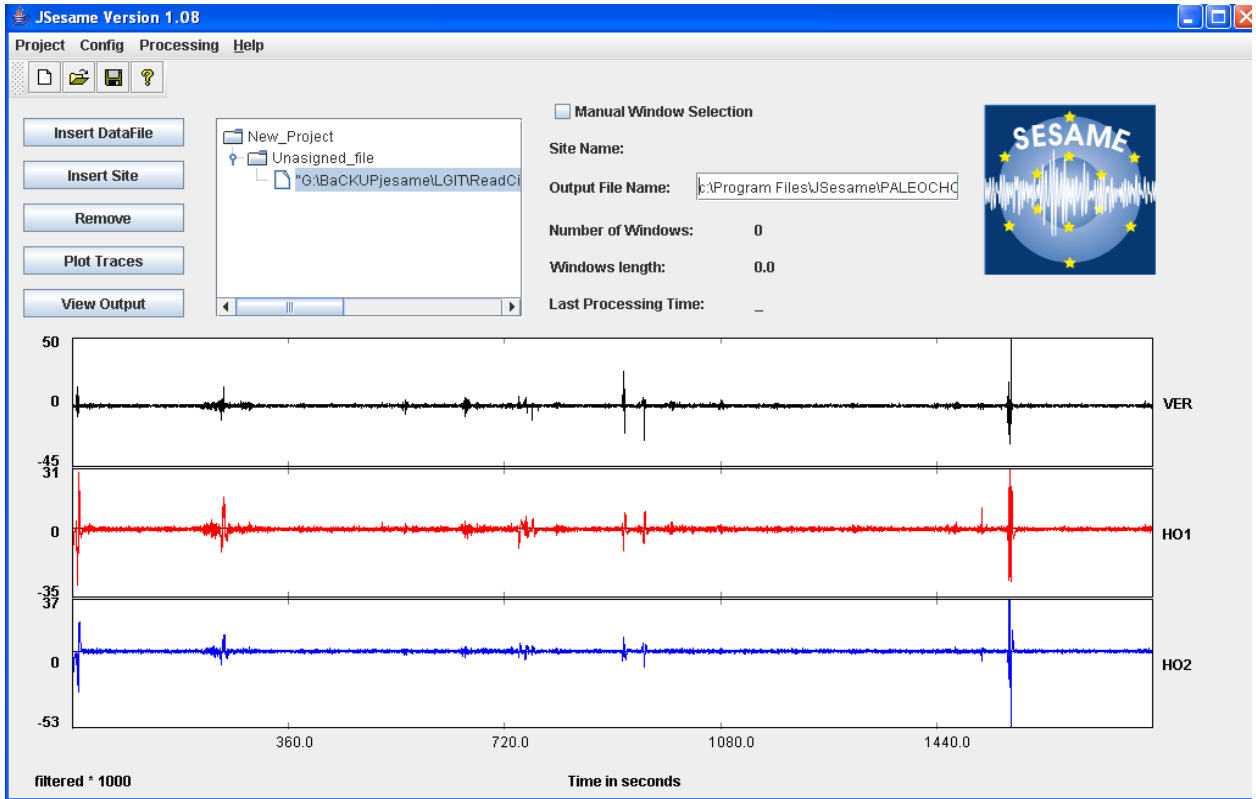


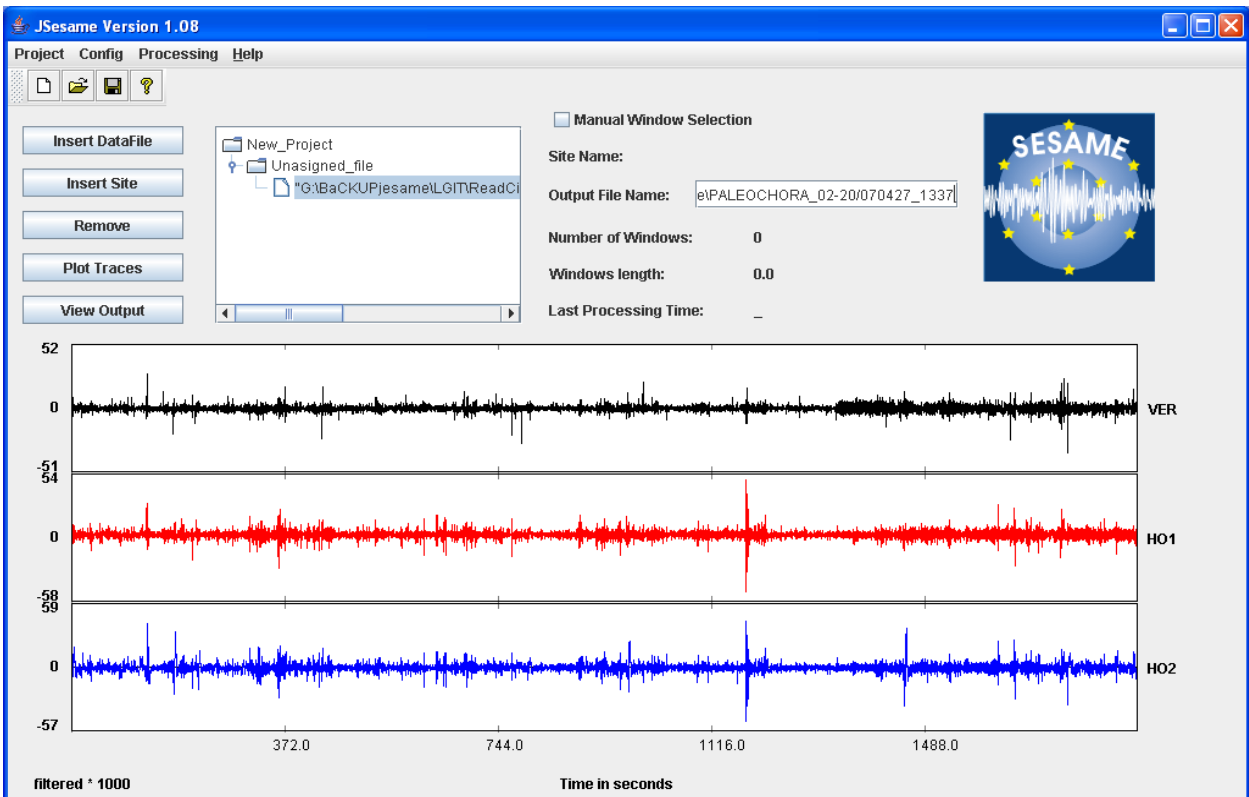
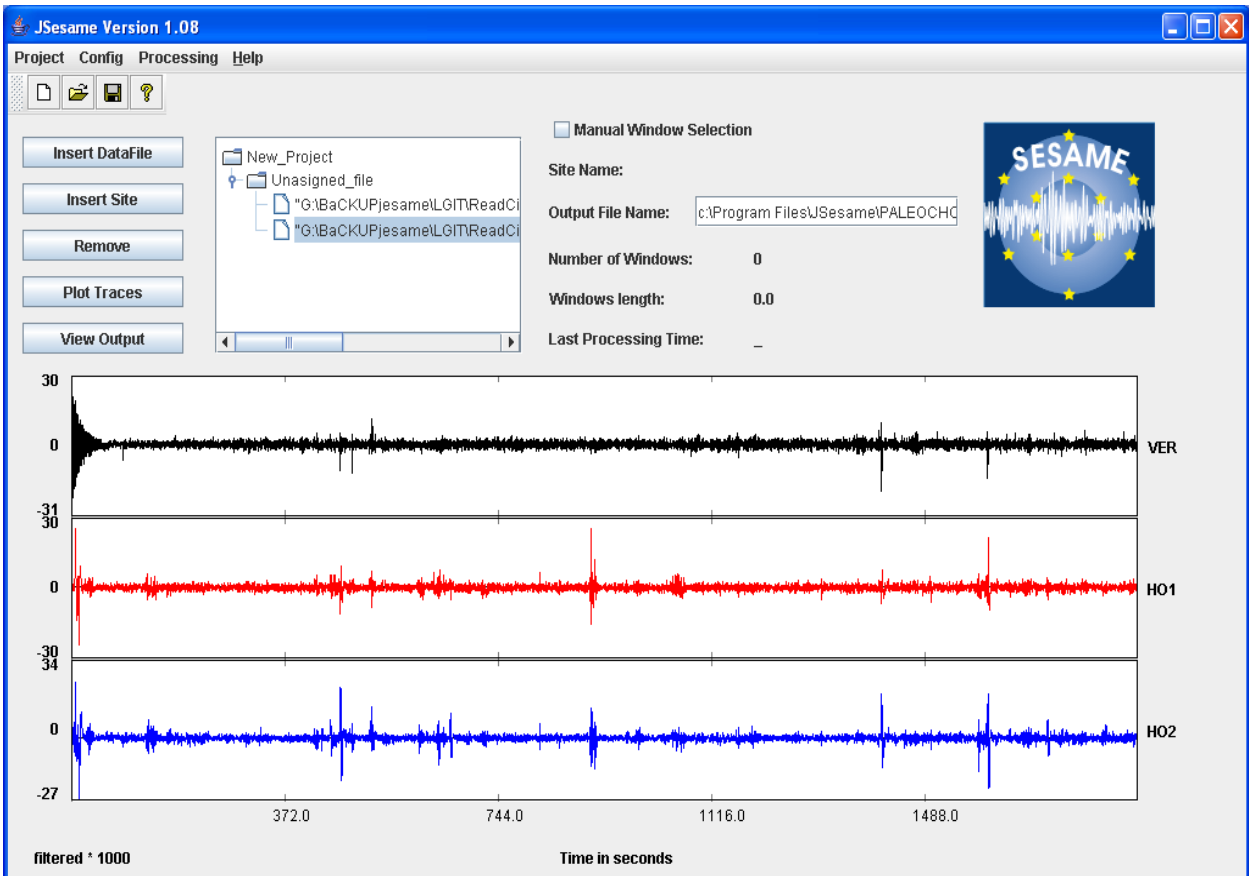


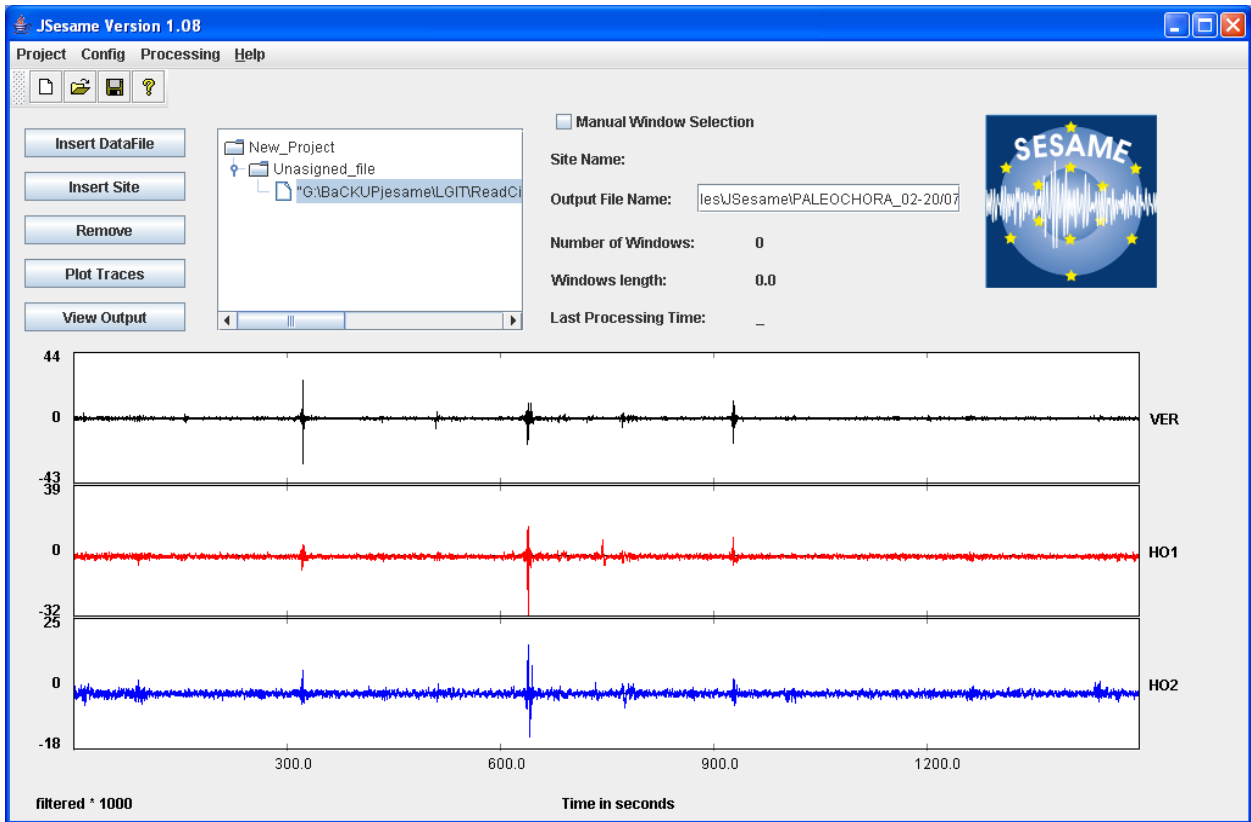
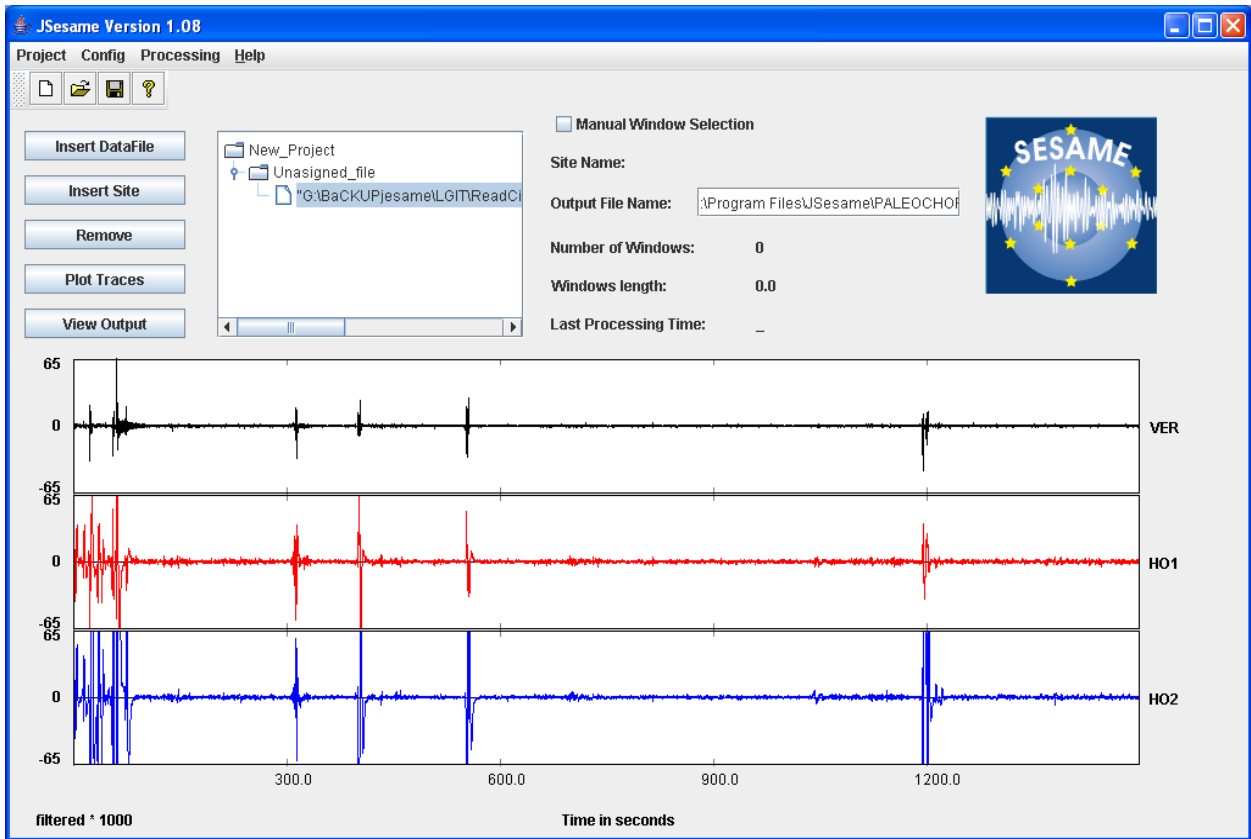


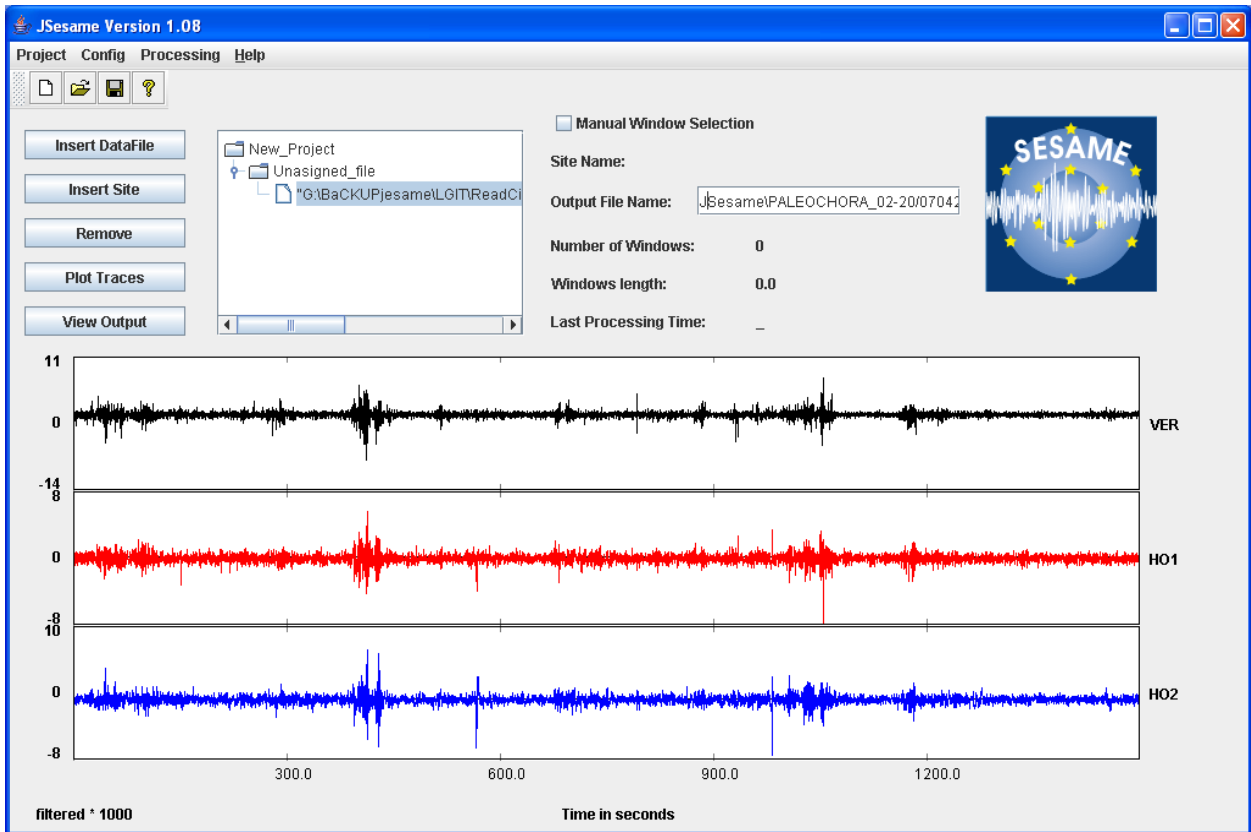
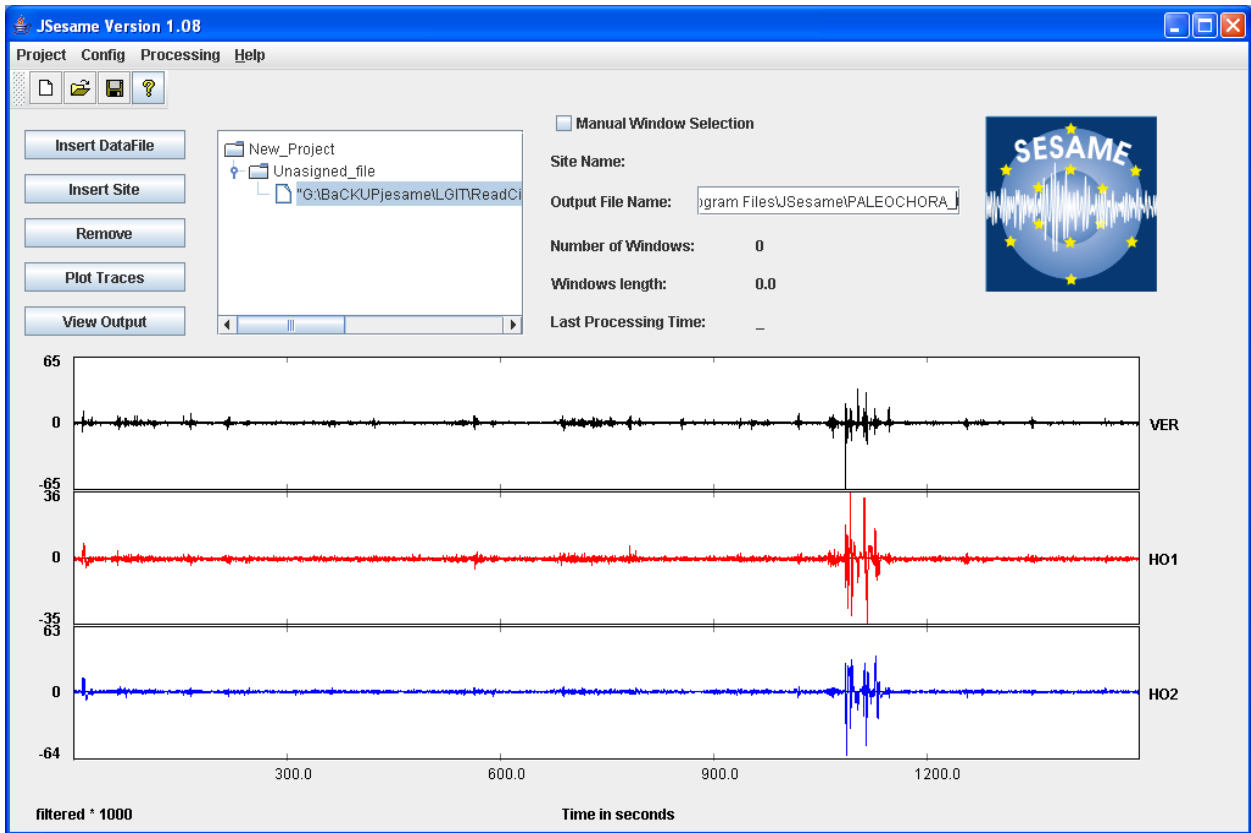


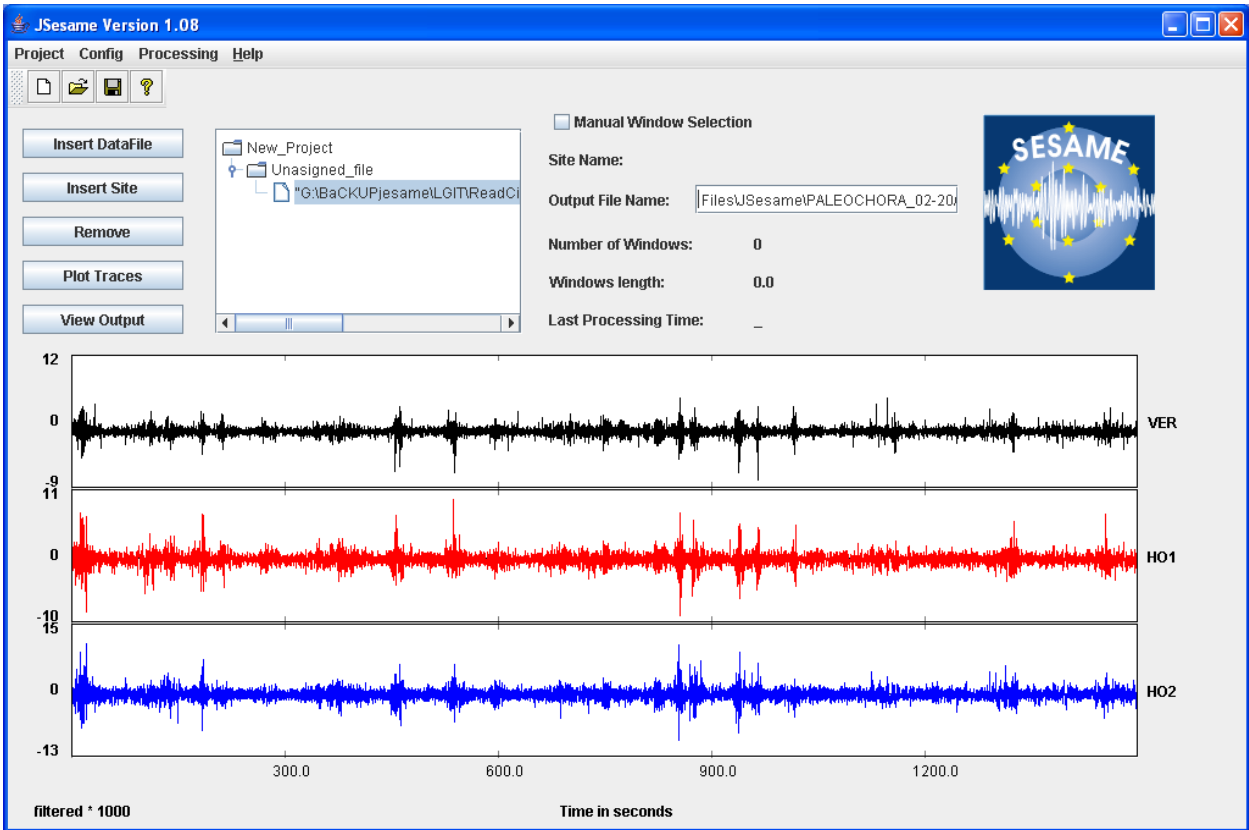
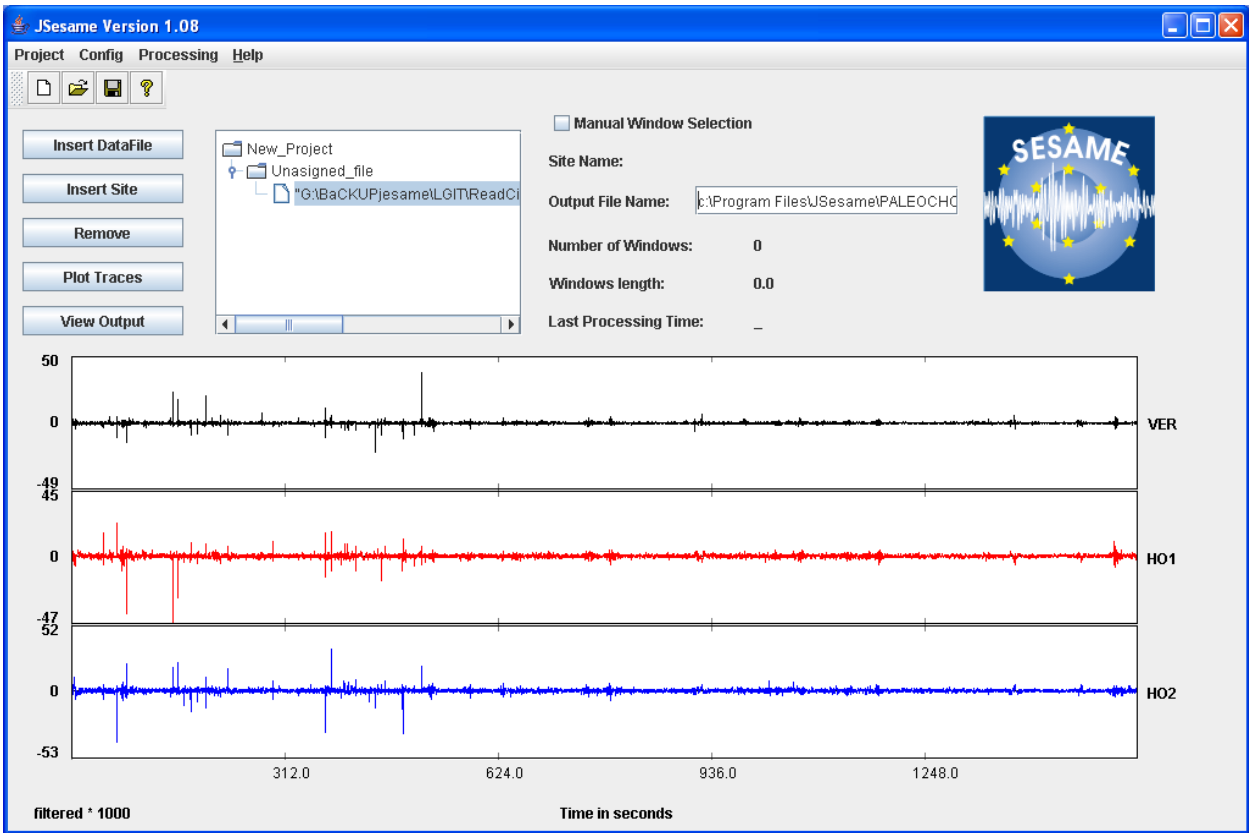
## A2: MICROTREMOR RECORDINGS IN PALEOHORA BASIN

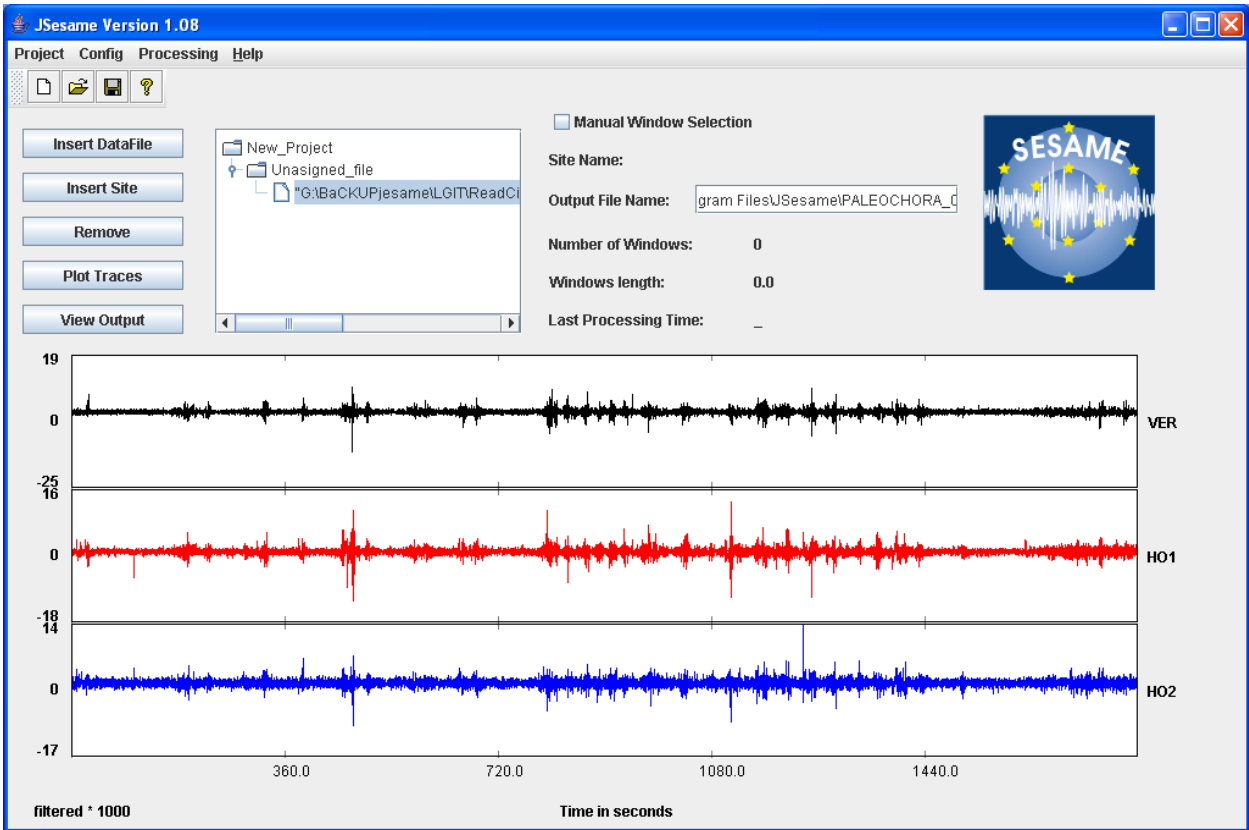
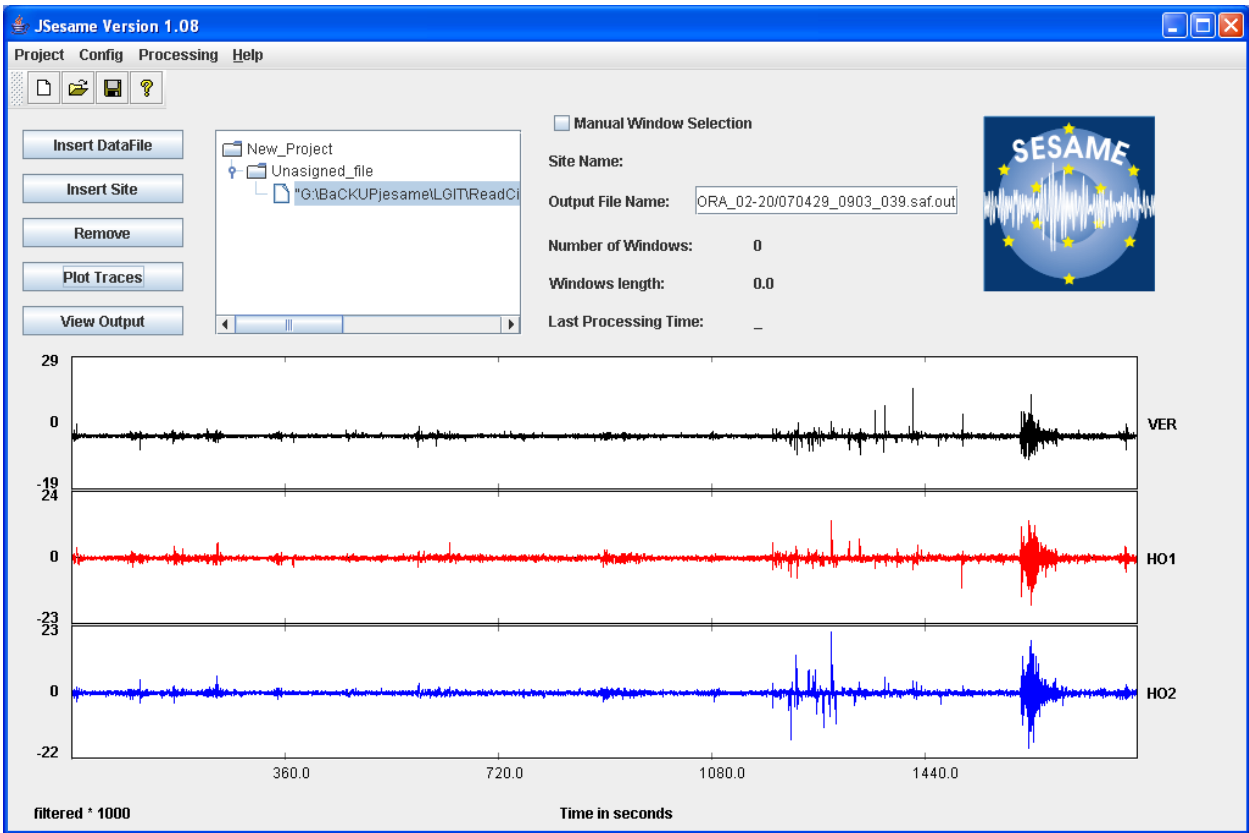


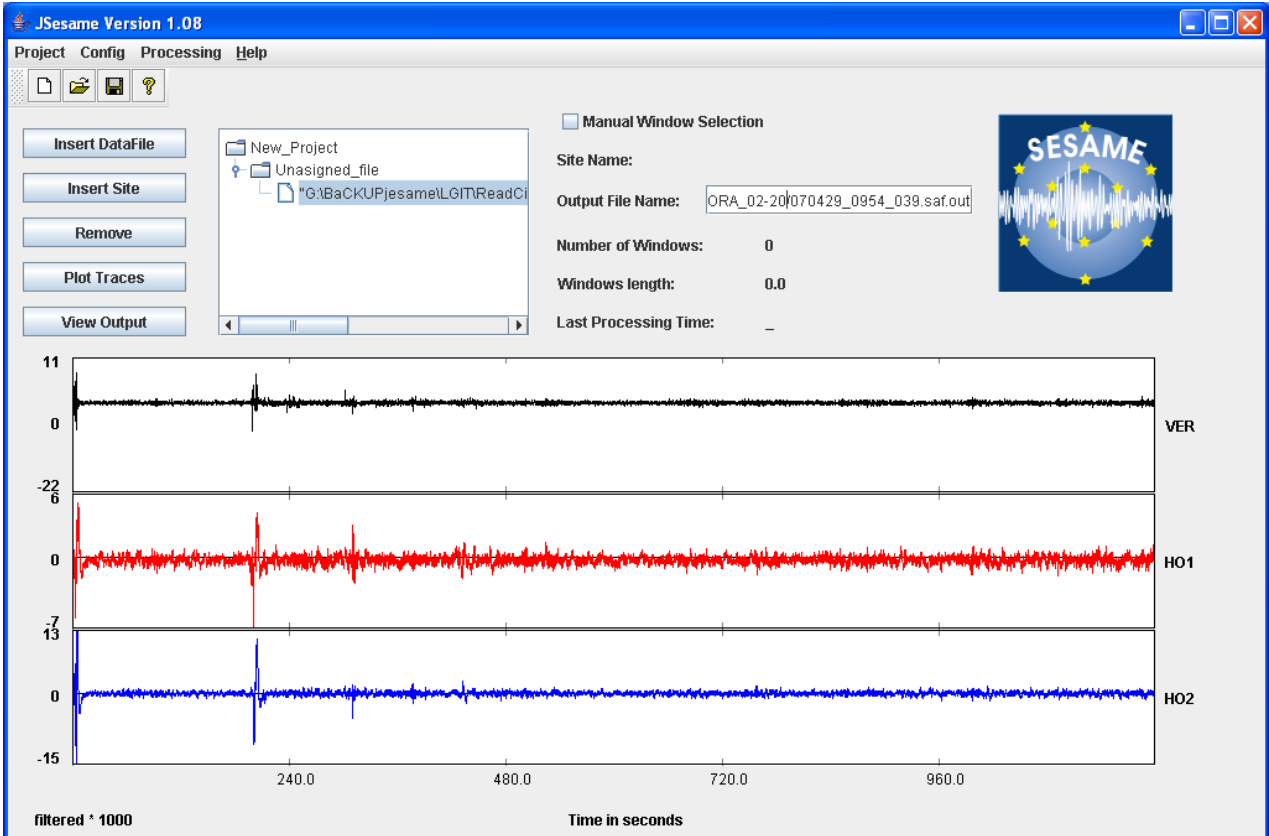
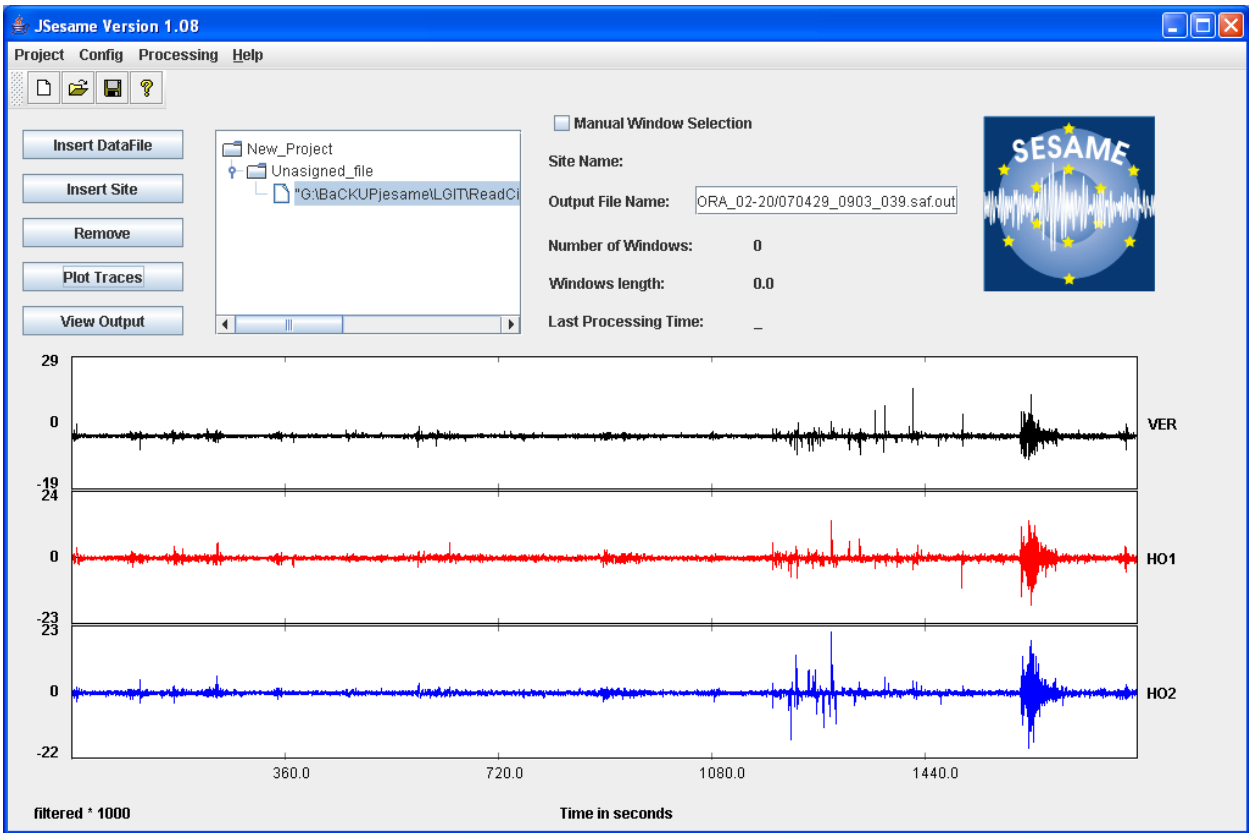


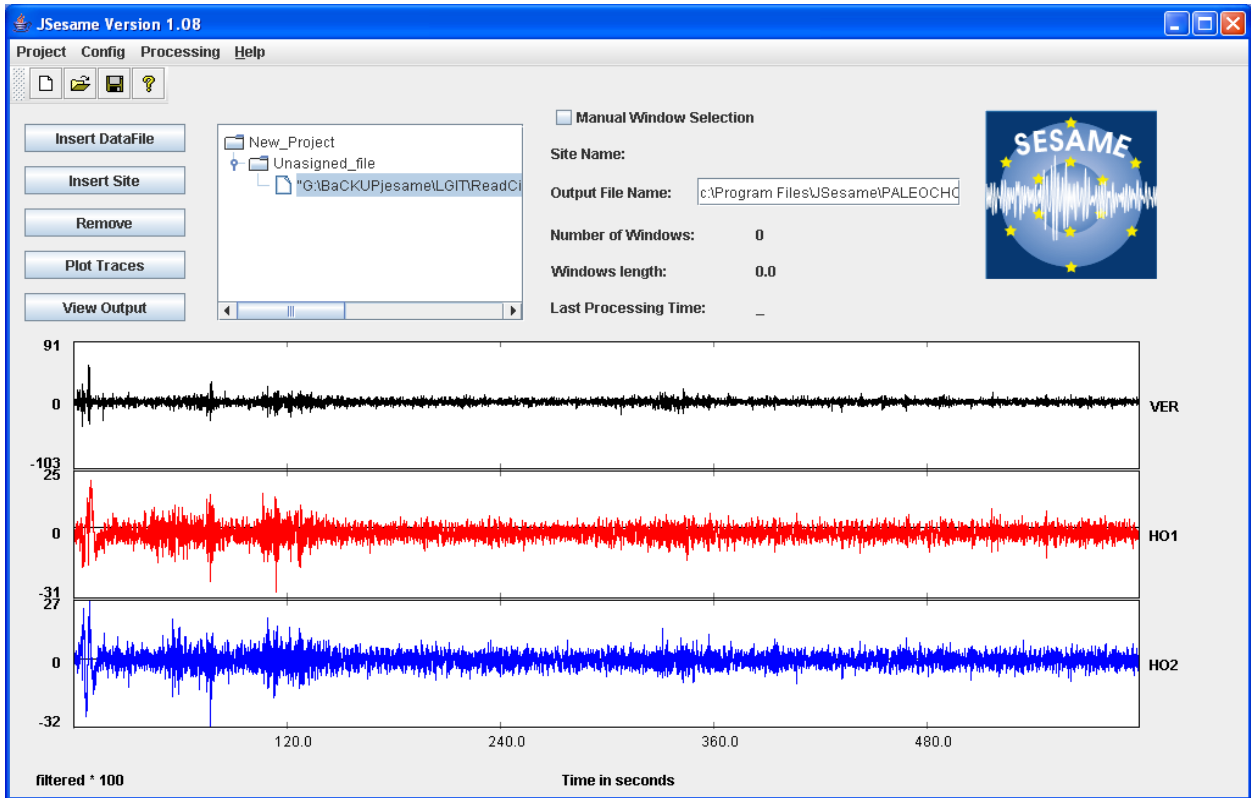
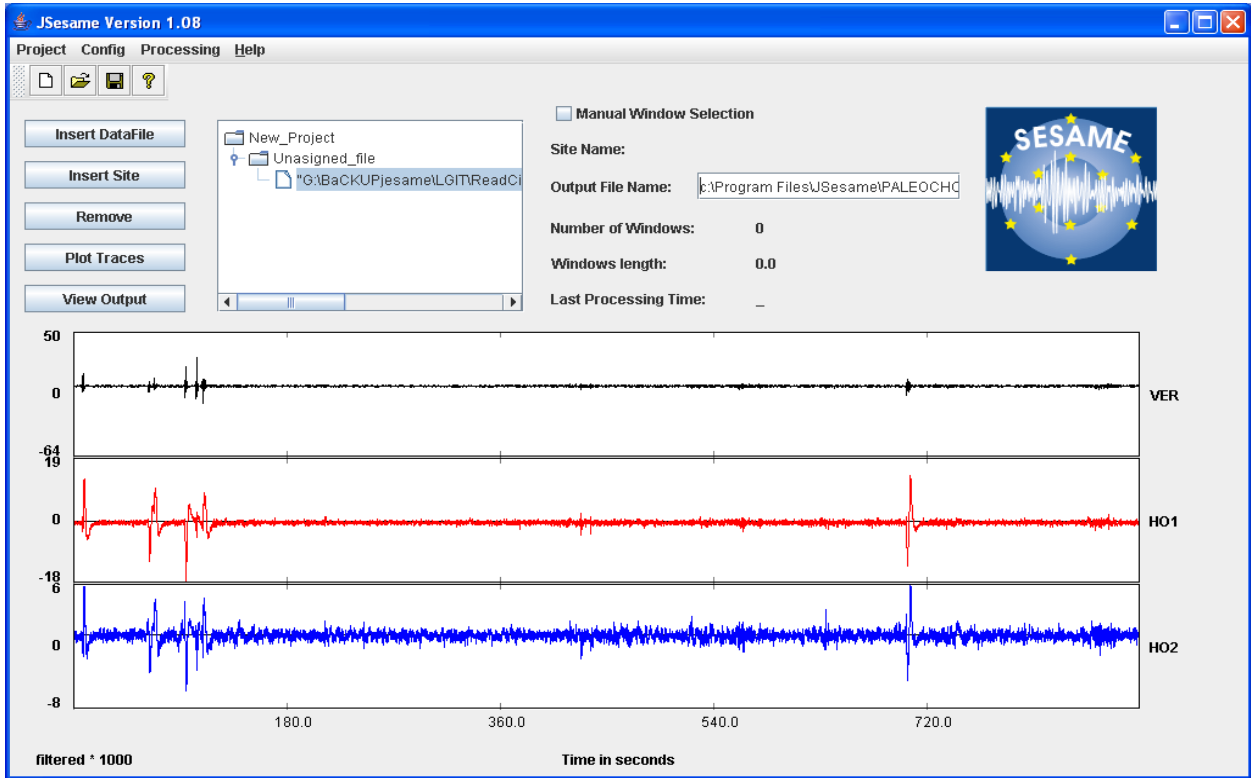




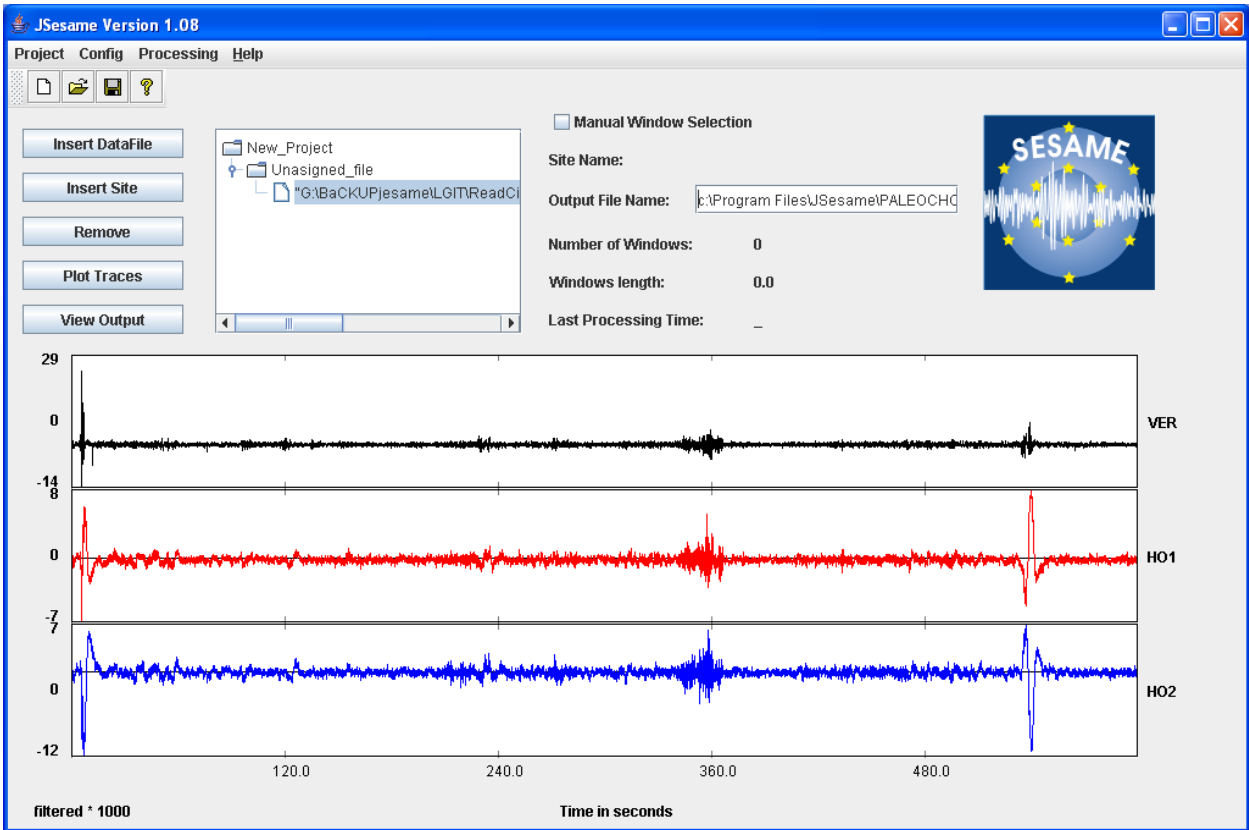
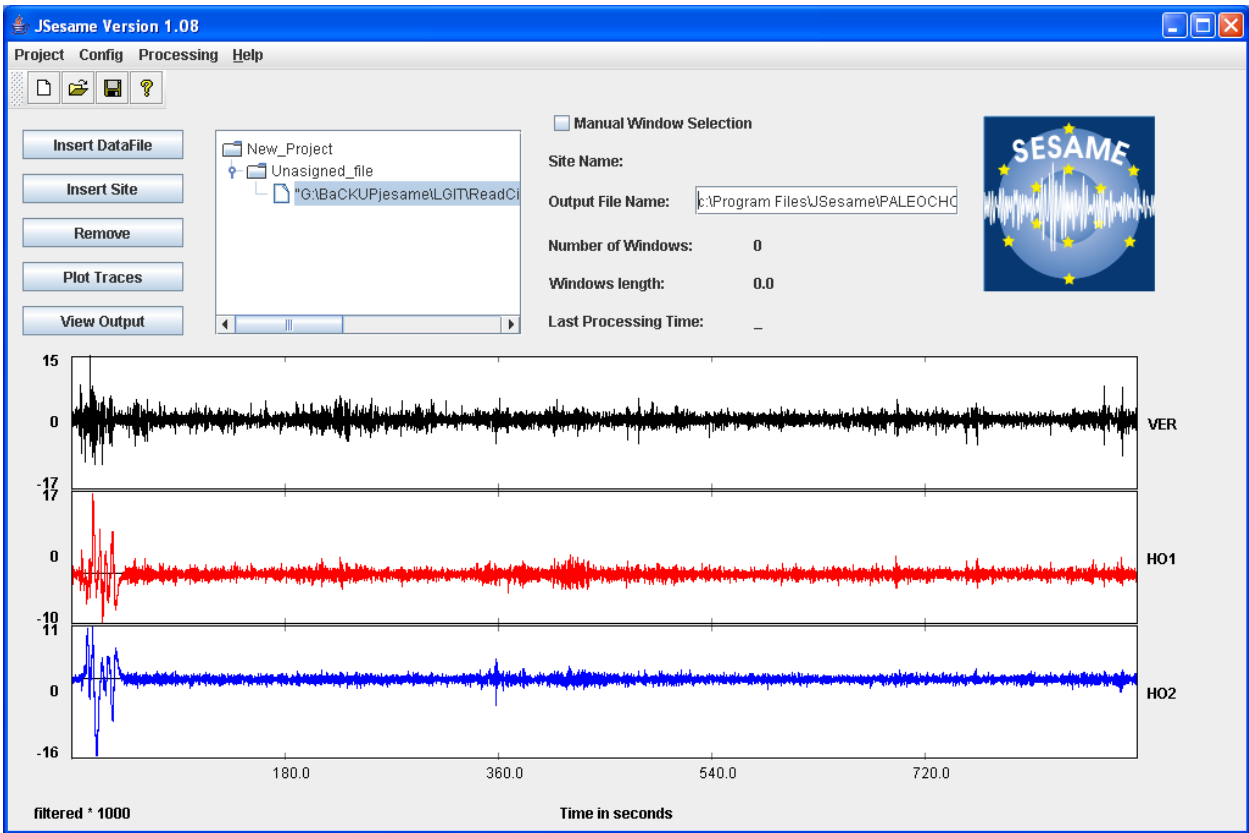


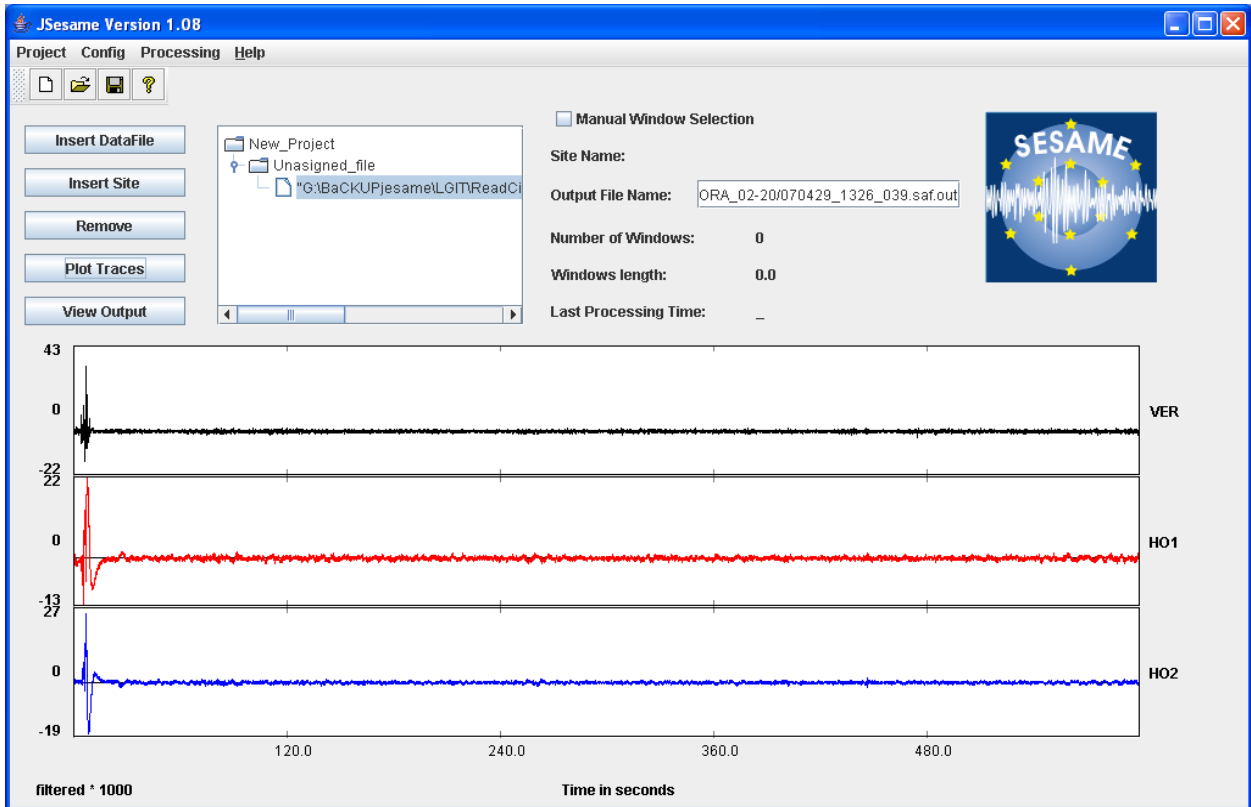
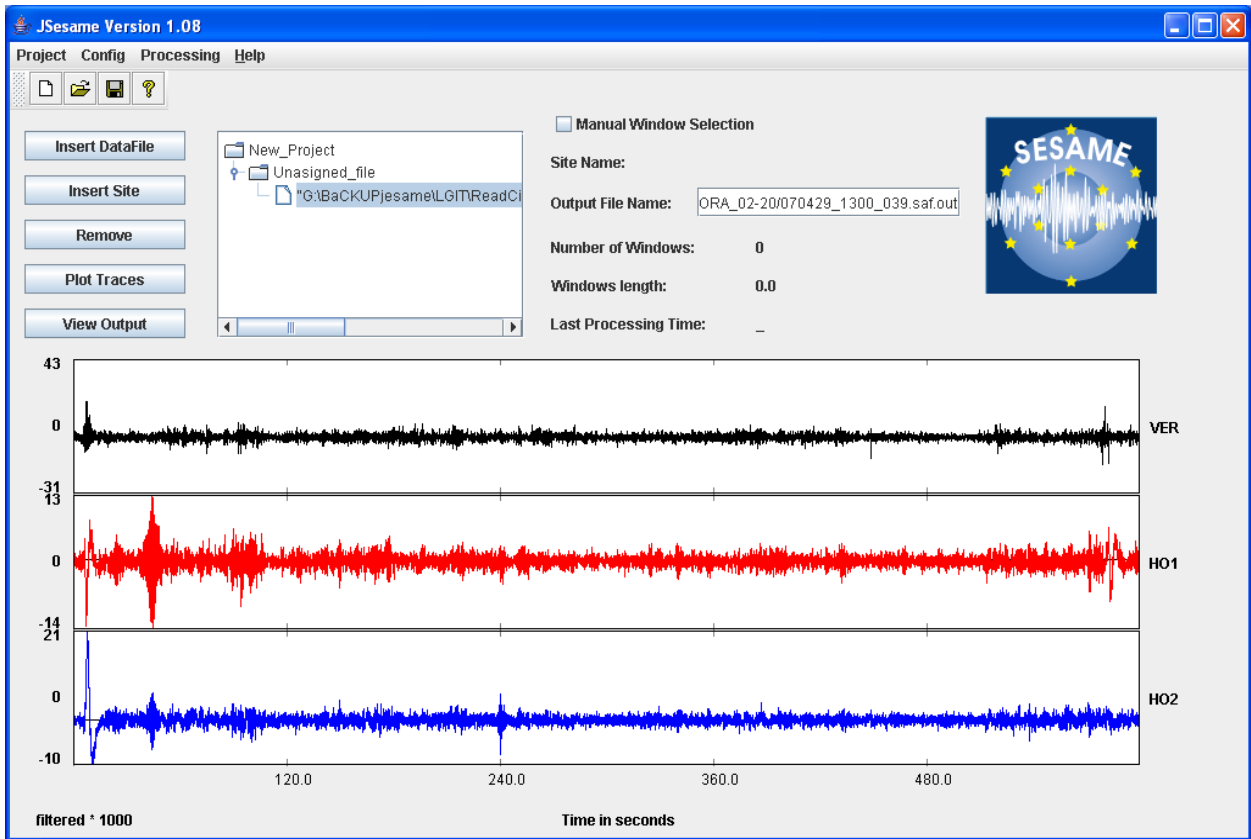


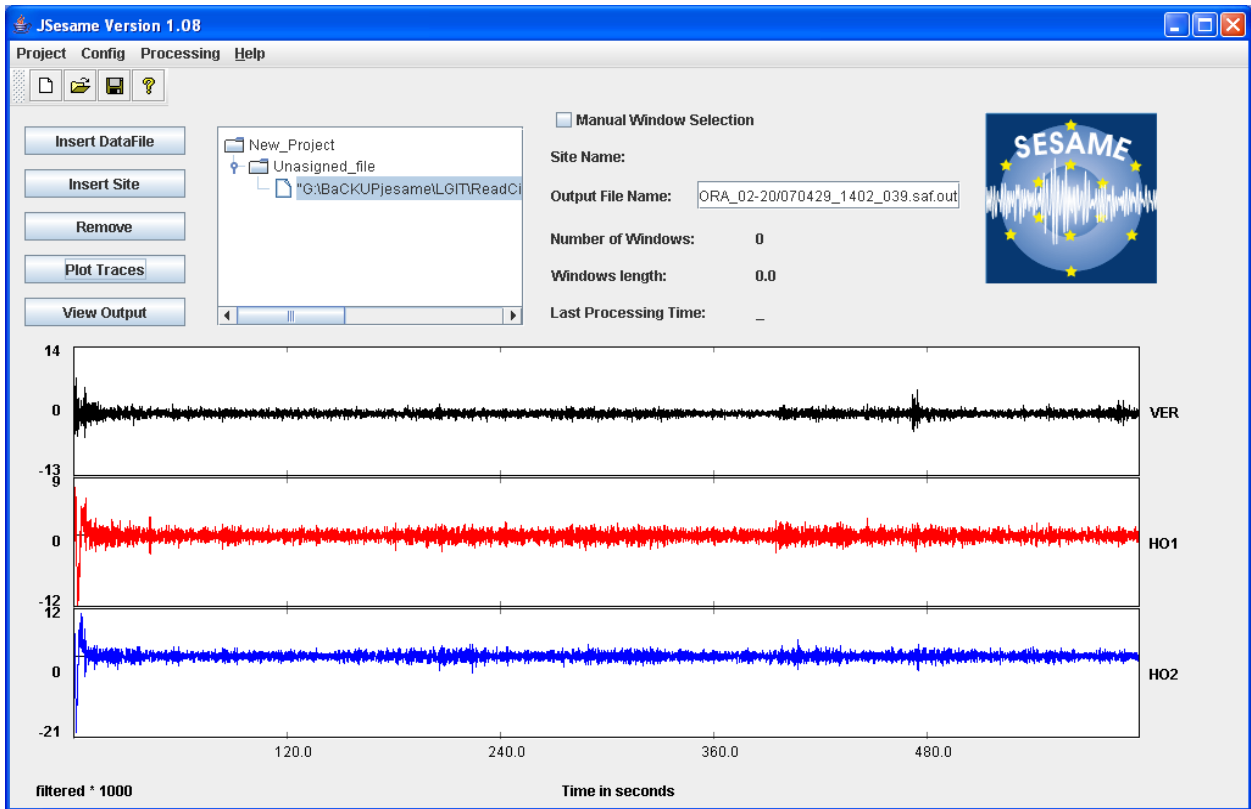
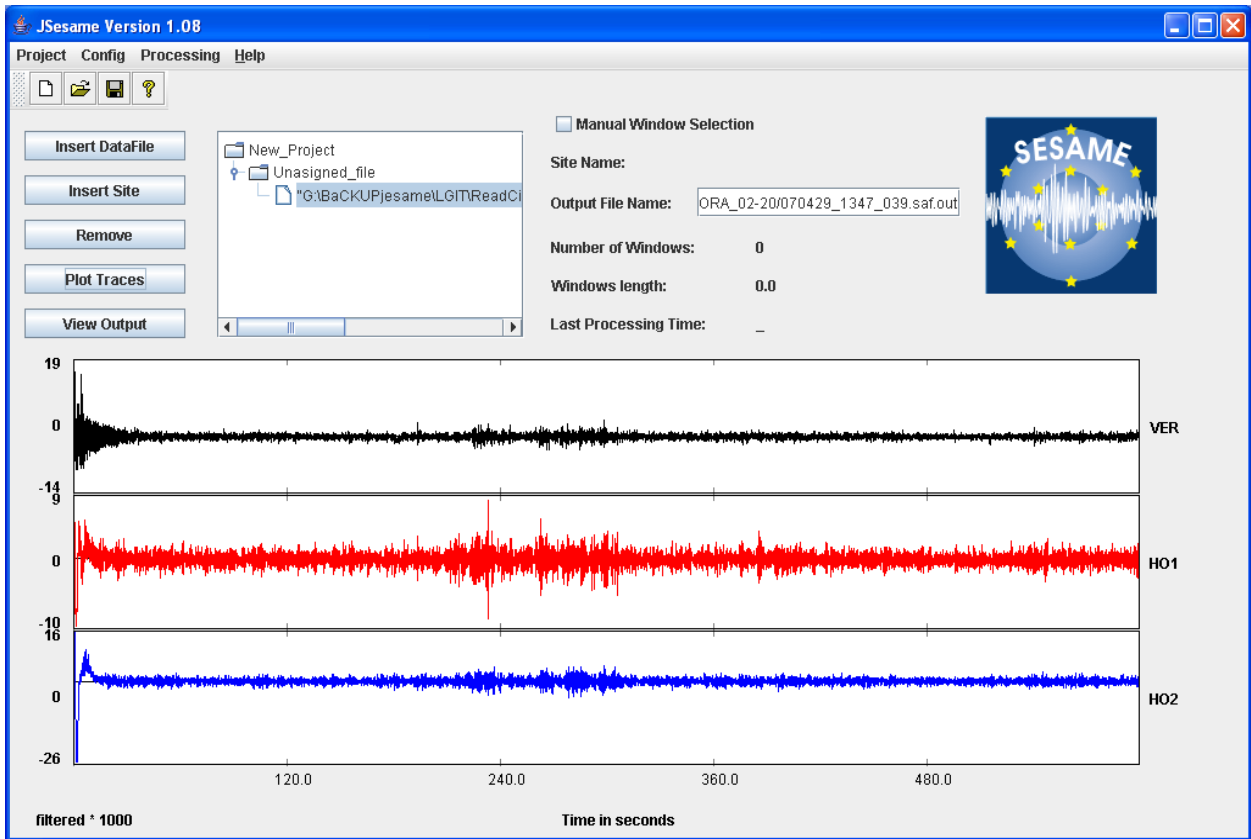


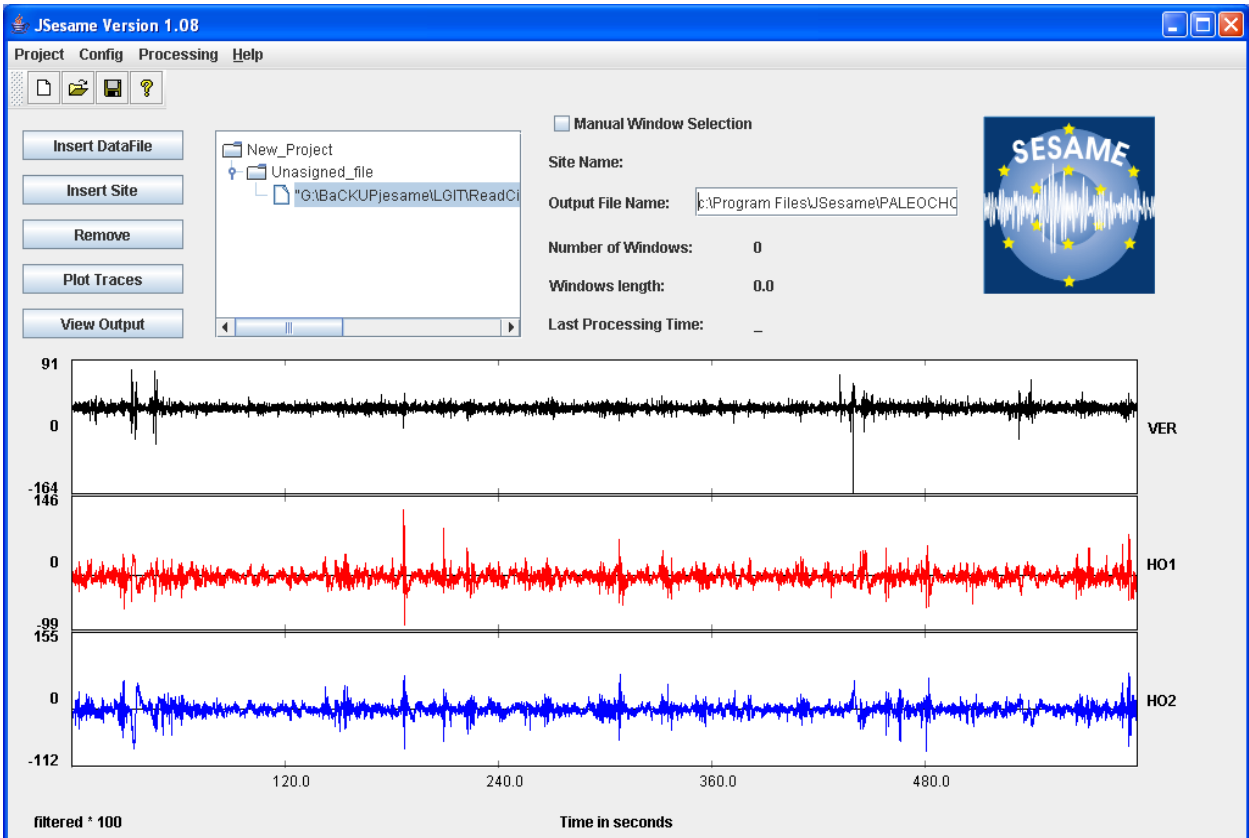
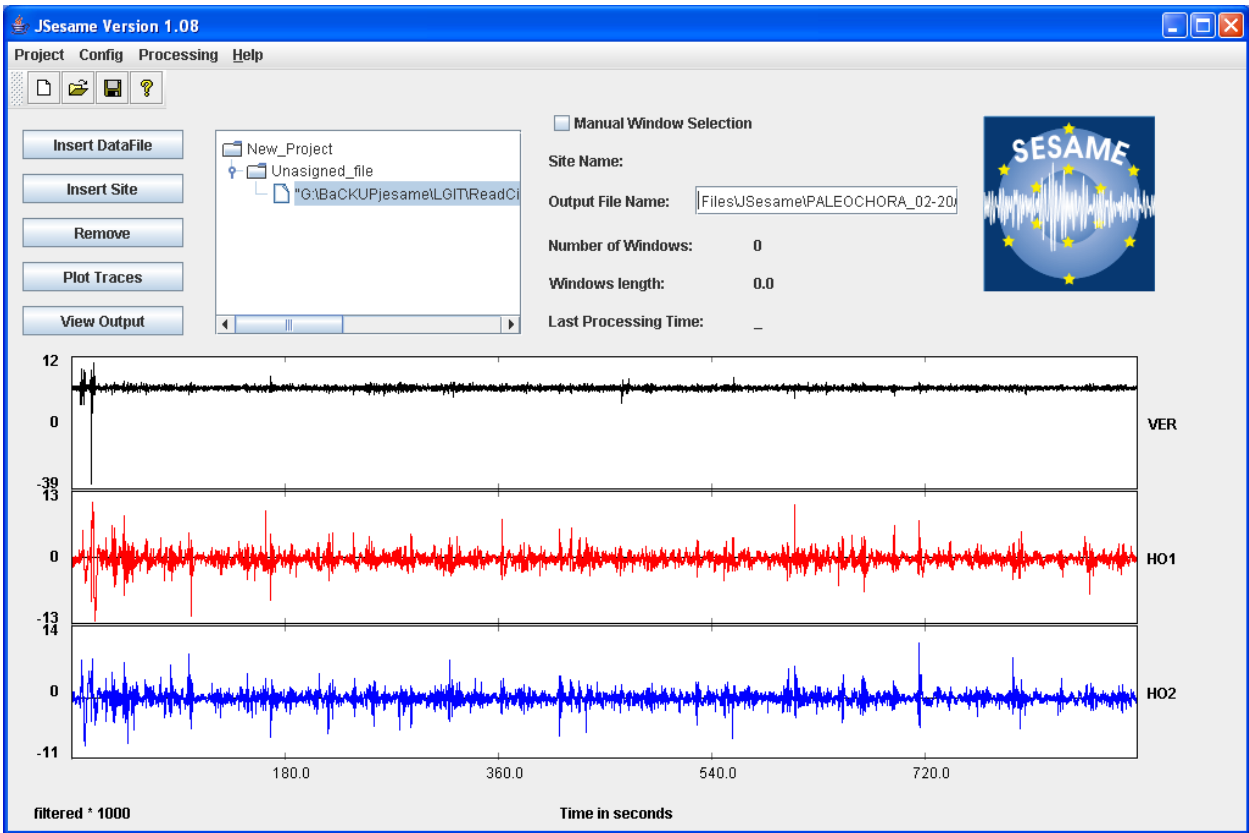


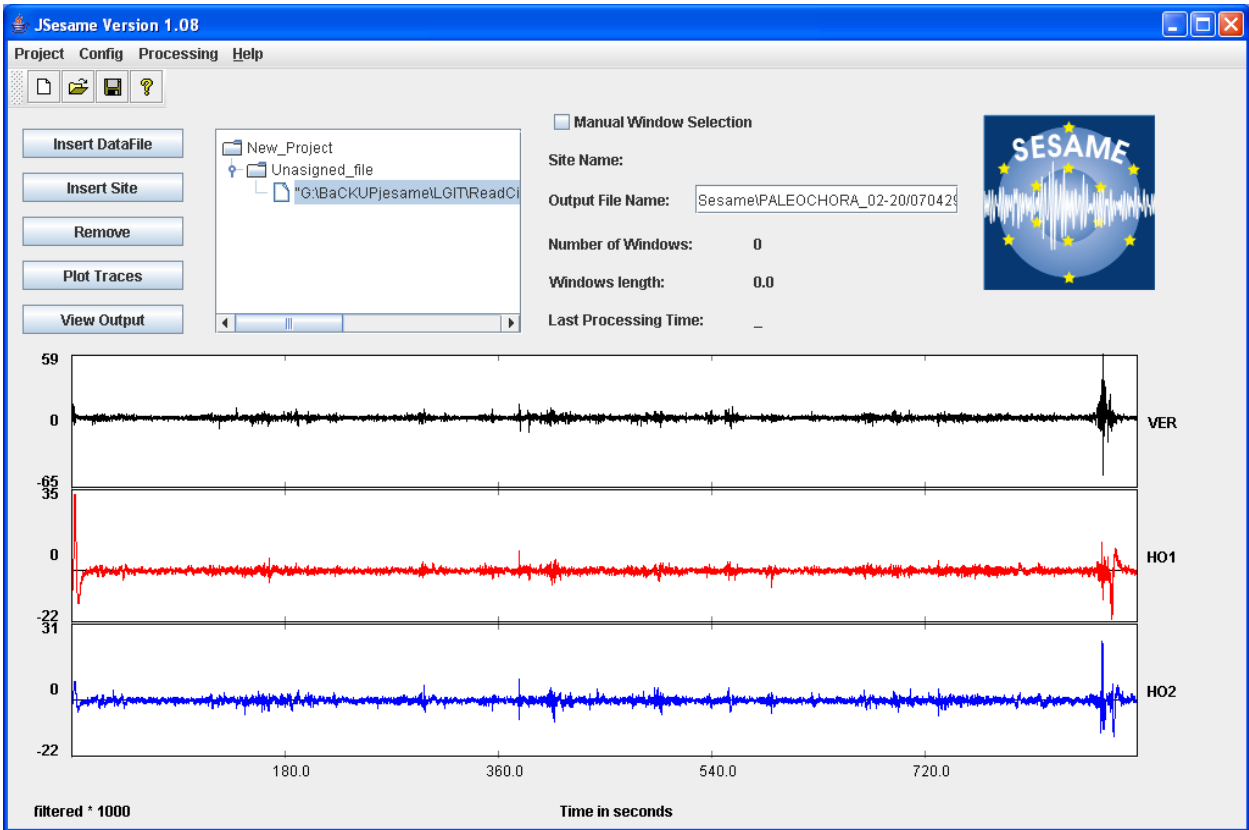
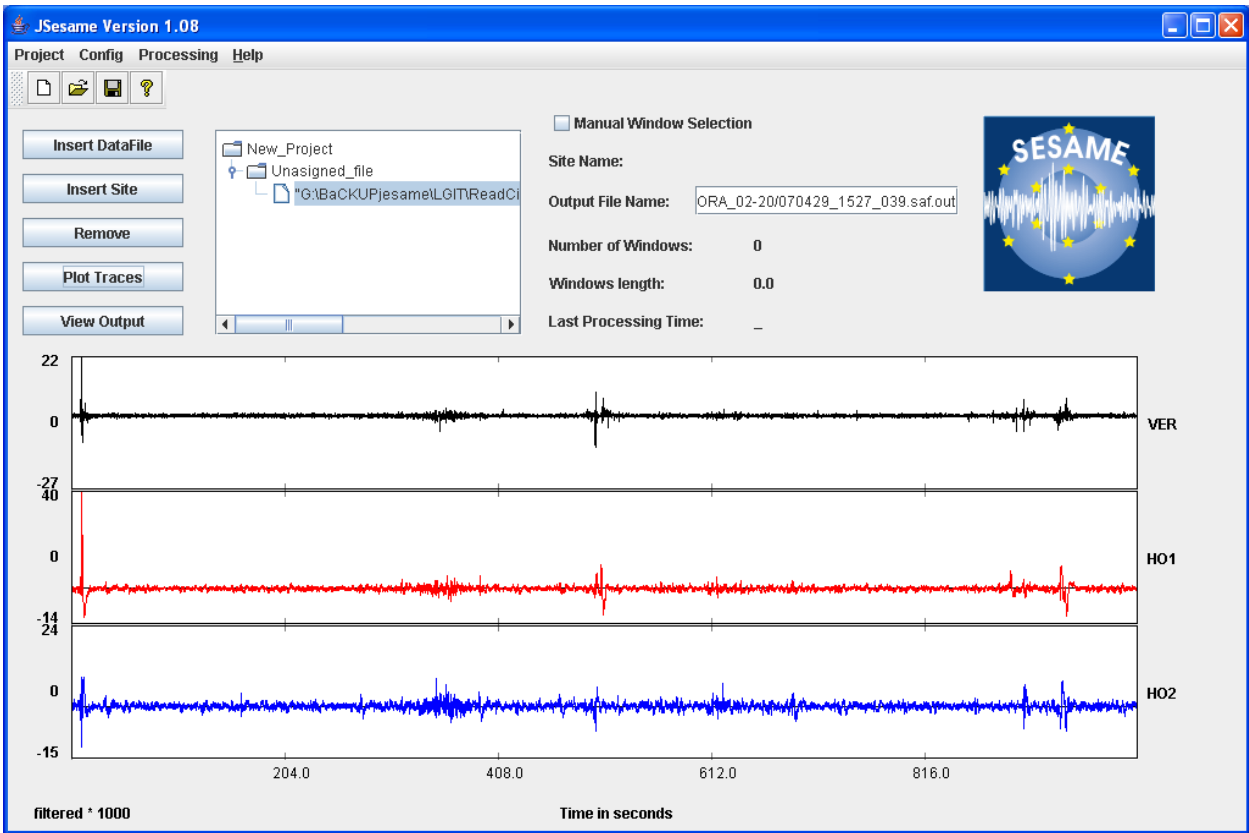


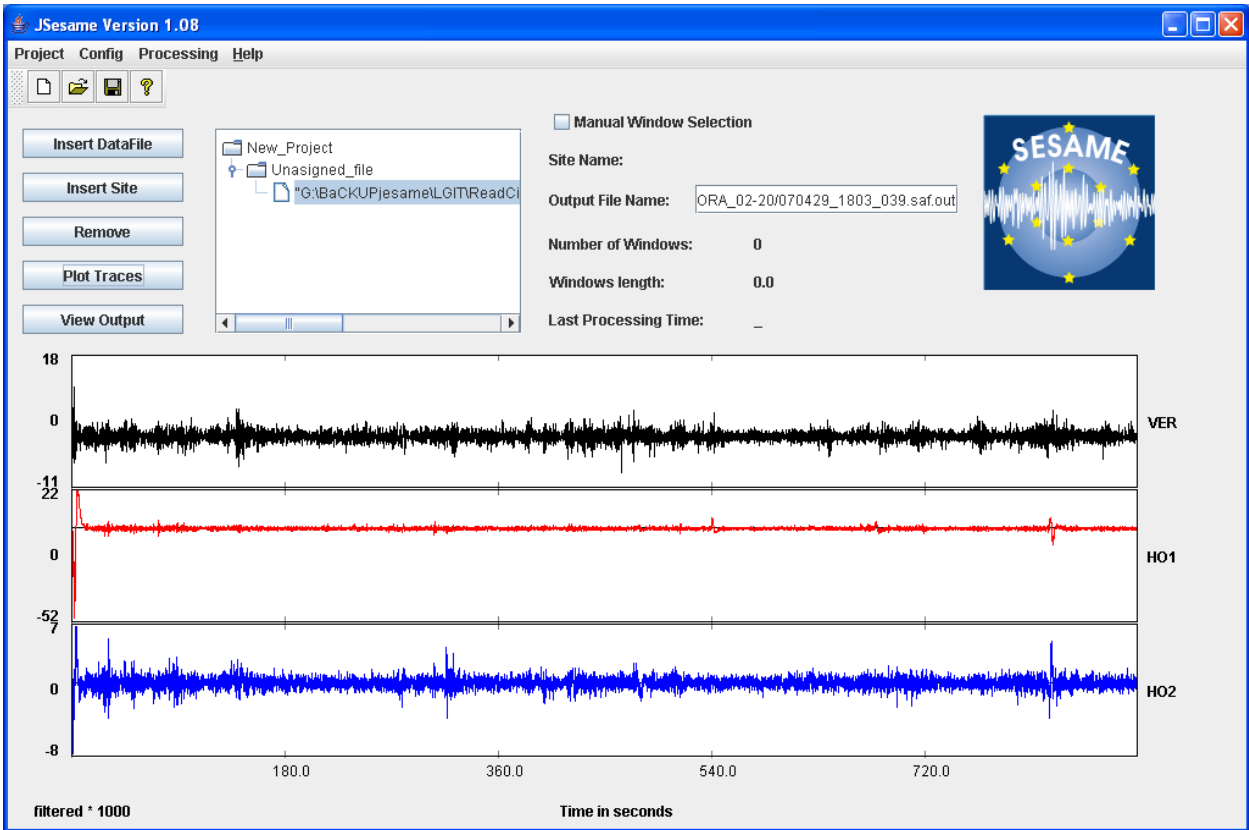
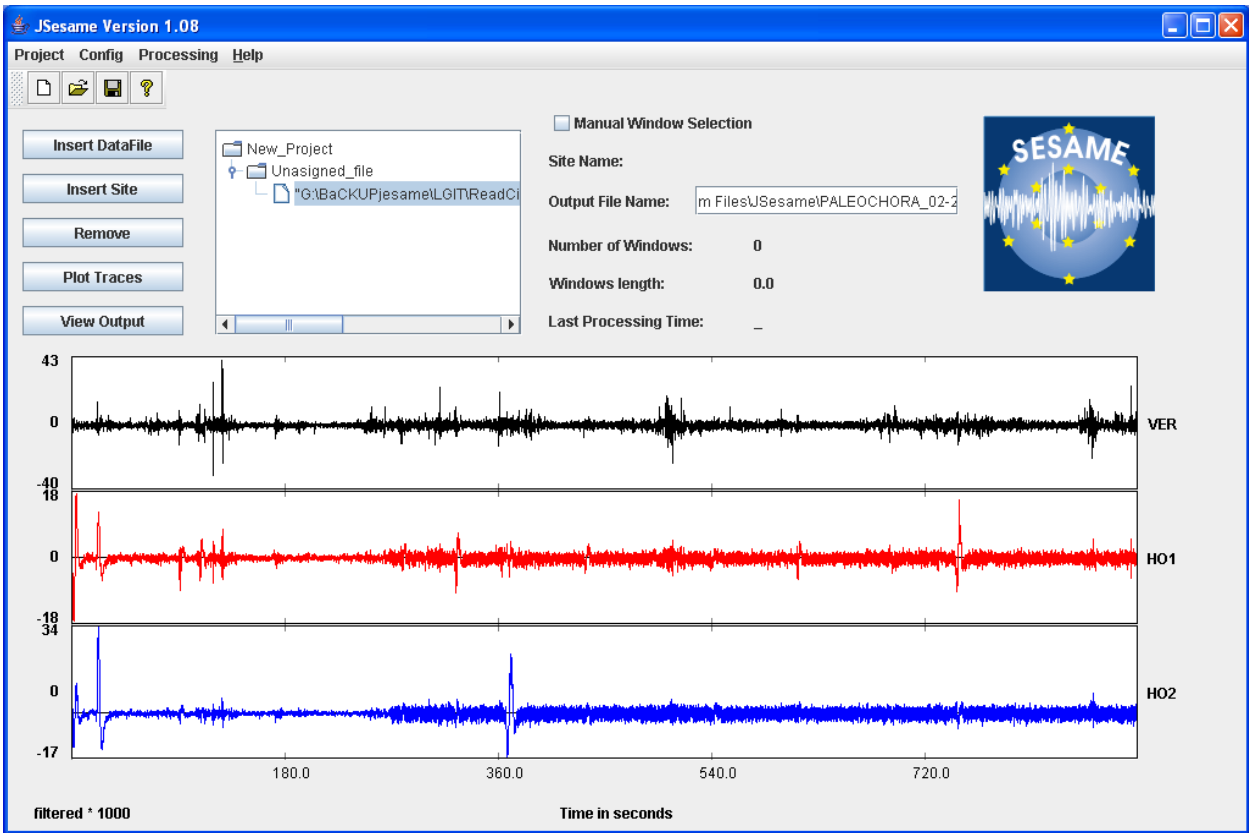


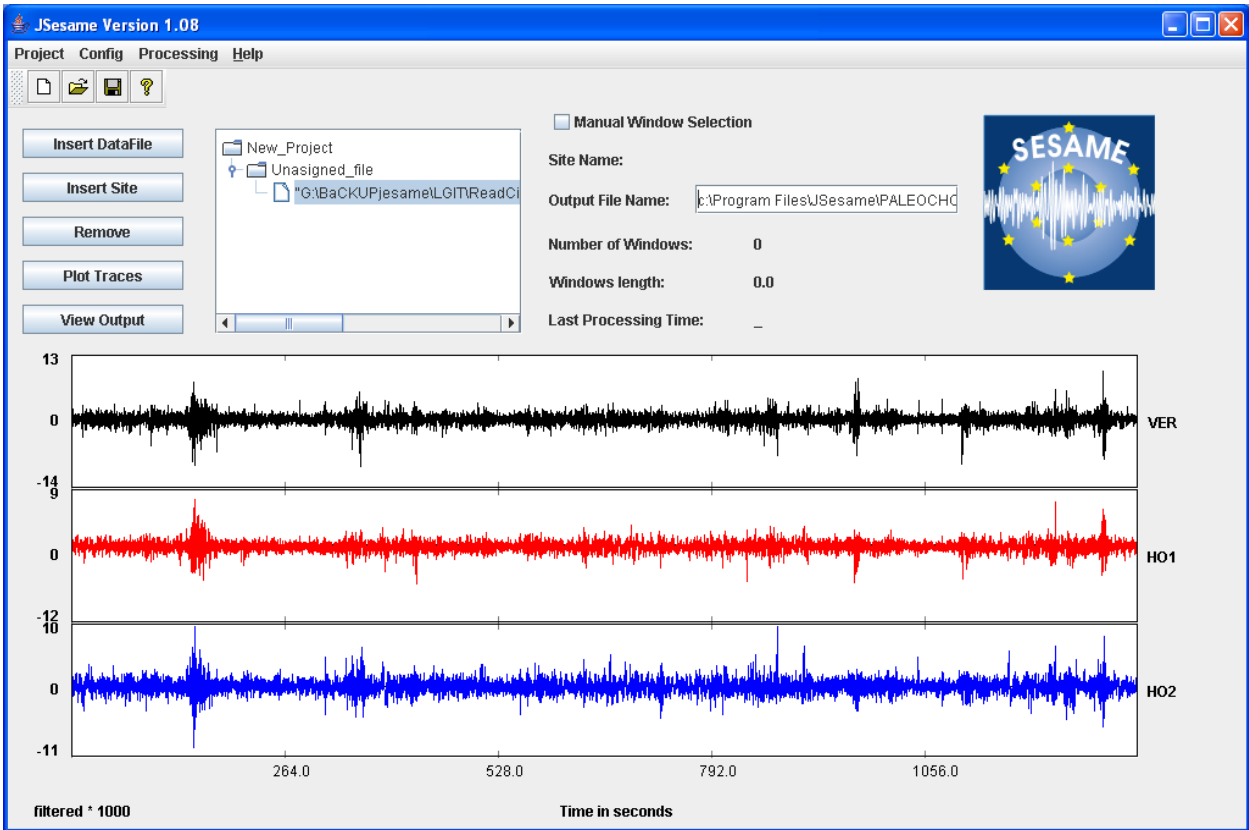
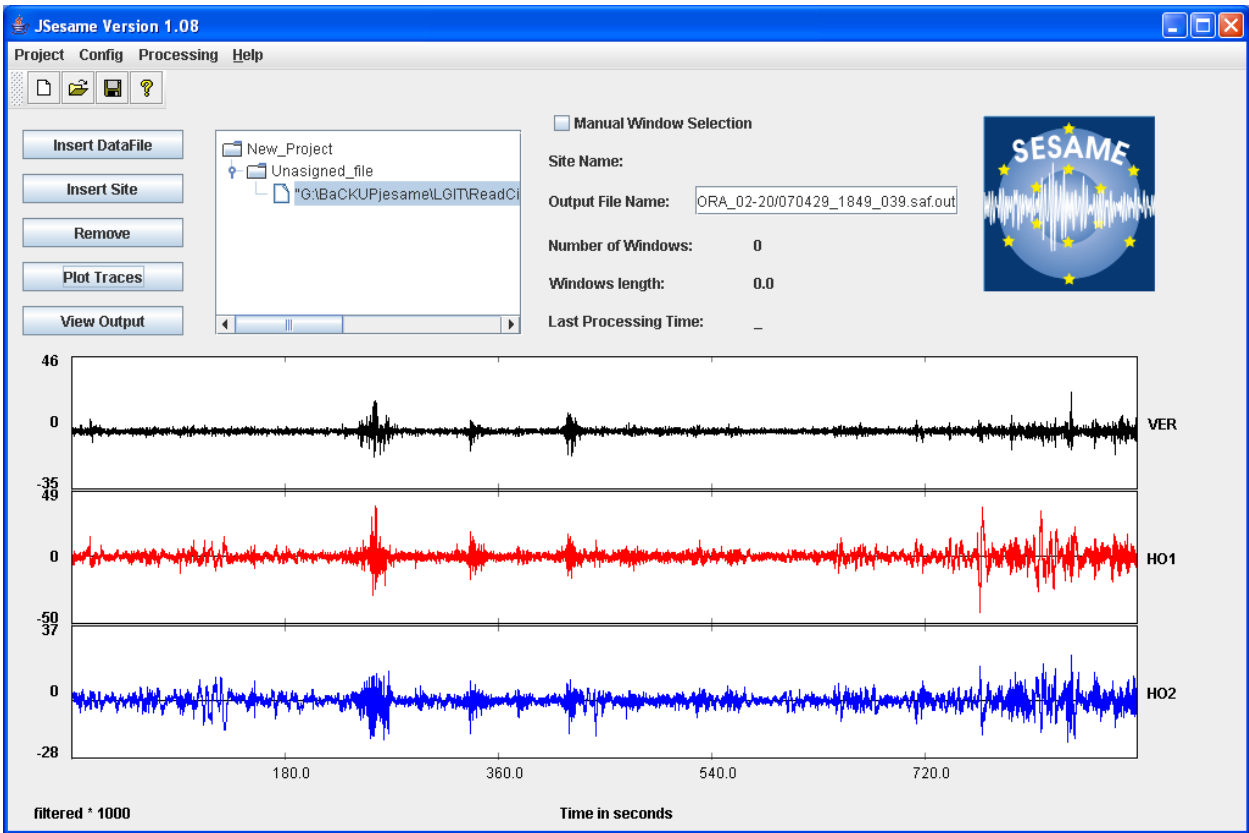


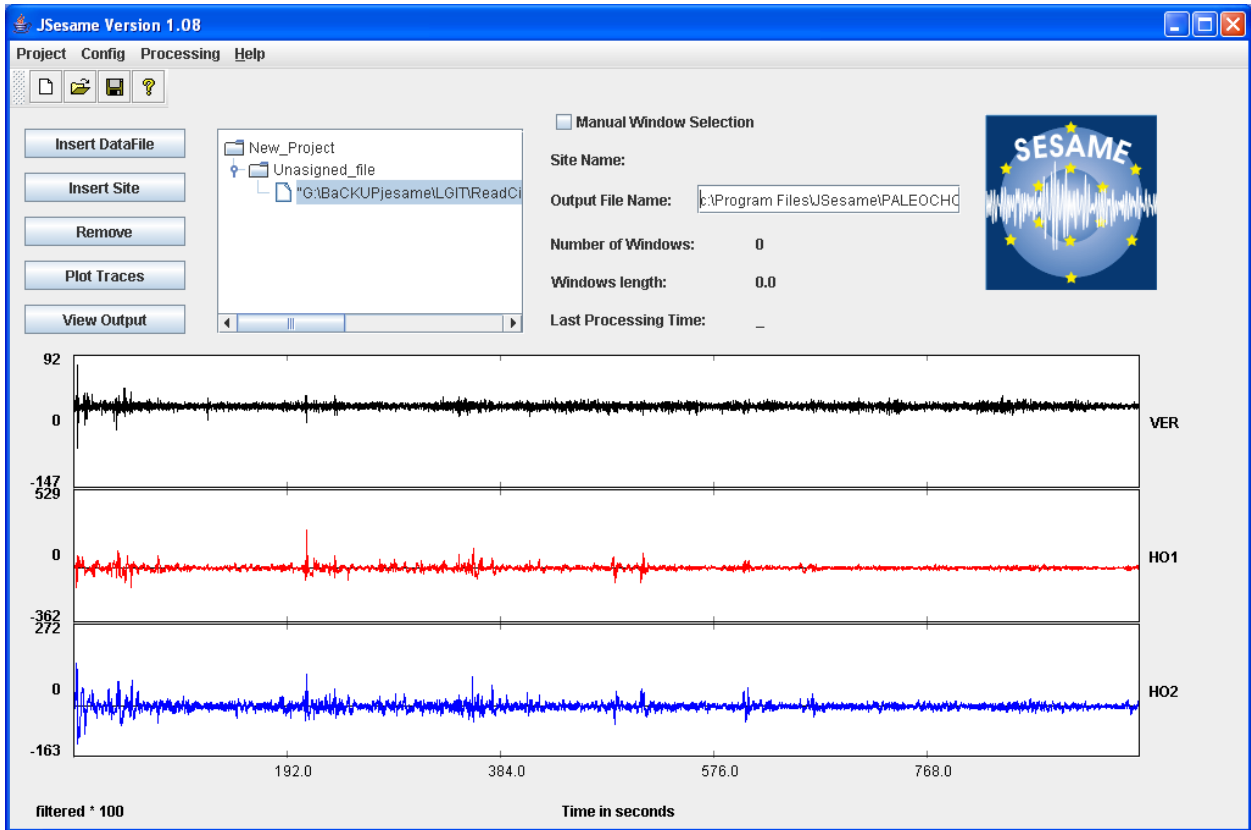
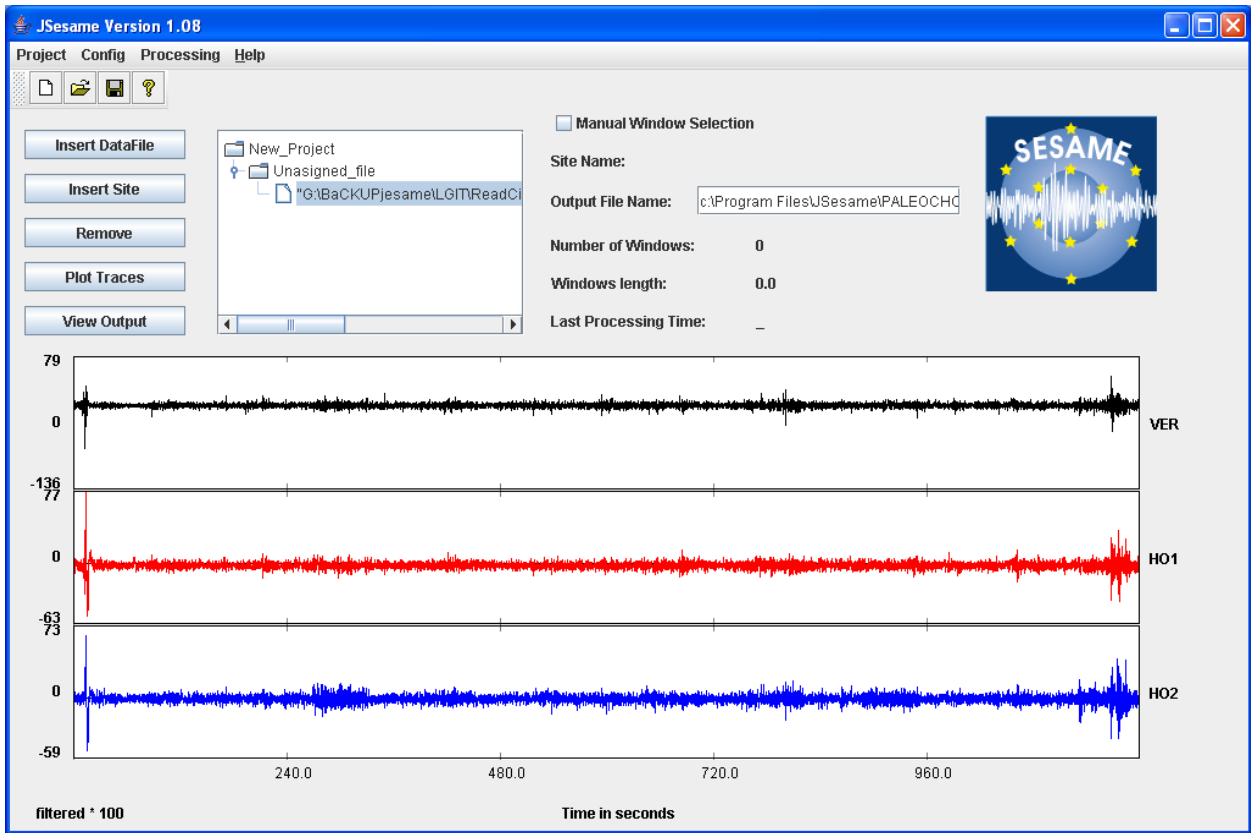




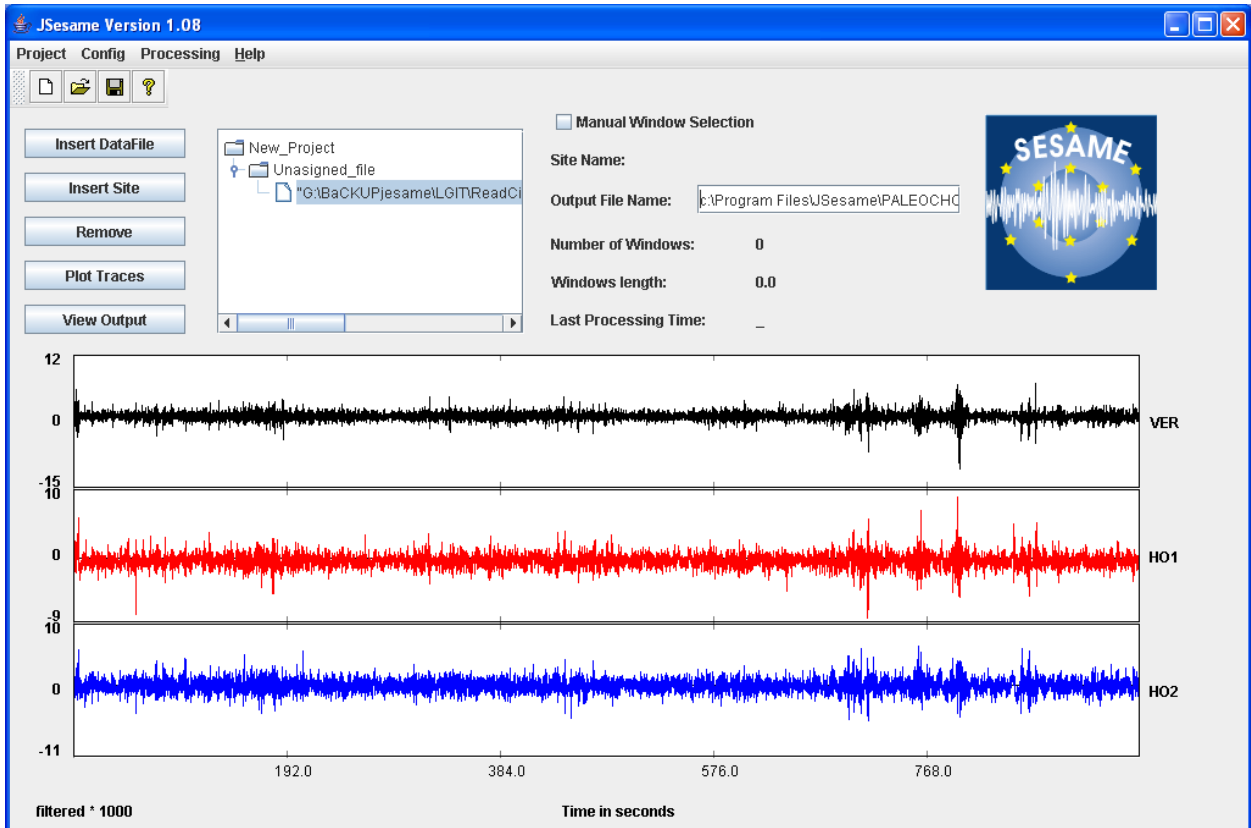
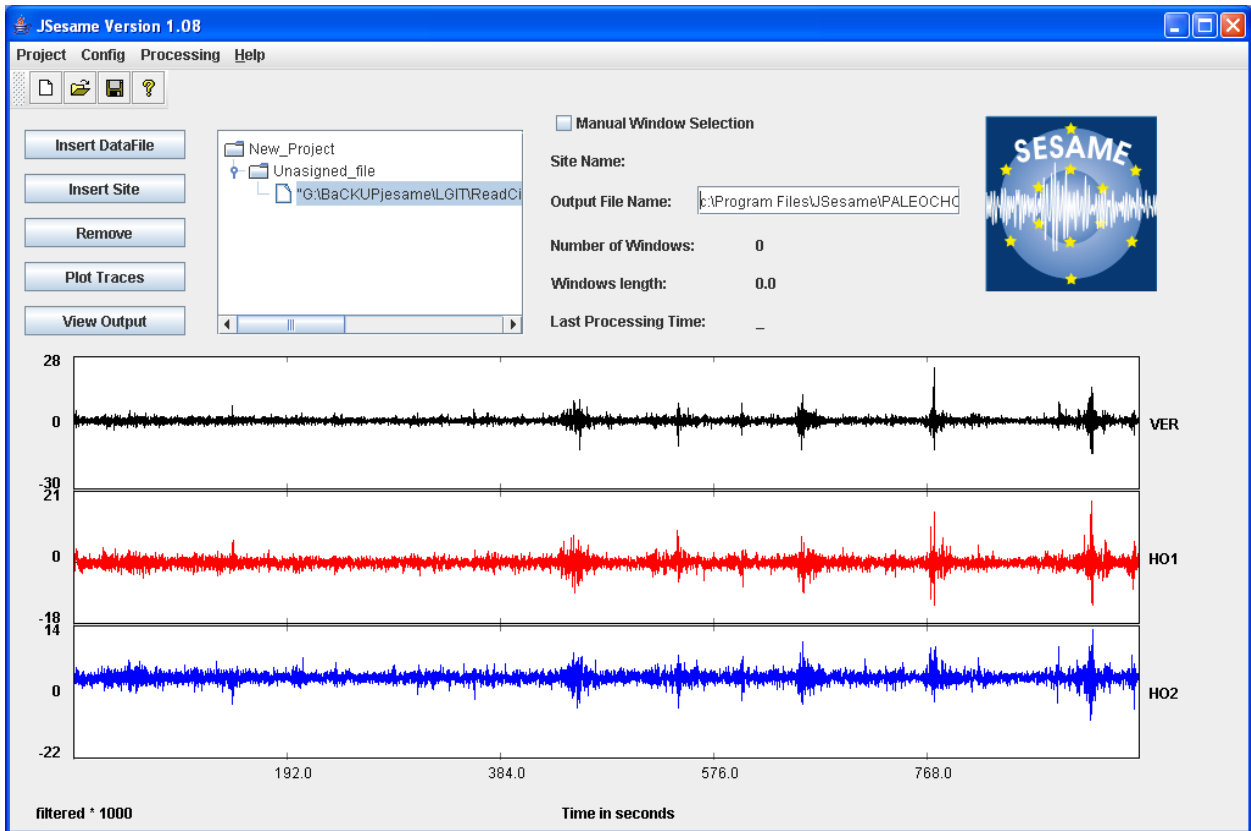


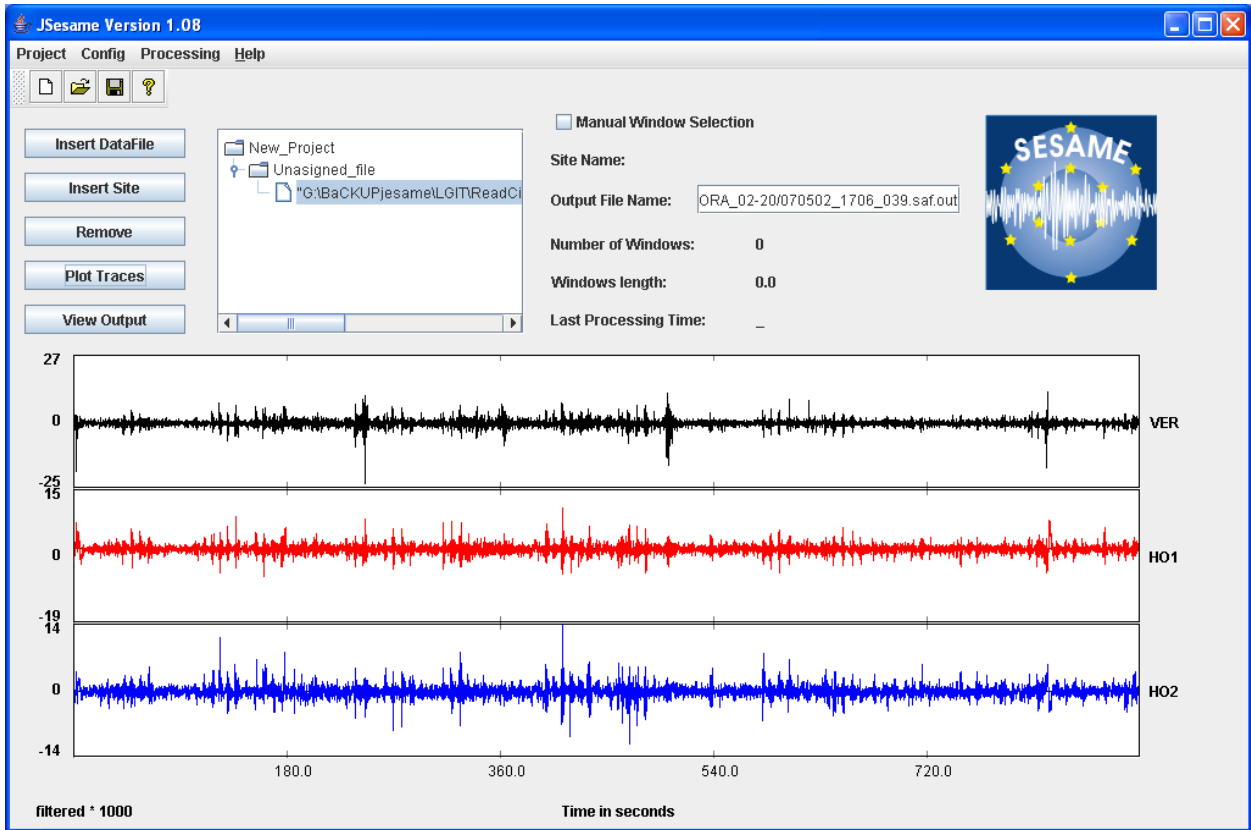
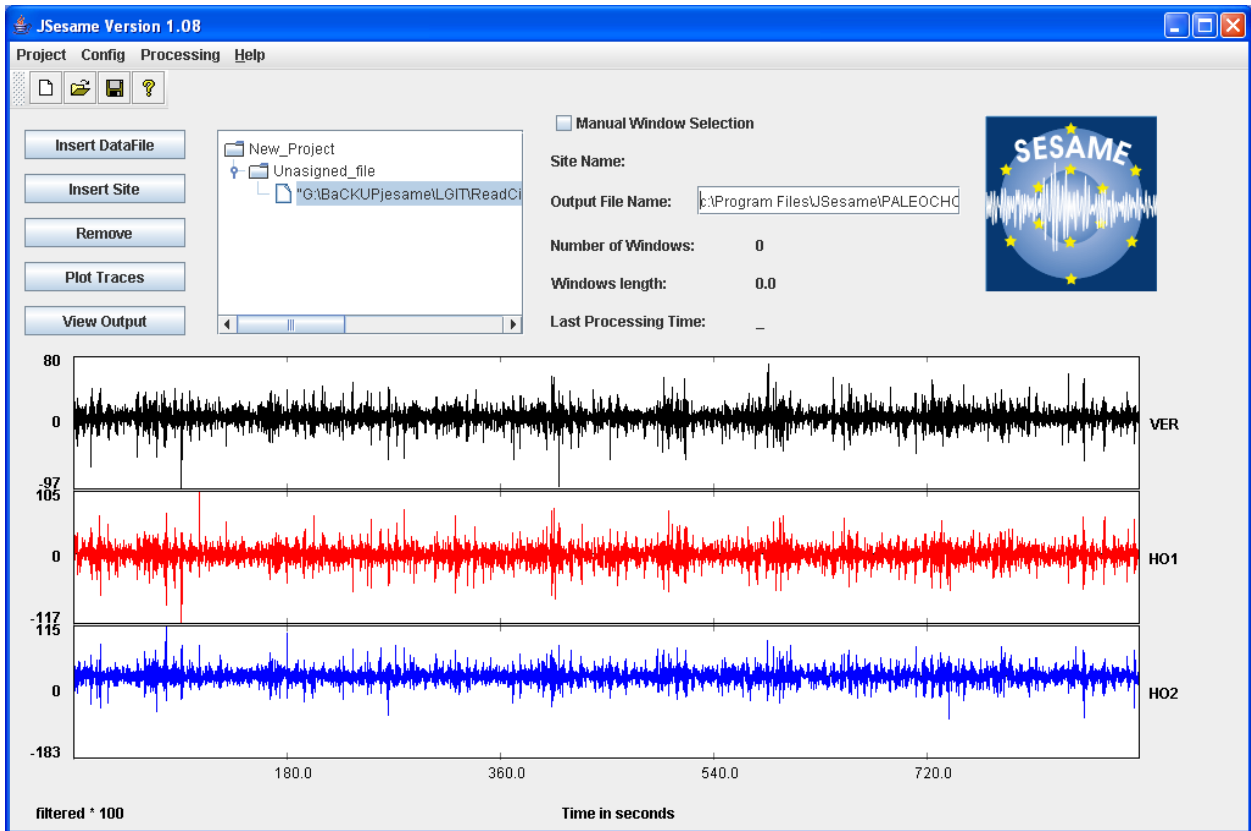


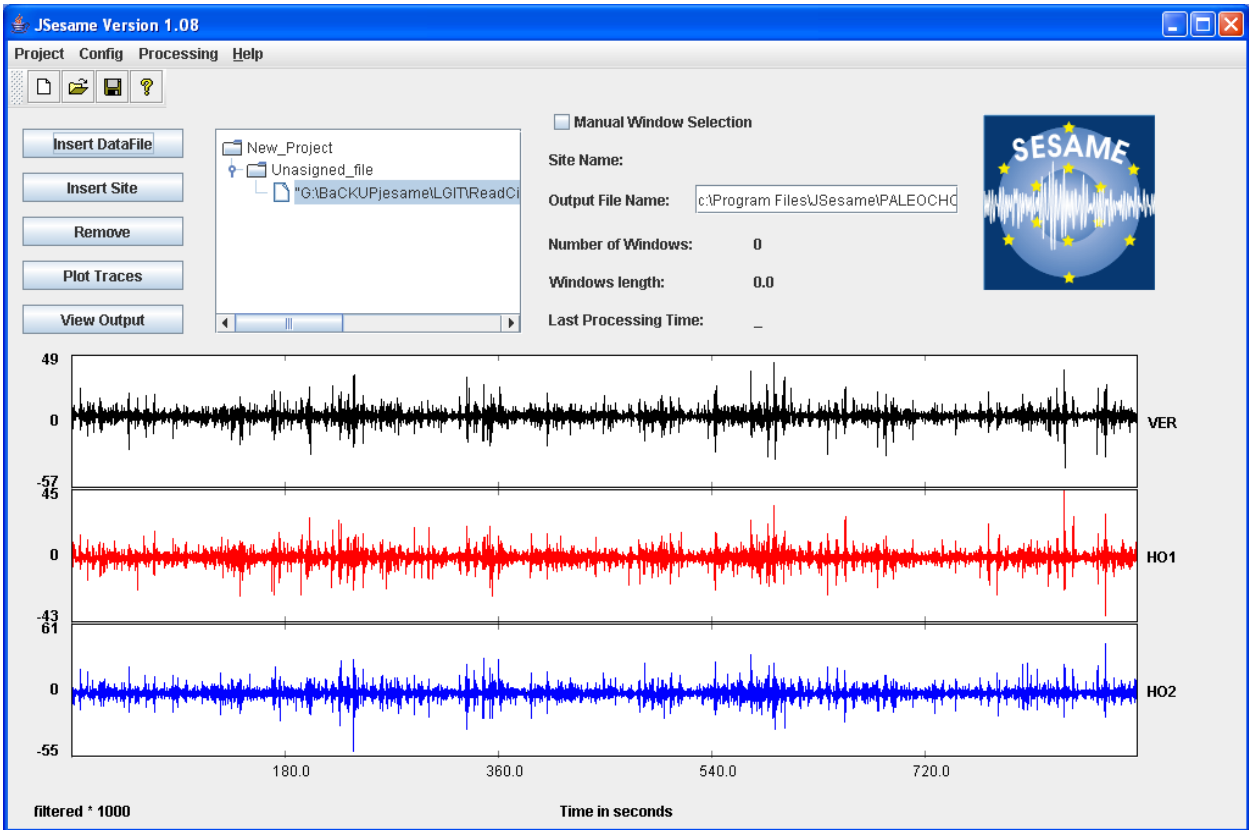
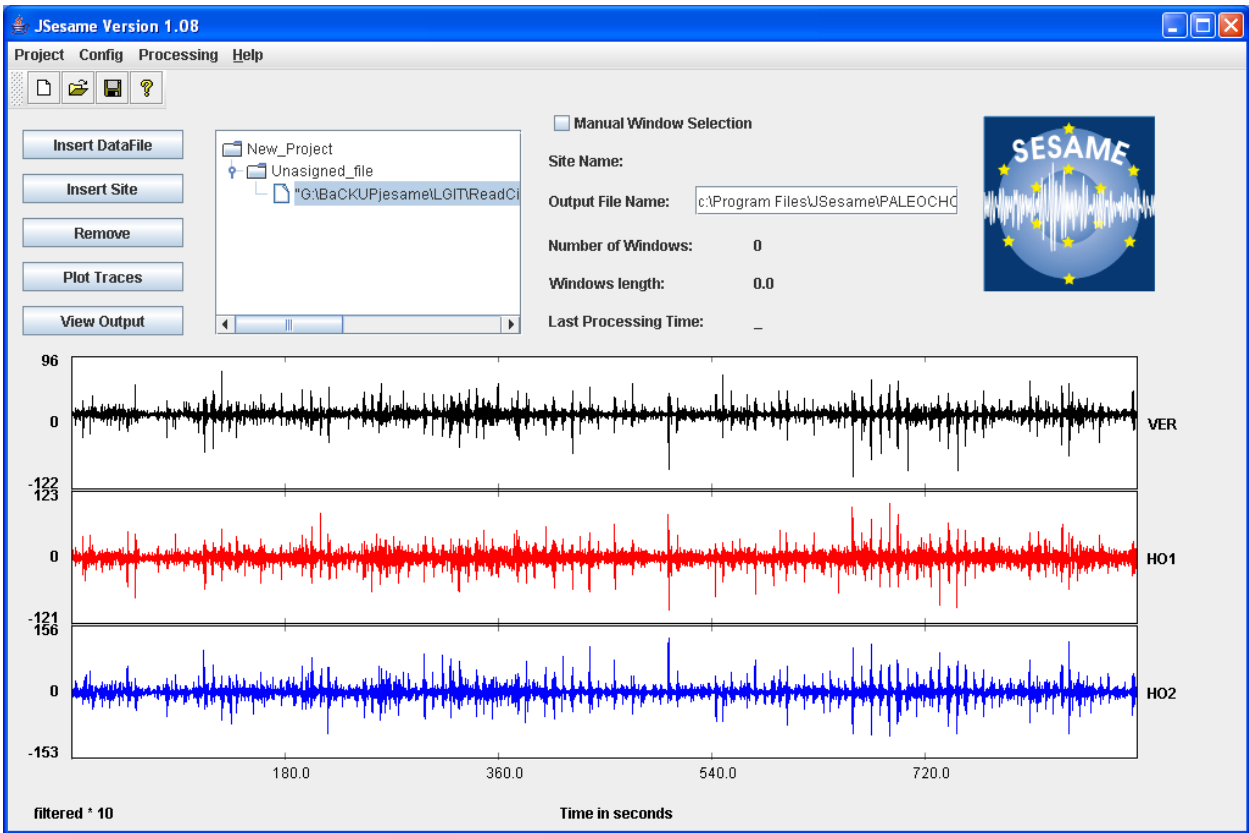


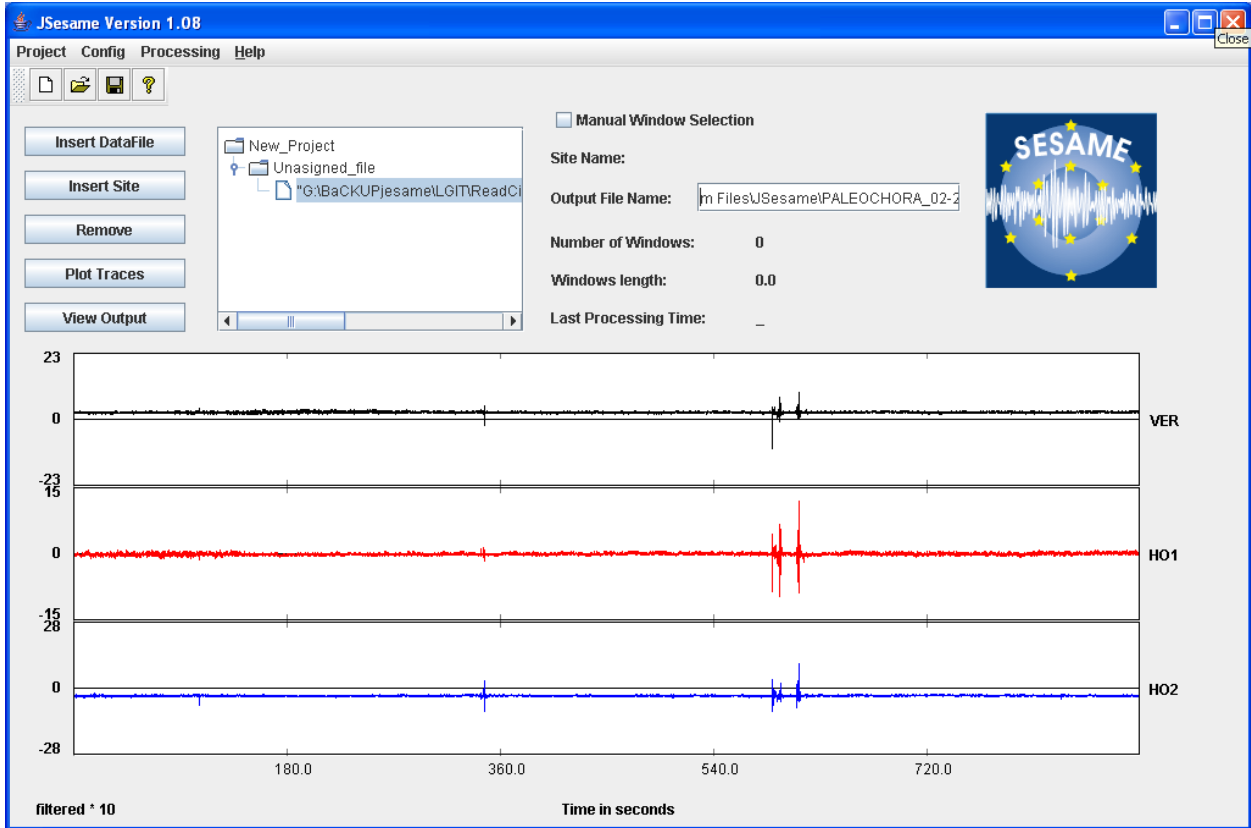
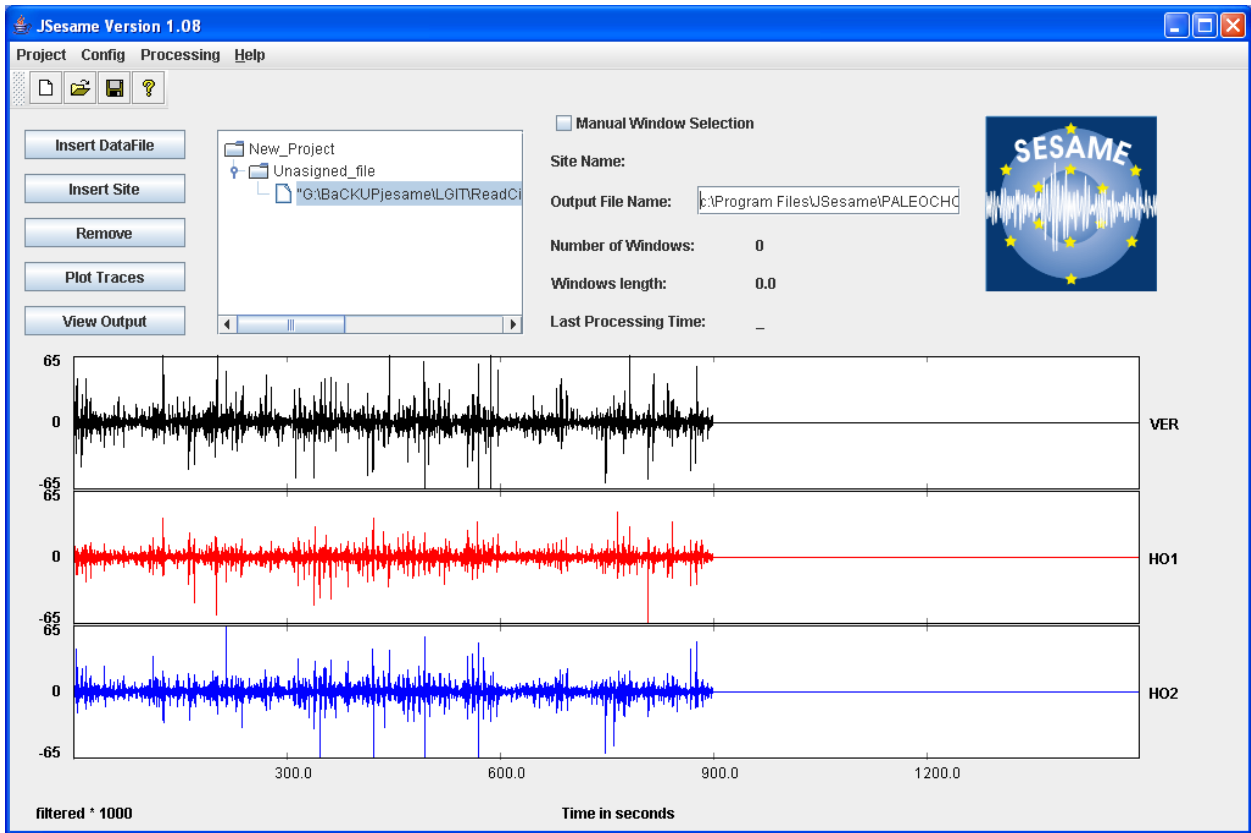


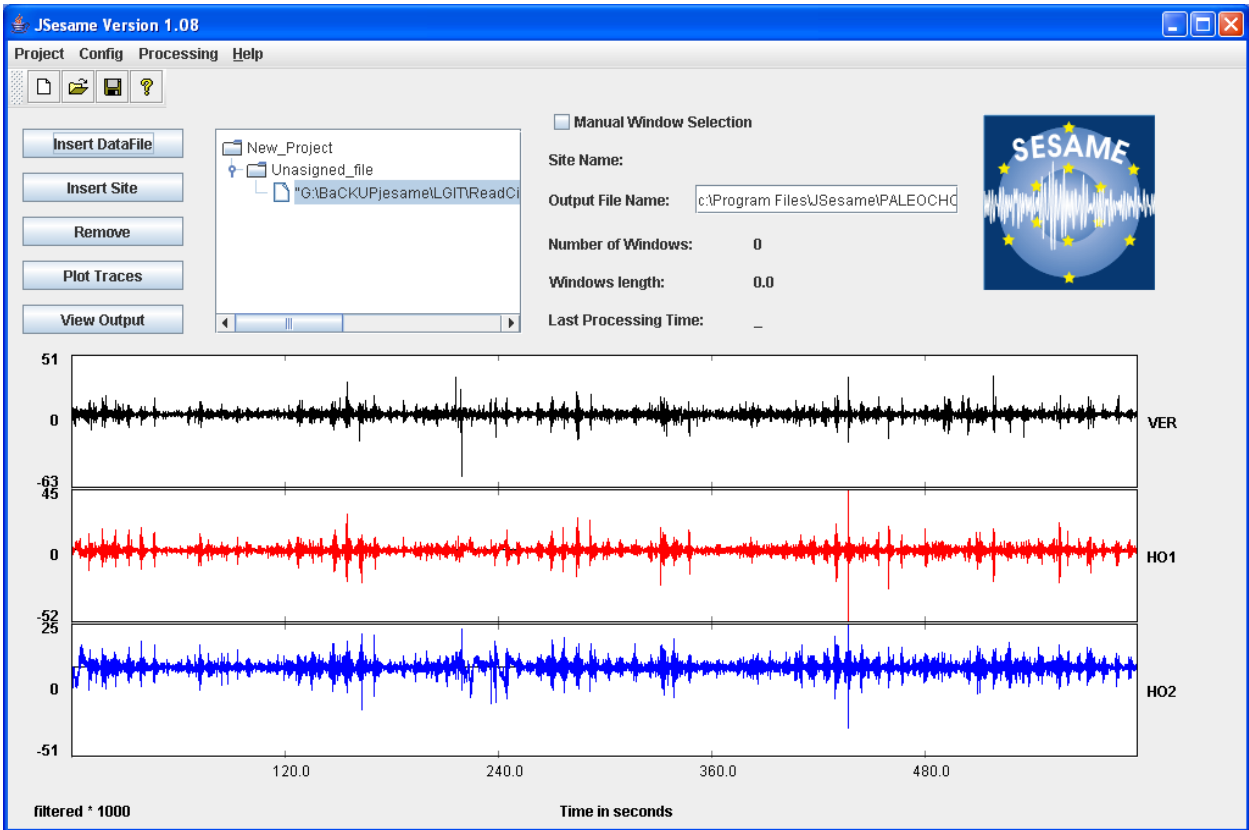
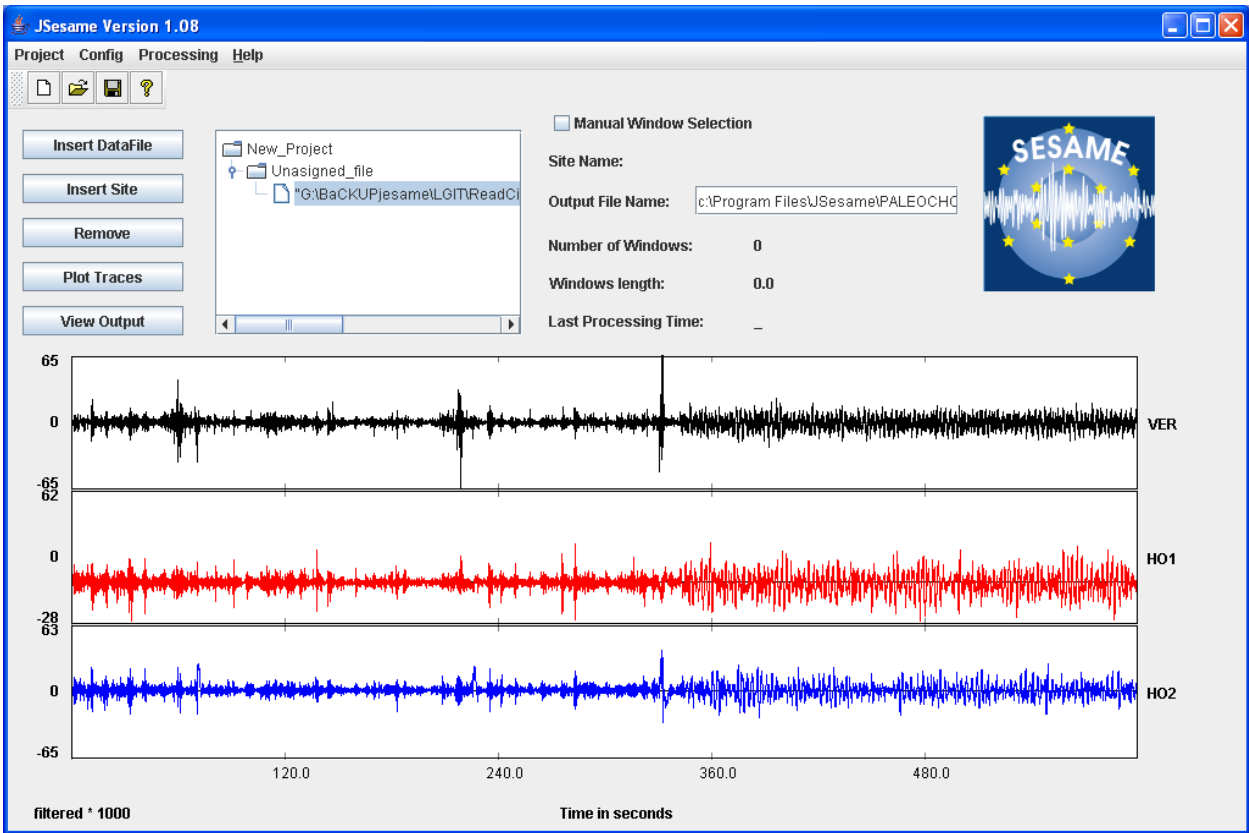


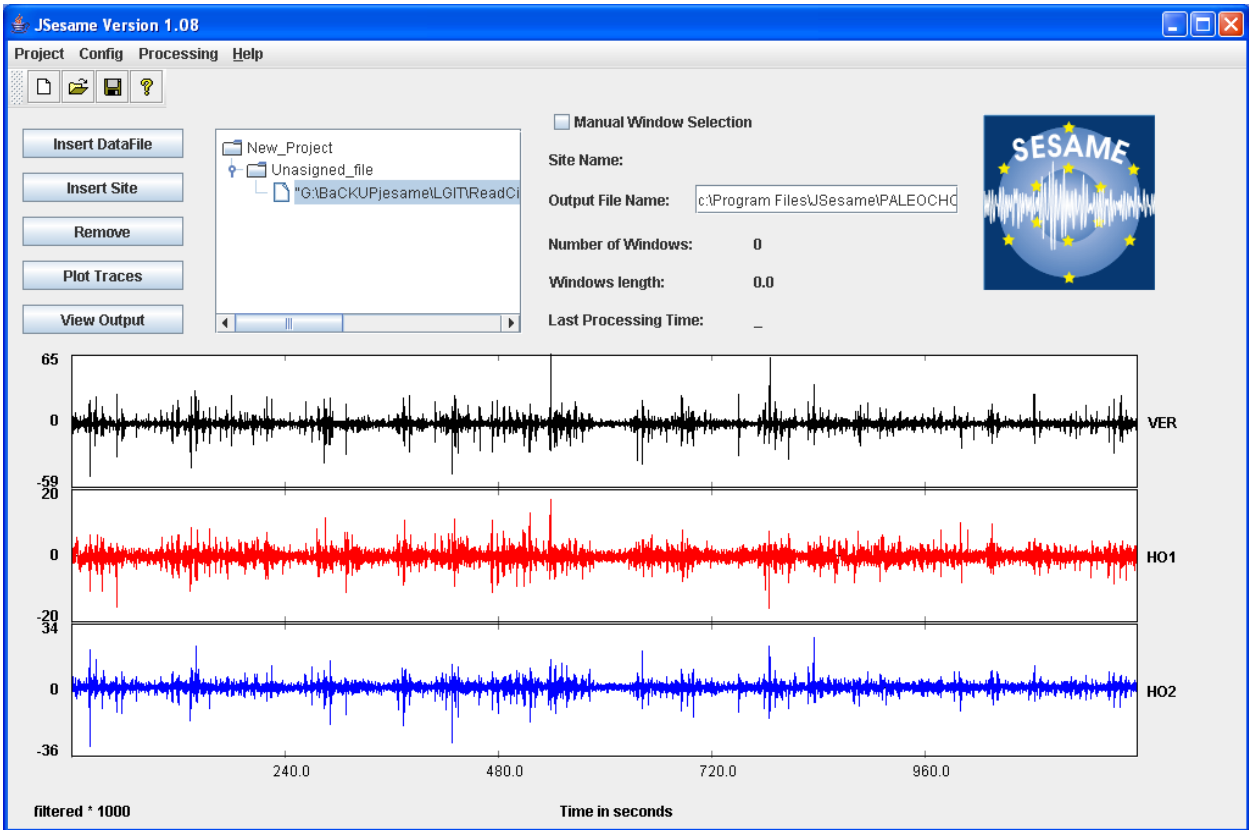
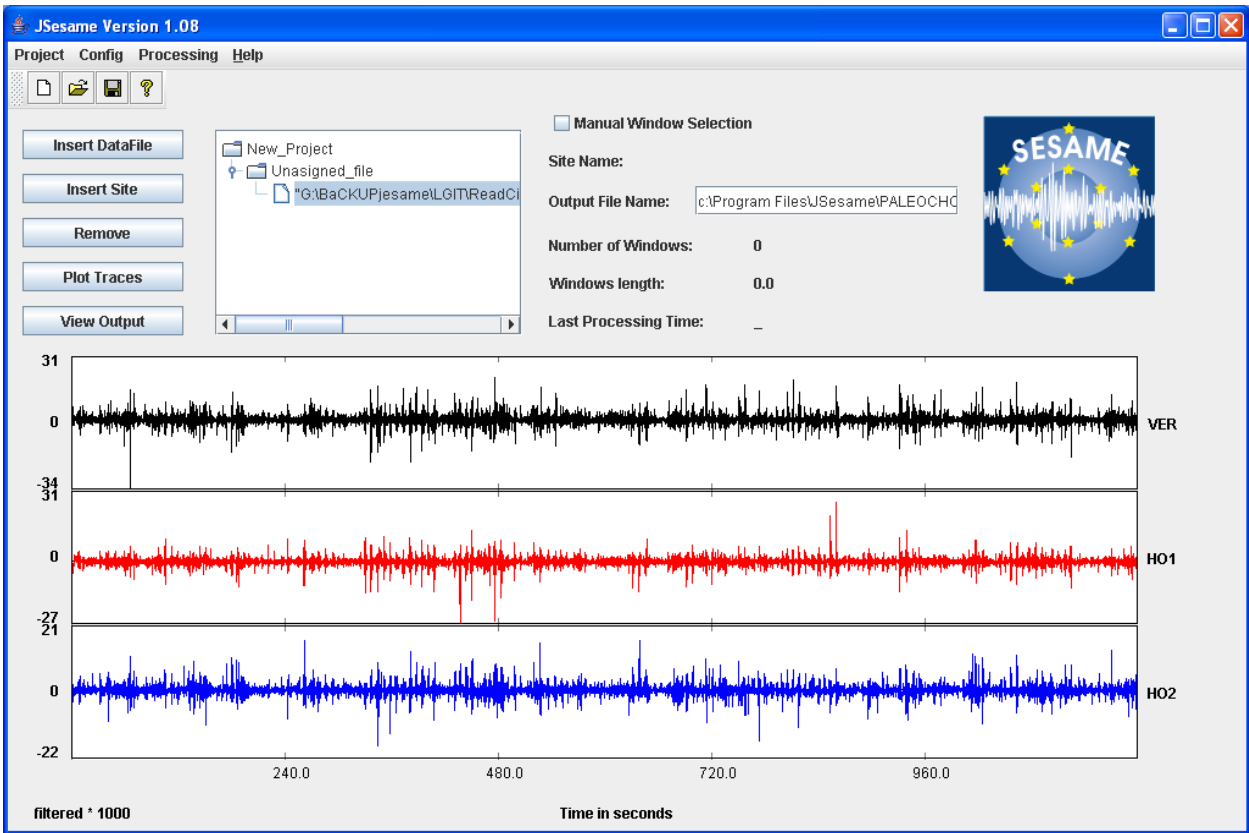


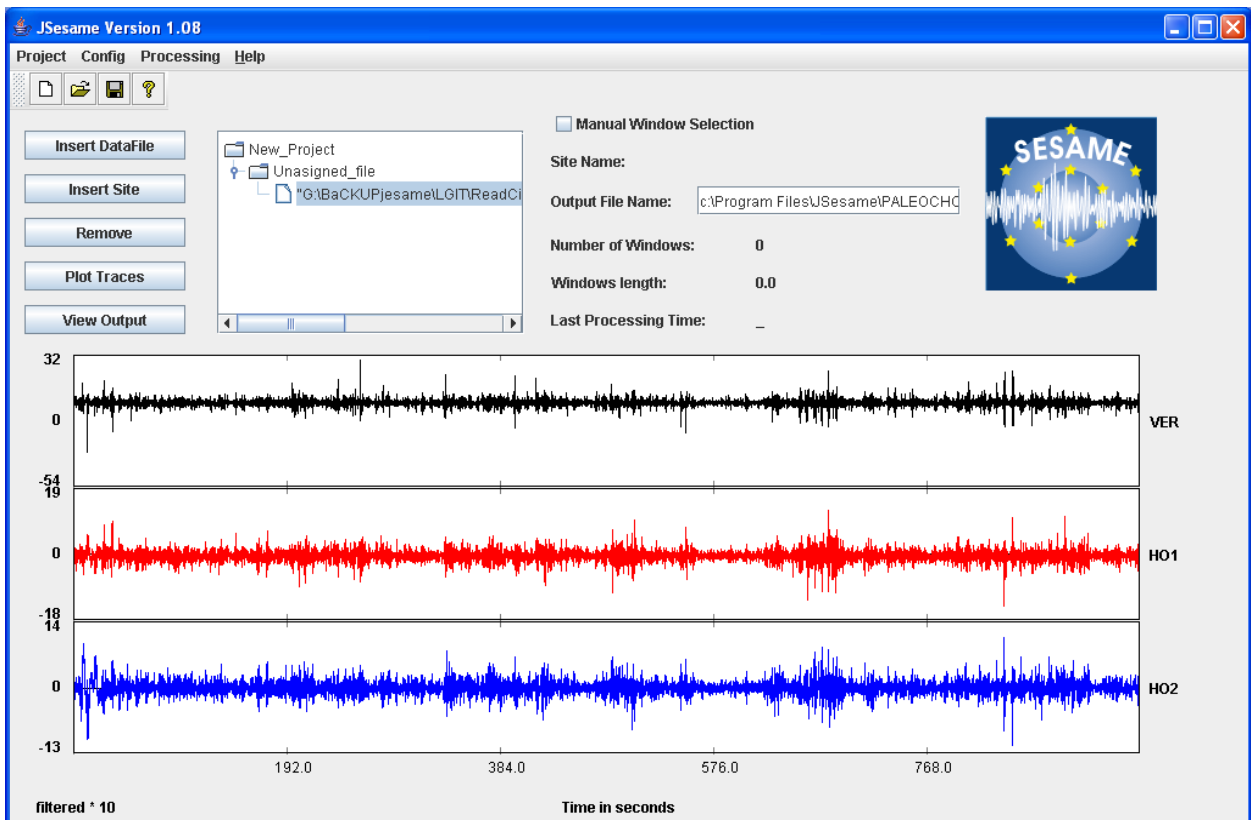
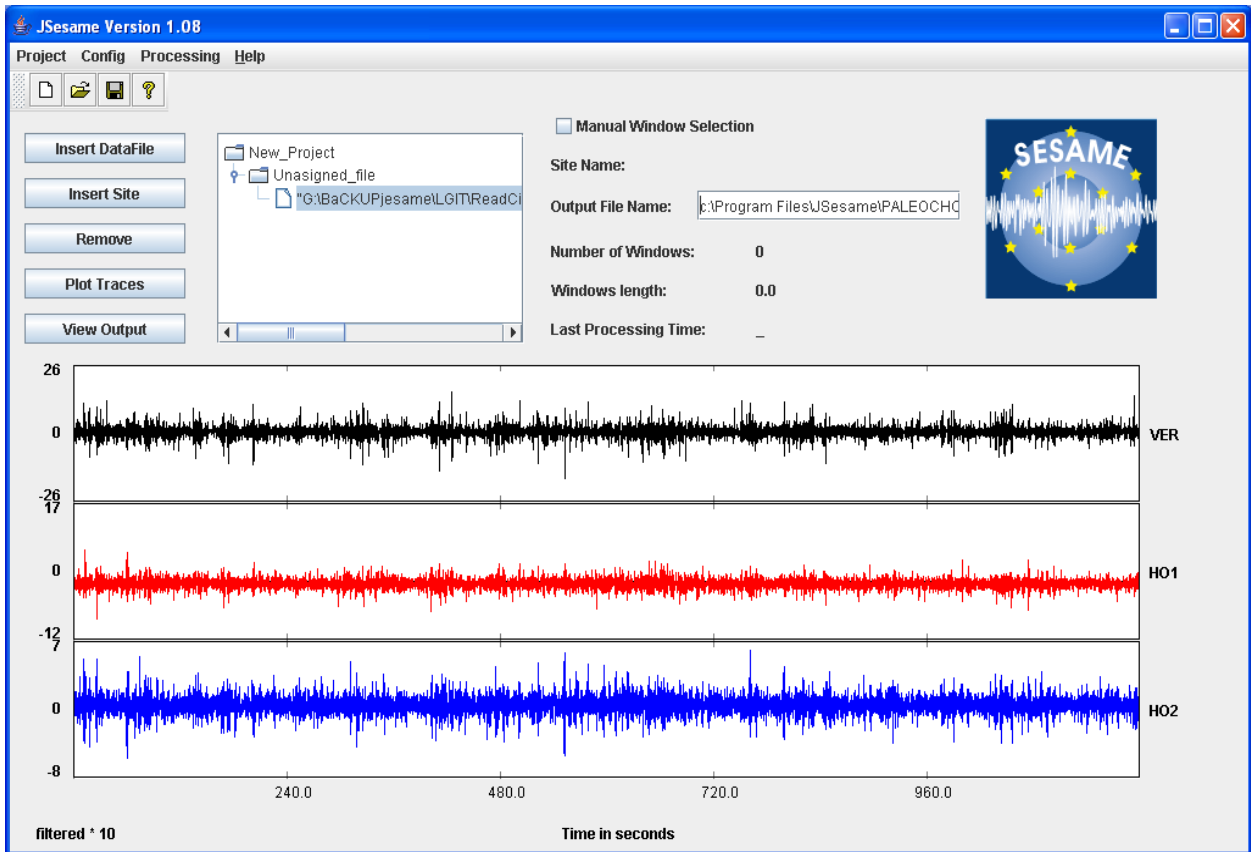


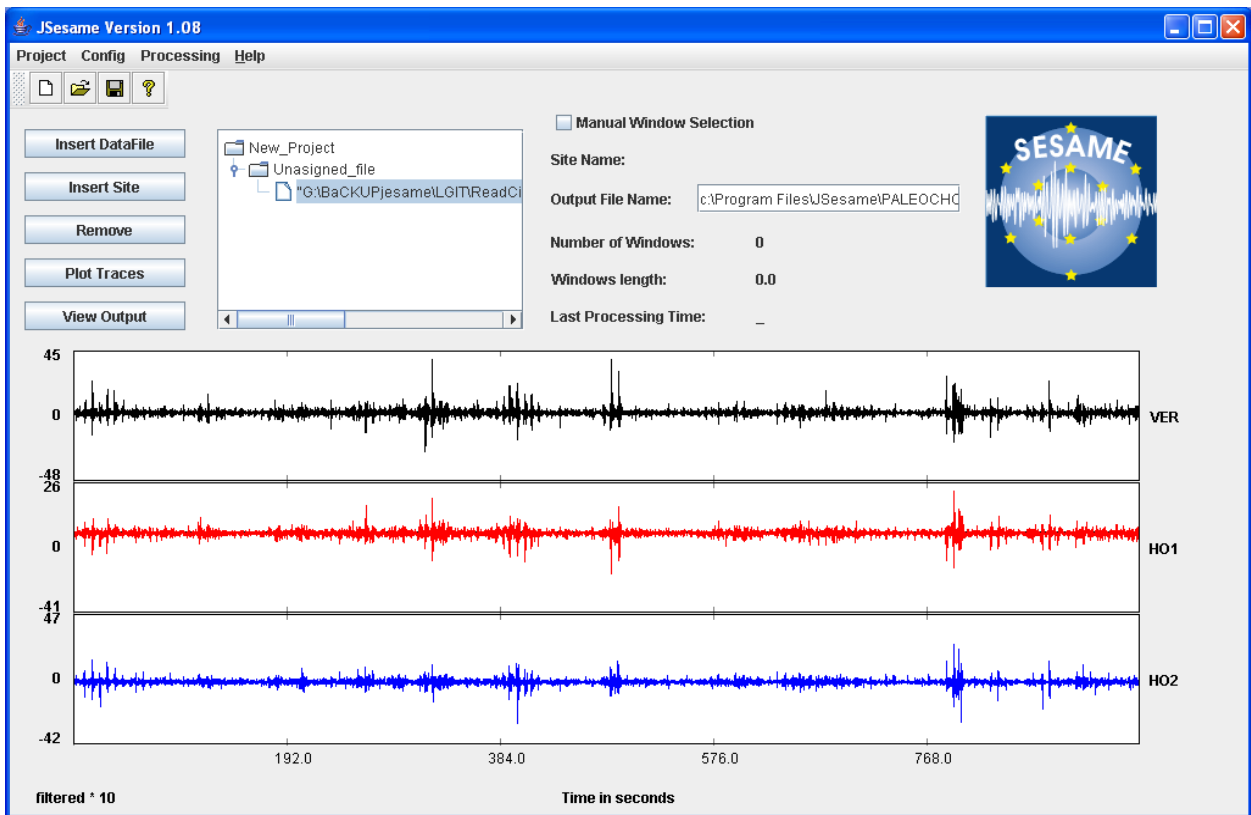
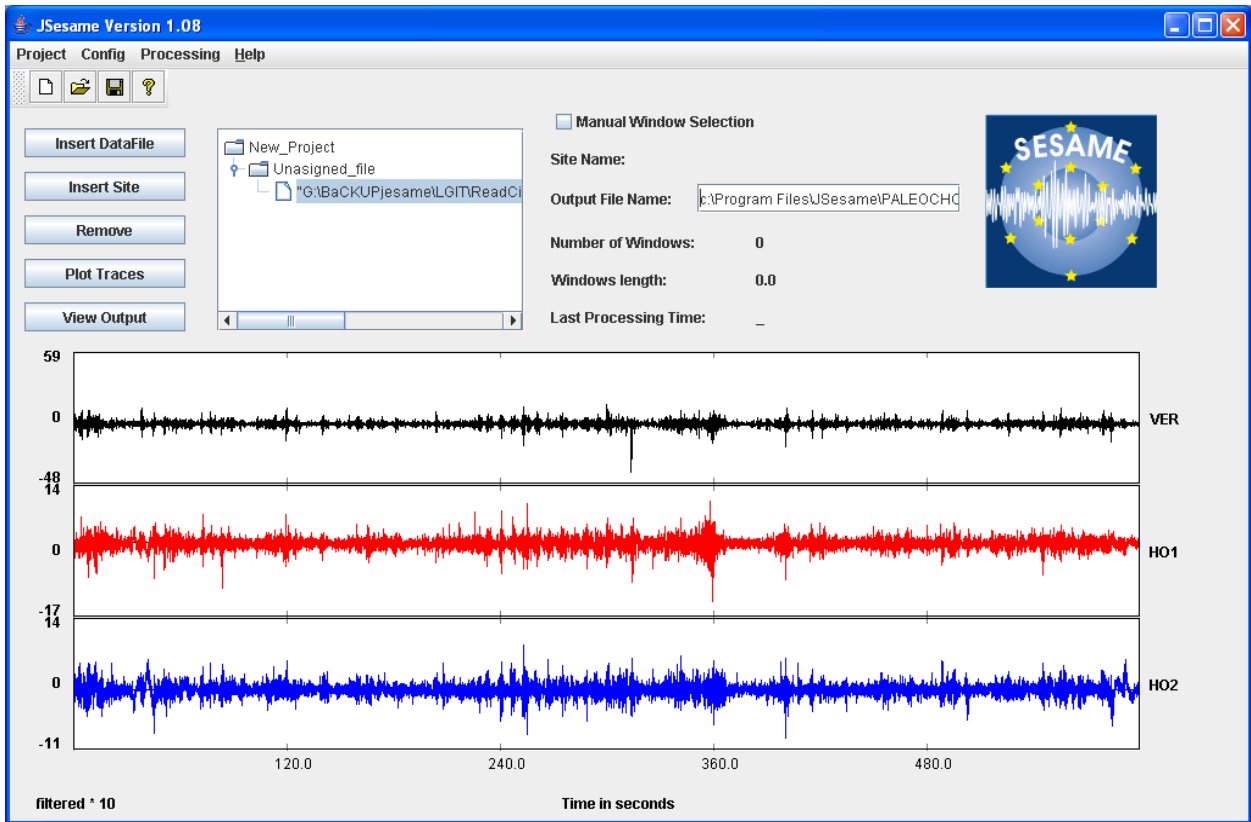




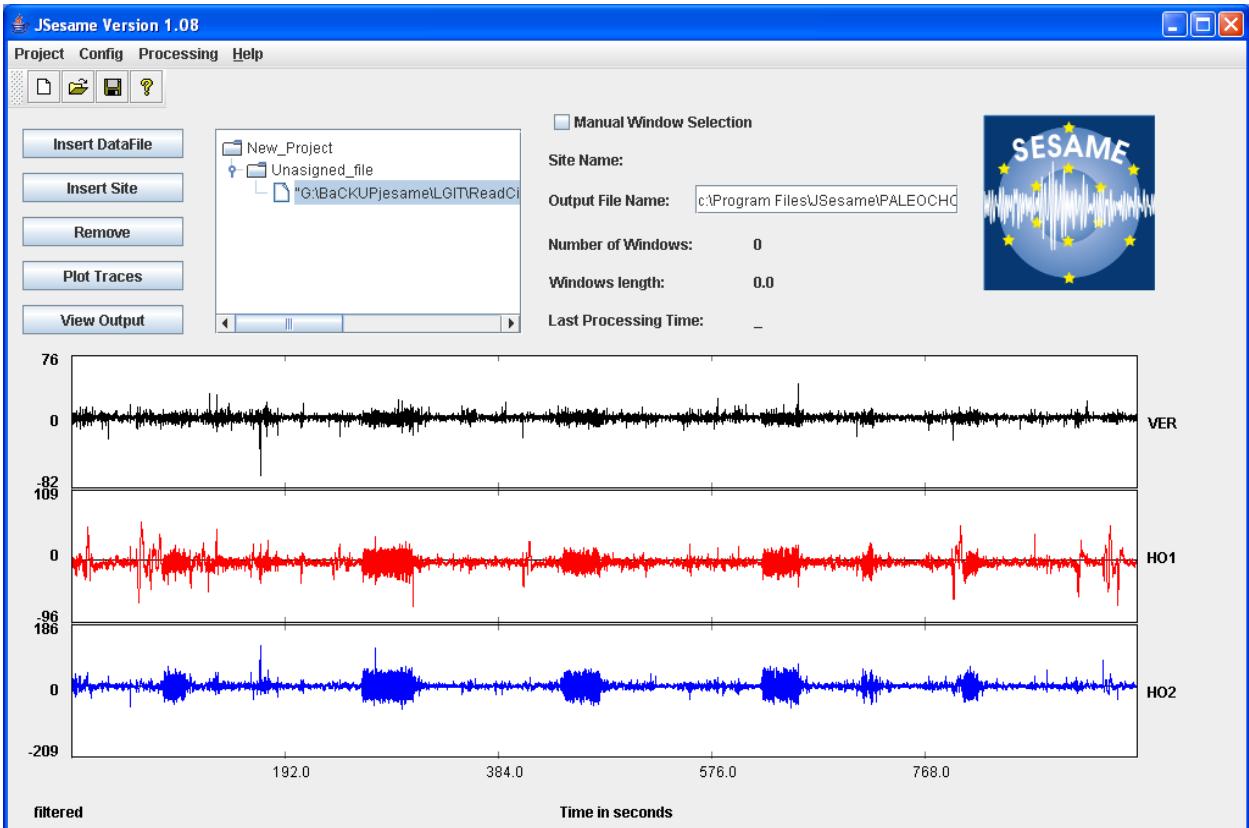
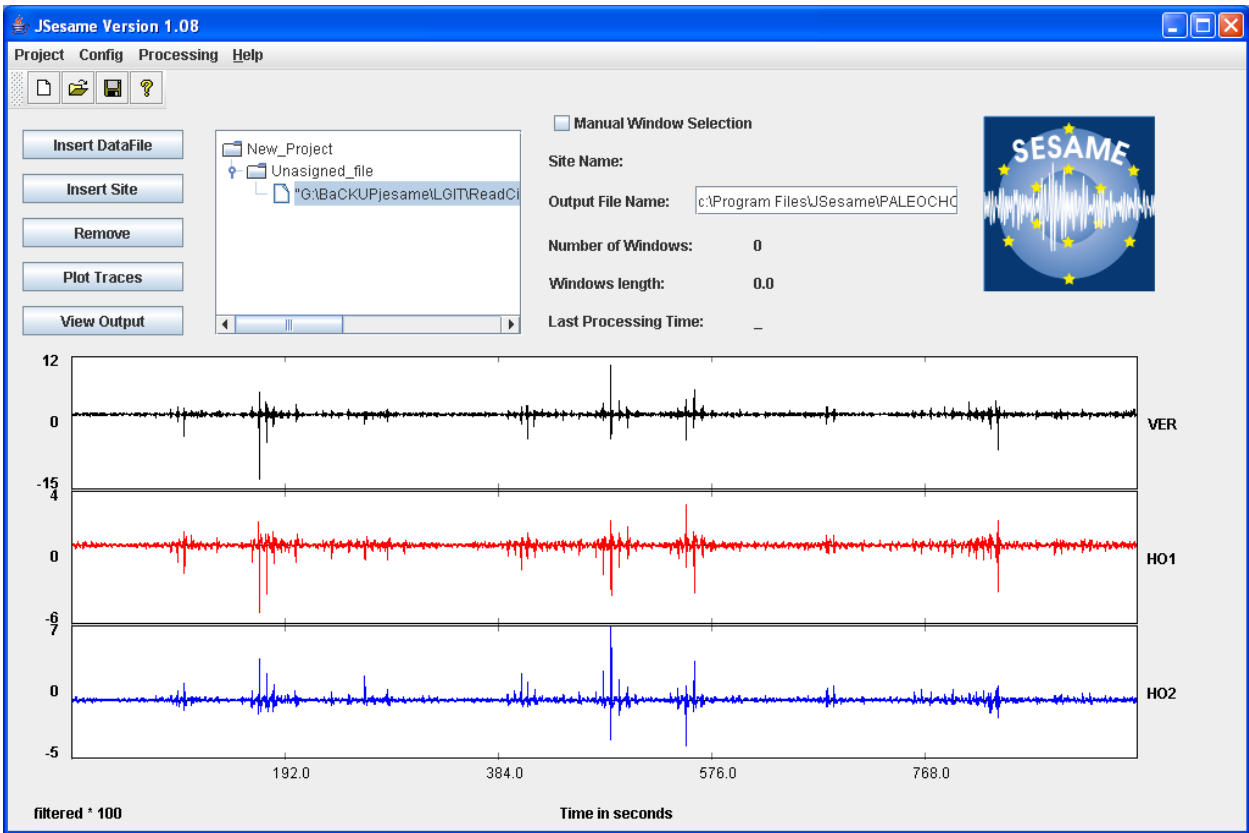


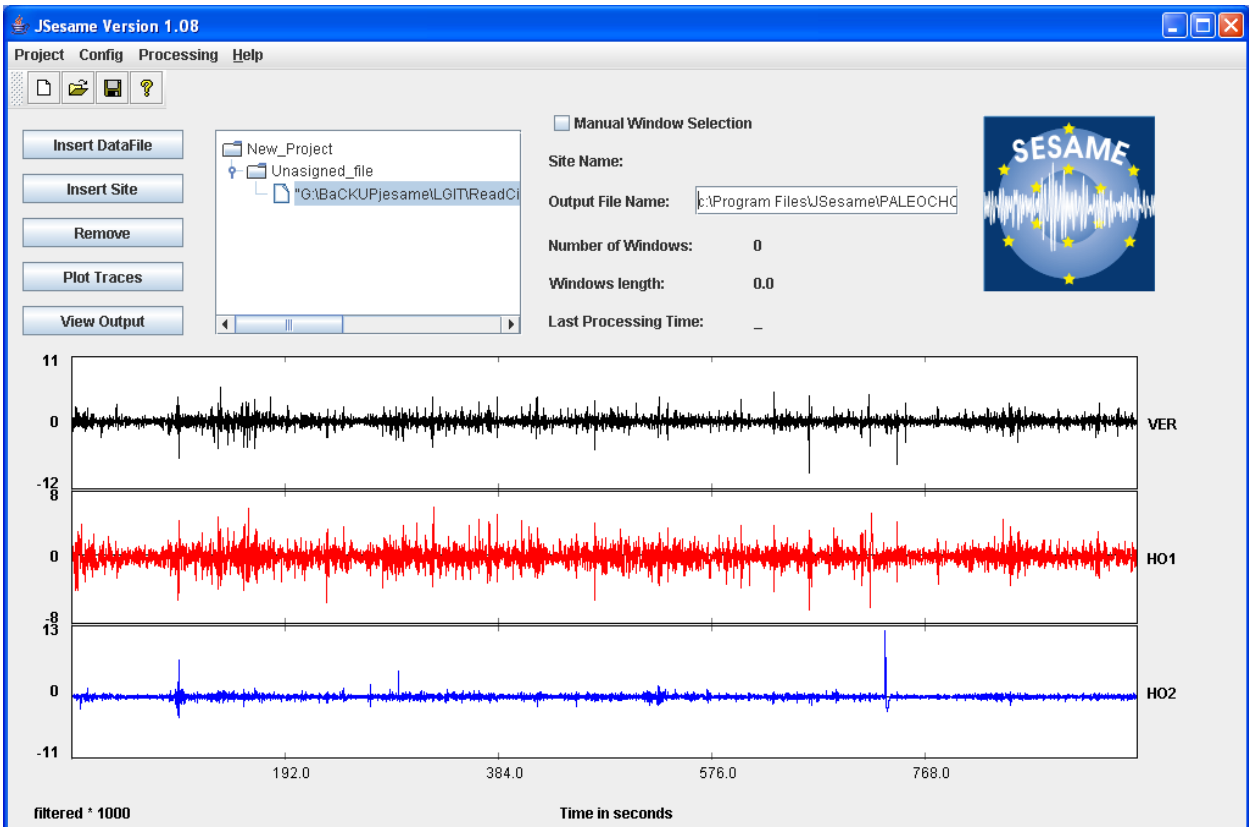
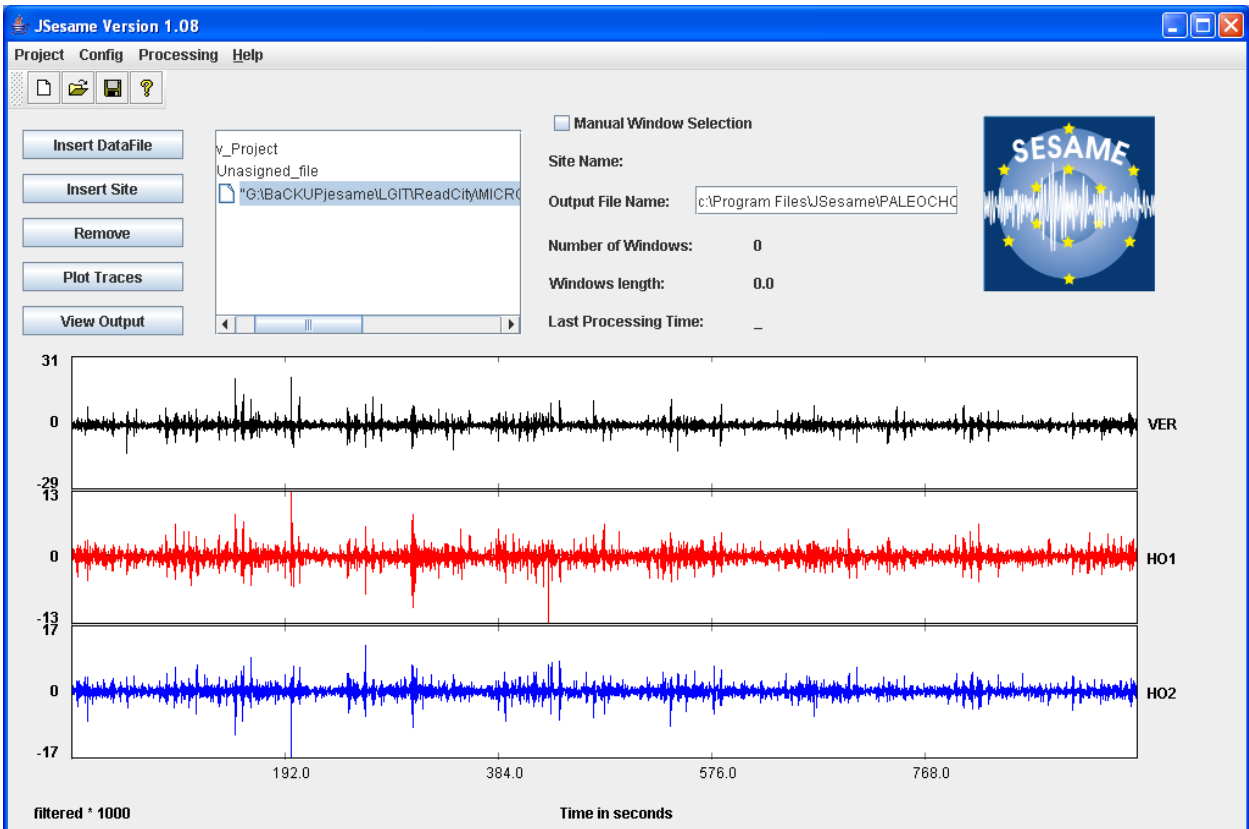


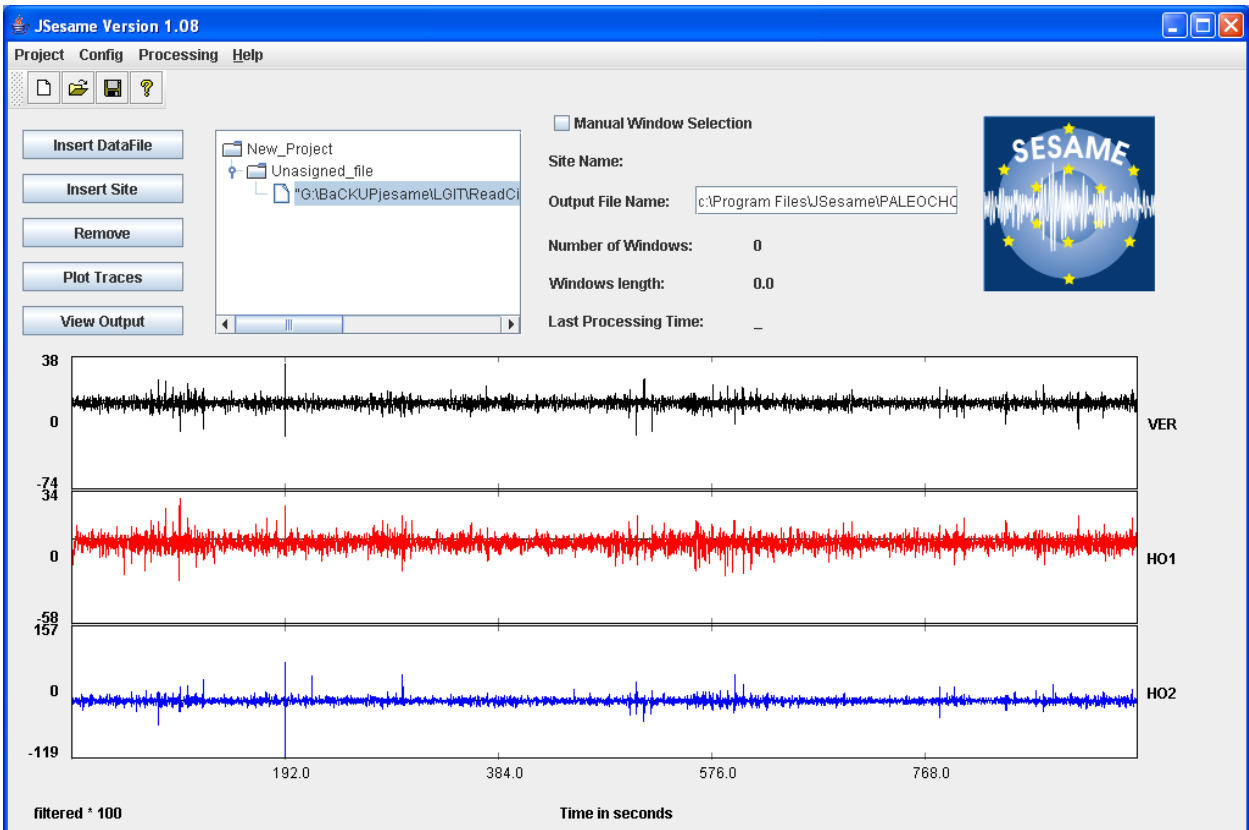
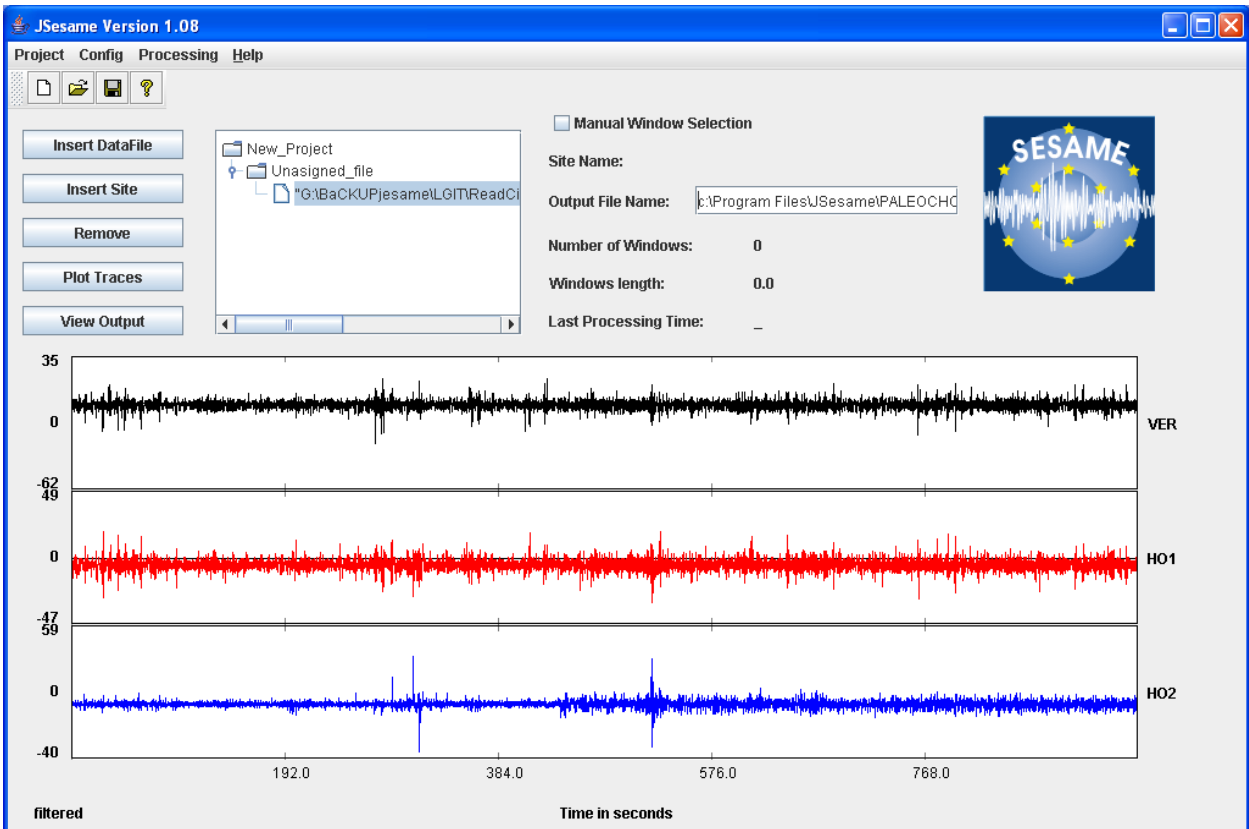


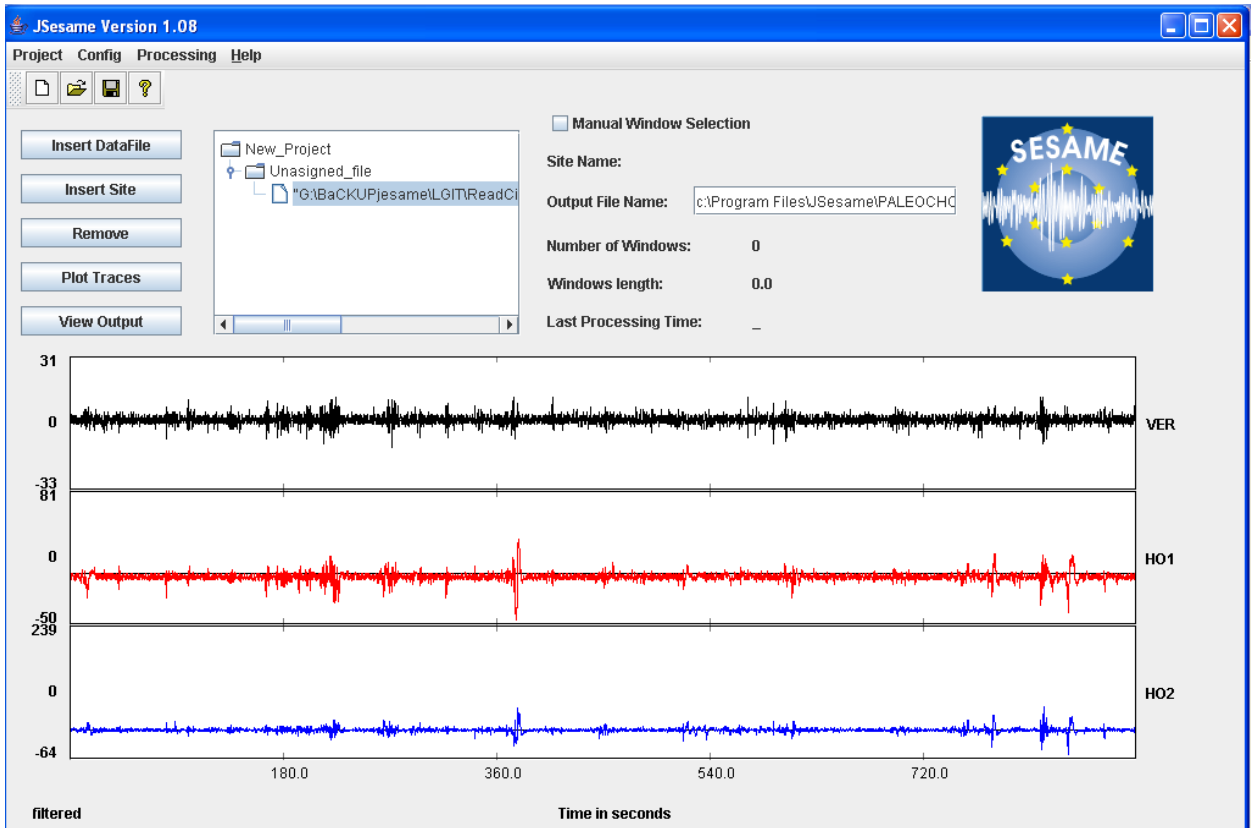
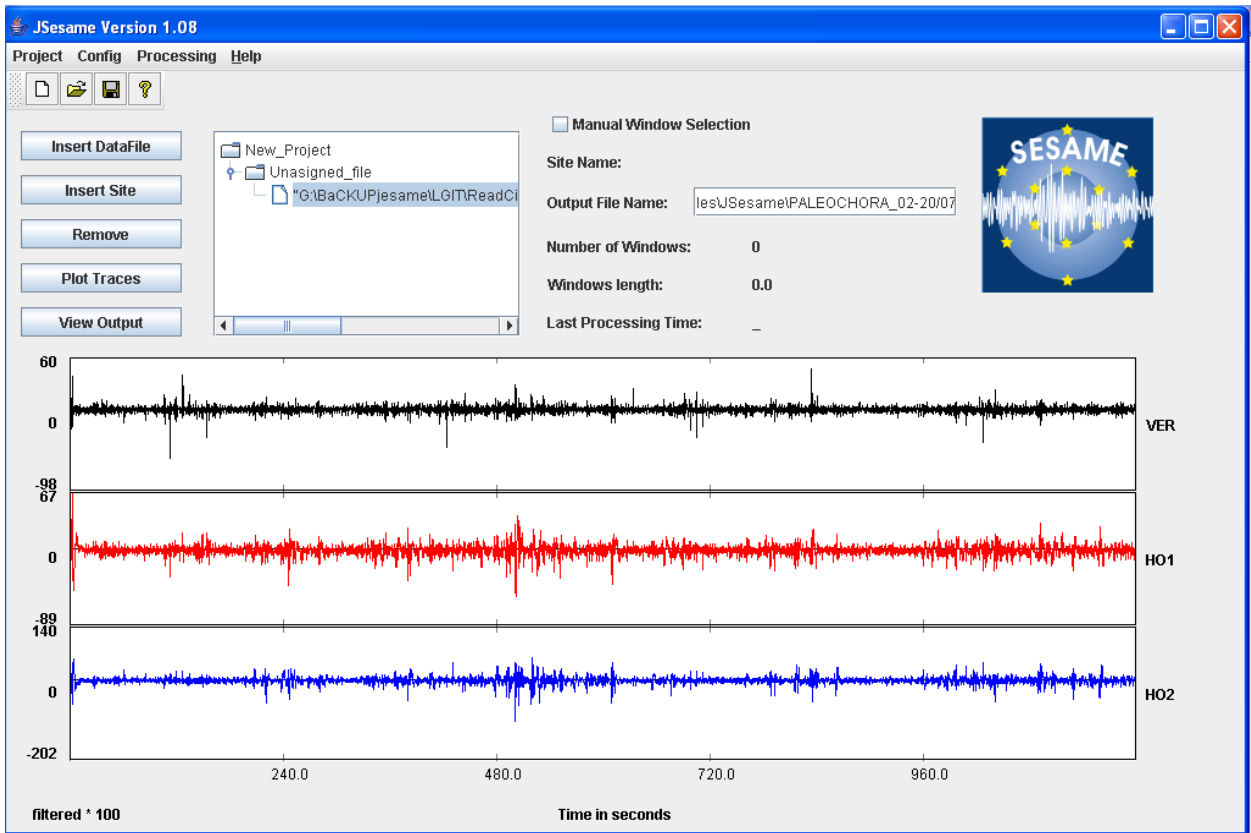


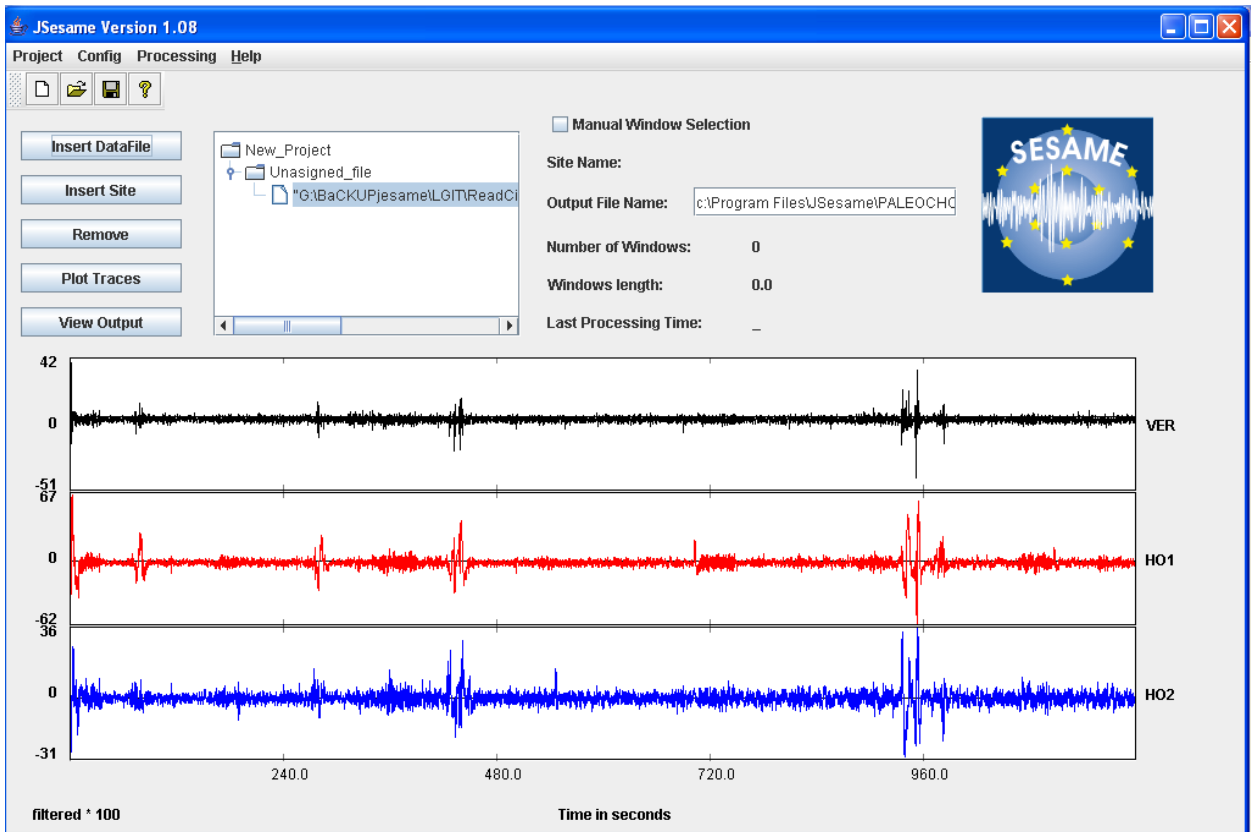
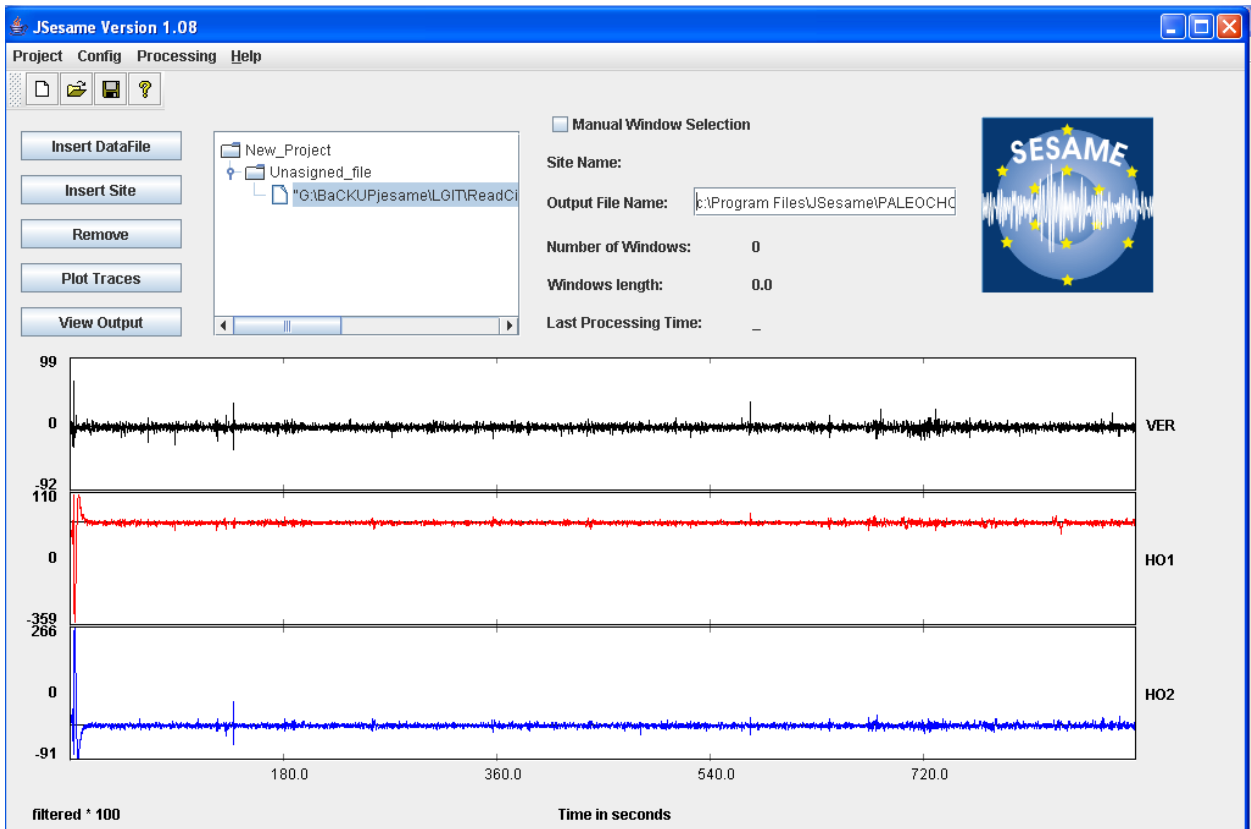


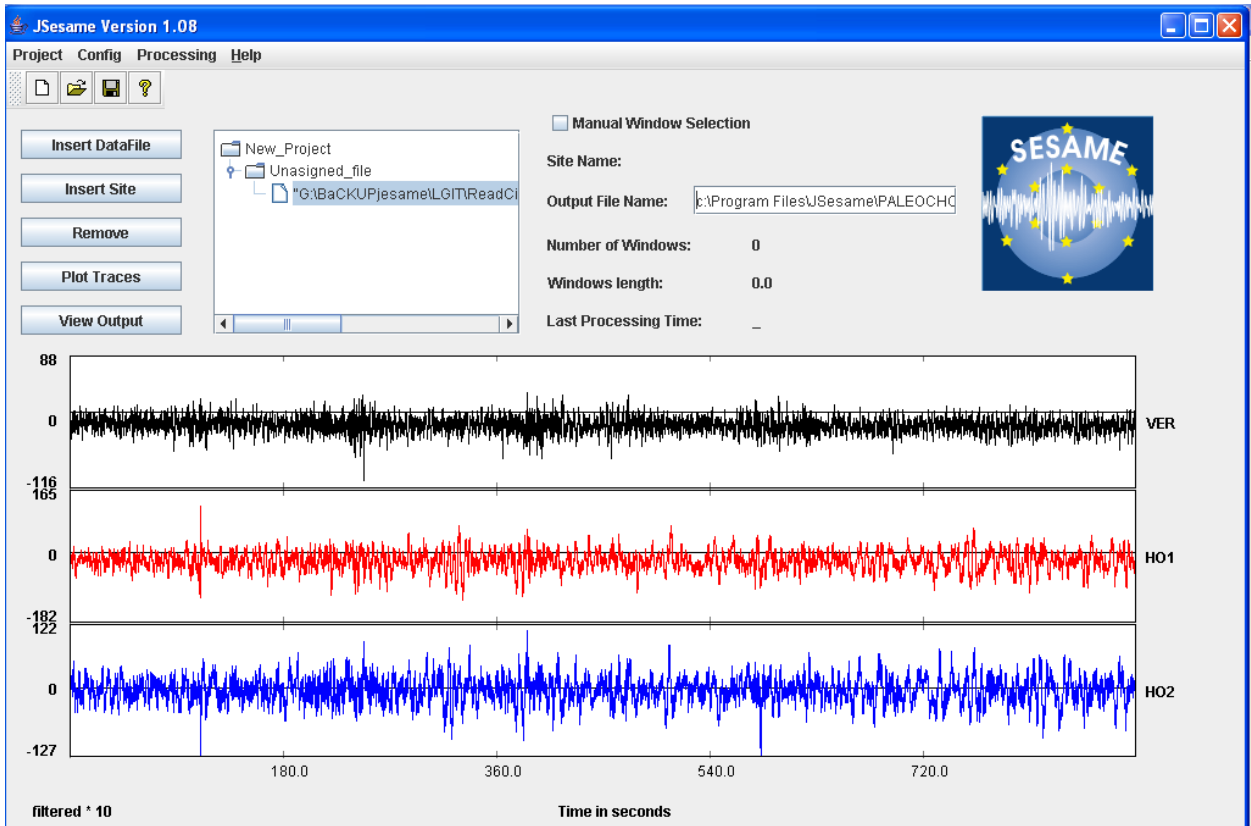
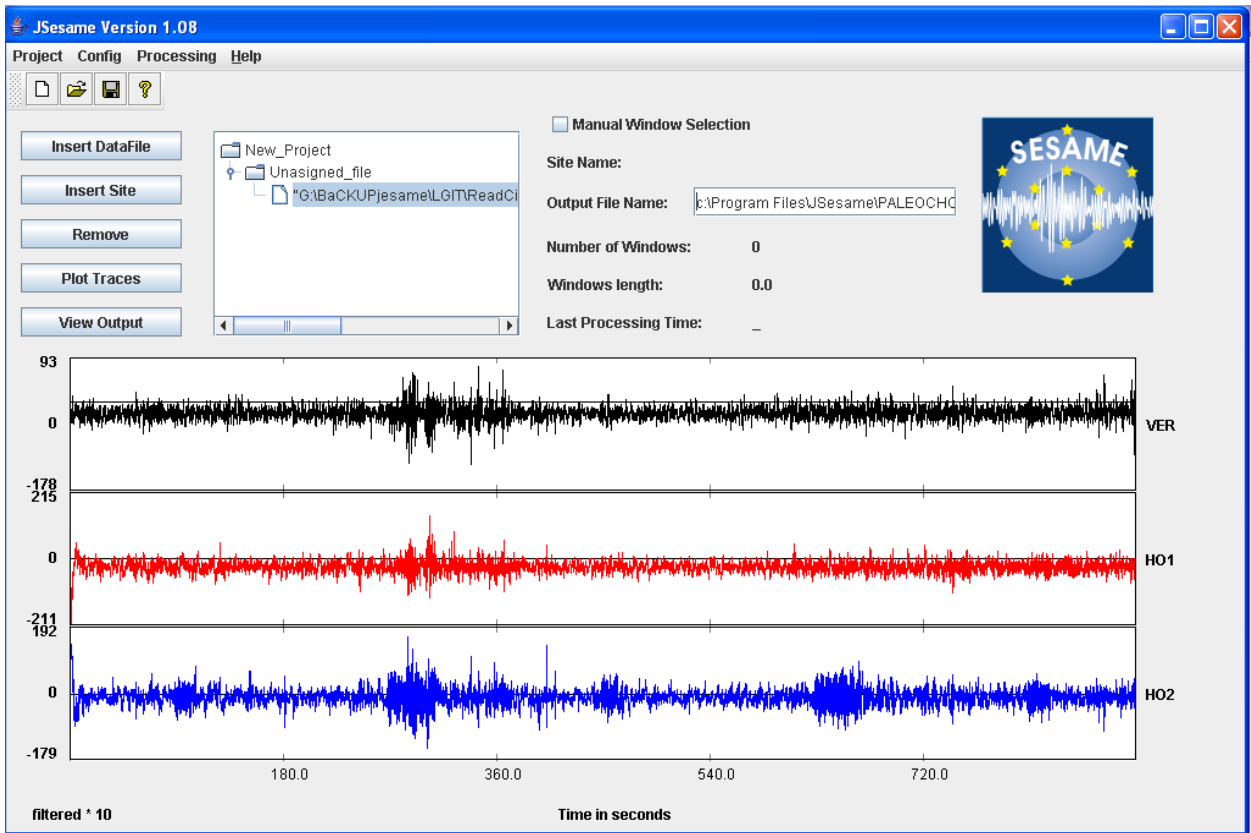


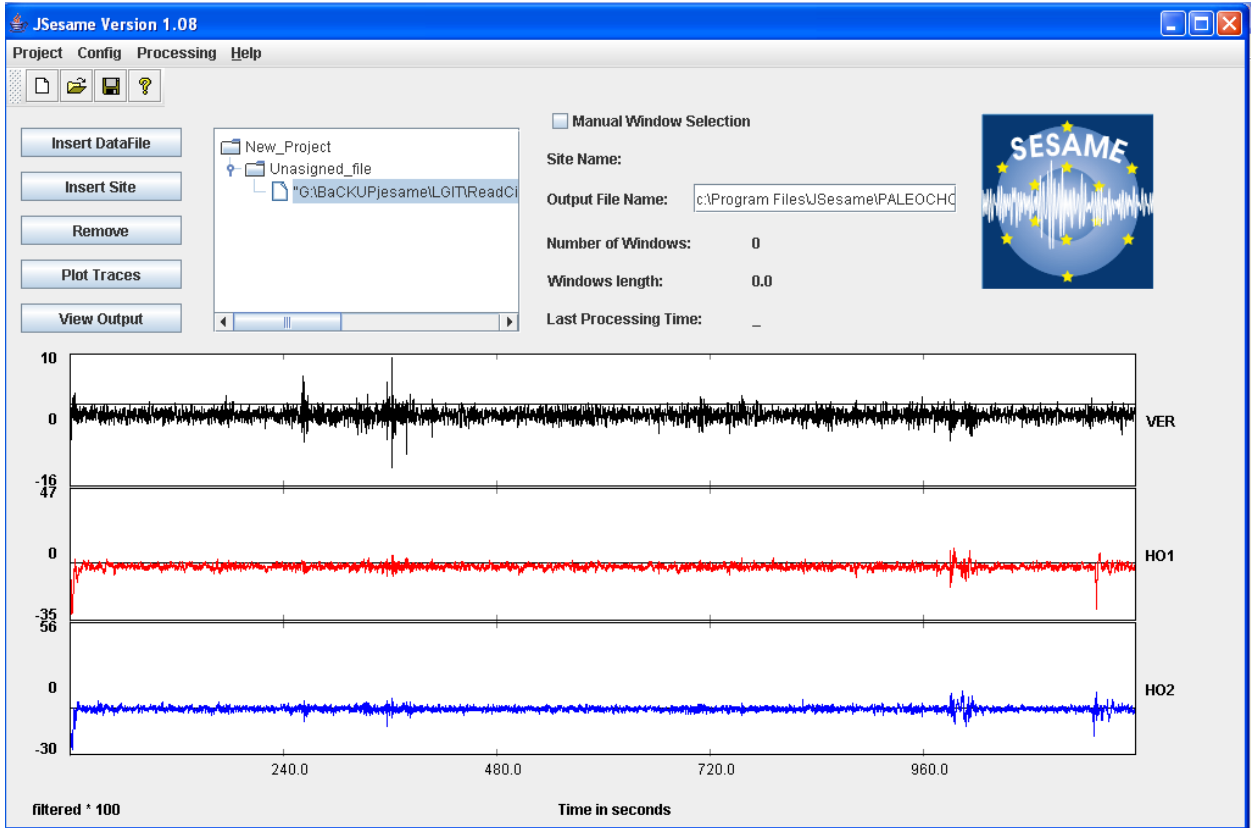
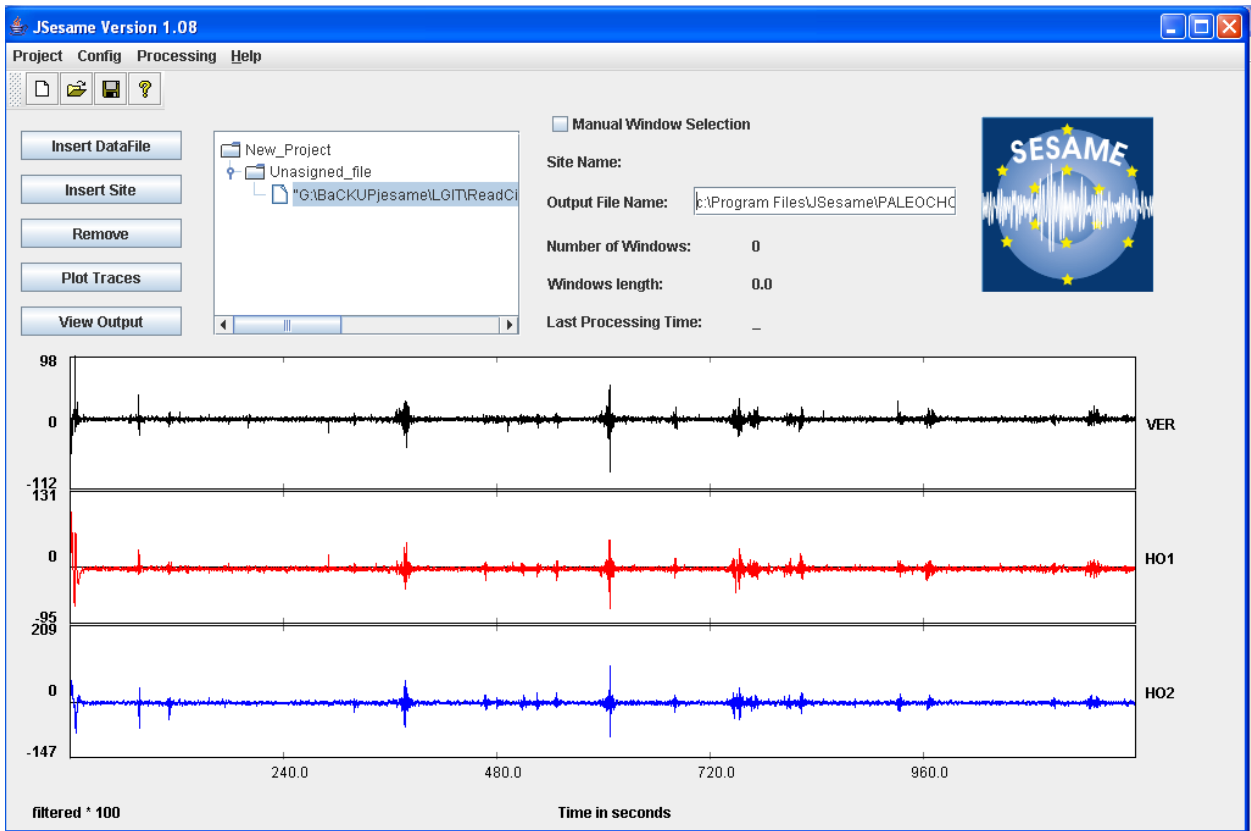


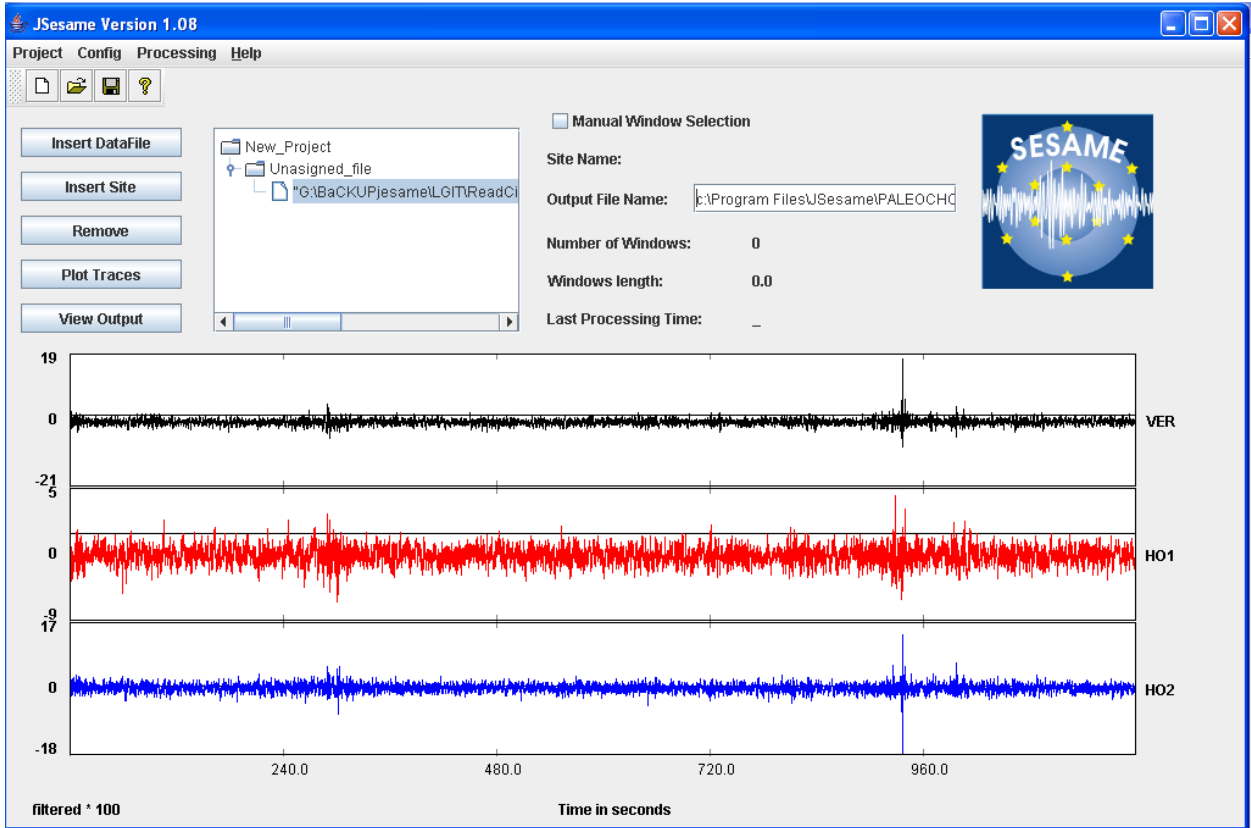
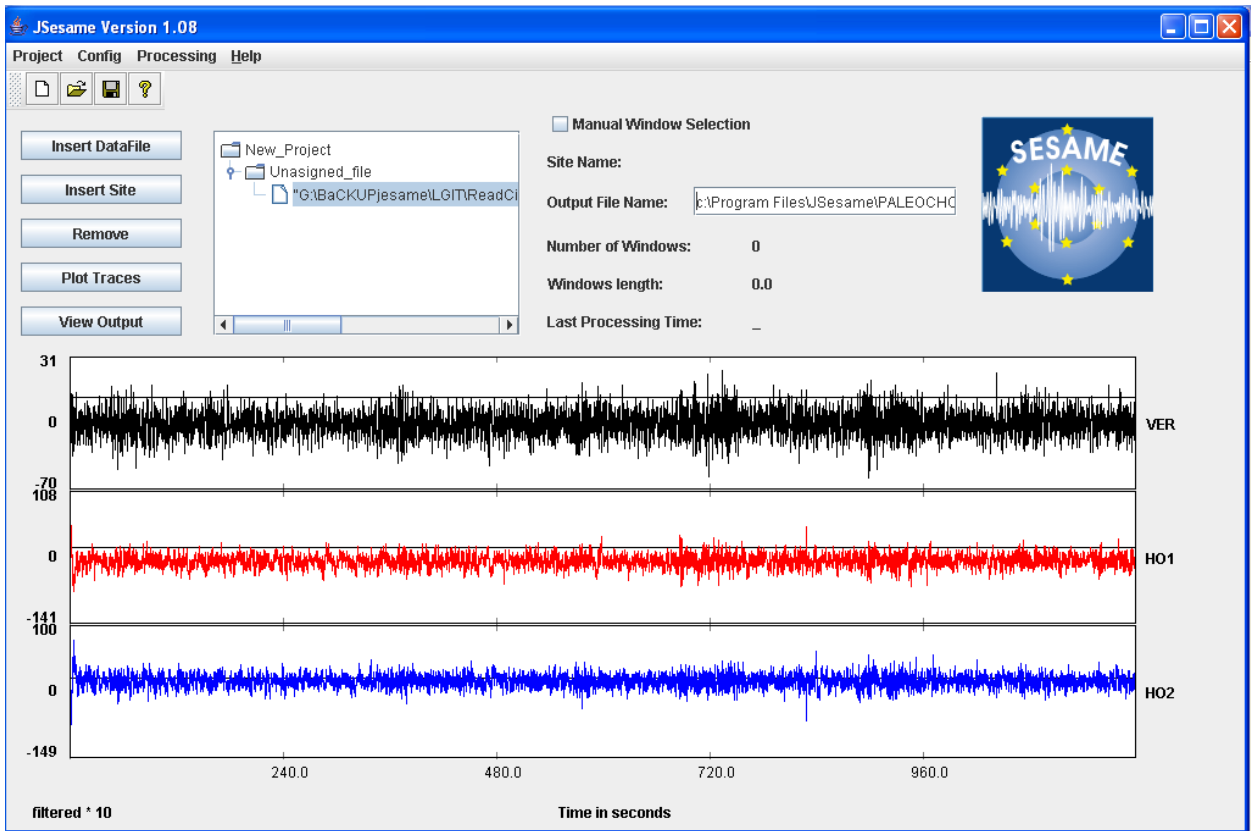




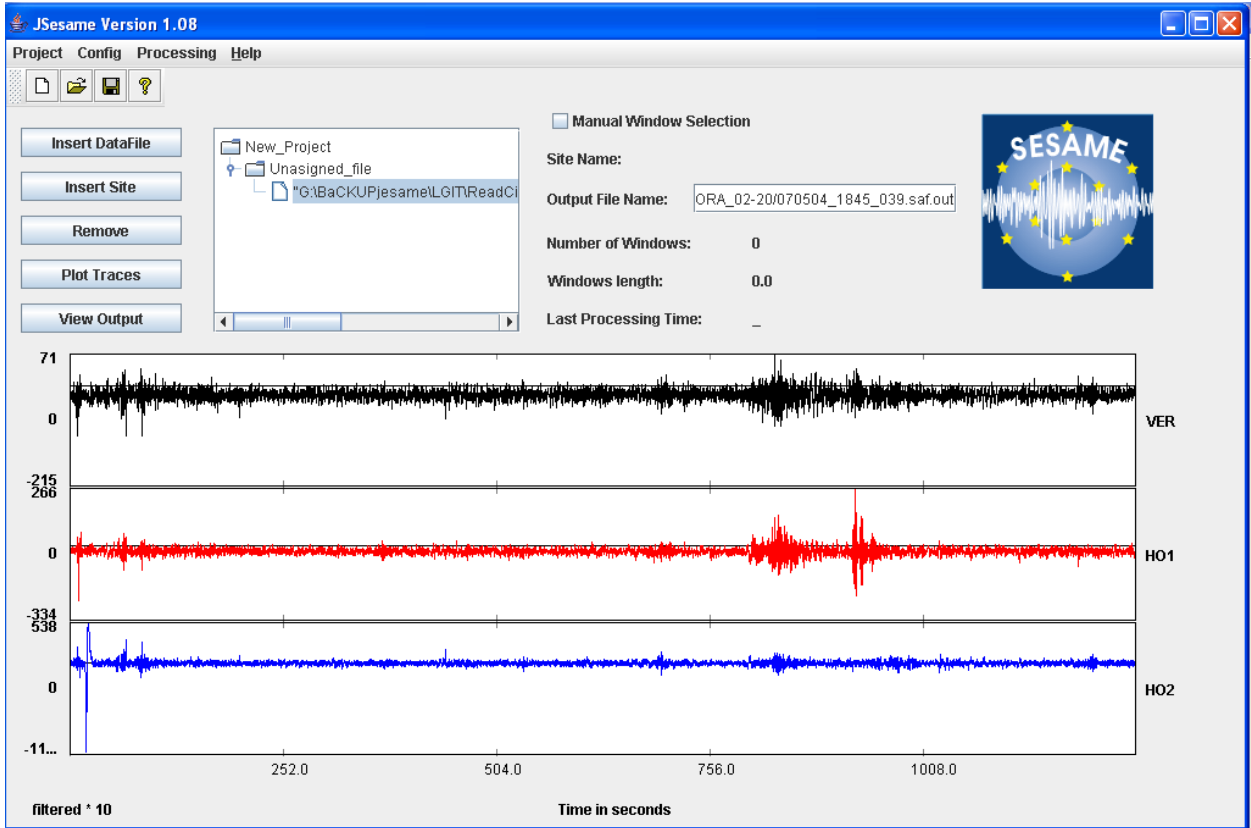
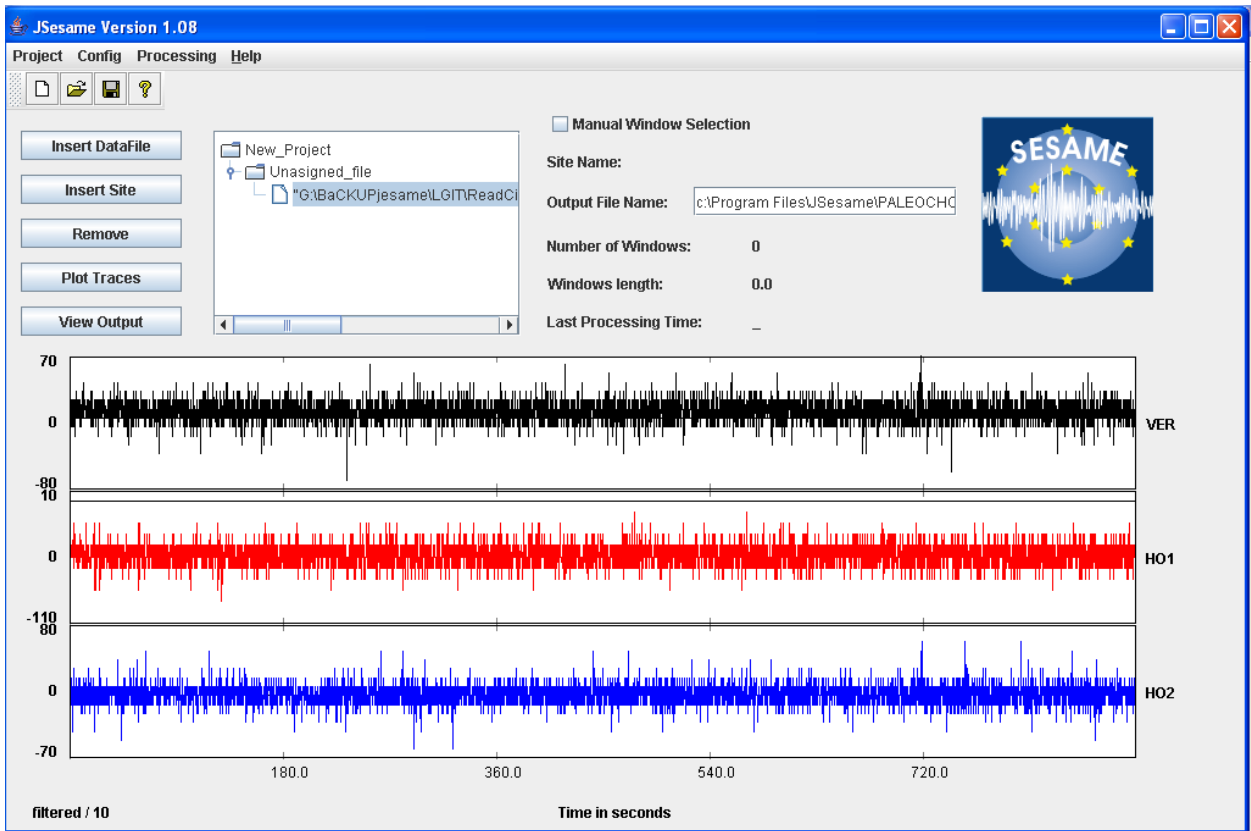


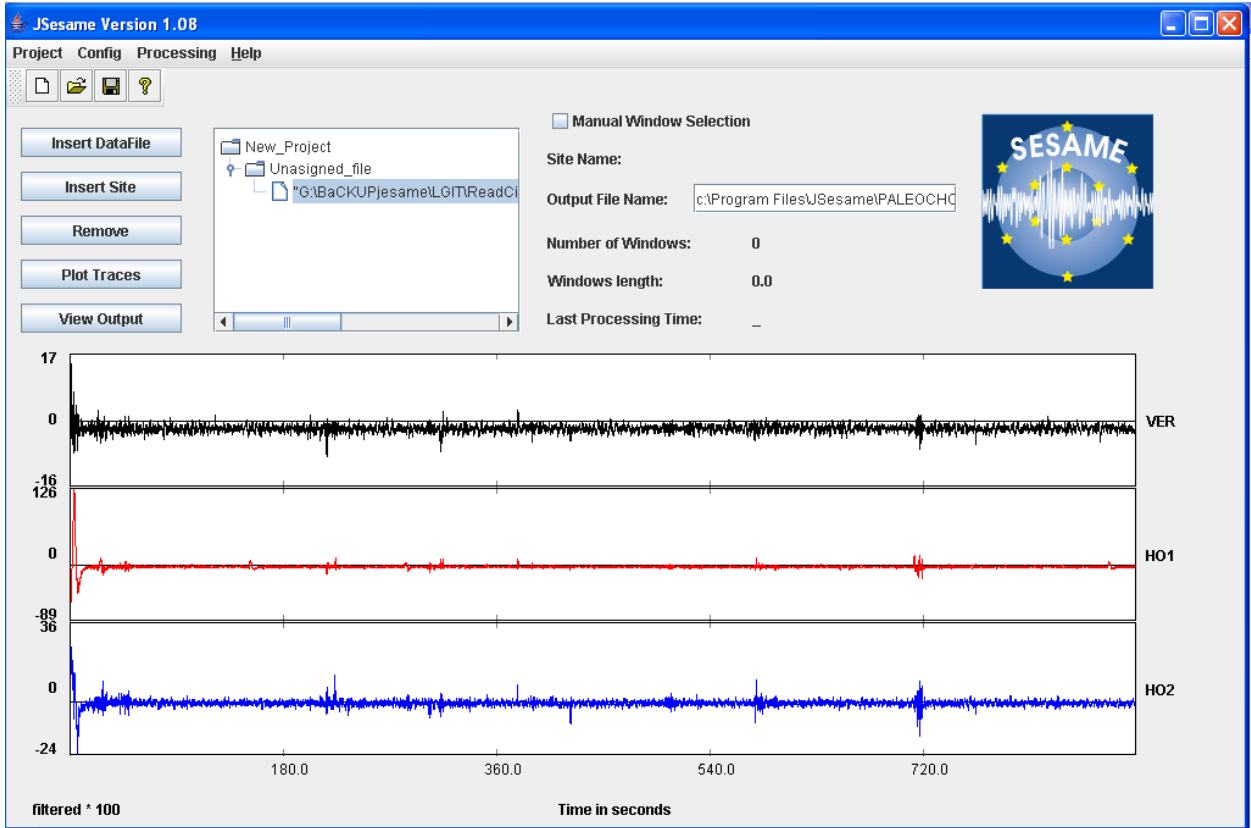
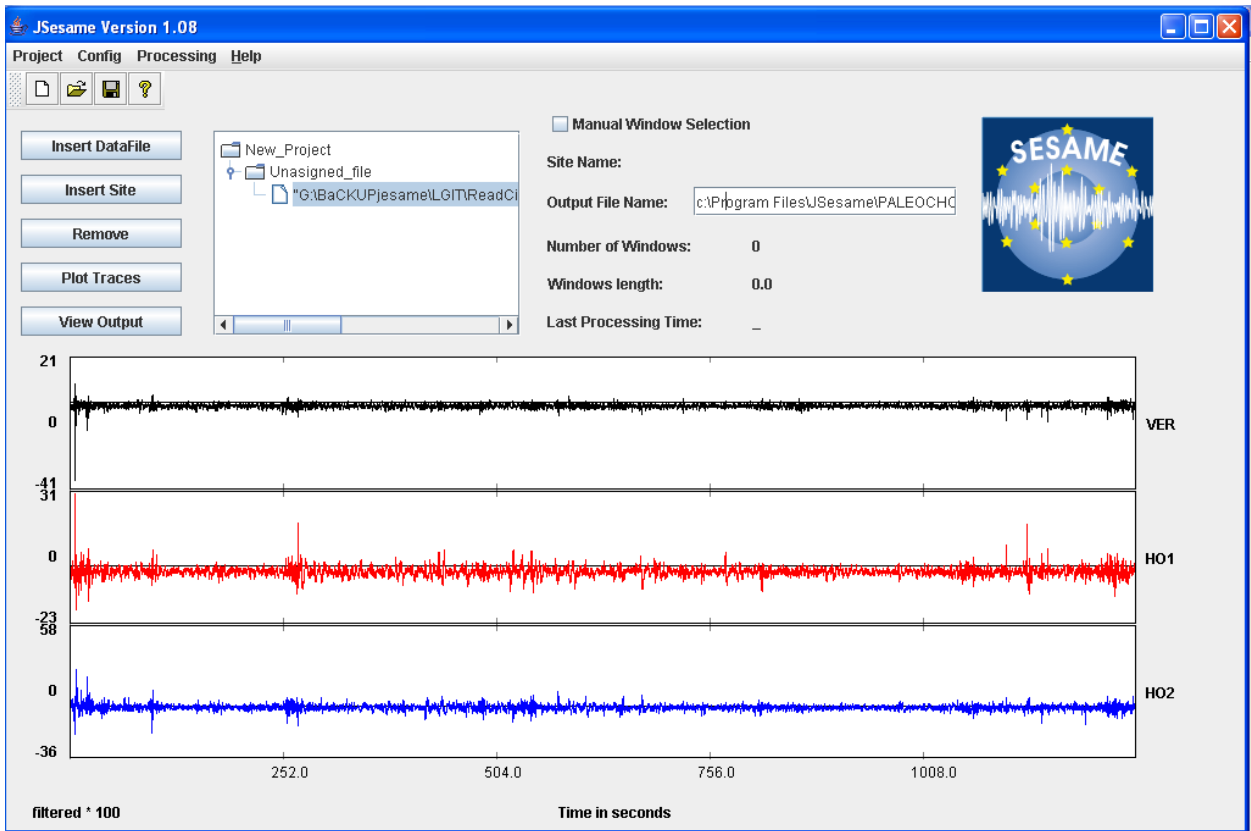


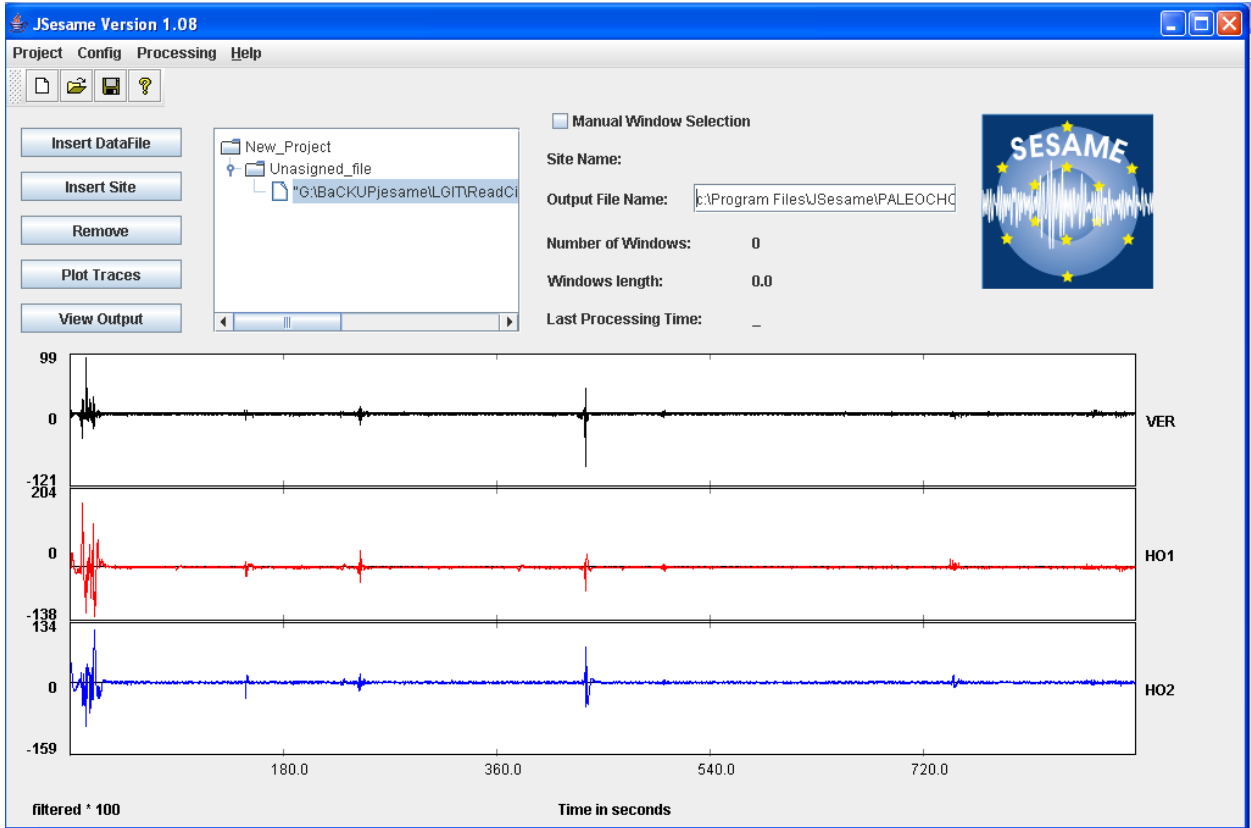
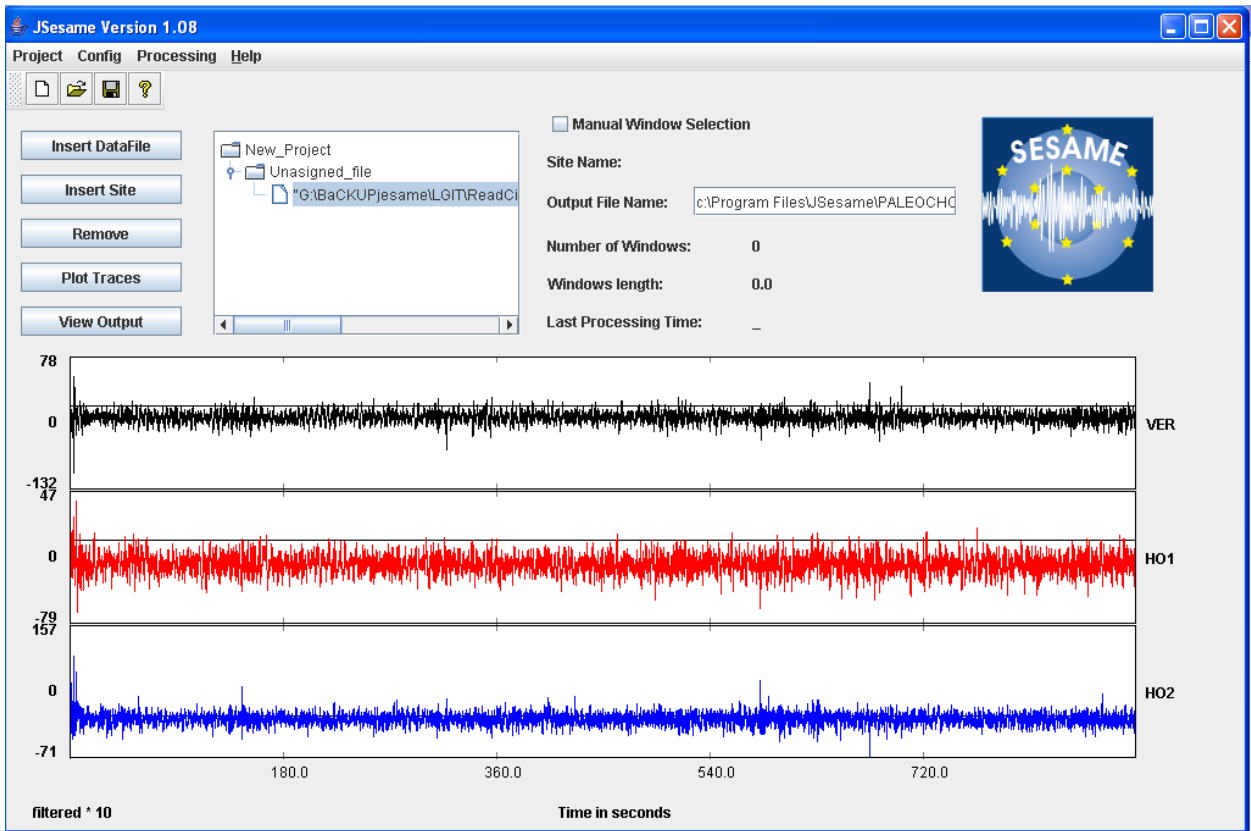


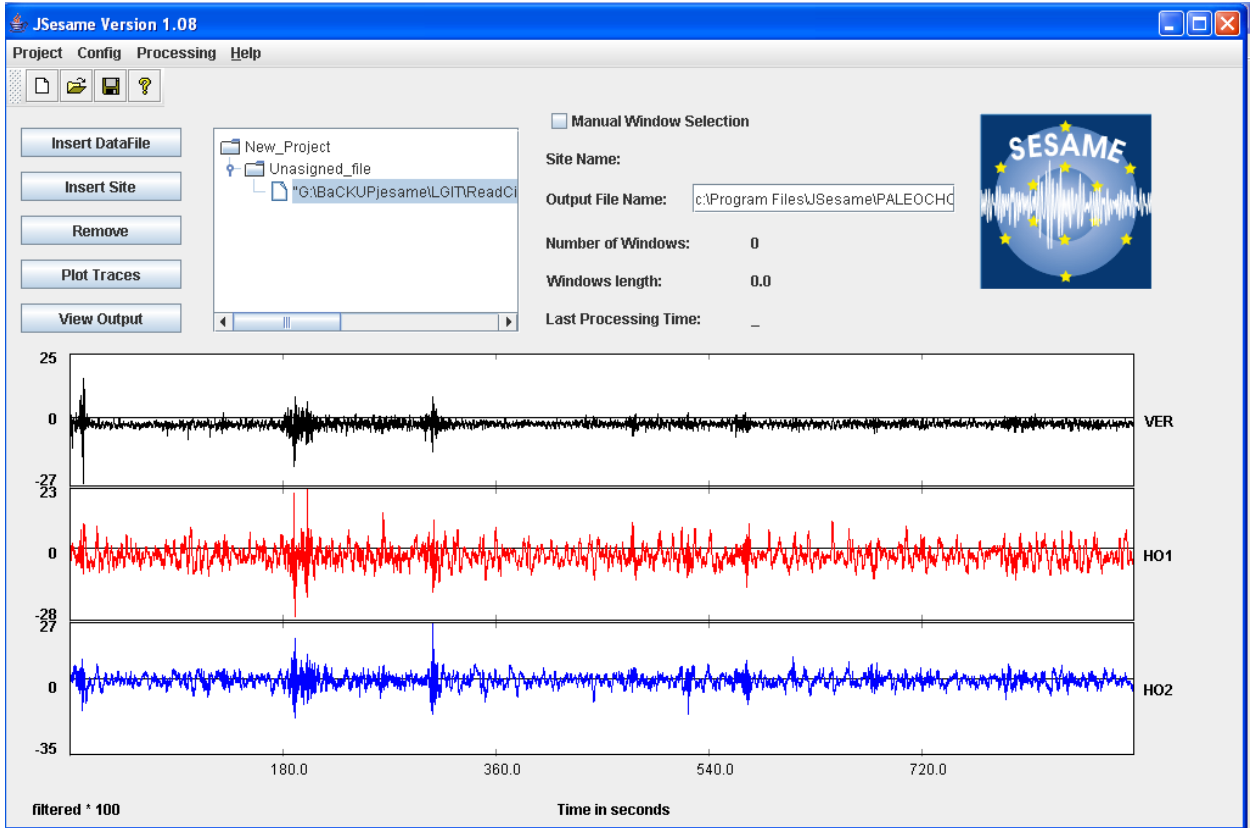
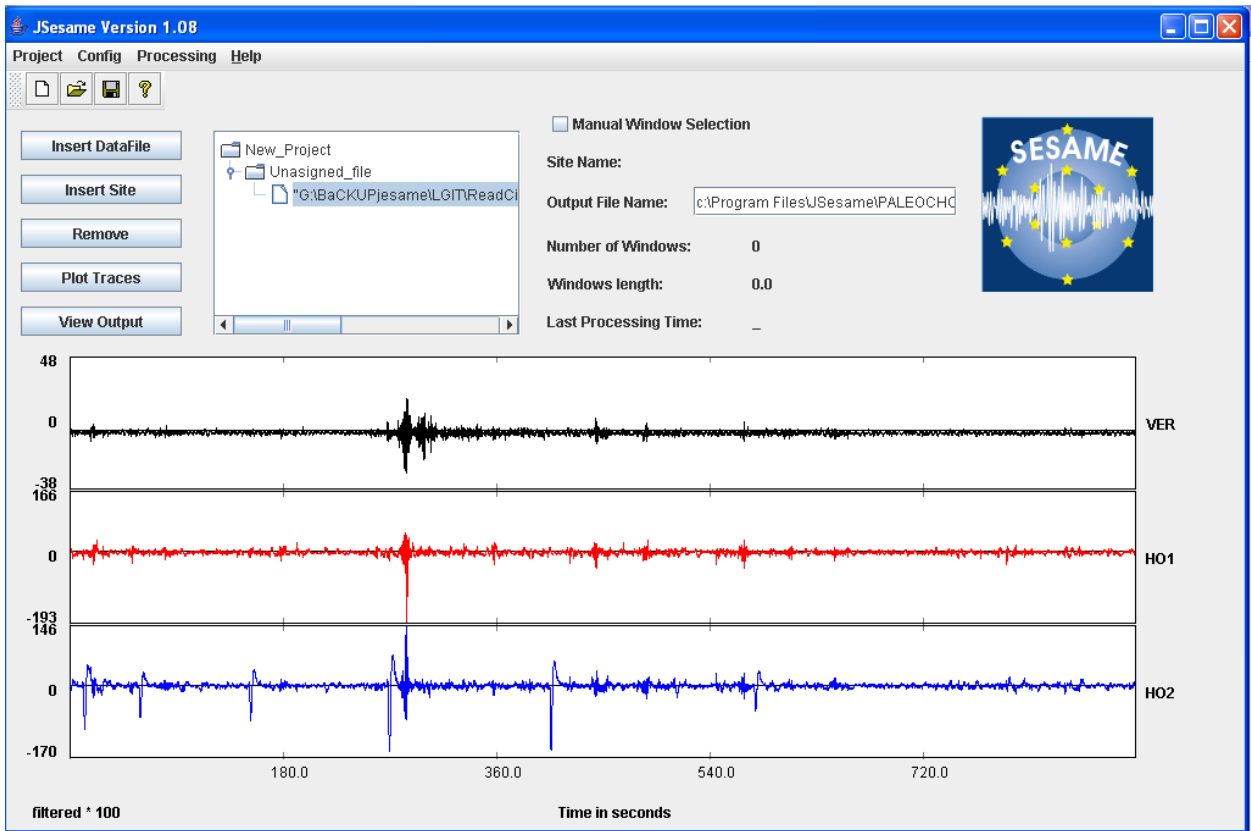


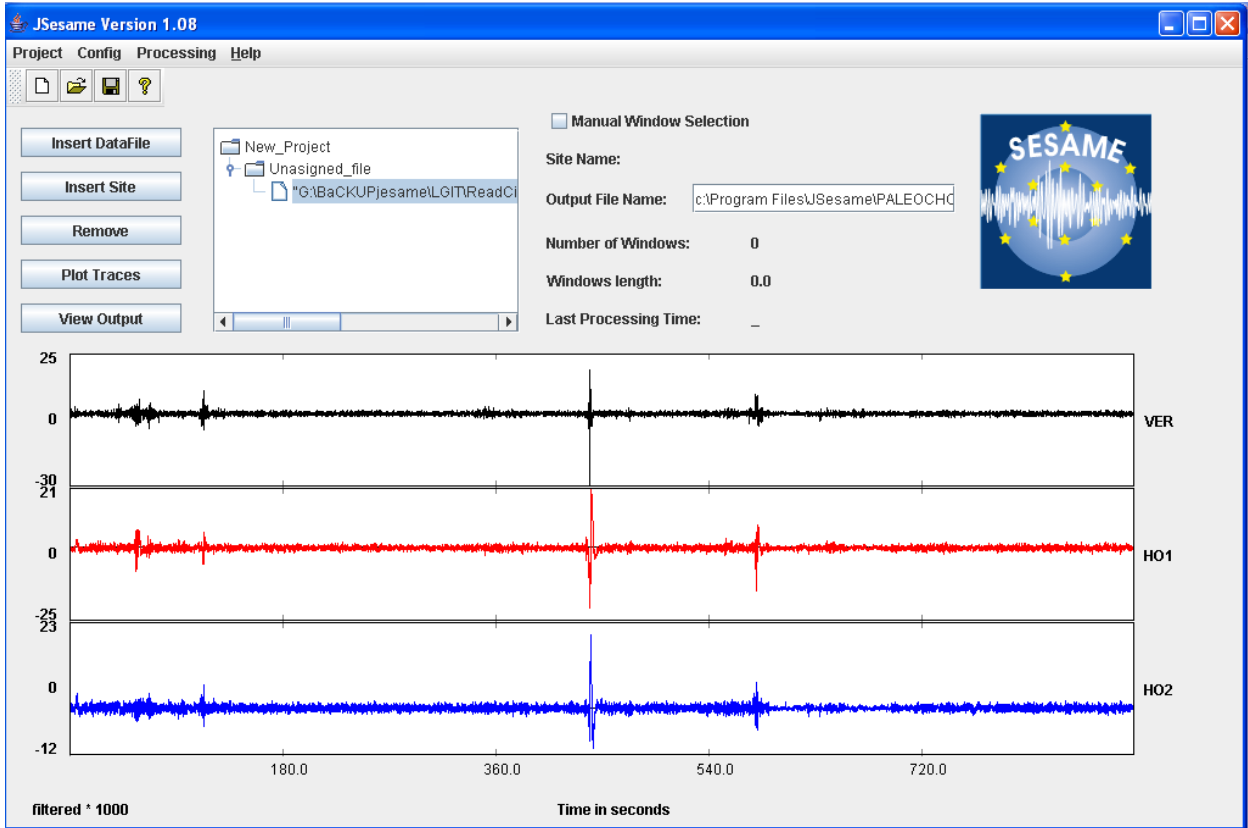
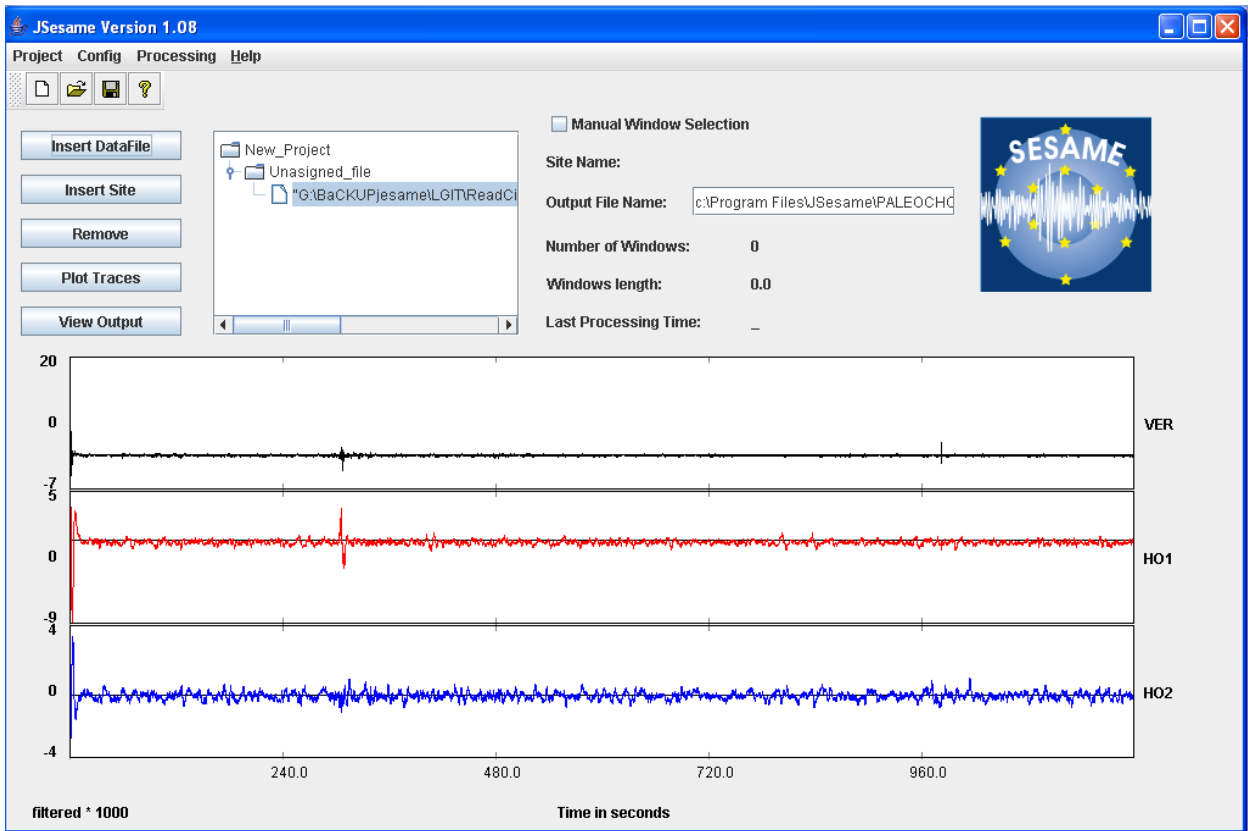


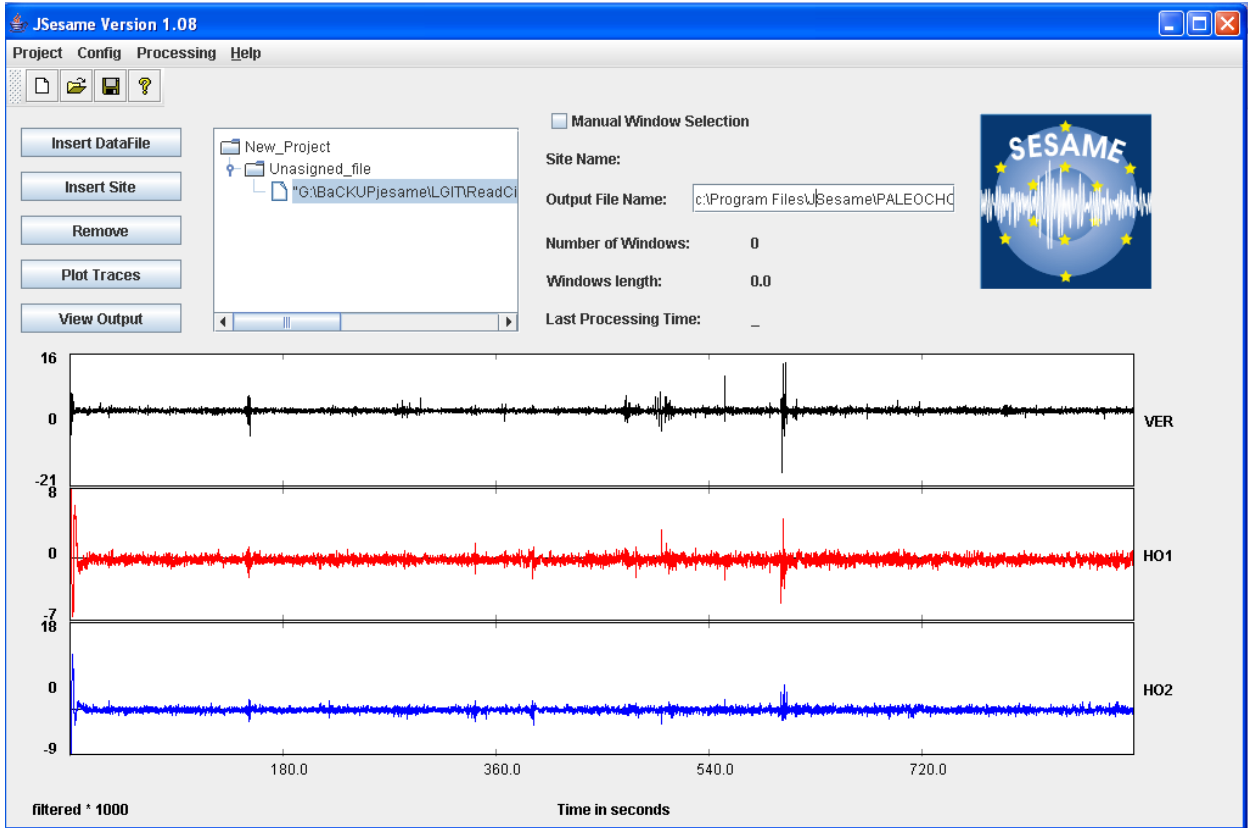
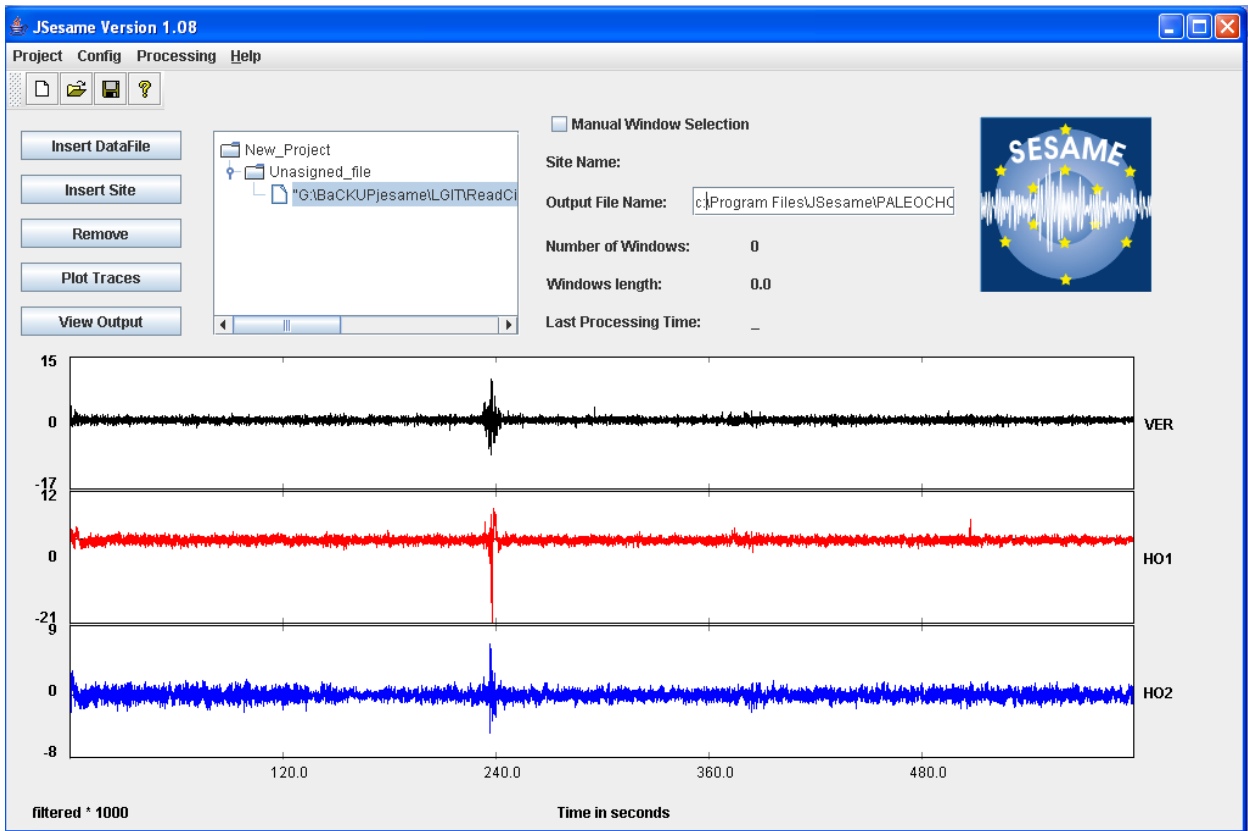


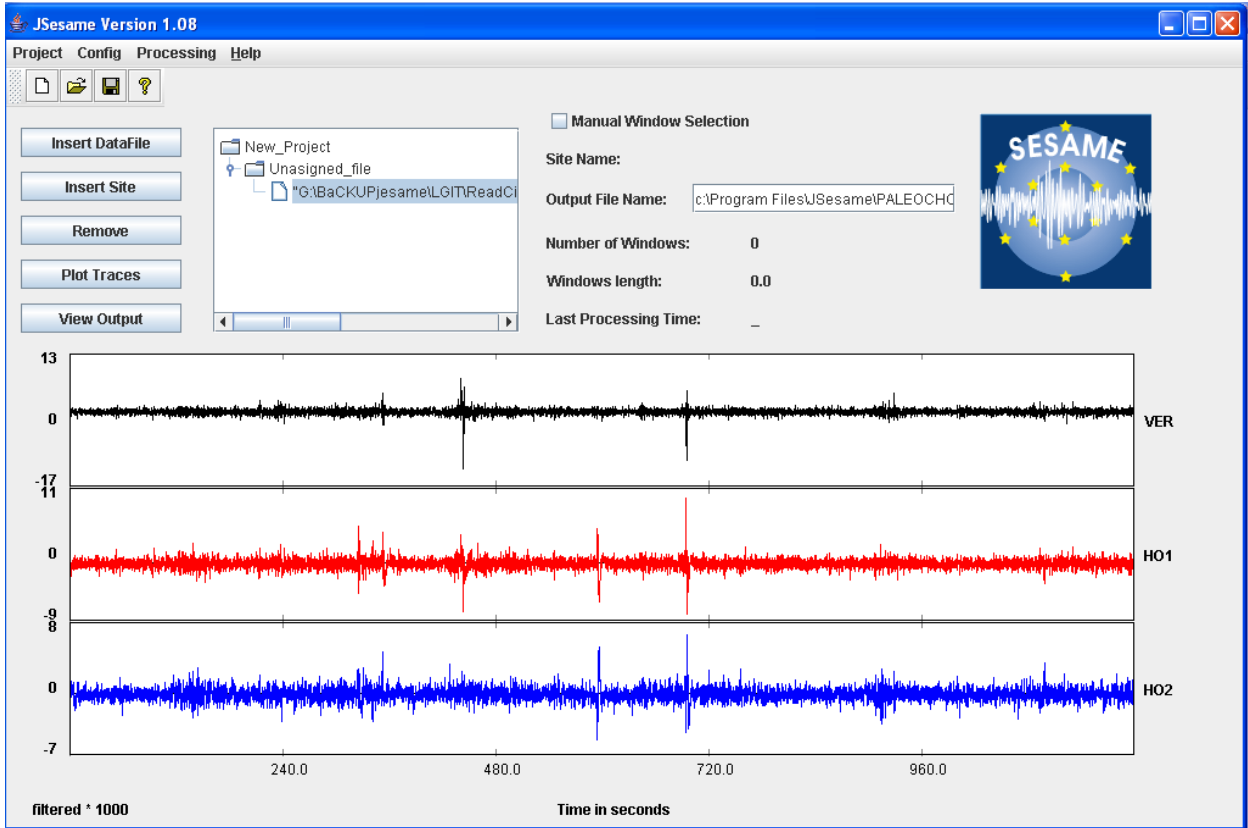
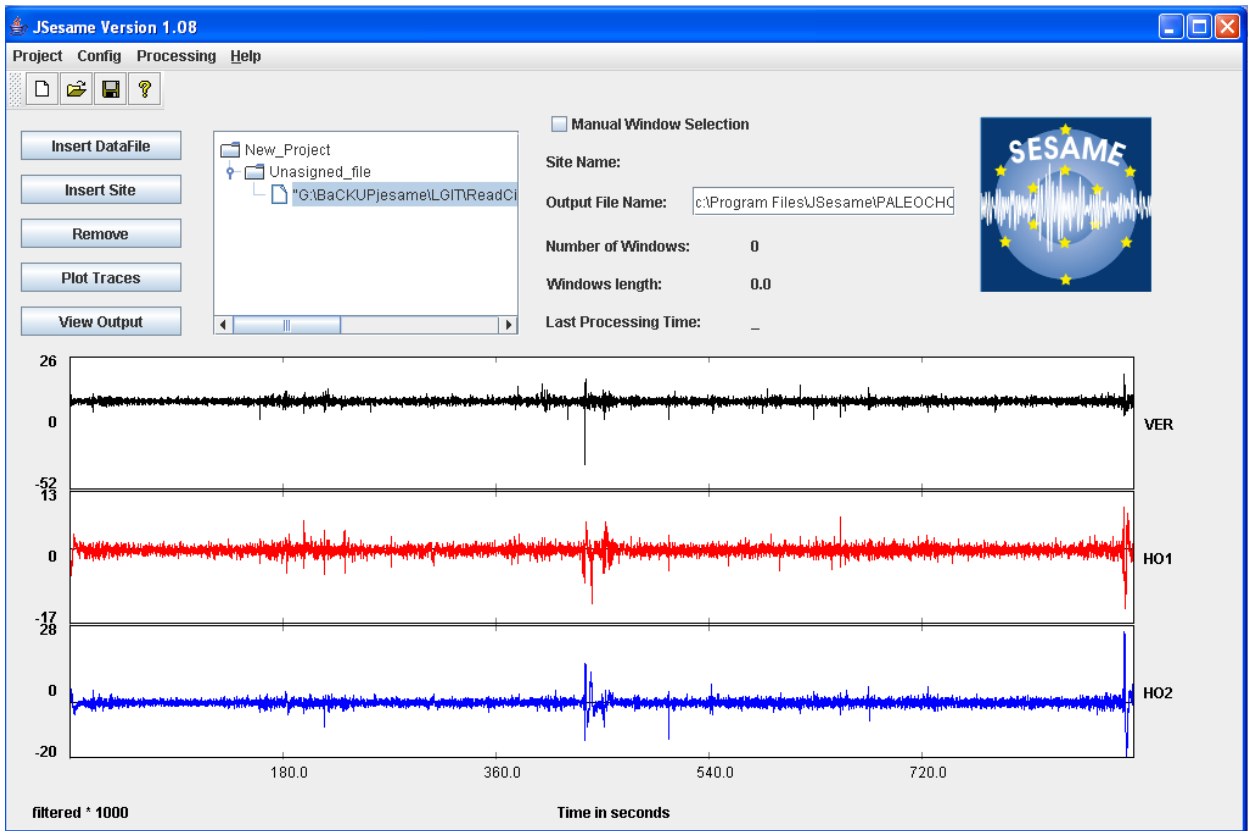


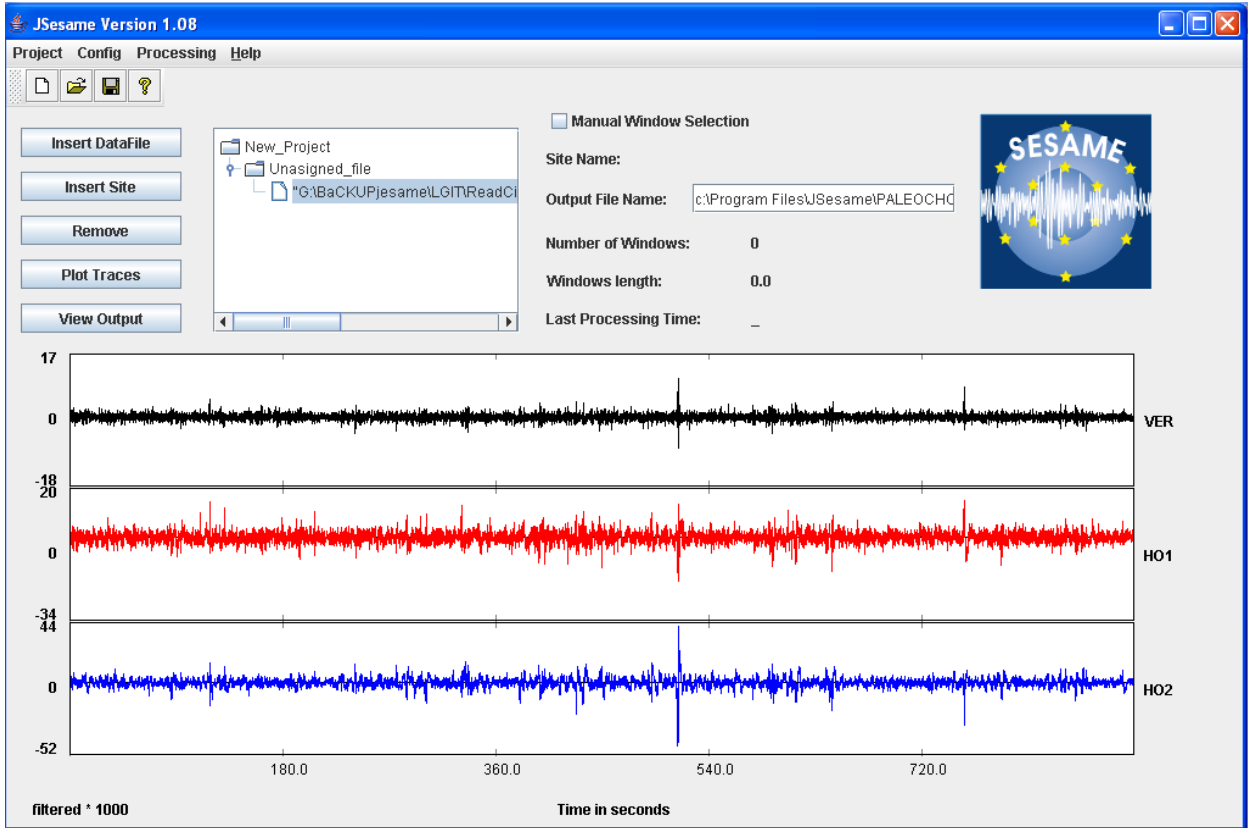
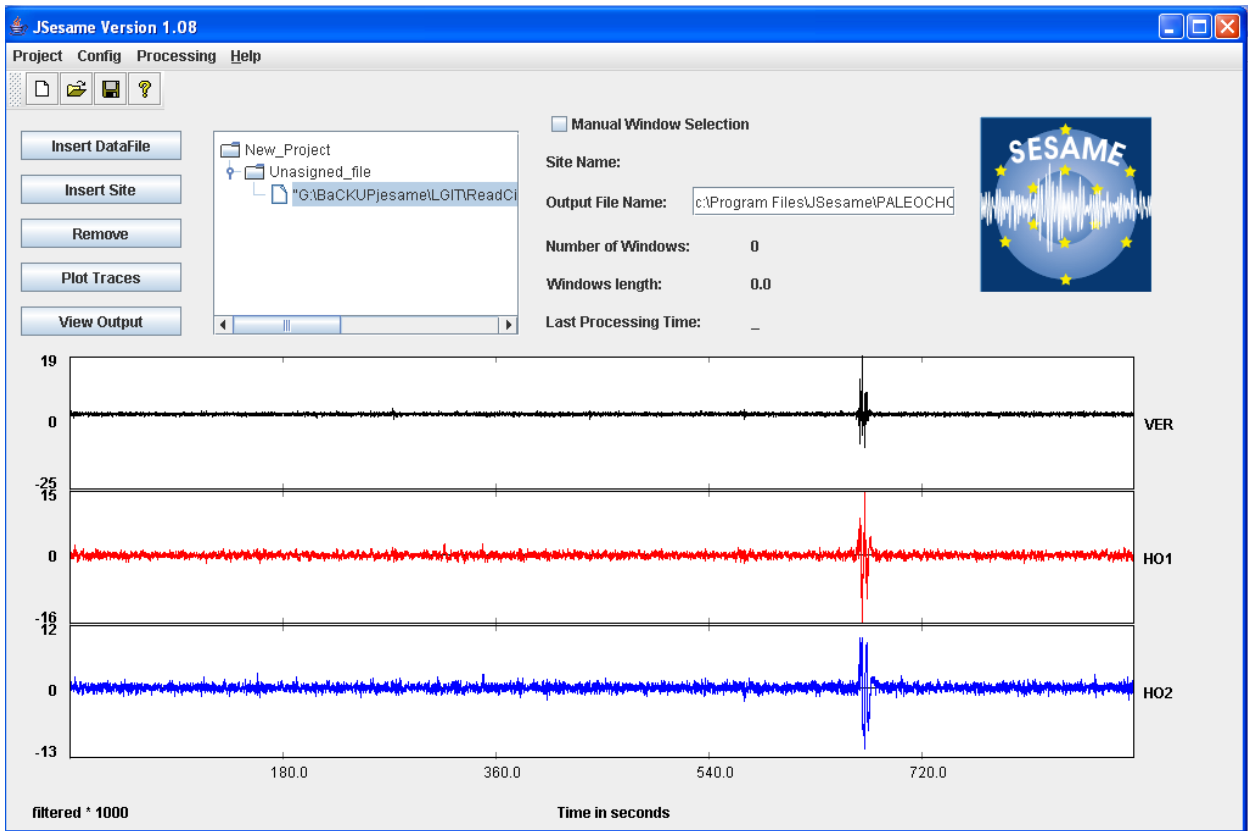




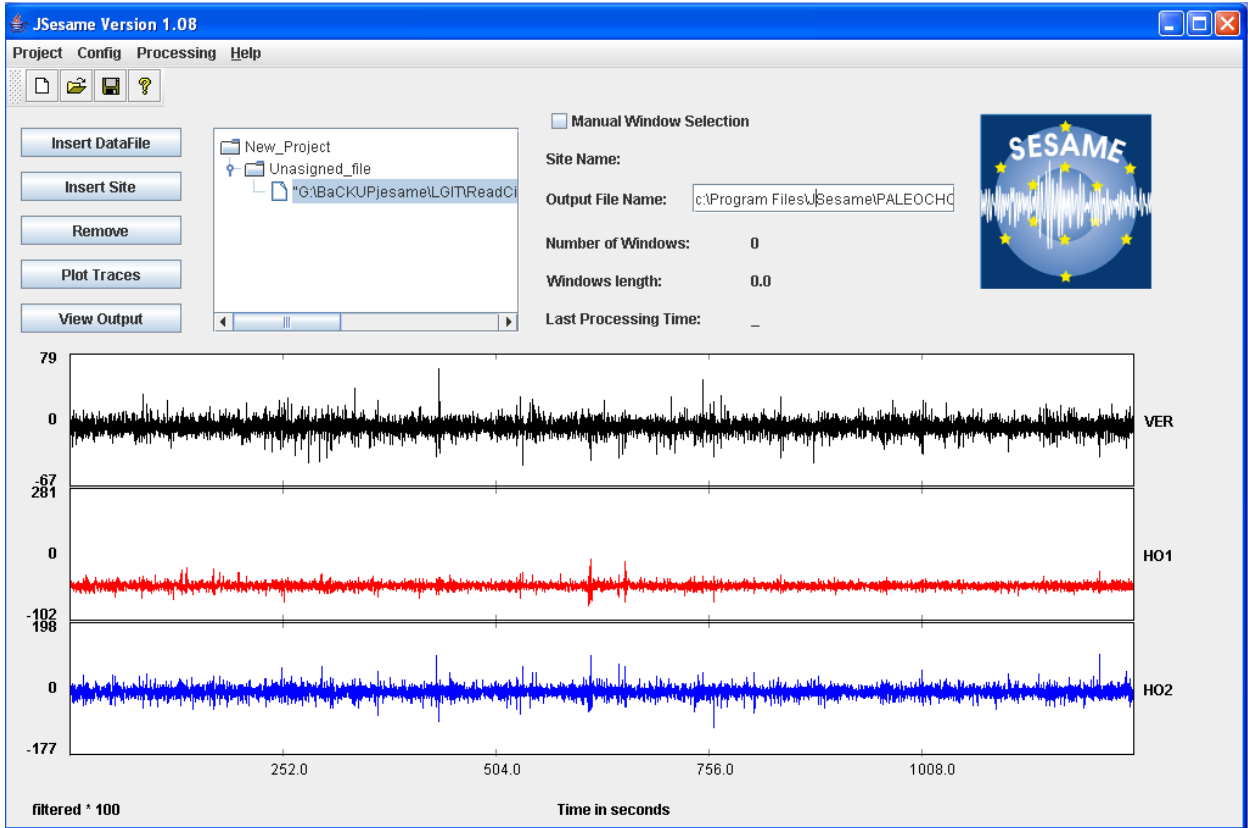
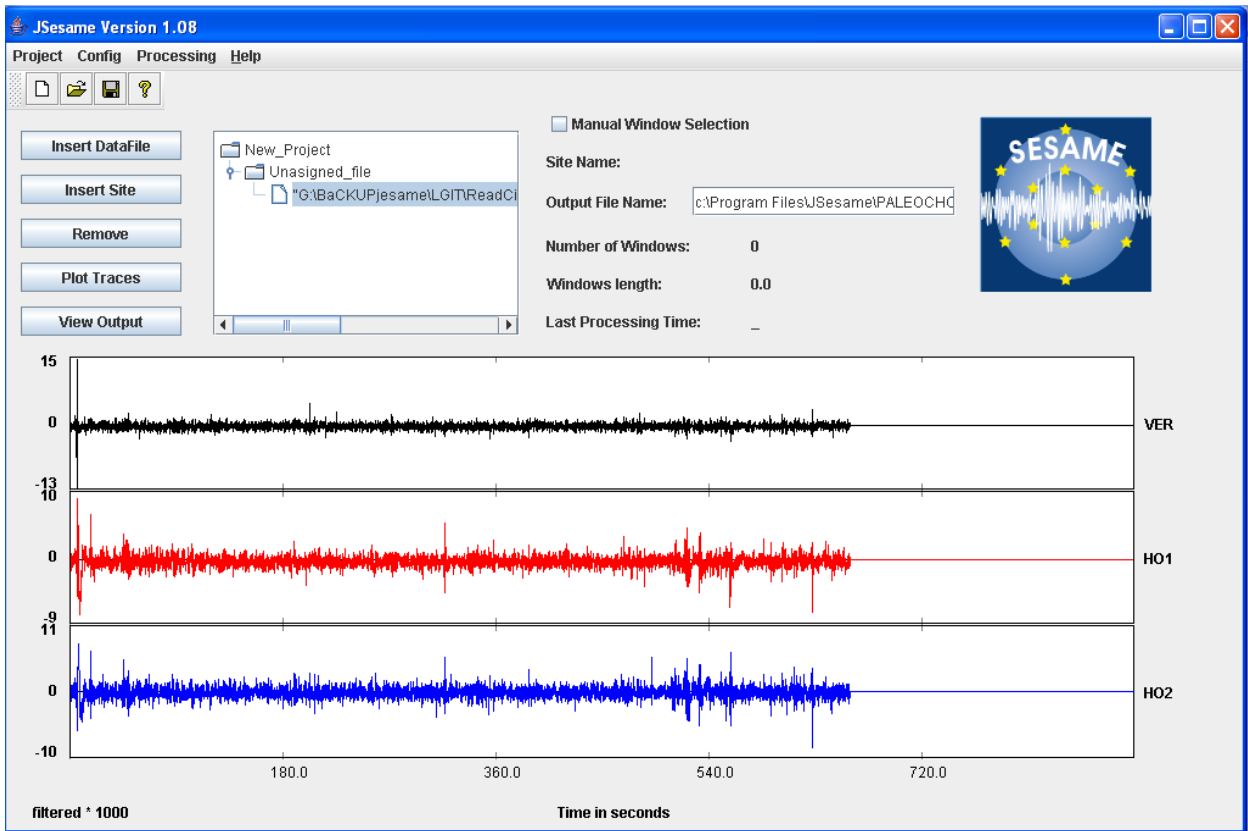


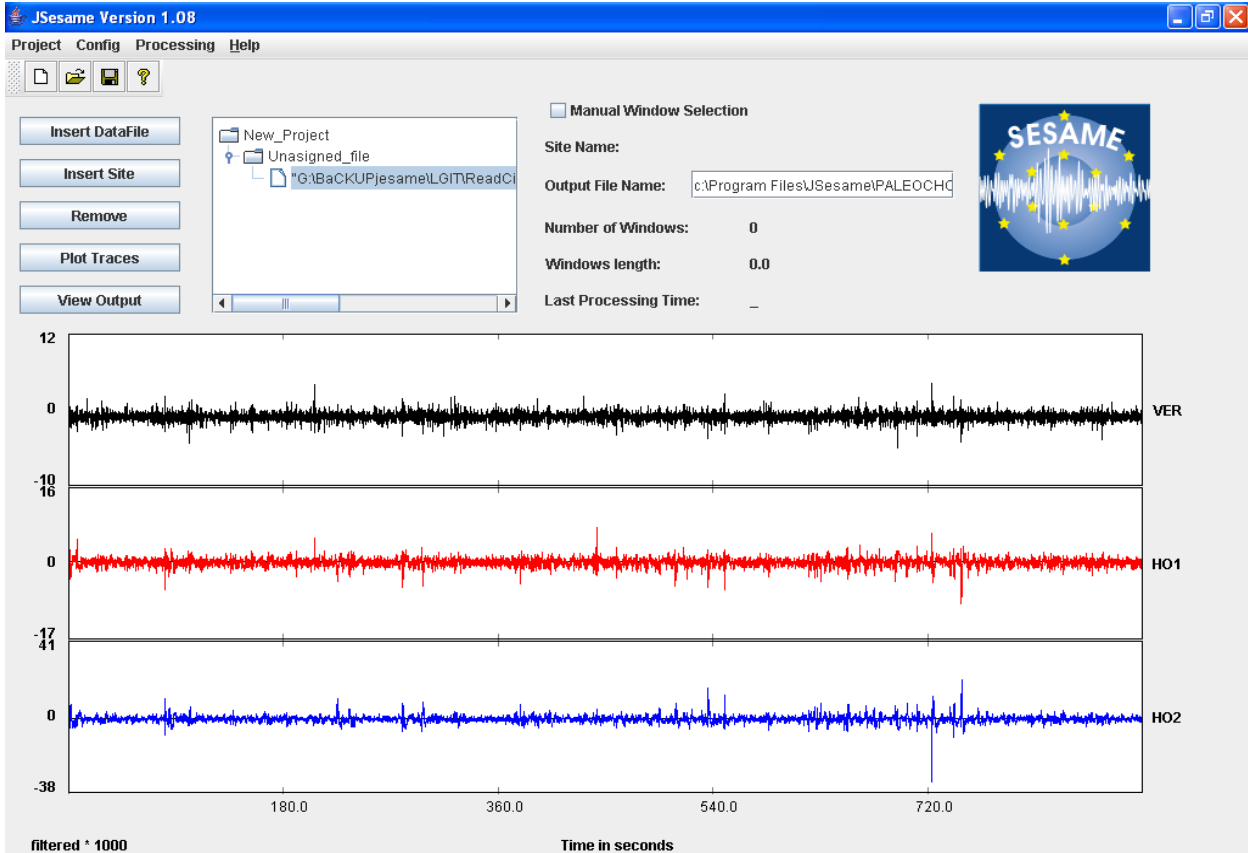
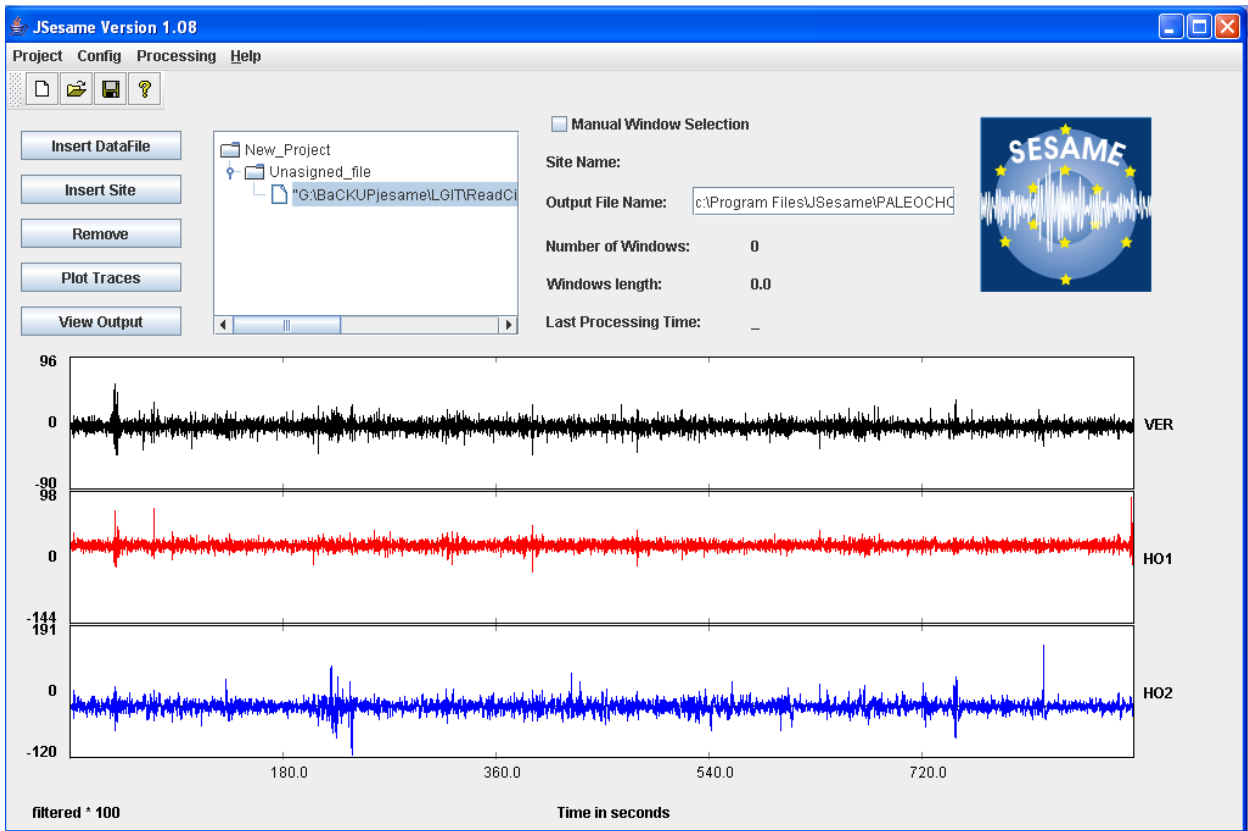


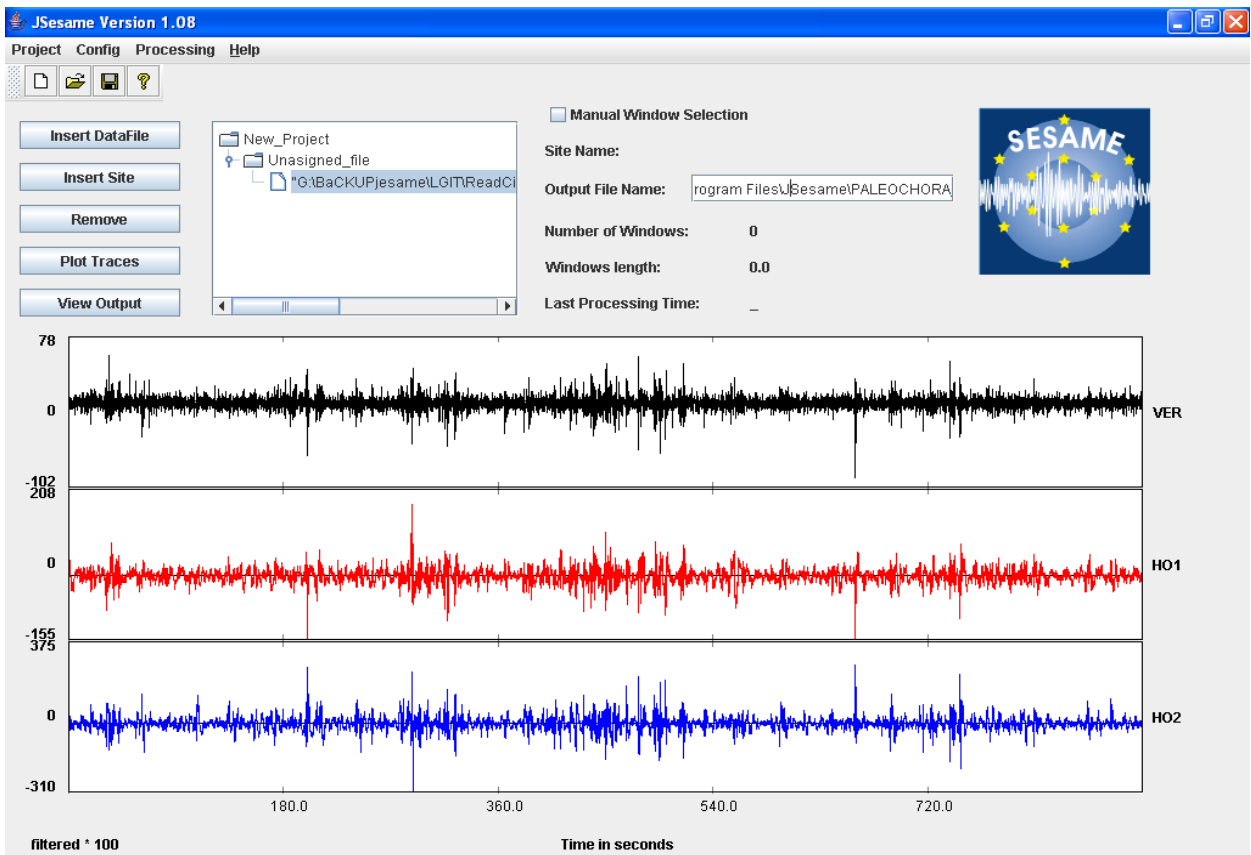
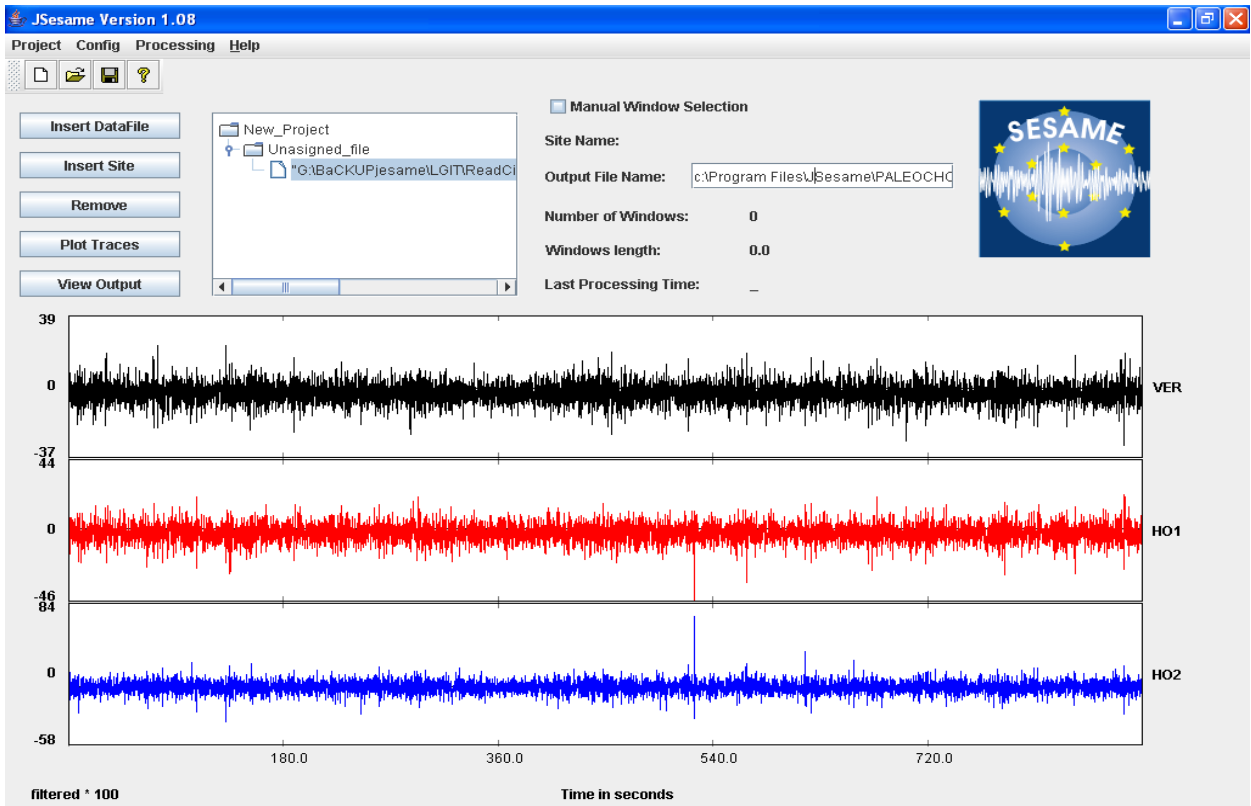


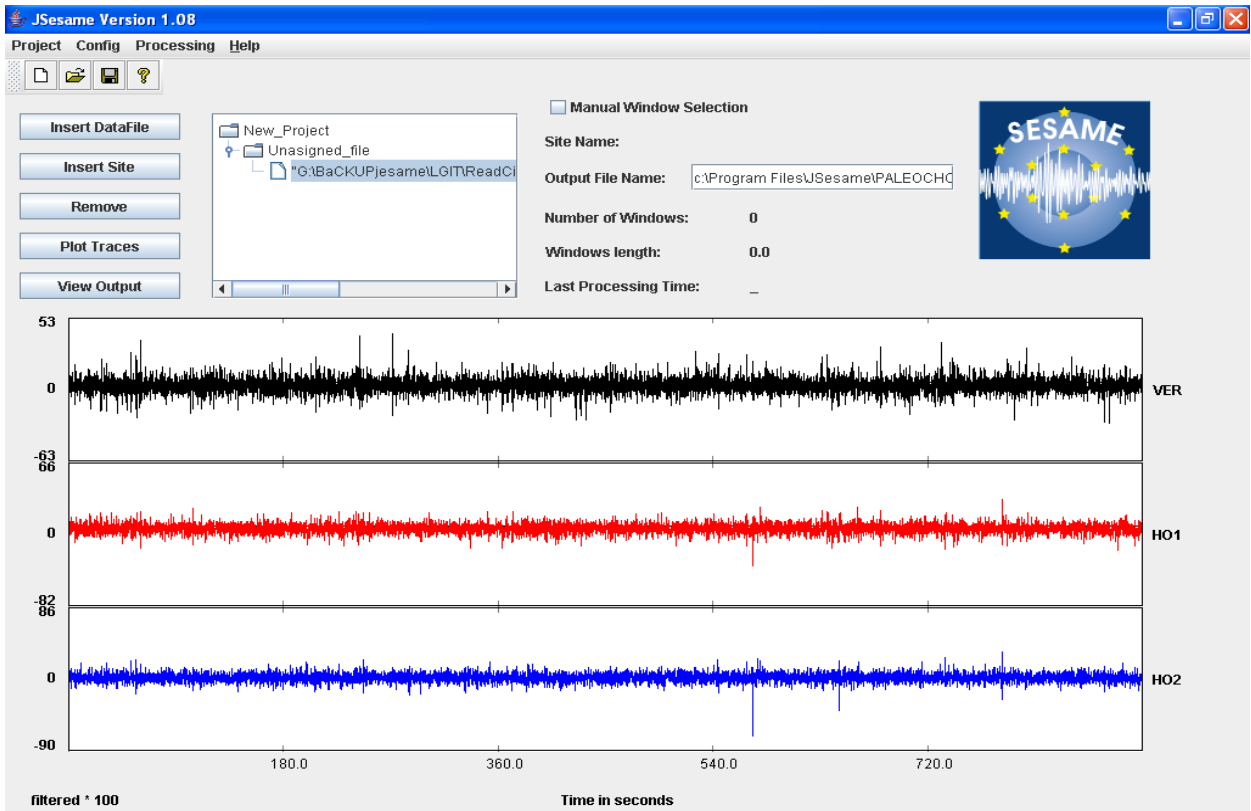
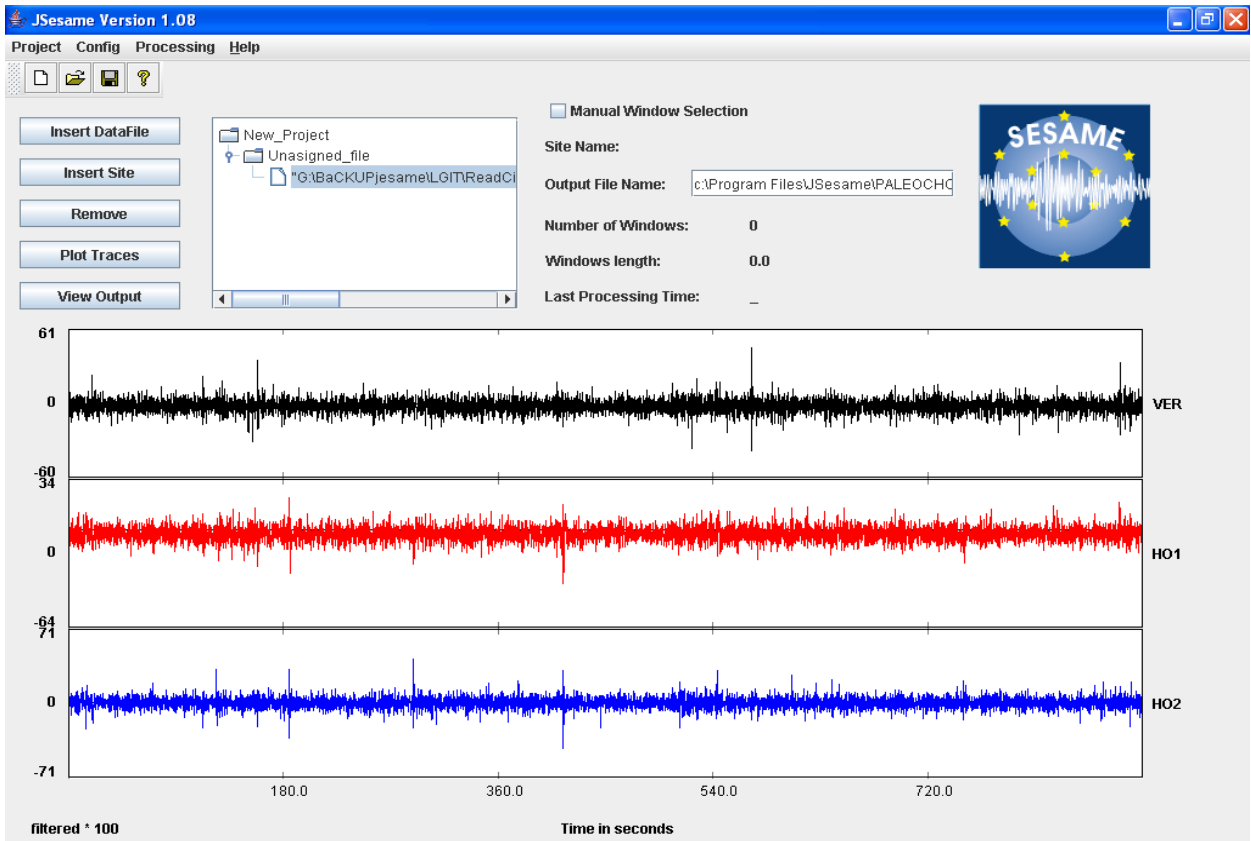


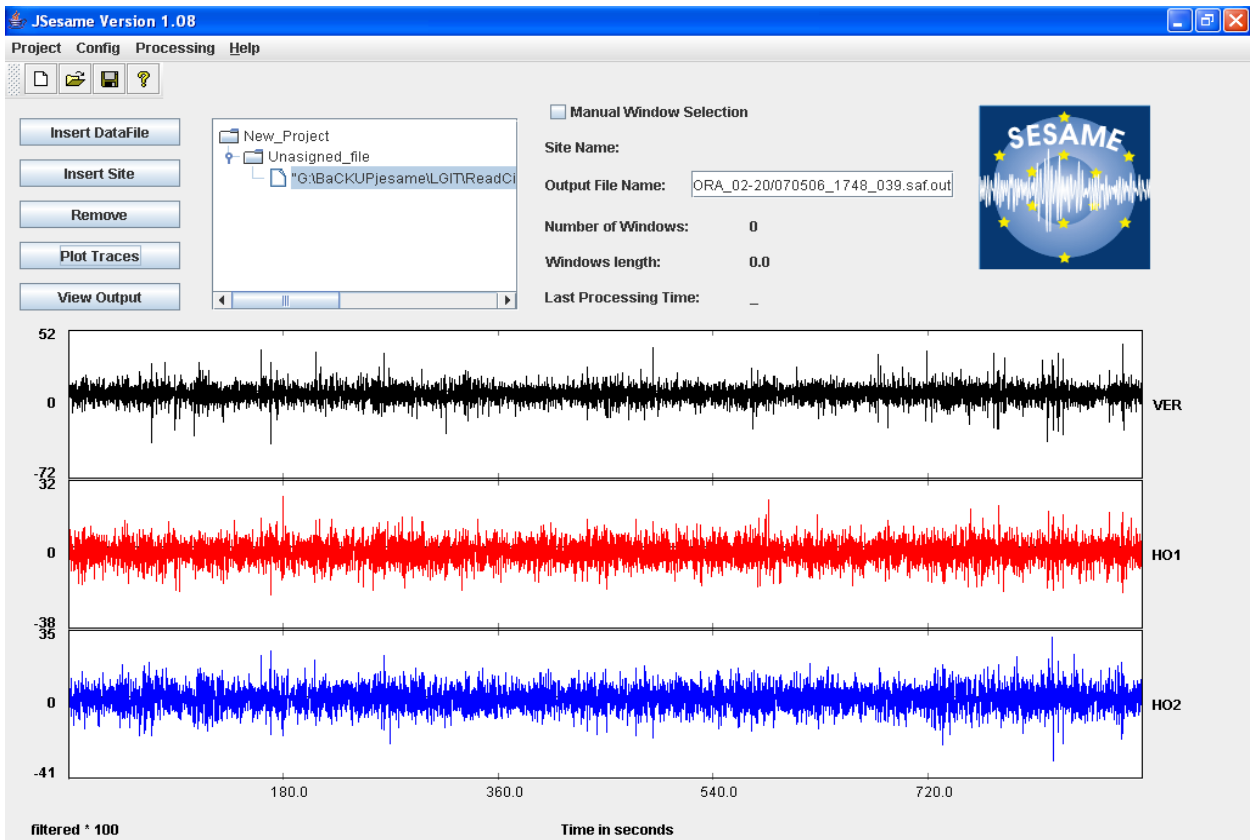
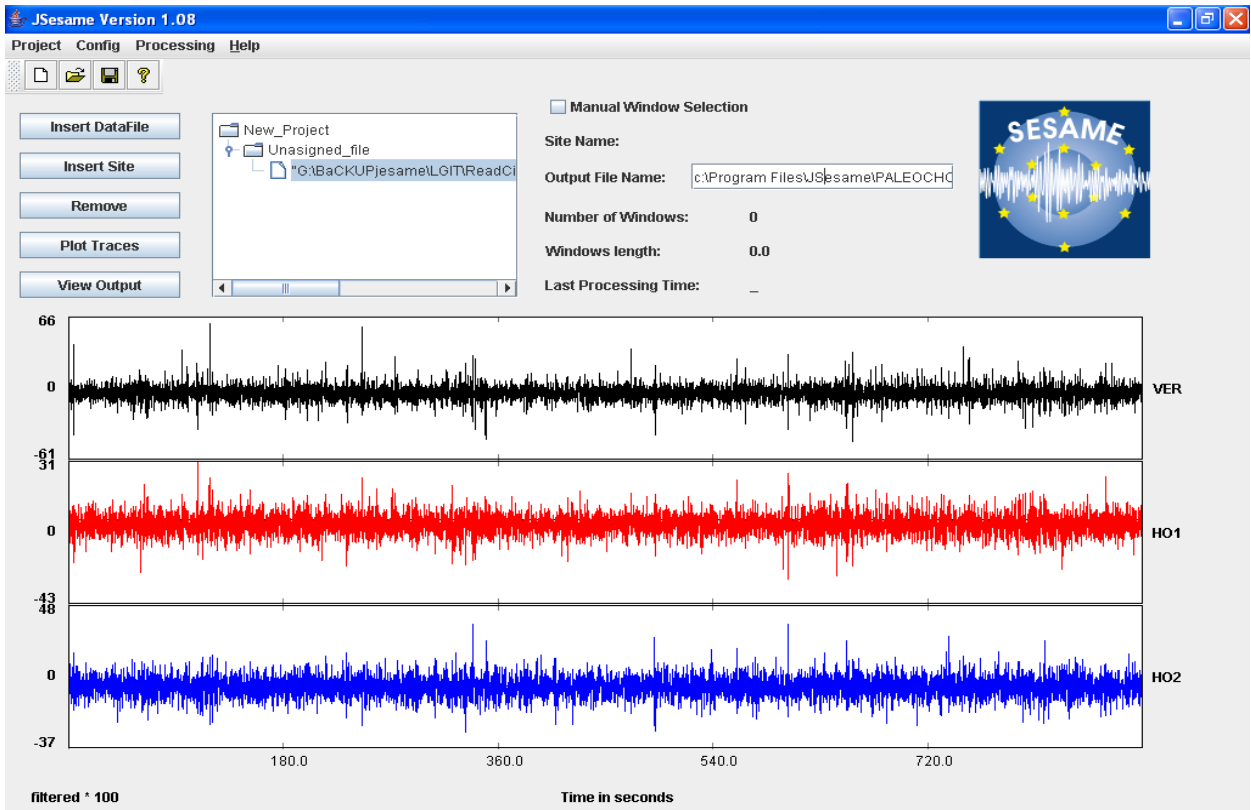


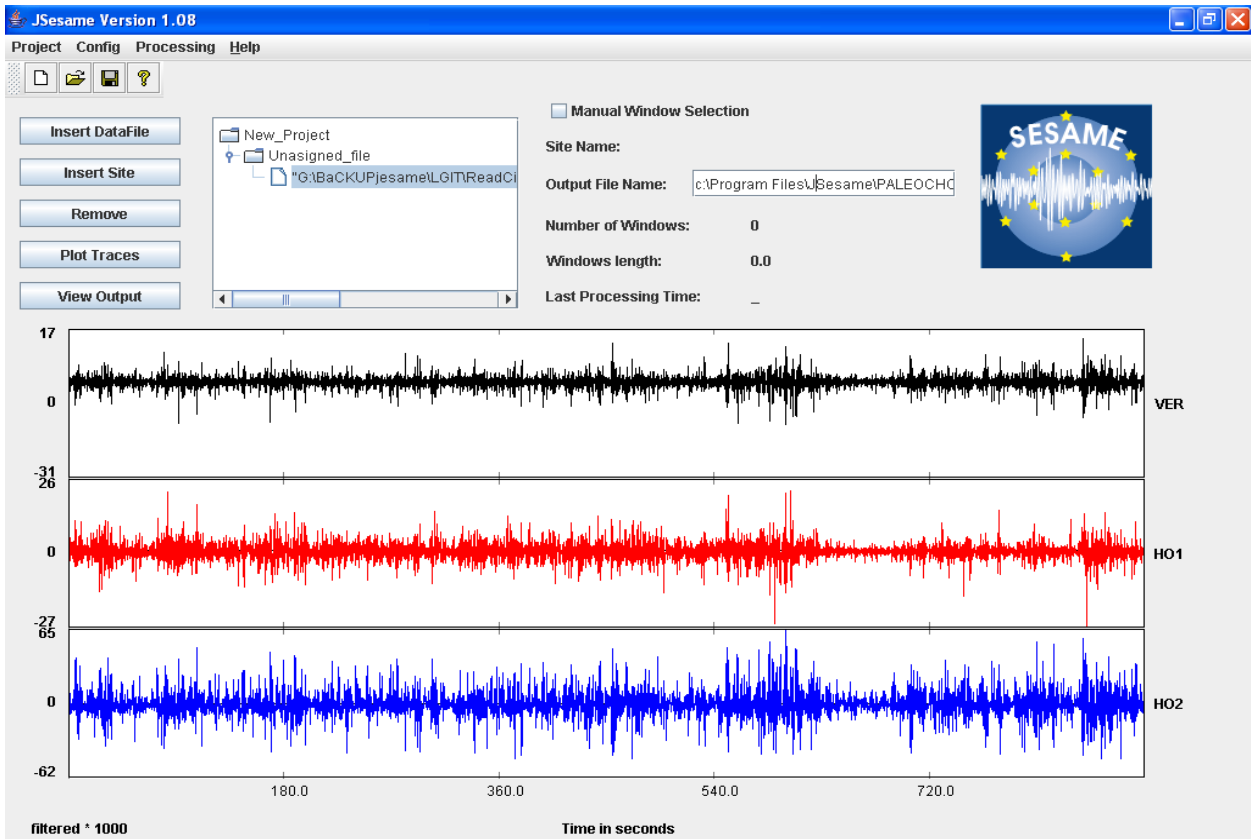
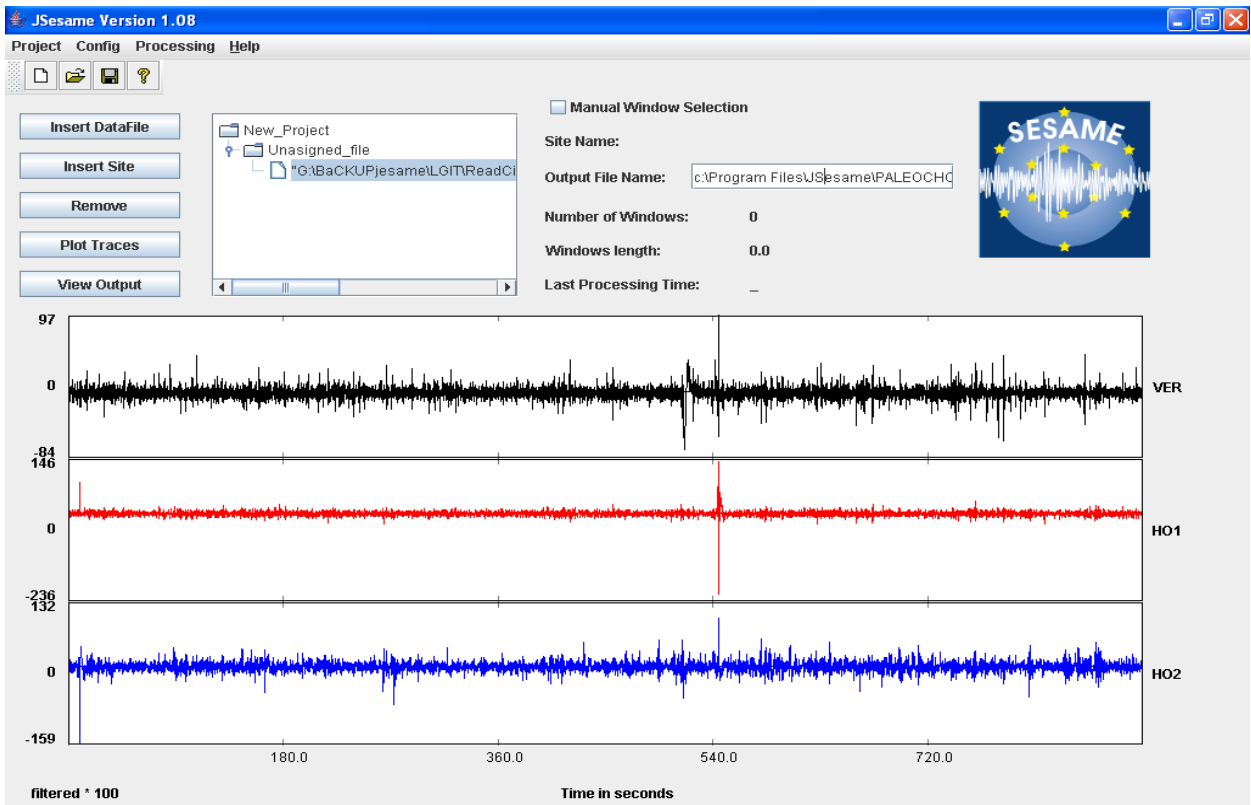


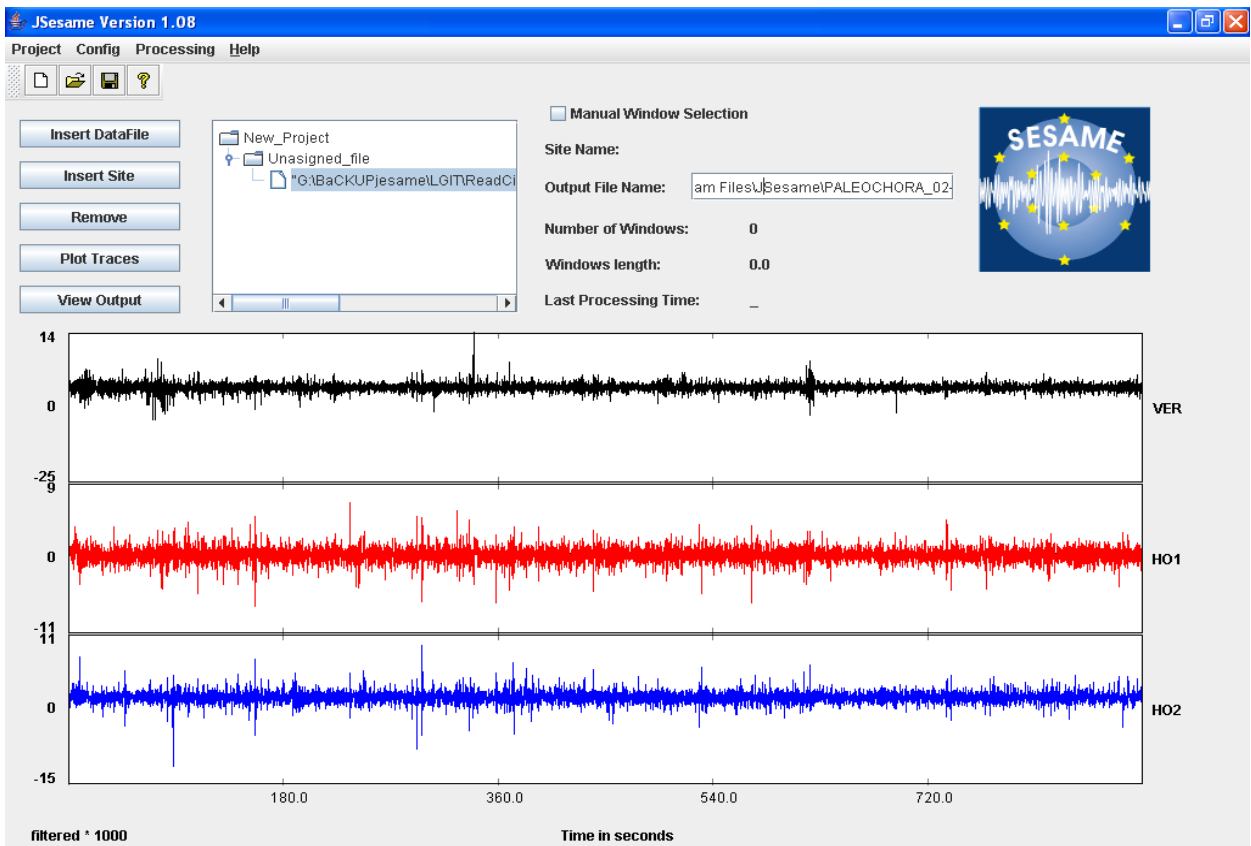
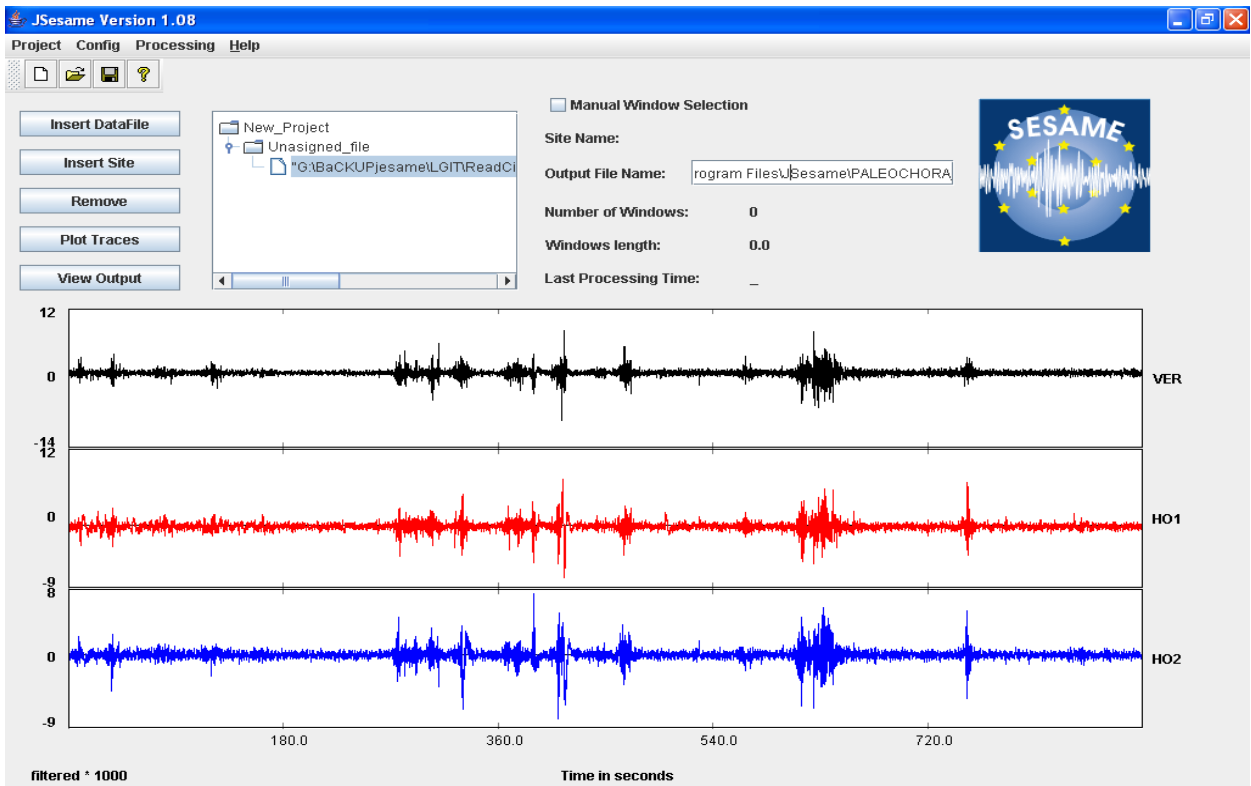


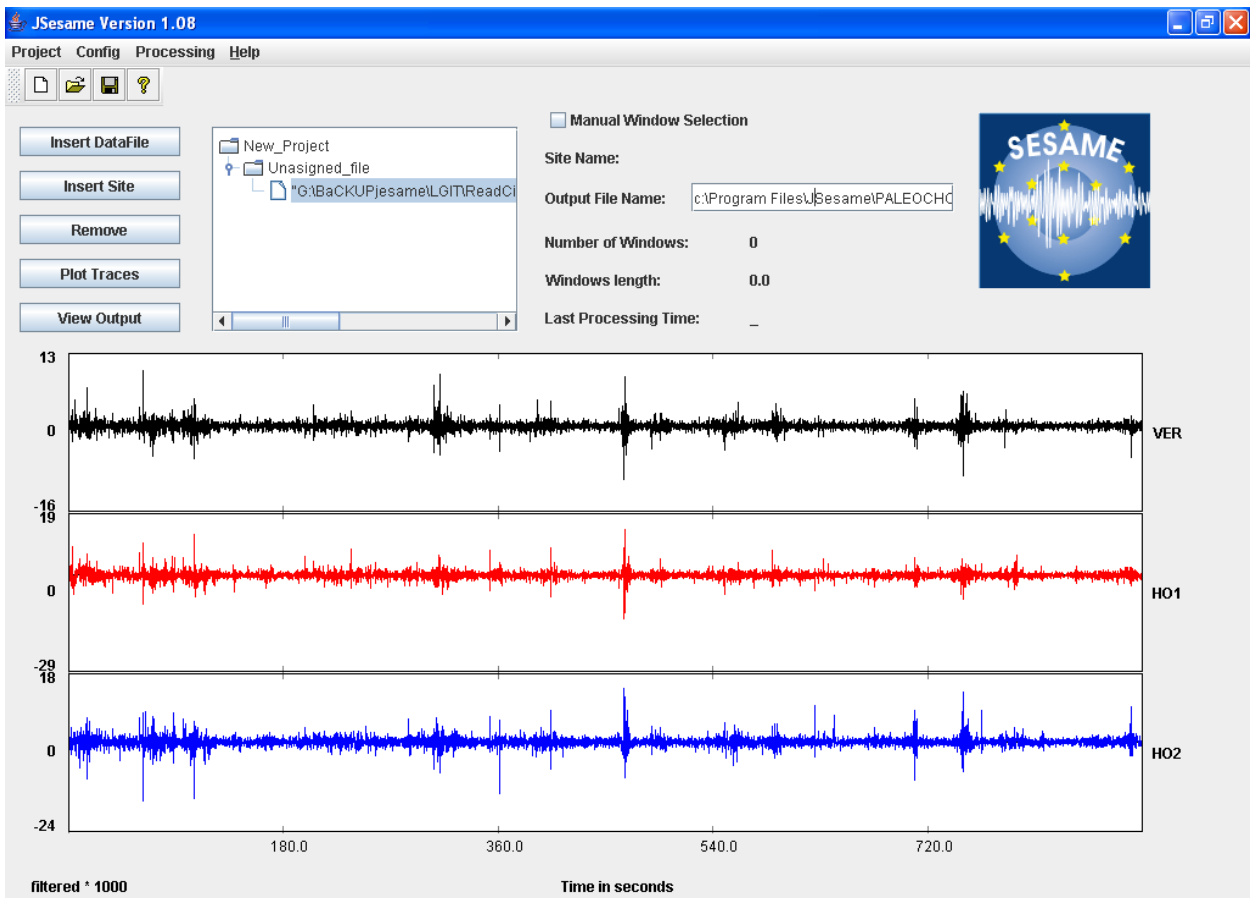
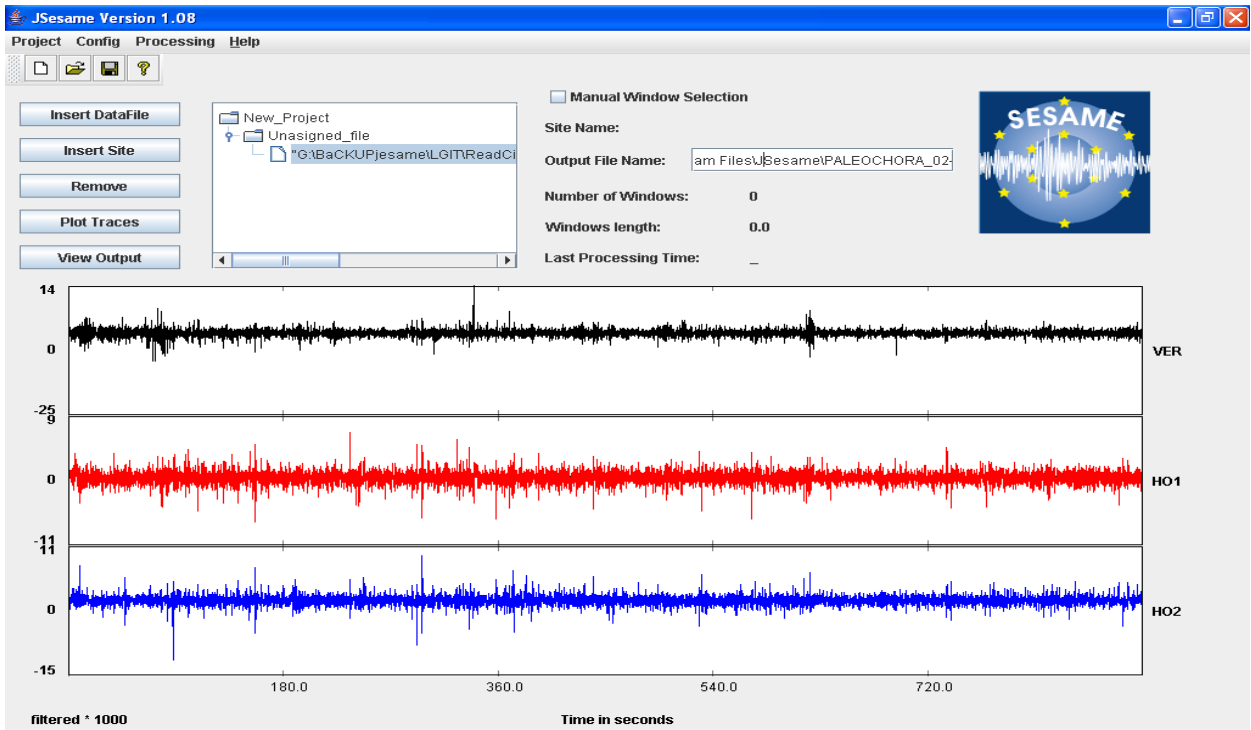




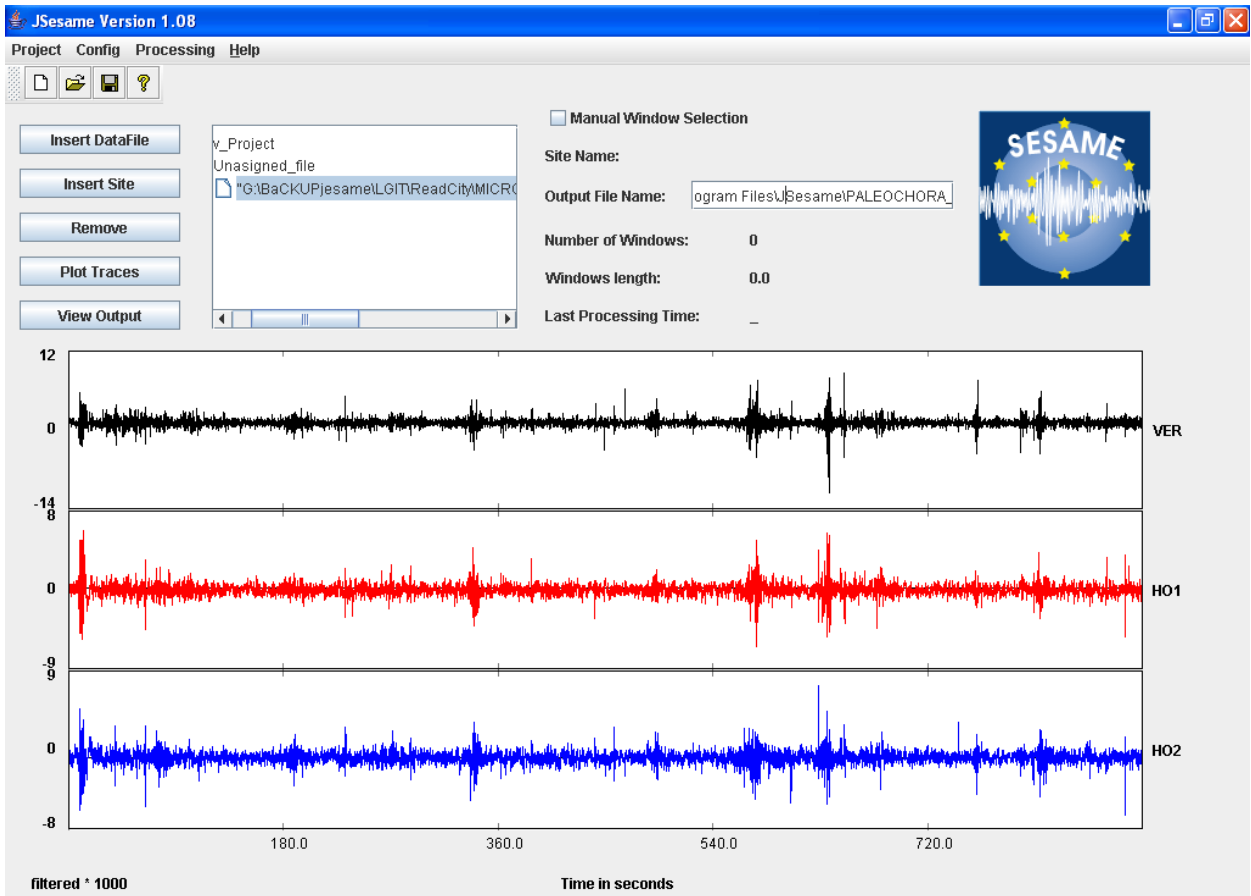
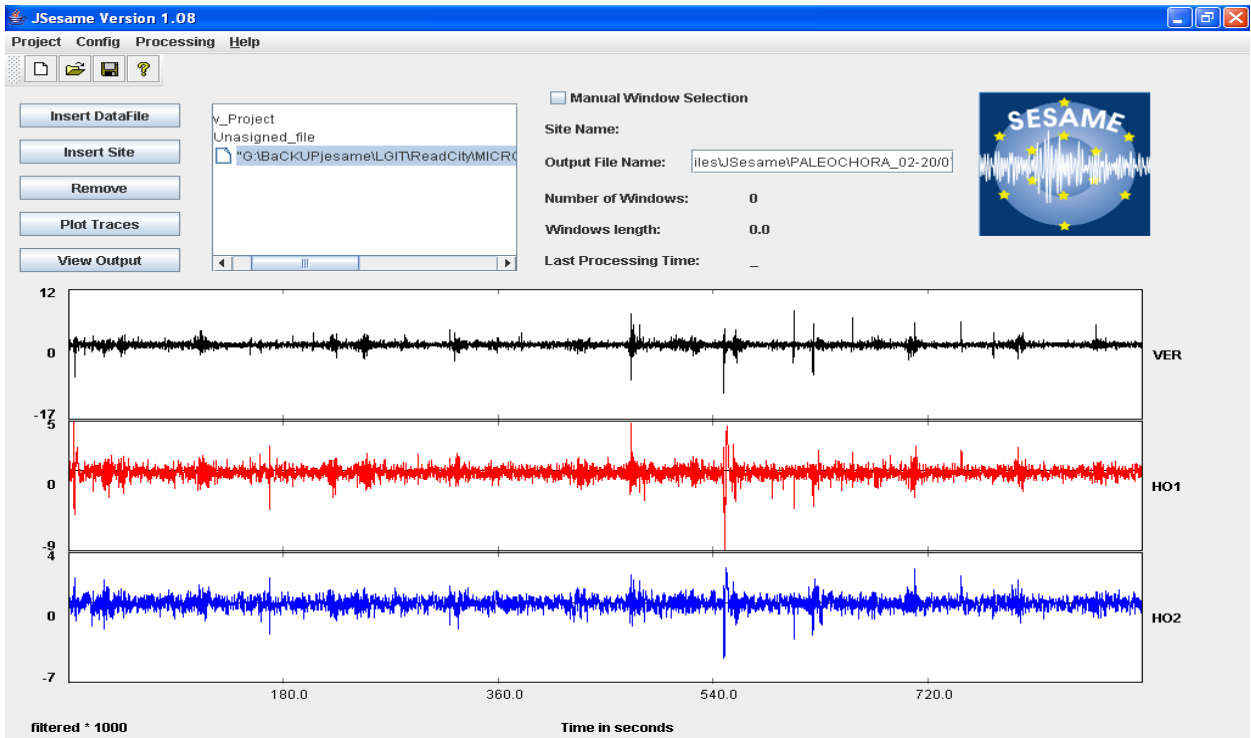


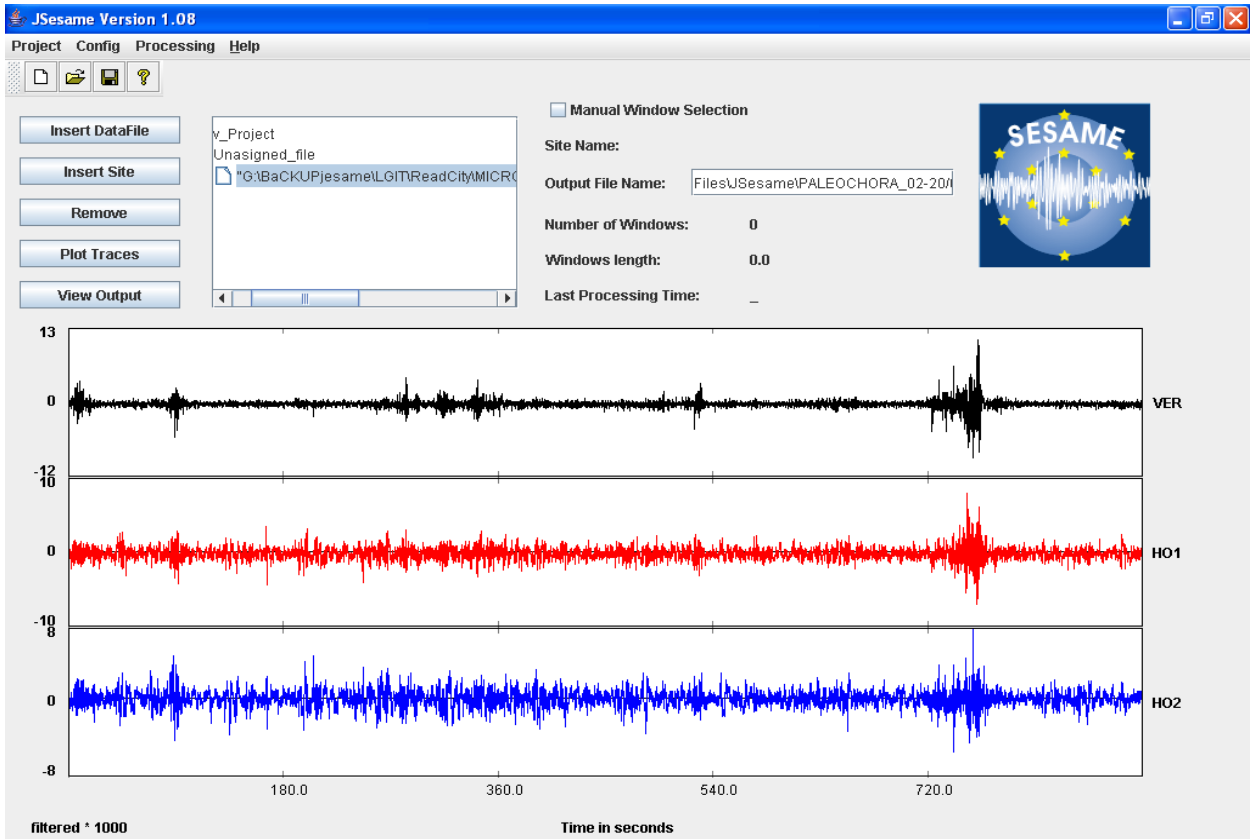
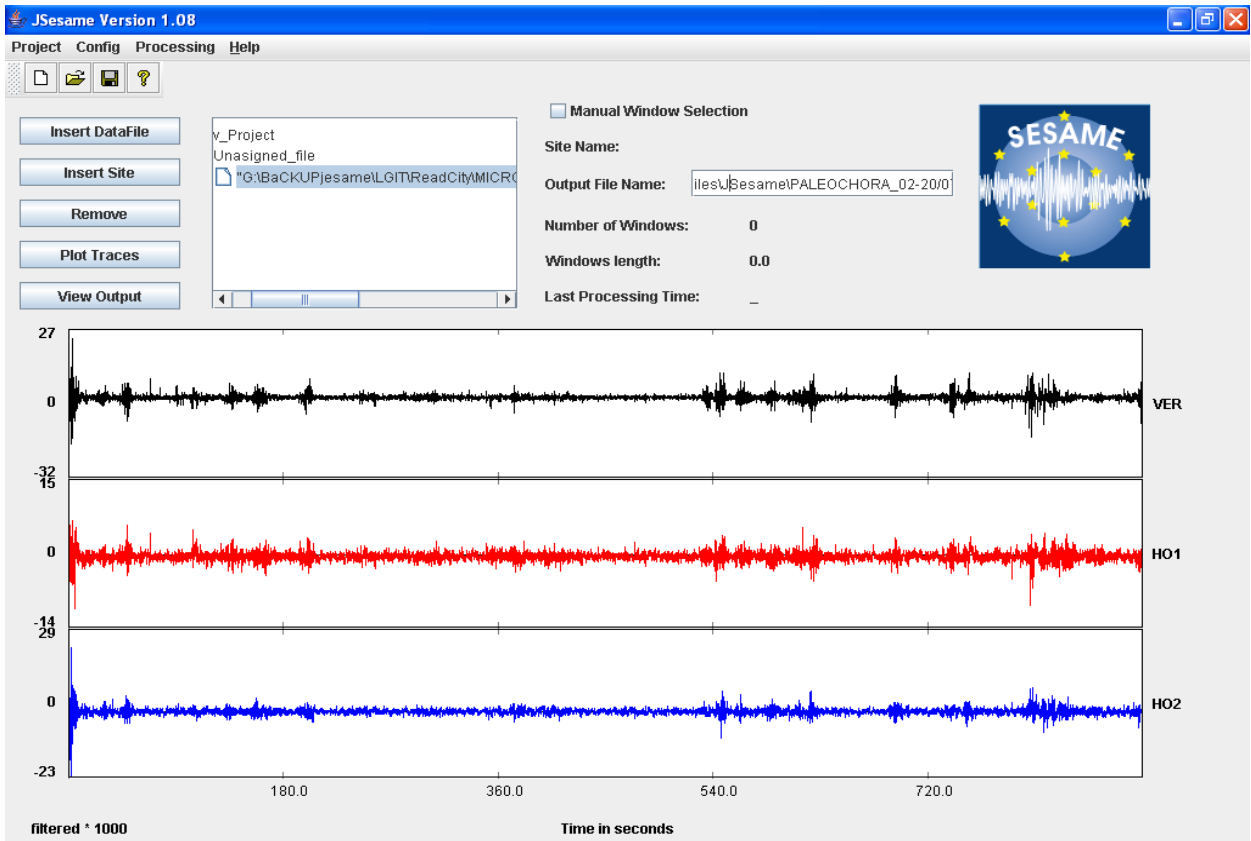


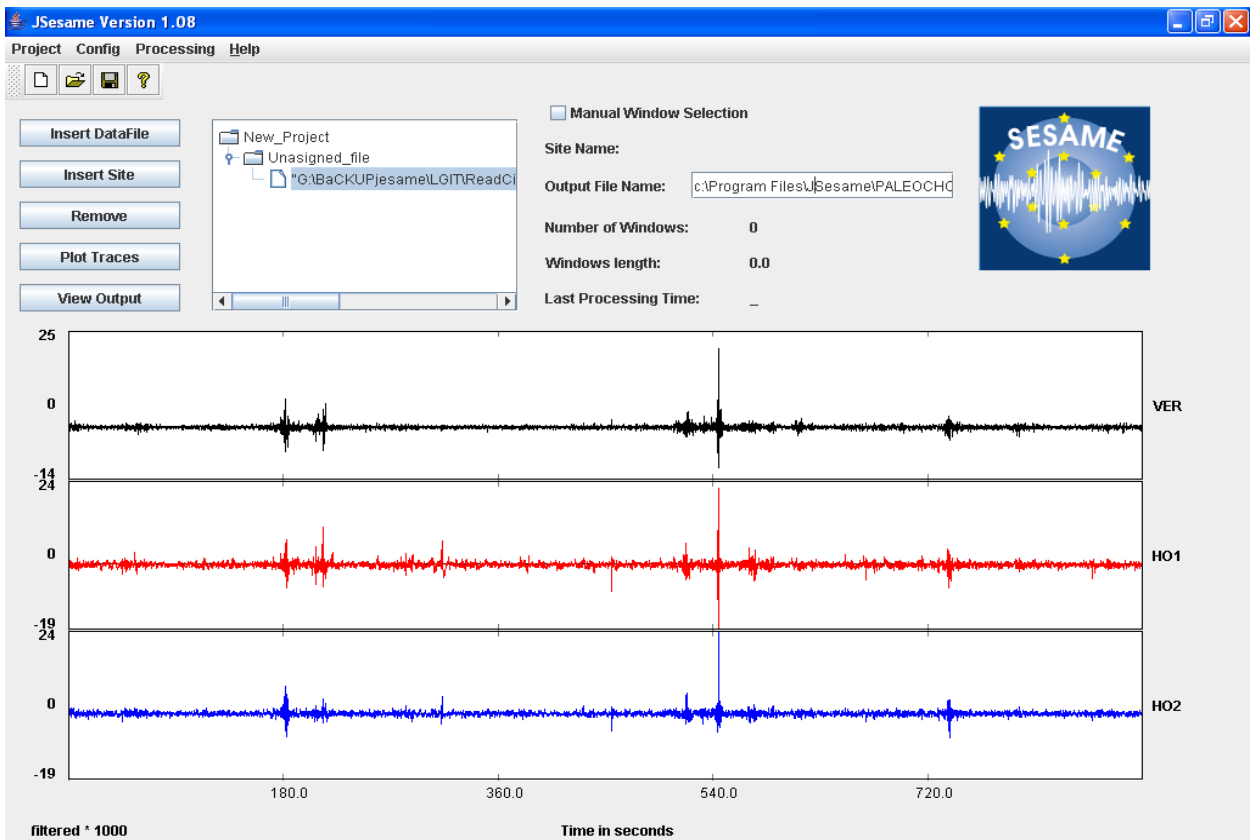
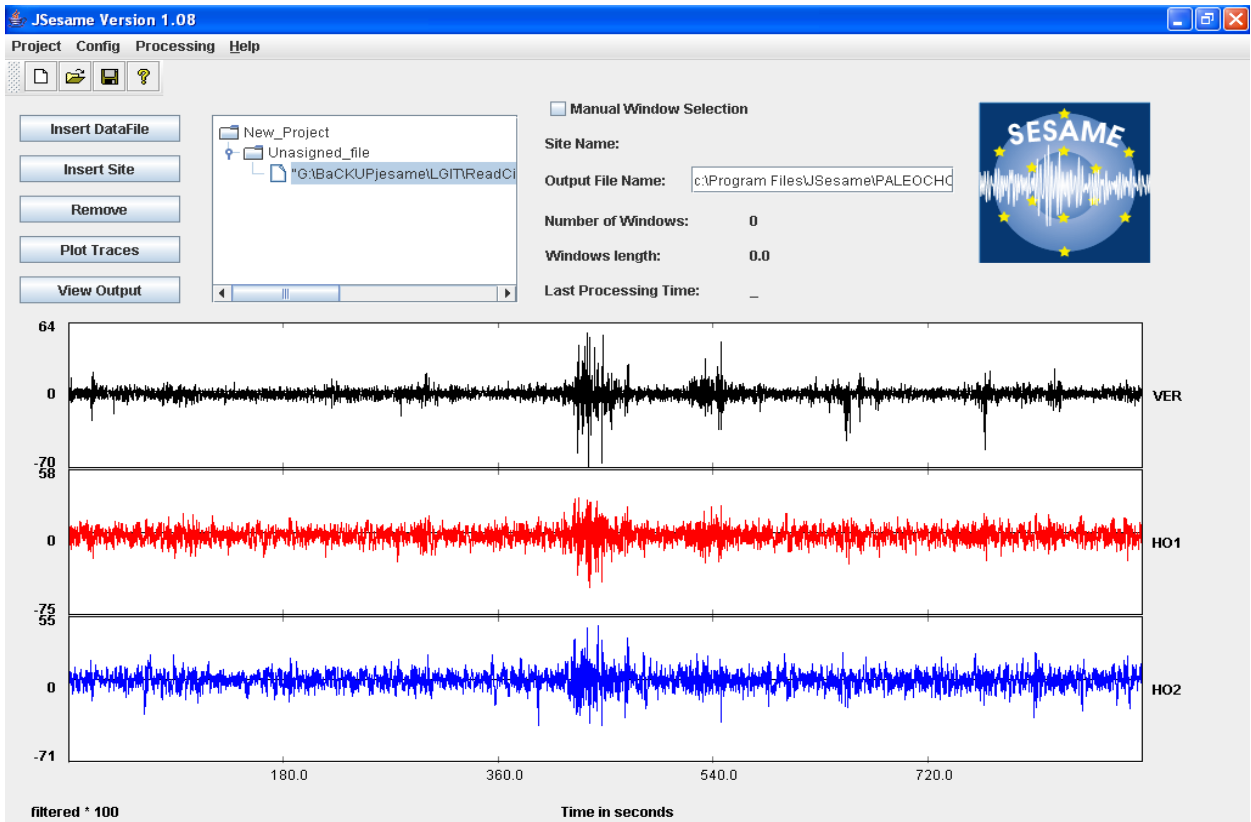


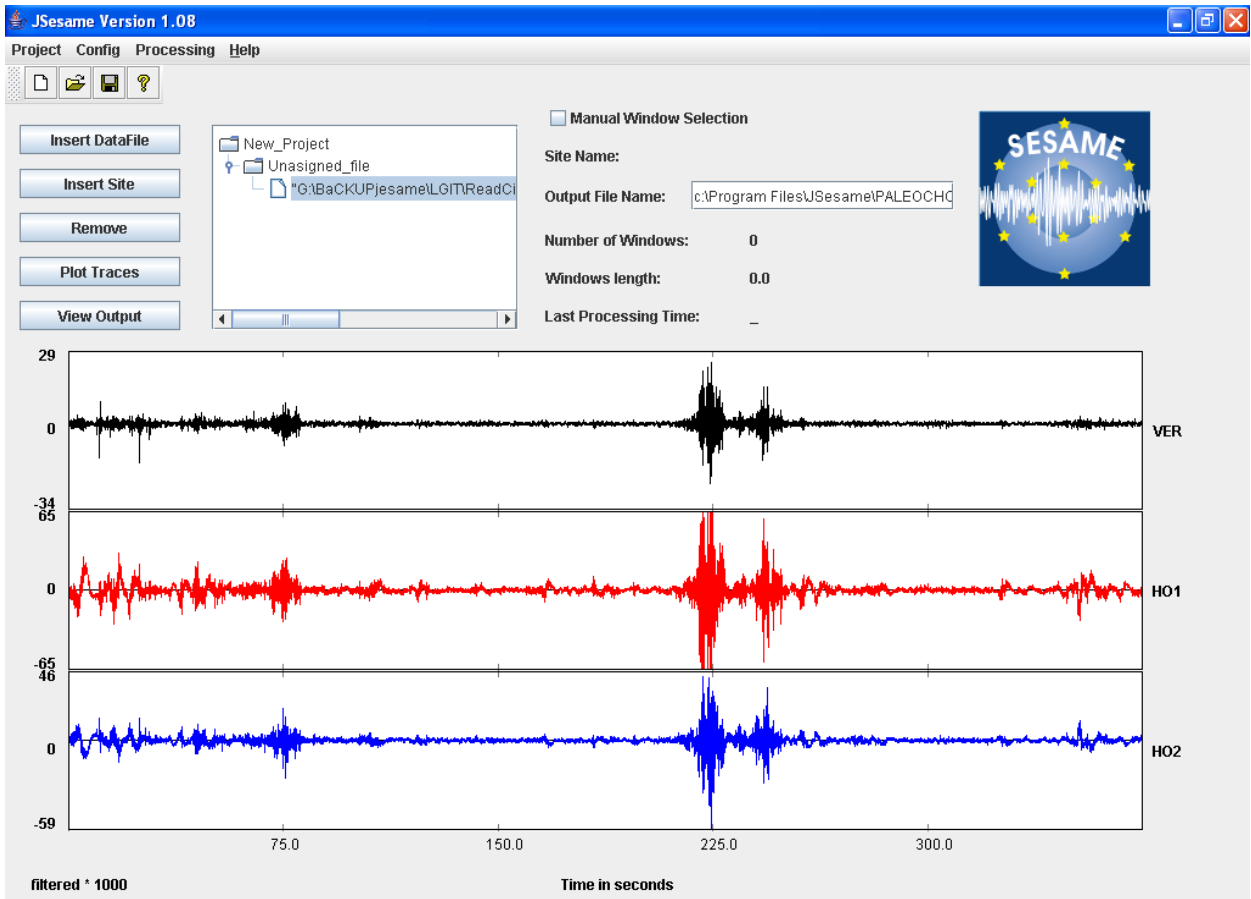






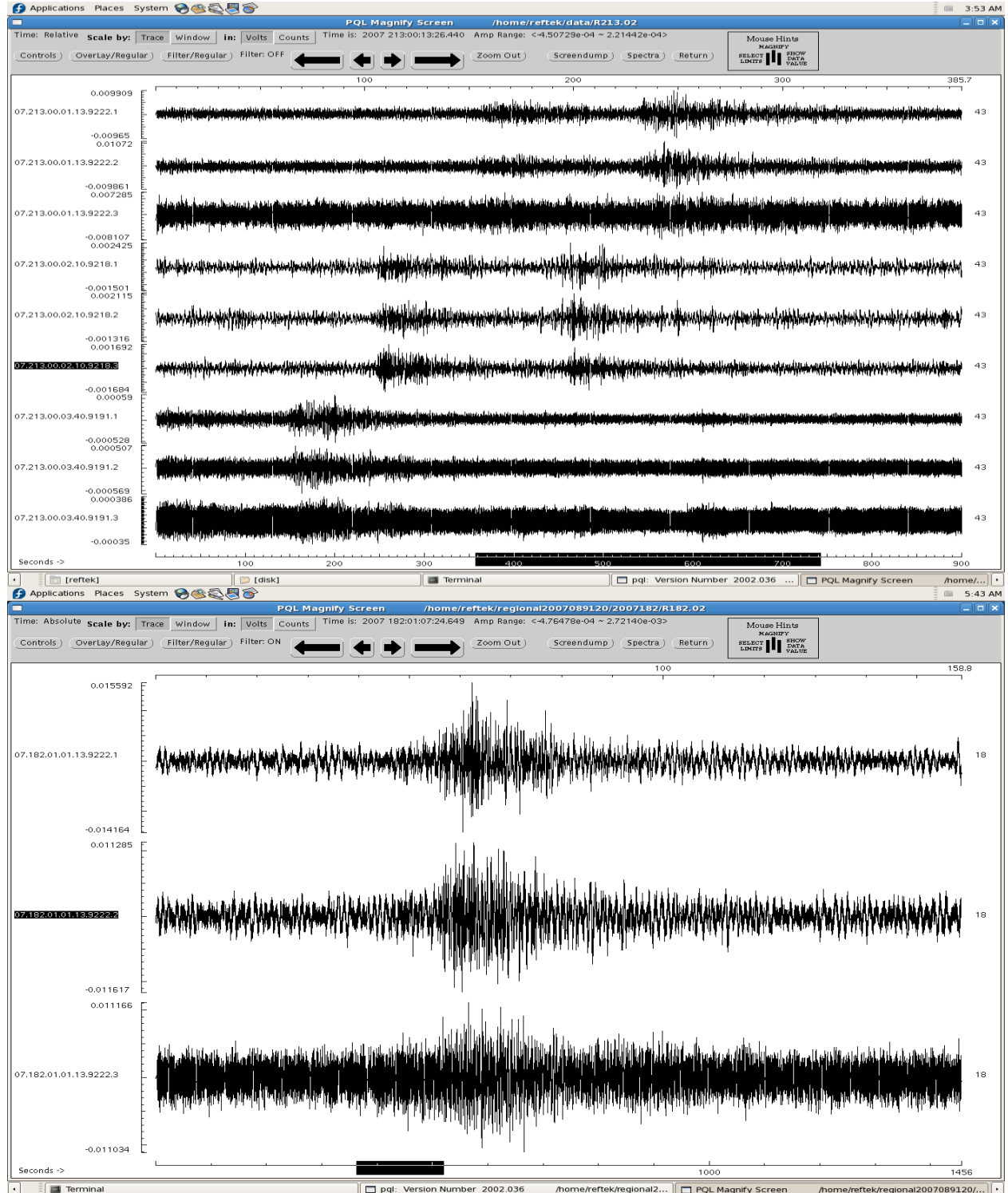


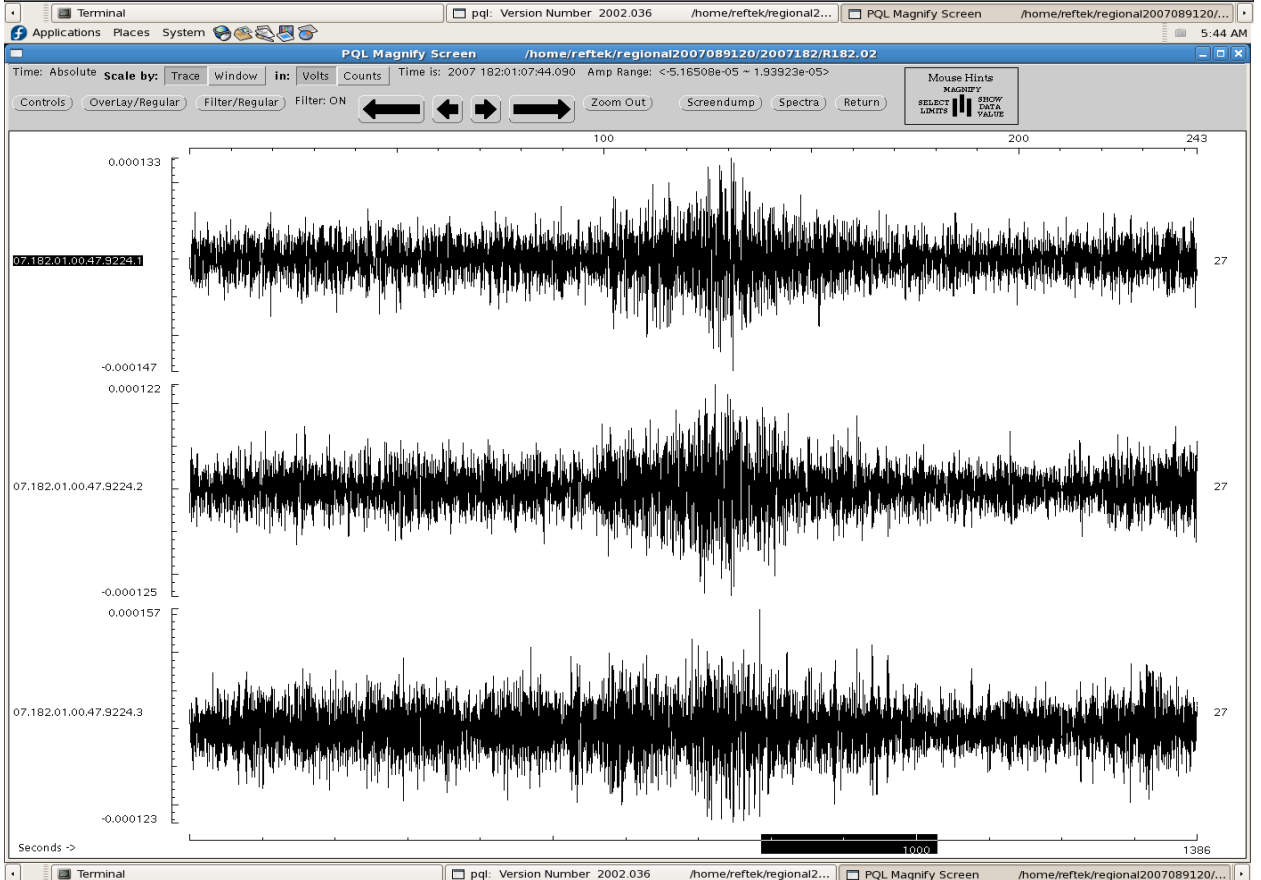
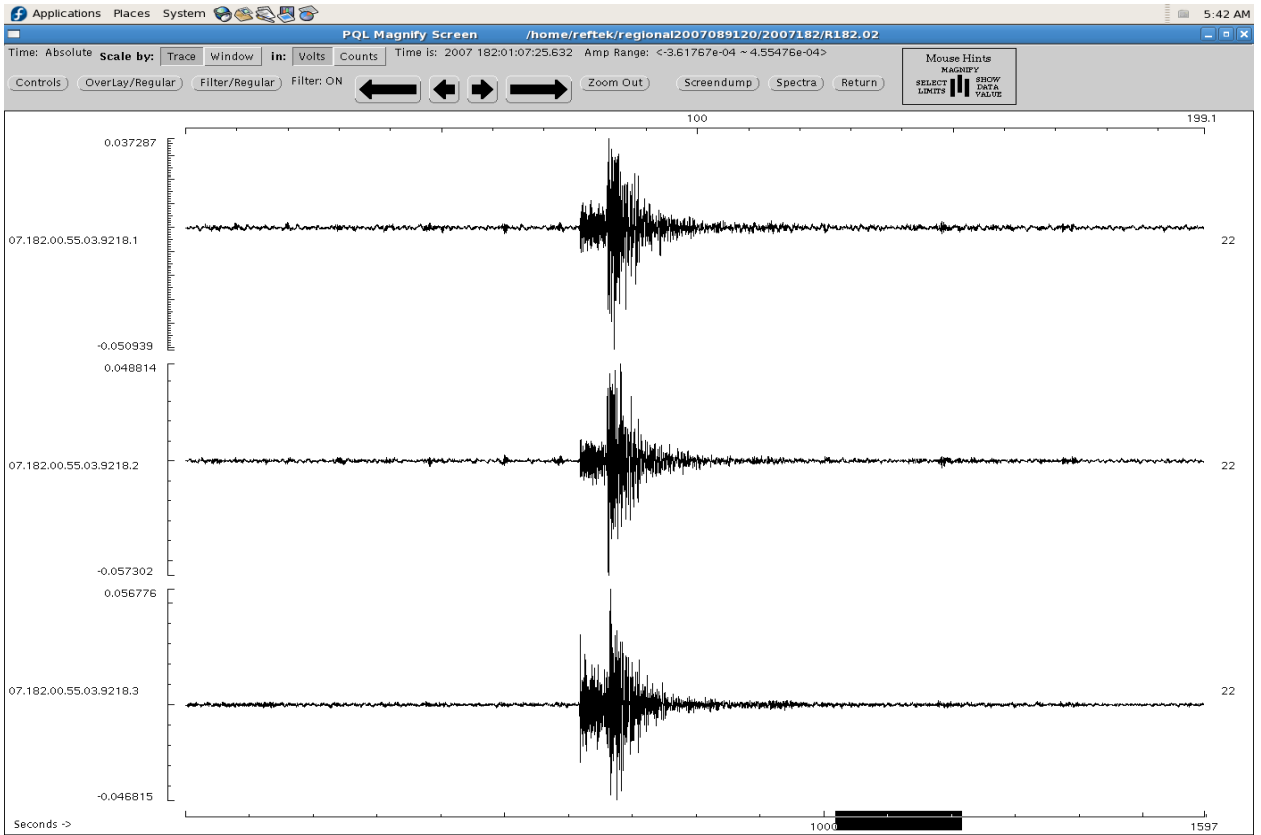


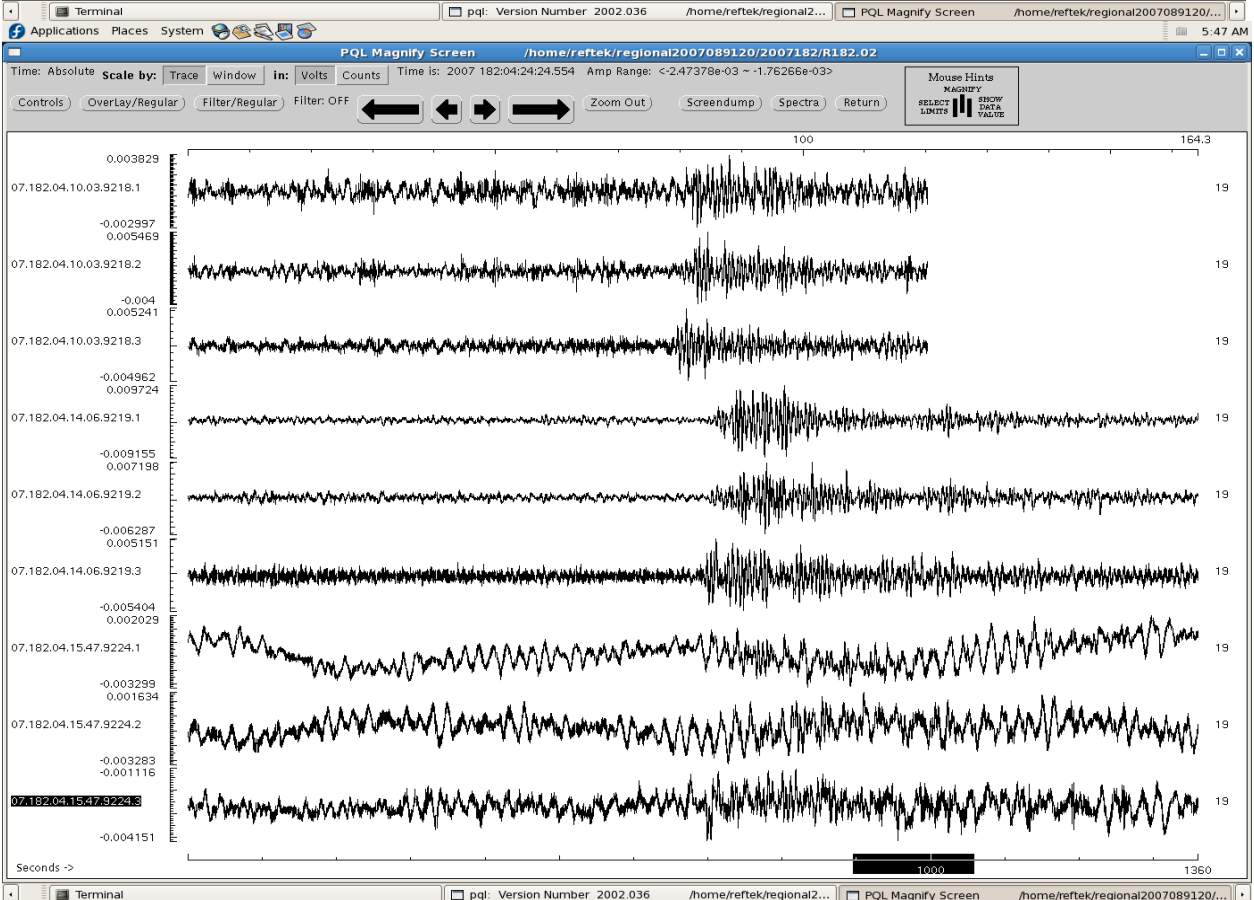
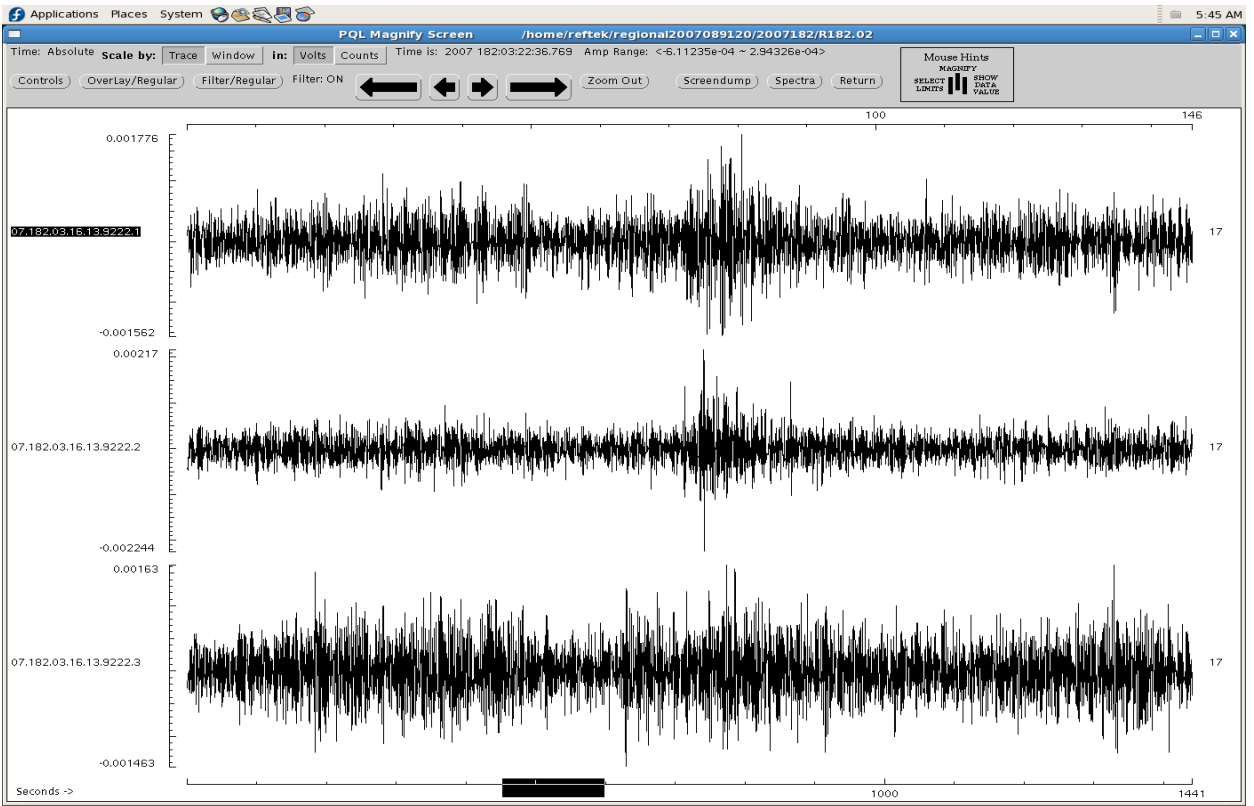


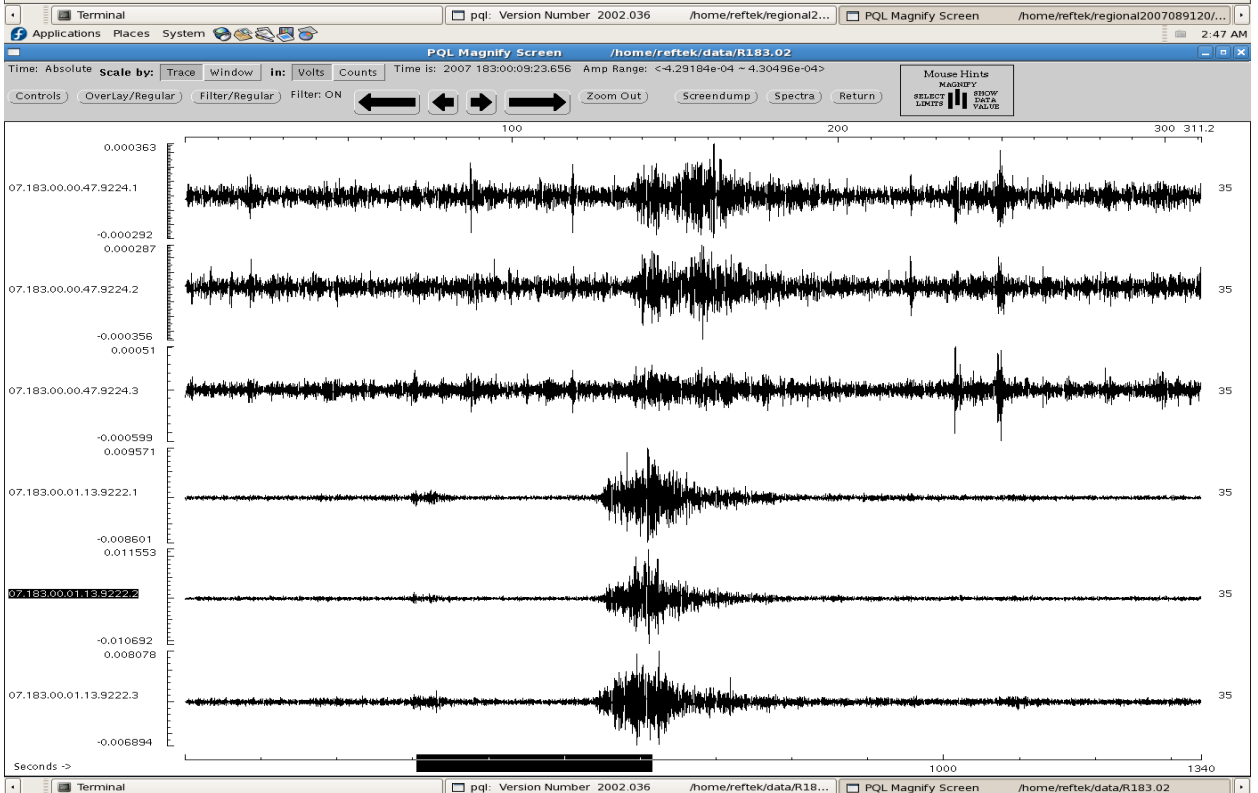
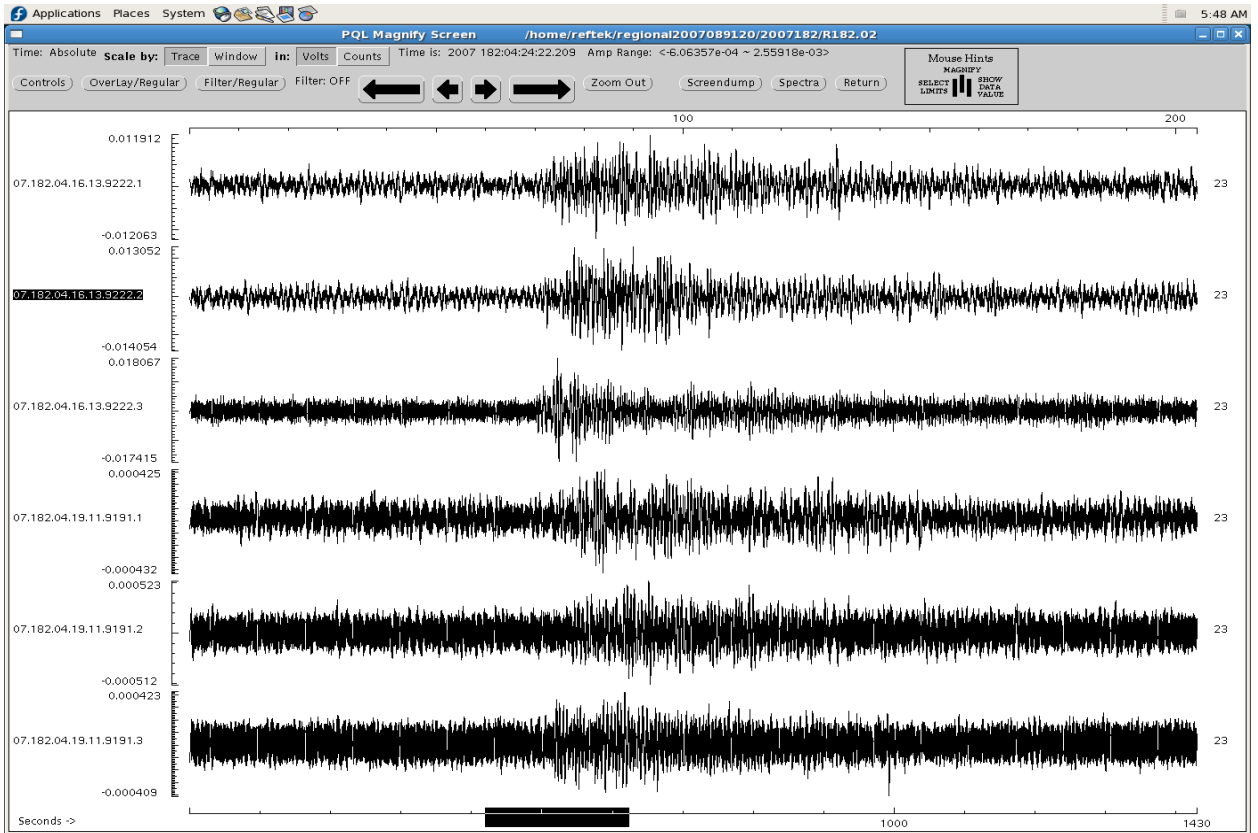
## APPENDIX IV: EARTHQUAKE SAMPLES RECORDED FROM THE PERMANENT AND TEMPORAL SEISMOLOGICAL NETWORK OF CRETE

### A1: EARTHQUAKE SAMPLES RECORDED FROM THE PERMANENT SEISMOLOGICAL NETWORK OF CRETE

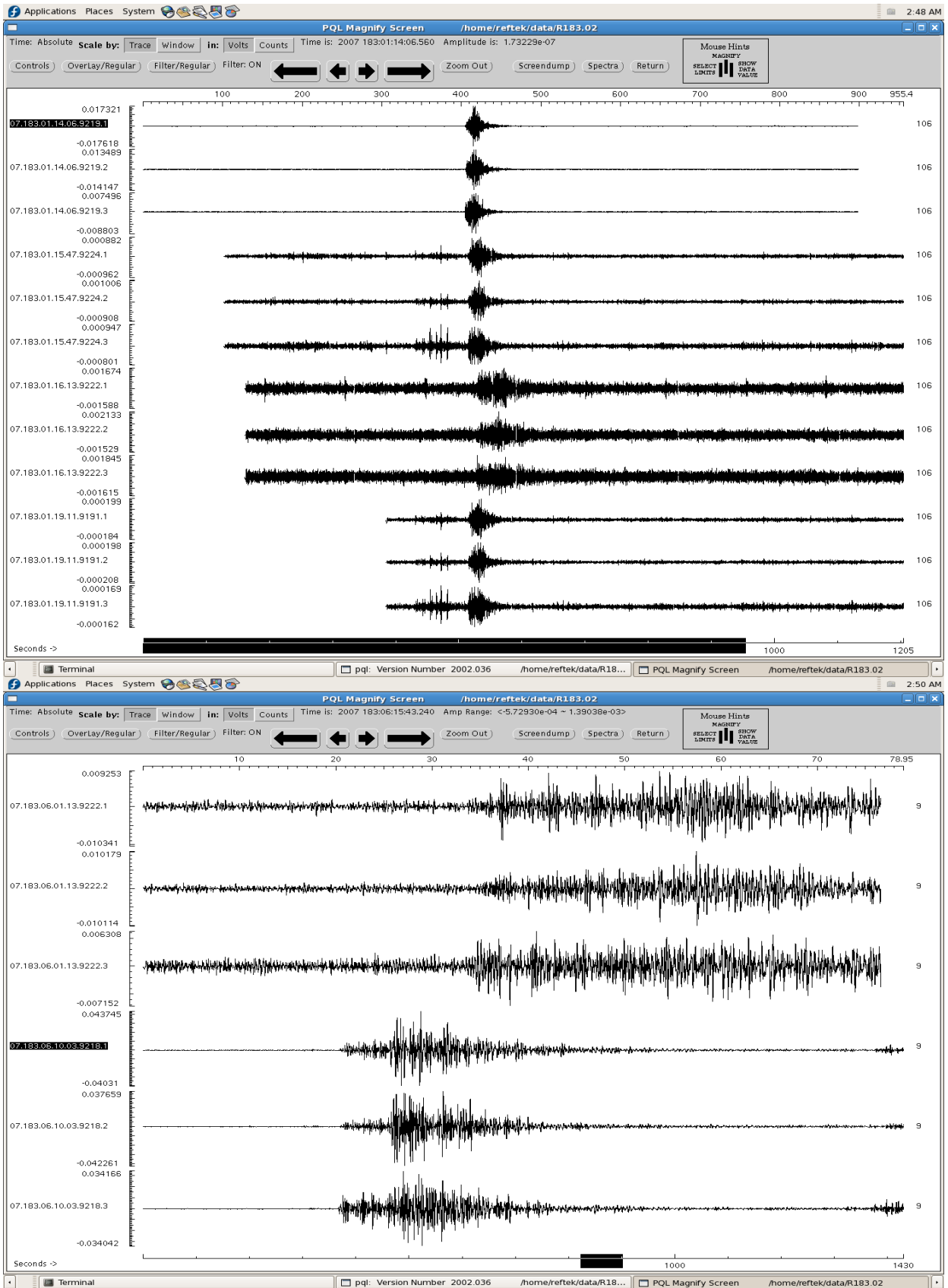


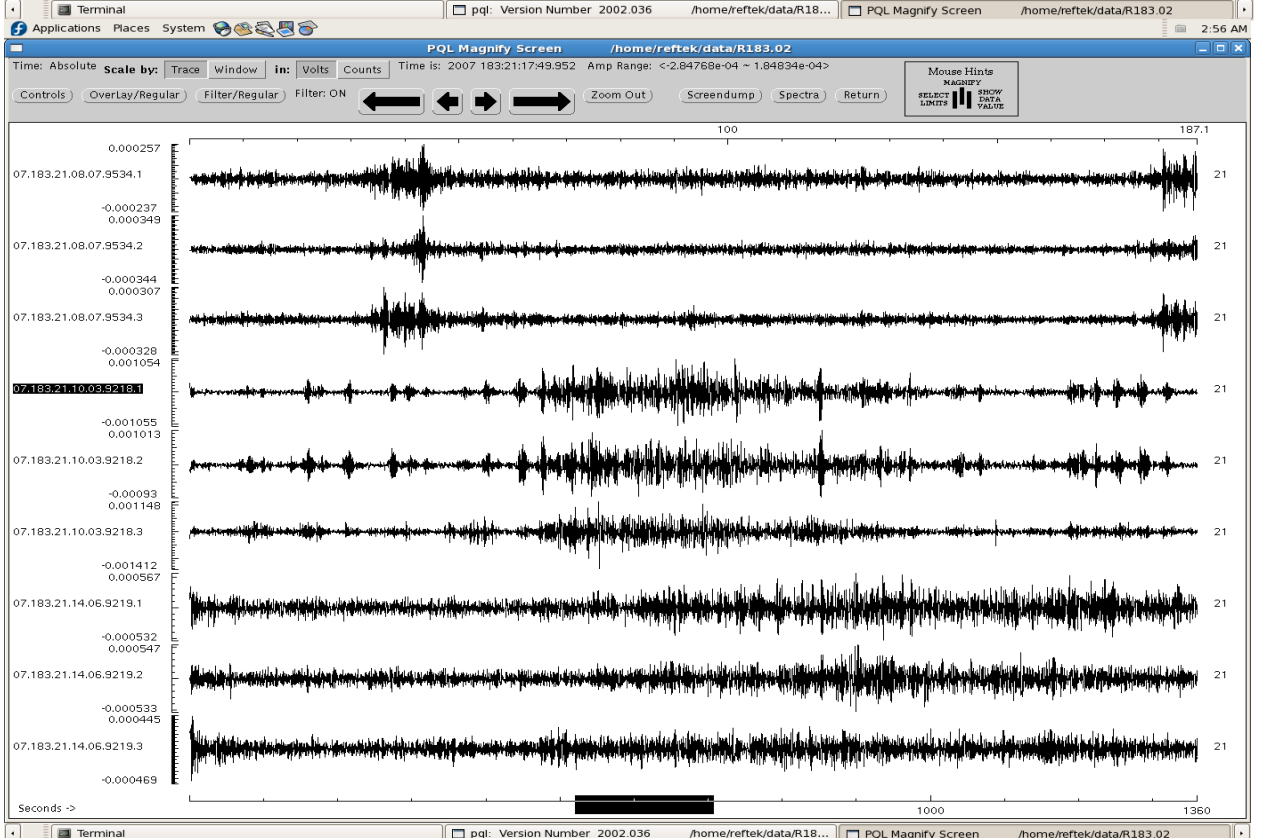
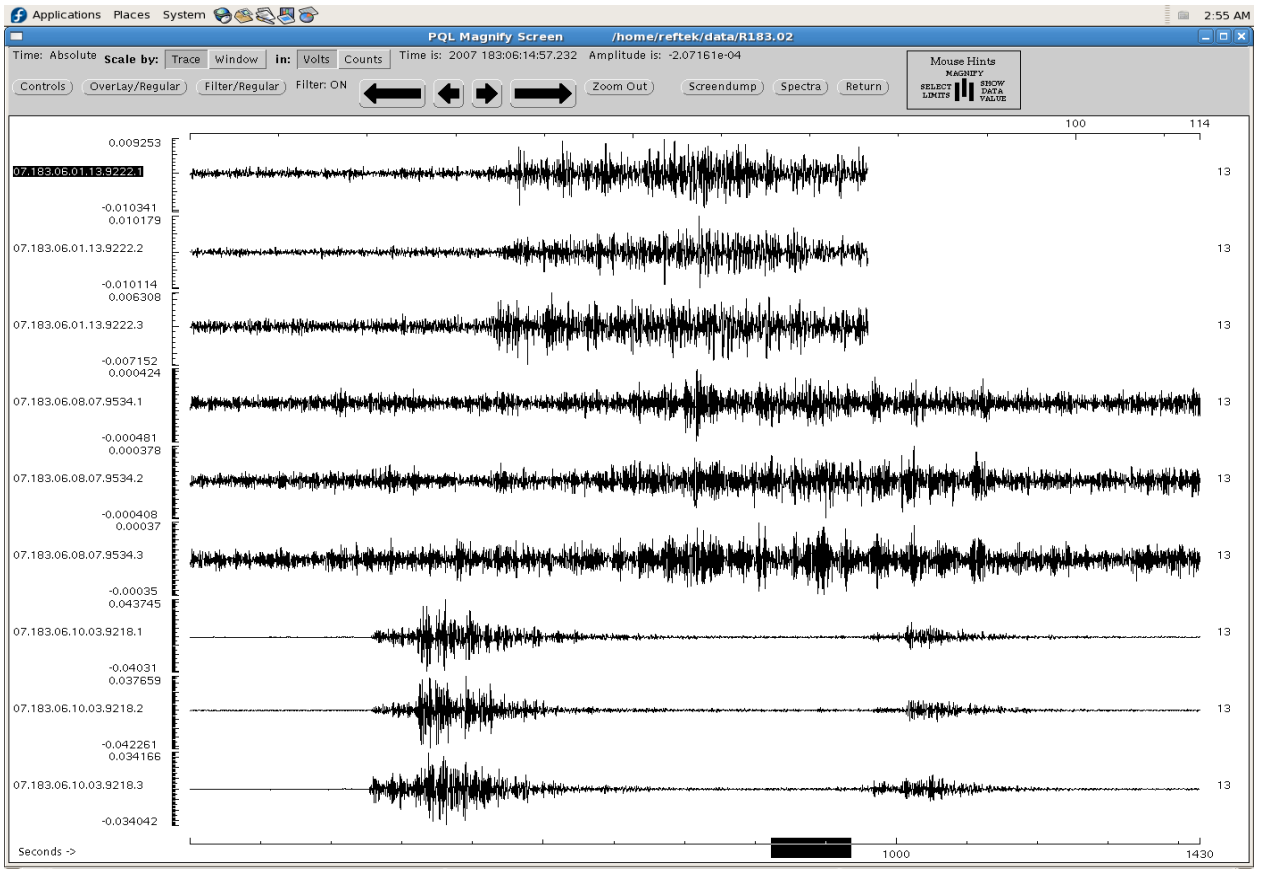


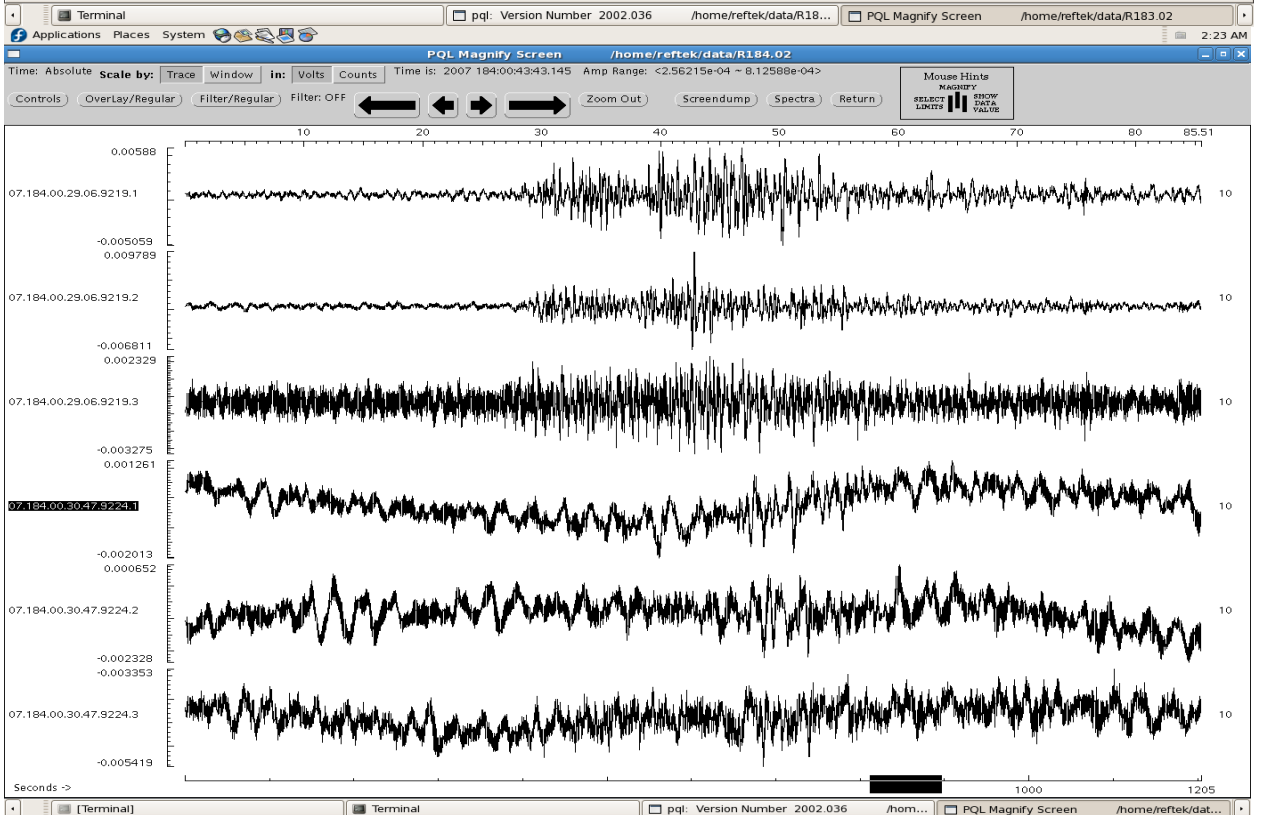
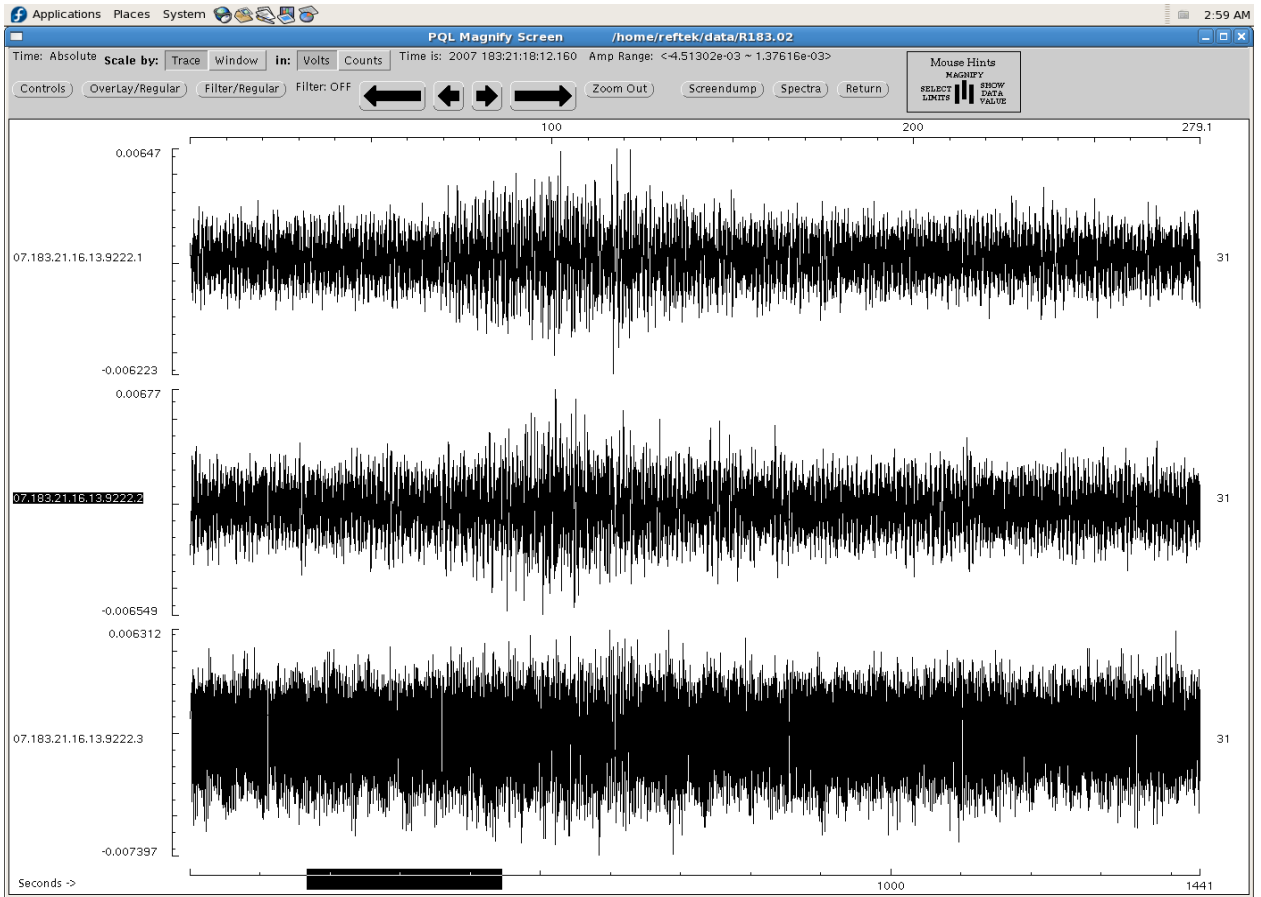


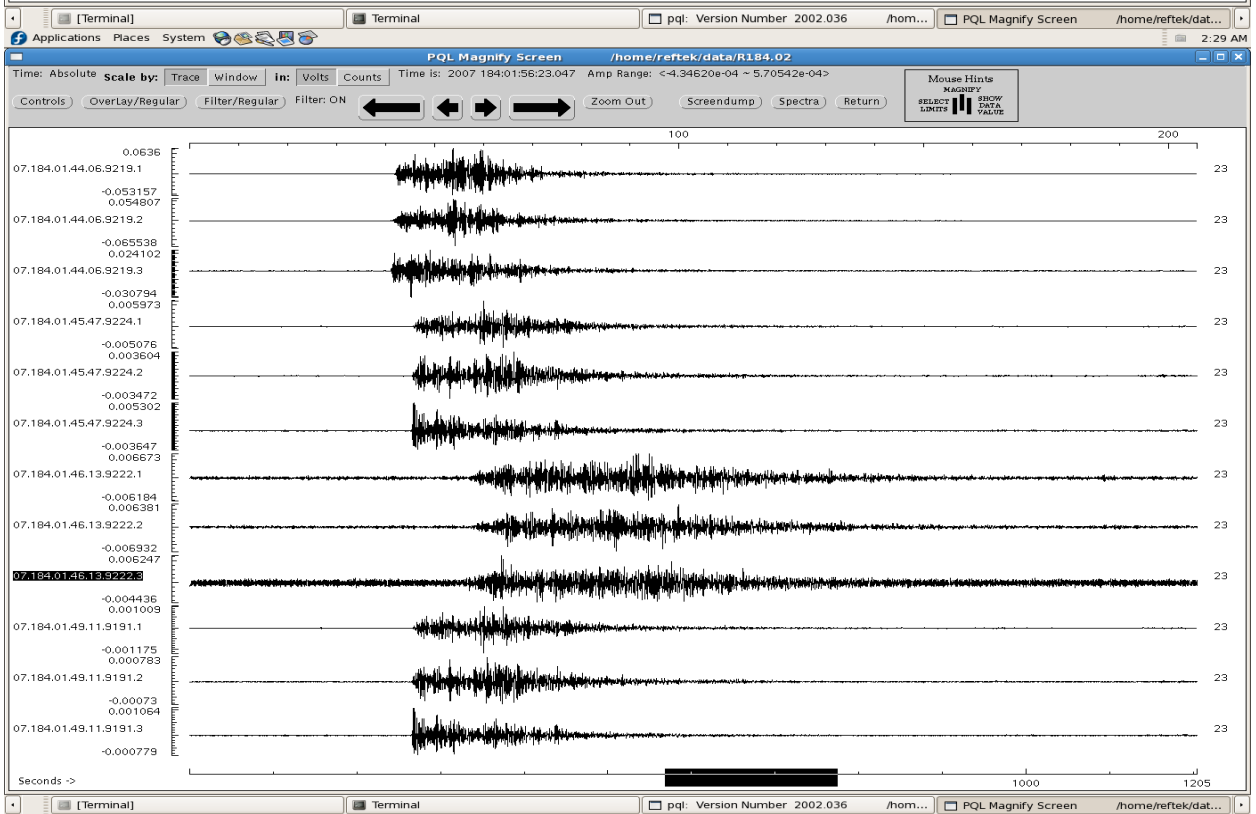
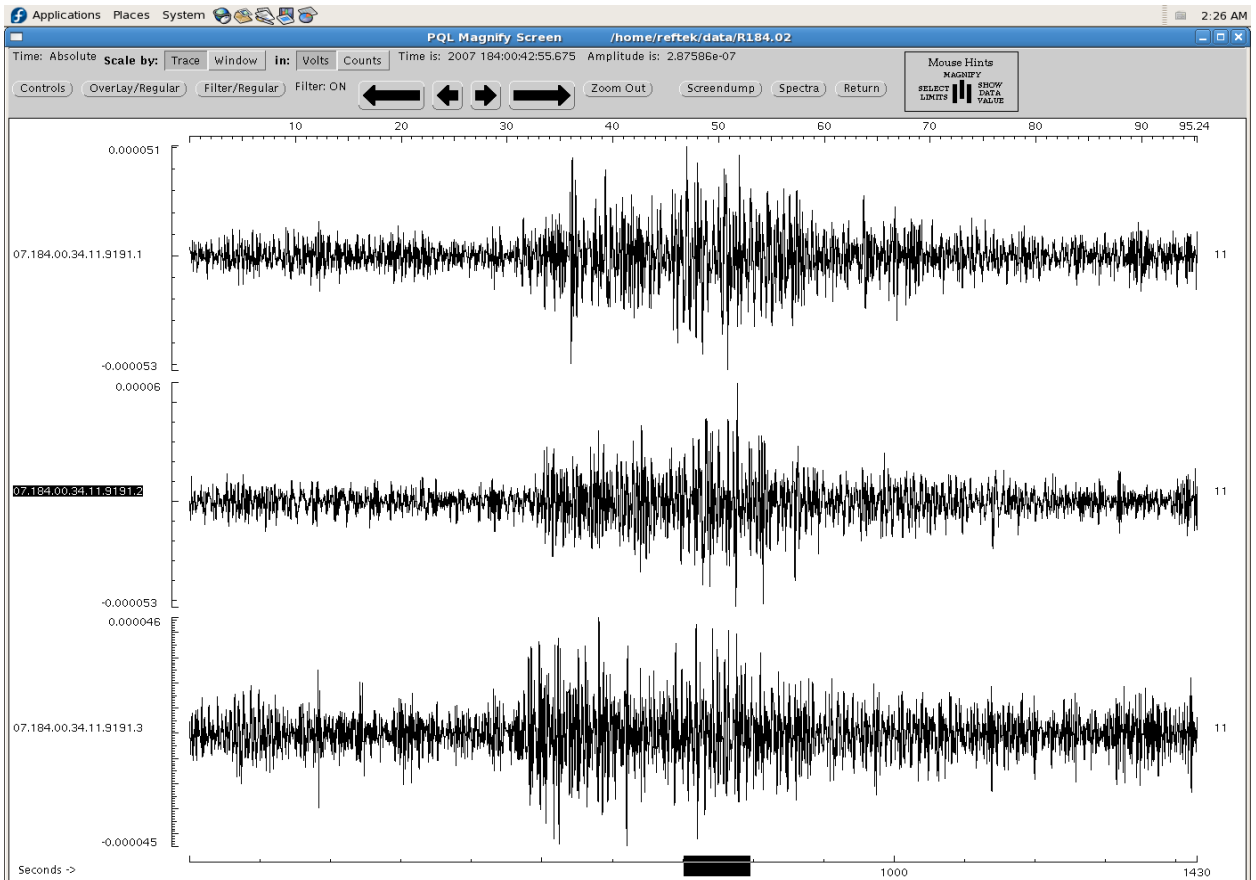


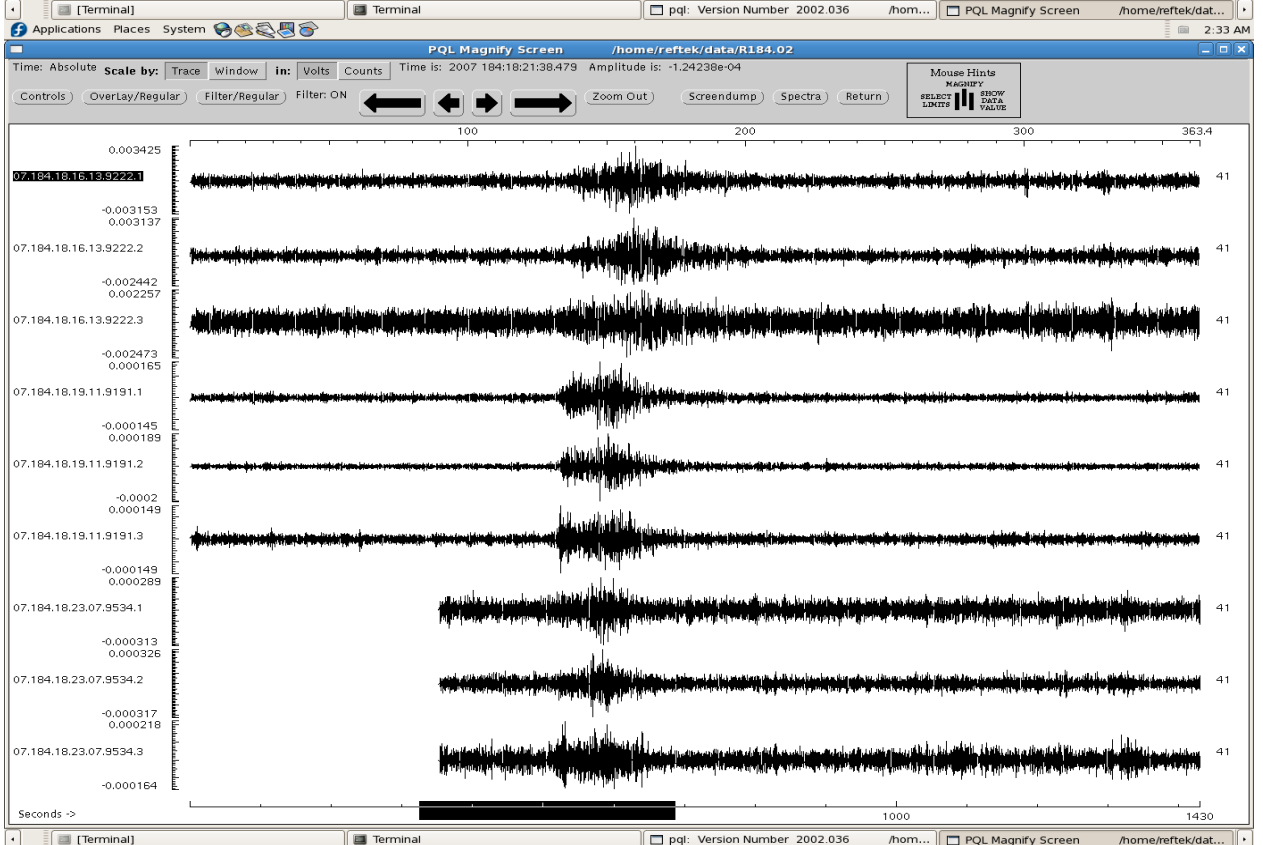
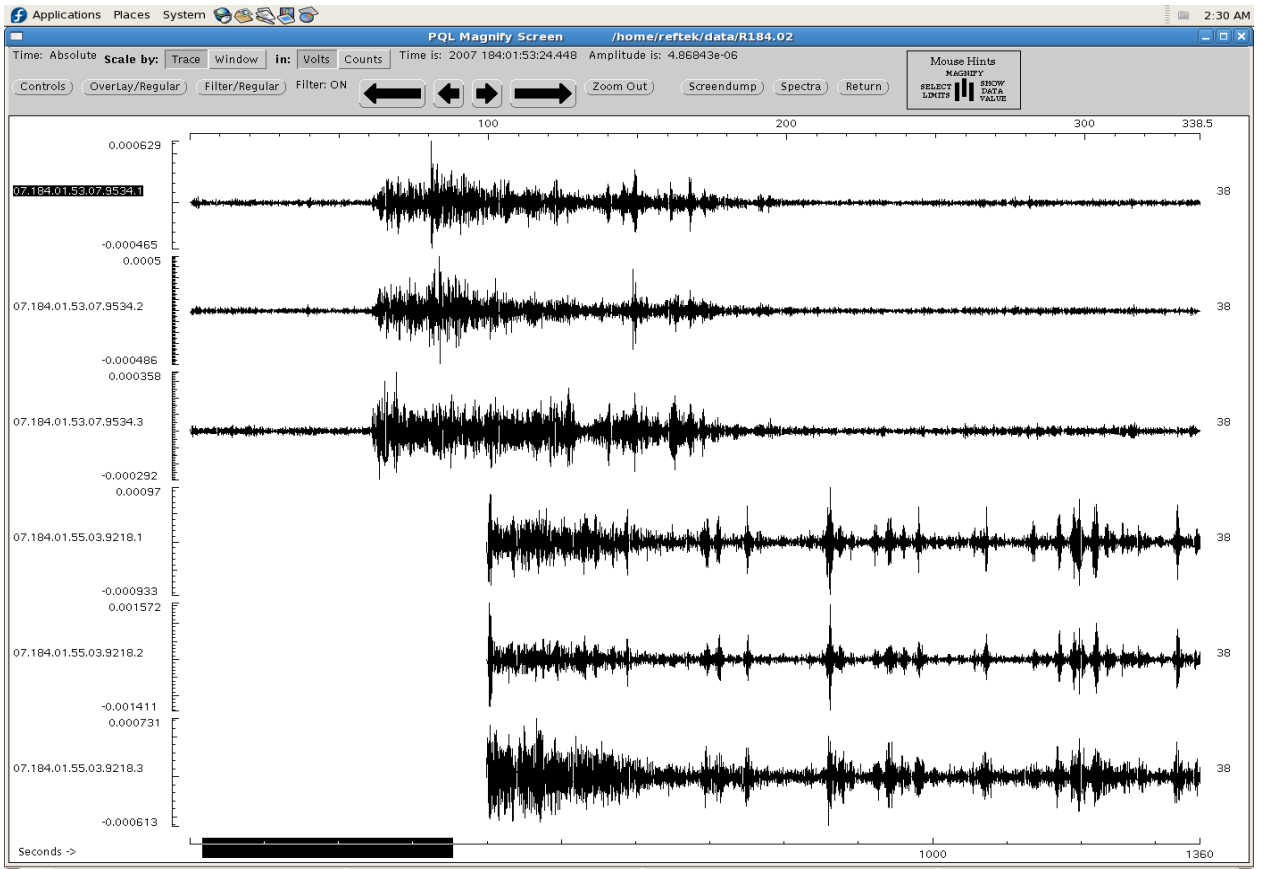


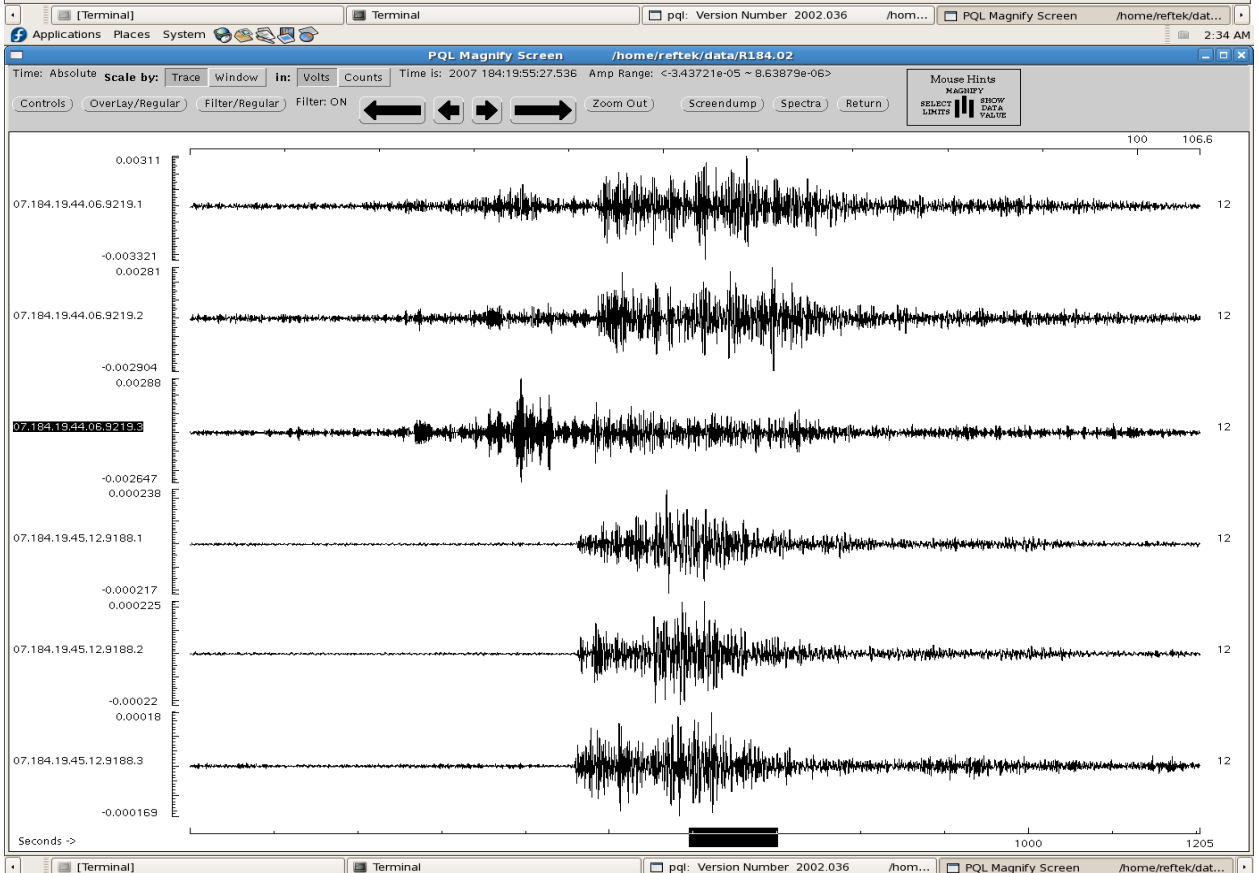
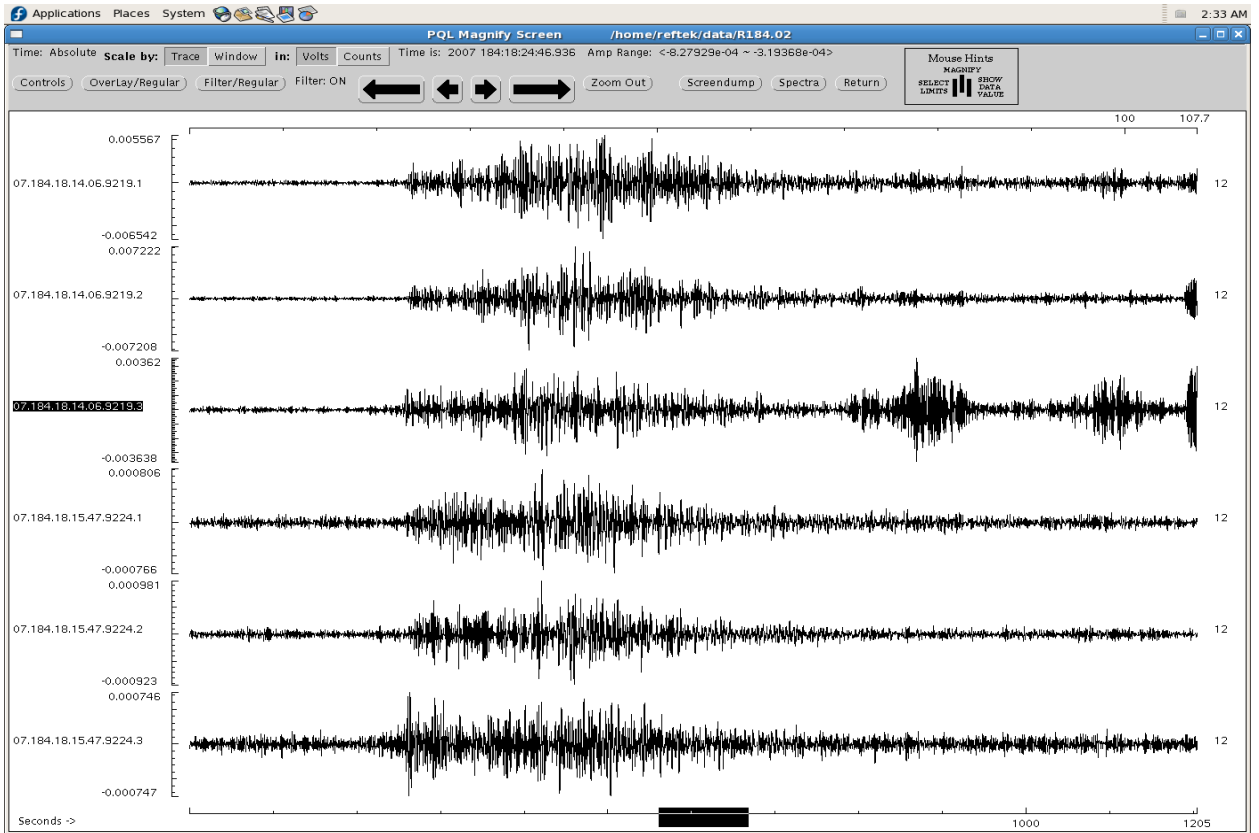


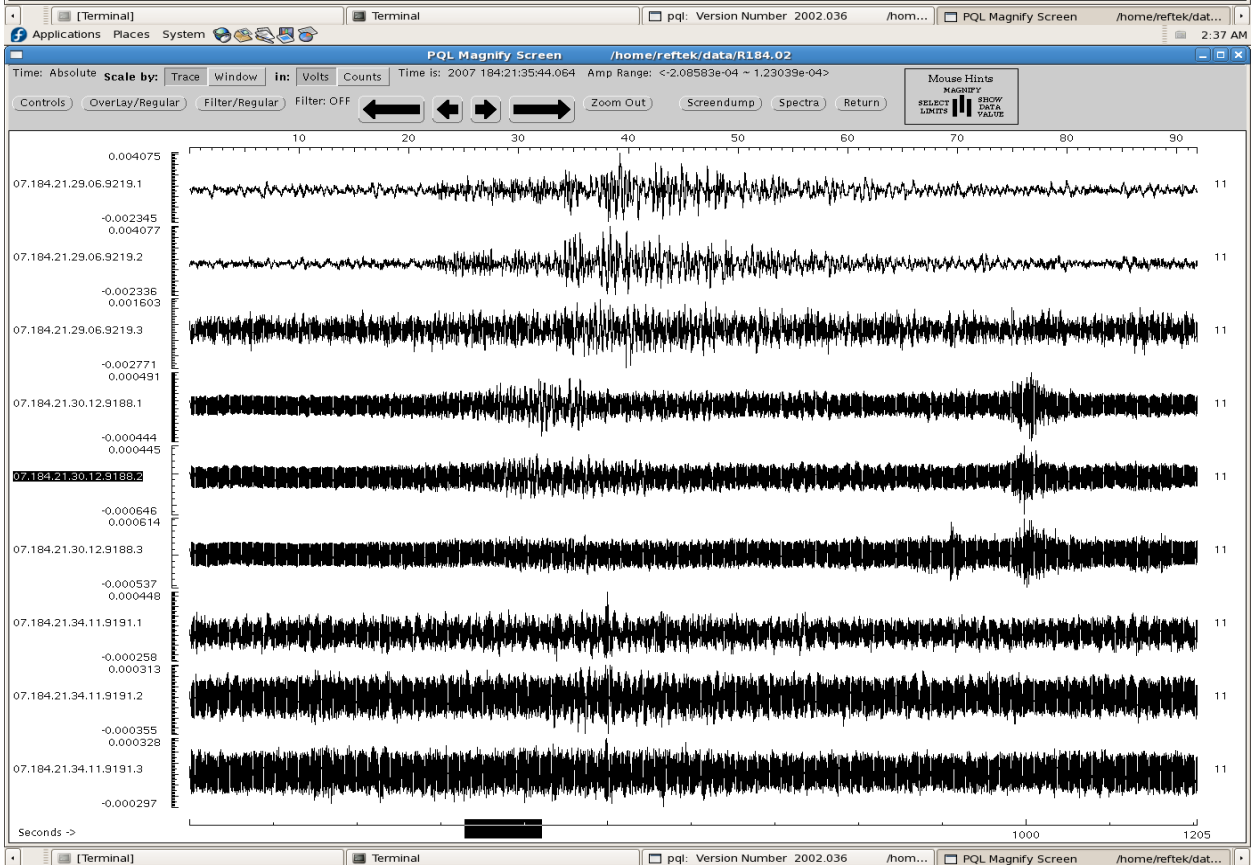
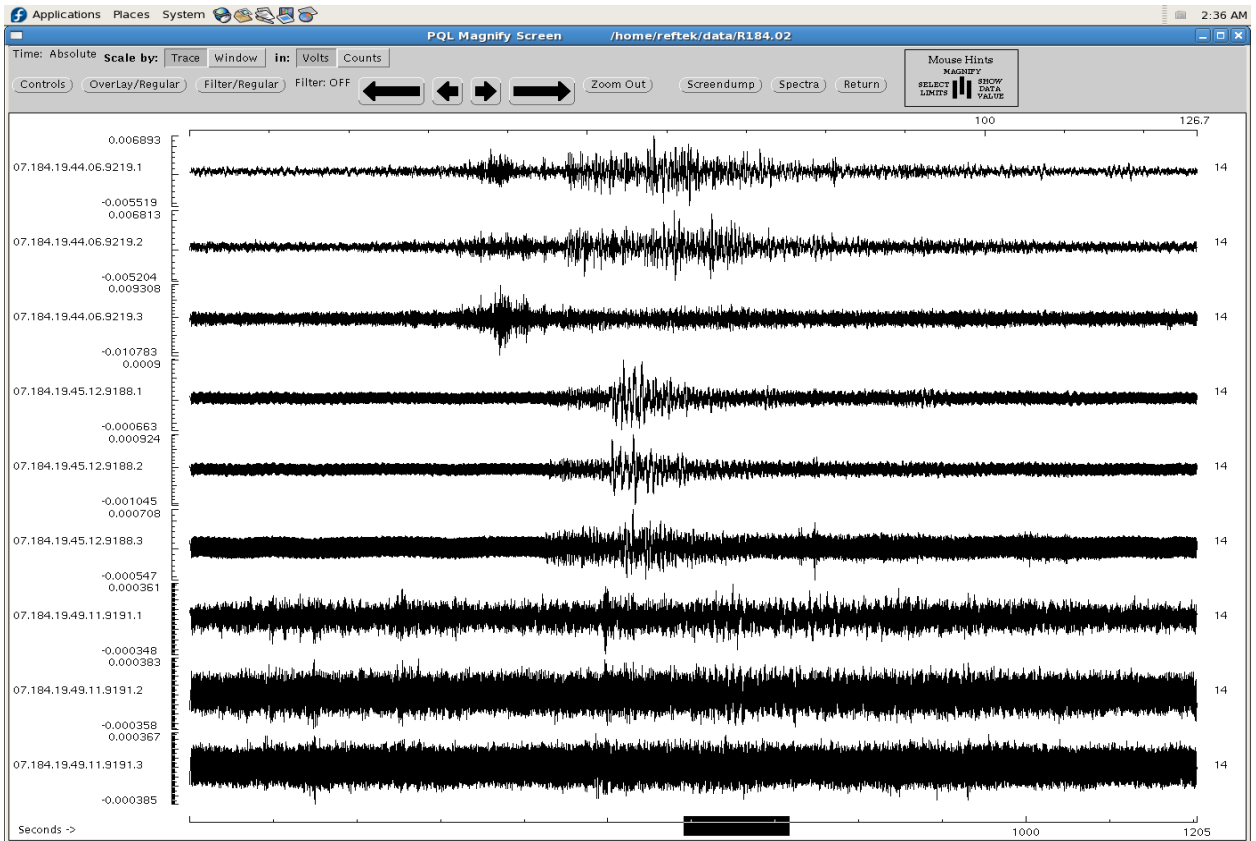


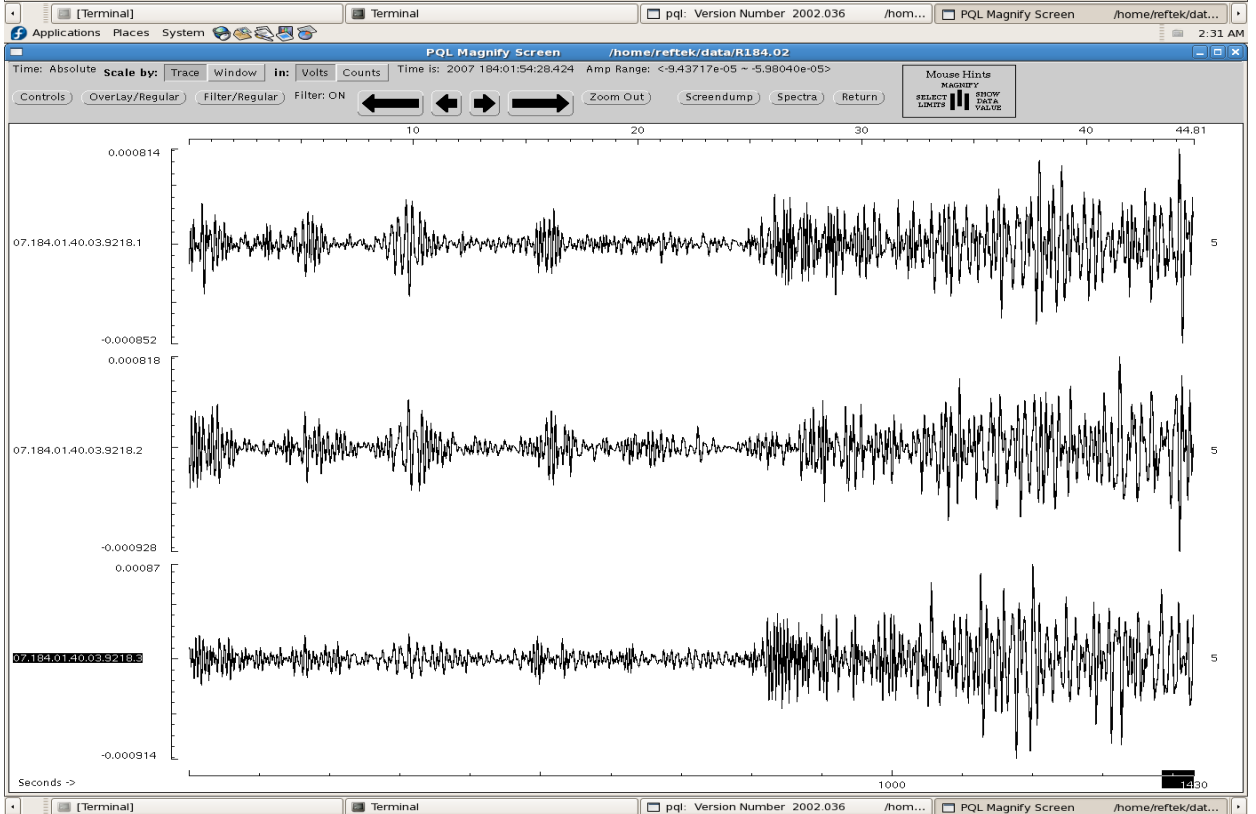
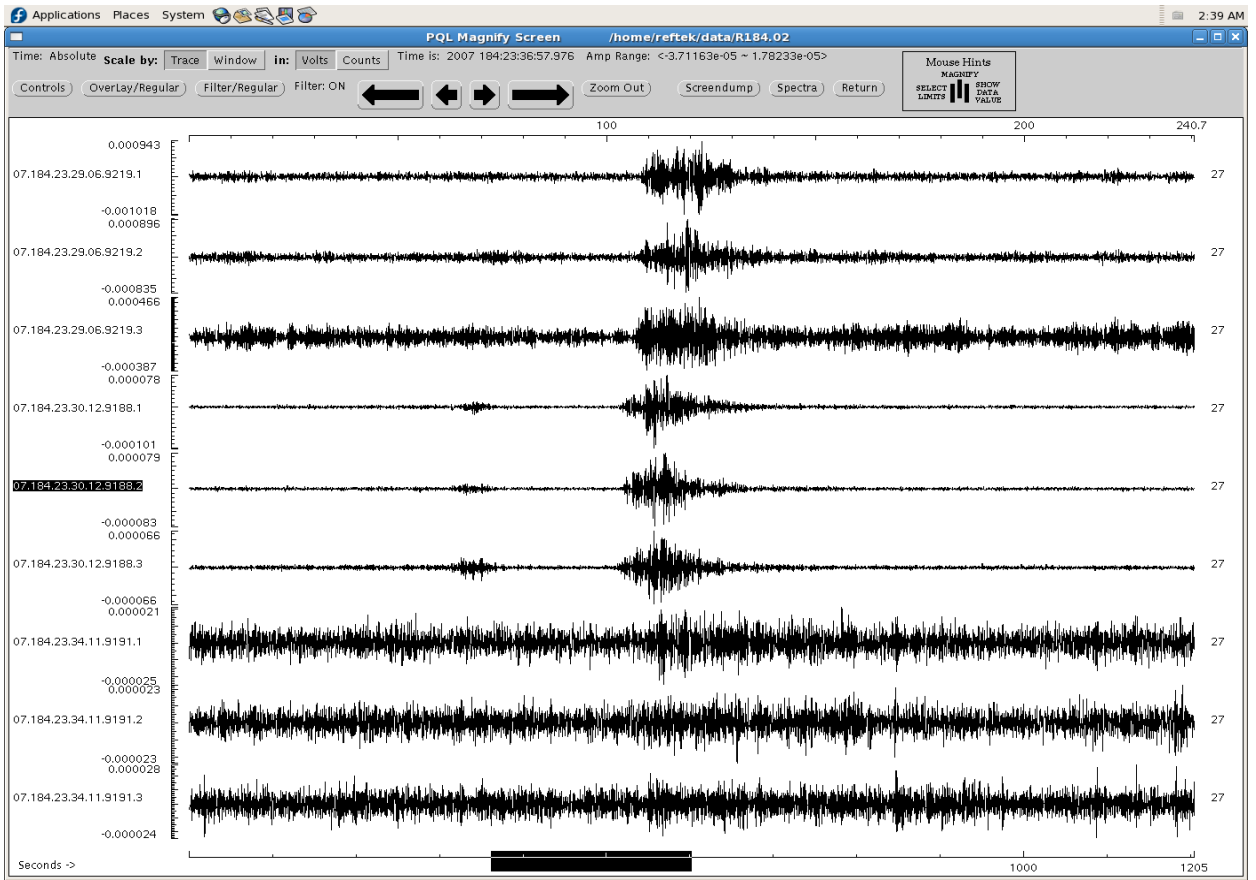




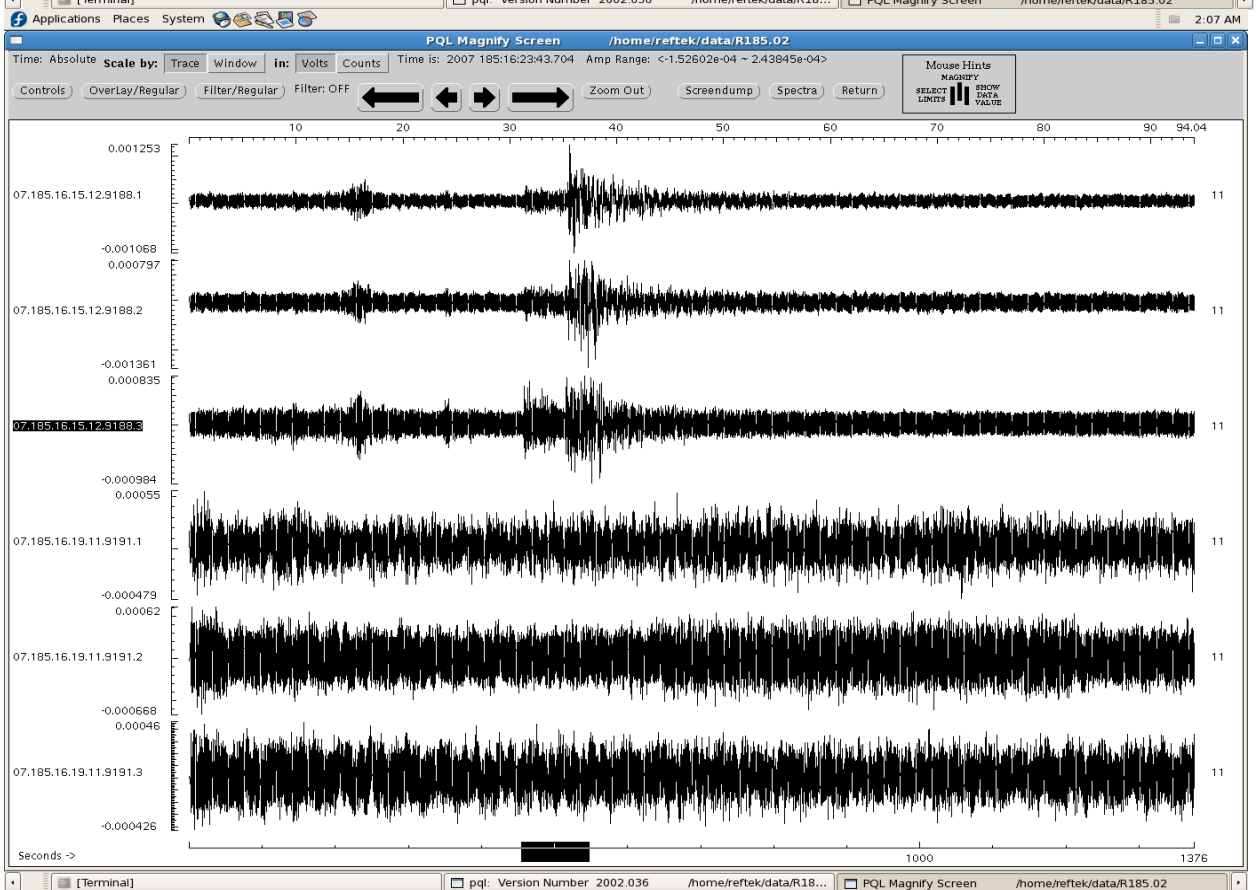
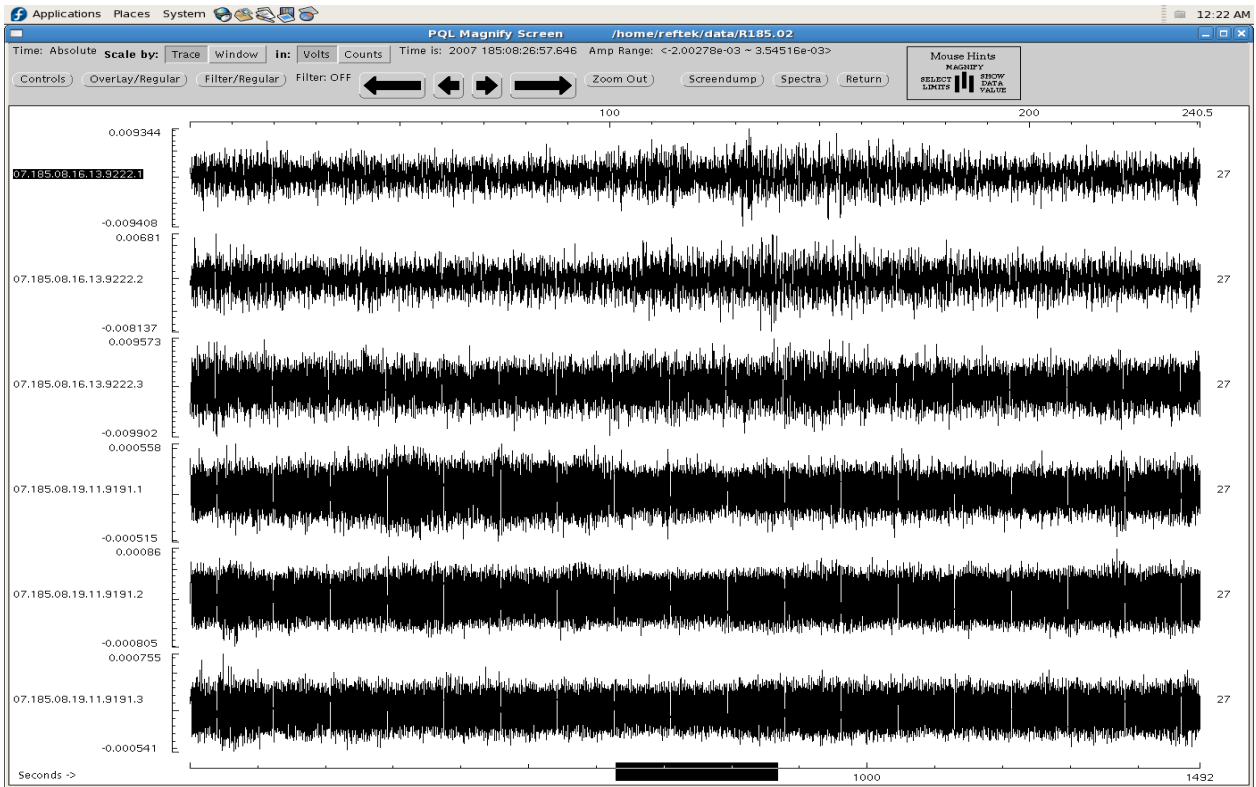


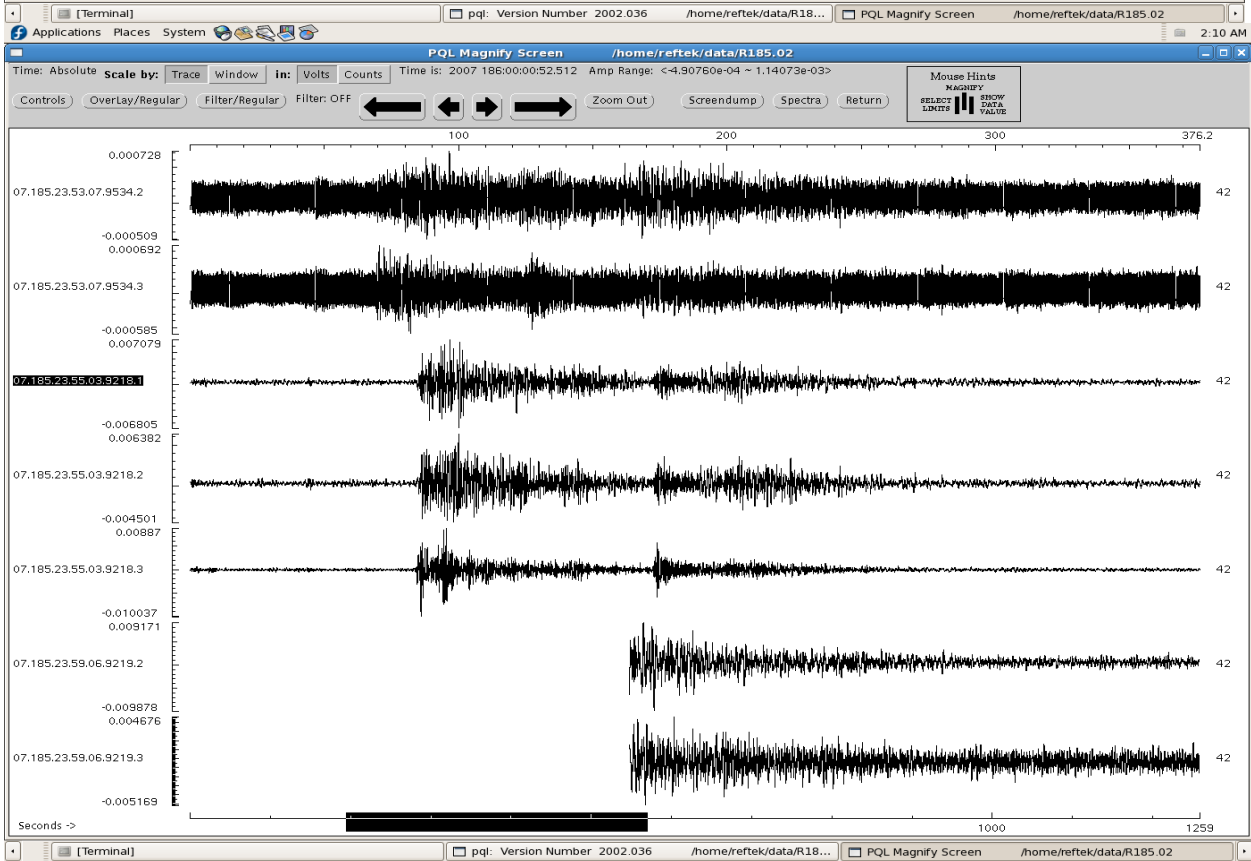
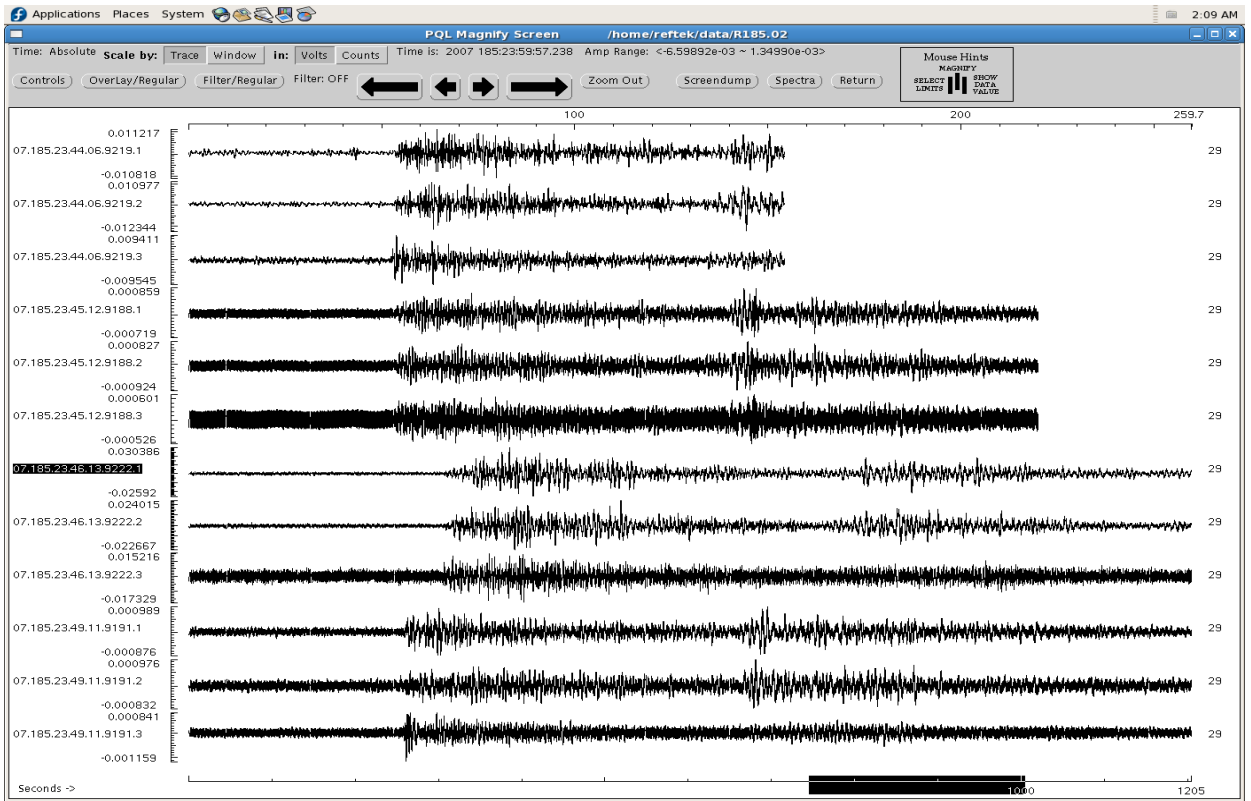


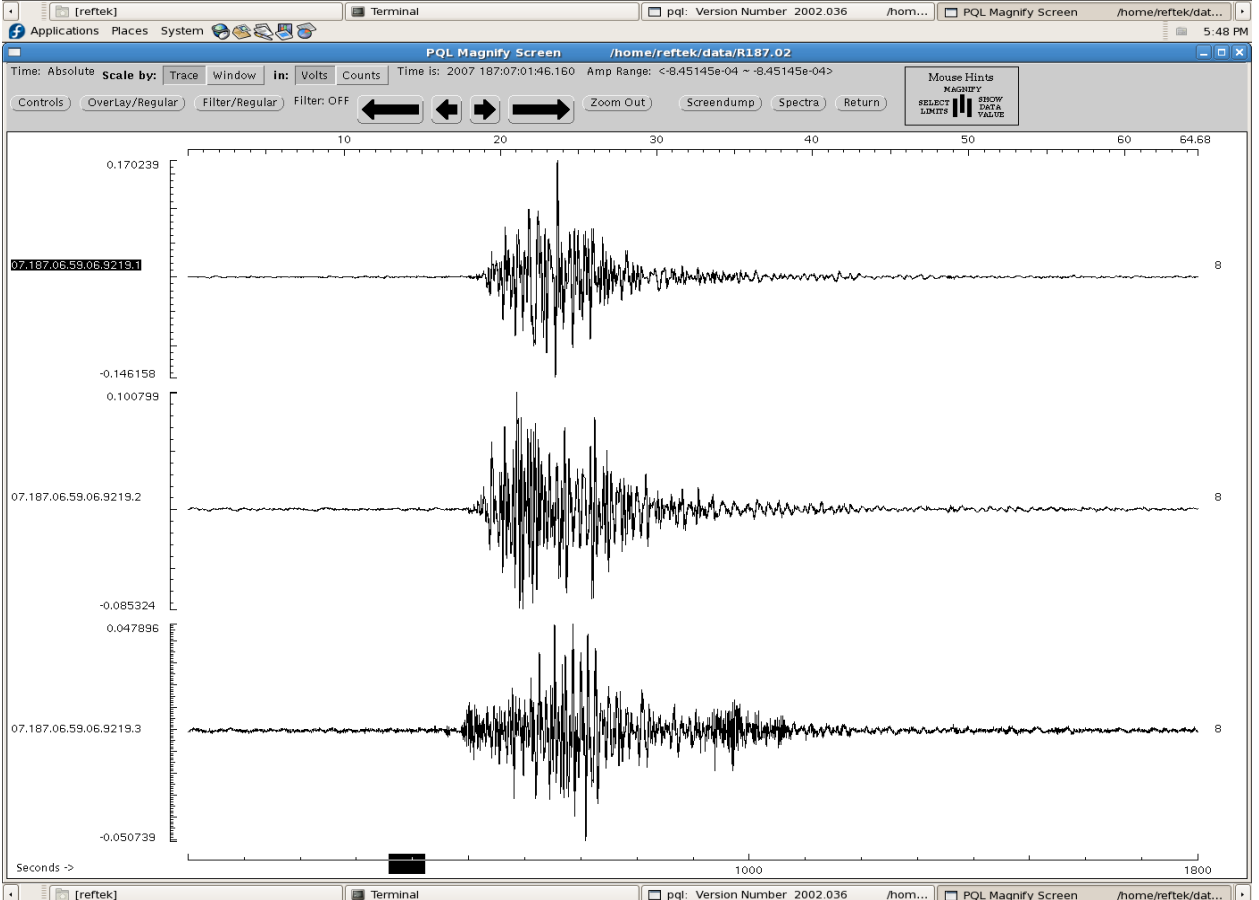
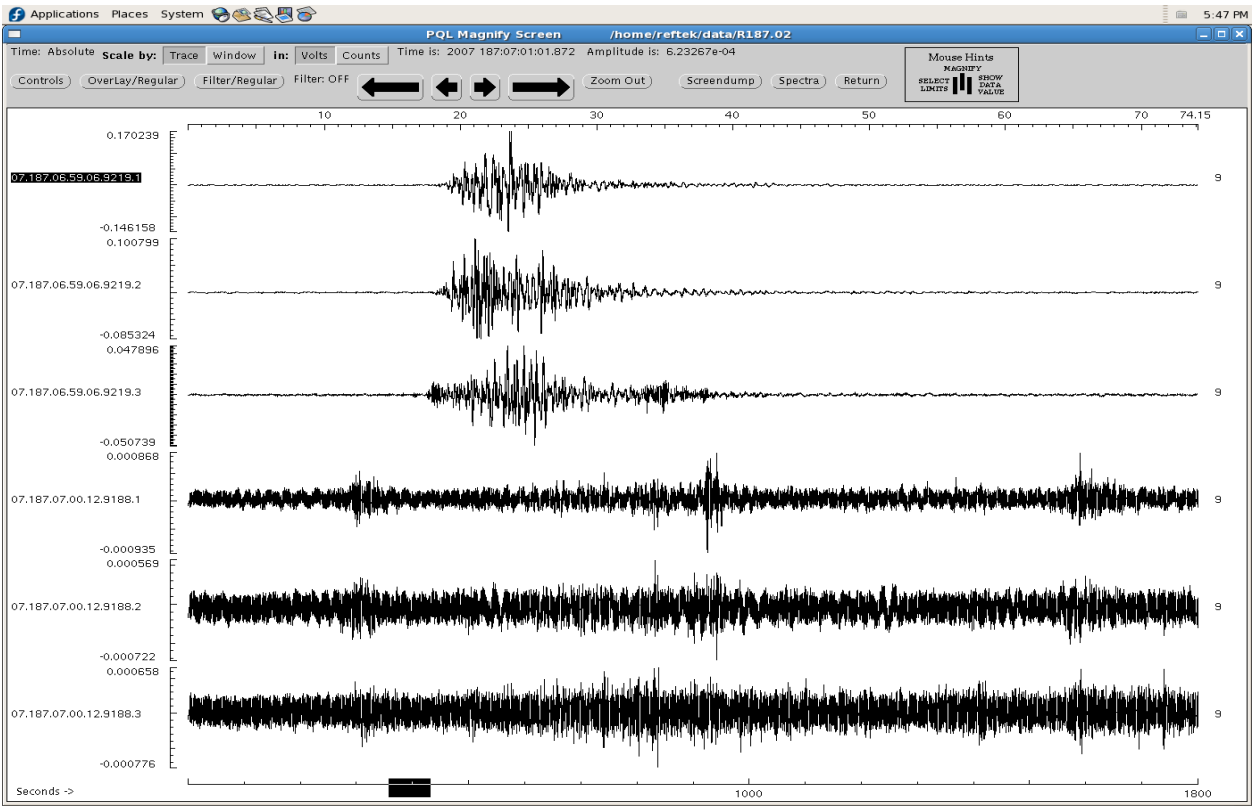


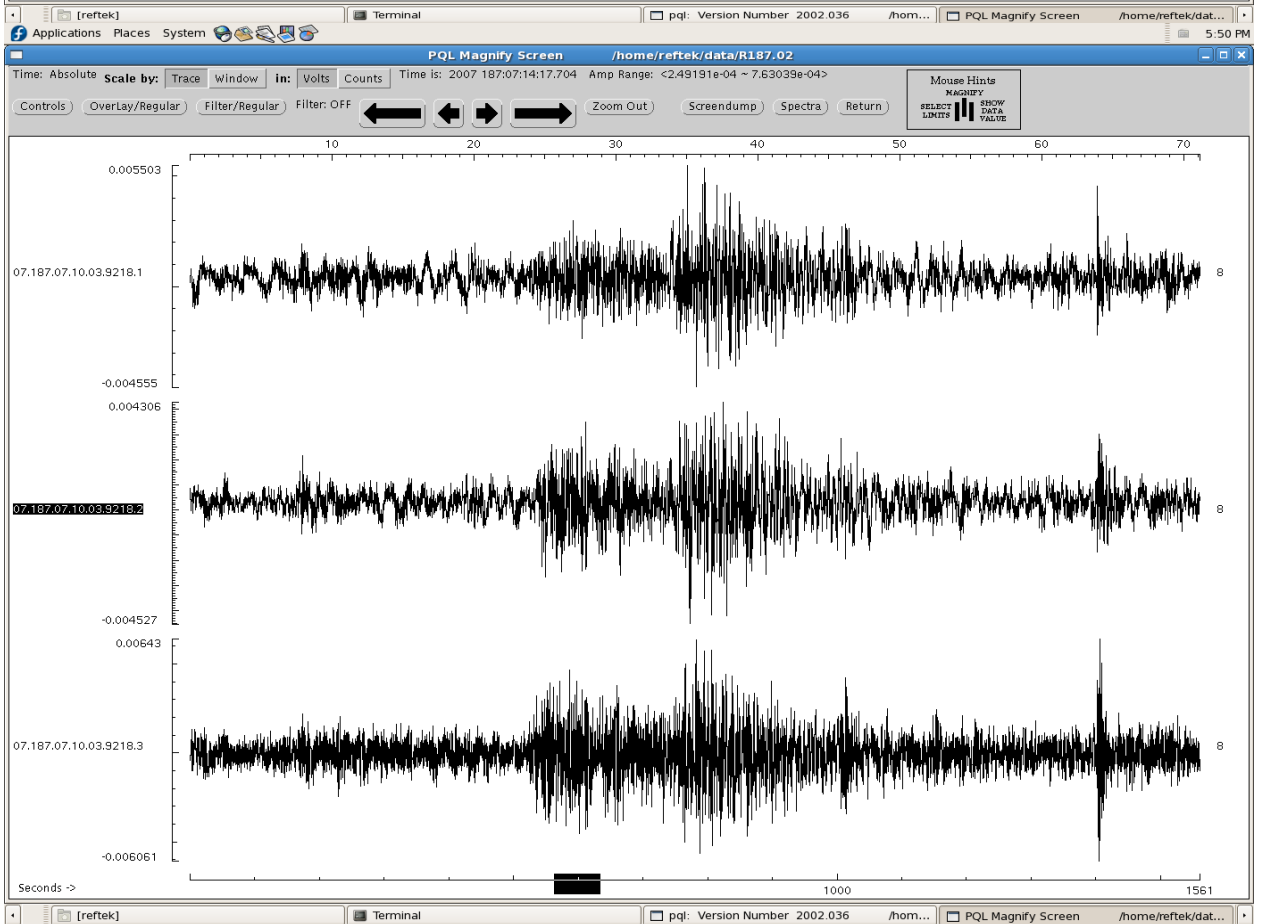
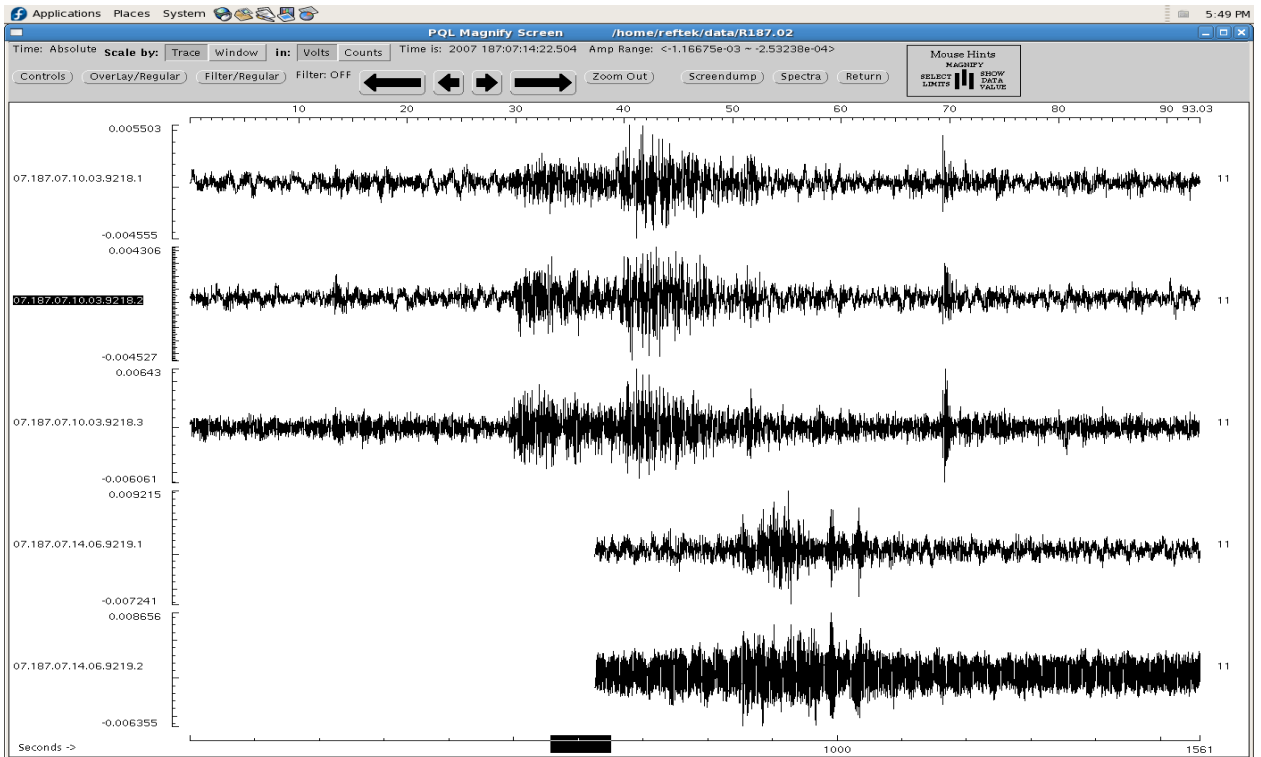


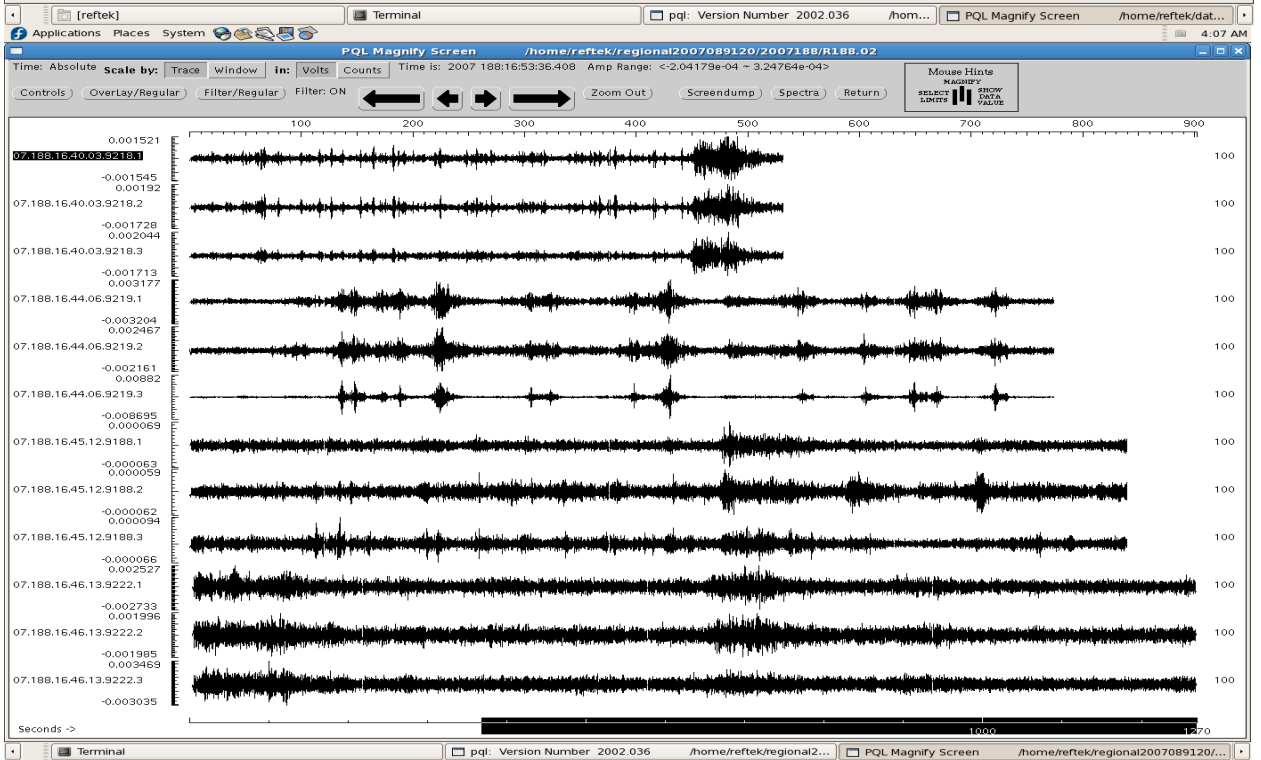
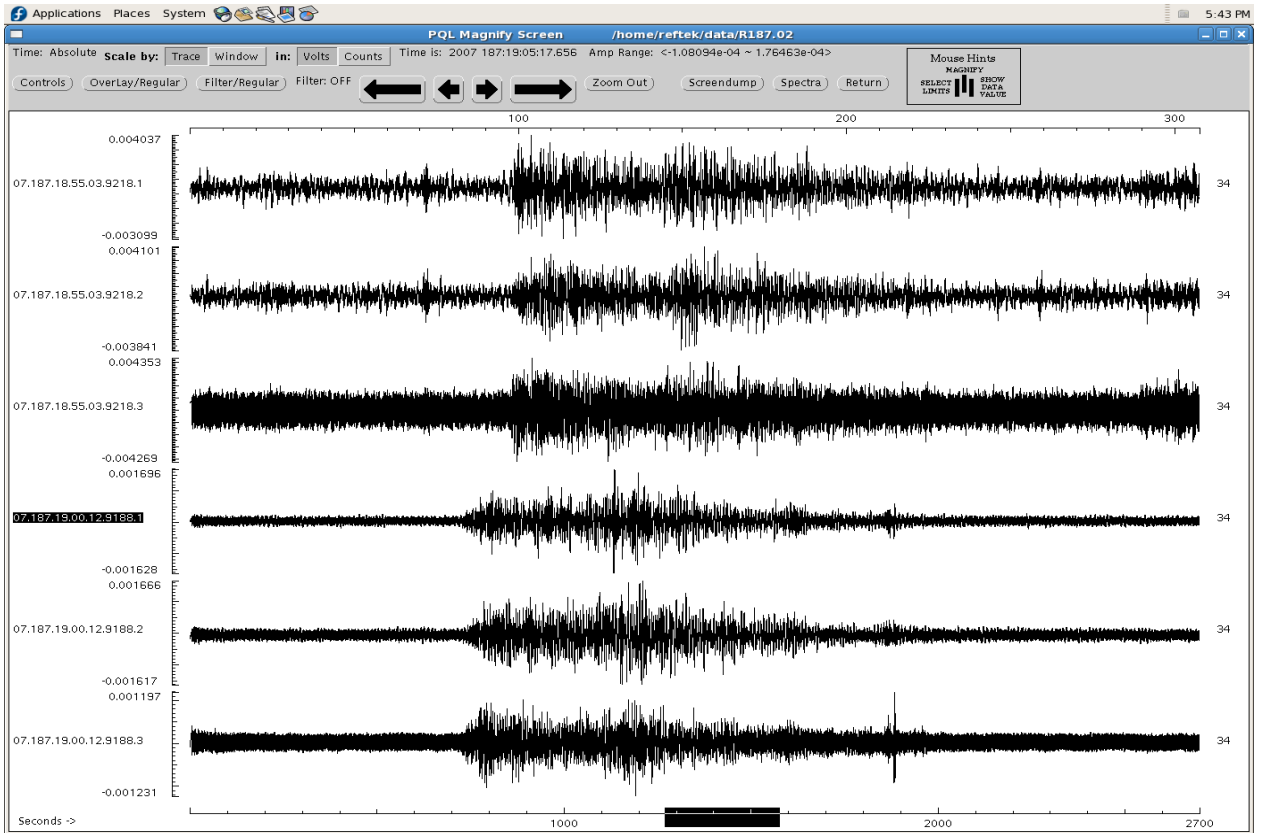


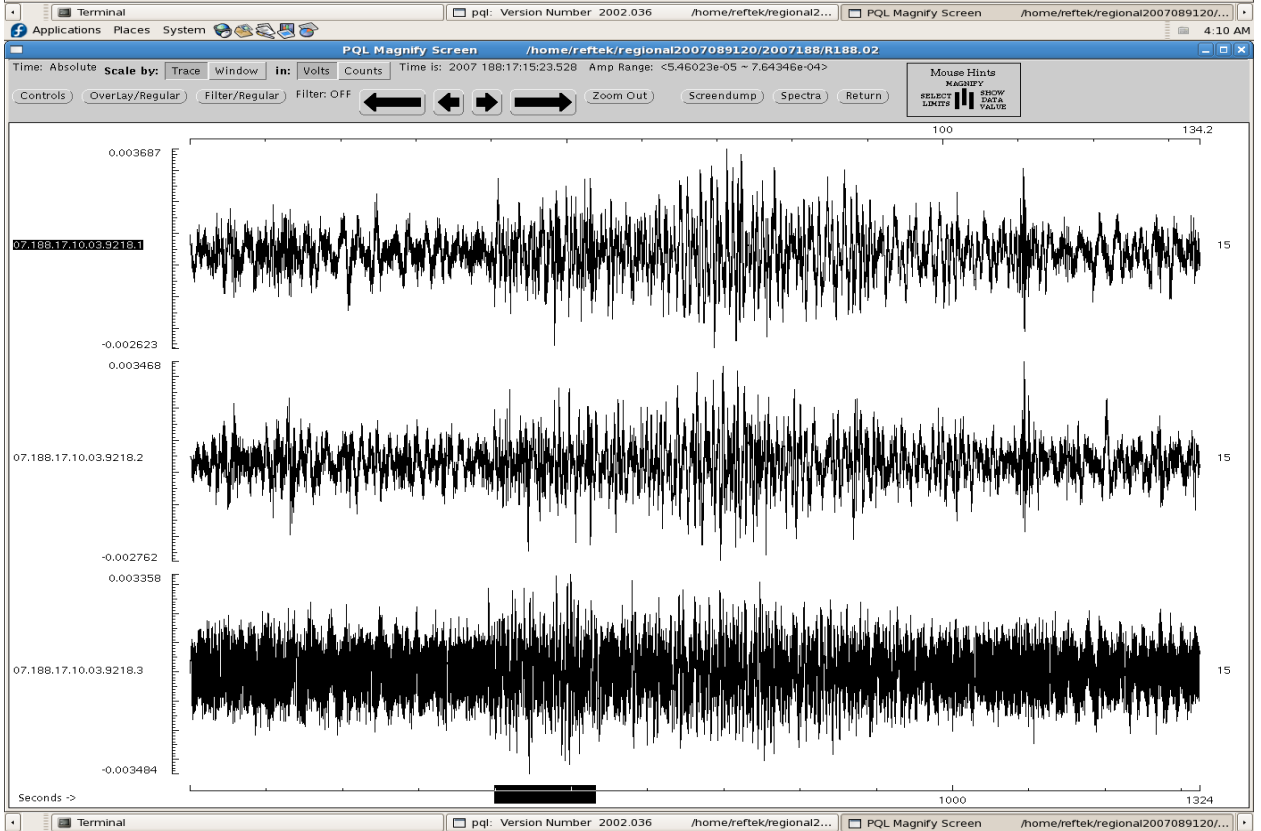
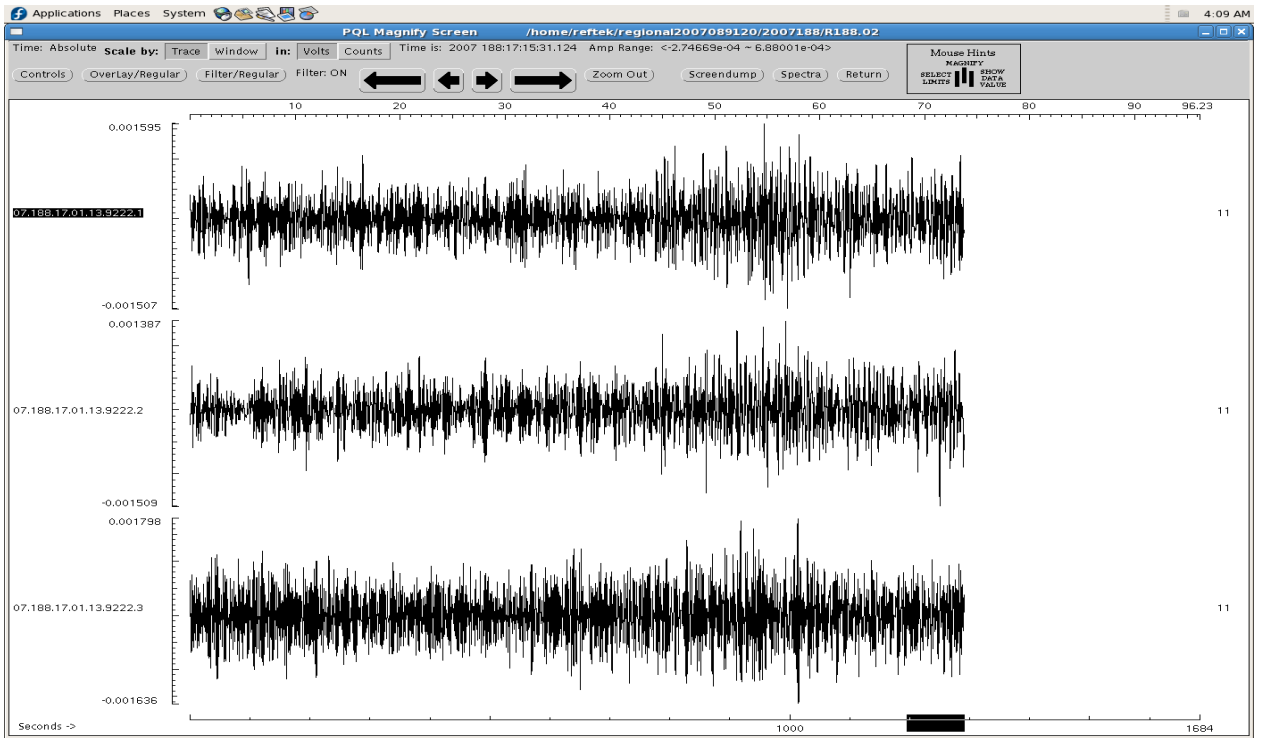


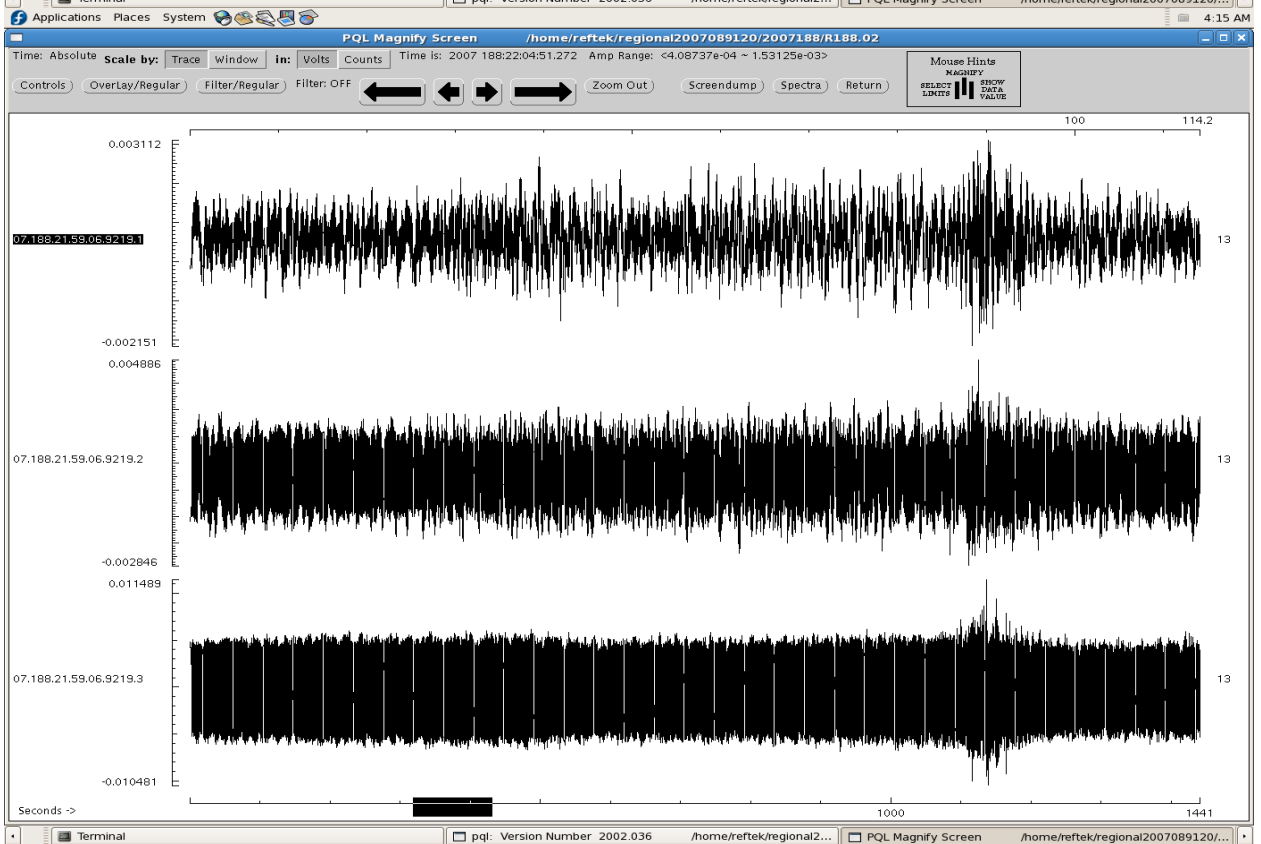
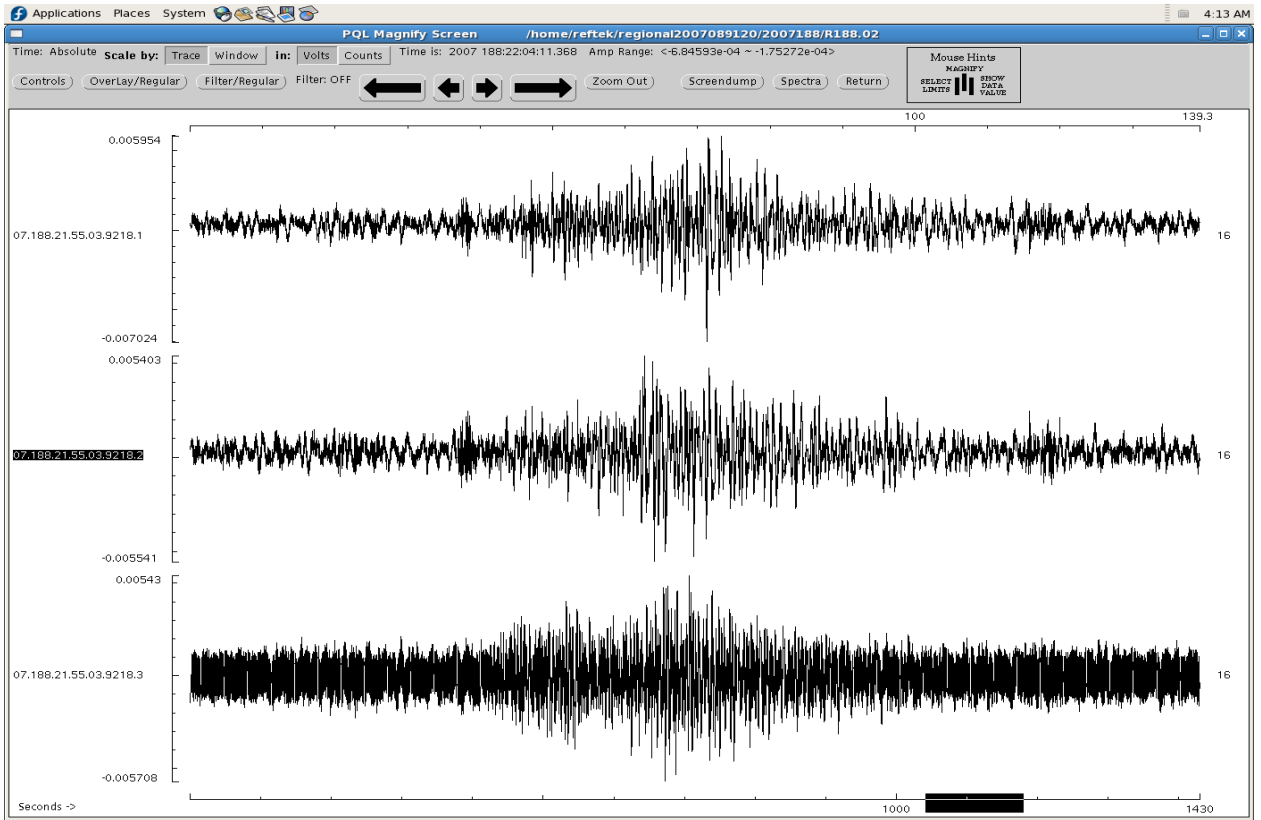


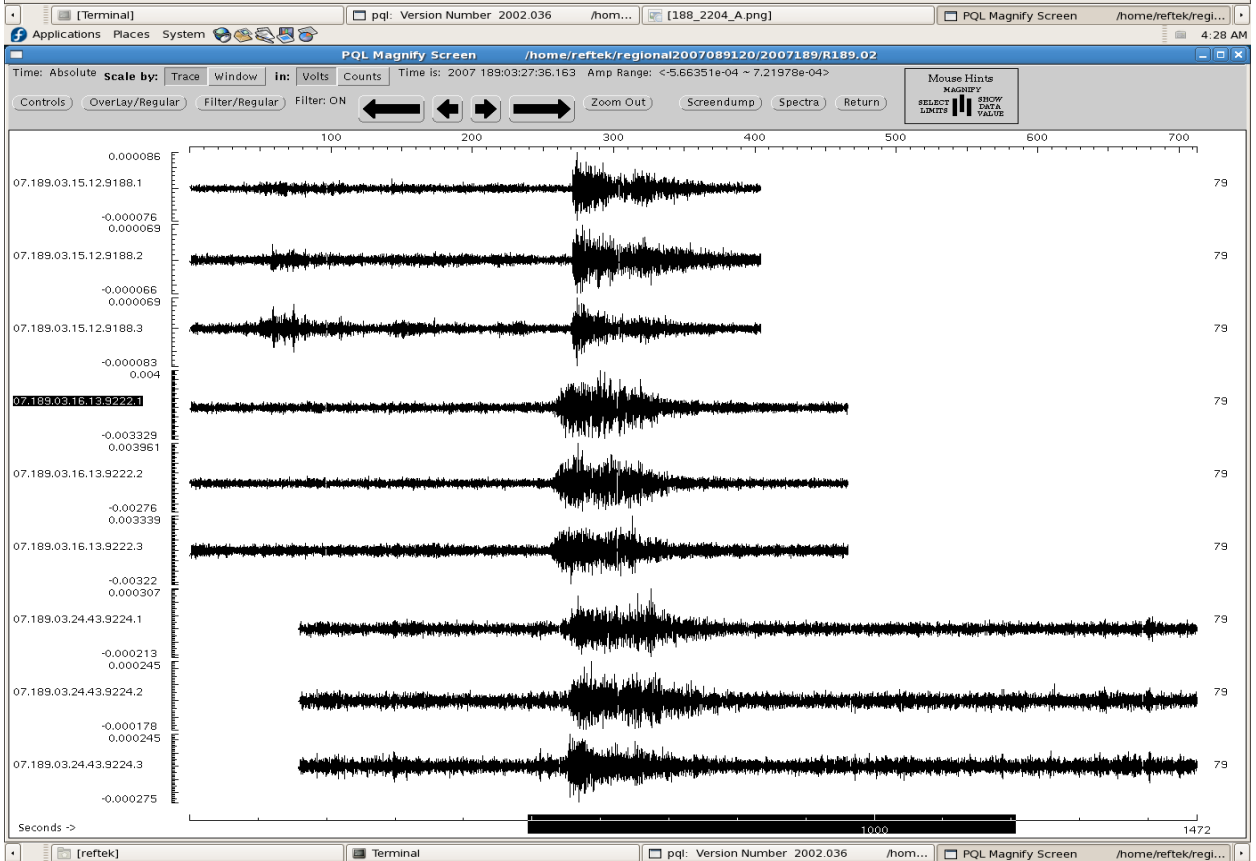
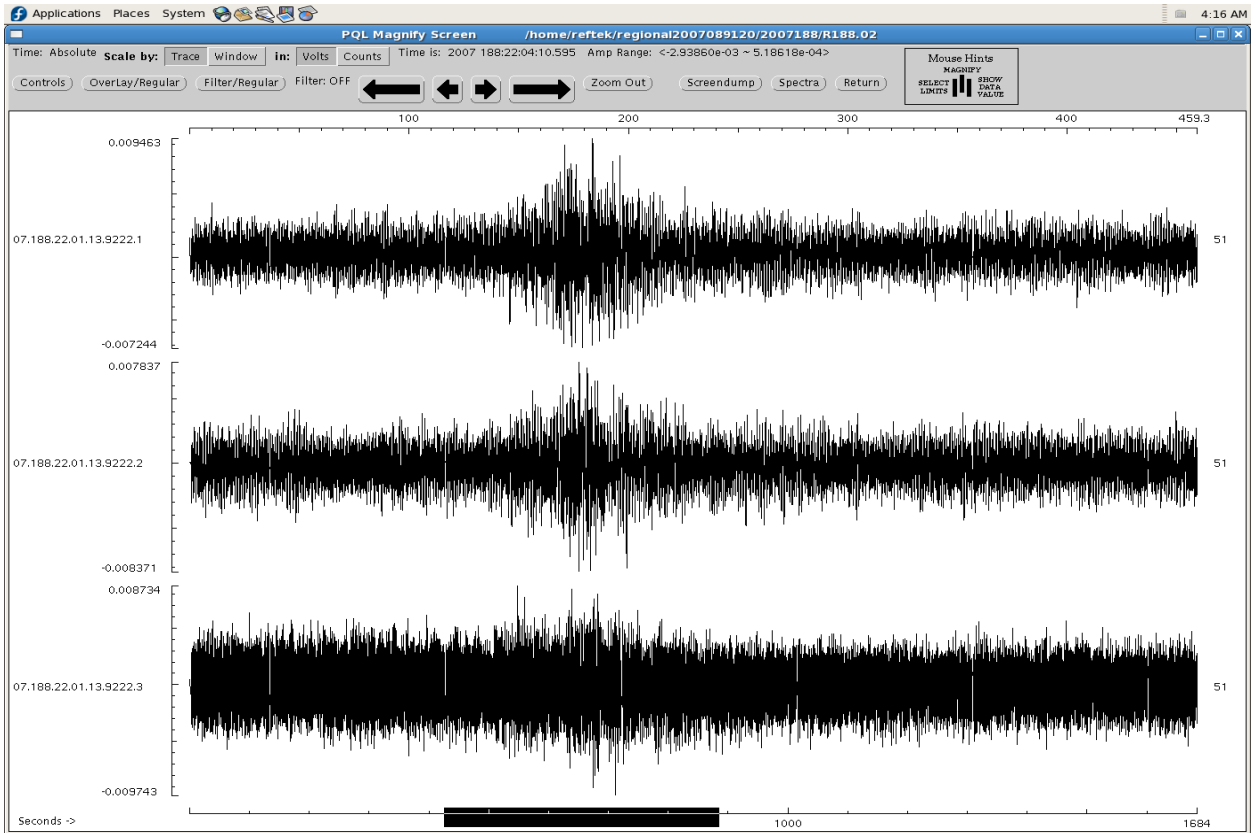




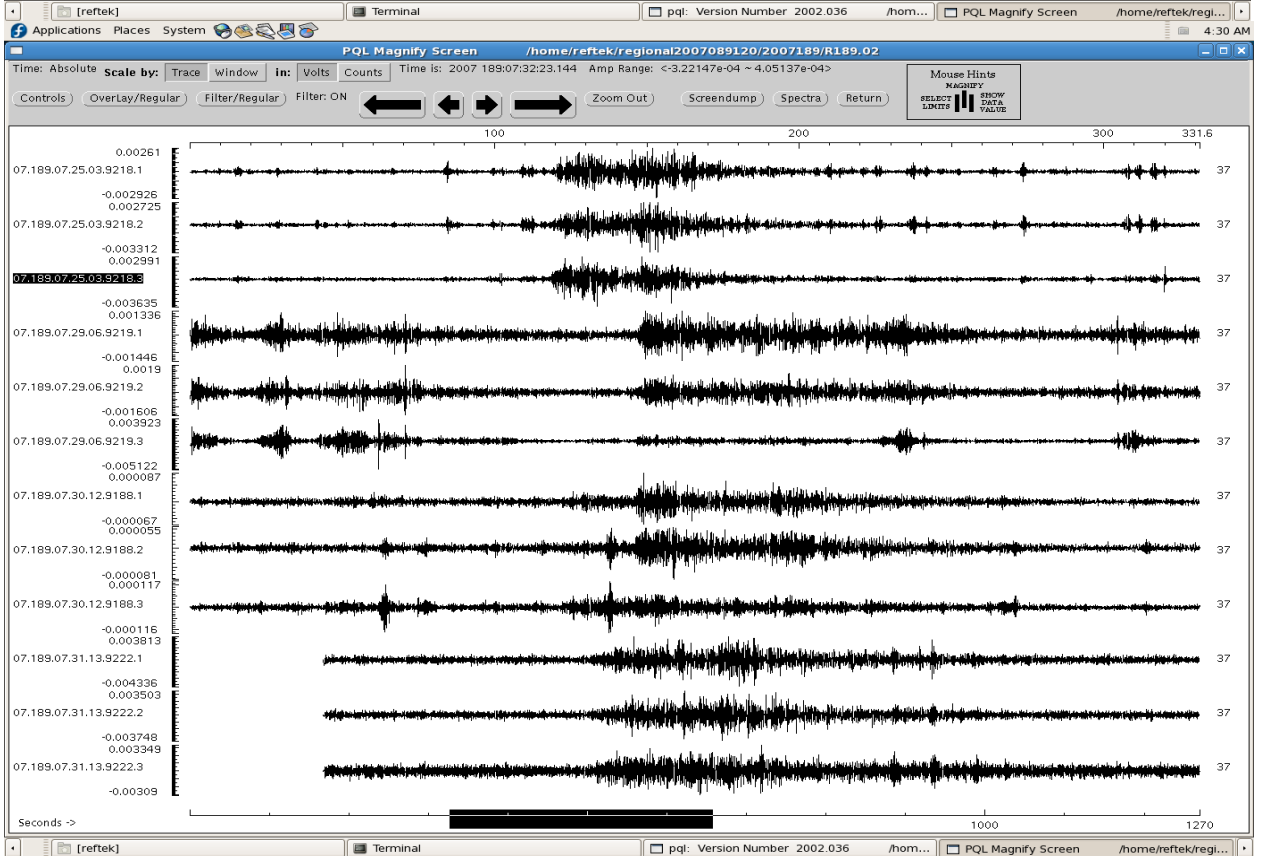
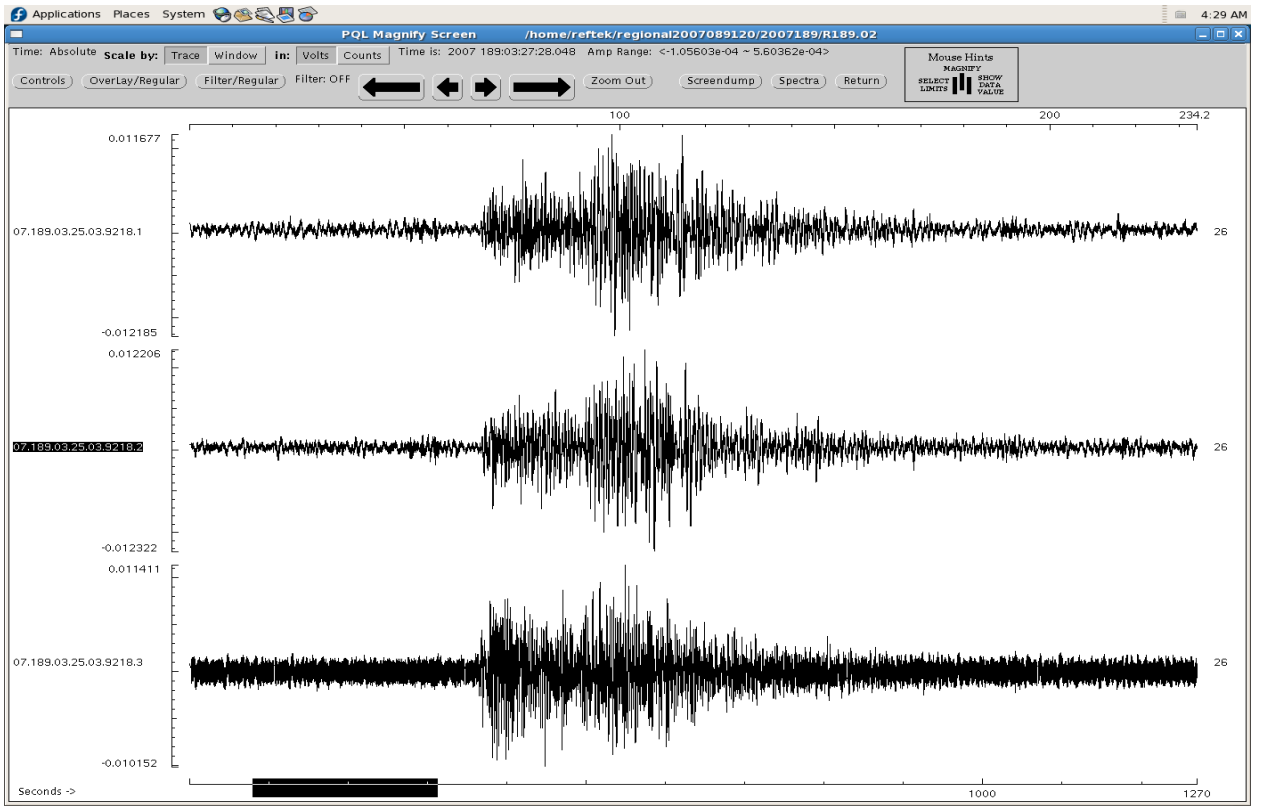


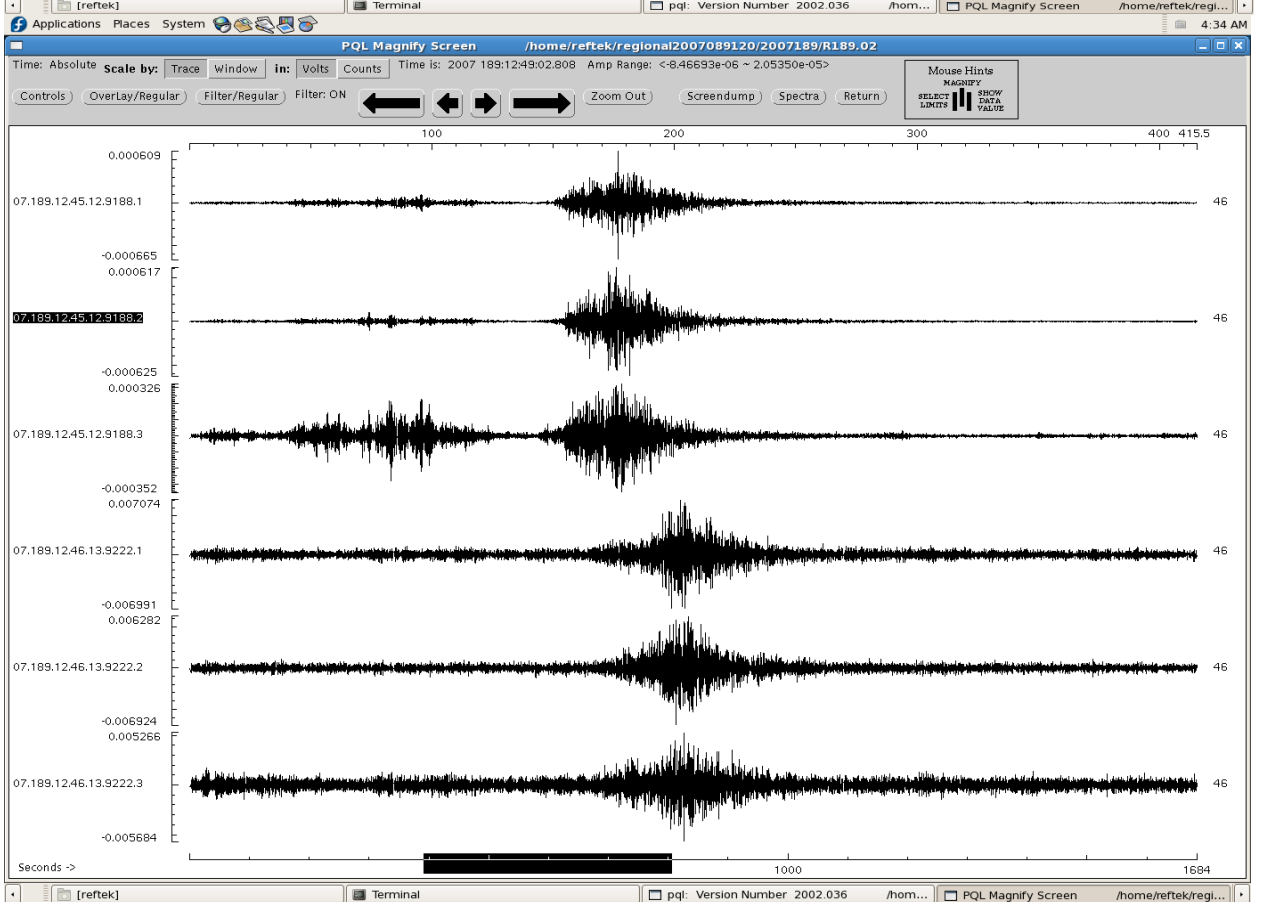
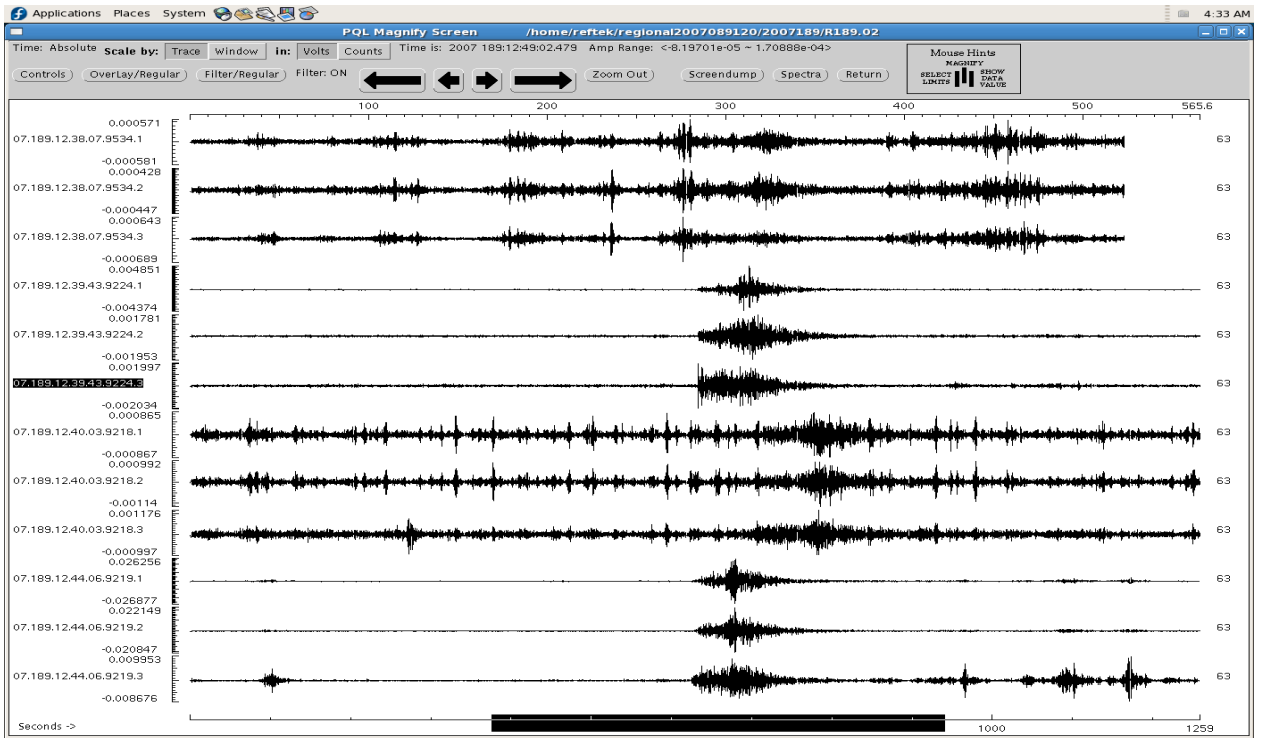


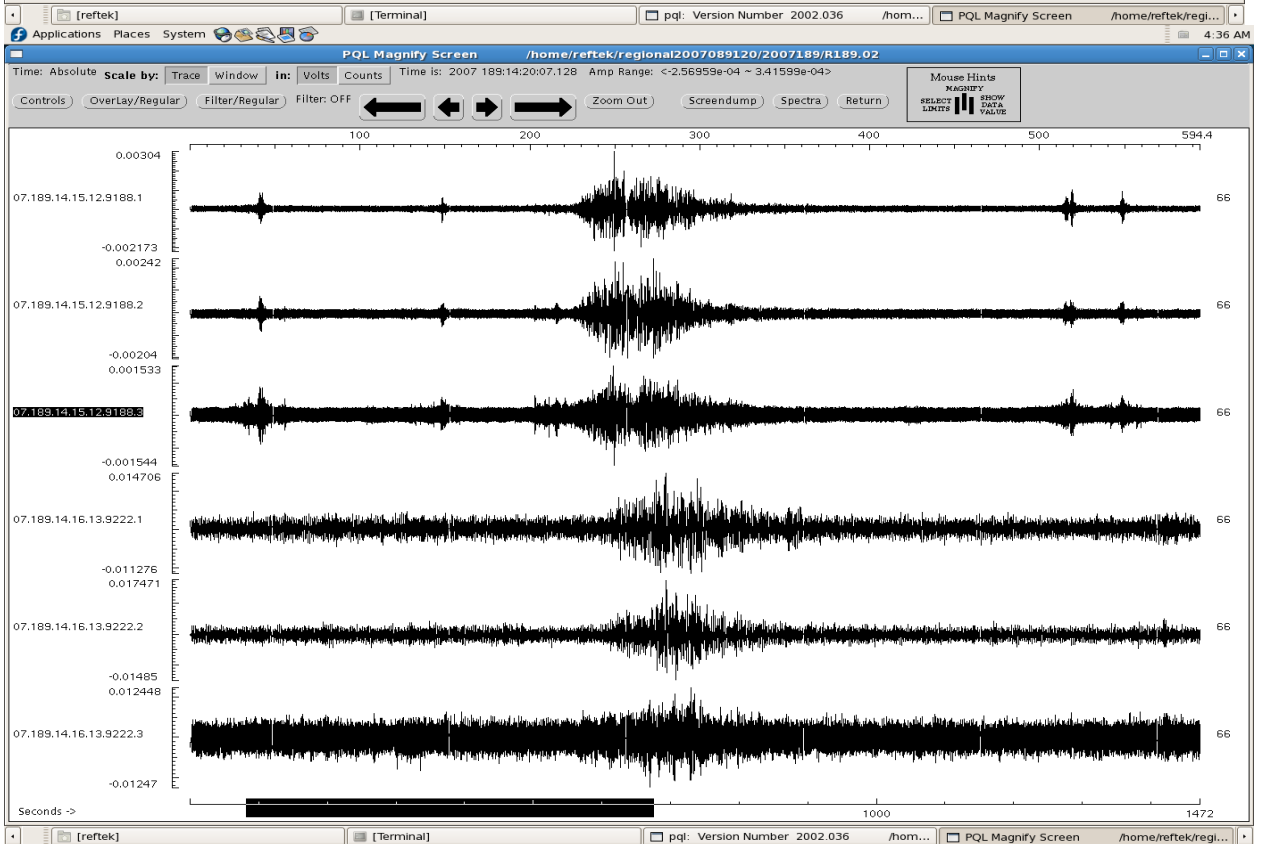
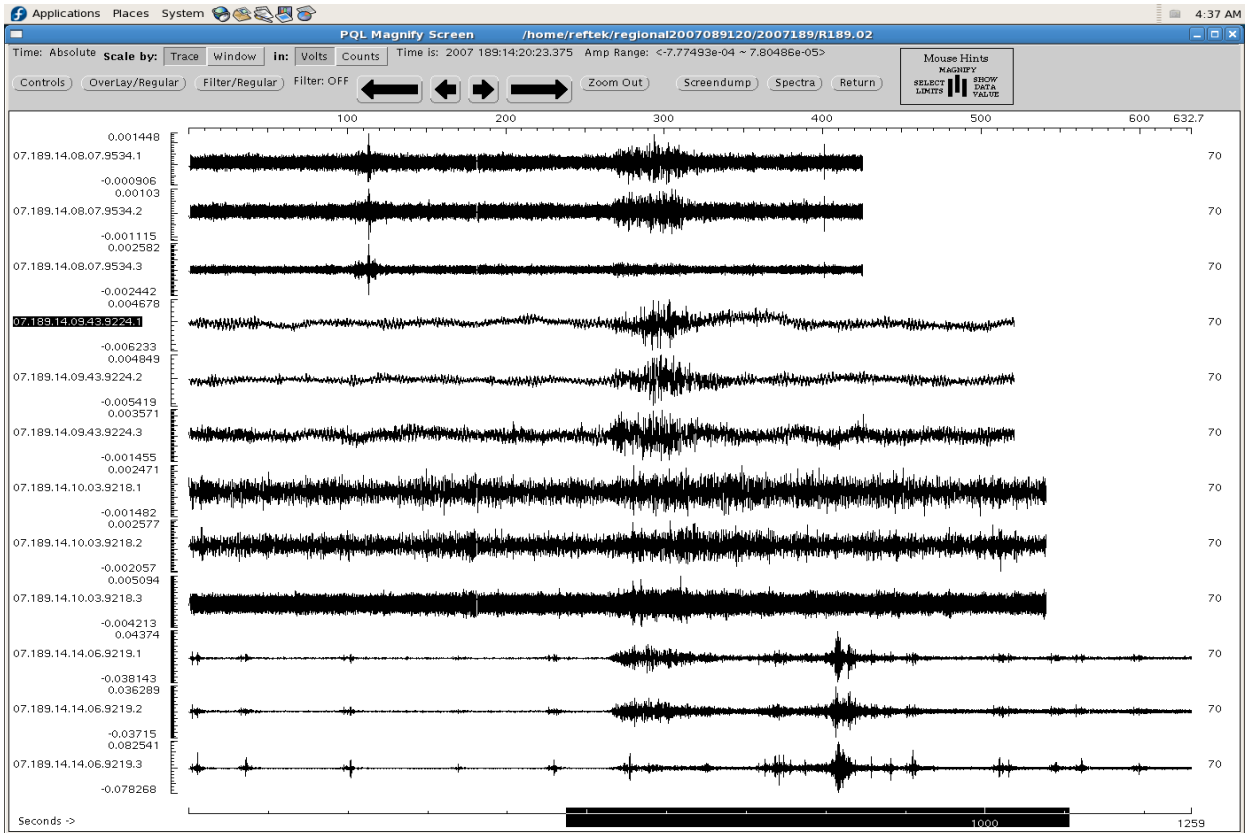


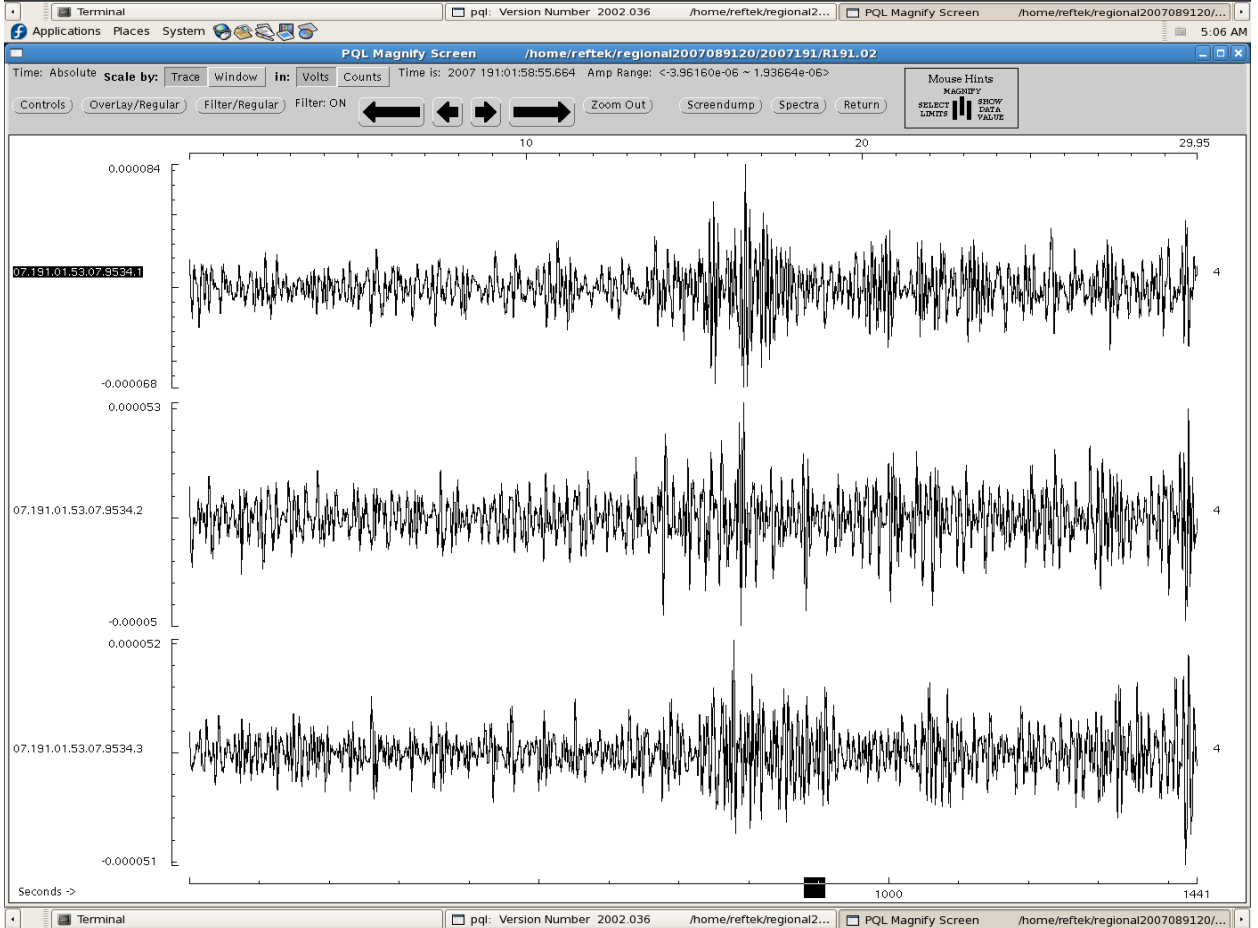
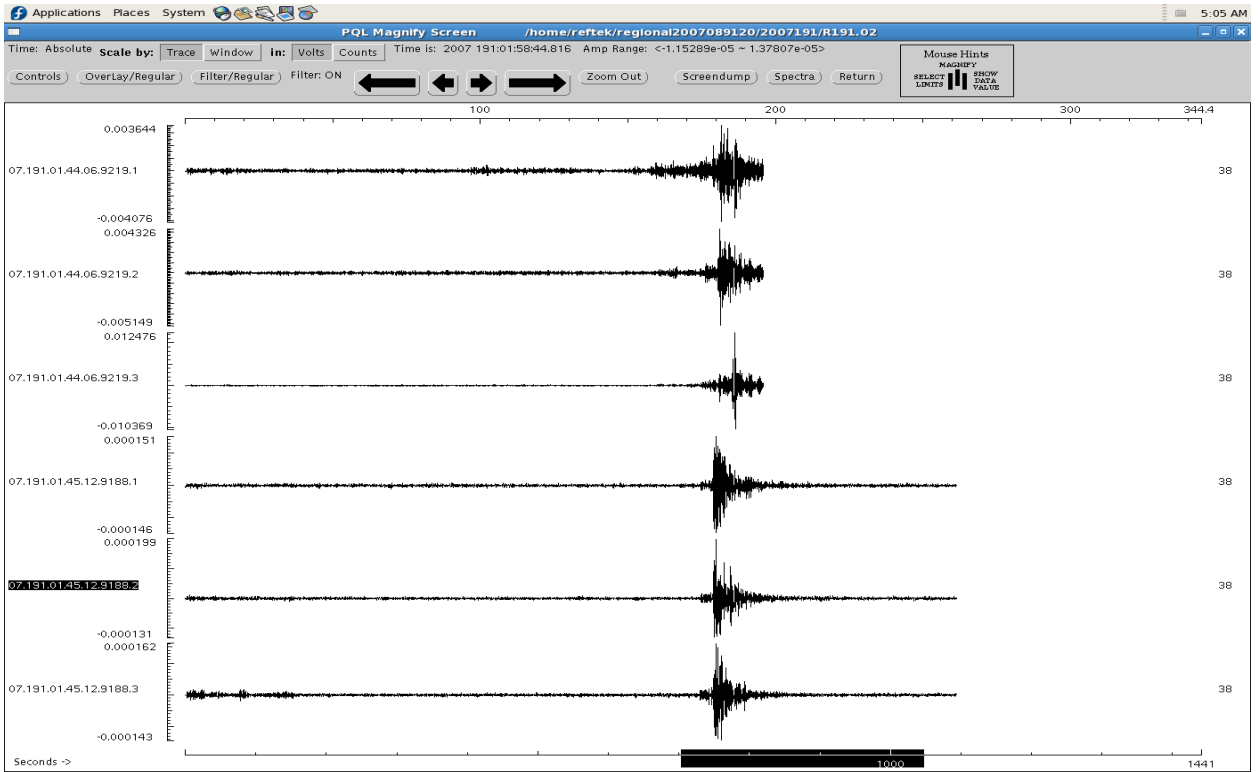


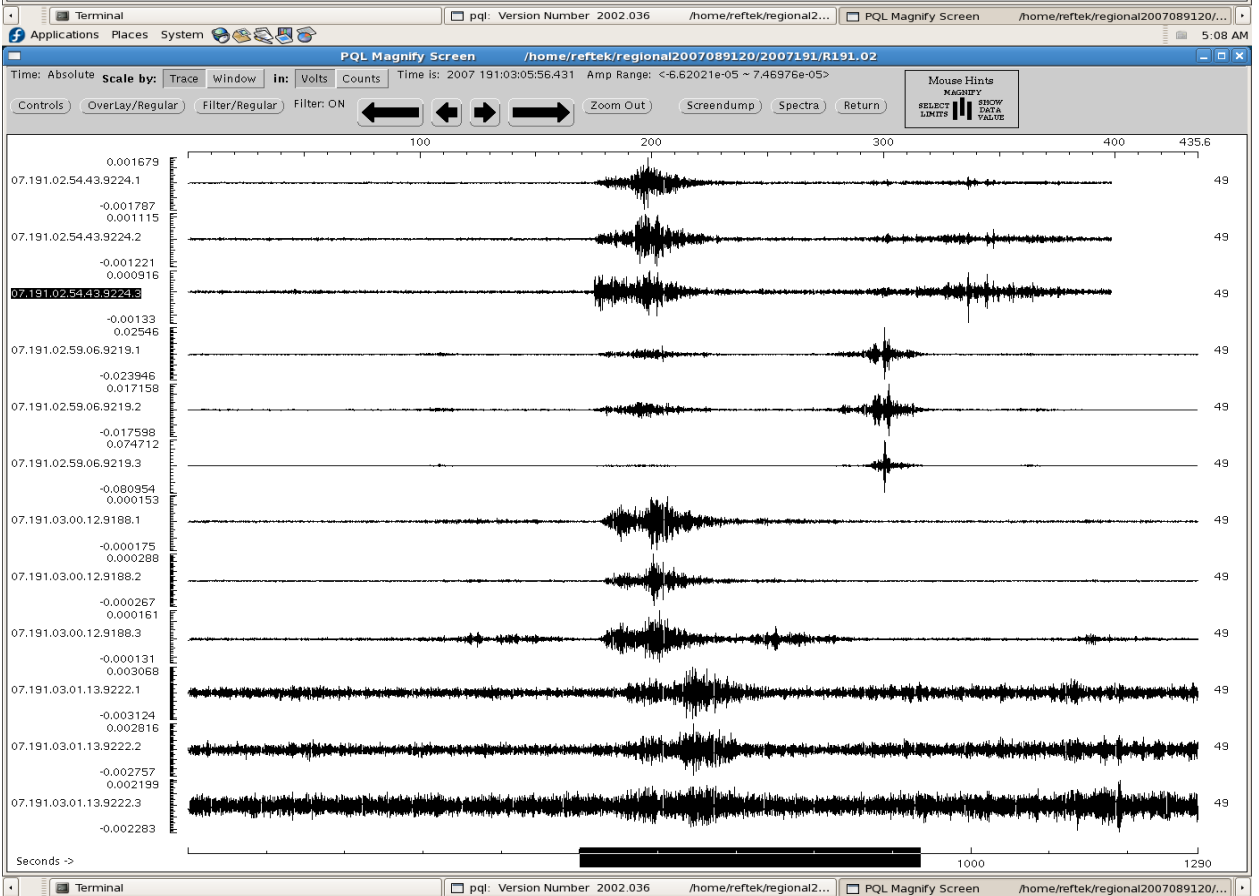
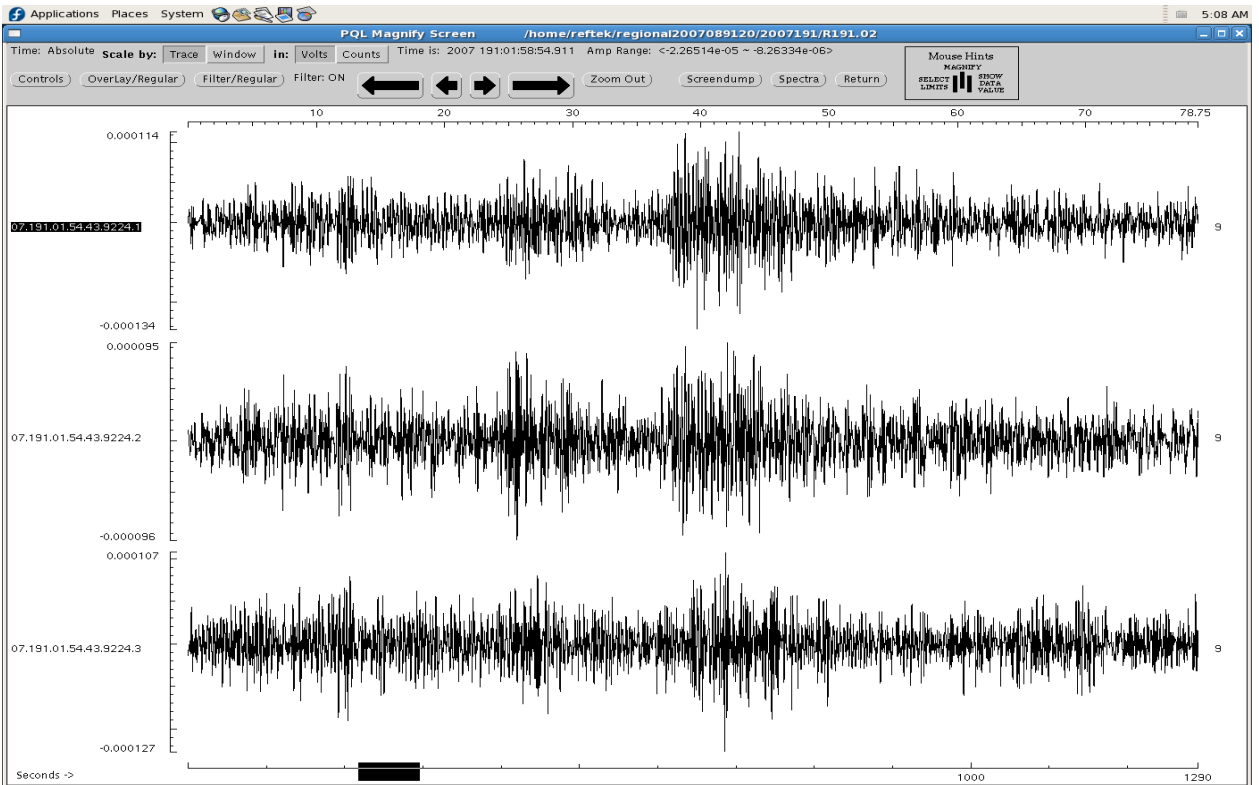


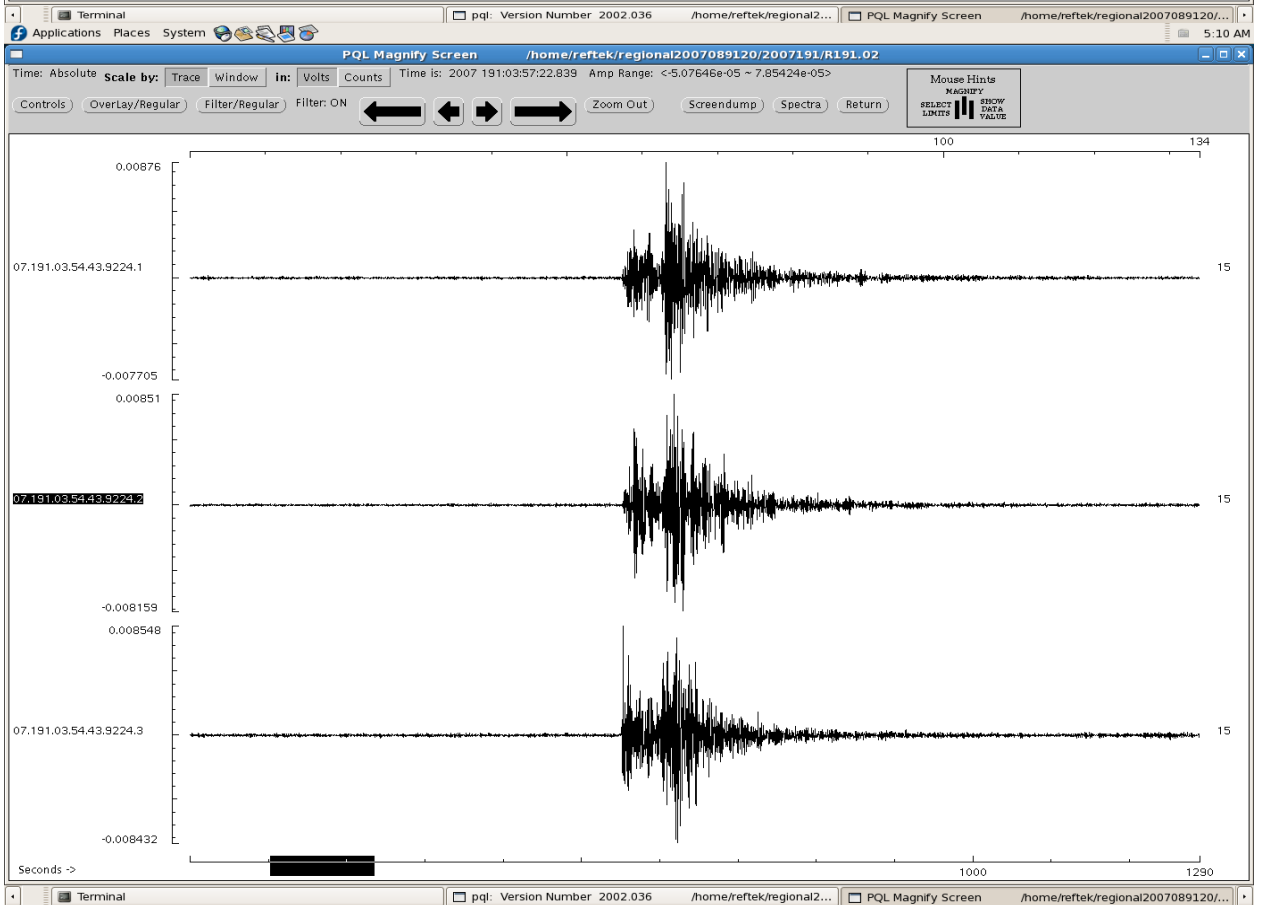
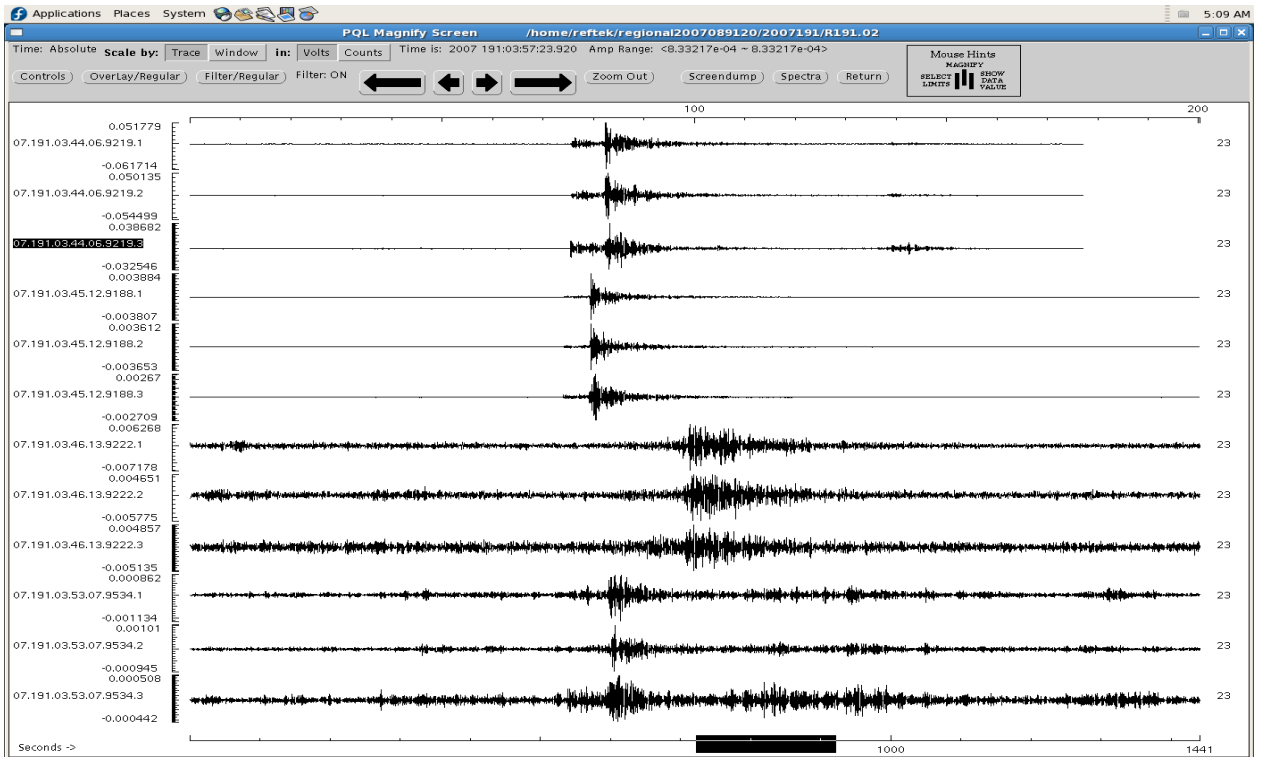


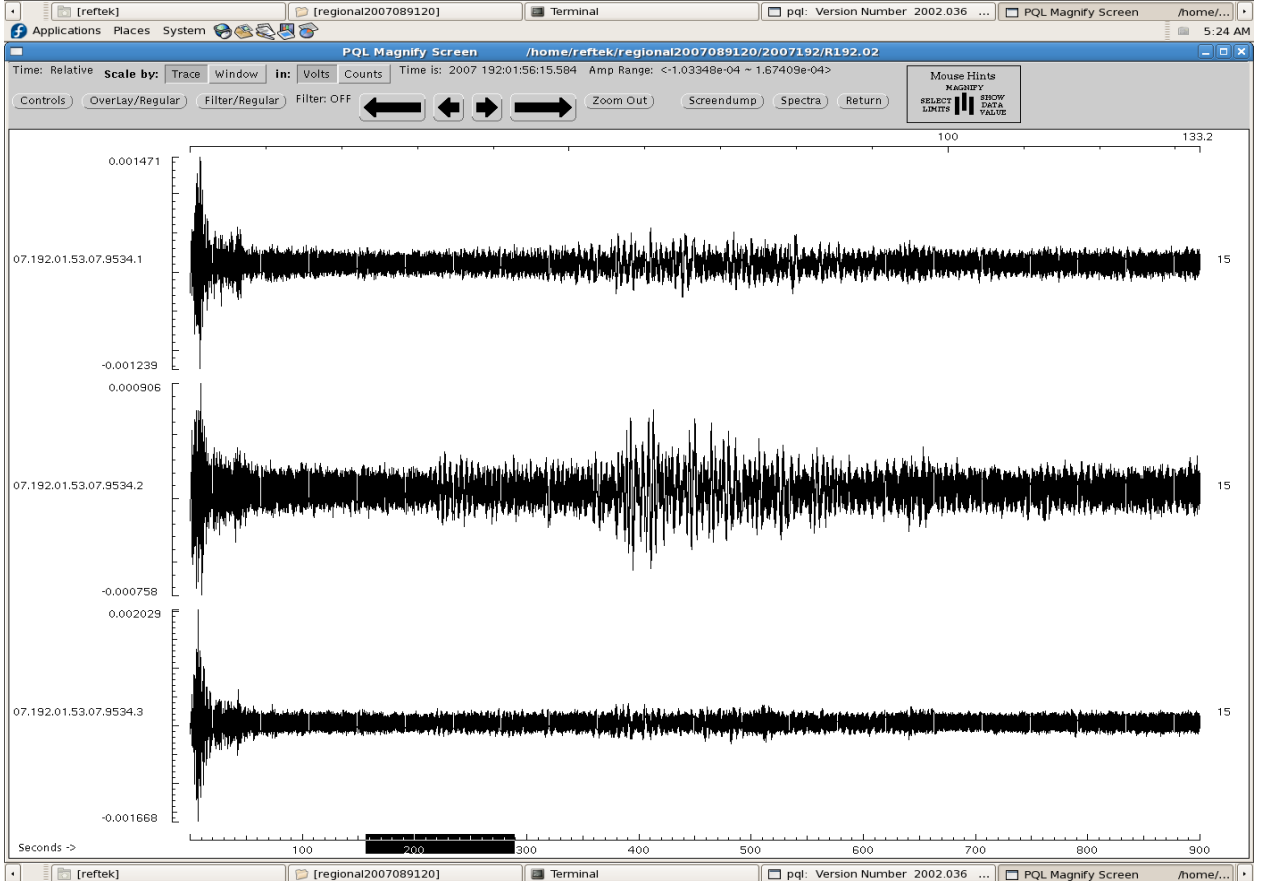
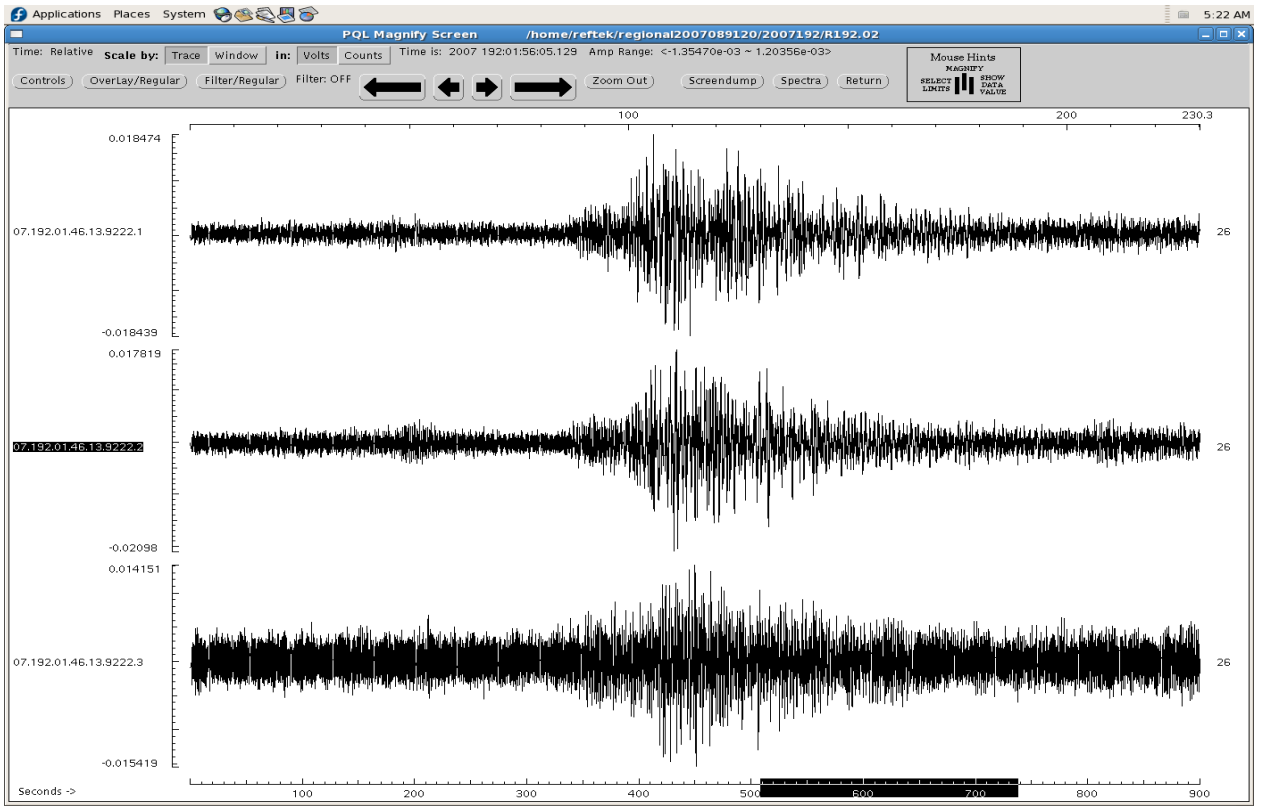


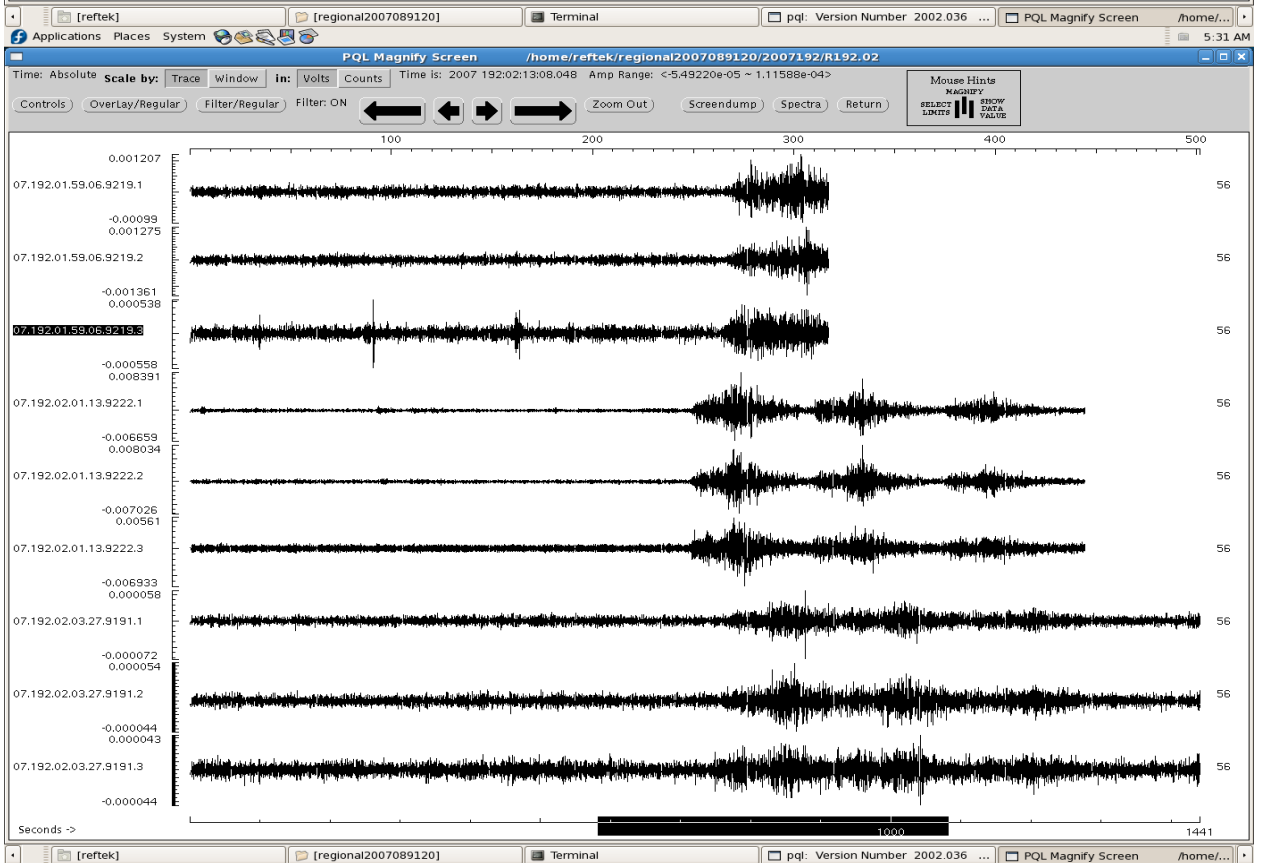
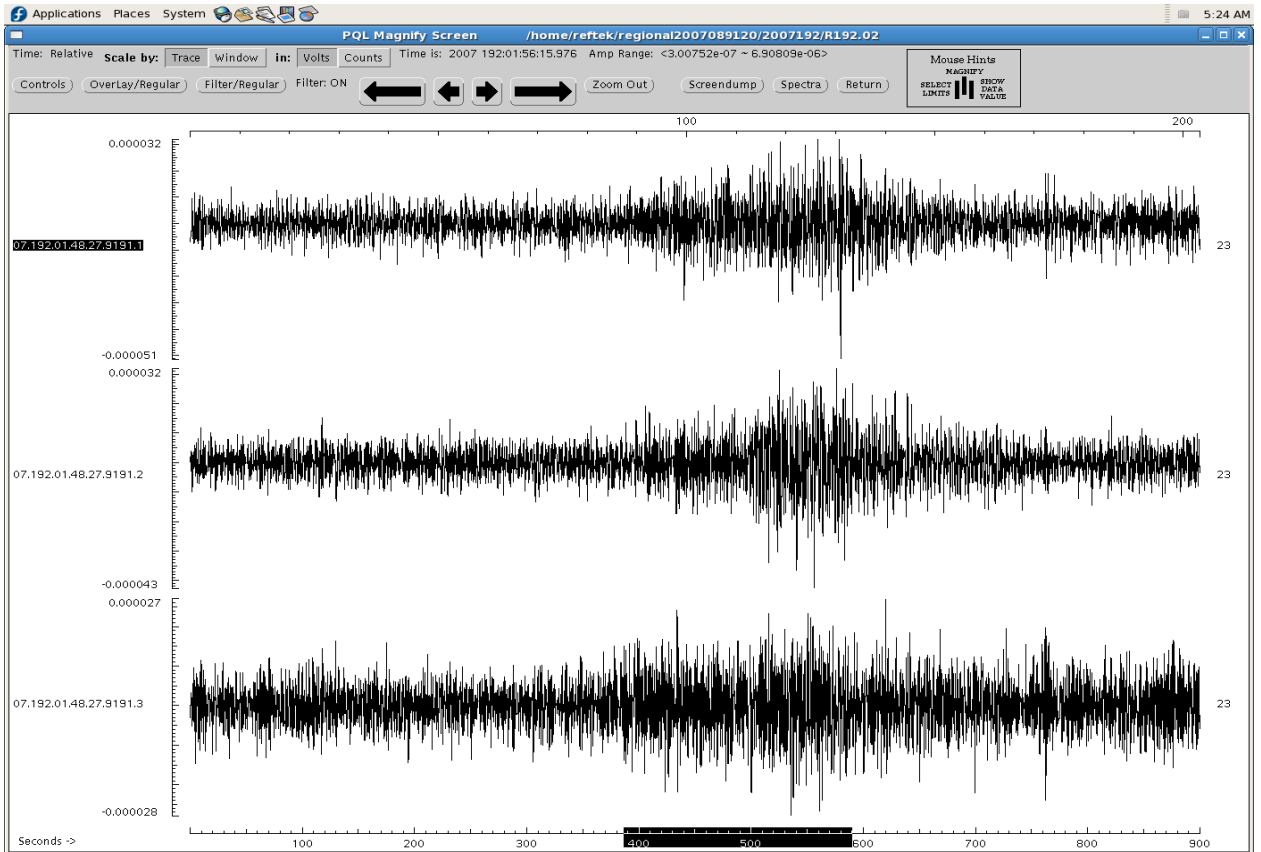




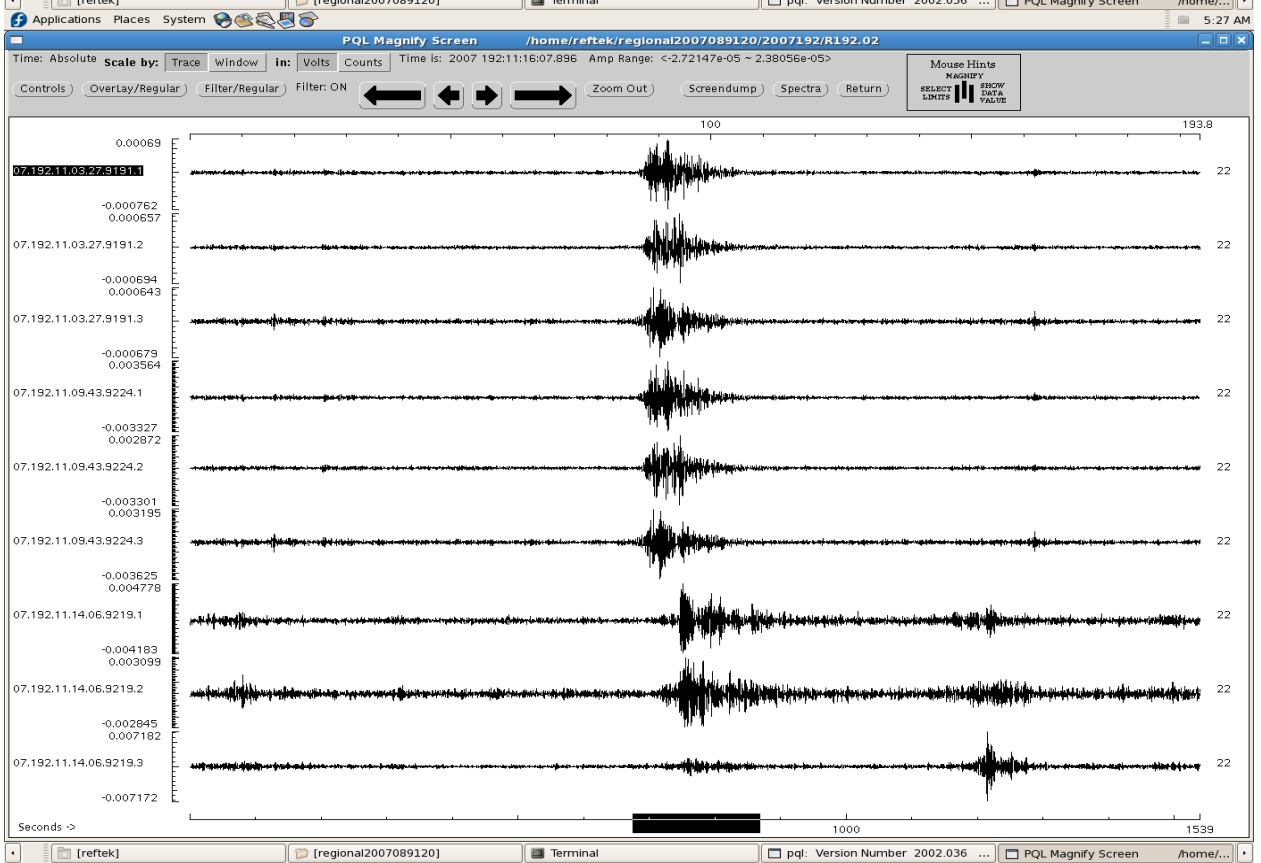
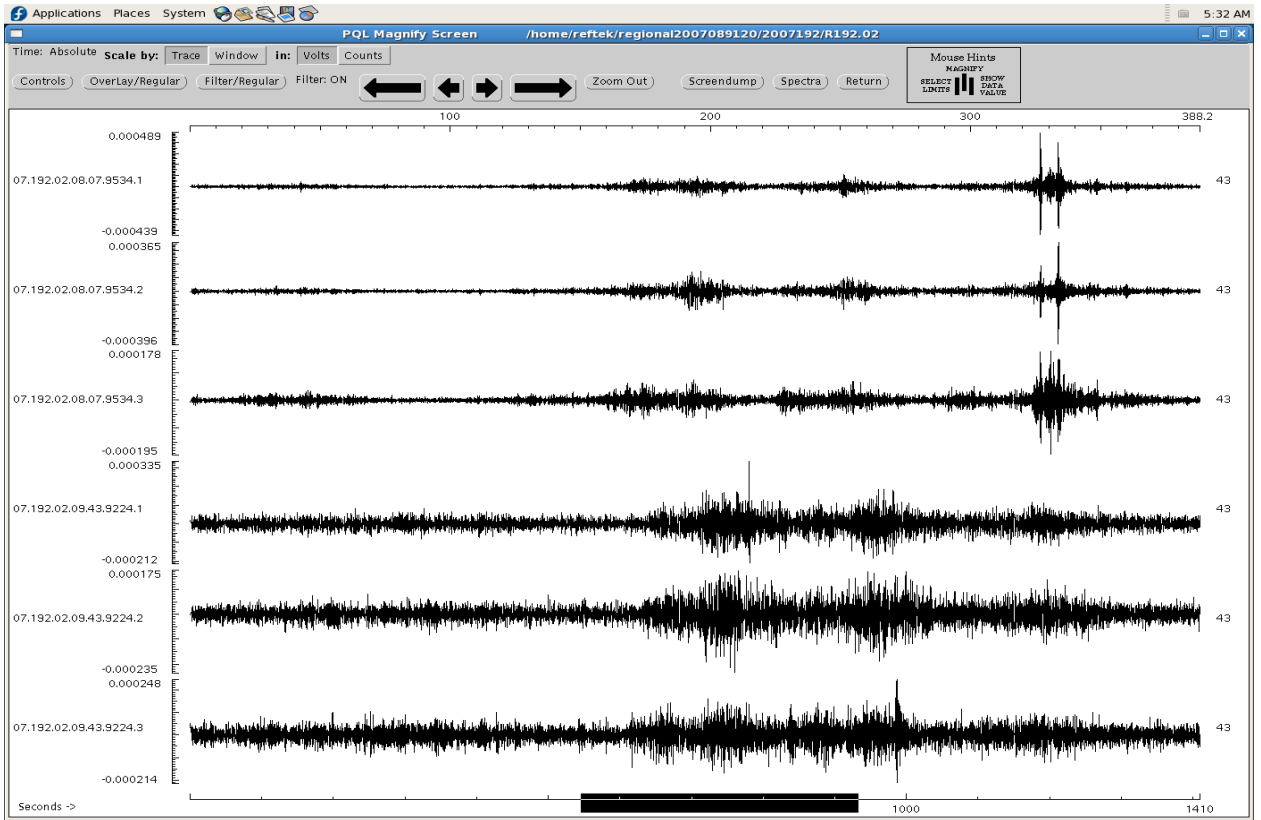


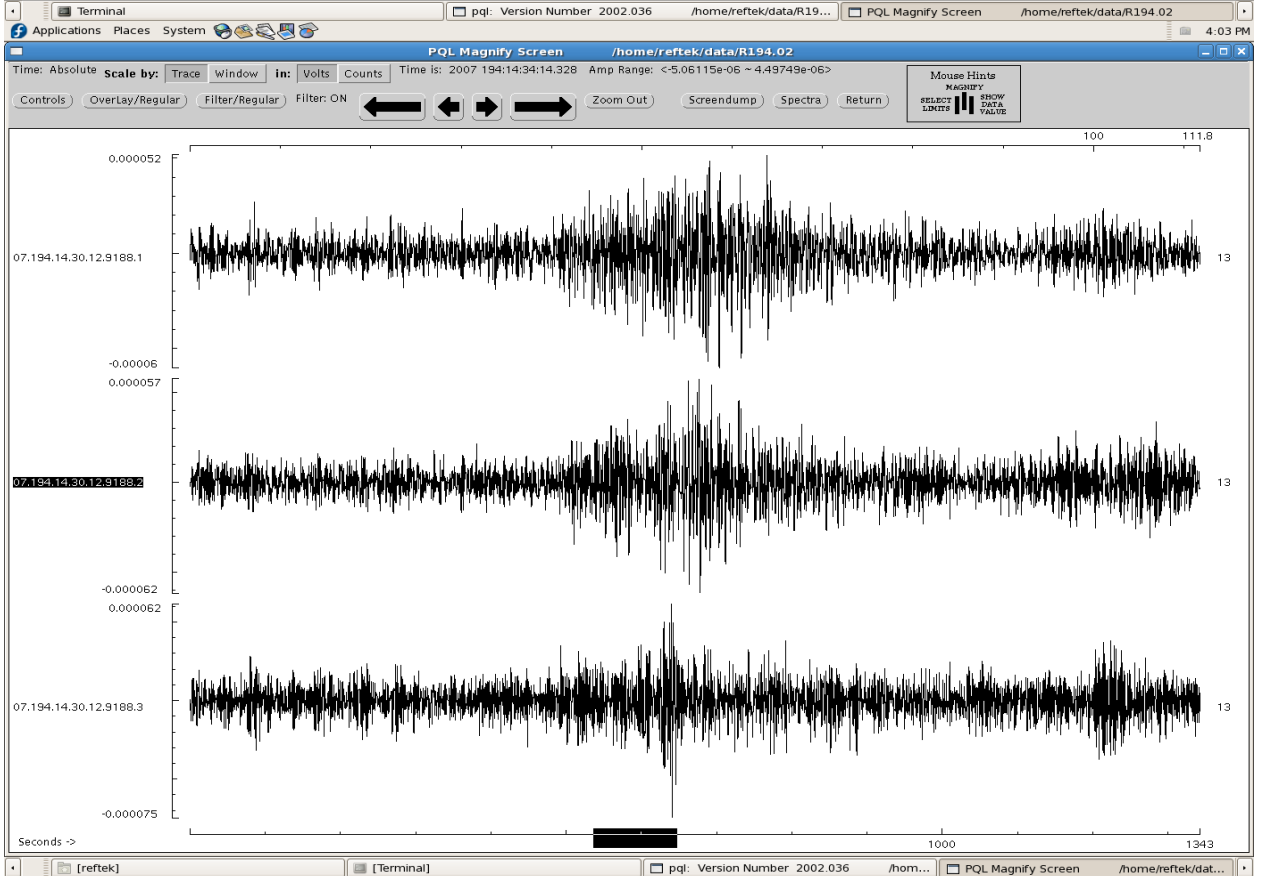
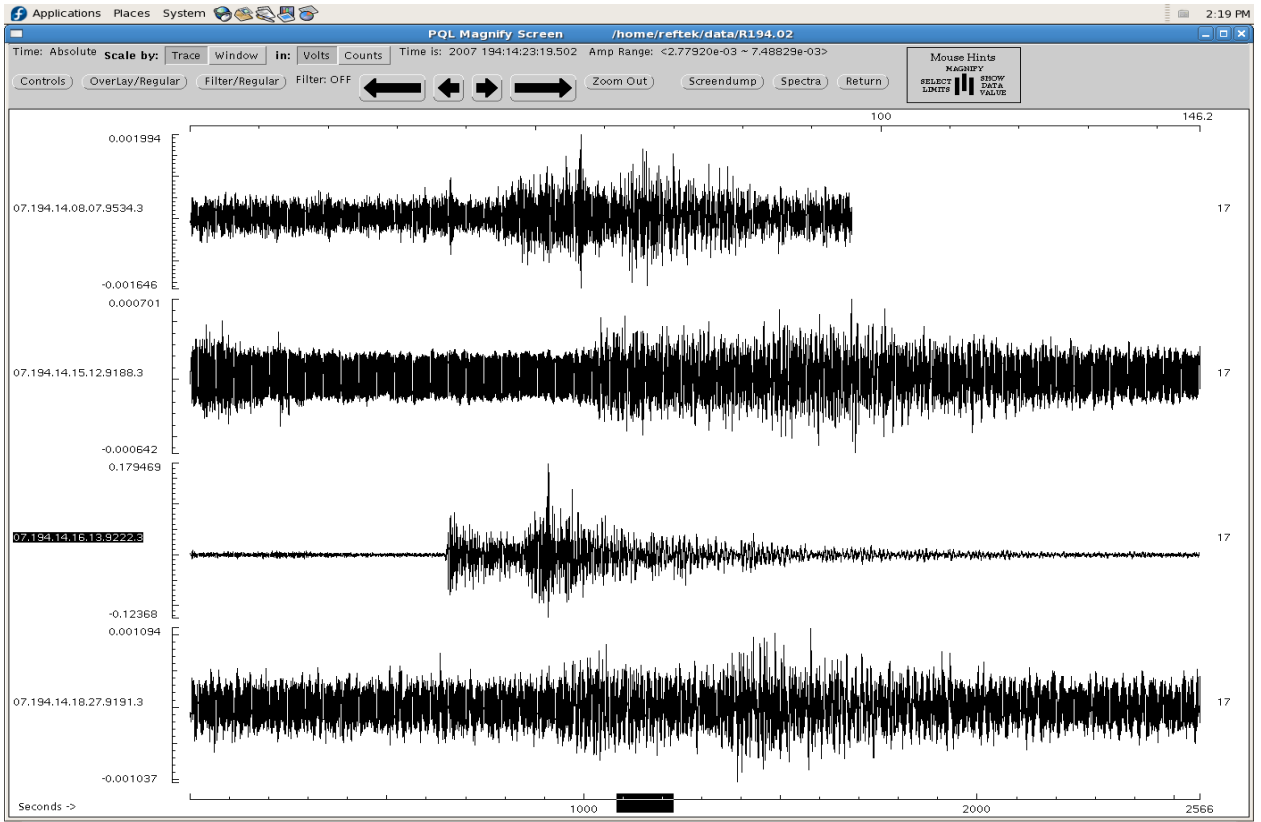


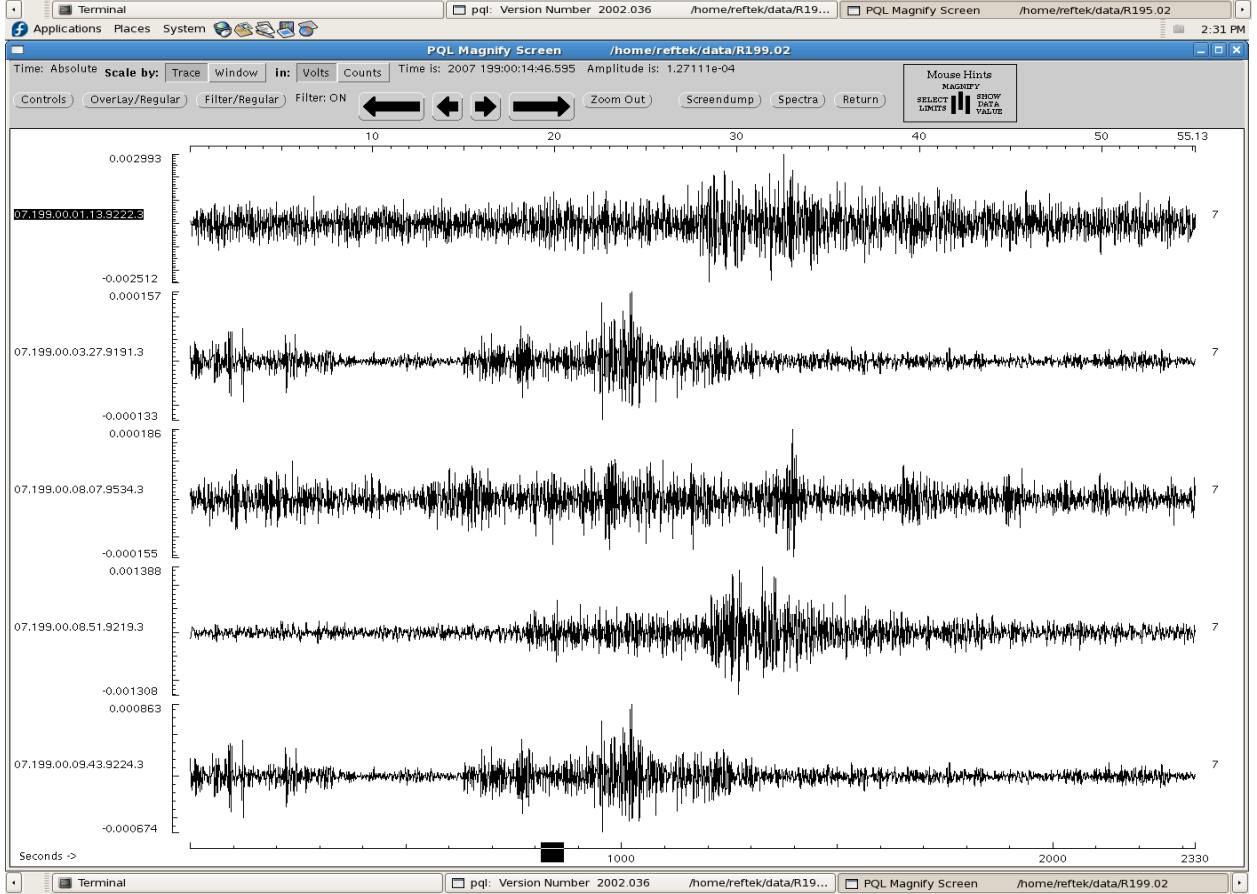
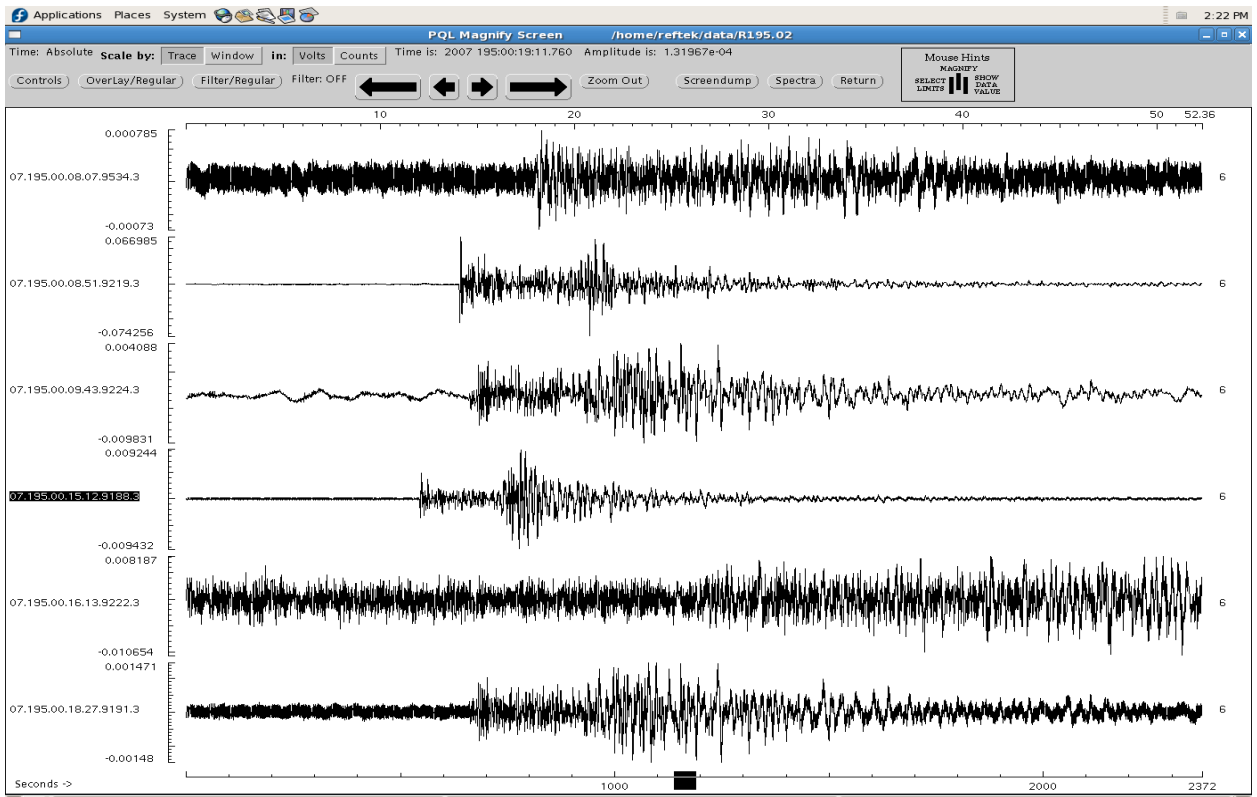


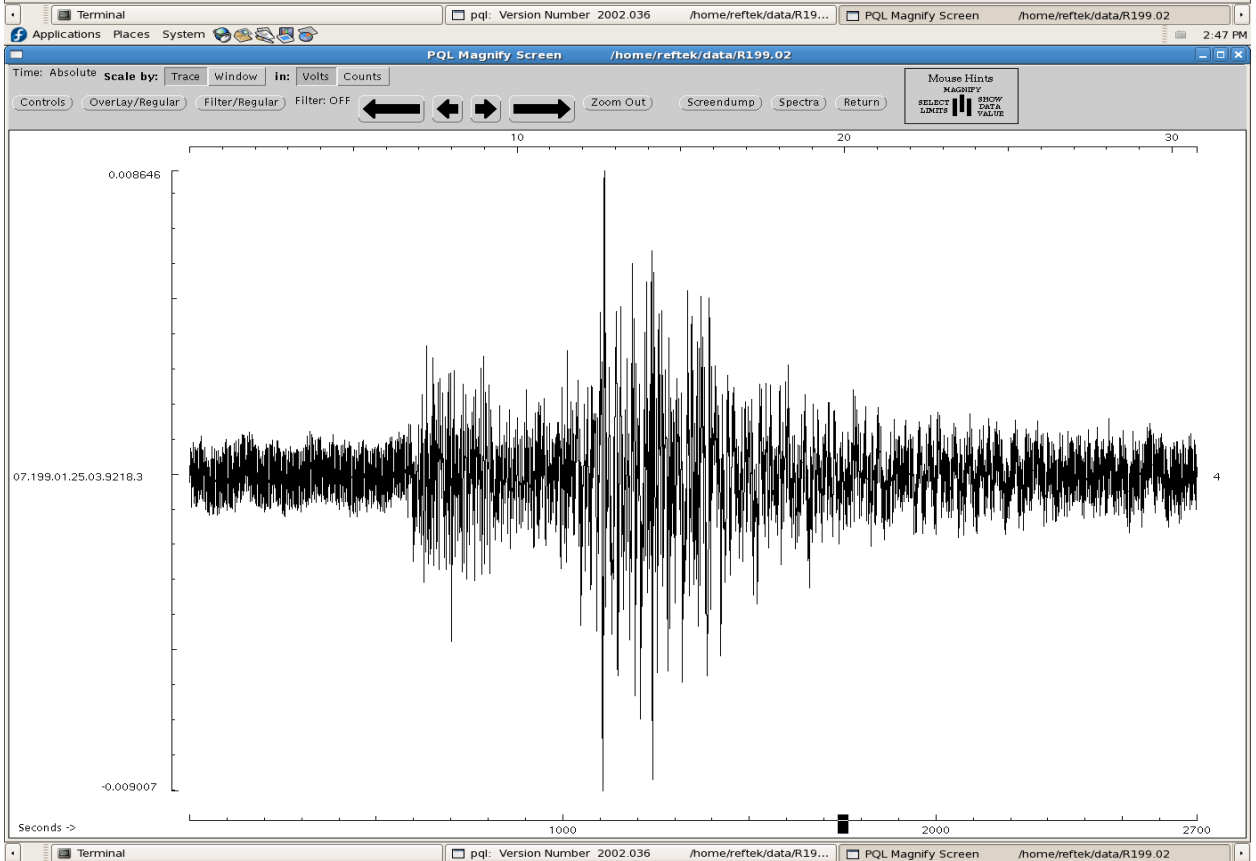
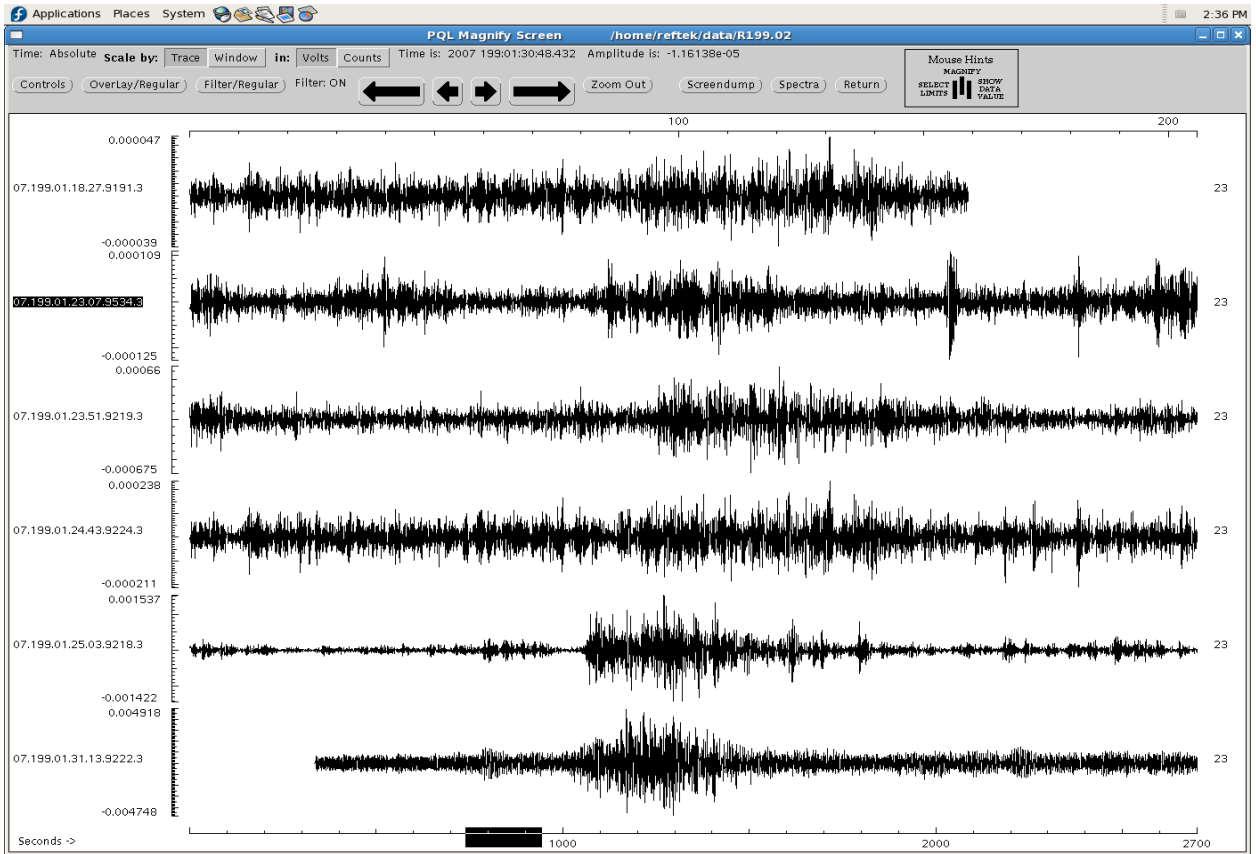


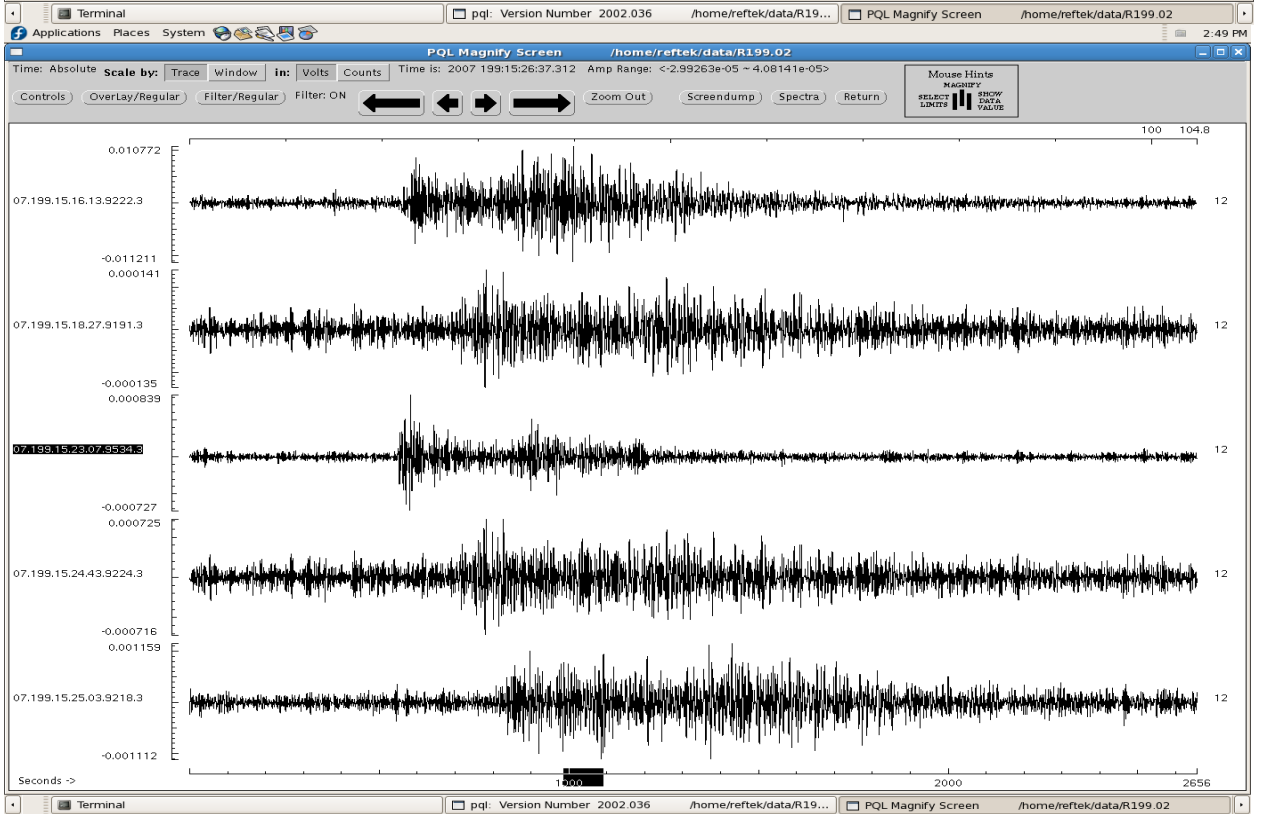
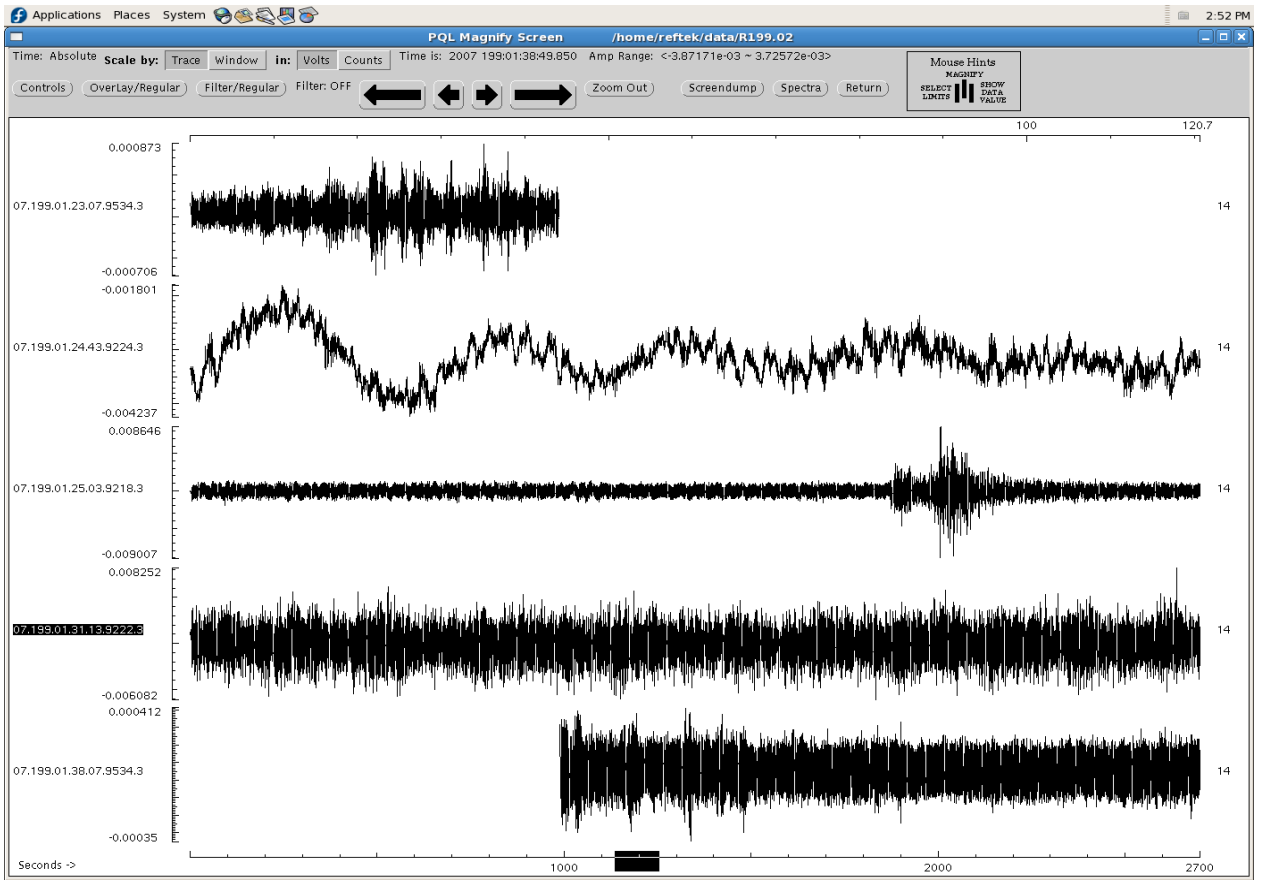


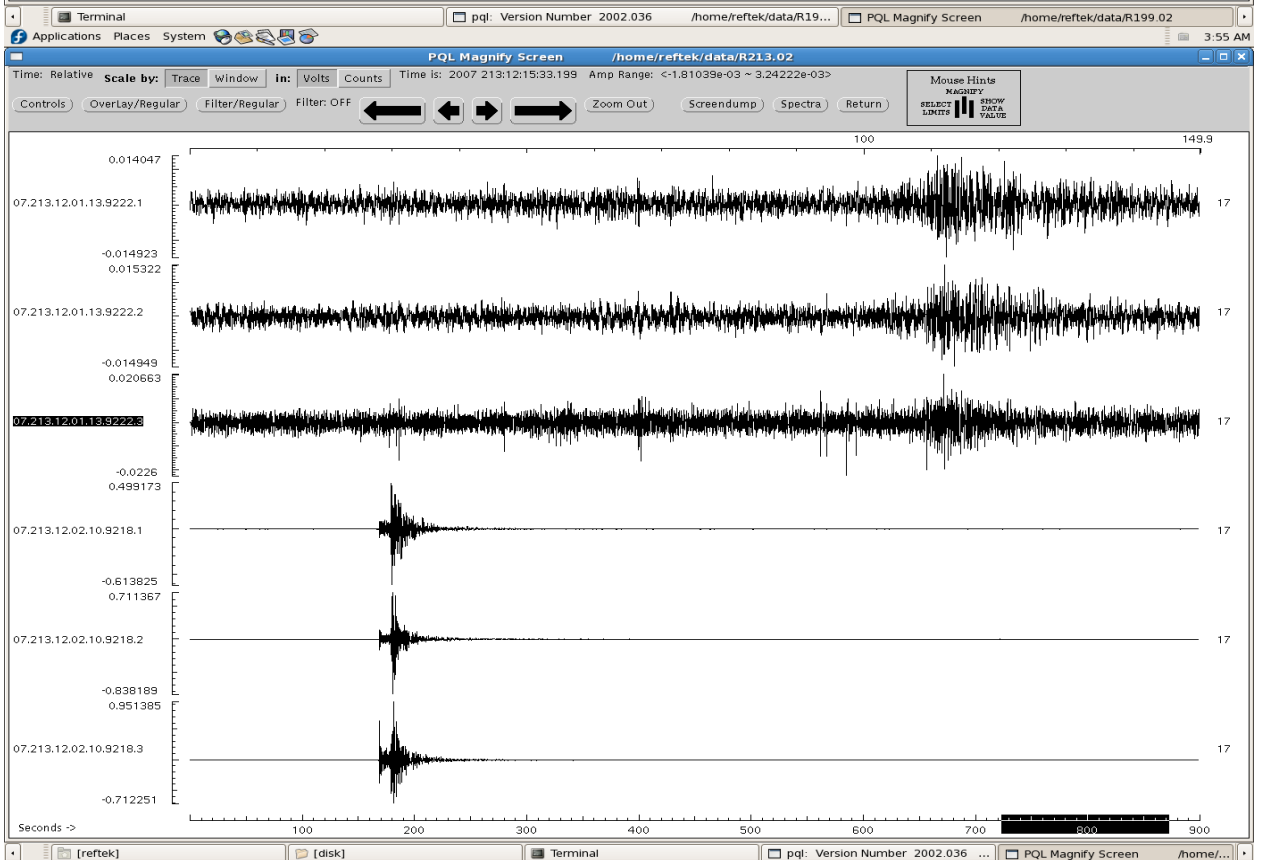
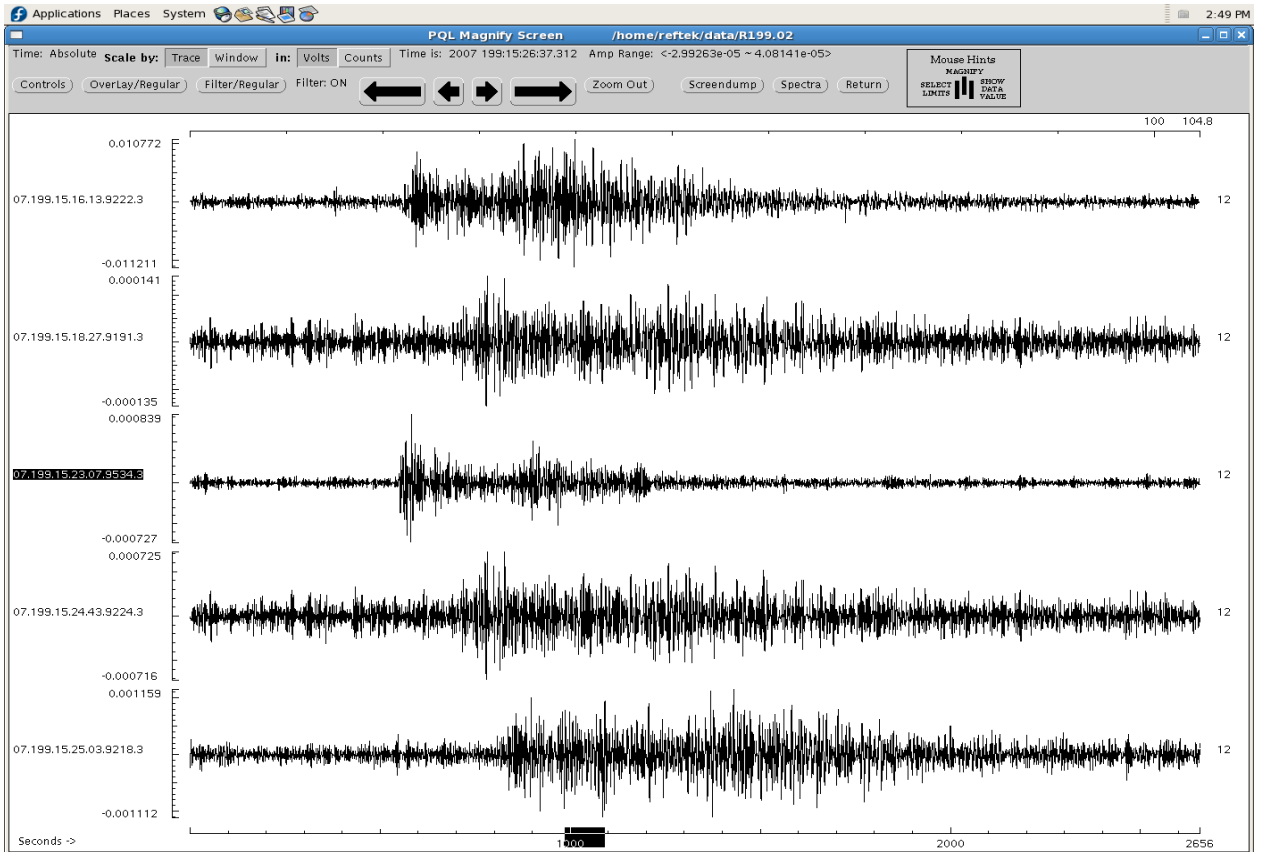


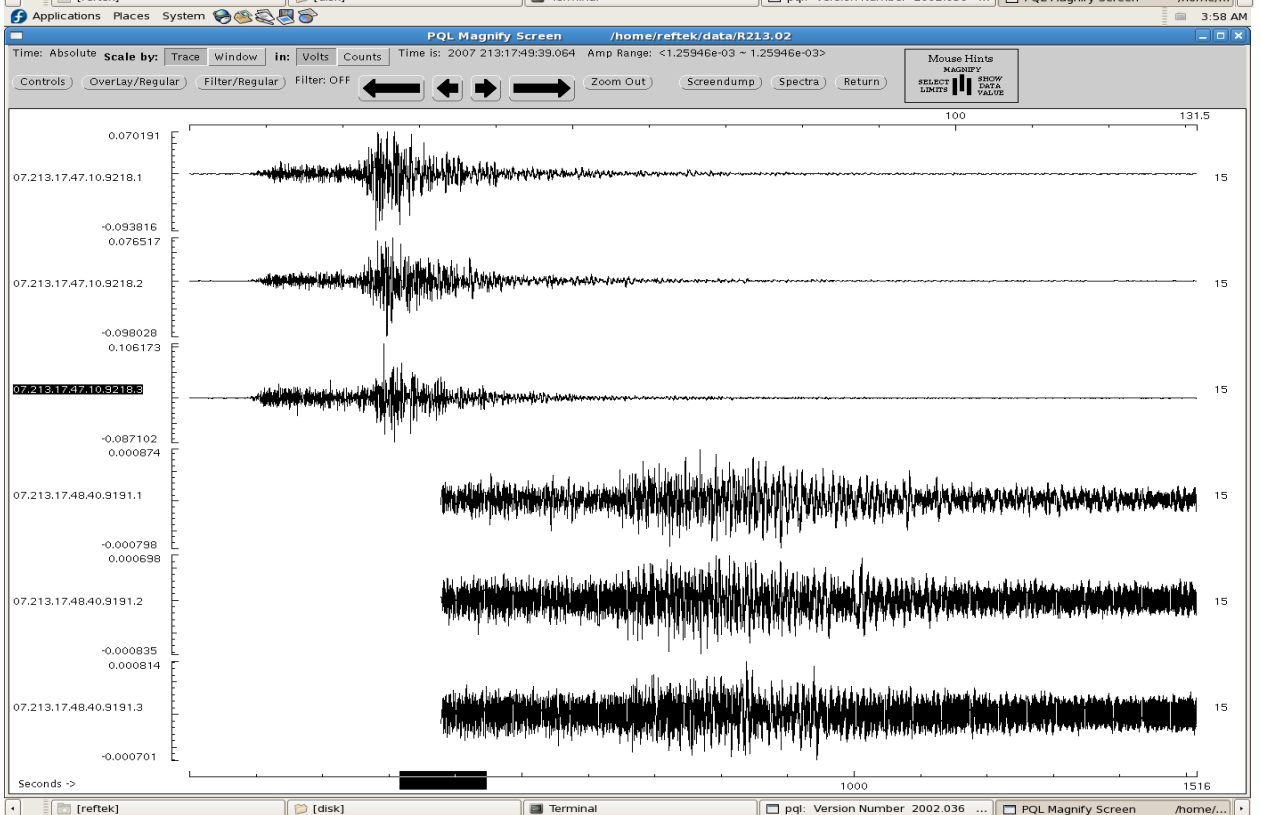
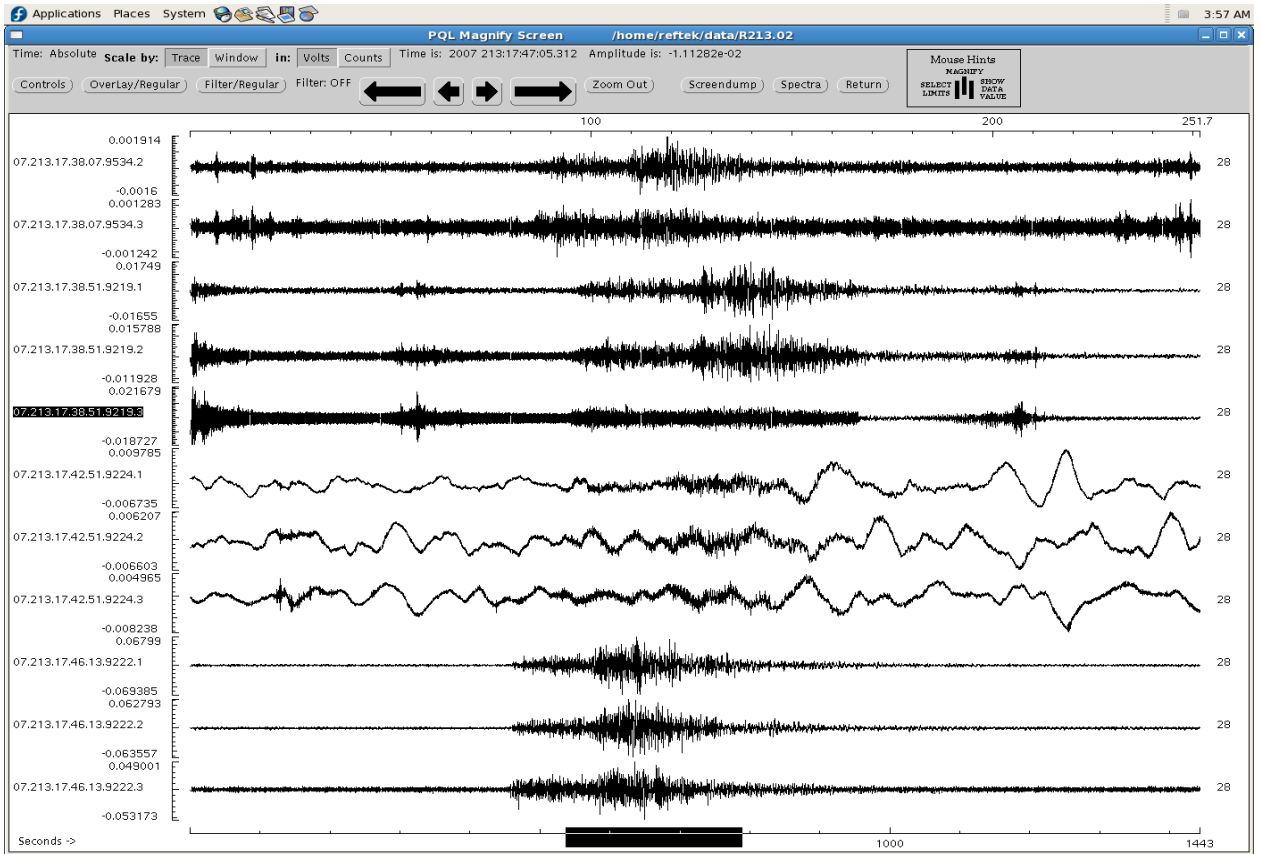


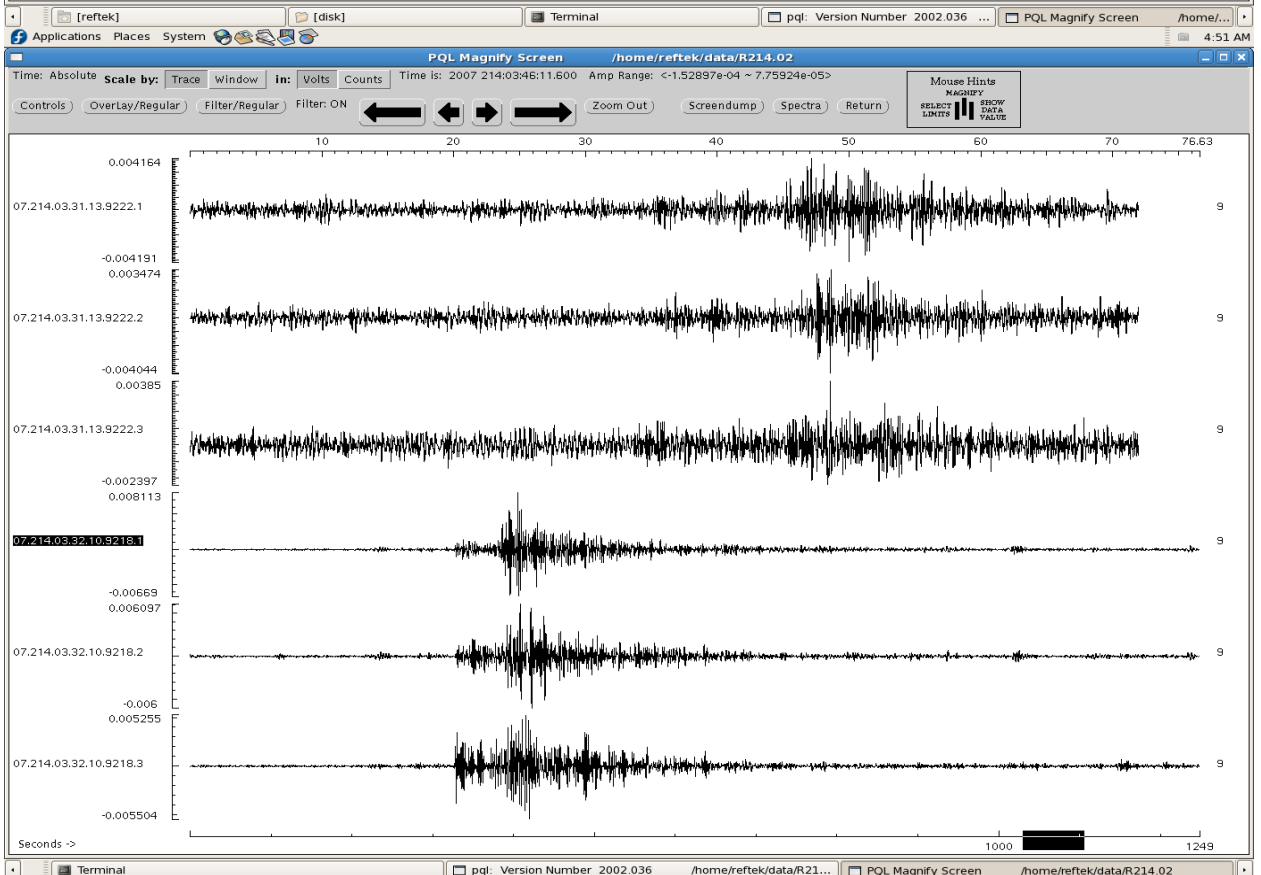
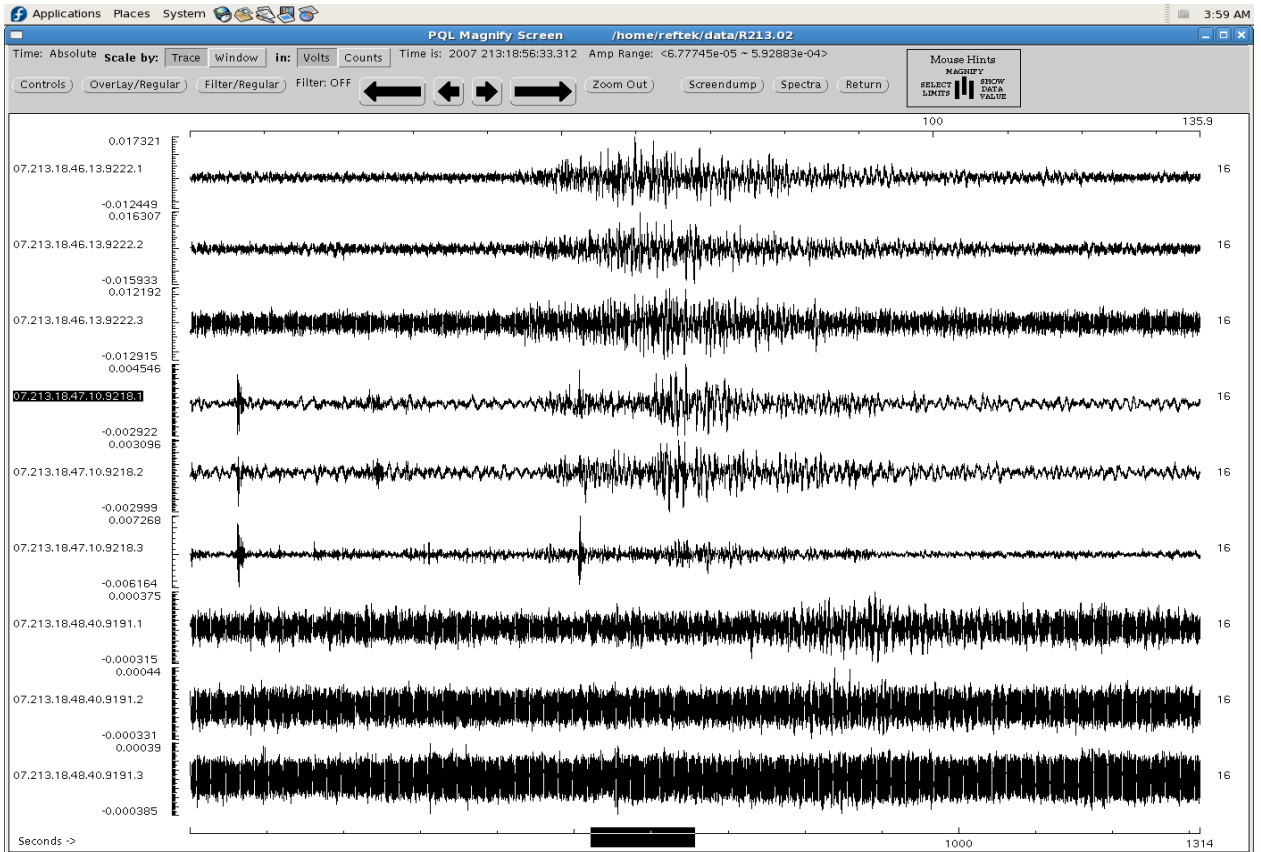




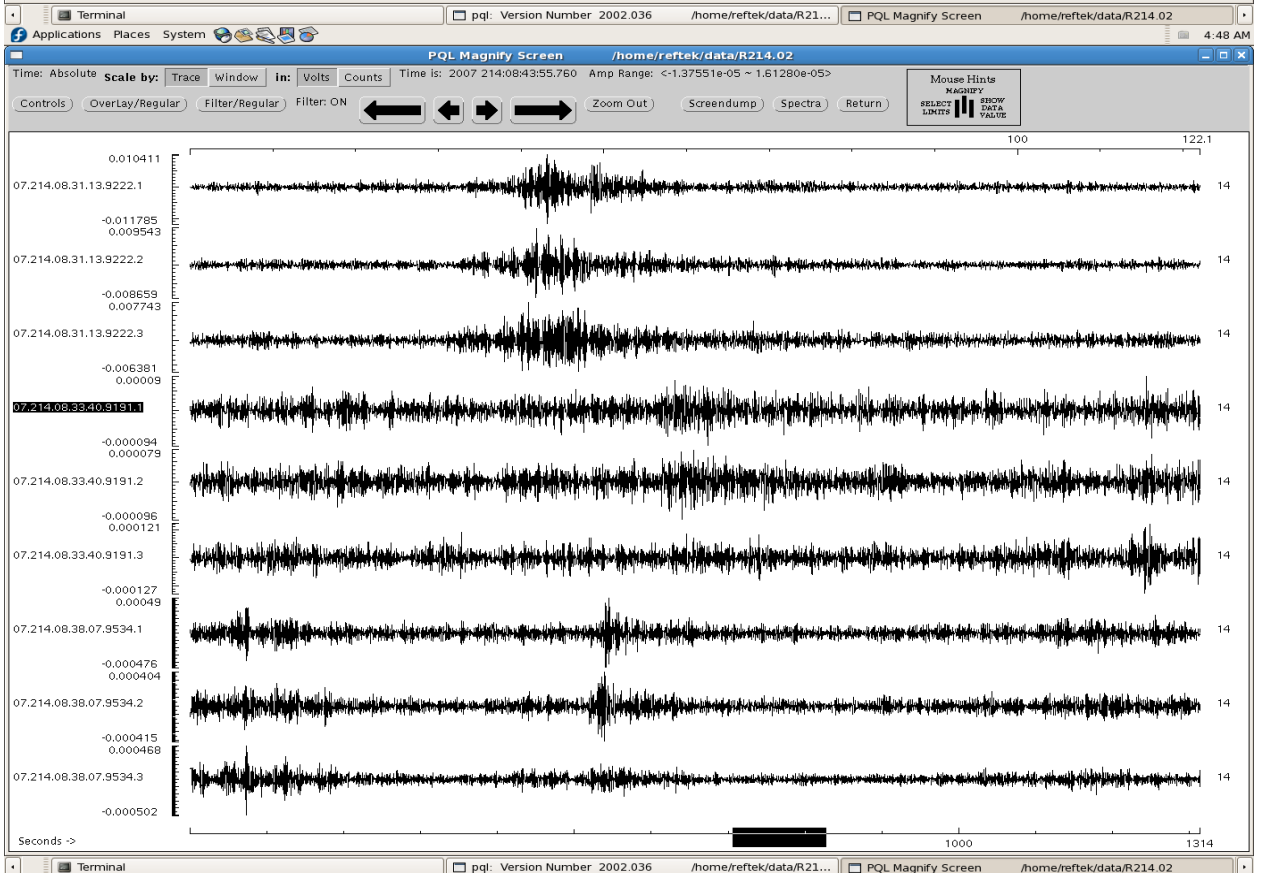
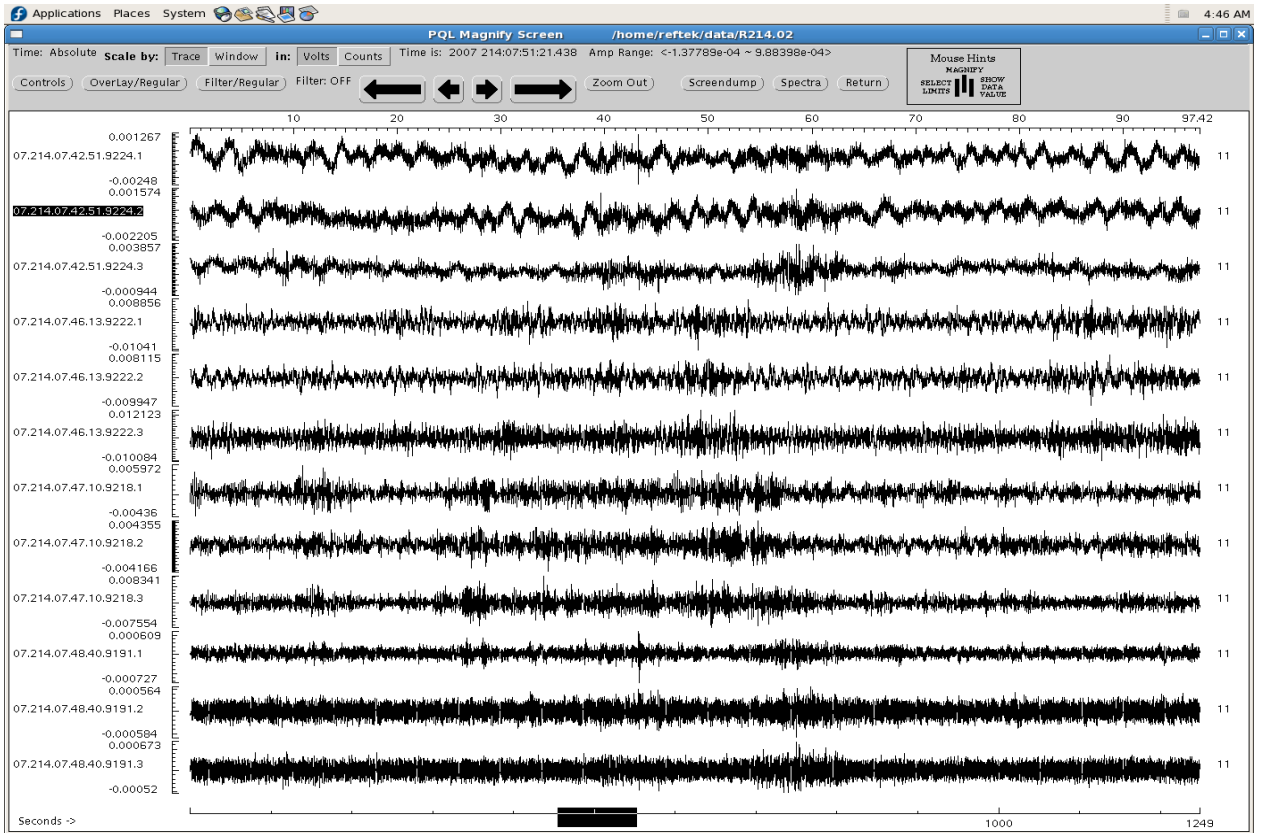


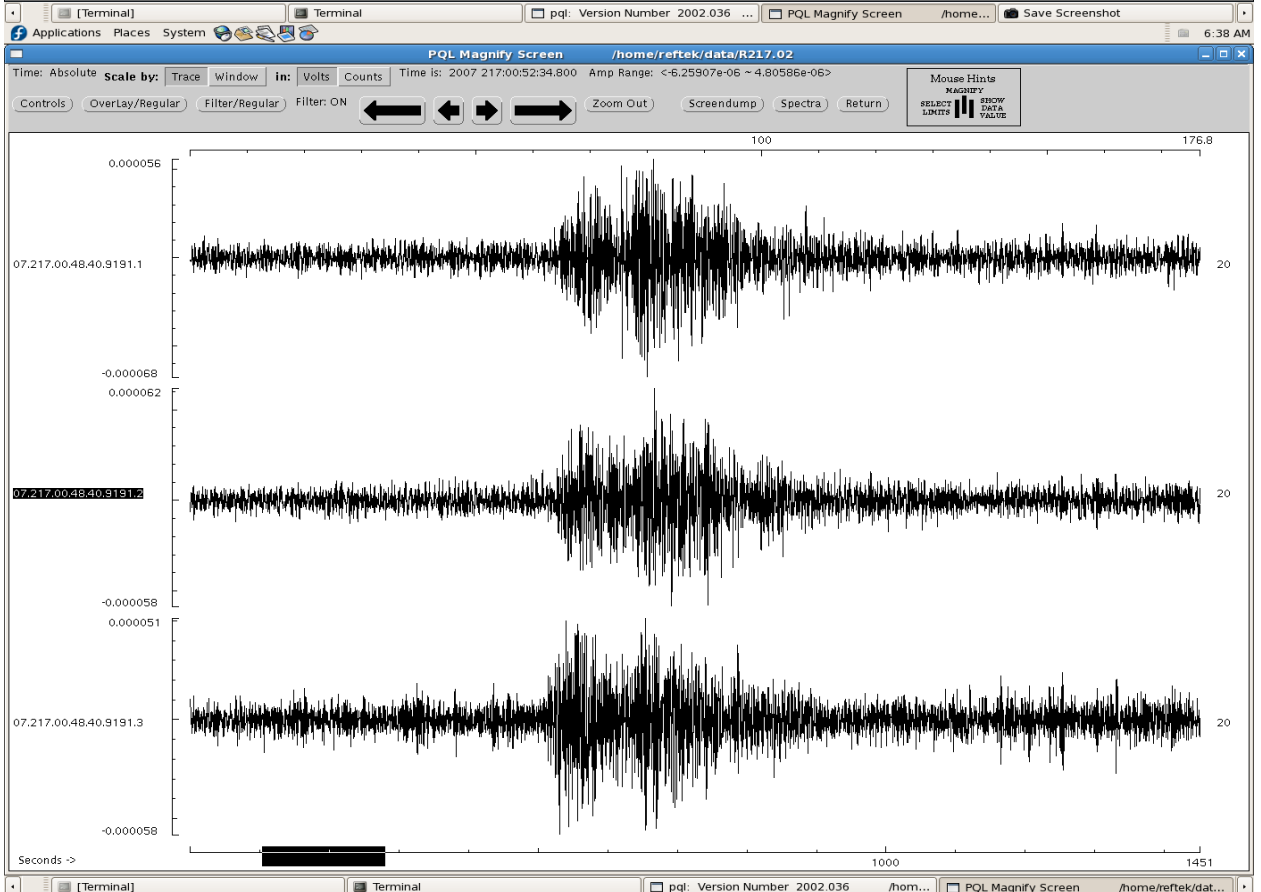
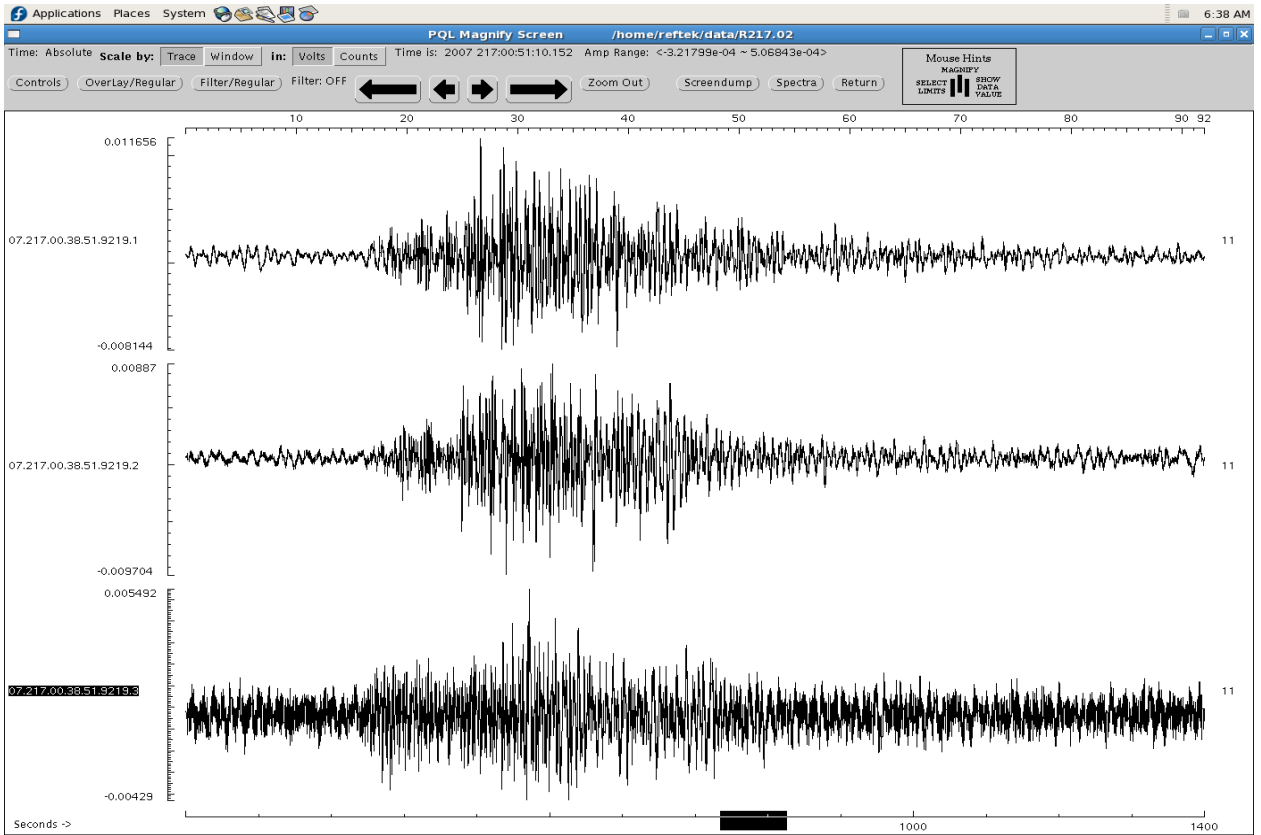


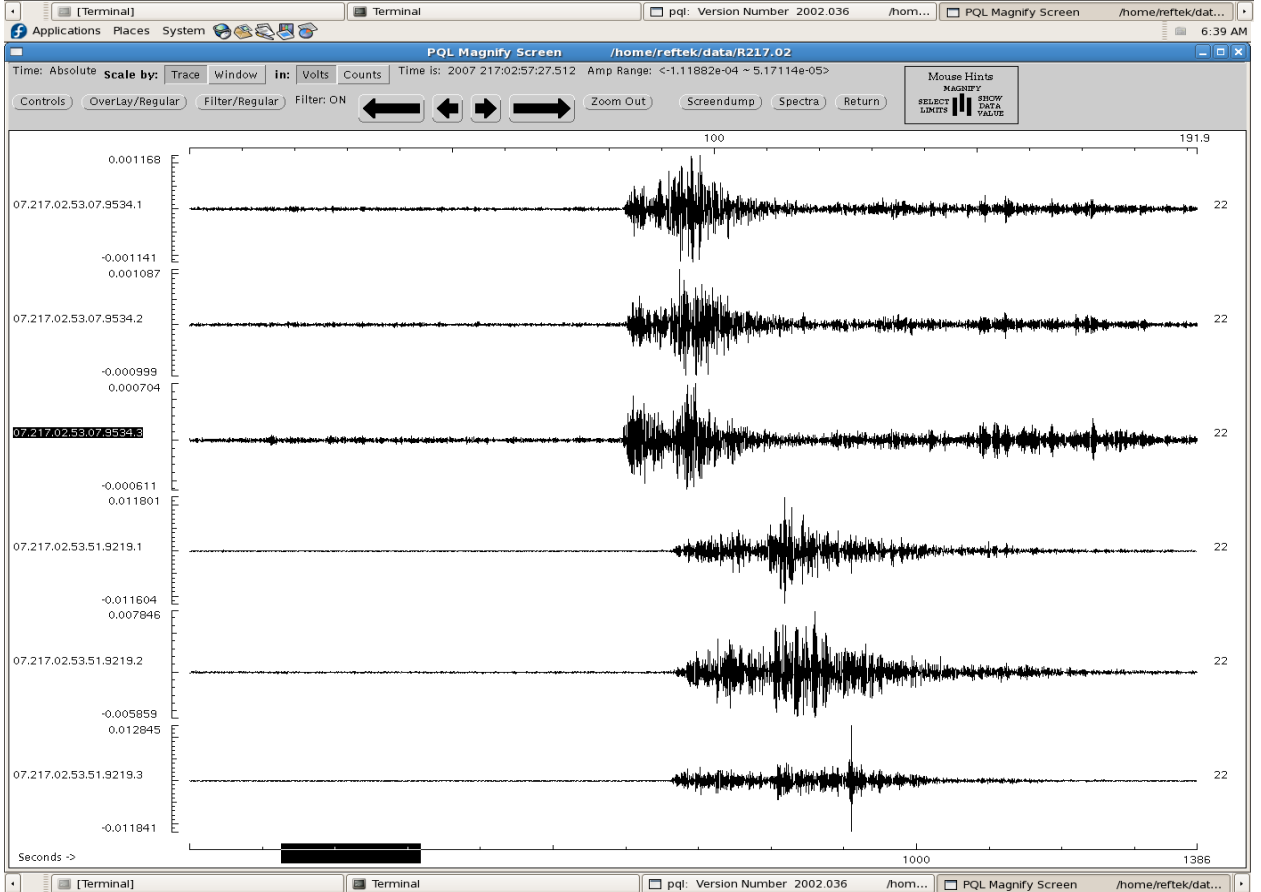
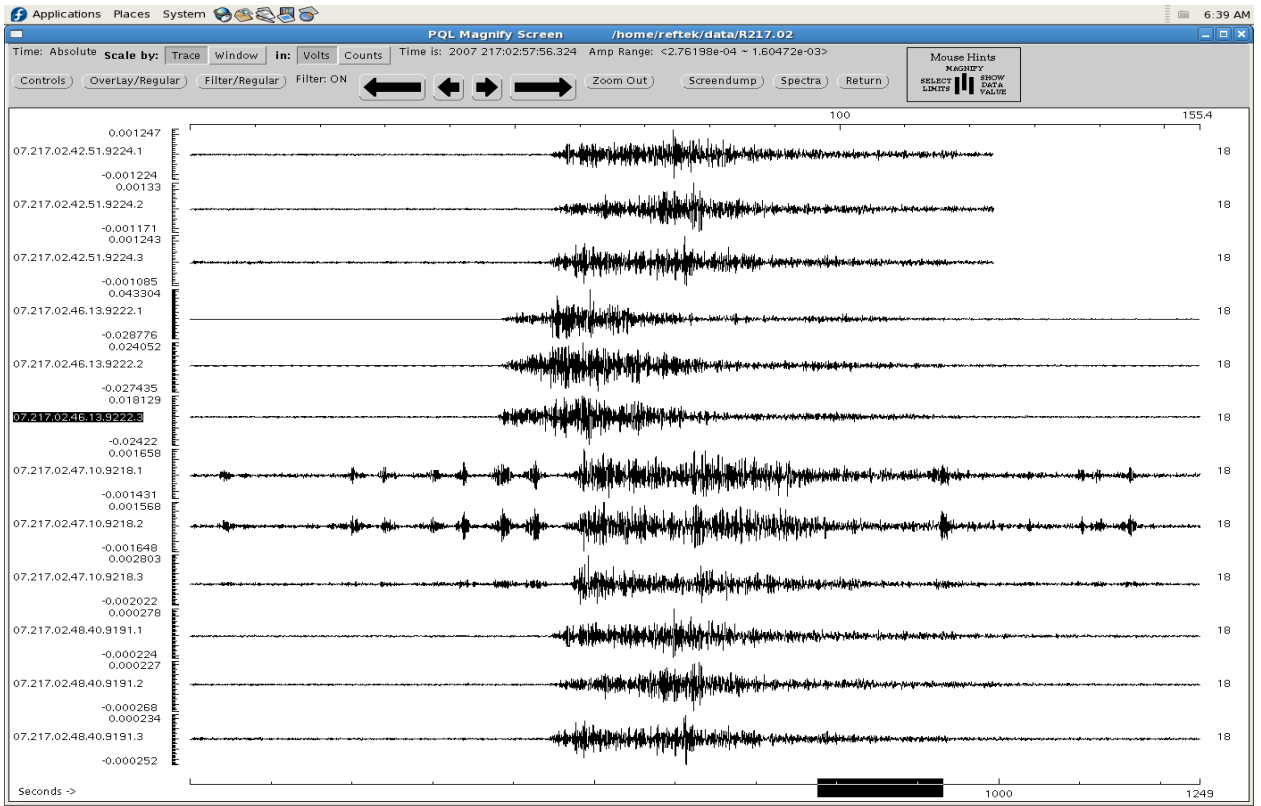


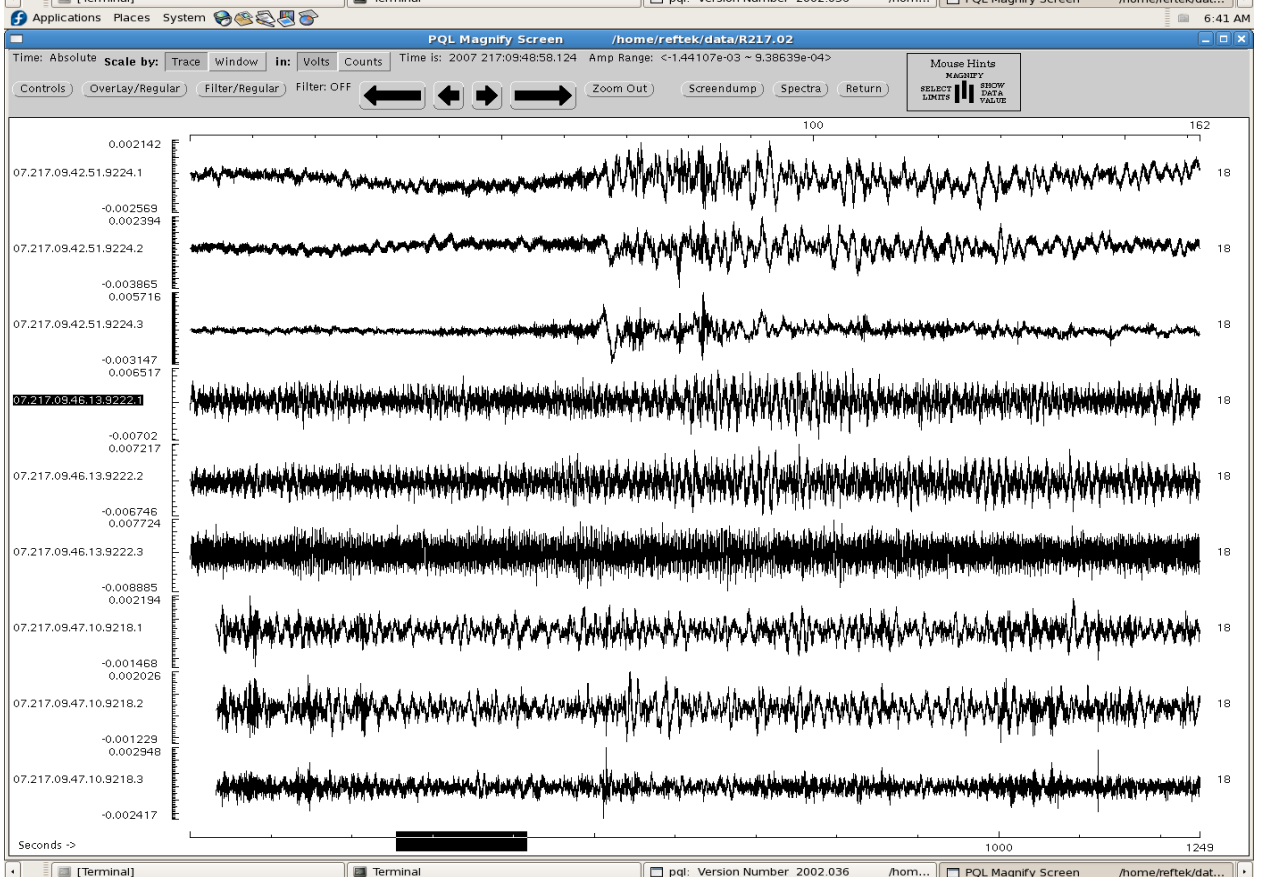
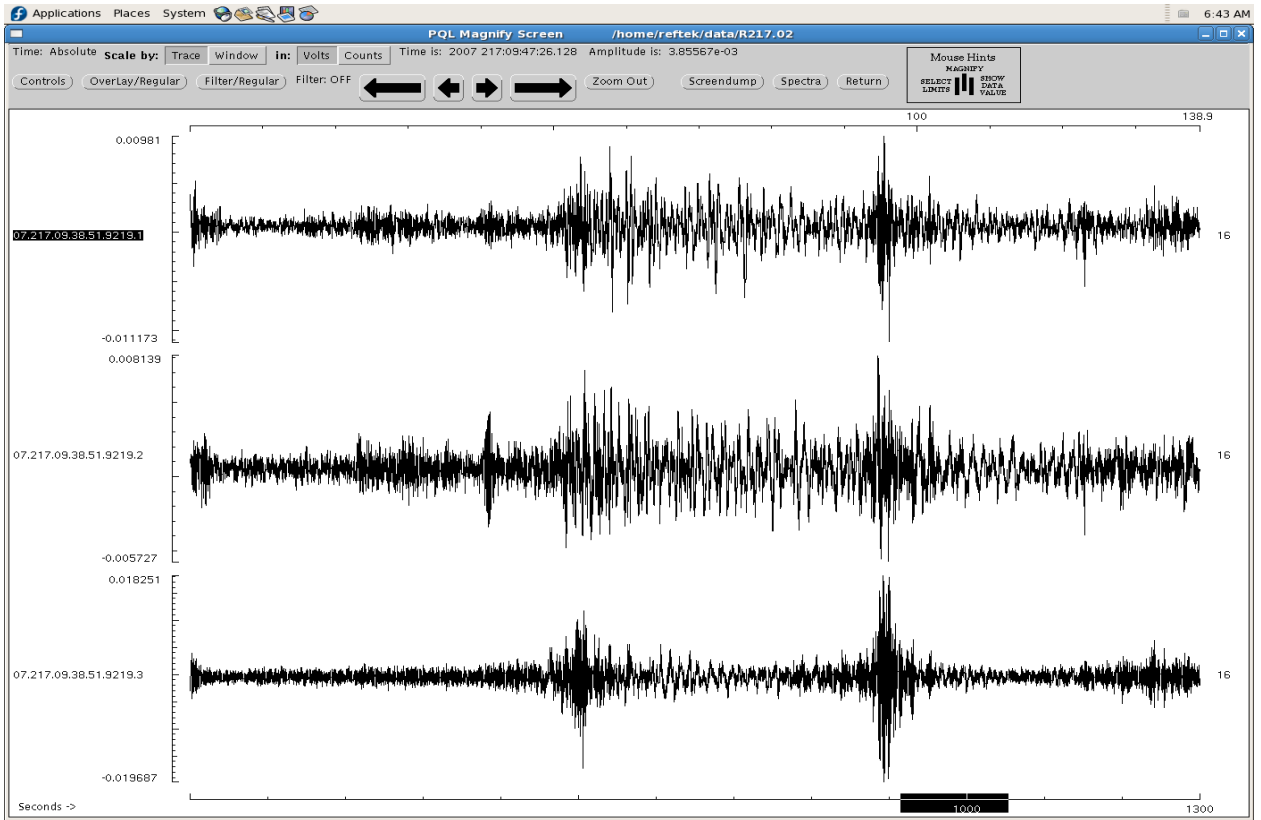


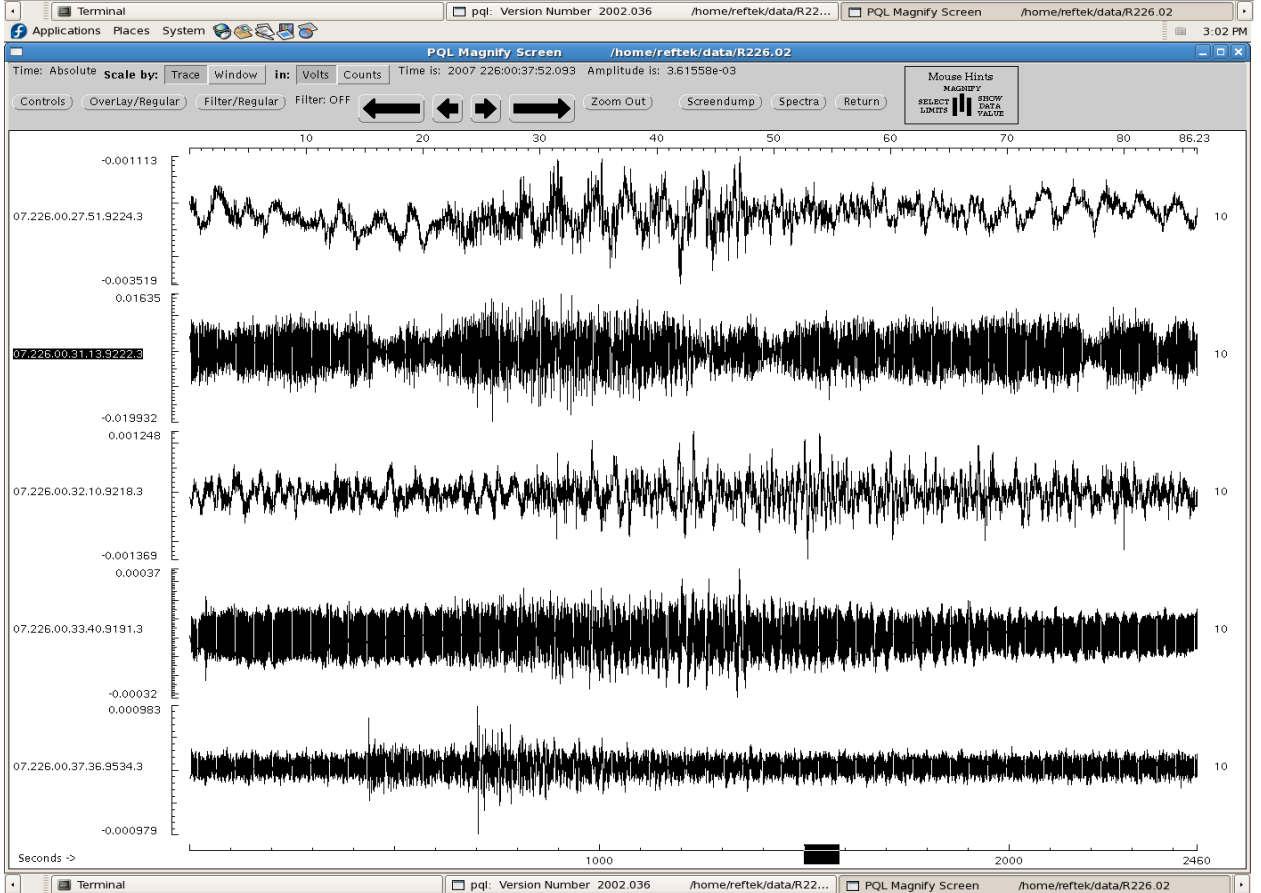
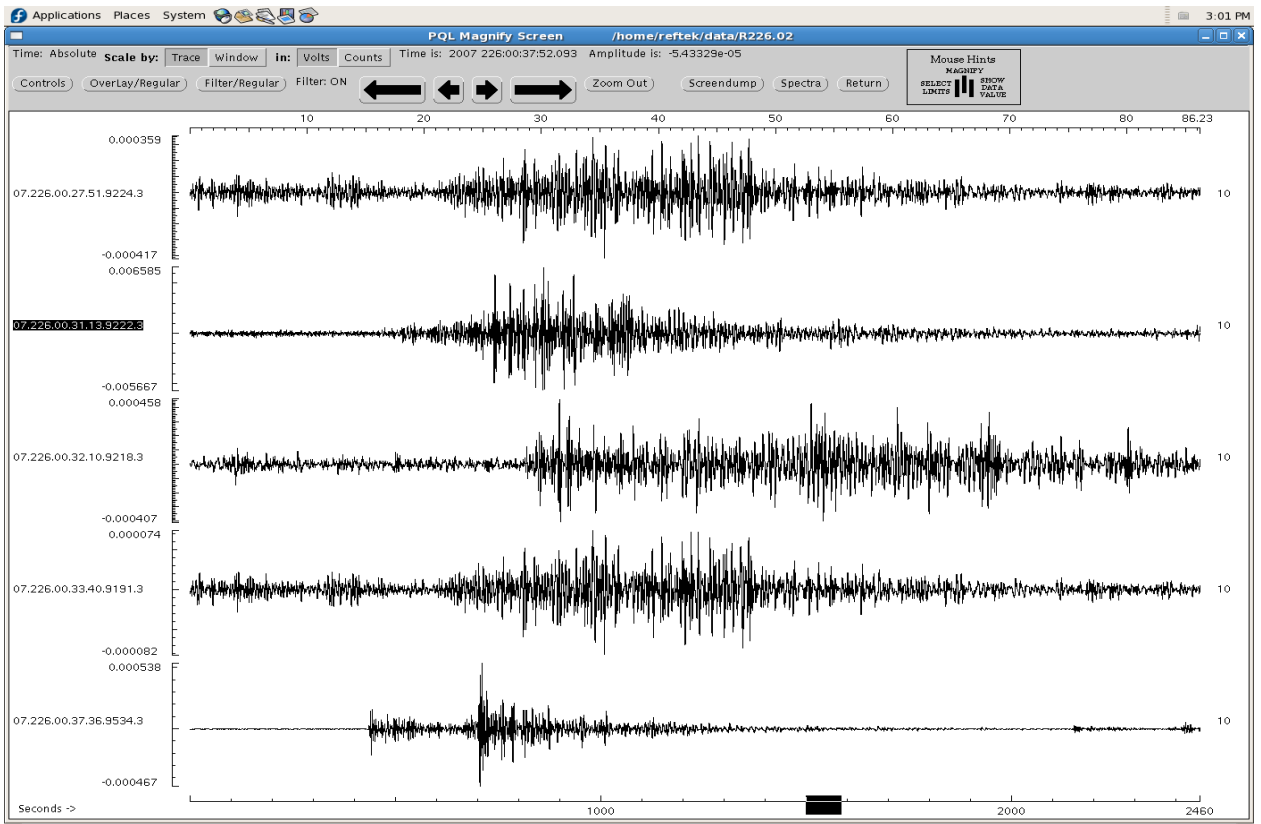


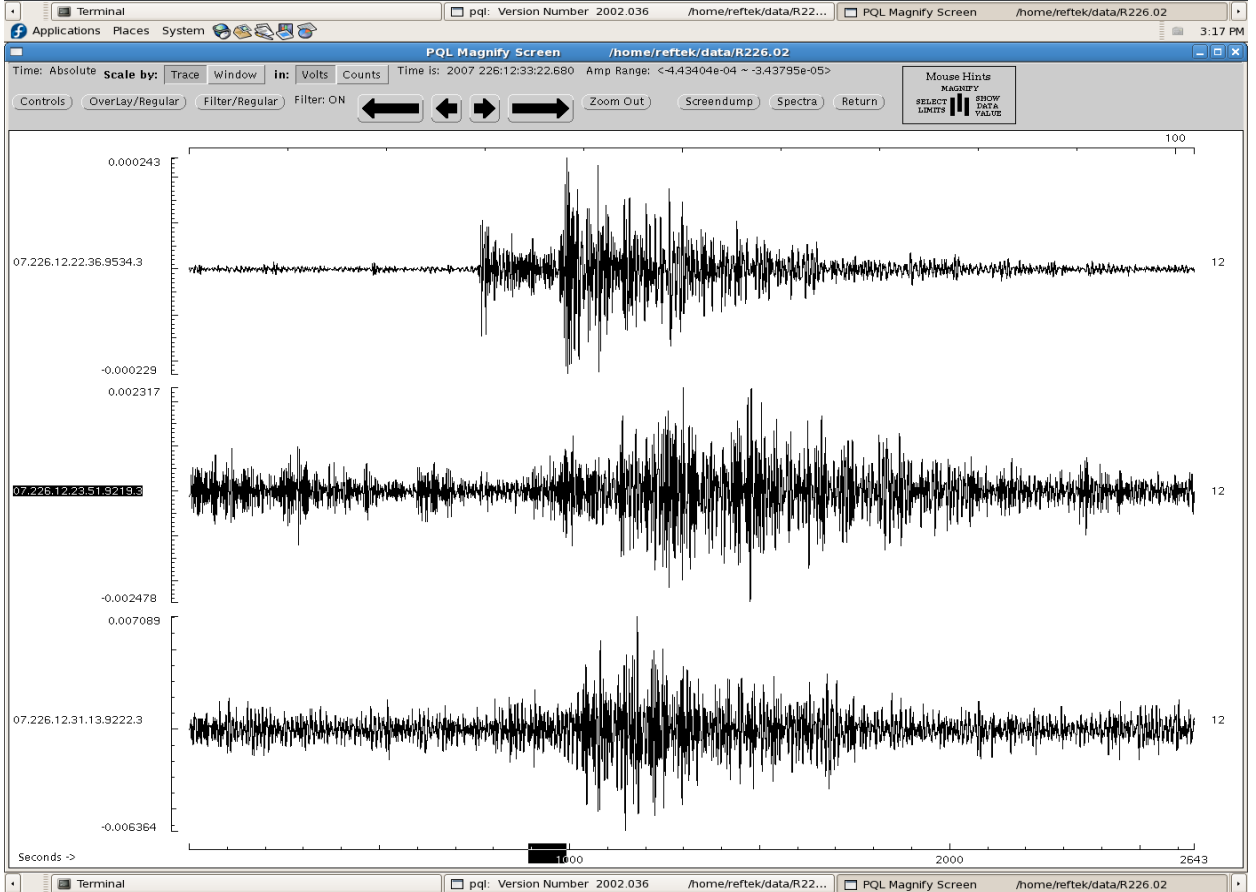
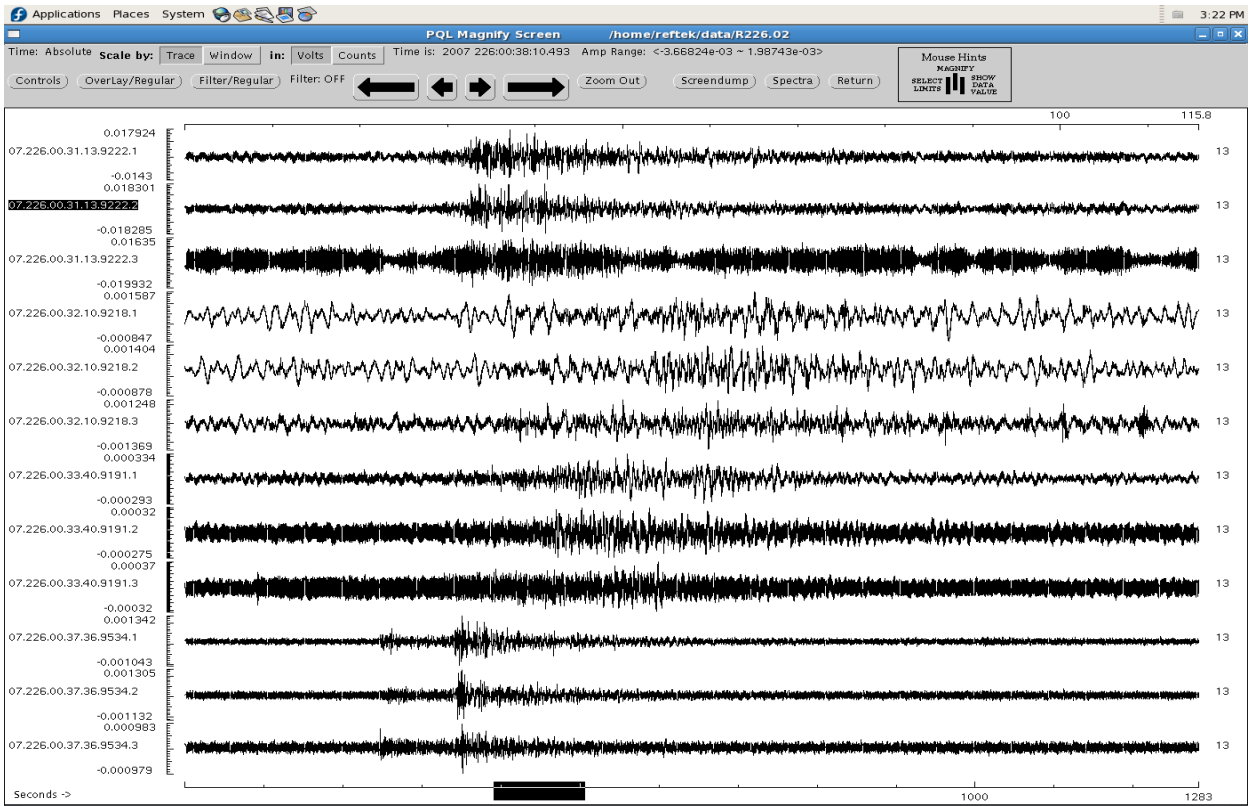


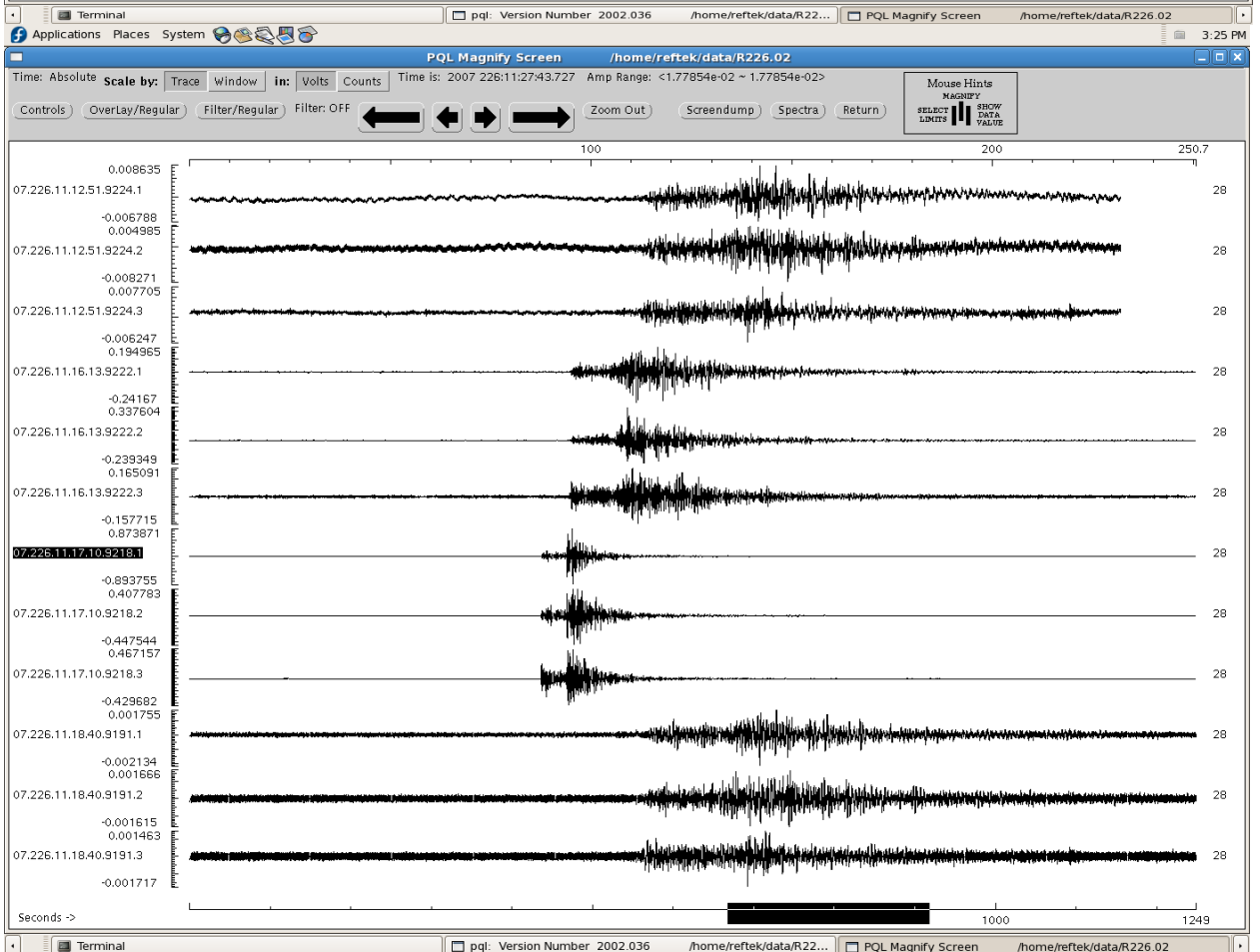
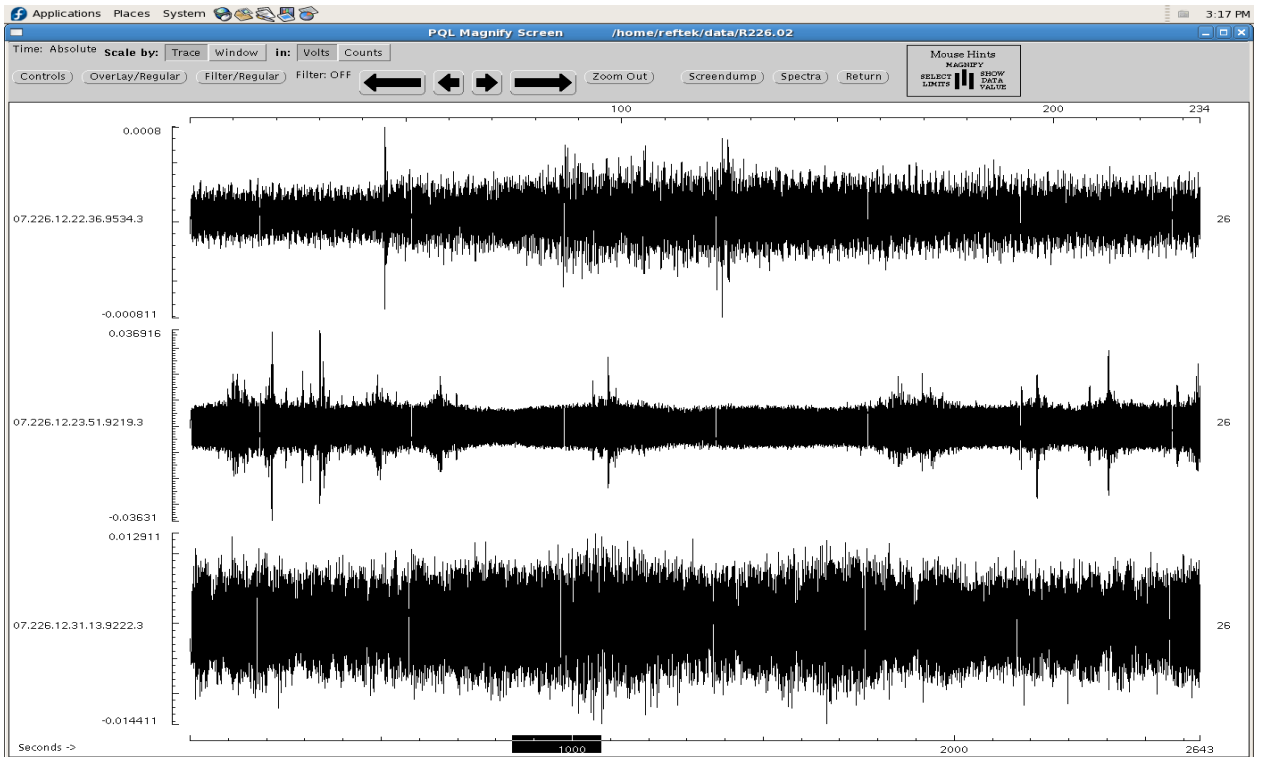


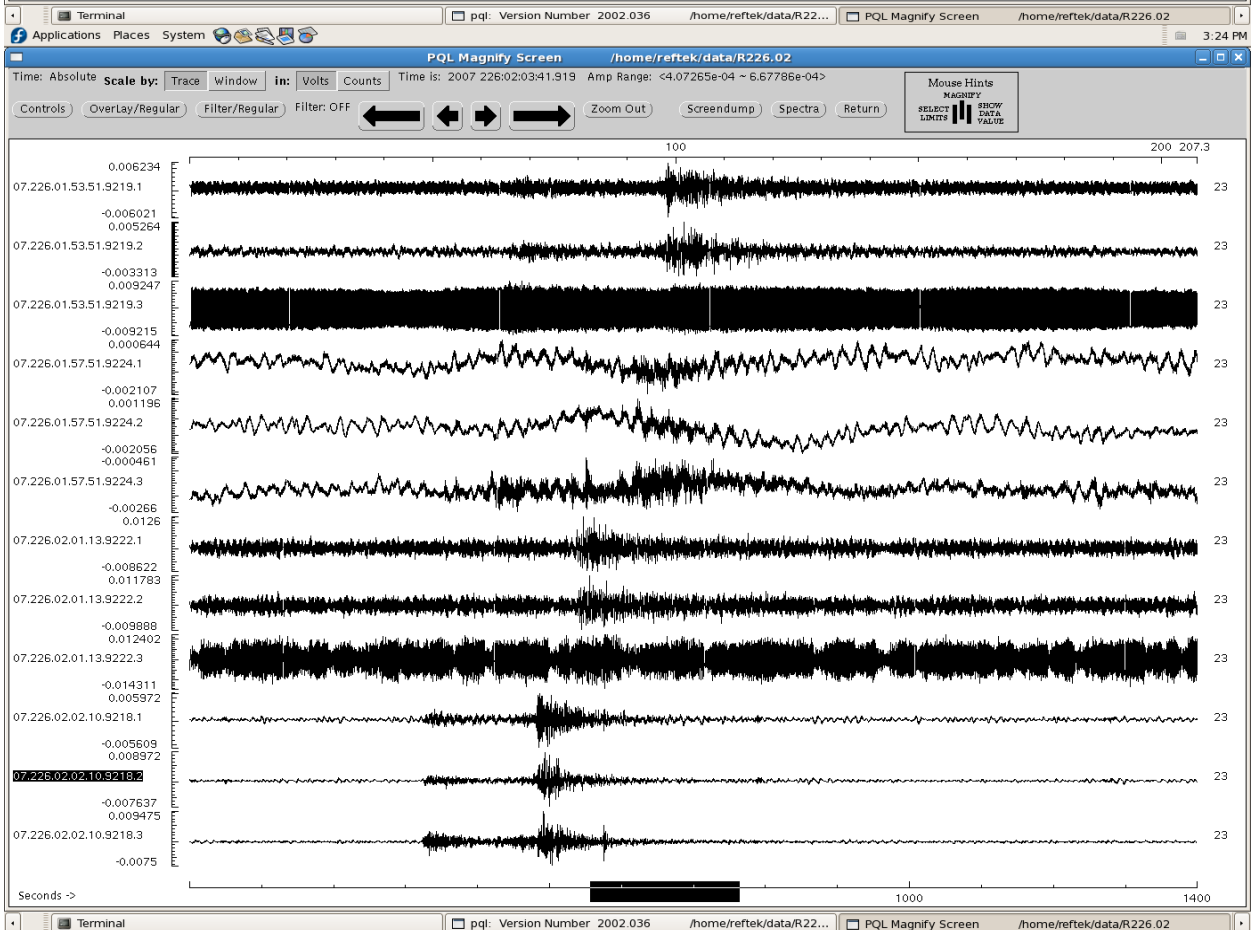
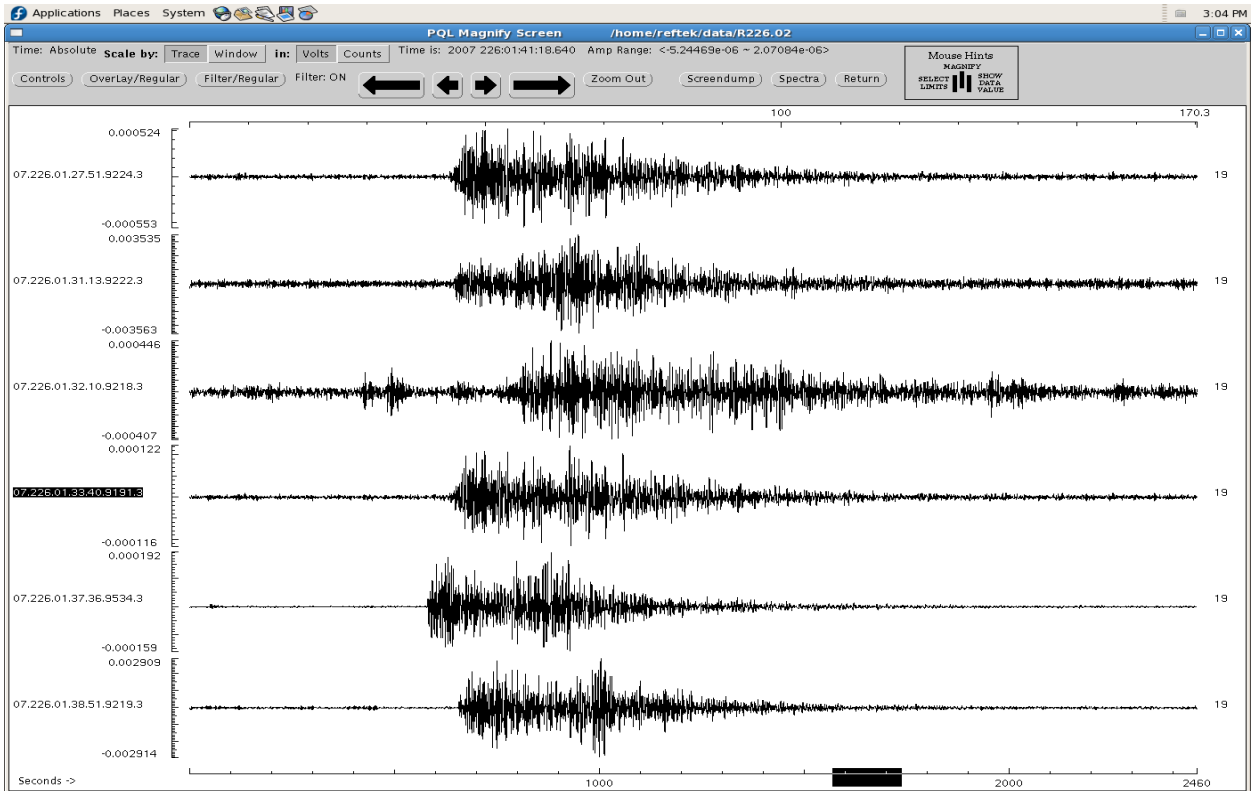




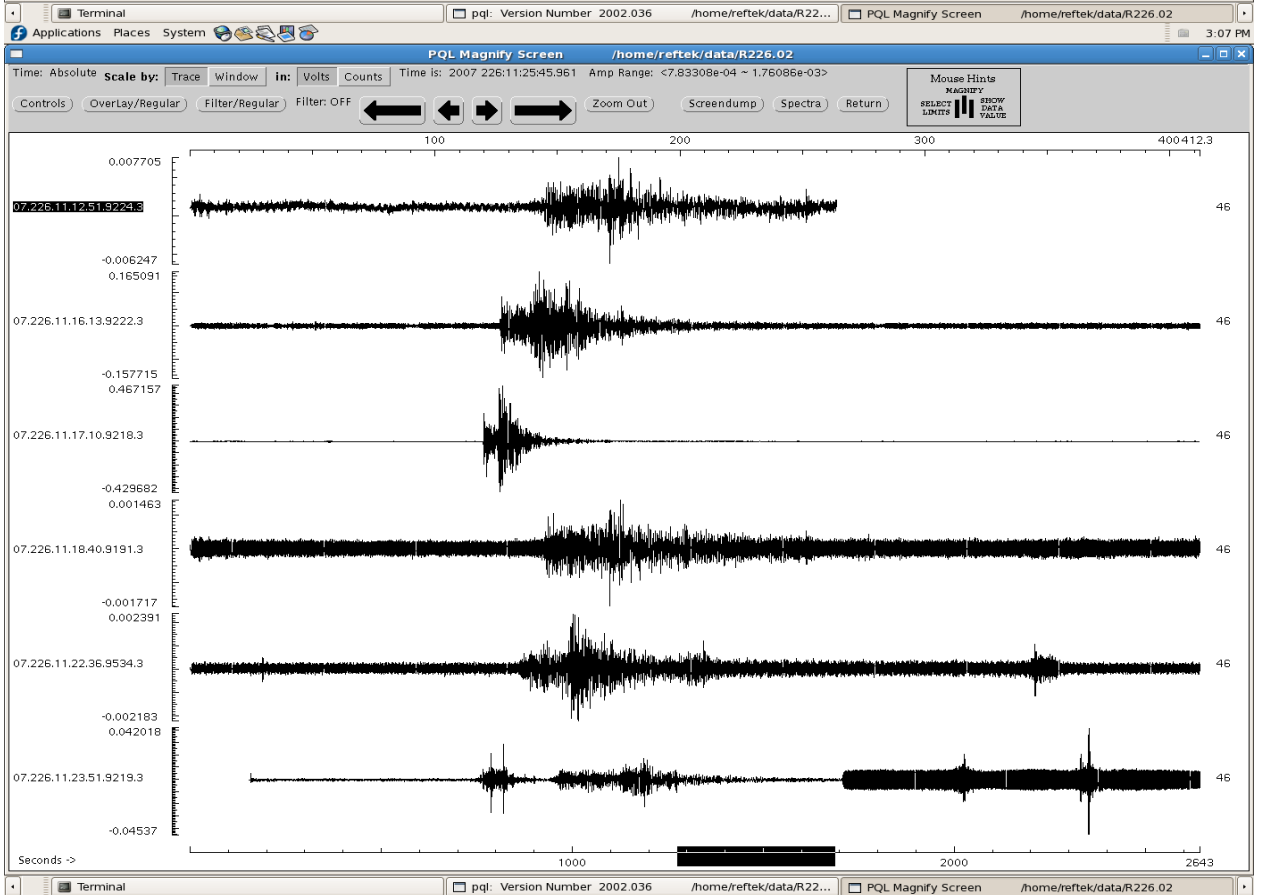
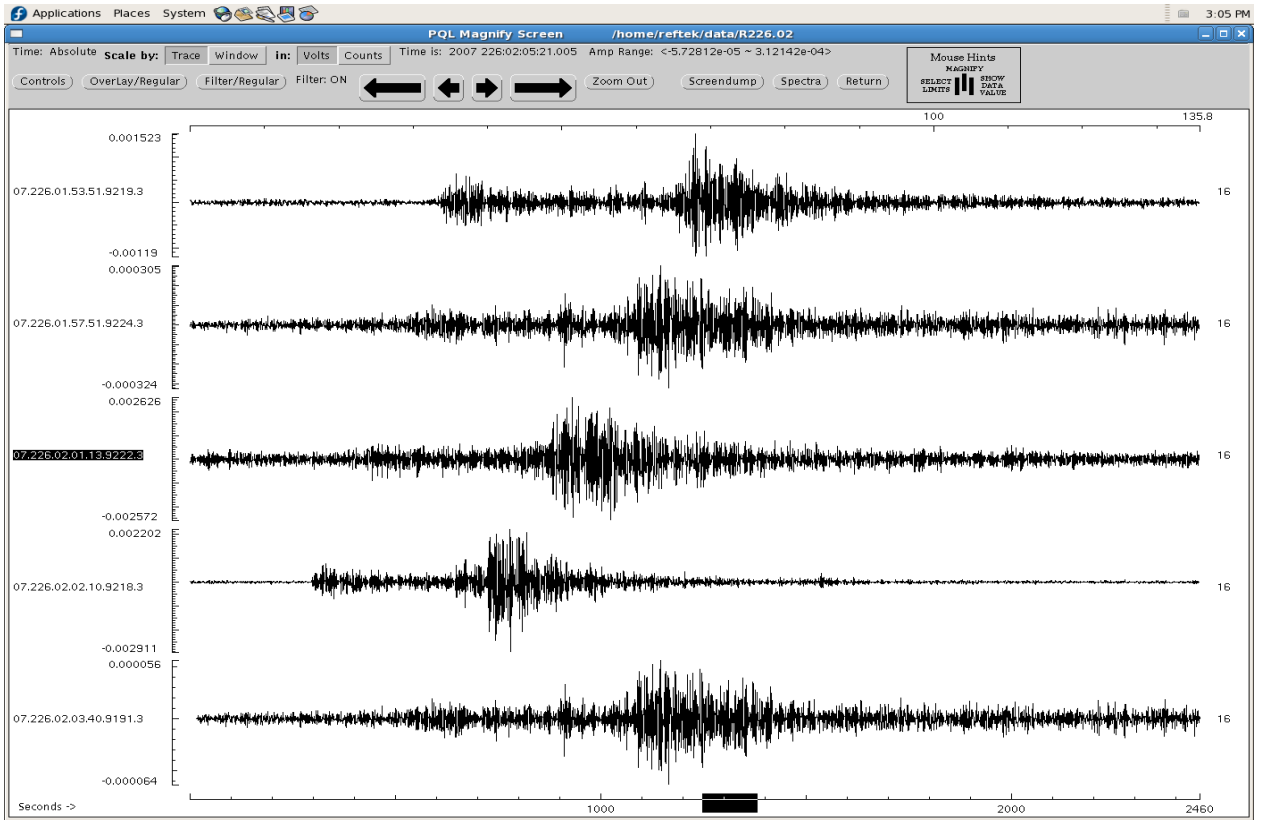


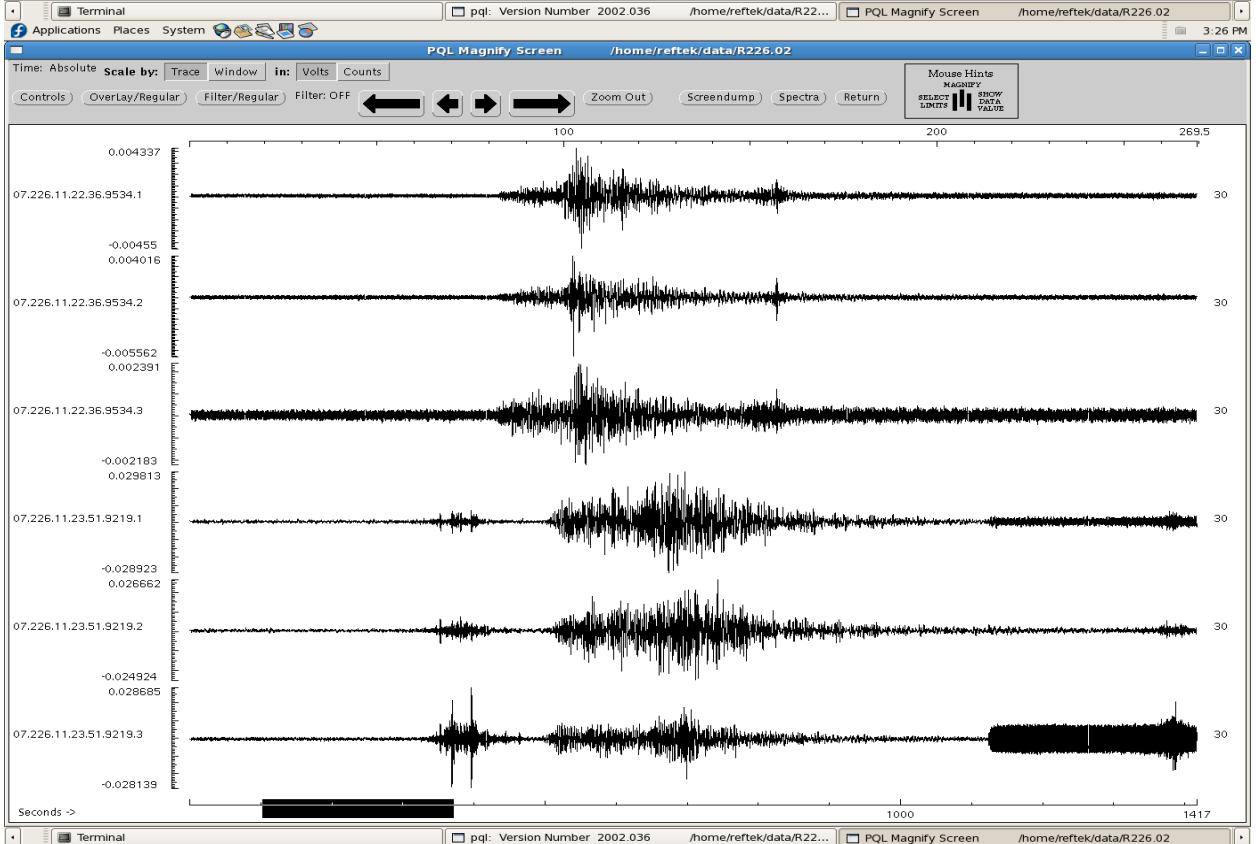
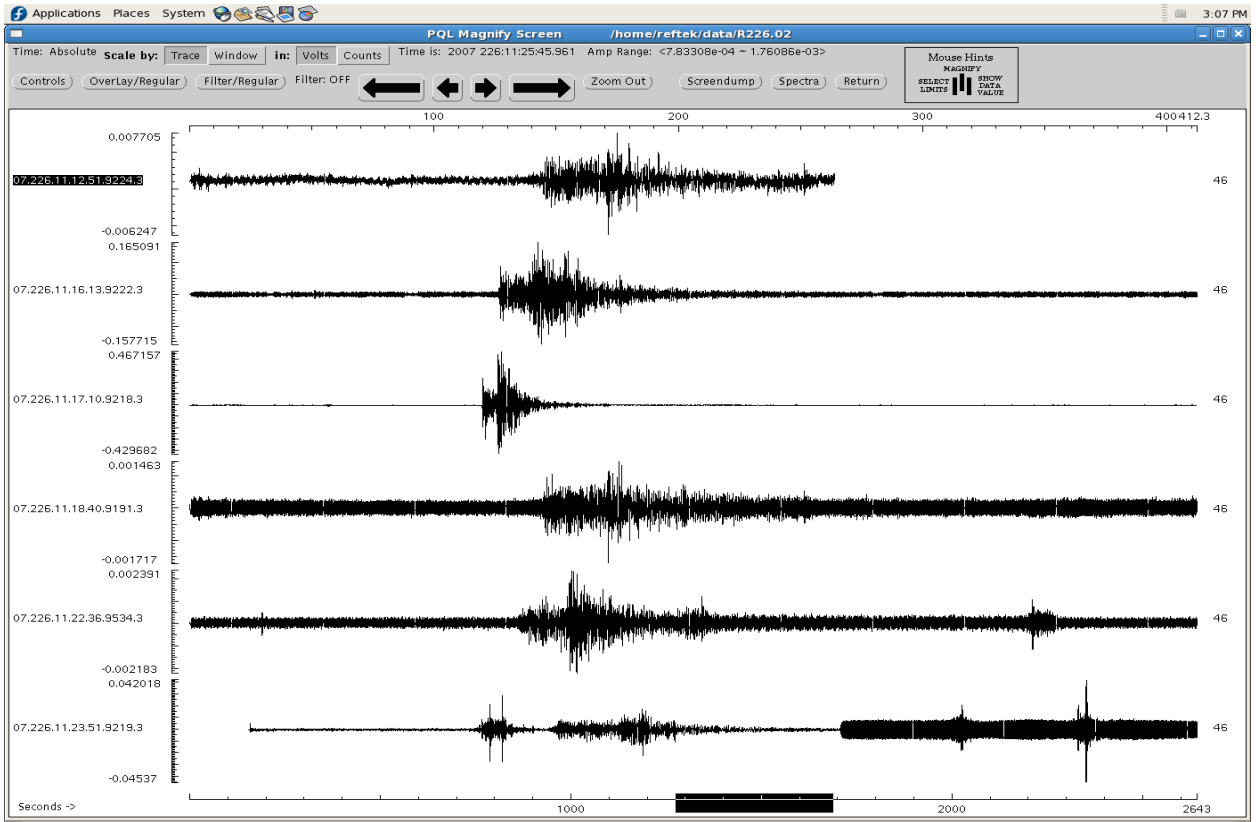


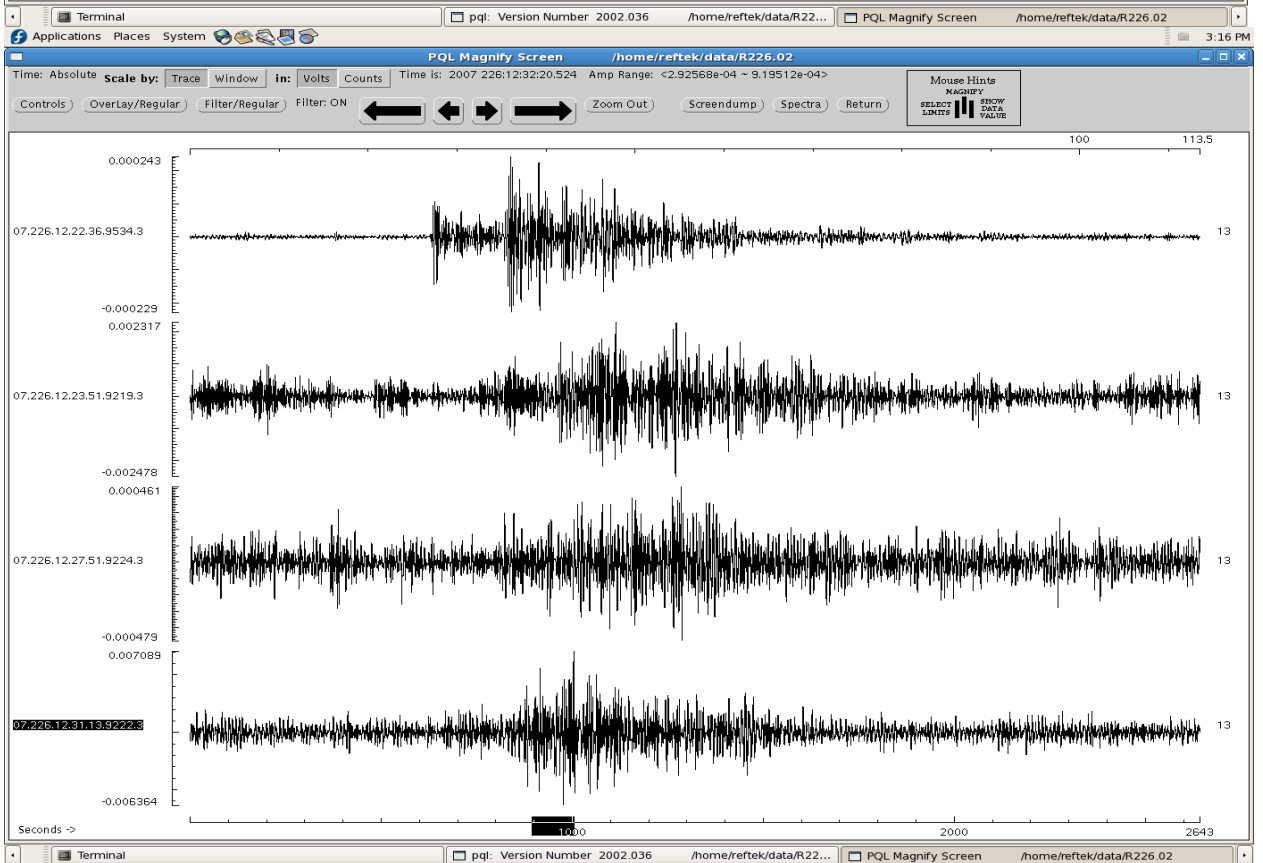
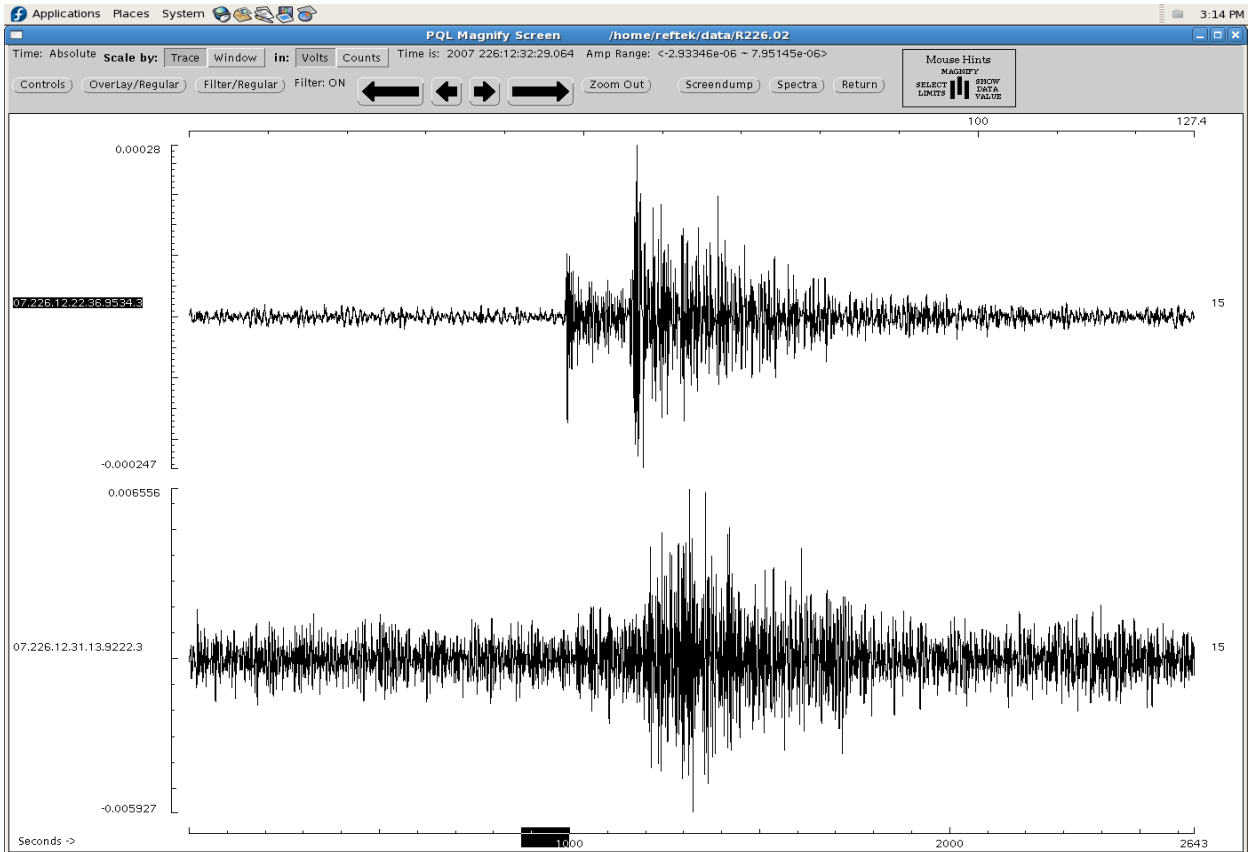


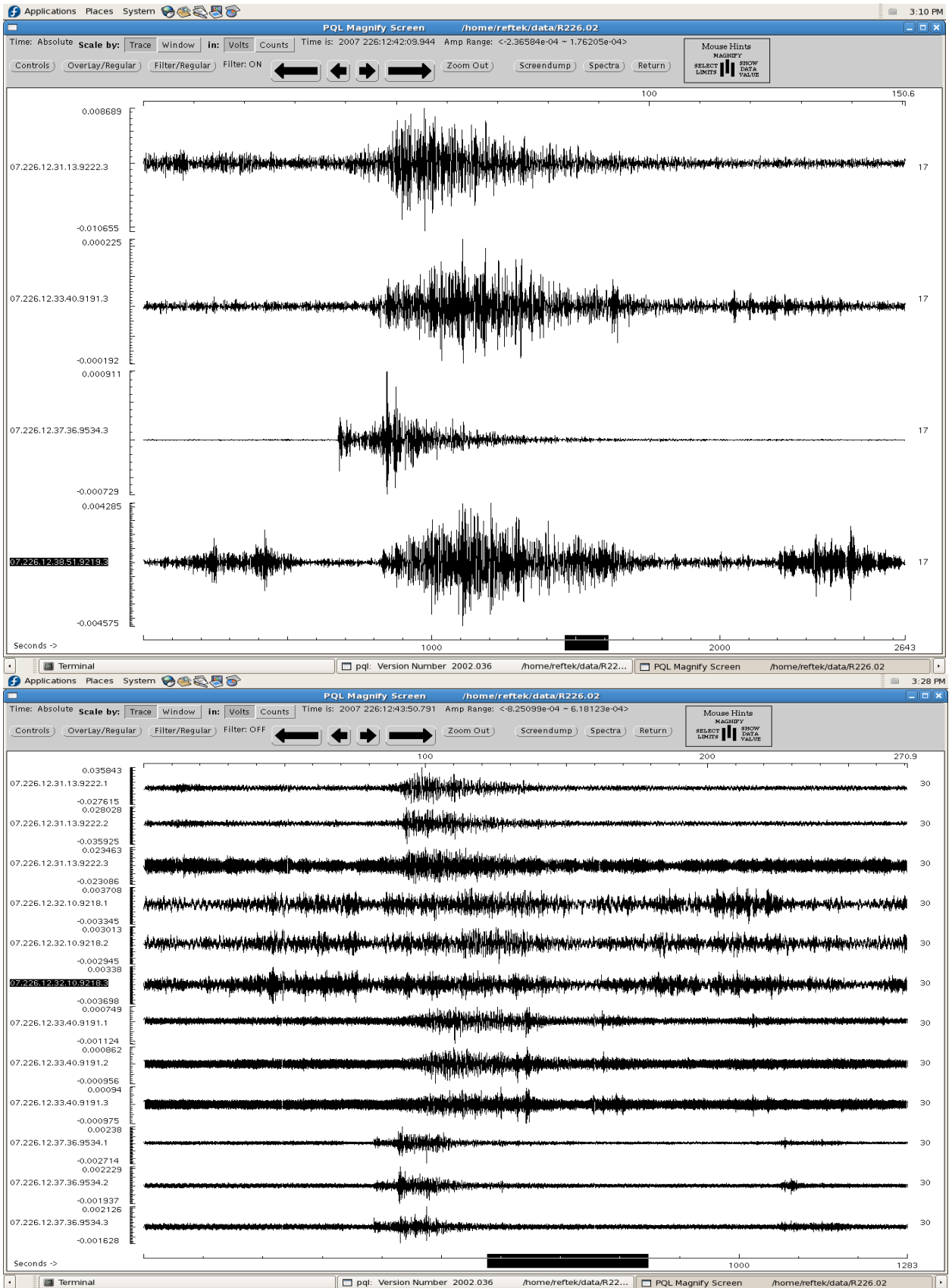


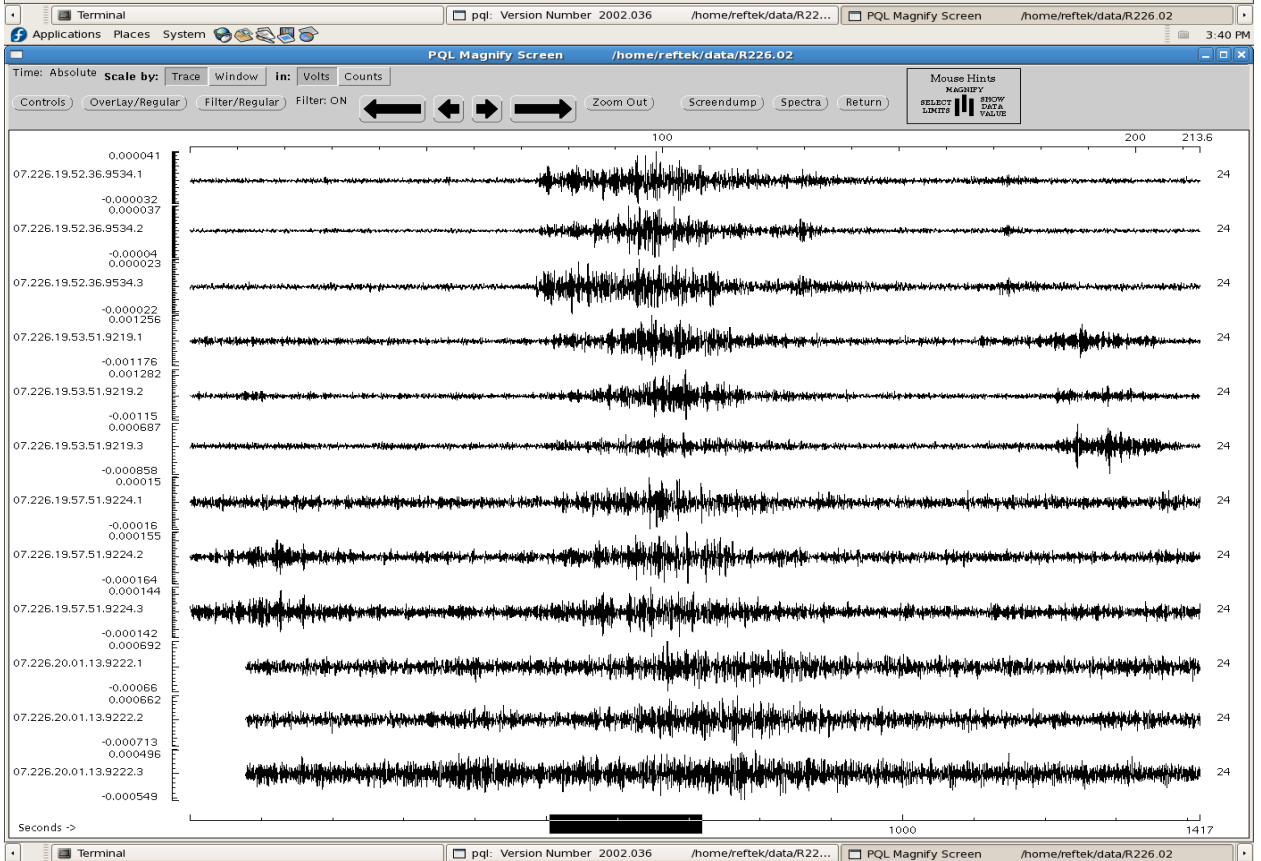
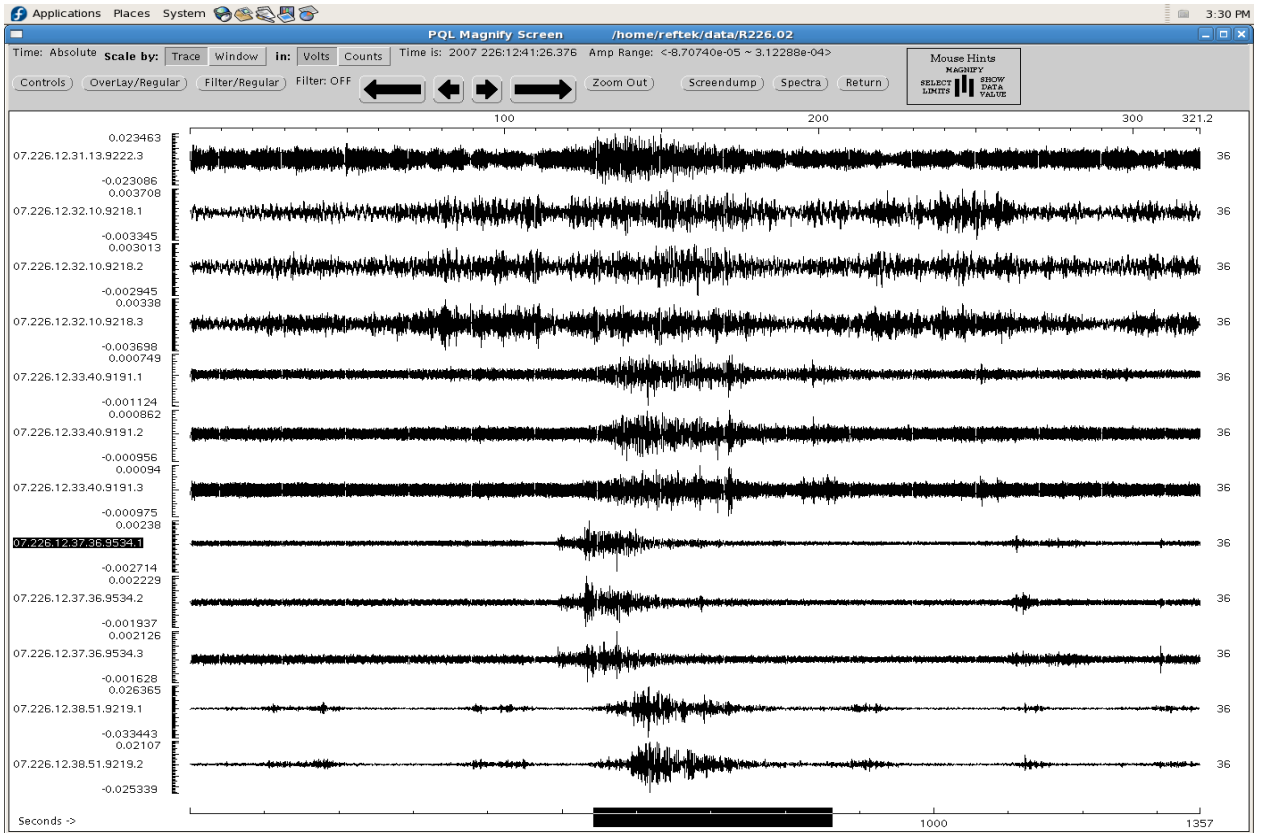


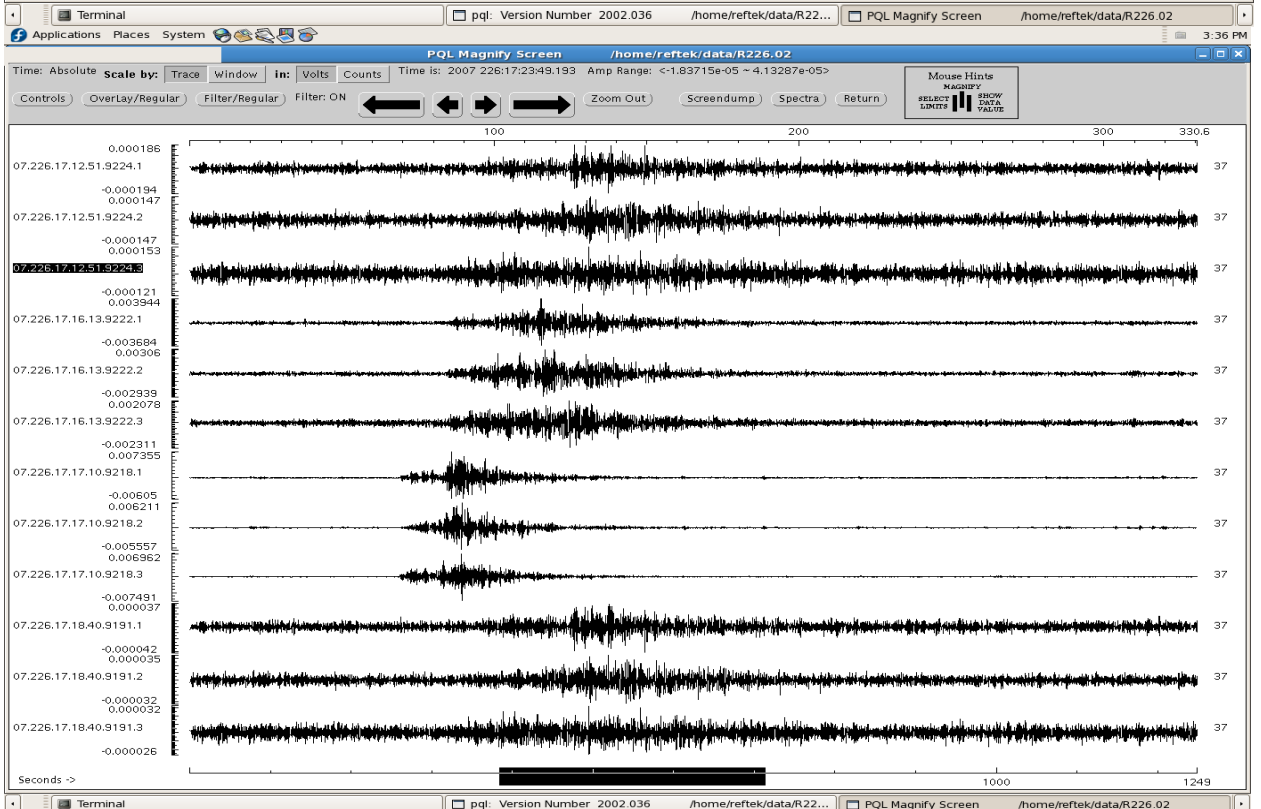
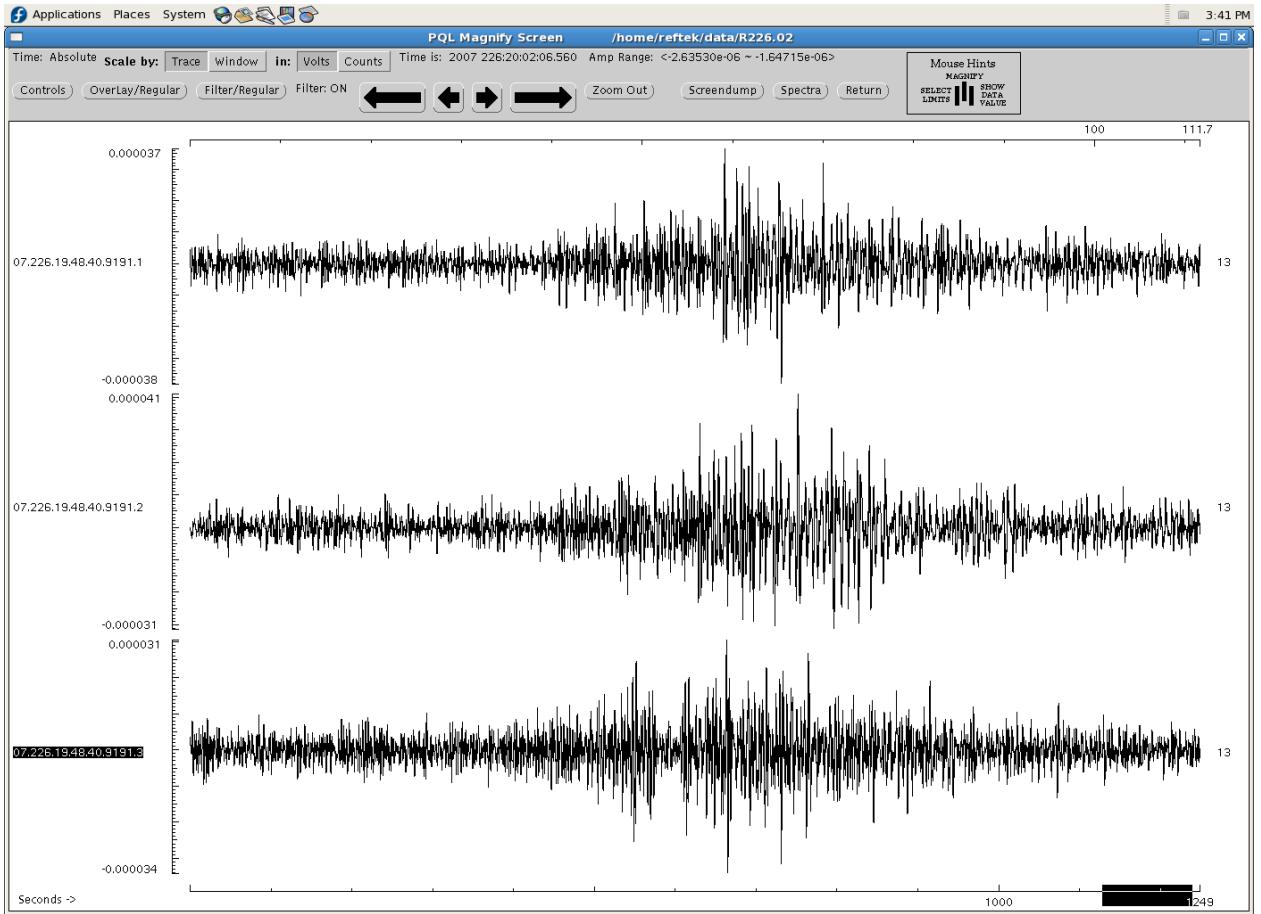


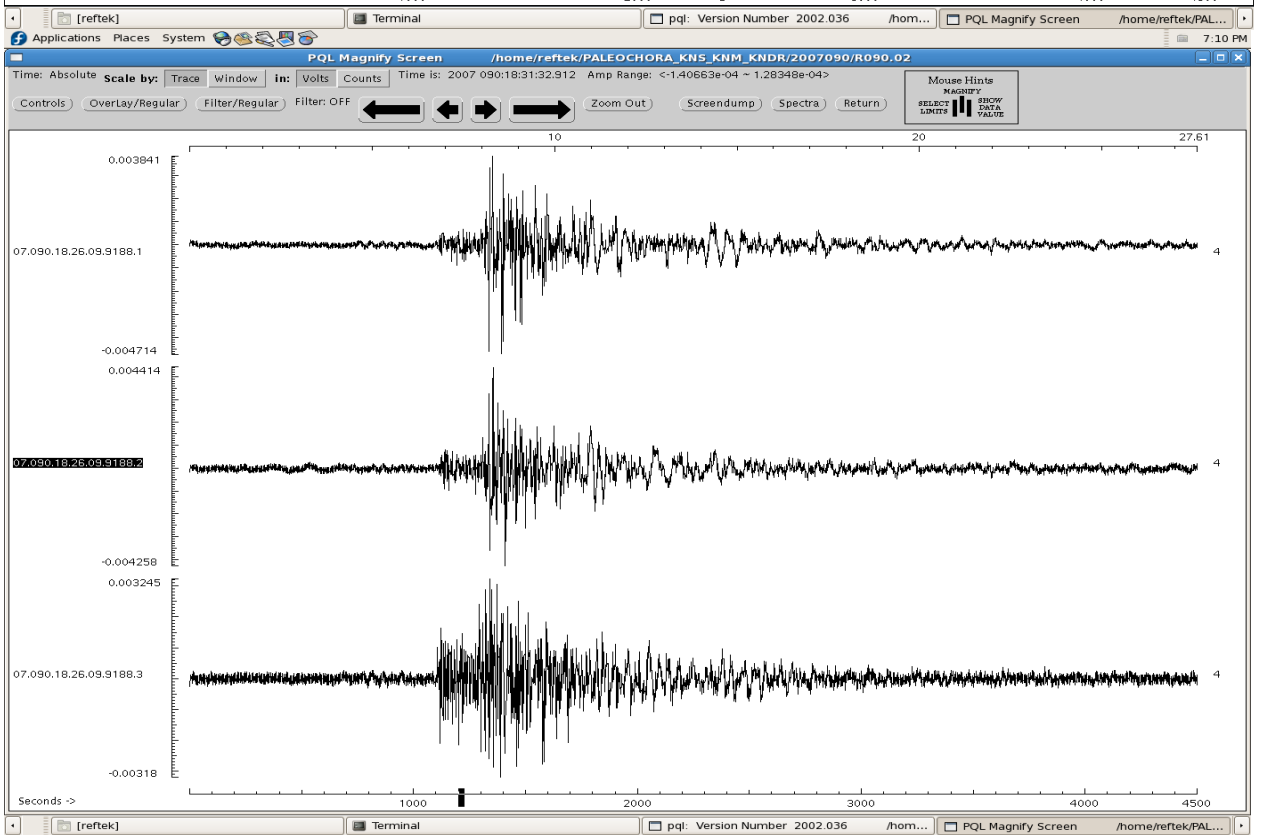
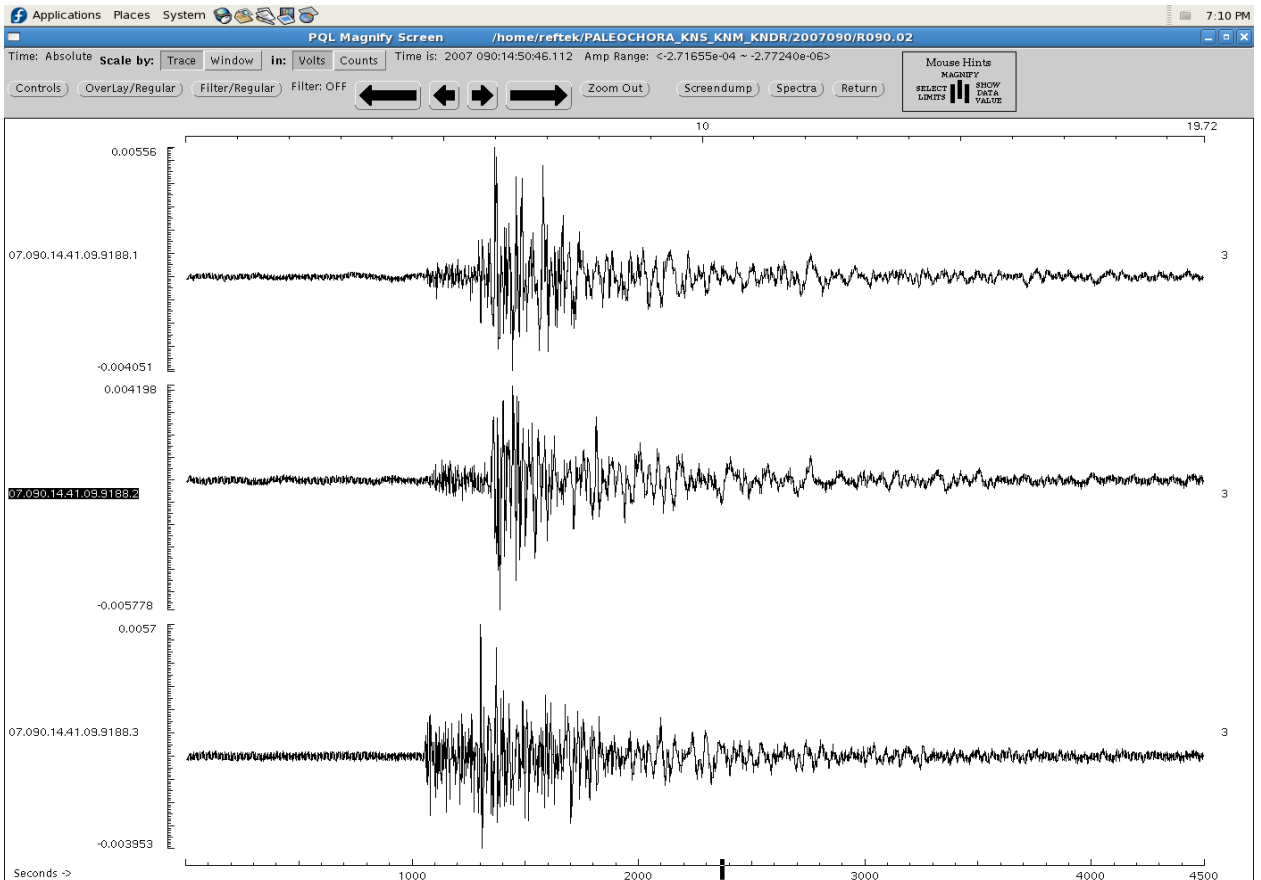


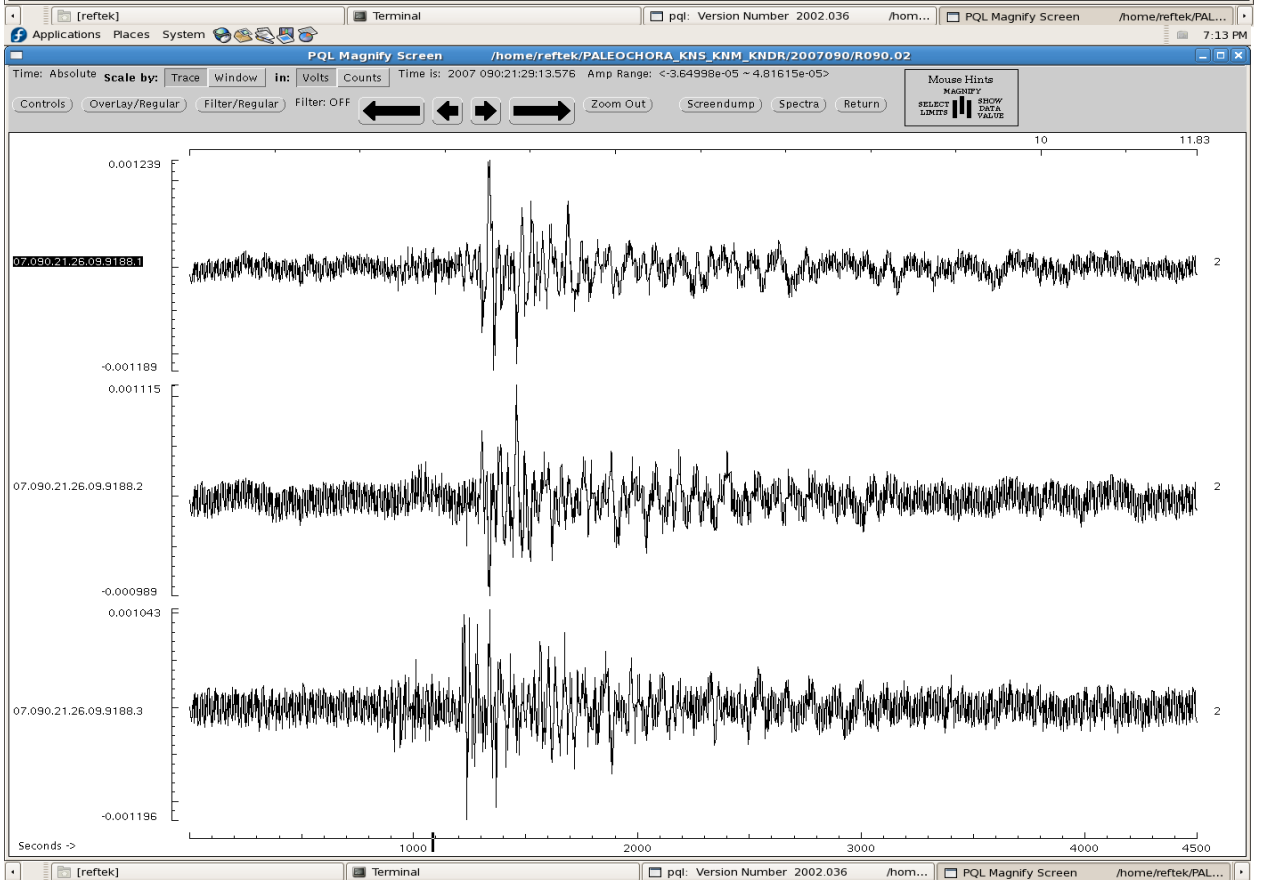
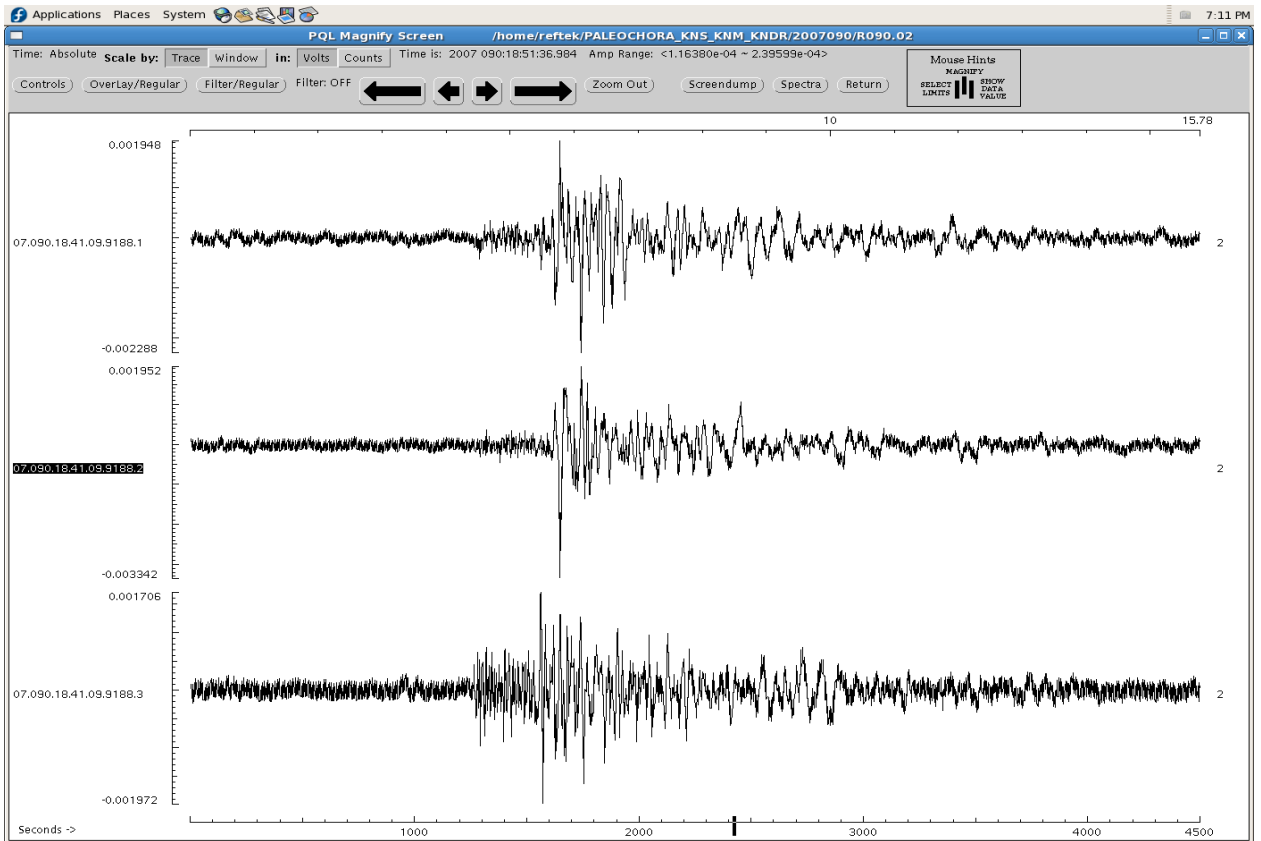




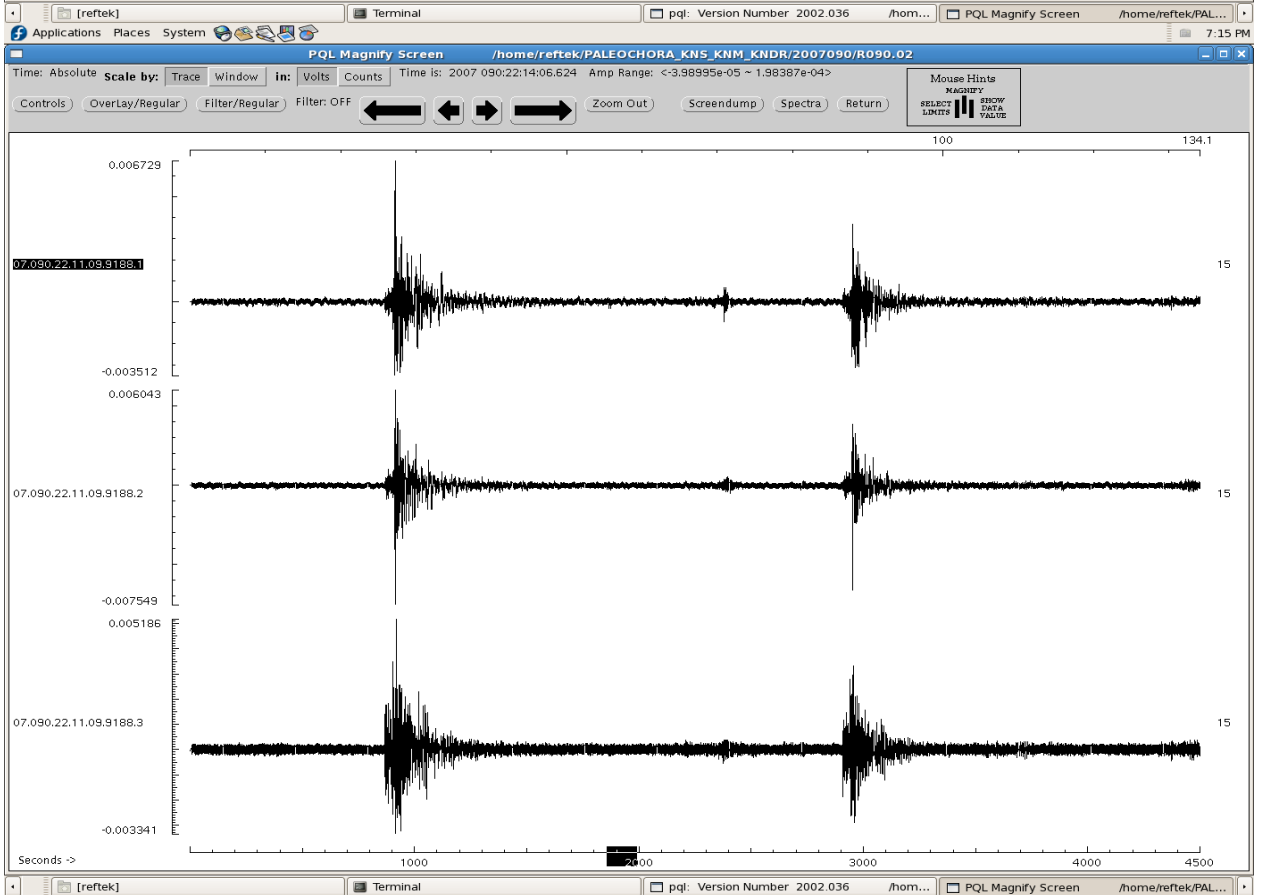
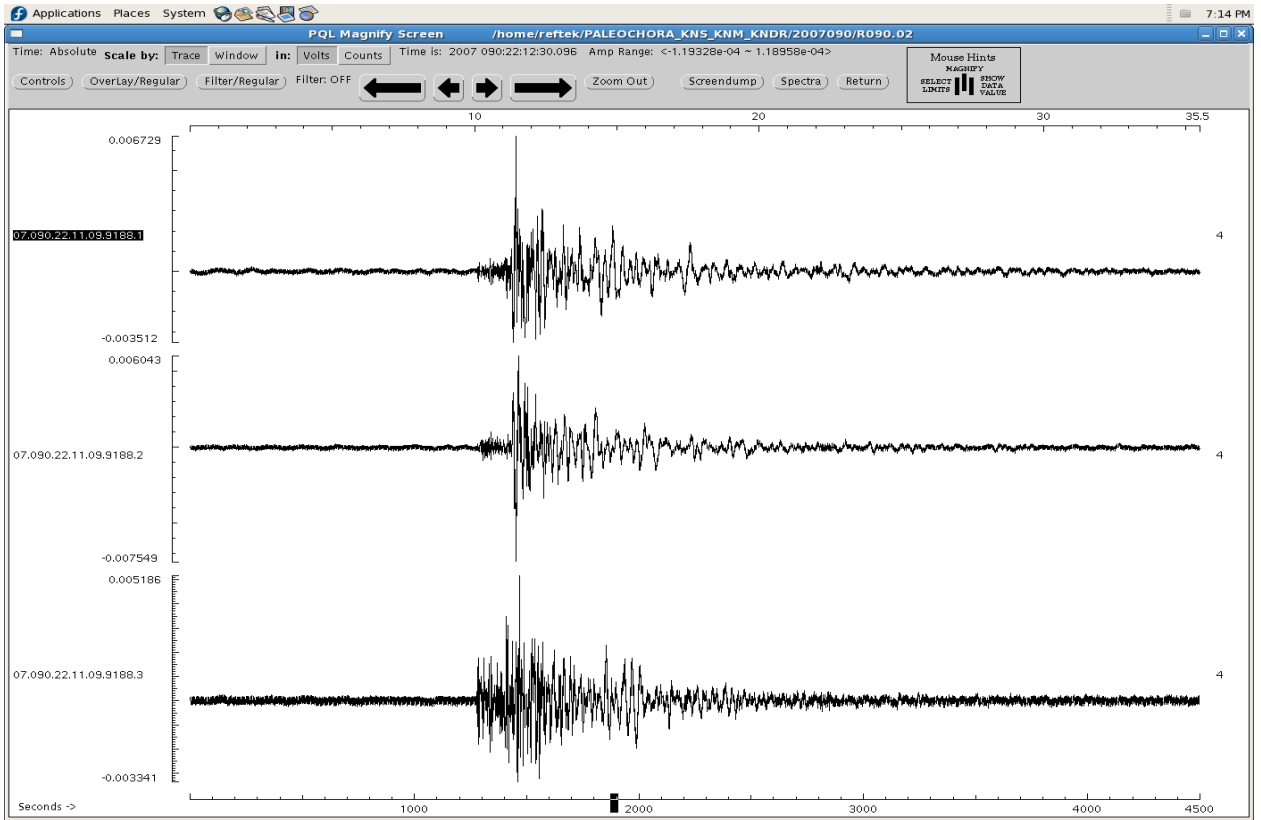


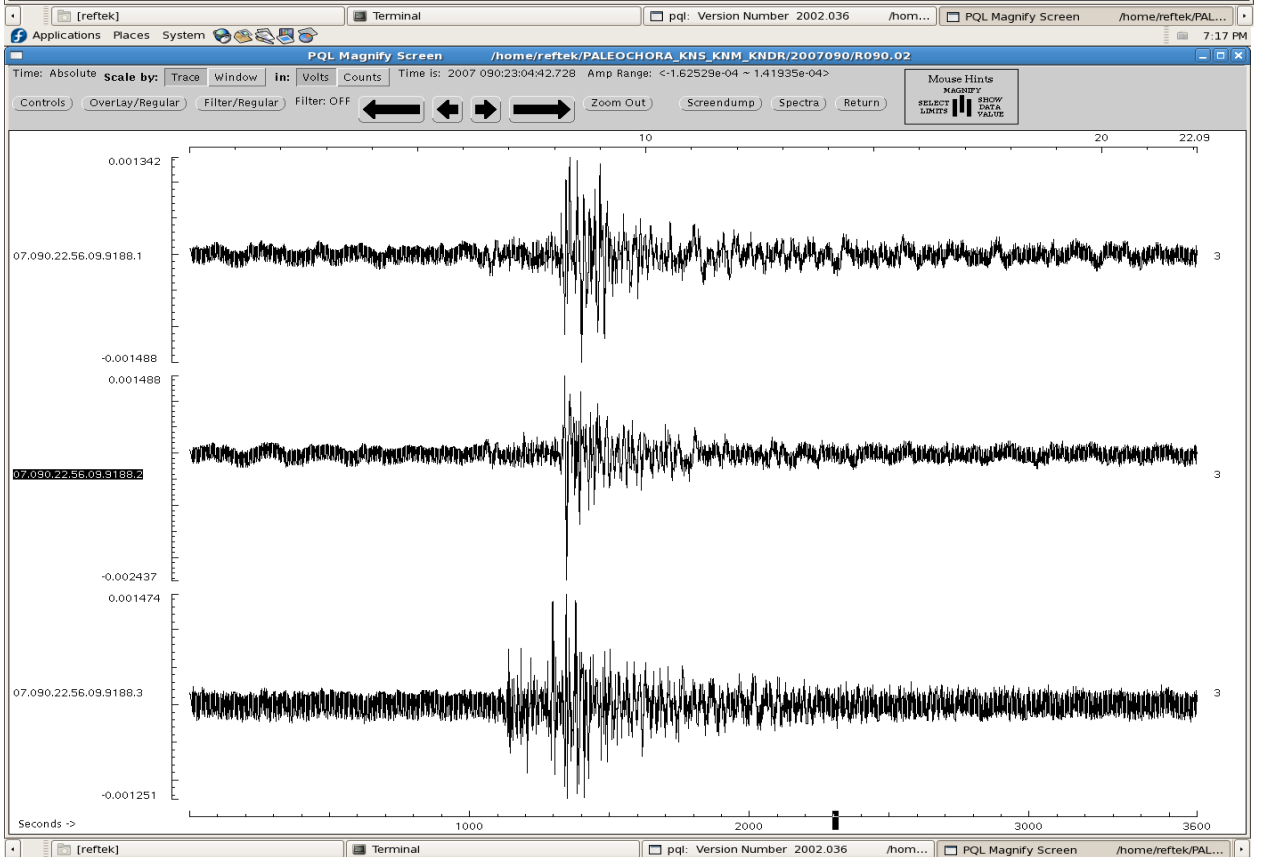
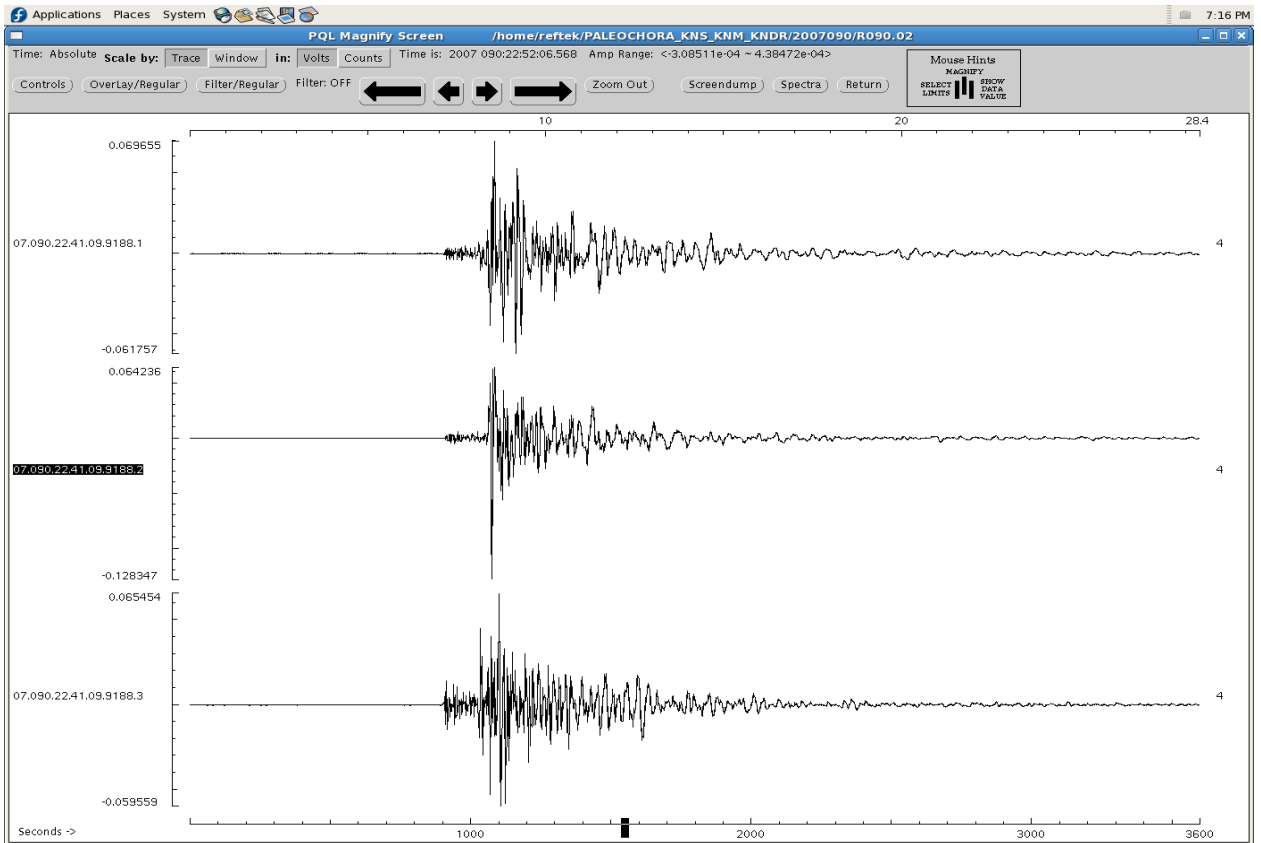


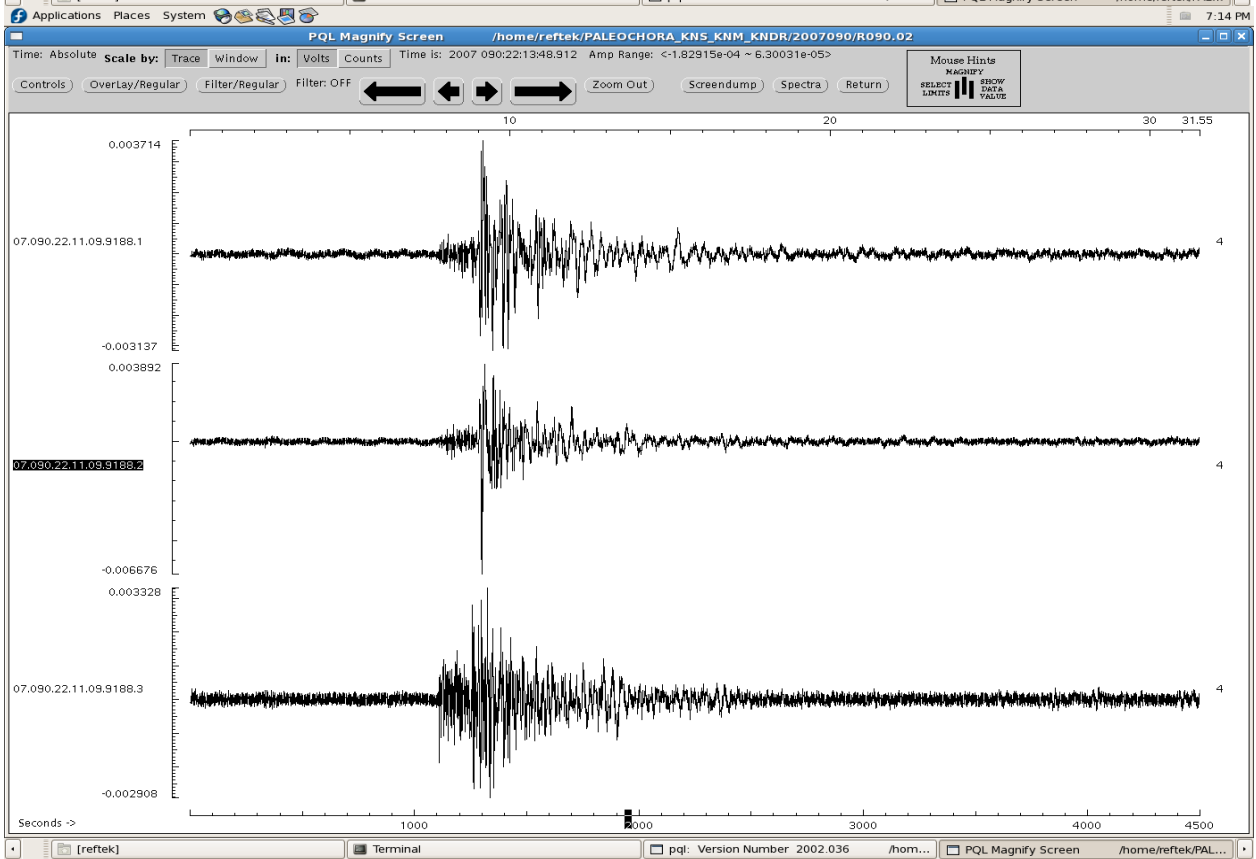
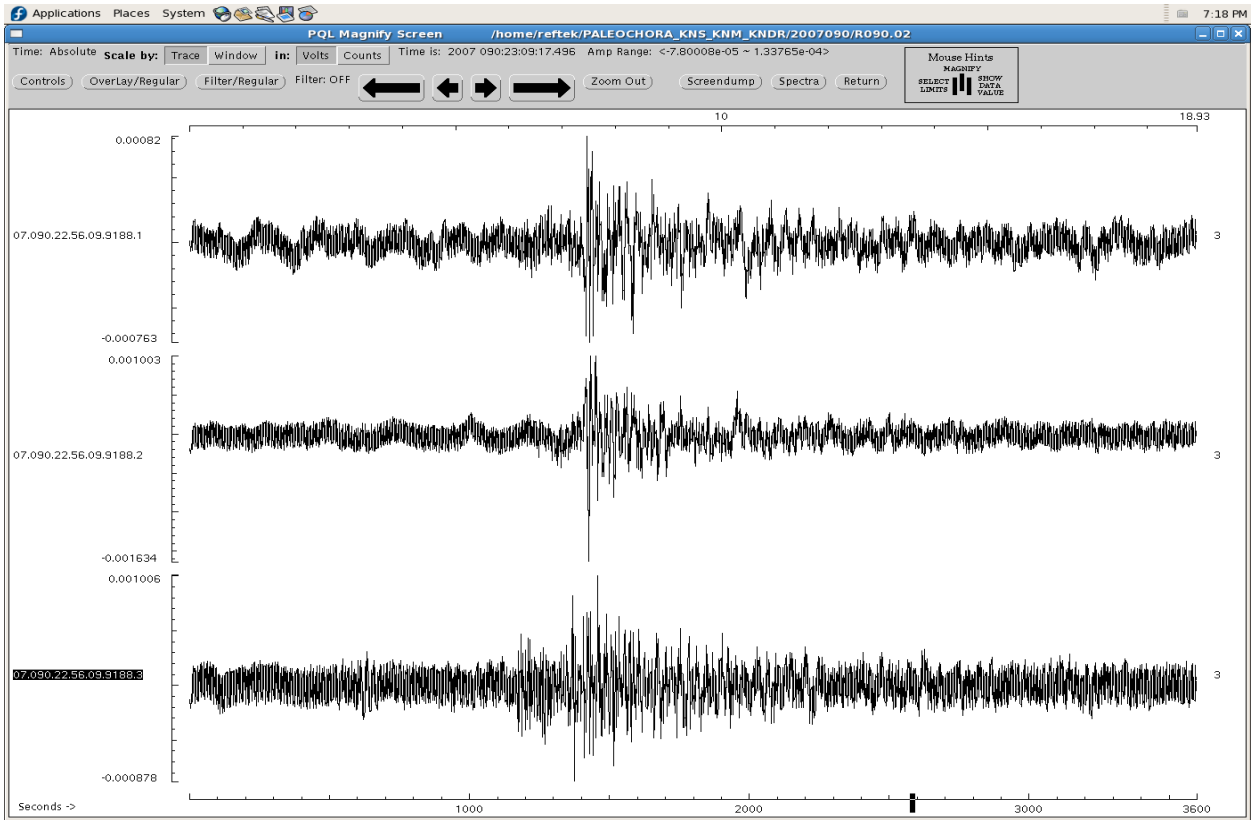


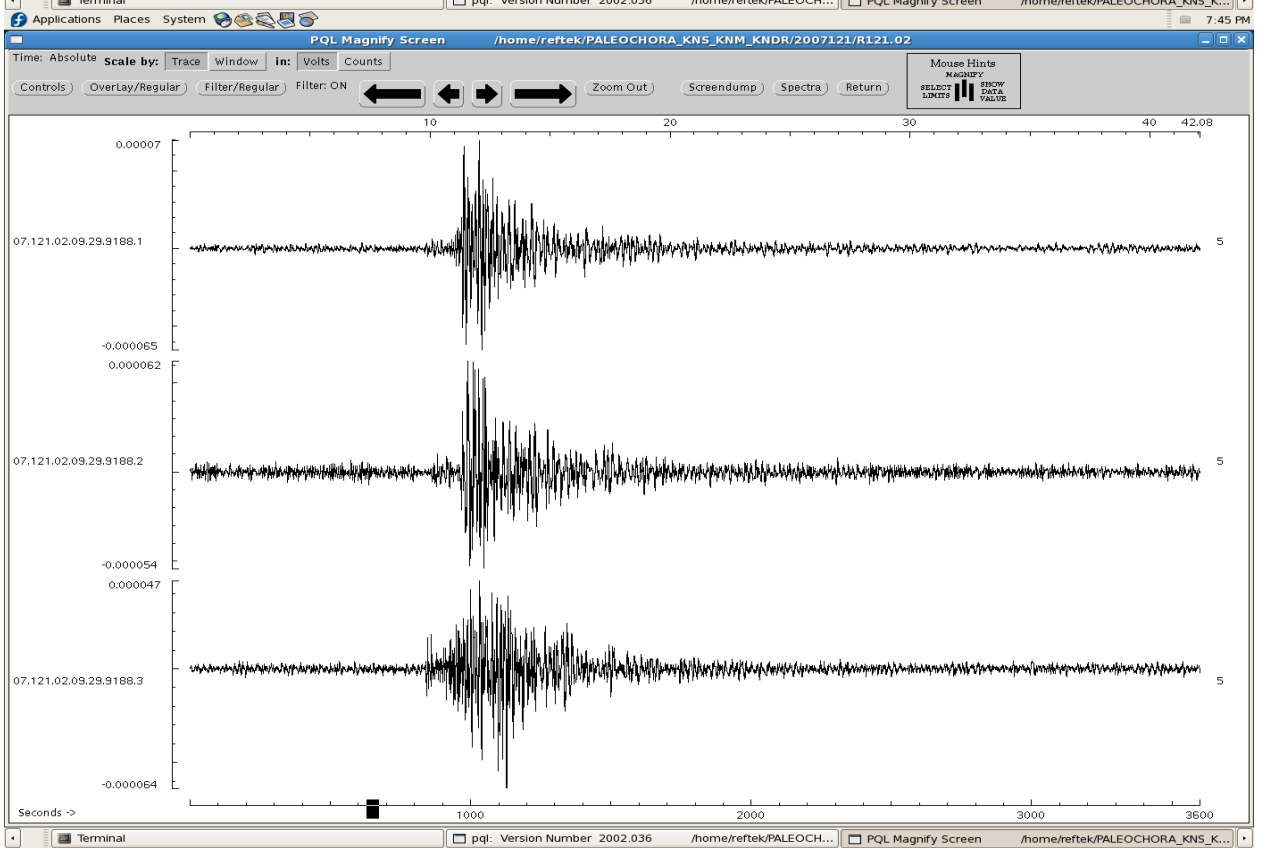
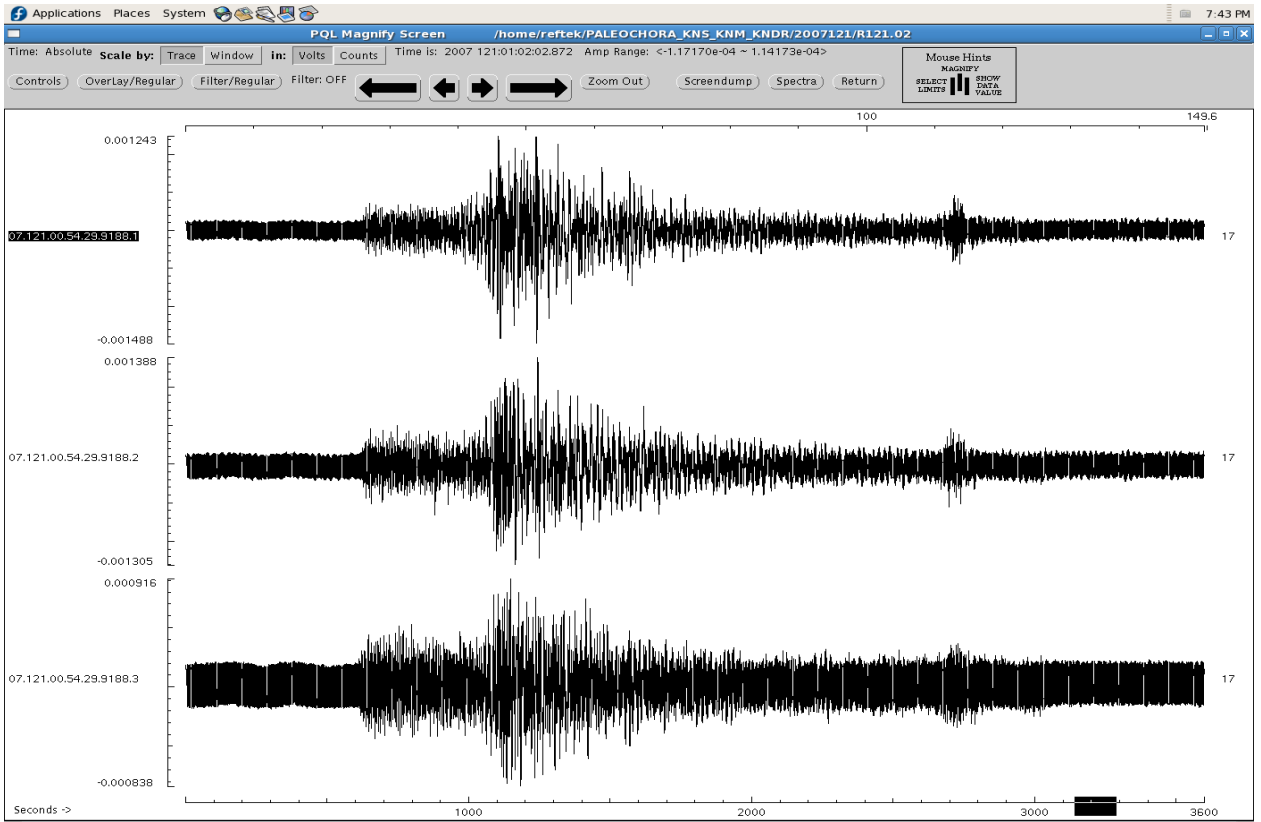


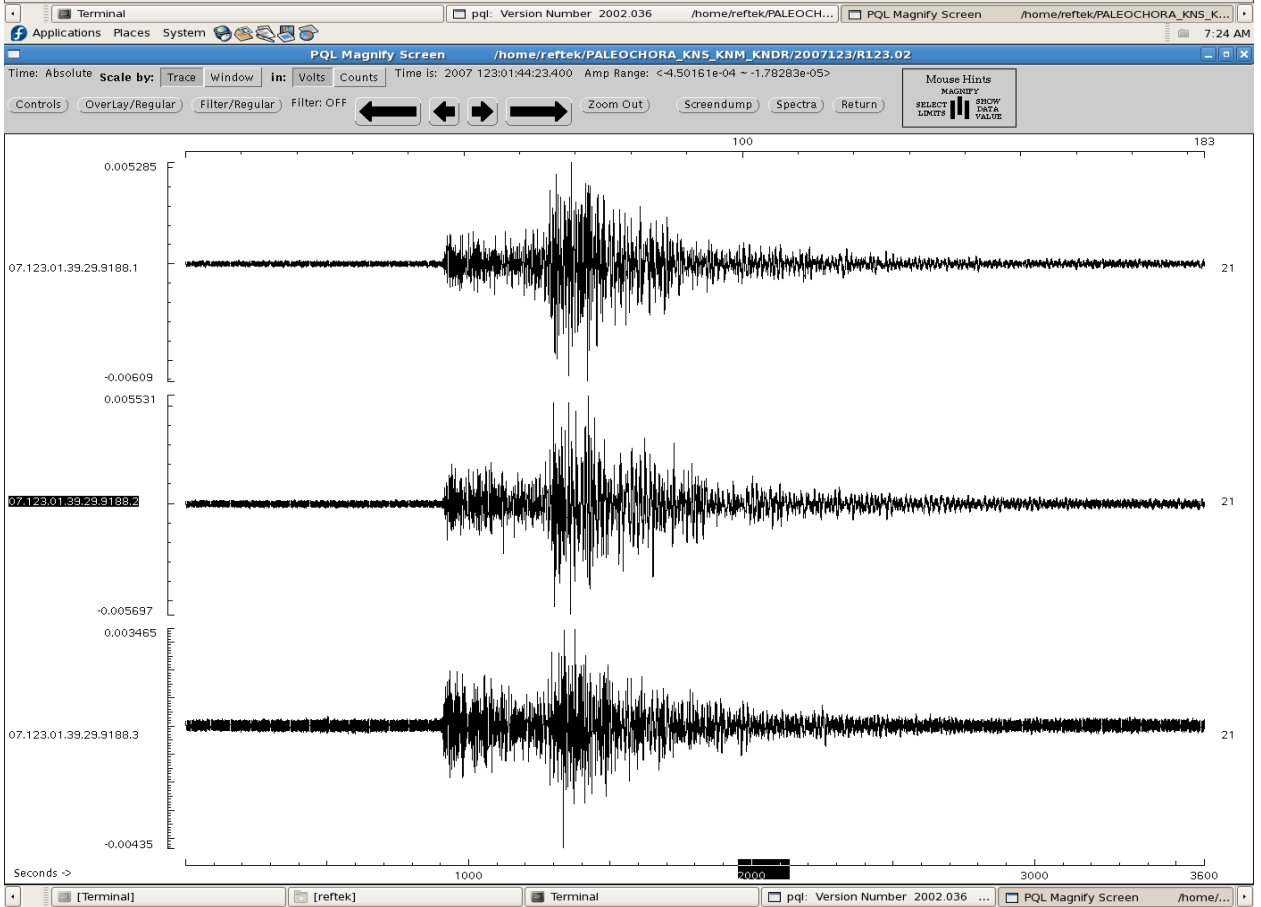
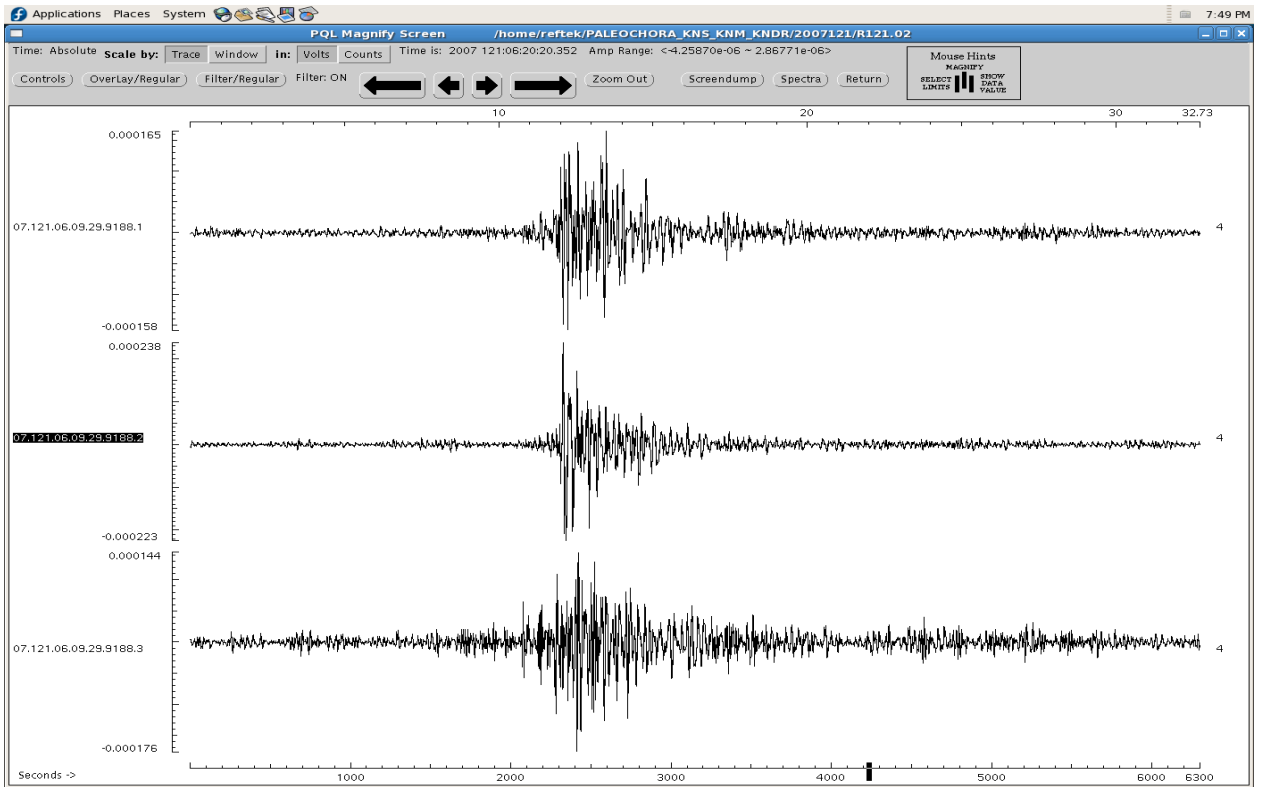


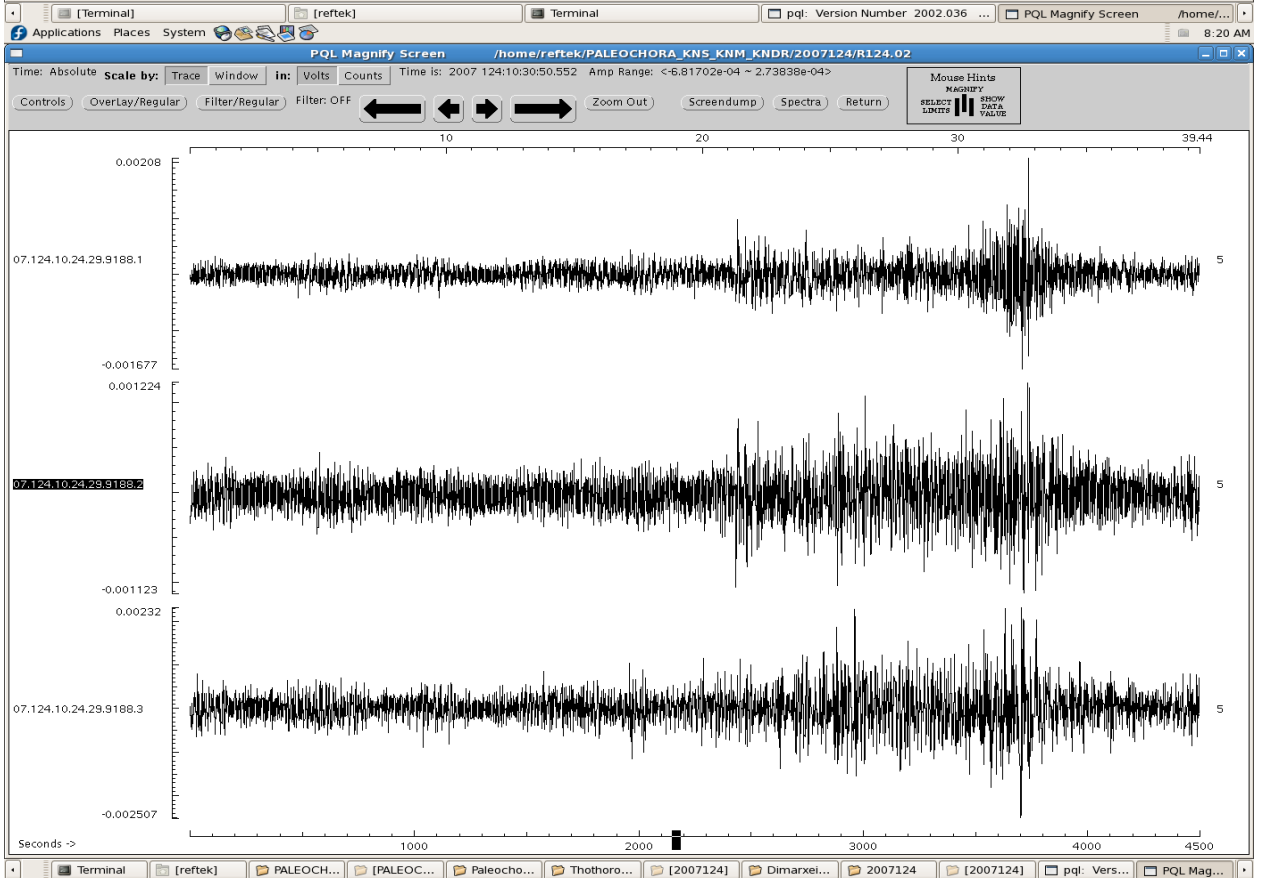
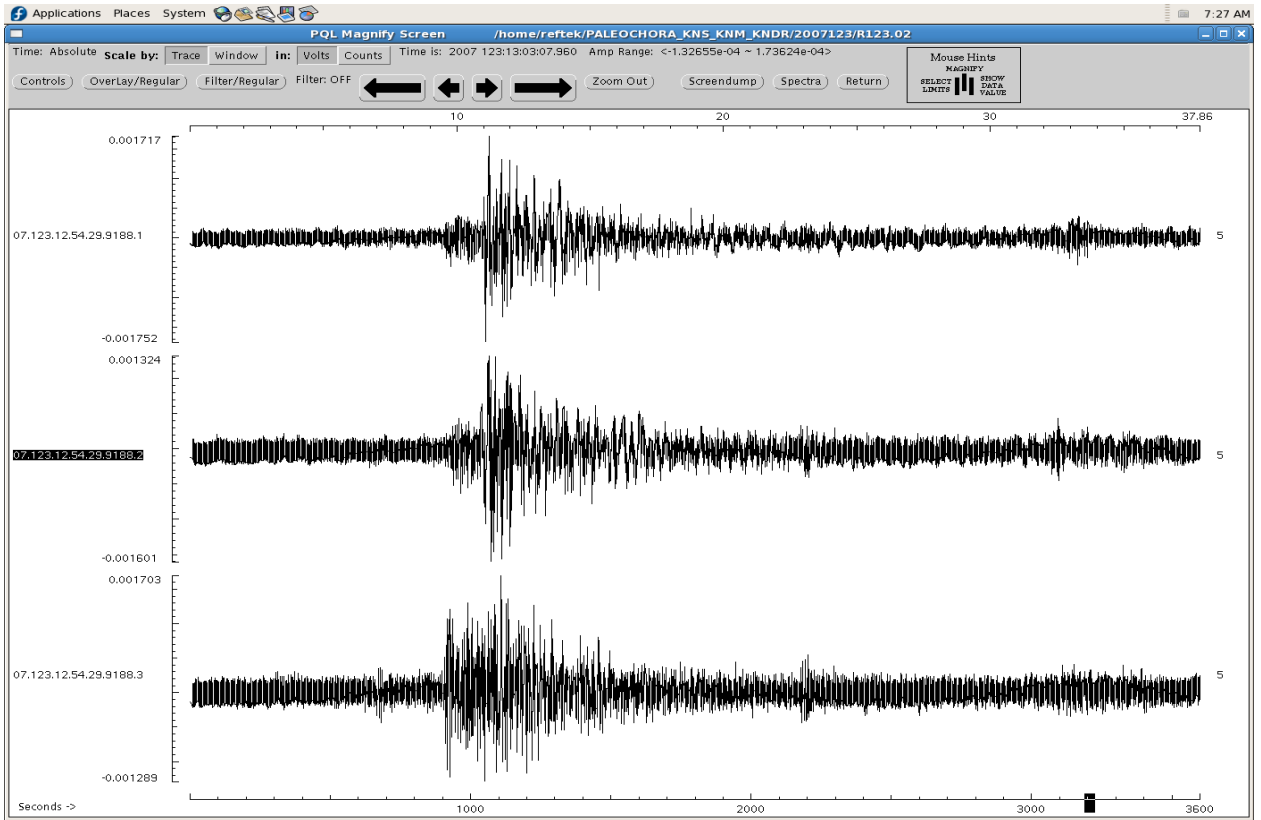


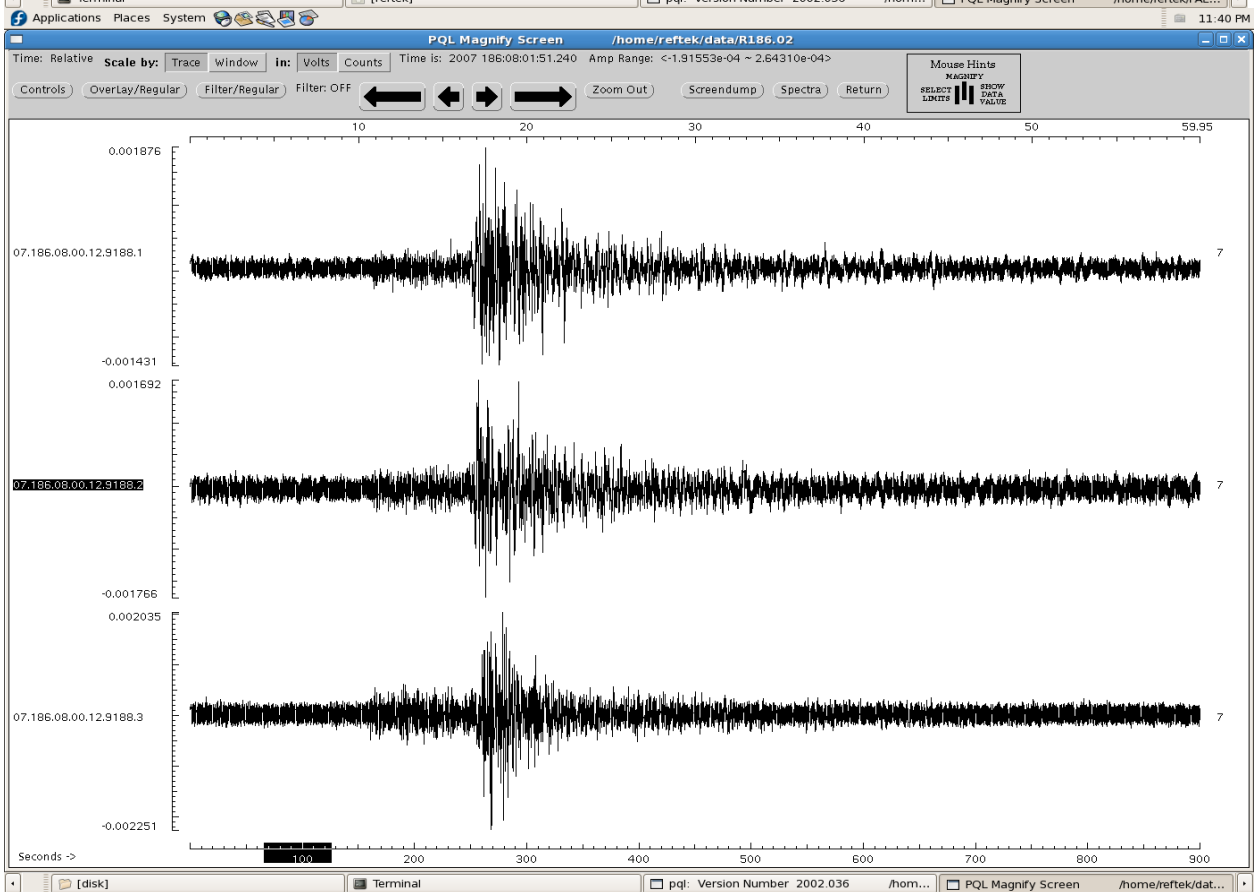
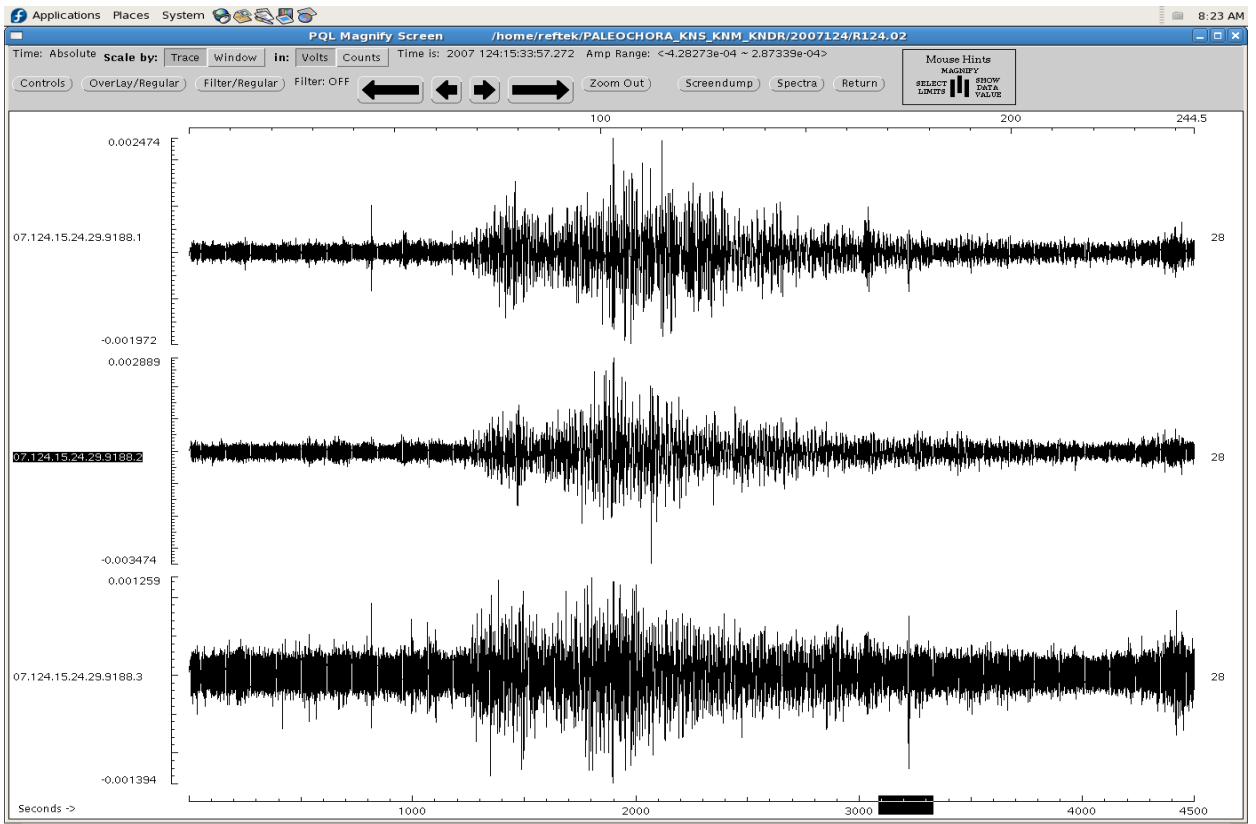


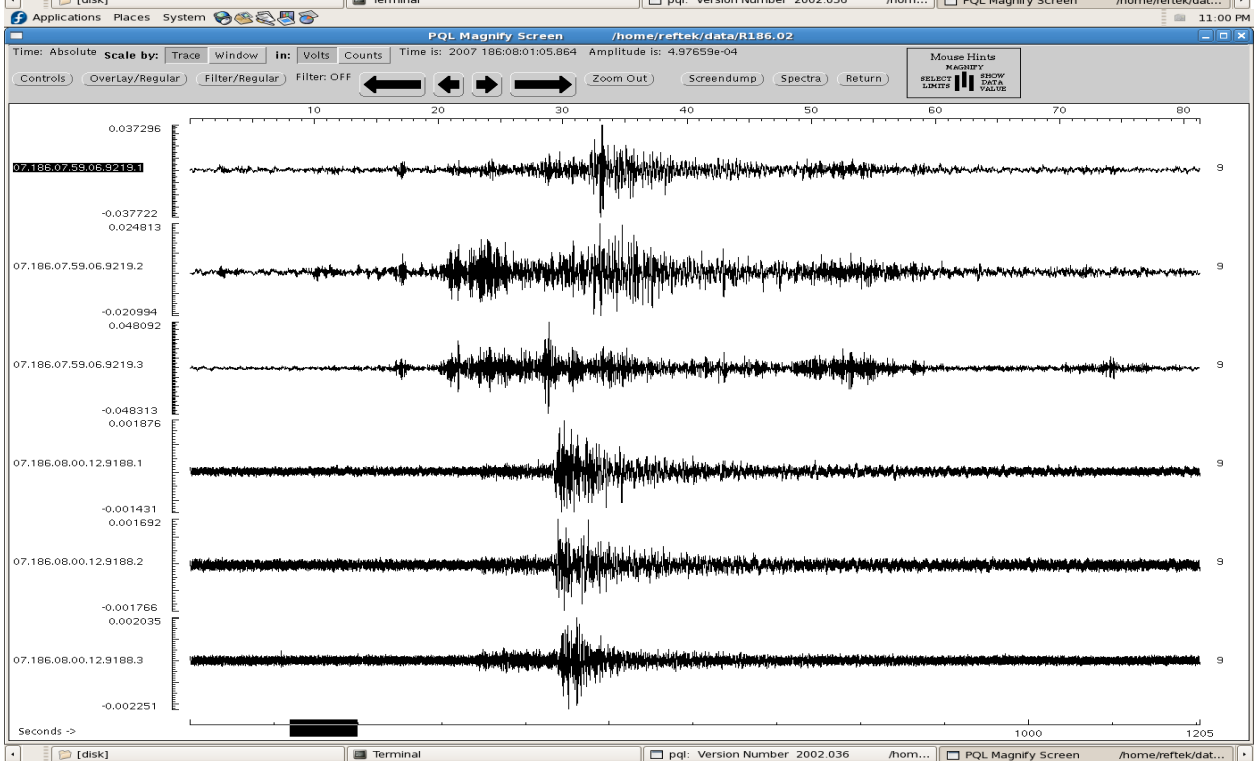
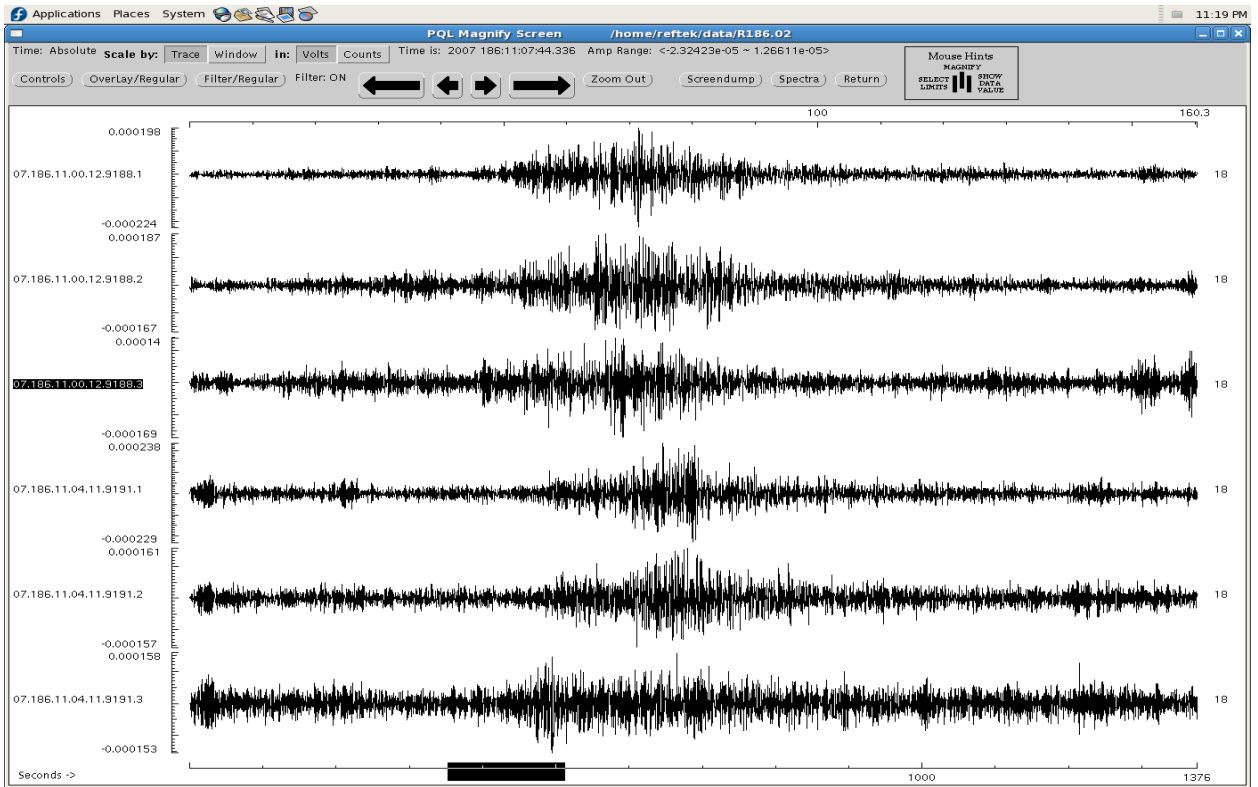




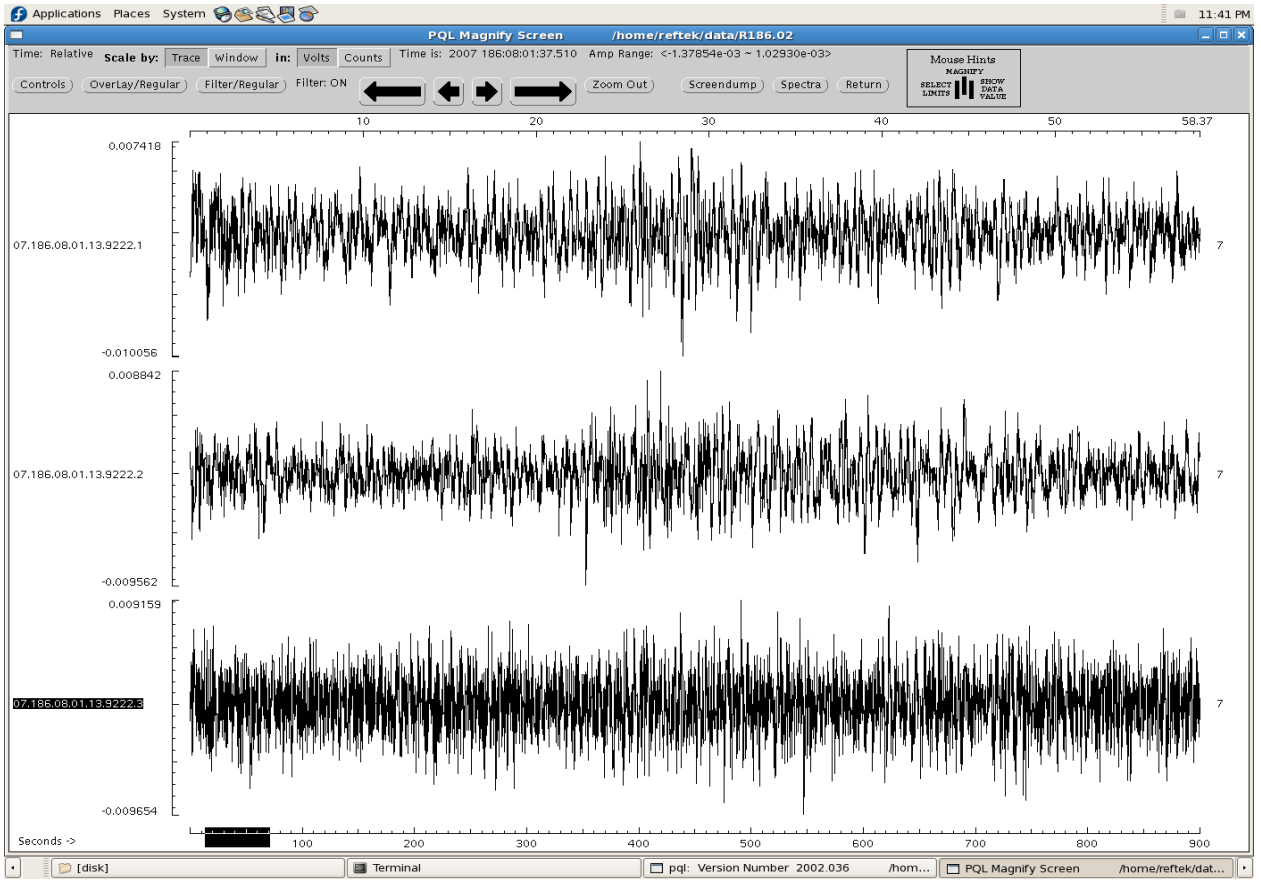


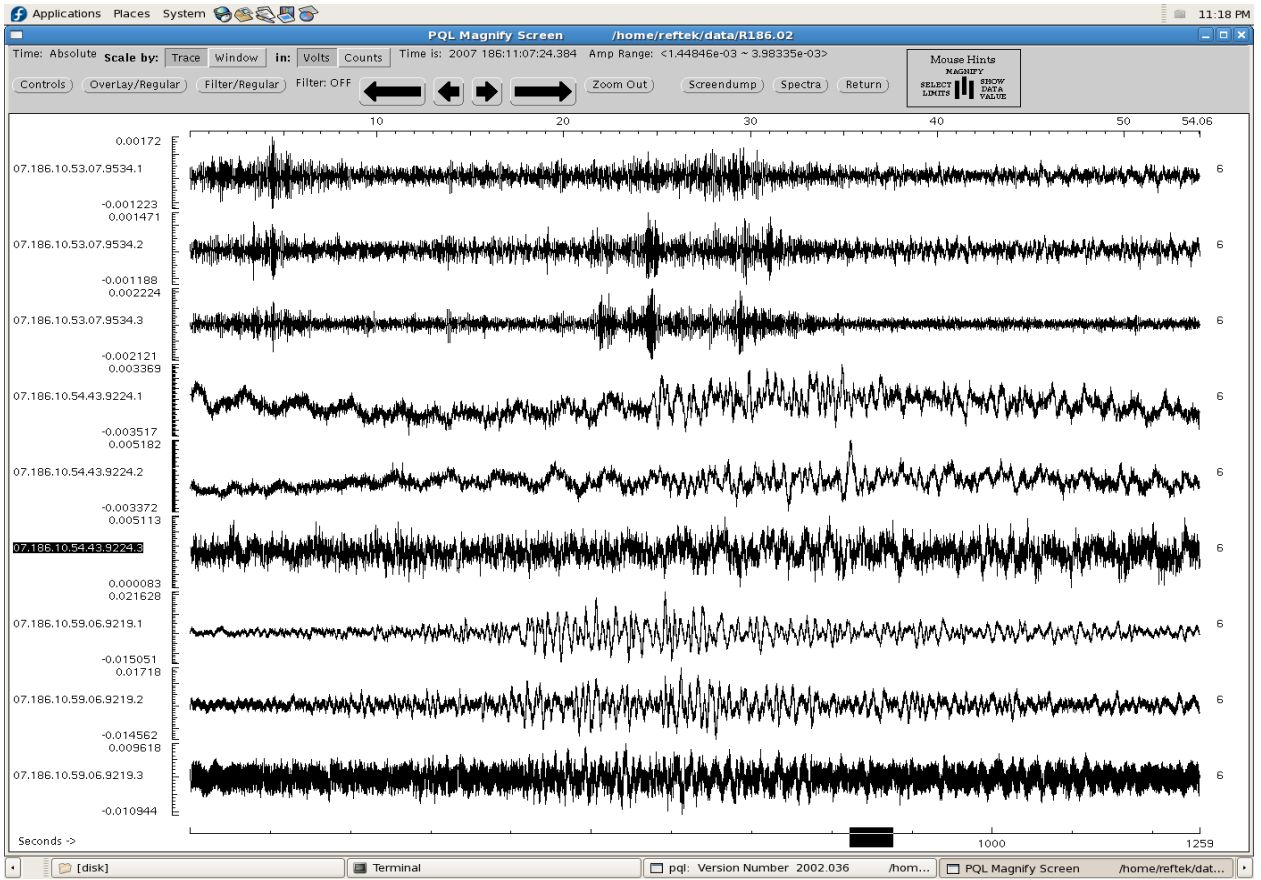


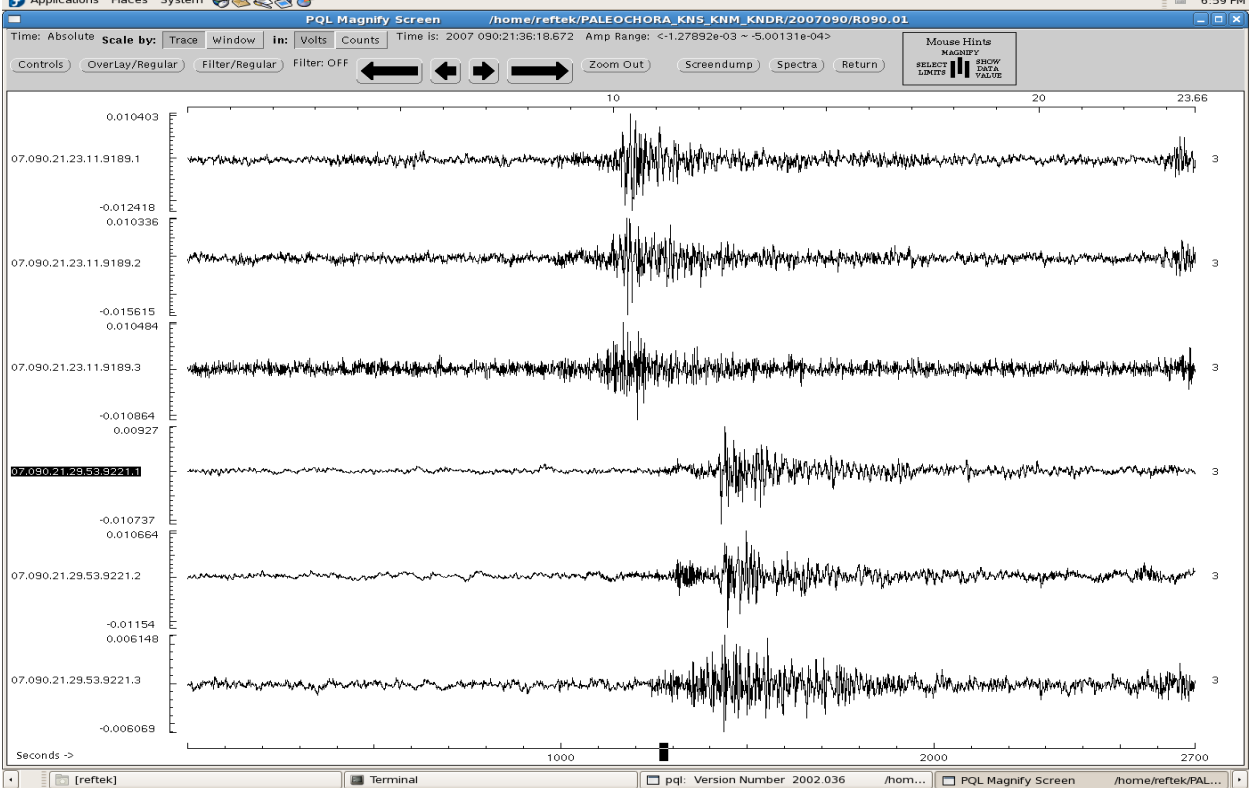
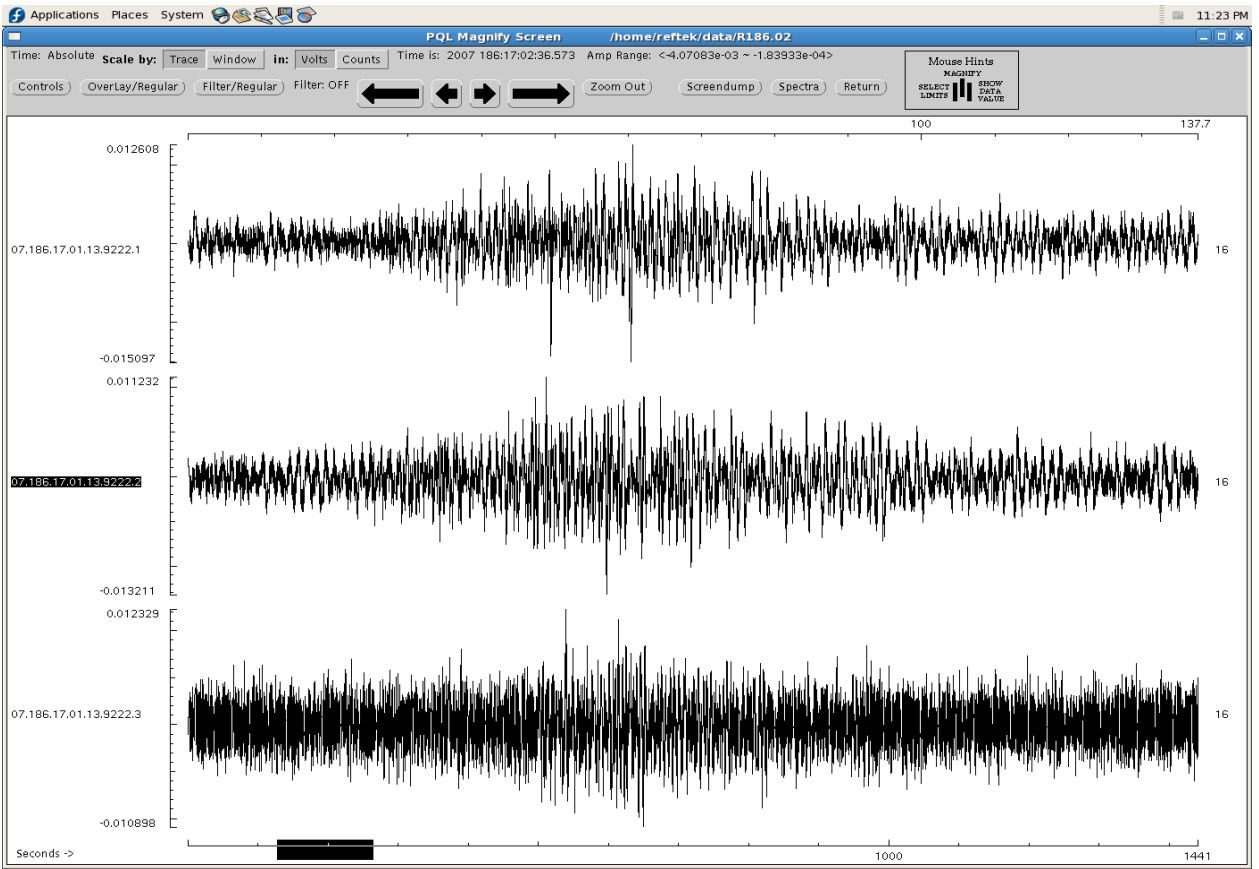


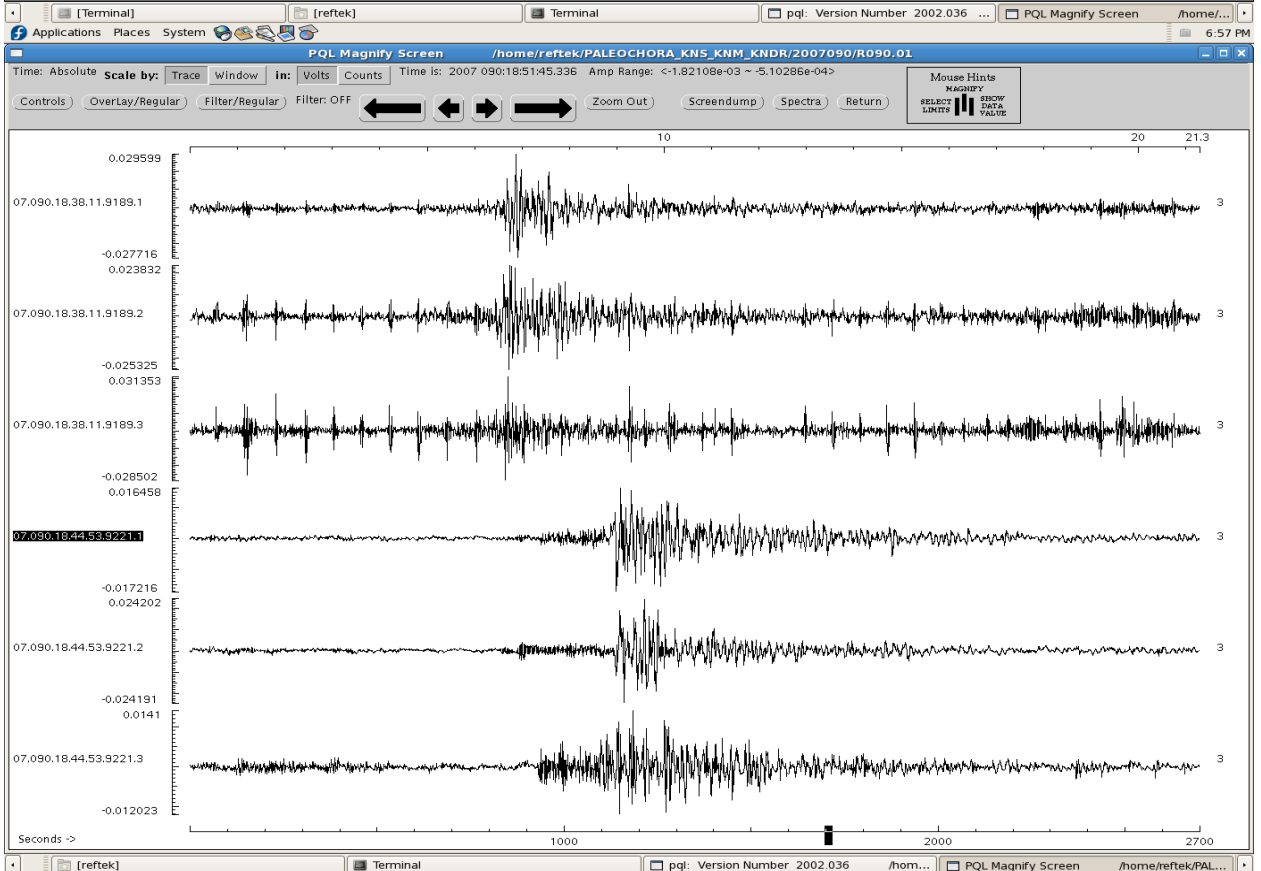
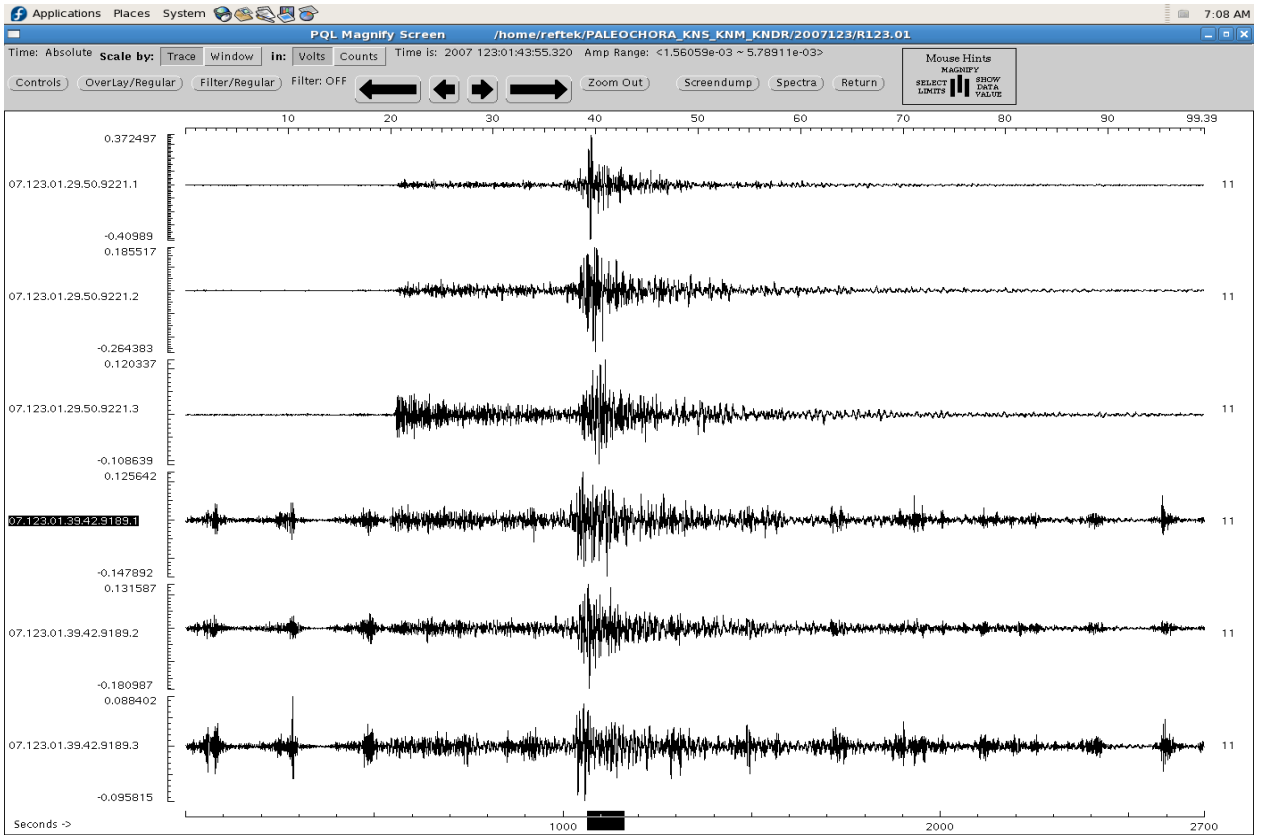


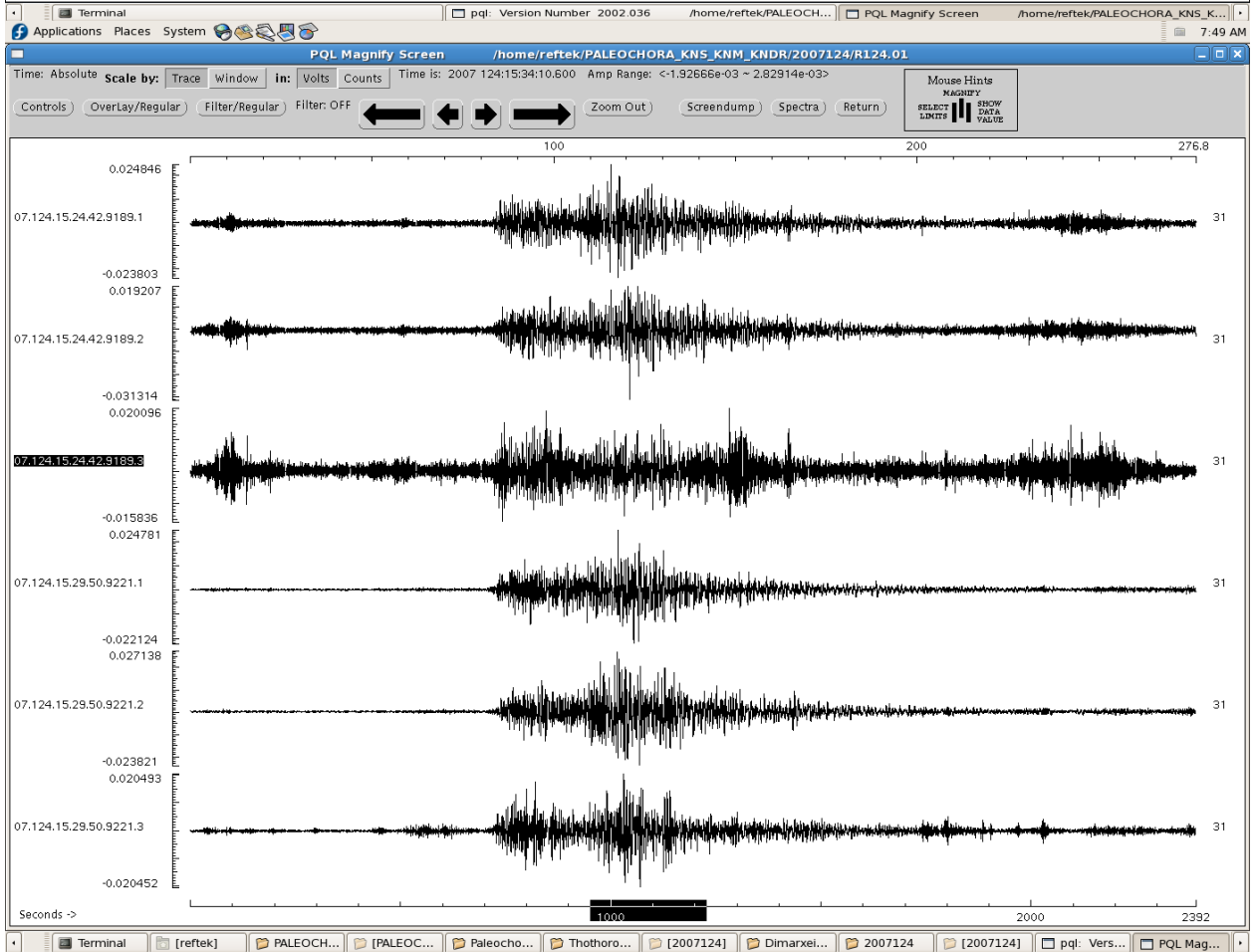
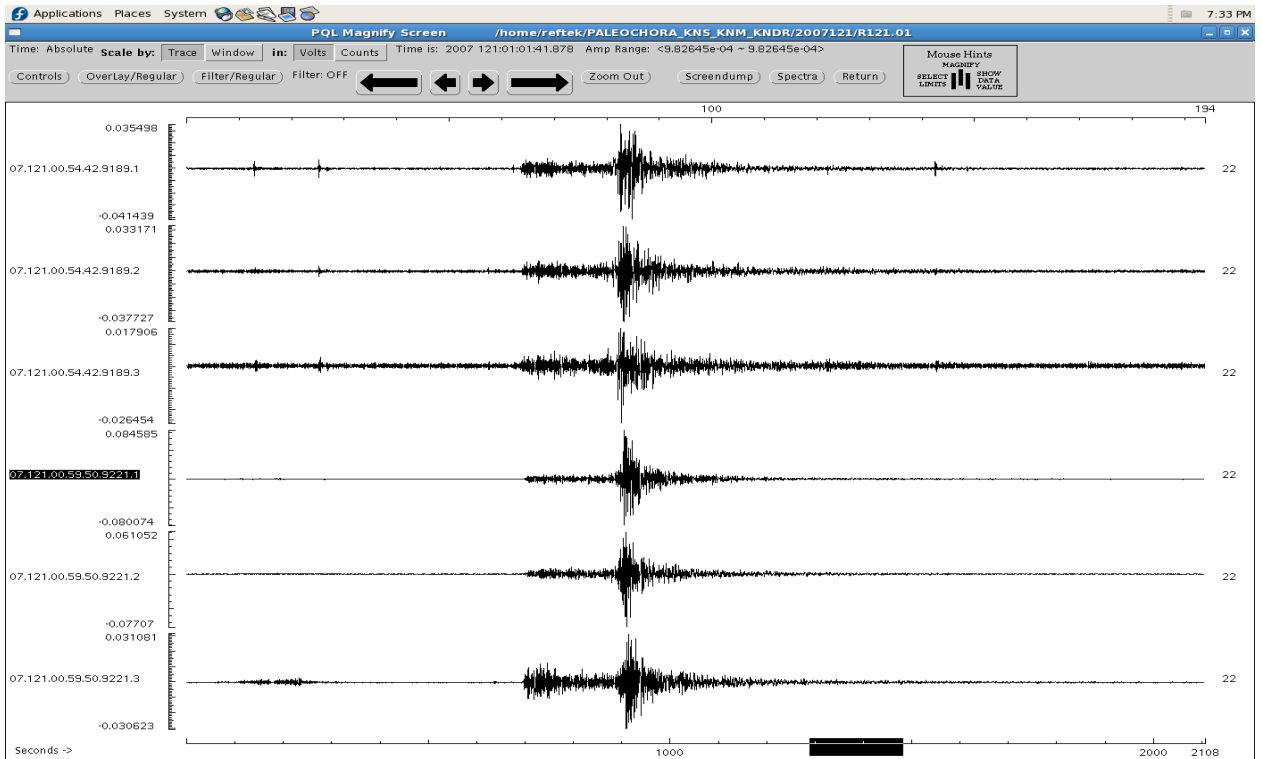


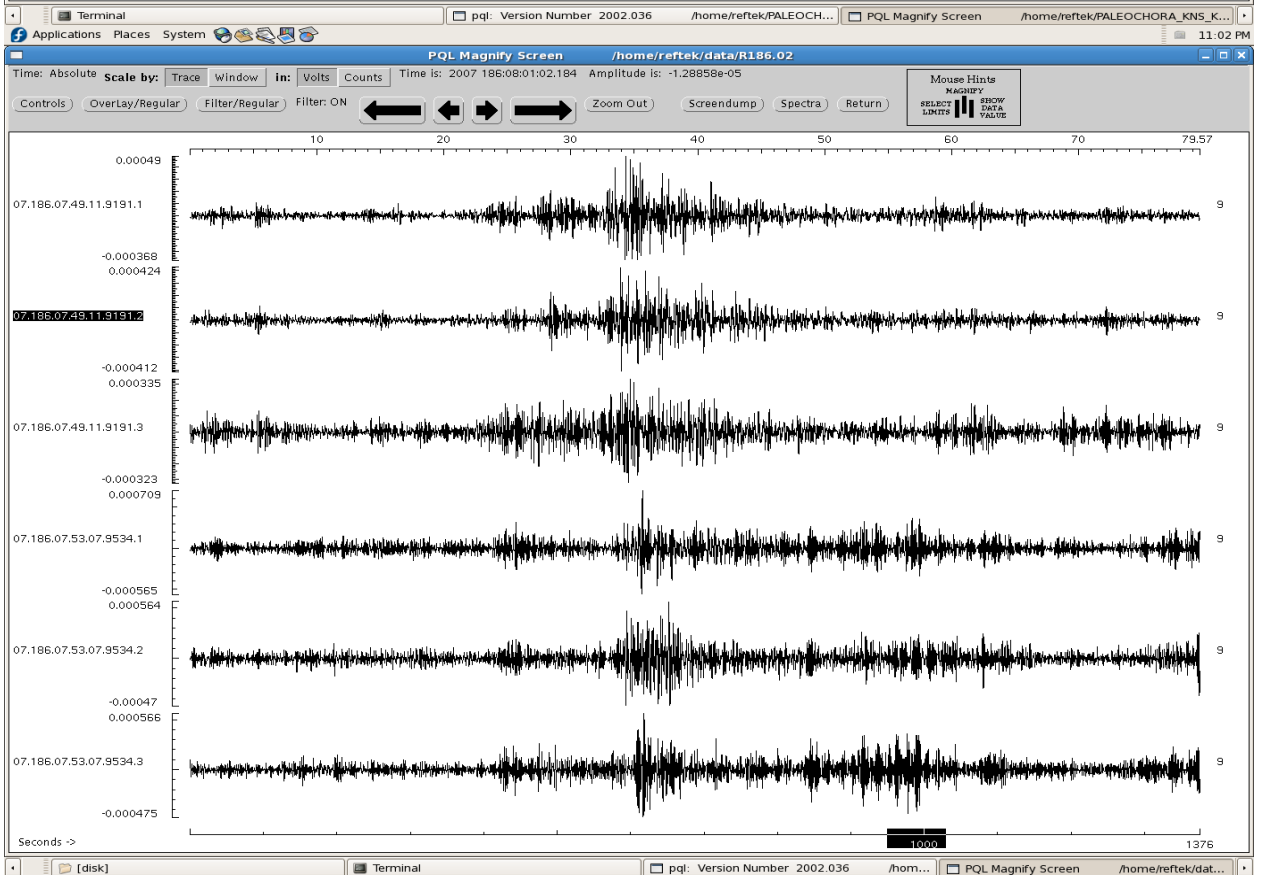
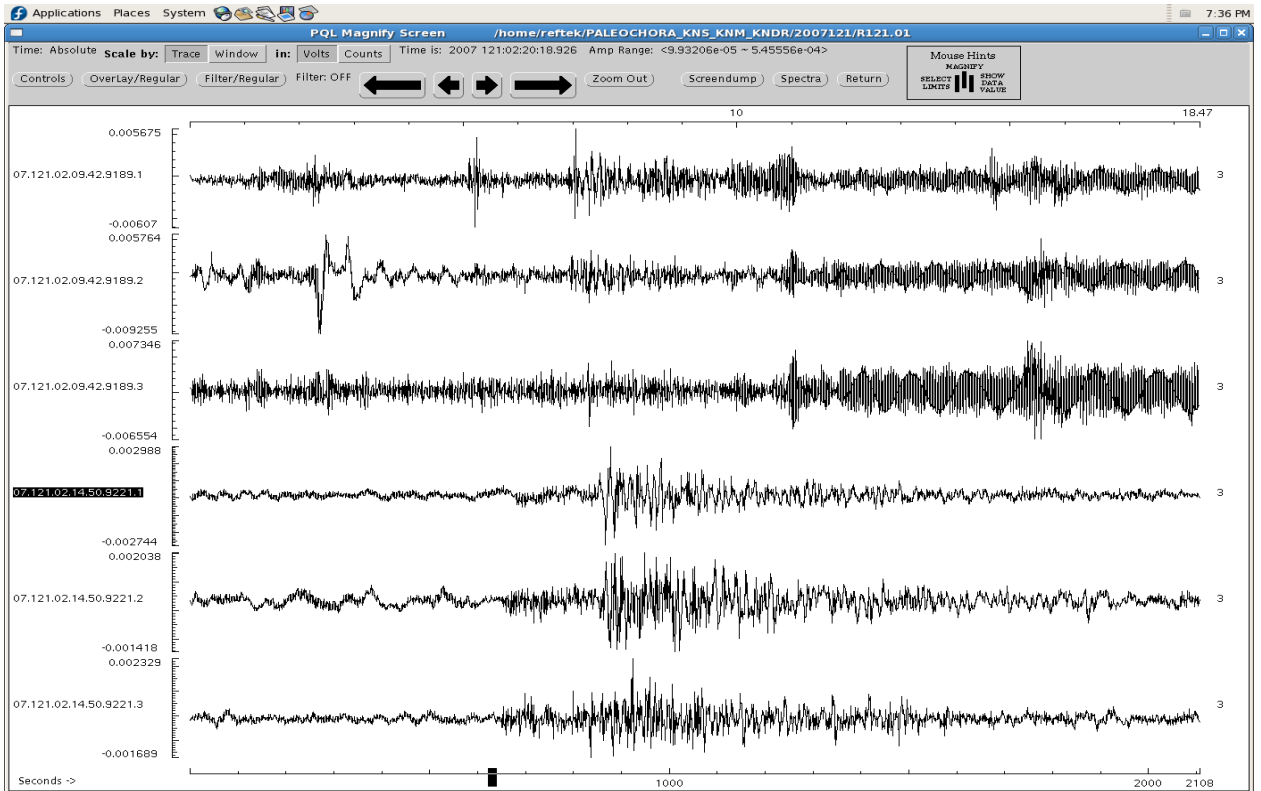


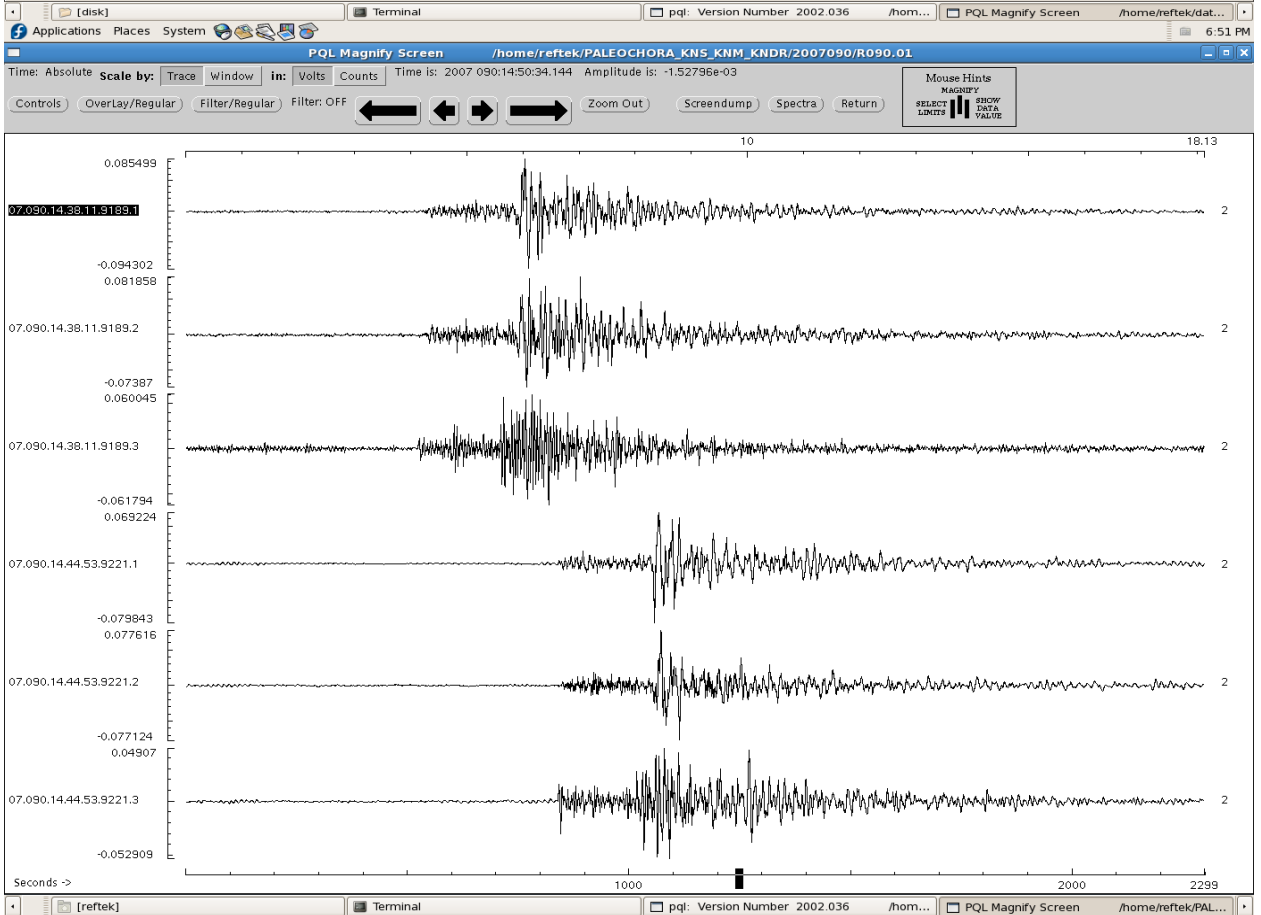
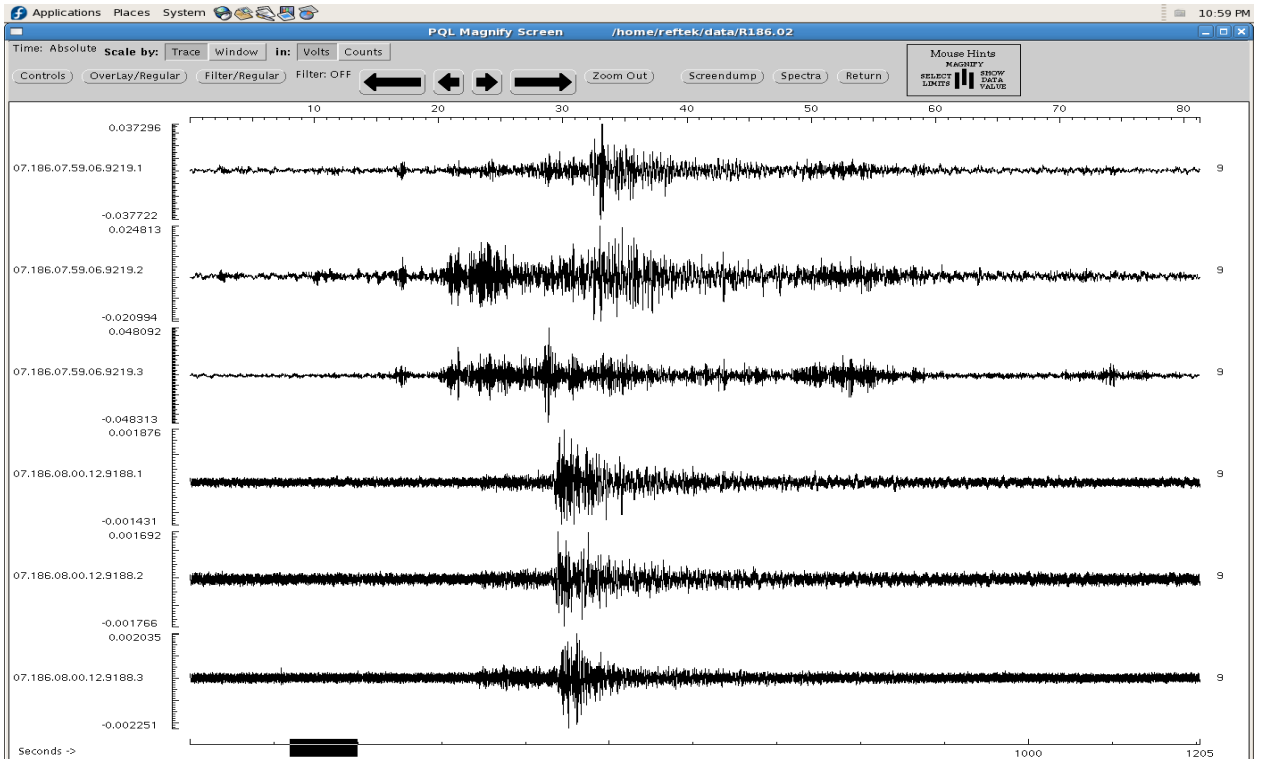


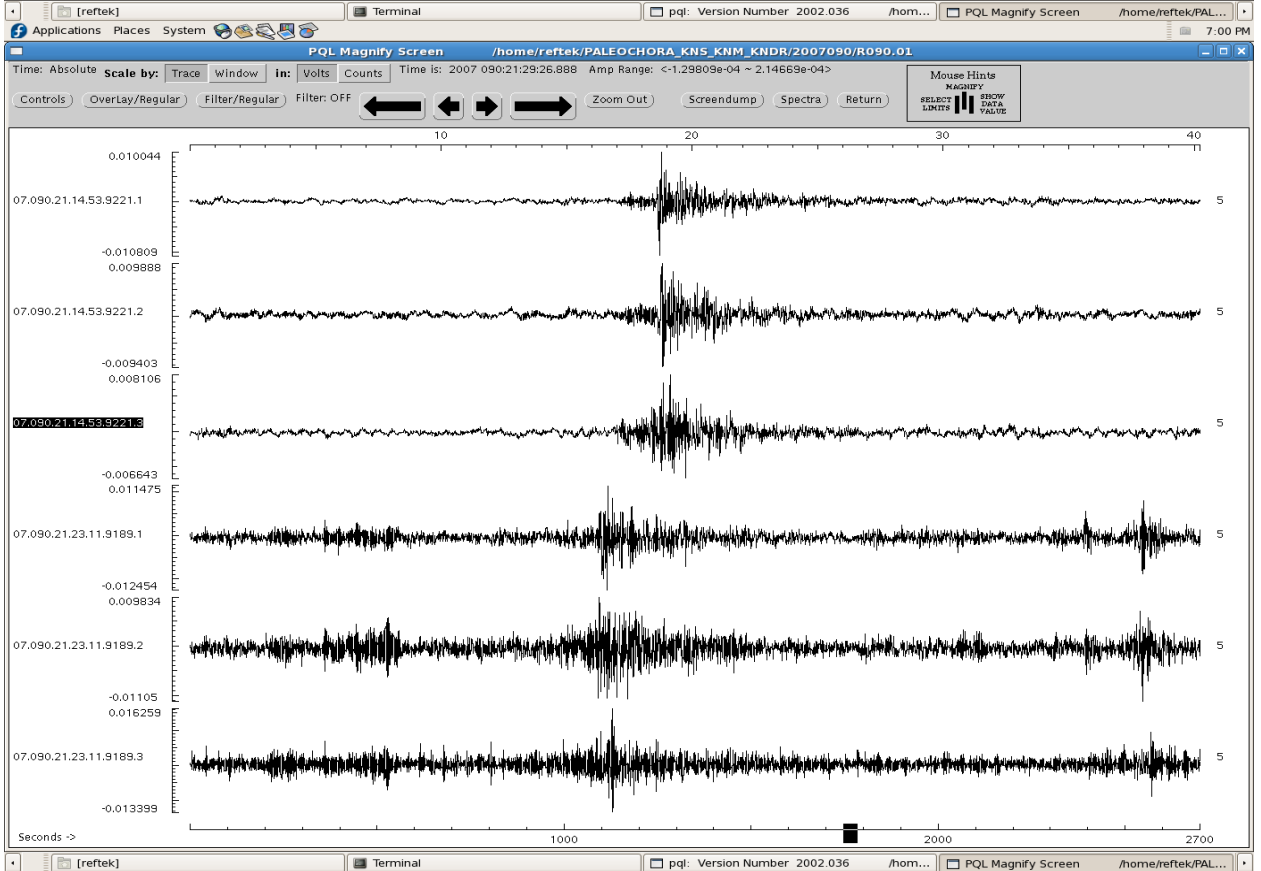
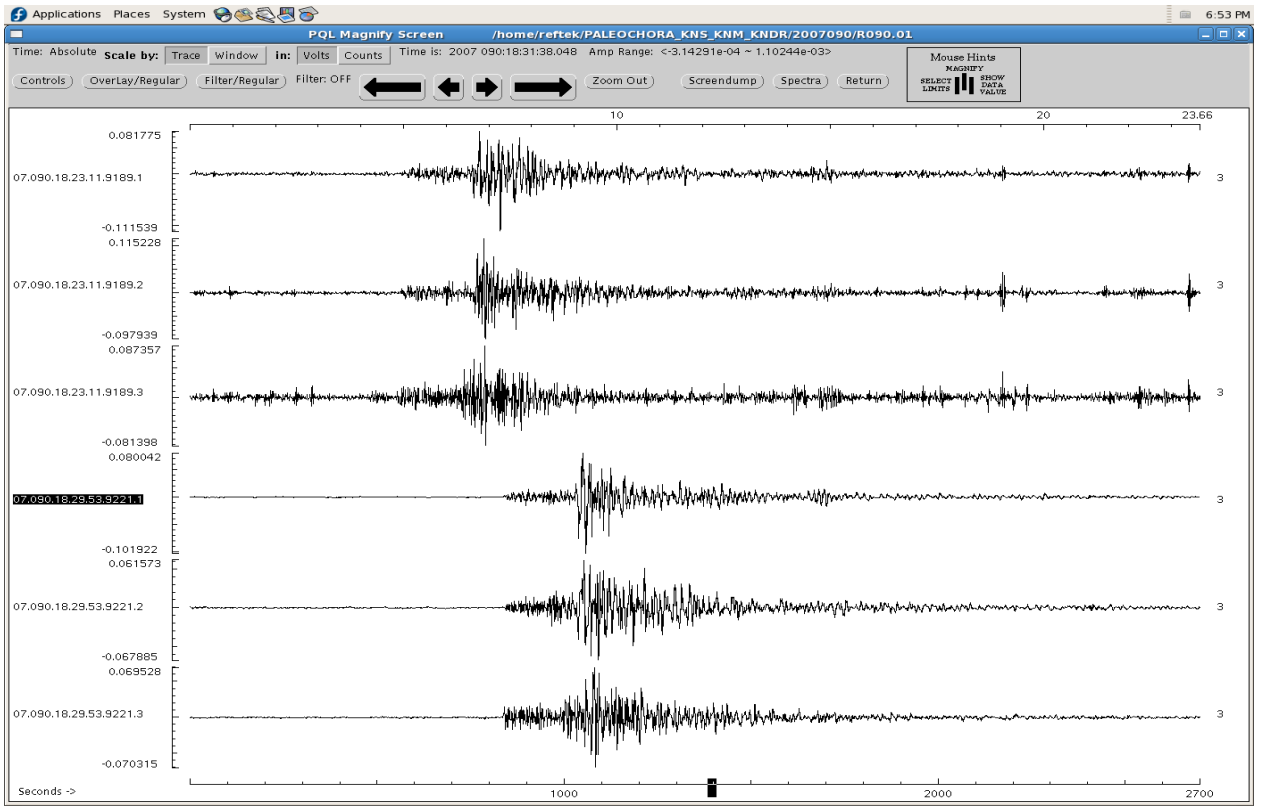




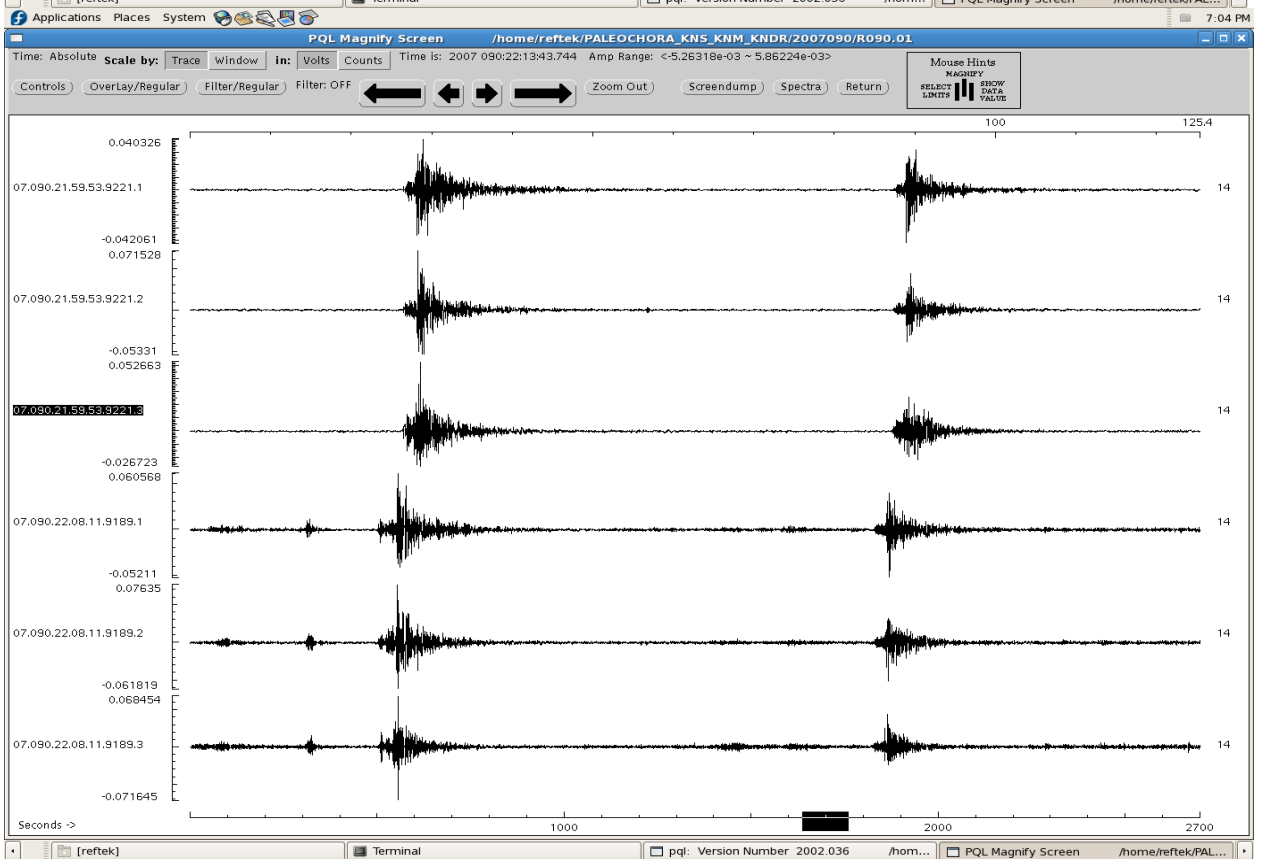
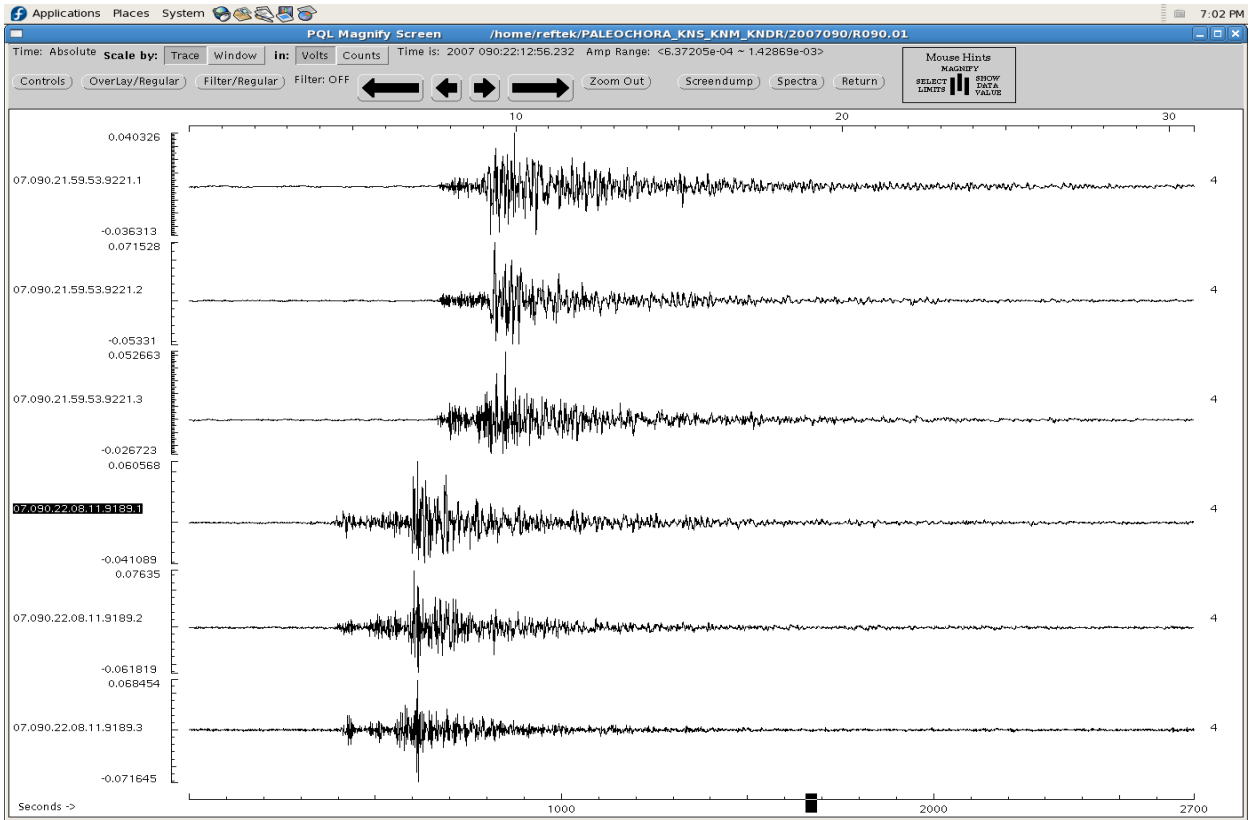


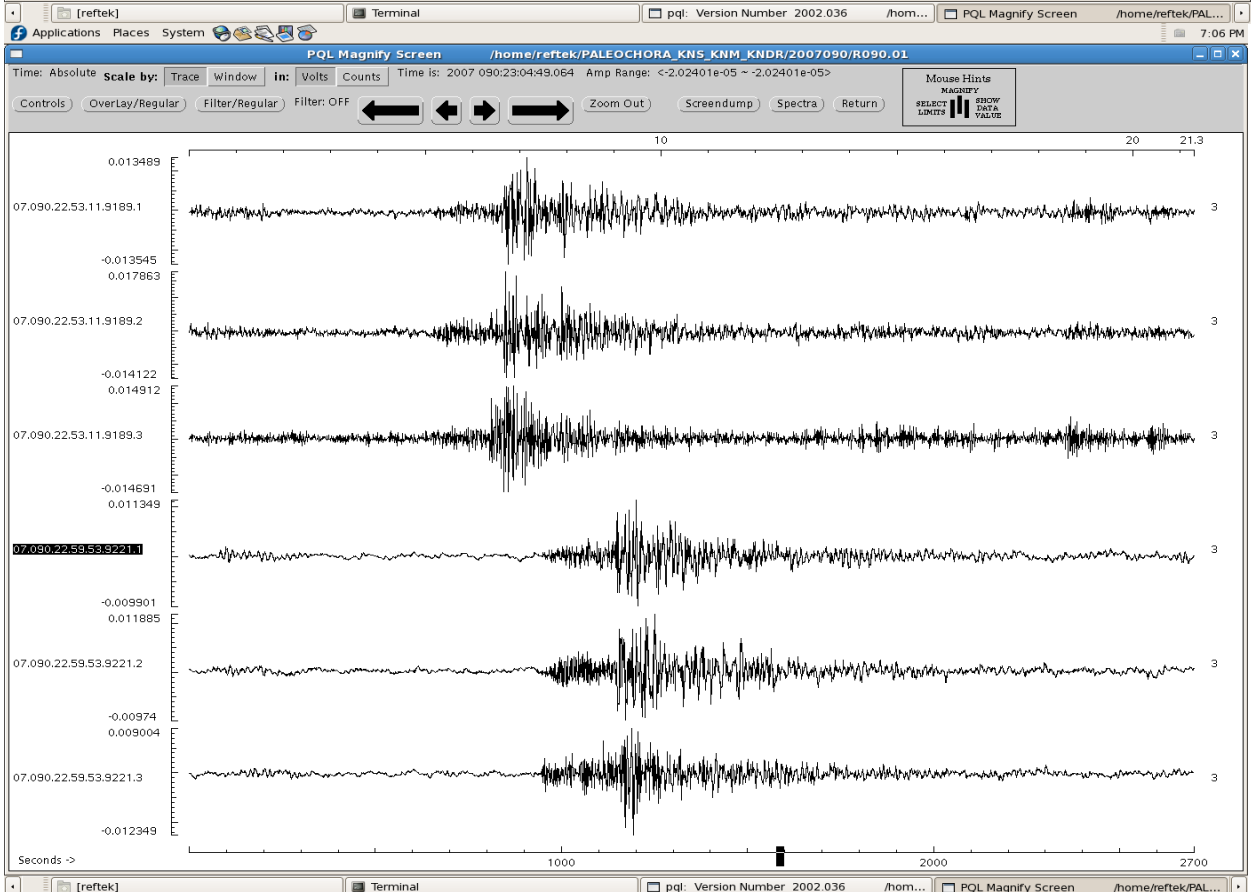
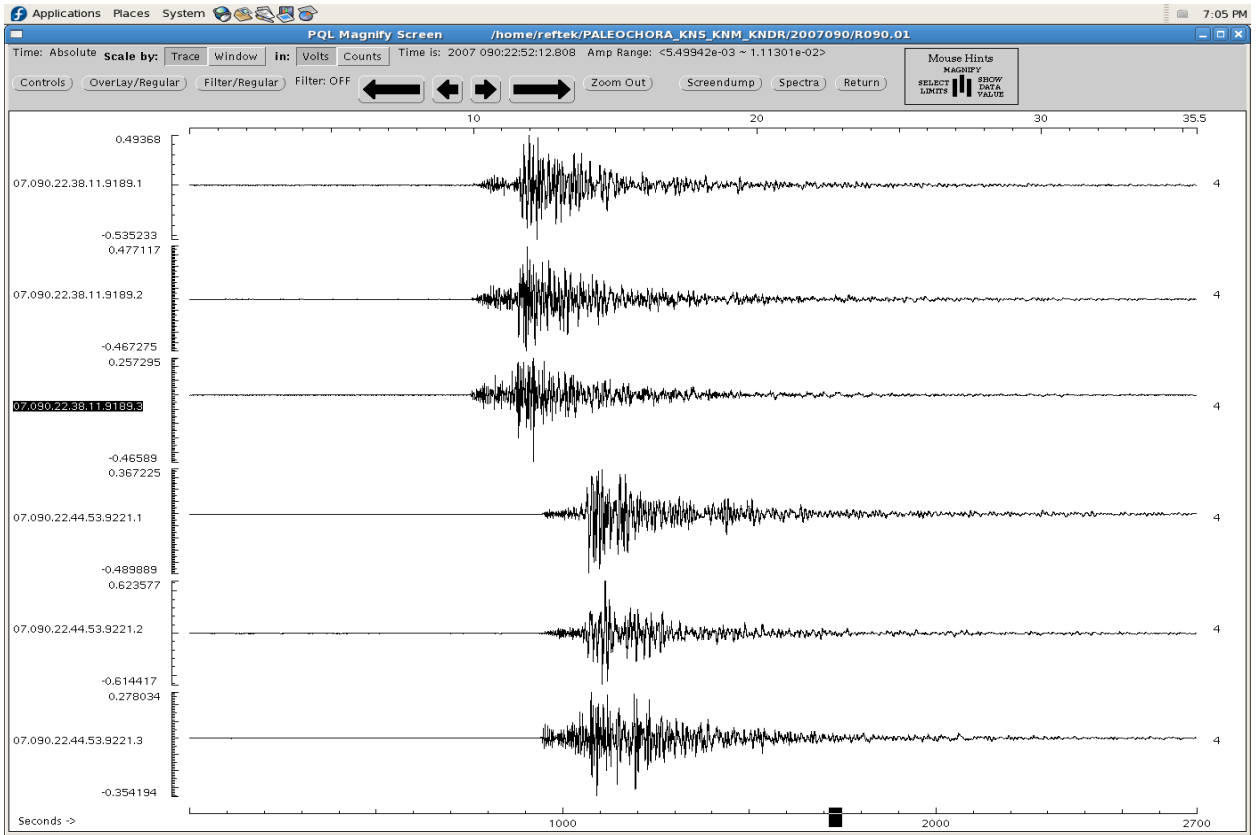


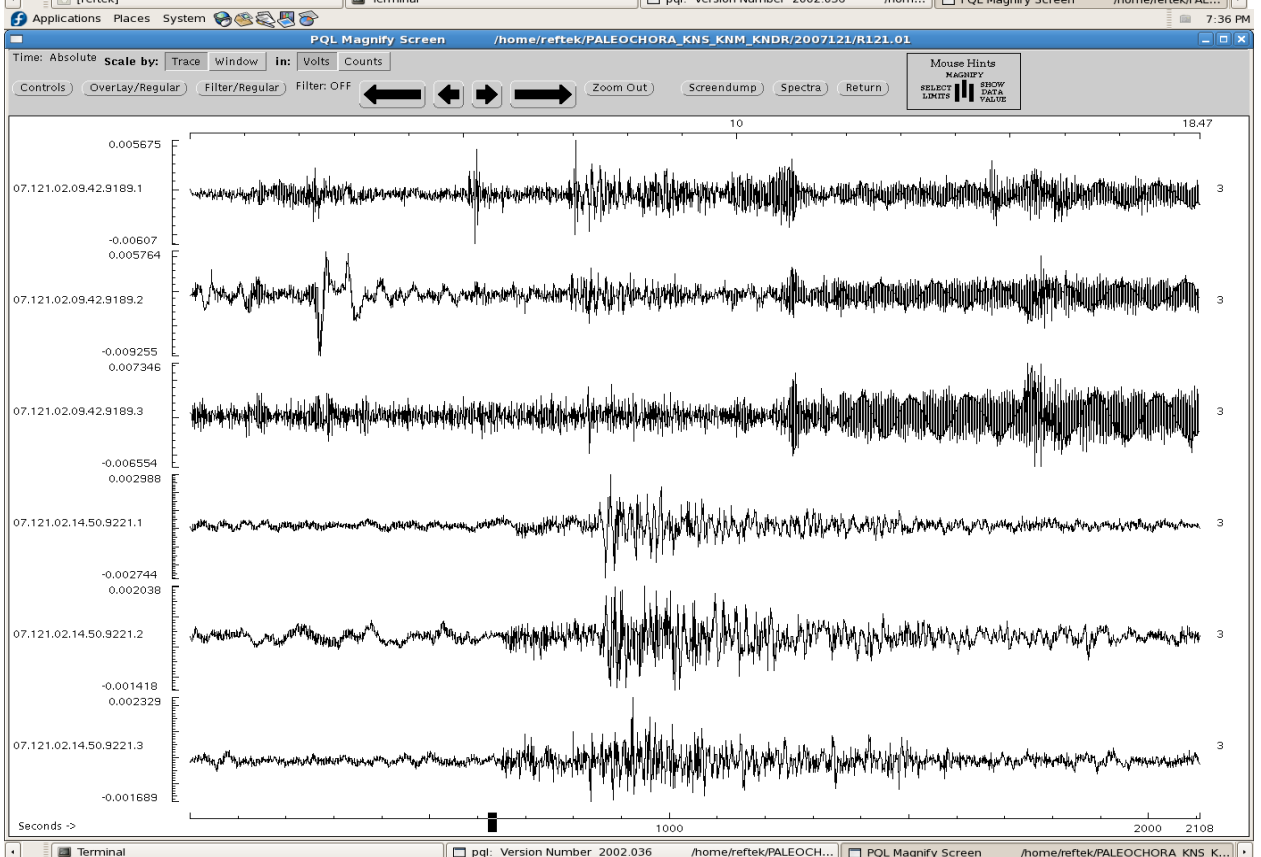
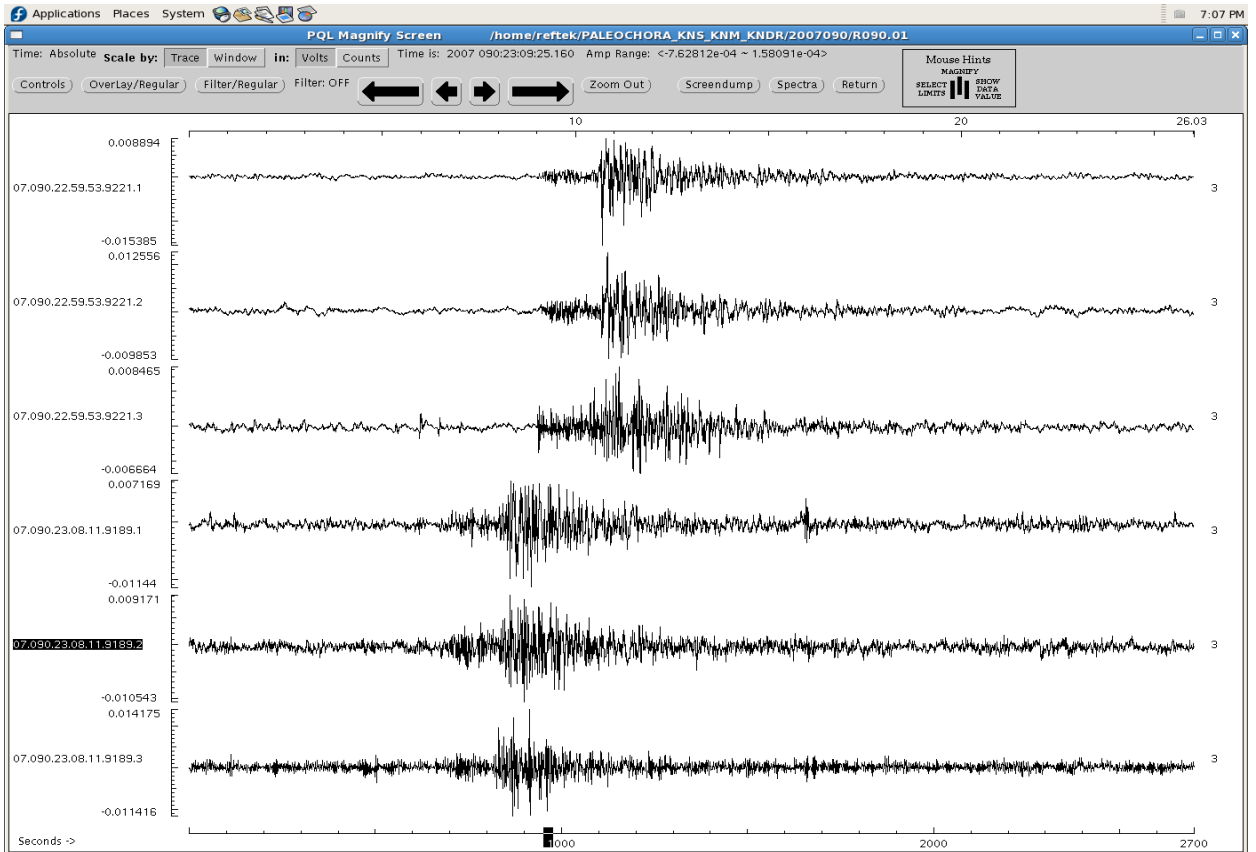


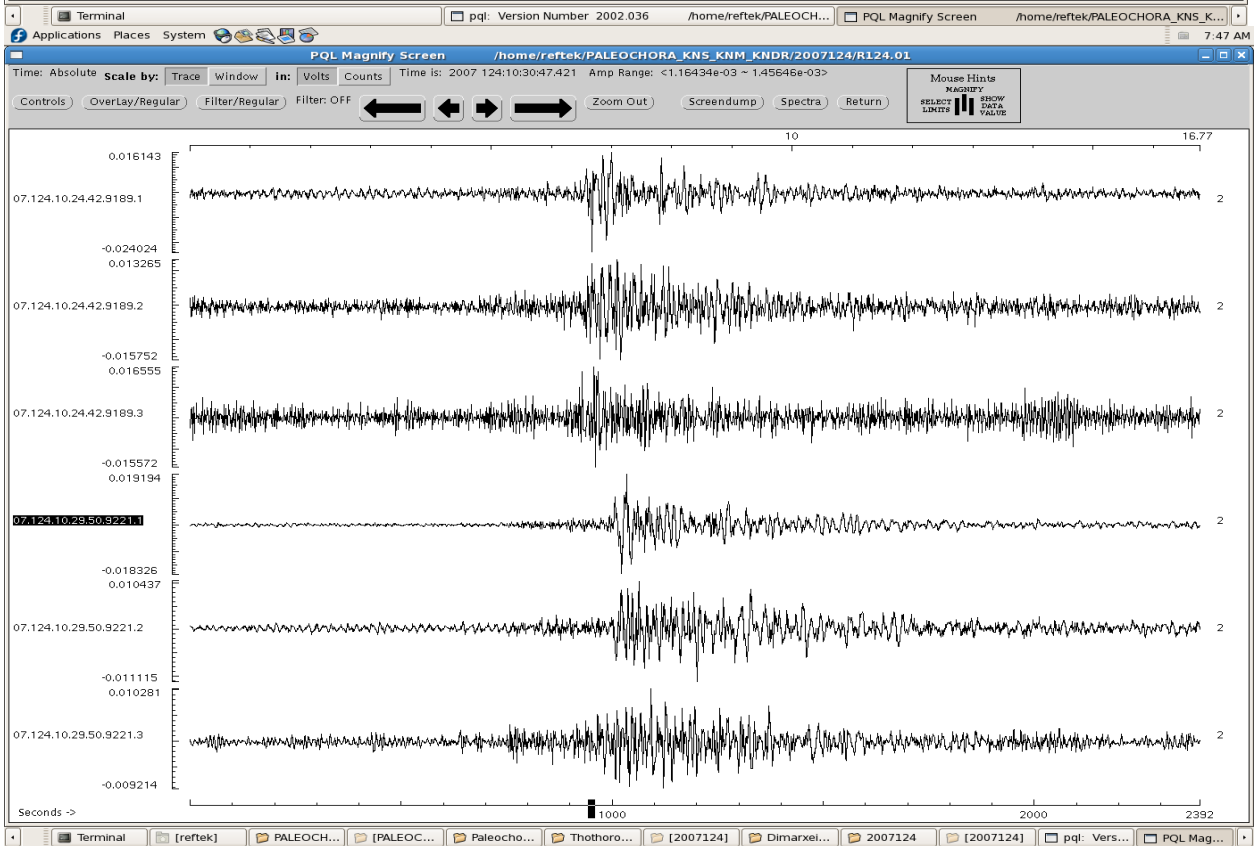
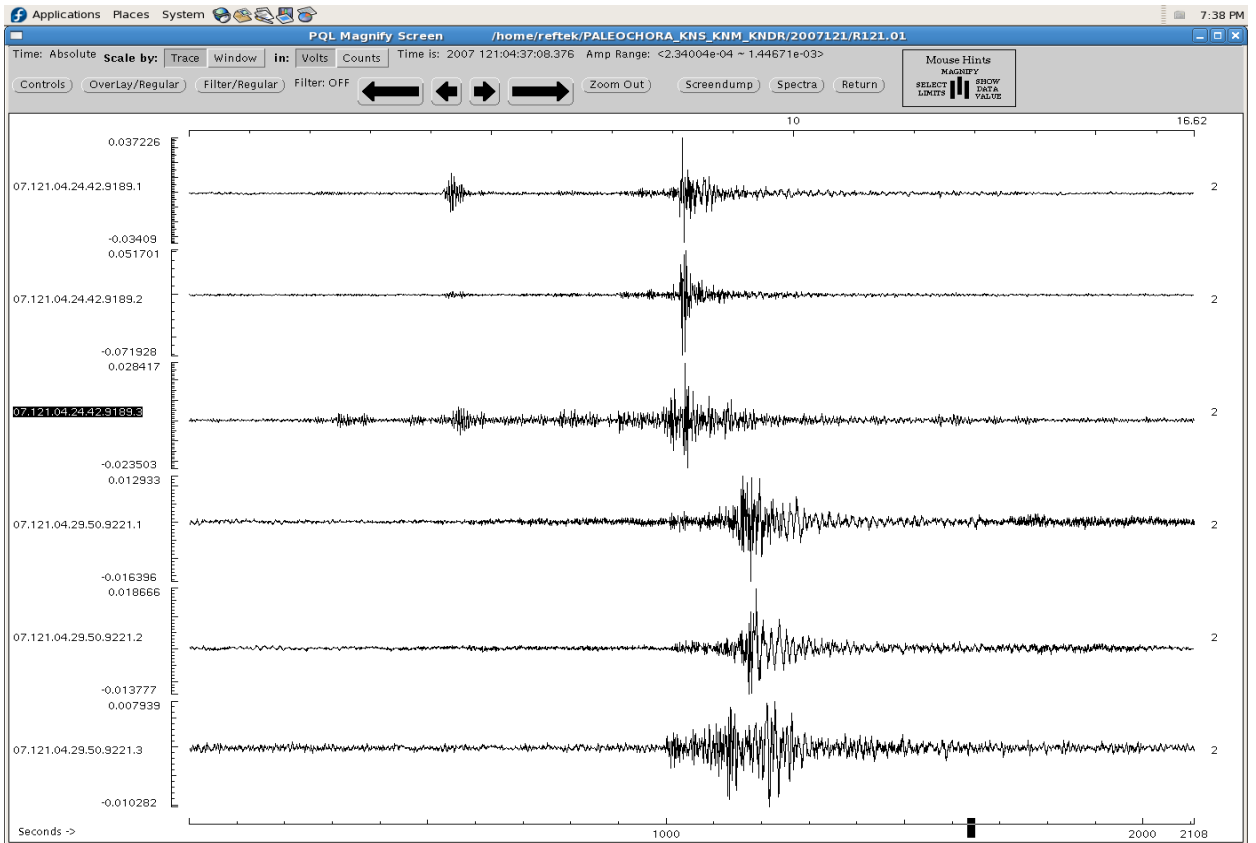


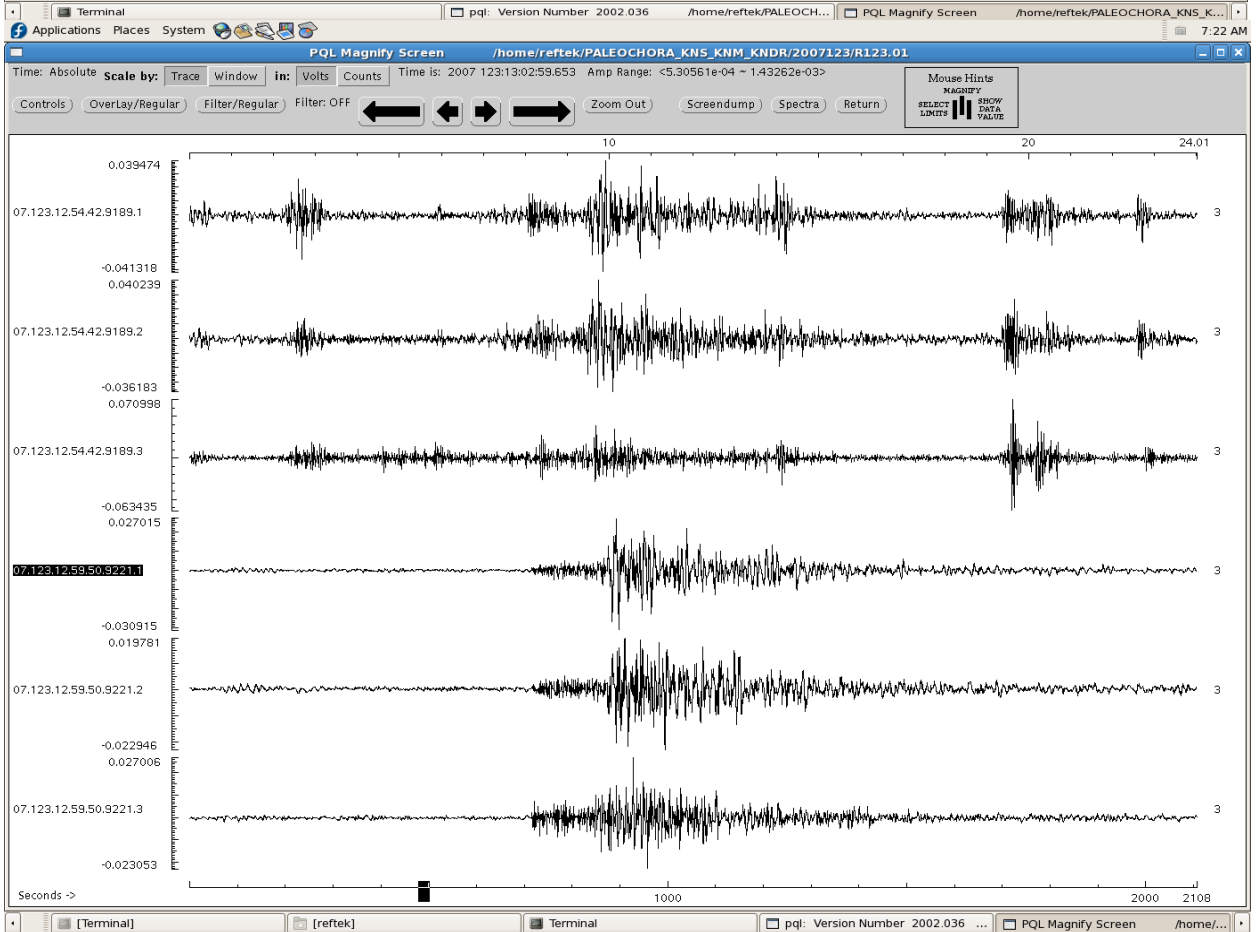
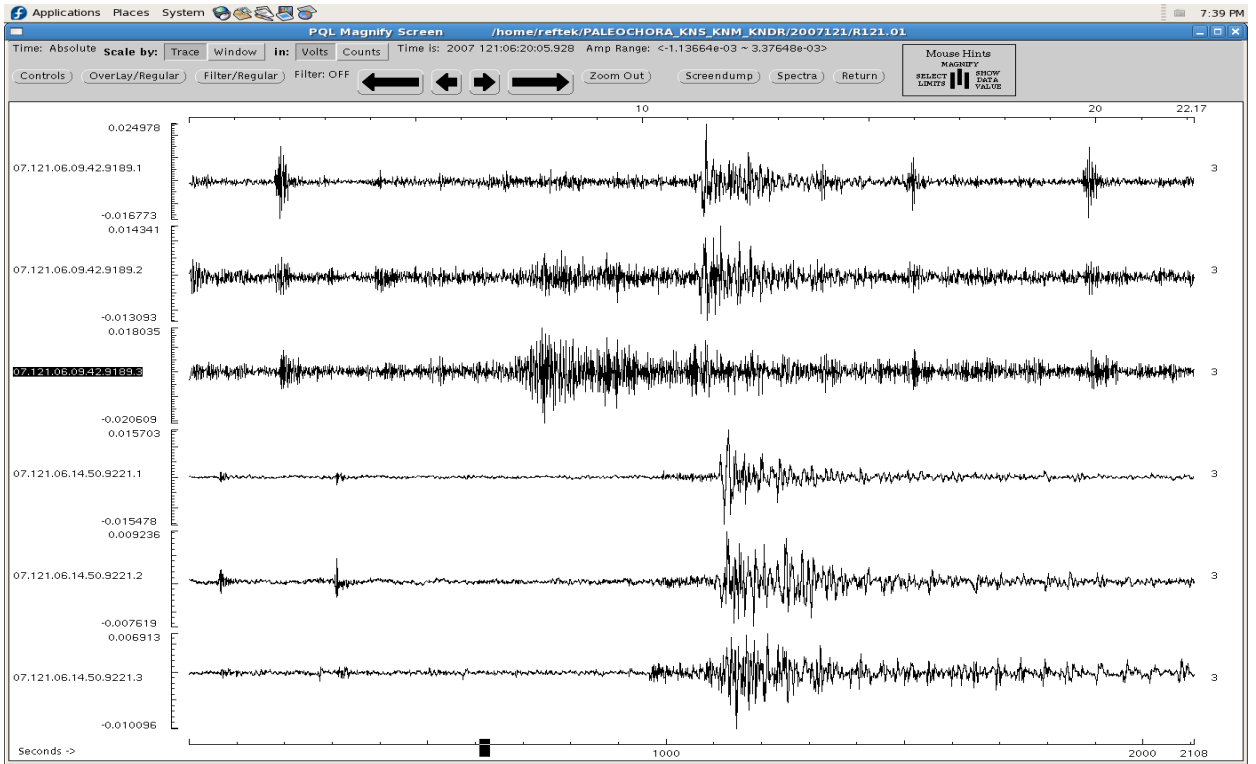


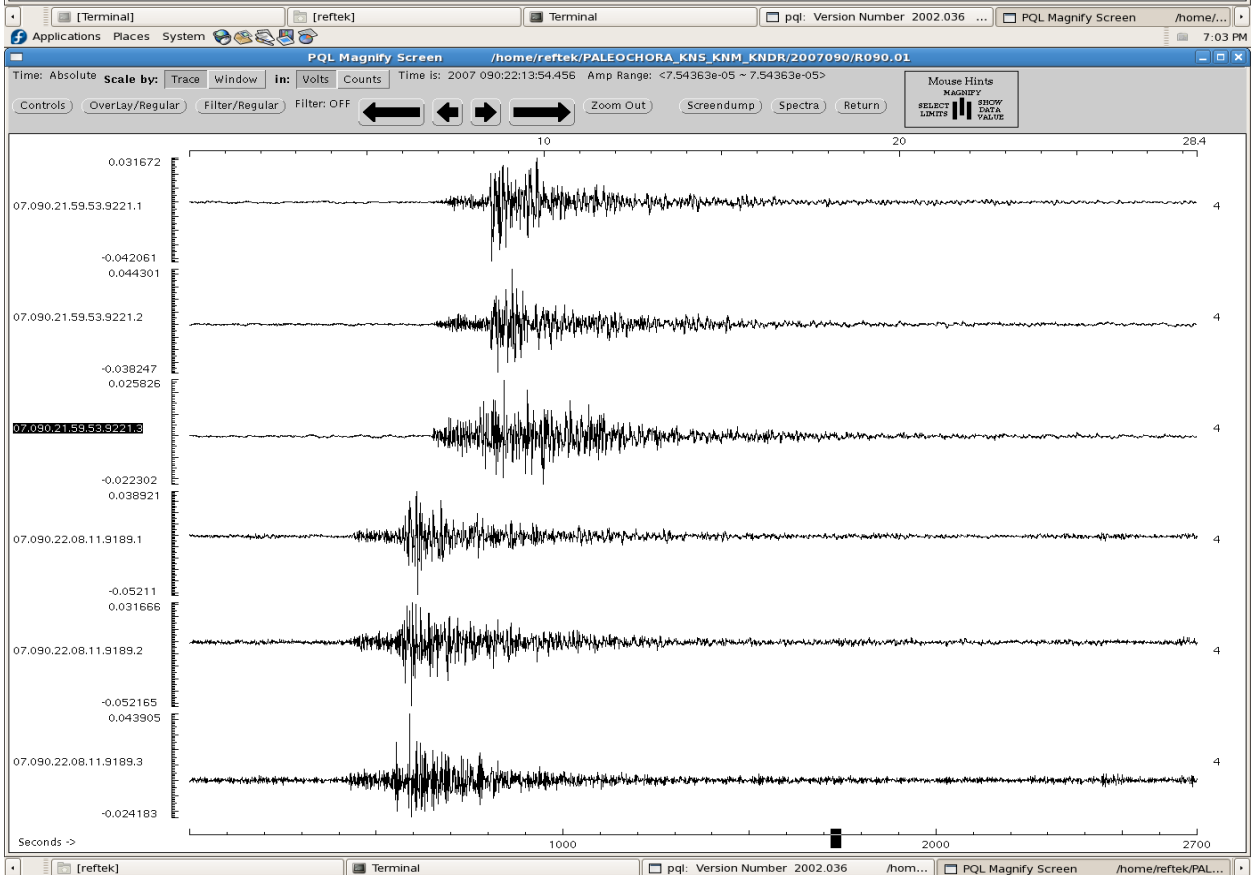
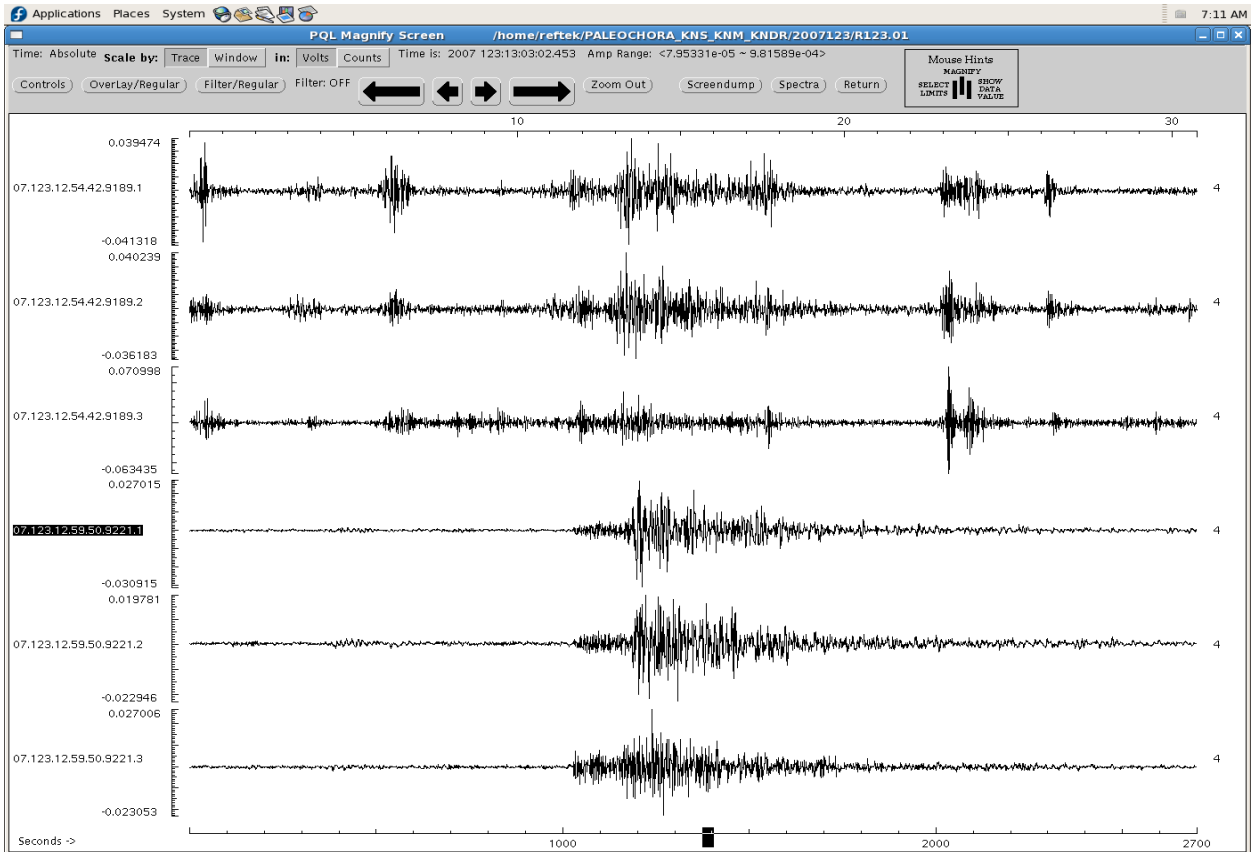


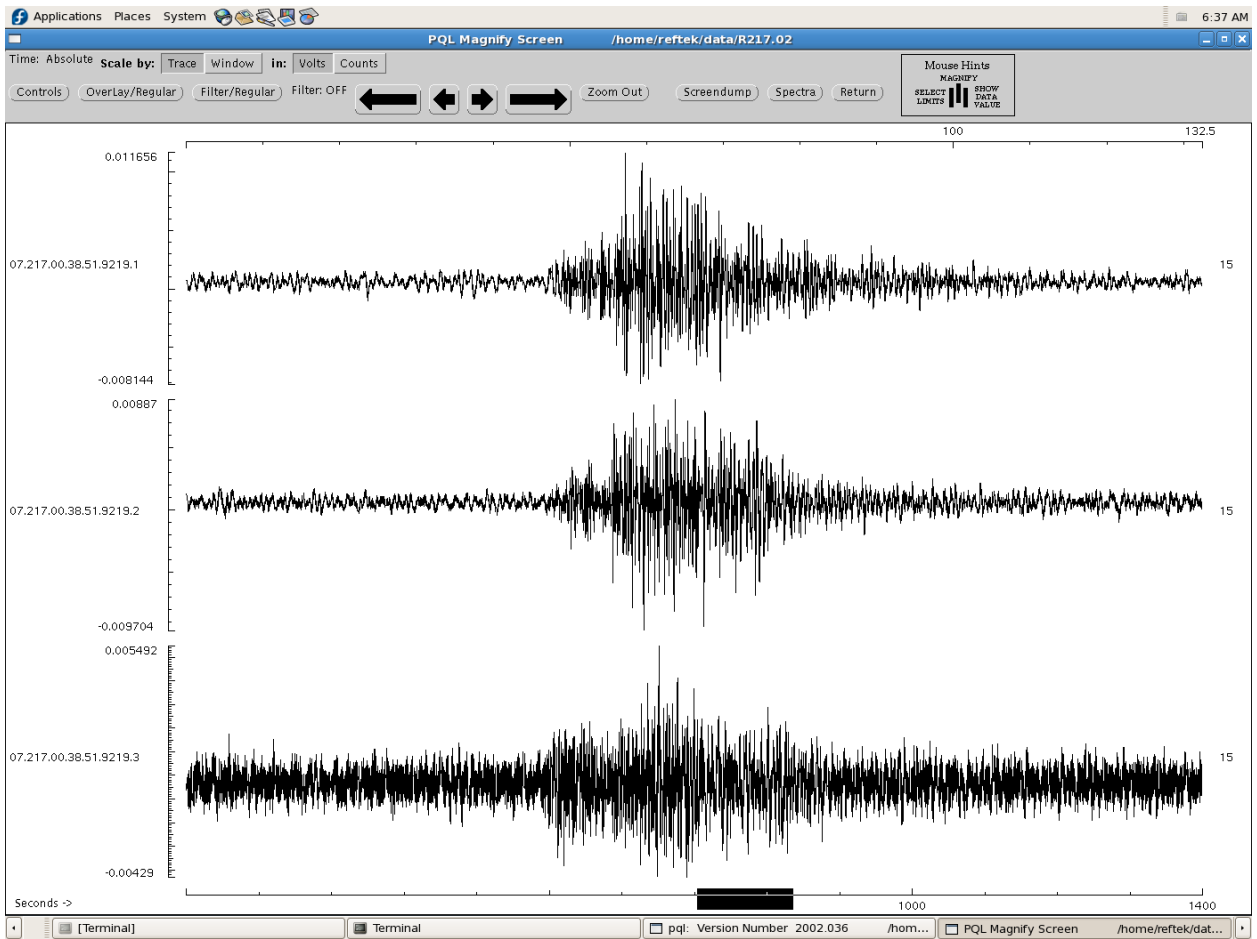




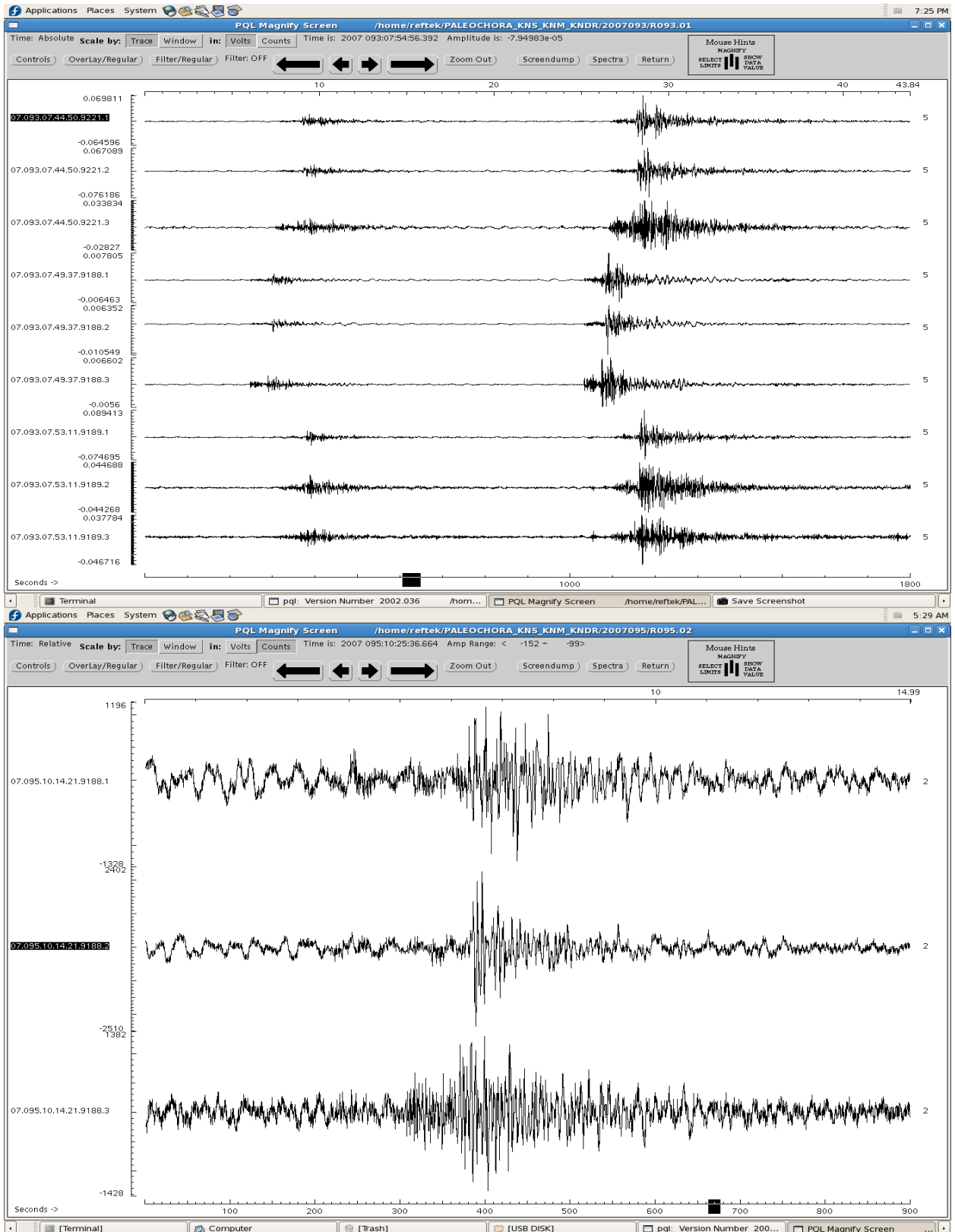




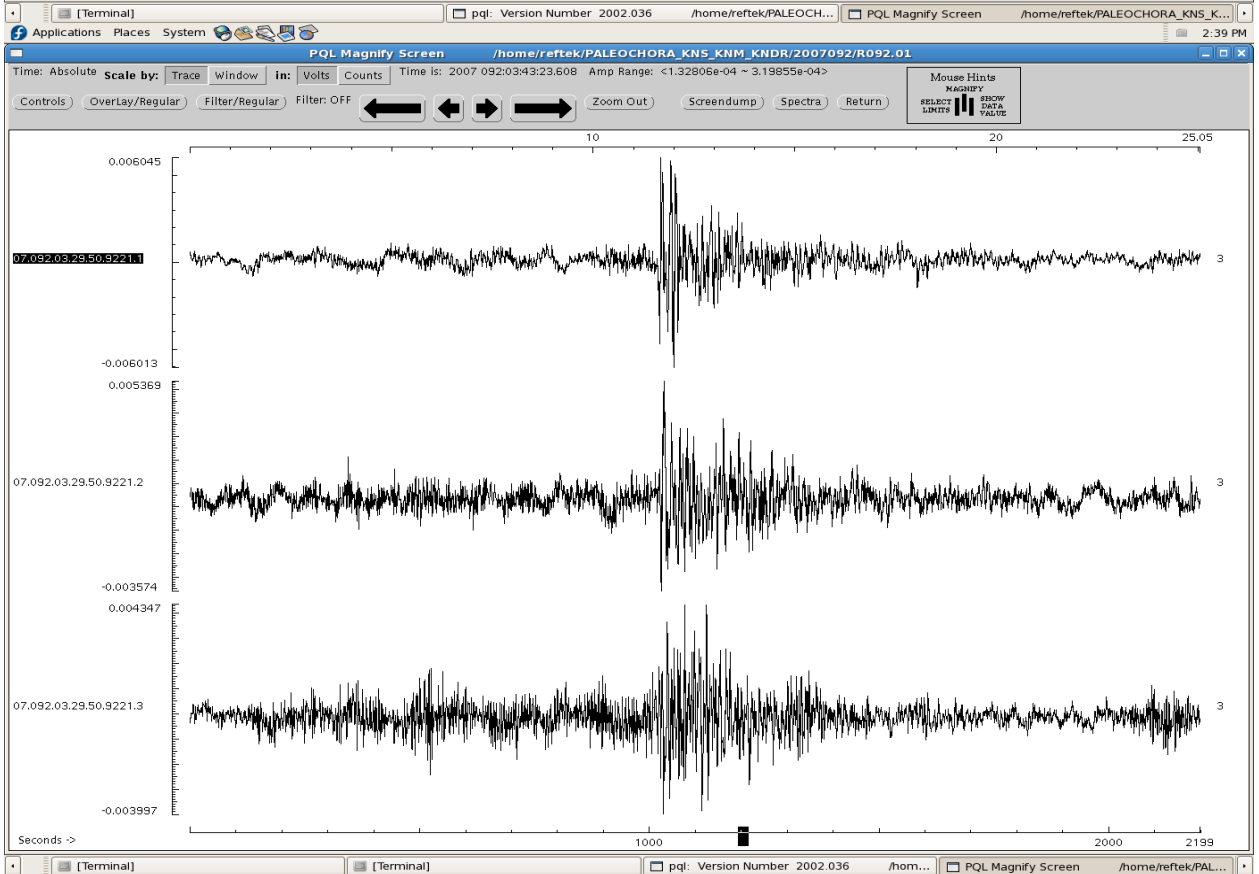
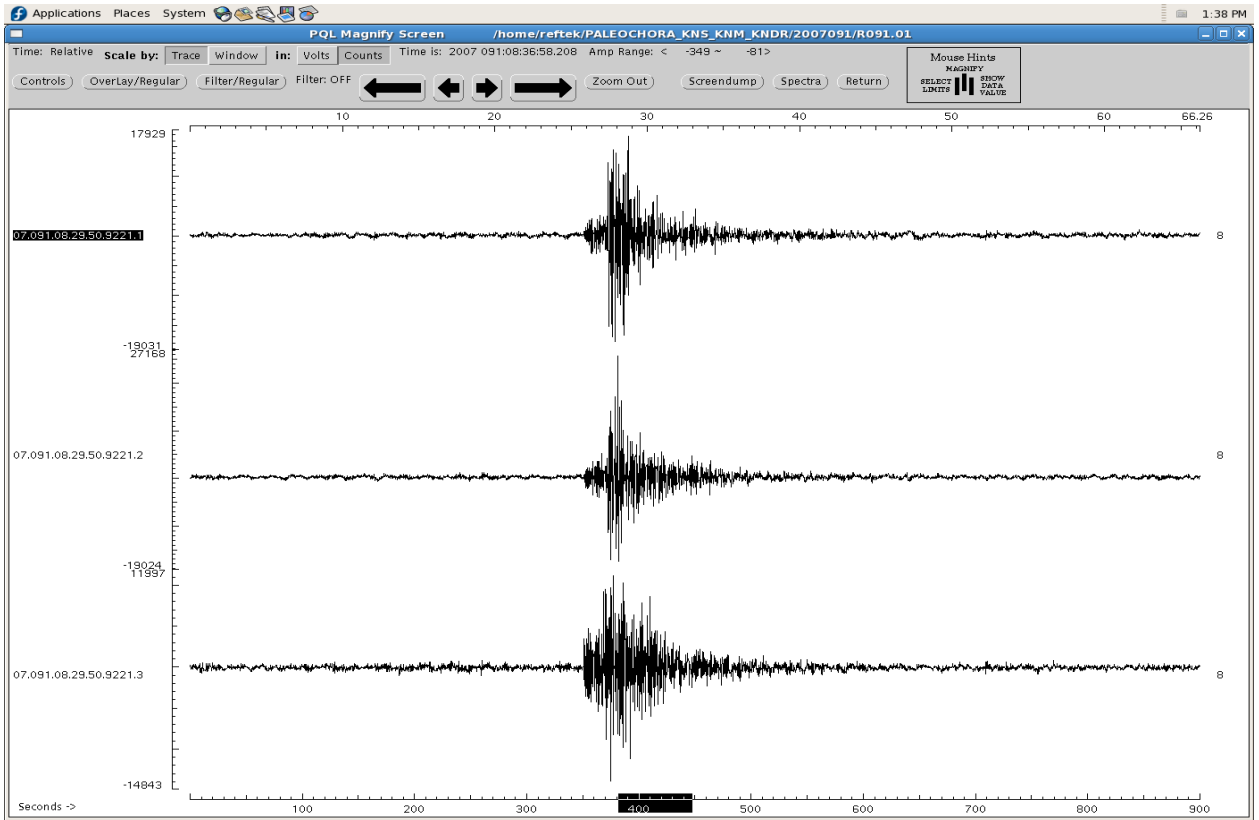


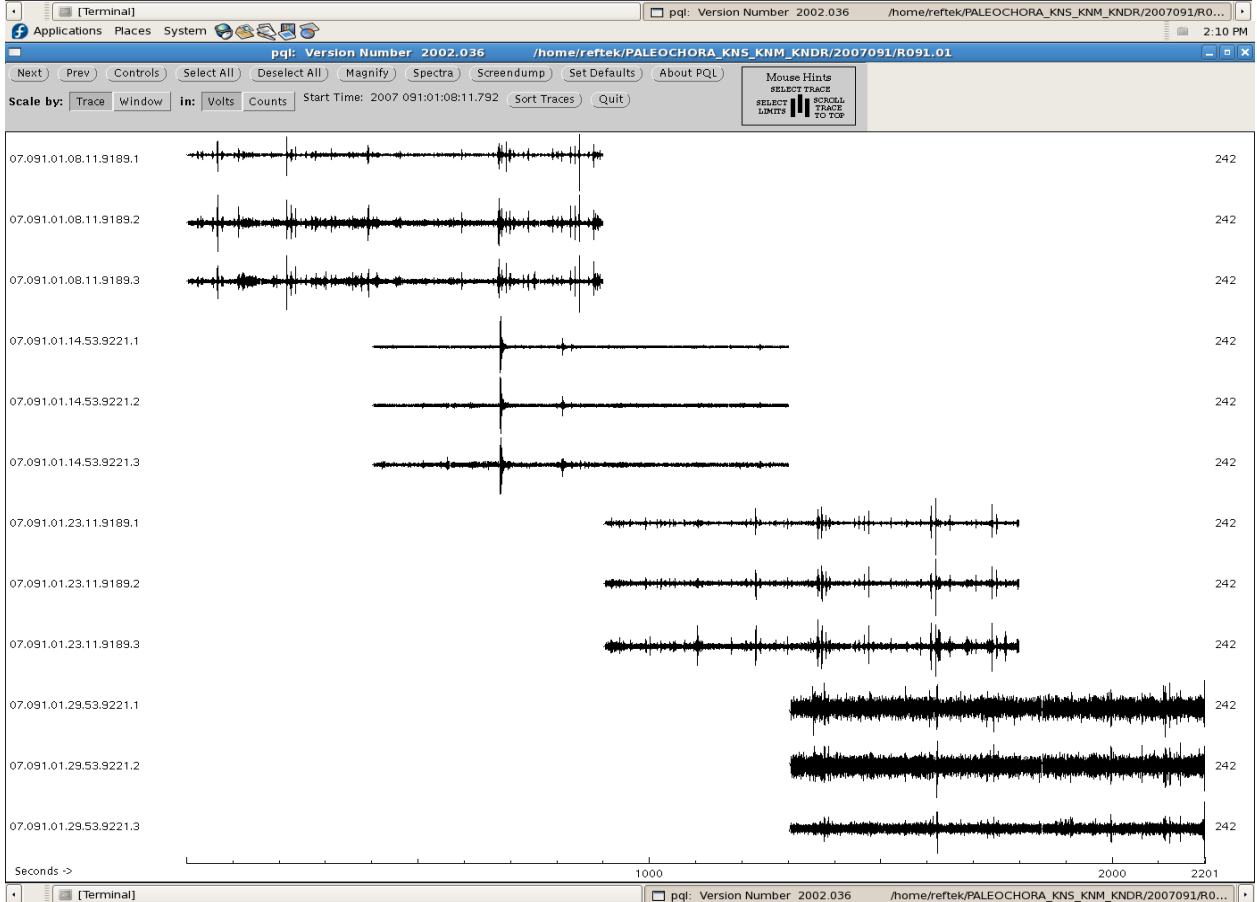
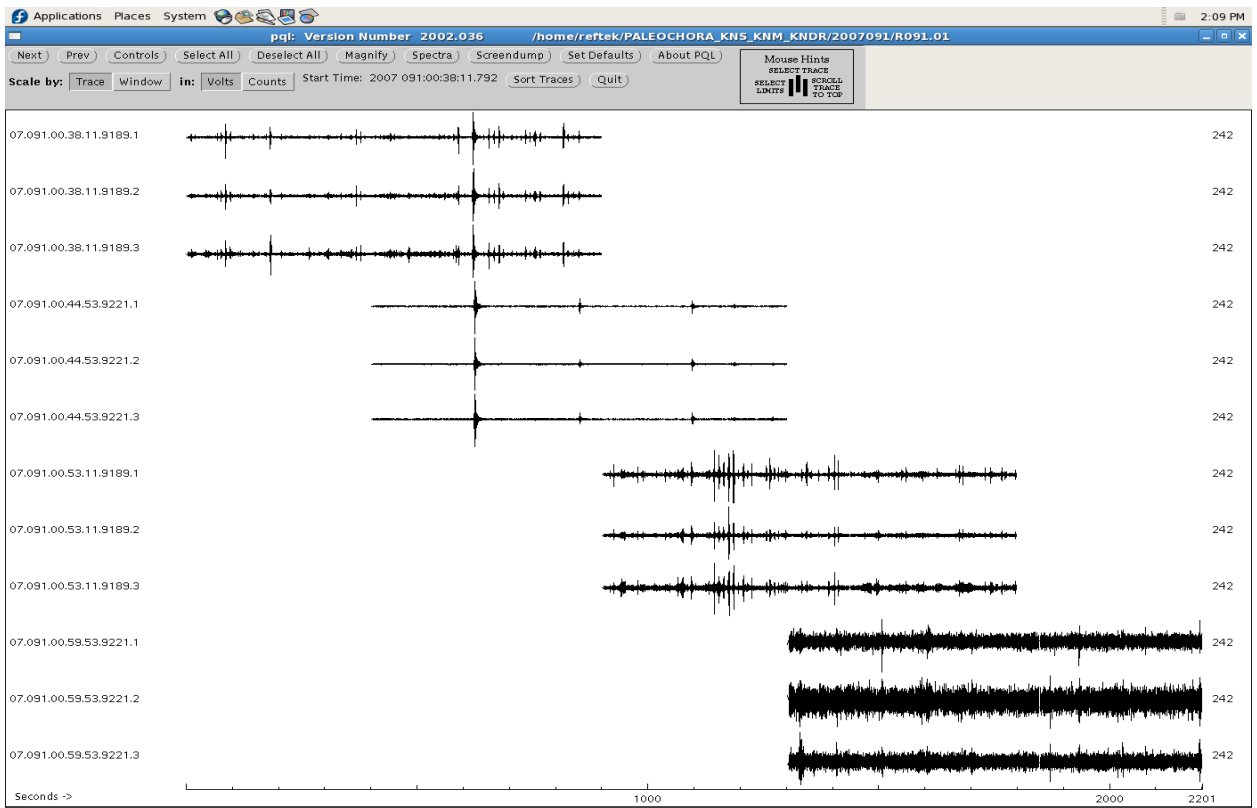


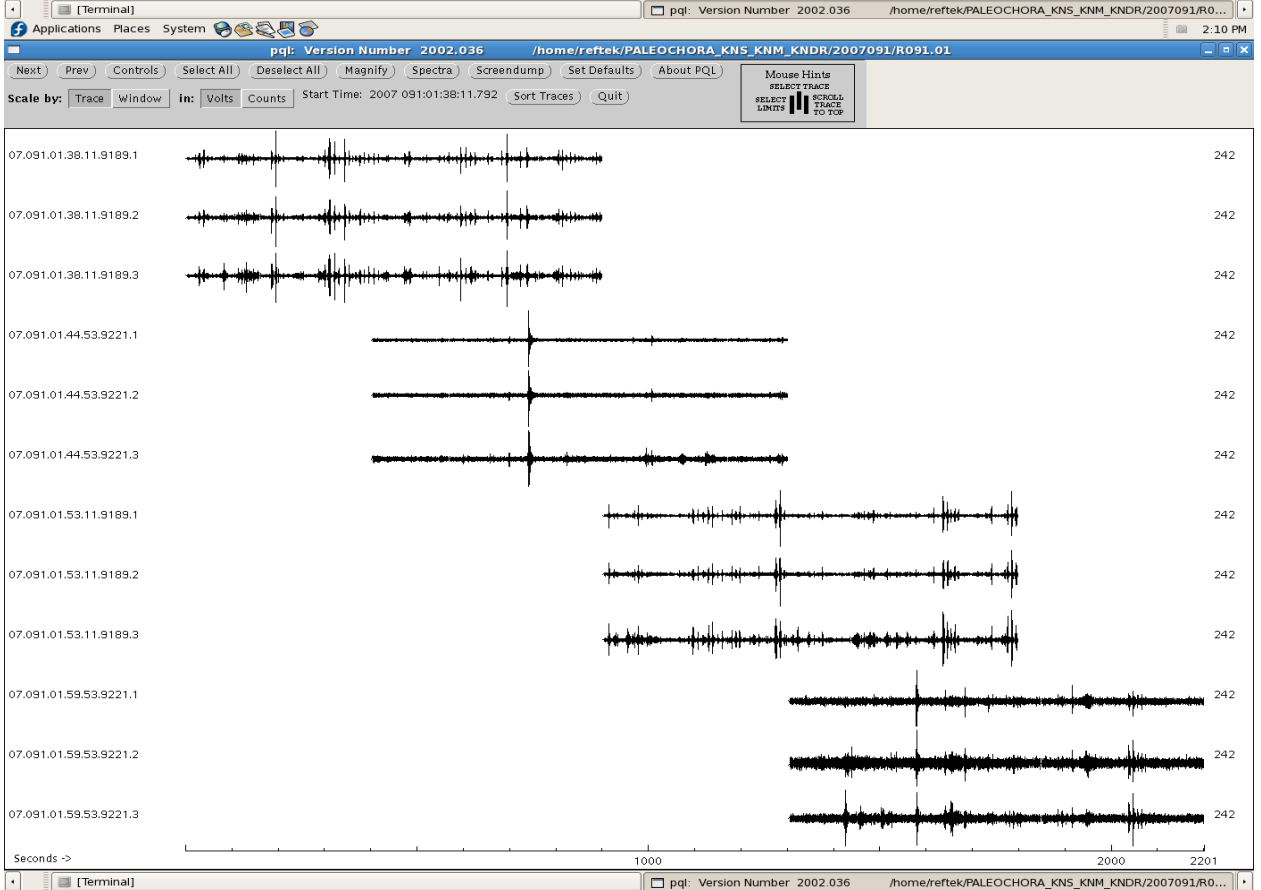
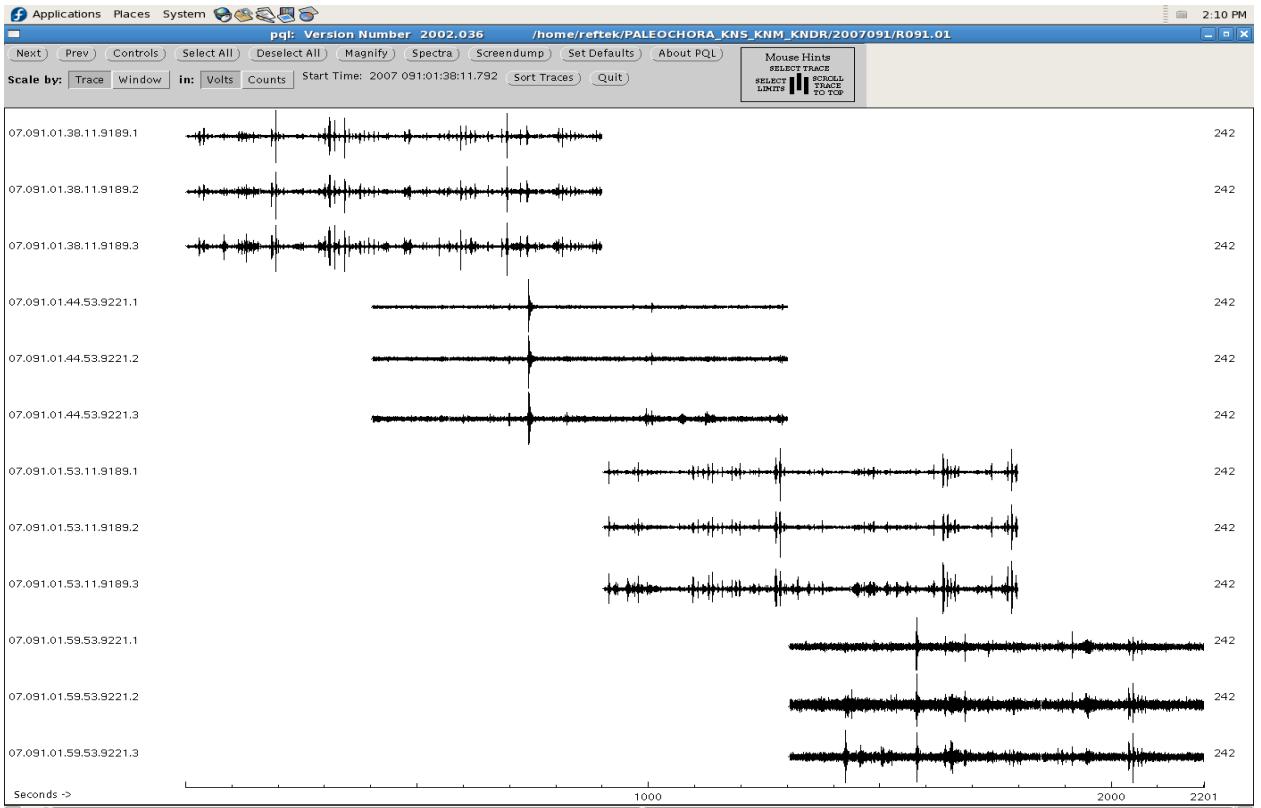
## A2: EARTHQUAKE SAMPLES RECORDED FROM THE TEMPORAL SEISMOLOGICAL NETWORK OF CRETE

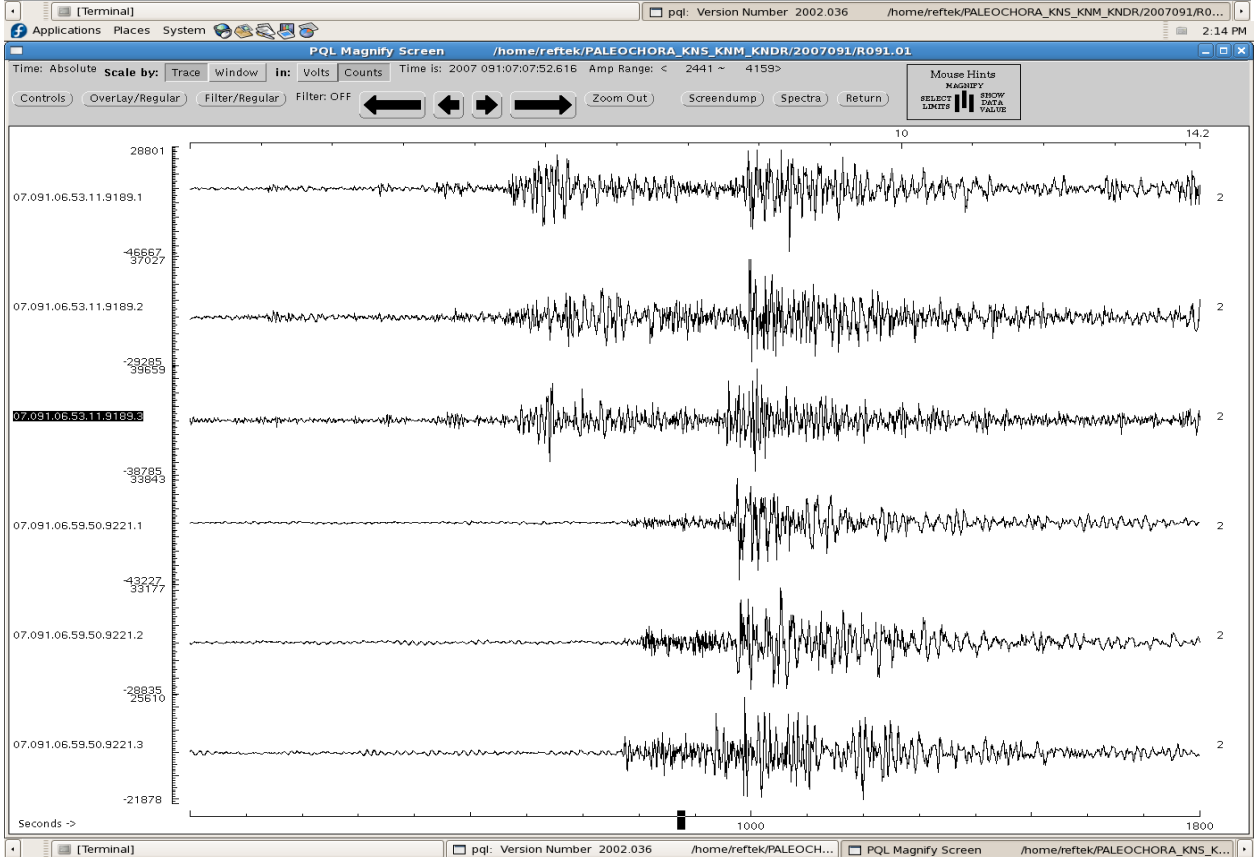
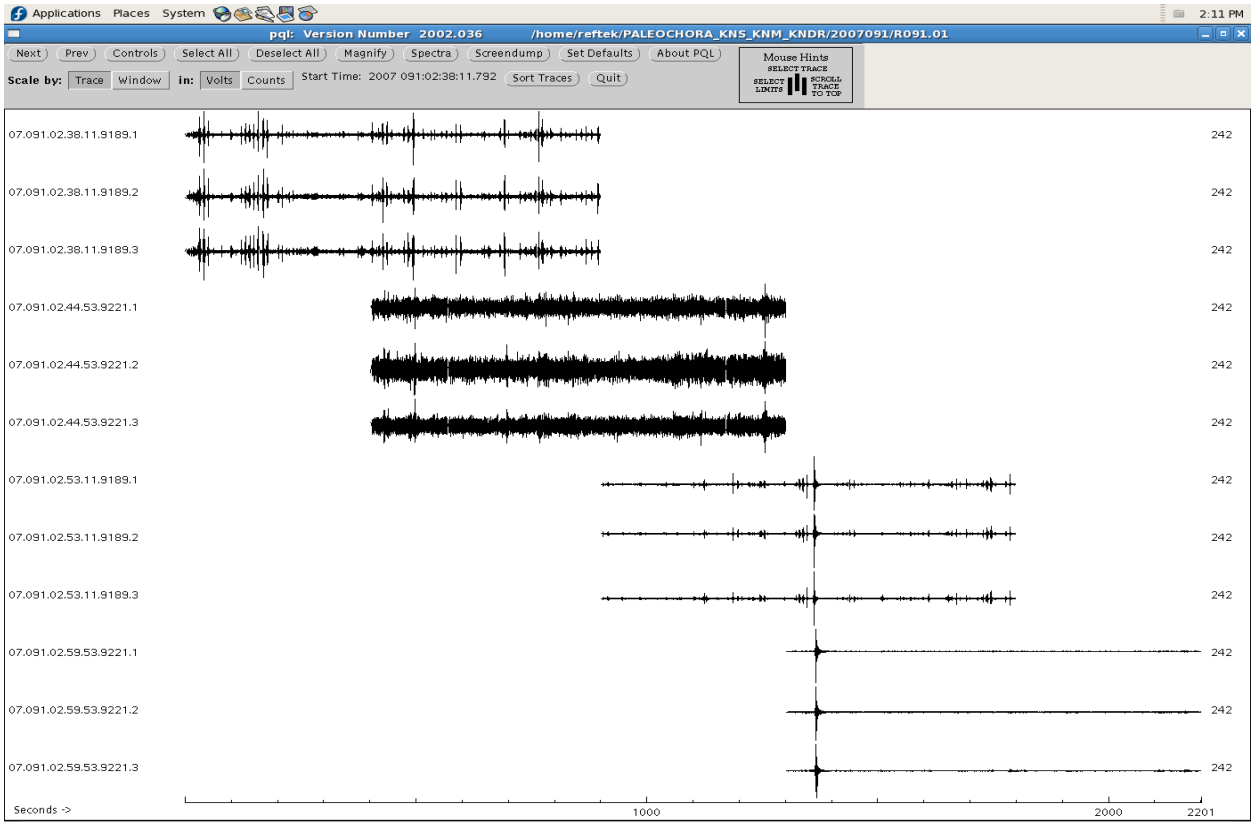


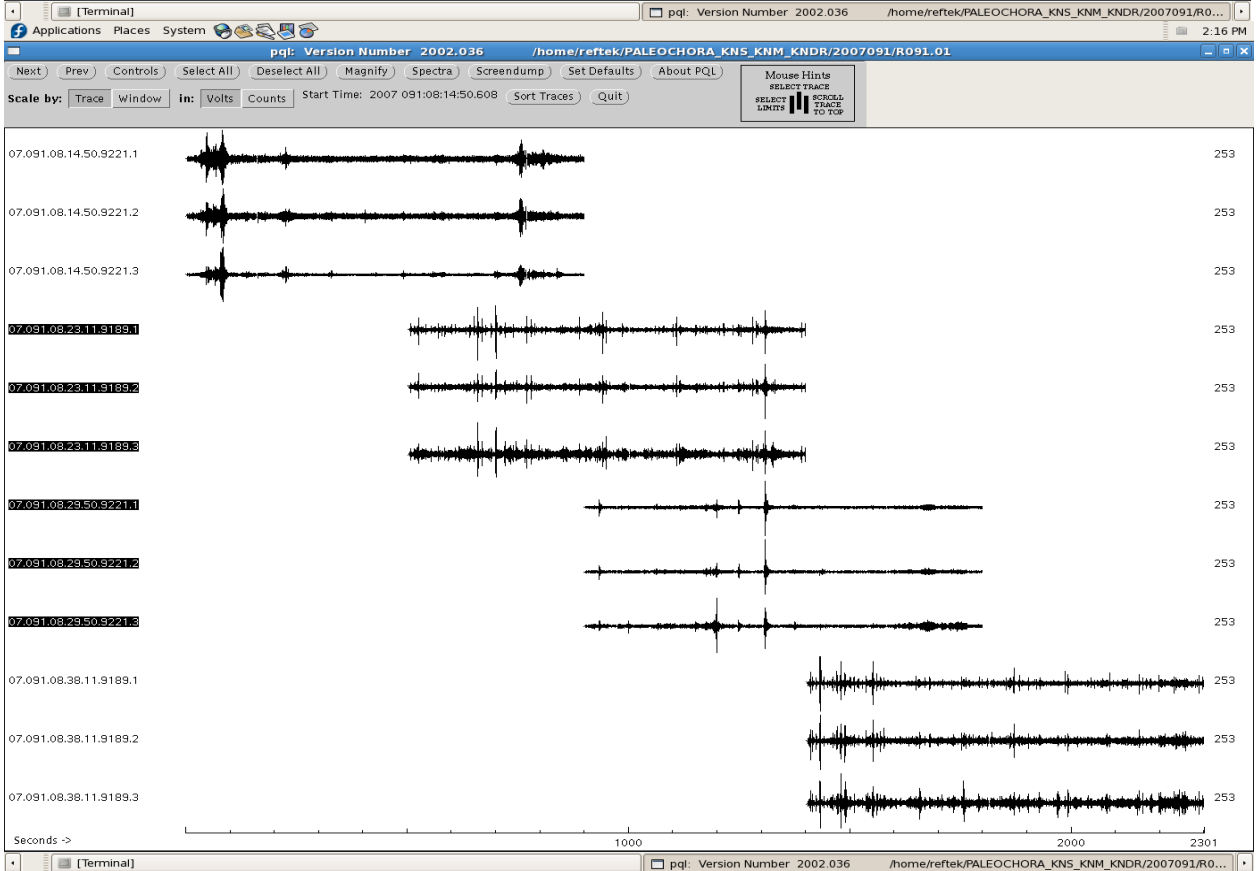
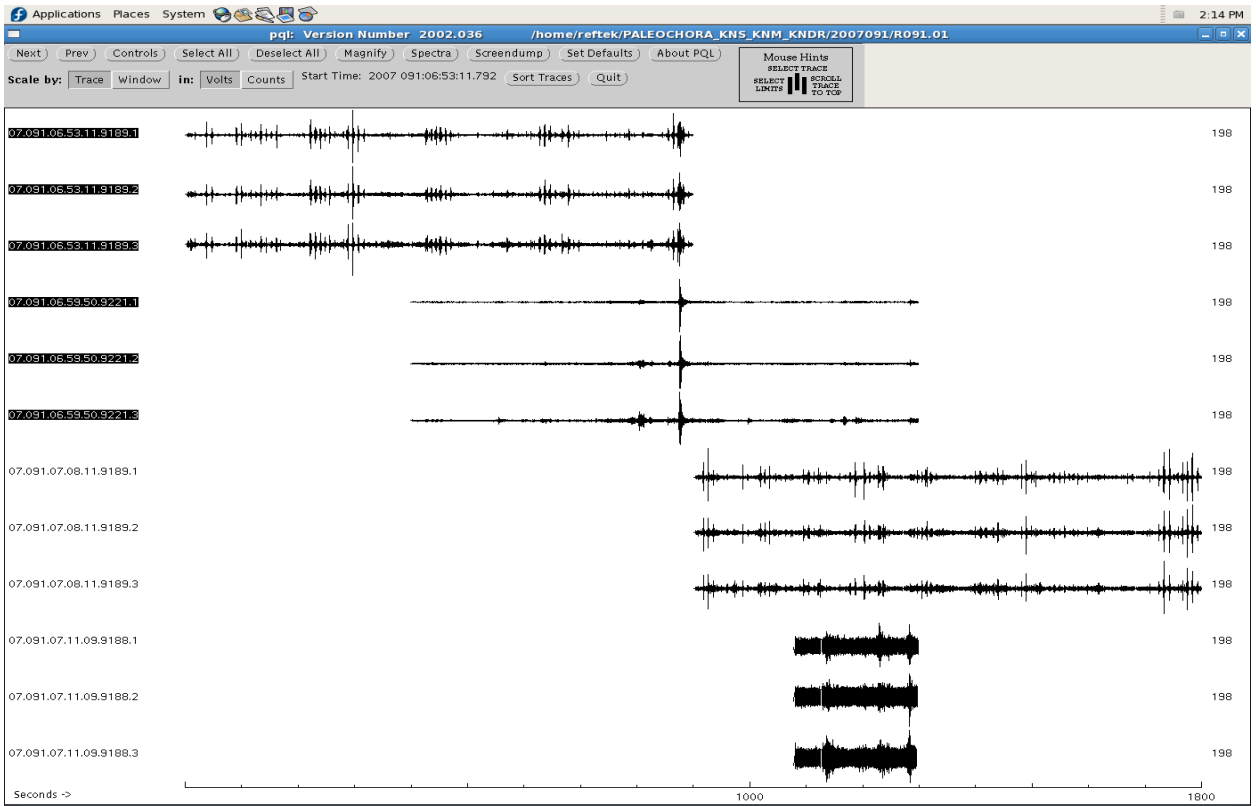


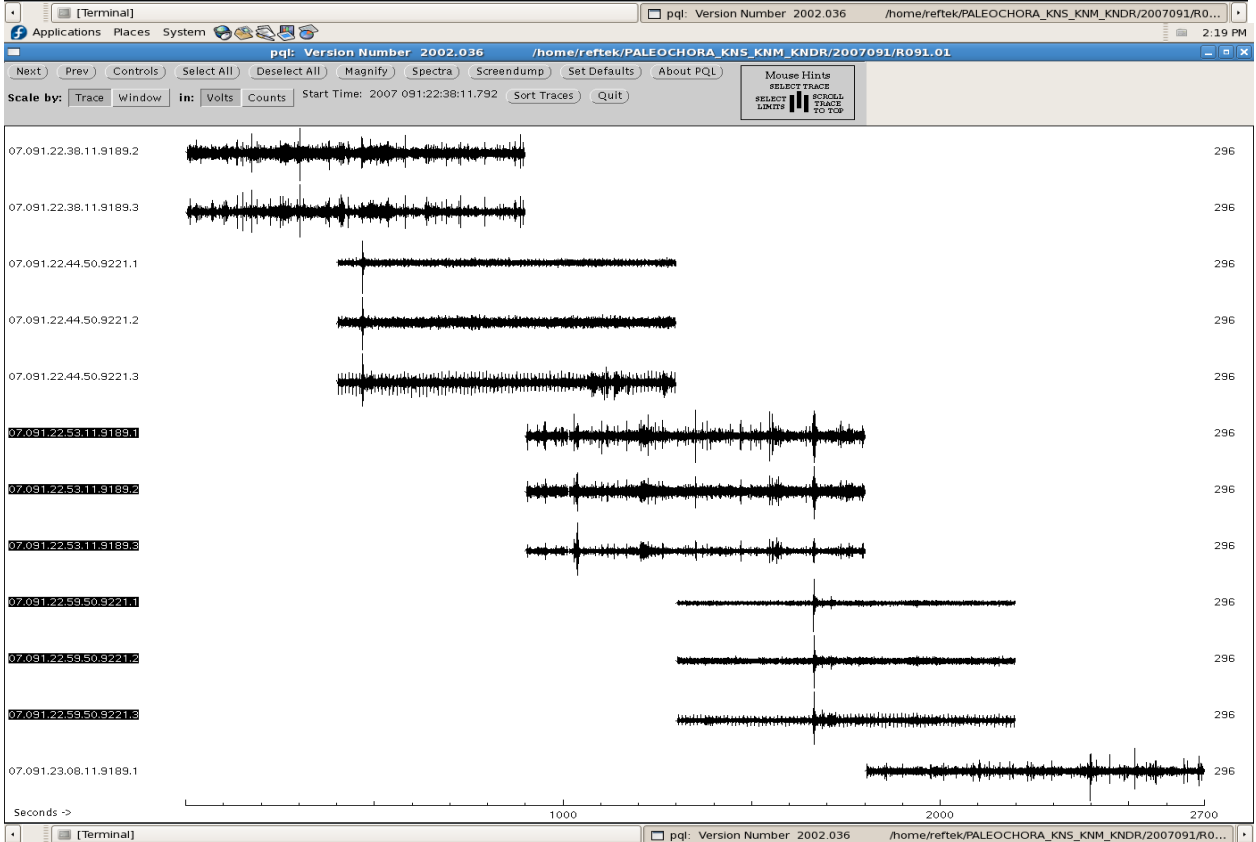
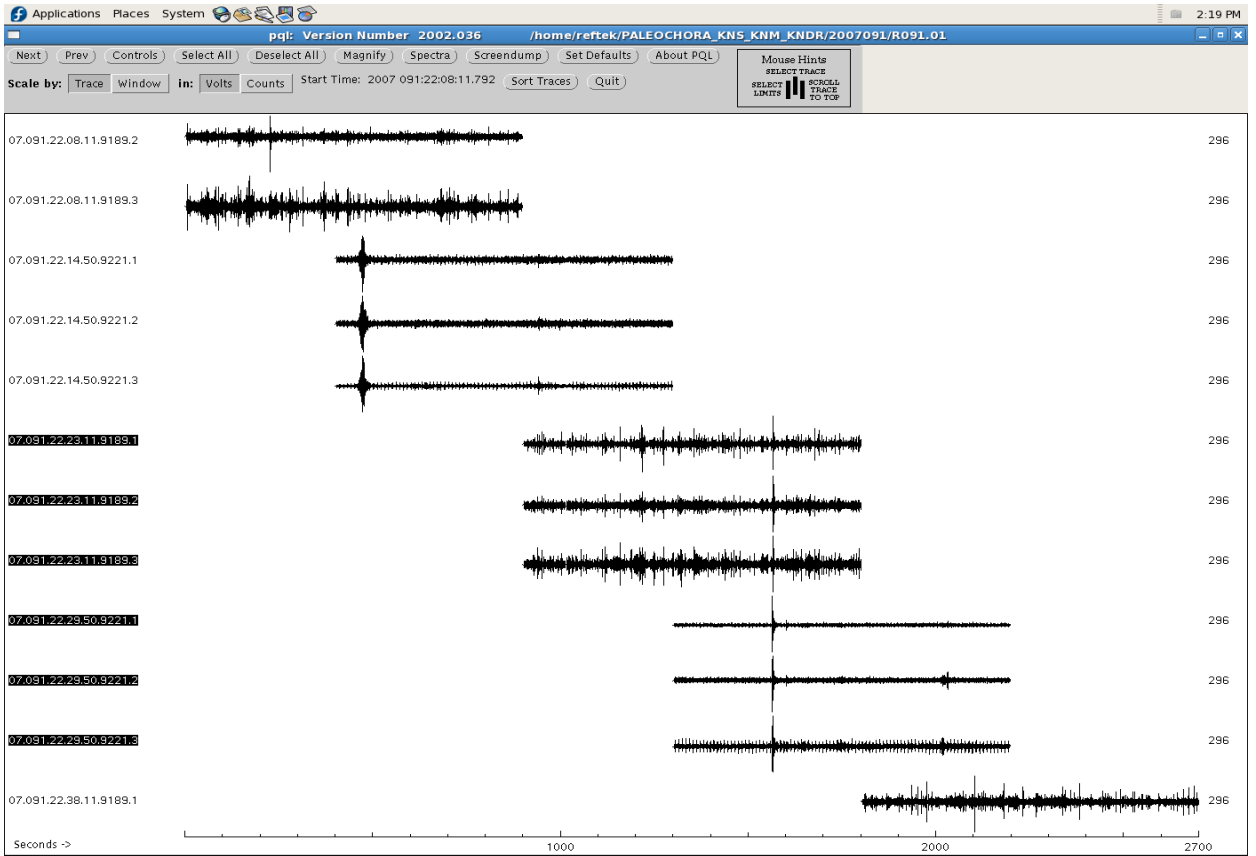


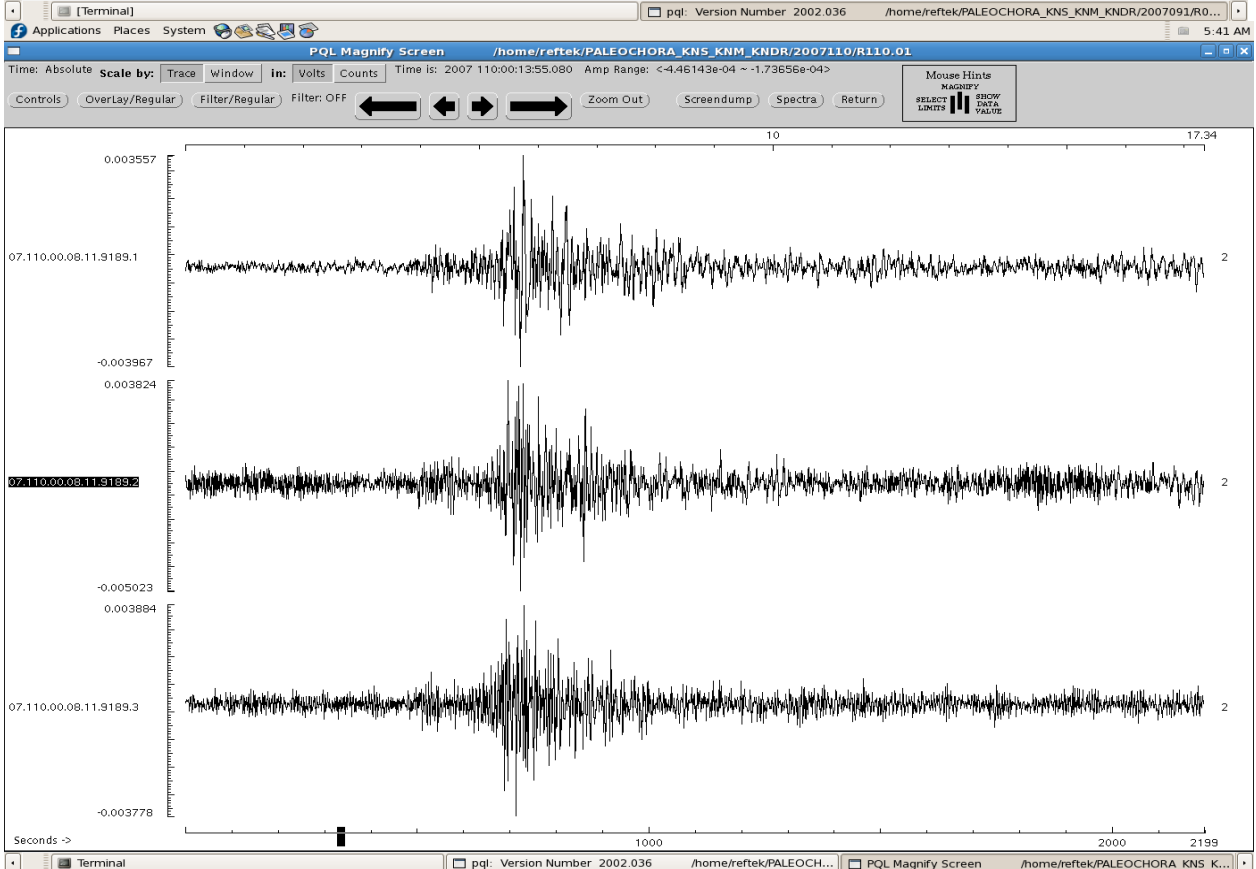
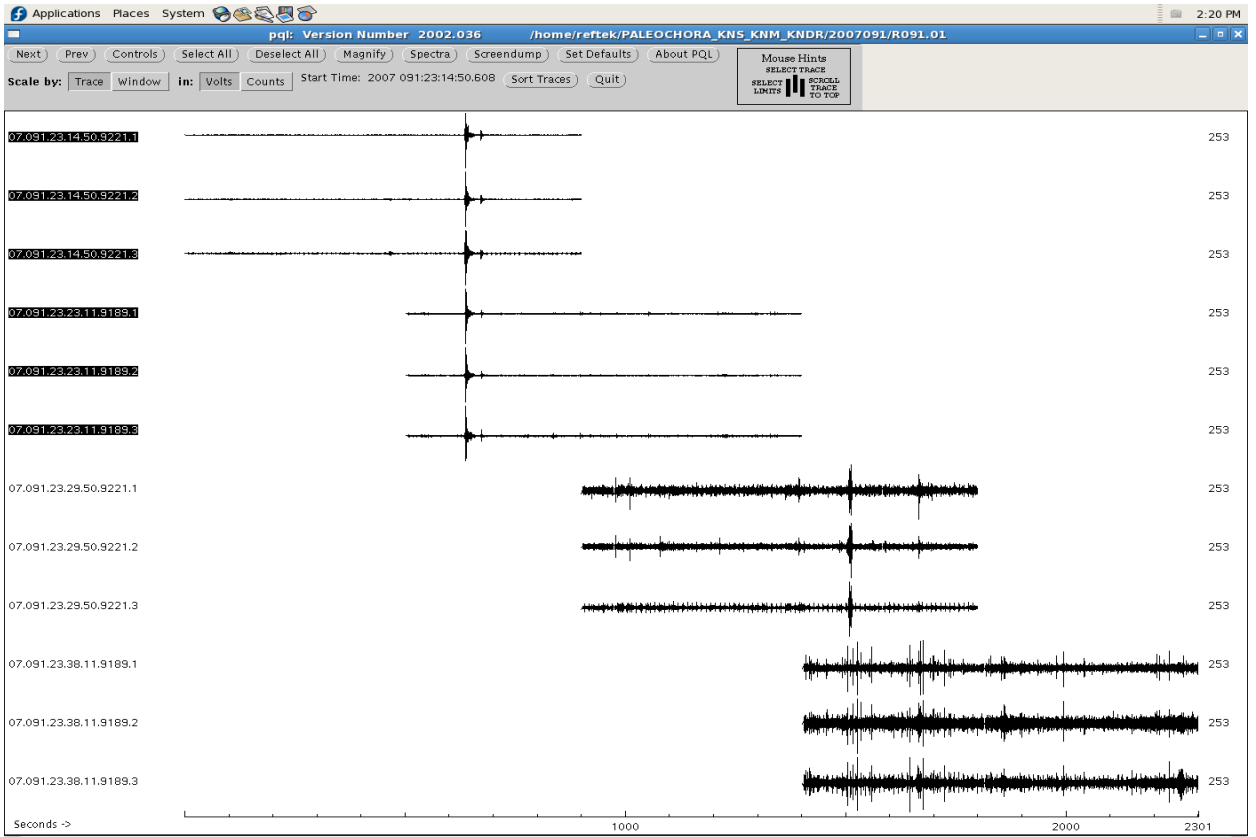


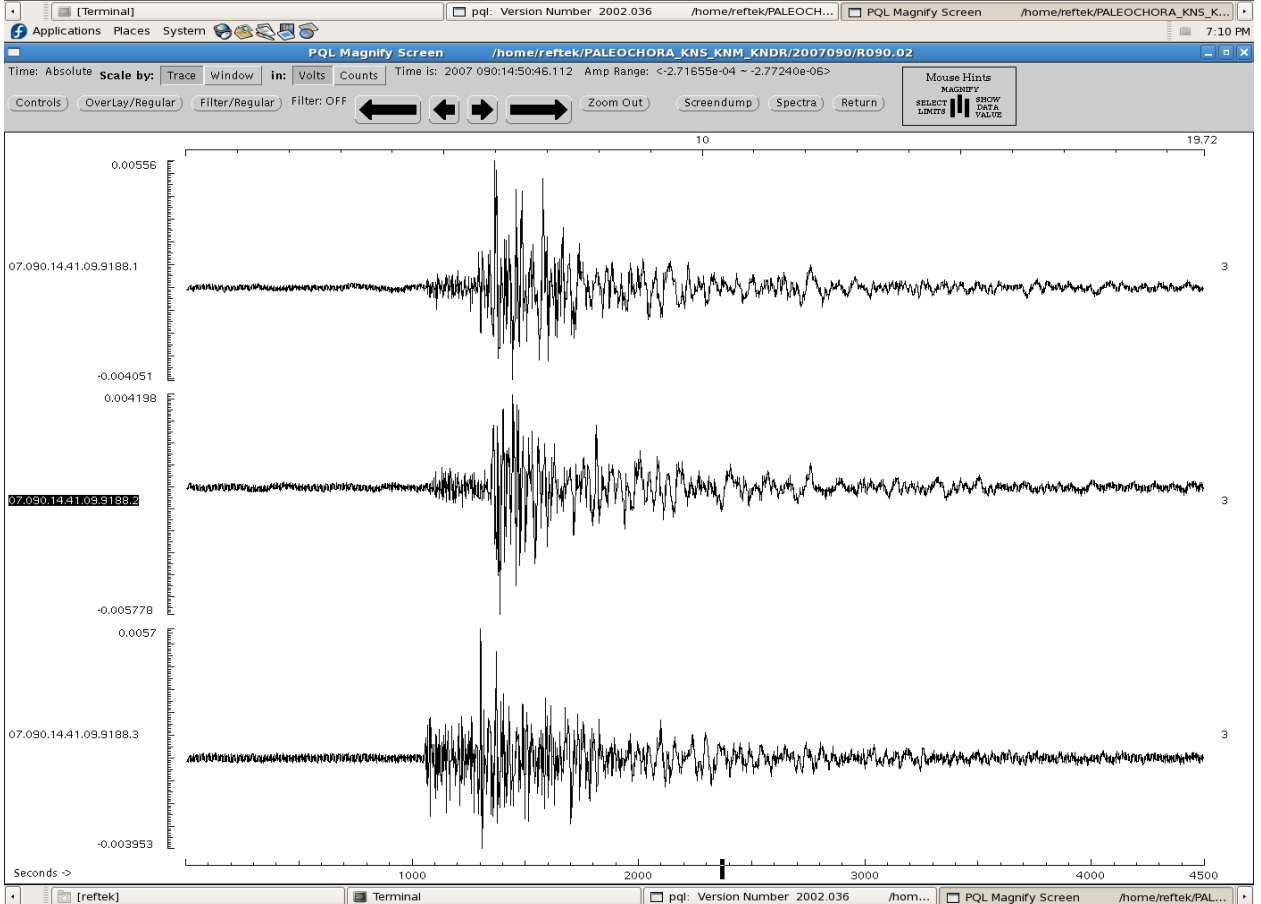
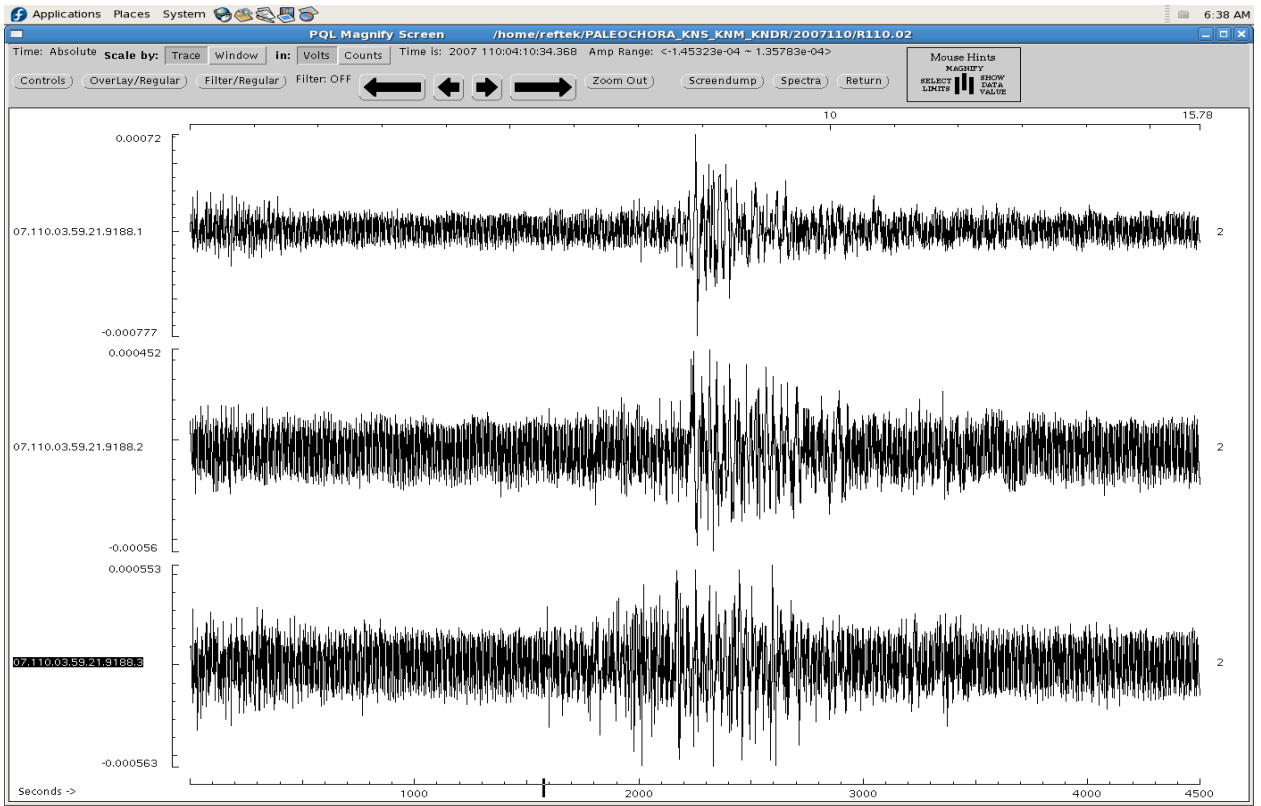




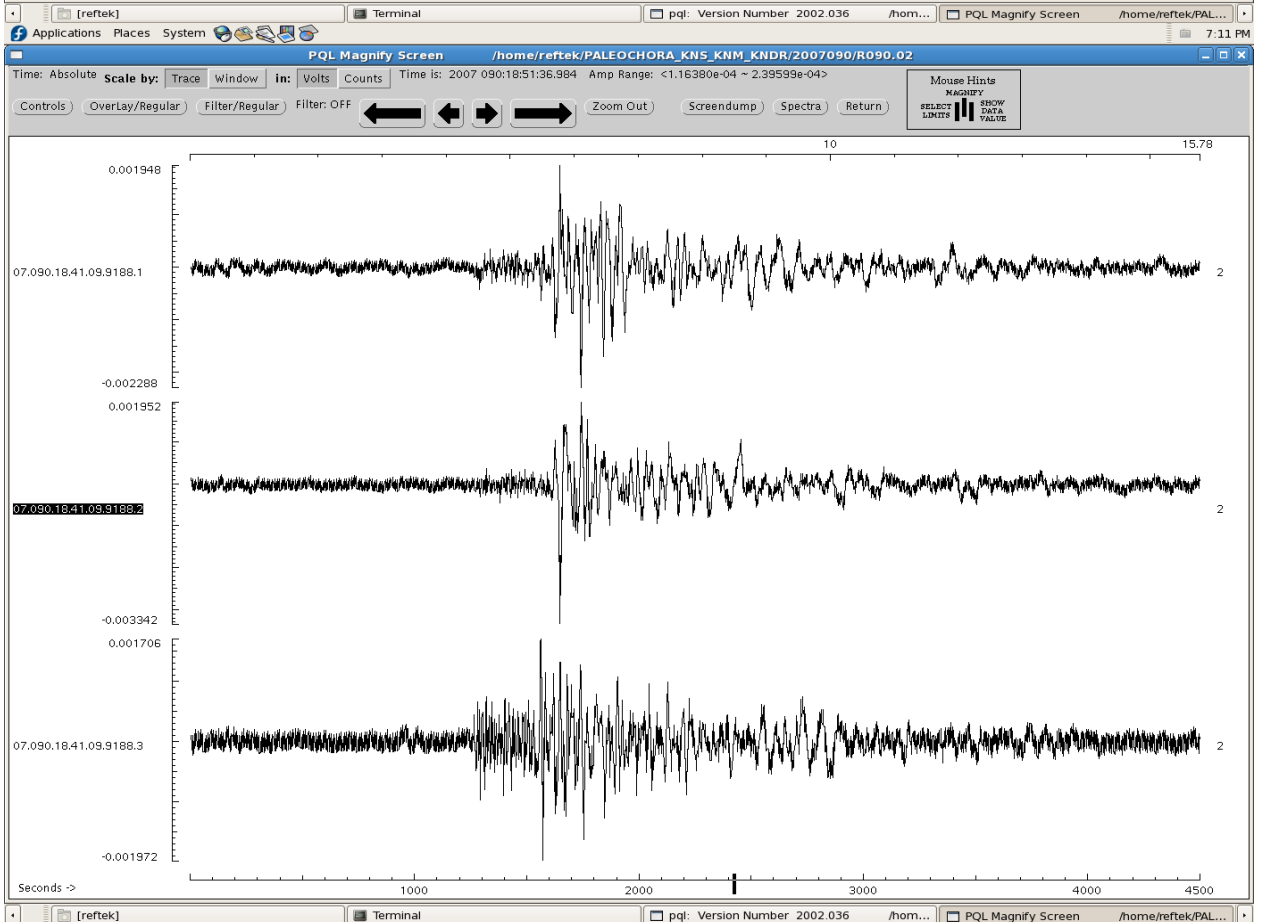
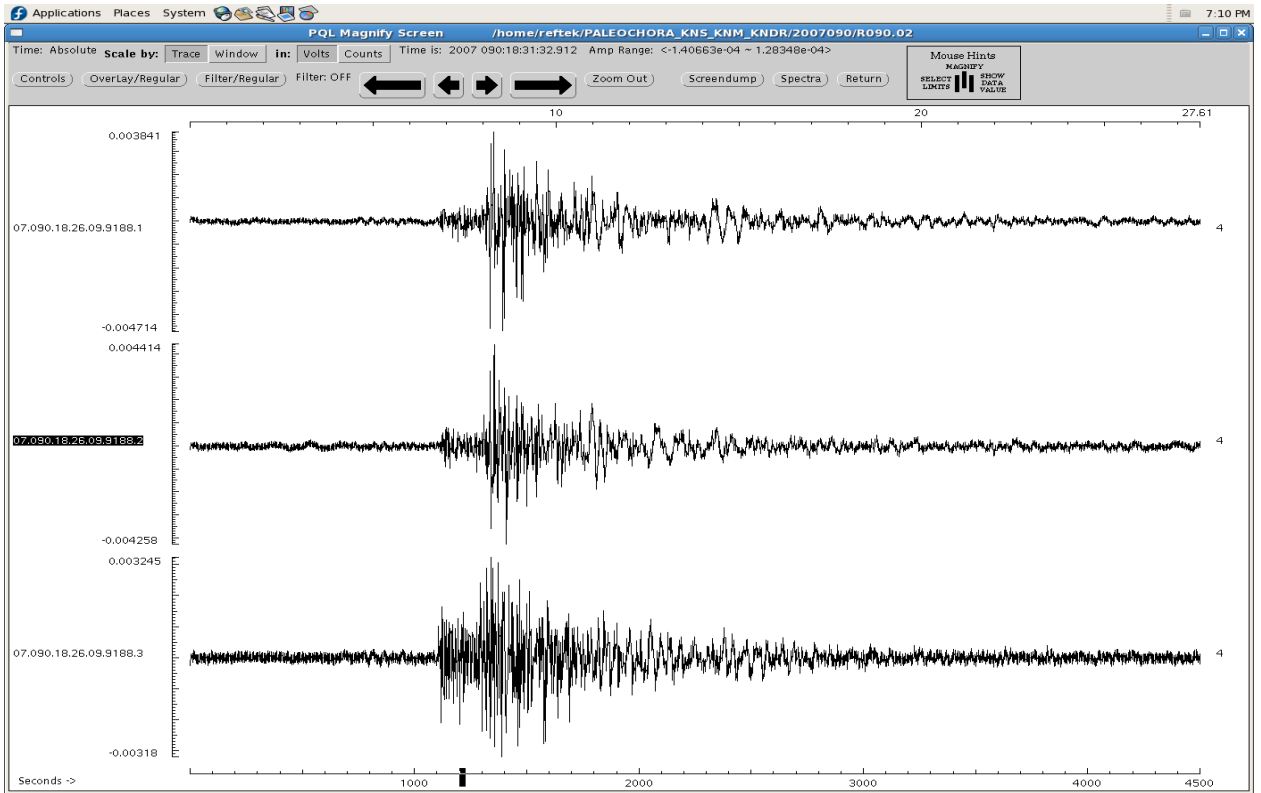


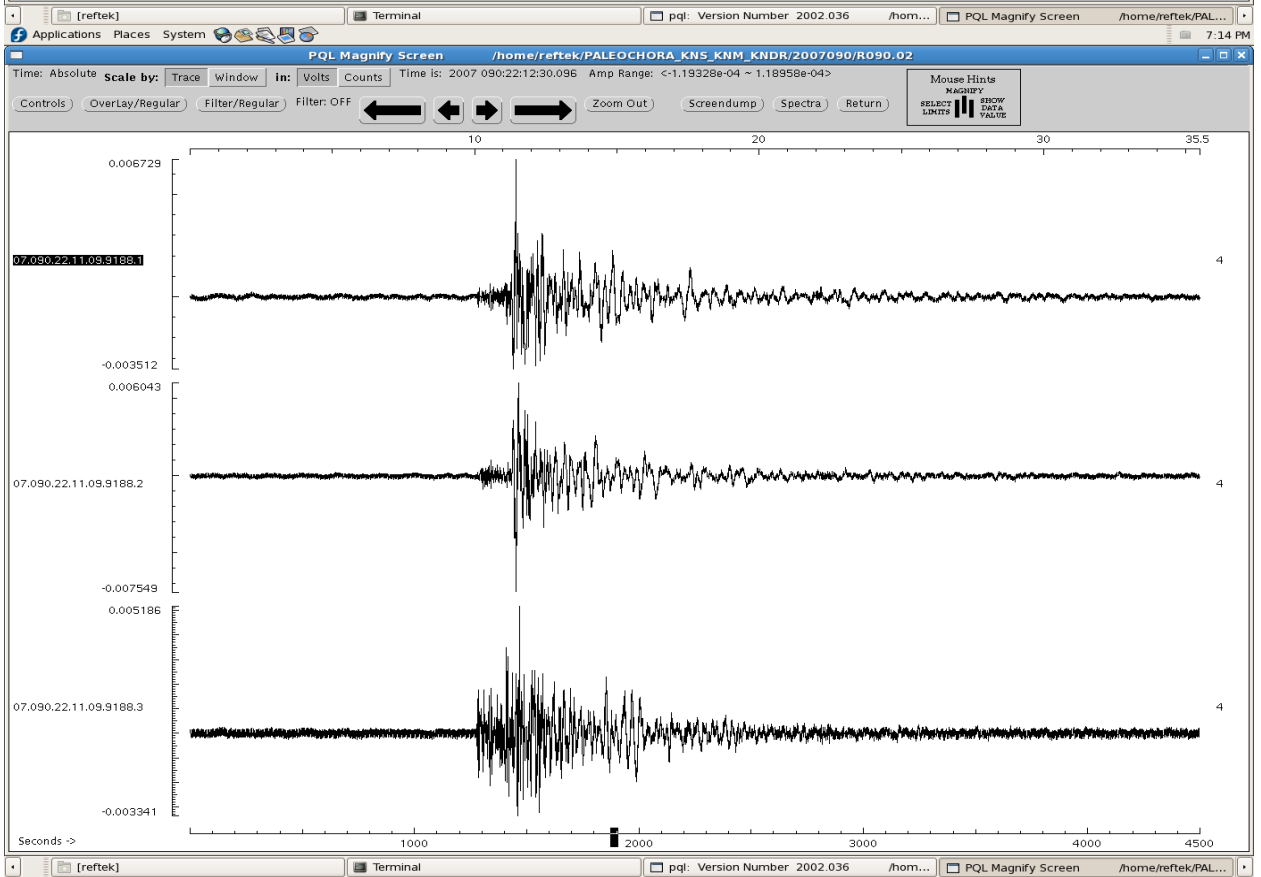
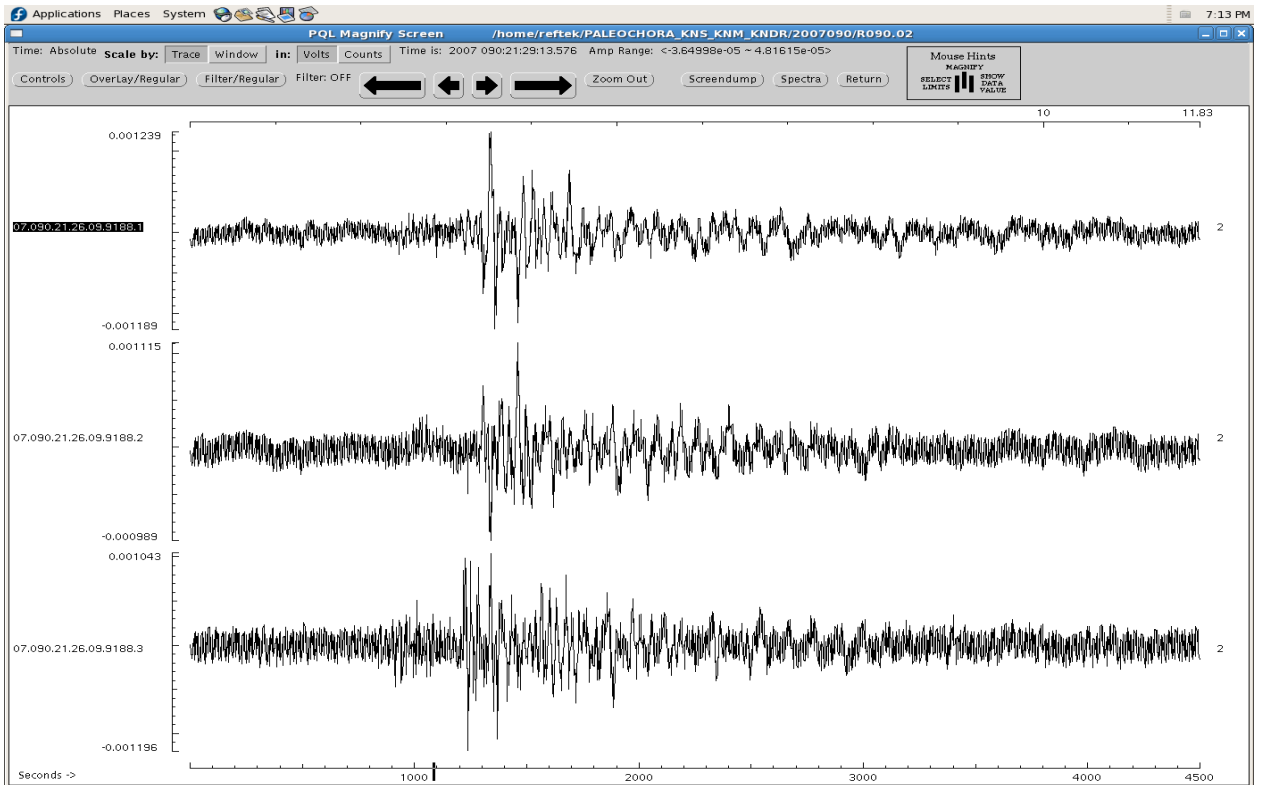


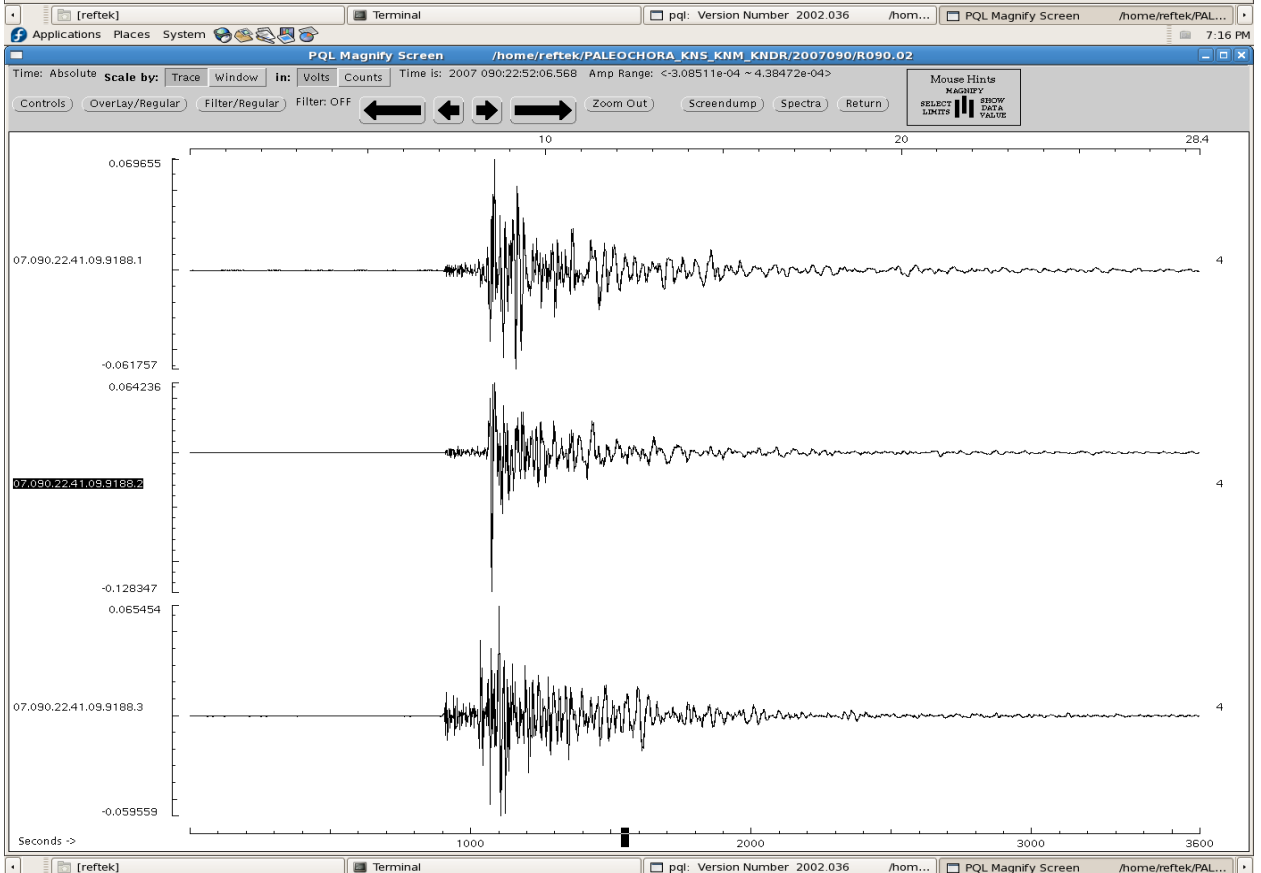
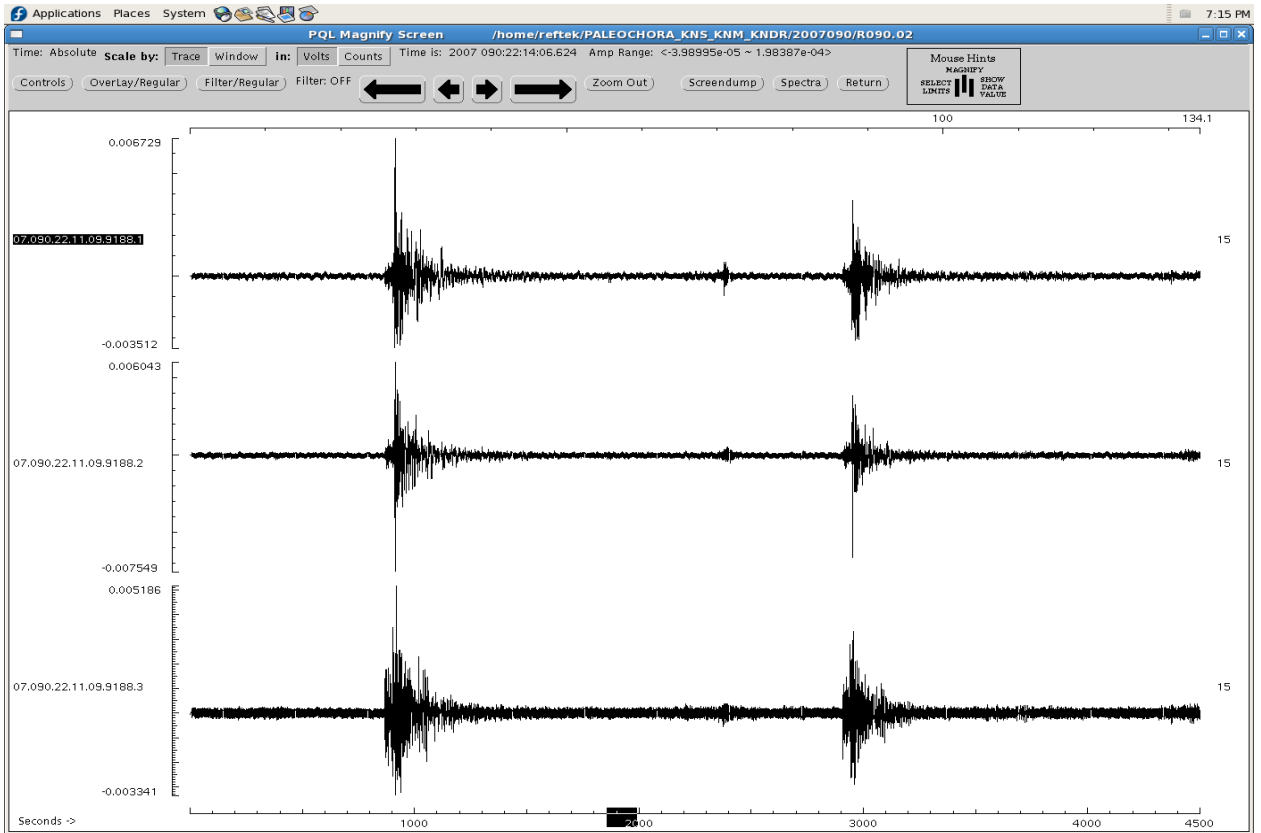


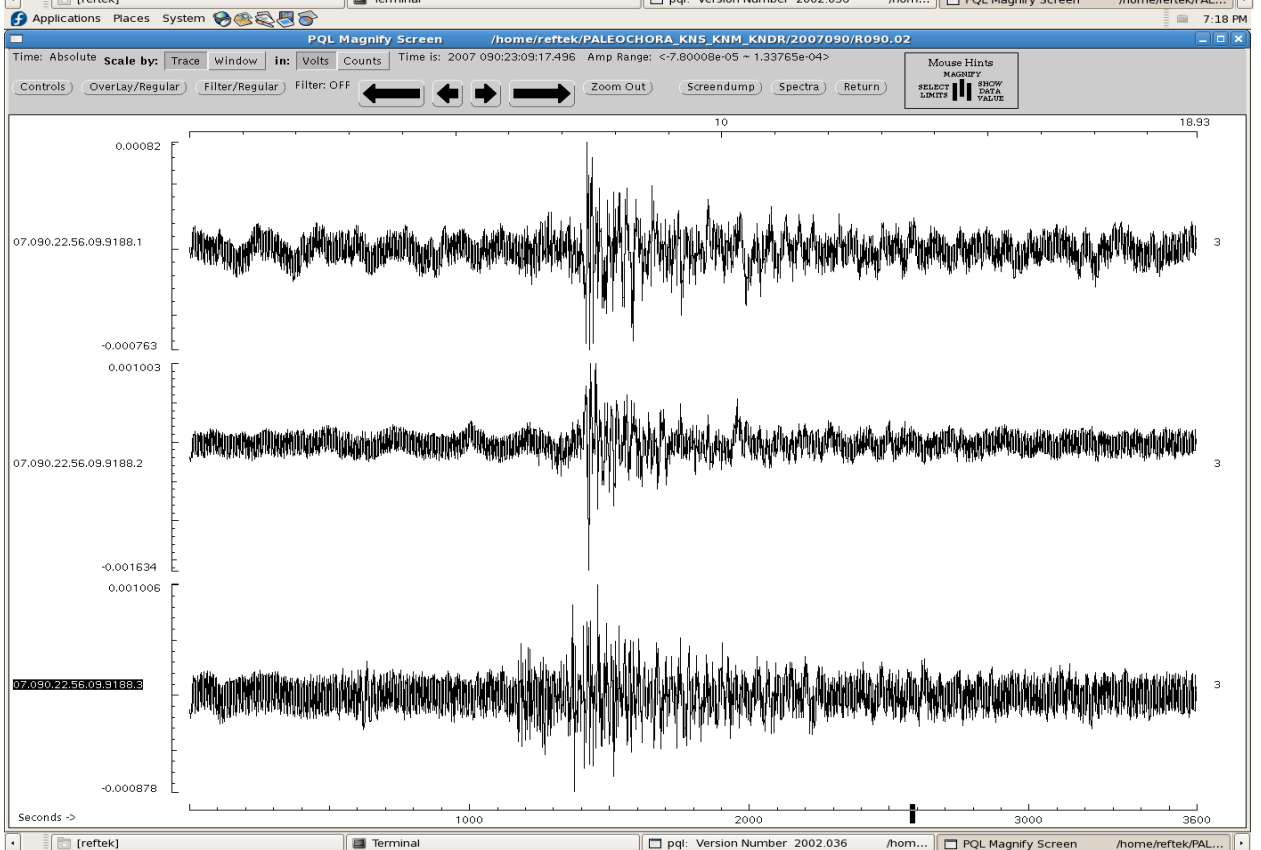
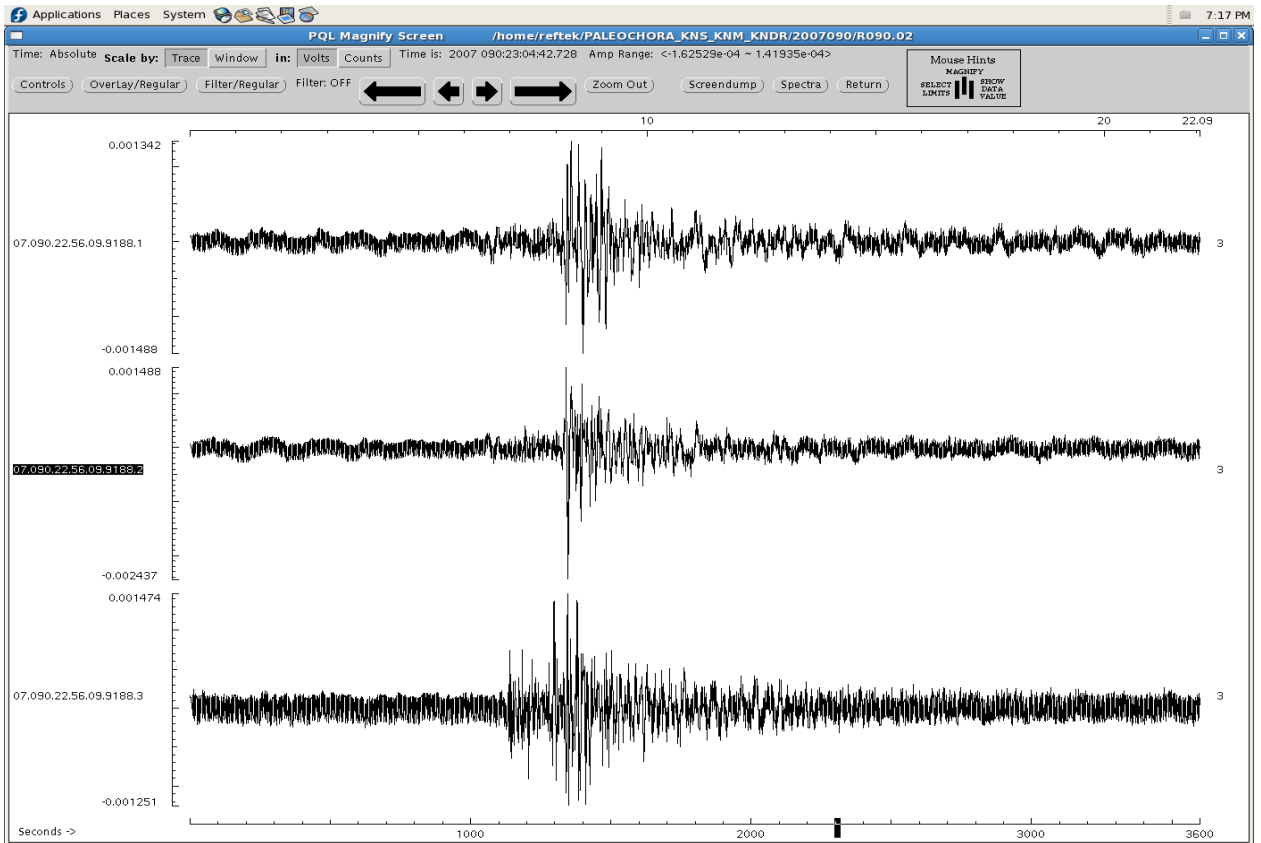


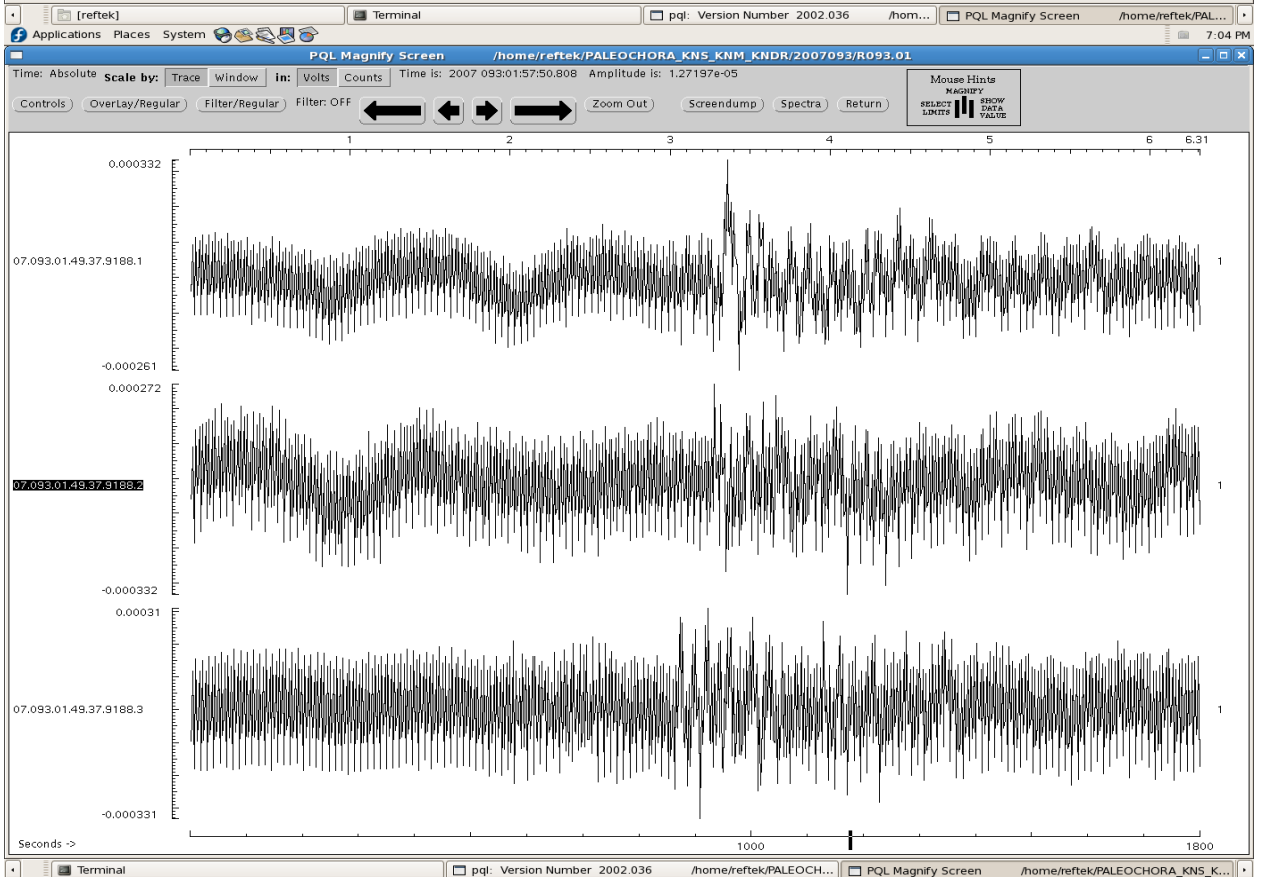
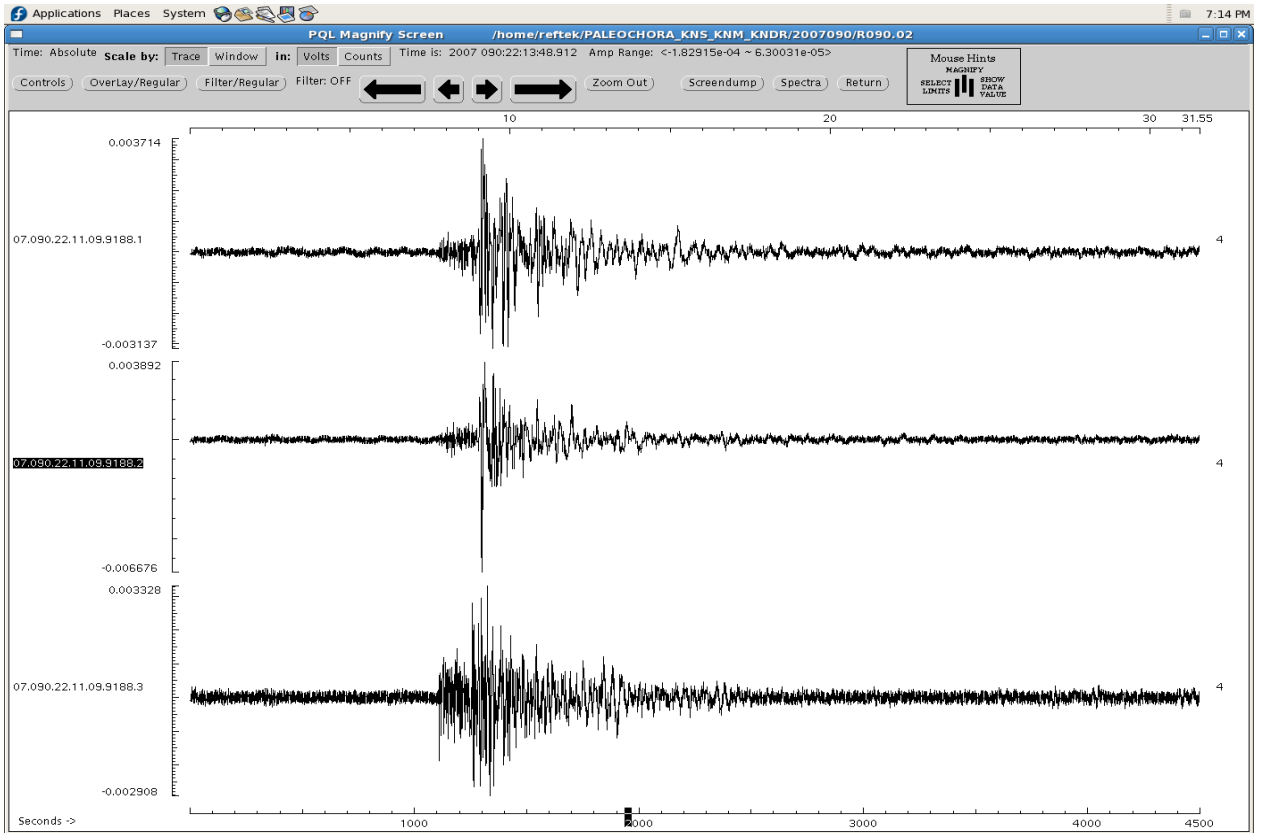


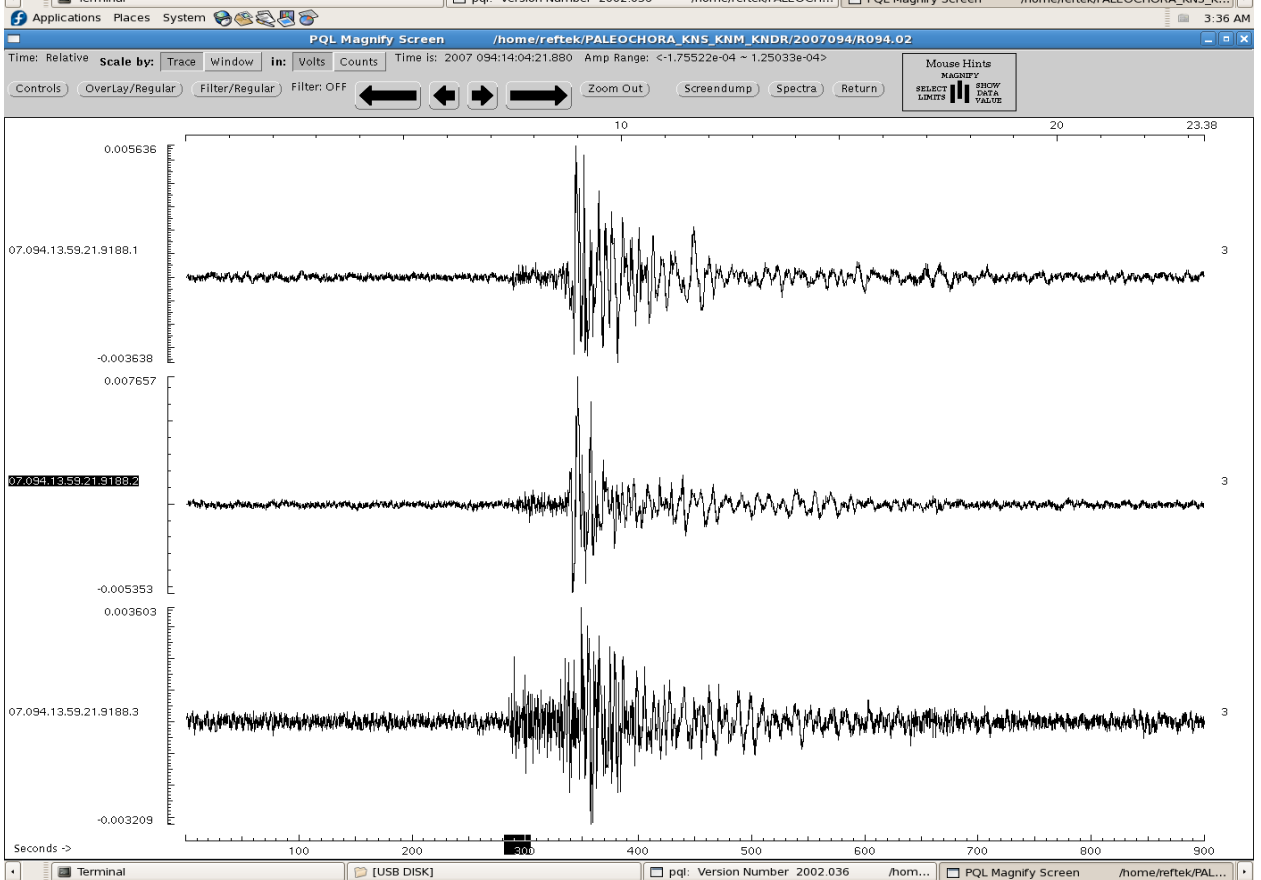
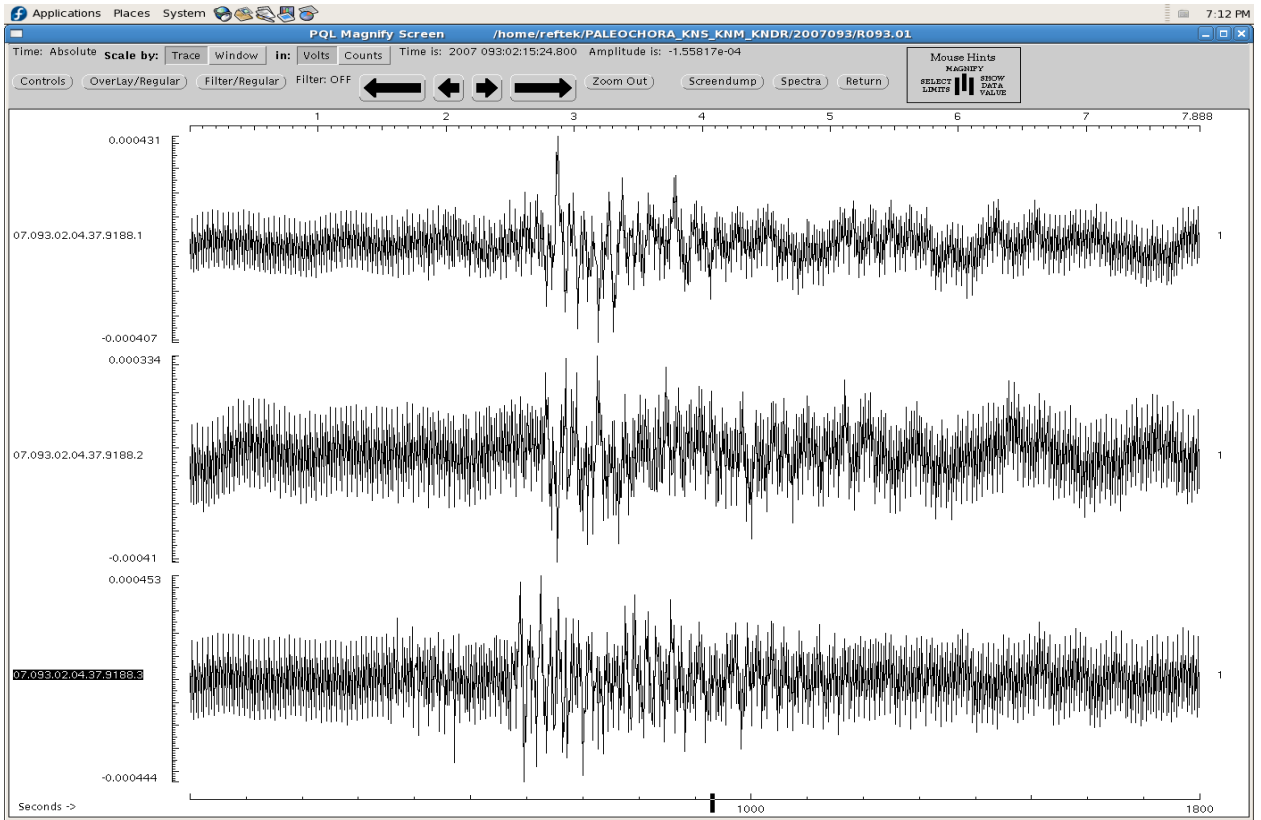


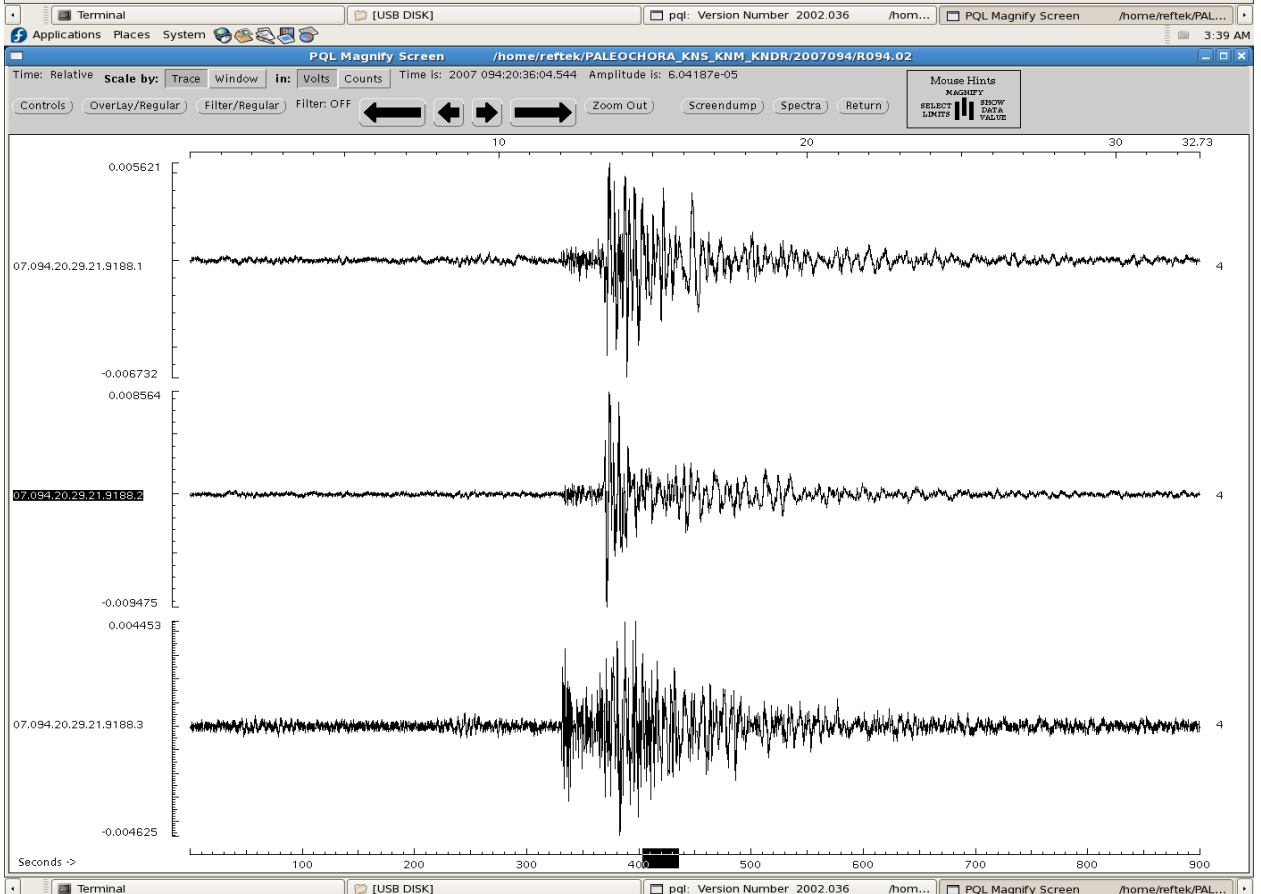
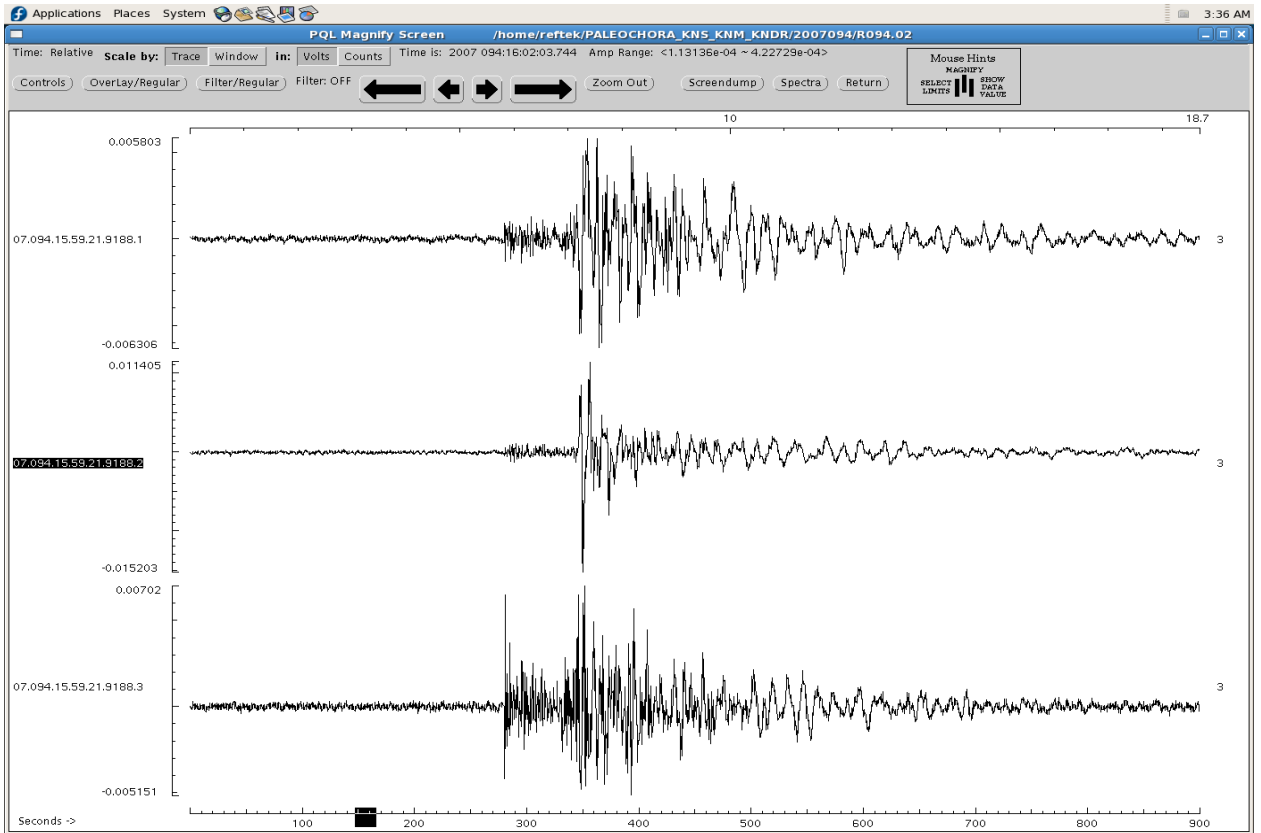


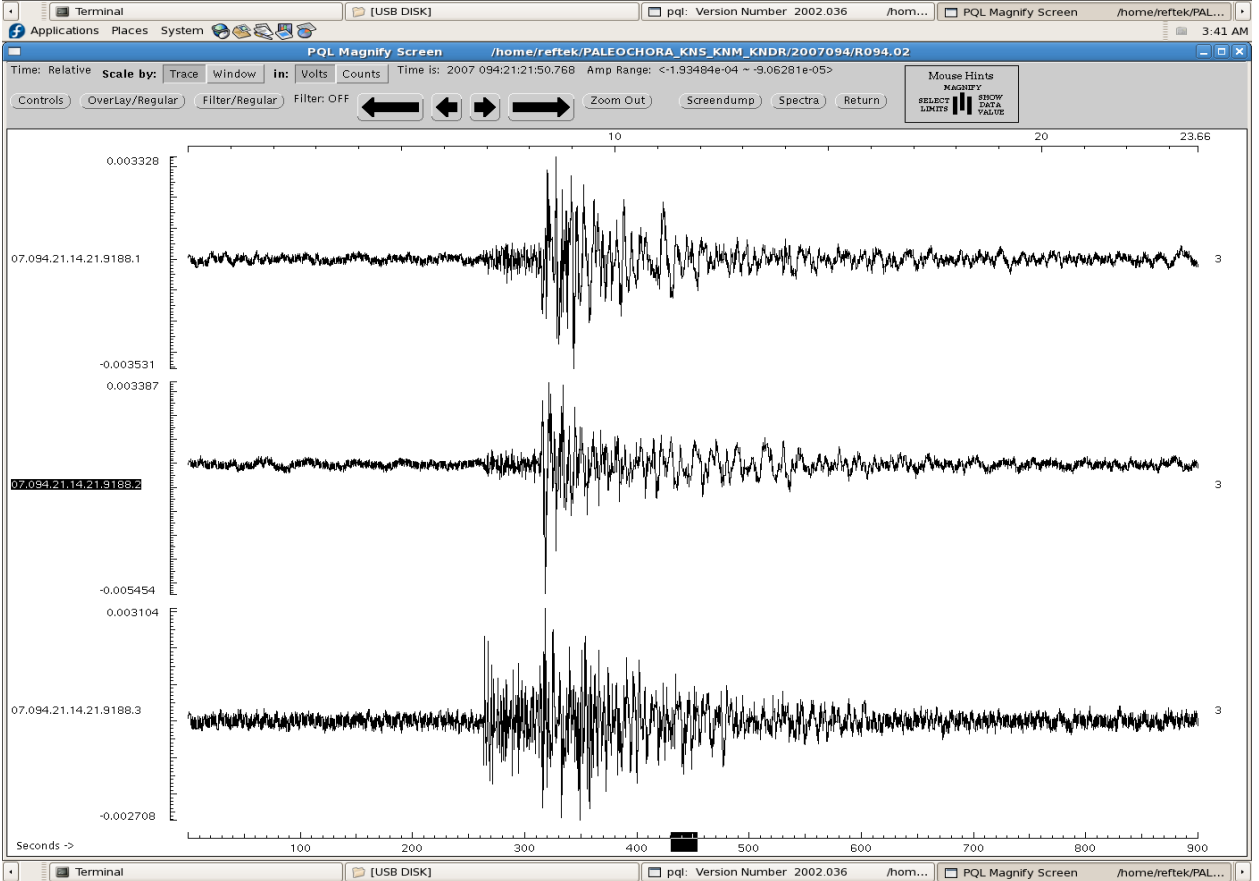
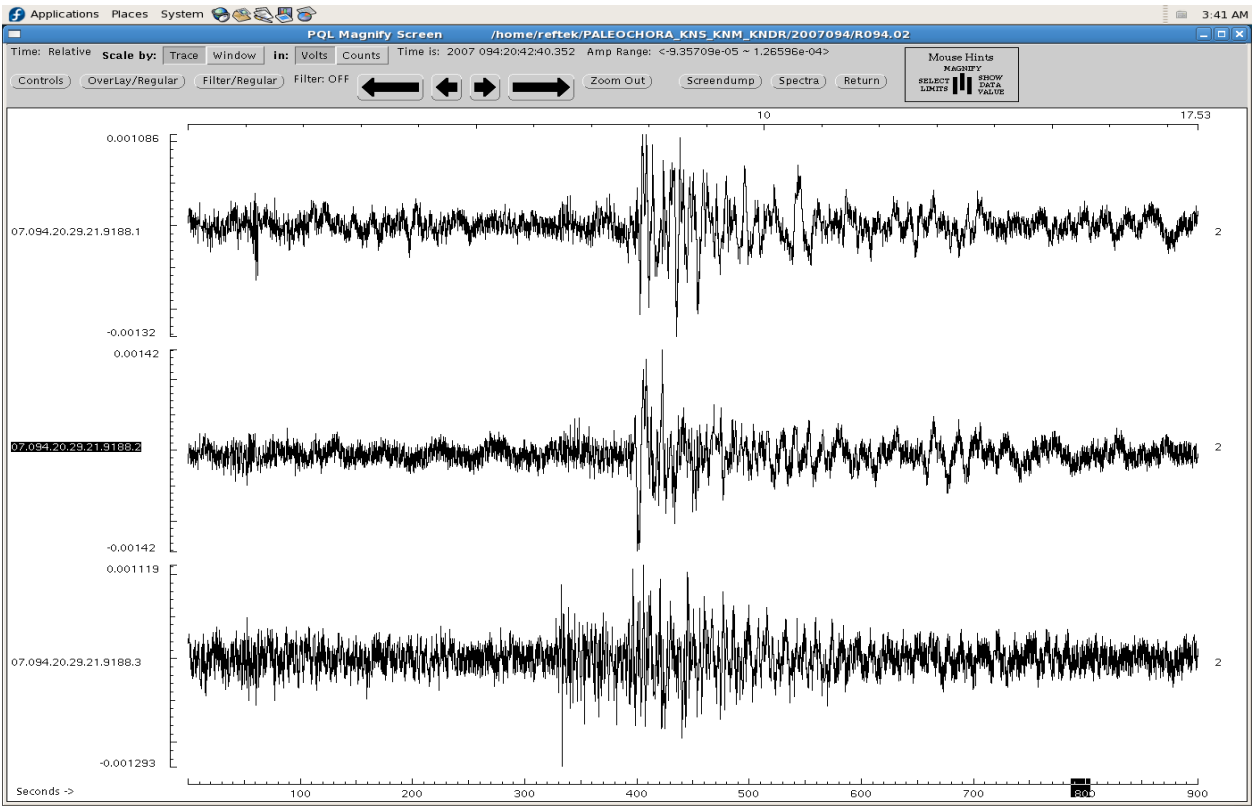




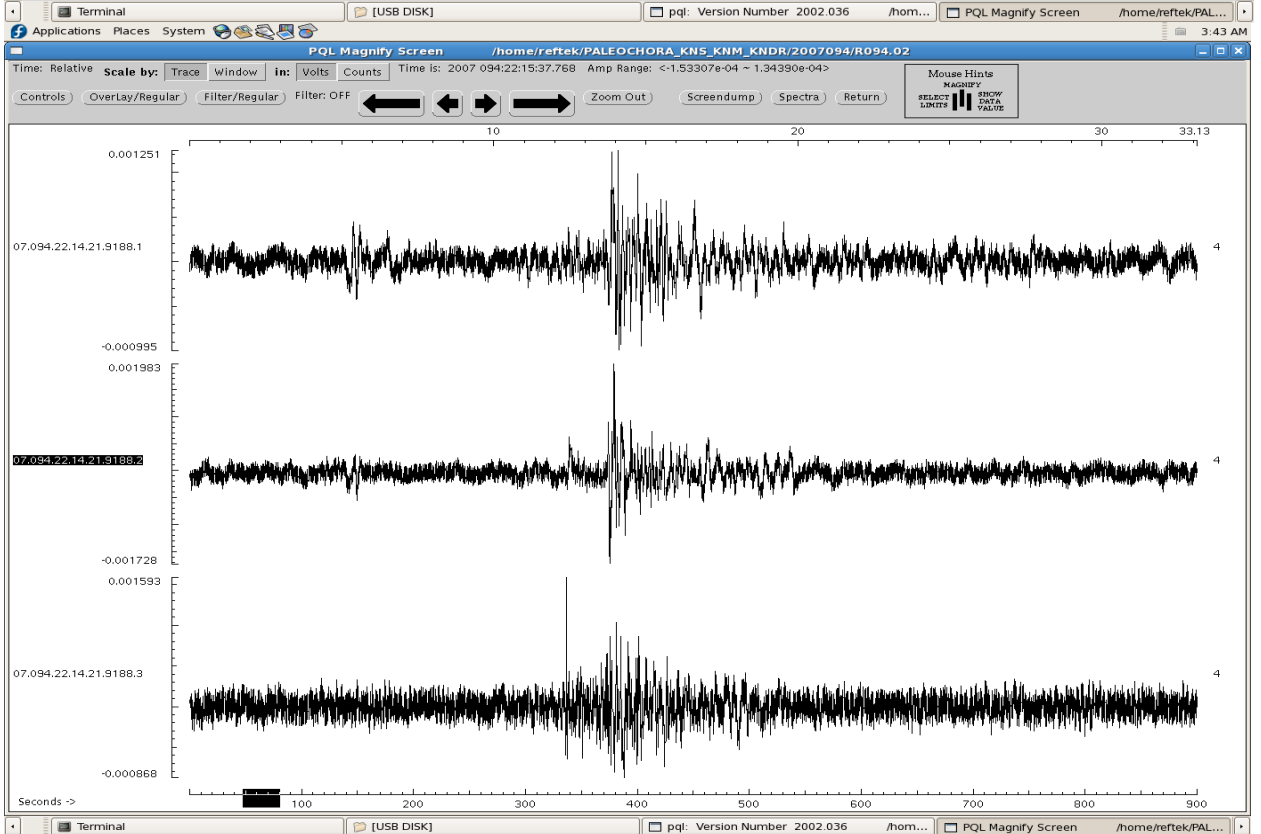
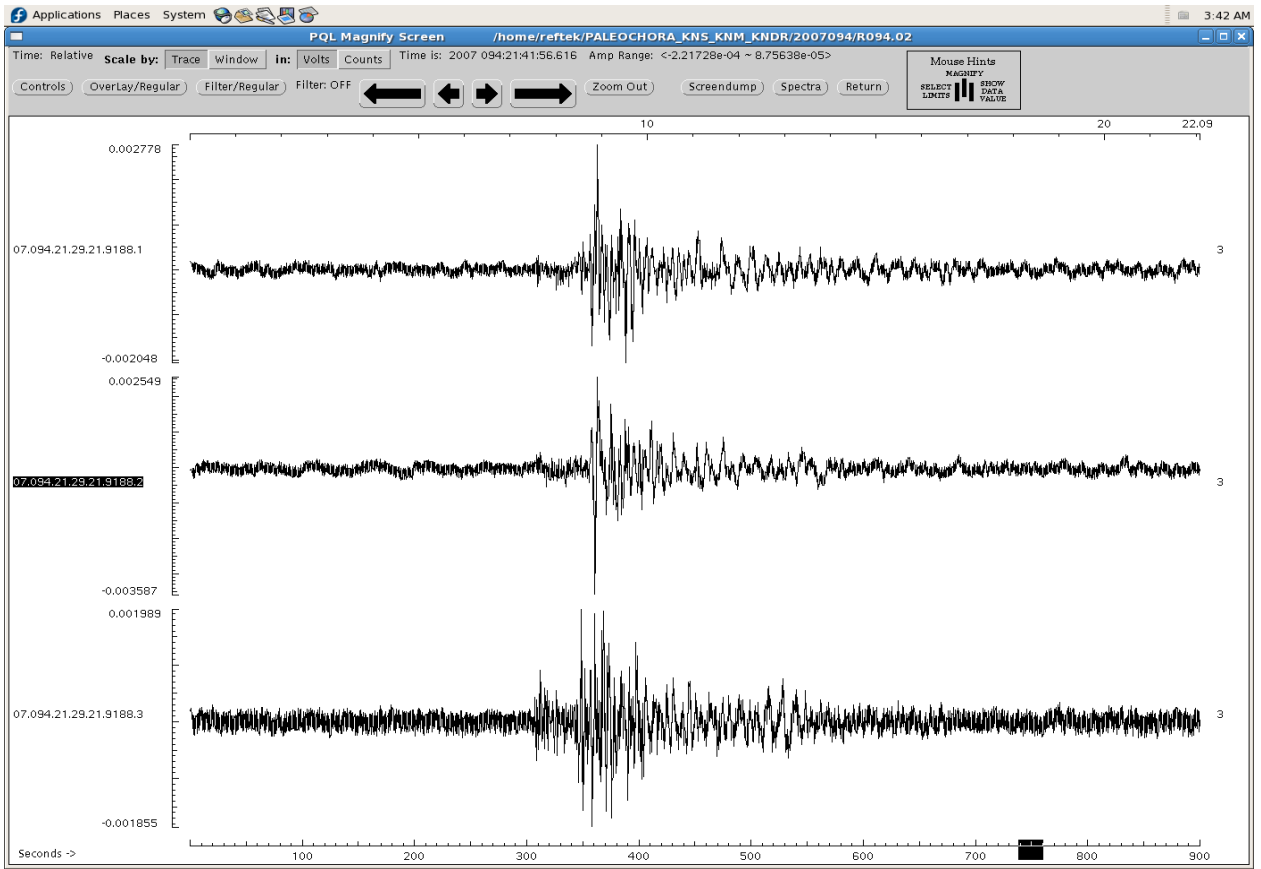


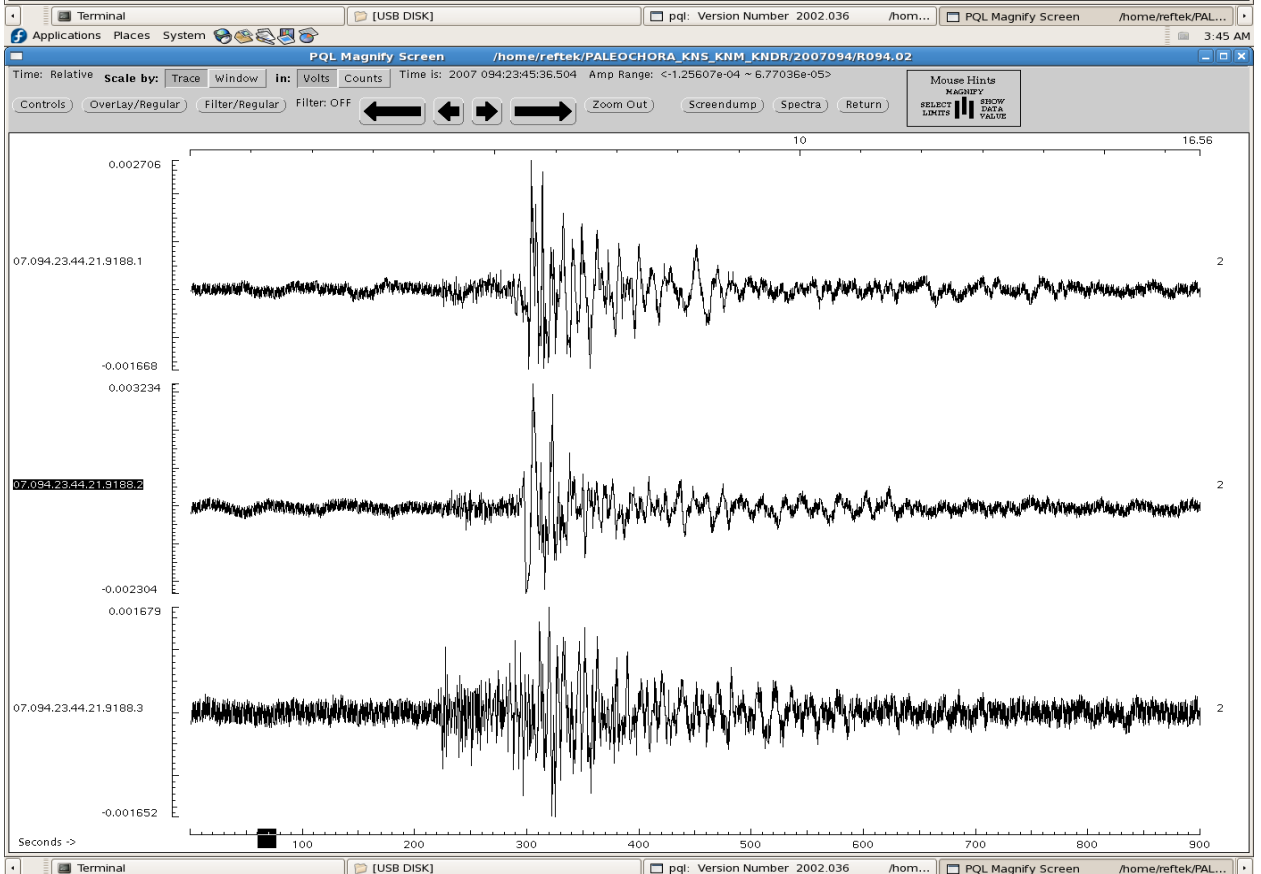
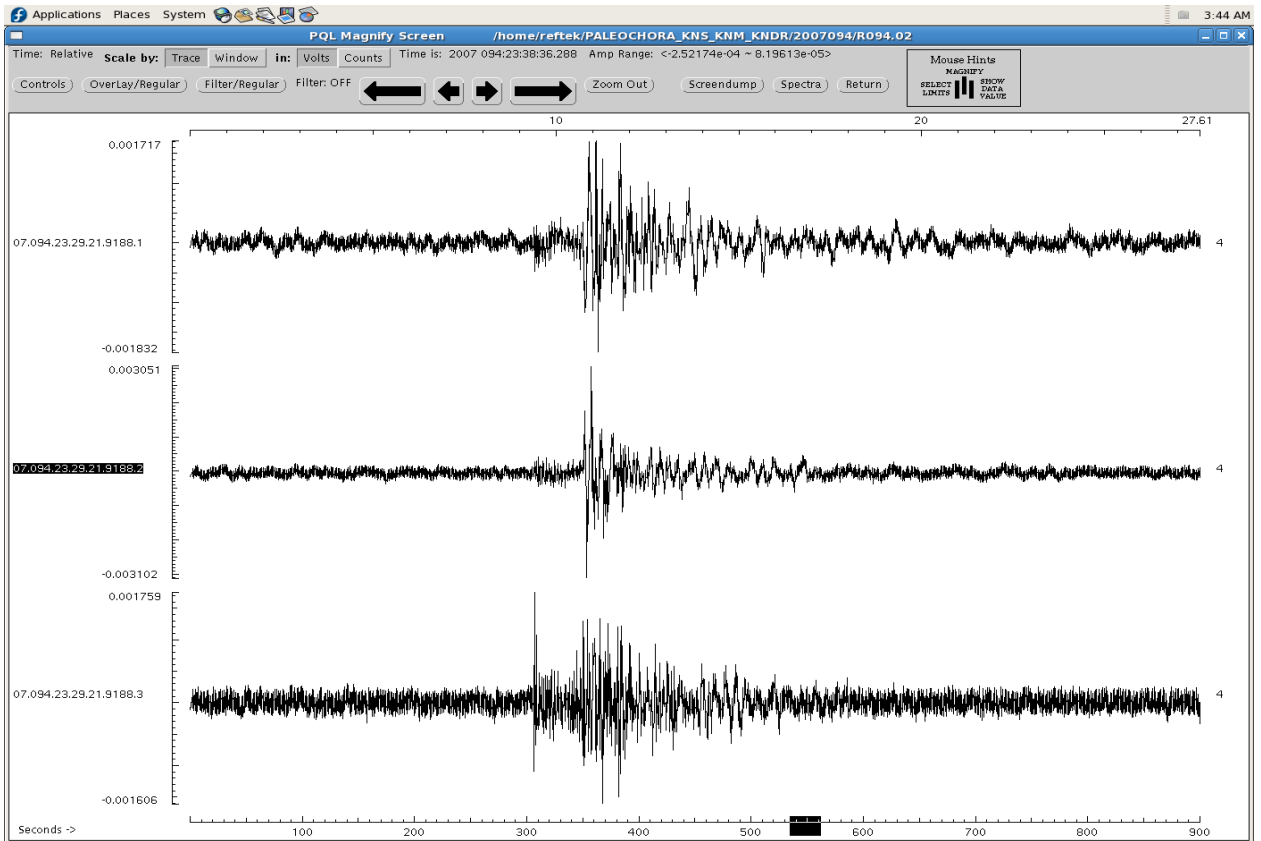


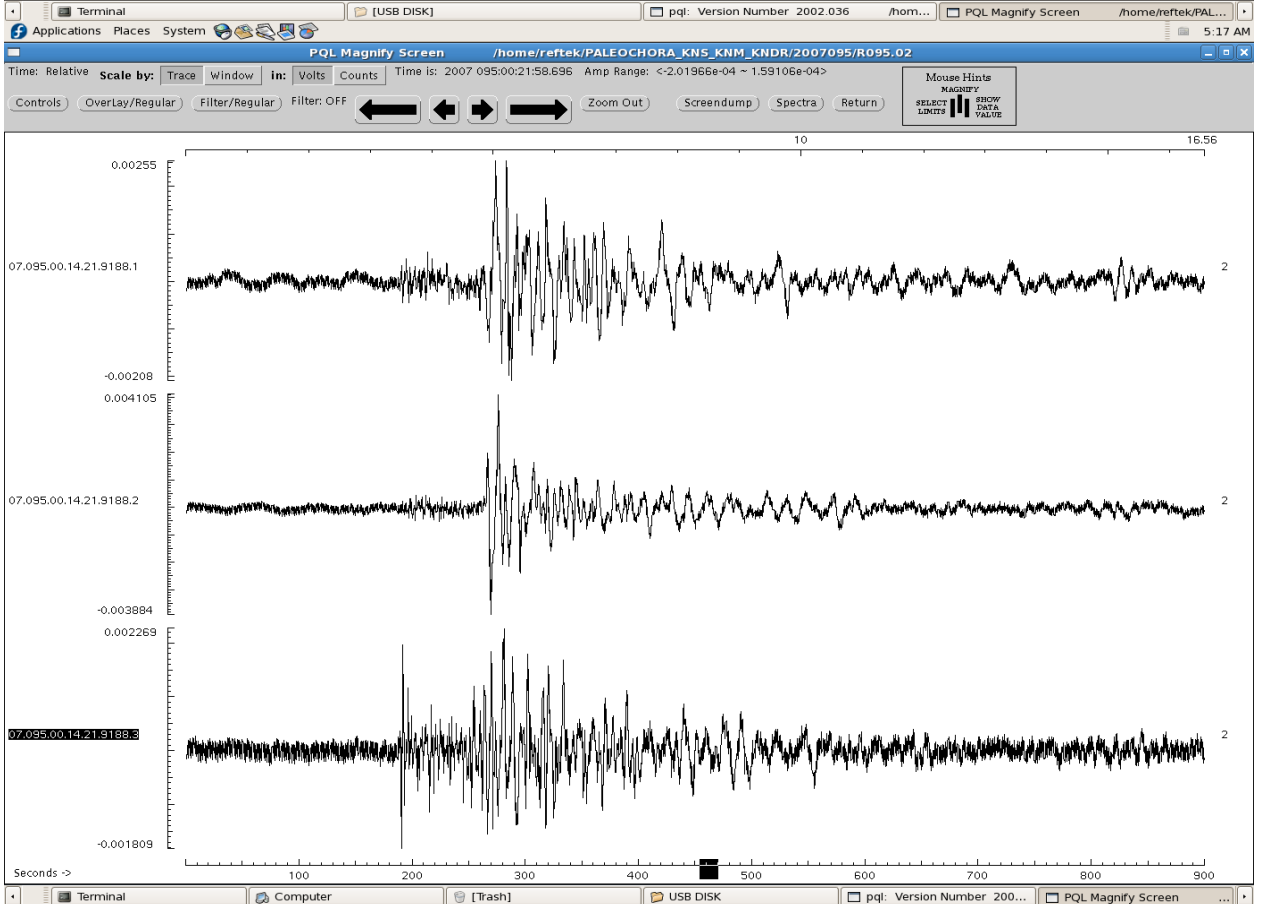
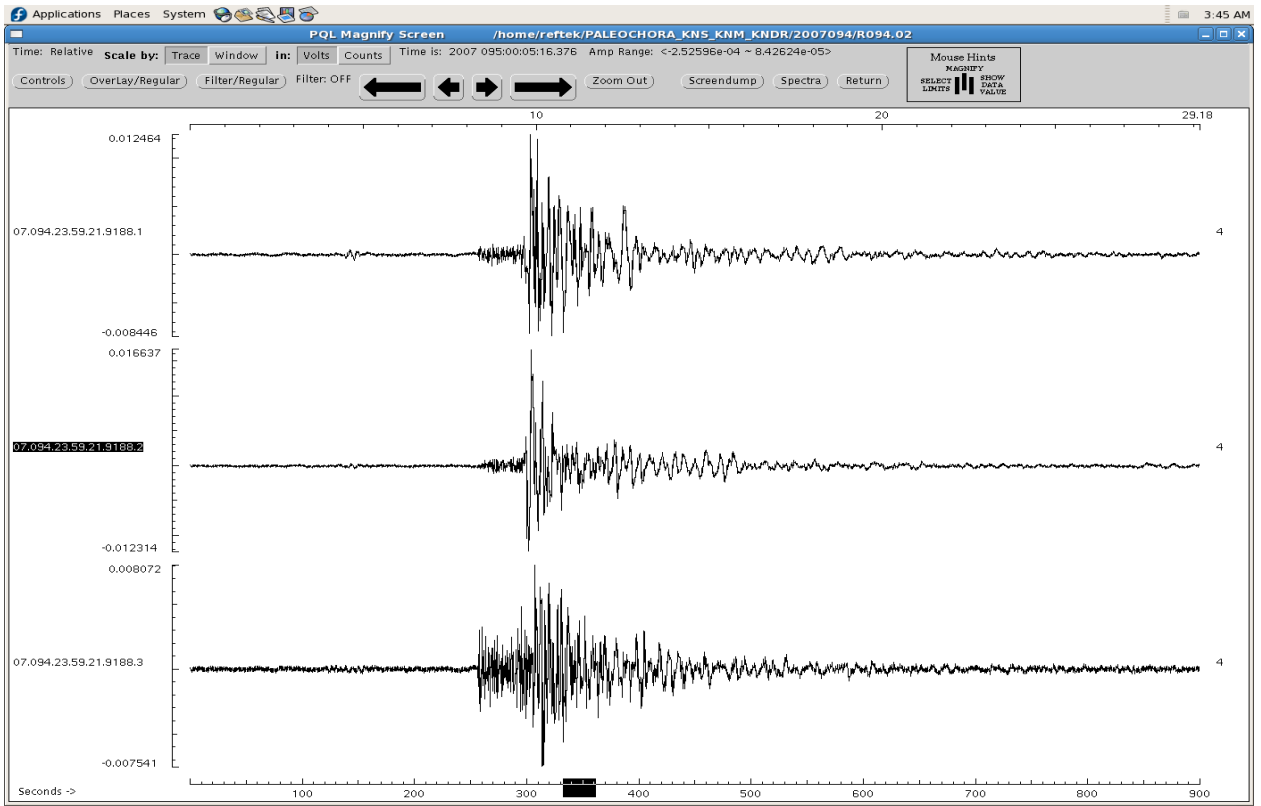


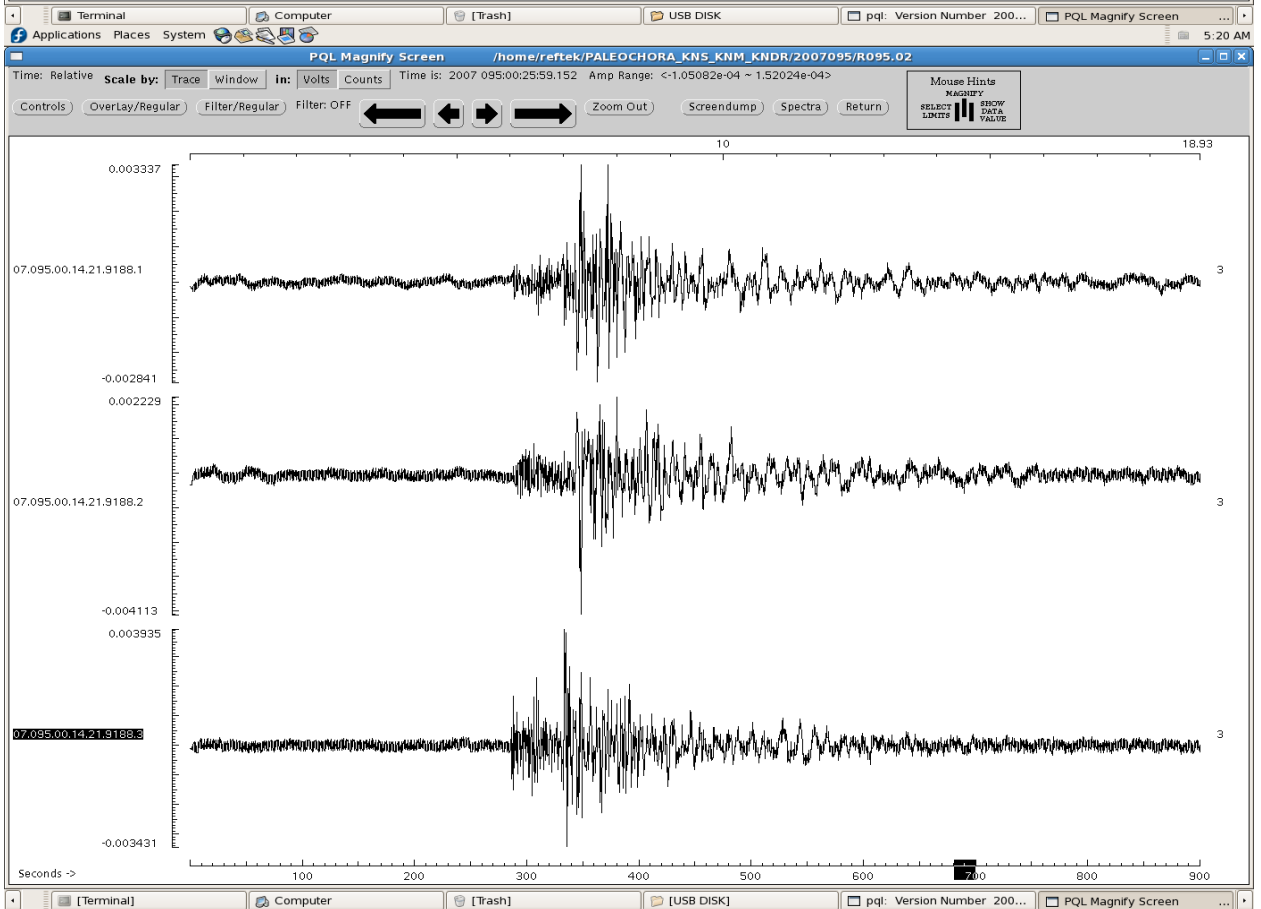
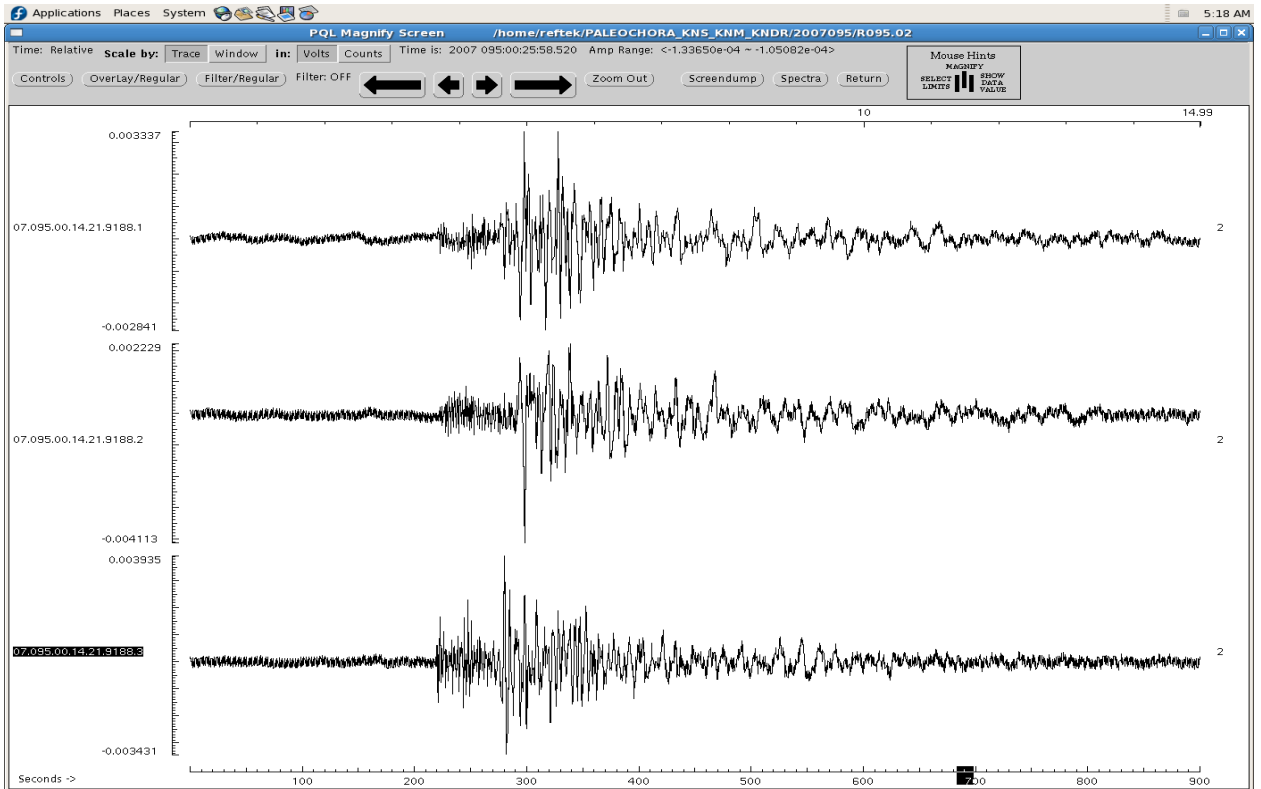


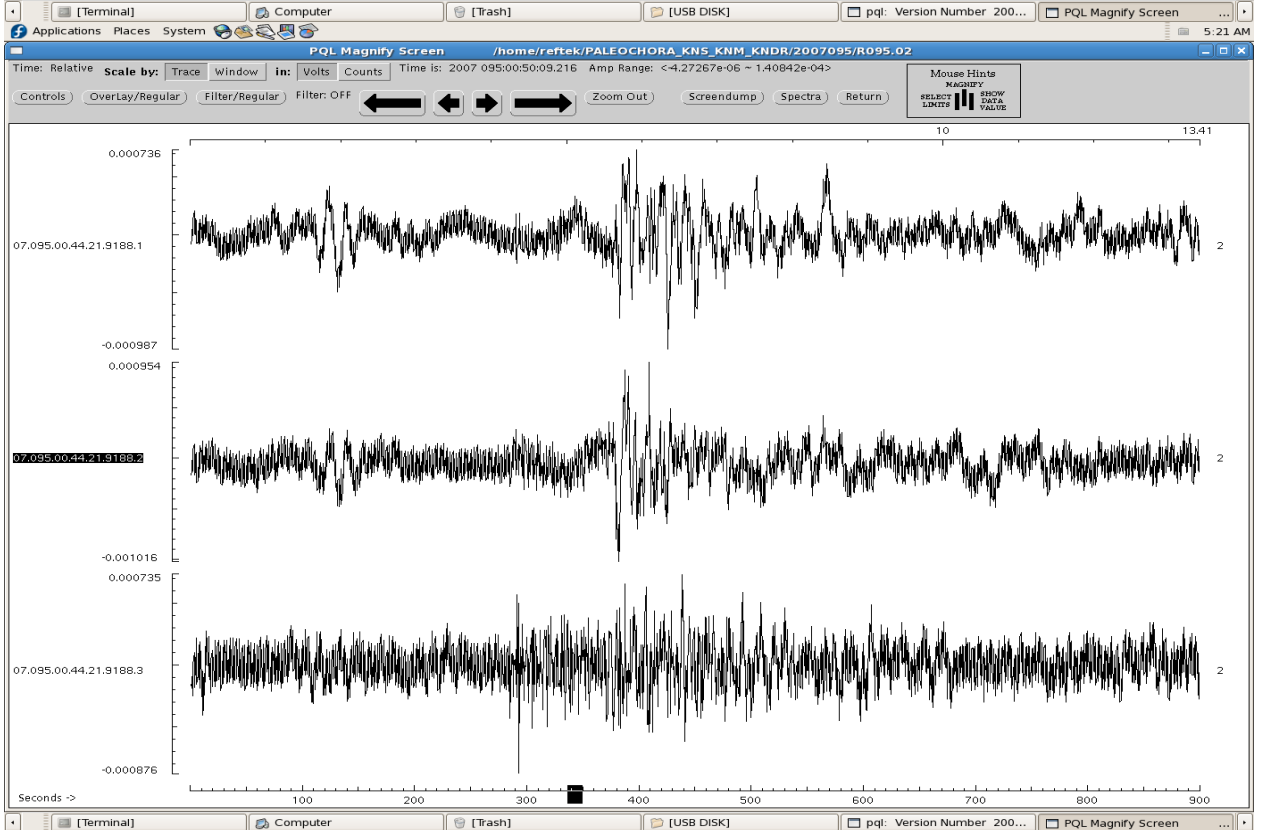
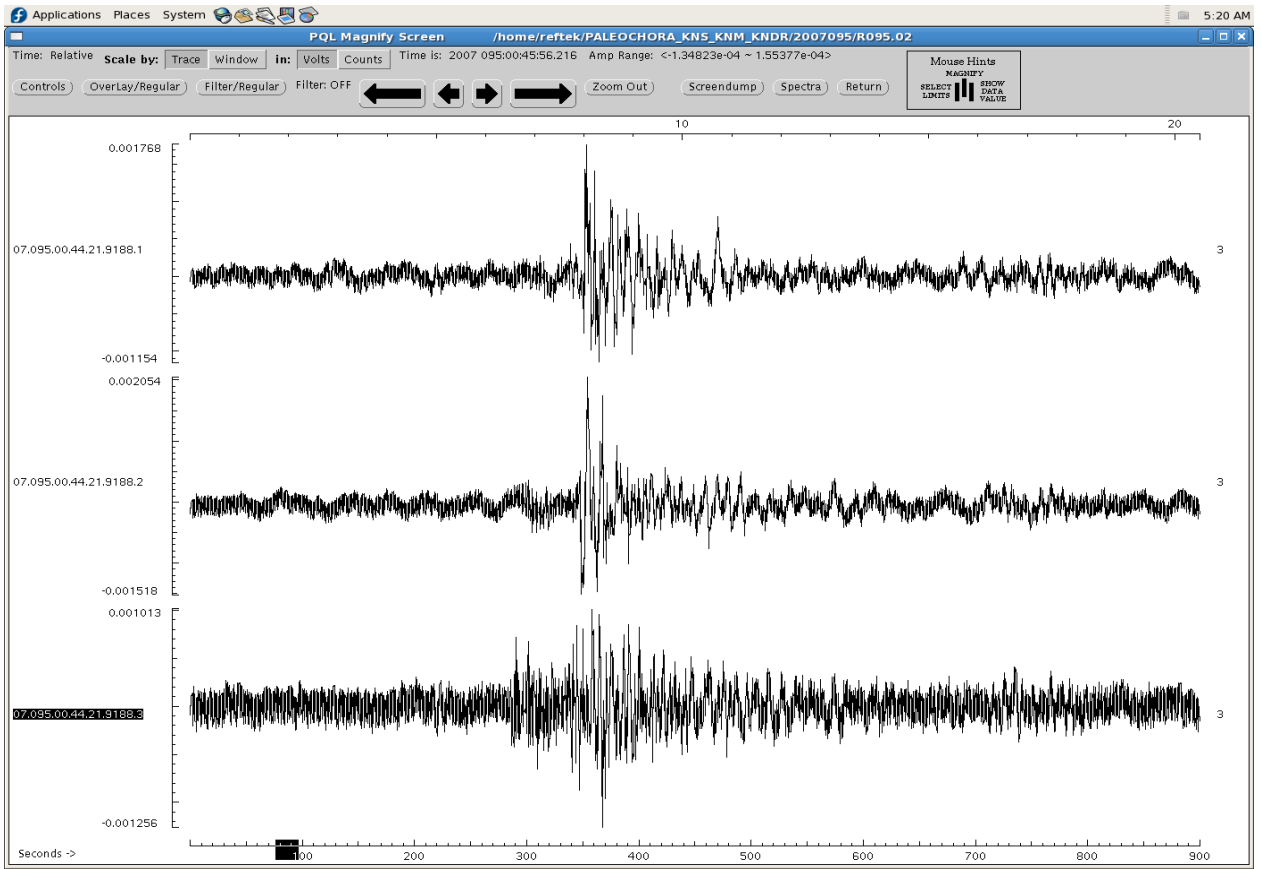


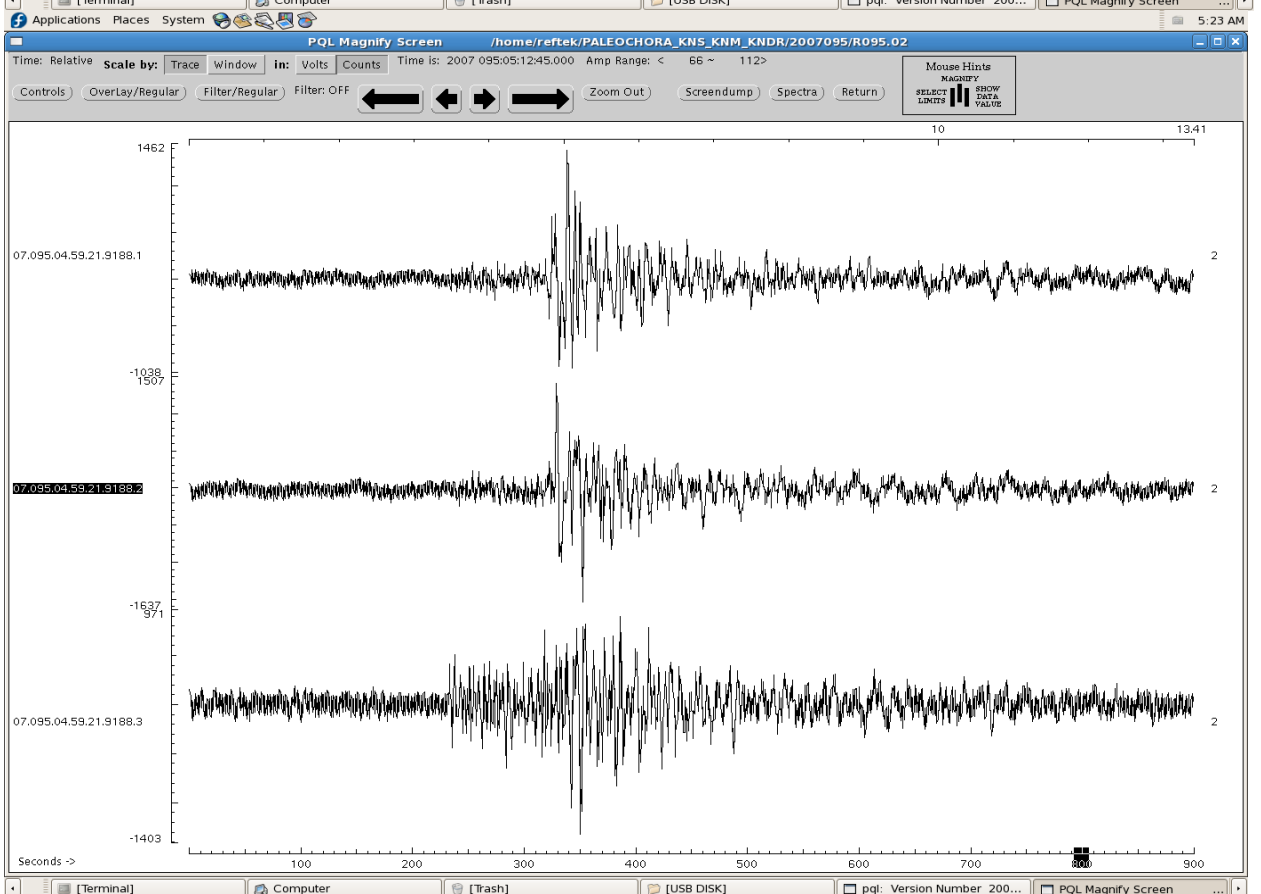
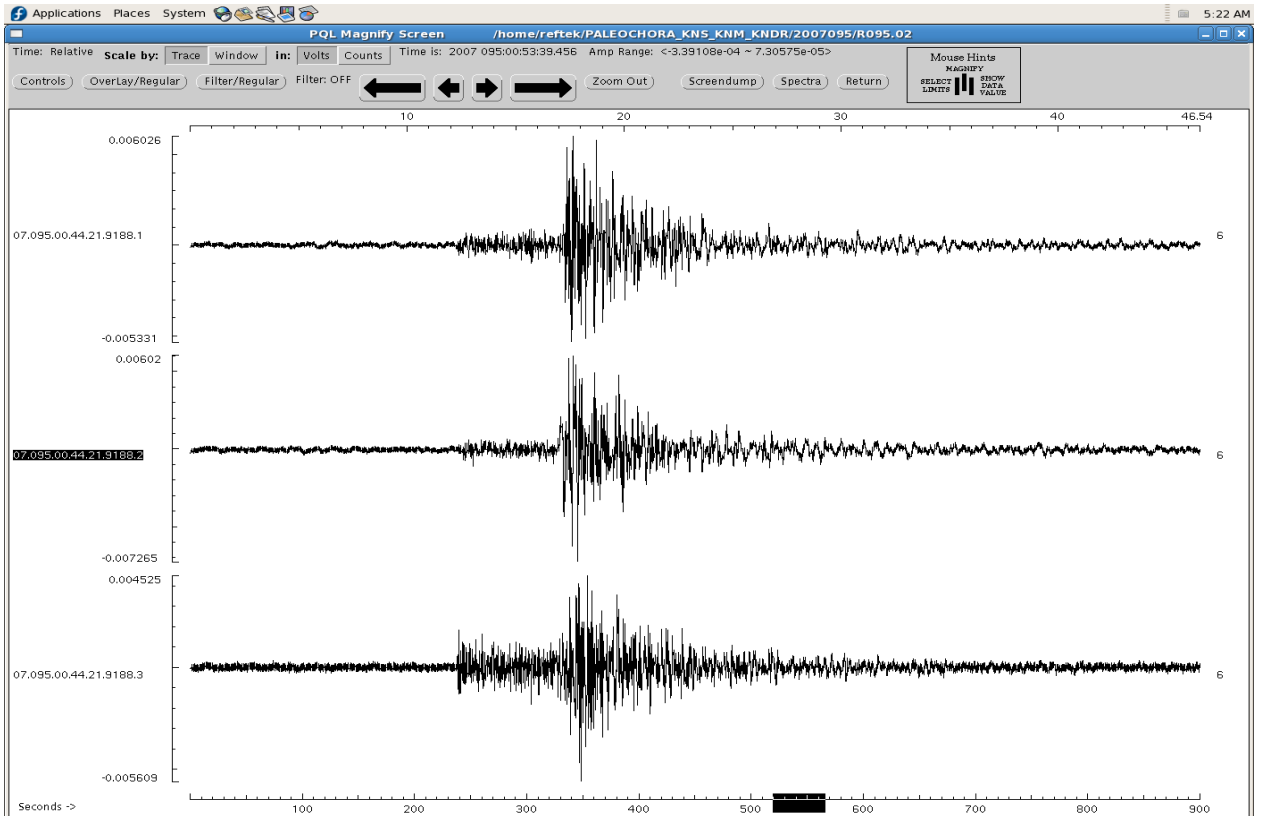


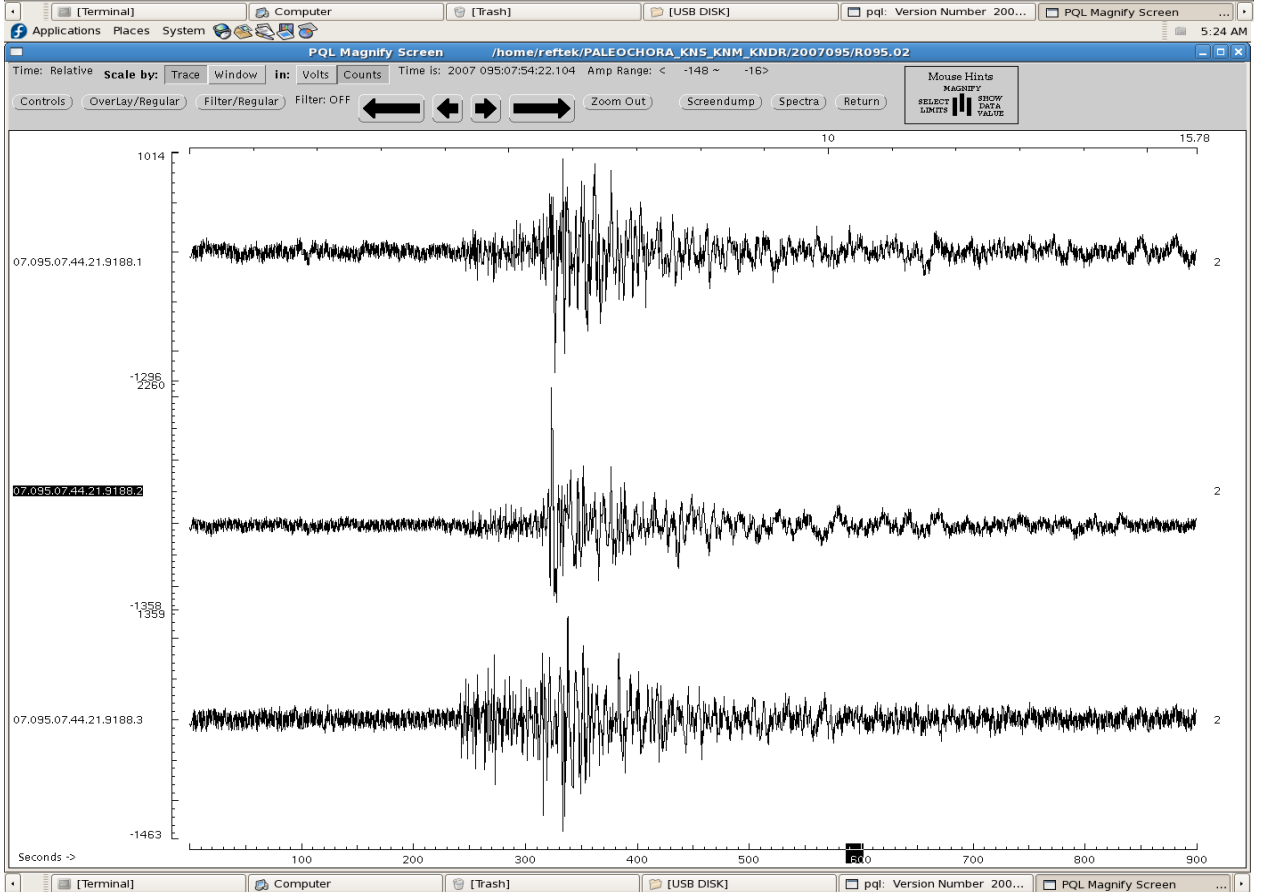
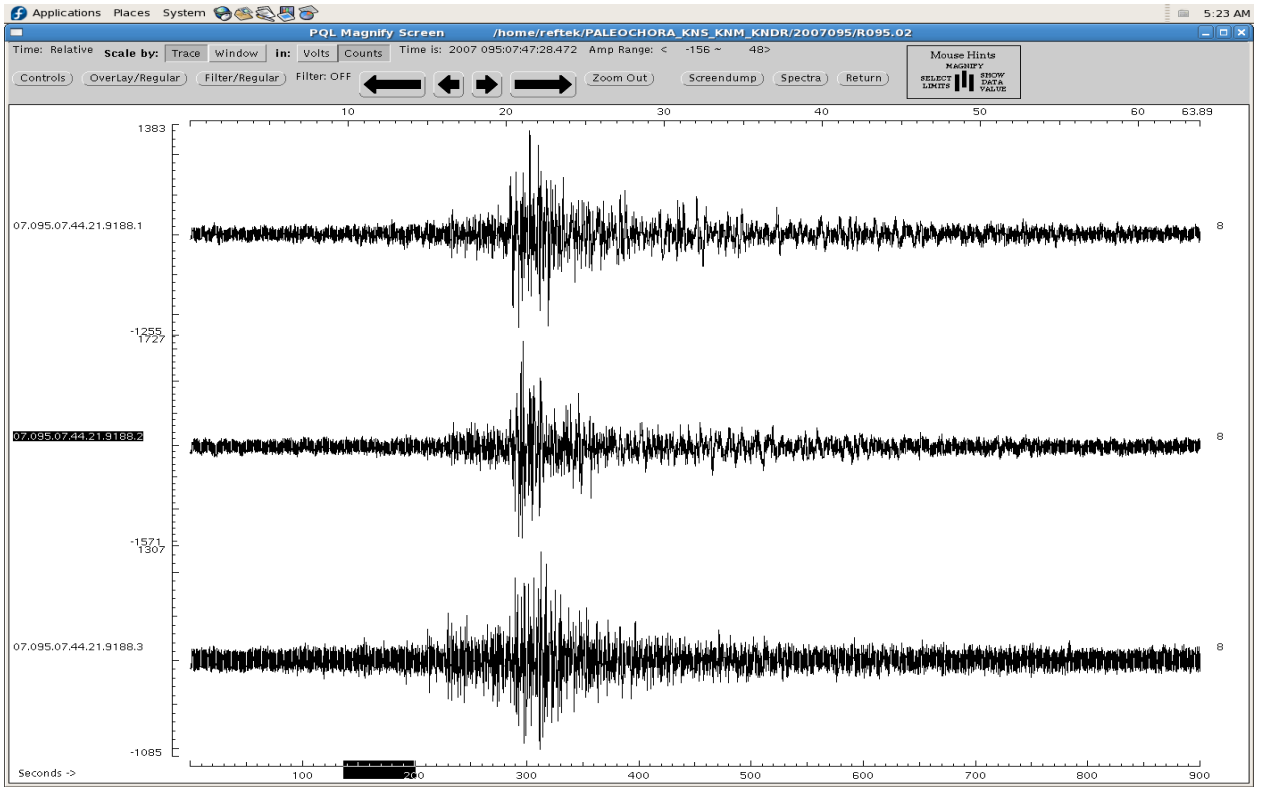


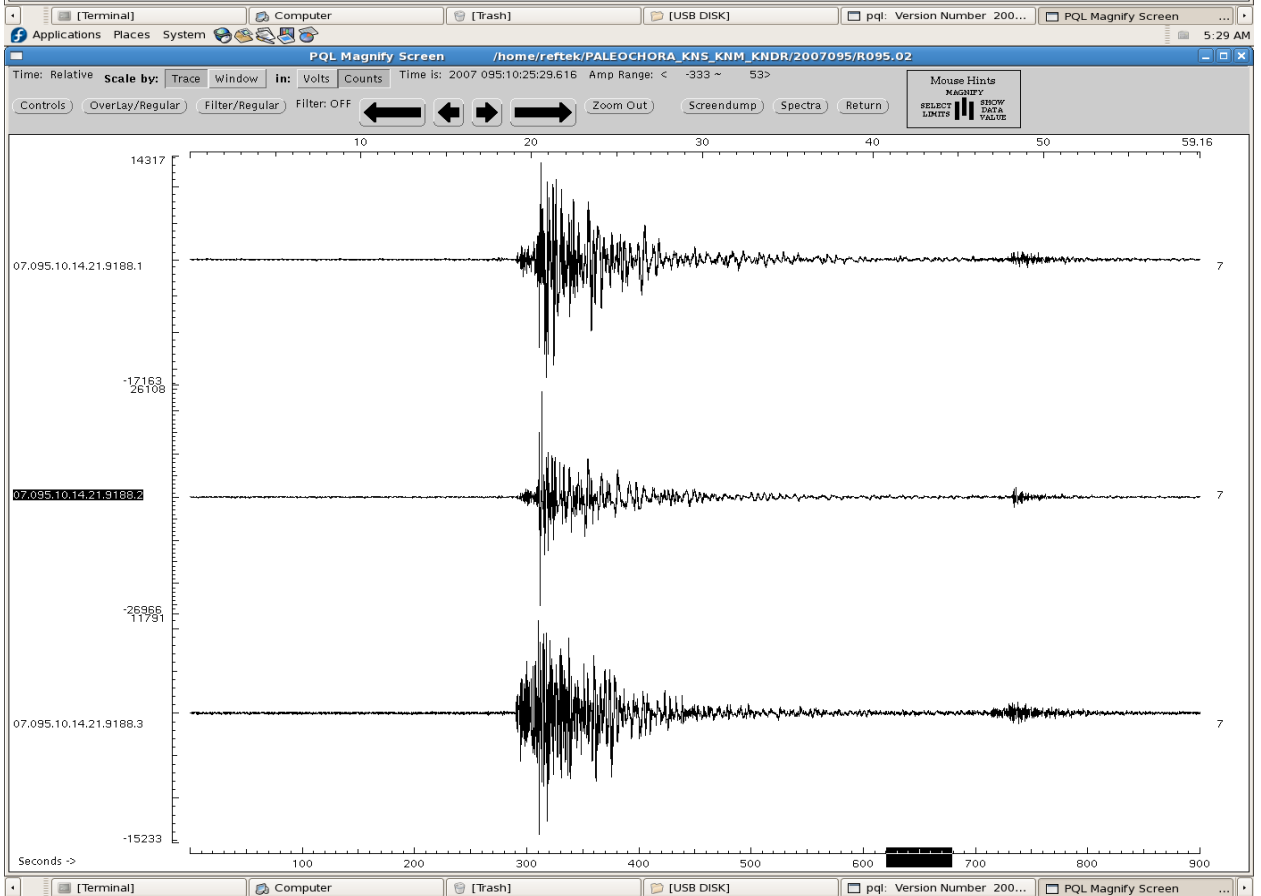
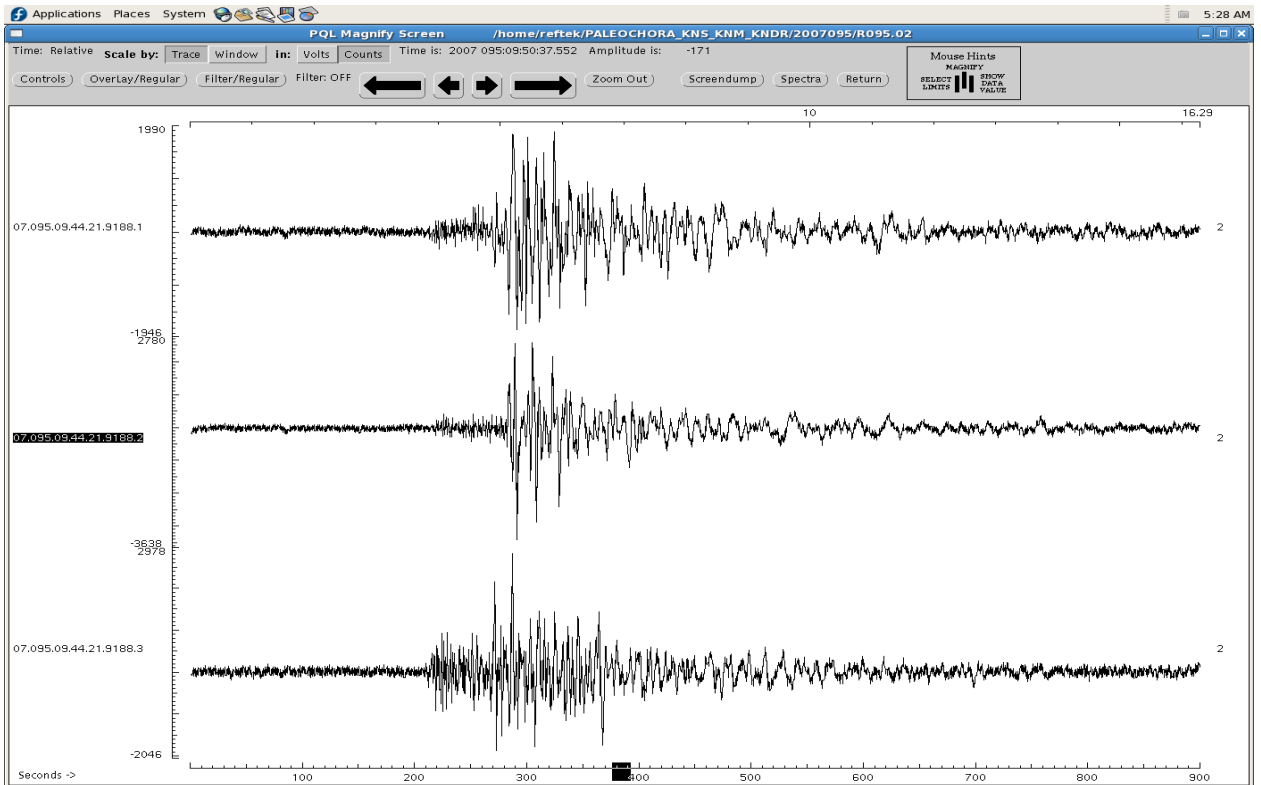




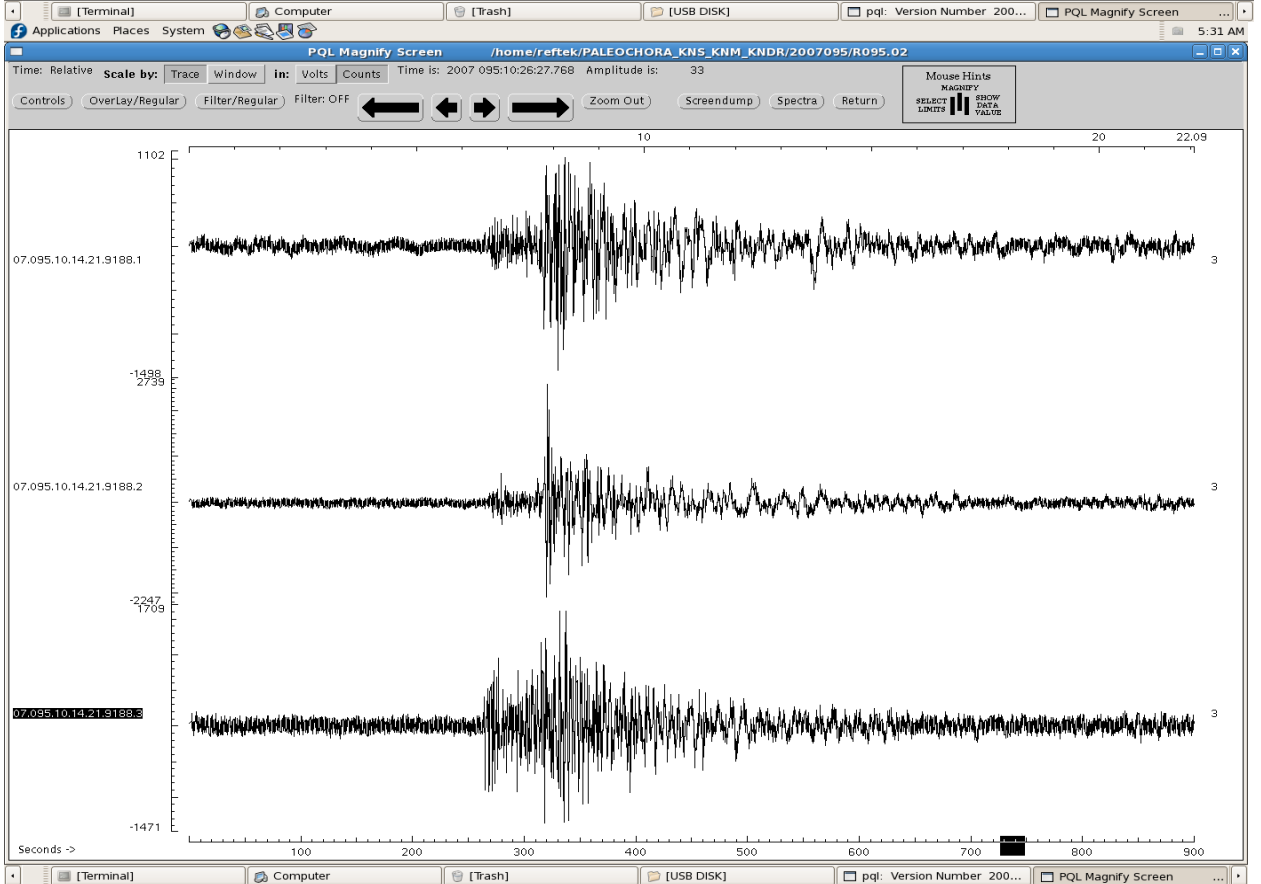
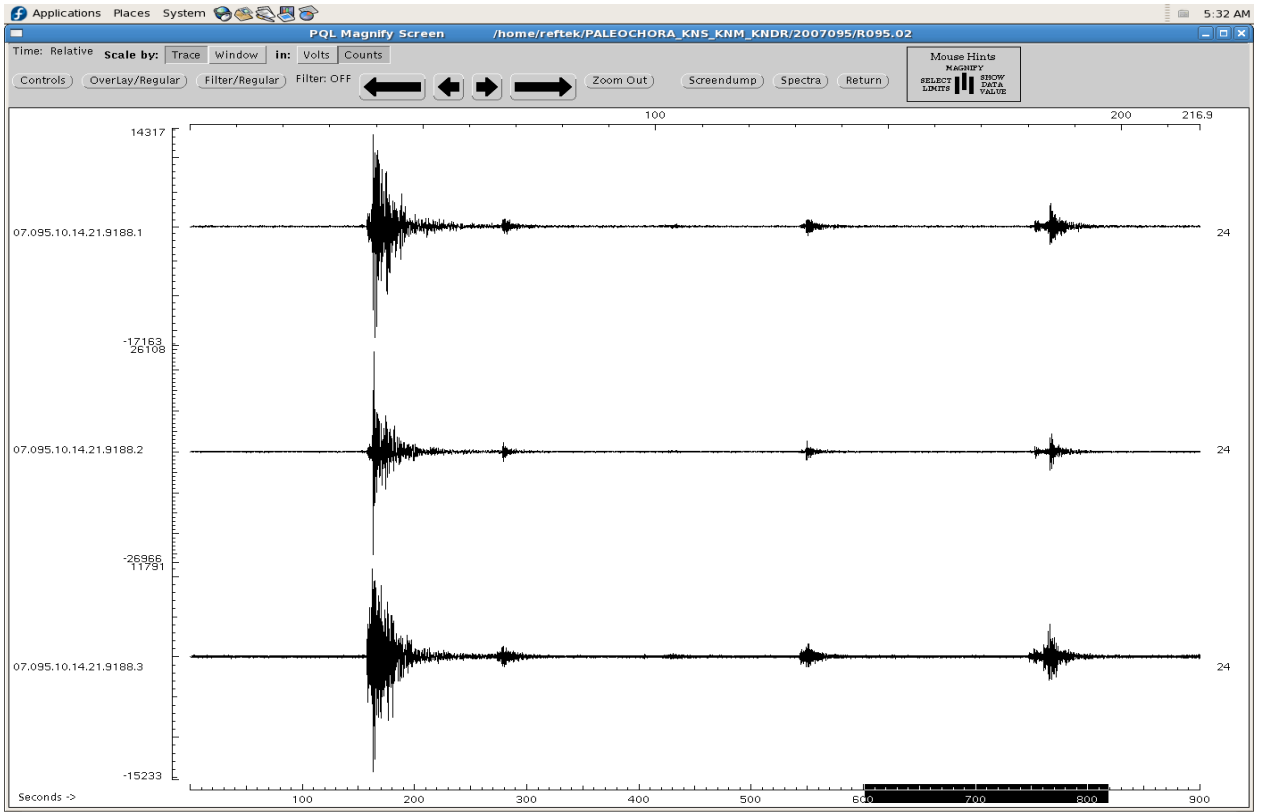


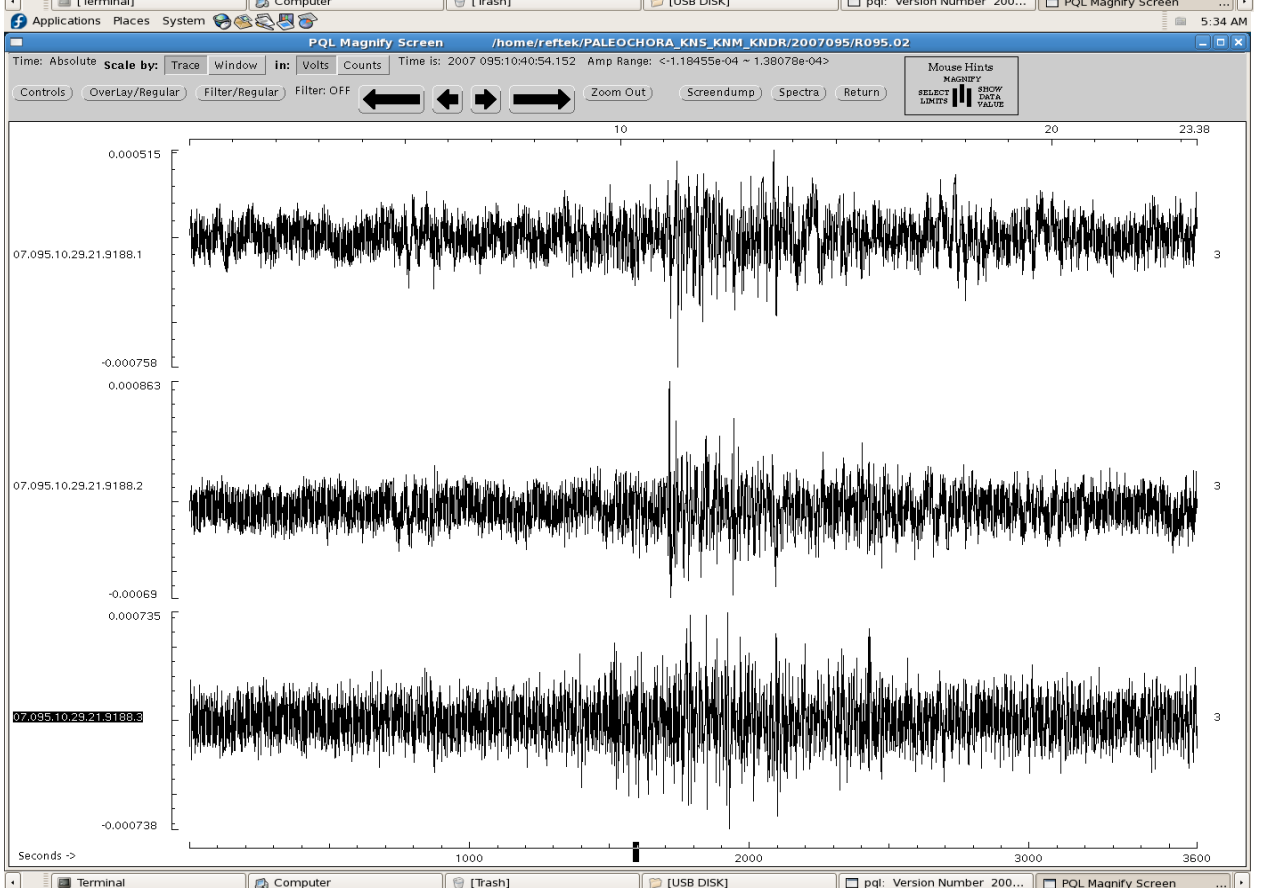
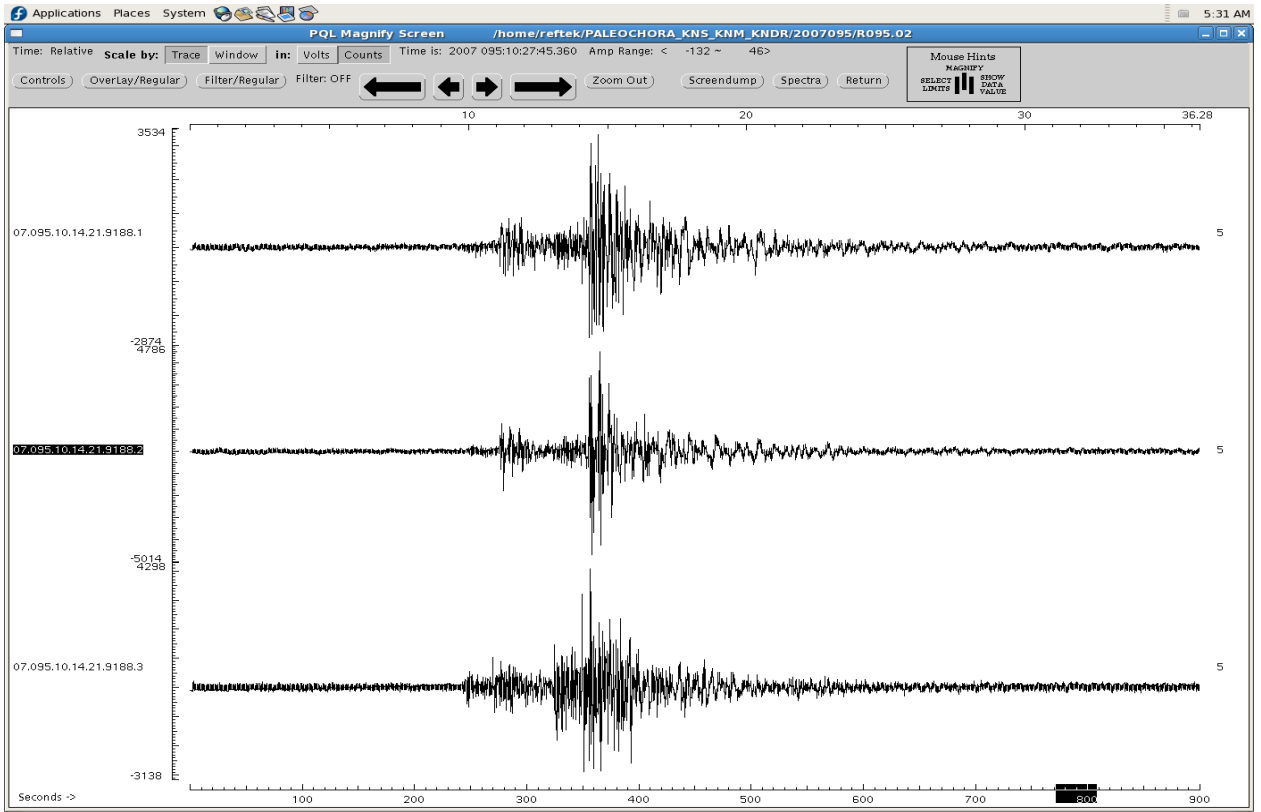


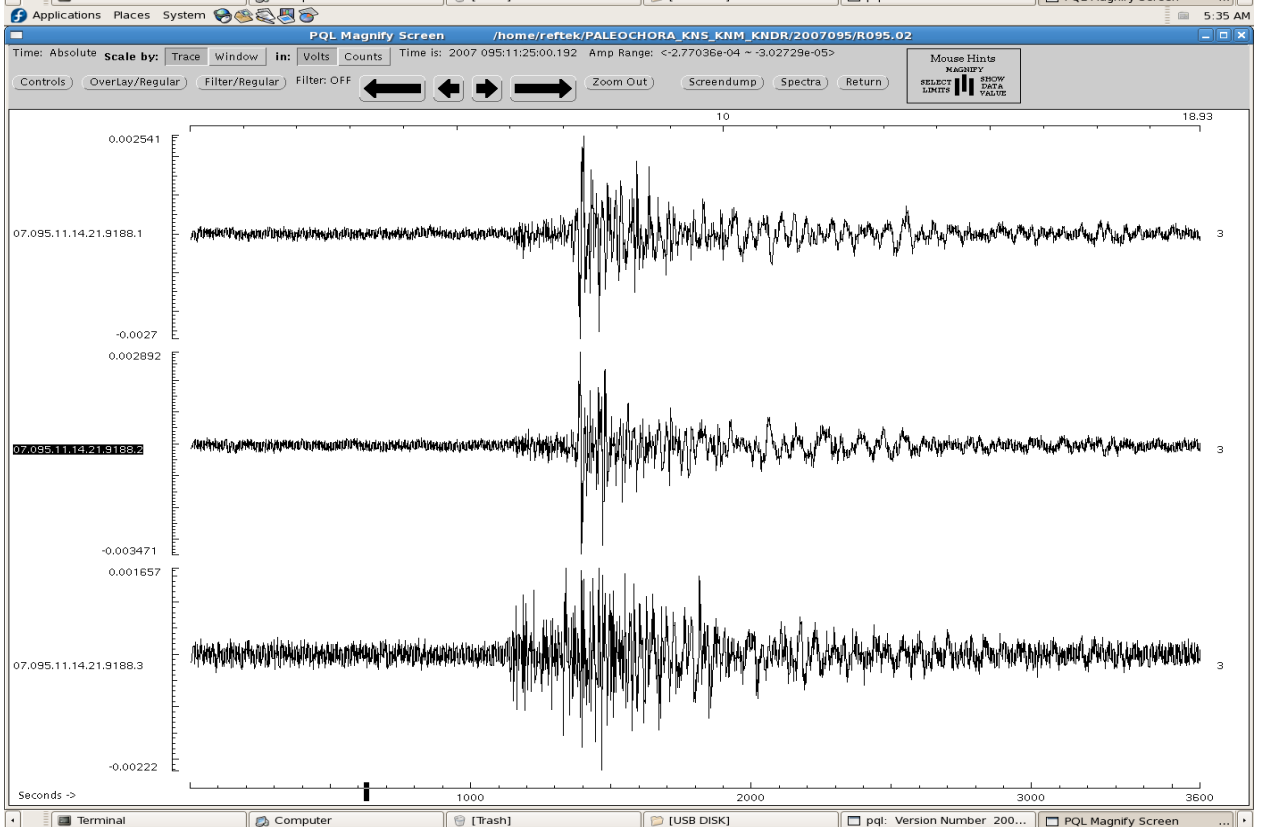
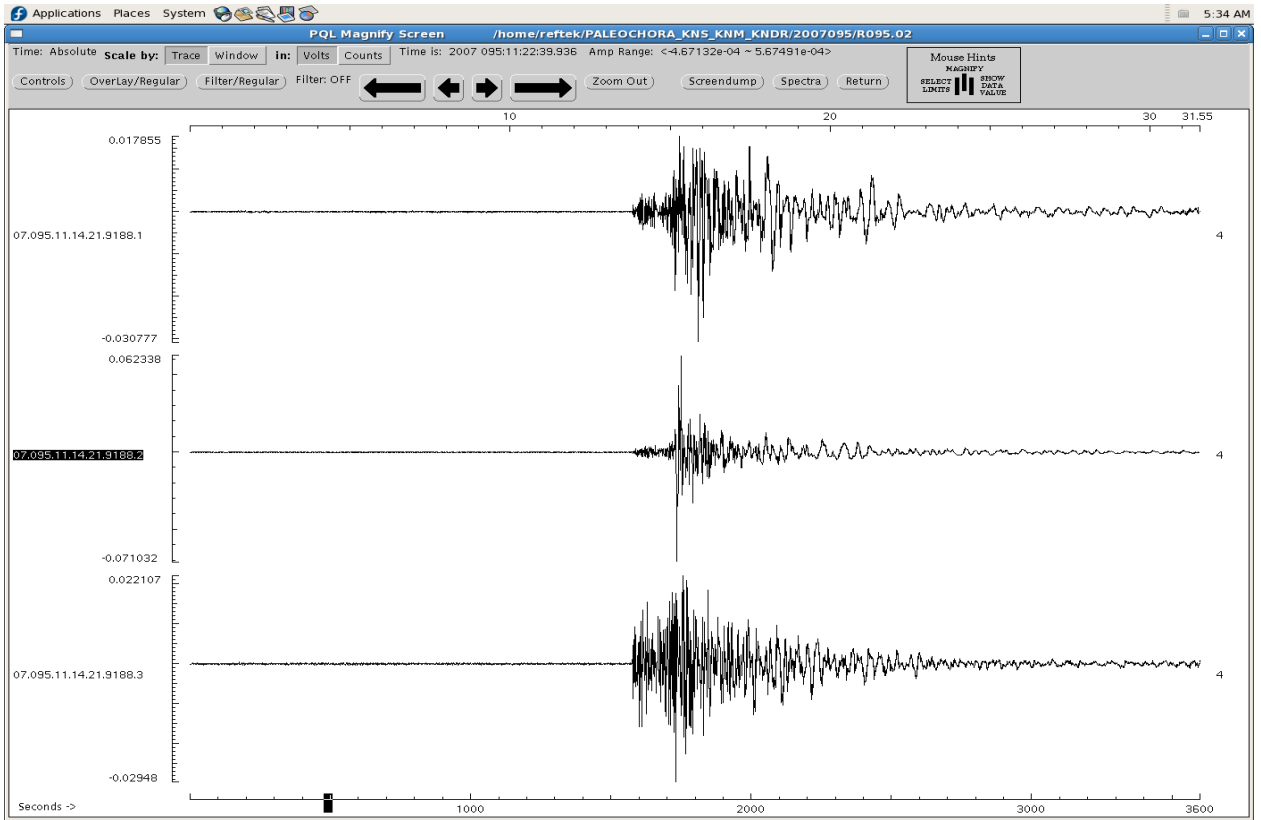


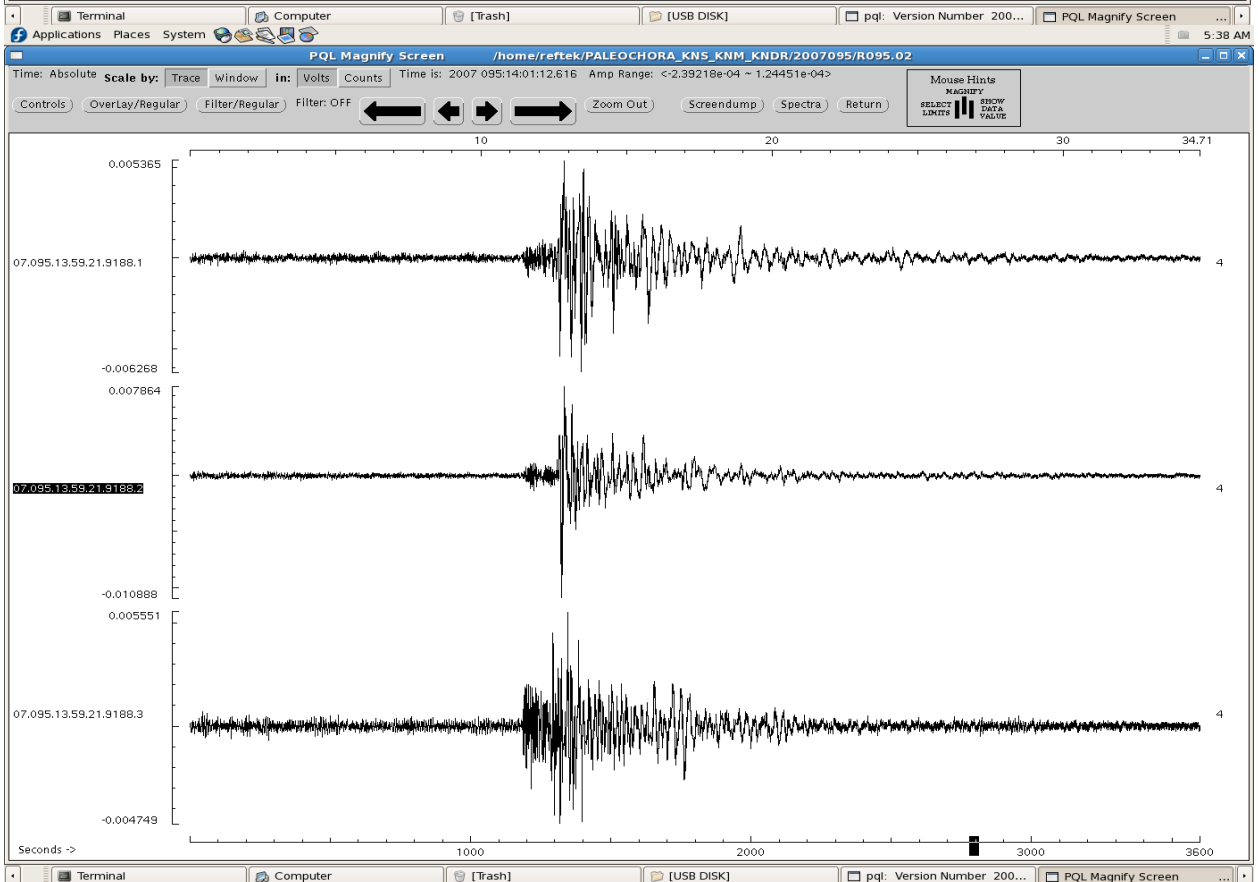
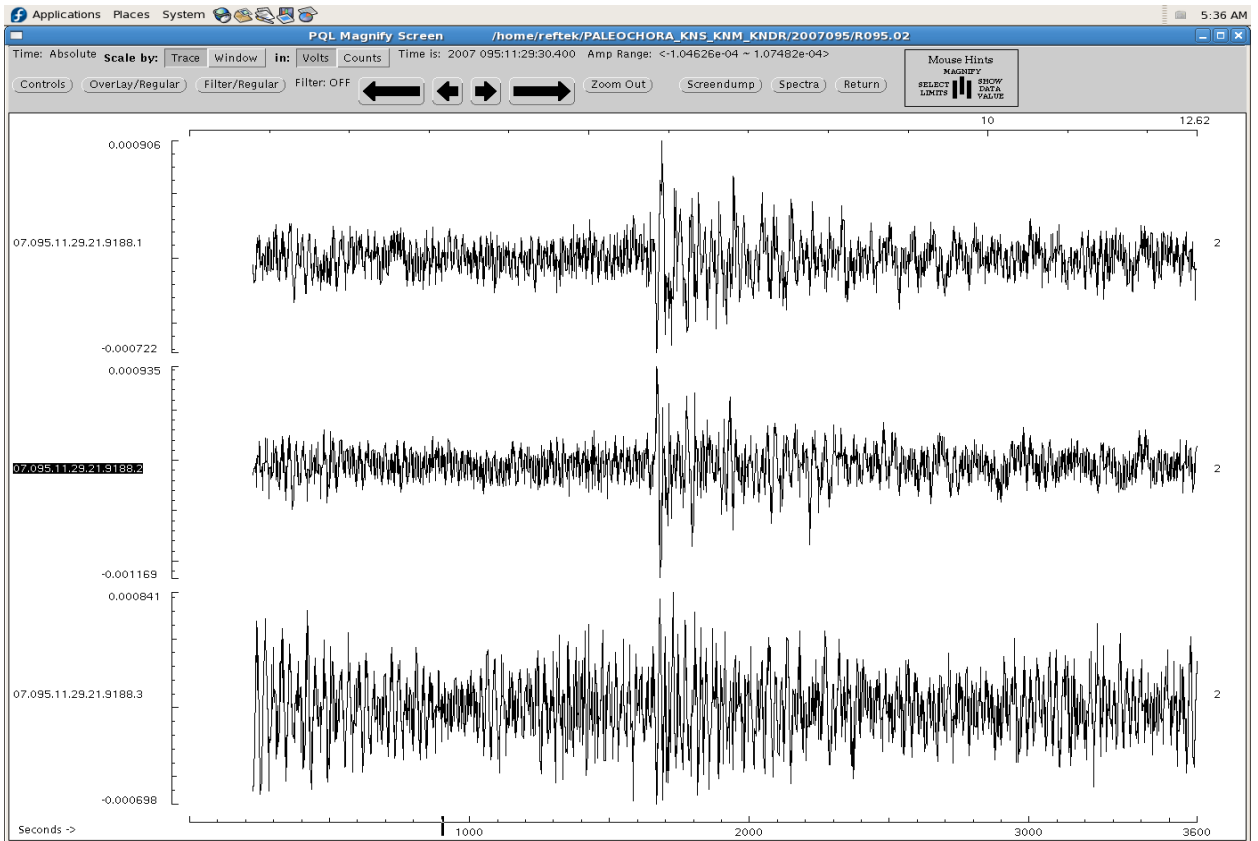


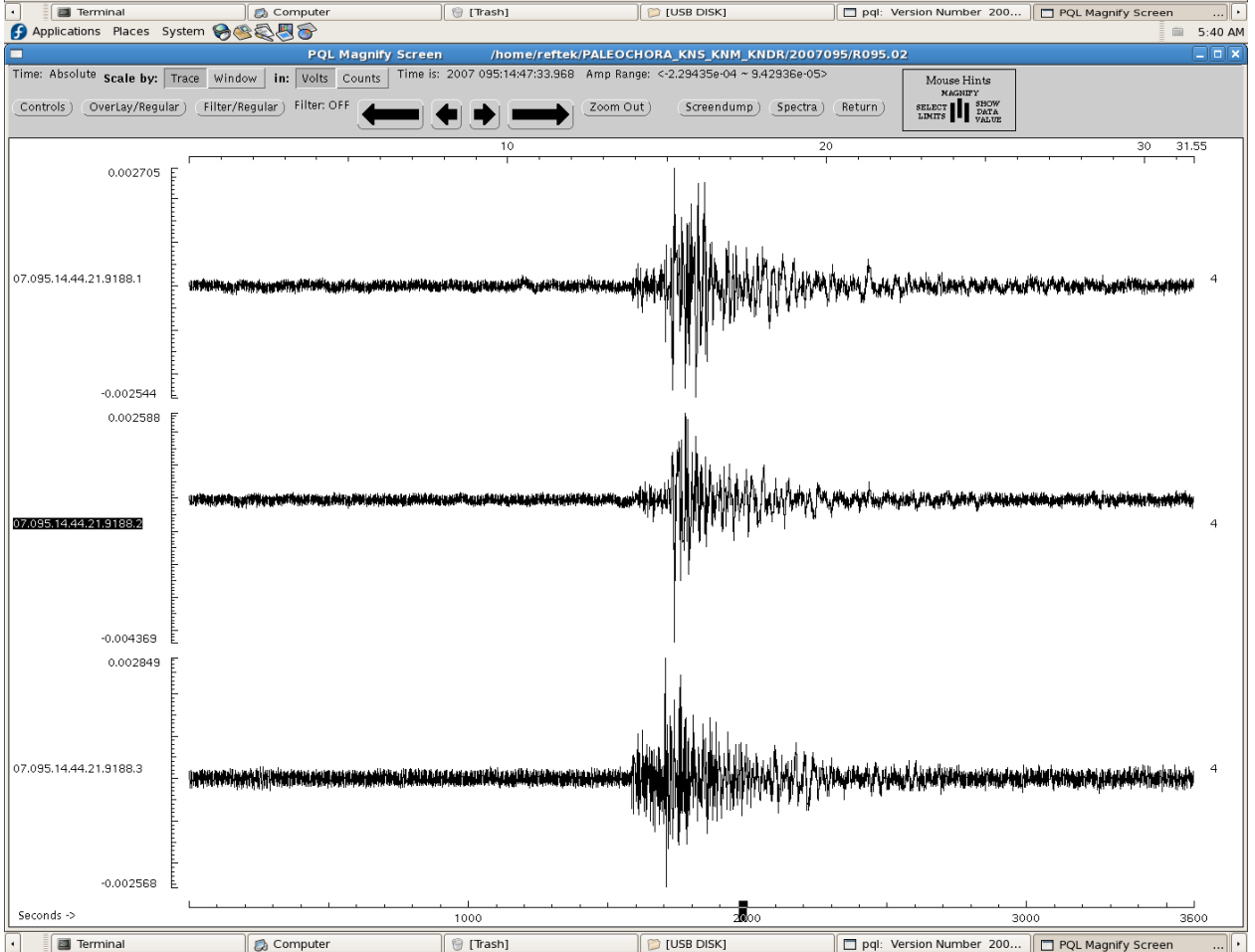
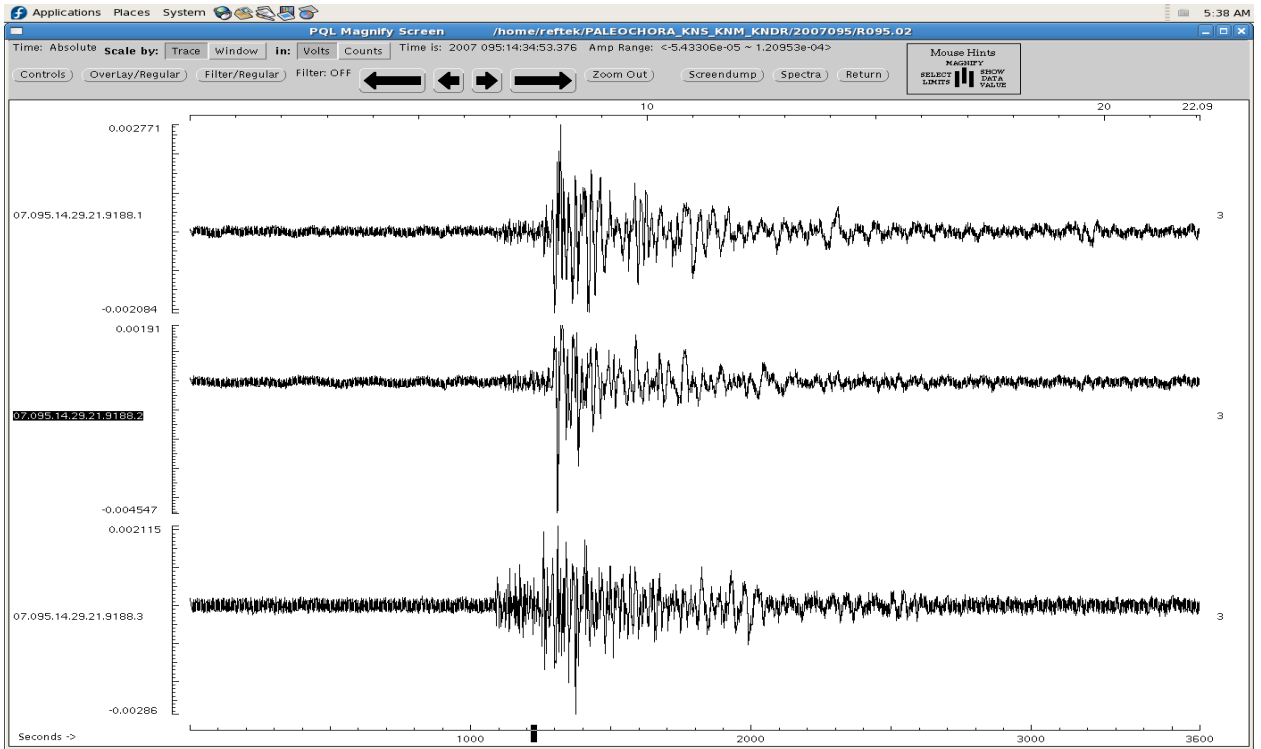


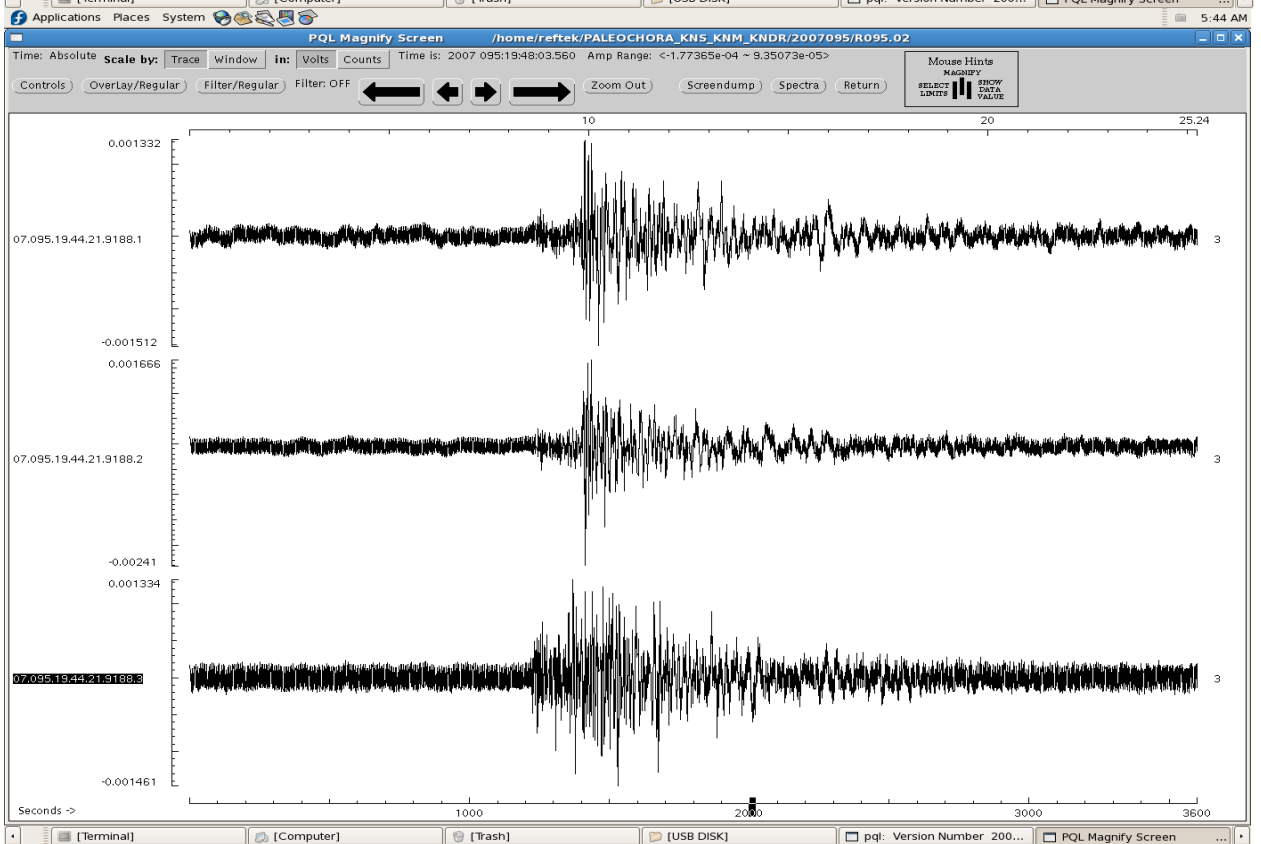
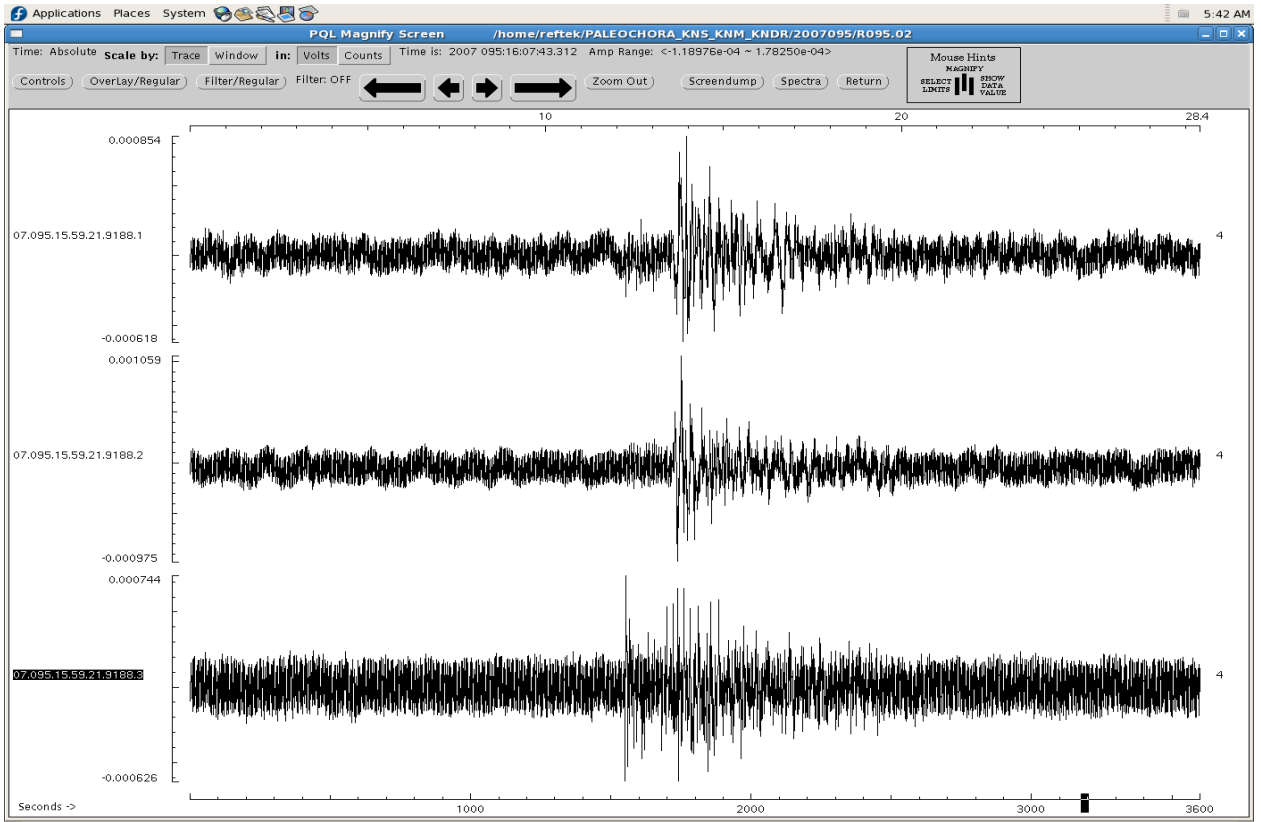


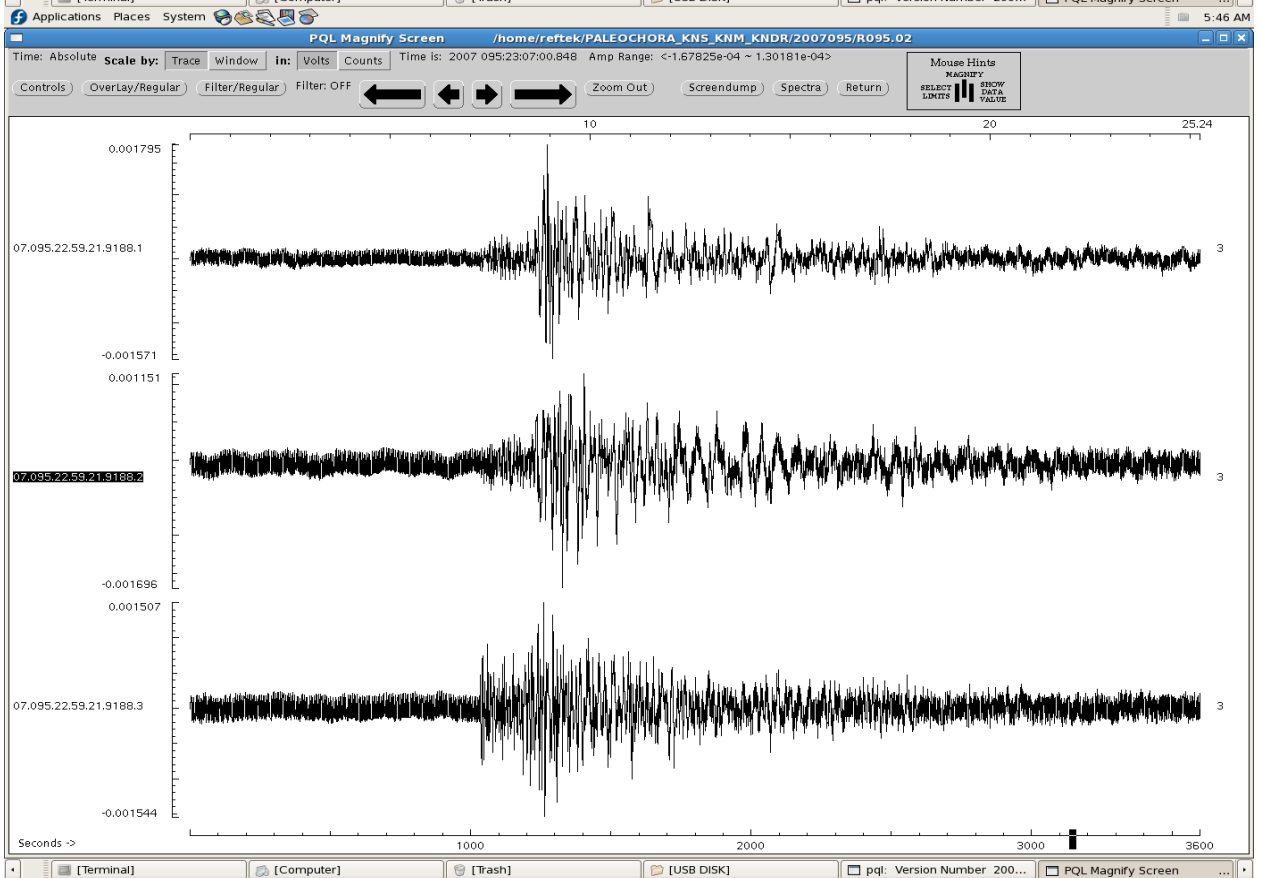
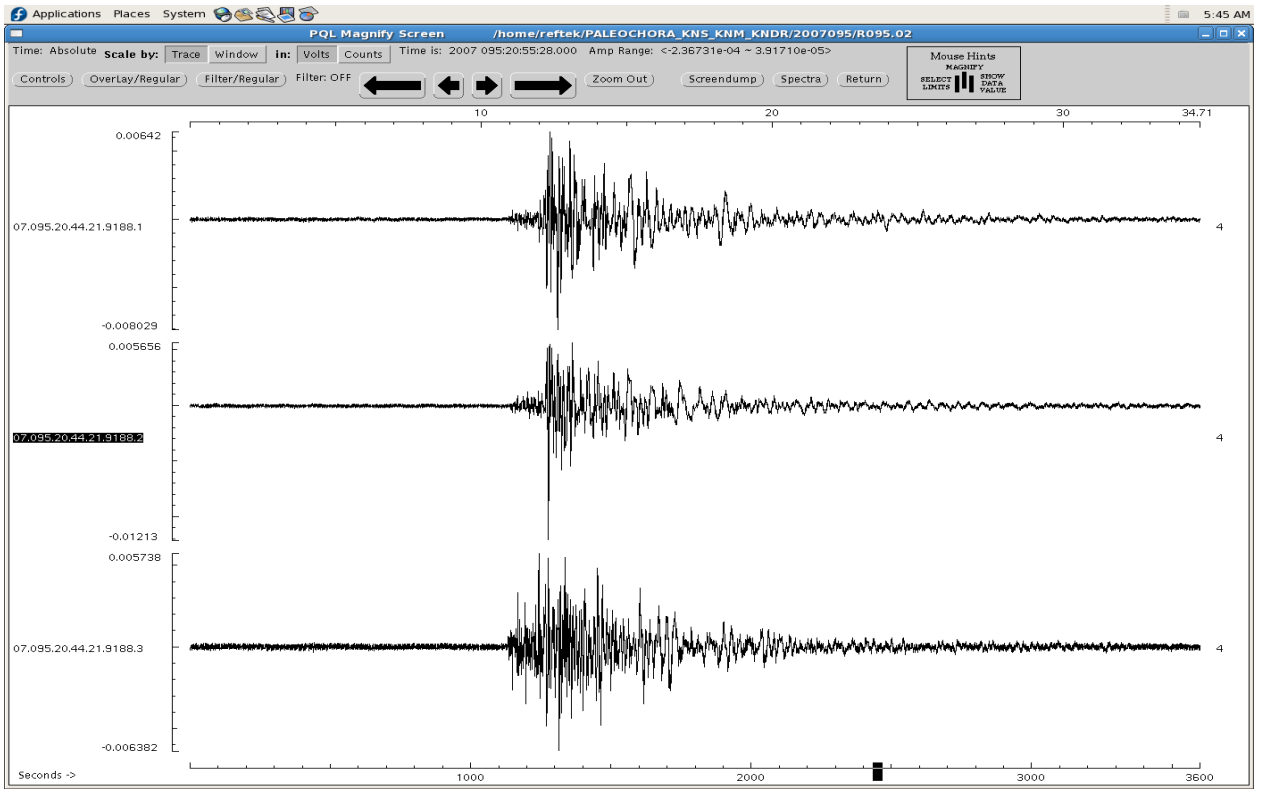


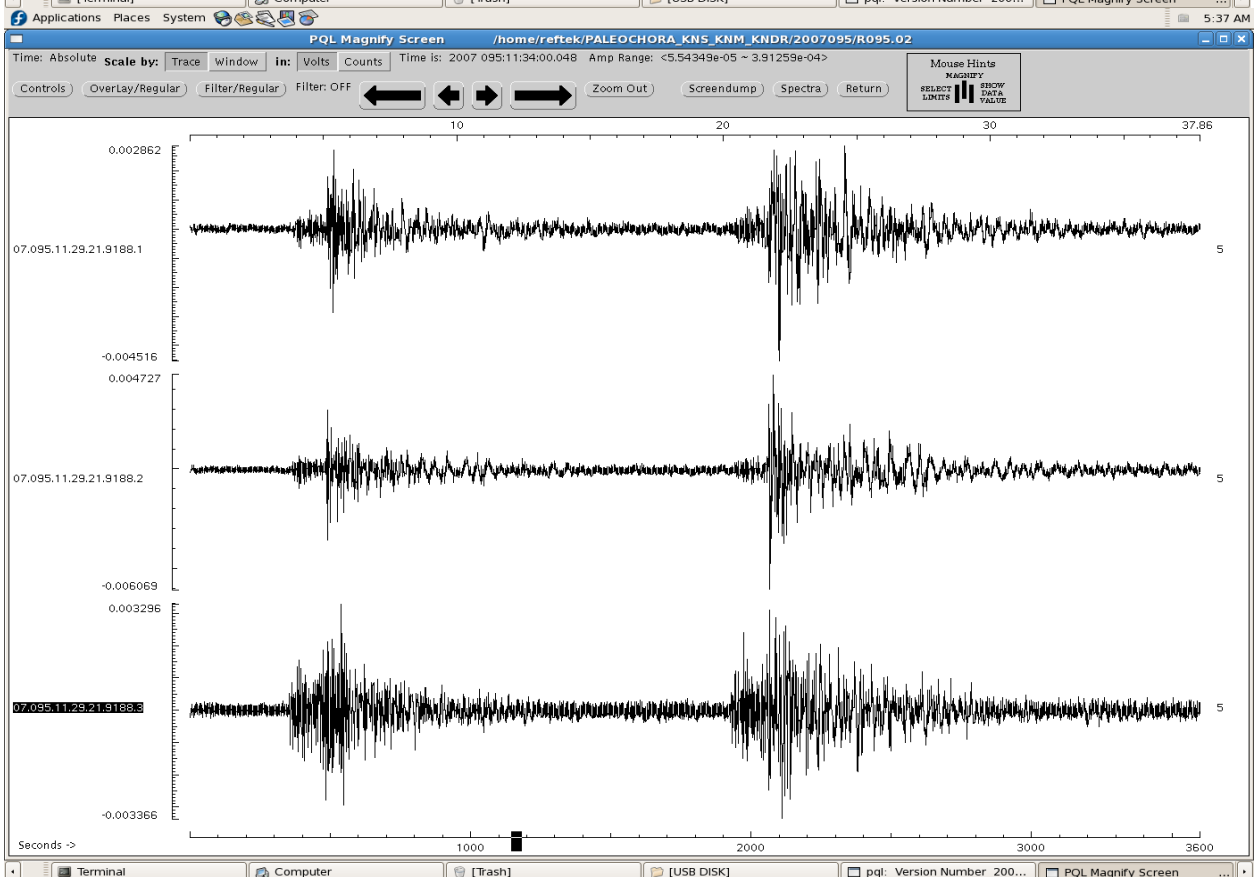
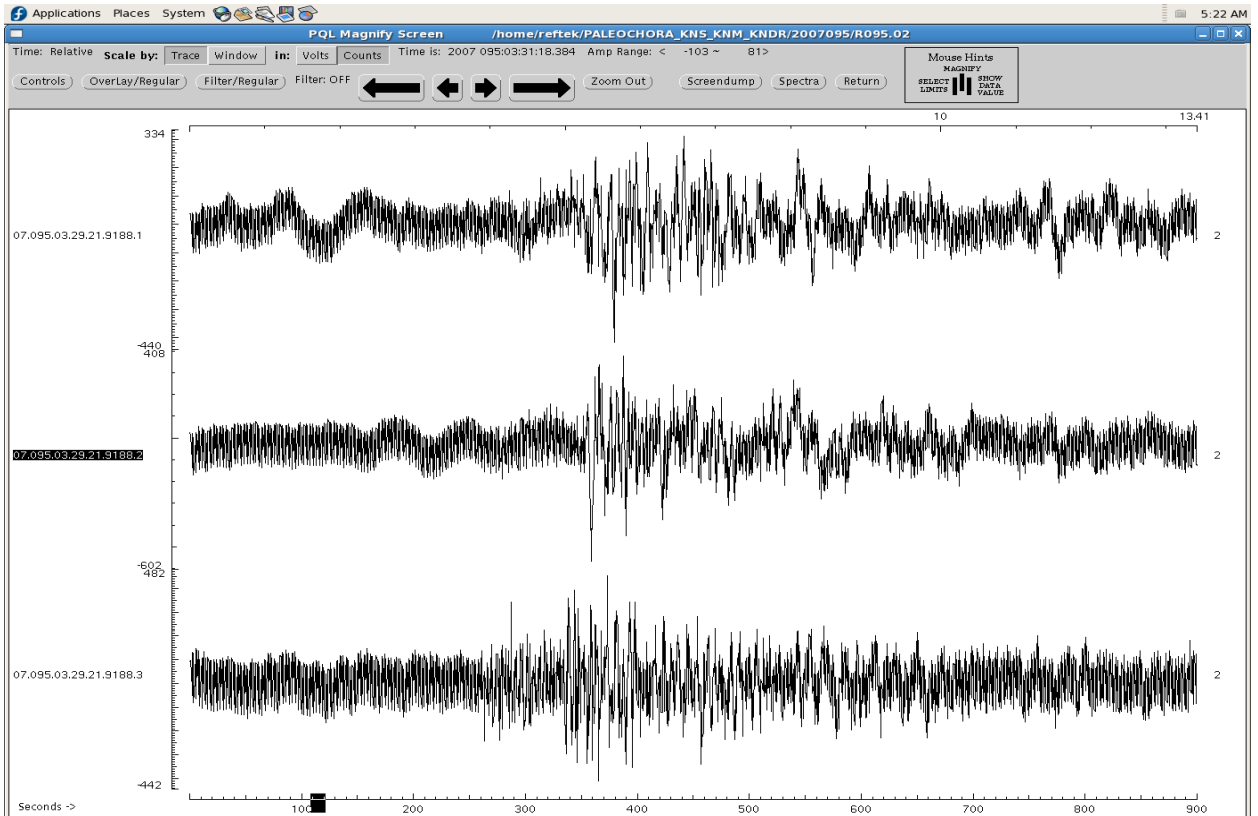




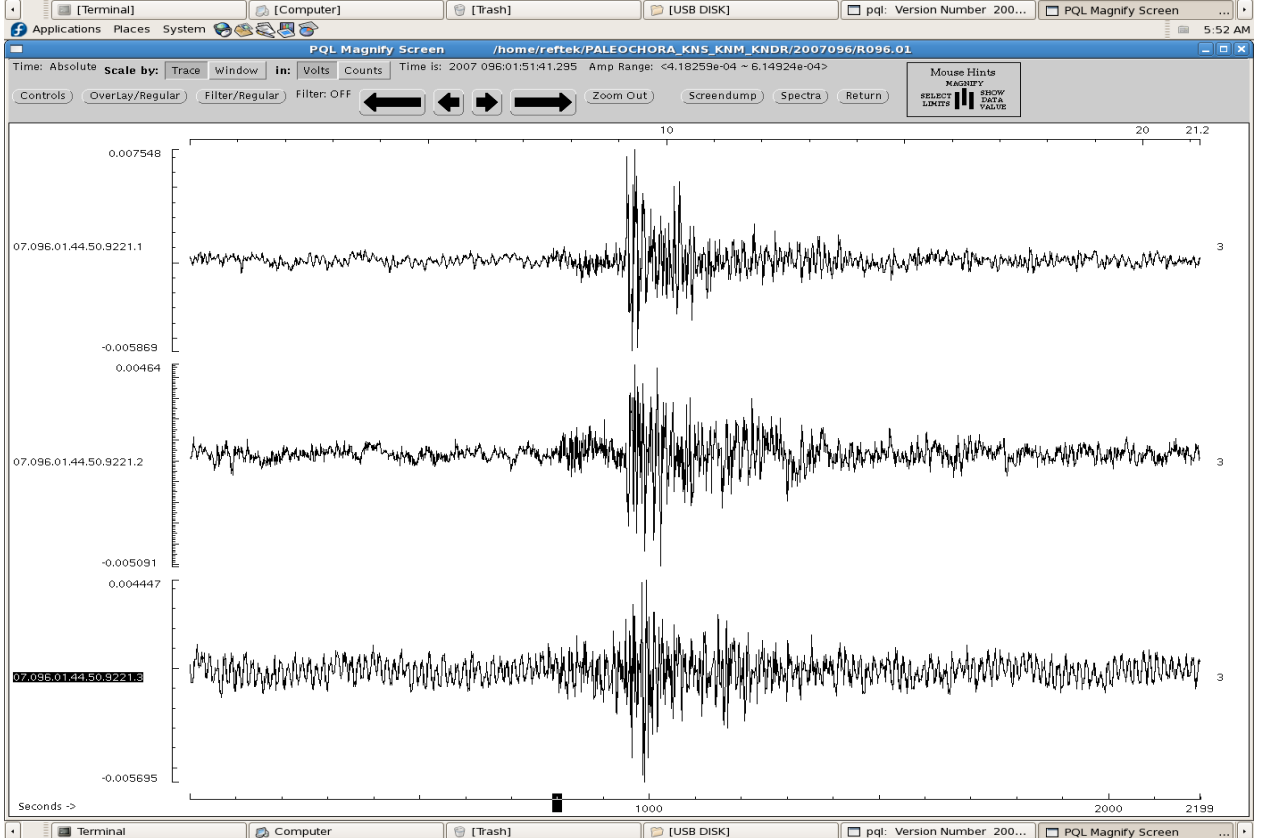
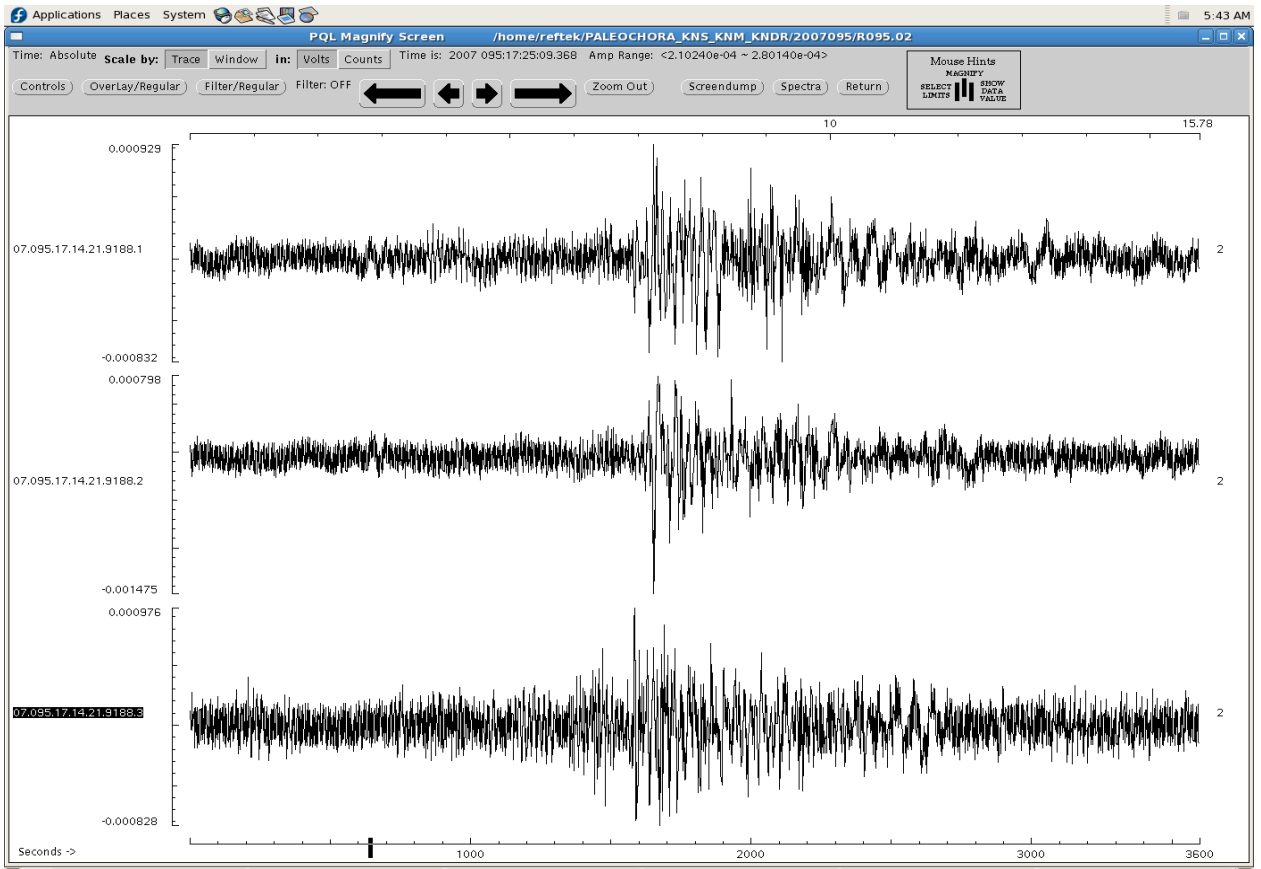


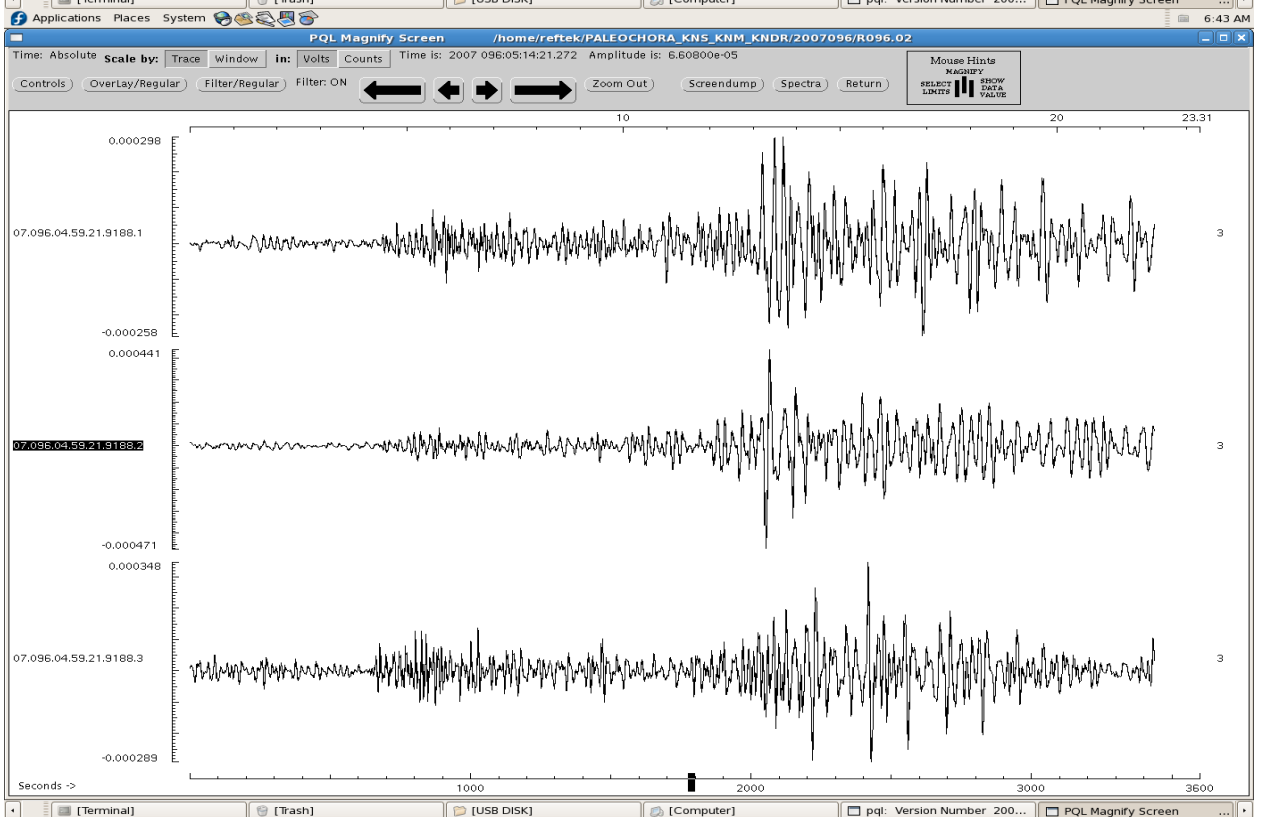
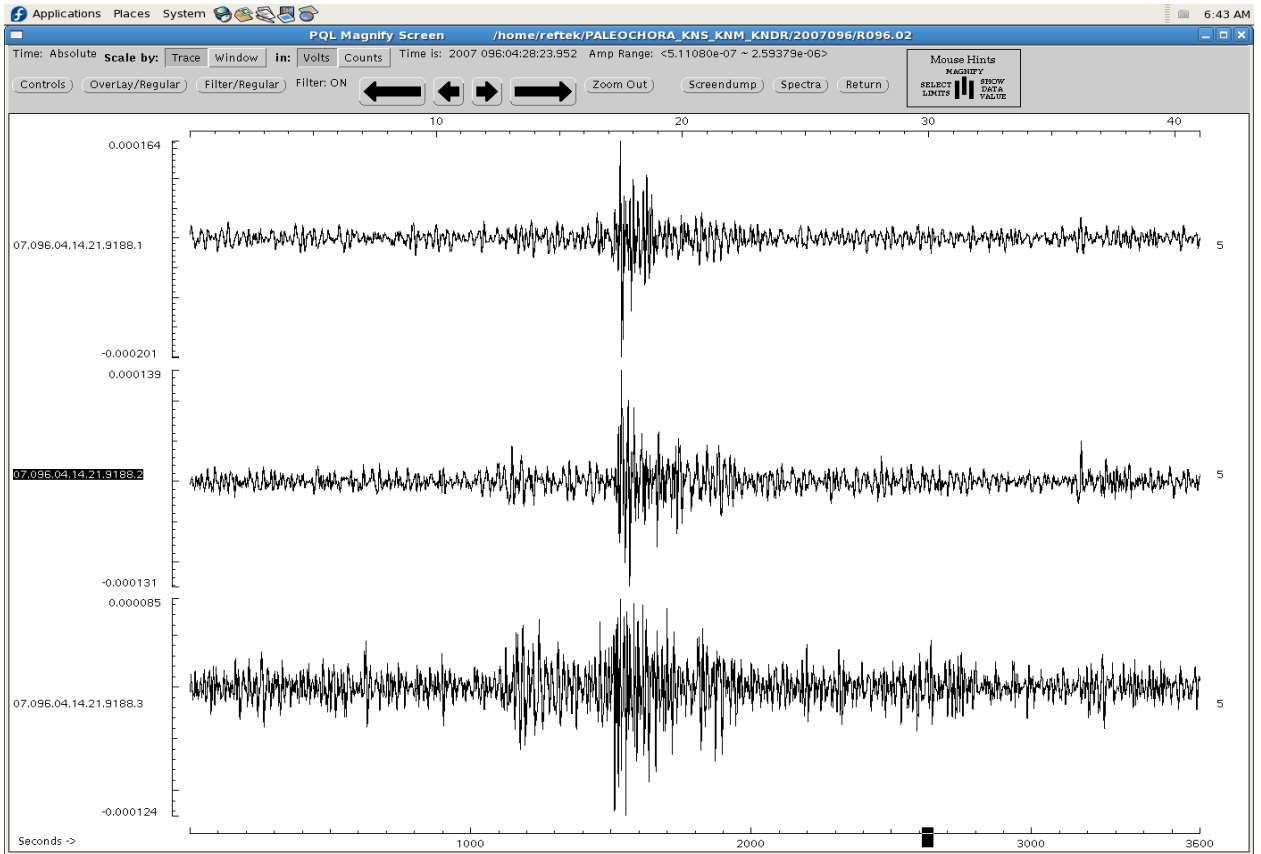


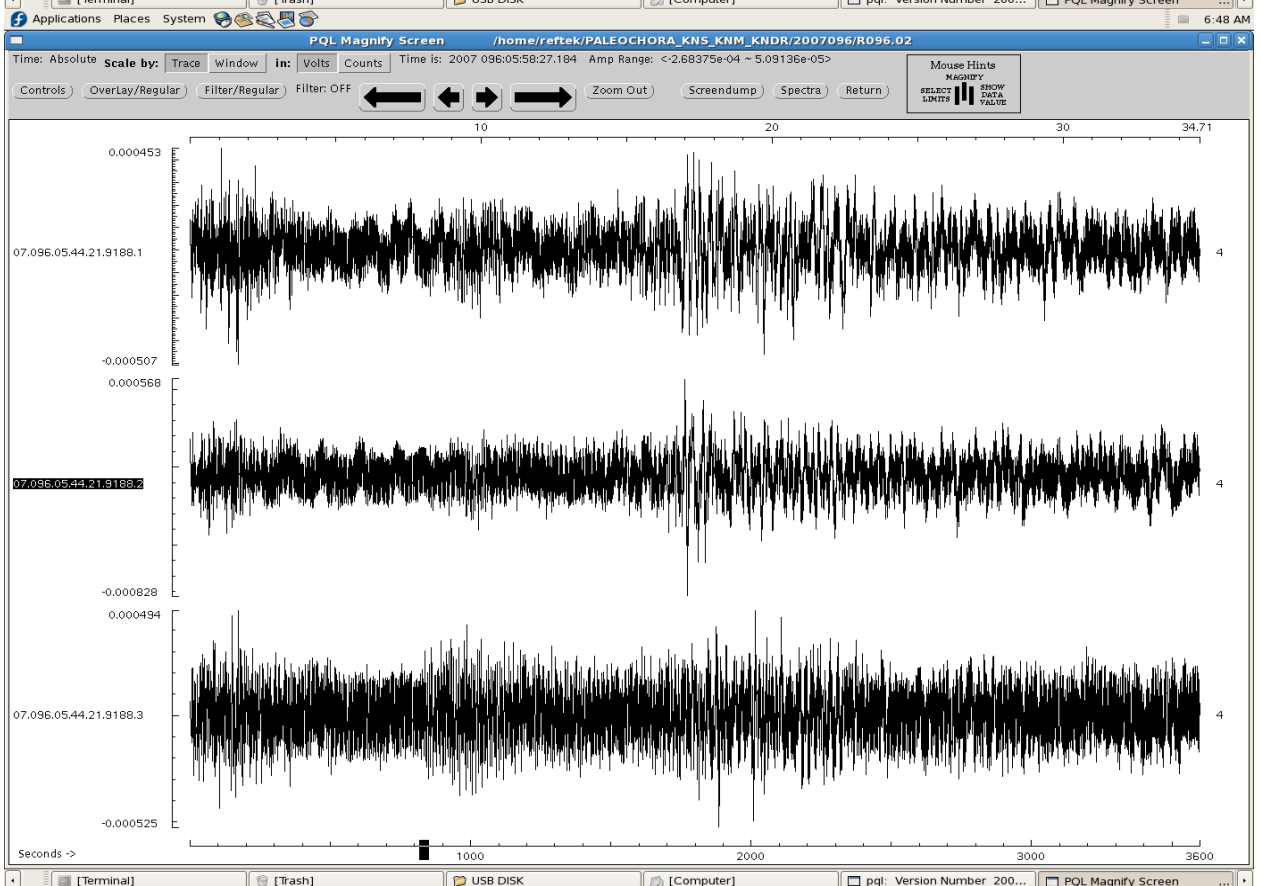
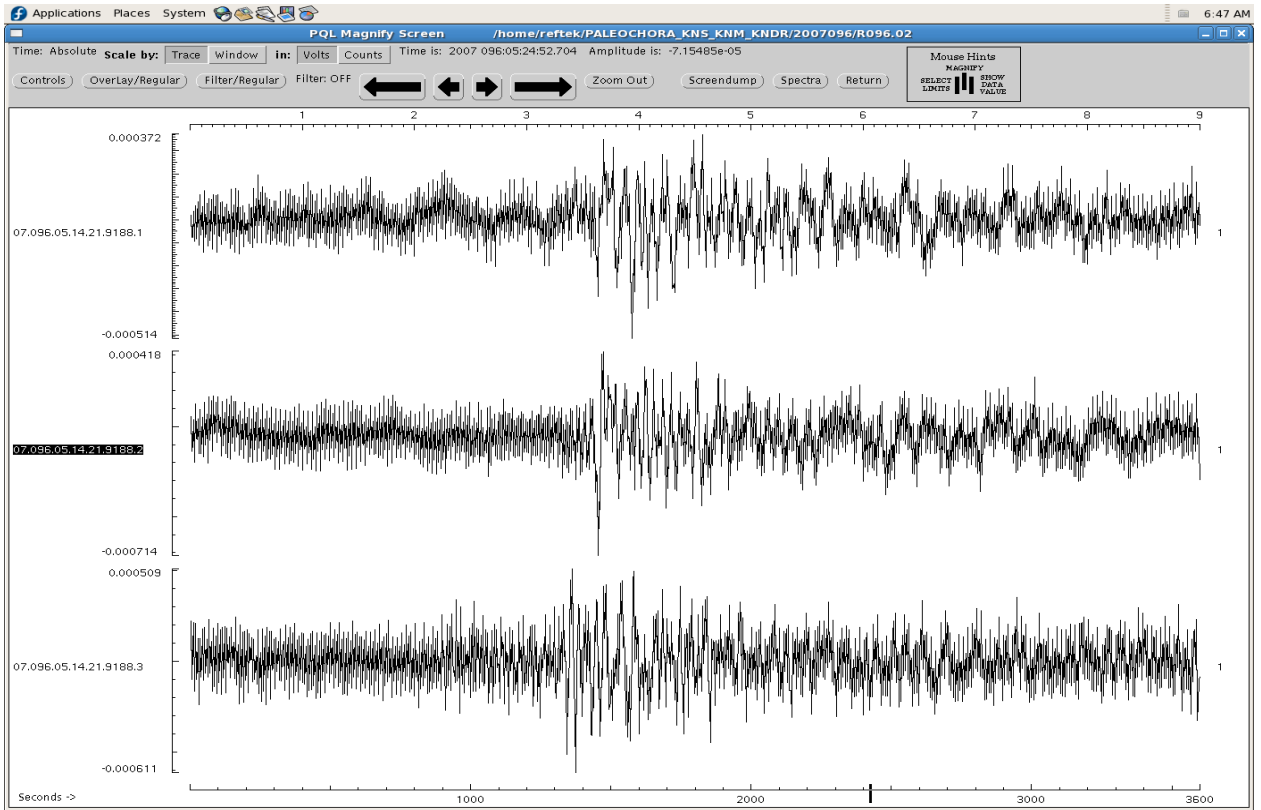


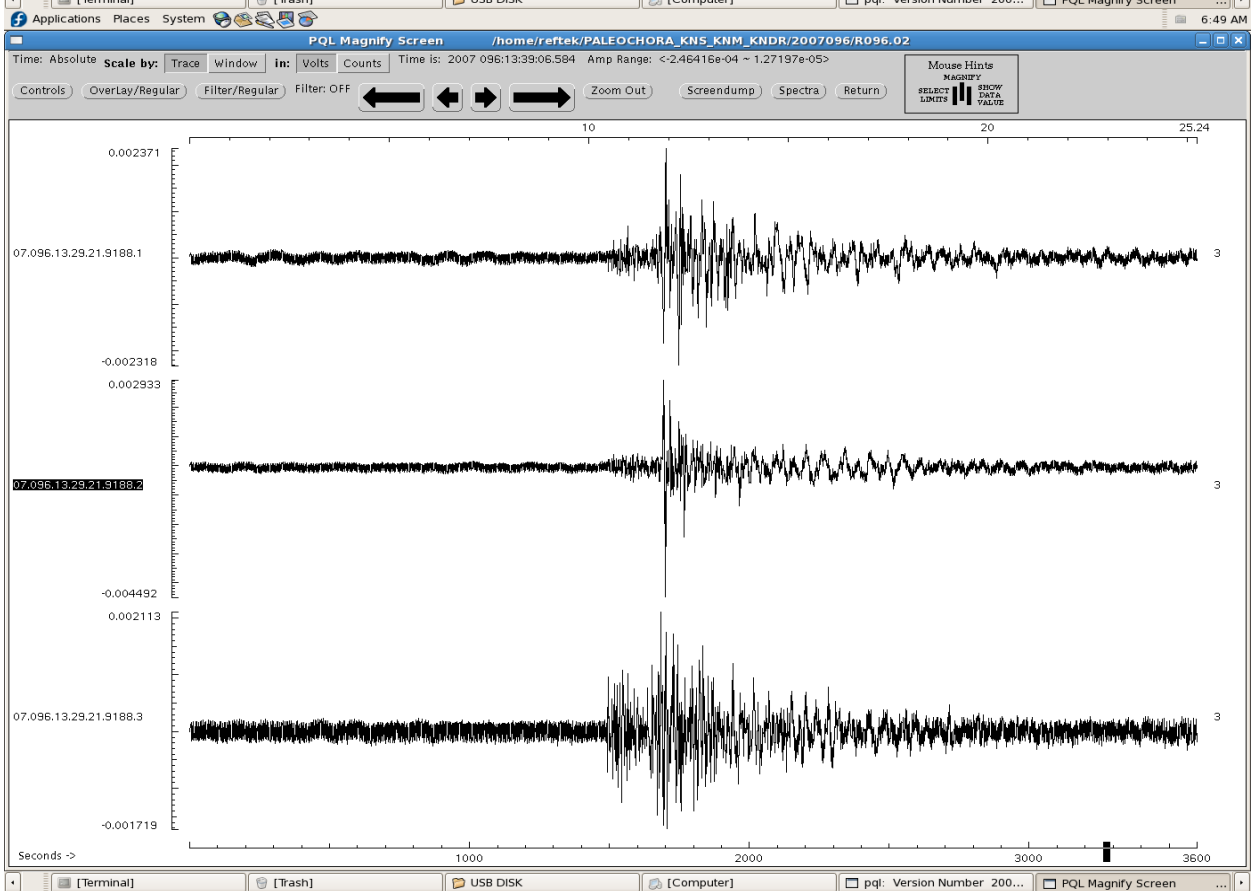
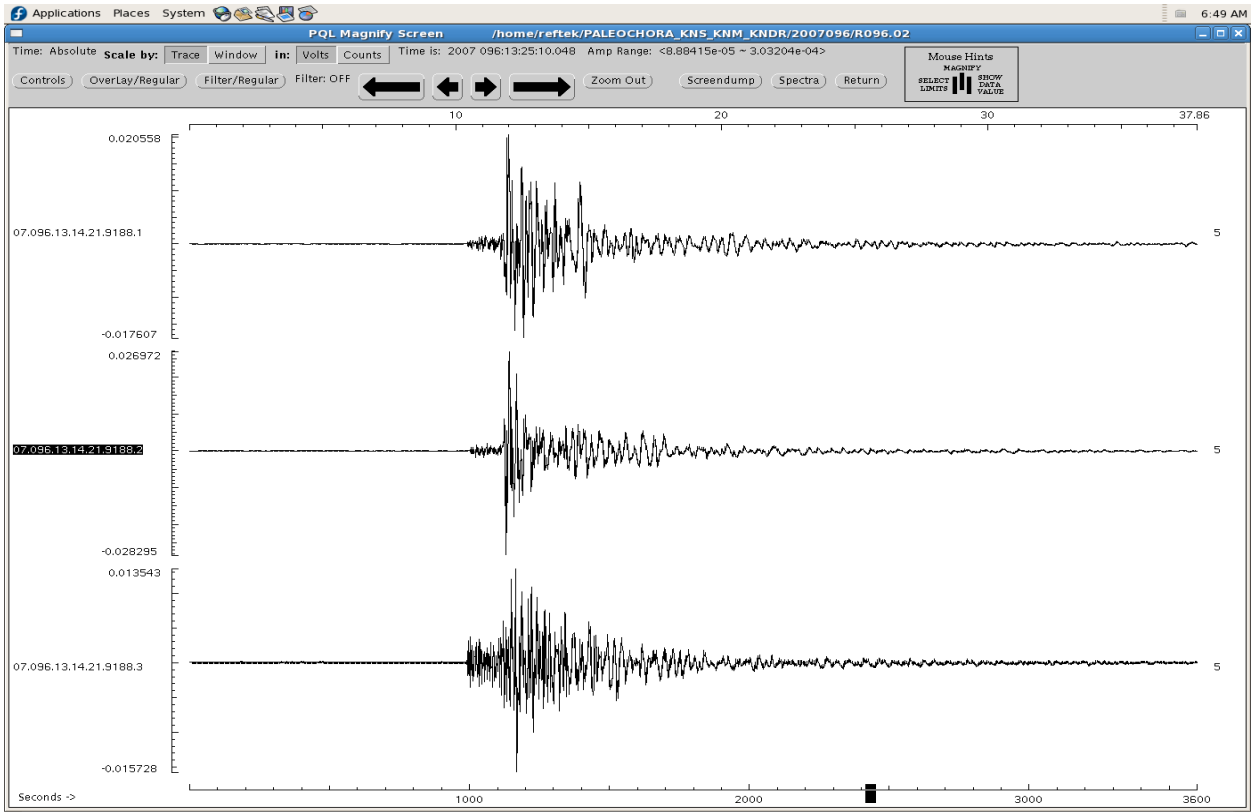


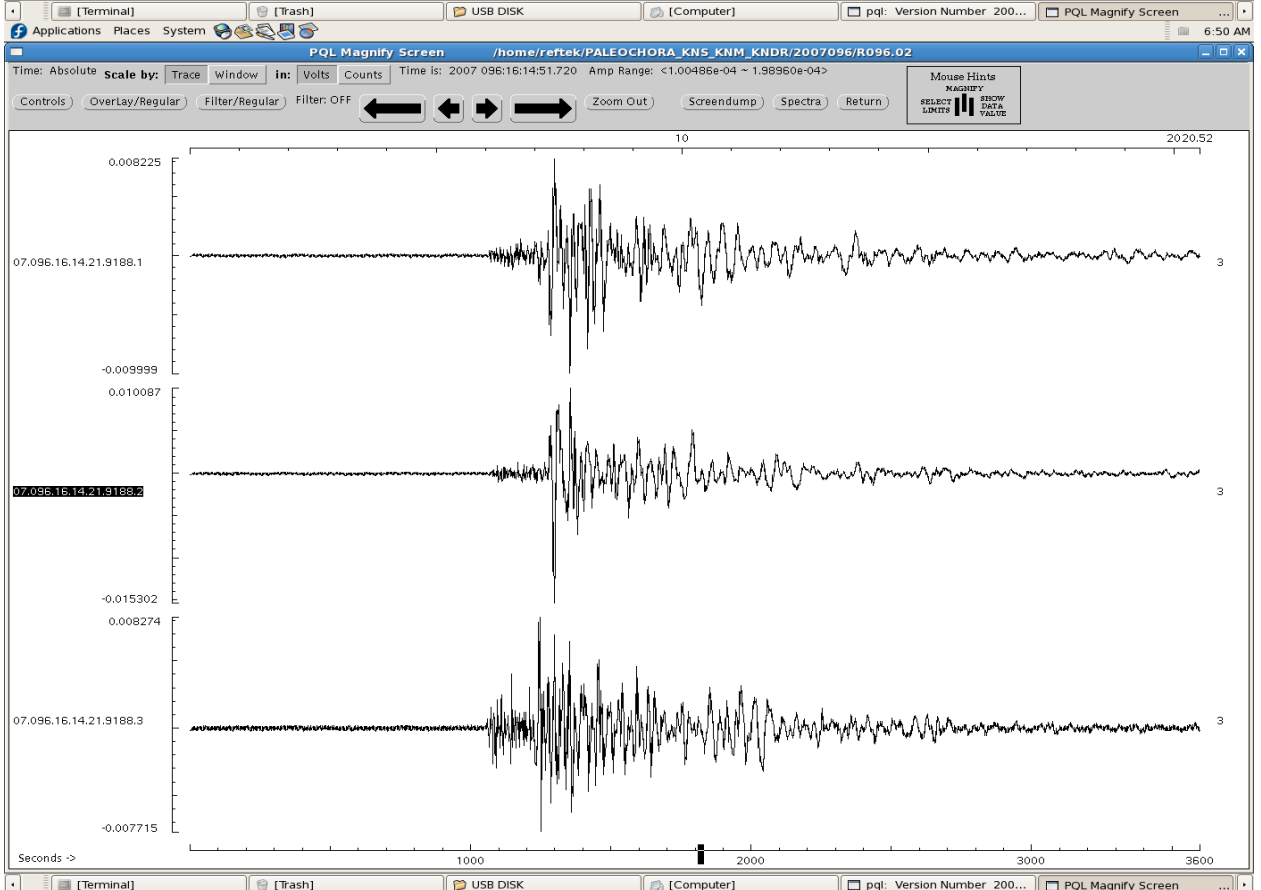
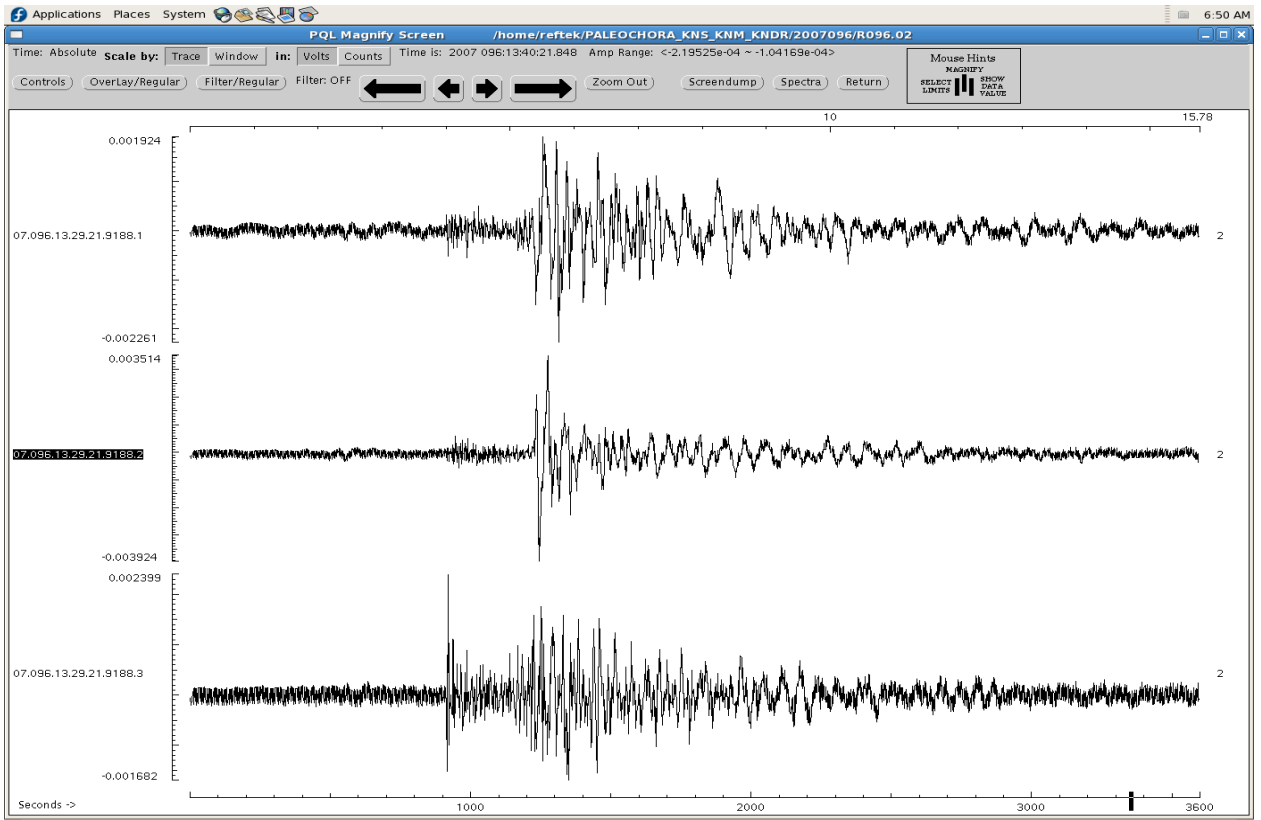


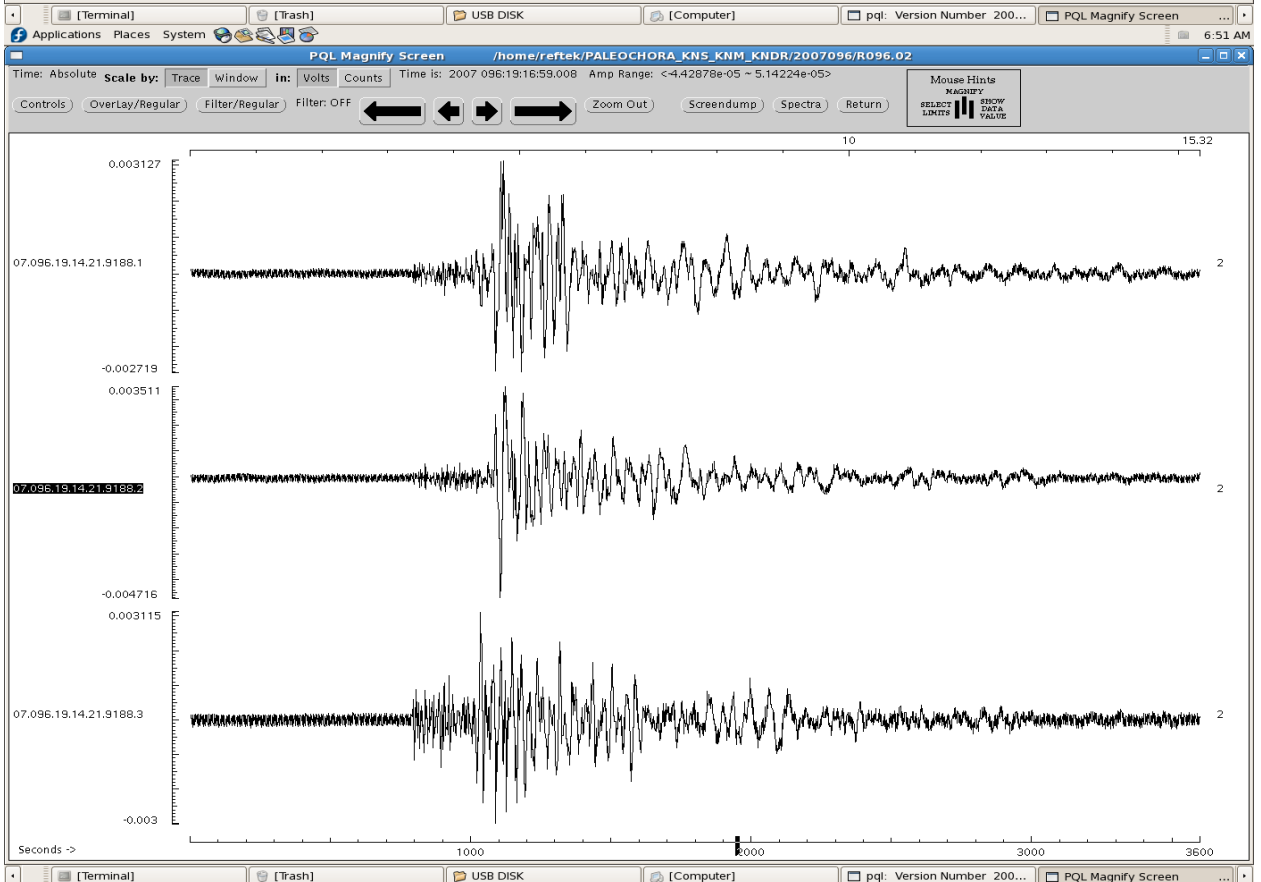
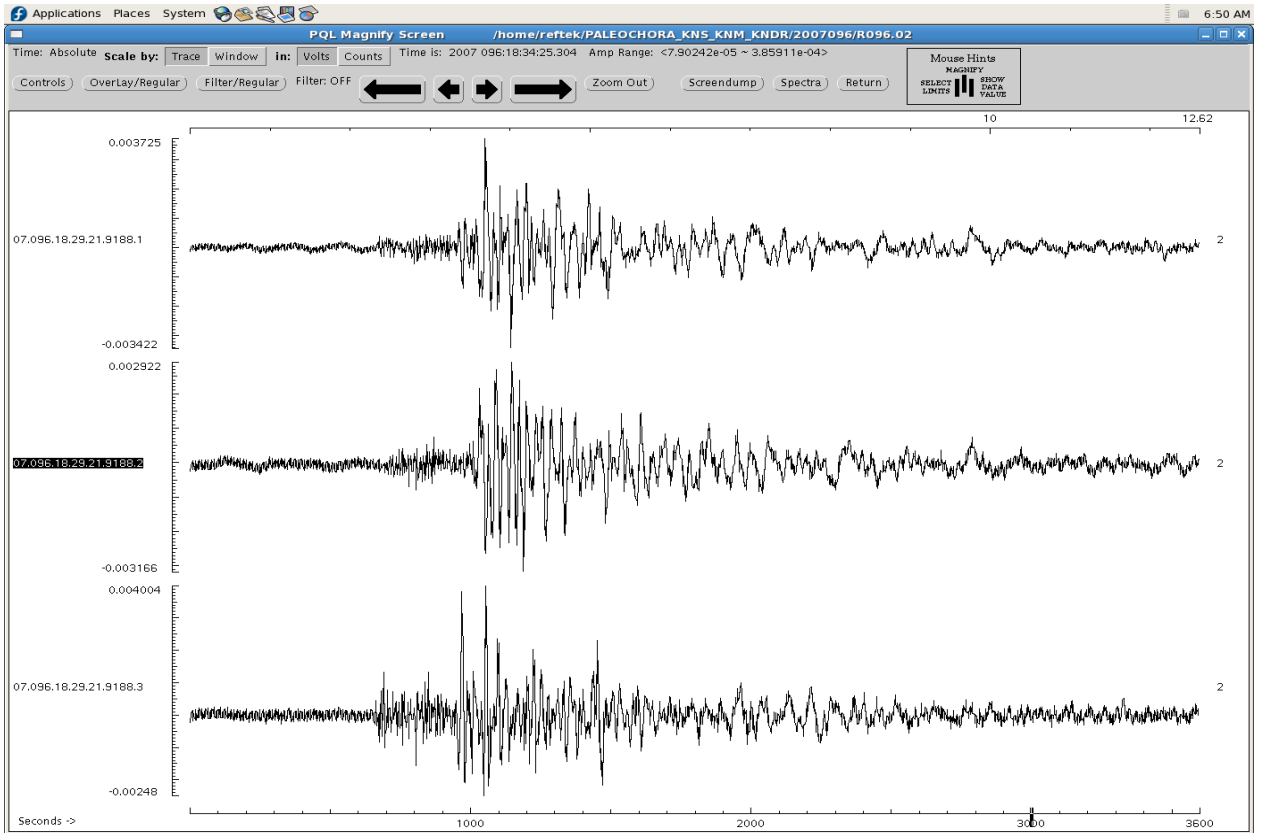


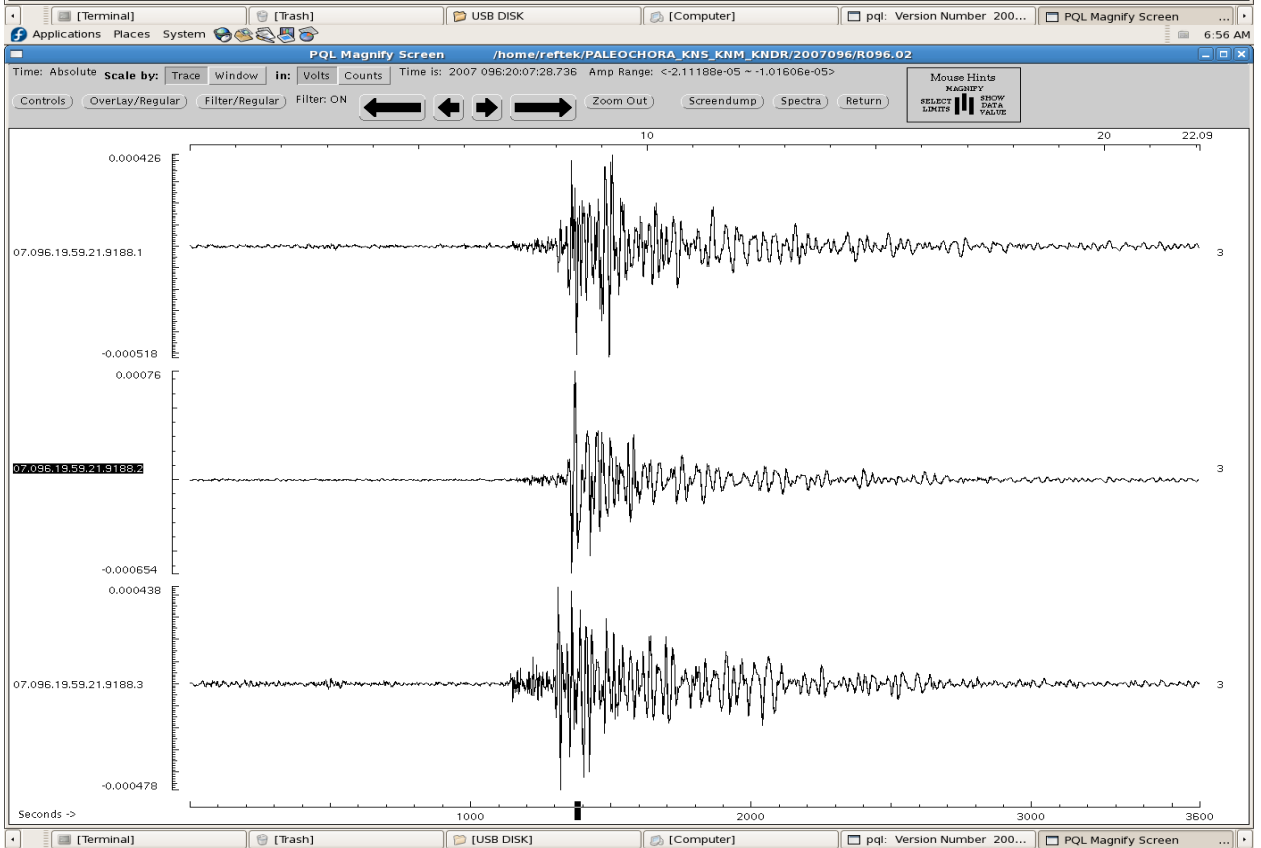
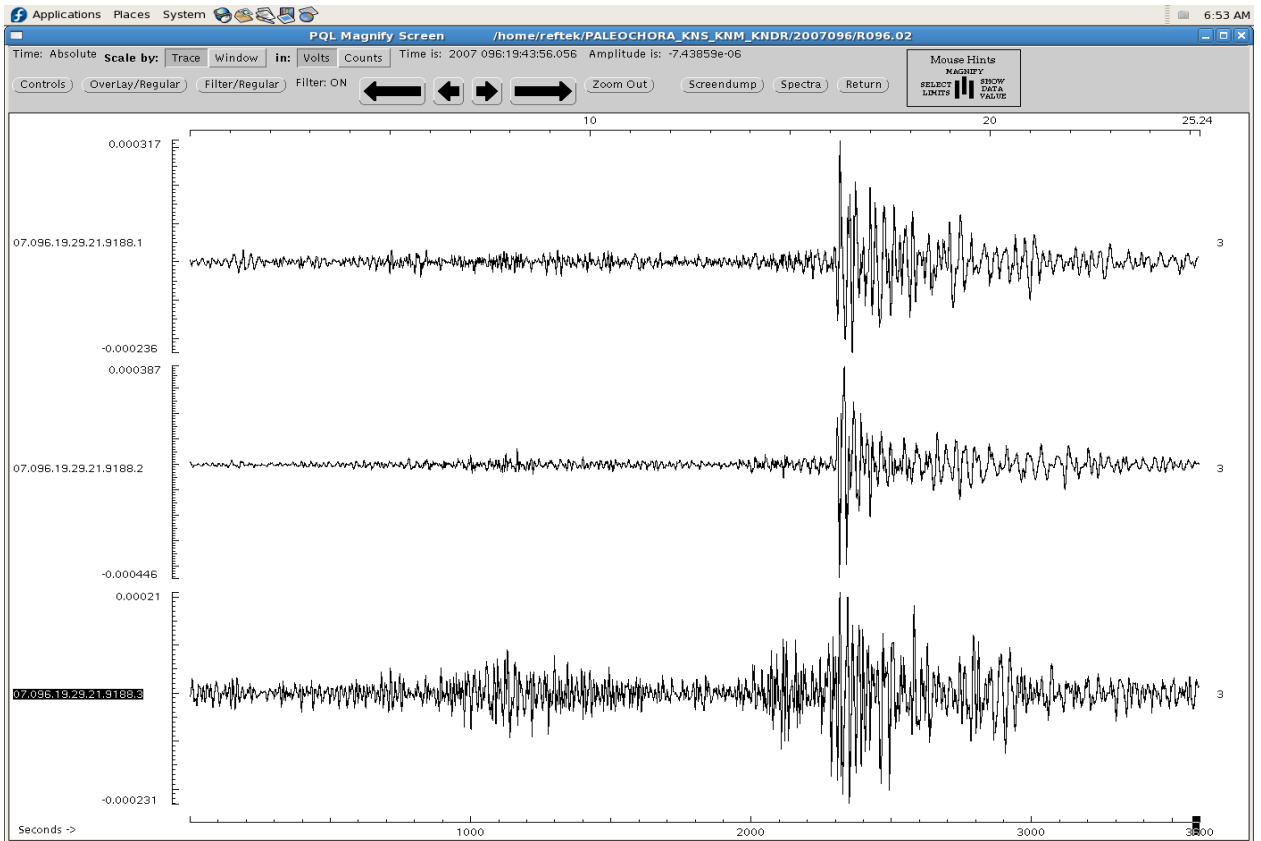


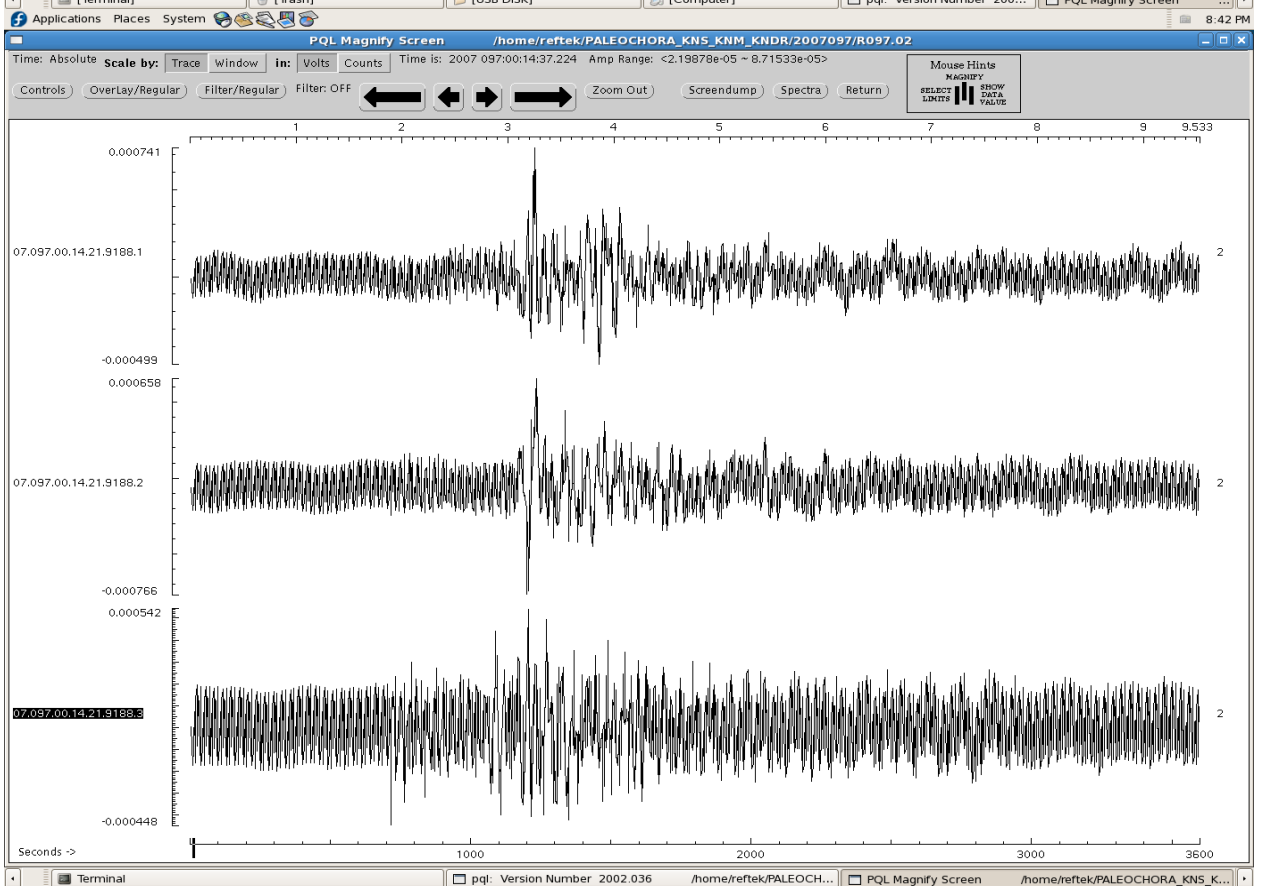
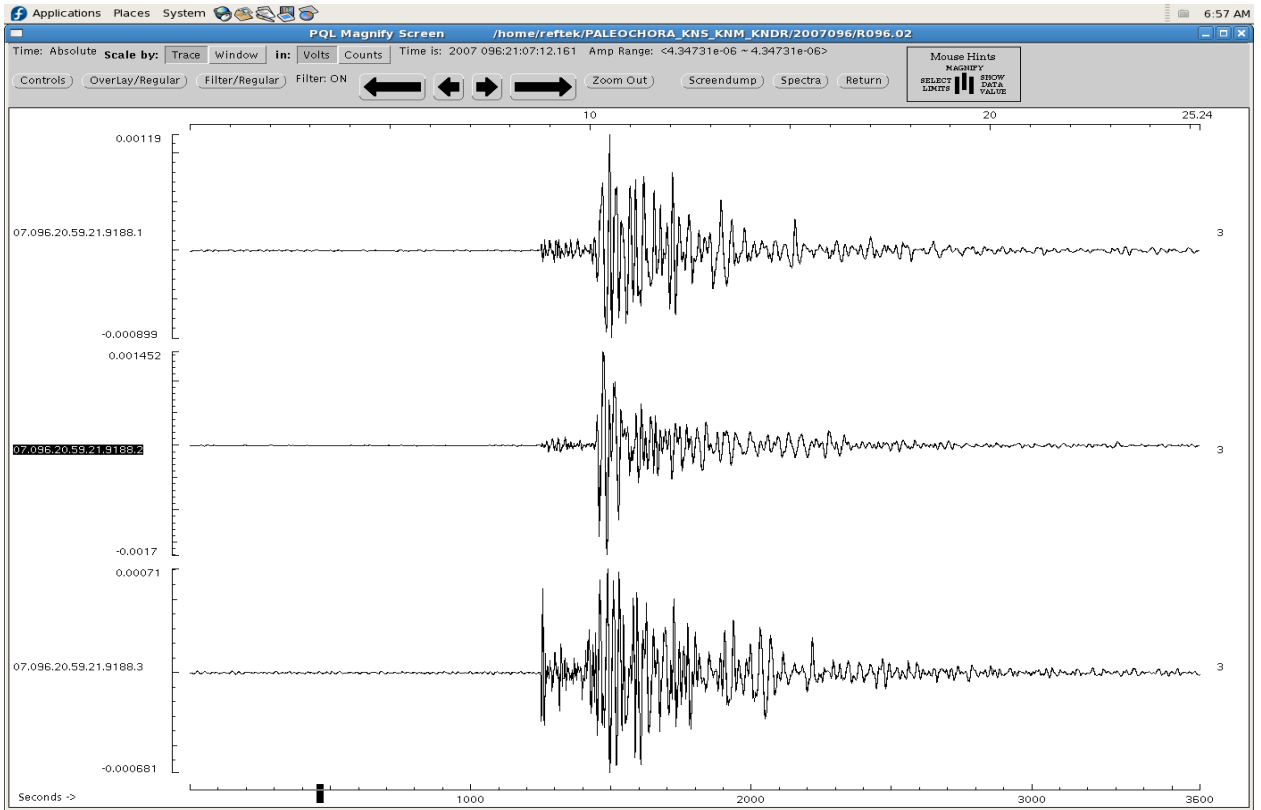




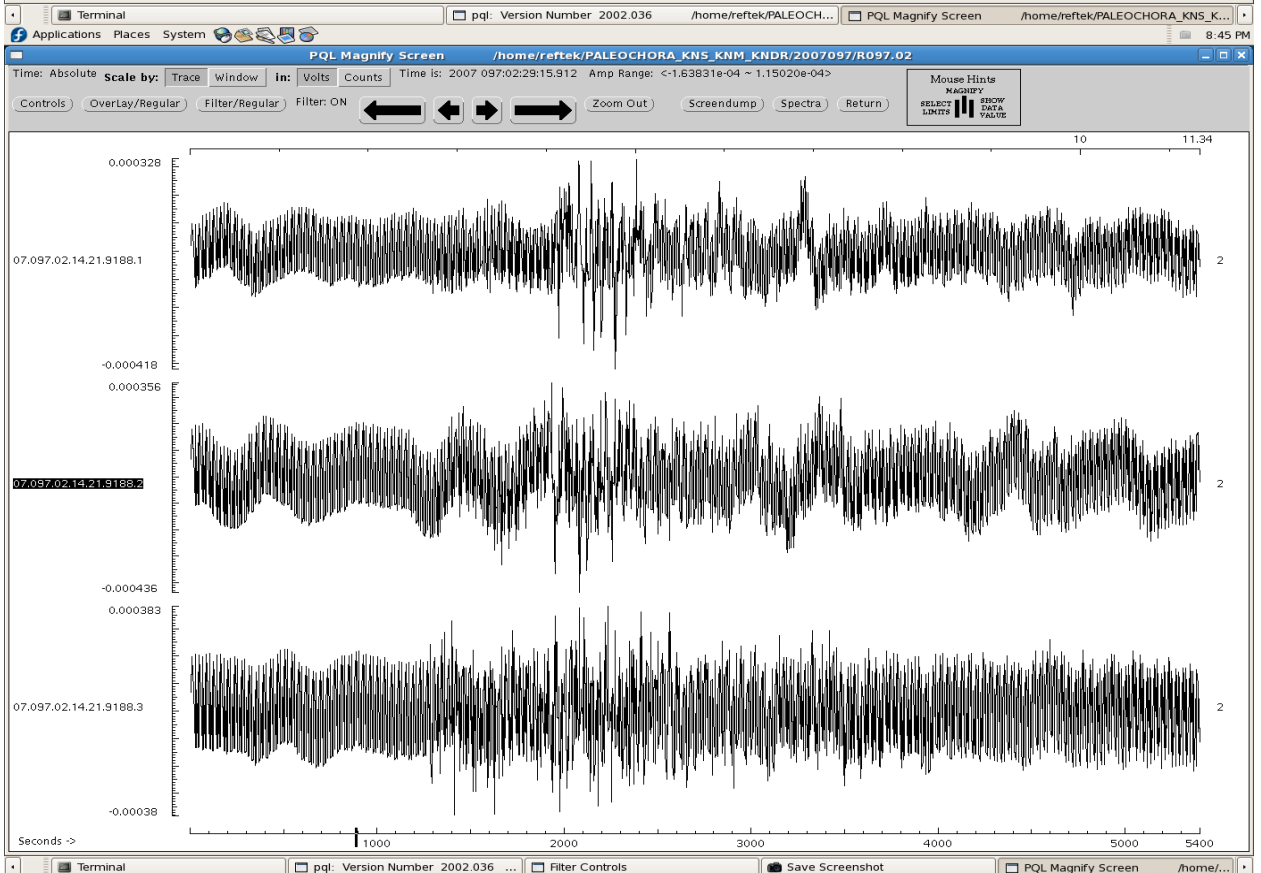
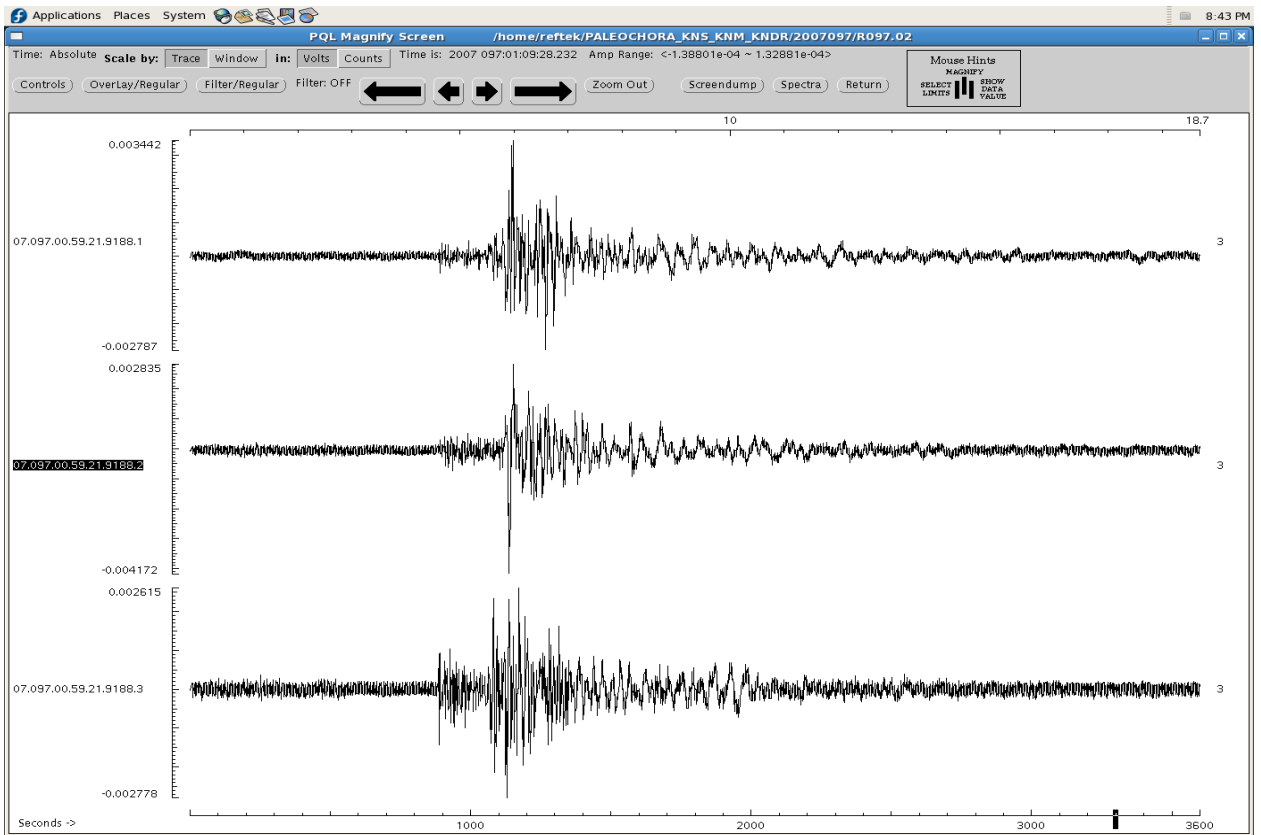


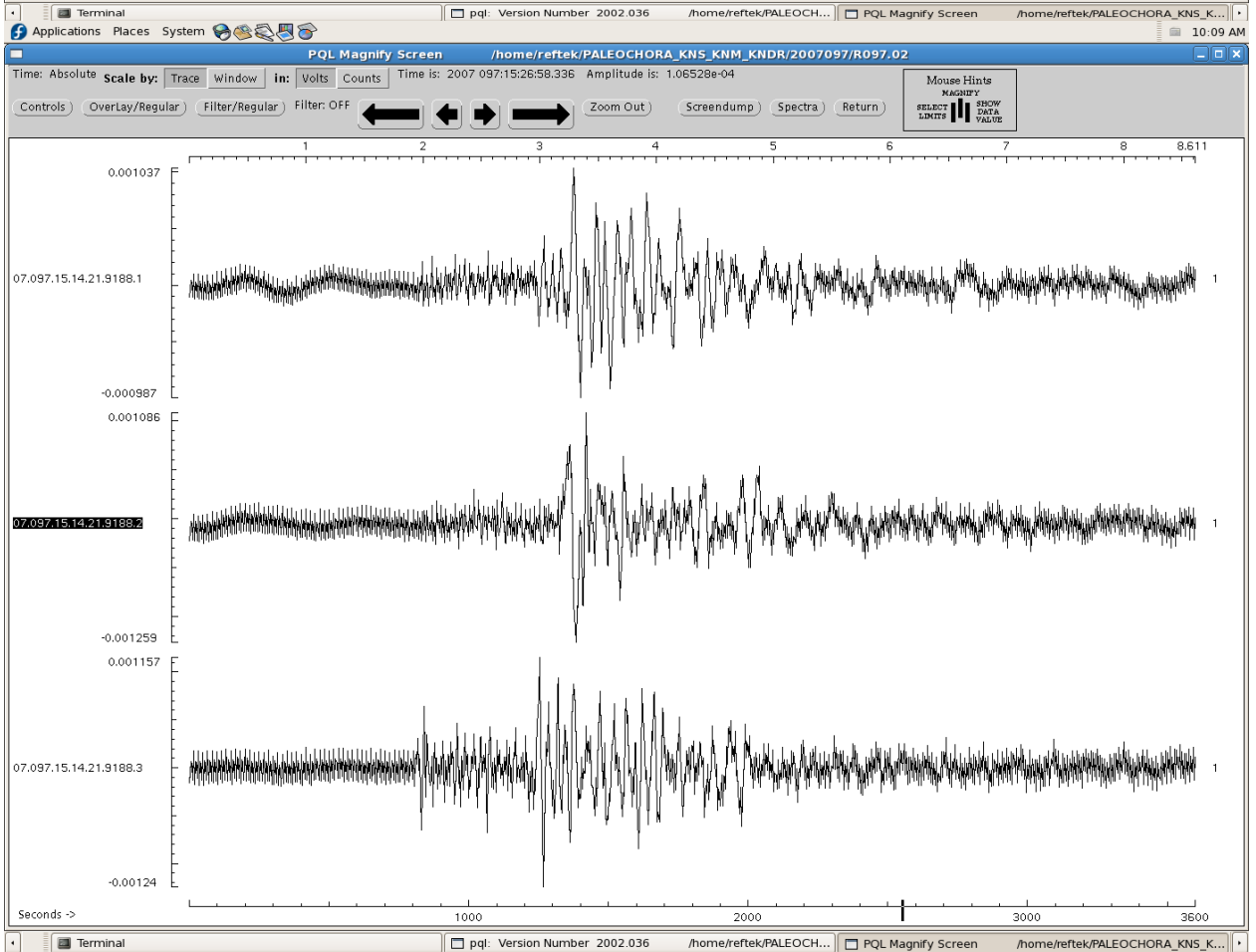
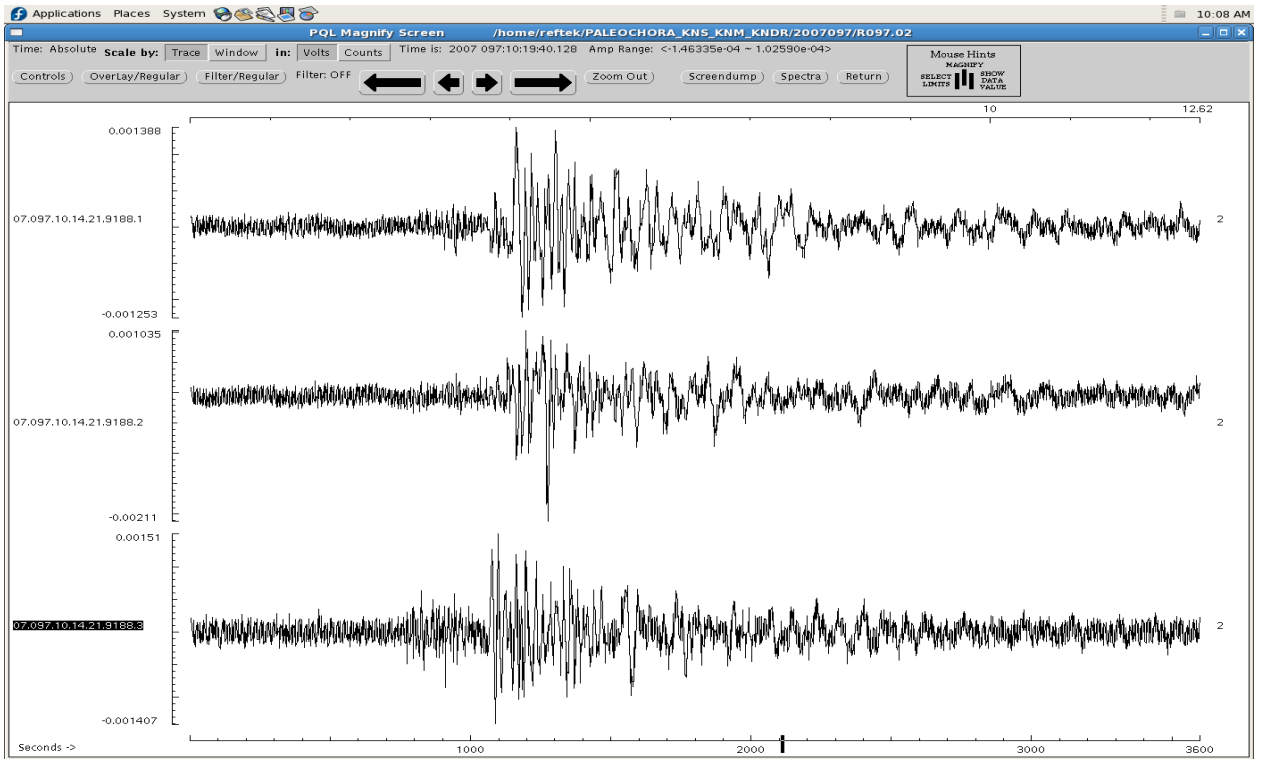


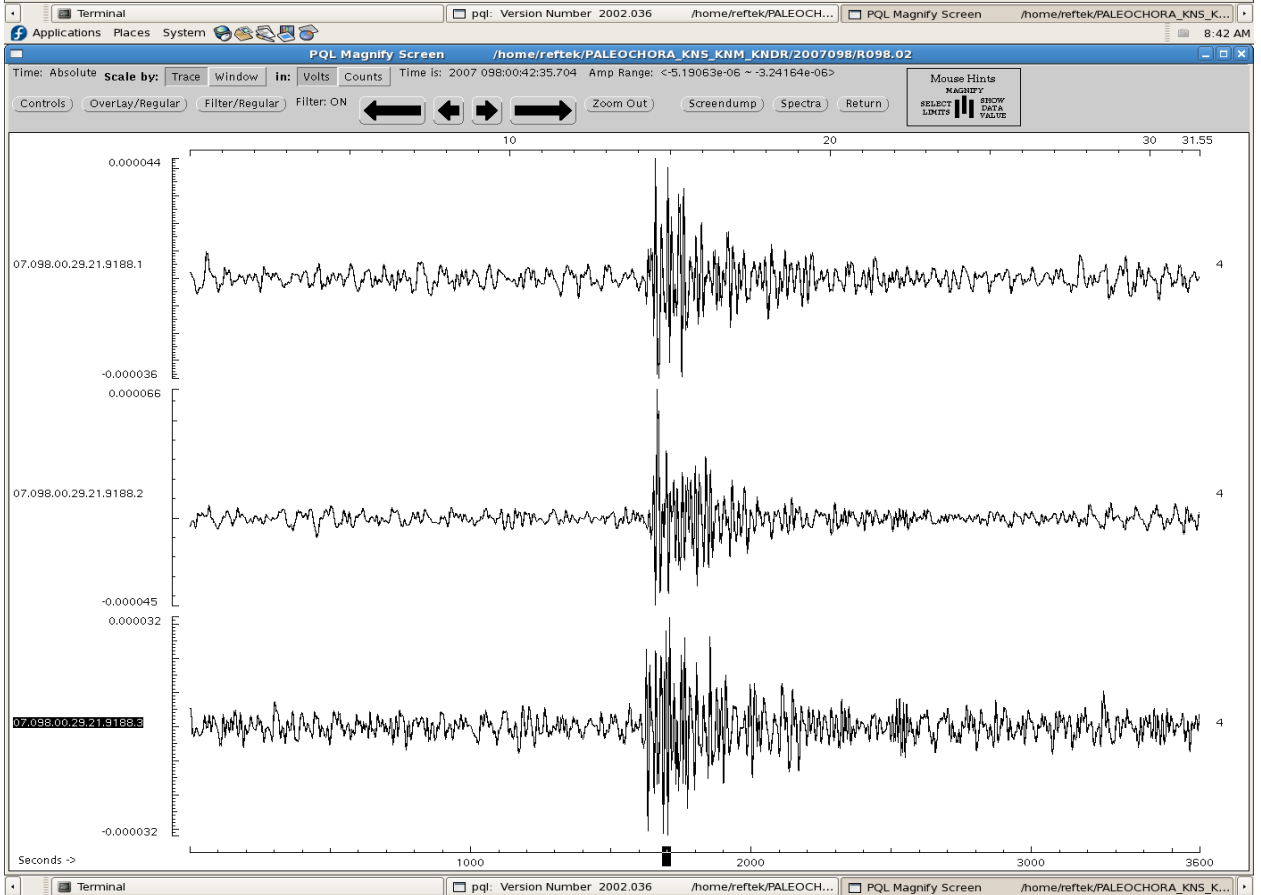
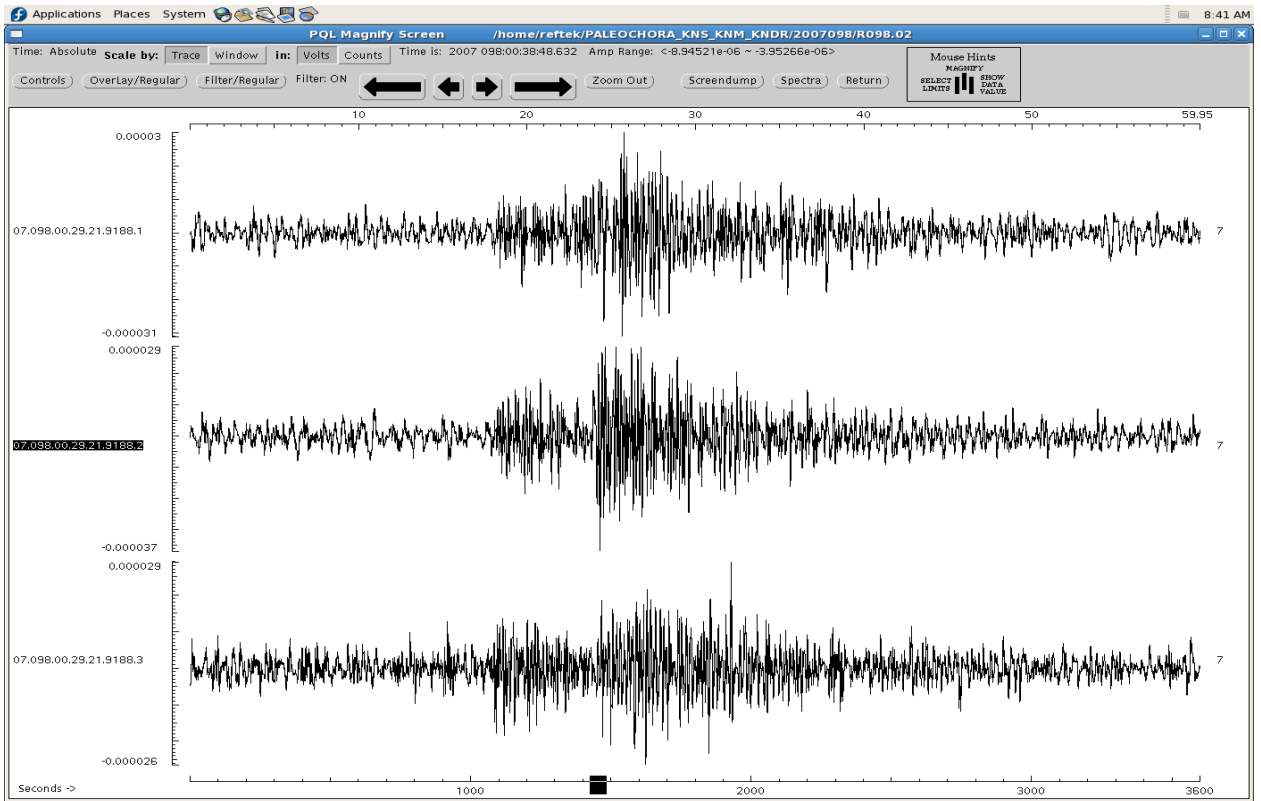


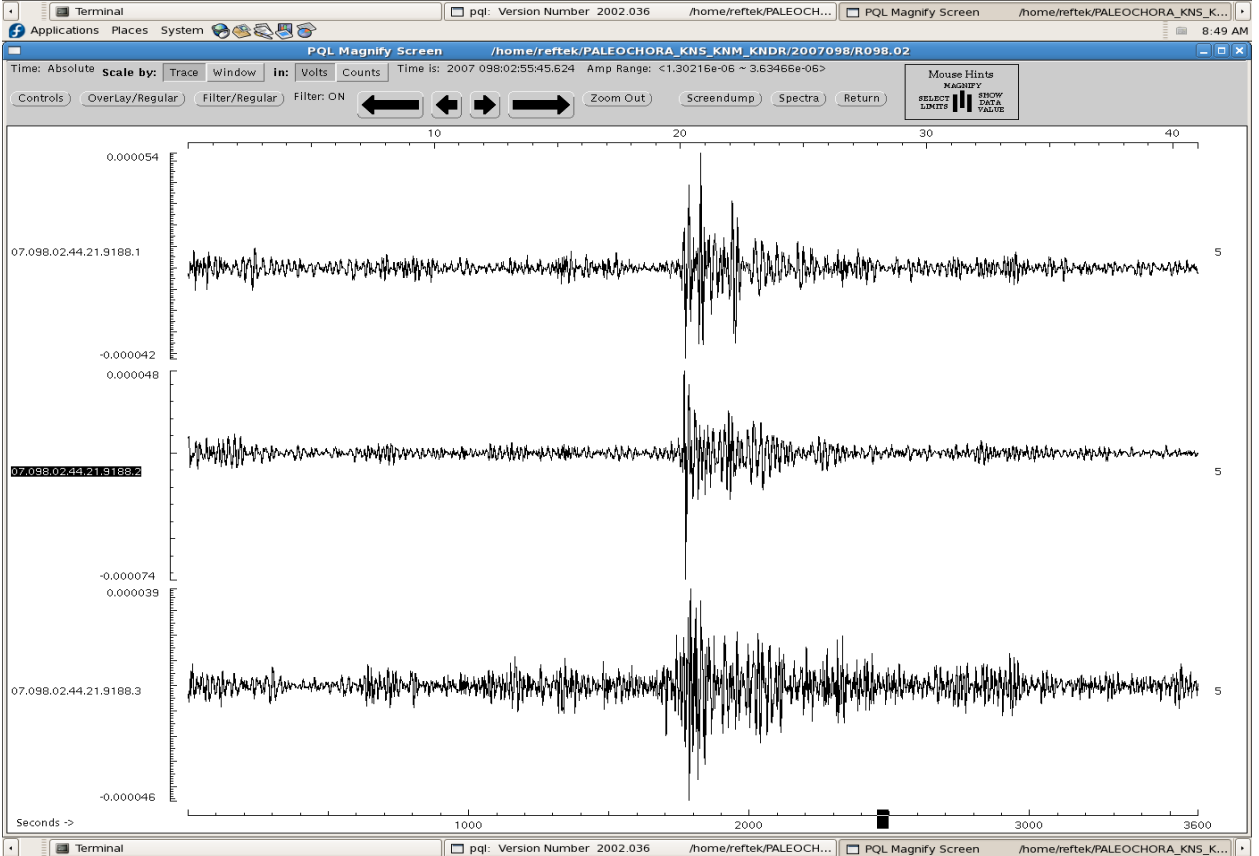
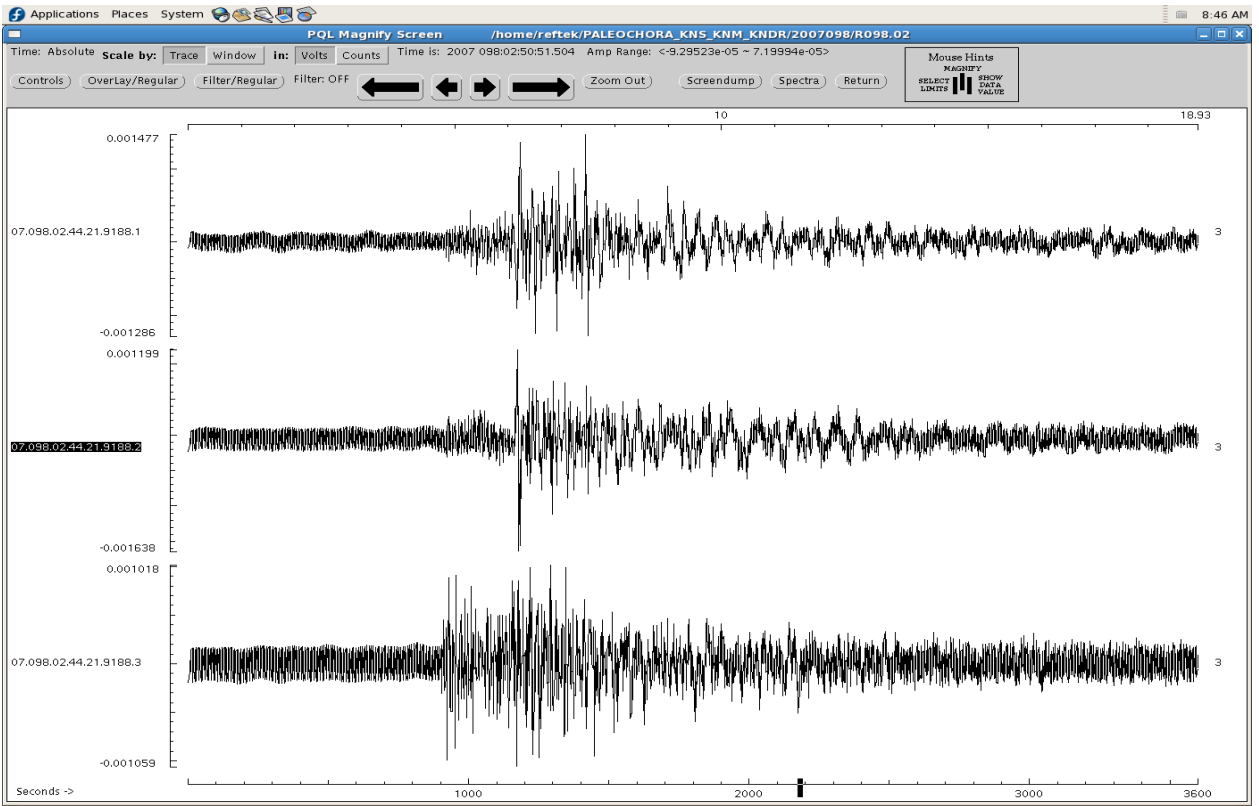


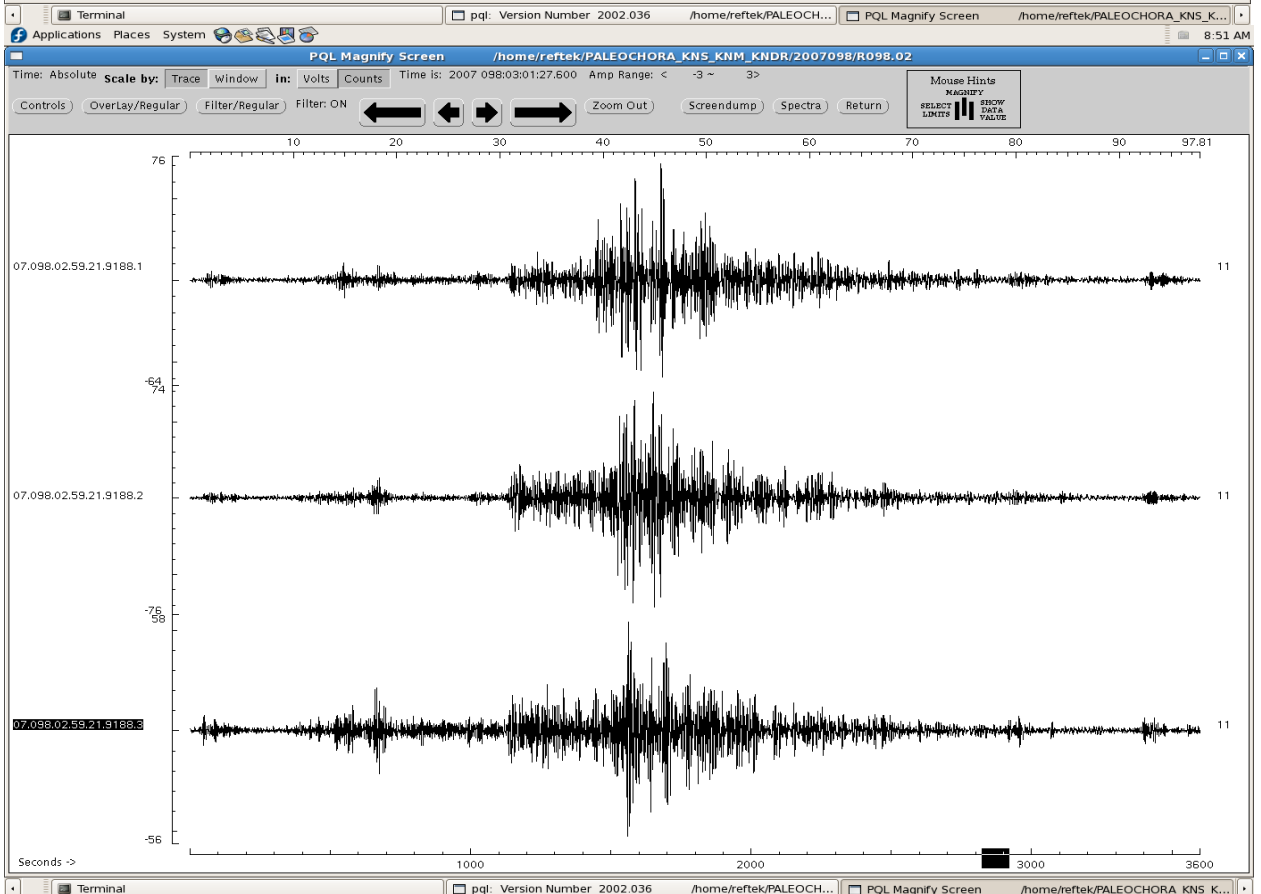
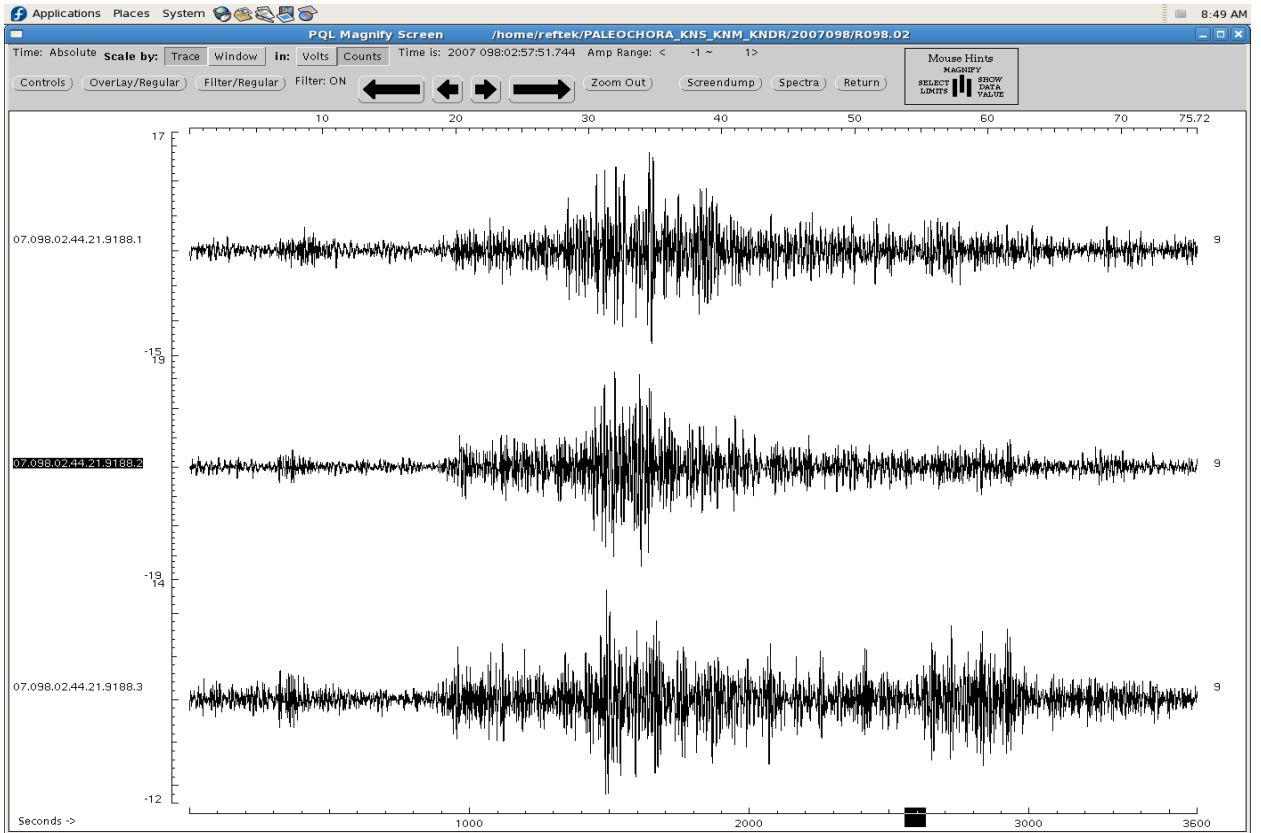


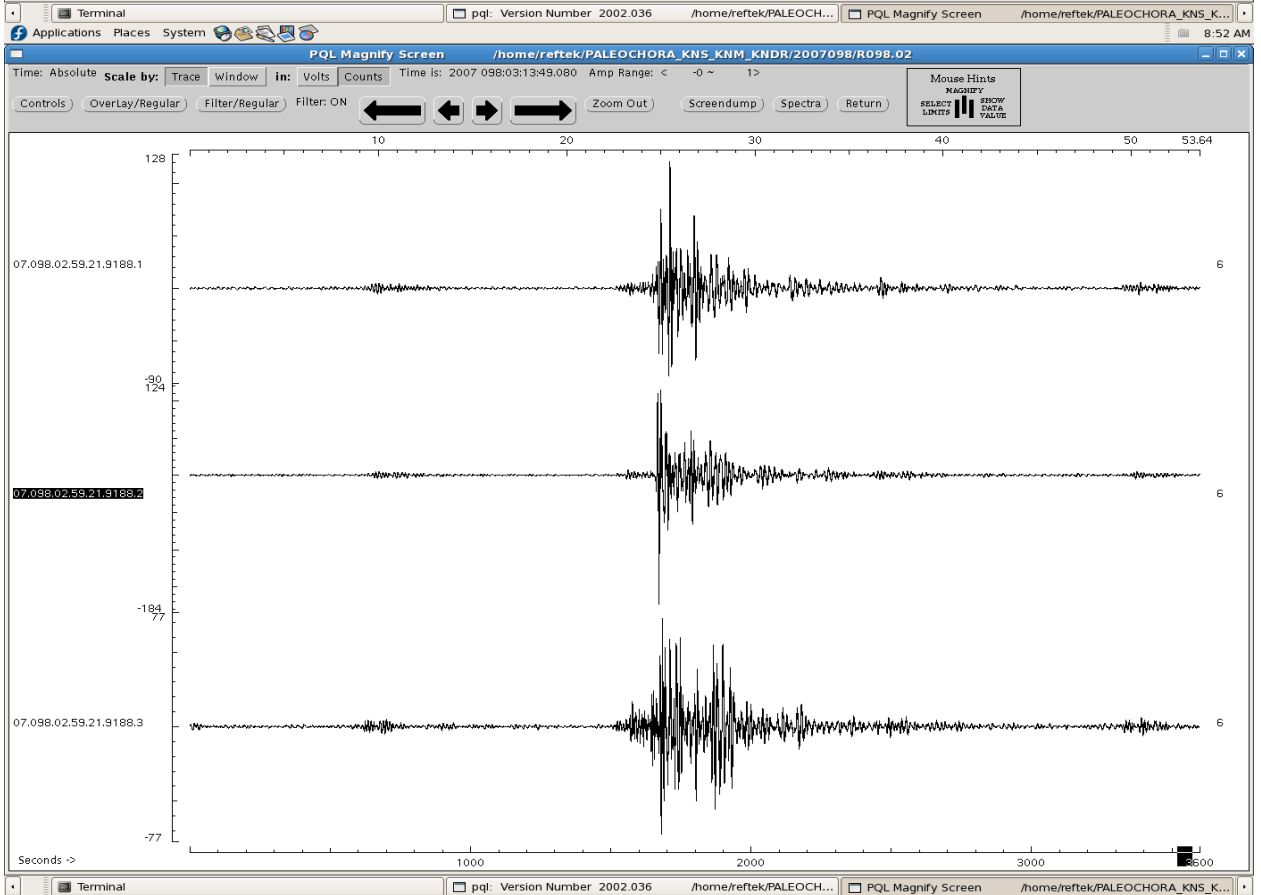
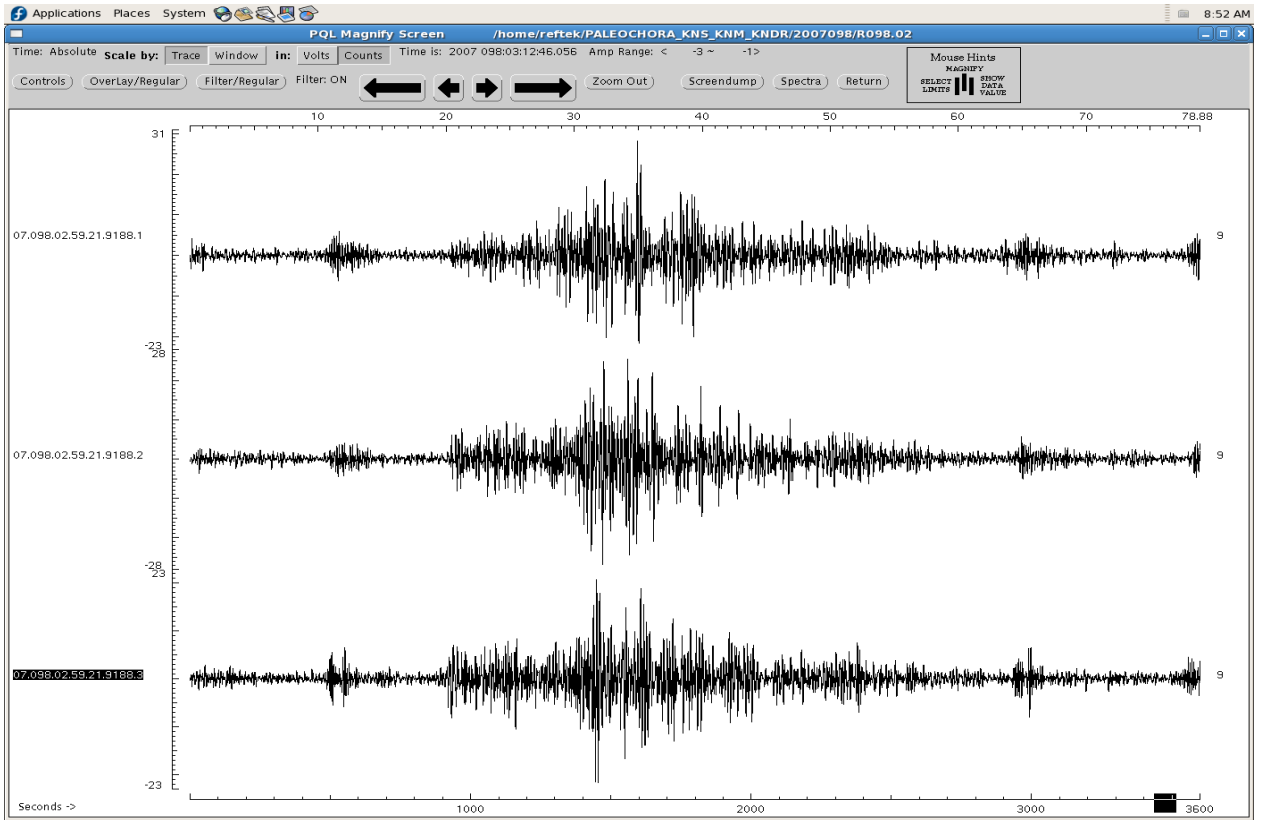


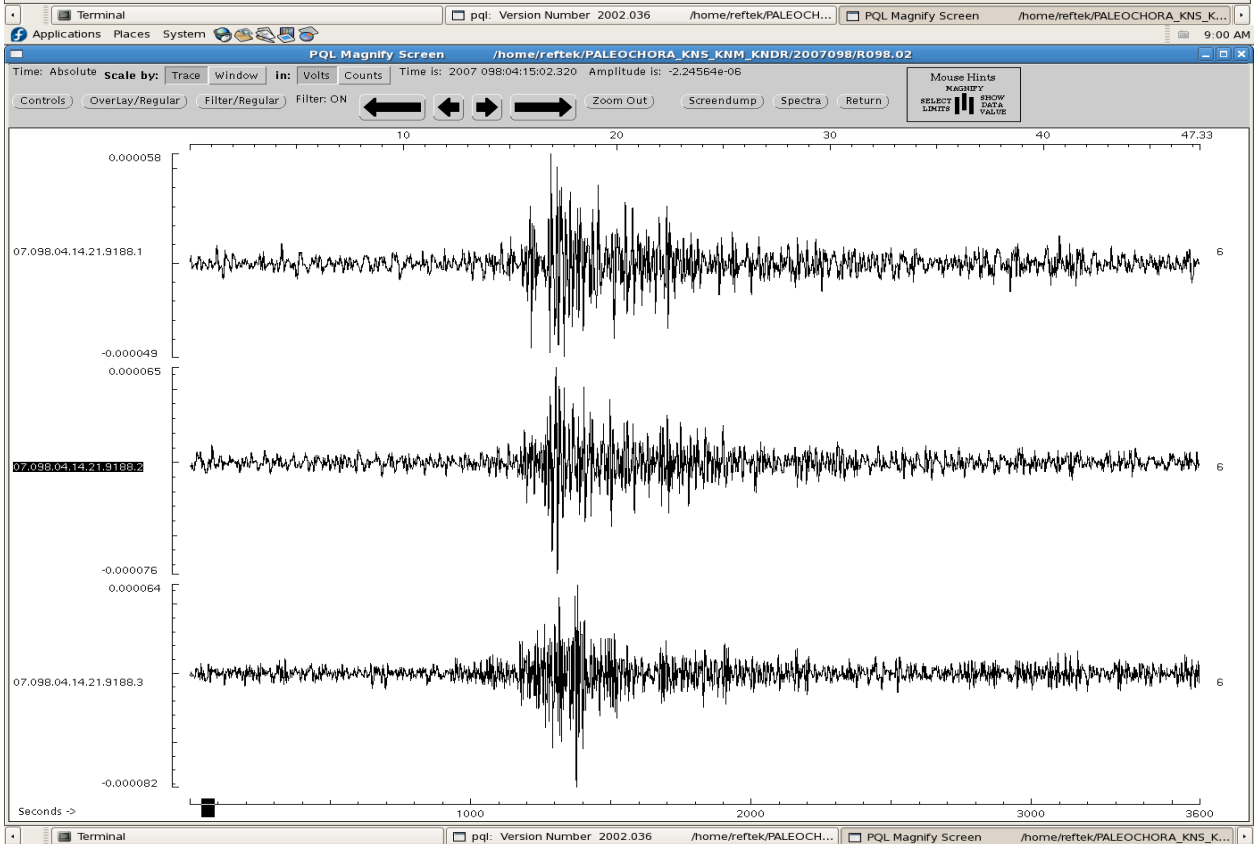
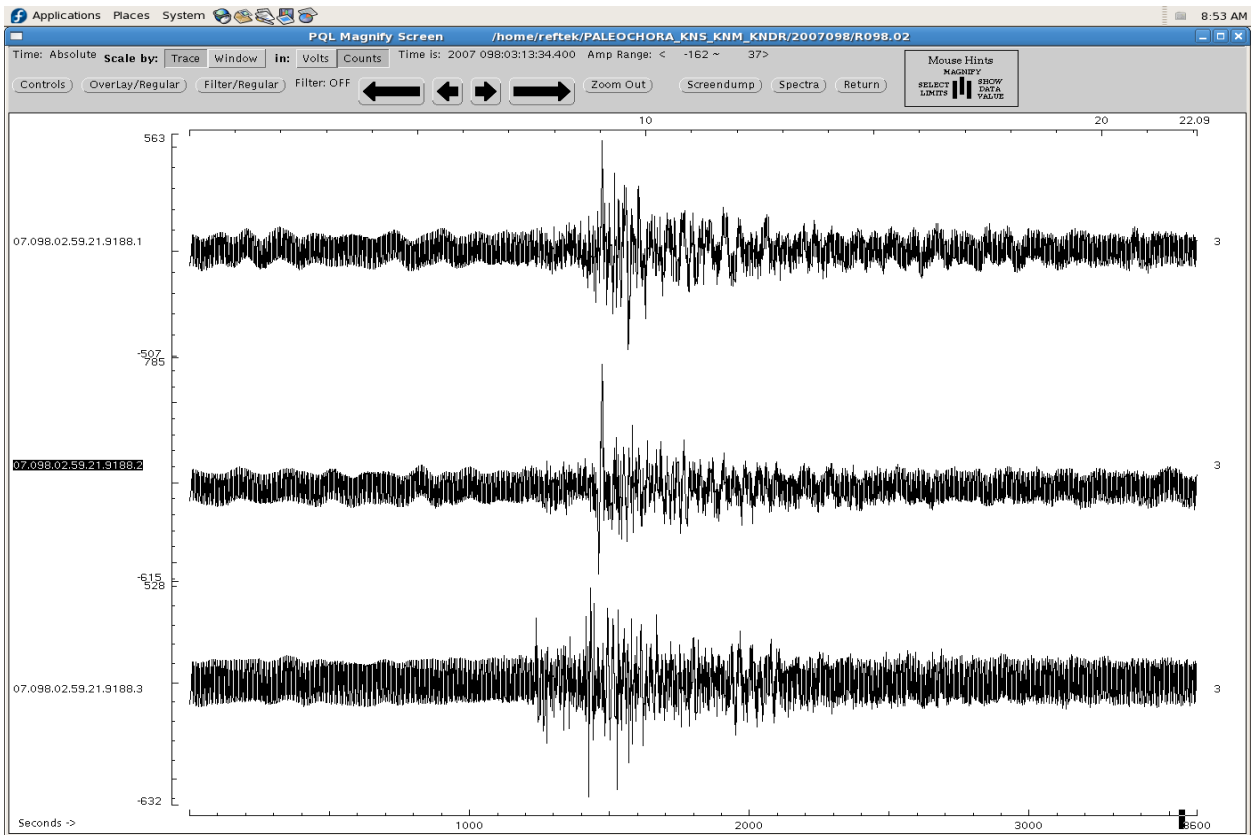


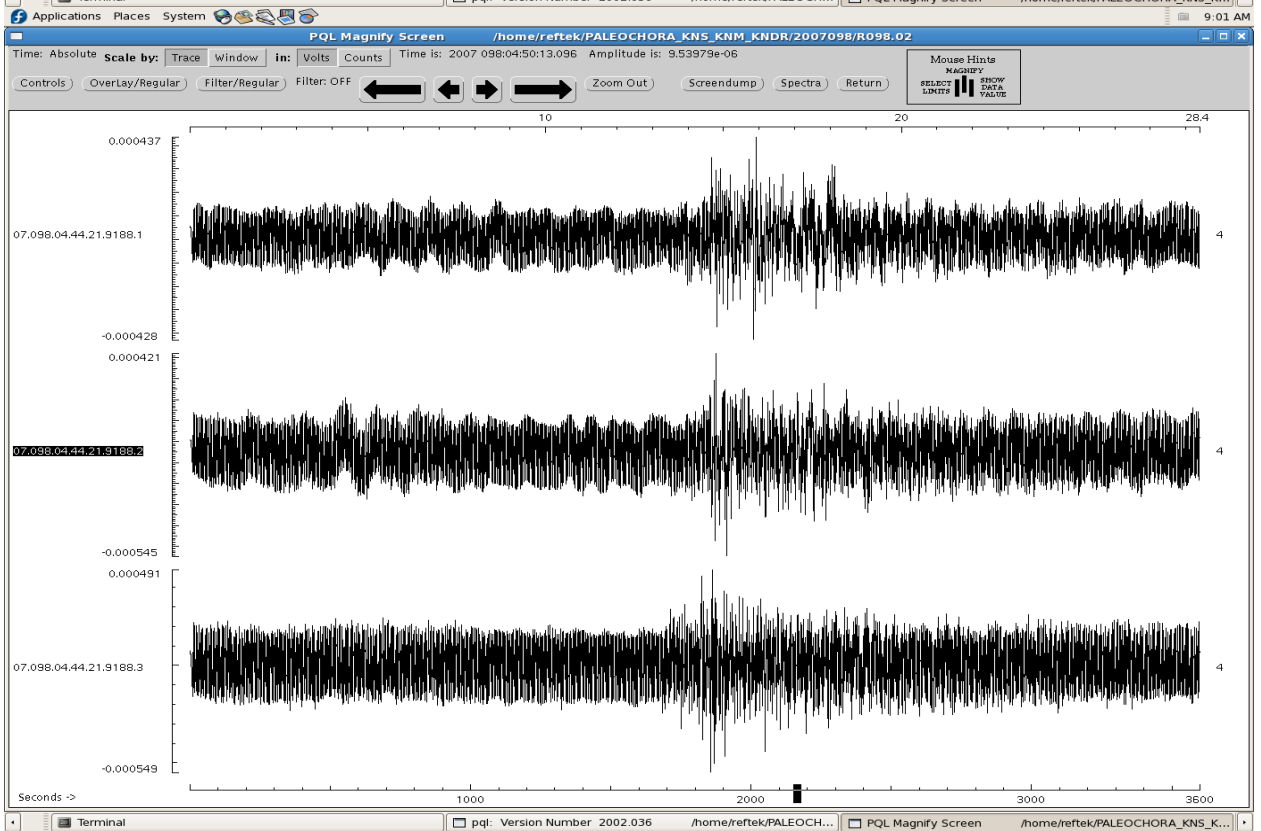
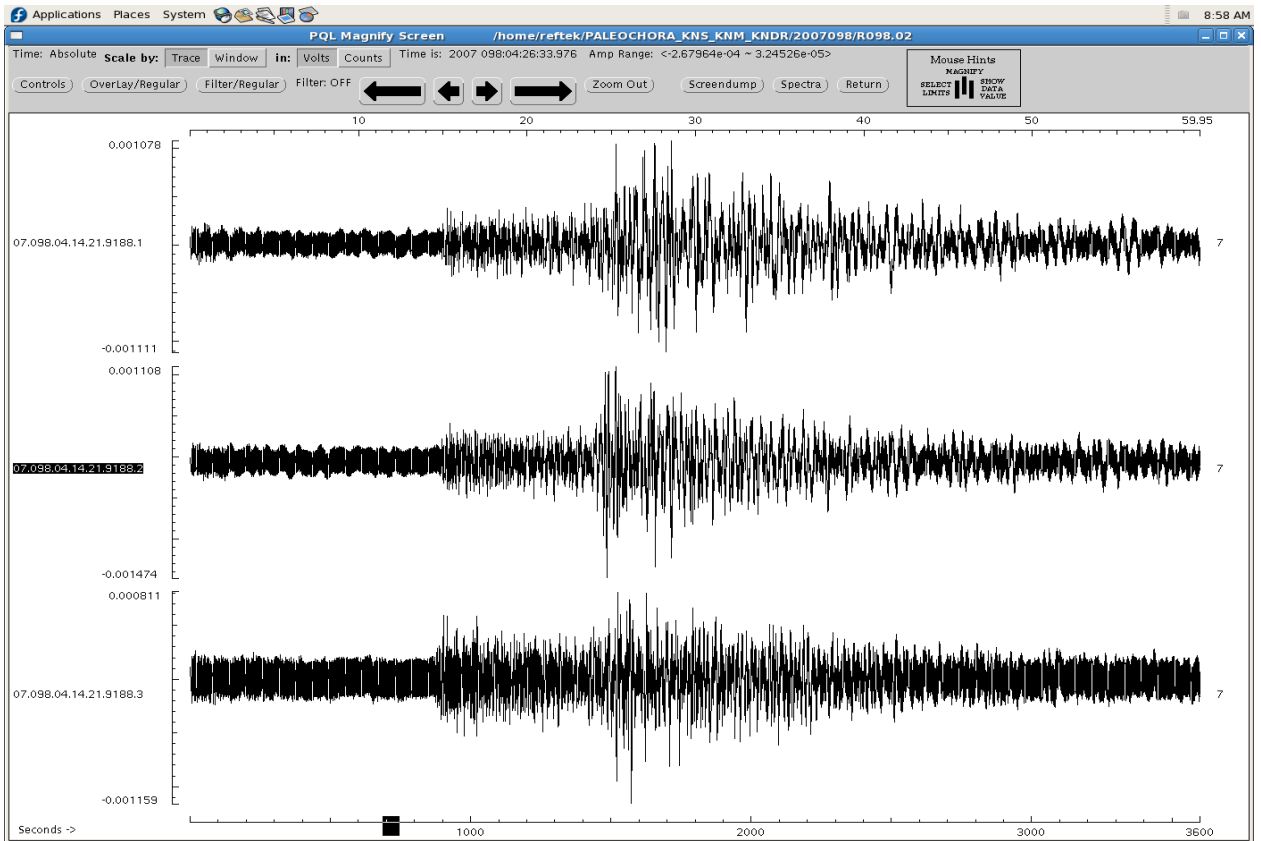




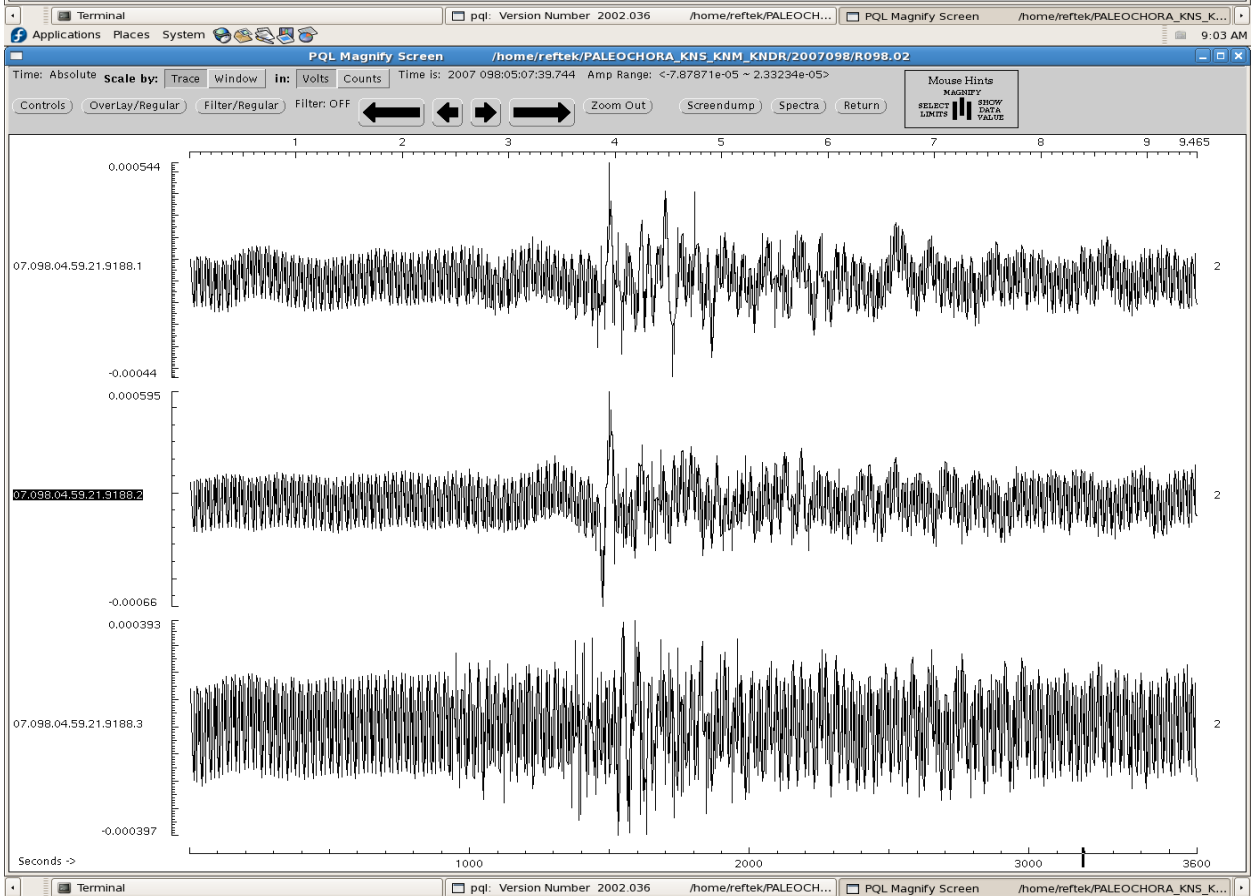
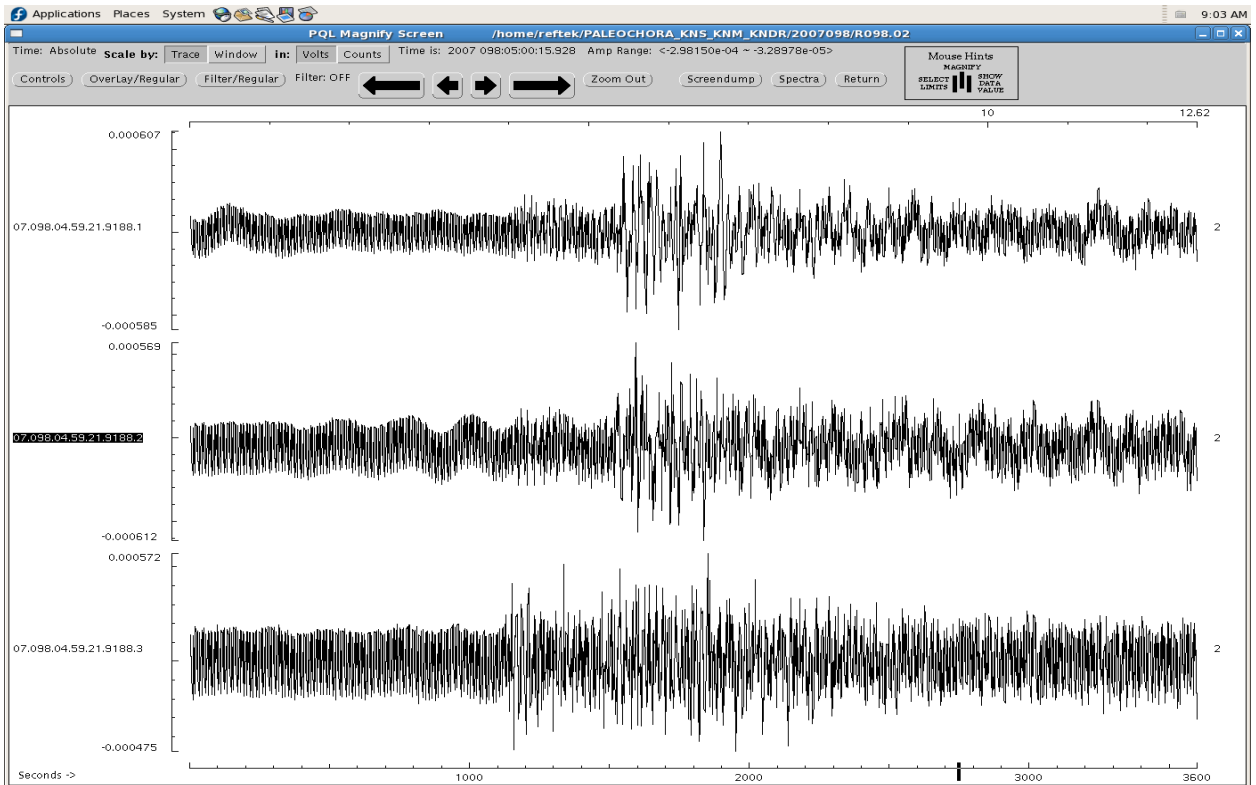


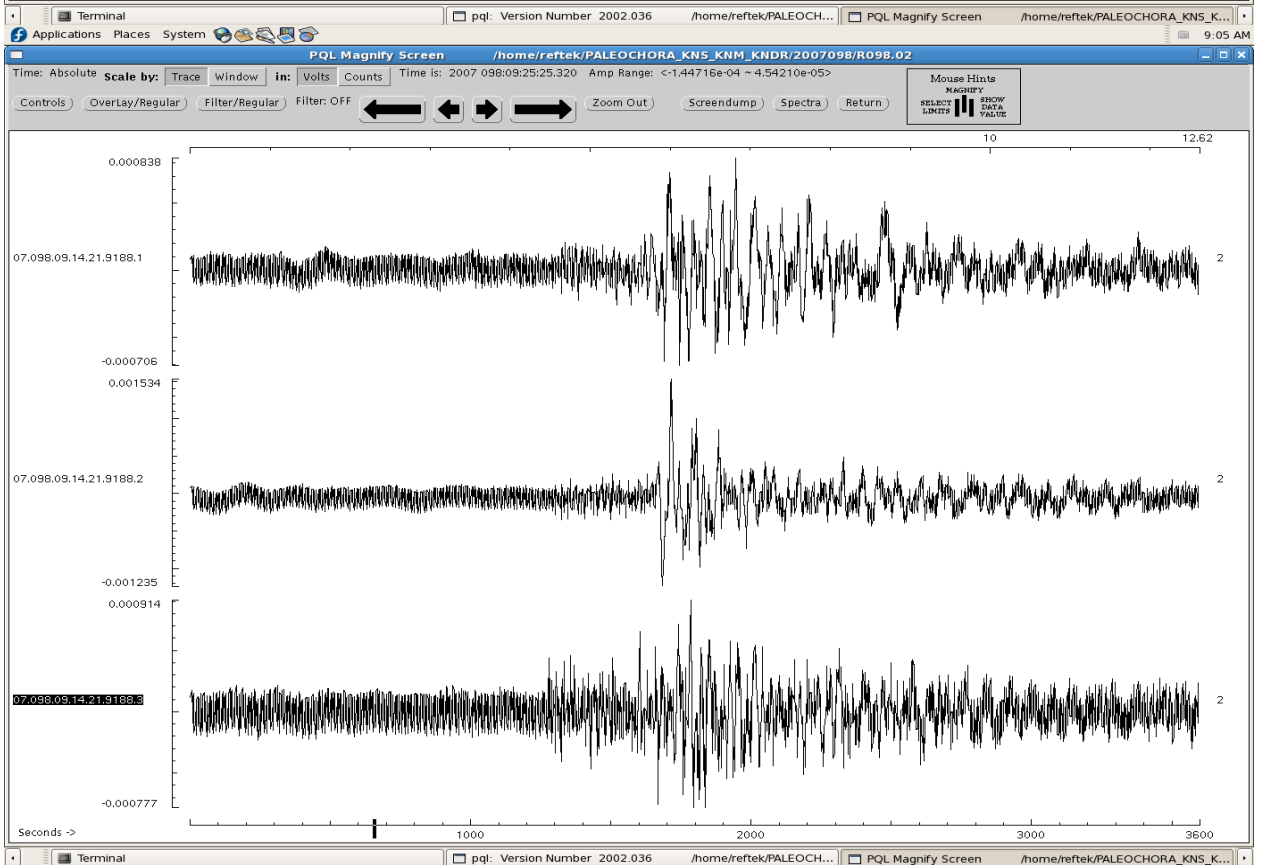
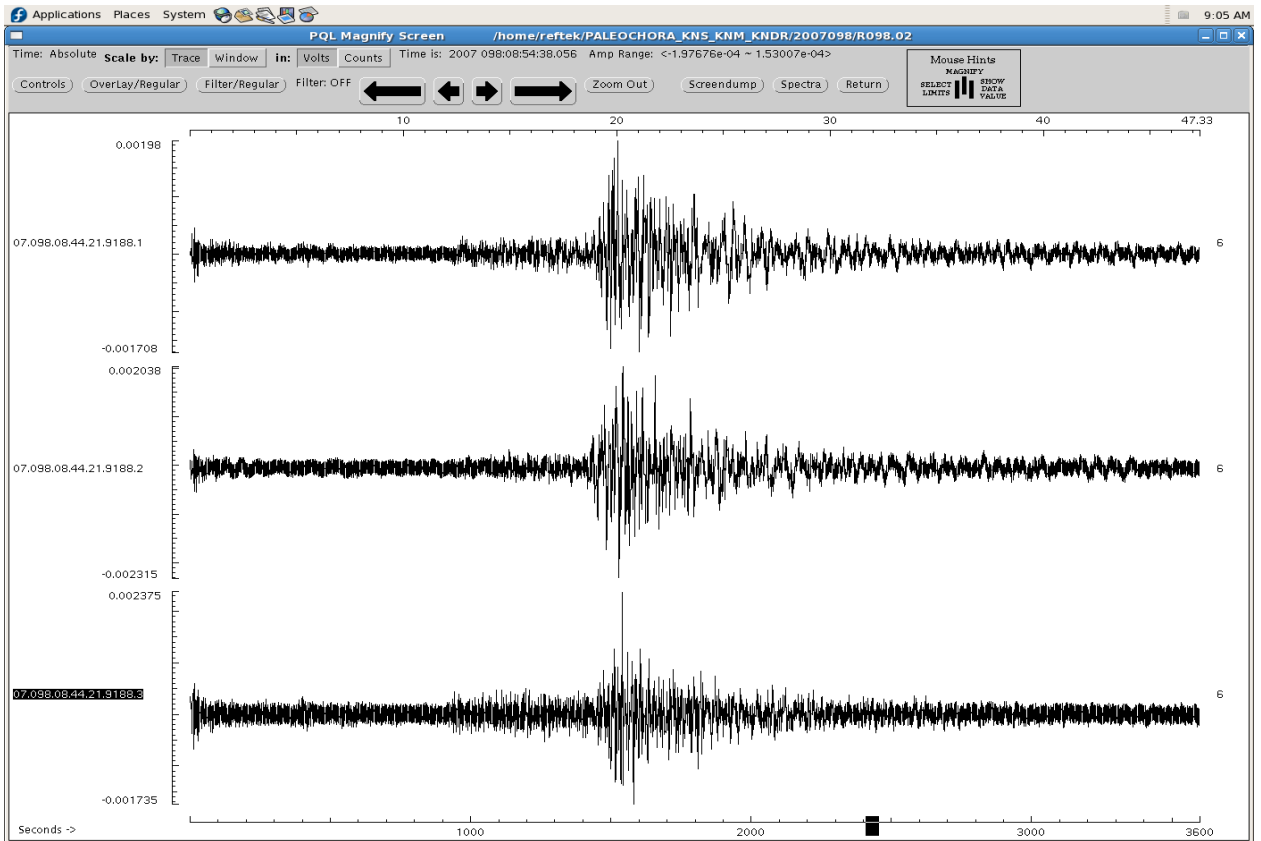


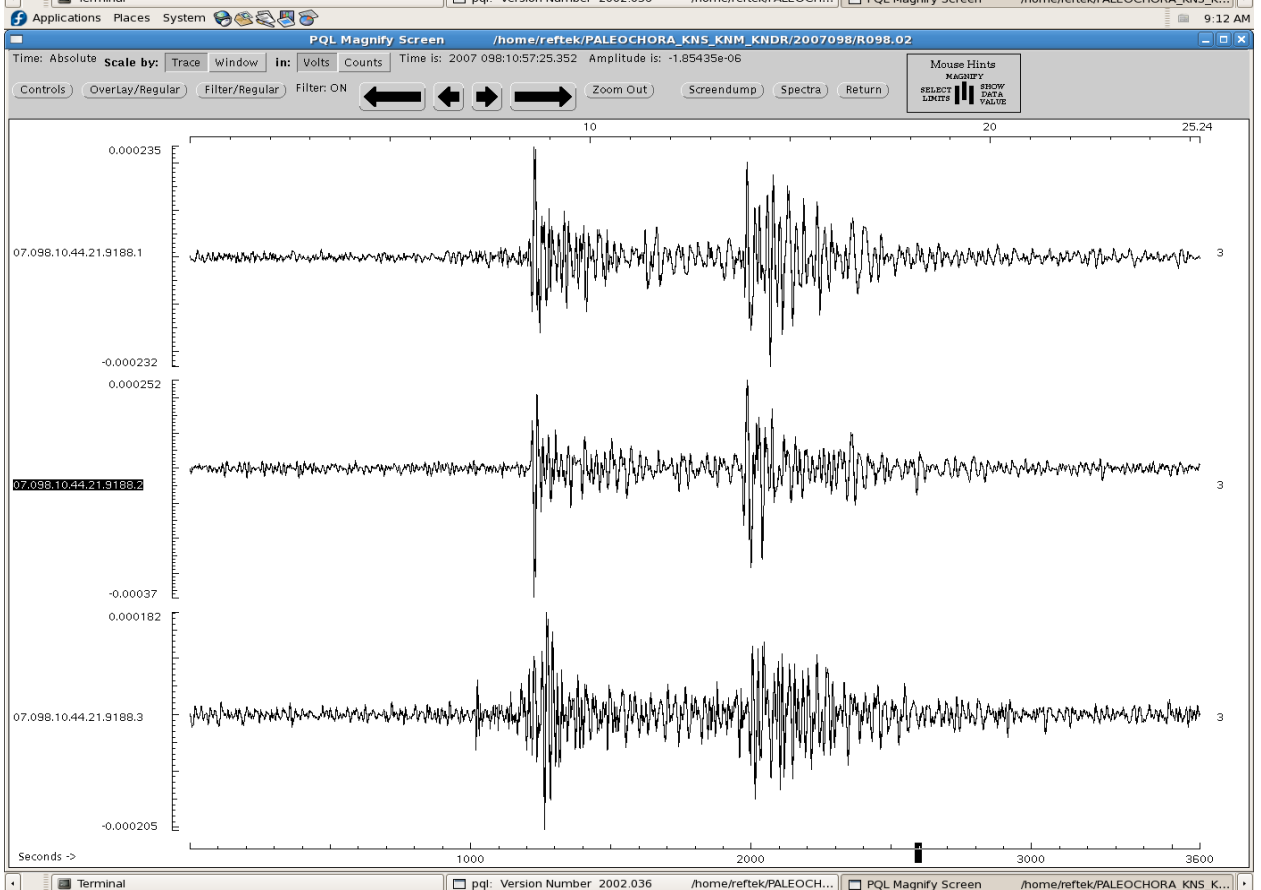
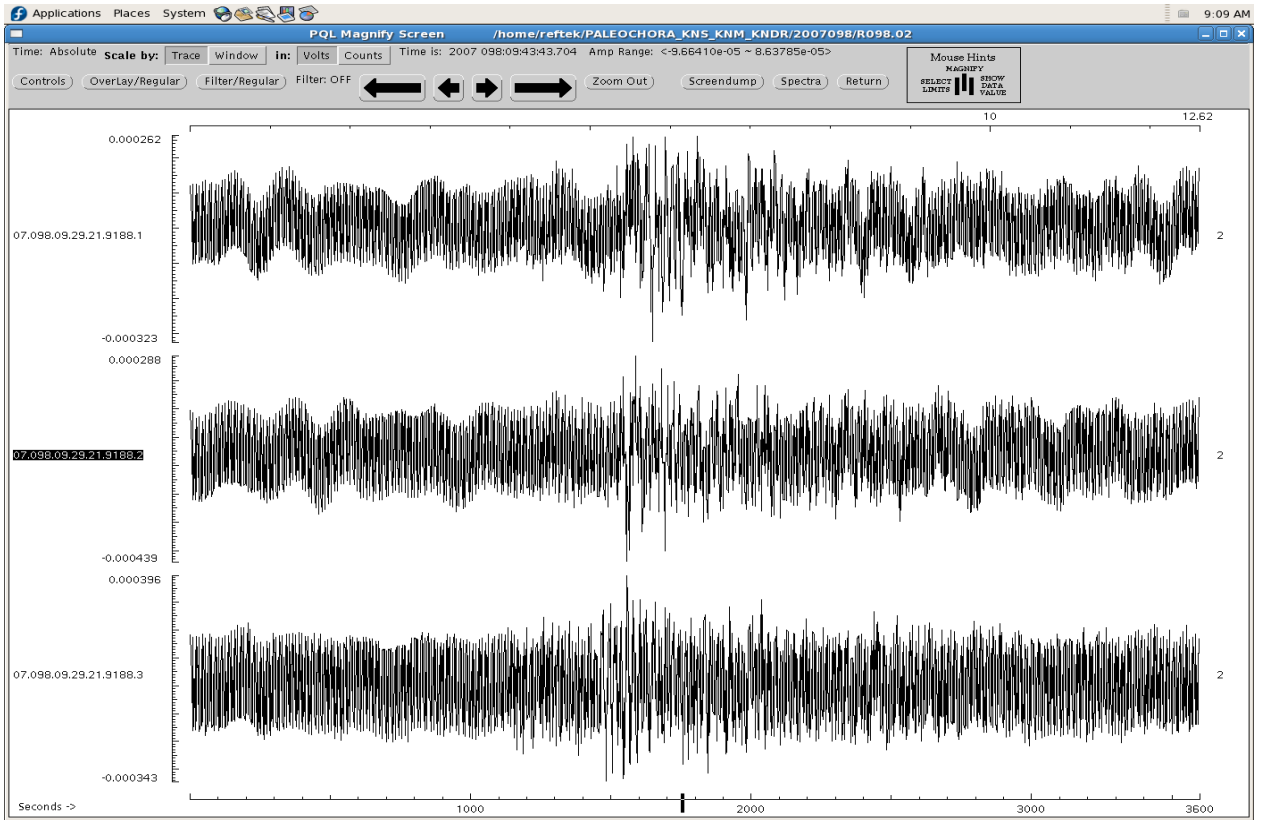


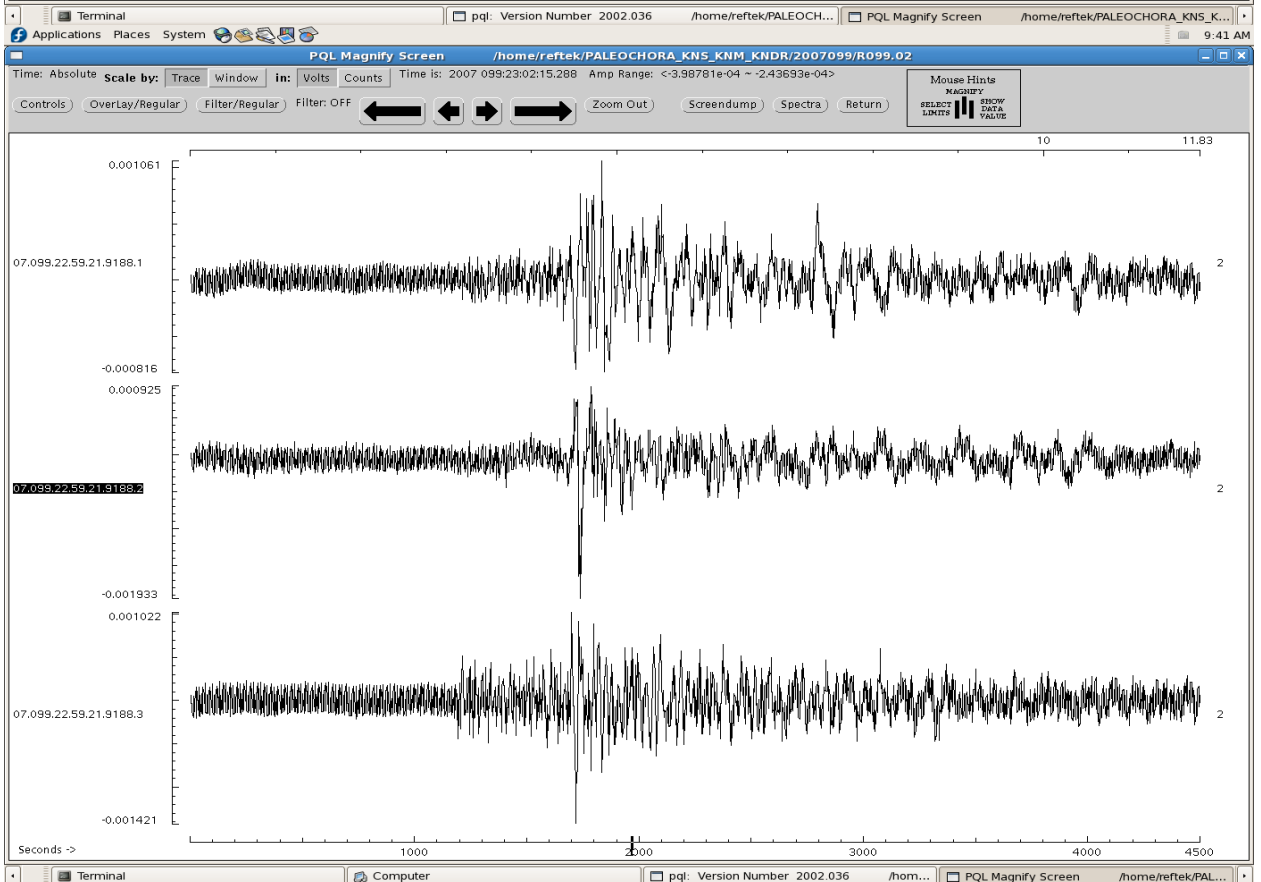
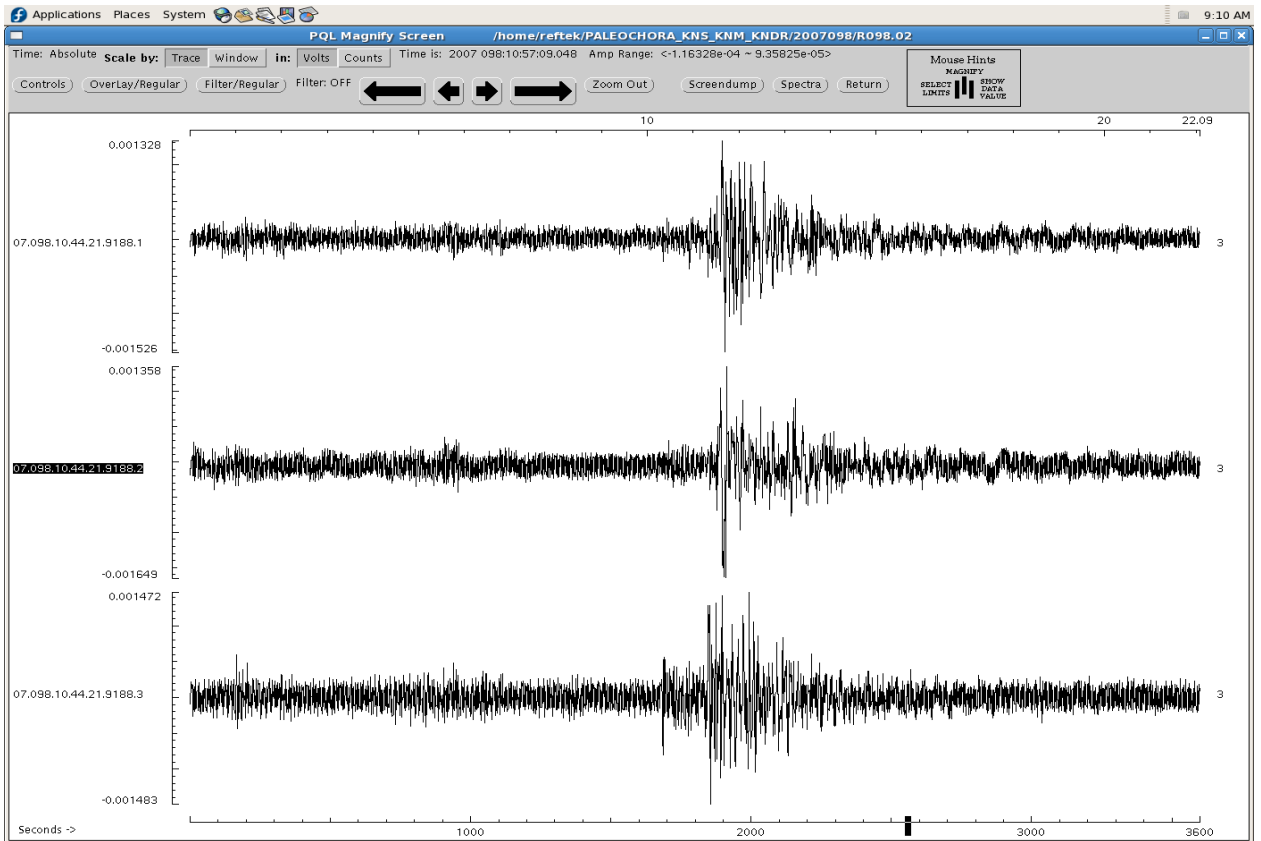


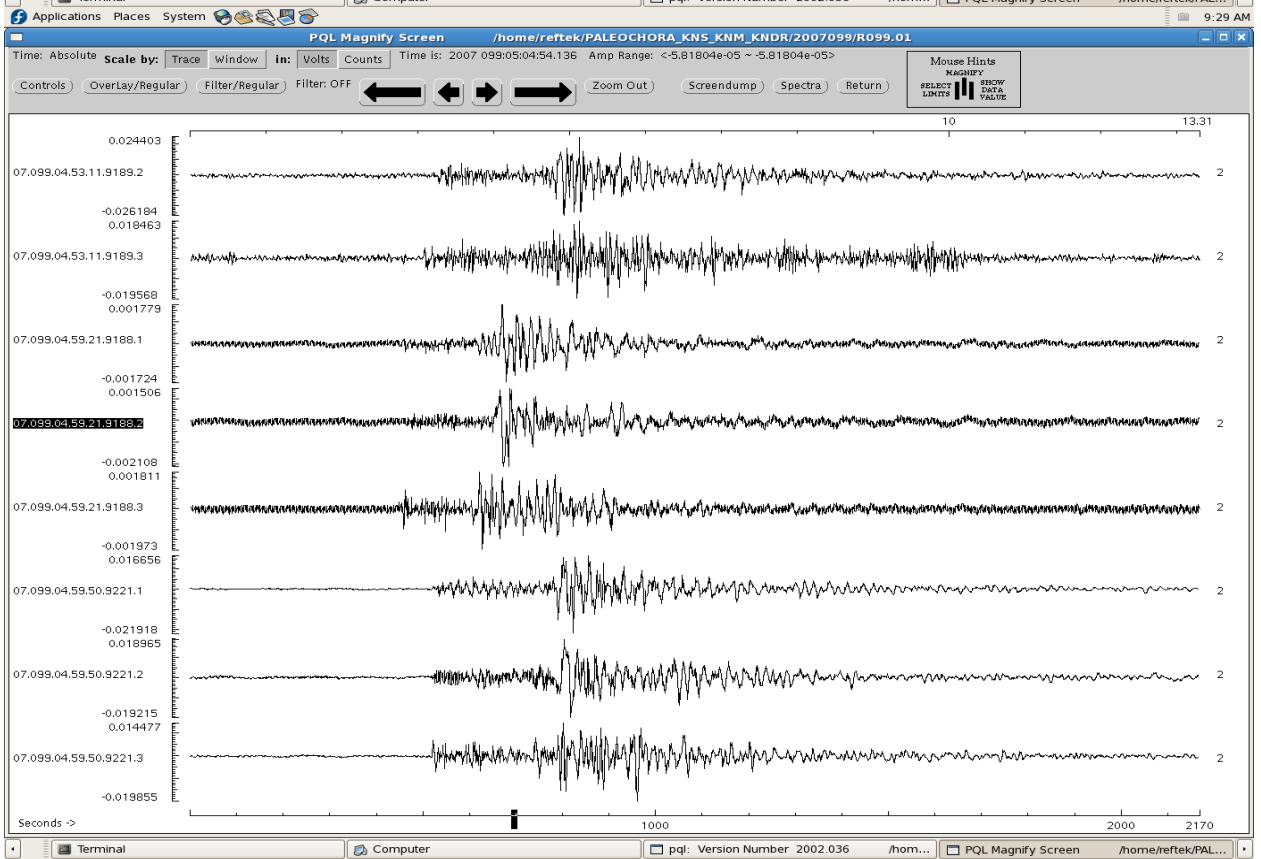
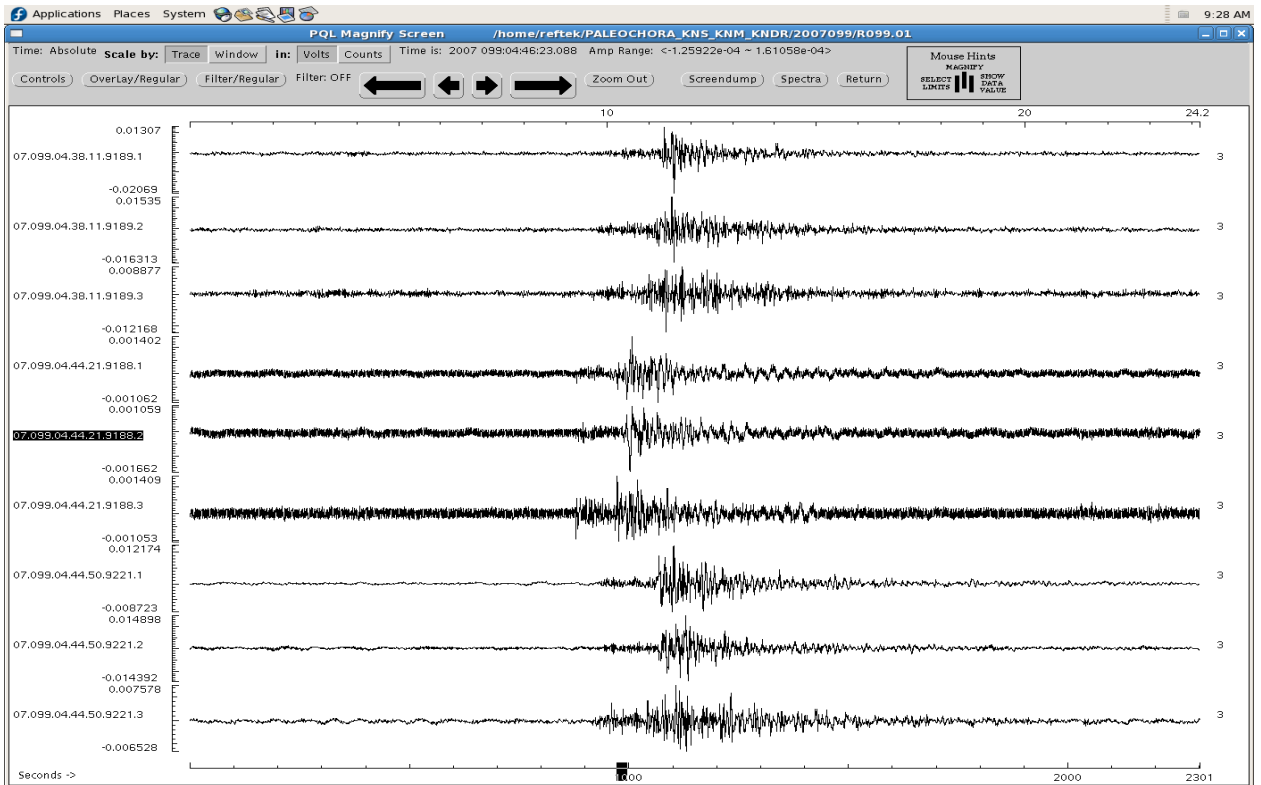


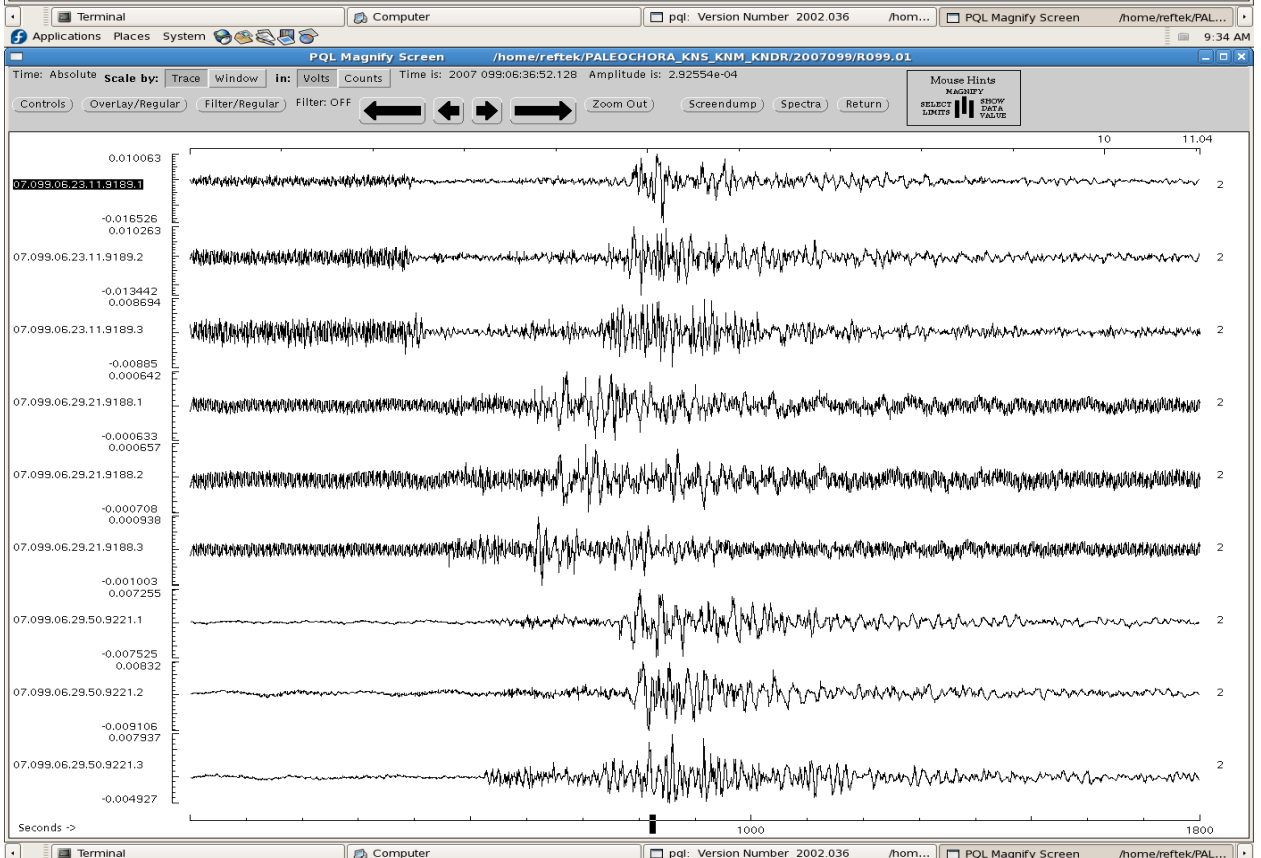
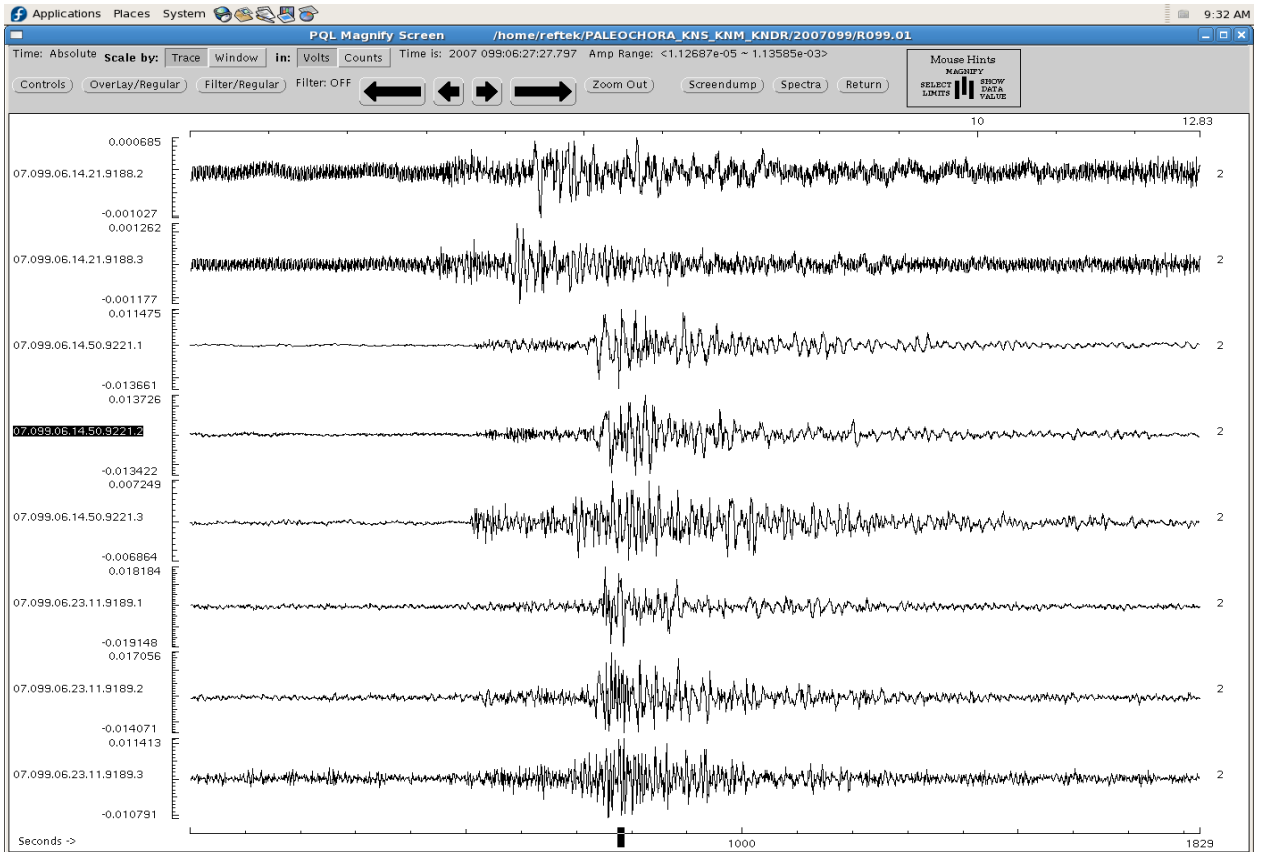


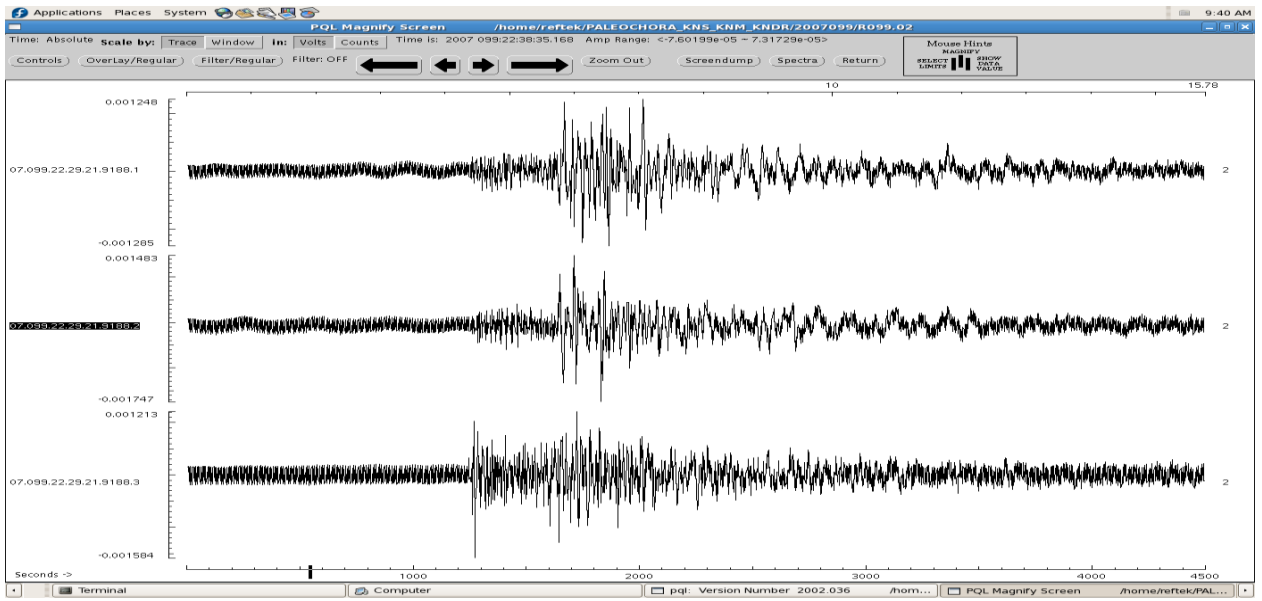


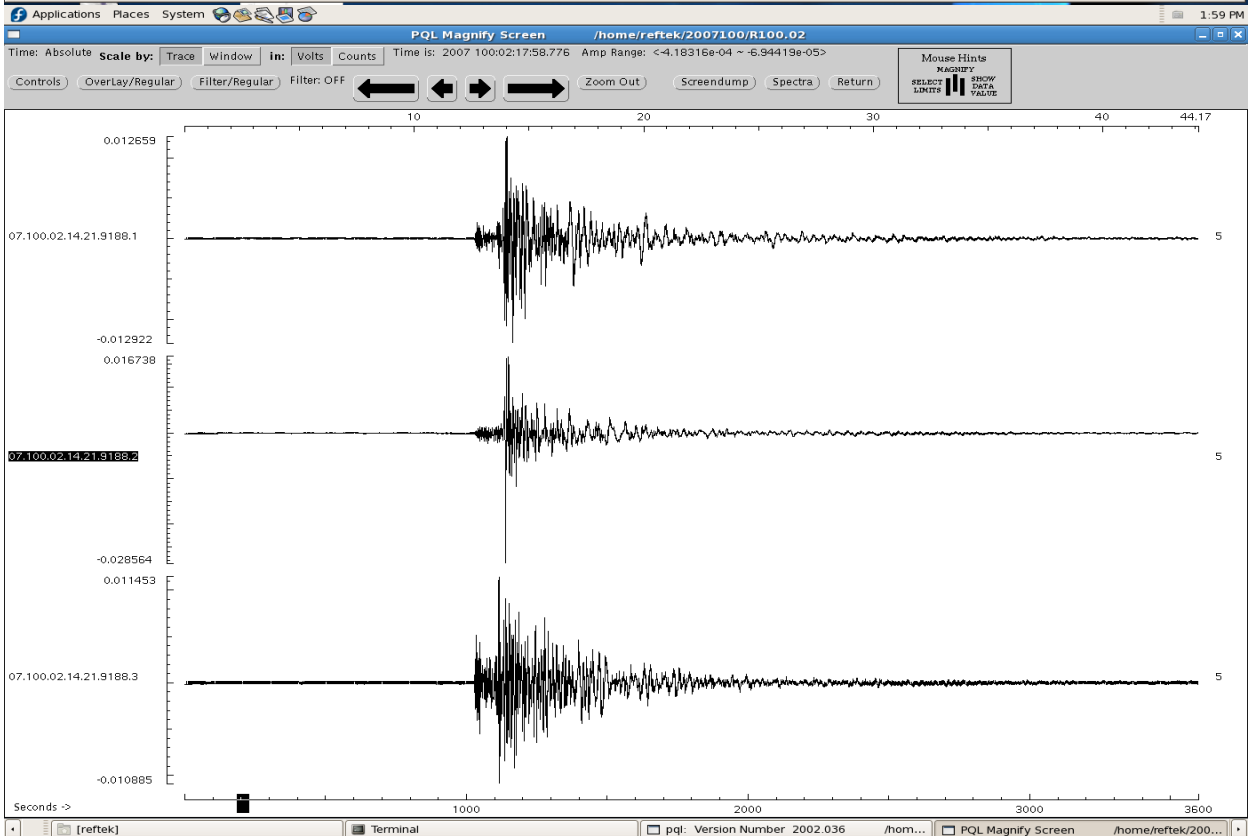
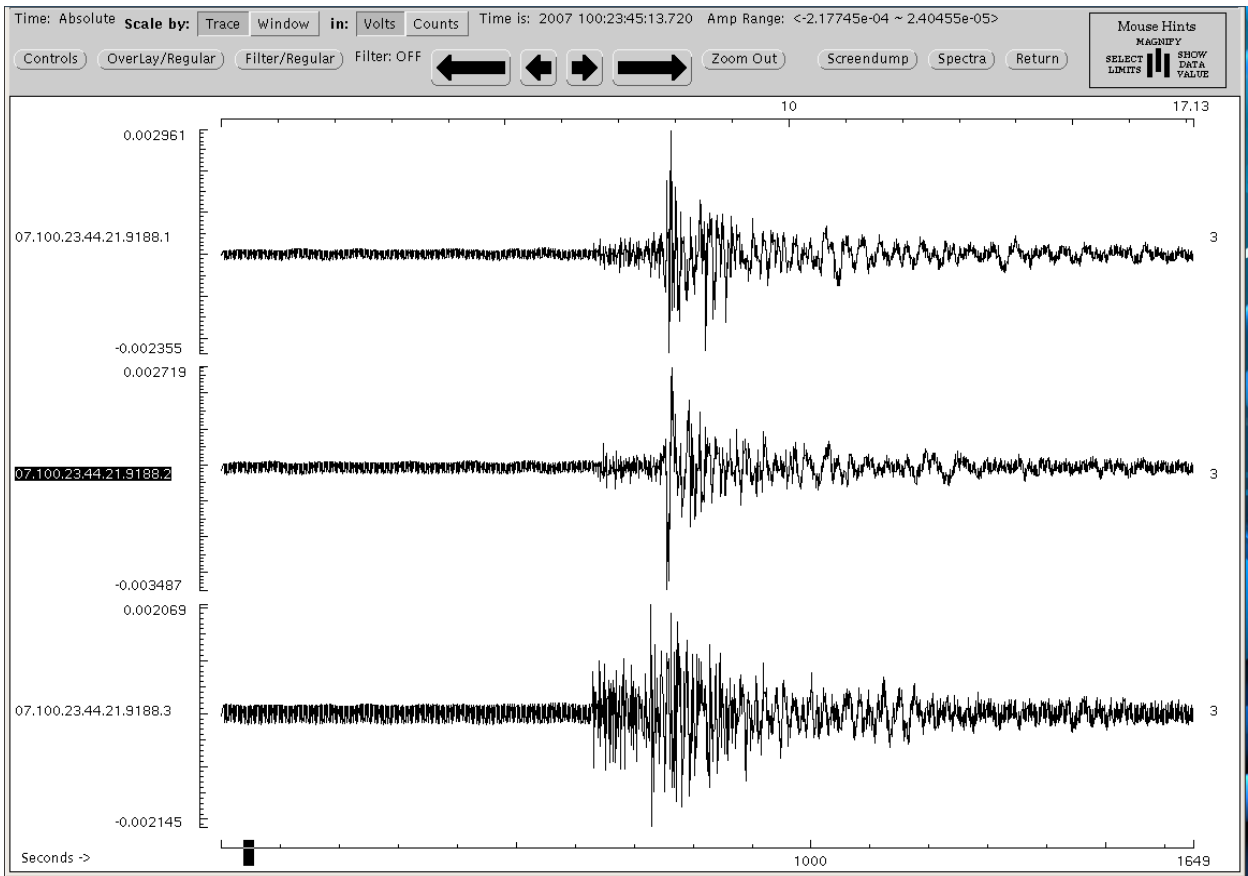




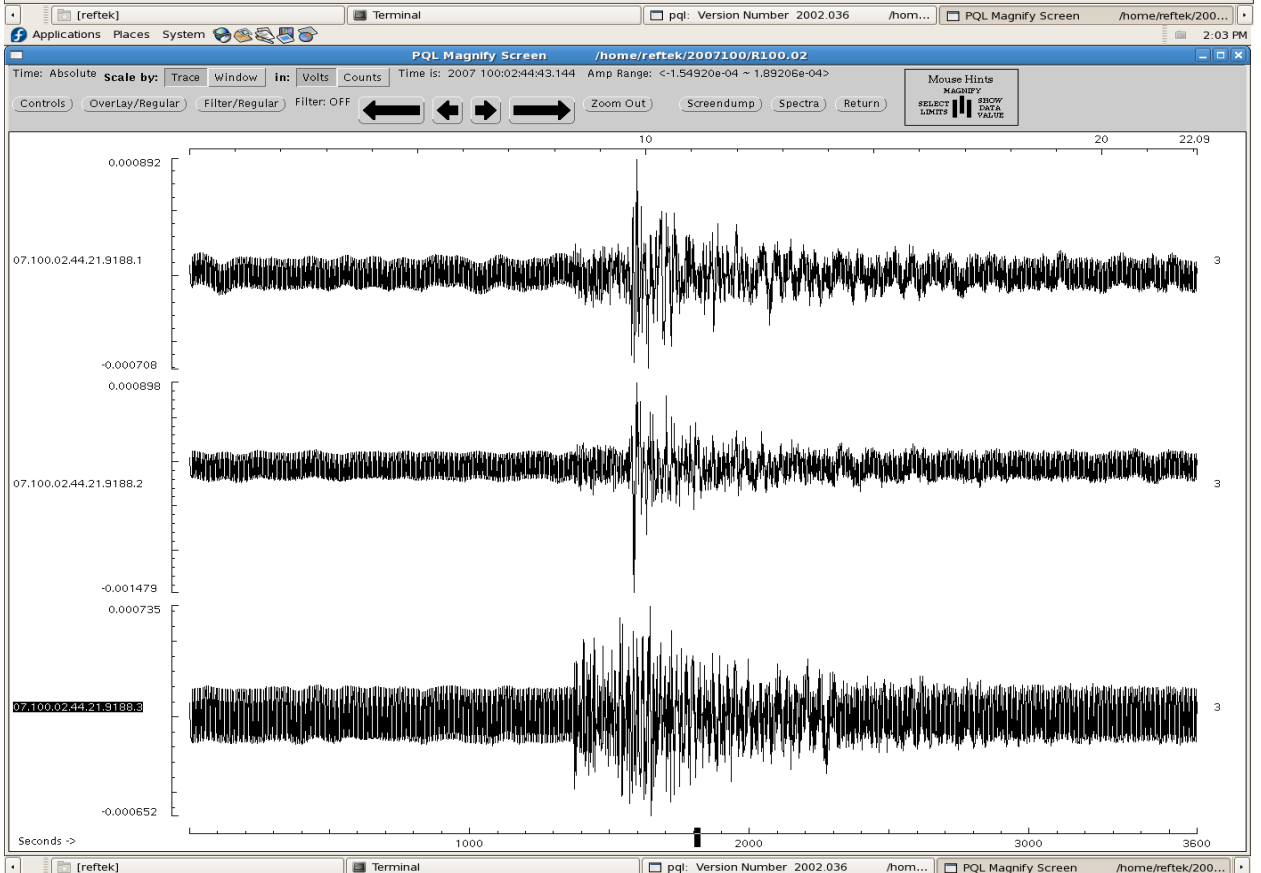
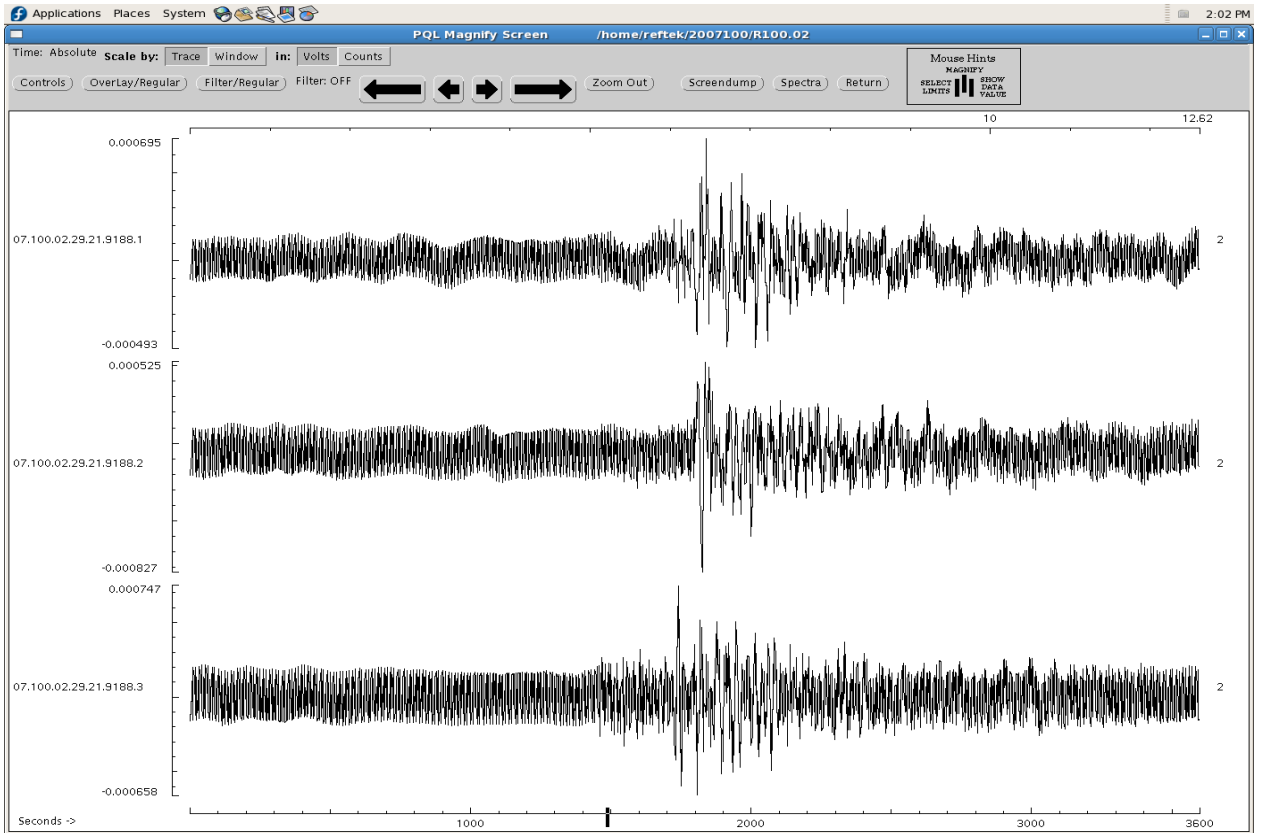


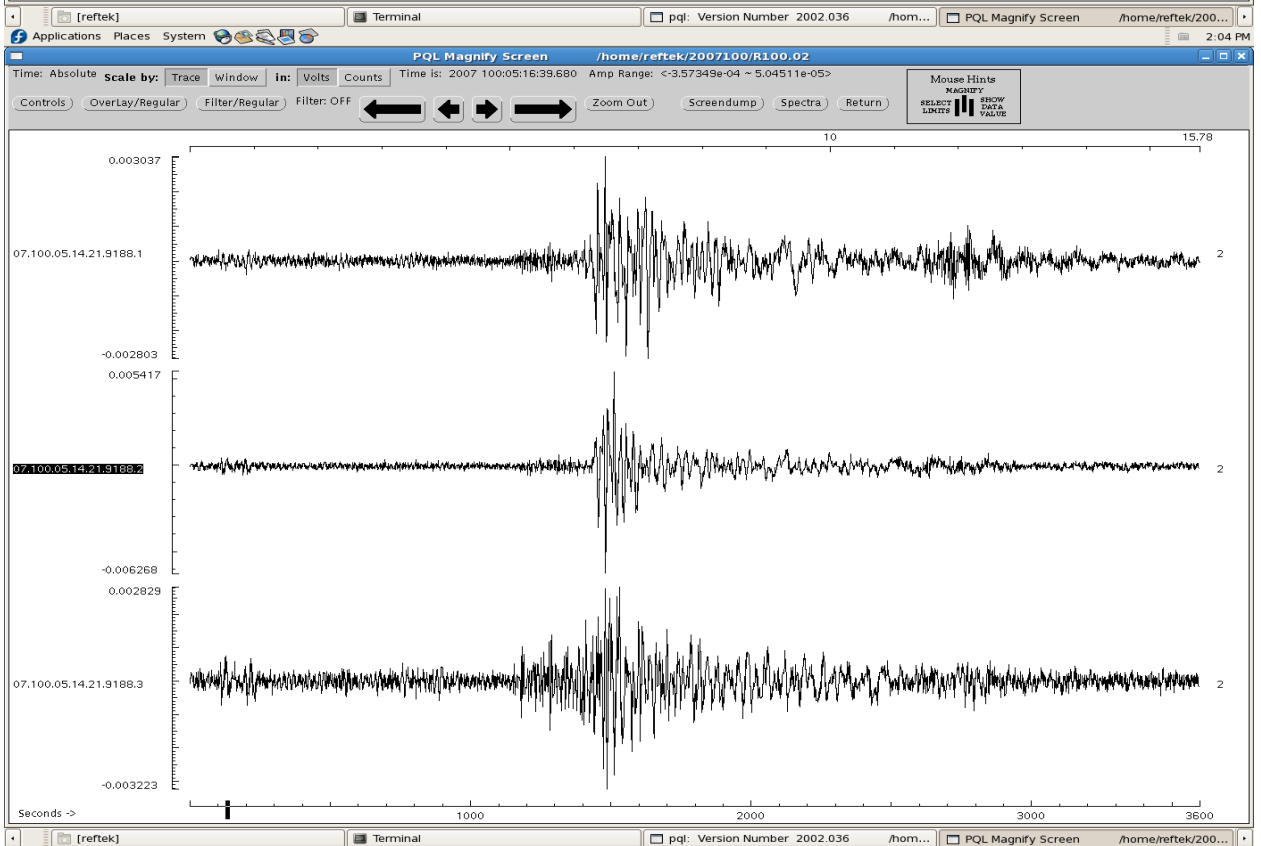
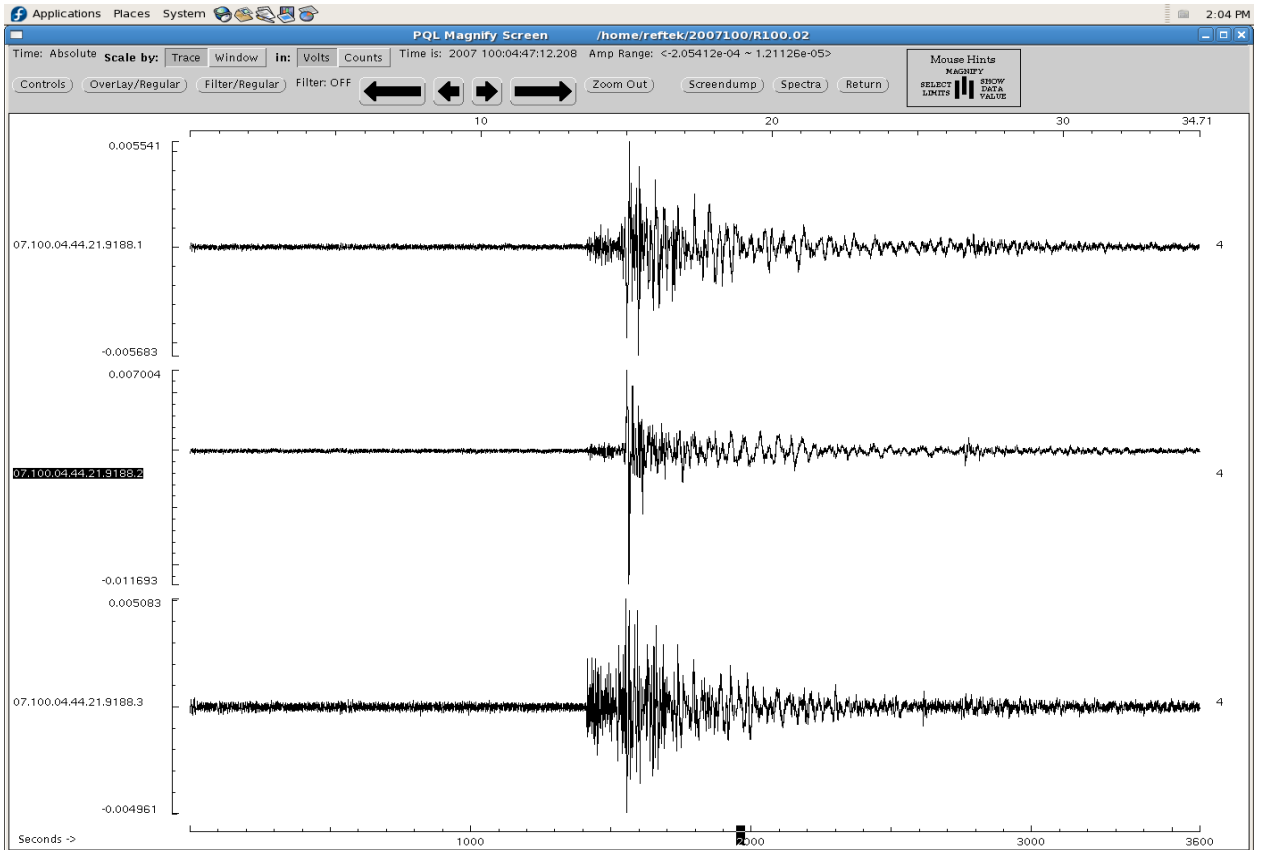


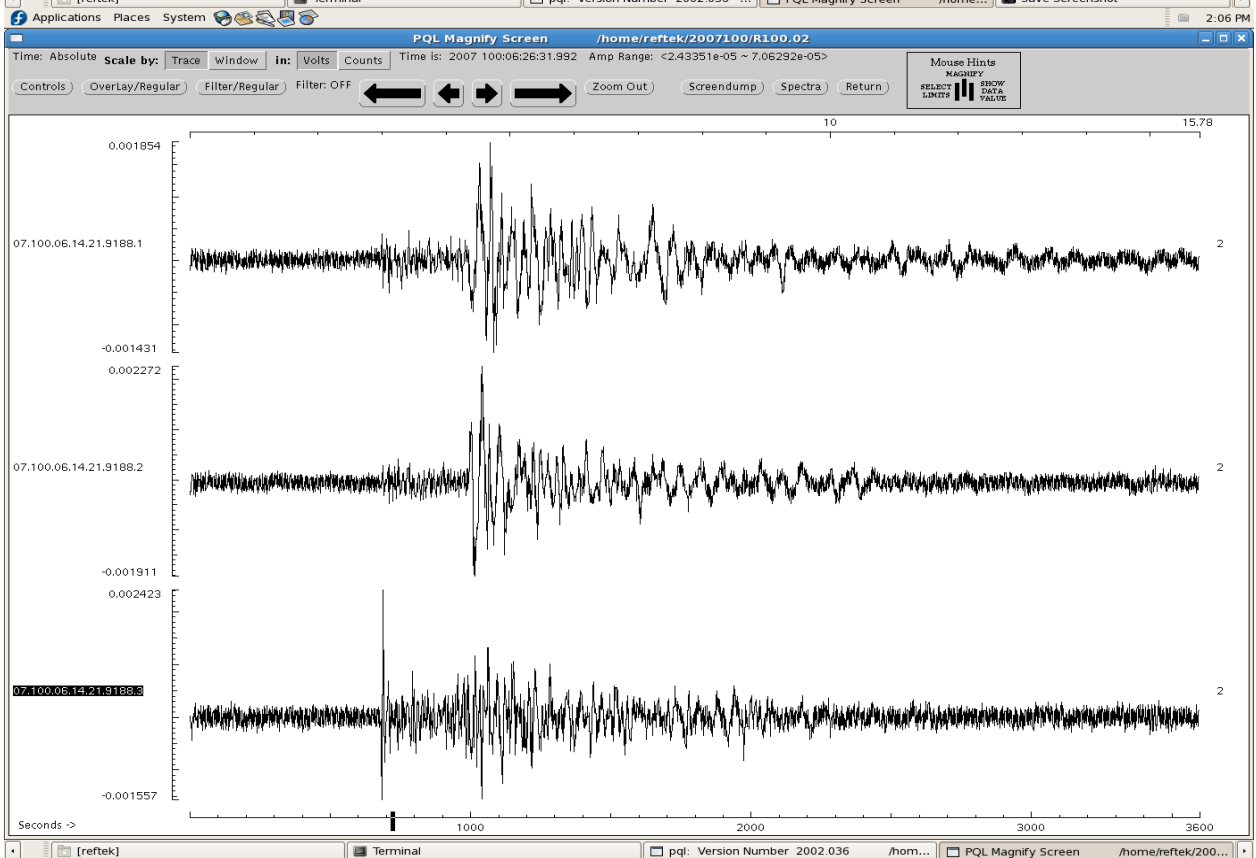
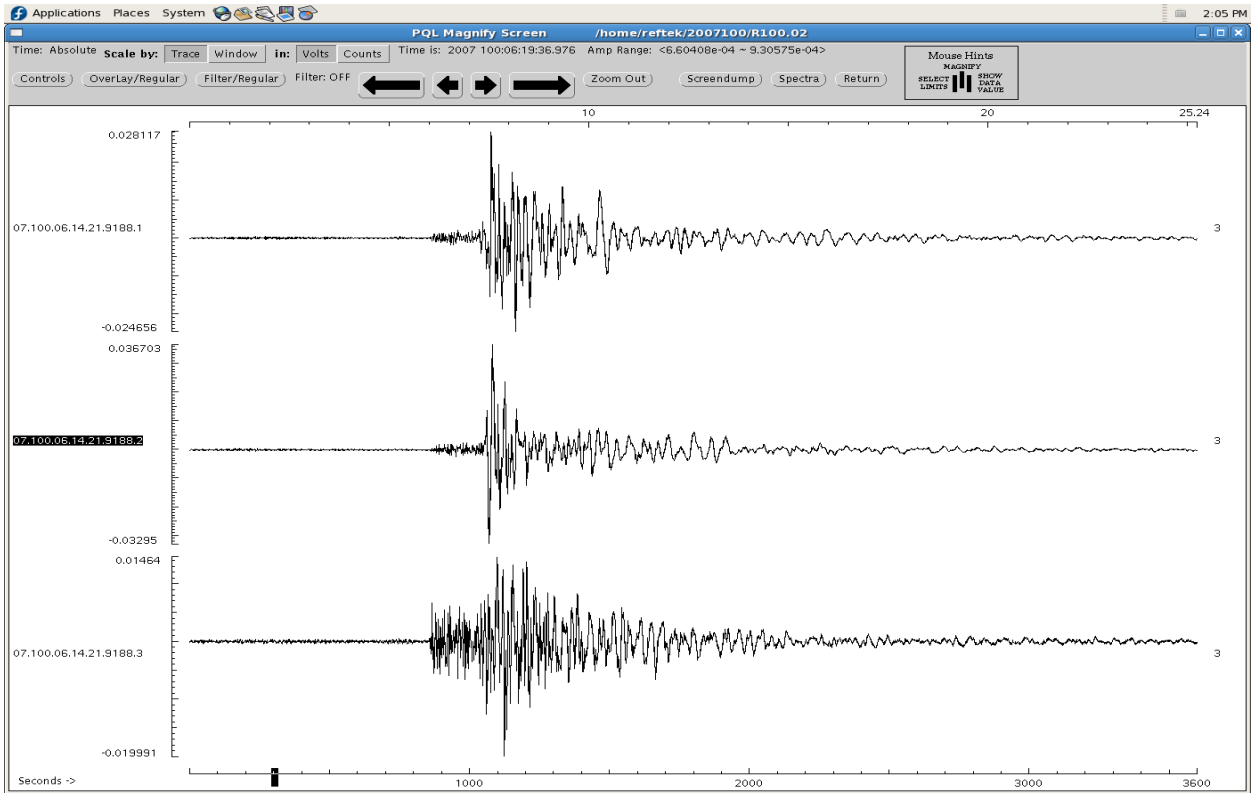


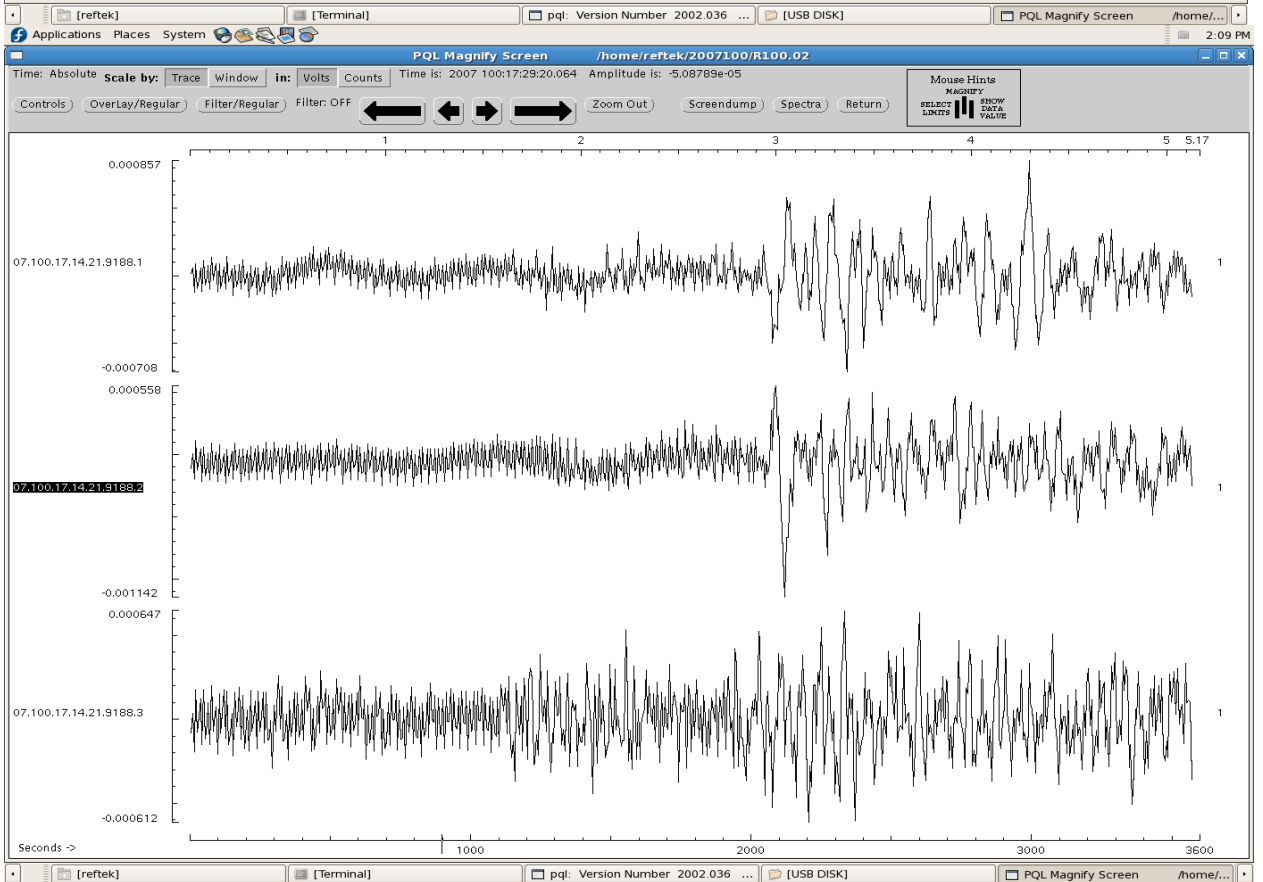
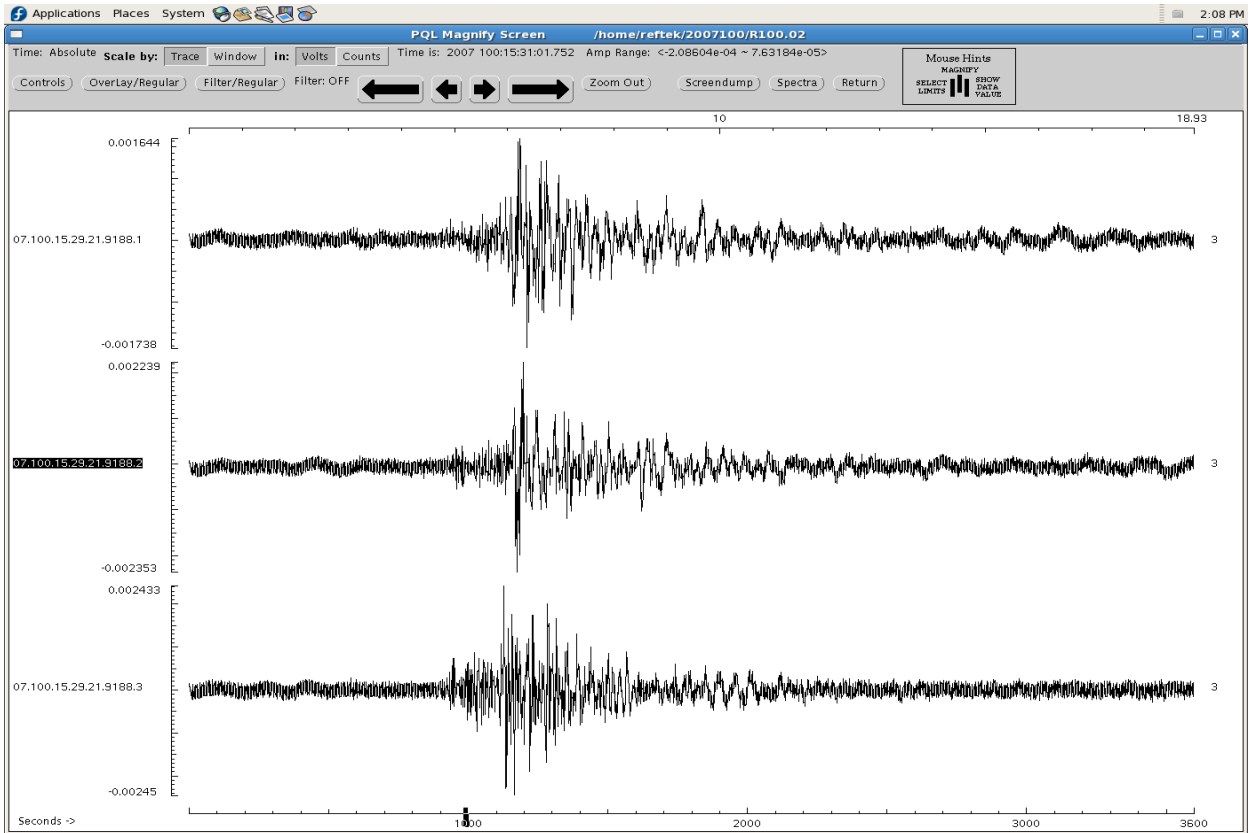


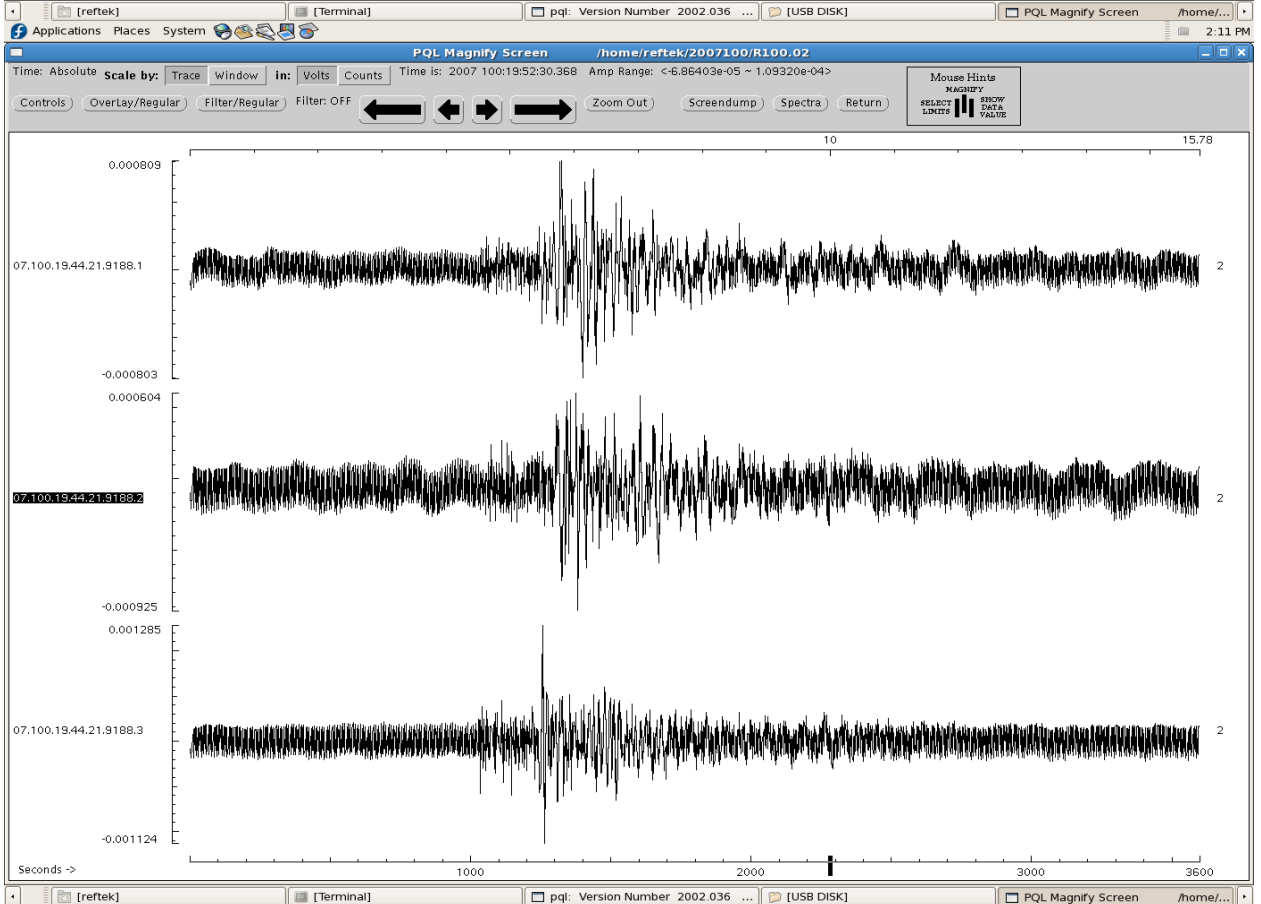
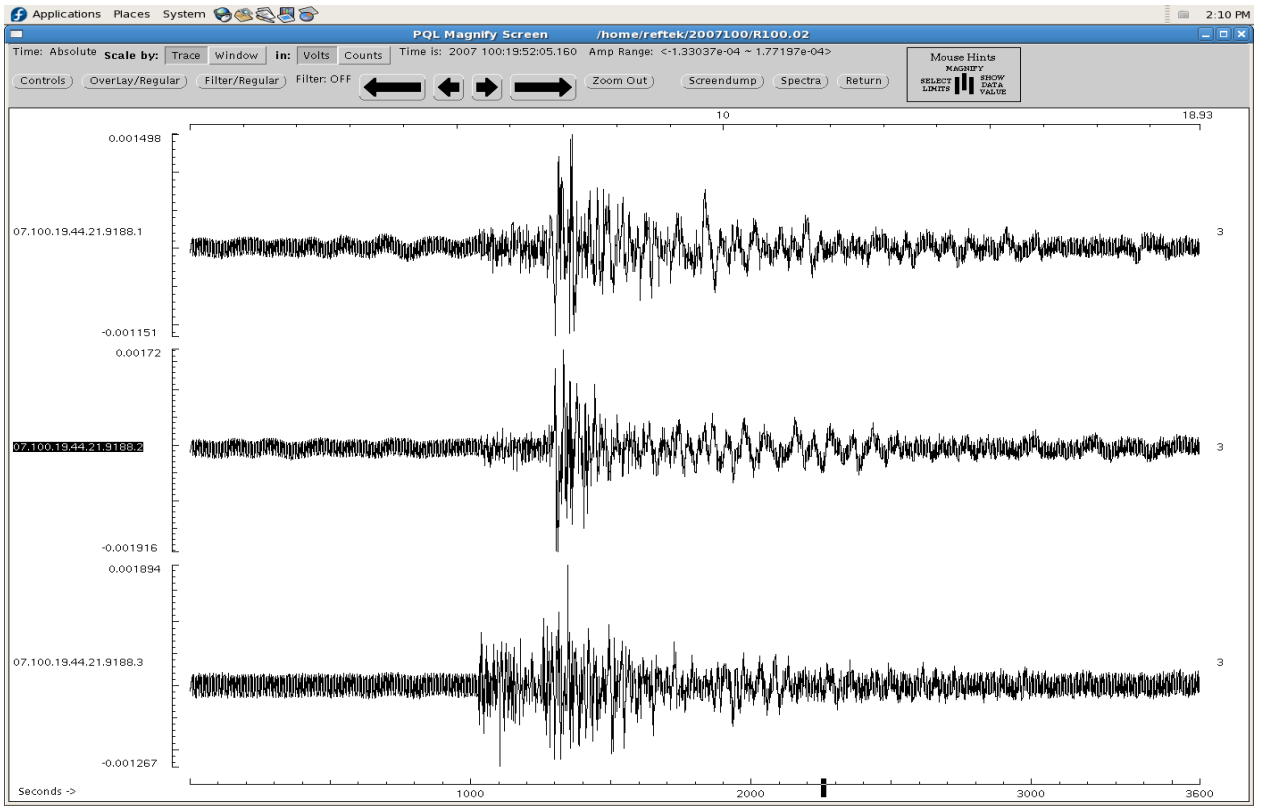


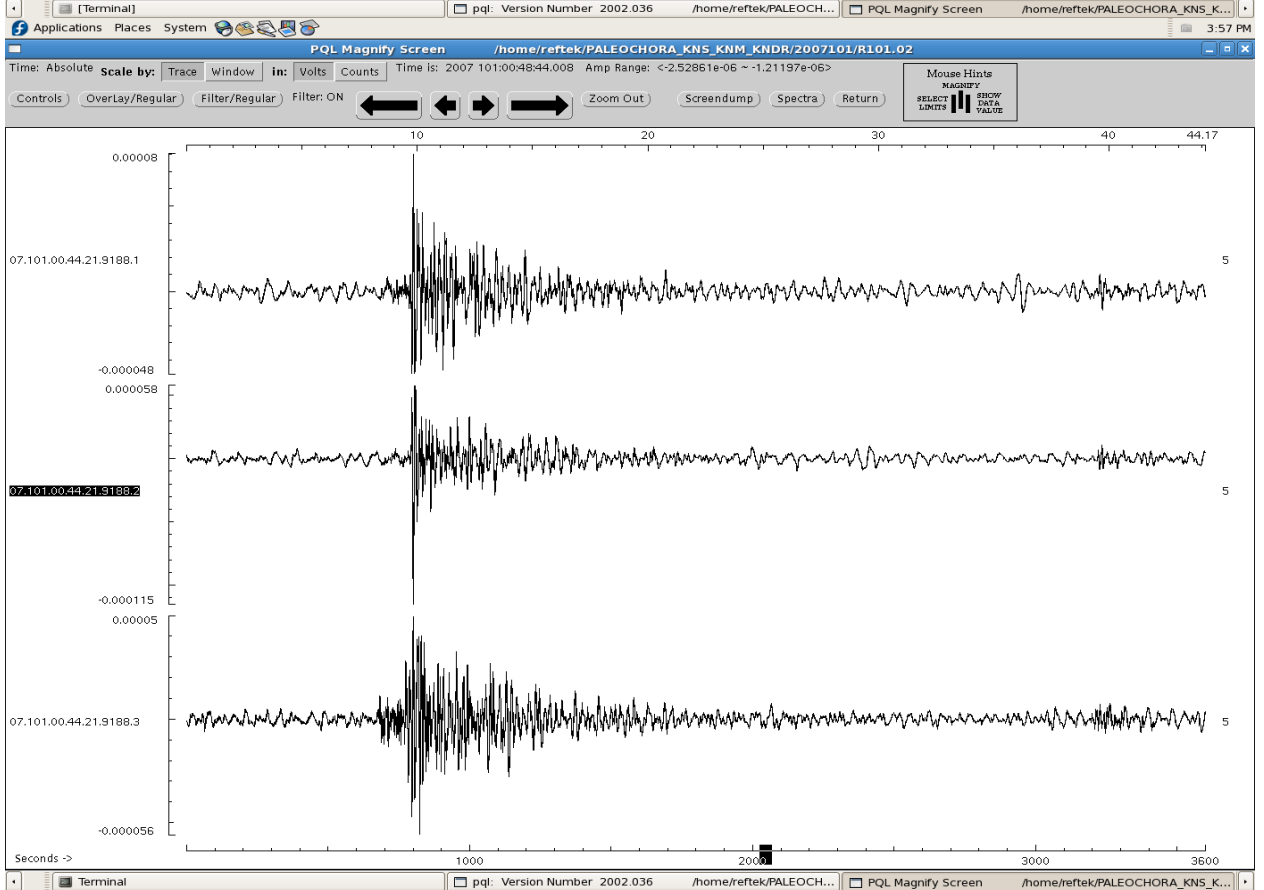
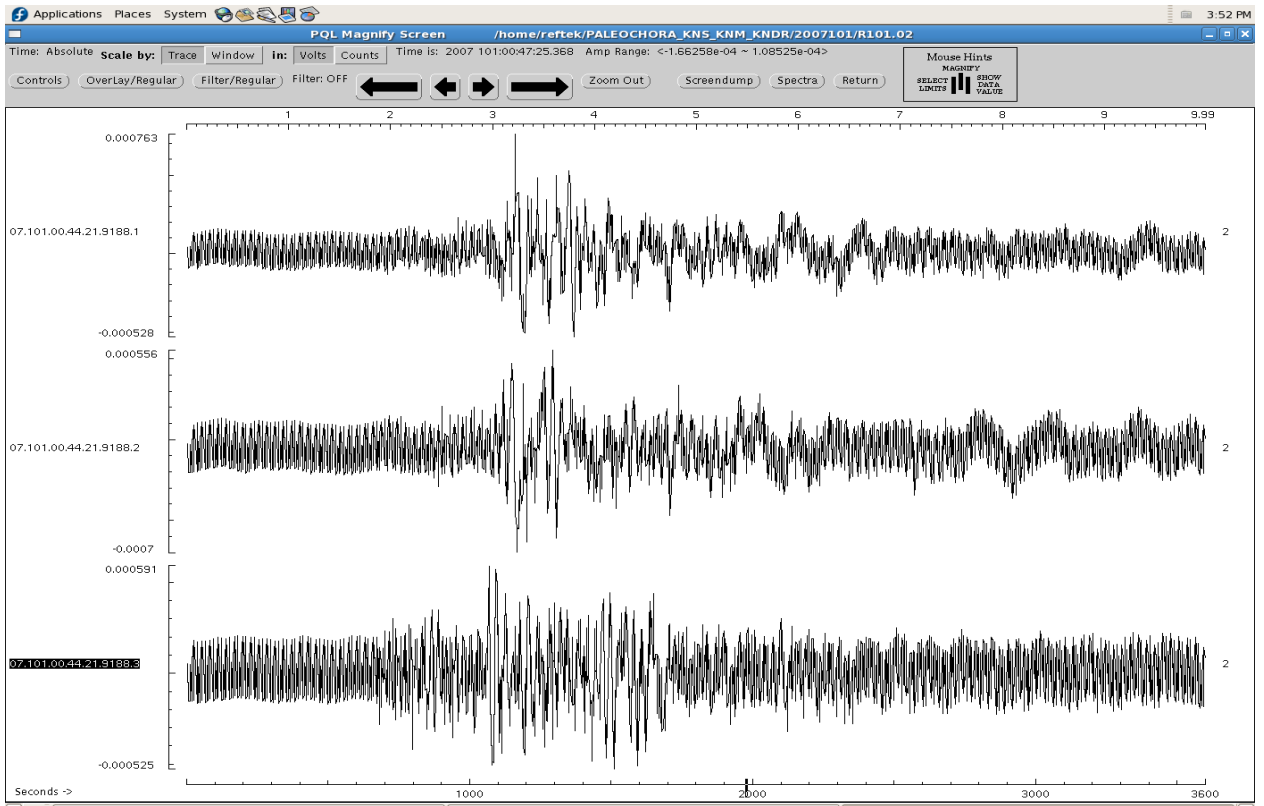


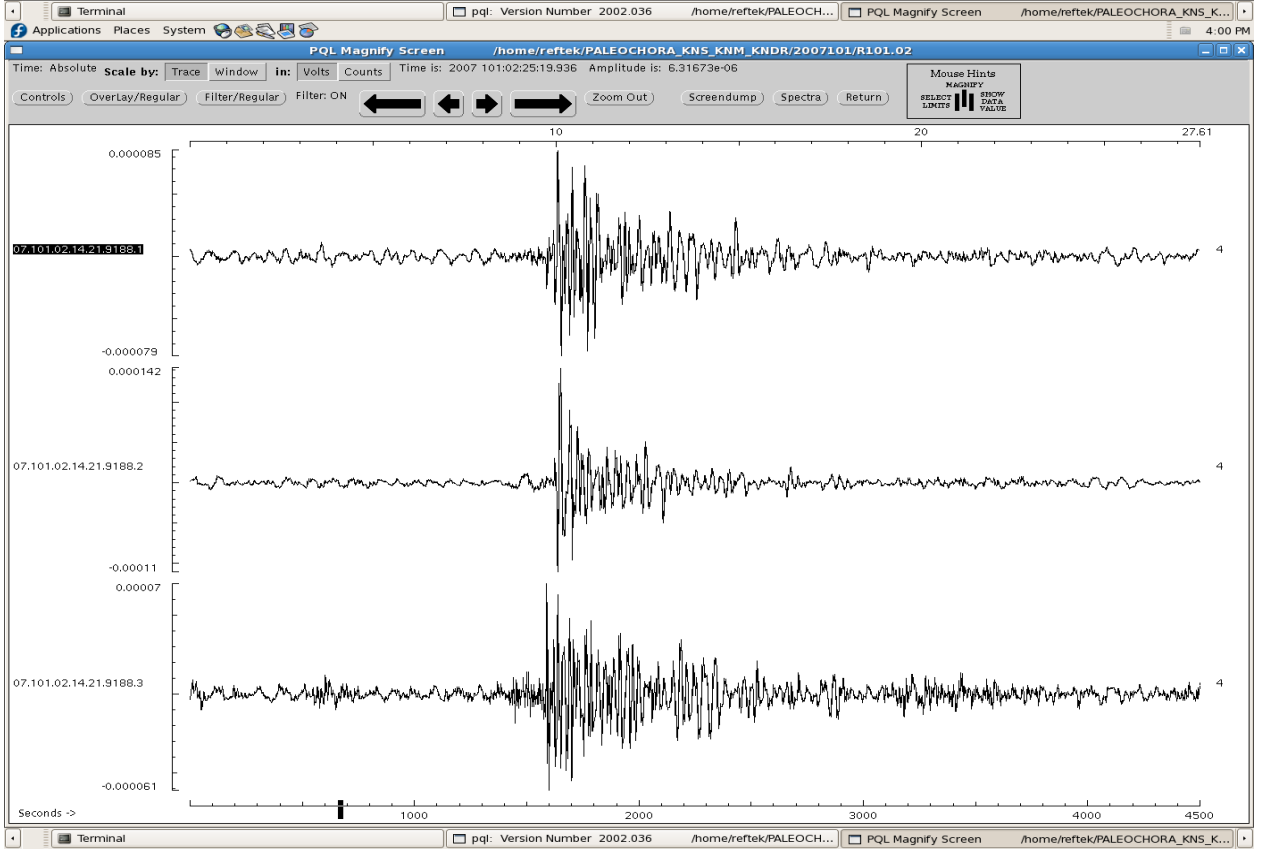
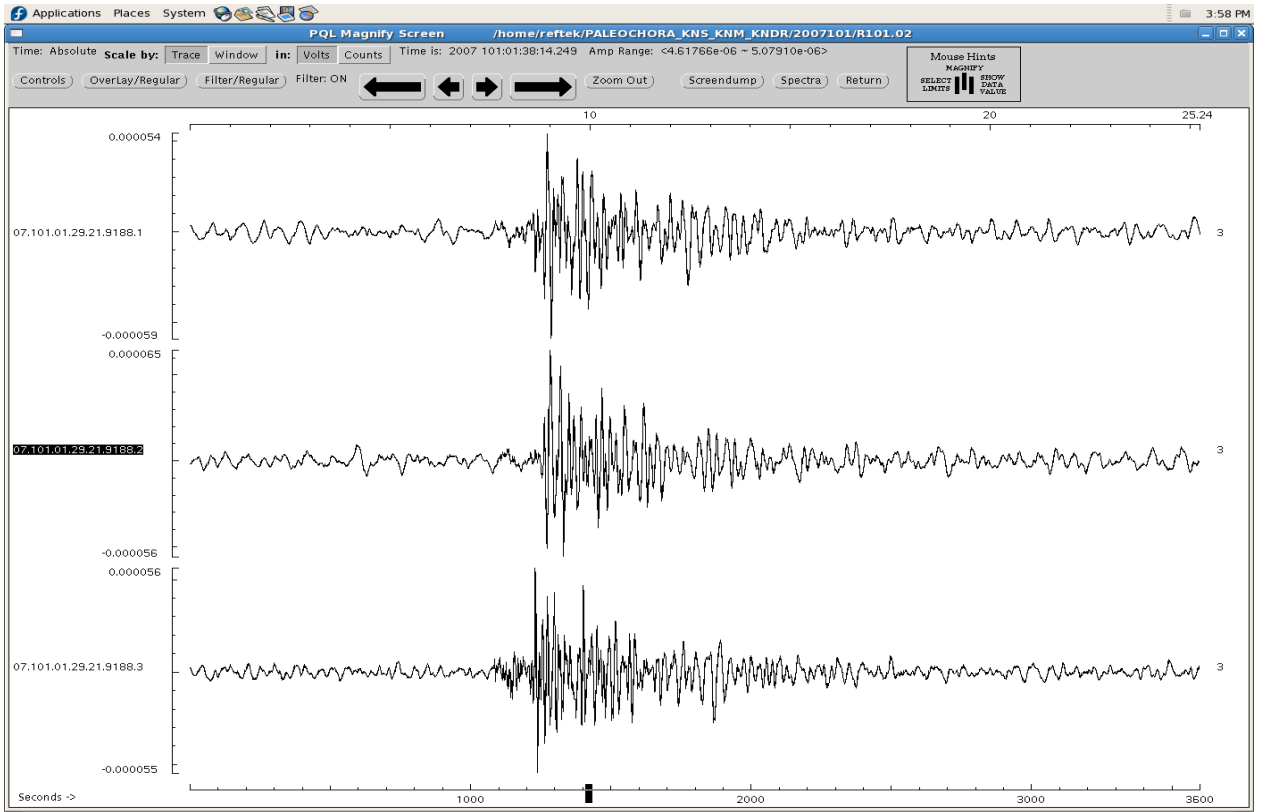


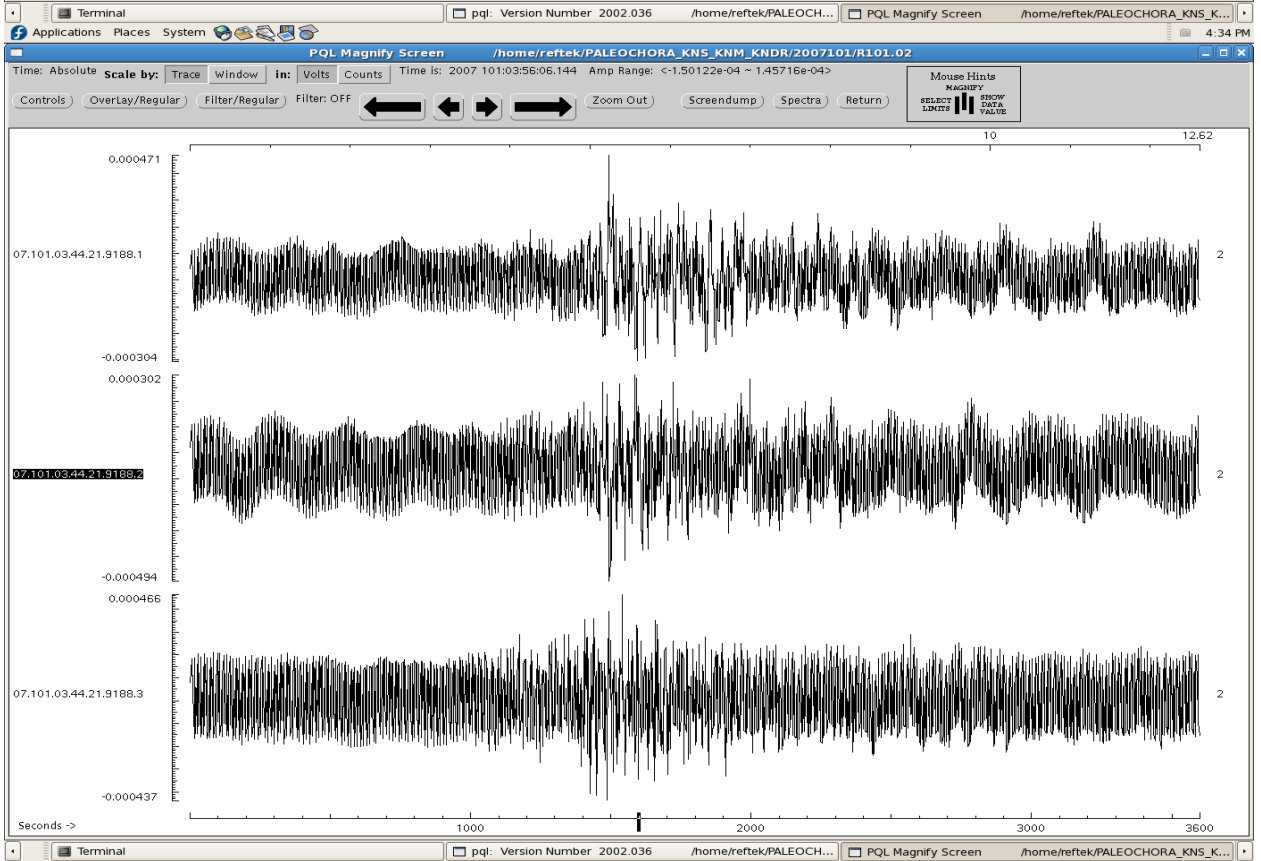
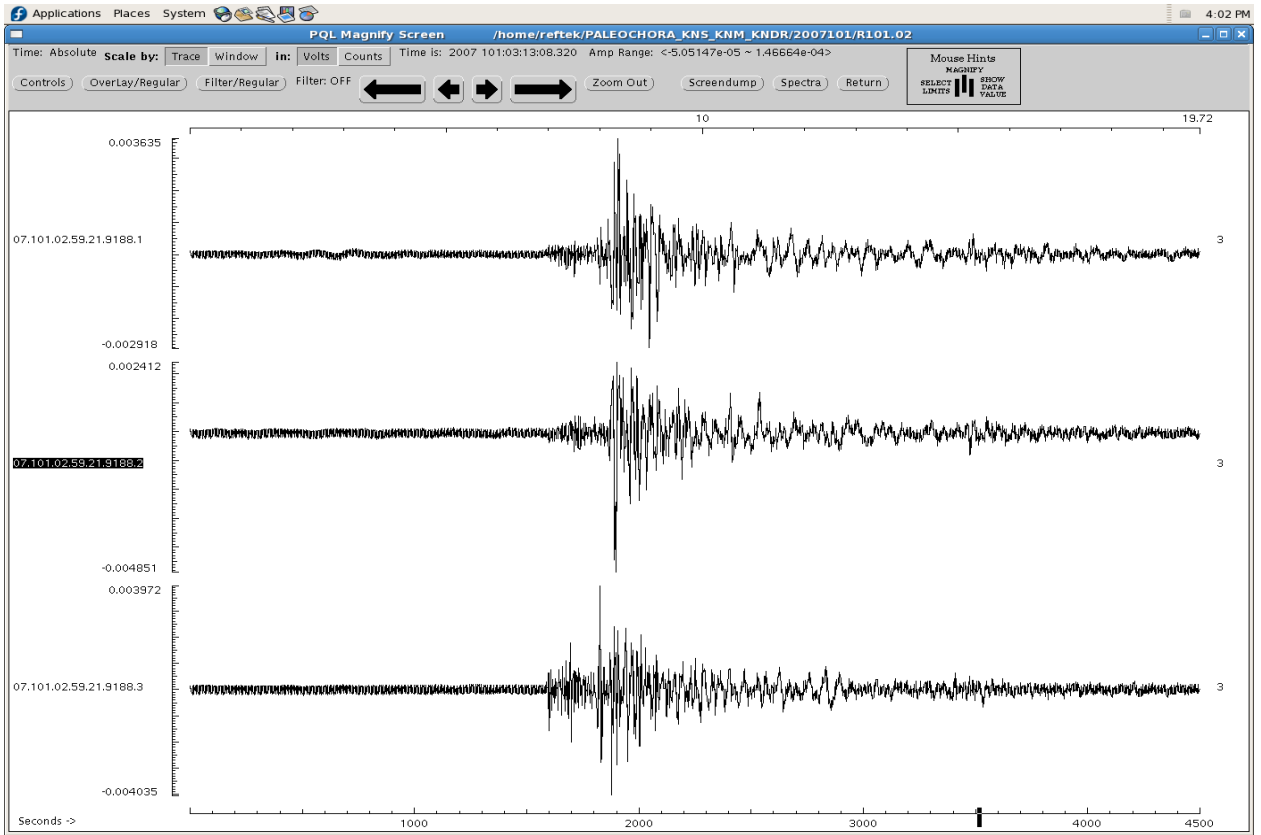




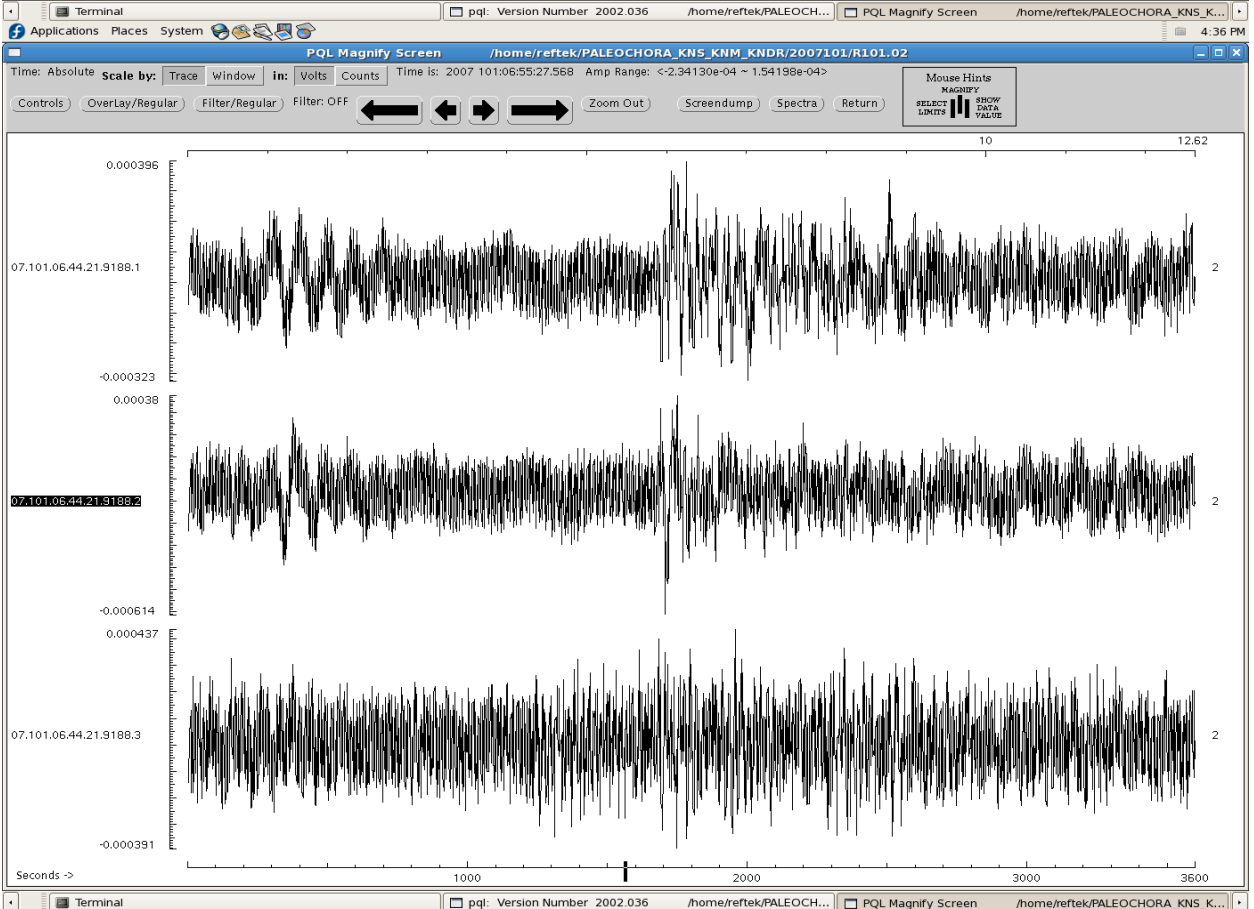
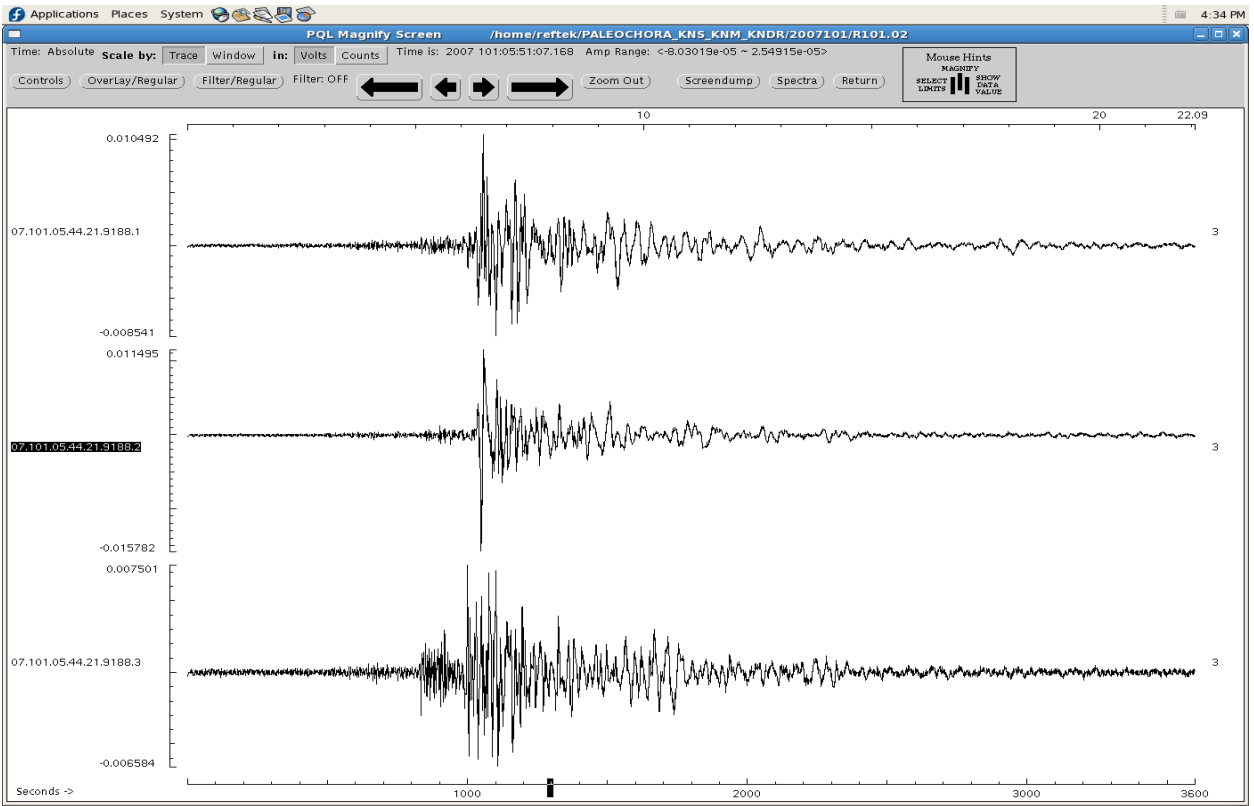


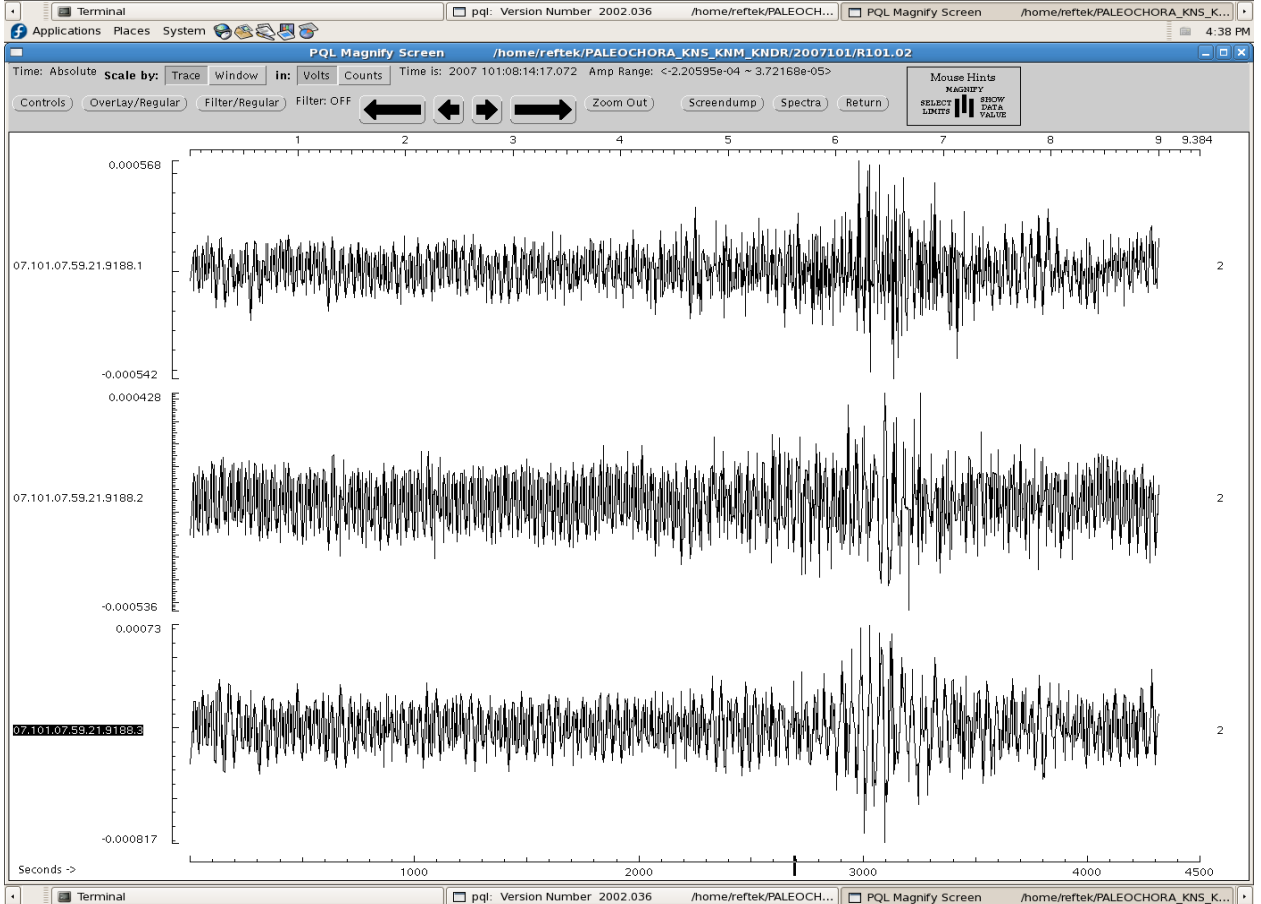
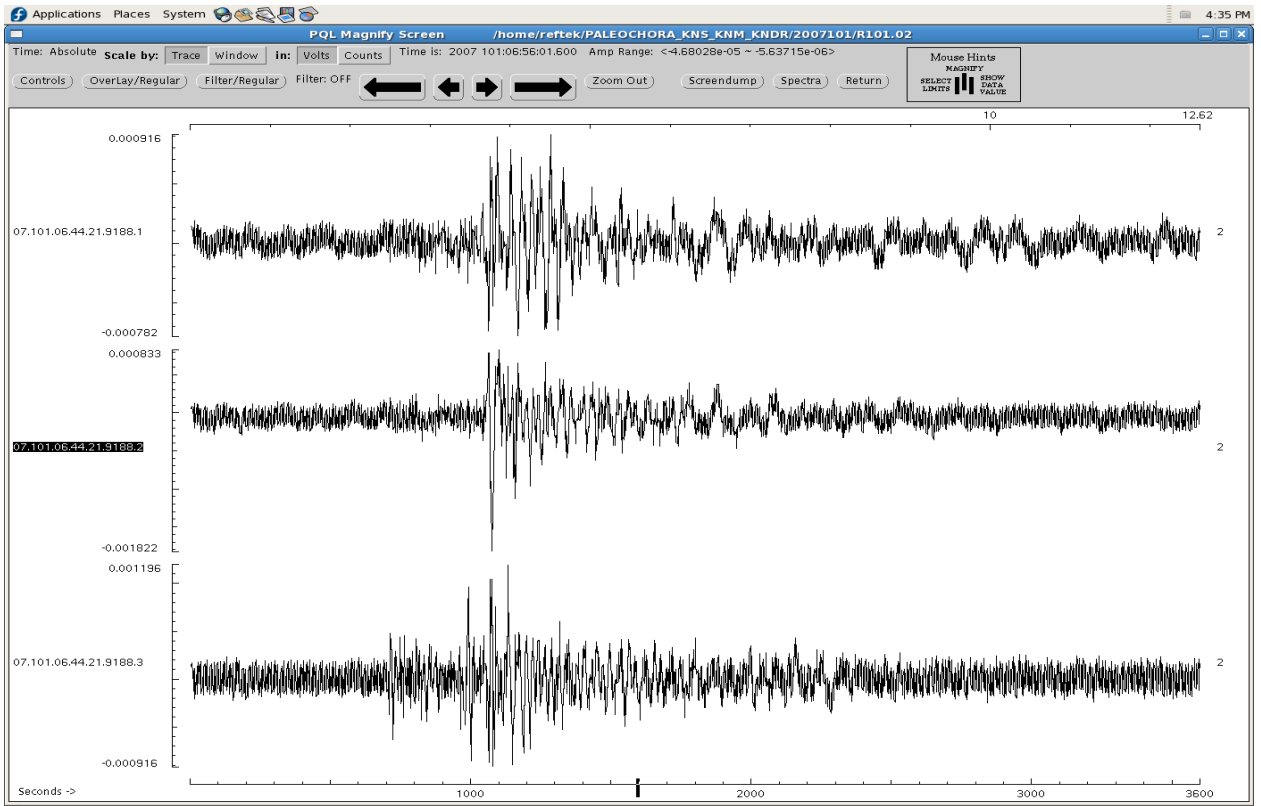


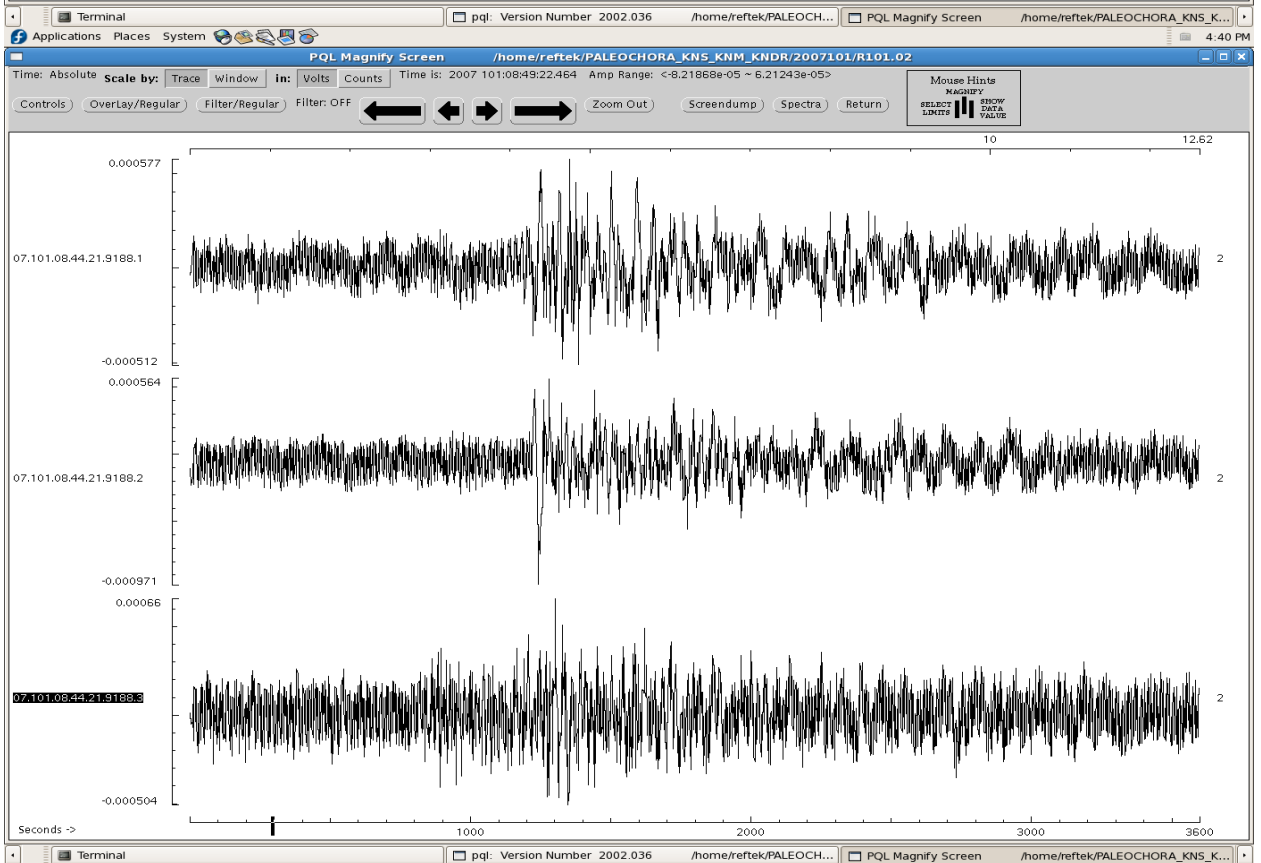
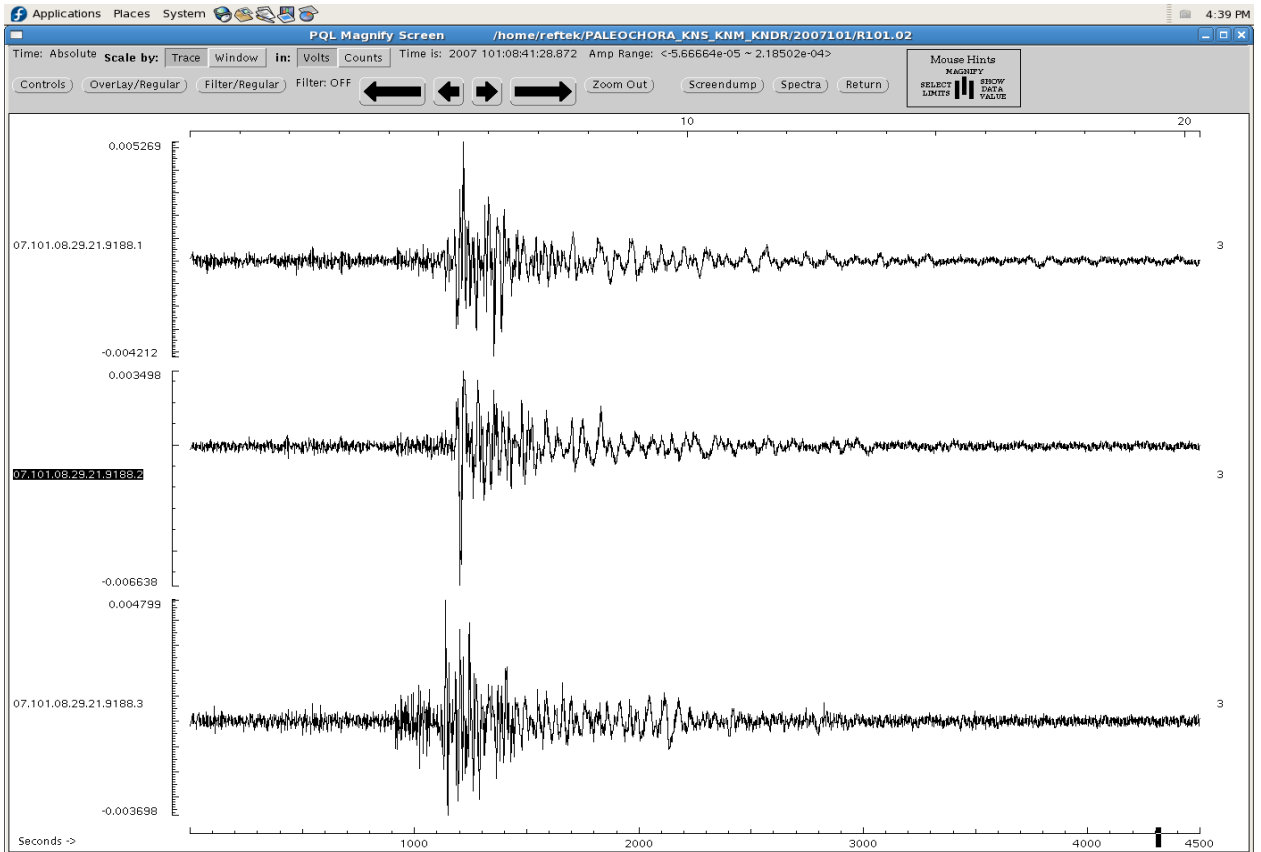


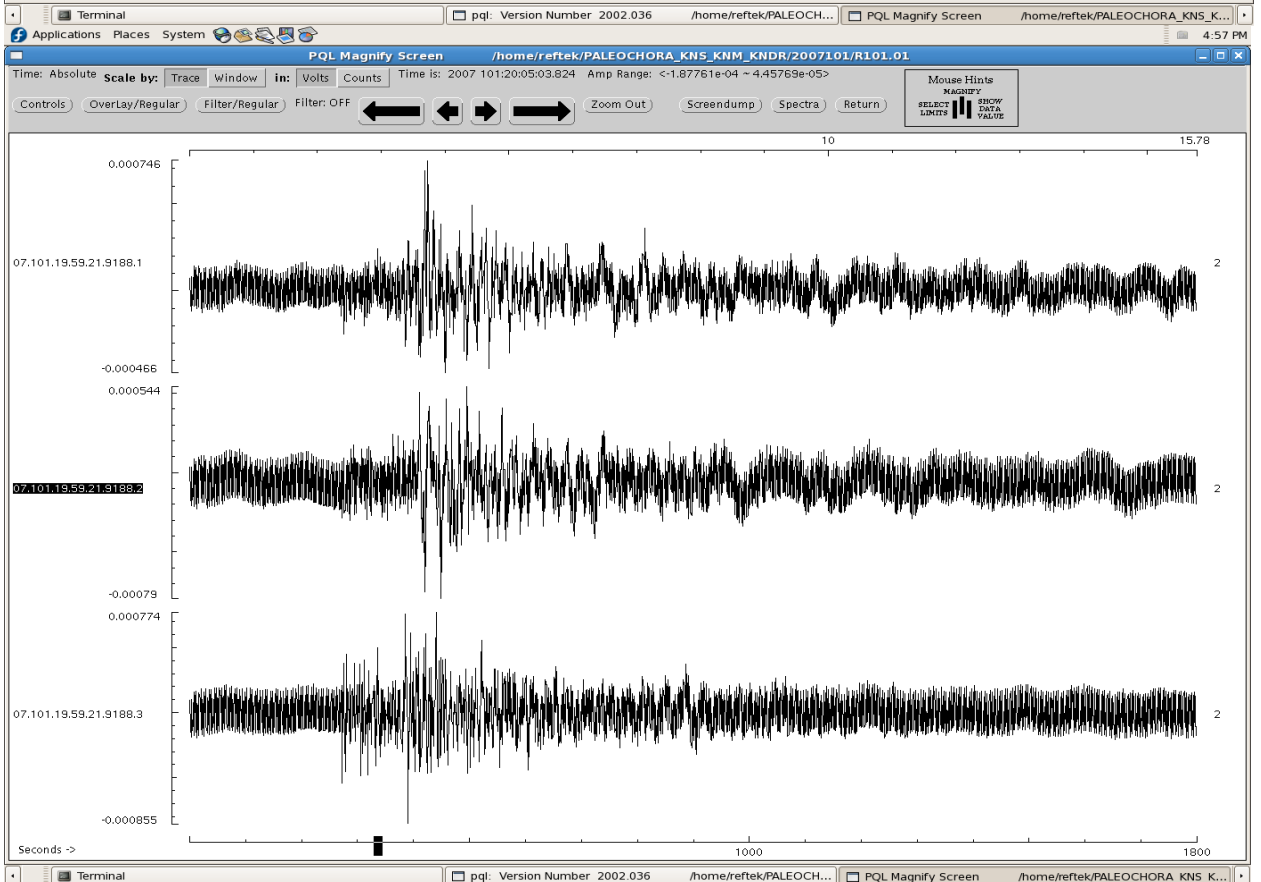
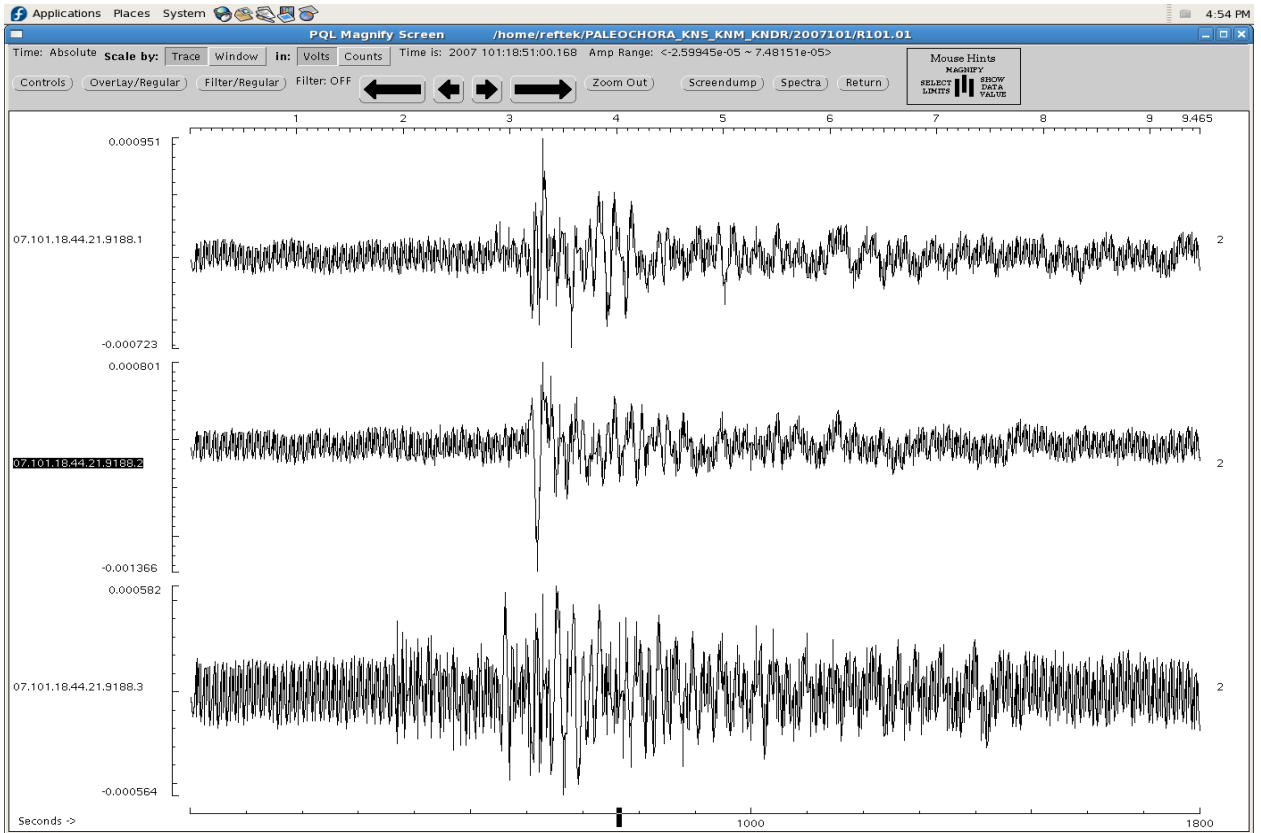


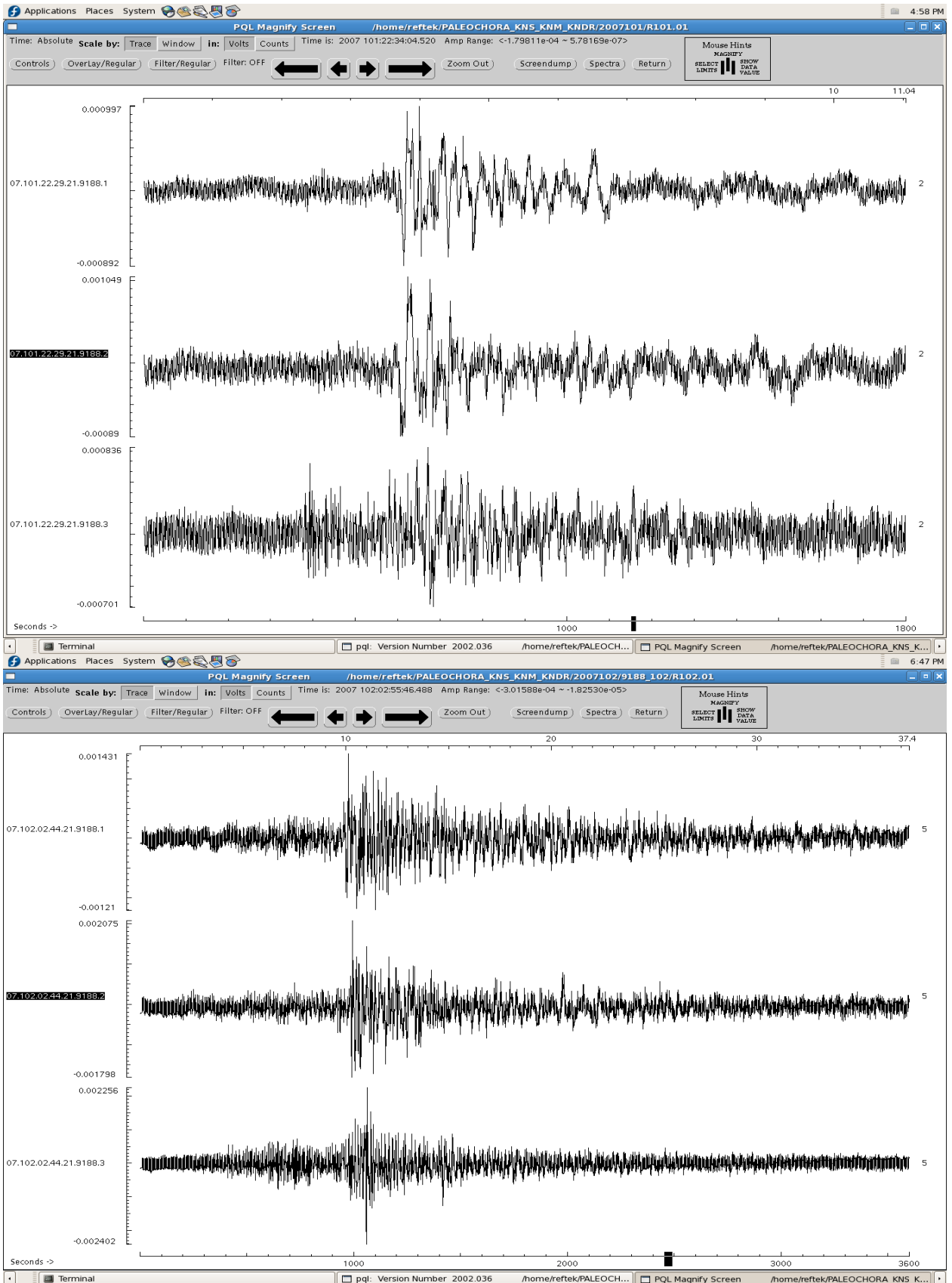


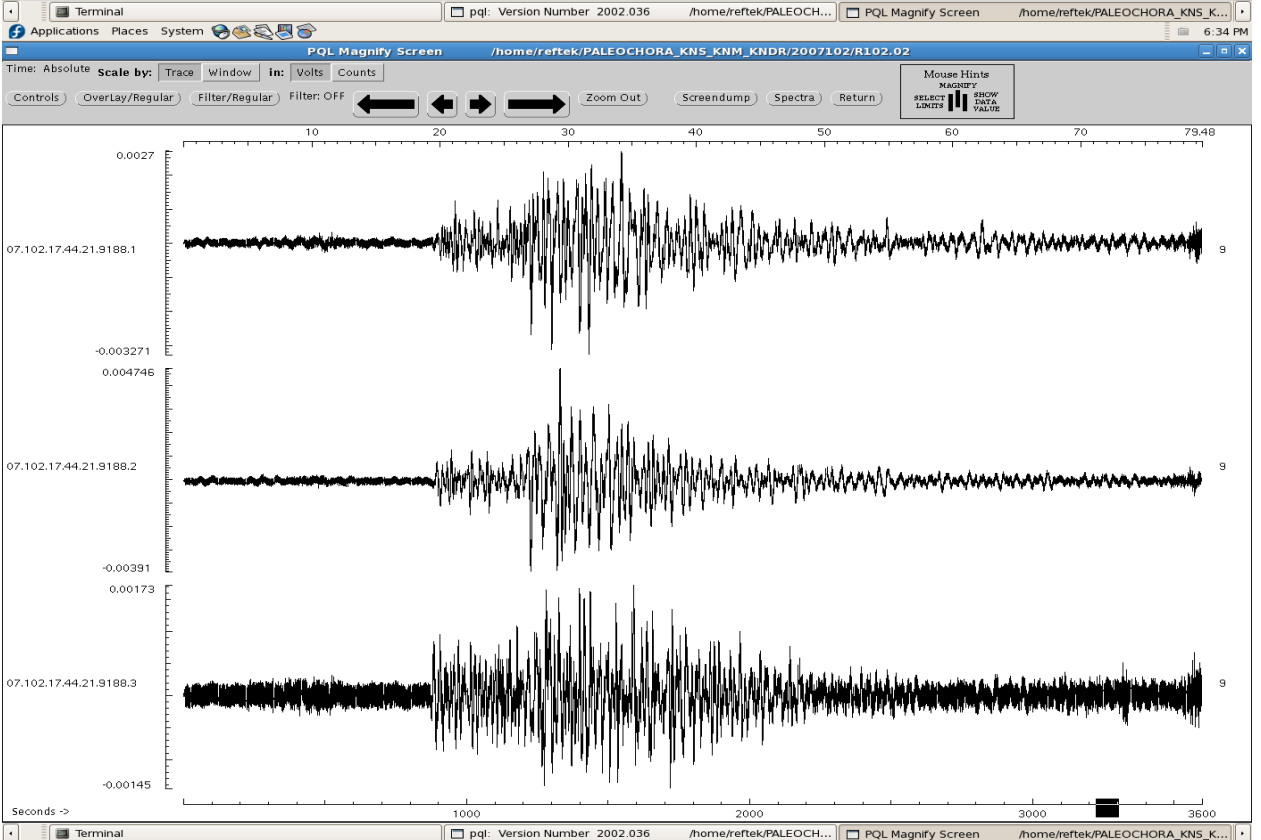
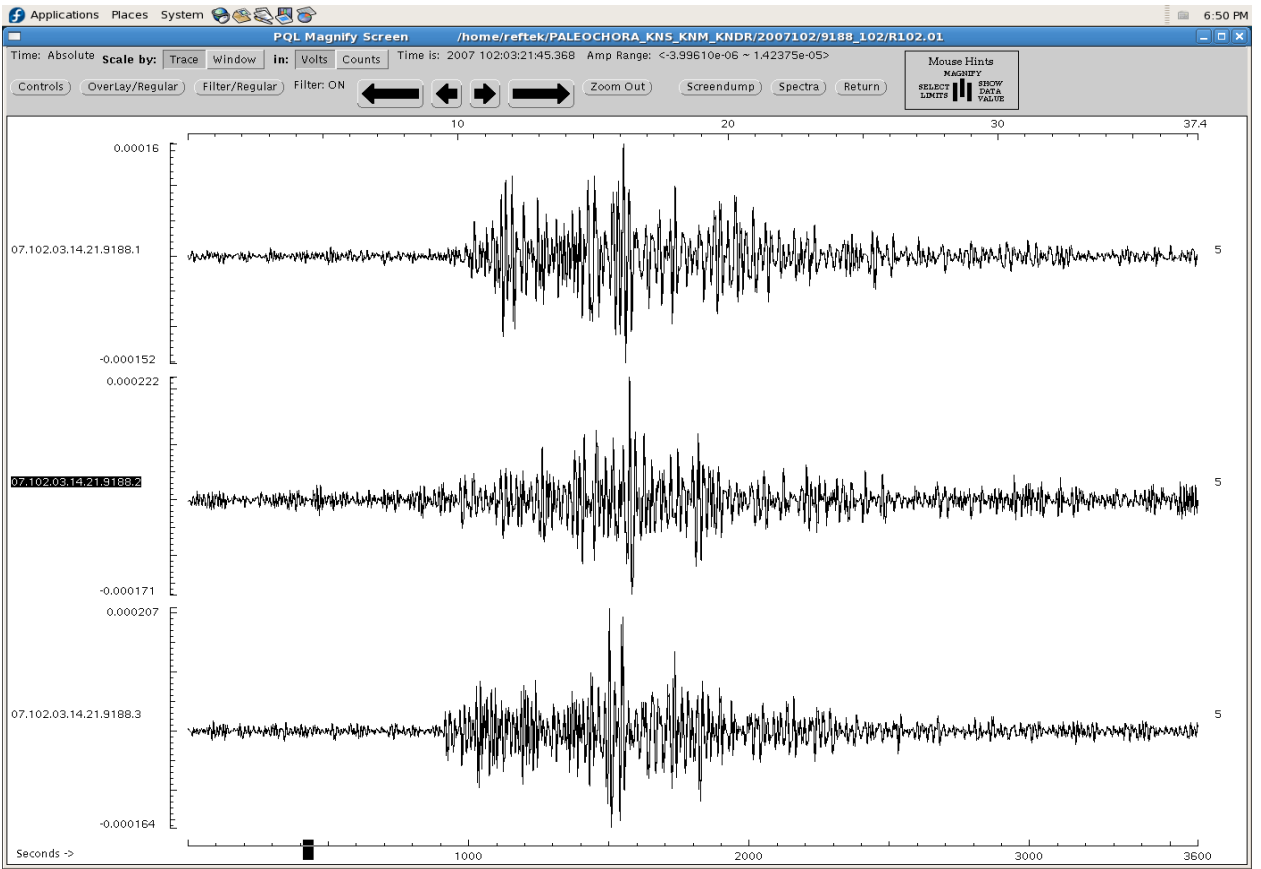


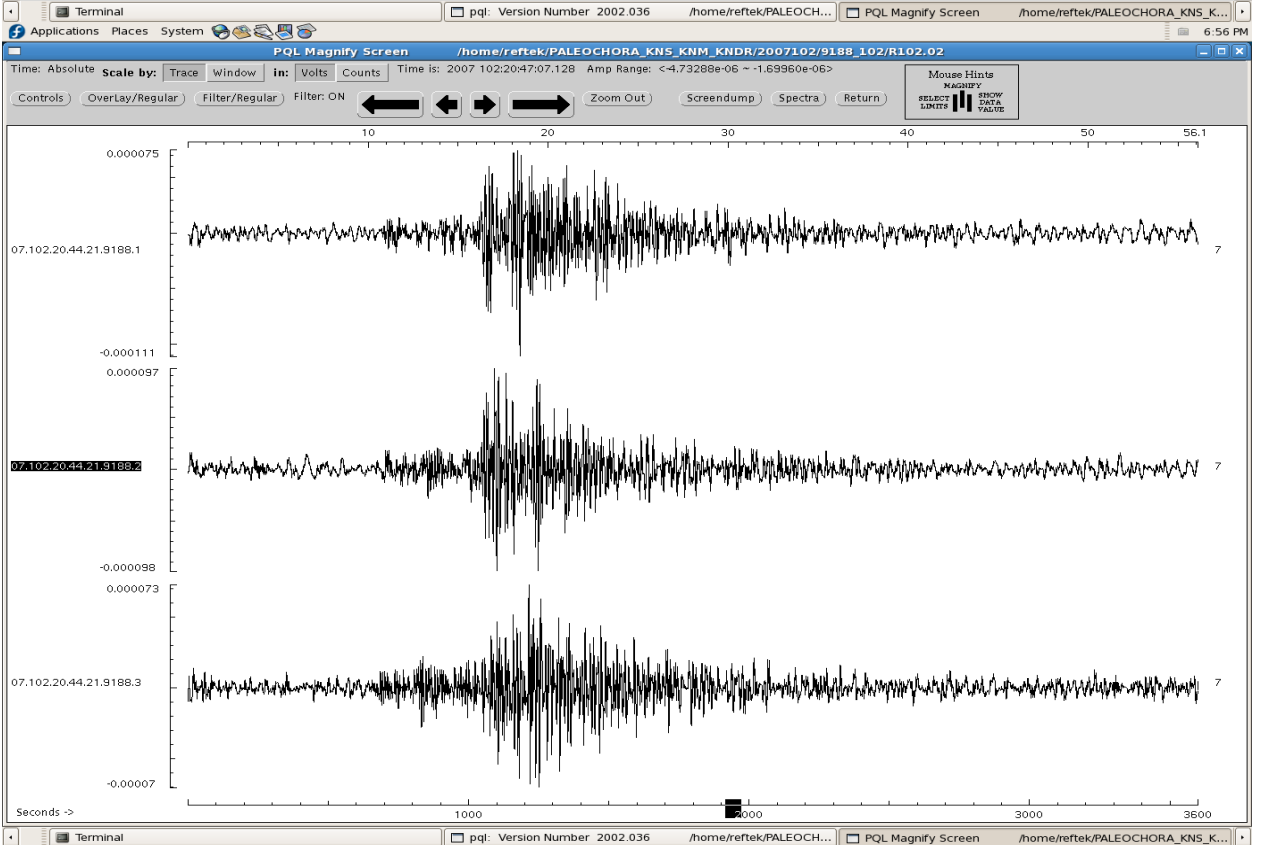
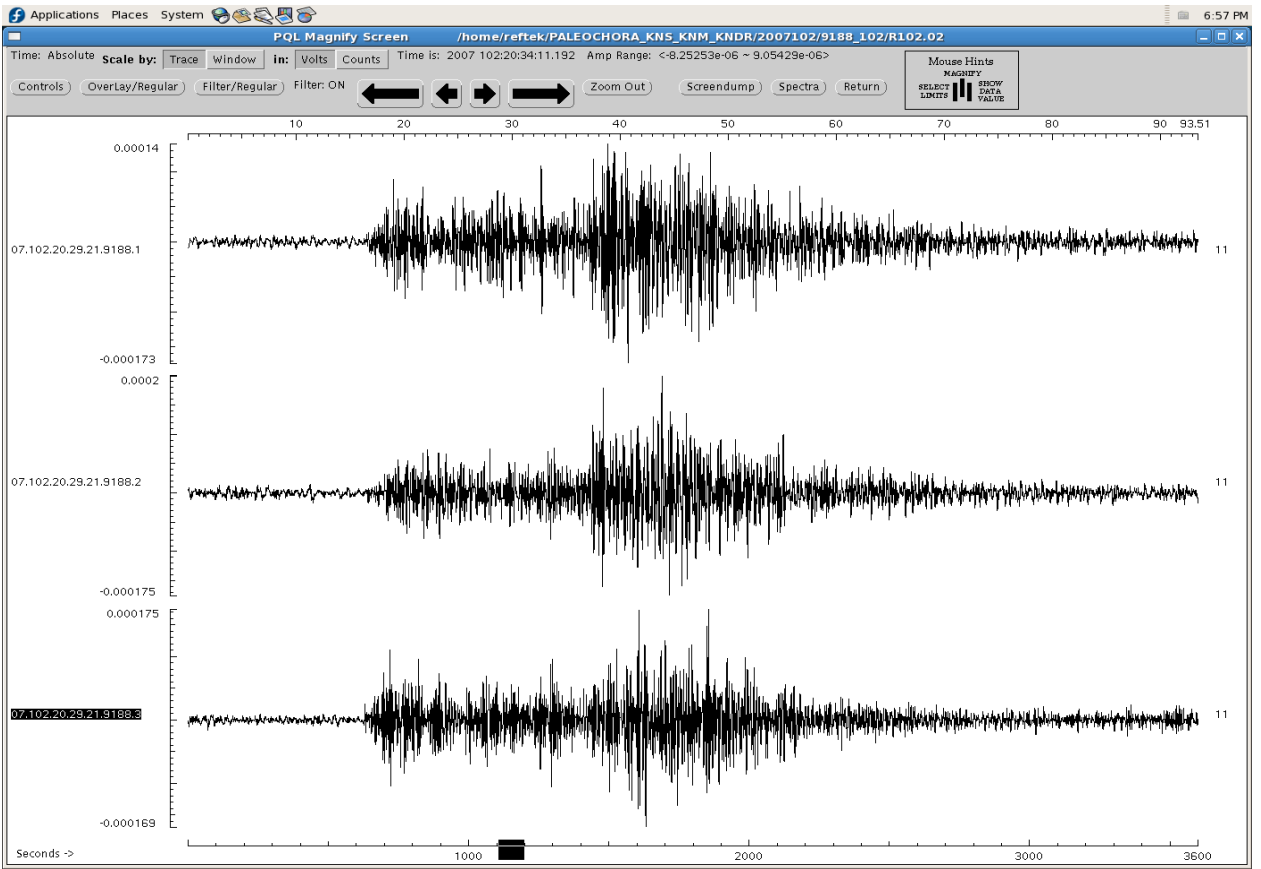


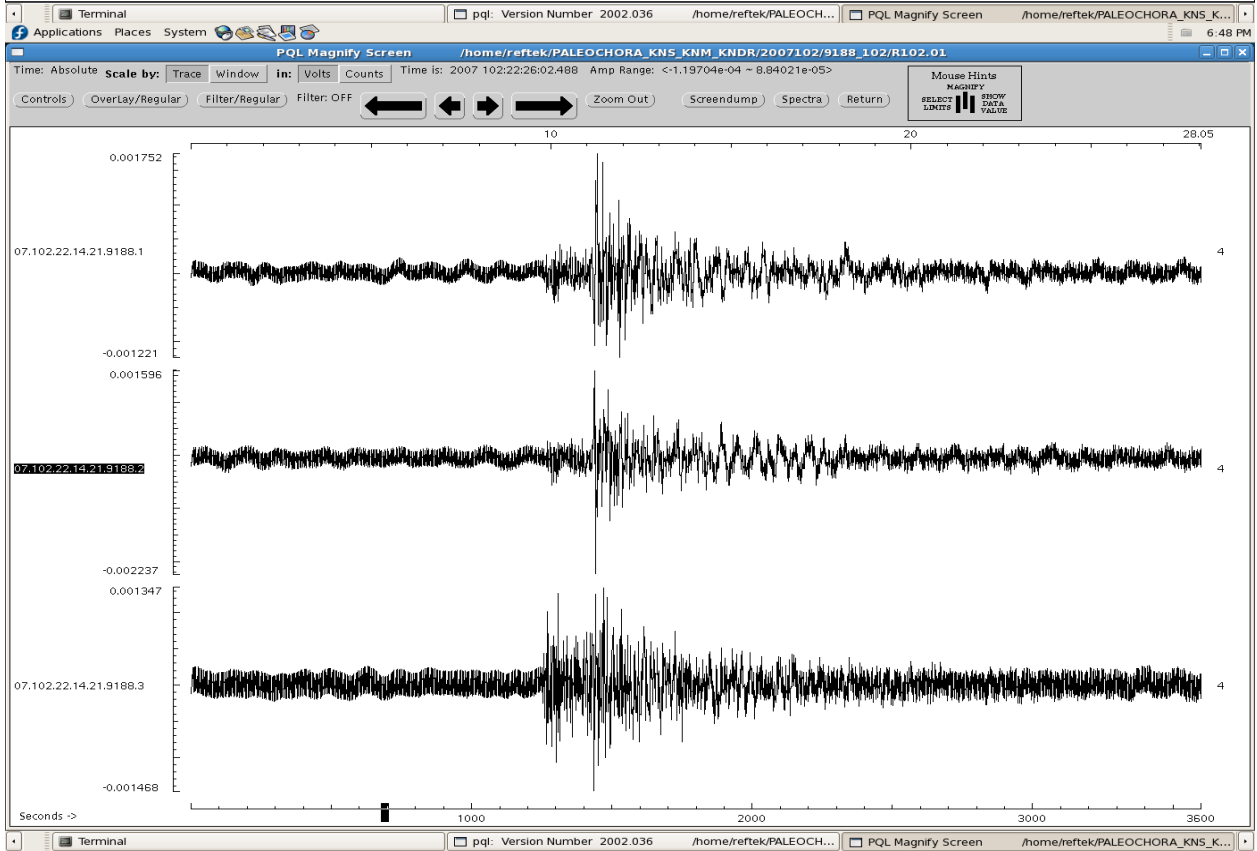
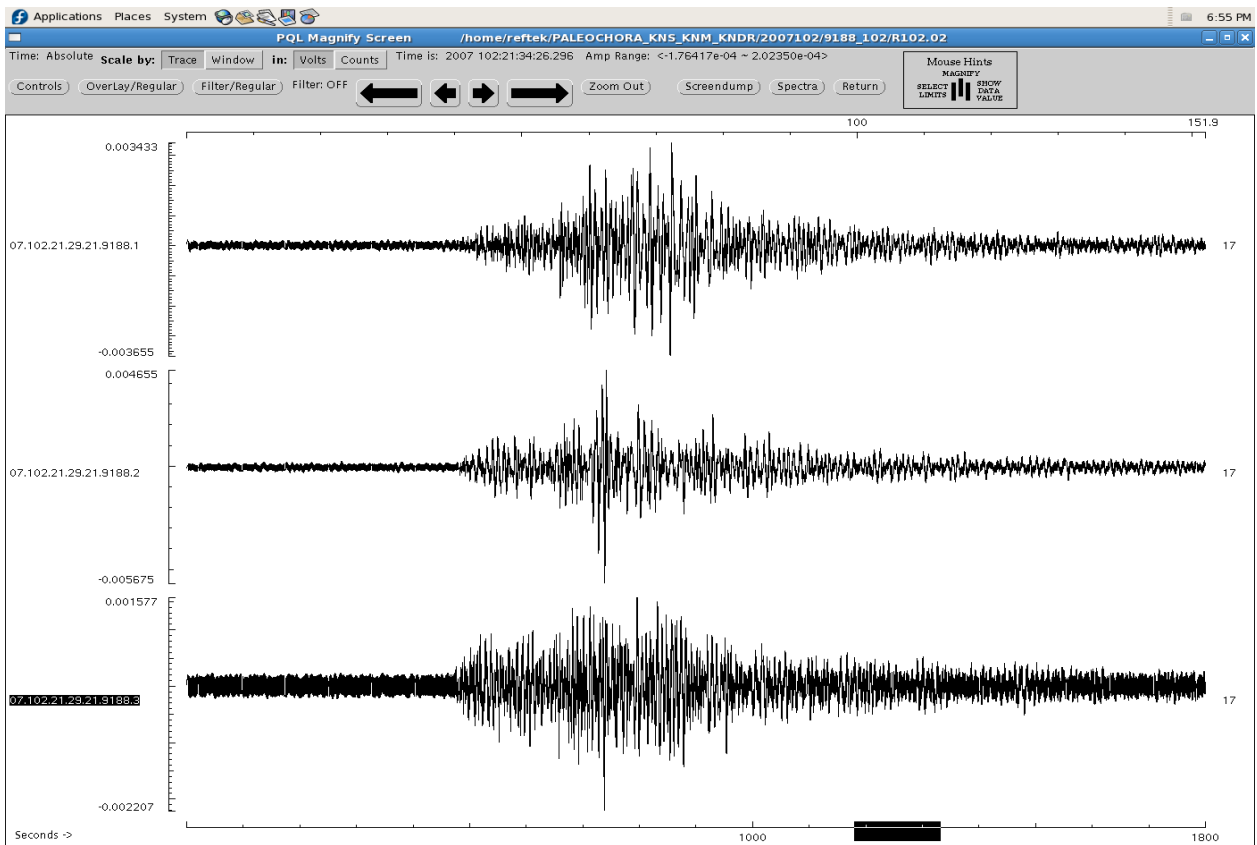




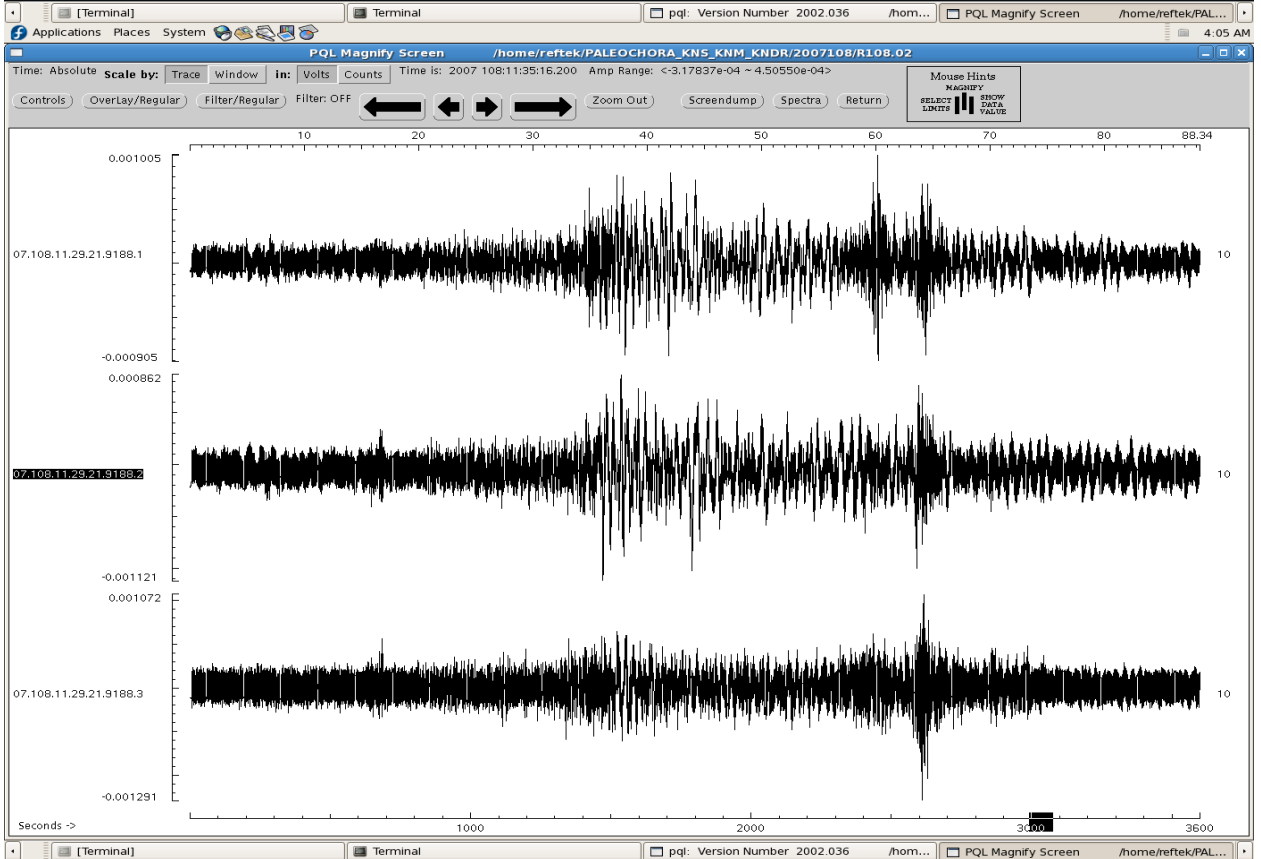
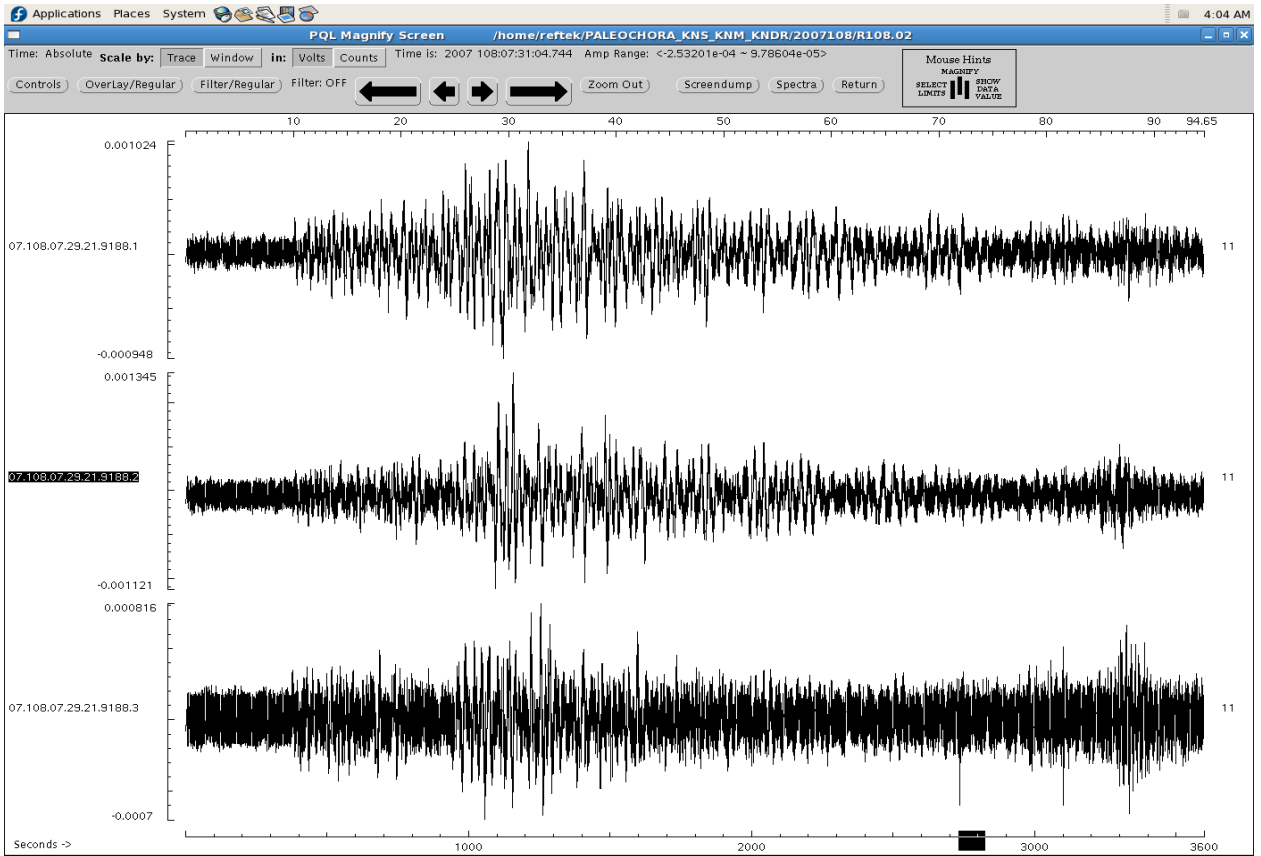


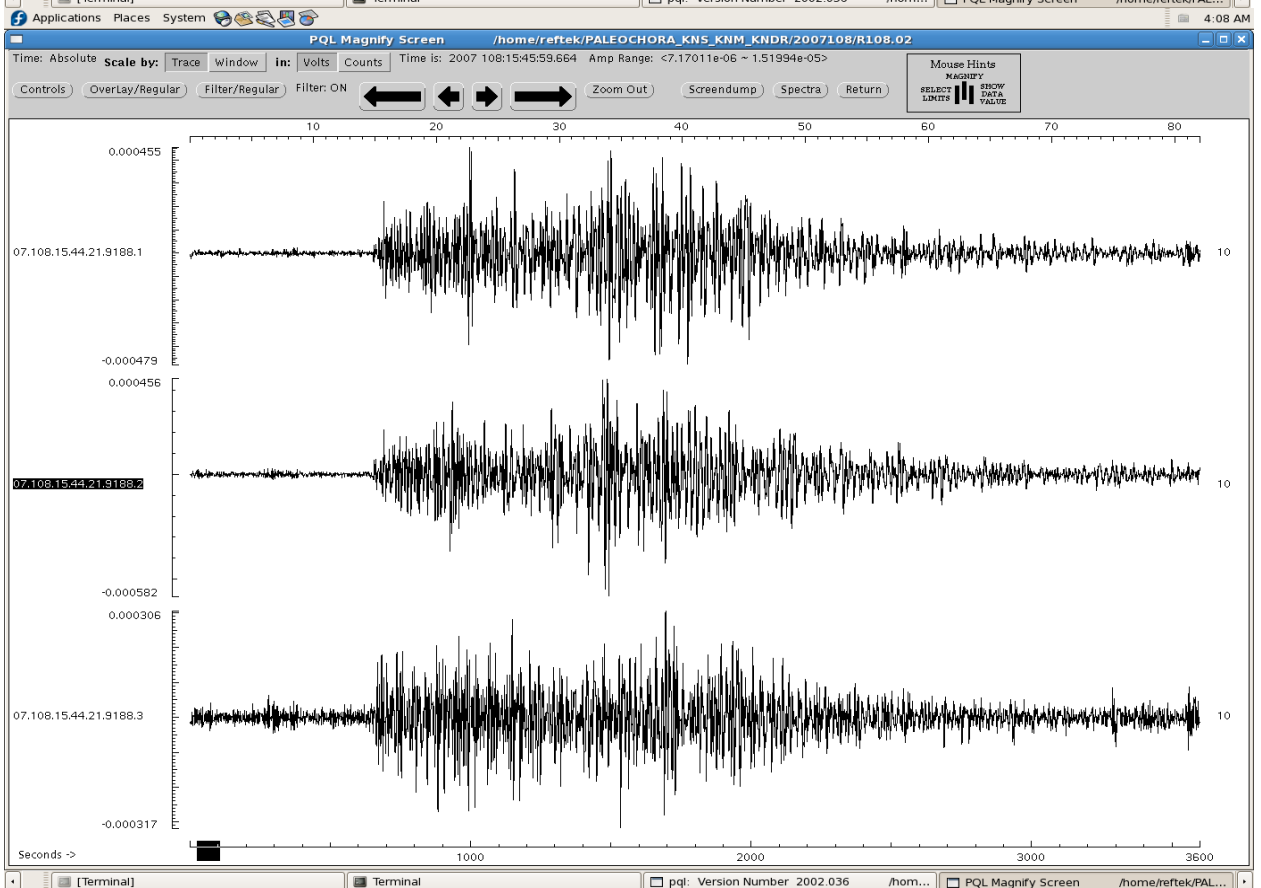
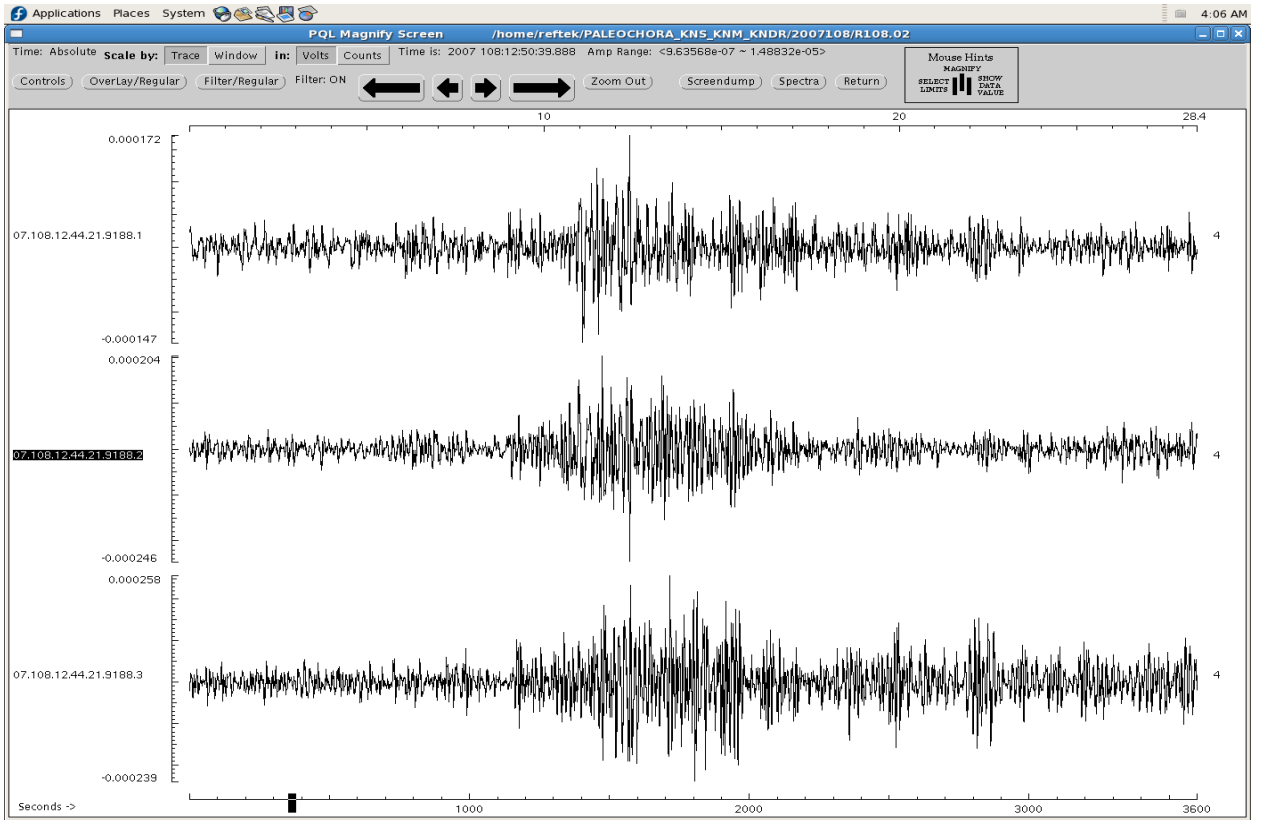


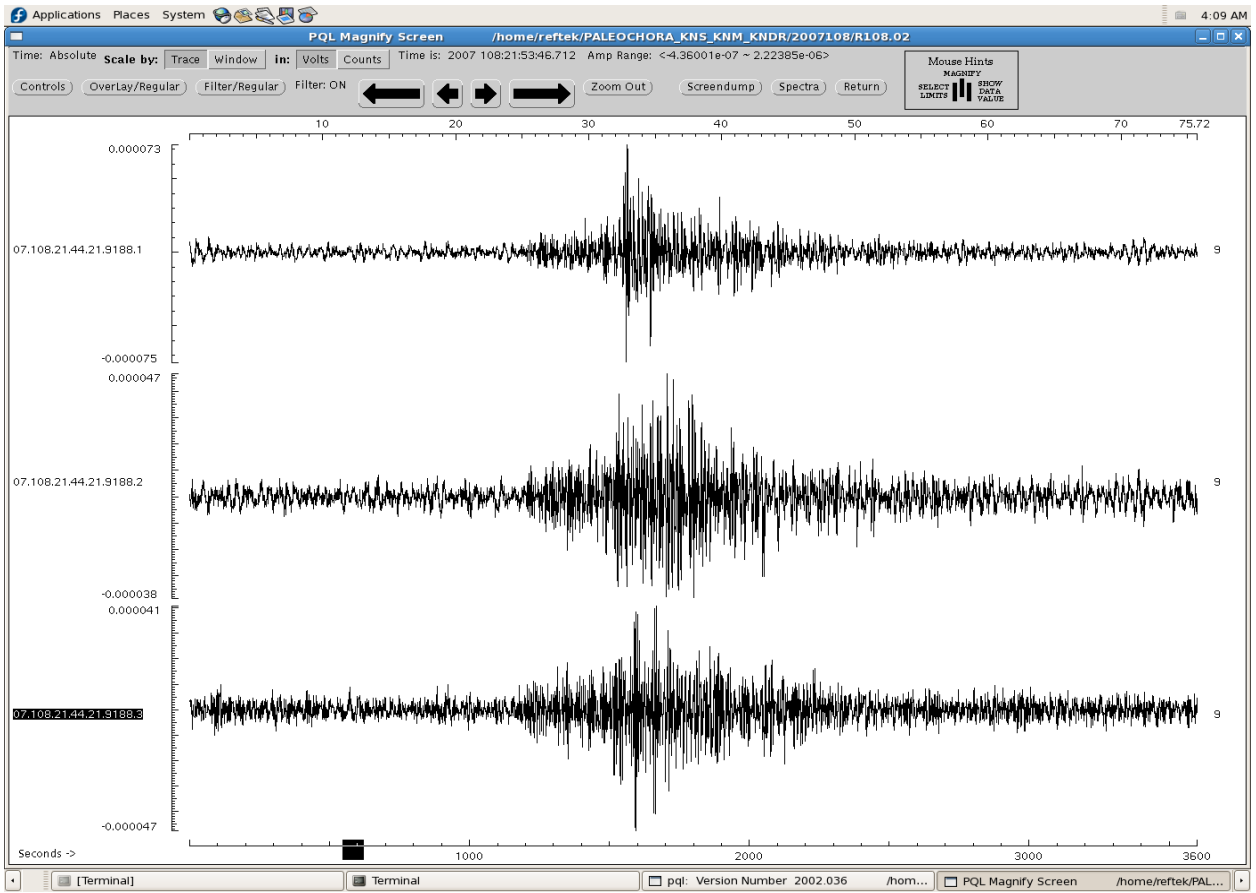


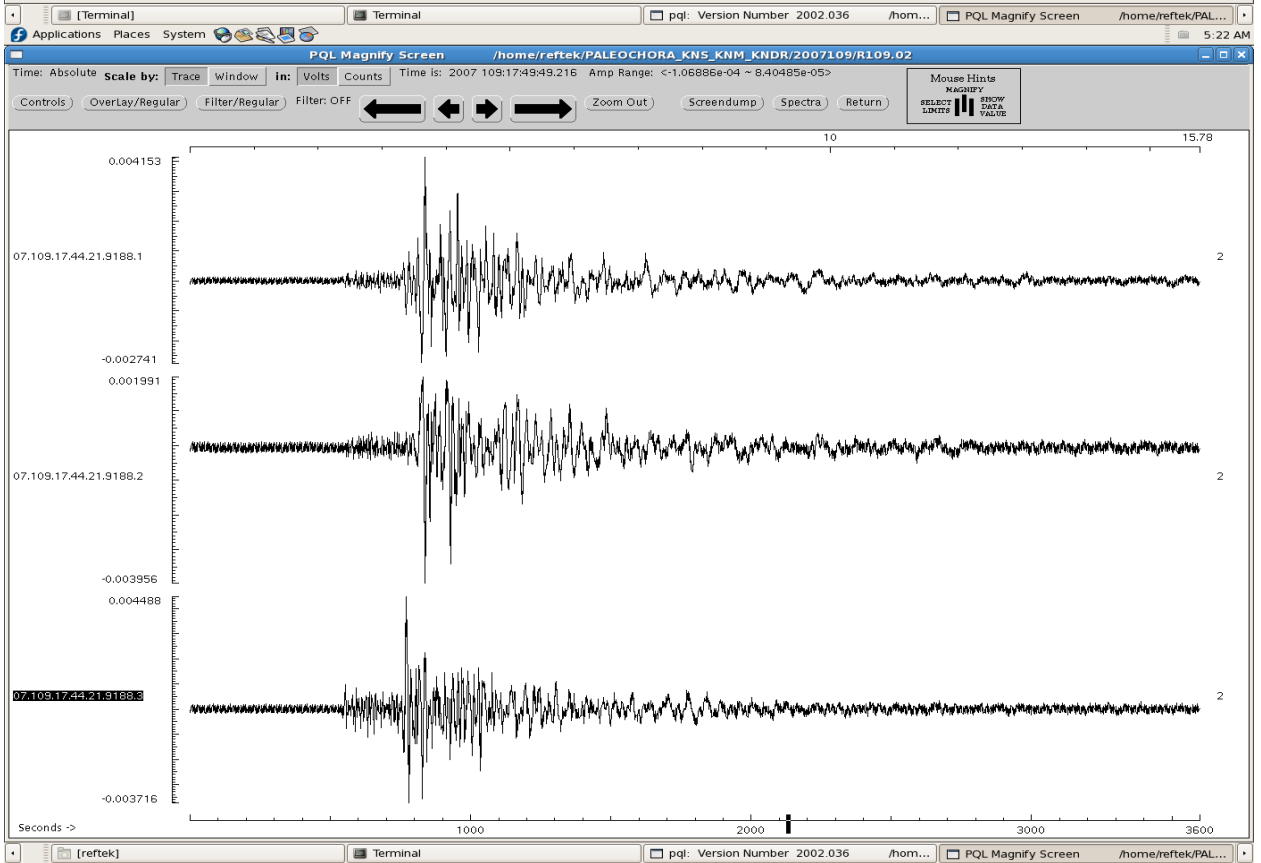
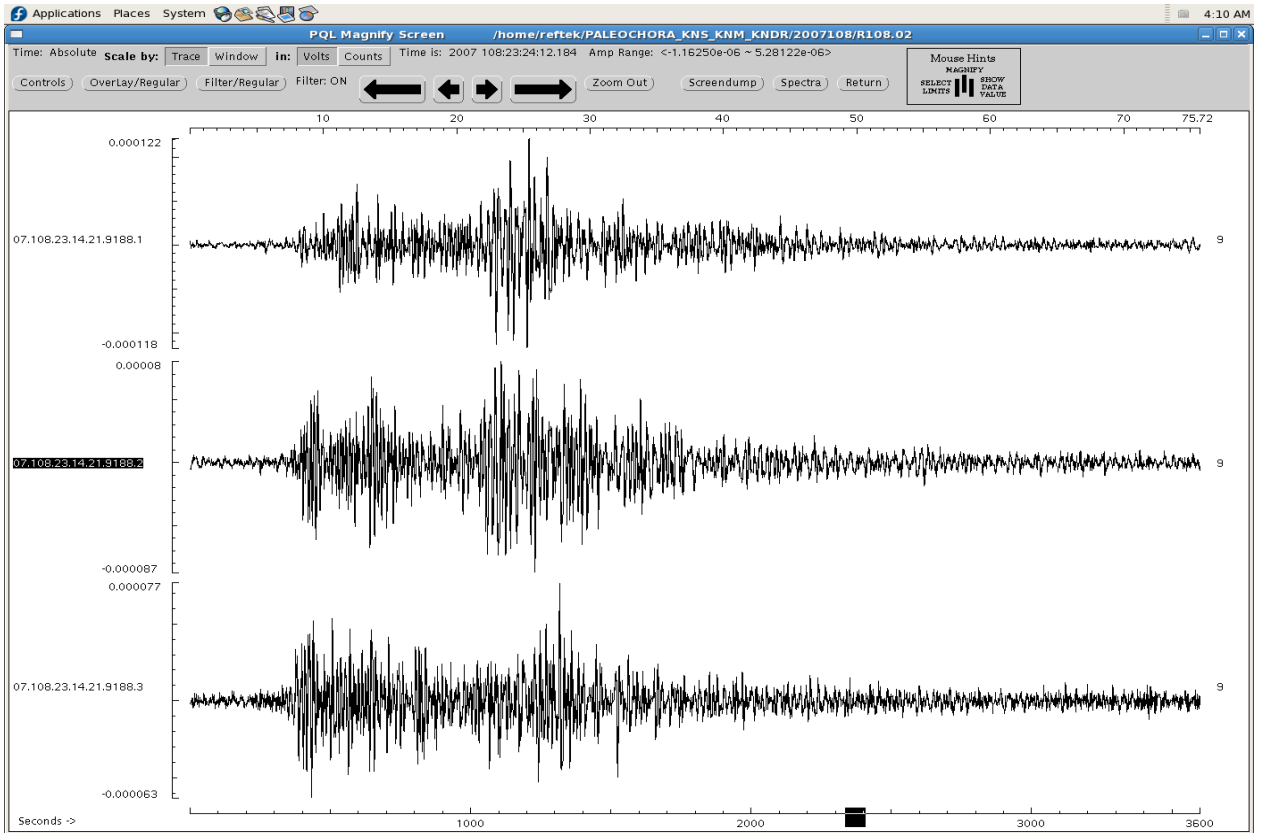


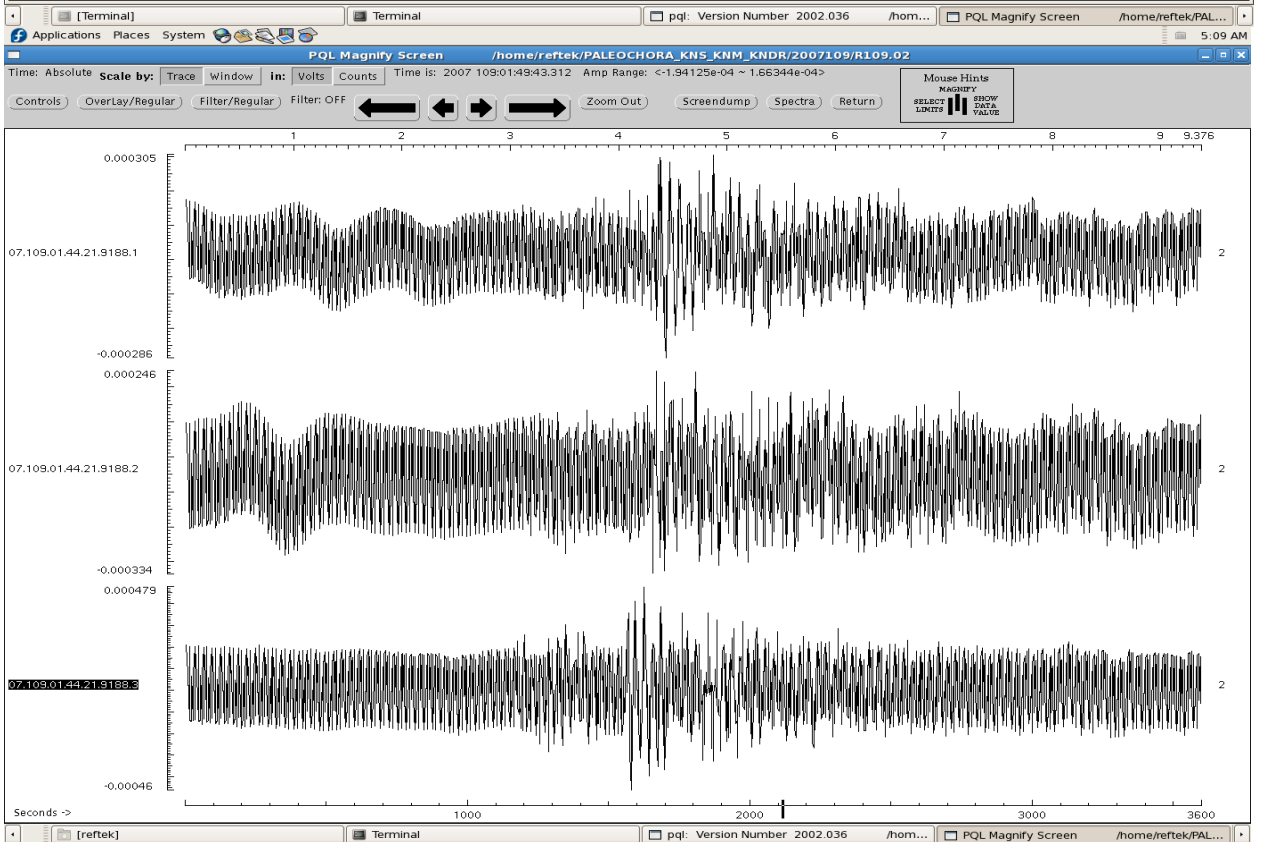
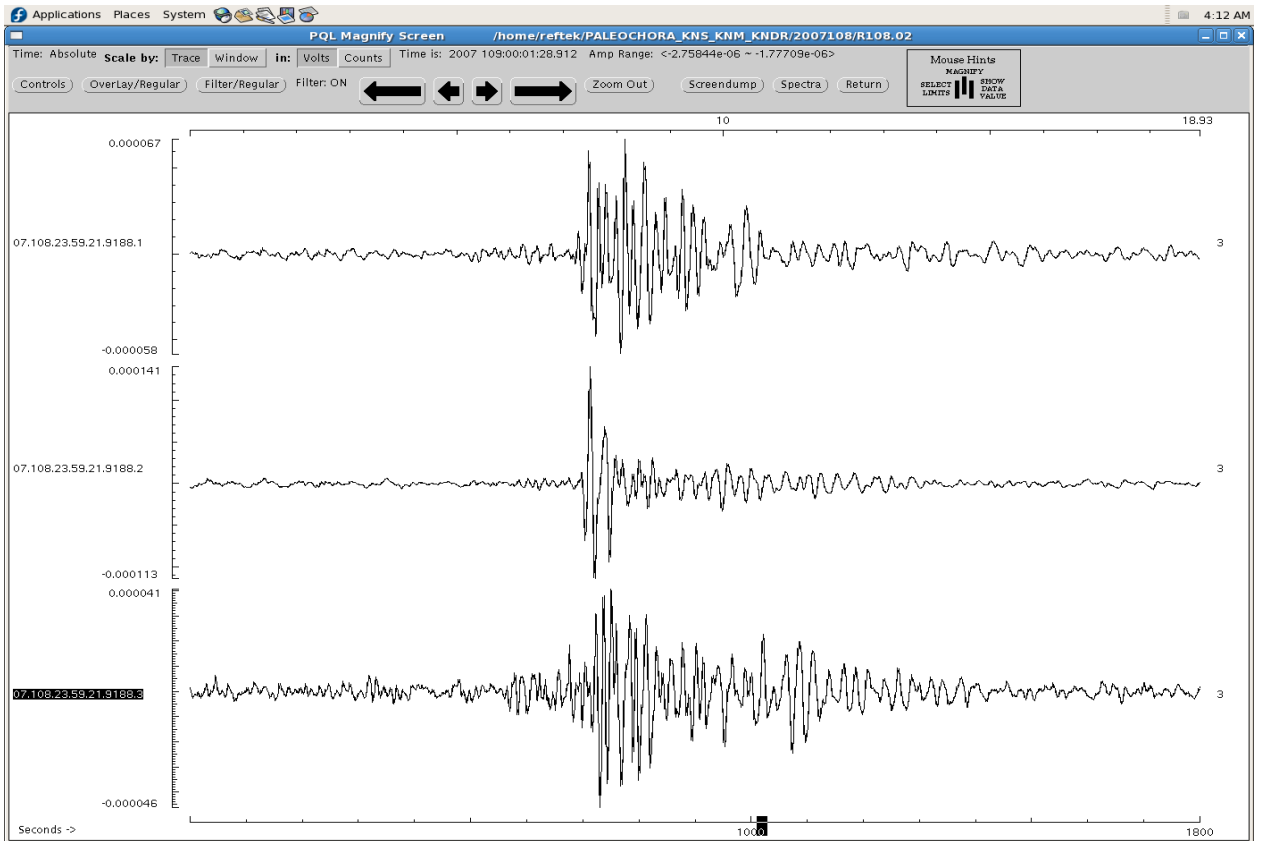


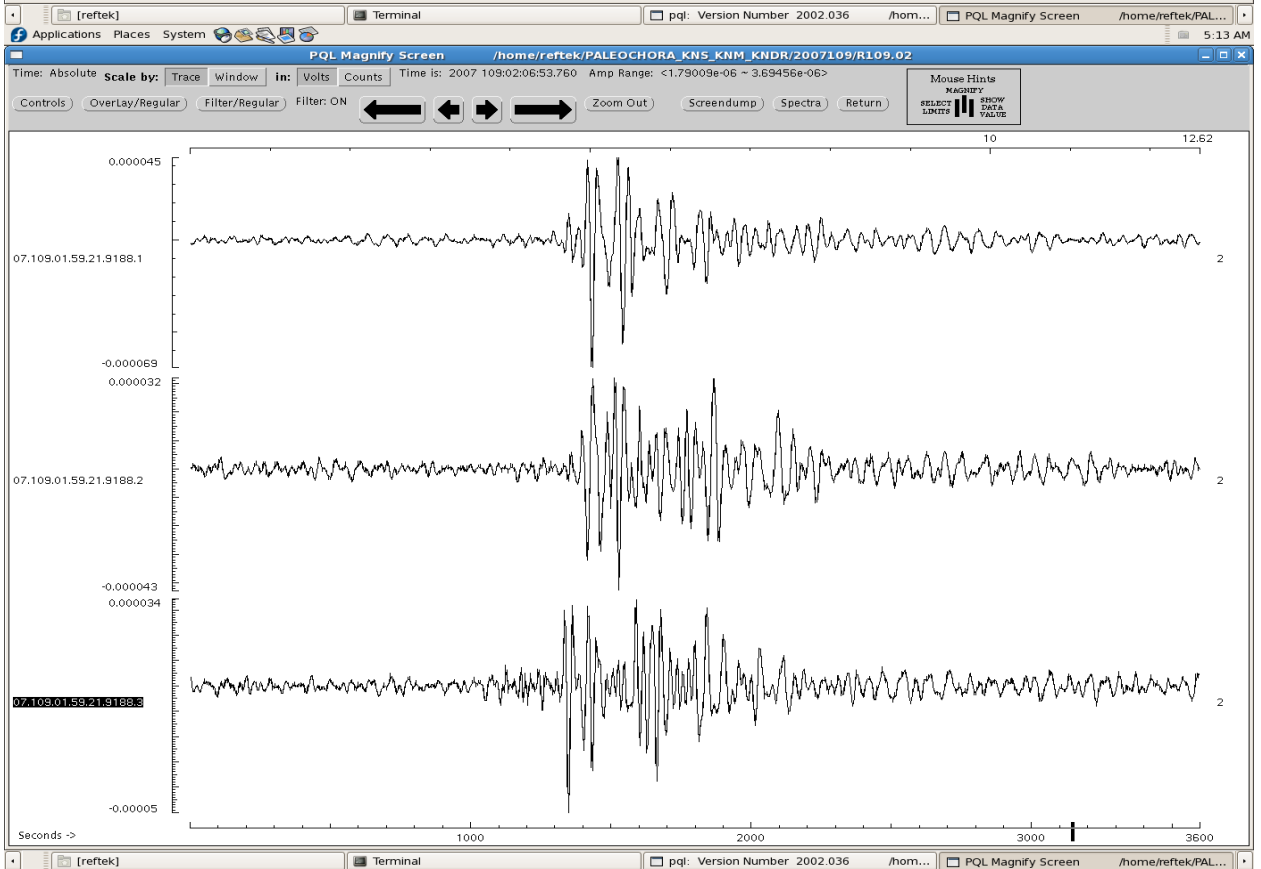
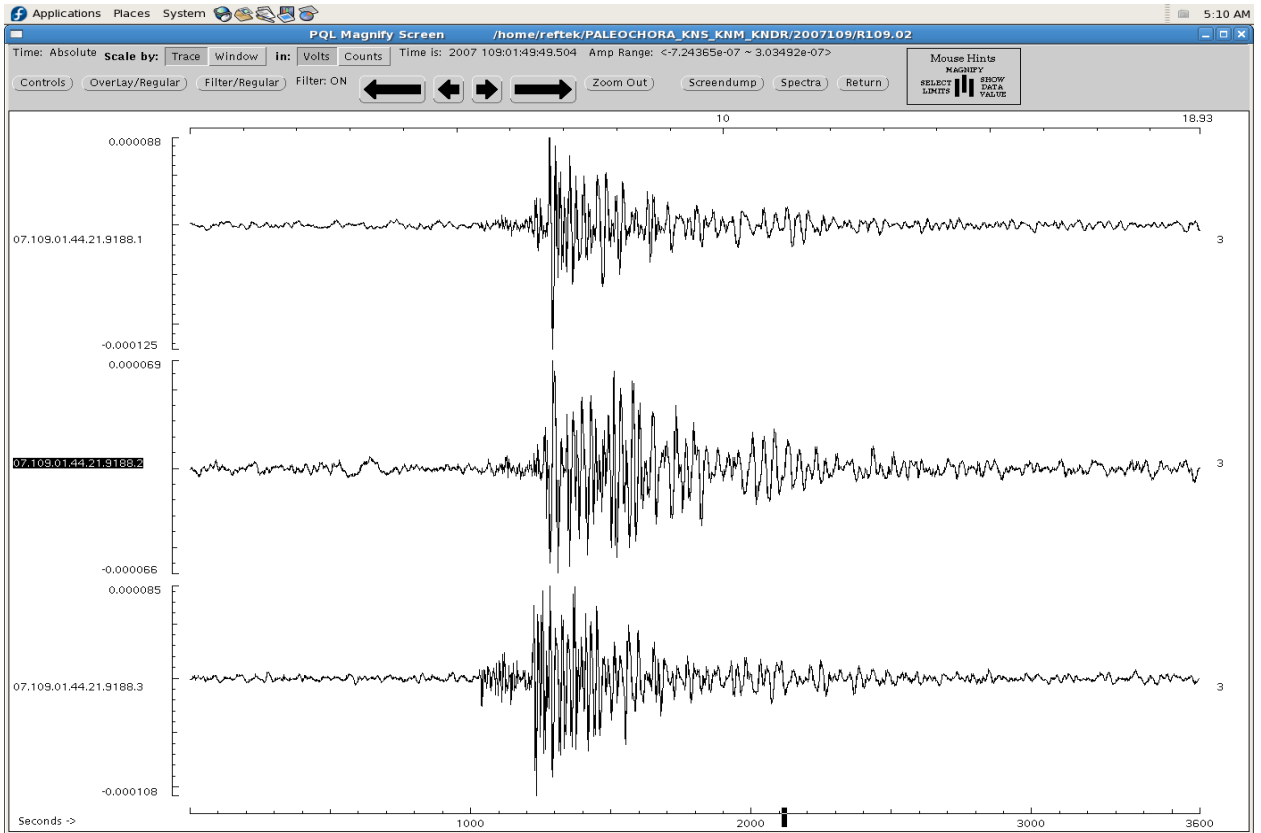


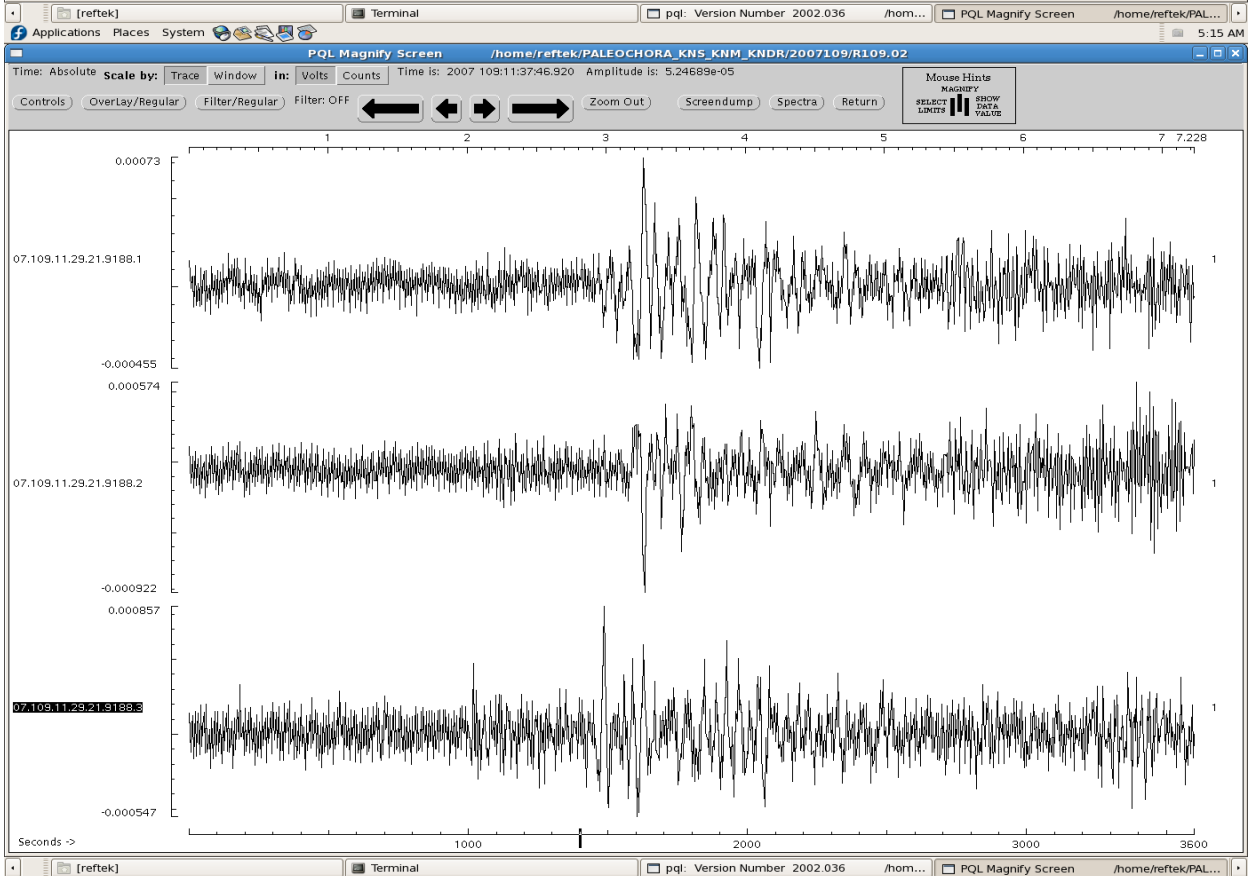
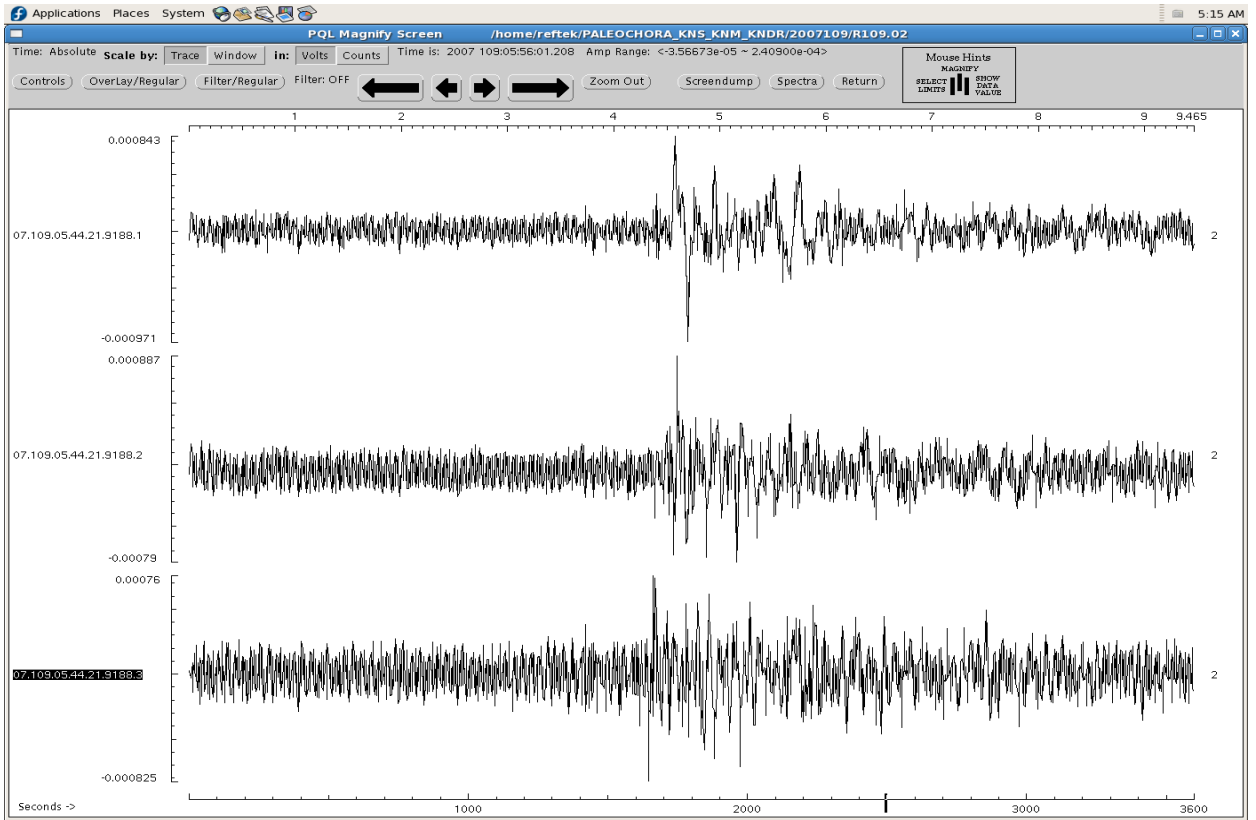


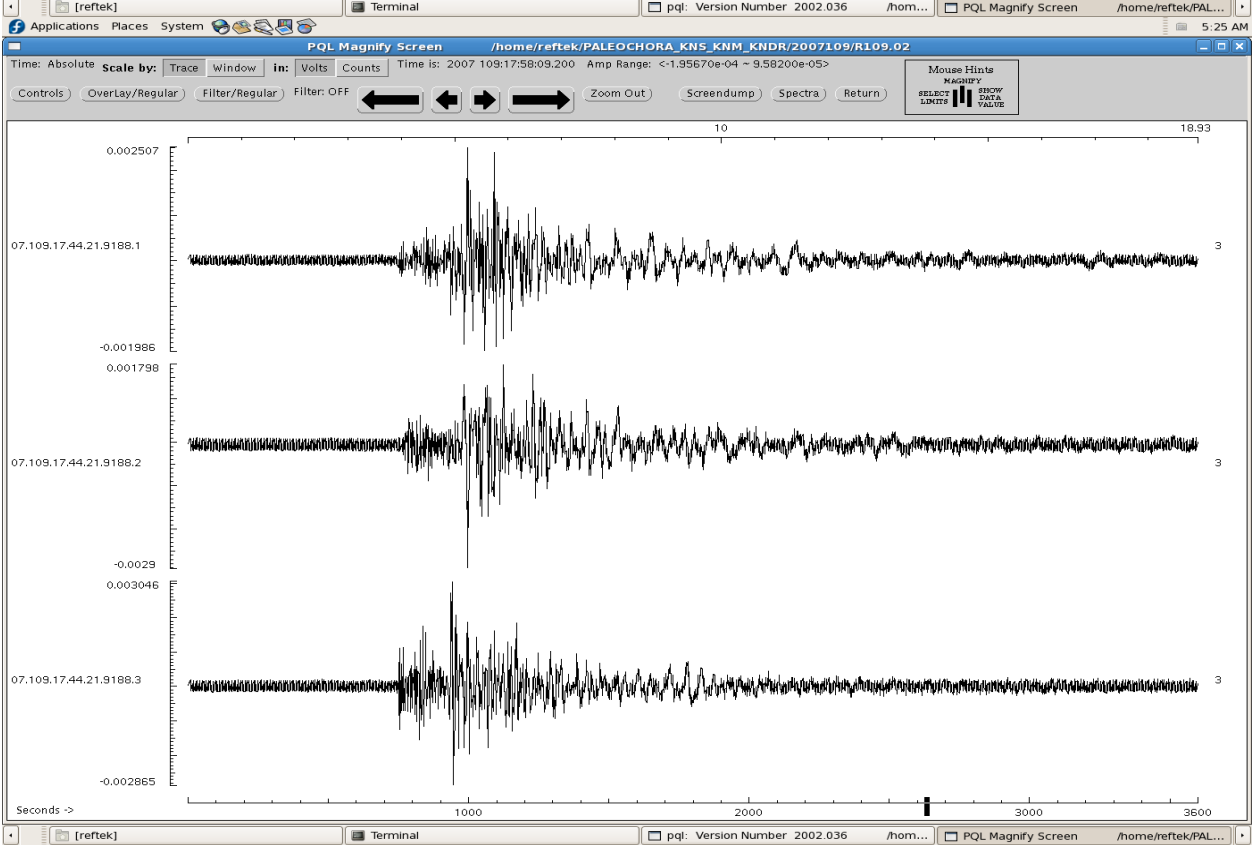
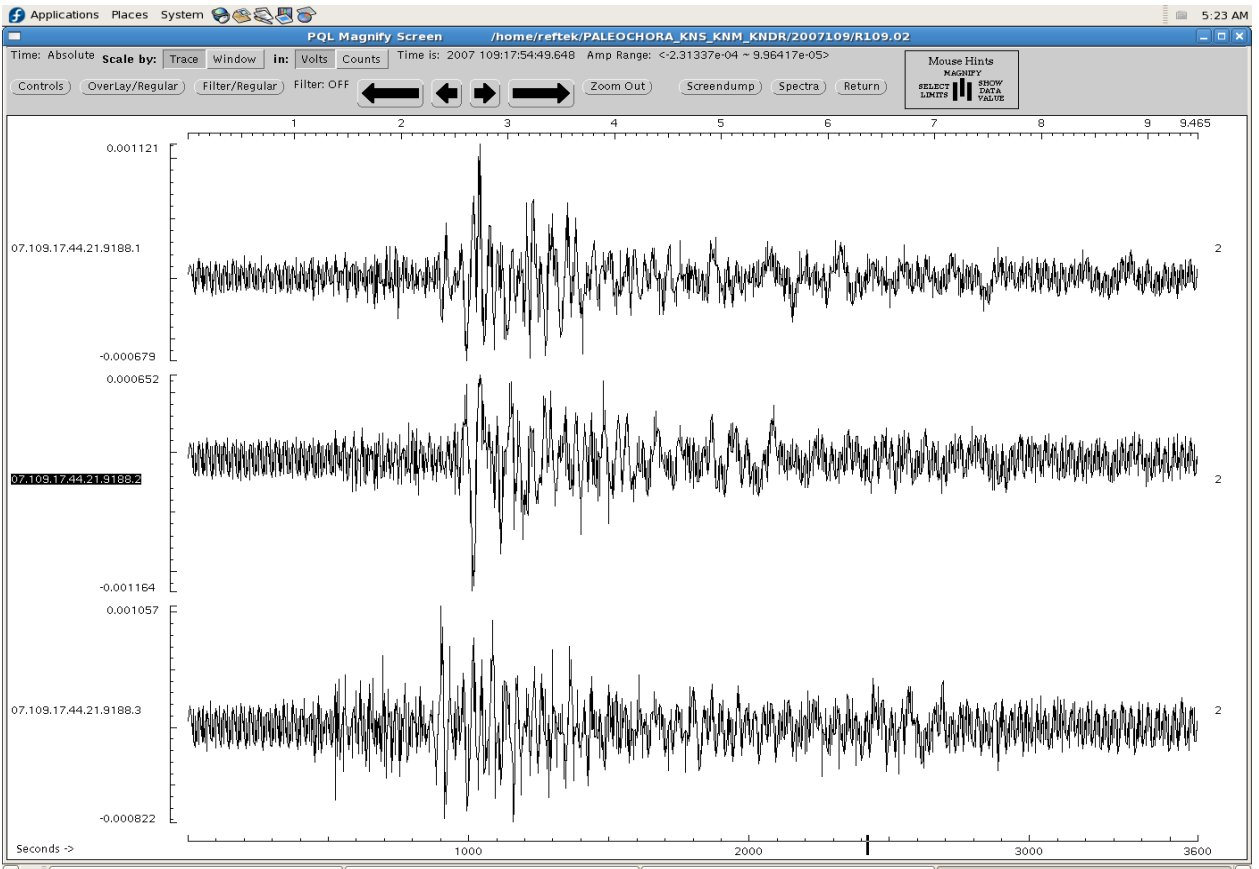




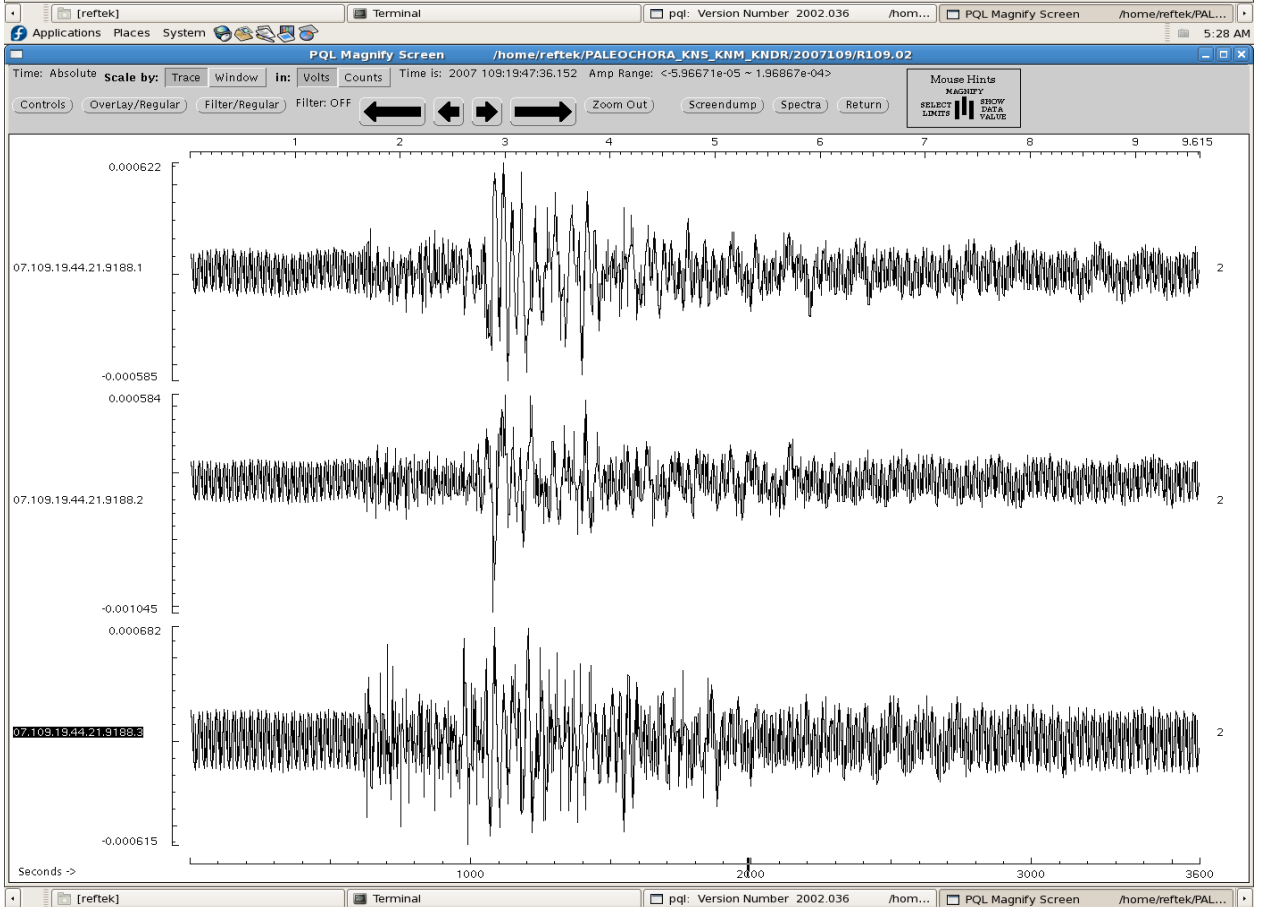
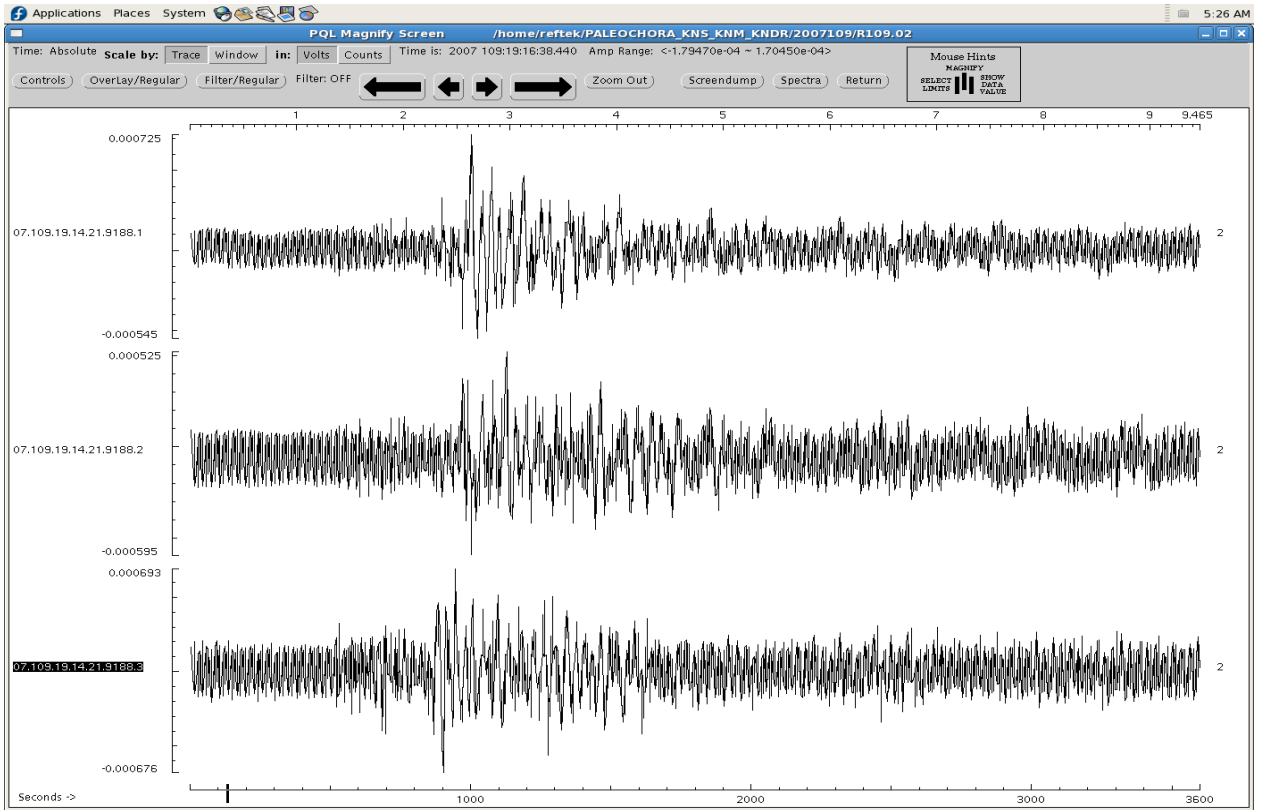


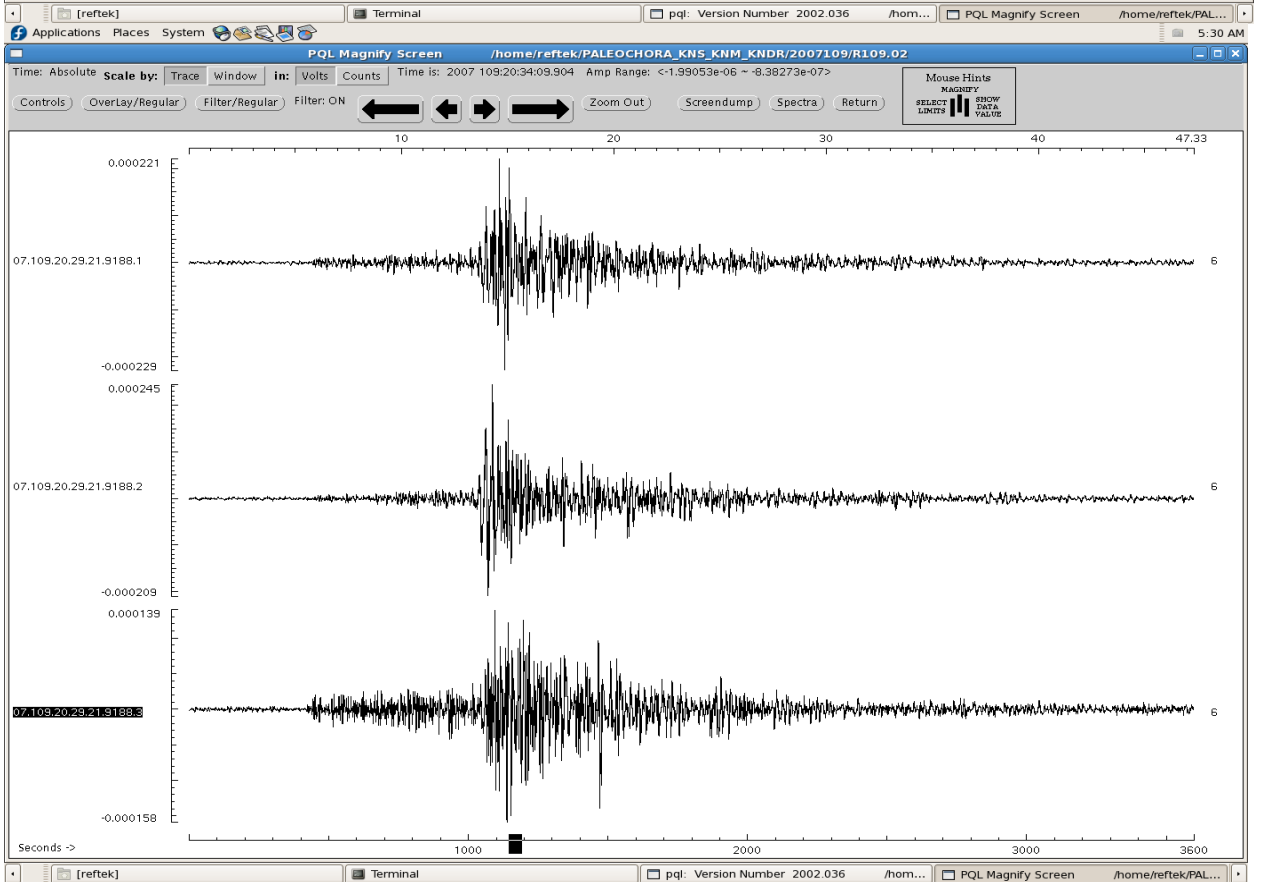
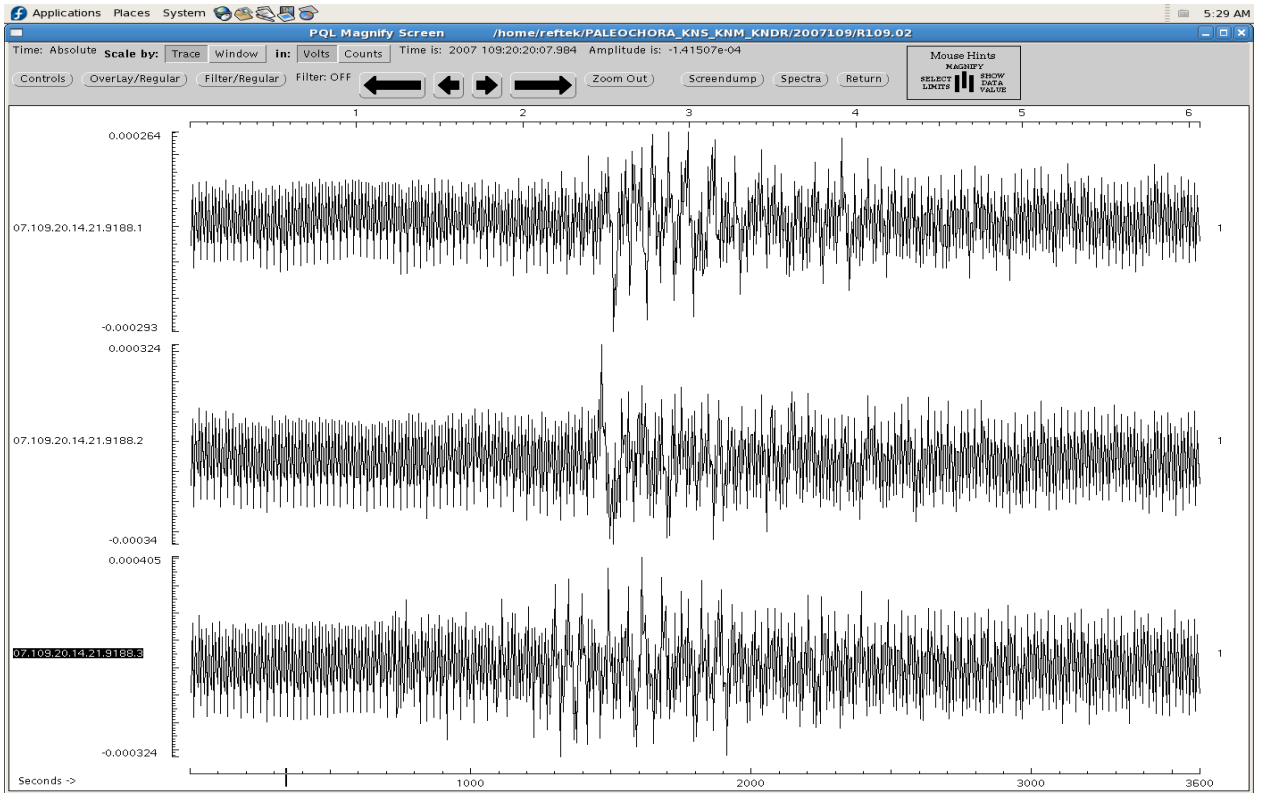


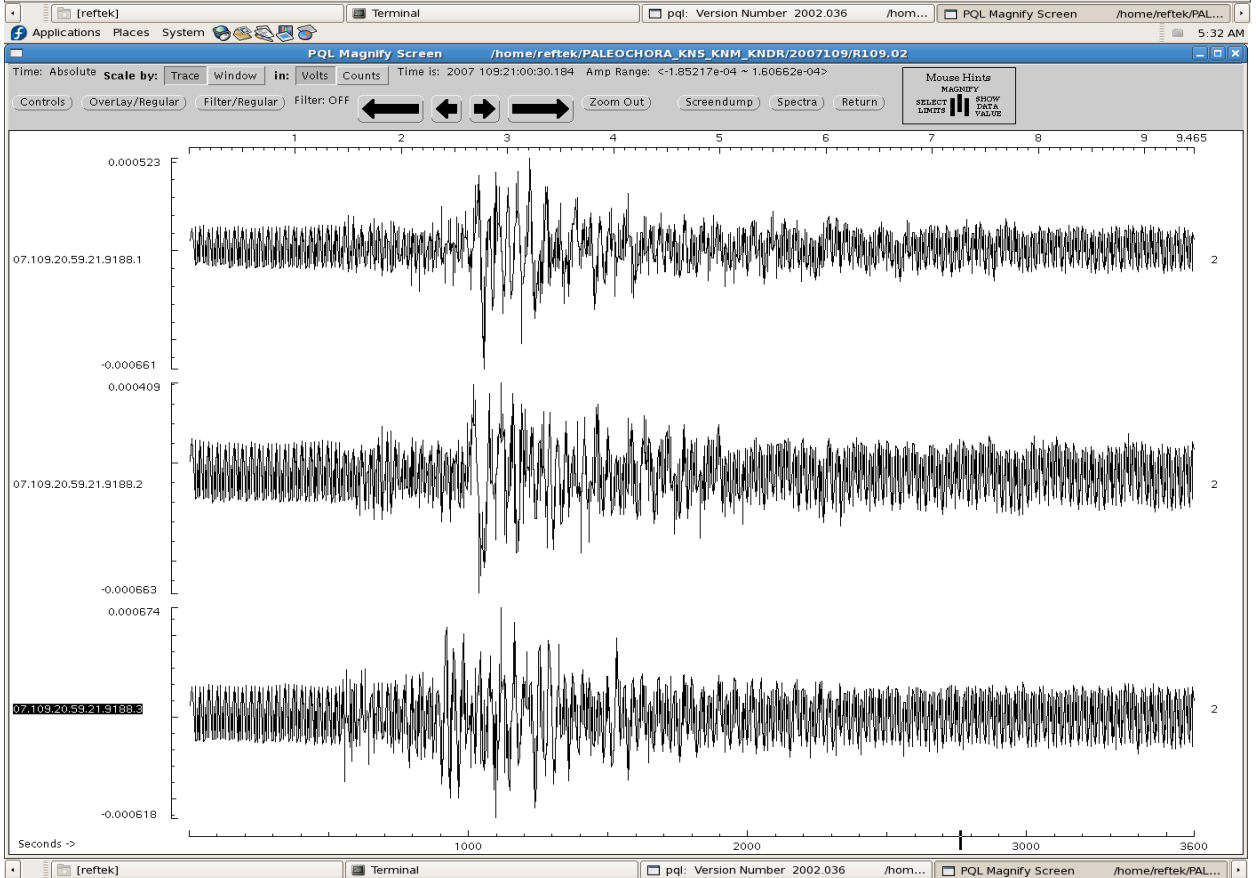
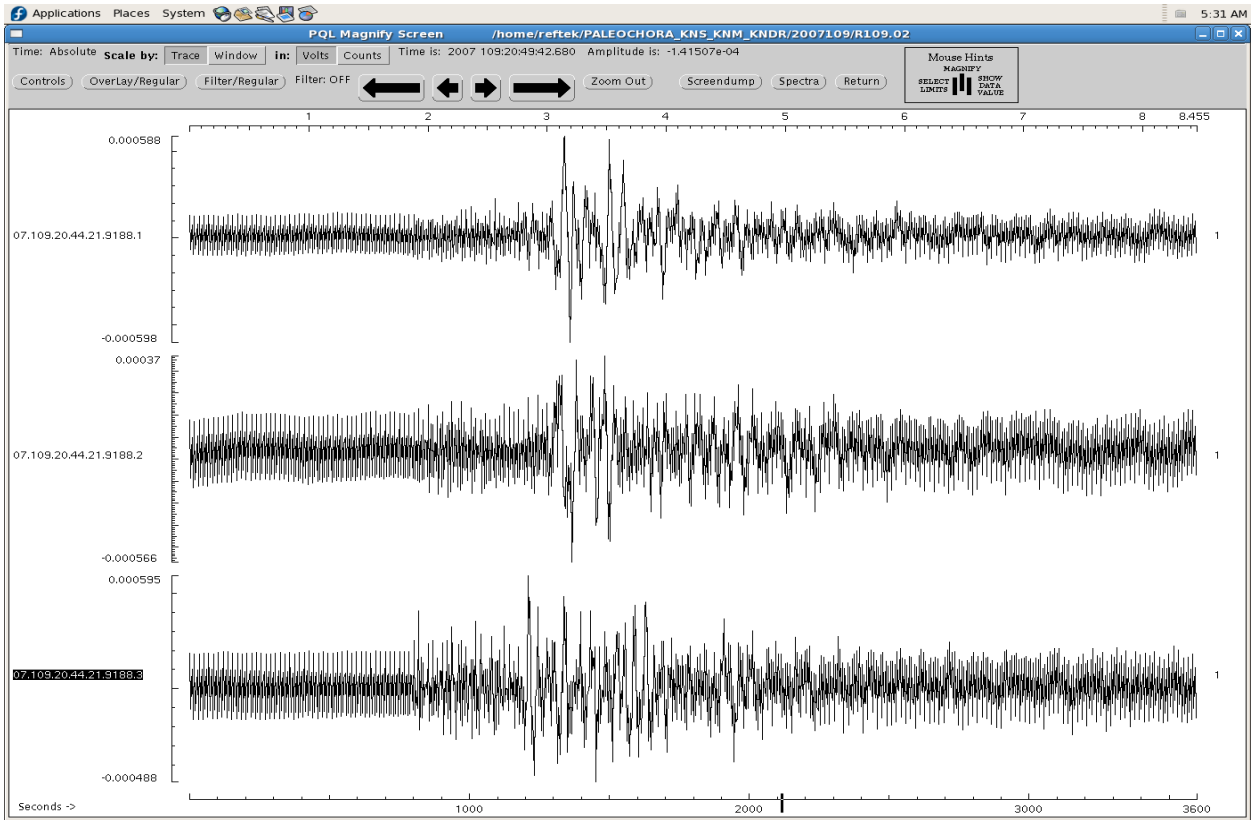


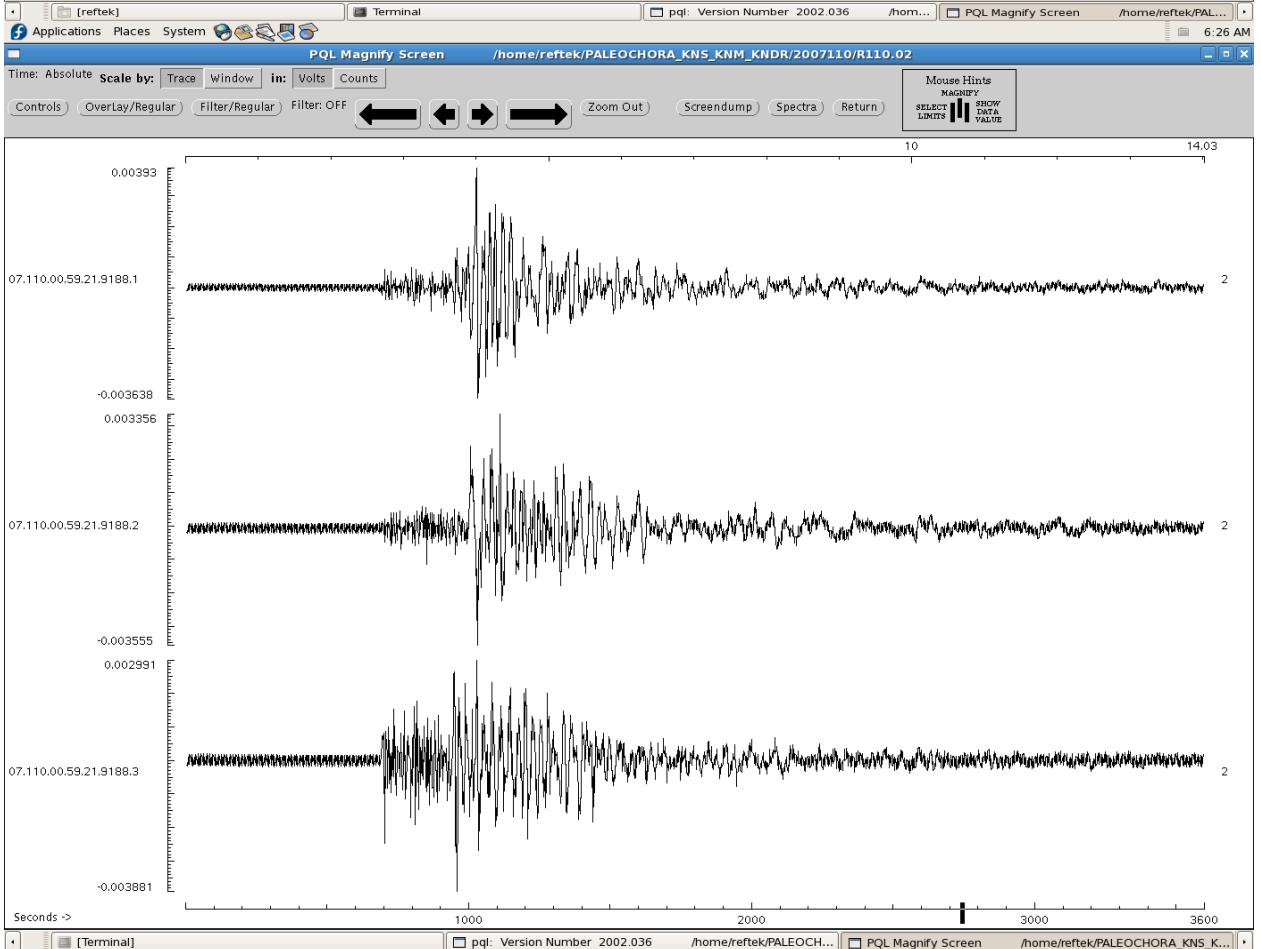
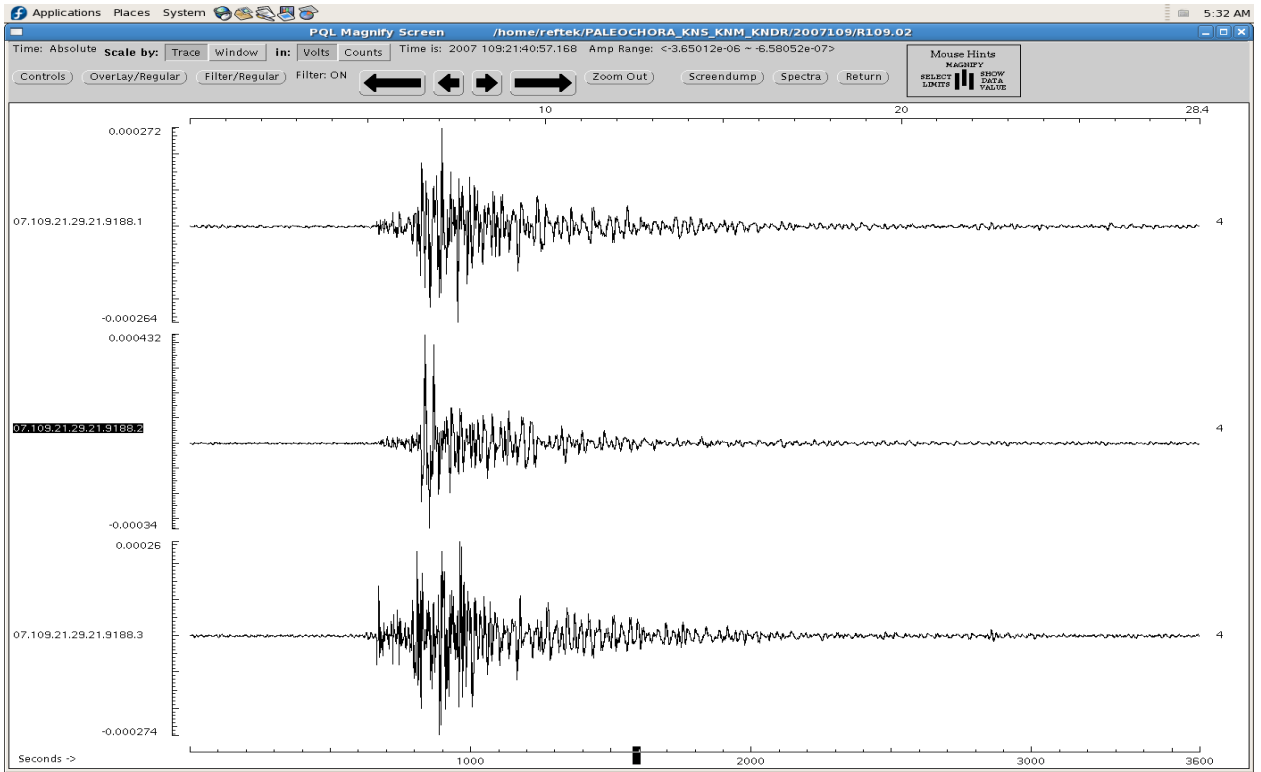


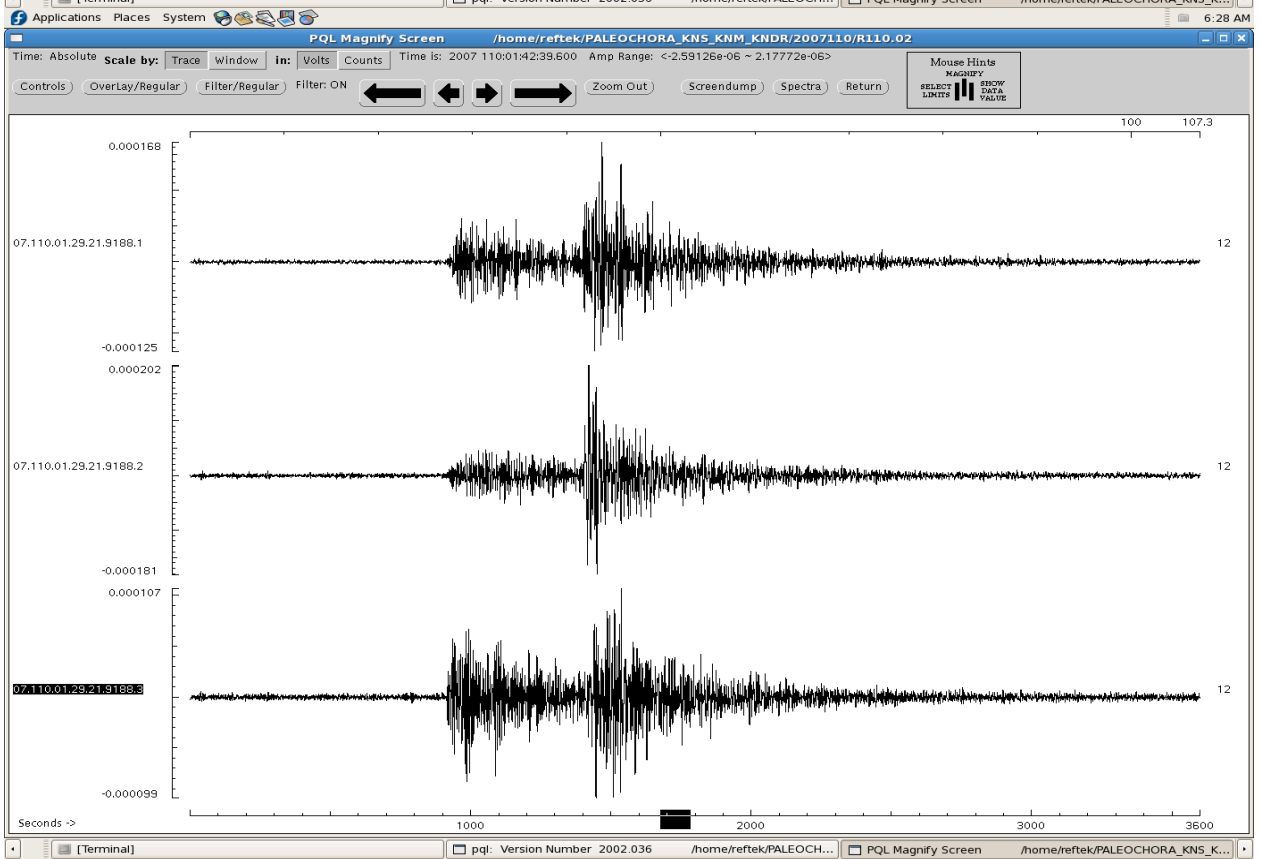
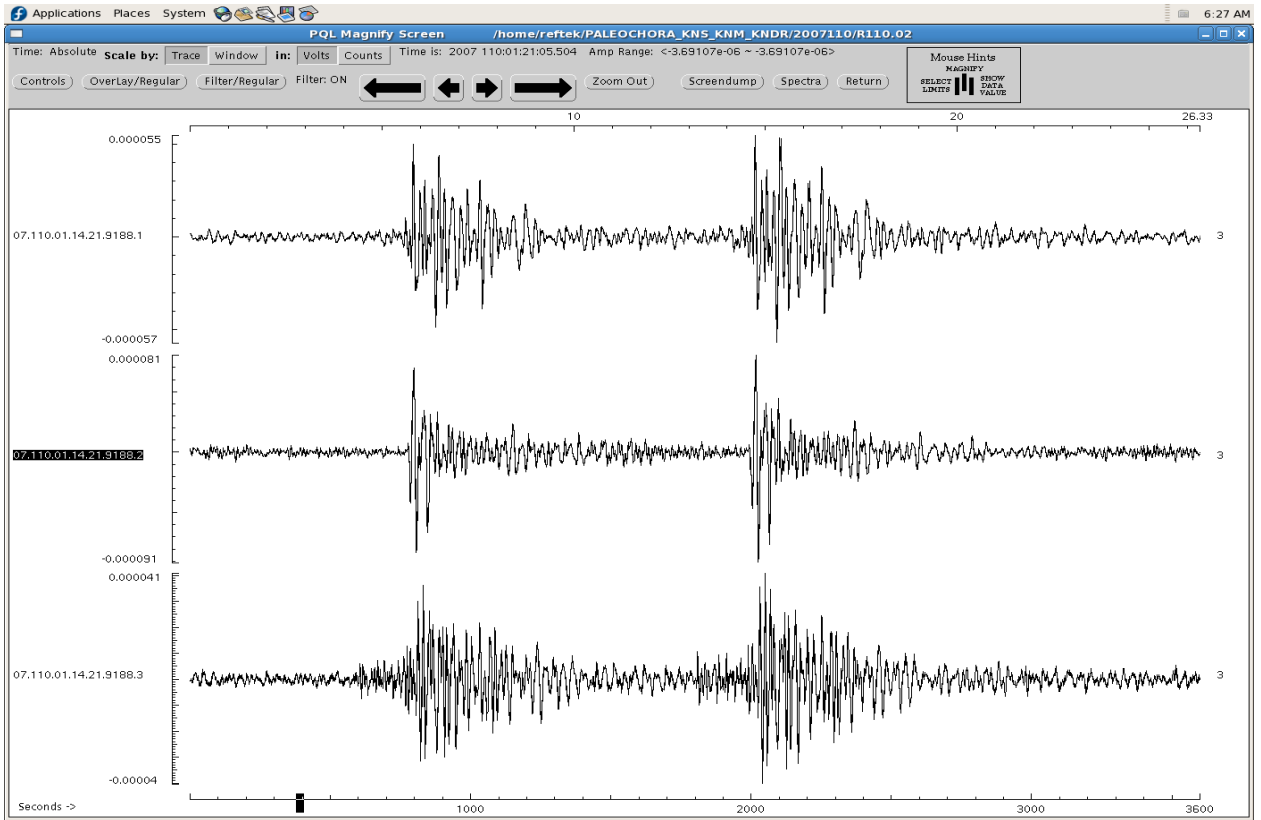


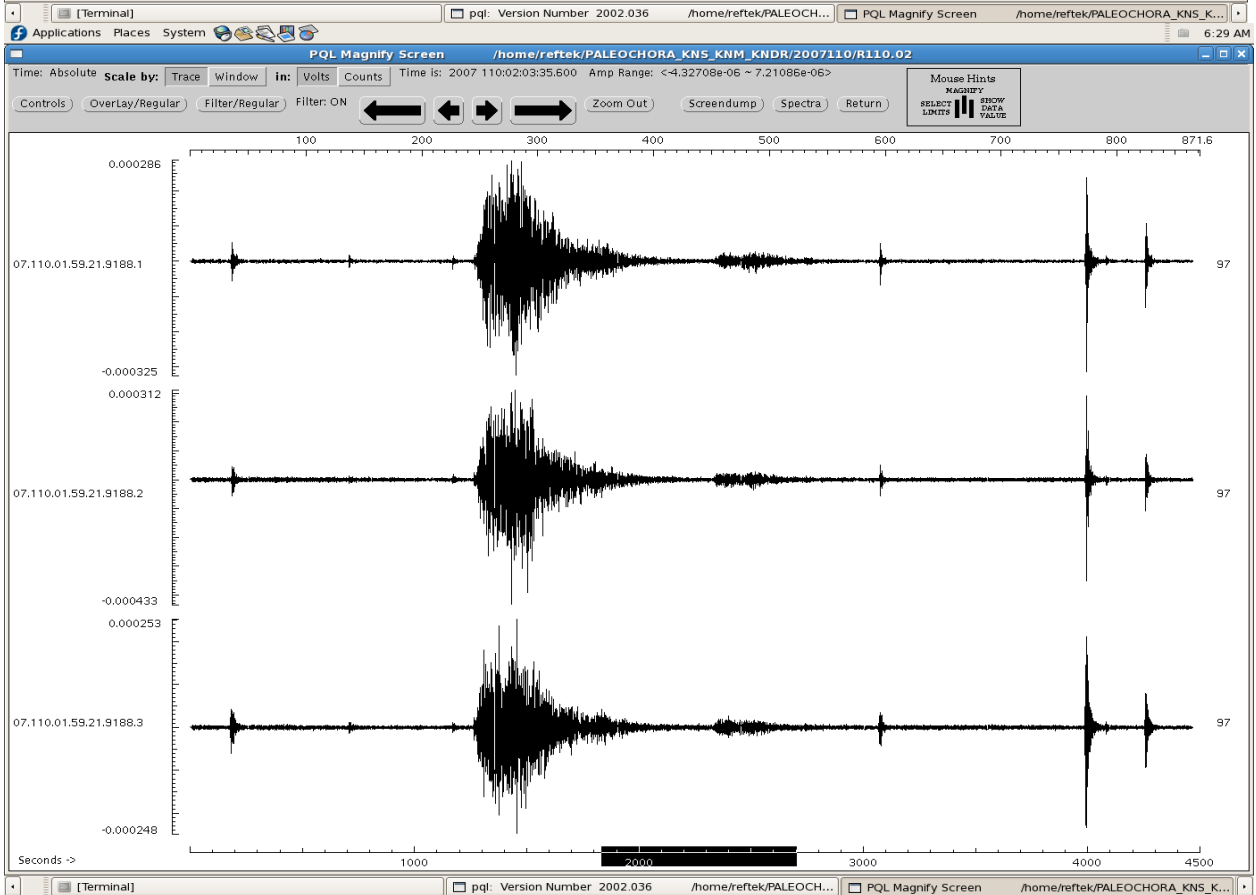
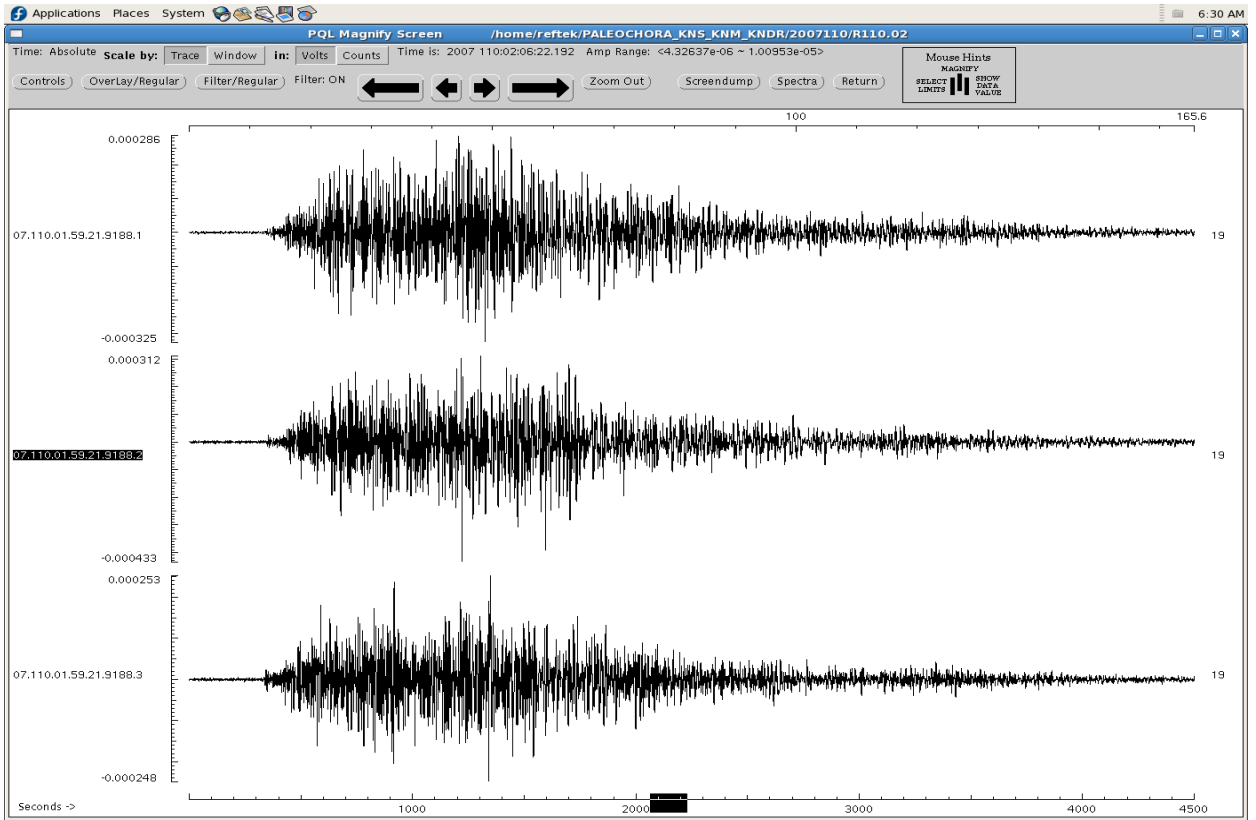


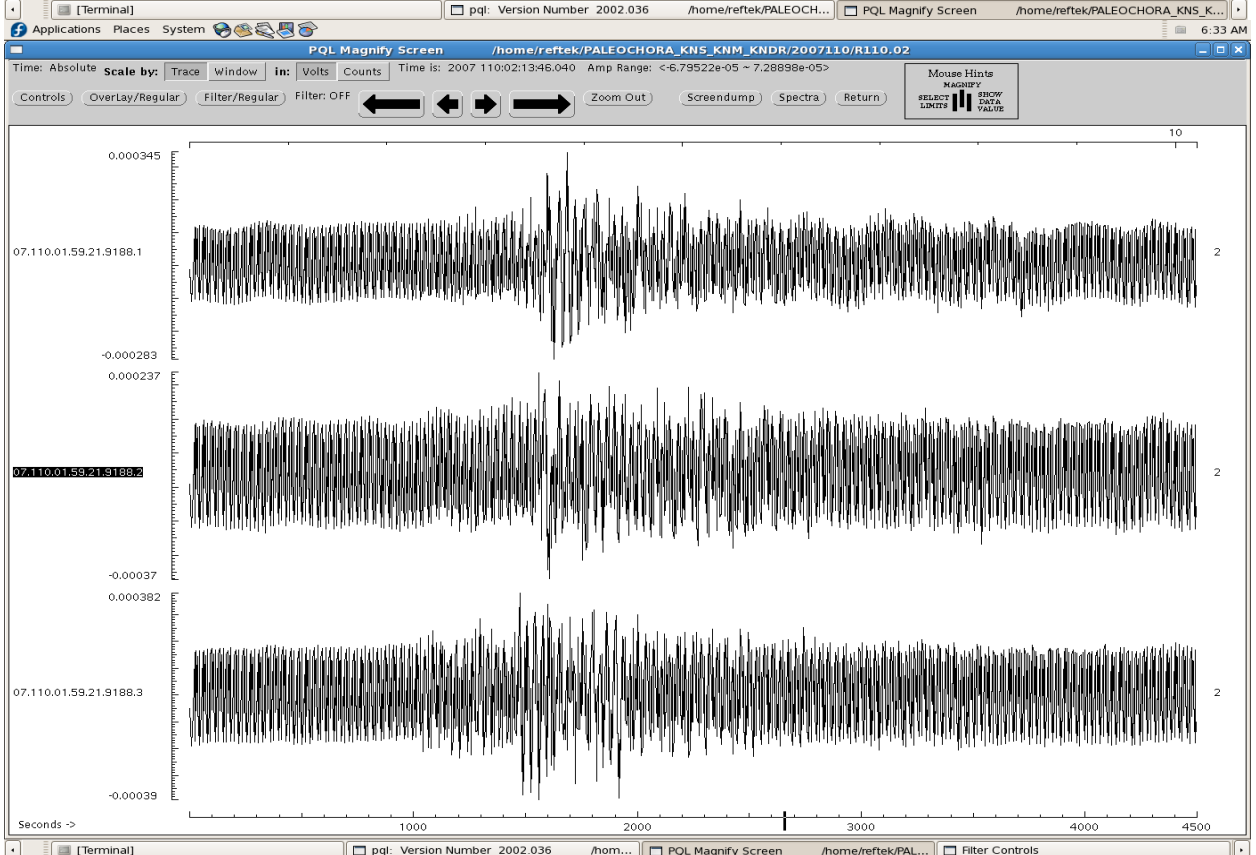
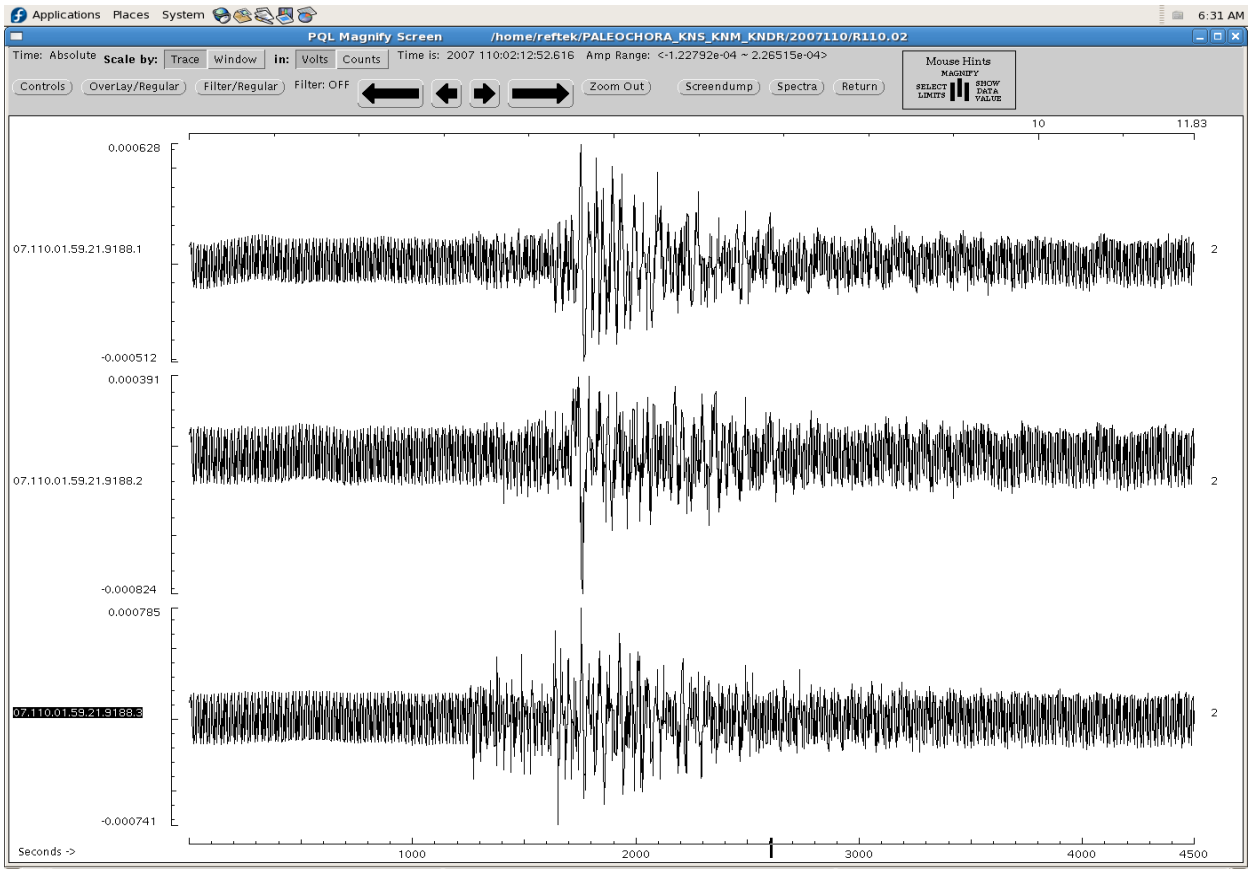


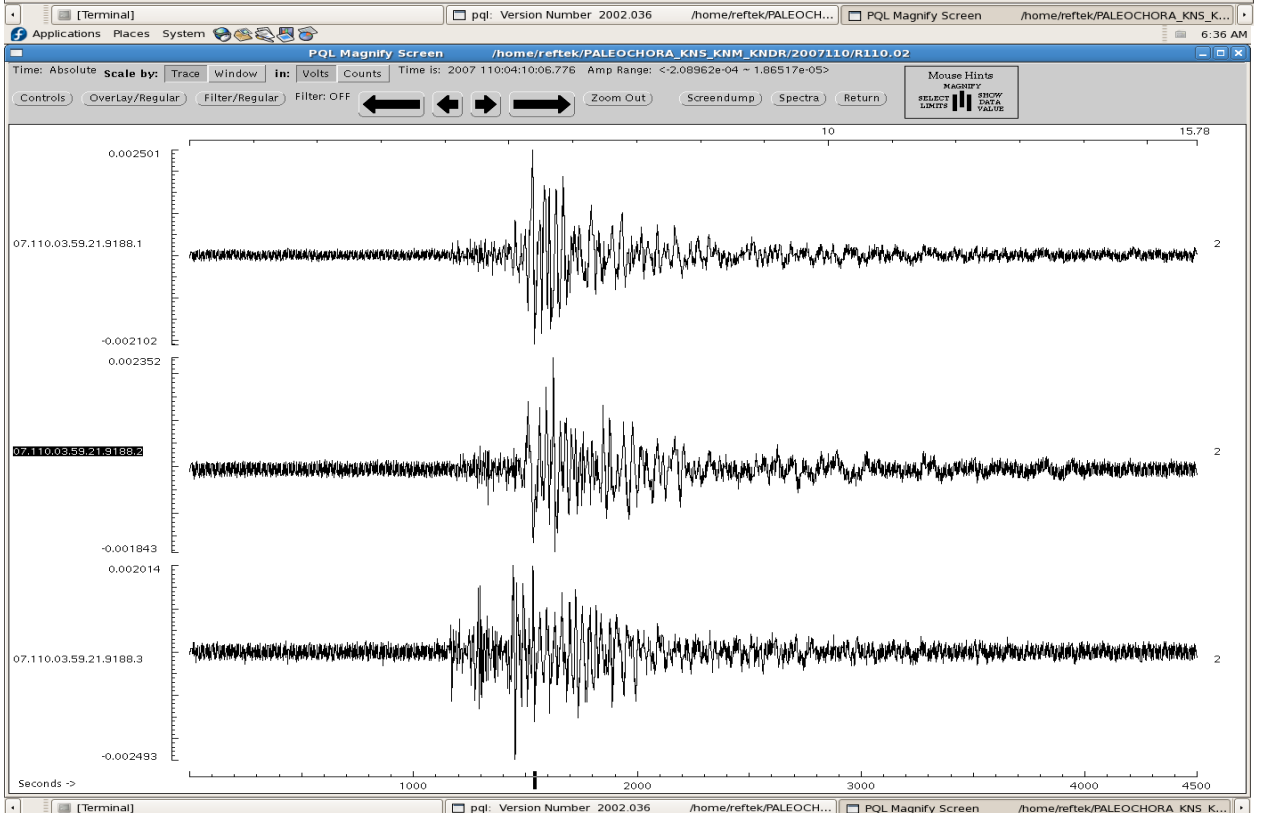
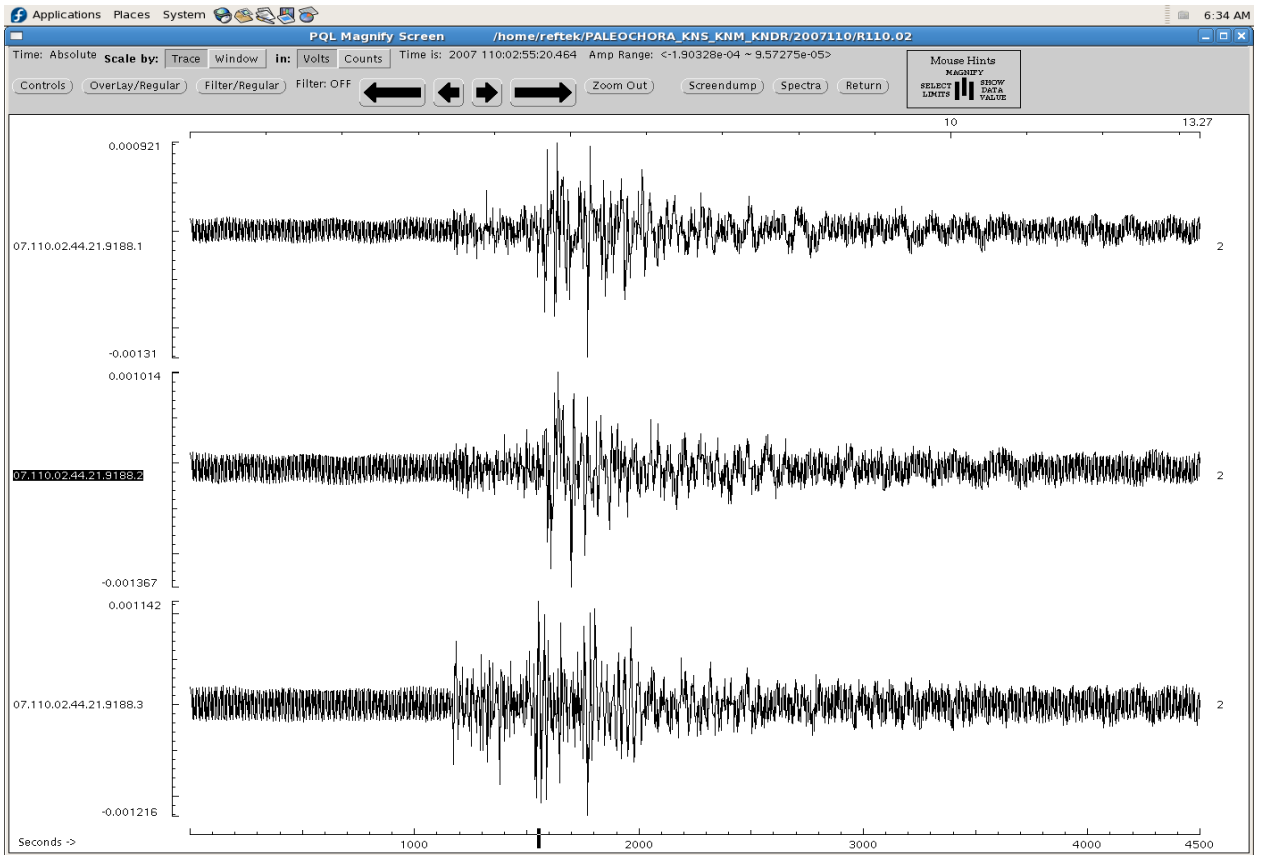




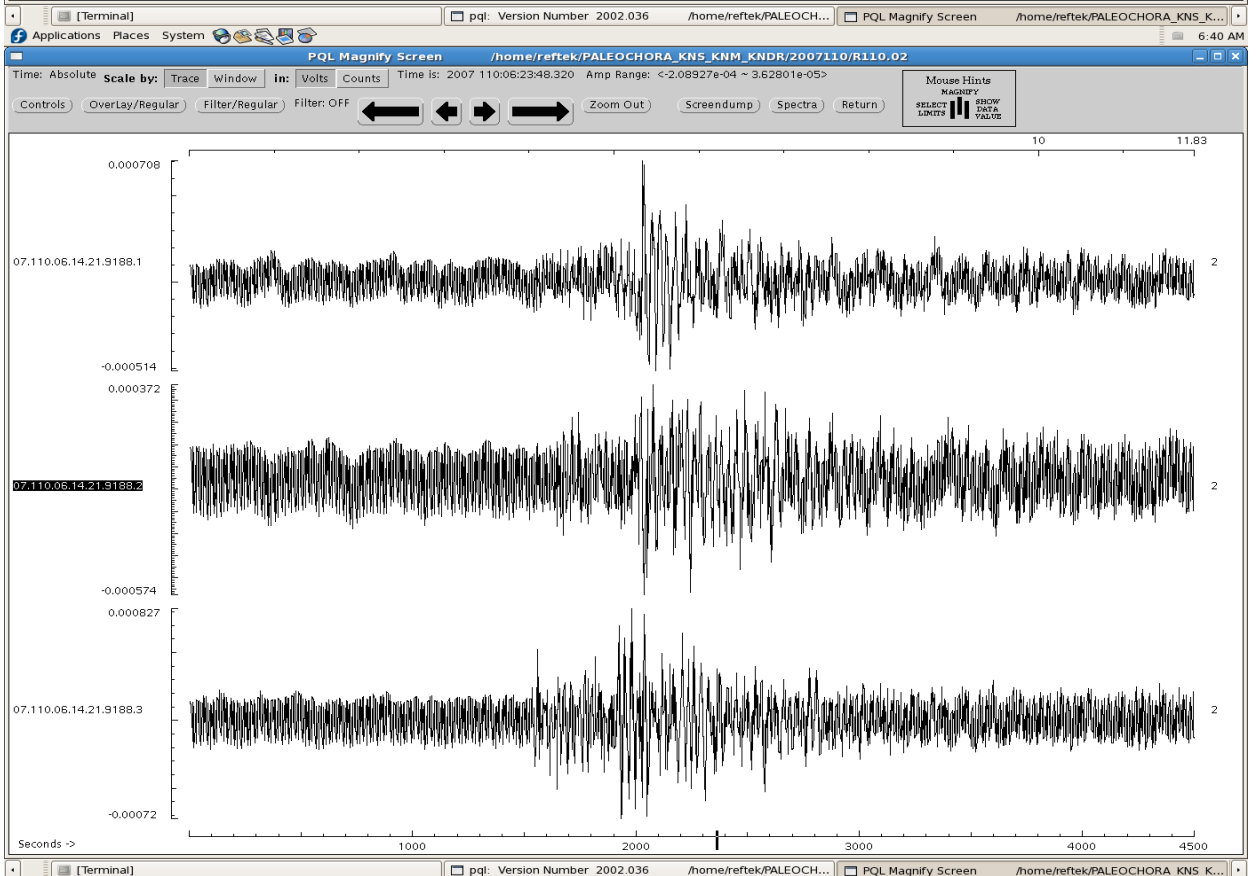
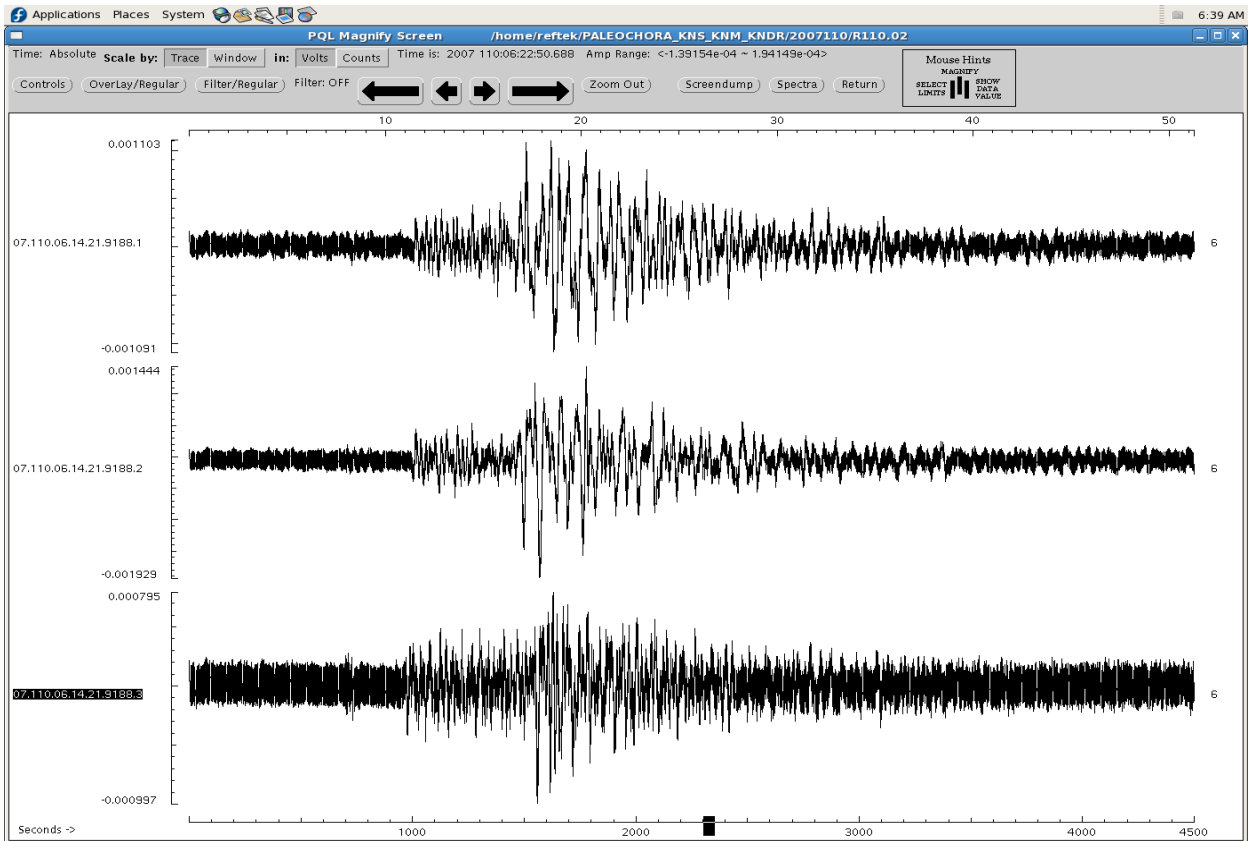


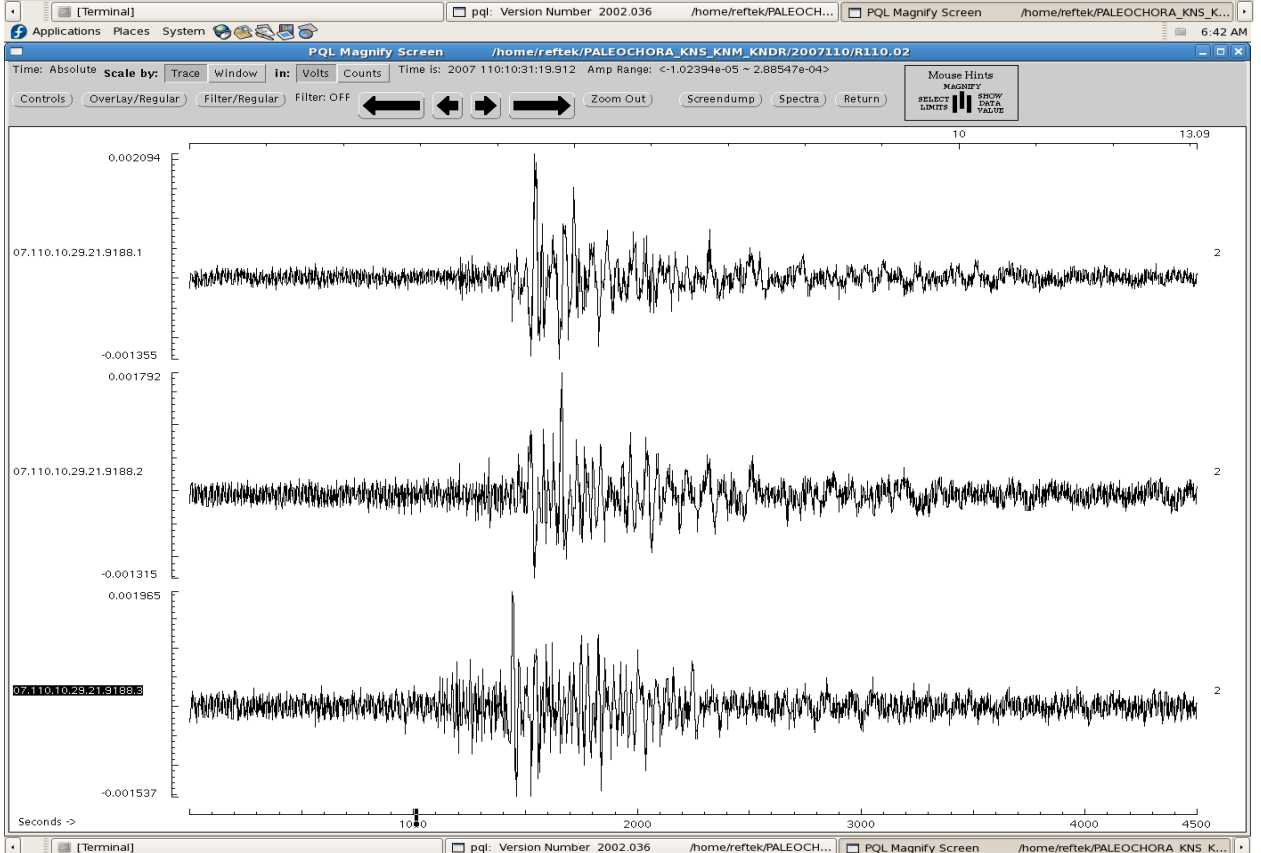
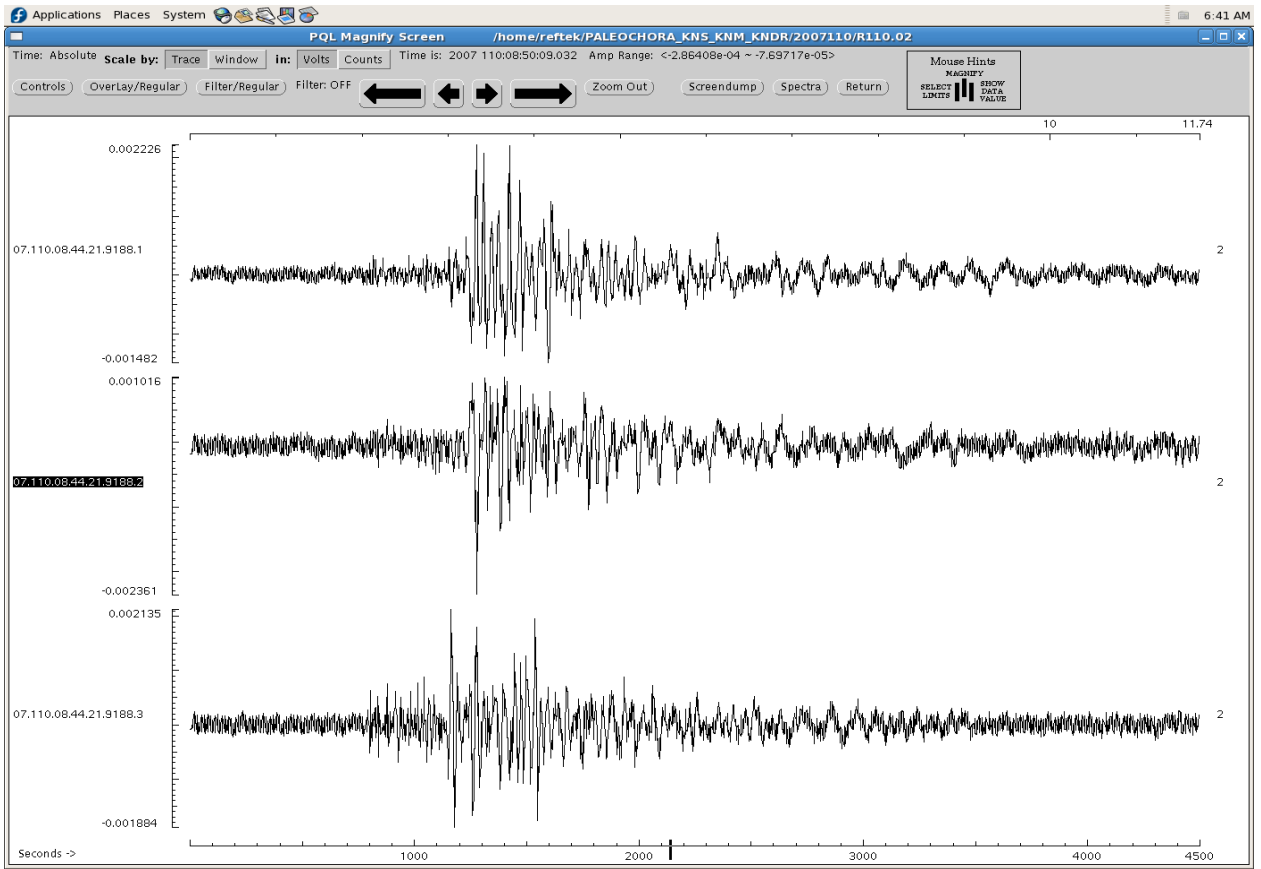


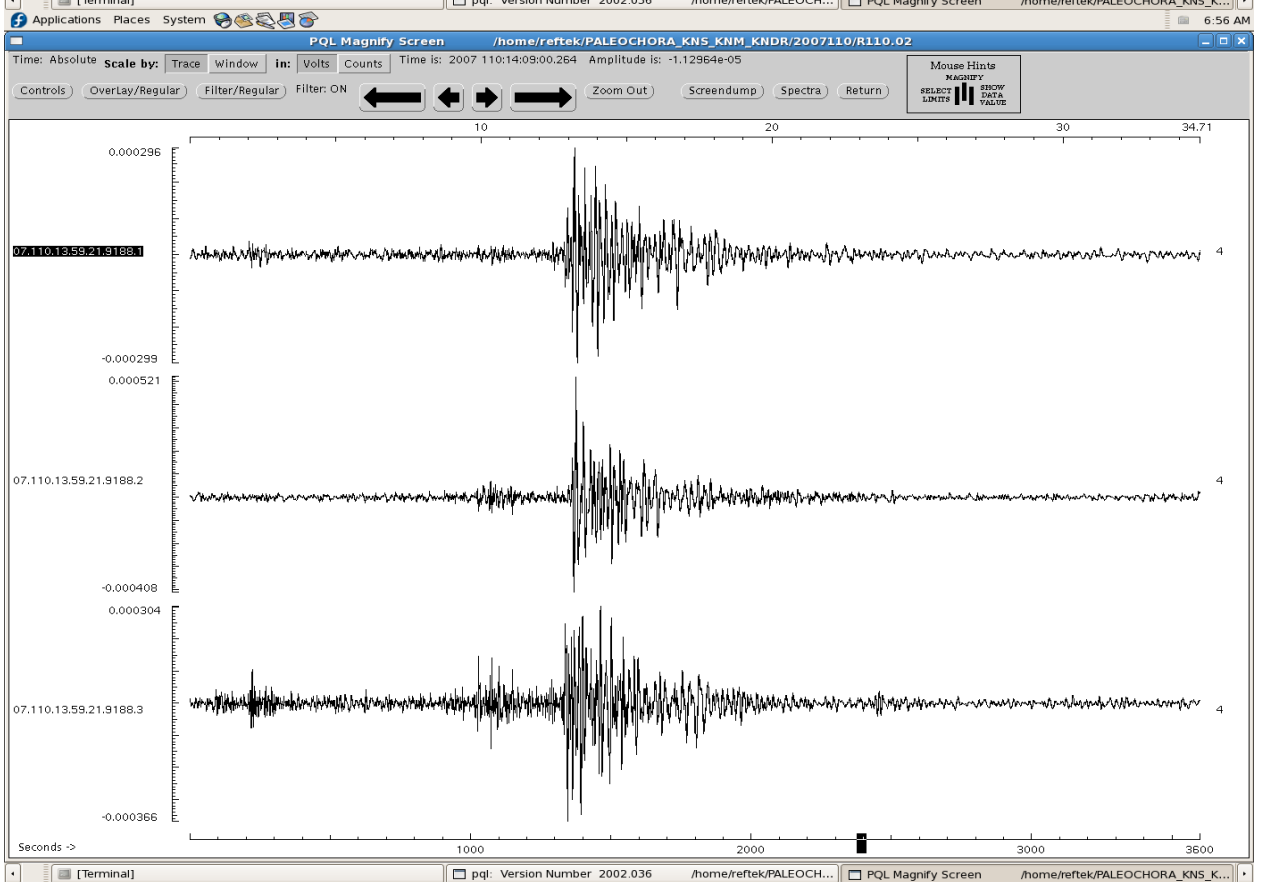
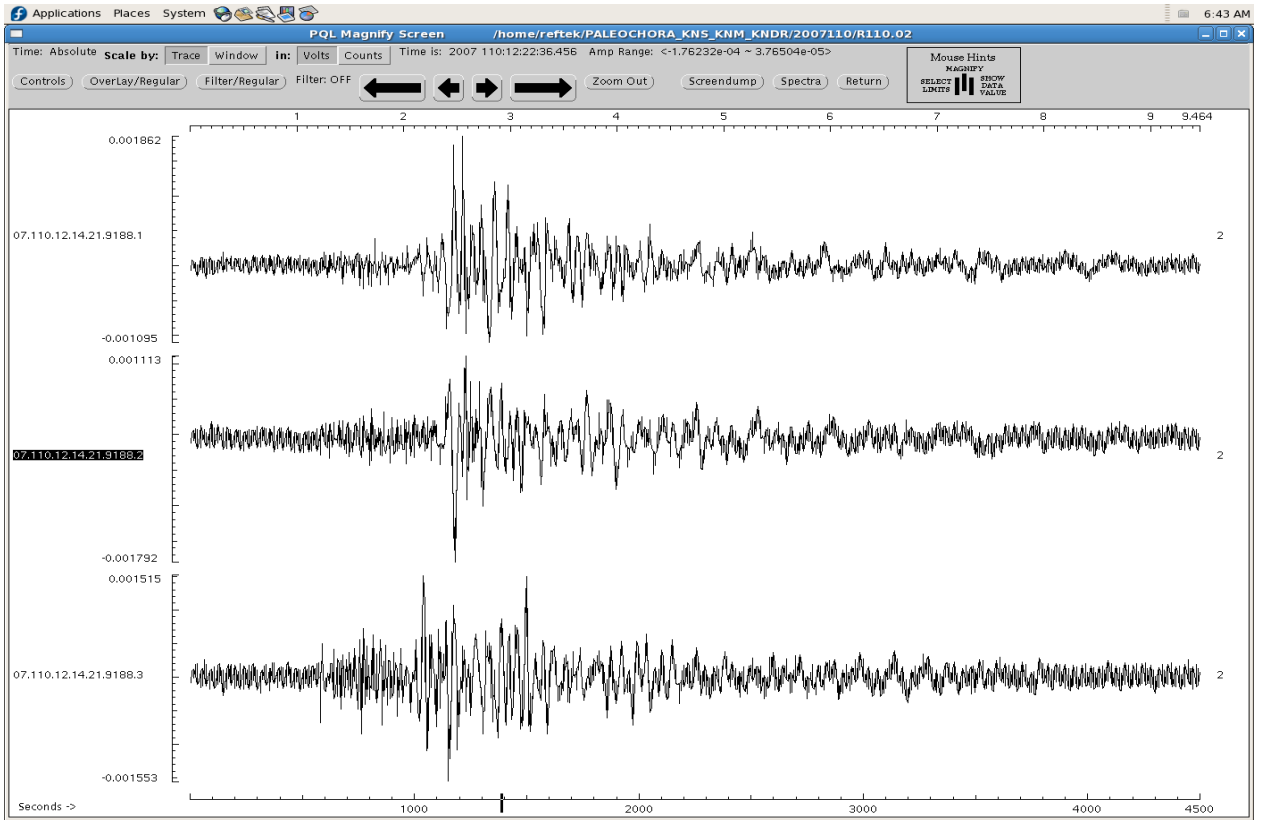


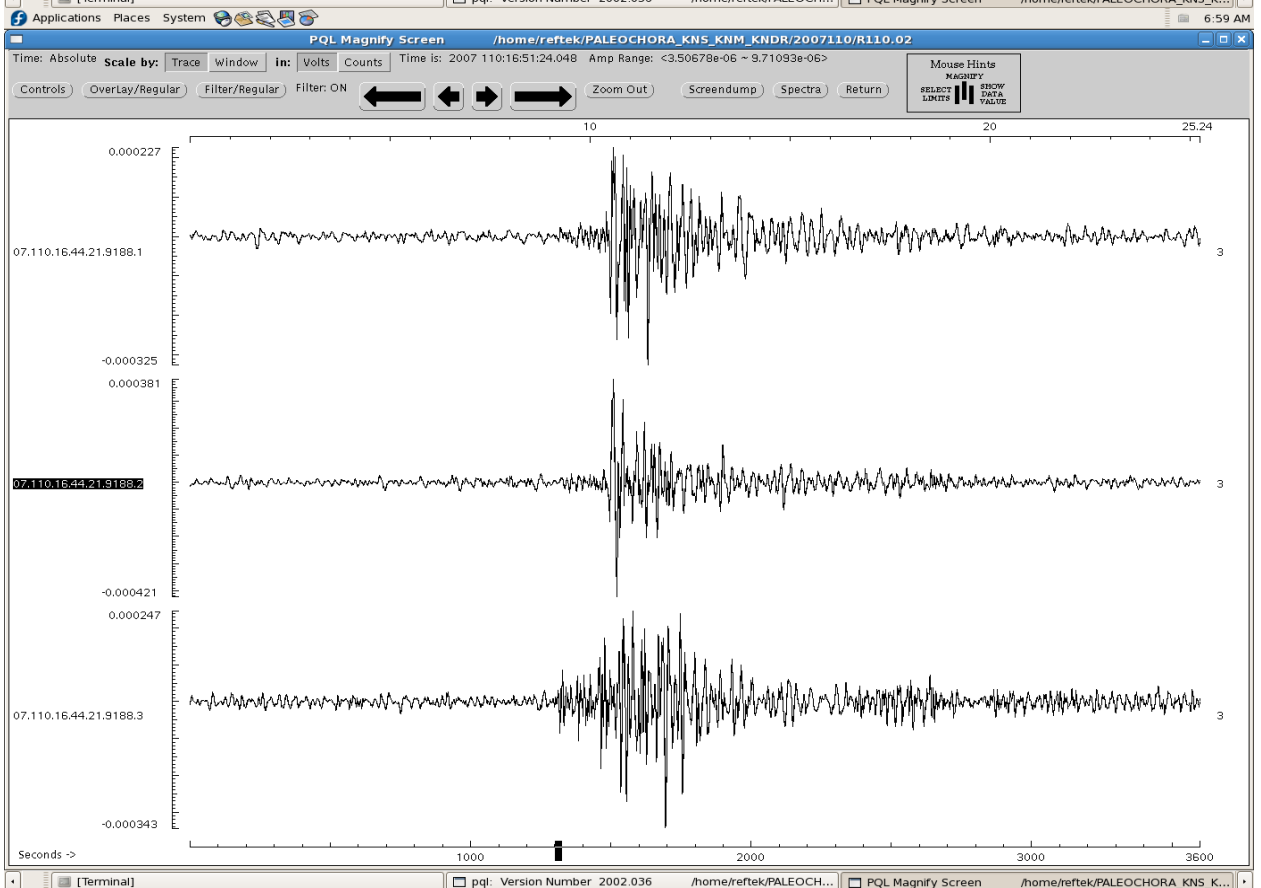
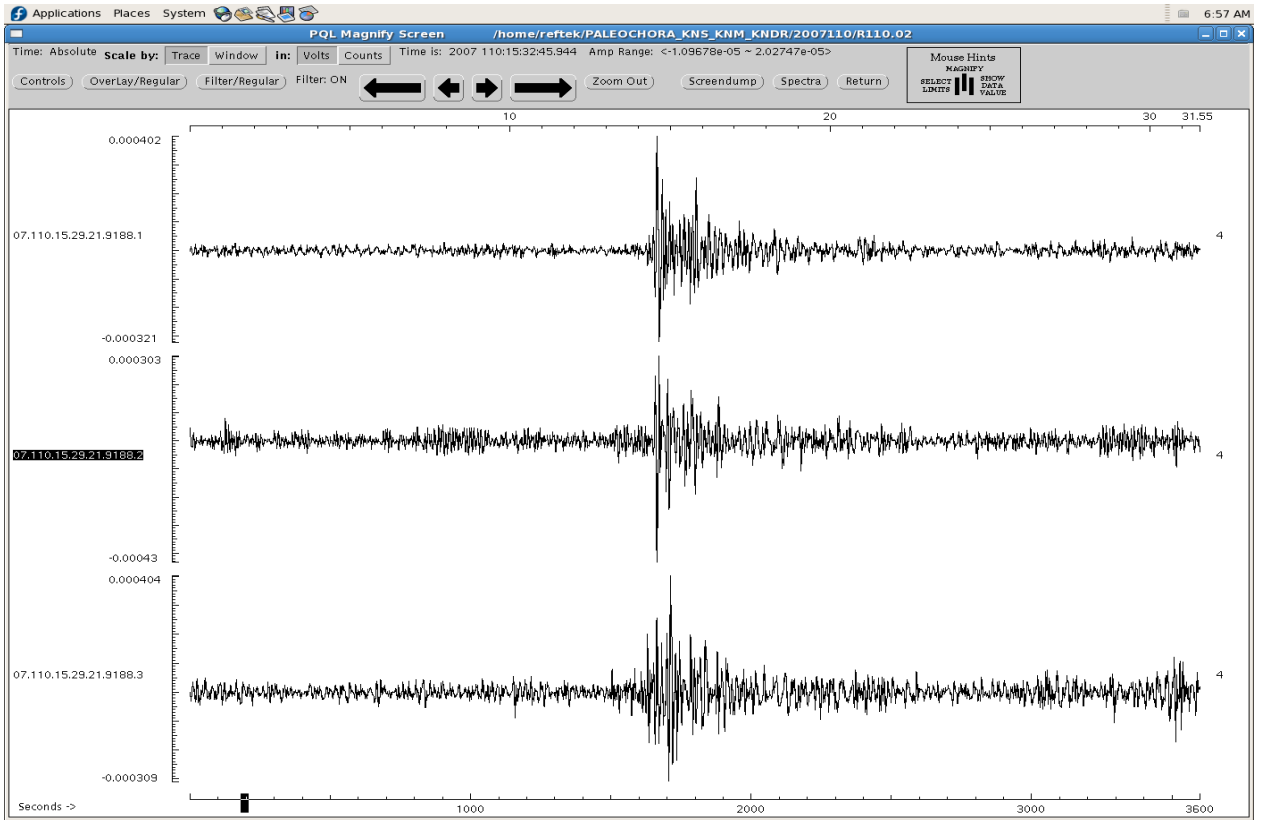


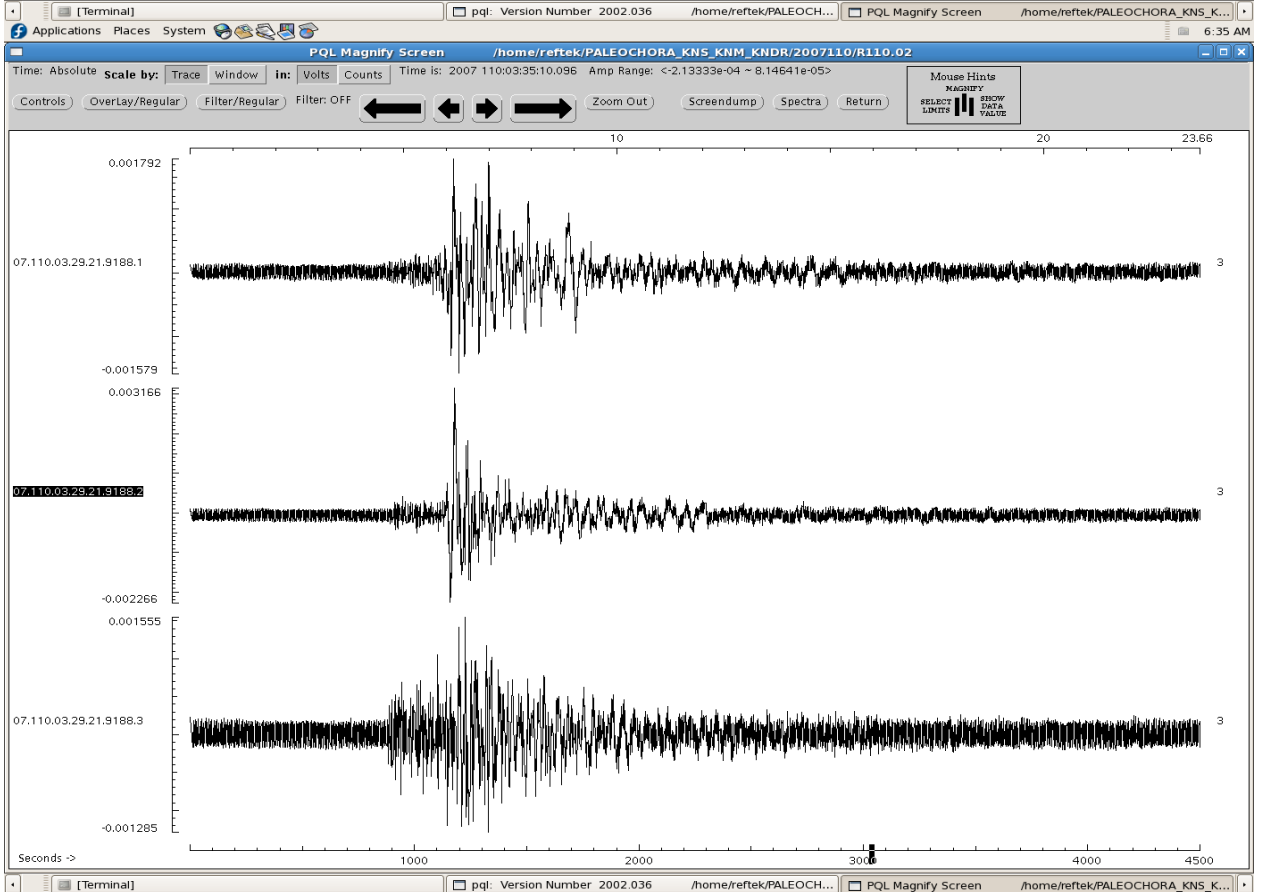
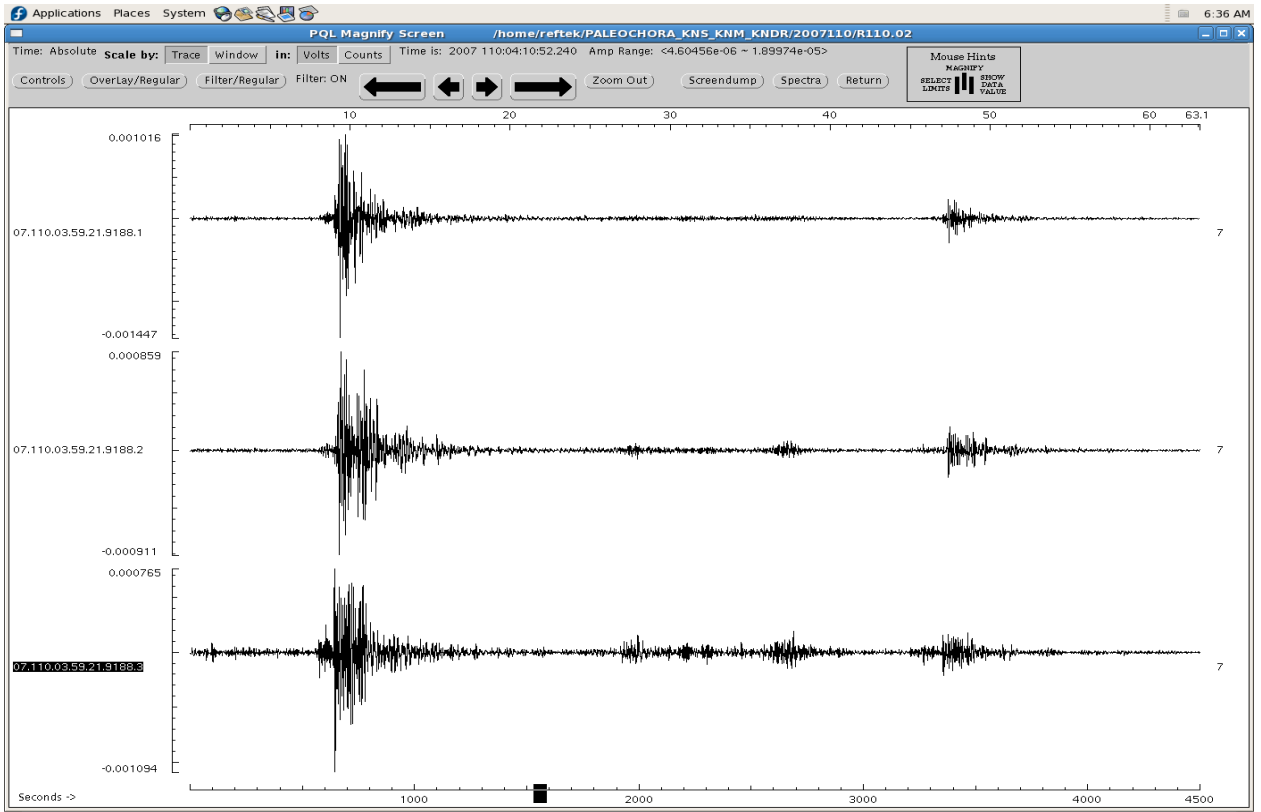


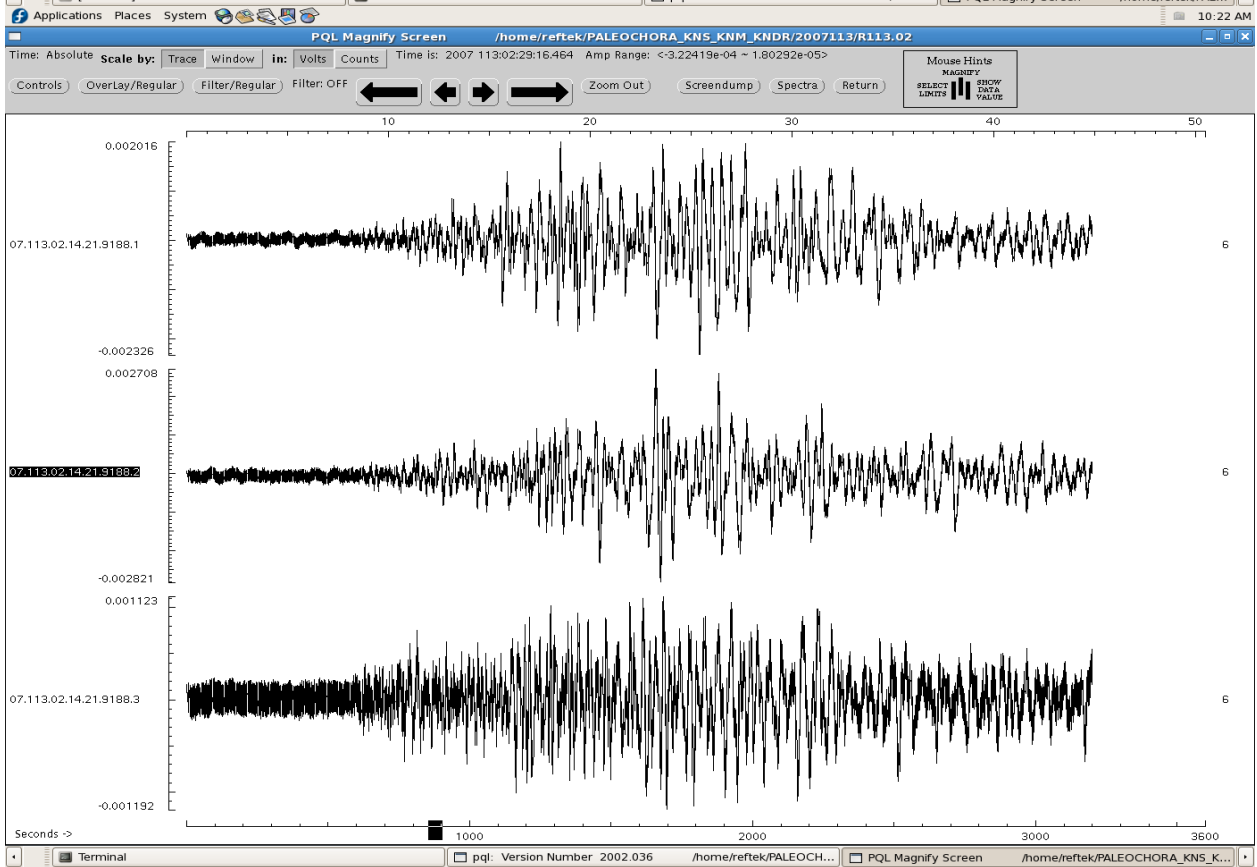
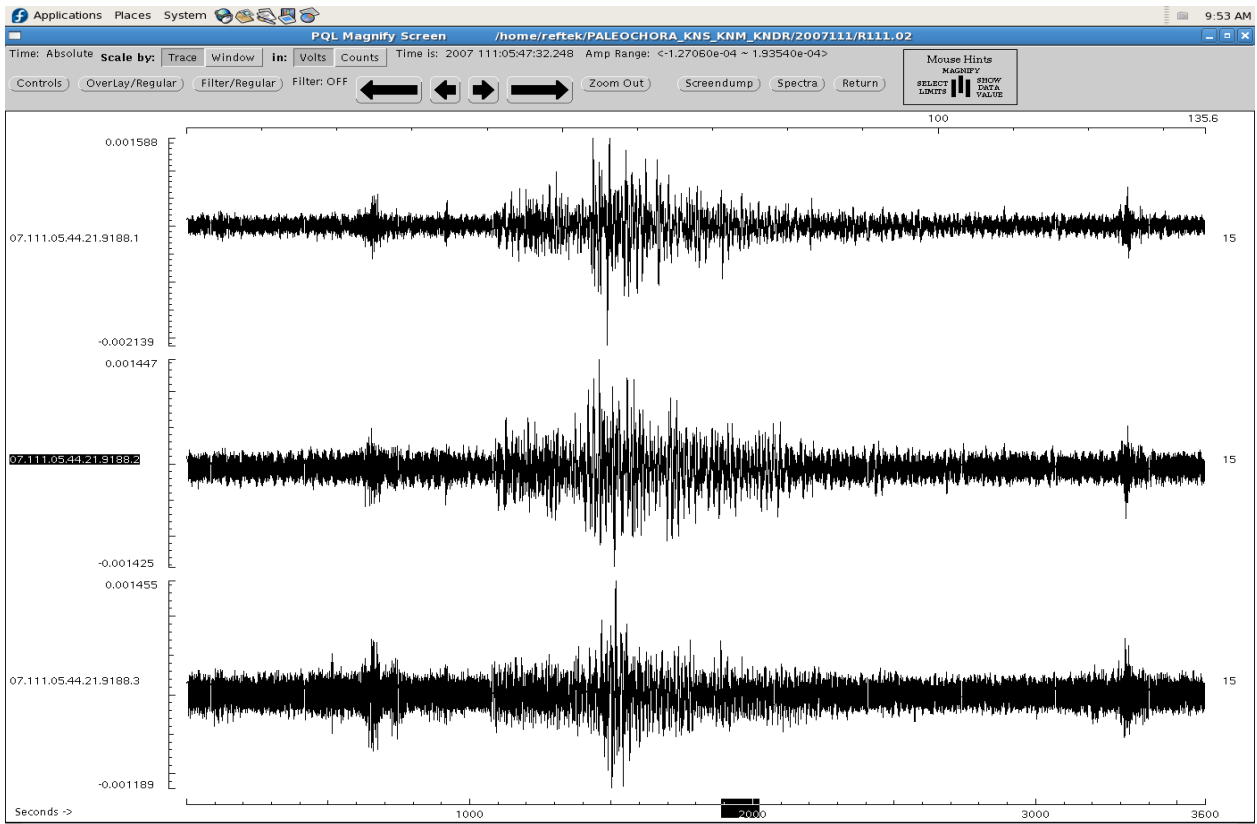


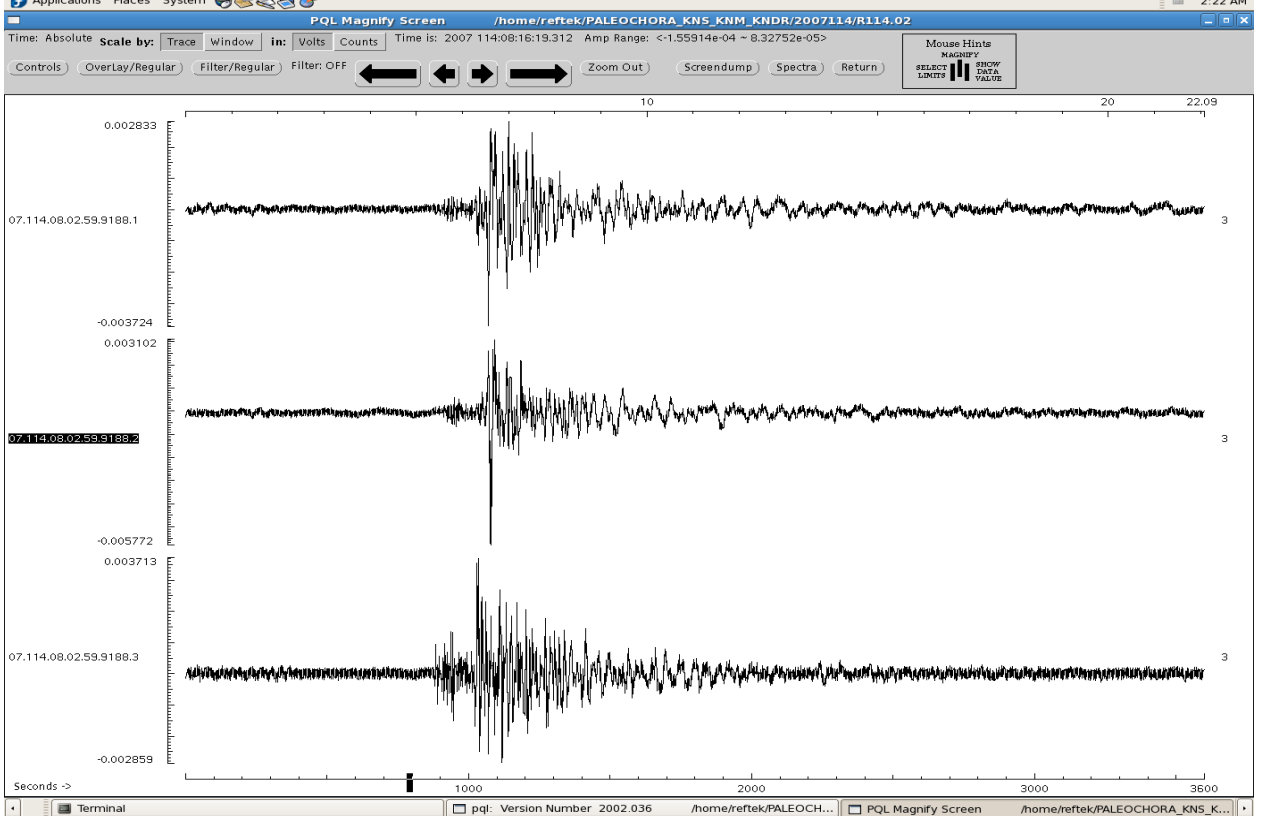
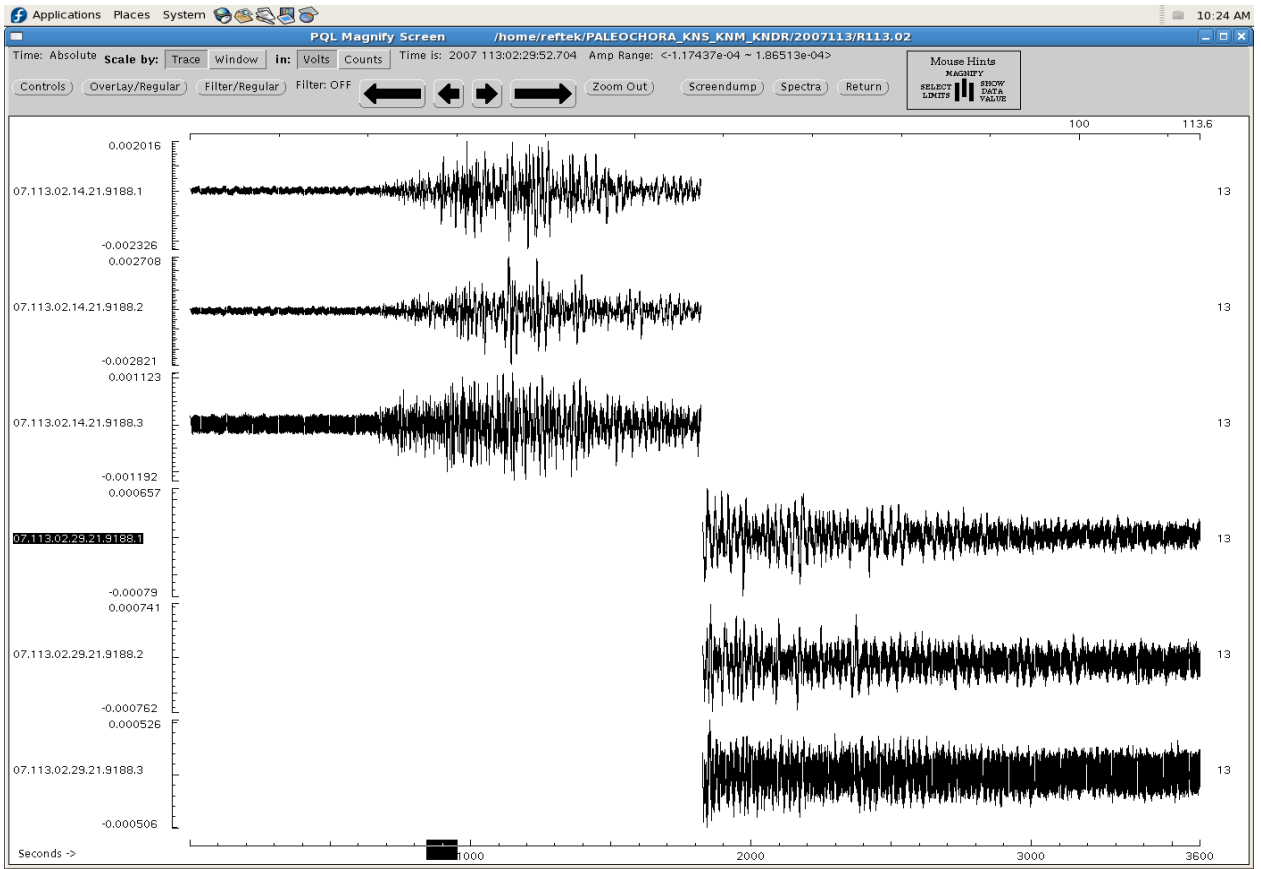


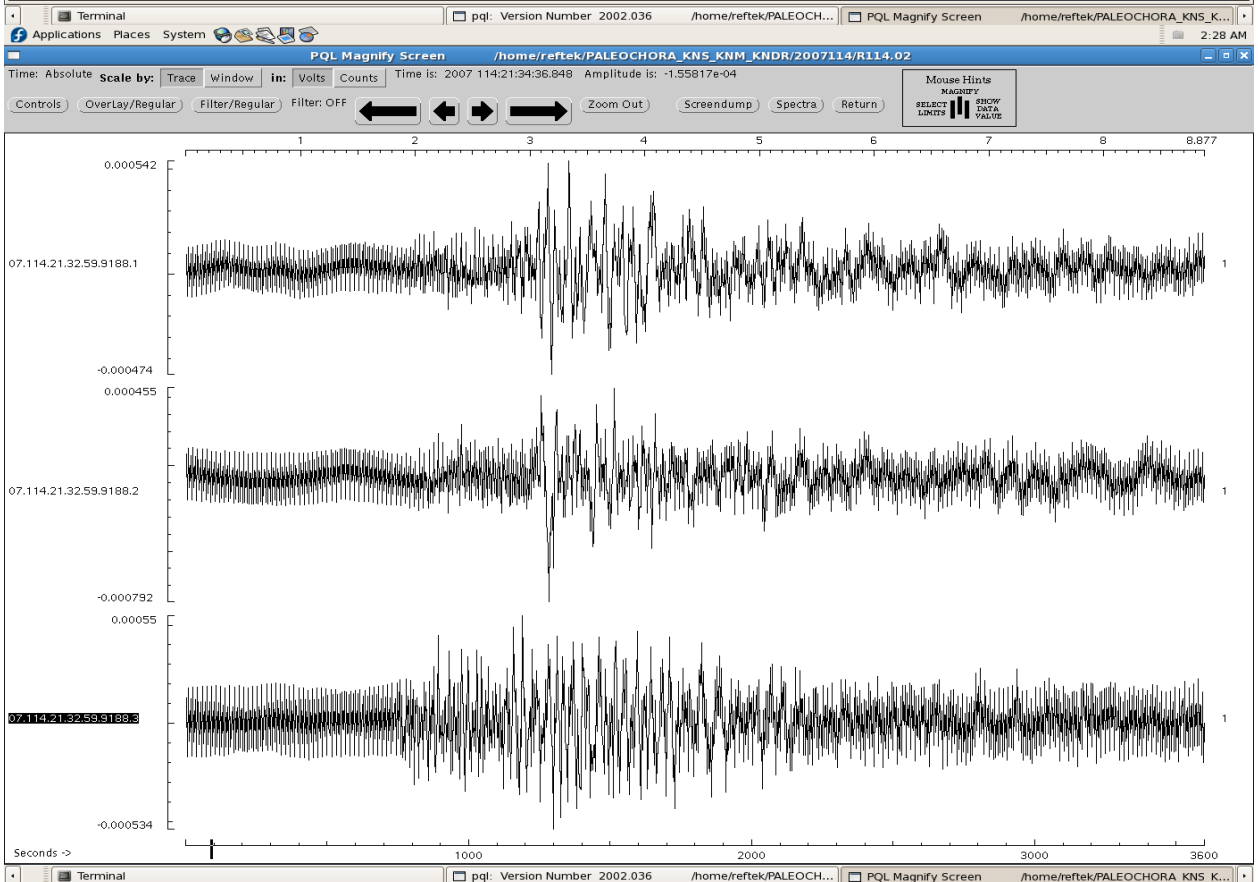
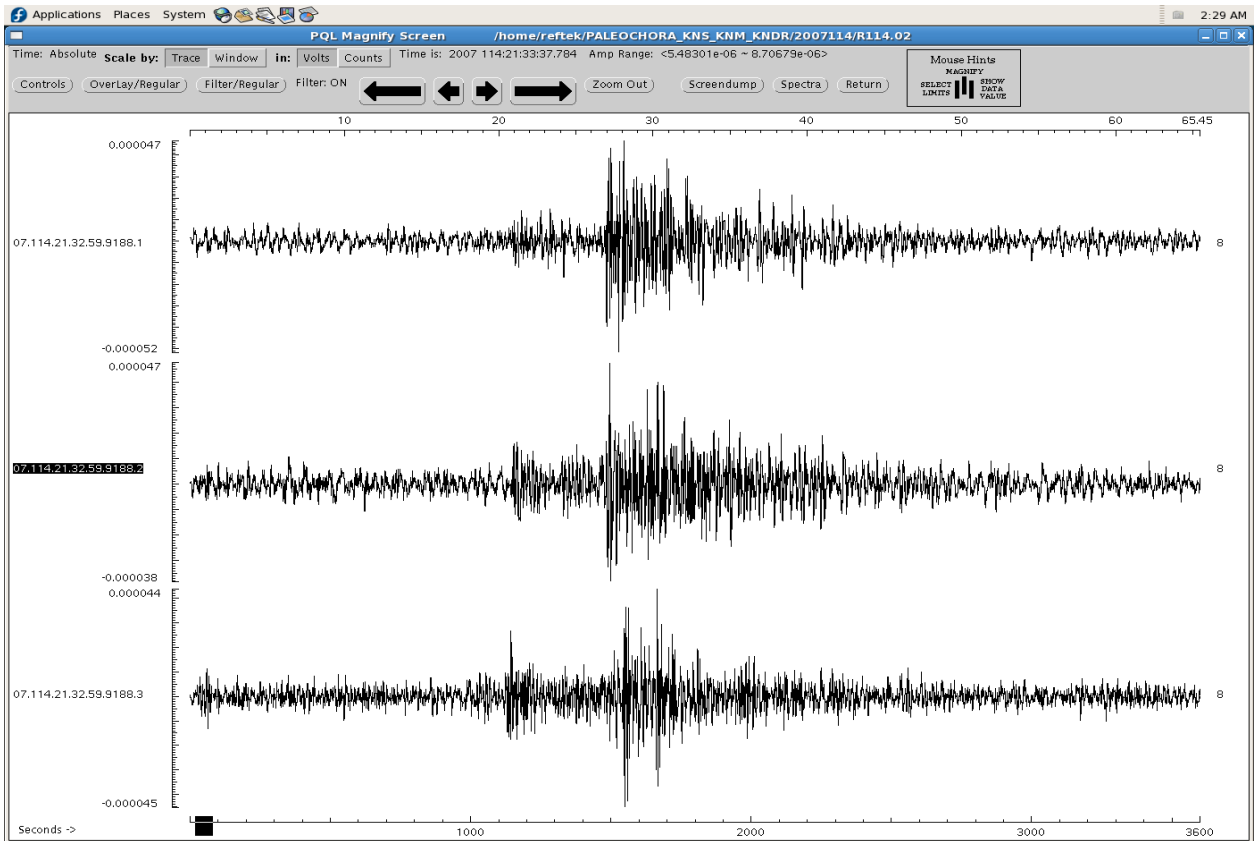




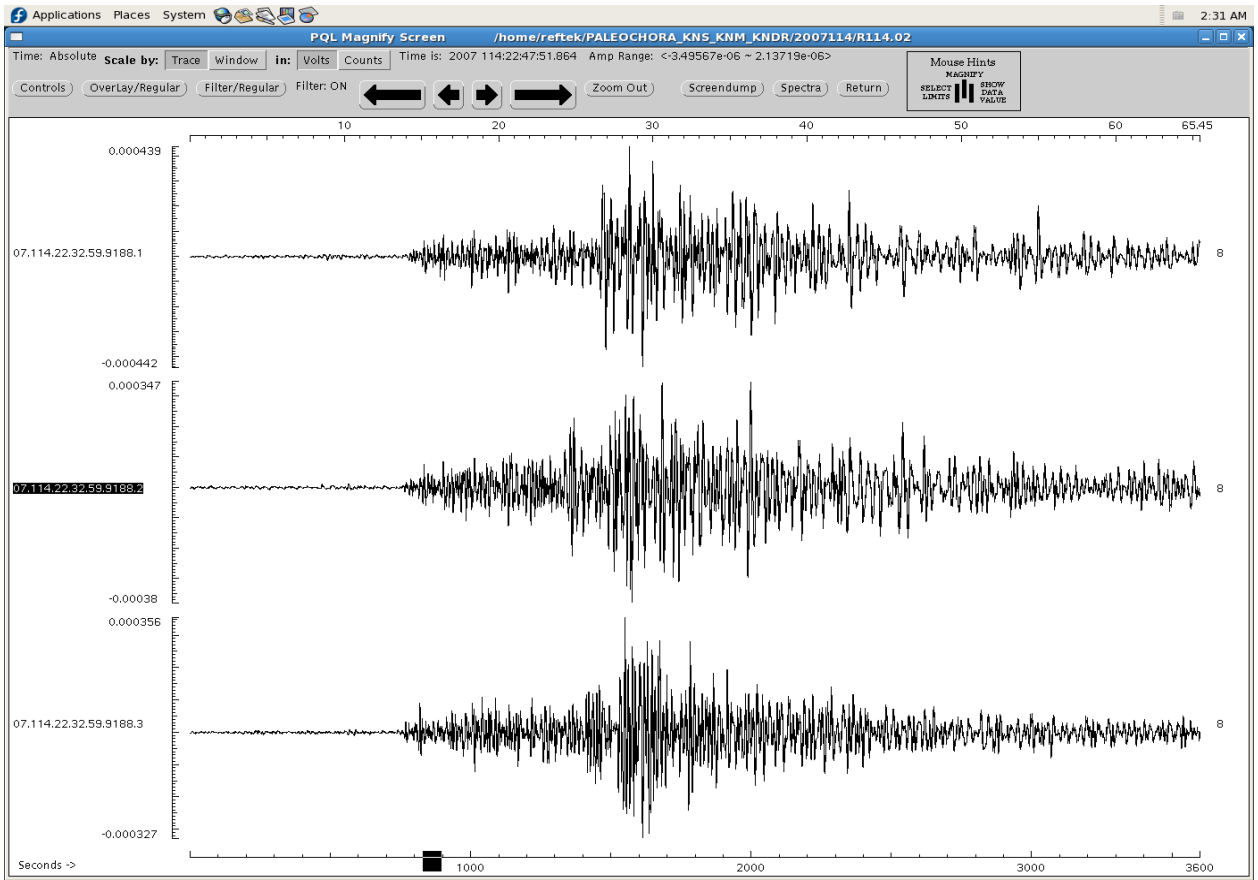




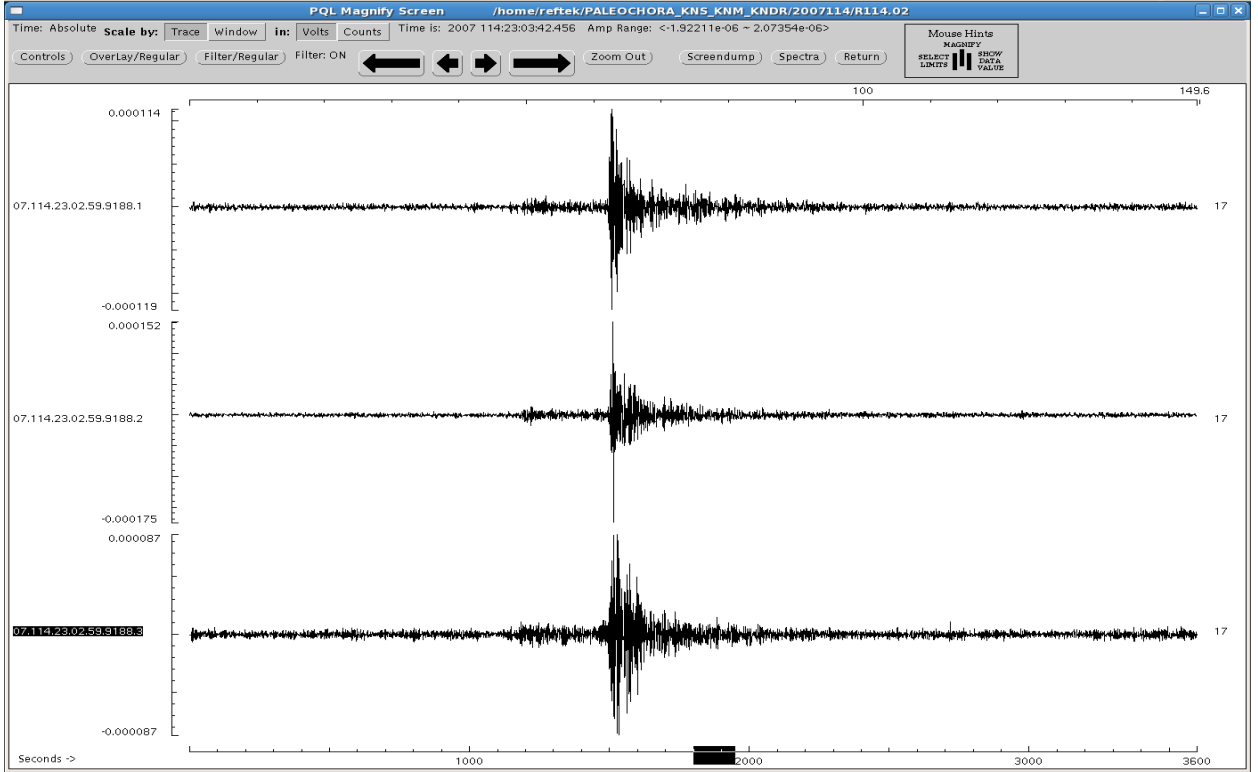




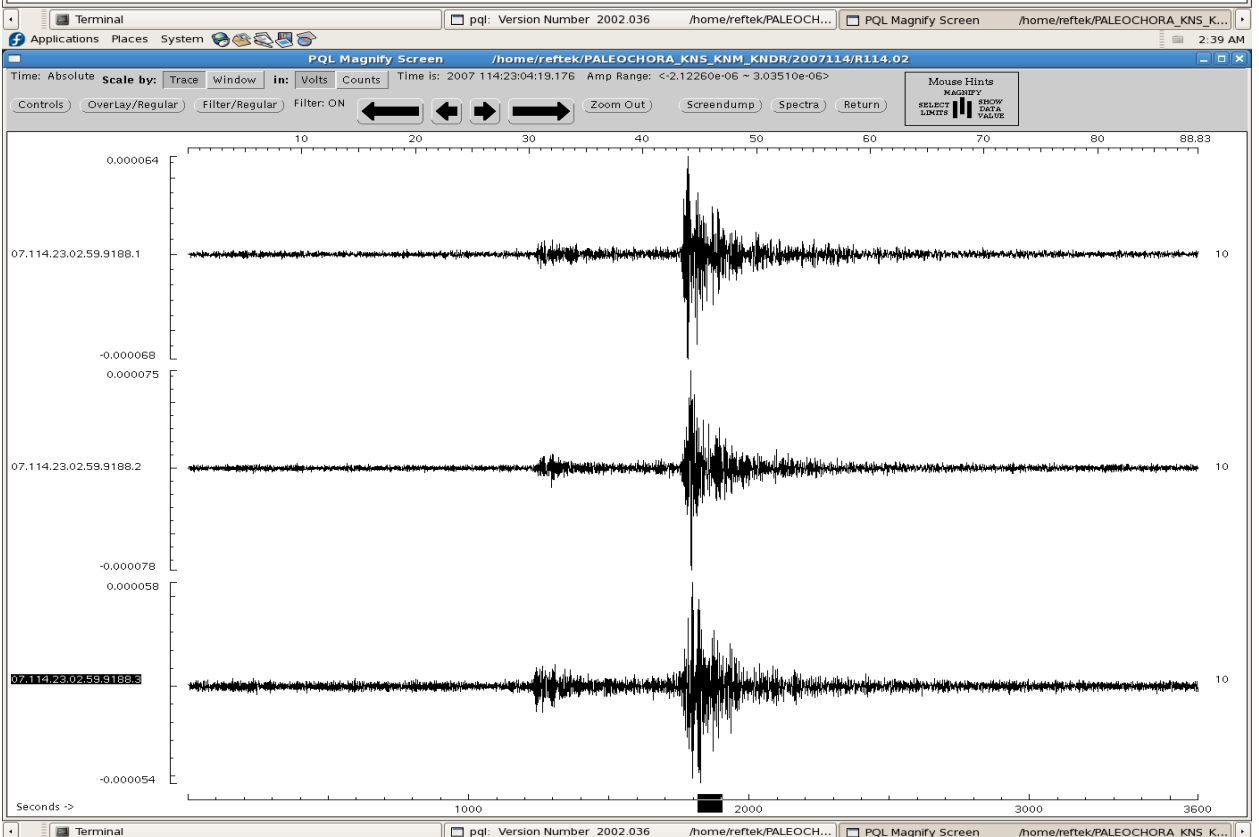
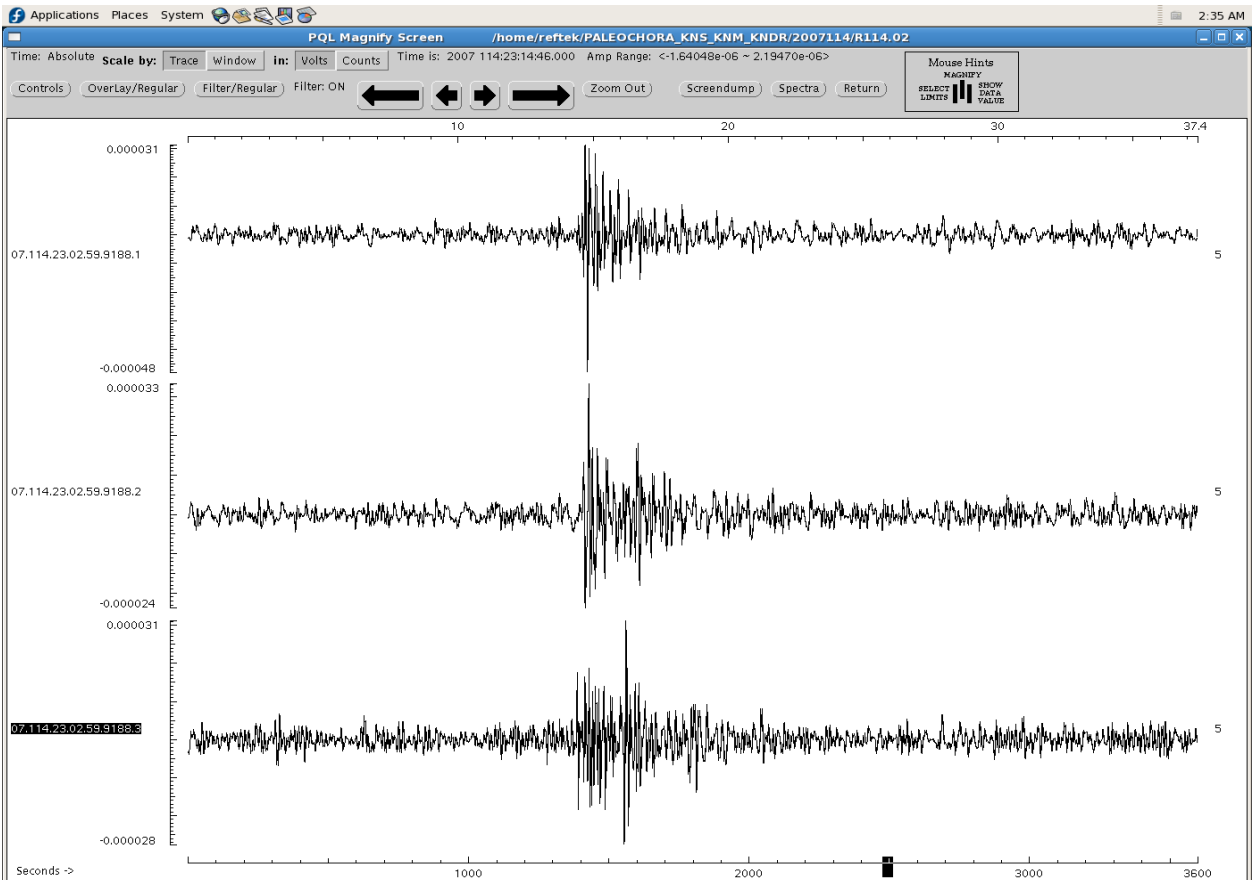


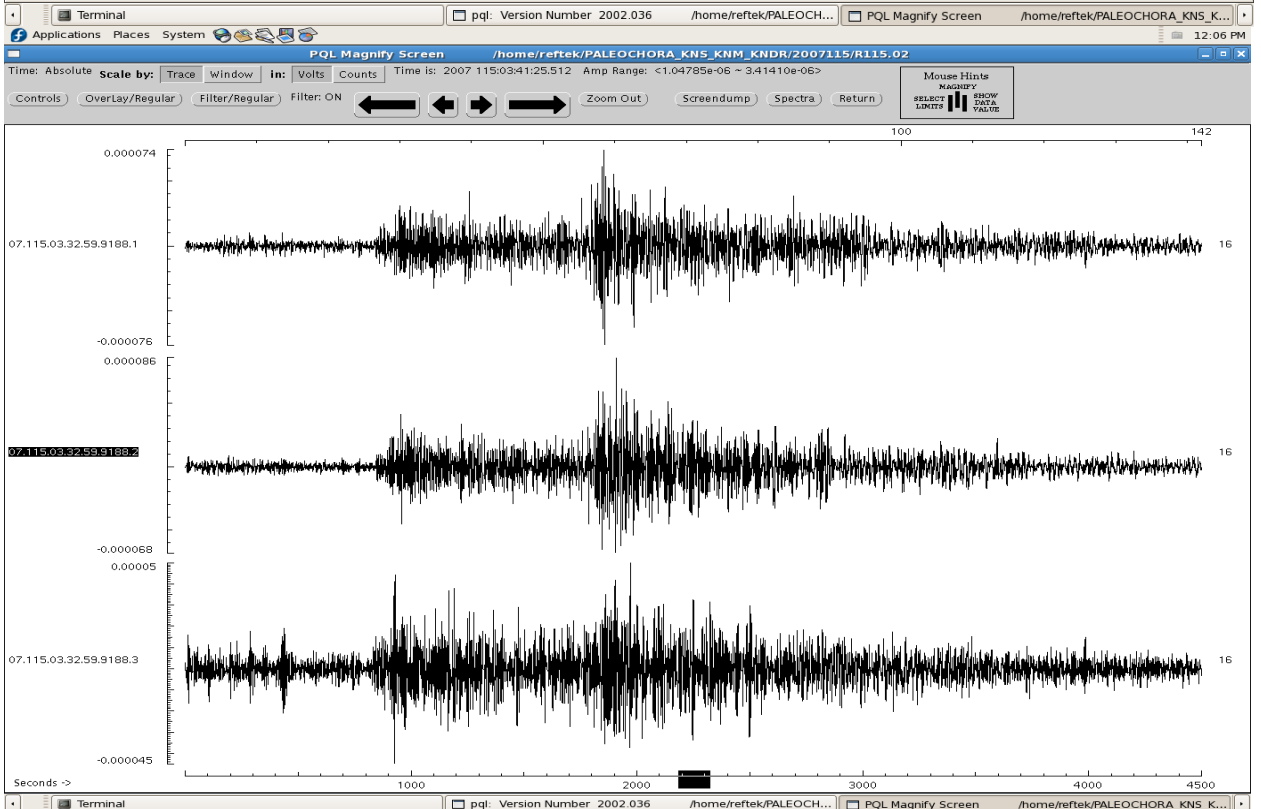
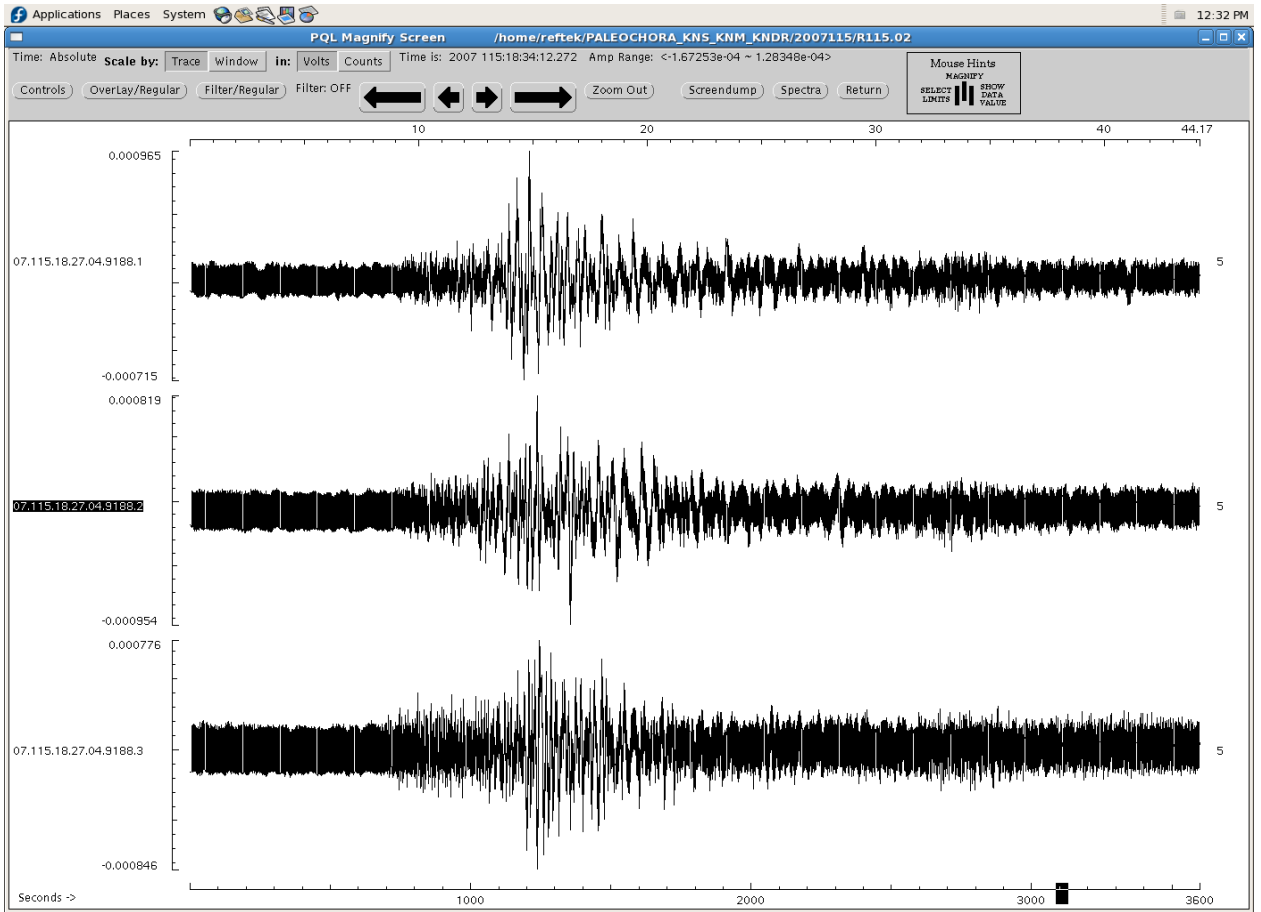


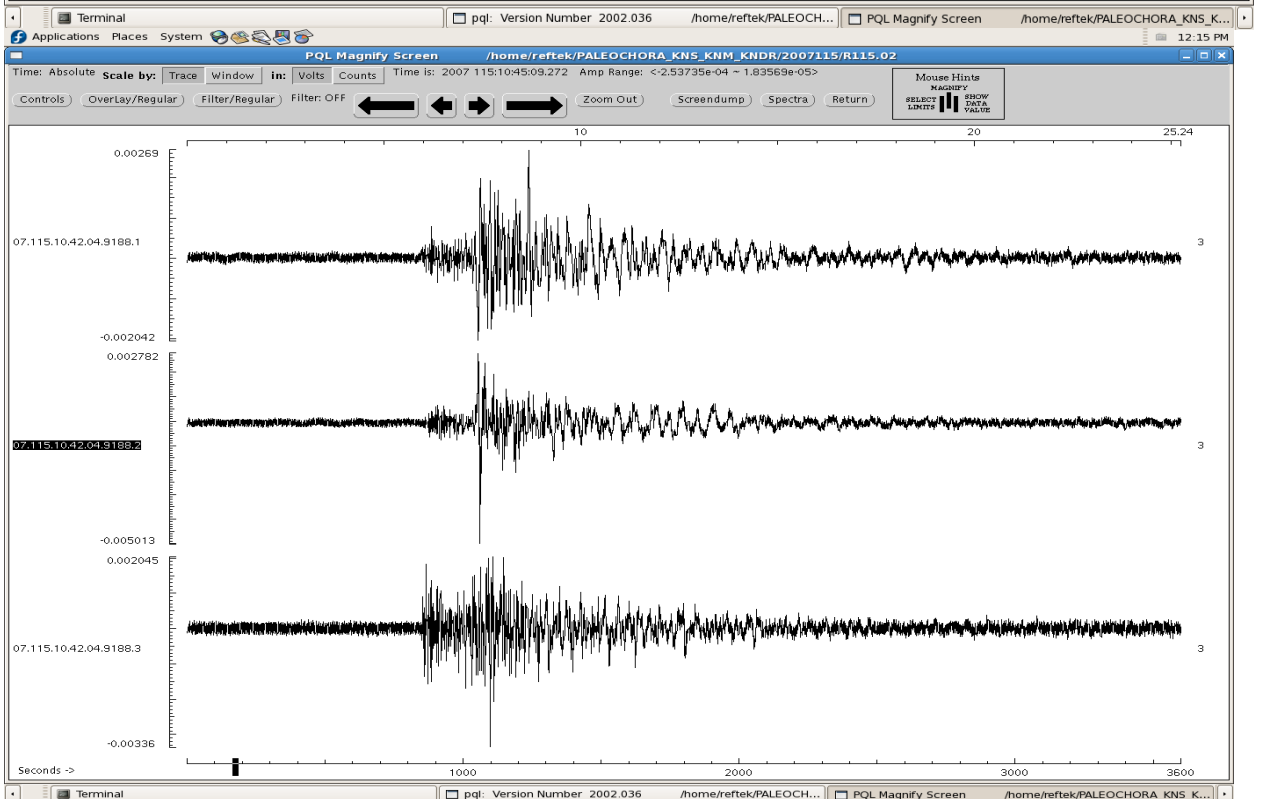
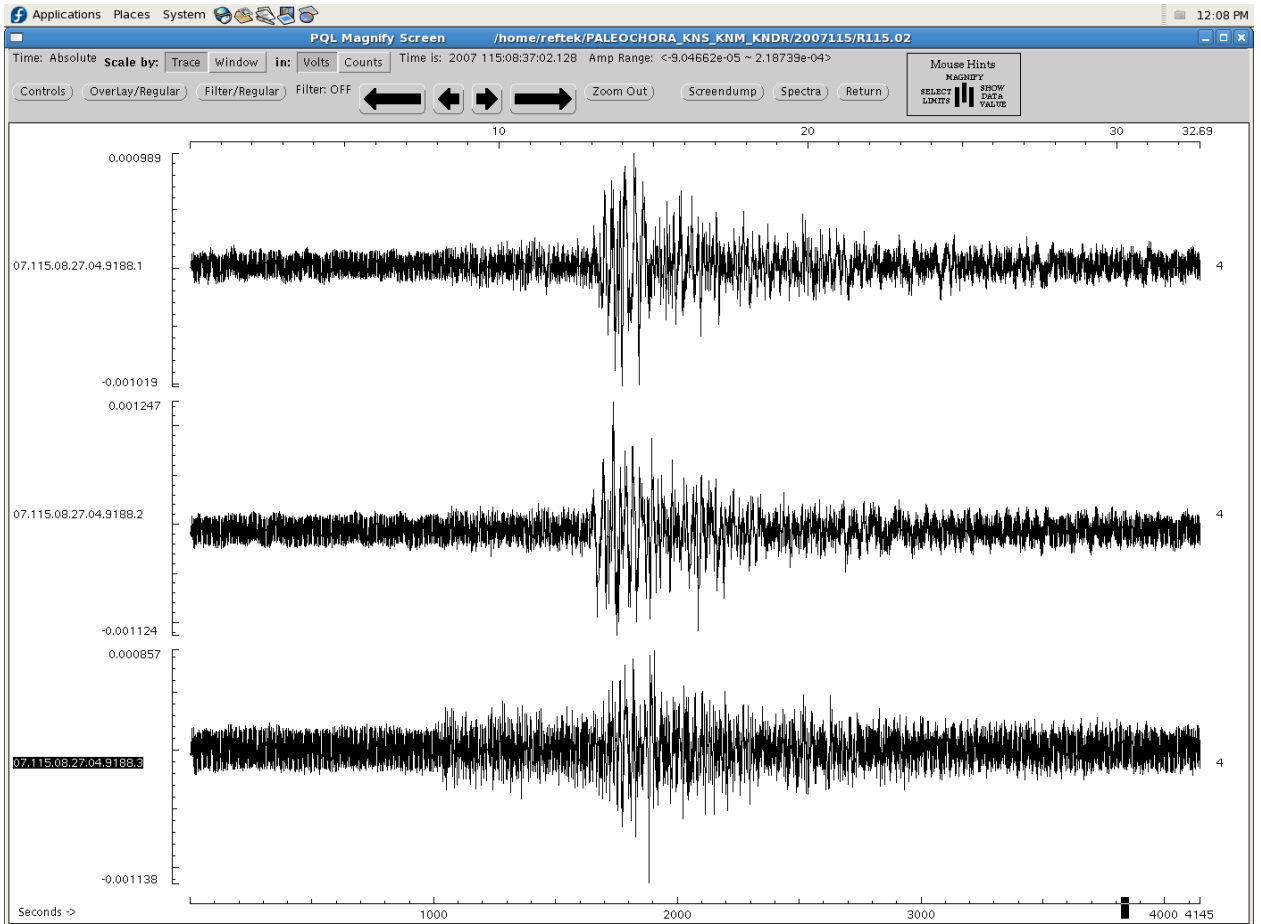
Terminal pql: Version Number 2002.036 /home/reftek/PALEOCH... PQL Magnify Screen /home/reftek/PALEOCHORA\_KNS\_K...

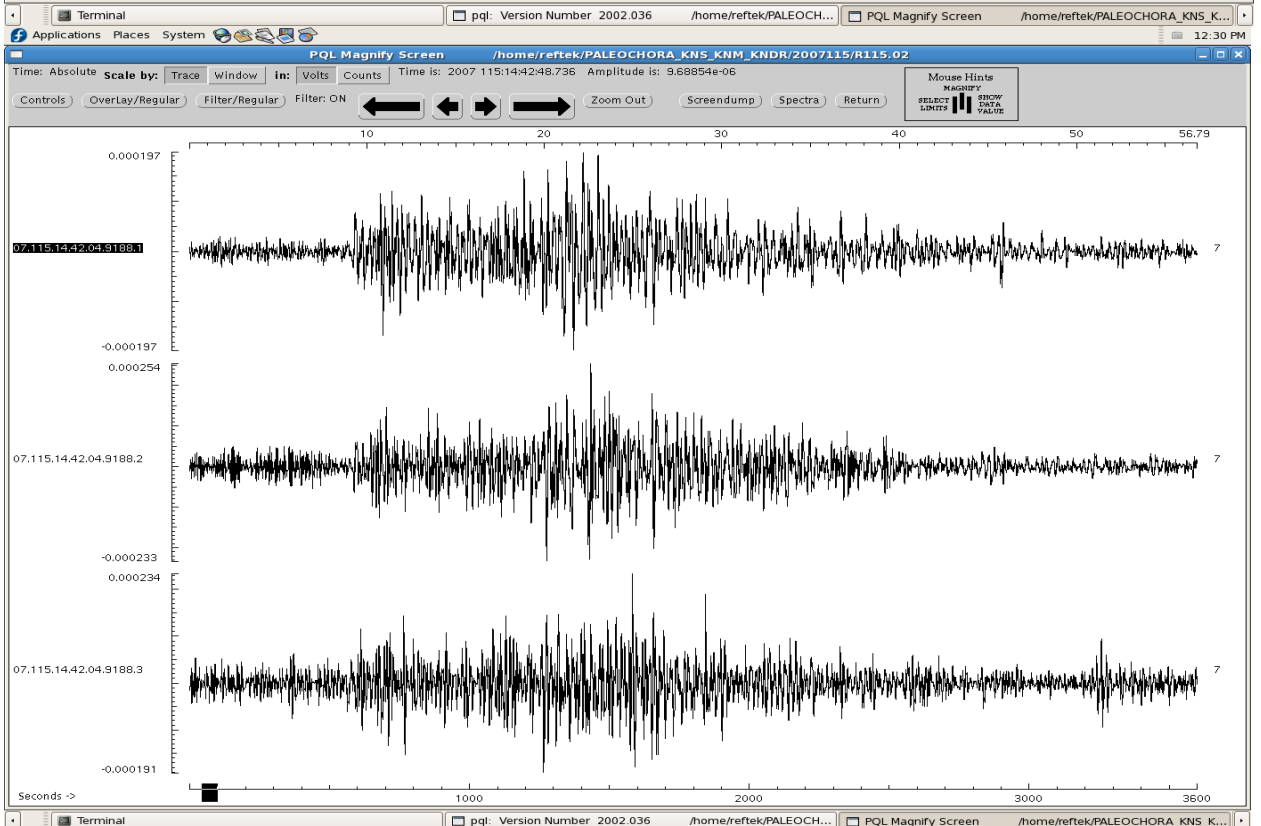
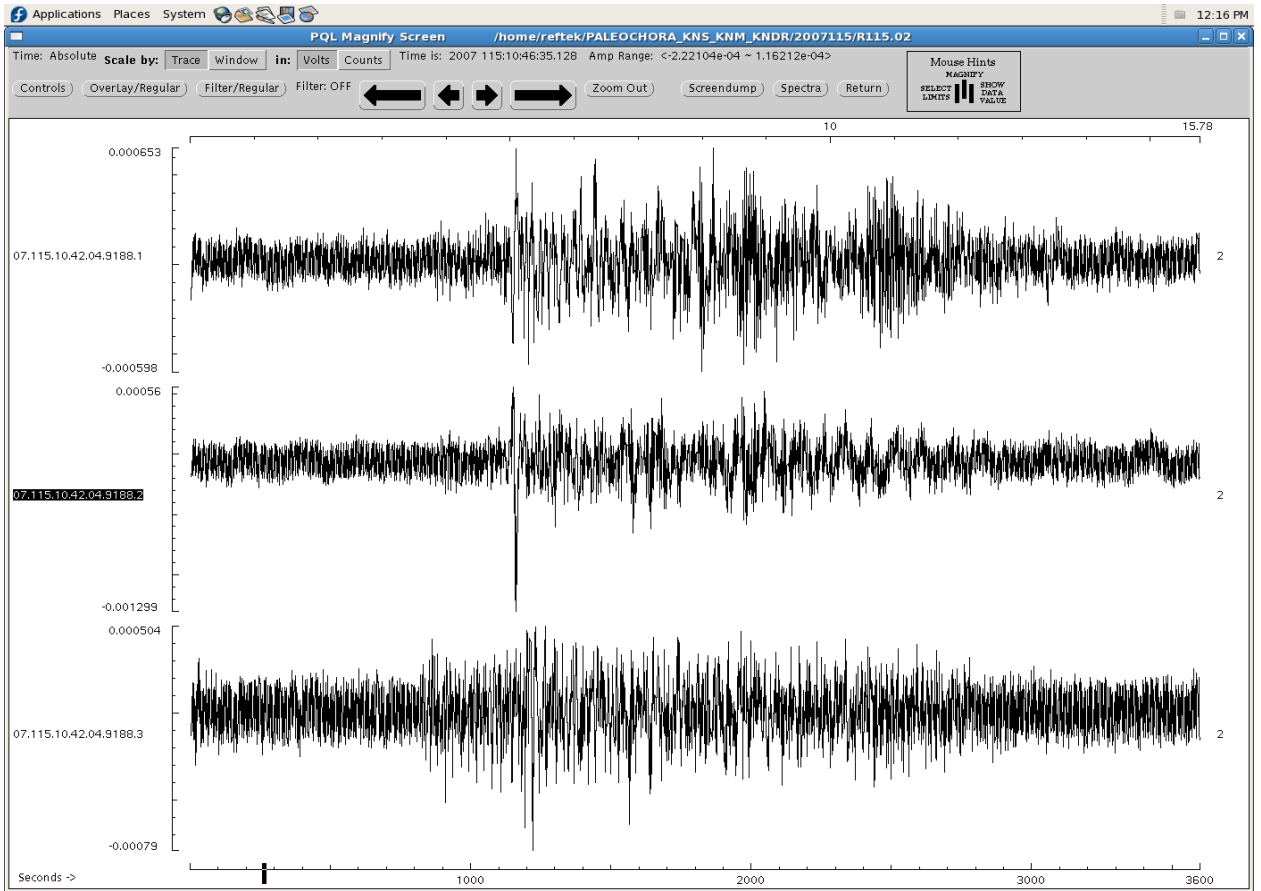


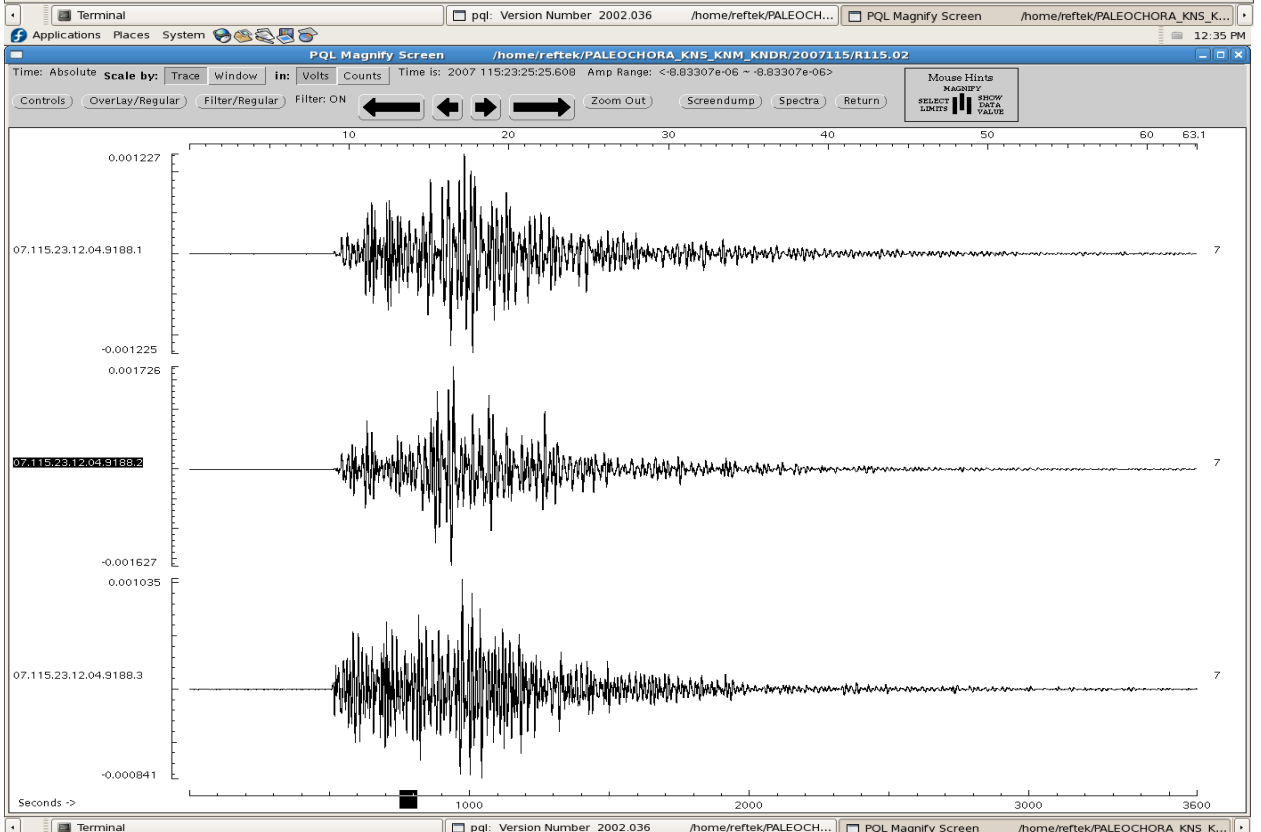
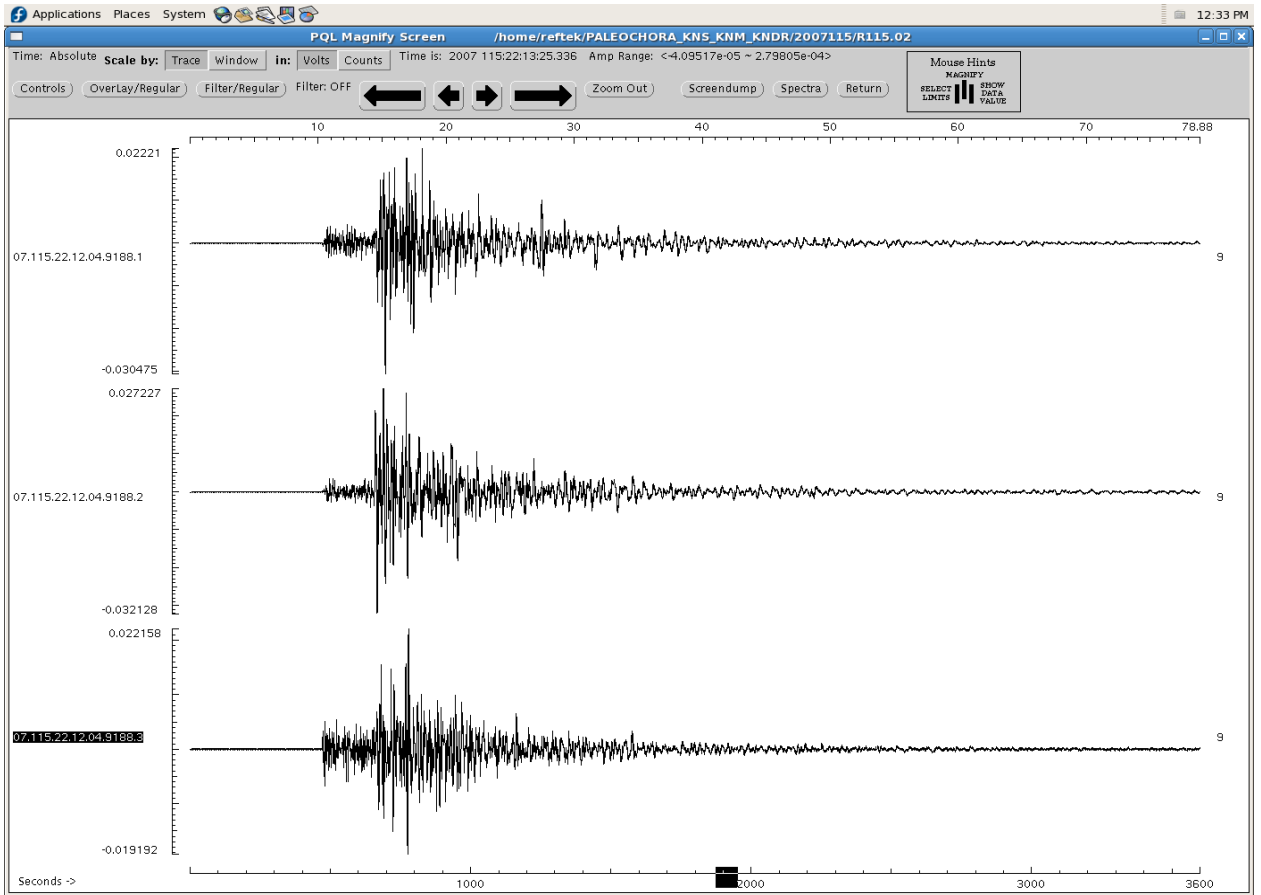
Terminal pql: Version Number 2002.036 /home/reftek/PALEOCH... PQL Magnify Screen /home/reftek/PALEOCHORA\_KNS\_K...

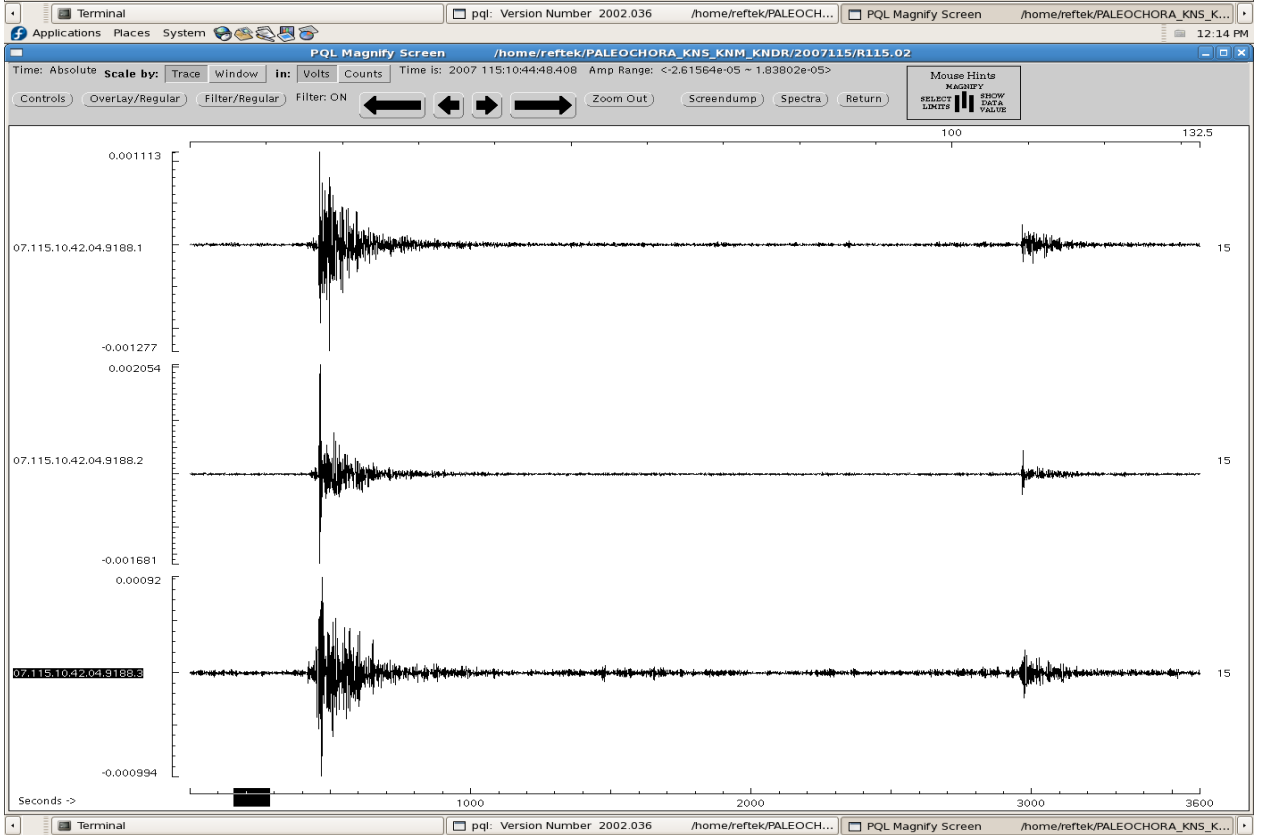
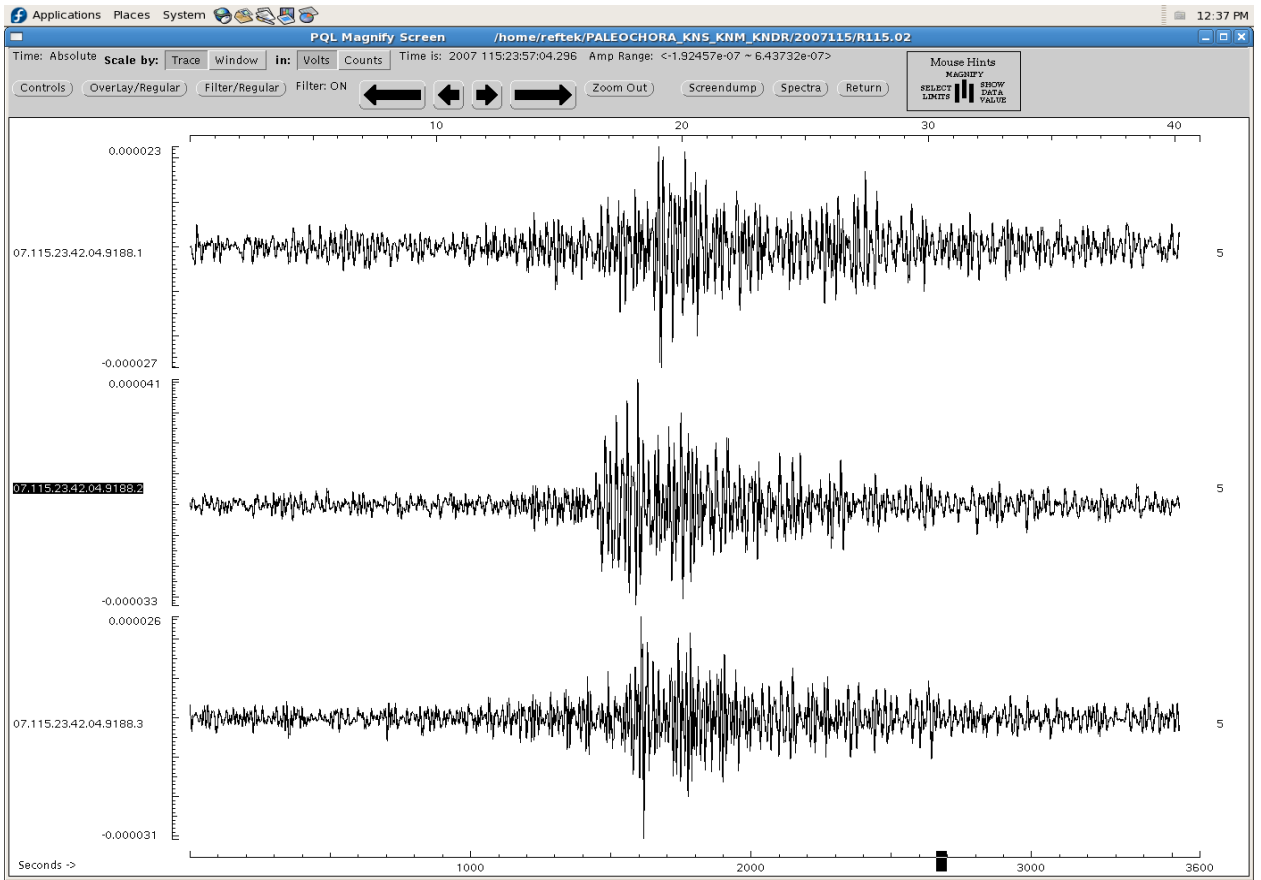


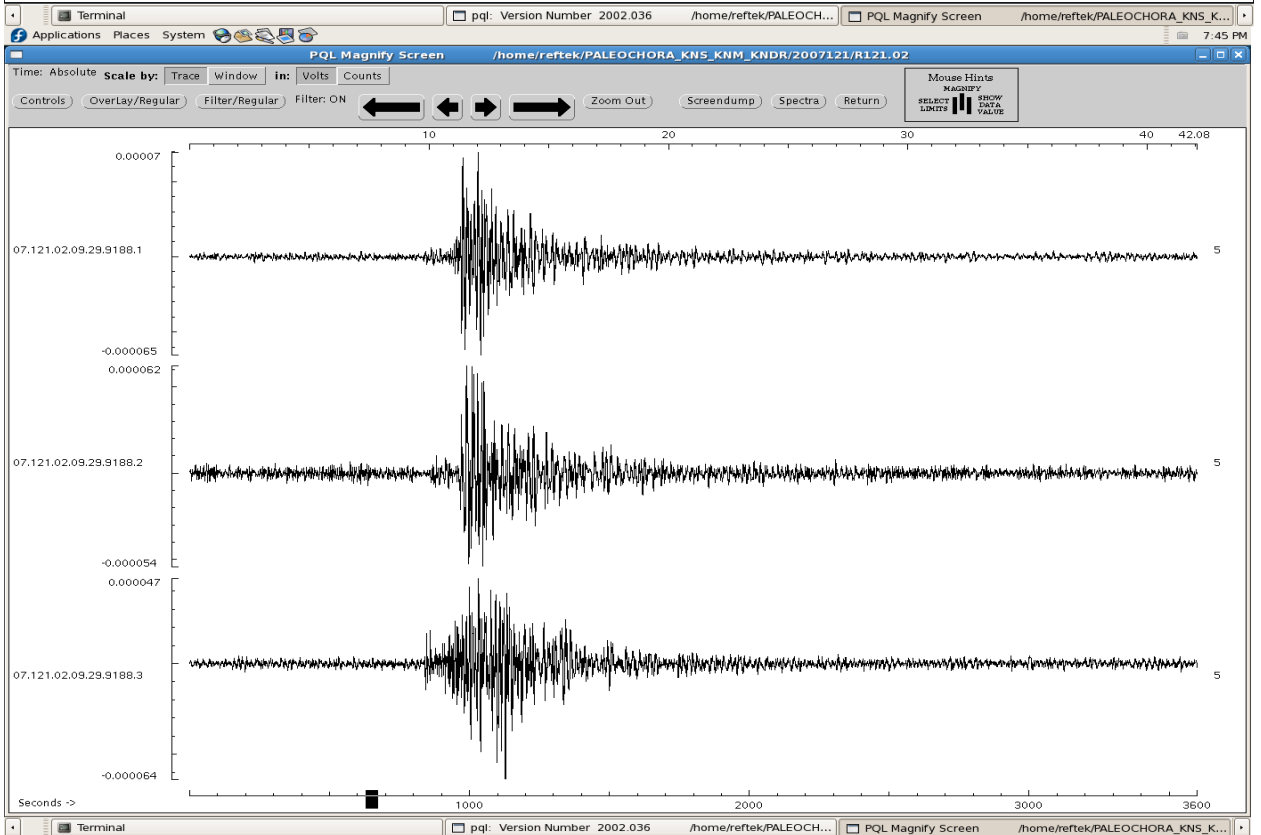
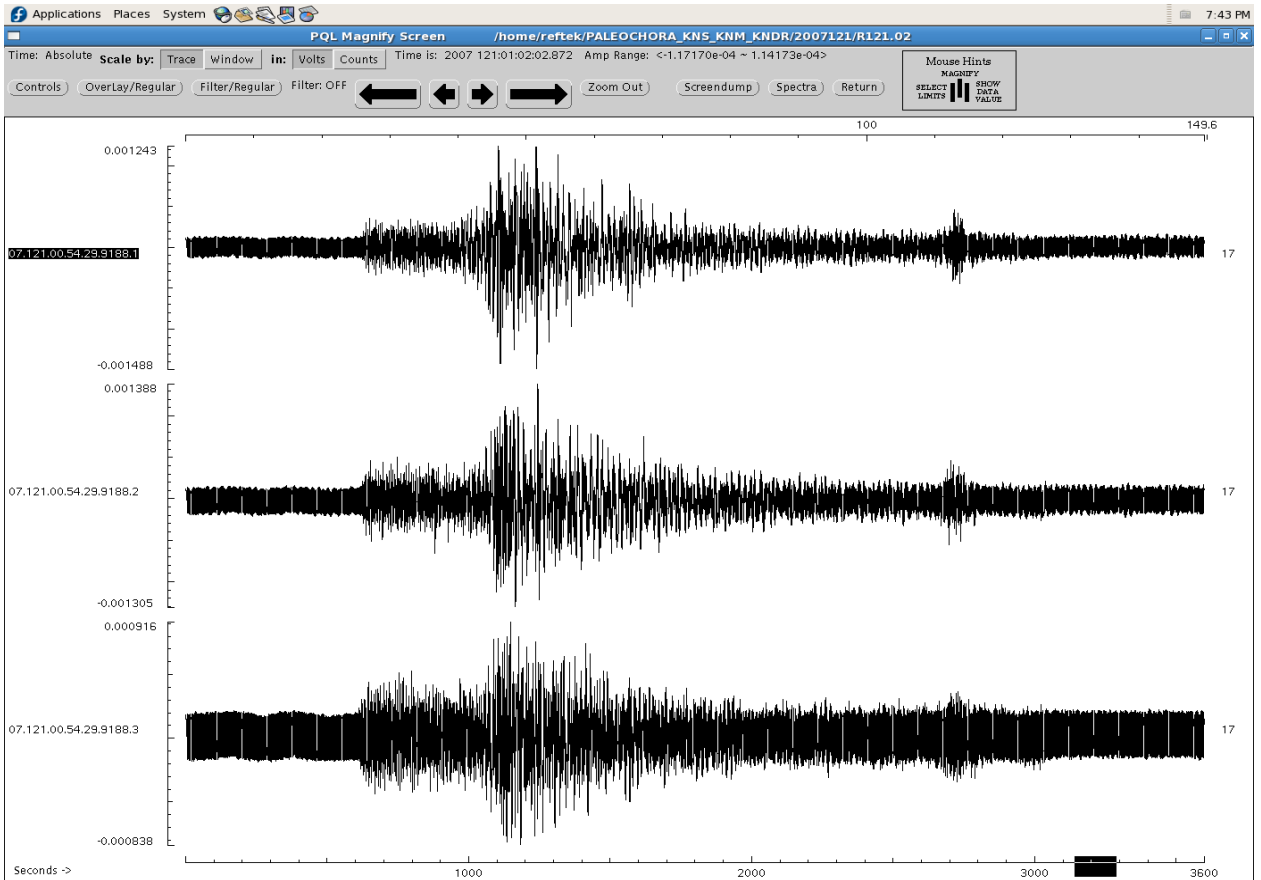




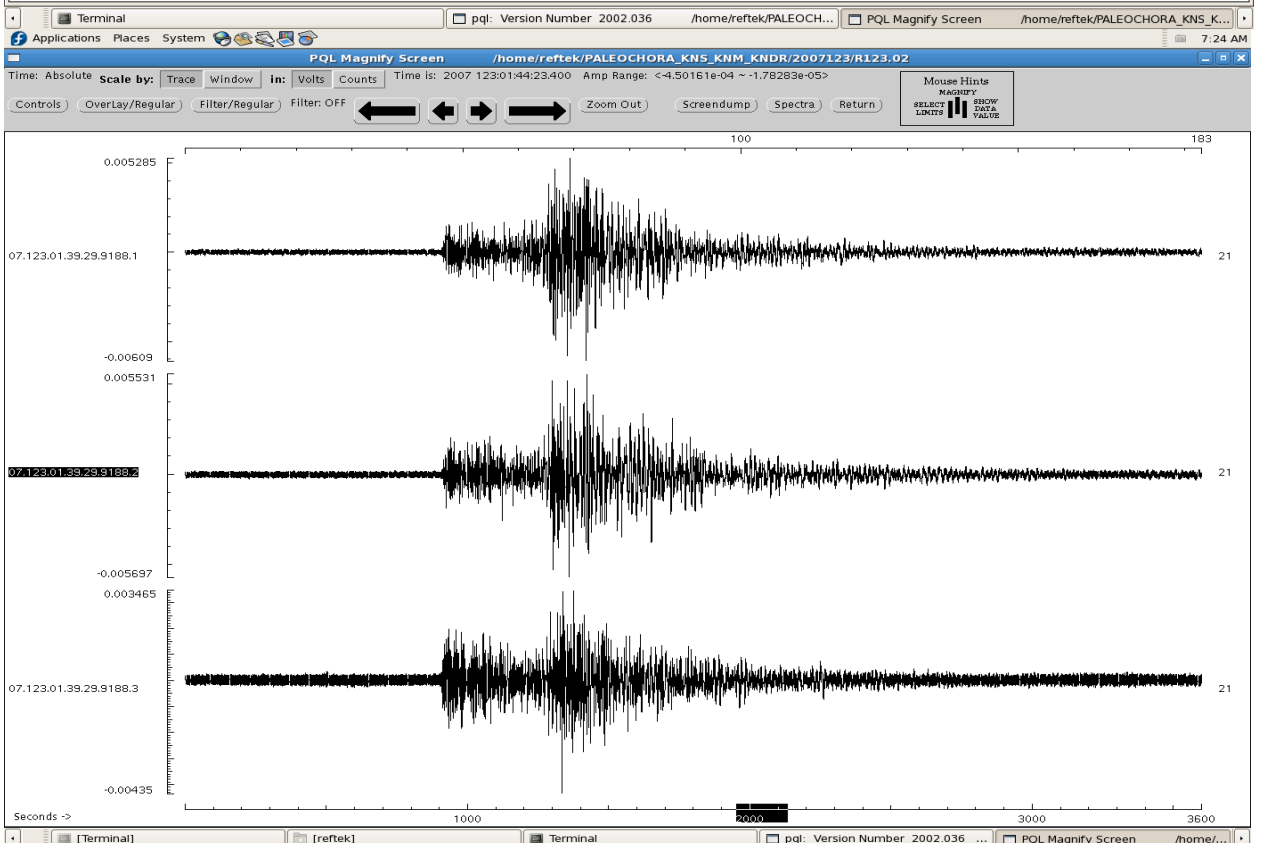
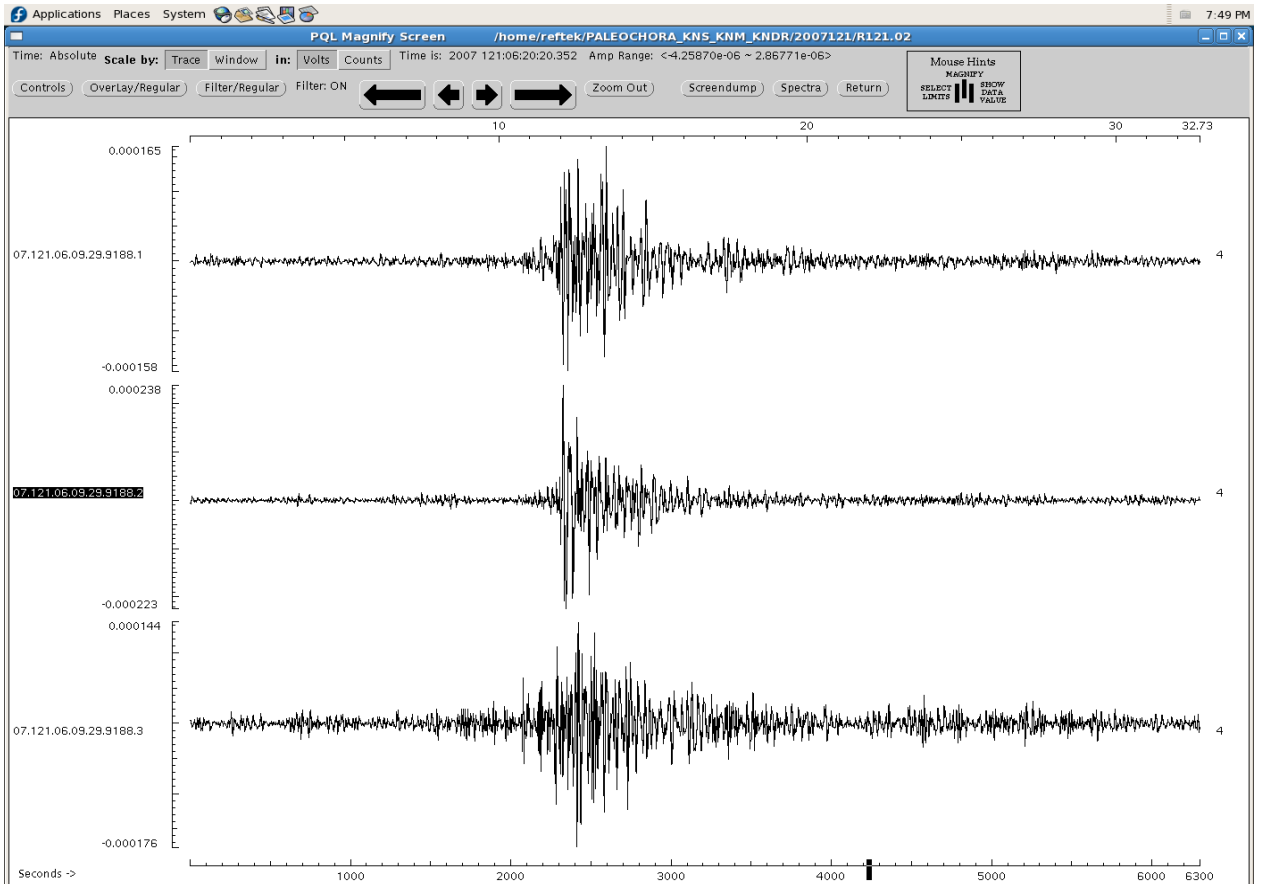


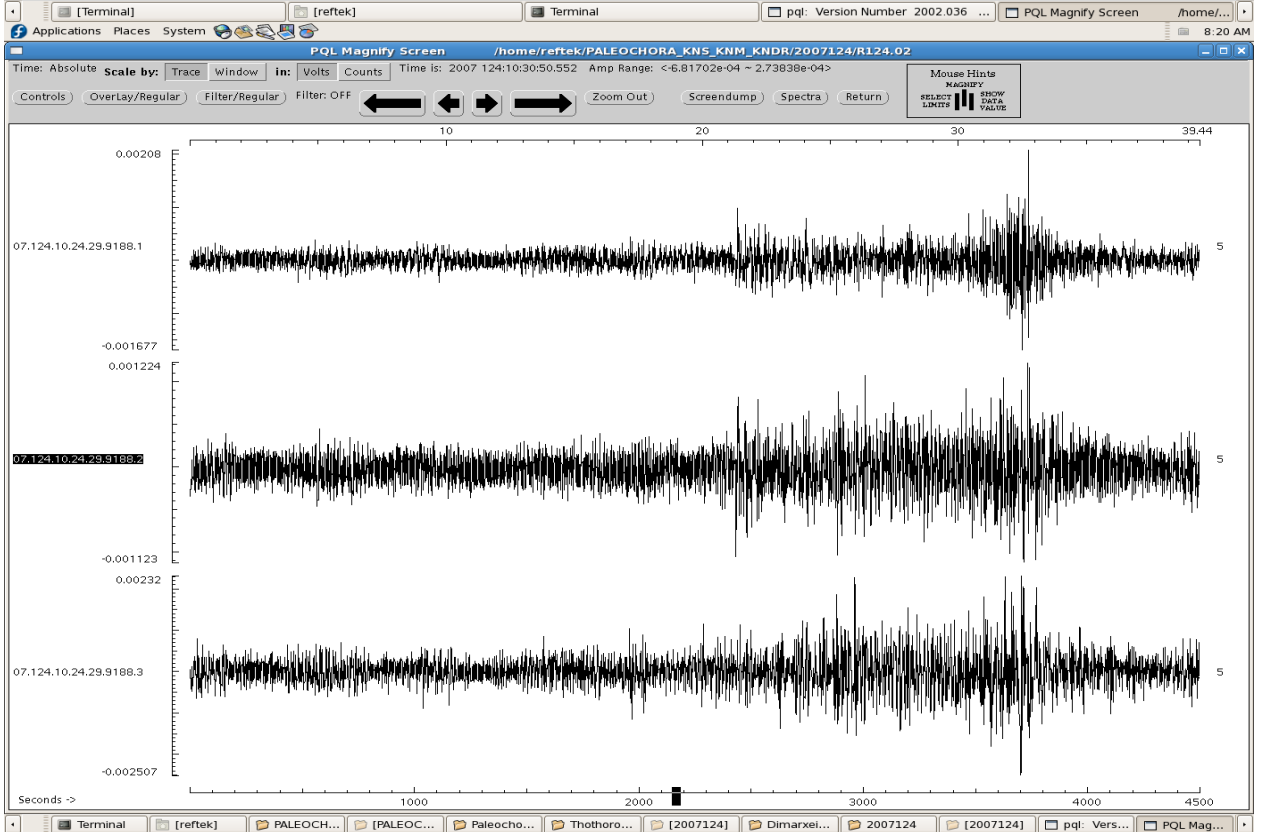
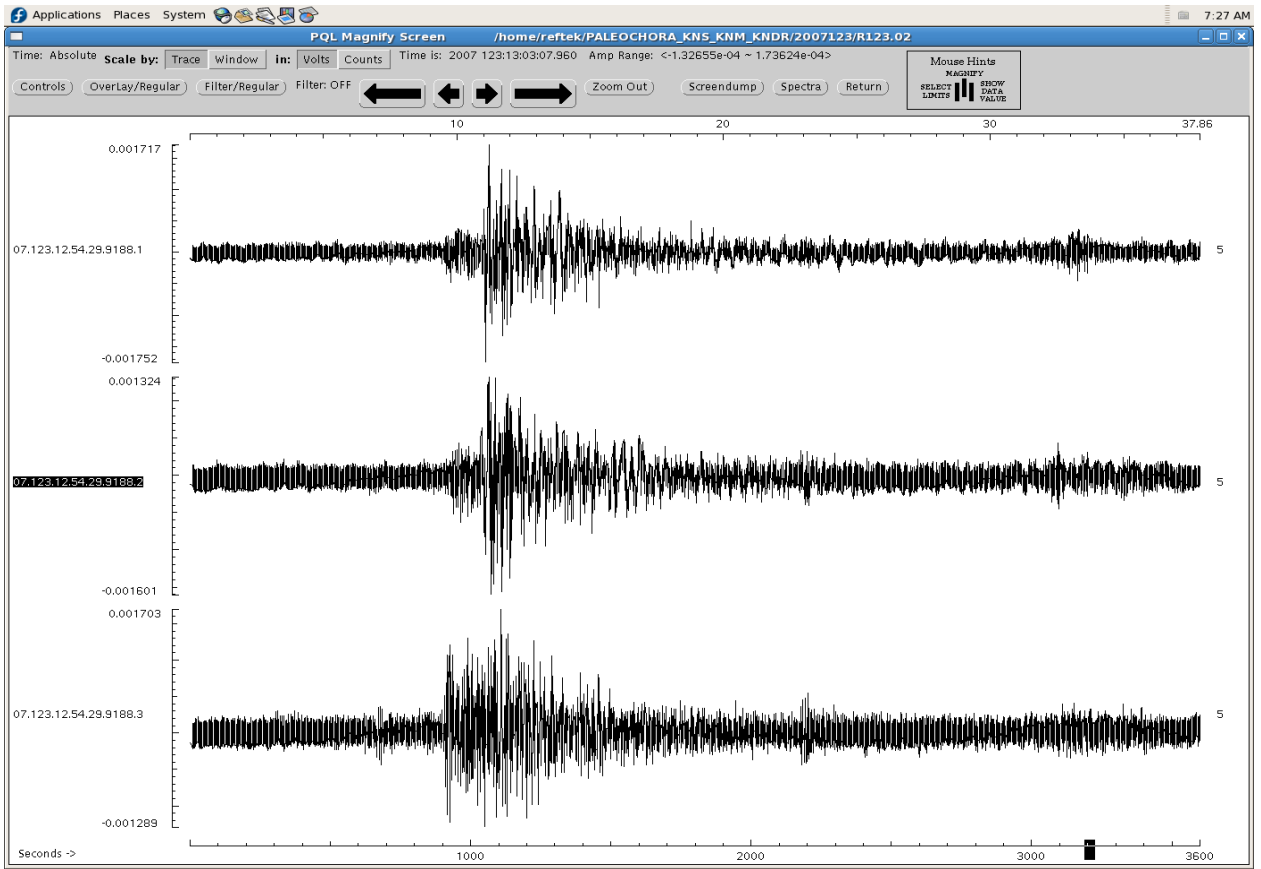


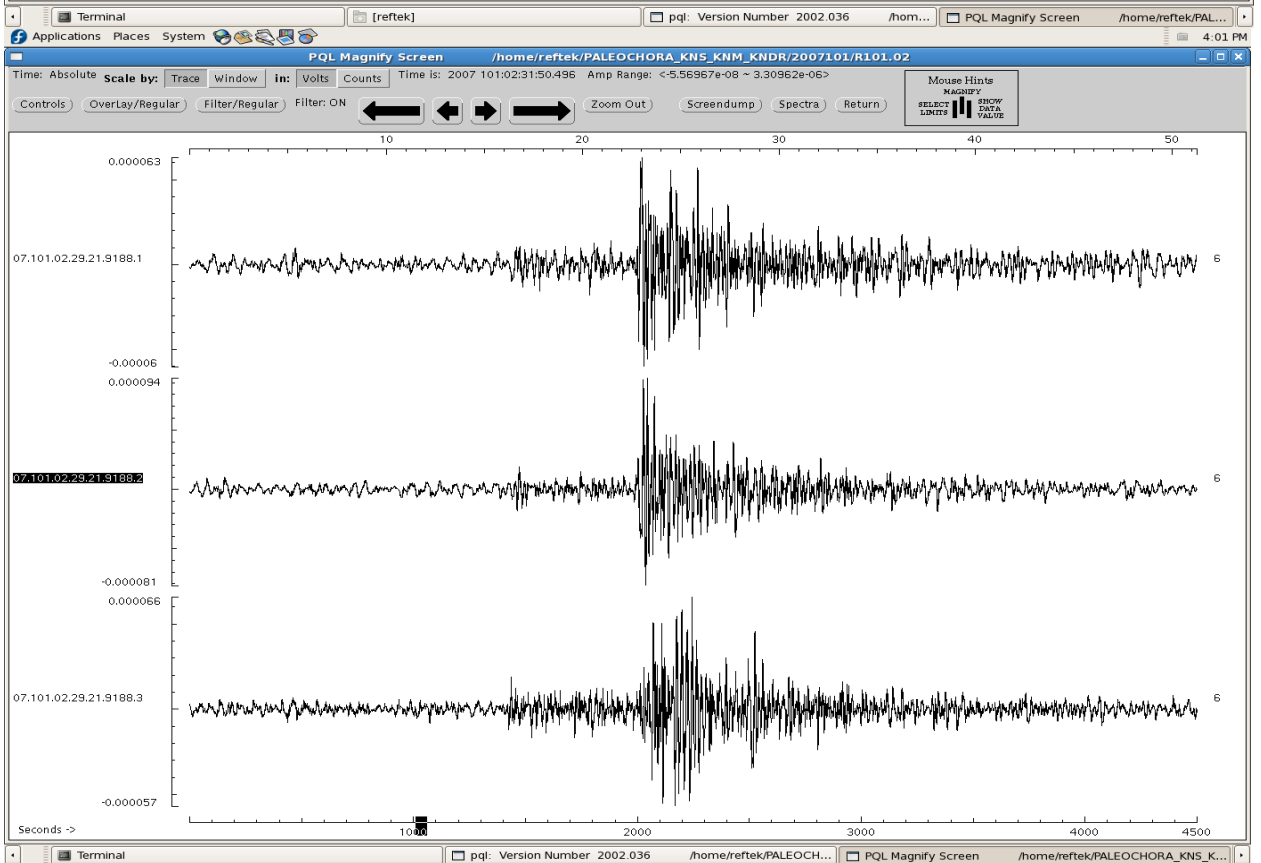
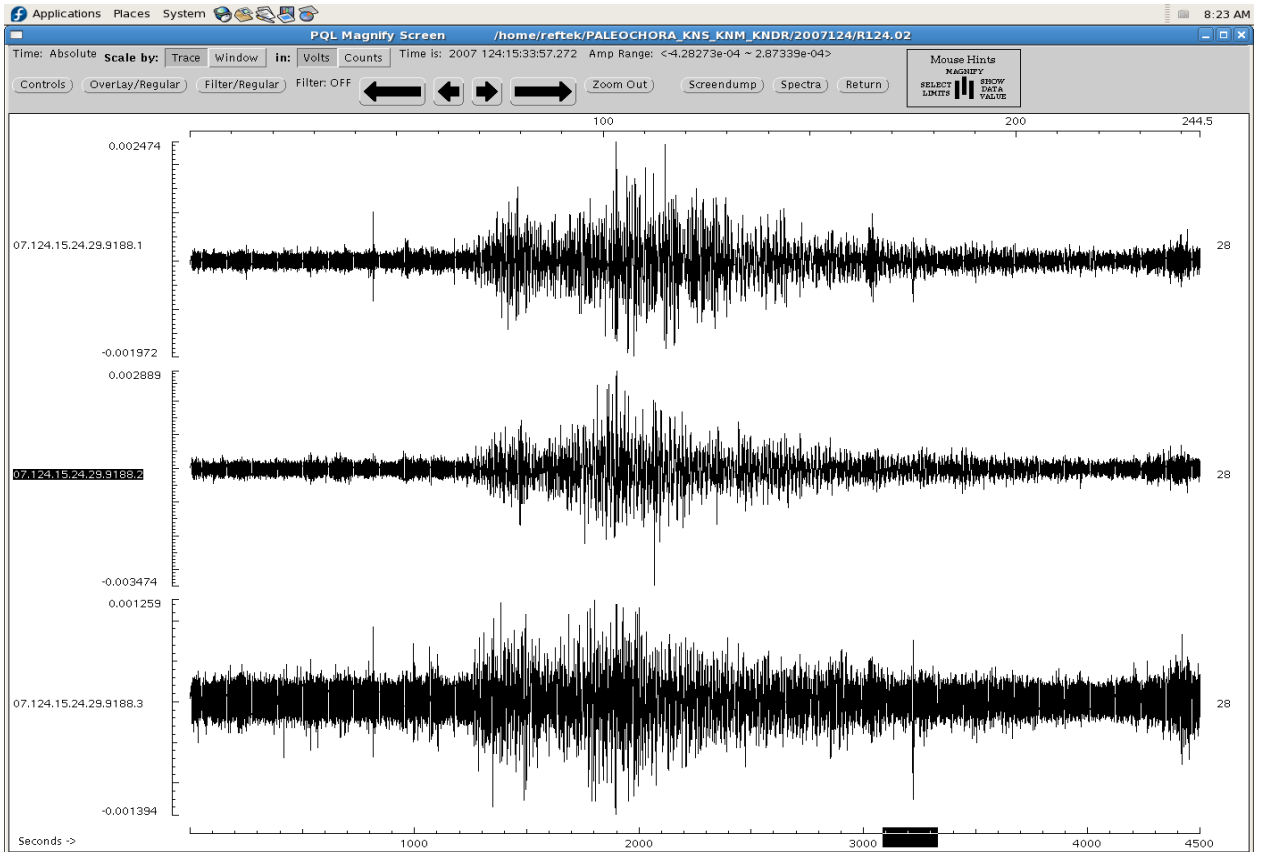


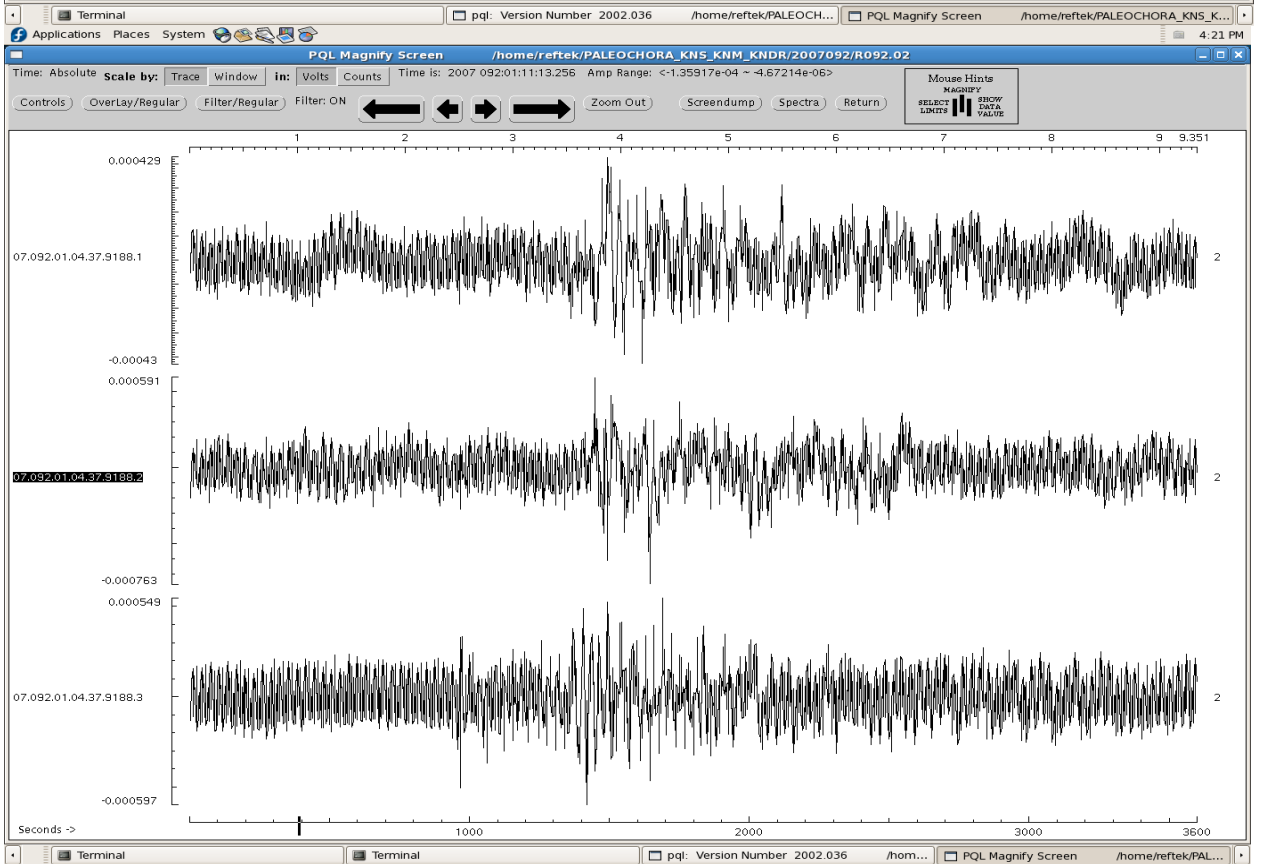
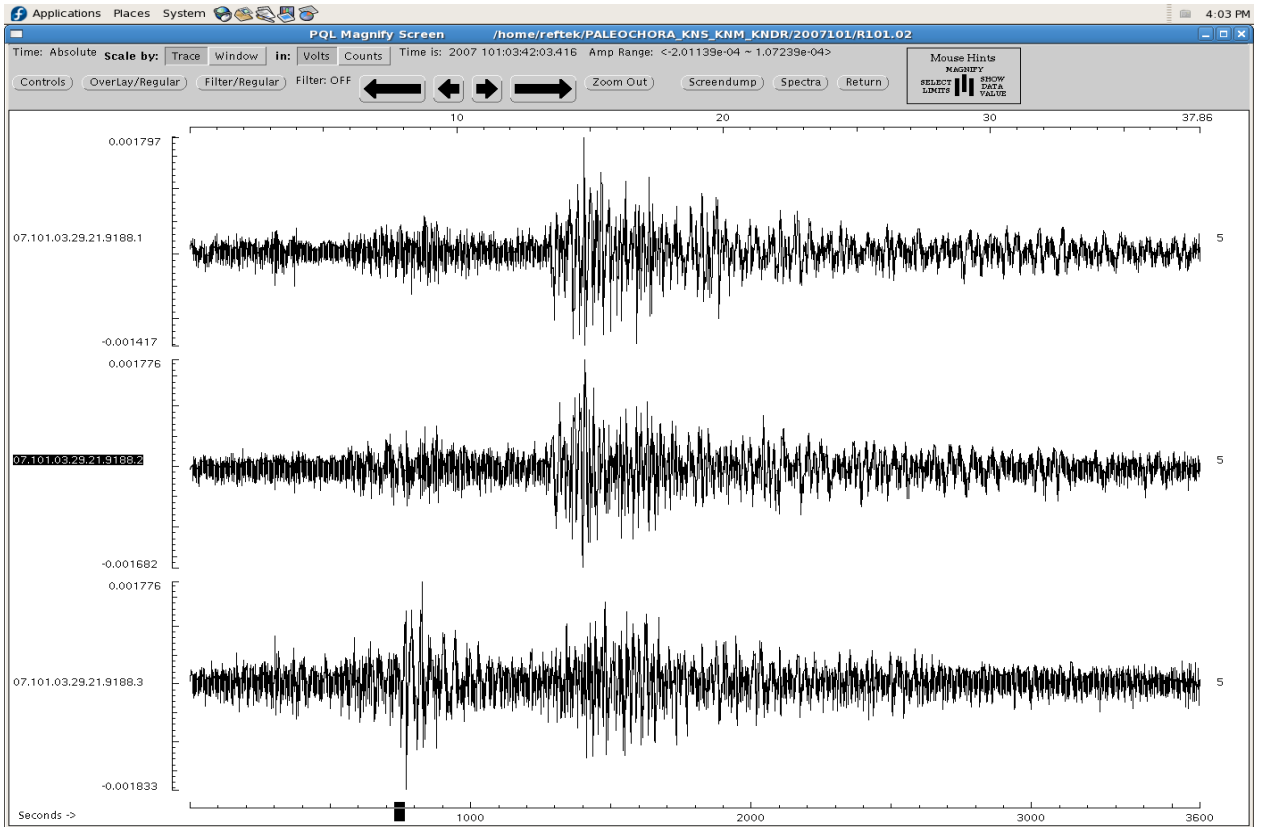


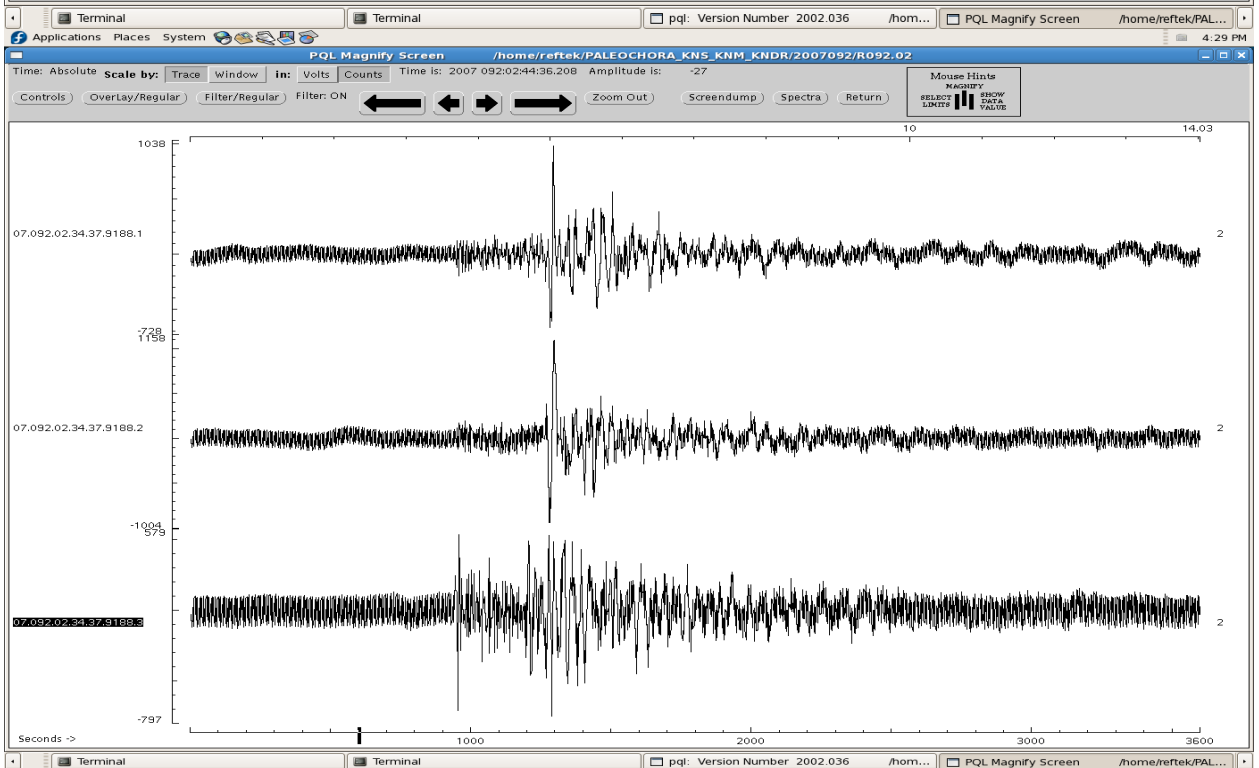
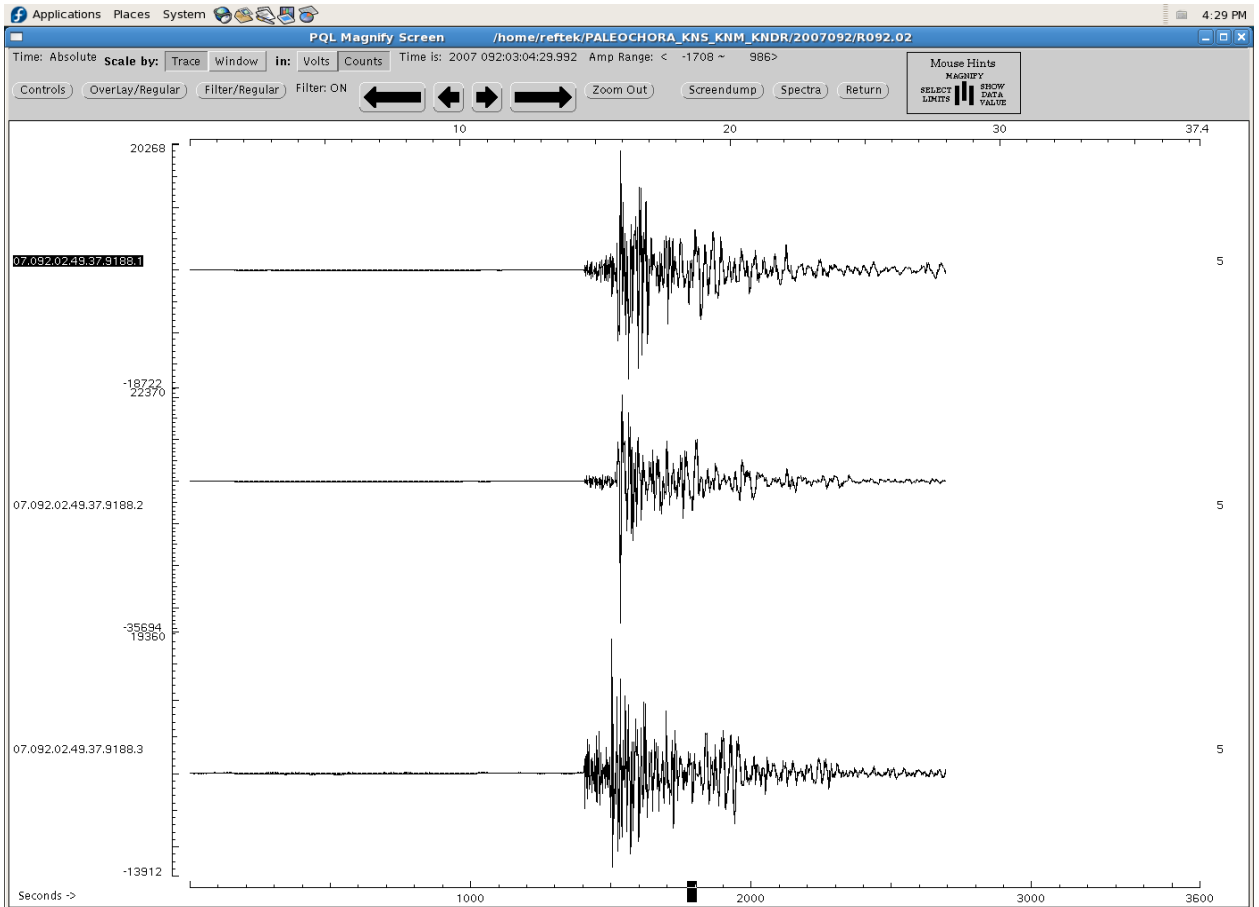


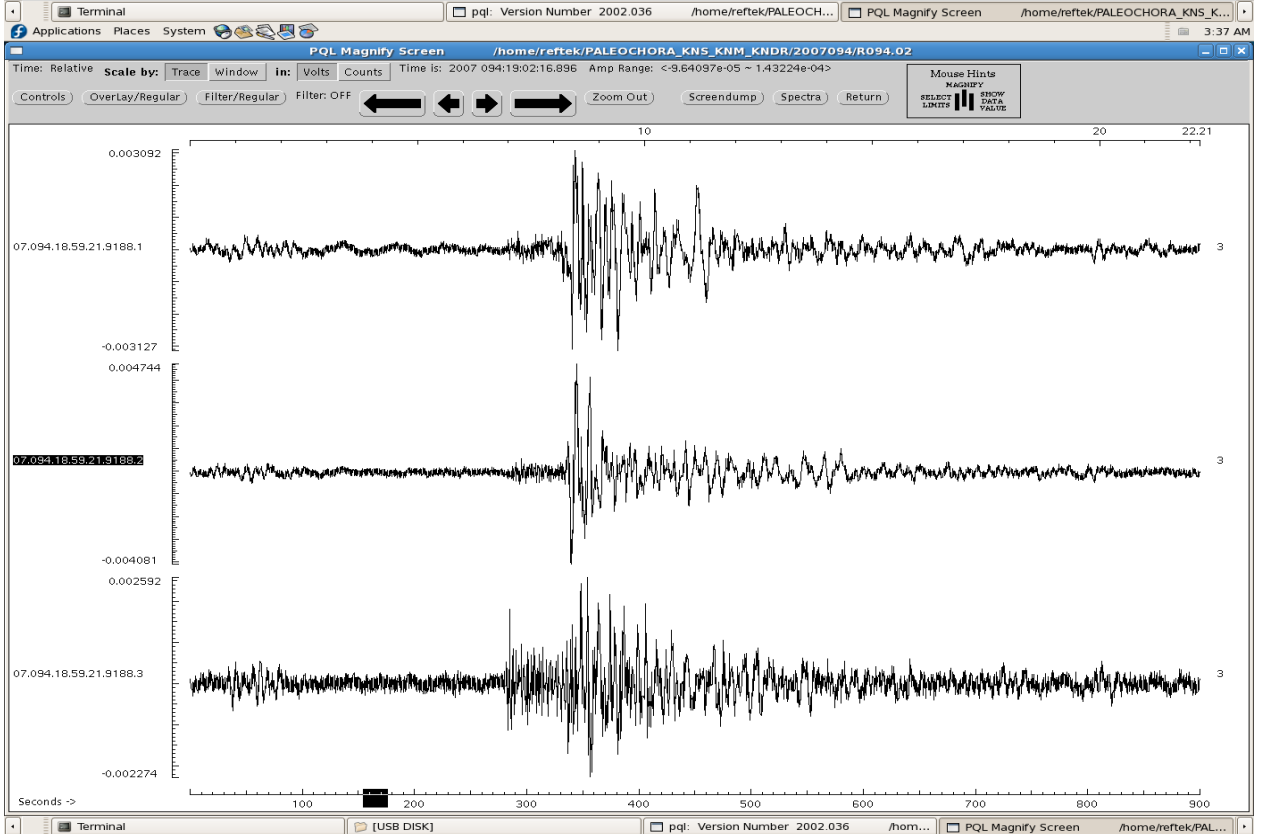
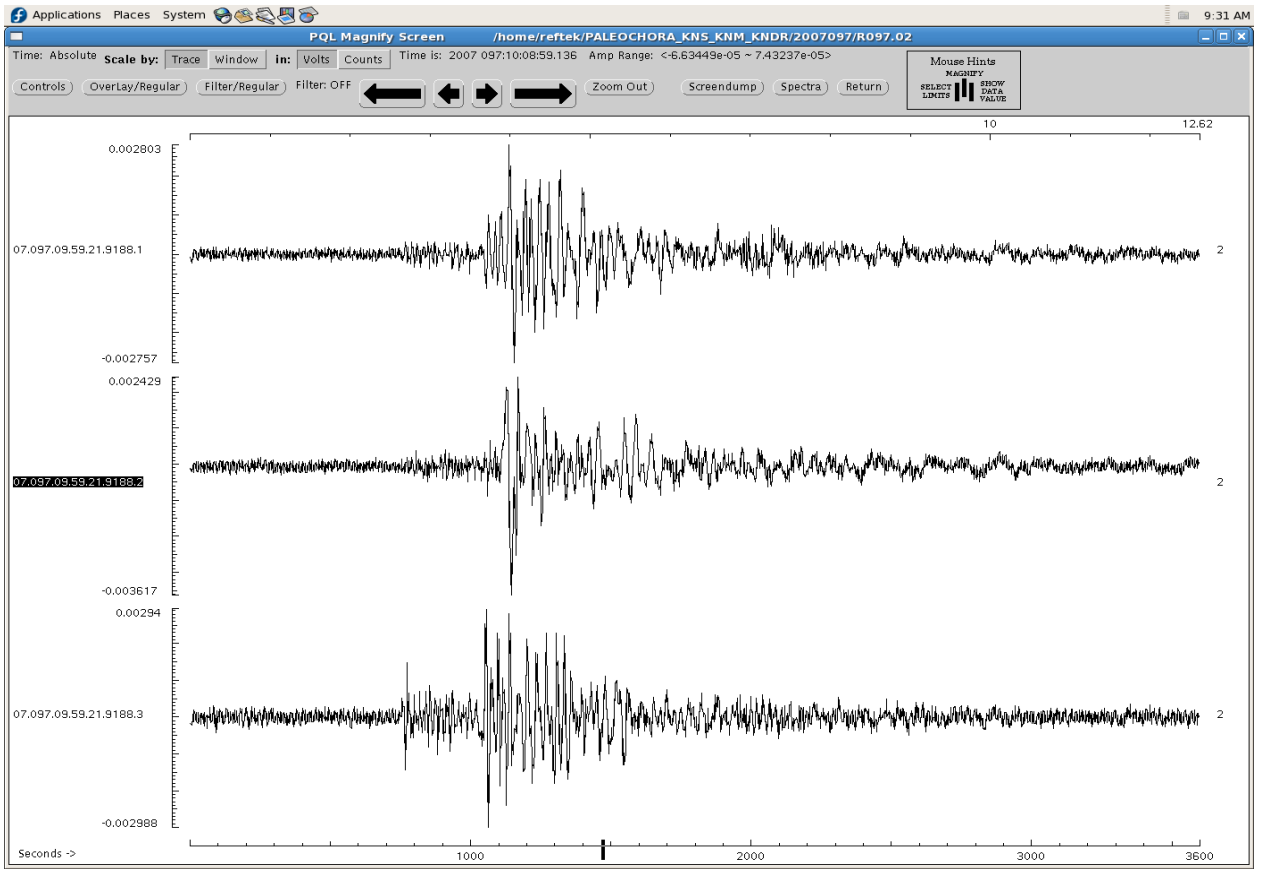


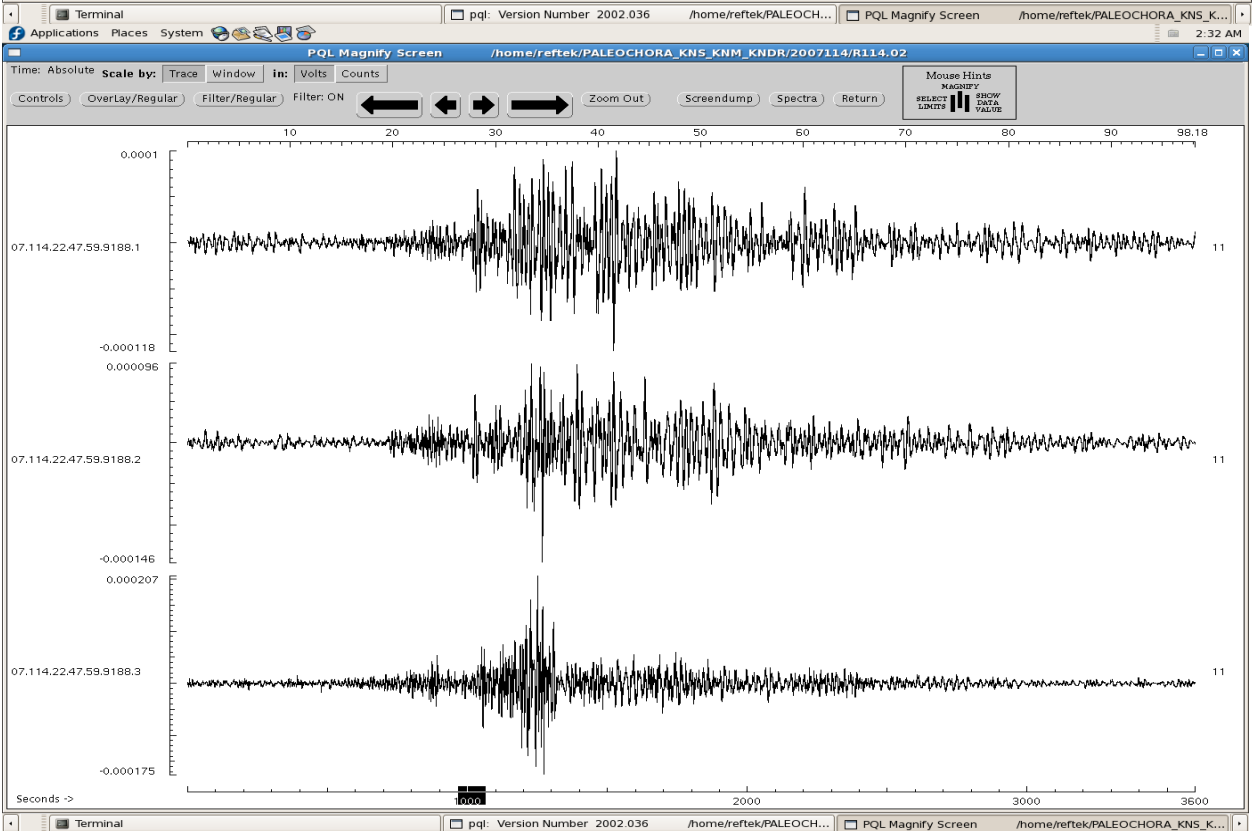
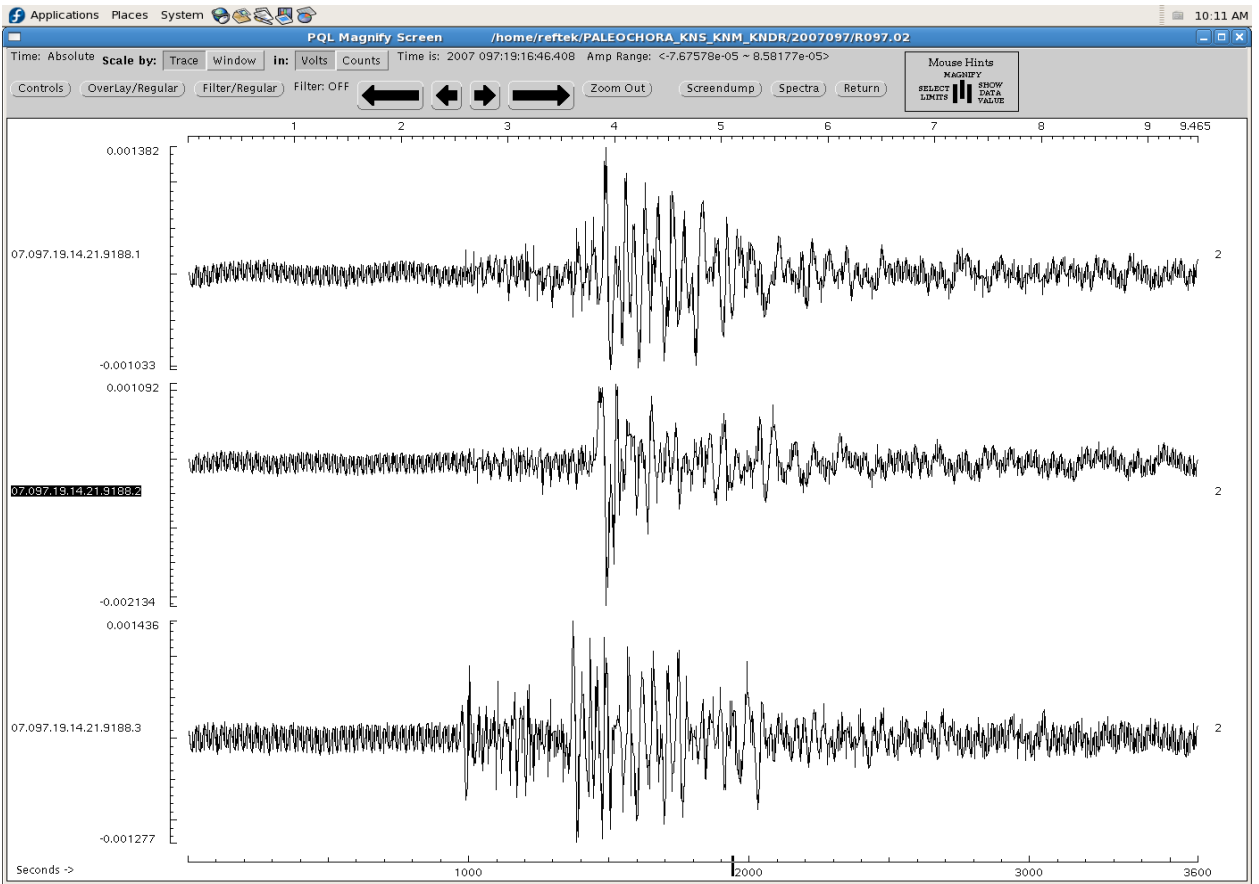


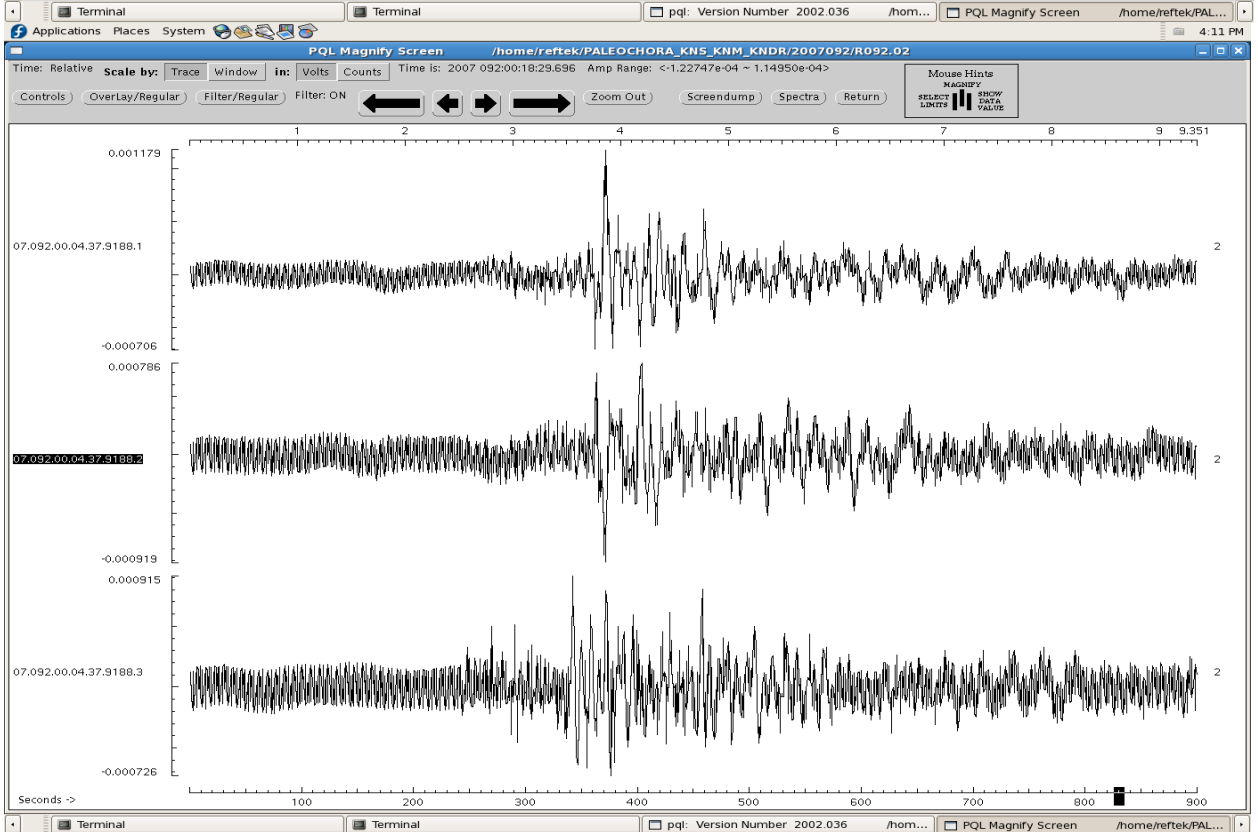
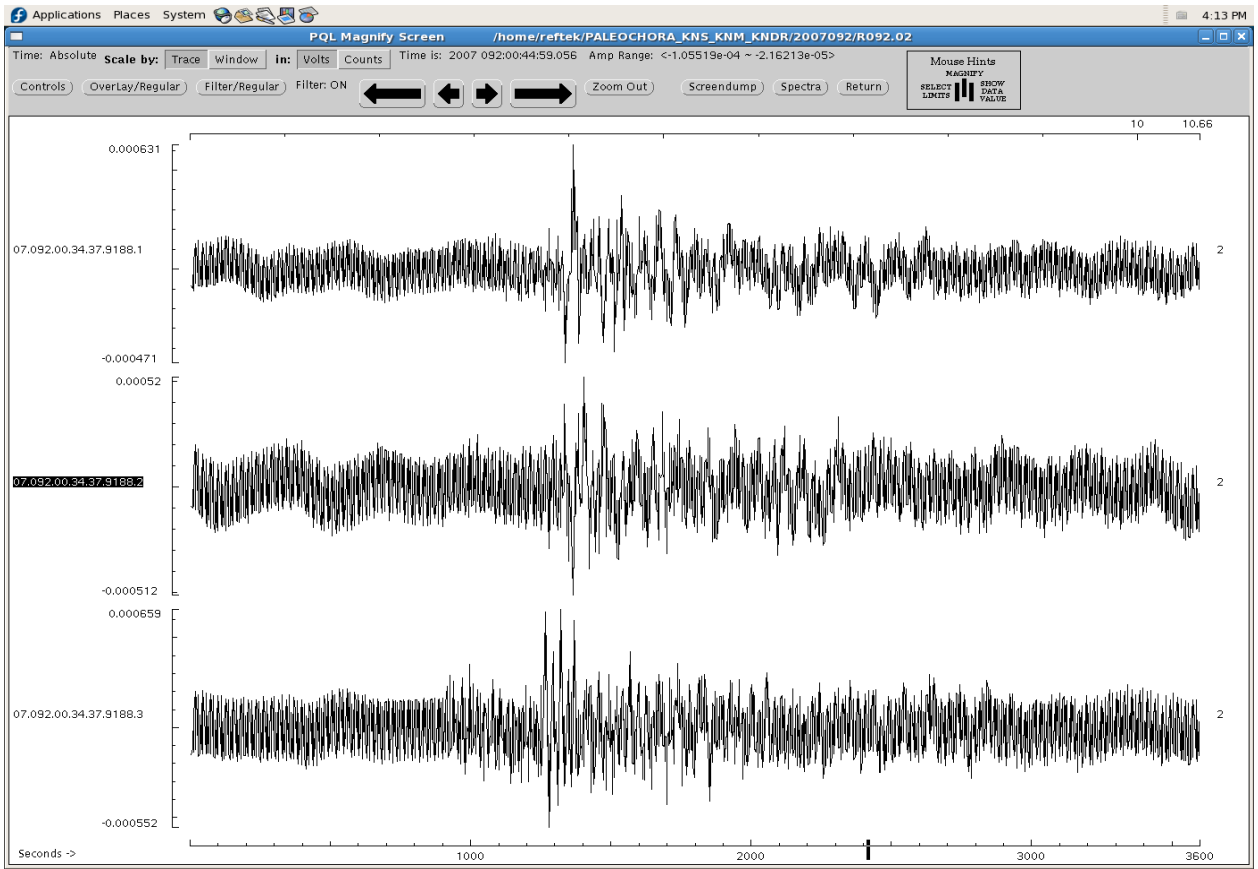




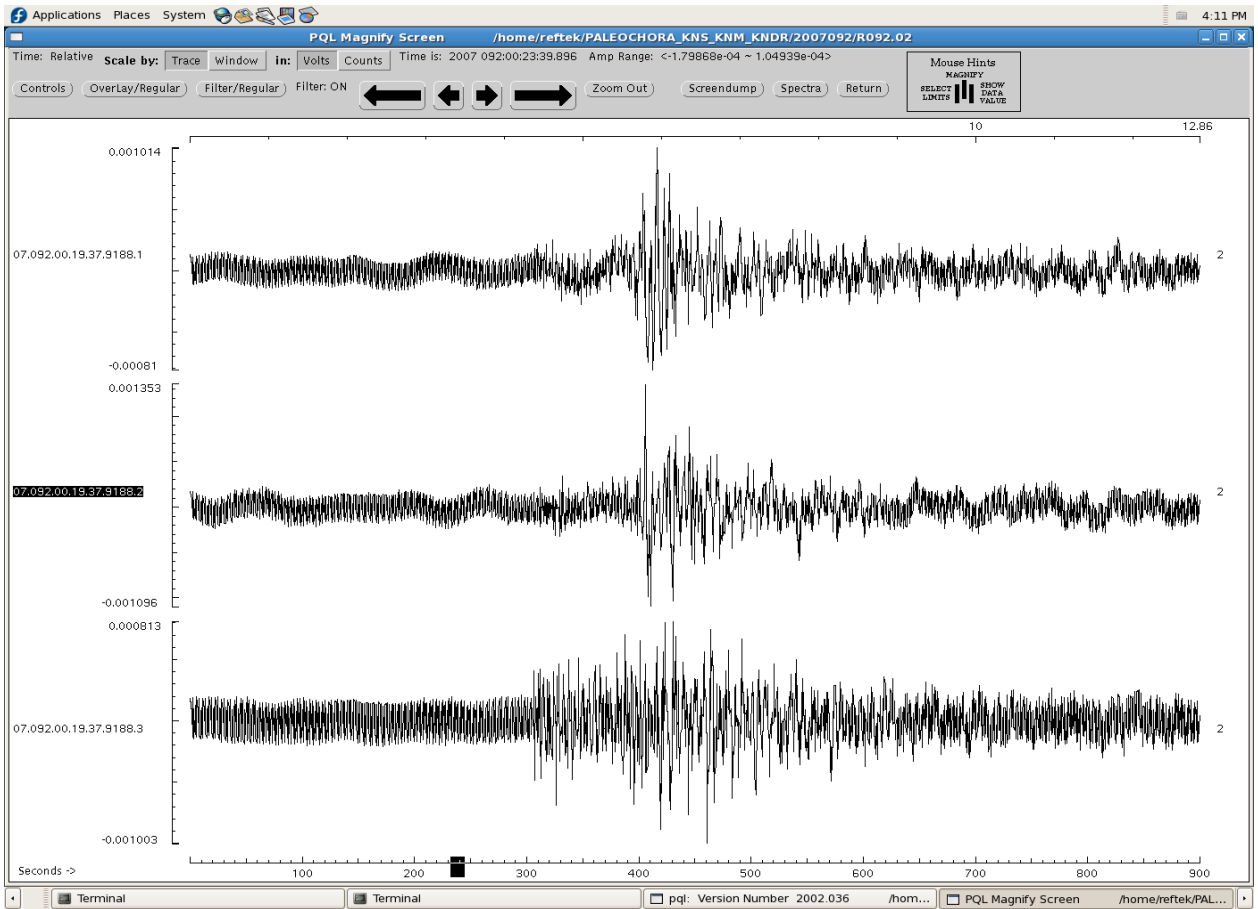


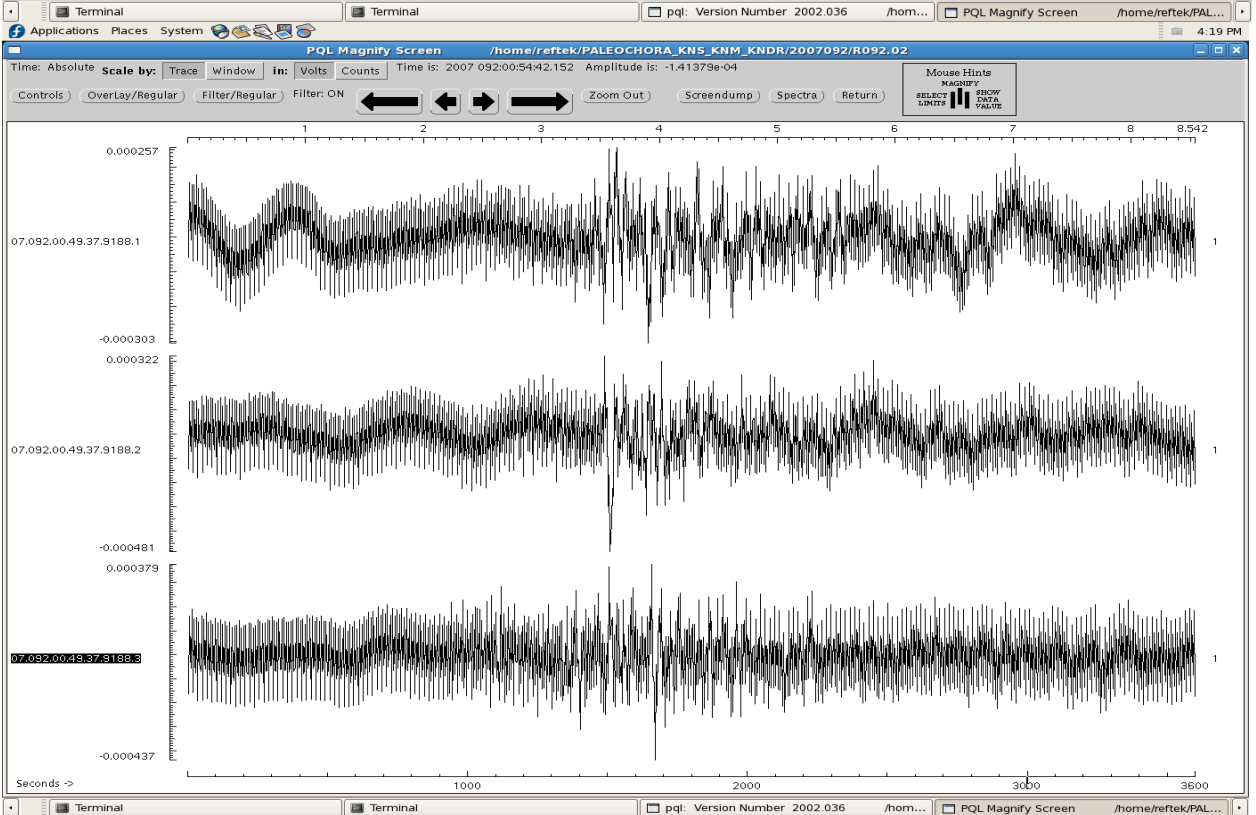
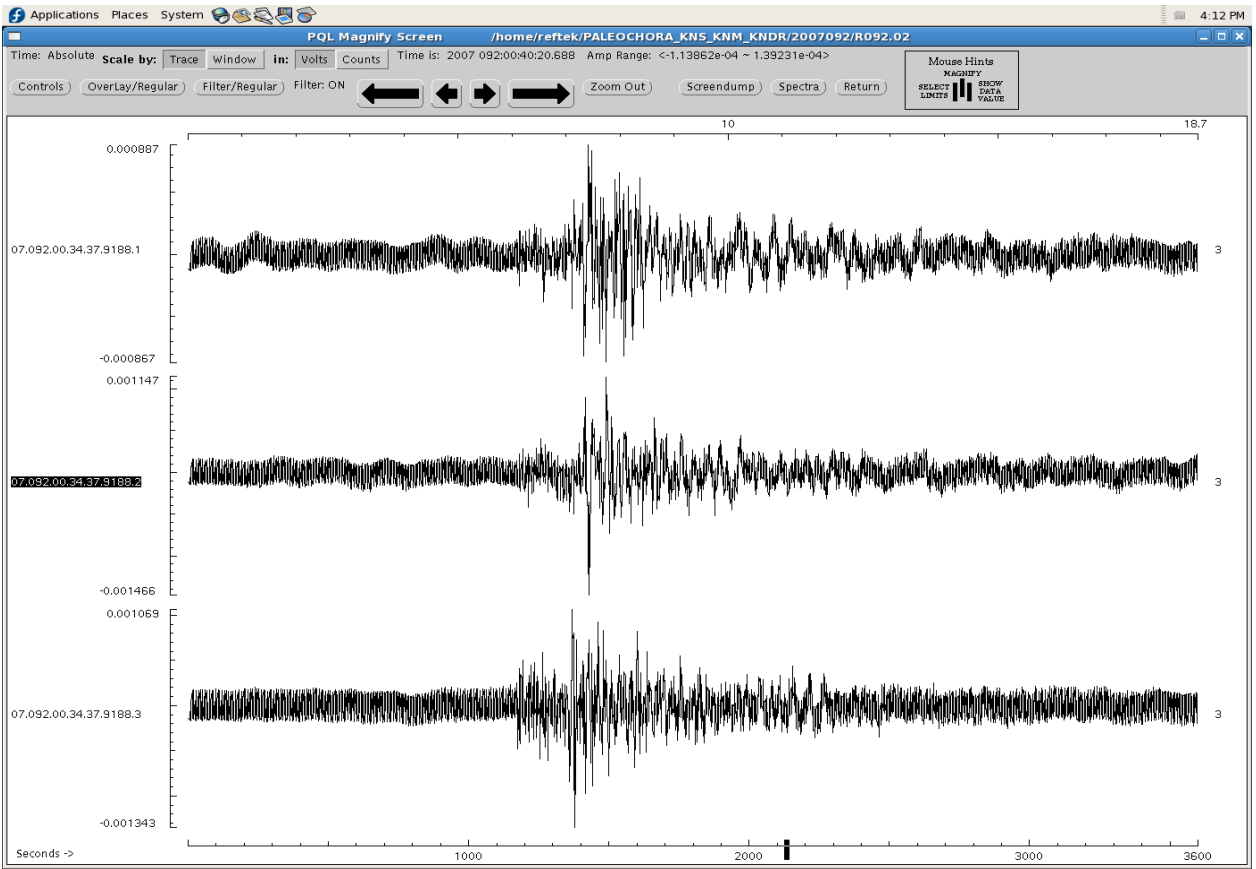


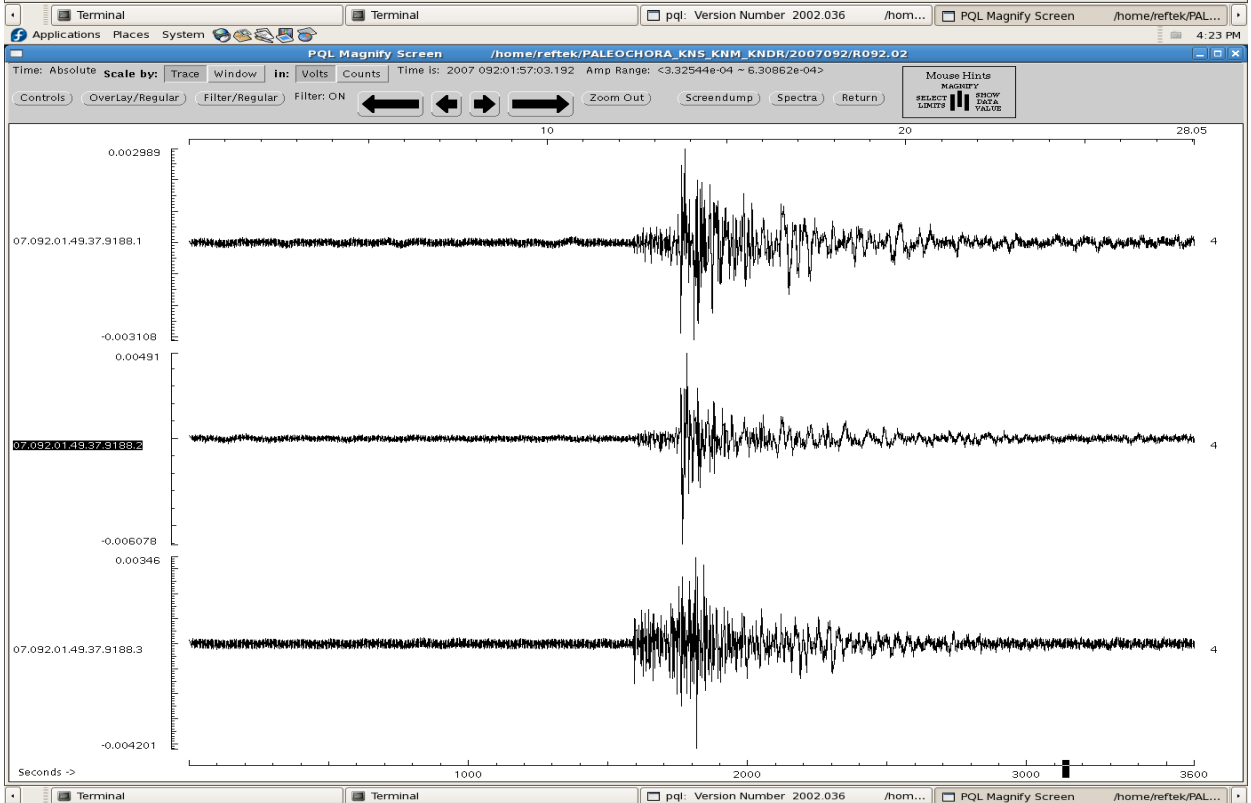
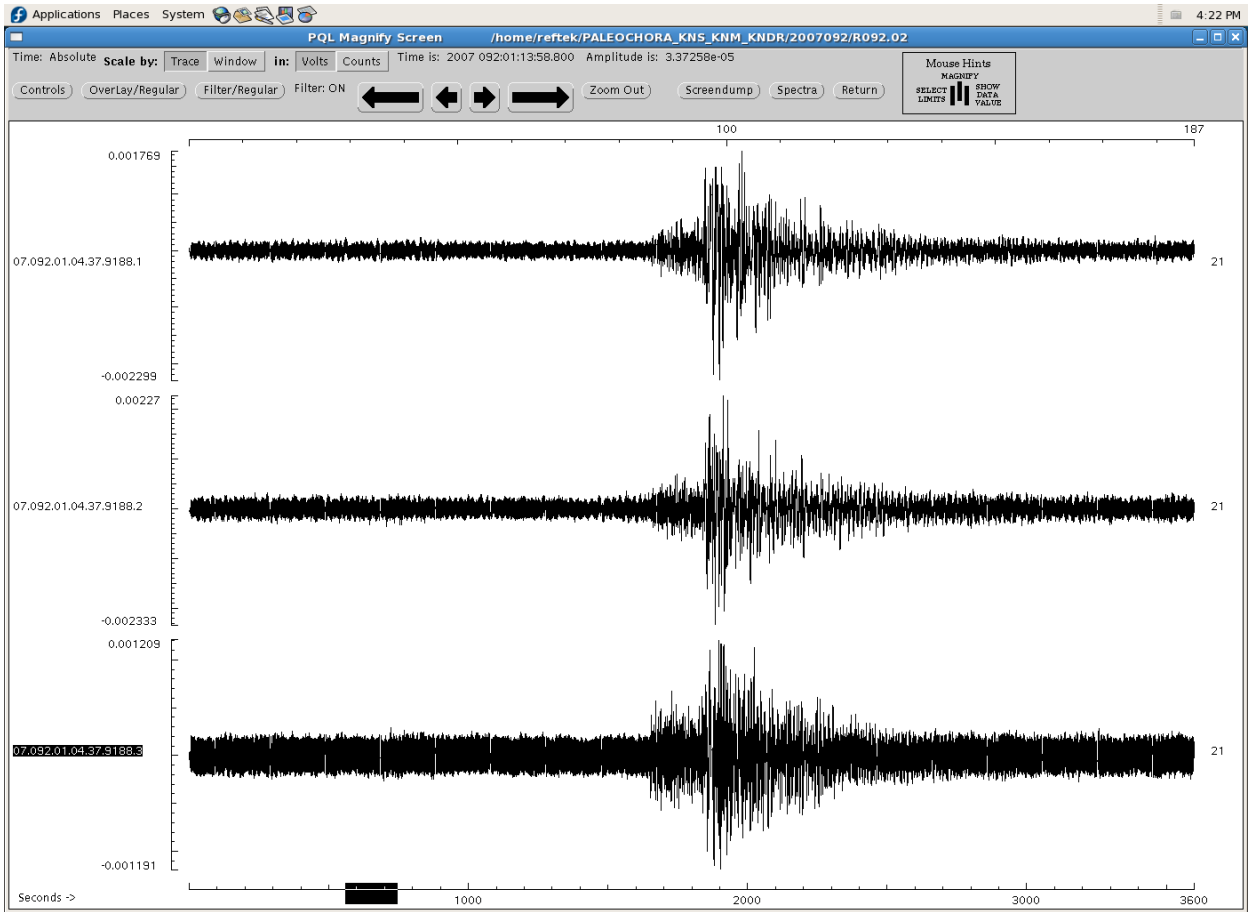


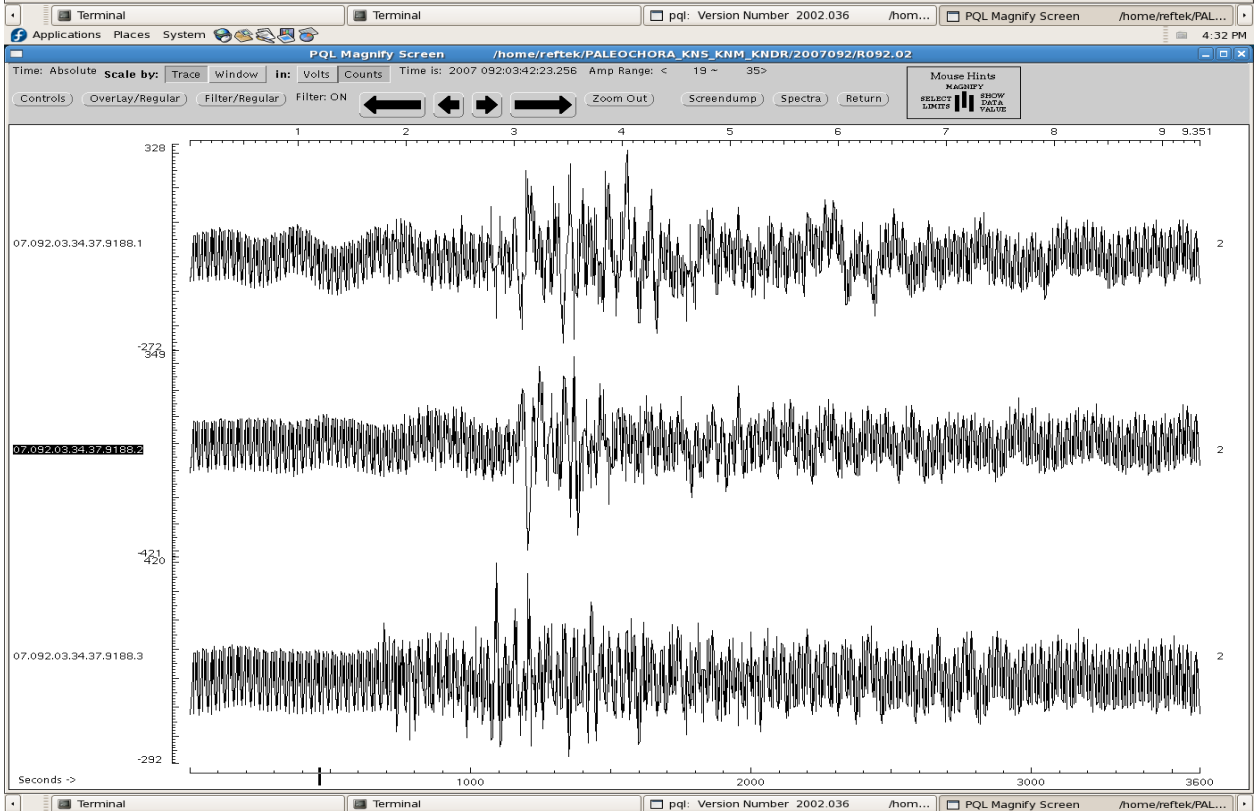
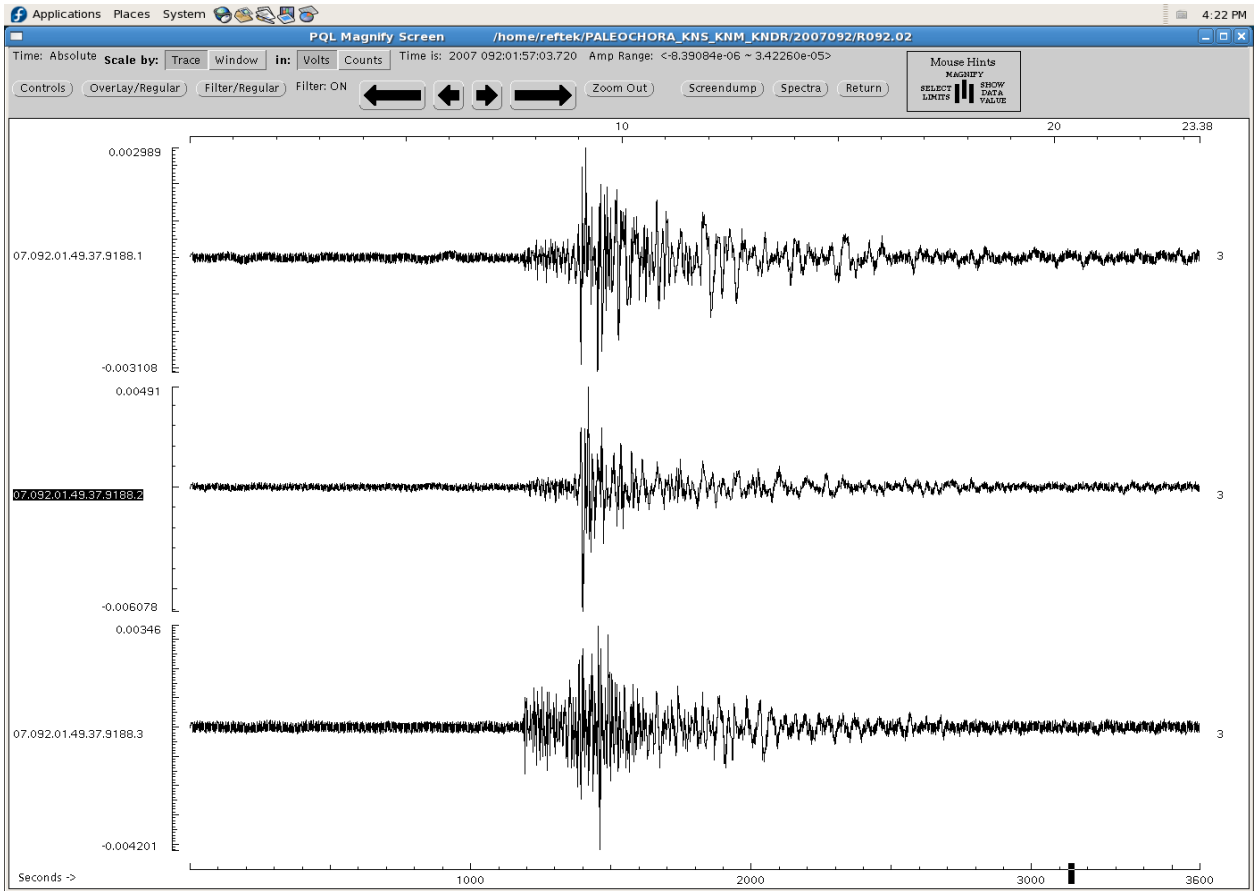


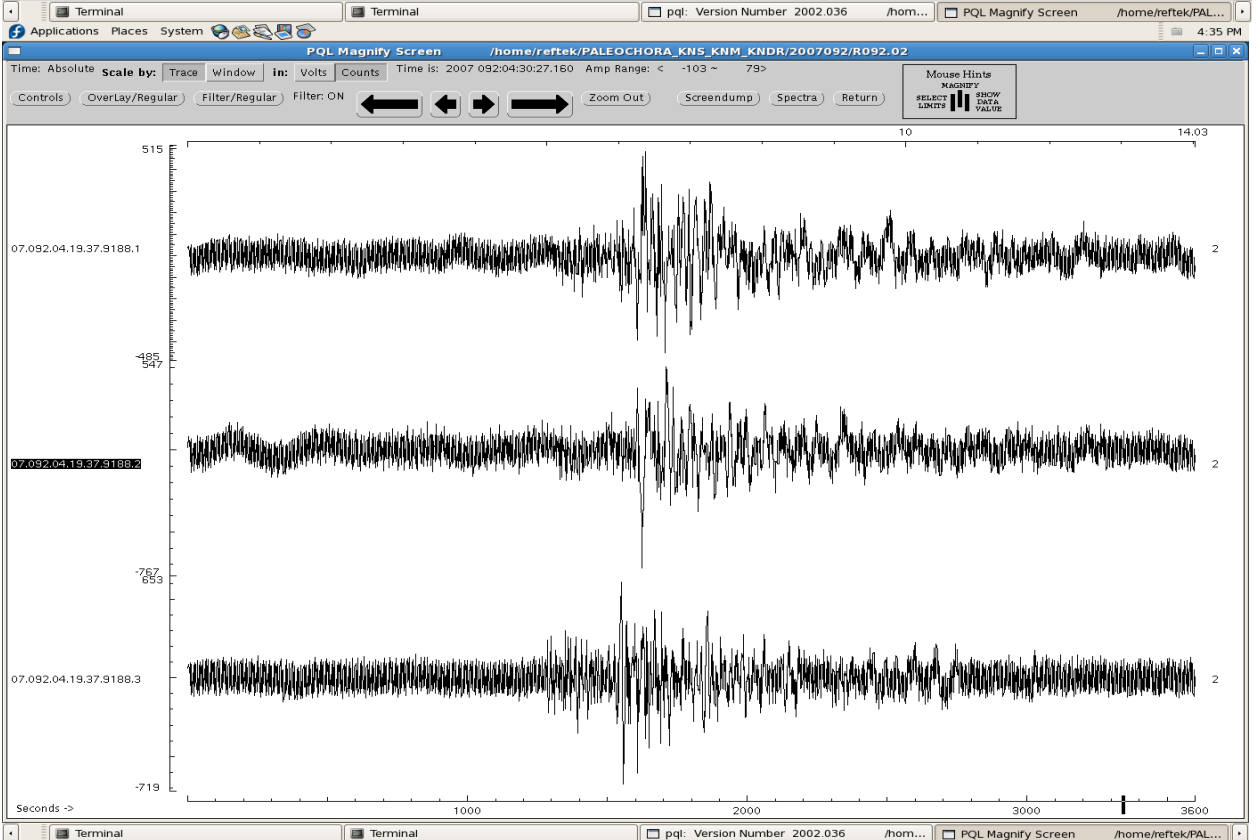
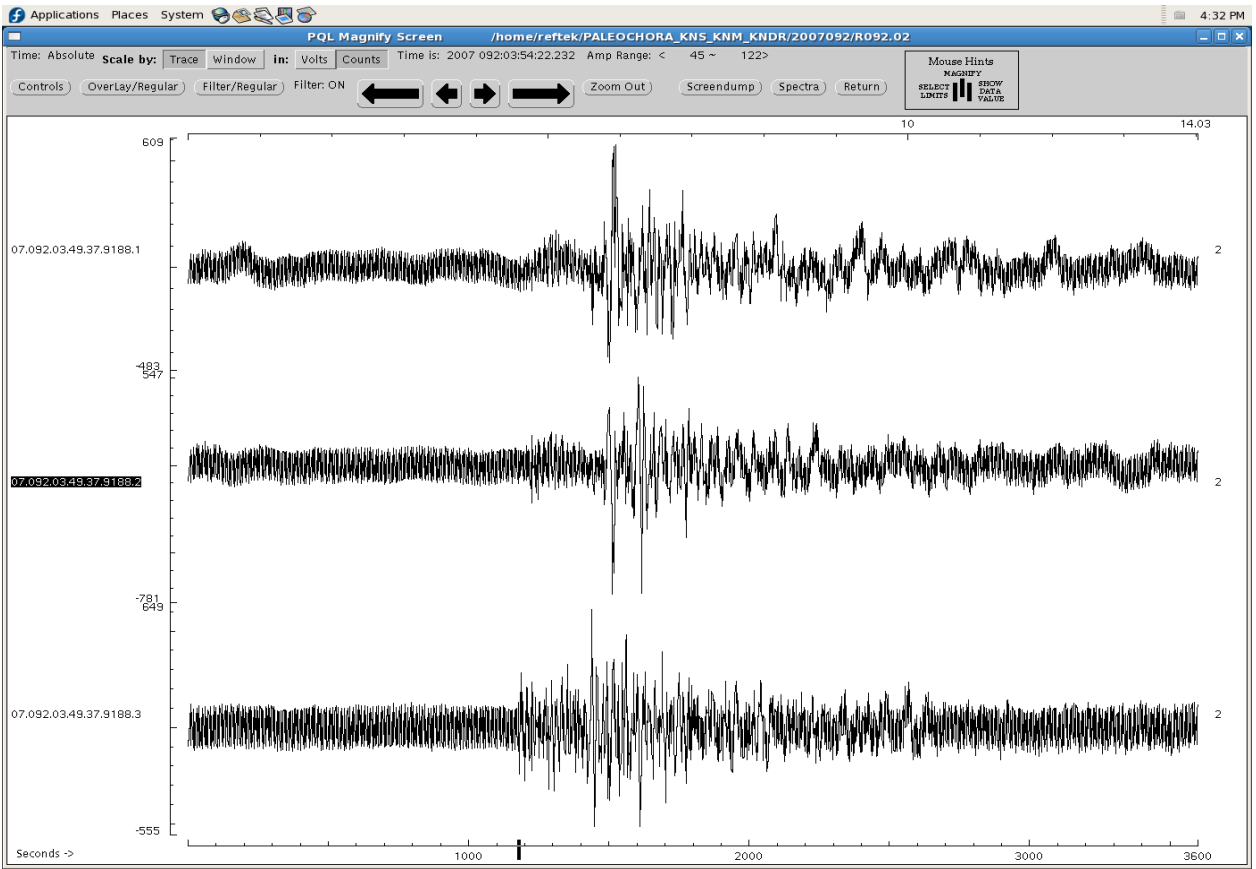


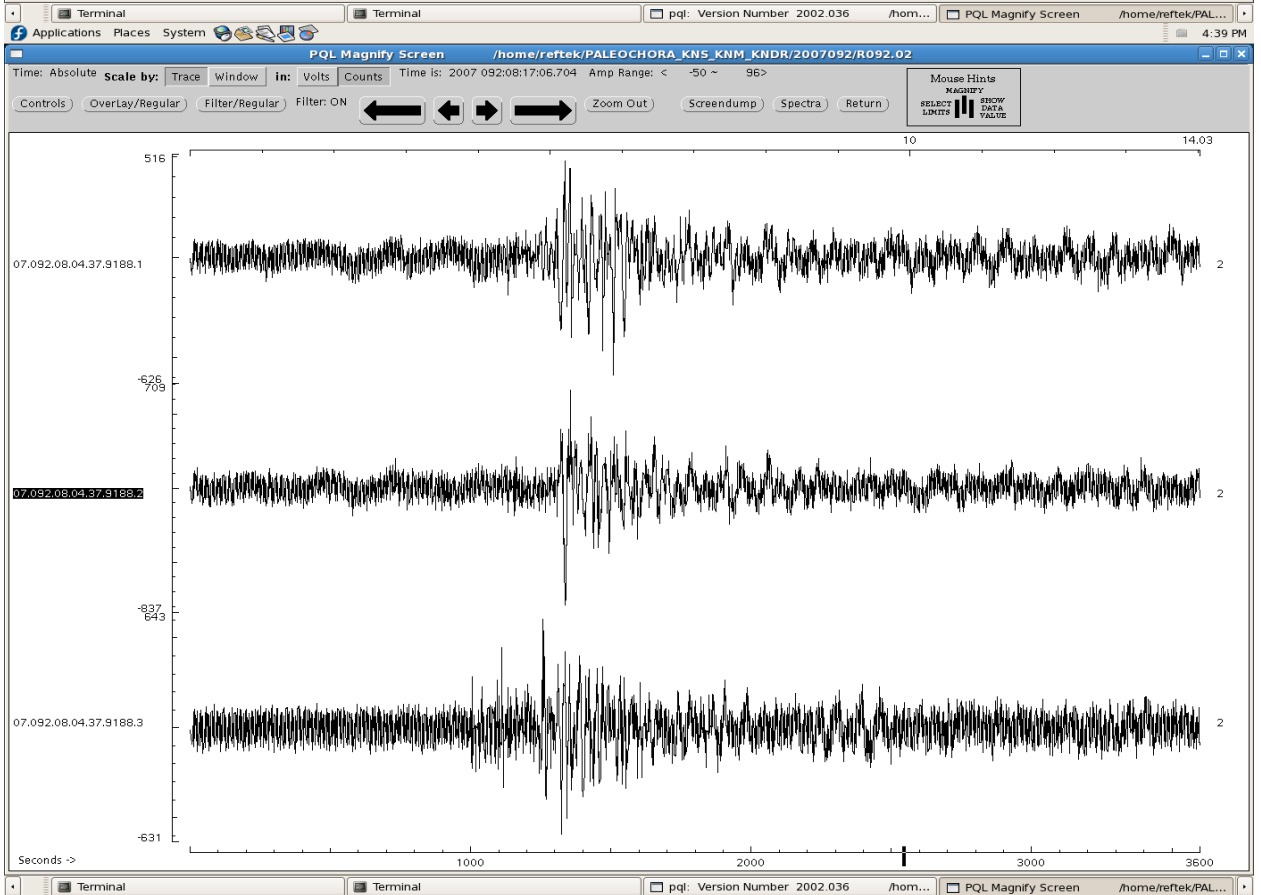
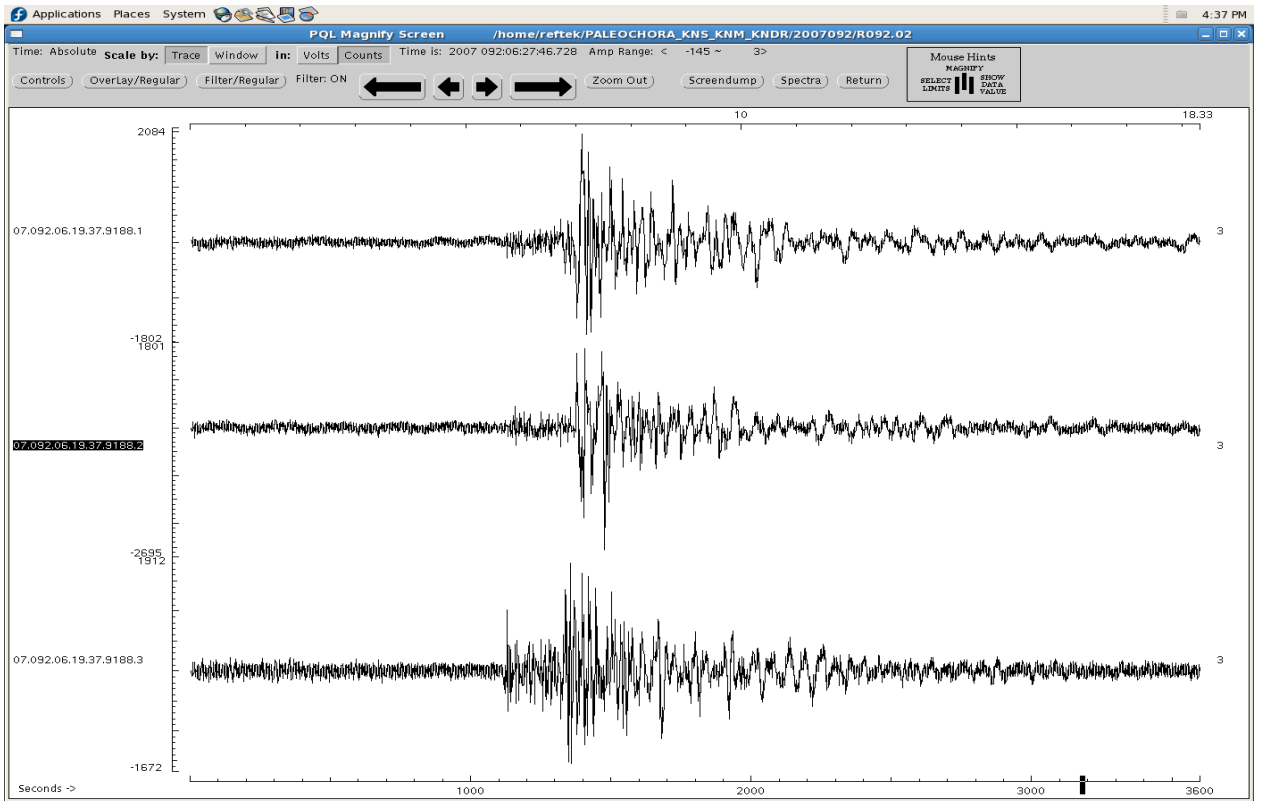


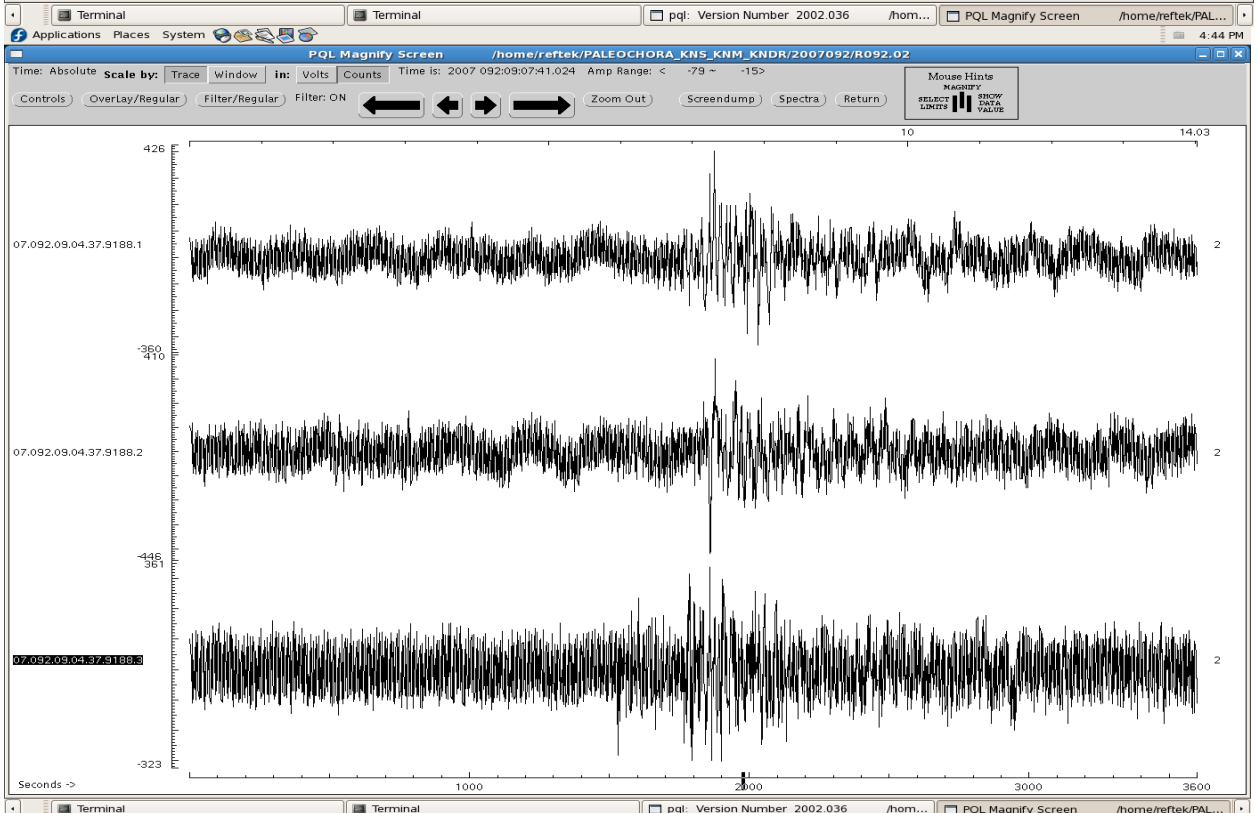
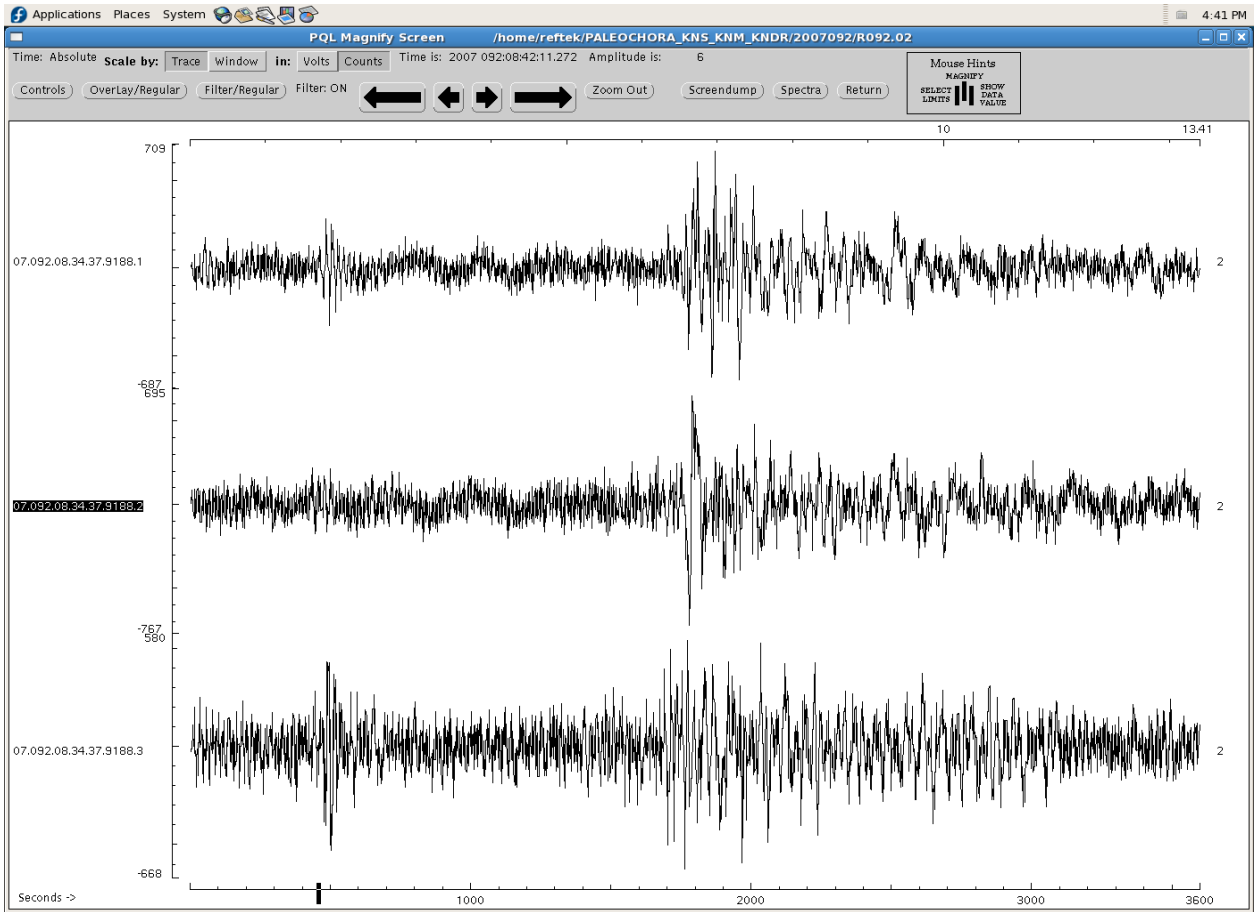


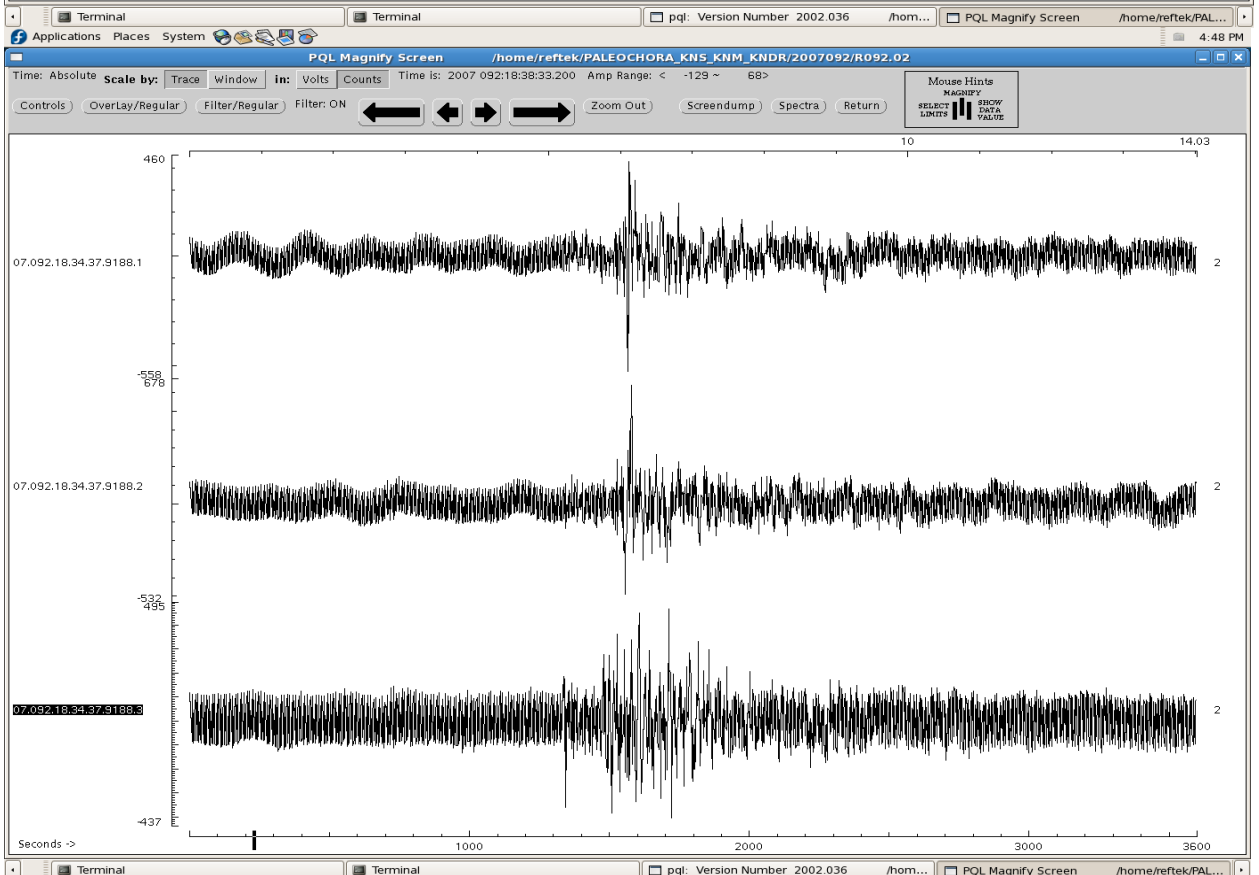
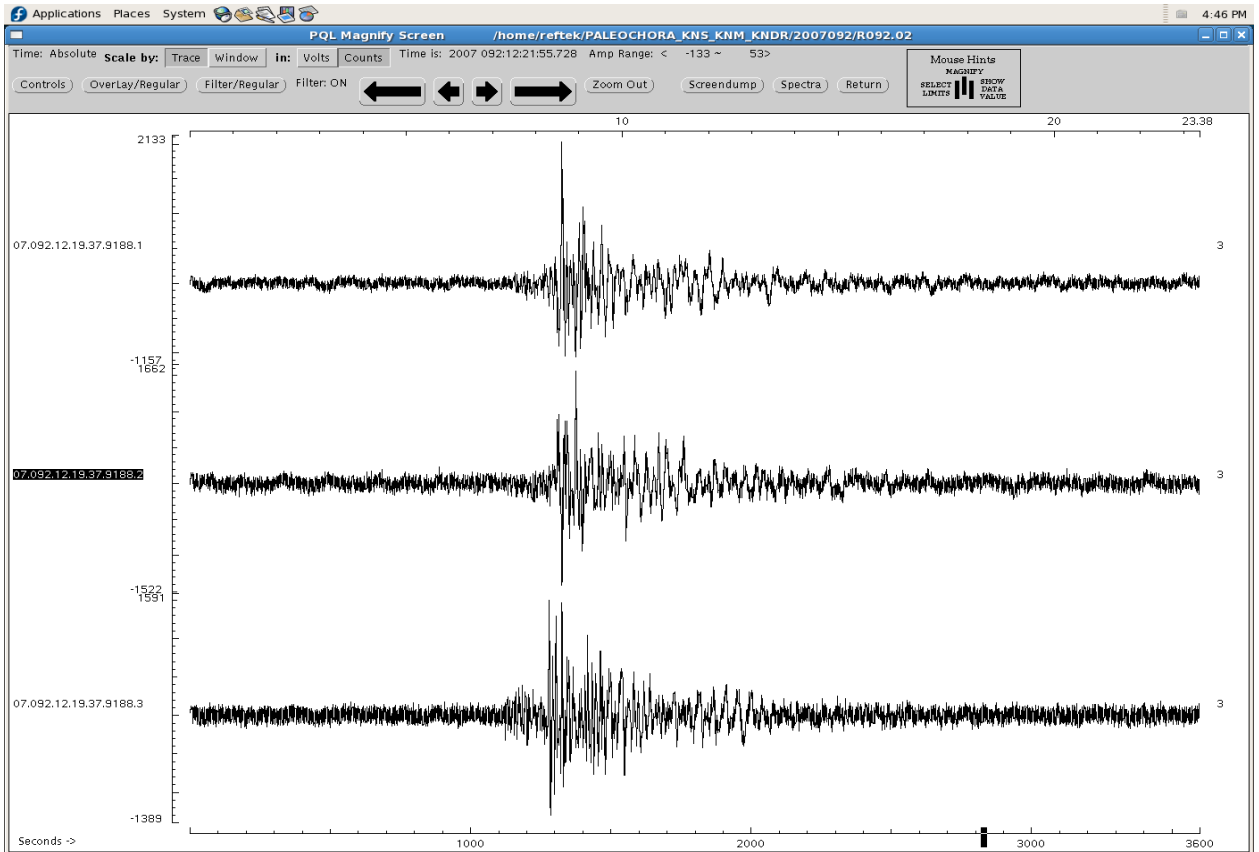




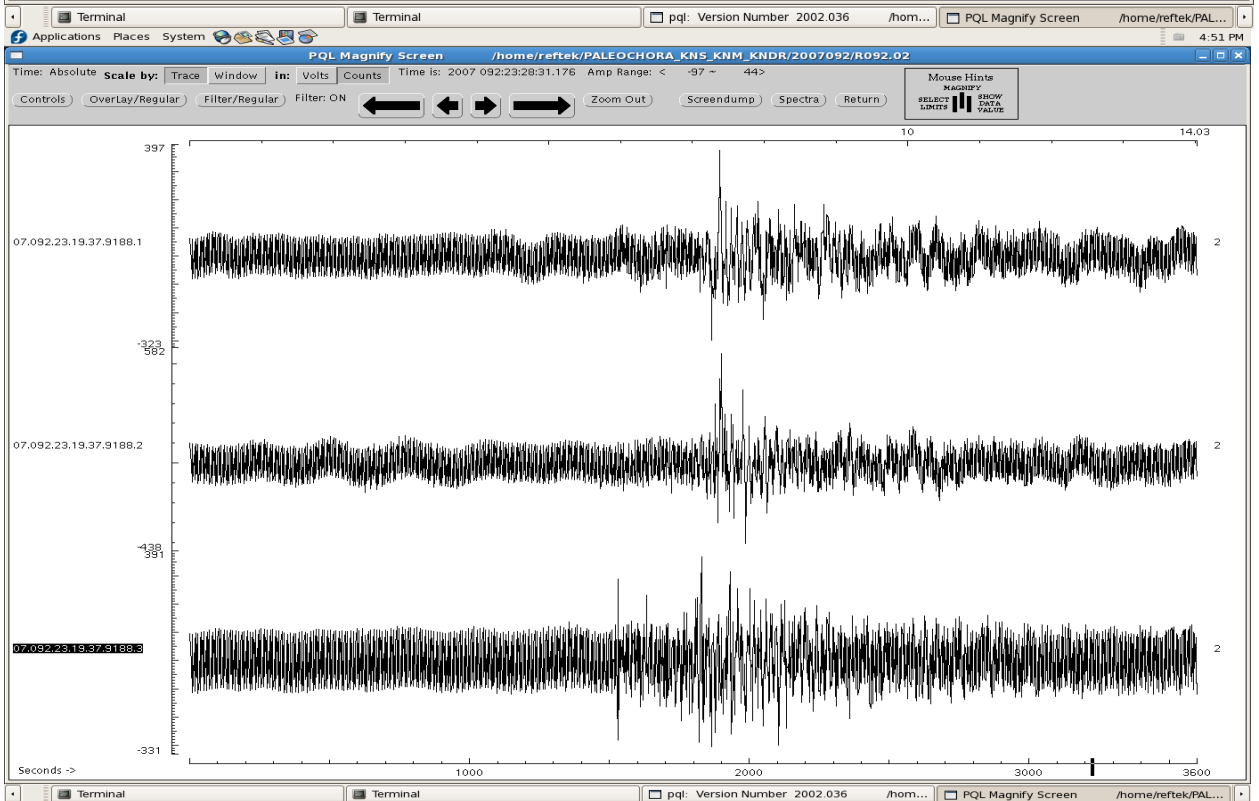
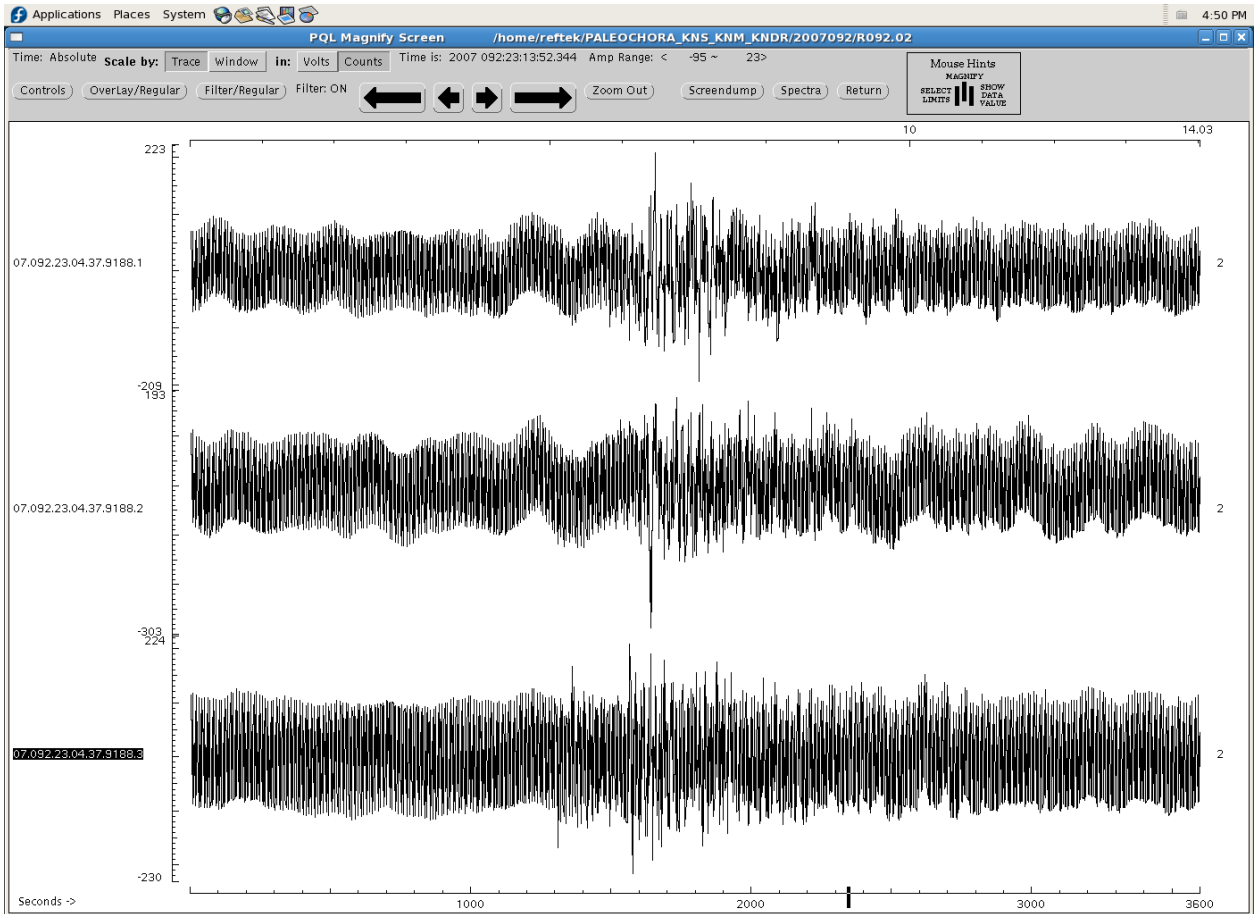


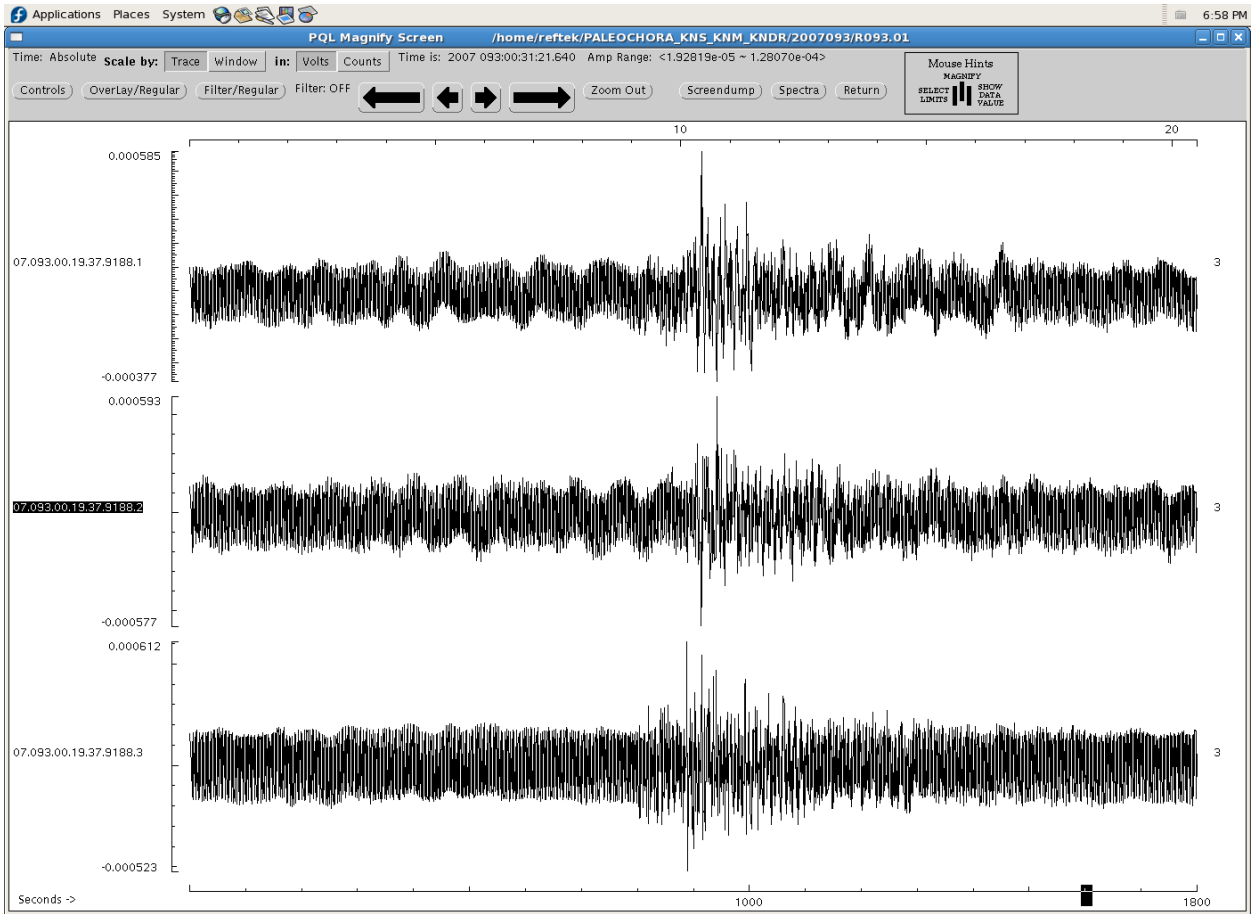




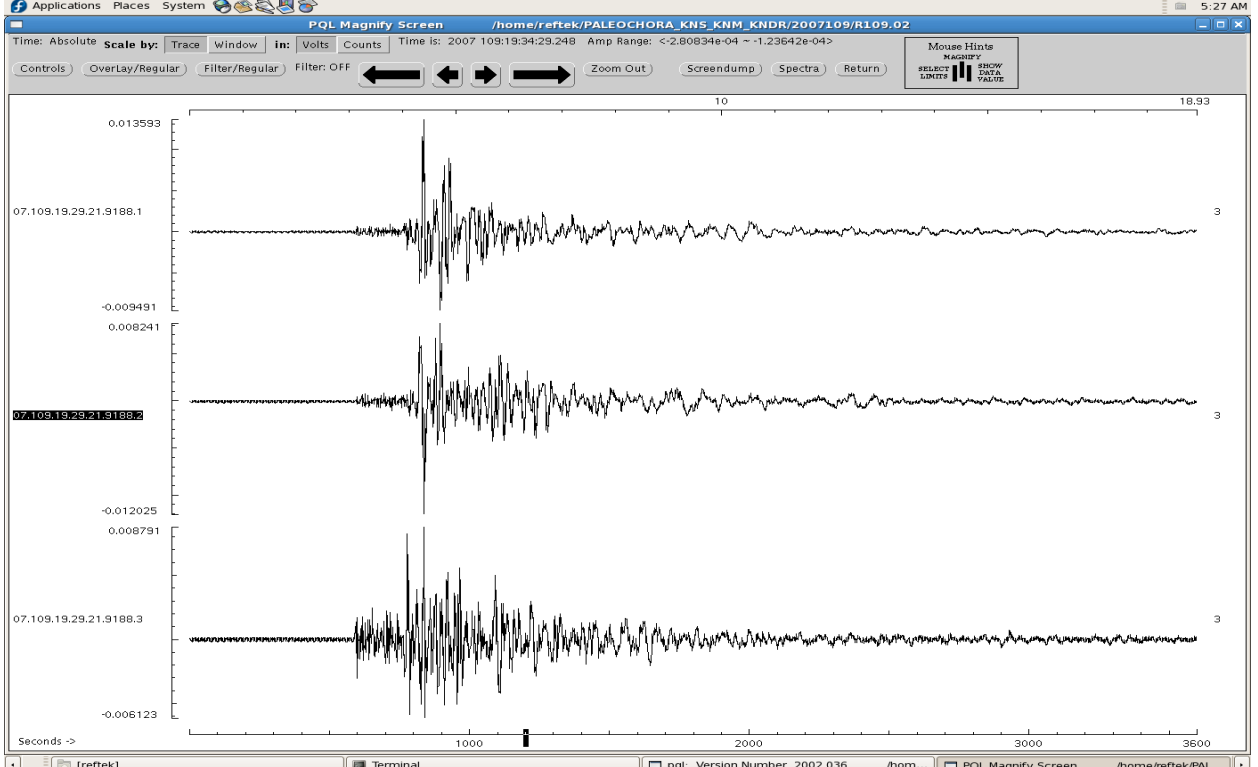




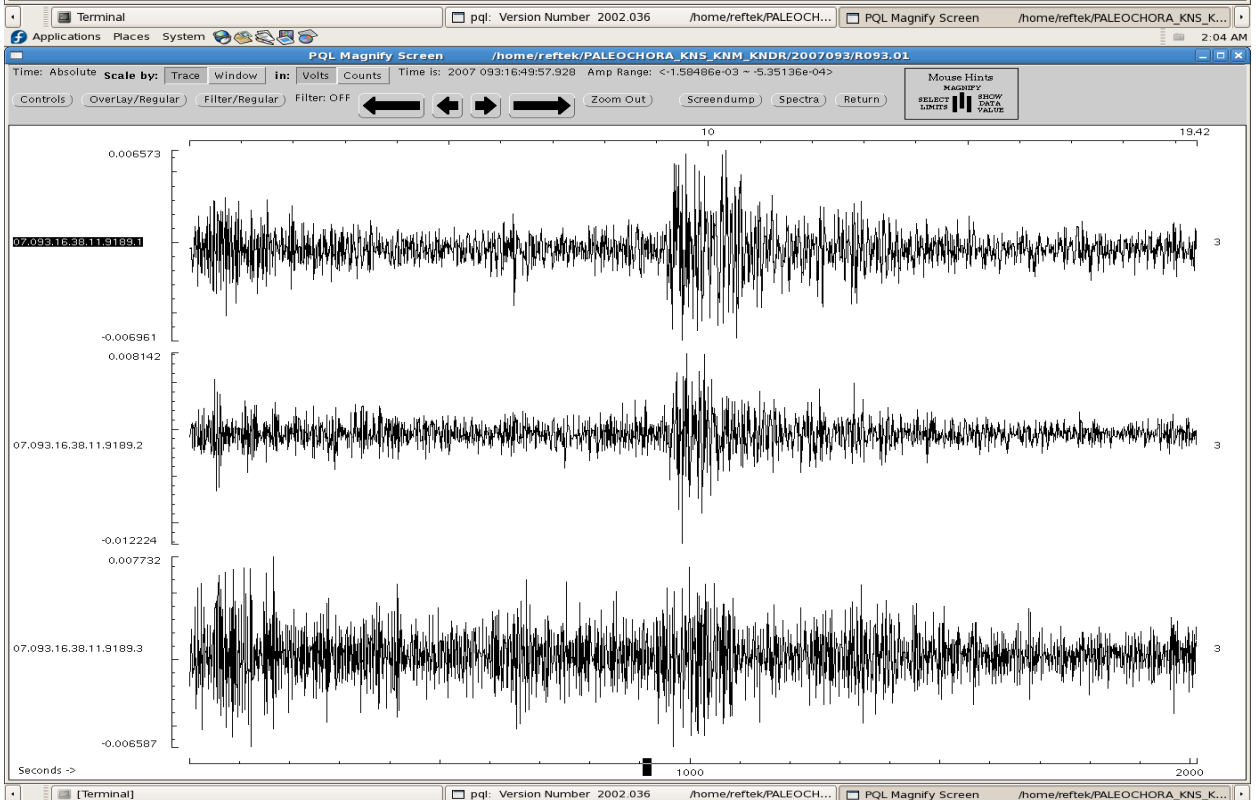
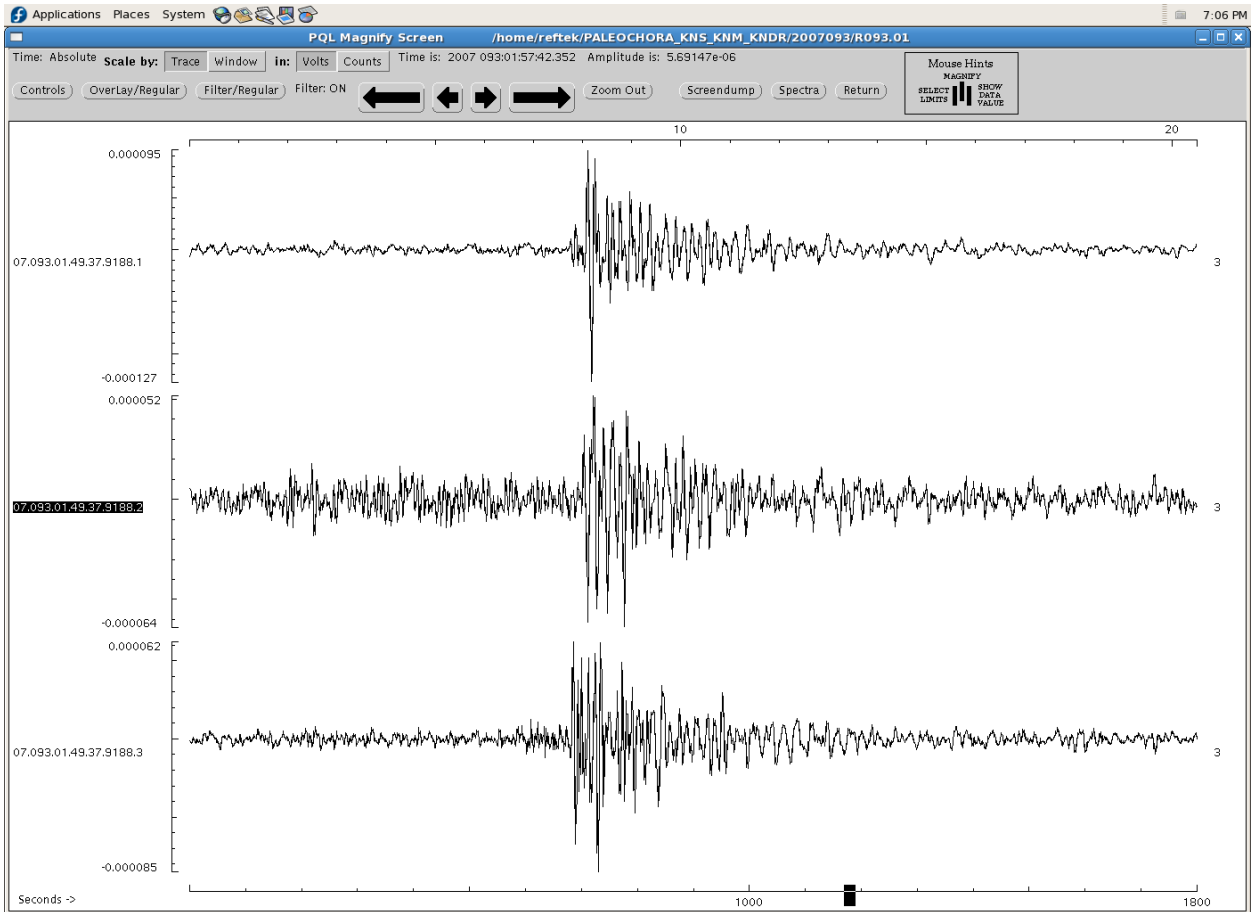


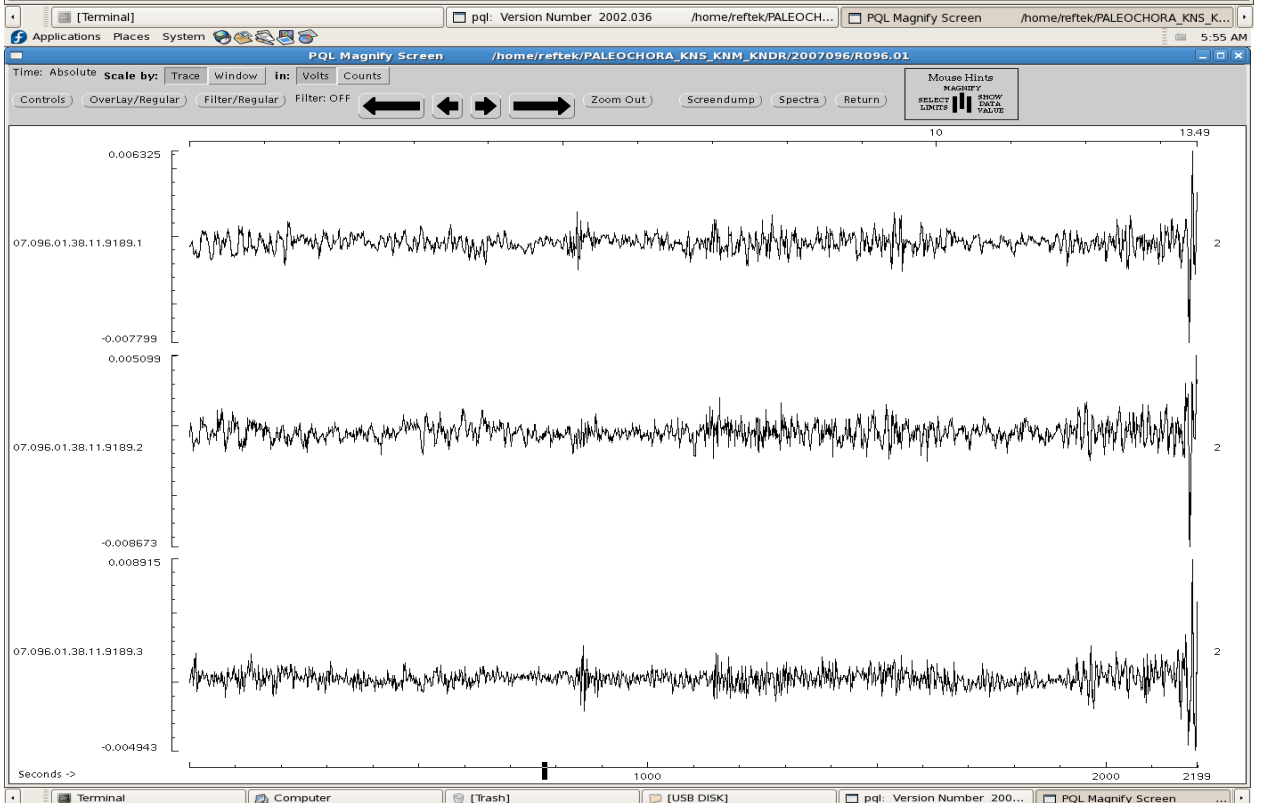
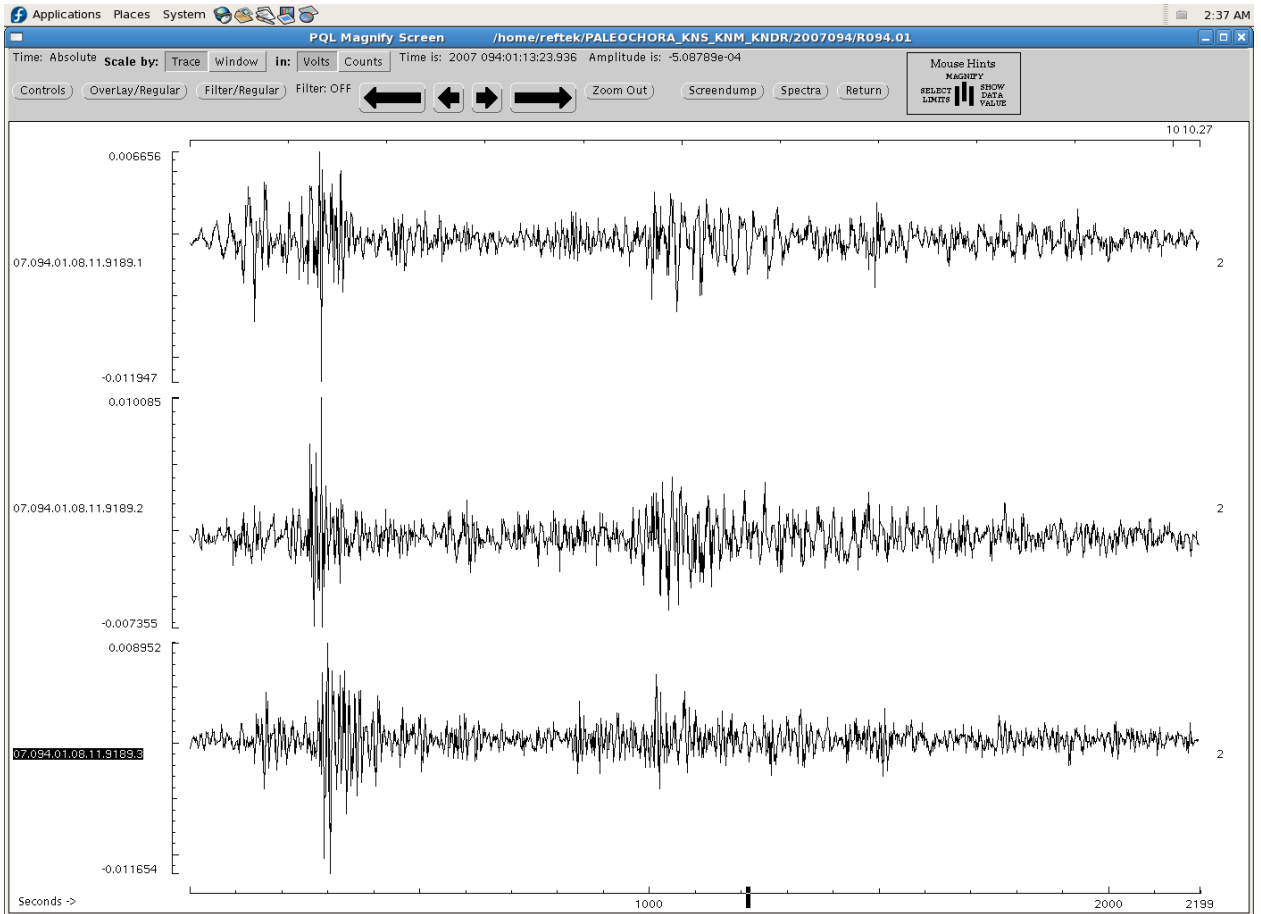


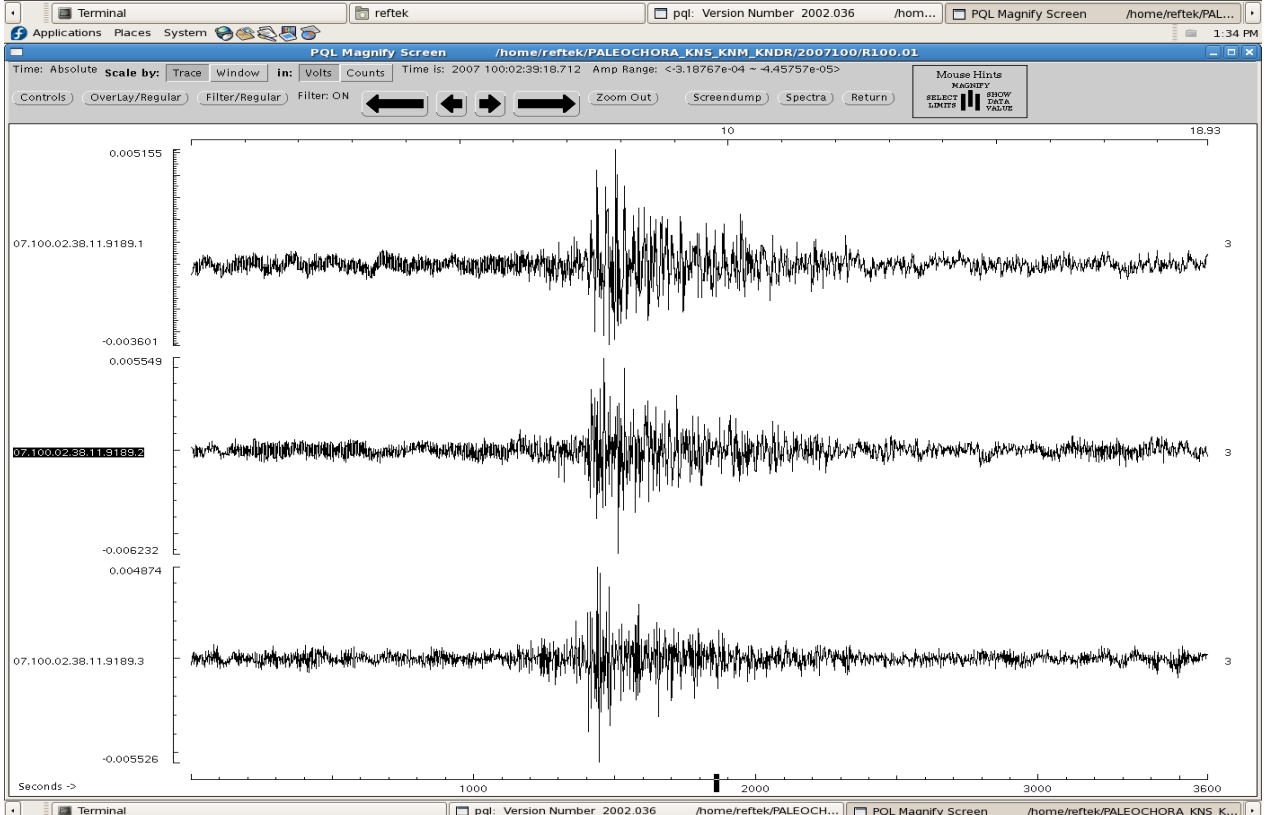
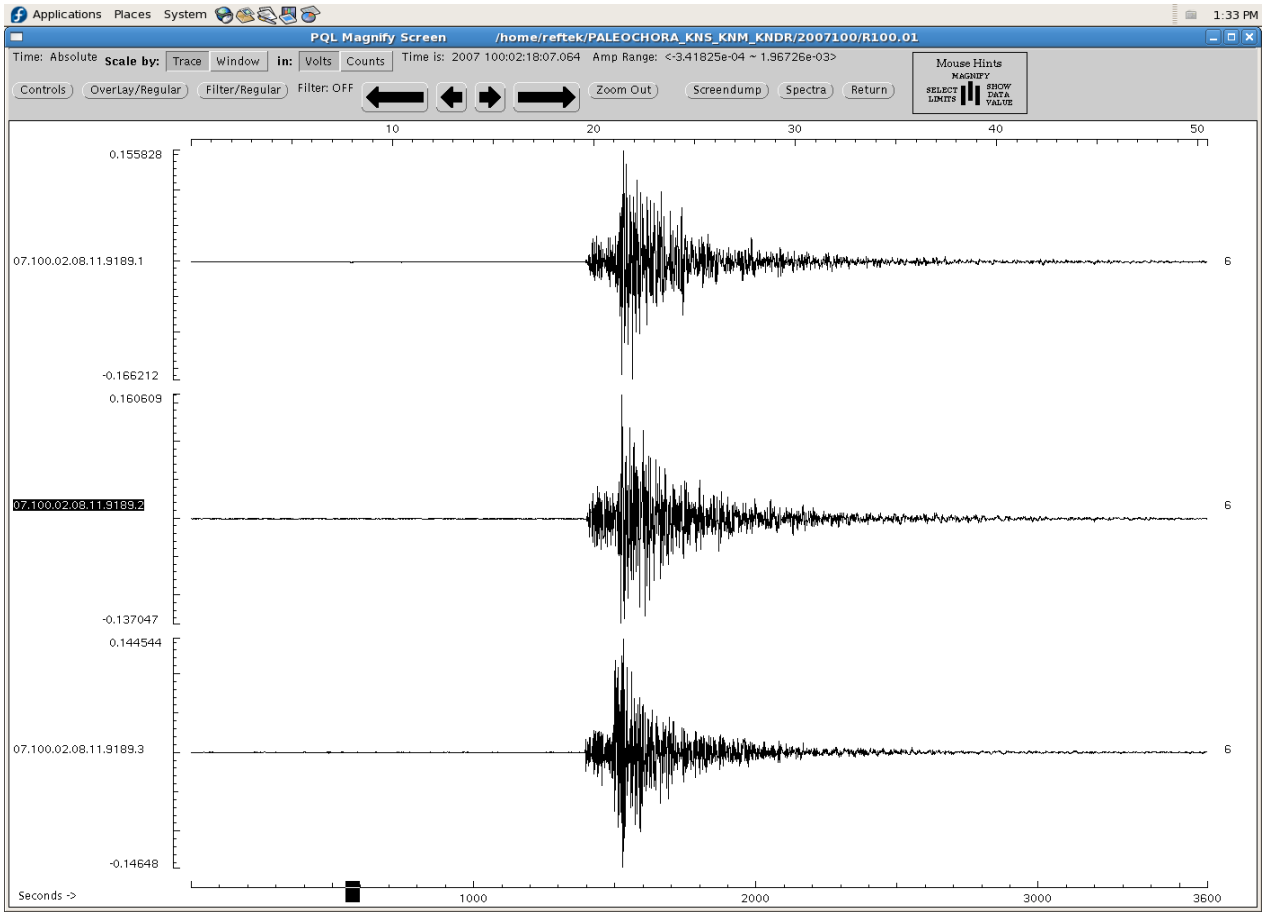
Terminal pql: Version Number 2002.036 /home/reftek/PALEOCH...

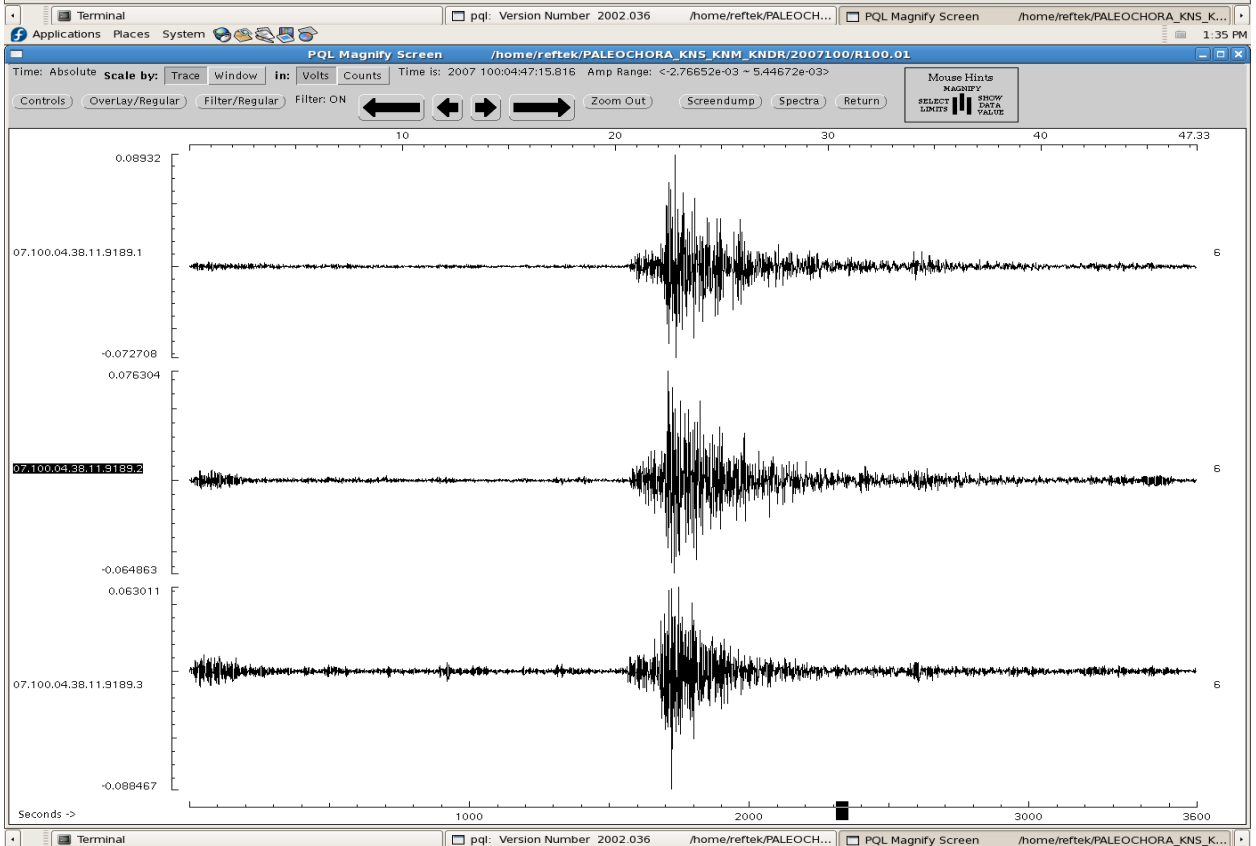
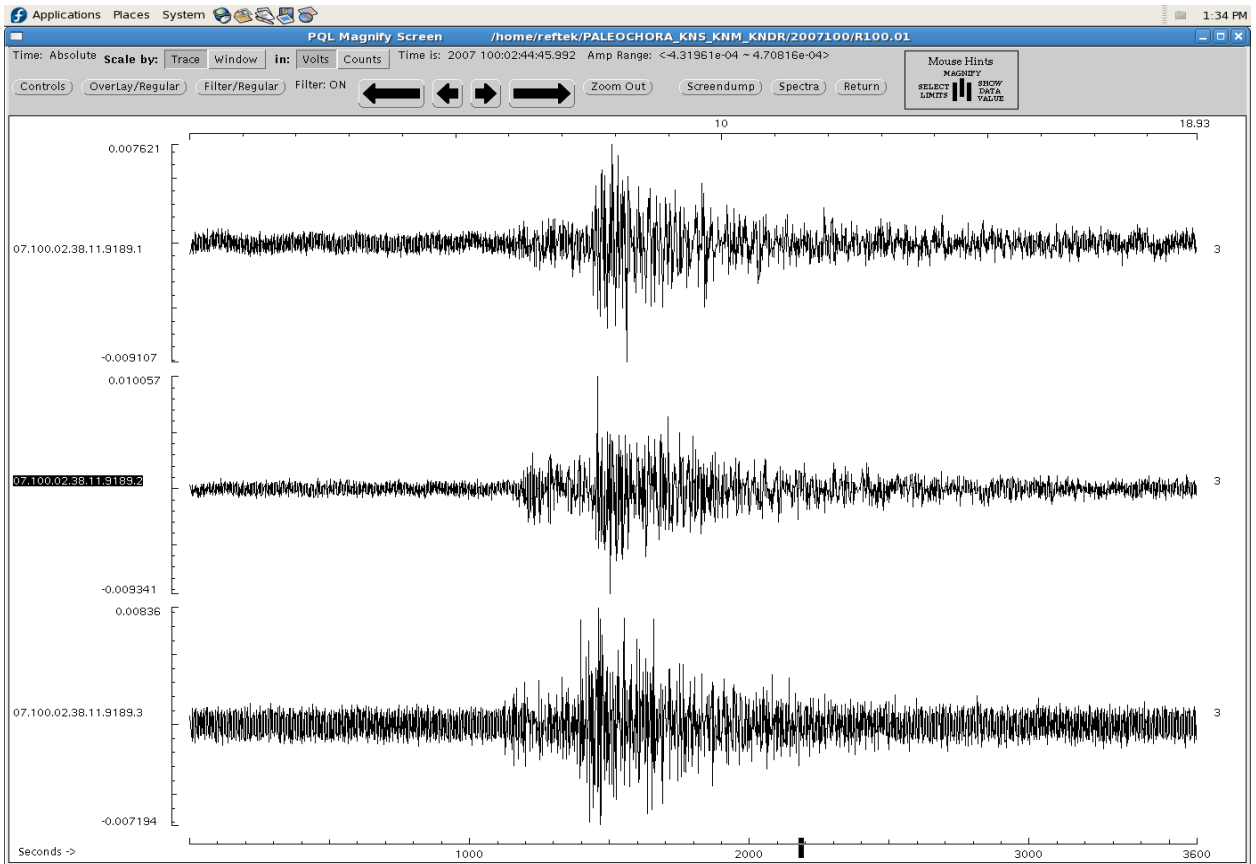


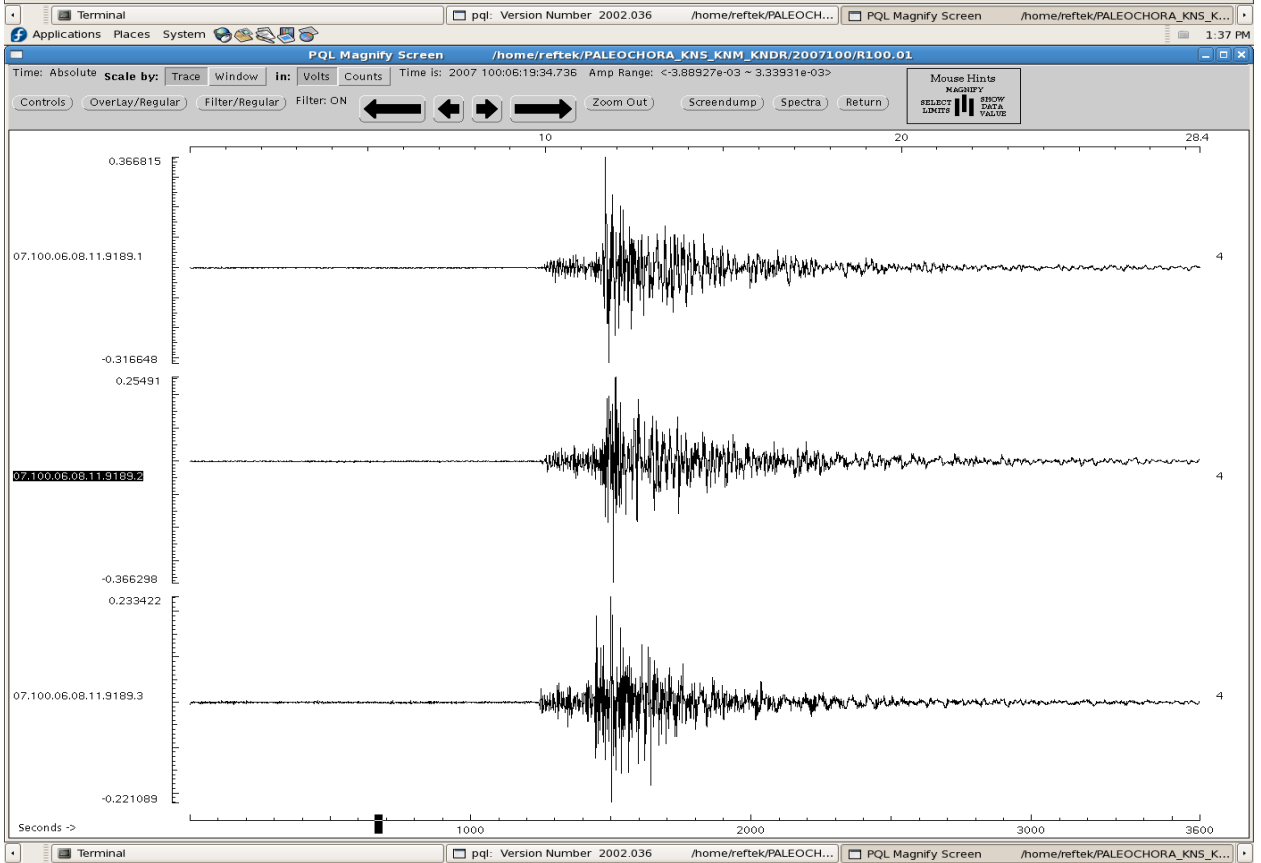
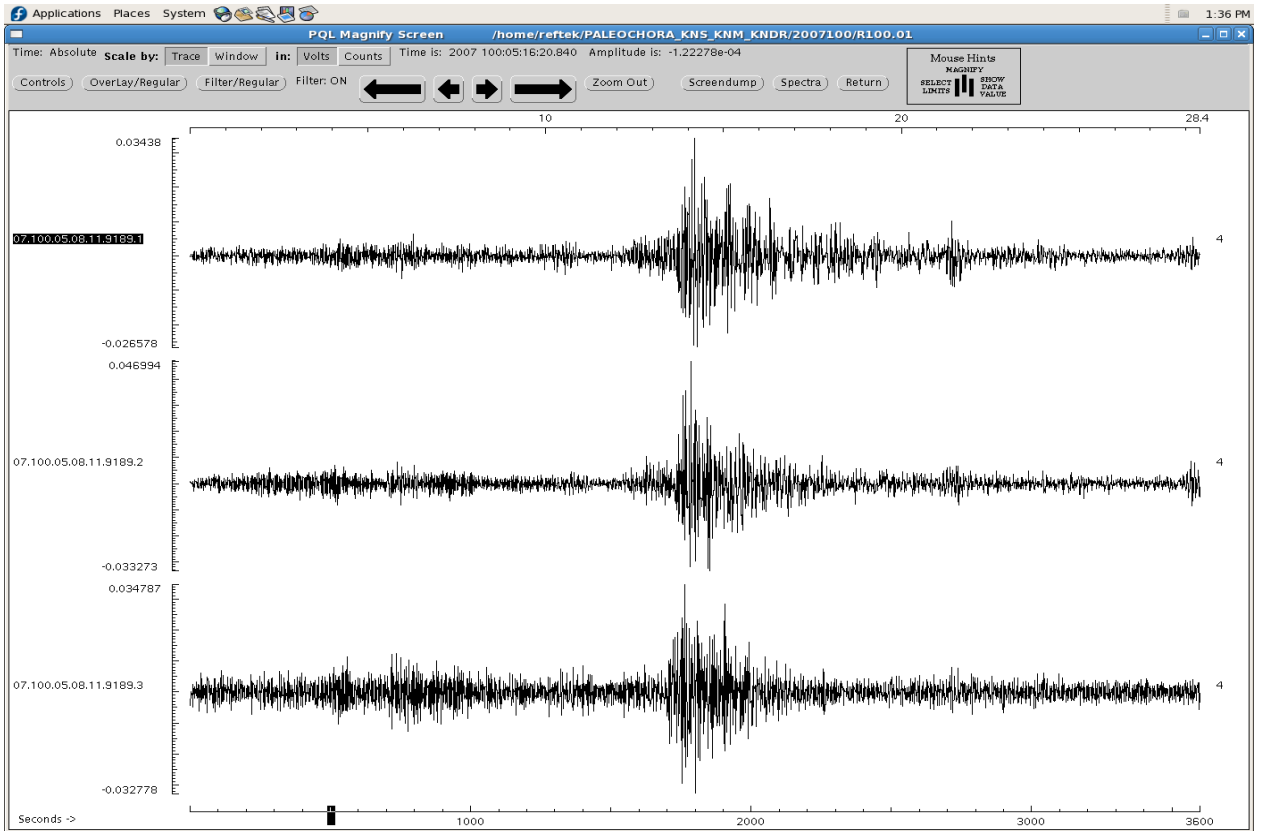
[reftek] Terminal pql: Version Number 2002.036 /hom... PQL Magnify Screen /home/reftek/PAL...

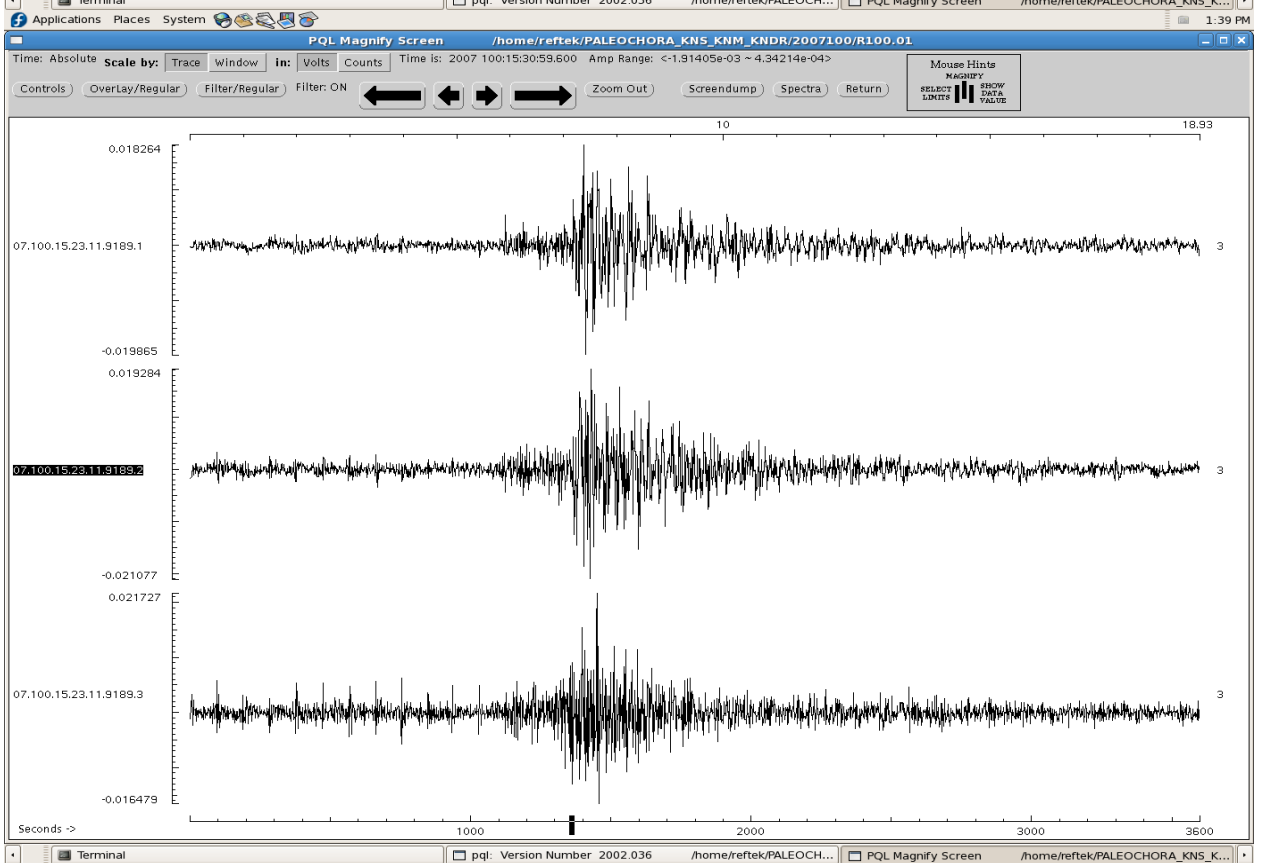
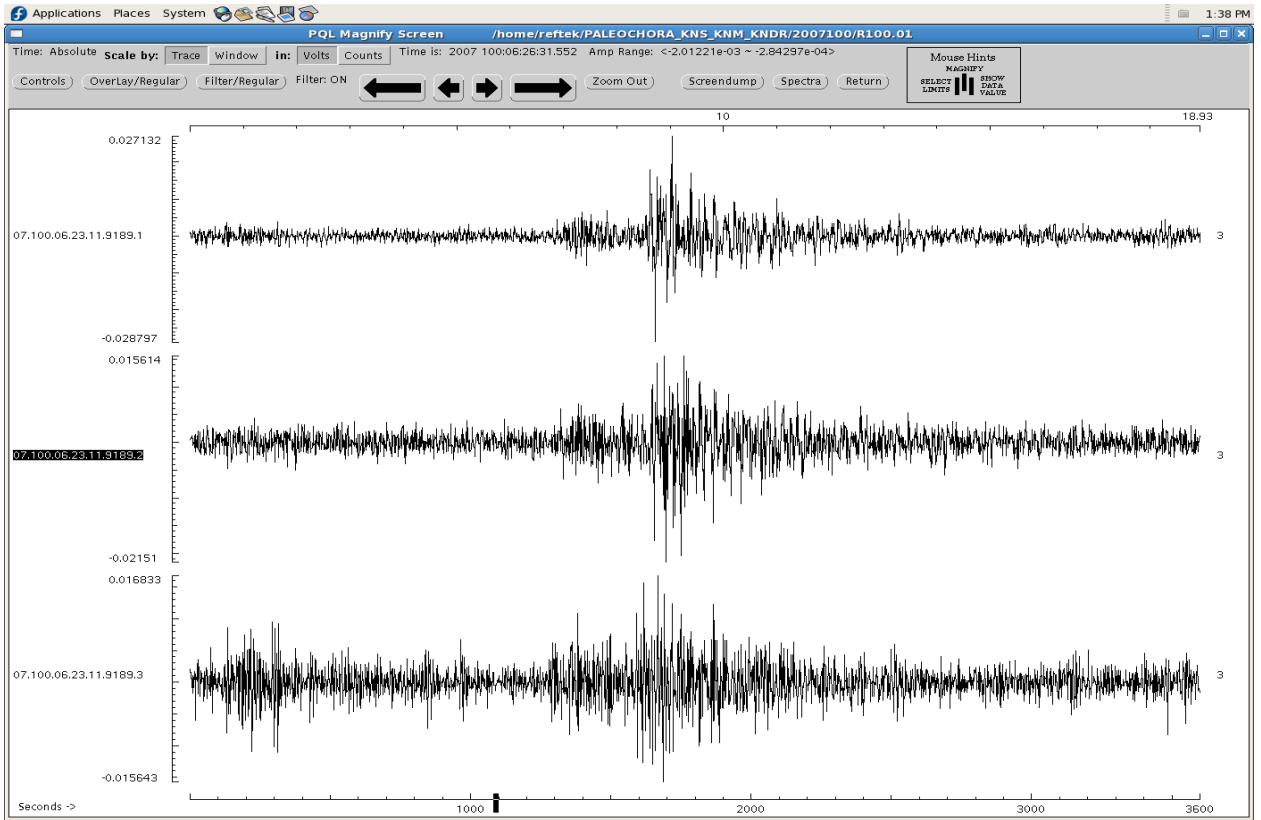




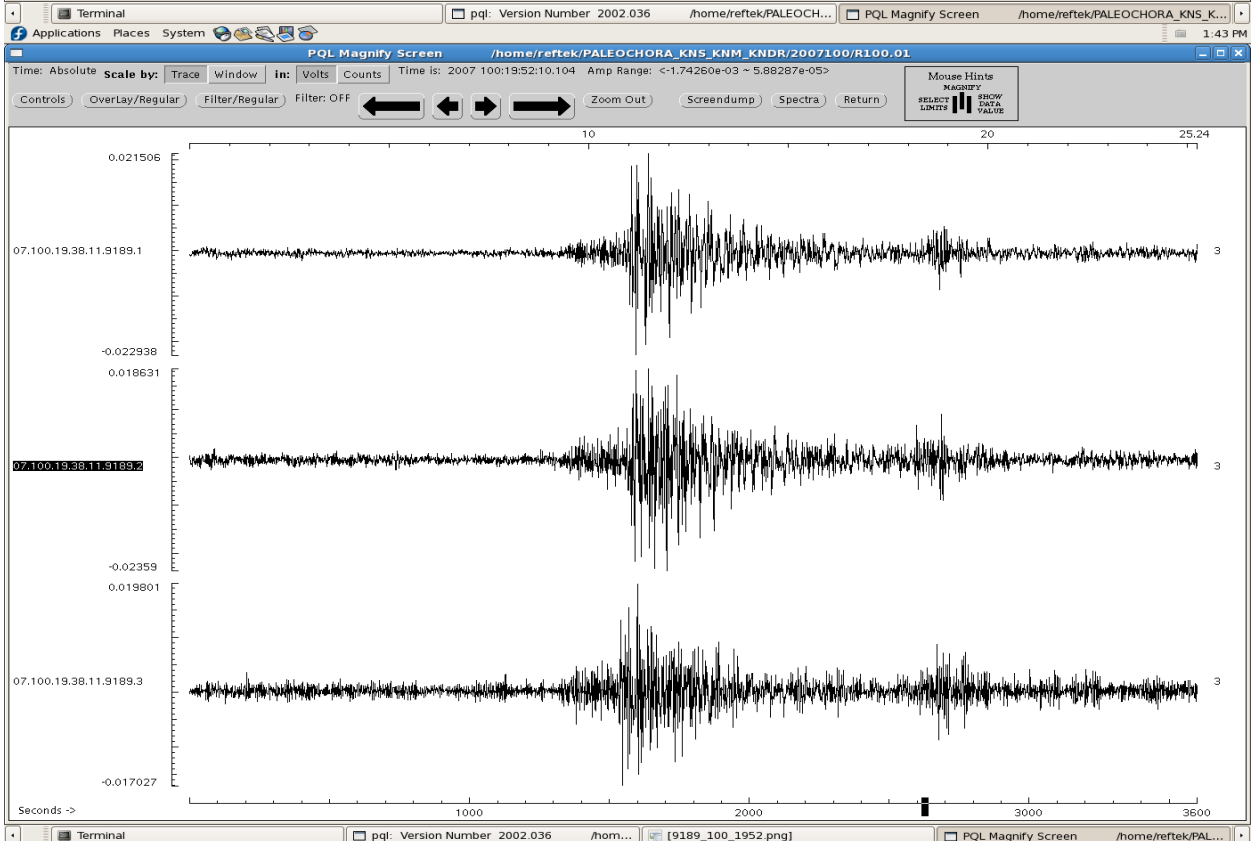
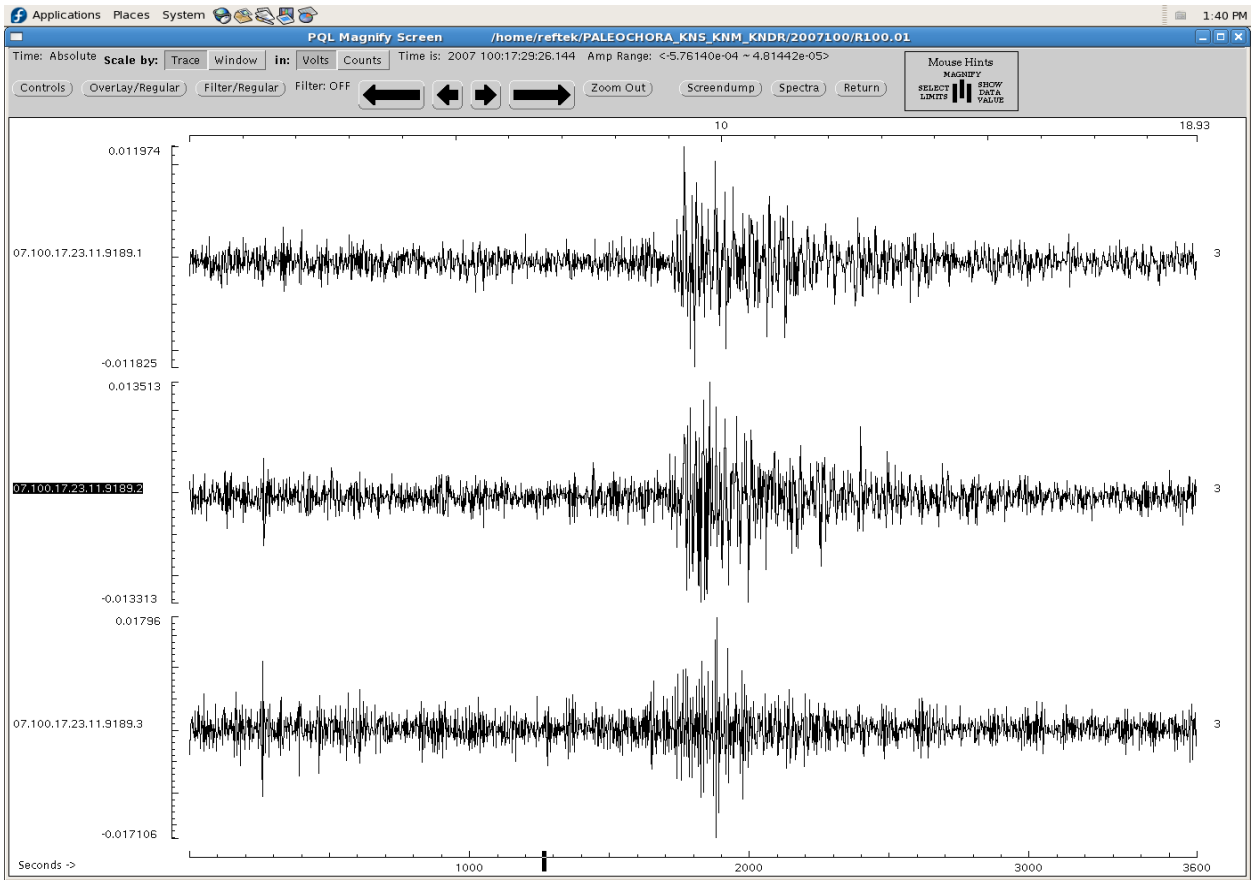


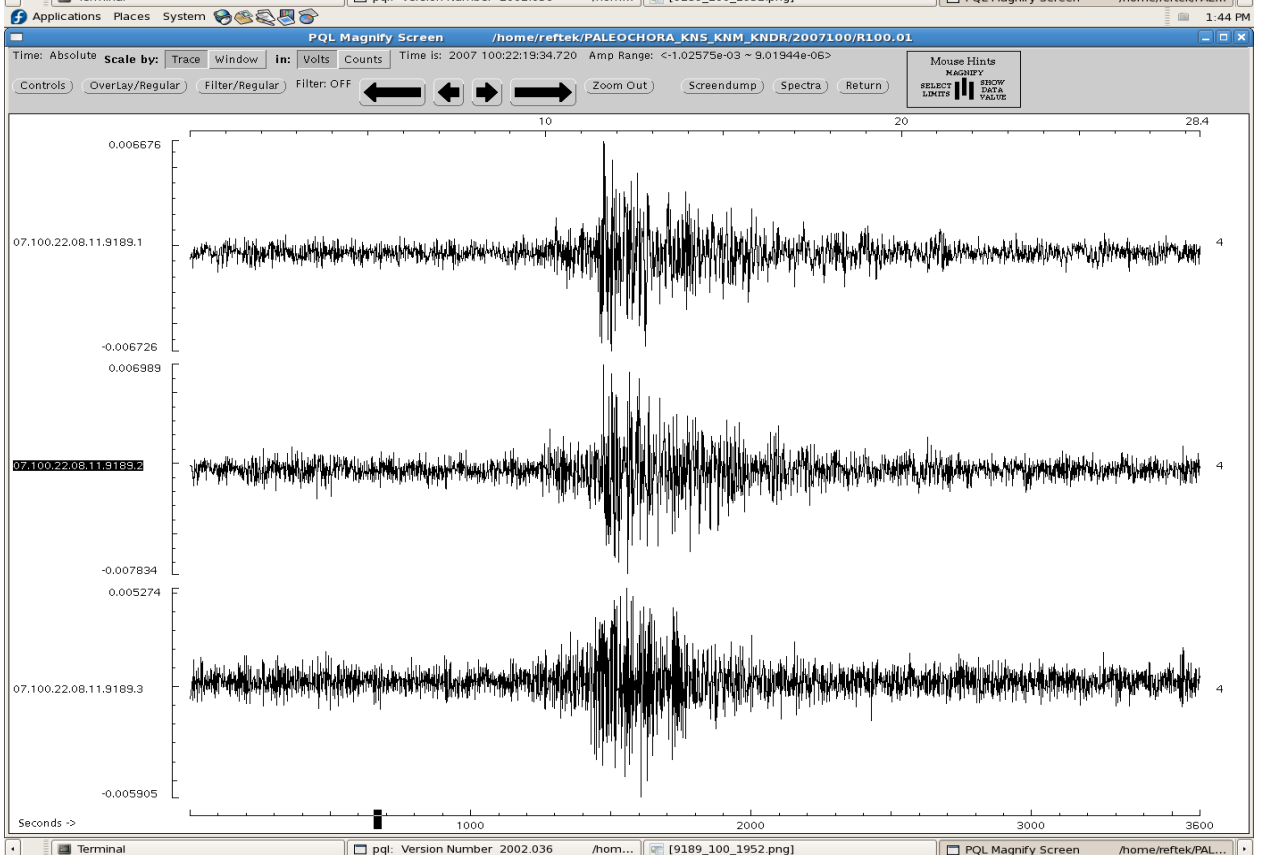
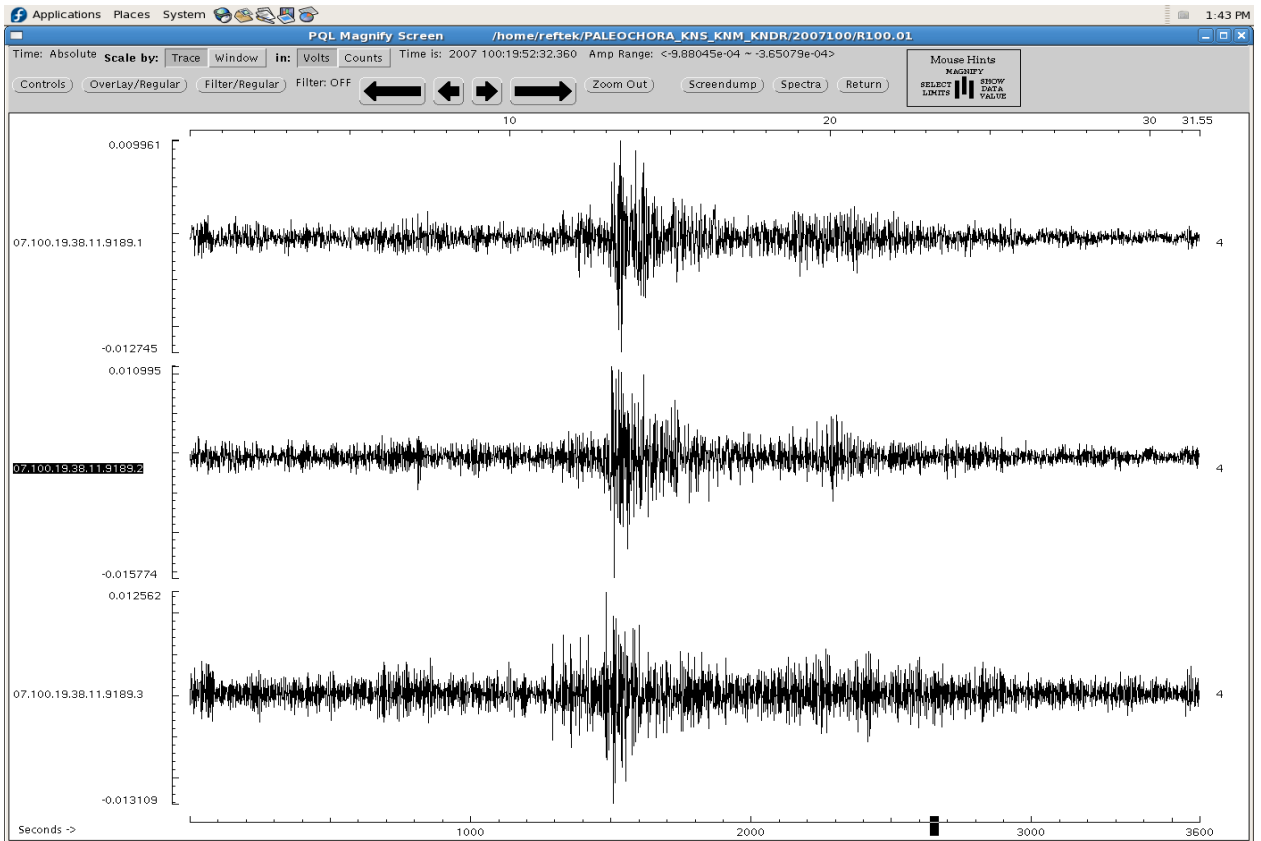


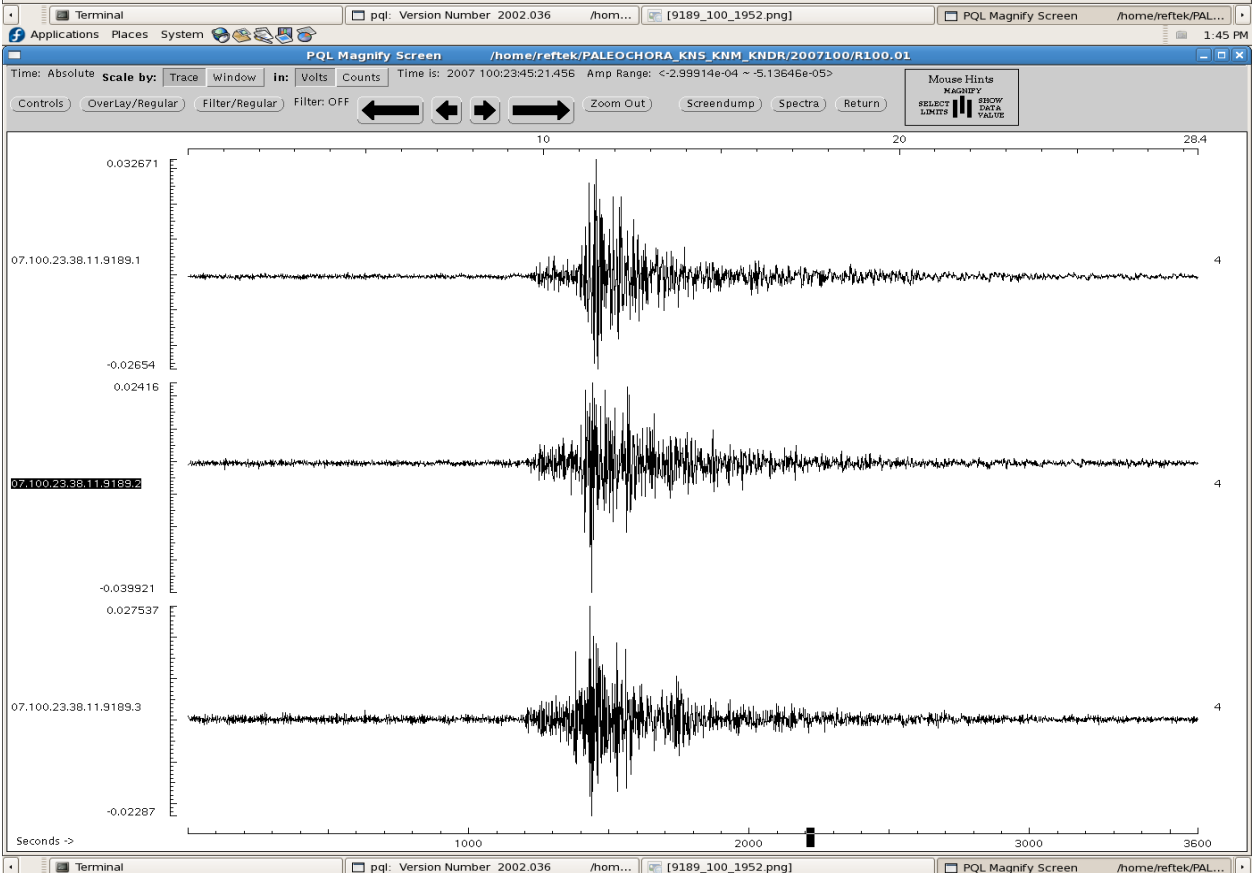
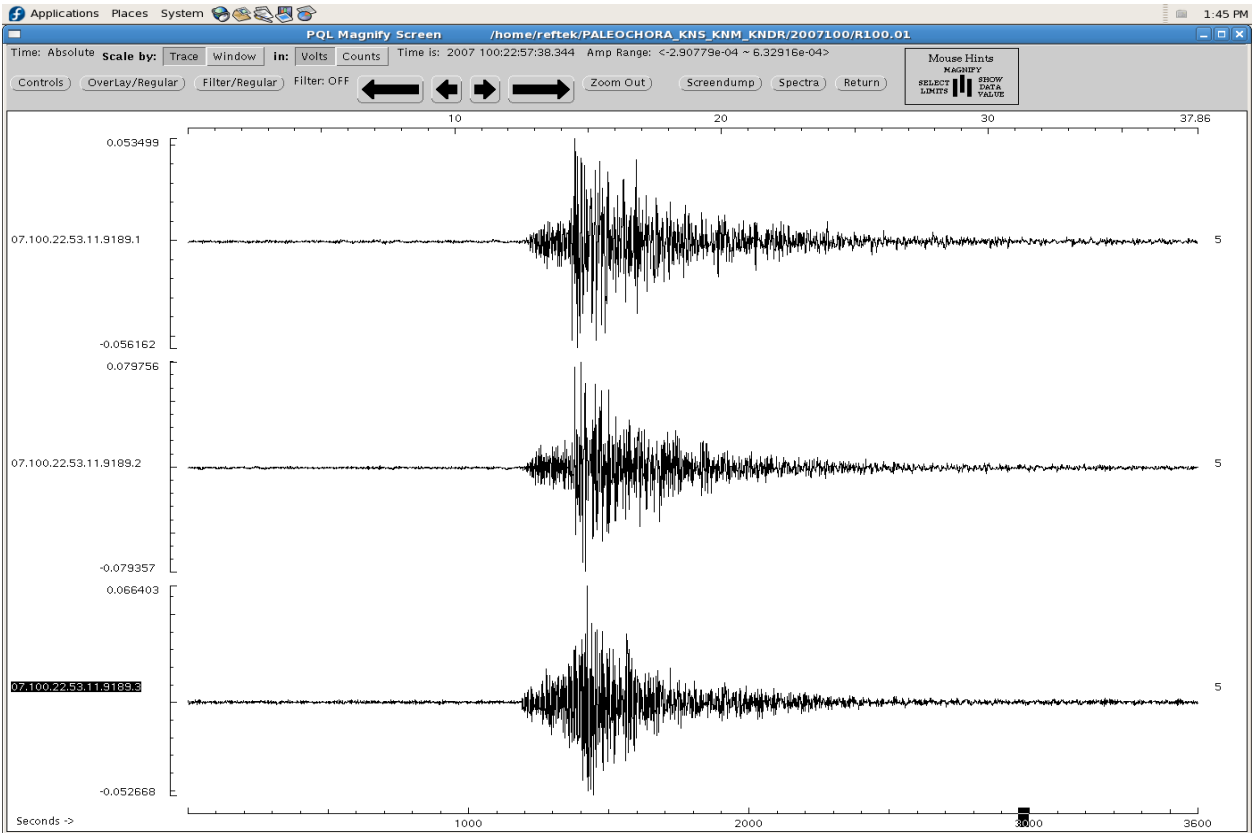


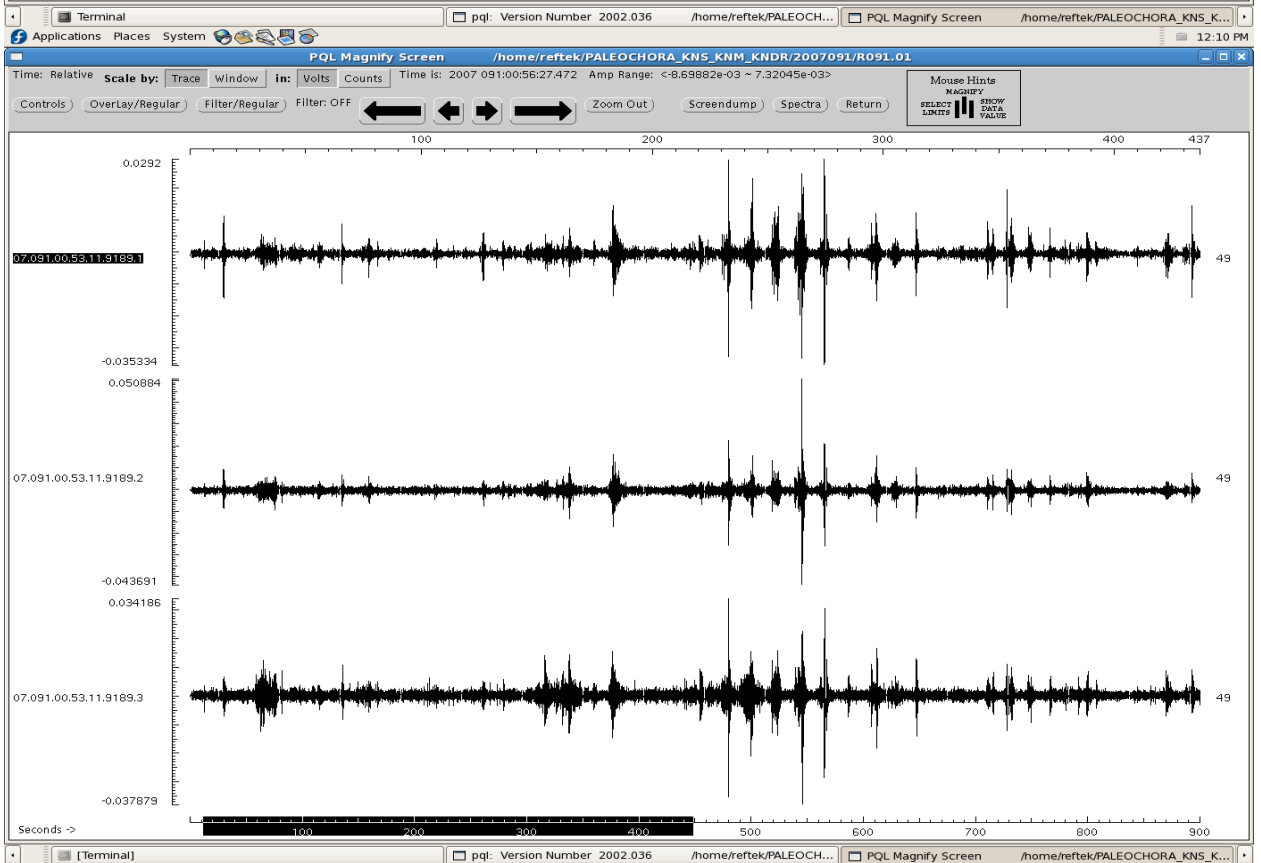
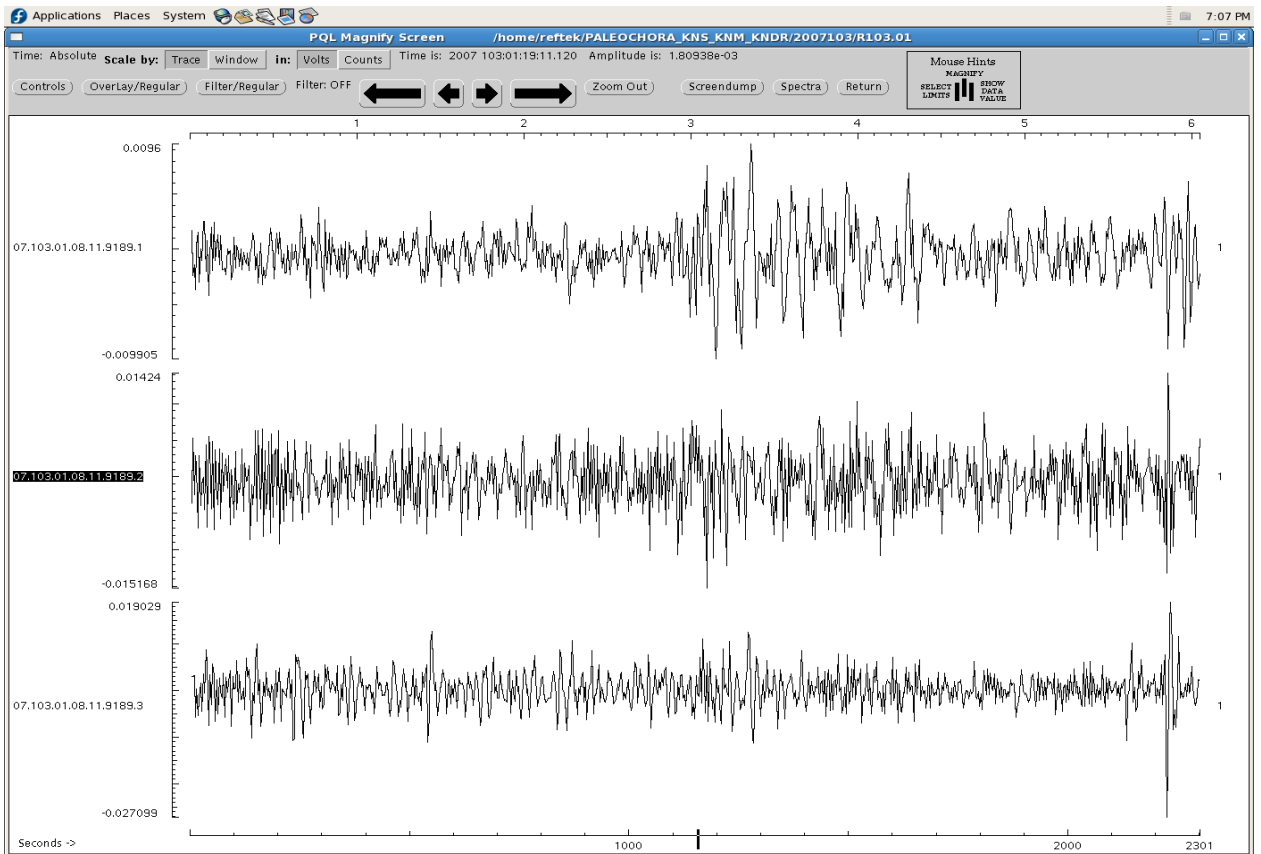


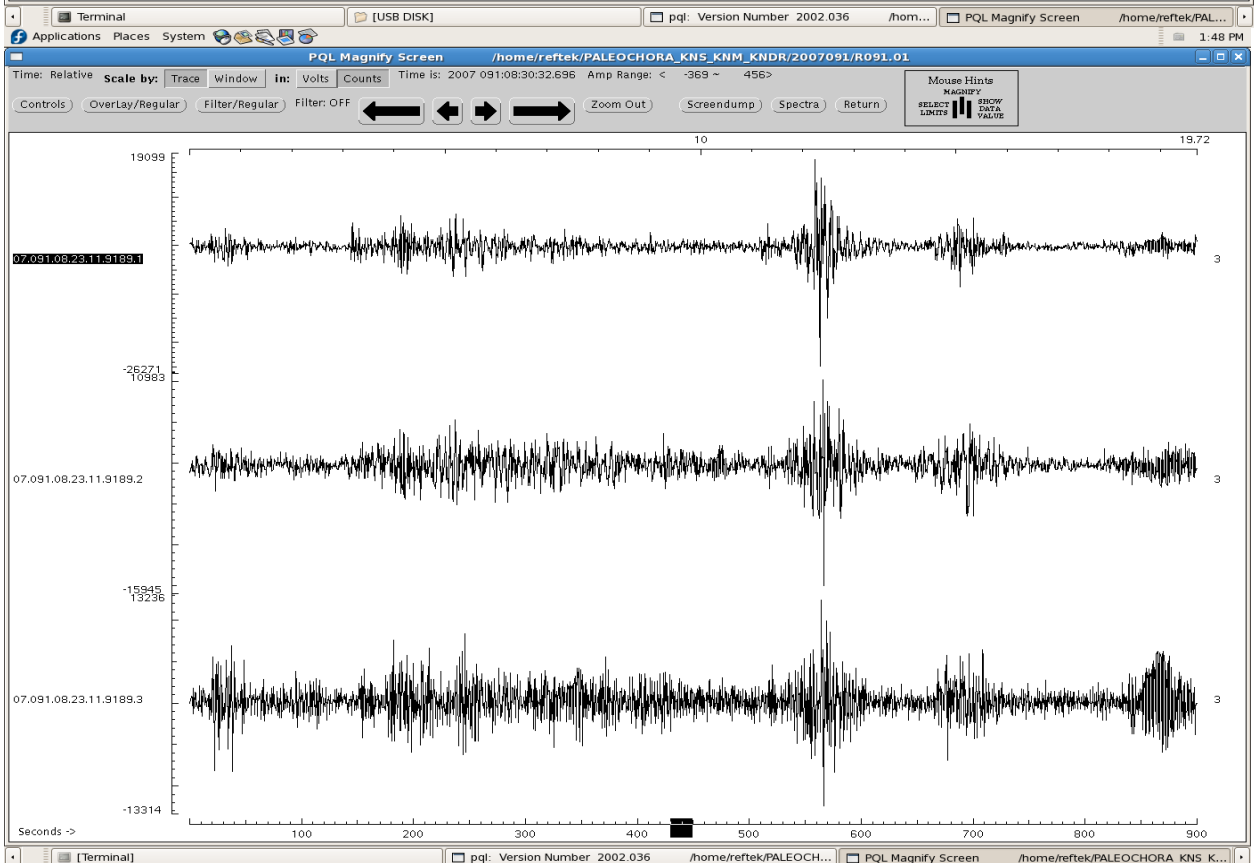
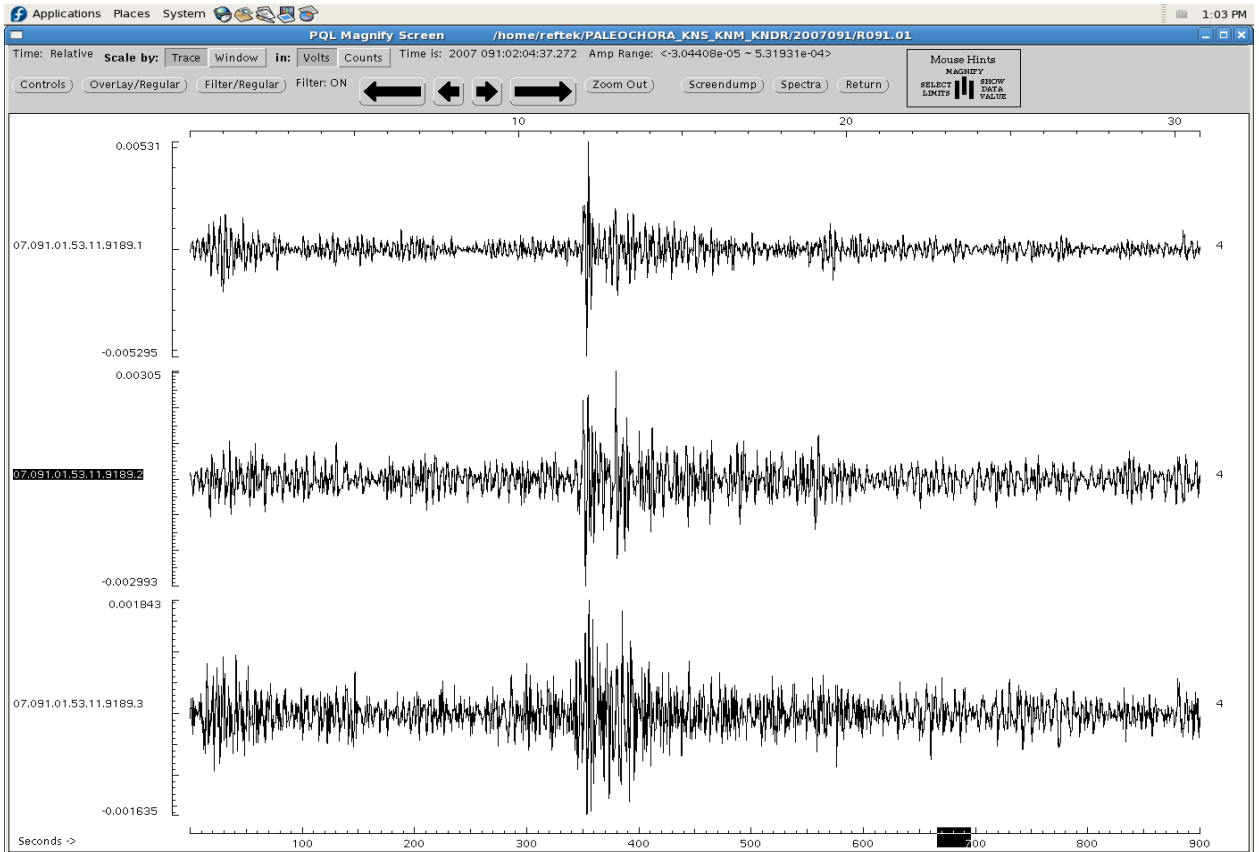


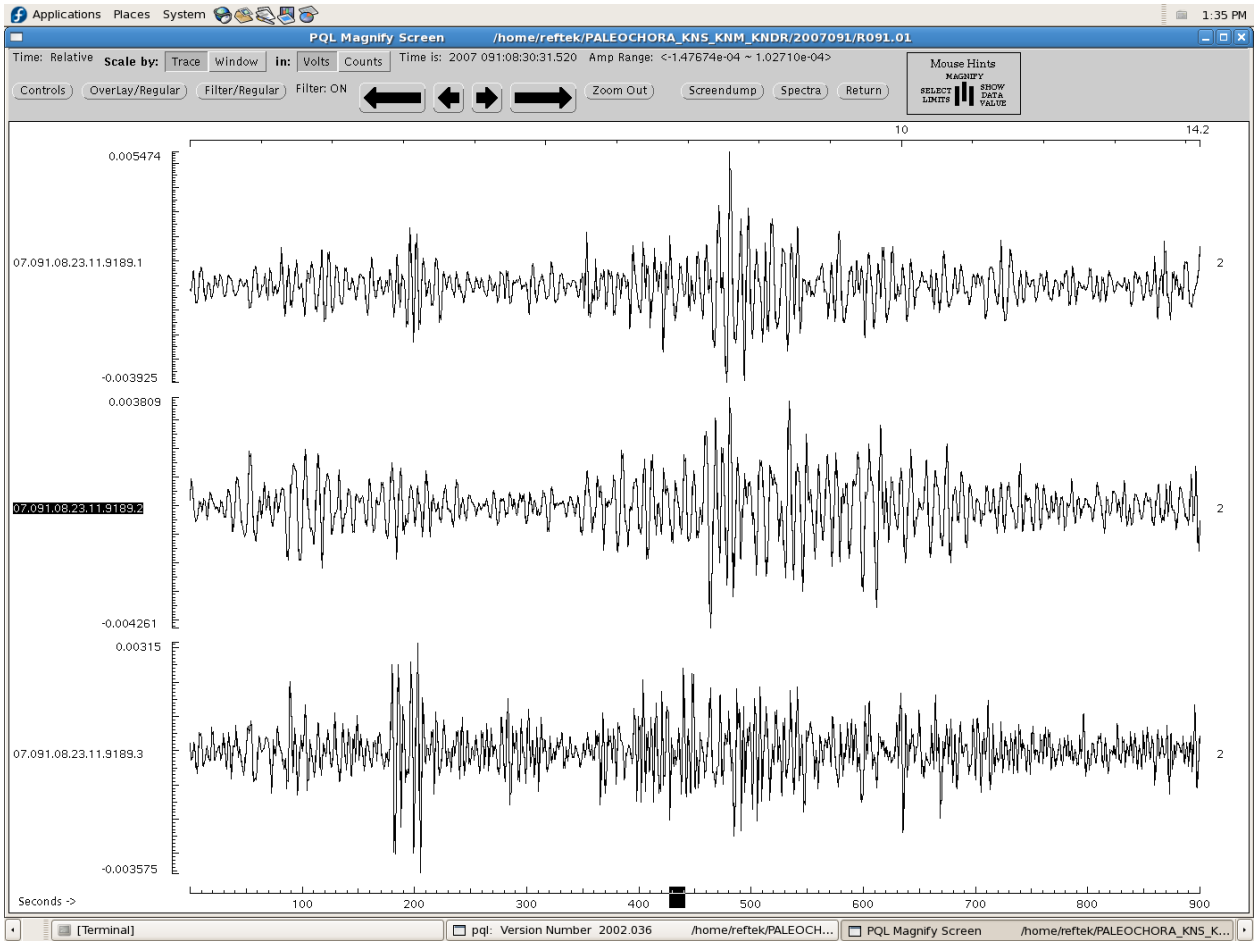


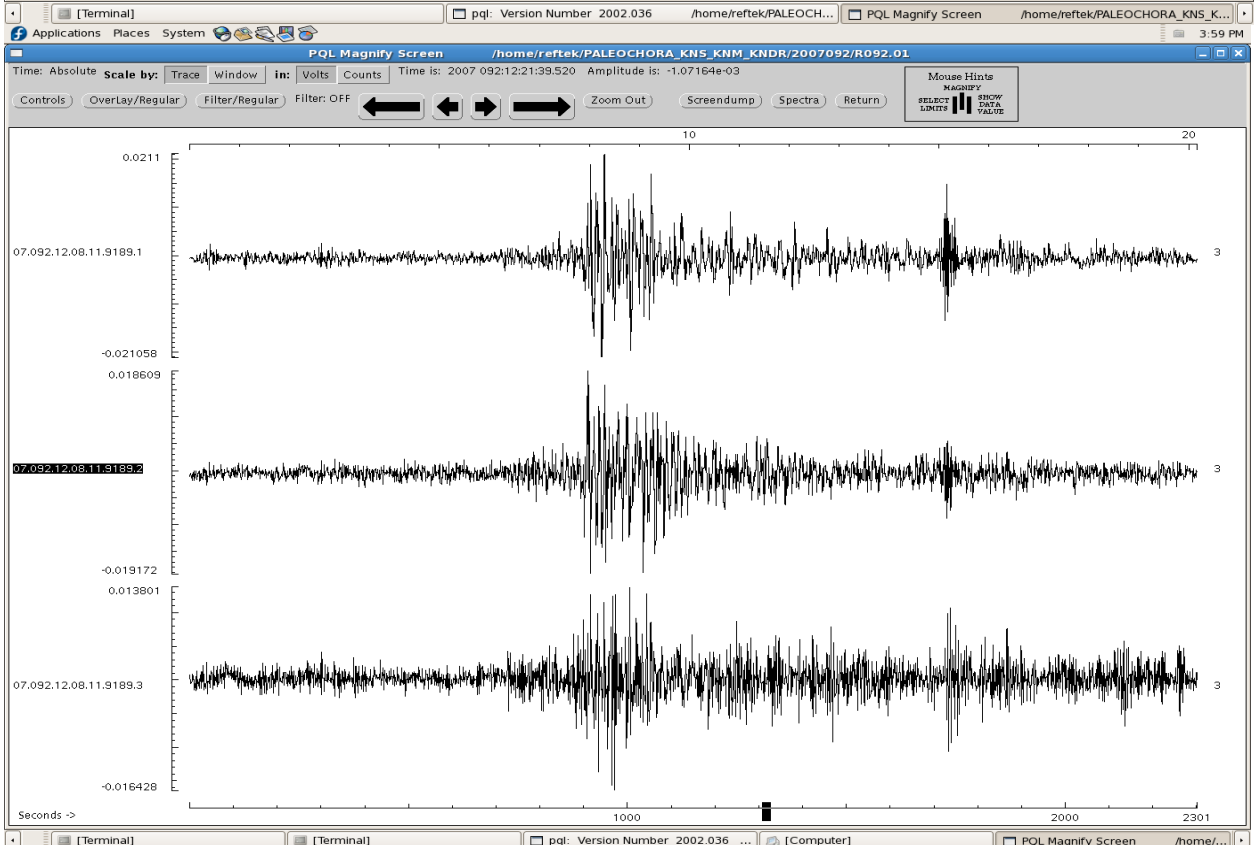
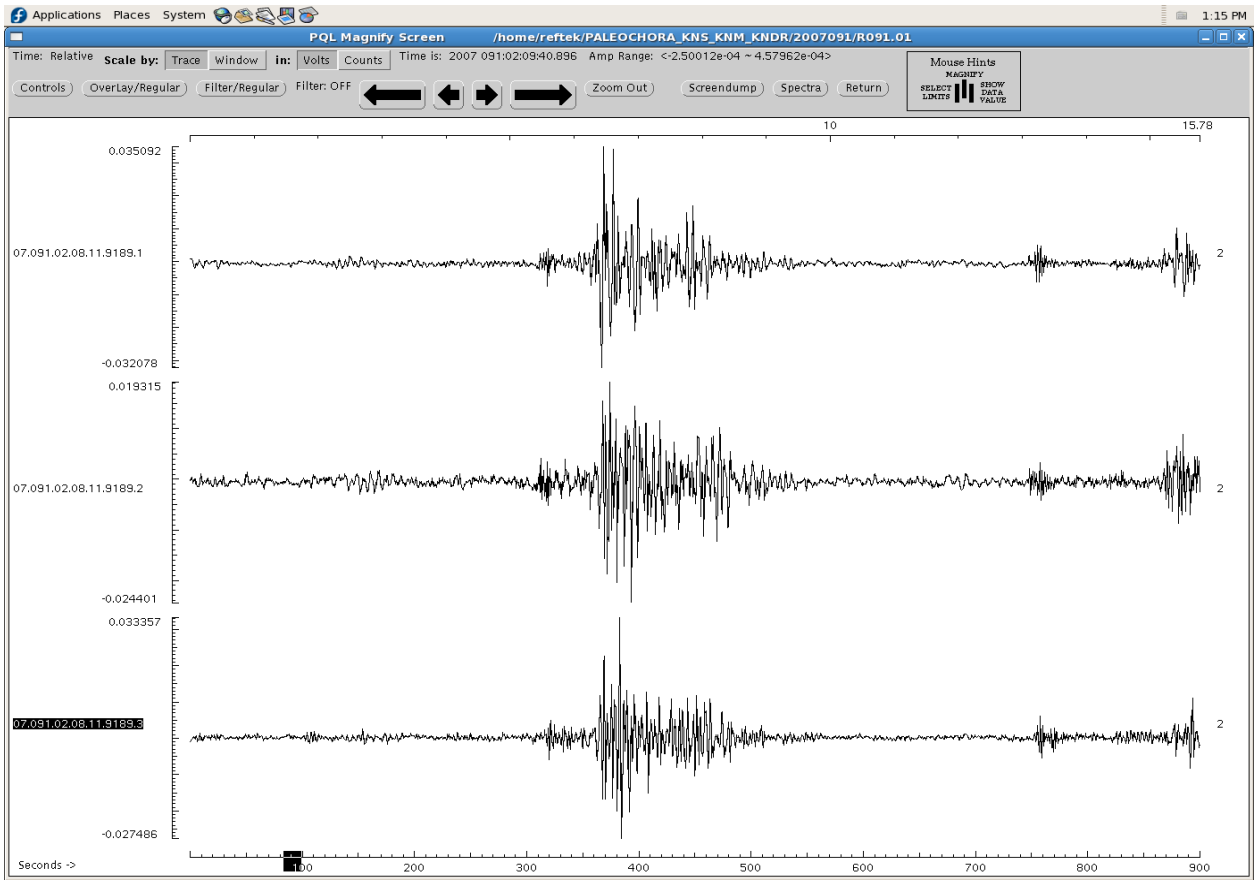


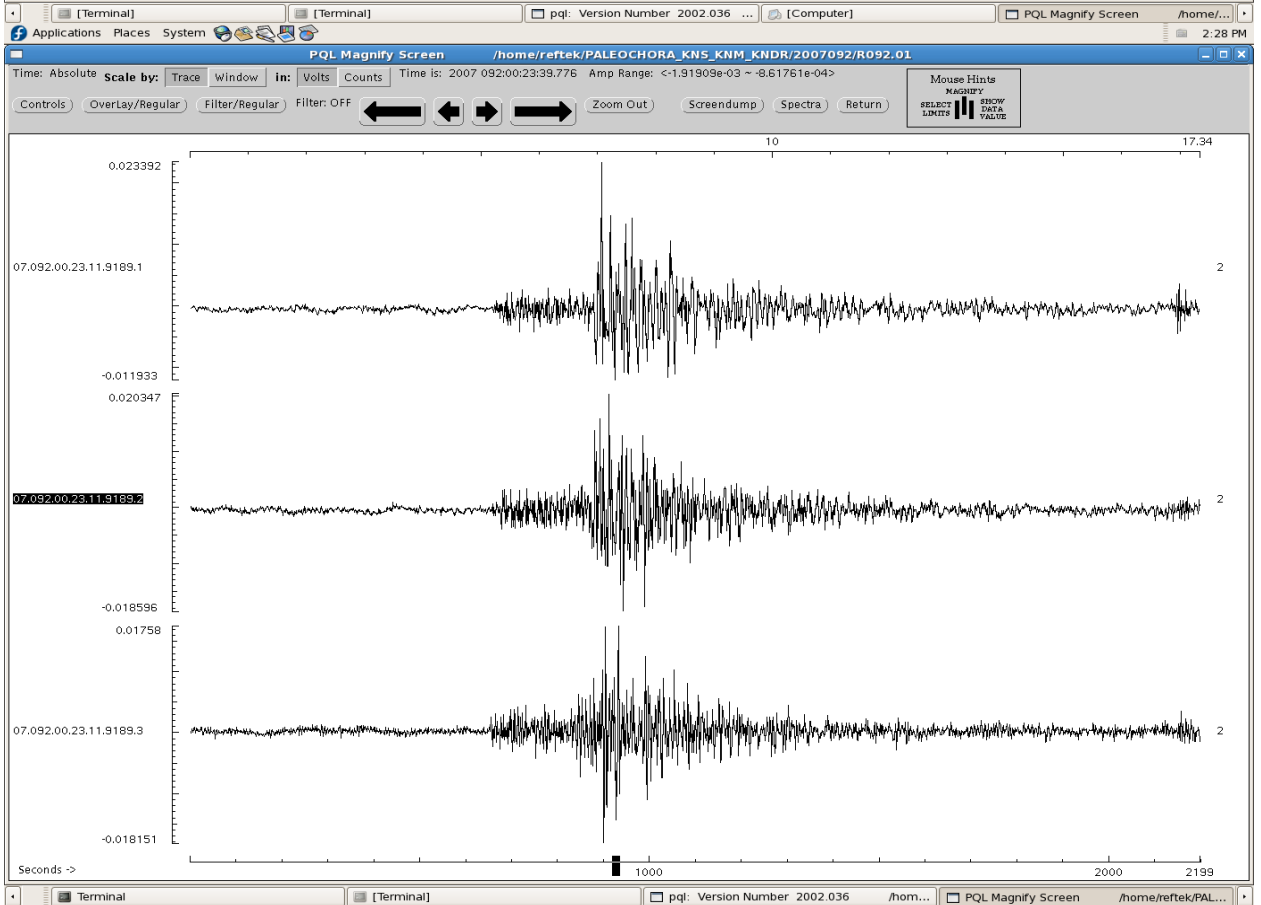
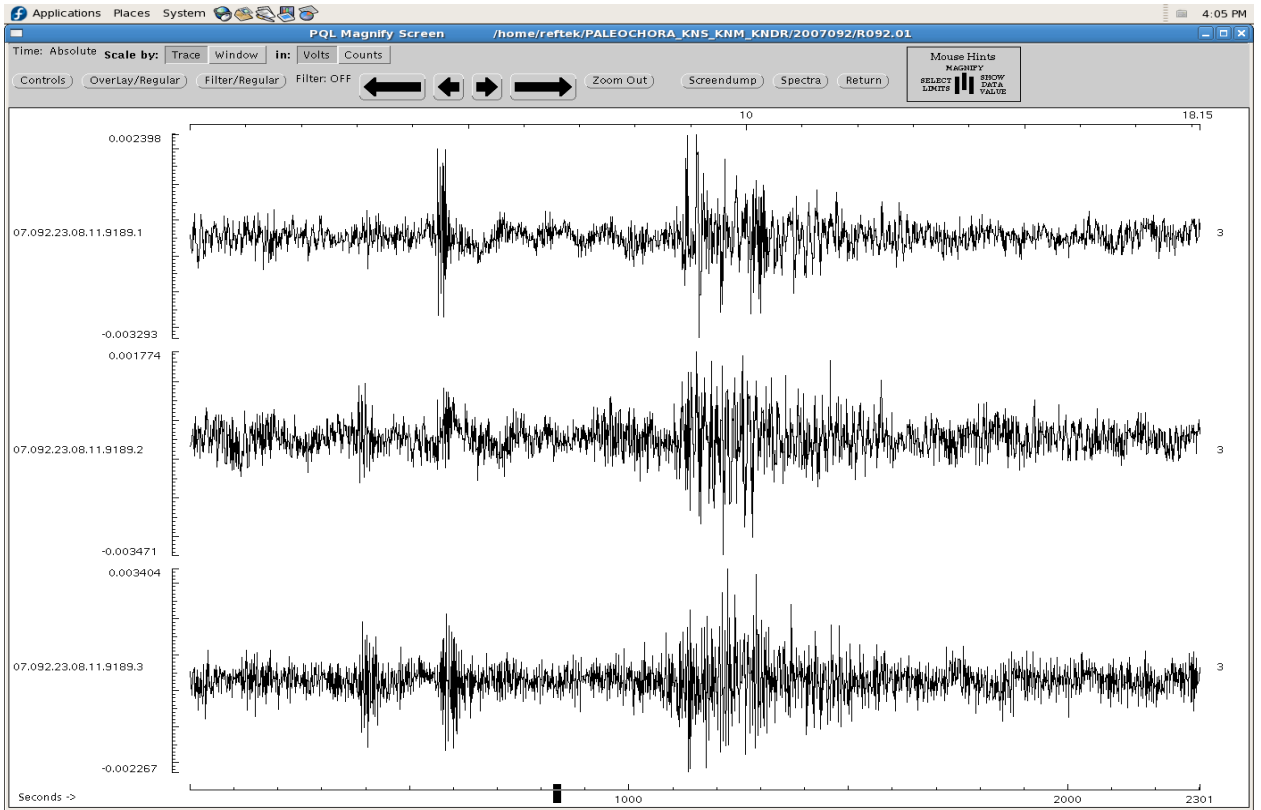




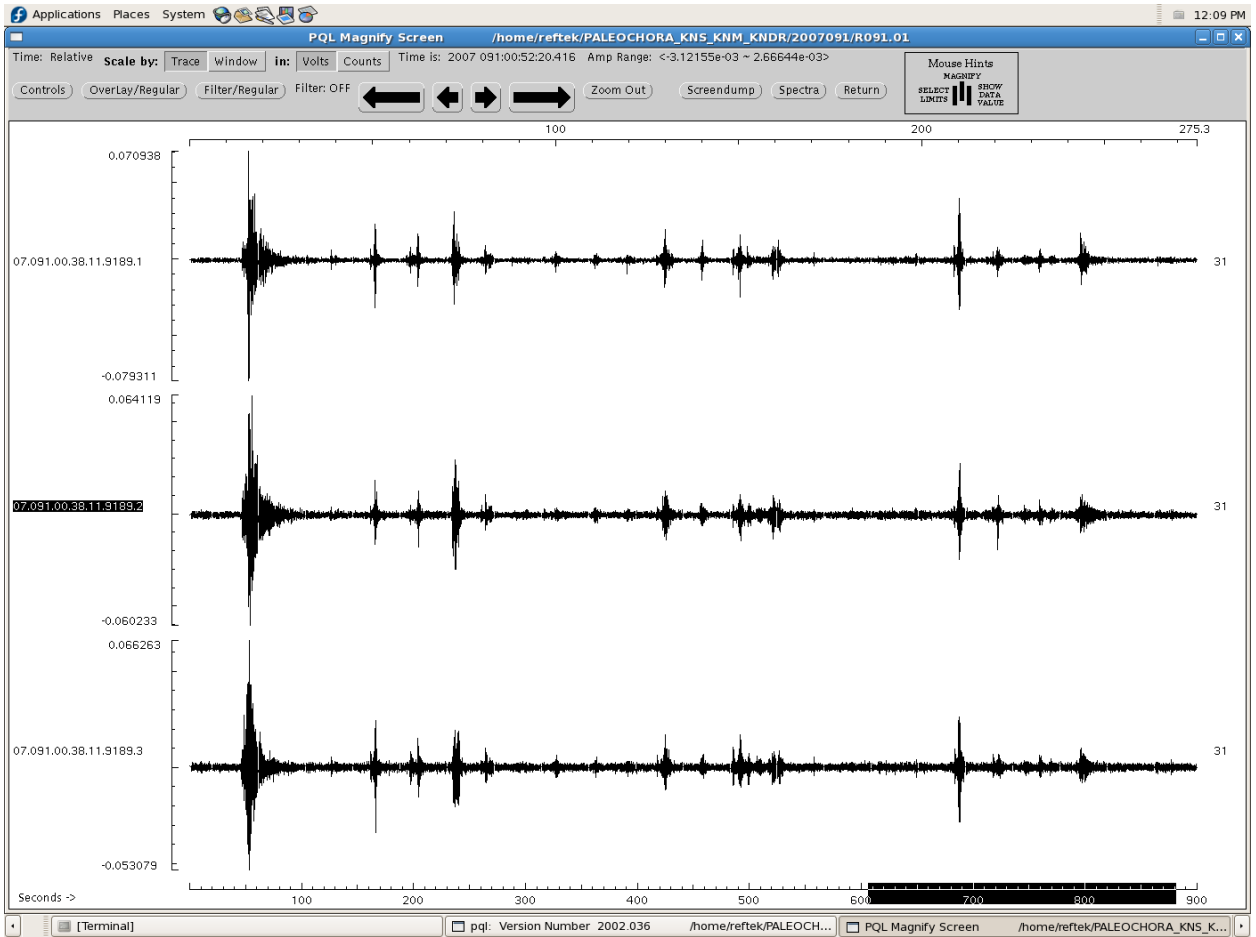


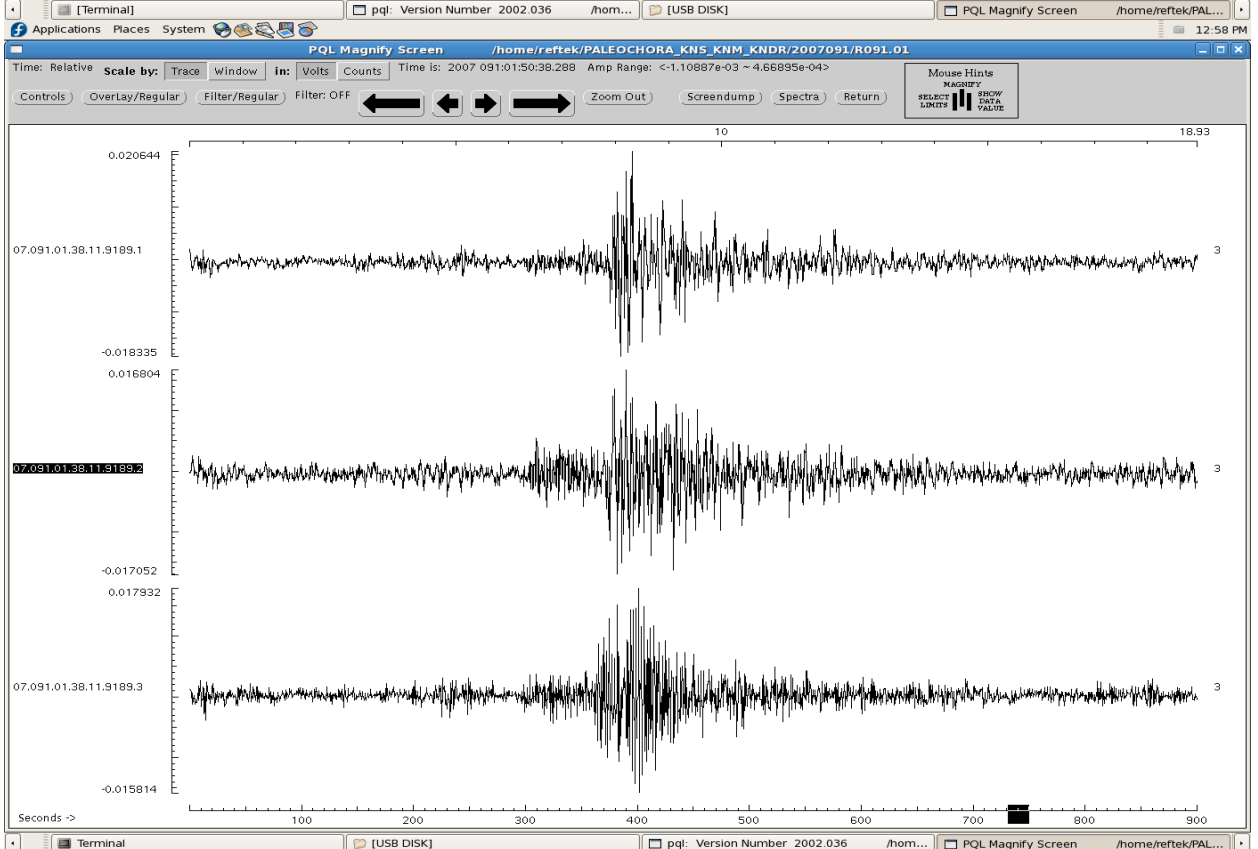
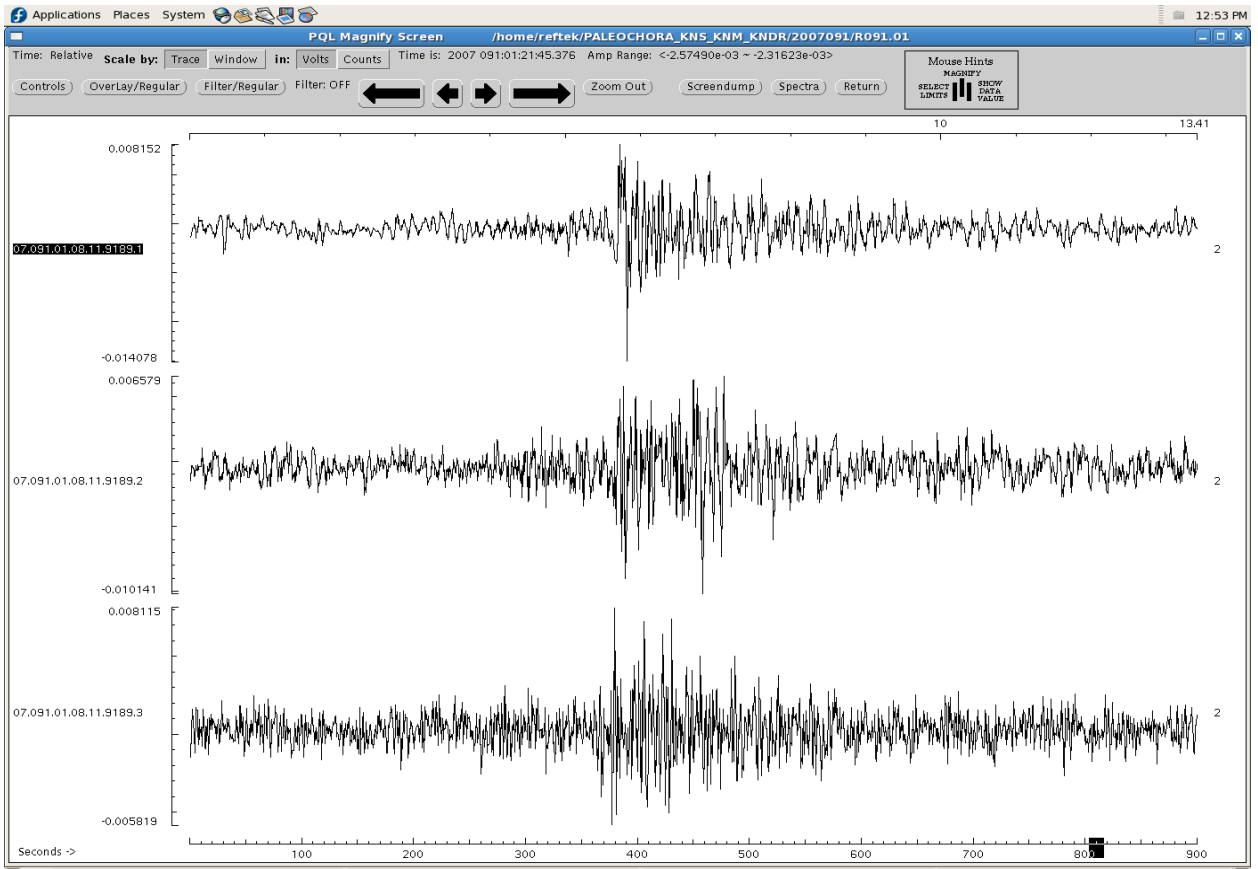


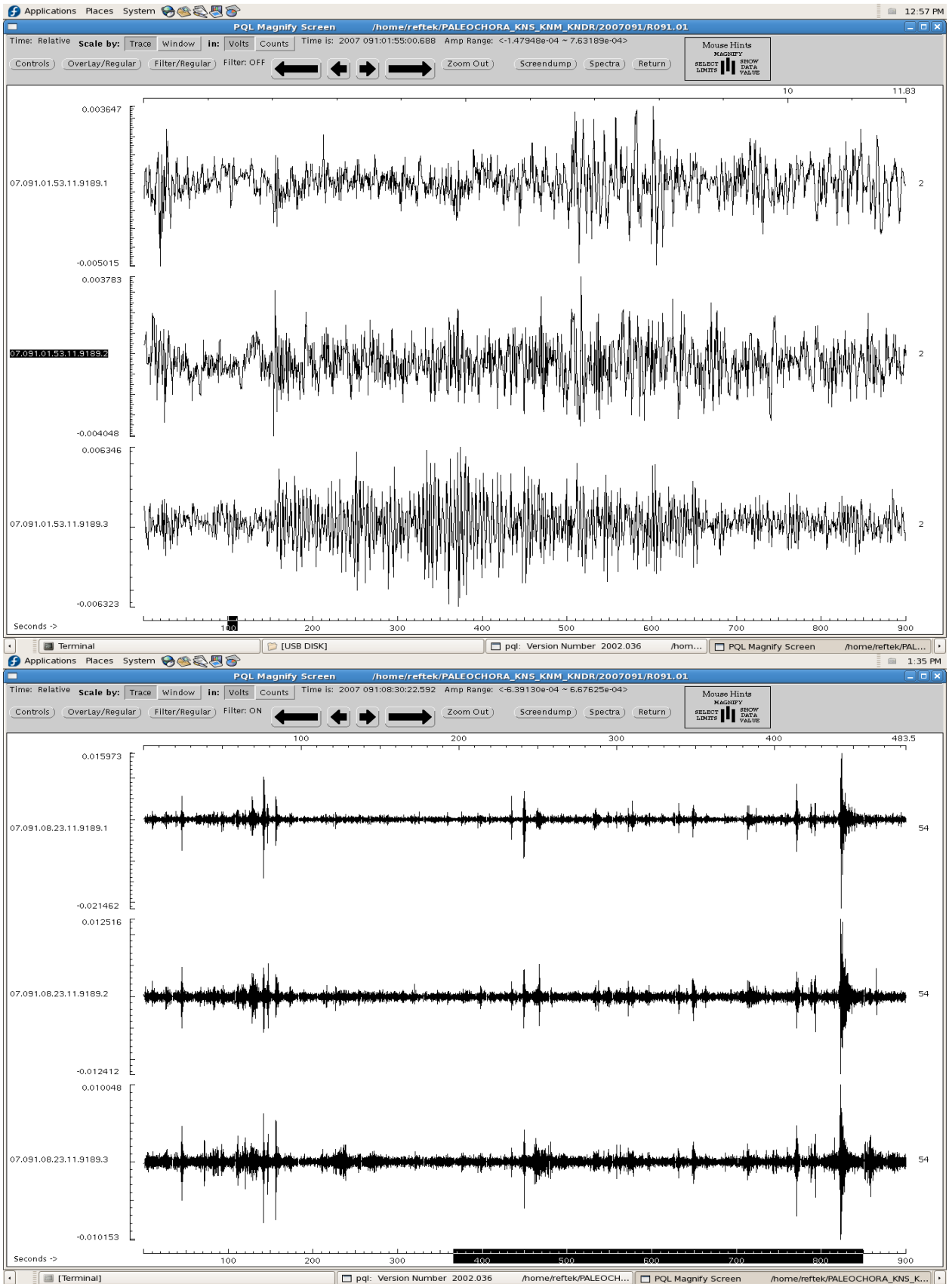


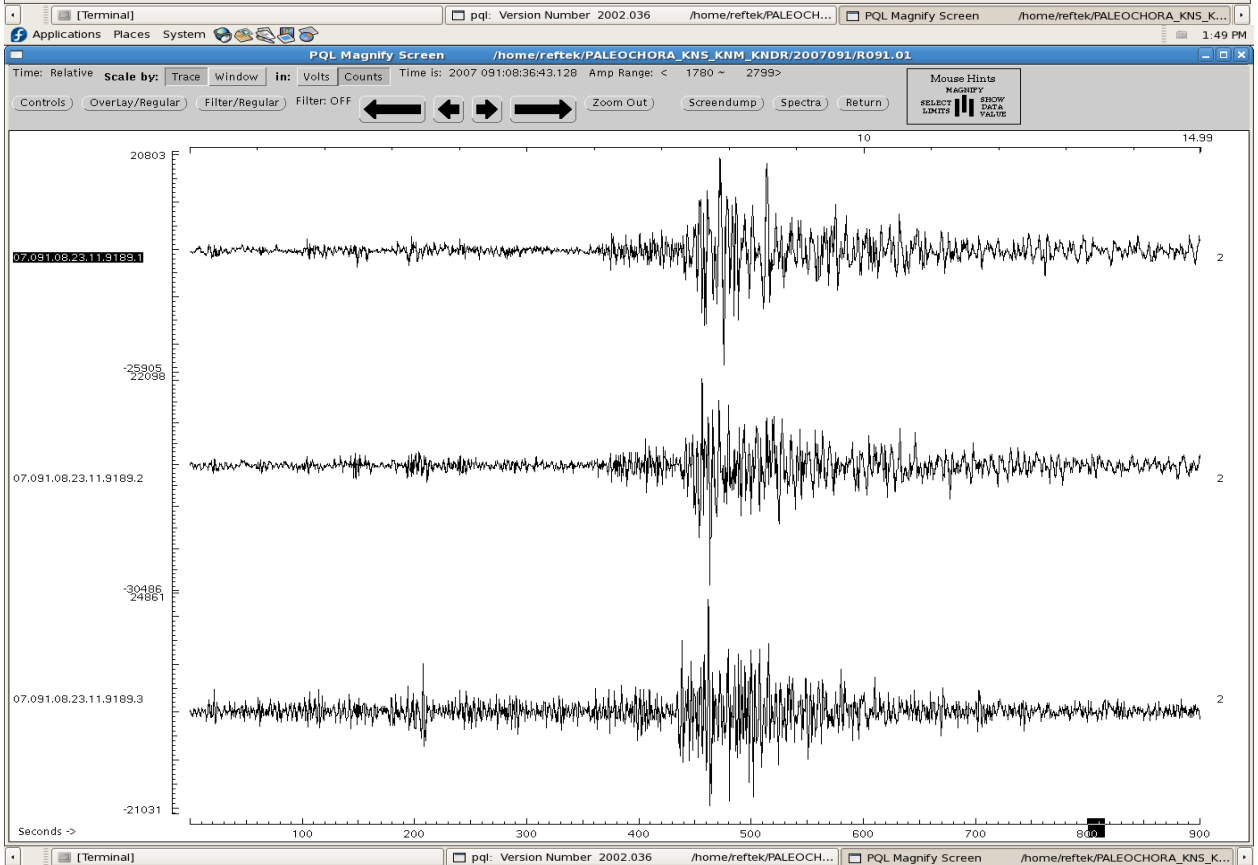
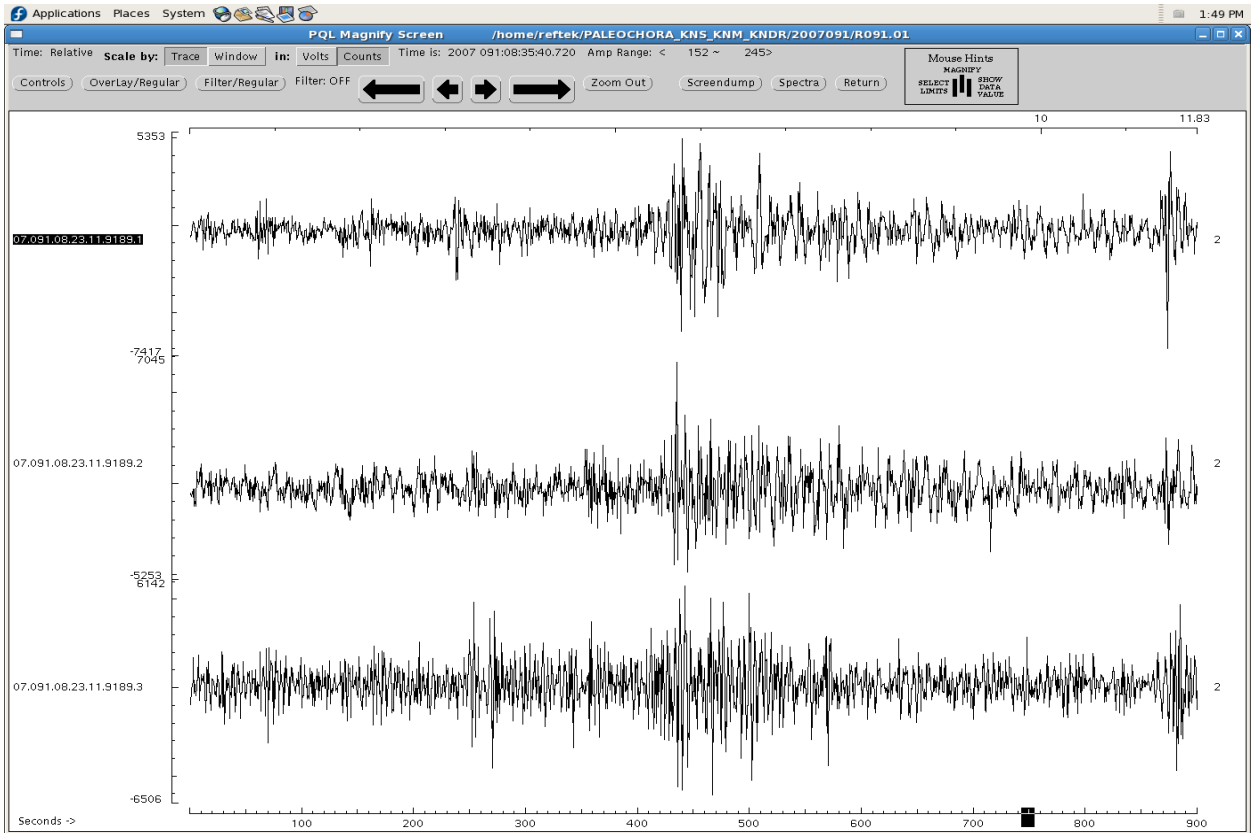


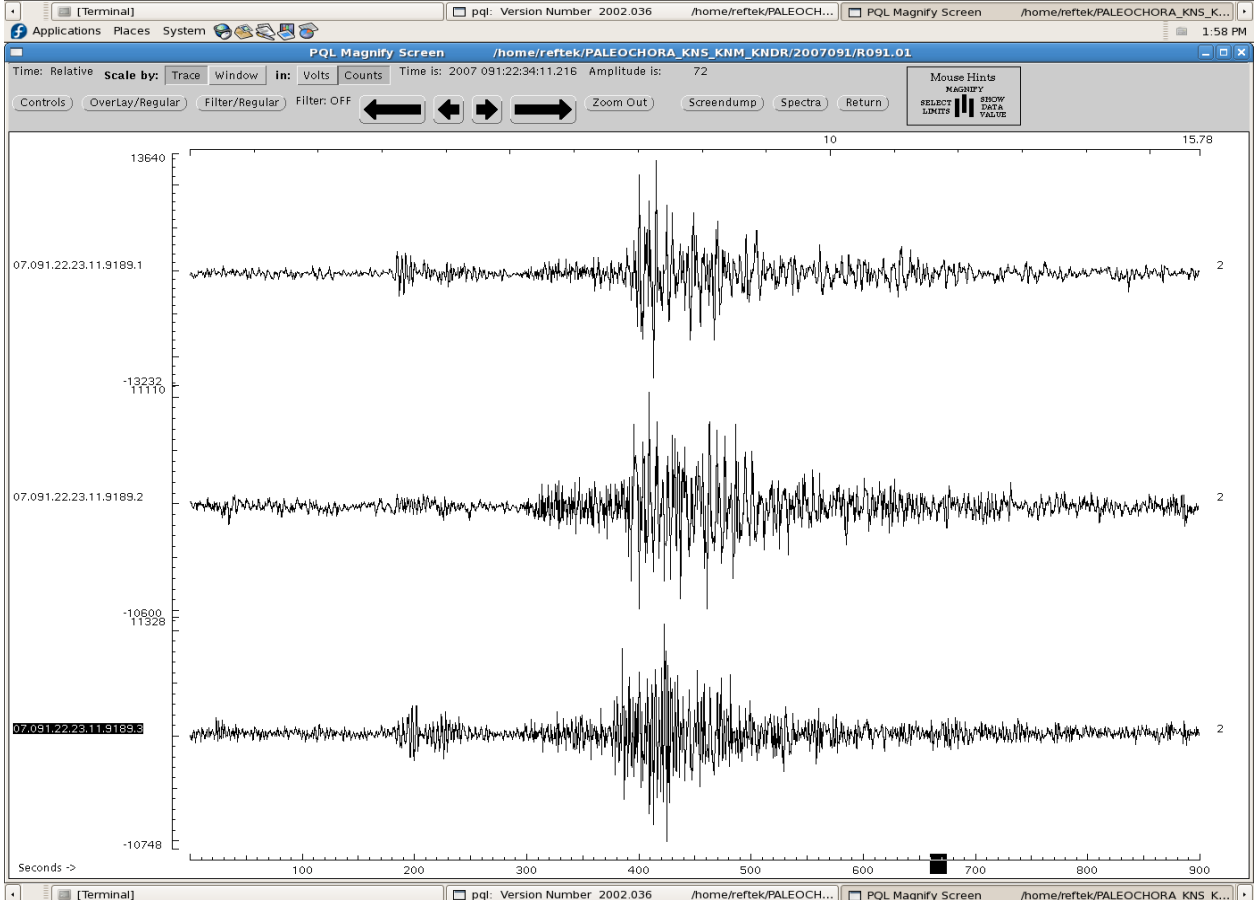
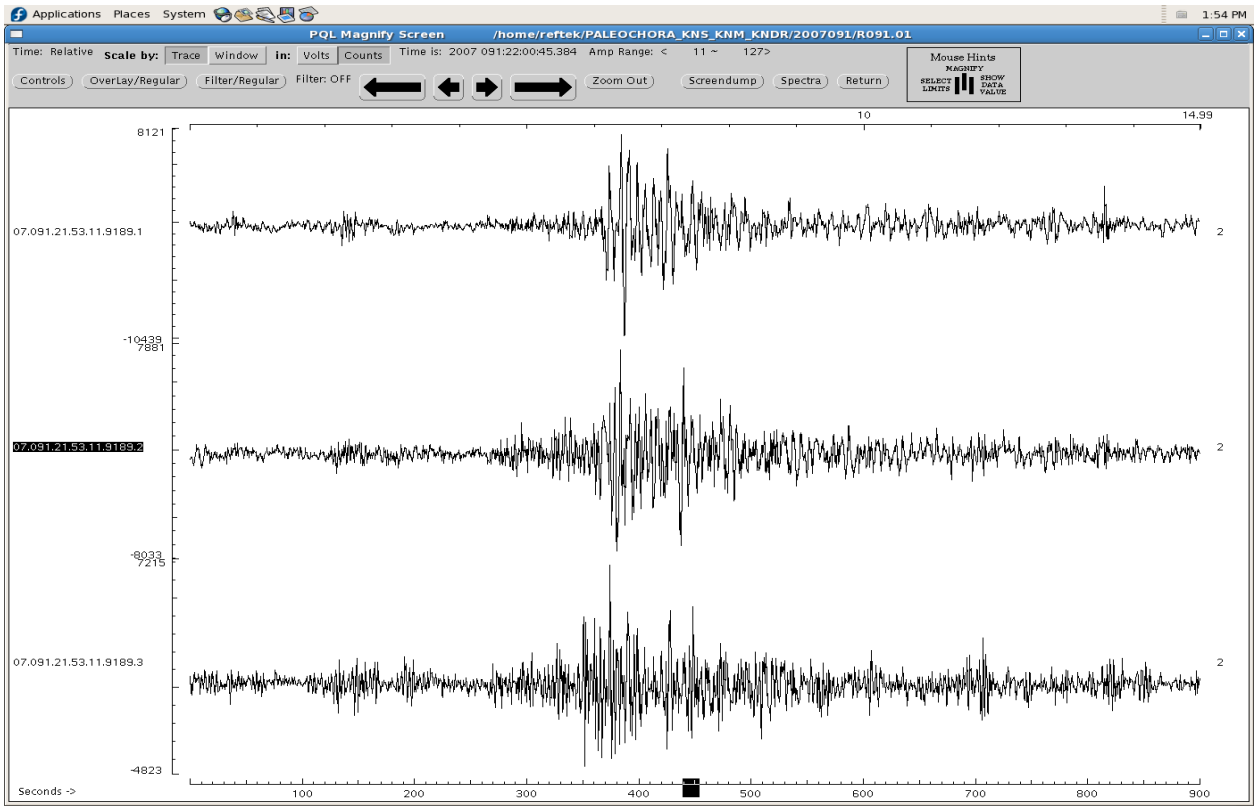


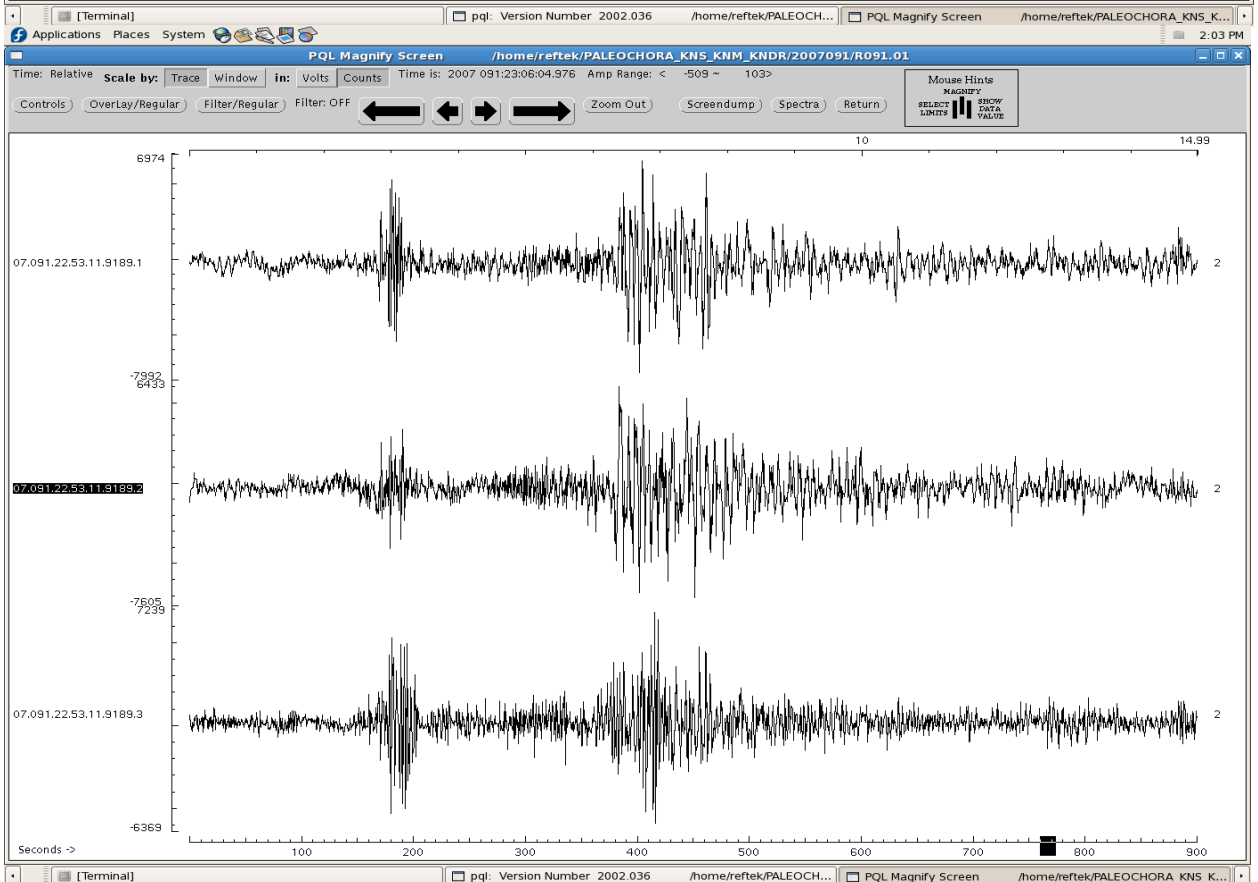
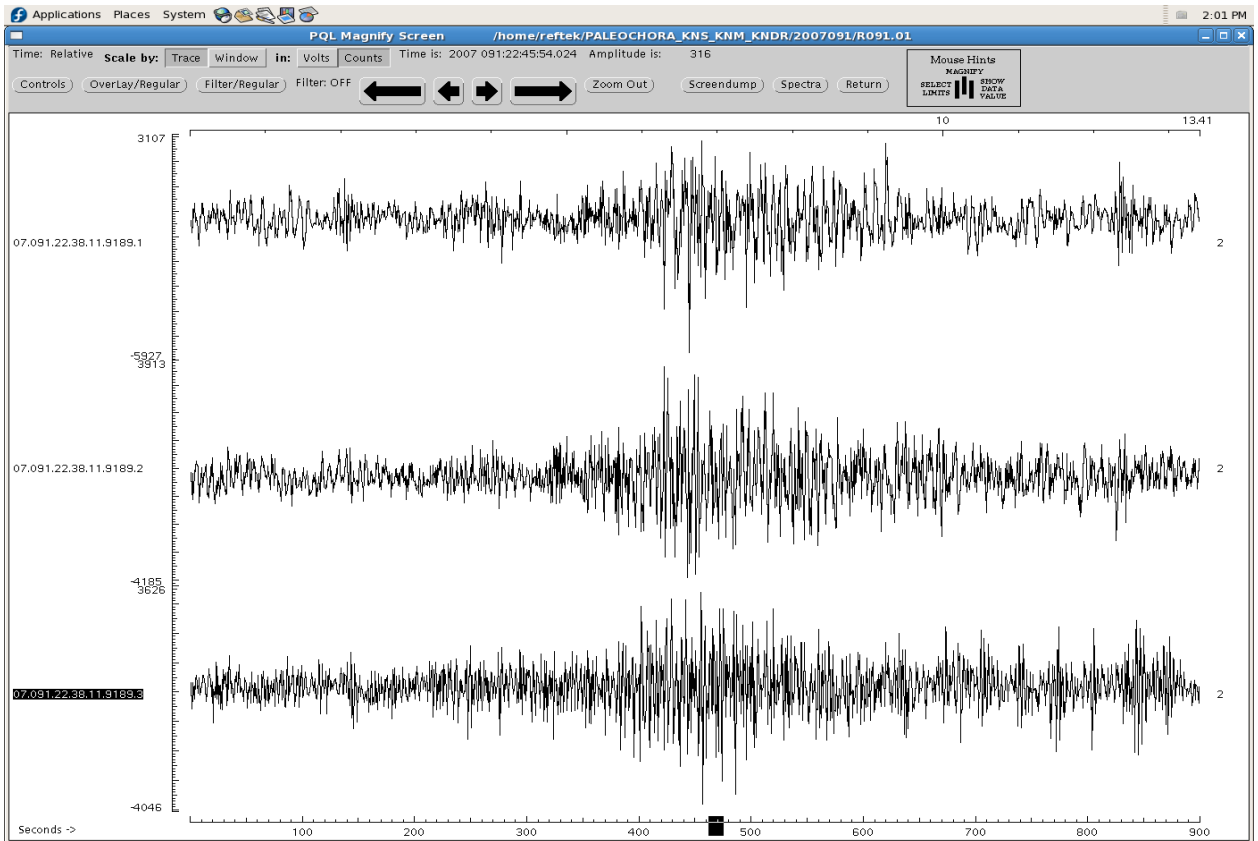


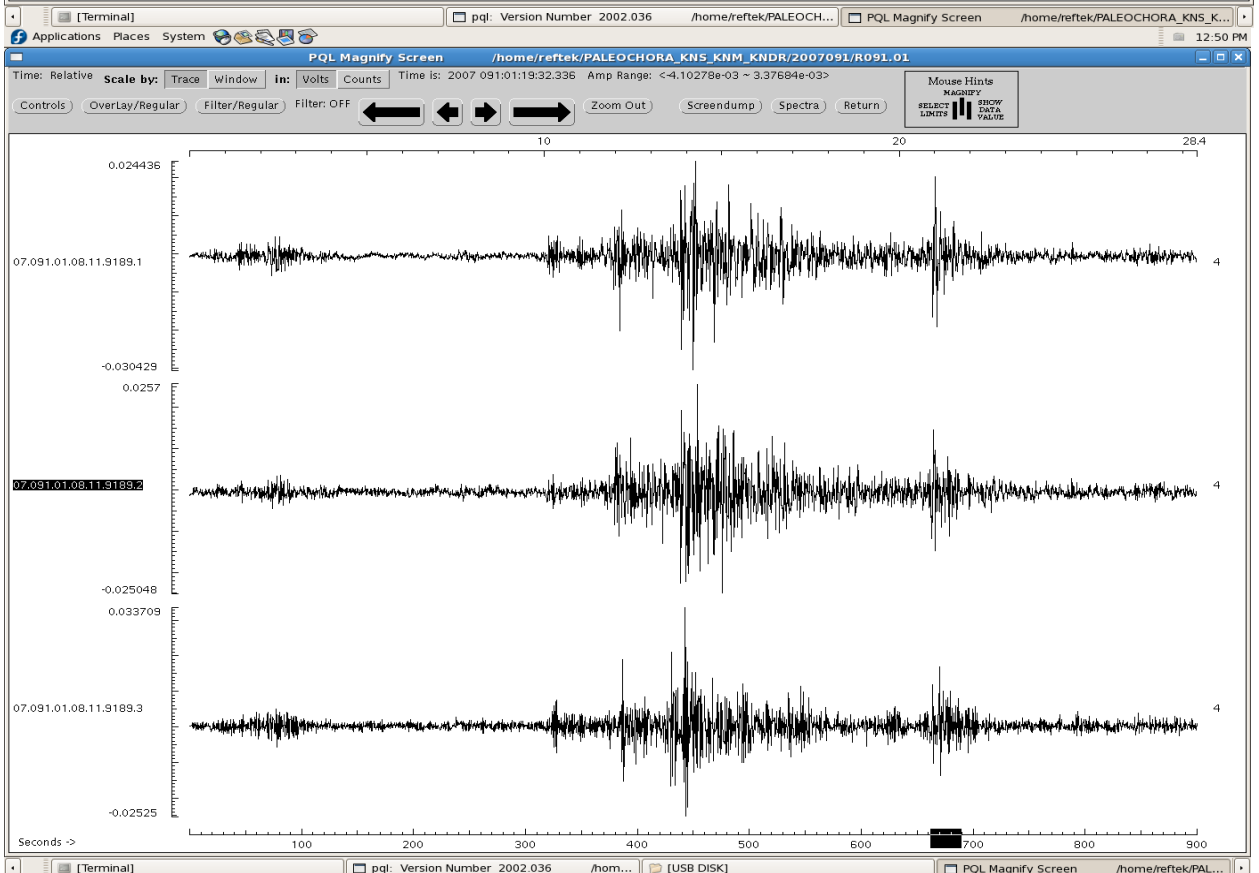
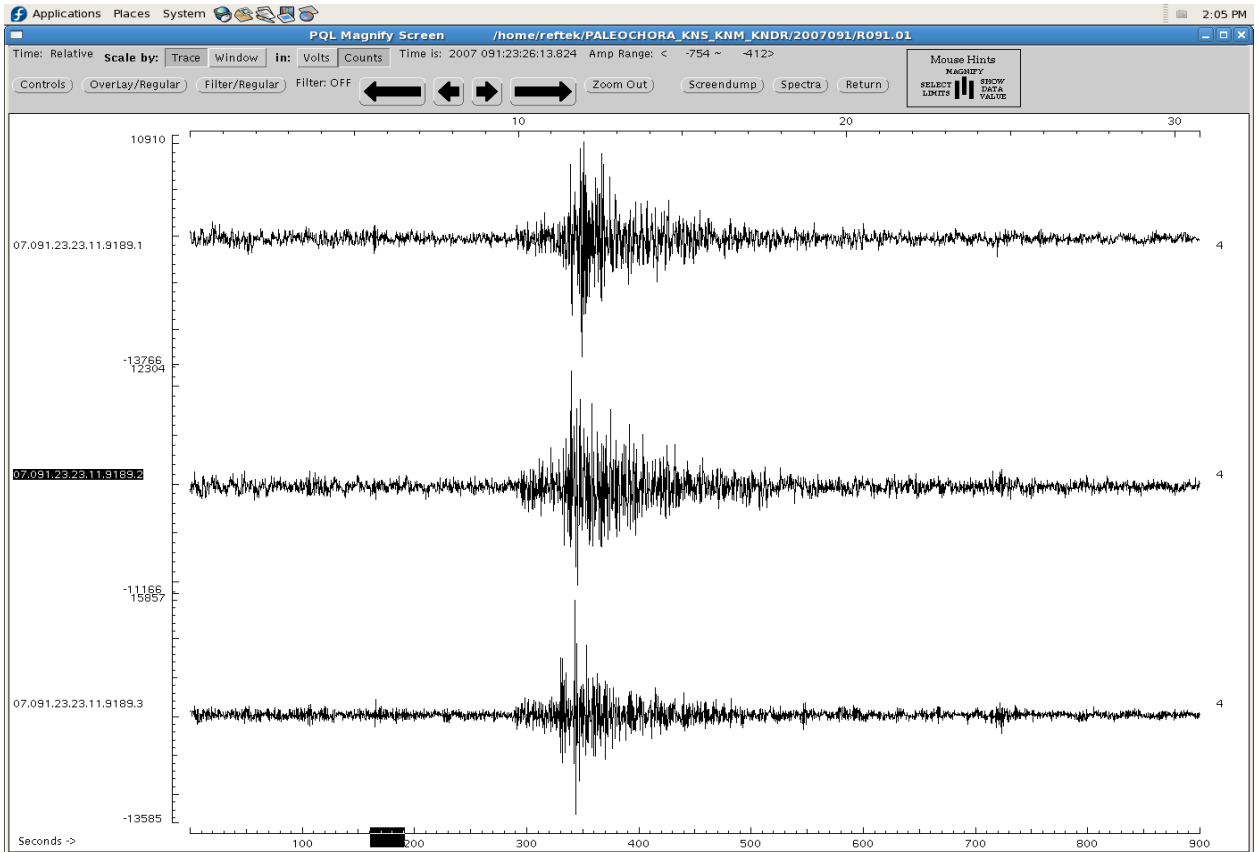


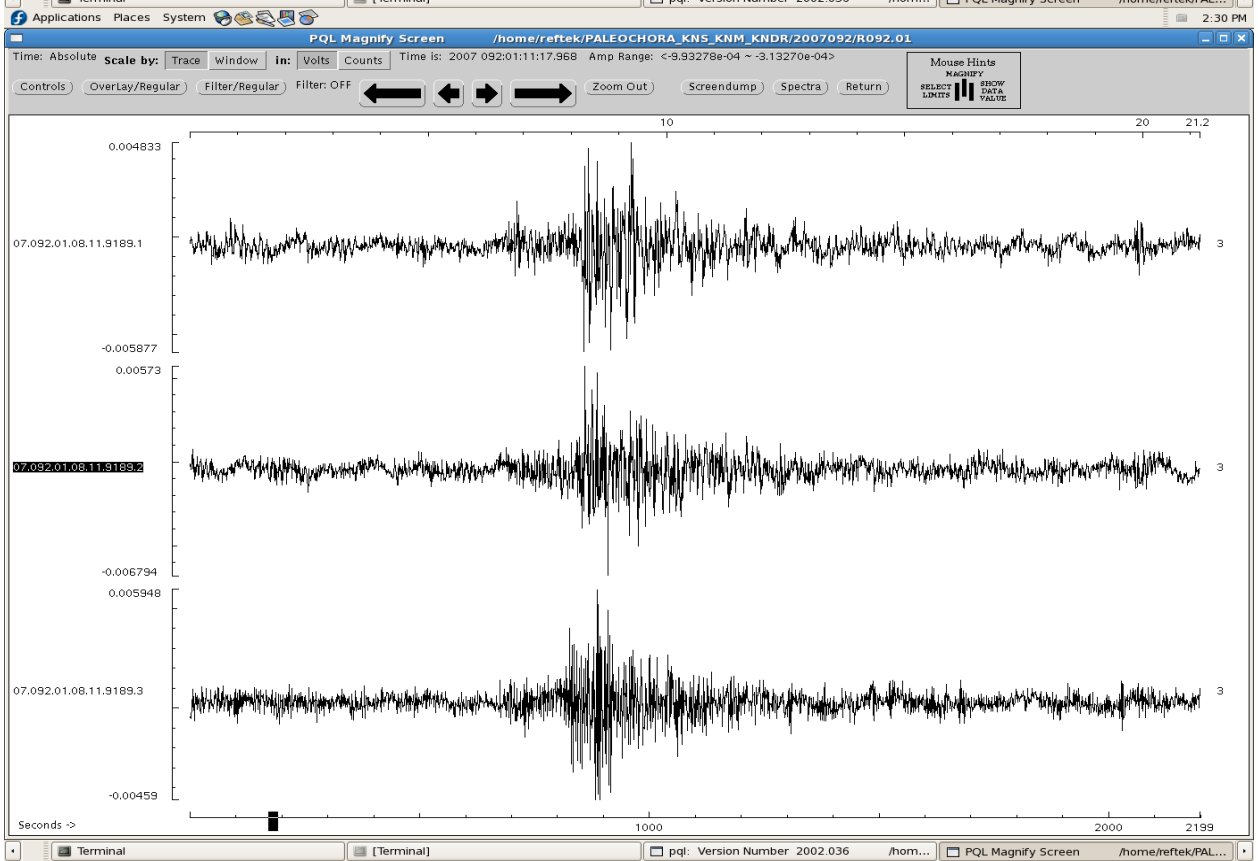
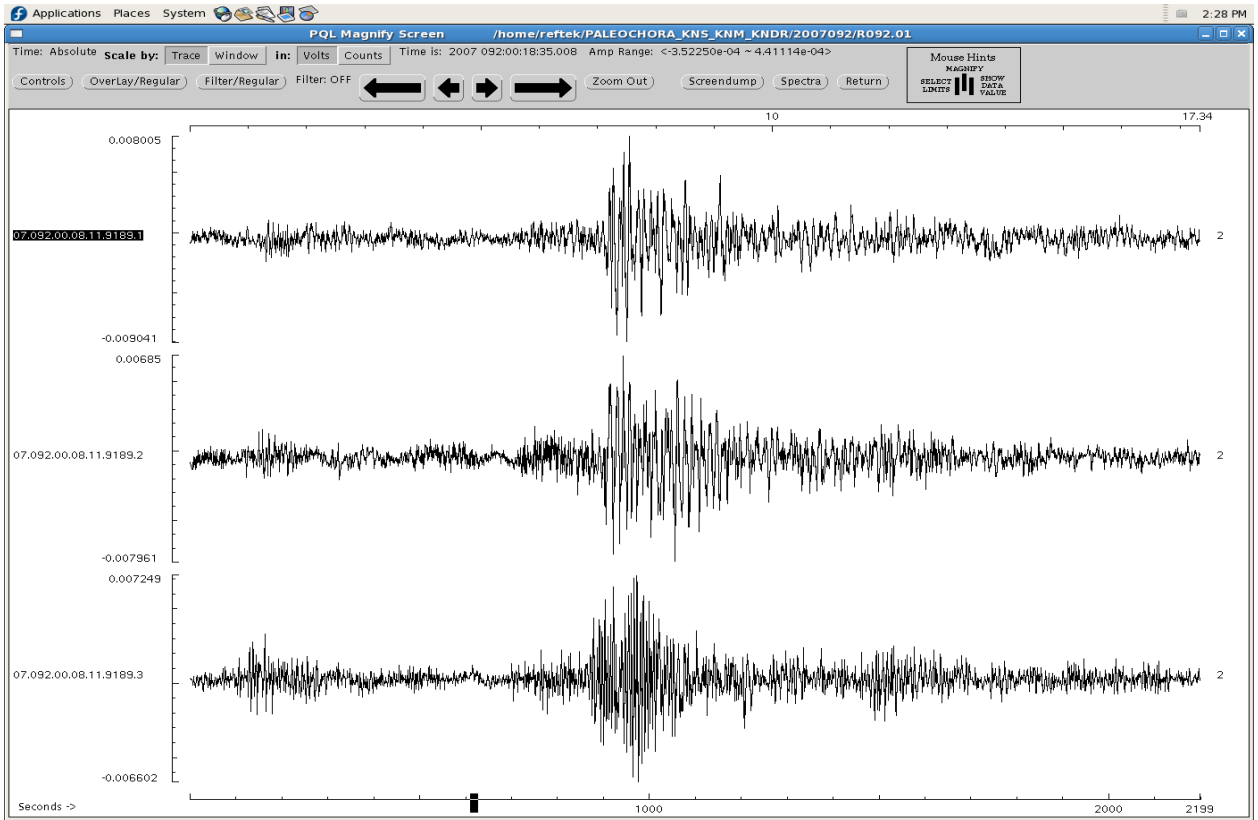




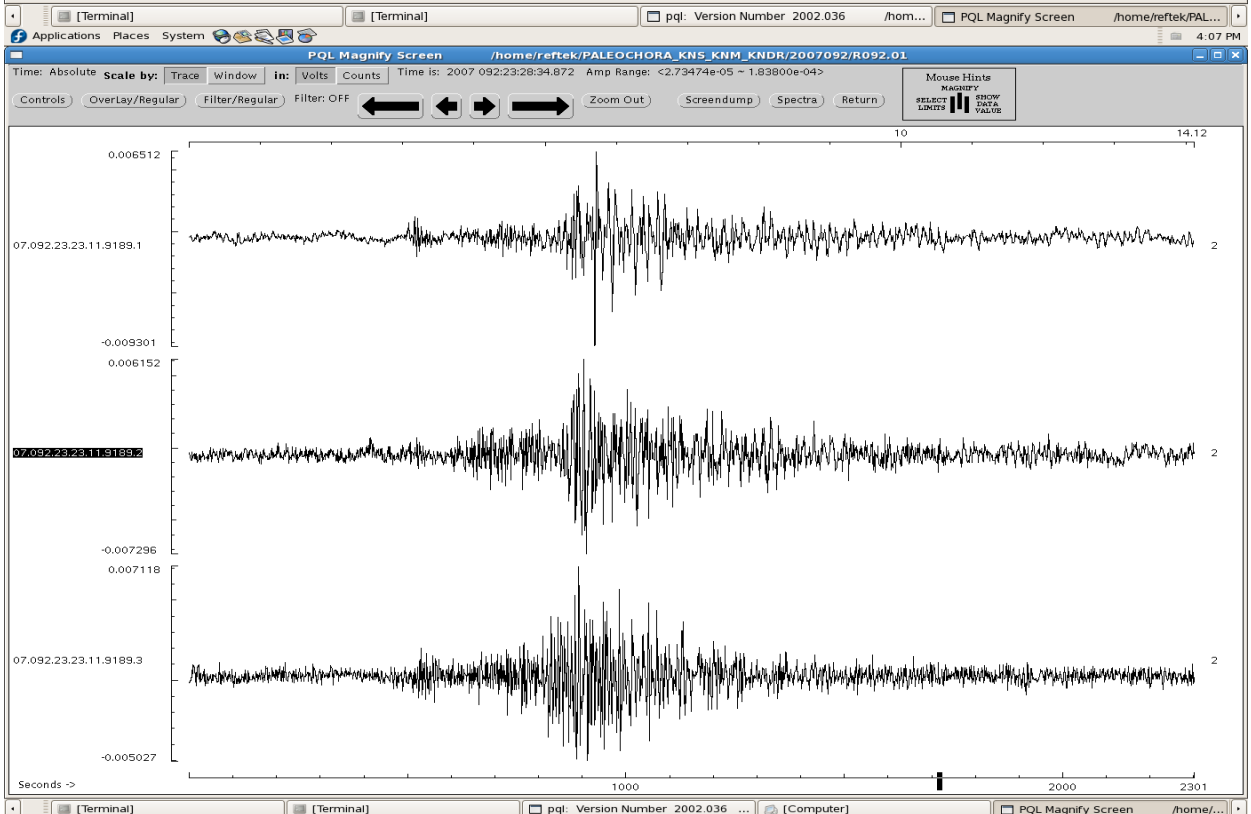
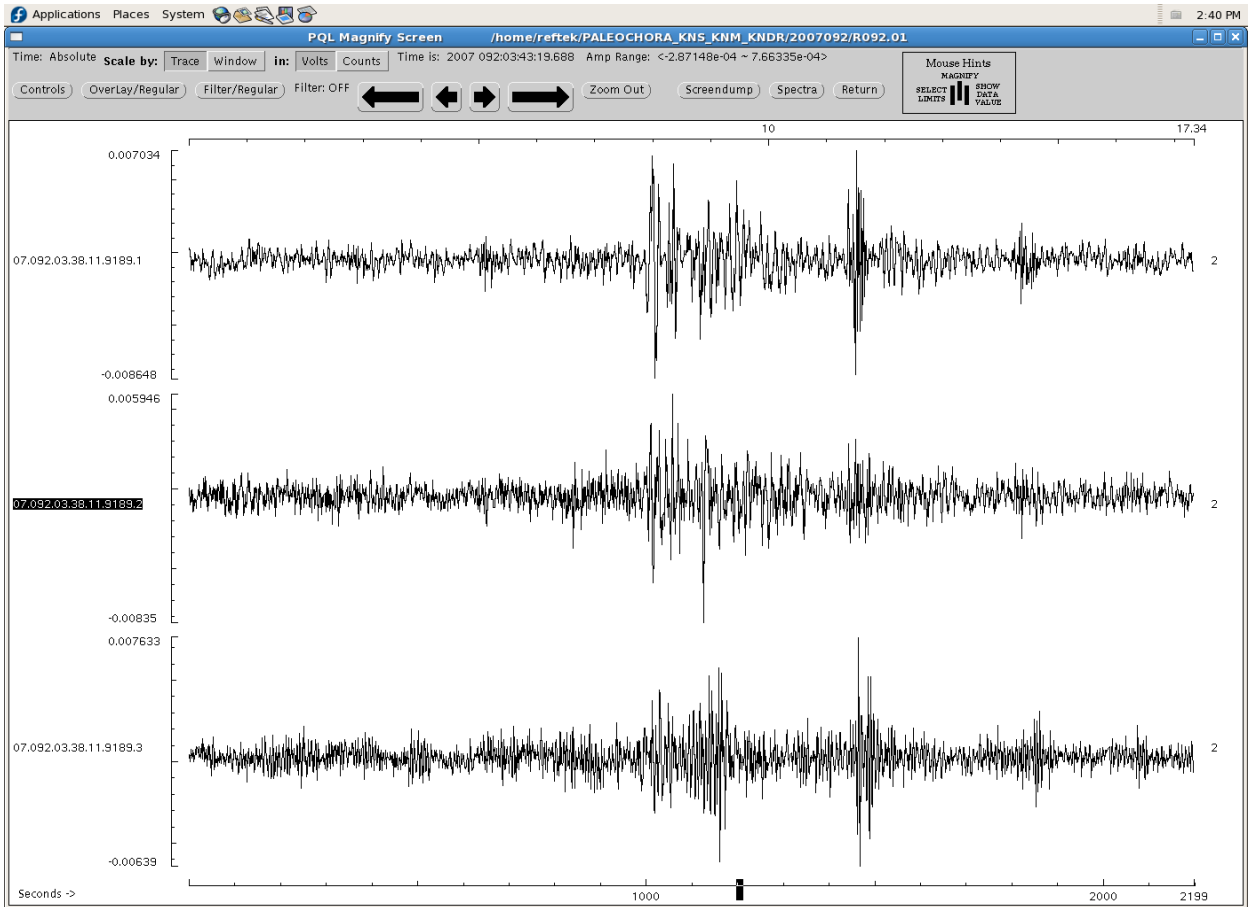


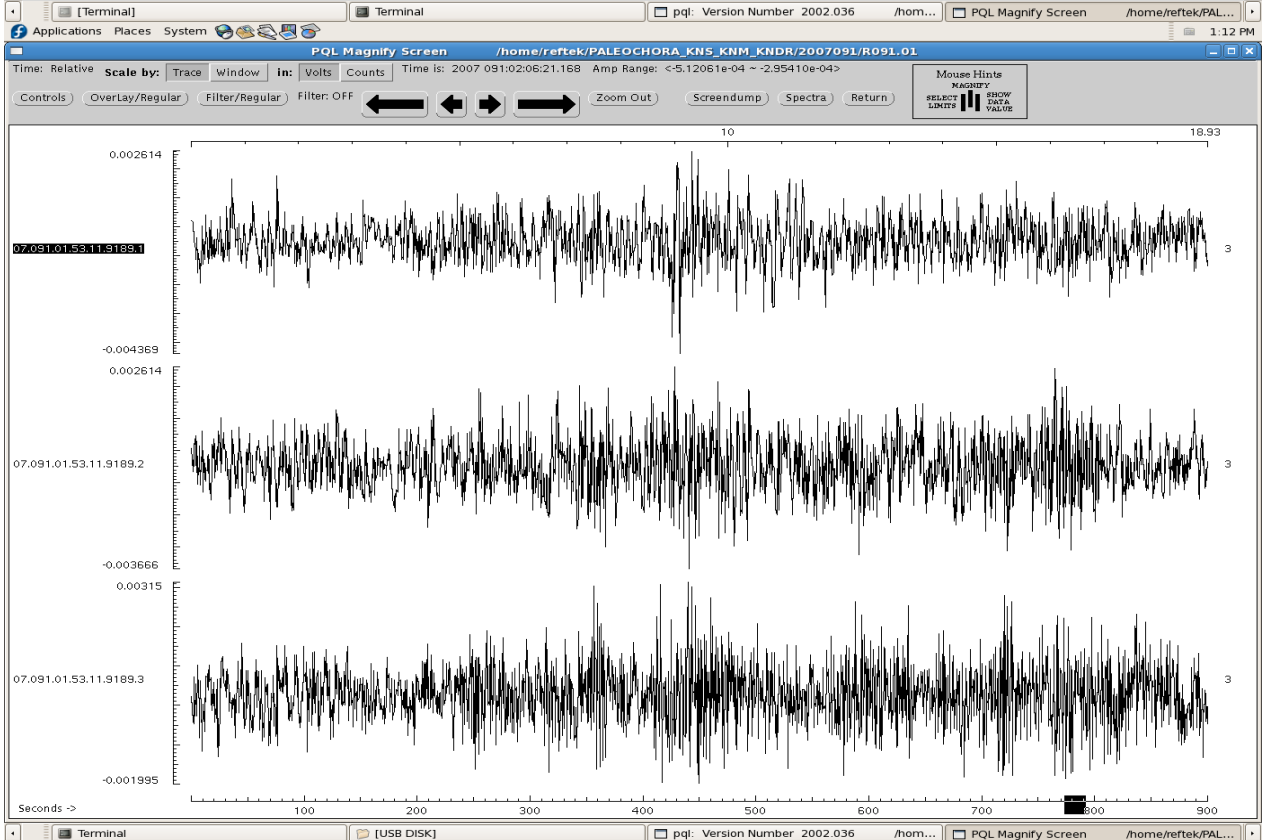
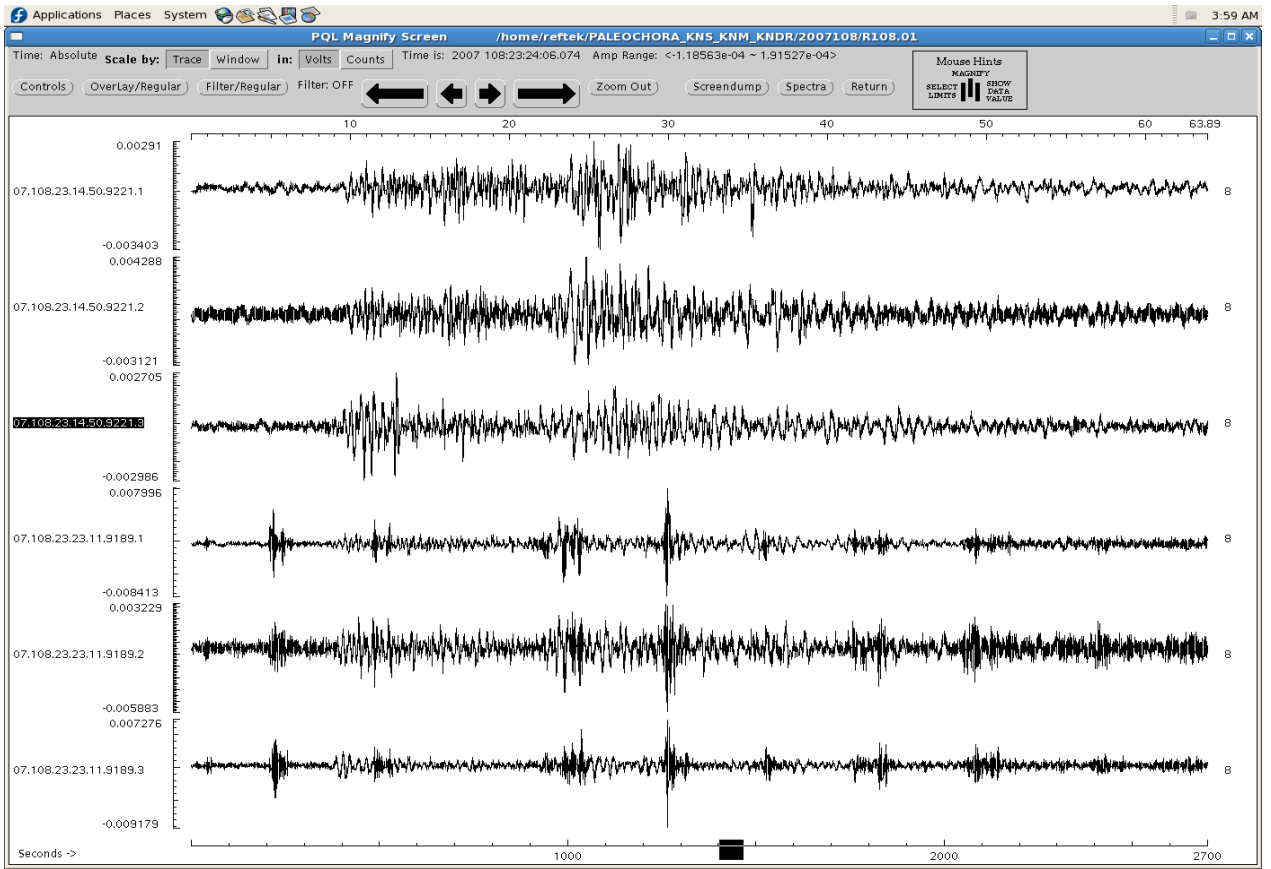


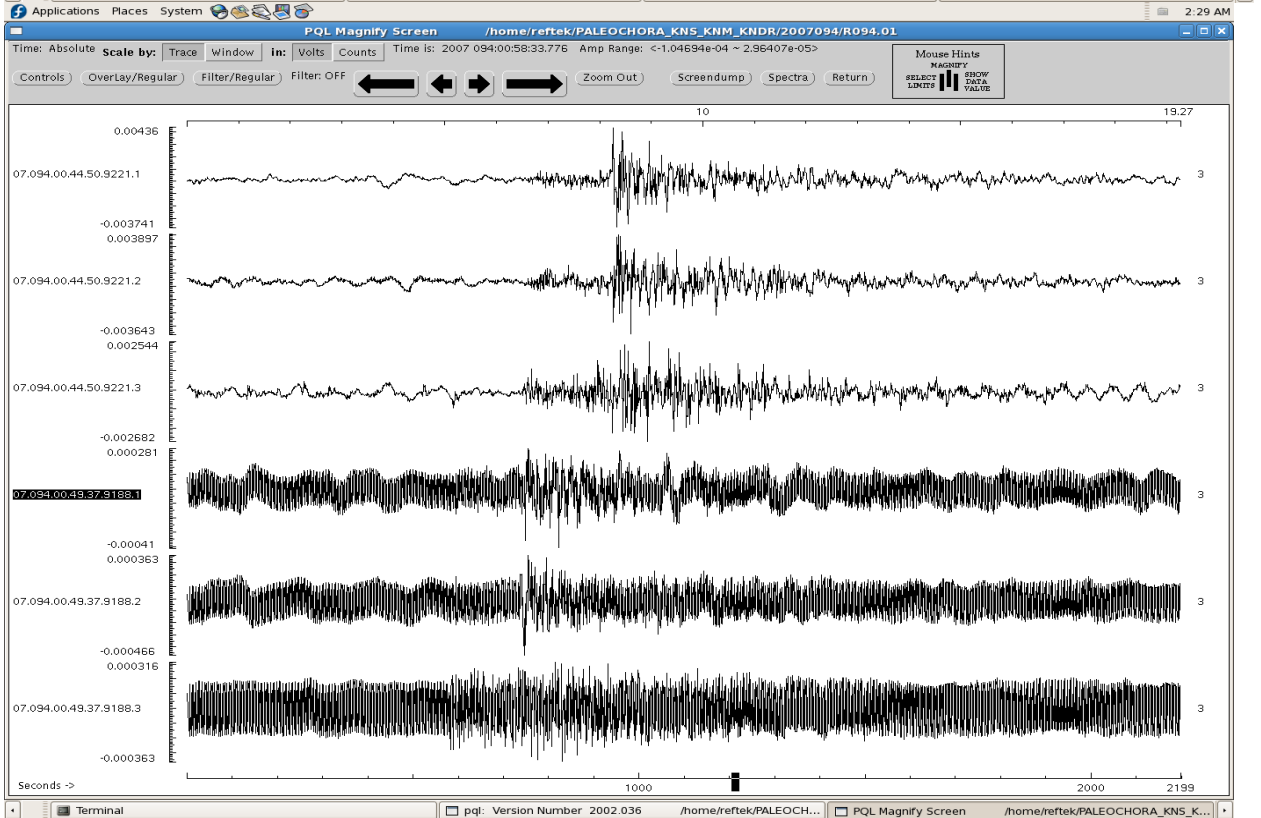
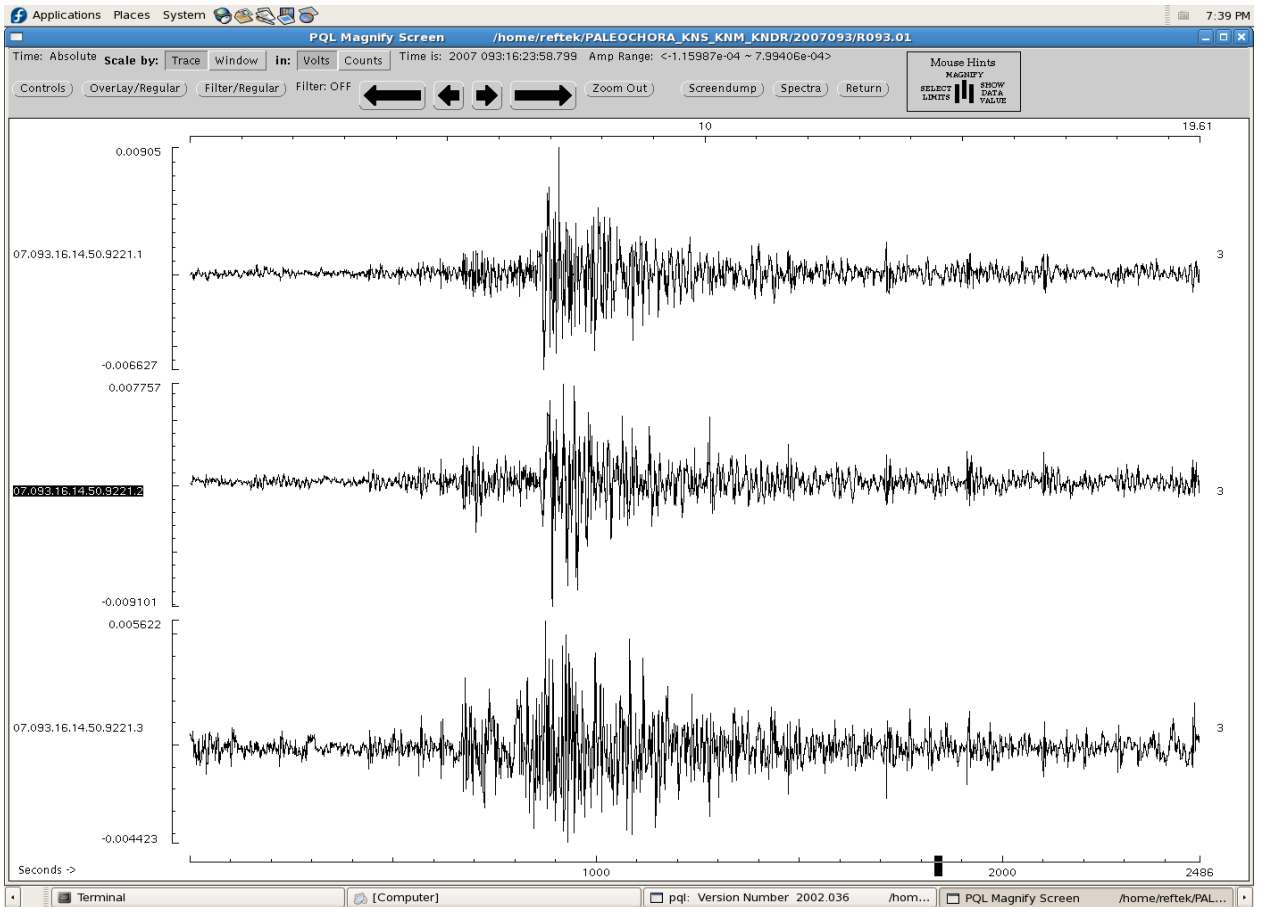


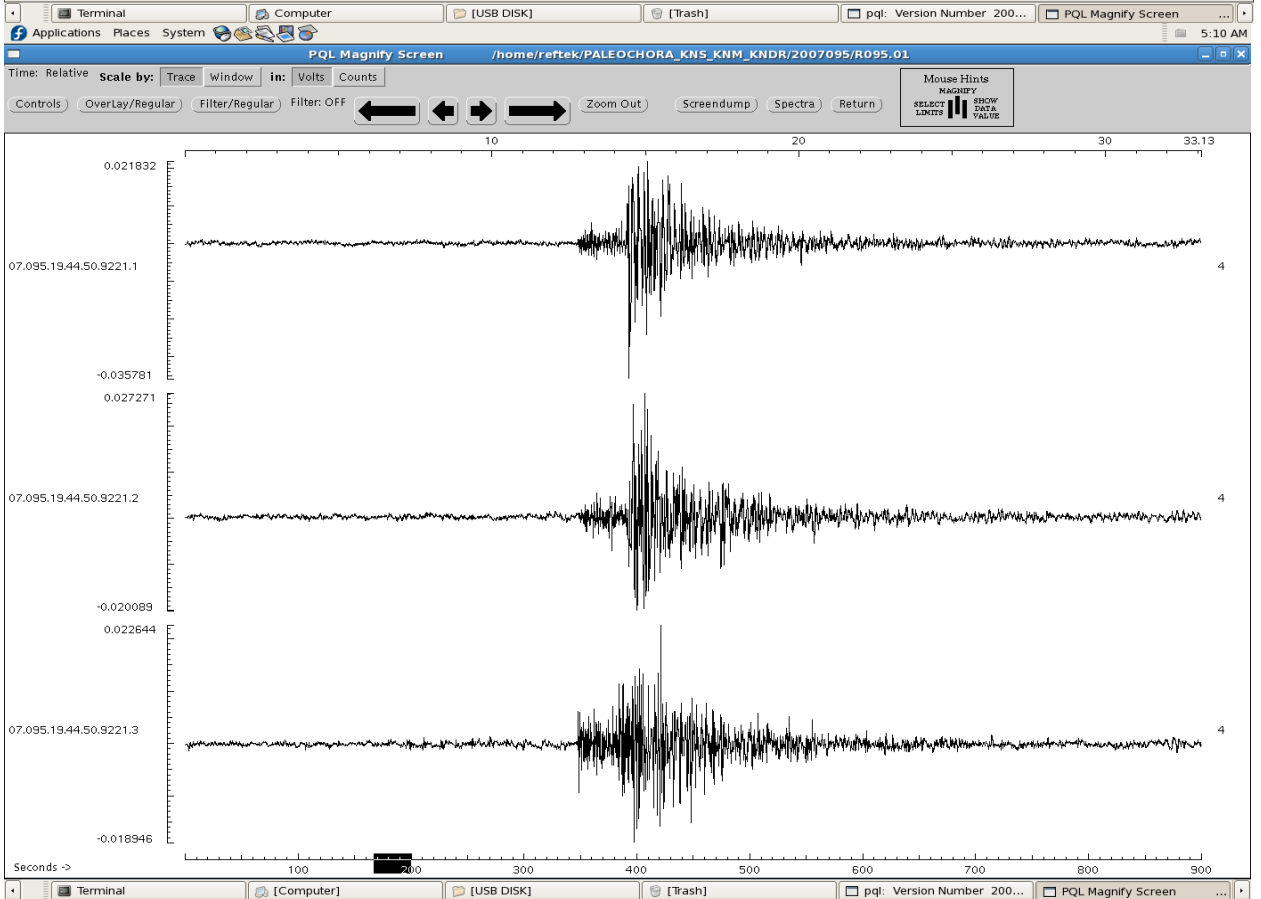
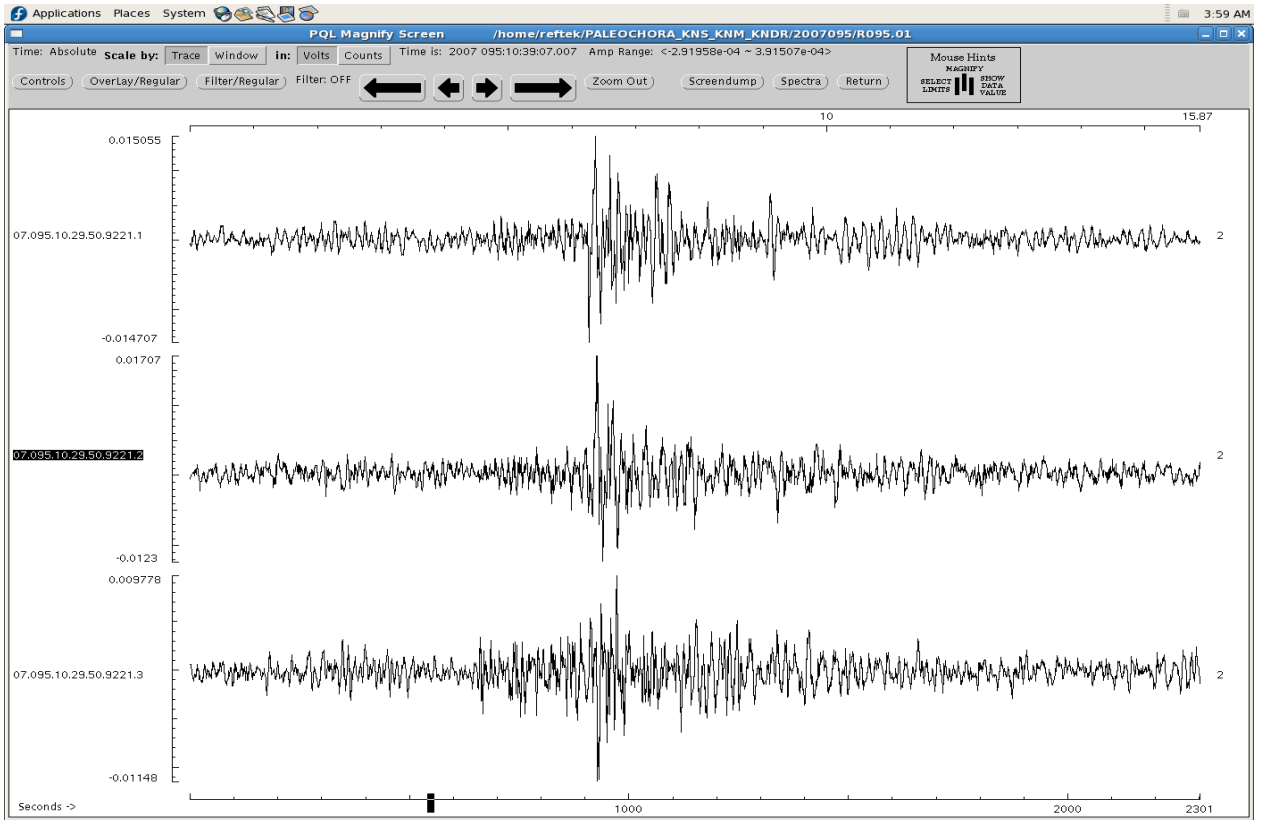


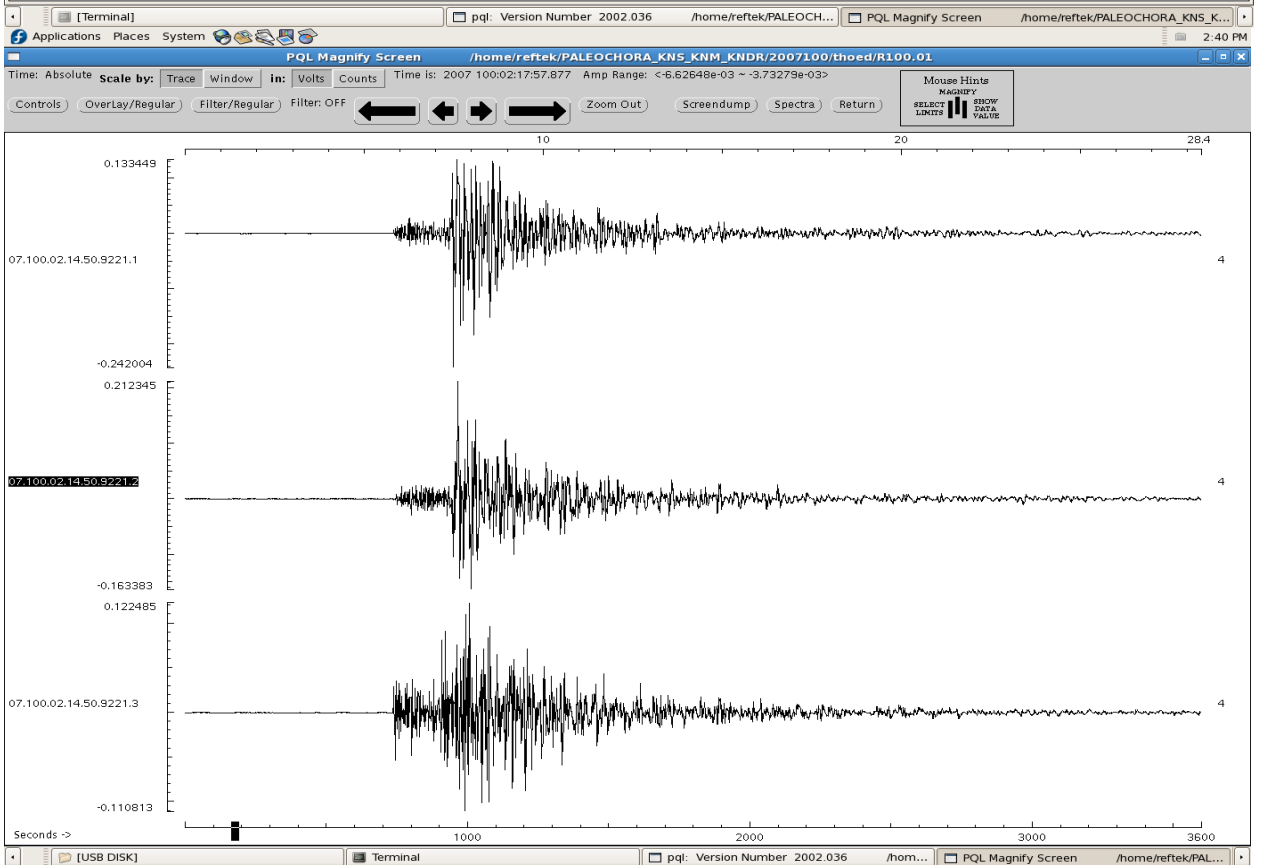
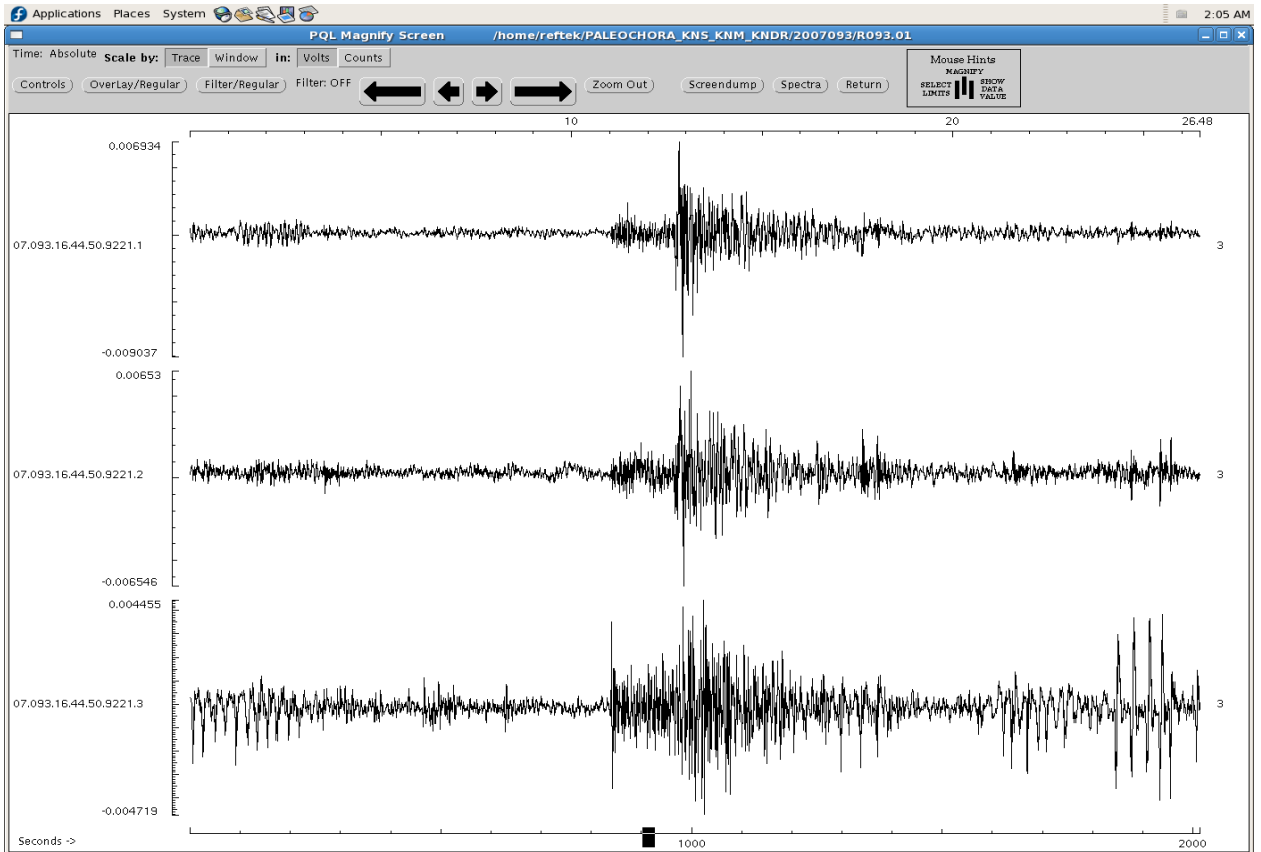


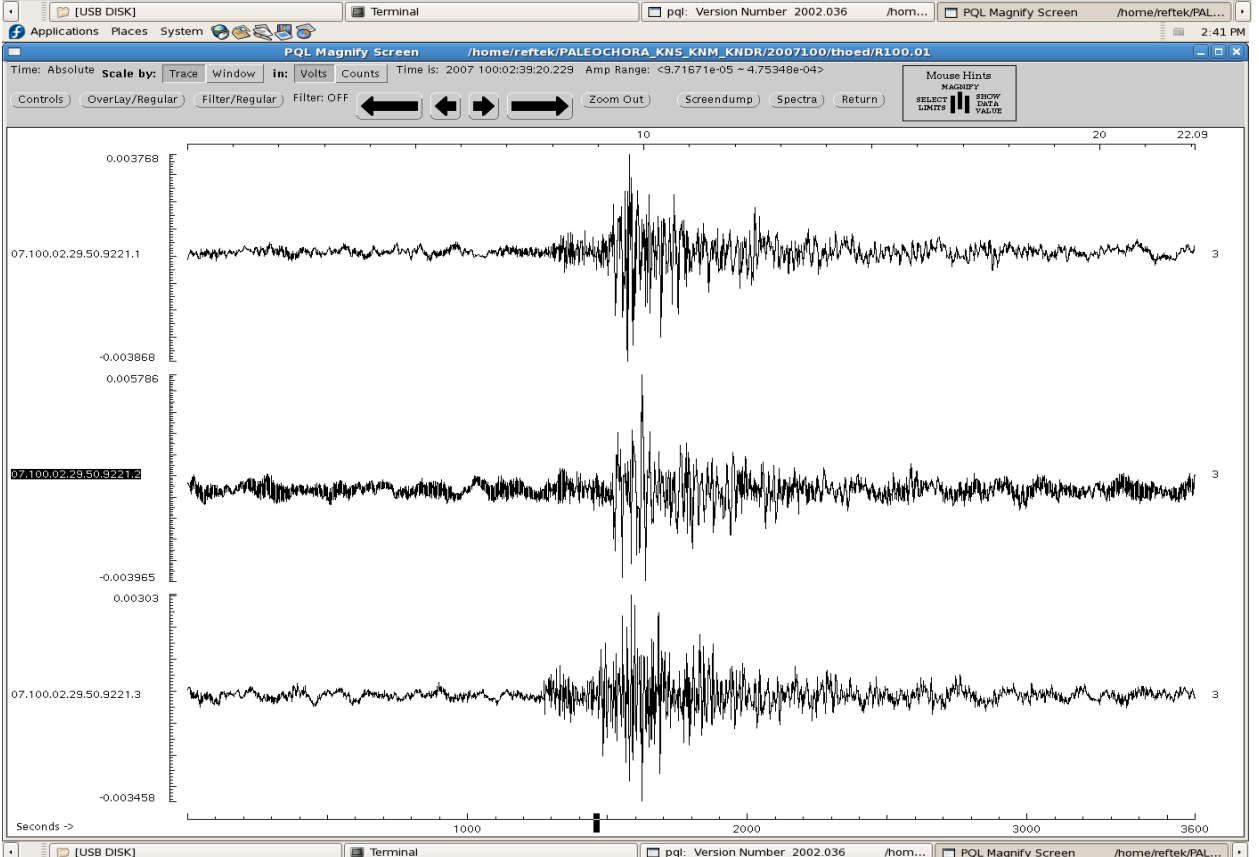
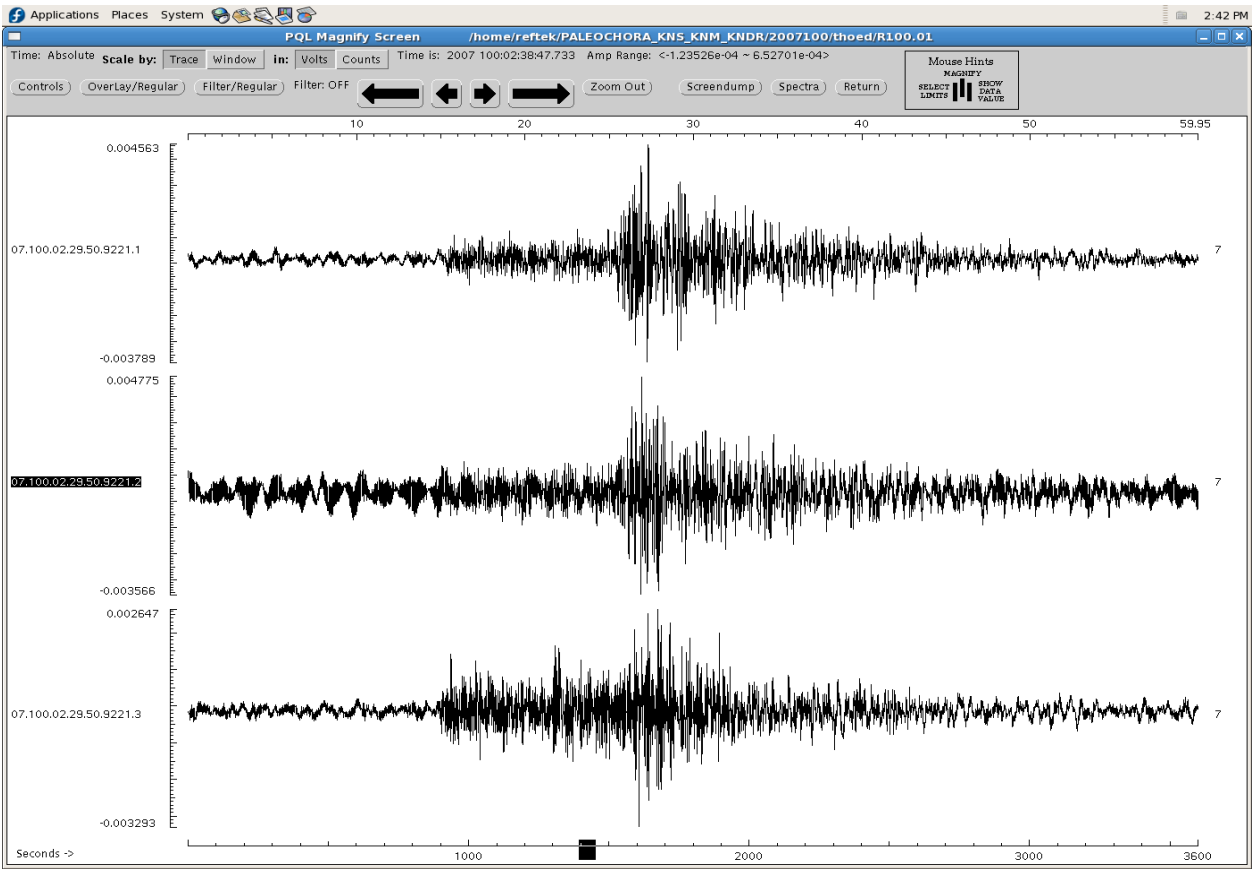


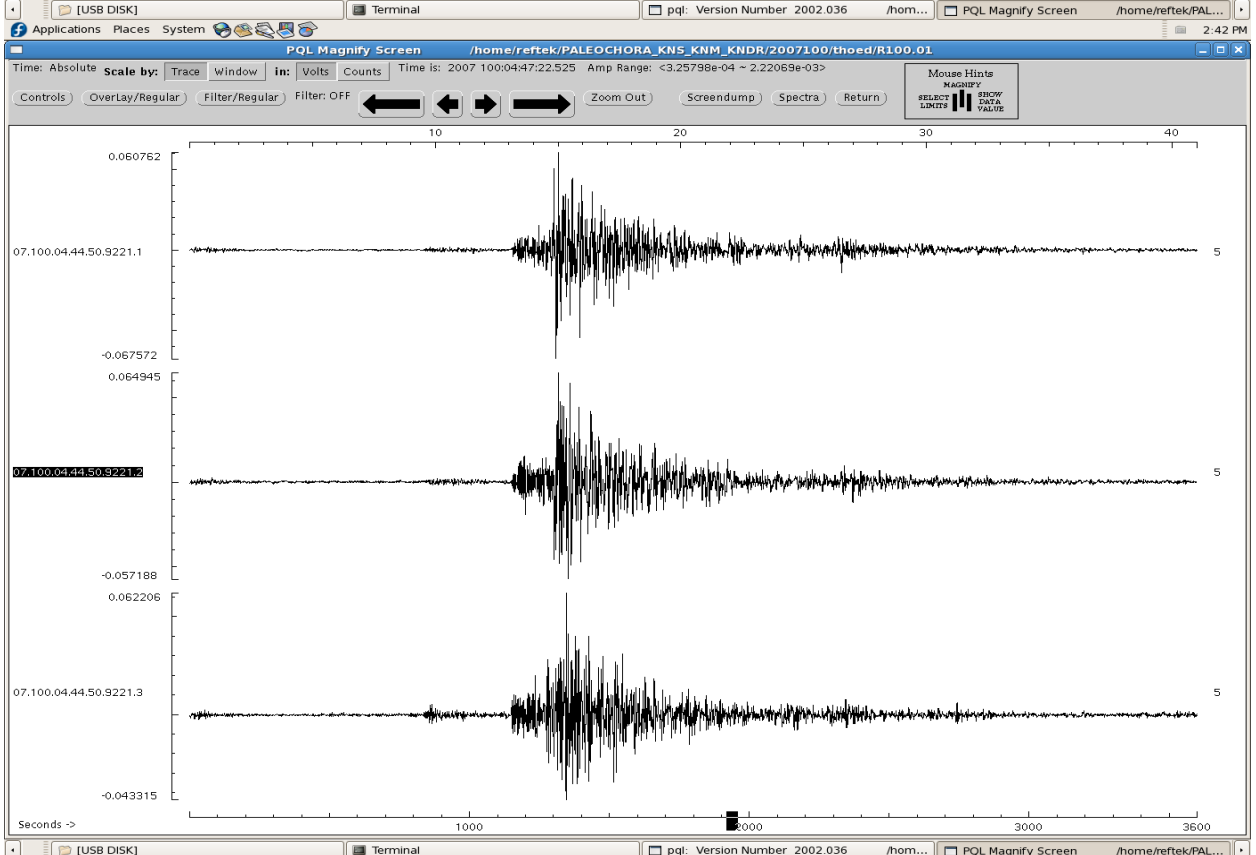
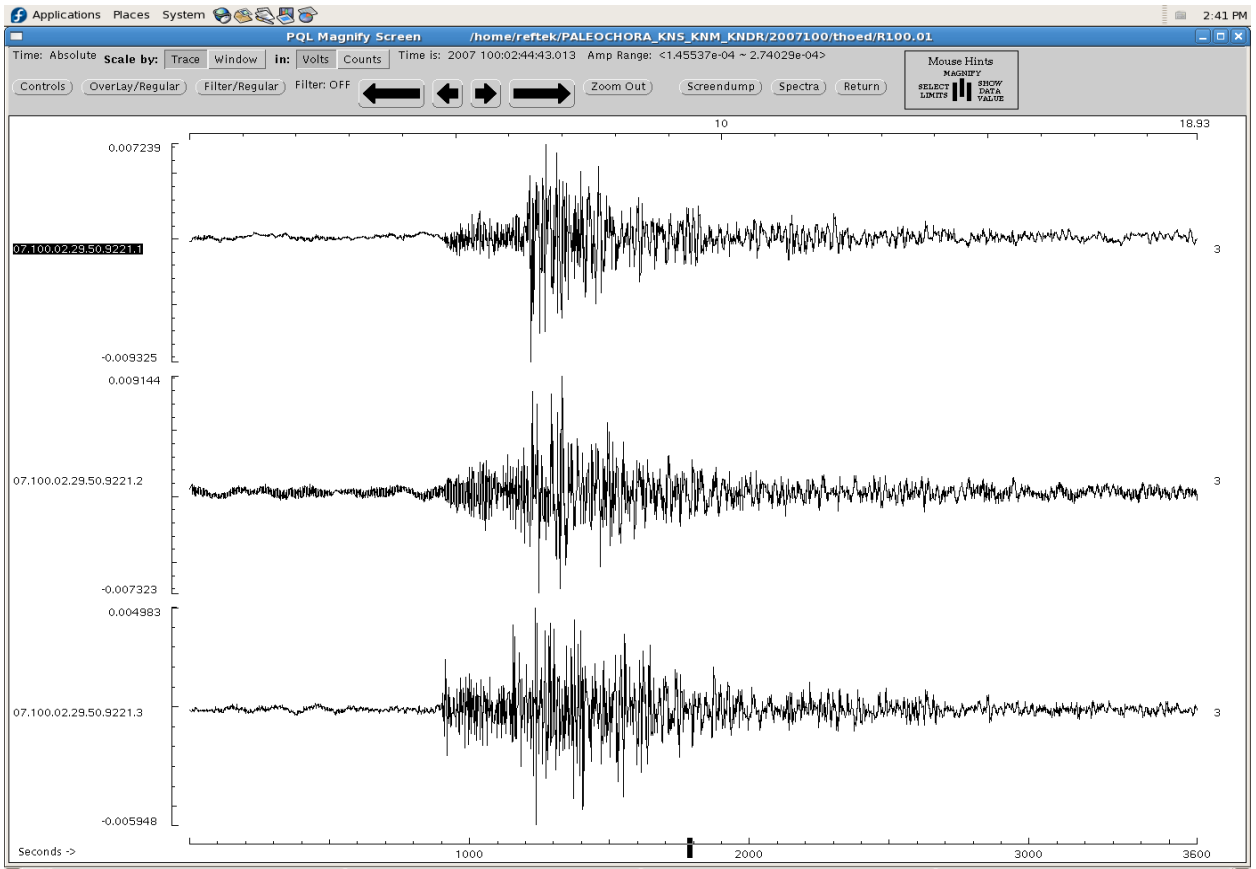


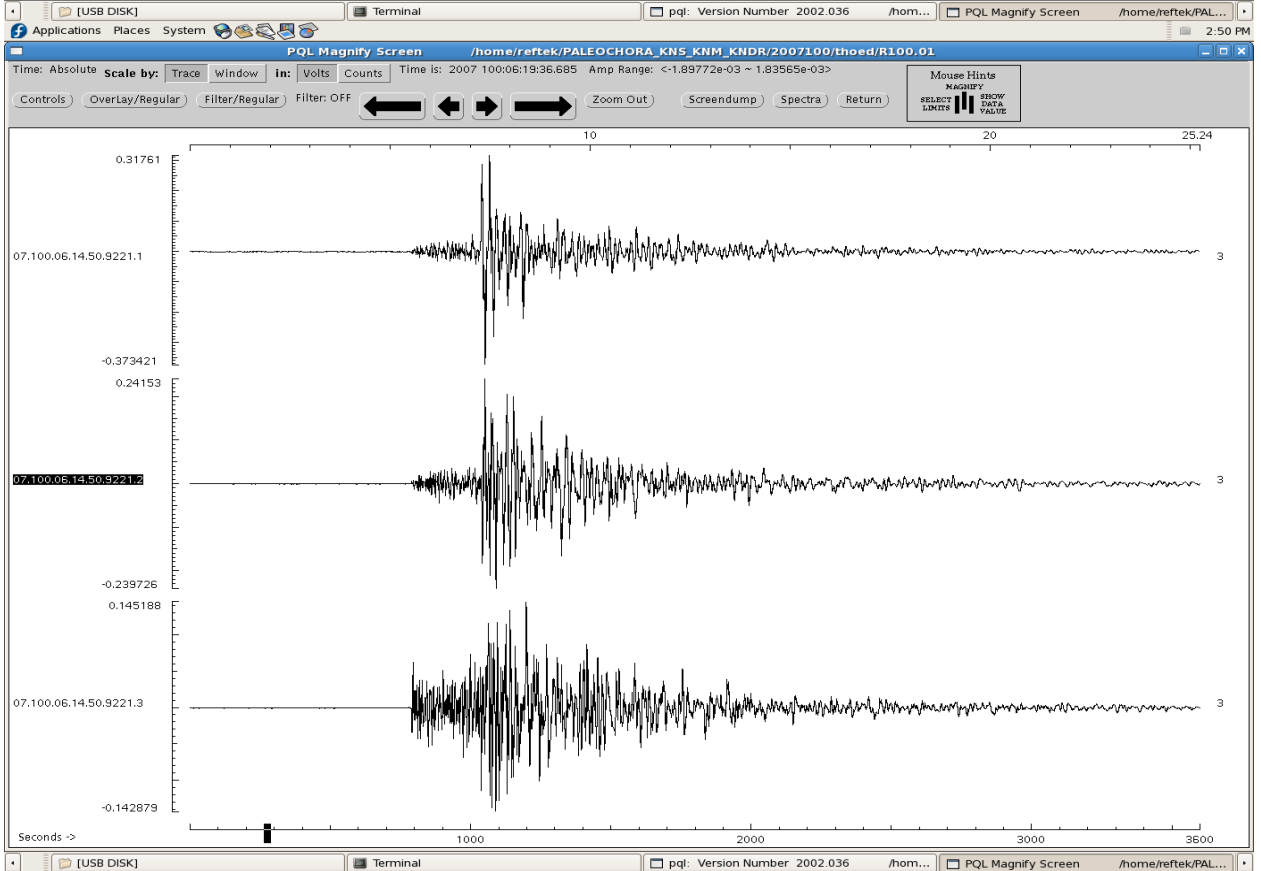
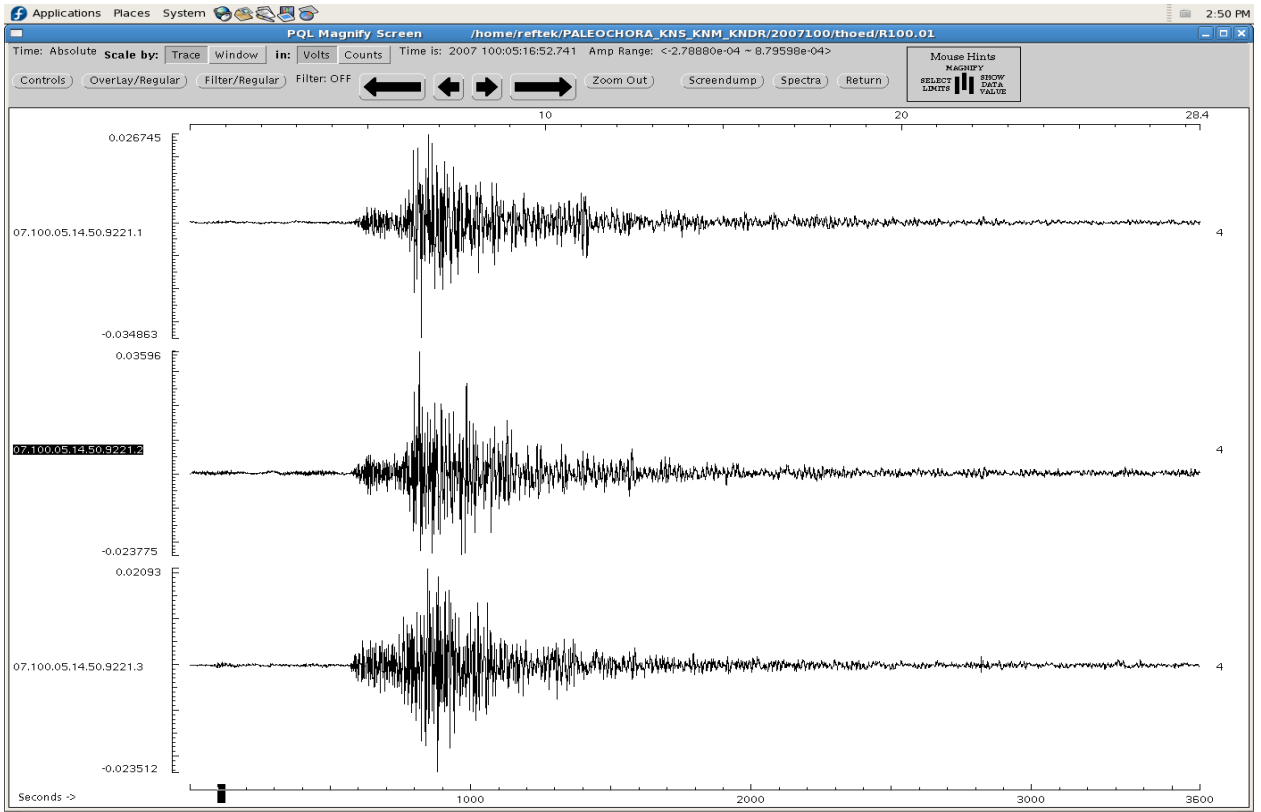




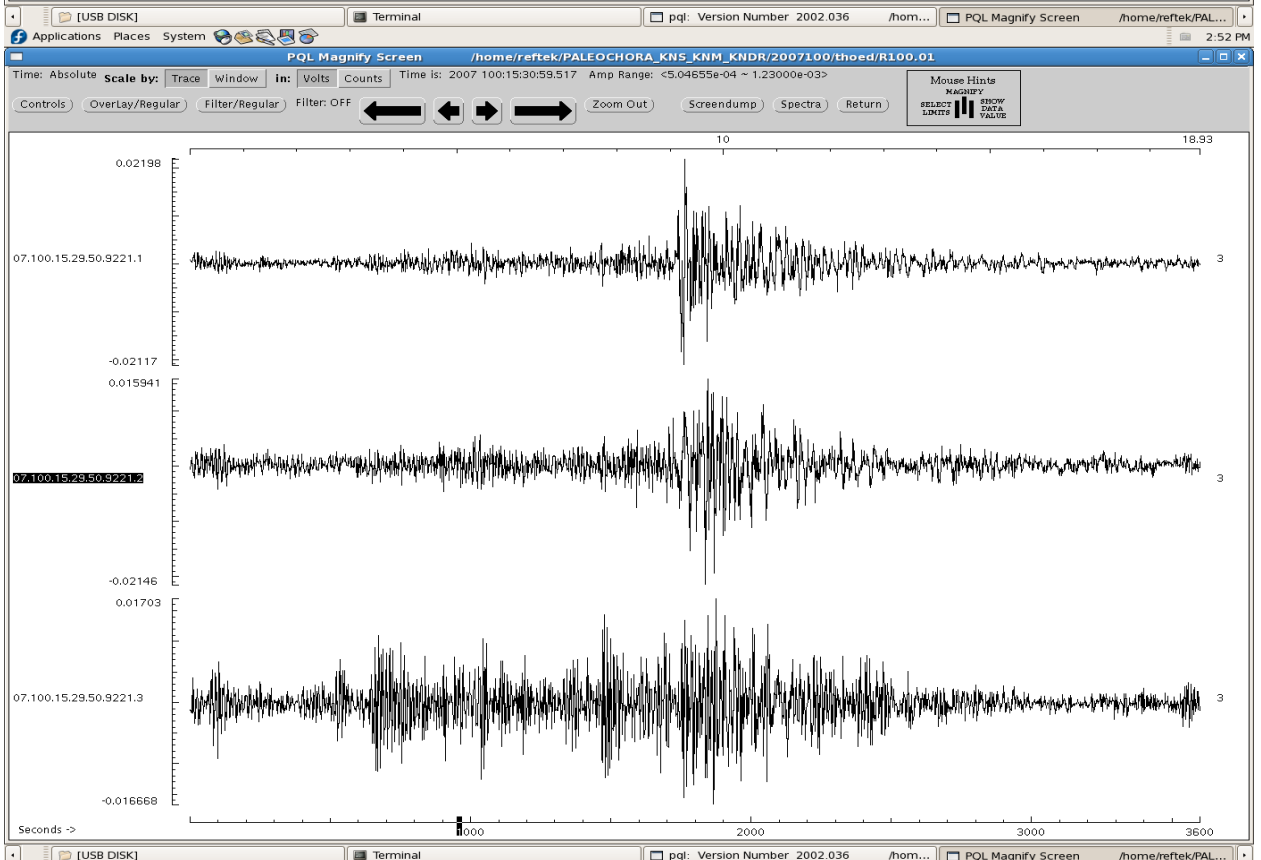
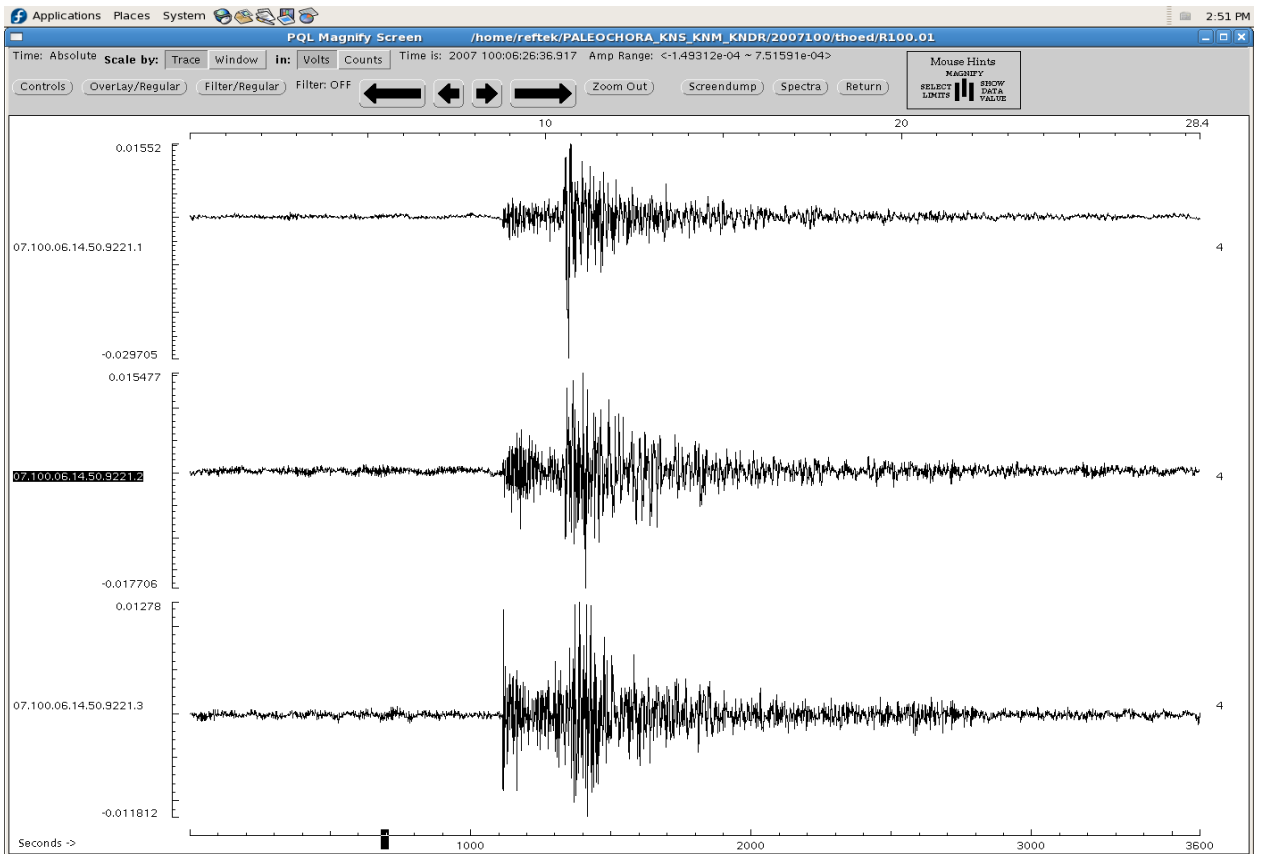


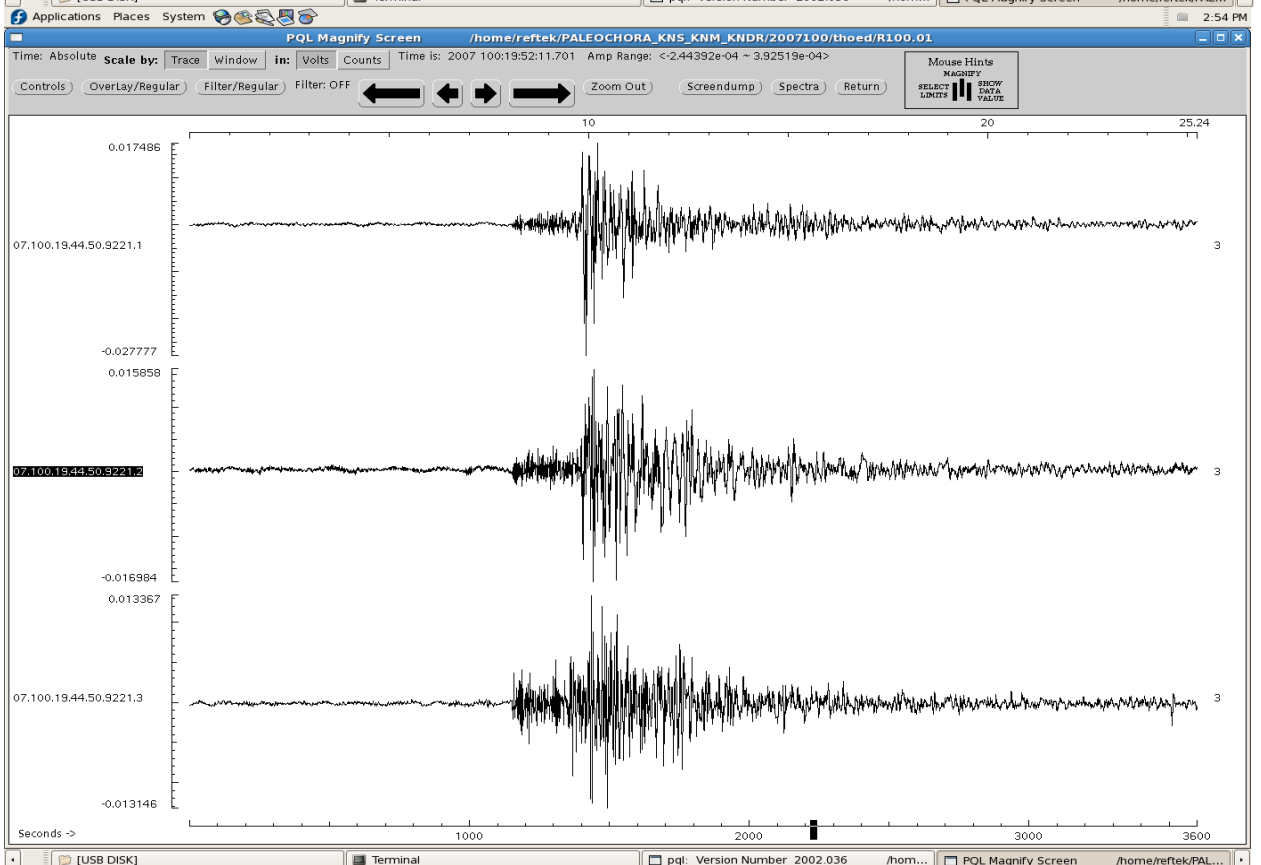
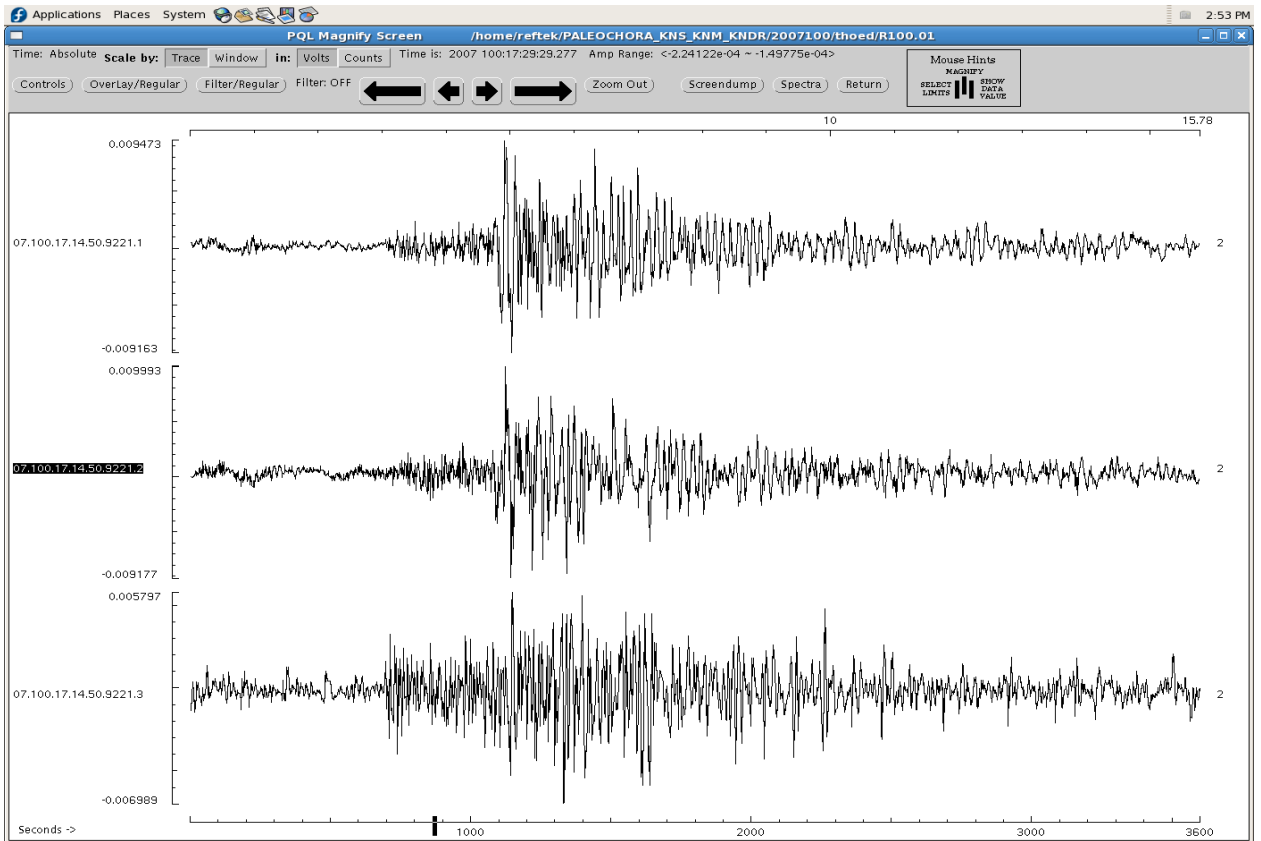


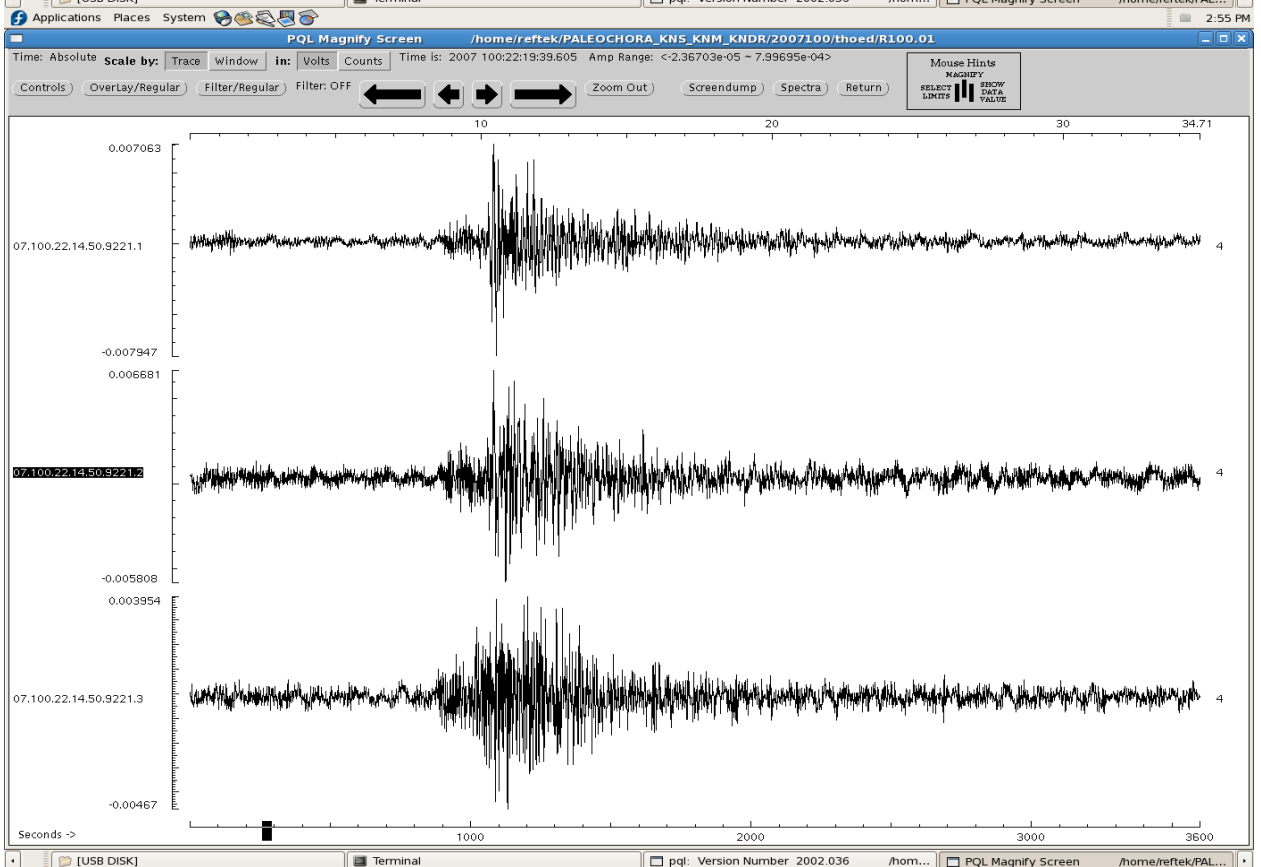
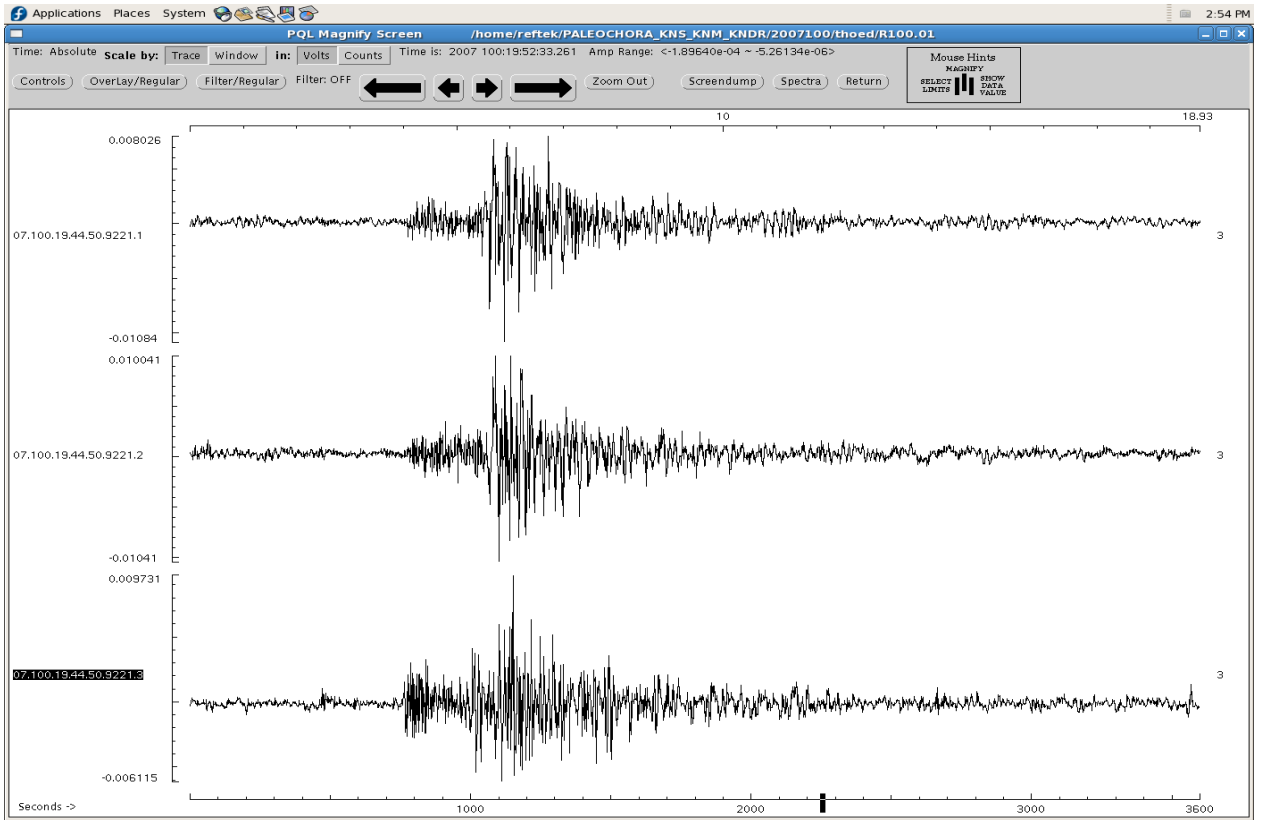


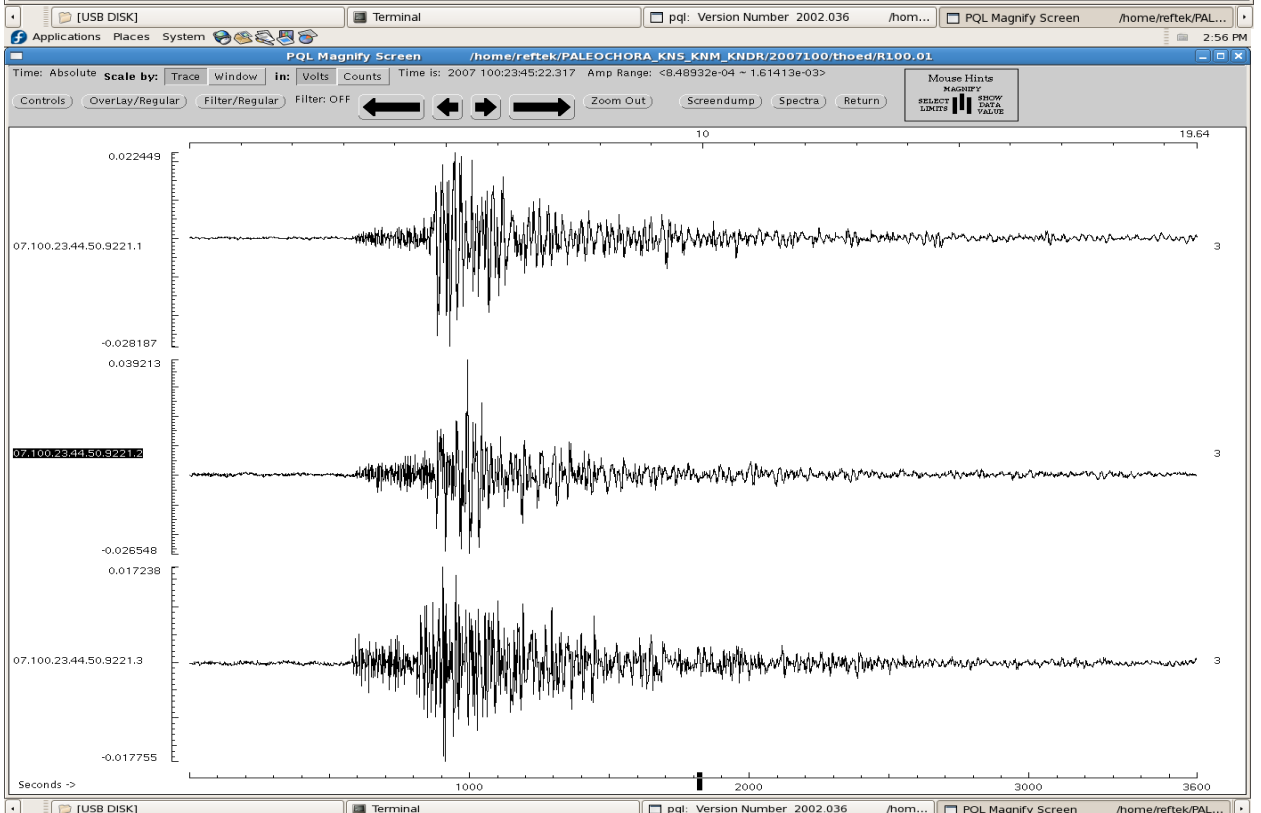
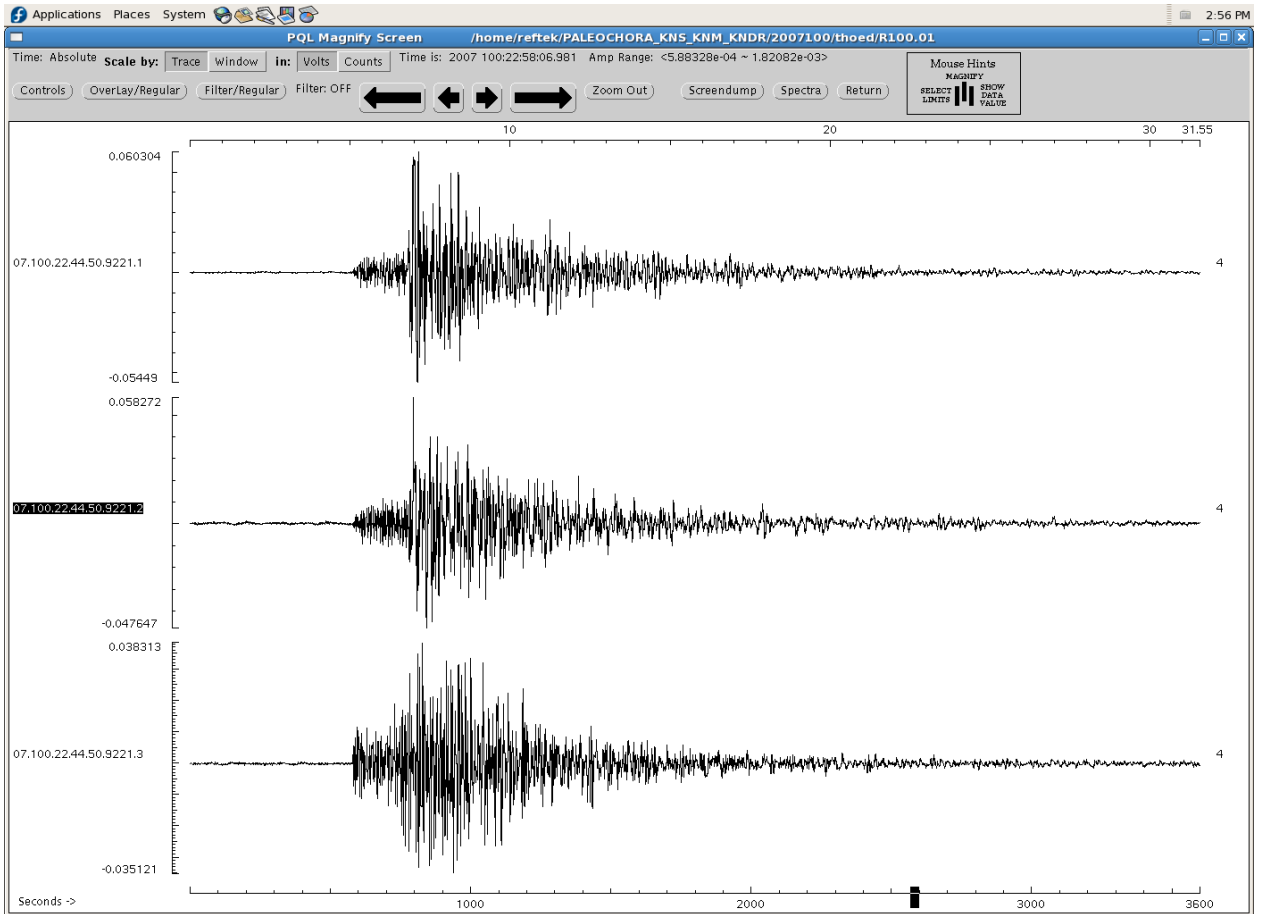


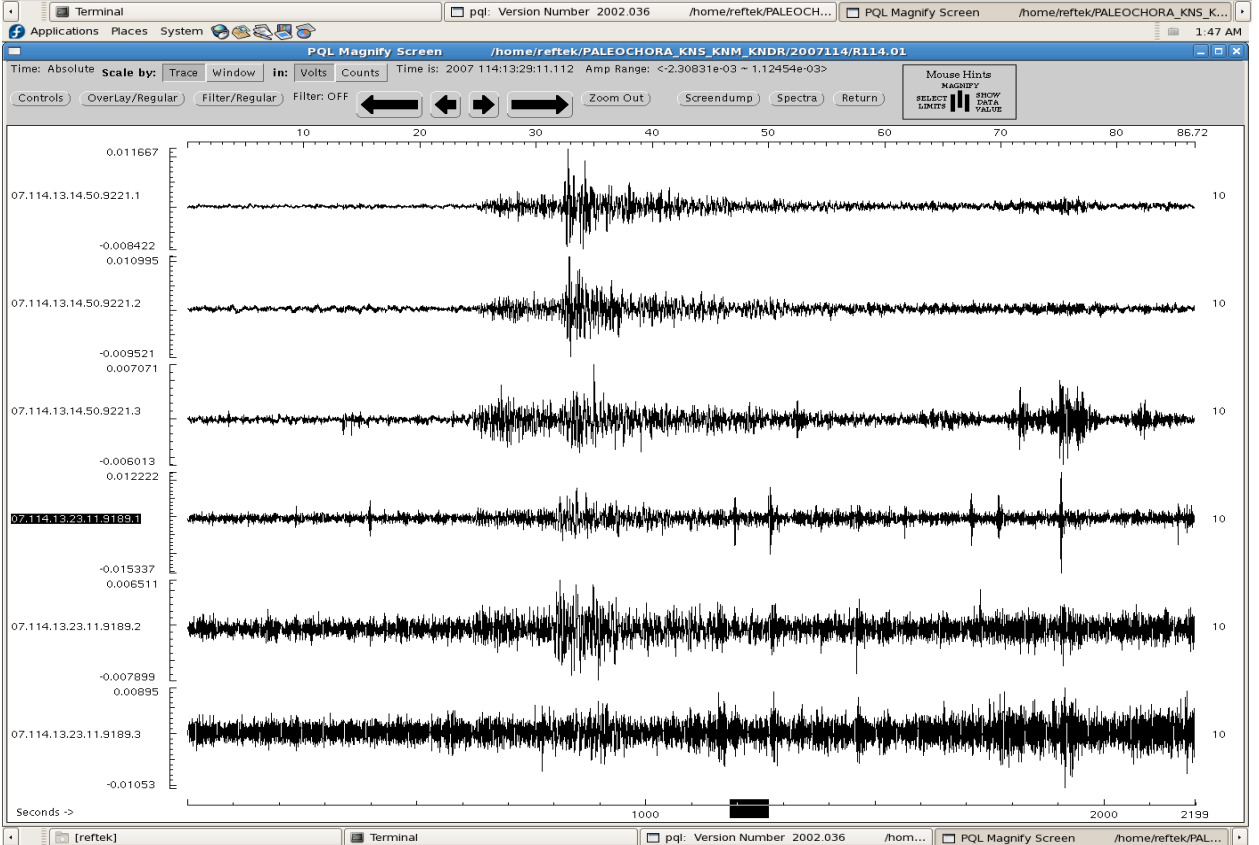
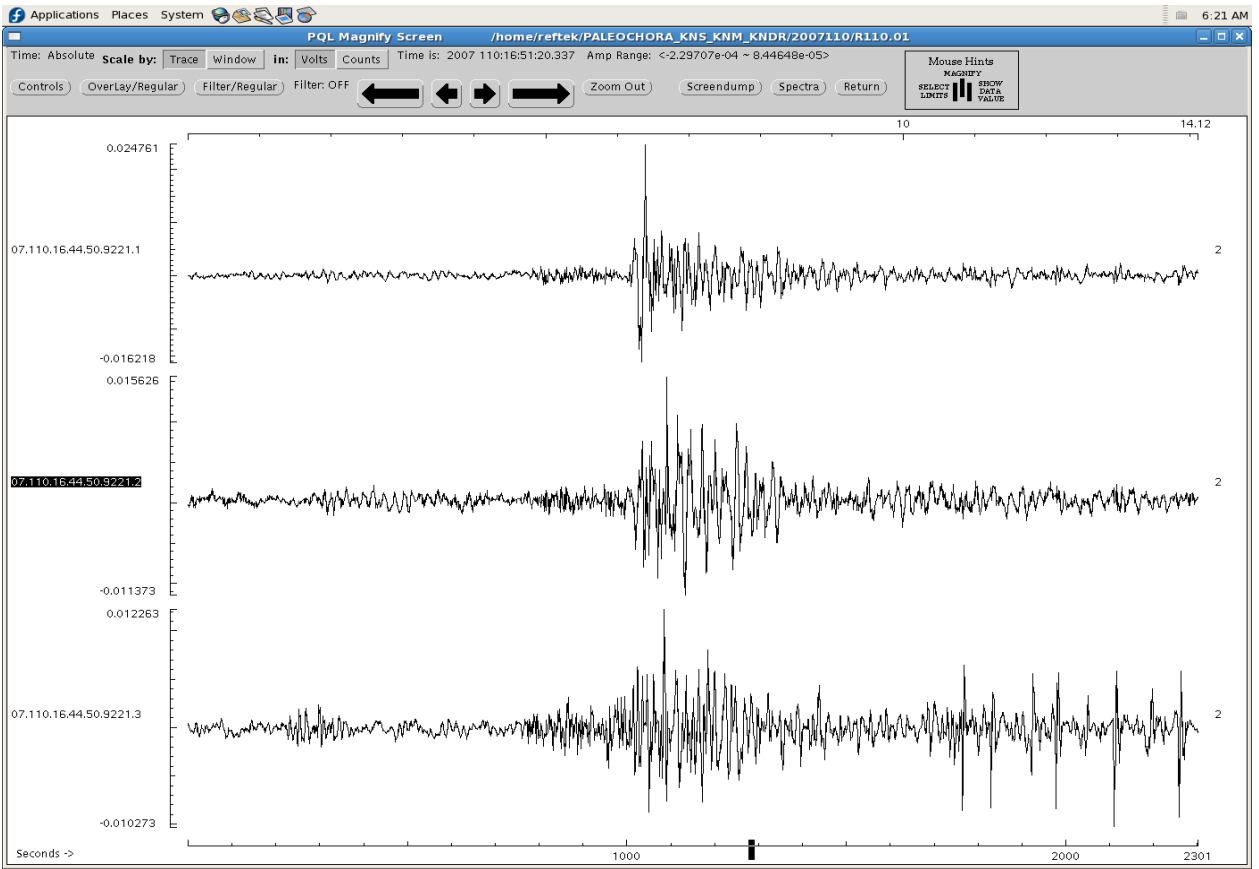


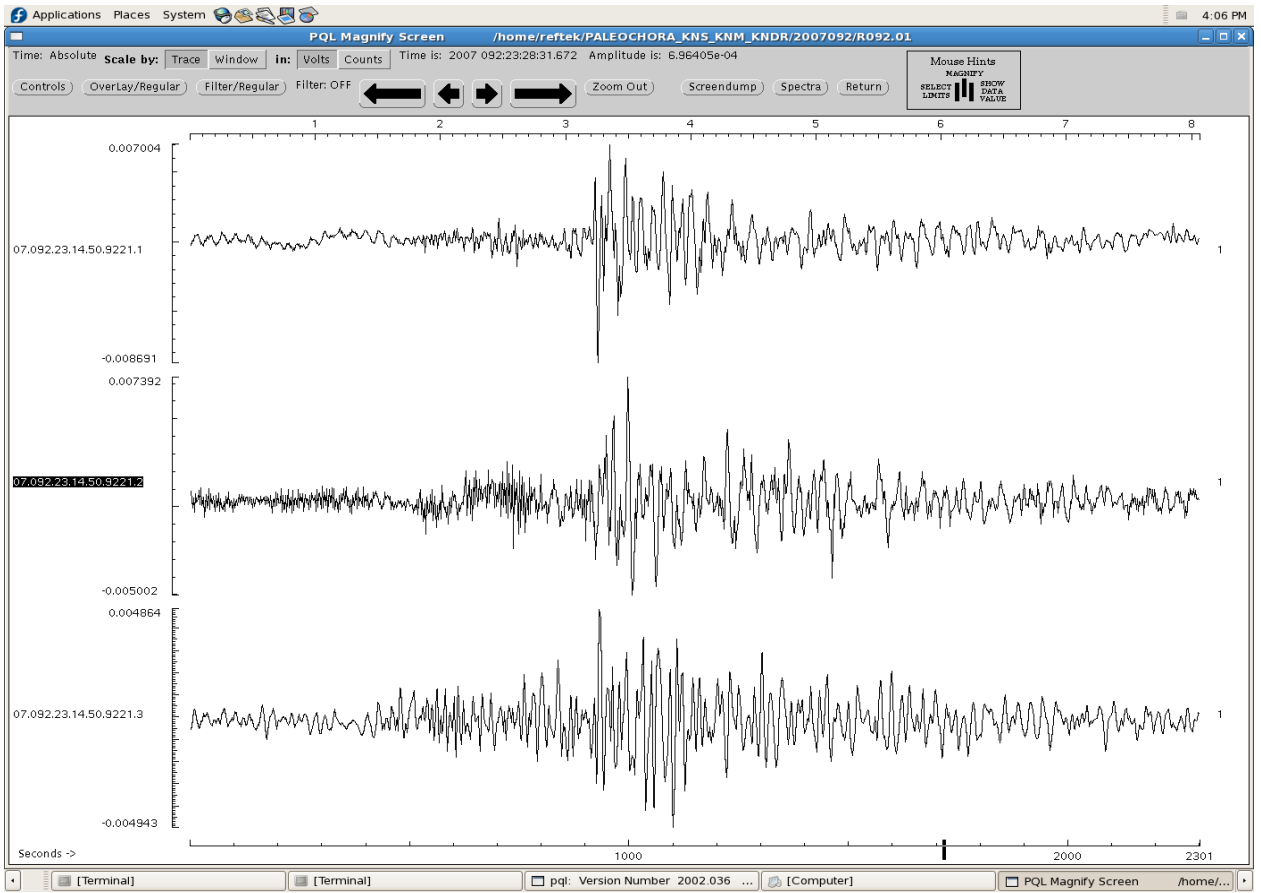


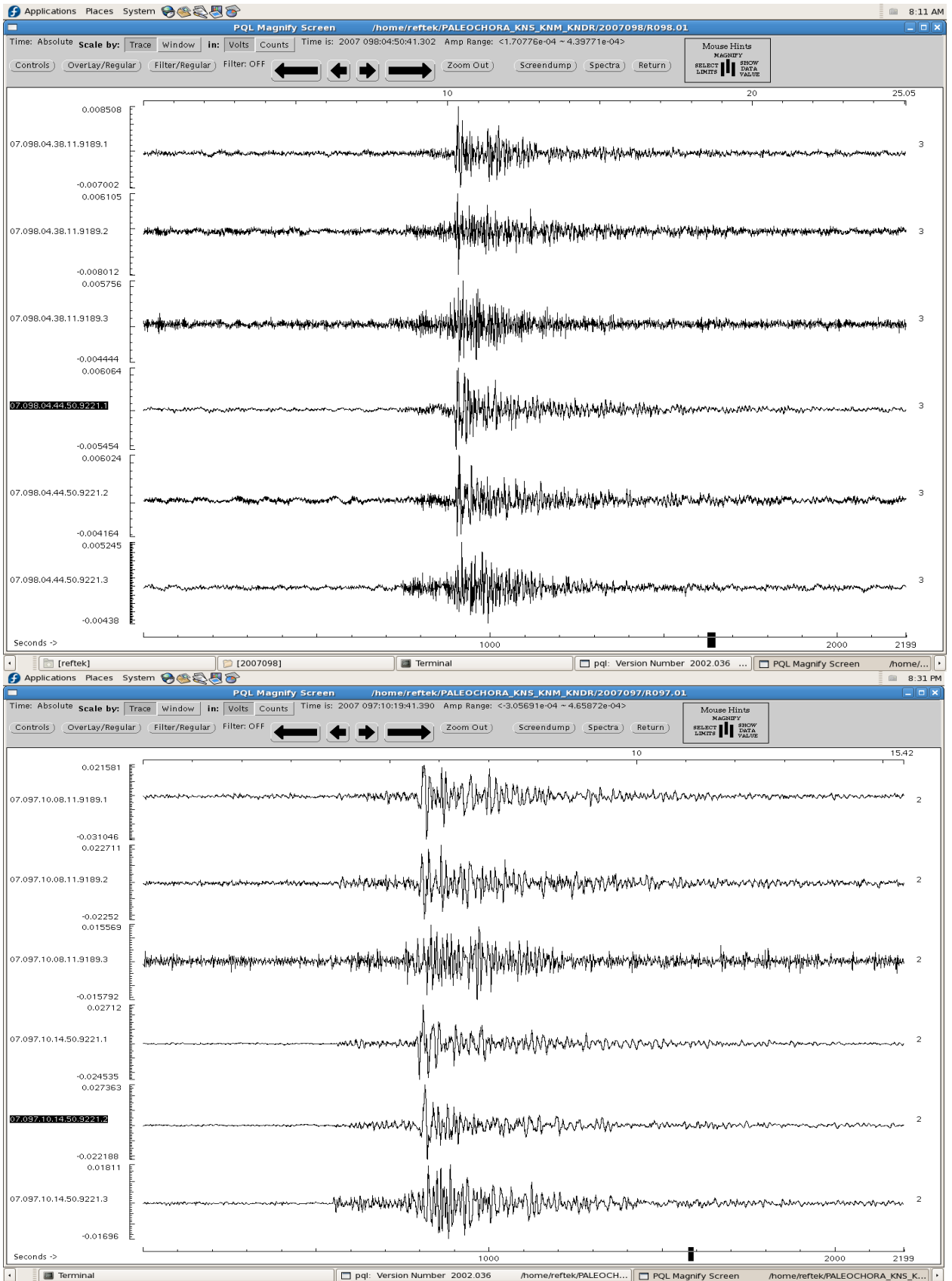


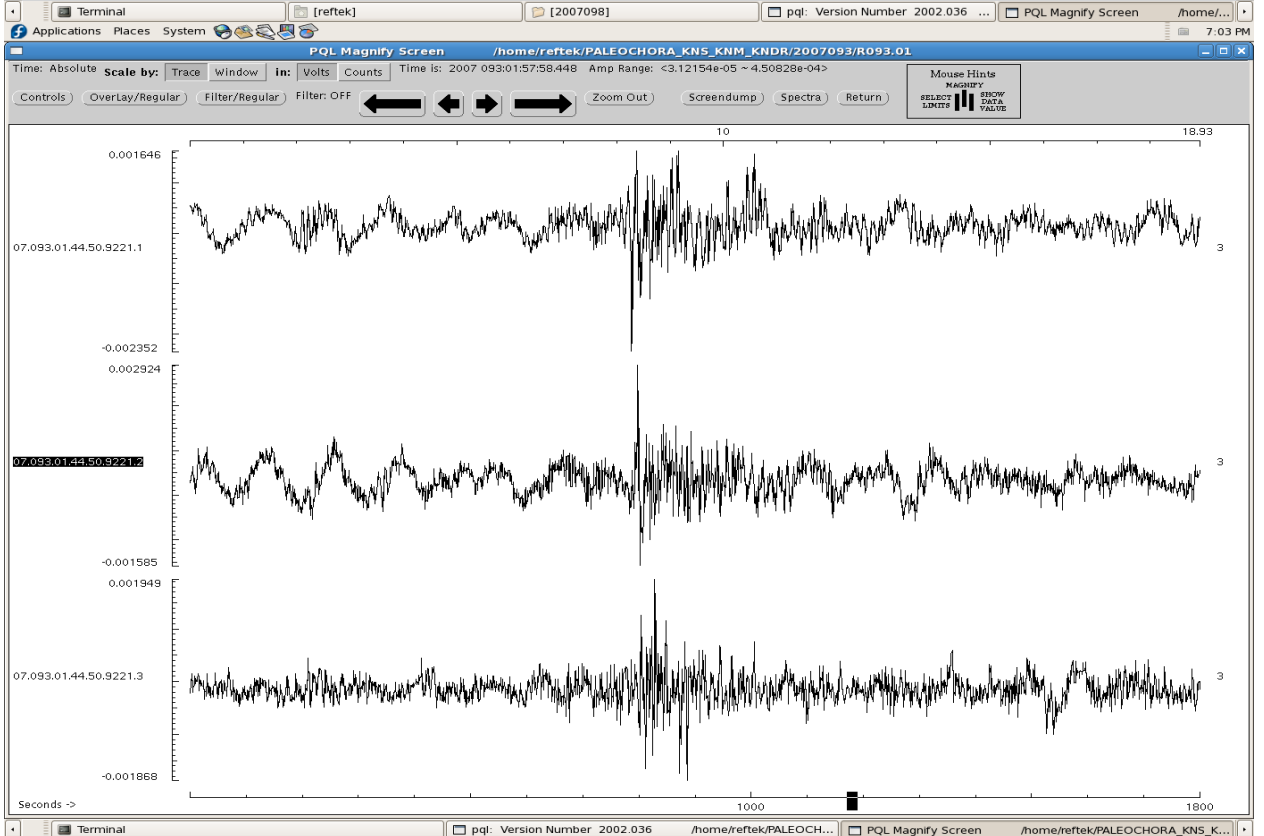
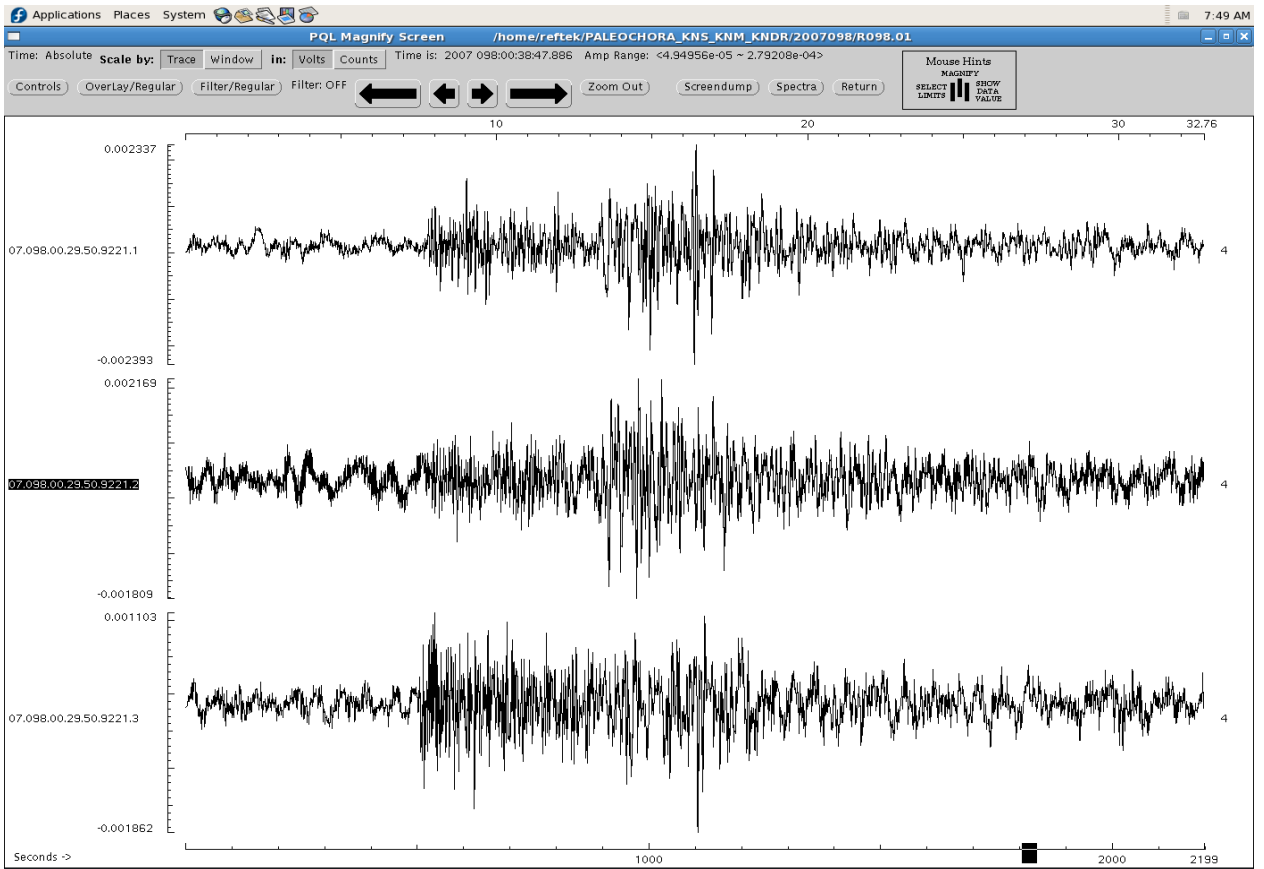




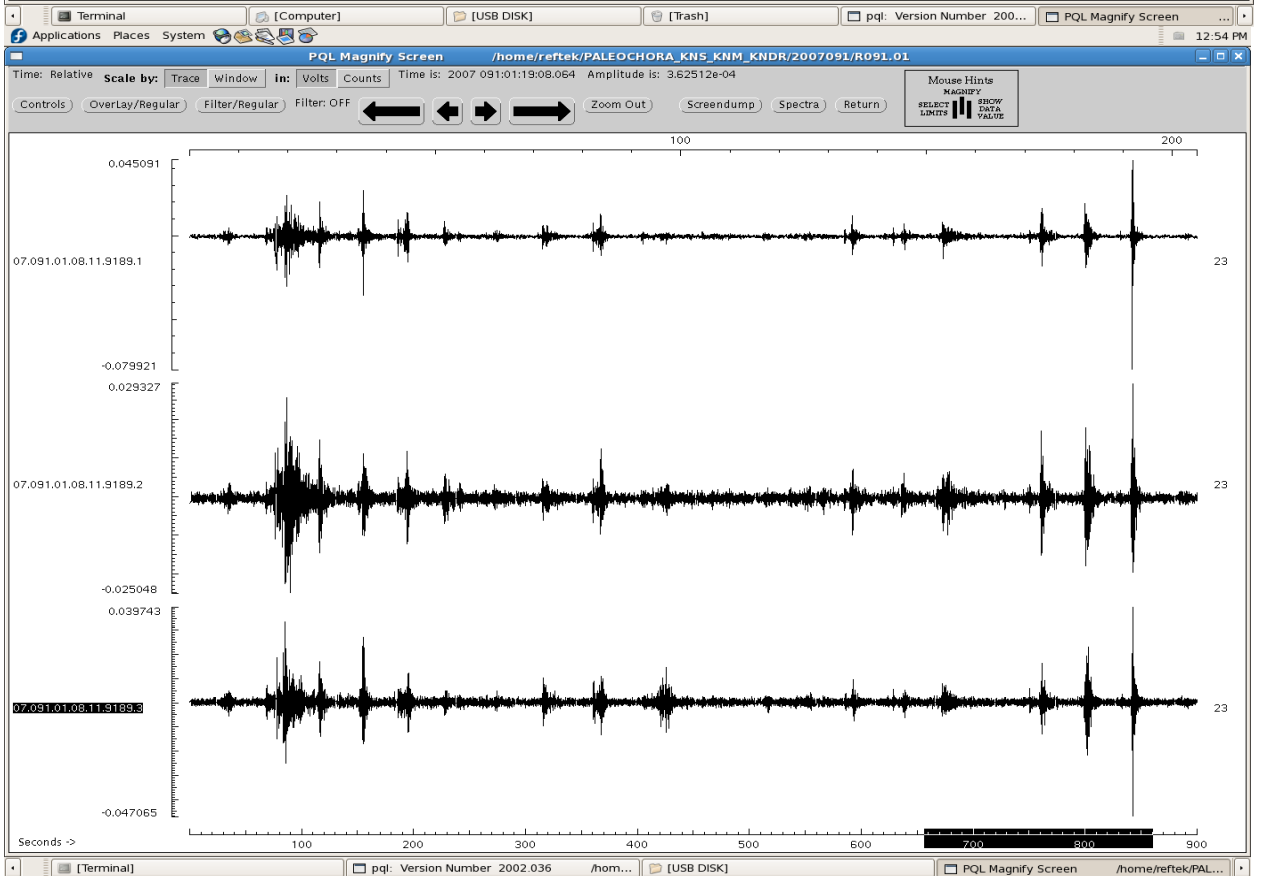
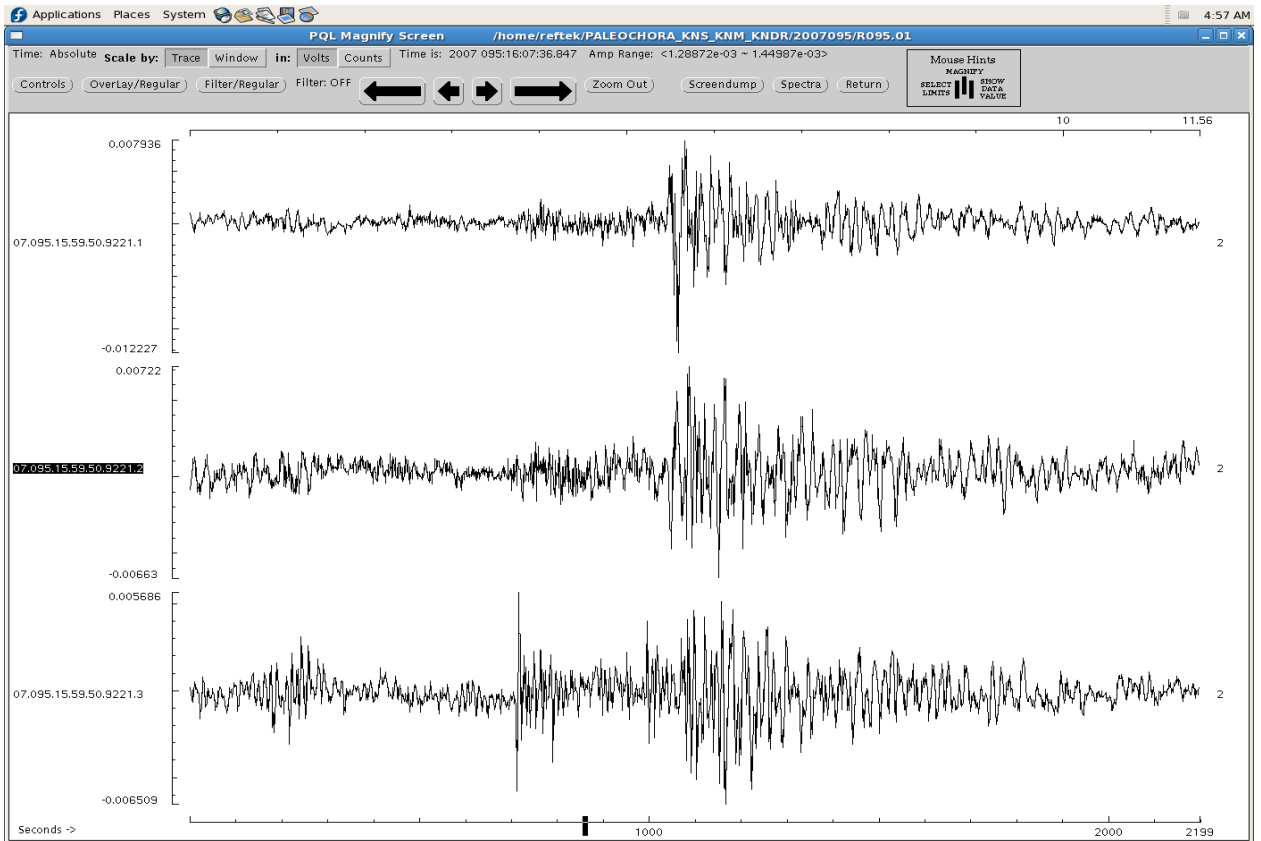


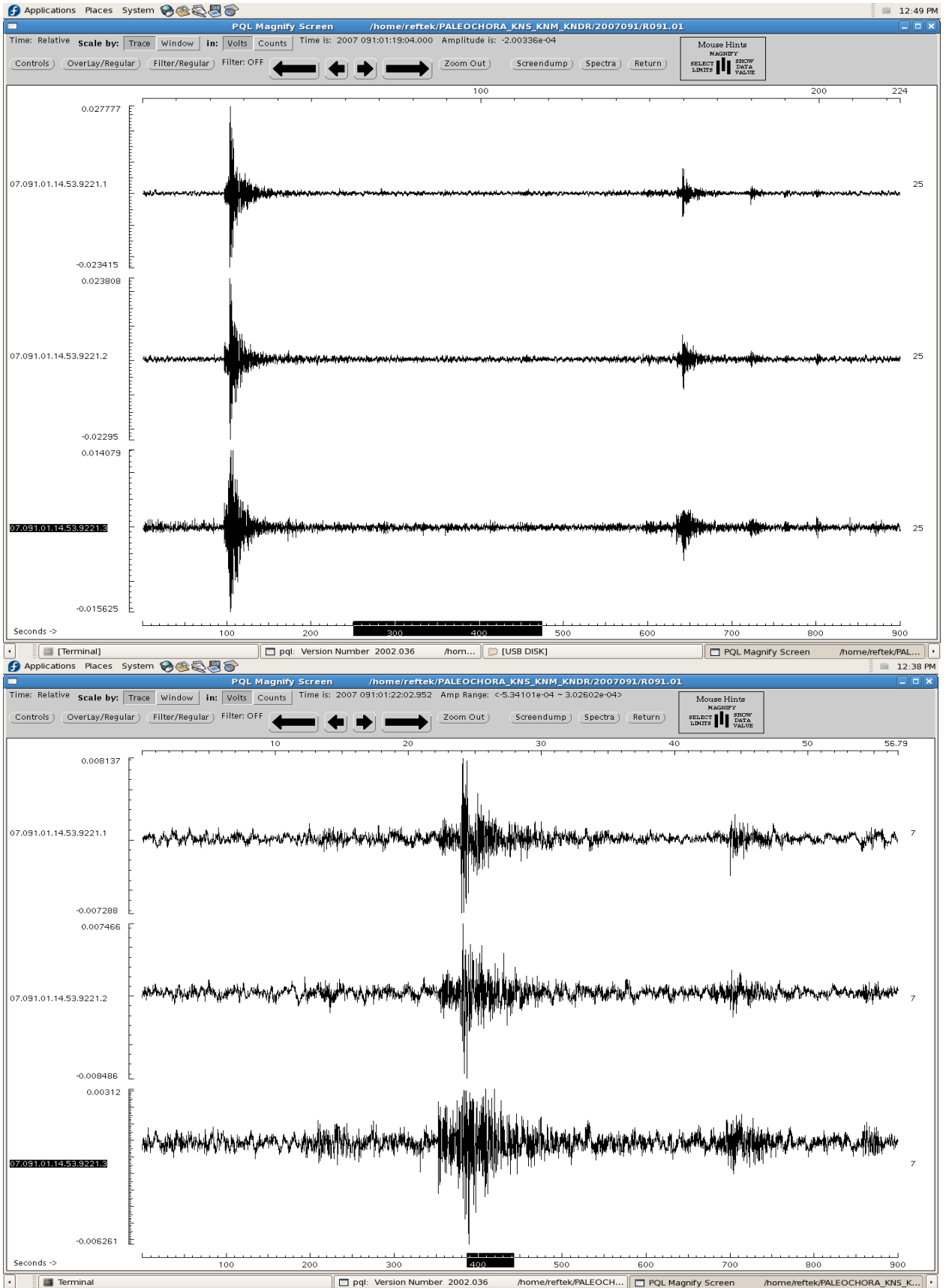


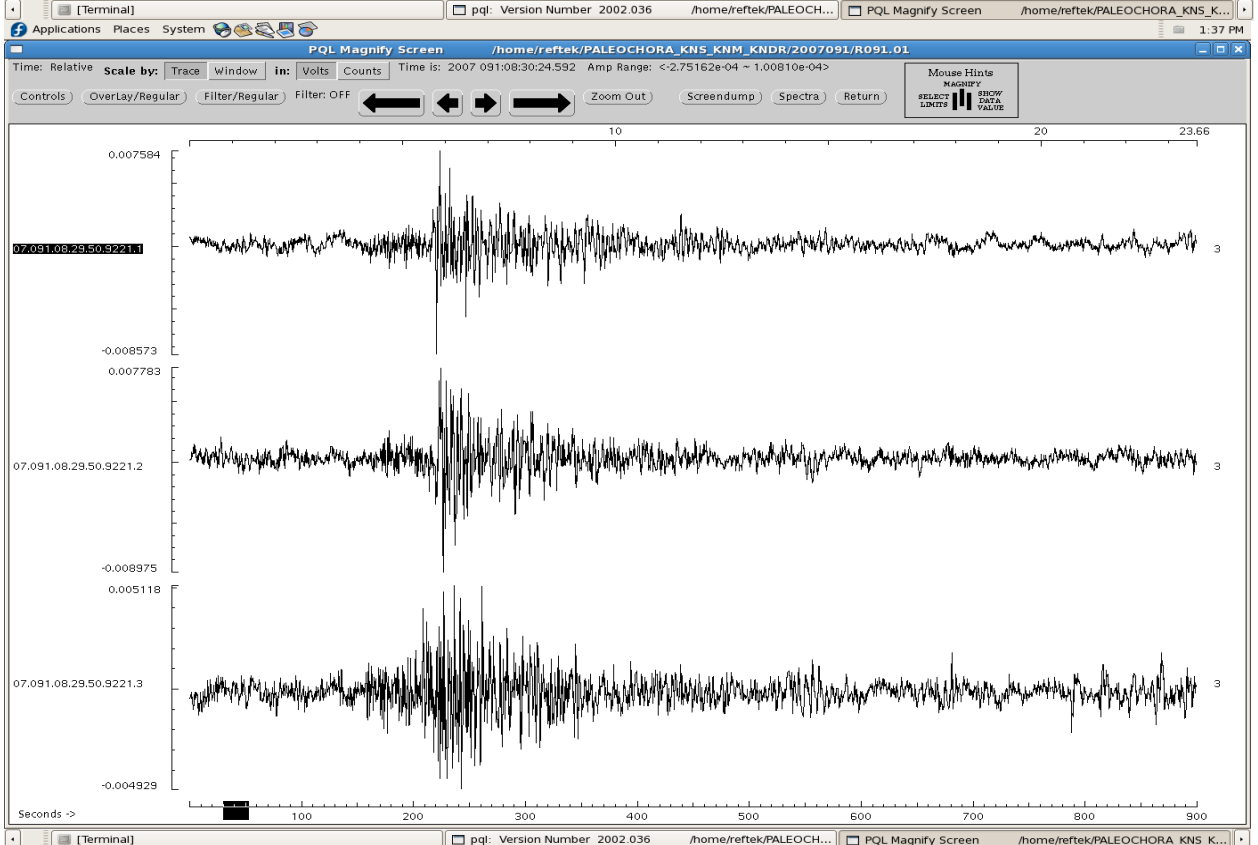
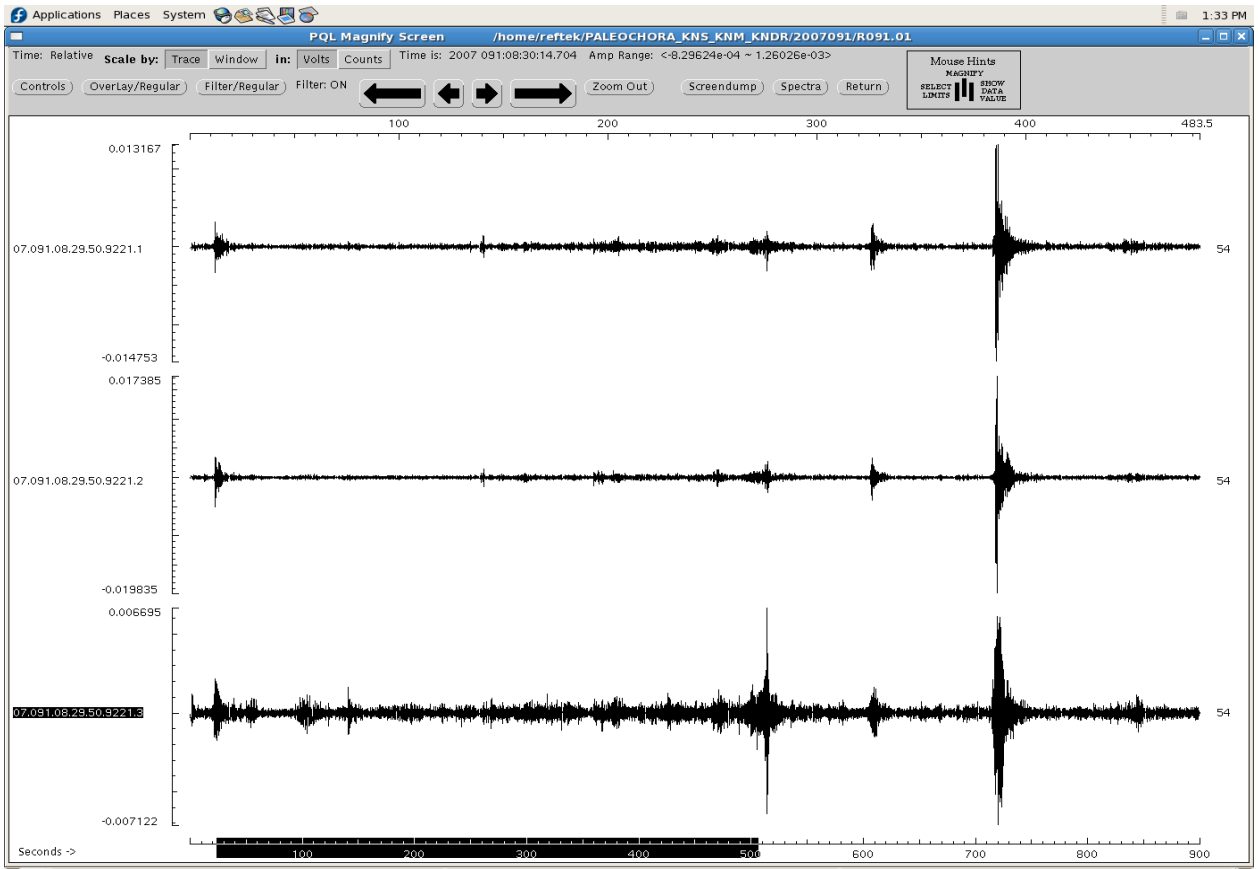


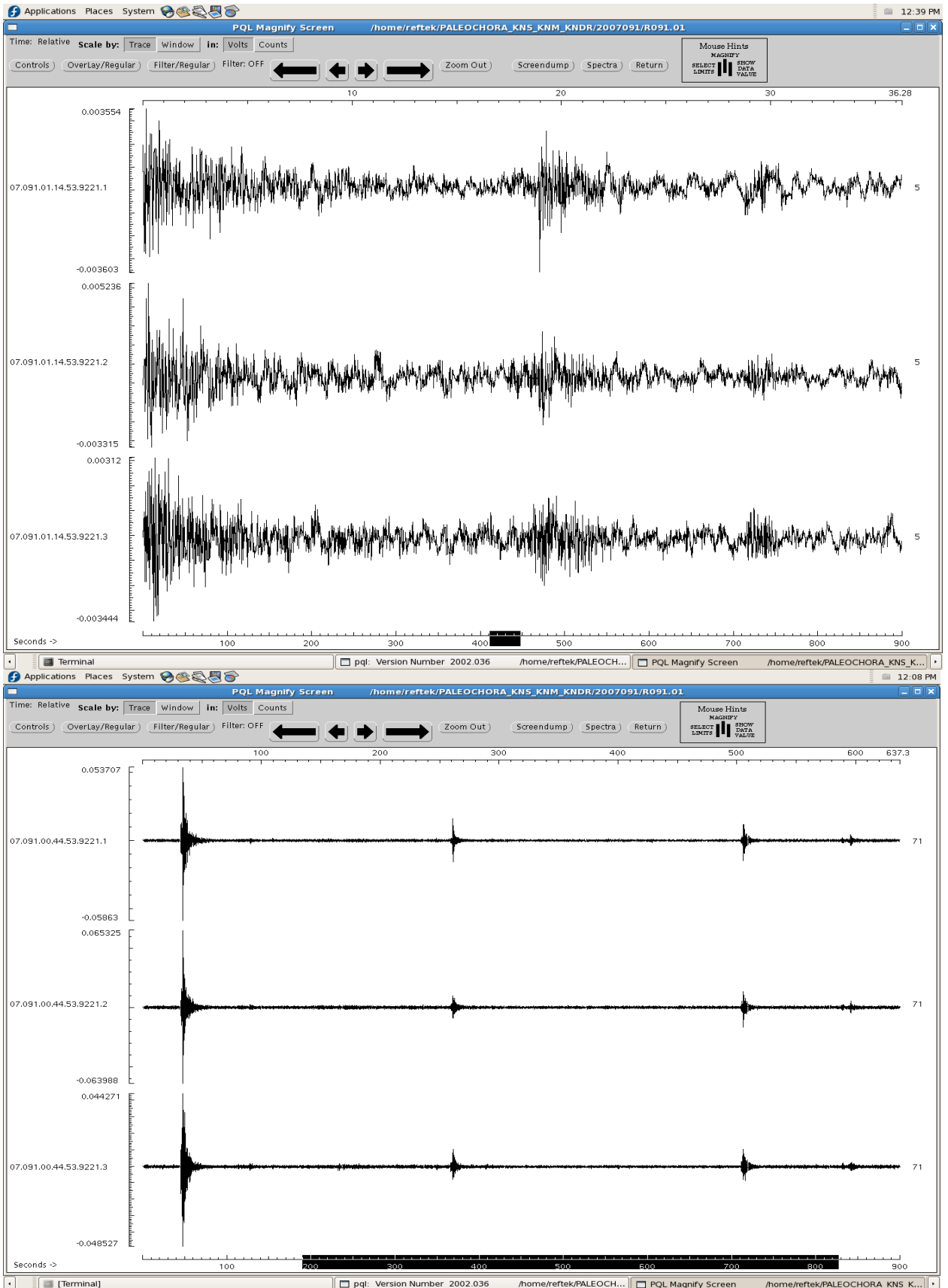


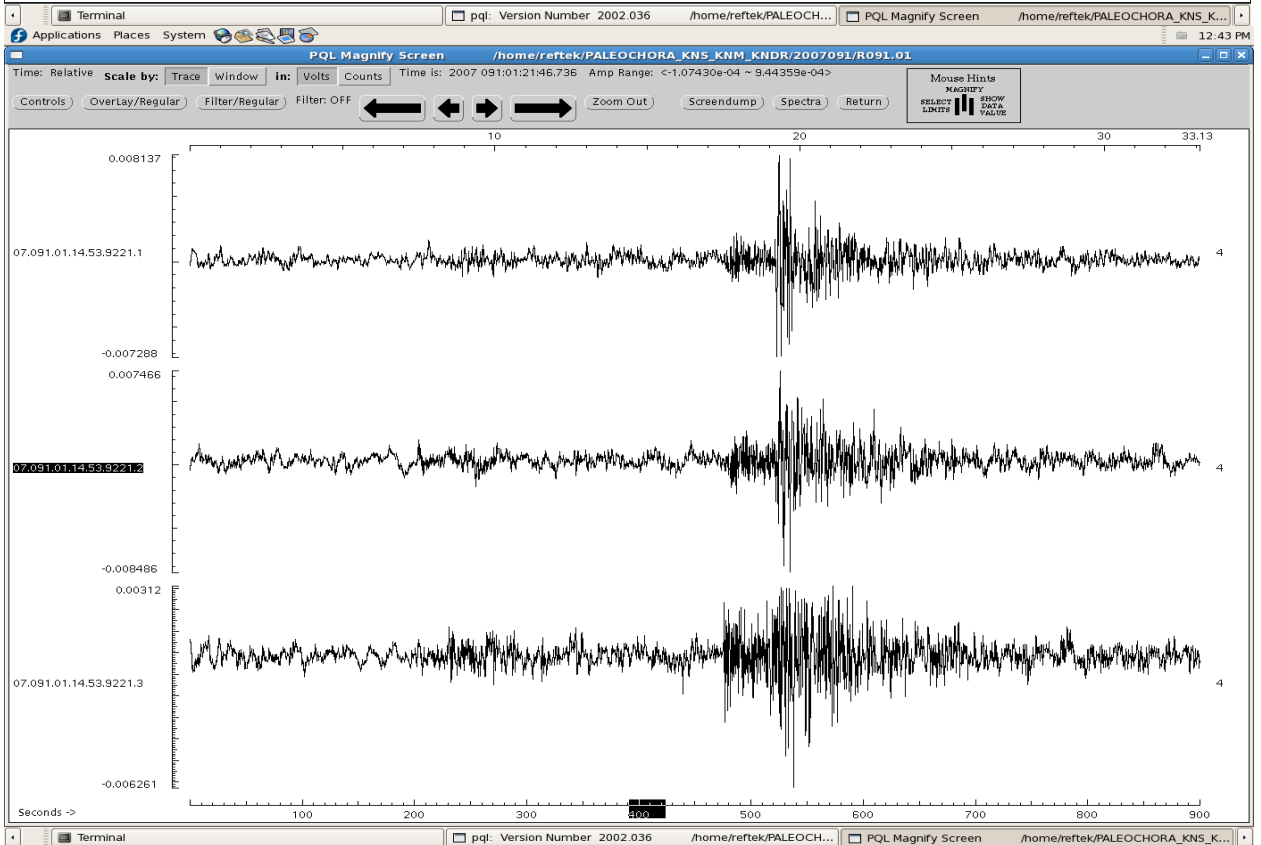
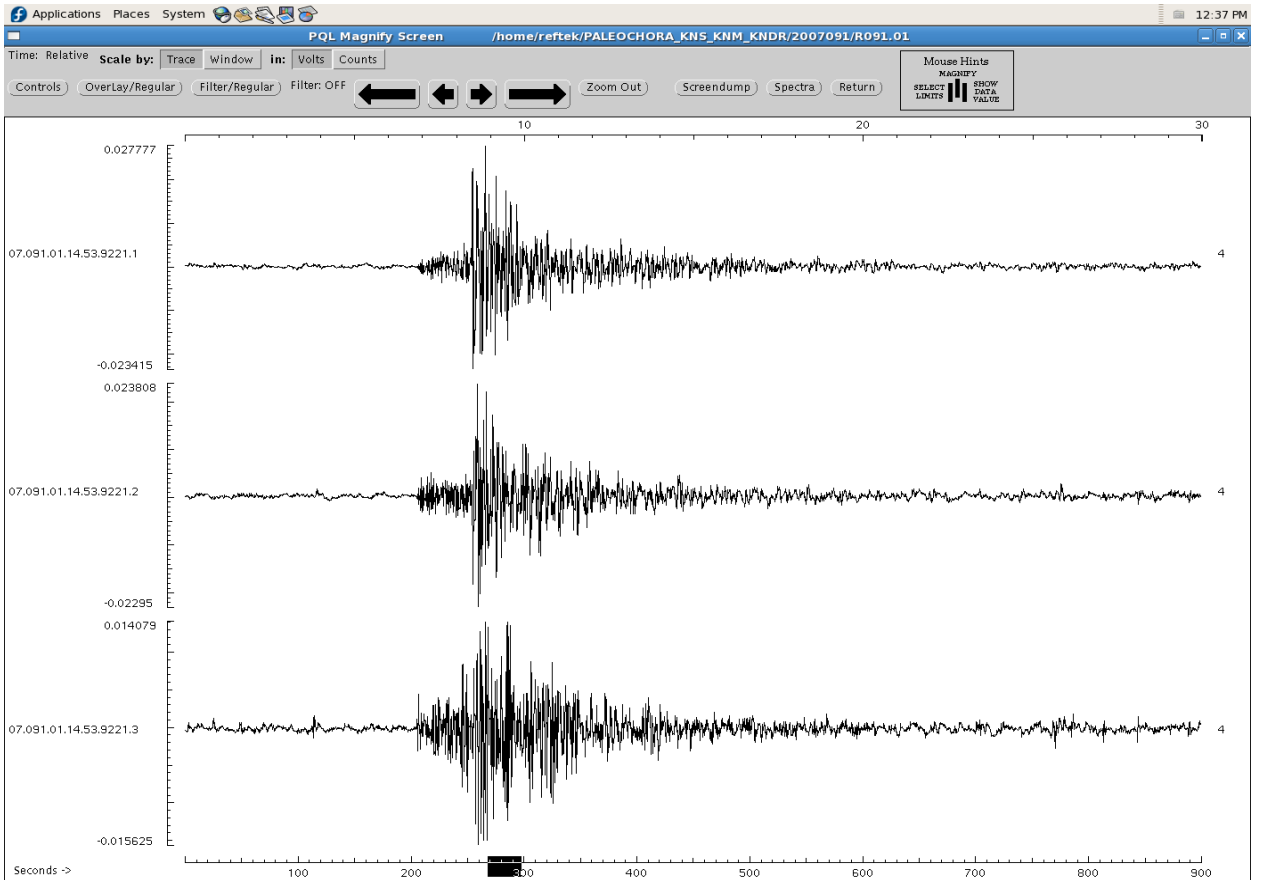


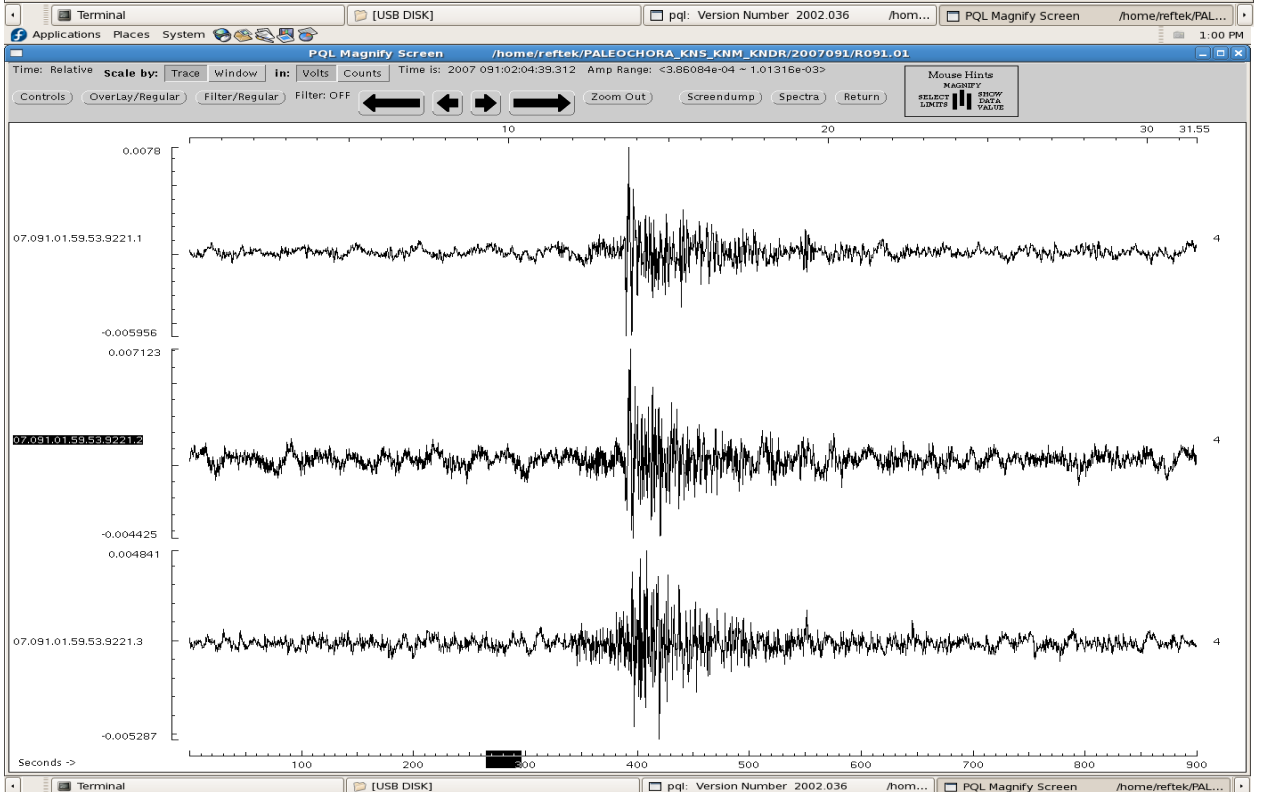
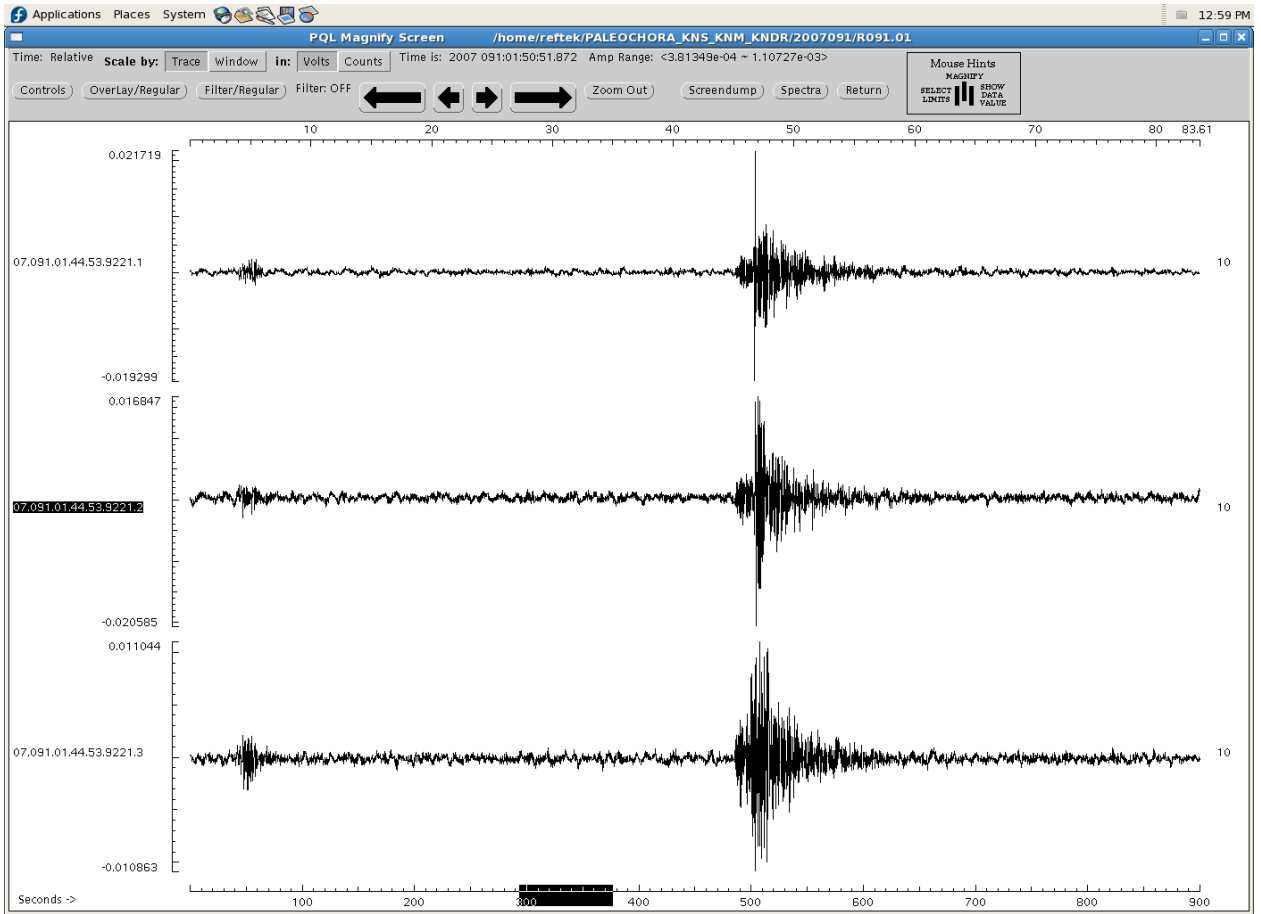


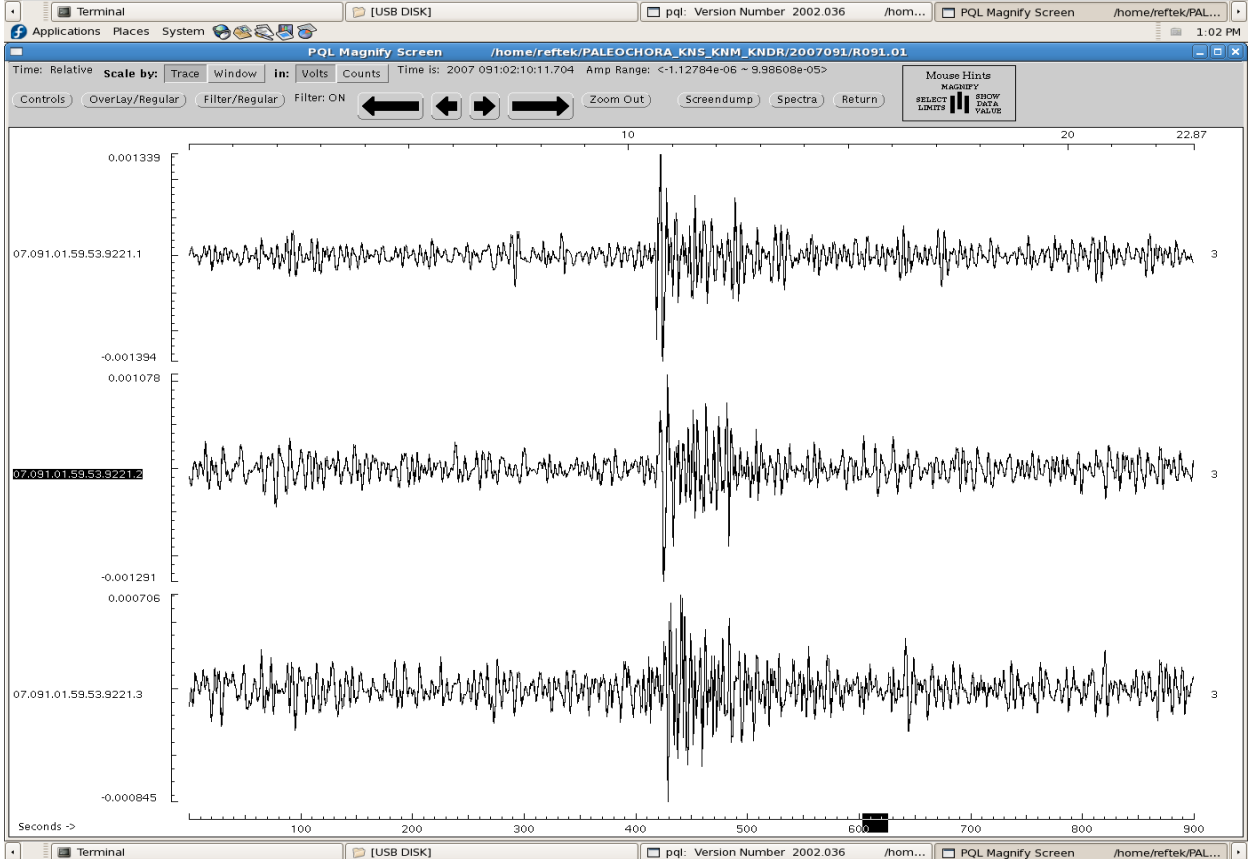
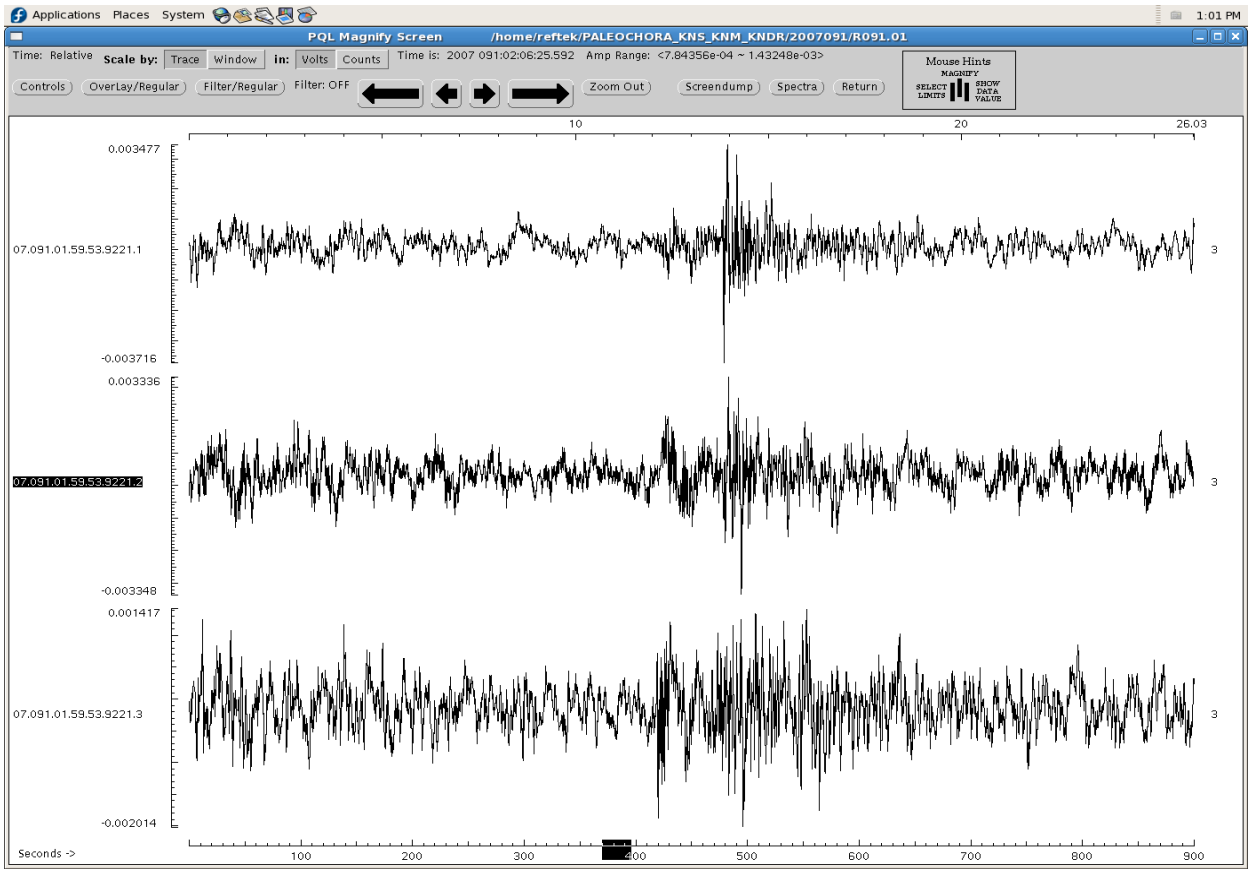


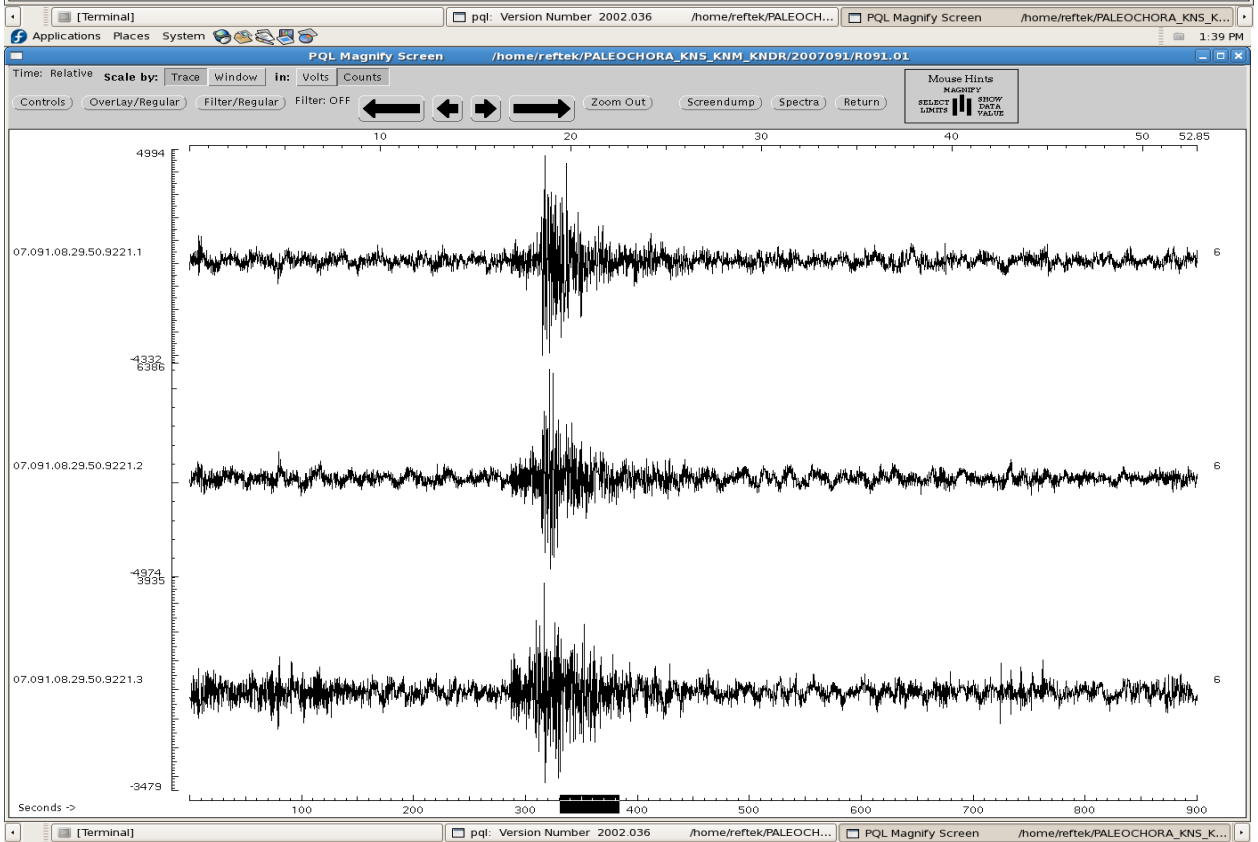
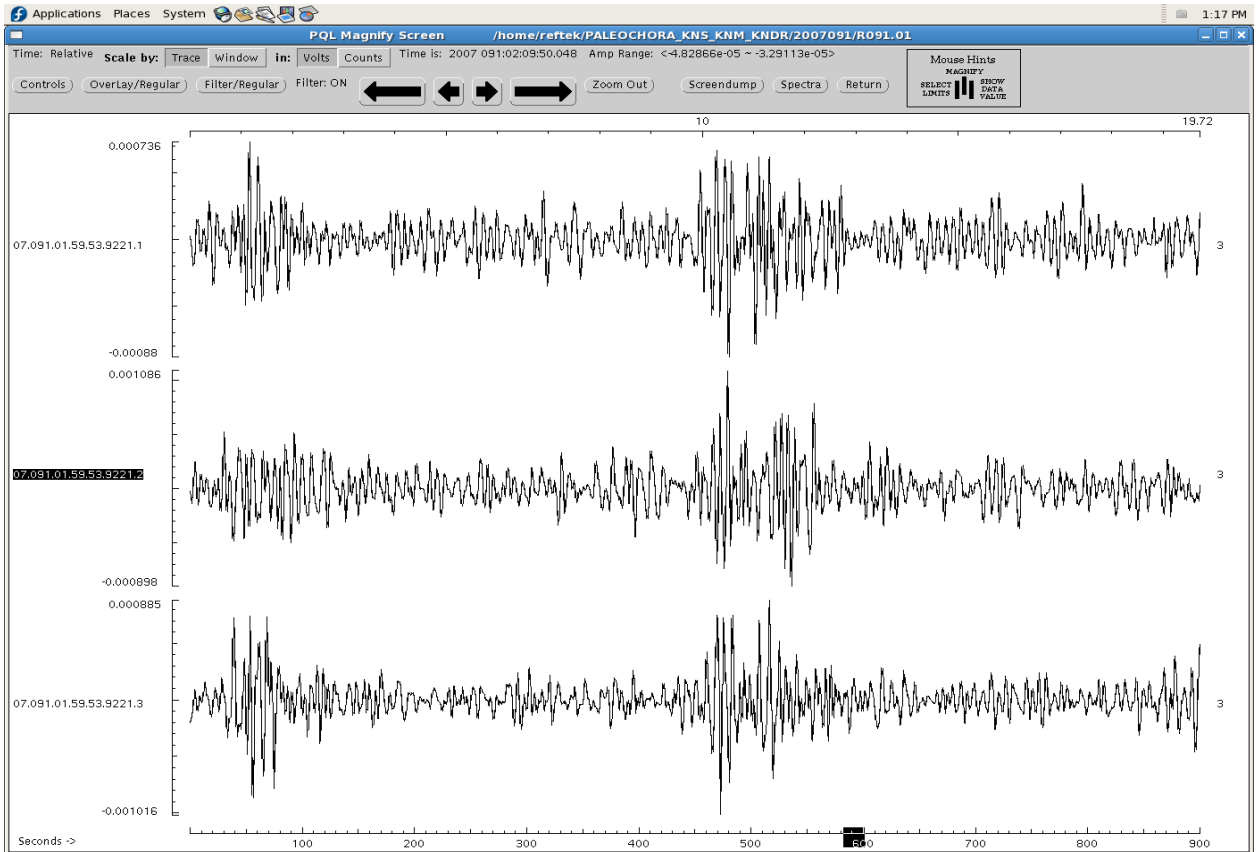




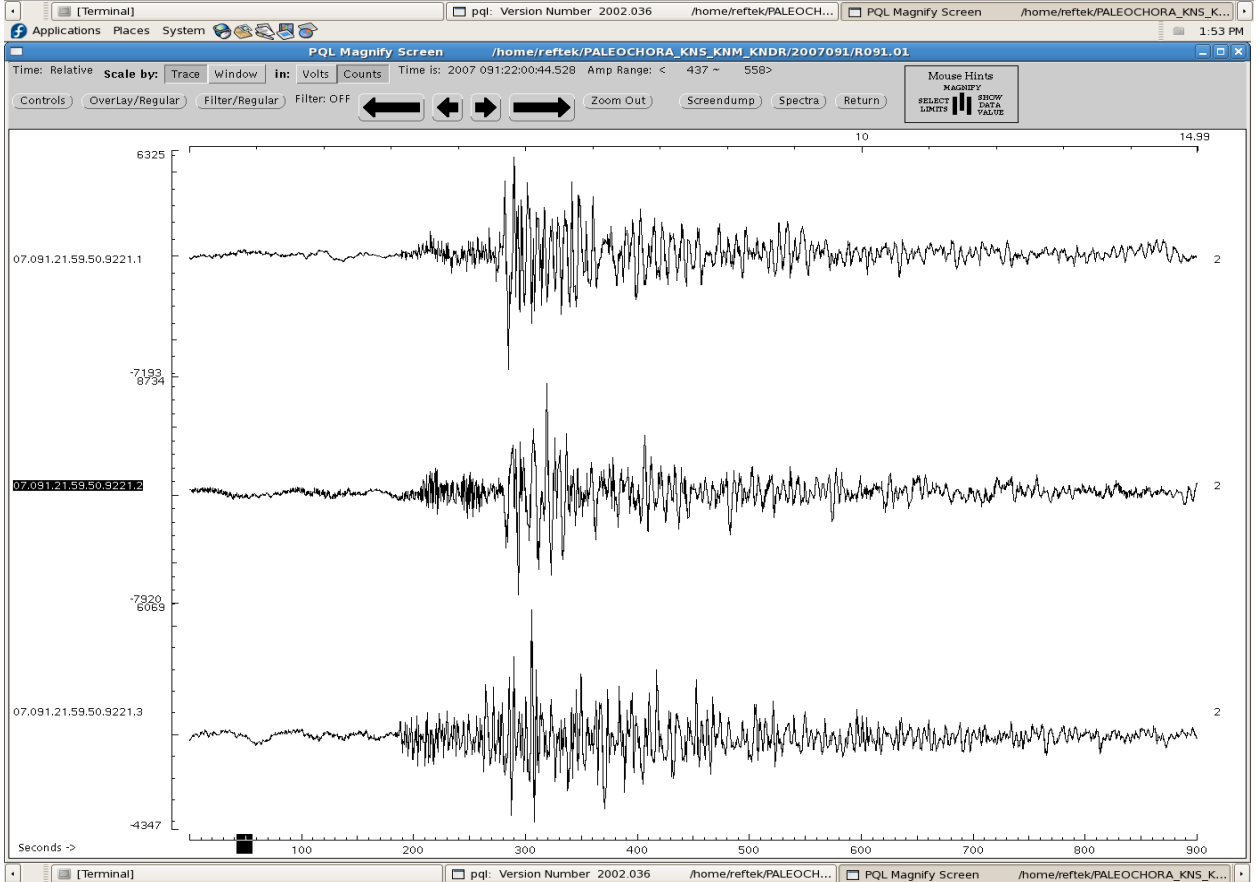
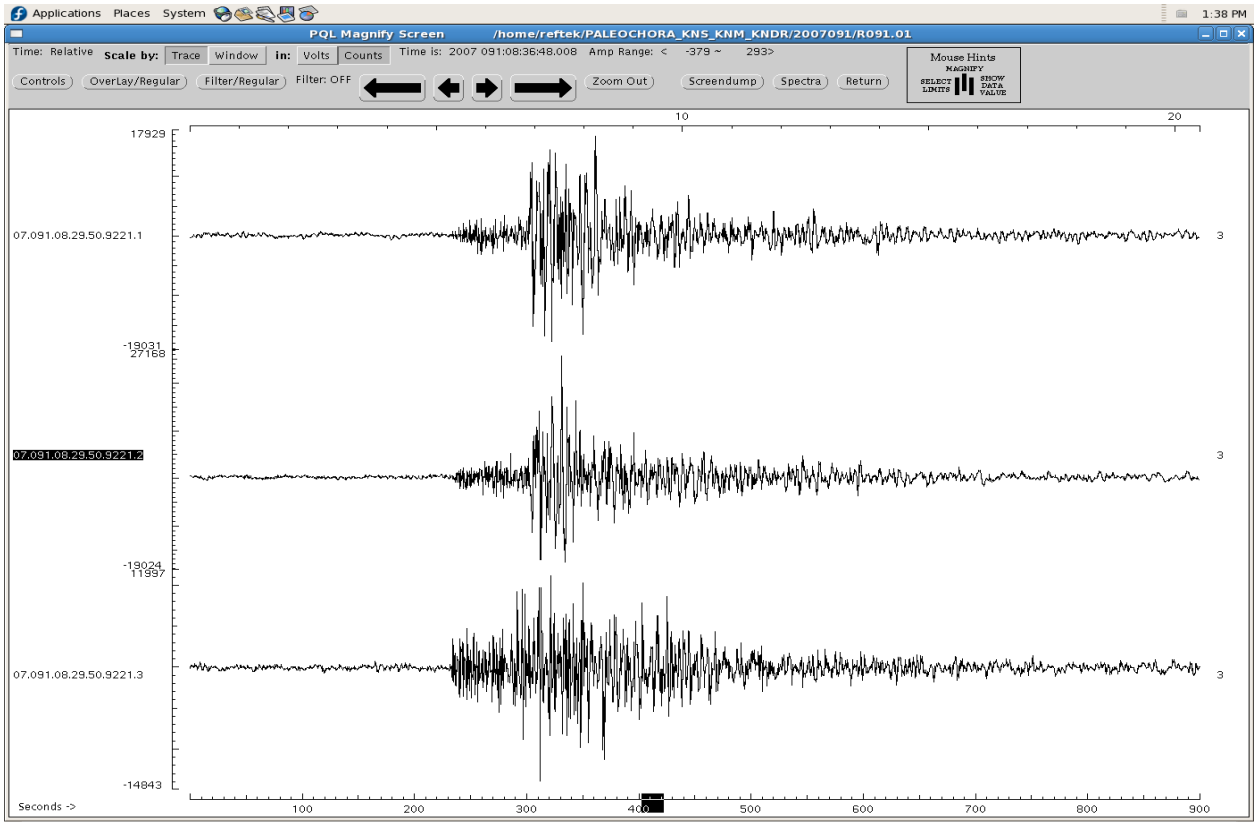


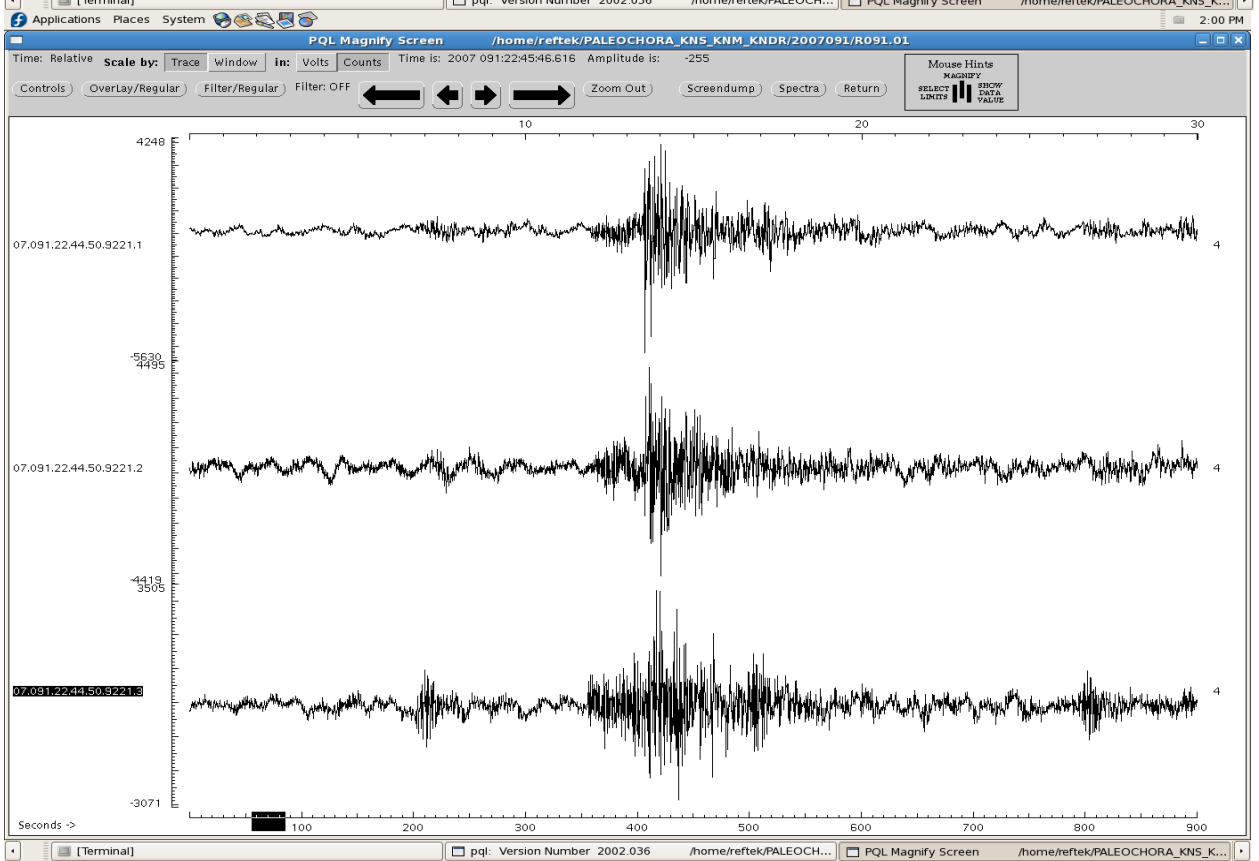
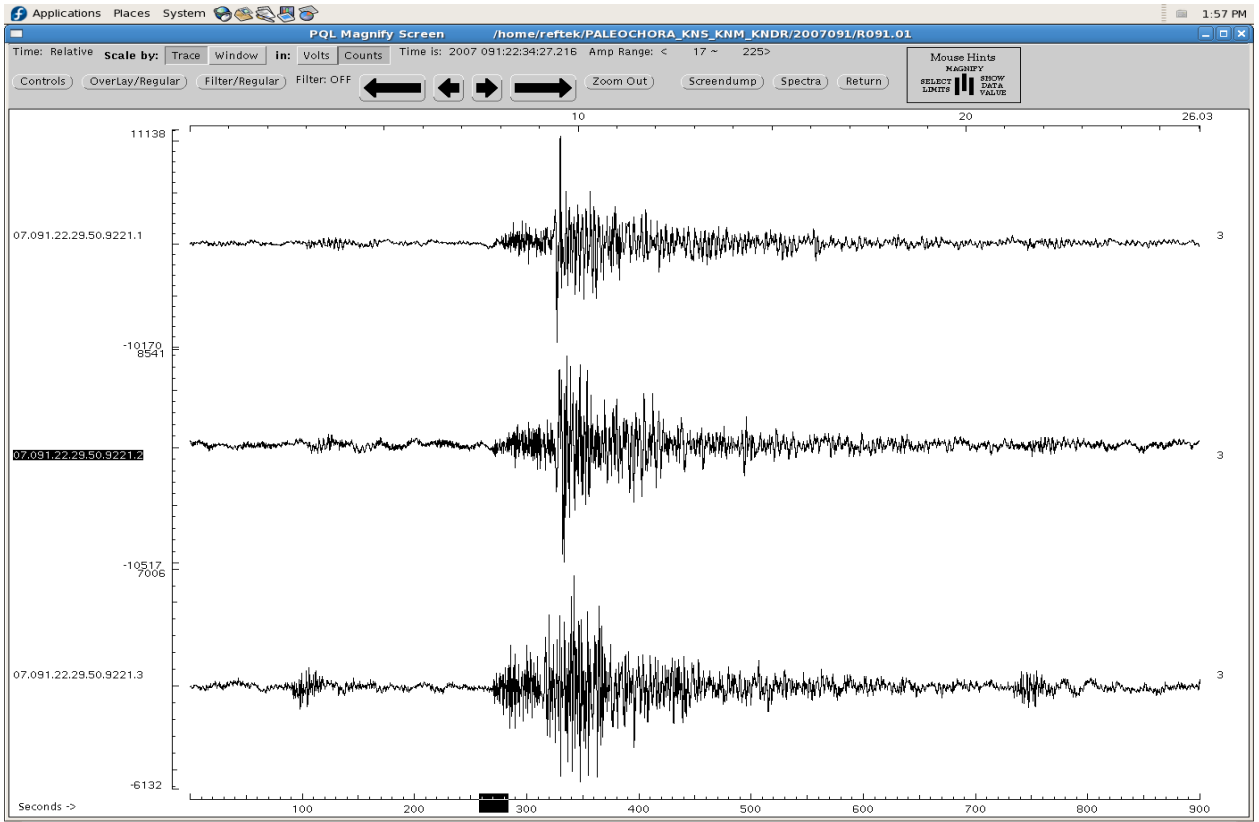


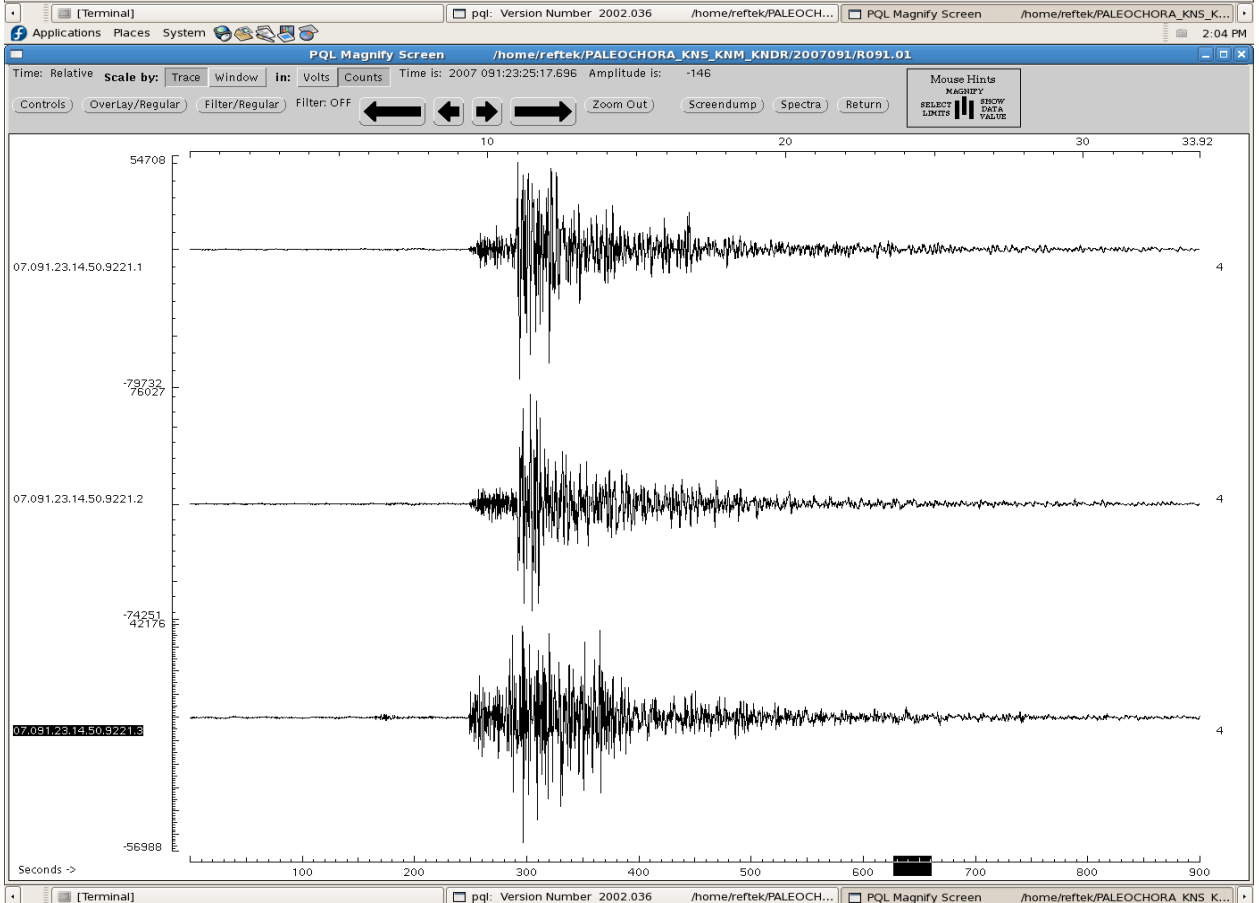
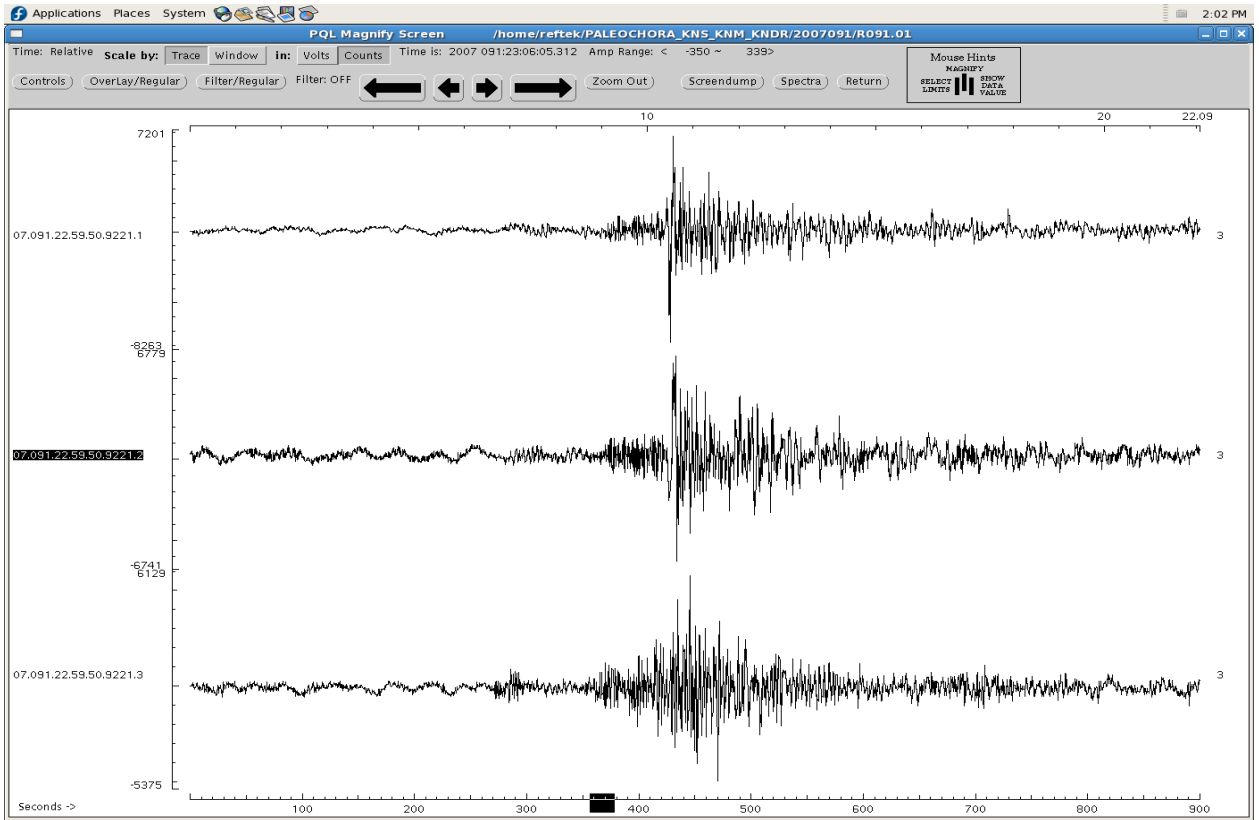


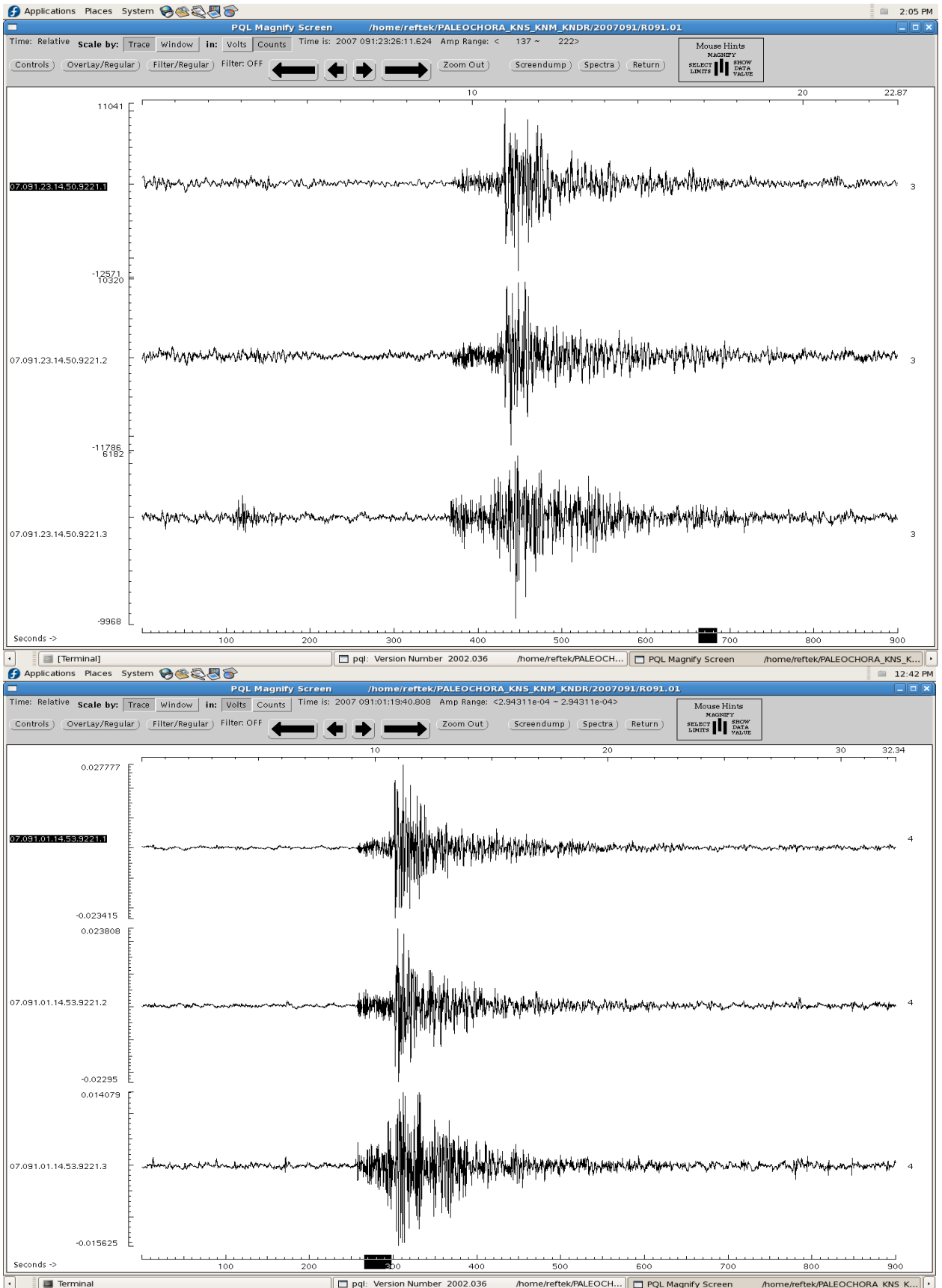


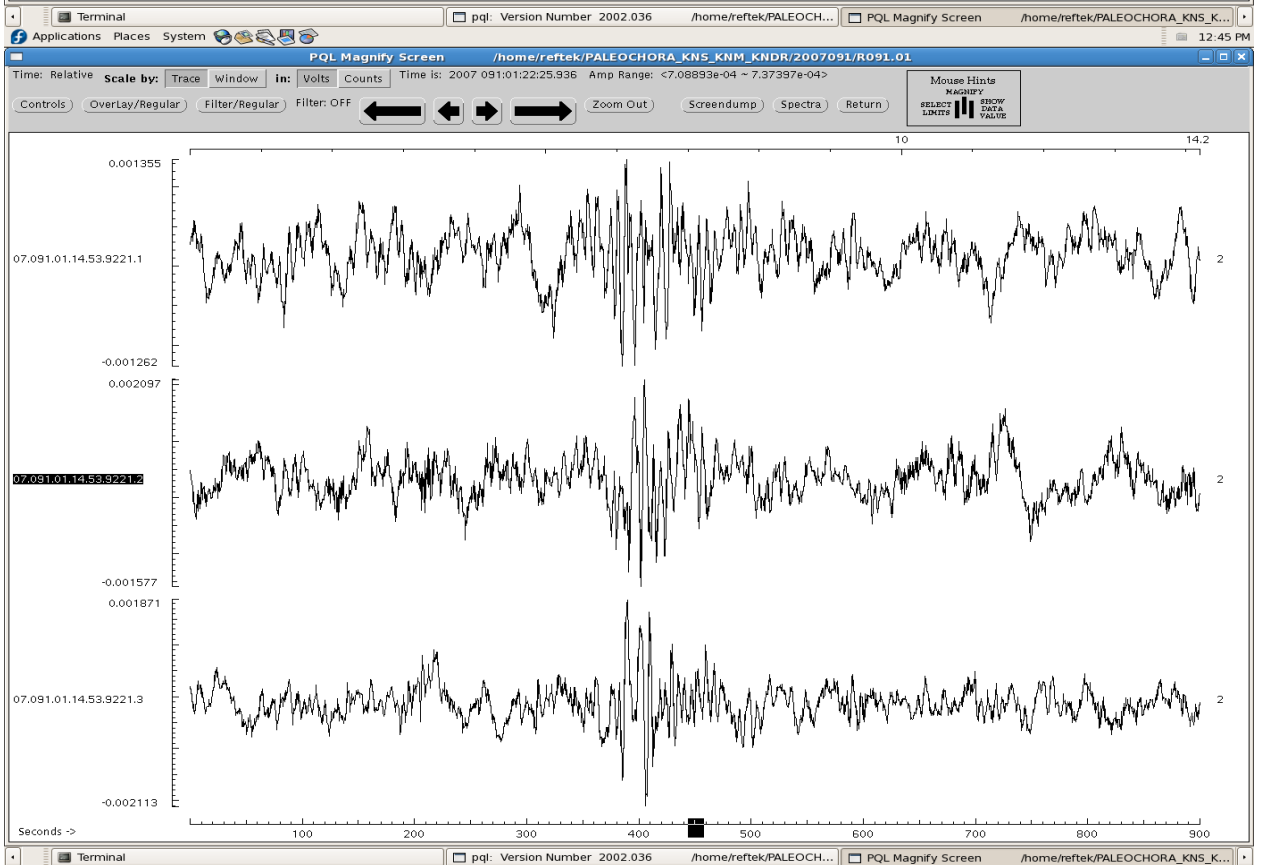
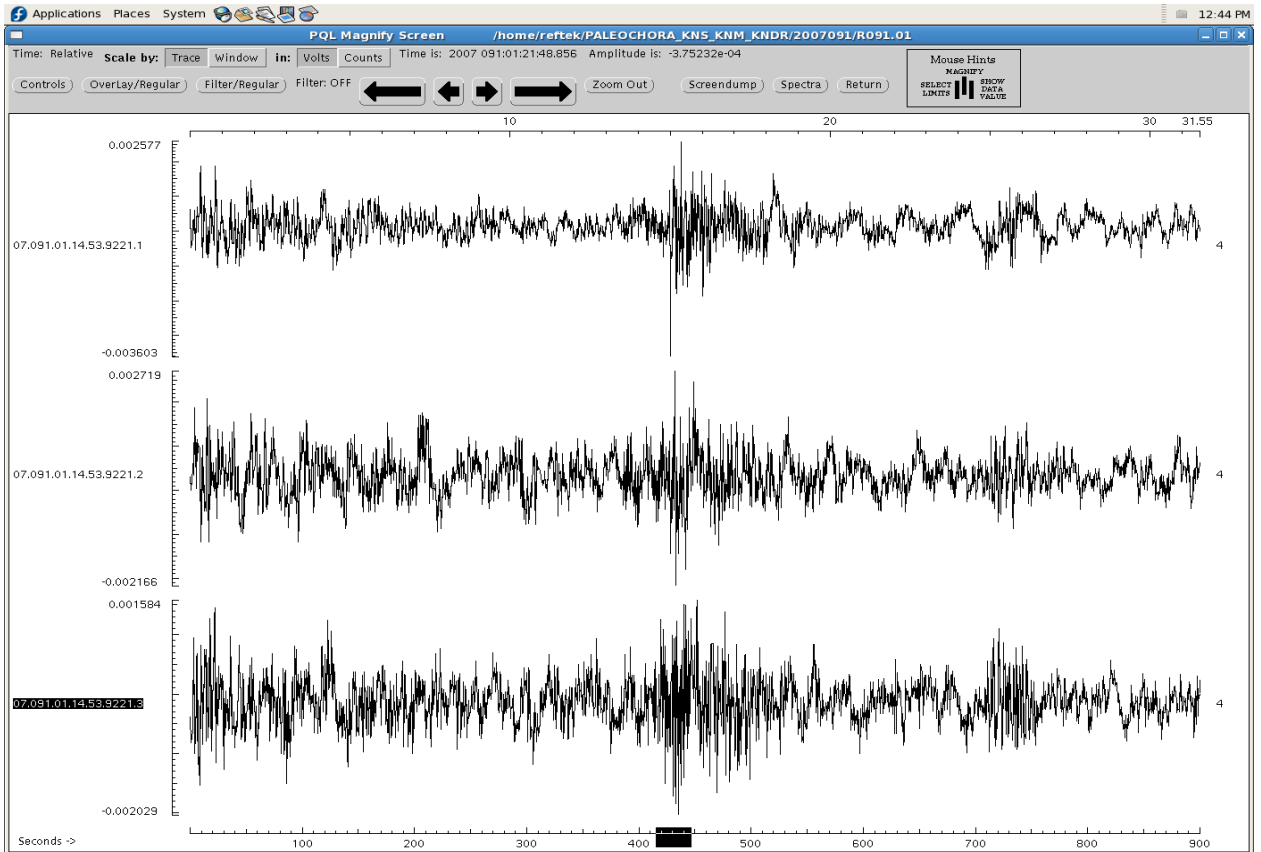


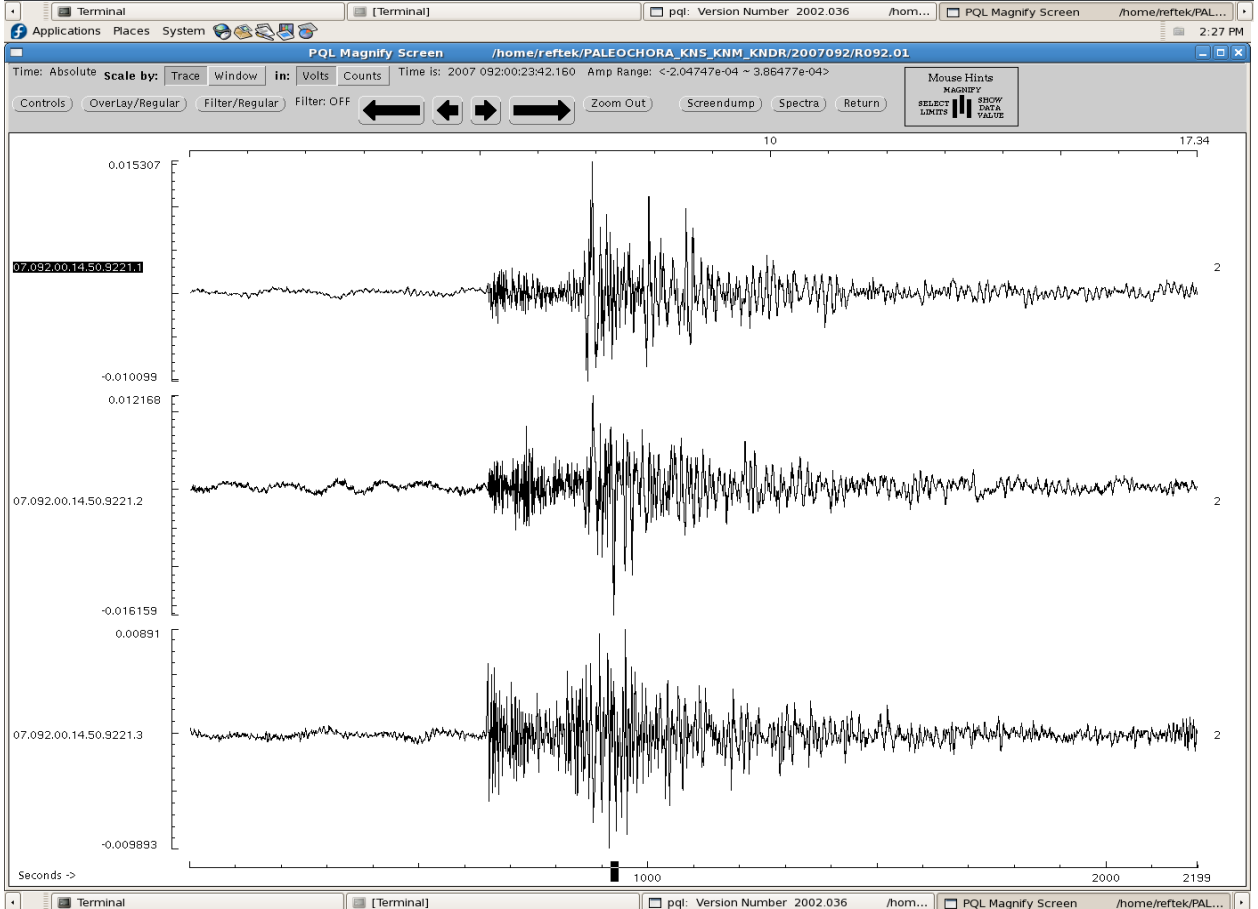
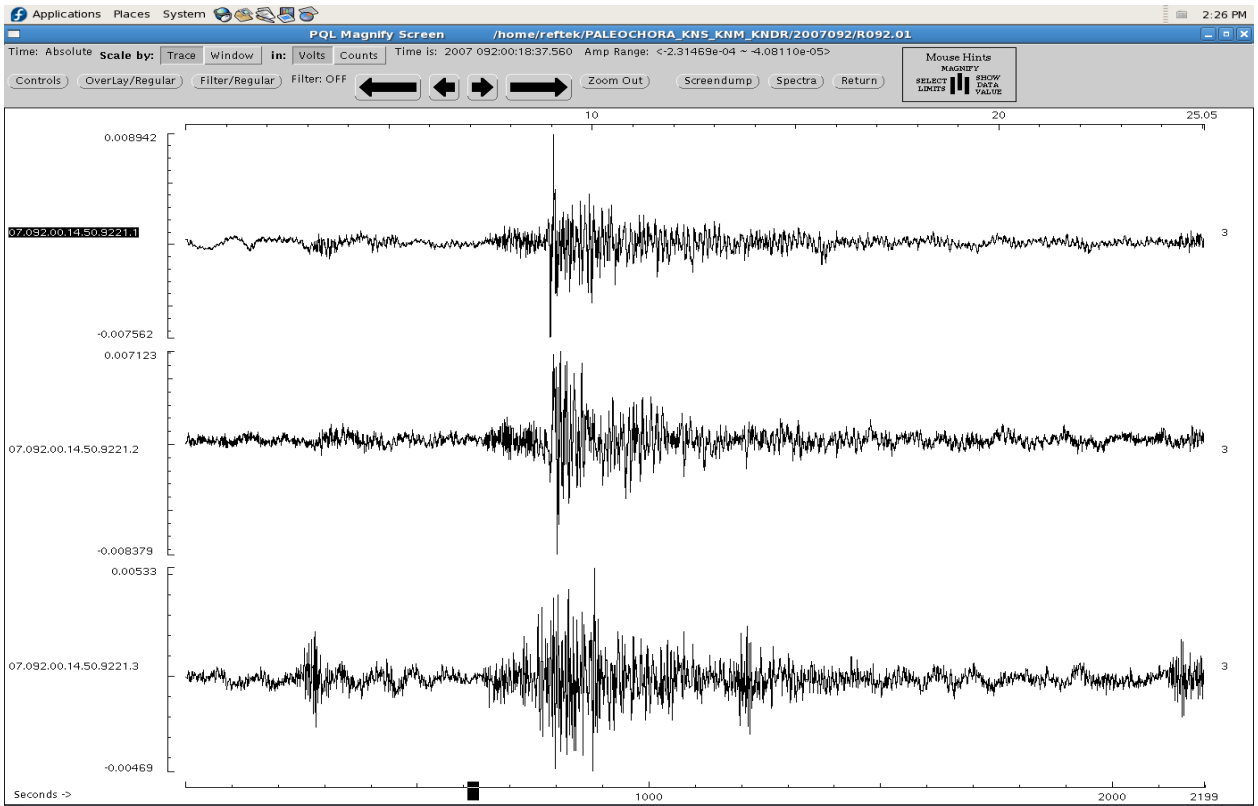


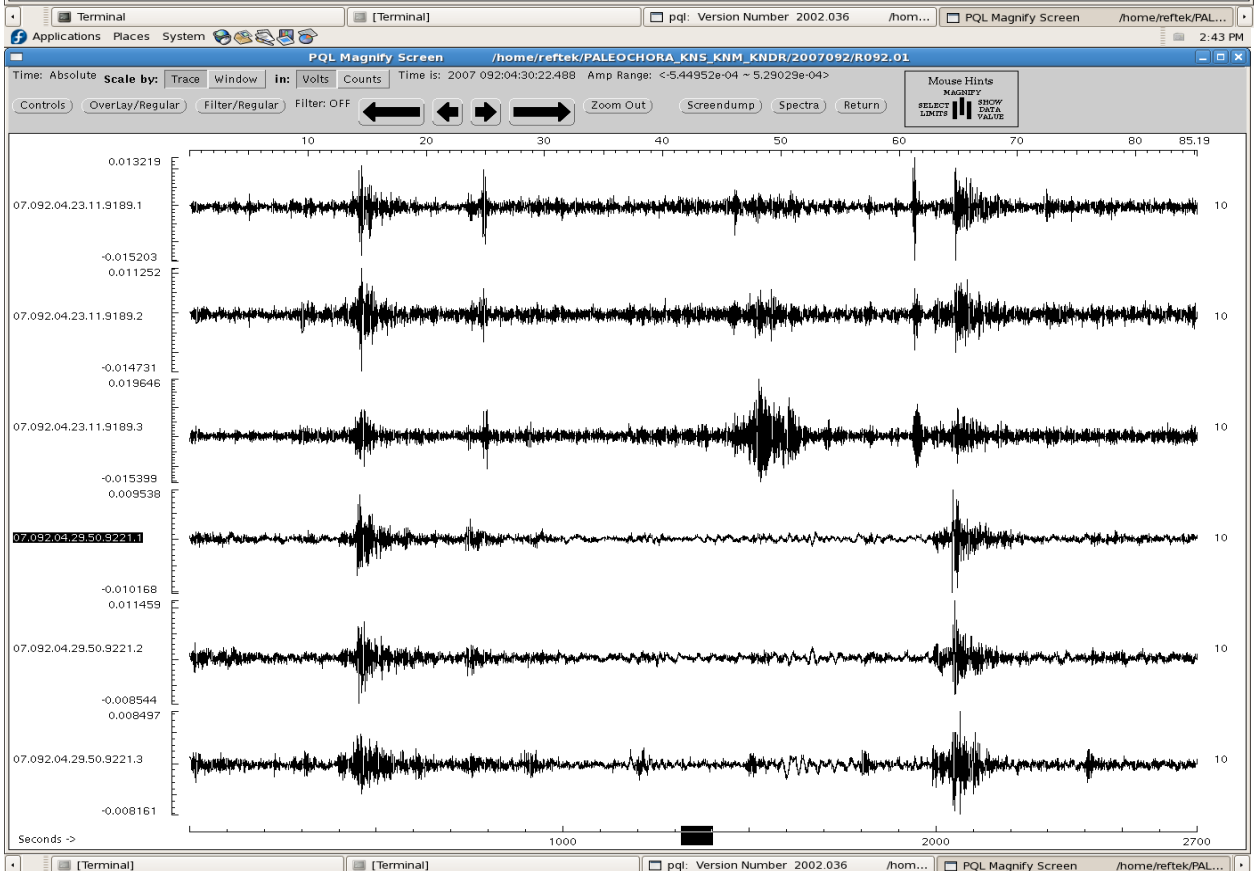
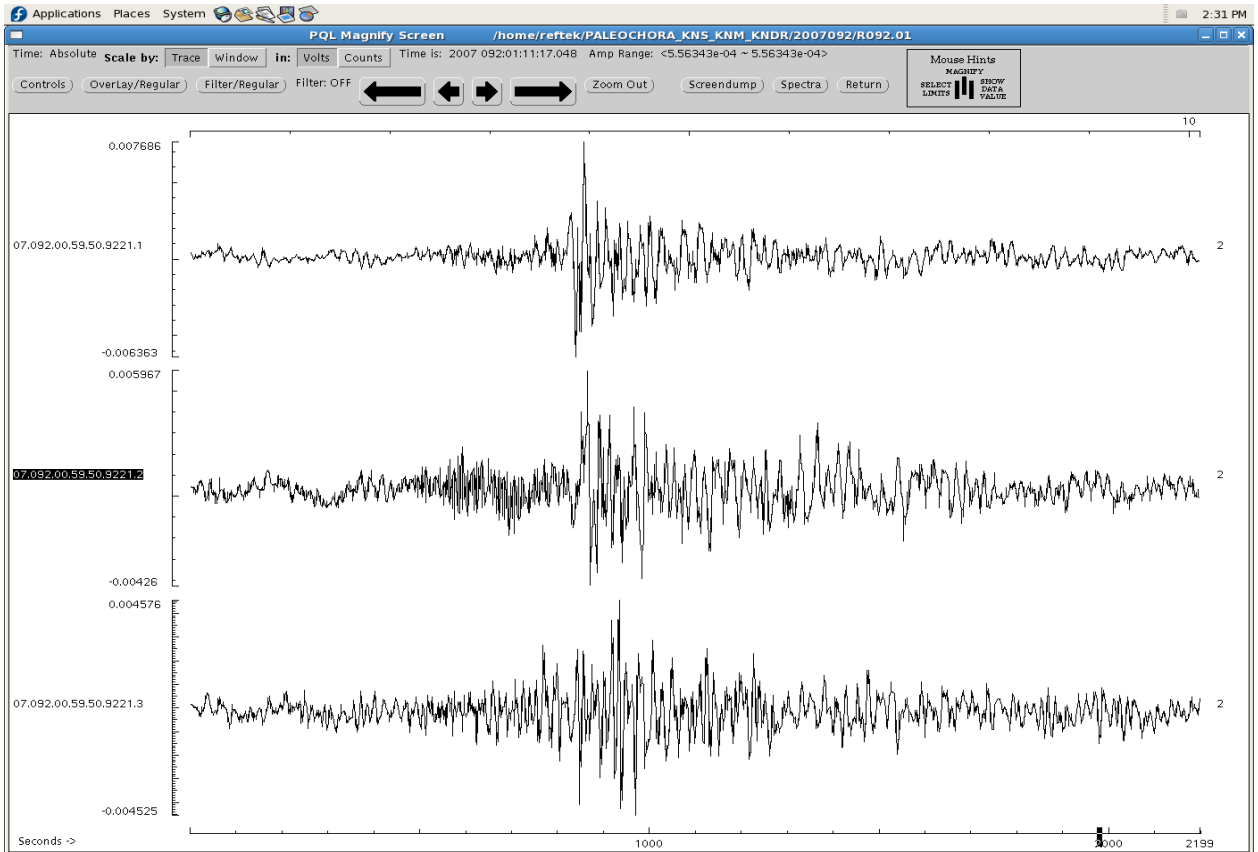


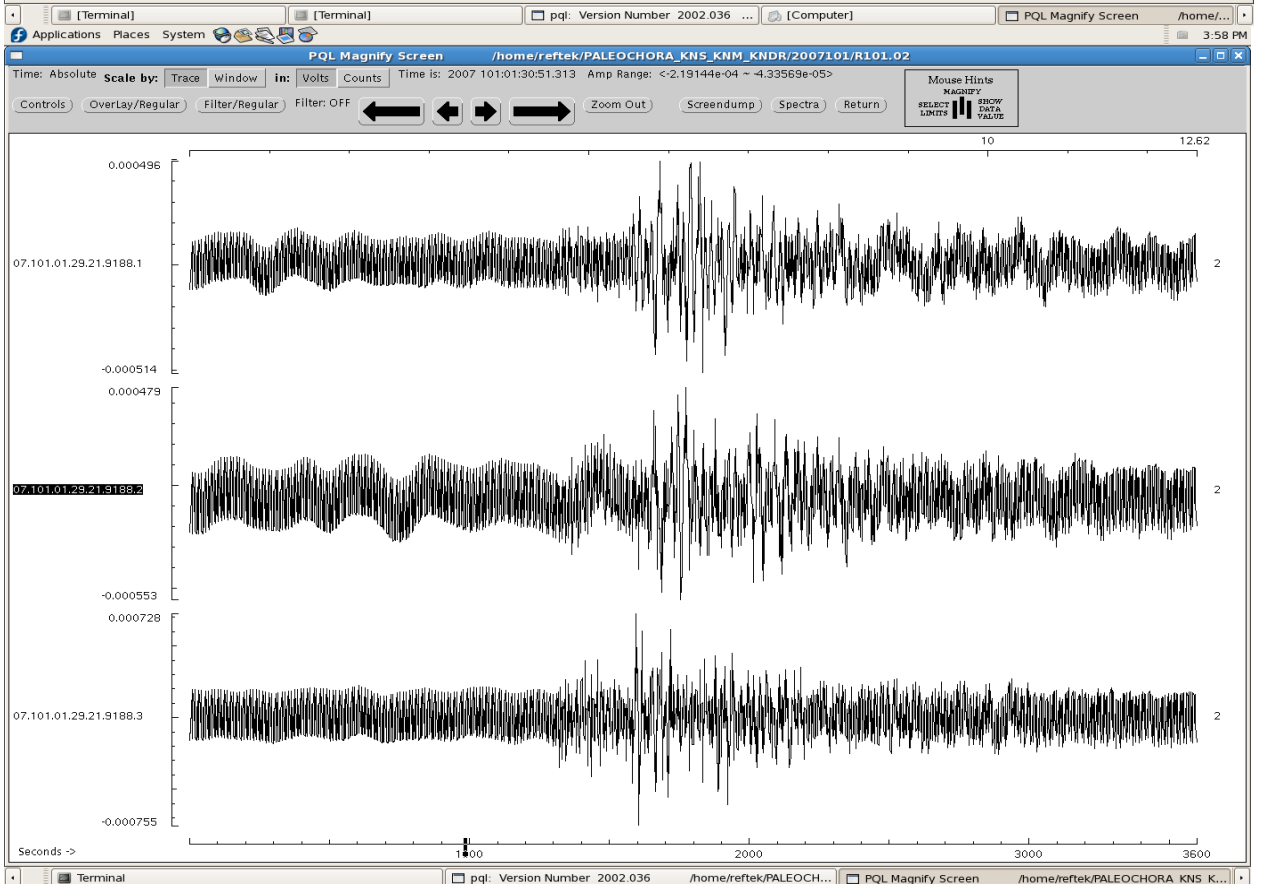
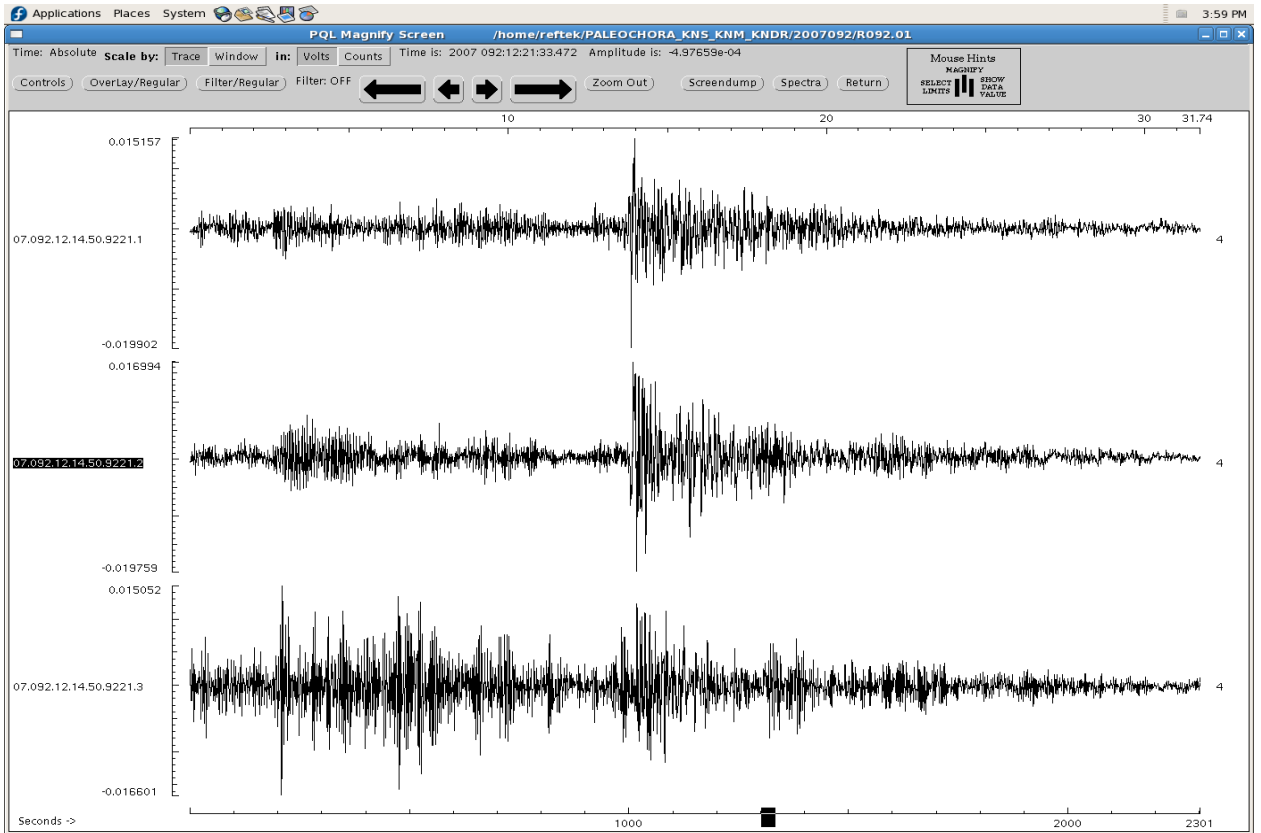




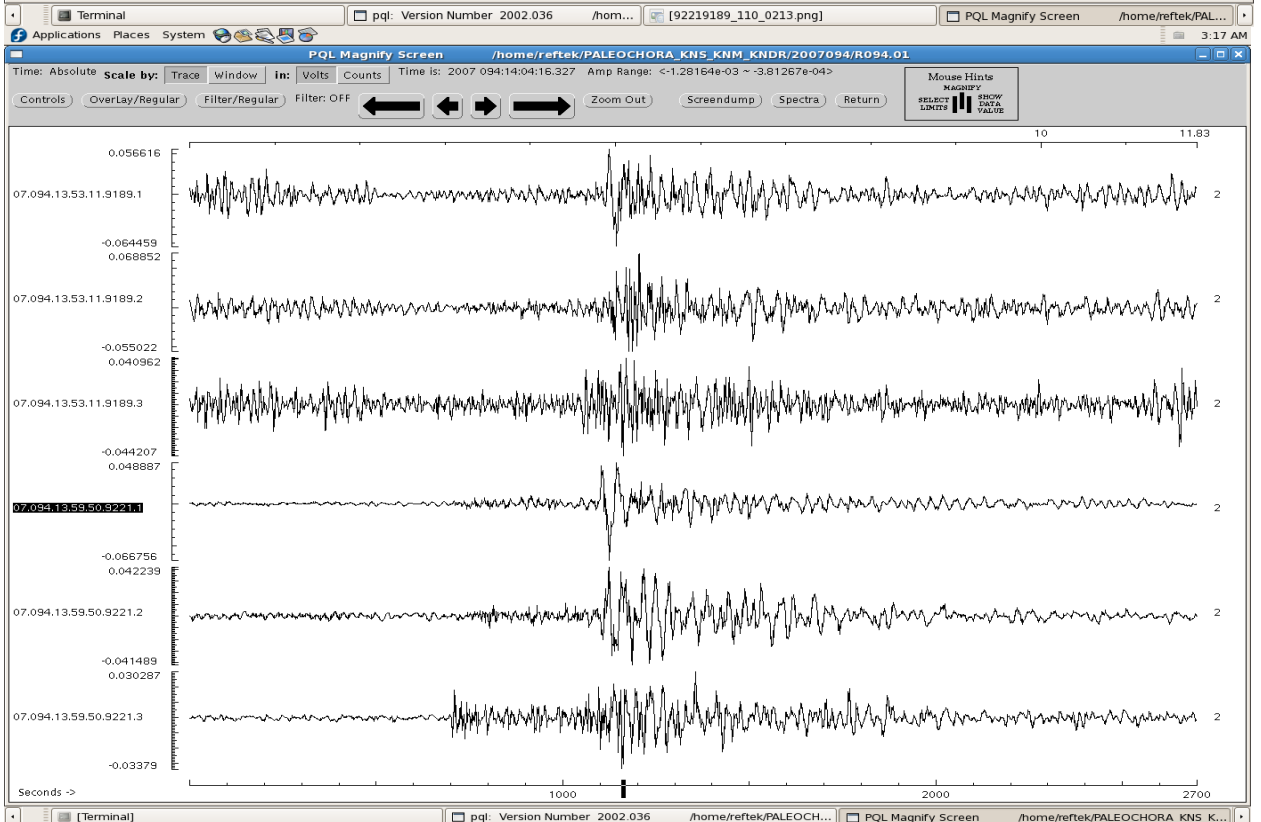
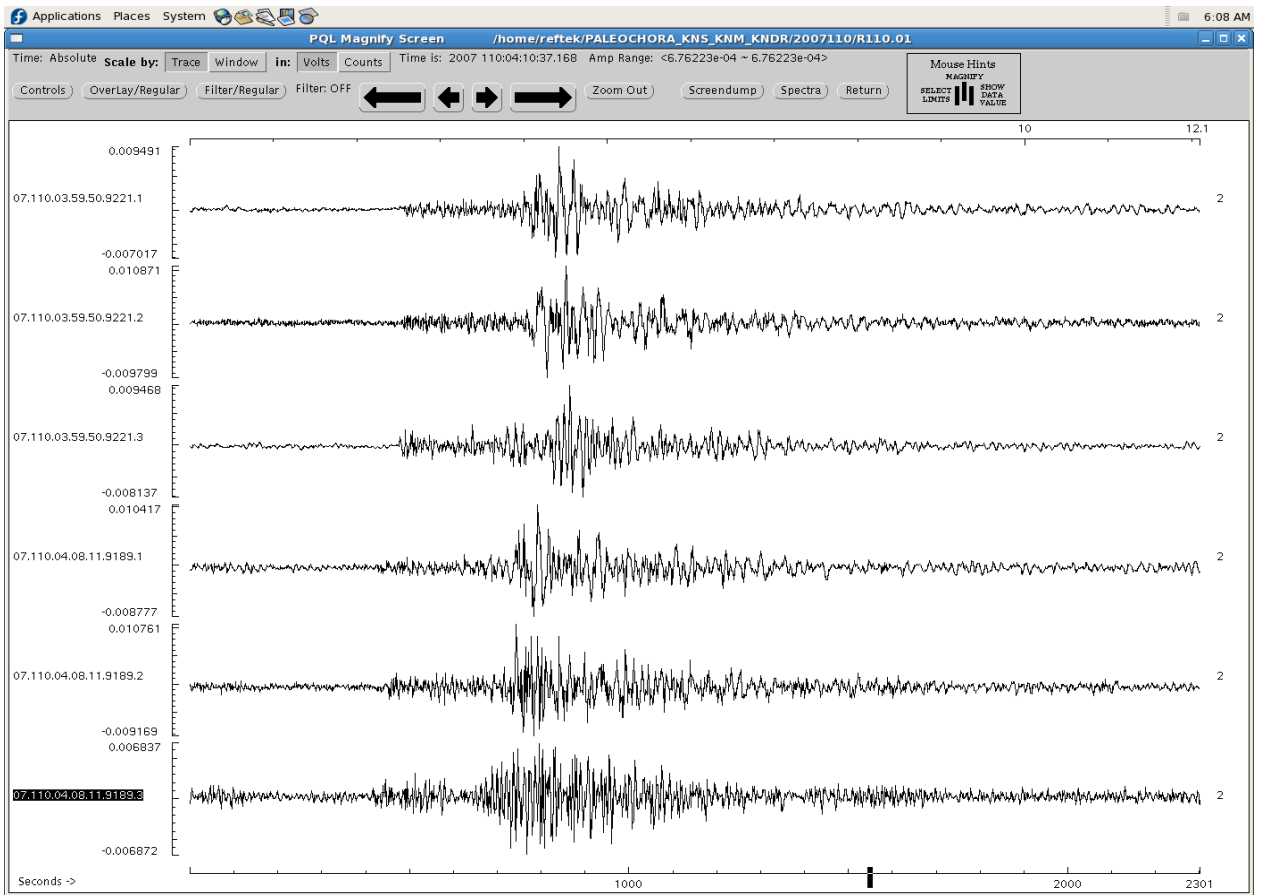


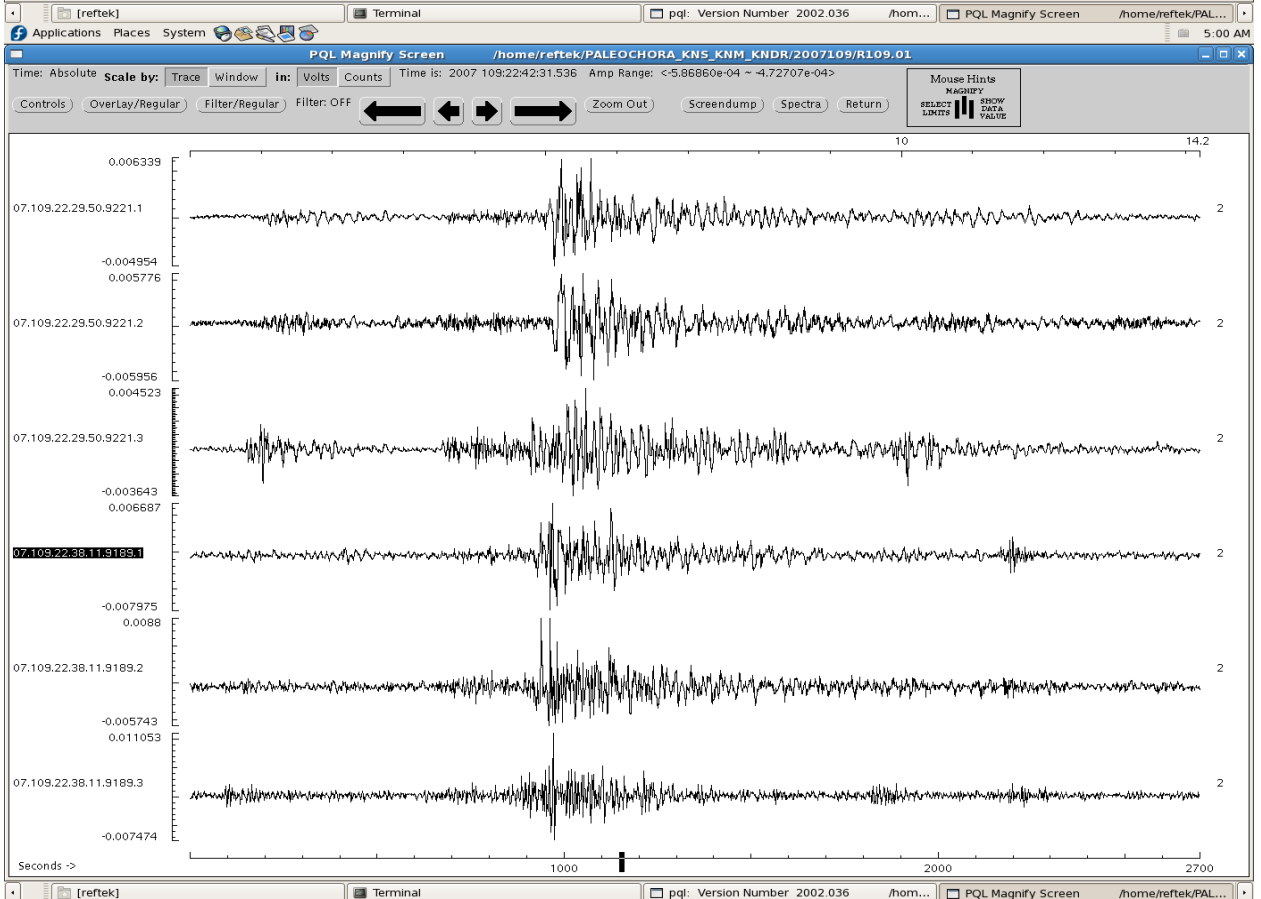
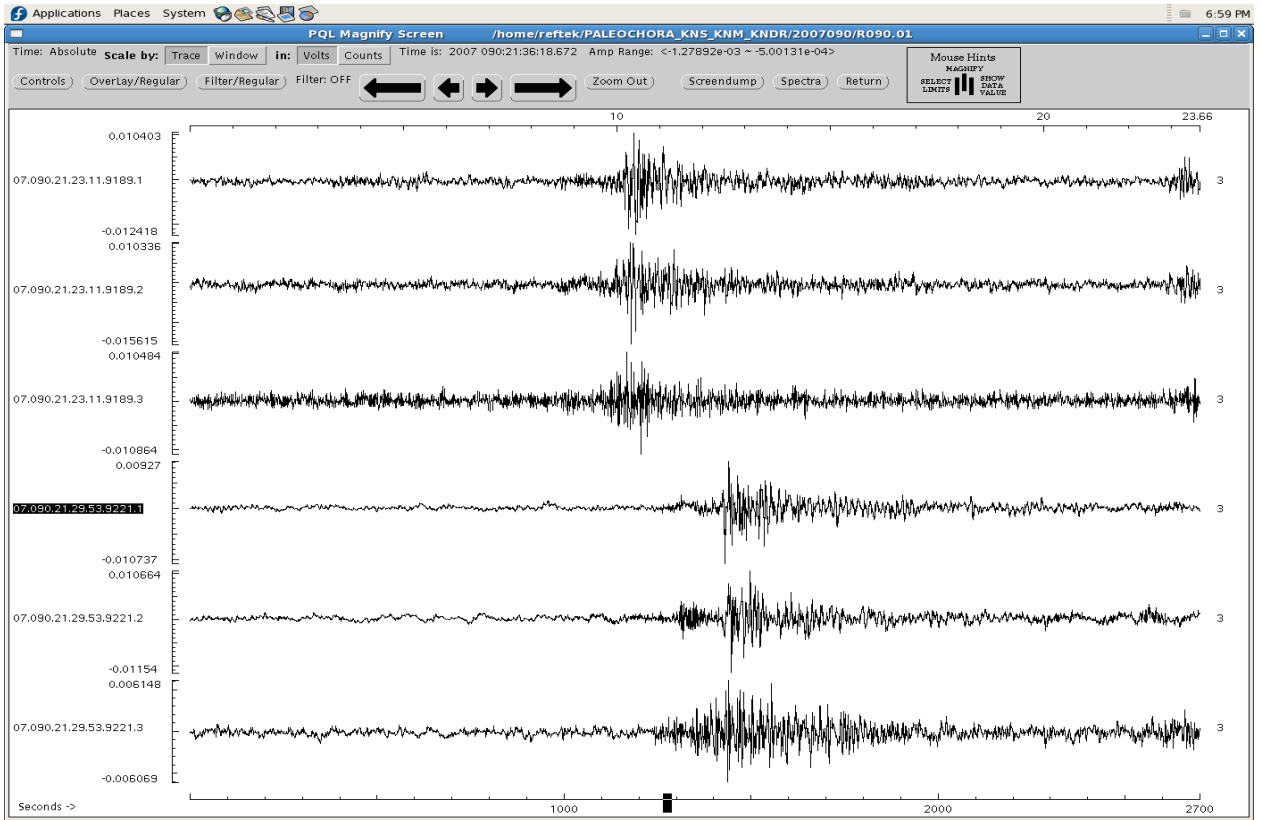


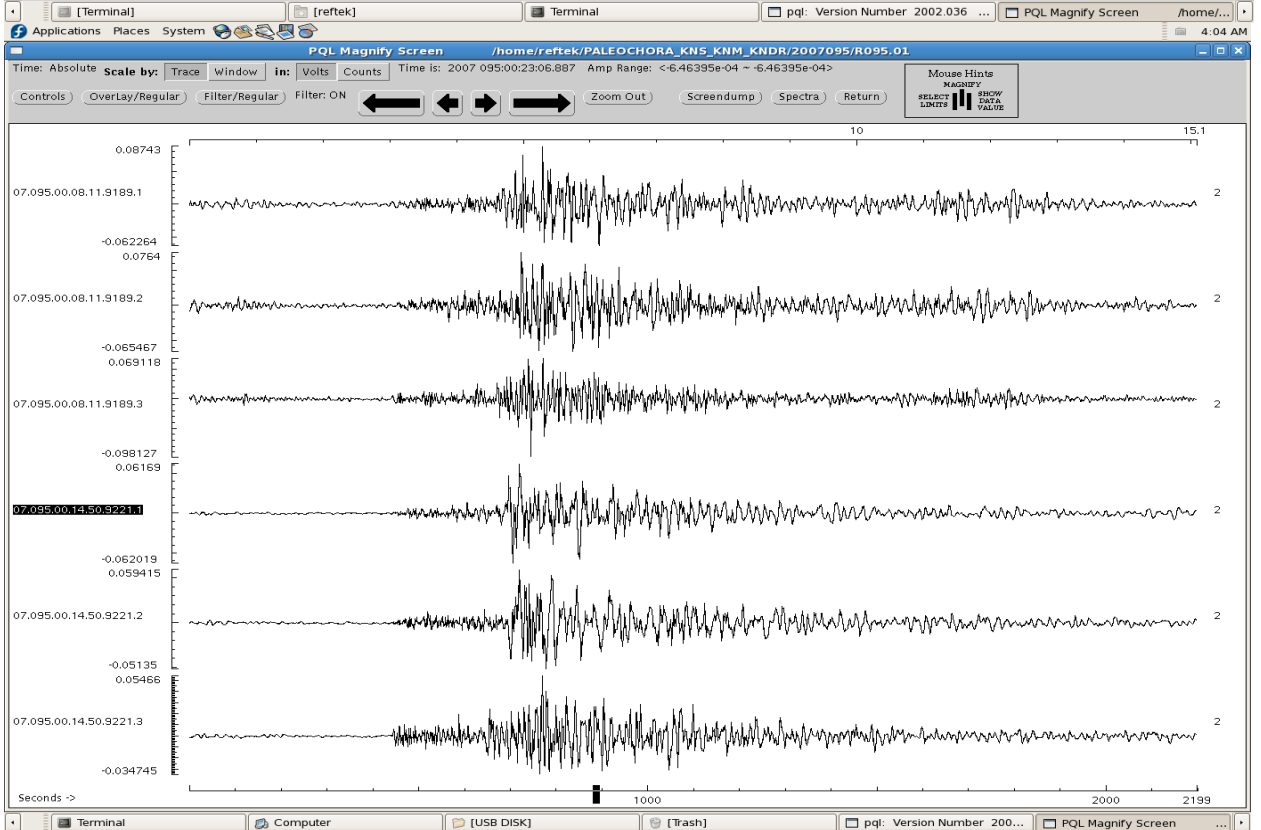
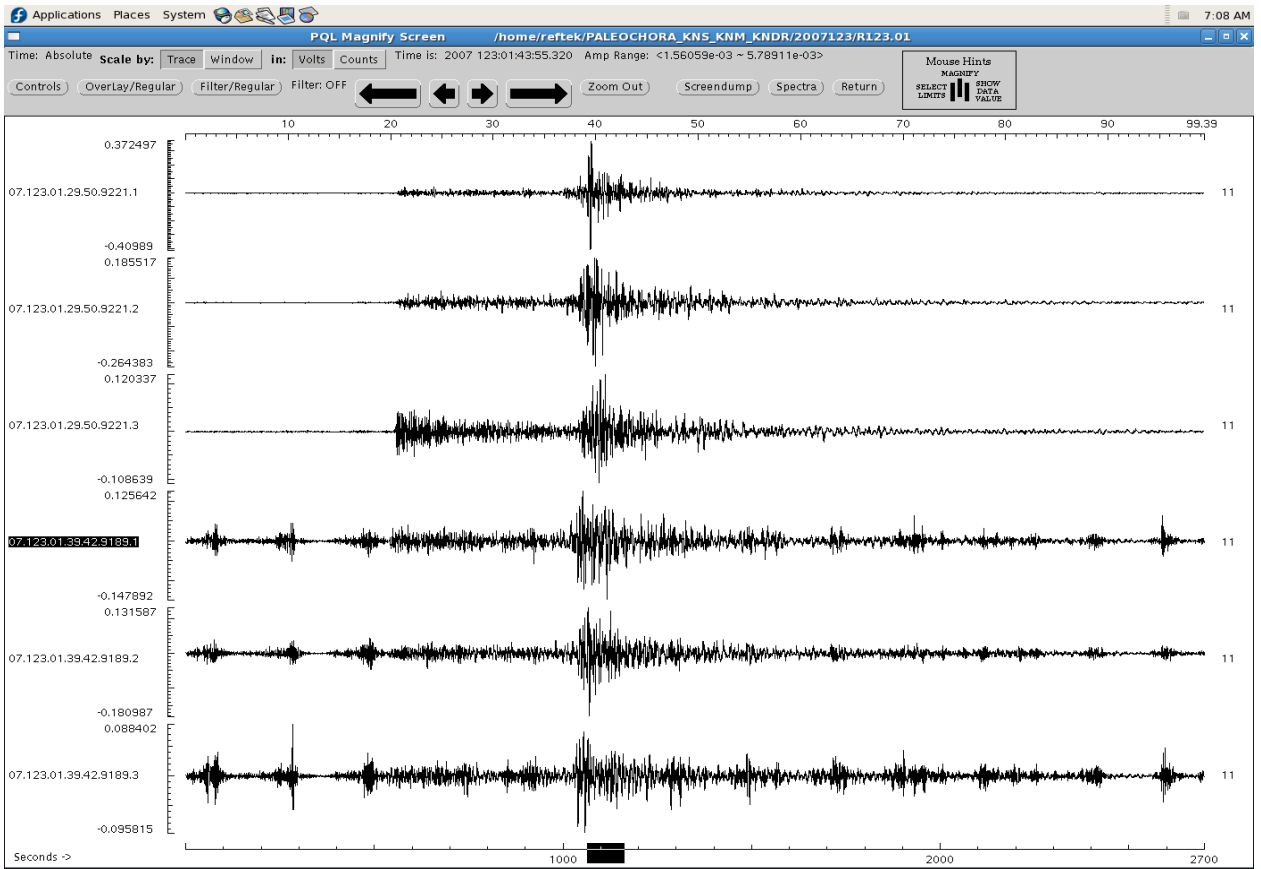


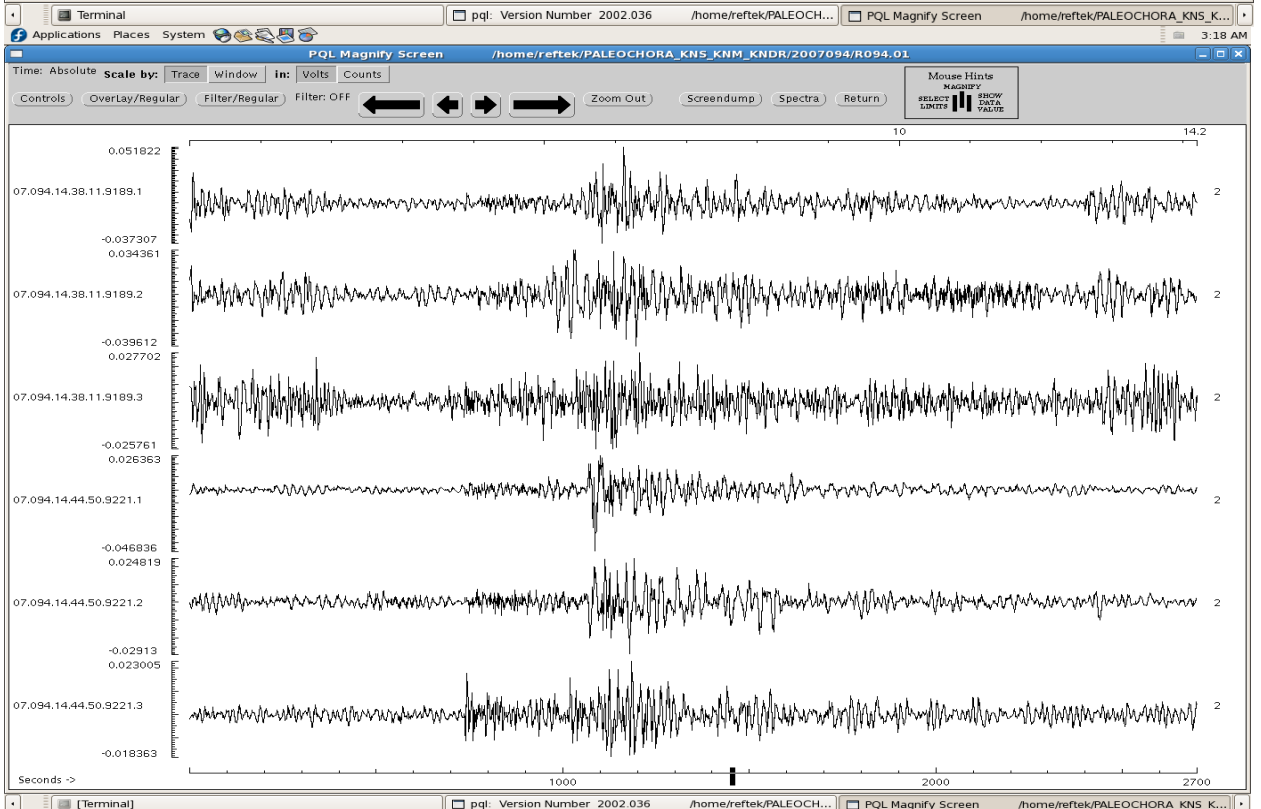
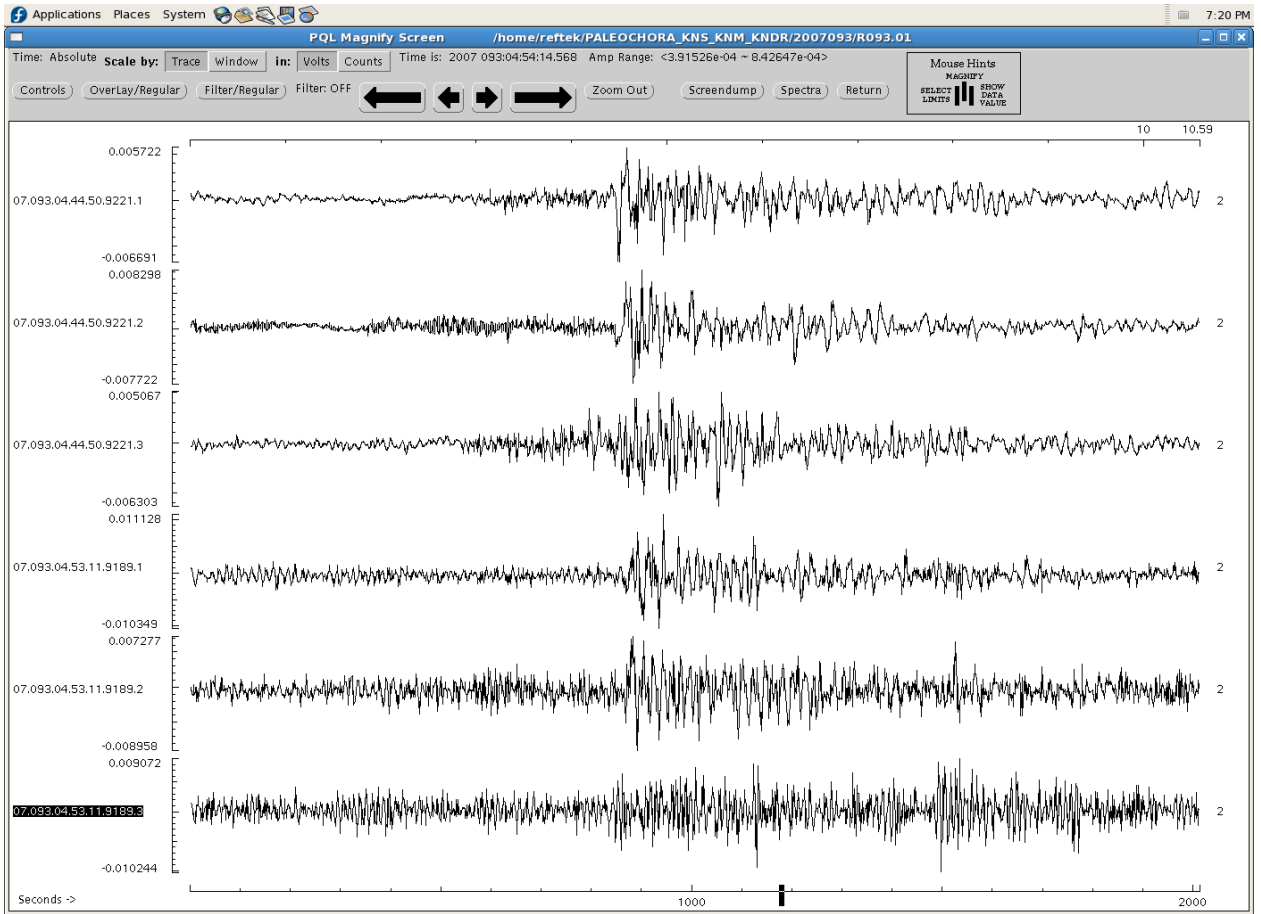


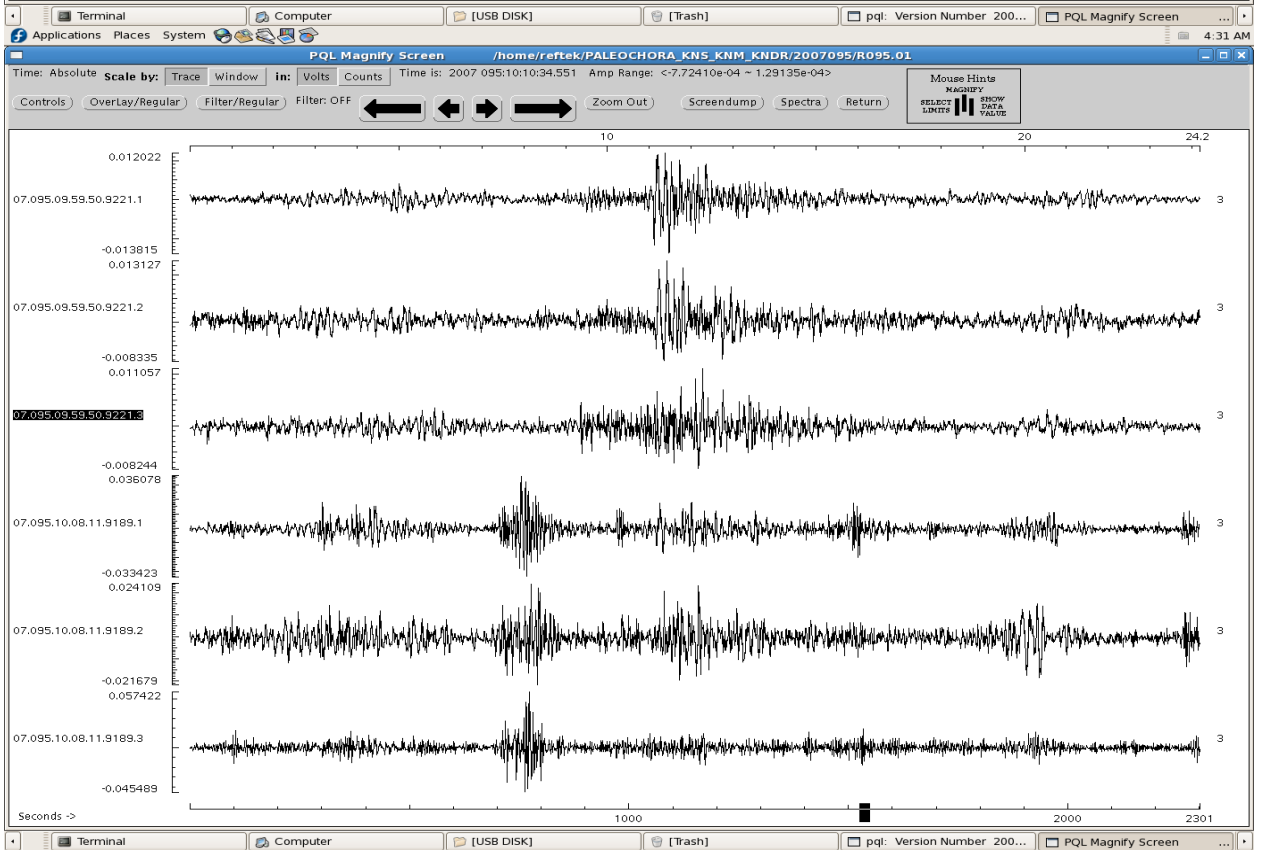
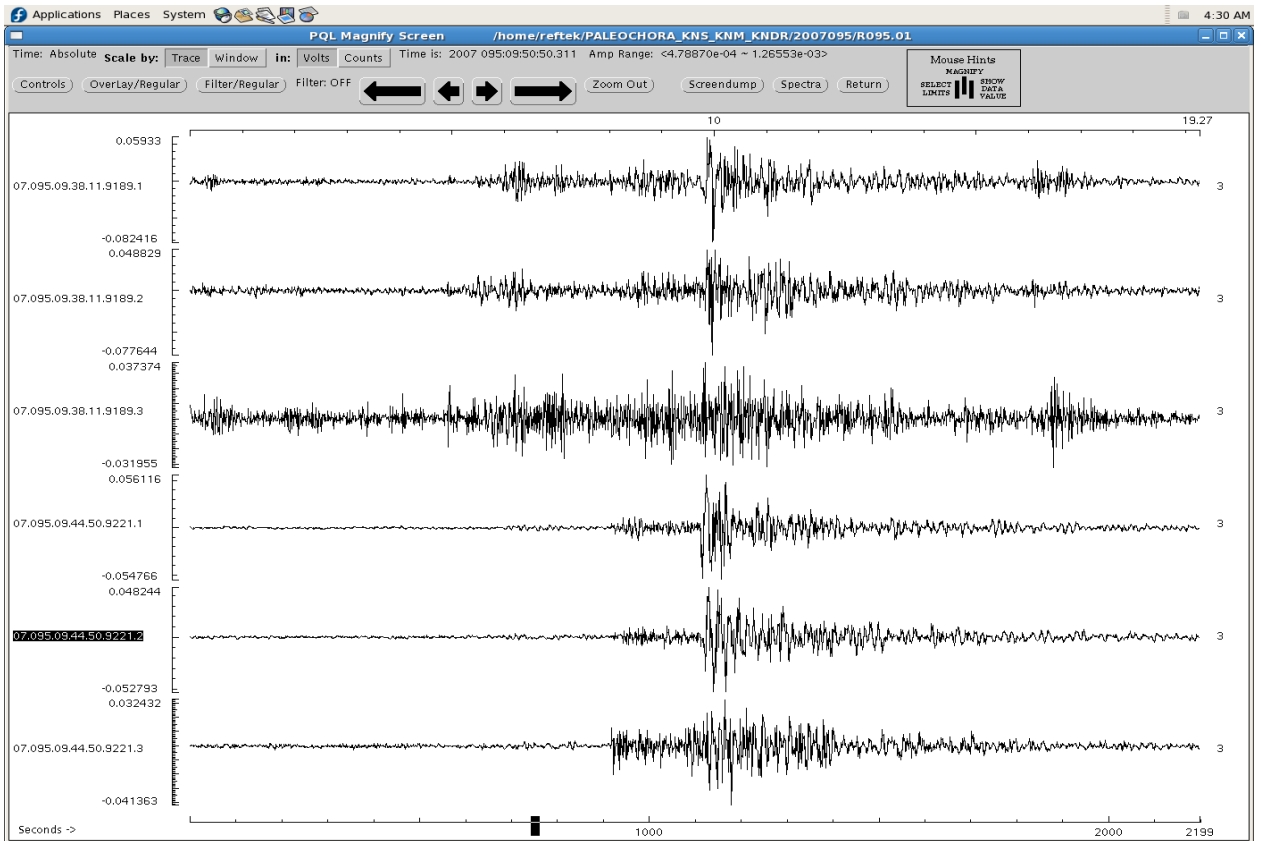


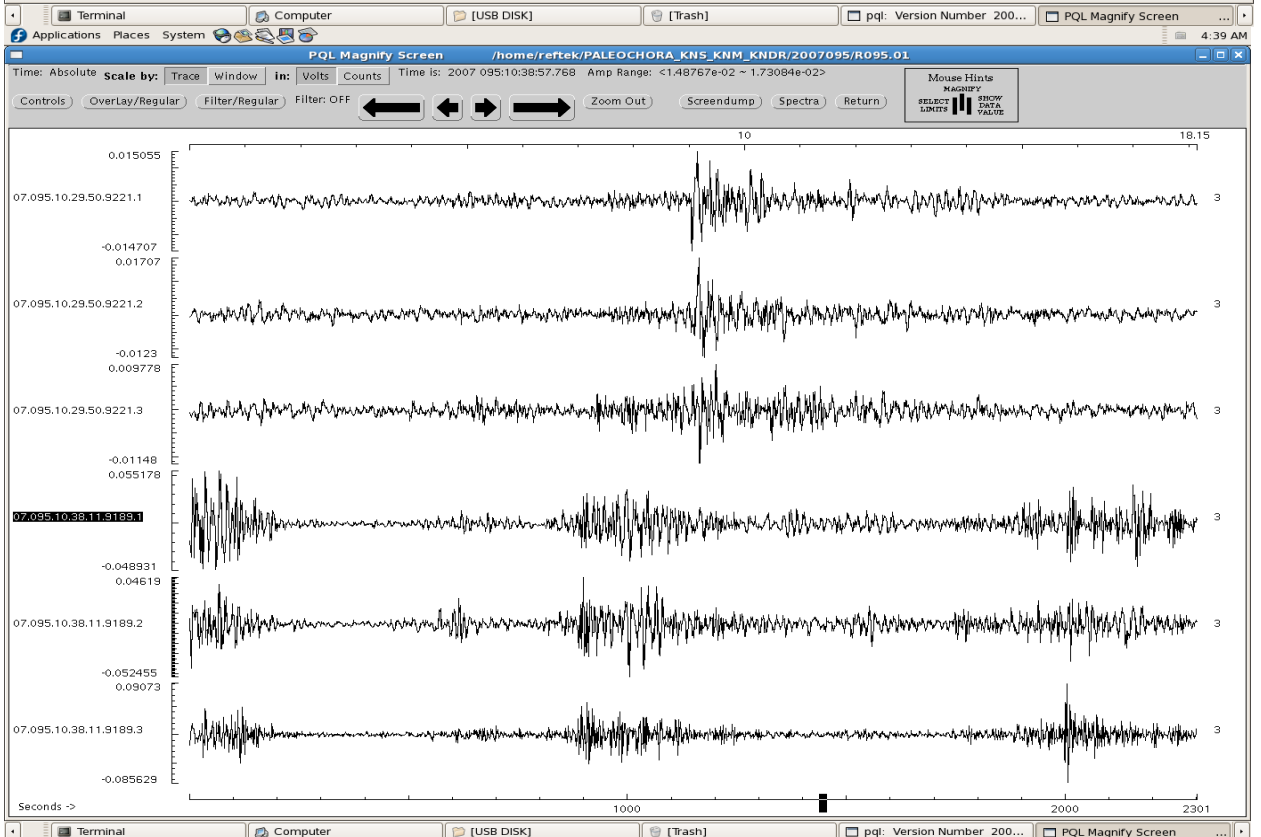
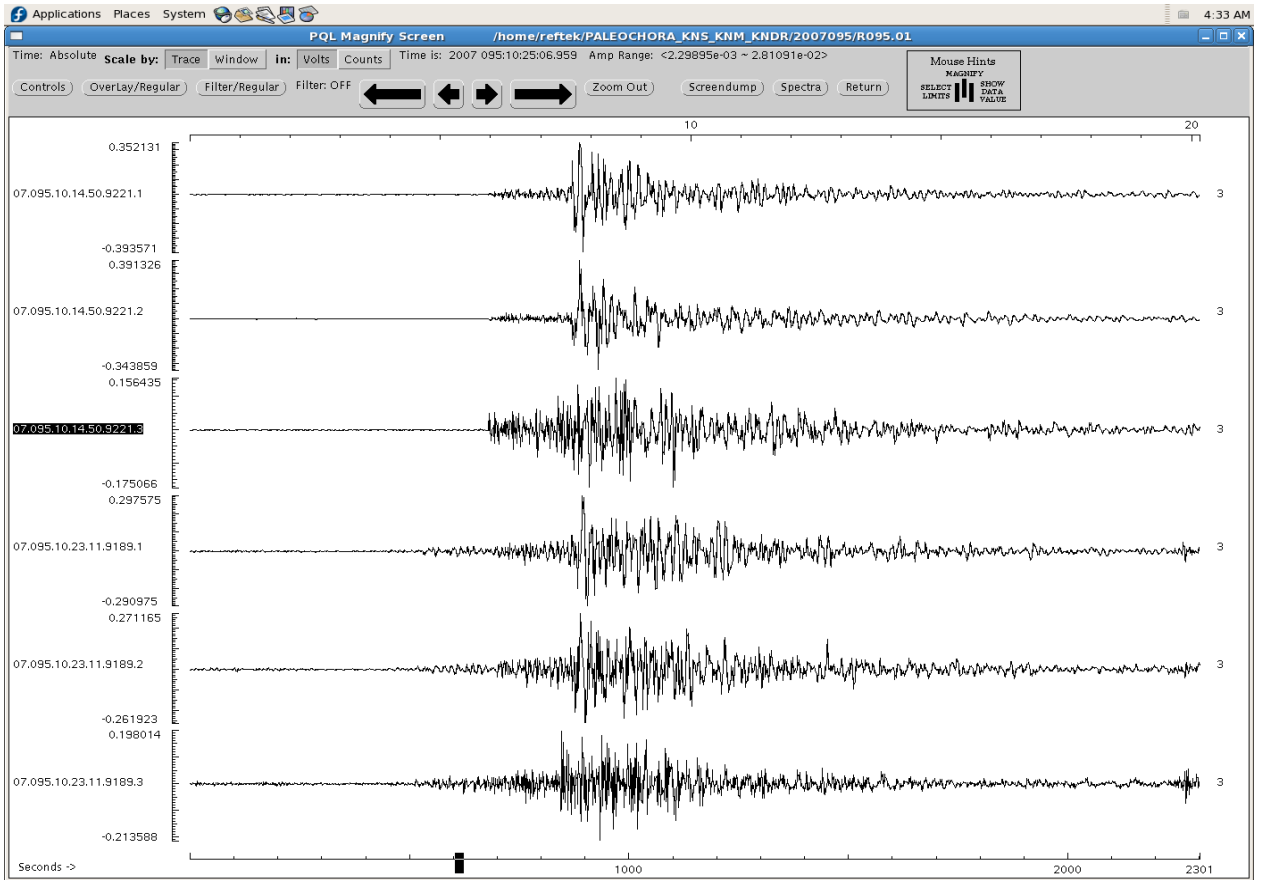


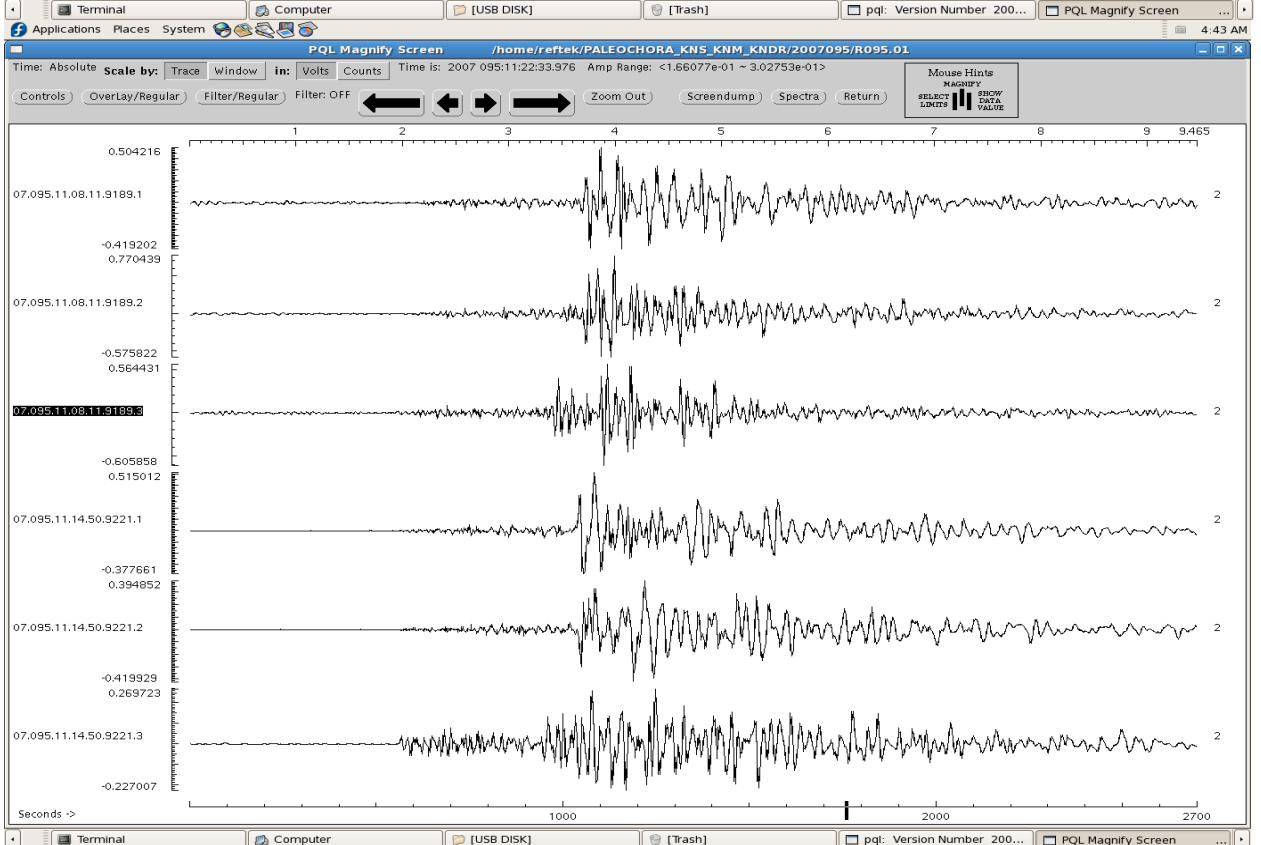
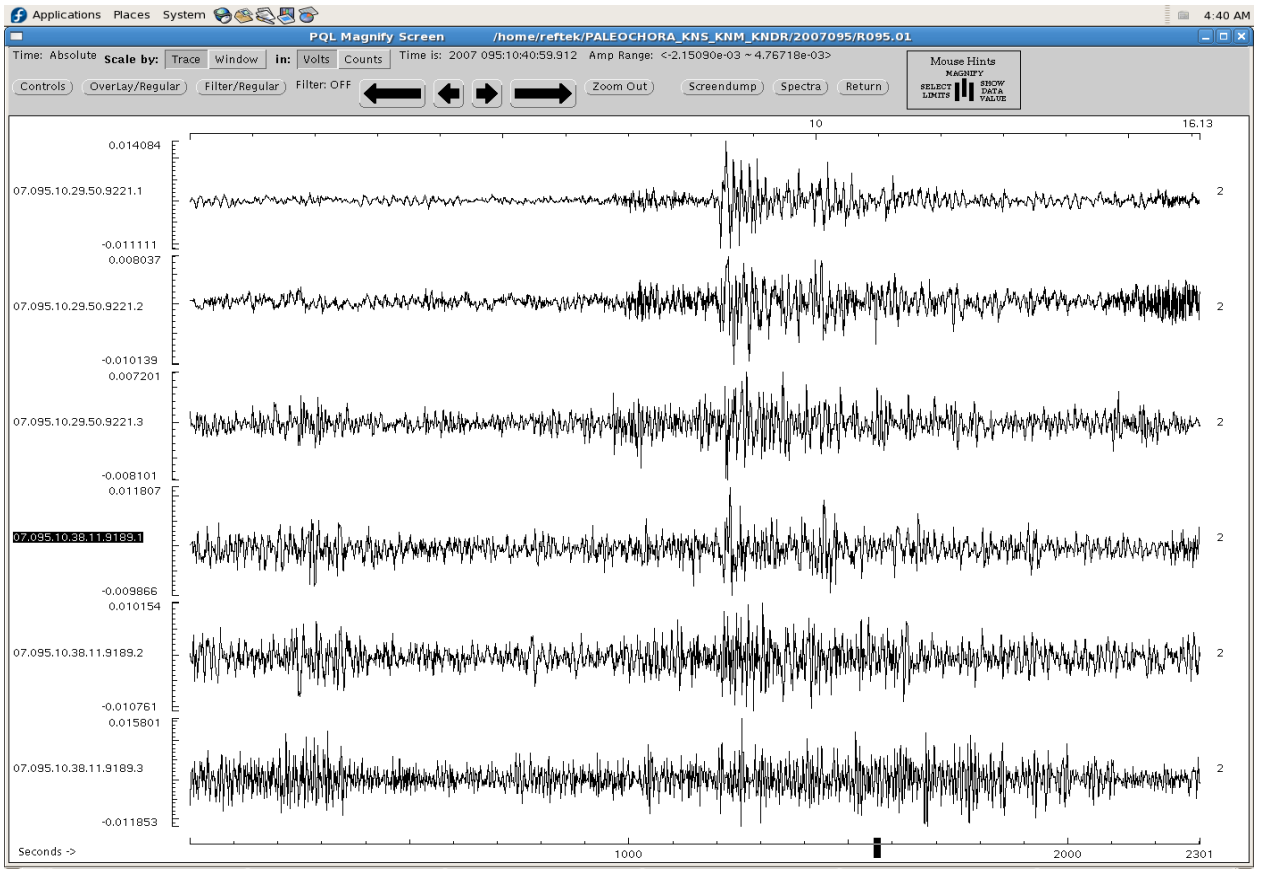


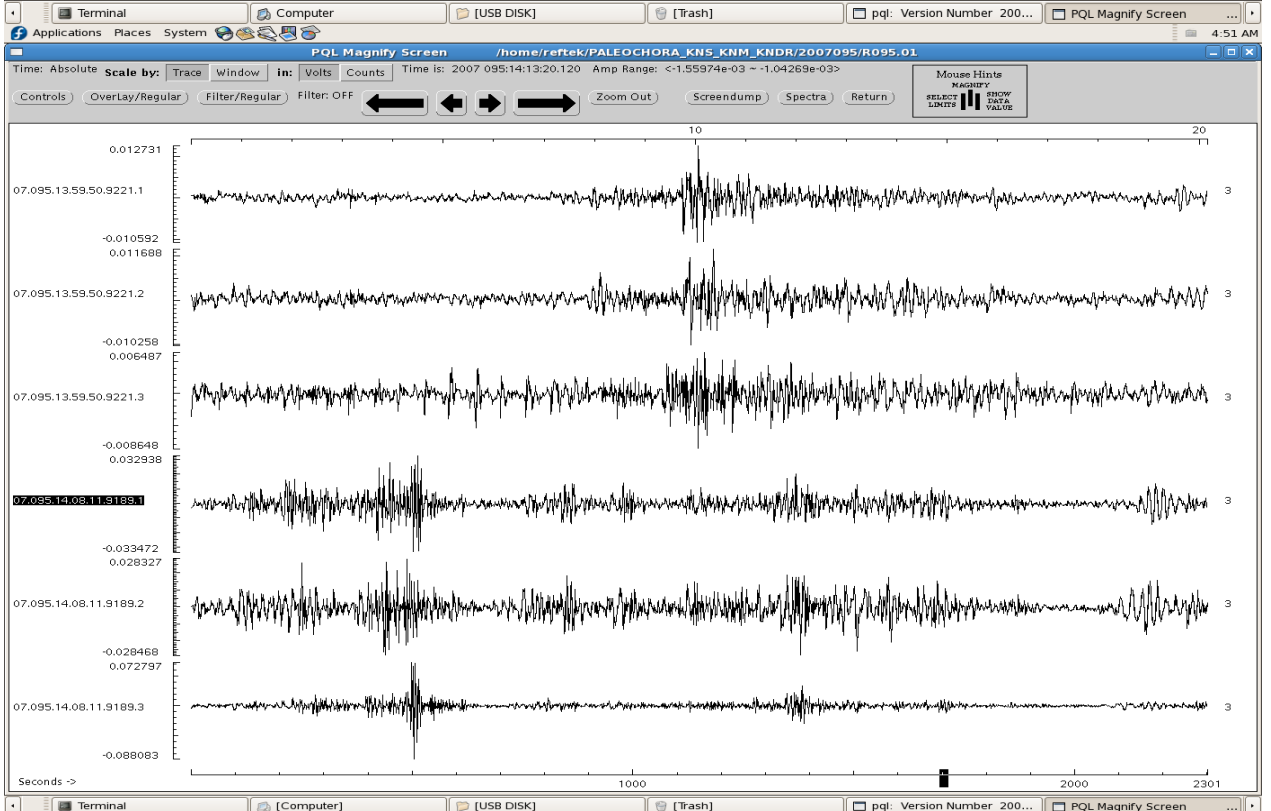
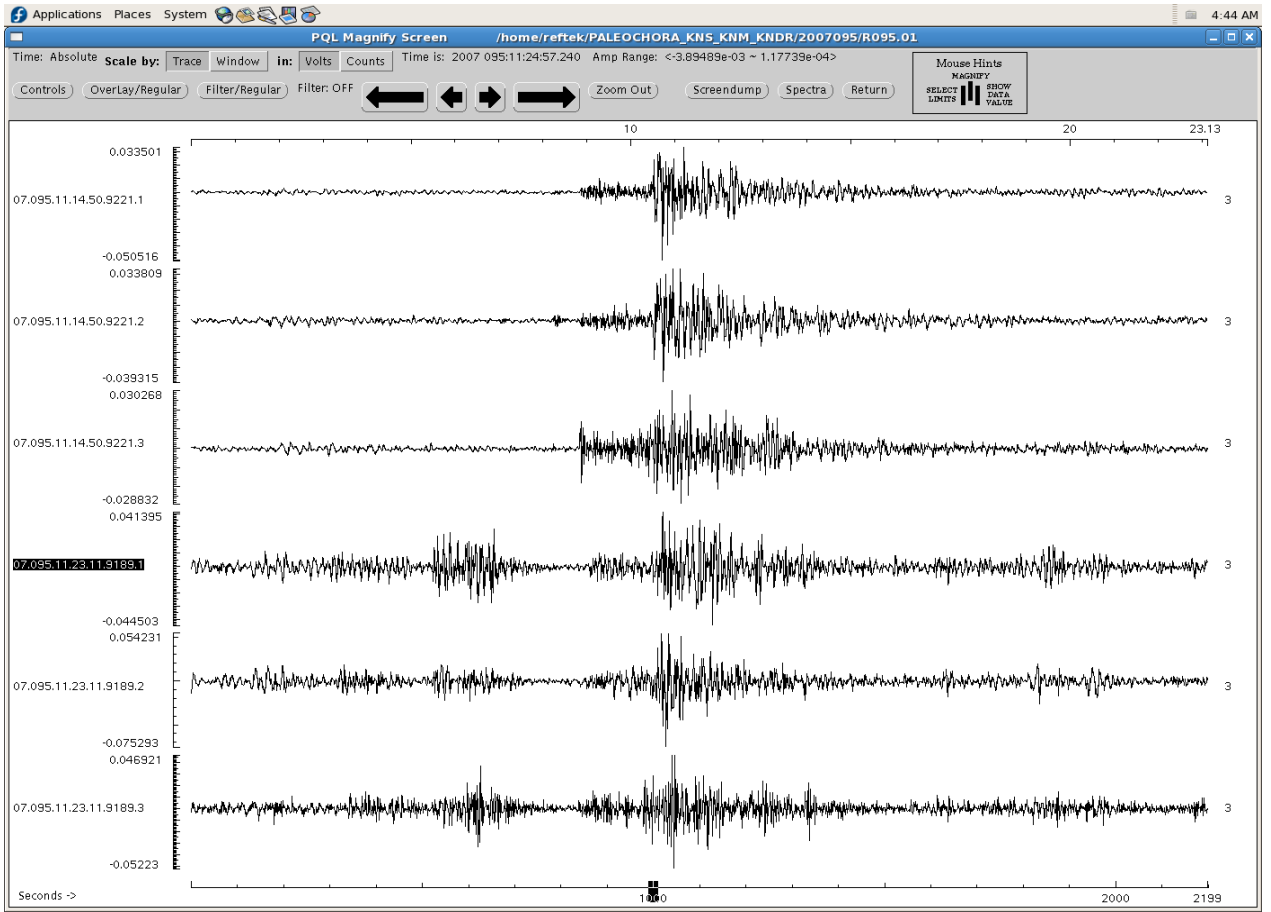




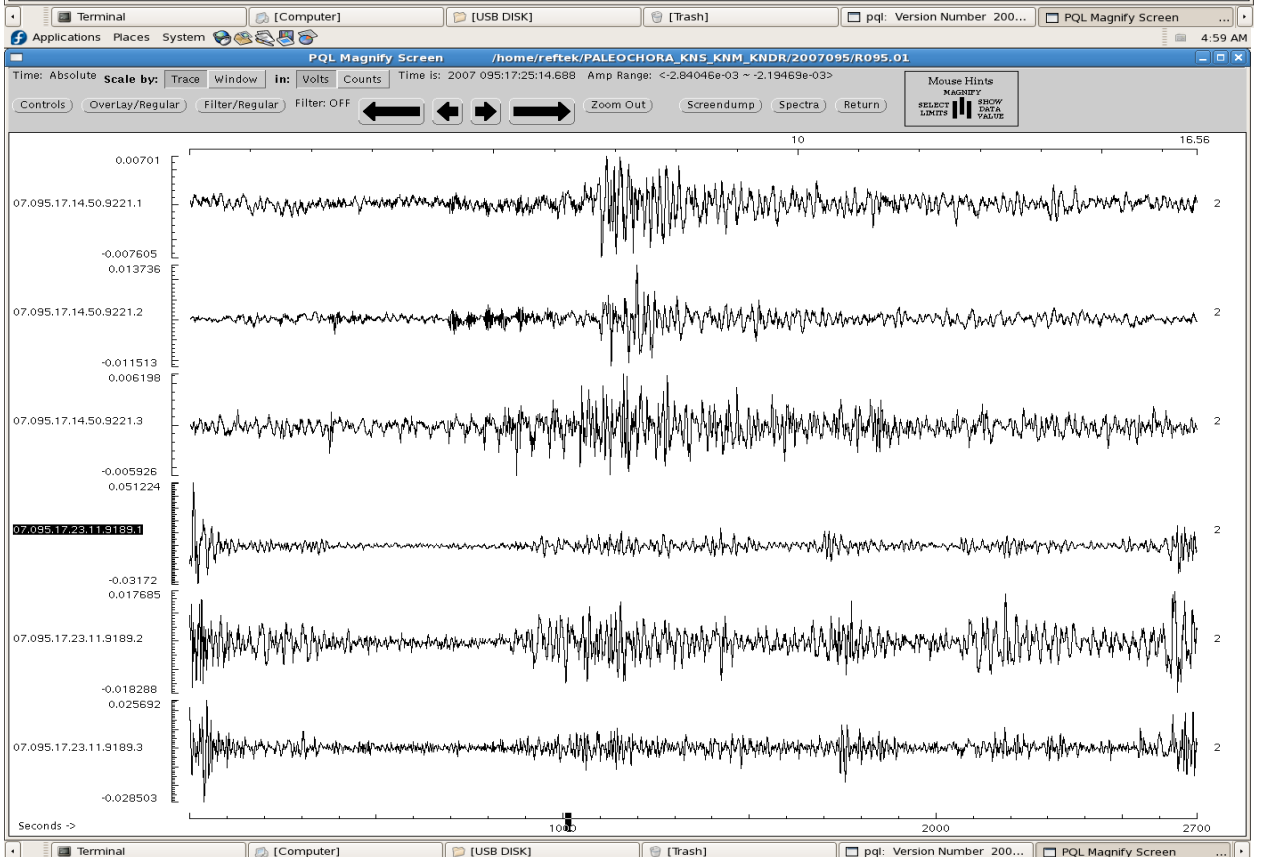
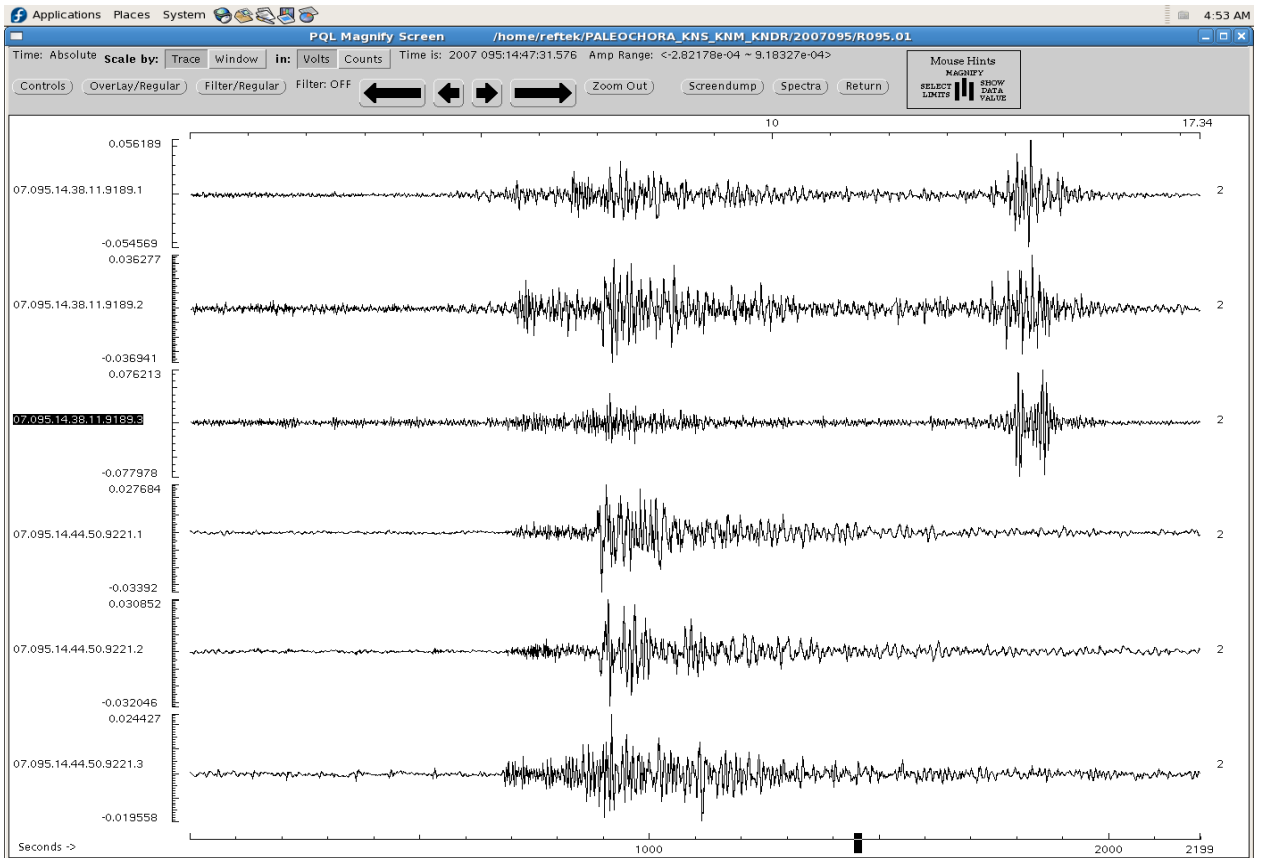


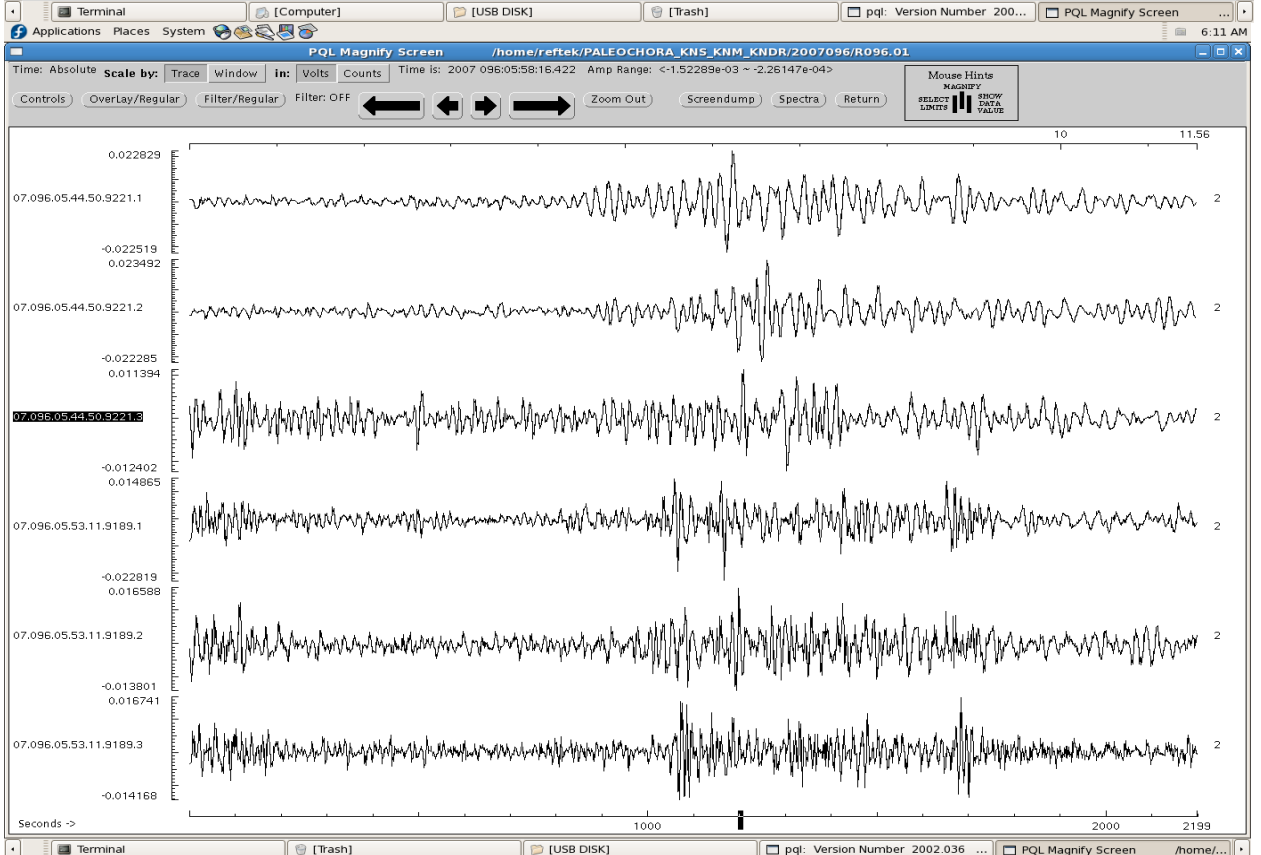
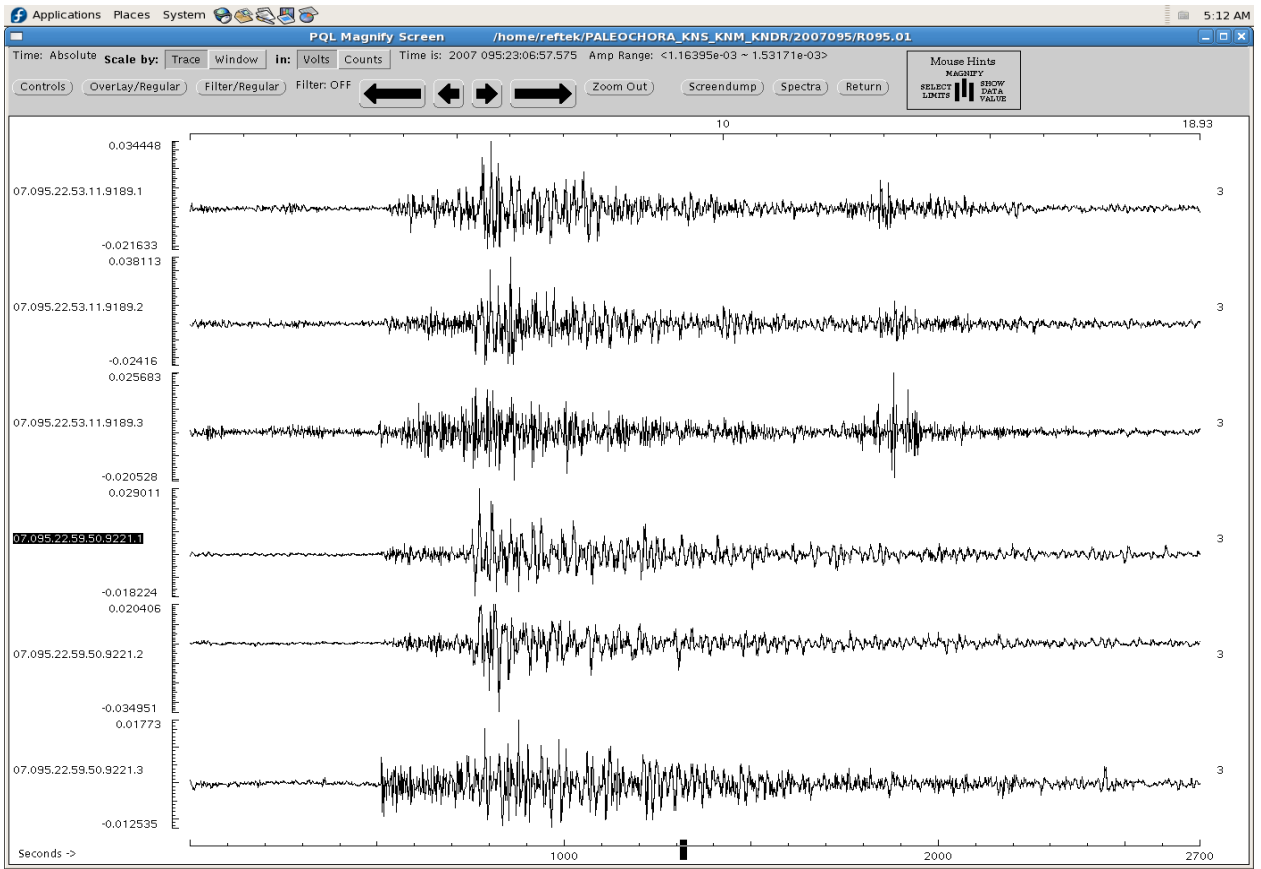


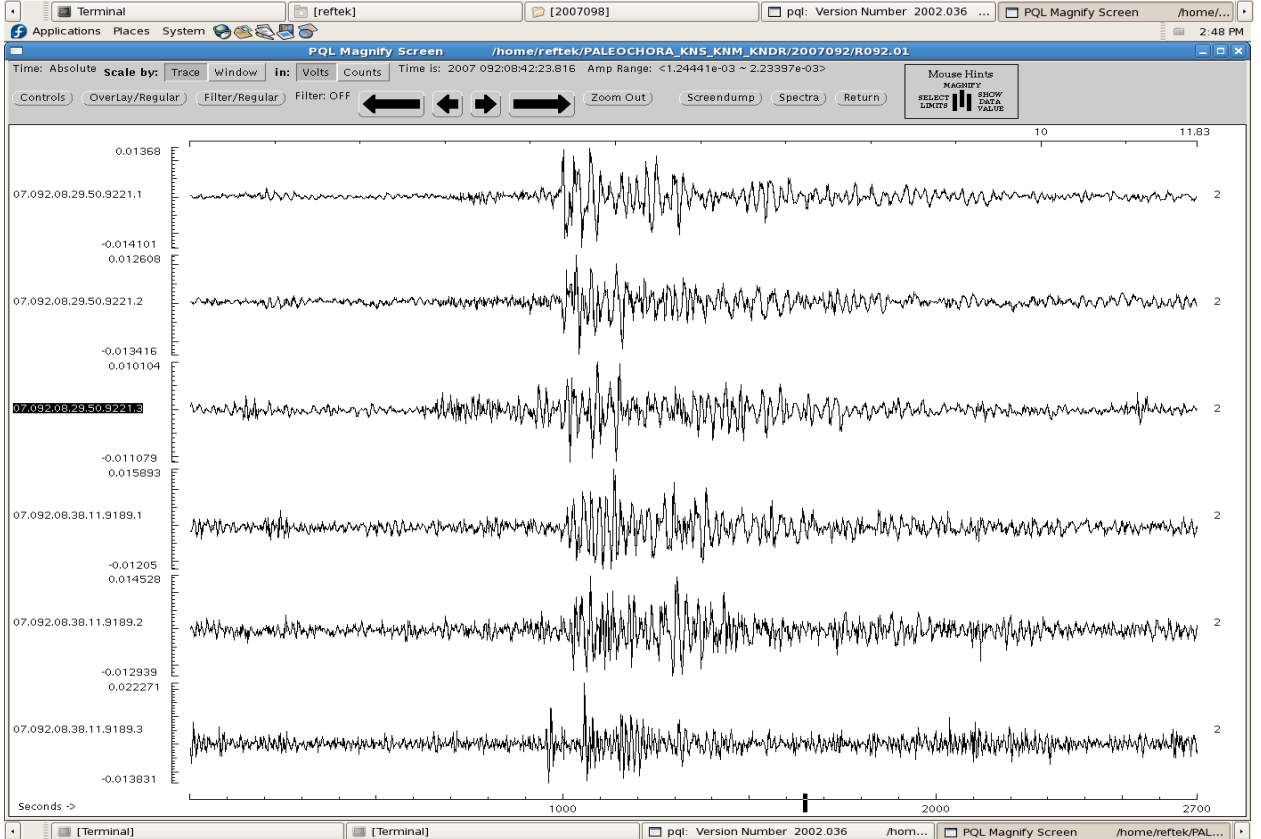
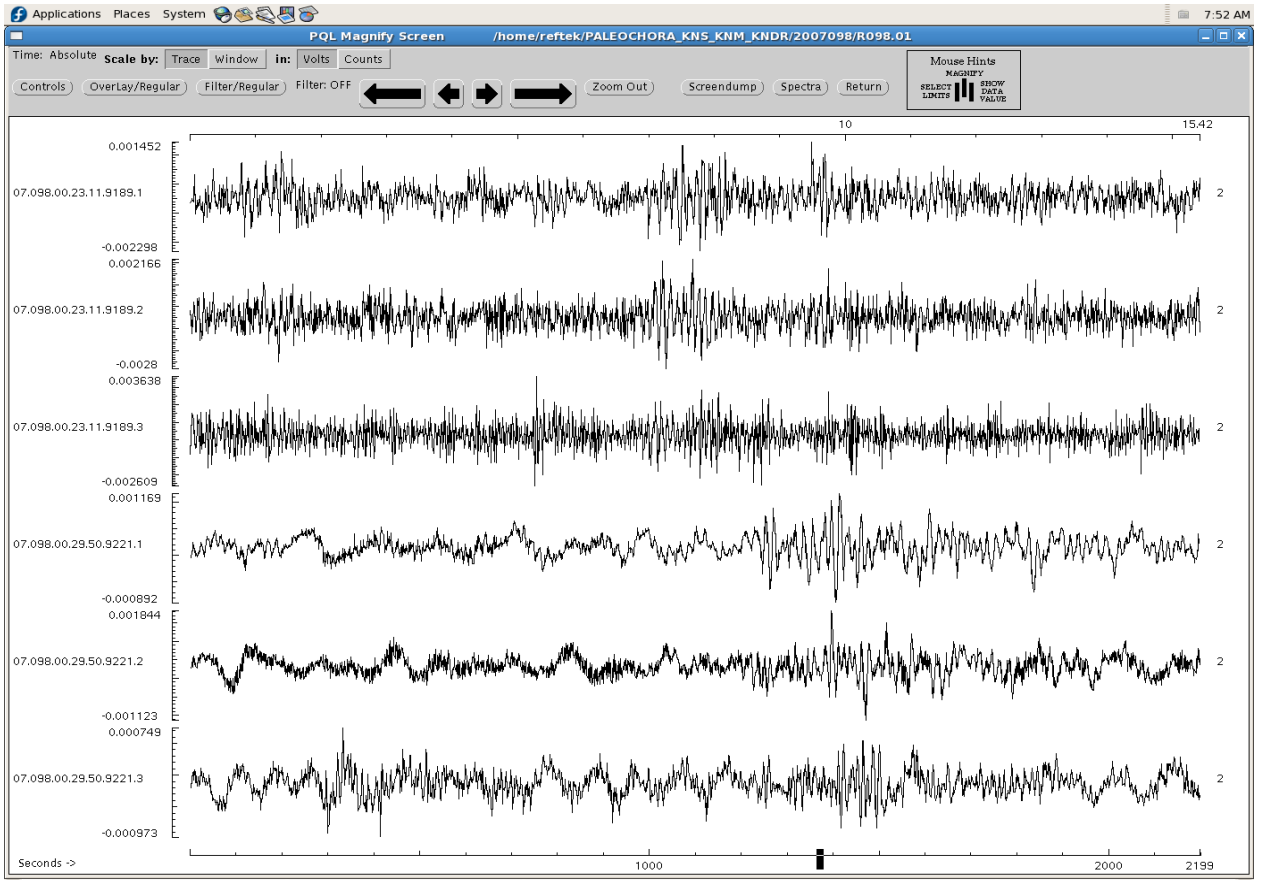


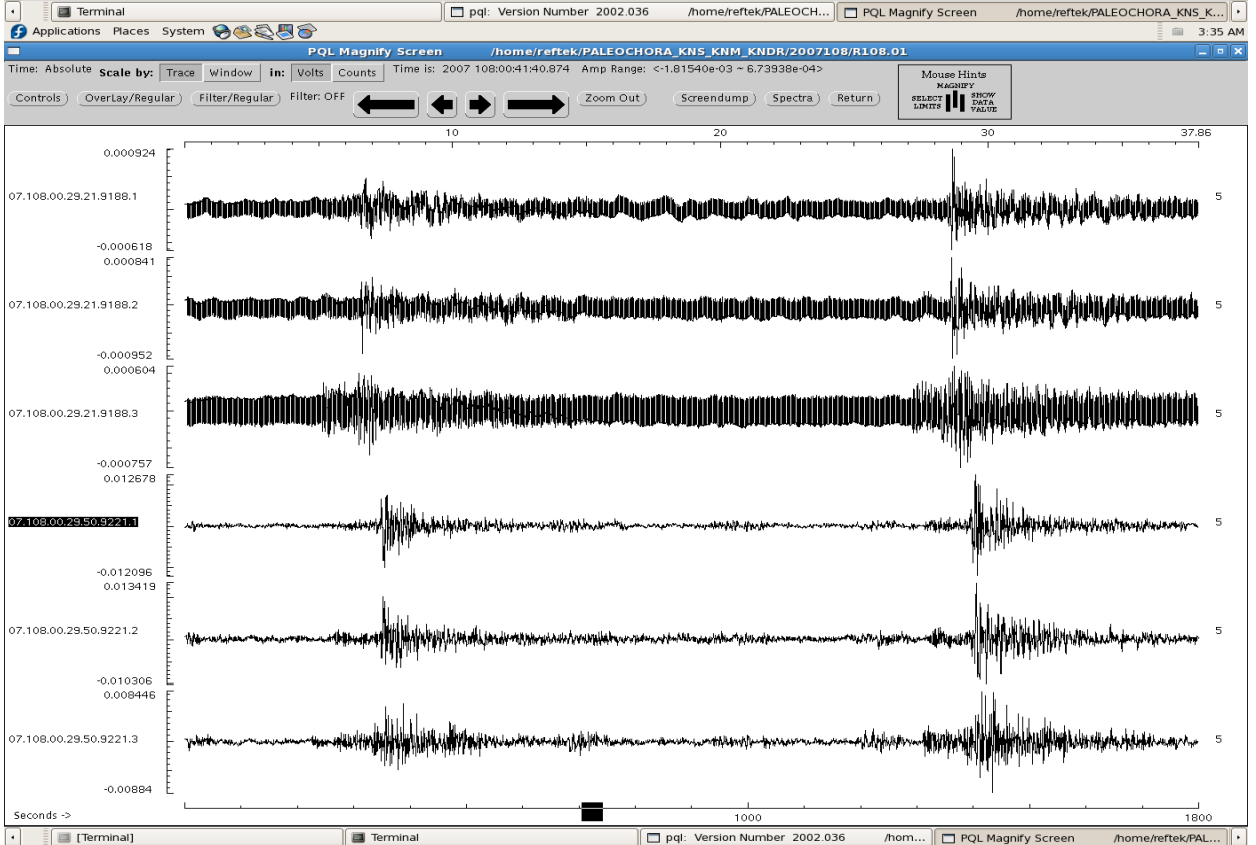
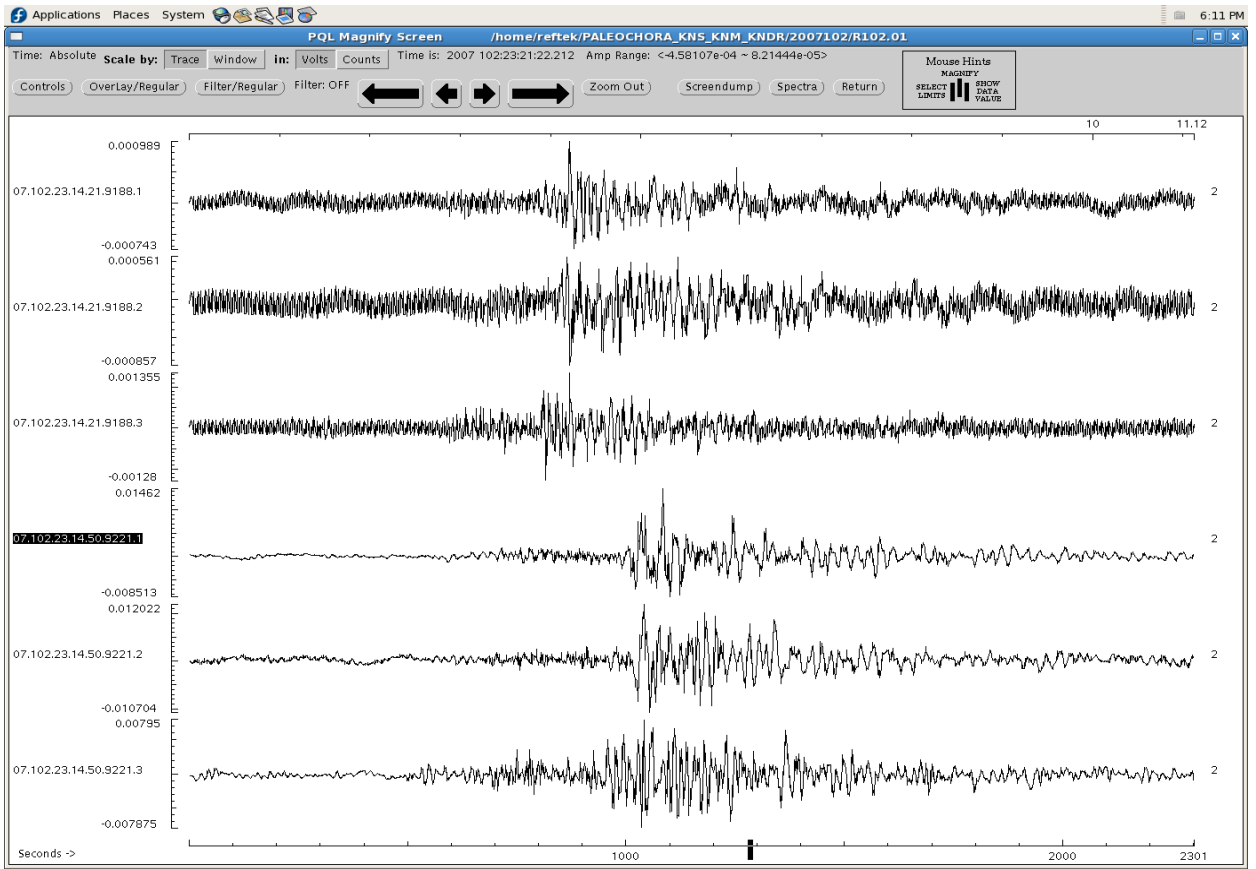


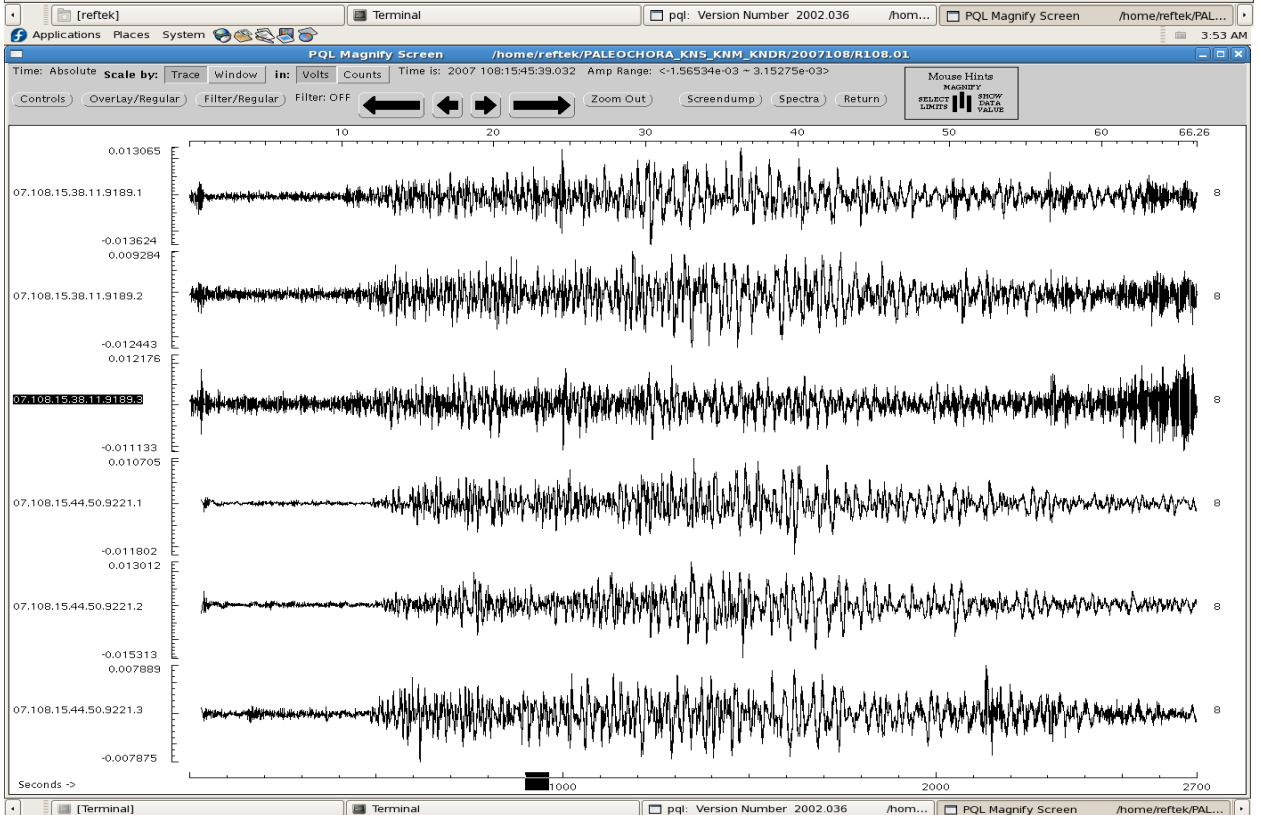
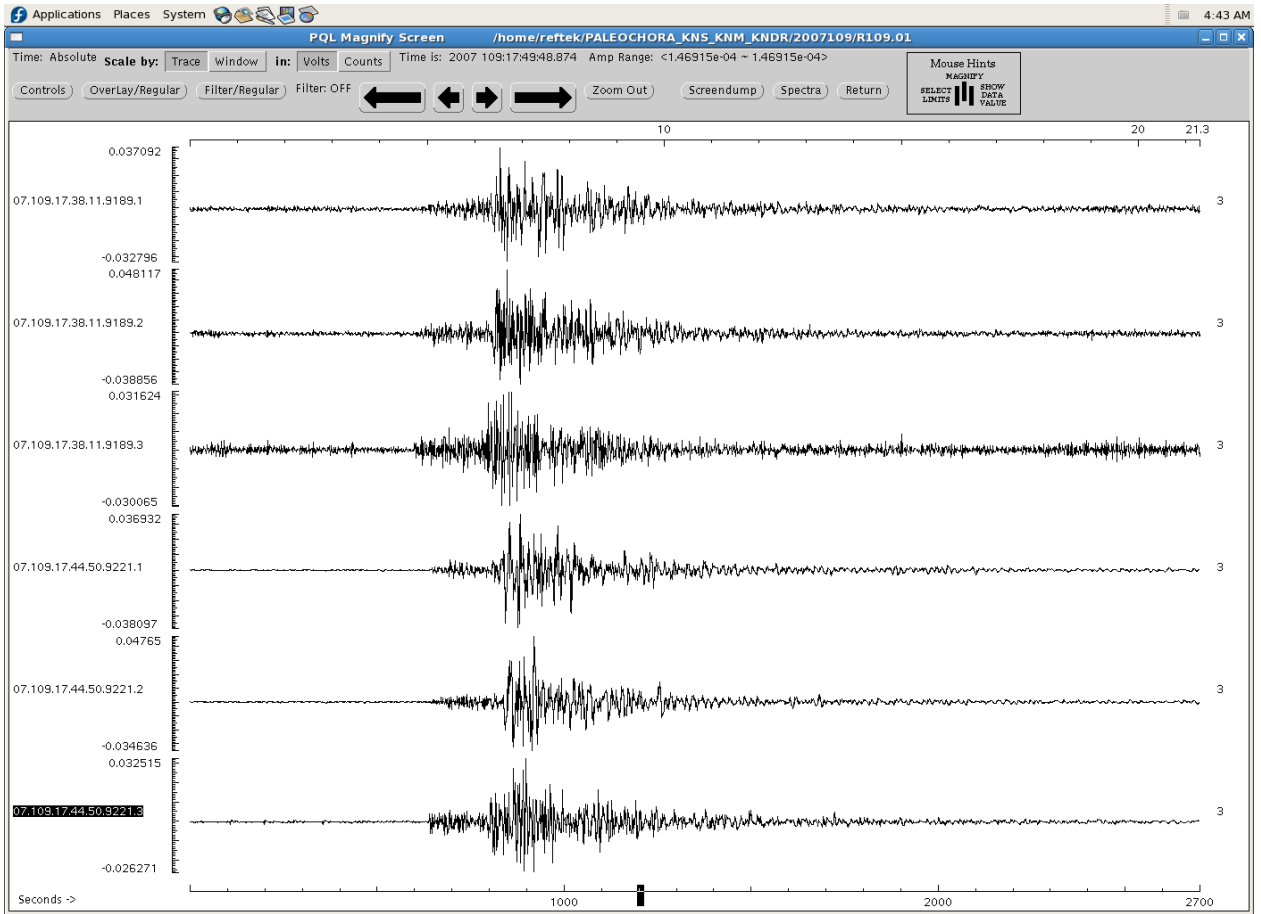


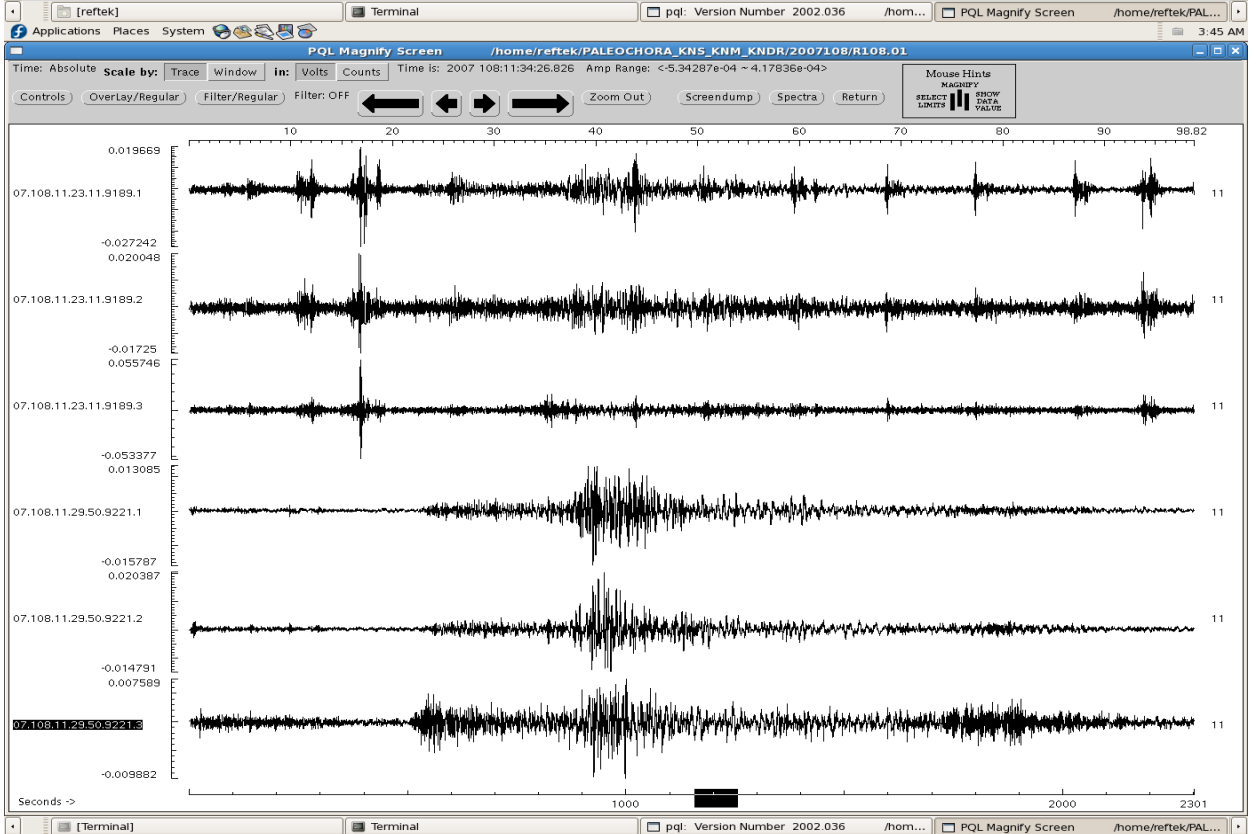
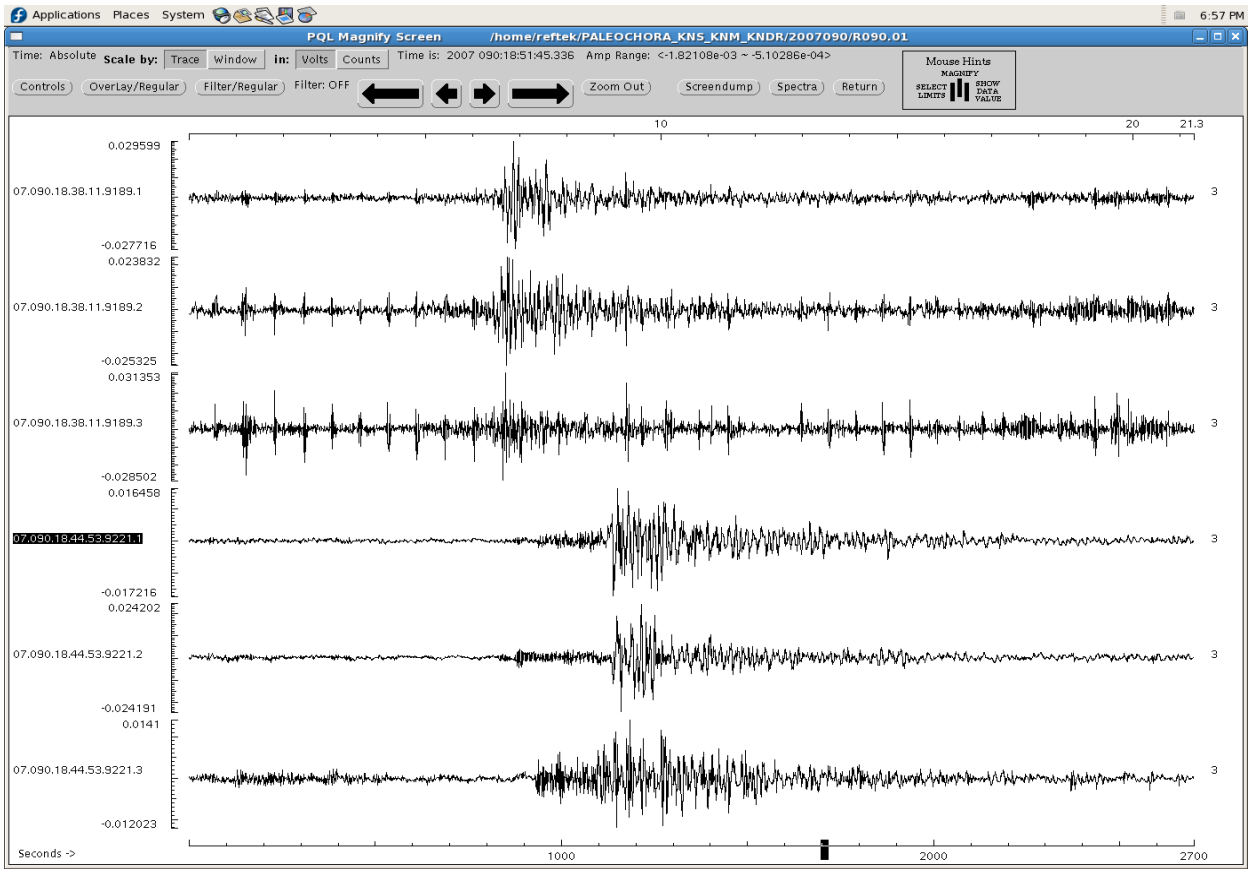


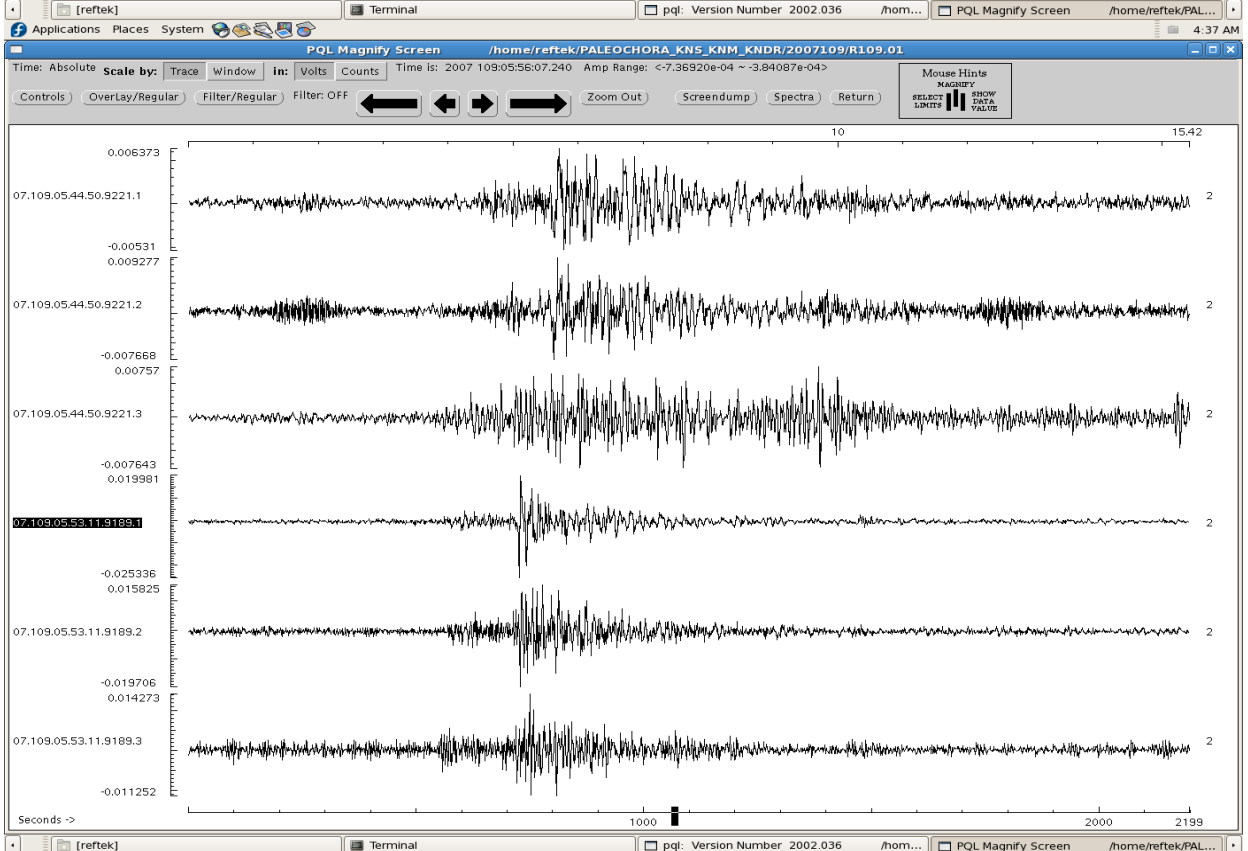
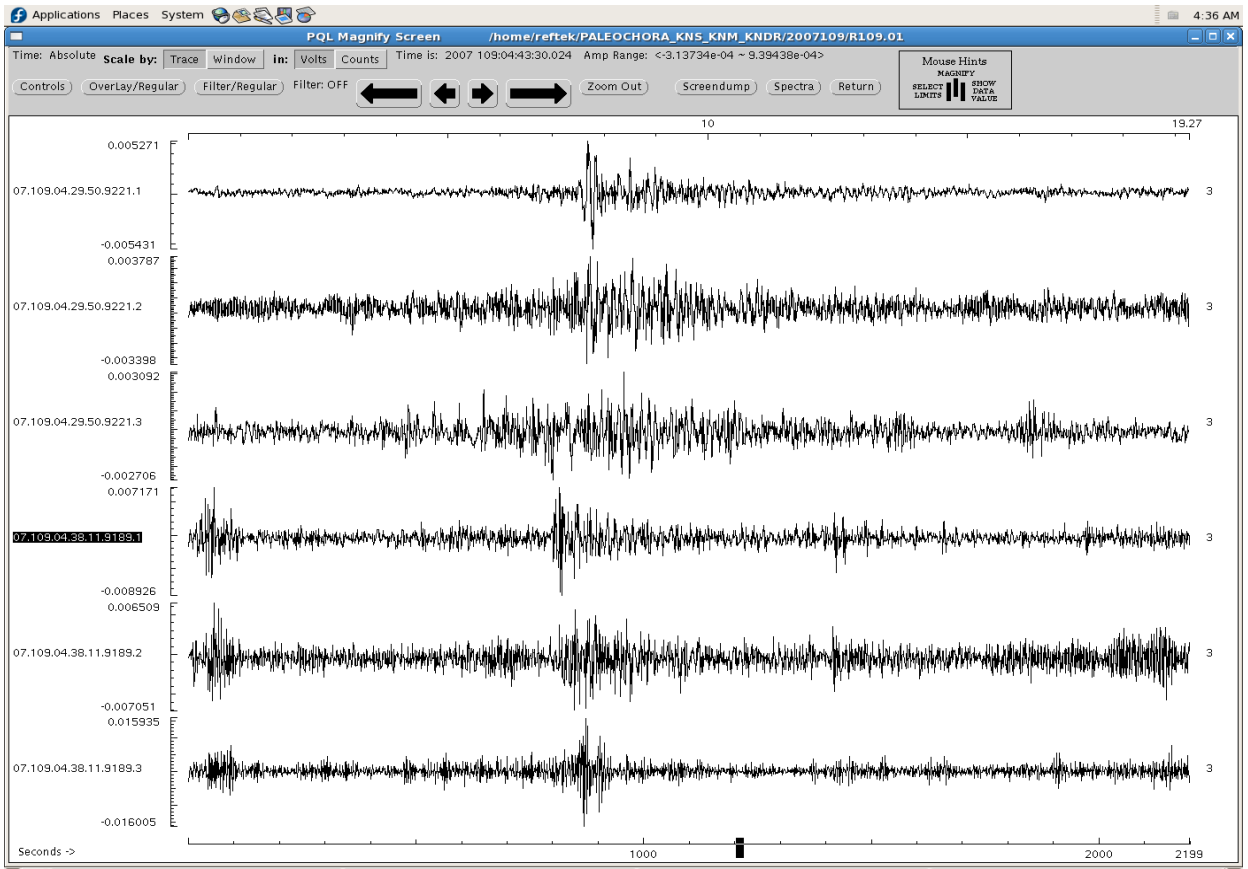


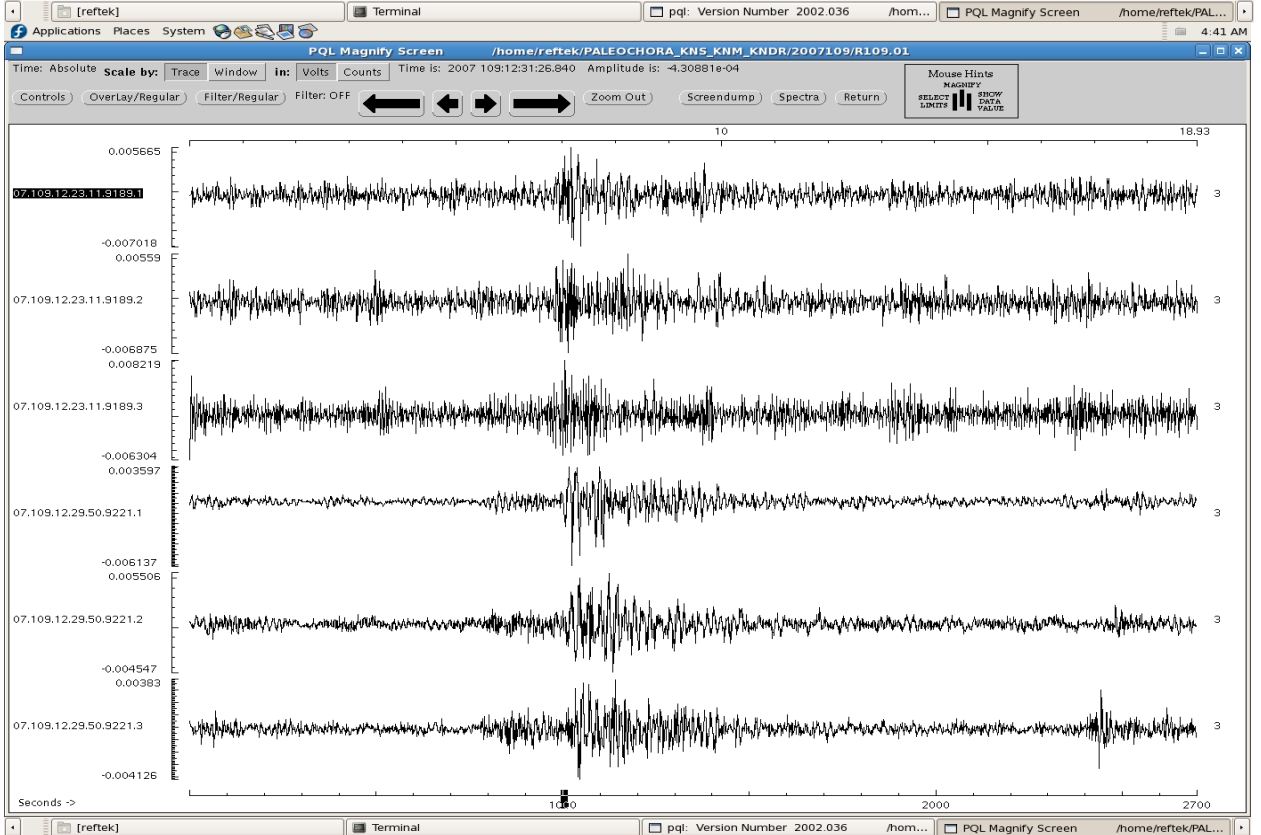
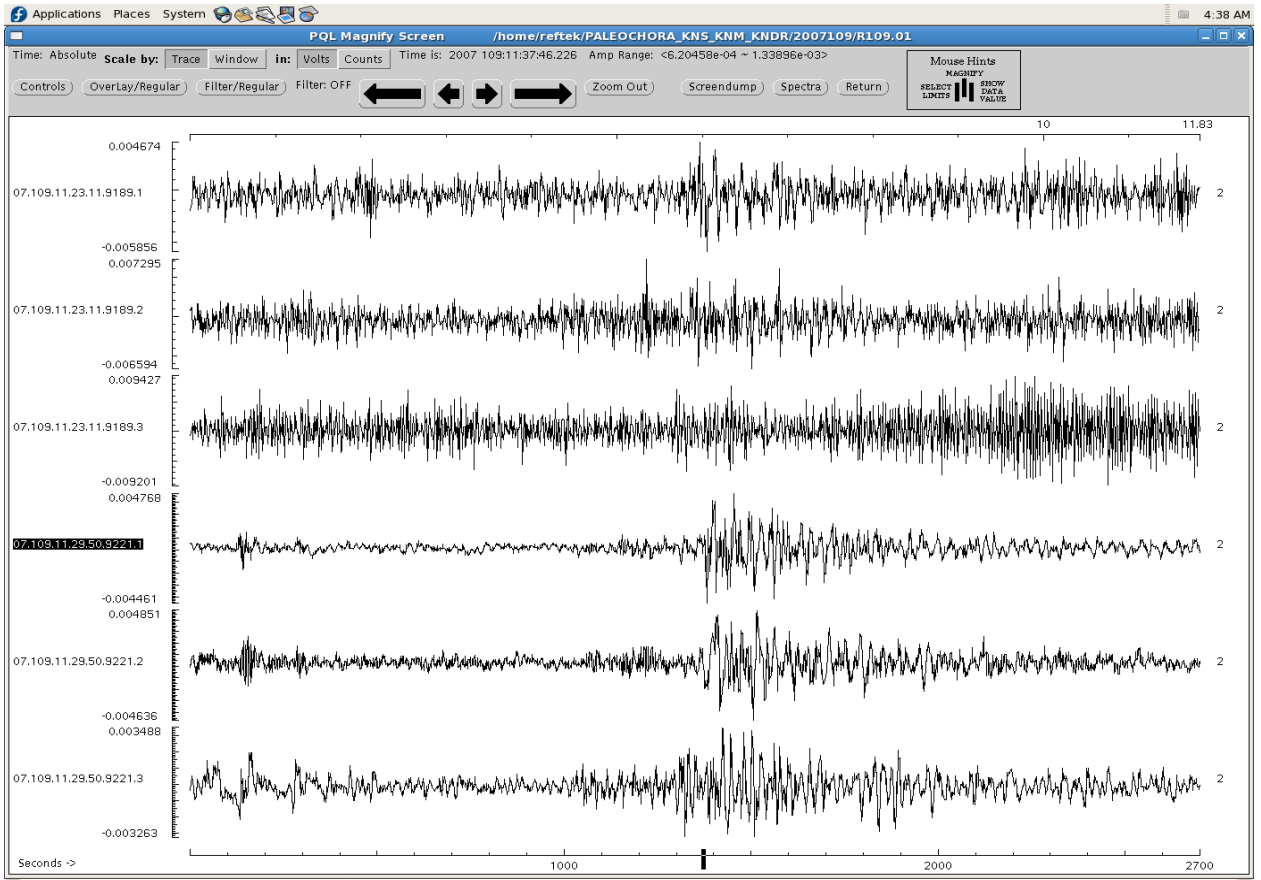




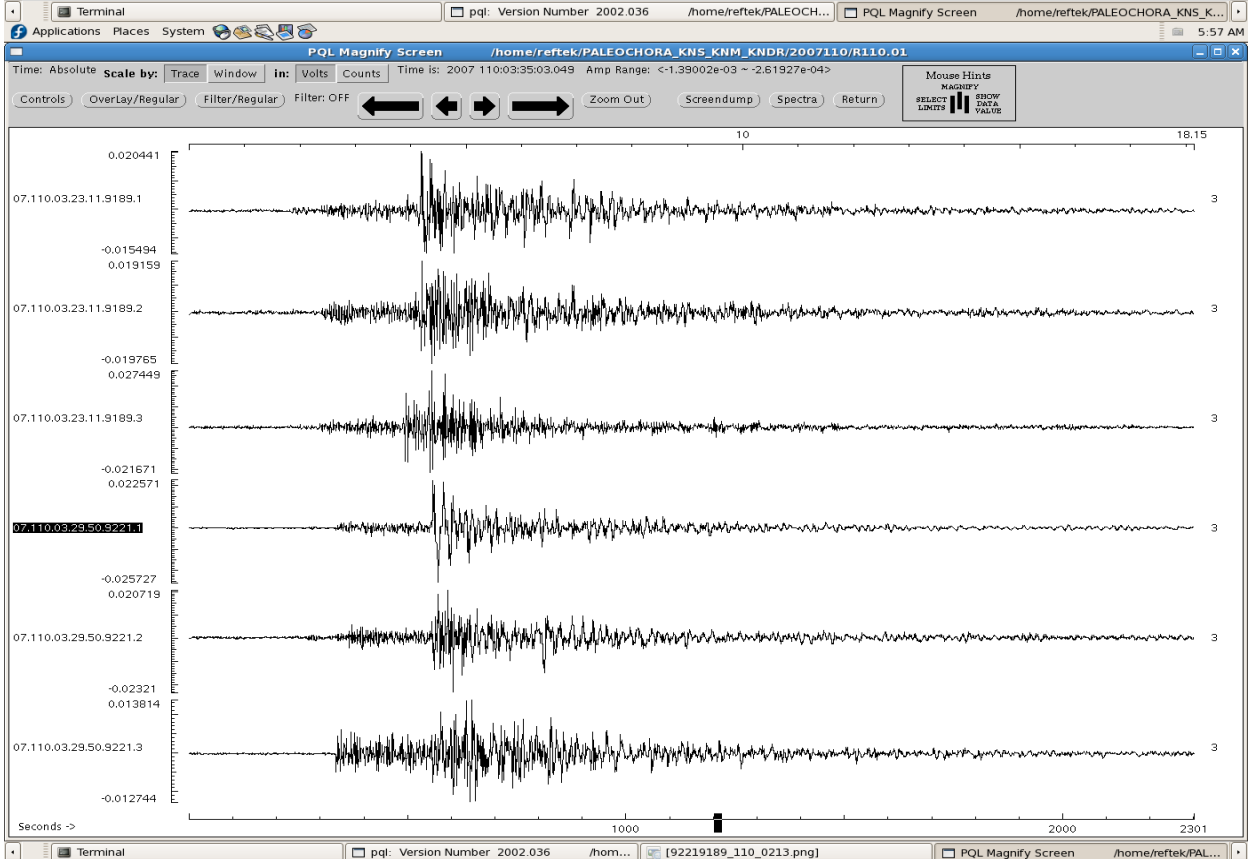
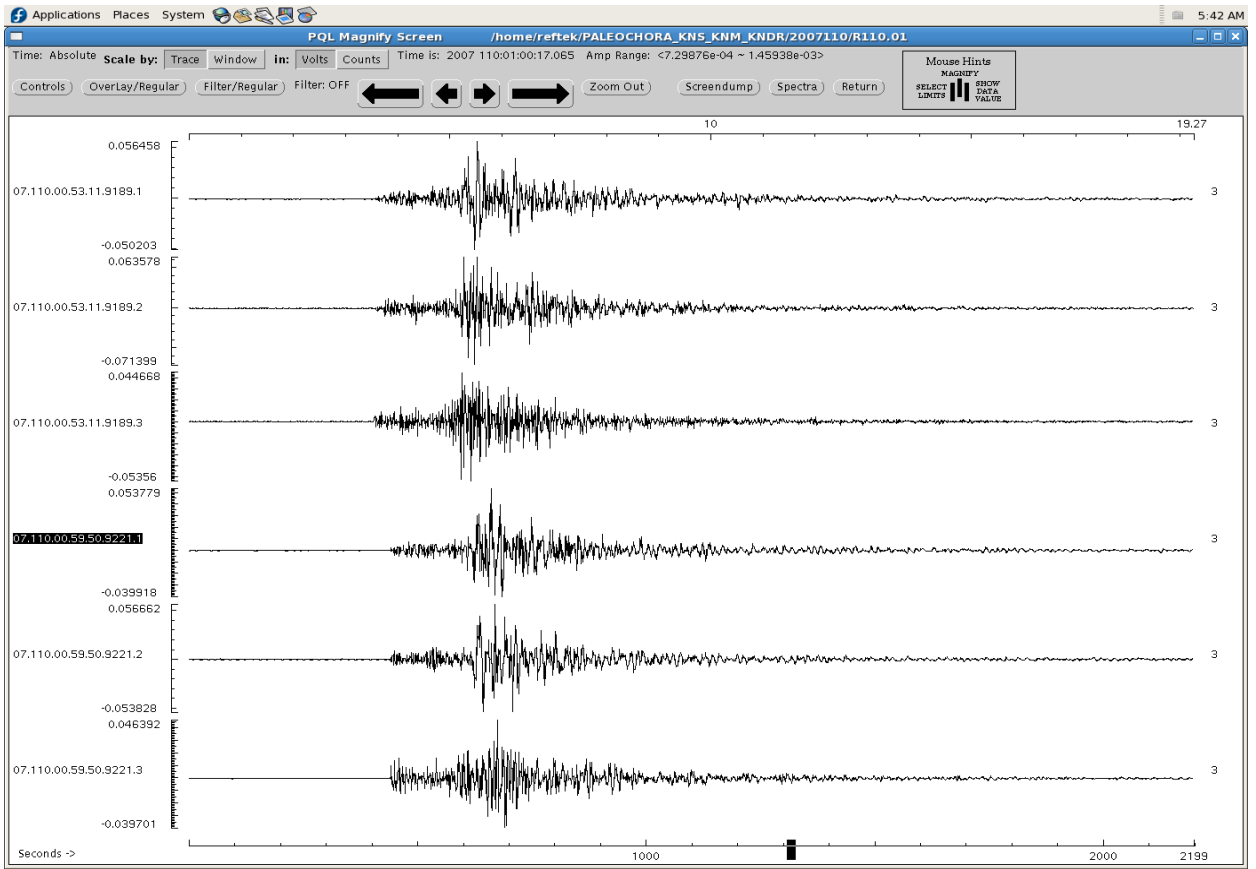


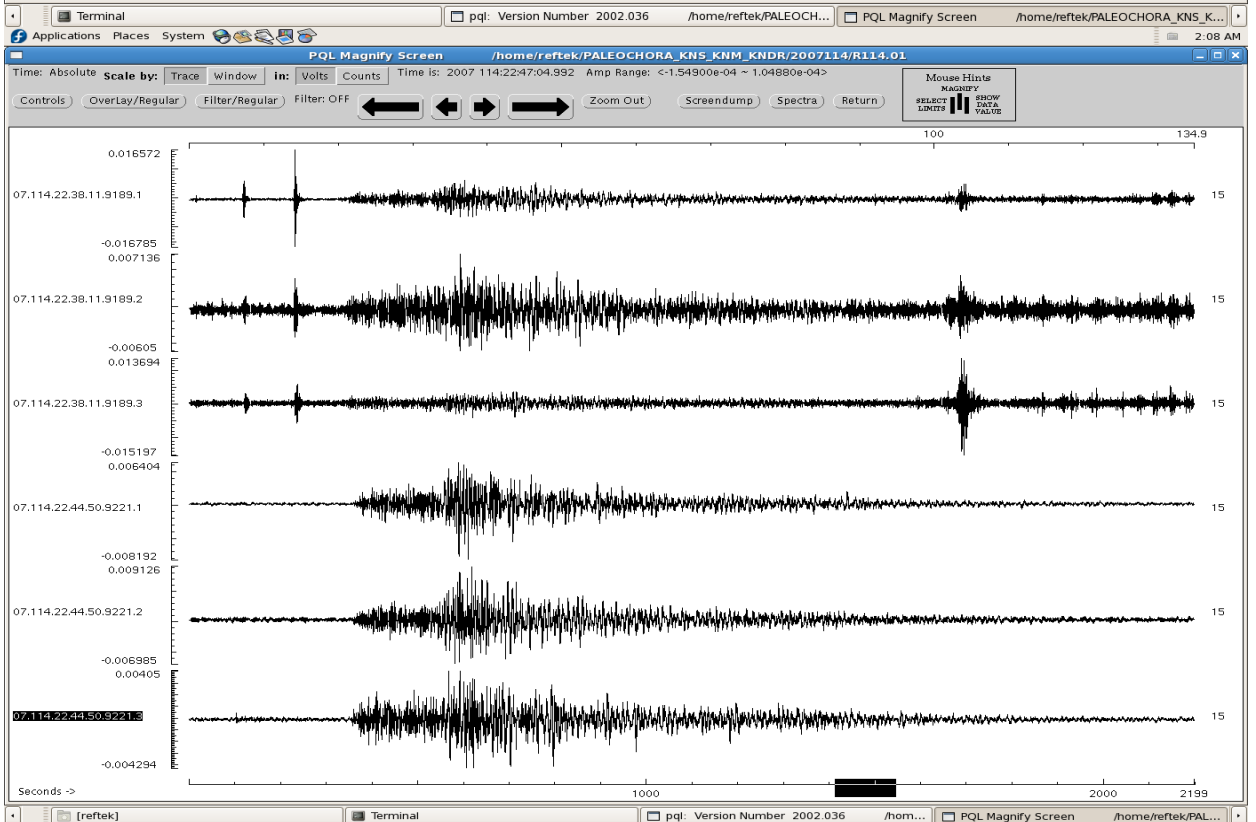
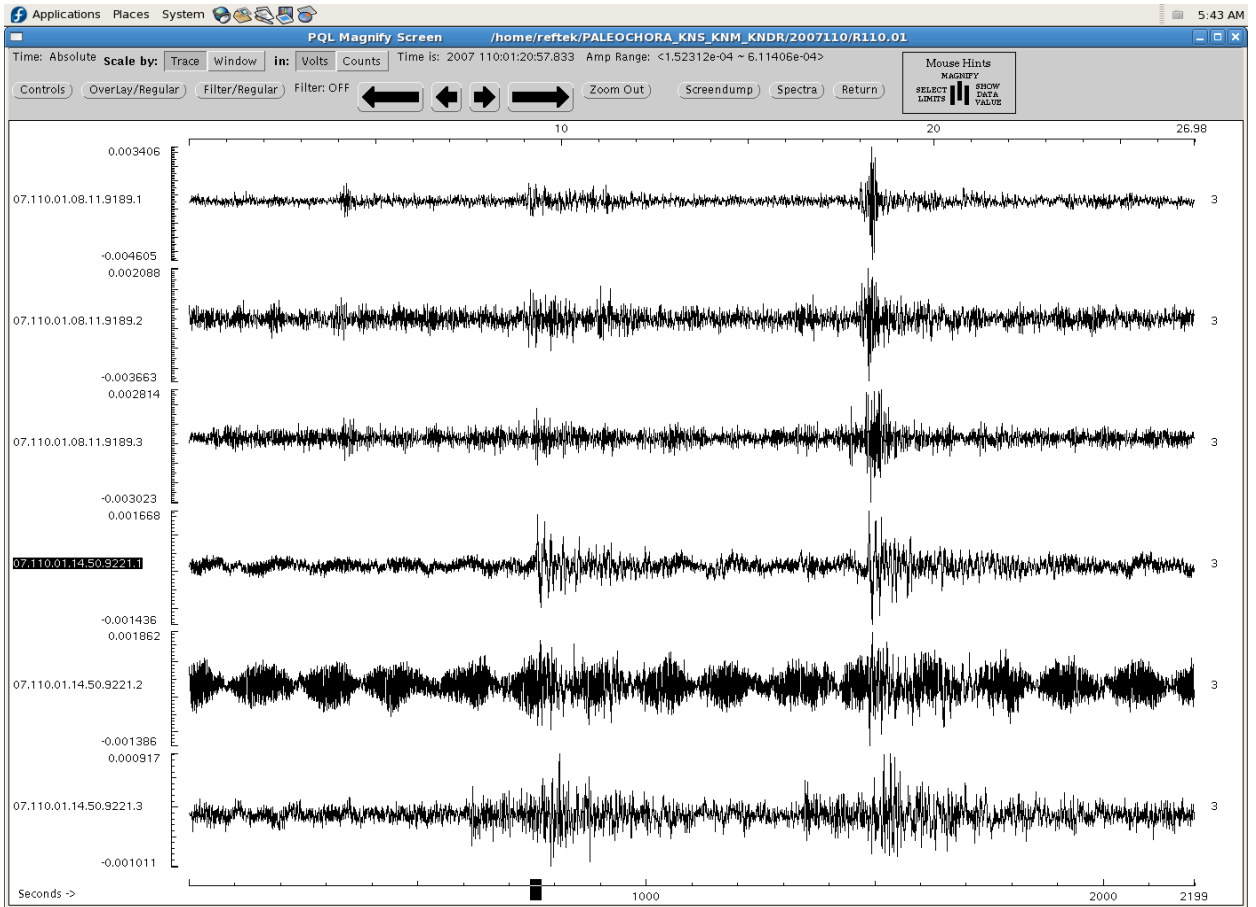


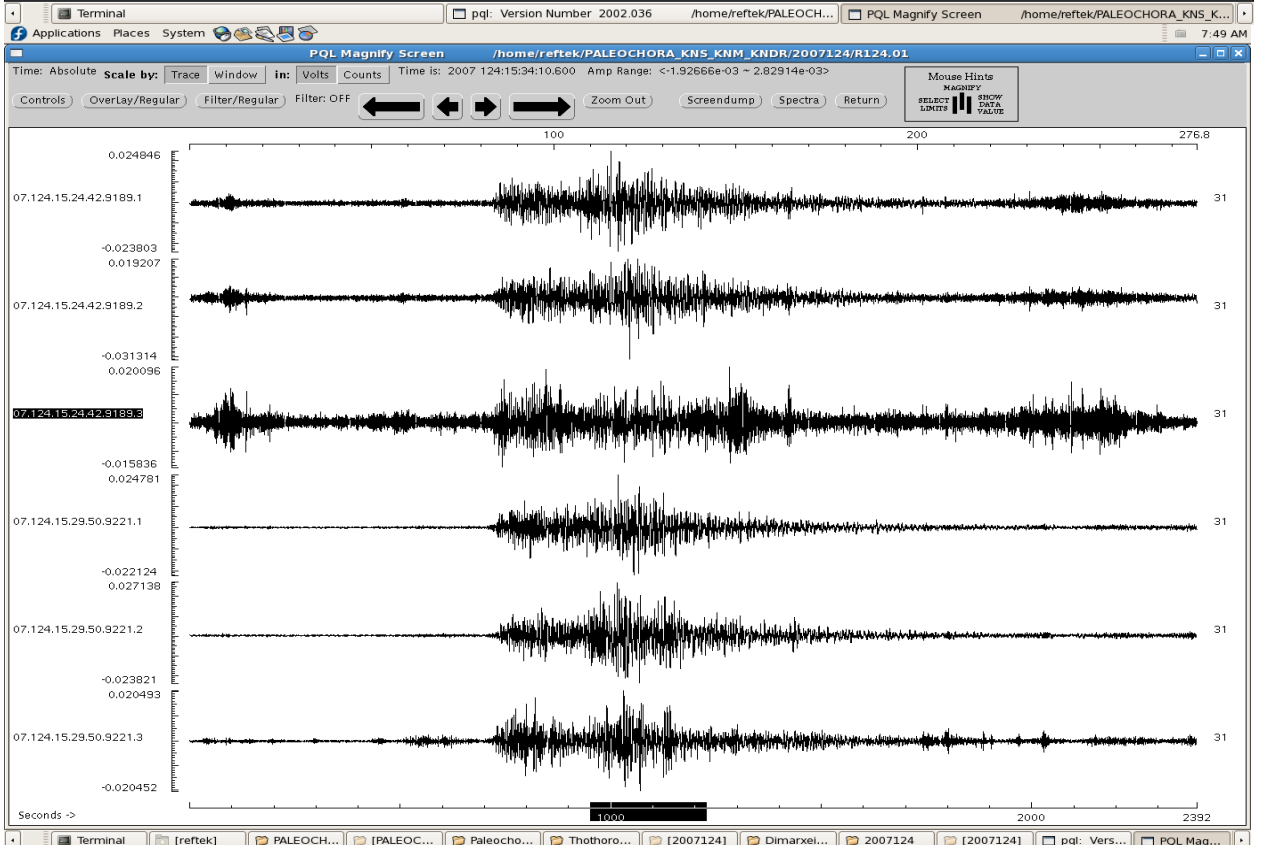
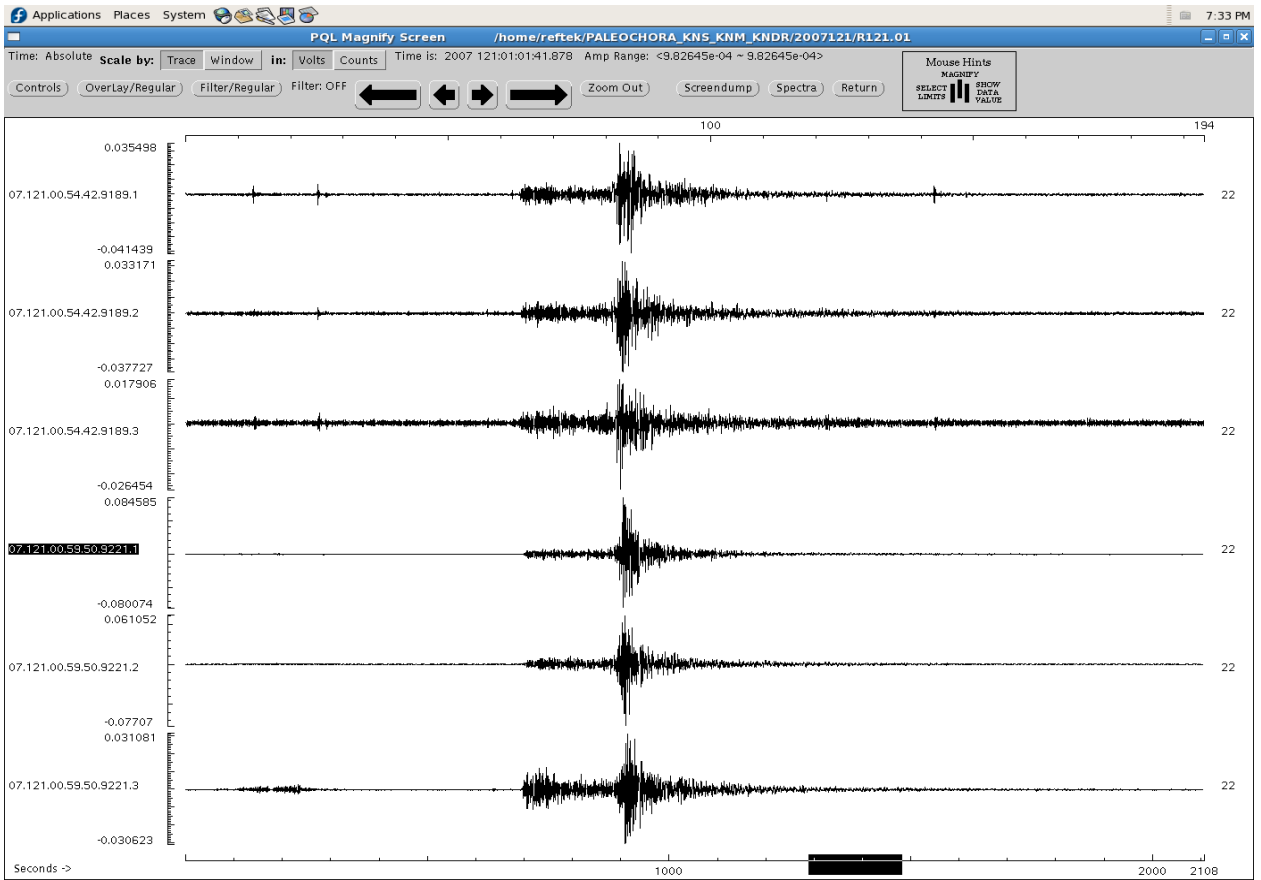


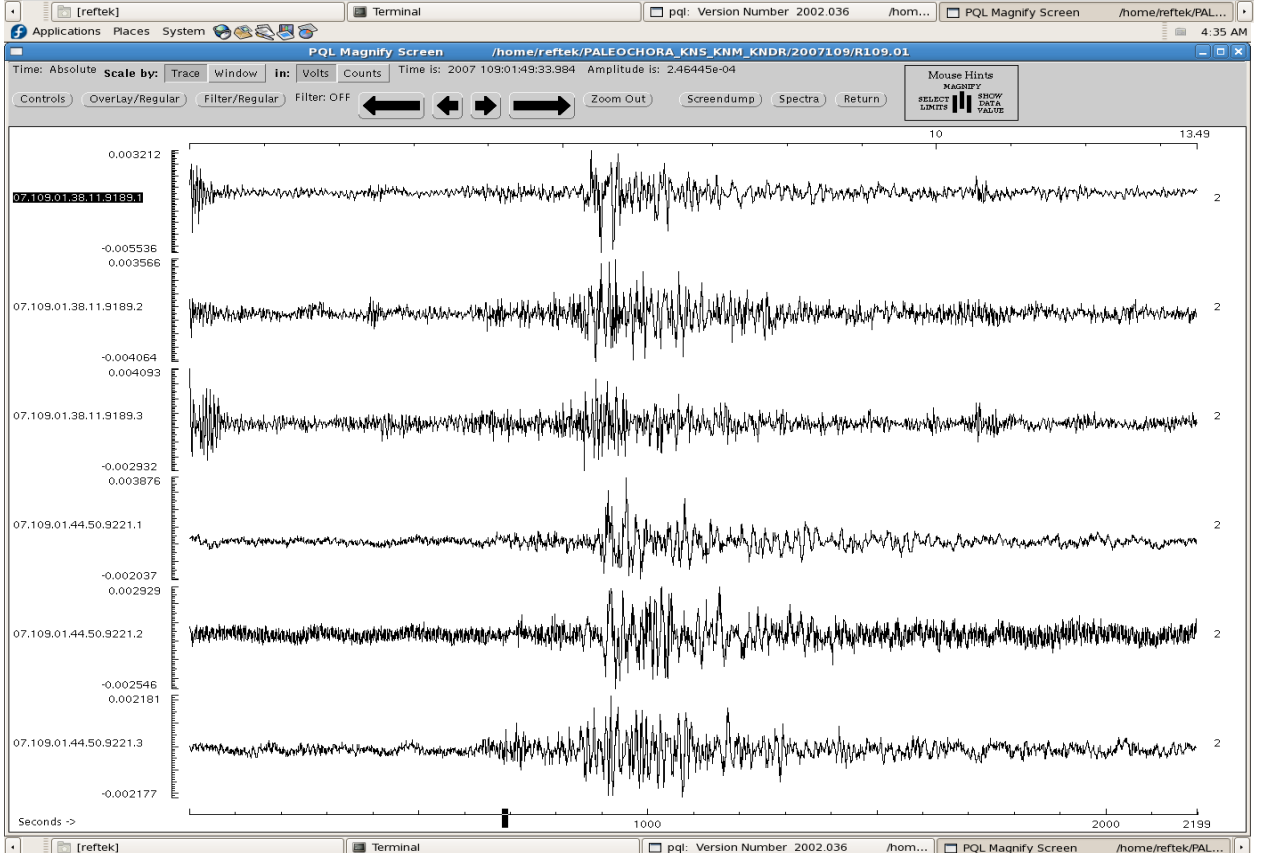
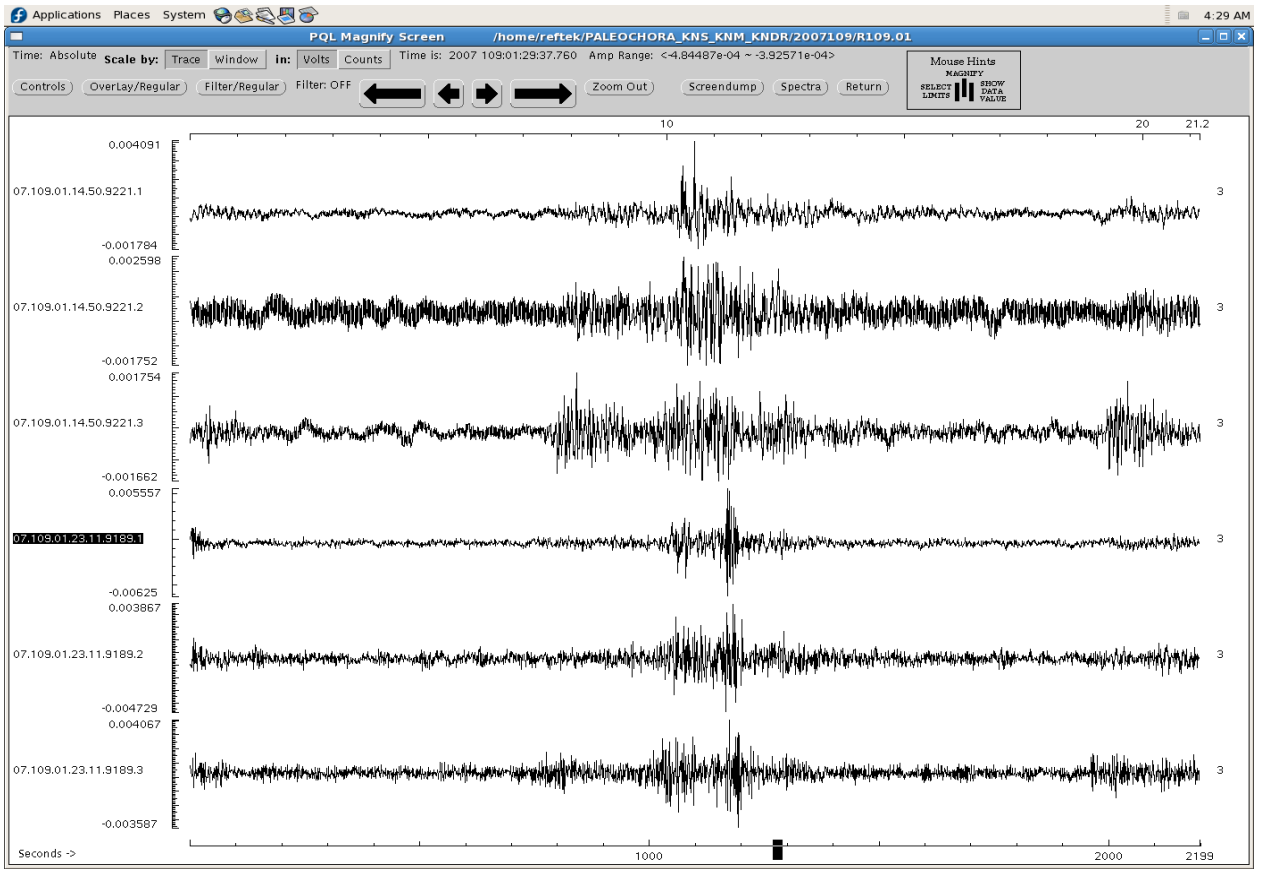


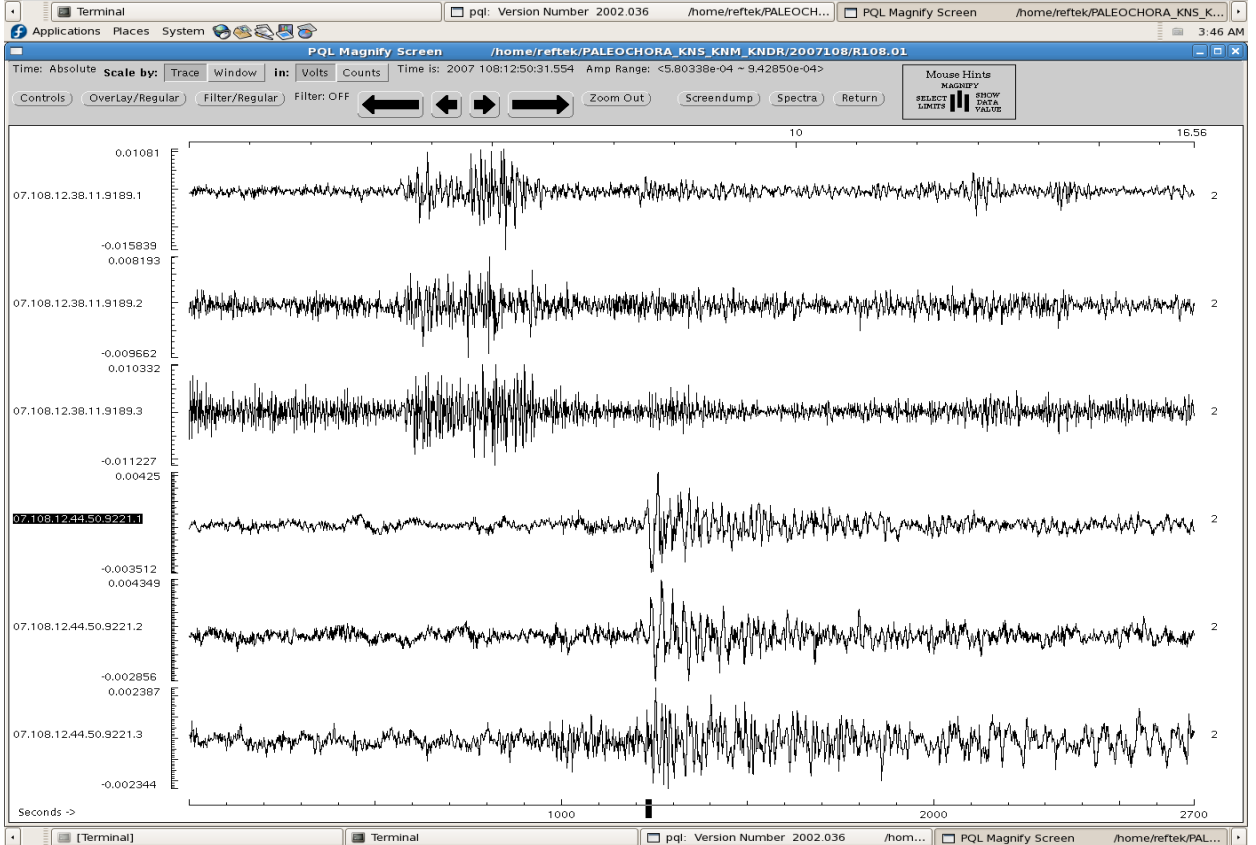
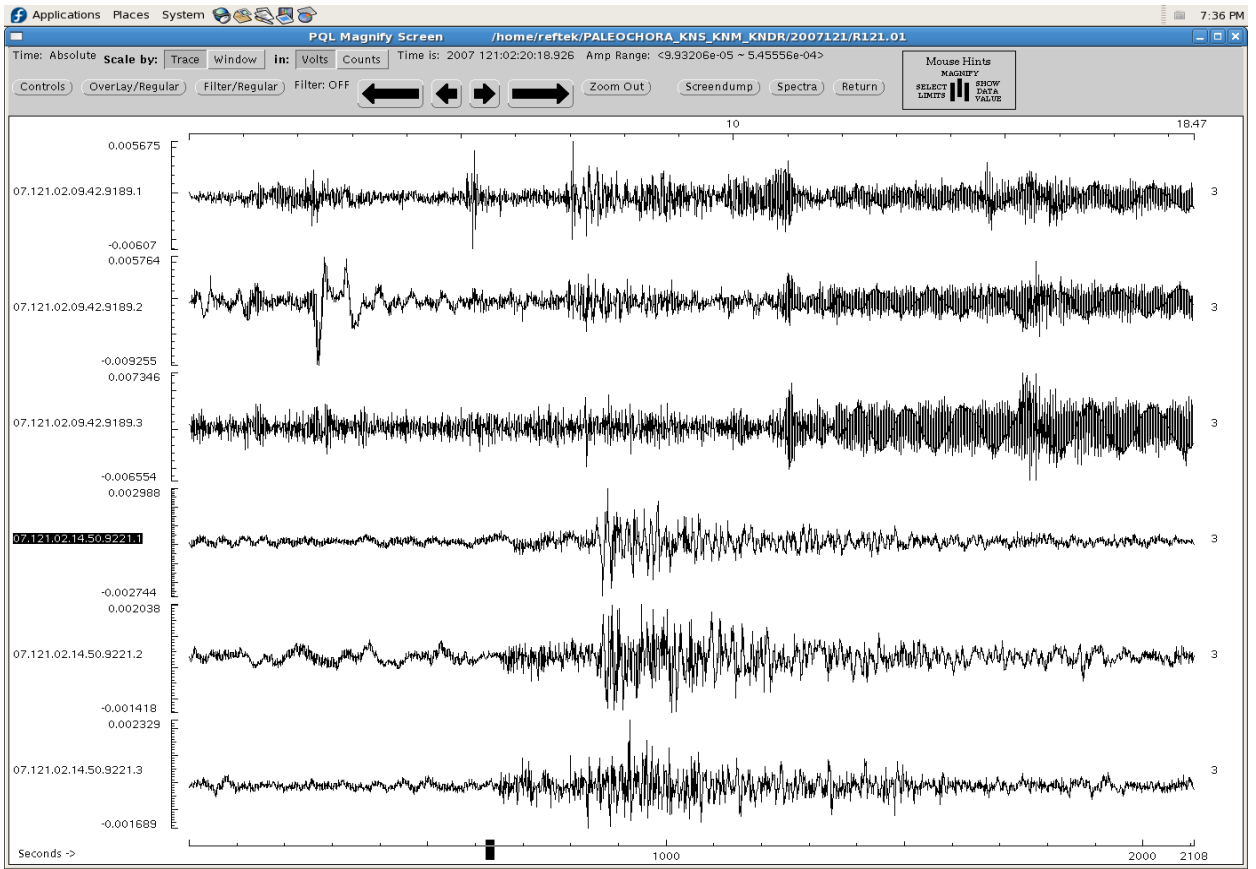


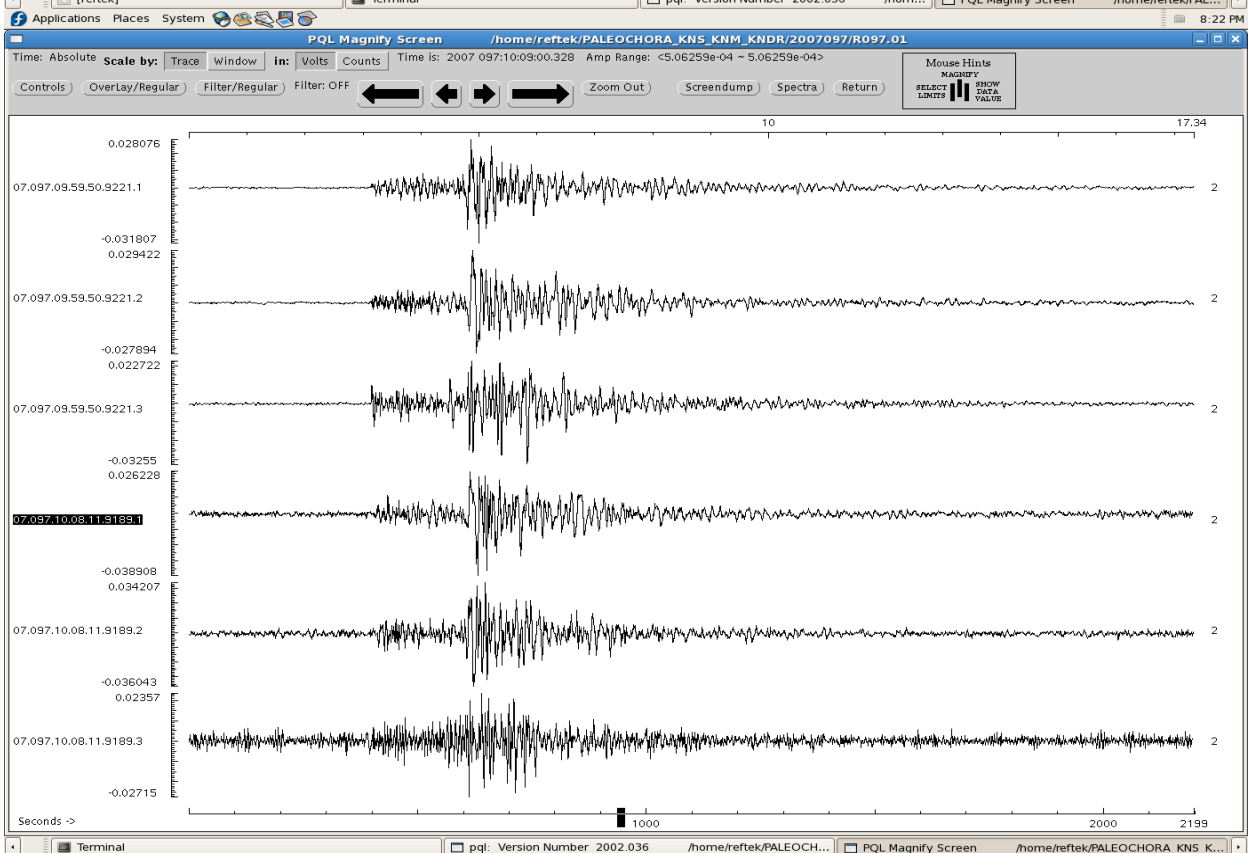
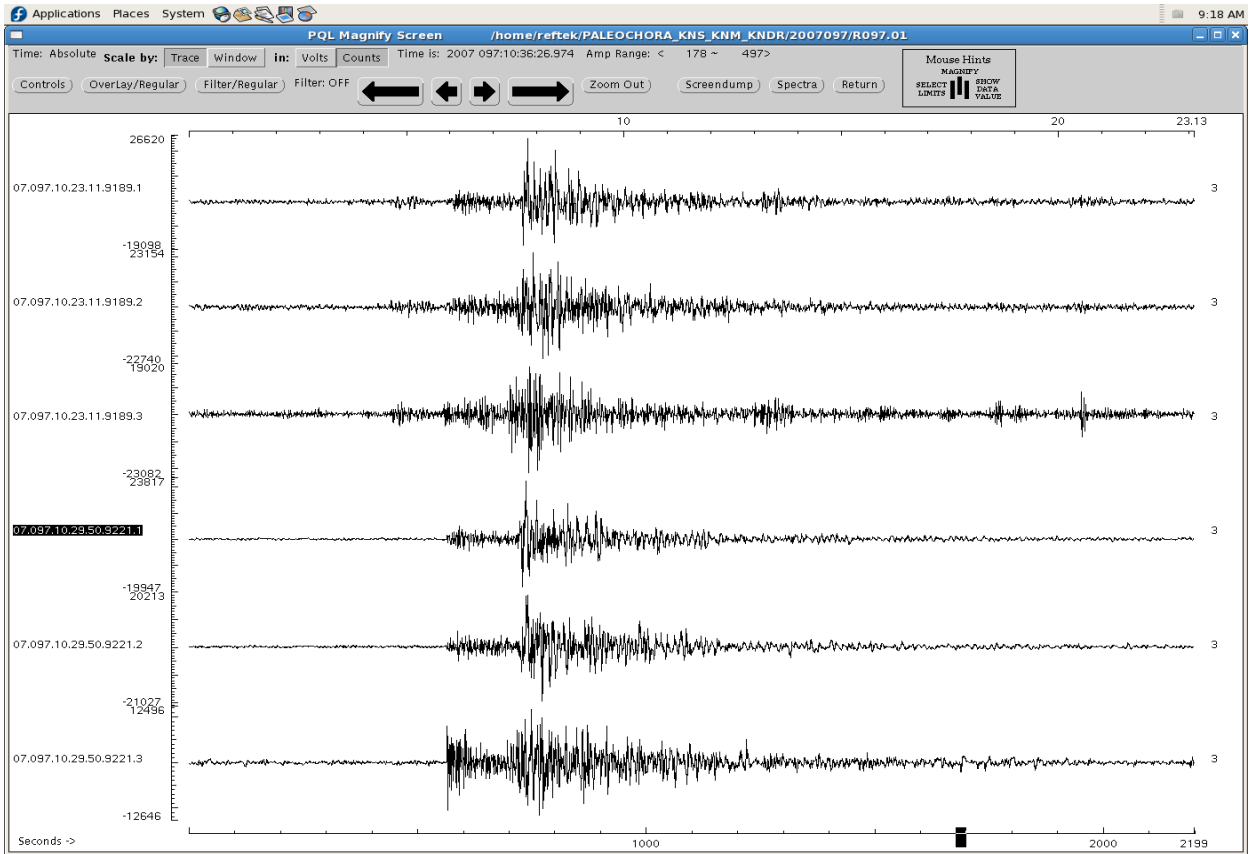


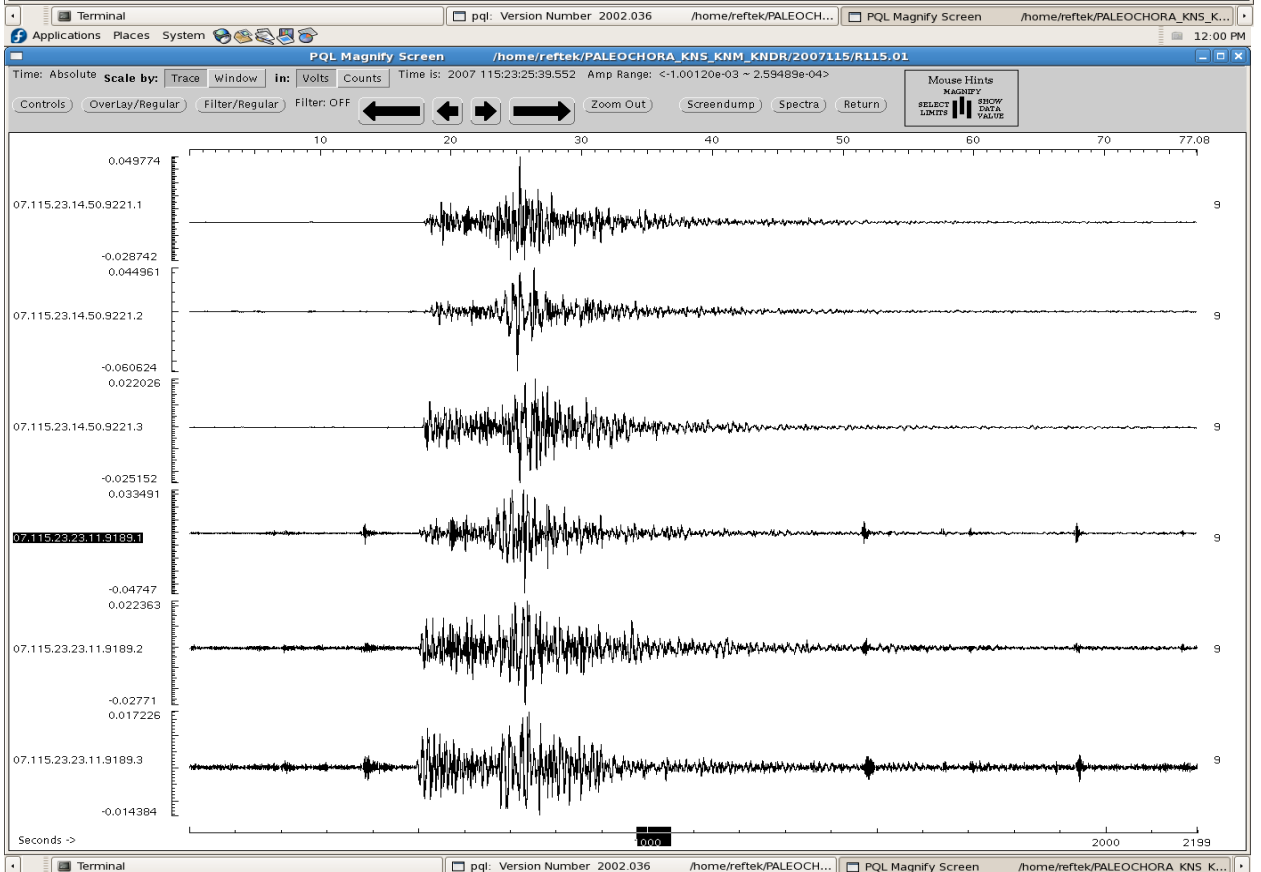
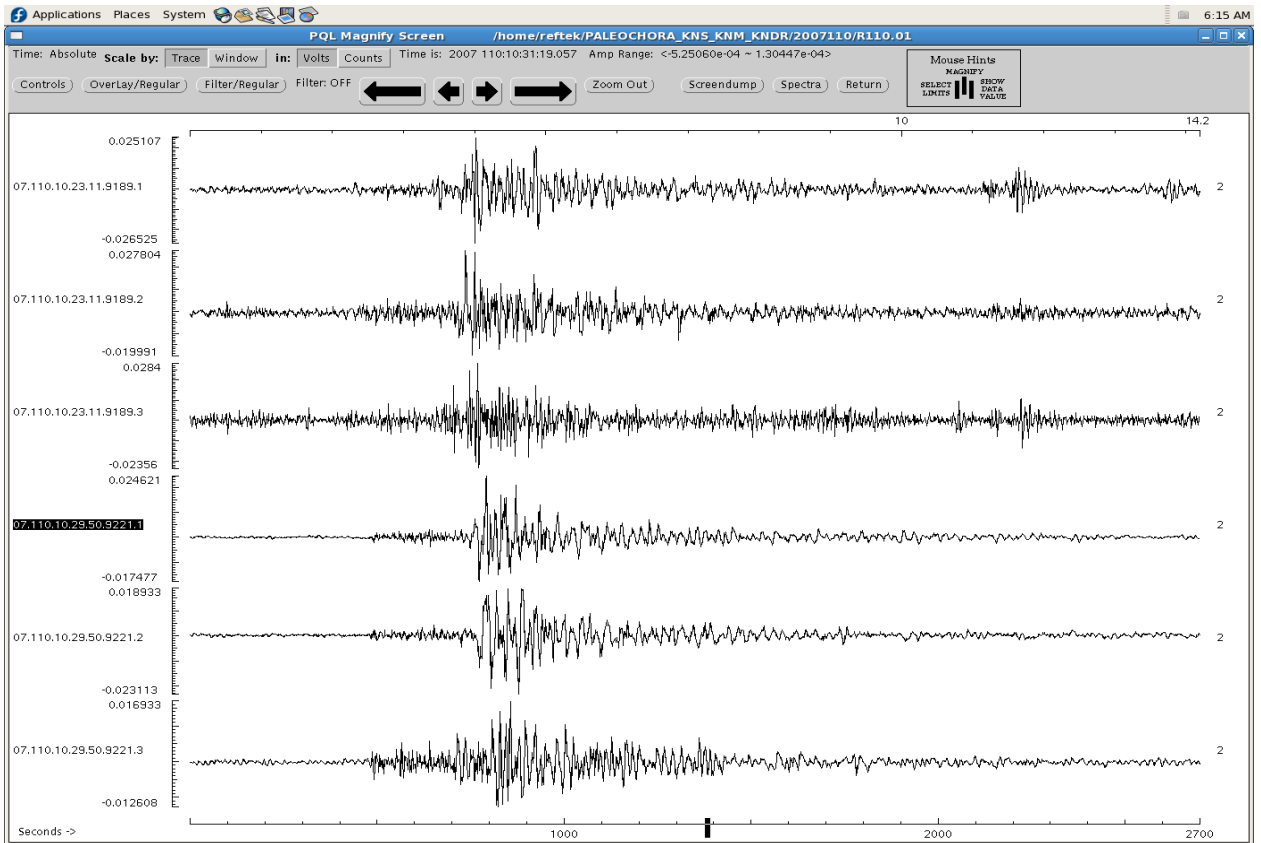


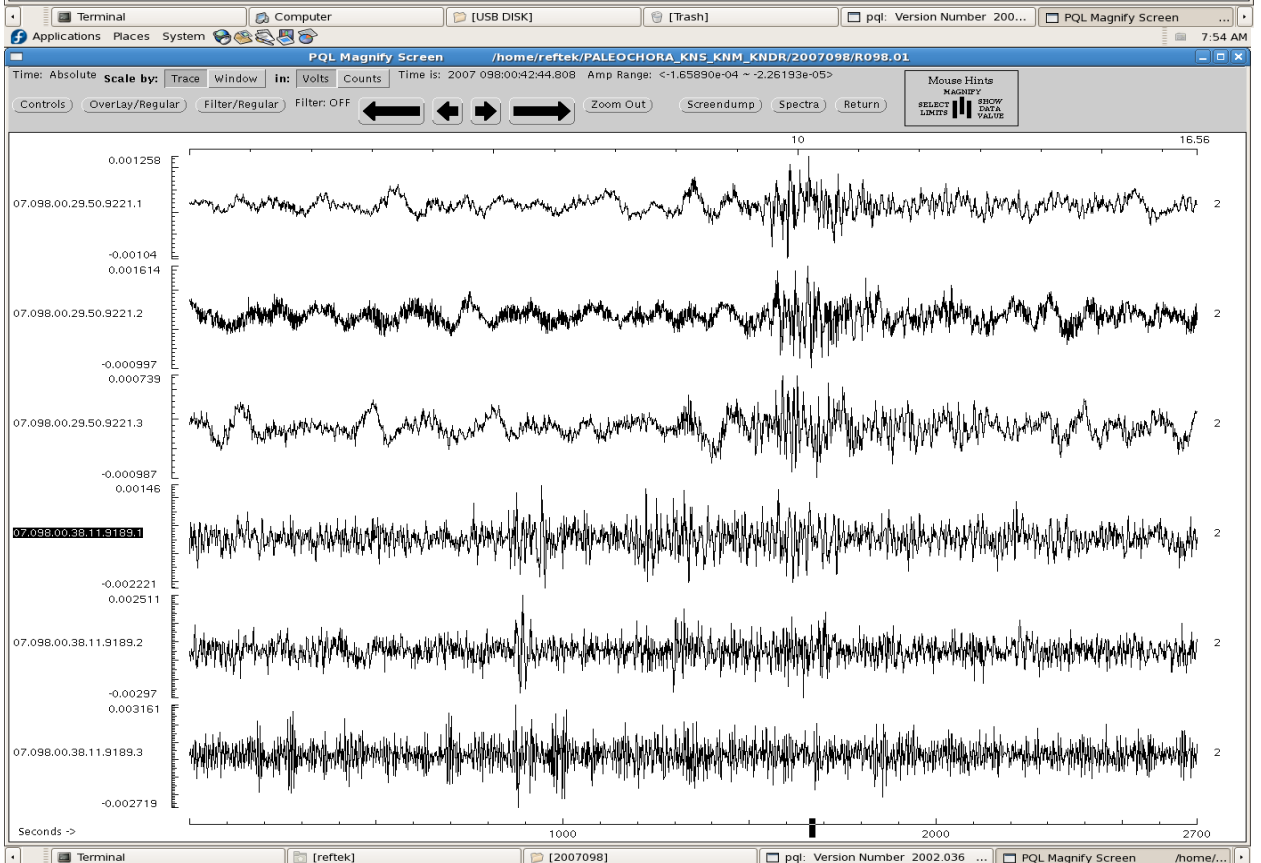
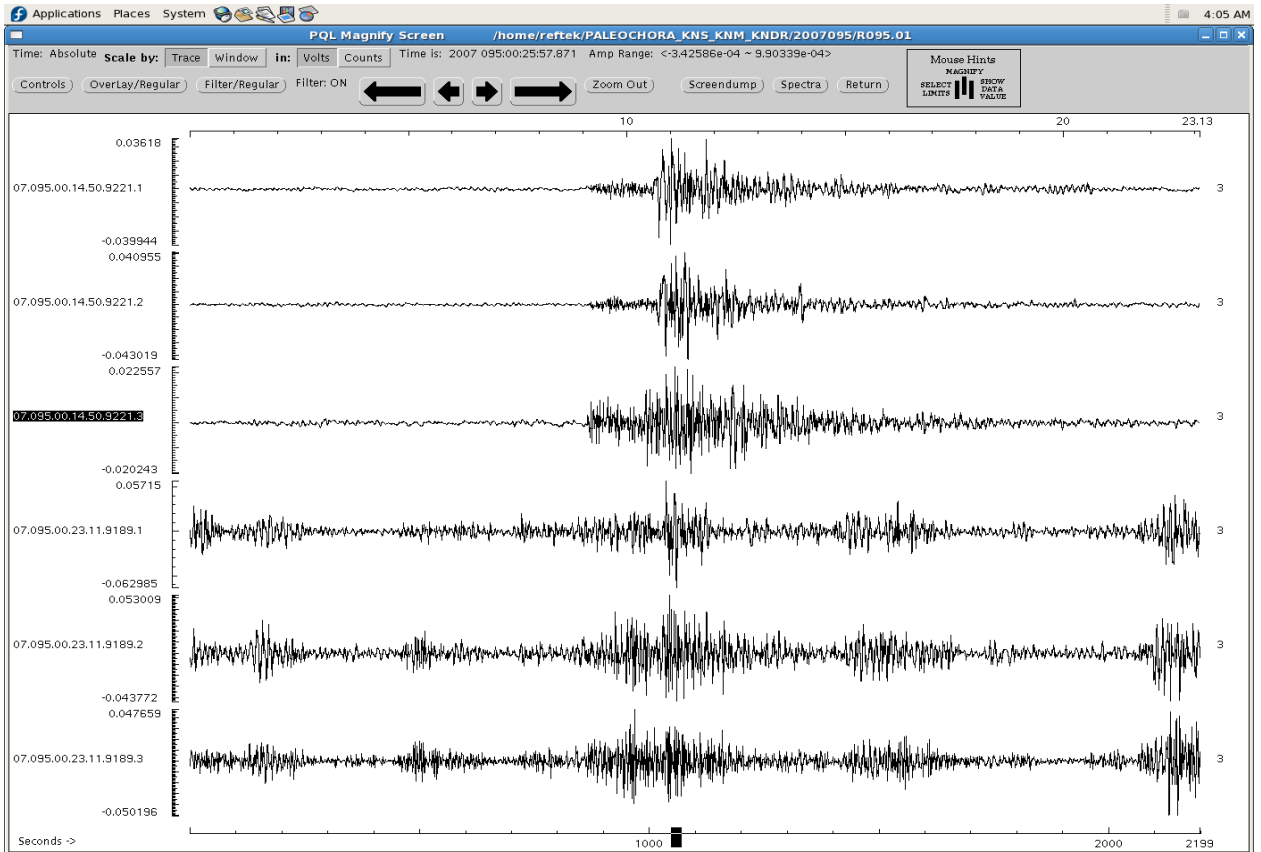




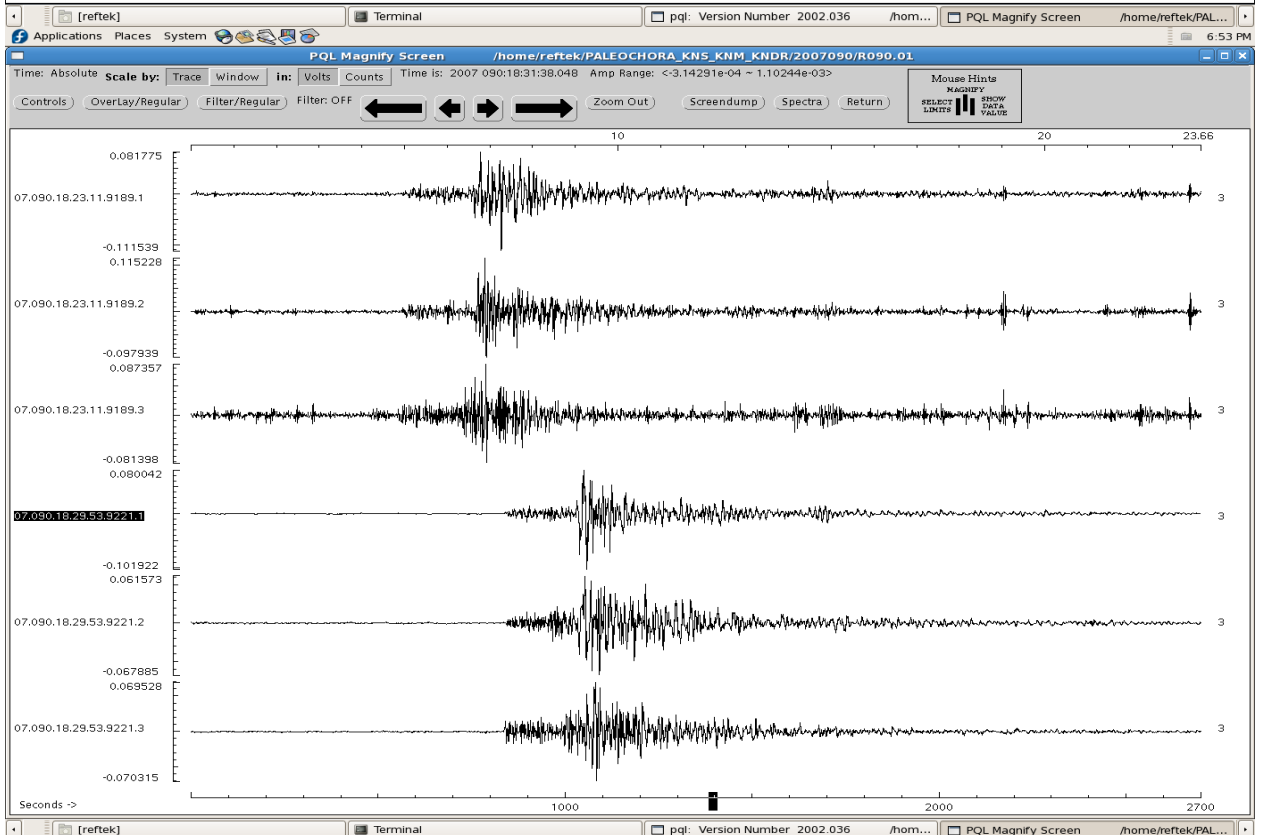
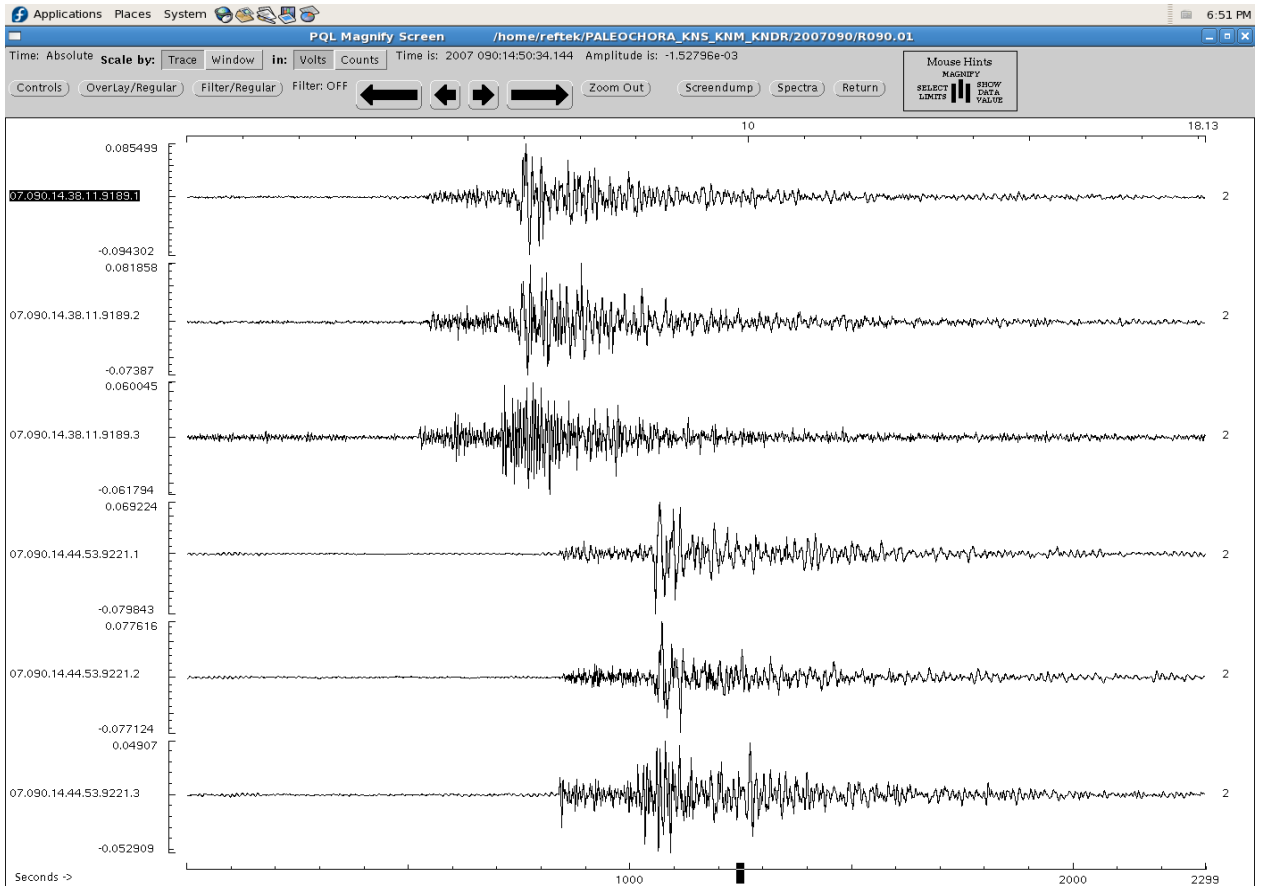


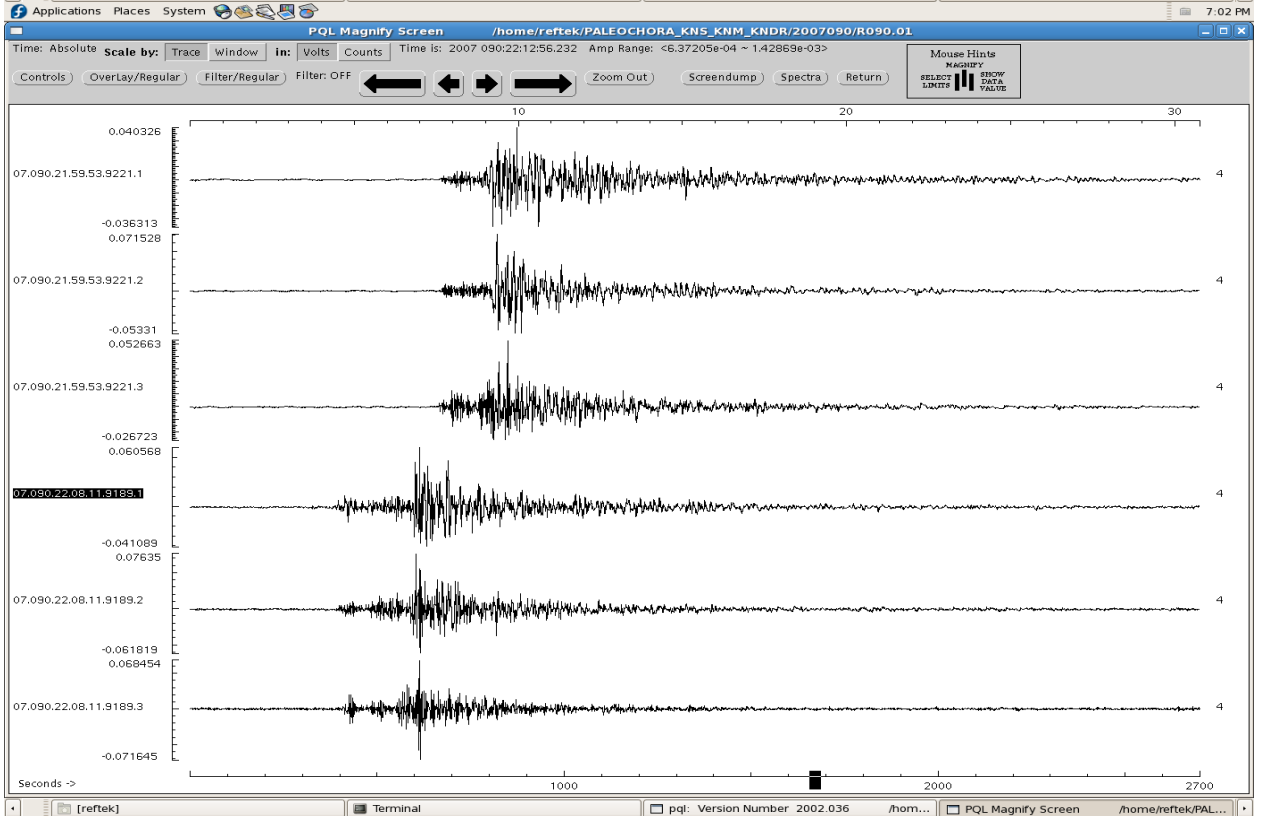
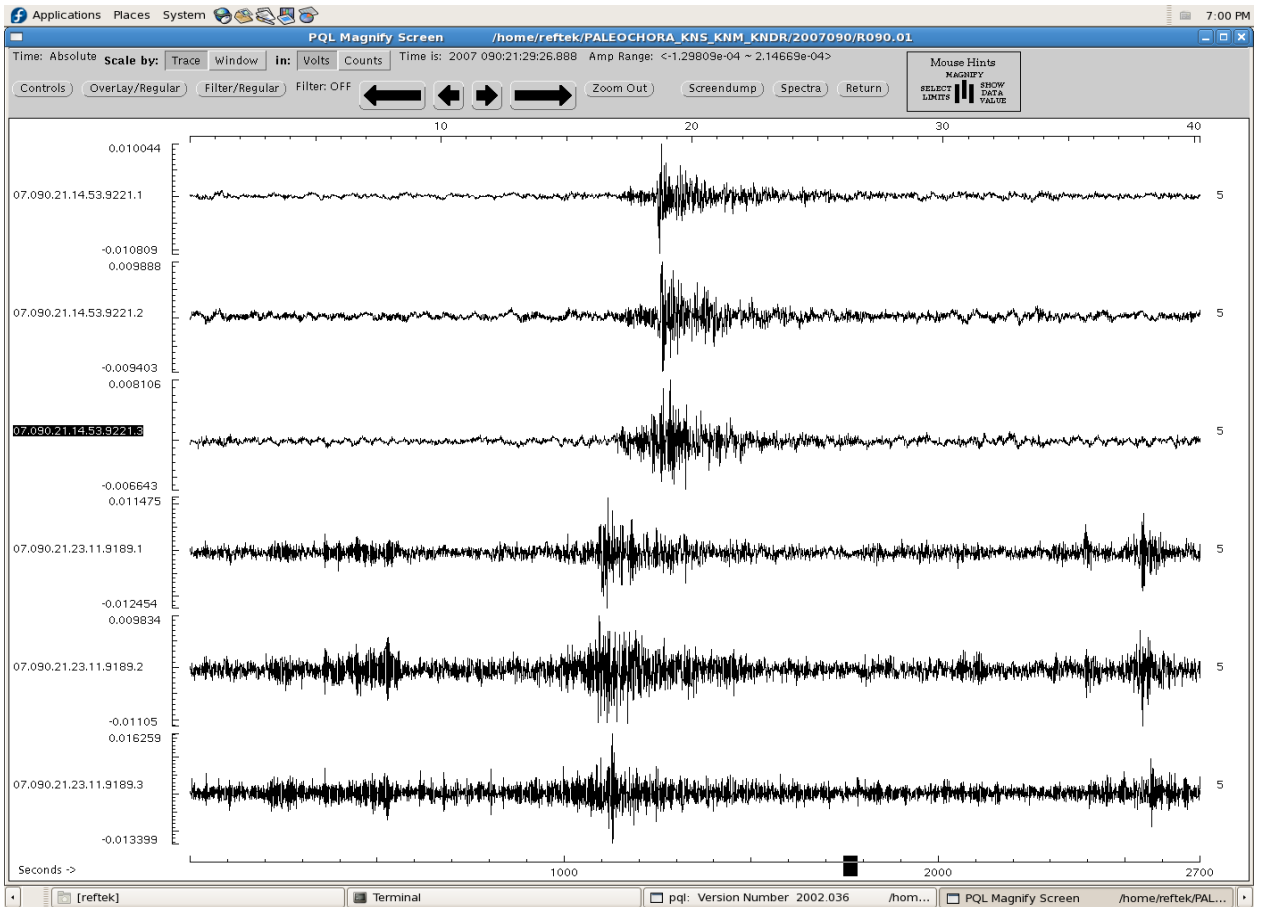


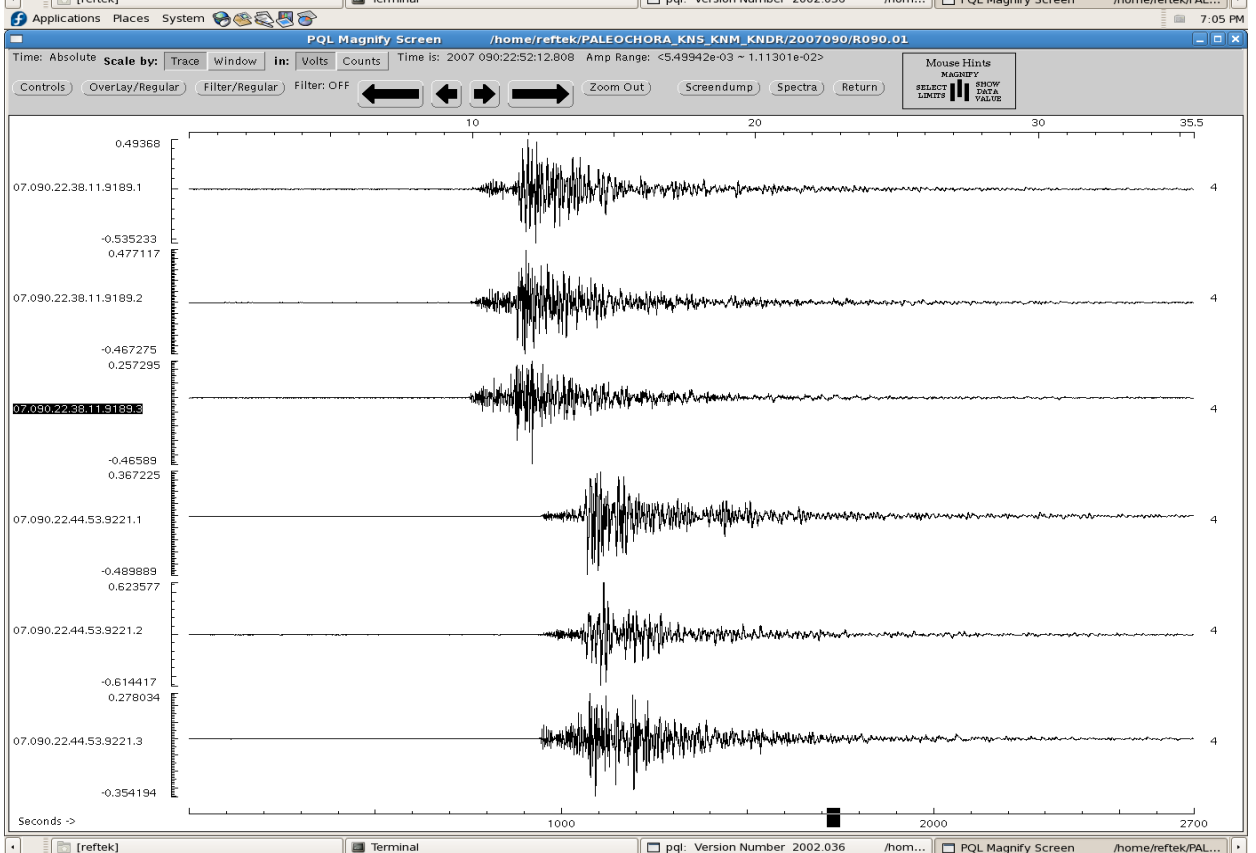
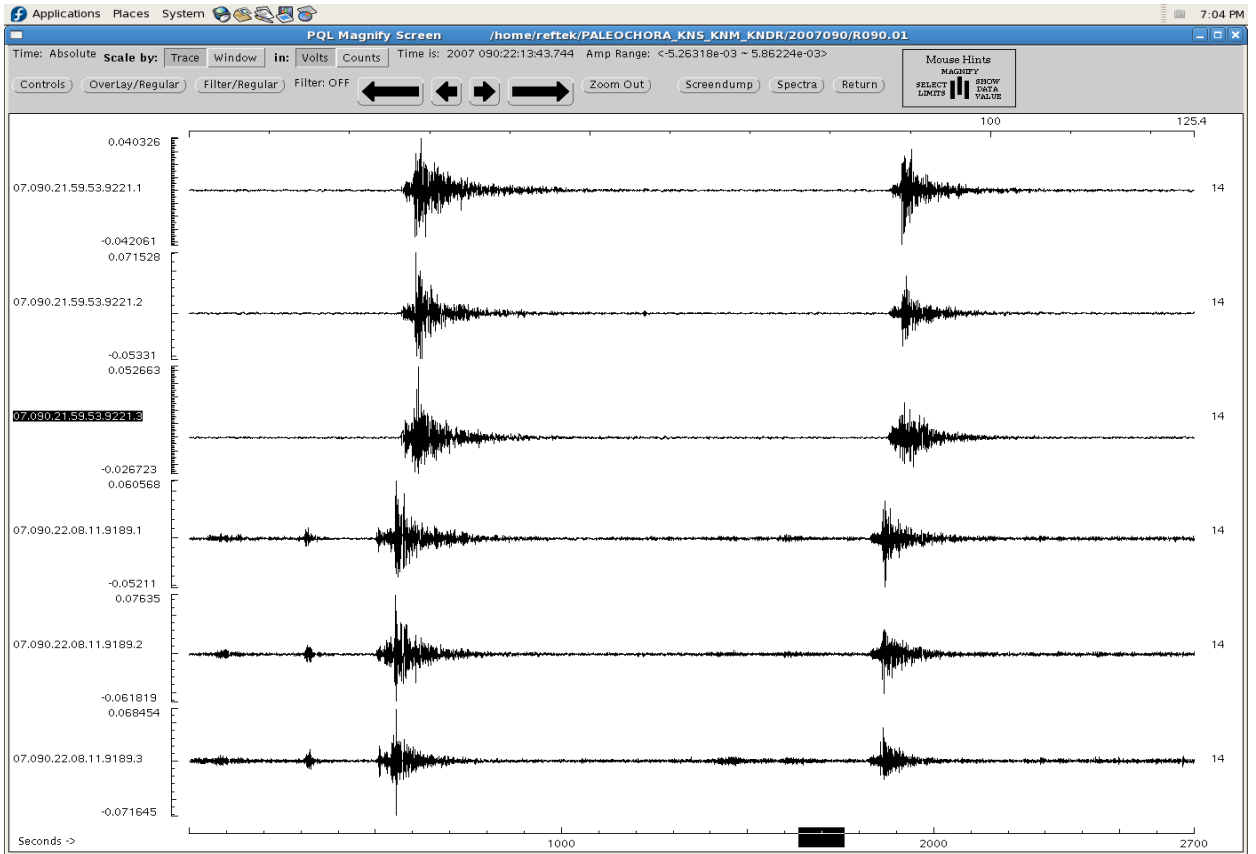


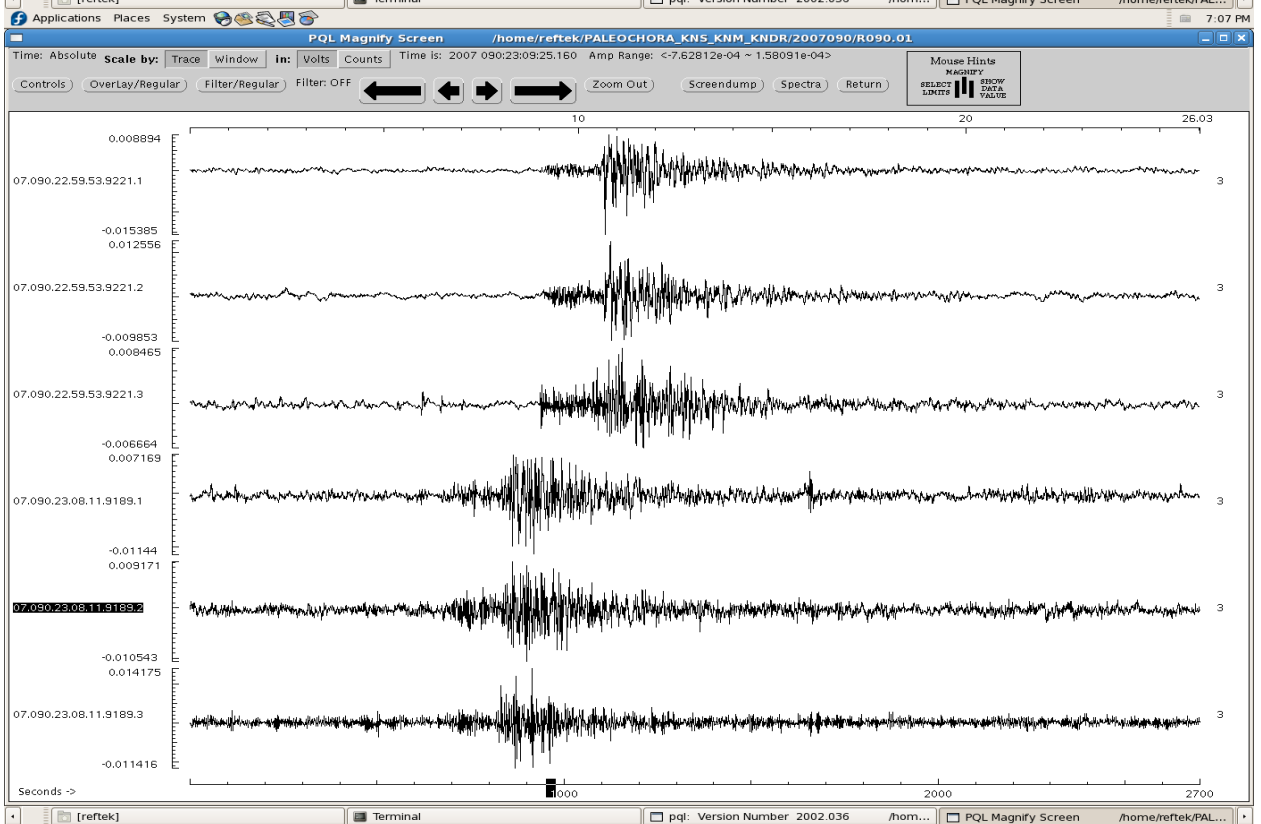
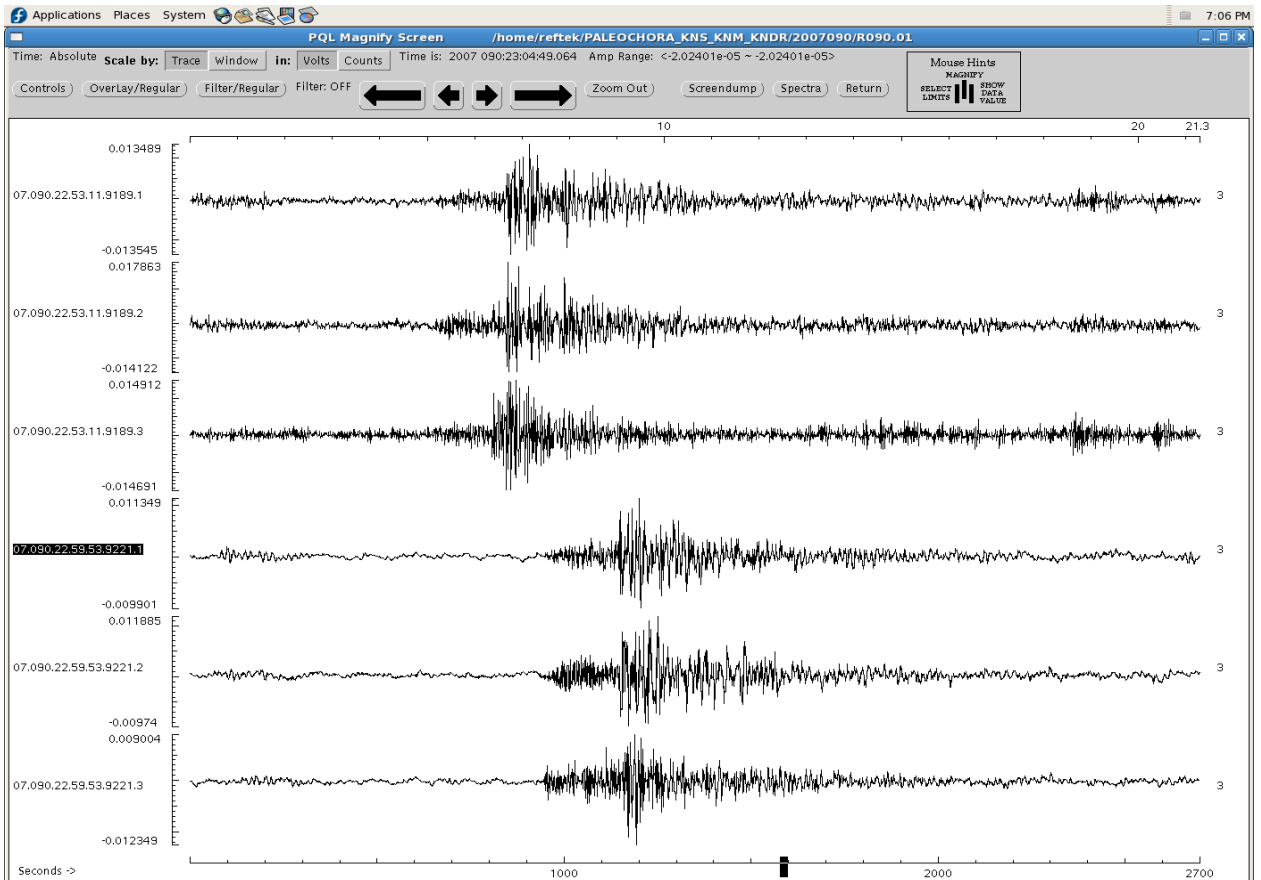


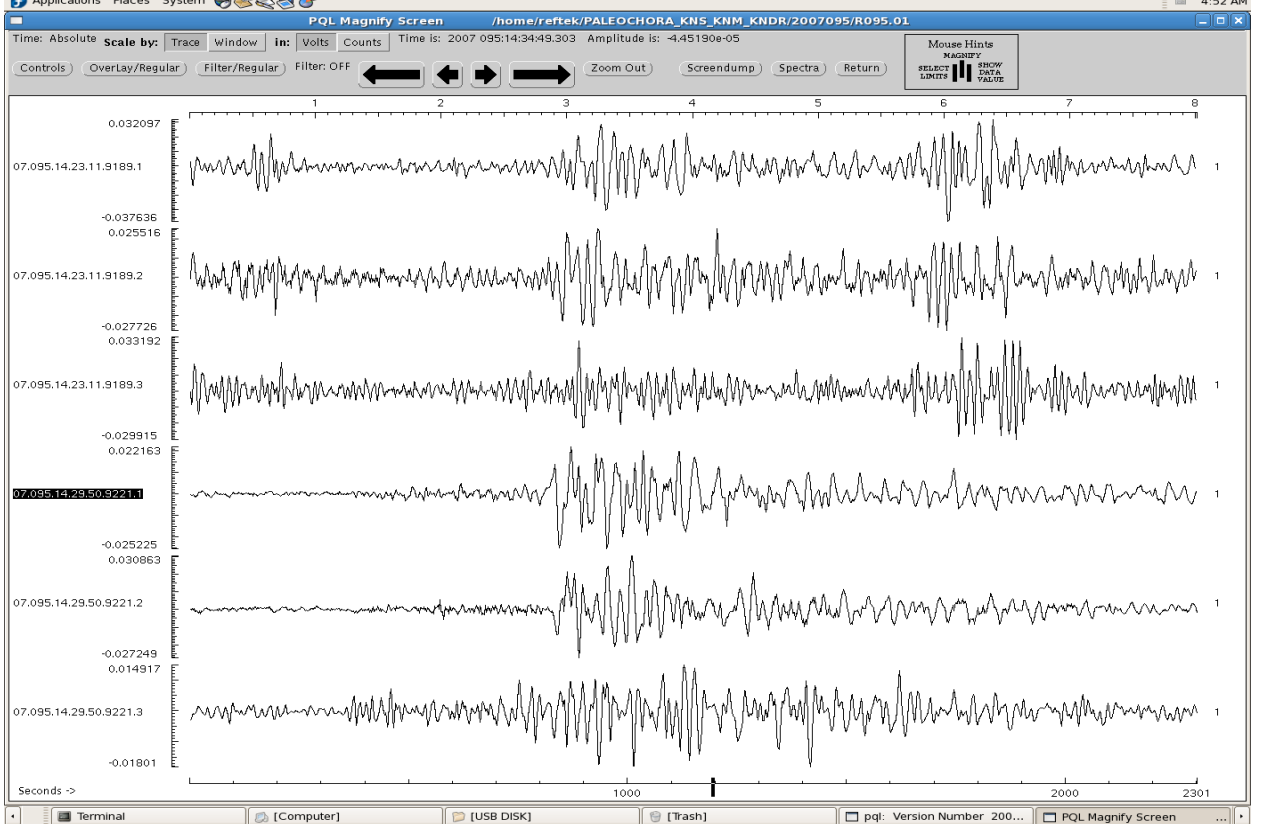
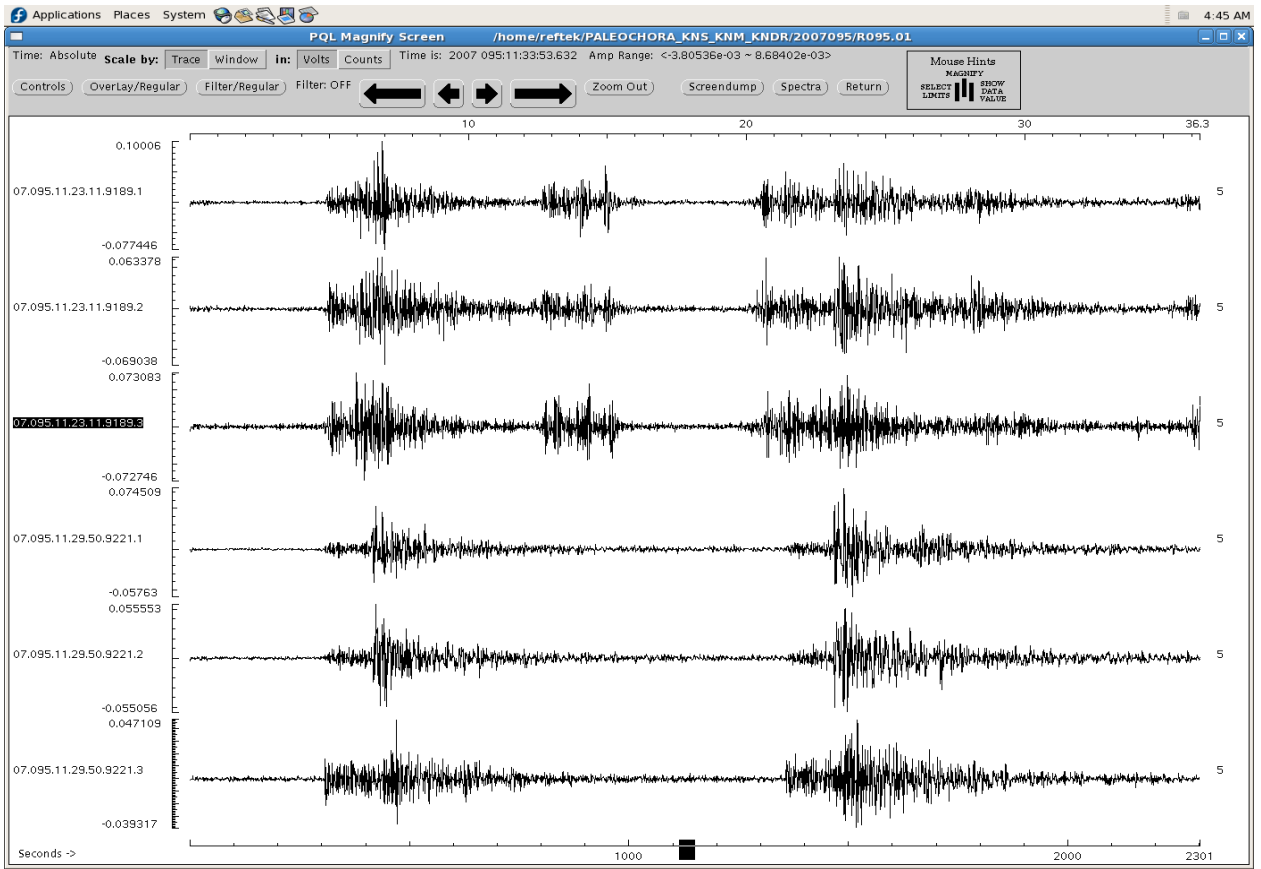


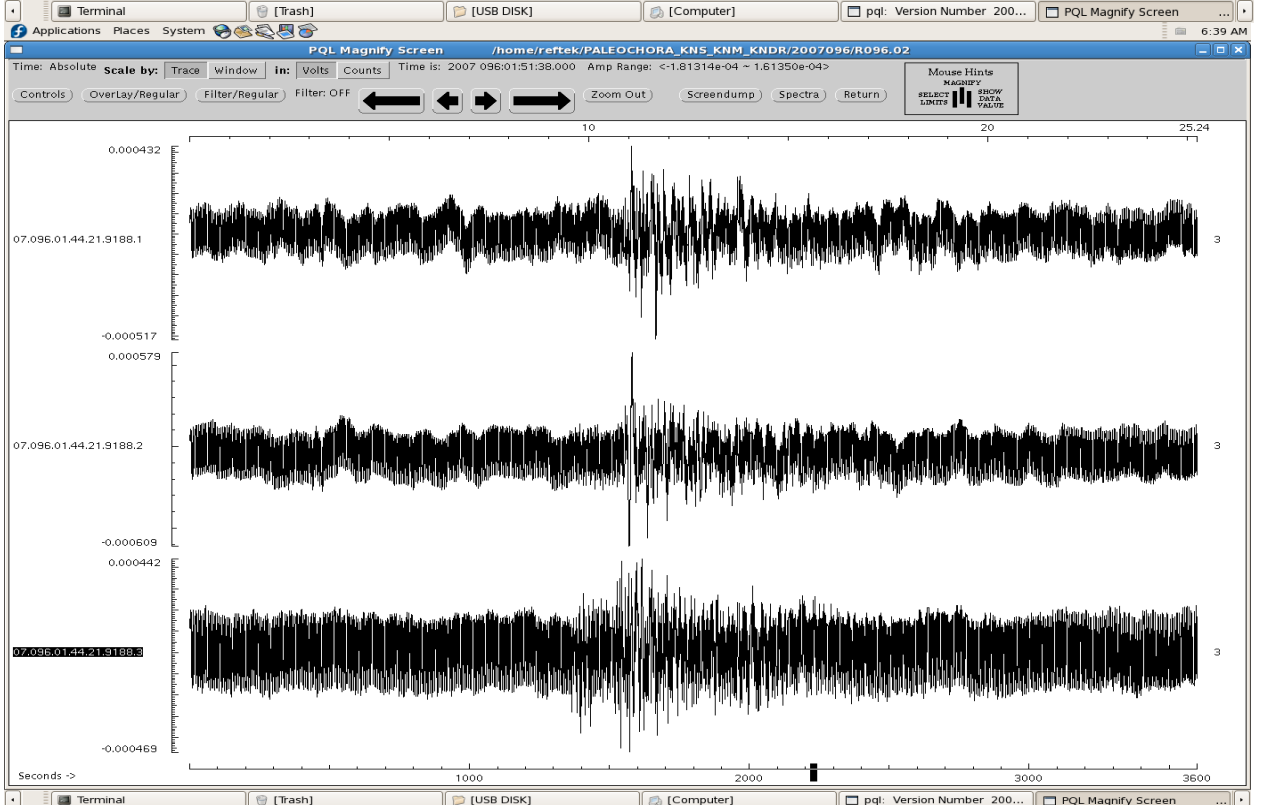
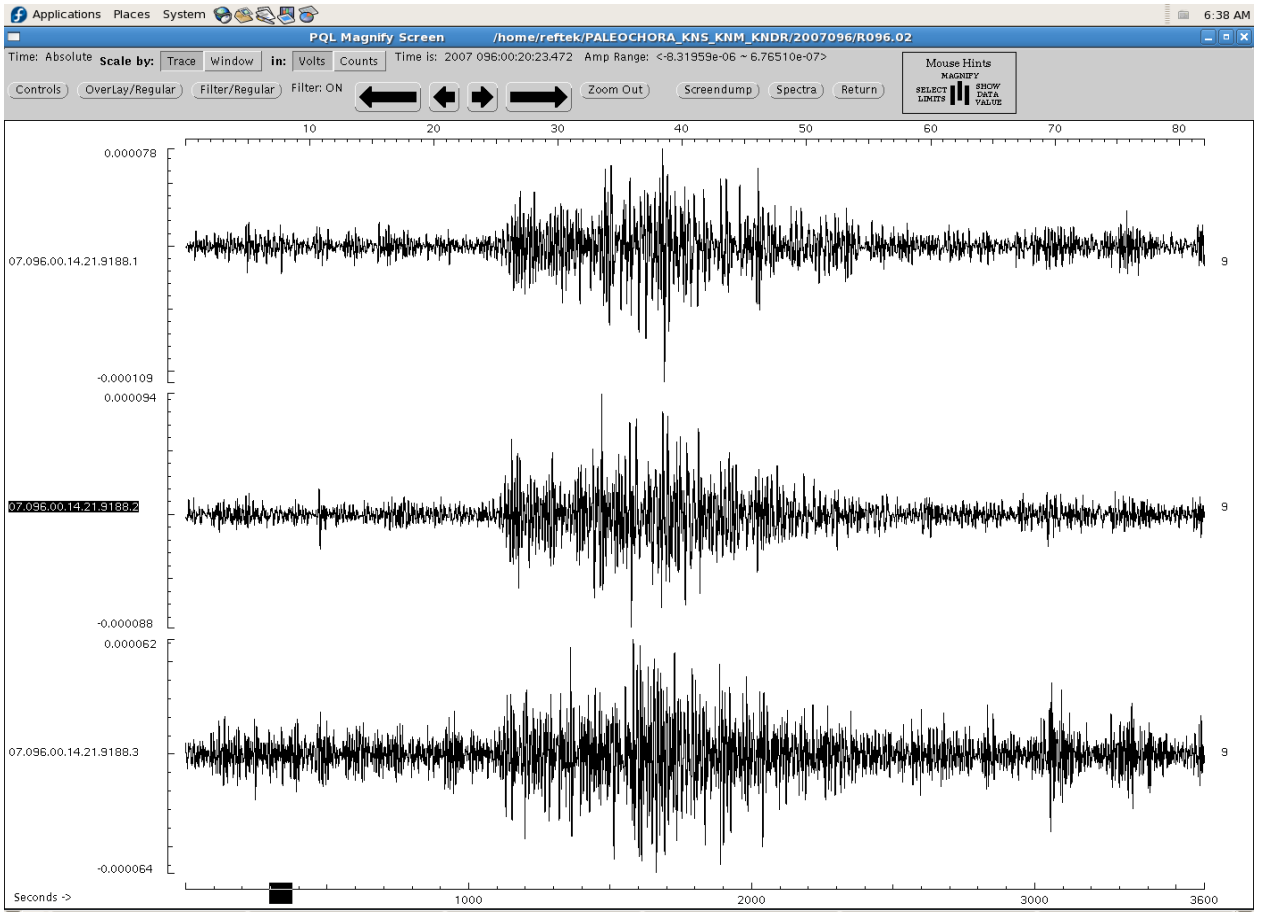


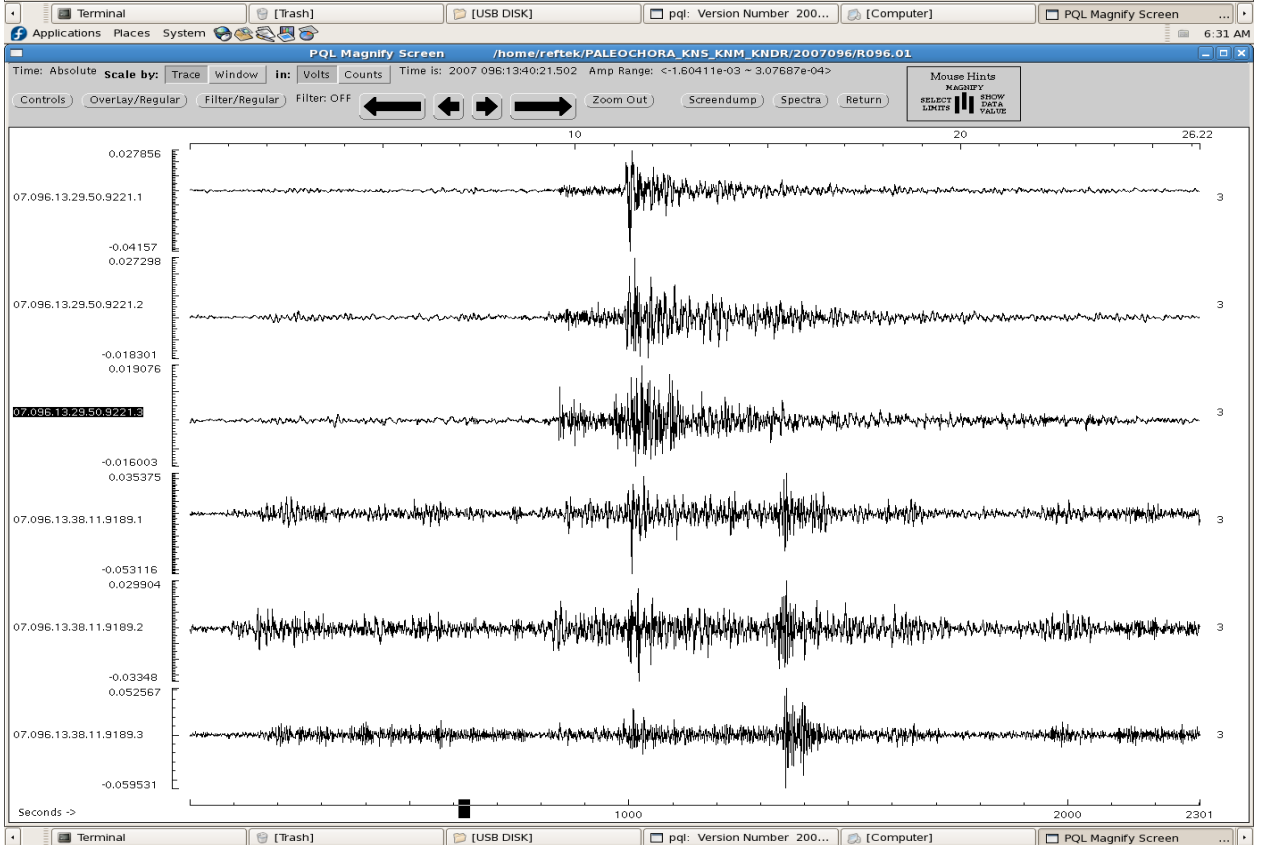
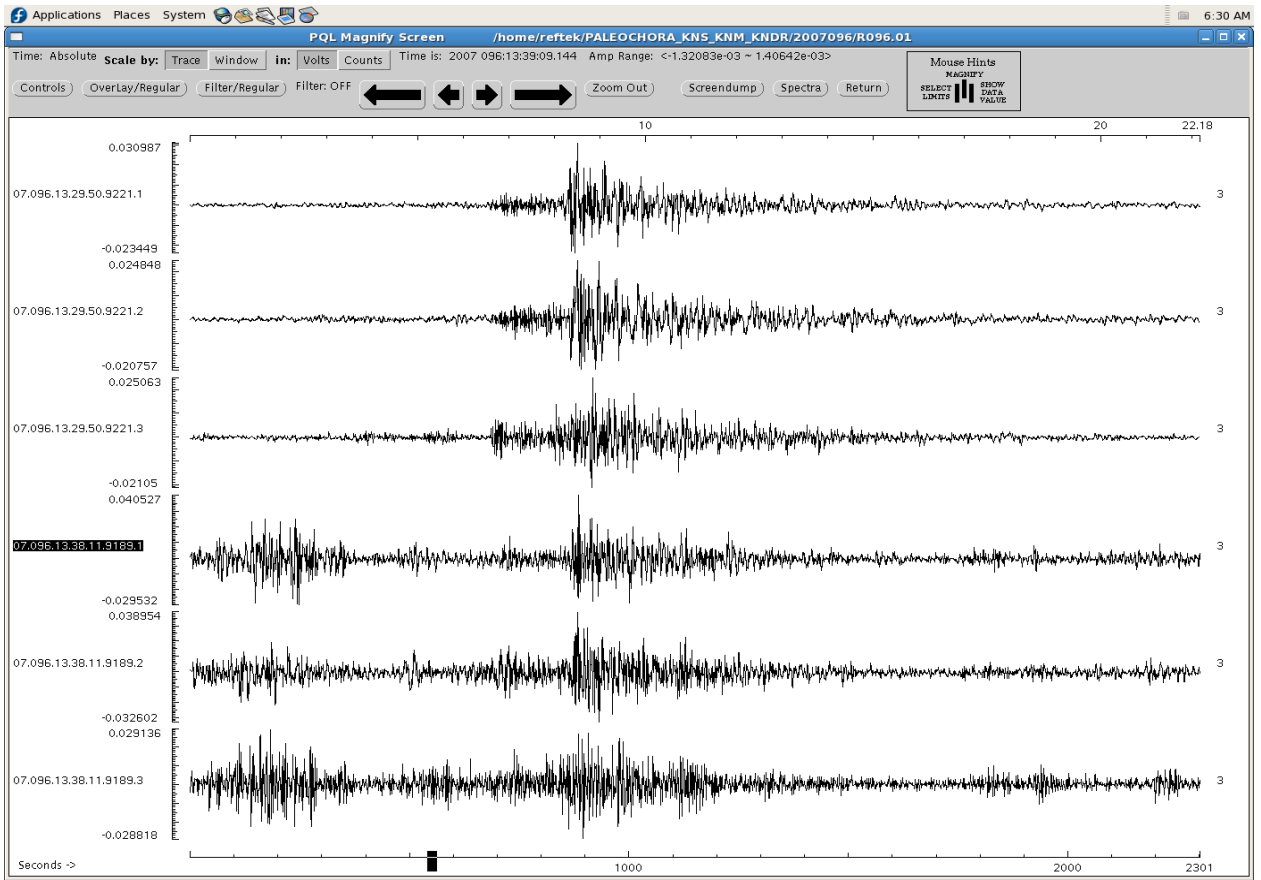


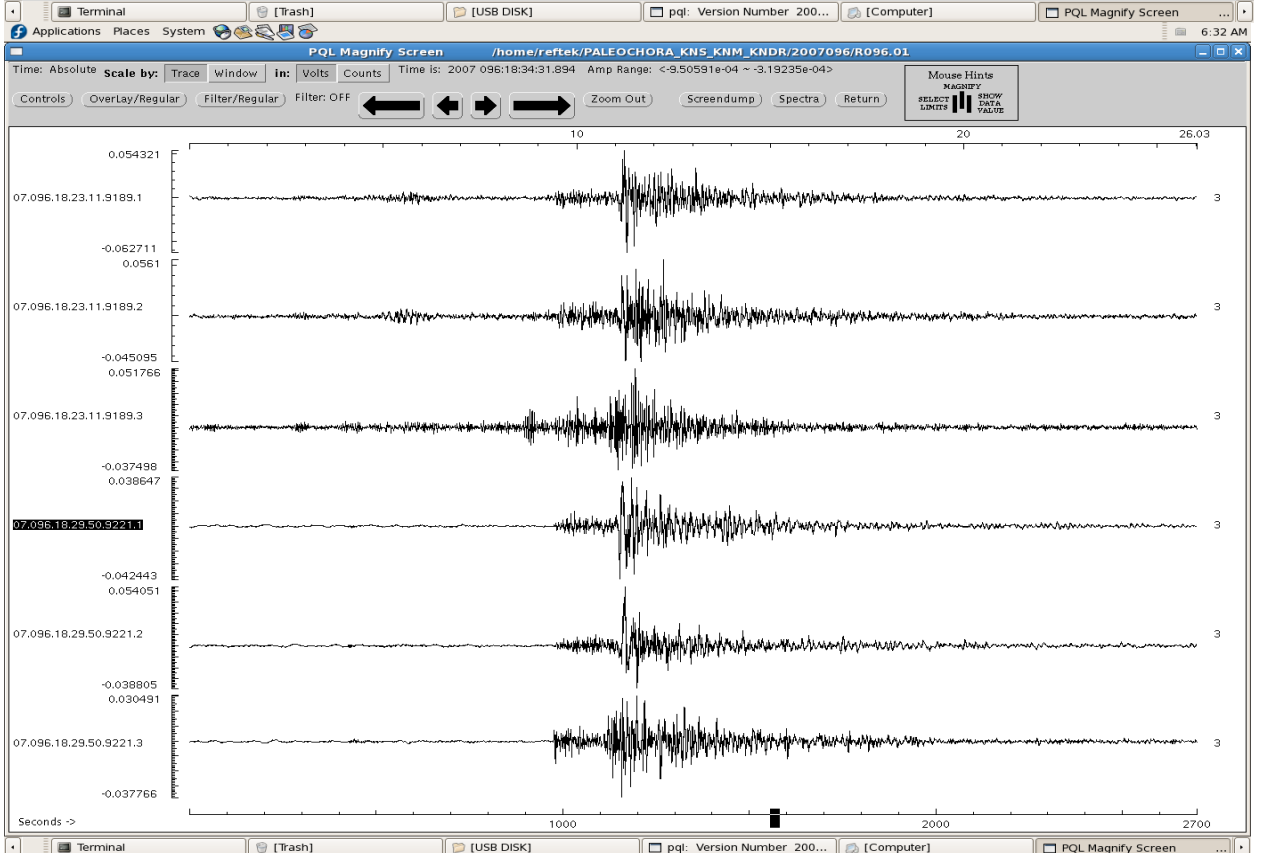
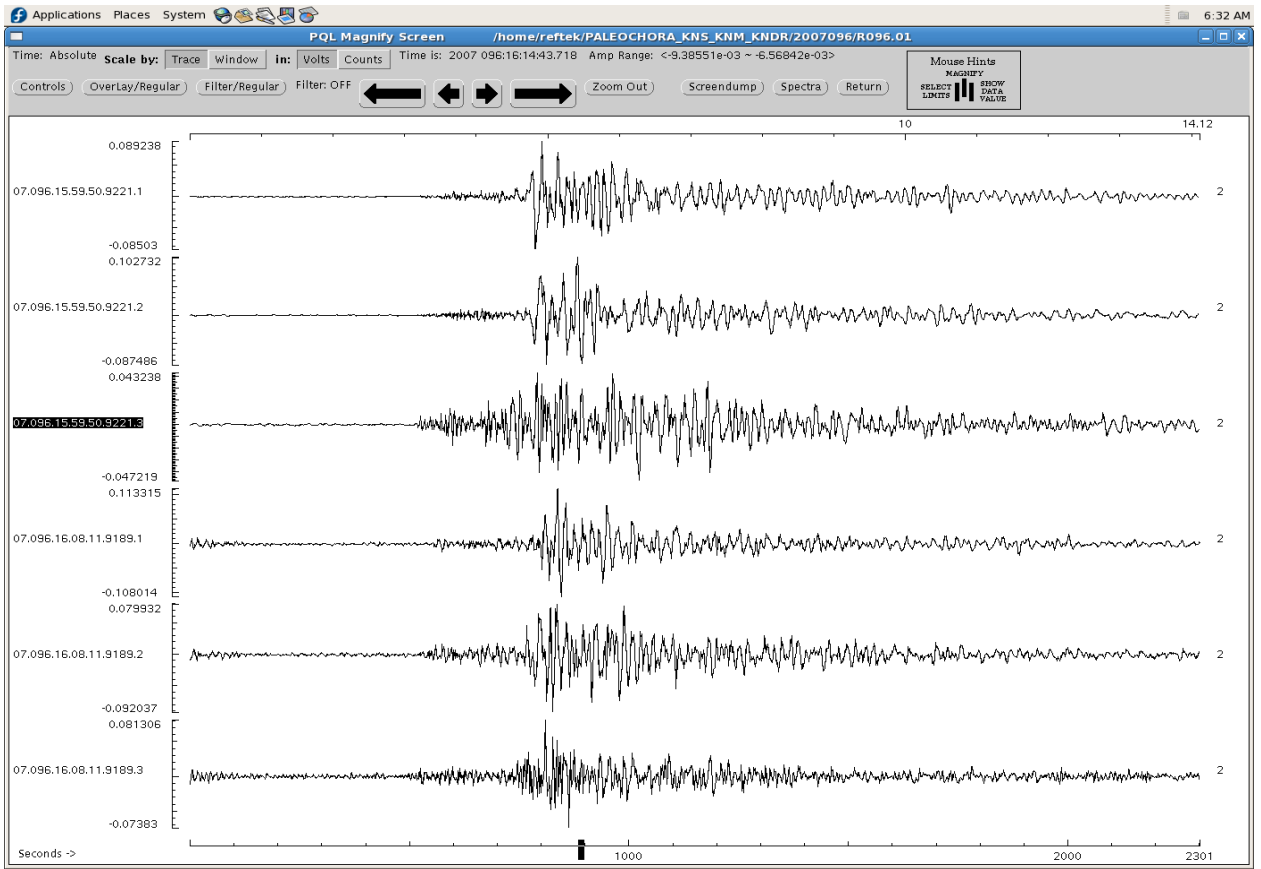




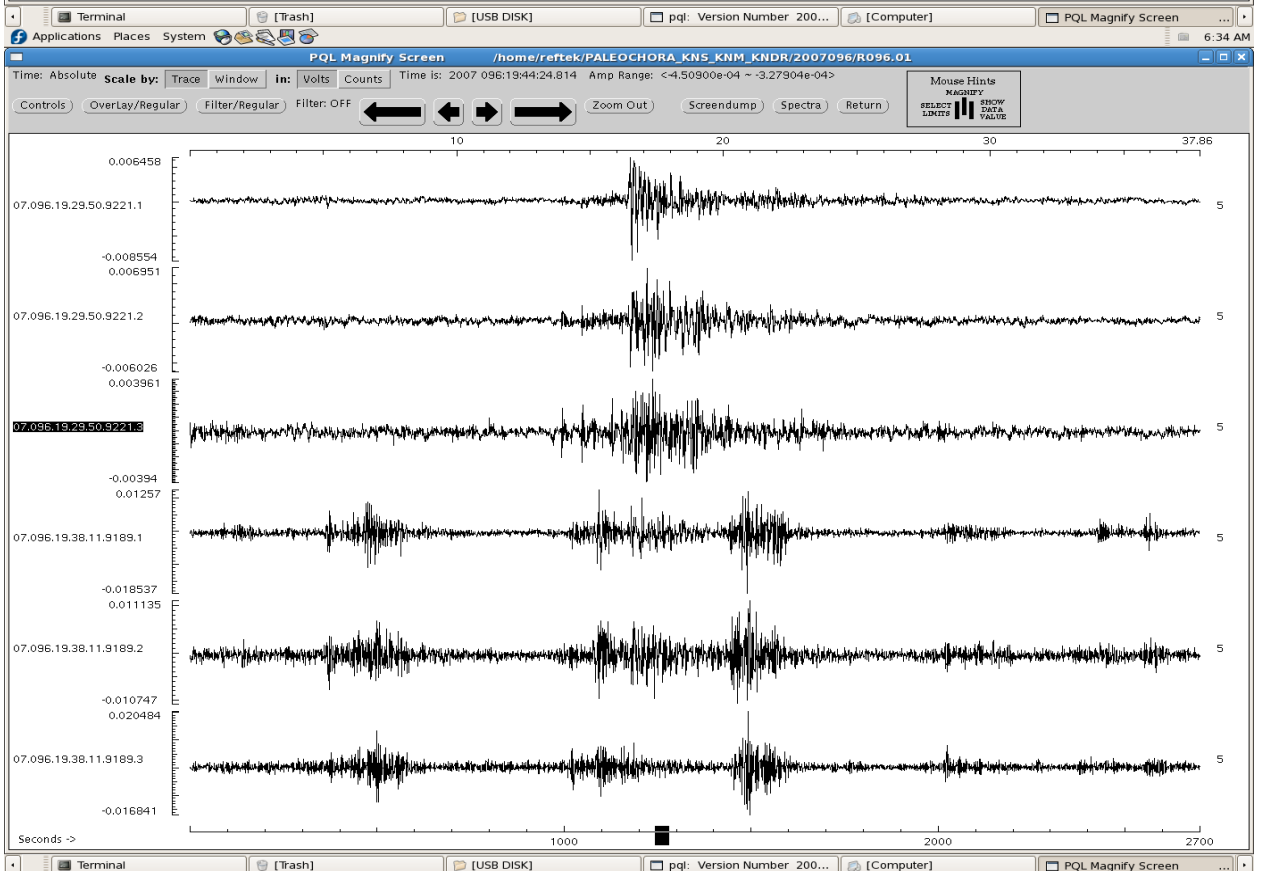
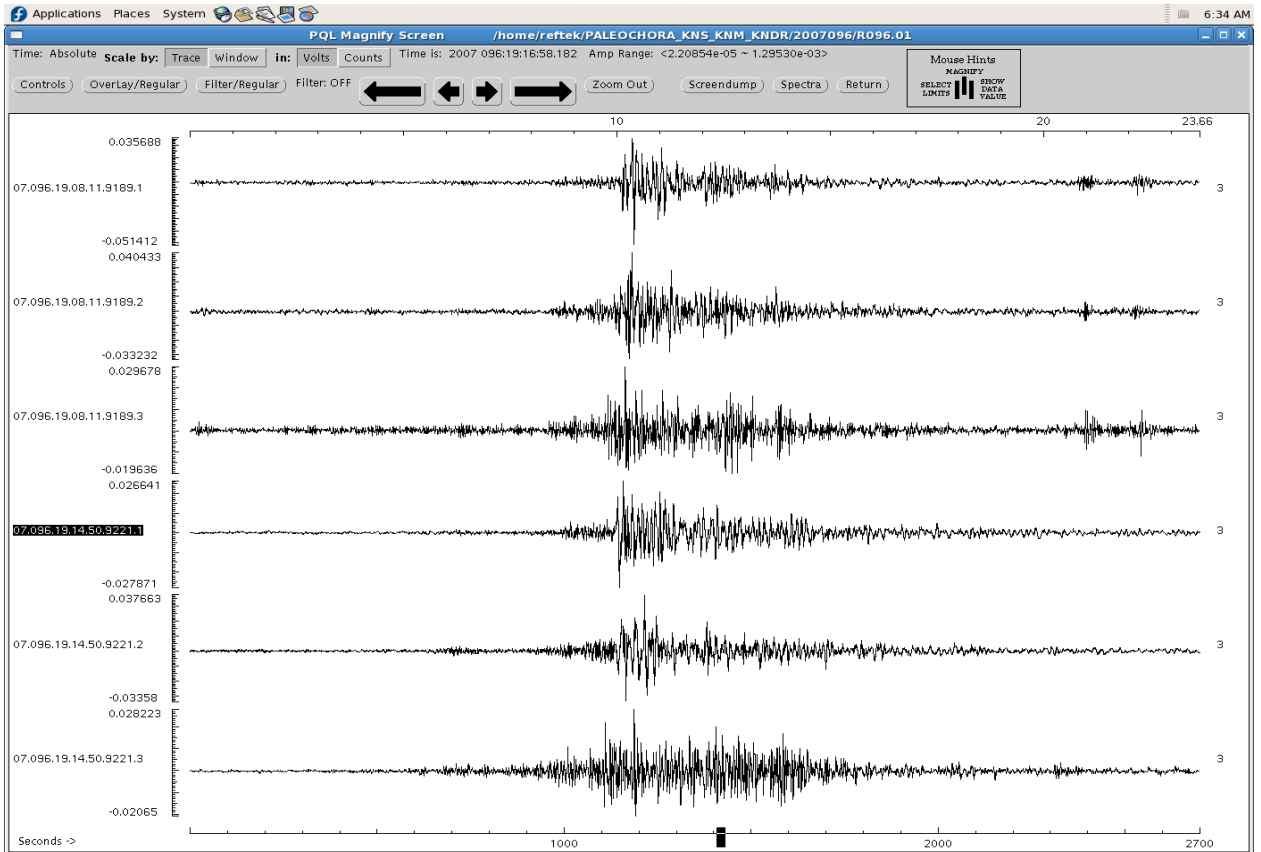


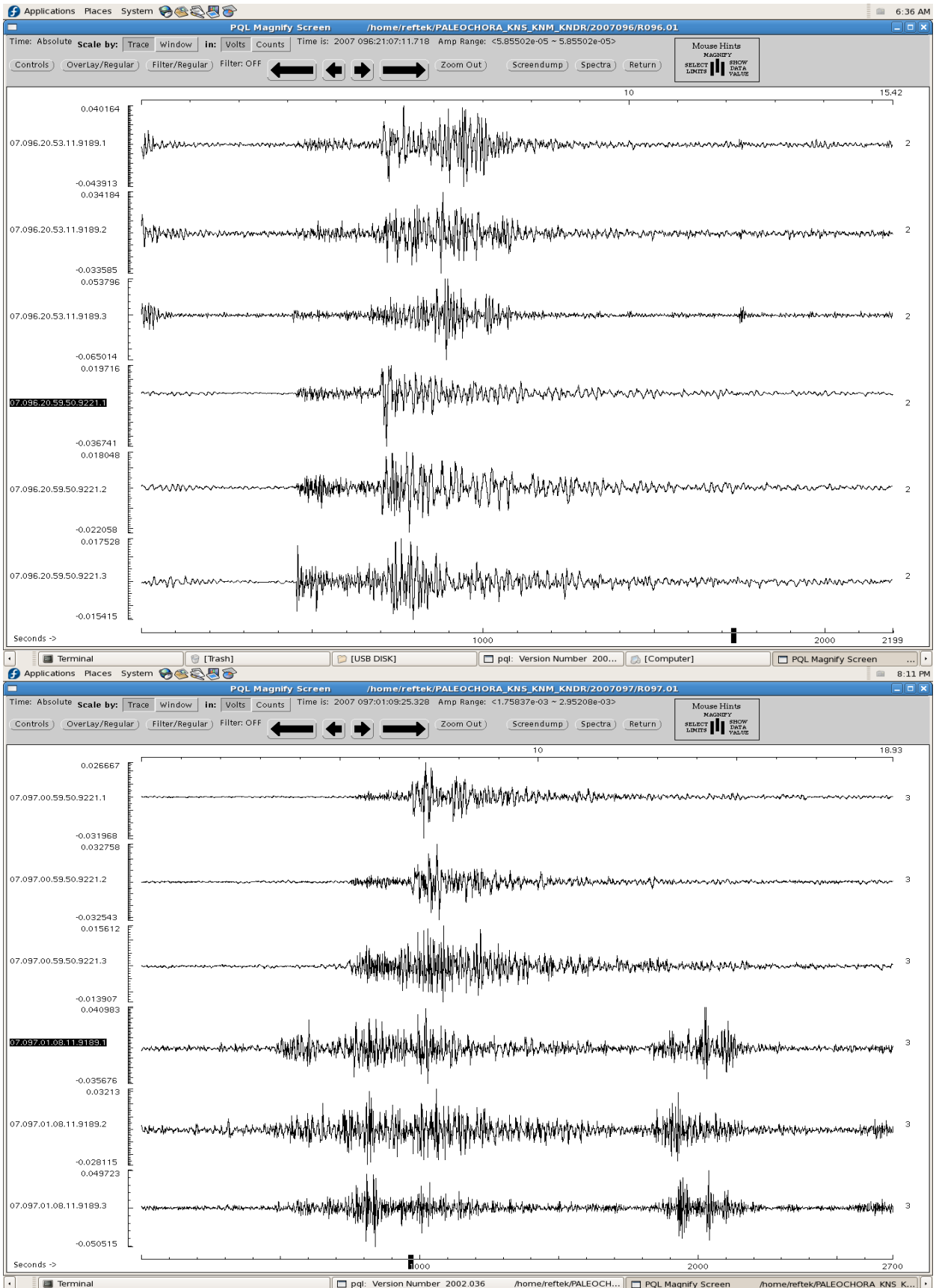


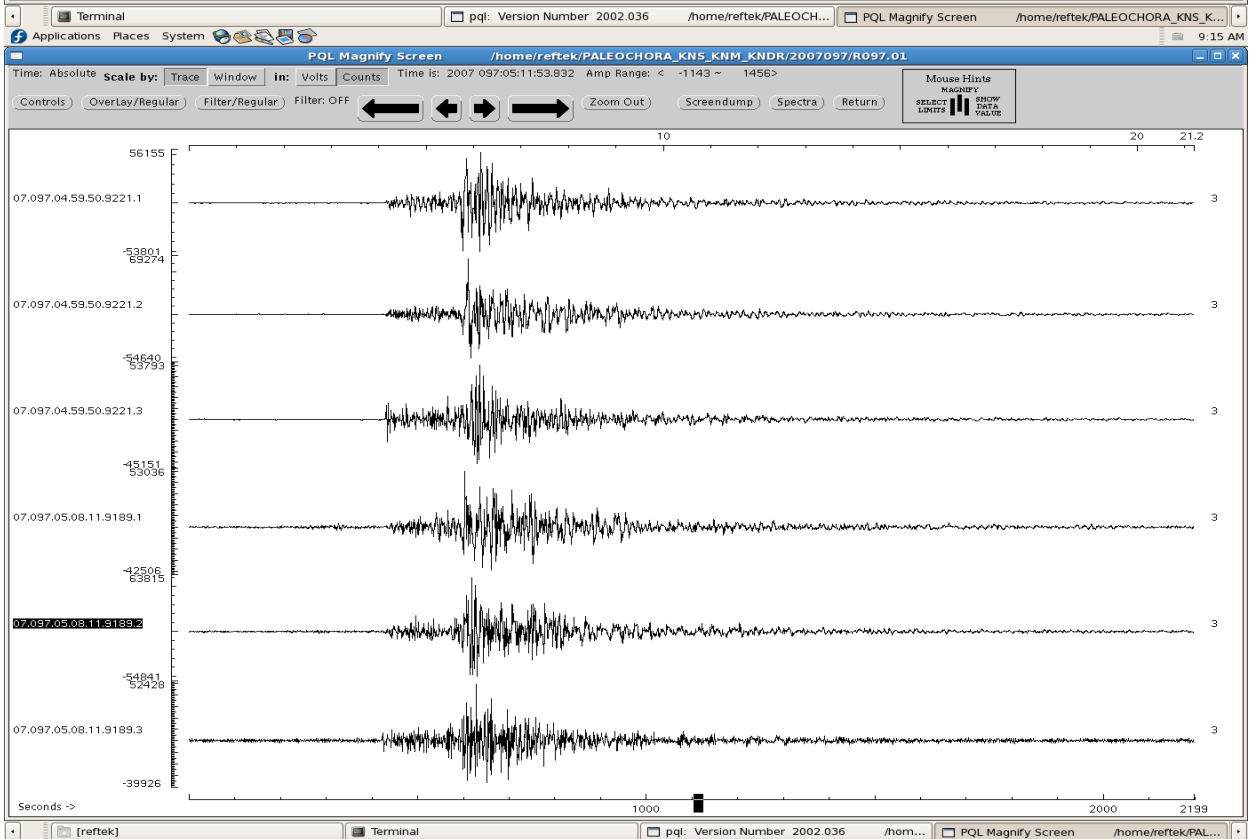
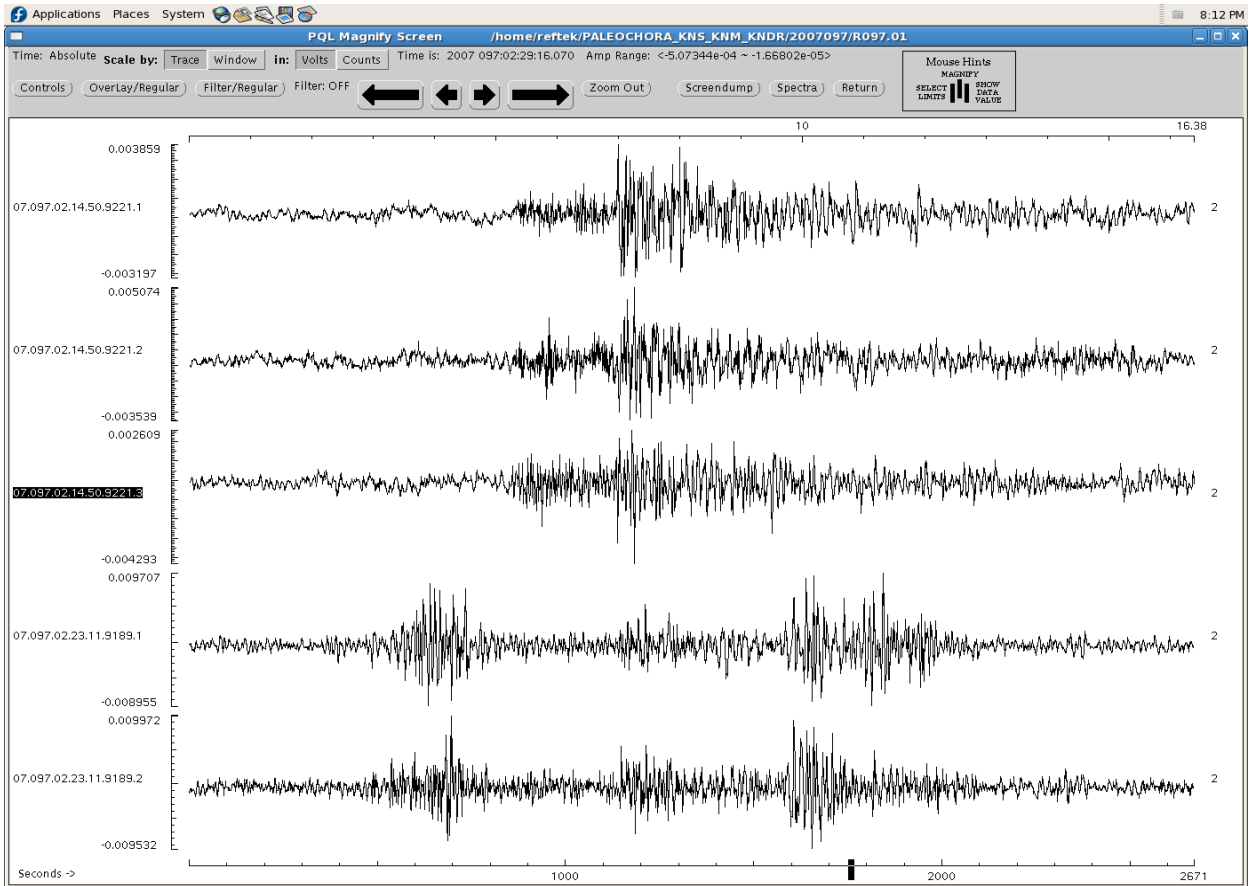


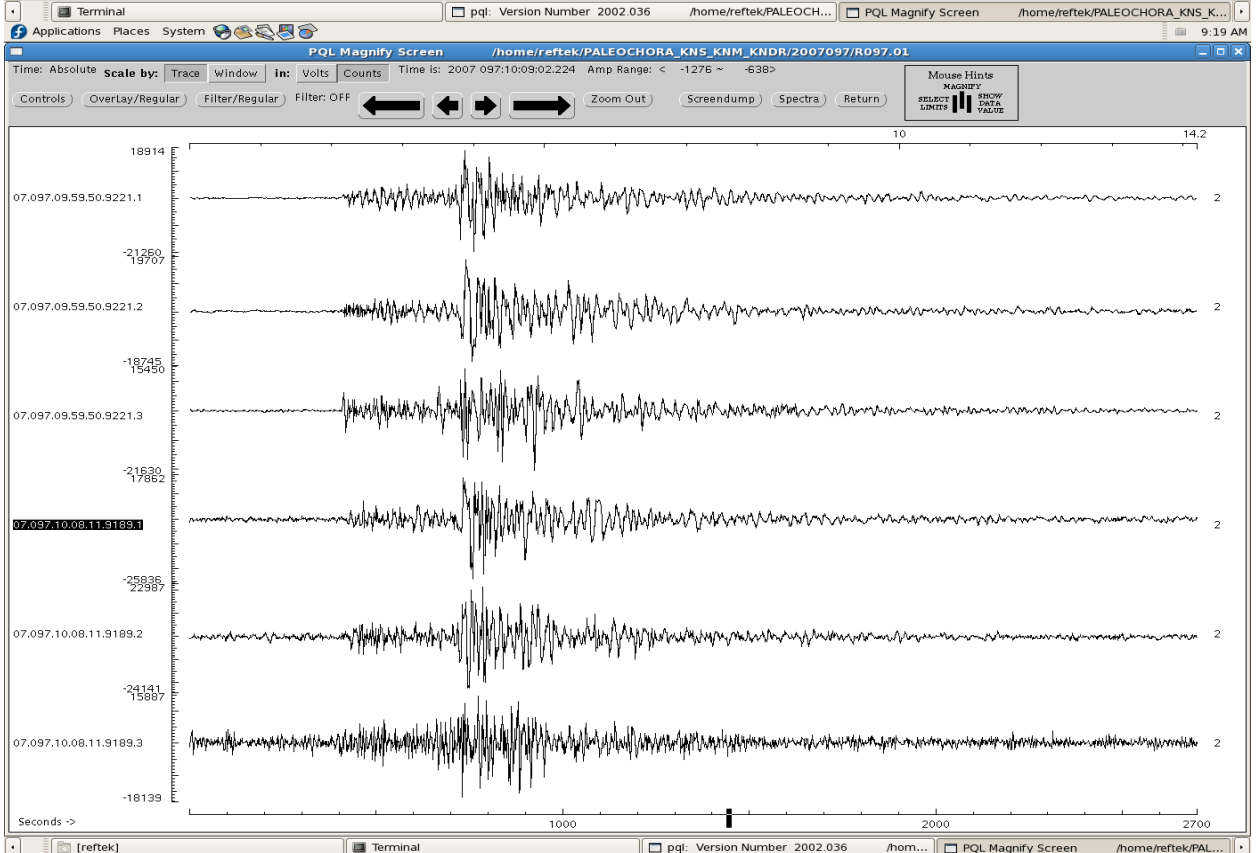
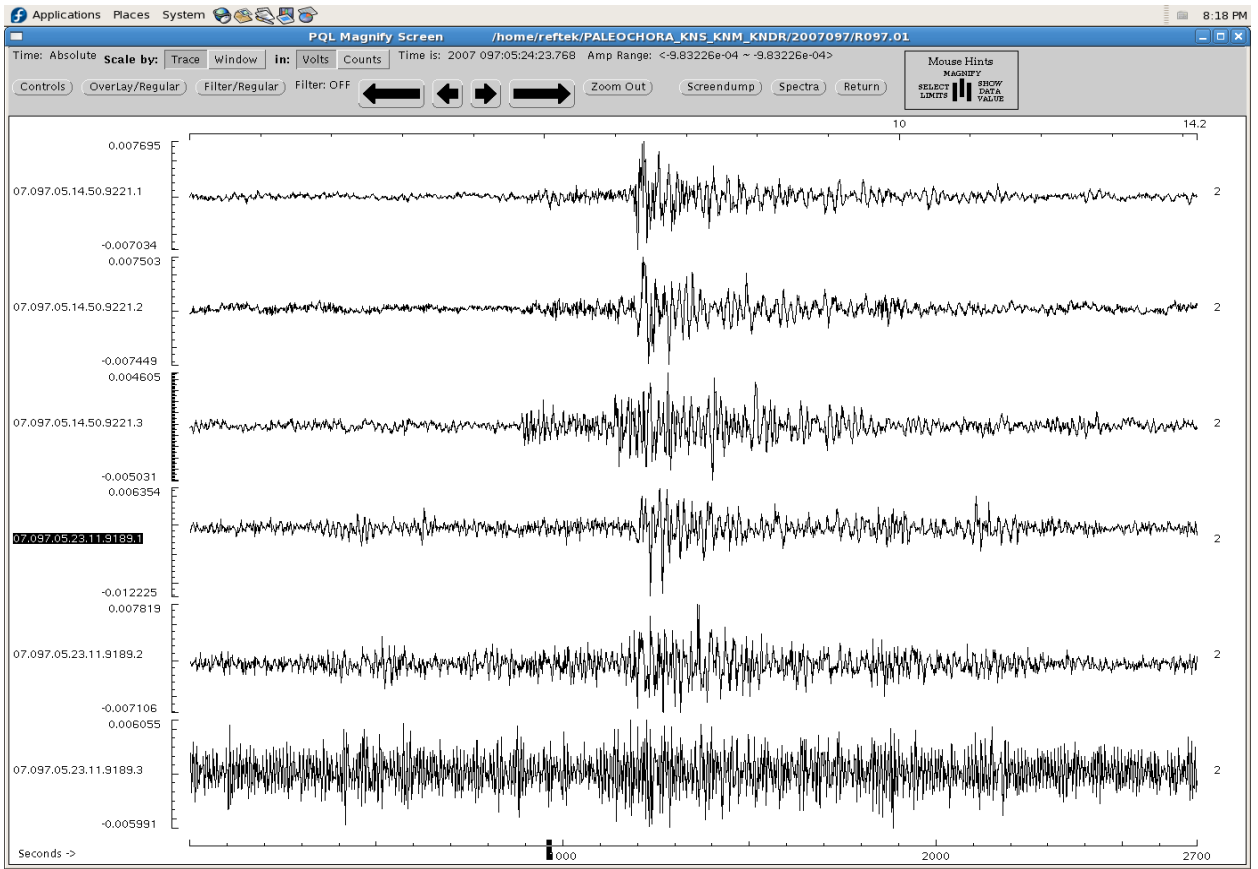


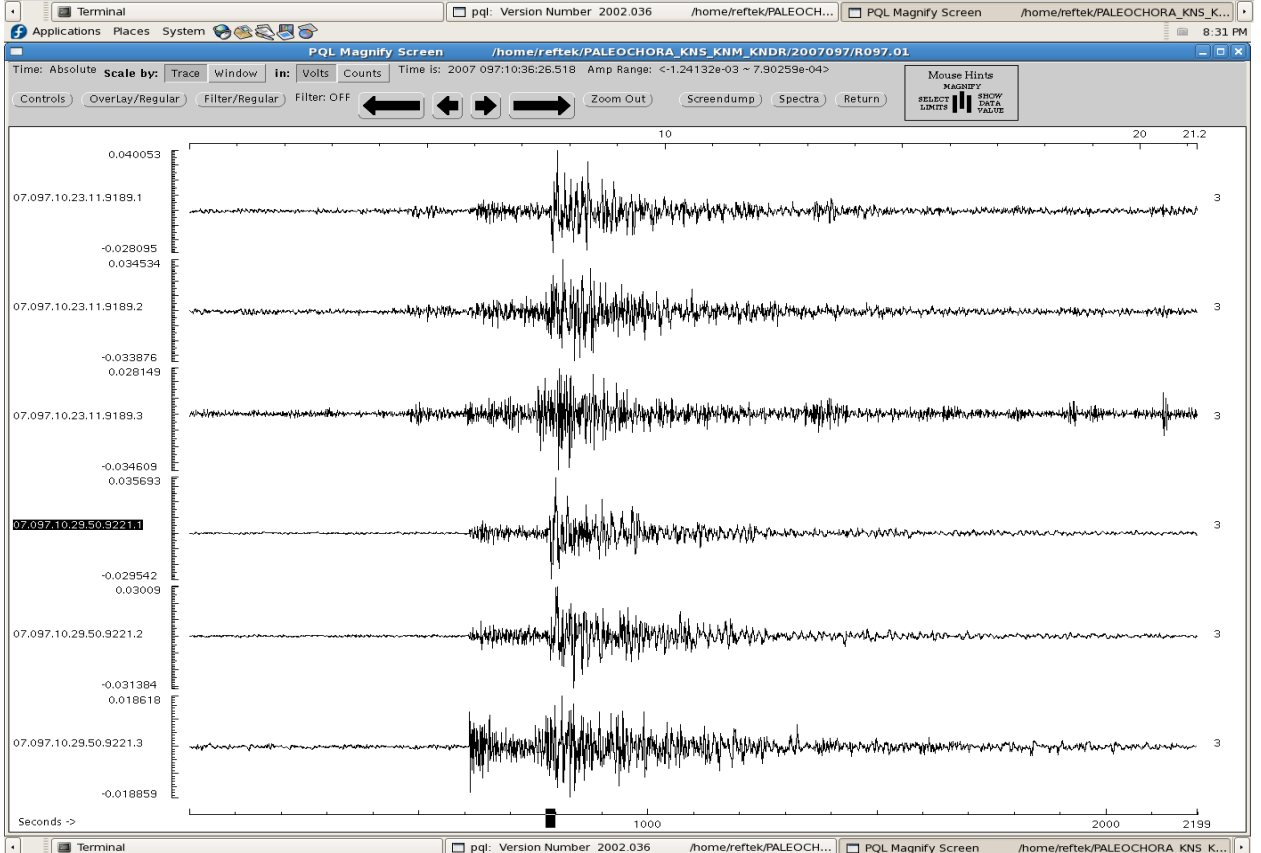
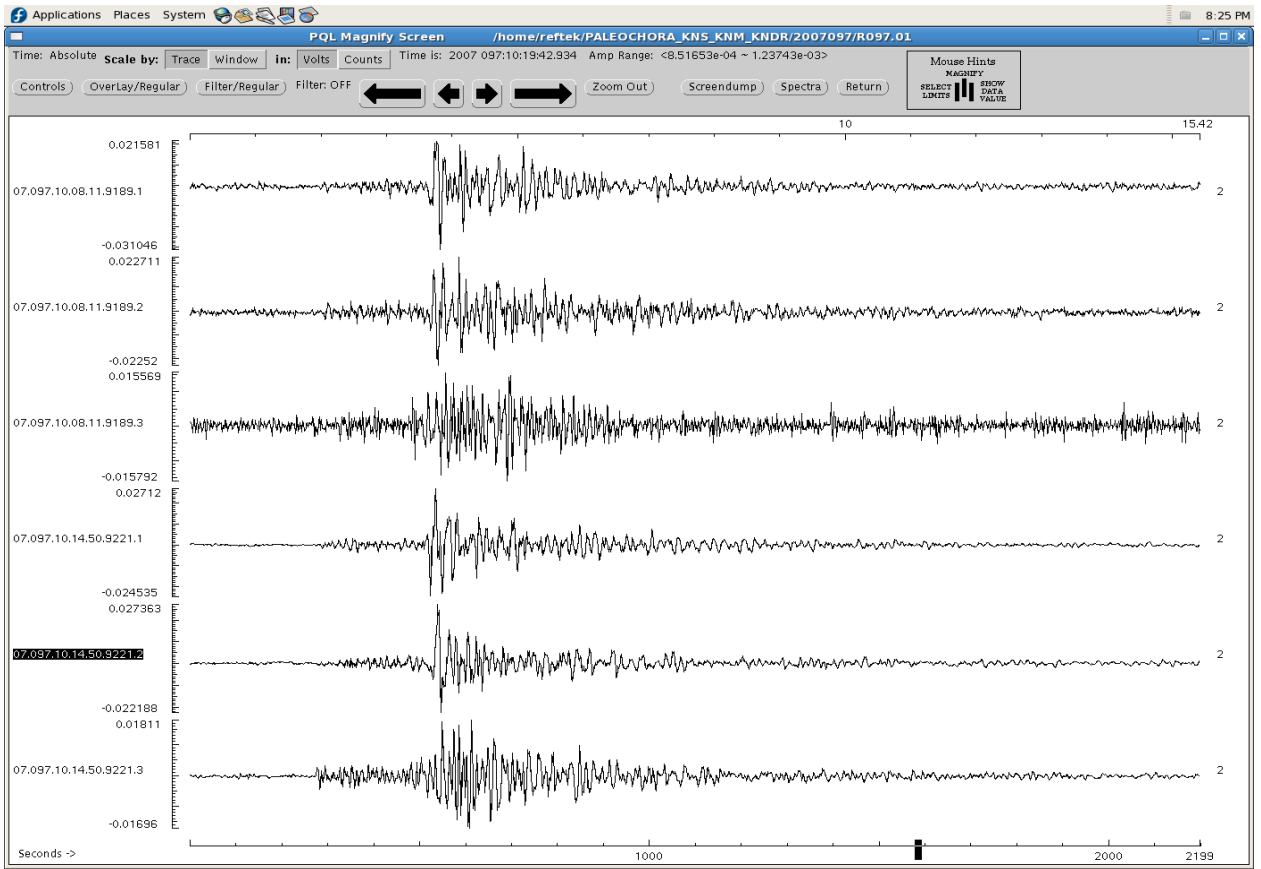


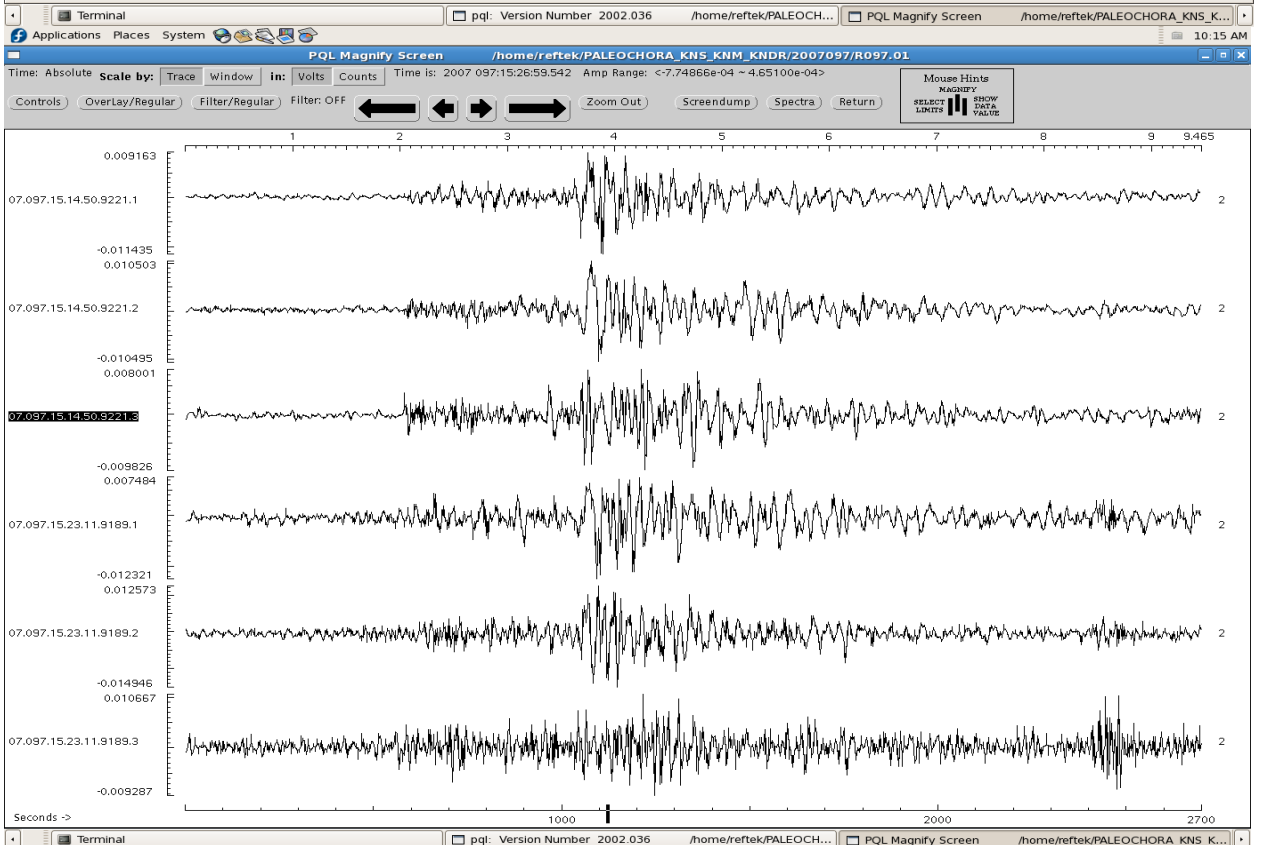
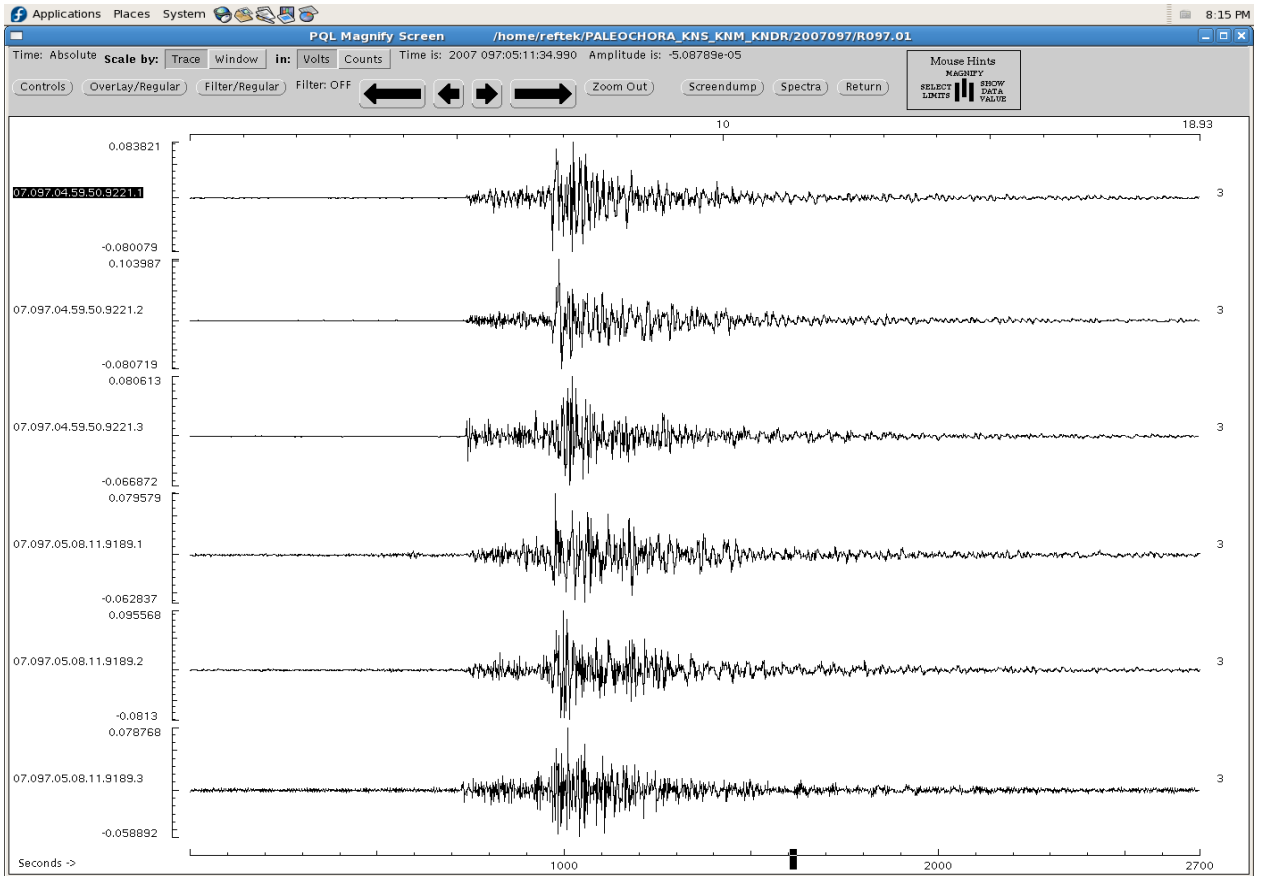


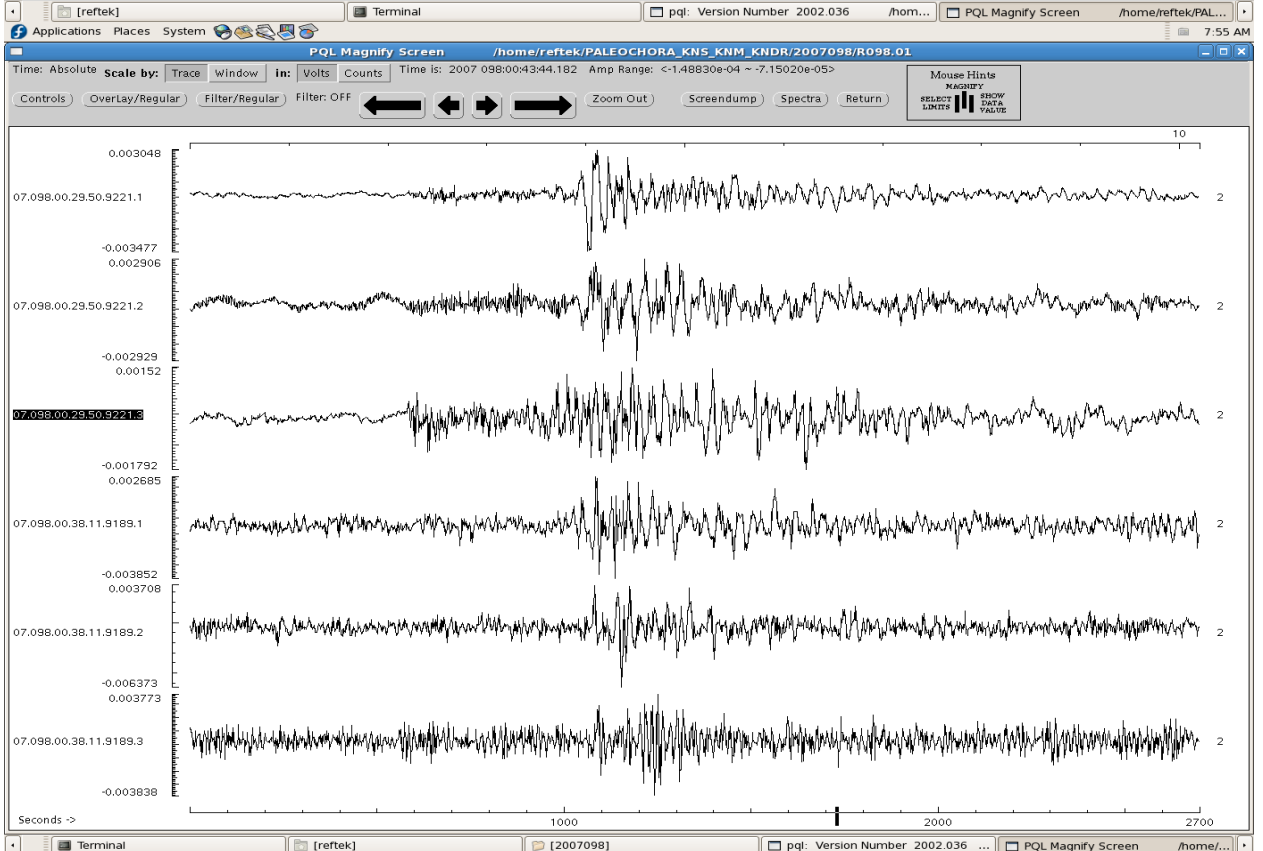
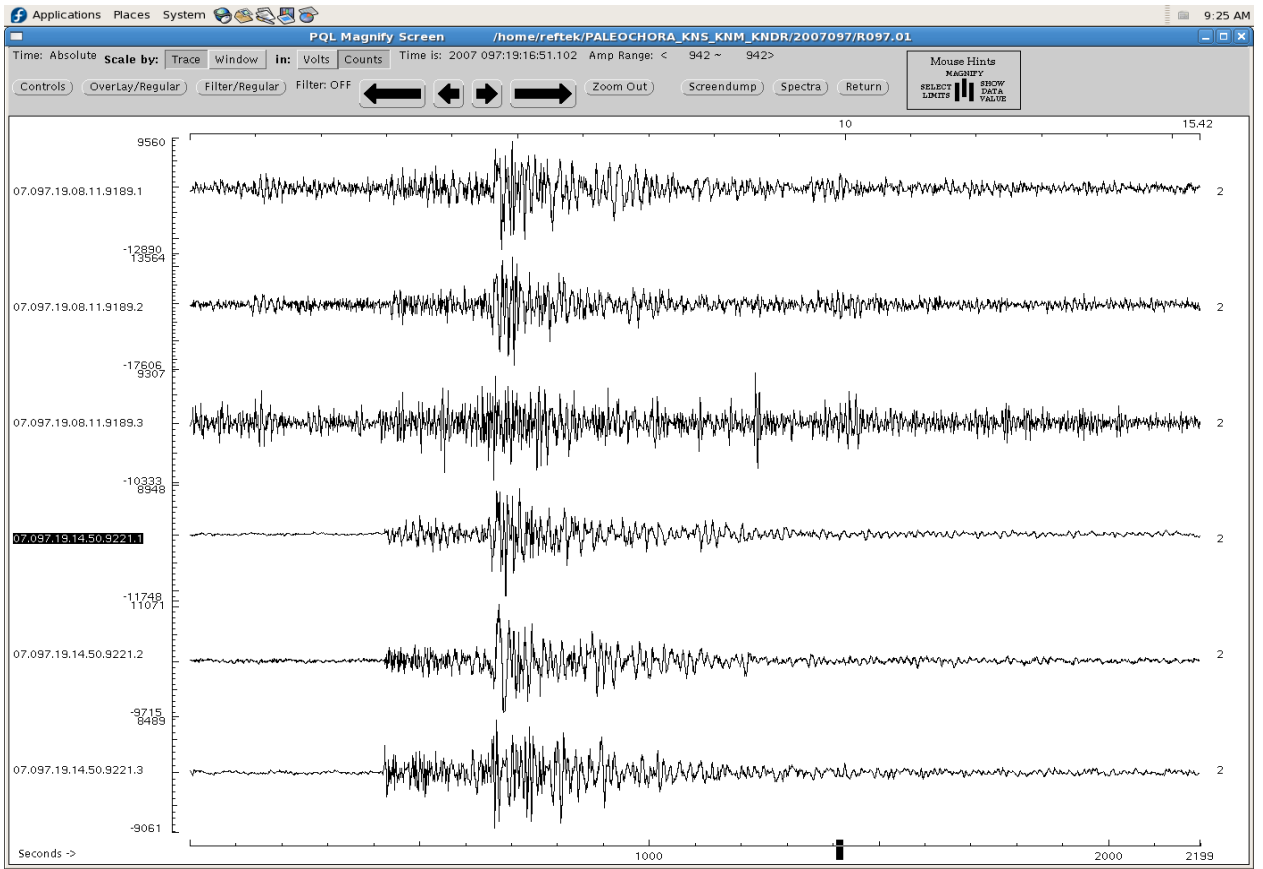


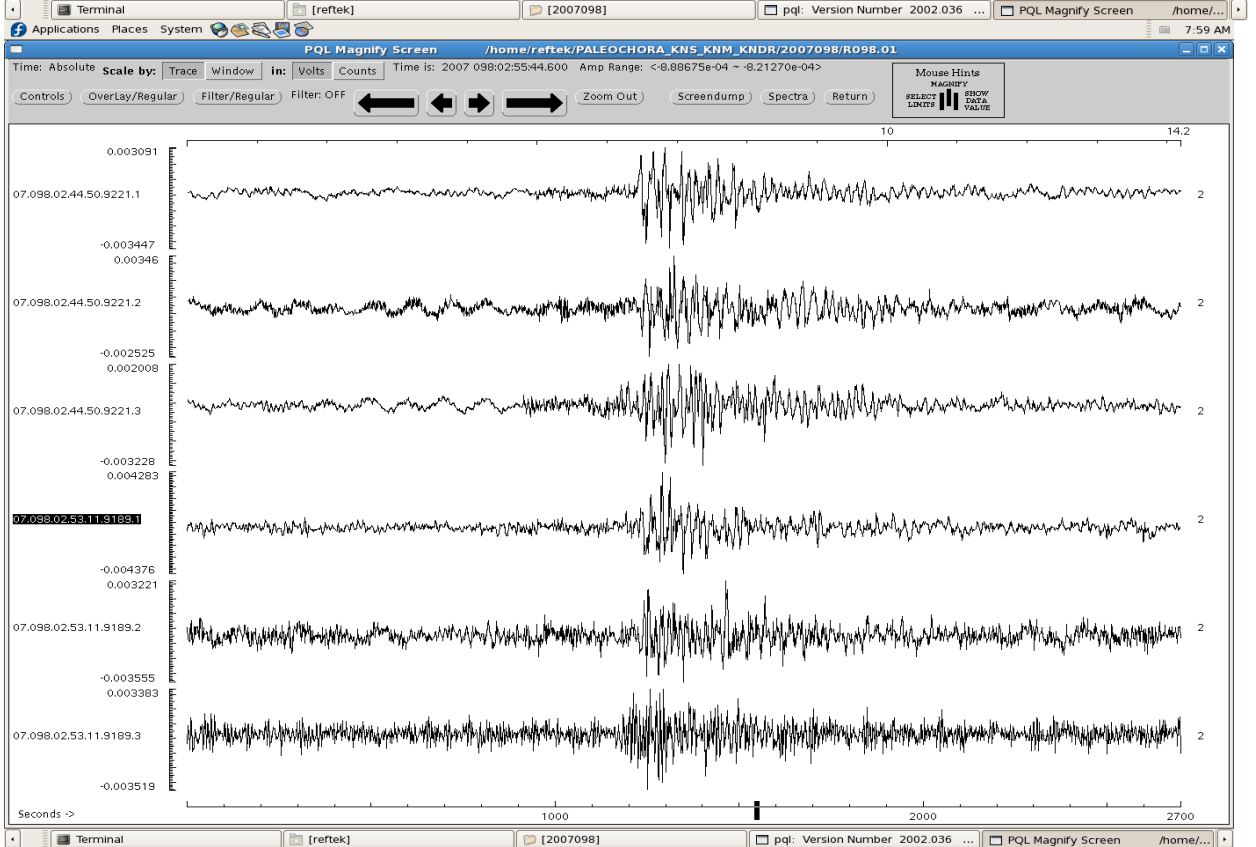
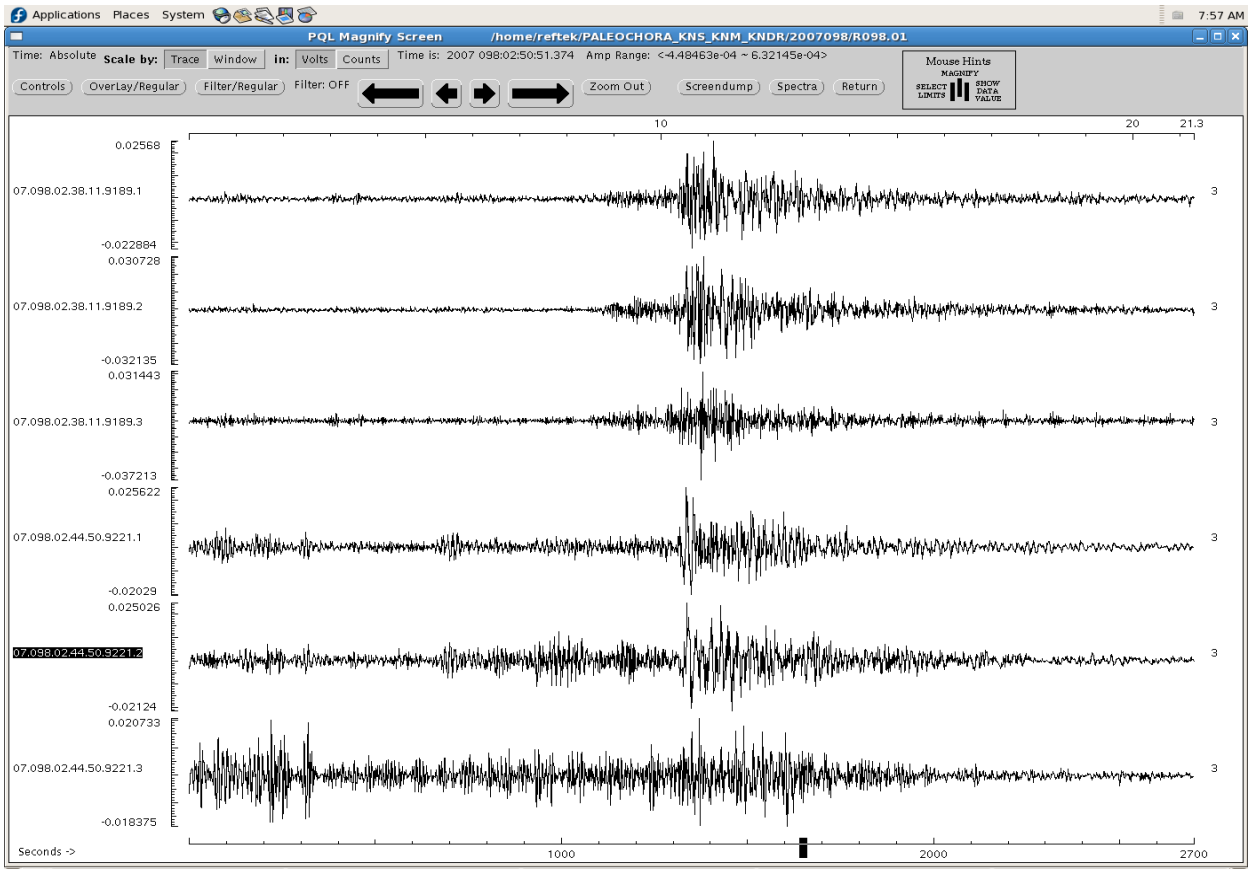




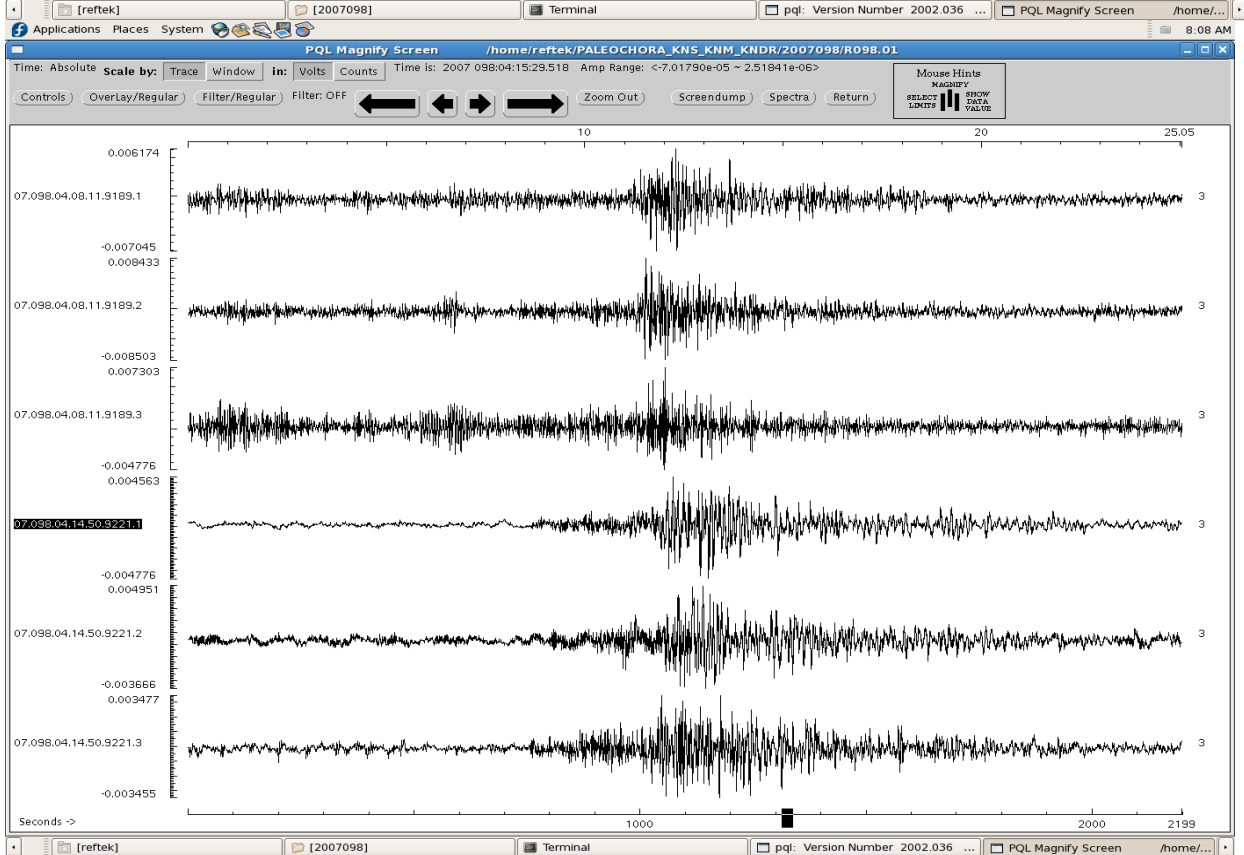
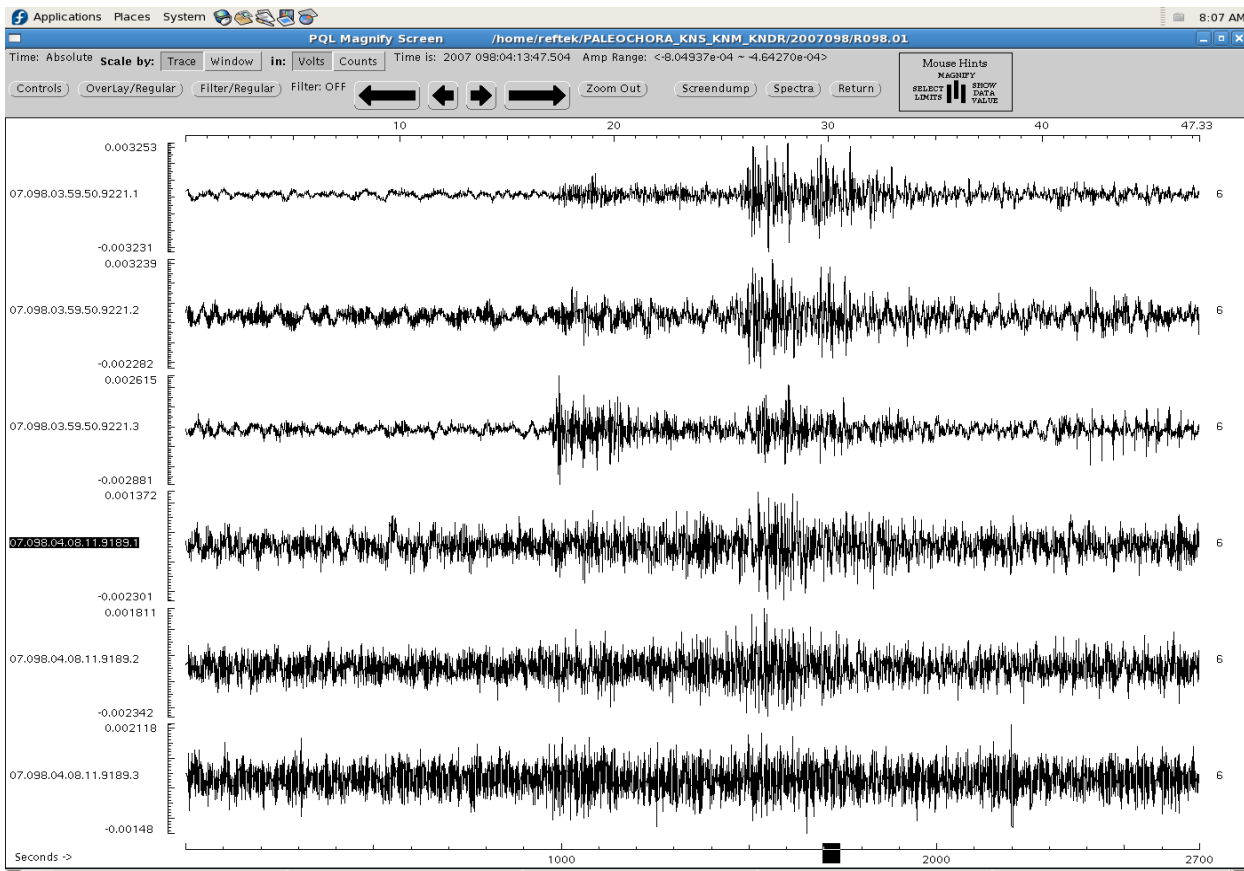


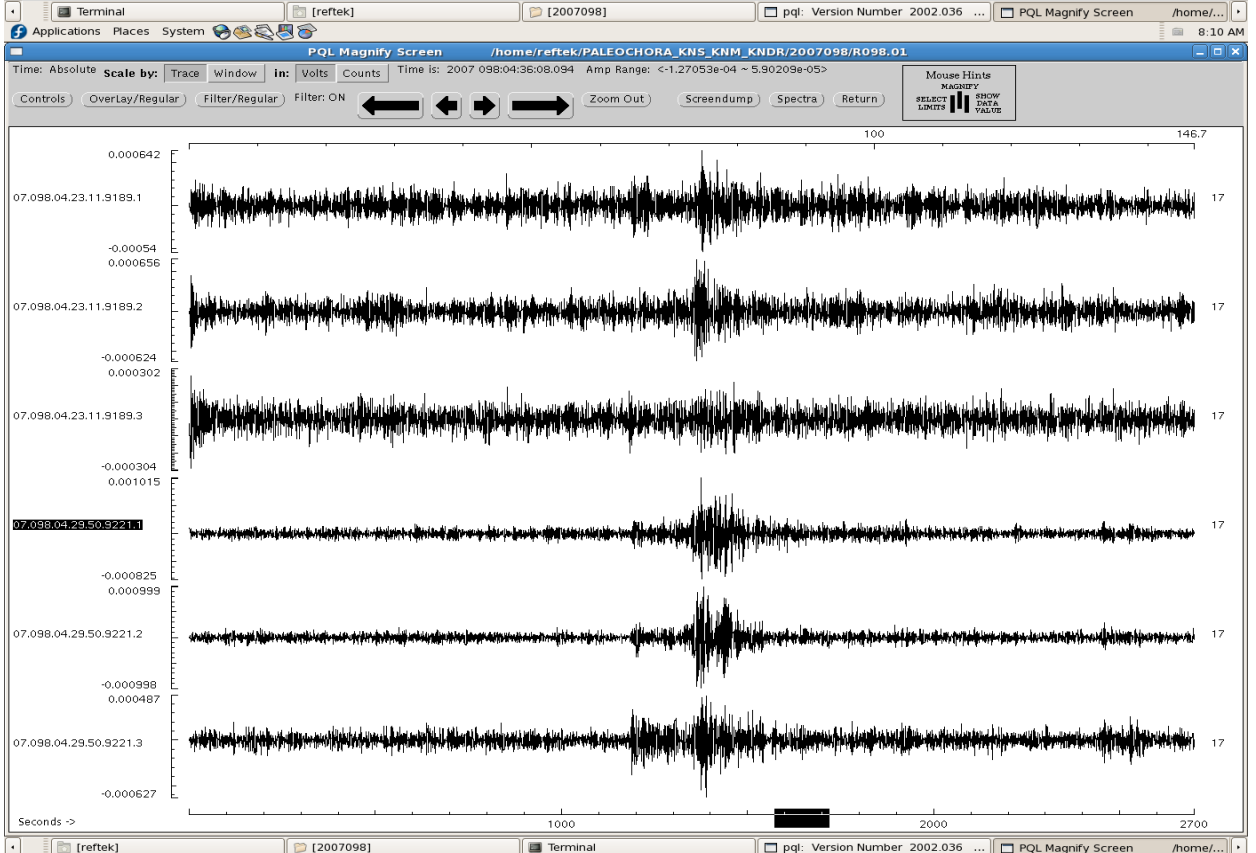
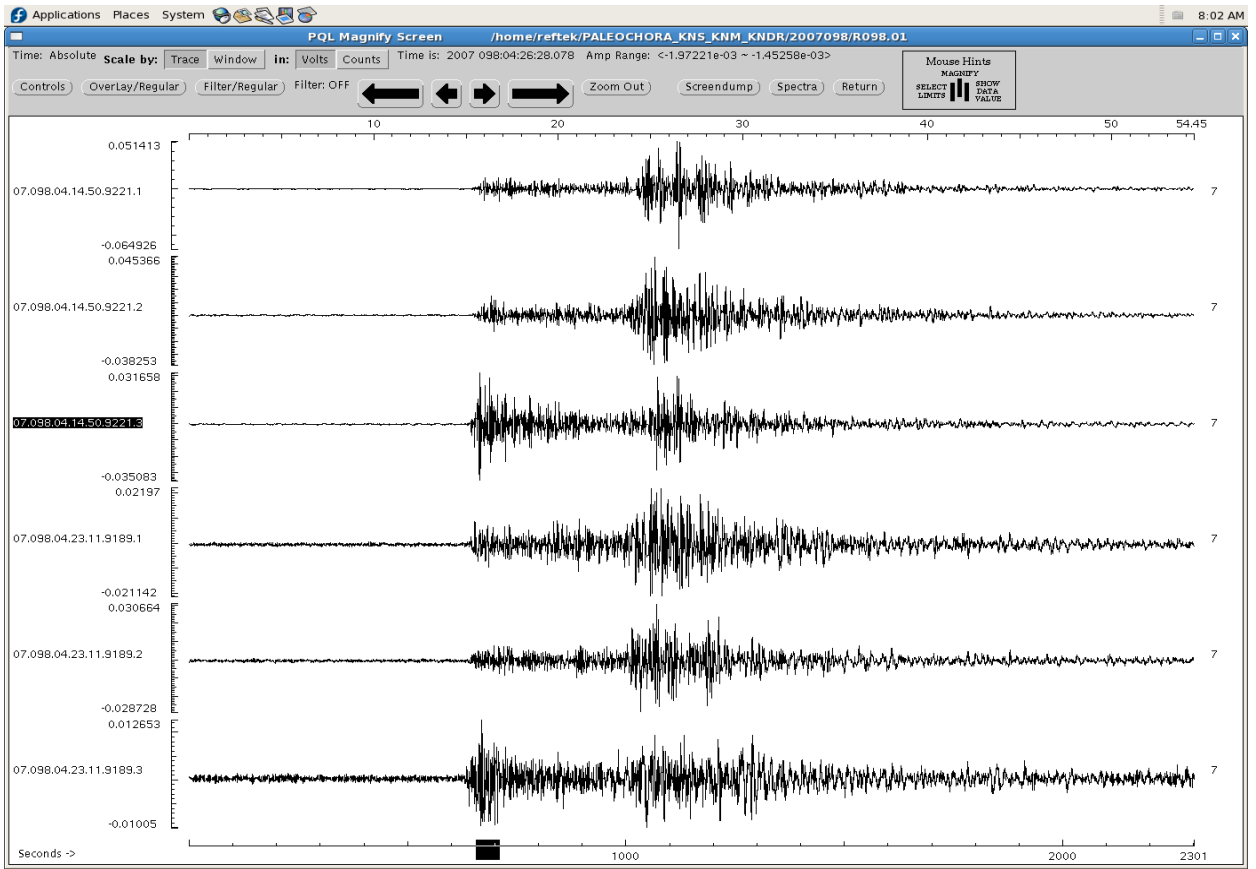


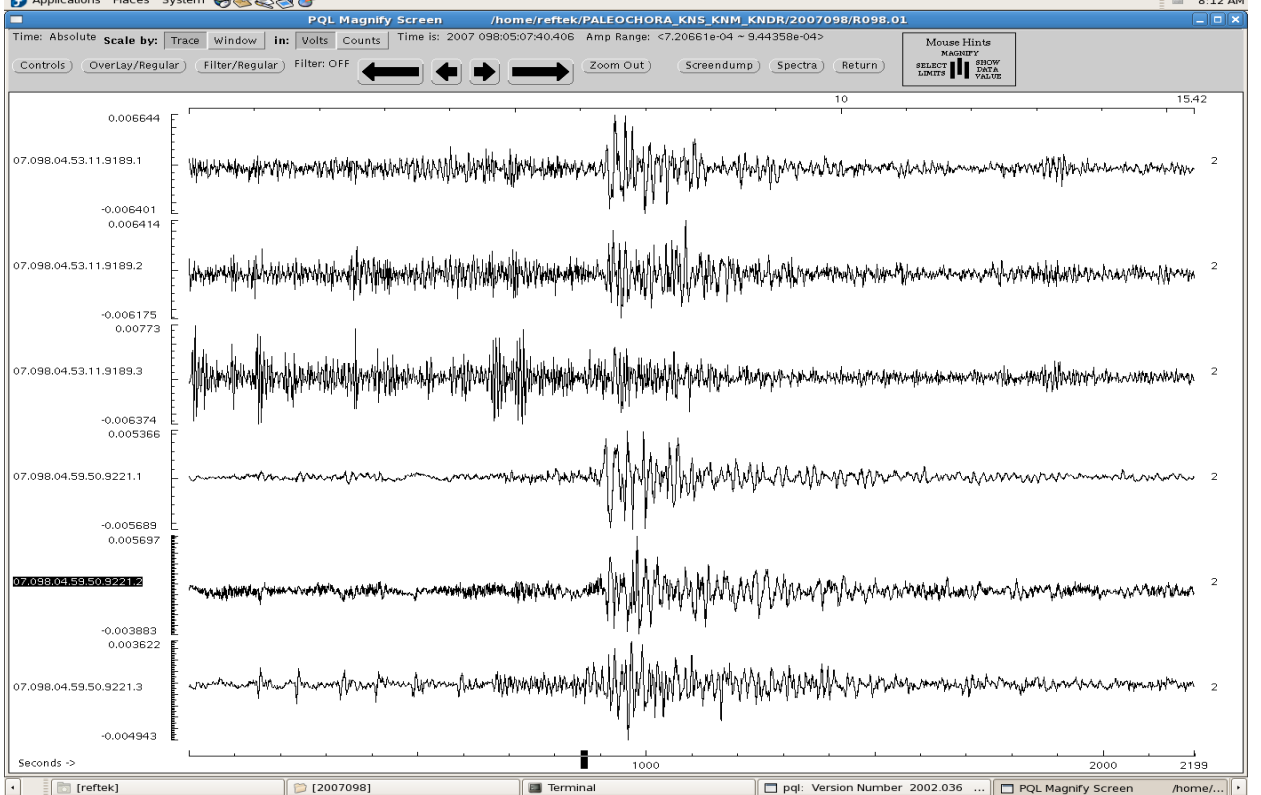
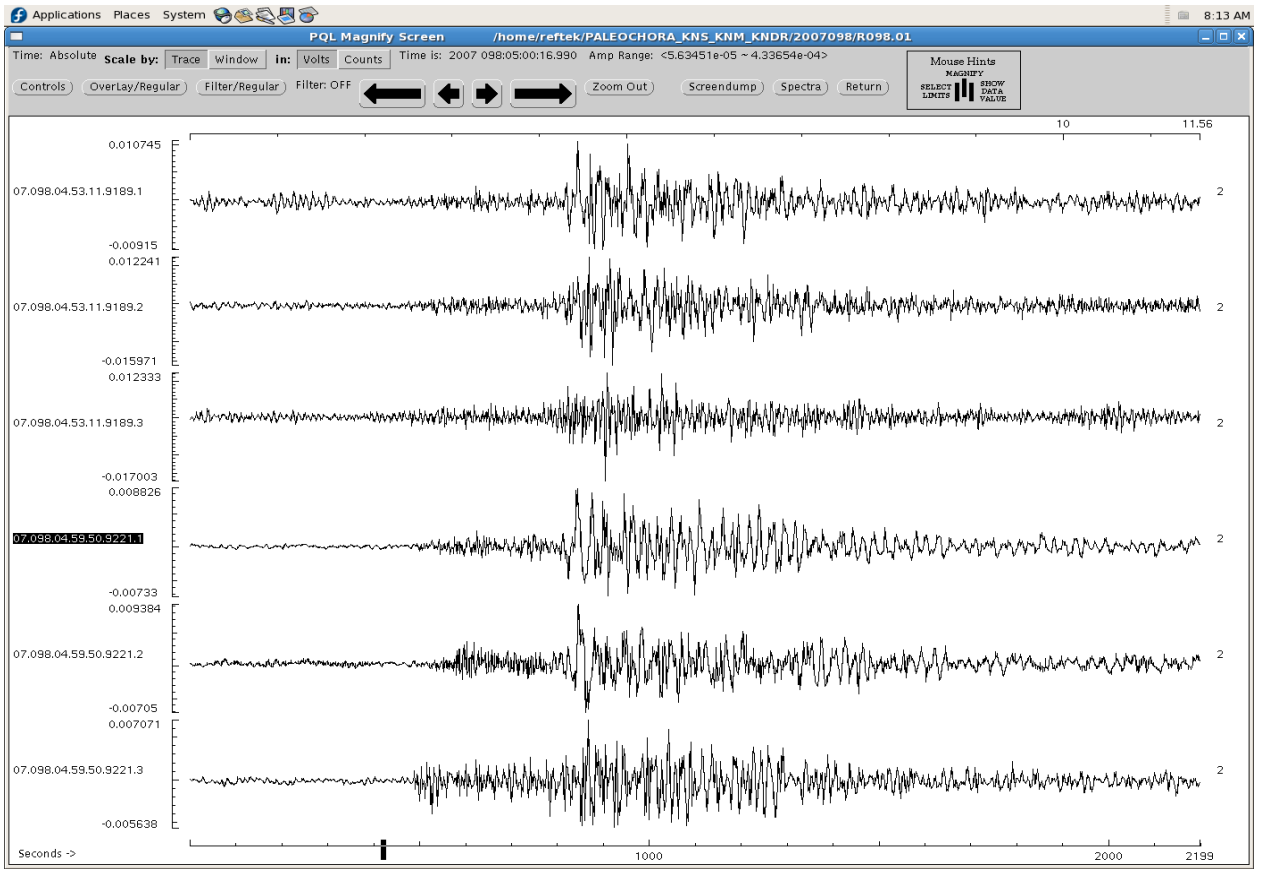


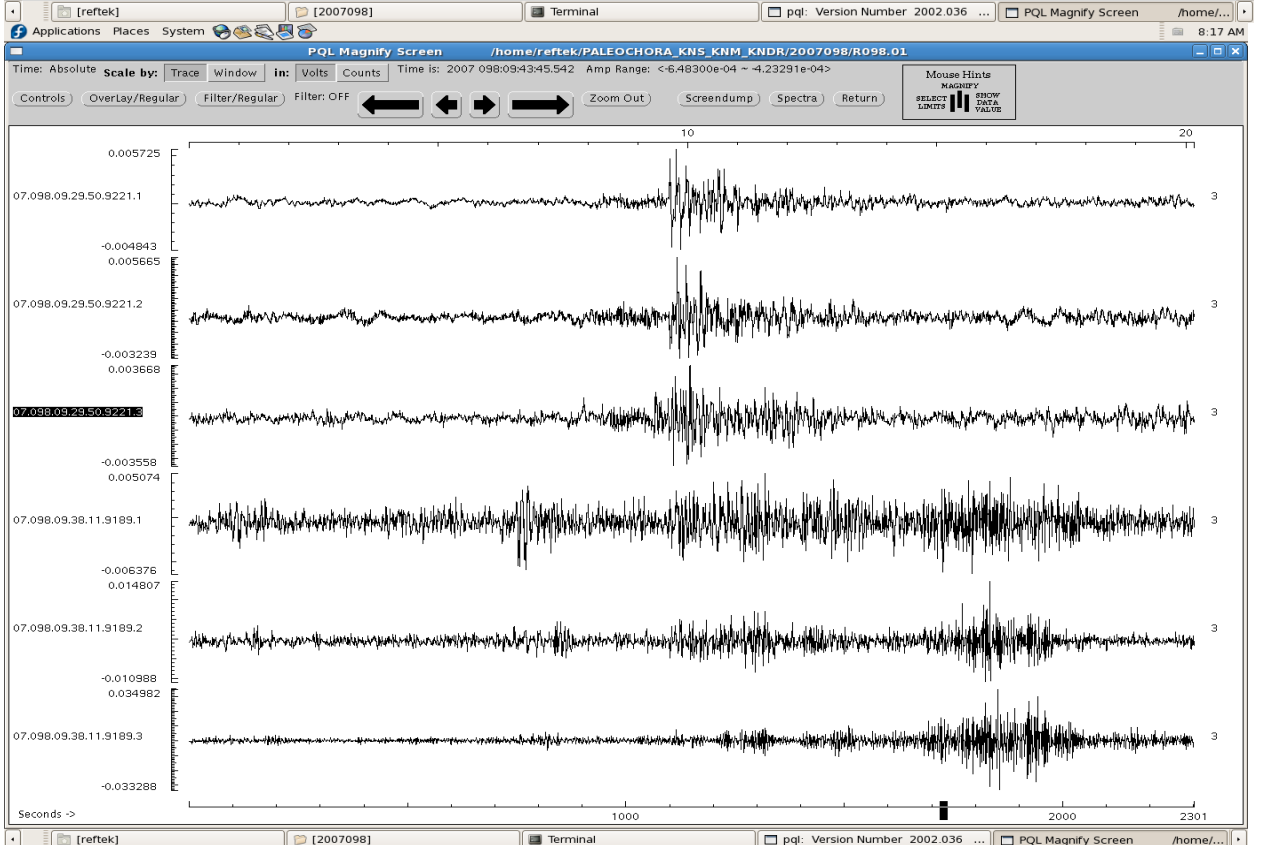
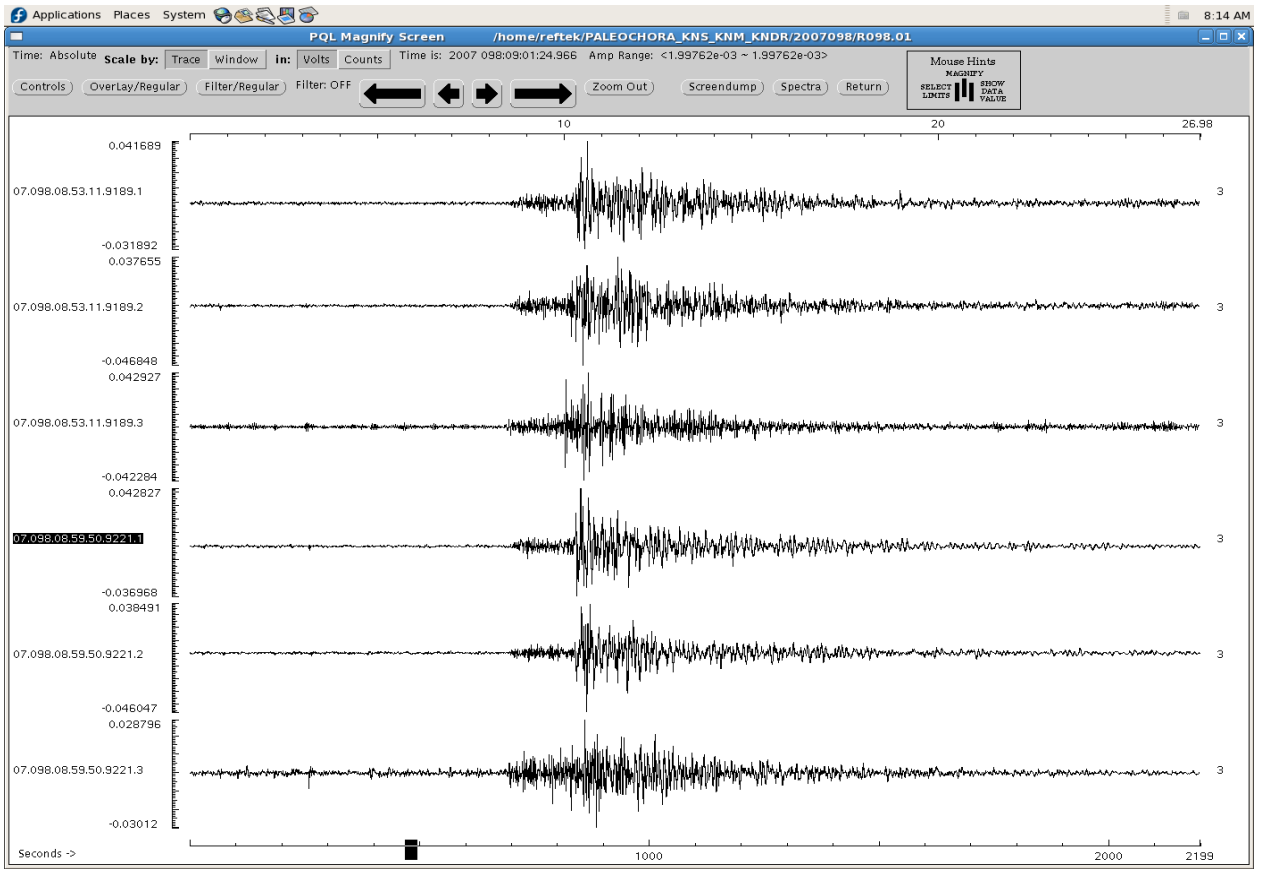


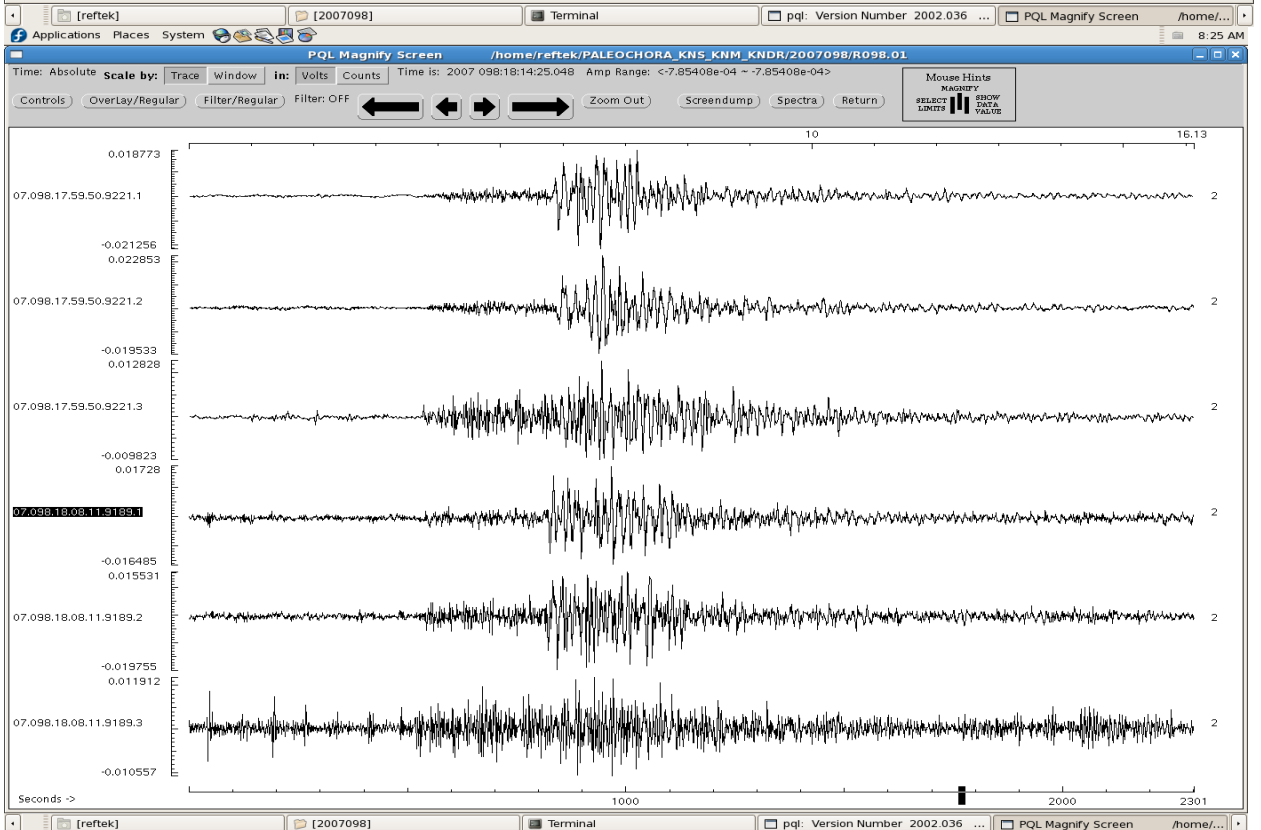
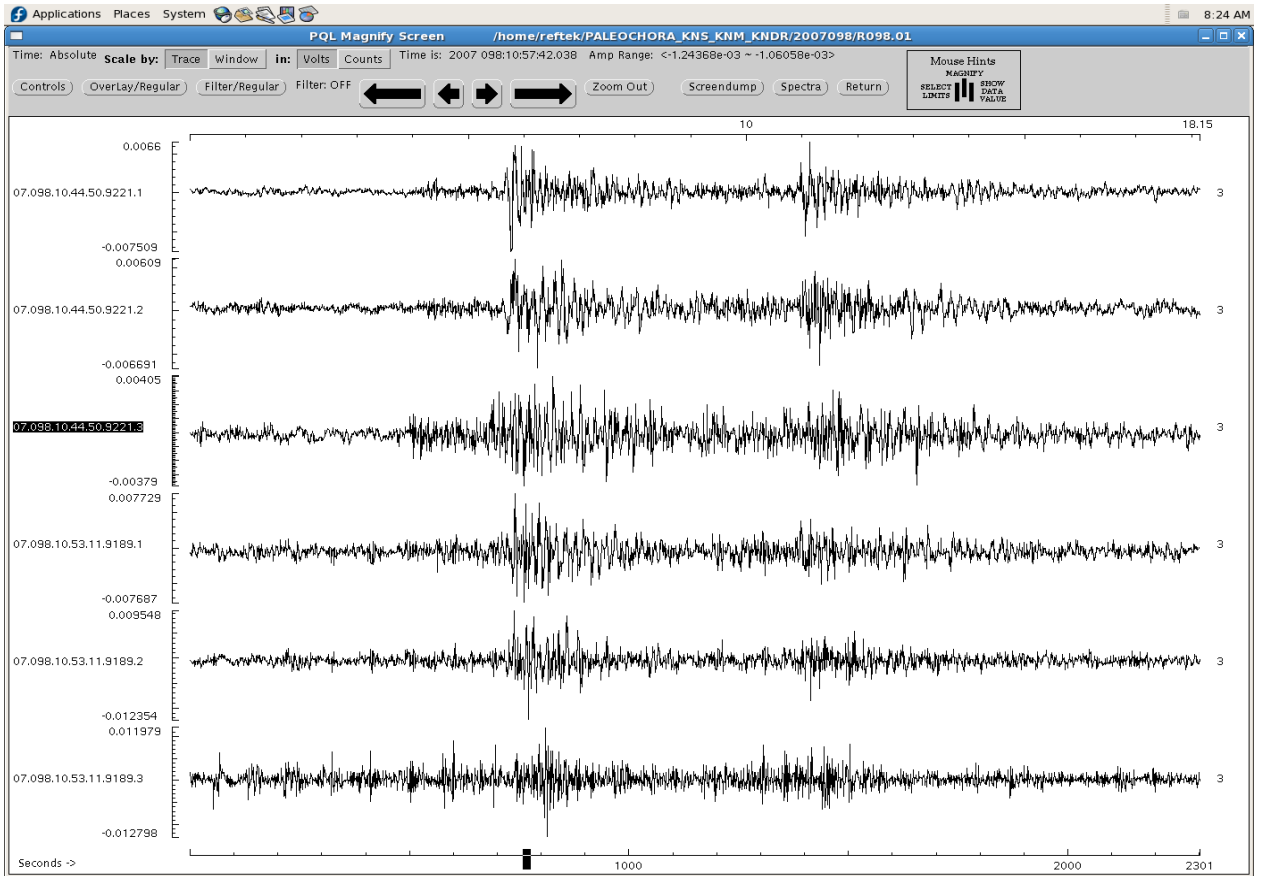


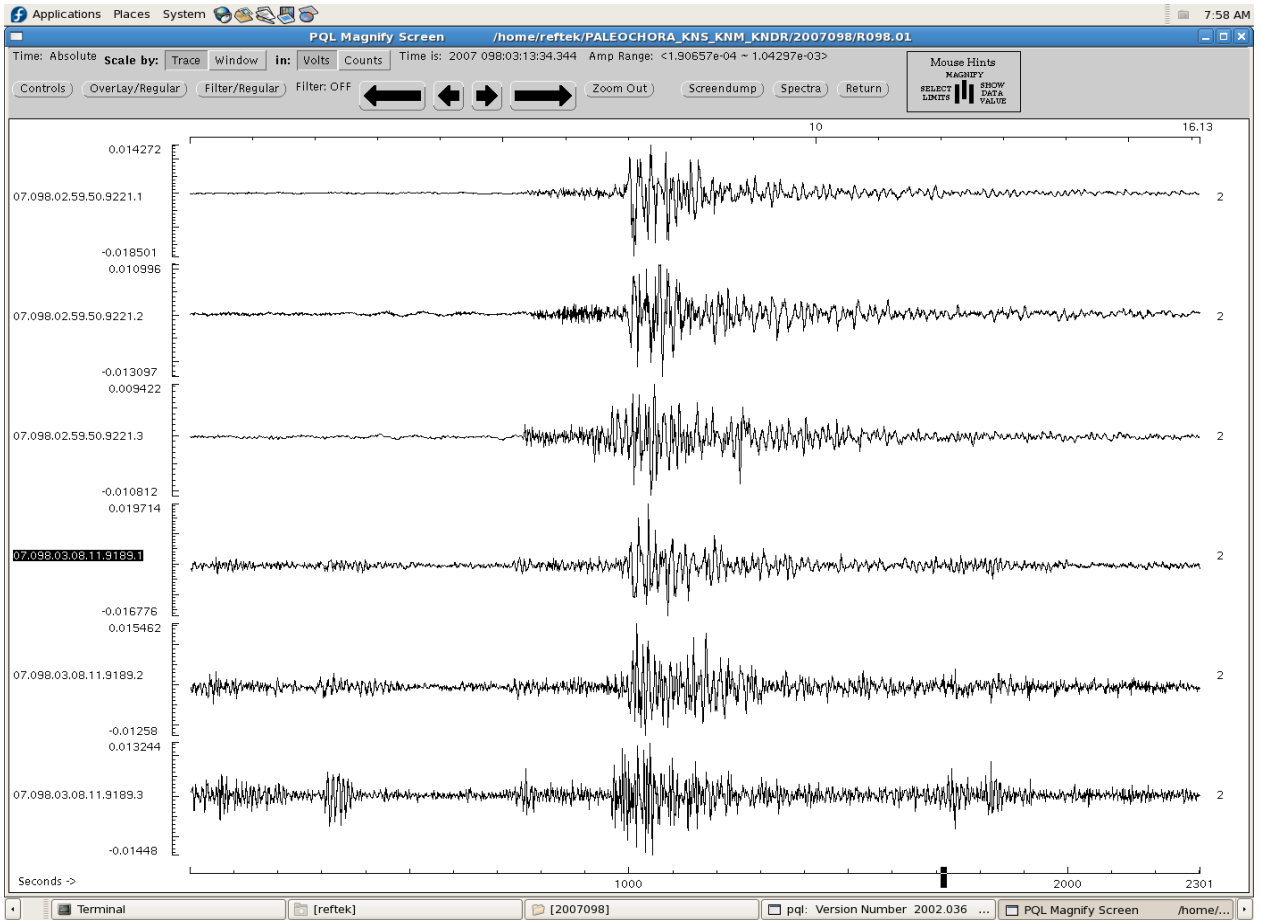


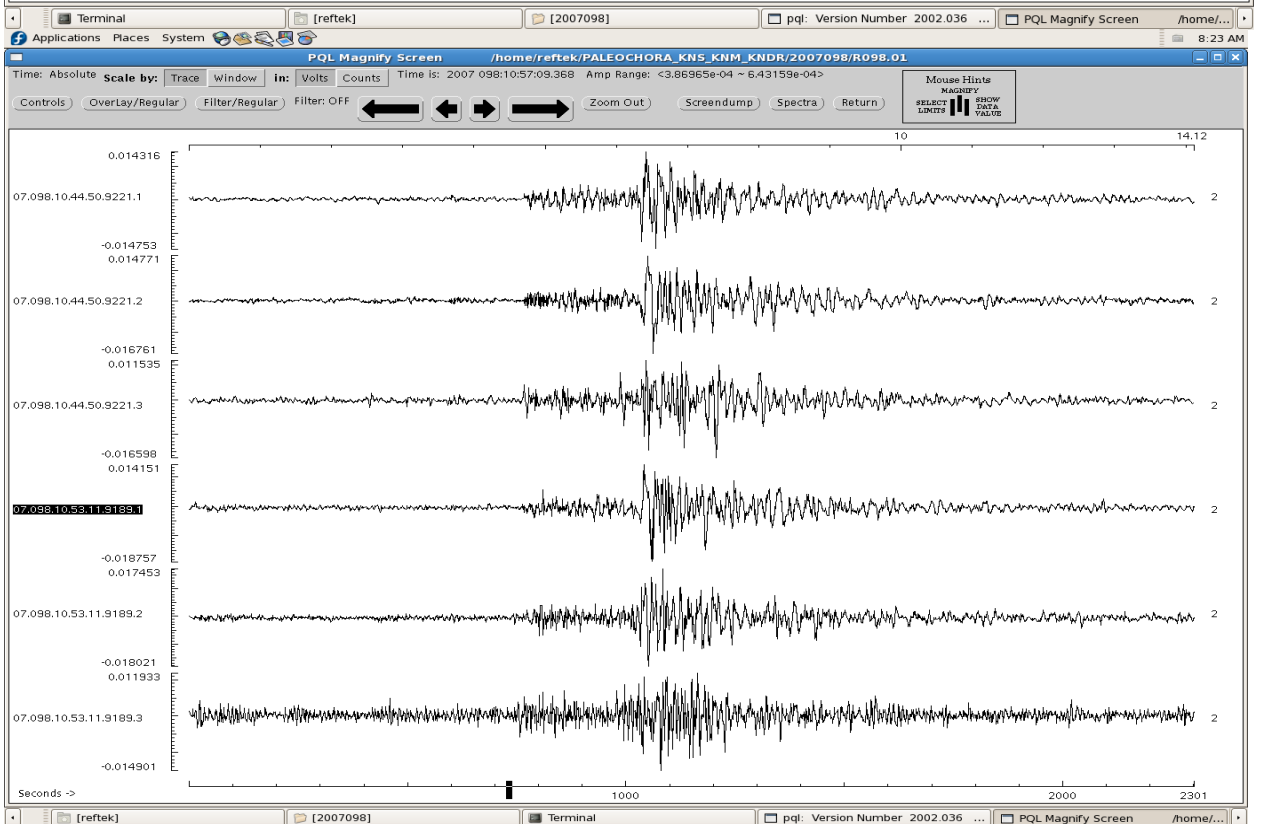
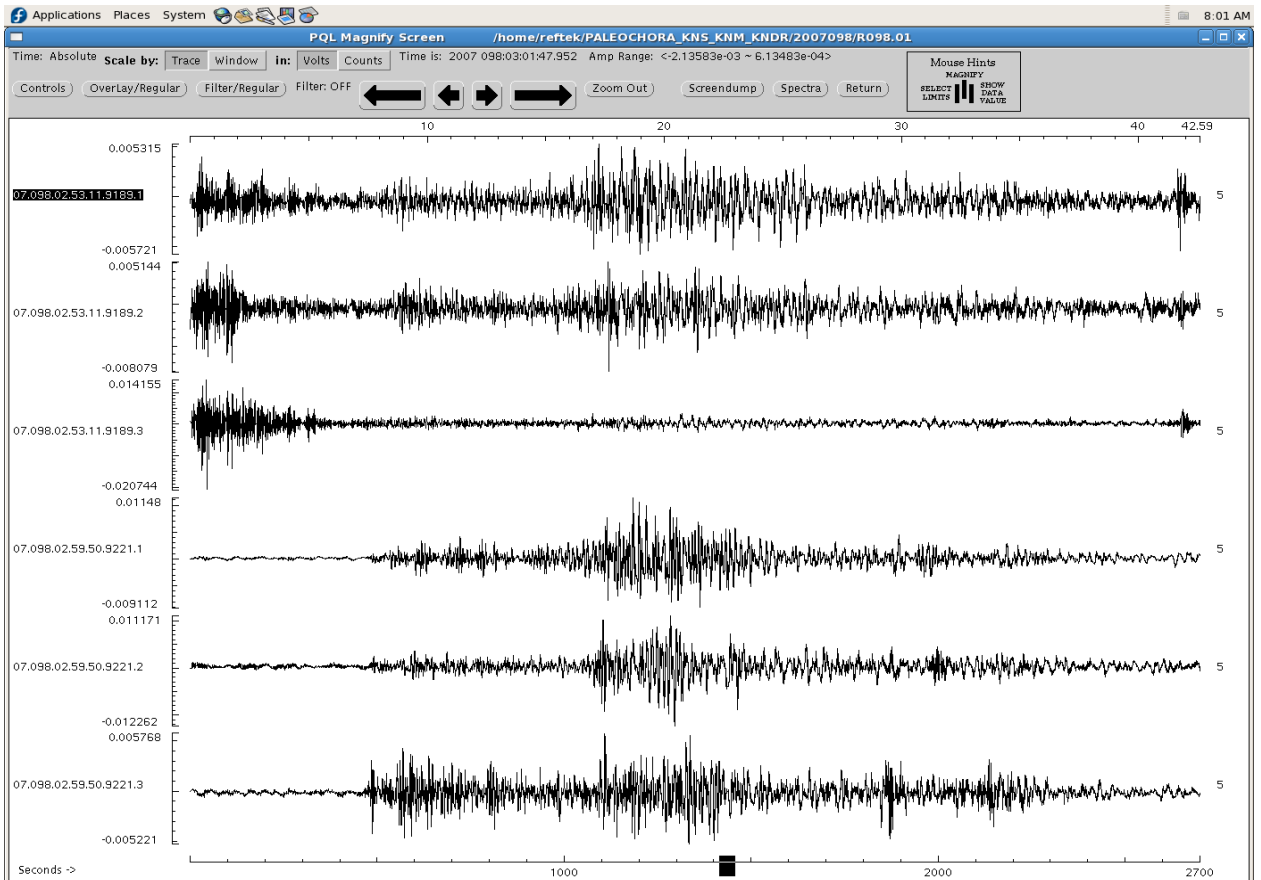


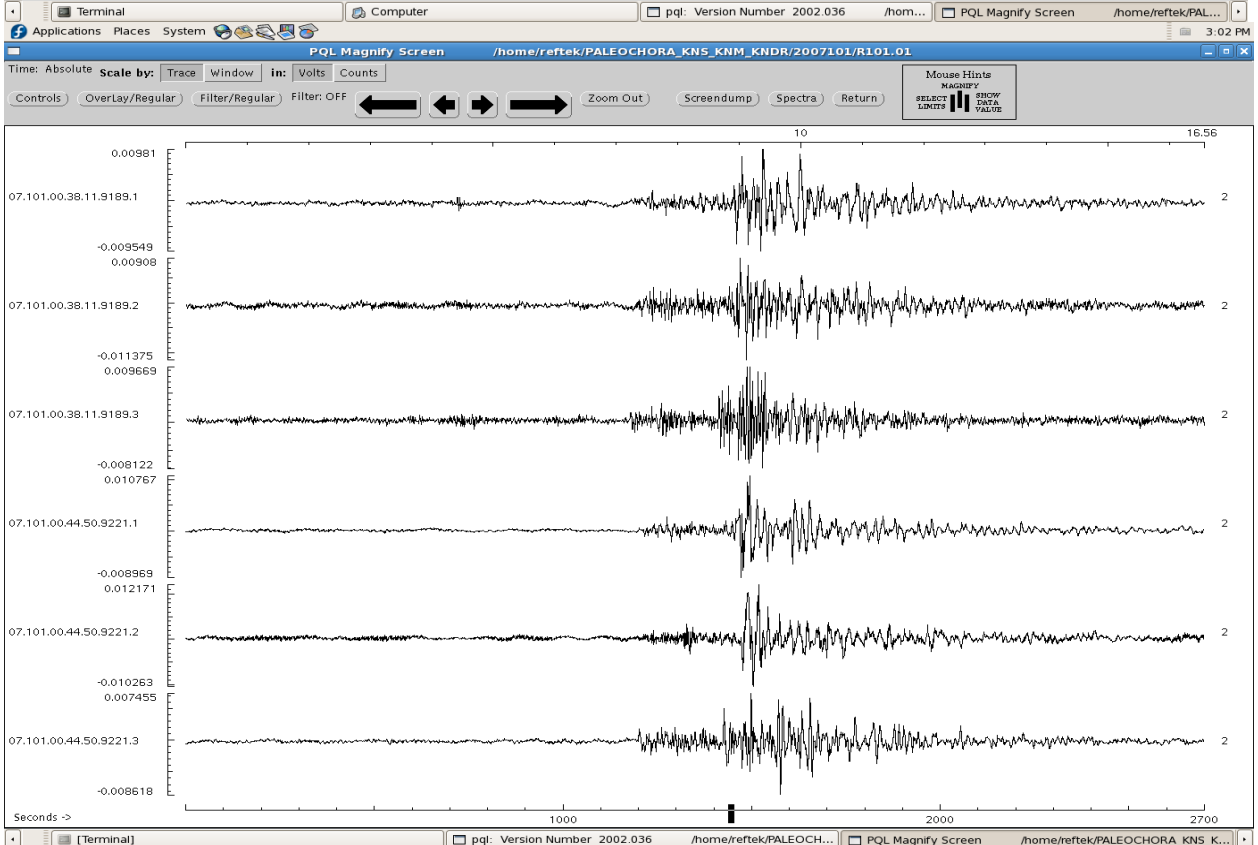
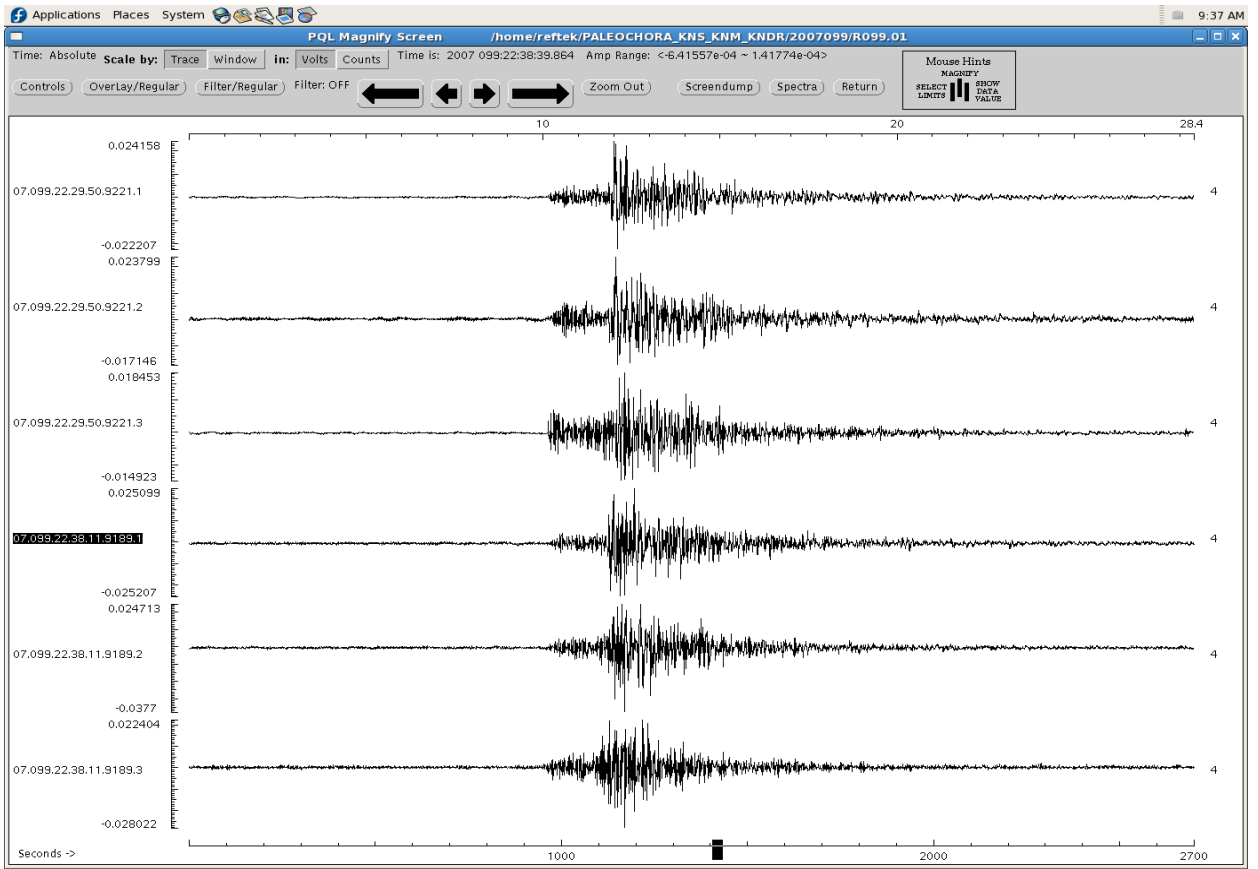




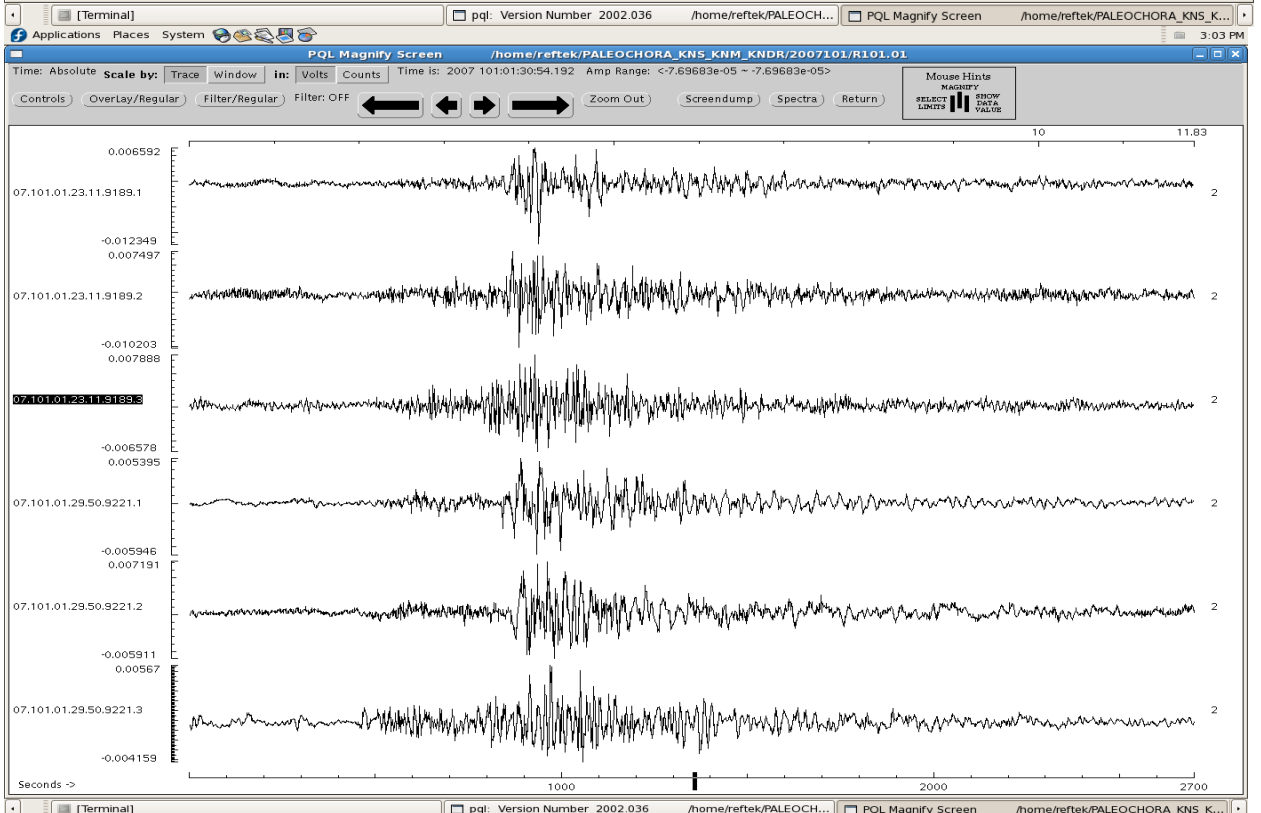
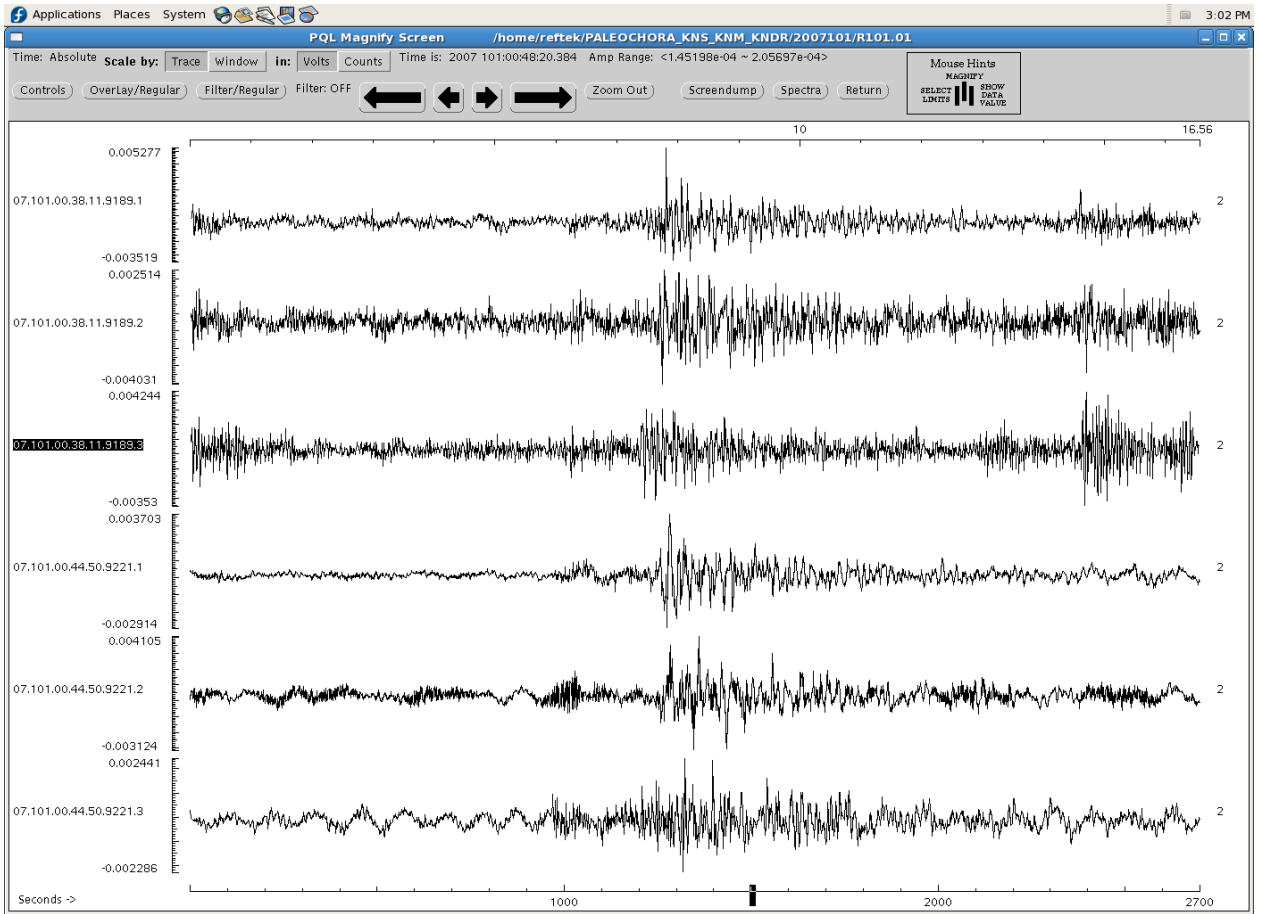


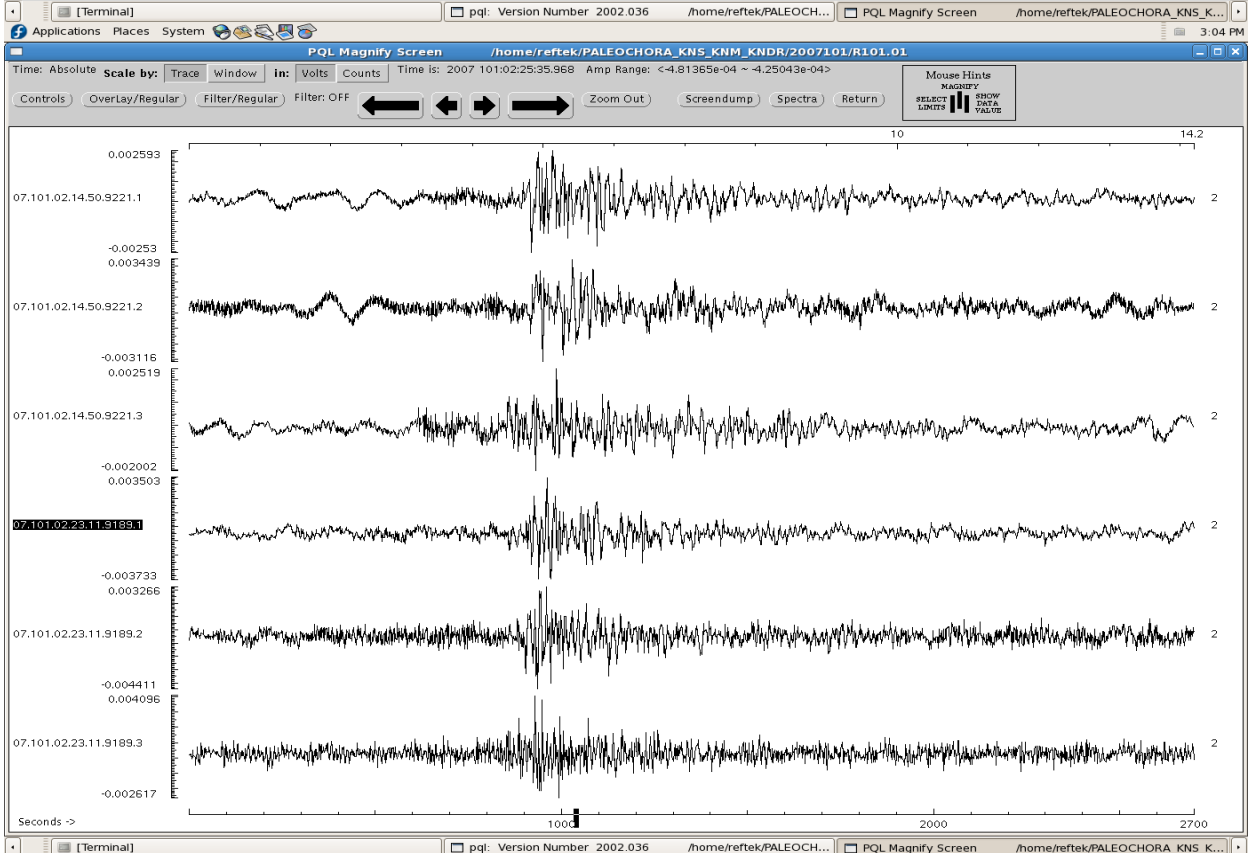
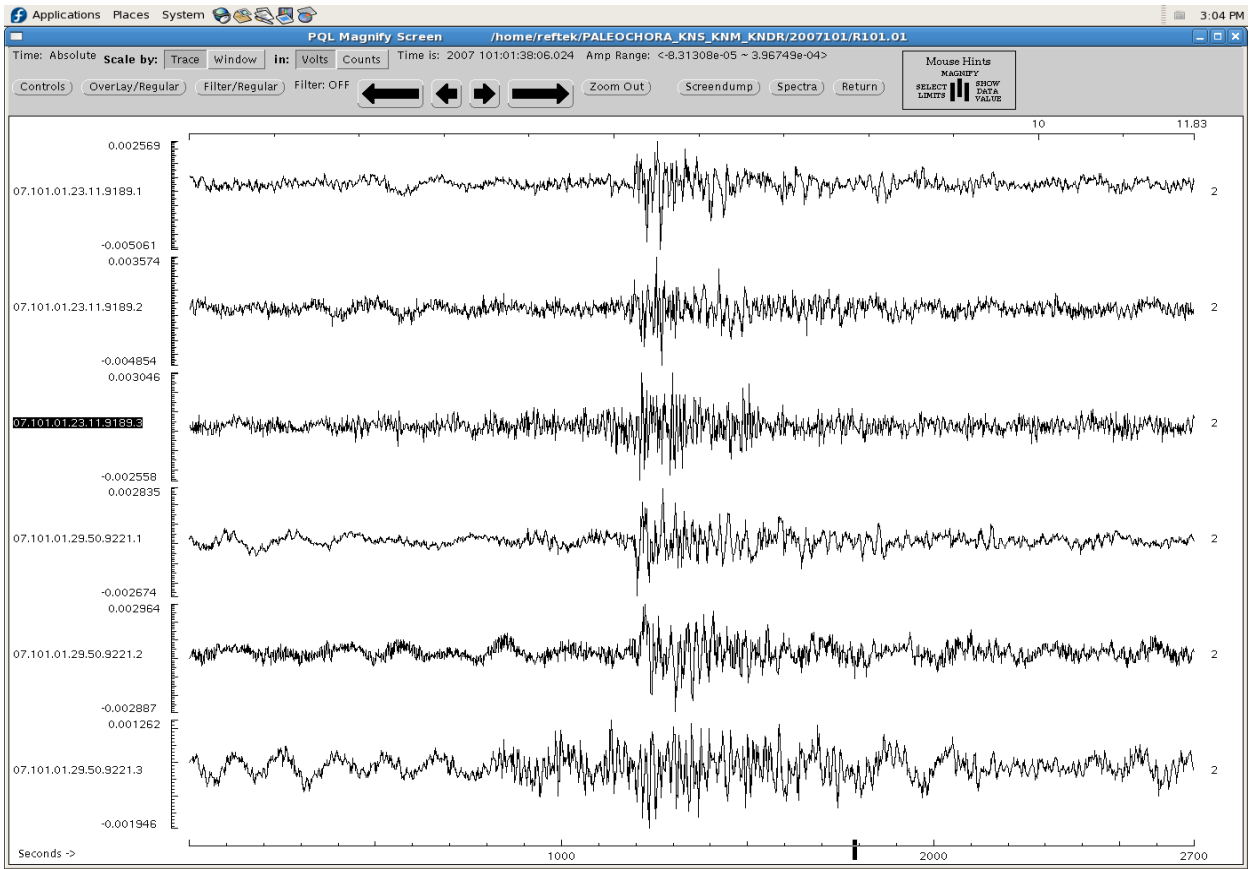


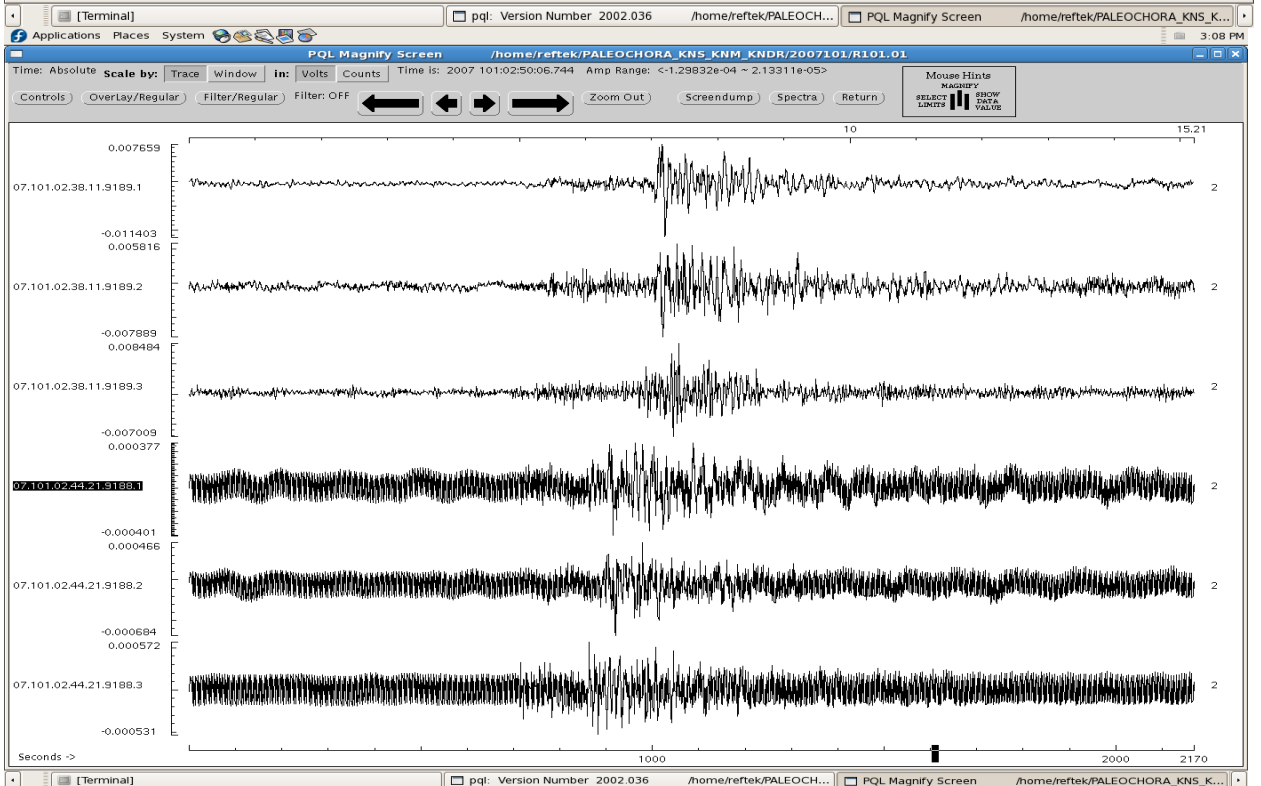
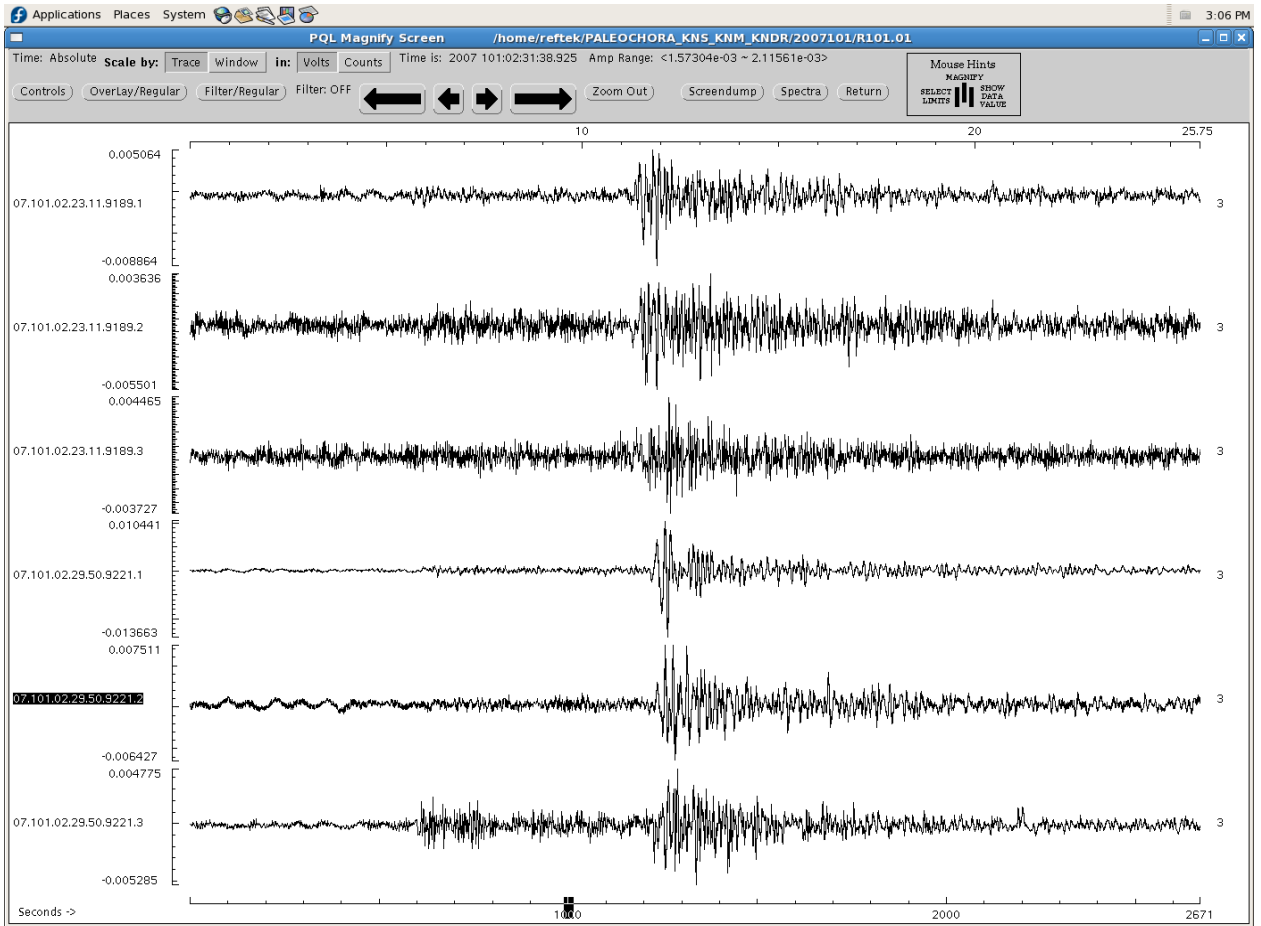


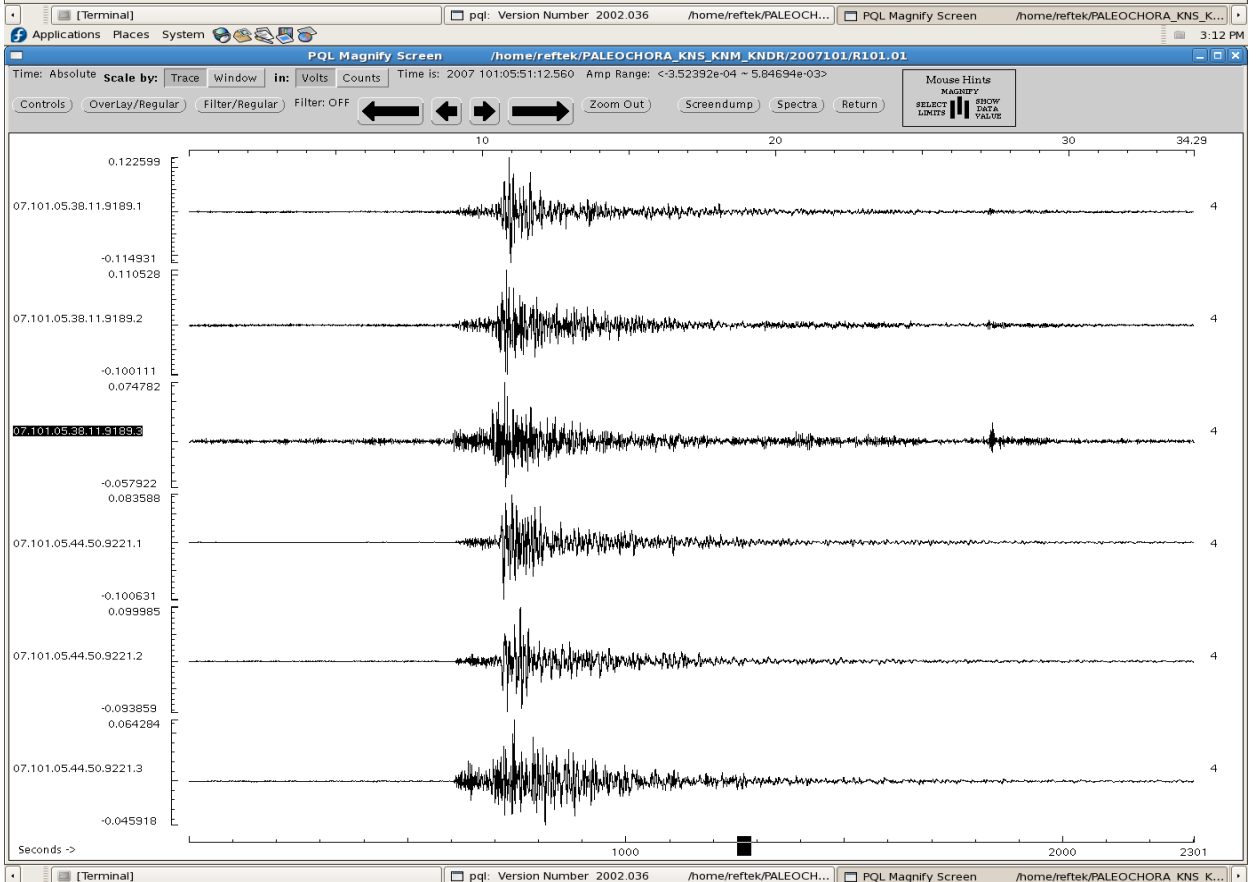
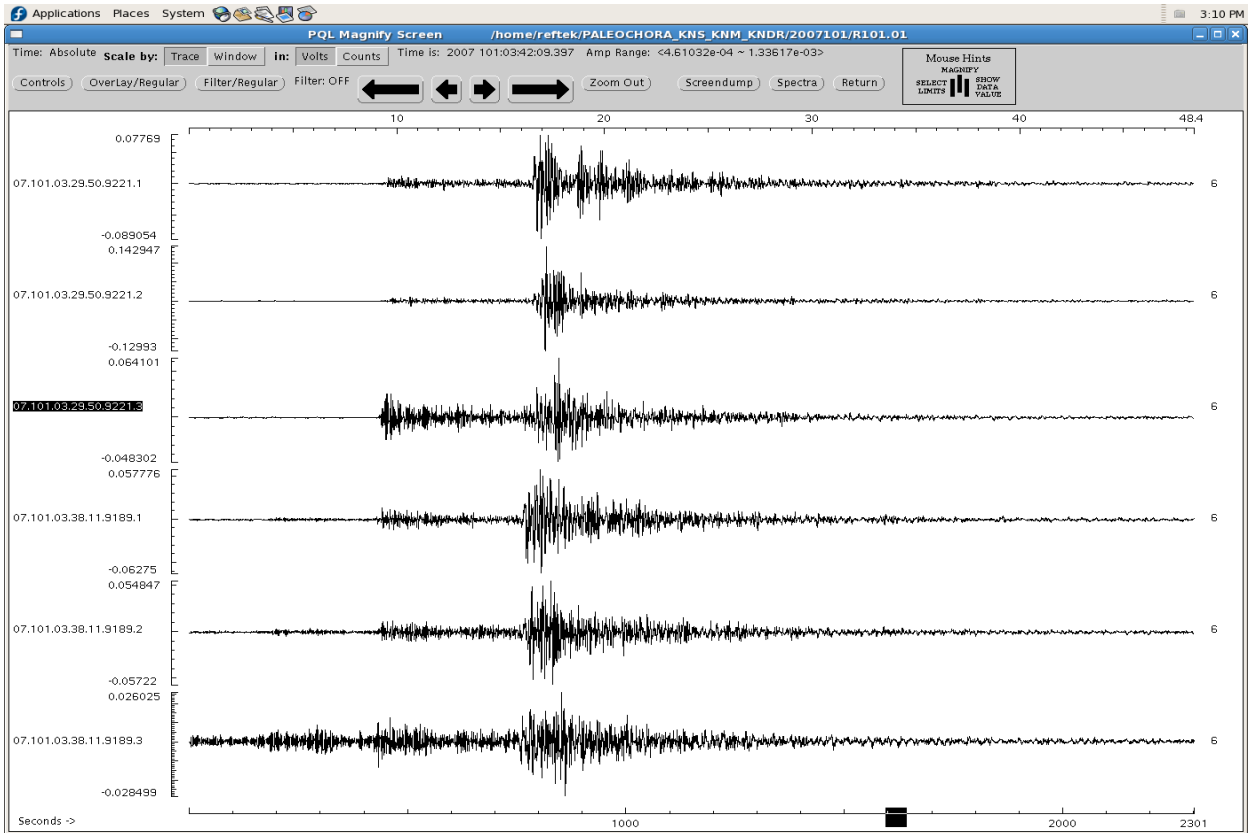


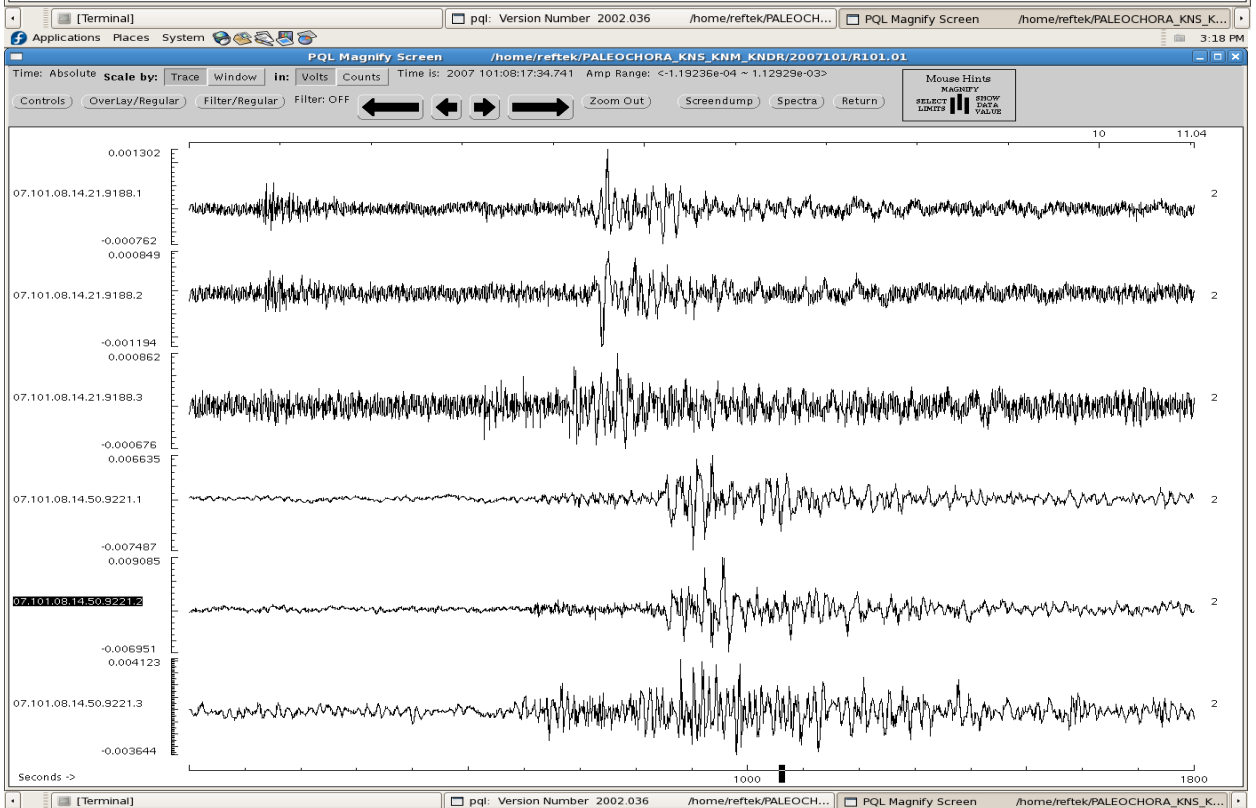
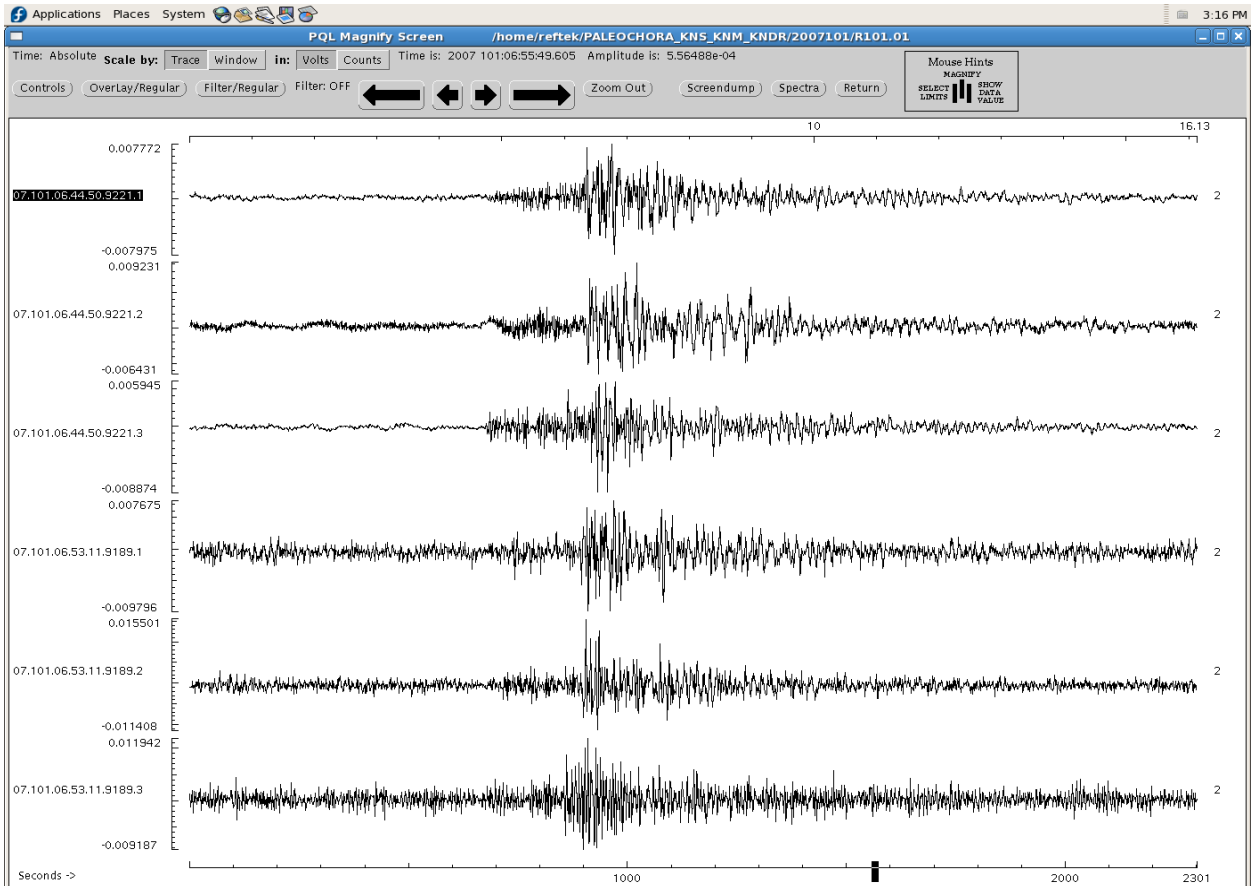


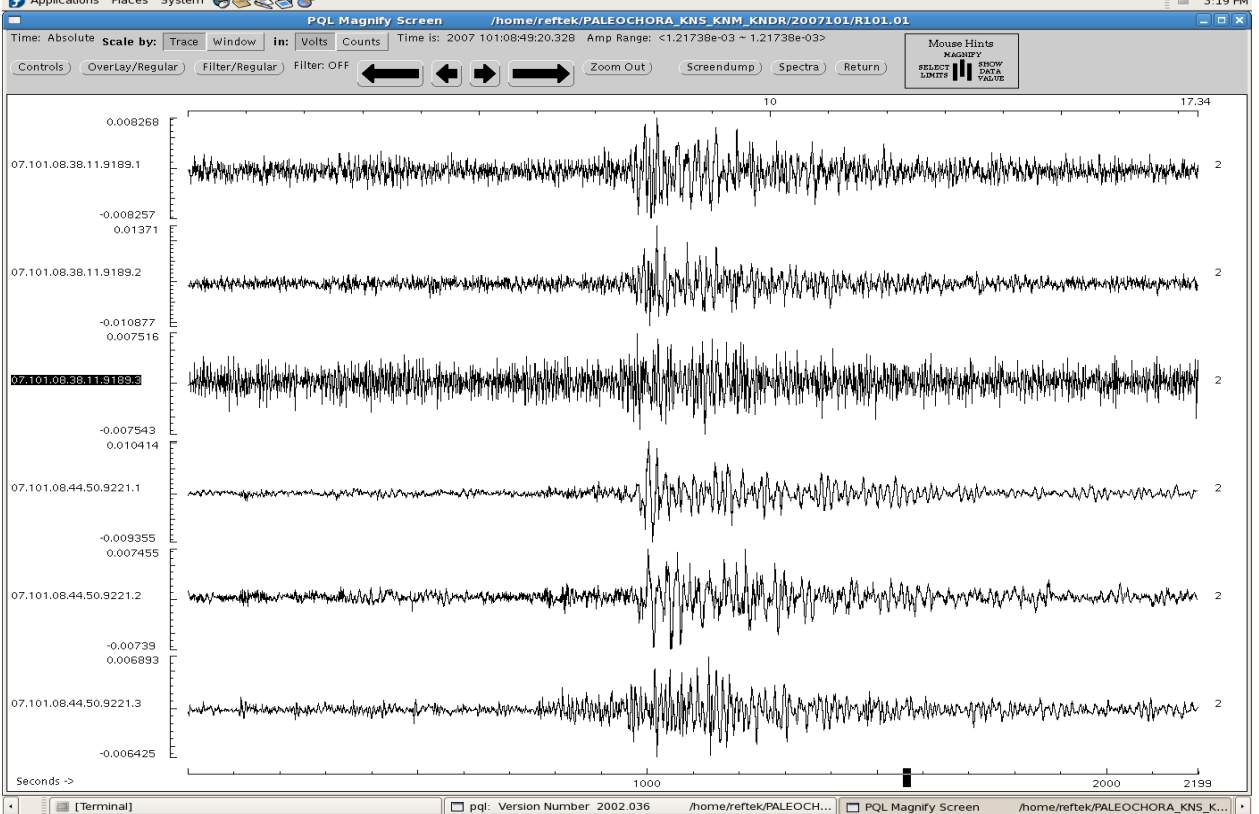
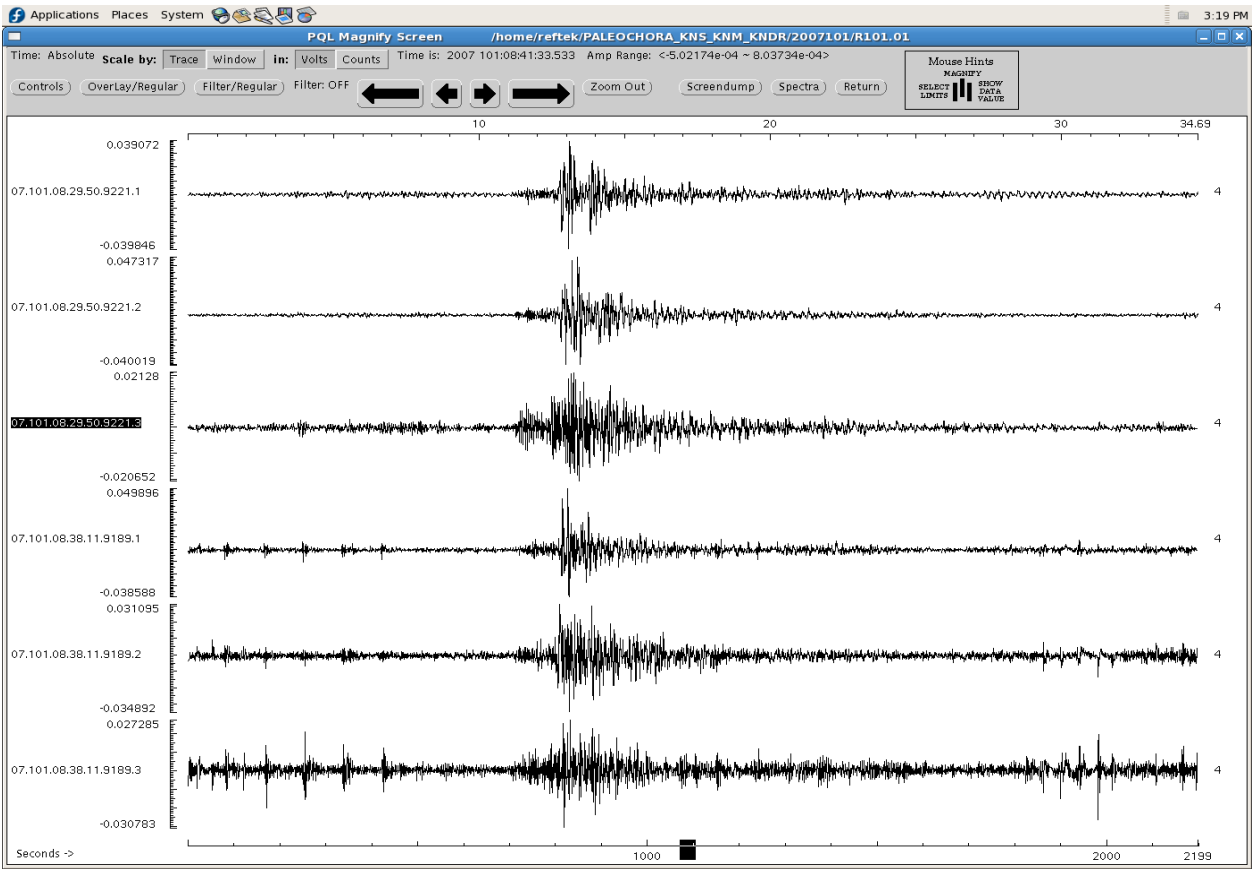


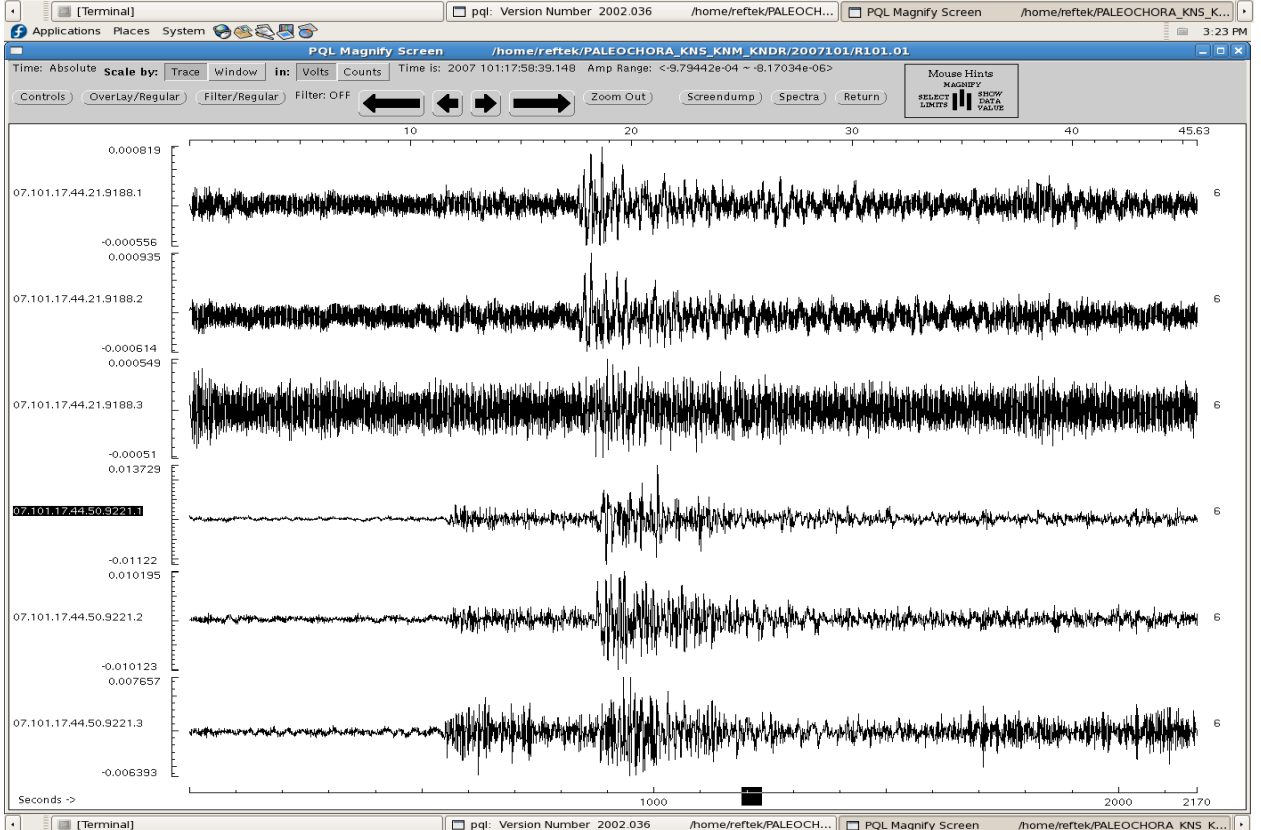
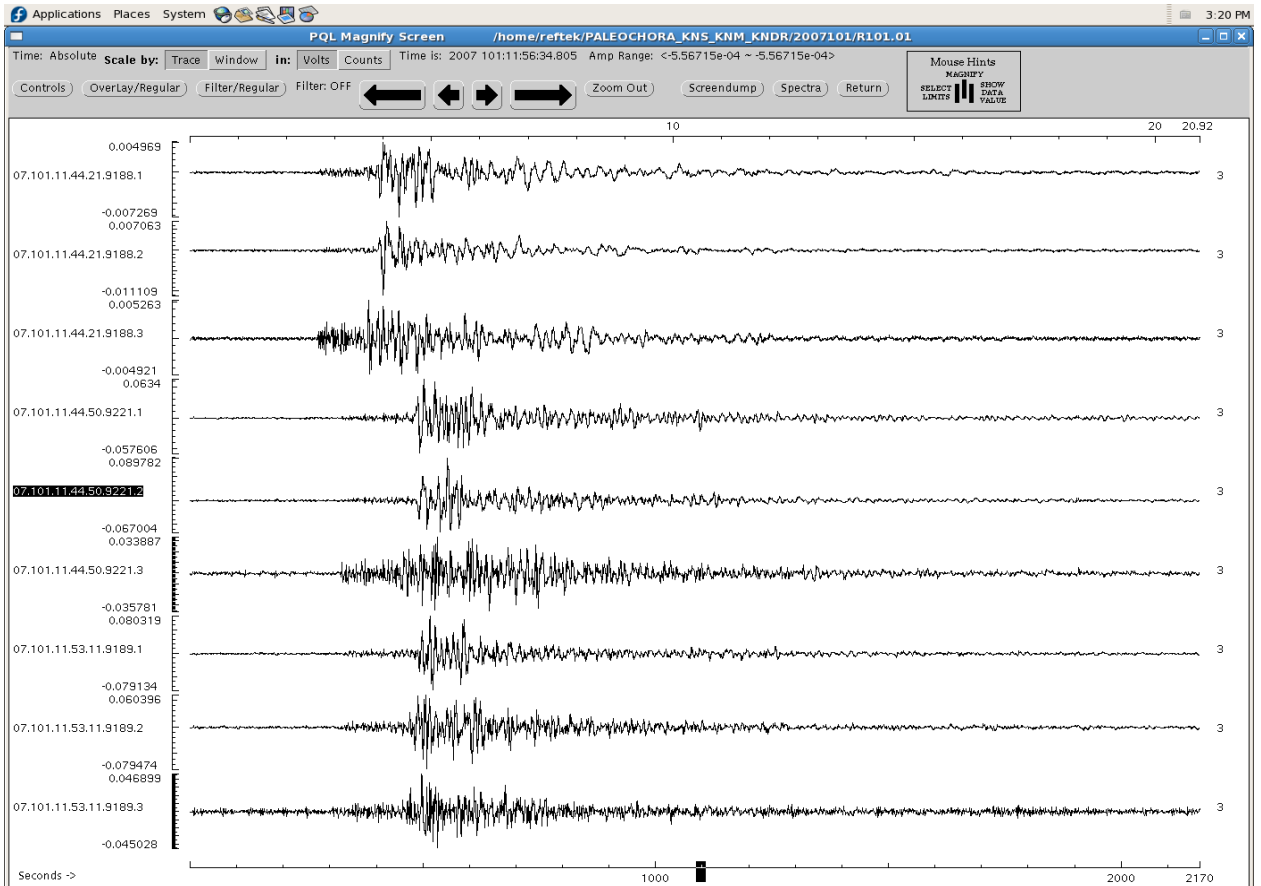


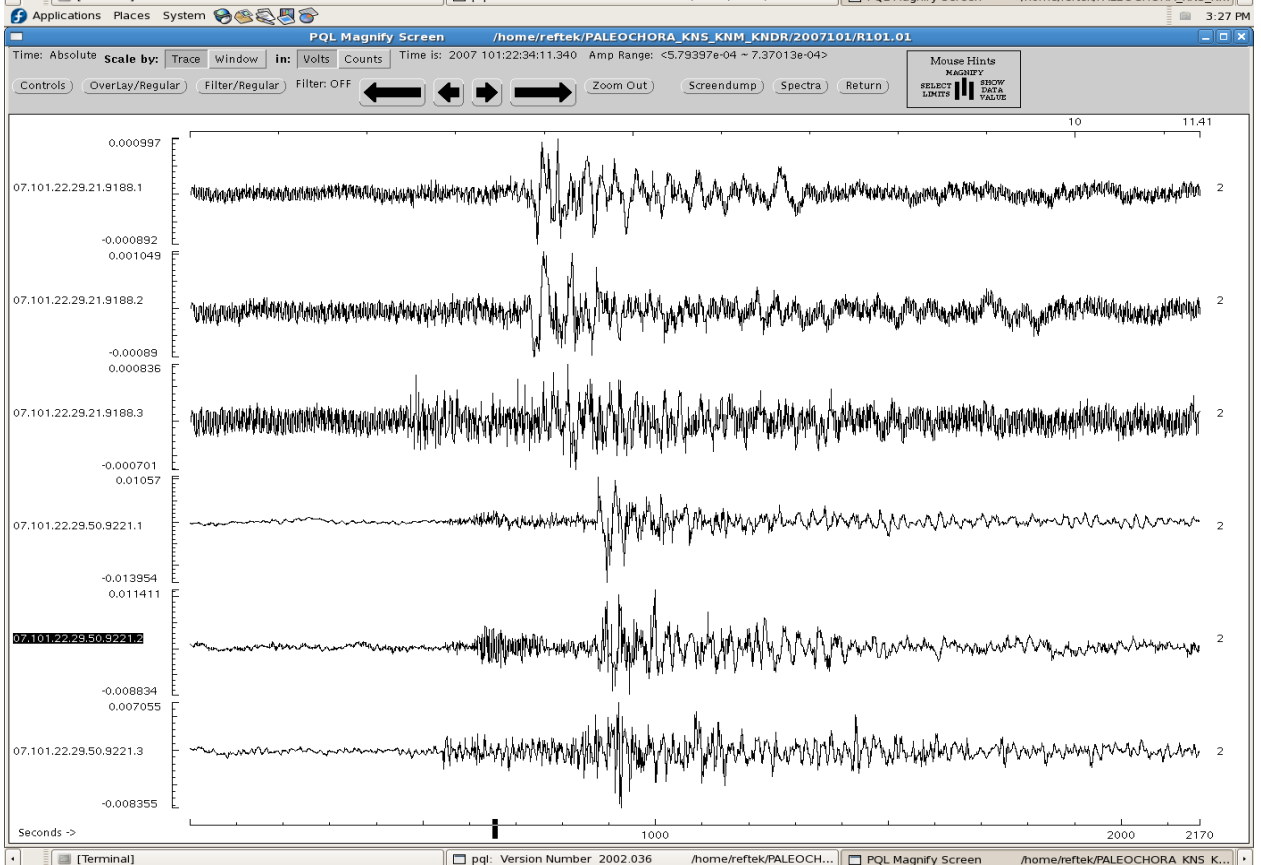
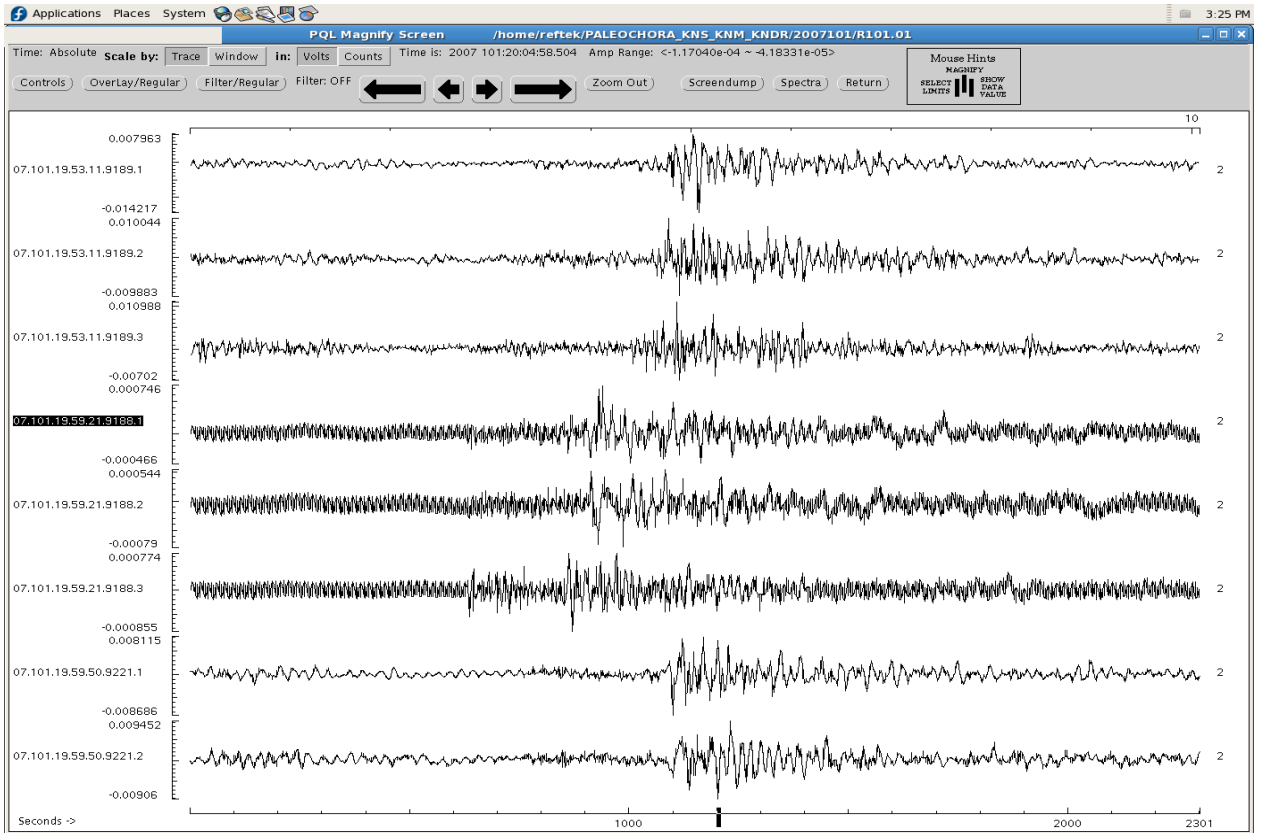




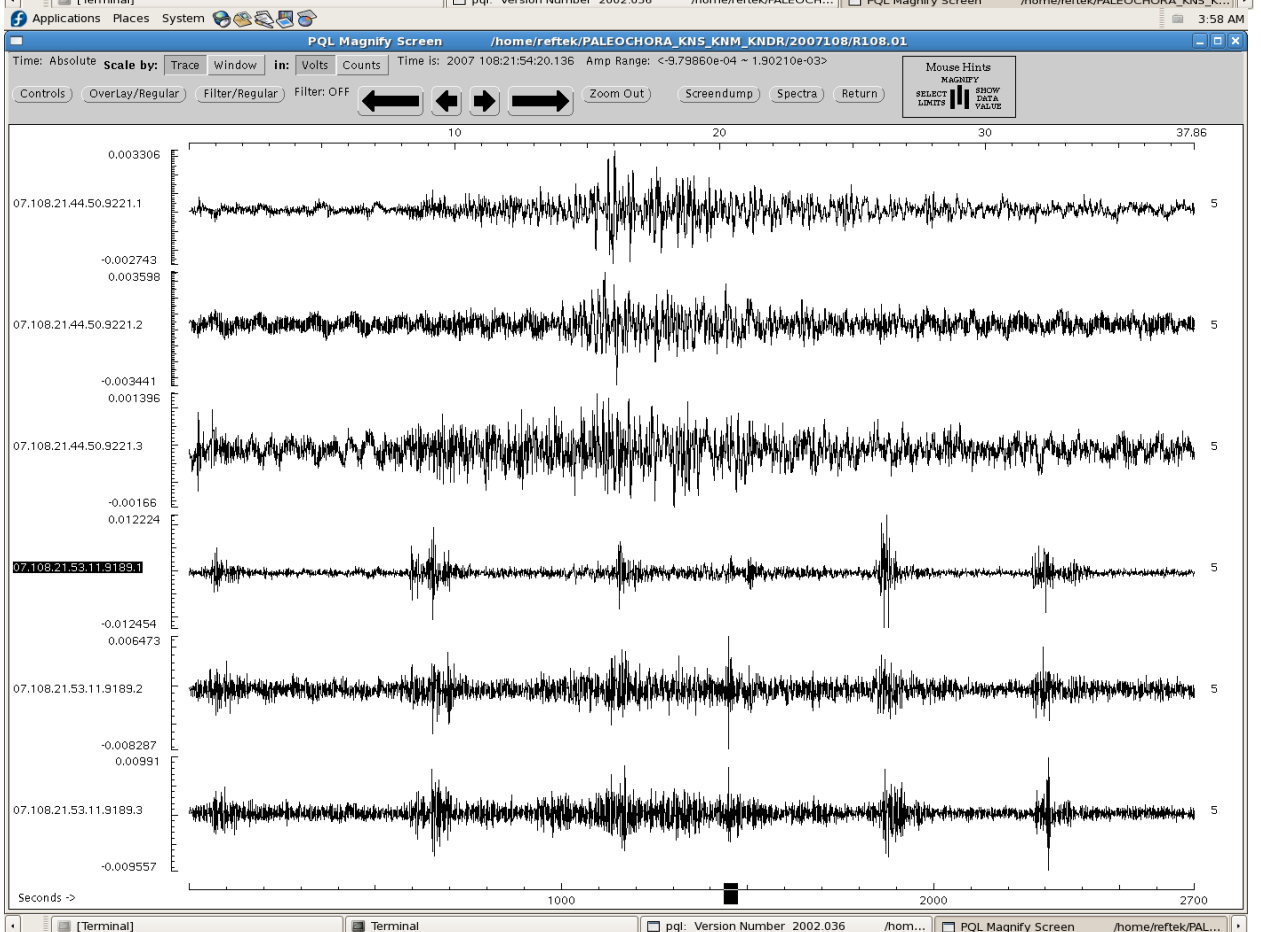
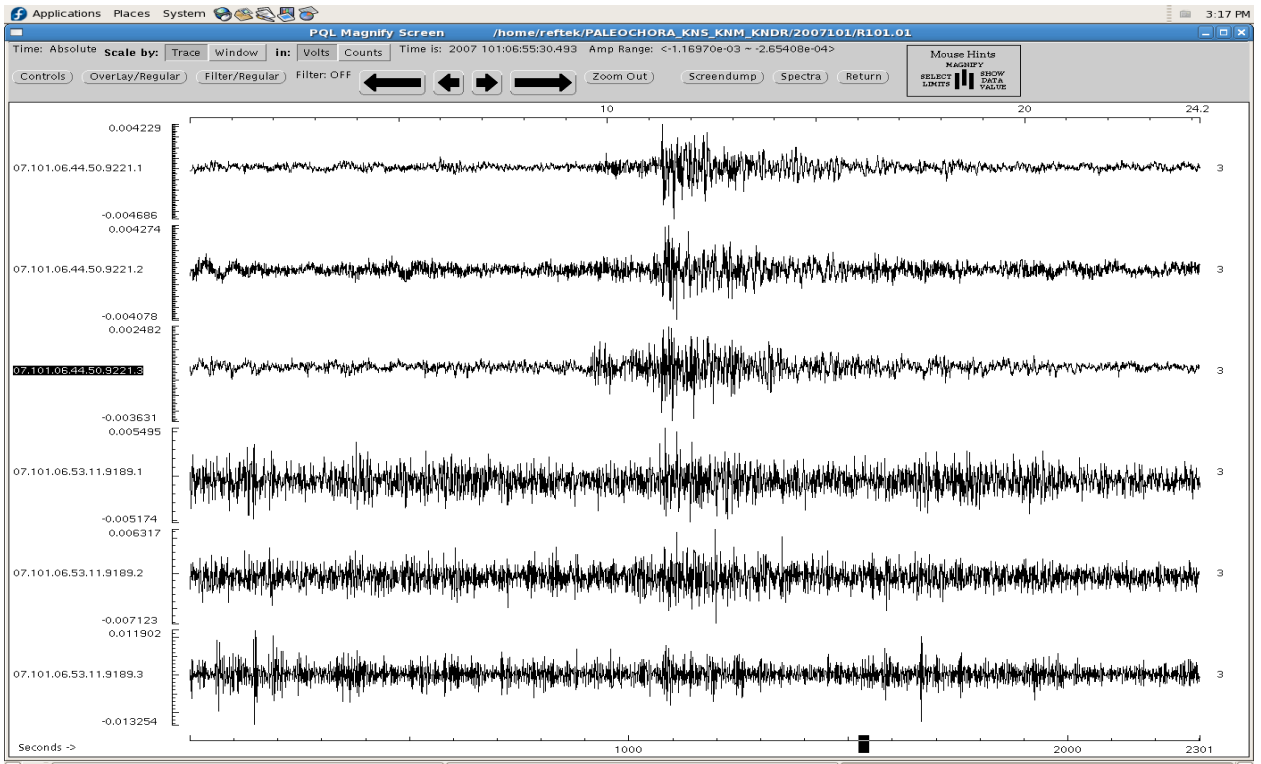


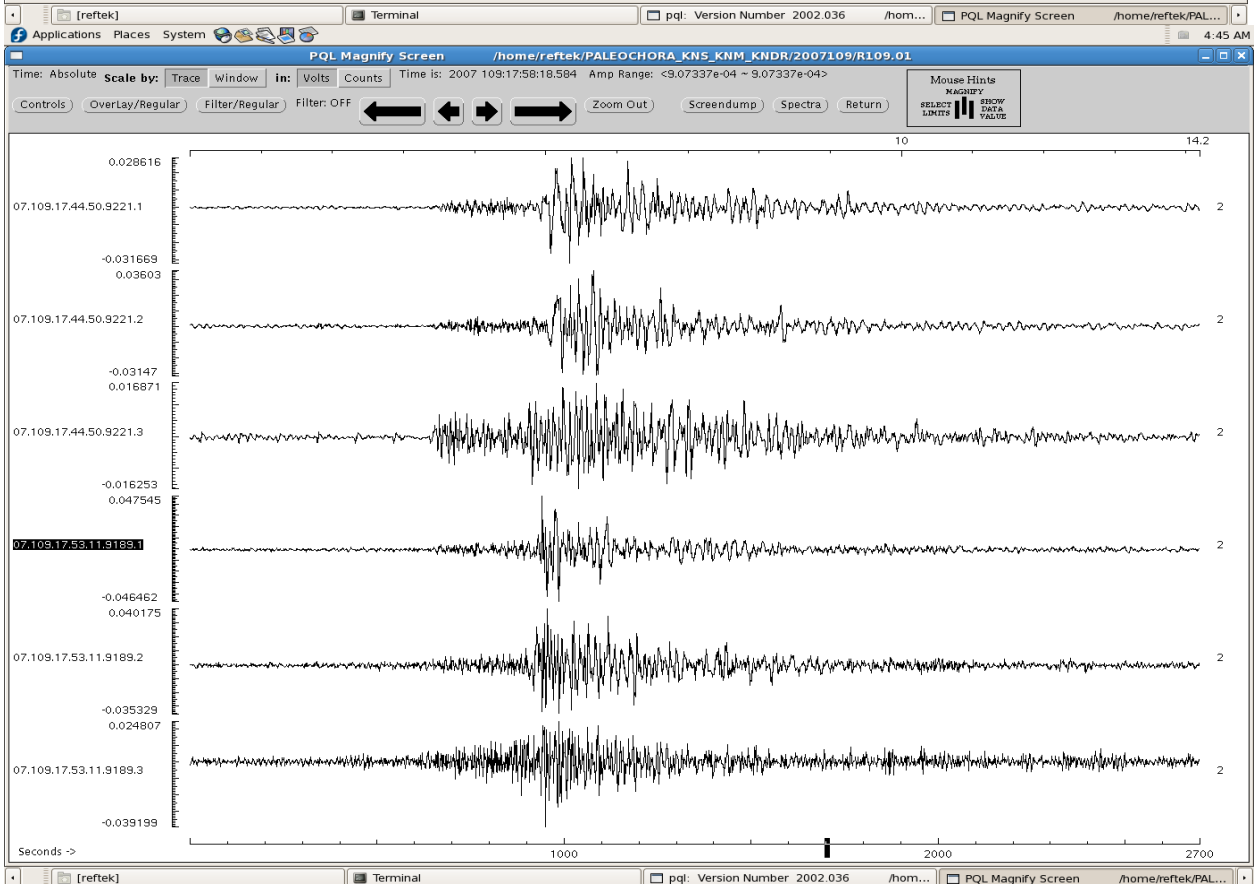
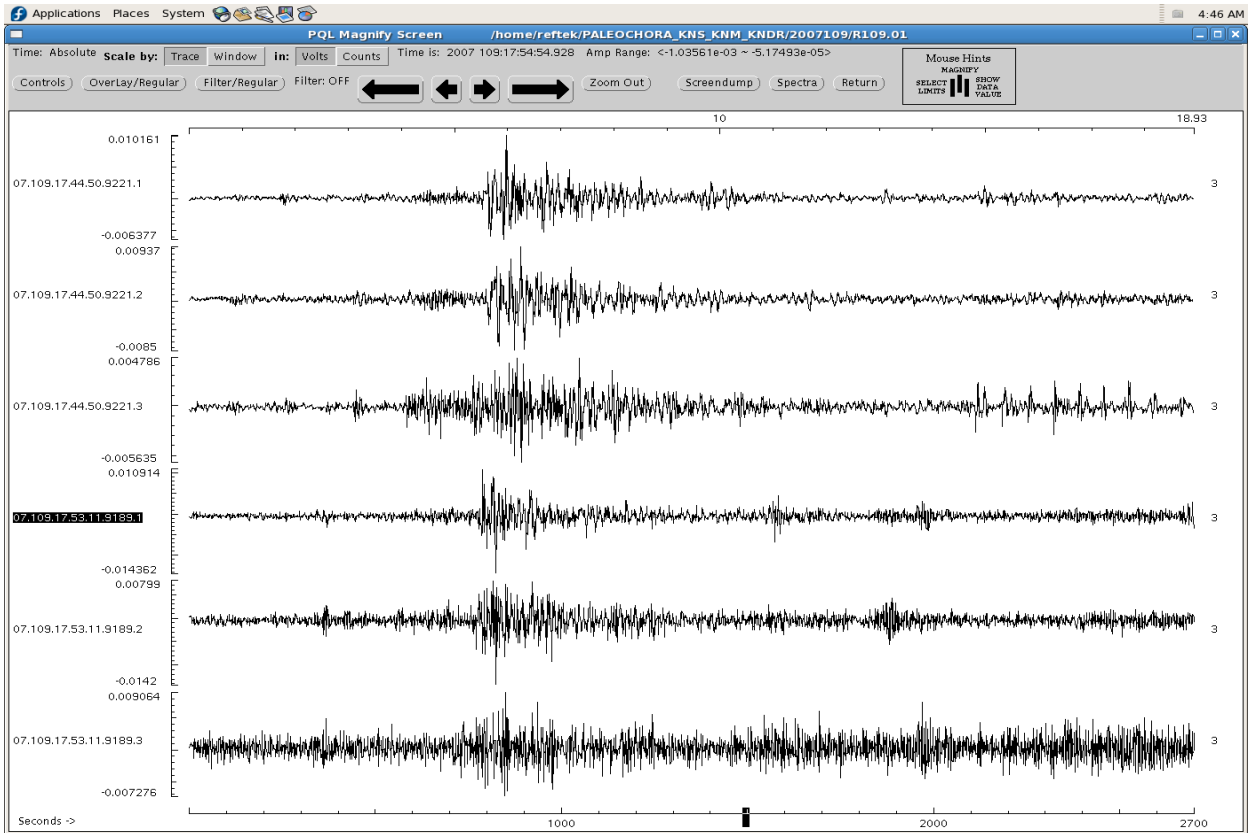


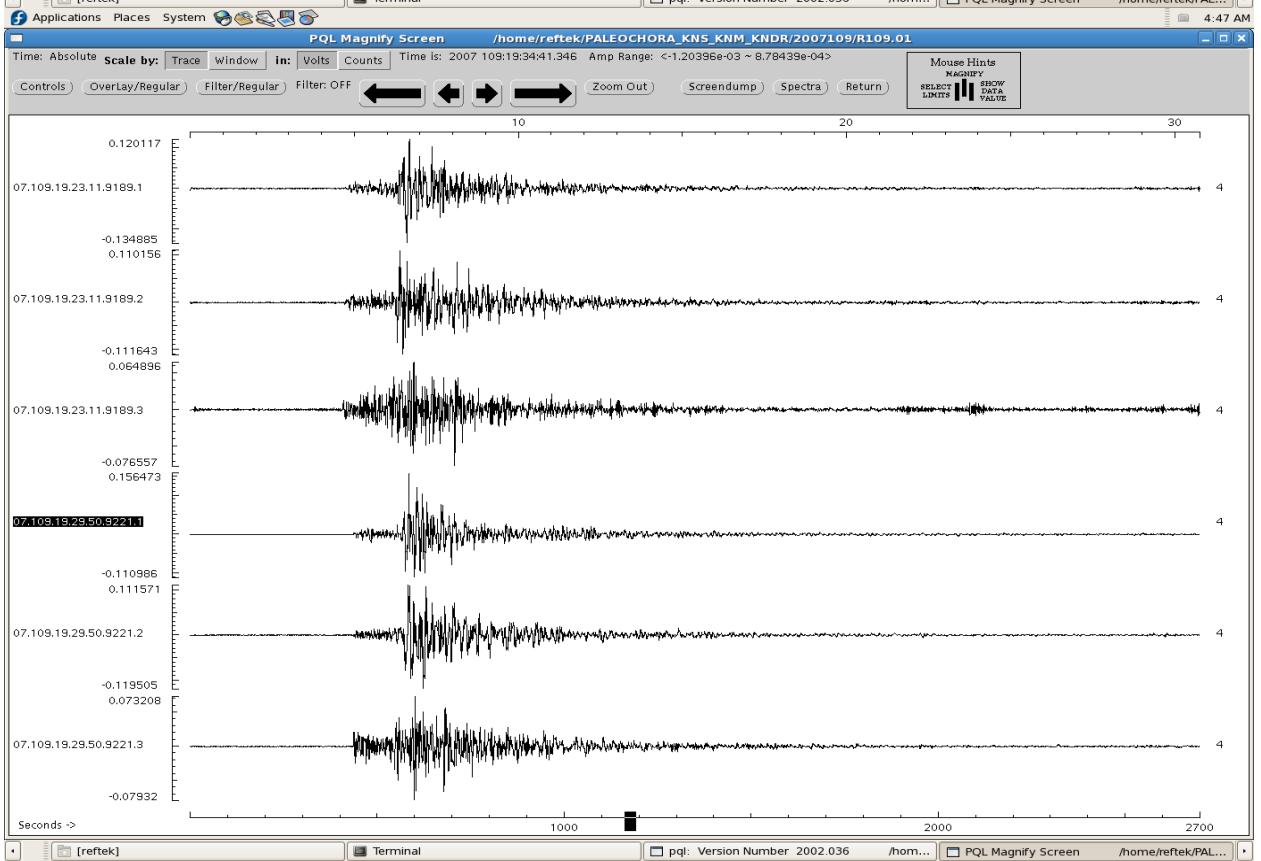
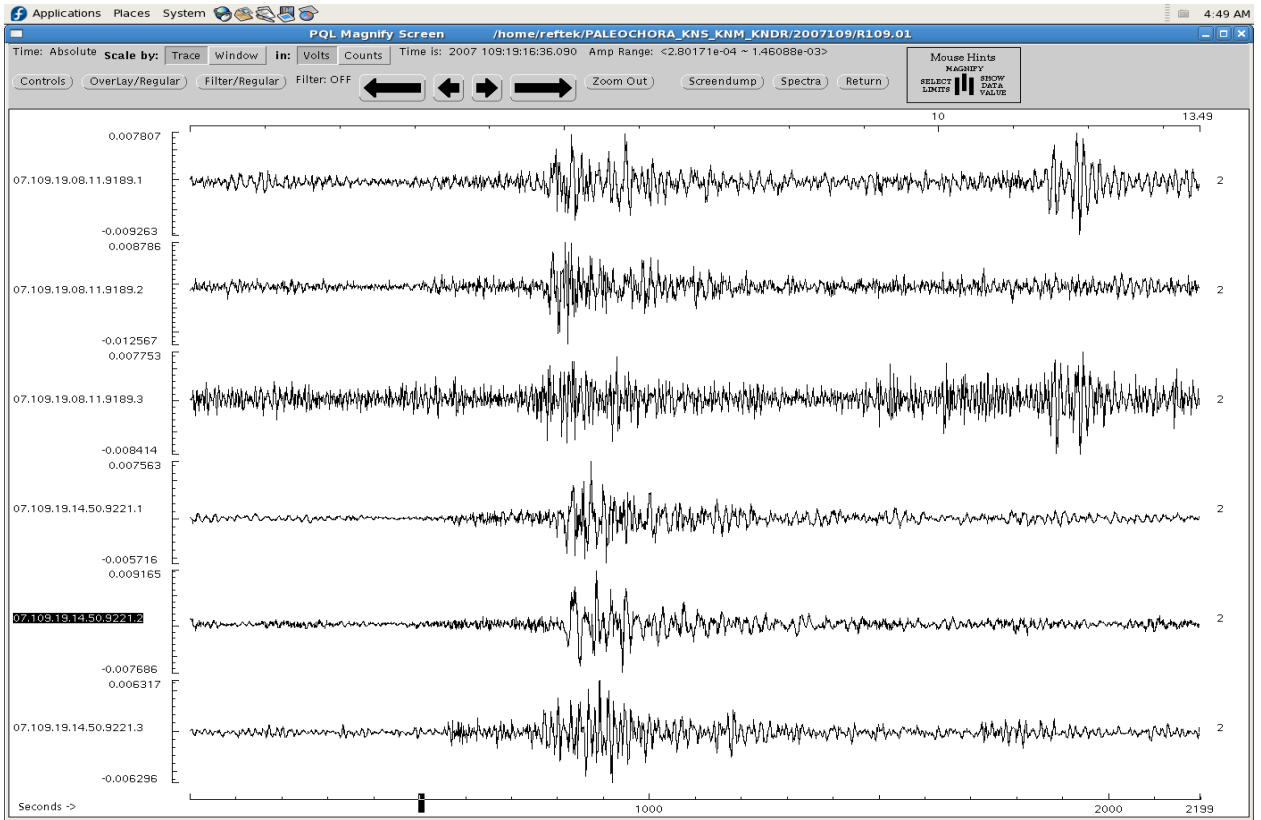


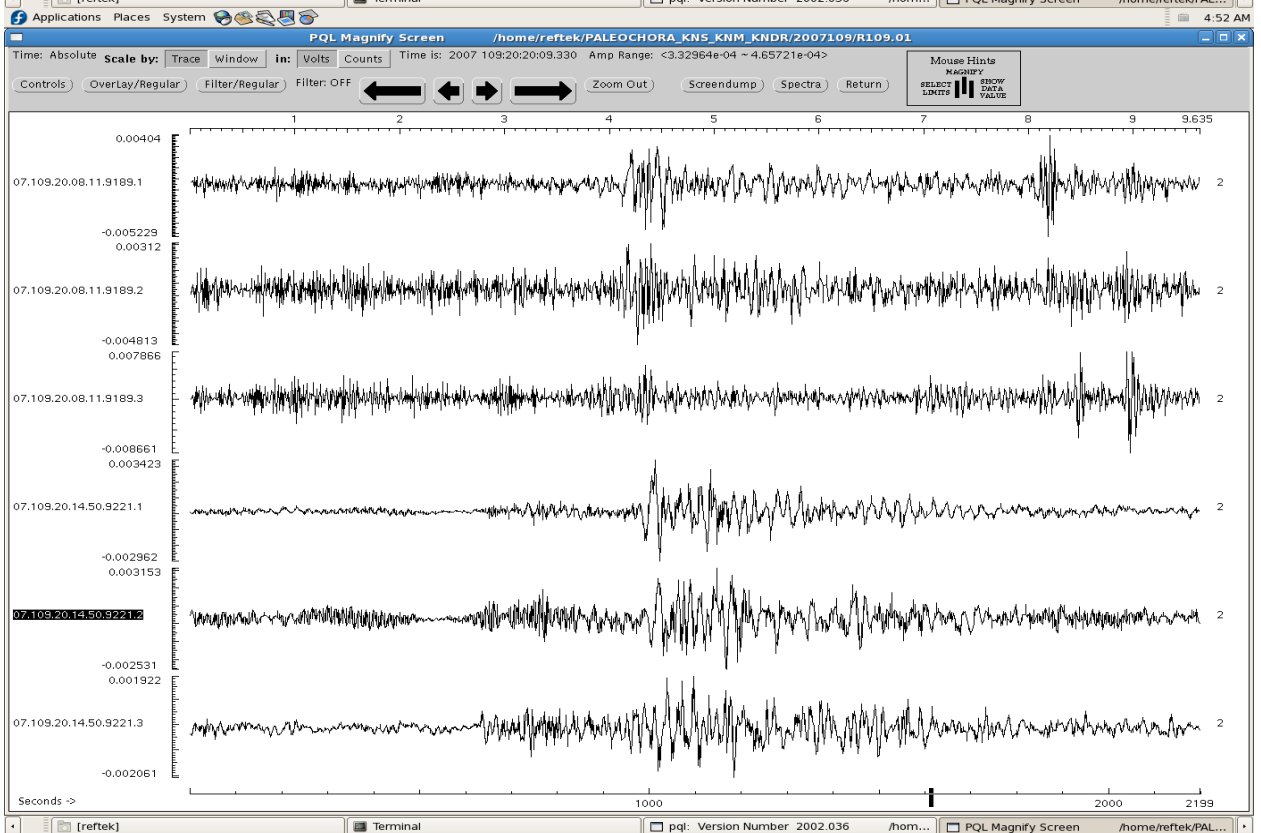
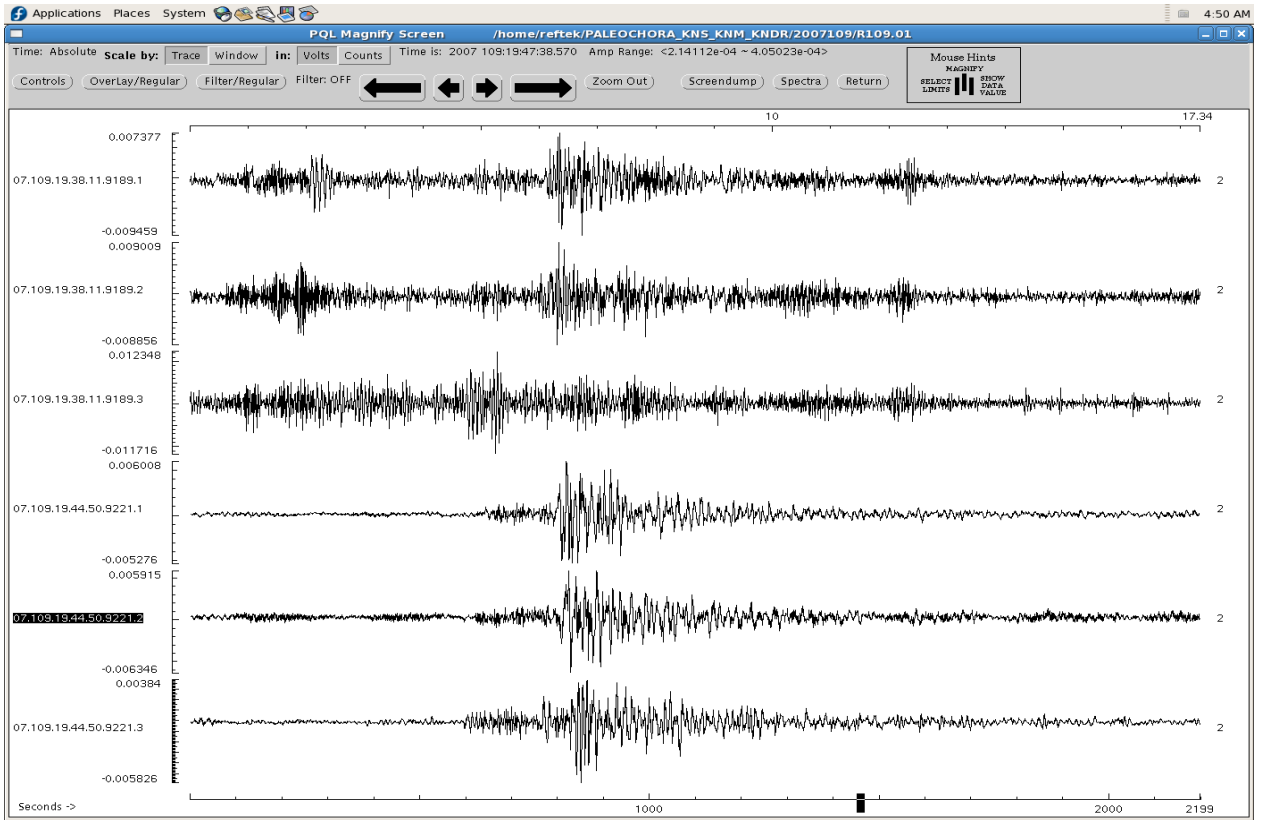


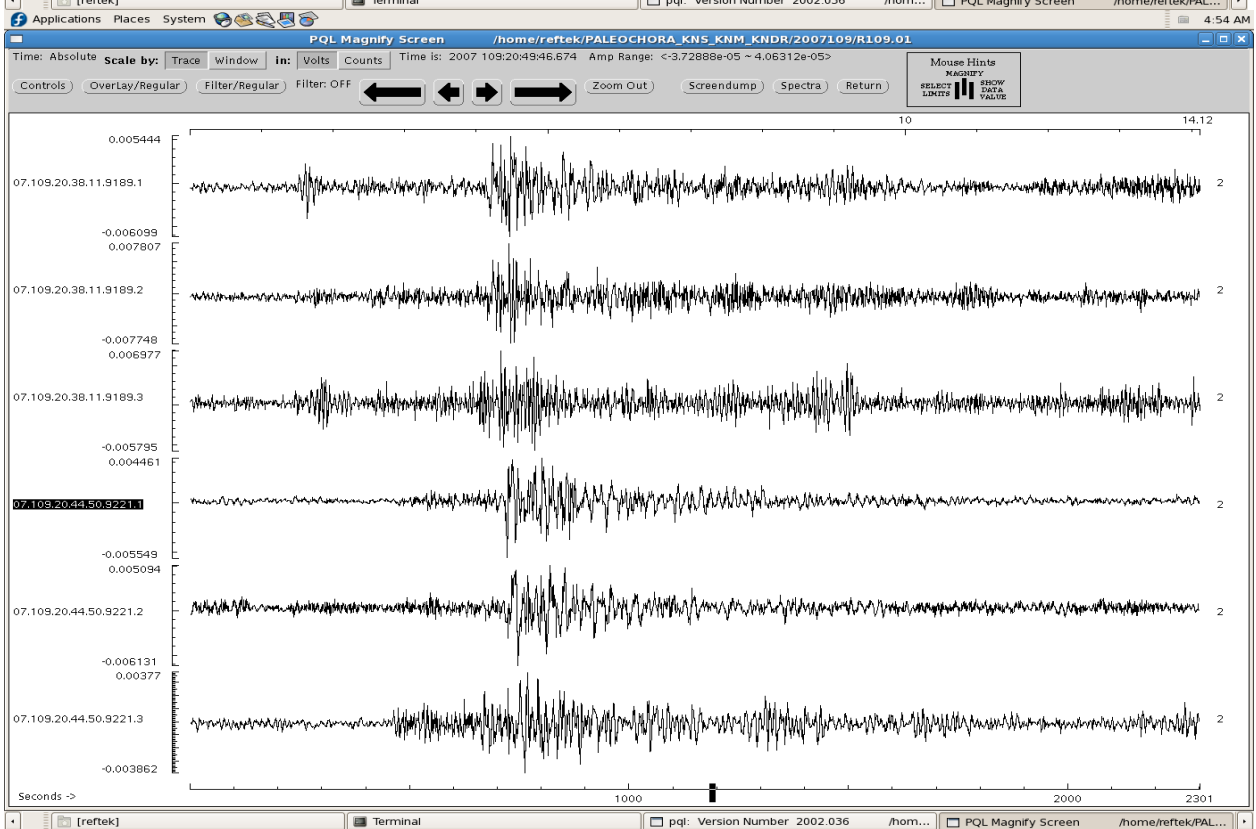
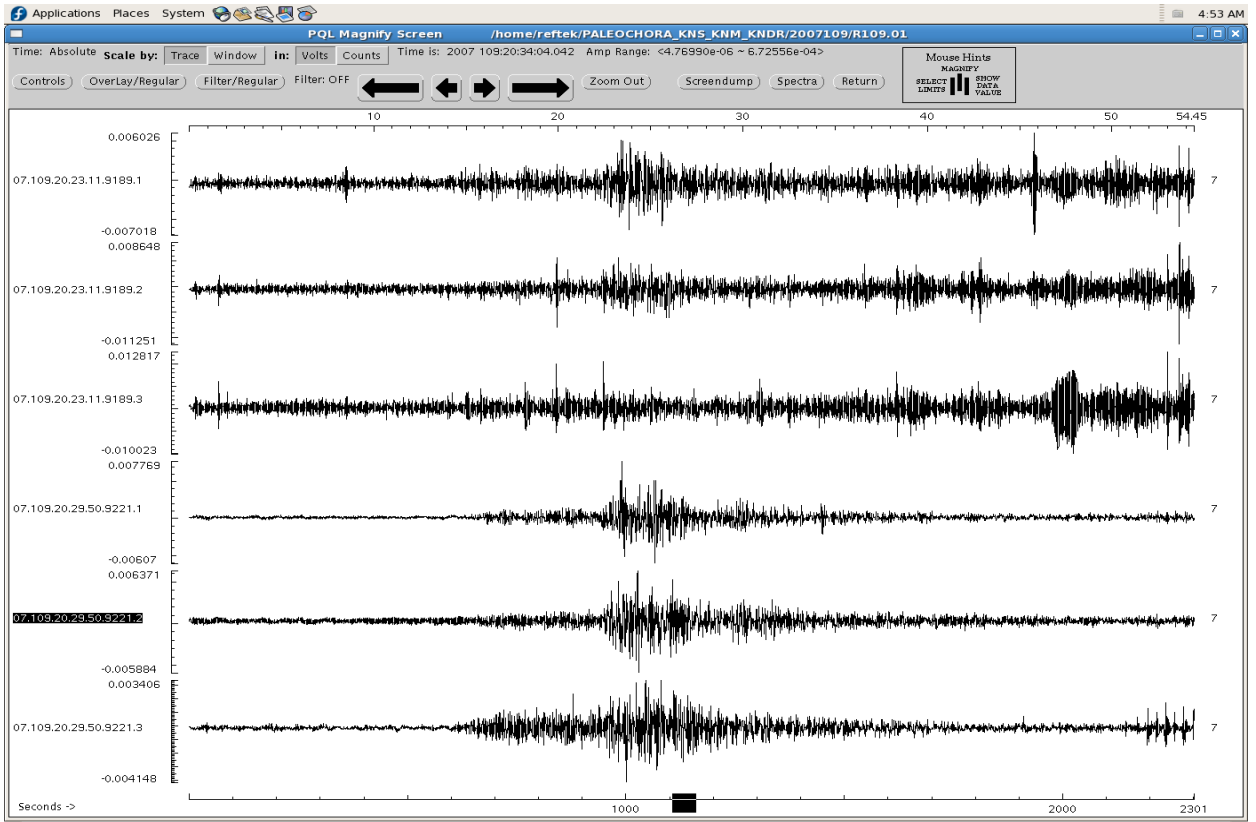


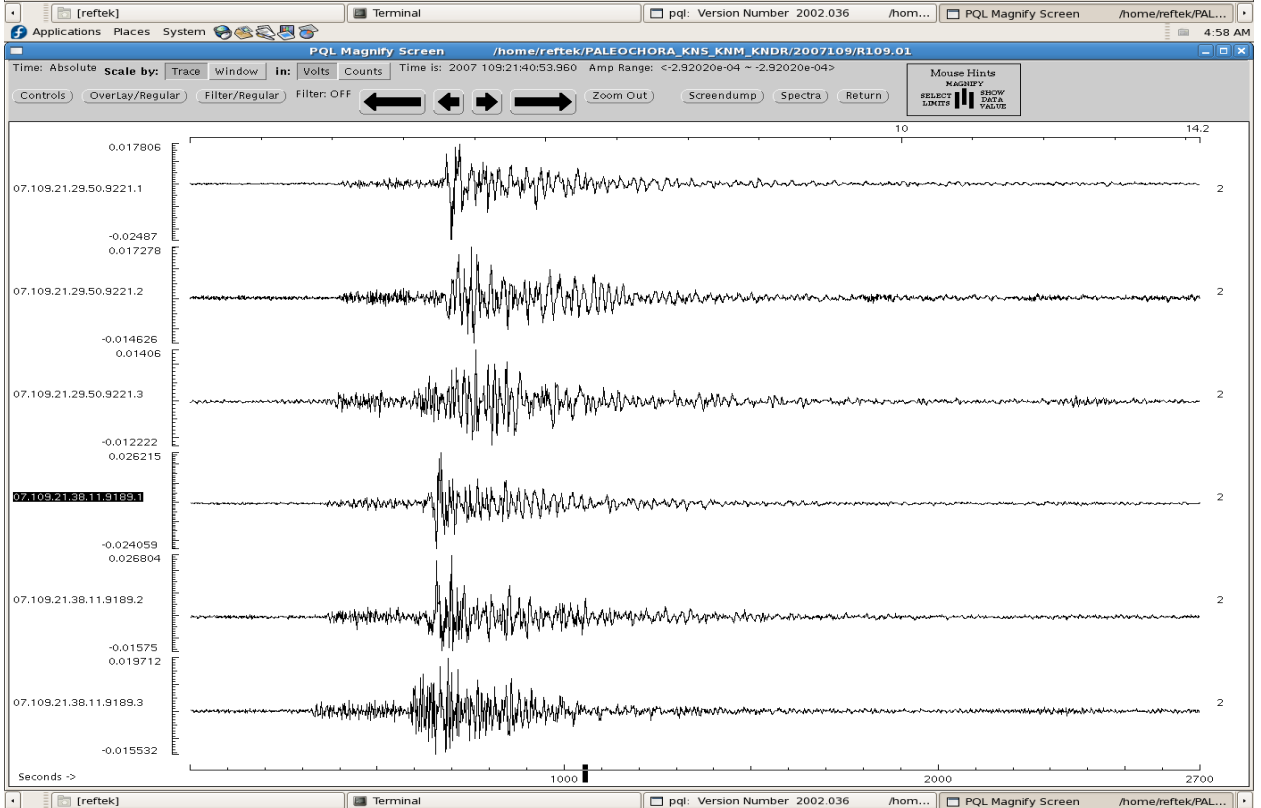
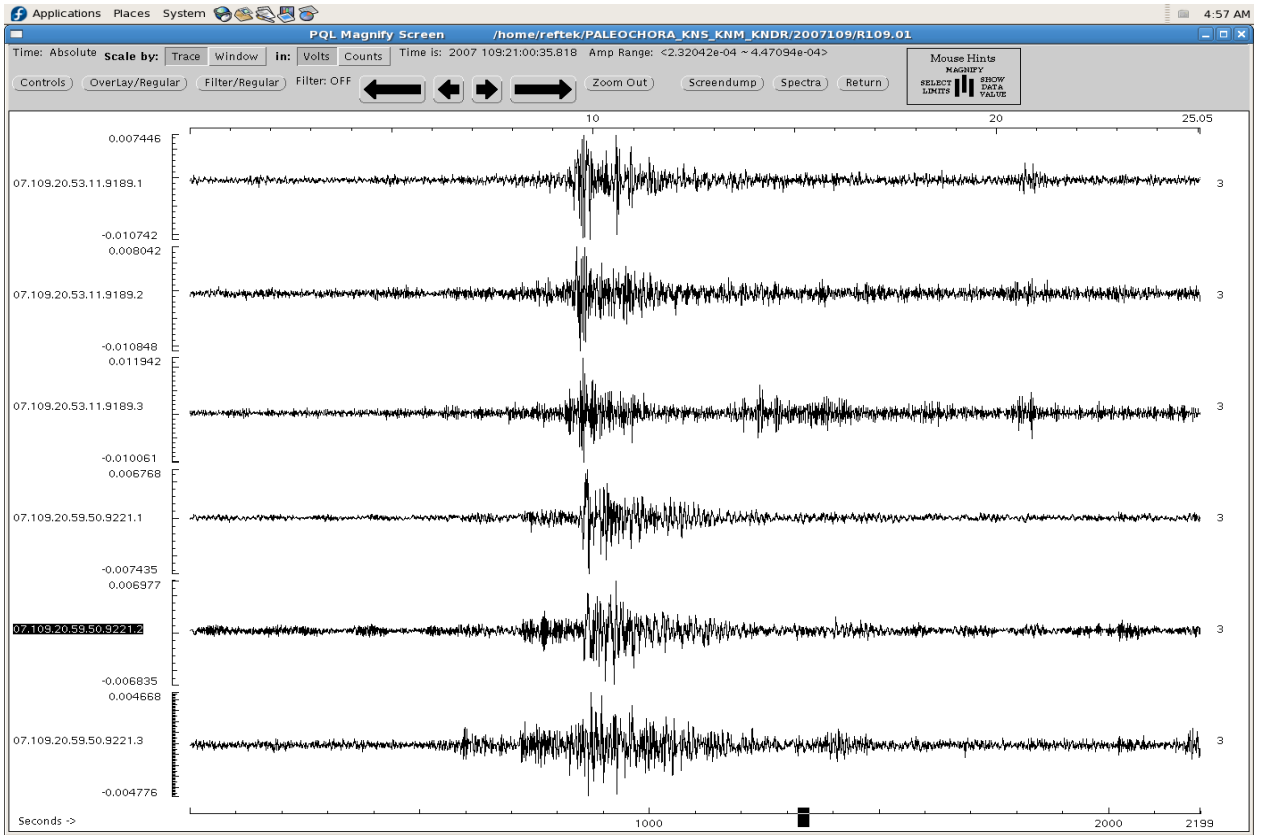


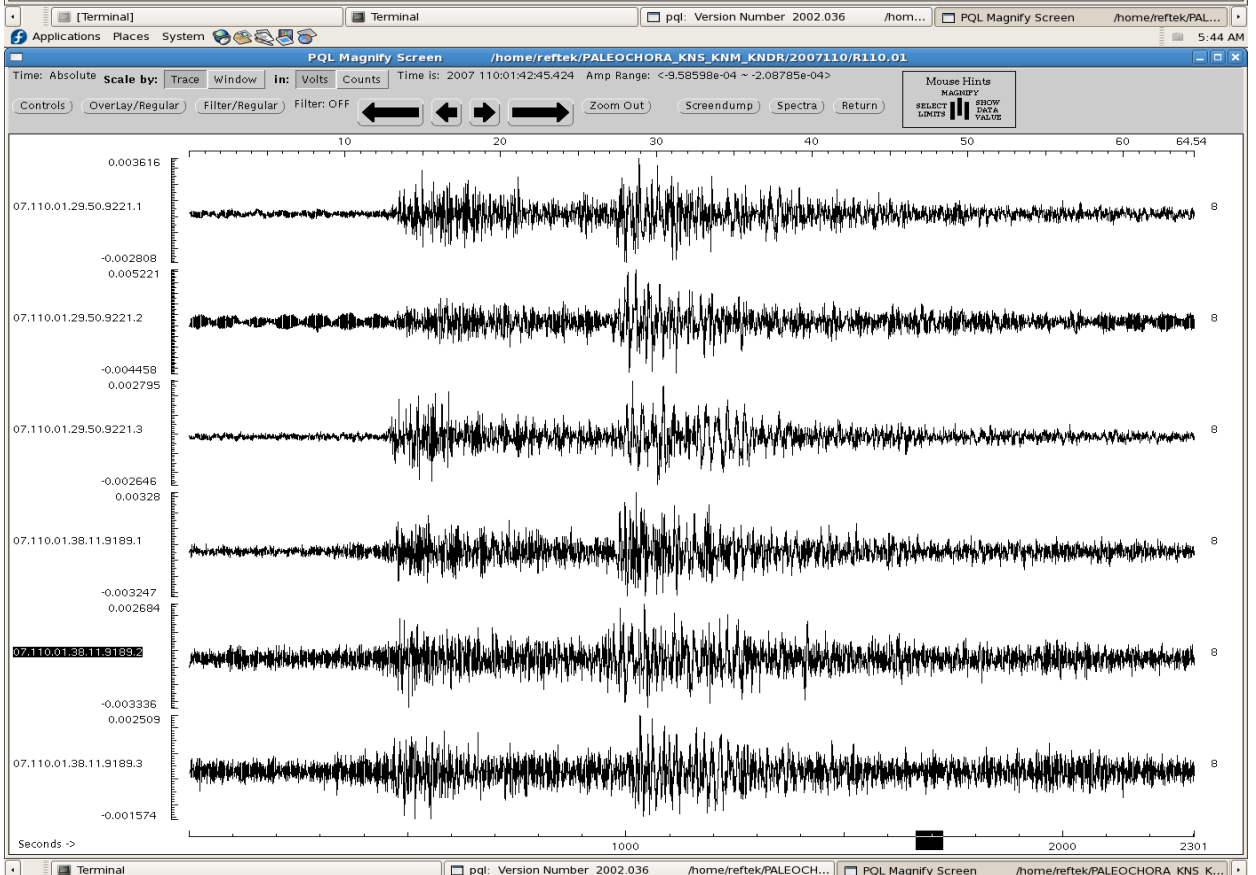
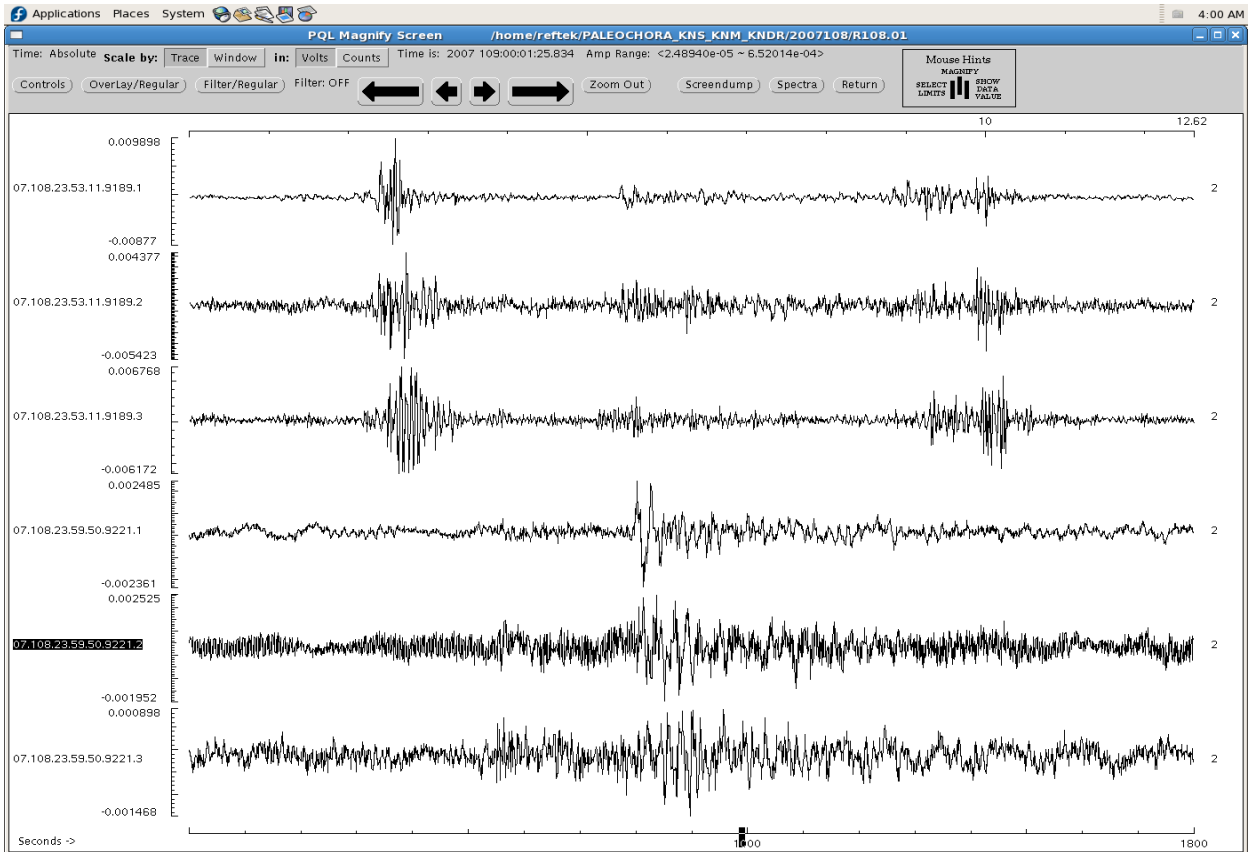


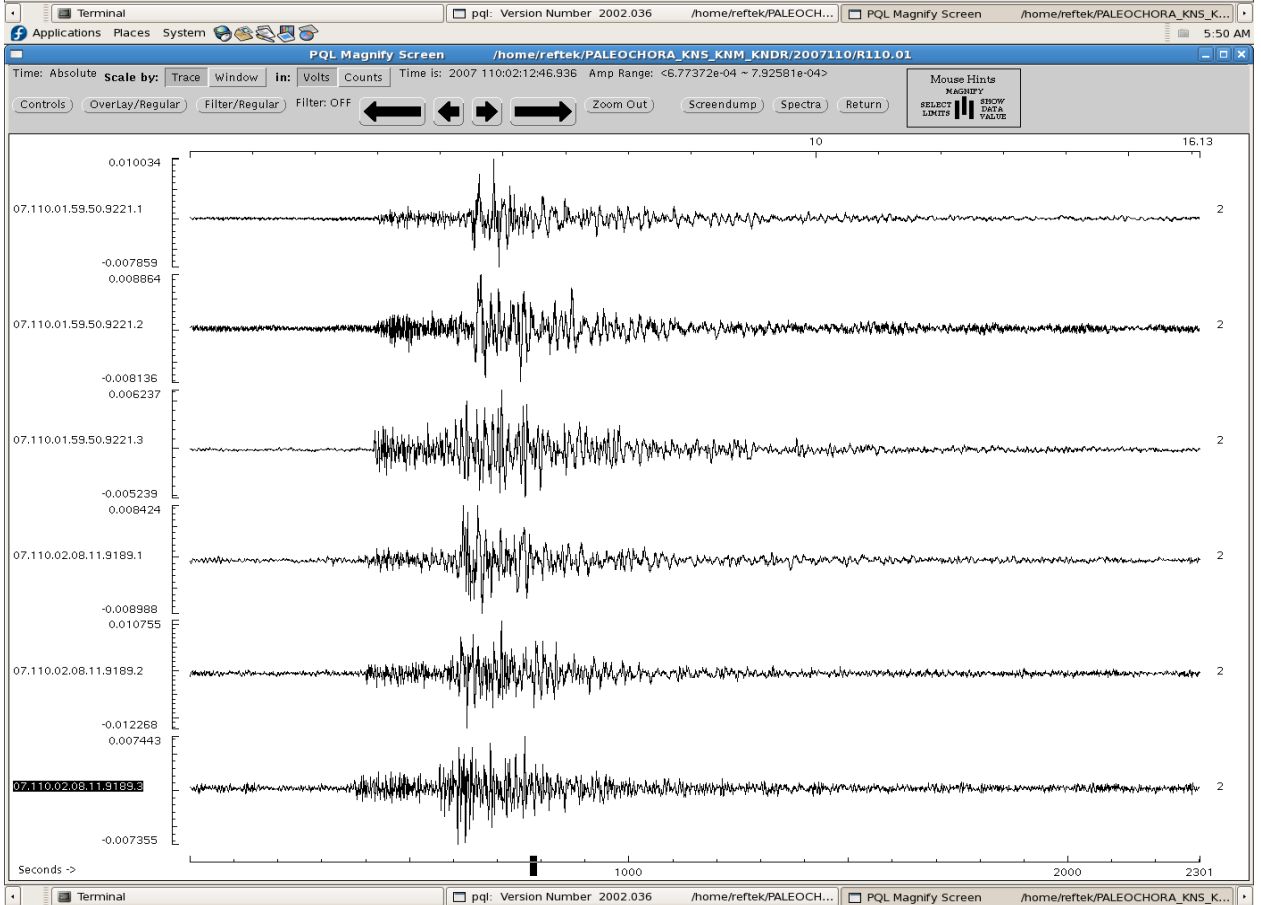
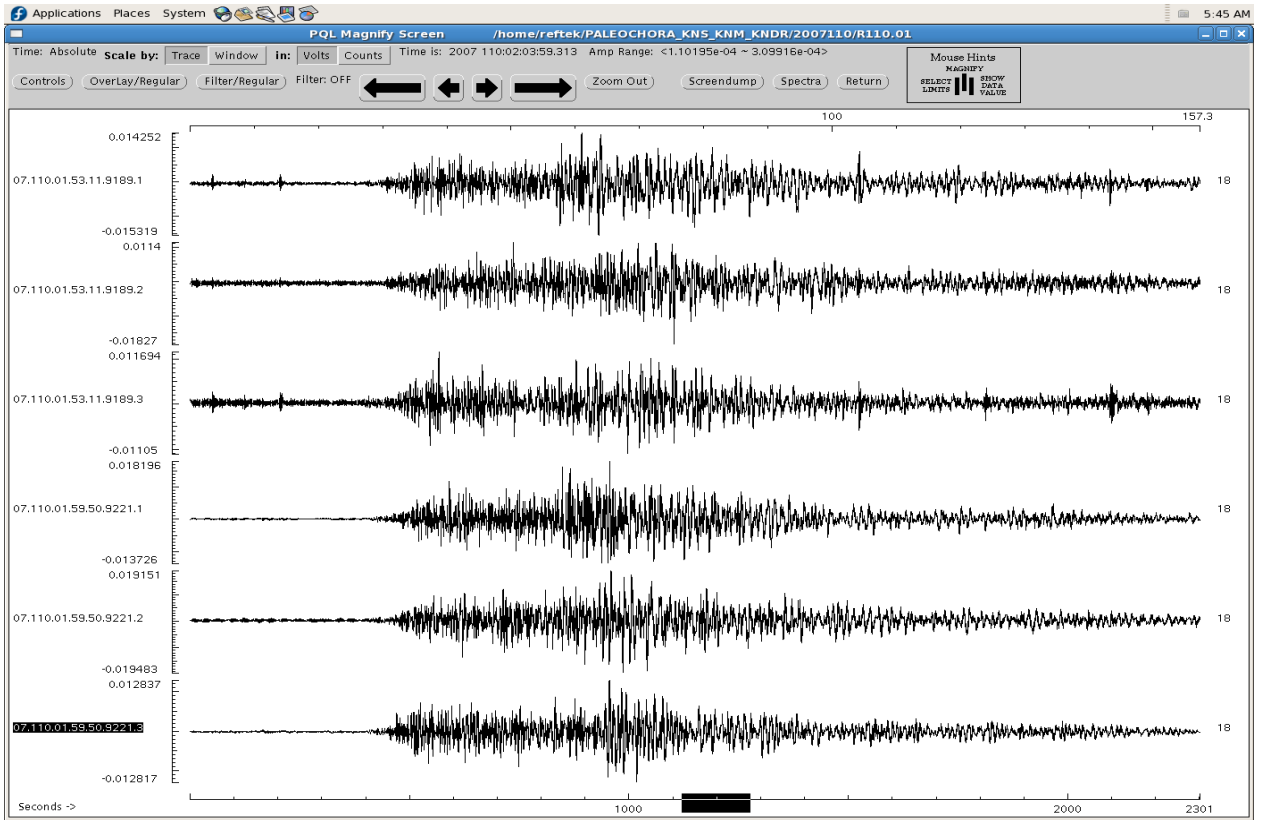




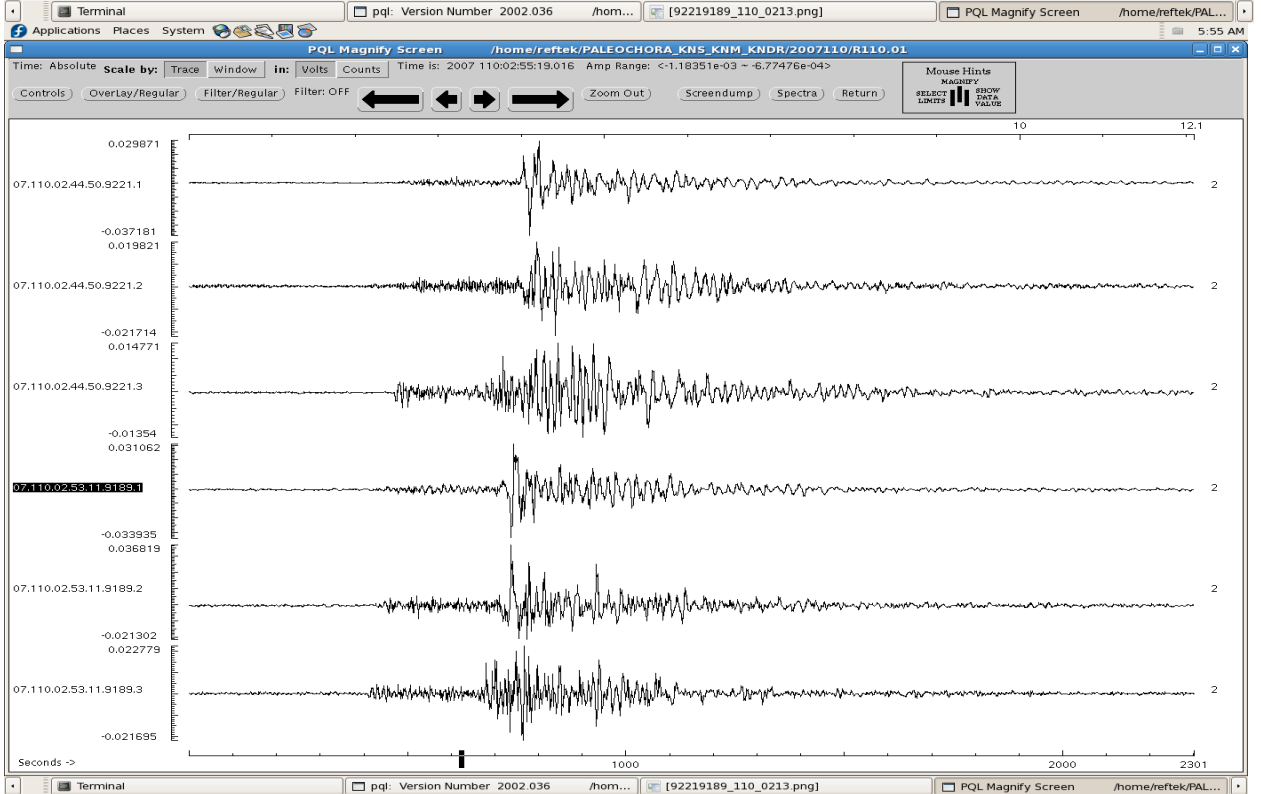
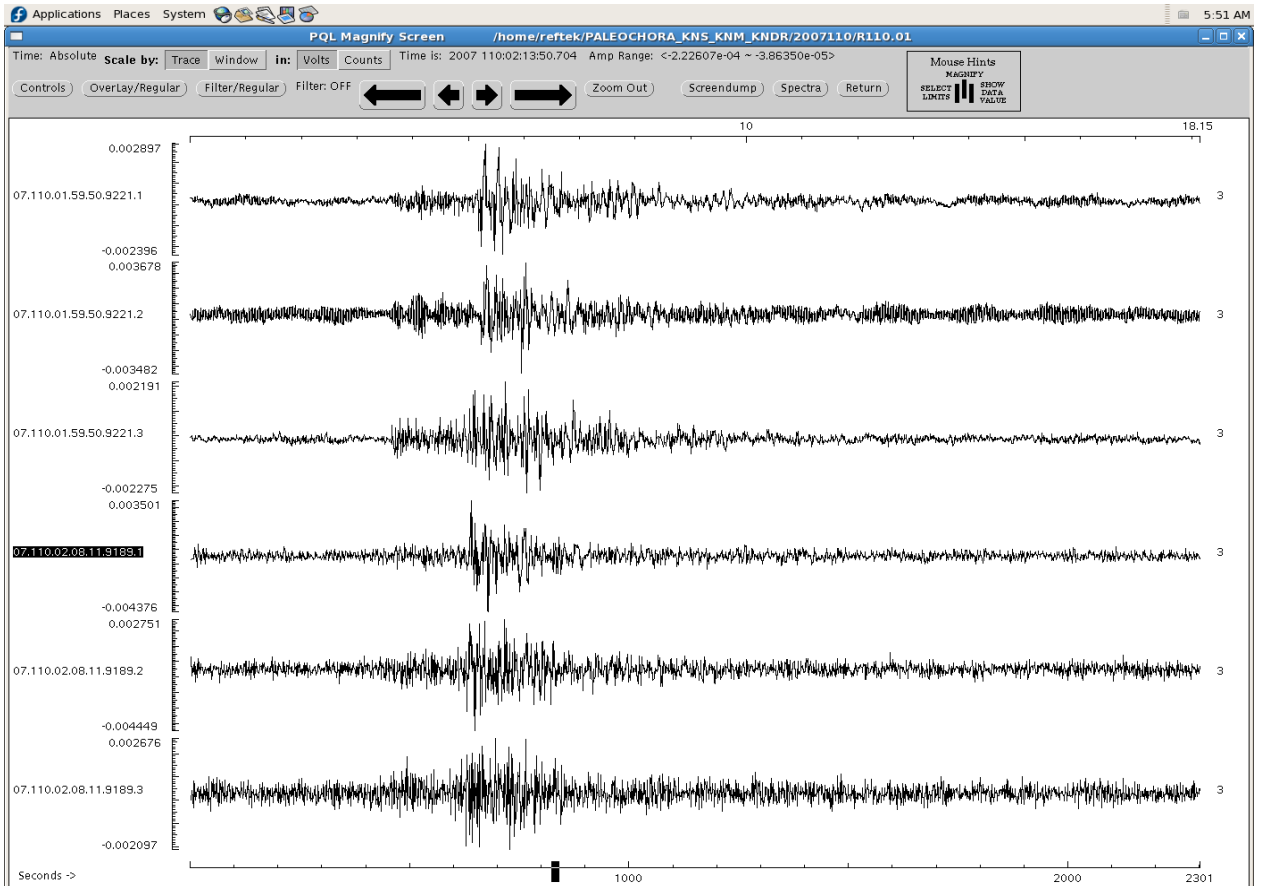


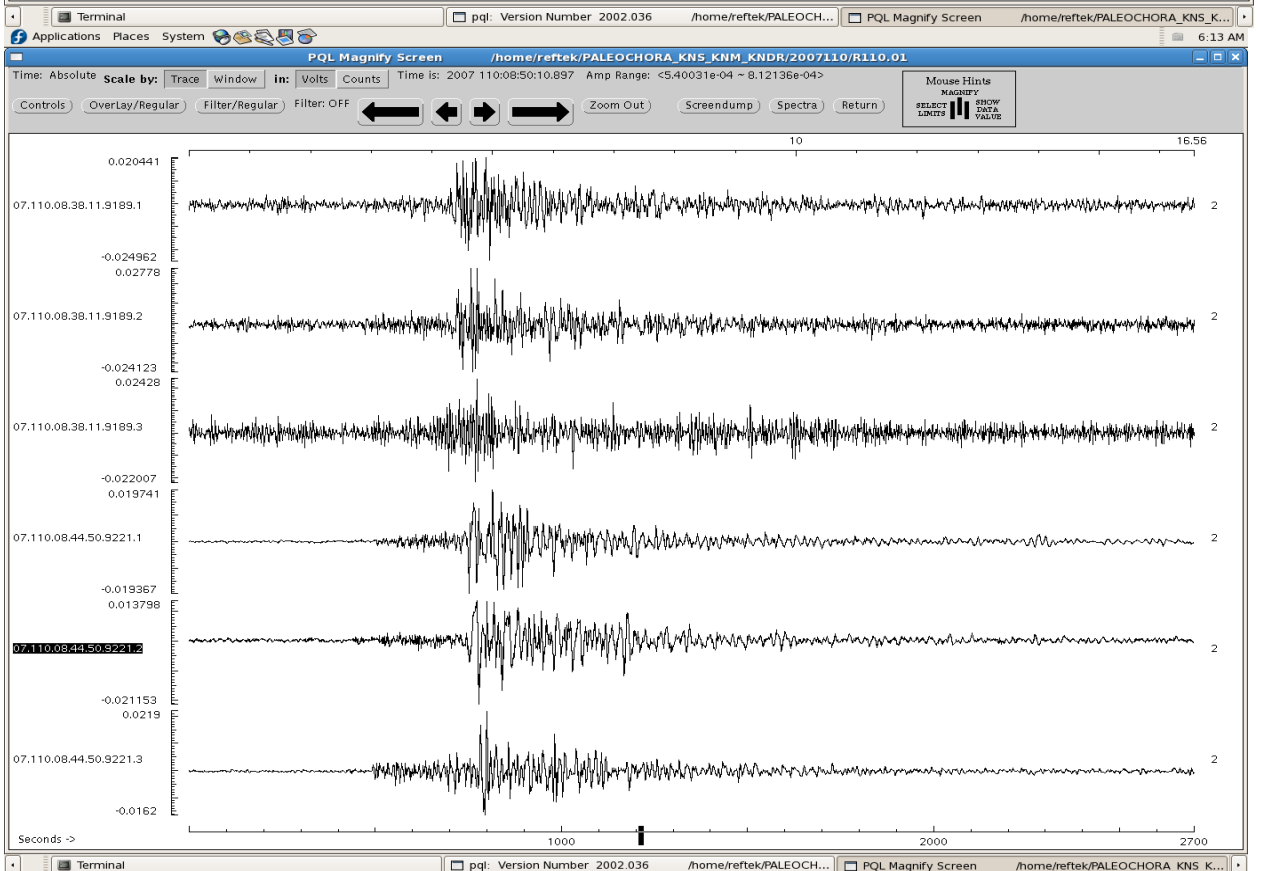
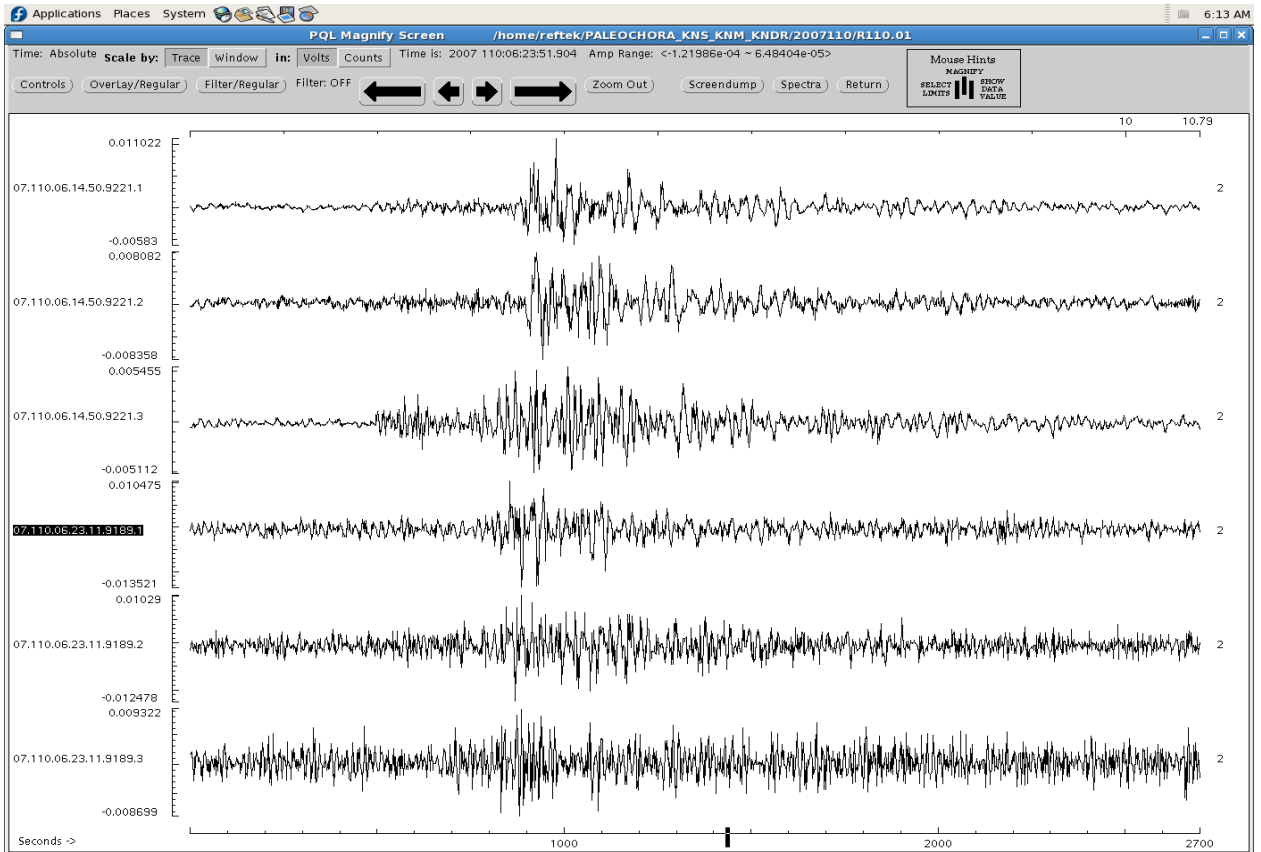


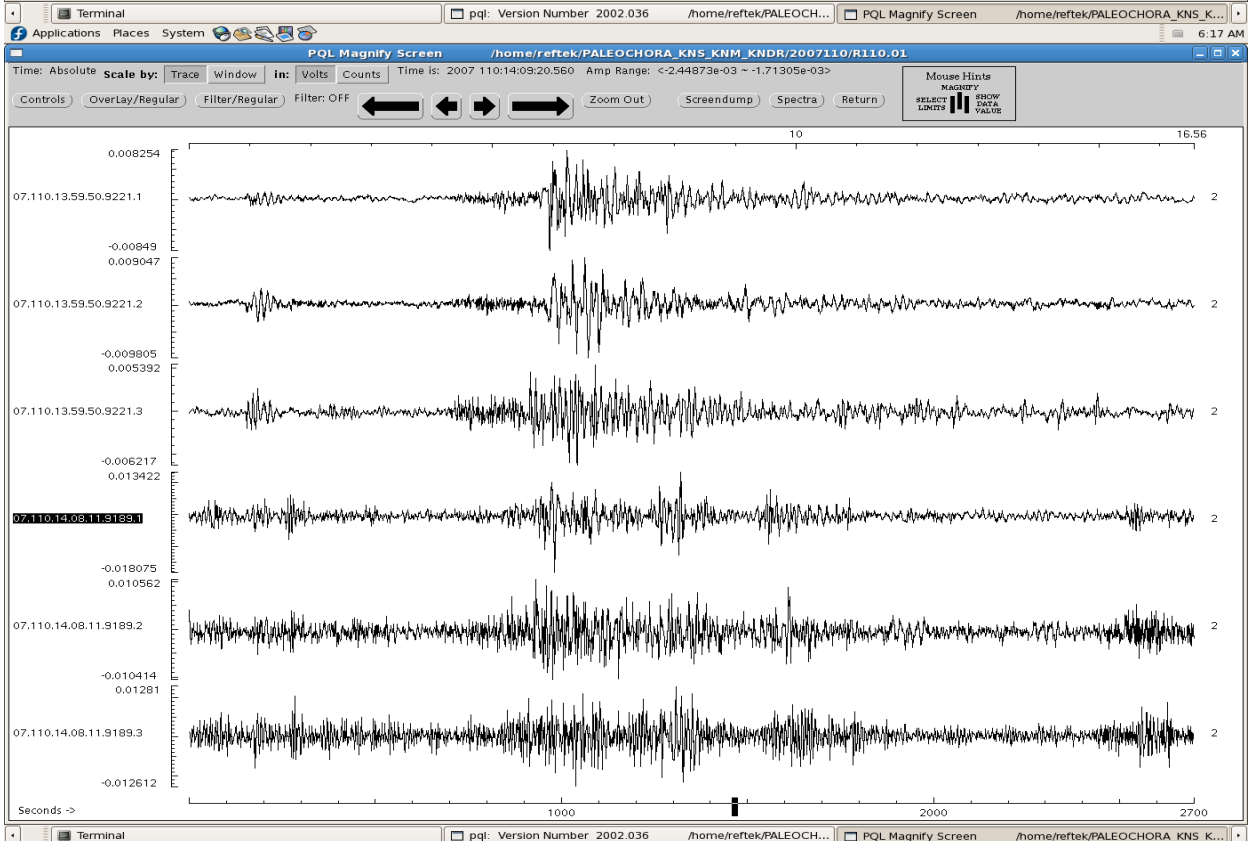
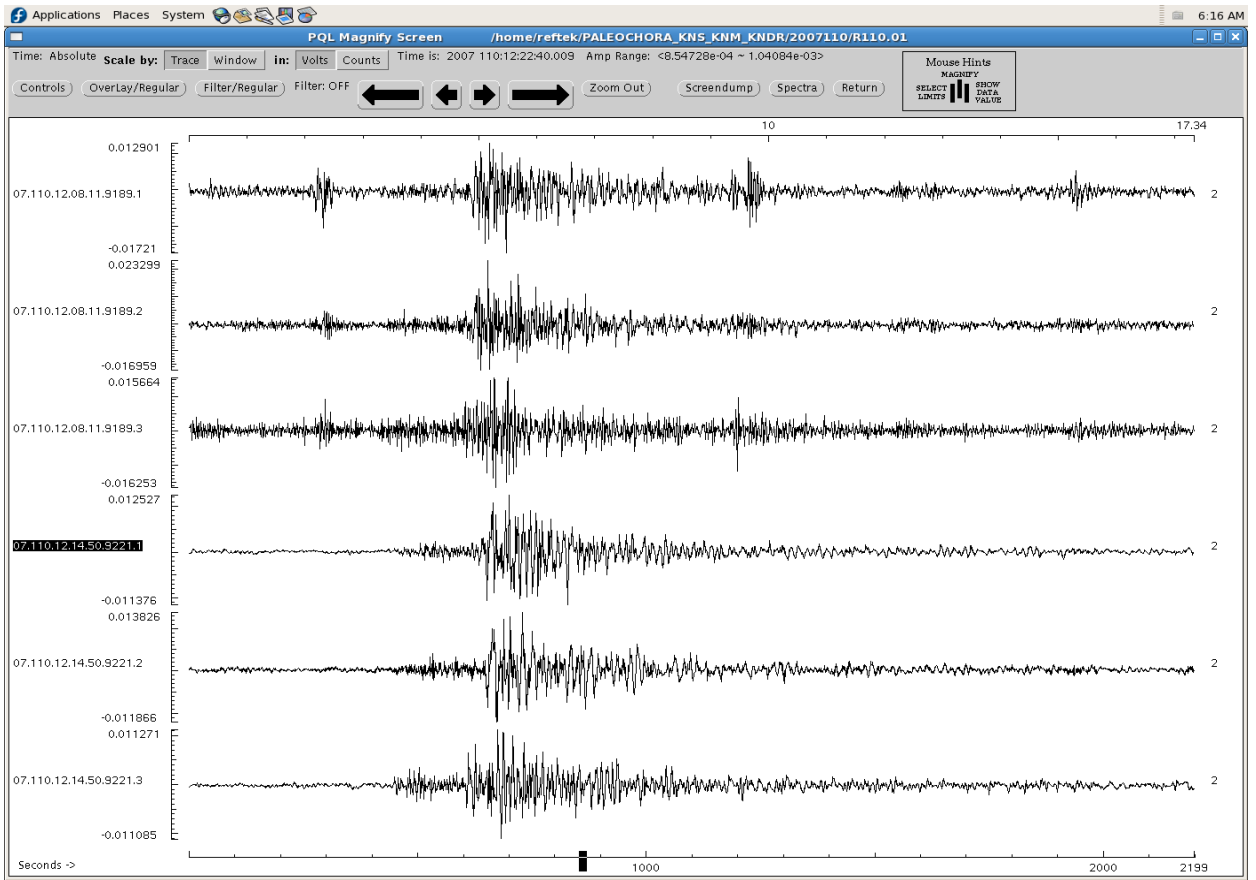


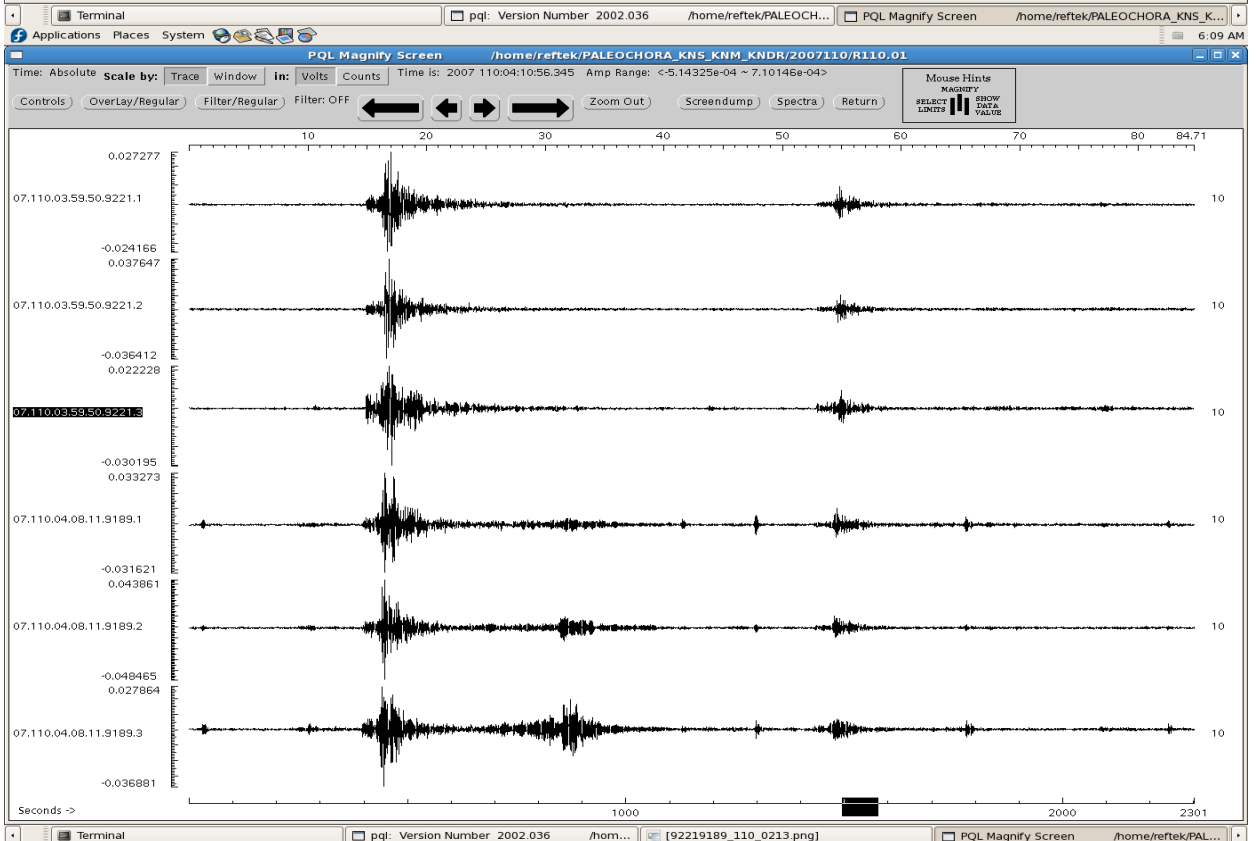
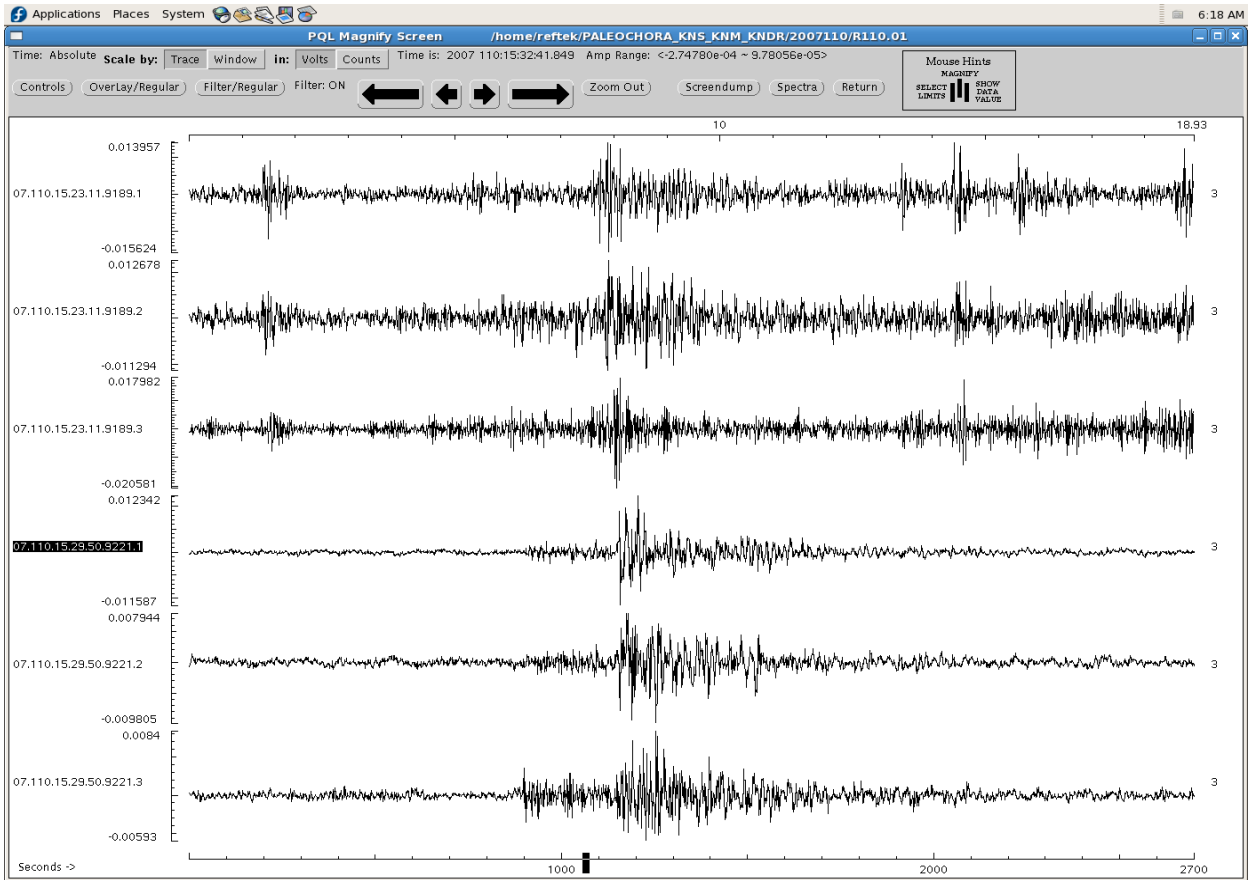


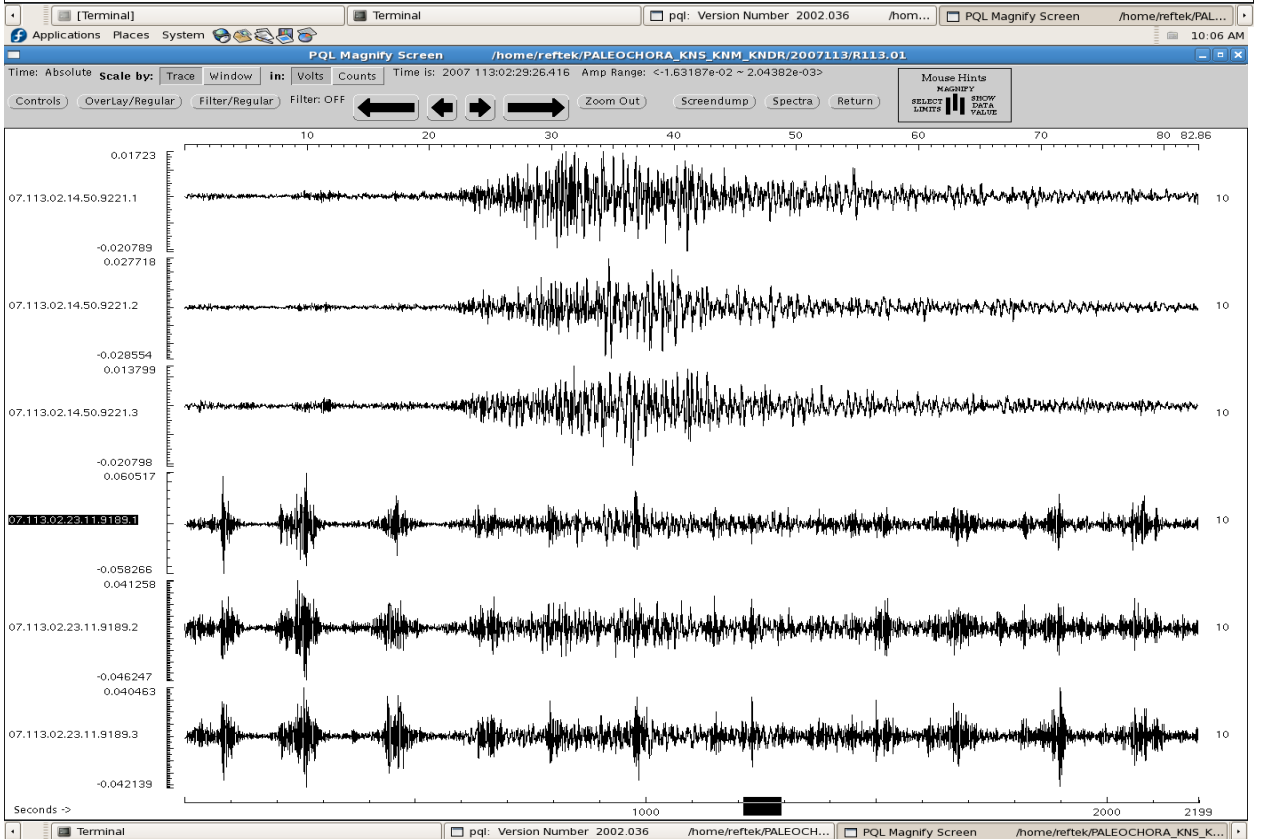
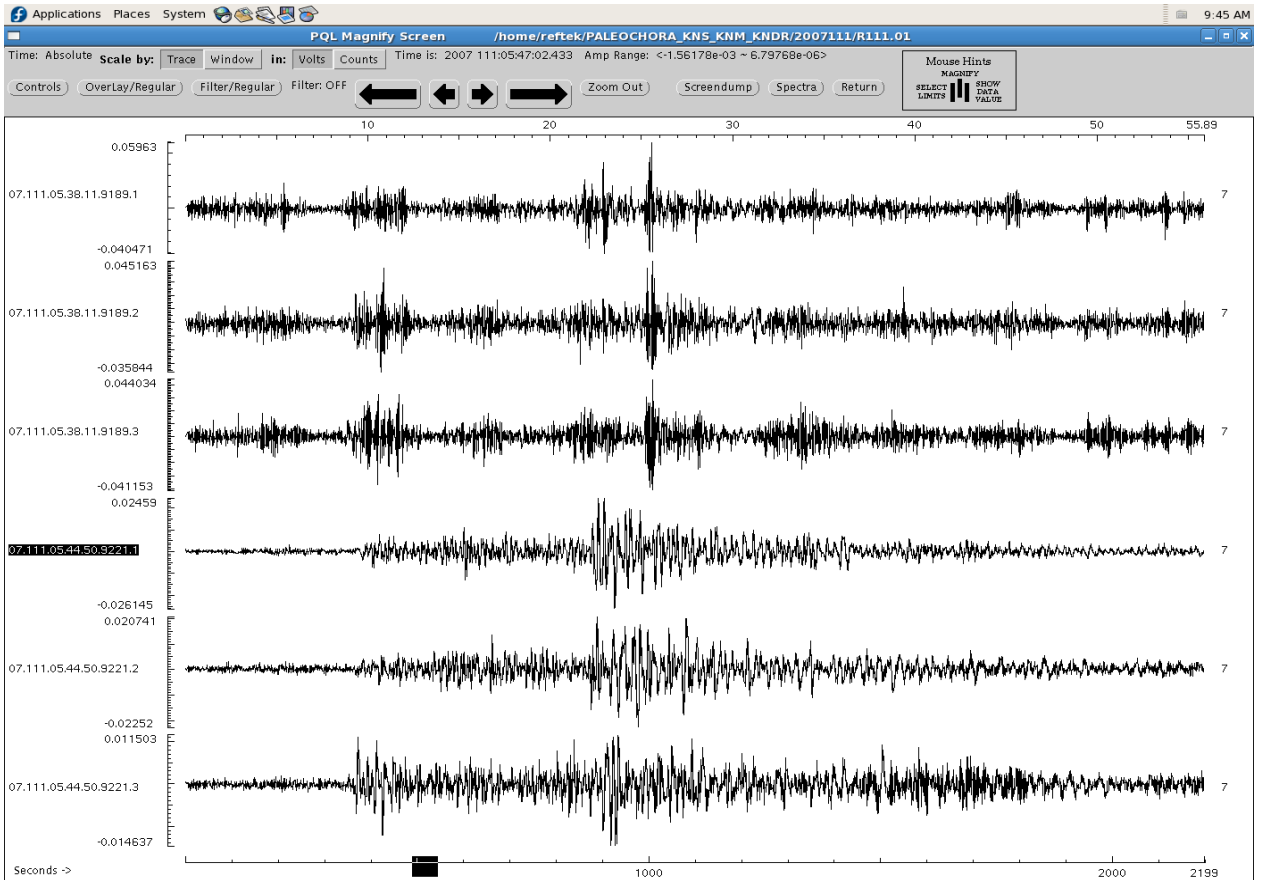


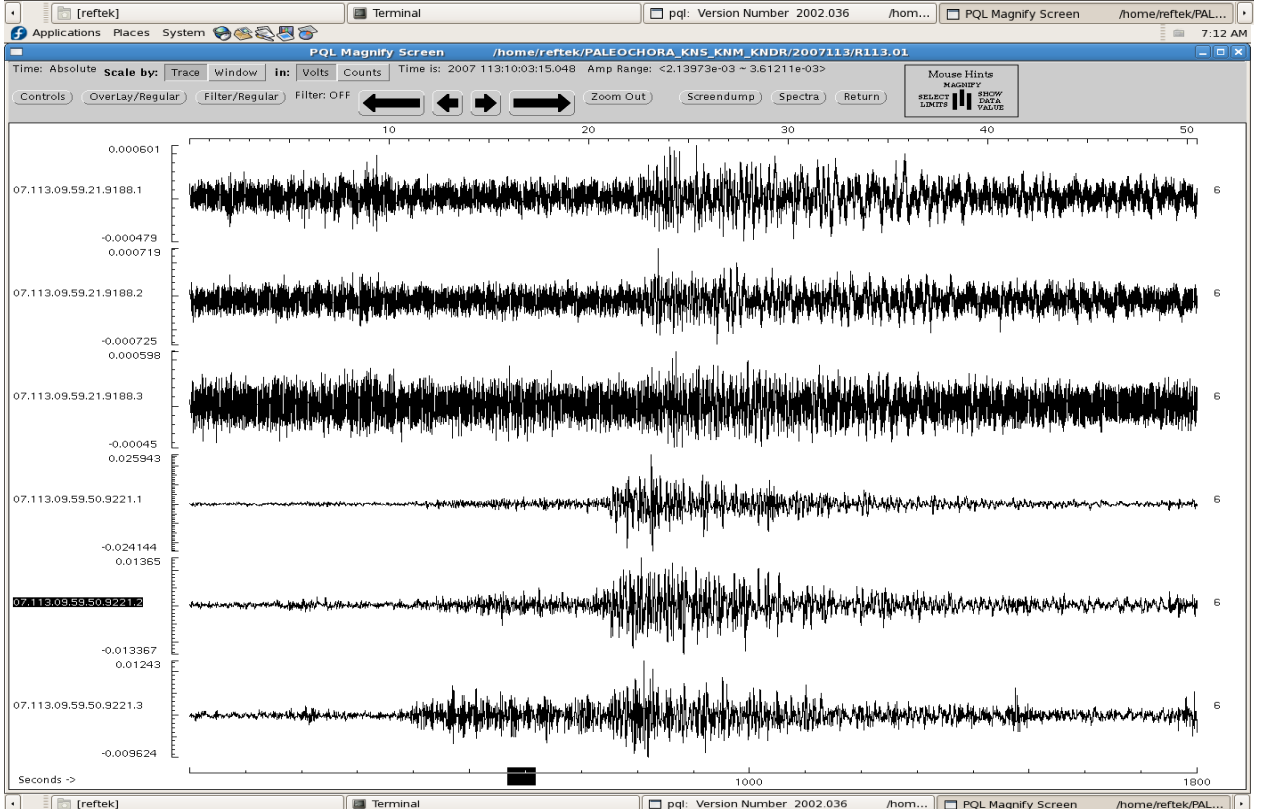
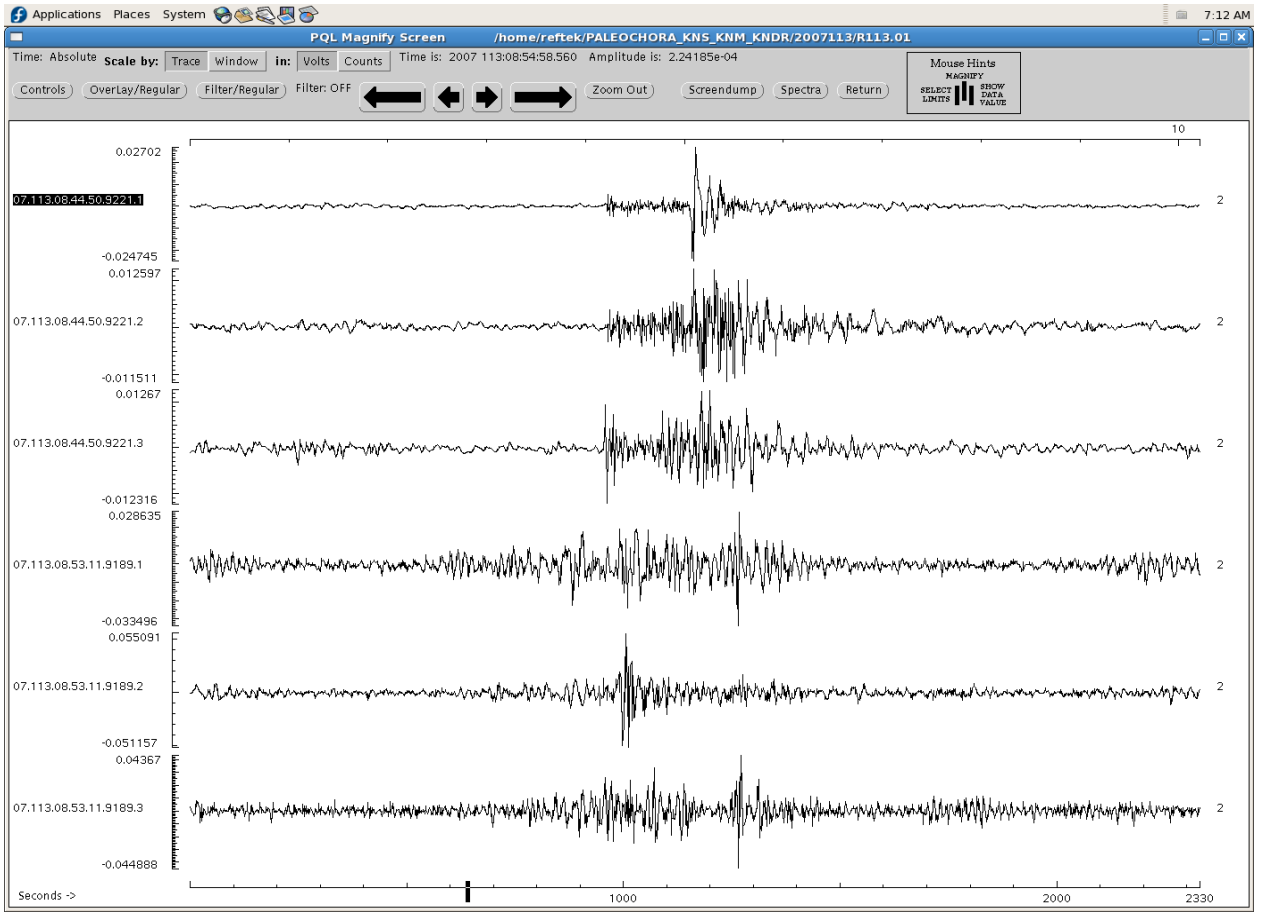


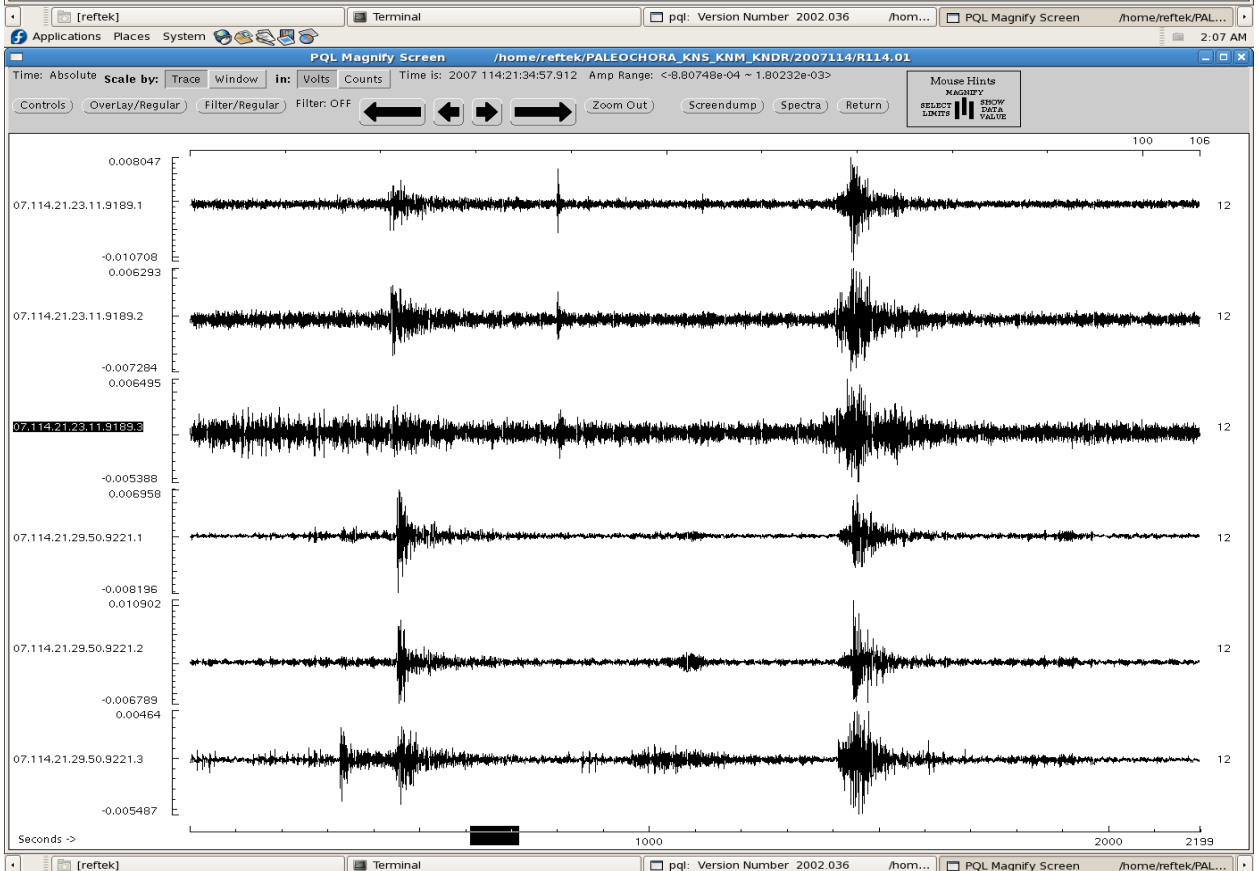
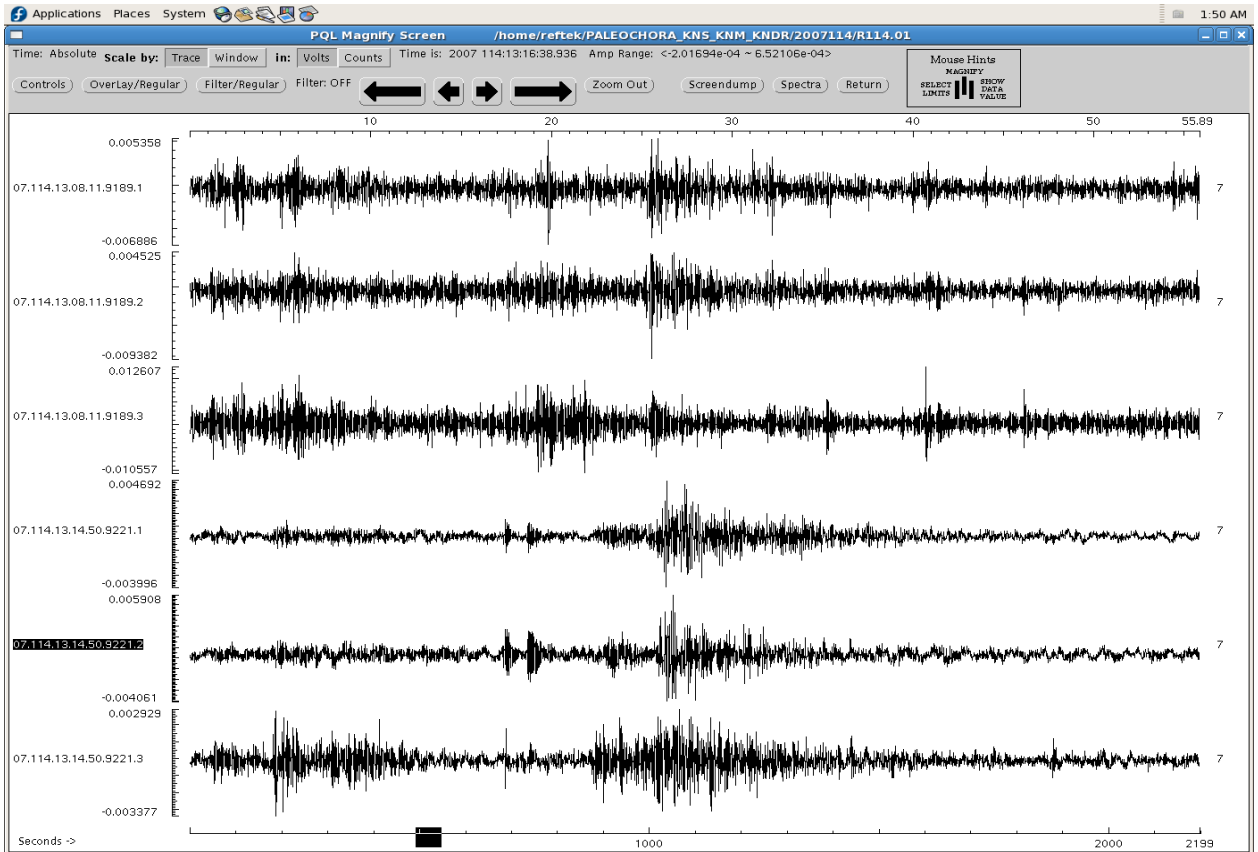


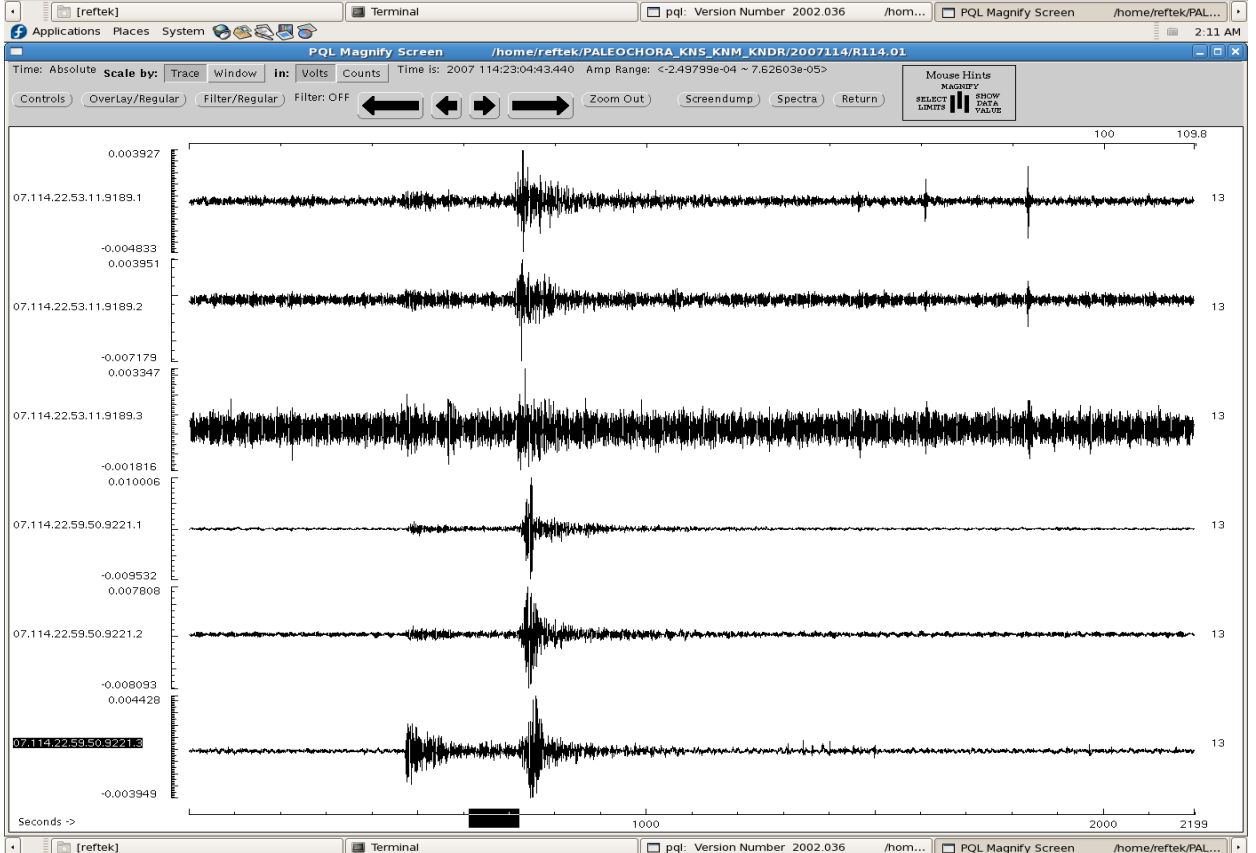
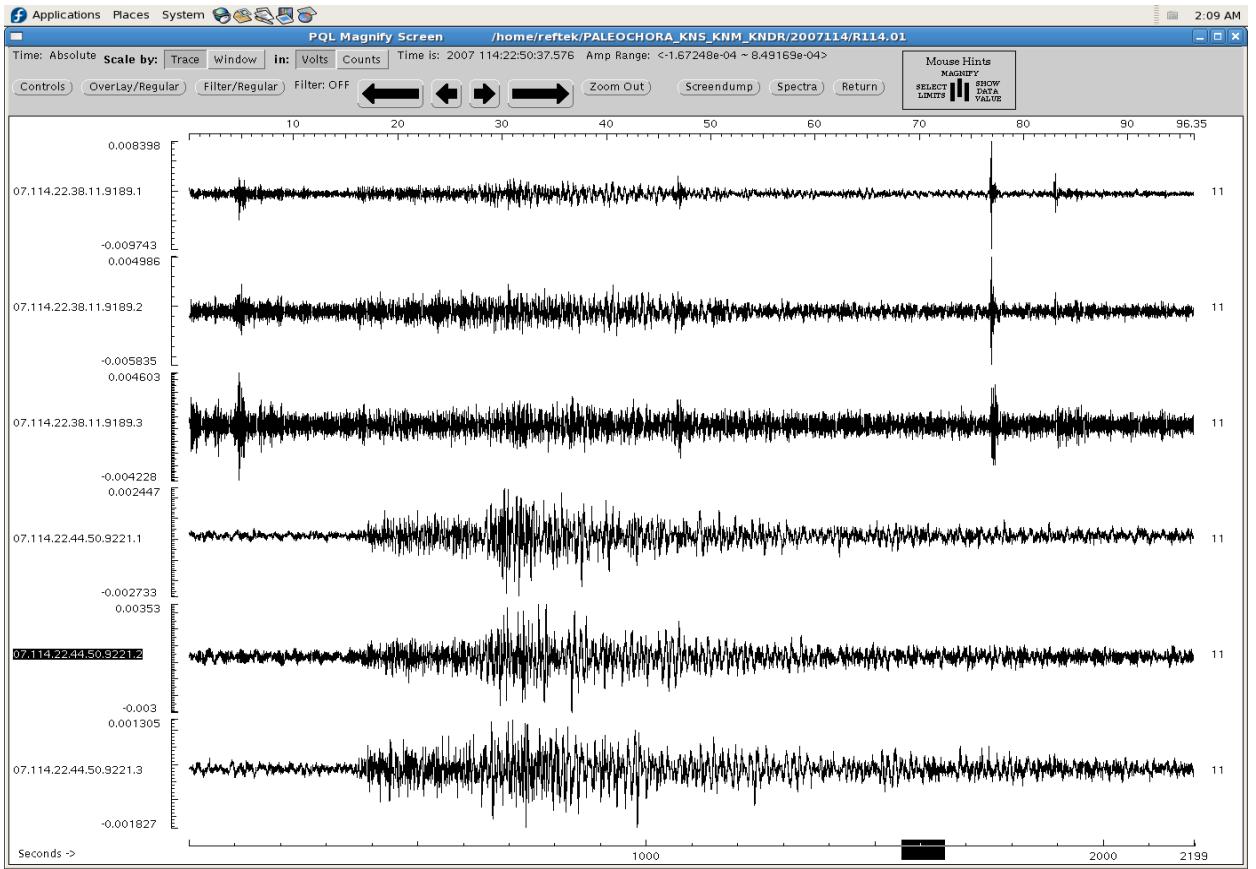




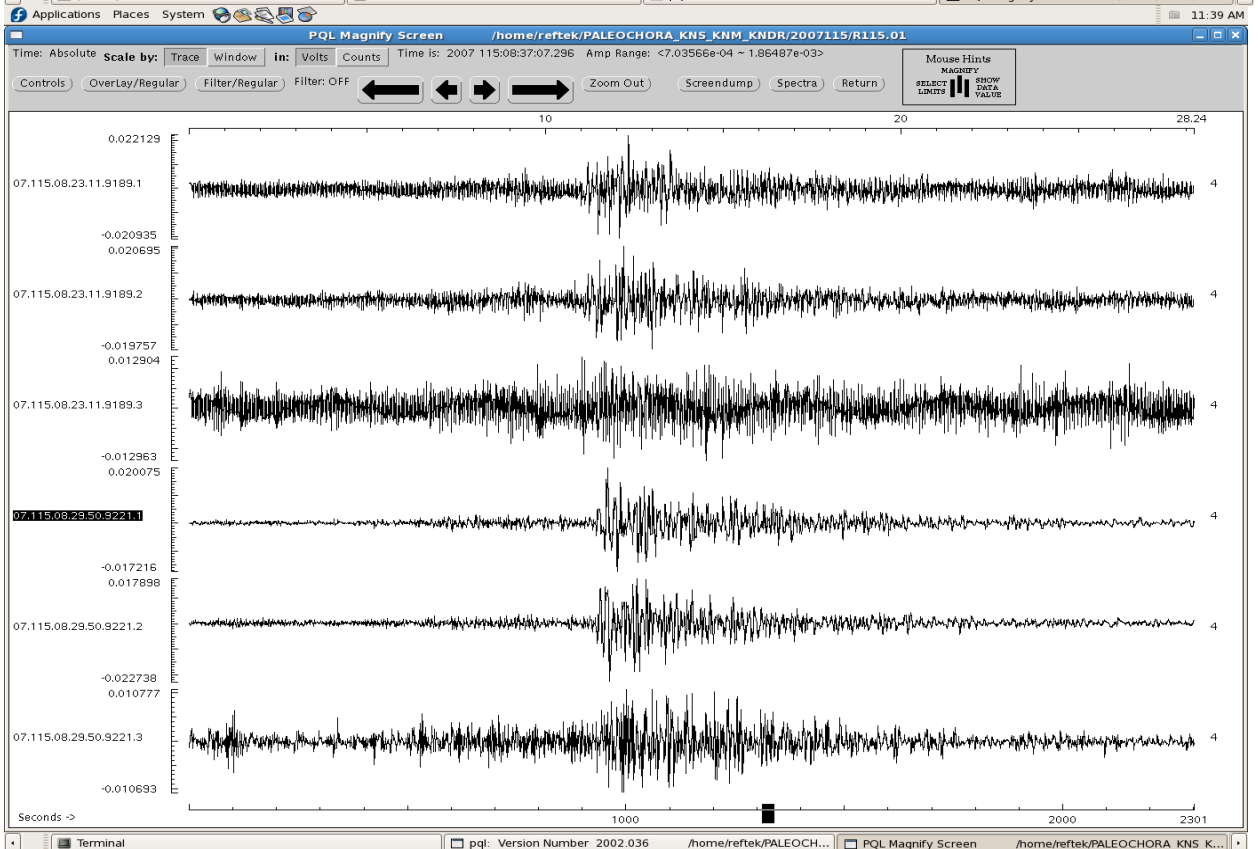
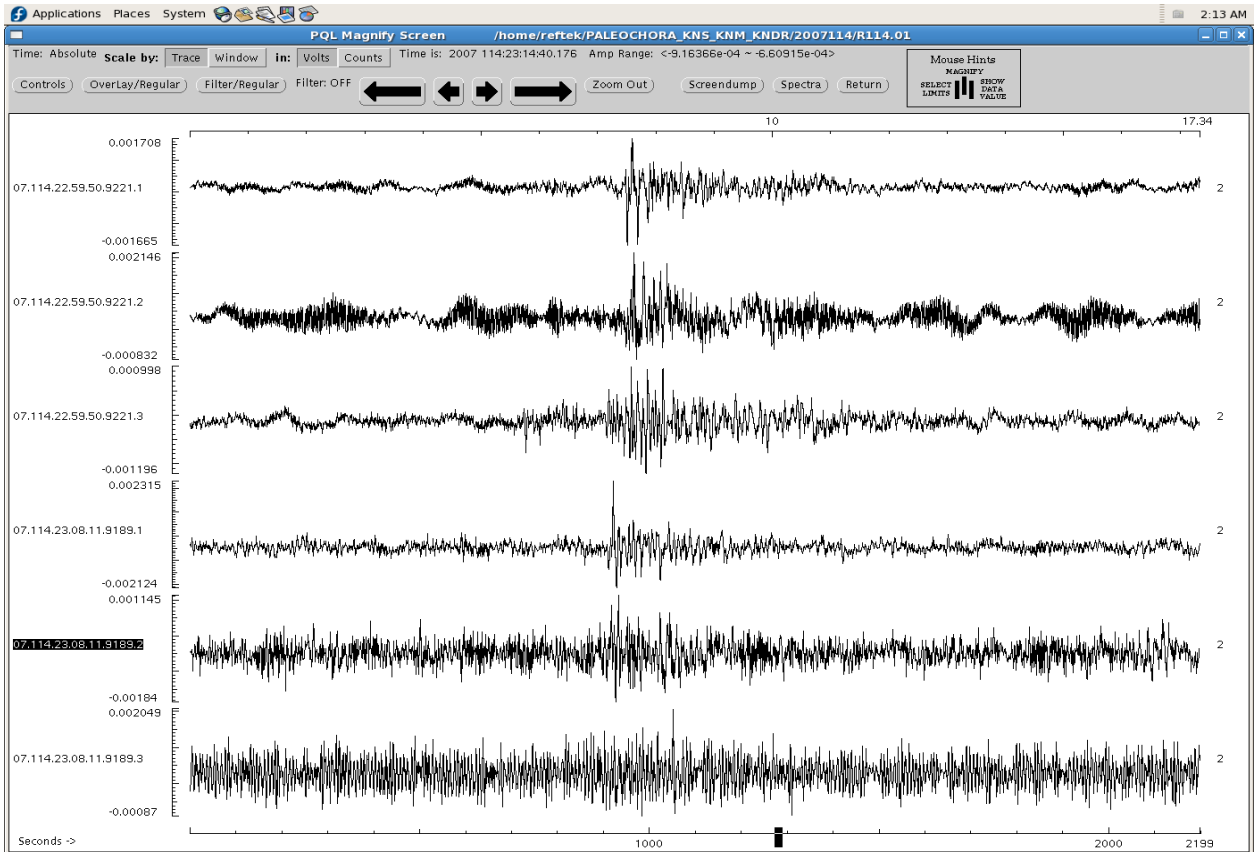


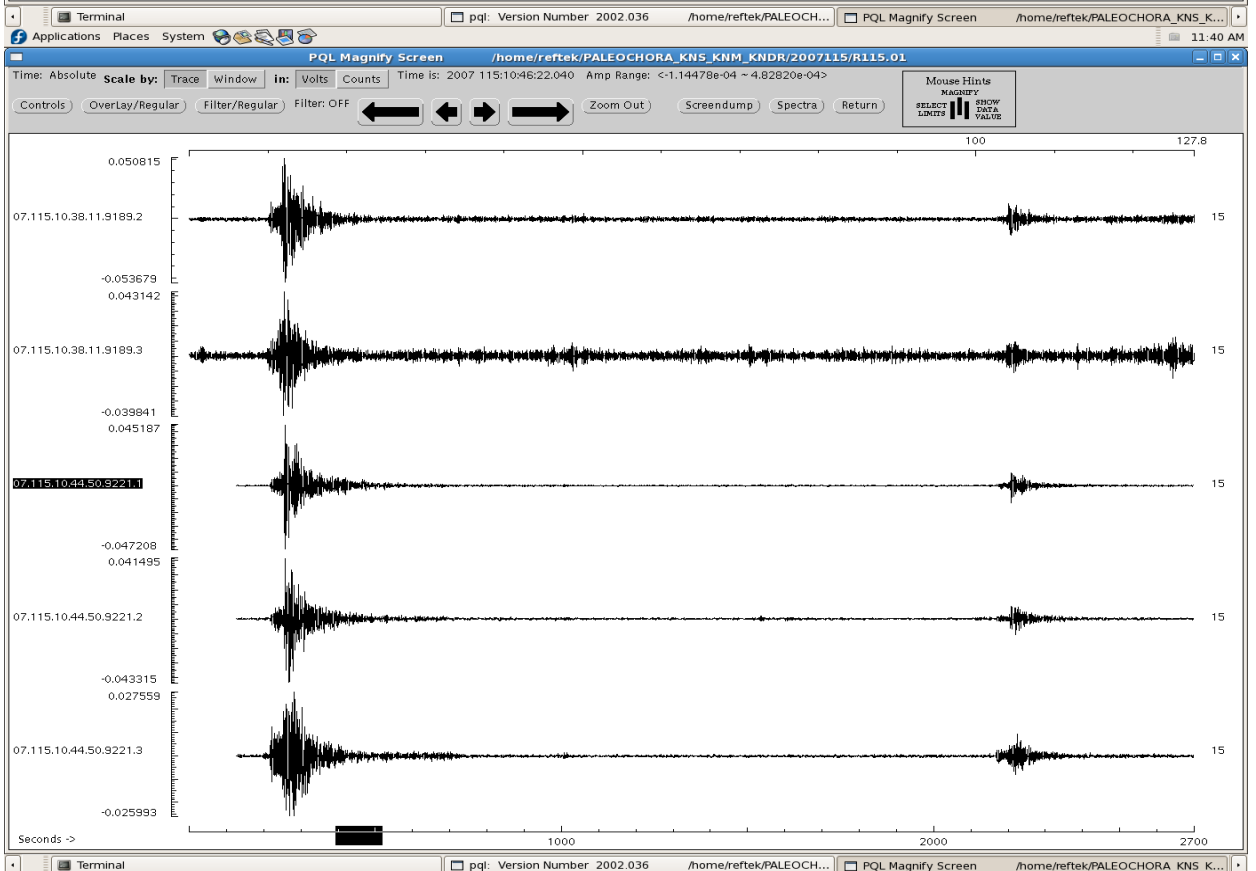
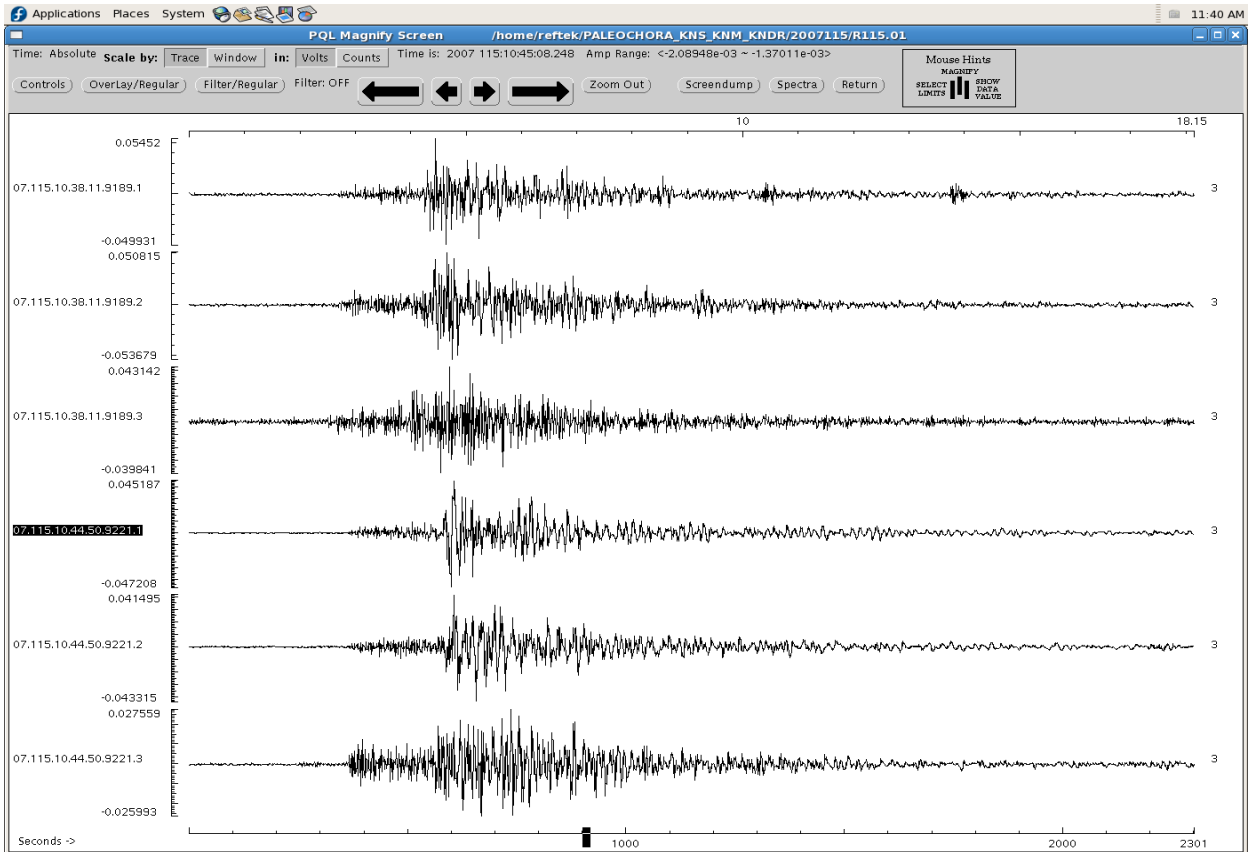


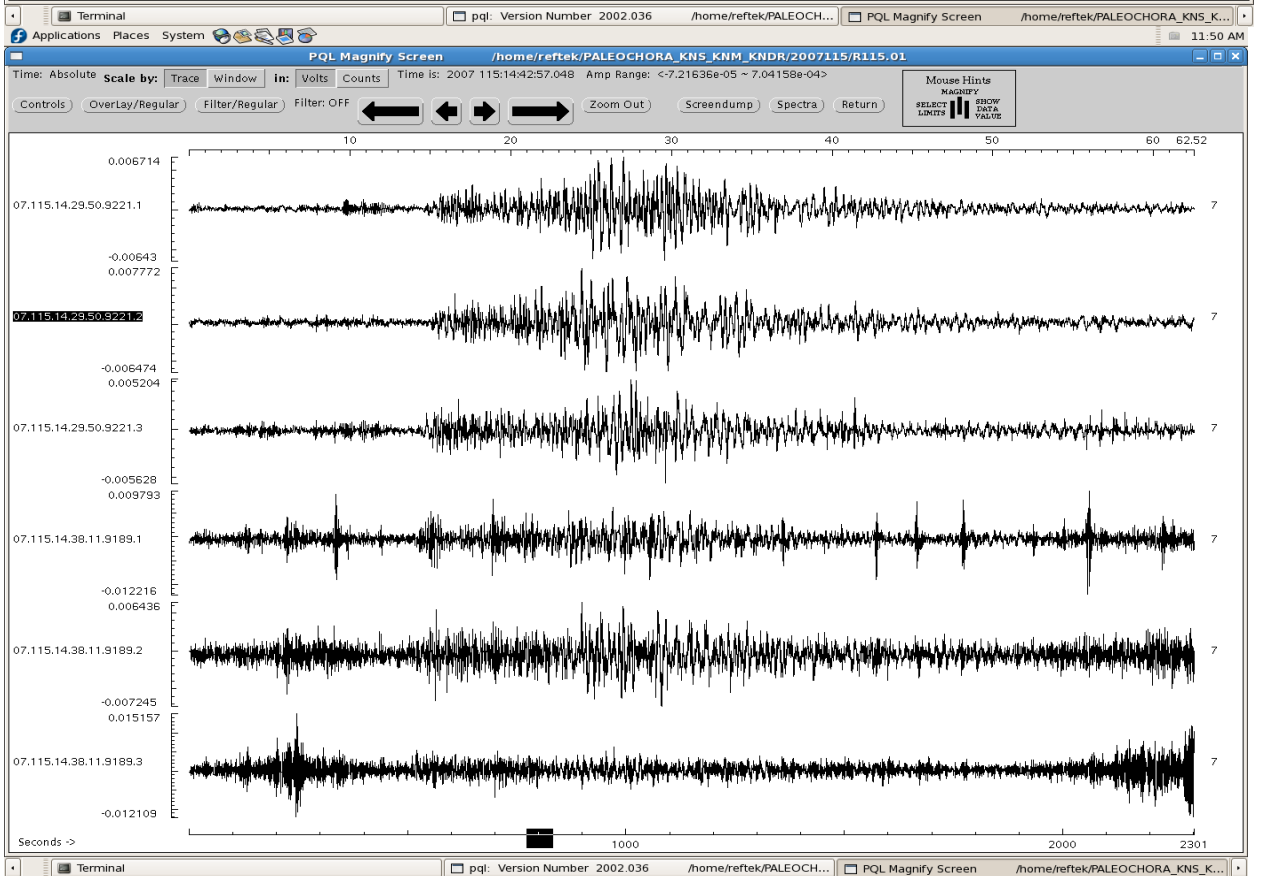
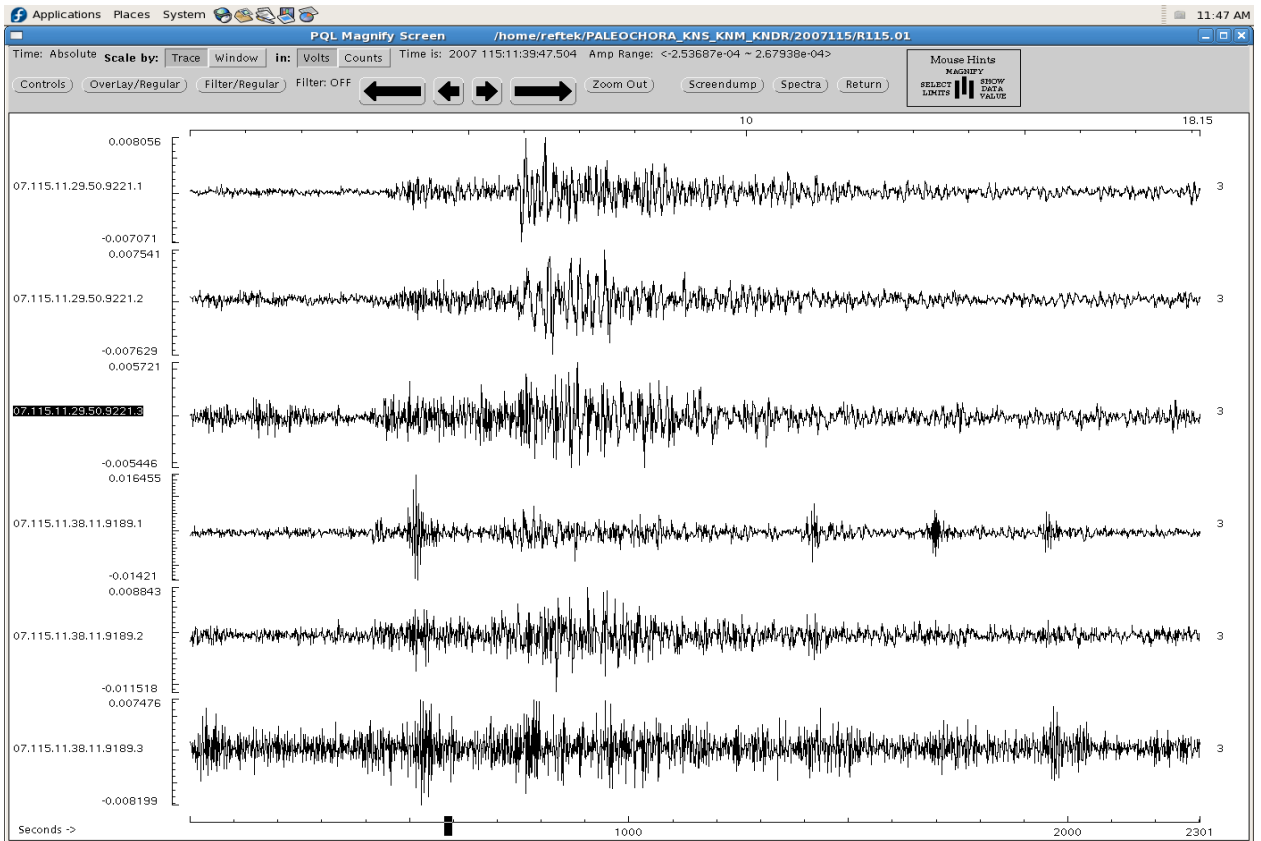


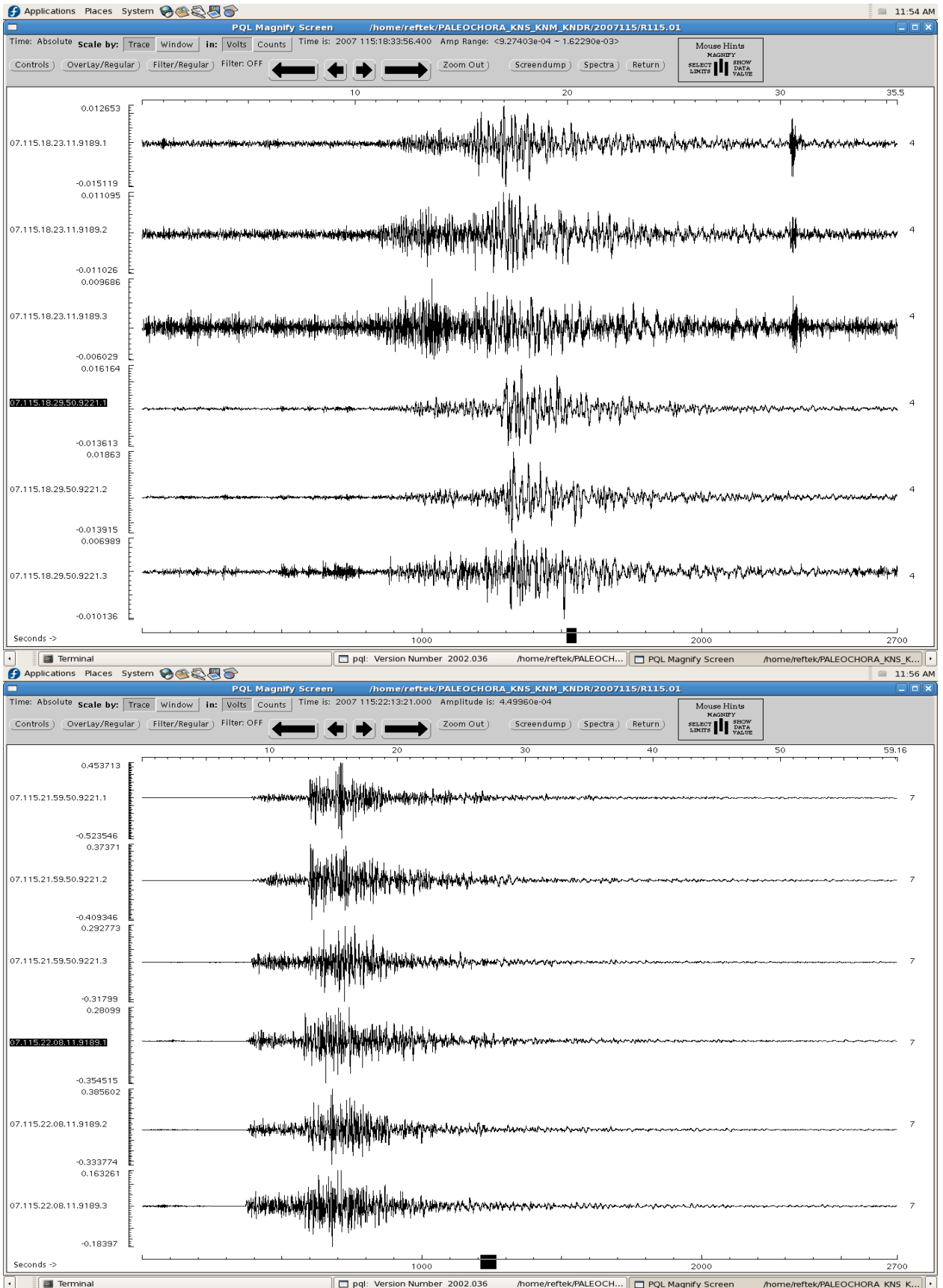


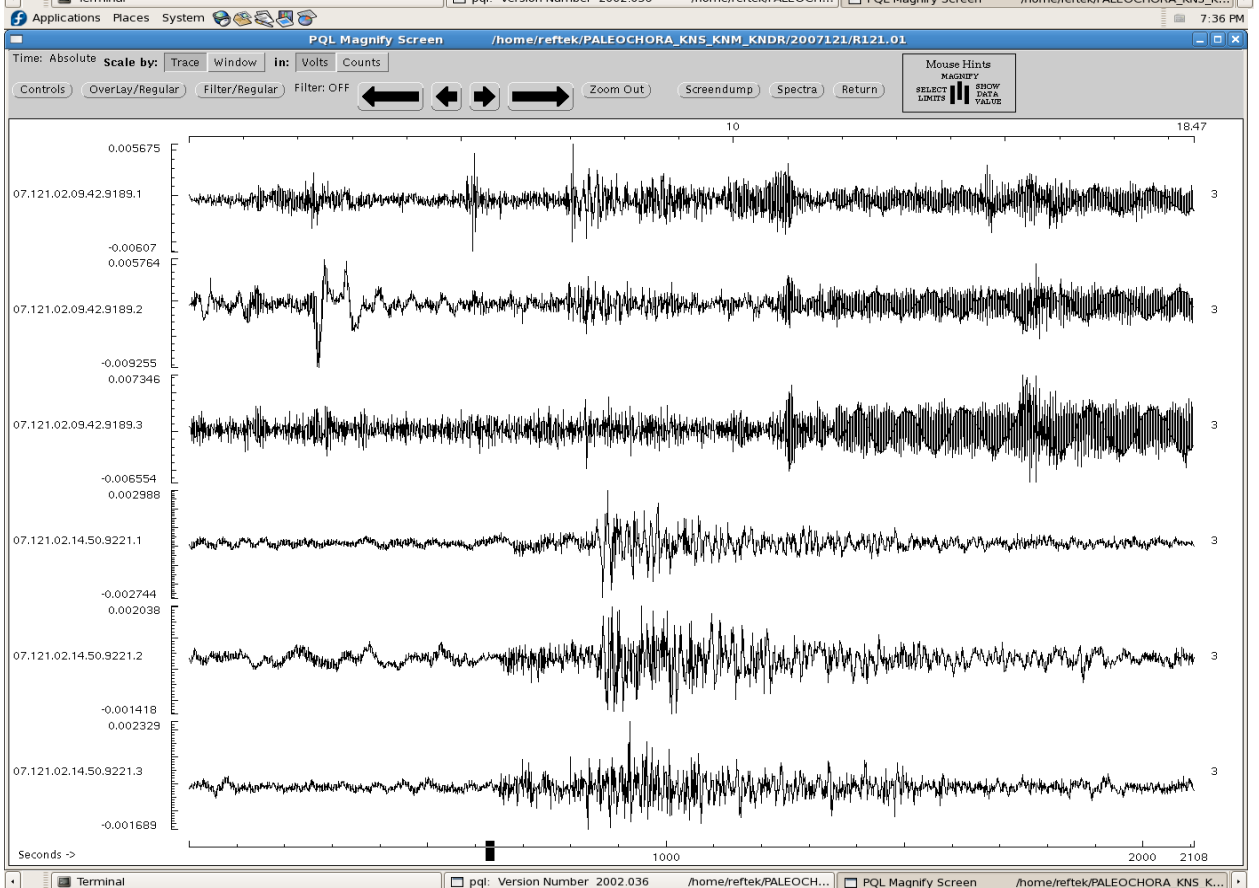
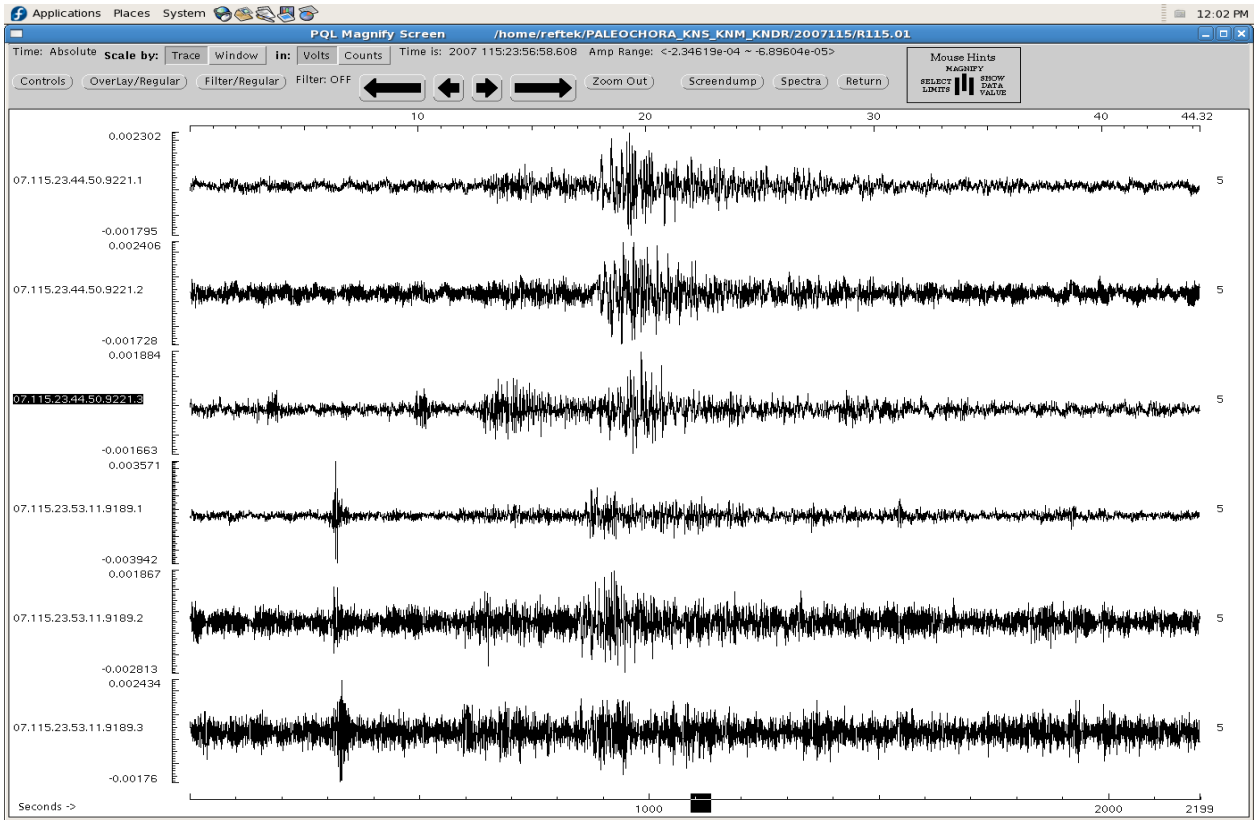


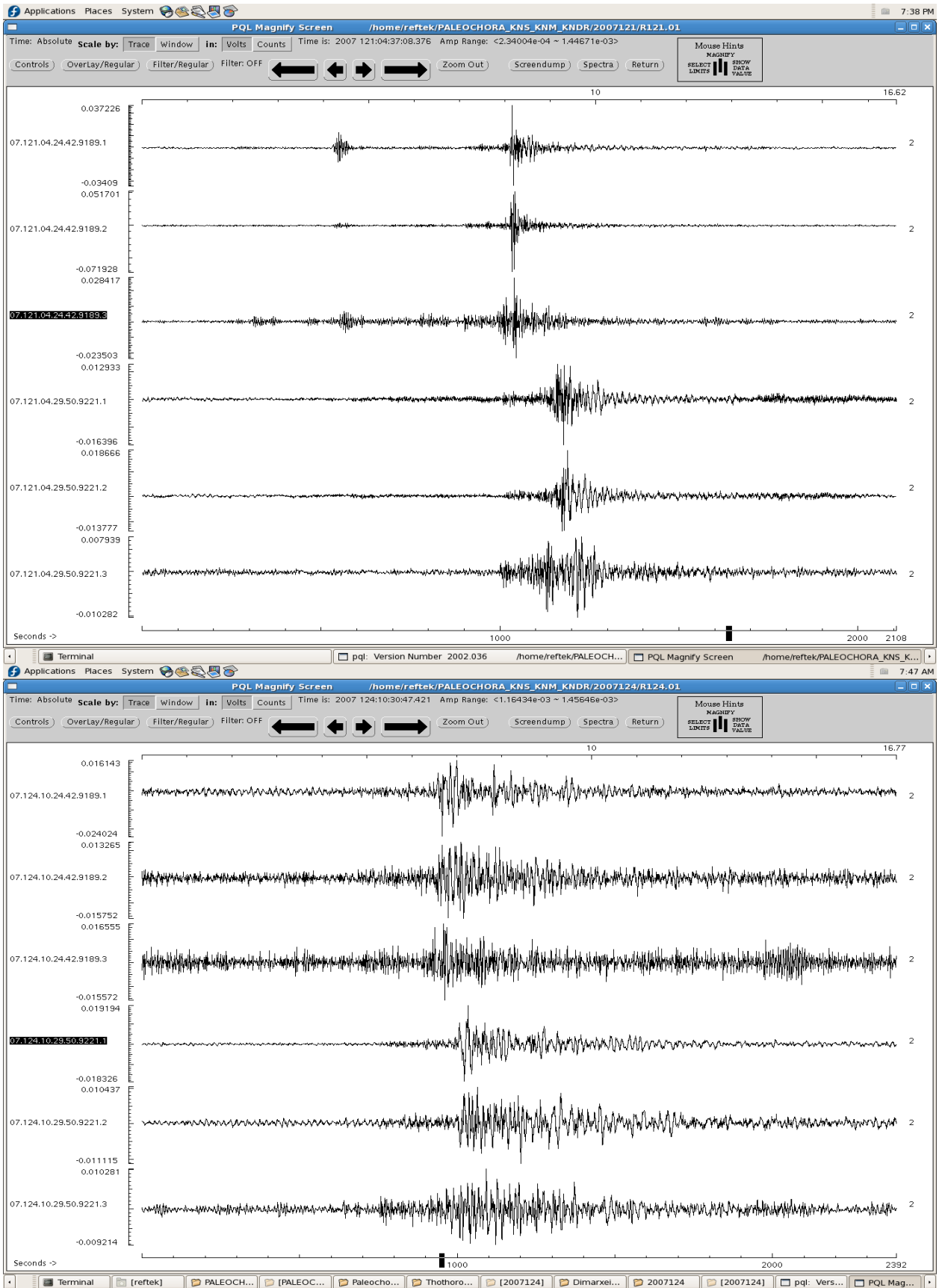


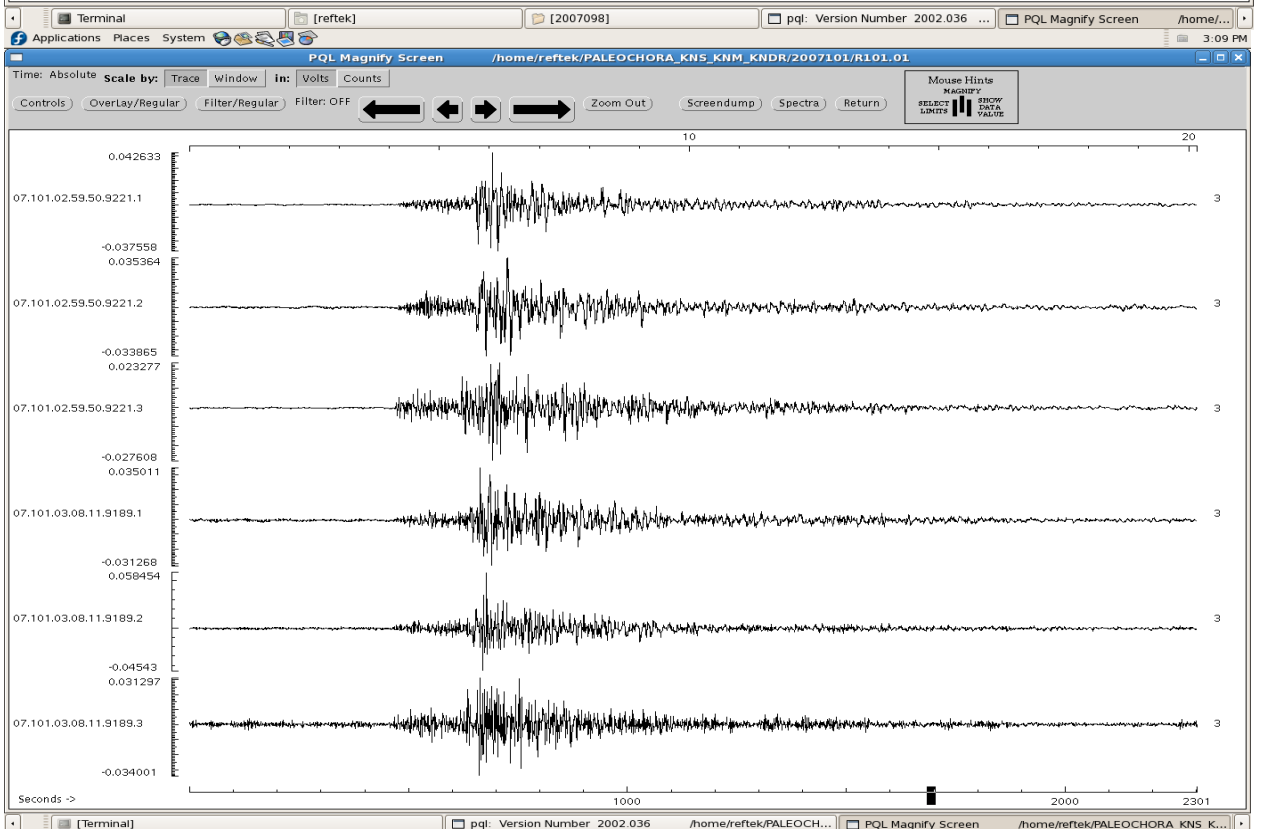
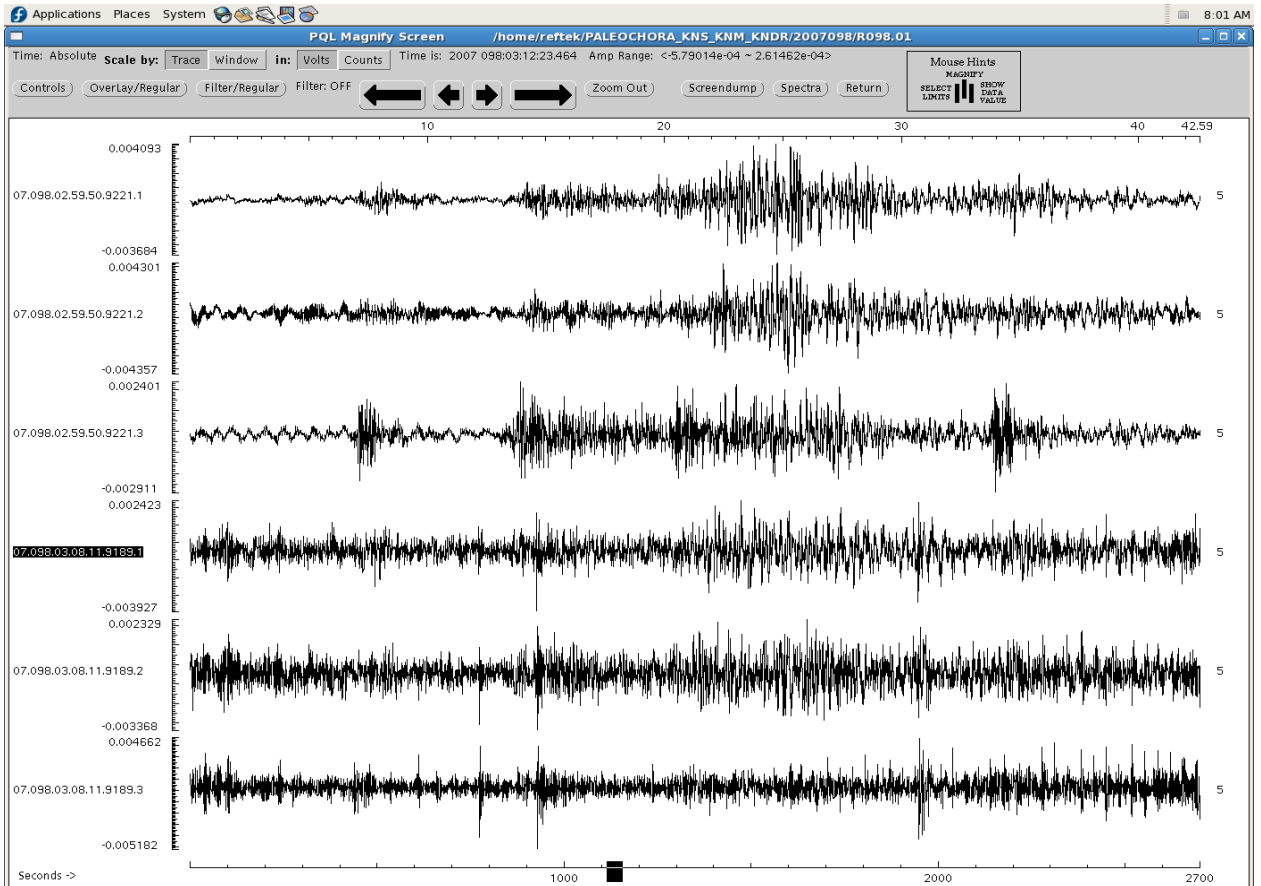


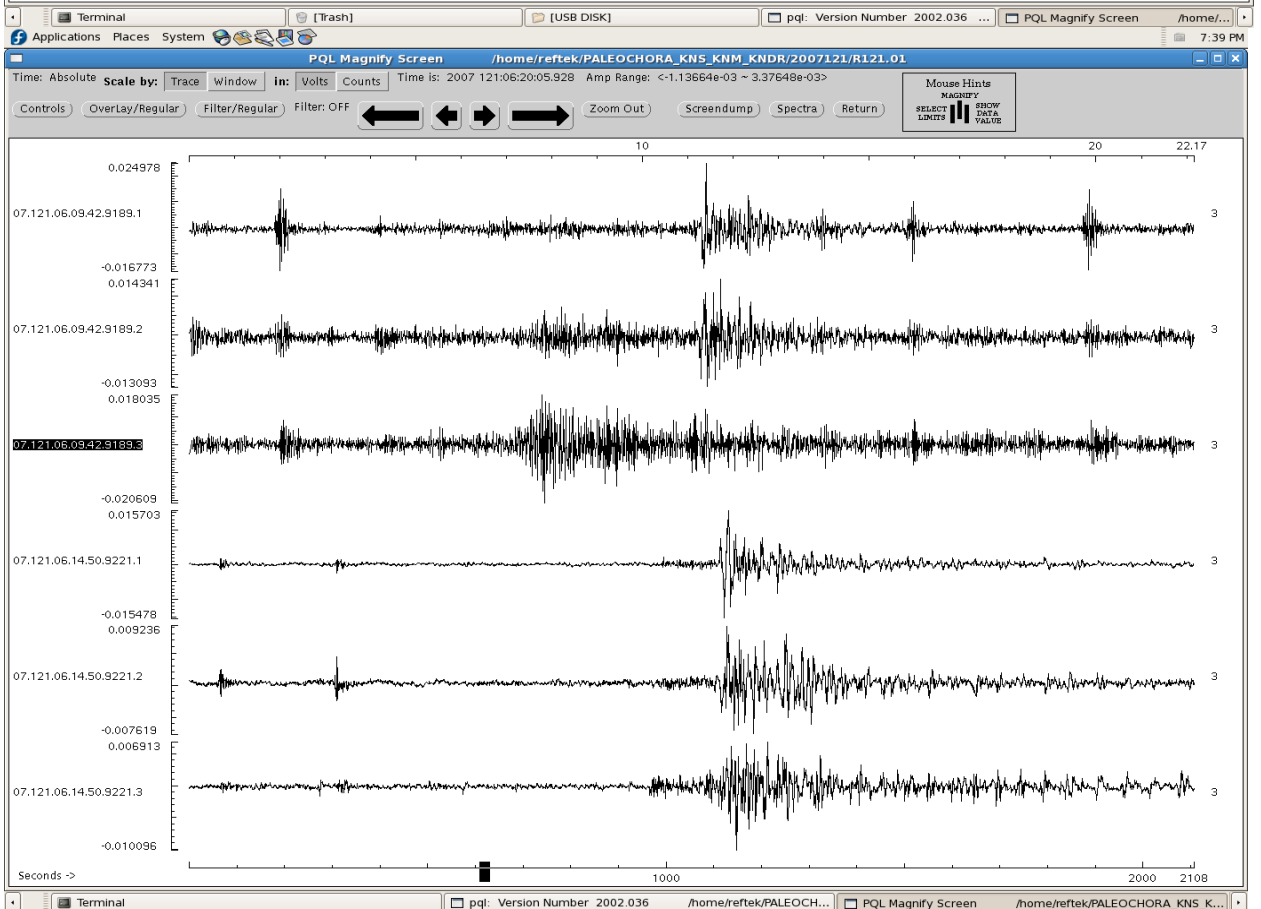
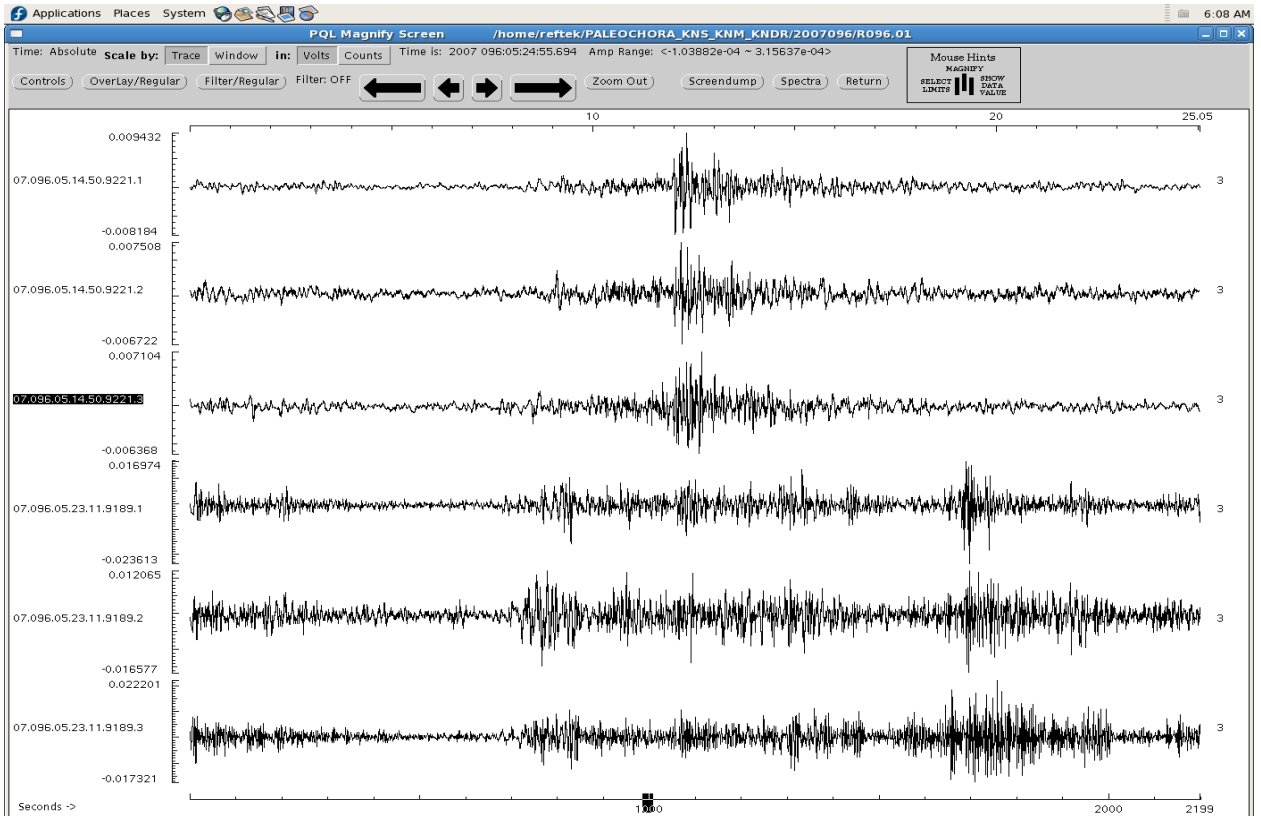




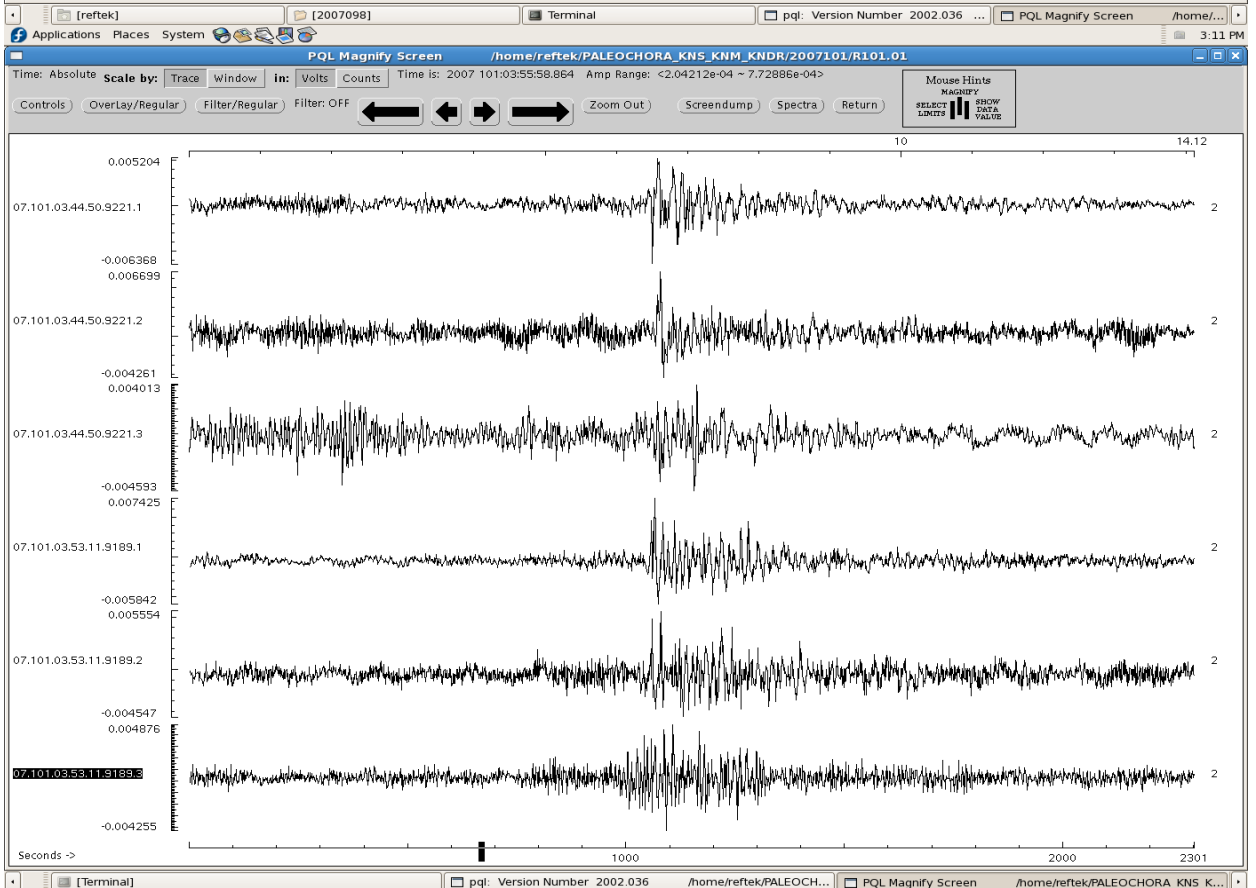
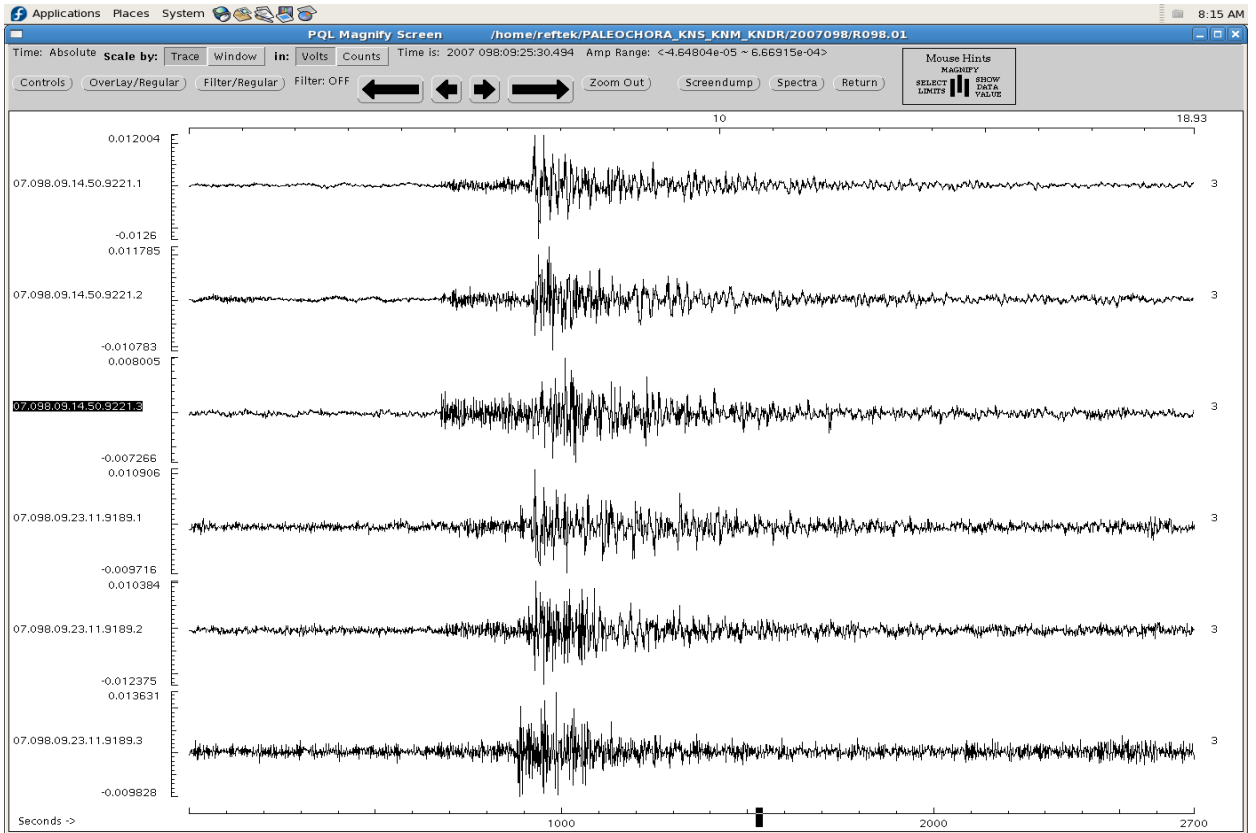


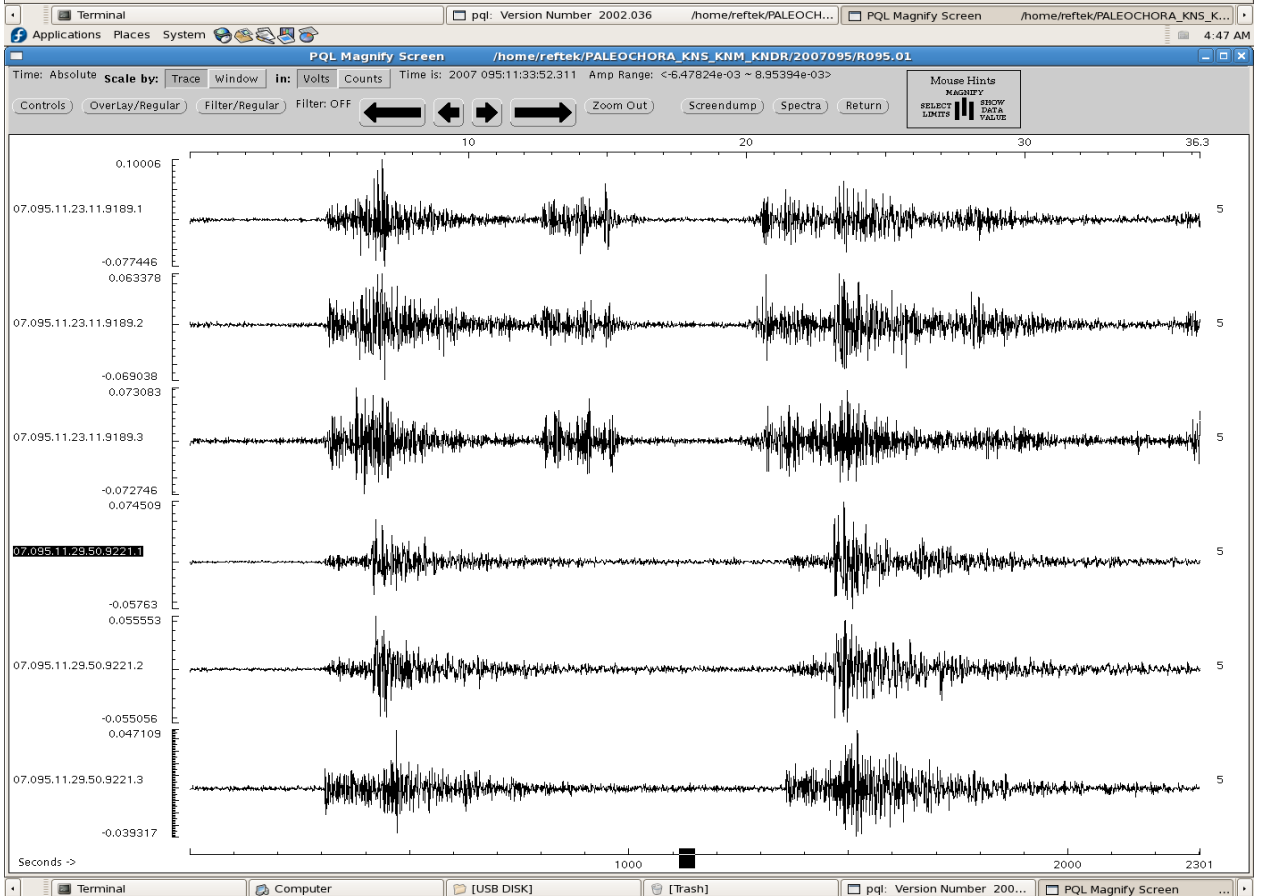
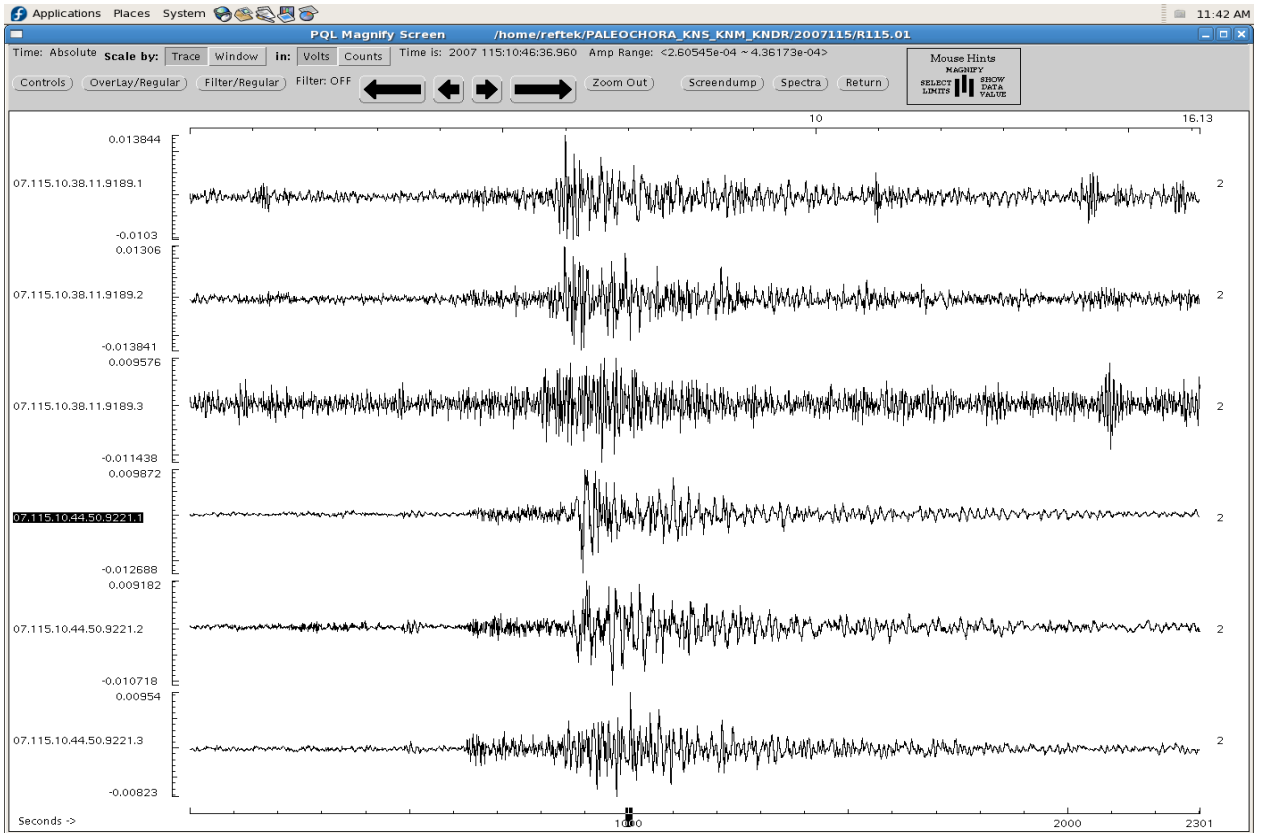


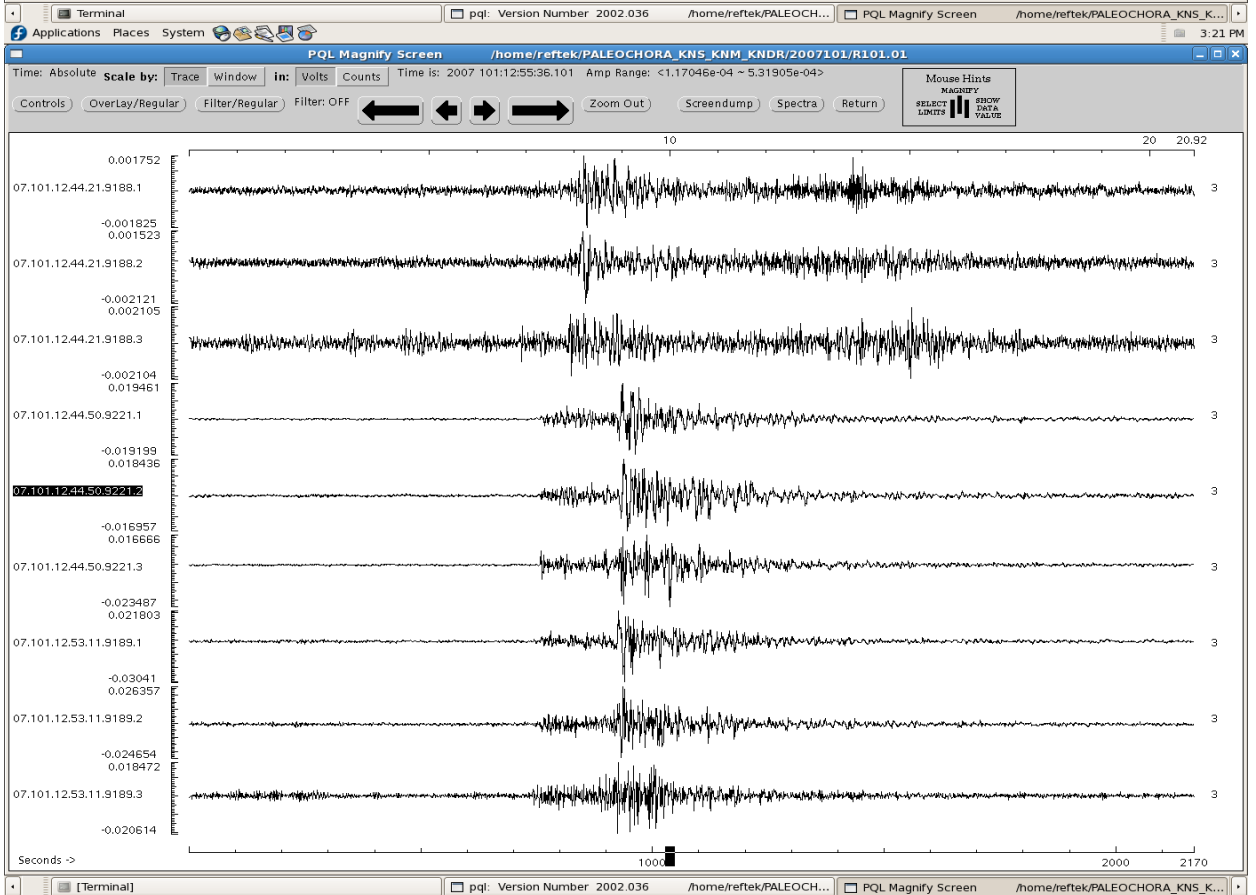
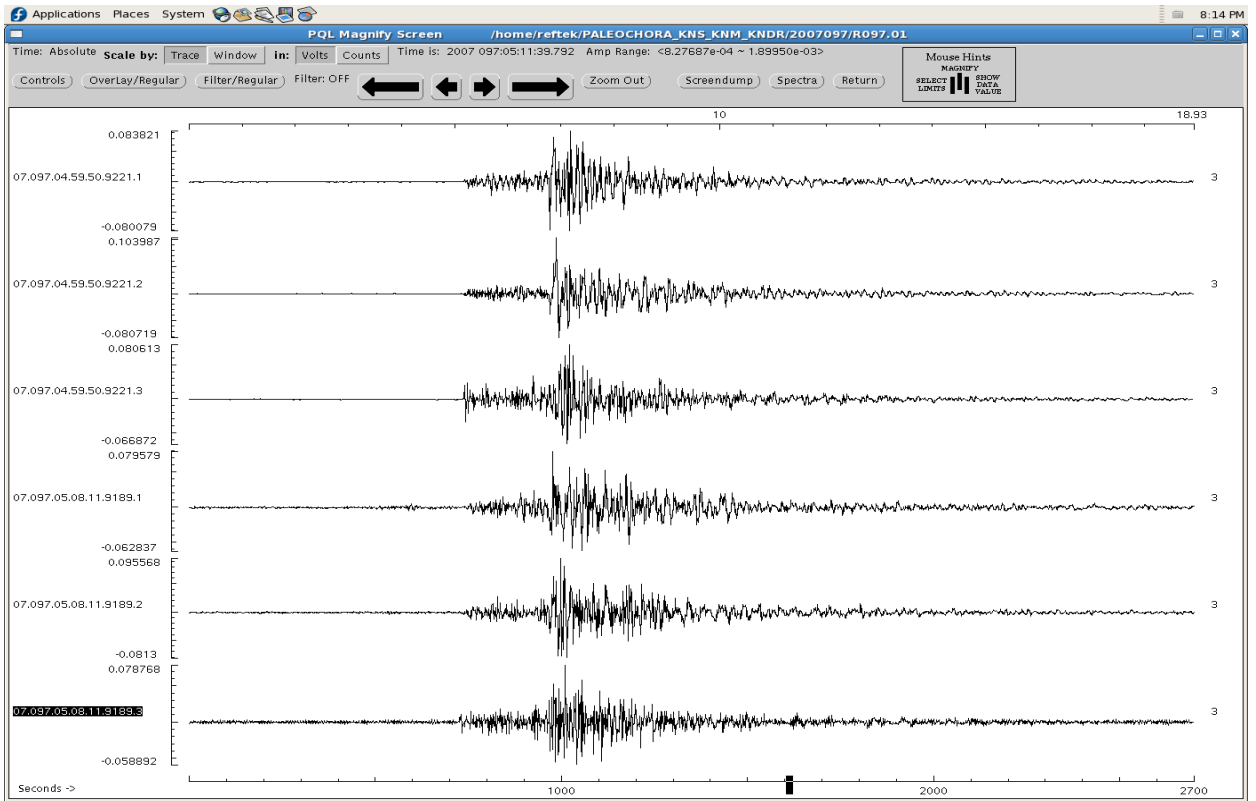


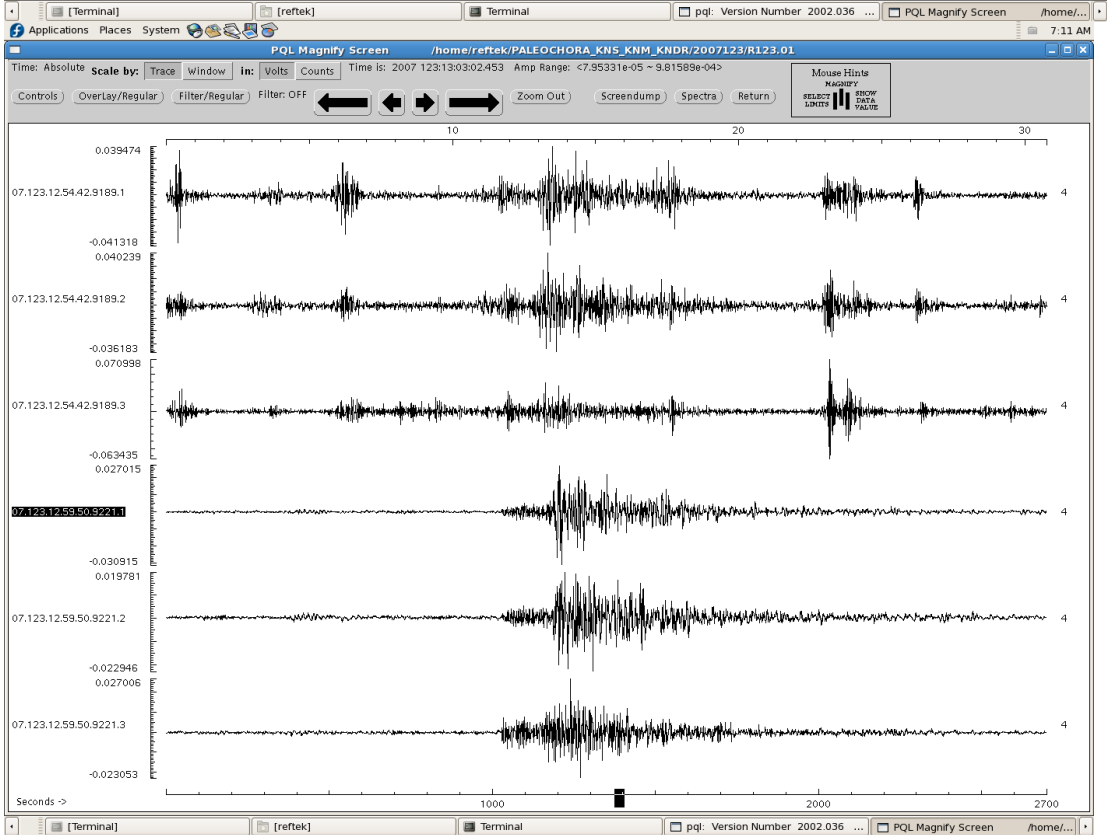
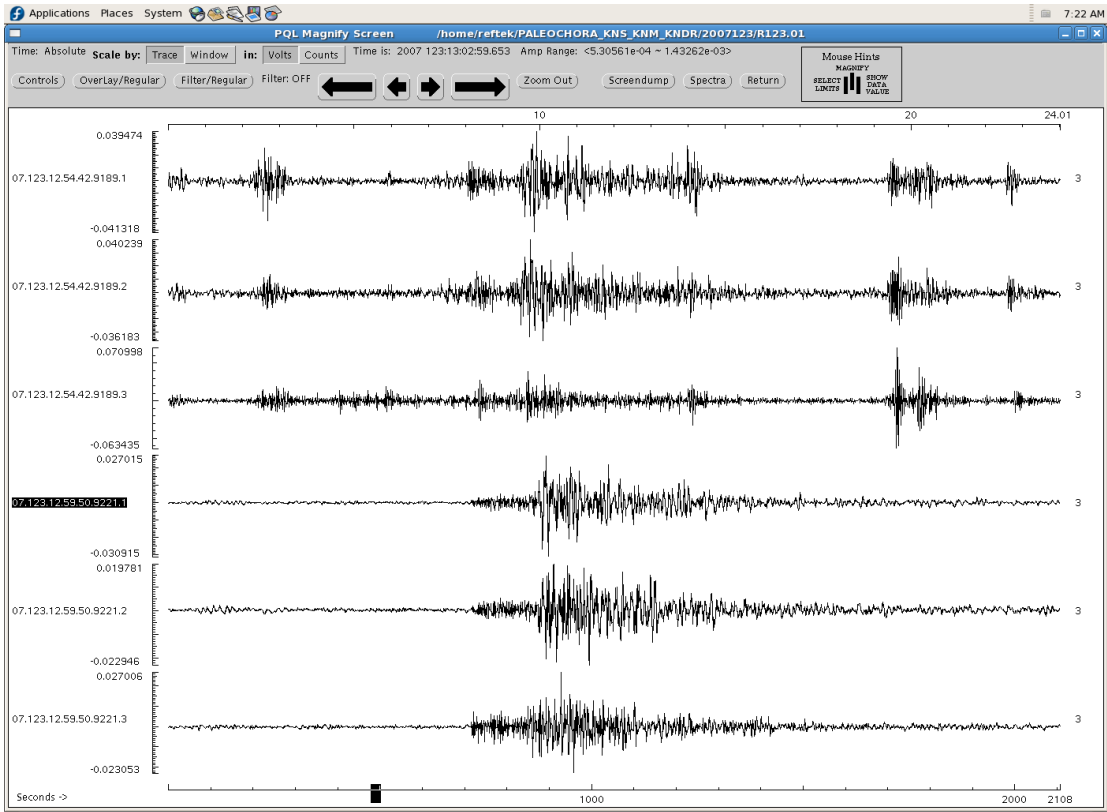


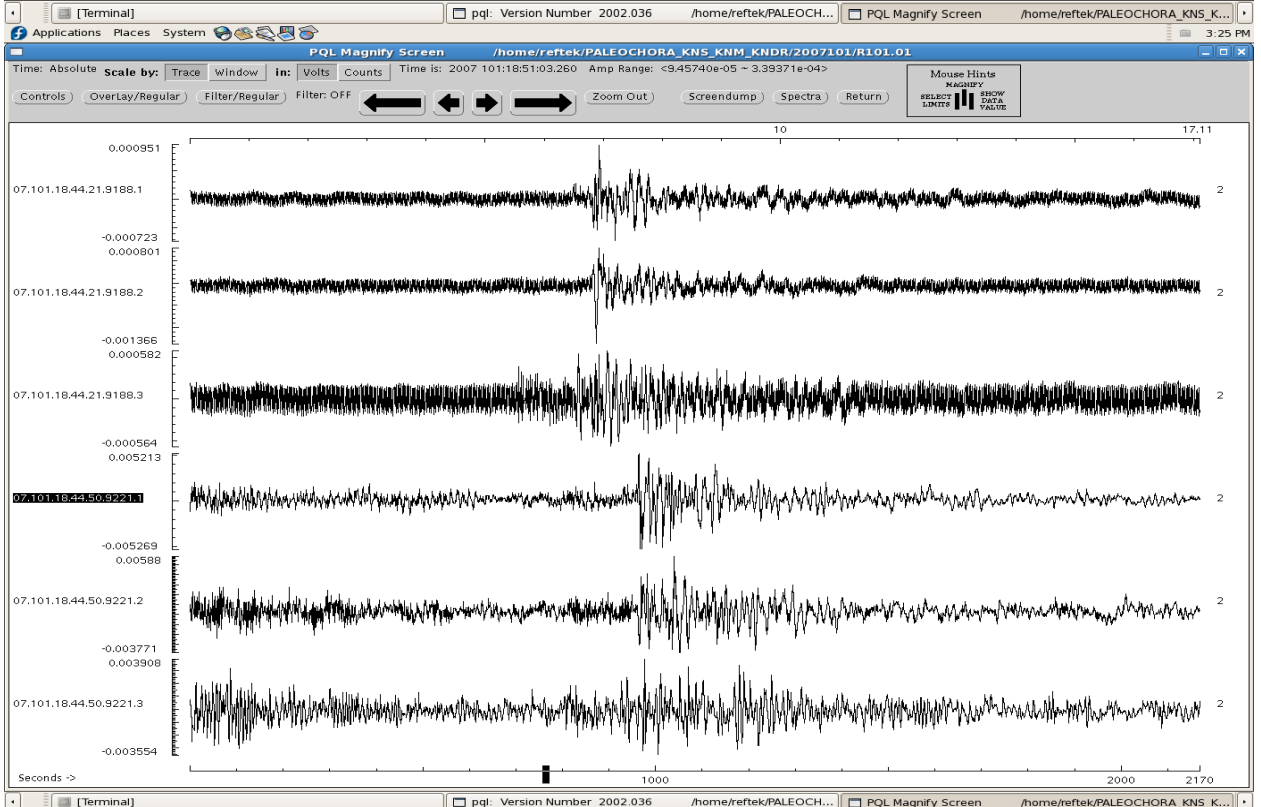
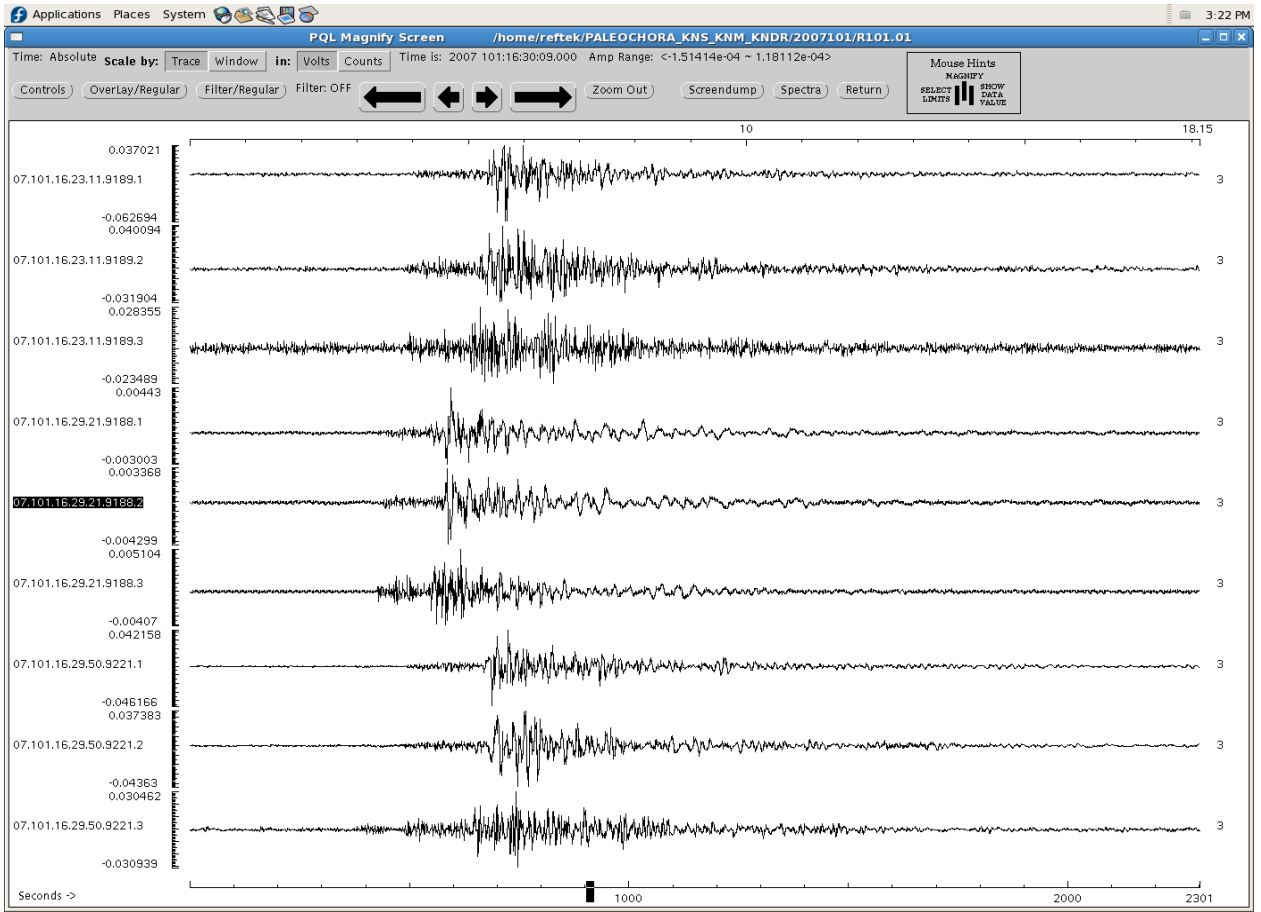


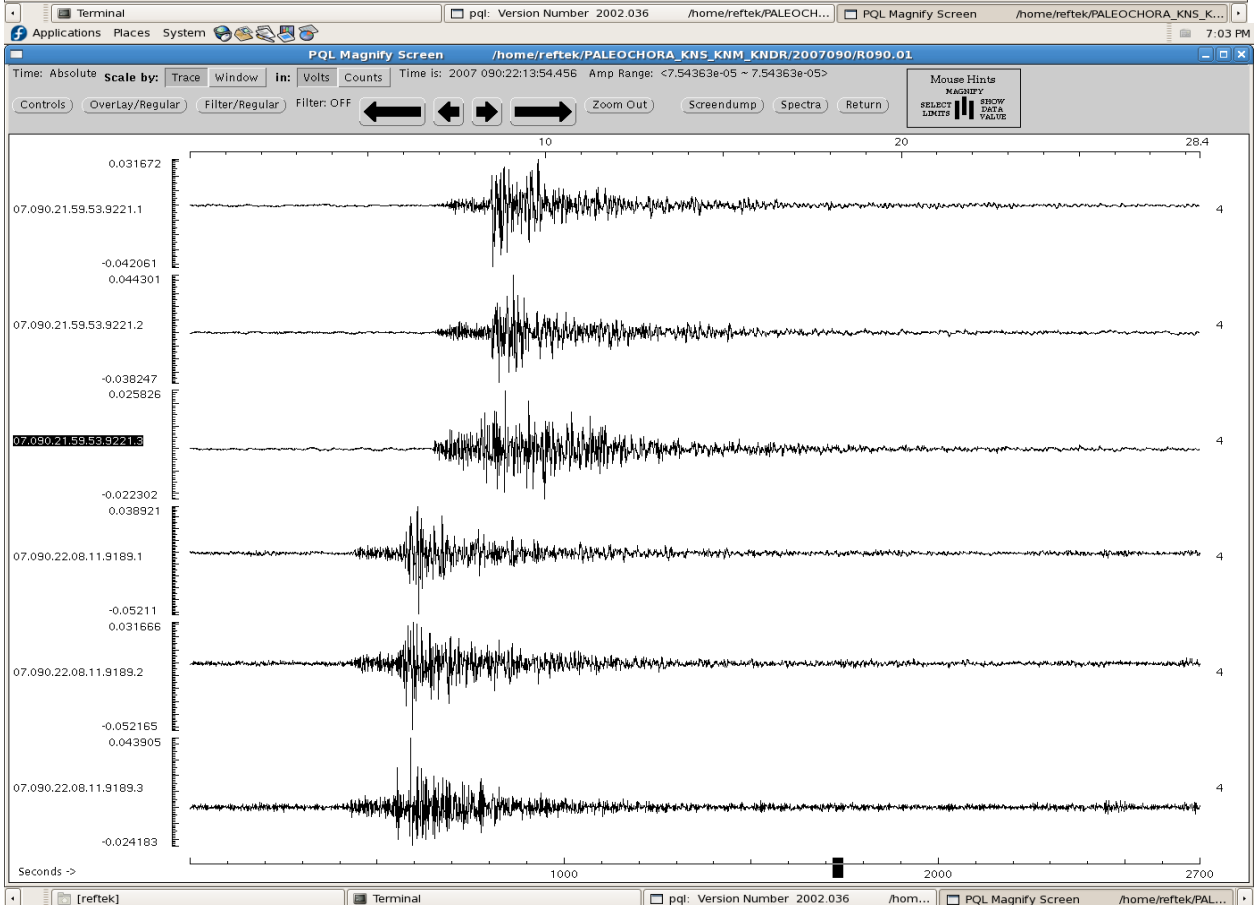
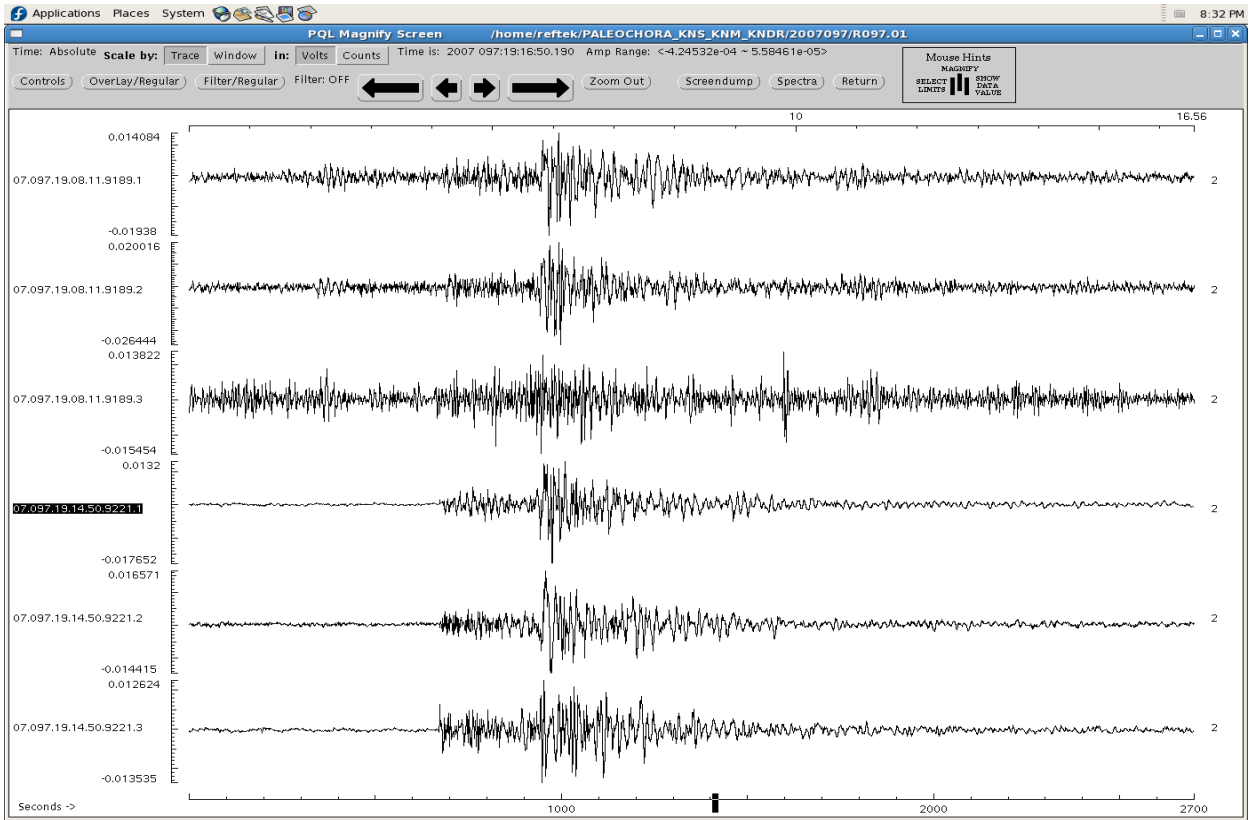


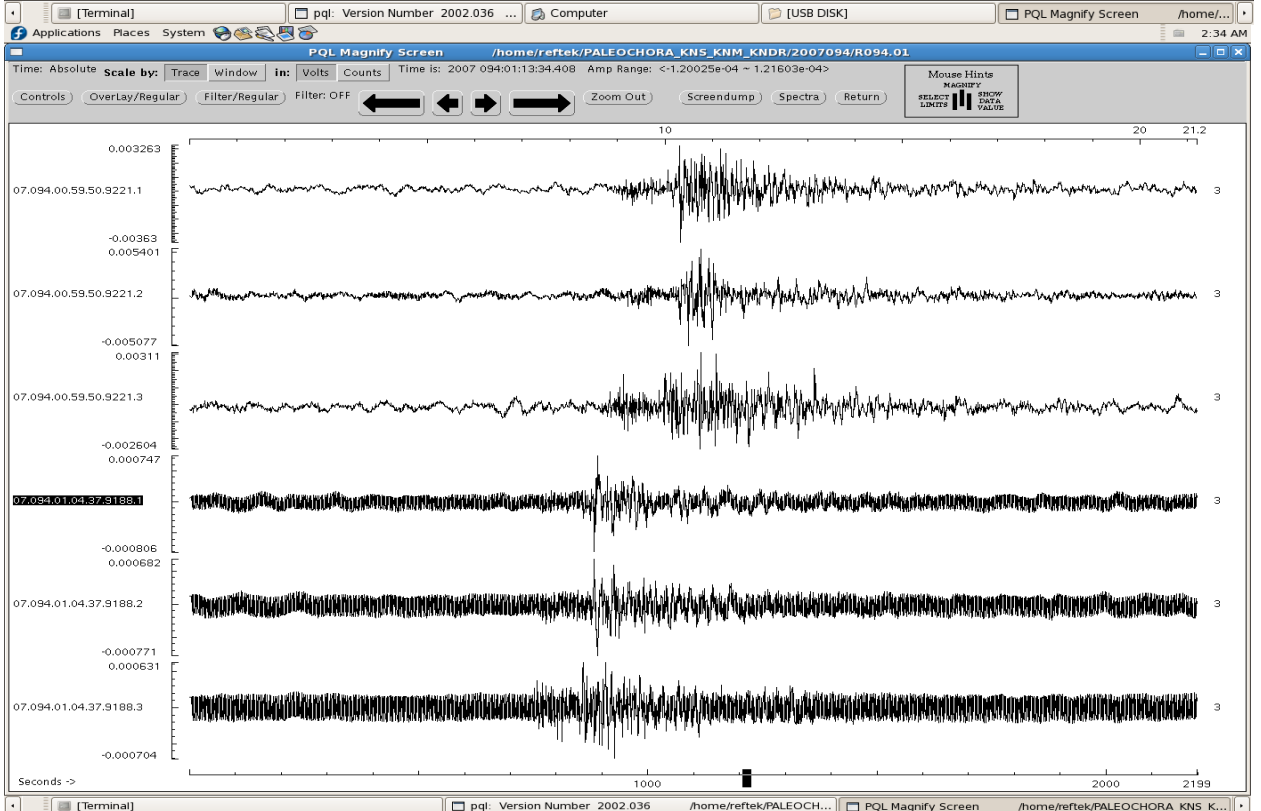
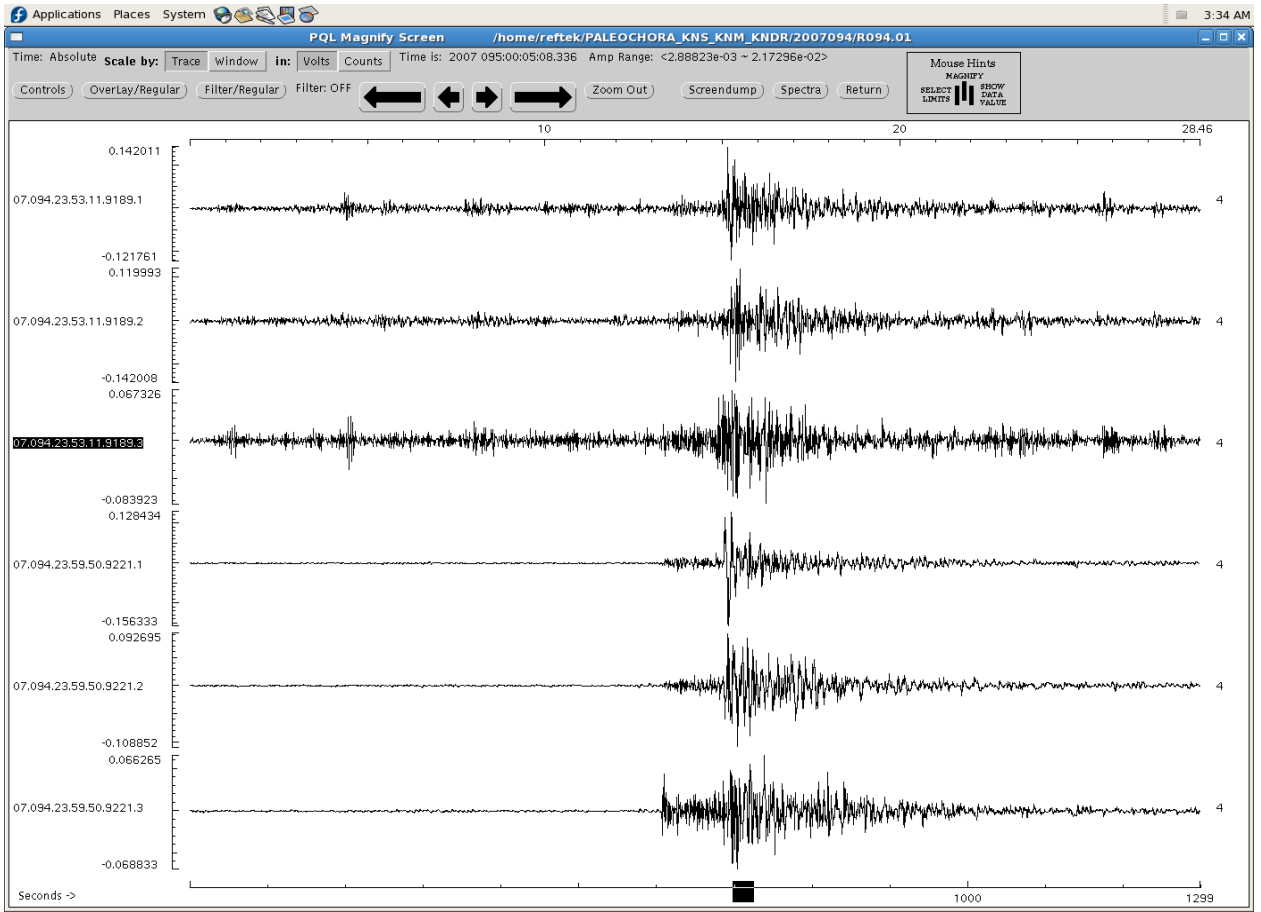


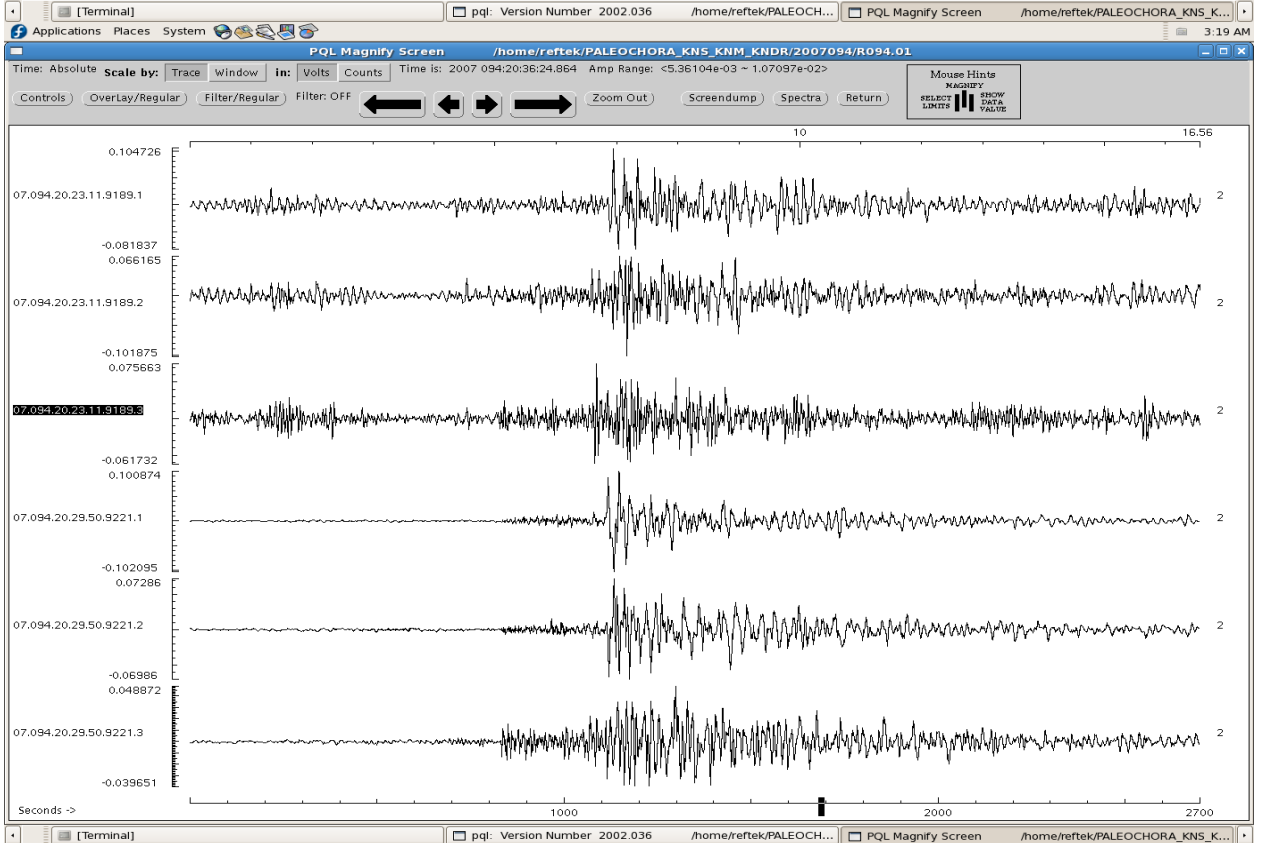
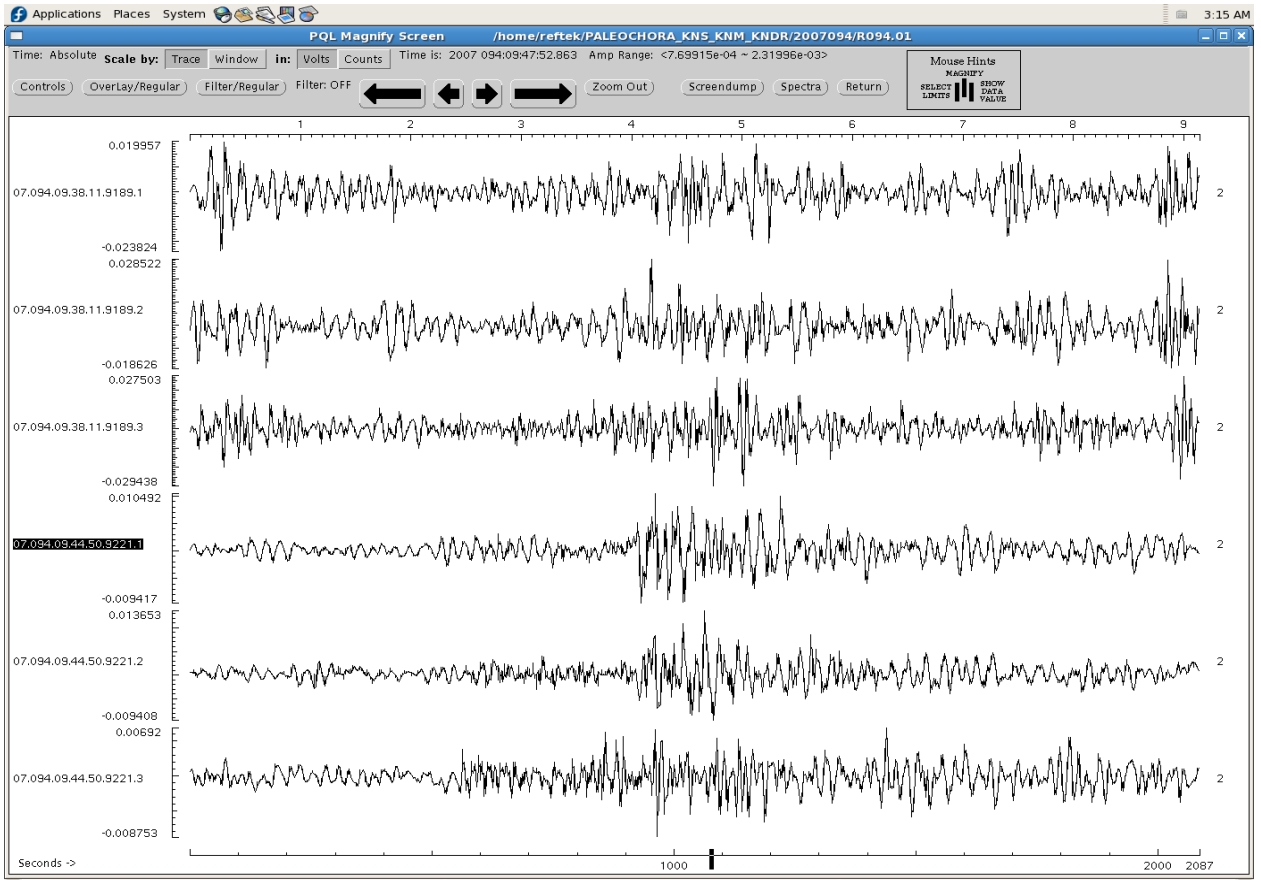




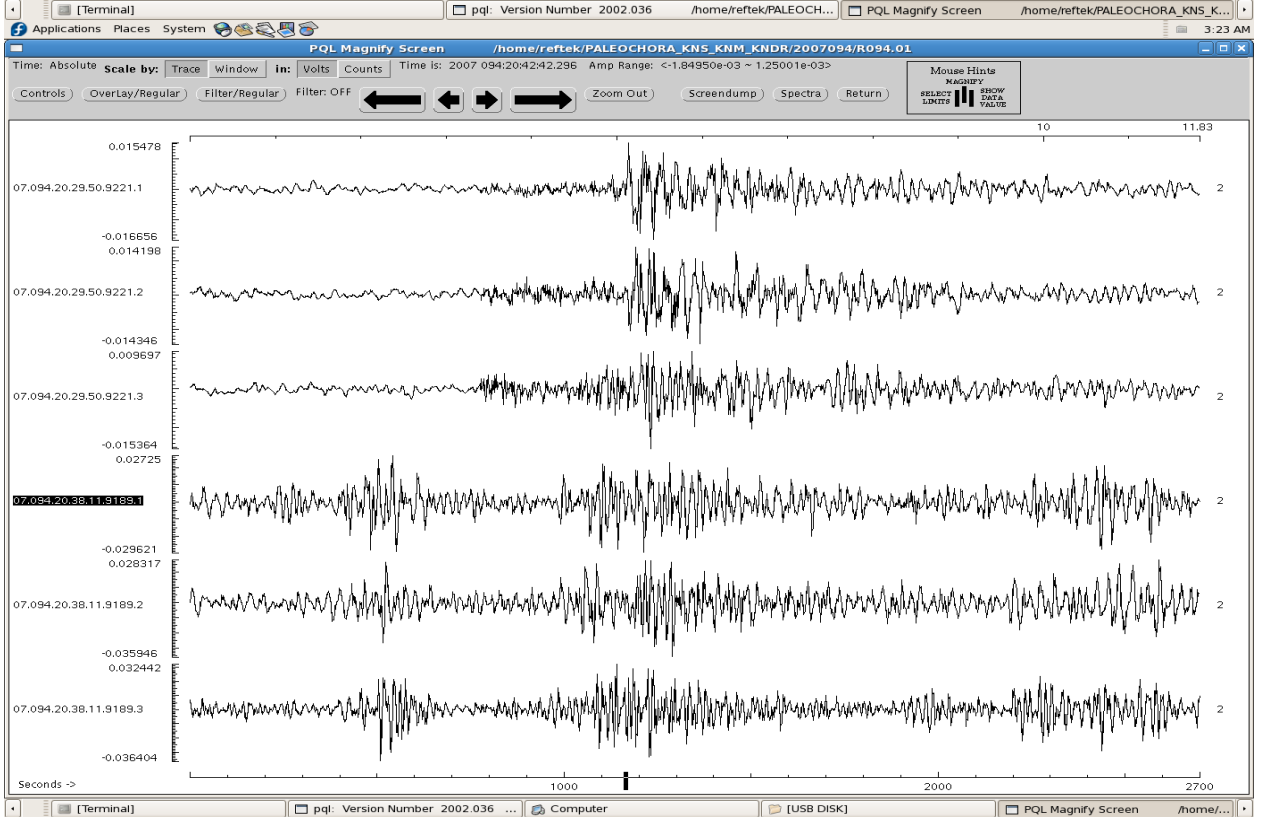
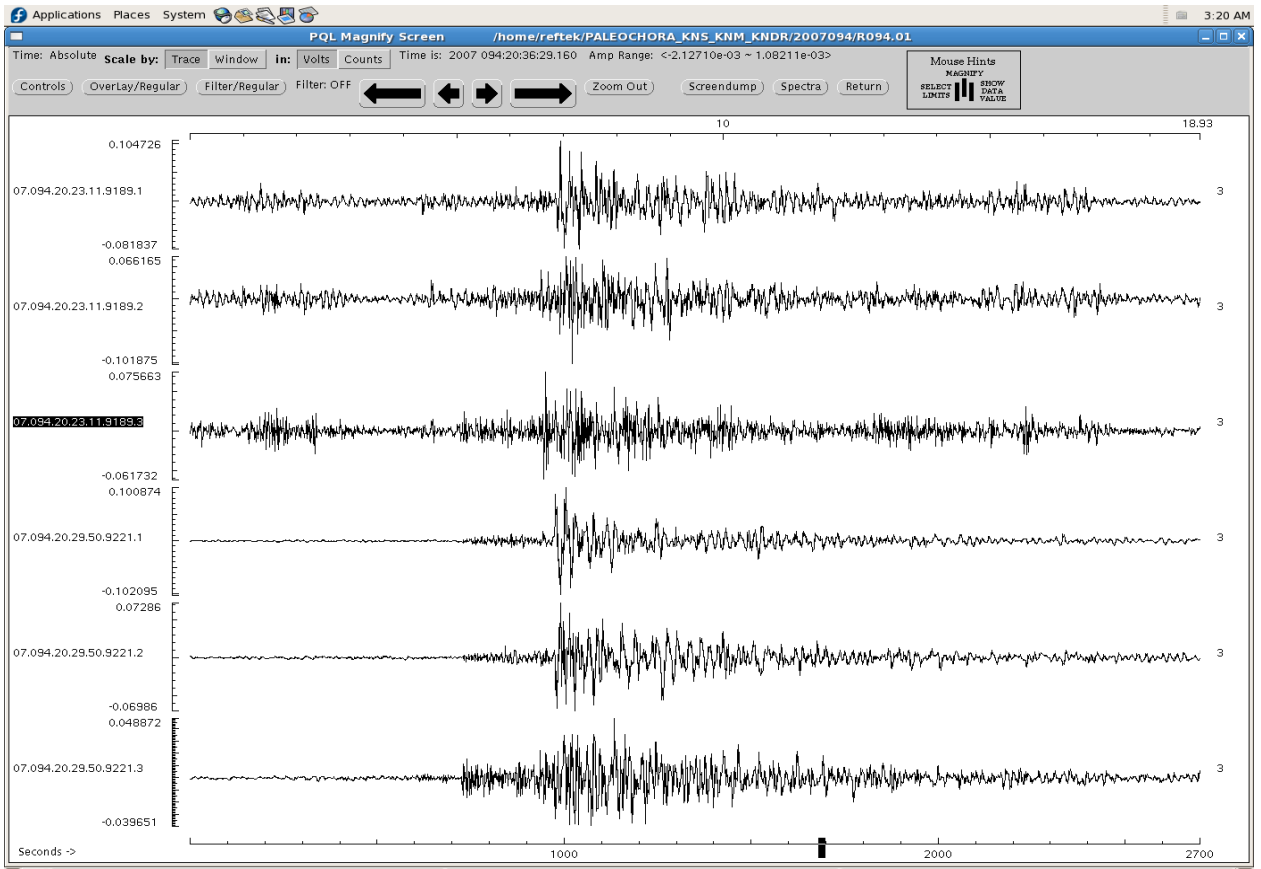


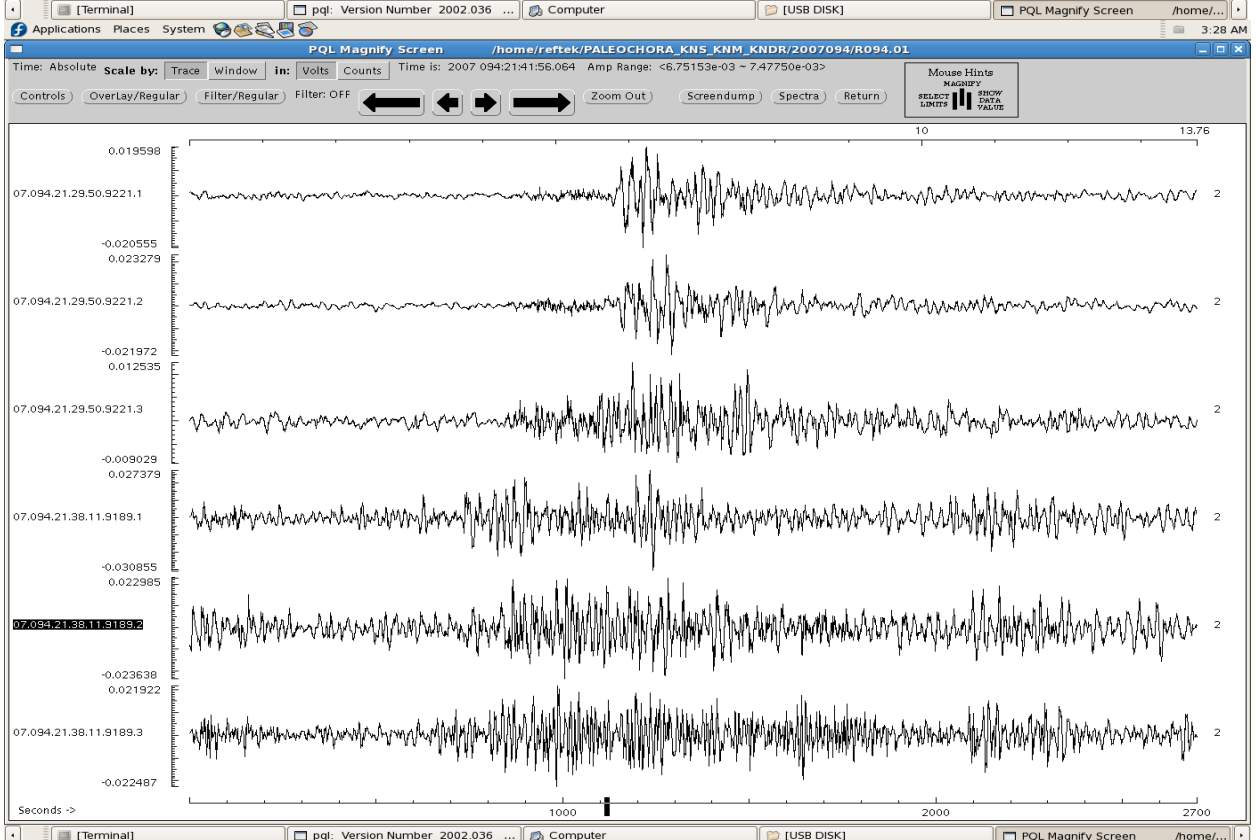
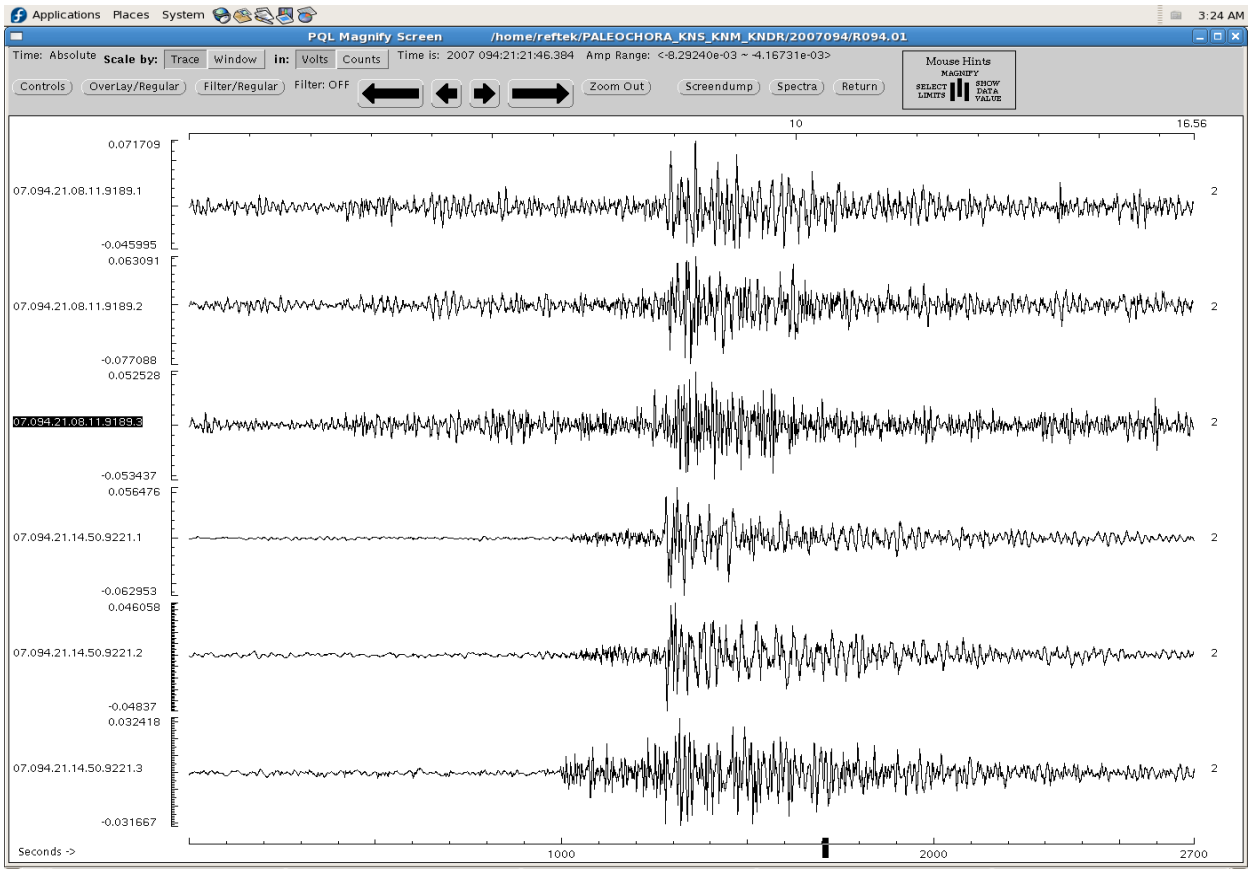


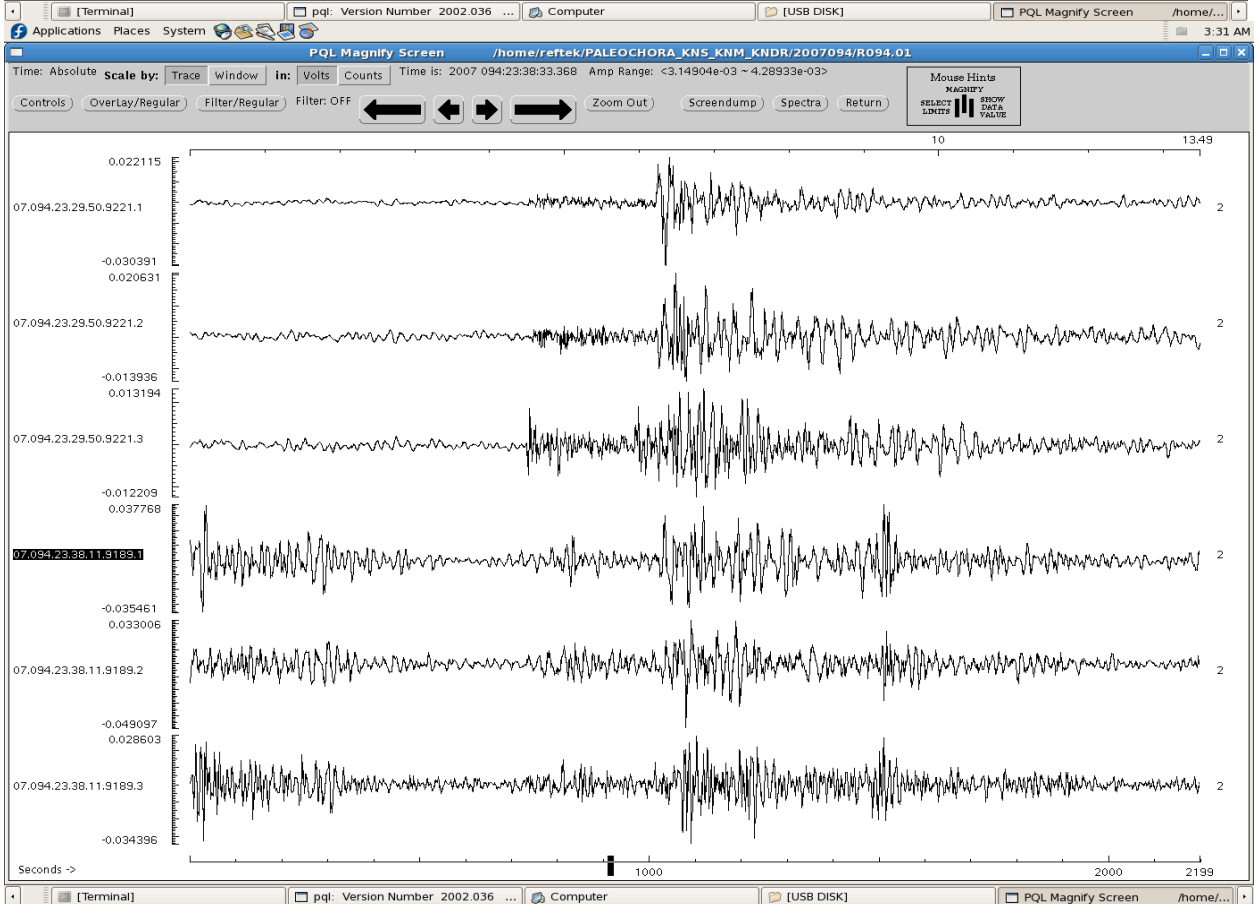
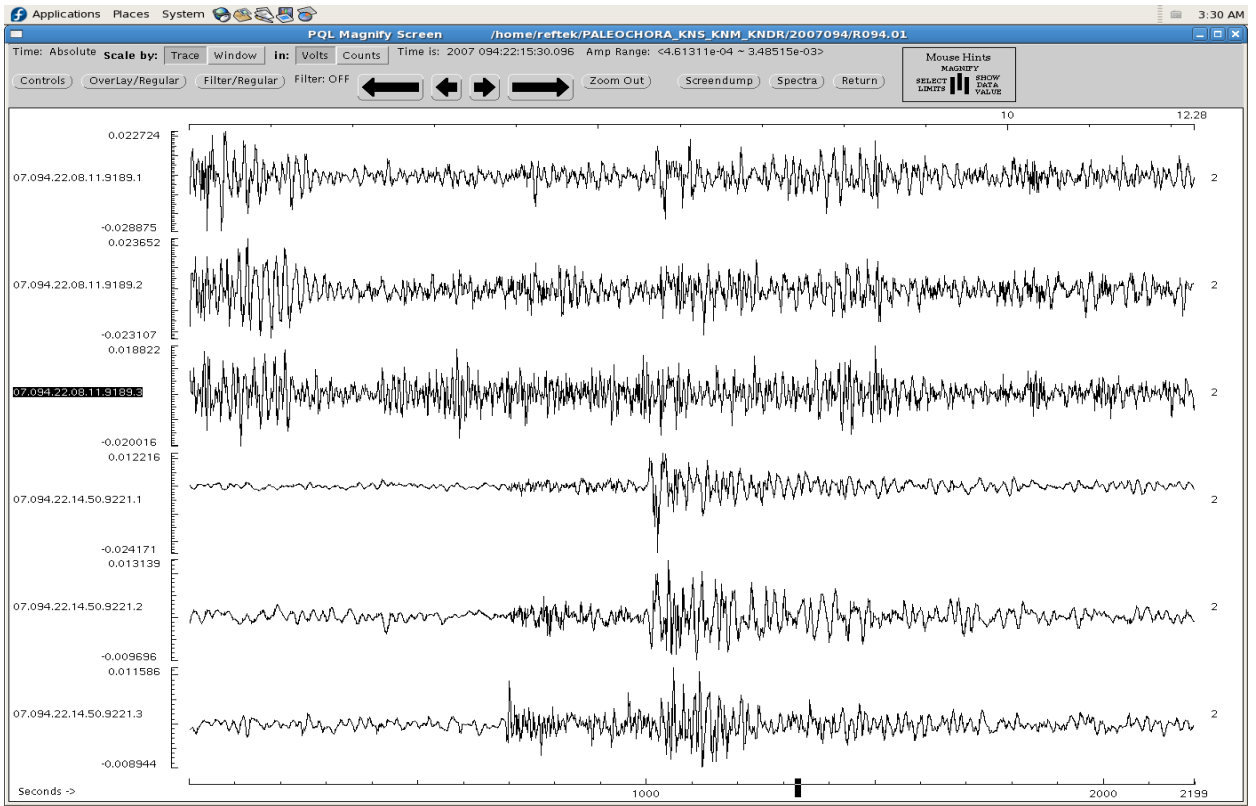


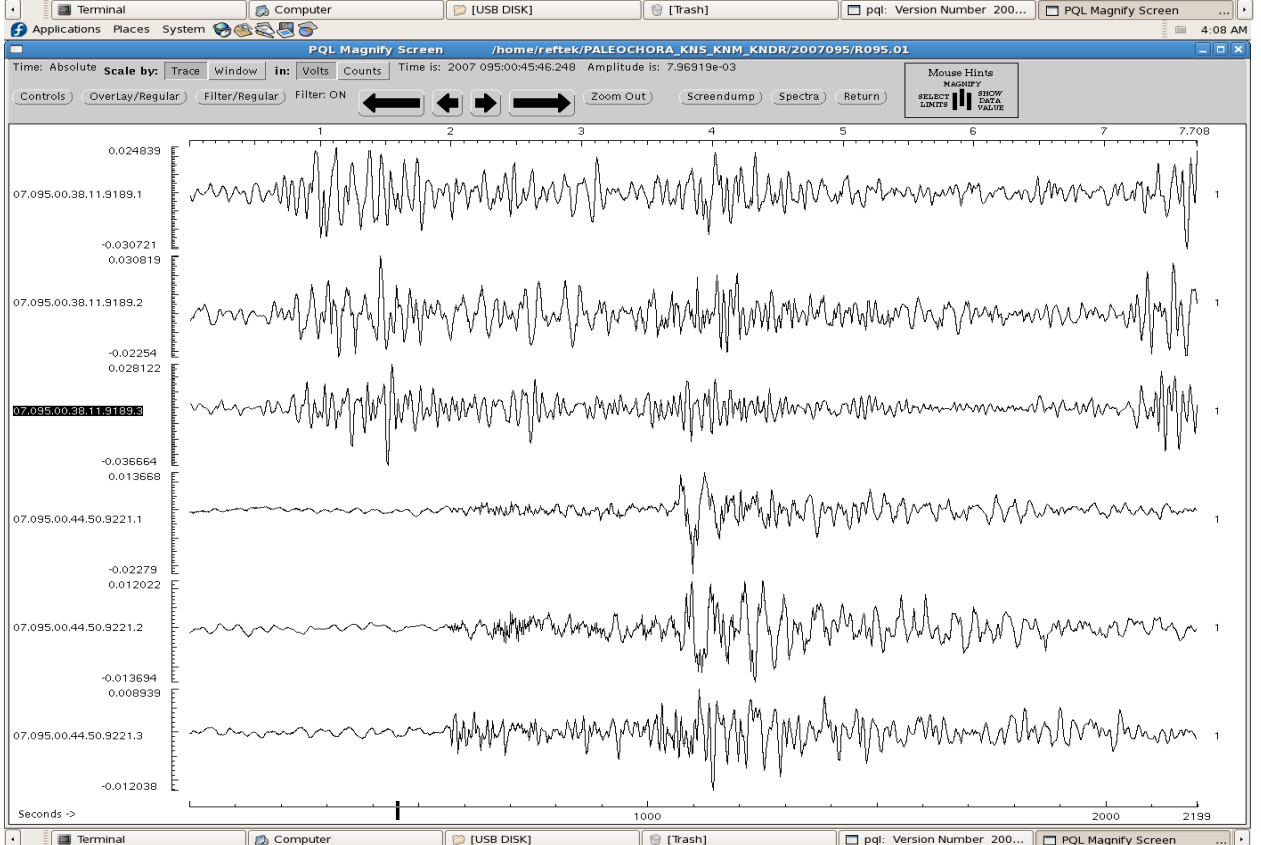
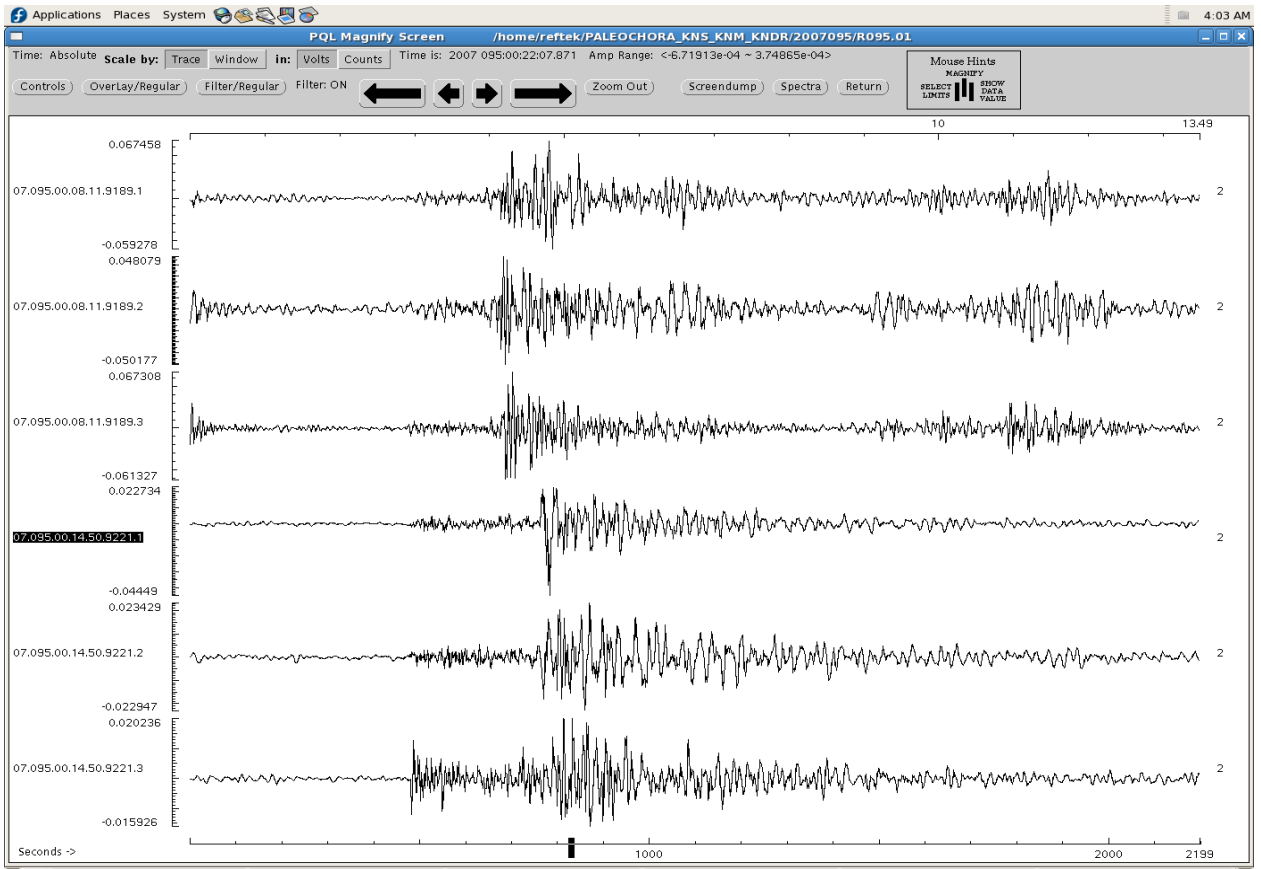


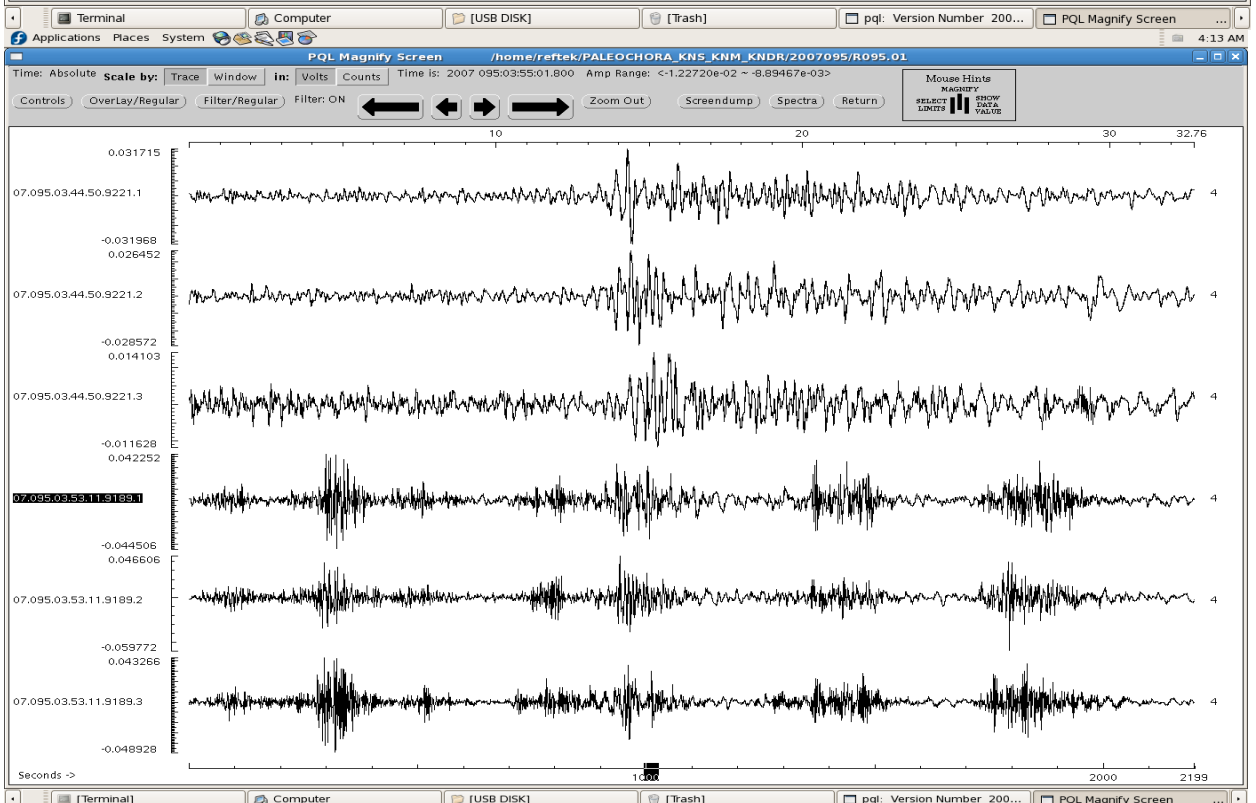
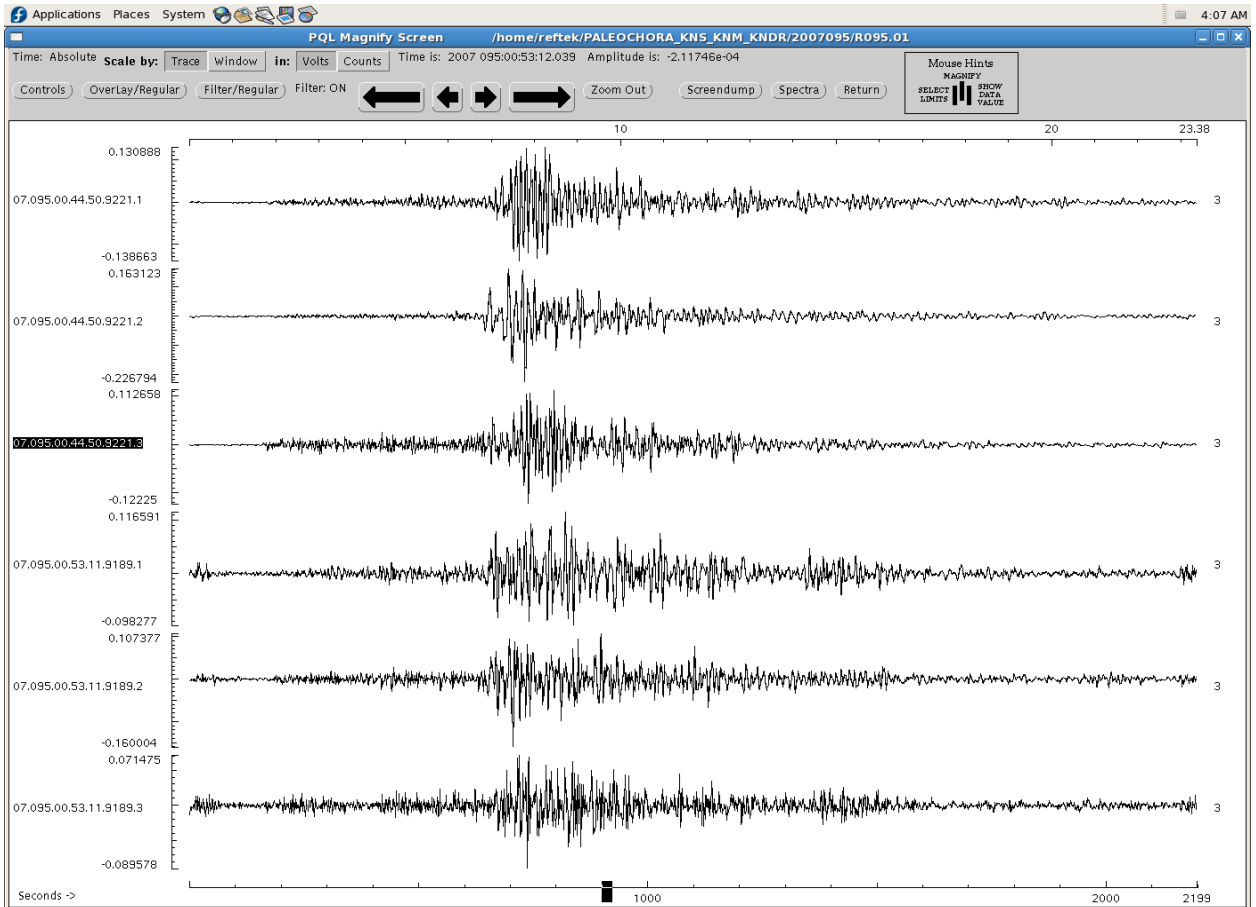


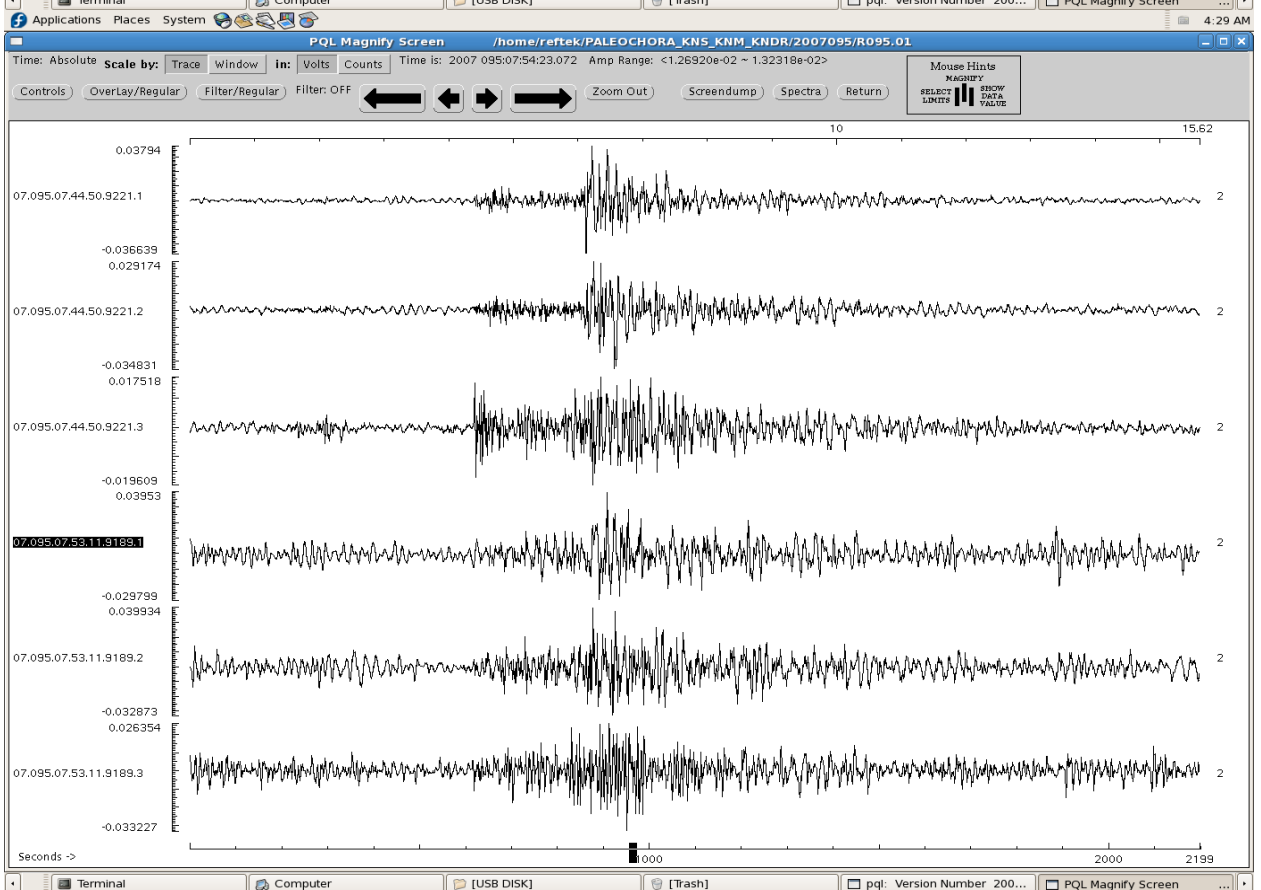
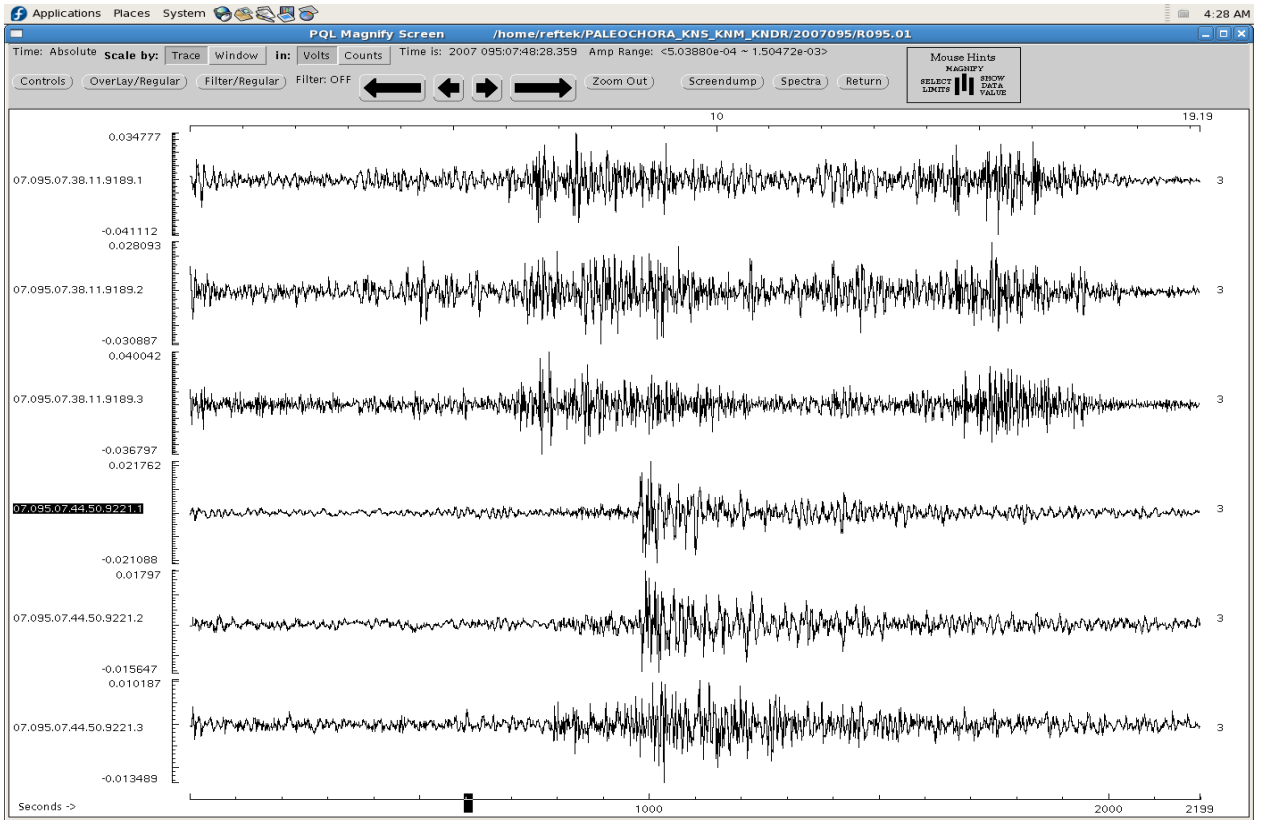


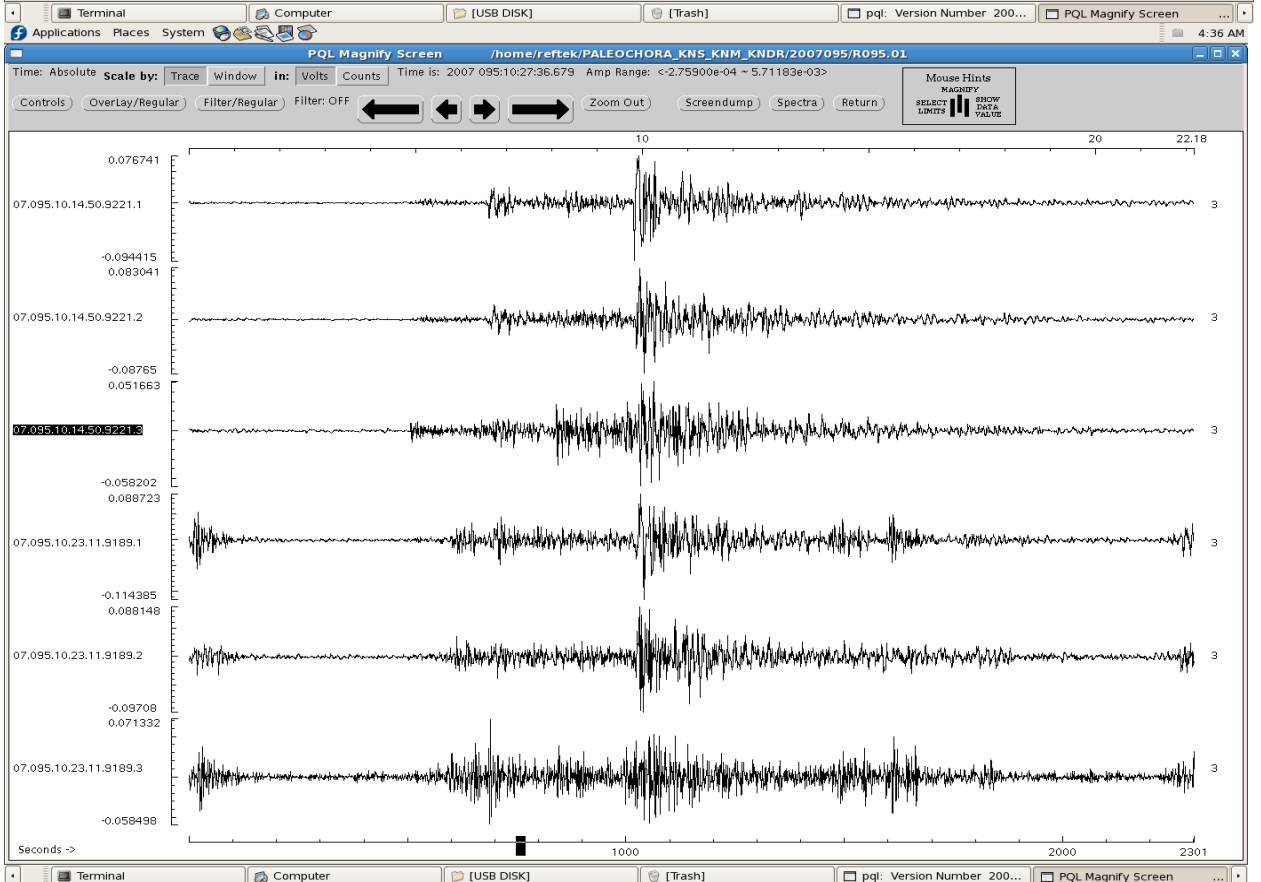
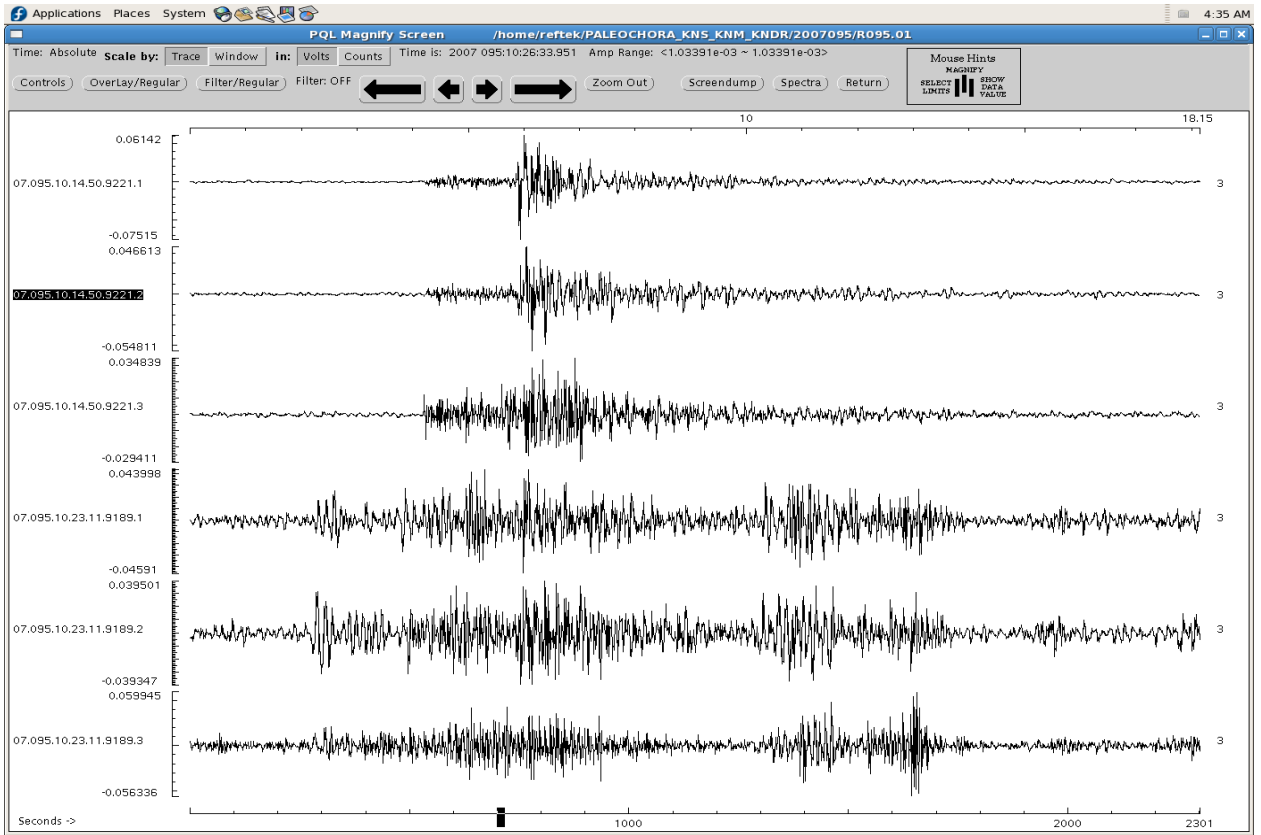


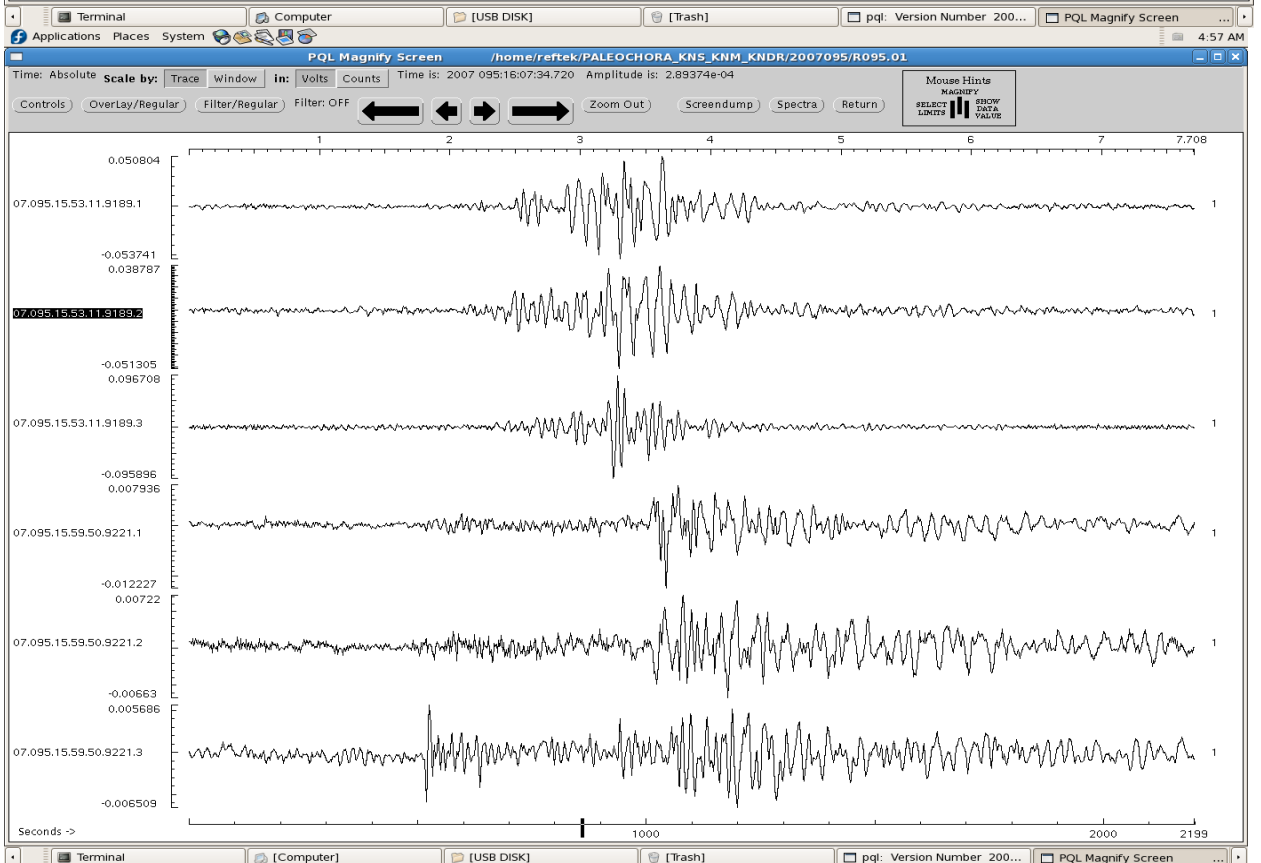
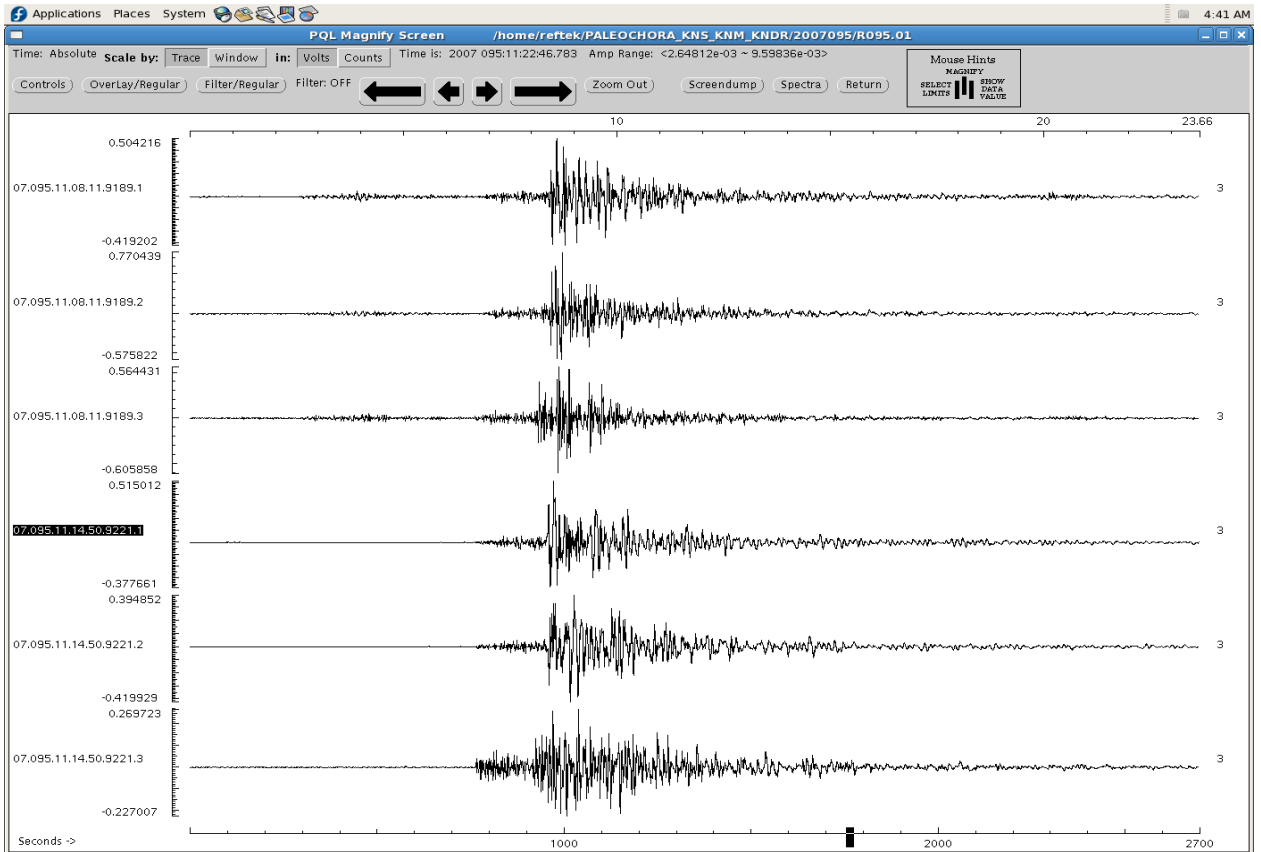




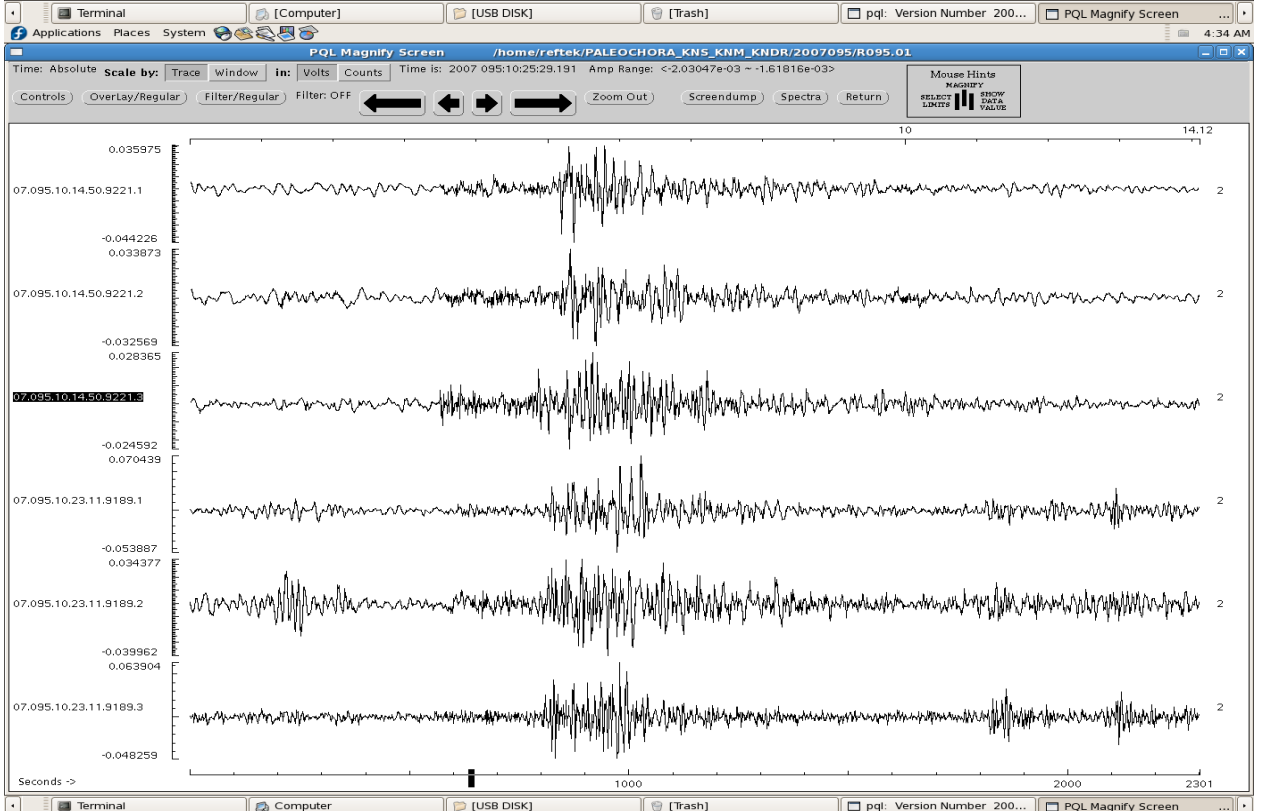
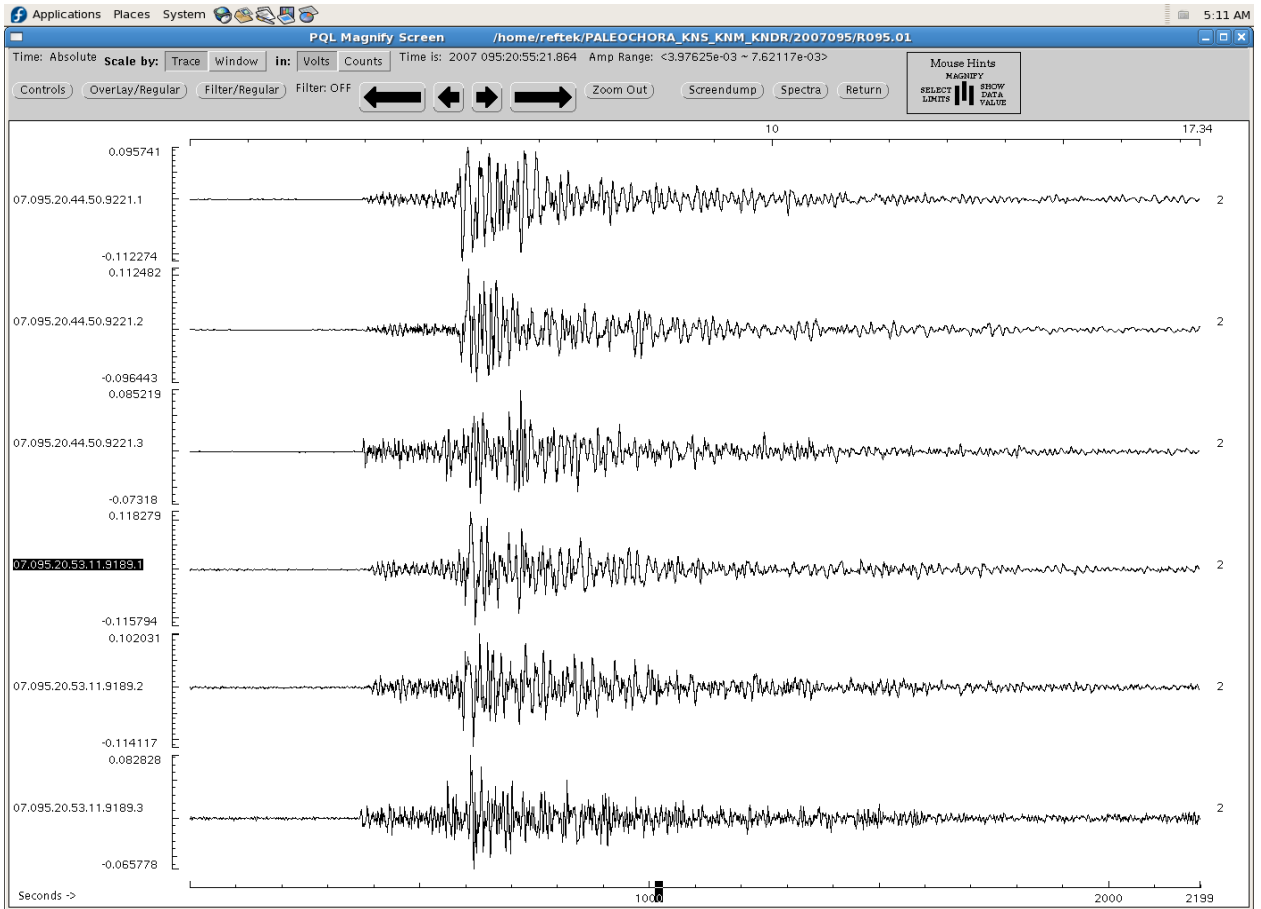


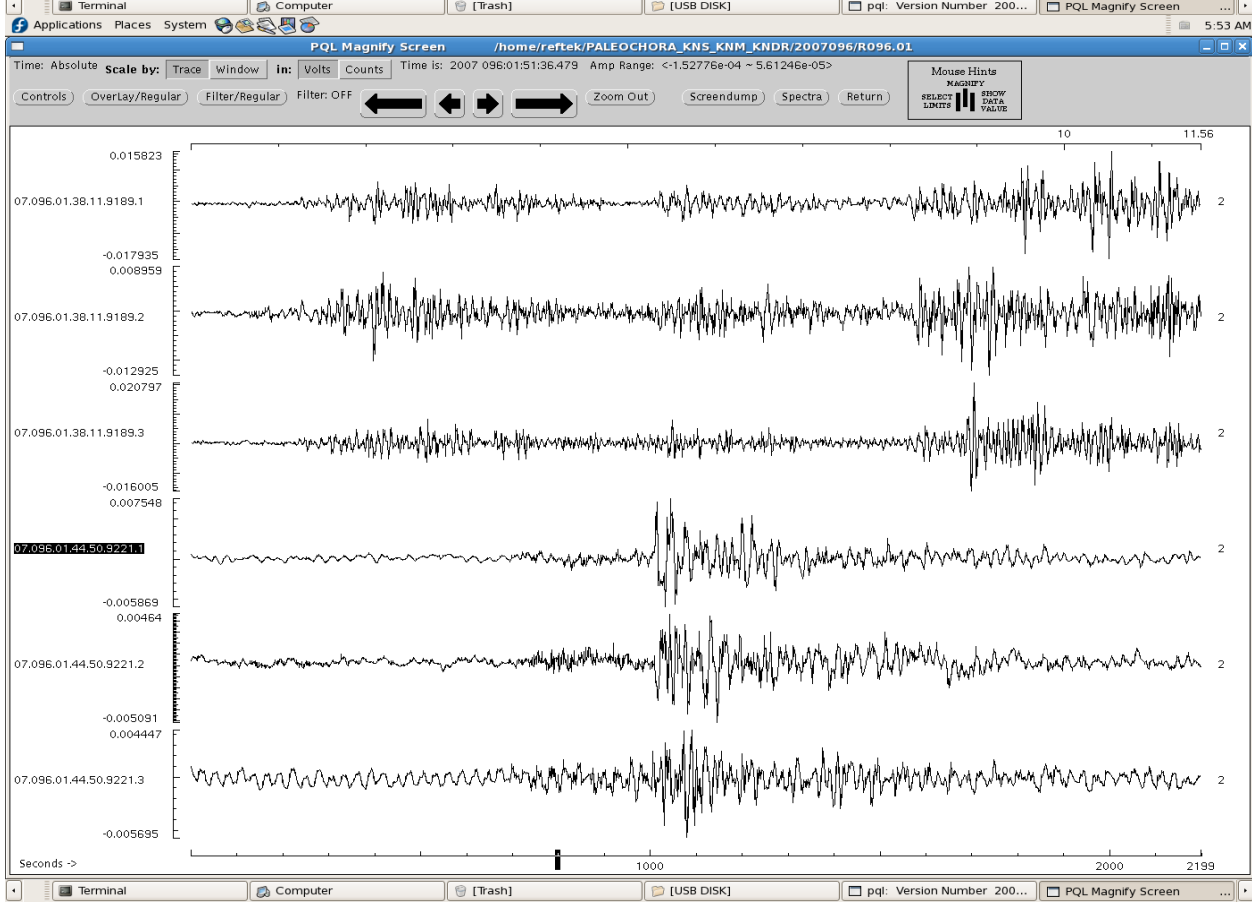
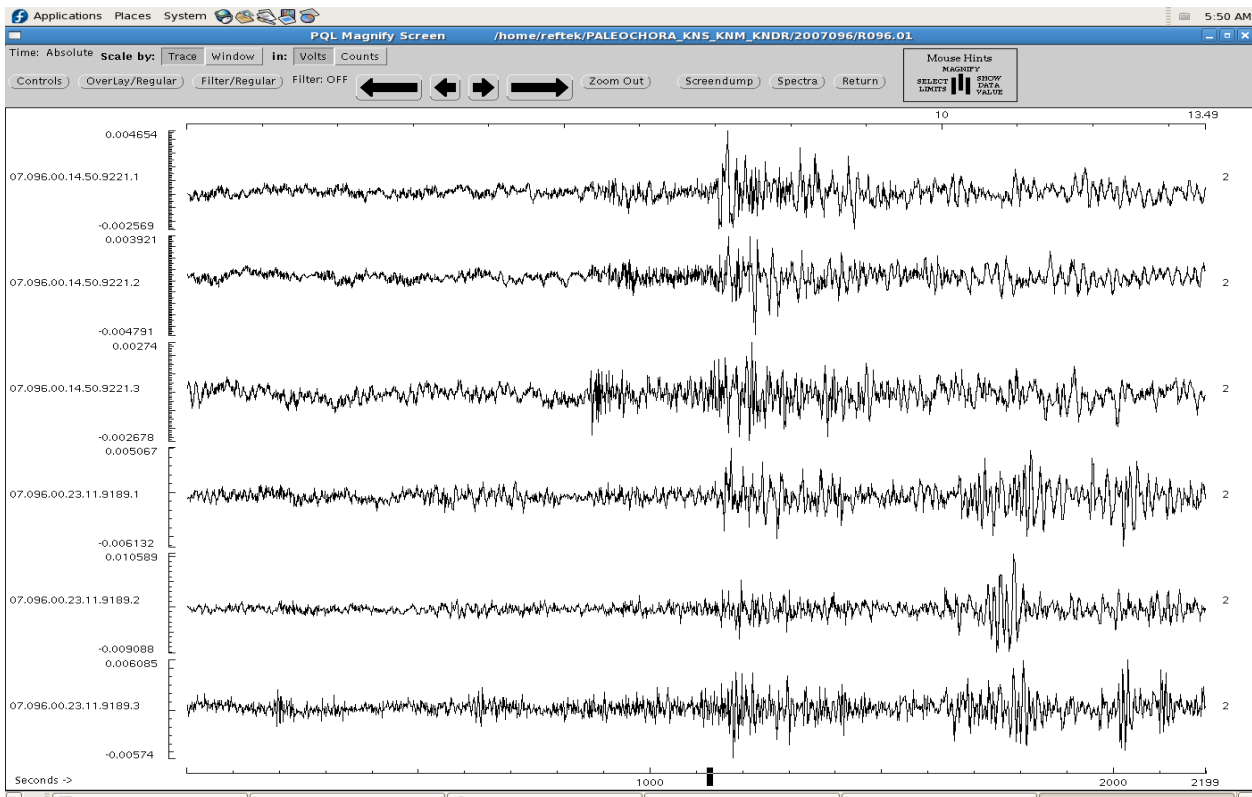


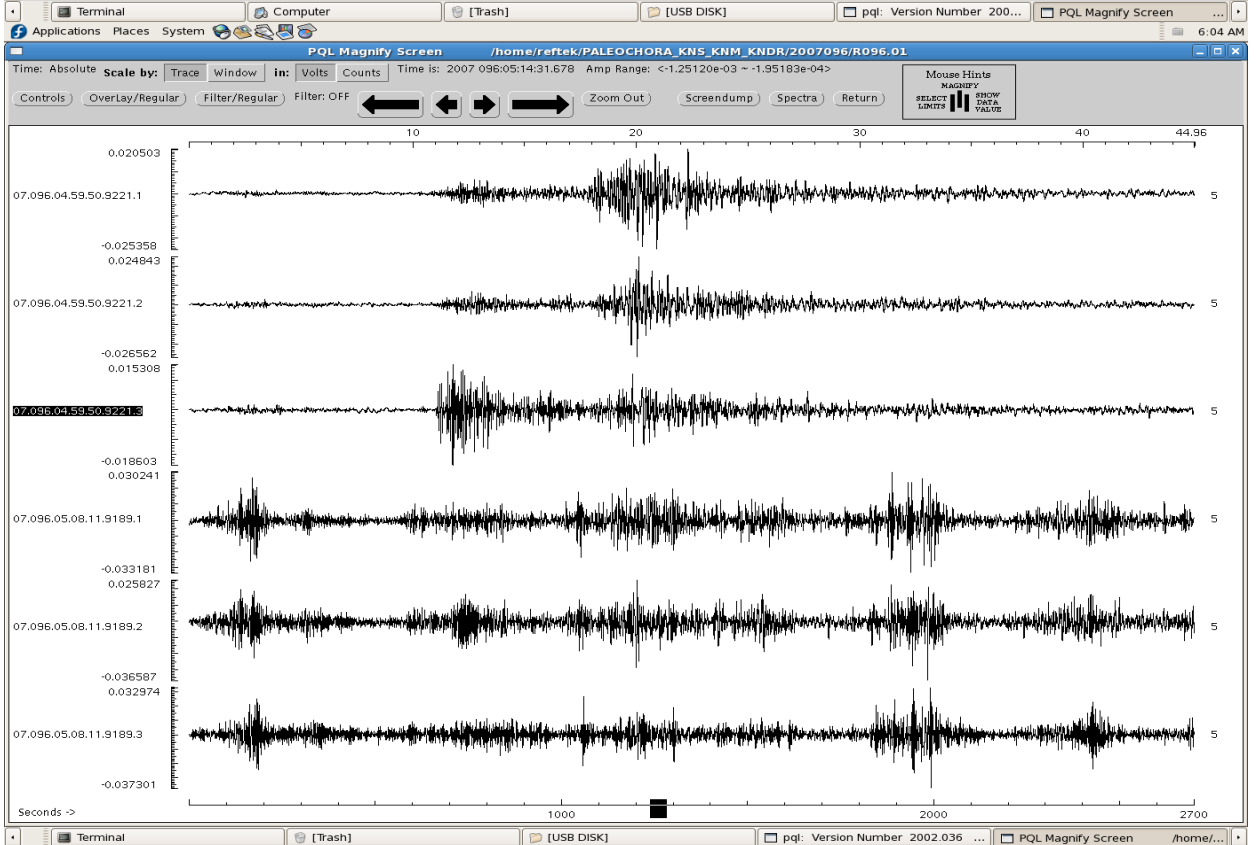
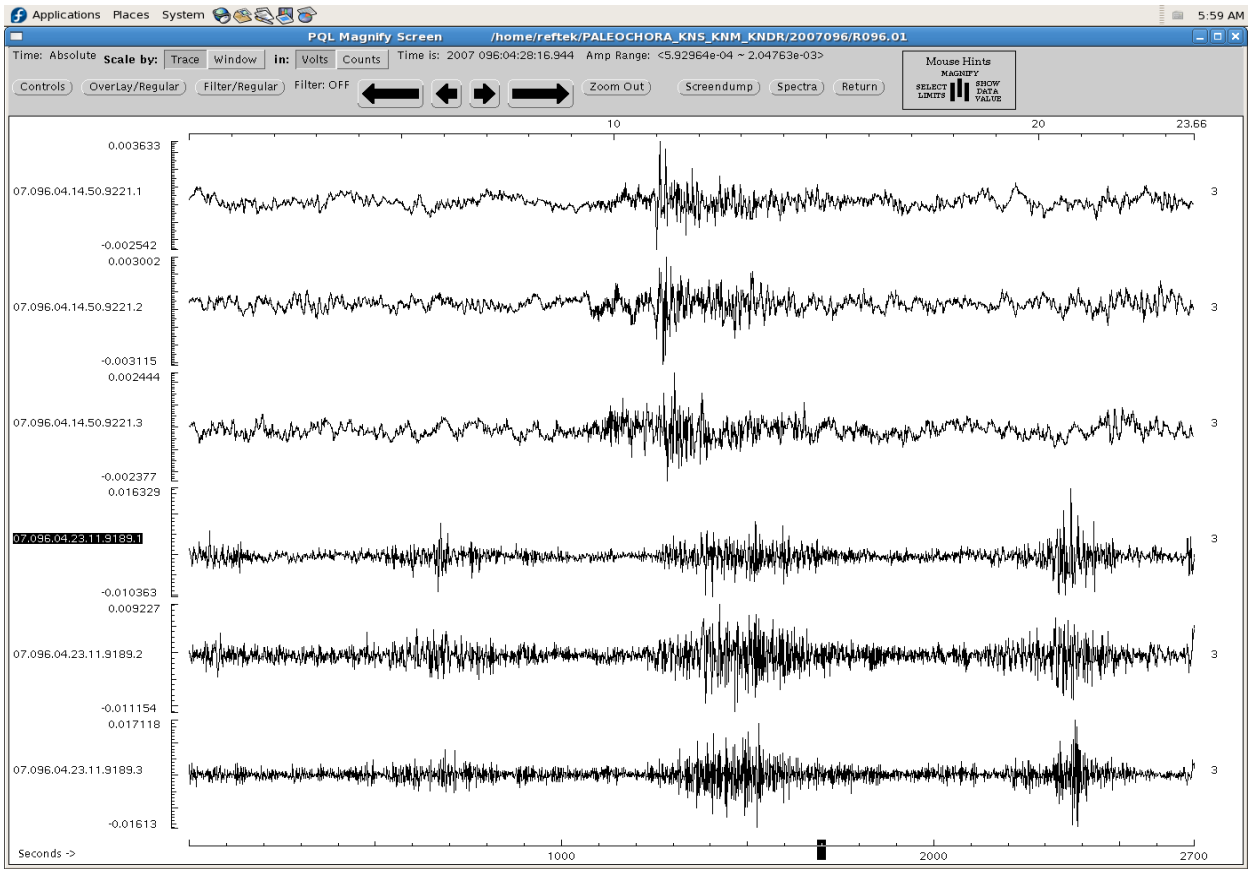


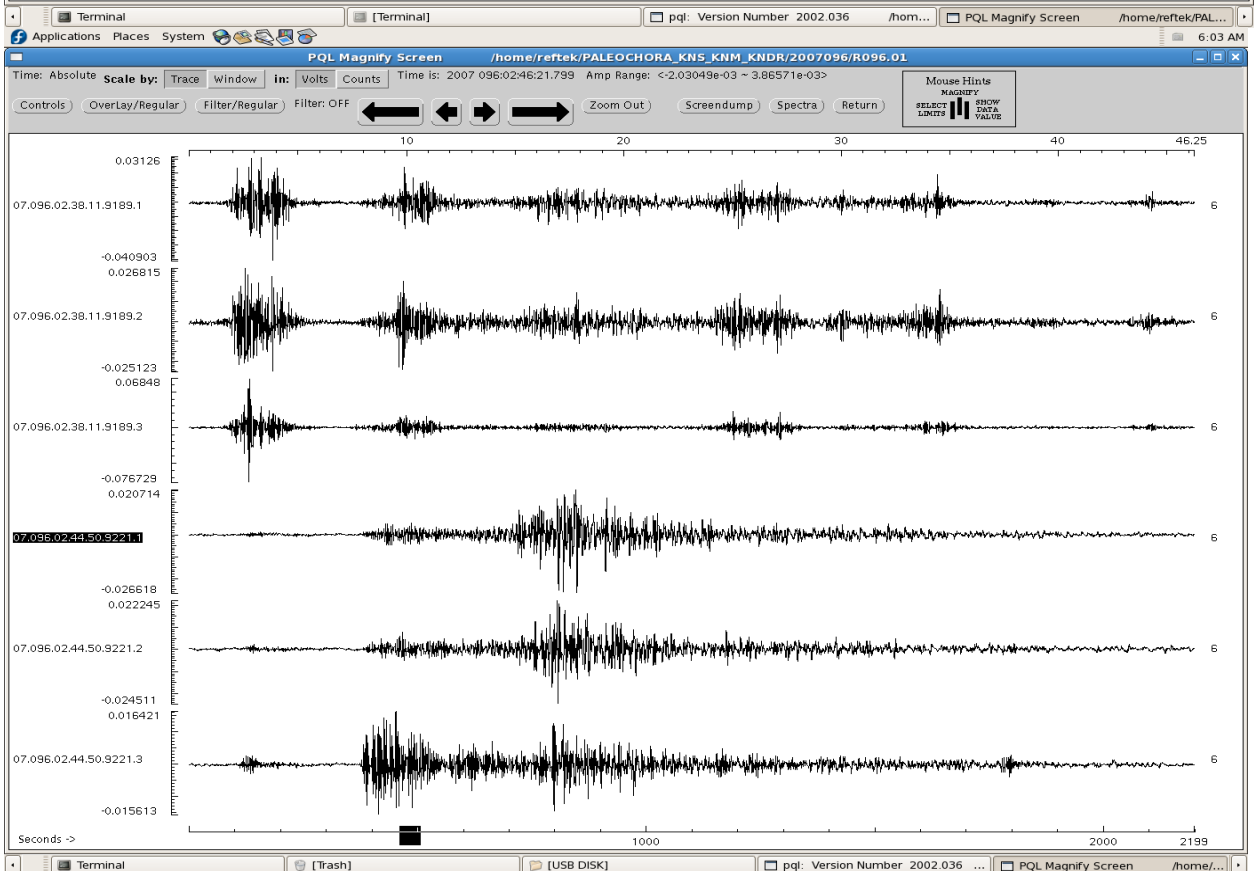
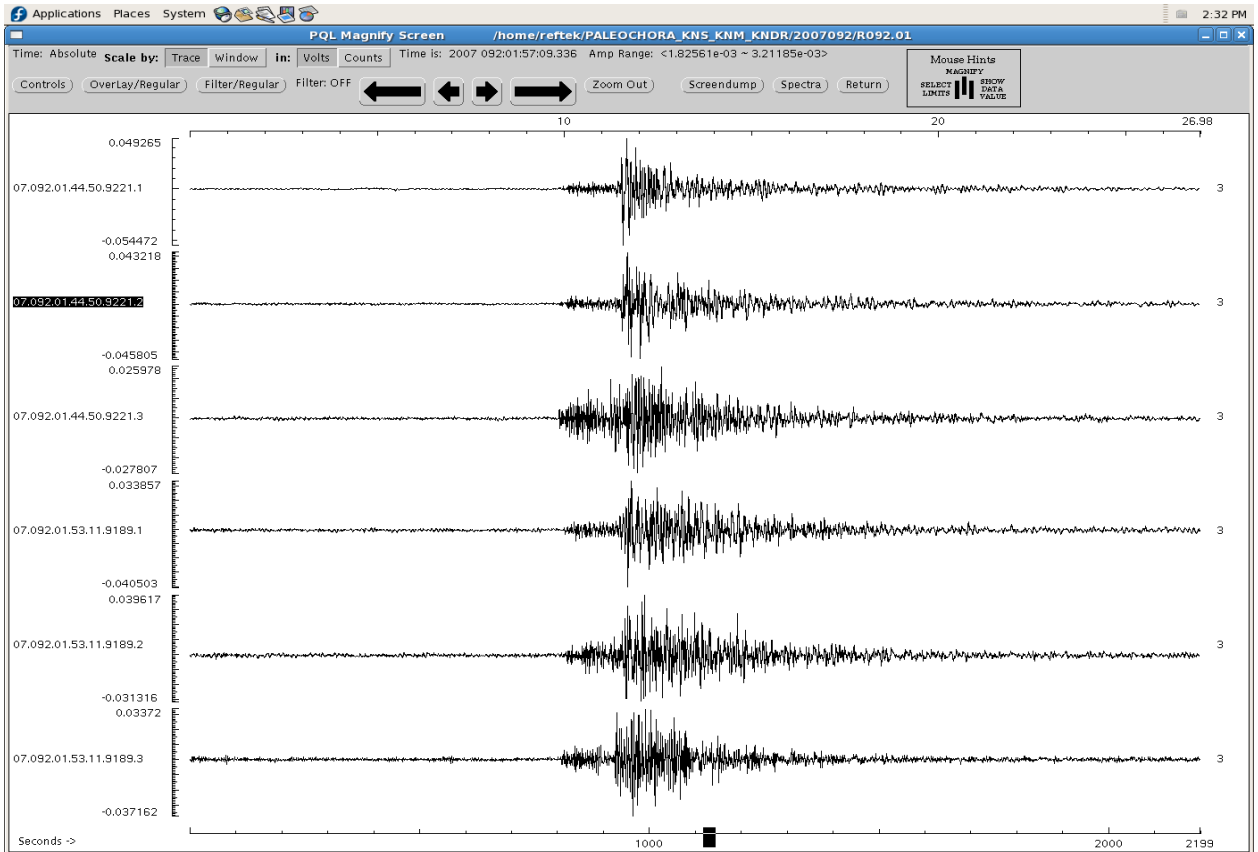


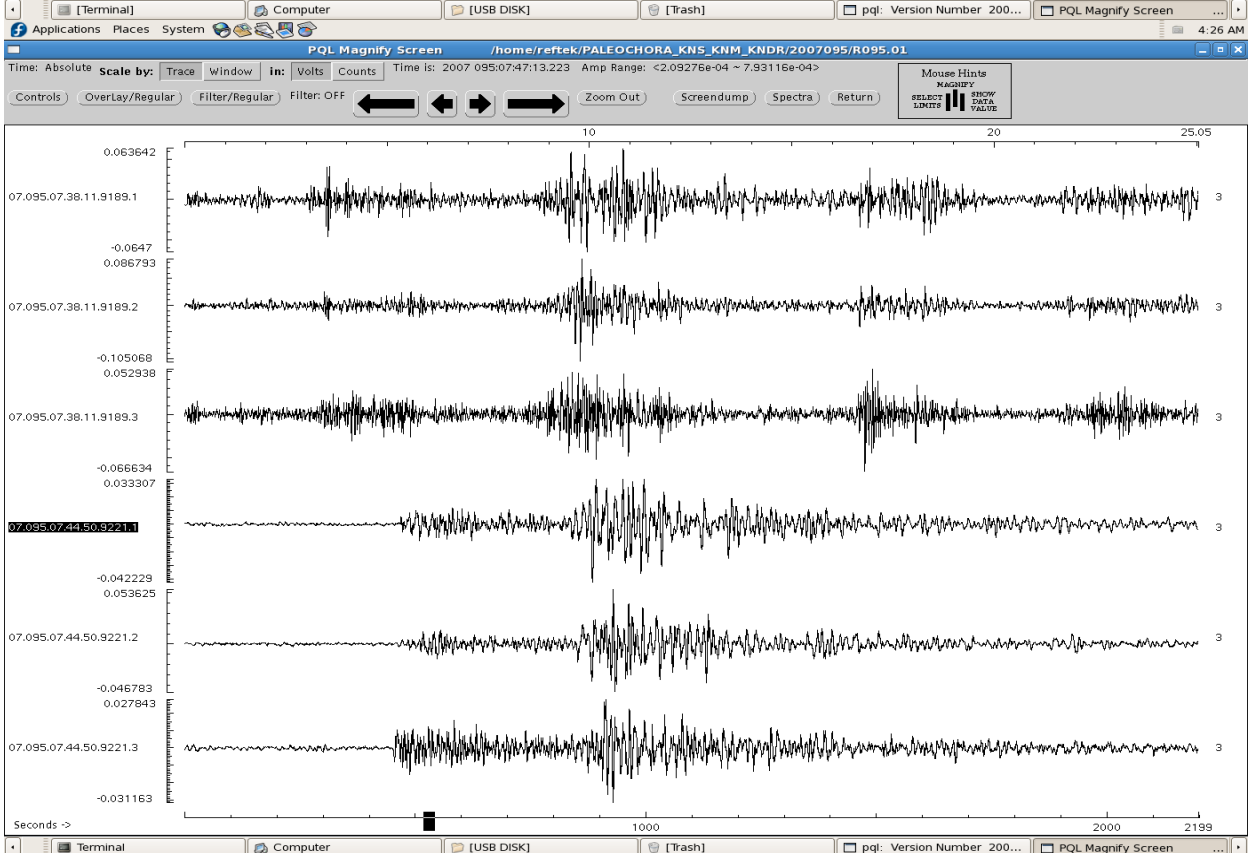
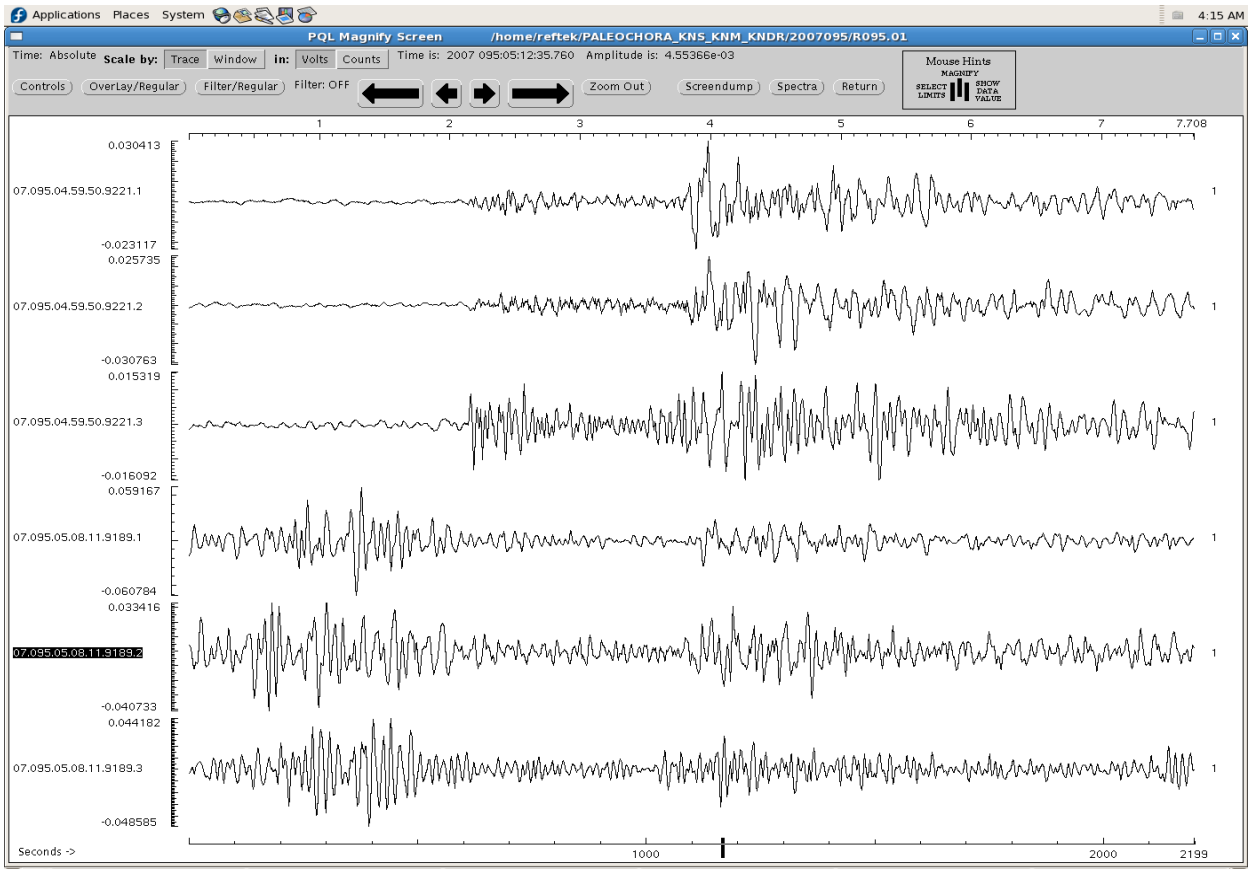


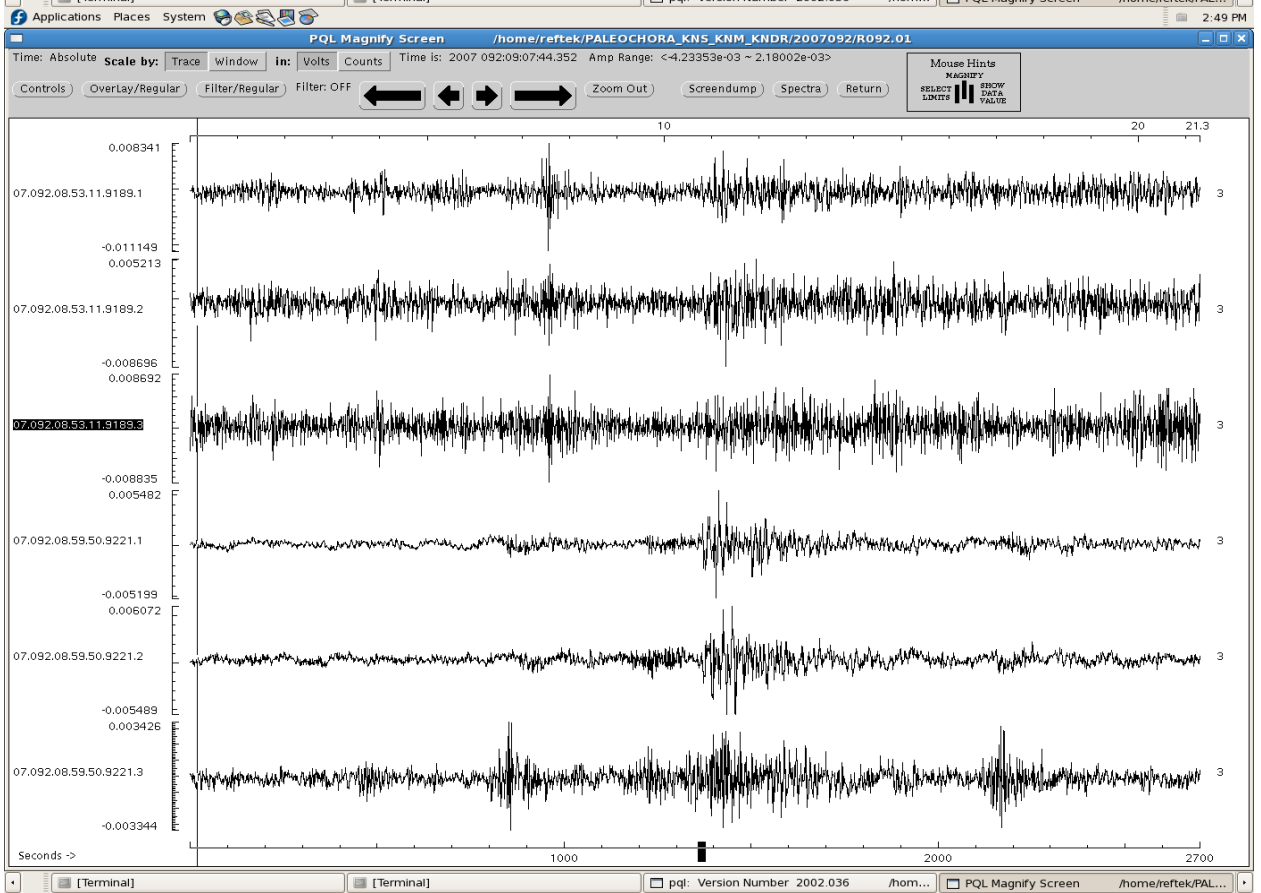
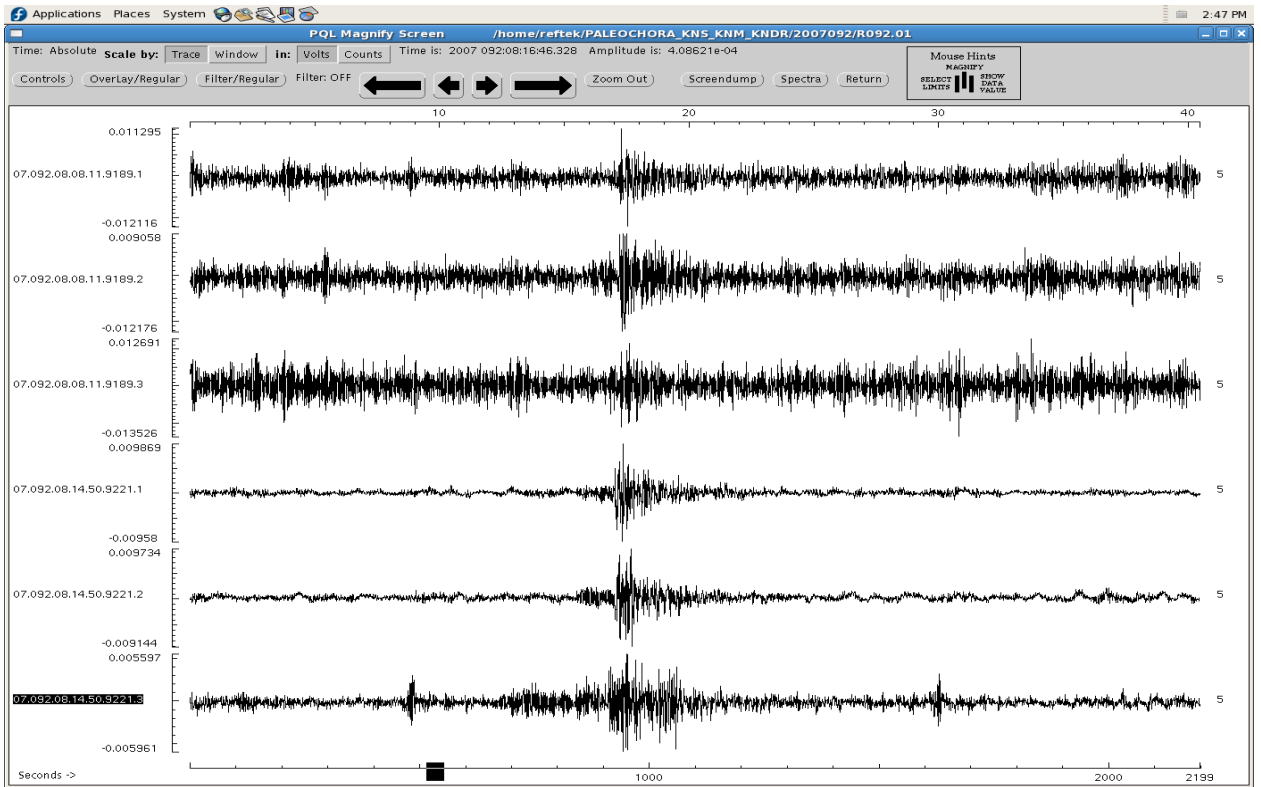


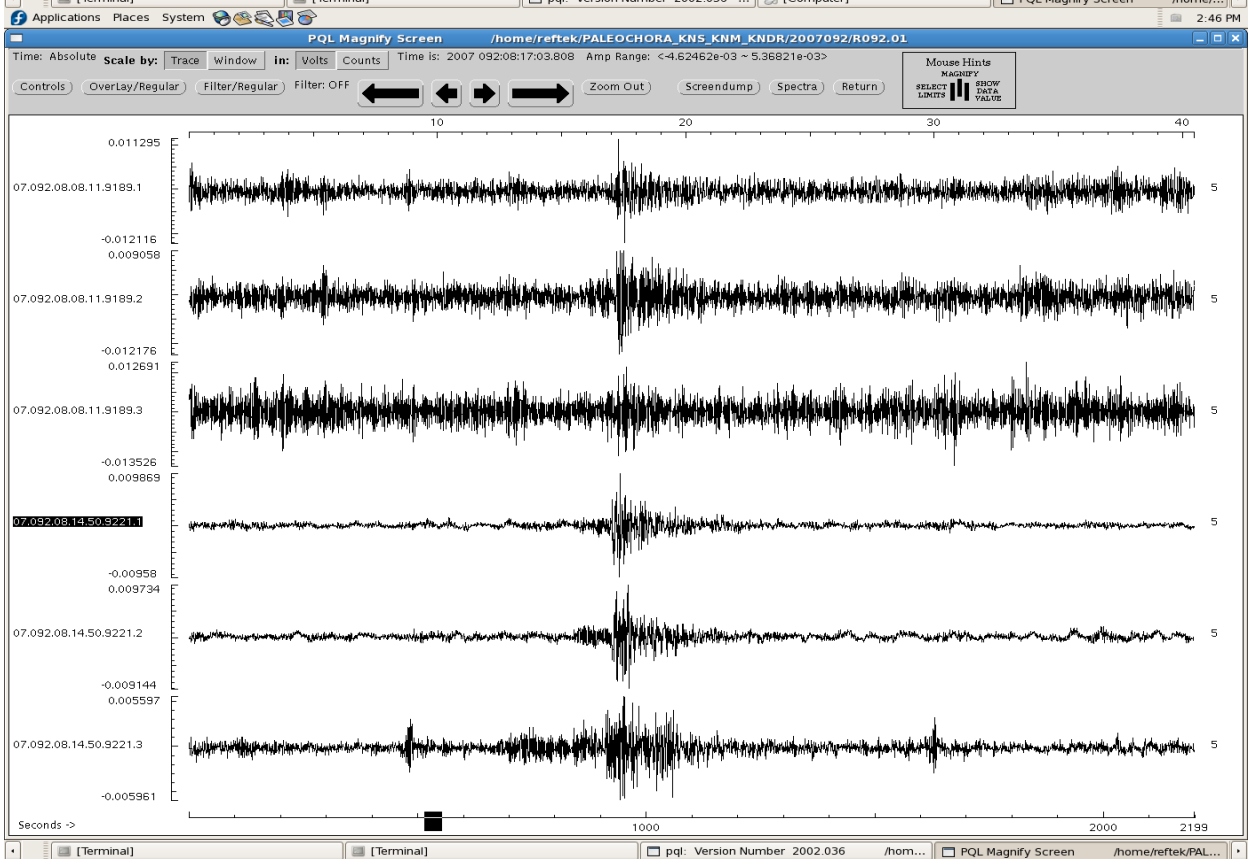
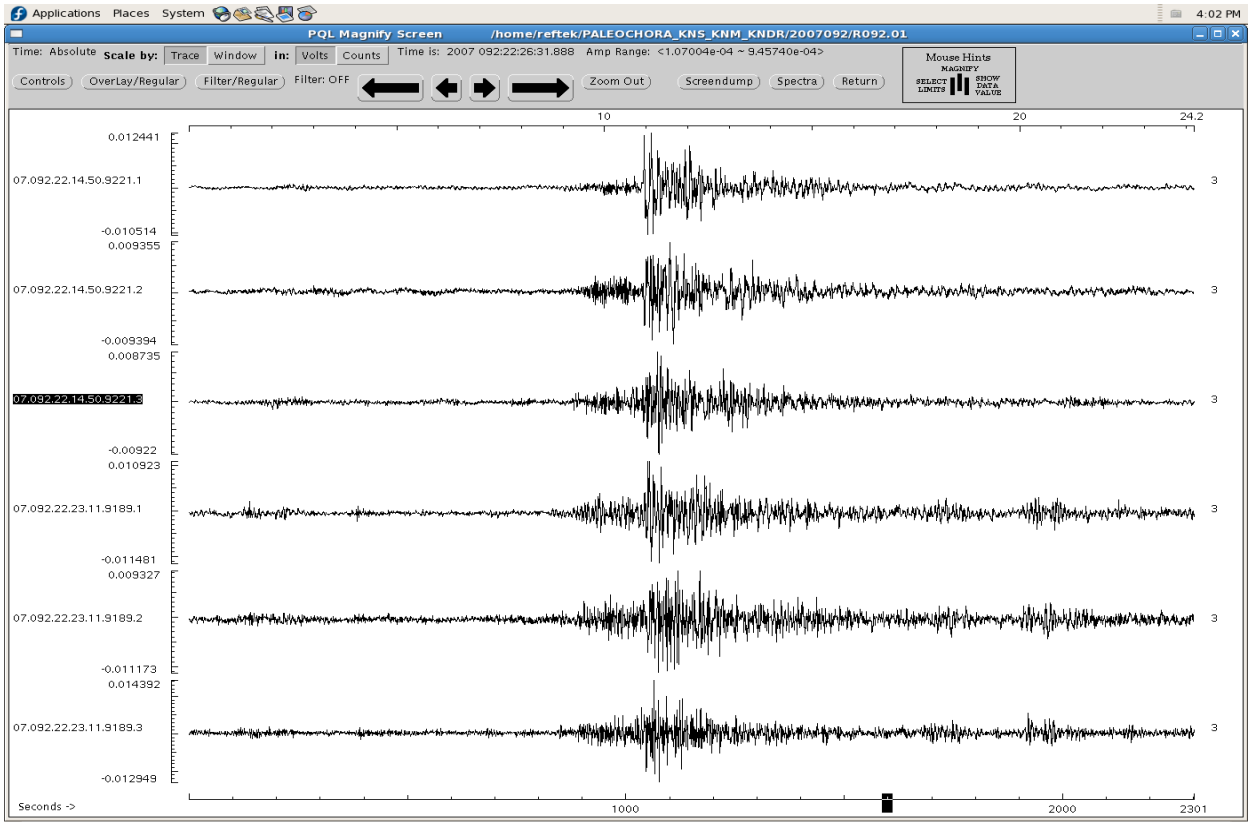


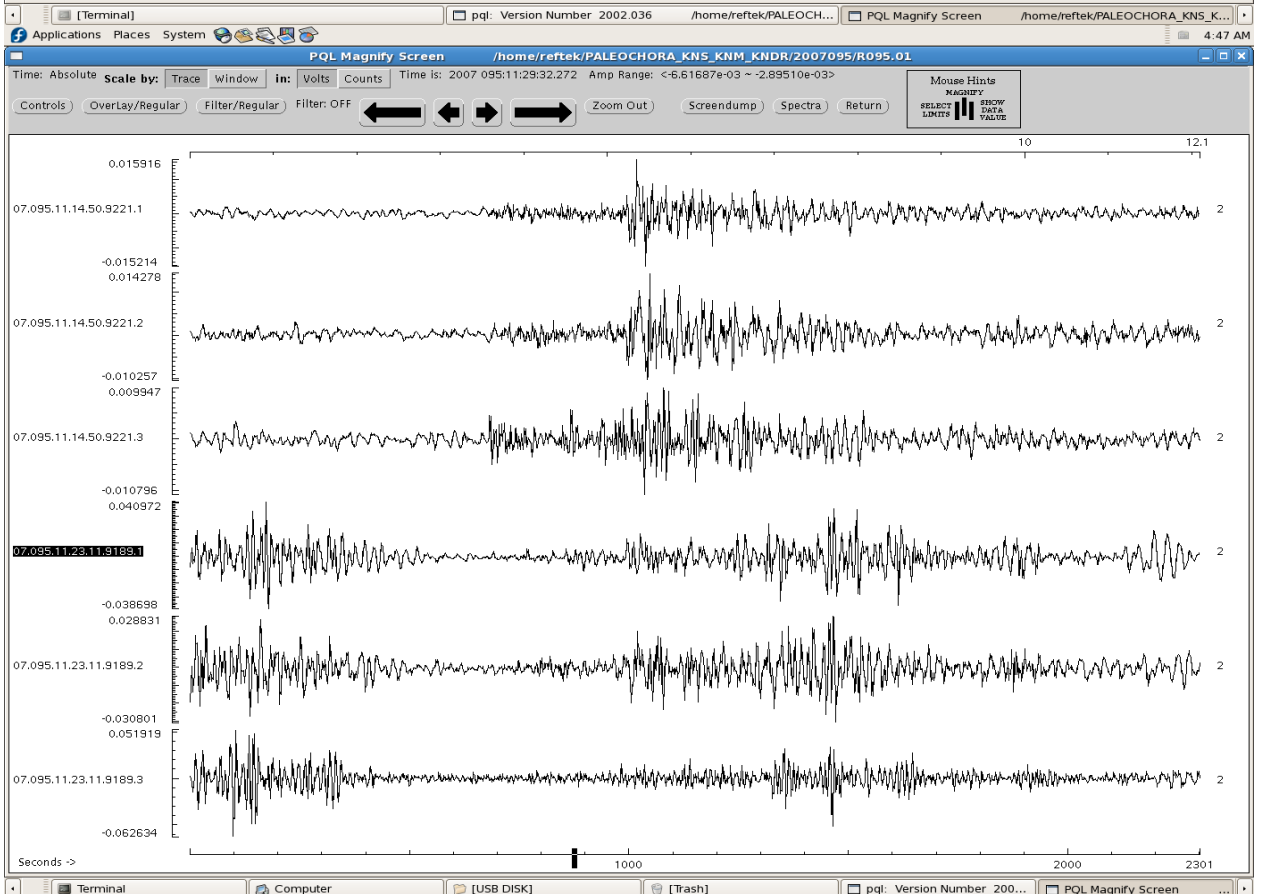
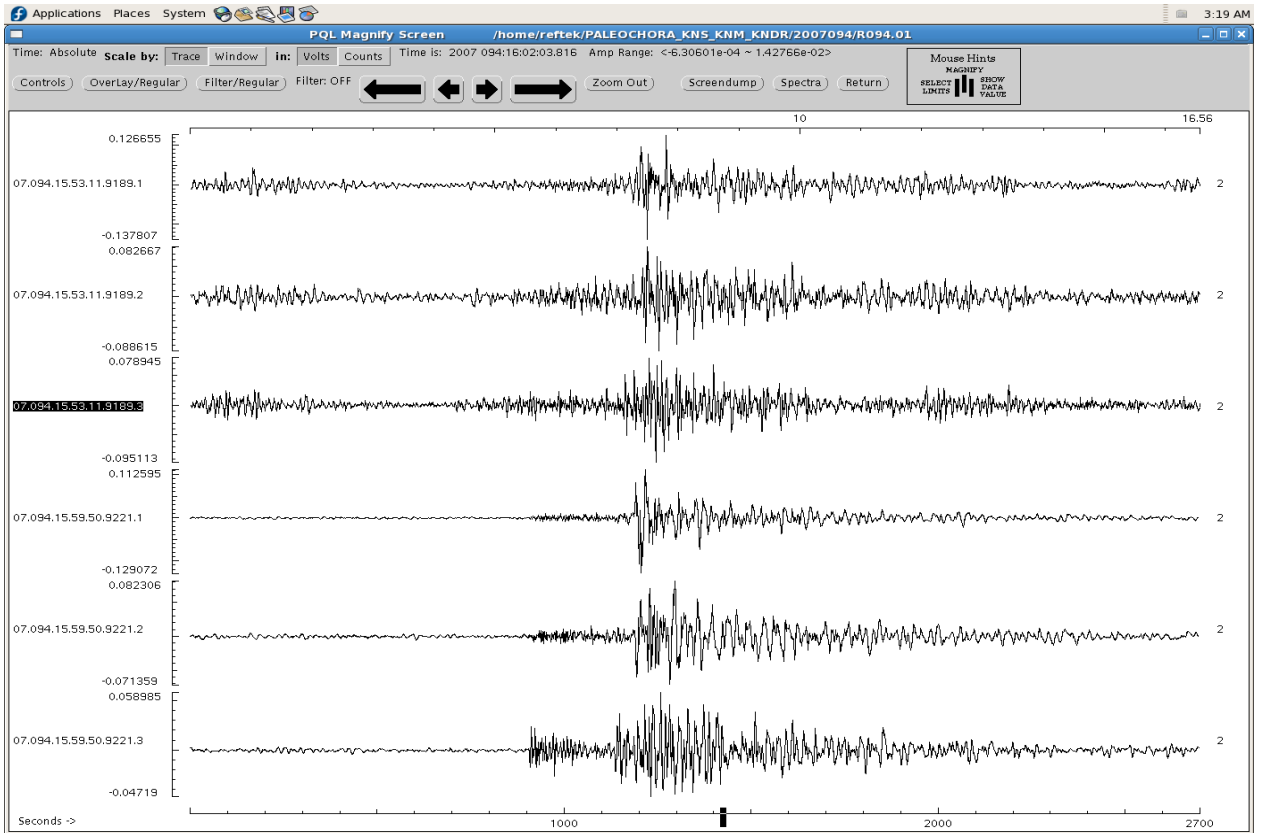




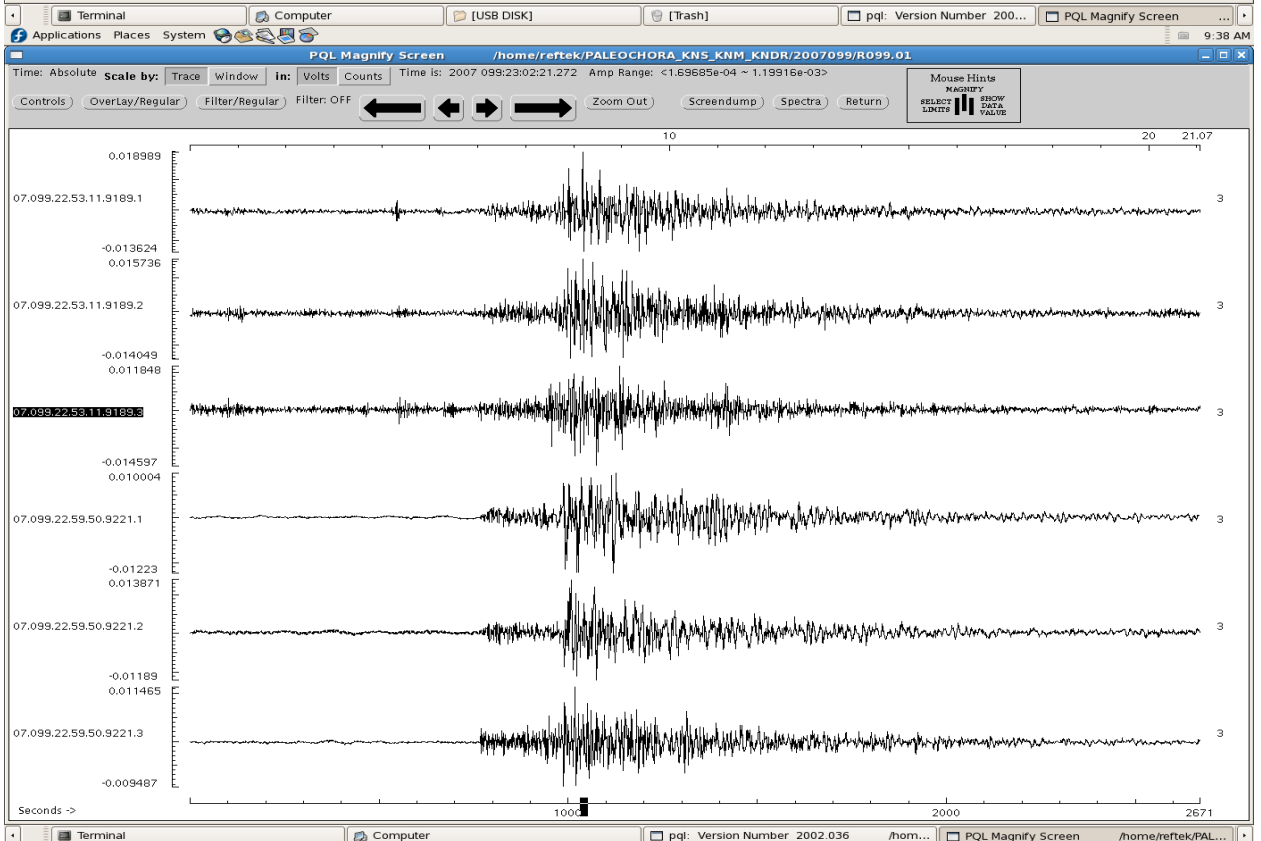
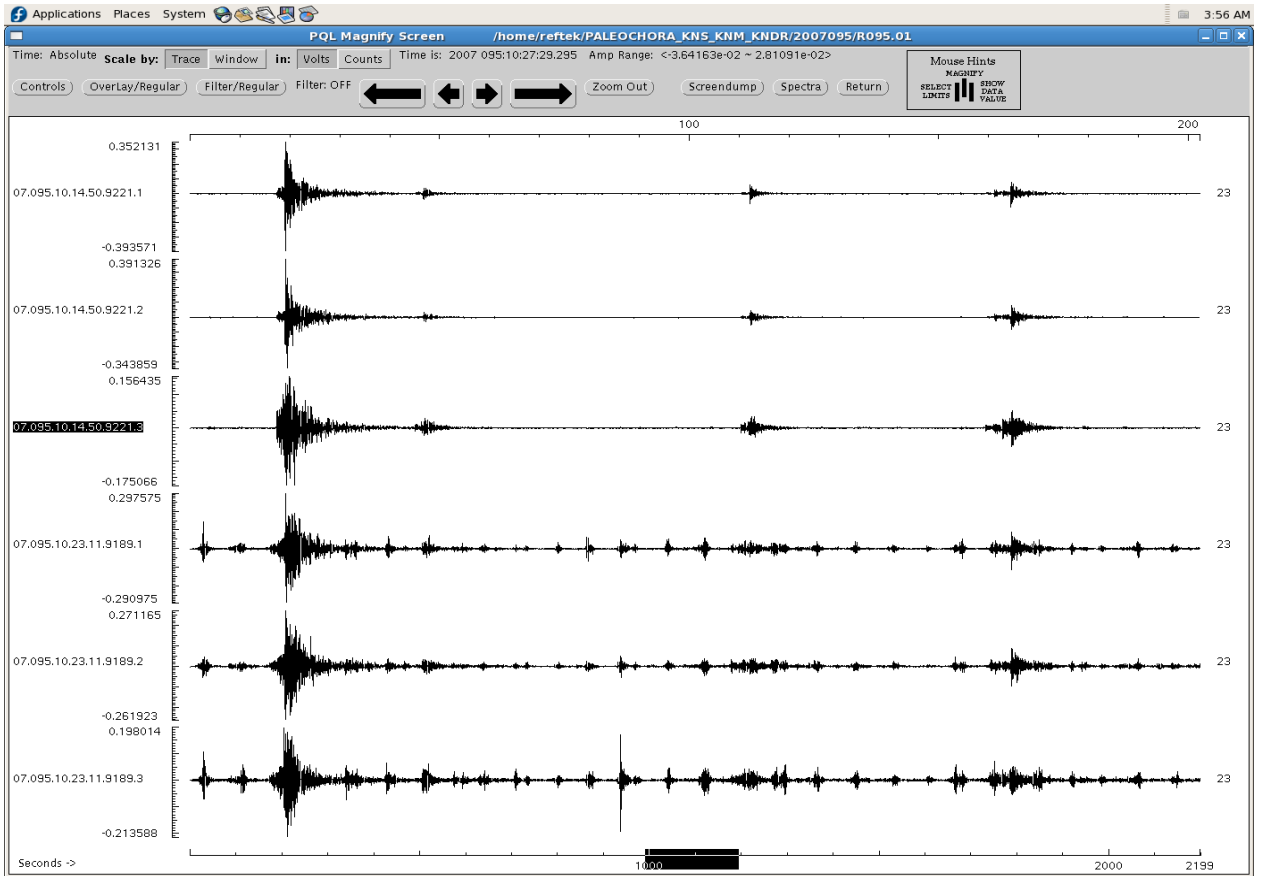


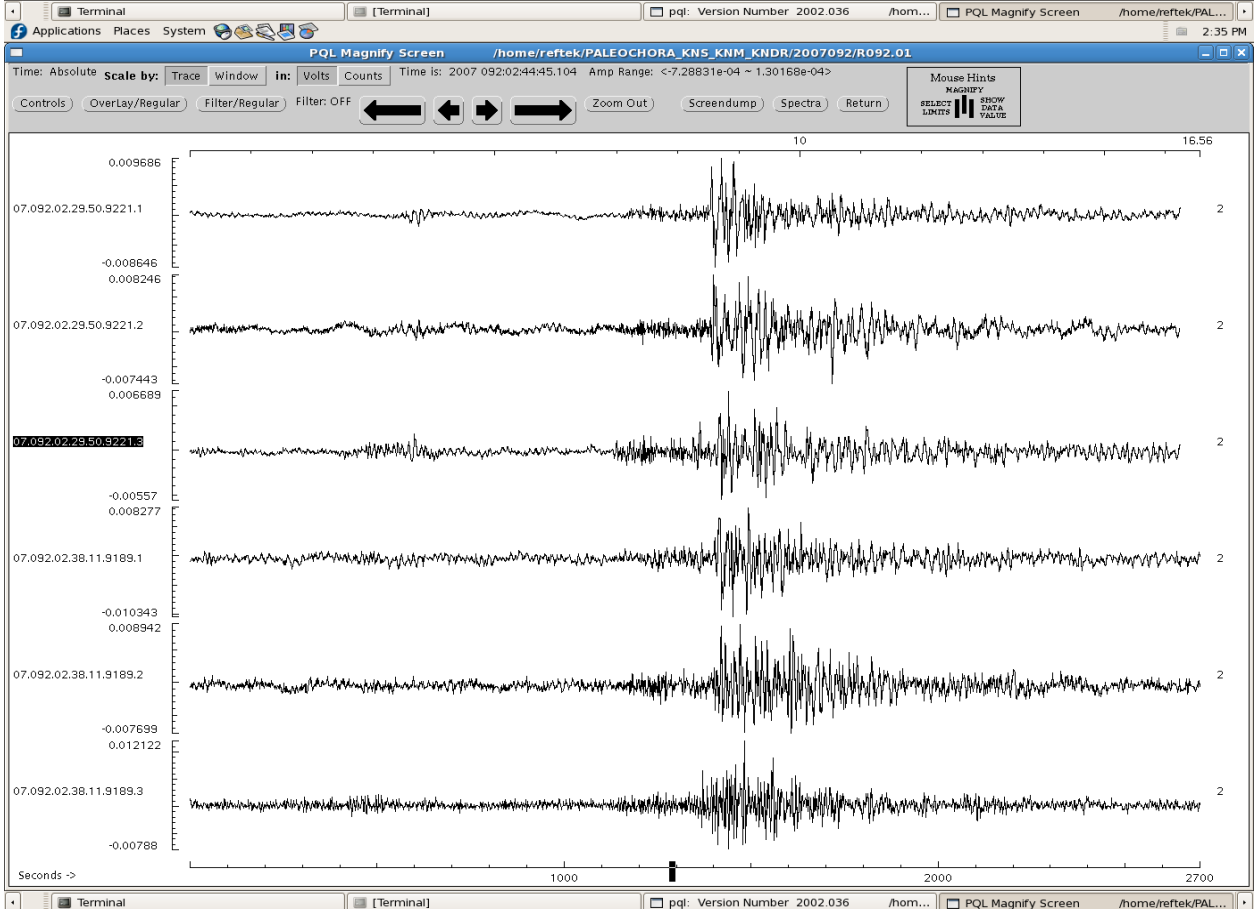
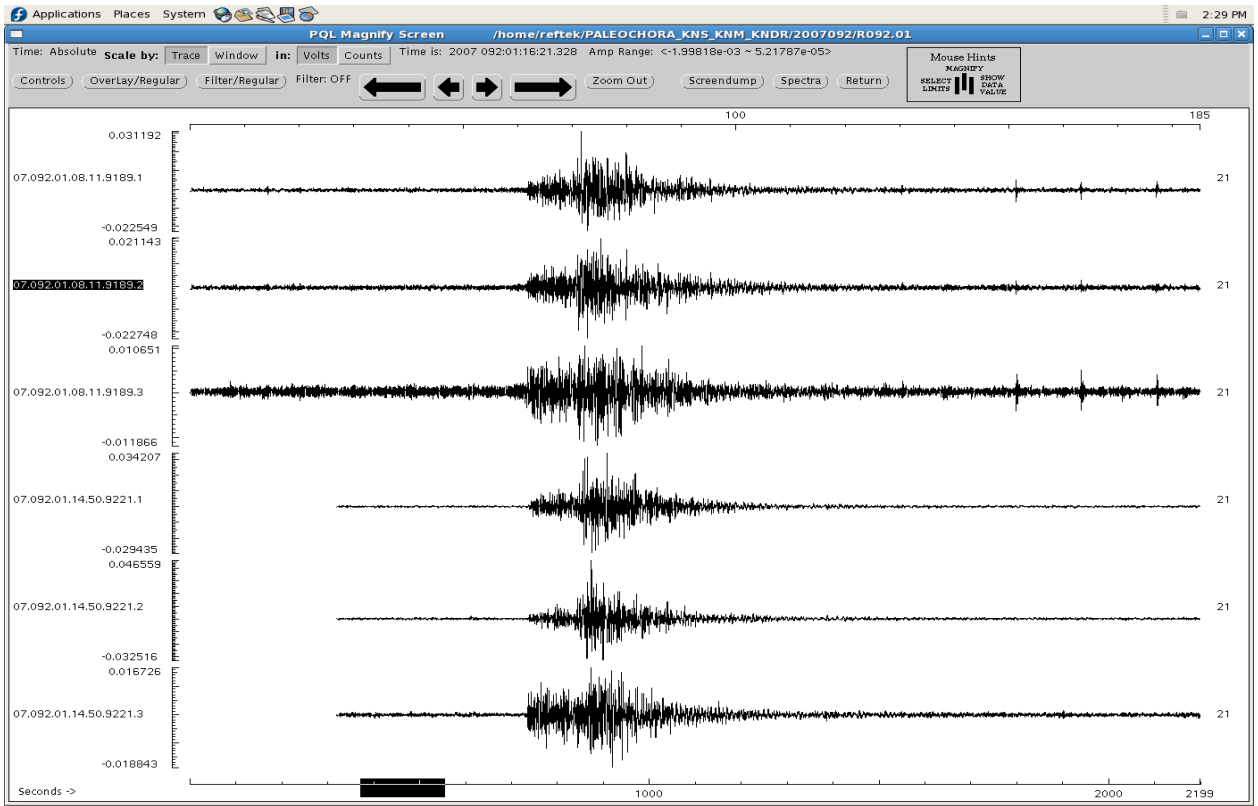


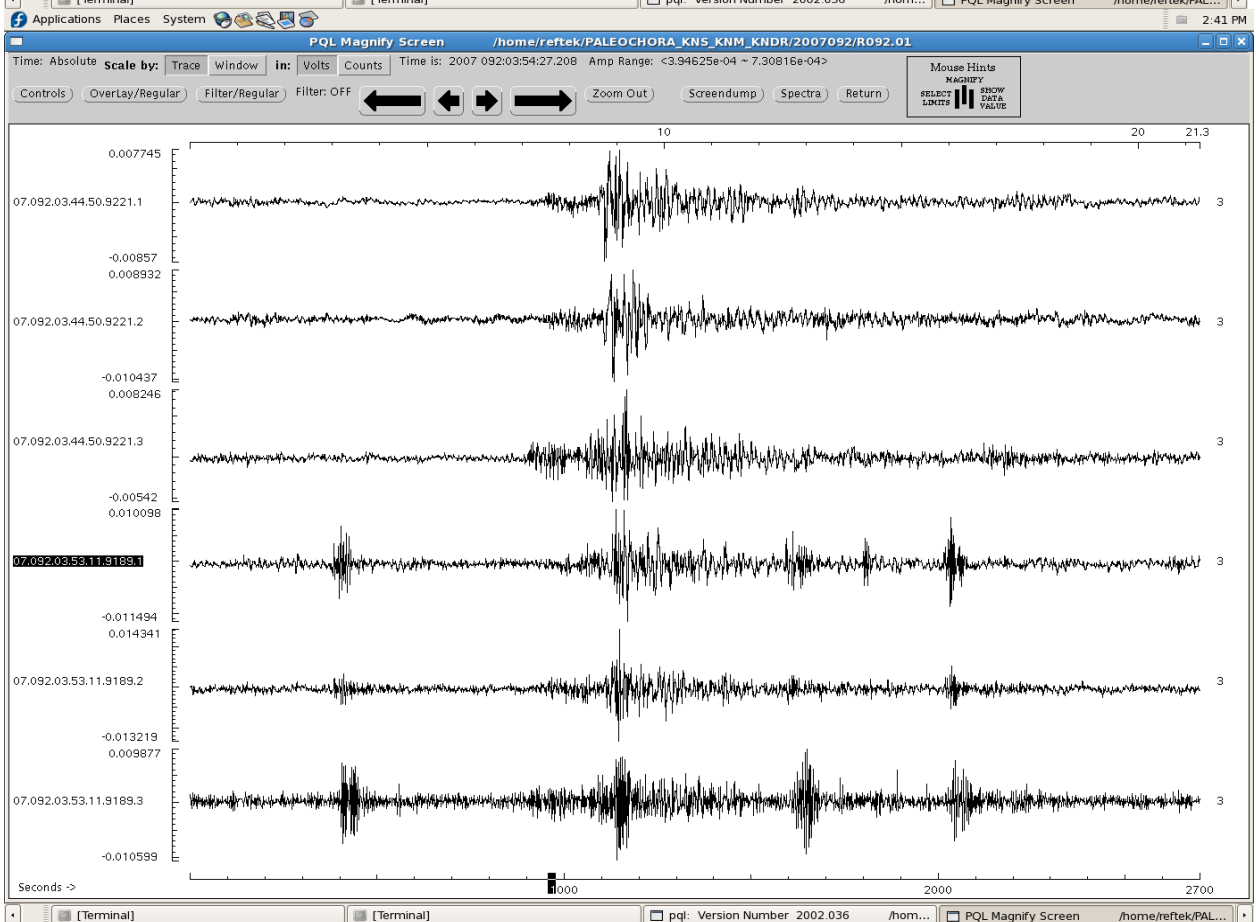
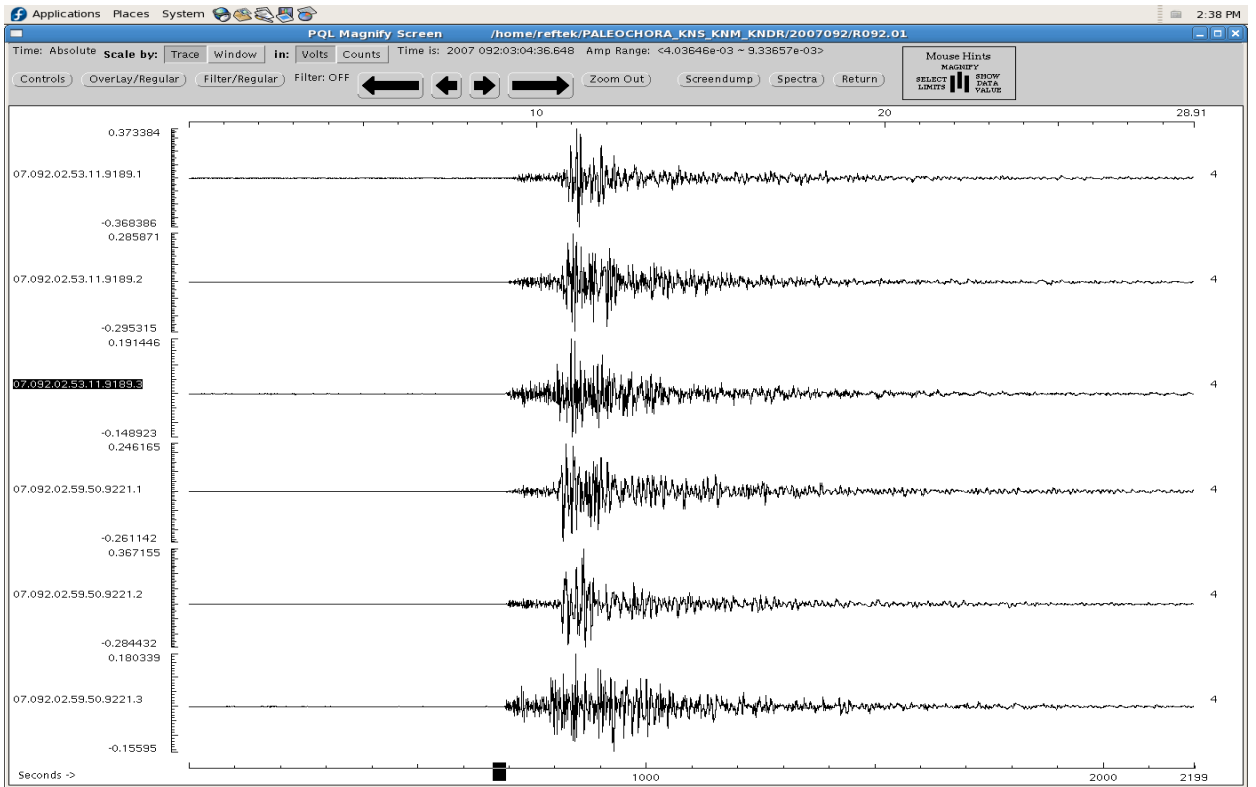


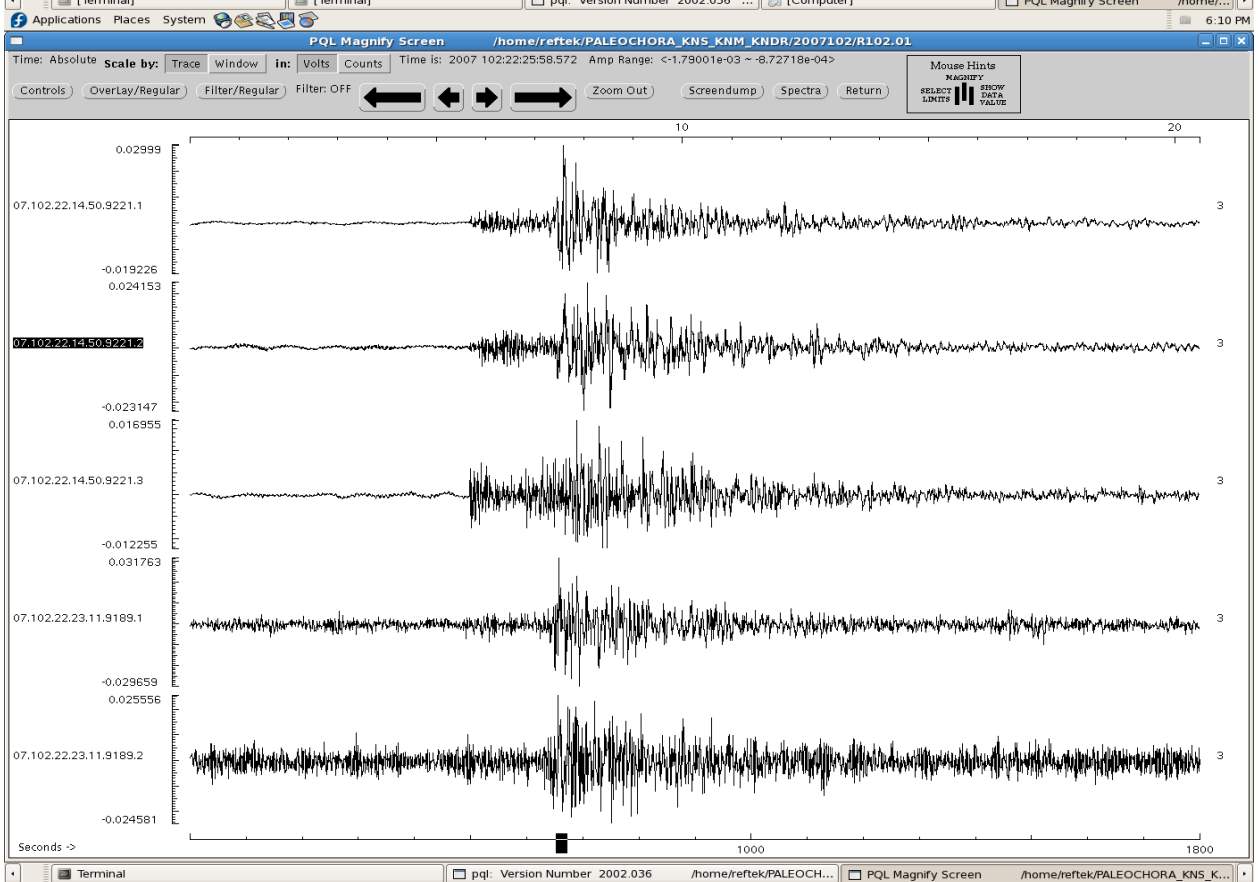
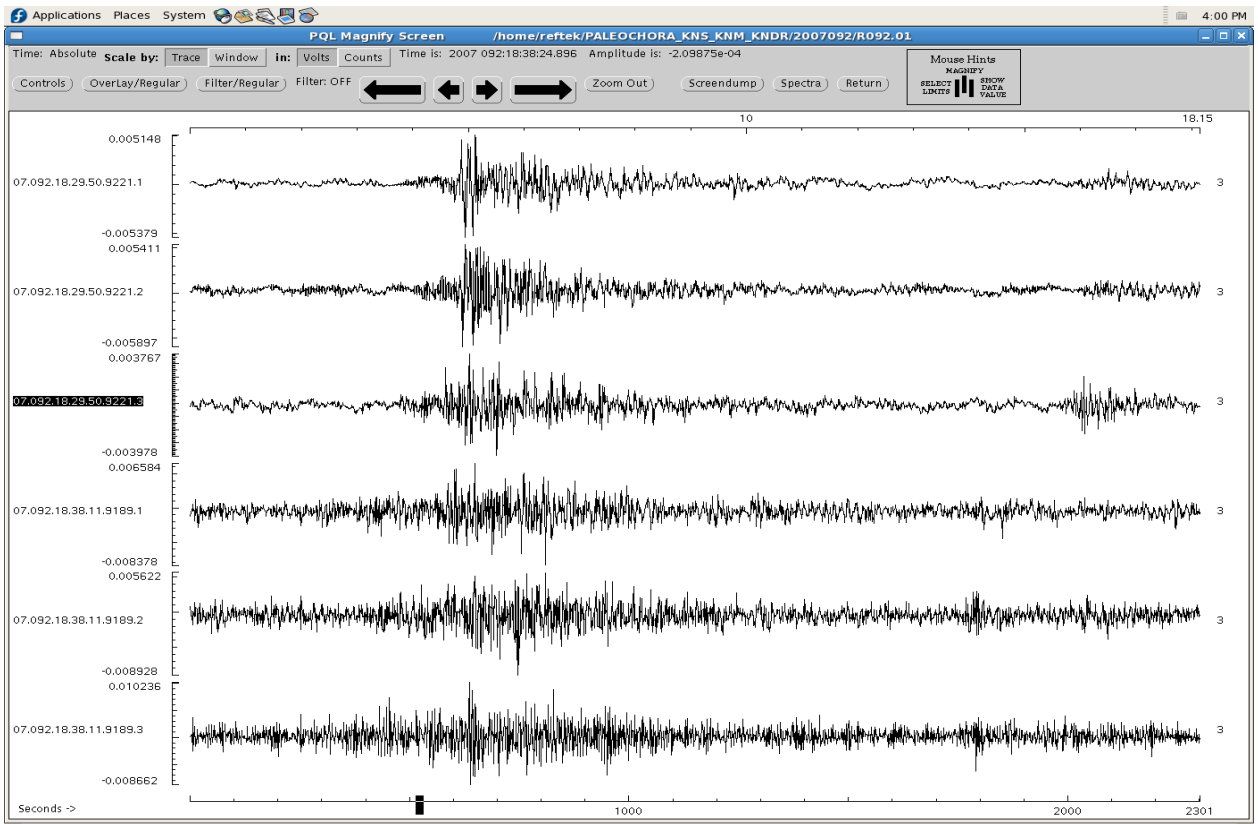


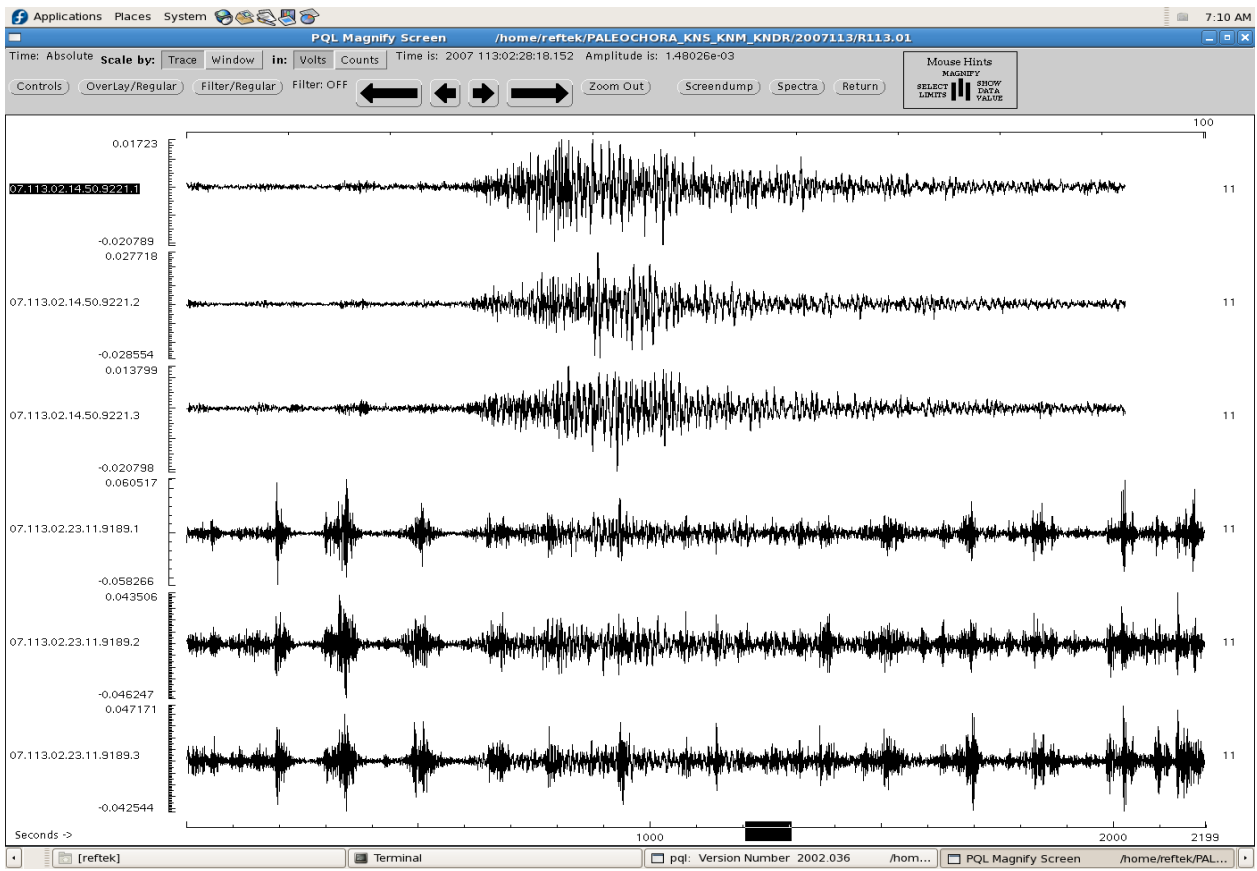


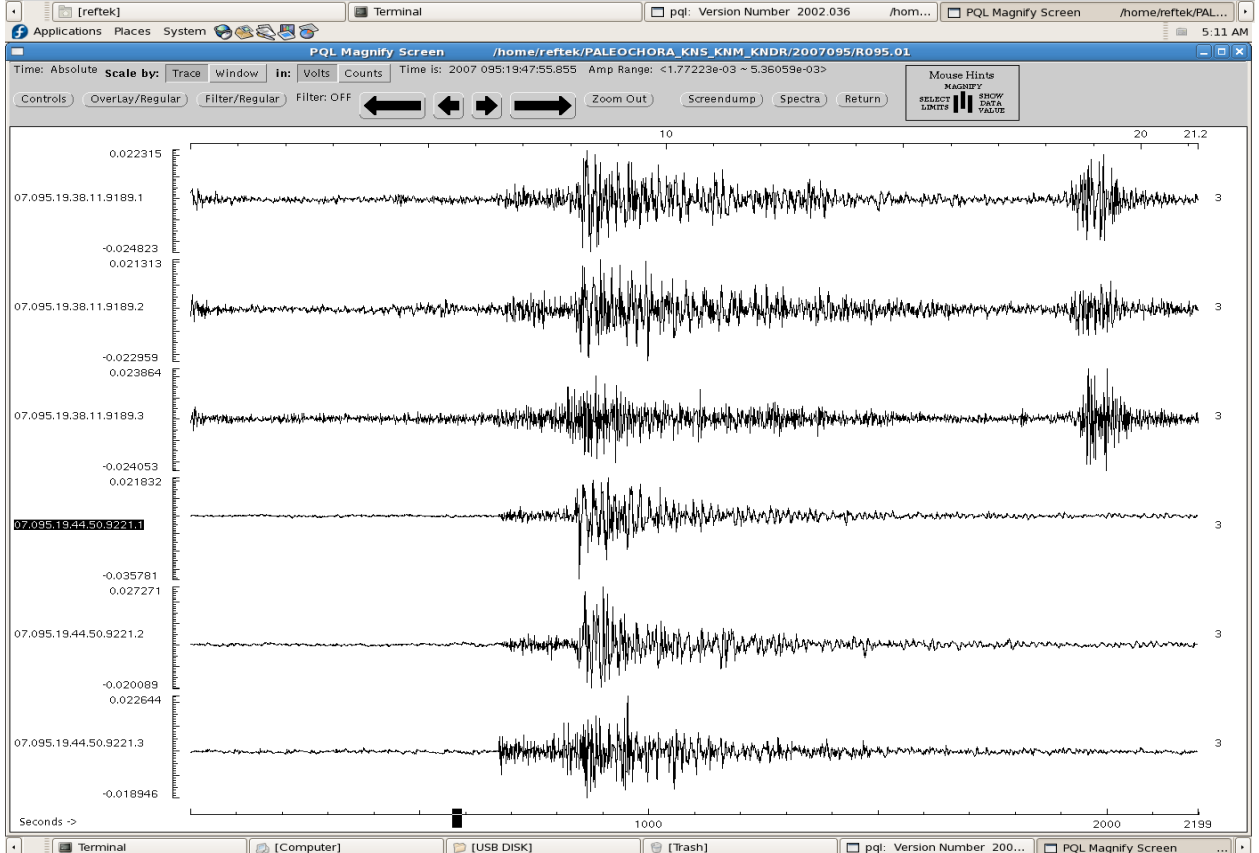
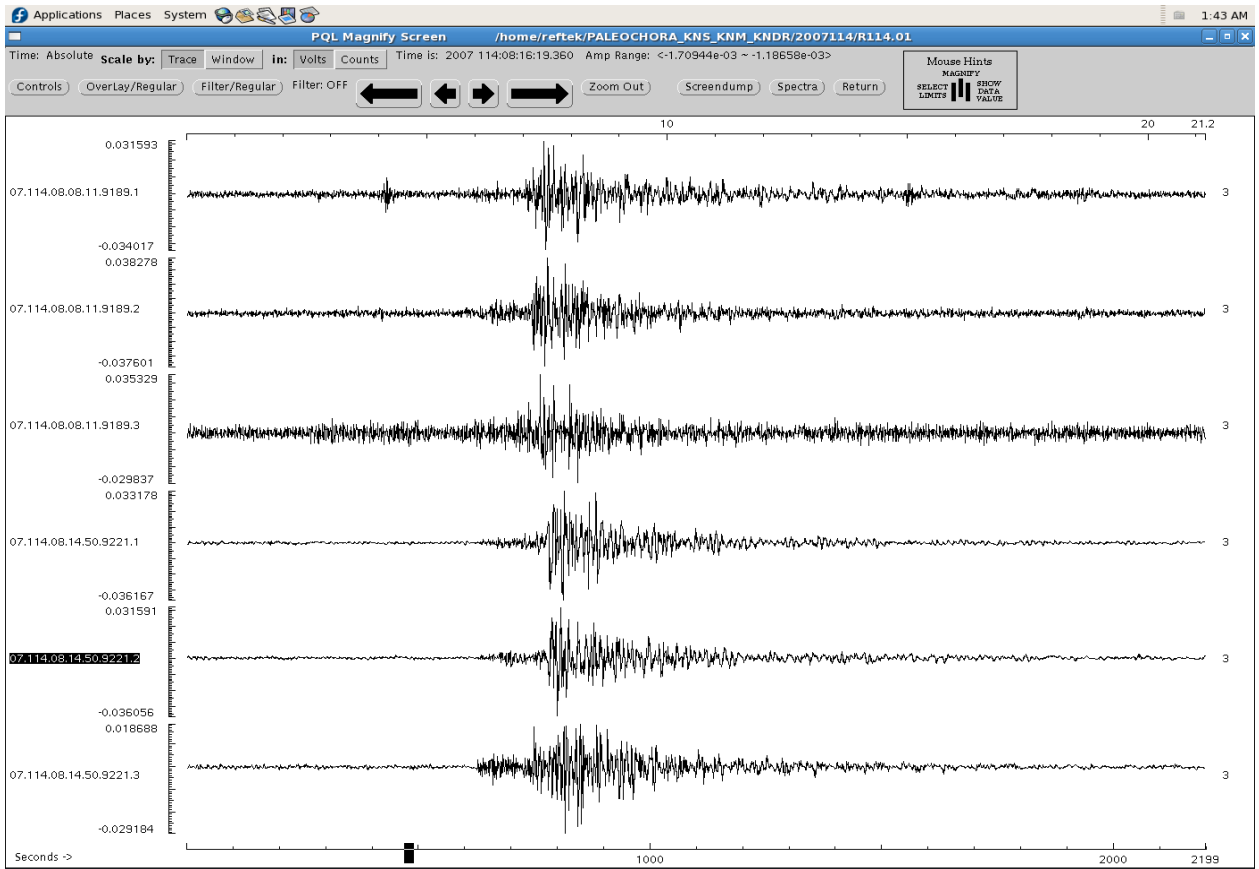


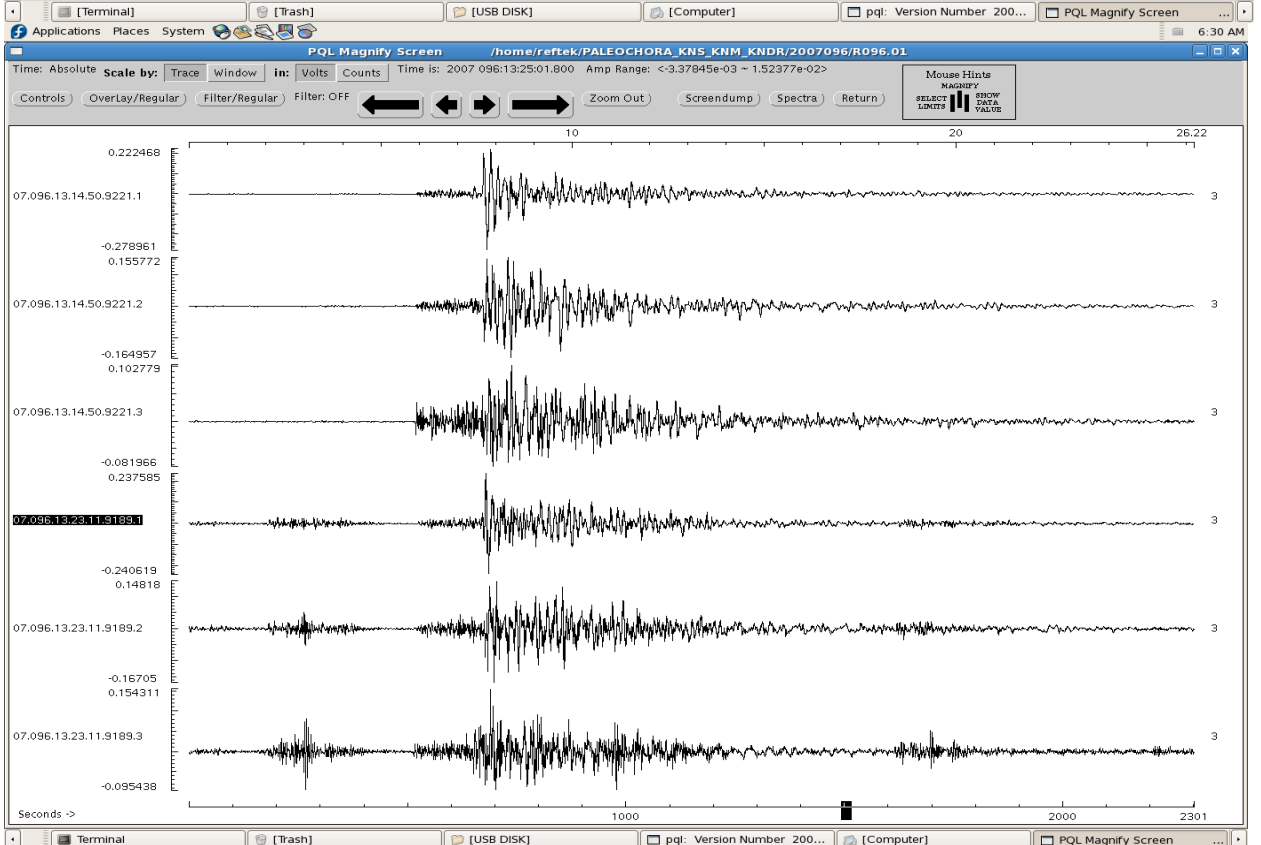
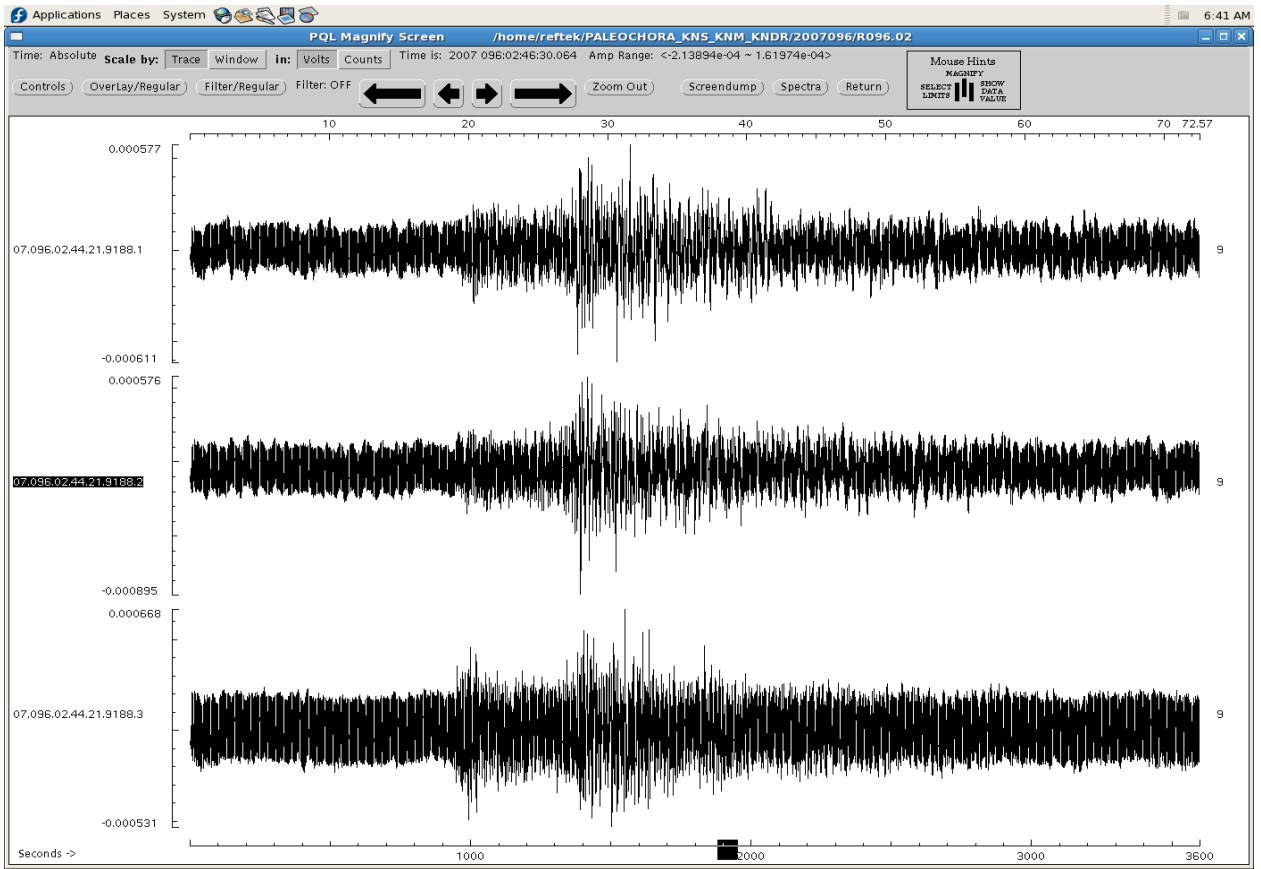


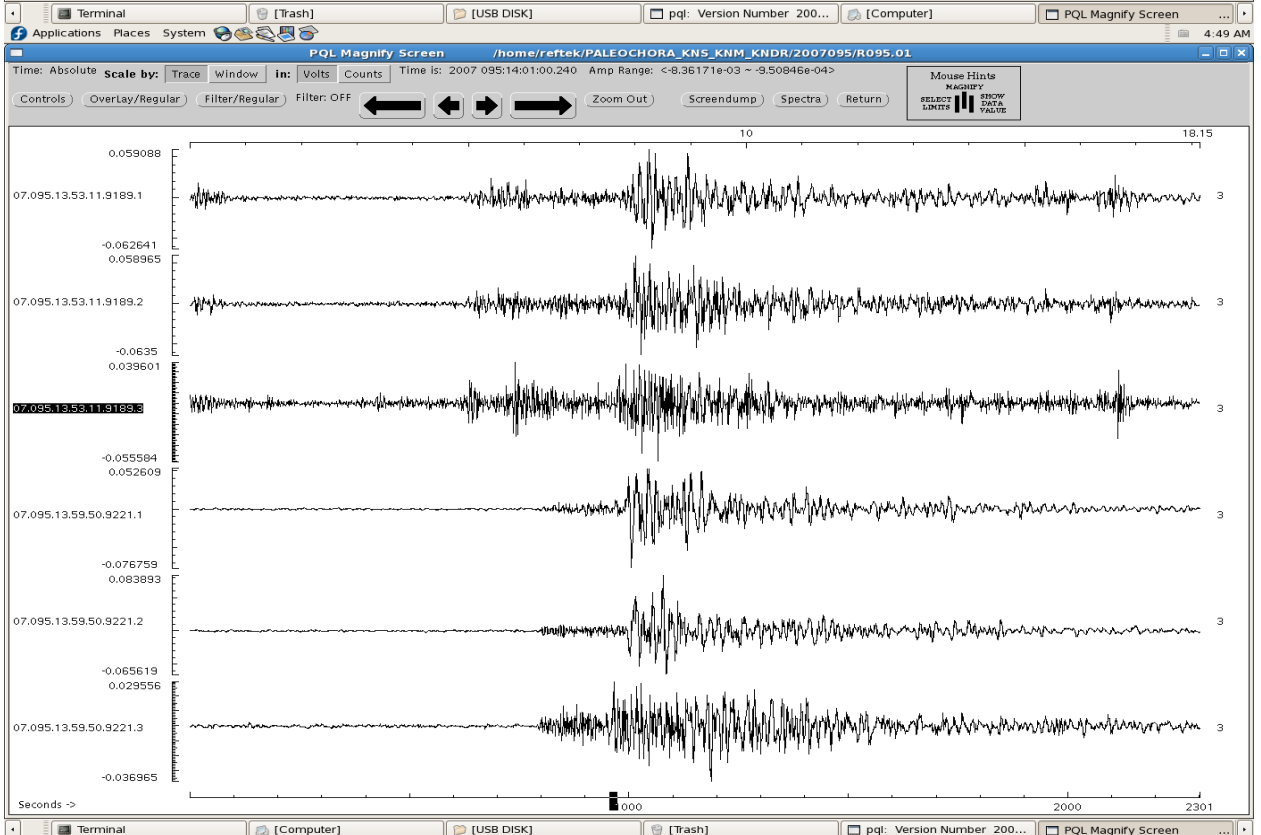
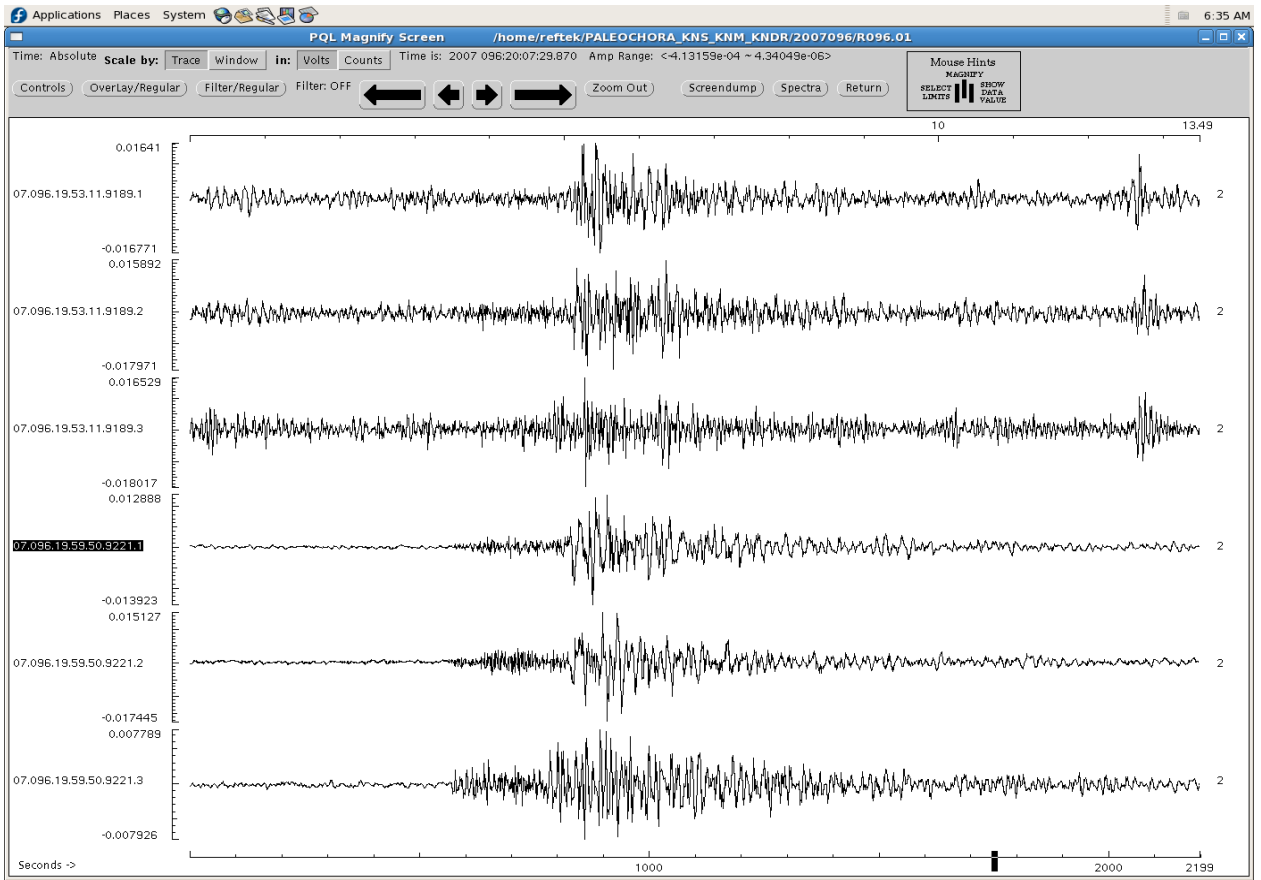




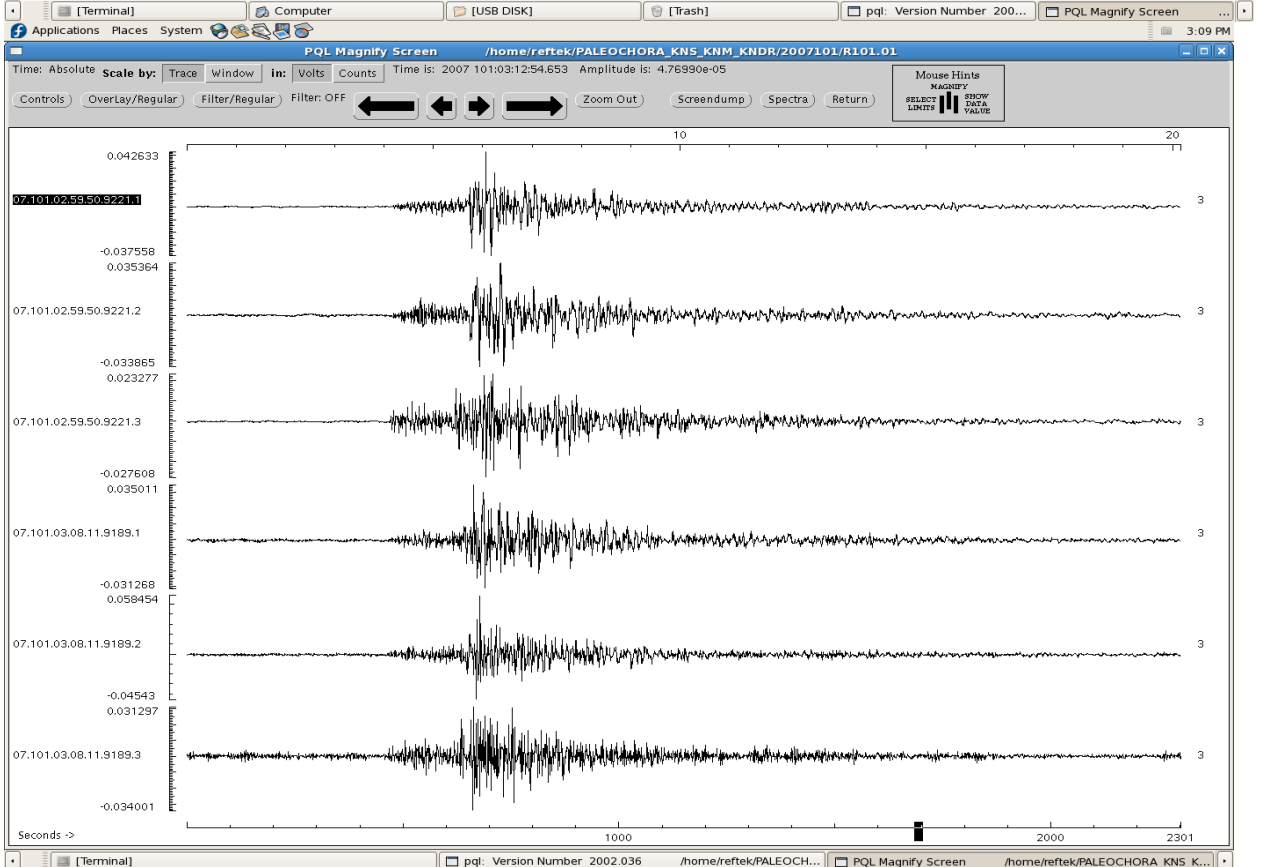
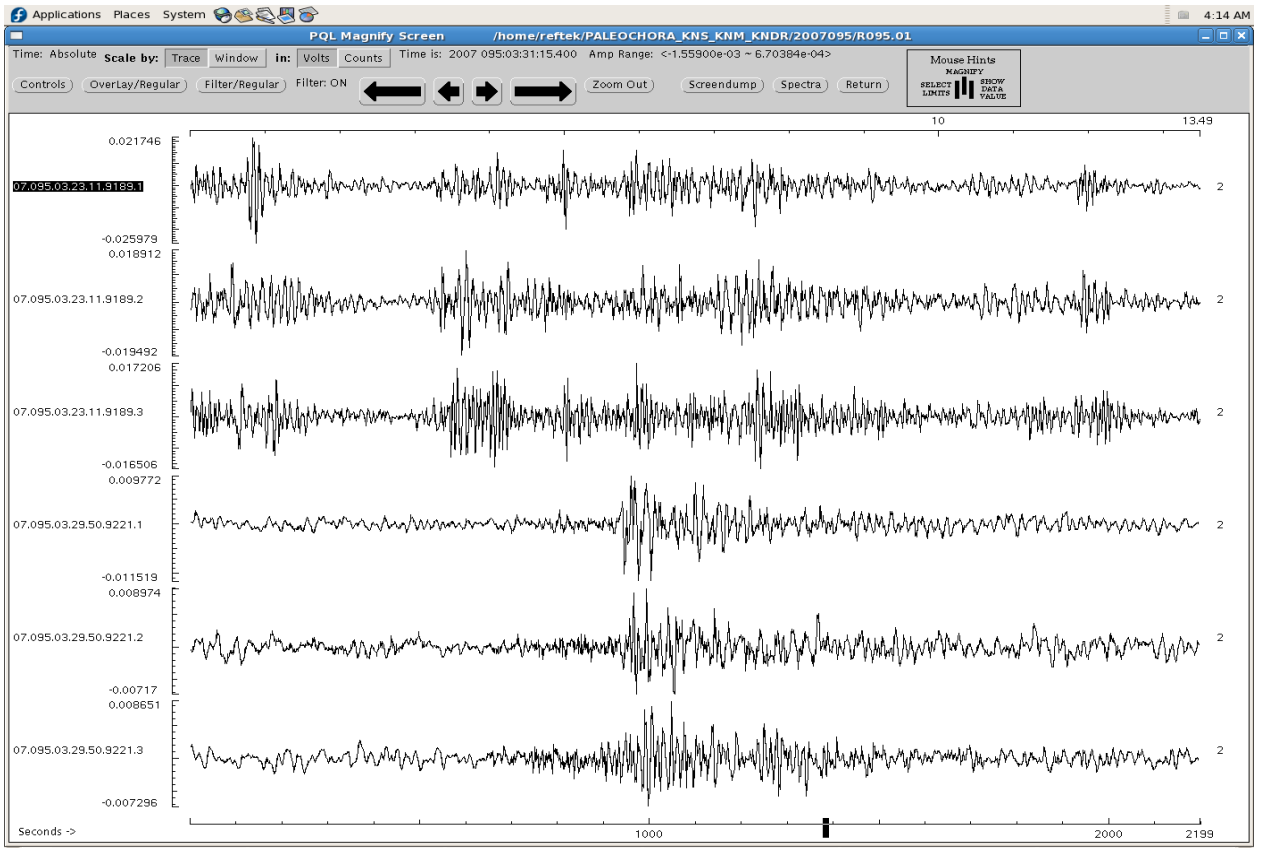


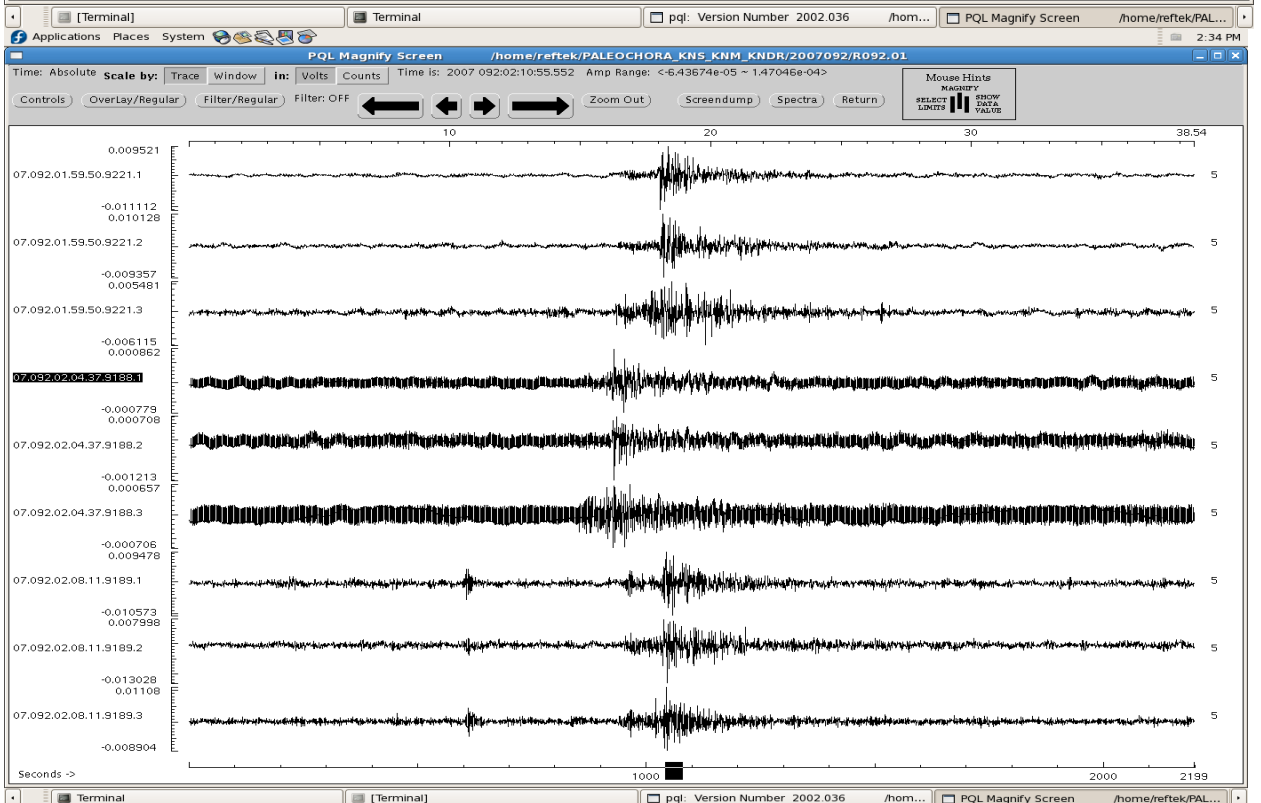
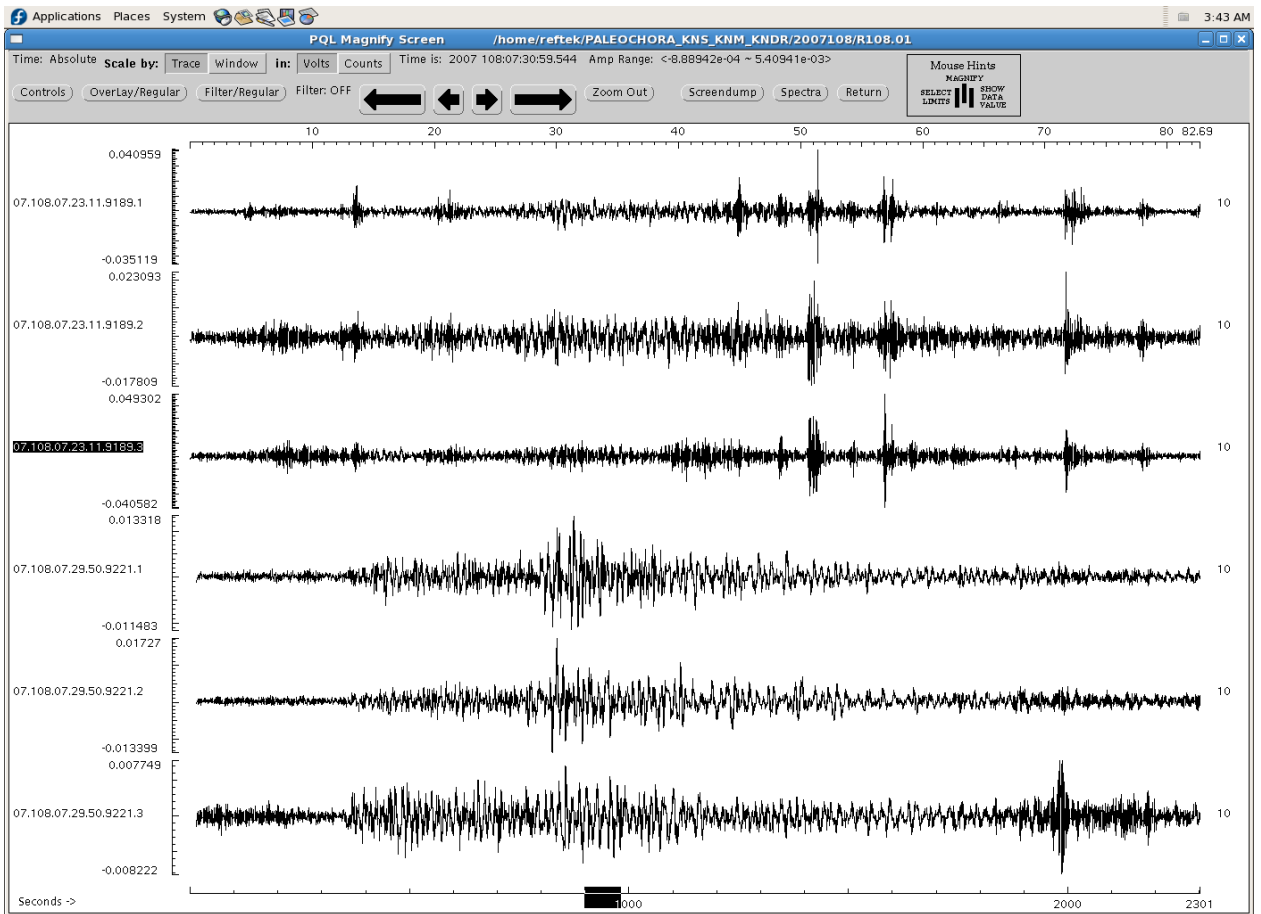


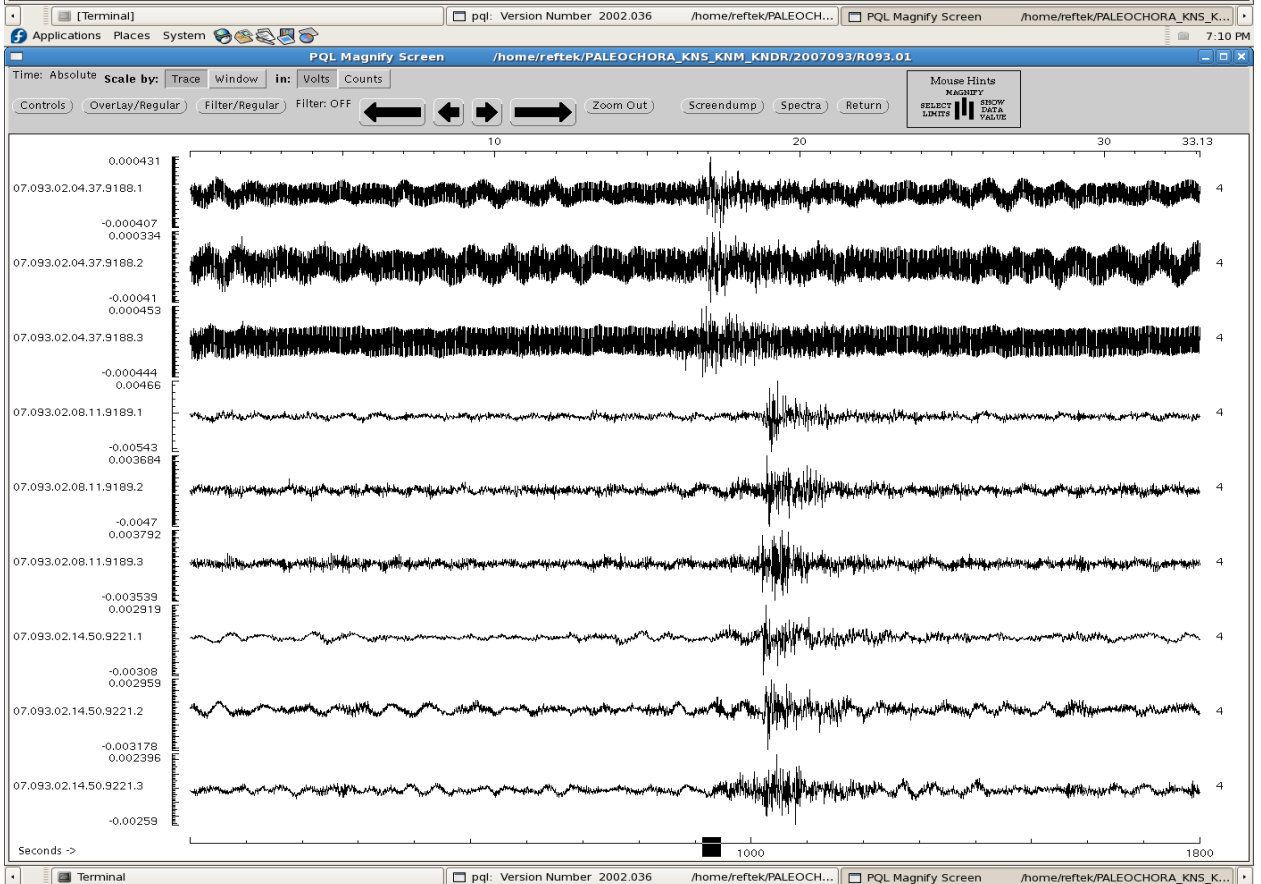
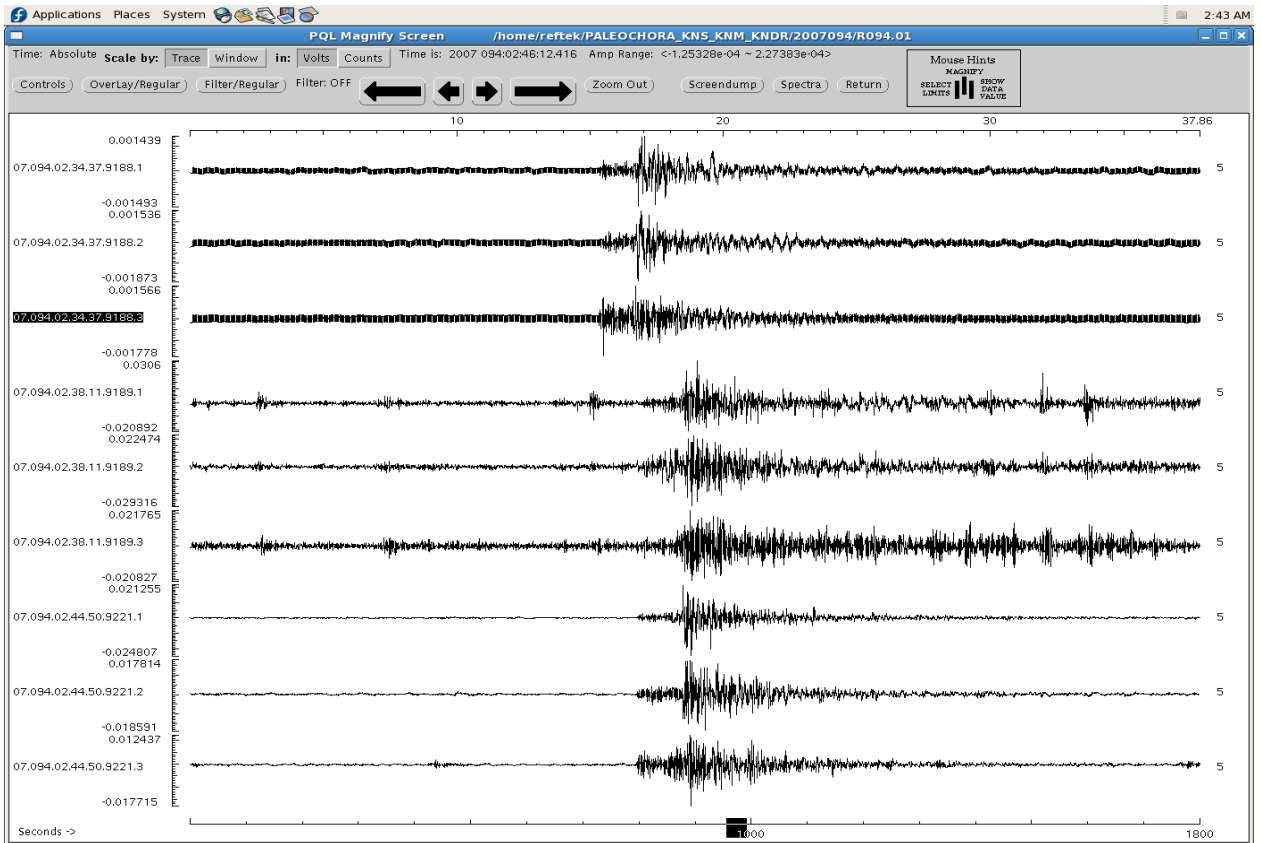


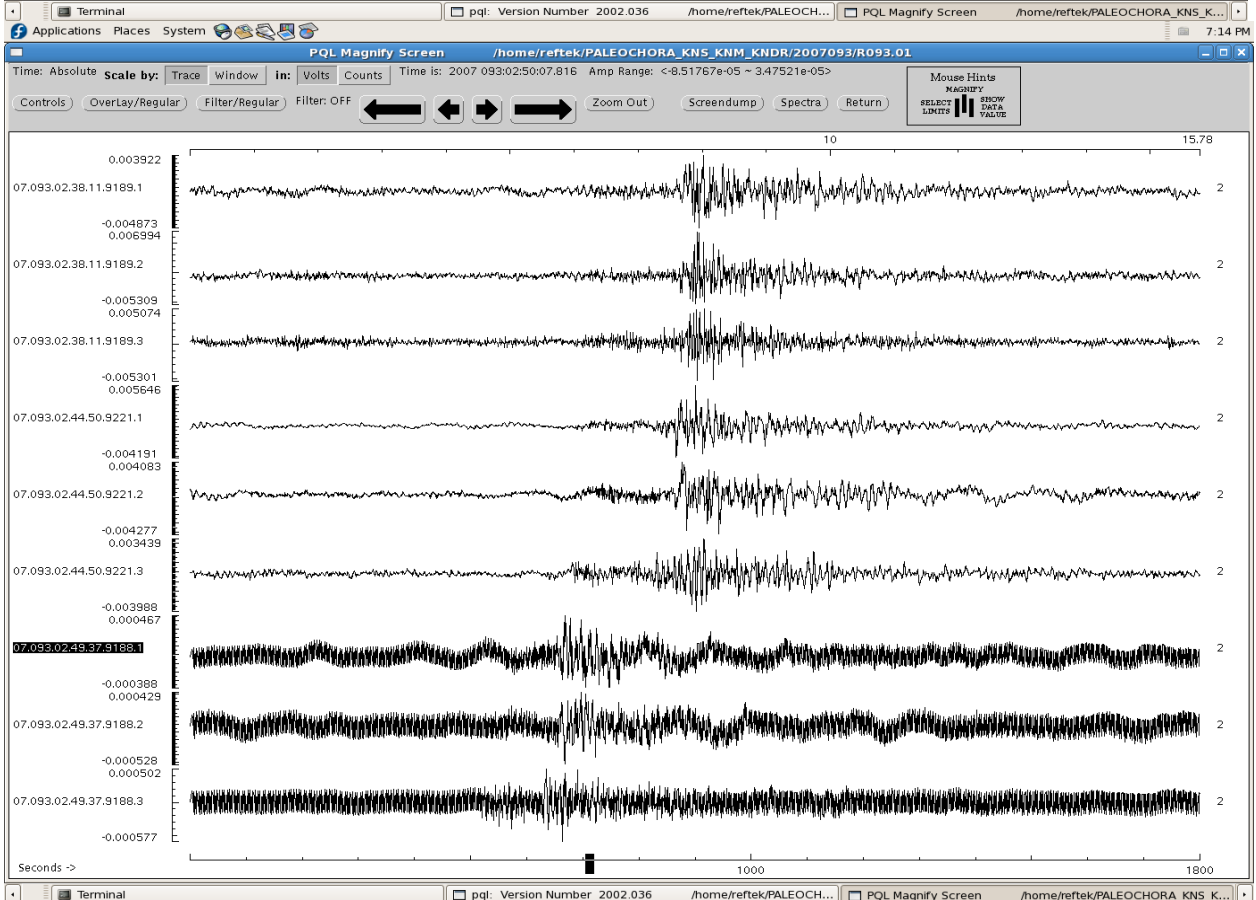
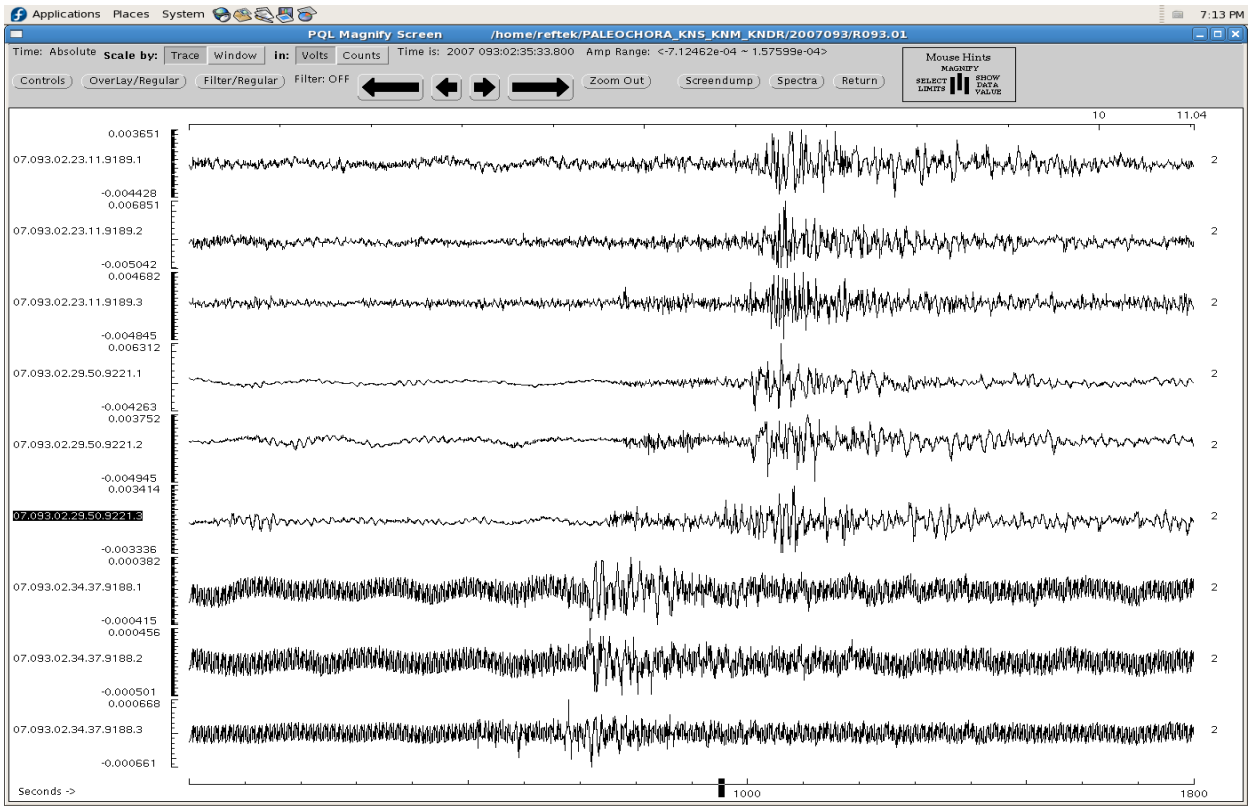


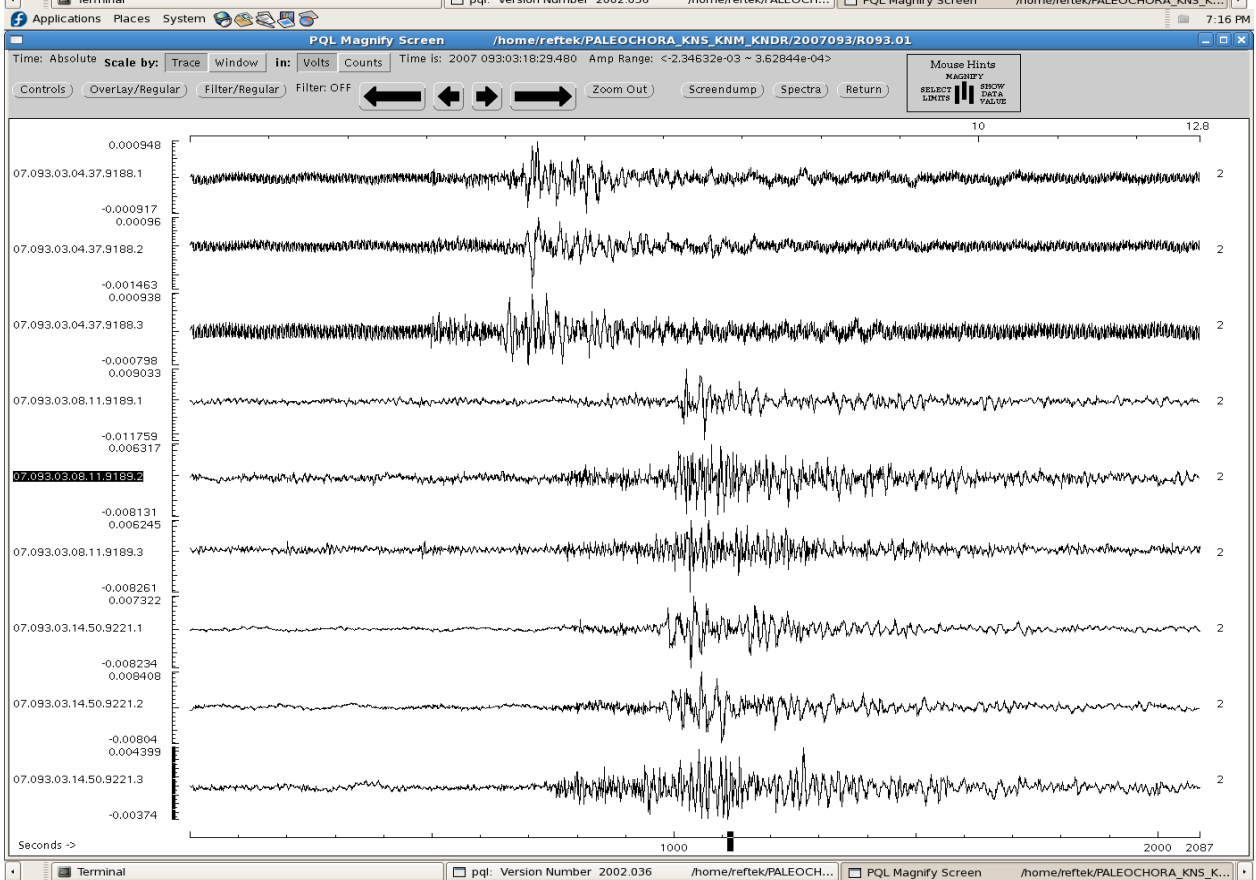
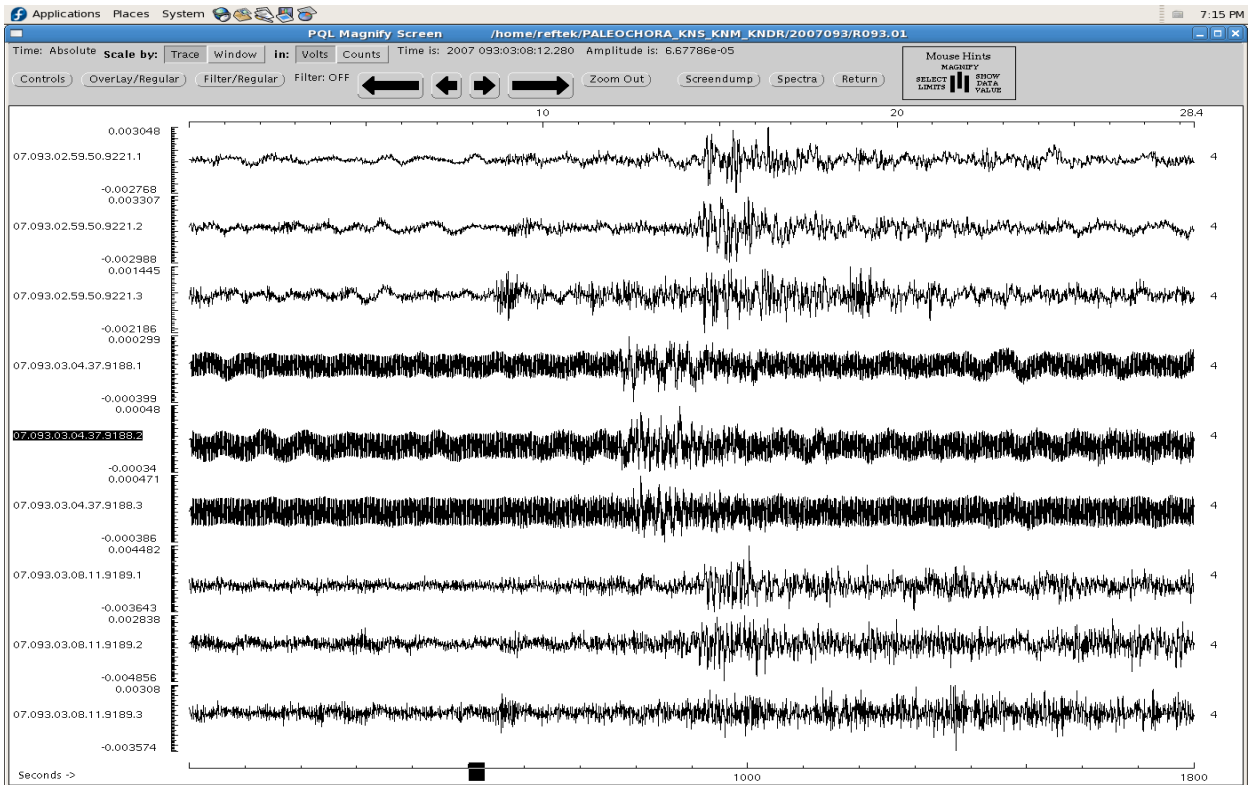


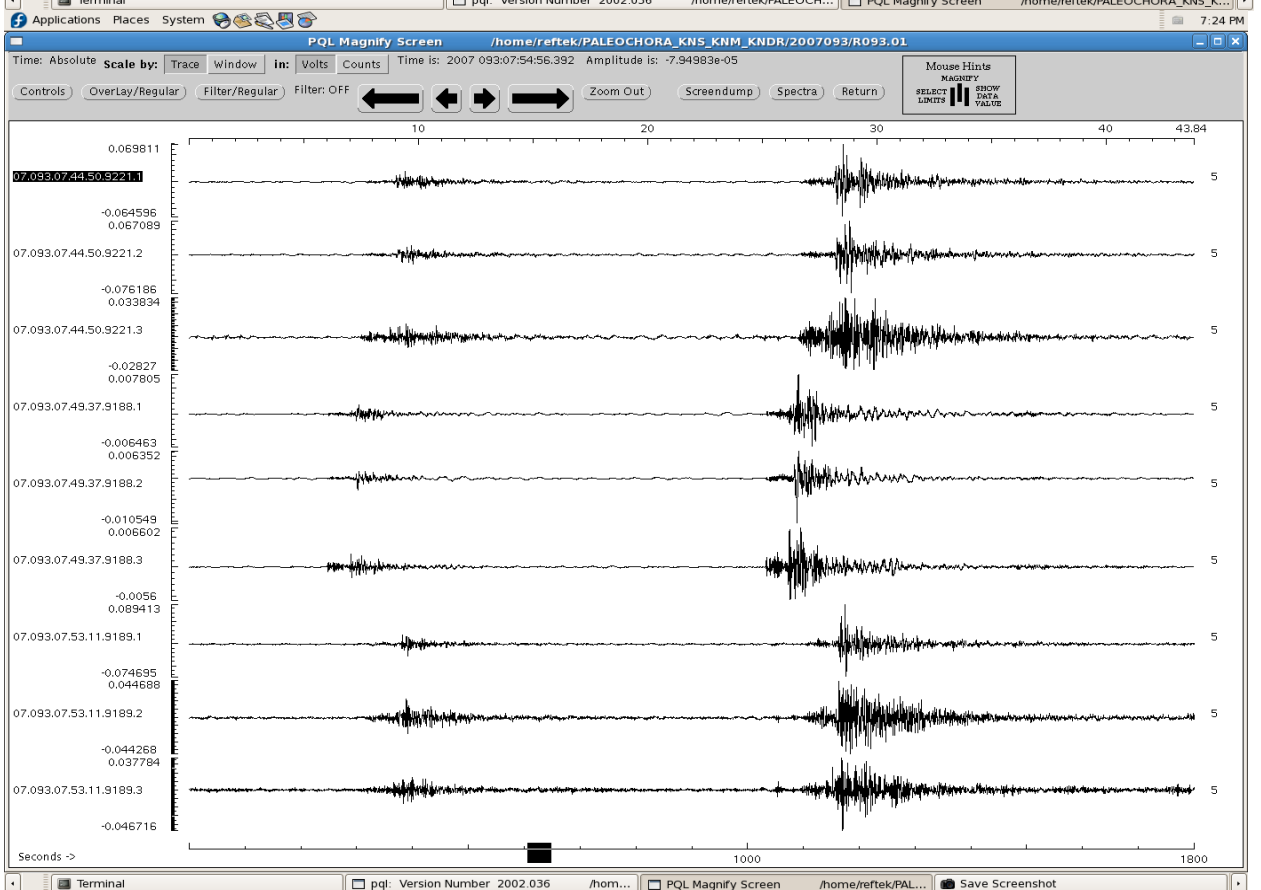
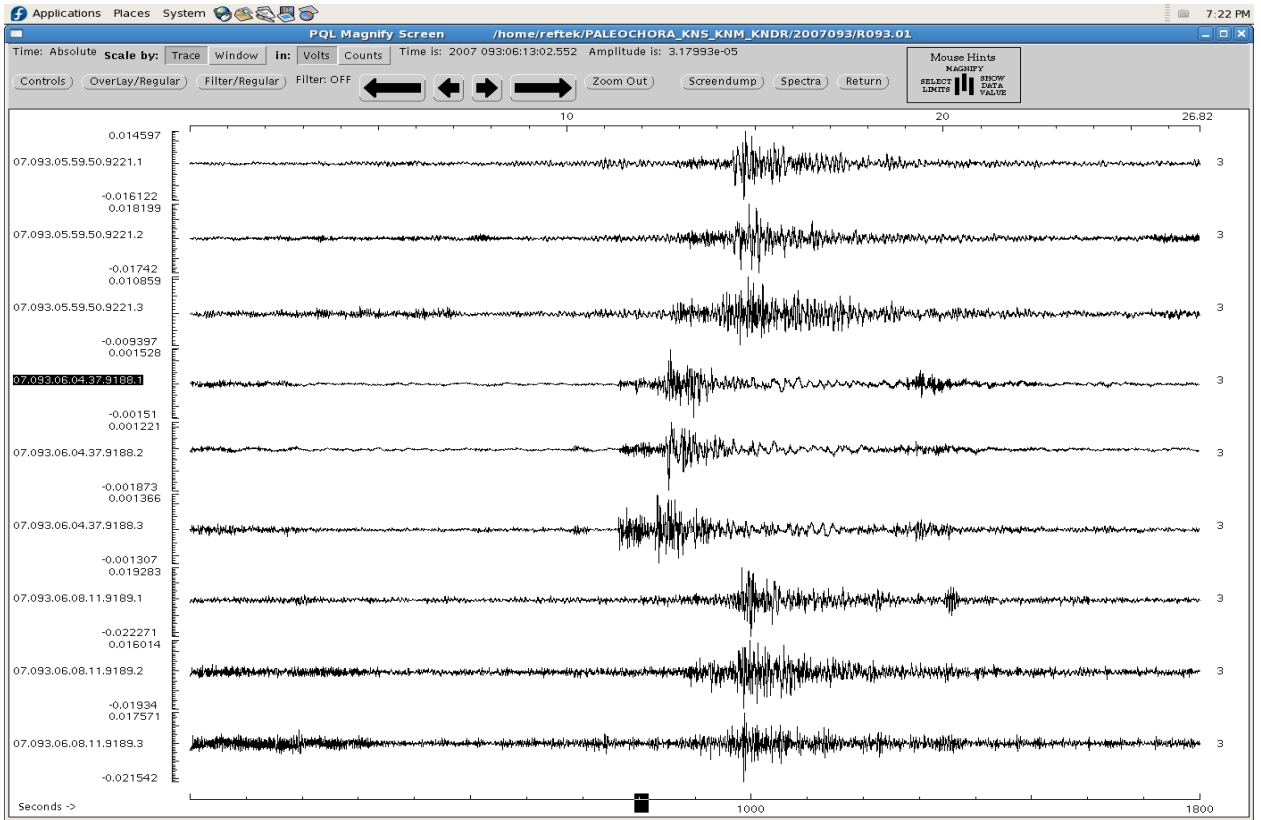


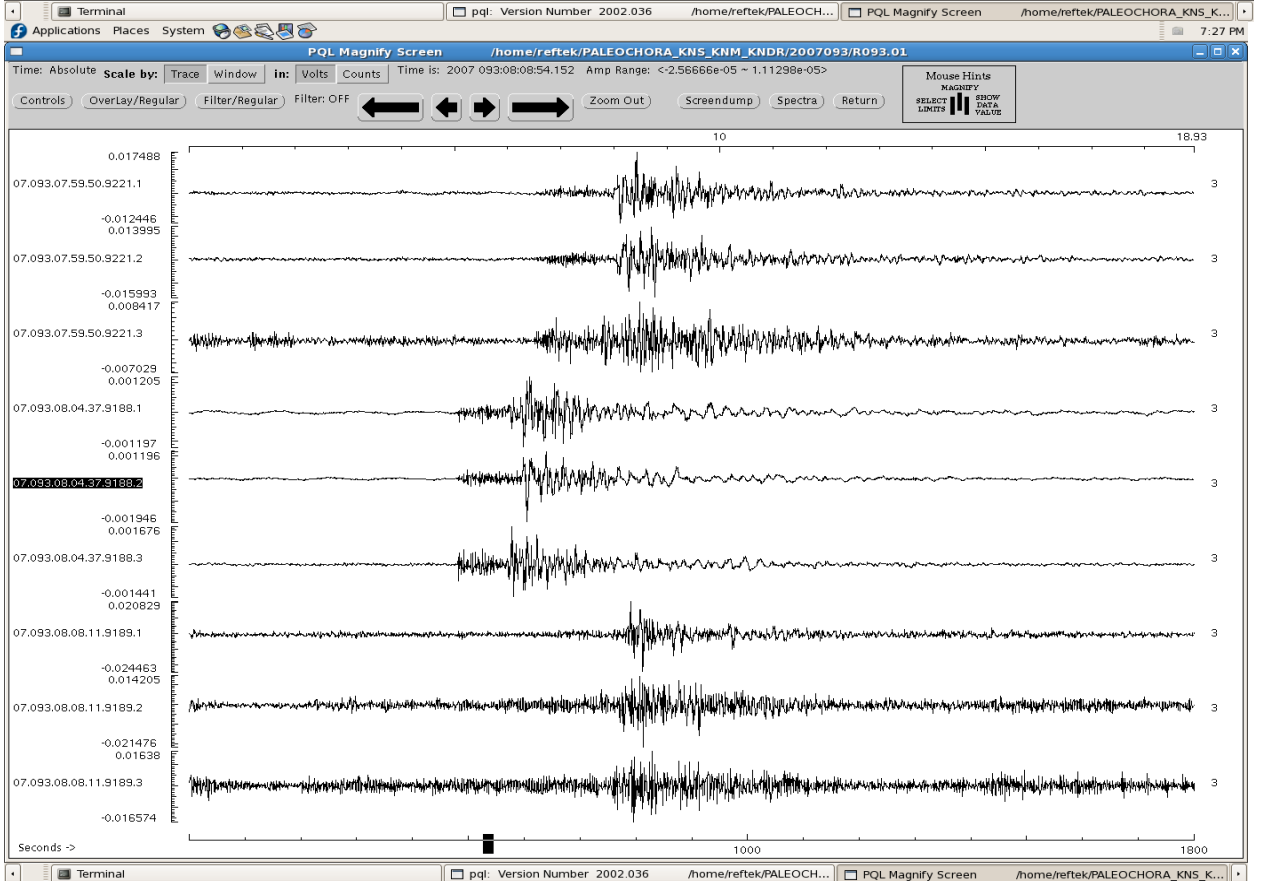
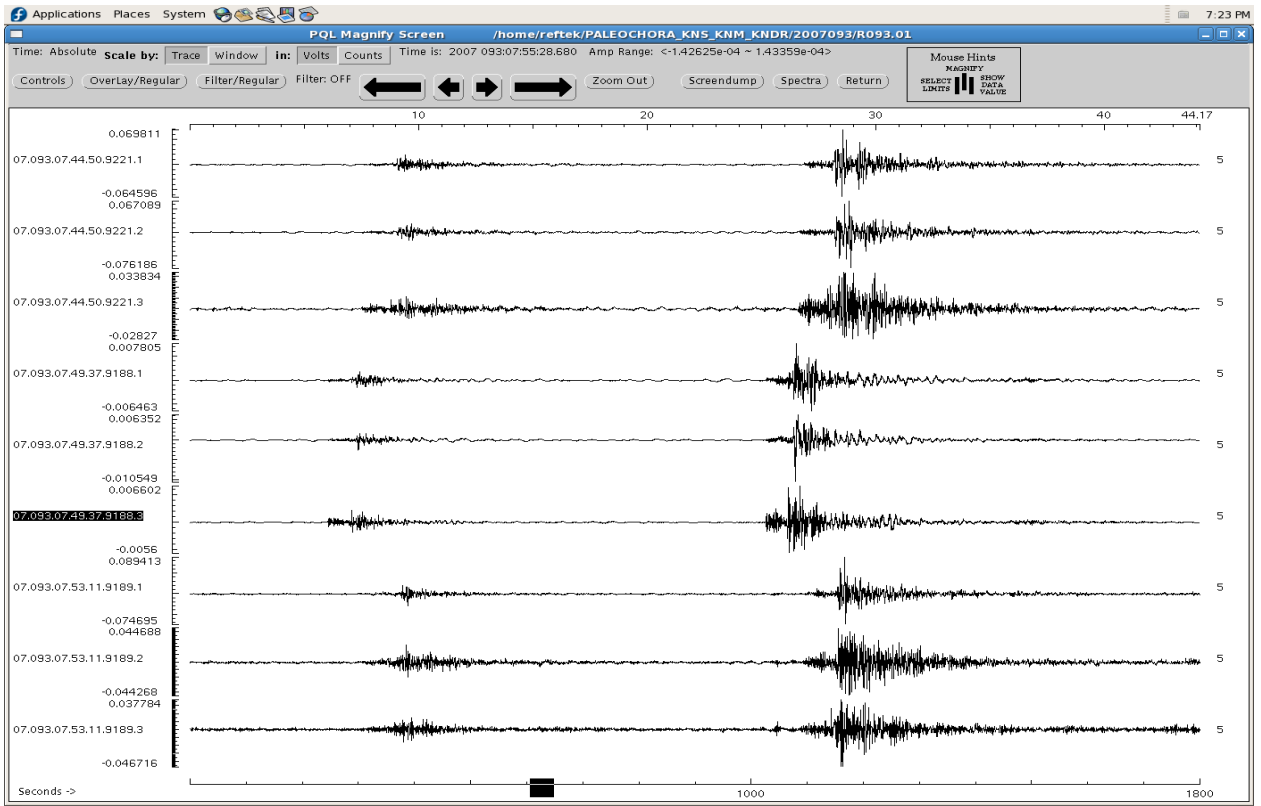


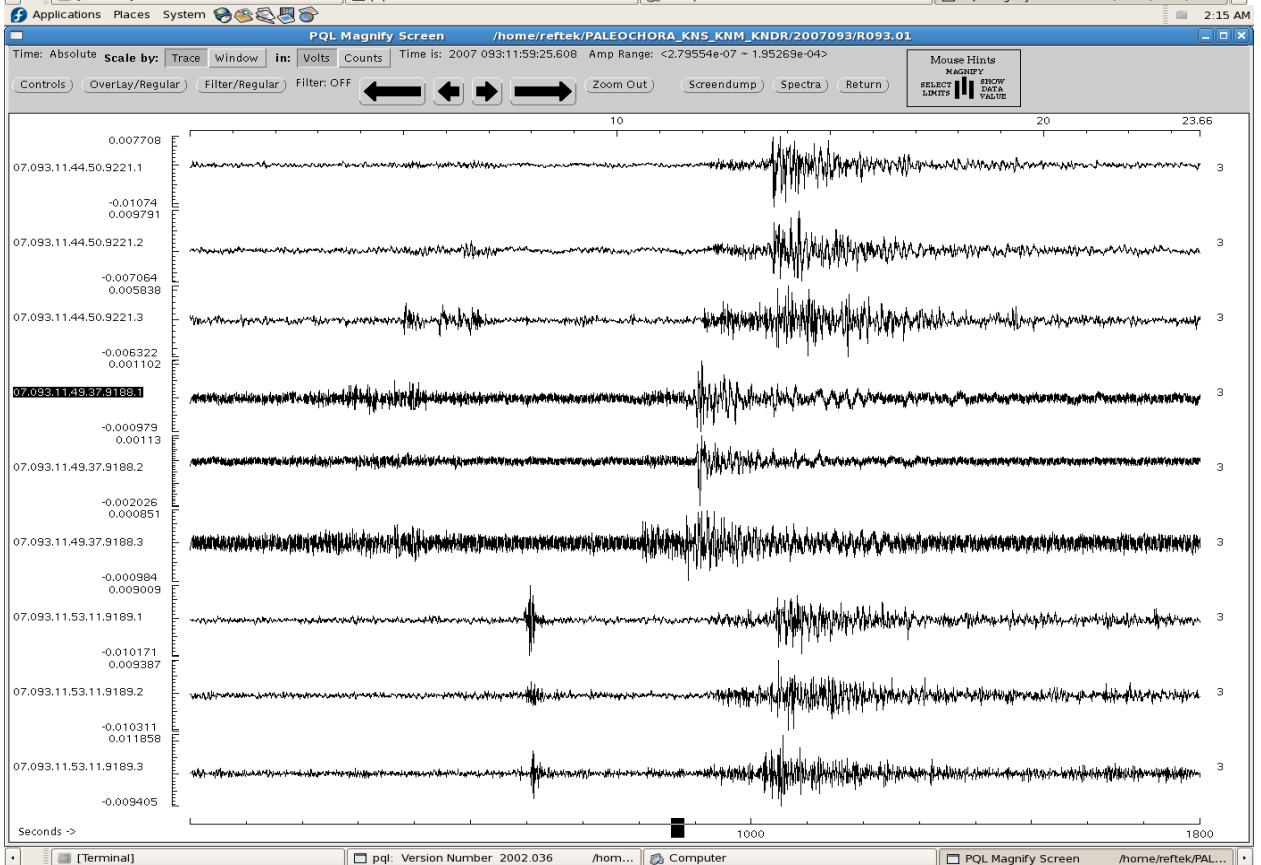
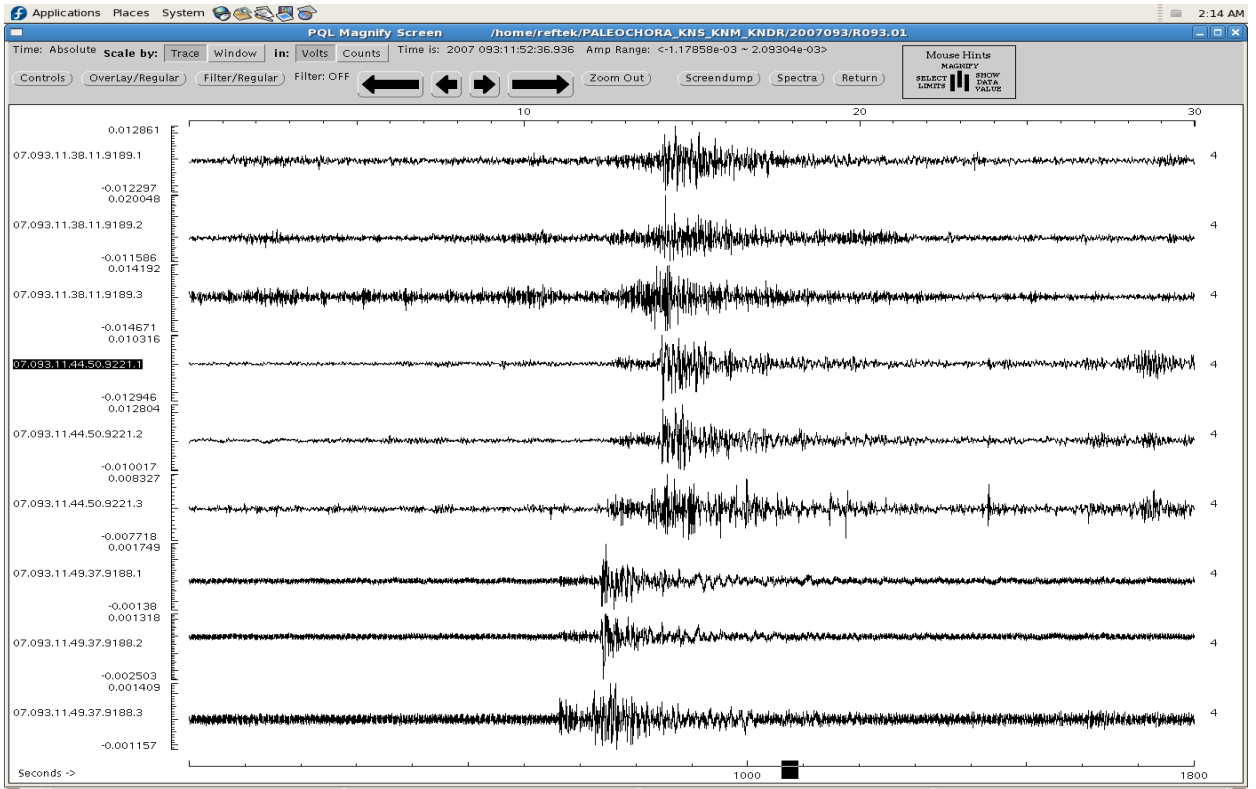




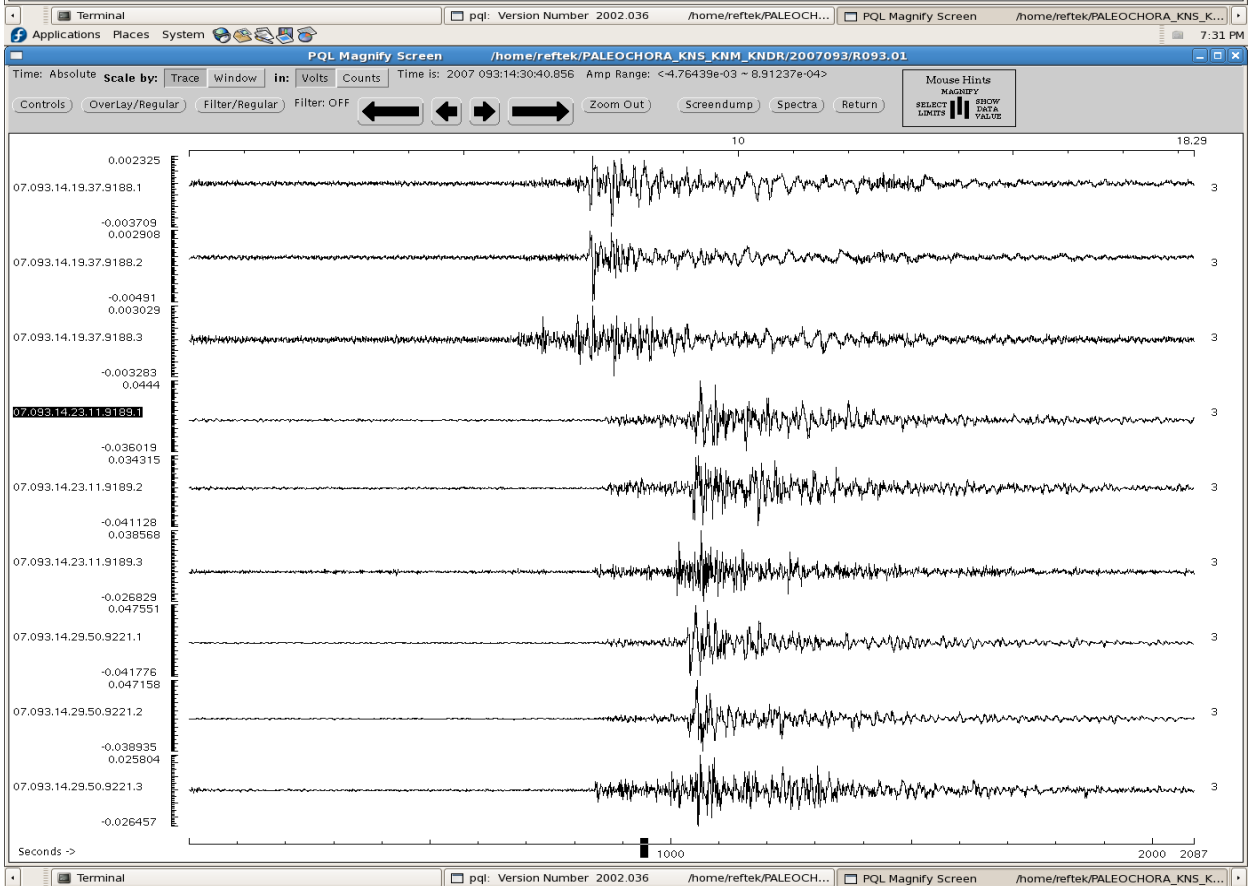
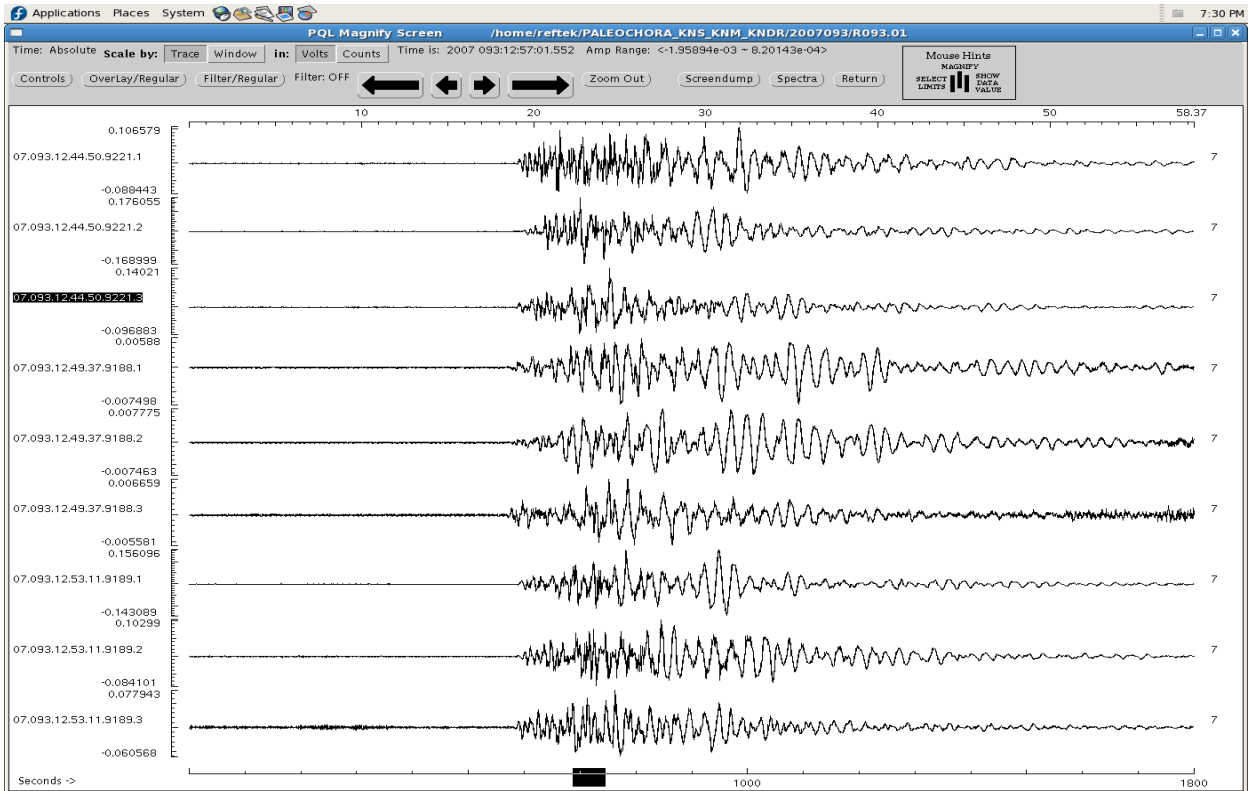


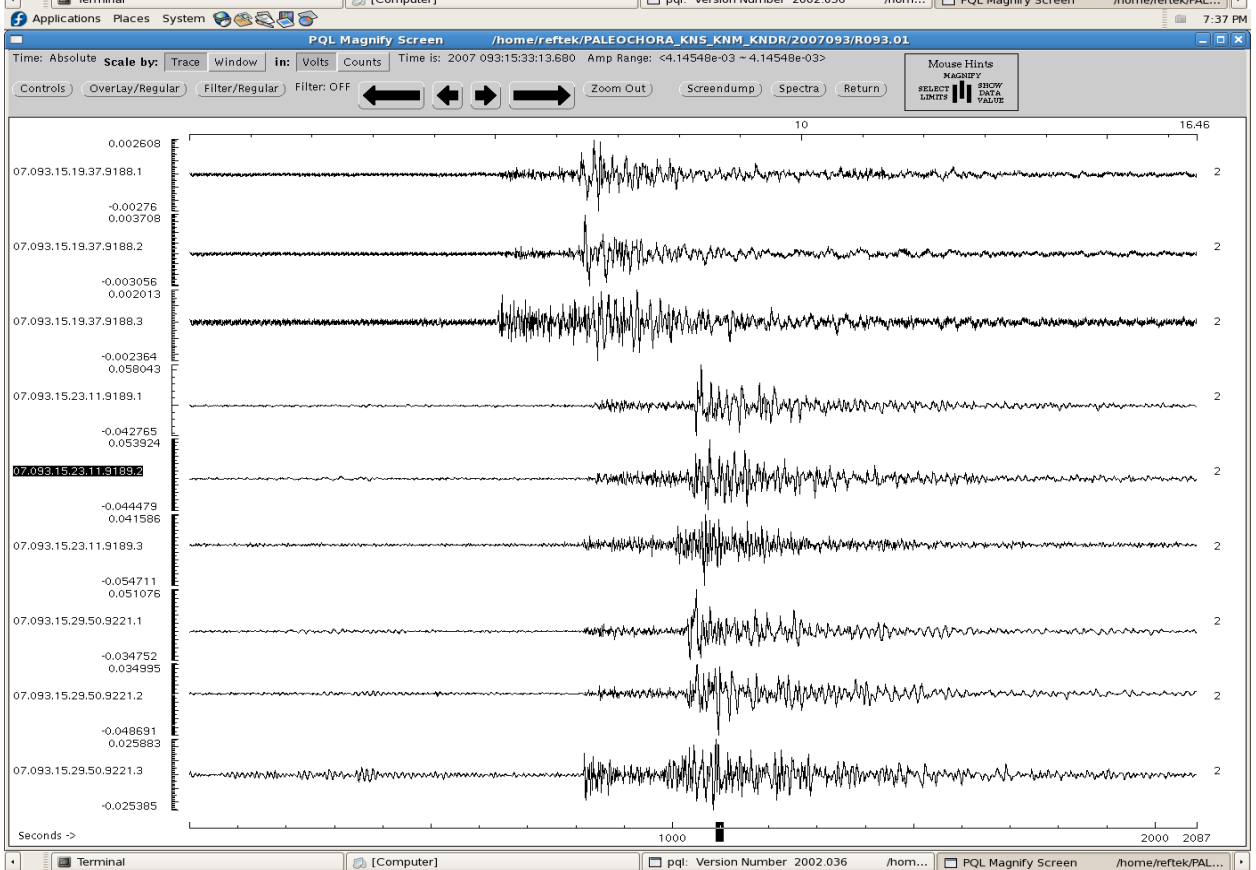
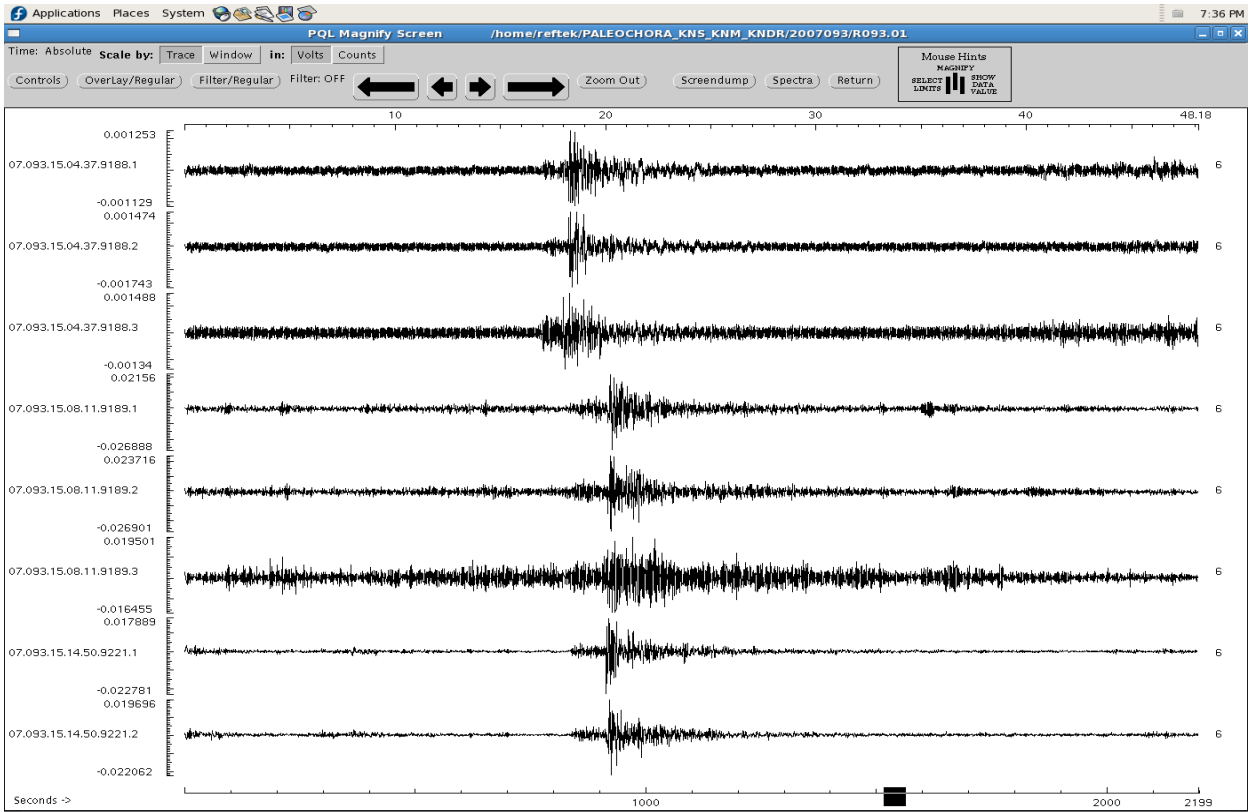


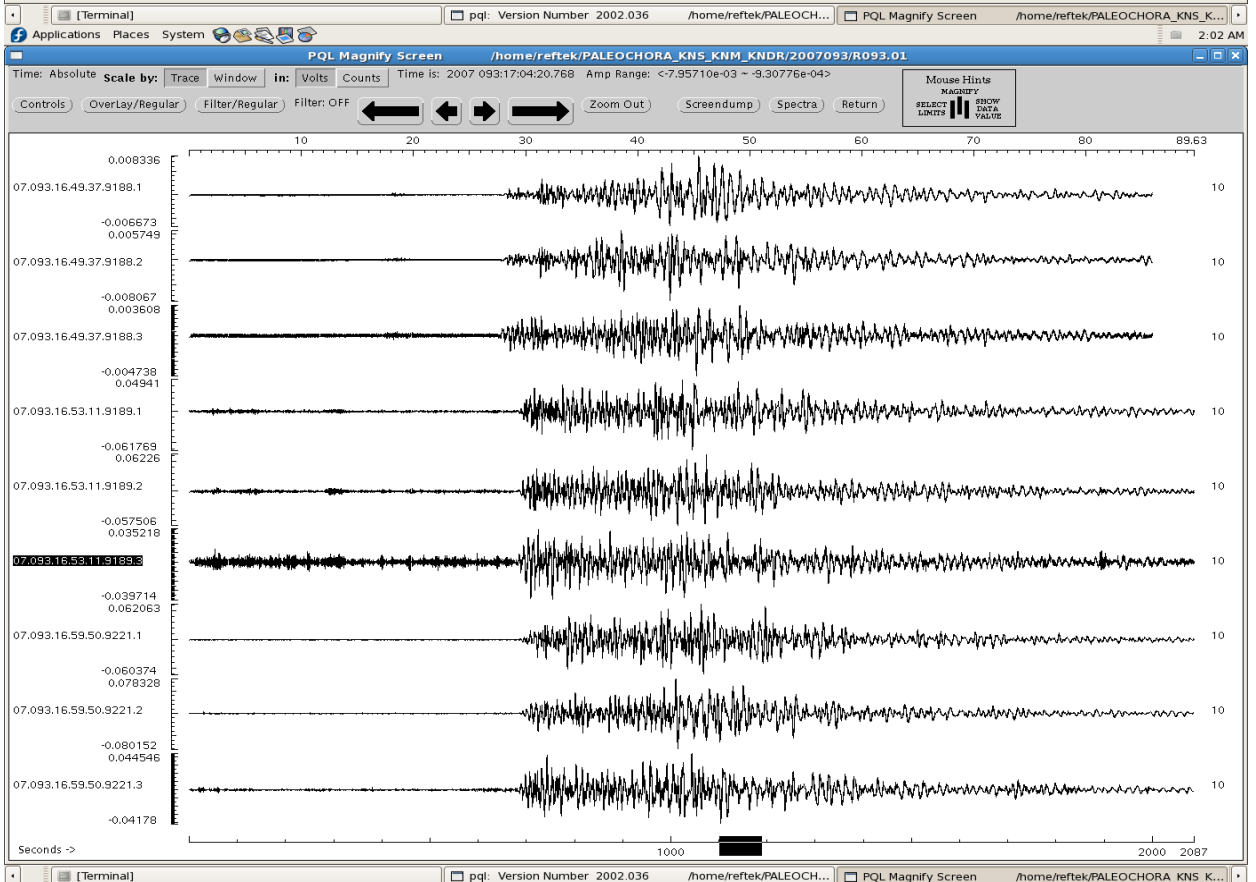
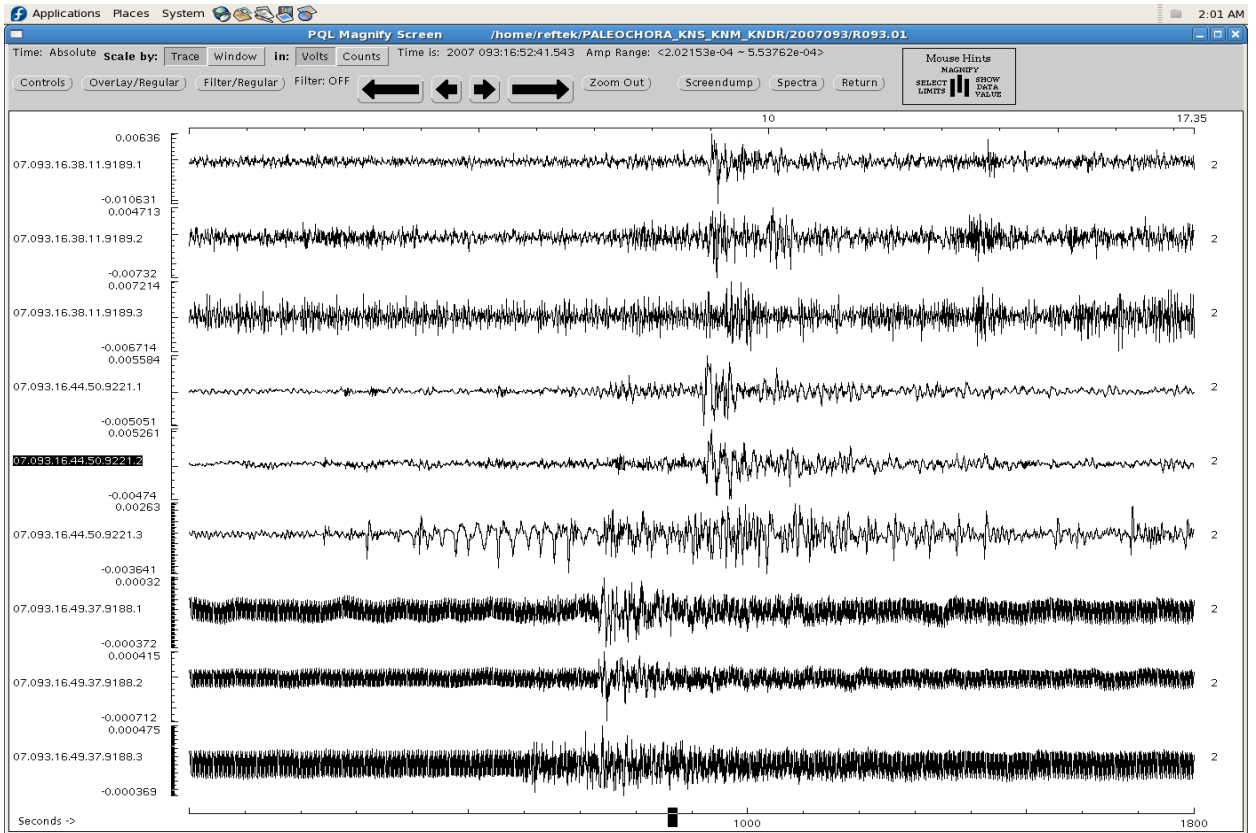


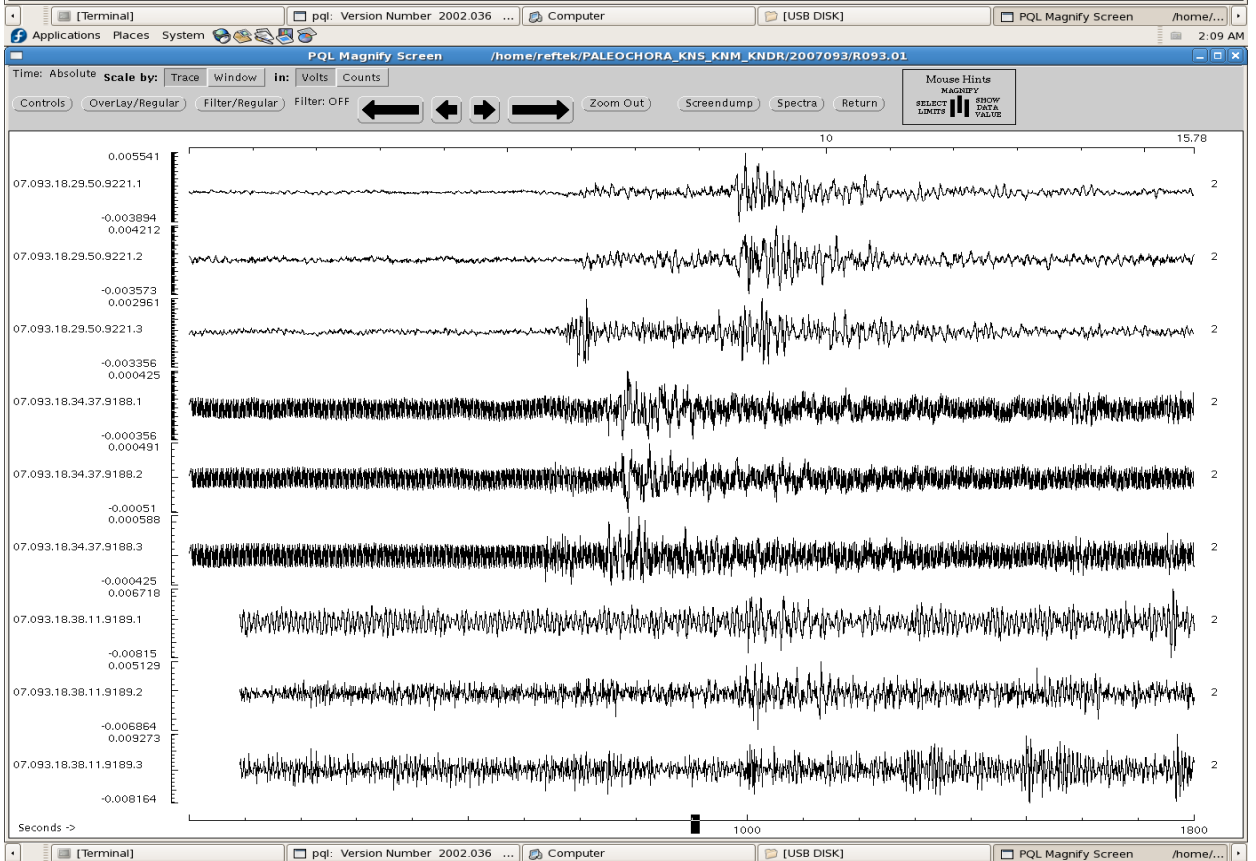
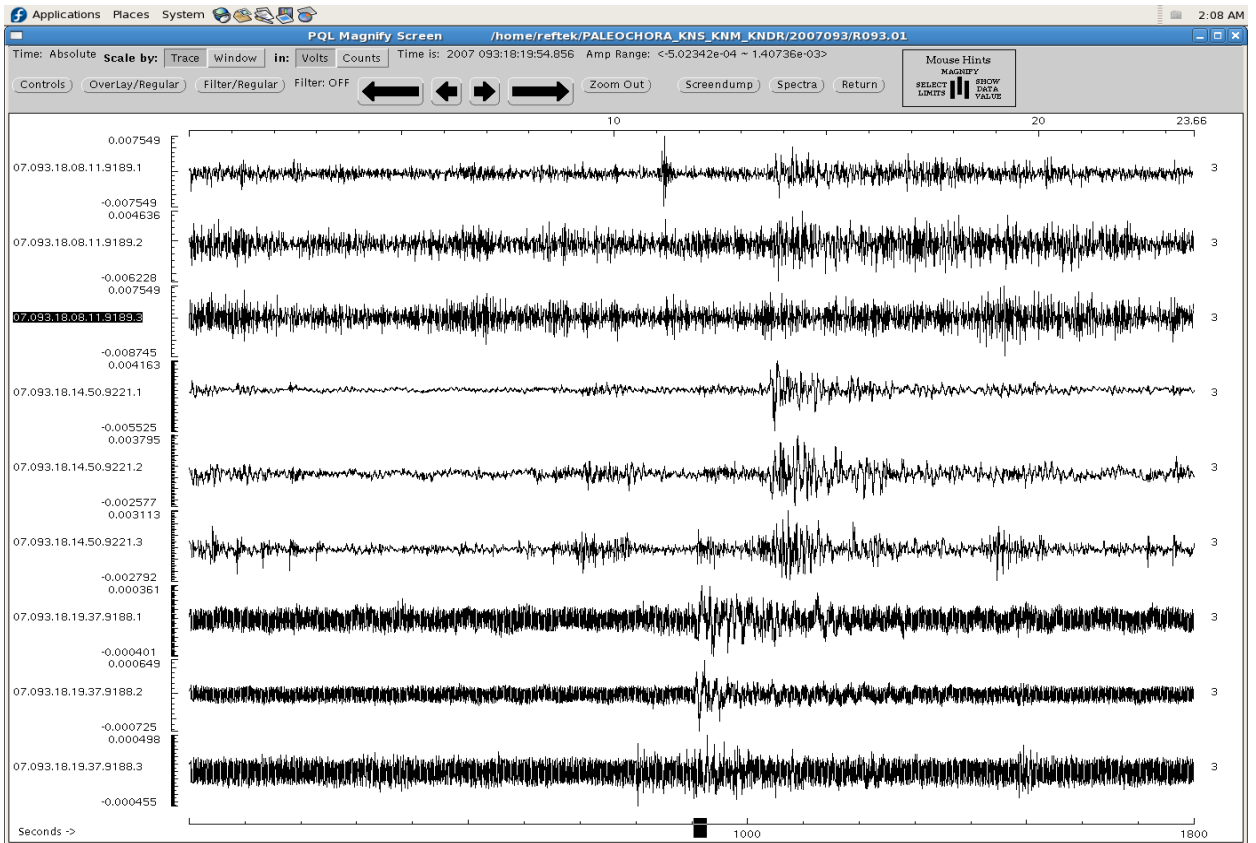


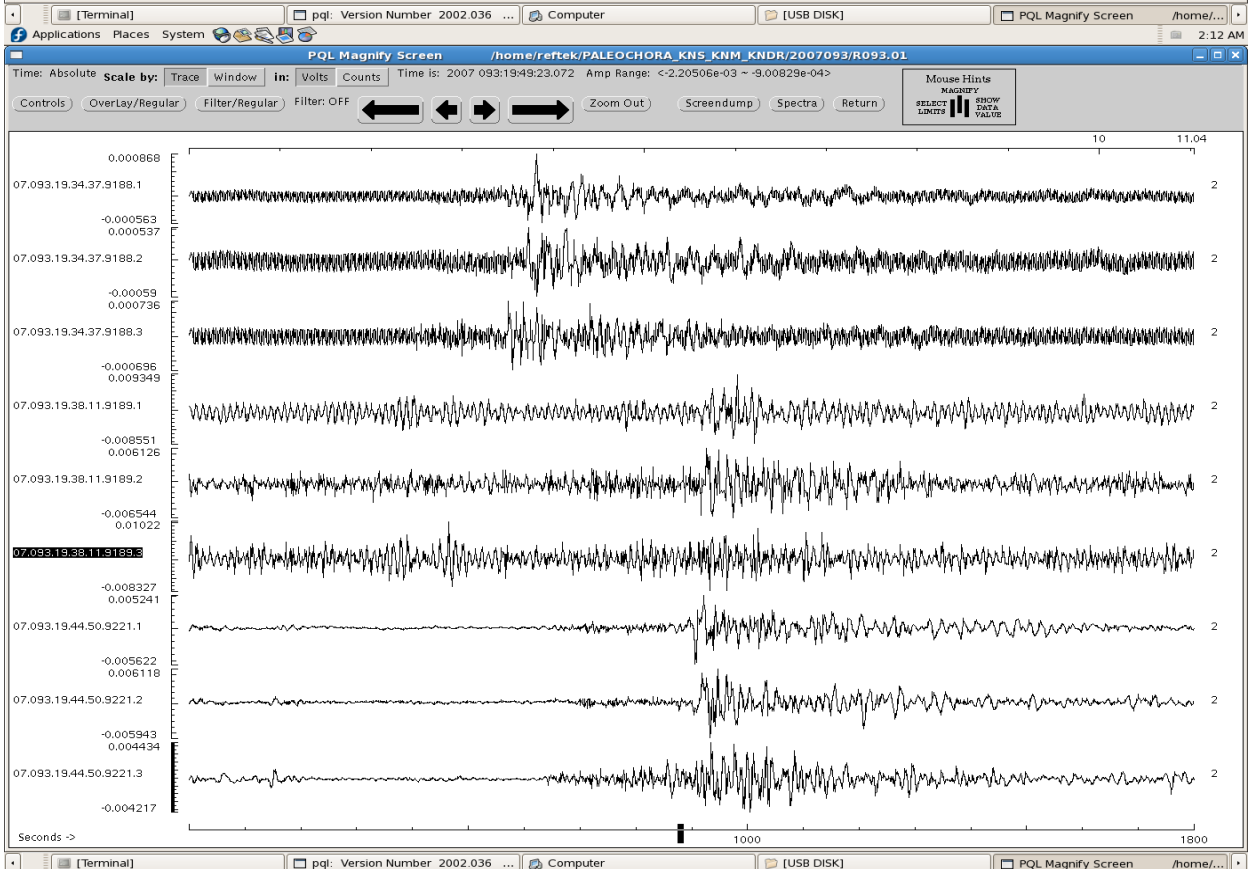
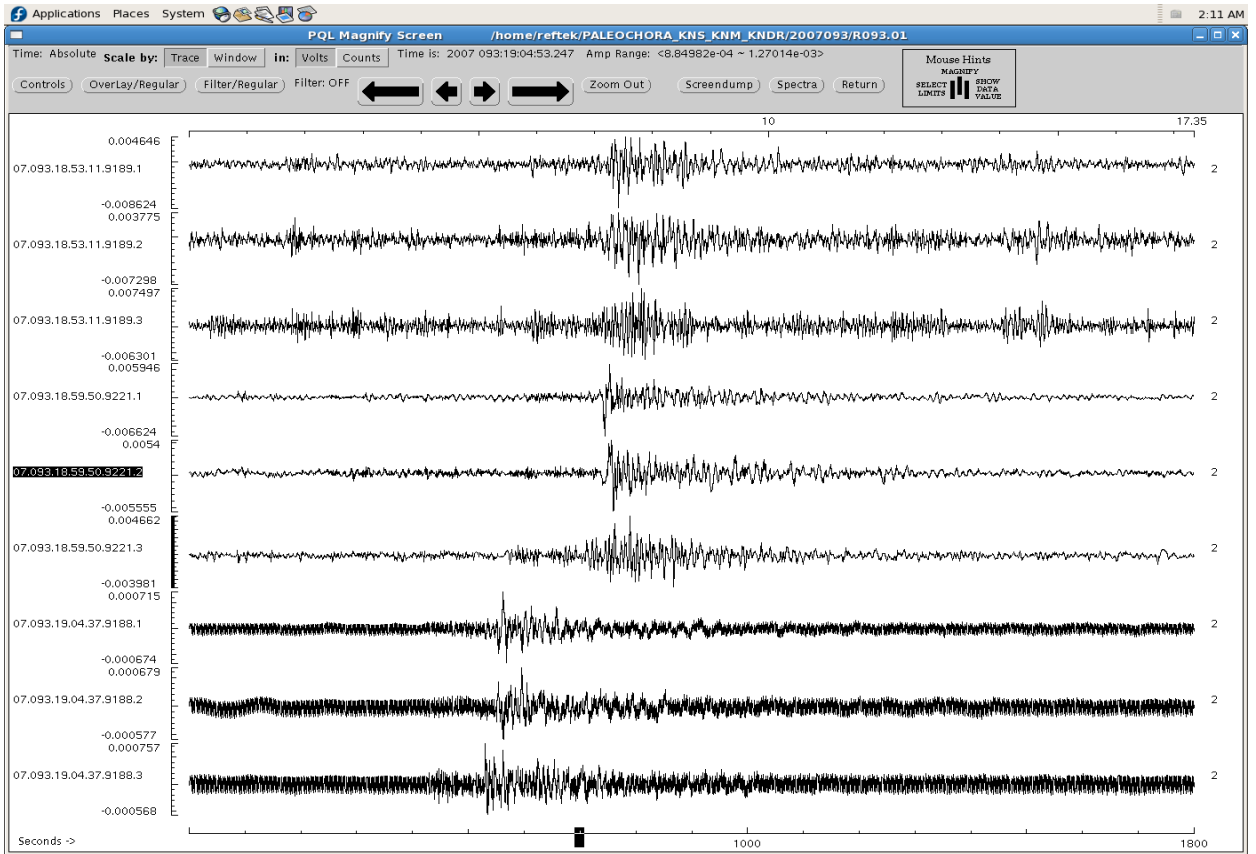


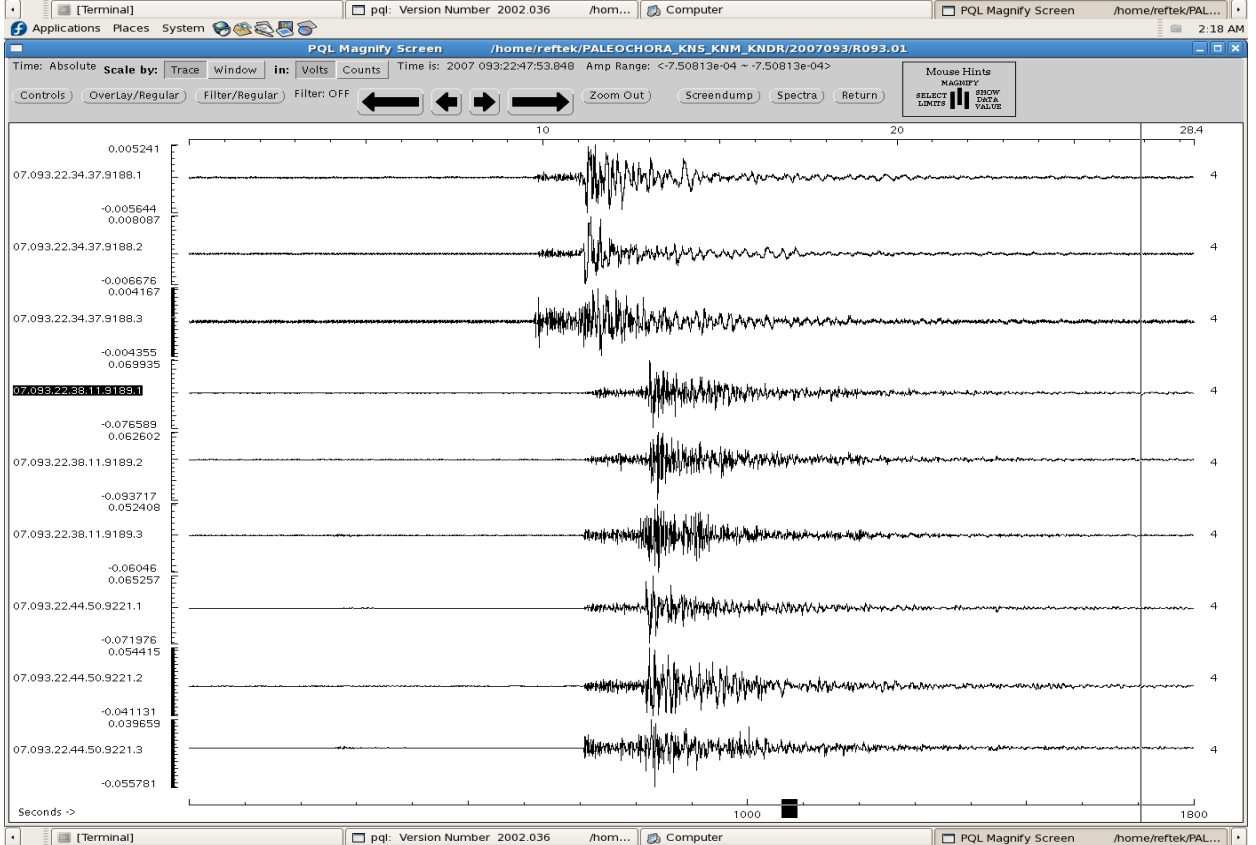
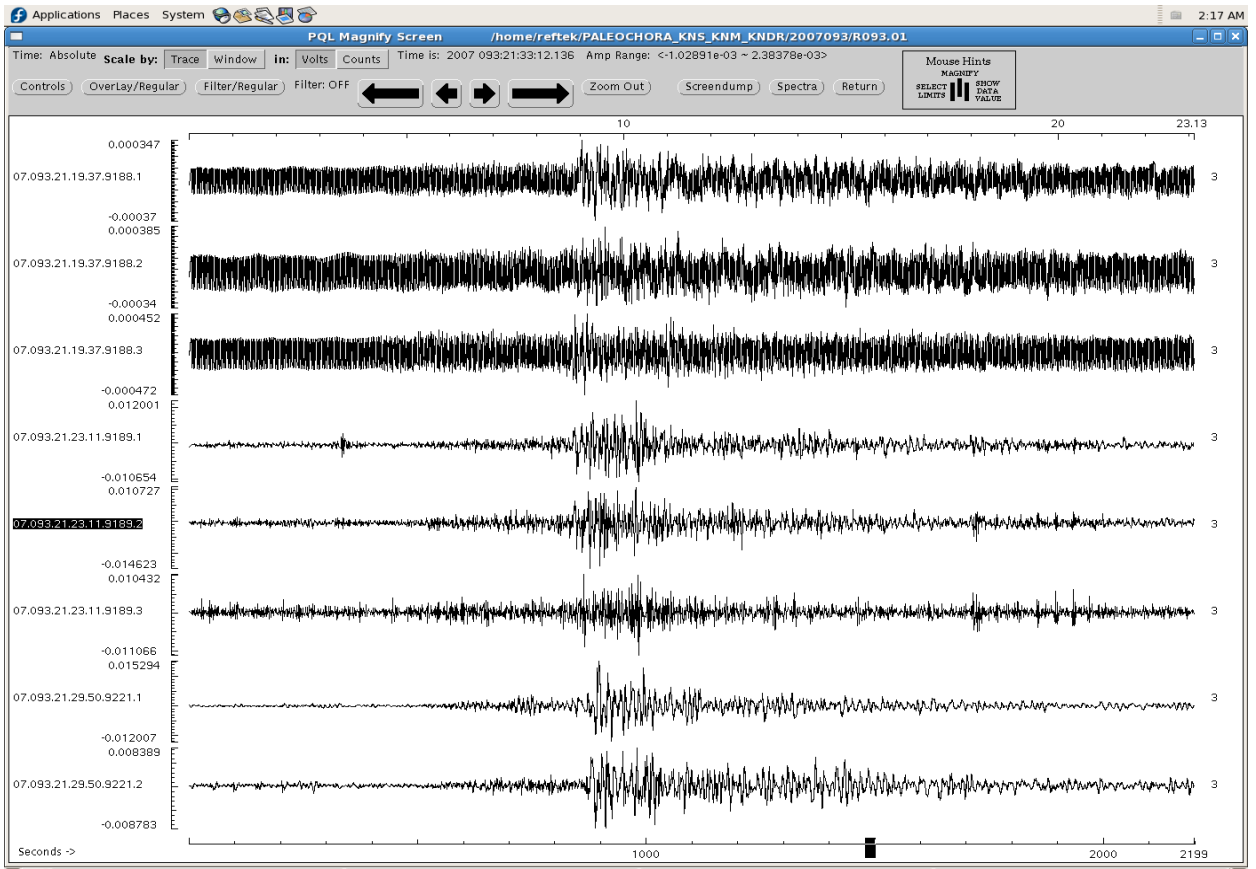


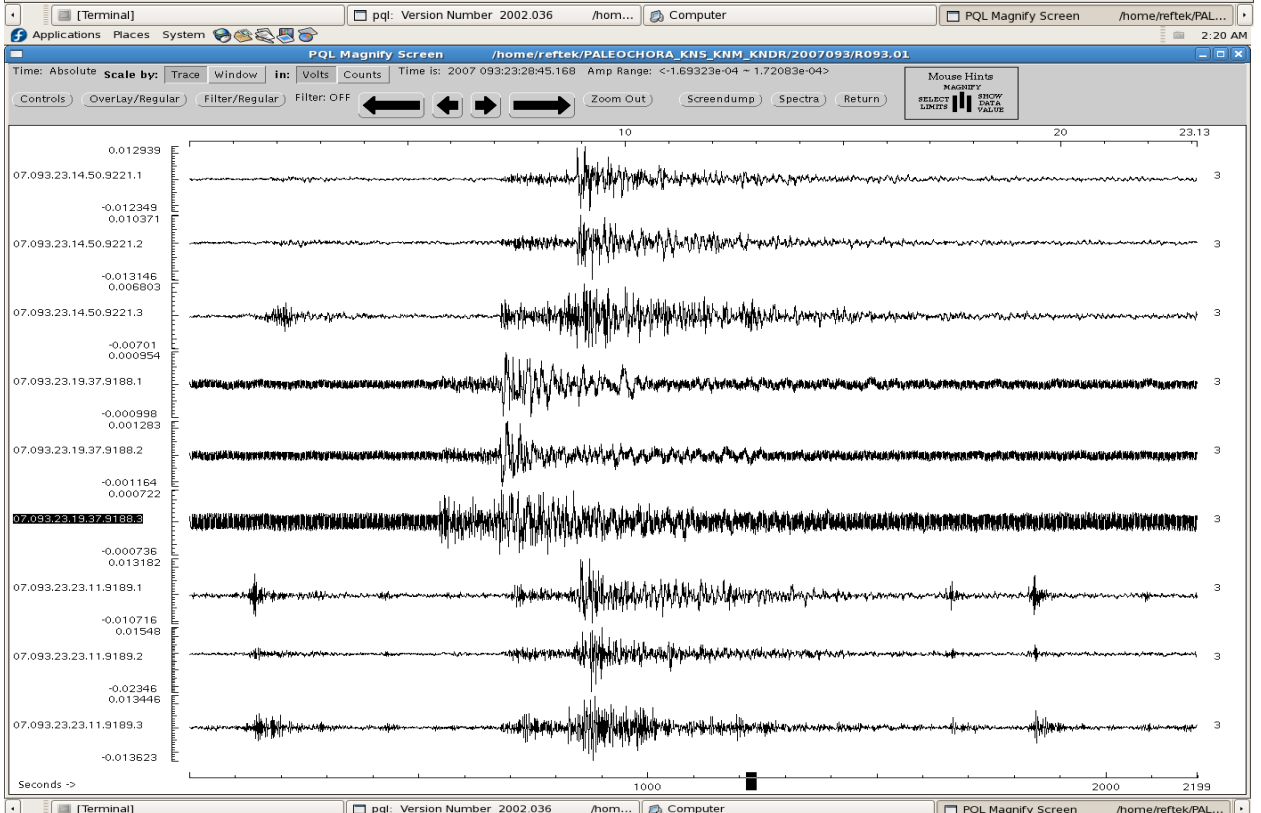
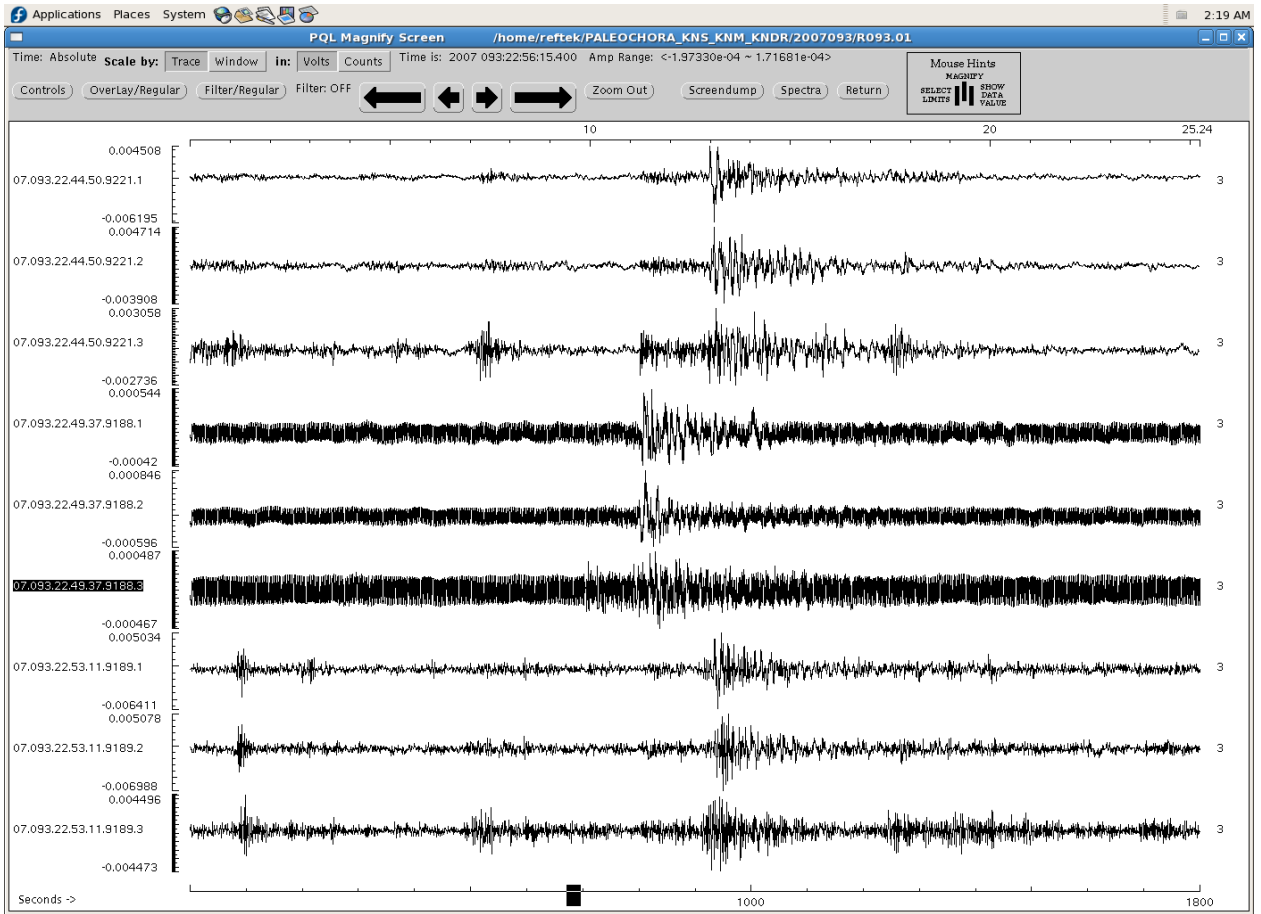


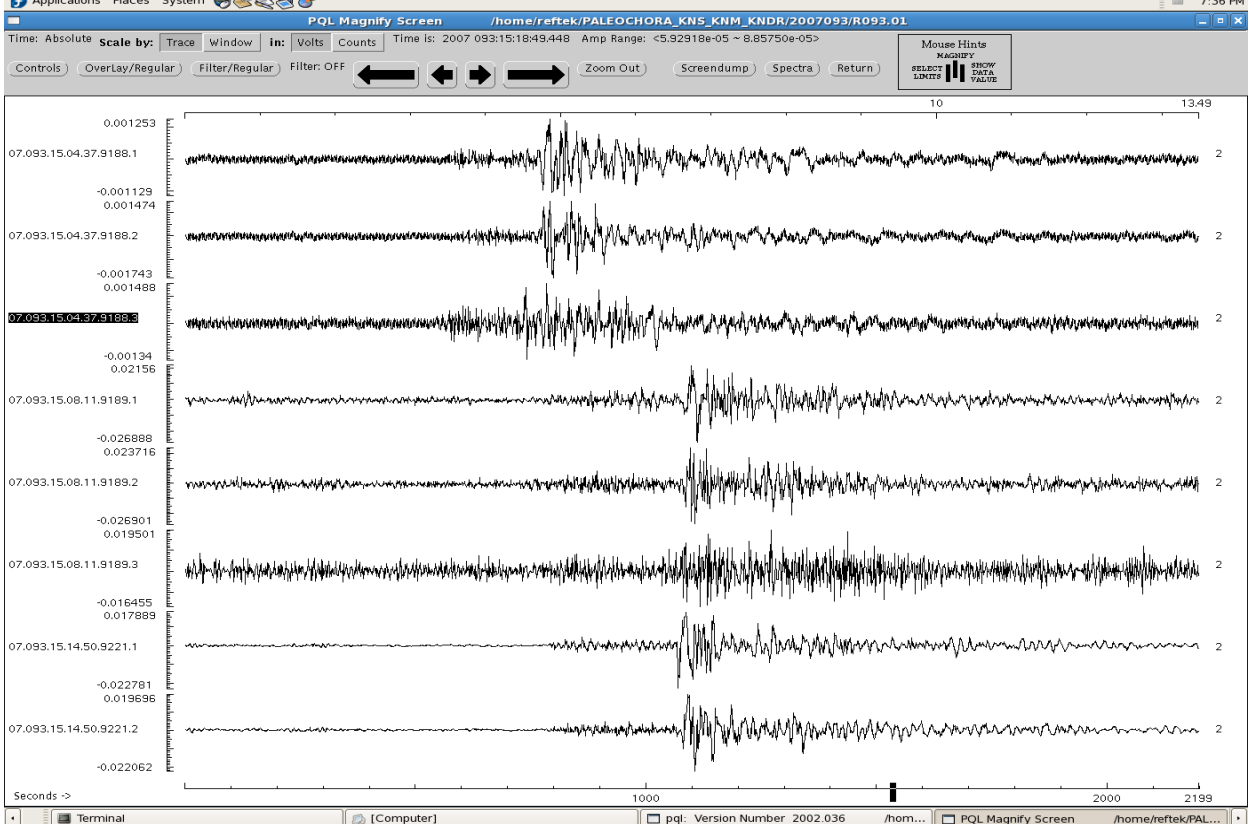
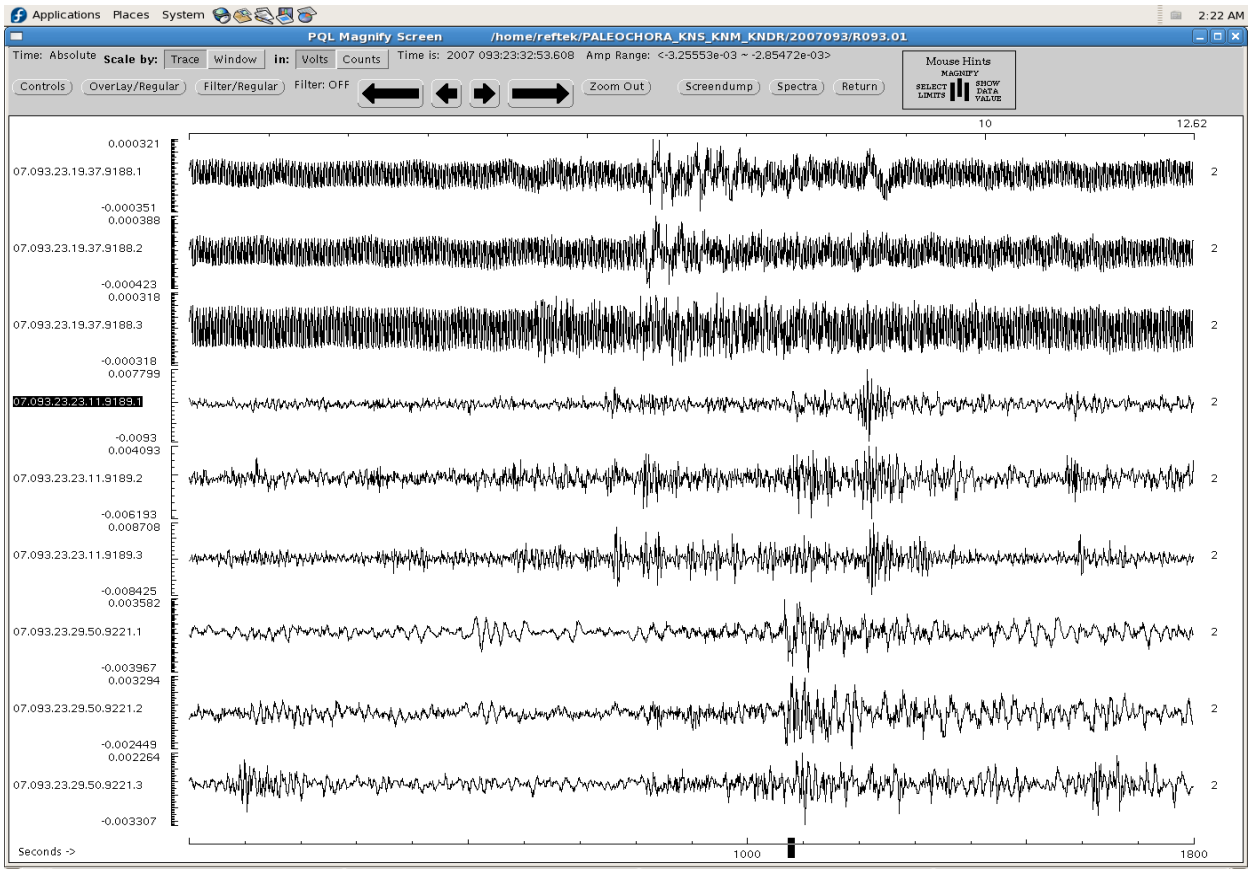




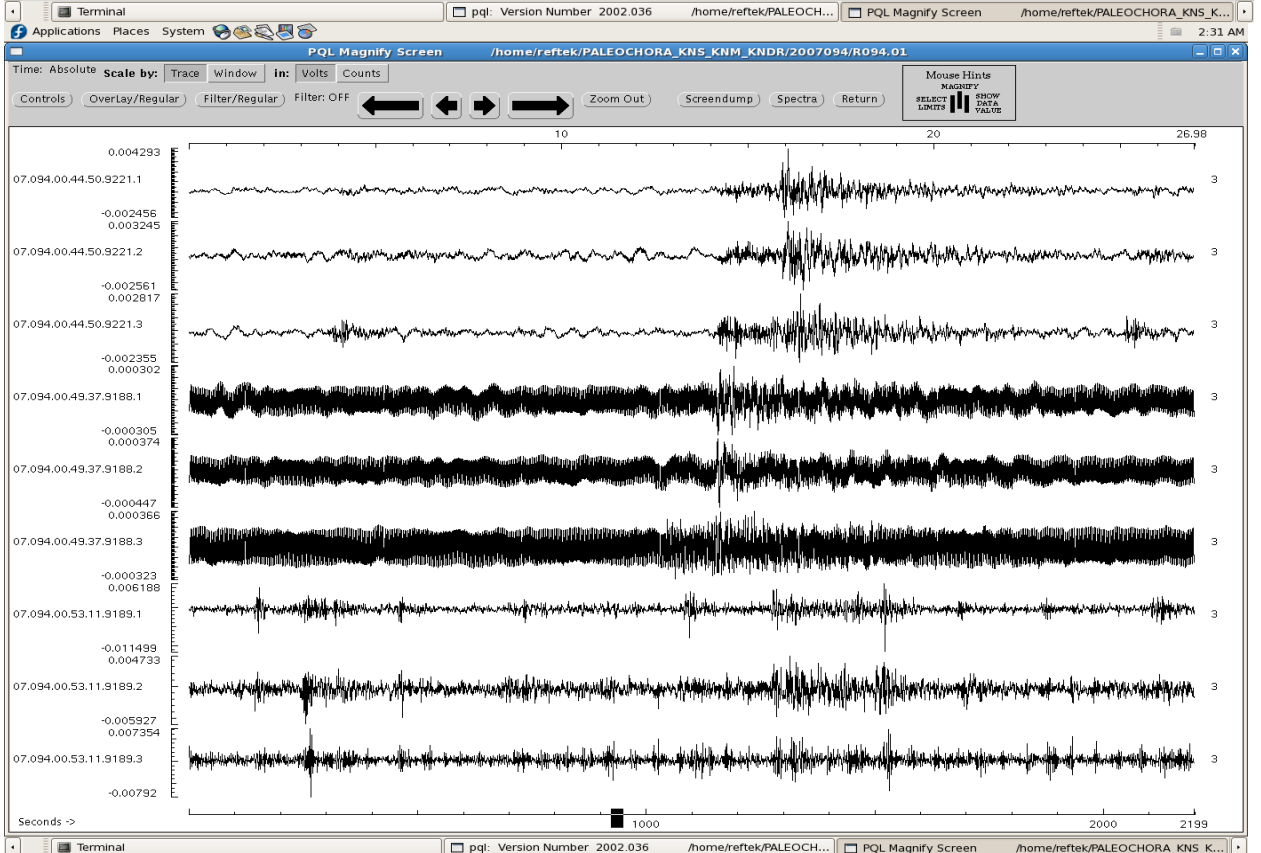
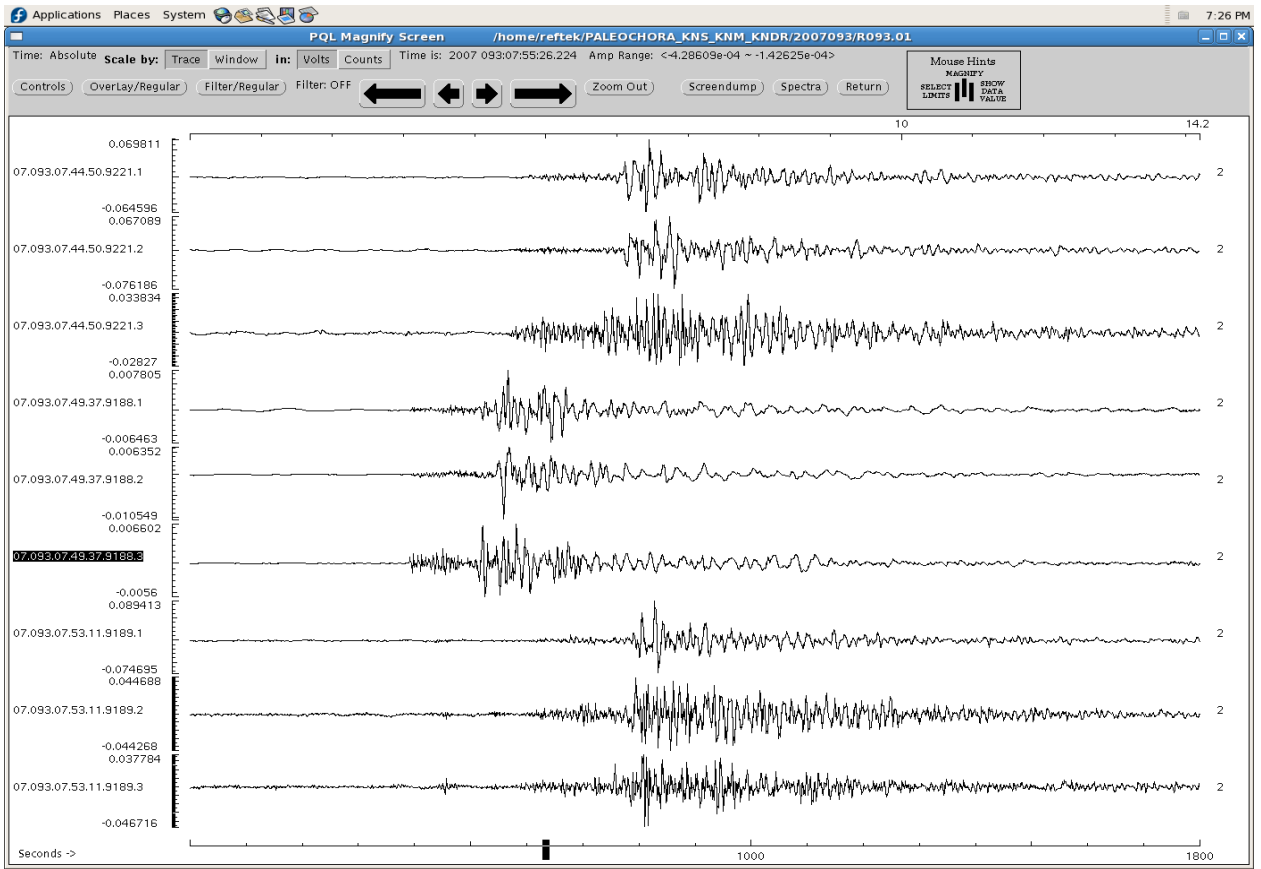


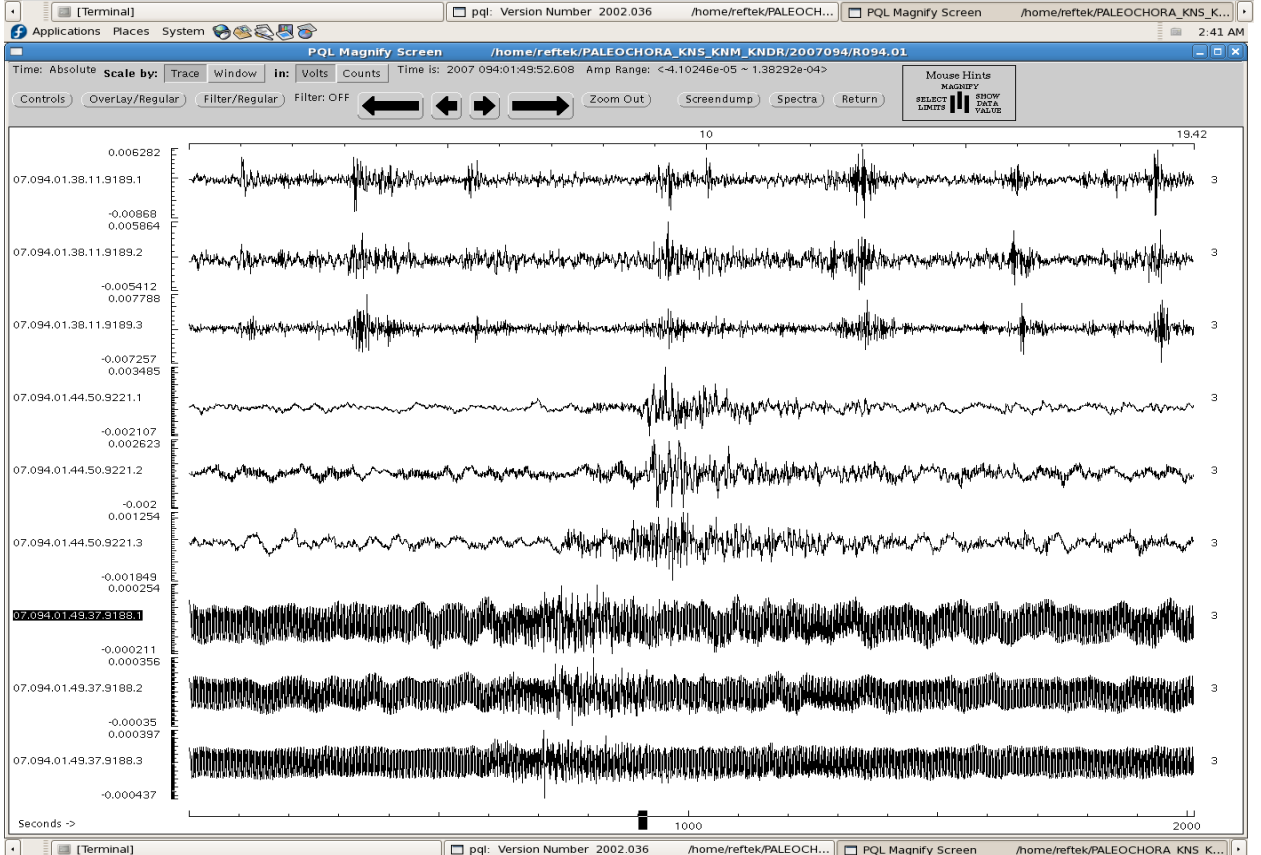
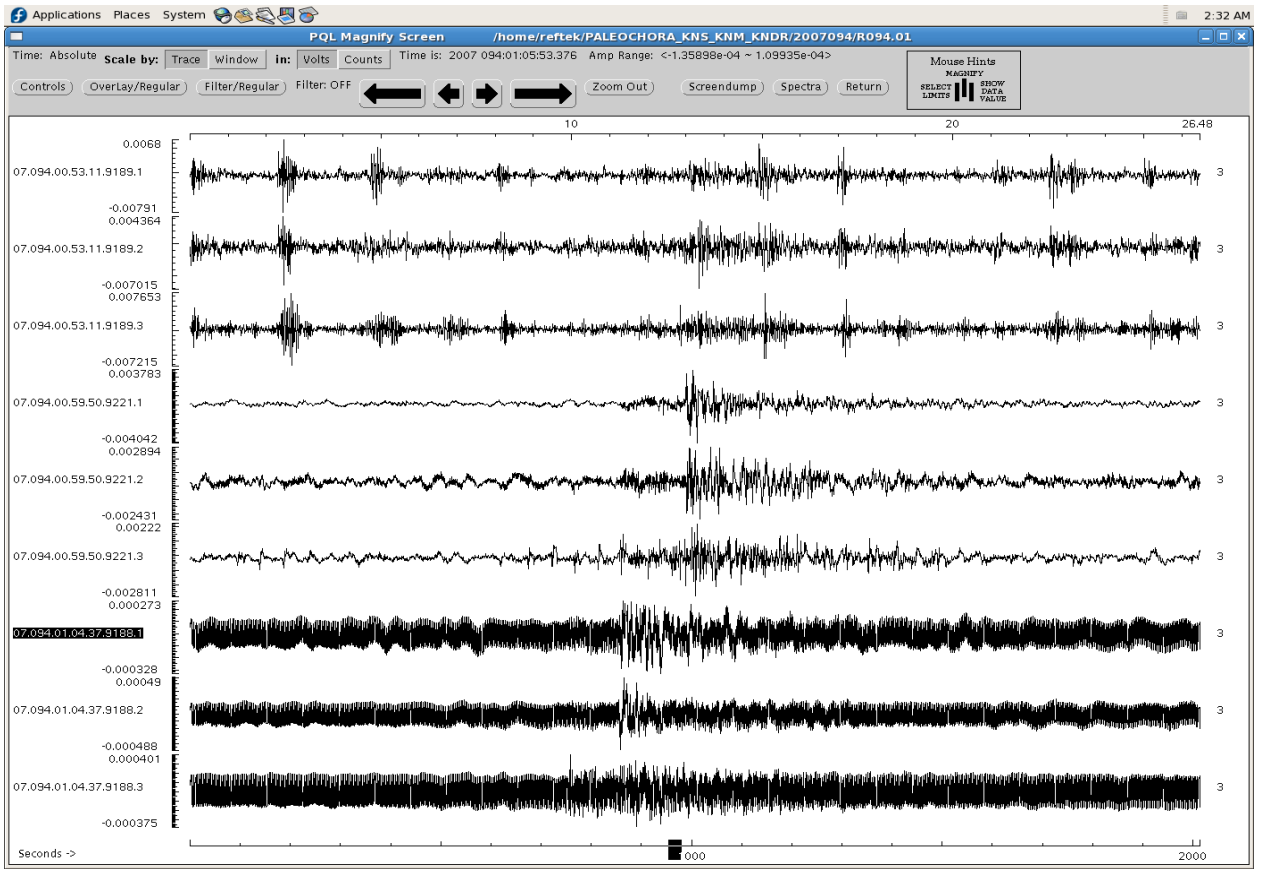


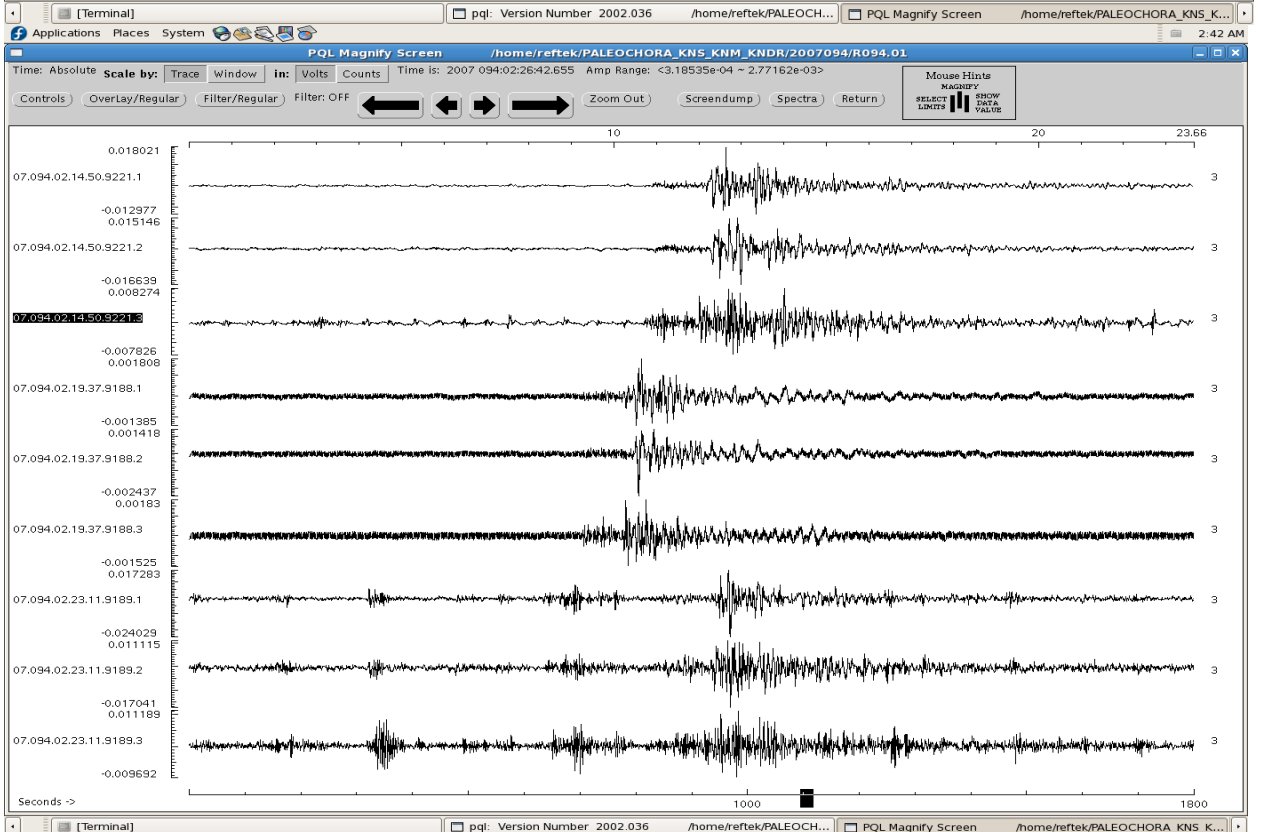
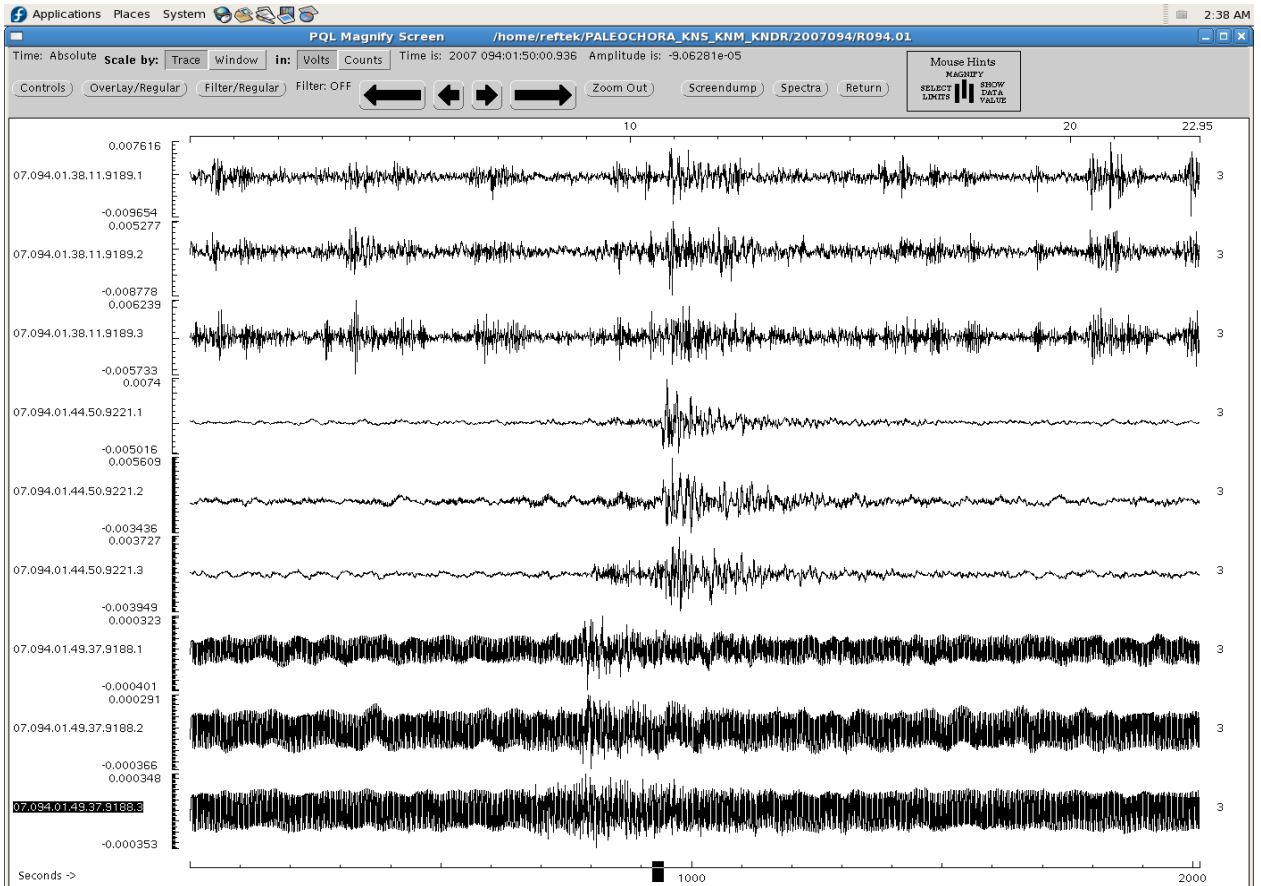


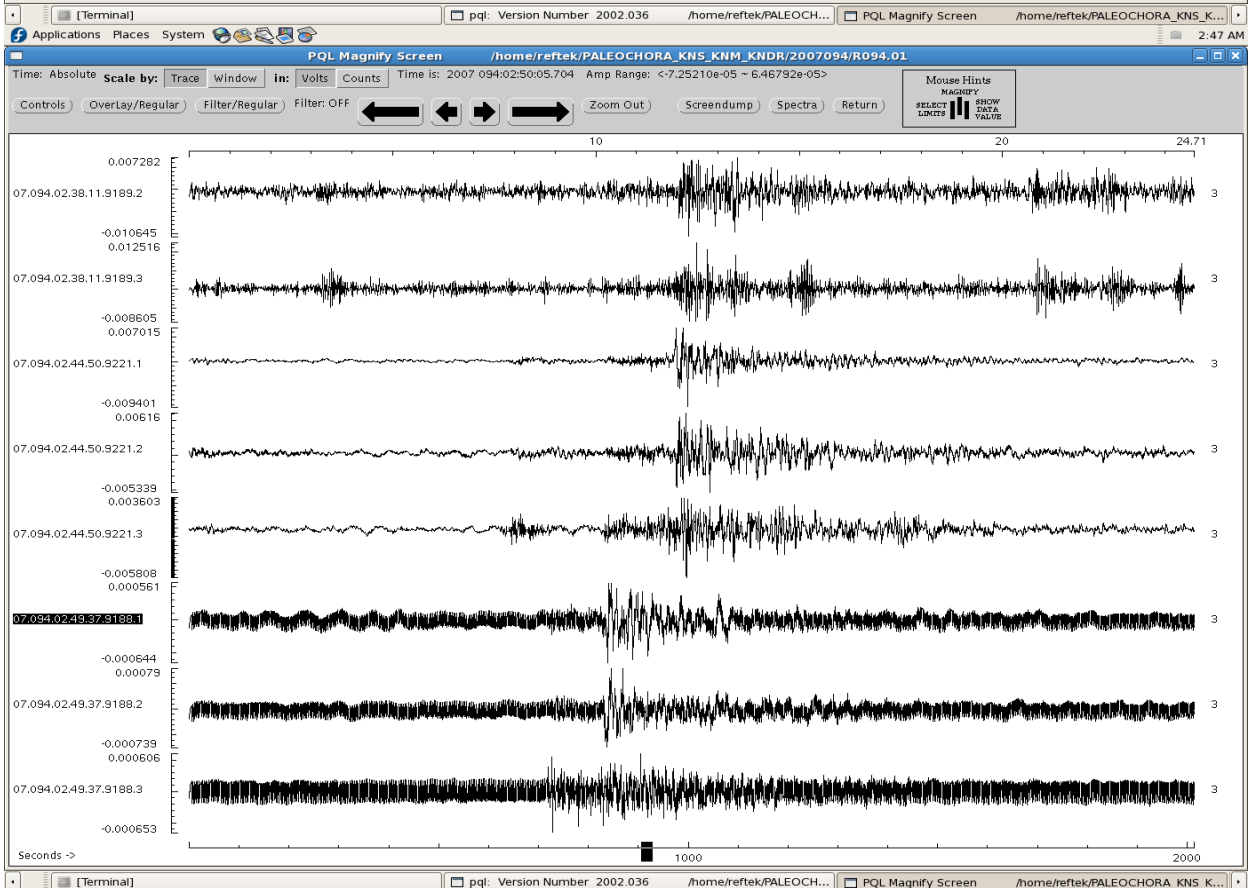
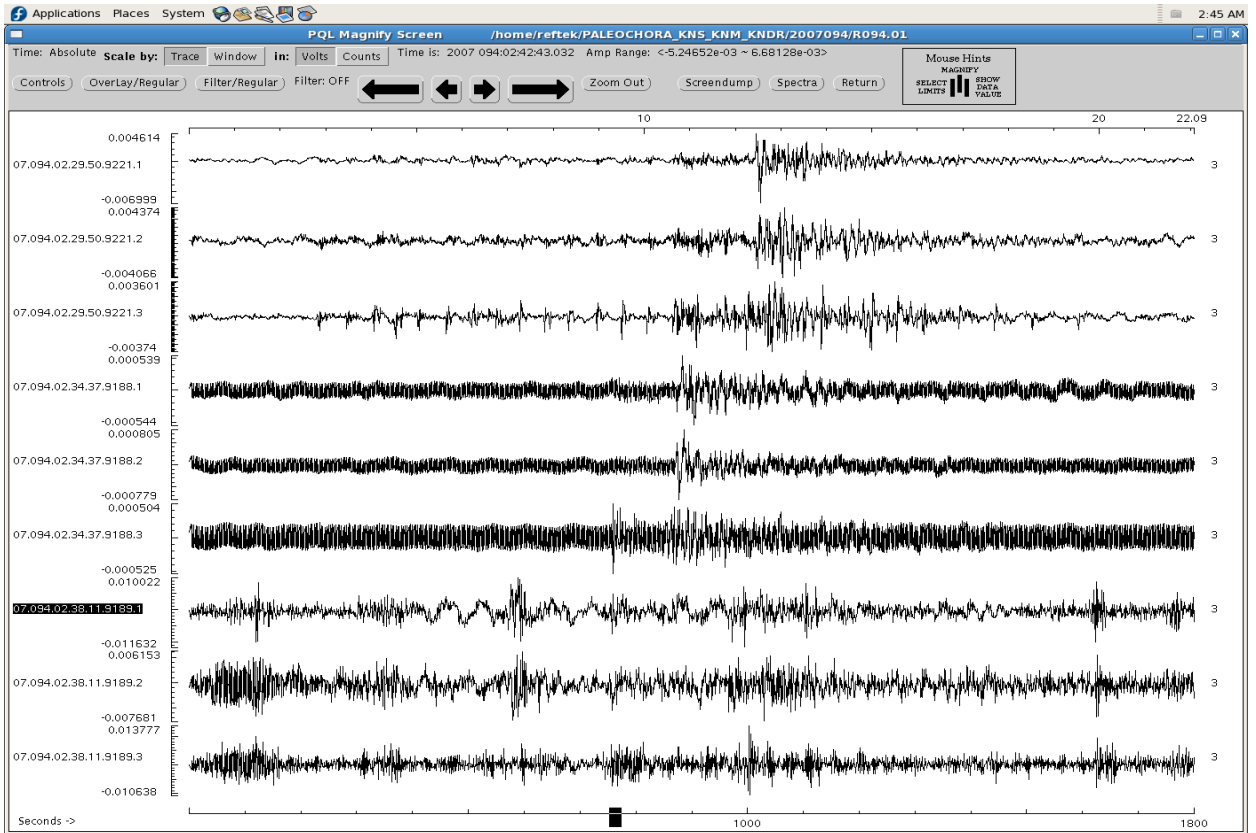


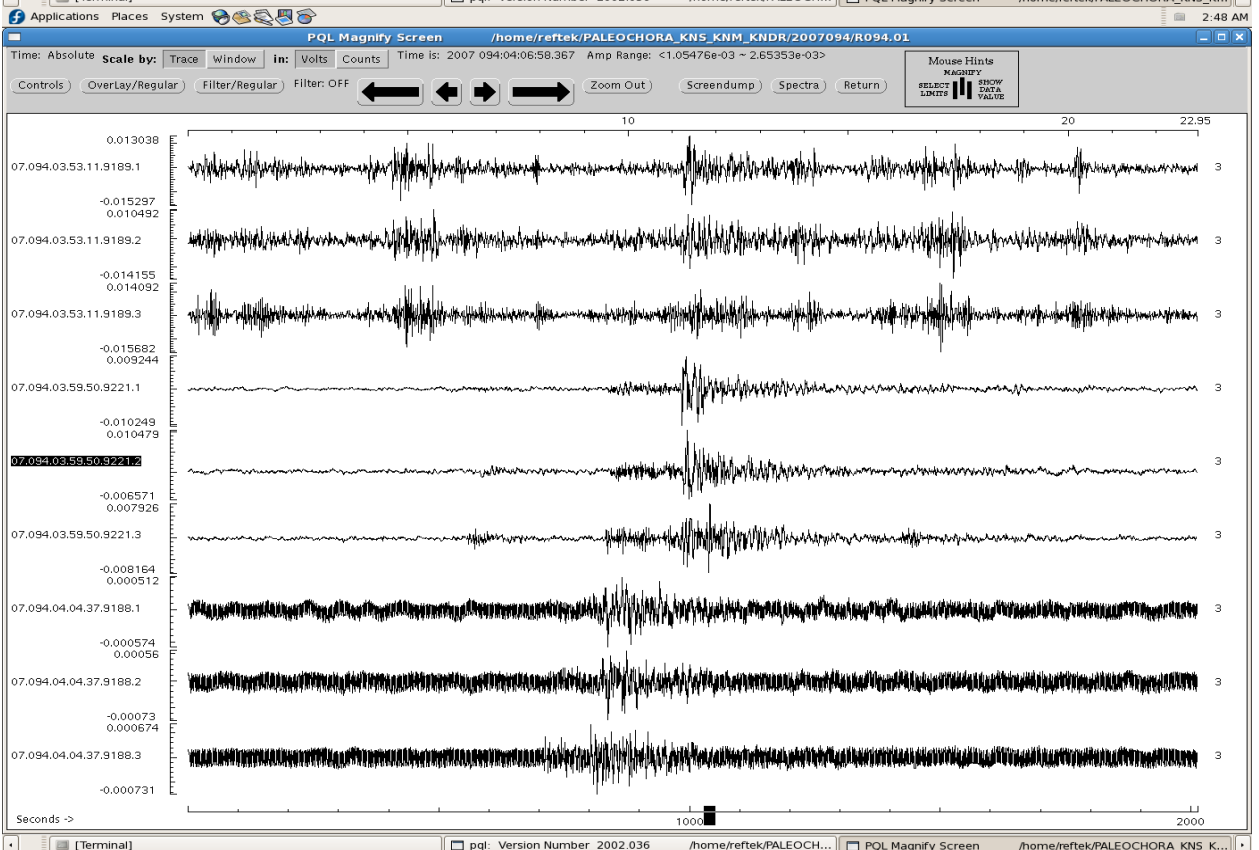
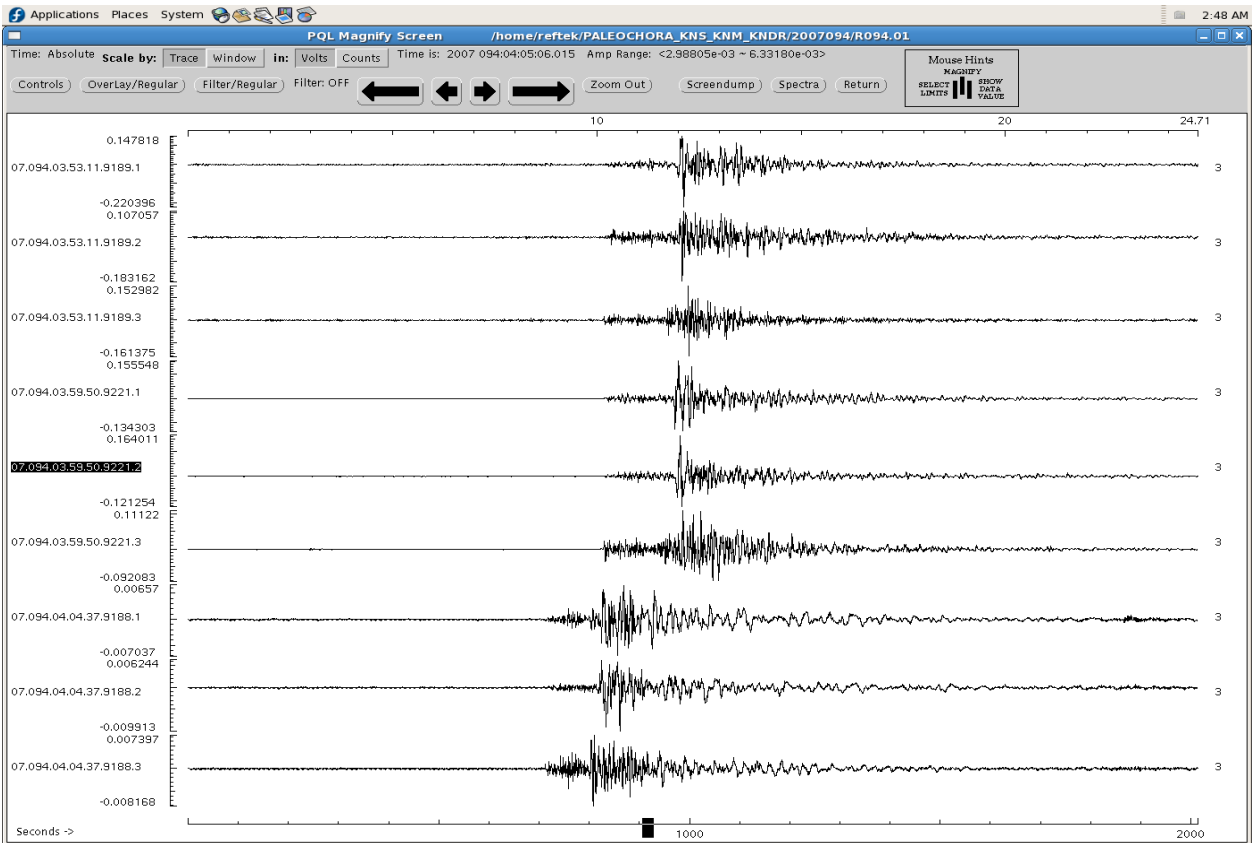


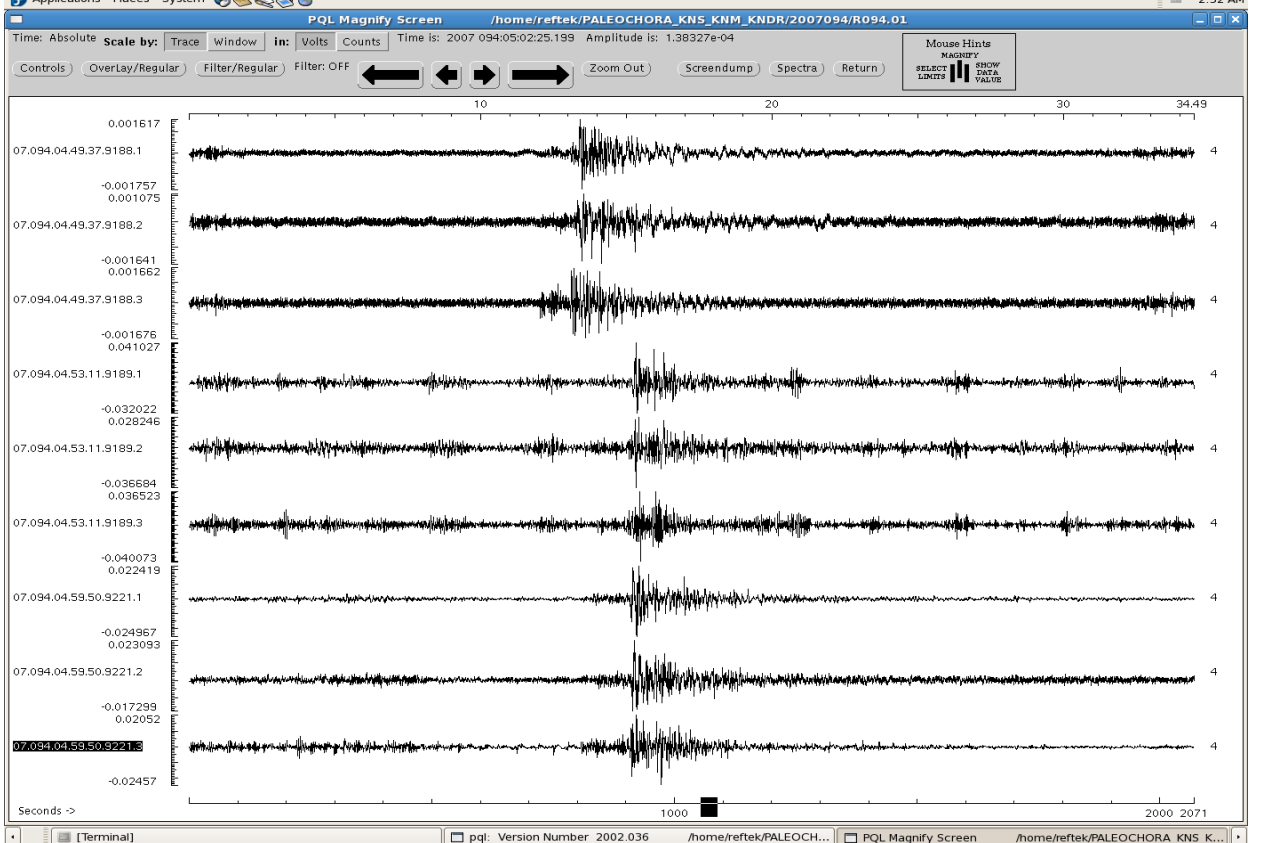
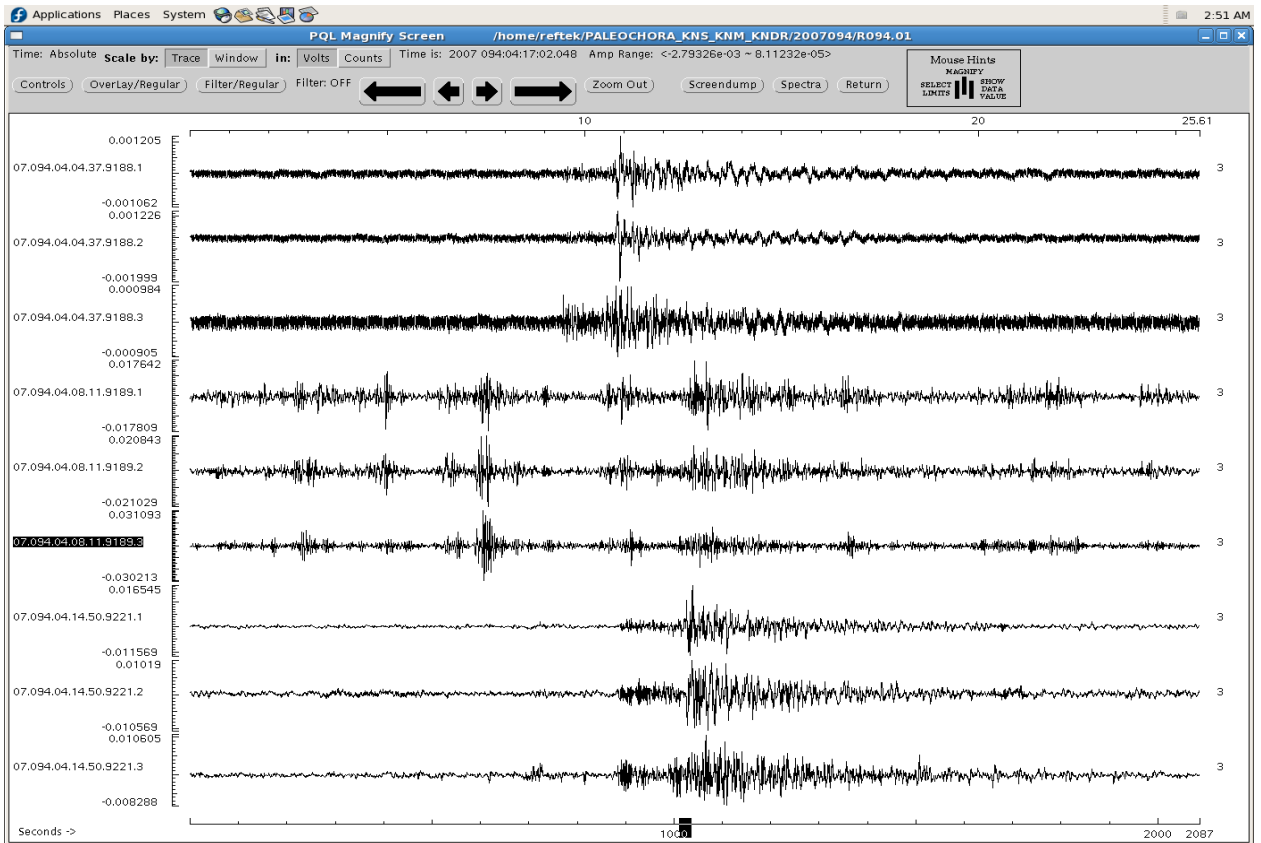


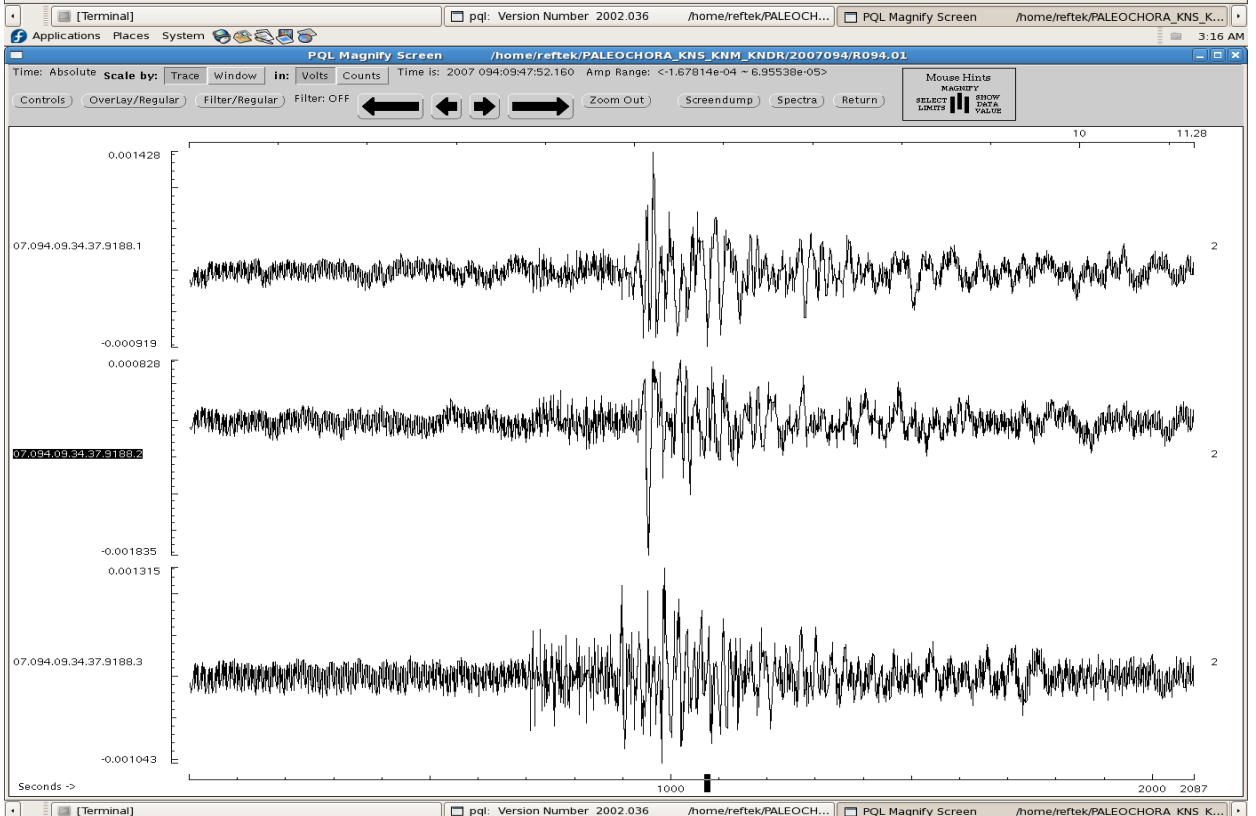
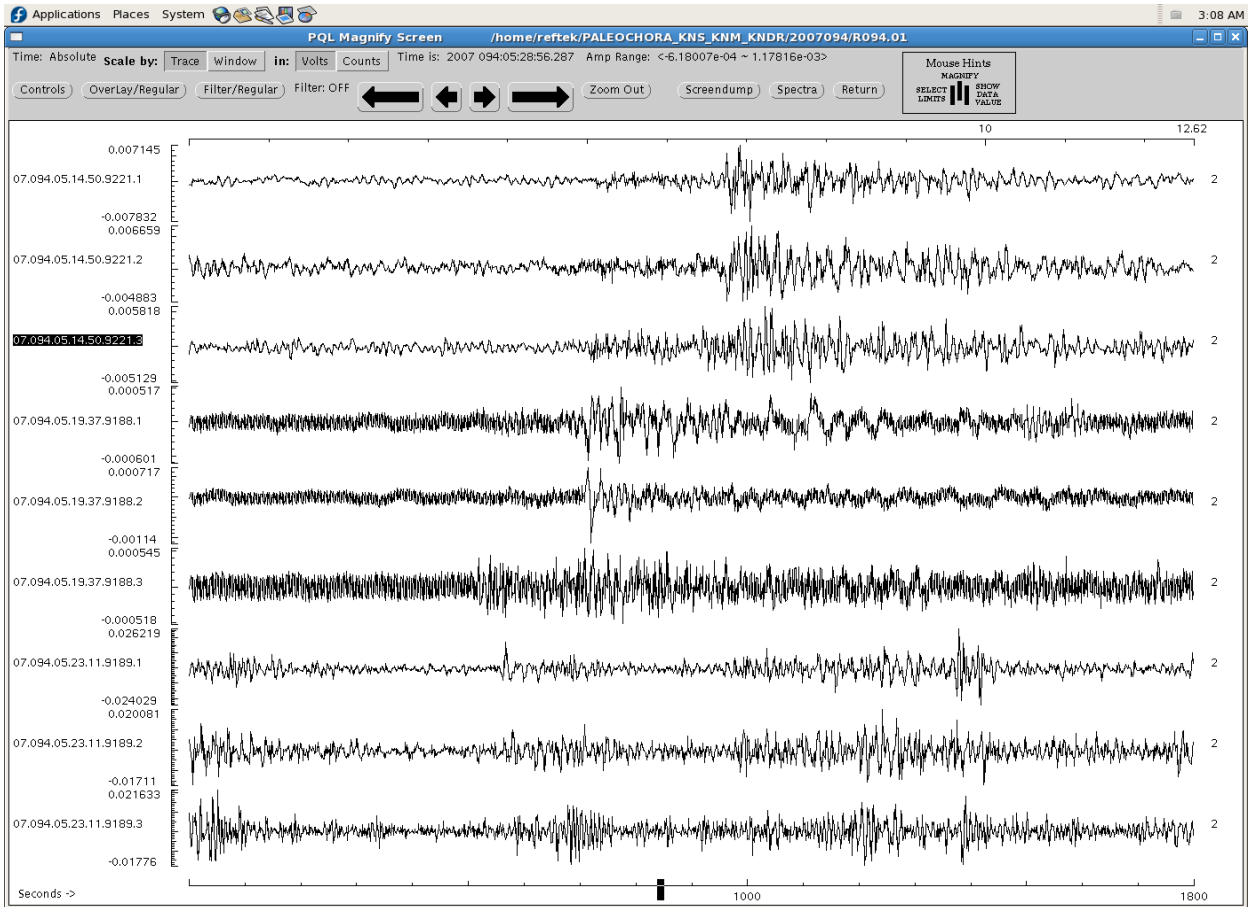


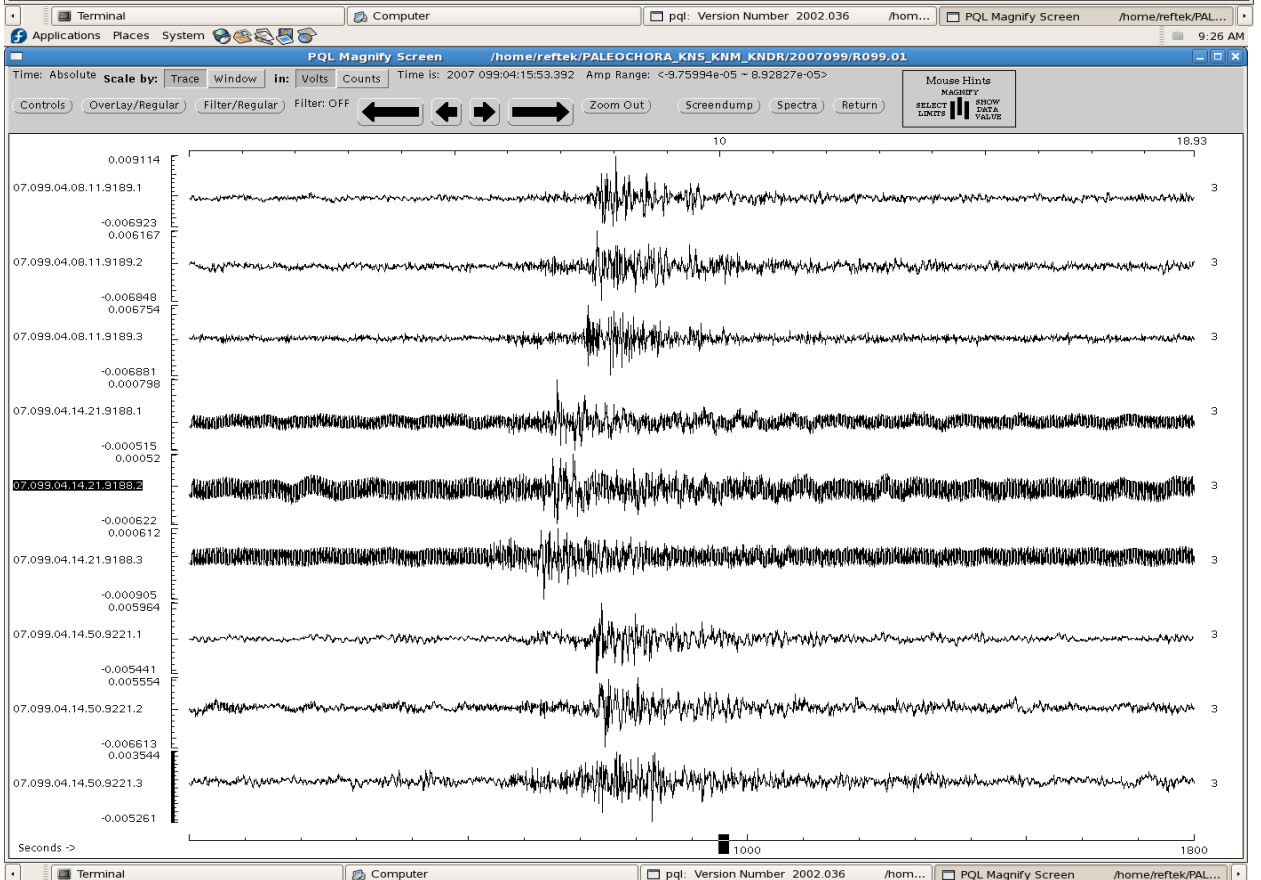
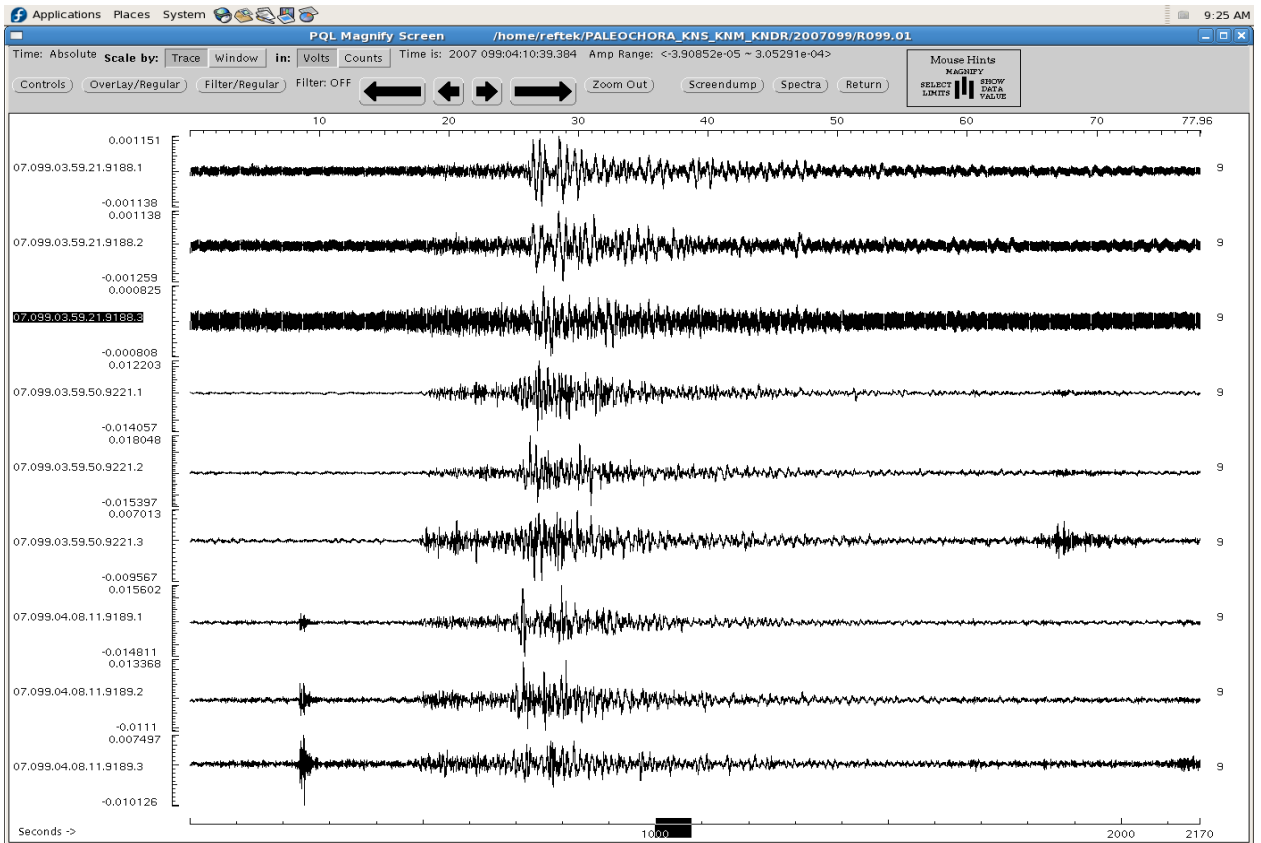




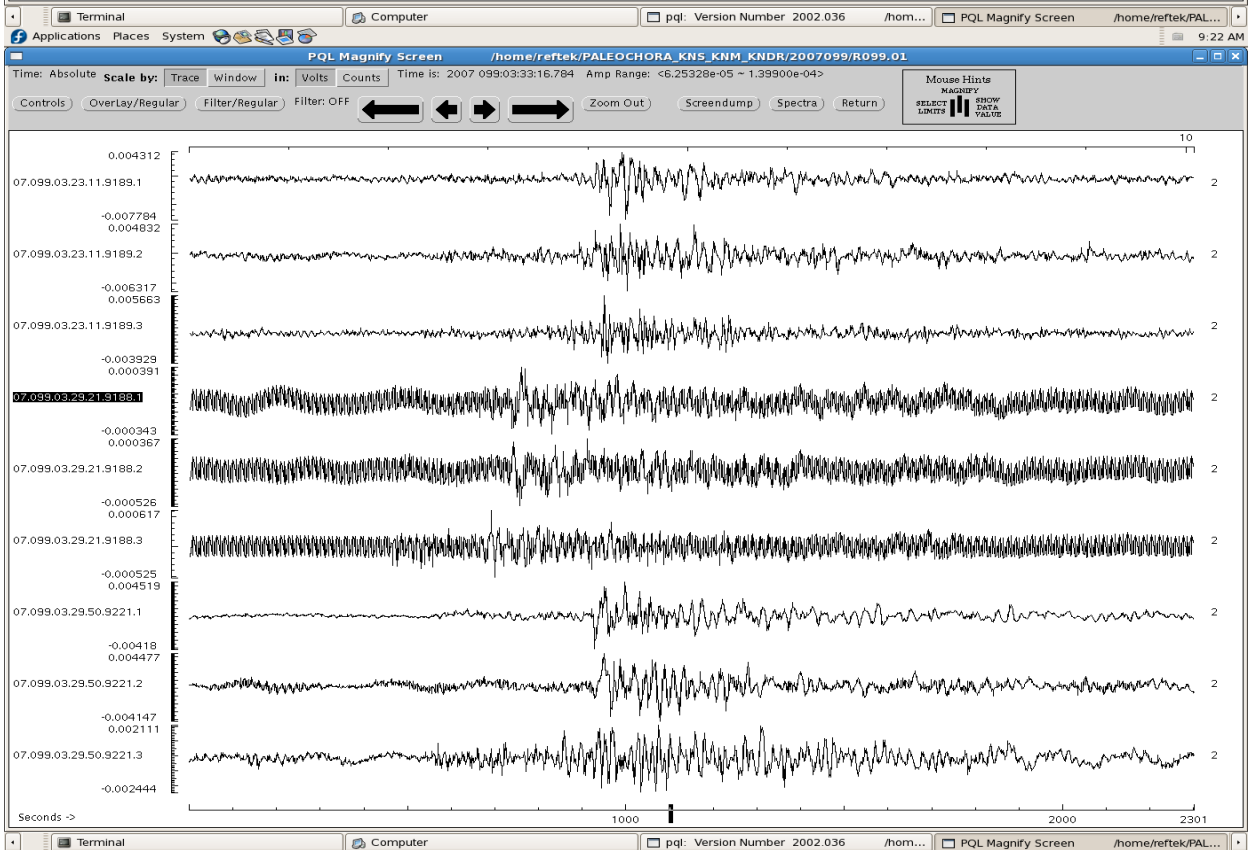
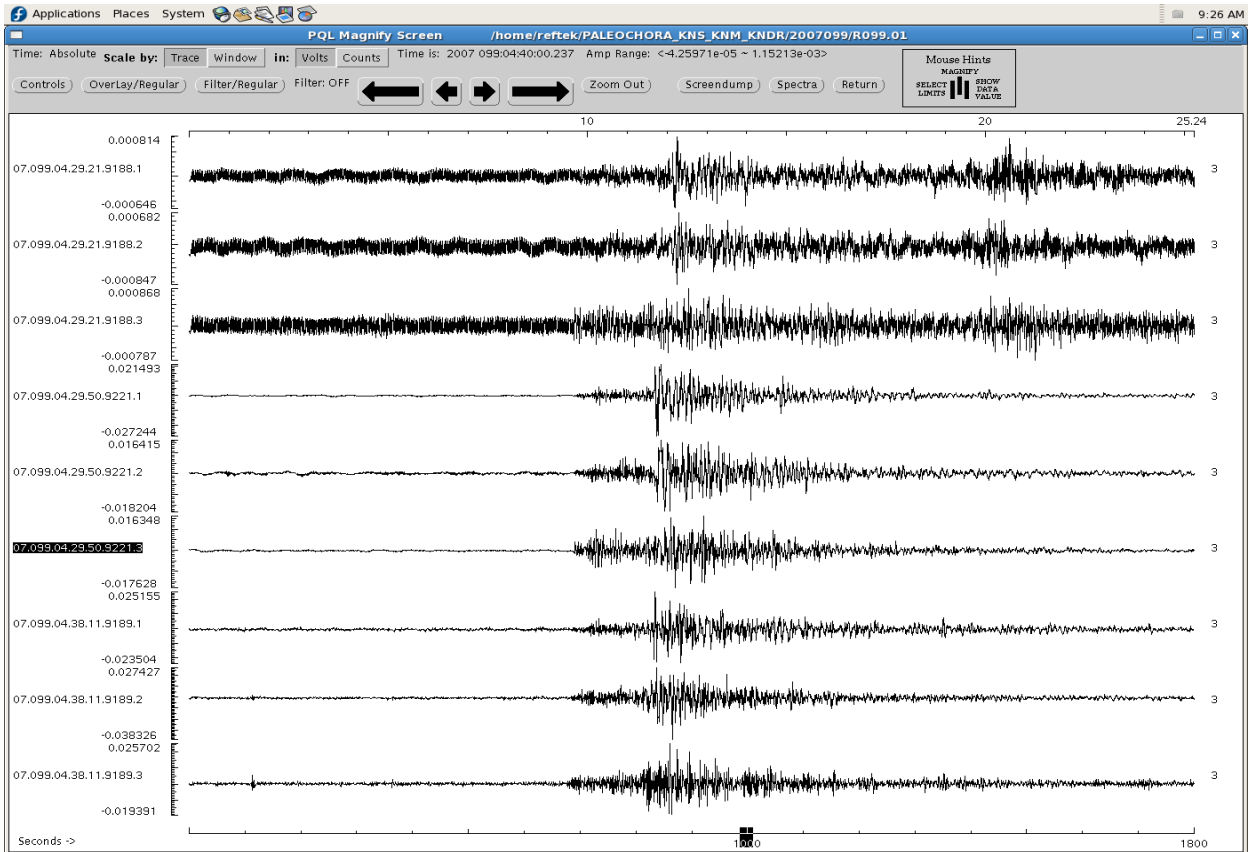


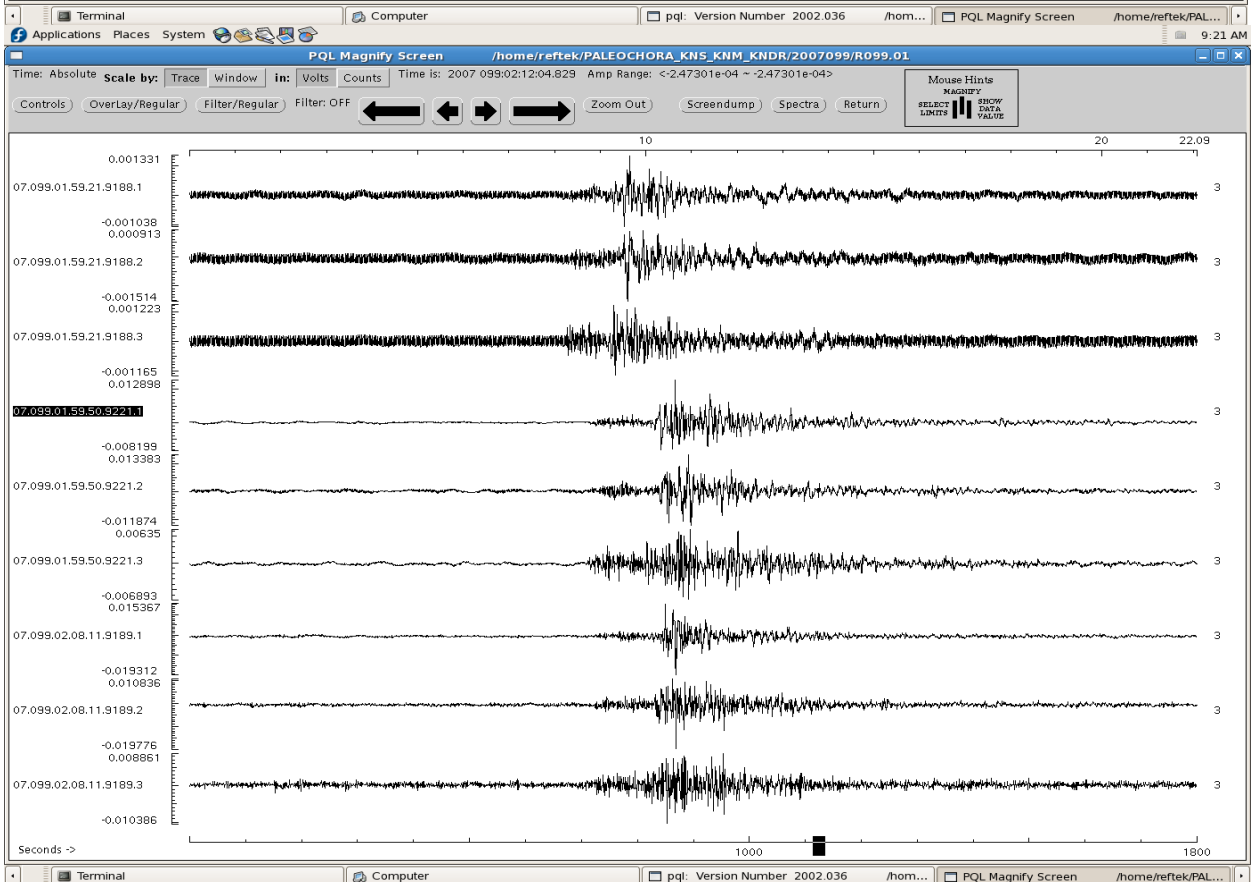
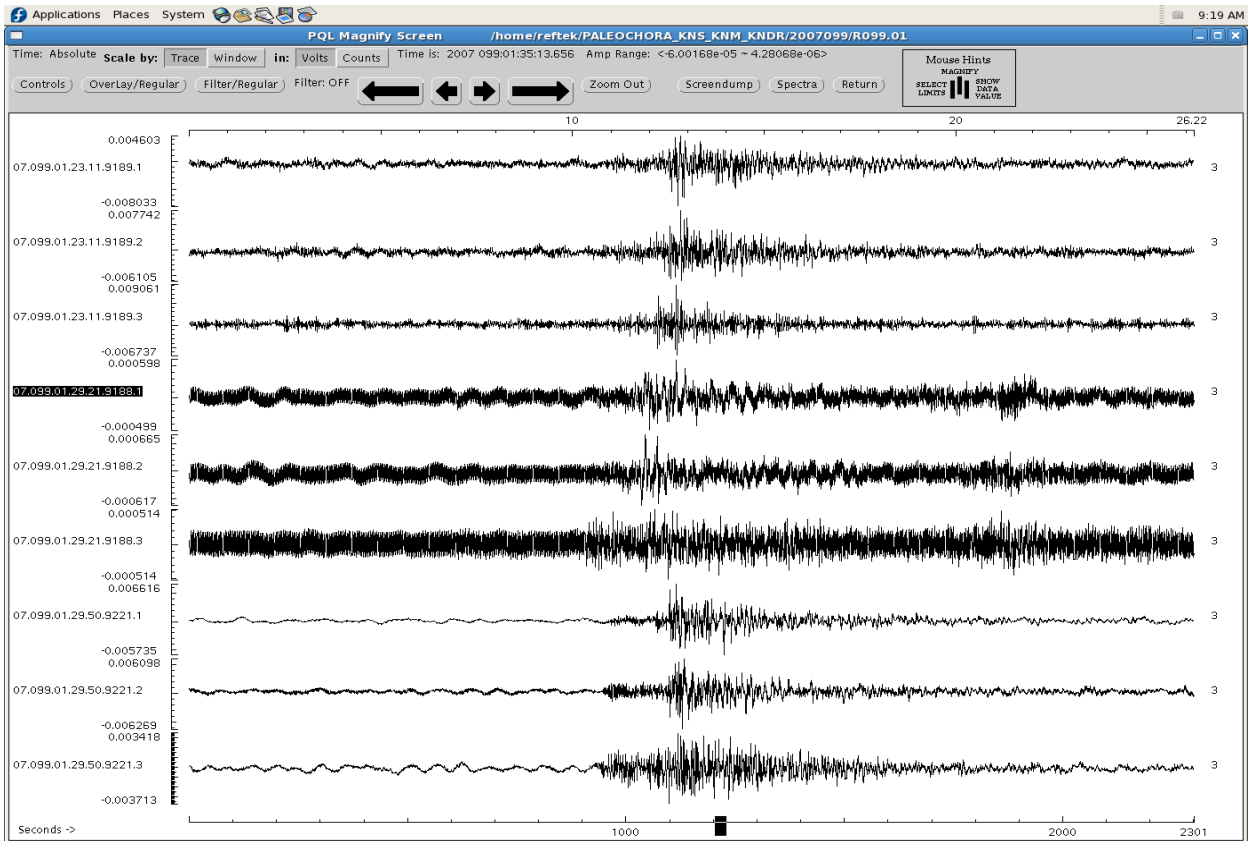


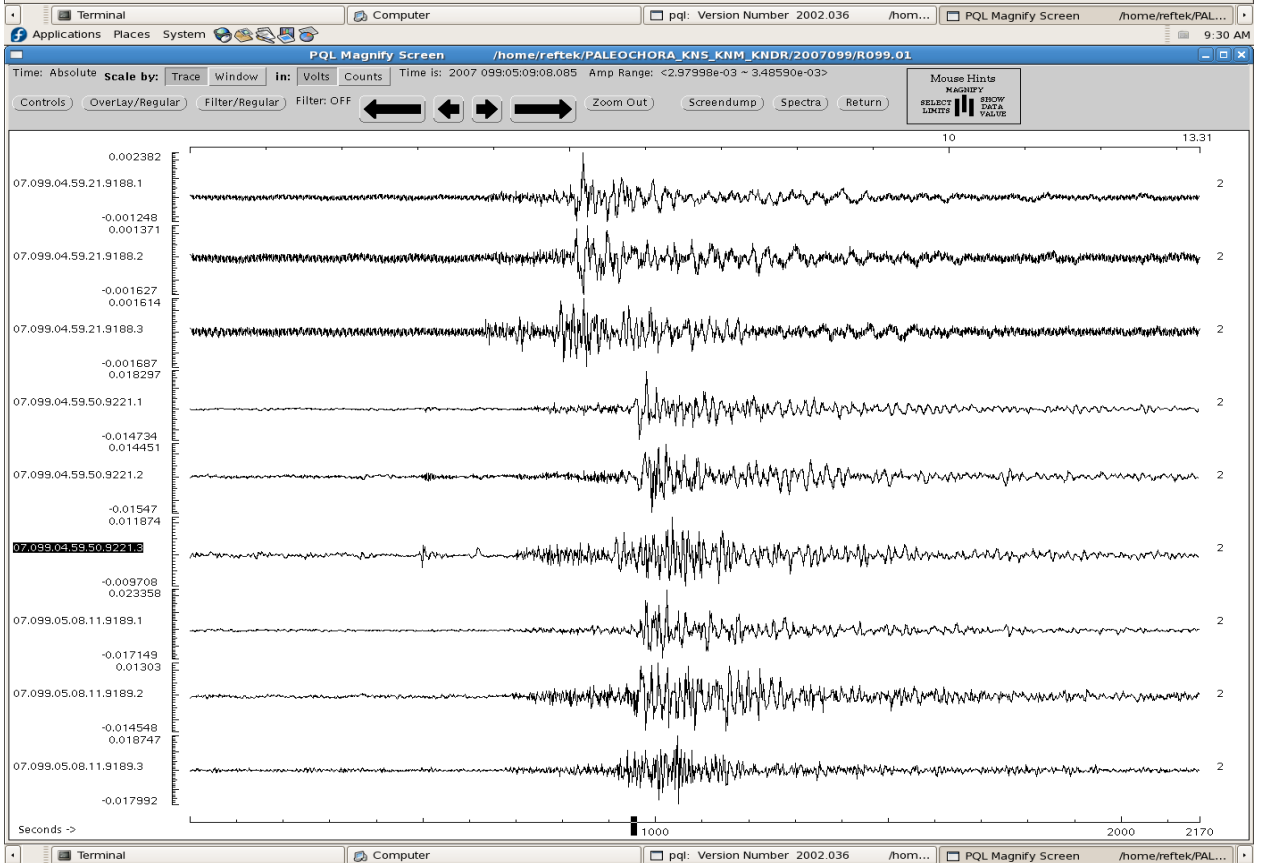
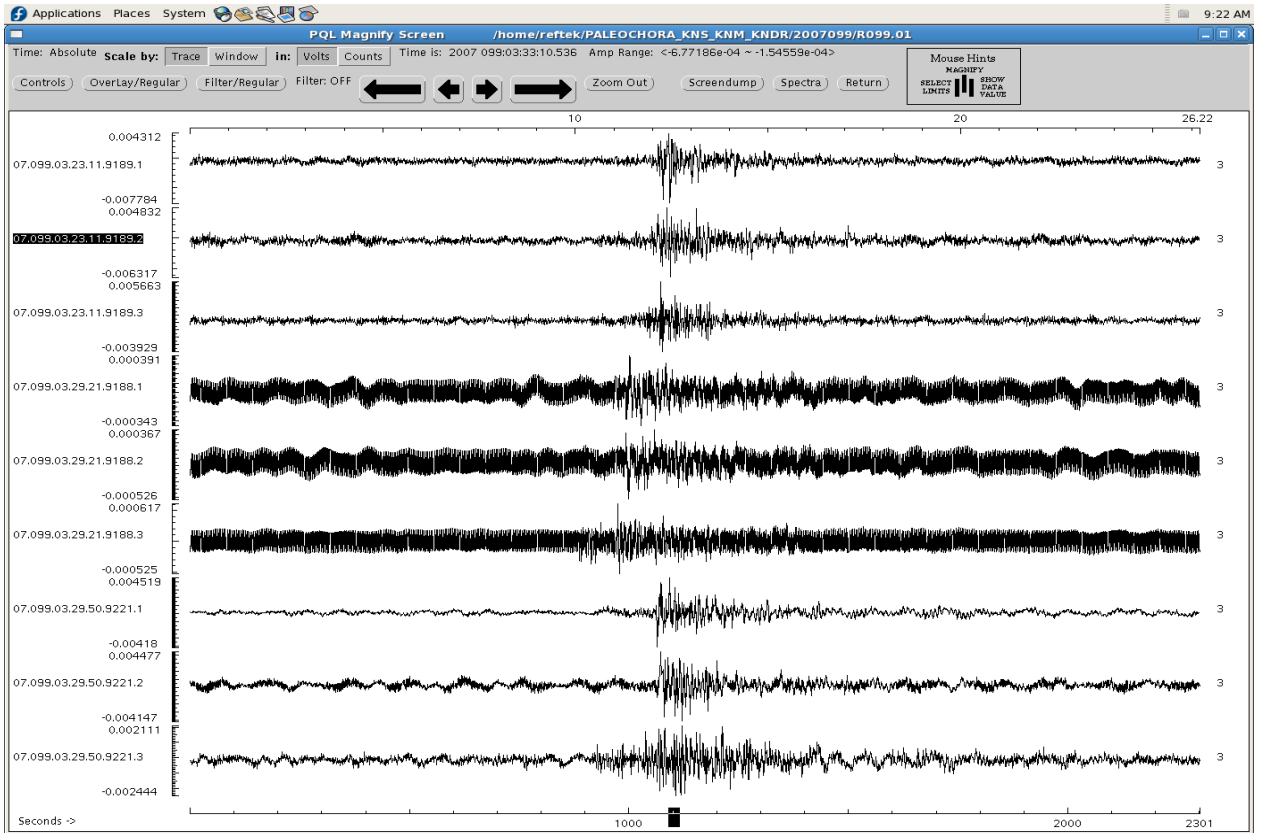


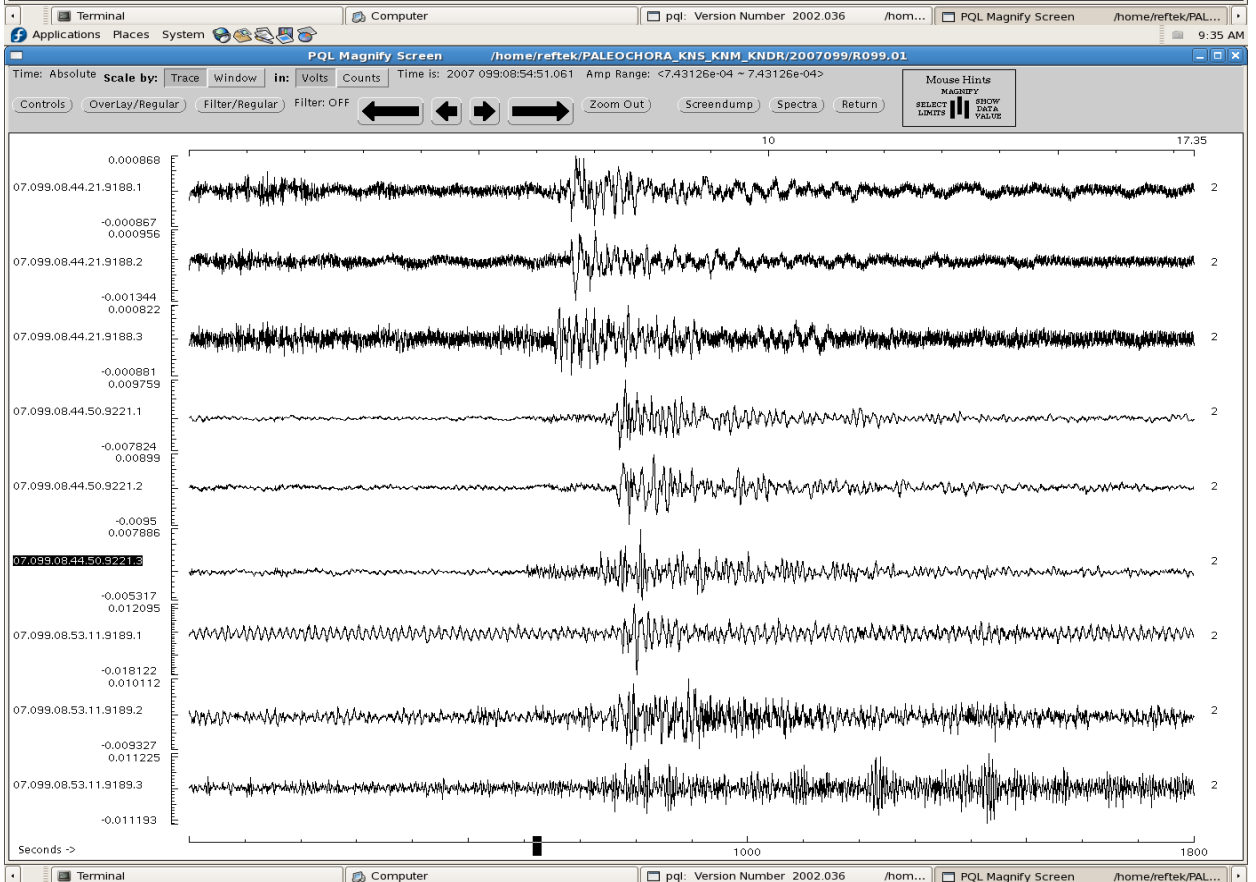
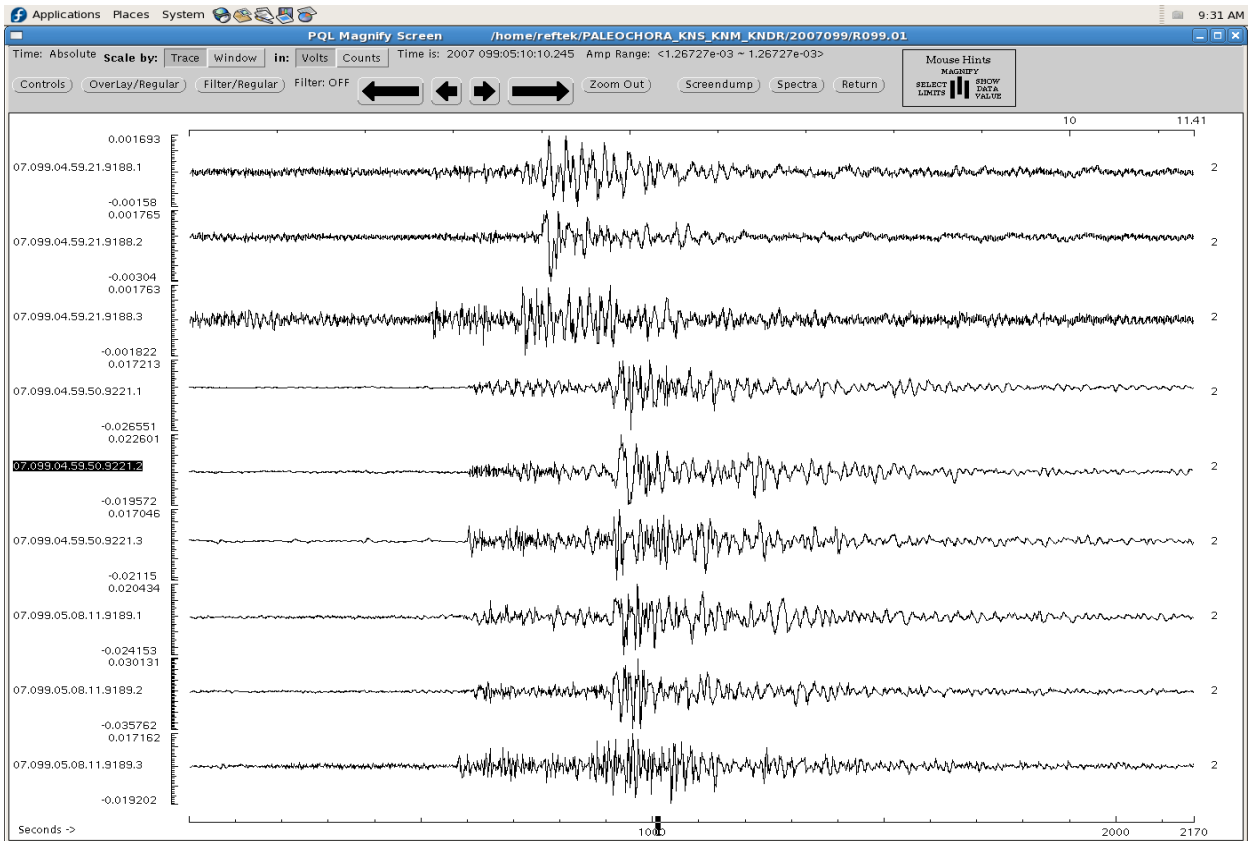


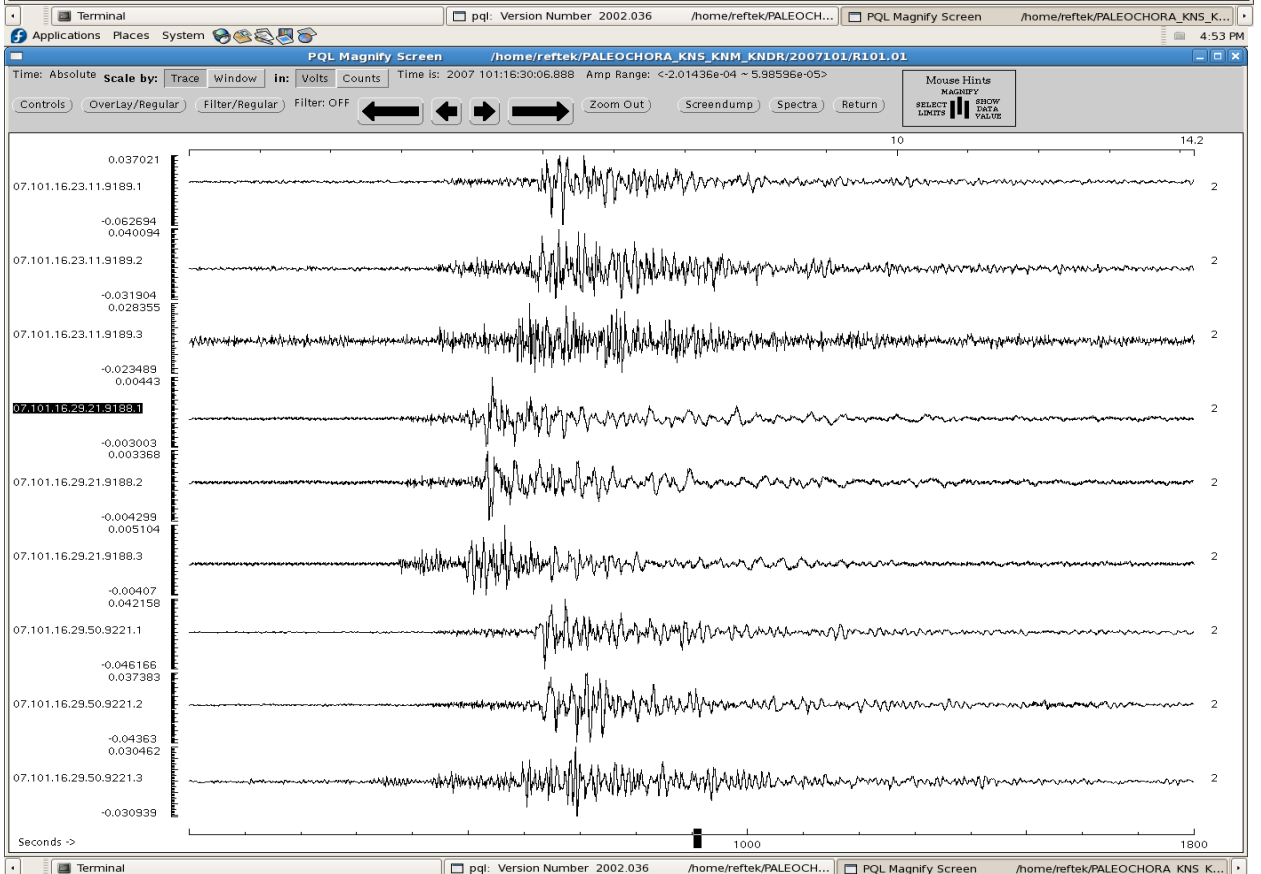
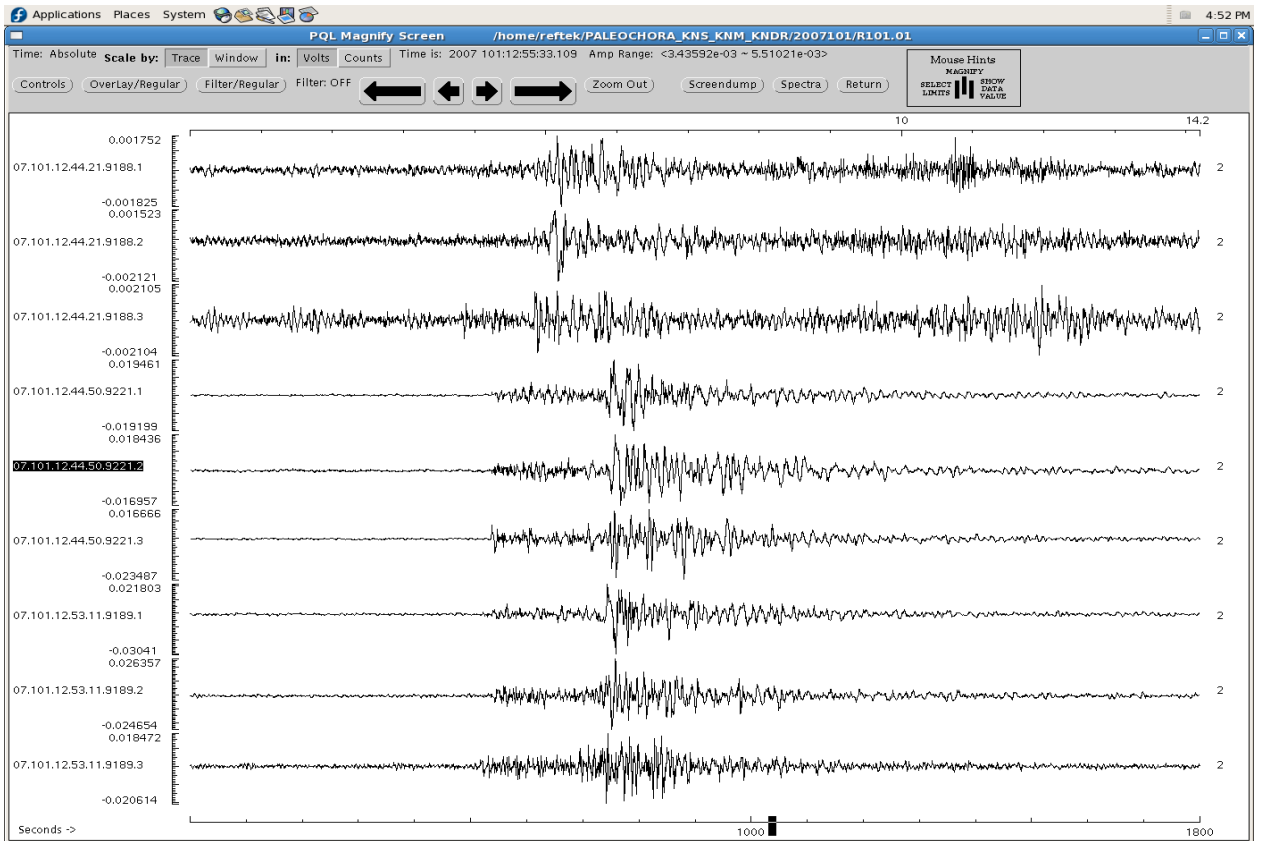


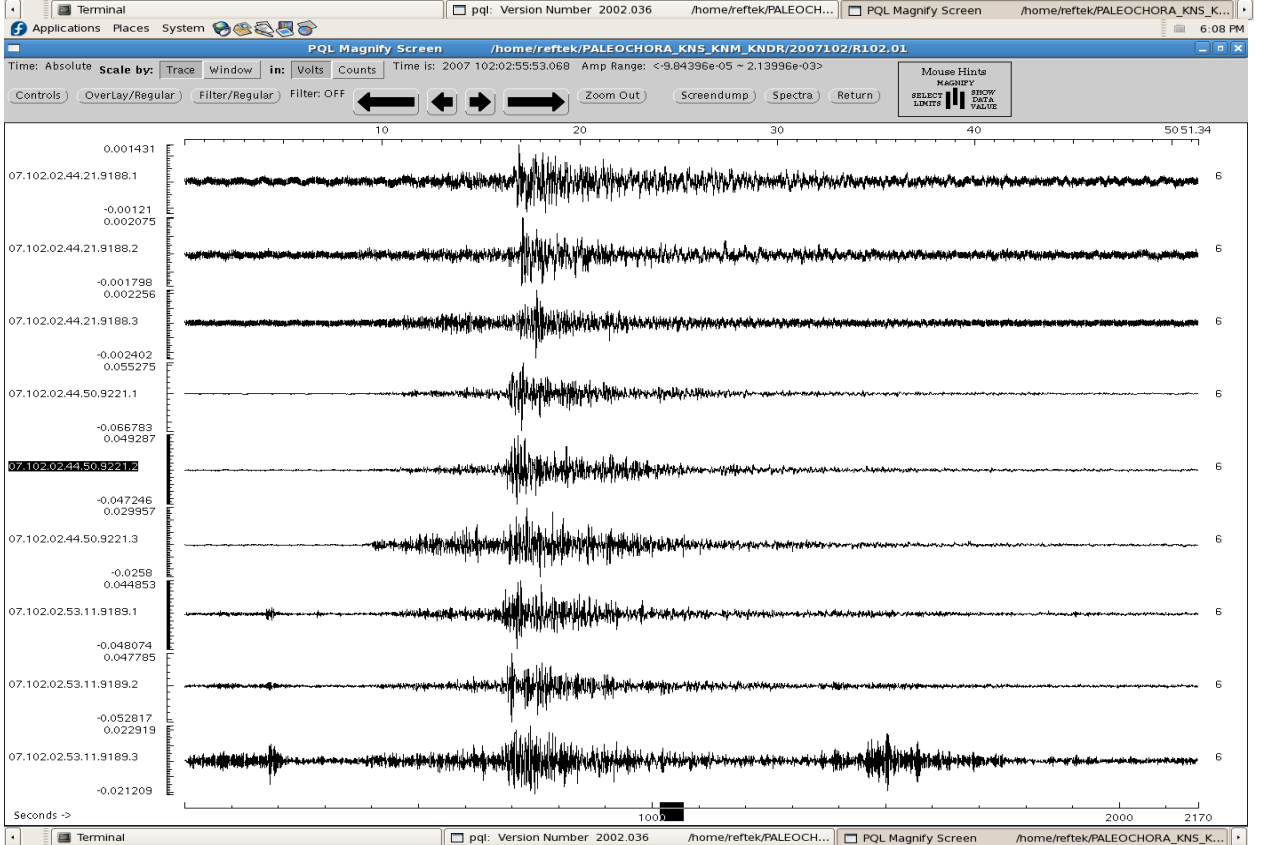
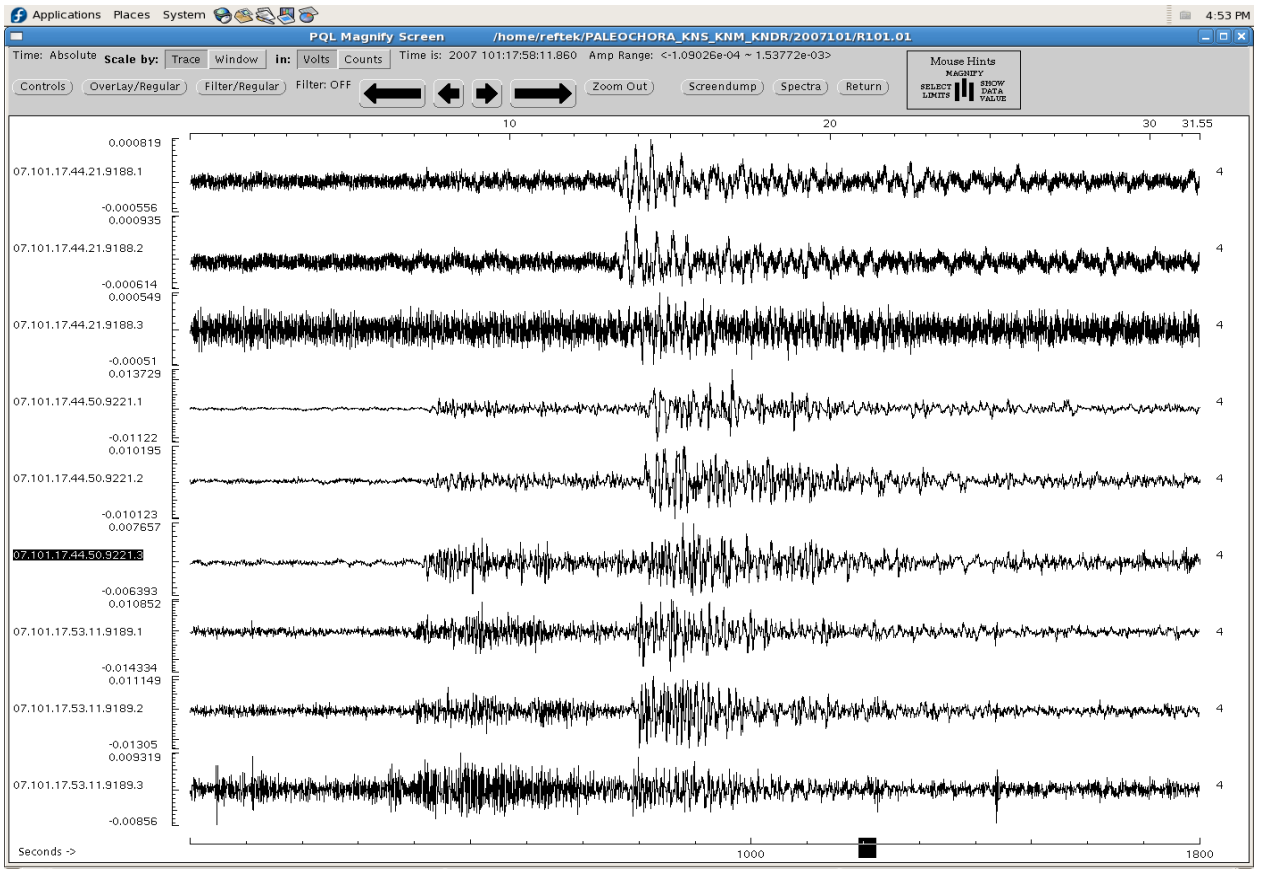


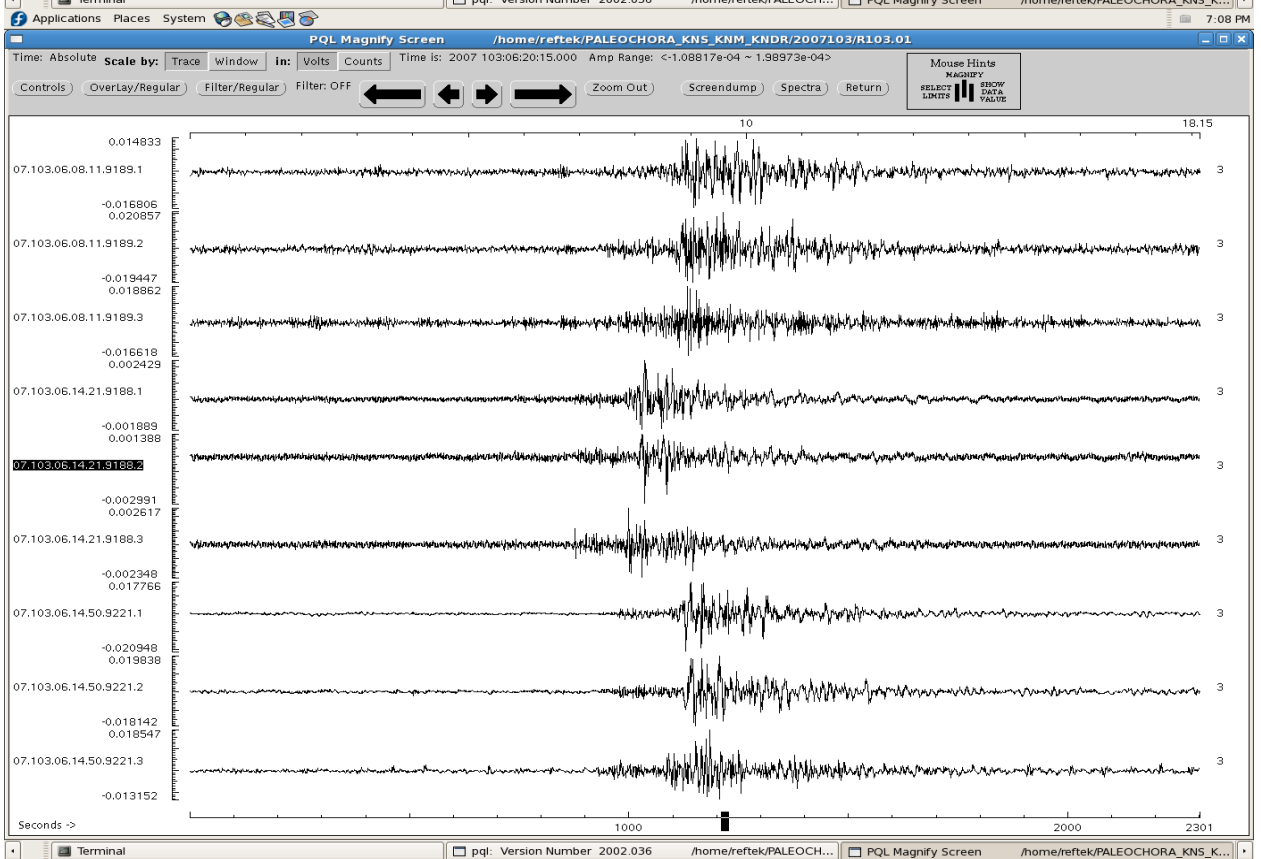
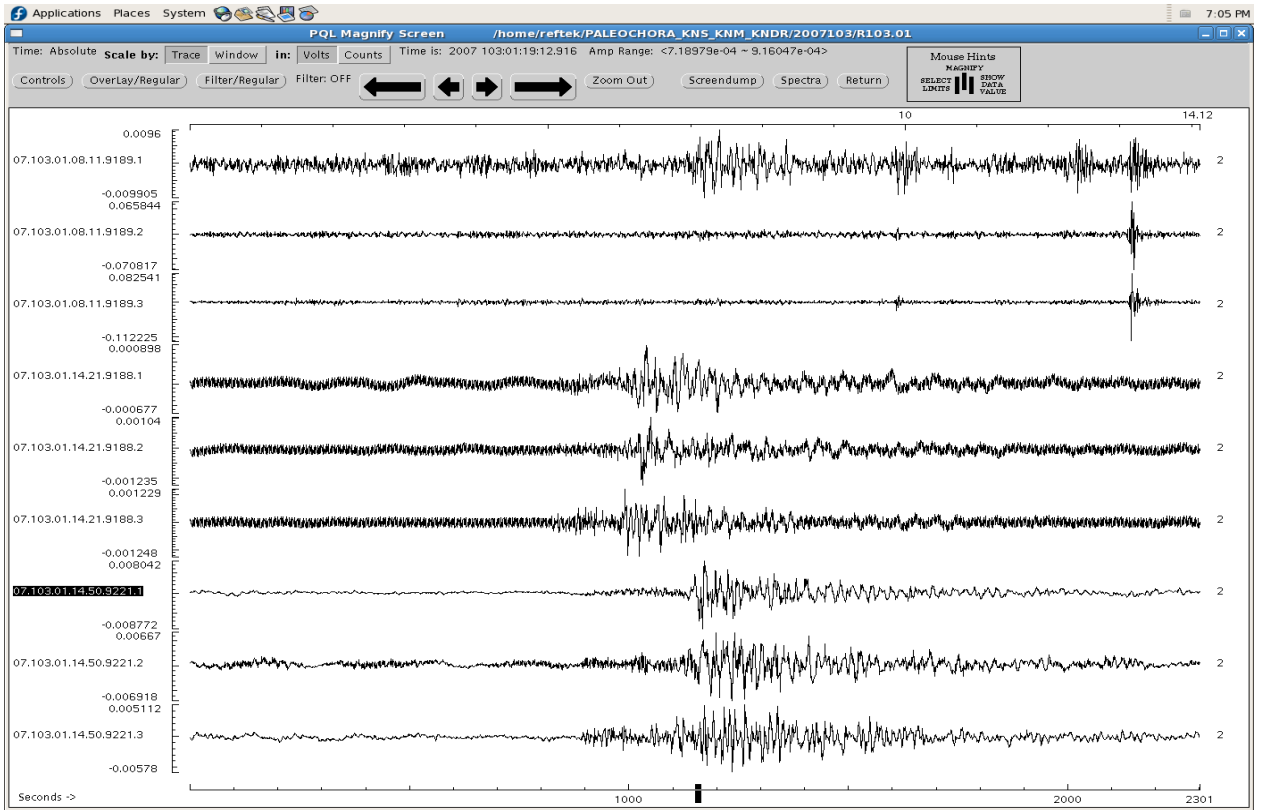


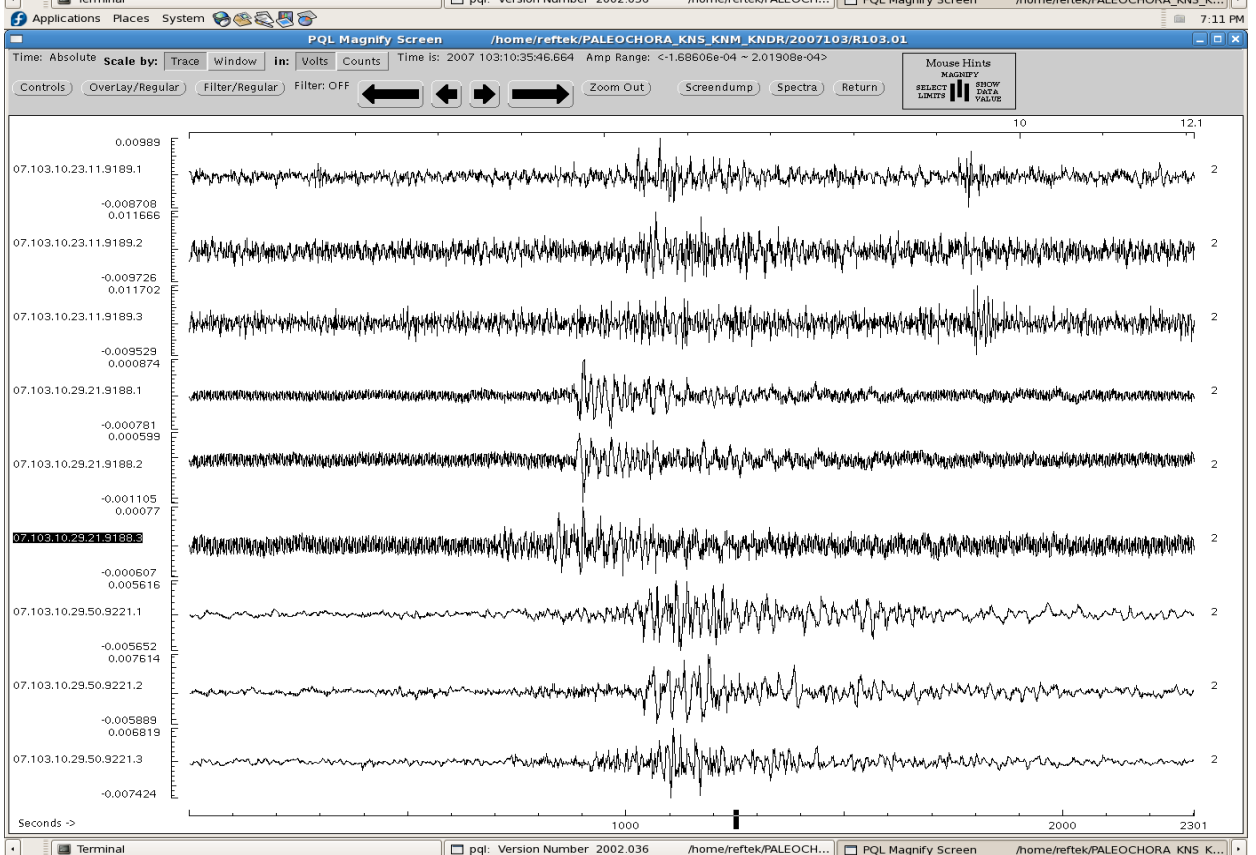
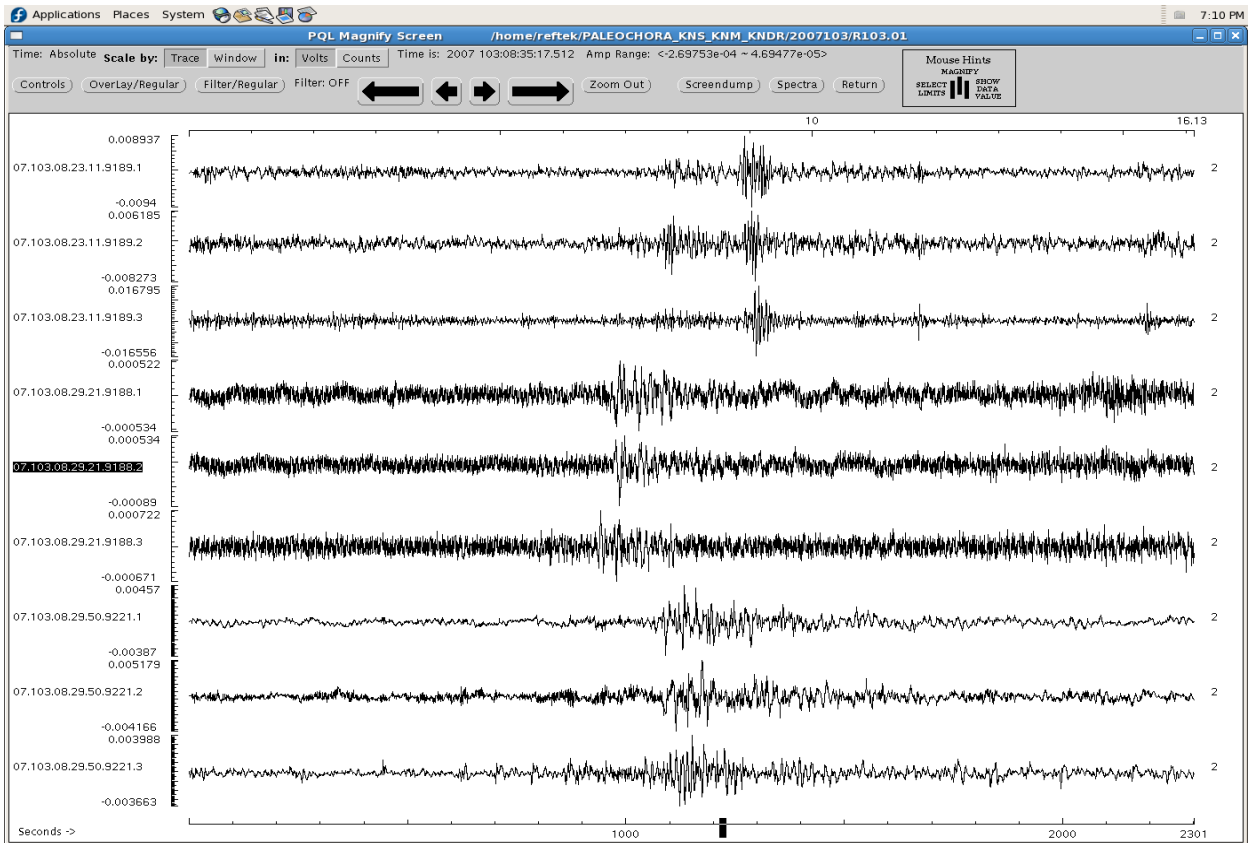




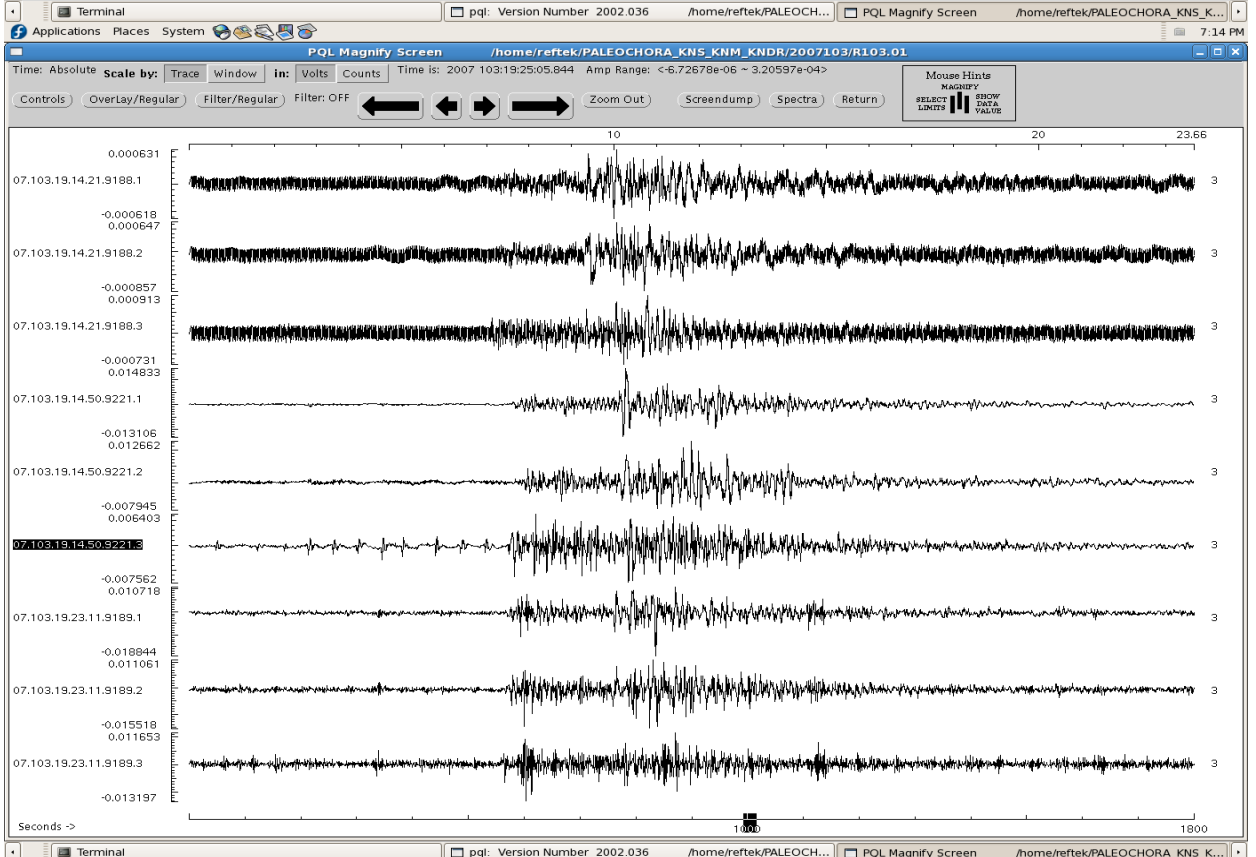
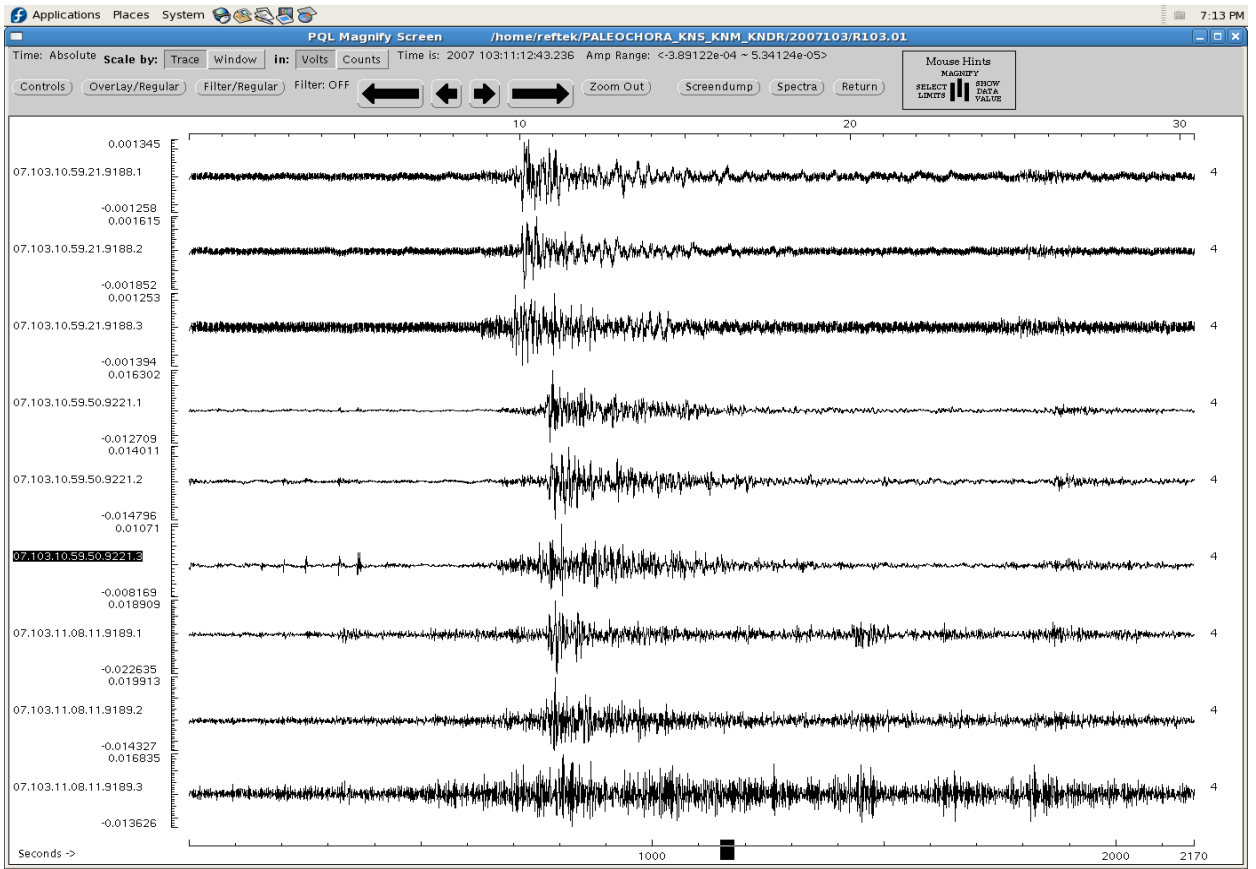


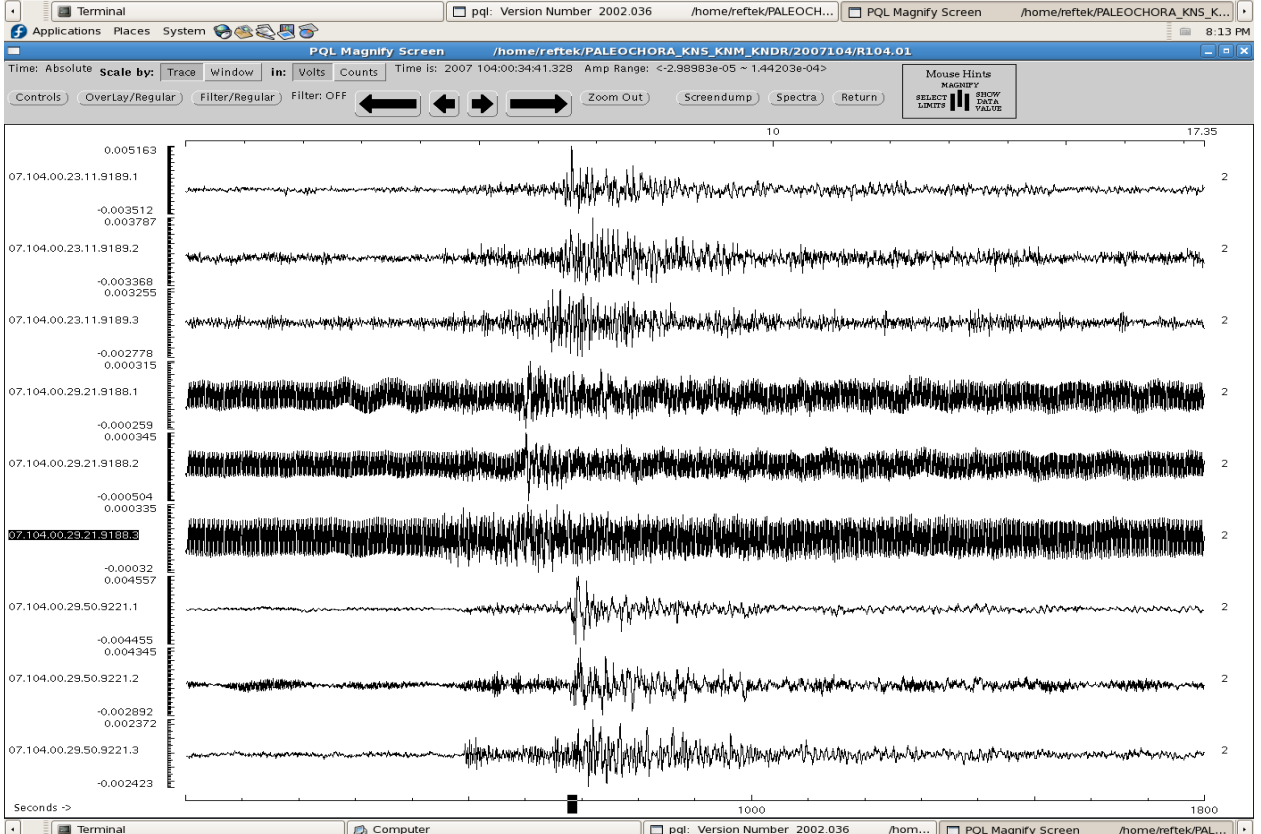
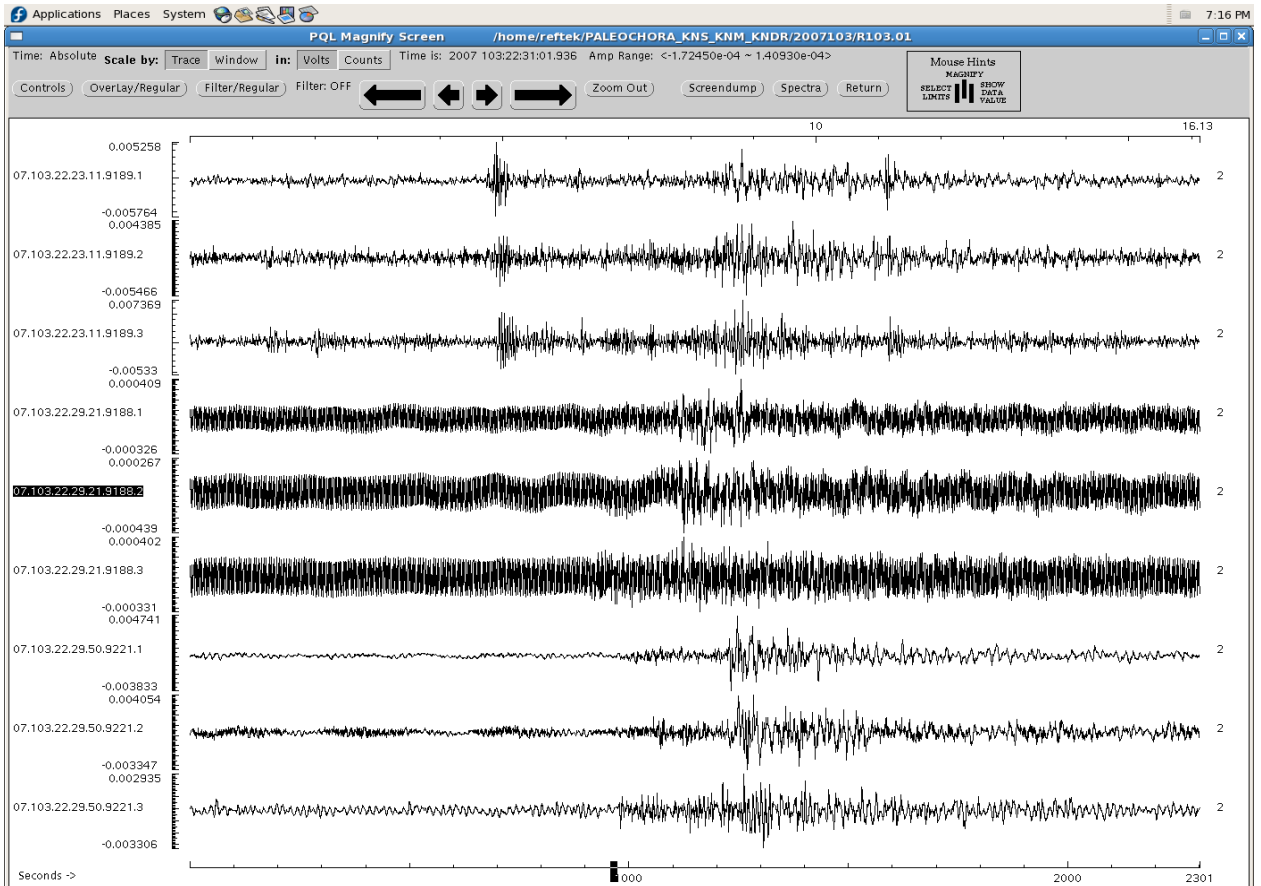


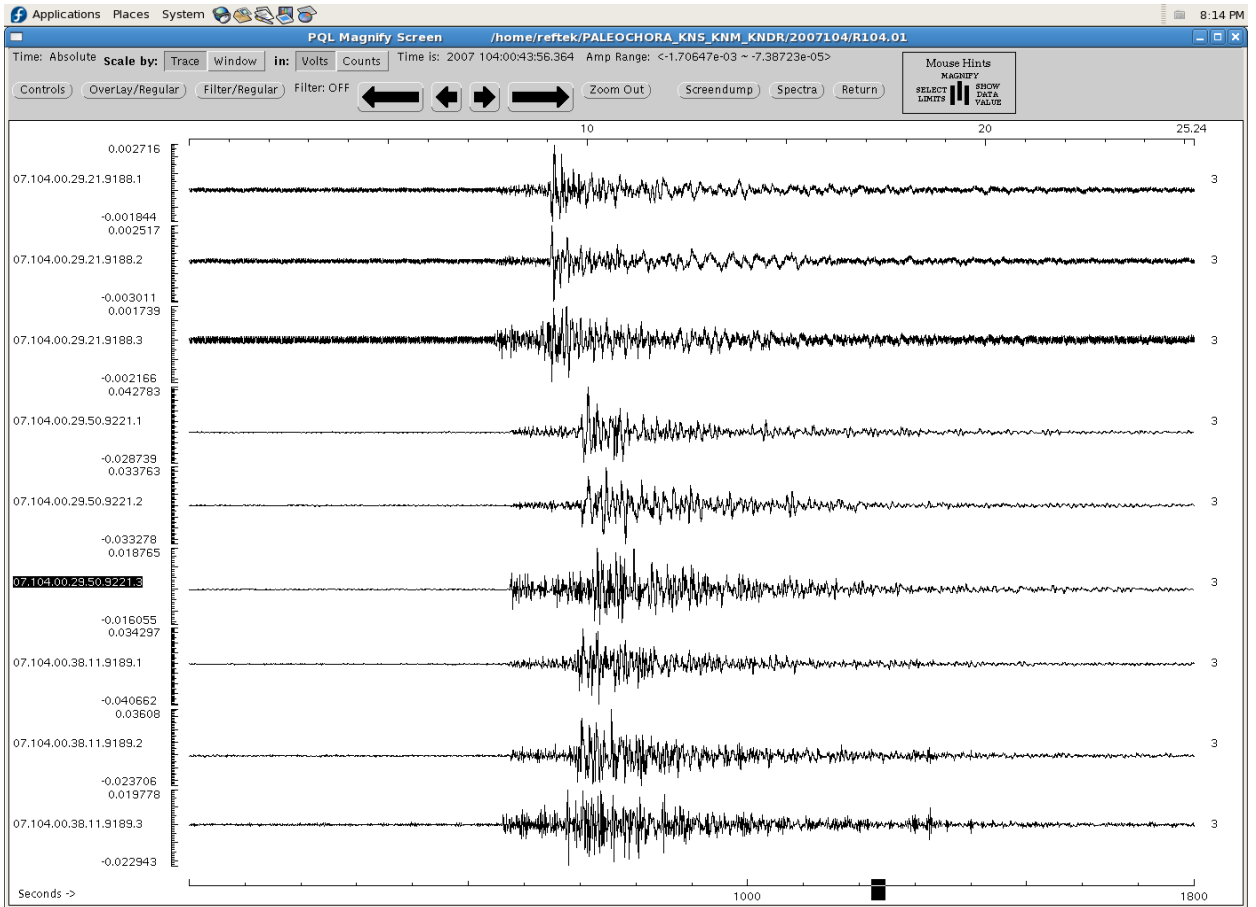




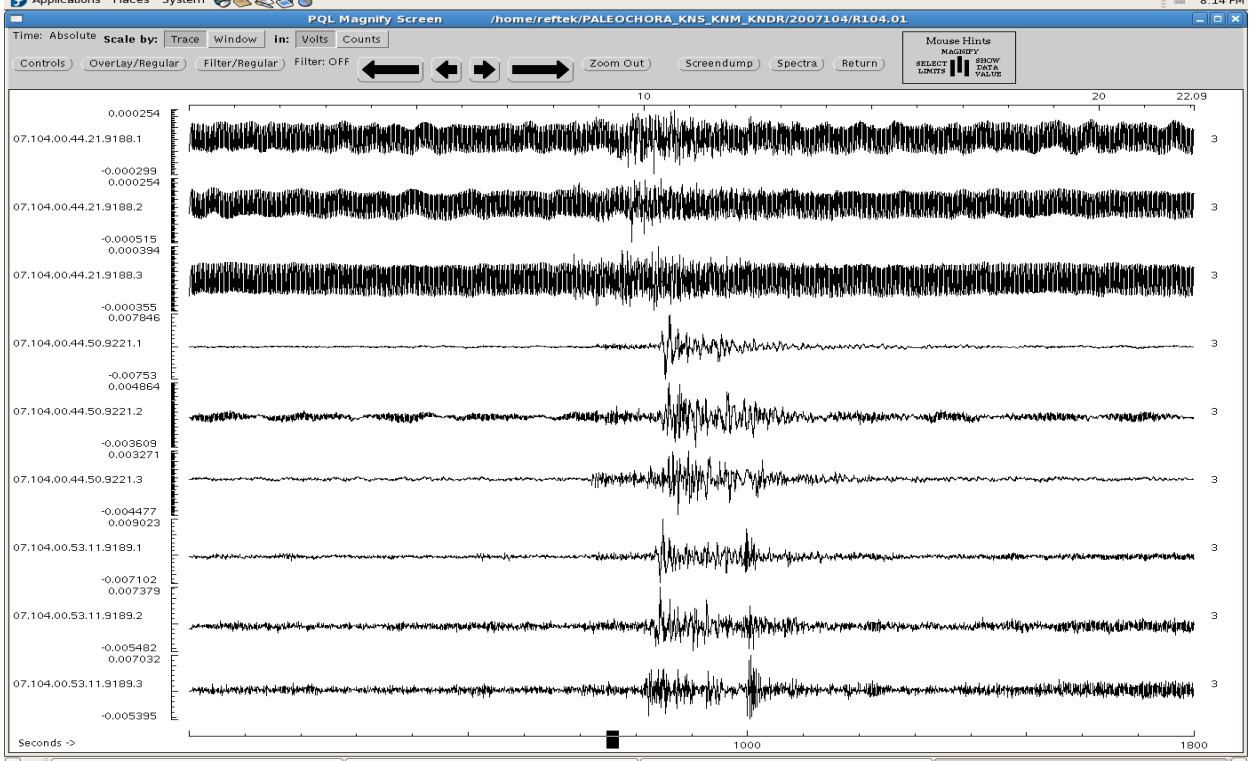




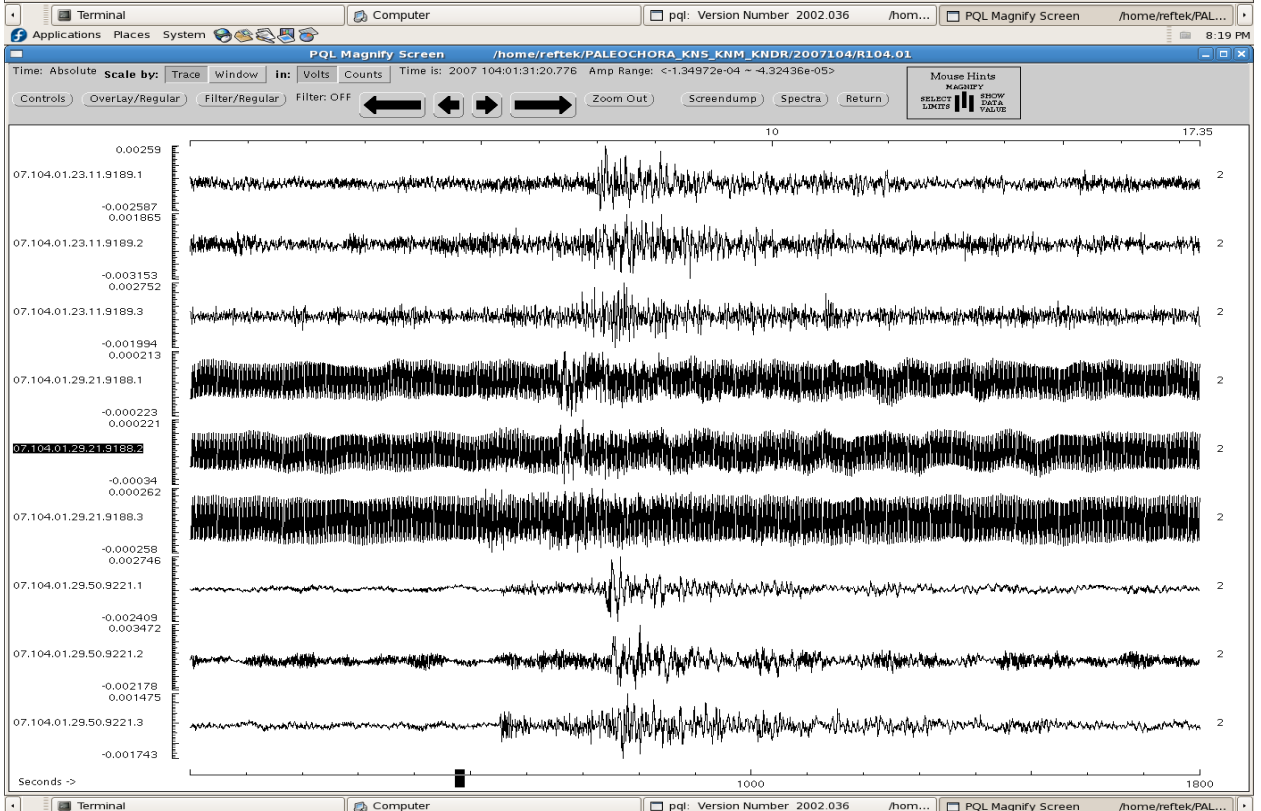
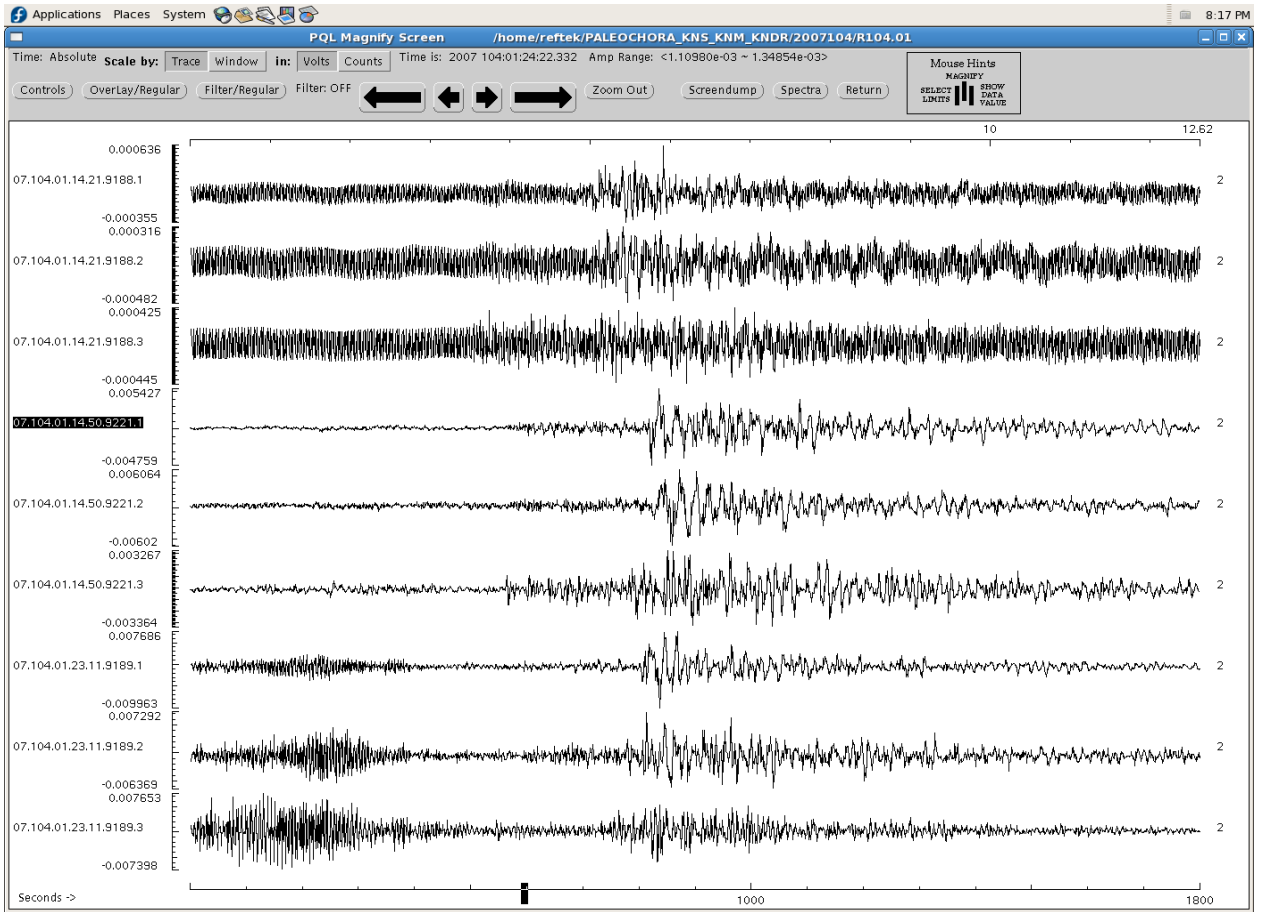


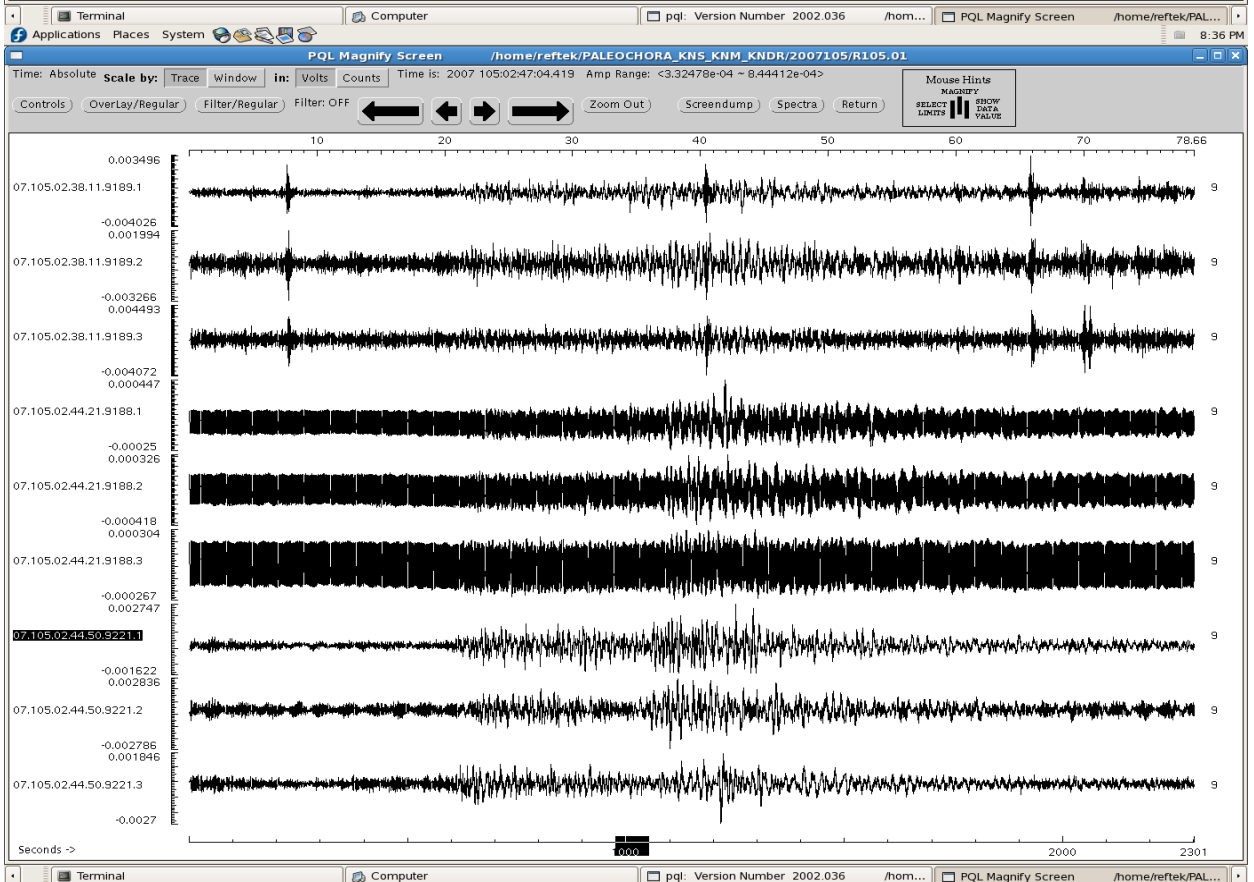
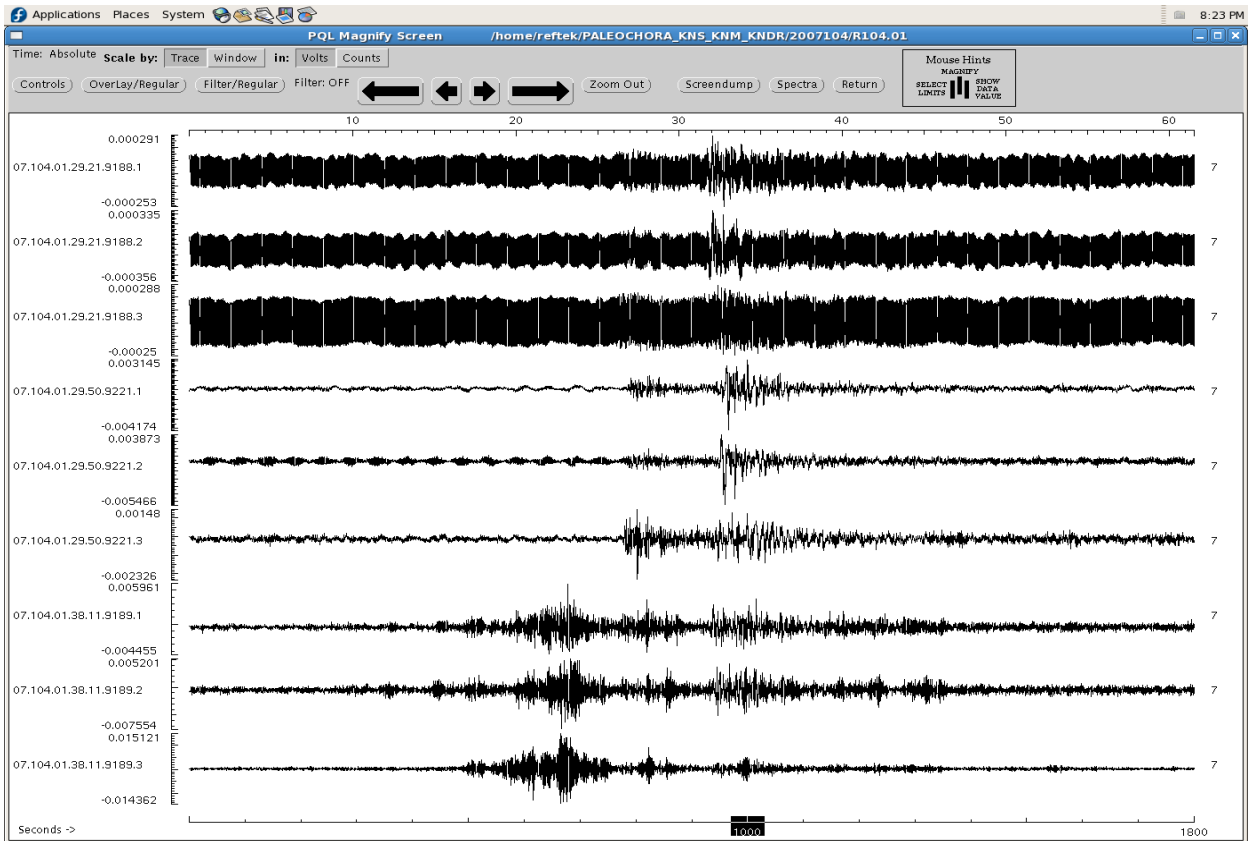


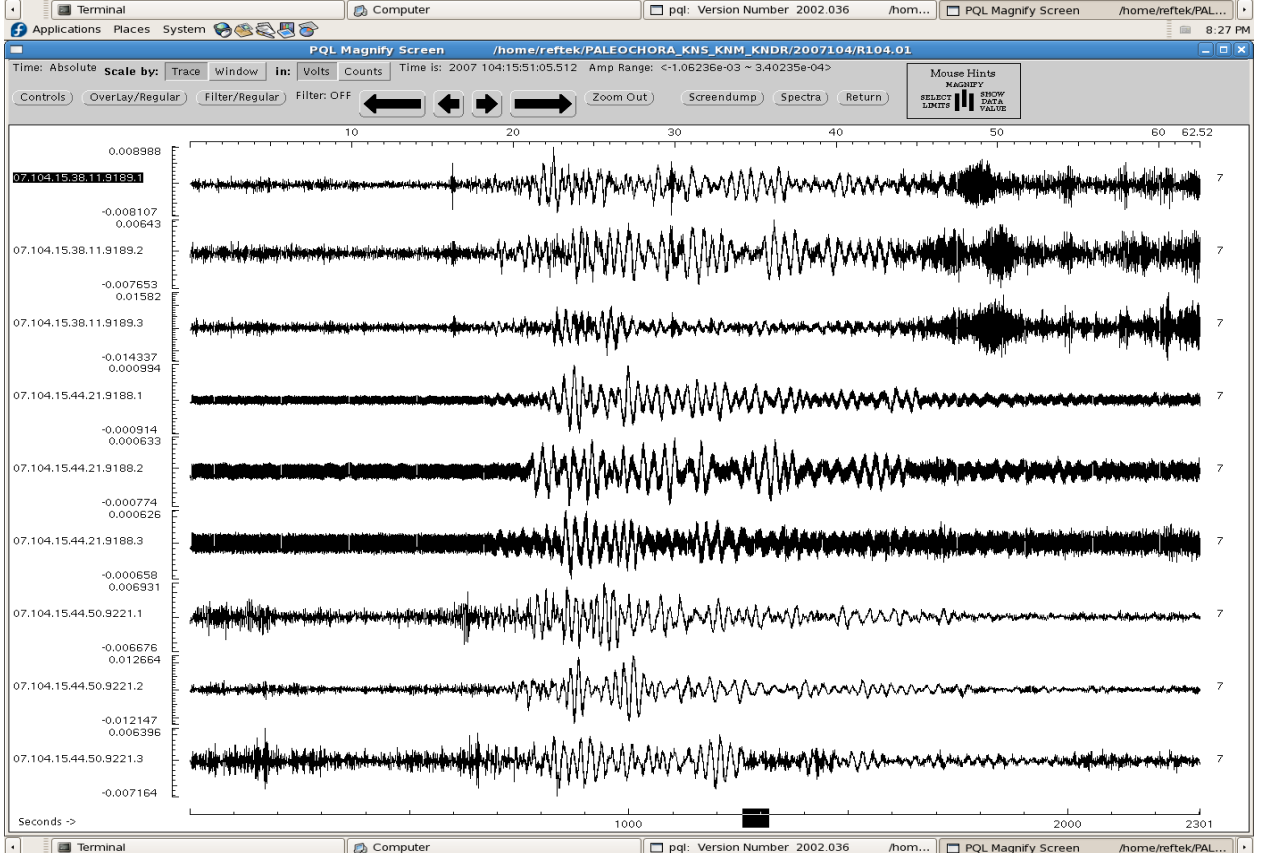
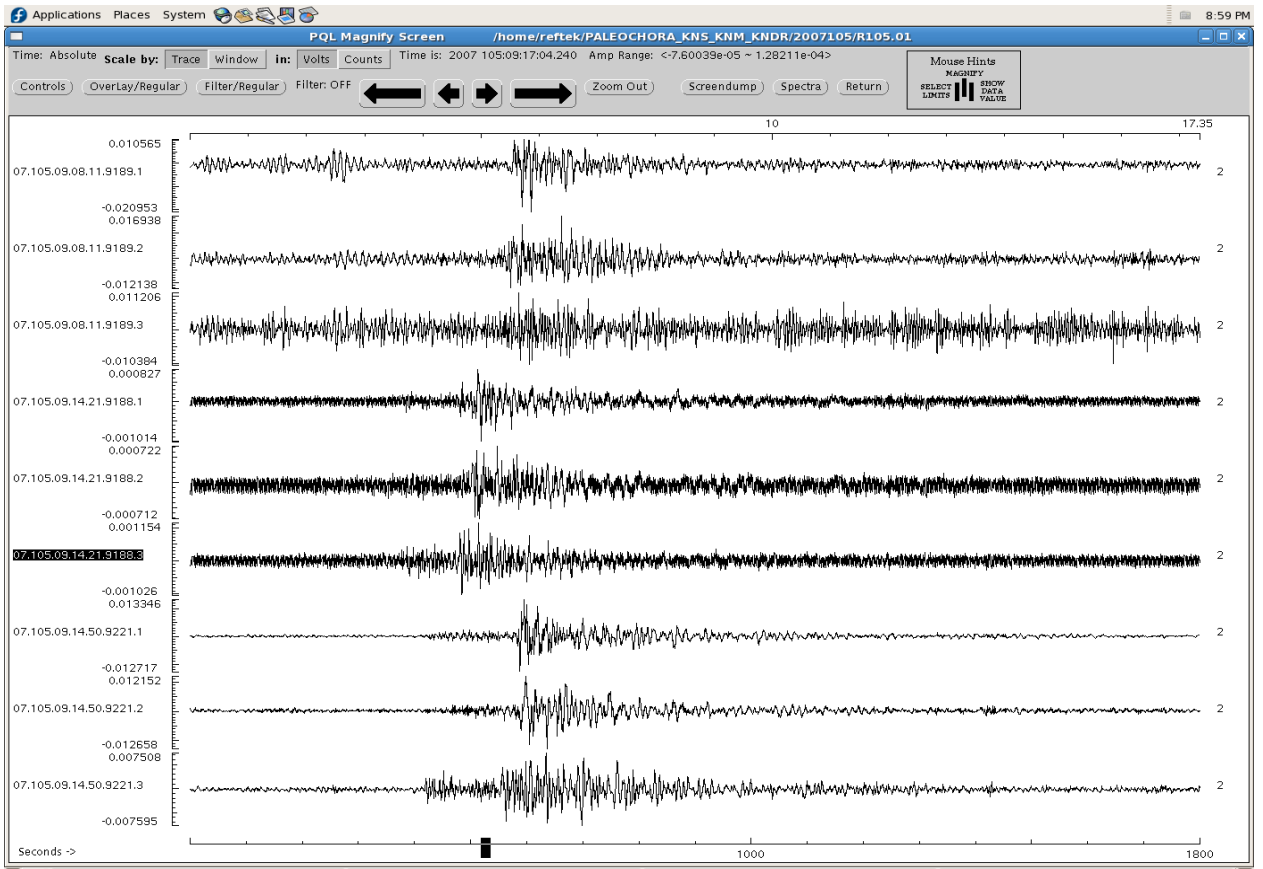
Terminal Computer pql: Version Number 2002.036 /hom... PQL Magnify Screen /home/reftek/PAL...

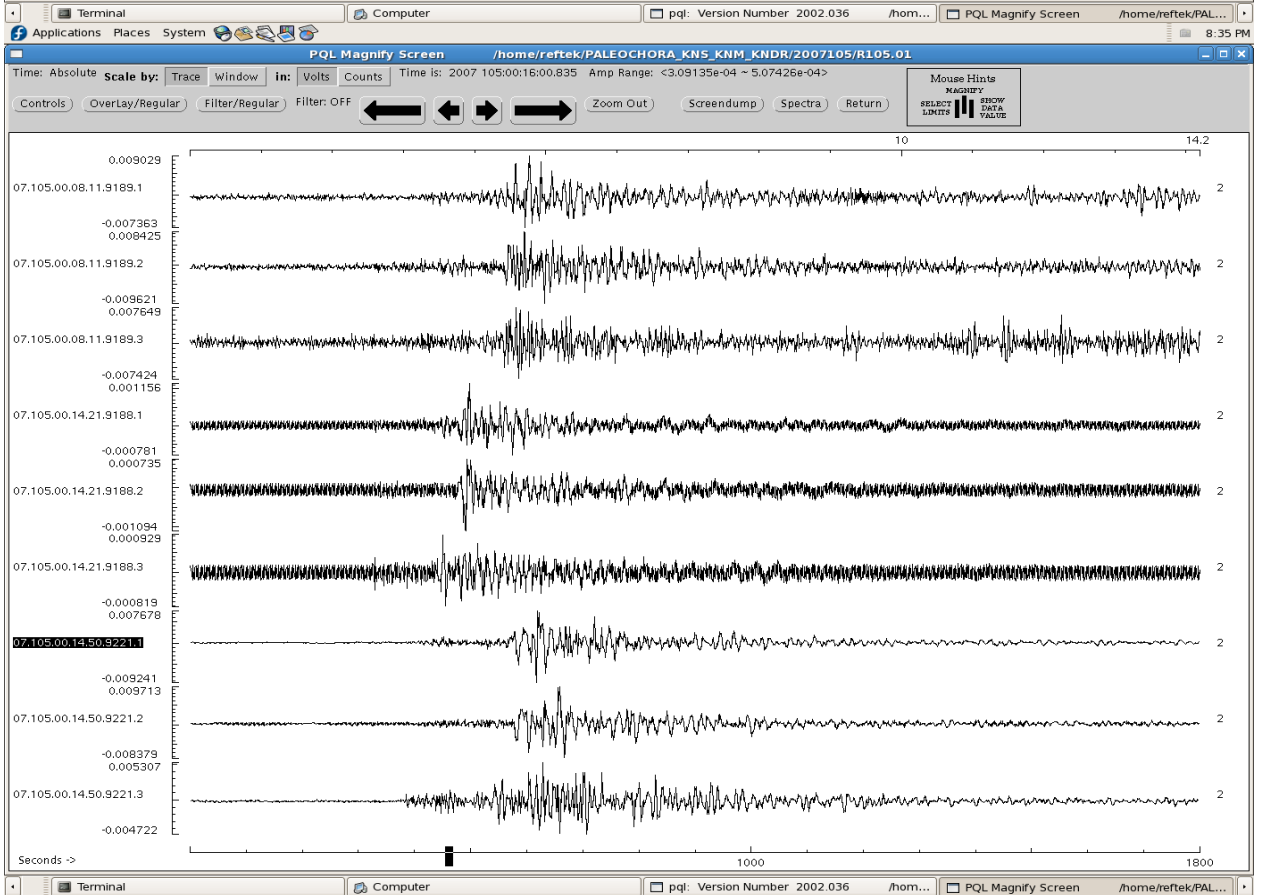
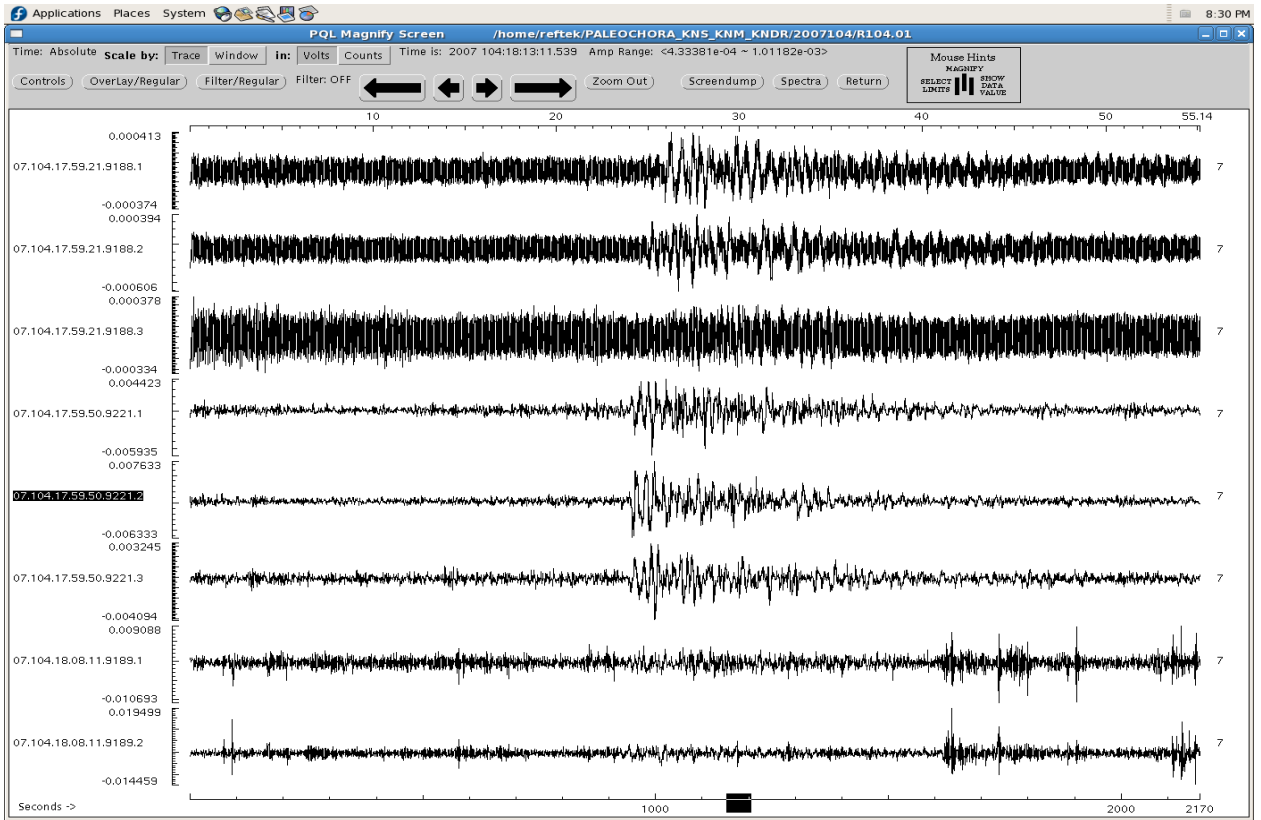


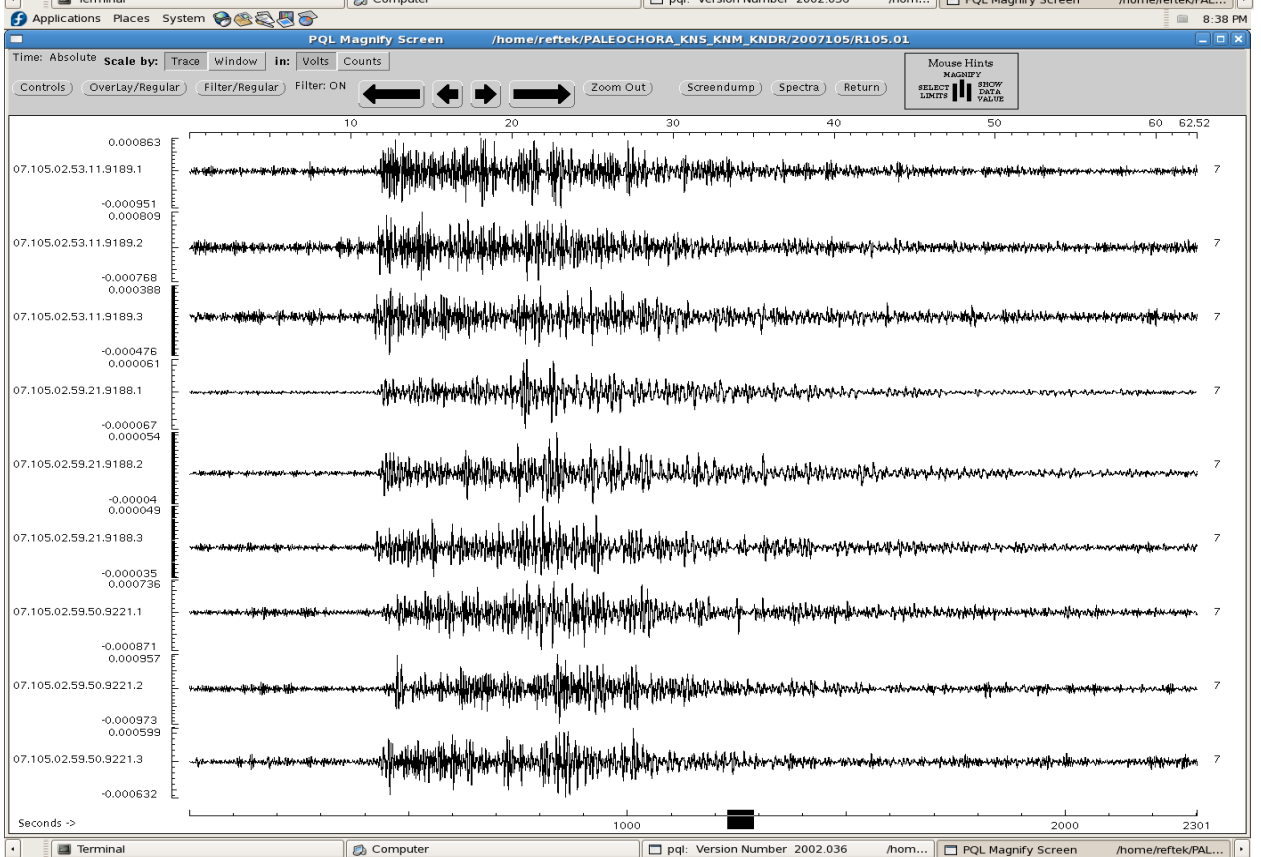
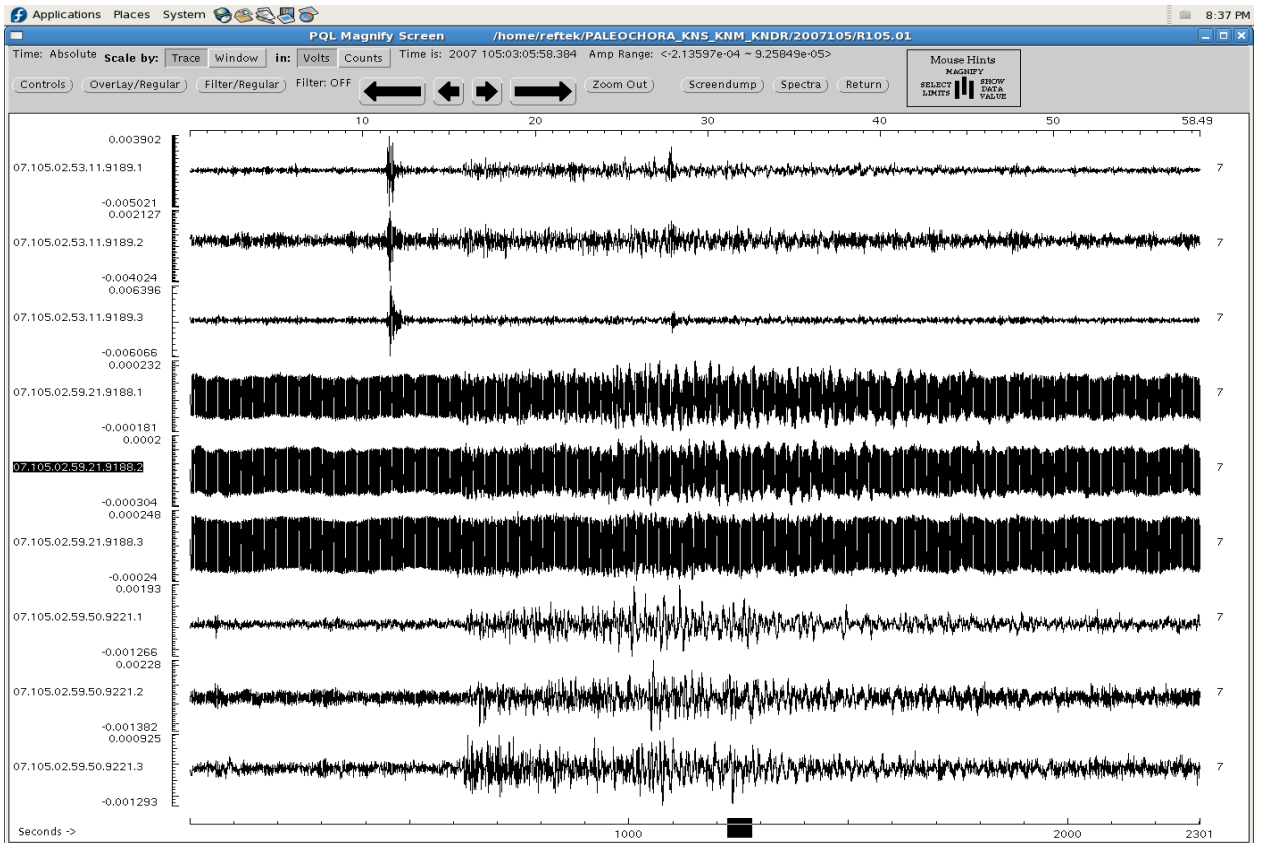
Terminal Computer pql: Version Number 2002.036 /hom... PQL Magnify Screen /home/reftek/PAL...



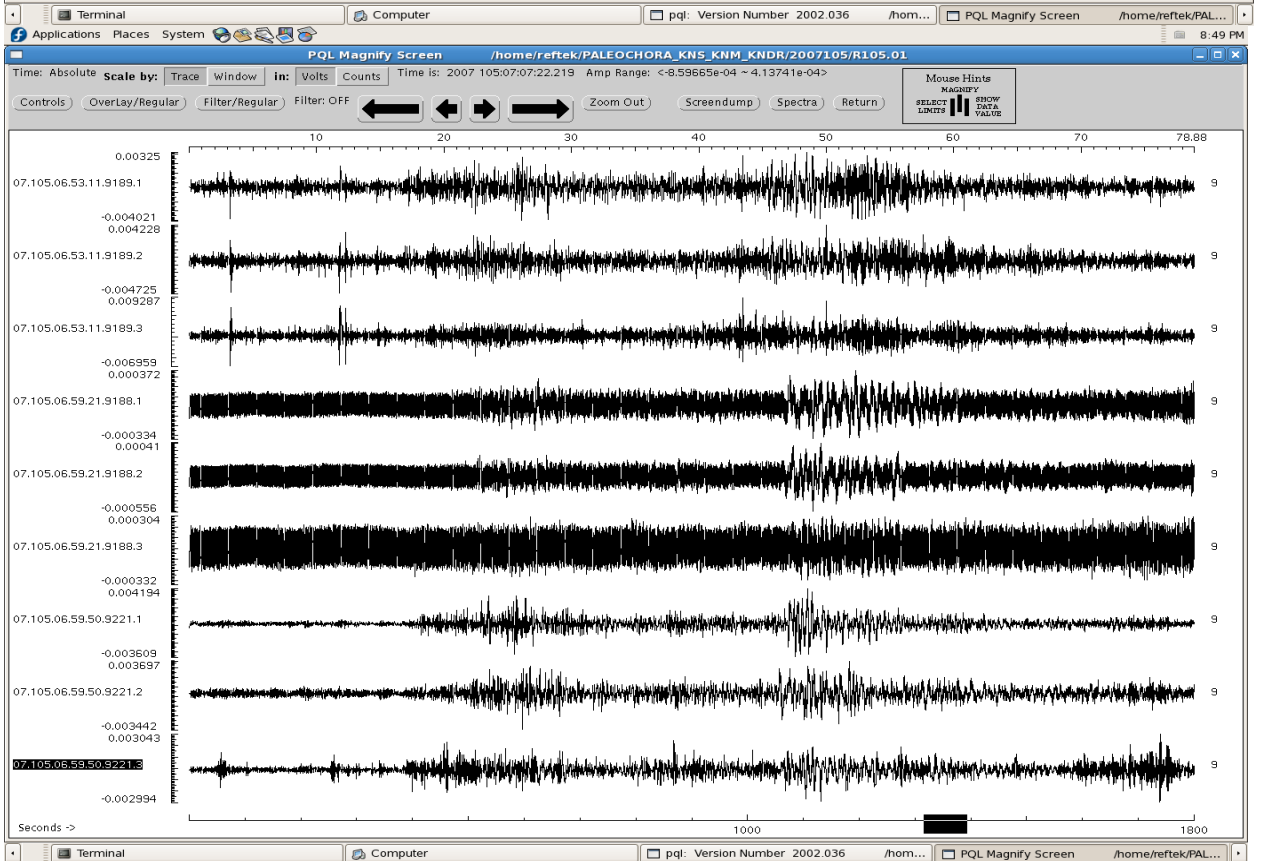
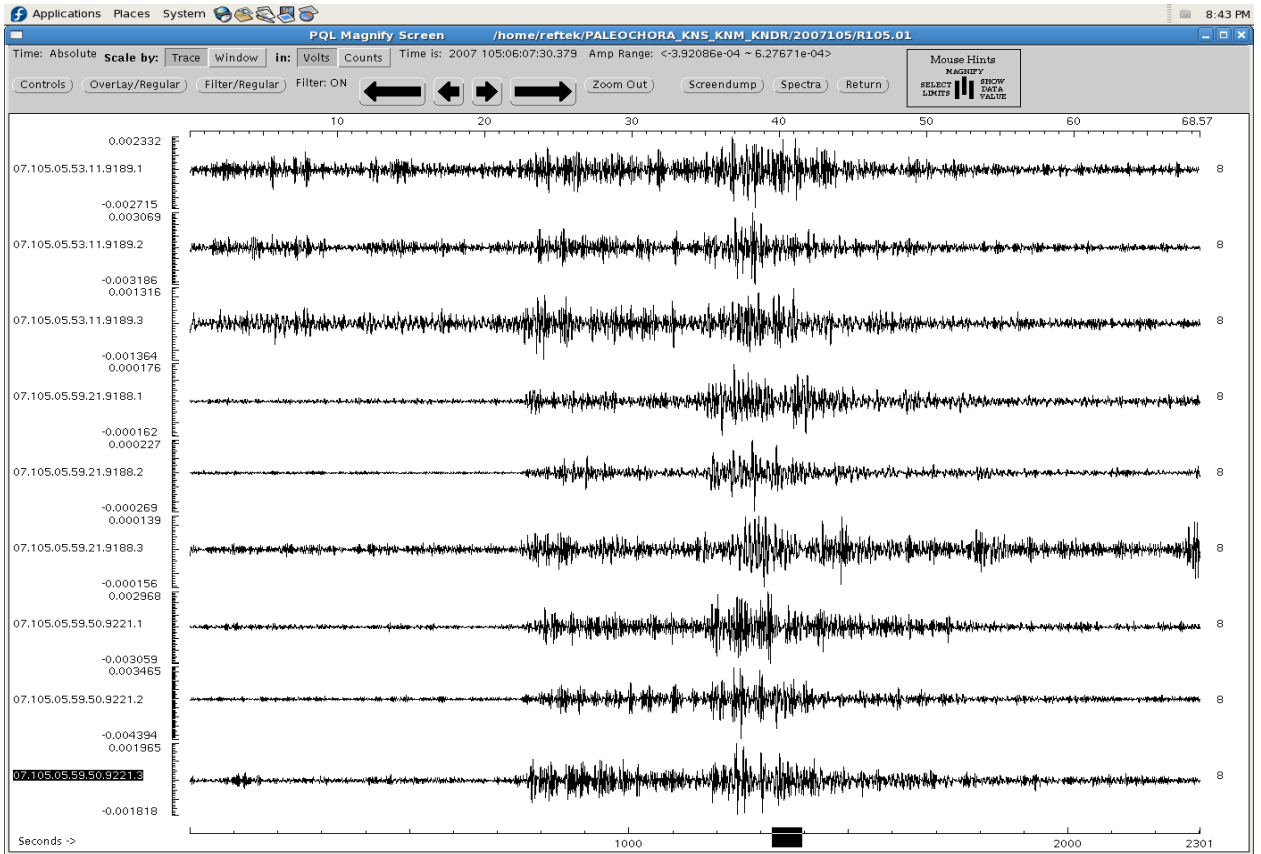


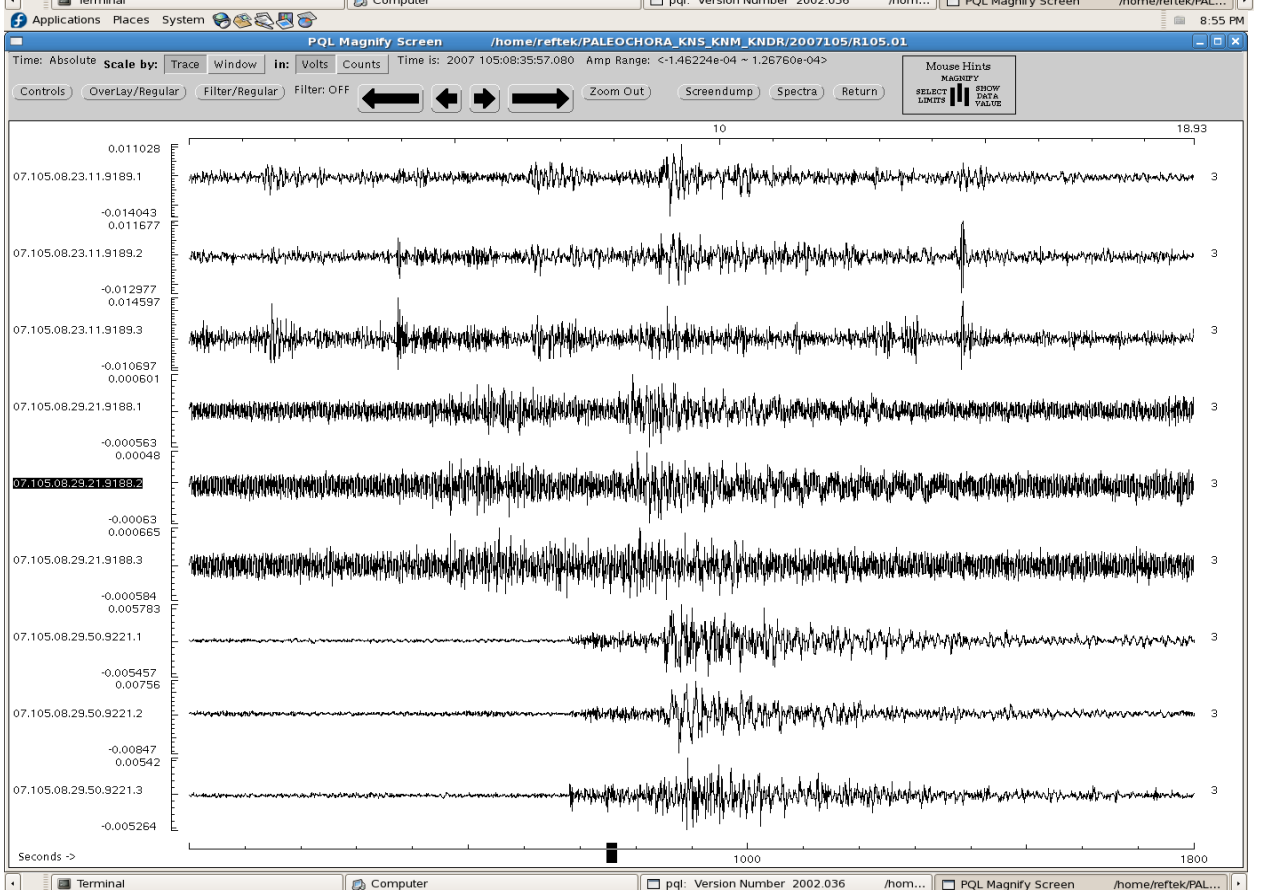
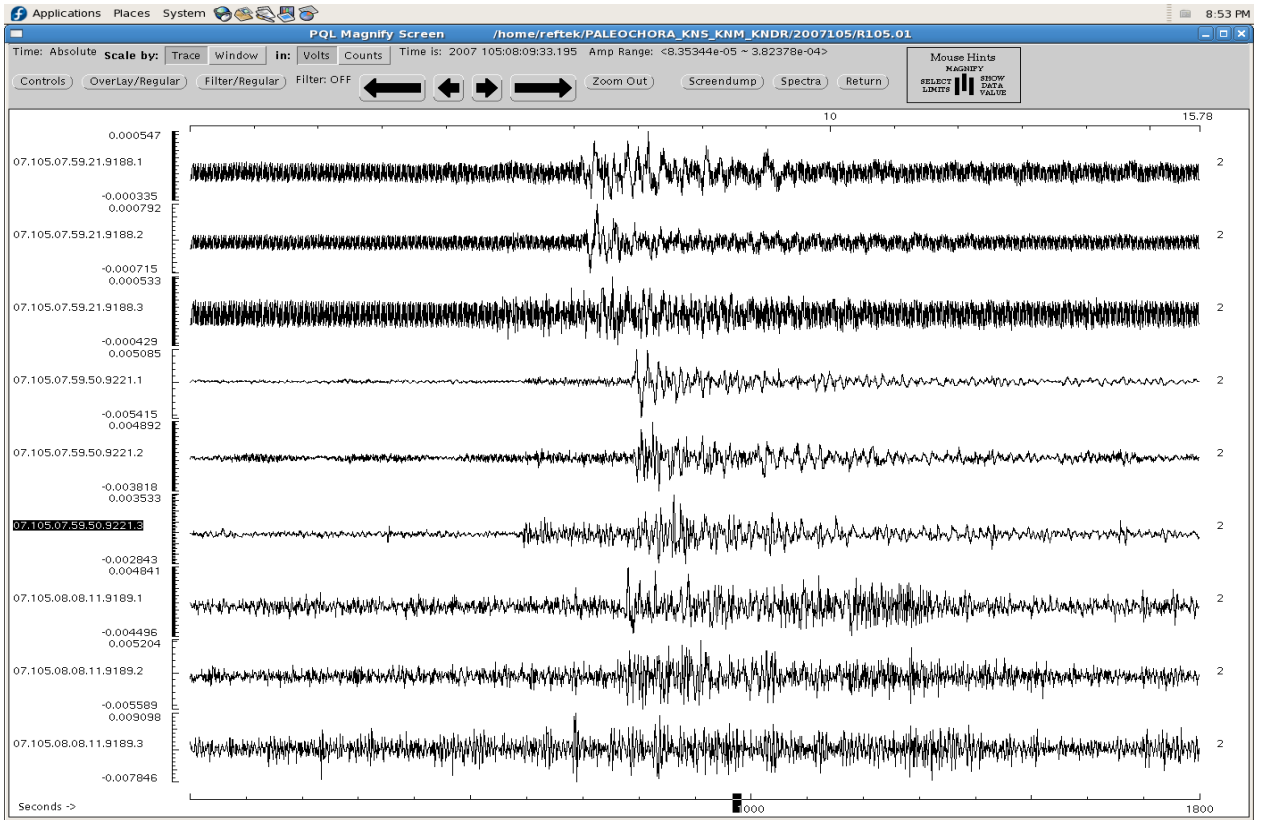


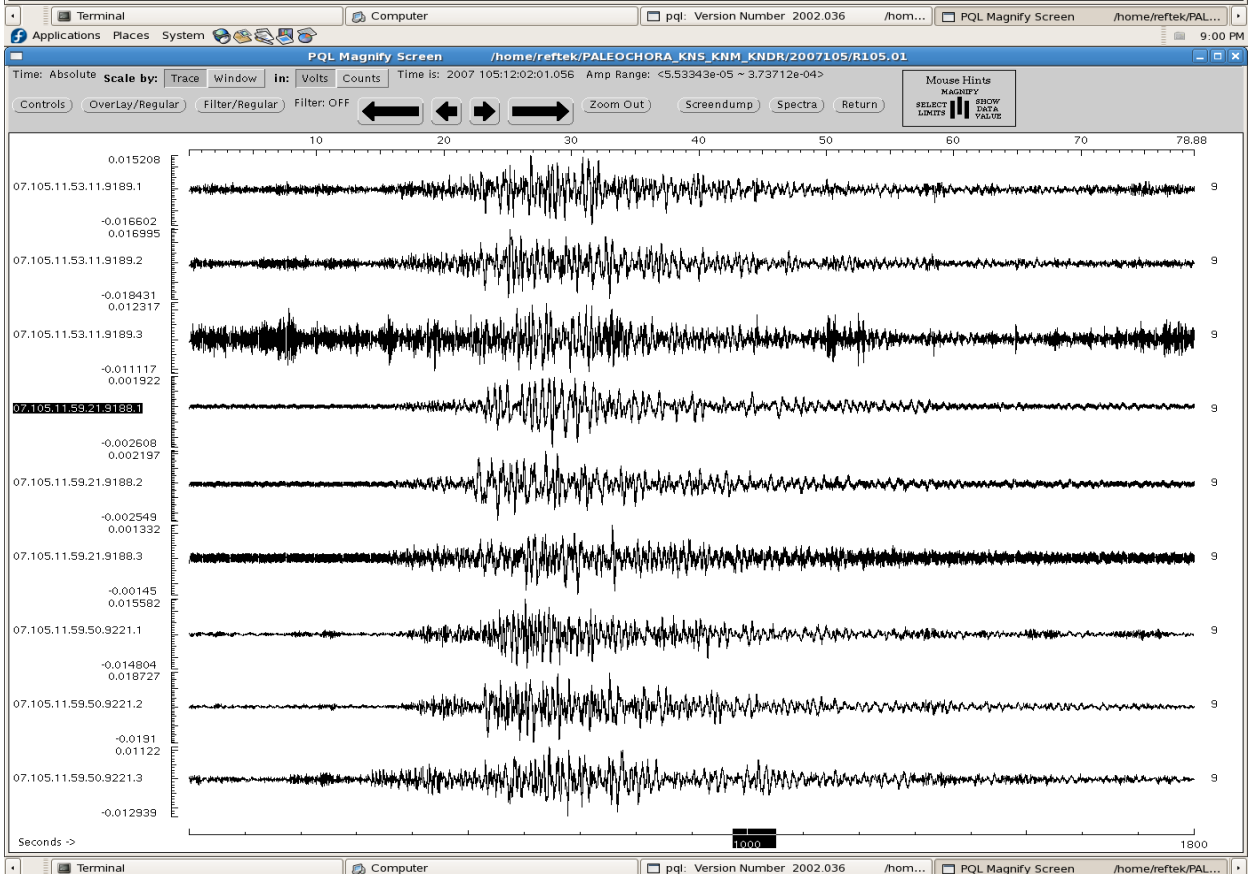
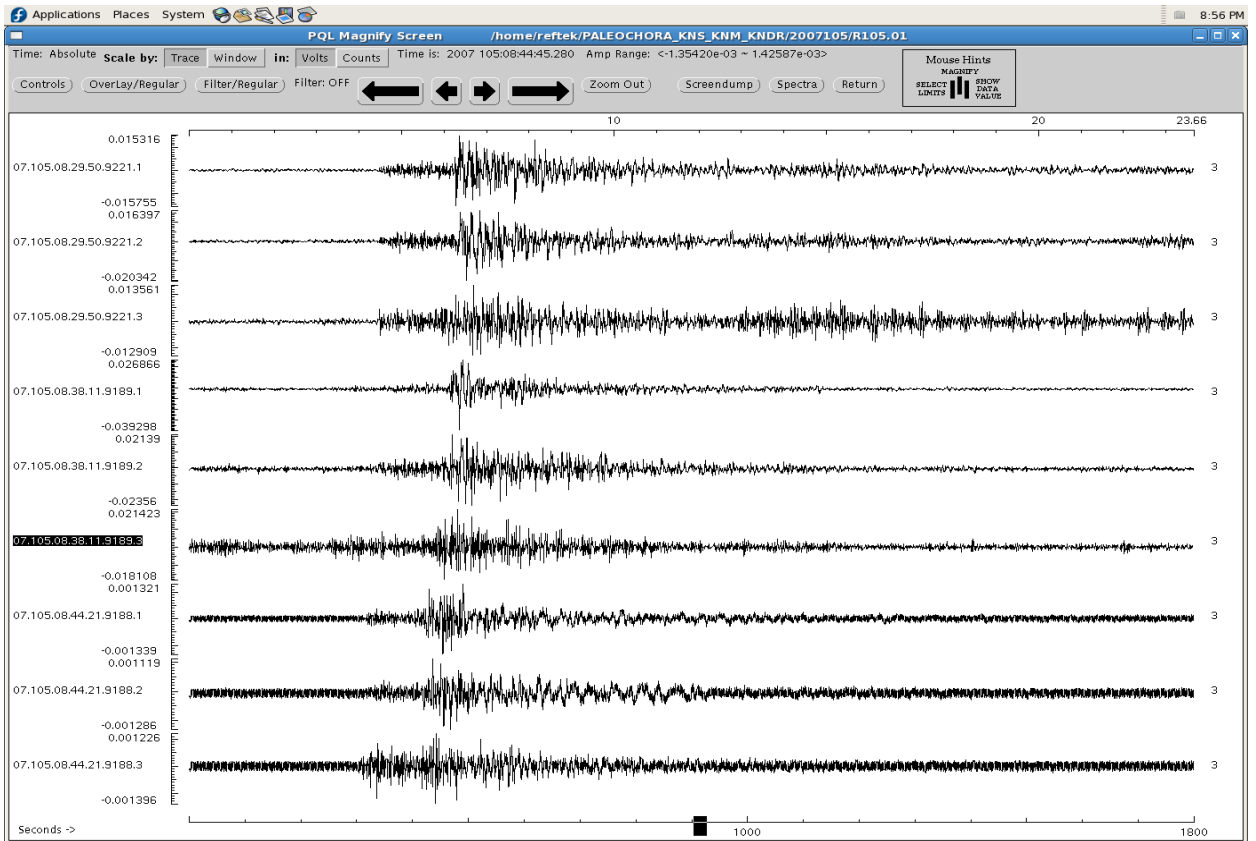


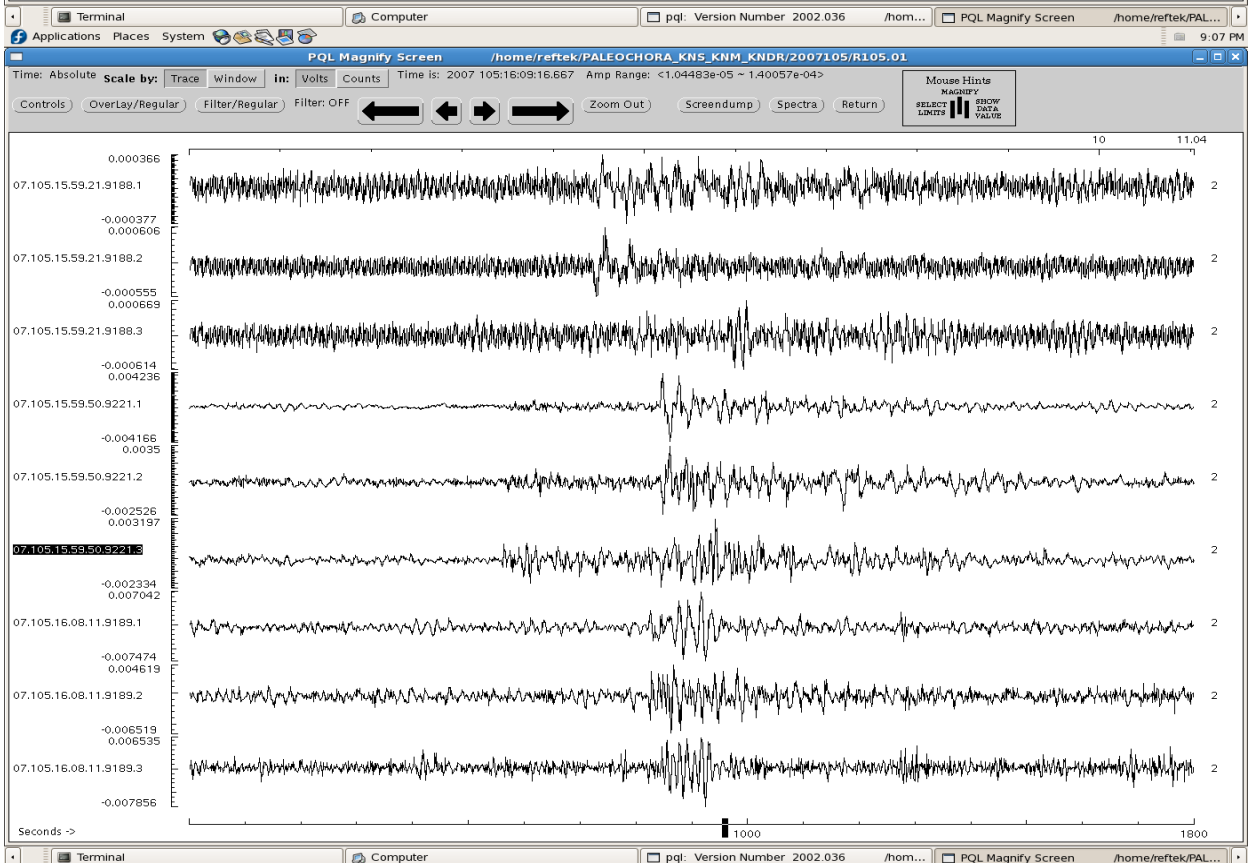
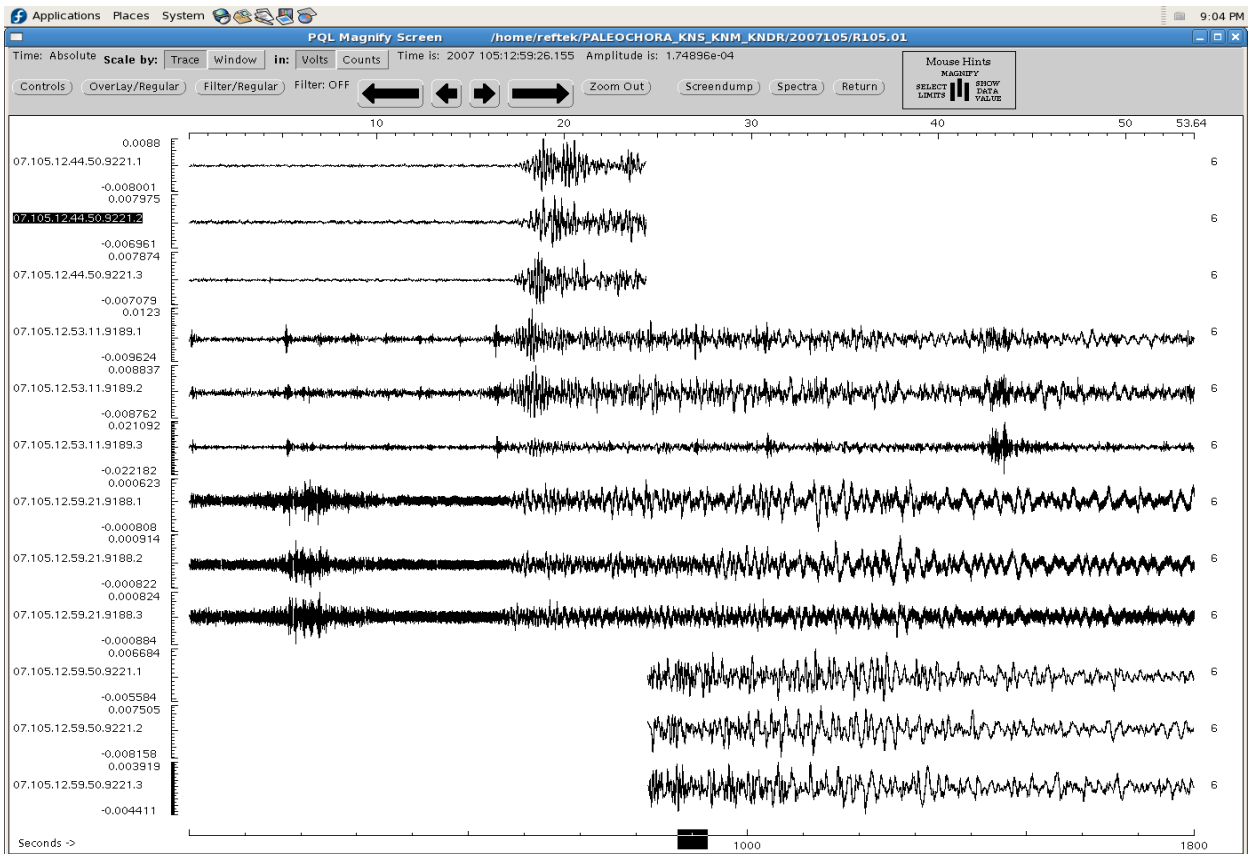


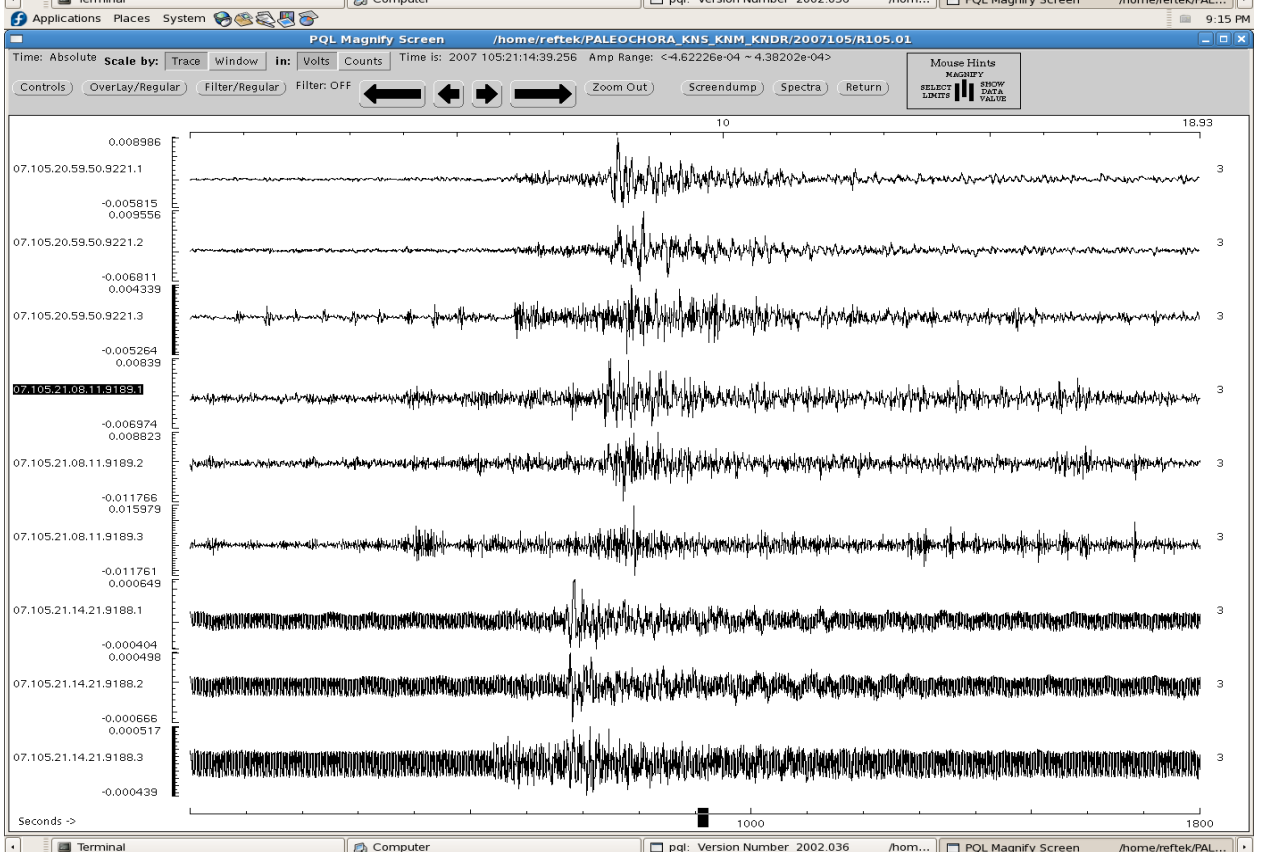
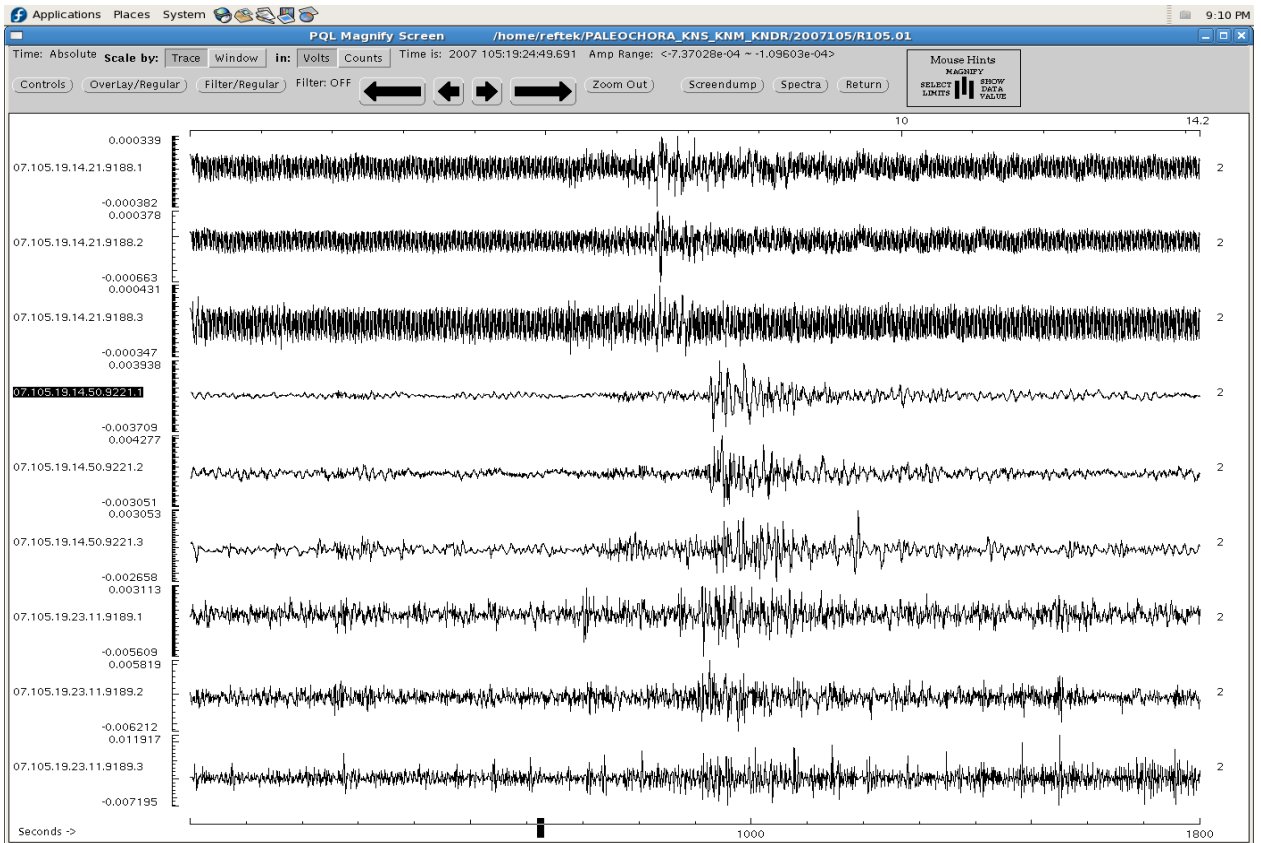


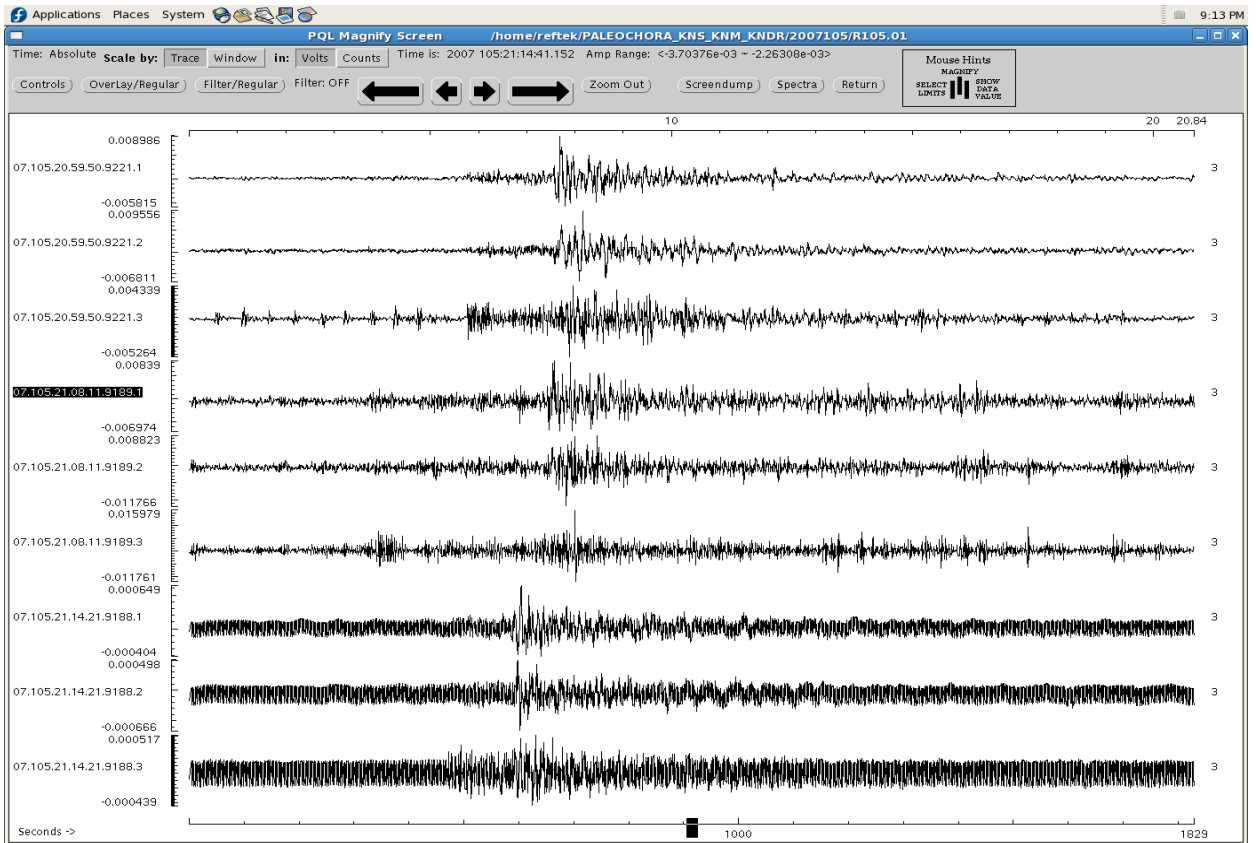




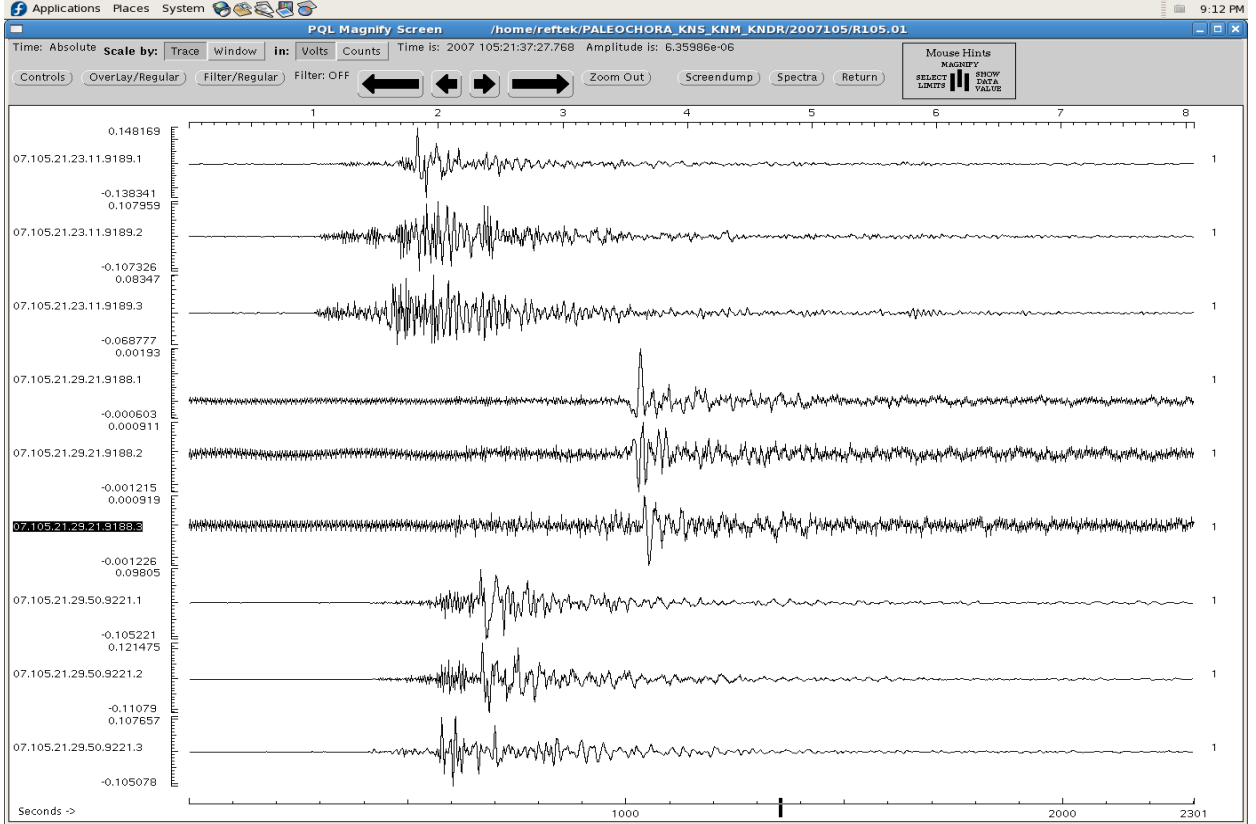




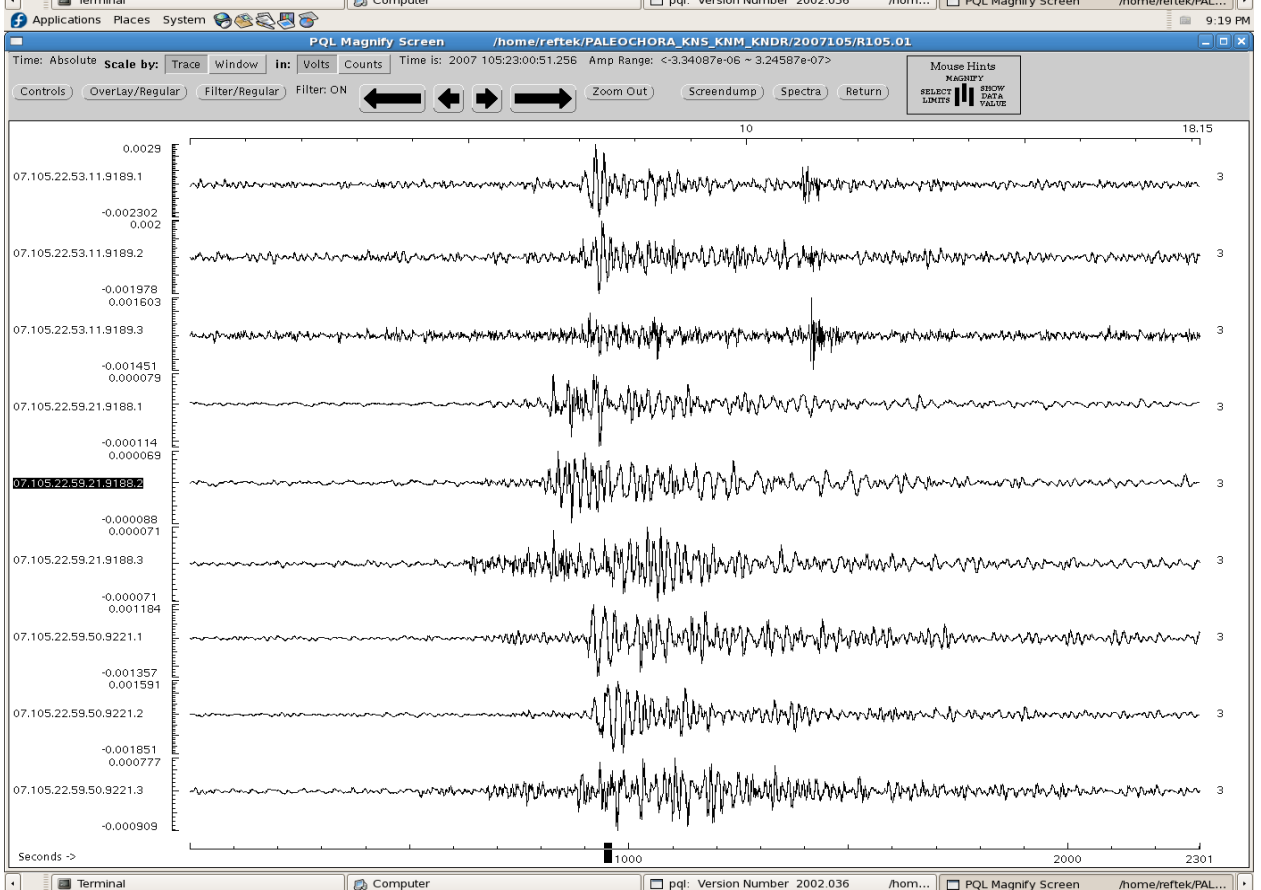
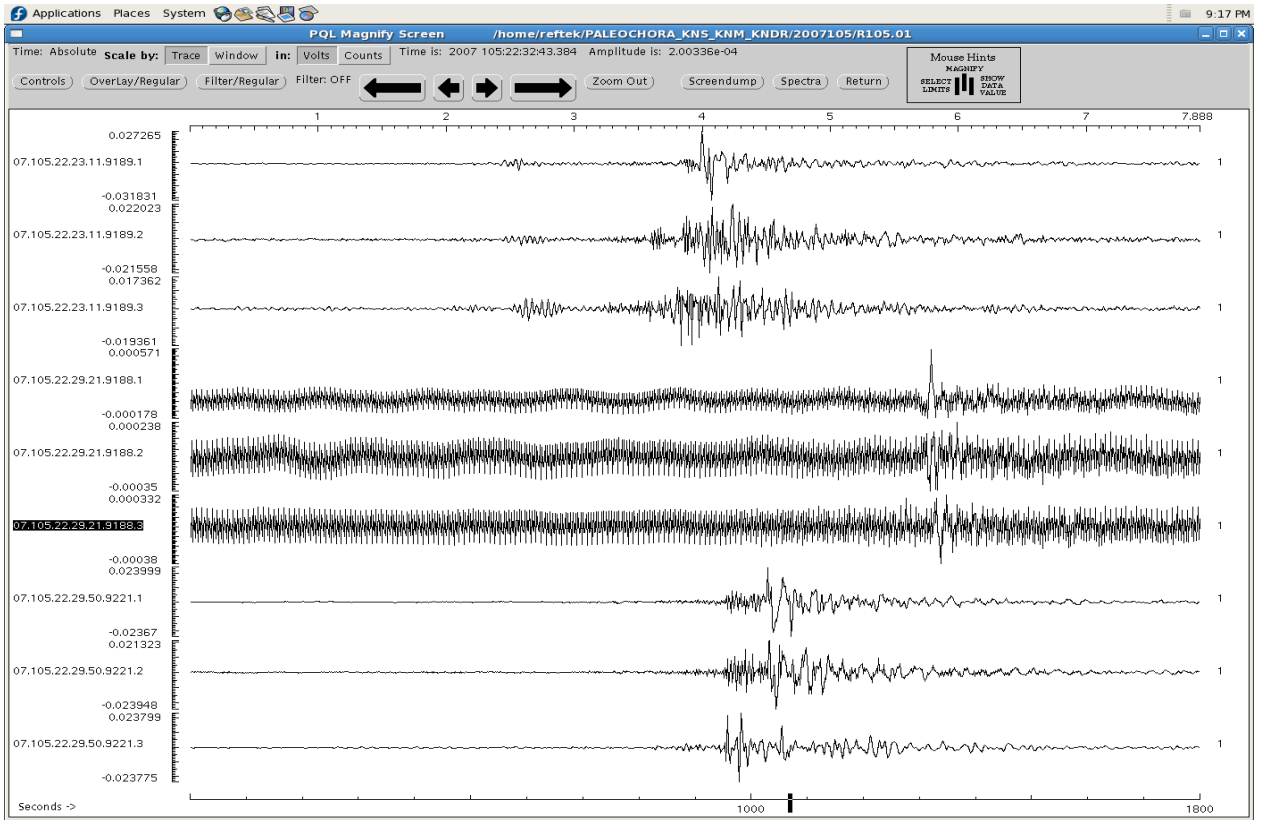


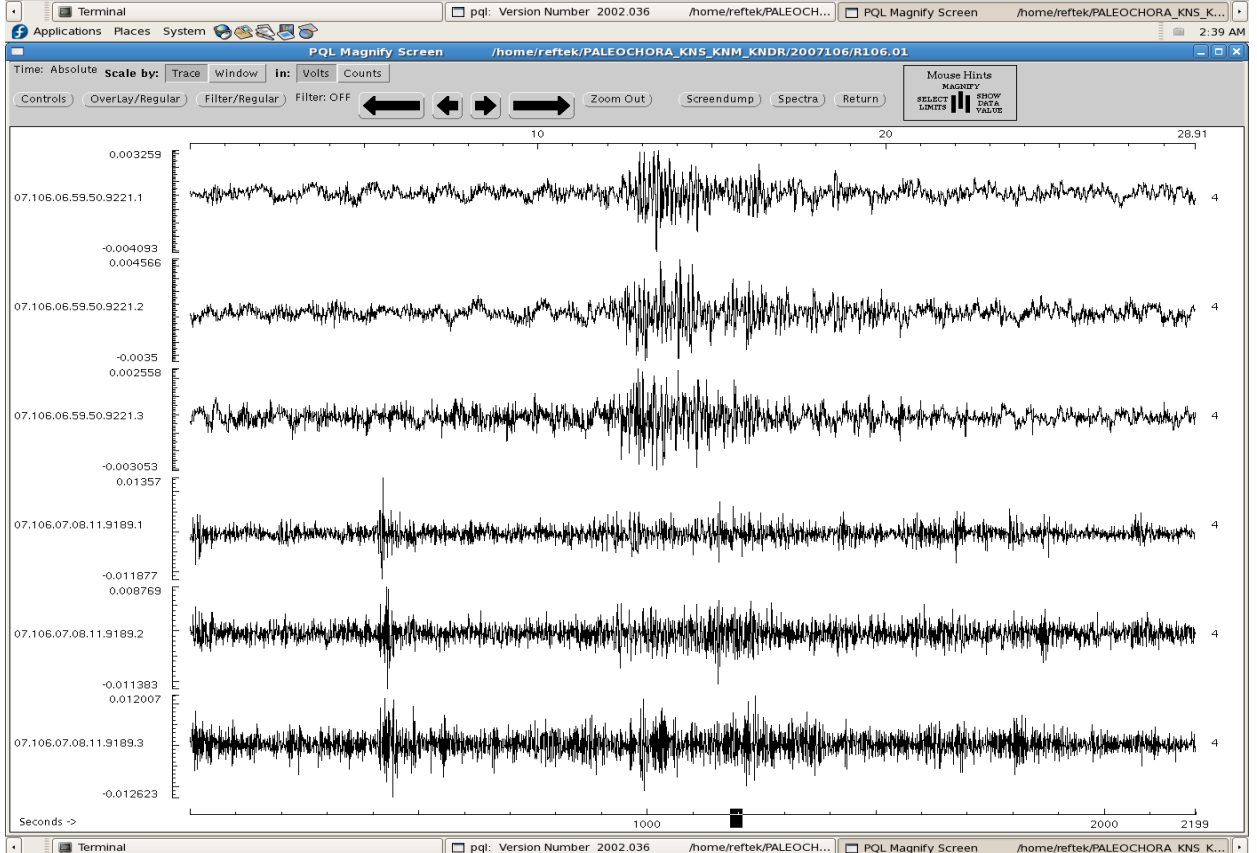
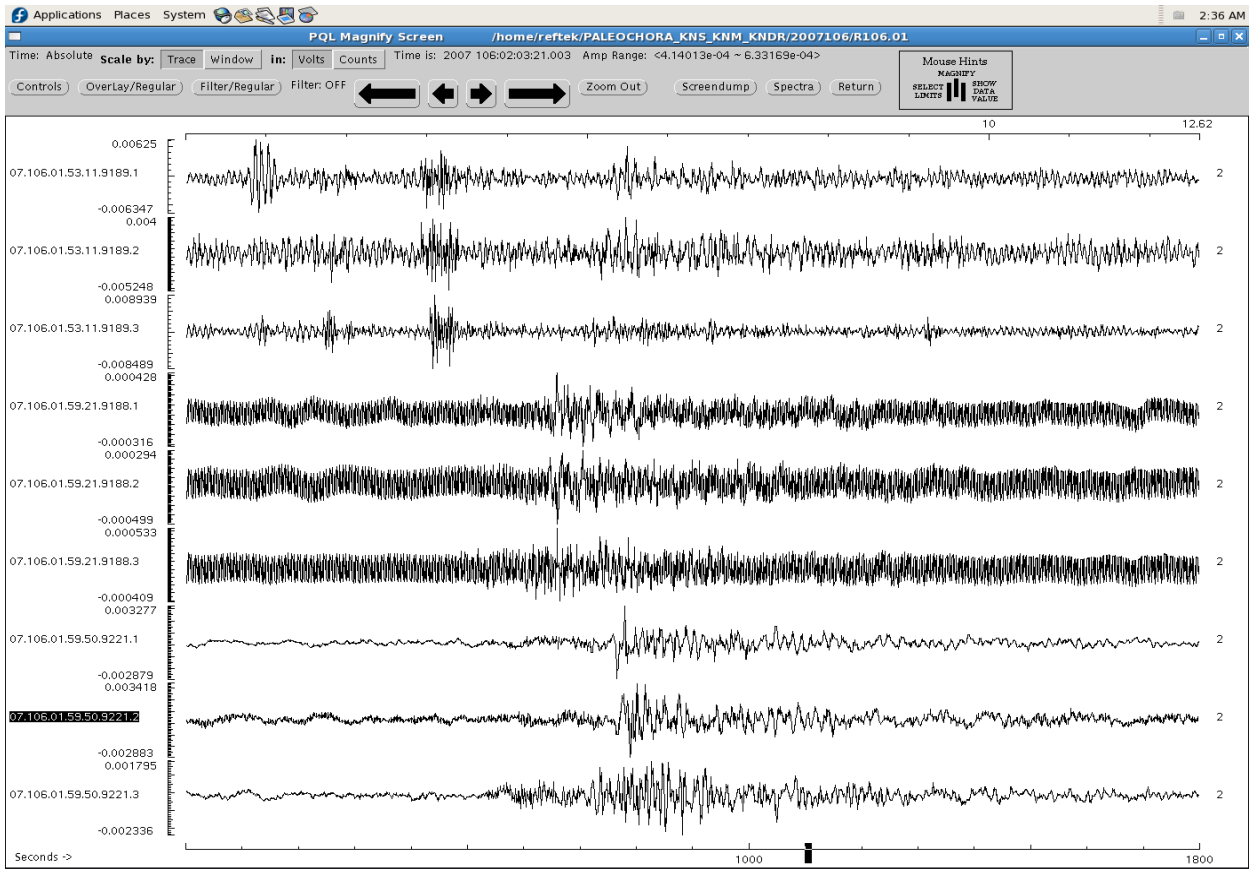


Terminal Computer pql: Version Number 2002.036 /home/ PQL Magnify Screen /home/reftek/PAL...

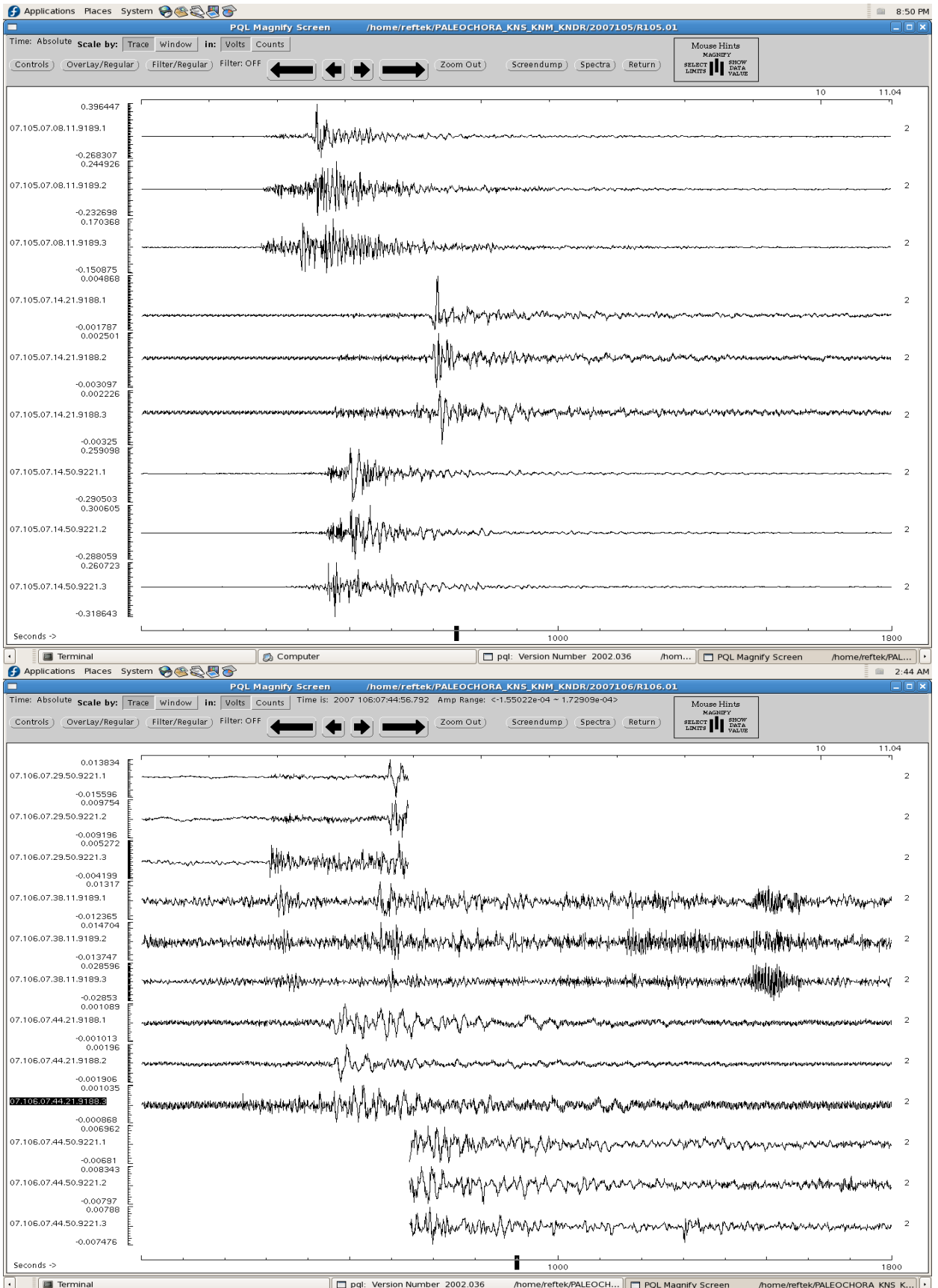


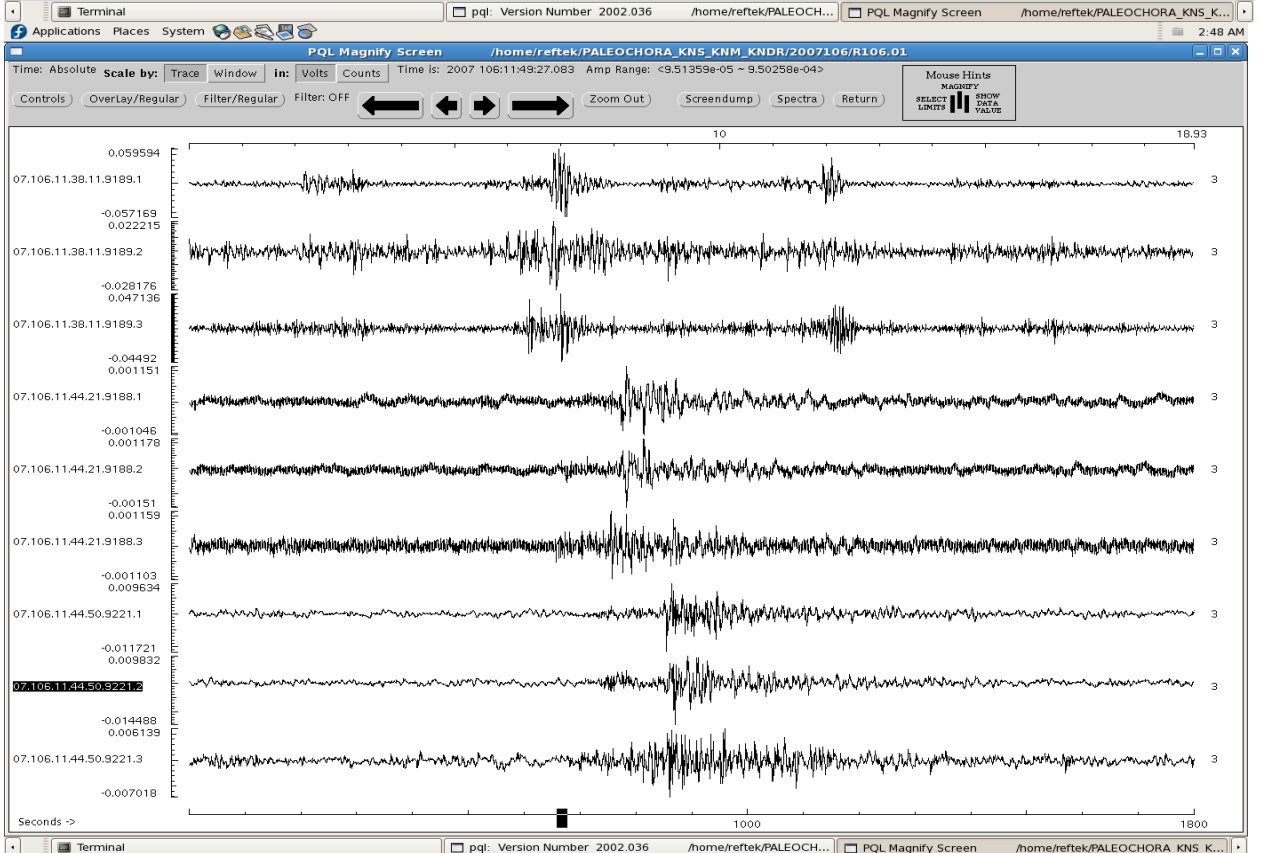
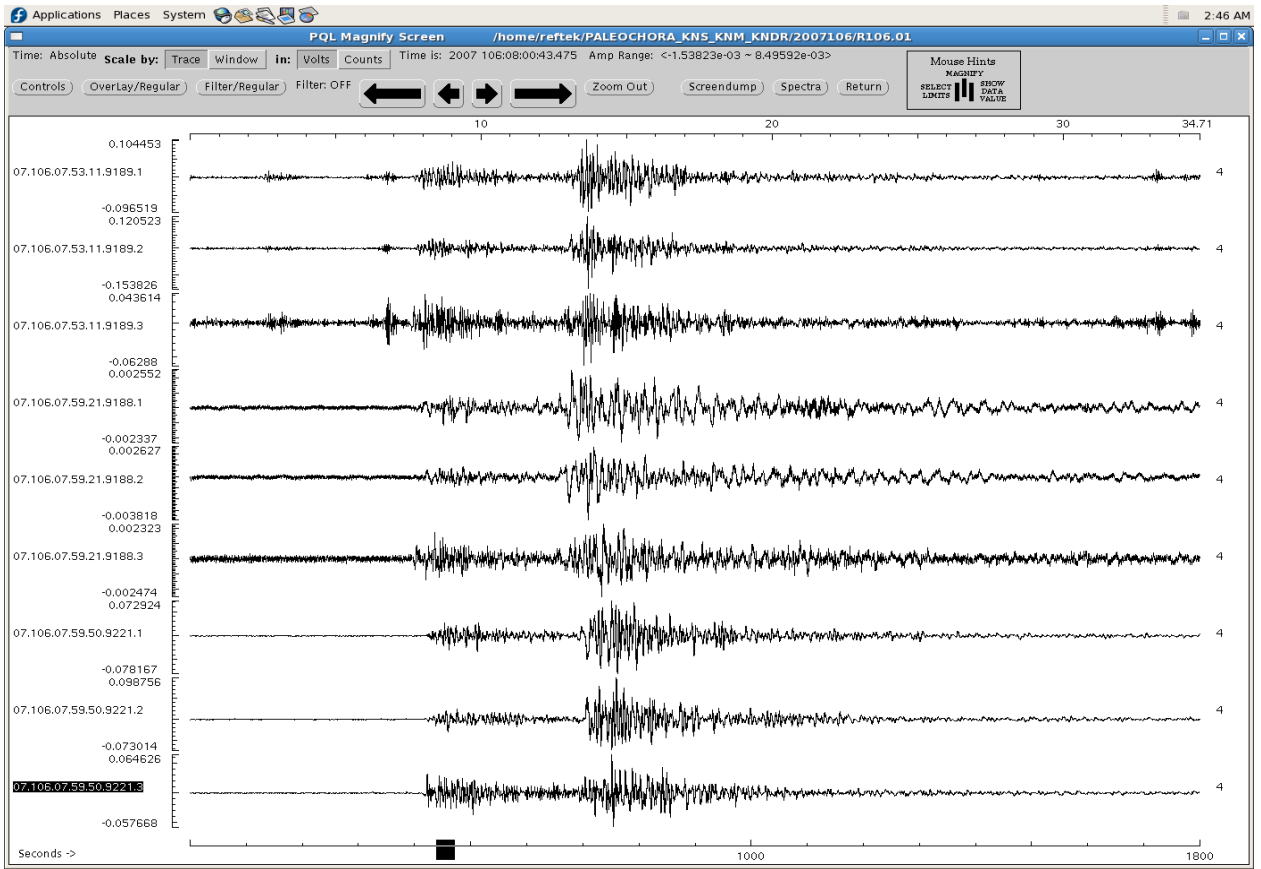
Terminal Computer pql: Version Number 2002.036 /home/ PQL Magnify Screen /home/reftek/PAL...

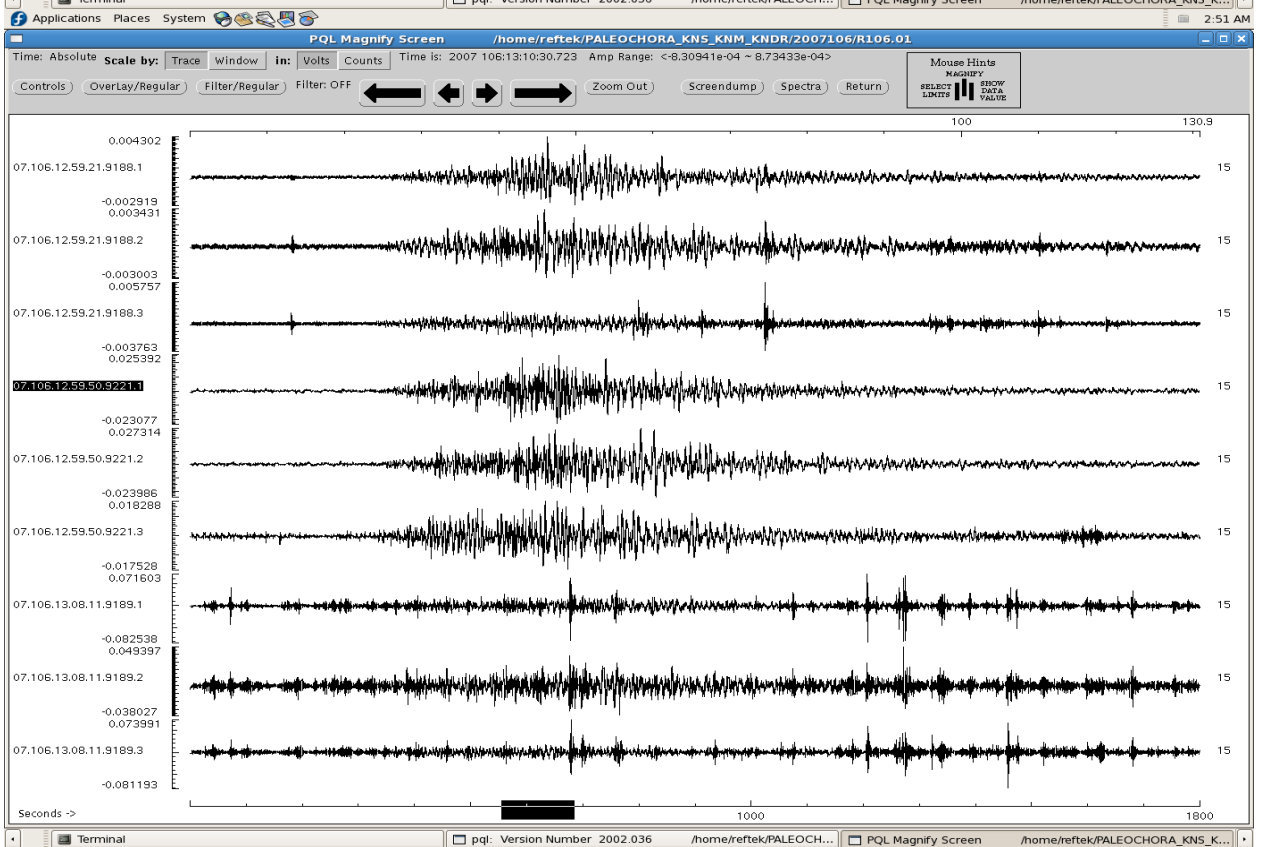
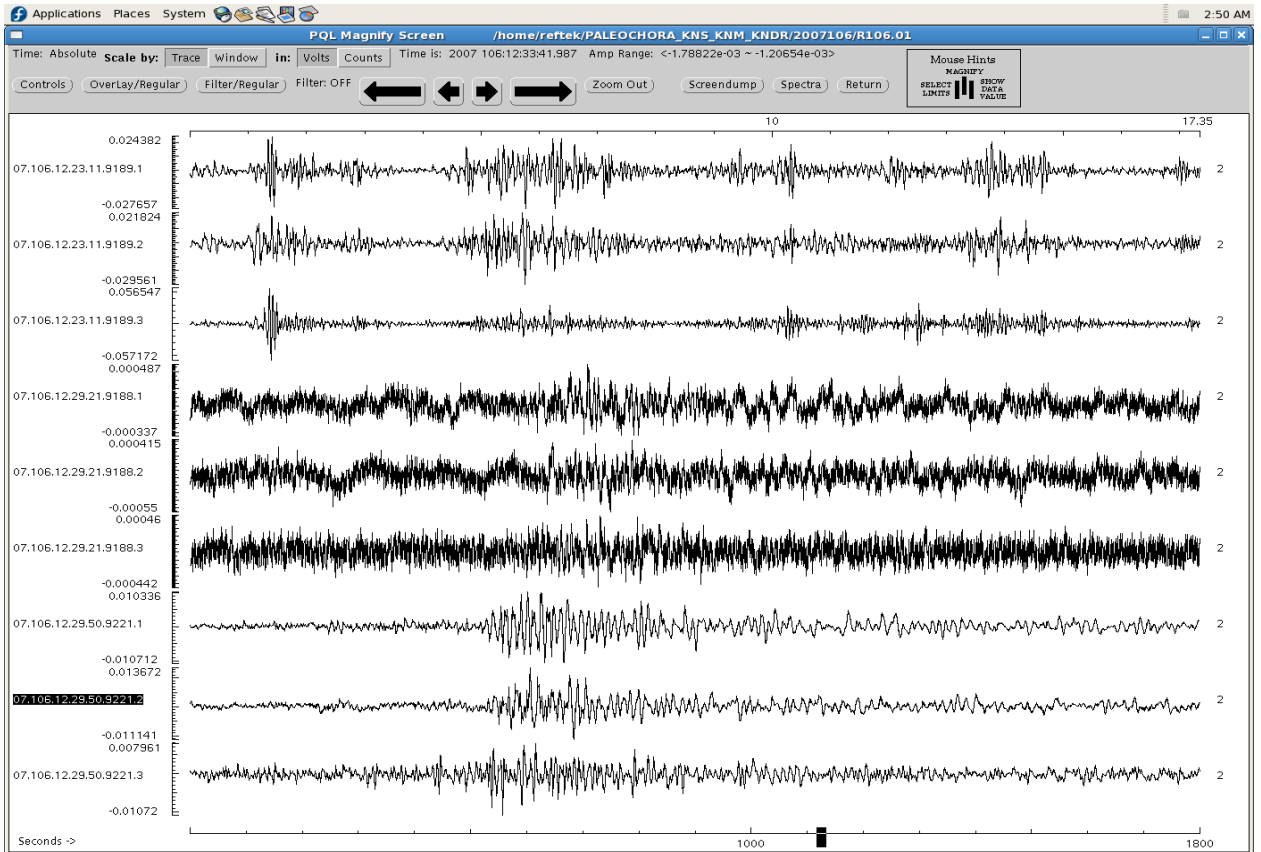


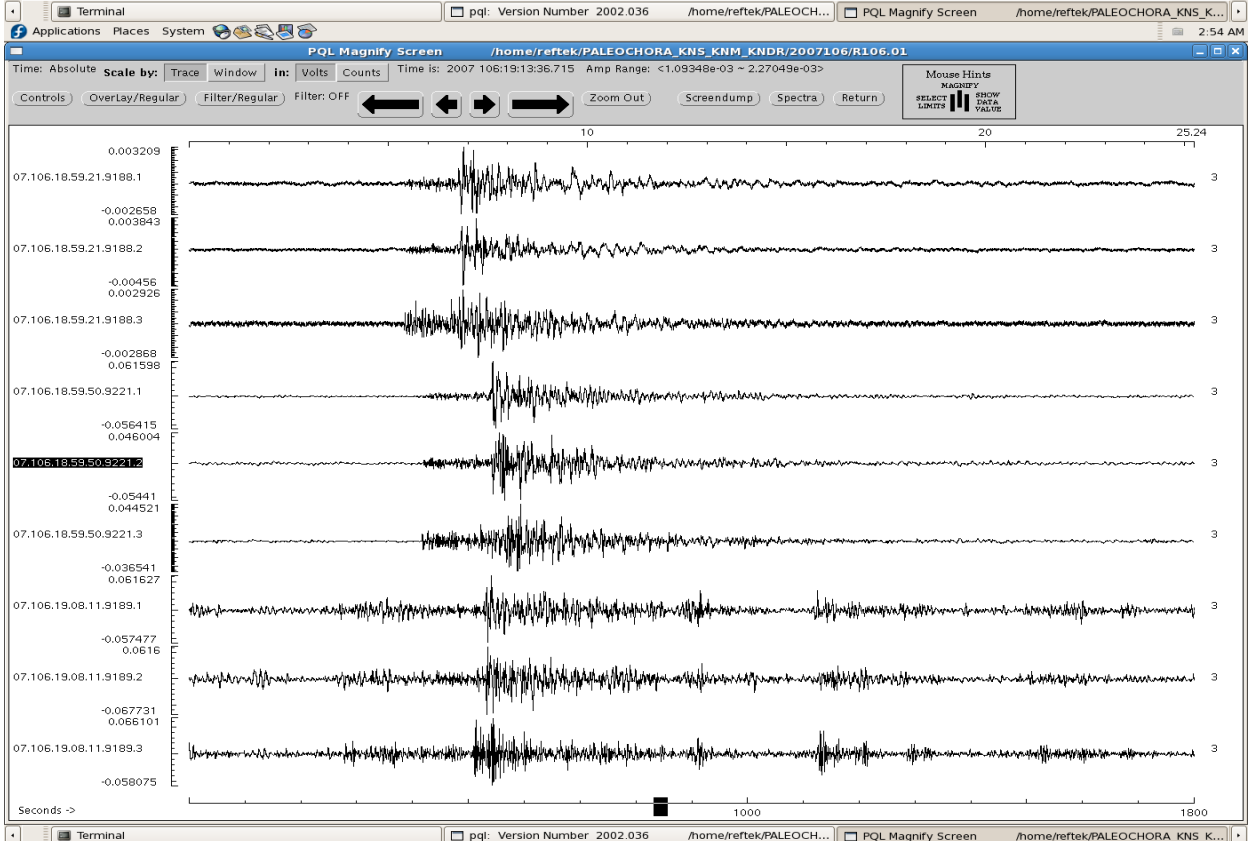
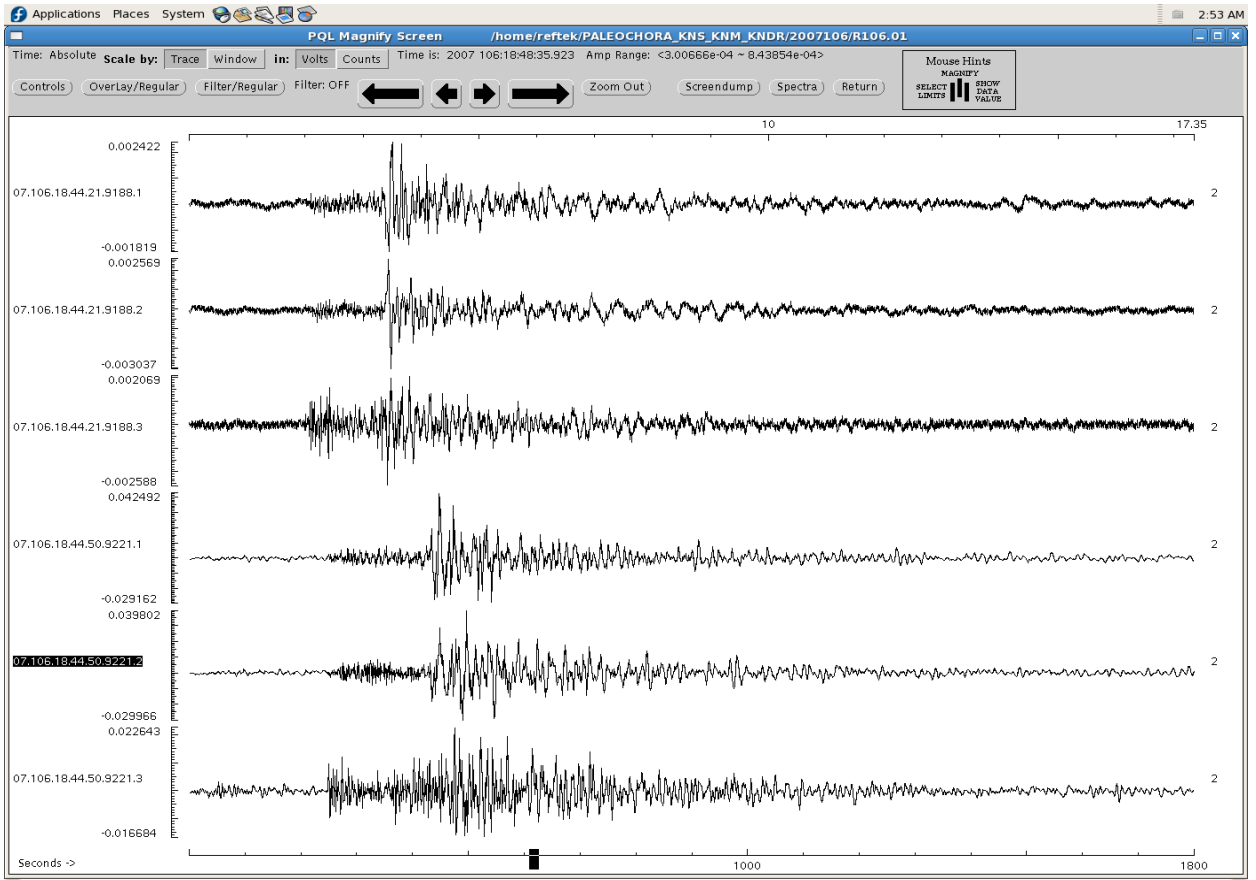


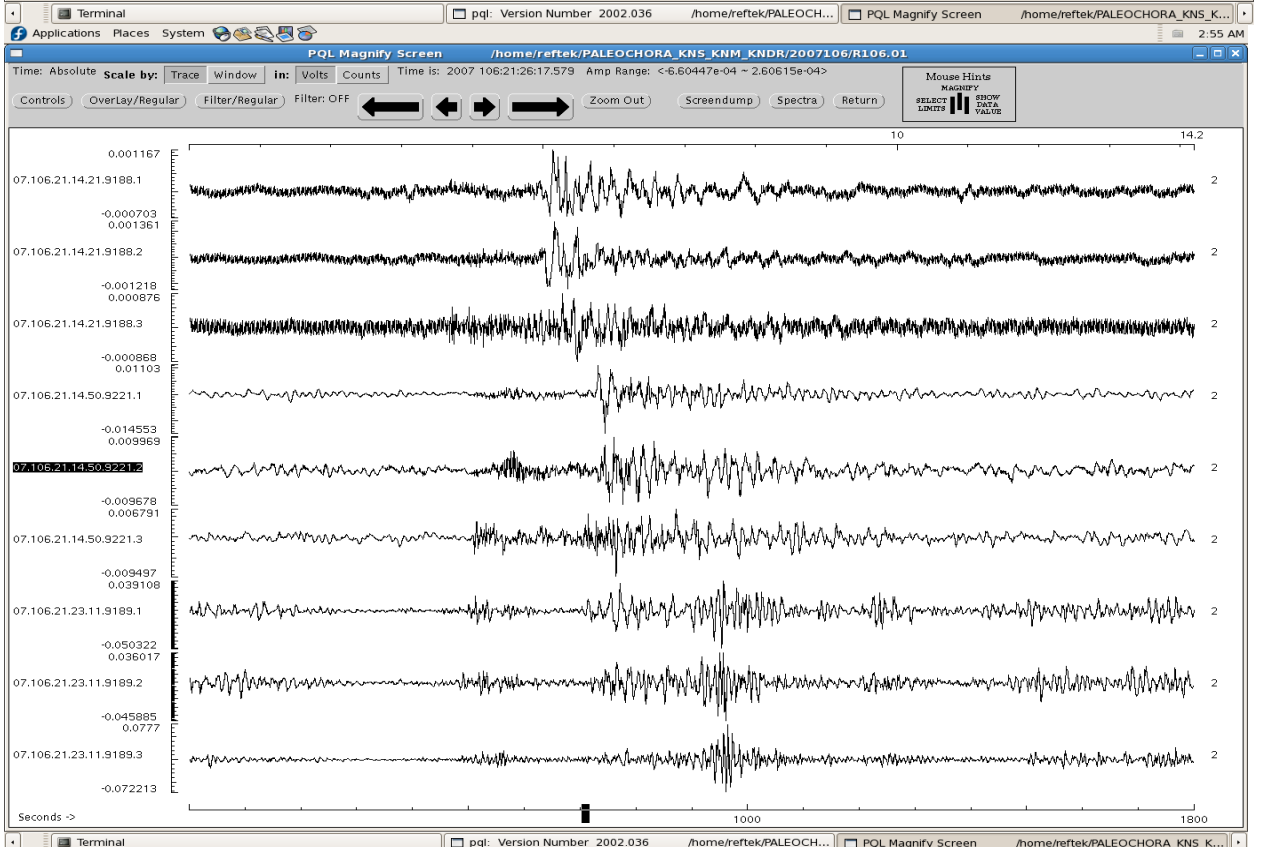
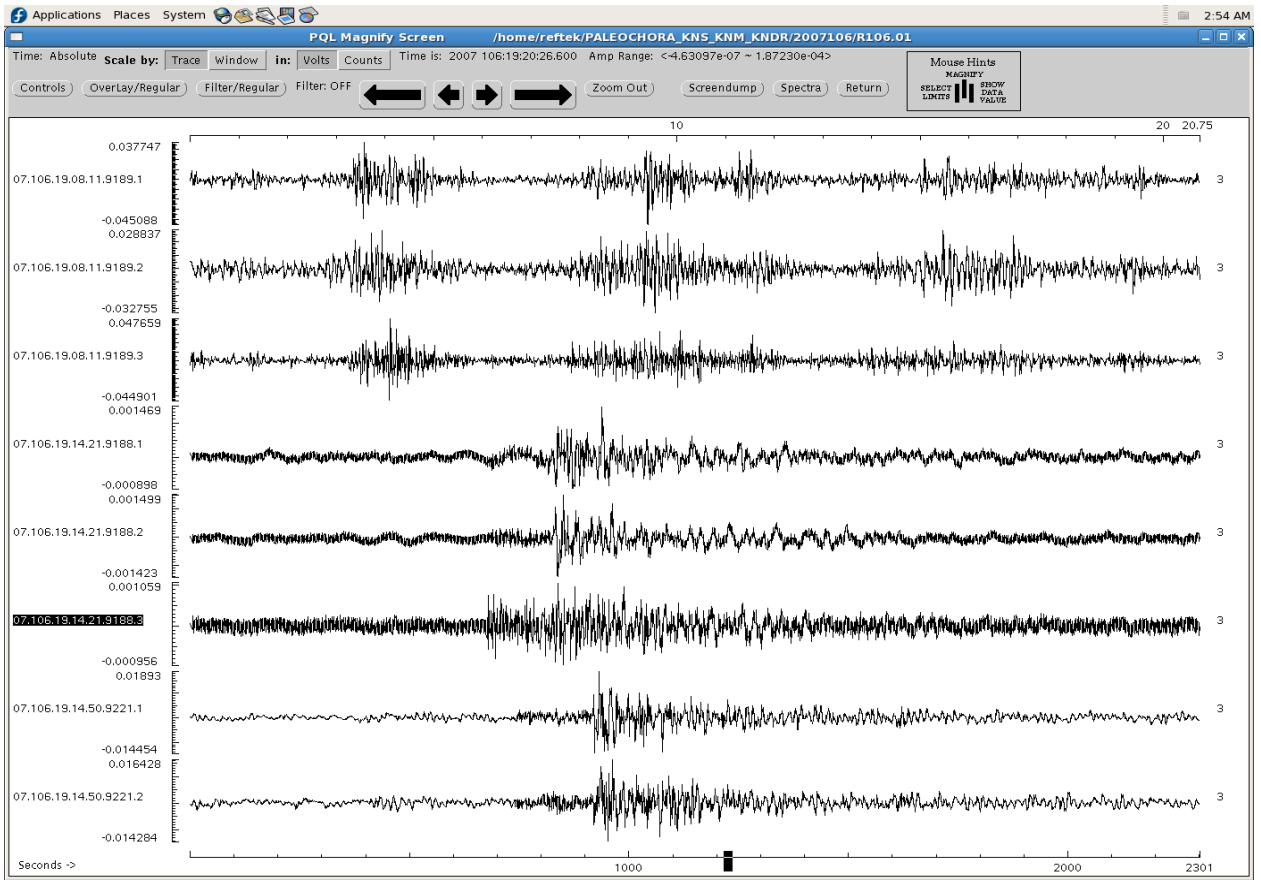


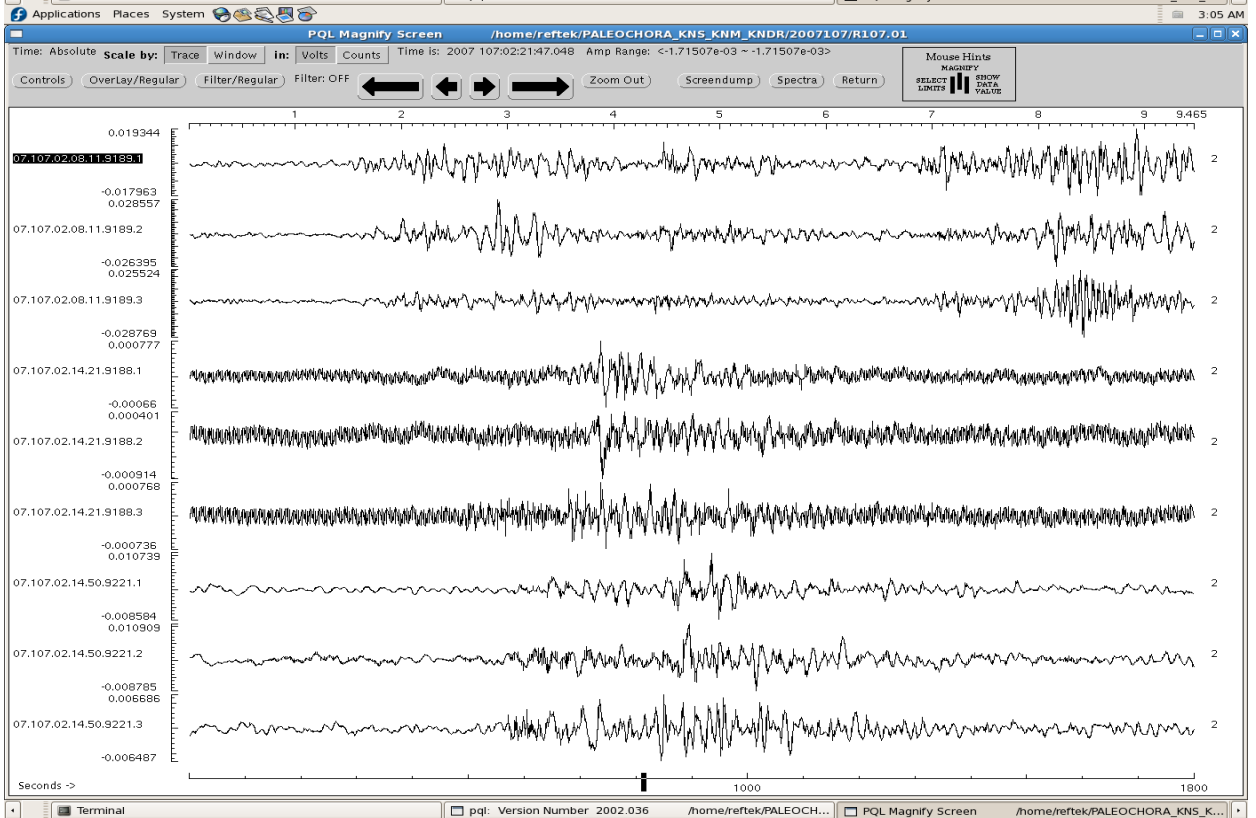
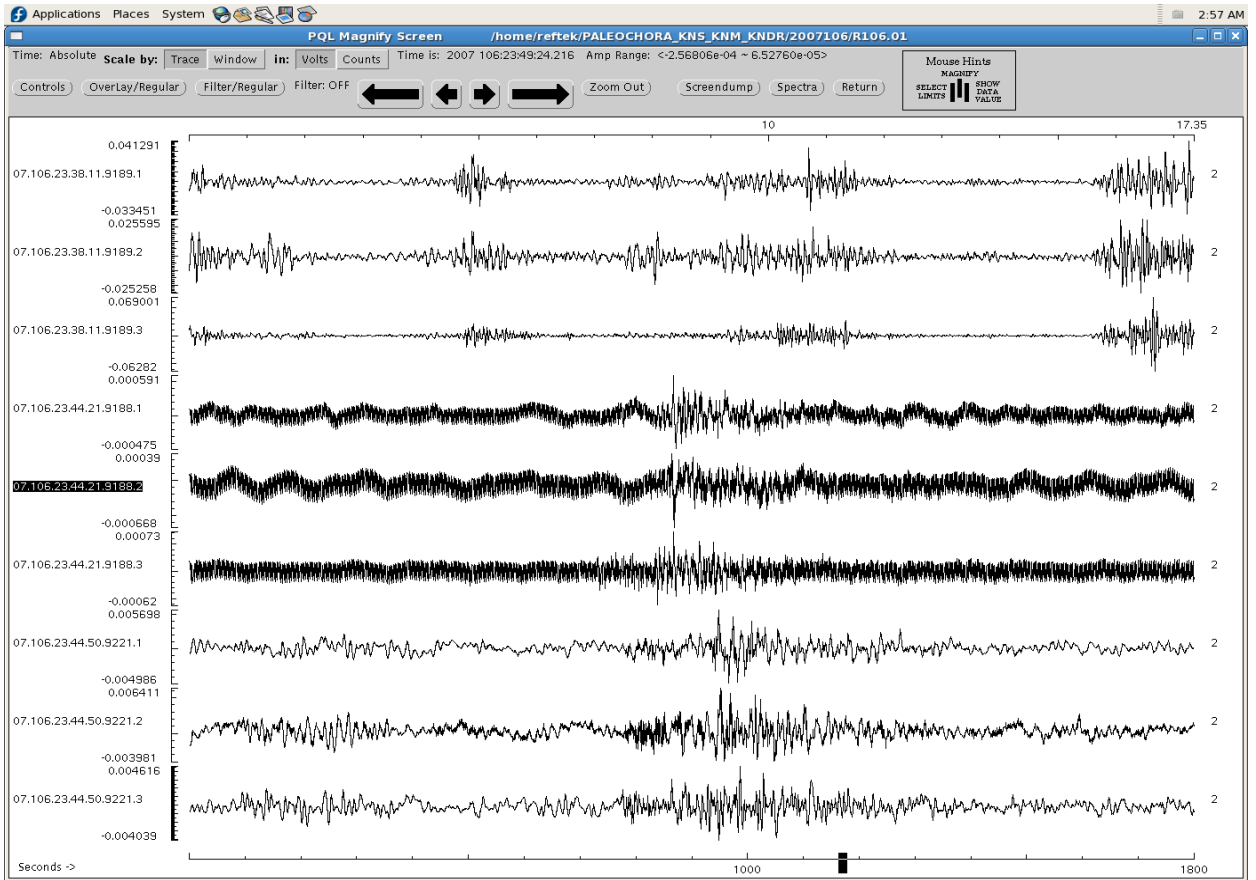


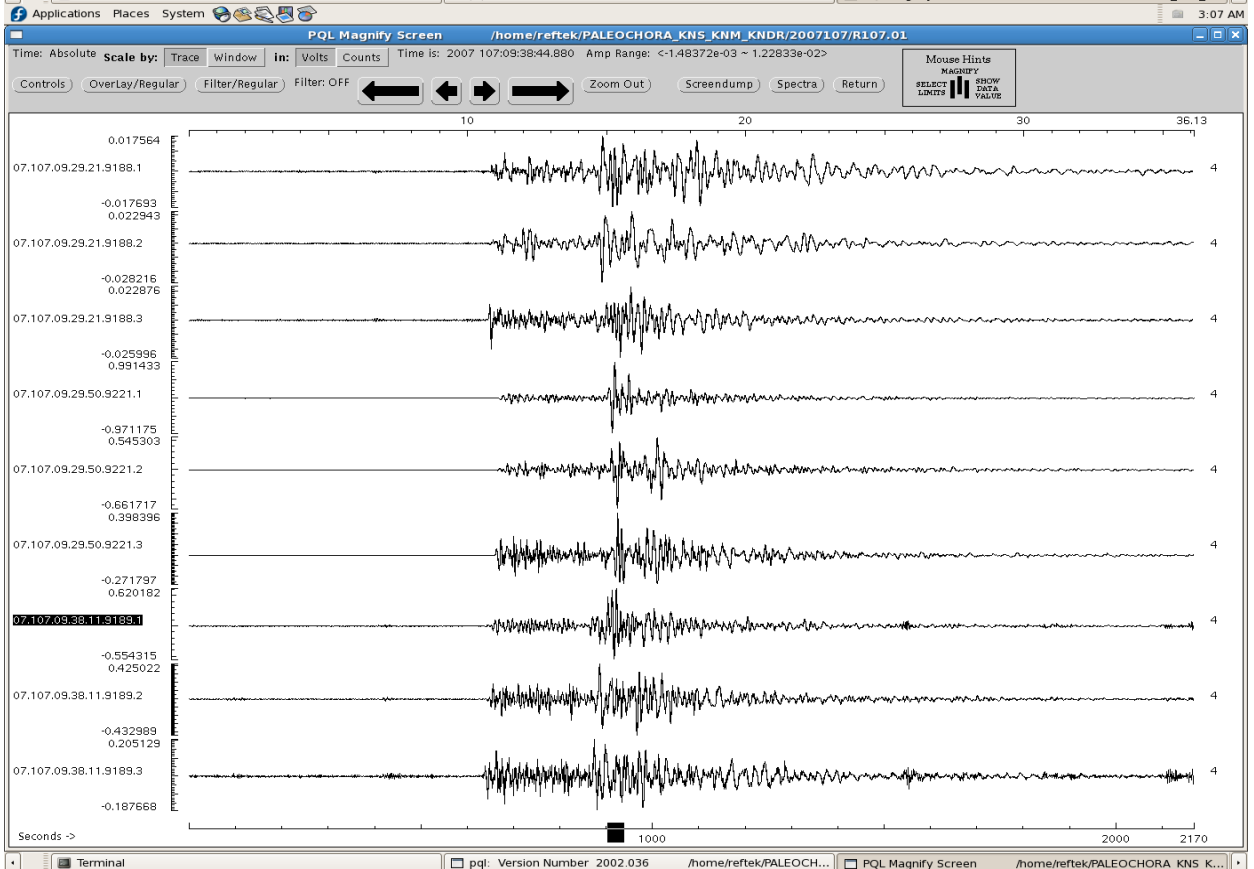
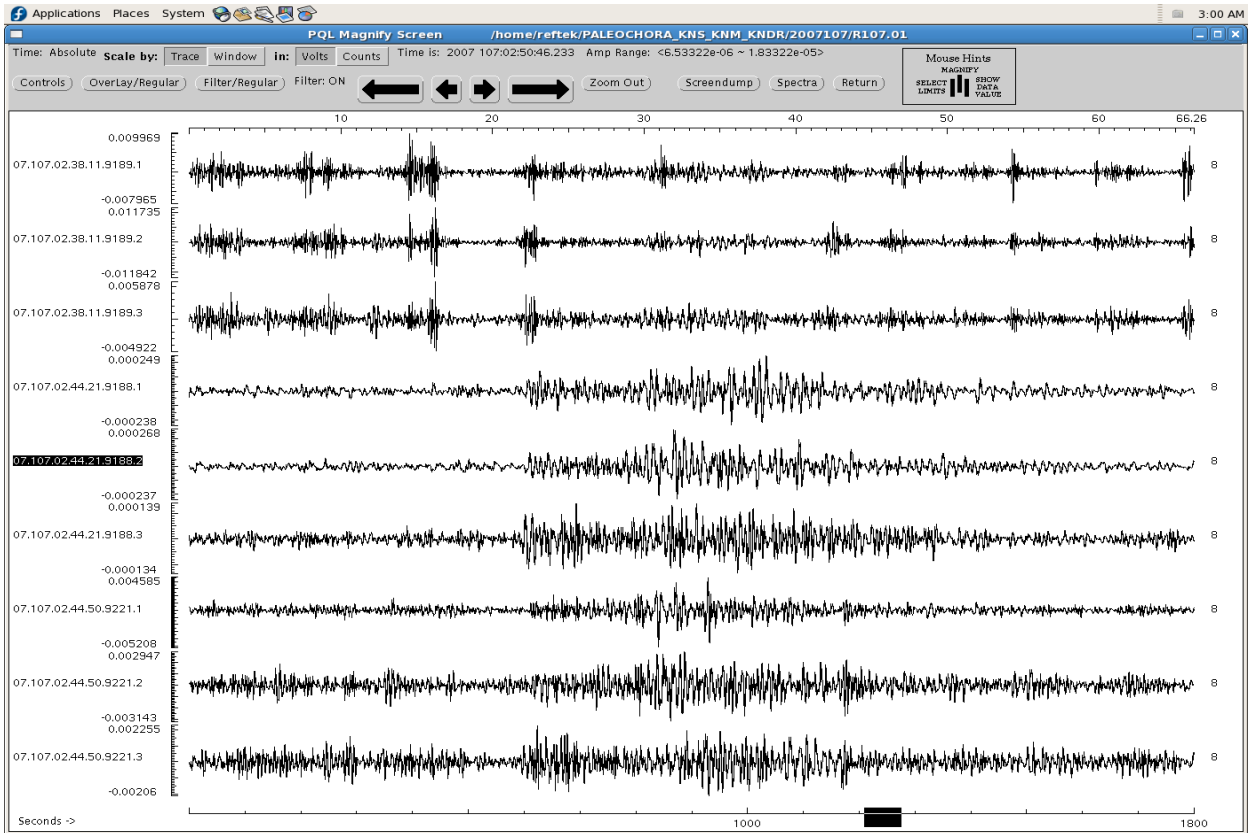


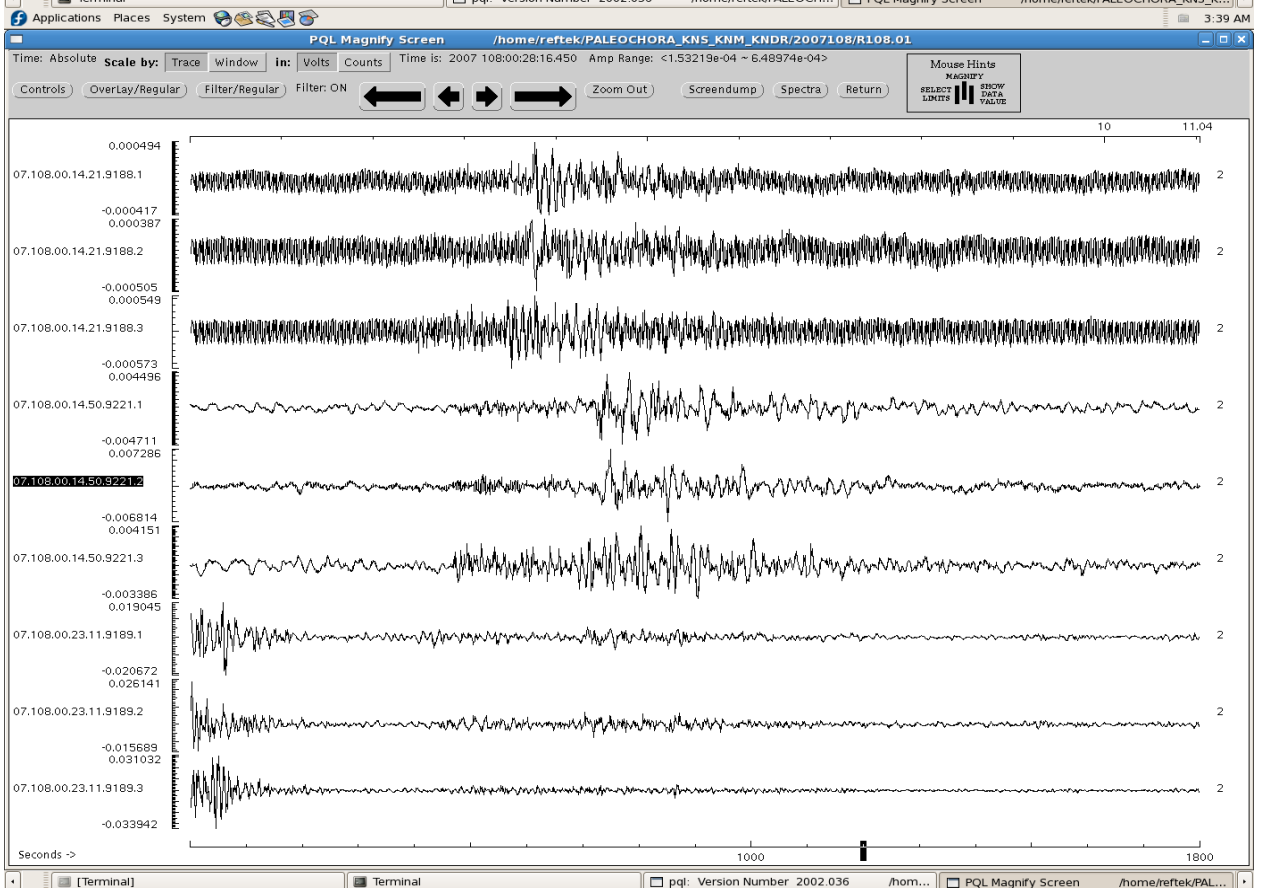
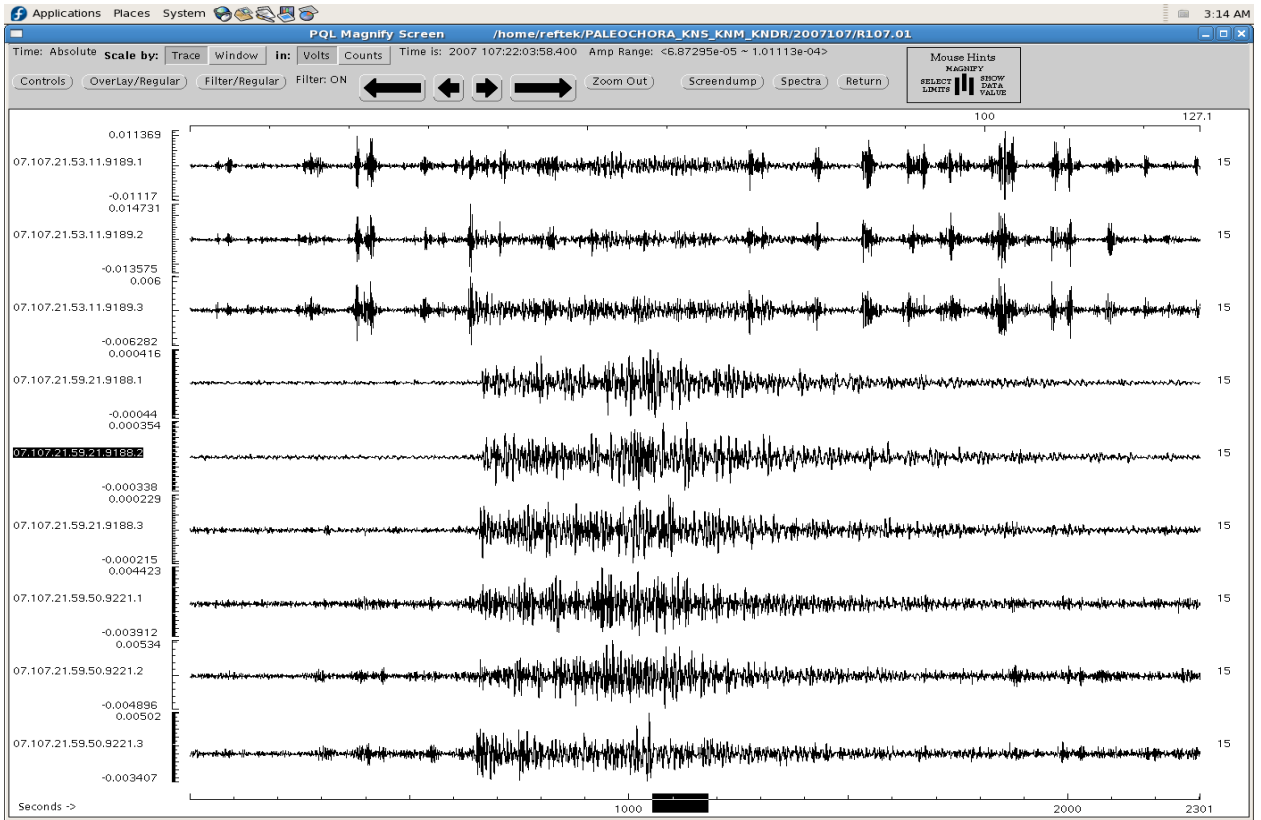




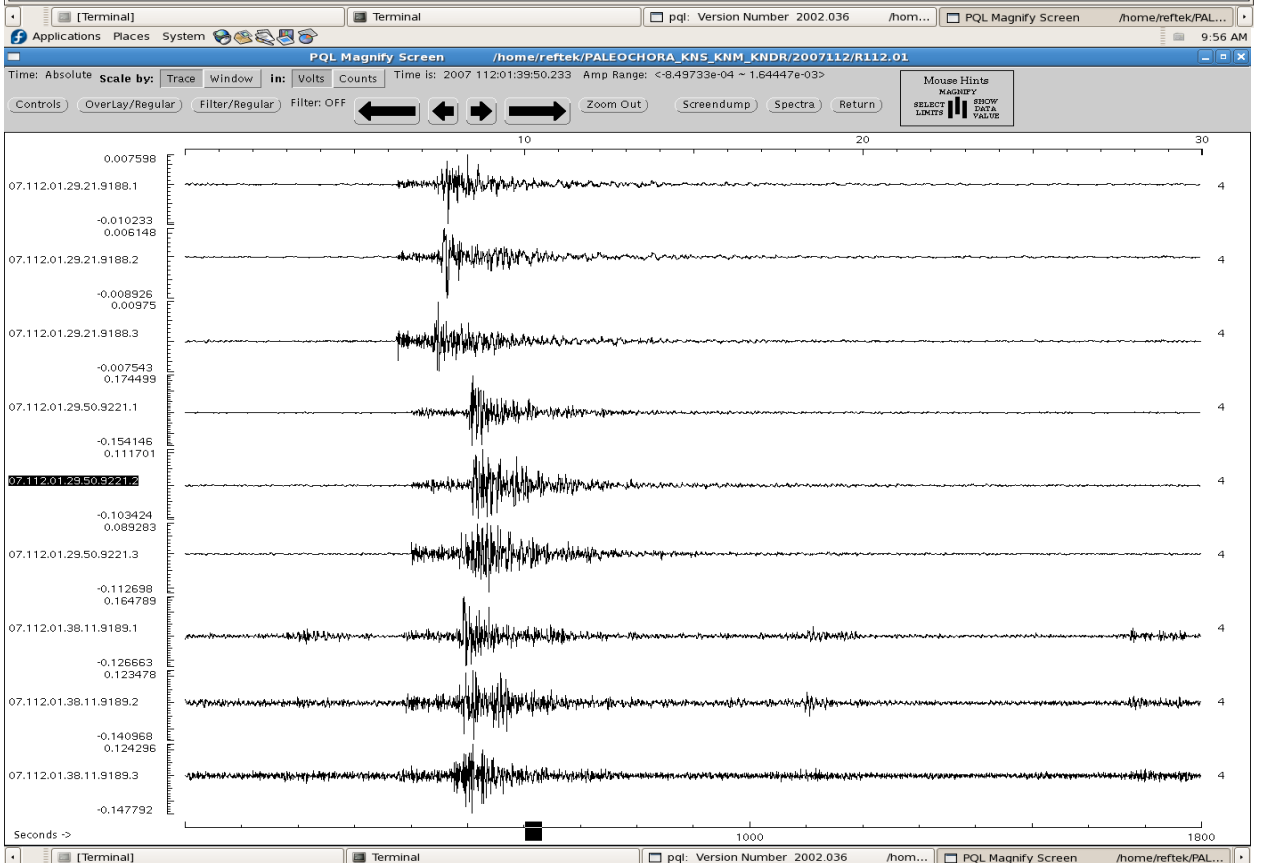
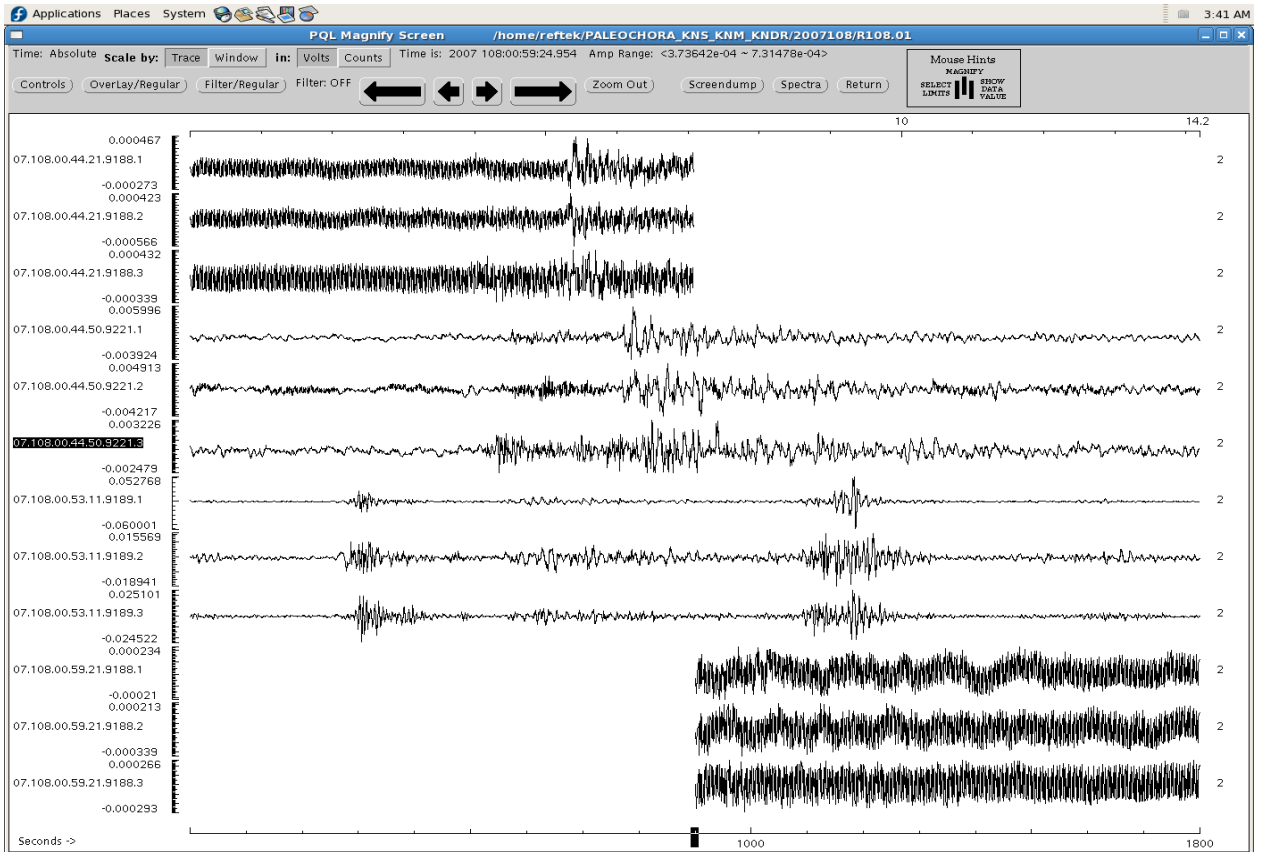


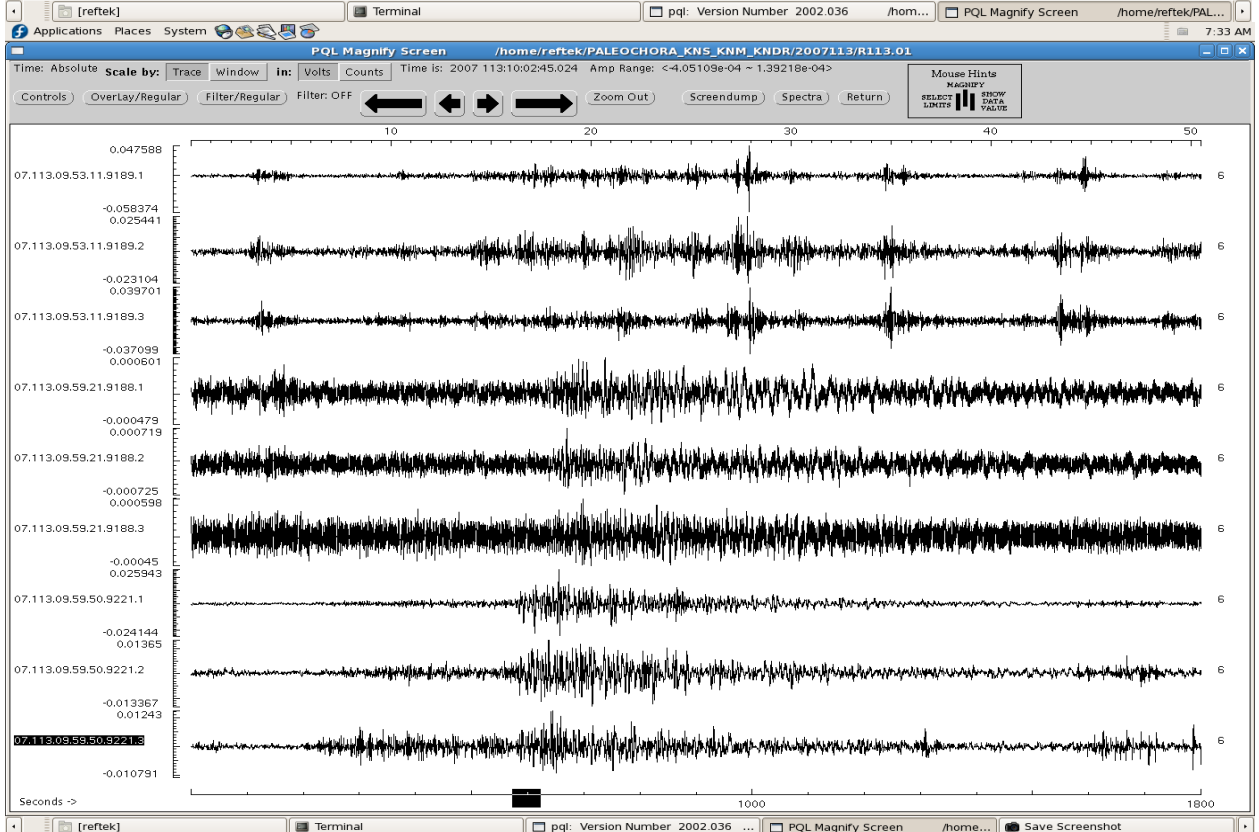
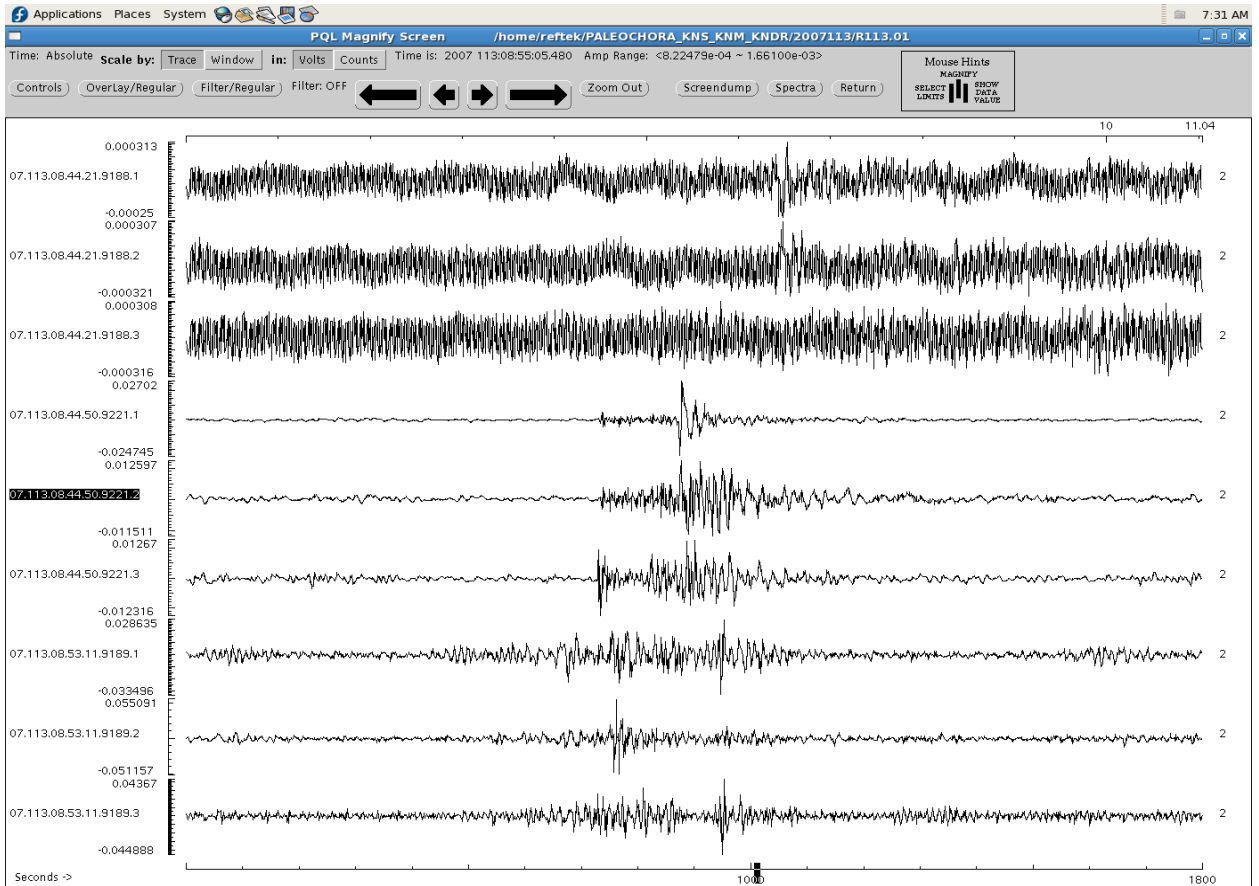


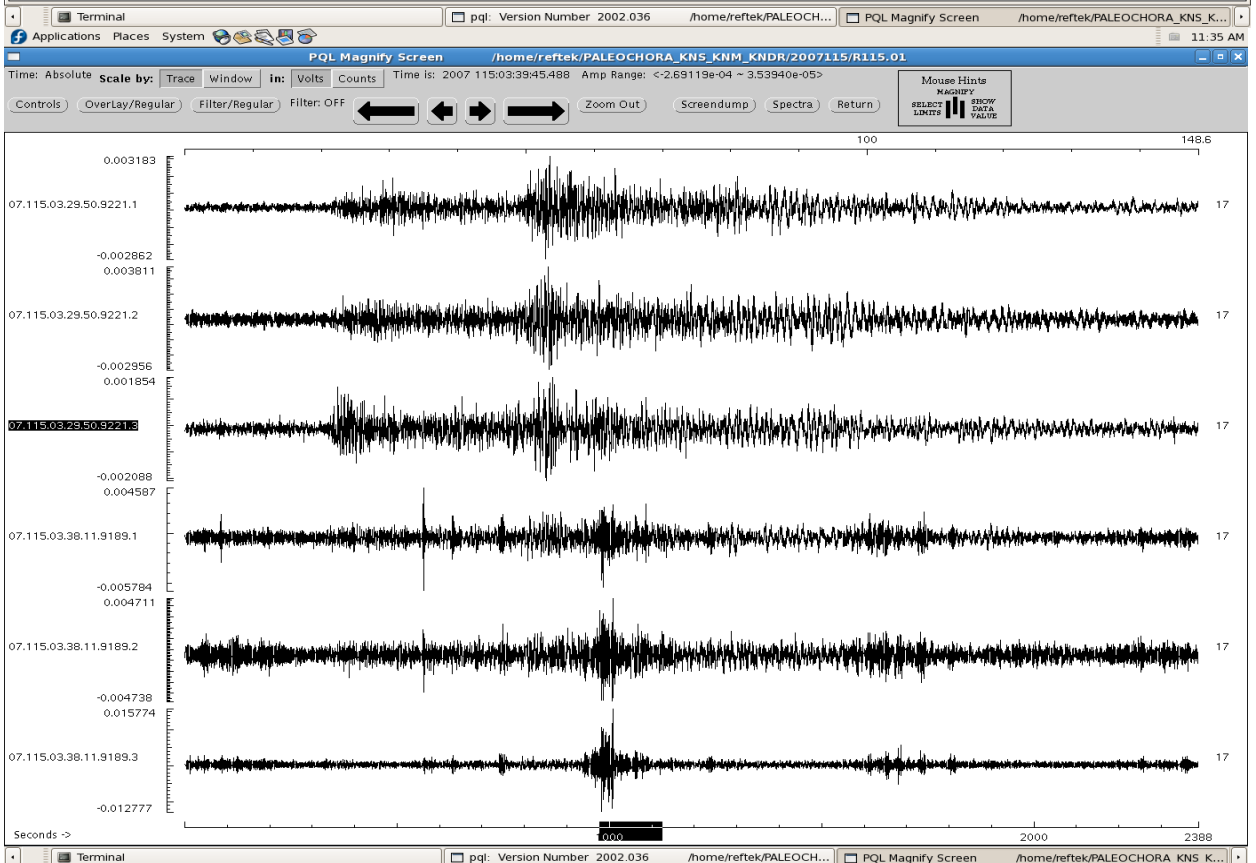
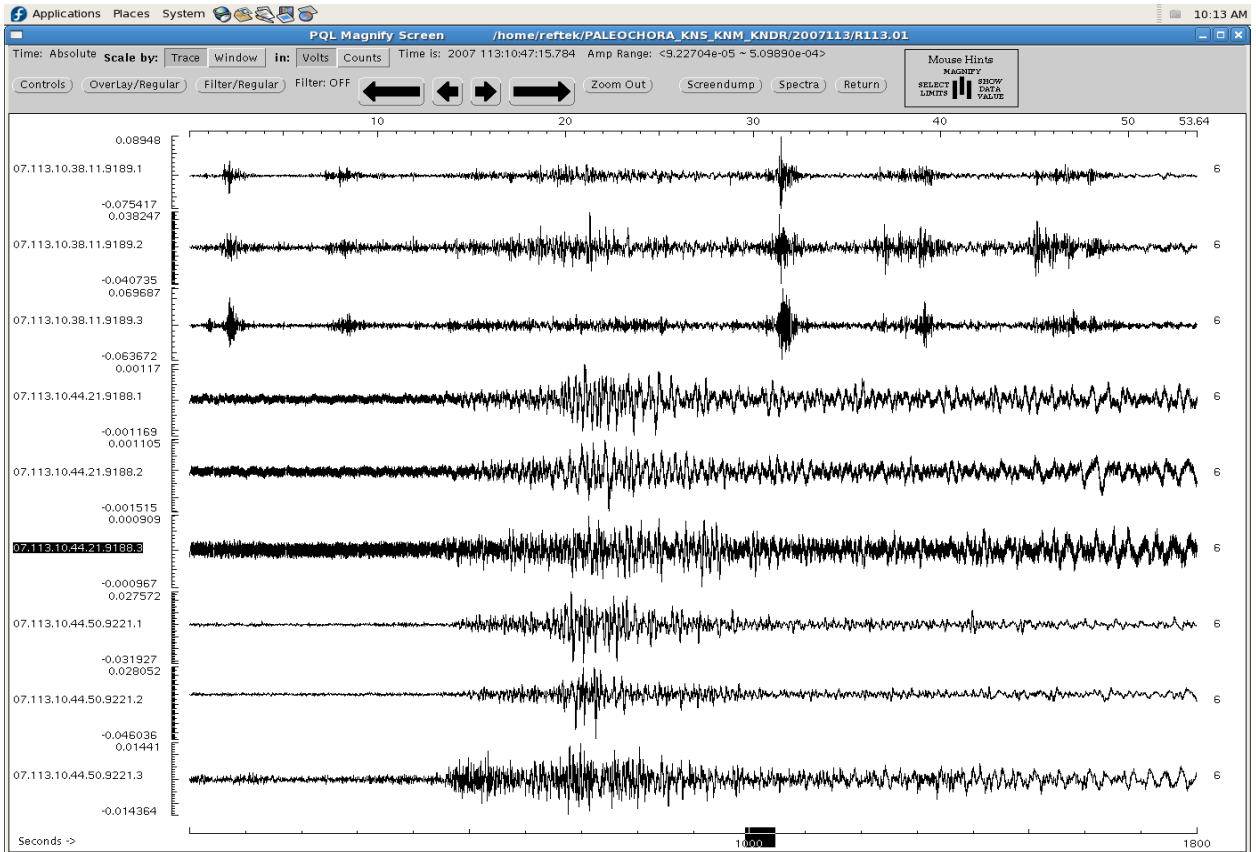


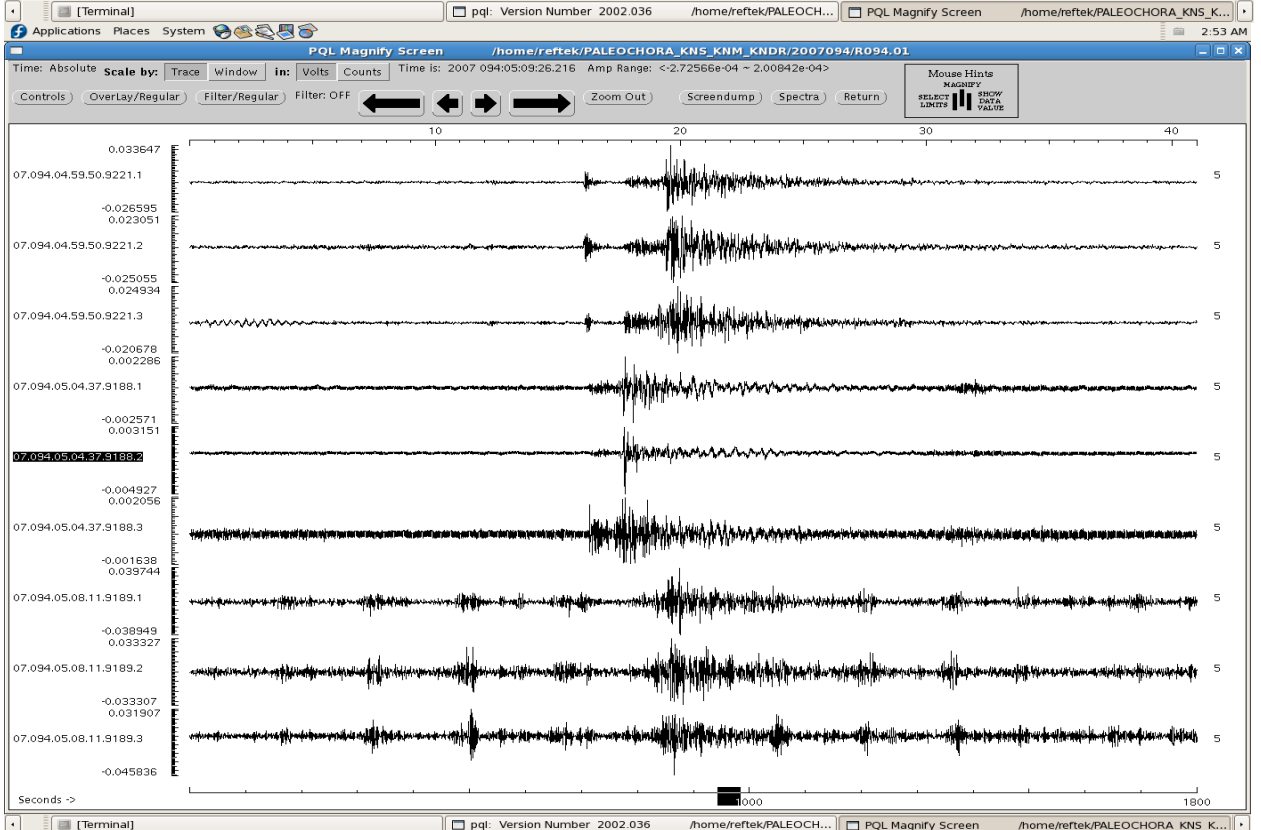
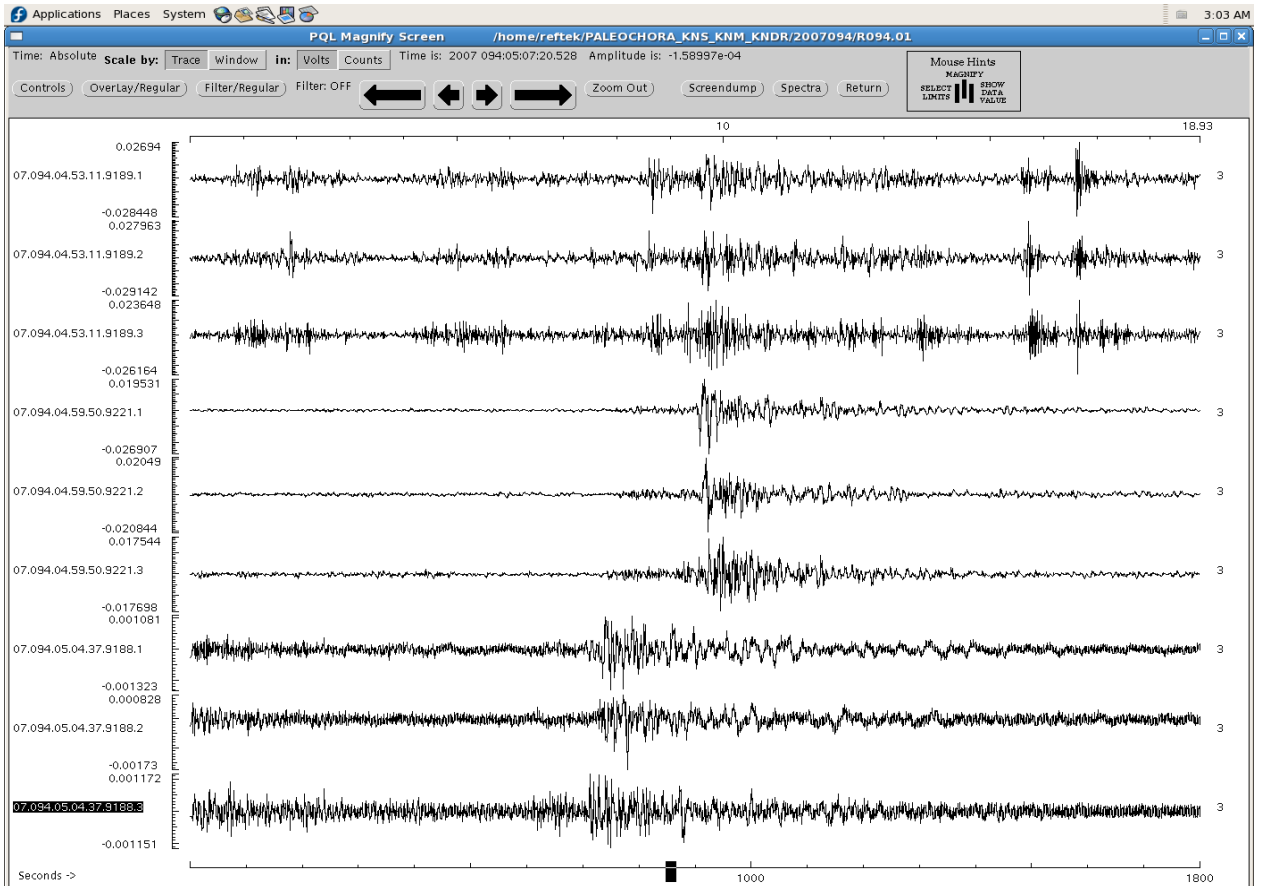


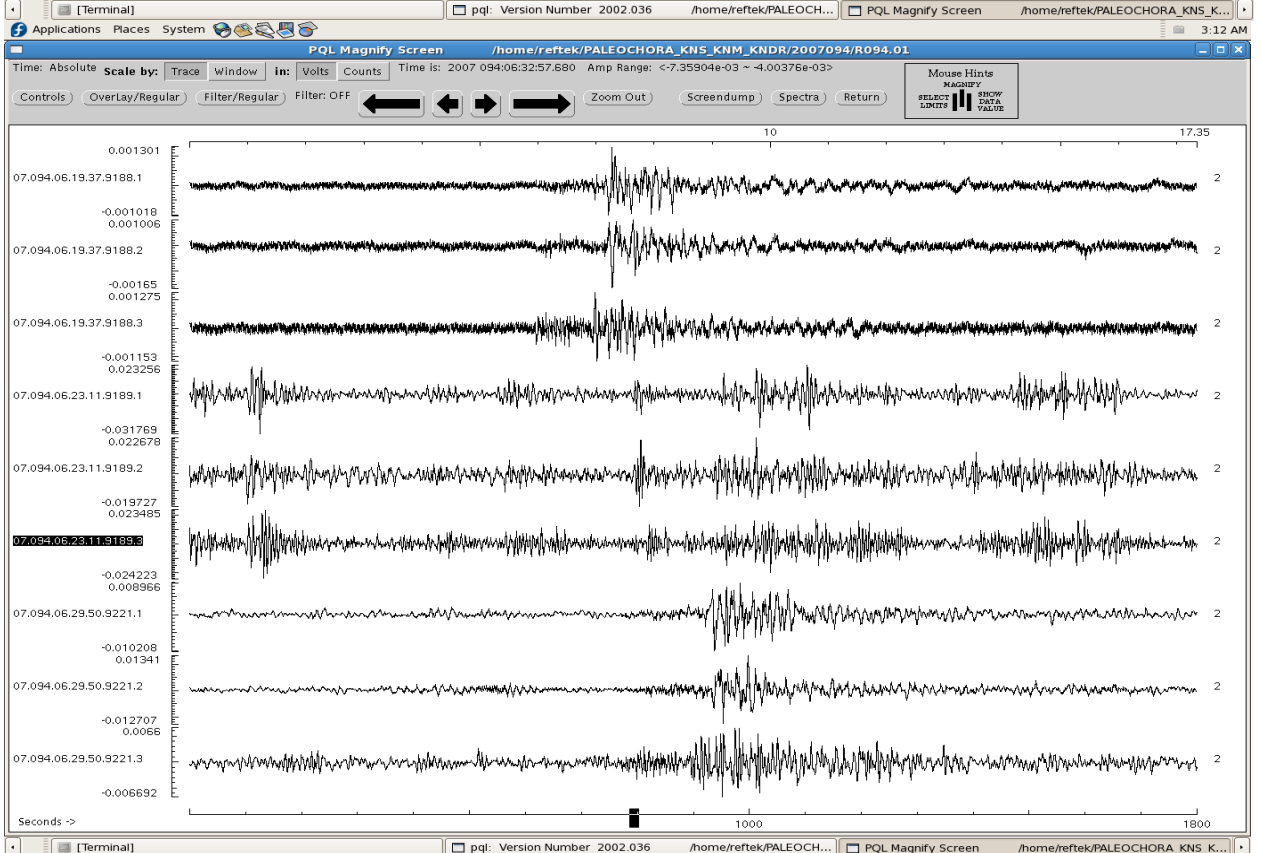
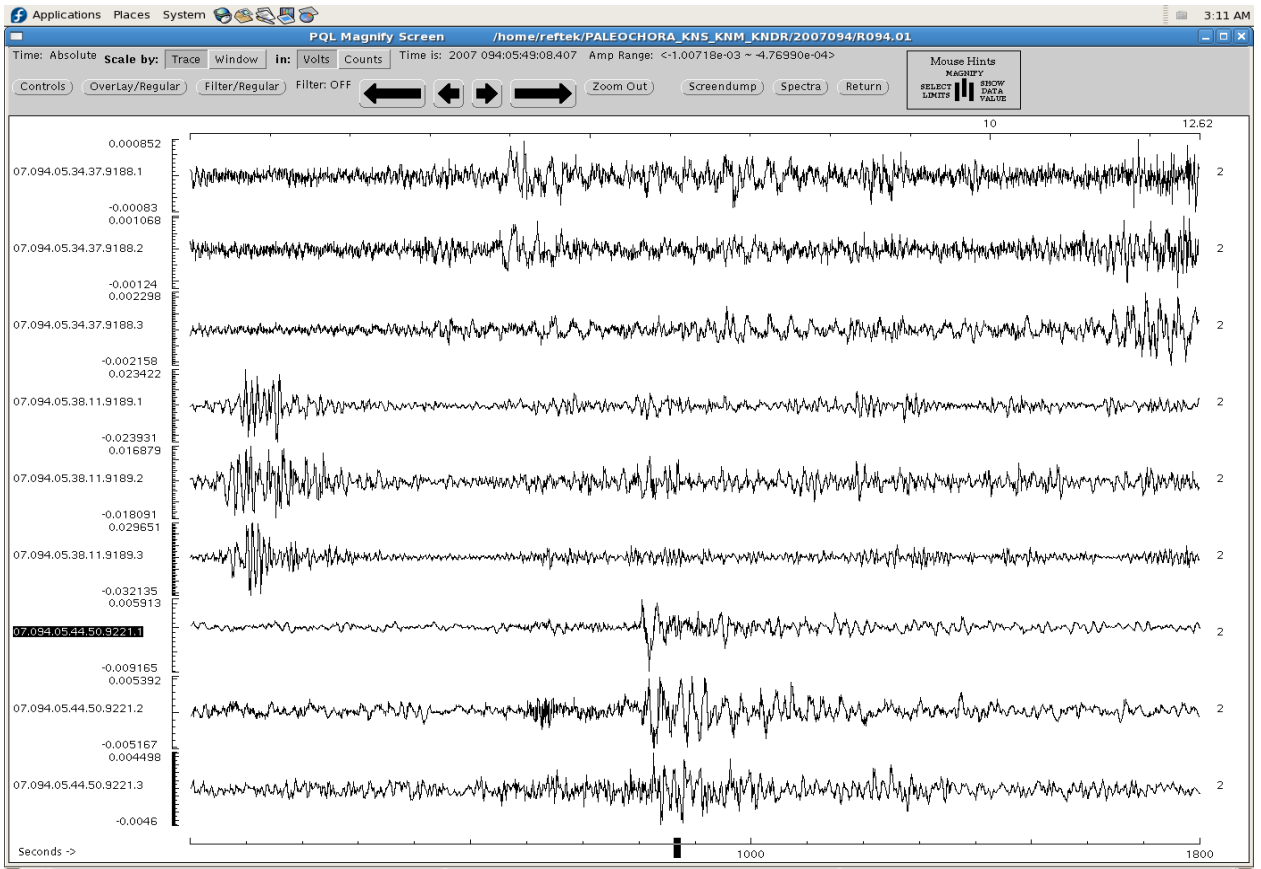


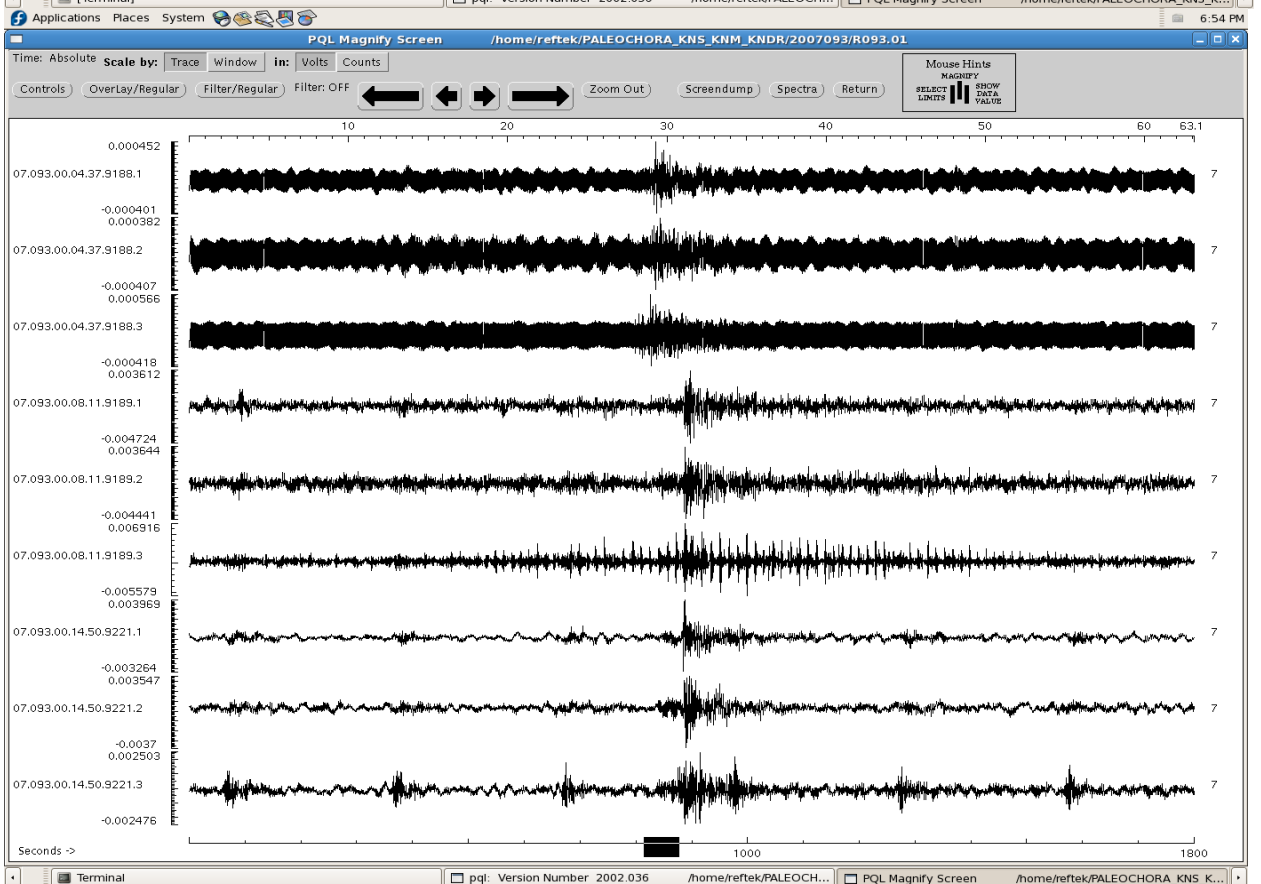
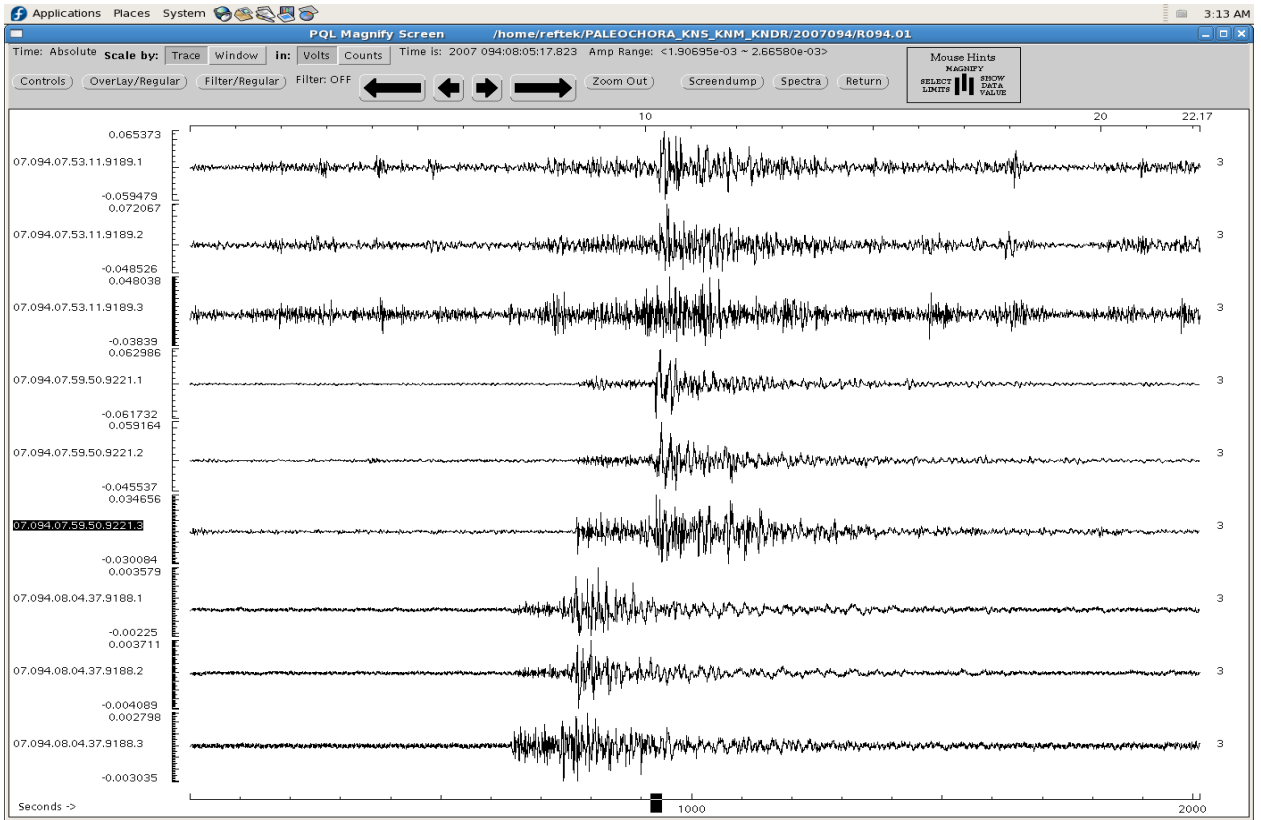


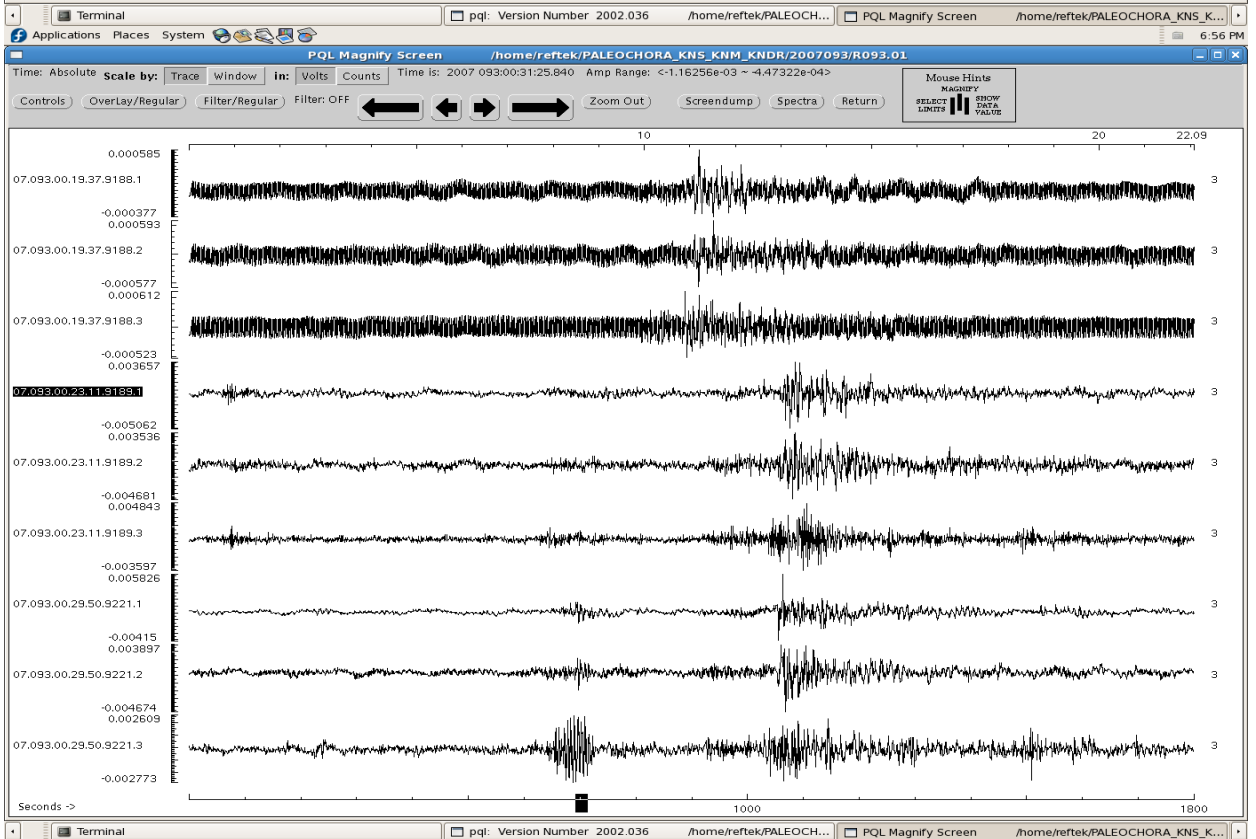
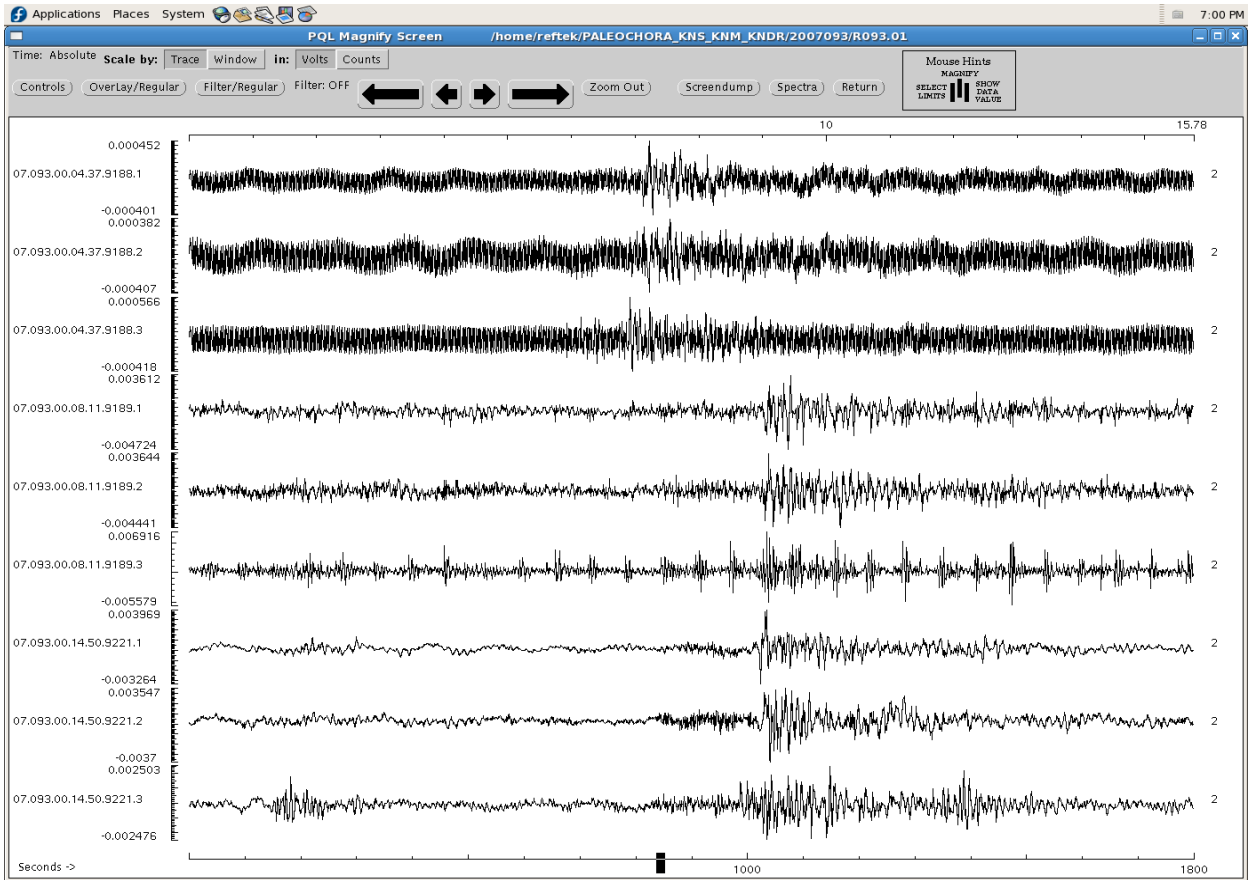


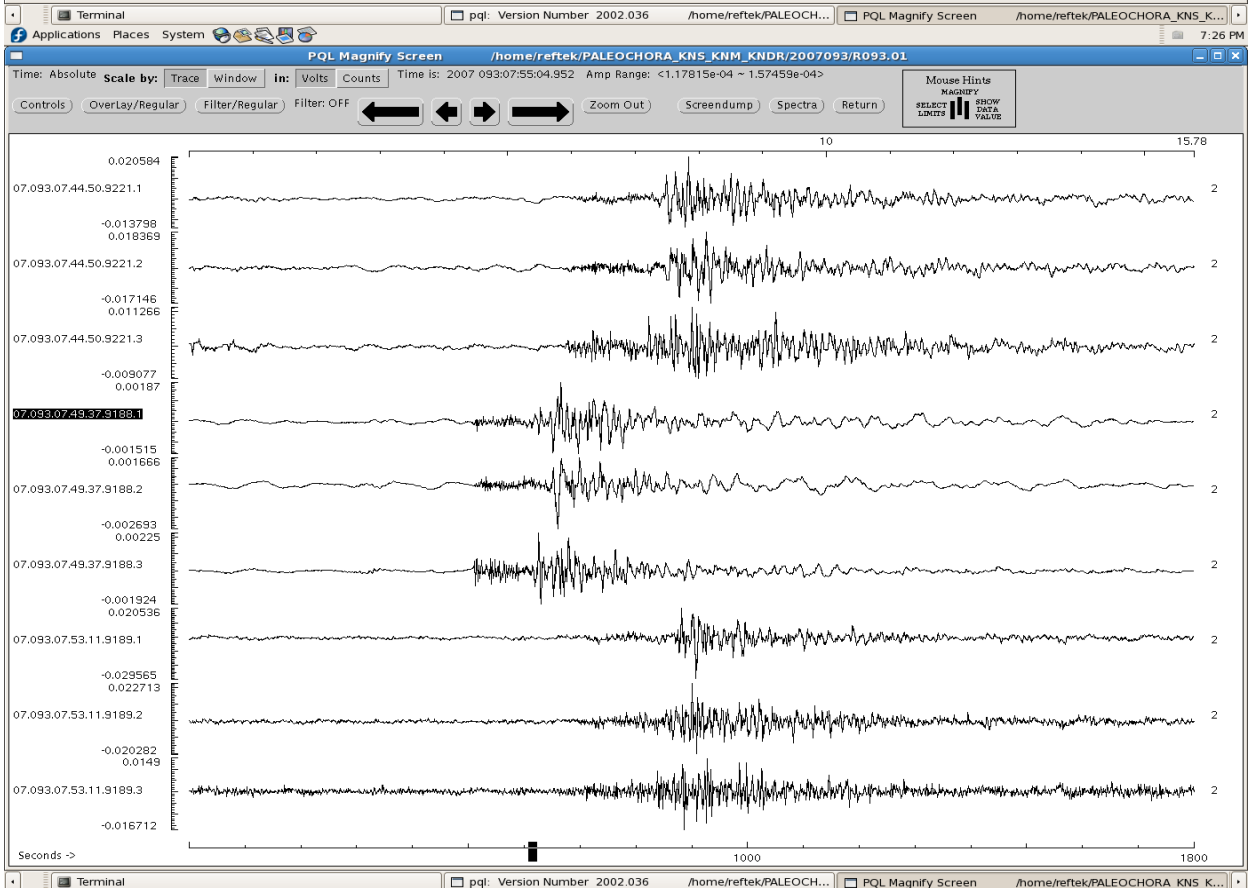
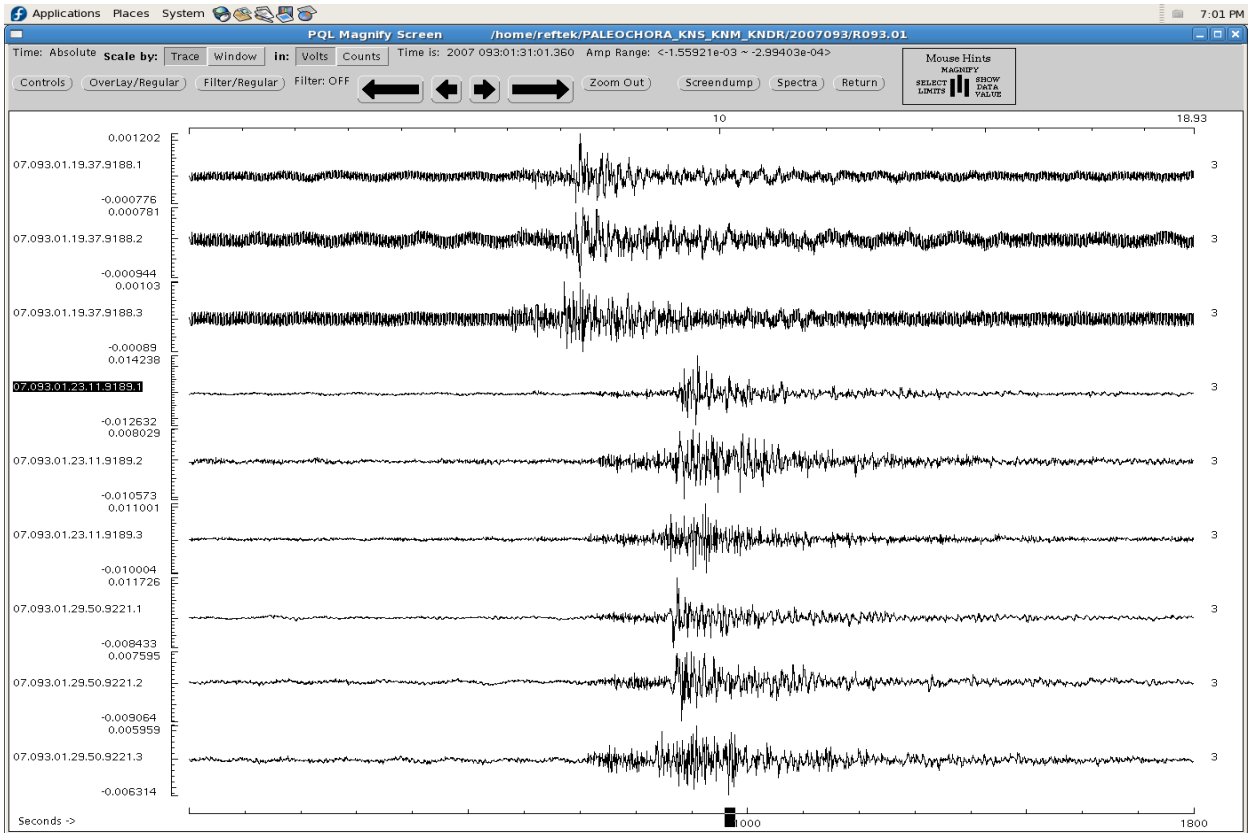




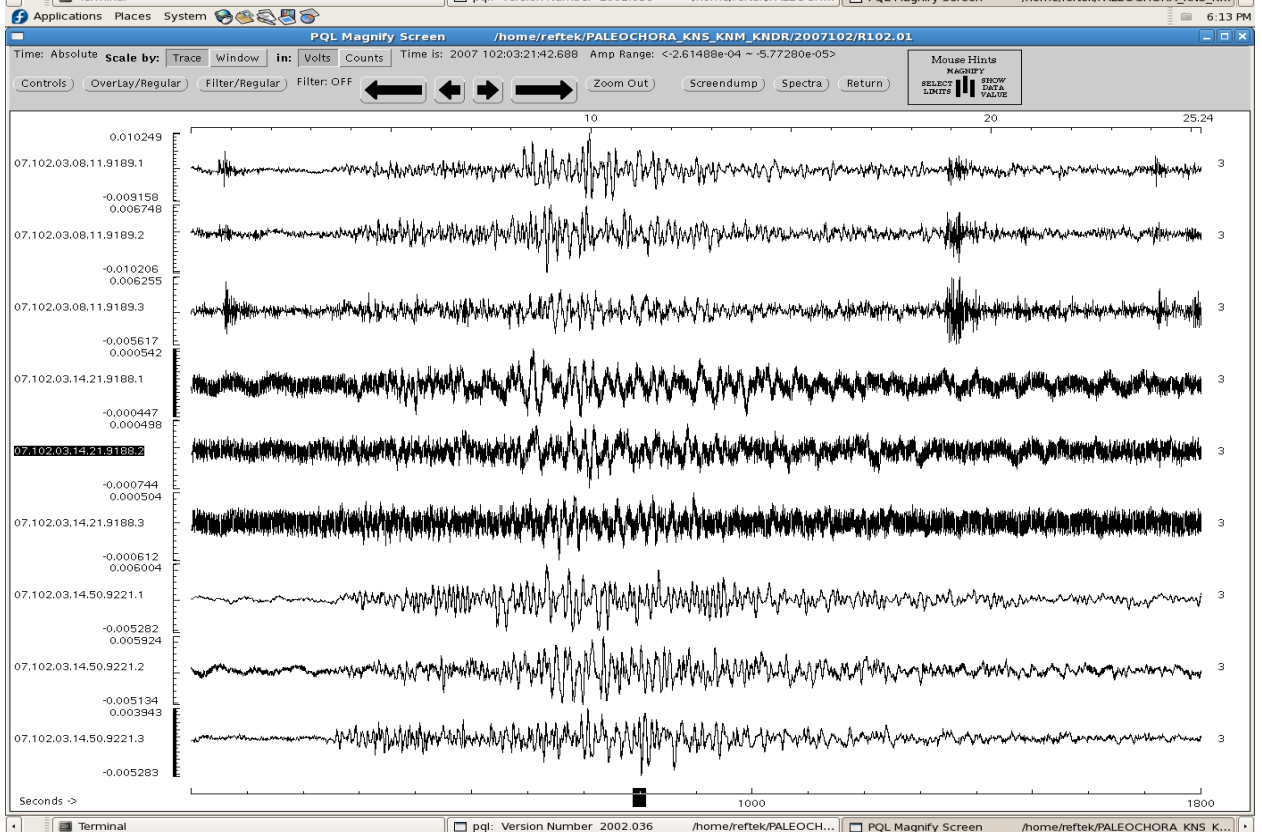
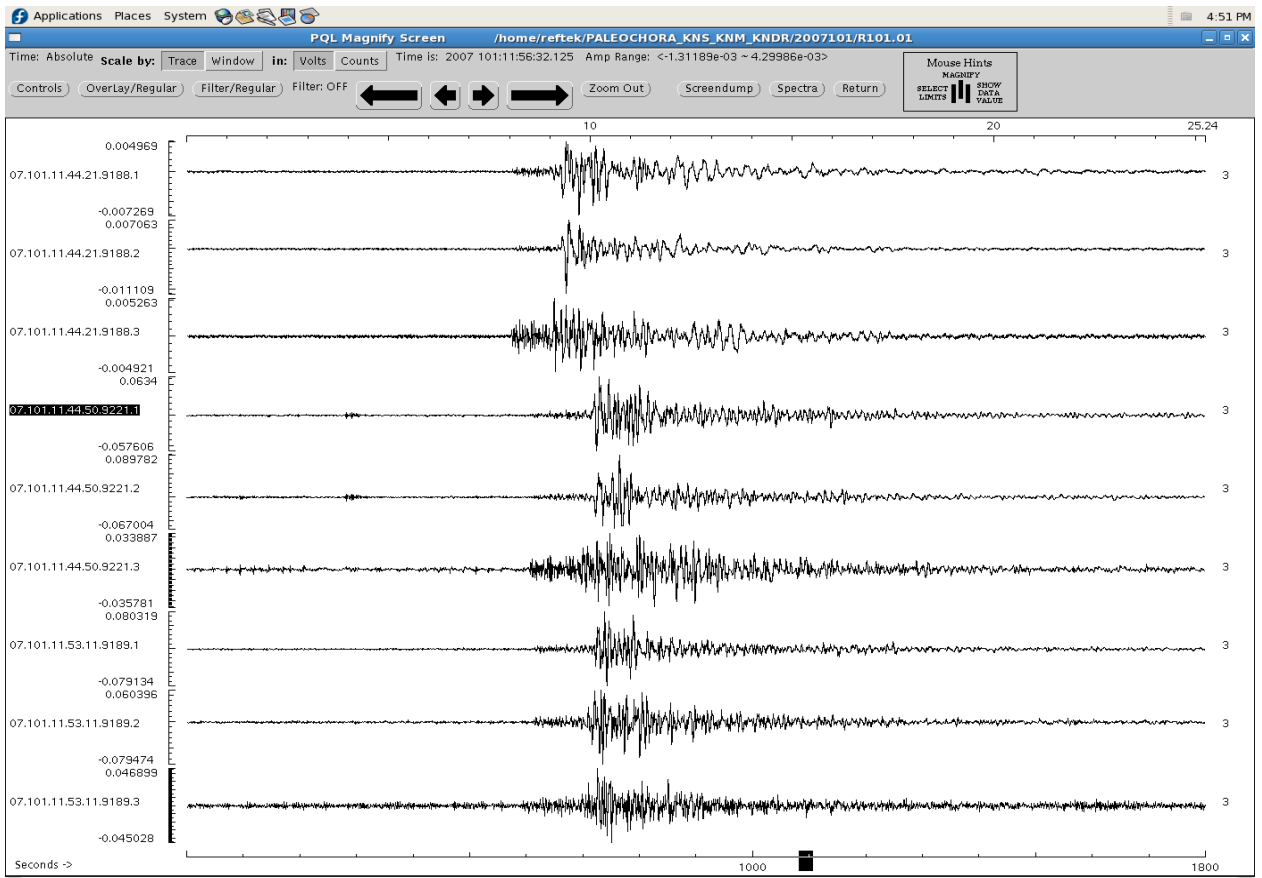












**APPENDIX VI: SAMPLES OF SITES OF MICROTREMOR RECORDINGS USING LENNARTZ 3D/5sec SEISMOMETER**

---

